Spectral Hole Burning in Dye Solutions

GERARD MOUROU

Abstract—**Using picopulses generated by a mode-locked ruby laser, we have measured the 3-8-Å bandwidth of a hole burned in the 0–0 transition of cryptocyanine in methanol and demonstrated the inhomogeneous character of this transition.**

The population-rate equations are written for an inhomogeneous transition with two and four energy levels interacting with continuous or pulsed excitation. Using the numerical solutions of this model together with the experimental result we determine a transverse relaxation time T_2 = 0.6–1 ps for cryptocyanine in methanol.

Introduction and Summary

In order to explain the spectral condensation of the Q-switched ruby-laser emission, some authors [1] introduced the concept of spectral hole burning in dye solutions and devised experiments to observe either directly [2], [3], [7], [8] or indirectly [4]–[6], [9], [10] the spectral behavior of the transition when the solutions were excited by the strong monochromatic light from a Q-switched laser. Very disparate results were obtained because, in our opinion, of the quasi-continuous[1] excitation used in all these experiments. In effect, as we will show in the theoretical model described in the following, the depth of the hole created by continuous excitation is small and not easily detected even for an extremely inhomogeneous line. Using short-test and excitation pulses one may improve considerably the detection of hole burning.

This paper presents an experimental and theoretical line-shape analysis of the absorption bands of dye solutions commonly used in the laser field. Experimental measurements of the hole-burning bandwidth of cryptocyanine dissolved in methanol were obtained using short pulses generated by a mode-locked ruby laser. The estimated 3-8-Å bandwidth is within the range of values of 30 and 0.5 Å given by Spaeth and Sooy [7] and Giuliano and Hess [5]. From this value a dephasing time $T_2 \approx 0.6$–1 ps is deduced for the solution. A similar time will be deduced from the line-shape analysis of the transition.

The inhomogeneous broadening of the dye transition is attributed to the different solvent cages, as well as the different configurations adopted by the solute molecule. This hypothesis is supported by the Gaussian shape of the absorption band.

A theoretical treatment will be presented where we will consider the population rate equations for an inhomogeneous transition with two-level and four-level models. From these equations we will find the solution of the hole burning for continuous monochromatic excitation and the spectral behavior of the absorption band during mode-locked excitation.

Manuscript received April 25, 1974; revised September 12, 1974. This work was supported by the Petroleum Research Fund.

The author was with the Laboratoire de Recherche en Optique et Laser, Laval University, P.Q., Canada. He is now with the Department of Chemistry, San Diego State University, San Diego, Calif. 92115.

[1] Quasi-continuous since the pulse duration T is greater than the fluorescence decay time T_1, typically $T \sim 50$ ns, $T_1 < 5$ ns.

Direct Measurement of Hole Burning in Cryptocyanine [8]

As shown schematically in Fig. 1, a train of pulses of 7-ps duration was used both to bleach the dye solution and to generate the spectrally broadened picopulses which probed the shape of the absorption band in the vicinity of the excitation wavelength. A beam splitter (B) divided the ruby-laser output in two parts. One part was focused into a 20-cm path length CS_2 cell. There the spectrum of the pulse was broadened by self-phase modulation. Immediately after the CS_2 cell a lens L_2 brought into focus the parallel light not trapped in filaments and this light was blocked by a small-diameter mask (M) at the focal point. The light trapped in filaments (and therefore strongly broadened) was collected by a lens L_3, passed through the 2-mm dye cell, and imaged on the slit of a spectrograph. The other beam (transmitted by B) passed through an adjustable delay line and bleached the dye. The low-intensity transmission of the dye T_0 is 10^{-3} for a concentration of 10^{-4} M. At this concentration there is no evidence for dimerization since the absorbance obeys the Beer–Lambert law. In addition, it is worth noting that, according to the work of Dempster *et al.* [11], no photoisomers have been found.

A diaphragm D with the same dimensions as the pump beam (7 mm) was set against the cell. The synchronization of the two beams was obtained by varying the delay line and observing the signal of a photomultiplier placed at the position of the spectrograph slit.

First, we checked that the film was not exposed by the probe beam when the exiting beam was blocked [Fig. 2(b)]. The Raman-scattered light did expose the film since this light is outside the 0–0 absorption band of cryptocyanine in methanol. Then we recorded the test beam spectrum when the exciting beam bleached the dye [Fig. 2(c)]. The input spectrum

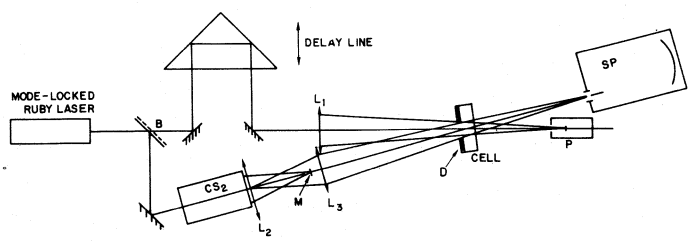

Fig. 1. The experimental arrangement which was used to demonstrate hole burning in the absorption band of cryptocyanine in methanol is shown. A beam splitter B divides the mode-locked ruby-laser output into a test pulse and a pump pulse. The test pulse is spectrally broadened by self-focusing in a cell of CS_2. A lens L_2 collects the light which is not trapped in filaments (and therefore not spectrally broadened) and brings it to a focus on a mask M. The lens L_3 images the light which was trapped in filaments in the CS_2 cell onto the slit of the spectrograph SP. The pump beam travels through an adjustable delay line and through the lens L_1 which focuses the beam into a light trap P. A diaphragm D is placed adjacent to the cell so that only that part of the test beam which overlaps with the pump beam in the 2-mm dye cell enters the spectrograph. The cell contains cryptocyanine in methanol and the transmission at 6963 Å is initially 0.001.

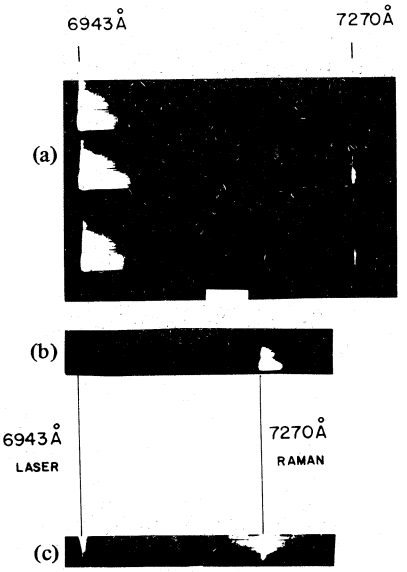

Fig. 2. (a) Spectrum of the incident test beam. The cryptocyanine has been removed and replaced by pure methanol. (b) Spectrum of the transmitted test beam when the cell contains the cryptocyanine (T_0 = 0.001) and the pump beam is off. The light at 6943 Å has been absorbed, while the CS_2 Raman-scattered light which is outside the absorption band is slightly attenuated. (c) Typical output spectrum obtained when the pump beam and the test beam are synchronous.

[Fig. 2(a)] was recorded by substituting pure methanol for the dye solution and setting a neutral density filter ($T = 0.50$) before the spectrograph slit in order to work in the same range of light intensity. From this we surmise that the transmission when the dye is bleached is in the range from 50 to 100 percent.

The densitograms of Fig. 2(a) and (c) (Fig. 3) show that a very narrow part of the probe beam, 5–10 Å wide, is transmitted when the dye is bleached. This observation leads us to conclude that there was a hole burned in the dye transition. On account of the spectral bandwidth of the laser, 2 Å, we estimate that the hole is 3–8 Å wide, and with the help of the theoretical treatment to be developed, we will determine that the dephasing time T_2 is between 0.6 and 1 ps.

Nature and Shape of the Dye Transition

Two mechanisms in dye solutions inhomogeneously broaden the transition. The first is related to the differences in the solvent cage surrounding each dye molecule, while the second is connected with the variation of the molecular configuration of the dye. For instance, for a polymethine cyanine dye such as cryptocyanine, formed by two heterocyclic nuclei linked by a conjugated chain, the transition frequency of these dyes should be very sensitive to the twisting of the heterocyclic nuclei with respect to the conjugated chain [15].

The variation of the solvent cages and molecular configurations are random quantities which exhibit Gaussian probability density. The numerical analysis of the absorption band for the cryptocyanine dye solutions shows that the long wavelength portion of the absorption band is approximately Gaussian, corroborating the hypothesis that the dye molecule's transition is inhomogeneous.

More precisely, Fig. 4 shows that the absorption curve can be fit with a convolution of a Gaussian 225 ± 5-Å full width at half maximum (FWHM) and a Lorentzian 15 ∓ 5-Å FWHM.

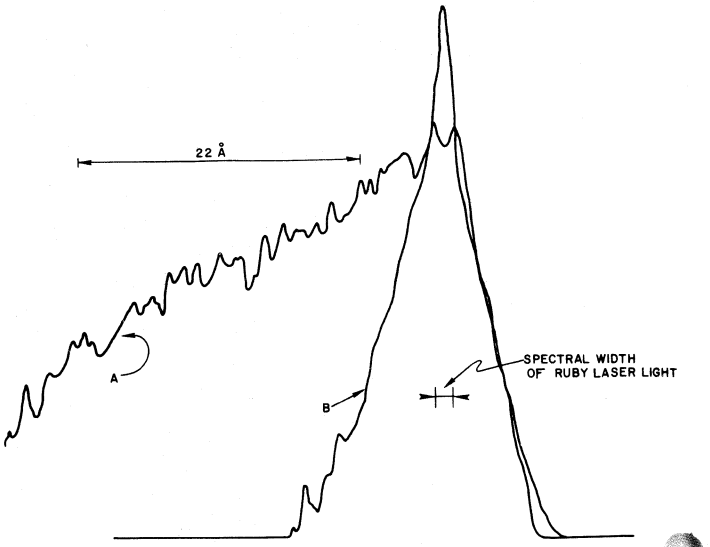

Fig. 3. Spectral selection carried out by the hole burning. Curve *A*: Input spectrum of the test beam. Curve *B*: Test-beam spectrum filtered by the hole burning.

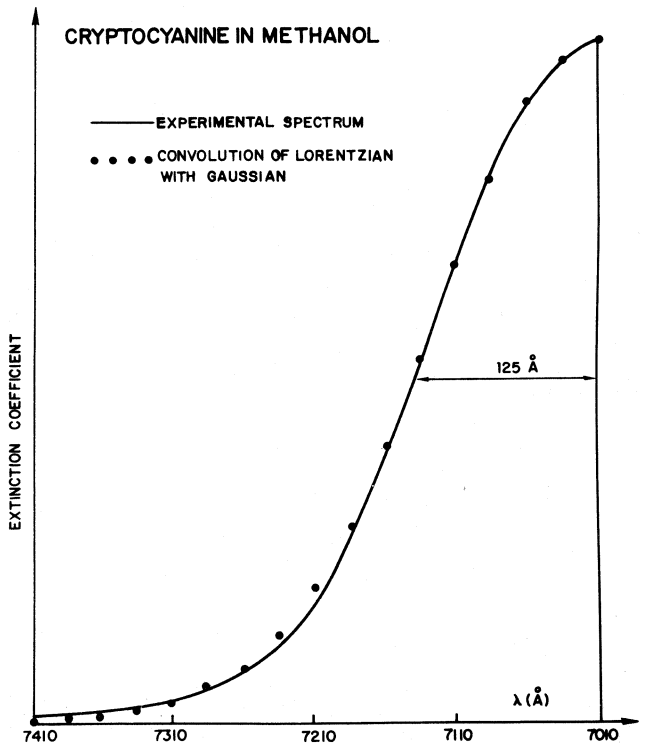

Fig. 4. Best fit of the experimental spectrum (–) of a cryptocyanine in methanol solution by the convolution (•) of a Gaussian (225-Å bandwidth) with a Lorentzian (15-Å bandwidth).

The Lorentzian bandwidth, which must be the homogeneous bandwidth of the solute molecule, is in good agreement with that deduced from the hole-burning experiment. Therefore, the line-shape analysis seems to be a convenient method to deduce the value of the homogeneous response of the solute molecule.

Inhomogeneous Transition Excited by Intense Monochromatic Field

Now, what is the behavior of the inhomogeneous transition when excited by an intense monochromatic light? Basically, since the super molecules (i.e., the dye molecules and their

solvent cage) making up the population are dissimilar, one needs to apply the population rate equations for all the different kinds of molecules at each frequency of the inhomogeneous line. However, all the frequencies ω will be coupled by spectral diffusion. The molecular agitation in the solution randomly forces each solvent cage and each solute molecule to adopt another configuration involving a different transition frequency for the super molecules. Let us call T_3 the time required to change the frequency. We will hypothesize that the probability for a molecule with a frequency ω' to adopt a frequency ω after a "collision" is proportional to $D(\omega)$, the molecular distribution. So we state that the probability rate per frequency of frequency change is

$$P(\omega' \to \omega) = \frac{1}{T_3} D(\omega) \tag{1}$$

with

$$\int_0^\infty D(\omega)\, d\omega = 1. \tag{2}$$

Now, let us write the population rate equations for a two-level and a four-level model.

Two-Level Model

Let us consider the energy diagram sketched in Fig. 5 and let us assume that the following is true.

1) The molecular distribution $D(\omega)$ is independent of the population of the ground 1 and excited state 2 so that

$$D(\omega) = n_1(\omega, t) + n_2(\omega, t) \tag{3}$$

where $n_1(\omega, t)$ and $n_2(\omega, t)$ are the number for the time t of molecules at the frequency ω in the states 1 and 2.

2) Since the halfwidth of the molecule distribution $D(\omega)$ is large compared to the homogeneous response of each super molecule, the extinction coefficient is proportional to the molecular distribution.

Let $I(\omega_L)$ and $\sigma(\omega)$ be the excitation intensity and the homogeneous cross section of the super molecule, respectively. On account of (1) and assumptions 1) and 2), the population rate equations for each frequency can be written

$$\frac{dn_1}{dt}(\omega, t) = -I(\omega_L)\, \sigma(\omega)\, n(\omega, t) + \frac{n_2(\omega, t)}{T_1} - \frac{n_1(\omega, t)}{T_3} + \frac{D(\omega)}{T_3} \int_0^\infty n_1(\omega', t)\, d\omega' \tag{4}$$

$$\frac{dn_2}{dt}(\omega, t) = +I(\omega_L) \cdot \sigma(\omega) \cdot n(\omega, t) - \frac{n_2(\omega, t)}{T_1} - \frac{n_2(\omega, t)}{T_3} + \frac{D(\omega)}{T_3} \int_0^\infty n_2(\omega, t)\, d\omega \tag{5}$$

with

$$\sigma(\omega) = \frac{T_2'}{T_1} \frac{\sigma_0}{1 + (2(\omega_L - \omega) T_2')^2} \tag{6}$$

$$n(\omega, t) = n_1(\omega, t) - n_2(\omega, t) \tag{7}$$

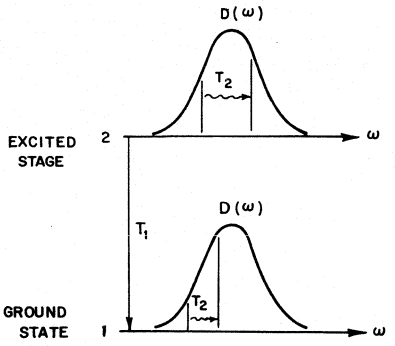

Fig. 5. Scheme of the two-level model with inhomogeneous population distribution adopted in the theoretical treatment.

where $1/T_2' = (1/T_1) + (2/T_2)$, and σ_0 is the maximum cross section when $T_2' = T_1$.

In (4) and (5) the first term is the number of stimulated transitions, the second relates spontaneous emission, while the third and the fourth are the terms associated with the spectral diffusion.

From (1)-(7) the expression of the population inversion for each frequency will be

$$\frac{dn}{dt}(\omega, t) = -2 \cdot I(\omega_L)\, \sigma(\omega)\, n(\omega, t) - \left(\frac{1}{T_3} + \frac{1}{T_1}\right) n(\omega) + \frac{D(\omega)}{T_1} + \frac{D(\omega)}{T_3} \int_0^\infty n(\omega, t)\, d\omega. \tag{8}$$

Equation (8) is expressed as a function of the homogeneous cross section $\sigma(\omega)$. Let us write this expression as a function of the classically measured[2] cross section $\sigma_M(\omega)$ and a parameter T_2' to be determined.

Assuming that $\sigma_M(\omega)$ is Gaussian, as shown previously, and since the oscillator strength is independent of the broadening mechanism, we can write

$$\int_0^\infty \sigma(\omega)\, d\omega = \int_0^\infty \sigma_M(\omega)\, d\omega. \tag{9}$$

Using (6) the homogeneous cross section can be expressed as

$$\sigma(\omega) = \frac{T_2' \cdot \Delta\omega_T}{\sqrt{\pi \cdot \ln 2}} \cdot \frac{\sigma_M(\omega_0)}{1 + (2(\omega - \omega_0) T_2')^2} \tag{10}$$

where $\Delta\omega_T$ is the Gaussian half-power bandwidth and ω_0 is the center frequency. If $I_S(\omega_0) = [(\sigma_M(\omega_0) \cdot T_1)/2]^{-1}$ is the saturation intensity, then (8) will take the form for $\omega_0 = \omega_L$

$$\frac{dn}{dt}(\omega, t) = \sqrt{\frac{1}{\pi \cdot \ln 2}} \cdot \Delta\omega_T \left(\frac{T_2'}{T_1}\right) \cdot \frac{B(\omega_L)\, n(\omega, t)}{1 + (2(\omega_L - \omega) T_2')^2} + n(\omega) \cdot \left(\frac{1}{T_2} + \frac{1}{T_1}\right) + \frac{D(\omega)}{T_1} + \frac{D(\omega)}{T_3} \int_0^\infty n(\omega, t)\, d\omega \tag{11}$$

where $B(\omega_L) = I(\omega_L)/I_S(\omega_0)$.

[2] $\sigma_M(\omega)$ is obtained by dividing the extinction coefficient by the number of molecules per unit volume.

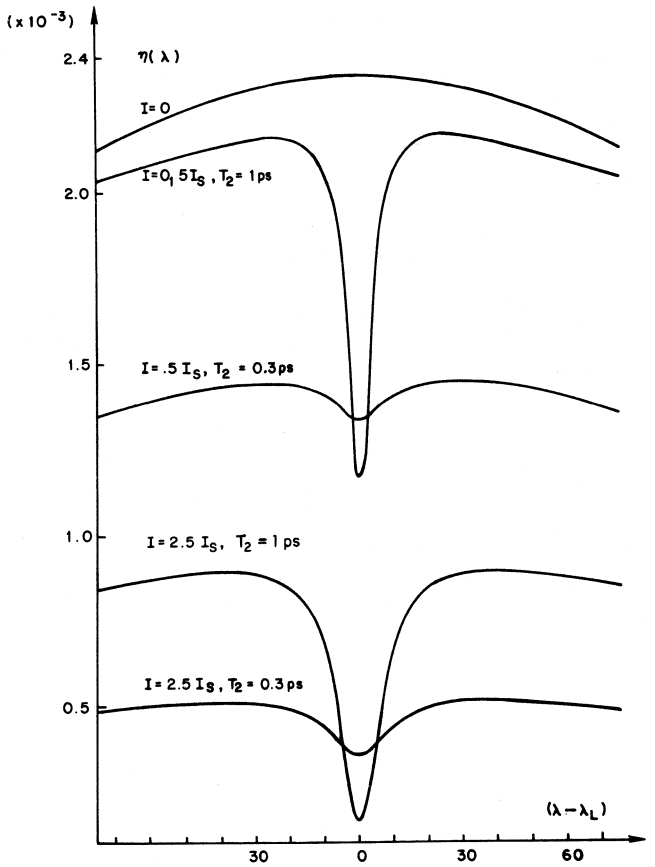

Fig. 6. Population inversion for a two-level inhomogeneous distribution when the solution is excited by continuous monochromatic light.

The steady-state solution for (11) is obtained numerically by applying a step function of amplitude B and assuming that each solvent collision alters the phase and the frequency of the molecule, in this case $T_2 = T_3$. After a time on the order of T_1 the solution of (11) does not change and may be considered steady state.

Fig. 6 shows the spectral distribution for two values of B and T_2, keeping $\Delta\omega_T = 1.54\ 10^{+14}$ rad/s and $T_1 = 50$ ps [12], [14] constant. $\Delta\omega_T$ and T_1 correspond approximately to the known parameters of cryptocyanine in methanol. The hole is narrower and deeper for larger values of T_2 because of the influence of molecular agitation both on the broadening of the homogeneous response and on the spectral diffusion. The excitation intensity also contributes to the width of the hole burned in the absorption band. The ratio between the minimum and the maximum absorption rapidly approaches unity when the spectral diffusion and dephasing times decrease. So we see that it is difficult to measure the hole-burning bandwidth with a continuous technique such as used by others [2]-[7]. The calculations made with pulse duration shorter than T_1 will show an improvement in the detection even for short T_2.

From (11) we can obtain the population inversion versus the intensity for homogeneously and inhomogeneously broadened lines with continuous excitation. Fig. 7 shows the variation of the population inversion at ω_L versus the excitation intensity for different values of T_2, keeping T_1 and $\Delta\omega_T$ constant. We notice significantly different behavior for each value, so that one may deduce T_2 from a study of optical saturation. However, this method supposes detailed knowledge of the specific parameters of the dye, such as the excited-singlet decay time, the solvent-solute relaxation time [12], and the anisotropic distribution of the excited oscillators, which makes the interpretation difficult.

Four-Level Model

Let us improve the previously developed theory by introducing the solvent cage and molecular-configuration effects which shift the ground and excited states after each transition. We will label these states 1, 2, 3, and 4 as shown in Fig. 8, for the stable ground state, the unstable excited state, the stable excited state, and the unstable ground state, respectively. We will assume that 1 and 2 are connected by T_1, while 2 and 3, like 4 and 1, will be connected by T_S, the solvent-solute relaxation time. Basically, the same treatment as for the two-level model will be used. Since it is not necessary to suppose any distribution for the states 3 and 4, the rate equations will be written

$$\frac{dn_1(\omega,t)}{dt} = -I(t)\,\sigma(\omega)\cdot n(\omega,t) - \frac{n_1(\omega,t)}{T_3} + \frac{D(\omega)}{T_3}\int_0^\infty n_1(\omega,t)\,d\omega + \frac{n_2(\omega,t)}{T_1} + \frac{n_4(t)\cdot D(\omega)}{T_S} \tag{12}$$

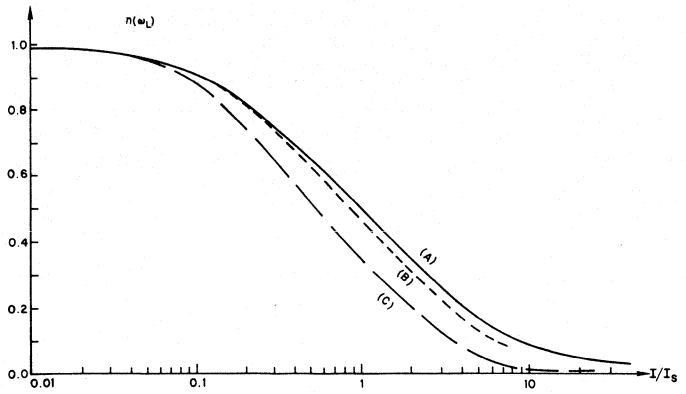

Fig. 7. Population inversion versus continuous monochromatic intensity shown by the following curves. *A:* for homogeneous broadening. *B:* for inhomogeneous broadening (T_2 = 0.3 ps). *C:* for inhomogeneous broadening (T_2 = 1 ps).

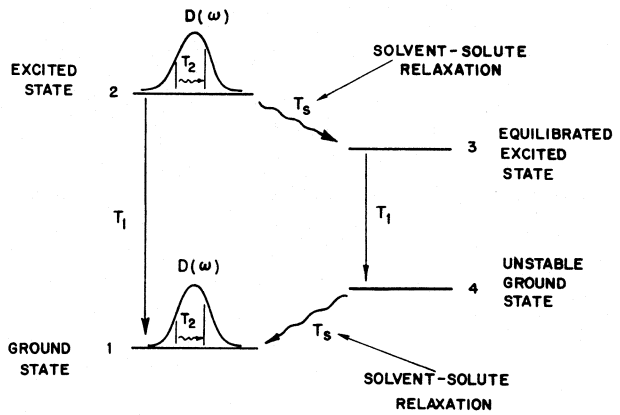

Fig. 8. Scheme of the four-level model with inhomogeneous population distribution adopted in the theoretical treatment. Stable ground state 1; unstable excited state 2; stable excited state 3; unstable ground state 4.

$$\frac{dn_2}{dt}(\omega,t) = +I(t)\cdot\sigma(\omega)\cdot n(\omega,t) - \frac{n_2(\omega,t)}{T_3} + \frac{D(\omega)}{T_3}\int_0^\infty n_2(\omega,t)\,d\omega - \frac{n_2(\omega,t)}{T_S} - \frac{n_2(\omega,t)}{T_1} \tag{13}$$

$$\frac{dn_3}{dt}(t) = \frac{1}{T_S}\int_0^\infty n_2(\omega,t)\,d\omega - \frac{n_3(t)}{T_1} \tag{14}$$

$$\frac{dn_4}{dt}(t) = \frac{n_3(t)}{T_1} - \frac{n_4(t)}{T_S} \tag{15}$$

$$n(\omega,t) = n_1(\omega,t) - n_2(\omega,t) \tag{16}$$

$$1 = \int_0^\infty n_1(\omega,t)\,d\omega + \int_0^\infty n_2(\omega,t)\,d\omega + n_3(t) + n_4(t). \tag{17}$$

With the help of (10) the system (12)–(17) is numerically resolved for a Gaussian pulse excitation, with 7-ps half-power duration. For T_1 = 50 ps and T_S = 10 ps [12], Fig. 9 shows the behavior of the spectral transition for the different times *A–F* during the excitation.

Now, in order to compare these curves with the experimental data, one must deal with the transmission versus wavelength which will be deduced using the simple expression

$$T(\lambda) = T_0^{n(\lambda)} \tag{18}$$

at the instant D, when the maximum of probe light goes through the cell. Fig. 10 shows that for T_1 = 50 ps and T_2 = 0.6–1 ps, a hole of 10-Å bandwidth is burned in the transition, as was observed experimentally.

Conclusion

By means of the ultrafast excitation and test pulses (pulse duration < excited-singlet lifetime) generated by a mode-locked ruby laser, we observed a 3–8-Å hole burned in the absorption band of cryptocyanine dissolved in methanol. The study of the line shape corroborated the experimental result and the idea of the inhomogeneous character of the dye transition. The population rate equations were written for the inhomogeneous case and resolved for two- and four-level models with the assumption that the spectral diffusion time T_3 is equal to the dephasing time T_2.

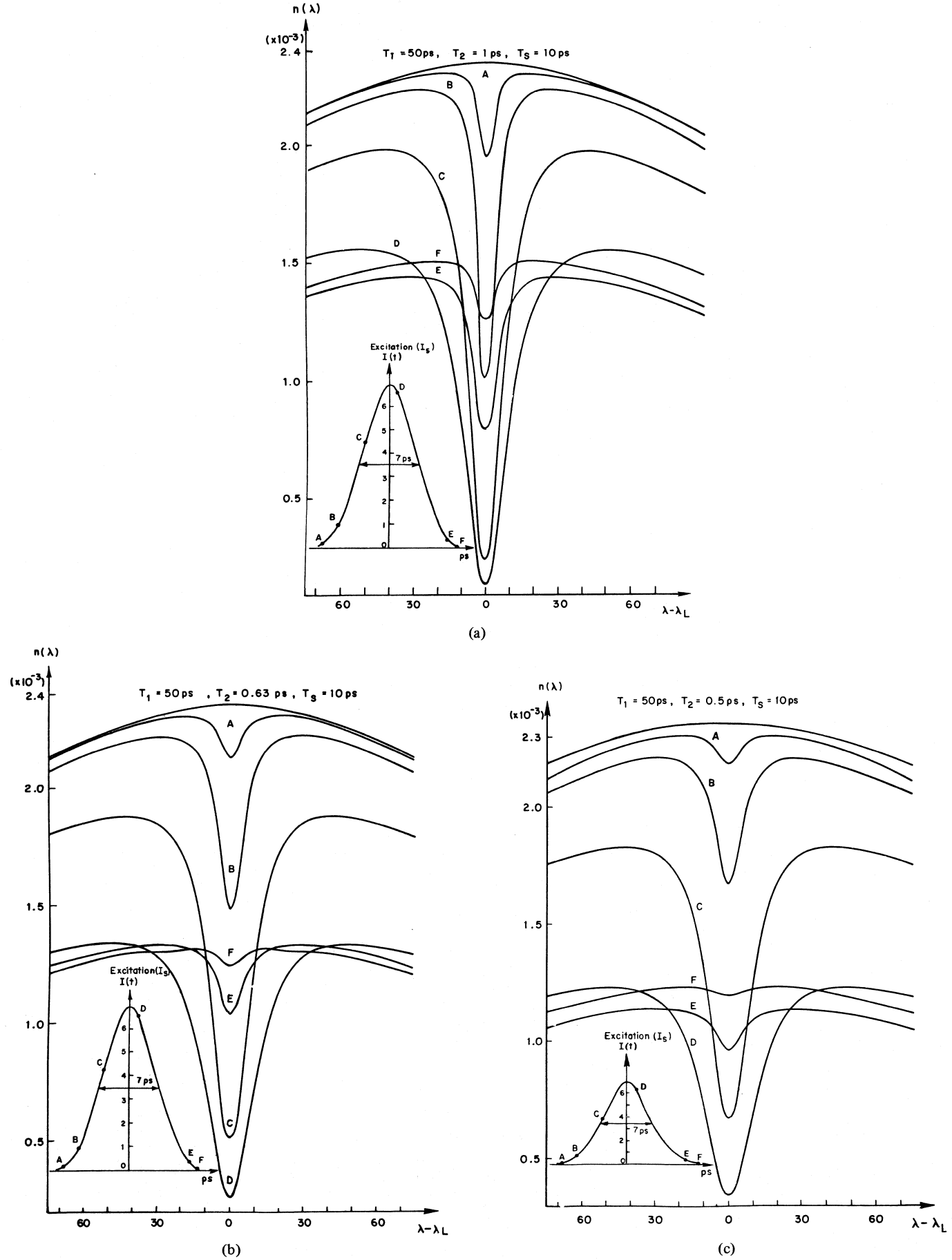

Fig. 9. Population inversion for an inhomogeneous distribution when excited by a strong monochromatic pulse at different times. $T_1 = 50$ ps, $T_S = 10$ ps. (a) $T_2 = 1$ ps. (b) $T_2 = 0.6$ ps. (c) $T_2 = 0.5$ ps.

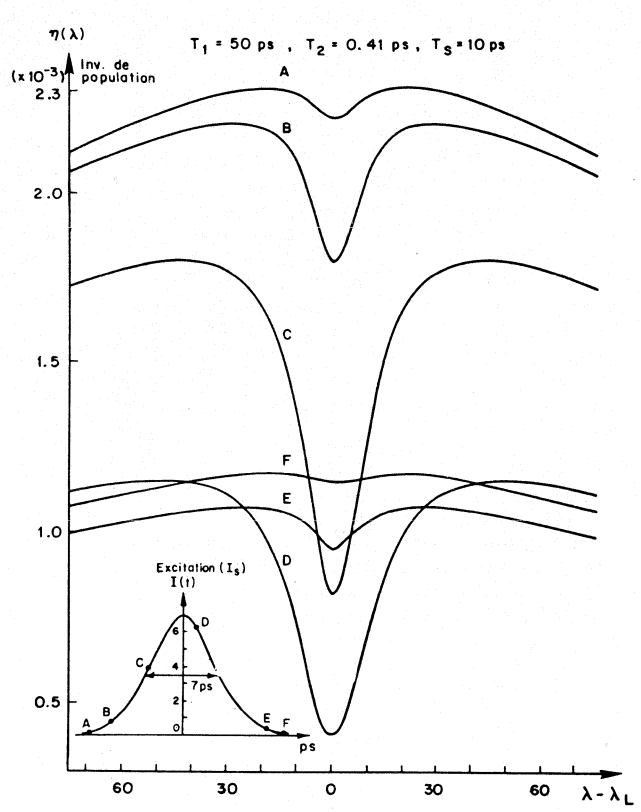

(d)

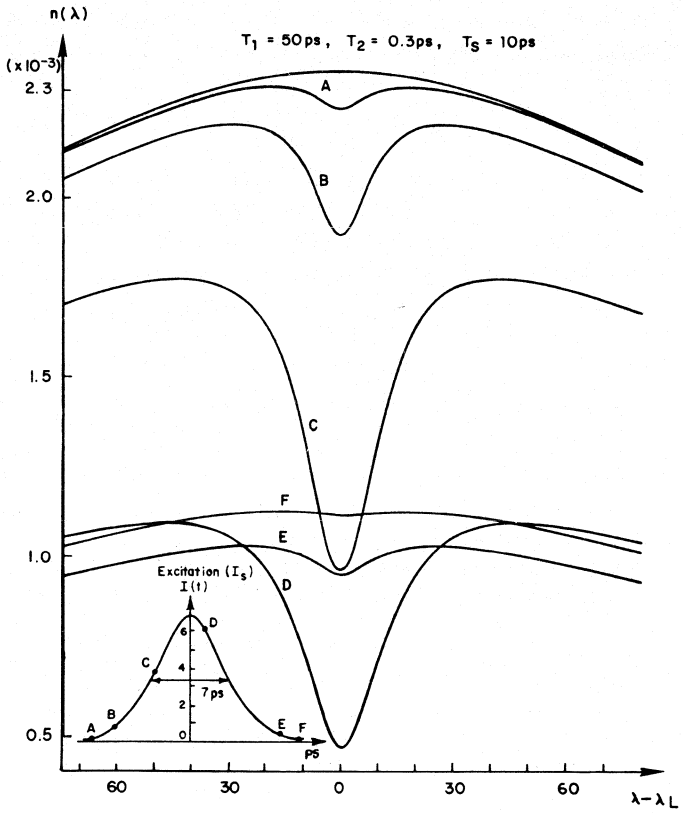

(e)

Fig. 9. (continued). (d) $T_2 = 0.4$ ps. (e) $T_2 = 0.3$ ps.

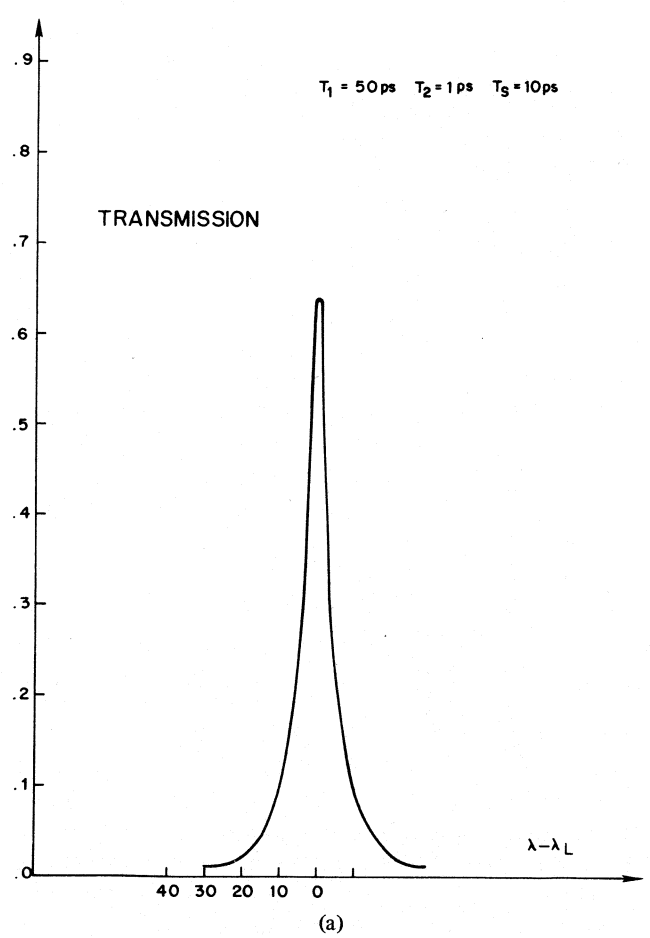

(a)

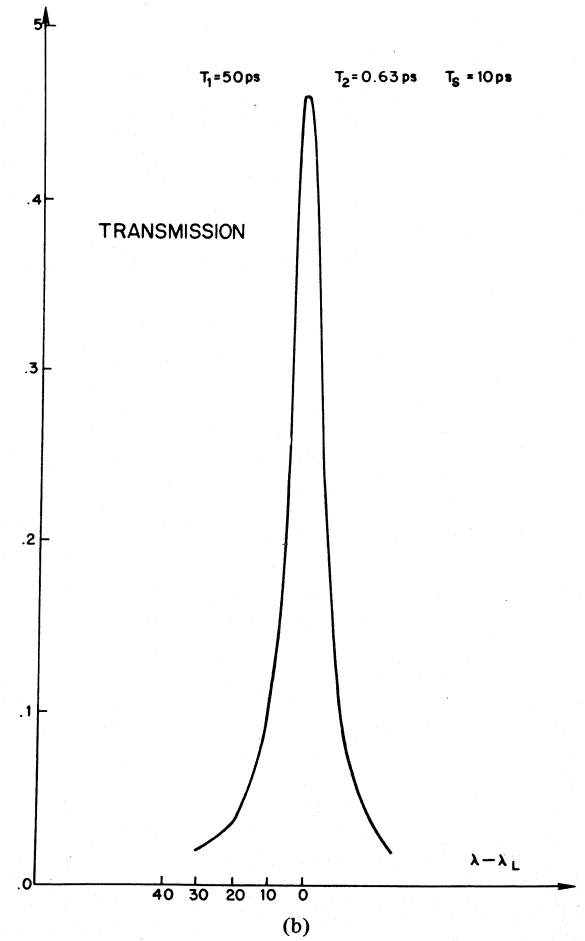

(b)

Fig. 10. Transmission across the wavelength deduced from the population inversion sketched on Fig. 9(a). (a) $T_2 = 1$ ps. (b) $T_2 = 0.6$ ps.

By using the experimental value for the bandwidth of the hole, we are able to estimate that the dephasing time is between 0.6 and 1 ps.

ACKNOWLEDGMENT

The author wishes to thank Prof. M. M. Denariez-Roberge and the Laboratoire de Recherche en Optique et Laser of Laval University for their continued interest, Prof. M. M. Malley for reading the manuscript, and B. Drouin for his expert technical assistance.

REFERENCES

[1] B. H. Soffer, "Giant pulse laser operation by a passive reversibly bleachable absorber," *J. Appl. Phys.*, vol. 35, p. 2551, Aug. 1964.
[2] F. Gires and F. Combaud, "Saturation de l'absorption optique de certaines solutions de phtalocyanines," *J. Phys.* (Paris), vol. 26, pp. 325-330, June 1965.
[3] F. Gires, "Etude de l'absorption saturable," *J. Phys.* (Paris), vol. 30, pp. 203-213, Feb./Mar. 1969.
[4] V. de Giorgio and G. Potenza, "Saturation effects in the absorption of the laser light by organic dyes," *Nuovo Cimento*, vol. 141, pp. 254-257, Feb. 1966.
[5] C. R. Giuliano and L. D. Hess, "Investigation of spectral bleaching in passive *Q*-switch dye," *Appl. Phys. Lett.*, vol. 9, pp. 196-198, Sept. 1968.
[6] B. H. Soffer and B. B. McFarland, "Frequency locking and dye spectral hole burning in *Q*-spoiled laser," *Appl. Phys. Lett.*, vol. 8, pp. 166-168, Apr. 1968.
[7] M. L. Spaeth and W. R. Sooy, "Fluorescence and bleaching of organic dyes for a passive *Q*-switch laser," *J. Chem. Phys.*, vol. 48, pp. 2315-2323, Mar. 1968.
[8] G. Mourou, B. Drouin, and H. H. Denariez-Roberge, "Observation du 'hole burning' dans une solution de cryptocyanine dans le methanol," *Opt. Commun.*, vol. 8, pp. 56-59, May 1973.
[9] D. W. Vahey and A. Yariv, "The effect of spectral cross relaxation and collisional dephasing on the absorption of light by organic dye solutions," to be published.
[10] —, "Measurements of spectral cross relaxation and collisional dephasing in organic dye solutions," to be published.
[11] D. N. Dempster, T. Morrow, R. Rankin, and G. F. Thompson, "Photochemical characteristics of the mode-locking dye, 1,1'-diethyl-4,4' carbocyanine iodide (cryptocyanine, DCI) and 1,1'-diethyl 2,2' dicarbocyanine iodide (DDI)," to be published.
[12] G. Mourou, B. Drouin, M. Bergeron, and M. M. Denariez-Roberge, "Kinetics of bleaching in polymethine cyanine dyes," *IEEE J. Quantum Electron.*, vol. QE-9, pp. 745-748, July 1973.
[13] G. Mourou and M. M. Denariez-Roberge, "Polarization of fluorescence and bleaching of dyes in a high-viscosity solvent," *IEEE J. Quantum Electron.*, vol. QE-9, pp. 787-790, Aug. 1973.
[14] M. A. Duguay and J. W. Hansen, "Direct measurement of picosecond lifetimes," *Opt. Commun.*, vol. 1, pp. 254-256, Nov./Dec. 1969.
[15] J. R. Platt *et al.*, *Systematics of the Electronic Spectra of Conjugated Molecules.* New York: Wiley, 1964, pp. 71-123.

The Fluctuation Model of a Passively Mode-Locked Laser

WILLIAM H. GLENN, MEMBER, IEEE

Abstract—**The "Fluctuation Model" for the generation of ultrashort pulses by a saturable absorber has been discussed by a number of authors. This model has provided valuable insights into the mechanisms involved in passive mode locking; however, previous treatments have been incorrect in several important respects. These treatments have attempted to describe the behavior of the laser in terms of the evolution of a statistically independent set of fluctuations (pulses) circulating in the laser. It is shown here that such a description is impossible in principle. This paper discusses in detail the problem with the previous treatments and presents an alternate treatment of the evolution of the ultrashort pulses during the nonlinear phase of development. The model is capable of predicting the conditions under which good mode locking will occur, the probability of the appearance of secondary pulses and their relative intensities, the peak intensity of the output pulse train and its statistical variation, and the duration and time of appearance of the output pulse train. The analysis has also been formulated in such a way that the evolution of the signal can be followed by measurement of experimentally observable quantities.**

Manuscript received June 7, 1974; revised September 18, 1974. This work was supported by the Air Force Cambridge Research Laboratories under a contract.

The author is with the United Aircraft Research Laboratories, East Hartford, Conn. 06108.

I. INTRODUCTION

THE "Fluctuation Model" of the passively mode-locked pulsed laser has been discussed by a number of authors [1]-[5]. The basic idea of this model is that the ultrashort pulse output from the laser results from the selection and temporal shaping of the fluctuations initially present in the spontaneous noise of the laser. When the flashlamp pumping begins, ions are excited to the upper laser level and produce spontaneous emission. The bandwidth of this emission is characteristic of the full inhomogeneous linewidth of the laser (~200 Å for Nd-glass) and the emission is noiselike. As the pumping continues, the laser gain builds up and the radiation in the cavity acquires a periodic structure with the cavity period $T = 2L/c$, while still retaining its noiselike structure within this period. With further increase in gain the radiation experiences a period of linear amplification resulting in a decrease in the bandwidth of the radiation. By the time the intensity reaches a point where the nonlinearity of the dye becomes important, the bandwidth of the radiation is such

that the time scale of the random variation of the intensity is a few picoseconds, and the radiation can be described by a collection of pulses of this duration and with random intensities. At this point the critical period for the development of mode locking takes place. Through the combined action of the nonlinearity of the dye, the laser gain saturation, and other possible nonlinearities, this random collection of pulses evolves to a condition where one of the pulses grows to an intensity that is much larger than any of the other pulses. This surviving pulse undergoes some narrowing in duration and spectral broadening in this process. Finally, it grows to such an intensity that electronic nonlinearities in the dye, solvent, and laser rod produce a further increase in the bandwidth to the observed output bandwidth. These nonlinearities can also impose complicated phase structures on the pulse. The analysis of this paper is concerned solely with the evolution of the radiation in the nonlinear period where the random fluctuations evolve into a single or multiple pulse train, and the description here is fundamentally different than previous treatments.

II. Formulation of the Model

A simple model of the behavior of the laser and bleachable dye will be used, and it is identical to previously described models. The dye cell will be treated as an inertialess bleachable absorber and the laser will be assumed to saturate on the total energy extracted. The transmission of the dye cell is determined by the dye transmission coefficient κ_0. The transmission is

$$\exp - \kappa = \exp - [\kappa_0/(1+I)]. \tag{1}$$

Here κ_0 is the unbleached absorption coefficient. A unit length is assumed. All intensities are normalized to the dye saturation intensity $I_s \sim 50$ MW/cm^2. The linear losses of the cavity are represented by a round-trip transmission of $\exp - \gamma$. The gain of the laser is given by $\exp \alpha$ where

$$\frac{d\alpha}{dt} = \frac{-2\sigma\alpha I}{h\cup} I_s + f. \tag{2}$$

Here σ is the cross section for stimulated emission and f is the rate of pumping due to the flashlamp.

We consider now a sample of the radiation field existing in the cavity at the kth pass. This intensity obeys the equation

$$\frac{dI_k}{dk} = I_k \left(\alpha_k - \gamma - \frac{\kappa_0}{1+I_k} \right) + \left(\frac{dI_k}{dk} \right)_{sp} \tag{3}$$

The last quantity represents the contribution of spontaneous emission. The gain coefficient α obeys the equation

$$\frac{d\alpha_k}{dk} = -\alpha_k \left(\frac{2\sigma}{h\cup} I_s T \right) I_k + fT \tag{4}$$

where T is the cavity transit time. It will be assumed that the flashlamp pumping is such that acting alone it produces a linearly increasing value of α.

The behavior of the laser is illustrated schematically in Fig. 1. The pumping begins at $t = 0$ and begins to excite the laser. In region I, the intensity is small and is dominated by the spontaneous emission term of (3). At the end of region I

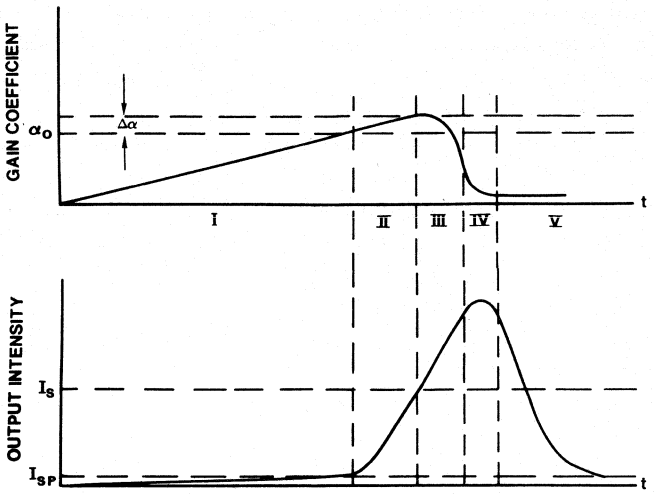

Fig. 1. Behavior of the gain and average intensity in a mode-locked laser.

the gain coefficient has increased to the threshold value

$$\alpha = \alpha_0 = \kappa_0 + \gamma. \tag{5}$$

In region II the intensity undergoes a linear period of amplification and acquires a periodic structure with period T. The bandwidth is reduced and the time scale of the random fluctuations is correspondingly increased. The increase in duration has been treated adequately elsewhere [1]. The end of region II occurs when the intensity has grown to such a point that nonlinearities in the dye become important. This represents the starting point for the mode-locking process. At this point, the radiaiton field in the cavity consists of a noiselike signal. It can be described by a collection of M pulses of duration T/M and with random intensities. The probability density of the intensities can be taken as

$$W_1(I) = \langle I \rangle^{-1} \exp - (I/\langle I \rangle) \tag{6}$$

characteristic of white noise. At the end of this period the gain has also increased from its threshold value α_0 to

$$\alpha_1 = \alpha_0 + \Delta\alpha. \tag{7}$$

It will be seen that this quantity $\Delta\alpha$ is of extreme importance in determining the behavior of the laser.

Region III is the critical period for mode locking. During this period, if the laser is to be well mode locked, the random ensemble of pulses evolves to a state where one pulse has an intensity that is much larger than any of the other pulses. During this period the pulses undergo some distortion and shortening in duration. This latter effect is of secondary importance and will not be treated here. It will be assumed that the pulses remain of constant duration, i.e., that they are effectively "square" pulses. The primary mechanism is one of pulse selection and discrimination.

III. Discussion of Previous Treatments

The behavior of the pulse intensities in region III is determined by

$$\frac{dI_{ki}}{dk} = I_{ki} \left(\alpha_{ki} - \gamma - \frac{\kappa_0}{1+I_{ki}} \right) \tag{8}$$

where the i subscript denotes the ith member of the set of M pulses circulating in the cavity. In general, the gain coefficient will depend on all previous pulses that have passed through the laser. Most previous treatments have assumed, however, that α is constant in region III and equal to $\alpha_0 + \Delta\alpha$, its value at the start of the period. This implies that the selection process is essentially complete before appreciable gain saturation sets in. The change in α during this period is quite small but small changes can be extremely important. We will return to this point in Section IV.

The basic approach used in previous treatments is to subject the starting ensemble of pulses to the nonlinear transformation of (8) and to calculate the statistical properties of the output set of pulses. This procedure assumes that the pulses are statistically independent, which in fact they would be if they were governed only by (8) with constant α. This approach, in spite of its apparent success, suffers from two fundamental errors.

1) It is impossible in principle to describe the output of a mode-locked laser in terms of a cavity containing a set of statistically independent pulses (fluctuations).

2) Even if the pulses were statistically independent, the statistics would be such that there would be no reason to expect that an ensemble average of any property of the pulses would correspond to a sample average as actually observed.

These difficulties may now be examined in detail.

If we assume that the pulses are statistically independent, then after passing through the dye and laser a number of times, the probability density given in (6) will be transformed into some new distribution $W_2(I)$. This may be calculated, but for the present purpose it may be allowed to be arbitrary. The implications of this may now be examined.

Let us take as a working definition of a "well mode-locked" laser, one that produces an output set of pulses in which one and only one is larger than some threshold value (say the triggering level of an oscilloscope), for a large percentage of the time. We now attempt to describe this situation by a set of M independent pulses with a probability density $W_2(I)$. The probability that one pulse exceeds the threshold I_t is

$$P_1 = Mpq^{M-1} \tag{9}$$

where

$$p = \int_{I_t}^{\infty} W_2(I)\, dI \tag{10}$$

$$q = \int_{0}^{I_t} W_2(I)\, dI. \tag{11}$$

Similarly, the probability that two and only two pulses exceed this threshold is

$$P_2 = \frac{M(M-1)}{2} p^2 q^{M-2} \tag{12}$$

and in general, for N pulses

$$P_N = \binom{M}{N} p^N q^{M-N}. \tag{13}$$

This is simply the binomial probability distribution. If many observations are made, the average number of pulses exceeding I_t will be Mp, and ideally $Mp = 1$. The case of large M and small p is the case where the Poisson approximation to the binomial distribution applies and we have

$$P_N \approx \frac{(Mp)^N}{N!} e^{-Mp} = \frac{\lambda^n e^{-\lambda}}{N!}$$

$$\lambda \equiv Mp. \tag{14}$$

P_1 has a maximum for $\lambda = 1$ and for this case $P_0 = 0.368$, $P_1 = 0.368$, and $P_2 = 0.184$. Thus the model predicts that a "single pulse" train can be achieved only 36.8 percent of the time. This is contrary to experimental observation. Note that this result is independent of the statistical distribution; it is a result only of the statistical independence.

From the previous discussion, it is clear that the pulses in the output cannot be statistically independent. Nevertheless, several authors [1], [3], [5] have calculated that the probability of the appearance of a single, large pulse is high. The basic argument is that the nonlinear transformation is so strong that initial pulses of very nearly the same intensity emerge after the transformation with much different intensities. The objection to this is that the nonlinear transformation is in fact so strong that it is not valid to expect that the statistical average will correspond to the actually observed average over a set of pulses. The situation is that the final probability density $W_2(I)$ calculated from the nonlinear transformation in (8) is so "spread out" that an enormous number of samples would be required for the sample average to approach the statistical average. We are considering a finite number M of samples and the number is simply not large enough to apply the statistical average. This statement may be proved by means of the Central Limit Theorem and a proof is given in Appendix I. There is no paradox involved in the fact that the statistically independent model predicts a high probability of a single isolated pulse for a fixed number of starting pulses. If a sufficient number of starting pulses were used to allow valid application of statistical averaging, then it would be found that in fact the probability of obtaining a single isolated large pulse would be small. A simple example of this is given in Appendix I.

IV. Formulation of the Alternate Approach

From the discussion of the previous section it is clear that the pulses cannot be treated as statistically independent. In more physical terms, it is necessary to invoke some mechanism by means of which one pulse can capture the stored energy of the laser at the expense of the other pulses. Only in this way can an output consisting of a single large pulse be obtained consistently. In terms of the statistics, the joint probability distribution must be such that the presence of a large-intensity pulse implies that the intensities of the other pulses are low. There are a number of mechanisms that could cause this. Perhaps the simplest is gain saturation. The net gain experienced by a pulse is a function of its intensity. The effective gain coefficient is

$$\alpha_{\text{net}} = \alpha - \gamma - \kappa_0/(1 + I_{ki}). \tag{15}$$

At the start of region III, this quantity is positive for all pulses, although it may be quite small. Only a minute amount of saturation is necessary, however, before this quantity can become negative for pulses of very low intensity while remaining positive for pulses of higher intensity. The higher intensity pulses continue to grow while the lower intensity pulses decay. This provides a powerful discriminant. It is convenient to think of a critical intensity I_c for which

$$\alpha - \gamma - \kappa_0/(1 + I_c) = 0 \tag{16}$$

$$I_c = \frac{\kappa_0}{\alpha - \gamma} - 1 = \frac{\kappa_0}{\kappa_0 + \Delta\alpha} - 1. \tag{17}$$

At the start of region III, $I_c < 0$, i.e., all pulses have gain. As the gain becomes depleted, $\Delta\alpha = \alpha - \gamma - \kappa_0$ goes to zero and becomes negative, and $I_c > 0$. Only pulses with greater intensity than this continue to grow. Clearly, the presence of a very large pulse will deplete the gain faster and will cause I_c to rise more rapidly. This results in more effective elimination of the smaller pulses. To achieve good mode locking, one wants to have the intensity of only the largest pulse "outrun" the rising value of I_c. This picture is borne out in detail in the results to be described below.

The treatment of a large number of statistically dependent variables is a formidable mathematical task. It was decided to resort to a simulation to verify the picture previously described. The simulation that was used started with an ensemble of pulses of low intensity. For each pass through the laser, the gain was assumed to be constant, but at the end of each pass, the total energy extracted from the laser was computed and the gain was recalculated for the next pass. The intensity of the pulses was assumed to obey (8), which in difference equation form is

$$\log I_{k+1,i} = \log I_{k,i} + \left(\alpha_k - \gamma - \frac{\kappa_0}{1 + I_{ki}}\right) \tag{18}$$

i.e., α was independent of i but a function of k. The dependence of α was

$$\alpha_{k+1} = \alpha_k - \frac{2\sigma\alpha_k}{h\upsilon} T \sum_{n=1}^{M} I_{ki}. \tag{19}$$

Before presenting the results of the simulation it is necessary to discuss the choice of the starting set of pulses. The starting set could simply be chosen by a computer-generated set of random intensities having the proper statistics (6). This was, in fact, how the fruitfulness of the present approach was initially discovered. Such an approach does not provide a good picture of the statistical variation that would be expected in the output without a large number of trials for each set of laser parameters. A better approach is to consider the statistics of all possible ensembles of M starting pulses (as opposed to the statistics of the individual pulses). For any given set of starting pulses the behavior is completely determined by (18) and (19). The problem is thus one of analyzing the properties of the starting set of pulses that are likely to lead to good mode locking, determining the statistical distribution of these properties, and running judiciously chosen sets of input pulses to determine the statistical behavior of the output.

We consider a set of M starting pulses having the probability density

$$W(I) = e^{-I} \tag{20}$$

and ask what is the probability density of the Nth largest pulse in the set. It may be shown (see Appendix II) that this is

$$U_N(I) = \frac{M!}{(N-1)!\,(M-N)!} e^{-NI} [1 - e^{-I}]^{M-N}. \tag{21}$$

The most probable intensity of the Nth largest pulse, I_{mp}, is determined by

$$\frac{d\,U_N(I)}{dI} = 0 \tag{22}$$

which gives

$$I_{mp} = \log (M/N). \tag{23}$$

A reasonable starting set of pulses is one in which the intensity of each pulse is assigned its most probable value, i.e., the largest is $\log M$, next $\log M/2$, next $\log M/3$, etc. The output from this set will thus represent the most probable output of the laser. For the case $M = 100$, the most probable amplitudes of the largest pulses are 4.6, 3.9, 3.5, and 3.2.

We must now consider what properties of the input set of pulses will lead to significant variations in the output. In this we may be guided by the picture presented earlier of a rising value of the critical intensity that gradually "eliminates" the pulses starting from the least intense pulse. For good mode locking only a few pulses will be able to outrun this critical intensity. Very close to the conditions for optimum mode locking the behavior will depend on the competition between the two largest pulses, i.e., whether their growth rate is such that they both survive or whether the rising critical intensity finally eliminates the second largest pulse, leaving only one pulse of large intensity. Thus one is led to the conclusion that for conditions close to those for optimum mode locking, the most important property of the starting set of pulses is the ratio between the intensities of the largest and the second largest pulse. The probability that the largest pulse is C times larger than the second largest pulse may be shown to be (see Appendix II)

$$V(M, C) = \frac{\Gamma(C+1)\,\Gamma(M+1)}{\Gamma(M+C)} \approx \frac{C}{(M+1)^{C-1}}. \tag{24}$$

The approximation is valid for C slightly greater than 1. The behavior of this function for $M = 100$ is shown in the following table:

C	1	1.01	1.02	1.04	1.10	1.20	1.50	2.0
V	1.0	0.96	0.93	0.86	0.69	0.48	0.15	0.02

If the pulses are assigned their most probable value, the ratio between the two largest pulses is ~1.18 and from (24) the ratio should be this large or larger approximately 50 percent of the time. Conditions could be found using this set of pulses

for which only the largest pulse survived to grow to an appreciable intensity. To further investigate the behavior, another starting set of pulses was chosen. In most cases, this was taken as a set in which all pulses had their most probable intensities except the second largest and the ratio of the largest to the second largest was taken as 1.02. The ratio would be expected to exceed this value 93 percent of the time. By varying the ratio of the two largest pulses, an excellent picture of the statistical behavior of the output near the conditions for good mode locking could be obtained. The results are discussed in the following sections.

V. Results of the Simulation

Equations (18) and (19) were simply computed for every pass and every pulse in the starting set. A flowchart for the simulation is shown in Fig. 2. The program was run on-line on a time-shared PDP-6 computer. The inputs to the program were the linear loss γ, the small-signal dye absorption κ_0, the laser cross section σ (taken as $\sigma/h\upsilon = 0.16$ cm^2/J characteristic of Owens Illinois ED-2 glass), the dye saturation intensity (taken as 50 MW/cm^2), the gain at the start of the calculation $\alpha = \alpha_0 + \Delta\alpha$, and the cavity transit time T (taken as 5 ns). The laser area is assumed to be 1 cm^2. The mean value of the starting set of pulses was taken as 0.002 (normalized to the dye saturation intensity), and all pulse intensities were assigned their most probable values with the exception of the second largest pulse. This intensity was also a variable input to the program. In all cases to be discussed, it was assumed that $M = 100$.

The output available consisted of a) the number of passes from the starting point, b) the intensity of any or all of the pulses at any pass (at the discretion of the operator), c) the average intensity of the M pulses at any pass, d) the ratio of the two largest pulses, e) the second-harmonic intensity that would be observed (i.e., the average of I^2 over the M pulses), f) the second-harmonic enhancement ratio (SHER) [i.e., the ratio of e) to the square of c)], g) the value of the gain and critical intensity, and the h) total energy extracted from the laser.

Of these quantities c), e), and f) are of particular significance since they are experimentally observable quantities. The intensities of the various pulses cannot be observed since detectors of sufficient speed, sensitivity, and dynamic range are not available.

The behavior of the laser was investigated for values of κ_0 of 0.1, 0.2, 0.3, and 0.4 and for a range of values of the gain α_0. The linear loss γ was usually taken as 0.1. For every case, it was found that a range of values of the gain α could be found for which excellent discrimination took place. The critical parameter is the "excess gain," $\alpha - \gamma - \kappa_0$ that is present at the start of the calculation. Space will not permit a complete presentation of all the results obtained, but several interesting cases will be discussed. Figs. 3-7 show the behavior for the case $\kappa_0 = 0.2$, $\gamma = 0.1$ for various values of the gain.

Fig. 3 shows the behavior of the intensity (within the cavity) of the largest pulse. As the excess gain is decreased, the peak output occurs later and later. For the value $\alpha - \gamma - \kappa_0 = 0.01$,

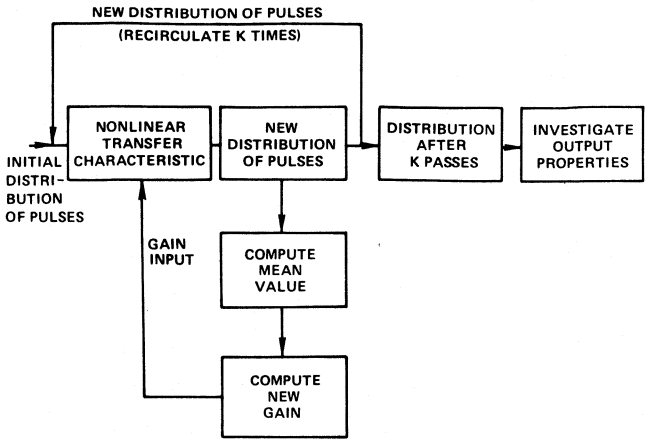

Fig. 2. Flowchart for the numerical simulation.

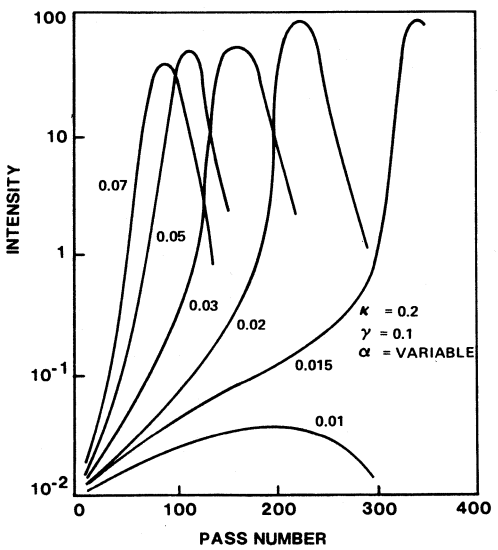

Fig. 3. Behavior of the intensity of the largest pulse. Conditions are $\kappa_0 = 0.2$, $\gamma = 0.1$, $\Delta\alpha$ is the parameter.

the output remains small throughout. In this case, the gain is depleted before any pulse saturates the dye. For values slightly greater than this, there is a long delay followed by a rapid increase in intensity. This, as we shall see, corresponds to the best mode locking.

Fig. 4 shows the behavior of the average intensity of all the pulses. These curves display, for $\Delta\alpha = 0.015$ and 0.02 a very interesting feature, namely a growth, followed by a dip and then a very rapid growth.

The reason for this is clear. In the region of the dip very strong discrimination of the pulse intensities is taking place. The largest pulses are growing while all the others are decaying. For a time this result in a decrease in the average intensity before the largest pulse reaches its peak.

Fig. 5 shows the behavior of the SHER. The positions of the peak output, from Fig. 3, are indicated by the arrows. The cases $\Delta\alpha = 0.015$ and $\Delta\alpha = 0.02$ represent essentially perfect mode locking as indicated by the enhancement ratio of 100 (the maximum possible value with $M = 100$ corresponding to 100 modes locked). For larger values of the excess gain, the

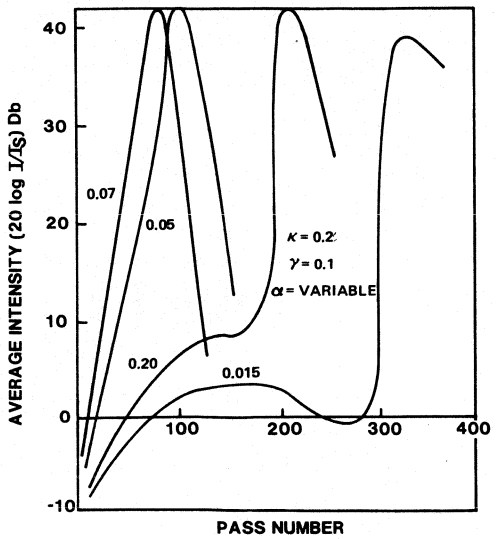

Fig. 4. Behavior of the average intensity. Same conditions as in Fig. 3.

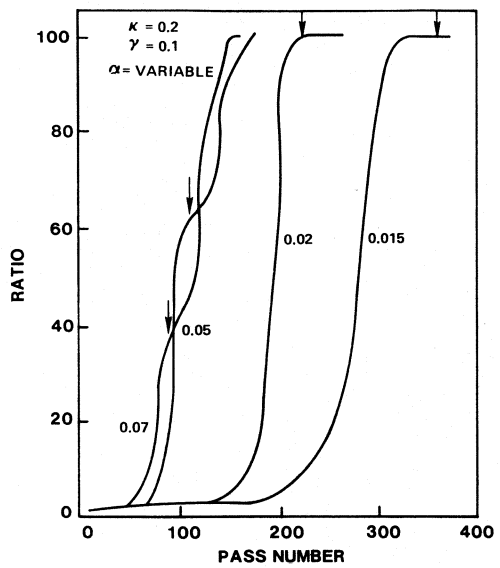

Fig. 5. Behavior of the SHER. Same conditions as in Fig. 3.

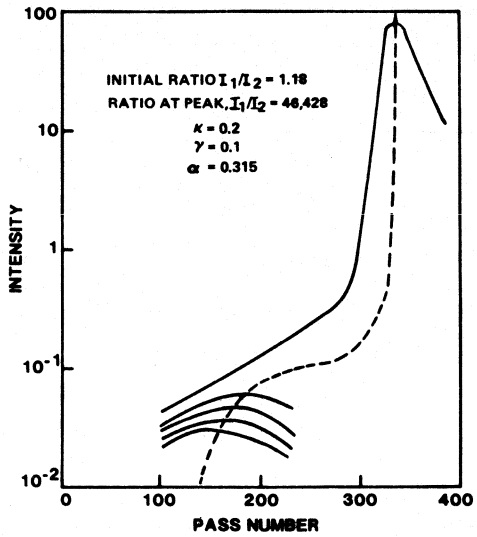

Fig. 6. Behavior of the five largest pulses for the most probable starting set. The initial ratio of the two largest pulses was 1.18. Conditions were $\kappa_0 = 0.2$, $\gamma = 0.1$, $\alpha = 0.315$ ($\Delta\alpha = 0.015$).

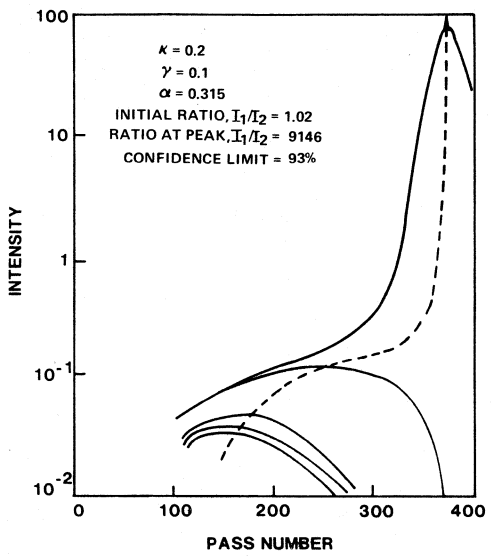

Fig. 7. Behavior of the five largest pulses for an initial ratio of 1.02 between two largest pulses. Other conditions as in Fig. 6.

mode locking is incomplete. The shoulder in the curves is easy to understand. Initially, the SHER grows as the pulse intensities pass through the nonlinear region of the dye characteristics. Finally, several pulses "break through" and grow to large values. At the peak, the dye is ineffective and the SHER slows its rate of growth. As the pulses decay they again pass through the nonlinear region and the SHER again grows and saturates at a value which may be less than 100 as all the pulses drop to low intensities.

Fig. 6 shows the behavior of the five largest pulses for $\Delta\alpha = 0.015$. In this case, all pulses were assigned their most probable value. The dotted line shows the behavior of the critical intensity defined earlier. The discrimination is dramatic. The initial intensity ratio of the two largest pulses was 1.18. At the peak, the ratio is in excess of 46 000. Fig. 7 shows the case where the initial ratio of the two pulses was taken as 1.02, which should be exceeded 93 percent of the time. The discrimination is still intense, with a final ratio in excess of 9000.

The critical role of the gain saturation may be readily seen. Fig. 8 shows the behavior of the five largest pulses for a case of good mode locking. The parameters were $\kappa_0 = 0.3$, $\Delta\alpha = 0.02$. Fig. 9 shows the behavior for the same parameters with the gain saturation removed. In this case, of course, the pulses continue to grow without limit; however, the discrimination is extremely weak.

The results of all the cases run can be combined to describe those conditions necessary for good mode locking. The SHER at the peak of the output may be taken as a measure of the quality of the mode locking. This is plotted in Fig. 10 as a function of the excess gain $\alpha - \gamma - \kappa_0$, with κ_0 as a parameter. As can be seen, there is a narrow window just above threshold for which mode locking will occur. For values that are too

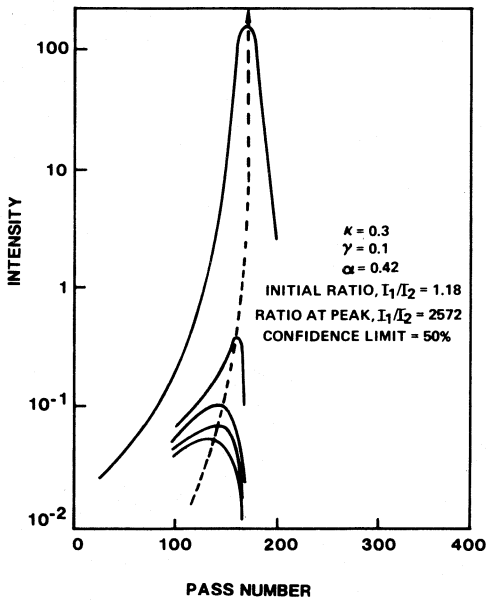

Fig. 8. Behavior of the five largest pulses for $\kappa_0 = 0.3$, $\gamma = 0.1$, $\alpha = 0.42$ ($\Delta\alpha = 0.02$).

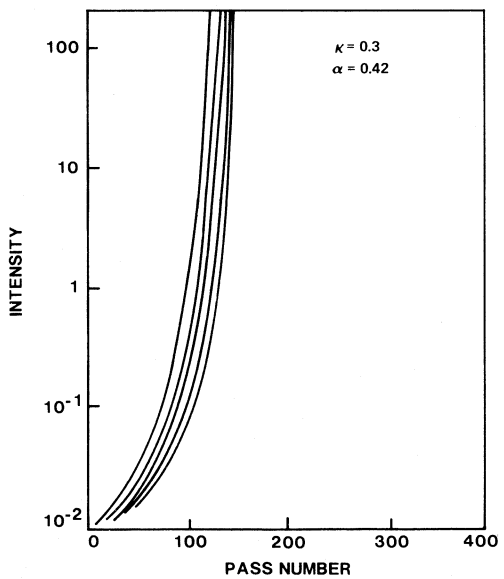

Fig. 9. Behavior of the five largest pulses in the absence of gain saturation. Conditions were the same as in Fig. 8.

low, the intensity never breaks through the dye. For values too high, the discrimination is poor. These curves were plotted for the 50-percent confidence level corresponding to the most probable set of starting pulses. Use of a higher confidence level would result in a narrowing of the window.

VI. Discussion

It has been shown that it is impossible to describe the the behavior of a mode-locked laser in terms of the evolution of a statistically independent set of fluctuations arising from spontaneous emission. It is necessary to invoke some mechanism to introduce a statistical dependence among the pulses. The simplest mechanism is the saturation of the laser gain. The introduction of the statistical dependence leads to formidable difficulties in the analytical description of the

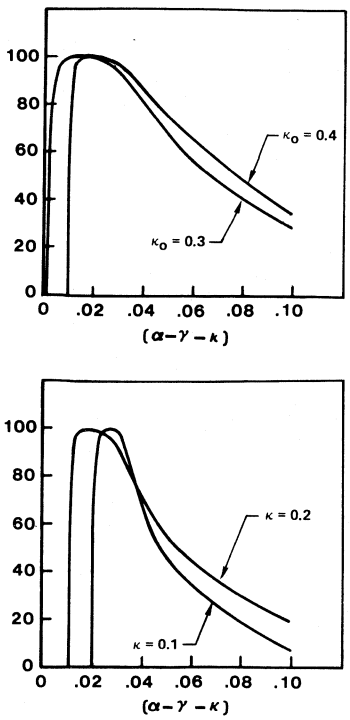

Fig. 10. SHER at peak output as a function of the excess gain.

evolution of the radiation field. A numerical simulation of the behavior, however, is straightforward. The results of the simulation provide a very clear picture of the mode-locking process. The most important parameter governing the behavior of the laser is the excess gain $\Delta\alpha = \alpha - \gamma - \kappa_0$ that exists at the start of the nonlinear phase of the process. For a small range of value of $\Delta\alpha > 0$, the combination of the dye nonlinearity and the laser saturation provides an extremely powerful discriminant that allows only the largest of the initial fluctuations to grow to a large intensity. The importance of this parameter has emerged from previous treatments of the problem. The present model, however, provides a much stronger discrimination of pulse intensities.

The present model is in excellent qualitative agreement with experimental observations. Quantitative agreement should not be expected since a number of effects have been neglected. The change in pulse duration during the nonlinear phase could be treated by an extension of the present approach which characterizes each pulse by an energy and duration rather than simply by an intensity as was done here. The present treatment has also tacitly assumed a undirectional ring-type geometry. In a linear laser, pulses traveling in opposite directions overlap in the dye cell leading to a further statistical dependence. This effect is somewhat more difficult to treat since it is sensitive to the time ordering of the starting set of pulses. The result of this effect is the development of satellite pulses, and it should be possible to estimate the statistical distribution of the intensity of these pulses. The introduction of a finite relaxation time of the saturable absorber can be readily incorporated into the simulation; however, this too introduces a dependence on the time ordering of the initial set of pulses and would require a large number of trials to determine the statistical behavior of the output.

It should be possible to verify the predictions of the model presented here experimentally. The average intensity and the average second-harmonic intensity can be observed experimentally by means of a reasonably slow detector, one with a response time of the order of the cavity transit time. The only problem is one of dynamic range in recording the signals. Logarithmic amplifiers may be used to compress the dynamic range required in the recording of the signals. The initial slope of the average intensity gives a measure of the excess gain while the behavior of the SHER gives a good indication of the amount of pulse-intensity discrimination taking place. Thus all parameters of the model can be determined.

Appendix I

In Section III it was stated that for a sufficiently severe nonlinear transformation, it is not reasonable to expect that the sample average and the statistical average should correspond. This may be shown rigorously by means of the Central Limit Theorem. As an example, suppose we wish to calculate the average intensity of a set of M statistically independent pulses each having a probability density $W(I)$. The sample average is

$$\langle I\rangle_{sa} = M^{-1}\sum_{i=0}^{M} I_i \tag{25}$$

while the statistical average is

$$\mu \equiv \langle I\rangle_{st} = \int_0^\infty IW(I)\,dI. \tag{26}$$

The Central Limit Theorem states that the sum of a number M of statistically independent random variables, each with a mean μ and a variance σ, is itself a random variable whose distribution approaches a normal distribution with a mean value $M\mu$ and a variance $M^{1/2}\sigma$. More precisely, for every fixed β [6]

$$P\left\{\frac{\Sigma_i I_i - M\mu}{\sigma M^{1/2}} < \beta\right\} \longrightarrow \Phi(\beta) \tag{27}$$

or

$$P\{M^{-1}\Sigma_i I_i - \mu < \sigma M^{1/2}\beta\} \longrightarrow \Phi(\beta) \tag{28}$$

where

$$\Phi = (2\pi)^{-1}\int_{-\infty}^{\beta} e^{-x^2/2}\,dx. \tag{29}$$

Let us now determine the probability that the sample mean and the statistical mean differ by no more than a fixed amount with a probability of 0.5. This is

$$P\{M^{-1}\Sigma_i I_i - \mu < \sigma M^{-1/2}\beta\} - P\{M^{-1}\Sigma_i I_i - \mu < -\sigma M^{-1/2}\beta\} = \Phi(\beta) - \Phi(-\beta). \tag{30}$$

The value of β for which $\Phi(\beta) - \Phi(-\beta) = 0.5$ is $\beta = 0.678$ so that

$$P\{|M^{-1}\Sigma_i I - \mu| < 0.678\sigma M^{-1/2}\} = 0.5. \tag{31}$$

That is, the sample average and the statistical average will differ by more than $0.678\sigma M^{-1/2}$ for 50 percent of the time.

Let us require that this deviation be no greater than $\frac{1}{2}\mu$. This implies

$$\tfrac{1}{2}\mu > 0.678\sigma M^{-1/2} \tag{32}$$

or

$$M > \left|\frac{1.356\sigma}{\mu}\right|^2$$

This provides an estimate of the sample size required for even a rather poor agreement between the sample average and the statistical average.

Let us now consider a strong nonlinear transformation of the type

$$I_k = I_0^n \tag{33}$$

where n is a reasonably large number (10–100). This transformation has been used by a number of authors. We may calculate the mean and variance of the transformed distribution where the distribution of I_0 is

$$W(I_0) = e^{-I_0}. \tag{34}$$

We find

$$\mu = \langle I_k\rangle = \int_0^\infty I_0^n\, e^{-I_0}\,dI_0 = n!$$

$$\langle I_k^2\rangle = \int_0^\infty I_0^{2n}\, e^{-I_0}\,dI_0 = (2n)!$$

$$\sigma^2 = [\langle I^2\rangle - \langle I^2\rangle] = (2n)! - n!. \tag{35}$$

Using the approximation

$$\log n! \approx n\log n \tag{36}$$

we have

$$\sigma \approx [e^{2n\log 2n} - e^{2n\log n}]^{1/2} \approx e^{n\log 2n} \tag{37}$$

and

$$\mu \approx e^{n\log n}. \tag{38}$$

Consequently,

$$\sigma/\mu \approx \frac{e^{n\log 2n}}{e^{n\log n}} = e^{n\log 2}. \tag{39}$$

Referring to (32), we have

$$M > 1.838e^{2n\log 2}.$$

For $n = 30$, this becomes $M > 1.838e^{41.6}$. This is an extremely large number of samples. M is the number of pulses in the cavity or, equivalently, the number of modes. It is at most a few thousand and this does not constitute a sufficiently large sample.

The hypothetical transformation in (33) does not, of course, correspond to the actual transformation that is produced by

(8). A similar situation occurs, however, if the actual transformation is used. Equation (8) has an exact solution for constant α; it was given by Kryukov and Letokhov [1] and is, in the present notation,

$$I_k^{-1}[(\alpha-\gamma-\kappa_0)+(\alpha-\gamma)I_k]^{\kappa_0/\alpha-\gamma} = I_0^{-1}[(\alpha-\gamma-\kappa_0)+(\alpha-\gamma)I_0]^{\kappa_0/\alpha-\gamma} \cdot \exp[-(\alpha-\gamma-\kappa_0)k]. \quad (40)$$

This is not an explicit solution for I_k in terms of I_0, but it may readily be solved numerically. If this is done, the mean and the variance of the new distribution may be computed. It is found that, as a function of k, the quantity σ/μ grows so rapidly that the sample size soon becomes too small for the valid application of statistical averaging.

A further point should be noted with regard to (40). One might be led to consider the case when I_0 is very small, $I_0 \ll (\alpha-\gamma-\kappa_0)/(\alpha-\gamma)$ and I_k very large, $I_k \gg (\alpha-\gamma-\kappa_0)/(\alpha-\gamma)$. If this approximation is made, (40) becomes

$$[(\alpha-\gamma)^{\kappa_0/\alpha-\gamma} I_k^{\kappa_0/(\alpha-\gamma)-1}] = (\alpha-\gamma-\kappa_0)^{\kappa_0/\alpha-\gamma} I_0^{-1} \exp[-(\alpha-\gamma-\kappa_0)k]. \quad (41)$$

Rearrangement gives

$$I_k^{(\kappa_0/\alpha-\gamma)-1} = I_k^{-(\alpha-\gamma-\kappa_0)/(\alpha-\gamma)} = \left(\frac{\alpha-\gamma-\kappa_0}{\alpha-\gamma}\right)^{\kappa_0/(\alpha-\gamma)} I_0^{-1} \exp-[(\alpha-\gamma-\kappa_0)k]. \quad (42)$$

Now let

$$n = \frac{\alpha-\gamma}{\alpha-\gamma-\kappa_0}. \quad (43)$$

Equation (43) becomes

$$I_k^{-1/n} = \left(\frac{1}{n}\right)^{(\kappa_0/\alpha-\gamma)} I_0^{-1} \exp-[(\alpha-\gamma-\kappa_0)k]$$

$$I_k = I_0^n (n)^{(\kappa_0 n)/(\alpha-\gamma)} \exp[(\alpha-\gamma)k] = DI_0^n$$

$$D = (n)^{(\kappa_0 n)/(\alpha-\gamma)} \exp[(\alpha-\gamma)k]. \quad (44)$$

We note

$$n = \frac{\alpha-\gamma}{\alpha-\gamma-\kappa_0} \approx \frac{\alpha_0-\gamma}{\Delta\alpha}. \quad (45)$$

This is simply the nonlinearity parameter μ introduced by Letokhov. This approximation results in the power-law dependence of the output intensity upon the input intensity, such as was used in (33). In fact, (44) constitutes a very poor approximation to (40) as may be verified by direct numerical computation.

As a final point on this topic, we may illustrate by an example the failure of the statistically independent model. According to [1], the probability of generating a double pulse train with an amplitude ratio not exceeding S is

$$\rho(2) = \frac{\log S \log \cdot M}{en}. \quad (46)$$

Here n (or μ in [1]) is the coefficient of the power law. In order for the statistical averaging to be valid we must have

$$M \gtrsim e^{2n \log 2}. \quad (47)$$

Thus

$$\rho(2) > \log S \frac{2 \log 2}{e}. \quad (48)$$

This is totally independent of the nonlinearity parameter and there is no way to make it small for any value of S that would represent good mode locking. For $S = 2$, $\rho(2) = 0.35$.

Appendix II

In Section IV, two probability densities were employed. The probability density for the intensity of the Nth largest pulse in a set of M pulses is

$$U_N(I)dI = KW(I)\left[\int_I^\infty W(I')dI'\right]^{N-1} \cdot \left[\int_0^I W(I')dI'\right]^{M-N} dI. \quad (49)$$

The $W(I)$ term is the probability density for the pulse in question. The first term in brackets is the probability that $N-1$ pulses are larger in intensity and the second term is the probability that the remaining $M-N$ pulses are smaller. The constant K can be determined by combinatorial analysis or by normalization. We require

$$\int_0^\infty U_N(I)dI = 1. \quad (50)$$

Let

$$x = \int_0^I W(I)dI \qquad dx = W(I)dI$$

then

$$\int_0^\infty U_N(I)\,dI = K\int_0^1 (1-x)^{N-1}x^{M-N}\,dx = KB(N, M-N+1) \quad (51)$$

$$= K\frac{\Gamma(N)\,\Gamma(M-N+1)}{\Gamma(M+1)} = 1. \quad (52)$$

Thus

$$K = \frac{\Gamma(M+1)}{\Gamma(N)\,\Gamma(M-N+1)} = \frac{M!}{(N-1)!\,(M-N)!}. \quad (53)$$

Here B and Γ are the beta and gamma functions as conventionally defined. Substituting the function $W(I)$ into (49) gives the result of (21).

The probability that the largest pulse is more than C times

larger than the second largest pulse is

$$V(M, C) = M \int_0^\infty W(I') \left(\int_0^{I'/C} W(I) dI \right)^{M-1} dI'. \quad (54)$$

The term $W(I')$ is just the probability density for the largest pulse. The term in parenthesis is the probability that the remaining $M-1$ pulses are at least C times smaller. The expression is integrated over all possible values of the largest pulse. The factor M arises because there are M ways to choose the largest pulse. Substituting $W(I)$ into this expression gives

$$V(M, C) = M \int_0^\infty e^{-I'} \left(\int_0^{I'/C} e^{-I} dI \right)^{M-1} dI'$$

$$= M \int_0^\infty e^{-I'} \left[1 - e^{-I'/C} \right]^{M-1} dI'$$

$$= MC \int_0^1 t^{C-1} \left[1 - t \right]^{M-1} dt (t = e^{-I'/C})$$

$$= MC\mathrm{B}(C, M)$$

$$V(M, C) = \frac{\Gamma(C+1)\,\Gamma(M+1)}{\Gamma(M+C)}. \quad (55)$$

It should be noted here that it is perfectly valid to apply statistical averages to the starting set of pulses. They are independent and there is an adequate number of samples.

References

[1] P. G. Kryukov and V. S. Letokhov, "Fluctuation mechanism of ultrashort pulse generation by laser with saturable absorber," *IEEE J. Quantum Electron.*, vol. QE-8, pp. 766–782, Oct. 1972.

[2] V. S. Letokhov, "Generation of ultrashort light pulses in a laser with a nonlinear absorber," *Sov. Phys.–JETP*, vol. 28, pp. 562–568, Mar. 1969.

[3] T. J. Kuznetsova, "On the statistics of appearance of ultrashort light pulses in a laser with a bleachable absorber," *Sov. Phys.–JETP*, vol. 30, pp. 904–909, May 1972.

[4] N. G. Basov, P. G. Kriukov, V. S. Letokhov, and Yu. V. Senatskii, "Generation and amplification of ultrashort optical pulses," *IEEE J. Quantum Electron. (Special Issue on International Quantum Electronics Conference: Part I)*, vol. QE-4, pp. 606–609, Oct. 1968.

[5] B. Hausherr, E. Mathieu, and H. Weber, "Influence of saturable-absorber transmission and optical pumping on the reproducibility of passive mode locking," *IEEE J. Quantum Electron.*, vol. QE-9, pp. 445–449, Apr. 1973.

[6] See, for example, W. Feller, *An Introduction to Probability Theory and its Applications*, vol. I. New York: Wiley, 1957, p. 229.

Pulse Stretching and Shape Control by Compound Feedback in a Q-Switched Ruby Laser

R. V. LOVBERG, ERIC R. WOODING, AND MICHAEL L. YEOMAN

Abstract—**Feedback control is employed to stabilize the output of a Q-switched ruby laser. A computational model of the rate equations plus feedback terms is used to examine pulse shapes with changing feedback parameters. It is shown that a lengthened flat-top pulse cannot be obtained with negative feedback alone, a compound feedback arrangement is suggested to facilitate this. A practical laser system is constructed with an associated feedback loop, good agreement is found between theory and experiment. Pulses flat to within ±5 percent are obtained with durations up to 600 ns and are amplified with no apparent saturation. Output powers of 15 MW are achieved for hundreds of nanoseconds with a divergence of 7 mrad and a spectrum consisting of transform-limited lines separated by the axial mode spacing.**

Manuscript received July 10, 1974; revised August 26, 1974.

R. V. Lovberg is with the Department of Physics, University of California-San Diego, La Jolla, Calif.

E. R. Wooding is with Royal Holloway College, Englefield Green, Surrey, England.

M. L. Yeoman was with Royal Holloway College, Englefield Green, Surrey, England. He is now with AERE Harwell, Oxono, England.

Introduction

ULTRAHIGH-frequency drift waves in a plasma are expected to scatter laser light by acting as a diffraction grating. A preliminary study [1] showed the need for a rectangular pulse of light lasting about 200 ns. Long pulses have been obtained from Q-switched lasers by introducing nonlinear materials into the cavity [2]–[5], lengthening the cavity [1], or by use of a feedback loop to control the switching of an electrooptic shutter [6]–[8]. The first two methods produce light pulses whose time variation is either approximately Gaussian or asymmetric with a fast rise and a decay time of several hundred microseconds. The feedback technique with a Kerr cell has converted the random relaxation oscillations of a ruby laser to a steady flux which decays exponentially in several hundred microseconds [6], but the resulting output

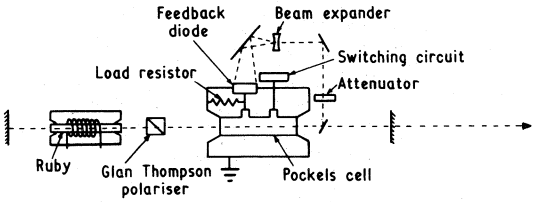

Fig. 1. Laser cavity with feedback elements.

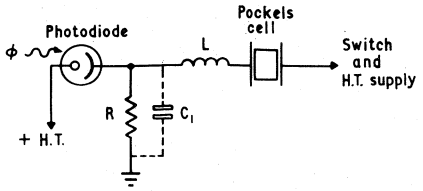

Fig. 2. Feedback control circuit with parasitic inductance and shunt capacitance.

power is low (<100 kW) and high-frequency oscillations occur [7].

The laser pulse for the proposed scattering experiment is required to have a power of at least 10 MW, a duration of about 200 ns, and rise and decay times less than 20 ns. Any ripple in the power should be less than 5 percent of the peak value and should occur at a frequency of less than 10 MHz.

The laser which produced the pulse is represented in Fig. 1 and contains a feedback loop consisting of a pellicle beam splitter and a photodiode which applies a negative feedback potential to a Pockels-cell shutter. Initially, the Pockels cell is biased for zero transmission by applying the quarter-wave voltage. As soon as this voltage is reduced the optical transmission rises and laser action begins. Five percent of the intercavity photon flux is used in the feedback loop.

After some preliminary experiments, a numerical analysis was carried out to determine which were the significant terms in the control equations governing the system. The mathematical model consists of a system of first-order linear differential equations with specific initial conditions. In these equations the terms corresponding to the circuit parameters may easily be varied, permitting a study of a wide range of operating conditions to be made in a short time. As a result of the computer experiments the system may be modified until the requisite pulse shape and duration are obtained.

Numerical Analysis

Previous calculations [4], [7] had shown that lengthened pulses could be generated by a Q-switched laser with the disadvantage that high-frequency oscillations occurred for an appreciable part of the pulse. The present analysis makes use of the rational extrapolation method of Burlisch and Stoer [9] through a software facility (ORDIFFS) for solving up to ten coupled first-order differential equations with Teletype printout.

Elementary Feedback System

The laser rate equations of Wagner and Lengyel [10] are used to describe the growth of photon flux which results from gain in the ruby and losses within the laser cavity. The rate of growth of photon density is given by

$$\frac{d\phi}{dt} = \frac{1}{t_1}(\alpha_0 nL - \gamma)\phi \tag{1}$$

and the rate of decay of the population inversion in the ruby is

$$\frac{dn}{dt} = -\frac{2\alpha_0 L}{t_1} \cdot n\phi \tag{2}$$

where $\phi = \Phi/N_0$ is the normalized photon density, Φ the total photon density (photons cm^{-3}), and N_0 is the chromium-ion density ($Cr^{+++}cm^{-3}$) in the ruby. The time taken for a photon to traverse the cavity is t_1, and the fraction of photons lost per traverse is γ. The fractional population inversion is $n = (N_2 - N_1)/N_0$. The absorption coefficient of the unexcited ruby is α_0 which becomes a gain parameter when n is greater than zero. L is the length of the ruby rod, N_2 the density of chromium ions excited to the upper level, and N_1 the density in the ground state.

These rate equations have been solved and yield giant pulses. However, in the present application γ is not constant but is made explicitly dependent upon ϕ by the feedback loop, i.e.,

$$\gamma = \gamma_c + \gamma(\phi) \tag{3}$$

where γ_c is the constant loss term, which is mainly attributable to the output mirror transmission T_1 and may be written $\gamma_c = -\ln(1 - T_1) = -\ln R_1$, while $\gamma(\phi)$ includes the transfer function of the feedback loop and shutter characteristics. It is assumed that the photodetector output current i is directly proportional to the input light flux so that $i = M\phi$. Then a voltage V may be produced by the load resistance R of Fig. 2 with

$$V = iR = MR\phi.$$

The transmission of the Pockels cell is

$$T = \cos^2\left(\frac{\pi}{2}\frac{V}{V_0}\right)$$

where V_0 is the quarter-wave bias-voltage. Then

$$\gamma(\phi) = -\ln\left[\cos^2\left(\frac{\pi}{2}\frac{V}{V_0}\right)\right]. \tag{4}$$

Before inserting (4) and (3) into (1) for solution, terms must be added to account for the stray series inductance and shunt capacitance of the feedback circuit. Since the photodiode is a pure current generator the voltage at its output is determined by the impedance of the circuit connected to it; with capacitance C_1 in shunt to earth, V cannot rise to the level iR until C_1 is charged in a time of the order $C_1 V/i$. Thus a time lag is introduced into the loop. It will be seen that values of C_1 of a few picofarads can produce destabilizing delays, whereas typical amounts of series wiring inductance do not seem significant.

The effect of shunt capacitance requires that the V in (4) be the solution of the circuit equation

$$C_1\frac{dV}{dt} = M\phi - \frac{V}{R}. \tag{5}$$

Computations

Equations (1), (2), (4), and (5) were integrated by the ORDIFFS routine which is capable of handling up to ten coupled first-order ordinary differential equations. No algebraic expressions may be used in addition to the differential equations so that parameters may be treated as time-dependent variables. The normalized photon density in the Pockels cell was assumed to be 10^{-4} at the instant of switching with t_1 = 4 ns, L = 10 cm, and $\alpha_0 = 0.4\ \text{cm}^{-1}$. The value of the load resistor R was chosen as 200 Ω after some experience; larger values produced instability because C_1 could not be less than a few picofarads, but smaller values required more current than the available photodiode could supply.

An initial computation was carried out with $M = 0$, corresponding to zero feedback and resulting in a conventional Q-switched pulse having a peak flux 400 times the initial value as shown in Fig. 3(a).

When negative feedback is introduced with $M = 10^3$ and the stray capacitance C_1 in parallel with the 200-Ω load resistor is 20 pF, the pulse shown in Fig. 3(b) is obtained. A small initial overshoot occurs as the capacitor charges making the feedback momentarily ineffective. Subsequently, the output falls almost exponentially with a decay time of 80 ns which is determined by C_1/M.

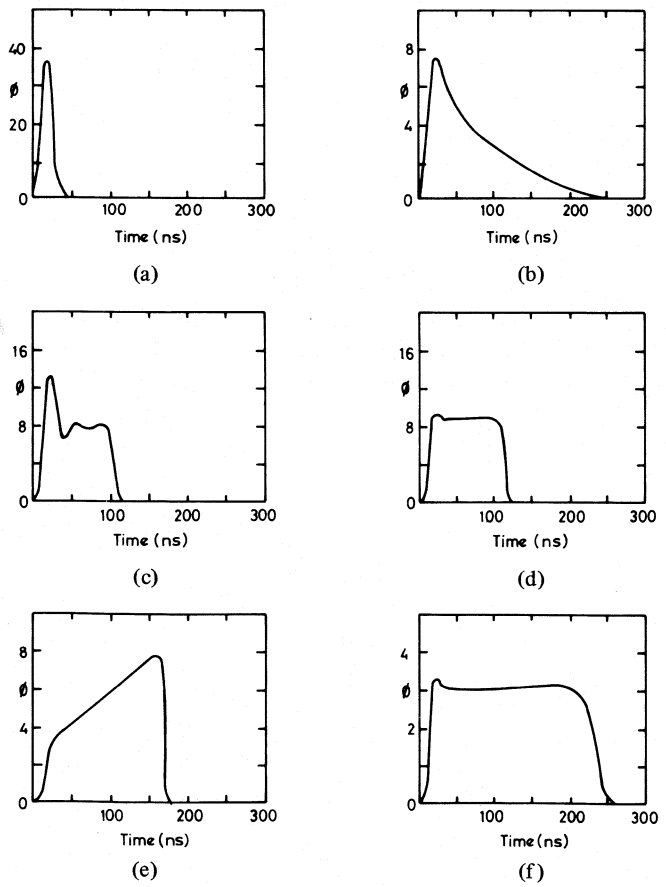

Fig. 3. Computed output for a controlled laser in units of 10^{-3} photons cm^{-3}/chromium-ion density. (a) No feedback. (b) Negative feedback only. (c) Compound feedback with $n = 0.5$. (d) Compound feedback with $n = 0.3$. (e) Increased feedback-loop gain, L_1 = 20 μH. (f) Increased feedback-loop gain, L_1 = 120 μH.

Compound Feedback

The purpose of introducing the feedback mechanism was to generate a rectangular pulse, but the circuit of Fig. 2 will always give a monotonic decay even with RC_1 made small enough to reduce the initial spike. To make the pulse rectangular the feedback must be reduced as time progresses. This is accompanied by adding an auxiliary positive-feedback loop consisting of an inductance L_1 in series with capacitor C_2 having a time-constant comparable with C_1/M.

The resulting feedback circuit is shown in Fig. 4. It is assumed that C_2 is initially uncharged but at a time approximately RC_1 after the laser pulse begins, a voltage appears on the Pockels cell and partially closes it. At the same time this voltage produces a current i_2 rising at a rate V/L_1, which charges the capacitor C_2 and reduces the net bias on the Pockels cell, tending to reopen it. For a constant input voltage the series circuit L_1C_2 produces a potential V_2 on C_2 which increases as $(1 - \cos 2\pi t/(L_1C_2)^{1/2})$ so that the shutter reopening does not become very rapid until about a quarter period after the pulse onset.

From Fig. 4 it is seen that the single-circuit equation (5) must be replaced by a set of three new equations given below, and that V in (4) must be replaced by $V_1 - V_2$.

$$C_1 \frac{dV_1}{dt} = i_1 = i_0 - i_2 - i_3$$

$$= M\phi - \frac{V_1}{R} - i_3$$

$$C_2 \frac{dV_2}{dt} = i_3$$

$$L_1 \frac{di_3}{dt} = V_1 - V_2.$$

Pulse shapes computed from these equations combined with (1)-(4) are given in Fig. 3(c)-(f). A value of 0.5 was assumed for the population inversion ratio, 20 μH for the inductor L_1, and 200 pF for C_1, the combined capacitances of the Pockels cell (6 pF), photodiode (6 pF), and circuit stray capacitance. This last value is slightly larger than the realizable minimum and results in a giant spike at the beginning of the output as shown in Fig. 3(c). This spike takes a large part of the available ruby energy from the rest of the pulse but is reduced if the pumping energy is lowered. The laser gain is then reduced, resulting in a lower pulse rise rate and a voltage rise of C_1 which

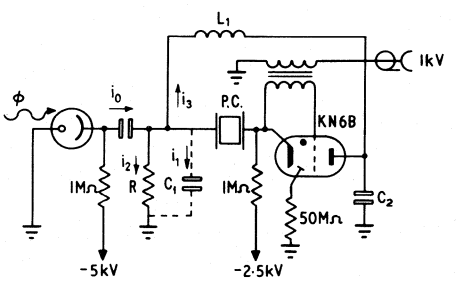

Fig. 4. Compound-feedback circuit with a Krytron switch.

follows the photon pulse more closely. In Fig. 3(d) the ruby is pumped to $n = 0.3$ which is more realistic than 0.5, and C_1 is made equal to 20 pF. The pulse overshoot is now seen to be negligible.

An increase in the pulse length must result in a decrease in pulse amplitude so that a longer pulse should be attained by increasing the feedback loop gain M. In Fig. 3(e) the gain M is increased from 10^3 to 3.10^3 resulting in a decrease in the initial pulse level but the amplitude rises steadily until its sudden collapse after about 150 ns. To recover a flat-topped pulse, the L_1C_2 product of the positive-feedback loop must be increased. In Fig. 3(f), L_1 has been increased to 120 μH and the resulting pulse is slightly longer than 200 ns, but over 150 ns the amplitude varies by less than 5 percent.

The abrupt turnoff of the pulses in Fig. 3 is obtained because the voltage V_2 rises quite rapidly in the later stages, exceeding V_1, causing momentary complete opening of the shutter. This sustains a high output, but V_2 continues to swing upwards and recloses the shutter. V_1 then drops, further increasing the value $V_1 - V_2$, and causes the final shutter closure to be very rapid. Some part of the population inversion remains and must be included in the final optimization of the system.

By solving the Frantz and Nodvik [11] equation for the gain of a laser amplifier it was shown that amplification of the laser pulse [Fig. 3(f)] causes a departure from the flat-topped structure of not greater than 10 percent when the pulse power at the amplifier input is as much as 15 MW.

A Q-Switched Long-Pulse Laser

A laser was constructed with a cavity 100 cm long and an output mirror of 50-percent reflectivity. The feedback loop consisted of an ITT FW114A photodiode and a KD*P Pockels cell, with the photodiode mounted so close to the Pockels cell that connections between terminals were only a few centimeters in length to minimize the stray capacitance. A 200-Ω load resistor R was employed as shown in Fig. 4. The Pockels cell was switched on initially by means of a Krytron switch type KN6B. The cavity flux was polarized with a Glan-Thompson prism and about 5 percent was diverted by a pellicle beam splitter into the feedback loop. All other optical surfaces were antireflection coated.

To operate the system the Pockels cell was initially biased to its quarter-wave voltage thereby preventing laser action. On firing the Krytron tube the Pockels cell bias falls to zero and light amplification begins. The switching time of about 1 ns determined by the load resistor and the Pockels cell capacitance, is insignificant compared with the pulse build-up time of about 200 ns. The megohm isolation resistor prevents C_2 charging from the power supply during the laser pulse duration but is low enough to keep the Krytron conducting.

It was shown that a conventional Q-switched pulse of 40-ns duration, as seen in Fig. 5(a), could be obtained by making the optical attenuator of Fig. 1 completely opaque to laser light and thereby eliminating all feedback. With simple feedback-omitting inductor L_1, the laser pulse and feedback voltage shown in Fig. 5(b) were obtained. It is apparent that control of the kind observed by Marshall and Roberts [6] has been effected since the fast rise and long decay is the same as the computed shape of Fig. 3(b). Compound feedback was achieved with the addition of a random-wound inductor of 75 μH together with a capacitor of 240 pF. An early result employing both positive and negative feedback is shown in Fig. 5(c), where the shunt capacitance to earth was high. The difference in shape between the feedback voltage and the laser pulse is due to ringing in the LC circuit. The initial spike and following hump of the laser pulse is the same as the computed shape of Fig. 3(c). On reducing the shunt capacitance the flat-topped pulse of 160-ns duration shown in Fig. 5(d) was obtained. When the feedback-loop gain M was increased without increasing the inductance, the laser pulse rose with time as in Fig. 5(e) until the surge in the positive-feedback voltage reduced it to zero. This figure compares with the computational shape of Fig. 3(e). Finally, in Fig. 5(f) we show the pulse shape obtained when the inductance was increased to 160 μH, the flat top in the computed curve of Fig. 3(f) is reproduced with a deviation from flatness of ±5 percent for 130 ns of the total pulse duration of 240 ns.

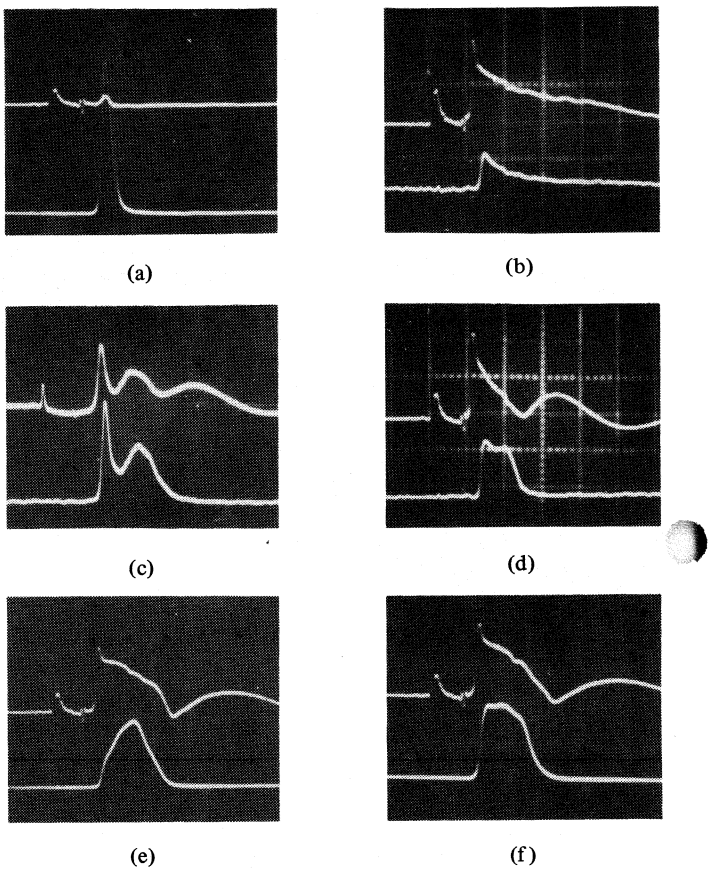

Fig. 5. The upper trace is the feedback voltage and the lower trace the laser pulse. 200 ns/major division. (a) No feedback. (b) Negative feedback only. (c) Compound-feedback large shunt capacitance. (d) Compound-feedback low shunt capacitance. (e) Increased feedback-loop gain, inductance 75 μH. (f) Increased feedback-loop gain, inductance increased to 160 μH.

Measurements of the output pulse made with a cone calorimeter showed that between 80 and 90 percent of the energy of the Q-spoiled pulse is retained in the extended pulse.

The spectrum of the laser pulse was determined in a photomixing experiment. An attenuated pulse was allowed to fall on a biplanar photodiode (ITL HCB2) with a 125-Ω load. The

output voltage was analyzed up to 30 MHz with a Heathkit RG52 communications receiver and up to 870 MHz with an Eddystone 990S UHF receiver. The spectrum was found to consist of lines having a transform-limited halfwidth of 2.5 MHz with subsidiary satellites, separated by the axial mode spacing of 125 MHz.

Conclusions

It has been shown that the shape of a ruby laser pulse can be controlled by the use of a Pockels cell whose transmission is governed by the intensity of light in the laser cavity. The latter is related to the potential difference across the Pockels cell by the use of a photodiode and a combination of negative and positive feedback.

Using the Wagner and Lengyel's giant-pulse equations coupled with the equations of the electric circuit, pulse shapes have been computed which bear a close resemblence to those actually measured in the laboratory.

A correct choice of feedback parameters permits the generation of approximately rectangular laser pulses whose length can be varied at will between 120 and 600 ns, and which, moreover, are free from high-frequency oscillations. 15-MW rectangular pulses have been amplified without distortion.

Acknowledgment

The authors wish to thank Dr. H. A. B. Bodin for inviting them to carry out this work as part of the Toroidal Pinch program at Culham, and are grateful to the UKAEA for the facilities provided. They also wish to thank P. Tripathi of the University of California for assistance in setting up the computational model, and R. Hamilton for experimental assistance.

References

[1] E. R. Wooding and M. L. Yeoman, "A laser scattering homodyne technique for studying plasma drift waves," in *Proc. 10th Int. Conf. Phenomena in Ionized Gases* (1971), p. 417.
[2] W. R. Callen, R. H. Pantell, and J. Warszawski, "Phase stretching of *Q*-switched lasers," *Opto-Electron.*, vol. 1, pp. 123–127, Aug. 1969.
[3] R. H. Pantell and J. Warszawski, "Laser power stabilisation by means of non-linear absorption," *Appl. Phys. Lett.*, vol. 11, pp. 213–215, Oct. 1967.
[4] A. Hordvik, "Pulse stretching utilizing two-photon-induced light absorption," *IEEE J. Quantum Electron.*, vol. QE-6, pp. 199–203, Apr. 1970.
[5] J. F. Young, J. E. Murrey, R. B. Miles, and S. E. Harris, "*Q*-switched laser with controllable pulse length," *Appl. Phys. Lett.*, vol. 18, pp. 129–130, Feb. 1971.
[6] F. R. Marshall and D. L. Roberts, "Use of electro-optical shutters to stabilize ruby laser operation," *Proc. IRE* (Corresp.), vol. 50, p. 2108, Oct. 1962.
[7] C. H. Thomas and E. V. Price, "Feedback control of a *Q*-switched ruby laser," *IEEE J. Quantum Electron. (1966 International Quantum Electronics Conference)*, vol. QE-2, pp. 617–623, Sept. 1966.
[8] V. I. Mishin, "Ruby laser for generating microsecond light pulses having a narrow spectrum," *Pri. Tekh. Eksp.*, no. 4, pp. 181–182, July/Aug. 1971.
[9] R. Burlisch and J. Stoer, "Numerical treatment of ordinary differential equations by extrapolation methods," *J. Num. Maths*, vol. 8, pp. 1–13, 1966.
[10] W. G. Wagner and P. A. Lengyel, "Evolution of the giant pulse in a laser," *J. Appl. Phys.*, vol. 34, pp. 2040–2046, July 1963.
[11] L. M. Frantz and J. S. Nodvik, "Theory of pulse propagation in a laser amplifier," *J. Appl. Phys.*, vol. 34, pp. 2346–2349, Aug. 1963.

A Theory of the Mode-Locked, Internally Frequency-Doubled Laser

JOEL FALK, MEMBER, IEEE

***Abstract*—An AM mode-locked laser with a frequency doubler internal to the laser cavity is analyzed. Mathematical expressions are derived for laser pulsewidth, saturated gain, and second-harmonic output power. It is shown that the maximum second-harmonic power output available from the mode-locked laser is a factor of $\sqrt{2}$ less than that available from an identical free-running laser.**

Numerical examples are given for an Nd:YAG laser with a $Ba_2NaNb_5O_{15}$ internal frequency doubler.

Manuscript received June 26, 1974; revised September 17, 1974. This work was partially supported by the Advanced Development Program 405B, Air Force Avionics Laboratory, Wright-Patterson AFB, Ohio, under a subcontract from the McDonnell Douglas Astronautics Company East.

The author is with the Electro-Optics Organization, GTE Sylvania Inc., Mountain View, Calif. 94042.

I. Introduction

A MODE-LOCKED LASER provides an attractive means of producing a stream of high repetition-rate pulses useful for optical communication. Frequency doubling of a mode-locked laser is often useful for shifting the output of a laser source from a wavelength of limited utility to a more useful region of the optical spectrum. Limited atmospheric transmission, poor detector, and modulator response at the fundamental wavelength are three possible reasons for considering frequency doubling of a mode-locked laser designed for optical communications applications. Frequency doubling may be accomplished internally or externally to the laser's optical cavity. The internally frequency-doubled laser, be-

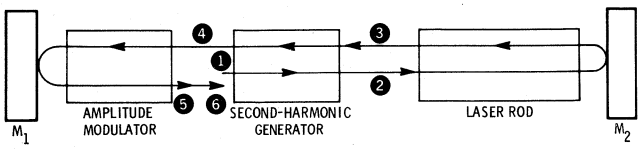

Fig. 1. The optical cavity.

cause of the higher fundamental fields available within the laser cavity, accomplishes the frequency doubling in a more efficient manner than if it is performed externally to the laser cavity. On the other hand, because the second-harmonic process provides a power-dependent loss to the mode-locked laser pulse, the laser's temporal width is increased by the doubling process [1]. This increase in pulsewidth at the fundamental wavelength is an important determinant of the pulse shape for the internally doubled laser.

This paper theoretically analyzes the mode-locked, *frequency-doubled*, homogeneously broadened laser. Mode locking produced by amplitude modulation is treated. The self-consistent approach introduced by Kuizenga and Siegman for describing a mode-locked homogeneously broadened laser is employed [2]. In the analysis that follows the propagation of a temporally Gaussian pulse is traced around the optical cavity shown schematically in Fig. 1. The effects of each component on the Gaussian pulse shape are considered, and it is required that the pulse envelope repeat itself after a round-trip traversal of the optical cavity. The principal extension of the Kuizenga-Siegman theory is the inclusion and analysis of a frequency doubler within the laser cavity.

Other authors have attempted to treat the mode-locked doubled laser analytically but analyses previously published [1], [3]:

1) have neglected the effects of laser fluorescent linewidth and hence present results which have only limited validity;
2) have not given an explicit expression for laser pulsewidth;
3) have not treated the effects of modulator detuning.

The analysis presented here leads to expressions for pulsewidth and laser power, and a prediction of laser performance when the modulator is detuned from its ideal driving frequency.

This paper first considers the component transforms of each of the elements in the cavity shown in Fig. 1. Self-consistent equations are then developed and simplified. Numerical examples relevant to the Nd:YAG laser are given.

II. Component Transforms

The effect of each of the intracavity components on a temporally Gaussian pulse is considered. The pulse is assumed to have a Gaussian spatial distribution with a $1/e$ beam size of w_0. The generalized electric-field pulse shape, including both time and radial variations, is

$$E_a(t,r) = A \exp(-r^2/w_0^2)\, E_a(t) \exp j\omega_a t + \text{c.c.} \tag{1}$$

where the function $E_a(t) = \exp - [\gamma(t+t_0)^2]$ describes the temporal variation of the envelope of $E_a(t,r)$. The parameters γ and t_0 determine the laser's pulsewidth and the time of the peak pulse amplitude. In the analysis that follows γ is assumed to be real, and any frequency chirping on the pulse is ignored.

The Fourier transform of $E_a(t,r)$, or a description of the propagating pulse in the frequency domain is

$$F[E_a(t,r)] = E_a(\omega,r) = A\sqrt{\pi/\gamma} \exp(-r^2/w_0^2) \cdot \exp[jt_0(\omega-\omega_a) - (\omega-\omega_a)^2/4\gamma]. \tag{2}$$

Thus the pulse's optical spectrum is centered at $\omega = \omega_a$.

A. The Laser Rod

The transfer function of the laser rod is best described in the frequency domain. For a homogeneously broadened medium, the amplifier single-pass field transfer characteristic $T_A(\omega)$ has a Lorentzian line shape [2]

$$T_A(\omega) = \exp[g/(1 + j2(\omega-\omega_a)/\Delta\omega_a)] \tag{3}$$

or

$$T_A(\omega) \cong \exp[g - (2jg(\omega-\omega_a)/\Delta\omega_a) - 4g(\omega-\omega_a)^2/\Delta\omega_a^2] \tag{4}$$

where g is the *saturated* single-pass field gain at line center ($\omega = \omega_a$), and $\Delta\omega_a$ is the homogeneous linewidth of the laser transition. The three-term Taylor-series expansion given in (4) for $T_A(\omega)$ is valid for $|\omega_a - \omega_a| << \Delta\omega_a$.

The temporal output field of the amplifier rod is given by

$$E_b(t,r) = F^{-1}[T_A(\omega)E_a(\omega,r)]$$

where F^{-1} indicates an inverse Fourier transform. Thus

$$E_b(t,r) = A' \exp(-r^2/w_0^2) \exp[-\gamma'(t+t_0')^2] \cdot \exp j\omega_a t + \text{c.c.} \tag{5}$$

and

$$A' \equiv A \exp(g)/\sqrt{G}, \quad \gamma' \equiv \gamma/G, \quad t_0' \equiv t_0 - 2g/\Delta\omega_0$$

where

$$G \equiv 1 + 16\gamma g/\Delta\omega_a^2.$$

Hence the output pulse from the laser amplifier remains Gaussian. The effects of the laser rod are to delay the pulse by $2g/\Delta\omega$, to lengthen it by decreasing γ to γ/G, and to increase the pulse amplitude. These effects have been previously reported by Kuizenga and Siegman and are repeated here only for completeness [2].

In writing (1)-(4) it was tacitly assumed that the center of the envelope of the optical spectrum of the Gaussian pulse lies exactly at the center of the amplifier's passband. In practice the centermost axial mode may be as far as one-half the longitudinal-mode spacing removed from line center. This small frequency displacement has no apparent practical consequence and is neglected in the remainder of this paper.

B. The Loss Modulator

The single-pass field transfer function of the loss modulator is [2]

$$a_L(t) = \exp[-\delta_L \sin^2(\omega_m t/2)] \tag{6a}$$

or

$$a_L(t) \cong \exp\left[-\delta_L\left[\sin^2(\omega_m t_0/2) - \frac{\omega_m(t+t_0)\sin(\omega_m t_0)}{2} + \frac{\omega_m^2(t+t_0)^2}{(2)(2!)}\cos\omega_m t_0)\right]\right] \quad (6b)$$

where $\exp(-\delta_L/2)$ is the time-average modulator amplitude transmission and $\omega_m/2$ is the modulator drive frequency. The loss seen by the laser varies with frequency ω_m, which is twice the modulator drive frequency. It is important to realize that the exact form of the modulator transfer function is dependent upon the physical means employed to loss modulate. Equation (6a) is only approximately correct for the two most common means of loss modulation, namely electrooptic or acoustooptic [4], [5]. However, (6b) is valid in the temporal region of interest, where $\delta_L \sin^2(\omega_m t/2) \ll 1$, i.e., when the optical pulse passes through the loss modulator with comparatively little loss.

C. The Second-Harmonic Generator

The frequency-doubling process has pronounced effects on both the spatial and the temporal shape of the Gaussian pulse. For this analysis the effects on the spatial variation can be treated in a conventional manner where coupling to the fundamental-field cavity mode is considered. Changes in the Gaussian temporal shape of the pulse, however, are not so easily treated. The investigation of the effect of second-harmonic generation on the temporal shape is facilitated by a physically reasonable approximation.

The analysis given is strictly valid only for small conversion efficiency to the second harmonic. As a practical matter this limitation is of little consequence because most internally frequency-doubled lasers produce the maximum output power with only a small conversion of the fundamental-wavelength circulating power to second-harmonic output power.

1) Spatial-Mode Considerations: In this section the effect of the second-harmonic generation process on the spatial variation of the generalized Gaussian pulse given by (1) is considered. For notational simplicity the time variation of every electric field is rewritten as a product of an optically varying phase and of an envelope that varies both in time and in space

$$E_a(t,r) = |E_a(t,r)| \exp -j\omega_a t + \text{c.c.} \quad (7)$$

where

$$|E_a(t,r)| \equiv AE_a(t)\exp(-r^2/w_0^2). \quad (8)$$

If second harmonic is generated with 90° phase matching, i.e., without Poynting-vector walkoff, the envelope of the second-harmonic field produced in the doubler crystal is

$$|E_{2\omega}(t,r)| = j|E_a(t,r)| \tanh[K|E_a(t,r)|] \quad (9)$$

where K is dependent solely upon crystal parameters [6]. Similarly, the envelope of the fundamental frequency field emerging from the crystal is

$$|E_b(t,r)| = |E_a(t,r)| \operatorname{sech}[K|E_a(t,r)|]. \quad (10)$$

If the conversion efficiency is small, i.e., if $K|E_a(t,r)| \ll 1$, (10) becomes

$$|E_b(t,r)| \cong E_a(t)A\exp(-r^2/w_0^2)[1-(K^2A^2/2)E_a^2(t)\cdot\exp(-2r^2/w_0^2)]. \quad (11)$$

For a laser operating in the TEM_{00} mode the only part of $|E_b(t,r)|$ which couples to the cavity mode is that which overlaps a Gaussian beam of radius w_0. In general, $|E_b(t,r)|$ can be expanded as a sum of products of Gaussian and higher order Hermite or Laguerre polynomials. The envelope of the TEM_{00} mode exiting from the crystal can then be calculated using the orthogonality properties of the Laguerre functions. Hence, if $|E_b'(t,r)|$ is the TEM_{00} component of $|E_b(t,r)|$,

$$|E_b'(t,r)| = \exp(-r^2/w_0^2)\frac{\int_0^\infty |E_b(t,r)|\exp(-r^2/w_0^2)\,2\pi r\,dr}{\int_0^\infty [\exp(-r^2/w_0^2)]^2\,2\pi r\,dr} \quad (12)$$

$$|E_b'(t,r)| = |E_a(t,r)|[1-(KA/2)^2 E_a^2(t)]. \quad (13)$$

Thus the time-varying loss seen by the Gaussian envelope $|E_a(t,r)|$ is $(KA/2)^2 E_a^2(t)$.

2) Temporal Considerations: An exact analysis of the temporal effects of the second-harmonic process within the framework of Gaussian pulses is impossible because the second-harmonic process does not maintain the envelope of Gaussian input pulse. That is, treatment of the second-harmonic generation process by use of the transfer function described in (13) destroys the Gaussian temporal pulse shape.

However, it has been noted that the experimentally observed pulse shape and optical spectrum observed from a mode-locked frequency-doubled laser are very nearly Gaussian [7]. The effect of many passes through the doubling crystal is to alter the Gaussian-pulse parameters γ and t_0 while essentially maintaining a Gaussian envelope.

Therefore, the temporal effect of the second-harmonic generation is treated as if it maintains the Gaussian envelope of an input pulse, and produces an output whose peak amplitude and curvature at the time of the peak pulse amplitude are the same as the actual TEM_{00} output pulse described by (13). Thus the output of the doubler crystal is approximated by

$$|E_b'(t,r)| \cong A\exp(-r^2/w_0^2)(\exp -a)\exp[-\gamma b(t+t_0)^2] \quad (14)$$

where a and b are the curve-fitting parameters that can be adjusted so that (13) and (14) yield identical 1) peak amplitudes,

$$|E_b'(t=-t_0,r)|$$

and 2) curvatures

$$\frac{\partial^2}{\partial t^2}|E_b'(t=-t_0,r)|.$$

We note that both expressions for $|E_b'(t,r)|$ yield equal (zero) slopes at $t=-t_0$. These three time derivatives, which are

identical if calculated from either (13) or (14), are the first three coefficients of a Taylor expansion for $|E_b'(t,r)|$. Thus, with parameters a and b appropriately chosen, (14) describes the nonlinear transmission of the doubler crystal correctly to second order in $t + t_0$. This is the same degree of accuracy used for the description of both the amplitude modulator (6b) and the amplifier rod (4).

Equating the three time derivatives, as outlined above, it is found that the parameters a and b are given by

$$a = -\ln [1 - (KA/2)^2], \quad a \cong (KA/2)^2 \tag{15}$$

$$b = [1 - 3(KA/2)^2] [1 - (KA/2)^2]^{-1},$$

$$b \cong 1 - (KA)^2/2 \tag{16}$$

where the approximate values hold for $(KA)^2 \ll 1$.

Equations (15) and (16) relate curve-fitting variables a and b to physical parameters K and A. Although, in principle, K and A are either measurable or calculable precise evaluation of either is difficult and furthermore is unnecessary because only the product KA appears in (13)-(16). It is more convenient and physically meaningful to relate KA, hence a and b, to the single-pass power loss associated with the second-harmonic process. This time-varying loss $\alpha(t) \equiv [P_2(t)]/[P_1(t)]$ = (second-harmonic power)/(fundamental power) can be calculated from (9), (14)-(16). The peak value of $\alpha(t)$, i.e., the peak conversion efficiency or peak single-pass power loss to the second harmonic, is the conversion efficiency at the peak of the fundamental pulse and is given by

$$\alpha_{\text{peak}} = \alpha(t = -t_0) = (KA)^2/2. \tag{17}$$

Similarly, it can be shown that the average single-pass power loss to the second harmonic,

$$\alpha_{\text{SHG}} = \frac{\int_{-\infty}^{\infty} P_2(t)\,dt}{\int_{-\infty}^{\infty} P_1(t)\,dt}$$

is related to KA via

$$\alpha_{\text{SHG}} = (KA)^2 \sqrt{2}/4. \tag{18}$$

Hence the peak loss to the second harmonic is $\sqrt{2}$ times the average power loss. It will later become apparent that the difference between peak and average second-harmonic losses leads to a unique power saturation behavior for the mode-locked frequency-doubled laser.

With values of α_{SHG}, the average single-pass power loss or second-harmonic conversion efficiency, determined by (18), the parameters a and b may be rewritten

$$a = (\sqrt{2}/2)\,\alpha_{\text{SHG}} \tag{19a}$$

$$b = 1 - \sqrt{2}\,\alpha_{\text{SHG}} \tag{19b}$$

for $\alpha_{\text{SHG}} \ll 1$.

III. Self-Consistency

It is required that after one round-trip traversal of the optical cavity, the pulse envelope repeat itself. With the required component transforms developed in the preceding sections of this paper the mathematical formalism necessary to follow a pulse around the optical cavity now exists.

Consider a pulse with electric-field envelope at point 1 (input to the doubler crystal) in Fig. 1 given by the generalized Gaussian

$$|E_1(t,r)| = A \exp(-r^2/w_0^2) \exp[-\gamma(t + t_0)^2]. \tag{20}$$

The TEM_{00} output pulse resulting from a single pass through the second-harmonic crystal and thus the pulse into the amplifier rod is determined from (14). The output resulting from two passes through the amplifier rod is found by two applications of (5). Hence the rod output is

$$|E_3(t,r)| = A'' \exp(-r^2/w_0^2) \exp[-\gamma''(t + t_0'')^2] \tag{21}$$

where

$$A'' \equiv \frac{A \exp(-a + 2g)}{\sqrt{G'}}, \quad \gamma'' = \gamma b/G',$$

$$t_0'' = t_0 - 4g/\Delta\omega_a \tag{22}$$

and

$$G' = 1 + 32\gamma b g/\Delta\omega_a^2. \tag{23}$$

Similarly, $|E_3(t,r)|$ is the input for the second pass through the doubler crystal, so that the output-field envelope $|E_4(t,r)|$ is

$$|E_4(t,r)| = (A/\sqrt{G'}) \exp(-r^2/w_0^2) \exp(-2a' + 2g) \cdot \exp[(-\gamma b'/G')(t + t_0 - 4g/\Delta\omega_a)^2] \tag{24}$$

where

$$2a' = \frac{\sqrt{2}}{2}[\alpha_{\text{SHG1}} + \alpha_{\text{SHG2}}] = \sqrt{2}\,\alpha_{\text{SHG}} \tag{25}$$

$$b' = 1 - \sqrt{2}(\alpha_{\text{SHG1}} + \alpha_{\text{SHG2}}) = 1 - 2\sqrt{2}\,\alpha_{\text{SHG}}. \tag{26}$$

Note that α_{SHG2}, the efficiency of conversion to the second-harmonic for the second pass through the doubler crystal, is not necessarily equal to α_{SHG1} (the first pass conversion efficiency) [8]. The parameter, $\alpha_{\text{SHG}} \equiv (\alpha_{\text{SHG1}} + \alpha_{\text{SHG2}})/2$, defines a measure of the effective single-pass losses to the second harmonic. Continuing the tracing of the optical pulse with two passes through the loss modulator

$$|E_5(t,r)| = |E_4(t,r)| \cdot a_L^2(t) \tag{27}$$

where $a_L(t)$, the loss modulator's amplitude transmission is given by (6b).

Finally, the round trip for the pulse is completed by including an additional time delay $2L_0/c$, and an effective loss α. The time delay allows for the time of round-trip propagation through the cavity of optical length L_0 and the effective loss α accounts for all linear cavity losses.

For self-consistency the envelope of the pulse at any point in the cavity must repeat itself after one period of the modulation cycle. Thus

$$E_1(t - T_m, r) = E_6(t, r) \exp(-j\theta) \tag{28}$$

where $T_M = 2\pi/\omega_m$ and θ allows for an optical phase precession [2].

Equation (28) may be rewritten by using (24)-(27) and by equating powers of t. This leads to three coupled complex equations which completely describe the behavior of the mode-locked frequency-doubled laser. These equations are

$$\gamma = \gamma b'/G' + (\delta_L \omega_m^2/2) \cos \omega_m t_0 \tag{29}$$

$$T_m - 2L_0/c = 4b'g/(G'\Delta\omega_a) + [\delta_L \omega_m/(2\gamma)] \sin \omega_m t_0 \tag{30}$$

and

$$\exp[-\gamma(T_M - 2L_0/c)^2] = (G')^{-1/2} \exp[2g - 2a' - \alpha + j\theta + j\omega_p(T_M - 2L_0/c) - 16g^2 \gamma b'/(\Delta\omega_a^2 G') - 2\delta_L \sin^2(\omega_m t_0/2)]. \tag{31}$$

In the absence of second-harmonic generation these equations, with minor notational changes, reduce to those given in [2].

Although (29)-(31) provide a complete description of the laser's performance, their complexity precludes any meaningful physical understanding without further simplification.

Fortunately, simplification is possible if a low-gain laser ($g \ll 1$), such as CW-pumped Nd:YAG is considered, and if note is taken of the usual magnitudes of the variables in (29)-(31). First, for internal frequency doubling, the conversion efficiency α_{SHG} must be much less than unity if overcoupling [9] of the laser is to be avoided. Further, the pulse spectral extent $\Delta\omega_p$, defined at its 10-percent power points, must be less than the laser fluorescent linewidth. Subject only to these two assumptions, (29) becomes

$$\gamma = -\frac{\sqrt{2}\,\alpha_{SHG}}{32g/\Delta\omega_a^2} + \frac{1}{2}\left[\frac{8\alpha_{SHG}^2}{(32g/\Delta\omega_a^2)^2} + \frac{2\delta_L \omega_m^2 \cos \omega t_0}{32g/\Delta\omega_a^2}\right]^{1/2}. \tag{32}$$

This equation essentially describes laser pulsewidth as a function of modulation depth (δ_L), second-harmonic conversion efficiency (α_{SHG}), and detuning. Pulsewidth (τ_p) is defined as the full pulsewidth of the second-harmonic output as measured as its 10-percent power points. This definition of pulsewidth is useful when dealing with optical communication systems because it represents the time which an optical shutter or modulator must be open in order to pass almost all (97 percent) of the energy in the second-harmonic output pulse [10]. Pulsewidth and γ are related by $\tau_p = [\ln 10/\gamma]^{1/2}$. Note that maximum γ, or minimum pulsewidth (τ_p), occurs with $\omega_m t_0 = 0$, i.e., when there is no phase shift between the optical pulse train and the loss modulation. Further note that minimum pulsewidth occurs at minimum value of α_{SHG}, i.e., where the effects of second-harmonic generation are least. It should be pointed out that although α_{SHG} is treated as an independent variable in (32) it is in fact an implicit function of pulsewidth (e.g., α_{SHG} increases for shorter pulsewidths) and hence cannot simply be varied at will.

It is interesting to evaluate the expression for pulsewidth in the region of large second-harmonic generation, i.e., where

$$\alpha_{SHG}^2 \gg 8g\delta_L(\omega_m^2/\Delta\omega_a^2) \cos \omega_m t_0. \tag{33}$$

In this case a Taylor expansion of (32) yields

$$\gamma = (\omega_m^2 \delta_L/4\sqrt{2})(\cos \omega_m t_0)/\alpha_{SHG} \tag{34}$$

and

$$\tau_p = 2[\sqrt{2} \ln 10]^{1/2} \frac{1}{\omega_m}\left[\frac{\alpha_{SHG}}{\delta_L \cos \omega_m t_0}\right]^{1/2}. \tag{35}$$

In this regime γ and τ_p are independent of g and $\Delta\omega_a$. That is, for high second-harmonic conversion efficiency, pulsewidth is independent of the characteristics of the laser amplifier medium and dependent only upon a competition between the doubler which favors long pulses and the modulator which prefers short pulses [1]. The simple explicit dependence of pulsewidth on ω_m and δ_L, given in (35), is markedly different from that which occurs for the mode-locked, nondoubled laser [2] where $\tau \sim (1/\omega_m)^{1/2}(1/\delta_L)^{1/4}$. It is interesting to note that the dependence of τ on α_{SHG}, ω_m, and δ_L given implicitly by Bernecker [3] (who neglects the effects of laser fluorescent linewidth) is identical to that predicted by (35).

The phase shift, described by (30), between the optical pulse train and modulator drive, may also be simplified using the small gain, small α_{SHG} approximation. Then

$$\Delta f = \omega_m^2/(4\pi^2)[4g/\Delta\omega_a + (\delta_L/2\gamma)\omega_m \sin \omega_m t_0] \tag{36}$$

where $\Delta f = c/2L_0 - \omega_m/2\pi$ is the deviation of twice the modulator drive frequency from the cavity axial mode spacing. In a practical laser system this phase-shift-detuning characteristic may be used as a discriminant in order to maintain mode locking with $\omega t_0 = 0$ over long periods of time [11].

Similarly, (31), which determines laser saturated gain and hence laser output power, may be written

$$2g = \sqrt{2}\,\alpha_{SHG} + \alpha + 2\delta_L \sin^2(\omega_m t_0/2) - 2(\ln 10)\delta_L^2(\omega_m/\Delta\omega_p)^2 \sin^2 \omega_m t_0 - 4g\delta_L(\omega_m/\Delta\omega_a) \sin \omega_m t_0 + (2g/\ln 10)(\Delta\omega_p/\Delta\omega_a)^2 \tag{37}$$

where $\Delta\omega_p$ is the pulse spectral width measured at its 10-percent power points. The terms on the right-hand side of (37) can be physically identified. The first three terms are due to the second-harmonic conversion, linear loss, and loss produced by the modulator if the pulse center does not pass through the modulator at a time of zero loss. The next three terms are a consequence of the finite amplifier linewidth and finite pulse spectral width. Typical values for an Nd:YAG mode-locked frequency-doubled laser are $\omega_m = 2\pi(250\ \text{MHz})$, $\Delta\omega_a = 2\pi(120\ \text{GHz})$, and $\Delta\omega_p = 2\pi(10\ \text{GHz})$. Hence $\omega_m/\Delta\omega_a \ll 1$,

$(\Delta\omega_p/\Delta\omega_a)^2 \ll 1$, and the last two terms are negligible. The fourth term, $-2(\ln 10)\delta_L^2 \cdot (\omega_m/\Delta\omega_p)^2 \sin^2 \omega_m t_0$ is maximum when $\Delta\omega_p$ is minimum. This occurs when the coupling to the second harmonic α_{SHG} is large. In that case $\Delta\omega_p$ can be determined from (35) and therefore an upper bound for the fourth term is given by $\sqrt{2}\,\delta_L\,\alpha_{SHG} \sin^2 \omega_m t_0/\cos \omega_m t_0$. In the usual frequency-doubled Nd:YAG laser, $\alpha_{SHG} \leqslant 0.01$, and therefore the fourth term of (37) is negligible compared to $+2\delta_L \sin^2 (\omega_m t_0/2)$ over nearly the entire detuning range.

Hence the saturated round-trip field gain is determined approximately by

$$2g = \sqrt{2}\,\alpha_{SHG} + \alpha + 2\delta_L \sin^2 (\omega_m t_0/2). \tag{38}$$

The form of this equation determines the power output from the mode-locked frequency-doubled laser discussed in the next section.

IV. Laser Saturation and Output Power

It has been noted previously [12] that the gain of a homogeneously broadened laser saturates according to

$$g = G_0/(1 + \beta P_c) \tag{39}$$

where G_0 is the unsaturated or small-signal single-pass electric-field amplitude gain, β is a saturation parameter which depends only upon laser-material parameters and the cross-sectional area of the oscillating mode, and P_c is the laser's average circulating power. Equations (38) and (39) thus serve to determine the circulating power that can be expected internal to a mode-locked frequency-doubled laser. Harmonic output power is given by $P_{out} = 2\alpha_{SHG} P_c$, and

$$P_{out} = \frac{2\alpha_{SHG}}{\beta}\left[\frac{2G_0}{\sqrt{2}\,\alpha_{SHG} + \alpha + 2\delta_L \sin^2 (\omega_m t_0/2)} - 1\right]. \tag{40}$$

Maximum power output occurs with $\omega_m t_0 = 0$ and

$$\alpha_{SHG} = (\sqrt{2}/2)\,[(2G_0)^{1/2}\,\alpha^{1/2} - \alpha] \tag{41}$$

and is given by

$$P_{max} = (\sqrt{2}/\beta)\,[(2G_0)^{1/2} - \alpha^{1/2}]^2. \tag{42}$$

These values of optimum output coupling and optimum output power are a factor of $\sqrt{2}$ less than those expected from either a frequency-doubled non-mode-locked laser or a mode-locked laser operating at its fundamental wavelength.

For either of these lasers, power gain saturates at a value equal to single-pass power loss. For the frequency-doubled free-running laser, this means that saturated gain is found from $2g = \alpha + \alpha_{SHG}$. Similarly, gain saturation in the mode-locked fundamental-wavelength laser reduces gain until $2g = \alpha + T/2$, where T is the power transmission of the output coupler. The maximum power available from either of these lasers is $2/\beta\,[(2G_0)^{1/2} - \alpha^{1/2}]^2$ and occurs with $\alpha_{SHG} = (2G_0)^{1/2} \cdot \alpha^{1/2} - \alpha$ for the doubled laser and with $T/2 = (2G_0)^{1/2}\,\alpha^{1/2} - \alpha$ for the mode-locked fundamental-wavelength laser [9].

The basic mathematical difference that distinguishes the mode-locked frequency-doubled laser from these lasers is that in the mode-locked frequency-doubled laser saturation is affected by $\sqrt{2}\,\alpha_{SHG}$, while only α_{SHG} contributes to the single-direction output power. For either a frequency-doubled free-running laser or for a mode-locked fundamental-wavelength laser, all loss terms which contribute to output power appear in an identical form in both output-power and laser-saturation equations.

There is one basic physically distinctive feature of the mode-locked frequency-doubled laser that accounts for a reduction in its available power output as compared to the free-running or fundamental-wavelength laser. In contrast to the latter two lasers, the loss encountered by the Gaussian pulse in passing through the amplitude modulator of a frequency-doubled laser is not negligible and is in fact proportional to α_{SHG}.

For the special case of a long pulsewidth, without detuning, a simple physical explanation exists which clarifies this result. In this case, the Gaussian pulse occupies a relatively narrow spectral width and the amplifier saturated gain may be considered a temporal constant g. In the steady state the sum of all single-pass cavity power-losses must be equal to $2g$ and thus must be time independent. Although second-harmonic loss and modulator losses each vary with time, their sum must be a constant if the total cavity loss is to be time invariant. At $t = 0$, i.e., at the peak of the Gaussian pulse, modulator loss is zero and second-harmonic loss is maximum and given by $\sqrt{2}\,\alpha_{SHG}$. As time increases from $t = 0$, doubling losses are reduced and modulator losses increase. Their sum nevertheless remains constant and may be calculated by its value at $t = 0$ and is thus given by $\sqrt{2}\,\alpha_{SHG}$.

In the case of no detuning and where the line shape of the amplifying medium is unimportant, the dependence of the sum of modulator and second-harmonic loss on α_{SHG} is mathematically easily demonstrated. Consider the field-amplitude transmission of a modulator as given by (6b). For a laser operating without detuning, i.e., for modulator-drive frequency adjusted such that $t_0 = 0$, this transmission may be written $a_L(t) = \exp[-\delta_L(\omega_m t)^2/4]$. The amplitude transmission through the second-harmonic generator is found from (7) and (14) and is given by

$$T_{SHG}(t) = (\exp - a) \exp[-\gamma t^2 (b - 1)] \tag{43}$$

where $a = (\sqrt{2}/2)\,\alpha_{SHG}$ and $b = 1 - \sqrt{2}\,\alpha_{SHG}$. Thus a single pass through the modulator, frequency-doubler combination results in a power-transmission function

$$T = [T_{SHG}(t)\,a_L(t)]^2 = \exp(-2a) \cdot \exp[-2t^2[\gamma(b - 1) + \delta_L \omega_m^2/4]]. \tag{44}$$

The pulse propagation constant γ is determined from (34) and hence the single-pass modulator, frequency-doubler power loss is

$$1 - T = 1 - \exp - 2a \cong \sqrt{2}\,\alpha_{SHG}. \tag{45}$$

Consequently, $\sqrt{2}\,\alpha_{SHG}$ accounts for the effect of both the modulator and the doubler in saturating the laser gain. On the other hand, only α_{SHG}, the time average losses to the second harmonic, is available as single-direction output coupling. The remaining loss is caused by the modulator and does not contribute to output power.

V. Some Numerical Examples

A. The Significance of α_{SHG}: Laser Performance as a Function of α_{SHG}

Before considering the analytical implications of the theory developed in this paper it is useful to examine further the physical significance of α_{SHG}, the second-harmonic conversion efficiency. Although in the theory herein α_{SHG} is treated as an independent variable and as a determinant of circulating power and pulsewidth, α_{SHG} actually changes both with circulating power and with pulsewidth.

The treatment of α_{SHG} as an independent, rather than dependent variable, has the advantage that it decouples the analysis of effects of laser saturation from the analysis of the effects of mode locking and frequency doubling. Hence it allows the characterization of the output mode-locked pulsewidth given in Section III without direct reference to laser saturation. This treatment permits the generation of generalized curves which describe the pulsewidth τ_p and phase shift $\omega_m t_0$ of the mode-locked pulse as a function of second-harmonic conversion efficiency α_{SHG}, and detuning parameter Δf. Figs. 2-4 present these curves for a internally frequency-doubled Nd:YAG laser. The laser parameters used to calculate the curves are $\Delta\omega_a = 2\pi(120\text{ GHz})$, $\omega_m = 2\pi(250\text{ MHz})$, and $2g = 0.05 + \sqrt{2}\,\alpha_{SHG}$.

Fig. 2 shows, for various modulation indices, δ_L the variation of pulsewidth τ_p with increasing second-harmonic conversion efficiency α_{SHG}. This curve is plotted from (32) for zero phase shift between the amplitude-modulation and the mode-locked pulse train ($\omega_m t_0 = 0$). Note that even for small α_{SHG} rather substantial broadening of the laser pulsewidth from its second-harmonic-free value occurs. It is interesting to note that for α_{SHG} greater than approximately 0.3 percent the pulsewidth follows a square-root dependency on α_{SHG}, as described by (35), and is consequently independent of the assumed value of saturated laser gain. That is, for $\alpha_{SHG} > 0.3$-percent pulsewidth is determined solely by the modulator and second-harmonic process and does not depend on the amplifier line shape.

Fig. 3 shows the variation of pulsewidth τ_p with detuning Δf. The detuning characteristic is approximately symmetric about a detuning $\Delta f = (\omega_m/2\pi)^2 (4g/\Delta\omega_a)$. A positive Δf corresponds to a modulation frequency lower than the axial mode spacing, $c/2L_0$. The occurrence of a minimum pulsewidth at a modulation period different from the round-trip cavity time is due to the time delay seen by the pulse passing through the Nd:YAG amplifier rod. Note also that as α_{SHG} is increased the effect of detuning is decreased.

The change in the mode-locked pulse phase shift $\omega_m t_0$ with detuning Δf is shown in Fig. 4. A positive value of $\omega_m t_0$ denotes that the laser pulse train leads the amplitude modulation. Here again note that detuning effects are less pronounced at high α_{SHG}. The reduced sensitivity of the phase shift $\omega_m t_0$ to detuning may be viewed as the cause of the insensitivity of pulsewidth to changes in modulation frequency when α_{SHG} is large. That is, from (32) it is seen that the primary way detuning affects pulsewidth is via a change in pulse position $\omega_m t_0$. Hence, if pulse position is insensitive to detuning, pulsewidth will also vary slowly with changes in modulation frequency.

Physically, the lessened sensitivity of pulse position to detuning at higher second-harmonic conversion efficiencies is due to the relatively long pulse durations associated with large values of α_{SHG}. This can be understood by examining the physical implications of modulator detuning. For any modulation period, the requirement that the pulse envelope repeat itself after a cavity round trip determines $\omega_m t_0$, the phase shift between the modulation and the output pulse train.

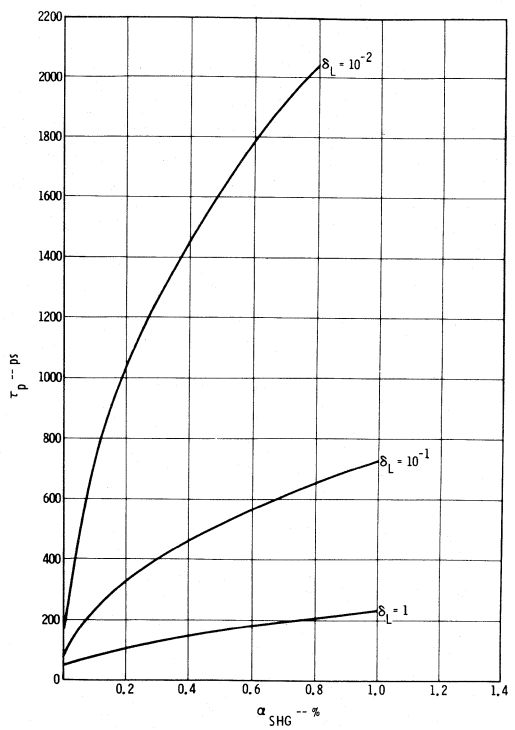

Fig. 2. Second-harmonic pulsewidth τ_p (10-percent power points) as a function of the second-harmonic conversion efficiency α_{SHG}.

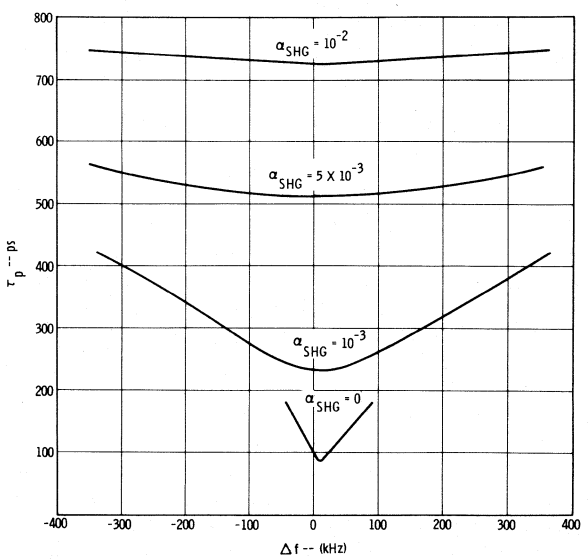

Fig. 3. Second-harmonic pulsewidth τ_p (10-percent power points) as a function of detuning Δf. The modulation depth δ_L is 0.1.

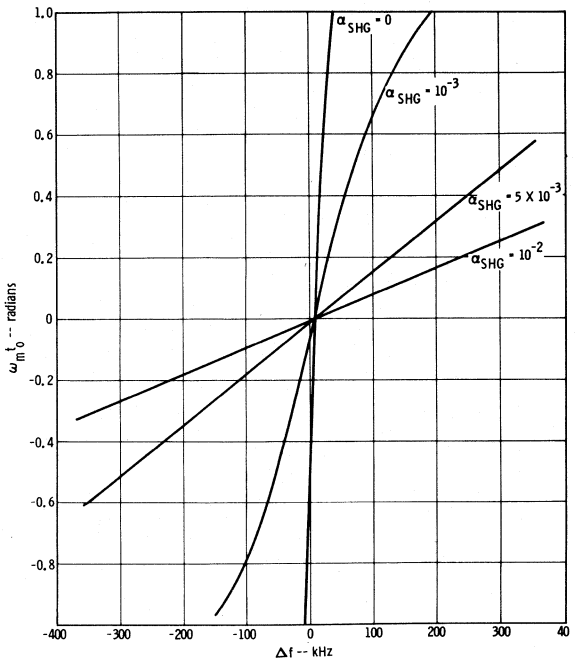

Fig. 4. Pulse position $\omega_m t_0$ relative to the amplitude modulation, as a function of detuning Δf. The modulation depth δ_L is 0.1.

If the drive frequency is chosen optimally, i.e., for minimum pulsewidth, then the pulse train will leave the modulator in phase with the modulation, complete a traversal through the optical cavity, and return in phase with the modulation waveform. A pulse thus propagating will suffer minimum loss in the modulator. In that case the modulation period T_M is the sum of the linear cavity propagation time and the two-pass amplifier delay time, i.e.,

$$T_M \text{ (optimum)} = 2L_0/c + 4g/\Delta\omega_a. \tag{46}$$

Now what happens if the modulation period is not chosen according to (46)? A pulse leaving the modulator in phase with the amplitude modulation will return to the modulator after a cavity round trip with a nonzero phase shift (ϕ) with respect to the amplitude modulation. First consider the case shown in Fig. 5 where the modulation period is slightly less than T_M (optimum) so that when the pulse reenters the modulator, $\phi > 0$. At $0 < \phi < \pi$ the modulator loss is increasing with increasing time and hence the pulse's trailing portion is attenuated more strongly than its leading edge. As seen in Fig. 5, this nonsymmetrical loss results in a negative delay of the pulse centroid. Steady-state operation of the detuned laser is achieved when the pulse leaving the modulator with phase ϕ returns to it with the same phase ϕ. Thus in the steady state the phase shift between the modulation and pulse train determines a delay in the modulator. This delay exactly compensates for the deviation of modulation period from T_M (optimum). The delay in the modulator is determined from the generalized Gaussian pulse shape given by (1) and the amplitude modulator transfer function given by (6b). From these equations it can be shown that the delay t_D, due to the amplitude modulator, is given by

$$t_D = (\delta_L \omega_m \sin \omega_m t_0)/(2\gamma) \tag{47}$$

or in terms of the pulsewidth

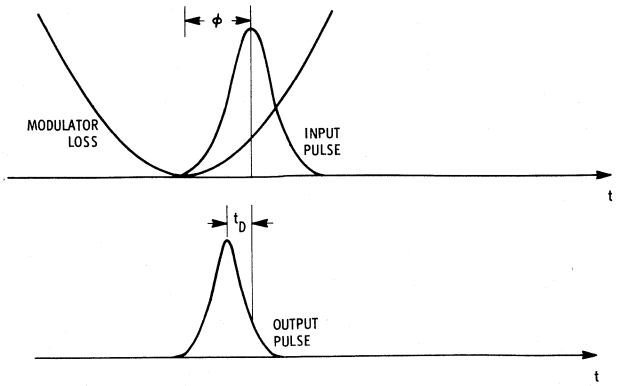

Fig. 5. Pulse delay in the amplitude modulator. If the pulse enters the modulator with a phase ϕ relative to the modulation it experiences an effective delay t_D.

$$t_D = (\delta_L \omega_m \sin \omega_m t_0)\, \tau_p^2/(2 \ln 10). \tag{48}$$

In Fig. 5 steady-state operation occurs with $\omega_m t_0 < 0$ so that t_D is negative.

On the other hand, if the modulation period is greater than T_M the pulse's leading edge sees more loss than its trailing portion and in the steady state the pulse position $\omega_m t_0 > 0$ so that a positive pulse delay results.

The delay t_D, required by the modulator, is determined solely by the deviation of the modulation period from T_M (optimum). From (48) it is seen that the phase shift $\omega_m t_0$ required for a particular delay t_D is least when the laser produces long pulses. Longest pulsewidth occurs when the conversion to the second harmonic is greatest and hence the sensitivity of pulse phase shift to detuning is least at highest conversion to the second harmonic.

B. Laser Performance as a Function of Beam Size in the Frequency-Doubler Crystal

Thus far this paper has analyzed the performance of modelocked internally frequency-doubled laser in terms of a single parameter, α_{SHG}, the second-harmonic conversion efficiency. Because of the dependent nature of α_{SHG}, a parametric analysis based only on α_{SHG} is necessarily incomplete and the variation of α_{SHG} with circulating power, laser beam size, and pulsewidth must be unraveled before a prediction of laser performance as a function of independent variables can be made. That is, a prediction of laser performance as a function of cavity mode sizes or pump-lamp input power requires an evaluation of α_{SHG} in terms of more basic laser parameters.

Recall that α_{SHG} is defined as the ratio of average single-direction second-harmonic power generated to the average circulating fundamental power, i.e.,

$$\alpha_{SHG} = \overline{P_2(t)}/P_c \tag{49}$$

where the overbar denotes a time average.

The average second-harmonic power produced can be found from the single-pulse second-harmonic shape, (9), by integrating over both the spatial and temporal pulse extent. Assuming the maximum instantaneous conversion efficiency is small the second-harmonic power may be written

$$\overline{P_2(t)} = [K^2 A^4 \pi w_0^2/(8 z_{2\omega})]\, (c/2L_0)\, [\pi/(4\gamma)]^{1/2} \tag{50}$$

where $z_{2\omega}$ is the crystalline impedance at the second harmonic, w_0 is the $1/e^2$ fundamental wavelength beam radius, and $c/2L_0$ is the pulse repetition frequency. Other quantities in (50) are defined in (1) and (9).

The average fundamental power, calculated from (1) in a similar manner, is given by

$$P_c = [A^2 \pi w_0^2/(4z_\omega)]\,(c/2L_0)\,[\pi/(2\gamma)]^{1/2} \tag{51}$$

where z_ω is the crystalline impedance of the fundamental wavelength. Thus the second-harmonic conversion efficiency can be described in terms of incavity beam sizes, fundamental circulating power, and second-harmonic pulsewidth as

$$\alpha_{SHG} = [2K^2/(\pi w_0^2)]\,[z_\omega^2/z_{2\omega}] \cdot P_c(2L_0/c)\sqrt{\ln 10}/(\sqrt{\pi}\,\tau_p). \tag{52}$$

In performing the temporal integrations necessary to evaluate P_c and $\overline{P_2(t)}$ it was implicitly assumed that $\tau_p \ll 2L_0/c$, so that temporal overlap of consecutive pulses is negligible.

It is instructive to compare the evaluation of α_{SHG} for the mode-locked laser to that of a identical single axial mode [6, p. 133] free-running laser. A similar calculation of the second-harmonic conversion efficiency for the free-running laser and a comparison with (52) shows that the factor

$$(2L_0/c)\,[\sqrt{(\ln 10)}/\sqrt{\pi}\,]\,(1/\tau_p) \simeq (2L_0/c)(0.85/\tau_p)$$

is the enhancement due to the mode locking.

Now with a mechanism established to relate α_{SHG} to basic cavity parameters, the results of this paper can be well illustrated by a numerical example. An Nd:YAG laser, AM mode locked and internally frequency doubled by a $Ba_2NaNb_5O_{15}$ crystal is considered. Where appropriate, parameters are taken equal to those analyzed in [2]. This choice of numerical values facilitates comparison with the mode-locked fundamental-wavelength laser.

A laser pumped by a single krypton lamp is considered, and the unsaturated power gain $2G_0$ is assumed to vary linearly with lamp input power and to be described by [13]

$$2G_0 = k[P_{lamp} - P_0]. \tag{53}$$

This linear approximation to unsaturated gain is approximately valid for $P_{lamp} \geqslant 2P_0$. The parameter k depends on the electrical efficiency of the pump lamp, on the efficiency of coupling into the Nd:YAG rod, and upon Nd:YAG material parameters. The parameter P_0 is the value of power input to the pump lamp at which the gain G_0 equals zero in the linear approximation. P_{lamp} is the input power to the pump lamp.

Assumed values for these parameters and other parameters are given in Table I. The values given are typical values for a laser consisting of a 3-mm-diam, 50-mm-long Nd:YAG laser crystal pumped by a 4-mm-bore krypton lamp.

Fig. 6 shows the predicted variation in second-harmonic output power as a function of lamp power for various beam sizes in the frequency-doubler crystal. For reference, the mode-locked second-harmonic power P_{max} available from the laser is also shown (42). The curve for a beam size of $w_0 = 100\ \mu$ is slightly under coupled over much of the range of pumping powers. Hence while decreasing the beam size in the doubler crystal to slightly below $100\ \mu$ would provide a small increase in output power, decreasing the beam size well below $100\ \mu$ would actually lead to a reduction of output power. A curve of second-harmonic output power for $w_0 = 50\ \mu$ falls nearly coincident with the 100-μ curve.

Fig. 7 shows predicted second-harmonic pulsewidths over the same range of pump powers and spot sizes. As lamp input

TABLE I
LASER PARAMETERS: FIGS. 6-10

k	pumping-efficiency constant = 2.2×10^{-4} $(W)^{-1}$
P_0	lamp-threshold parameter = 385 W
α	single-pass linear power loss = 0.05
$\frac{c}{2L_0}$	laser axial mode spacing = 250 MHz
L_0	laser-cavity optical length = 60 cm.
$\Delta\omega_a$	laser fluorescent linewidth (full width at half maximum) = 2π(120 GHz)
ω_m	AM frequency = $2x$ modulation drive frequency = 2π (250 MHz)
β	saturation parameter = 0.1 $(W)^{-1}$
K	second-harmonic nonlinearity[a] = 1.96×10^{-7} m/V

[a]The second-harmonic nonlinearity K (9) is calculated assuming a 90° phase-matched $Ba_2NaNb_5O_{15}$ of 5-mm length. The crystal parameters used in evaluation of K are from S. Singh, D. A. Draegert, and J. E. Geusic, "Optical and ferroelectric properties of barium sodium niobate," *Phys. Rev. B*, vol. 2, pp. 2709-2724, Oct. 1970.

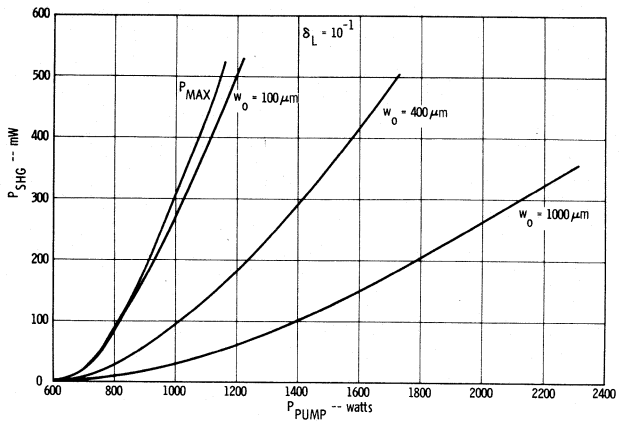

Fig. 6. Second-harmonic output power P_{SHG} as a function of the krypton-lamp input power P_{lamp}. The modulation depth δ_L is 0.1.

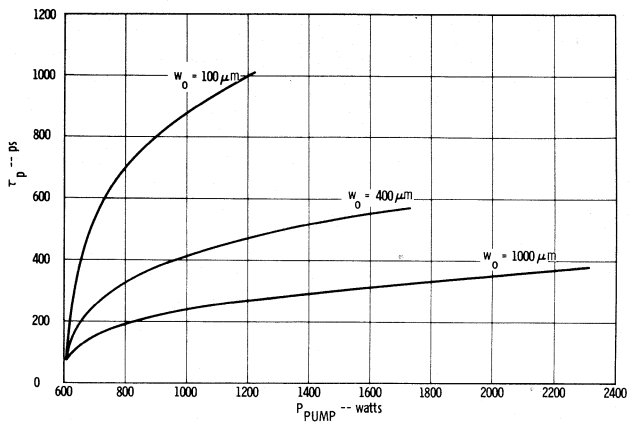

Fig. 7. Second-harmonic pulsewidth (10-percent power points) τ_p as a function of the krypton-lamp input power P_{lamp}. The modulation depth δ_L is 0.1.

power increases, pulses broaden due to the increase of second-harmonic conversion efficiency. Because pulsewidths increase monotonically with decreasing beam sizes (increasing α_{SHG}) a decrease in the beam size in the doubler crystal below 100 μ would result in a large increase in pulsewidth with only a small increase in power output.

Figs. 8–10 show the response of the frequency-doubled laser to detuning of the modulation drive frequency. As expected from Fig. 4, detuning effects are less pronounced for smaller beam sizes in the frequency doubler, i.e., at higher values of α_{SHG}. Figs. 8–10 show, respectively, the change in pulse position, output power, and pulsewidth with detuning. This large

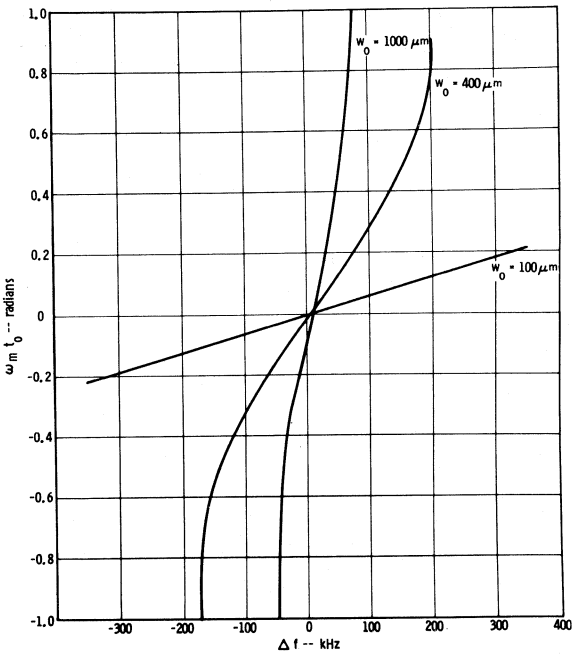

Fig. 8. Pulse position $\omega_m t_0$ relative to the amplitude modulation as a function of detuning Δf. The lamp input power P_{lamp} is 1000 W and the modulation depth δ_L is 0.1.

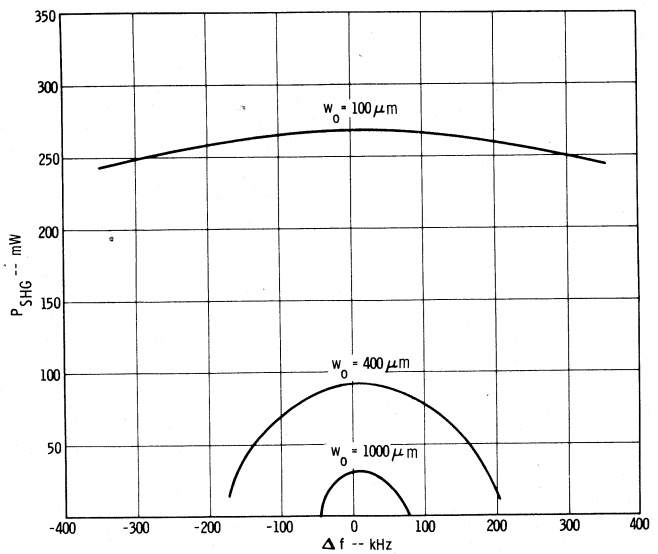

Fig. 9. Second-harmonic power P_{SHG} as a function of detuning Δf. P_{lamp} = 1000 W, δ_L = 0.1.

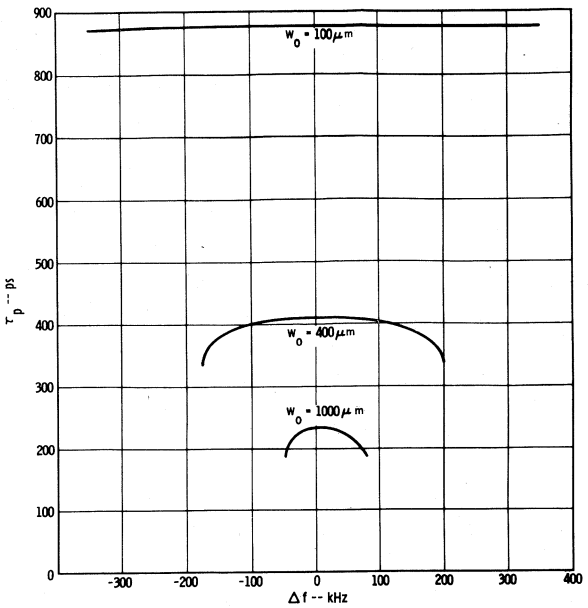

Fig. 10. Second-harmonic pulsewidth (10-percent power points) as a function of detuning Δf. P_{lamp} = 1000 W, δ_L = 0.1.

theoretical detuning range is not apt to be achieved in practice because the most common types of amplitude modulators, acoustooptic or electrooptic, do not usually present constant modulation depths over frequency ranges as large as the 700-kHz range shown in Figs. 8–10 [14].

The reduction in pulsewidth with detuning shown in Fig. 10 is caused by the reduction in circulating power due to modulator loss as the modulator is detuned from its optimal drive frequency (or as the cavity length is changed from optimum). As the detuning is increased the pulse position changes and the modulator presents an internal cavity loss that reduces P_c. This decrease in circulating power results in a decrease in α_{SHG} and hence reduction in the laser's pulsewidth.

VI. Experimental Results

A preliminary confirmation of this theory was made with a frequency-doubled Nd:YAG laser pumped by a K-Rb lamp. The frequency doubler was a barium sodium niobate crystal and relevant laser parameters were $g \cong 0.01$, $\delta_L = 0.03$, $c/2L = 5 \cdot 10^8$ Hz, and $\alpha_{SHG} \cong 0.005$. The theory developed here predicts a pulsewidth of 460 ps in rough agreement with the measured pulsewidth (corrected for detector response) of 390 ps.

VII. Summary

This paper has analyzed the performance of an internally frequency-doubled mode-locked laser. The results reported herein have been derived by considering the effects of each intracavity component upon a generalized Gaussian pulse shape. This technique was introduced by Kuizenga and Siegman [2] for the analysis of a mode-locked fundamental-wavelength laser. The effects of the internal frequency doubler are accounted for by a single parameter α_{SHG}, defined as the average power conversion efficiency to the second-harmonic wavelength. The second-harmonic process provides a power-

dependent loss to the intracavity propagating pulse, presenting more loss at its peak than at its extremities. This nonlinear loss leads to substantial broadening of the laser pulsewidth. The variation of pulsewidth, pulse position, and laser saturated gain with α_{SHG} has been predicted. The equations derived differ markedly from those describing the fundamental-wavelength laser. The pulse broadening caused by second-harmonic generation has been shown to be substantial even at small α_{SHG}.

In contrast to the fundamental-wavelength mode-locked laser, losses due to the amplitude modulator have been shown to be an important determinant of total laser losses and hence greatly affect the available second-harmonic output power. In fact, unavoidable modulator losses limit the output power theoretically extractable from the mode-locked frequency-doubled laser to a factor of $\sqrt{2}$ less than that available from an identical free-running laser. It has been further shown that, if the value of α_{SHG} necessary to extract the maximum available laser power is exceeded, the pulsewidth increases while the output power decreases with increasing α_{SHG}.

The response of the mode-locked frequency-doubled laser to detuning has been predicted. It has been shown that at higher values of α_{SHG} the laser is less affected by detuning of the modulator from its optimal frequency.

Numerical examples have been given for predicted laser performance for an Nd:YAG laser, internally frequency doubled by a $Ba_2NaNb_5O_{15}$ crystal.

Acknowledgment

The author wishes to thank A. E. Siegman for discussions regarding the treatment of second-harmonic generation used in Section II of this paper. He also wishes to thank J. D. Barry, C. B. Hitz, C. J. Kennedy, D. J. Kuizenga, N. Blackman, R. S. Reynolds, W. A. Specht, and P. J. Titterton for suggestions and comments on the manuscript. He especially wants to thank this JOURNAL's reviewers for valuable criticisms of the manuscript.

References

[1] C. B. Hitz and L. M. Osterink, "Simultaneous intracavity frequency doubling and mode locking in a Nd:YAG laser," *Appl. Phys. Lett.*, vol. 18, pp. 378–380, May 1, 1971.

[2] D. J. Kuizenga and A. E. Siegman, "FM and AM mode locking of the homogeneous laser–Part I: Theory," *IEEE J. Quantum Electron.*, vol. QE-6, pp. 694–708, Nov. 1970.

[3] O. Bernecker, "Limitations for mode-locking enhancement of internal SHG in a laser," *IEEE J. Quantum Electron.*, vol. QE-9, pp. 897–900, Sept. 1973.

[4] A. E. Siegman and D. J. Kuizenga, "Active mode-coupling phenomena in pulsed and continuous lasers," *Opto-Electron.*, vol. 6, pp. 43–66, 1974.

[5] A. Yariv, *Quantum Electronics*. New York: Wiley, 1967, pp. 310–312.

[6] N. Bloembergen, *Nonlinear Optics*. New York: W. A. Benjamin, 1965, pp. 85–89.

[7] C. B. Hitz, GTE Sylvania, Mountain View, Calif., private communication.

[8] J. M. Yarborough, J. Falk, and C. B. Hitz, "Enhancement of optical second harmonic generation by utilizing the dispersion of air," *Appl. Phys. Lett.*, vol. 18, pp. 70–72, Feb. 1, 1971.

[9] R. G. Smith, "Theory of intracavity optical second-harmonic generation," *IEEE J. Quantum Electron.*, vol. QE-6, pp. 215–223, Apr. 1970.

[10] P. J. Titterton, "Effect of system inaccuracies on the probability of bit error for pulsed communication systems," *Appl. Opt.*, vol. 13, pp. 1034–1040, May 1974.

[11] T. S. Kinsel, "A stabilized mode-locked Nd:YAlG laser using electronic feedback," *IEEE J. Quantum Electron. (Part I of Two Parts)*, vol. QE-9, pp. 3–8, Jan. 1973.

[12] A. Yariv, *Introduction to Optical Electronics*. New York: Holt, Rinehart and Winston, 1971, pp. 109–112.

[13] G. A. Massey, "Measurement of device parameters for Nd:$YAlO_3$ lasers," *IEEE J. Quantum Electron.*, vol. QE-8, pp. 669–674, July 1972.

[14] I. P. Kaminow and E. H. Turner, "Electrooptic light modulators," *Proc. IEEE (A Special Joint Issue on Optical Electronics with Applied Optics)*, vol. 54, pp. 1374–1390, Oct. 1966.

Mode Conversion in Planar-Dielectric Separating Waveguides

WILLIAM K. BURNS AND A. FENNER MILTON

Abstract—**The mode-conversion behavior of branching or separating planar-dielectric waveguides is studied theoretically as a function of branch asymmetry and taper slope. When the taper slope is large in a near-symmetric structure, considerable mode conversion will occur and the structure will act as a power divider. In an asymmetric structure with small taper slope, mode conversion is negligible and the structure will act as a mode splitter. A quantitative formula is presented which can be used to determine the behavior of a given separating structure.**

I. Introduction

IT IS ANTICIPATED that separating optical waveguides will become important in integrated optics. They will be encountered whenever a branching optical waveguide, as shown in Fig. 1(a), is used or whenever two parallel waveguides in close proximity are separated, as shown in Fig. 1(b). These structures are expected to find widespread use in electrooptical amplitude modulators and switches.

The distinguishing characteristics of optical separating waveguides in dielectric media are that the evanescent fields of the guided modes exist outside the boundaries of the guiding layers and power transfer between the individual waveguides or arms of the branching waveguide can occur due to the overlap of the evanescent fields. In this study we will confine our attention to planar-dielectric waveguides due to their mathematical simplicity, recognizing that the same mode-conversion considerations will apply to the separation of dielectric channel guides.

We use the term separating optical waveguide to apply to either of the structures in Fig. 1 since the separation of parallel waveguides is equivalent to a branching waveguide starting from a nonzero branch separation. The mode-conversion problem can be treated in the same way for each structure except for a different starting separation.

Yajima [1] showed experimentally that modes incident on an asymmetric planar-dielectric branching waveguide with a shallow taper propagate such that the mode power is transferred to one arm of the branch or the other. The principle was established that a mode would choose the arm in which it could propagate with an effective index closest to the effective index that characterized its propagation before the waveguide divided. An asymmetric branching waveguide with a shallow taper can thus be considered to act as a mode splitter [Fig. 2(a)]. Yajima recognized that branching waveguides with steeper tapers would not behave as ideal mode splitters due to mode conversion between the normal modes of the five-layer structure and power transfer to unguided radiation modes. Symmetry considerations lead us to believe that in extreme cases of steep tapers or near-symmetric branches the branching waveguide will act not as a mode splitter but rather as a power divider [Fig. 2(b)]. If the device acts as a power divider, incident power concentrated in the upper part of the structure will end up in the upper arm and incident power concentrated in the lower part of the structure will end up in the lower arm, independent of the modal evolution graphically described in Fig. 2(a).

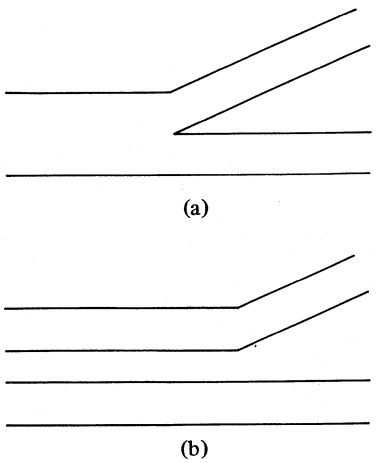

Fig. 1. Two types of separating optical waveguides. Propagation in both structures can be described in an equivalent manner if the parallel sections are sufficiently close in (b) for the normal modes to have power in both guiding regions.

Recently Yajima calculated many such cases of mode conversion [2], [3], starting with the approximate step theory of Marcuse [4]. We have extended the same step theory to include power transfer between two guided modes. By including a more rigorous treatment of the phase difference between the guided modes, we present results of more precise mode-conversion calculations for separating waveguides as a function of the rate of separation and mode synchronism, which is adjusted by the index asymmetry of the structure. The correct treatment of the phase difference between the two modes leads to a distinctly different dependence of mode conversion on taper slope for near-symmetric structures, and allows us to rigorously investigate the transition region between the two limiting modes of operation of a separating waveguide. We will thus explore the difference in behavior between separating

Manuscript received July 18, 1974; revised September 27, 1974. This research was partially supported by the Advanced Research Projects Agency and the Office of Naval Research.

The authors are with the Naval Research Laboratory, Washington, D.C. 20375.

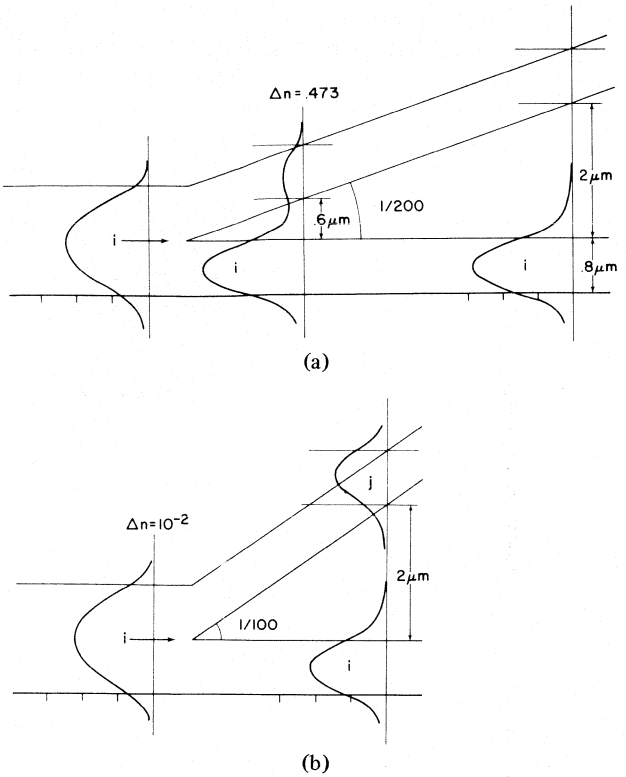

Fig. 2. Examples of a branching waveguide operated as a mode splitter (a) and as a power divider (b). Mode electric field is plotted for various waveguide cross sections, with indices as shown in Fig. 3. In (a) 98 percent of the input power remains in mode *i*. In (b) output powers are 55 percent for mode *i* and 36 percent for mode *j*.

asymmetric waveguides which separate slowly with a shallow taper and separating symmetric guides (where the two guides or branches are more nearly identical) which separate quickly with a steep taper.

II. Theory

We consider a planar, five-layer waveguide, which consists of two waveguiding layers and three regions of lower index boundary media that separate and clad the two waveguiding branches. Unless stated otherwise, use of the term "mode" will refer to the local normal modes of this five-layer waveguide for a given guide separation, which may be 0 or ∞. Thus propagation in the structures shown in Fig. 1(a) and (b) can be described by the same formulism with a different starting separation. With this approach the individual modes of a structure which consists of two guiding layers will evidence power in *both* layers if the guiding layers are in close enough proximity. Except in the case of exact symmetry (where the two guiding layers considered separately would have modes with exactly the same propagation constant), the modes of the five-layer structure with a large enough separation between guiding layers will concentrate power in one guiding layer or the other. Mode propagation is assumed in the z direction, the x direction is normal to the waveguiding layers, and fields and geometry are assumed unchanged in the y direction. The mode-dispersion equation can be obtained by solving the boundary value problem, and is given by Yajima [2], [3] for transverse electric modes

$$\{(\gamma_1+\gamma_3)\gamma_2+(\gamma_1\gamma_3-\gamma_2^2)\tan\gamma_2 d_2\}\cdot\{(\gamma_3+\gamma_5)\gamma_4+(\gamma_3\gamma_5-\gamma_4^2)\tan\gamma_4 d_4\}-\exp(-2\gamma_3 d_3)\{(\gamma_3-\gamma_1)\gamma_2+(\gamma_1\gamma_3+\gamma_2^2)\tan\gamma_2 d_2\}\cdot\{(\gamma_3-\gamma_5)\gamma_4+(\gamma_3\gamma_5+\gamma_4^2)\tan\gamma_4 d_4\}=0. \quad (1a)$$

Here γ_l is the transverse wave vector

$$\gamma_l=\sqrt{|n_l^2k^2-\beta^2|}, \quad l=1\text{-}5 \quad (1b)$$

and β is the mode wave vector in the direction of propagation, k is the free-space wave vector, and d_l and n_l are waveguide layer thicknesses and indices, as shown in Fig. 3. The roots of this equation yield mode wave vectors (β), which are then used to calculate the mode electric-field distributions. By plotting these mode electric-field distributions as a function of increasing branch separation, one can see how an individual mode transforms itself as the branch separation changes and which arm of the branch it chooses. All these considerations are calculations at a given position z and are independent of the rate at which the arms of the branch separate, or taper slope.

For a waveguide branch with an infinitely slow taper slope, we assume mode conversion to be negligible and mode power to be conserved for propagation through the branch. This corresponds to adiabatic passage. However, as taper slope is increased we expect that the adiabatic approximation will break down and power transfer will occur from an input mode to other guided and radiation modes, both transmitted and reflected. This problem is conveniently treated by the step approximation method of Marcuse [4]. The continuous-branch taper is approximated by a series of discontinuous, abrupt steps, separated by regions of parallel, five-layer waveguide (Fig. 3). We assume the waveguide modes of interest to be incident on a step and compute the transmitted mode amplitudes by requiring the transverse-field components to be continuous at the step. By breaking up the taper into a large number of small steps and repeating this process at each step, a reasonable approximation to the effect of a given taper slope is obtained.

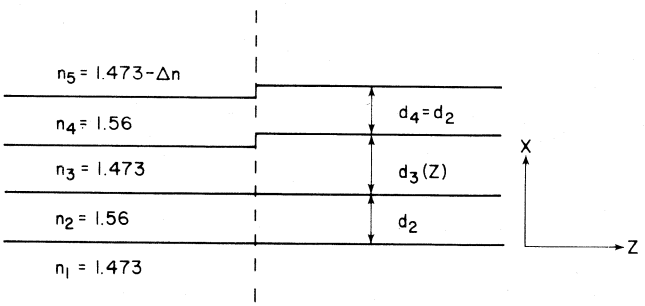

Fig. 3. Model of one of the steps used to approximate a continuous taper slope. The indices shown are used in most of the calculations in this paper. Note the geometric asymmetry assumed to approximate a planar geometry.

We restrict attention to two transverse electric guided modes, i and j. Guided-mode electric fields are written

$$e_y = E(z)\,\mathcal{E}(x,z)\exp(-i\alpha(z)) \tag{2a}$$

where

$$\alpha(z) = \beta z + \phi. \tag{2b}$$

$E(z)$ is the real amplitude at a point z, $\mathcal{E}(x,z)$ the real, x dependent field distribution, β the mode wave vector, and ϕ a phase constant. We will show that the effect of reflected radiation into unguided modes e^{ref} is small and can ultimately be neglected. Transmitted radiation into unguided modes e^{trans} is treated exactly. Boundary conditions for TE modes require e_y and h_x to be continuous across a step at z. We obtain the equations

$$\begin{aligned} e_y: {} & E_{i0}\mathcal{E}_{i0}\exp(-i\alpha_{i0}) + E_{j0}\mathcal{E}_{j0}\exp(-i\alpha_{j0}) \\ & + E^R_{i0}\mathcal{E}_{i0}\exp(i\alpha^R_{i0}) + E^R_{j0}\mathcal{E}_{j0}\exp(i\alpha^R_{j0}) + e^{\text{ref}} \\ & = E_{i1}\mathcal{E}_{i1}\exp(-i\alpha_{i1}) + E_{j1}\mathcal{E}_{j1}\exp(-i\alpha_{j1}) + e^{\text{trans}} \end{aligned} \tag{3a}$$

$$\begin{aligned} h_x: {} & \beta_{i0}E_{i0}\mathcal{E}_{i0}\exp(-i\alpha_{i0}) + \beta_{j0}E_{j0}\mathcal{E}_{j0}\exp(-i\alpha_{j0}) \\ & - \beta_{i0}E^R_{i0}\mathcal{E}_{i0}\exp(i\alpha^R_{i0}) - \beta_{j0}E^R_{j0}\mathcal{E}_{j0}\exp(i\alpha^R_{j0}) + h^{\text{ref}} \\ & = \beta_{i1}E_{i1}\mathcal{E}_{i1}\exp(-i\alpha_{i1}) + \beta_{j1}E_{j1}\mathcal{E}_{j1} \\ & \cdot \exp(-i\alpha_{j1}) + h^{\text{trans}} \end{aligned} \tag{3b}$$

where the subscripts 0 and 1 are used to denote the incident and transmitted fields across the step, and E^R is the amplitude of reflected guided modes. Multiplication by a transmitted mode field and integration over x eliminates the transmitted unguided radiation modes, because of orthogonality.

Our goal now is to obtain iterative equations for E_{j1} and α_{j1} from (3). If we consider cross reflection between modes i and j to be small, multiplication of (3) by $\int \mathcal{E}_{i1}\,dx$ gives an approximate equation for E^R_{i0}.

$$\begin{aligned} E^R_{i0}\exp(i\alpha^R_{i0}) \simeq {} & \left(\frac{\beta_{i0}-\beta_{i1}}{\beta_{i0}+\beta_{i1}}\right)E_{i0} \\ & \cdot \exp(-i\alpha_{i0}) + 0\left(E_{j0}\int \mathcal{E}_{j0}\mathcal{E}_{i1}\,dx\right). \end{aligned} \tag{4}$$

Now multiply (3) by $\int \mathcal{E}_{j1}\,dx$ and subtract out the term in E^R_{j0}. Using (4) in the resulting equation gives

$$\begin{aligned} & (\beta_{j0}+\beta_{j1})E_{j1}I_{j1,j1} \\ & \cdot \exp(-i\alpha_{j1}) = 2\beta_{i0}\left(\frac{\beta_{j0}+\beta_{i1}}{\beta_{i0}+\beta_{i1}}\right)E_{i0}I_{i0,j1} \\ & \cdot \exp(-i\alpha_{i0}) + 2\beta_{j0}E_{j0}I_{j0,j1} \\ & \cdot \exp(-i\alpha_{j0}) + 0(E_{j0}I_{j0,i1}I_{i0,j1}) \end{aligned} \tag{5a}$$

where

$$I_{\gamma,\delta} = \int \mathcal{E}_\gamma \mathcal{E}_\delta\,dx, \qquad \gamma,\delta = i,j. \tag{5b}$$

Equation (5a) is conveniently normalized by introducing a mode amplitude (E^s) which corresponds to a mode power of unity. At any point z, E^s is related to mode power (P) by

$$\sqrt{P_\gamma} = 1 = E^s_\gamma\sqrt{\frac{\beta_\gamma}{2k}I_{\gamma,\gamma}}, \qquad \gamma = i,j \tag{6}$$

where k is the free-space wave vector. By dividing the terms of (5a) by appropriate factors of the right-hand side of (6), and neglecting terms which contain the square of an overlap integral between different modes on opposite sides of the step, we obtain

$$A_{j1}\exp(-i\alpha_{j1}) = c_{ij}A_{i0}\exp(-i\alpha_{i0}) + c_{jj}A_{j0}\exp(-i\alpha_{j0}). \tag{7}$$

Here $A_\gamma = E_\gamma/E^s_\gamma$ is the ratio of mode amplitude in the presence of mode conversion to that mode amplitude which corresponds to unity power. The coefficient c_{ij} is given by

$$c_{ij} = \frac{2\sqrt{\beta_{i0}\beta_{j1}}}{(\beta_{j0}+\beta_{j1})}\left(\frac{\beta_{j0}+\beta_{i1}}{\beta_{i0}+\beta_{i1}}\right)\frac{I_{i0,j1}}{\sqrt{I_{i0,i0}I_{j1,j1}}} \tag{8}$$

and c_{jj} by substituting j for i in (8).

The real and imaginary parts of (7) then completely describe the transmitted mode j in terms of the input modes.

$$A_{j1} = c_{ij}A_{i0}\cos(\alpha_{i0}-\alpha_{j1}) + c_{jj}A_{j0}\cos(\alpha_{j0}-\alpha_{j1}) \tag{9a}$$

$$\tan\alpha_{j1} = \frac{c_{ij}A_{i0}\sin\alpha_{i0} + c_{jj}A_{j0}\sin\alpha_{j0}}{c_{ij}A_{i0}\cos\alpha_{i0} + c_{jj}A_{j0}\cos\alpha_{j0}}. \tag{9b}$$

Equation (9) plus its counterpart for mode i provide iterative, coupled-mode equations to calculate mode conversion and radiation loss due to a branch taper which is approximated by a large number of small steps. Since terms containing the square of an overlap integral between different modes on opposite sides of the step are neglected, we might expect poorer results for very steep tapers. Note that the phase of the output mode is coupled to the input mode parameters through (9b).

III. Discussion of Results

Using the theory developed in the last section we have studied mode conversion in a planar-dielectric waveguide branch as a function of taper slope and index asymmetry. The model waveguide, adapted from Yajima [2], [3], has dimensions $d_2 = d_4 = 0.8$ μm and indices as shown in Fig. 3. The free-space wavelength is 0.6328 μm and the first- and second-order modes are referred to as i and j, respectively. The geometry of the step model used to approximate the taper was deliberately chosen to reflect the experimental situation, where the lower branch lies flat on the substrate and the upper branch moves upward as the separation between the branches increases. Note that in this case we would expect modes with power primarily in the upper branch to suffer more radiation loss than modes in the lower branch. Computer programs were written to compute the mode wave vectors and electric fields between steps, evaluate the mode-

conversion coefficients, and to perform the iterations describing changes in mode amplitude at each step.

For a branching waveguide with indices as given in Fig. 3 and positive Δn, it was found that mode i propagated into the lower branch, while mode j went into the upper branch. It is mode j then which primarily sees the abrupt steps which form the taper. It was found that about 80 iterations were satisfactory to describe the mode-conversion effects of a waveguide branch within the limitations of computer time. Doubling the number of iterations caused amplitude changes of $\lesssim 5$ percent for mode j and $\lesssim 1$ percent for mode i. These small amplitude changes do make significant changes in estimates of power lost to radiation modes. To compensate for the larger error in A_j, we typically take mode i to be the input mode, and look at the buildup of power in mode j.

Plots of mode electric-field distributions versus increasing branch separation (Fig. 4) showed that initially mode power was equally divided between the branches, but that index asymmetry eventually caused the mode power to shift to one branch. The more asymmetric the branching waveguide, the faster this power shift occurs, as measured by amount of branch separation. This effect is shown in Fig. 5(a). Fig. 5(b) is a plot of c_{ij} and c_{ji} as given by (8) as a function of branch separation for various index asymmetries. We see that for each case the mode-conversion coefficient c_{ij} is large in the region of branch separation where mode power is being transferred from both branches to a single branch. This implies that mode conversion will also occur in this region. Although the branch separation at which the peak in c_{ij} occurs is a function of Δn, the width of this peak is approximately constant. We show in the Appendix that this width is a function of the index of the separating region between the branches. We also see that the coefficients c_{ij} and c_{ji} are related by $c_{ij} \simeq -c_{ji}$, as expected from power-conservation considerations in coupled-mode theory.

We can now be more precise in stating under what conditions the case of separating parallel guides is equivalent to a branching waveguide for the purpose of calculating mode conversion. They will behave in exactly the same manner if the initial branch separation of the separating parallel waveguide is less than or equal to the branch separation at which power transfer begins or the mode-conversion coefficient c_{ij} becomes appreciable. In this case, mode-conversion results will be directly transferrable from a branching-waveguide calculation. For initial branch separations in the region of power transfer, the mode-conversion calculations must be done with the appropriate initial conditions, and we can expect that mode conversion will be reduced. For initial branch separations beyond the region of power transfer there will be no mode conversion. In the calculations which follow we will assume a branching waveguide with zero initial branch separation.

Fig. 5(b) shows that c_{ij} tends to be finite for small branch separation and, for the smaller asymmetries, changes sign as the separation is increased. This effect is a consequence of the fundamentally asymmetric step geometry we have used to represent the experimental situation for a planar branching waveguide. The contribution to c_{ij} from the geometric asymmetry is of opposite sign to the contribution from modal evolution, and is dominant at small branch separation before power transfer takes place. We would expect that for a symmetric geometry, with displacement of both branches at a step, that c_{ij} would be zero at small branch separations and would exhibit no sign change as separation increased. Such a symmetric geometry for separating waveguides is more likely to be realized with channel guides. The initial behavior of c_{ij} does have important consequences on cumulative mode conversion, as will be shown.

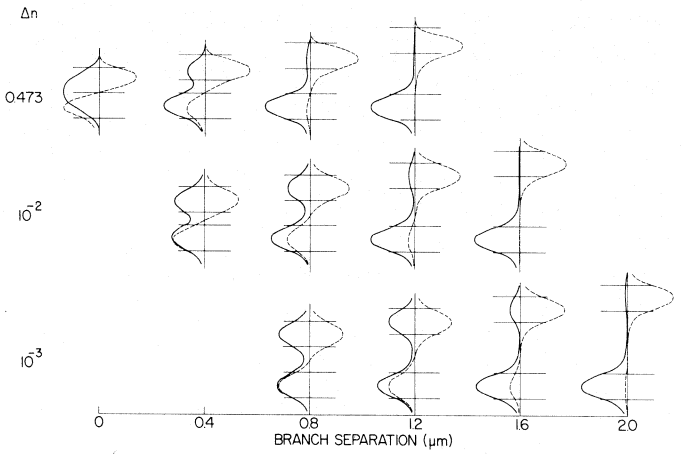

Fig. 4. Plots of adiabatic mode electric-field distributions in model waveguide versus branch separation for index asymmetry Δn of 0.473, 10^{-2}, and 10^{-3}. The solid curve is the first-order mode (i), and the dashed curve is the second-order mode (j). Each mode has unity power.

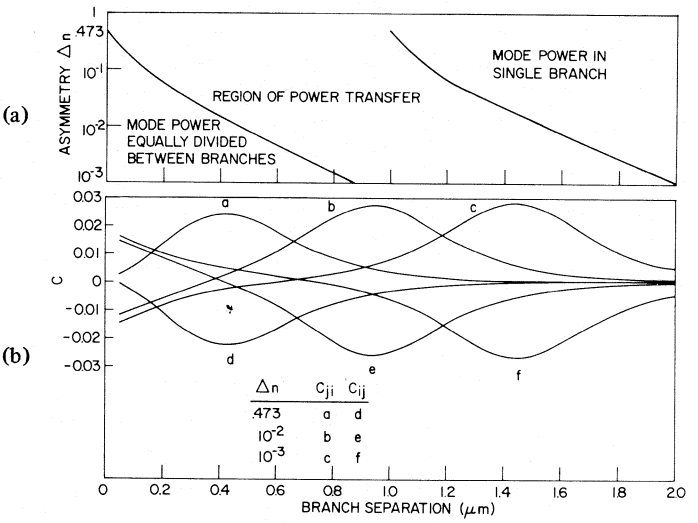

Fig. 5. (a) Branch separations at which power transfers from both branches to one as a function of branching waveguide index asymmetry for the model waveguide. (b) Plots of mode-conversion coefficients versus branch separation for various index asymmetries. The mode-conversion coefficients are large in the region of modal evolution.

The results of the mode-conversion calculations for the branching waveguides described by Fig. 3 with various index asymmetries and taper slopes are shown in Fig. 6. In each case, the input mode powers were 1 and 0 for modes i and j, respectively. The output mode amplitudes at branch separation $d_3 = 2$ μm ($d_3 = 2.4$ μm for the $\Delta n = 10^{-3}$ data) are plotted. Substantial mode conversion to mode j is observed

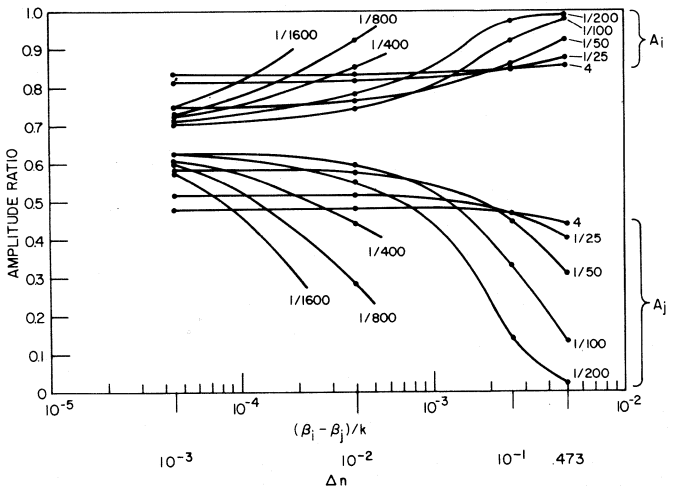

Fig. 6. Output-mode amplitude ratios illustrating mode conversion from mode i to mode j in the model branching waveguide with the indices given by Fig. 3 and $d_2 = d_4 = 0.8$ μm for various taper slopes. The abscissa shows both index asymmetry and difference in mode-effective indices at large branch separation ($\Delta\beta/k$).

in asymmetric branches (Δn large) as the slope increases. In the near-symmetric (Δn small) branches, substantial mode conversion occurs for nearly all slopes. This behavior can be understood by examining (7) when the condition

$$(\beta_{i0} - \beta_{j1})z \simeq 0 \tag{10a}$$

is satisfied over the length of the branch. For a small step $\beta_{j0} \approx \beta_{j1}$ so that we also have

$$(\beta_{j0} - \beta_{j1})z \simeq 0. \tag{10b}$$

Equation (10a) is obeyed for branches with steep slopes and for near-symmetric branches whose modes are nearly degenerate. Equation (7) can then be expressed in real form

$$A_{j1} = c_{ij}A_{i0}\cos(\phi_{i0} - \phi_{j1}) + c_{jj}A_{j0}\cos(\phi_{j0} - \phi_{j1}) \tag{11a}$$

$$0 = c_{ij}A_{i0}\sin(\phi_{i0} - \phi_{j1}) + c_{jj}A_{j0}\sin(\phi_{j0} - \phi_{j1}). \tag{11b}$$

If we assume a phase for mode i, $\phi_{i0} = 0$, and that the step is small enough so that the phase of mode j changes very little across a step, $\phi_{j0} - \phi_{j1} \simeq 0$, then (11) is satisfied by taking $\phi_{j1} = 0$ or π. A distinction can be made by expanding (11b) to give

$$\tan\phi_{j1} = \frac{c_{ij}A_{i0}\sin\phi_{i0} + c_{jj}A_{j0}\sin\phi_{j0}}{c_{ij}A_{i0}\cos\phi_{i0} + c_{jj}A_{j0}\cos\phi_{j0}}. \tag{12}$$

If c_{ij} were always negative, ϕ_{j1} would be locked at π and cumulative mode conversion would occur over the whole length of the taper. If c_{ij} is initially positive and then turns negative (asymmetric step displacement), $\phi_{j1} = 0$ until the denominator of (12) turns negative at

$$c_{ij} = -c_{jj}\frac{A_{j0}}{A_{i0}} \tag{13}$$

after which $\phi_{j1} = \pi$. After $\phi_{j1} = \pi$ cumulative mode conversion occurs.

Various cases of phase behavior are illustrated in Fig. 7. In

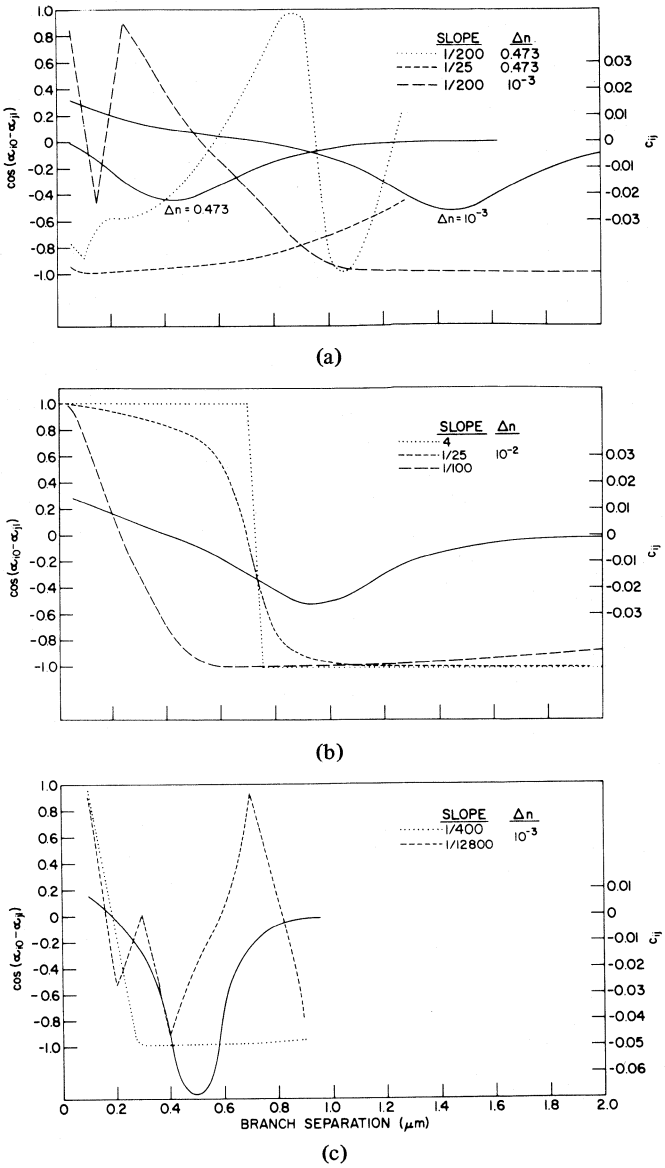

Fig. 7. Plots of the phase term and mode-conversion coefficient for various cases of slope, index asymmetry, and n_3 versus branch separation. (a) and (b): $d_2 = 0.8$ μm, $n_3 = 1.473$. (c): $d_2 = 0.6$ μm, $n_3 = 1.0$. In (b) an increase in slope reduces the range of mode-conversion coefficient over which the phase term has value −1. In (c) the slopes 1/400 and 1/12 800 correspond to converted mode amplitude of 62 and 7 percent, respectively.

Fig. 7(a) the terms c_{ij} and $\cos(\alpha_{i0} - \alpha_{j1})$ are plotted for waveguide branches with conditions of slope and Δn of 1/25, 0.473; 1/200, 0.473; and 1/200, 10^{-3}. For the first and last case the phase term is close to −1 when the overlap integral is large and negative, so that the converted mode amplitude builds up. In the case of large asymmetry and small slope, the phase term rapidly oscillates, and no accumulation of converted mode amplitude is possible. Plots of mode amplitude ratio (A_γ) versus branch separation for these 3 cases are shown in Fig. 8.

Fig. 6 shows that for near-symmetric branches mode conversion increases with increasing taper slope until it reaches a maximum value, after which it decreases. The phase behavior that causes this effect is shown in Fig. 7(b) for $\Delta n = 10^{-2}$. As the taper slope increases beyond 1/100, the phase term reaches

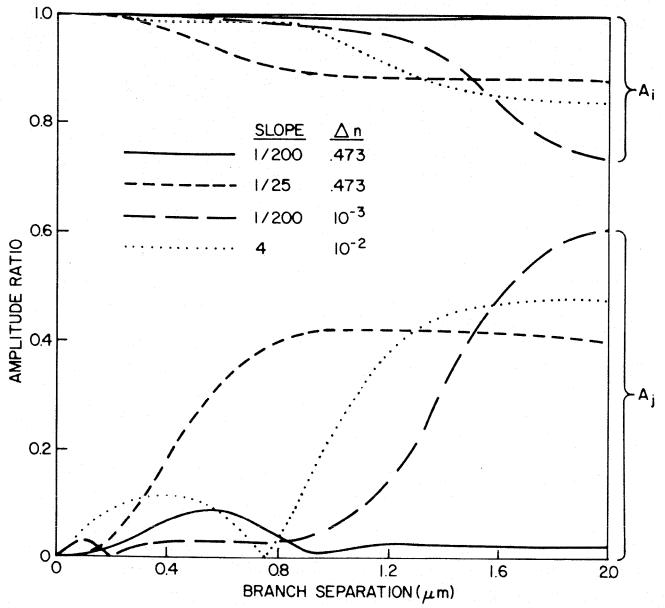

Fig. 8. Mode amplitude ratios versus branch separation for mode conversion from mode i to j in the model branching waveguide.

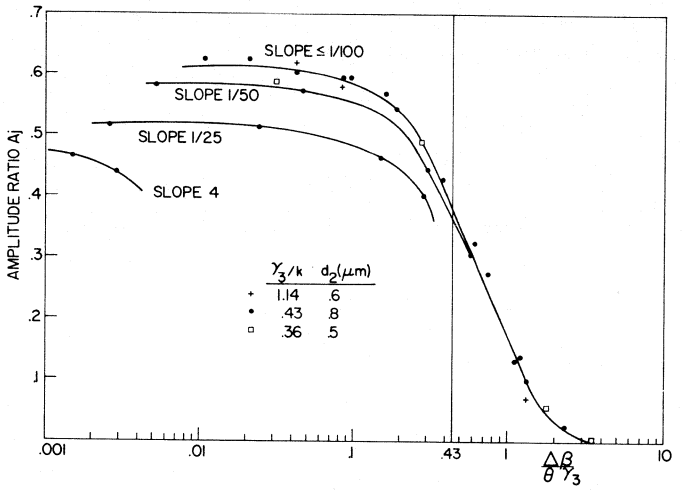

Fig. 9. Converted mode amplitude ratio A_j versus the calculated parameter $\Delta\beta/\theta\gamma_3$, which is indicative of mode-conversion magnitude. For abscissa values >0.43, the separating waveguide acts as a mode splitter; <0.43, as a power divider.

-1 more slowly and there is less cumulative mode conversion. The rate of development of the phase term to the -1 value depends in detail on the slope as defined by (2b) and (9b). The case of slope 4, $\Delta n = 10^{-2}$ in Fig. 8 shows the canceling effect of geometrical asymmetry at small branch separation for an abrupt taper. A physical interpretation is that with increasingly steep tapers the geometric asymmetry overrides the index symmetry due to small Δn, making the branches look asymmetric to the incoming modes. This asymmetry impedes the transfer of power between modes by causing a sign change in c_{ij} at small branch separations. In contrast we would expect a symmetrical step geometry to always show increasing mode conversion as the taper slope increased.

The important point is that for an asymmetrical taper geometry there is an optimum taper slope for maximum mode conversion for a given index asymmetry. This reduced mode conversion is limited by the data for slope 4 in Fig. 6, which is equivalent to an abrupt junction. No further changes were observed when this slope was increased by a factor of 100. We have also calculated mode conversion from mode j to i for the abrupt junction. In this case the mode-conversion coefficients and phase terms are mirror images of the case of i-j so that the converted amplitudes build up identically, except for slightly higher losses of mode j.

We have also calculated mode conversion for the case of thinner branches ($d_2 = d_4 = 0.5$ μm) where each branch can only support a single mode at large separation. These data are included in Fig. 9 and are similar to the data for $d_2 = d_4 = 0.8$ μm. We have assumed throughout this paper that any cumulative power transfer to higher order guided modes is small so that we can ignore any power transfer back from these modes. This assumption is justified by the large propagation-constant mismatch between the two modes of interest and the higher order guided modes, and is supported by the consistency of the data shown in Fig. 9.

An examination of the computer runs shows that the cumulative amount of mode conversion obtained depends critically on the behavior of the phase term $\cos(\alpha_{i0} - \alpha_{j1})$ in the region where c_{ij} is large. If the phase term oscillates rapidly in the region where c_{ij} peaks no cumulative mode conversion will occur and the device will act as a mode splitter; whereas, if the phase term is locked to ± 1 in that region, cumulative mode conversion will result and the device will act as a power divider. Quantitative examples of a branching waveguide acting as a mode splitter and a power divider are shown in Fig. 2. For the mode splitter of Fig. 2(a) (slope 1/200, $\Delta n = 0.473$) the corresponding phase and amplitude buildup is shown in Figs. 7(a) and 8. Mode conversion is essentially zero. The phase-term behavior for the power divider of Fig. 2(b) (slope 1/100, $\Delta n = 10^{-2}$) is shown in Fig. 7(b). This phase relationship between the output-mode amplitudes allows the power divider to operate as if the input mode is simply spatially divided between the branches.

Since negligible power conversion occurs until c_{ij} is appreciable, A_{j0} will remain small until the peak in c_{ij} is encountered. As long as A_{j0} is small the phases of the two modes are locked together by (9b). Thus the position of the peak in c_{ij} versus branch separation is not important to first order; only the behavior of the phase term over the width of the peak where the phase of A_{j0} is not locked is critical. Varying the index of the intermediate layer can cause a large shift in the position of the peak; however, under the conditions of near symmetry (small Δn) and a reasonable taper steepness considerable mode conversion will always occur.[1] This is illustrated in Fig. 7(c) where we show the phase-term behavior for a steep and very shallow slope when $n_3 = 1.0$.

The considerations used in the discussion of (10)–(12) lead us to conclude that as long as

$$(\beta_{i0} - \beta_{j1})\,\Delta z \ll \frac{\pi}{2} \tag{14a}$$

[1] This result is contrary to the initial suggestion by Yajima in [3] that the phase term does not depend on the position of the peak in c_{ij}.

considerable mode conversion will occur and the device will act as a power divider; whereas if

$$(\beta_{i0} - \beta_{j1})\,\Delta z \gg \frac{\pi}{2} \tag{14b}$$

cumulative mode conversion will not occur and the device will act as a mode splitter. Here Δz represents the width of the region where c_{ij} is appreciable. It is thus possible for the width of the peak in c_{ij} to influence the amount of cumulative mode conversion; however, the position of the peak will be unimportant. For a linear taper

$$\Delta z = \frac{\Delta d_3}{\theta} \tag{15}$$

where Δd_3 is the width of the peak in c_{ij} in units of branch separation (measured at the half-maximum points), and θ is the taper slope for the separating guides. Clearly, only the slope of the taper in the region of appreciable c_{ij} is important. It is also true, as is shown in the Appendix, that in the region of appreciable c_{ij} (where the coupling is caused by modal evolution, not geometric asymmetry)

$$\beta_{i0} - \beta_{j1} \approx \sqrt{2}\,\Delta\beta \tag{16}$$

where $\Delta\beta$ is the difference in propagation constant for infinite branch separation. In the Appendix we use an approximate coupled-mode formalism to show that the separation of the half-maximum points in c_{ij} versus d_3 is given by

$$\Delta d_3 \approx \frac{2.6}{\gamma_3}. \tag{17}$$

Here $\gamma_3 \simeq (\beta_0^2 - n_3^2k^2)^{1/2}$ is the decay constant of the field in the separating region, and β_0 is the average propagation constant for a large guide separation. Equation (17) indicates that Δd_3 reaches a minimum far from cutoff as β_j/k, $\beta_i/k \to n_2$. Near cutoff, if $n_3 \geqslant n_1, n_5$; β_i/k, $\beta_j/k \to n_3$, and Δd_3 can increase. This would tend to impede mode conversion in some circumstances, but here conclusions must be drawn with caution since the theory used in the Appendix breaks down for strong coupling between arms and significant coupling to radiation modes.

We can now describe the transition boundary between a mode splitter and a power divider approximately as

$$\frac{\Delta\beta}{\theta\sqrt{\beta_0^2 - n_3^2k^2}} \gtrless 0.43. \tag{18}$$

This equation can be used to predict the behavior of separating waveguides as well as a branching waveguide whenever the separating guides start out close enough together such that the normal modes of the five-layer structure contain appreciable power in both guiding regions at the starting separation. If this is the case as the guides separate they will pass through a region of appreciable c_{ij}. If the separating guides are initially further apart it will be impossible to distinguish between behavior as a mode splitter or behavior as a power divider since the normal modes will contain power only in a single guiding region. In Fig. 9 we plot the converted amplitude ratio A_j versus the quantity $\Delta\beta/\theta\gamma_3$ for all the cases previously discussed. We see that (18) is well obeyed with all the data lying near a single curve, except for those cases with slopes $\geqslant 1/50$ where the geometric asymmetry predominates.

IV. Summary

Paying careful attention to the phase relationship between the normal modes of a five-layer structure we have developed a theory of power transfer between two modes to use with the step transition model of Marcuse. This has allowed us to investigate branching and separating dielectric waveguides and to investigate in detail the transition region between the operation of these structures as mode splitters and as power dividers. We have developed approximate expressions which should be useful to the designers of integrated optical circuits. The amount of mode conversion can be described by a function of $\Delta\beta/\theta\gamma_3$.

We find that whenever the branches are symmetric ($\Delta\beta$ is small) and the taper slope θ is large the structure will act as a power divider; however, whenever the branches are asymmetric ($\Delta\beta$ is large) and the taper angle θ is small the structure will act as a mode splitter. The transition region is described by (18). It is expected that steeper tapers will evidence more loss to radiation modes so that a low-loss mode splitter will be easier to fabricate than a low-loss power divider. An evanescent coupler of the type envisioned for use in electro-optical amplitude modulators contains a region of separating waveguides which needs to act as a power divider. Unless the two separating guides are very similar a steep taper will be needed which will introduce losses into the device.

Appendix

In this section we will change representation to a more conventional coupled-mode theory appropriate for parallel waveguides with weak coupling to obtain approximation expressions for c_{ij} [5], [6]. The two coupled modes will now be considered to be the modes of each guiding layer taken separately, ϕ_a and ϕ_b, with mode amplitudes a and b and propagation constants β_a and β_b. With this representation the normal modes of the five-layer structure can be taken as linear combinations of these modes.

$$\psi_i = a\phi_a + b\phi_b \tag{A-1a}$$

$$\psi_j = b\phi_a - a\phi_b \tag{A-1b}$$

where $a^2 + b^2 = 1$; $\int_{-\infty}^{\infty} \phi_a\phi_a\,dx = 1$; $\int_{-\infty}^{\infty} \phi_b\phi_b\,dx = 1$; and b/a is constant as a function of z for a given guide separation. The ratio of b/a will depend upon guide separation d_3 (i.e., $b/a = f(d_3)$) approaching zero for large separation and one for small separation. If we consider a taper step there will be uncoupled modes ψ_{i0}, ψ_{j0} on one side with branch separation d_{30} and uncoupled modes ψ_{i1}, ψ_{j1} on the other with branch separation d_{31}. From the definition of c_{ij}:

$$c_{ij} \approx \int_{-\infty}^{\infty} \psi_{i0}\psi_{j1}\,dx \tag{A-2a}$$

$$= a_0 b_1 \int_{-\infty}^{\infty} \phi_{a0}\phi_{a1}\,dx - b_0 a_1 \int_{-\infty}^{\infty} \phi_{b0}\phi_{b1}\,dx + b_0 b_1 \int_{-\infty}^{\infty} \phi_{b0}\phi_{a1}\,dx - a_0 a_1 \int_{-\infty}^{\infty} \phi_{a0}\phi_{b1}\,dx. \tag{A-2b}$$

For a small symmetric step when the guides are far apart (weak coupling) we can approximate

$$\int_{-\infty}^{\infty} \phi_{a0}\phi_{a1}\,dx = 1; \quad \int_{-\infty}^{\infty} \phi_{b0}\phi_{a1}\,dx = 0$$

$$\int_{-\infty}^{\infty} \phi_{b0}\phi_{b1}\,dx = 1; \quad \int_{-\infty}^{\infty} \phi_{a0}\phi_{b1}\,dx = 0. \tag{A-3}$$

Using the above approximations

$$c_{ij} \approx a_0 b_1 - b_0 a_1 \tag{A-4a}$$

$$= a_0 a_1 \left(f(d_{31}) - f(d_{30})\right) \tag{A-4b}$$

$$= a_0 a_1 \frac{\partial f(d_3)}{\partial d_3}\delta d \tag{A-4c}$$

$$\approx \frac{1}{1 + (f(d_3))^2}\frac{\partial f(d_3)}{\partial d_3}\delta d \tag{A-4d}$$

where $\delta d = d_{31} - d_{30}$.

The conventional coupled-mode theory tells us that

$$b/a = -i\left[\frac{-(\beta_a - \beta_b) + \sqrt{(\beta_a - \beta_b)^2 + 4KK^*}}{2K}\right] \tag{A-5}$$

assuming $\beta_a - \beta_b$ is positive where K is the coupling coefficient. For the case of two parallel guides coupled-mode theory can be used to show that [7]

$$K = -iF\exp(-d_3\gamma_3) \tag{A-6}$$

where F is real and positive, $\gamma_3 \simeq (\beta_0^2 - n_3^2k^2)^{1/2}$, and $\beta_0 = (\beta_a + \beta_b)/2$. Then we can write expressions for $f(d_3)$ and its derivative by defining $\Delta\beta = \beta_a - \beta_b$ and $|K| = F\exp(-\gamma_3 d_3)$:

$$f(d_3) = \frac{-\Delta\beta + (\Delta\beta^2 + 4|K|^2)^{1/2}}{2|K|} \tag{A-7a}$$

$$\frac{\partial f(d_3)}{\partial d_3} = \frac{\gamma_3\Delta\beta}{2|K|}\left[\frac{\Delta\beta}{(\Delta\beta^2 + 4|K|^2)^{1/2}} - 1\right]. \tag{A-7b}$$

Substituting (A-7) into (A-4) then gives

$$c_{ij} \approx \frac{-\gamma_3\delta d\,|K|\Delta\beta}{(\Delta\beta^2 + 4|K|^2)}. \tag{A-8}$$

This function has a minimum value of $-\gamma_3\delta d/4$ for $|K| = 0.5\,\Delta\beta$ and has the half-minimum value $-\gamma_3\delta d/8$ for $|K| = 0.138\,\Delta\beta$ or $1.9\,\Delta\beta$. The minimum in c_{ij} will thus occur at

$$d_0 = -\frac{1}{\gamma_3}\ln\left(\frac{\Delta\beta}{2F}\right) \tag{A-9}$$

and the half width for c_{ij} will be

$$\Delta d_3 = \frac{\ln 1.9 - \ln 0.138}{\gamma_3} = \frac{2.6}{\gamma_3}. \tag{A-10}$$

Coupled-mode theory also tells us that

$$\beta_i - \beta_j = (\Delta\beta^2 + 4|K|^2)^{1/2} \tag{A-11a}$$

so that where c_{ij} is a minimum

$$\beta_i - \beta_j = \sqrt{2}\,\Delta\beta. \tag{A-11b}$$

This coupled-mode theory can only be rigorously defended when the peak in c_{ij} occurs in a region where K is small, i.e., for cases of small $\Delta\beta$. However, the exact computer-calculated results described in the main text are well described by the results of this approximate approach.

Acknowledgment

The authors wish to thank T. Giallorenzi and H. Yajima for useful discussions. They also wish to thank J. Weiss for programming advice.

References

[1] H. Yajima, "Dielectric thin film optical branching waveguide," *Appl. Phys. Lett.*, vol. 22, pp. 647–649, 1973.
[2] —, "Dielectric optical branching waveguide," to be published.
[3] —, "Theory and applications of dielectric branching waveguides," in *Proc. Symp. Optical and Acoustical Micro-Electronics* (New York, Apr. 1974).
[4] D. Marcuse, "Radiation losses of tapered dielectric slab waveguides," *Bell Syst. Tech. J.*, vol. 49, pp. 273–290, 1970.
[5] S. E. Miller, "Coupled wave theory and waveguide applications," *Bell Syst. Tech. J.*, vol. 33, pp. 661–719, 1954.
[6] A. Yariv, "Coupled-mode theory for guided-wave optics," *IEEE J. Quantum Electron.*, vol. QE-9, pp. 919–933, Sept. 1973.
[7] N. S. Kapany and J. J. Burke, *Optical Waveguides.* New York: Academic, 1972.

Bond-Orbital Model for Second-Order Susceptibilities

MICHAEL M. CHOY, SALIM CIRACI, AND ROBERT L. BYER

Abstract—**The bond-orbital model (BOM) for tetrahedral compounds is used self-consistently to calculate the second-order susceptibility. No adjustable parameters are used and agreement with experiment is good. The origin of the nonlinearity arises from a charge transfer as a result of the asymmetric polar energy between the anion and the cation. The model correctly predicts an optimum polarity to maximize second-order susceptibilities.**

I. Introduction

THE understanding of the origin of the nonlinear optical susceptibilities has been the subject of many investigations. This understanding is important in material assessment and prediction of new material characteristics in nonlinear optical devices such as harmonic generators, mixers, and parametric oscillators [1], [2]. In a more formal approach, quantum mechanical expressions are derived from perturbation expansion involving complex sums of matrix elements and energy denominators [3]-[5]. These fundamental expressions, even when simplified through the use of octupole moment of the ground-state charge distribution [6], or by employing ground-state wave functions [7], are still formidable to use in quantitative predictions. Exact wave functions in solids are often not known to high accuracy and the complete band structure is also required. Other complications from contributions to the nonlinearity from different points in the Brillouin zone can also arise [8], [9]. Another approach is to use simple phenomenological models such as the anharmonic oscillator model [10] and Miller's rule [11]. Included in this category are the universal semiconductor model [12], [13], the bond-charge model [14], the charge-transfer model [15], and the molecular-orbital model [16]. The latter three models all draw heavily from the results of Phillip's dielectric theory [17], [18].

In this paper we use an approach based on Harrison's bond-orbital model (BOM) [19], [20]. This is a more predictive model and only appeals to essentially two input factors, the dielectric constant and the $E_{2A}(X_4 - X_1)$ transition energy to calculate the model parameters. The model predicts useful properties related to valence electrons such as cohesive energy, band structure [21], etc. Using BOM parameters, we calculate the second-order susceptibility in the optical-transparency region of a crystal. The analysis clearly displays the physical origin of the nonlinearity. Perhaps more importantly, by expressing the nonlinearity in terms of the fundamental material parameters of polarity and the bond length, salient characteristics desirable for high optical nonlinearities are distinctly revealed.

Manuscript received August 6, 1974. This work was supported by ARPA Materials Science Division and the Honeywell Research Center.

M. M. Choy and R. L. Byer are with the Department of Applied Physics, Stanford University, Stanford, Calif.

S. Ciraci is with the Middle East Technical University, Ankara, Turkey. He is on leave at Stanford University, Stanford, Calif.

II. Bond-Orbital Model

In this section, we outline the BOM so that we can discuss its extension to the calculation of the second-order susceptibility. For a more complete discussion of the model and the implications of the approximations involved refer to the original papers [19], [20].

The model is based on a tight-binding approximation of sp^3 hybrid orbitals for tetrahedral compounds. Denoting an sp^3 hybrid orbital on an anion (cation) by $|h^a>$ ($|h^c>$), a bonding orbital is constructed from a linear combination of nearest neighbor hybrids on the anion and its adjacent cation directed along the same bond,

$$|b> = u_a|h^a> + u_c|h^c>. \tag{1}$$

The minimization of the expectation value of the Hamiltonian by a standard variation on the u_a and u_c results in a (2 X 2) secular equation. The solution of the equations gives the eigenvalue and the eigenvectors. They are

$$\epsilon_{b,a} = V_2 <h^c|h^a> \mp \sqrt{V_2^2 + V_3^2} \tag{2}$$

and

$$u_a = \sqrt{\frac{1+\alpha_p}{2}}$$

$$u_c = \sqrt{\frac{1-\alpha_p}{2}} \tag{3}$$

where the polarity is defined by Harrison [19], [20] as

$$\alpha_p = \frac{V_3}{(V_2^2 + V_3^2)^{1/2}}. \tag{4}$$

Here V_2 and V_3 are the energy parameters defined as

$$V_2 = -\frac{<h^c|\mathcal{H}|h^a>}{1 - |<h^c|h^a>|^2} \tag{5}$$

for the covalent energy where $<h^c|\mathcal{H}|h^a>$ corresponds to hopping between an anion hybrid and a cation hybrid along the same bond,

$$V_3 = \frac{[<h^c|\mathcal{H}|h^c> - <h^a|\mathcal{H}|h^a>]}{2(1 - |<h^c|h^a>|^2)^{1/2}} \tag{6}$$

for the polar energy where $<h^c|\mathcal{H}|h^c>$ and $<h^a|\mathcal{H}|h^a>$

denote the coulomb integrals at the cation site and the anion site, respectively. In addition, there is one more energy parameter $V_1^{a,(c)}$, which is defined as a matrix element of Hamiltonian between adjacent anion (cation) hybrids. This is related physically to the atomic *s-p* splitting and does not come into play in most optical properties.

The dielectric constant, which is the parameter of interest in optical properties, is calculated by considering an isolated bond dipole with an applied electric field. The field perturbation is treated by adding to the polar energy V_3 the potential energy of the bond dipole in the electric field. Then in the ground-state wave-function approximation, calculation of the induced polarization by a change of polarity α_p through a change of the polar energy V_3 gives the dielectric constant

$$\epsilon_0 = 1 + \frac{N\pi\gamma^2 (ed)^2 V_2^2}{3(V_2^2 + V_3^2)^{3/2}} \tag{7}$$

where N is the density of electrons, d is the bond length, and γ is a parameter defined in the BOM formulation relating microscopic dipole moments to macroscopic linear susceptibilities and is taken to be constant along a row of the periodic table except for correction for carbon row atoms.

To determine the energy parameters Harrison and Ciraci [20] appeal to experimental parameters. The principal optical absorption peak E_{2A} is identified with the bonding and antibonding gap

$$\epsilon_a - \epsilon_b = 2\sqrt{V_2^2 + V_3^2}.$$

This identification has been shown to be consistent with experiments.

First, the E_{2A} gap of the group IV elemental compounds gives V_2 directly for each row of the periodic table, since $V_3 = 0$ in elemental compounds. The geometric mean is taken for compounds involving two rows. Then using (7) the dielectric constant gives γ for each row. A value for γ of 1.08 is found for diamond and 1.2 for silicon. When row three is reached, there are contributions from the polarizable d core electrons as noted by Phillips [17]. This is taken into account by introducing a correction factor θ in addition to γ. γ is taken at the silicon value and a value of $\theta = 1.18$ is obtained for germanium and $\theta = 1.41$ for the tin row. With these values of V_2 and γ, V_3 for any binary compound is derived from its dielectric constant using (7). This completes the summary of the BOM as originally stated by Harrison [19].

III. Calculation of $\chi^{(2)}$

The second-order susceptibility is defined by expanding the macroscopic polarization in a power series in the field

$$\boldsymbol{P}(\boldsymbol{E}) = \chi^{(1)}\boldsymbol{E} + \chi^{(2)}:\boldsymbol{EE} + \cdots \tag{8}$$

where $\chi^{(1)}$ and $\chi^{(2)}$ are the field-independent susceptibilities. In the independent bond formulation these macroscopic susceptibilities are related to their corresponding microscopic bond polarizabilities through geometrical factors as [21], [22]

$$\chi_{IJ}^{(1)} = \frac{1}{V}\sum_{s,i,j} a_{Ii}^{(s)} a_{Jj}^{(s)} \alpha_{ij} \tag{9}$$

$$\chi_{IJK}^{(2)} = \frac{1}{V}\sum_{s,i,j} a_{Ii}^{(s)} a_{Jj}^{(s)} a_{Kk}^{(s)} \beta_{ijk} \tag{10}$$

where a_{Ii} are the direction cosines between the macroscopic crystal axis I and the bond axis frame i. The index s identifies the different bonds in the periodic lattice structural unit whose volume is V. To apply the BOM, we confine ourselves to sp^3-bonded tetrahedral compounds with the zinc blende and wurtzite structures. In the former case, with crystal class point group $\bar{4}3$ m, (9) and (10) reduce to

$$\chi_{ii}^{(1)} = \frac{4n}{3}(\alpha_\parallel + 2\alpha_\perp) = \frac{4n}{3}\alpha_\parallel(1 + 2\kappa) \tag{11}$$

$$\chi_{14}^{(2)} = \frac{4n}{3\sqrt{3}}(\beta_\parallel - 3\beta_\perp) \tag{12}$$

where $\kappa = \alpha_\perp/\alpha_\parallel$ and $\alpha_\parallel$ and $\alpha_\perp$ are the parallel and perpendicular components of the bond polarizability.

Here $n = 3\sqrt{3}/16\, d^3$ is the number of tetrahedral unit cells per unit volume. In this case $\chi^{(1)}$ is a scalar, and $\chi_{14}^{(2)}$ is the only nonvanishing tensor component in Voigts notation. $E_\parallel$ is along the bond axis (111) and with axially symmetric $C_{\infty v}$ bonds, the independent nonvanishing components are $\alpha_\parallel = \alpha_{zz}$, $\alpha_\perp = \alpha_{xx} = \alpha_{yy}$, and $\beta_\parallel = \beta_{zzz}$, $\beta_\perp = \beta_{xzx} = \beta_{yzy}$. For the case of wurtzite structure the two inequivalent tetrahedra can be obtained from standard zinc-blende orientation by simple rotational matrices, the result is [23]

$$-\chi_{31}^{(2)} = -\chi_{15}^{(2)} = \chi_{33}^{(2)} = \frac{2}{\sqrt{3}}\chi_{14}^{(2)}.$$

It can be shown from an abinitio calculation that $\beta_\perp \ll \beta_\parallel$ [24]. In a bond-charge approach, $\beta_\perp = 0$ to first order [25]. Accordingly, we neglect $\beta_\perp$ relative to $\beta_\parallel$ in our formulation.

To calculate $\beta_\parallel$ we need to determine the variation of the linear polarizability α with an electric field. Physically, we expect a redistribution of charge density in the presence of the field. This manifests itself as an induced dipole as a result of an additional charge transfer. In the context of the BOM there is a change in the bond polarity α_p through a change in the bond-polar energy V_3. Harrison defines an effective charge on an anion (in units of $-e$) as

$$Z^* = 4\alpha_p - \Delta Z \tag{13}$$

where ΔZ is half of the nominal valence difference. Then the additional charge incurred by the applied field on a per-bond basis is

$$\Delta Z^* = \frac{\partial \alpha_p}{\partial V_3}\Delta V_3 = \frac{V_2^2}{(V_3^2 + V_2^2)^{3/2}}\Delta V_3 \tag{14}$$

where the main contribution is from the change in polar energy V_3. The covalent energy V_2 is constant since the bond length remains fairly undistorted. This is valid in the optical-transparency region above the phonon-lattice resonance frequencies, where the lattice and the bonds stay relatively stationary compared to the motion of the electronic-charge cloud. Here we have to stay below the interband electronic absorption, as the assumption of a bonding state of the hybrid orbitals implies that we are dealing with valence electrons

only. In the transparency region the optical response is fairly insensitive to frequency and hence our dispersionless approach should be adequate.

In the formulation of the BOM, when the macroscopic dielectric constant is used to calculate the microscopic bond parameters, the effects of charge-distribution scaling and the bond anisotropy are automatically included in the parameter γ. If we let γ^* be the charge-distribution scaling and $\kappa = \alpha_\parallel/\alpha_\perp$ be the anisotropy, then as in the derivation in BOM, the inclusion of the dipole potential energy in an electric field as a change in the polar energy gives in terms of γ^*

$$\alpha_\parallel = \frac{\gamma^{*2}\,(ed)^2\,V_2^2}{2(V_2^2 + V_3^2)^{3/2}}. \tag{15}$$

Putting this into (11) and comparing the result with (7) we find that $\gamma^2 = \gamma^{*2}(1 + 2\kappa)$, where $\epsilon = 1 + 4\pi\chi^{(1)}$ has been employed. There is no easy analytical calculation for the bond anisotropy. By simple extrapolation on values obtained from Kerr constants on diatomic molecules [26], we estimate $\kappa \approx 0.5$. Essentially the same estimate was employed previously [16]. With this value for the anisotropy factor and the BOM value of 1.2 for γ, γ^* is found to be 0.85.

To introduce the explicit field dependence we note that the induced bond dipole is

$$\Delta p = \gamma^* ed\,\Delta Z^* = \alpha_\parallel E_\parallel. \tag{16}$$

As explained earlier an electric field induces an additional charge transfer resulting in a change in the polar energy V_3. The second-order polarizability can be related to its linear counterpart by $\alpha_\parallel(E_\parallel) = \alpha_\parallel + \beta_\parallel E_\parallel + \cdots = \alpha_\parallel + \Delta\alpha_\parallel + \cdots$. Now $\Delta\alpha_\parallel = \beta_\parallel E_\parallel$ can be calculated from (15) through a change in polar energy ΔV_3. Elimination of ΔV_3 through (14) and (16) in terms of $E_\parallel$ gives

$$\beta_\parallel = \frac{3\alpha_p}{ed(1 - \alpha_p)^2}\,\alpha_\parallel^2. \tag{17}$$

To convert to experimental macroscopic quantities, (11) and (12) give

$$\chi_{14}^{(2)} = \frac{4d^2\,\alpha_p}{e\gamma^*(2\kappa + 1)^2\,(1 - \alpha_p^2)}\,|\chi^{(1)}|^2 \tag{18}$$

where the tetrahedral cell density ($n = 3\sqrt{3}/16d^3$) has been used. Since α_p can be calculated from the linear dielectric constant in BOM theory, (18) shows that $\chi^{(2)}$ can be estimated essentially from just the knowledge of the linear susceptibility alone. This is an important point. The independent bond formulation is only approximate in the sense that correlation effects between neighboring bonds do give rise to local-field corrections which are not subject to easy deductive analysis. By appealing to the macroscopic linear susceptibility as an input parameter, most of these local-field effects are accounted for in the BOM model.

To demonstrate the dependence of $\chi^{(2)}$ on polarity and to display some underlying physics, we transform (18) by casting $\chi^{(1)}$ in terms of polarity with the help of (7). Using the relation [20] $V_2 \propto 1/d^2$ we obtain

$$\chi_{14}^{(2)} \cong \text{constant}\;\alpha_p(1 - \alpha_p^2)^2\,d^4 \tag{19}$$

where the constant contains γ, and is constant for one row in the periodic table.

The dependence of $\chi^{(2)}$ on polarity is shown in Fig. 1, where $\chi_{14}^{(2)}/d^4$ is plotted against α_p. The upper boundary corresponds to the fifth row, and the lower one, the third row. Because of differences in geometric factors, we have only included the case of zinc blende. Note the interesting maximum at $\alpha_p \approx 0.44$, corresponding to an ionicity $f_i = 0.28$ in Phillip's model [$f_i = 1 - (1 - \alpha_p^2)^{3/2}$]. Tang [15] and Levine [14] have predicted an optimum value of $f_i \approx 0.17$. However, available experimental data seem to show a peak at around $\alpha_p = 0.45 (f_i \cong 0.3)$ in better agreement with our results. The physics of this maximum warrants some comment. In the complete polarity limit of $\alpha_p = 1$, i.e., full ionicity, all excess valence electrons from the cation are transferred to the anion. The anion in turn binds these electrons fairly tightly in its locality, resulting in a big forbidden energy gap characteristic of all ionic compounds. Actually, it can be shown that the energy gap of tetrahedral binary compounds scales linearly with ΔZ [18b]. Thus there is no more charge transfer ($\Delta Z^* \propto V_3^{-3}$) to respond to any applied field and hence the vanishing of $\chi^{(2)}$. In the covalent limit of $\alpha_p = 0$, we approach the transition of zinc blende into the elemental diamond structure and the center of inversion symmetry completely cancels all even order of nonlinearities. In a sense, the system overcompensates itself because the gain in the covalent "bond charge" is completely cancelled by the perfectly symmetric lattice environment. A minor word of caution seems to be appropriate here, since we must remember that in actual practice we have to stay within $f_i < 0.78$ for tetrahedral coordination. Any higher ionicity results in rock-salt structure, a hexacoordination typical of most ionic compounds.

To further test the accuracy of our analysis we choose materials of roughly equal polarity, i.e., ΔZ = constant, and plot $\log_{10}[\chi_{\text{expt}}^{(2)}\,10^7]$ against $\log_{10}[d]$ in Fig. 2. Lines of slope 4 are drawn and agreement is good with (18).

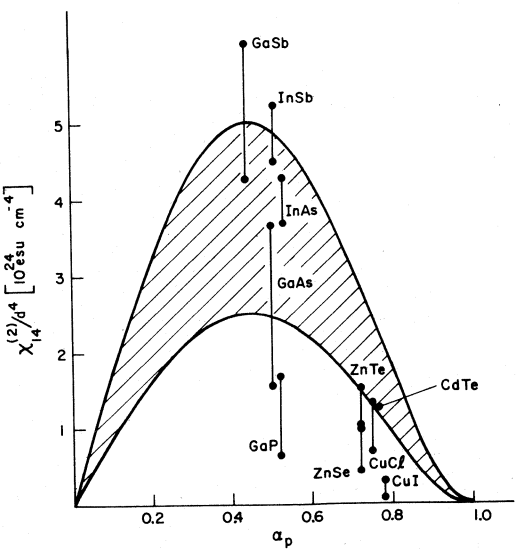

Fig. 1. The scaling of $\chi_{14}^{(2)}/d^4$ with α_p, the polarity. The upper boundary corresponds to materials from the fifth row and the lower one from the third row.

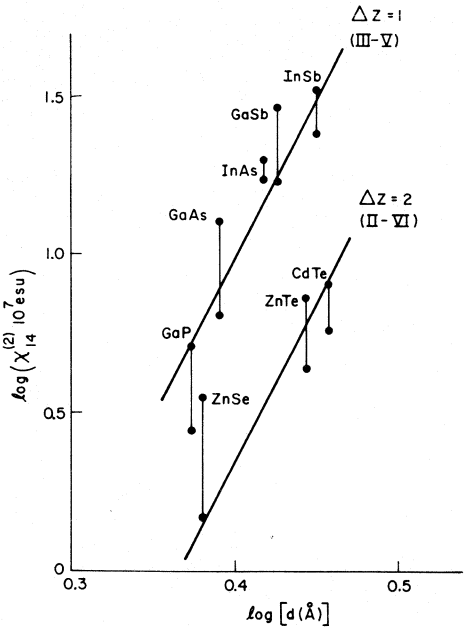

Fig. 2. The dependence of $\chi^{(2)}_{expt}$ on bond length d for materials of roughly constant polarity.

Thus, for large second-order nonlinearities, it is desirable to have a covalency high enough (α_p around 0.44) to give considerable polarizability from charge transfer but low enough such that inversion symmetry is not a detriment. We also want long bond lengths, which, from empirical evidence, means a high atomic number. As high covalency means proximity to group IV, the previous two criteria could be summarized in the context of the periodic table by saying that for high $\chi^{(2)}_{14}$ we want materials with small ΔZ and high atomic number.

These criteria are well borne out by experimental evidence. The III-V compounds are in general more nonlinear than the II-V, and among the III-V themselves the more metallic elements, InSb and InAs, which are from the fifth rows and fifth and fourth rows, respectively, are more nonlinear than GaAs and GaP, being compounds from the fourth rows and fourth and third rows. In Fig. 3 we plotted $\chi^{(2)}_{14}$ against the average quantum number $\bar{n}$ introduced first by Mooser and Pearson [27], verifying the above arguments.

However, for any device applications employing the second-order nonlinearity, the parameter of interest is the parametric gain coefficient [2] defined by

$$\Gamma^2 = \frac{9.10^8\,\omega_1\omega_2\,|\chi^{(2)}|^2 I_3}{8c^3 n_1 n_2 n_3}$$

where I_3 is the pump intensity and n_i are the refractive indices at ω_i.

From the device standpoint, besides the magnitude of $\chi^{(2)}$, there are also additional transparency factors in the frequency dependence of the gain coefficient. As one goes towards higher atomic numbers one loses ground in the transparency range as determined by the bandgap cutoff frequency. Experimentally, a material is chosen with the smallest bandgap consistent with transparency in the wavelength region of interest, as pointed out by Levine [14]. If half the bandgap frequency is taken for both ω_1 and ω_2 to avoid two-photon absorption,

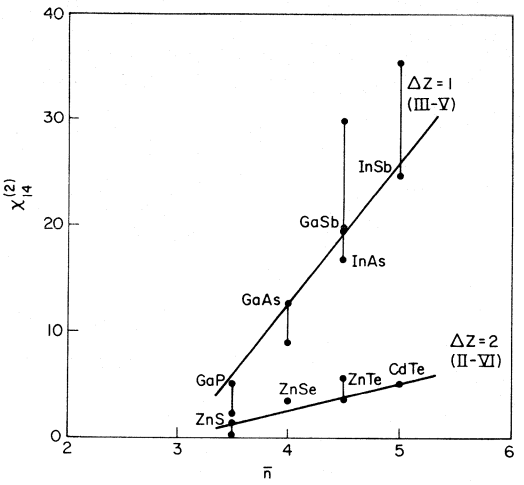

Fig. 3. A plot of $\chi^{(2)}_{14}$ versus $\bar{n}$, the average quantum number, showing the dependence within a vertical family in the periodic table.

it turns out that in some cases of high atomic numbers, e.g., InAb and InAs, the increase in $\chi^{(2)}$ is largely offset by frequency factors in the gain expression due to the narrow bandgap.

Another parameter which has proven to be very useful as a scale for nonlinearity is the Miller's delta, Δ_{ijk}, which is defined by

$$\frac{\chi^{2\omega}_{ijk}}{2} = \Delta_{ijk}\chi^{2\omega}_{ii}\,\chi^{\omega}_{jj}\,\chi^{\omega}_{kk}.$$

In the context of our model Miller's delta can be obtained by transforming (18) through use of $\chi^{(1)}$ expressed in polarity α_p and bond length d. We find that $\Delta_{ijk} \propto \alpha_p d/(1-\alpha_p)^{5/2}$. Thus we see that for materials of the same average quantum number $\bar{n}$, where the bond length is essentially constant and for materials of the same vertical family, i.e., of constant polarity, the Miller's delta should be constant. Essentially, a similar conclusion is reached by Tang and Flytzanis [15], though they employed slightly different parameters, namely the normalized-valence difference and the atomic-radii difference. In Miller's formulation, which is essentially an anharmonic oscillator model, Miller's delta is found to be a function of the asymmetric potential. Because polarity (charge transfer) is a direct result of the asymmetry between the cation and anion, and bond length also affects the potential, the dependence of Miller's delta on the previously given BOM parameters is not surprising.

The main results and parameters used are summarized in Table I. We have chosen the most recent data or that which we believe to be the most reliable. Correlation with experimental values is in general very good. It should be observed that there are two general classes of compounds where the relative discrepancy warrants some discussion. They are the narrow-bandgap materials; for example, InSb, InAs, GaSb, and the copper compounds.

As pointed out in the original formulation of BOM [20], the use of the E_{2A} peak for the bonding and antibonding gap works especially well for the large-bandgap materials. For narrow-bandgap materials, the minimum optical gap could be

TABLE I
COMPARISON BETWEEN THEORETICAL $\chi_{14}^{(2)}$ (CALC) AND EXPERIMENTAL $\chi_{14}^{(2)}$ (EXPT) TOGETHER WITH THE RELEVANT BOM PARAMETERS IN ZINC-BLENDE AND WURTZITE STRUCTURES

Compound	Bond length d [Å]	α_p	$\chi^{(1)}$	$\chi_{14}^{(2)}$(cal) 10^{-7} esu	$\chi_{14}^{(2)}$(expt) 10^{-7} esu
GaP	2.36	0.52	0.65	4.1	5.2 a
GaAs	2.44	0.50	0.79	6.1	6.4 b
GaSb	2.65	0.44	1.07	10.8	20.0 c
InP	2.54	0.58	0.68	6.5	8.0 d
InAs	2.61	0.53	0.90	10.0	17.4 c
InSb	2.80	0.51	1.17	18.3	24.8 c
ZnTe	2.64	0.72	0.50	6.4	7.3 e
ZnSe	2.45	0.72	0.39	3.4	3.7 f
CdTe	2.80	0.76	0.49	8.4	8.0 e
CuCl	2.34	0.75	0.22	1.1	0.2 g
CuBr	2.49	0.79	0.27	2.34	0.4 g
CuI	2.62	0.78	0.36	4.4	0.4 g
SiC	1.88	0.39	0.45	0.93	0.78 h
ZnO	1.98	0.70	0.24	0.88	0.33 i
Zns	2.34	0.73	0.33	2.64	1.8 f
CdS	2.53	0.77	0.33	3.74	2.1 f
CdSe	2.63	0.77	0.38	5.35	3.8 j

[a] J. J. Wynne and N. Bloembergen, "Measurement of the lowest order nonlinear susceptibility in III-V semiconductors by second harmonic generation with a CO_2 laser," *Phys. Rev.*, vol. 188, pp. 1211–1220, 1969.

[b] J. H. McFee, G. D. Boyd, and P. H. Schmidt, "Redetermination of the nonlinear optical coefficients of Te and GaAs by comparison with Ag_3SbS_3," *Appl. Phys. Lett.*, vol. 17, pp. 57–59, 1970.

[c] R. K. Chang, J. Ducuing, and N. Bloembergen, "Dispersion of the optical nonlinearity in semiconductors," *Phys. Rev. Lett.*, vol. 15, pp. 415–418, 1965.

[d] R. Braunstein and N. Ockman, "Interactions of coherent optical radiation with solids," Office of Naval Research, Department of the Navy, Washington, D.C., Contract NONR-4128100, ARPA Order 306-62, Final Rep., Aug. 1964.

[e] R. A. Soref and H. W. Moos, "Optical second harmonic generation in ZnS–CdS and CdS–CdSe alloys," *J. Appl. Phys.*, vol. 35, pp. 2152–2158, 1964.

[f] C. K. N. Patel, "Optical harmonic generation in the infrared using a CO_2 laser," *Phys. Rev. Lett.*, vol. 16, pp. 613–616, 1966.

[g] D. Chemla, P. Kupecek, C. Schwartz, C. Schwab, and A. Goltzene, "Nonlinear properties of cuprous halides," *IEEE J. Quantum Electron.*, vol. QE-7, pp. 126–132, Mar. 1971.

[h] S. Singh, J. R. Potopowiez, L. G. Van Uitert, and S. H. Wemple, "Nonlinear optical properties of hexagonal silicon carbide," *Appl. Phys. Lett.*, vol. 19, pp. 53–56, 1971.

[i] R. C. Miller, "Optical second harmonic generation in piezoelectric crystals," *Appl. Phys. Lett.*, vol. 5, pp. 17–19, 1964.

[j] R. L. Herbst, "CdSe infrared parametric oscillator," Ph.D. dissertation, Stanford Univ., Stanford, Calif., 1972.

almost an order of magnitude smaller than the E_{2A} gap. For example, in InAs $E_0 = 0.33$ eV and $E_{2A} = 3.9$ eV, so one might expect the Γ point in the Brillouin zone to modify the BOM energy parameters. As a result, the application of the BOM to these compounds is not as successful.

For the copper compounds, it is known that the *d* bands are strongly hybridized with the valence *s* and *p* bands. These delocalized *d* electrons at these noble-metal cations have been found experimentally to give an anomalous contribution to the second-order nonlinearity [28], [29]. This effect is discussed by Levine [14] in his bond-charge model and by Tang [16] in terms of a charge redistribution and a reversal of the direction of the bond dipole. Since the BOM deals with the sp^3 electrons, the *d* electrons are accounted for phenomenologically and the formulation overestimates the nonlinearity of these compounds. If we stay away from these noble-metal compounds and consider compounds where there is no appreciable hybridization of the *d* bands, then the BOM predictions agree well with experiment.

IV. Summary and Comments

Using a more predictive theory, the BOM, we have calculated the second-order susceptibility for tetrahedral compounds. Agreement with experiment is good, especially in light of the simplicity of the model. The approach is self-consistent, as the linear susceptibility is used to calculate the second-order susceptibility. Compared to other phenomenological models, our approach is more self-contained, as no adjustable parameter is used and all parameters are defined in the BOM.

The physical origin of the nonlinearity is seen to arise from the charge transfer as a result of the asymmetric polar energy between the anion and the cation. Chemical-trend considerations reveal an optimum value of polarity for a maximum second-order nonlinearity in zinc-blende and wurtzite structures. This, together with the bond-length dependence, gives a rule-of-thumb estimate on the choice of elements in the periodic table which will result in tetrahedral compounds of high second-order nonlinearity. It is found that for these tetrahedral structures, it is desirable to have high covalency and a high metallicity consistent with transparency region of interest. This means that one should stay close to group IV elements and high atomic numbers. We include the parametric gain parameter in our discussion showing that the bandgap is again important through the short wavelength frequency cutoff in the transparency range. The BOM is also quantitatively and qualitatively related to the Miller's rule through the concept of polarity.

Acknowledgment

The authors wish to thank Prof. W. Harrison for helpful discussions.

References

[1] S. E. Harris, "Tunable optical parametric oscillators," *Proc. IEEE*, vol. 57, pp. 2096–2113, Dec. 1969.

[2] R. L. Byer, "Optical parametric oscillators," in *Treatise in Quantum Electronics*, H. Rabin and C. L. Tang, Ed. New York: Academic, 1973.

[3] J. A. Armstrong, N. Bloembergen, J. Ducuing, and P. S. Pershan, "Interactions between light waves in a nonlinear dielectric," *Phys. Rev.*, vol. 127, pp. 1918–1939, 1962.
[4] P. N. Butcher and T. B. McLean, "The nonlinear constitutive relation in solids at optical frequencies," *Proc. Phys. Soc., Ser. A.*, vol. 81, pp. 219–239, 1963.
[5] P. L. Kelley, "Nonlinear effects in solids," *J. Phys. Chem. Solids*, vol. 24, pp. 607–616, 1963.
[6] F. N. H. Robinson, "Nonlinear optical coefficients," *Bell Syst. Tech. J.*, vol. 46, pp. 913–956, 1967.
[7] S. S. Jha and N. Bloembergen, "Nonlinear optical susceptibilities in group IV and III-V semiconductors," *Phys. Rev.*, vol. 171, pp. 891–898, 1968.
[8] D. E. Aspnes, "Energy-band theory of the second order nonlinear optical susceptibility of crystals of zinc blende symmetry," *Phys. Rev.*, vol. B6, pp. 4648–4659, 1972.
[9] M. I. Bell, in *Electronic Density of States*, L. H. Bennett, Ed. (Special Publ. 323). Washington, D.C.: NBS, 1971.
[10] a) C. G. B. Garrett and F. N. H. Robinson, "Miller's phenomenological rule for computing nonlinear susceptibilities," *IEEE J. Quantum Electron.* (Corresp.), vol. QE-2, pp. 328–329, Aug. 1966.
b) C. G. B. Garrett, "Nonlinear optics, anharmonic oscillators, and pyroelectricity," *IEEE J. Quantum Electron.*, vol. QE-4, pp. 70–84, Mar. 1968.
[11] R. C. Miller, "Optical second harmonic generation in piezoelectric crystals," *Appl. Phys. Lett.*, vol. 5, pp. 17–19, 1964.
[12] D. Penn, "Wave-number-dependent dielectric function of semiconductors," *Phys. Rev.*, vol. 128, pp. 2093–2097, 1962.
[13] D. A. Kleinman, "Nonlinear optical susceptibilities of covalent crystals," *Phys. Rev.*, vol. B2, pp. 3139–3142, 1970.
[14] B. F. Levine, "Bond charge calculation of nonlinear optical susceptibilities for various crystal structures," *Phys. Rev.*, vol. B7, pp. 2600–2626, 1973.
[15] C. L. Tang and C. Flytzanis, "Charge transfer model of the nonlinear susceptibilities of polar semiconductors," *Phys. Rev.*, vol. B4, pp. 2520–2524, 1971.
[16] C. L. Tang, "A simple molecular-orbital theory of the nonlinear optical properties of group III-V and II-VI compounds," *IEEE J. Quantum Electron.*, vol. QE-9, pp. 755–762, July 1973.
[17] a) J. C. Phillips, "A posteriori theory of covalent bonding," *Phys. Rev. Lett.*, vol. 19, pp. 415–417, 1967.
b) —, "Covalent bonds in crystals, I Element of a structural theory," *Phys. Rev.*, vol. 166, pp. 832–838, 1968.
c) —, "Covalent bonds in crystals, III Anisotrophy and quadrupole moments," *ibid.*, vol. 168, pp. 912–917, 1968.
d) —, "Ionicity of the chemical bond in crystals," *Rev. Mod. Phys.*, vol. 42, pp. 317–356, 1970.
[18] a) J. A. Van Vechten, "Quantum dielectric theory of electronegativity in covalent systems, I Electronic dielectric constant," *Phys. Rev.*, vol. 182, pp. 891–905, 1969.
b) —, "Quantum dielectric theory of electro-negativity in covalent systems, II Ionization potentials and interband transition energies," *ibid.*, vol. 187, pp. 1007–1020, 1969.
[19] W. A. Harrison, "Bond-orbital model and the properties of tetrahedrally coordinated solids," *Phys. Rev.*, vol. B8, pp. 4487–4498, 1973.
[20] a) W. A. Harrison and S. Ciraci, "Bond orbital model II," *Phys. Rev. B*, to be published.
b) S. Ciraci, Ph.D. dissertation, Stanford Univ., Stanford, Calif., 1974.
[21] J. Ducuing and C. Flytzanis, "Second order optical processes in solids," in *Optical Properties of Solids*, F. Abeles, Ed. Amsterdam, The Netherlands: North Holland, 1972, pp. 859–990.
[22] D. S. Chemla, "Dielectric theory of tetrahedral solids: Application to ternary compounds with chalcopyrite structure," *Phys. Rev. Lett.*, vol. 26, pp. 1441–1444, 1971.
[23] F. N. H. Robinson, "Relations between the components of the nonlinear polarizability tensor in cubic and hexagonal II-VI compounds," *Phys. Rev. Lett.*, vol. 26a, pp. 435–436, 1968.
[24] C. Flytzanis and J. Ducuing, "Second order optical susceptibilities of III-V semiconductors," *Phys. Rev.*, vol. 178, pp. 1218–1228, 1969.
[25] D. S. Chemla, R. F. Begley, and R. L. Byer, "Experimental and theoretical studies of the third-harmonic generation in the chalcopyrite $CdGeAs_2$," *IEEE J. Quantum Electron.*, vol. QE-10, pp. 71–81, Jan. 1974.
[26] K. G. Denbigh, "The polarizabilities of bonds," *Trans. Faraday Soc.*, vol. 36, pp. 936–948, 1940.
[27] E. Mooser and W. B. Pearson, "On the crystal chemistry of normal valence compounds," *Acta Crystallogr.*, vol. A12, pp. 1015–1022, 1959.
[28] R. C. Miller *et al.*, "Absolute signs of the second harmonic generation, electro-optic and piezoelectric coefficients of CuCl and ZnS," *Solid State Commun.*, vol. 9, pp. 1463–1465, 1971.
[29] B. F. Levine, W. A. Nordland, and J. W. Shiever, "Nonlinear optical susceptibility of AgI," *IEEE J. Quantum Electron.*, vol. QE-9, pp. 468–470, Apr. 1973.

Pulse Compression for More Efficient Operation of Solid-State Laser Amplifier Chains II

ROBERT A. FISHER AND WILLIAM K. BISCHEL

Abstract—**In a previous letter we proposed a compression scheme which reduces the intensity of a laser pulse in an Nd:glass amplifier chain and thereby allows more efficient energy extraction. In this scheme the nonlinear index of refraction (n_2) of the glass in the amplifier impresses a frequency sweep or "chirp" on the pulse. Further analysis is presented here. The stability to amplitude noise is demonstrated. We calculate that impressed periodic amplitude modulation is responsible for the growth of distinct spectral sidebands in the nonlinear host glass, and we find that the compressor converts these sidebands into temporal features which precede and follow the central compressed pulse. When a pulse with 10-percent peak-to-peak impressed periodic modulation passes through a sufficient length of glass so that the peak nonlinear phase is approximately 4π, these precursors are only about 1/20th the intensity of the main compressed pulse. RMS equivalent random noise has a flat sideband spectrum, and the precursors are found to be absent in the compressed pulses. The intensity averaging over possible transverse-mode structures is studied for some axially symmetric spatial mode shapes. This averaging somewhat reduces the compression ratio from the estimates in which the transverse modes were flat-topped. Finally, arguments are presented to explain why it is felt that a grating pair is not likely to be a suitable compressor for such intense nanosecond-duration pulses.**

I. Introduction

A COMPRESSION SCHEME for laser pulses was described in a previous letter [1]. The present paper primarily discusses that scheme's sensitivity to temporal and spatial pulse variations.

In [1] we proposed a scheme which reduces the intensity inside an Nd:glass amplifier chain by the injection of a longer duration and less intense pulse into the chain. By calculation the nonlinear index of refraction (n_2) of the glass host[1] was shown to impress upon the pulse a chirp which was suitable for subsequent temporal compression in a sequence of Gires–Tournois interferometers [2]. With this scheme energy extraction is far more efficient than if a pulse of the desired duration were amplified. This scheme is depicted in Fig. 1. It was shown in [1] that if a 1-ns (full $1/e$-duration) temporally Gaussian plane-wave pulse traveled 2 m through the glass chain with its peak intensity averaging 2 GW/cm^2 along the chain, the pulse could subsequently be compressed with high efficiency to 125 ps.[2] The Appendix presents the justification for averaging the intensity along the chain.

In [1] the influence of the dispersive-delay compressor was considered in terms of an expansion of the logarithm of the corresponding transfer function. The average phase shift and group delay do not affect pulse reshaping. The first term which is of influence is the group dispersion which is represented by the term quadratic in frequency offset [called $Q_2(\Delta\omega)^2$]. A pulse with a positive linear frequency sweep has a phase perturbation described by $\delta\phi = -\frac{1}{2}\beta t^2$ where $\beta > 0$. Such a pulse can be optimally compressed by a dispersive delay line adjusted so that $\beta Q_2 = -\frac{1}{2}$. This means that the low-frequency leading edge of the pulse is delayed half of the uncompressed pulse duration, and that the high-frequency trailing edge is correspondingly advanced. This assumes that higher terms in the logarithm of the transfer function ($\partial^3\Phi/\partial\omega^3$, $\partial^4\Phi/\partial\omega^4$, etc.) are of negligible consequence. A temporally Gaussian pulse in glass, for example, has a nonlinear phase given approximately by $\delta\phi = \delta\phi_{\max} \exp(-t^2/\tau^2)$ where 2τ is the full $1/e$ intensity duration of the uncompressed pulse. At the center time of the pulse, β is evaluated by taking the negative of the second derivative of $\delta\phi$ with respect to time; thus $\beta = (2\delta\phi_{\max}/\tau^2)$. From [1] the optimum compression ratio R can be written $R \simeq 1. + 0.65\delta\phi_{\max}$, from which β can be evaluated to find $\beta \simeq 2(R-1)/(0.65\tau^2)$. Therefore, for optimal compression in this scheme, only the initial and final pulse durations are sufficient to specify the necessary compressor dispersive delay. For the case of [1], ($\tau = 5 \times 10^{-10}$ s and $R = 8$) we estimate that $\beta = 8.6 \times 10^{19}$ s^{-2}. For optimal compression of this pulse ($\beta Q_2 = -\frac{1}{2}$), the required dispersive delay is given by $Q_2 = -5.8 \times 10^{-21}$ s^2. Although the compressor phase-shift terms through $Q_4(\Delta\omega)^4$ were analyzed for the case described in [1], the influence of terms above Q_2 can be made minimal. The new results we discuss in this paper are meaningful without consideration of the

Manuscript received August 7, 1974. This work was performed under the auspices of the U.S. Atomic Energy Commission. Part of this work was performed while R. A. Fisher was at the Lawrence Livermore Laboratory. W. K. Bischel's work was partially supported by an NDEA Title IV Fellowship.

R. A. Fisher is with the Los Alamos Scientific Laboratory, University of California, Los Alamos, N. Mex. 87544.

W. K. Bischel is with the Department of Applied Science and the Lawrence Livermore Laboratory, University of California, Livermore, Calif. 94550.

[1] The first measurement of this quantity in glasses was performed by M. A. Duguay, J. W. Hansen, and S. L. Shapiro, "Study of the Nd:glass laser radiation," *IEEE J. Quantum Electron.*, vol. QE-6, pp. 725–743, Nov. 1970. We chose our coefficient for Owens-Illinois ED-2 glass from the recent work of A. Owyoung, "Ellipse rotation studies in laser host materials," *IEEE J. Quantum Electron.*, vol. QE-9, pp. 1064–1069, Nov. 1973. The more recent work of E. S. Bliss and R. D. Speck (private communication) indicates that this coefficient may be 15 percent lower than the value (1.7×10^{-13} ESU) which we use. Reference to a company name or a product name does not imply approval or recommendation of the product by the University of California or the U.S. Atomic Energy Commission to the exclusion of others that may be suitable.

[2] Since the value of n_2 for the glass we considered is only known to within 30 percent, the results presented here and in [1] may undergo some refinement as the value becomes better known.

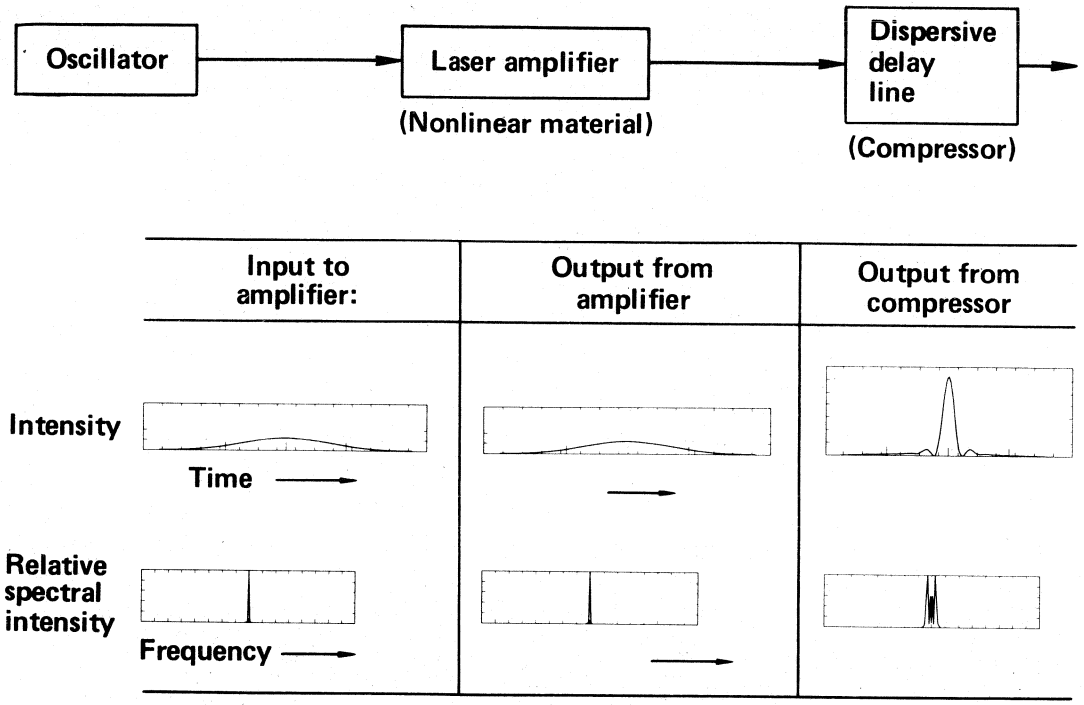

Fig. 1. A schematic of the pulse-compression proposal. The pulse spectrum is broadened due to the nonlinear effect of self-phase modulation in the laser amplifier. The pulse is then compressed by a dispersive delay line which takes advantage of the self-phase modulation "chirp." By this scheme it should be possible to get more energy out of a given amplifier system than if a short pulse were to be amplified.

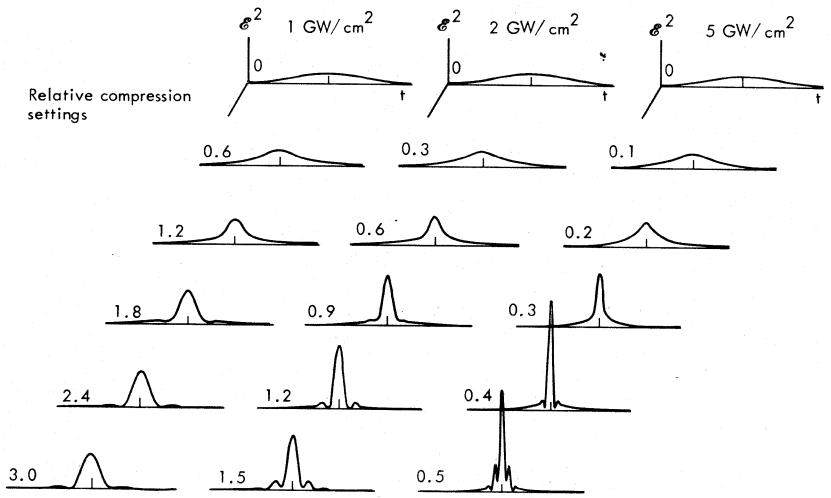

Fig. 2. Calculated dispersive compression of plane-wave pulses after they have traveled 2 m in an Nd:glass laser chain. Time is plotted horizontally and relative intensity is plotted vertically. Cases are shown for chain-averaged peak intensities of 1, 2, and 5 GW/cm^2. In each case, the initial full $1/e$ intensity duration is 1 ns. Spatial effects due to the radial intensity profile are not considered. Numbers associated with each graph are relative compression settings which are proportional to Q_2, with a setting of unity corresponding to $Q_2 = -6.4 \times 10^{-21}$ s^2. The optimally compressed pulse is next to the bottom in each column. The tic marks indicate where the center of the pulse would be if Q_2 were zero. The lateral displacement is of no consequence; it has been done in order that the 5-GW/cm^2 curves do not obscure each other. The intensity scales are different for each column so that the 3 cases may be readily seen on the figure.

higher order terms, and we therefore will restrict our attention to the calculations which only consider the influence of the Q_2 term.

In order that the more realistic cases we discuss in the remainder of the paper can be compared to the results for hypothetically perfect pulses, we have calculated (in the manner described in [1]) the dispersive temporal compression of various plane-wave 1-ns pulses. The results are shown in Fig. 2. In the calculation pulses traveled through 2 m of glass with their peak intensity averaging 1, 2, and 5 GW/cm^2 along the length of the chain. As one looks down any column of Fig. 2, dispersive delay is being increased. The relative com-

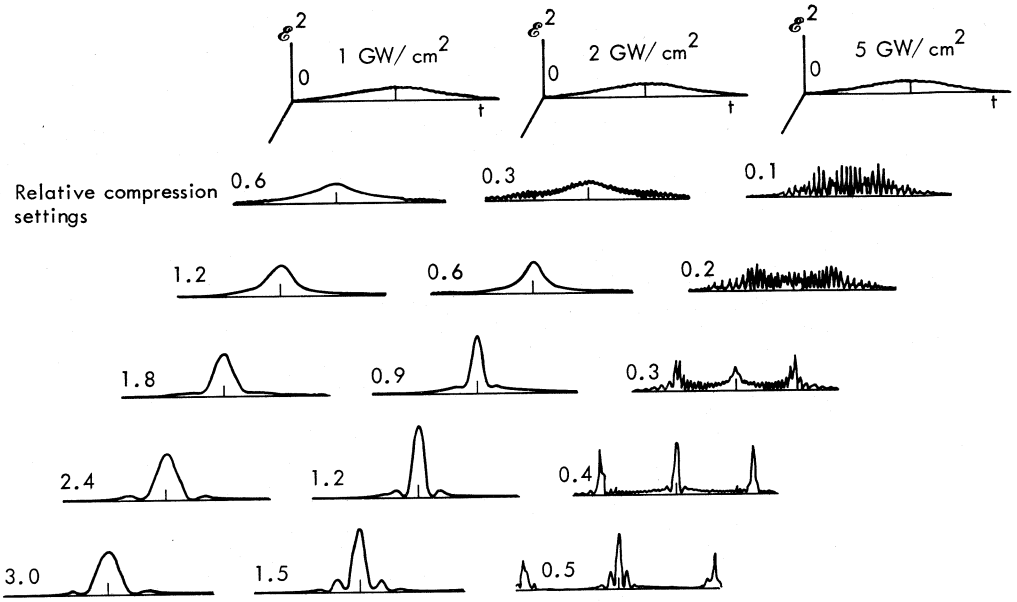

Fig. 3. A repeat of the calculation of Fig. 2 with the inclusion of 10-percent peak-to-peak amplitude ripple on the pulse which enters the laser chain. Note that compression of ripples occurs for far smaller compressor settings, so that the unwanted features are again temporally spread out at the optimally compressing dispersive delay setting. In the 5-GW/cm^2 case, the precursors (which are discussed in the text) are prominent features.

pression settings in the figure are proportional to the values of Q_2, and unity corresponds to $Q_2 = -6.4 \times 10^{-21}$ s^2. The relative compression setting of unity then should be fairly close to the optimally compressing setting for the 2-GW/cm^2 pulse of [1]. The optimally compressed pulse is next to the bottom in each column. Note that the less intense pulse develops less chirp, and therefore requires more dispersive delay for optimal compression. Note also that the more intense pulse can be compressed to a greater extent; this is because of the greater bandwidth expansion (i.e., greater chirp). The 2 GW/cm^2 case was the one considered in [1], and the other cases are shown for comparison.

II. Amplitude Noise Stability

Since the temporal shape of the input pulses may not be as smooth as in the calculated cases presented in [1], it is important that the pulse-compression scheme is not severely hampered by the presence of some temporal noise on the otherwise smooth input pulse. To study these stability considerations, we have repeated the plane-wave pulse-compression calculations shown in Fig. 2 with noise impressed upon the pulse which enters the chain. Terms in the compressor transfer function higher than Q_2 are neglected here. These calculations have been performed for 10-percent peak-to-peak periodic intensity modulation and for random amplitude modulation.

A. Periodic Amplitude Modulation

Fig. 3 shows the calculated attempt to compress the periodically modulated pulses. As $|Q_2|$ was increased from zero, the noise became accentuated because each feature had developed its own chirp. With further increase of $|Q_2|$ to the optimally compressing values, all amplitude fluctuations in the vicinity of the main pulses disappeared. This is because each ripple had generated a spectral content far richer than had the unmodulated pulses, and so each feature is quite smoothly dispersed (over-compressed) by the optimally compressing dispersive delay.

At optimum compression, the 10-percent modulated 2-GW/cm^2 case is indistinguishable from the smooth case (Fig. 2) in the time span we present. It is somewhat unfortunate, however, that during self-phase modulation the spectrum of the pulse develops sharp sidebands (at the modulation frequency) well separated from the smooth-pulse self-phase modulated spectrum. This can be seen in Fig. 4. These sidebands apparently have a spectral-intensity-dependent growth rate, and are ~1/20th the height of the spectral peak by the time the pulse exits the laser chain. At the optimally compressing dispersive delay (the setting 1.2 in Fig. 3), these "renegade" spectral components are delayed and advanced by approximately 2 ns with respect to the center of the compressed pulse. In the 5-GW/cm^2 case, the precursors are within the field of view because less dispersive delay is needed to optimally compress the pulse, and the precursors are prominent features. The precursor arrival time can be predicted by noting that the periodically modulated pulse develops spectral sidebands at the modulation frequency, which the compressor converts into temporal features. The anti-Stokes (Stokes) sideband is advanced (delayed) by $\sim 2Q_2$ times the modulation frequency. In the case presented here (50-ps ripple) these features for the 2-GW/cm^2 pulse precede and follow the central compressed pulse by ~2 ns. The difference in prominence of precursors in the 2- and 5-GW/cm^2 cases is because in the nonlinear chain, the sideband growth rate is spectral-intensity dependent. This can be seen in the relative heights of the spectral sidebands of the periodically modulated pulses in Fig. 4. Note in the same figure that nonlinear propagation in the 5-GW/cm^2 case has generated faint second spectral sidebands, and in the compressed pulse,

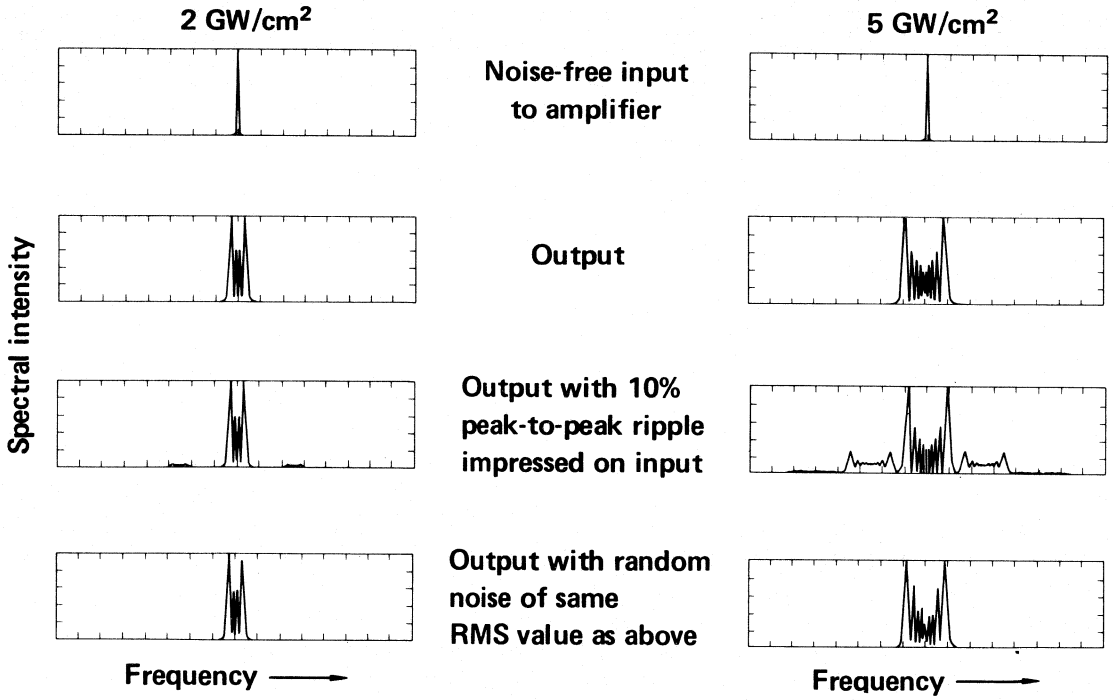

Fig. 4. Comparison of calculated spectra for pulses emanating from the laser amplifier chain. Cases of noise-free input, 10-percent peak-to-peak ripple, and random noise of the same rms deviation as in the 10-percent ripple are presented for 2-m propagation at chain-averaged peak intensities of 2 GW/cm^2 and 5 GW/cm^2.

they correspond to second precursors. These secondary features are 1/10th the height of the first precursor, and they are twice as far from the peak of the central compressed pulse.

B. Random Amplitude Modulation

The random modulation was generated by multiplication of of the original temporally Gaussian pulse-shape function at time N by the factor $[1 + \alpha A_N]$. Here α is an adjustable constant and $A_N = \sum_1^N R_i$, where $\{R_i\}$ is a set of random numbers distributed between the ranges +1 and −1. The value of α was adjusted so that after passing the calculated pulse through a 0.4-Å-bandwidth Lorentzian filter, the calculated rms deviation from the original Gaussian was equal to the calculated rms deviation for the 10-percent peak-to-peak periodic-ripple case previously discussed. The spectral filtering did not significantly reduce the rms deviation, yet it did remove the noise due to the finite temporal step size.

We have calculated the passage of the randomly modulated pulses through a 2-m laser chain, and have studied their compressibility. We find, as before, that for far less than the optimally compressing dispersive delay settings, the noise is accentuated, but at optimally compressing dispersive delay, the noise is not discernable. There is also no perceptible precursor, even in the 5-GW/cm^2 case, and it is because the spectrum as seen in Fig. 4 does not exhibit sidebands as had been observed in the periodic modulation case. Since the growth rate of a sideband is spectral-intensity dependent, the spectrally broader random noise did not have sufficient peak spectral amplitude to get significantly amplified during self-phase modulation in the laser chain.

From the comparison of the results just presented for periodic and random amplitude modulation, we conclude that although random amplitude modulation can be well tolerated, efforts must be made to limit periodic amplitude modulation in order to provide a pulse suitable for precursor-free dispersive compression.

III. Averages Over Spatial Profiles

In [1] the compression effect was intensity averaged over a Gaussian spatial profile. This neglects the influence of diffraction in the amplifier chain with the assumption that each radial zone in the amplifier chain acts independently and can therefore be treated in the plane-wave approximation. In the calculation, each radial zone is compressed and then the *intensities* are added to find the spatially averaged signal in the focal plane of a lens. In a laser fusion experiment, for example, this intensity averaging models the expected smoothing role of the electron thermal conductivity on the surface of the pellet. If the value of the conductivity proves to be insufficient, then spatially averaged quantities would not be meaningful, and one would have to consider the complicated time-dependent interference patterns produced by the laser pulse at the surface of the pellet. These interference effects have been studied by Campillo *et al.* [3].

Reference [1] presented the compression-effect intensity averaged over a spatially Gaussian pulse with a chain-averaged on-axis peak intensity of 2 GW/cm^2, and this was shown to be somewhat deleterious to the compression scheme. These intensity-averaging compression calculations have been extended here to include more typical spatial profiles. As a model of the various choices for spatial mode shapes which decrease monotonically with radius, consider the set of radial-intensity distributions given by the function $\exp\{-(R/R_0)^M\}$.

For $M = 2$, this is a Gaussian. In the design of a laser chain it is advantageous to run at higher M values. As M is increased, the central region becomes more flat-topped and the wings fall off faster. This means that higher M values allow R_0 to be chosen closer to R_A, the radius of the active medium which, in turn, results in more efficient extraction from the pumped laser amplifier. In addition, a higher M value gives more surface of relatively constant nonlinear phase, which brings compression results closer to the plane-wave case of [1]. The M value cannot be increased without limit, however, because of diffraction and self-focusing. The pulse-compression scheme presented here cannot improve the M-value limitations imposed by diffraction. If the M value is limited by self-focusing considerations, however, the reduction of the nonlinear-index change through this compression scheme can allow for an increased effective operating M value.

For temporally Gaussian 1-ns pulses we have repeated our spatial-intensity averaging calculations for M values from 2 through 6. In the calculation pulses traveled 2 m with their on-axis peak intensity kept at the chain-averaged value of 2 GW/cm^2. Fig. 5 shows the results of this spatial averaging for $M = 2$ (a Gaussian). For each M value the compression ratio R was estimated by measuring the $1/e$ intensity width of the compressed pulses, and the efficiency of compression ϵ was found by multiplying R times the ratio of the uncompressed maximum intensity to the maximum intensity of the compressed pulse. Results are shown in Table I. Since the cost of components for a constant energy subnanosecond Nd:glass laser system varies nearly inversely with pulse duration, we can estimate the potential savings if one were to convert from normal amplifier operation to this compression scheme. If the effective M value and output energy are not changed in the conversion, then we can define a figure of merit as $1 - 1/(\epsilon R)$. This denotes an estimate of the fractional-component cost savings which the compression scheme would provide if the compressor were free. The figure of merit is also shown in Table I. Note that the entries are only approximate because of our qualitative estimates of the optimally compressing conditions. The *additional* savings which can be achieved if, through its reduction of self-focusing problems, a compression scheme allows an increase in the operating M value can be estimated from the following. For a given M value, we assume that R_0 is chosen so that the intensity at R_A, the radius of the active medium, is approximately 10^{-3} of the intensity on-axis. This condition is written $\exp[-(R_A/R_0)^M] = 10^{-3}$. The mode-extraction efficiency is then estimated as $(R_0/R_A)^2$, which is approximately $7^{-(2/M)}$. This mode-extraction efficiency factor is also listed in Table I. As can be seen from Table I, there is an even greater benefit if the compression scheme can also allow the increase in effective operating M value.

TABLE I
COMPARISON OF CALCULATED RESULTS FOR INTENSITY AVERAGING OVER SPATIAL PROFILES

M-Value	Measured Compression Ratio:R	Efficiency ϵ	Figure of Merit $1-1/(\epsilon R)$	Mode Efficiency parameter $7^{-(2/M)}$
2	4.9	.56	.64	.14
3	5.5	.63	.71	.27
4	6.1	.64	.74	.37
5	6.3	.66	.76	.46
6	6.6	.68	.78	.52
∞ (plane-wave case)	7.8	.79	.84	1.0

Note: Temporal shape = $\exp\{-(t/\tau)^2\}$. Mode shape = $\exp\{-(R/R_0)^M\}$. Each pulse propagates 2 m through the chain with the peak intensity on axis averaging 2 GW/cm^2. The full $1/e$ intensity duration is given by $2\tau = 1$ ns.

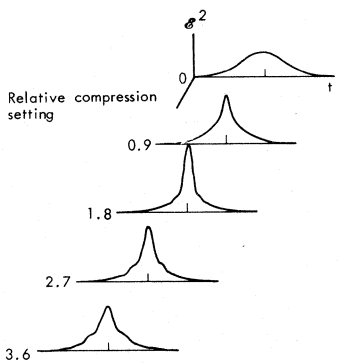

Fig. 5. Compression study of an intensity average over a Gaussian transverse mode with peak chain-averaged intensity on axis of 2 GW/cm^2. Time is plotted horizontally and intensity is plotted vertically. Note that ample compression can be achieved. As in Figs. 2 and 3, Q_3 and Q_4 terms were not included, and the numbers associated with each graph are relative compression settings which are proportional to Q_2, with a setting of unity corresponding to $Q_2 = -6.4 \times 10^{-21}$ s^2.

IV. Can a Grating Pair Compress Nanosecond Pulses?

There are two main candidates presently available for an anomalously dispersive compressor ($Q_2 < 0$). These are the Gires-Tournois interferometer and the grating pair. In [1] we considered only the Gires-Tournois interferometer because of the high damage threshold available from good coatings (approximately 5 J/cm^2 at 1.06 μm, 125-ps duration) and because of the low insertion loss. It is unfortunate, however, that there is only a narrow operating range over which the group delay depends linearly upon the center frequency, and hence sequential reflection from nine Gires-Tournois interferometers was required. The number of required interferometers might be reduced by designing more complex structures. Even though the proper alignment of as many as nine Gires-Tournois interferometers may be quite difficult, these interferometers most likely can be made the same diameter as the final output stage of the laser amplifier chain.

The second compressor candidate is the grating pair which has been studied by Treacy [4]. This device is very useful for compressing pulses from the 1-10-ps range, but we are not as confident that it can be used as a practical compressor for nanosecond-duration pulses. In general, we find that both required sizes of gratings and grating separation distances are

prohibitively large. For a single grating, the geometry of incident and diffracted rays is determined by the grating formula

$$N\frac{\lambda}{d} = \sin(\beta) + \sin(\gamma) \tag{1}$$

where N is the diffraction order, d^{-1} is the number of lines per centimeter, γ is the angle which the incident ray makes with the normal to the grating, and β is the angle between the diffracted beam and the normal to the grating. For a compressor phase-shift quadratic in frequency offset, we write $\Phi = Q_2(\Delta\omega)^2$. The quantity Q_2 has been derived for the grating pair [4], [5], and is written

$$Q_2 = -\left(\frac{\lambda}{4\pi c^2}\right)\left(\frac{N\lambda}{d}\right)^2 (b)\left(\frac{1}{\cos^3(\beta)}\right) \tag{2}$$

where b is the perpendicular distance between the two gratings. We find it quite difficult to make Q_2 sufficiently large. Note that increasing the order N or the grating constant d^{-1} will not significantly increase Q_2 because (1) limits the quantity $(N\lambda/d)^2$ to 4. Thus only the separation b and the geometric factor $[1/\cos^3(\beta)]$ can be adjusted to hopefully attain sufficiently large Q_2. The separation b could possibly be "folded" by a mirror system, but the increase of the geometric factor is accompanied by two distinct problems. First, high first-order blaze efficiency at these angles is not yet technologically possible for reflection gratings (transmission gratings may not be subject to this criticism). Second, if blaze efficiency could be kept high, operation would have to be near Littrow condition ($\beta \sim \gamma$), for which the size of the grating must be at least $D/\cos(\beta)$, where D is the beam diameter. For $D = 50$ cm and $\beta = 85°$, the grating would have to be 6 m across. This is exceedingly large.

As an example which could have high blaze efficiency, consider $\beta = 60°$, a grating spacing of 1200/mm and $\lambda = 1.06$ μm. Here only first-order diffraction can occur, and $(N\lambda/d)^2 = 1.6$. Equation (2) can be solved to find that under these circumstances, d must be 600 m in order to provide the Q_2 which was needed in [1]. Since d is the required *perpendicular* distance between gratings, their required physical separation will be 1200 m. Thus we see that at angles where the blaze will be efficient, the separation between gratings must be exceedingly large.

One must consider the additional difficulty that gratings may damage at much lower intensities than would the coatings of a Gires-Tournois interferometer. Although the damage susceptibility for gratings does not appear to be too well studied, one can surmise from the work of Bloembergen [6] that the preponderance of sharp corners could severely reduce the ability of a grating to tolerate high light fluxes. The possibility of standing waves with nodes at the periodically spaced sharp corners could further enhance the damage sensitivity. This damage consideration would probably require even larger surface gratings. If necessary, one might piece together several similar gratings, yet the accumulated list of design difficulties seems to rule out consideration of a grating pair for compressing nanosecond-duration pulses.

V. Concluding Remarks

Certain considerations have been described which are related to our previously presented pulse-compression scheme. The stability to amplitude noise was analyzed, and it was shown that a pulse could exit the compressor with precursors if it enters the chain with periodic amplitude modulation. For the case considered in [1], the addition of 10-percent peak-to-peak intensity ripple accounted for only a relatively small precursor, yet an increase of the operating intensity by a factor of $2\frac{1}{2}$ led to clearly unacceptable precursors. With the exception of causing these precursors, there is no other effect on the compressed pulse shapes. It was also shown that, unlike periodic modulation, random amplitude modulation (of the same rms value) did not produce the unwanted precursors. This was explained in terms of the nonlinear self-phase modulation effect, and is due to the broad spectral nature of the random modulation.

In order to help estimate the cost effectiveness of the pulse-compression scheme, the effects of intensity averaging the compression over reasonable spatial mode profiles were also tabulated. Our reasons were also stated for excluding consideration of the grating pair as a compressor.

Appendix

To justify the use of chain-averaged quantities, we consider a laser chain which consists of elements numbered from 1 through p. Each element is of length l_i, and the square of the maximum electric-field envelope is written $\mathcal{E}^2_{\max}(z_i)$, where z_i is the position in the ith element. The maximum nonlinear phase is written

$$\delta\phi_{\max} = \left(\frac{\omega_0}{c}\right)\left(\frac{n_2}{2}\right)\sum_{i=1}^{p}\int_0^{l_i} \mathcal{E}^2_{\max}(z_i)\,dz_i \tag{A1}$$

if both saturation of the transition and dispersion can be neglected. If we define the chain-averaged value of $\mathcal{E}^2_{\max}$ through the relationship

$$\overline{\mathcal{E}^2_{\max}} \equiv \left\{\sum_{i=1}^{p}\int_0^{l_i} \mathcal{E}^2_{\max}(z_i)\,dz_i\right\} \Big/ \left(\sum_{i=1}^{p} l_i\right) \tag{A2}$$

then the maximum nonlinear phase is written

$$\delta\phi_{\max} = \left(\frac{\omega_0}{c}\right) n_2 \frac{\overline{\mathcal{E}^2_{\max}}}{2}\left(\sum_{i=1}^{p} l_i\right). \tag{A3}$$

Thus we see that pulses can be treated as if they remained at their chain-averaged values. More precise calculations await the accurate specification of design parameters for a particular chain.

References

[1] R. A. Fisher and W. K. Bischel, "Pulse compression for more efficient operation of solid-state laser amplifier chains," *Appl. Phys. Lett.*, vol. 24, pp. 468–470, May 1974.

[2] F. Gires and P. Tournois, "Interférome utilisabe pour la compression d'impulsions lumineuses modulés en fréquence," *C. R. Acad. Sci.*, vol. 258, pp. 6112–6115, June 1964.

[3] A. J. Campillo, R. A. Fisher, R. C. Hyer, and S. L. Shapiro, "Streak camera investigation of the self-focusing onset in glass," *Appl. Phys. Lett.*, vol. 25, pp. 408–411, Oct. 1974.
[4] E. B. Treacy, "Optical pulse compression with diffraction gratings," *IEEE J. Quantum Electron.*, vol. QE-5, pp. 454–458, Sept. 1969.
[5] R. A. Fisher, P. L. Kelley, and T. K. Gustafson, "Subpicosecond pulse generation using the optical Kerr effect," *Appl. Phys. Lett.*, vol. 14, pp. 140–143, Feb. 1969.
[6] N. Bloembergen, "Role of cracks, pores, and absorbing inclusions on laser induced damage threshold at surfaces of transparent dielectrics," *Appl. Opt.*, vol. 12, pp. 661–664, Apr. 1973.

Correspondence

Radiation-Pressure Separation of Molecules and Atoms

JERRY GELBWACHS AND THOMAS S. HARTWICK

Abstract—**Radiation-pressure separation of molecules in a closed cylindrical geometry with radiation propagating along the axis has been analyzed. The degree of separation and separation efficiency are compared in the microwave, infrared, and visible-UV spectral regions for representative species.**

I. Introduction

The idea of using pressure induced by light to physically displace molecules is old [1]. Not until Ashkin and his colleagues [2]–[4] demonstrated vividly the utility of laser light did the use of radiation pressure merit serious consideration for applications. Since then, the old atomic-beam-deflection experiments have been repeated [5] and extended [6]. Due to the low density of atoms in an atomic beam, the yield of material separated by atomic-beam methods will be small. Our interest is to explore the usefulness of separation of isotopes by radiation pressure for a geometry that does not rely upon atomic beams and thus has potential for the separation of larger quantities of isotopes. A comparison of separation parameters in different spectral regions will be made.

II. Separation Parameters

Molecules are contained in a cylindrical tube of length L that is illuminated by radiation propagating along the axis of the cylinder. The molecular energy levels are modeled by a two manifold system with rotational line structure. The two levels describe electronic or vibrational transitions. Interaction between the radiation and the molecules changes the ground-state n_1 and excited-state n_2 populations. The spatial and temporal variation of the states is determined by the combination of stimulated absorption, radiative-momentum transfer, molecular diffusion, and relaxation of the upper state by spontaneous emission and collisional deactivation. The last process proceeds at a rate equal to $1/\tau$ and κp, respectively, where τ is the upper-state lifetime, κ is the collisional deactivation rate, and p is pressure. Assumptions are made to facilitate the calculation without significant loss of accuracy. These assumptions include: restricting the gas pressure to the regime where the mean free path is much less than the tube diameter; a constant gas temperature T; negligible radiation propagation losses; and uniform intensity I across the tube area. The stimulated absorption rate W is restricted to be less than the relaxation rate within the manifolds and the velocity cross-relaxation rate within the Doppler distribution. These restrictions eliminate hole-burning effects and permit the substitutions $f_{1,i}n = n_{1,i}$ and $f_{2,j}n_2 = n_{2,j}$, where the f's are Boltzmann coefficients.

Under the above constraints and assumptions, the time variations of the total population n and population difference δ is written as

$$dn/dt = -D\nabla^2 n + (Dhf/kT\lambda)\,\nabla \cdot W\delta\hat{z} \tag{1}$$

$$d\delta/dt = -D\nabla^2\delta - (Dhf/kT\lambda)\,\nabla \cdot Wn\hat{z} - 2Wf\delta + (n-\delta)(1/\tau + \kappa p) \tag{2}$$

where D is the diffusion coefficient, h is Planck's constant, k is Boltzmann's constant, λ is the excitation wavelength, and $\hat{z}$ is a unit vector in the longitudinal direction. For simplicity, the Boltzmann factors $f_{1,i}$, $f_{2,j}$ have been set equal to f.

The solutions to the coupled set of equations in the steady state are easily obtained by neglecting the slowly varying longitudinal drift and diffusion terms relative to the fast relaxation and stimulated absorption rates in (2). This produces

$$\delta = n[1 + 2Wf/(1/\tau + \kappa p)]^{-1}. \tag{3}$$

Substitution of (3) into (2) yields

$$0 = -D\nabla^2 n + \{hDfW/kT\lambda[1 + 2fW/(1/\tau + \kappa p)]\}\,\partial n/\partial z. \tag{4}$$

Only the longitudinal diffusion and drift terms remain.

The solution of (4) takes the form originally written by Ashkin [2]

$$n(z) = n(0)\exp \beta Z/L. \tag{5}$$

The exponential variation of the concentration with z fixes the degree of separation which is determined by the separation coefficient β. Solving (4) for β yields

$$\beta = \beta_s(I/I_s)[1 + (I/I_s)]^{-1} \tag{6}$$

Manuscript received April 1, 1974; revised September 20, 1974.
The authors are with the Electronics Research Laboratory, The Aerospace Corporation, Los Angeles, Calif. 90009.

TABLE I
LOW-INTENSITY SEPARATION COEFFICIENT AND EFFICIENCY FOR RADIATION-PRESSURE SEPARATION IN VARIOUS SPECTRAL REGIONS

Sprectral Region	Representative Molecule	Transition Wavelength	β^*/P (W^{-1})	η^* (Molecules/Joule)
Microwave	NH_3	12.6mm	2×10^{-4} [a]	1×10^{11}
Infrared	CO	4.7μm	5×10^{-3} [b]	1×10^{12}
uv-visible	NO	230nm	0.3 [b]	4×10^{13}
uv-visible	Na	589nm	10^{3} [b]	5×10^{17}

[a] Waveguide: $L = 100$ m; $A = \lambda^2$.
[b] $L/A = \lambda^{-1}$.

where

$$\beta_s = (h\nu L/2ckT)(1/\tau + \kappa p) \tag{7}$$

$$I_s = [4\pi h\nu/\lambda^2 f A_{ij} g(\nu)](1/\tau + \kappa p) \tag{8}$$

$$W = c^2 A_{ij} g(\nu) I/8\pi h\nu^3 \tag{9}$$

where c is the speed of light, A_{ij} is the spontaneous emission rate between the ith rotational state in the lower level and the jth rotational state in the upper level, $g(\nu)$ is the line-shape factor, and ν is the radiation frequency. This result demonstrates that saturation of the absorbing transition as measured by the saturation intensity I_s limits the amount of radiation pressure that can be exerted upon resonant molecules. The degree of separation that can be attained when maximum radiation pressure is exerted is β_s.

Until this point radiation pressure has been considered as a means to establish a concentration gradient of a resonant species along the length of a closed tube. For an open tube in which the initial mixture is continuously replenished at the input end and the separated species are removed at the output end, it is useful to define a separation efficiency η as the number of resonant molecules transported per incident radiant energy, i.e., the ratio of the drift current density to I. From (4) the drift current density is identified and it follows that

$$\eta = (nD\beta_s/LI_s)[1 + (I/I_s)]^{-1}. \tag{10}$$

III. CANDIDATE MOLECULES AND SPECTRAL COMPARISON

To determine the molecular species and spectral regime that are optimum for separation, it is useful to examine β and η at low-laser intensities (denoted by superscript *). Noting that the absorption coefficient in the absence of saturation is given by $\alpha = n_{1,i} c^2 A_{ij} g(\nu)/8\pi\nu^2$, (6) and (10) can be rewritten as

$$\beta^* = (\alpha/n)(LI/ckT) \tag{11}$$

$$\eta^* = D\alpha/ckT \tag{12}$$

where I_s has been eliminated in favor of α to facilitate computation of β^* and η^* from experimental parameters. The low-intensity value of β is a function of geometry through the dependence on length L. To compare values of β^* for different molecules in the optical region, a geometry is selected in which the focused laser radiation fills the area of the cylindrical tube A at its ends, i.e., $L/A \sim \lambda^{-1}$ for a single-mode Gaussian beam. Radiation pressure can be applied through the excitation of rotational, vibrational, and electronic transitions. In Table I values of β^*/P and η^* are compared in various spectral ranges for representative molecules. To avoid unduly penalizing the microwave spectral region, the L/A ratio has been calculated for a waveguide structure 100 m in length and $A = \lambda^2$ instead of $L/A = \lambda^{-1}$. In all spectral regions a sufficiently low pressure has been assumed so that the resonance lines are Doppler broadened. Values of β^*/P and η^* range over 7 orders of magnitude. For a given power P, atoms with strong resonance lines produce the largest separation coefficients and highest efficiencies in the absence of saturation.

IV. PRESSURE DEPENDENCE OF SEPARATION PARAMETERS

From (7) it is seen that maximum separation occurs when the excited state undergoes rapid deactivation. As discussed by Ashkin, the deactivation rate can be increased by introducing as the gas additive a collision partner with a large κ [2]. Three pressure regions are evident when the partial pressure of the resonant molecules is held constant and the variation of β_s and I_s with the pressure of the collision partner is considered. In the low-pressure region the absorption lines are Doppler broadened, and spontaneous emission relaxes the excited state so that β_s and I_s are independent of pressure. At higher pressure, collisions are mainly responsible for the decay of the excited state and both β_s and I_s vary directly as p. At still higher p, the line-shape factor $g(\nu)$ becomes Lorentzian and I_s varies as p^2. The lowest p region is characterized by small separation coefficients, low powers, and large separation efficiencies. At high p large separations are possible, but at the expense of a high-power requirement and, hence, reduced efficiency. In Fig. 1, β_s and saturation power $P_s (P_s = I_s A)$ are

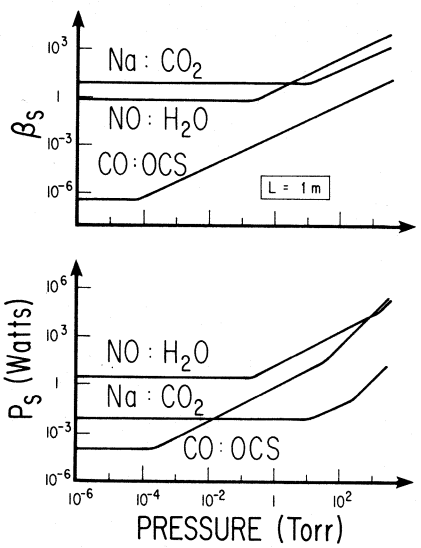

Fig. 1. Maximum degree of separation β_s and saturation power P_s versus the pressure of gas additive for various molecules and their collision partners.

plotted against the pressure of the gas additive for CO(4.7 μm), NO(0.23 μm), and Na(0.59 μm). A diffraction-limited geometry has been selected for which $L/A = \lambda^{-1}$ and $L = 1$ m. For example, consider that $\beta = 1.5$ is desired. When $\beta = \beta_s/2$ and $I = I_s$, good separation is achieved with only a slight reduction in separation efficiency due to saturation. These values for β and I are chosen in the examples. Under this condition, 30 kW of power and 1000 torr of OCS are necessary to separate CO isotopes. Isotopes of NO require 12 W and 1 torr of H_2O. Less than 10 mW is sufficient for the same separation of Na.

References

[1] R. Frisch, "Experimental detection of the Einstein recoil radiation," *Z. Phys.*, vol. 86, pp. 42–48, Oct. 1933.
[2] A. Ashkin, "Acceleration and trapping of particles by radiation pressure," *Phys. Rev. Lett.*, vol. 24, pp. 156–159, Jan. 1970.
[3] ——, "Atomic-beam deflection by resonance-radiation pressure," *Phys. Rev. Lett.*, vol. 25, pp. 1321–1324, Nov. 1970.
[4] A. Ashkin and J. M. Dziedzic, "Optical levitation by radiation pressure," *Appl. Phys. Lett.*, vol. 19, pp. 283–285, Oct. 1971.
[5] J. L. Picque and J. L. Vialle, "Atomic-beam deflection and broadening by recoils due to photon absorption or emission," *Opt. Commun.*, vol. 5, pp. 402–406, Aug. 1972.
[6] R. Schieder, H. Walther, and L. Woste, "Atomic beam deflection by the light of a tunable dye laser," *Opt. Commun.*, vol. 5, pp. 337–340, Aug. 1972.

Atomic Laser Action in Rare Gas–SF_6 Mixtures

D. G. SUTTON, L. GALVAN, P. R. VALENZUELA, AND S. N. SUCHARD

Abstract—**Pulsed-laser action is described on a number of atomic transitions of ArI, one of which has not been reported previously. The addition of SF_6 to Ar shifts the laser action in the Ar from the $3d'(3/2)_1^0 - 4p'(1/2)_1$ transition to six ArI transitions originating from the three lowest states of the $3p^5 3d$ electron configuration. Significant enhancement of the intensity is observed over that resulting from a discharge in pure argon. In addition, when a small amount of SF_6 is added to a He discharge, laser oscillation results from FI at 0.7129 μm. Increased SF_6 pressure produces an unidentified oscillation at 2.639 μm. These last two transitions have been observed also in He–NF_3, He–CF_4, and He–PF_3 mixtures.**

I. Introduction

Dissociative-excitation transfer has previously resulted in a number of atomic lasers in both pulsed and CW longitudinal discharge devices [1]–[3]. Transverse excitation has also proven effective in exciting atomic lasers at pressures up to 1 atm [4]. In addition, enhancement of certain CW ArI laser oscillations has been accomplished by the addition of chlorine to a mixture of argon and helium [5].

We have observed a total of seven laser transitions in Ar, one of which has not been previously reported. In pure Ar, only one transition was observed; however, the other six transitions were observed to lase simultaneously upon the addition of SF_6 to the discharge in Ar. These six transitions form a highly coupled system between three upper ($3d$) and three lower ($4p$) levels of the Ar.

Manuscript received July 2, 1974. This research was supported by the Defense Advanced Research Projects Agency of the Department of Defense under U.S. Air Force Space and Missile Systems Organization (SAMSO) Contract F04701-73-C-0074.

The authors are with The Aerospace Corporation, El Segundo, Calif.

The addition of less than 0.2 torr SF_6 to 49 torr He results in lasing on the FI($3p^2P^0_{1/2} \rightarrow 3s^2P_{1/2}$) transition at 0.7129 μm. However, the addition of several torr SF_6 to 49 torr He produces an unidentified oscillation at 2.639 μm. These last two transitions have also been observed to lase in He–NF_3, He–CF_4, and He–PF_3 mixtures.

II. Experimental Apparatus

The laser tube consists of a 3-m Lucite pipe fitted with a double helix of 470-Ω resistors. Each helix consists of 502 resistors with one wire lead penetrating the 1-in-ID tube at equally spaced intervals. The other lead is tied to a common bus line. One helix is connected via the bus to ground, and the other helix forms the anode of a pulsed power supply consisting of a 0.014-μF capacitor bank triggered at 1 Hz by a spark gap (EG&G GP-14B). The capacitor is connected to a dc supply (Universal Voltronics BAL 130-5.5) capable of delivering 130 kV. This configuration results in 502-pin-pair electrodes being opposed across a $\frac{3}{4}$-in gap. Actually, the tube is formed from two equal sections connected in the middle, where provision is made for evacuation by a mechanical pump, and the ends are sealed by CaF_2 windows at Brewster's angle. The gas mixture from a metered manifold flows into the tube from both ends. The cavity is formed by a 450-in focal-length silver-coated mirror and a silver-coated flat with a 1-mm-diam coupling hole. Both mirrors have a protective MgF_2 overcoat to prevent oxidation of the silver surface. These mirrors are spaced 6-in from the end windows, which yields a 3.2-m-long laser cavity. Output from the laser enters a screen room and is split into two beams by a sapphire flat at 45° to the beam. The beam reflected from the flat was monitored with an InSb photovoltaic detector at 77 K (Barnes Engineering). The transmitted portion of the laser beam was directed to a $\frac{1}{2}$-m McKee–Pedersen monochromator equipped with an infrared grating blazed at 3 μm. Output from the monochromator was focused onto an identical InSb detector by a gold-coated 8-in-radius of curvature mirror. Measured detector response was monitored by a Tektronix 7704 or 551 oscilloscope to be less than 20 ns.

III. Results

When the capacitor bank is charged to 25 kV and discharged through 5.0 torr or pure Ar, weak lasing occurs at 1.270 μm ($3d'(3/2)_1^0 \rightarrow 4p'(1/2)_1$). If the Ar pressure is maintained at 5 torr and 3 torr SF_6 is added, the peak laser intensity increases by two orders of magnitude. Spectral resolution of the laser output reveals six different laser oscillations occurring simultaneously between 1.652 and 2.397 μm from the Ar/SF_6 mixture. These transitions are cataloged in Table I. All transitions, except the first at 1.652 μm, have been observed previously, but under completely different conditions [6]. The temporal behavior of the six transitions resulting

TABLE I
Wavelengths of Observed Laser Transitions in Ar and Ar + SF_6 Mixtures

Transition	λ(μm)	Gas
$3d(3/2)^o_2 - 4p(3/2)_1$	1.652	Ar + SF_6
$3d(3/2)^o_2 - 4p(3/2)_2$	1.694	
$3d(1/2)^o_1 - 4p(3/2)_2$	1.791	
$3d(3/2)^o_2 - 4p'(1/2)_1$	2.153	
$3d(1/2)^o_1 - 4p'(1/2)_1$	2.313	
$3d(1/2)^o_0 - 4p'(1/2)_1$	2.397	
$3d'(3/2)^o_1 - 4p'(1/2)_1$	1.270	Ar

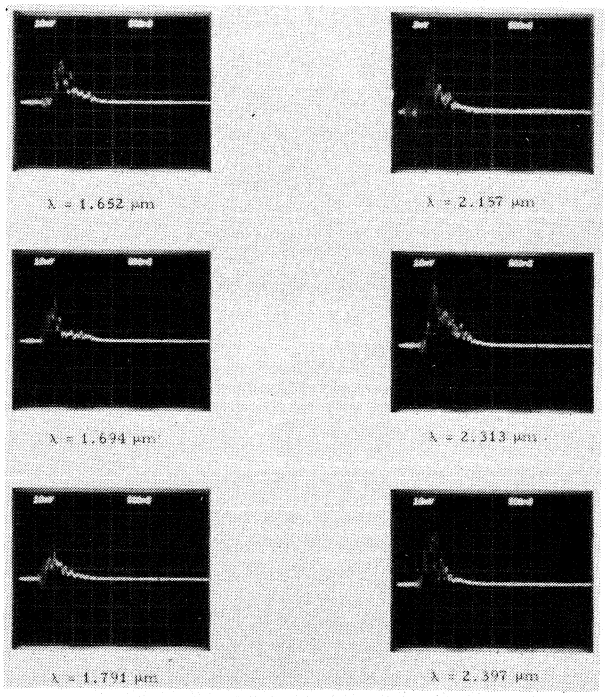

Fig. 1. Laser output at six wavelengths in ArI. (The signals at 1.791 and 2.397 μm were attenuated by a factor of 10 and 3.2, respectively. The time scale for all the oscilloscope traces is 500 ns/div.)

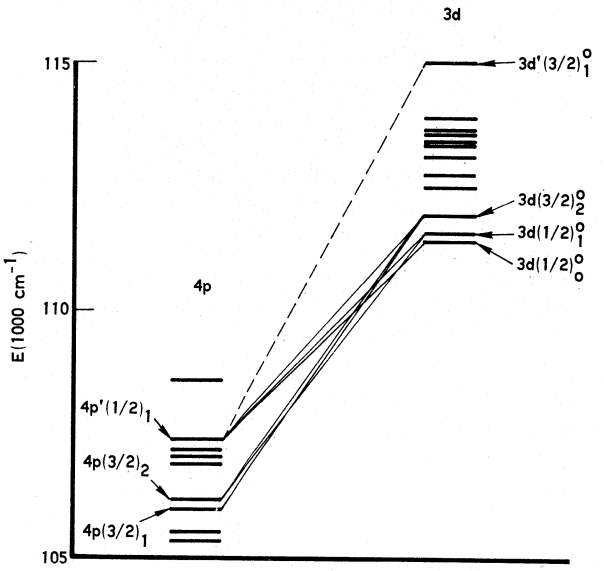

Fig. 2. Partial ArI energy-level diagram. (Dashed line shows weak laser transition occurring in pure Ar. Solid lines represent six strong transitions lasing simultaneously in Ar–SF_6 mixture.)

from the Ar/SF_6 mixture is shown in Fig. 1, and the relevant energy-level diagram of Ar is given in Fig. 2. It may be seen from Figs. 1 and 2 that the Ar/SF_6 mixture results in a highly coupled system of six transitions between six states, all lasing simultaneously.

When a mixture of 49 torr He and less than 0.2 torr SF_6 is discharged at 25 kV in the same device, lasing occurs at 0.7129 μm from FI atoms [7]. The laser pulse begins approximately 0.5 μs after initiation of the discharge and is 1 to 2 μs wide [full width at half maximum (FWHM)]. If the SF_6 pressure is increased to 18 torr, lasing occurs on an unidentified transition at 2.639 ± 0.002 μm. The output under these conditions (see Fig. 3) consists of a series of pulses beginning 10 μs after initiation and continuing for 50 μs. The pin discharge lasts no longer than 2 μs. Nearly identical results are obtained from He–CF_4 or He–PF_3 mixtures. A single 2-μs-wide pulse of laser light at 0.7129 μm is observed from a dilute (CF_4 or PF_3 = 0.2 torr, He = 49 torr) mixture. The laser output from a discharge in 25 torr CF_4 or PF_3 and 47 torr He occurs at 2.639 μm. The output consists of two or more pulses beginning 50 μs after initiation. In a mixture of NF_3 (0.2 torr) and He (47.8 torr), however, both the 0.7129- and 2.639-μm

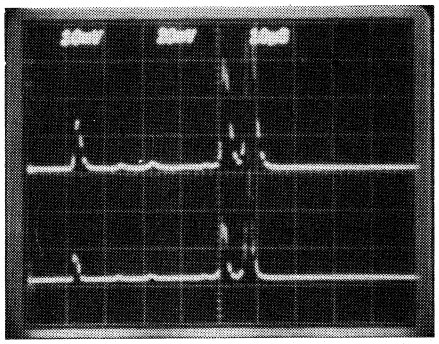

Fig. 3. Unidentified laser output at 2.639 μm in He–SF_6 gas mixture. (Top trace is the signal at the exit slits of the monochromator set at 2.639 μm. The bottom trace is the total laser output reflected from the front surface of the sapphire beam splitter. Reactant pressures are He = 49 torr and SF_6 = 18 torr. Time scale is 10 μs/div.)

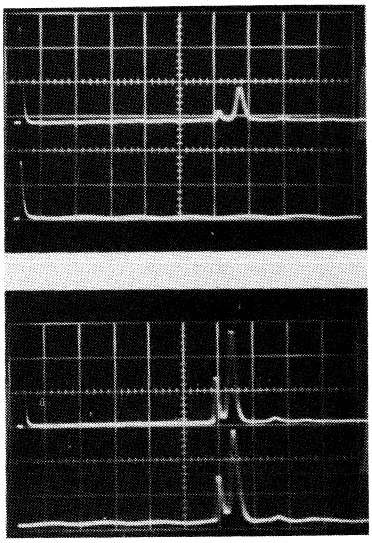

Fig. 4. Simultaneous laser oscillation on two lines from NF_3–He mixture. (The top trace in both photos is the total laser output. The bottom trace in the top photo is the output from the monochromator at 0.7129 μm. The bottom trace of second photo is from the monochromator set at 2.639 μm. Sweep time is 10 μs/cm. Sensitivity is 10 mV/cm. NF_3 = 0.2 torr and He = 47.8 torr.)

transitions lase simultaneously (Fig. 4). The time to threshold for the 2.639-μm line in this case is approximately 50 μs. Both of these laser oscillations are interpreted as arising from dissociative excitation transfer from metastable He to the F-atom bearing molecule.

In an attempt to identify the transition occurring at 2.639 μm, several additional experiments have been performed. The first of these was the interruption of the laser path, external to the optical cavity, by a cell with a path length of 2.0 cm containing HF at a pressure of 2 torr. Since a laser wavelength of 2.639 μm coincides with that of the $P_1(4)$ transition in the HF molecule, within the measurement accuracy of our spectral analysis apparatus, absorption of the laser radiation by the cell could be indicative of its source as HF radiation. Indeed, the laser radiation was greatly diminished in intensity by the HF cell. A possible source of H atoms for the production of the HF molecules could be an atmospheric water leak in our vacuum system. Test measurements made by adding water to the gaseous mixture did indeed demonstrate lasing from HF molecules, as has been reported previously by Florin and Jensen [8]; however, the laser action occurred from the $P_1(2)$–$P_1(10)$ transitions of the HF molecule. In our "pure" SF_6–He mixture, only laser radiation at the $P_1(4)$ wavelength was observed so, consequently, atmospheric water was not the H-atom source.

A second experiment in which the total gas pressure was increased to 300 torr was performed to ascertain if H-atom "contamination" was being formed by the discharge striking the laser-tube walls. As the gas pressure is increased, diffusion of vaporized Lucite into the laser zone should take longer, thereby increasing the time from the discharge to laser threshold. This increased threshold time was not observed; therefore, H-atom sources are not produced by laser-wall vaporization.

The results of the supporting experiments indicate that the laser oscillations at 2.639 μm do not originate from the HF molecule. Inspection of a table of atomic energy levels [9] indicates that this wavelength does not correspond to any known transitions in the neutral or ionized species possible in the gaseous mixture. Experiments are now under way to identify this laser-active species.

In addition to the FI transition at 0.7129 μm we have observed two additional laser oscillations that have been interpreted previously as arising from dissociative-excitation transfer from metastable He atoms [3]. The first of these occurs in a

mixture of 95 torr He with approximately 0.1 torr of N_2, N_2O, or NO discharged at 23 kV. The laser output is at 1.358 μm and is due to the $3p^2S^0_{1/2}$–$3s^2P_{3/2}$ transition of NI. The second oscillation is observed at 1.454 μm in mixtures of He (125 torr) and CO (0.1 torr). It has been assigned to the $3p^1P_1 - 3s^1P^0_1$ transition of CI. Both of these oscillations exhibit temporal behavior similar to the F-laser at 0.7129 μm.

In conclusion, we have observed laser action on seven transitions in ArI. Six of these are seen to lase simultaneously with enhanced output upon the addition of small amounts of SF_6. Oscillation in F, C, and N atoms in the near infrared occurs when small amounts of an appropriate compound are added to a He discharge. Discharging 18 torr SF_6 and 49 torr He results in an unidentified laser line at 2.639 μm that persists in multipulsing for >50 μs.

Acknowledgment

The authors wish to thank M. Lundquist and A. Ching for assisting with the design and construction of the pin discharge laser.

References

[1] C. K. N. Patel, R. A. McFarlane, and W. L. Faust, "Optical maser action in C, N, O, S, and Br on dissociation of diatomic and polyatomic molecules," *Phys. Rev.*, vol. 133A, pp. A1244–A1248, 1964.

[2] J. B. Atkinson and J. H. Sanders, "Laser action in C and N atoms following dissociative excitation transfer," *J. Phys. B (Proc. Phys. Soc.)*, vol. 1, pp. 1171–1179, 1968.

[3] G. L. De Poorter and G. Balog, "New infrared laser line in OCS and new method for C atom lasing," *IEEE J. Quantum Electron.* (Notes & Lines), vol. QE-8, pp. 917–918, Dec. 1972.

[4] O. R. Wood, E. G. Burkhardt, M. A. Pollack, and T. J. Bridges, "High pressure laser action in 13 gases with transverse excitation," *Appl. Phys. Lett.*, vol. 18, pp. 112–114, 1971.

[5] A. B. Dauger and O. M. Stafsudd, "Observation of CW laser action in chlorine, argon, and helium gas mixtures," *IEEE J. Quantum Electron.* (Corresp.), vol. QE-6, pp. 572–573, Sept. 1970.

[6] R. J. Pressley, Ed., *Handbook of Lasers*, Chemical Rubber Co. Cleveland, Ohio, 1971, p. 210.

[7] M. A. Kovacs and C. J. Ultee, "Visible laser action in fluorine I," *Appl. Phys. Lett.*, vol. 17, pp. 39–40, 1970.

[8] A. E. Florin and R. J. Jensen, "The F + H_2O chemical laser," *IEEE J. Quantum Electron.* (Notes & Lines), vol. QE-7, pp. 472–473, Sept. 1971.

[9] C. E. Moore, *Atomic Energy Levels* (Circular 467). Washington, D.C.: NBS, June 15, 1949.

Acoustooptic Bragg Deflection in $LiNbO_3$ Ti-Diffused Waveguides

R. V. SCHMIDT AND I. P. KAMINOW

Abstract—**A $LiNbO_3$ acoustooptic Bragg deflector utilizing a Ti-diffused optical waveguide and acoustic surface waves, which requires only 50 mW of electrical drive power to obtain 70-percent deflection, has been demonstrated.**

Recently, high-performance acoustooptic deflectors have been demonstrated using TeO_2 which require electrical drive powers as low as 35 mW for several hundred resolvable spots and random access times on the order of 10 μs [1]. These deflectors require low drive power because TeO_2 has a high acoustooptic figure of merit and the anisotropic Bragg-diffraction regime can be used at practical acoustic frequencies [1], [2]. In this correspondence we report on an acoustooptic Bragg deflector using $LiNbO_3$, which has an acoustooptic figure of merit about 100 times smaller than TeO_2, but has electrical drive power requirements similar to TeO_2 deflectors. In particular, 70-percent deflection of the incident light beam is obtained over a 3-dB bandwidth of 30-MHz with only 50 mW of electrical drive power. This deflector requires low electrical drive power because guided optical waves and acoustic surface waves are utilized which allows for a much more efficient interaction geometry than is possible with bulk deflectors.

Acoustic surface waves and guided optical waves lend themselves to low drive power deflectors because both waves are closely confined to the surface allowing long interaction lengths which are not obtainable in bulk deflectors because of diffraction. By analogy to bulk acoustooptic Bragg deflectors the power required for 70-percent deflection P_0 is given by [3]

$$P_0 = \frac{2\lambda_0^2}{\pi^2}\frac{H}{L}\frac{1}{M_{2\text{eff}}} \tag{1}$$

where L is the length of interaction, H is the depth of the sound wave, and λ_0 is the optical wavelength. The quantity $M_{2\text{eff}}$ is the effective acoustooptic figure of merit analogous to M_2 for bulk deflectors, but in addition to material properties it must also include the overlap integral of the acoustic and optical fields [3], [4]. For an efficient interaction requiring low drive power one desires H to be as small as possible and L to be large.

Acoustic surface waves and guided optical waves provide an ideal means of satisfying these requirements. An acoustic surface wave is predominantly contained within an acoustic wavelength Λ of the surface. Thus $H \approx \Lambda$ is as small as can be obtained with focused bulk waves. But since the surface wave is trapped near the surface there is no difficulty which can arise from the sound-wave depth expanding due to diffraction when the optical beam is very wide.

Because guided optical waves are also trapped near the surface, typically within 1 μ of the surface, the light can be contained within a sound column of depth H for arbitrarily long lengths L. In the case of bulk devices a light beam can be focused to a spot of diameter H only for a short distance on the order of H^2/λ before diffraction expands the optical beam to a diameter larger than the sound-column depth. Since there are no diffraction limitations on a guided optical beam to keep it contained within the sound column, the interaction length for surface-wave deflectors is set by the bandwidth requirements of the deflector. For a 3-dB deflection bandwidth Δf the maximum interaction length over which the light and sound waves can be Bragg phase matched in the isotropic case is

$$L_{\max} = 1.8\frac{nV^2}{\lambda_0 f_0 \Delta f} \tag{2}$$

where V and f_0 are the acoustic velocity and center frequency, respectively, and n is the index of refraction of the acoustooptic medium [5]. The interaction length $L_{\max}$ can be much greater than the interaction length limited by optical diffraction in bulk deflectors. If acoustic beam-steering techniques [6], [7] are used, the interaction can be even longer than $L_{\max}$.

The acoustooptic deflector reported on in this correspondence is illustrated in Fig. 1. The crystal is a Y-cut slab of $LiNbO_3$ with the Z axis oriented along the propagation direction of the sound wave. The optical waveguide was formed by an in-diffusion technique [8] similar to that used to form Nb-diffused $LiTaO_3$ waveguides [9]. A 500-Å-thick Ti film was

Manuscript received August 19, 1974.

The authors are with Bell Laboratories, Holmdel, N.J. 07733.

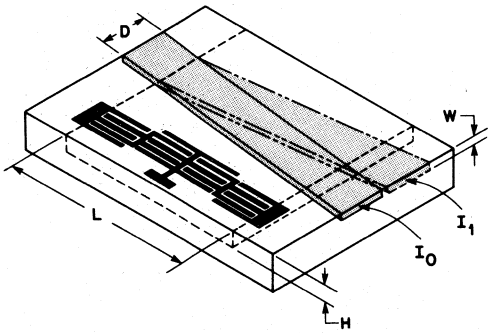

Fig. 1. Schematic of deflector illustrating optical beam of width D and sound beam of depth H and width L. Series-parallel connected transducer has center bonding pad wired to ground through inductor and outer two bonding pads wired together and connected to oscillator.

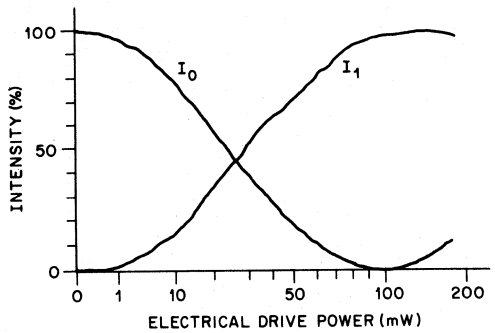

Fig. 2. Recorder trace of experimentally measured intensity of undeflected beam I_0 and deflected beam I_1 as a function of electrical drive power.

evaporated onto the Y-cut surface of a $LiNbO_3$ crystal and was heated for 6 h at 960°C in an argon atmosphere. However, no repoling was necessary since the diffusion took place below the Curie temperature. The waveguide whose losses were estimated to be approximately 1 dB/cm supported 4 TE modes and 1 TM mode. Each of the five modes could be excited independently with a prism coupler and there was insignificant scattering from one mode into the other modes. The waveguides were of good quality and confined the guided light to within 2 μ of the surface. The primary advantage of Ti-diffused waveguides for acoustooptic deflectors over out-diffused waveguides [10] is the tight surface confinement of the optical wave which allows the use of acoustic frequencies above 100 MHz.

A series-parallel connected interdigital transducer [11], illustrated in Fig. 1, was used in order to efficiently excite an acoustic surface wave over a long interaction length. This transducer consists of four 50-Ω, $4\frac{1}{2}$ finger-pair transducers which are series and parallel connected to give a transducer with 50-Ω input impedance, 175-MHz center frequency, and an active length L of 8.74 mm. This length corresponds to a 3-dB deflector bandwidth of 50-MHz as calculated from (2). The parameter $Q = 2\pi\lambda L/n\Lambda^2$ equals 40 indicating that the deflector is in the Bragg-deflection regime.

The efficiency of the deflector was measured by plotting the intensity of the undeflected and deflected optical beams as a function of electrical drive power. The results are presented in Fig. 2 for the TE_0 mode. Only 50 mW of electrical drive power are required for 70-percent deflection of the incident beam. The deflector had a measured 3-dB bandwidth of 30 MHz. This bandwidth is believed to be limited by the bandwidth of the transducer which had several broken electrodes. From measurements of the transducer input impedance the transduction loss was estimated to be greater than 7 dB indicating that less than 8 mW of acoustic power was necessary for 70-percent deflection. The higher order TE modes required slightly more drive power for a given deflection indicating a less efficient interaction geometry. When the TM_0 mode was launched, 140-mW electrical drive power gave 70-percent deflection. Presumably, this large increase in drive power is due to a smaller induced-index change in the ordinary index, which diffracts the TM mode, than in the extraordinary index which diffracts the TE modes.

The present deflector has ten resolvable spots with a 300-ns access time. The number of resolvable spots was limited by the width D over which a suitably uniform guided optical wave could be coupled into the waveguide with the available prism coupler arrangement, which was about 1 mm. However, the deflector has a time–bandwidth product which allows 300 resolvable spots with a 10-μs access time. Such performance would require an optical beamwidth of 35 mm. Such widths should be feasible if appropriate care is taken in coupling light into the deflector since Ti-diffused waveguides are extremely uniform and the guided light does not break up into filaments as is characteristic of many sputtered thin-film guides.

Optical damage may limit the optical power through the Ti-diffused $LiNbO_3$ deflector. For 6328-Å light, Ti-diffused waveguides normally show no signs of optical damage with power densities on the order of 5000 W/cm^2, but in some waveguides, similarly fabricated, rapid damage has been observed with power densities as low as 100 W/cm^2. The source of this optical damage is not understood and further work is necessary to determine the limitations on Ti-diffused $LiNbO_3$ waveguides set by optical damage.

In conclusion, an efficient acoustooptic deflector has been demonstrated on a $LiNbO_3$ crystal whose acoustooptic figure

of merit is approximately 100 times smaller than that of TeO_2. Such performance has been obtained by utilizing guided optical waves and acoustic surface waves which allow a more efficient interaction geometry than can be obtained in bulk deflectors. When optical waveguides become available on high acousto-optic figure-of-merit crystals such as TeO_2 one can expect even further reduction in electrical drive power.

References

[1] A. W. Warner, D. L. White, and W. A. Bonner, "Acoustooptic light deflectors using optical activity in paratellurite," *J. Appl. Phys.*, vol. 43, pp. 4489–4495, Nov. 1972.

[2] E. G. H. Lean, C. F. Quate, and H. J. Shaw, "Continuous deflection of laser beams," *Appl. Phys. Lett.*, vol. 10, pp. 48–51, Jan. 1967.

[3] Y. Ohmachi, "Acousto-optical light diffraction in thin films," *J. Appl. Phys.*, vol. 44, pp. 3928–3933, Sept. 1973.

[4] L. Kuhn, M. L. Dakss, P. F. Heidrich, and B. A. Scott, "Deflection of an optical guided wave by a surface acoustic wave," *Appl. Phys. Lett.*, vol. 17, pp. 265–267, Sept. 1970.

[5] E. I. Gordon, "A review of acoustooptical deflection and modulation devices," *Proc. IEEE (A Special Joint Issue on Optical Electronics with Applied Optics)*, vol. 54, pp. 1391–1401, Oct. 1966.

[6] D. A. Pinnow, "Acousto-optic light deflection: Design considerations for first order beam steering transducers," *IEEE Trans. Sonics Ultrason.*, vol. SU-18, pp. 209–214, Oct. 1971.

[7] R. M. DeLaRue, C. Stewart, C. D. W. Wilkinson, and I. R. Williamson, "Frequency-controlled beam steering of surface acoustic waves using a stepped transducer array," *Electron. Lett.*, vol. 9, pp. 326–327, July 1973.

[8] R. V. Schmidt and I. P. Kaminow, "Metal-diffused optical waveguides in $LiNbO_3$," *Appl. Phys. Lett.*, Oct. 1974.

[9] J. M. Hammer and W. Phillips, "Low-loss single-mode optical waveguides and efficient high-speed modulators of $LiNb_xTa_{1-x}O_3$ on $LiTaO_3$," *Appl. Phys. Lett.*, vol. 24, p. 545, 1974.

[10] R. V. Schmidt, I. P. Kaminow, and J. R. Carruthers, "Acousto-optic diffraction of guided optical waves in $LiNbO_3$," *Appl. Phys. Lett.*, vol. 23, pp. 417–419, Oct. 1973.

[11] K. M. Lakin, W. T. Mih, and R. M. Tarr, "The dog-leg transducer: A new IDT geometry," presented at the Ultrasonics Symp., Monterey, Calif., 1973, Talk D-4.

Mode Locking the Nd:Glass Laser with BDN: Measurements of Dye Recovery Times and Laser Pulse Lengths

R. C. GREENHOW AND A. J. STREET

***Abstract*—The recovery times for transient bleaching of the *Q*-switch dye bis(4-dimethylaminodithiobenzil)nickel (BDN) in the solvents dichlorethane and iodoethane have been determined. The lengths of pulses from an Nd:glass laser mode locked with BDN have also been measured by means of the two-photon fluorescence technique.**

A new dye, bis(4-dimethylaminodithiobenzil)nickel (or BDN), has recently emerged for *Q* switching the Nd:glass laser [1], which has the advantage over Kodak dyes 9860 and 9470 of being extremely stable. Compared with the latter dyes, however, which have lifetimes of 7 ± 1 ps and 11 ± 1 ps, respectively [2], BDN has a much longer lifetime, which varies markedly with solvent. In chloroform it is 6.2 ± 1.6 ns and in carbon disulphide it is 1.5 ± 0.2 ns [3]. In these solvents, therefore, the dye is ineffective in mode locking, although strongly modulated emission is observed in a proportion of cases [3]. New solvents have now been found which reduce the recovery time to such an extent that clean mode-locked pulse trains may be recorded on an oscilloscope [4]. One class of solvent, exemplified by iodoethane, is effective on account of the heavy-atom substituent (iodine), while another class, exemplified by methyl sulfoxide, is effective because of non-bonding (n^-) electron pairs [4].

We have measured the length of pulses from an Nd:glass laser mode locked with BDN in iodoethane, using the two-photon fluorescence (TPF) method [5]. We have also determined the decay times of transient bleaching of BDN in dichlorethane and in iodoethane.

The laser consisted of a $4\frac{1}{2} \times \frac{3}{8}$-in Brewster-angled, helically pumped Nd:glass rod in a plane-parallel cavity incorporating a +4-m lens. A 1-mm flowing dye cell was in contact with the 70-percent reflectivity output mirror. Using Kodak 9860 dye this laser produced clean pulse trains with 95-percent reliability. Measurements of TPF tracks in rhodamine 6G indicated pulse lengths between 5 and 10 ps with contrast ratios up to 2.7. Typically, the linear transmission of the dye cell was 80 percent, and the pulse-train length was 200–300 ns with about 3 mJ in each pulse. With BDN in iodoethane the dye-cell transmission used was 50 percent, and the pulse trains were about 50 ns long with up to 10 mJ in each pulse.

The TPF patterns observed when mode locking with BDN varied considerably. Frequently, an apparently good pulse train as seen on an oscilloscope failed to yield a recognizable pulse in the TPF cell—presumably because the pulses were very long ($\gtrsim 150$ ps). Others showed clear evidence of close satellite pulses. A number showed the broad, smooth shoulder with narrow "coherence spike" expected for a non-transform-limited (noisy) pulse.

A pulse train consisting of bursts of noise with zero intensity between pulses would give a TPF pattern with peak-to-shoulder-to-background ratios of 3:2:1 [6]. Even though the the 3:1 ratio was not observed for experimental reasons, one would still expect 2:1 for the shoulder-to-background ratio. In practice we observe, typically, 2:1.6:1 from which we deduce that there must be substantial energy between the pulses.

Pulse lengths measured (full width at half shoulder height of the TPF trace) were between 25 and 70 ps, although much longer pulses occur. Gillman and Dewhurst have used BDN to mode lock an Nd:YAG laser, the resulting pulses being 50 ± 10 ps long, as measured by two-photon fluorescence [7].

Measurements of the recovery times of transiently bleached BDN were made using the Nd:glass laser mode locked with Kodak 9860. For BDN in dichlorethane the method of [8] was used, in which the integrated transmission of an entire pulse train was measured as a function of delay time between bleaching and sampling pulses. This yielded the recovery time of 2.2 ± 0.4 ns. For BDN in iodoethane the technique of [2] was employed, in which bleaching due to individual pulses, selected from the beginning of the pulse train and with intensities uniform to within 10 percent, was measured, again as a function of probe-pulse delay time. A recovery curve is shown in Fig. 1. Each point is an average of up to eight measurements, and the errors shown are standard deviations. The recovery time as determined from the curve by means of a Swinbourne plot [9] was found to be 90 ± 20 ps. These measurements correlate well with the observed mode-locking performance.

We conclude that BDN is of limited use in mode locking the Nd:glass laser. It does provide a means of generating ~50-ps pulses, but the occurrence of clean pulse trains is less reliable and the lengths of the pulses more erratic than with Kodak 9860. The situation could probably be improved by reducing the oscillating bandwidth. This would not only result in the possibility of smooth transform-limited pulses, but, according to [10], would greatly increase the reliability of generation.

Manuscript received August 26, 1974.
The authors are with the Department of Physics, University of York, Heslington, York, England.

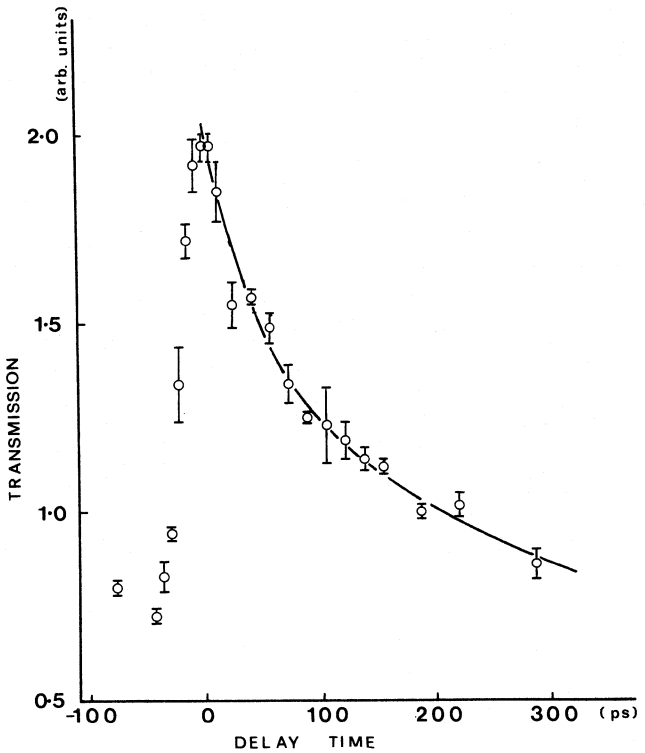

Fig. 1. Transmission of BDN in iodoethane as a function of delay time after bleaching pulse.

In this connection it is interesting to note that the Nd:YAG laser [7] with its smaller bandwidth, was much more reliable in its operation.

A disadvantage of BDN is that the pulses generated are much more destructive to the mirrors and the laser rod itself than the shorter pulses produced with Kodak 9860.

ACKNOWLEDGMENT

The authors wish to thank B. Knight of the Chemistry Department, University of York, for his synthesis of the BDN dye used in these experiments.

REFERENCES

[1] K. H. Drexhage and U. T. Müller-Westerhoff, "New Q-switch compounds for infrared lasers," *IEEE J. Quantum Electron.* (Notes & Lines), vol. QE-8, p. 759, Sept. 1972.

[2] D. Von der Linde and K. F. Rodgers, "Recovery time of saturable absorbers for 1.06 μ," *IEEE J. Quantum Electron.* (Corresp.), vol. QE-9, pp. 960–961, Sept. 1973.

[3] D. Magde, B. A. Bushaw, and M. W. Windsor, "Q switching and mode locking the Nd^{3+}–glass laser with nickel dithienes," *IEEE J. Quantum Electron.* (Notes & Lines), vol. QE-10, p. 394, Mar. 1974.

[4] K. H. Drexhage and G. A. Reynolds, "New dye solutions for mode locking infra red lasers," *Opt. Commun.*, vol. 10, pp. 18–20, Jan. 1974.

[5] J. A. Giordmaine, P. M. Rentzepis, S. L. Shapiro, and K. W. Wecht, "Two photon excitation of fluorescence by picosecond light pulses," *Appl. Phys. Lett.*, vol. 11, pp. 216–218, 1967.

[6] H. A. Pike and M. Hercher, "Basis for picosecond structure in mode-locked laser pulses," *J. Appl. Phys.*, vol. 41, pp. 4562–4565, 1970.

[7] G. Gillman and T. Dewhurst, Dep. Appl. Phys., Univ. Hull, England, private communication.

[8] R. I. Scarlet, J. F. Figueira, and H. Mahr, "Direct measurement of picosecond lifetimes," *Appl. Phys. Lett.*, vol. 13, pp. 71–73, 1968.

[9] E. S. Swinbourne, *Analysis of Kinetic Data.* London, England: Nelson, 1971, p. 81.

[10] P. G. Kryukov and V. S. Letokhov, "Fluctuation mechanisms of ultrashort pulse generation by laser with saturable absorber," *IEEE J. Quantum Electron.*, vol. QE-8, pp. 766–782, Oct. 1972.

Notes and Lines

Near-Infrared Dye Laser Emission from Ultraviolet Nitrogen-Laser-Pumped Dye Solutions

CHINLON LIN

Abstract—**We report "superradiant" near-IR dye laser emission, with peak of emission in the 690–930-nm range, from nitrogen-laser (λ = 337-nm)-pumped dye solutions including aluminum phthalocyanine chloride and seven polymethine cyanine dyes.**

Recently, Hilderbrand [1] reported near-IR dye laser emission from several polymethine dyes directly pumped by UV nitrogen-laser radiation. With a 100-kW N_2 laser he was able to obtain stimulated emission for highly concentrated dye solutions (10^{-1} M) in a cavity. The peaks of emission were in the 43–928-nm range.

In this note we report the observation of "superradiant" emission from eight dyes, including six of those reported in [1], using direct UV pumping by a 400-kW nitrogen laser. As shown in Table I the emission peaks fall within the range 690–930 nm, and have bandwidths of 20 to 30 nm. It may be noted that for the six dyes [dyes 2)–7)] which were also reported in [1], the emission peaks all occur at shorter wavelengths than listed in [1]. This is no doubt due to the much lower concentrations used here (5×10^{-4} M versus 10^{-1} M) and to the different solvent (acetone versus methyl sulfoxide). Dyes 1) and 8) have not been previously reported with direct UV pumping.

TABLE I
LIST OF DYE SOLUTION AND PEAK WAVELENGTHS OF SUPERRADIANT EMISSION[a]

	Dye/Solvent	Concentration	λ Peak
1)	Aluminum Phthalocyanine Chloride/methanol	10^{-3}M	690 nm
2)	3,3'-Diethyl-2,2'-thiadicarbocyanine iodide/acetone	2.5×10^{-4}M	695 nm
3)	3,3'-Diethyl-10-chloro-2,2'-(5,6,5',6'-dibenzo) thiadicarbocyanine iodide/acetone	2.5×10^{-4}M	720 nm
4)	3,3'-Diethyl-2,2'-oxatricarbocyanine iodide/acetone	5×10^{-4}M	770 nm
5)	3,3'-Diethyl-2,2'-thiatricarbocyanine iodide/acetone (DTTC iodide)	5×10^{-4}M	820 nm
6)	1,3,3,1',3',3'-Hexamethyl-2,2'-indotricarbocyanine iodide/acetone	5×10^{-4}M	840 nm
7)	3,3'-Diethyl-2,2'-(4,5,4',5'-dibenzo) thiatricarbocyanine iodide/acetone	5×10^{-4}M	870 nm
8)	1,1'-Diethyl-4,4'-dicarbocyanine iodide/methyl sulfoxide	10^{-3}M	930 nm

[a] Pumped with 10-ns 400-kW nitrogen-laser radiation (337 nm).

Manuscript received September 13, 1974.
The author is with Bell Laboratories, Holmdel, N.J. 07733.

REFERENCES

[1] O. Hilderbrand, "Nitrogen laser excitation of polymethine dyes for emission wavelengths up to 9500 Å," *Opt. Commun.*, vol. 10, pp. 310–312, Apr. 1974.

Contributors

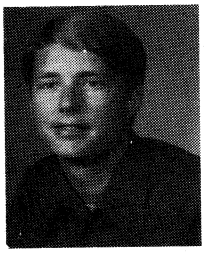

William K. Bischel was born in Houston, Tex., on June 9, 1948. He received the B.S. degree in physics and the M.S. degree in applied science, both from the University of California, Davis, in 1970 and 1972, respectively. He is currently working toward the Ph.D. degree in applied science at the Lawrence Livermore Laboratory, Livermore, Calif.

His current research interests include pulse compression, nonlinear optics, and nonlinear infrared laser spectroscopy.

Mr. Bischel is a member of the American Physical Society and the Optical Society of America.

*

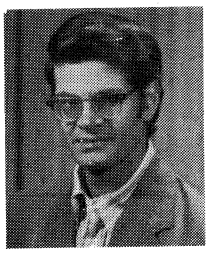

William K. Burns was born in Philadelphia, Pa., in June 1943. He received the B.S. degree in engineering physics from Cornell University, Ithaca, N.Y., in 1965, and the M.S. and Ph.D. degrees in applied physics from Harvard University, Cambridge, Mass., in 1967 and 1971, respectively.

During 1971 he was a Staff member at Arthur D. Little, Inc., Cambridge, Mass., where he contributed to various laser-related studies and surveys. Since 1972 he has been a Research Physicist in the Optical Sciences Division of the Naval Research Laboratory, Washington, D.C., where he is working on problems associated with integrated optics and optical communications systems.

Dr. Burns is a member of the American Physical Society and the Optical Society of America.

*

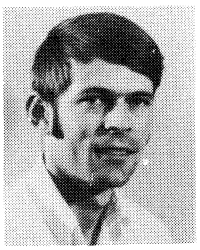

Robert L. Byer completed his undergraduate studies in physics at the University of California, Berkeley, in 1964.

He then joined Spectra Physics in research and development for one year prior to beginning graduate studies in quantum electronics in the Department of Applied Physics at Stanford University, Stanford, Calif. Following graduation he joined the Department of Applied Physics in 1969, where he is currently an Assistant Professor. His research areas include nonlinear materials studies, parametric devices, and applications of tunable coherent sources to spectroscopy.

*

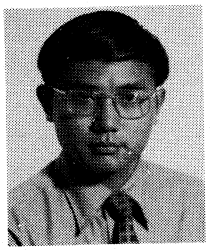

Michael M. Choy received the B.S. degree in engineering physics from the University of California, Berkeley, in 1971, and the M.S. degree in applied physics from Stanford University, Stanford, Calif., in 1973. Currently, he is completing the requirements for the Ph.D. degree, also at Stanford.

Since 1971 he has been a Research Assistant at the Microwave Laboratory at Stanford, where he has been working on tunable sources for the infrared, especially in the chalcopyrites. His research interests include nonlinear optics, solid-state physics, and lasers.

Mr. Choy is a member of Phi Beta Kappa.

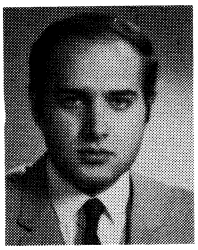

Salim Ciraci was born in Sivrihisar, Turkey, on August 30, 1942. He received the M.S. degree in mechanical engineering from the Technical University of Istanbul, Istanbul, Turkey, in 1965, and the B.S. and Ph.D. degrees in materials science from Stanford University, Stanford, Calif., in 1970 and 1973, respectively.

In 1973 he worked as a Research Associate at Stanford University on the theory of semiconductors. During 1974 he was engaged in research on surface physics at the IBM Research Laboratories in San Jose, Calif.

Dr. Ciraci is a member of the American Physical Society.

*



Joel Falk (S'64–M'70) was born in New York, N.Y., on February 12, 1945. He received the B.E.E. degree from the City College of New York, New York, in 1965, and the M.S. and Ph.D. degrees from Stanford University, Stanford, Calif., in 1967 and 1971, respectively.

He joined GTE Sylvania Inc., Mountain View, Calif., in April 1970, where he has done research and development work in the fields of nonlinear optics, dye lasers, high-power lasers, and laser mode locking.

*

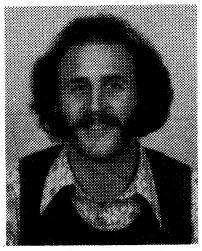

Robert A. Fisher was born in Berkeley, Calif., on April 19, 1943. He received the A.B., M.A., and Ph.D. degrees from the University of California, Berkeley, in 1965, 1967, and 1971, respectively.

He joined the Staff at the Lawrence Livermore Laboratory in 1971, where he was involved in work on nonlinear optics and lasers. Concurrently, he held a joint appointment as a Lecturer in the Department of Applied Science, University of California, Davis-Livermore. In 1974 he joined the Los Alamos Scientific Laboratory, Los Alamos, N. Mex.

Dr. Fisher is a member of the American Physical Society.

*



William H. Glenn (S'56–M'68) was born in Philadelphia, Pa., on December 22, 1937. He received the S.B. and M.S. degrees in electrical engineering in 1960, and the Ph.D. degree in physics in 1966, all from the Massachusetts Institute of Technology, Cambridge.

As a graduate student he was a member of the Plasma Physics Group of the Research Laboratory of Electronics of M.I.T. In 1966 he joined the United Aircraft Research Laboratories, East Hartford, Conn., and has been involved in the areas of nonlinear optics and studies of picosecond optical pulses. At the present time he is Principal Scientist of the Quantum Physics Group within the Quantum Physics Laboratory.

Dr. Glenn is a member of the American Physical Society, Tau Beta Pi, Eta Kappa Nu, and Sigma Xi.

R. V. Lovberg, photograph and biography not available at the time of publication.

*



A. Fenner Milton was born in New York, N.Y., on October 16, 1940. He received the B.A. degree from Williams College, Williamstown, Mass., in 1962, and the M.A. and Ph.D. degrees in applied physics, both from Harvard University, Cambridge, Mass., in 1963 and 1968, respectively.

He was a Technical Staff Member of the Science and Technology Division of the Institute for Defense Analyses from 1968 to 1971 when he joined the staff of the Naval Research Laboratory, Washington, D.C., as a Senior Staff Member of the Optical Sciences Division. His research interests have included photoconductivity, photo emission, nonlinear optics, fiber optics, and integrated optics.

*

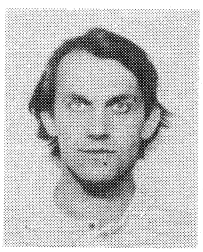

Gerard Mourou was born in Albertville, France, on June 22, 1944. He received the *licence de physique* degree from the University of Grenoble, Grenoble, France, in 1967, the *doctorat de 3ième cycle* and the *doctorat d'état* degrees from the University of Paris, Paris, France, in 1970 and 1973, respectively.

In 1968 he joined the Laboratoire Vignal de l'Ecole Polytechnique, France, where he did research on the frequency shift in Q-shifted ruby lasers. In 1970 he went to Laval University, where he was involved in measuring short fluorescence-decay time and nonlinear effects in saturable absorbers. In 1974 he joined the faculty at San Diego State University, San Diego, Calif.



Eric R. Wooding received the B.Sc. degree in 1948 and the Ph.D. degree in 1953, both from Imperial College, University of London, London, England.

From 1956 to 1960 he carried out research at the University of Sheffield, and then spent a year in the Engineering Science Laboratory at Oxford. From 1961 to 1966 he lectured in Electronic Physics at the University College of Wales, Aberystwyth. Since that time he has been Reader in Experimental Physics at Royal Holloway College, University of London. His main interest is in plasma physics, and he has collaborated with Culham Laboratory, UKAEA, on laser diagnostics for plasmas.

Dr. Wooding is a fellow of the Institute of Physics.

*

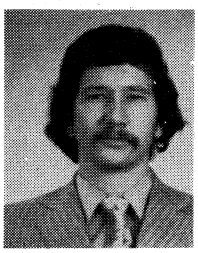

Michael L. Yeoman was born in the Principality of Wales on May 1, 1944. He received the B.S. degree in physics with honors from Swansea University, Swansea, Wales, in 1965. He then became a postgraduate student in Imperial College, University of London, London, England, where his masters degree was concerned with superconductivity and the science of materials, and his Ph.D. dissertation examined the effect of applied pressure and neutron irradiation on the electronic properties of the semimetal graphite.

On leaving Imperial College he joined the University of London as a Senior Research Fellow attached to the UKAEA Culham Laboratory for Plasma and Nuclear Fusion Research. His research work has included the use and development of novel laser diagnostic techniques for the observation of plasma parameters. He was involved in the development of a homodyne detection system for the study of laser light scattered by waves in a high-temperature plasma, and in tailoring the output of a Q-switched ruby laser in a controlled fashion. He is currently employed at AERE Harwell, Oxon., England.

Dr. Yeoman is an associate member of the Institute of Physics.

Table of Contents for Special Issue on Integrated Optics and Optical Waveguides, *IEEE Trans. Microwave Theory and Techniques*, vol. MTT-23, no. 1, January 1975

EDITORIAL . . . . . *D. Marcuse*

PAPERS

An Introduction to Integrated Optics . . . . . *H. Kogelnik*
The Progress of Integrated Optics in Japan . . . . . *Y. Suematsu*
Heterostructure Injection Lasers . . . . . *M. B. Panish*
Integrated Optics at 10.6-μm Wavelength . . . . . *W. S. C. Chang*
GaAs and GaAlAs Devices for Integrated Optics . . . . . *V. Evtuhov and A. Yariv*
Optical Waveguide Modulators . . . . . *I. P. Kaminow*
Nonreciprocal Magnetooptic Waveguides . . . . . *J. Warner*
Radiation Fields of a Tapered Film and a Novel Film-to-Fiber Coupler . . . . . *P. K. Tien, G. Smolinsky, and R. J. Martin*
Tapered Optical Directional Coupler . . . . . *M. G. F. Wilson and C. A. Teh*
Coupling from Multimode to Single-Mode Linear Waveguides Using Horn-Shaped Structures . . . . . *R. K. Winn and J. H. Harris*
Propagation, Attenuation, and Dispersion Characteristics of Inhomogeneous Dielectric Slab Waveguides . . . . . *E. F. Kuester and D. C. Chang*
Propagation Effects in Optical Fibers . . . . . *D. Gloge*
Pulse Propagation in Multimode Fibers with Frequency-Dependent Coupling . . . . . *R. Steinberg*
Theory of Periodic Dielectric Waveguides . . . . . *S. T. Peng, T. Tamir, and H. L. Bertoni*
Reflection at a Curved Dielectric Interface—Electromagnetic Tunneling . . . . . *A. W. Snyder and J. D. Love*
Radiation from Bends in Dielectric Rod Transmission Lines . . . . . *E.-G. Neumann and H.-D. Rudolph*
Ray, Beams, and Modes Pertaining to the Excitation of Dielectric Waveguides . . . . . *L. B. Felsen and S.-Y. Shin*
Modal Analysis of Coupling Problems in Optical Fibers . . . . . *A. Cardama and E. T. Kornhauser*
Quasi-Guided Modes and Related Radiation Losses in Optical Dielectric Waveguides with External Higher Index Layers . . . . . *Y. Suematsu and K. Furuya*

LETTERS

A Method for Measuring the Refractive Index Profile of Thin-Film Waveguides . . . . . *R. Mittra and T. Itoh*
Distributed Capacitance of a Thin-Film Electrooptic Light Modulator . . . . . *E. Yamashita and K. Atsuki*
Power Transfer of a Parallel Optical Fiber Directional Coupler . . . . . *H. Kuwahara, J. Hamasaki, and S. Saito*
Semitransparent Mirror-Type Directional Coupler for Optical Fiber Applications . *H. Kuwahara, J. Hamasaki, and S. Saito*

GaAs-Double-Heterostructure Lasers as Optical Amplifiers

D. SCHICKETANZ AND G. ZEIDLER

Abstract—**The results of measurements on a GaAs-double-heterostructure (DHS) laser used as an optical amplifier are reported. The laser's amplifying guide is coupled to an optical fiber with a rectangular core. The laser amplifier can be operated either in the traveling-wave or the resonator mode. The gain, noise, and performance of the amplifier when driven hard into saturation were measured as a function of various parameters.**

I. Introduction

MASER and laser amplifiers are, by accepted definition, simple configurations for the direct low-noise amplification of electromagnetic signals [1]. The intrinsic noise of such amplifiers when used to amplify optical signals may be so low as to be determined solely by fluctuations caused by the quantum nature of the optical power. Thus the recent development of low-loss optical fibers poses the question as to the possible use of laser amplifiers in fiber optic communications systems. Theoretical studies in [2] and [3] showed that even simple laser amplifiers can be meaningfully employed in fiber optic communications systems. First of all, they could be used in simple communications systems comprising only about 10–20 cascaded repeater sections with optical amplifiers, or in systems in which the pulse signal is regenerated 100 percent after passing through a few line sections with optical analog amplifiers in the baseband (hybrid-digital system).

Nonlinear laser amplifiers can be realized by, say, combining a laser amplifier with a saturable absorber. Such a configuration is capable of both amplifying pulses and regenerating them in their duration [4], so allowing the cascading of numerous optical repeater sections. Ultimately, it is to be expected that further work on integrated optics will result in the integration of laser amplifiers in a complex optical circuit configuration which directly performs all the functions of a regenerative baseband repeater also at optical frequencies.

These applications demand laser amplifiers of short structure which provide large gain accompanied by good pump efficiency. Of the amplifiers investigated so far, those with optically pumped solid-state lasers [5] and gas lasers [6] are too large, while the semiconductor laser amplifiers [7]–[9] satisfactorily meet the preceding demand. The amplifiers described in [7]–[9] were built with diffused GaAs laser diodes which were run cooled to the temperature of liquid nitrogen. For fiber optic systems [3], [10], on the other hand, double-heterostructure (DHS) diodes were used which can be run at room temperature [11] and whose optical amplification takes place in a dielectric guide that can be coupled to the guide of the fiber.

The present work will report the results of further measurements on this amplifier.

Manuscript received June 26, 1974; revised October 8, 1974. This work was supported by the Technological Program of the Federal Department of Research and Technology of the Federal Republic of Germany. The authors alone are responsible for the contents.

The authors are with Siemens Research Laboratories, Munich, Germany.

II. Experimental Configuration

Optical fibers usually have a core of circular cross section, whereas the amplifying guide in a GaAs-DHS laser diode has a flat rectangular cross section (e.g., 0.5 by 30 μm). In order to be able to use this laser diode as an amplifier in a fiber optic communications system, both guides have to be intercoupled. To avoid complicated optical systems (e.g., cylindrical lenses), we chose an optical fiber with a rectangular core as in [3], [10]. Fibers with this core cross section can be reliably fabricated by stretching appropriate preforms to fine fibers. Since the fibers used in the experiment were fabricated from commercial glass stock, the loss was rather high (about 500 dB/km) and we were only able to experiment with relatively short lengths of fiber. The coupling efficiency for intercoupling dielectric guides with a core of rectangular cross section was calculated in [12]. Relatively high efficiency (80 percent) is realized with a glass-to-GaAs interface if both guides have roughly the same core cross section. This simple possibility of coupling the fiber to the active guide of GaAs laser diodes (or to any other stripline in integrated optical systems) suggests two possible solutions, one being to use a fiber with a rectangular core cross section throughout the entire communications system and the other to splice lengths of fiber with a smooth tapered transition from a rectangular to a circular core to fibers with the conventional core cross section.

Fig. 1 shows the elementary configuration for this type of coupling and Fig. 2 the cross section of one of the fibers used. The fiber was scored and then broken. For coupling the fiber to the laser diodes, its ends were adjusted to within 0.1 μm with a piezoelectric drive. When coupling the fiber to the laser transmitter, the optical power in the fiber was measured with a photodetector and adjusted to maximum. When coupling the fiber to the amplifier, the amplifier output was observed through a microscope attached to a TV camera. Fig. 3 shows the coupling process. As the fiber is moved nearer to the laser diode, optical power is first coupled into all epitaxial layers of the laser diode (top photograph). When the fiber is almost touching the diode, the optical power enters only one guide. Given proper adjustment, this will be the amplifying guide (bottom photograph). During the adjustment of the optical fiber of both the laser and the amplifier, a droplet of immersion fluid or adhesive was added to improve the coupling efficiency. The coupling efficiency depends according to

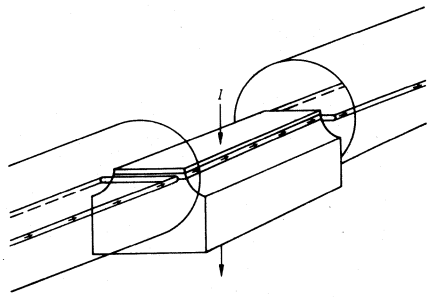

Fig. 1. Experimental configuration.



Fig. 2. Cross section of an optical fiber.

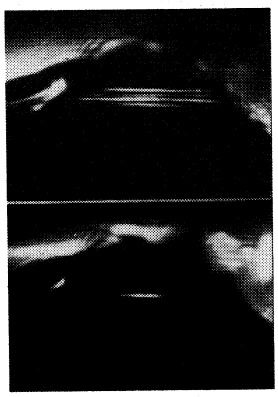

Fig. 3. Near-field of laser amplifier before and after it is coupled to the fiber. Top photograph: Fiber is still out of contact with the laser. Bottom photograph: Fiber is in contact with laser and properly adjusted.

[12] on the core dimensions of the two guides. After coupling the fiber shown in Fig. 2 (core dimensions about 2 by 30 μm) to a laser amplifier with a guide thickness of 0.5 μm, we obtained a coupling efficiency of only just under 10 percent. This value could certainly be improved by matching the two cross sections more closely.

The following measurements were obtained using laser diodes which were not mounted to a perfect heat sink. Therefore, the diodes could not be pumped continuously and they were pulsed in synchronism at a duty cycle of 10 percent, using different transmitter pulsewidths between 1 and 100 ns. Since the temperature of the active region rises during the applied pump pulse, all the following measurements were performed at the same relative phase of the pulse train. For that reason the results should also apply to CW diodes. The diodes used in the experiments were of the mesa type with a length of 150 μm and a width of 80 μm. The threshold current density was in the range of 1500 A/cm^2.

III. Some Measurements on a Nonresonant Amplifier

Subsequent to the experiments reported in [3] and [10] several gain and noise measurements were performed on simple GaAs-DHS laser amplifiers. Since the diodes were immersed in a fluid (monobromnaphthalene) with a refractive index of $n = 1.68$, the amplifier could only be run below its oscillation threshold. The laser transmitter was pumped so far above threshold as to cause the launching of a large number of axial modes in a broad frequency band. Since the length of the amplifier's cavity differed from that of the laser, no matching occurred between the launched modes and the gain resonances occurring just below the threshold of the amplifier [see (4)] and a gain averaged over the various modes was observed. The gain was measured by mapping the amplifier output by way of a grating monochromator onto a photodetector. The sensor's output signal was displayed on a CRT screen with and without the amplifier pump current i. For the power amplification factor G, the following relation with the pump current i is to be expected from theory [13], [14]:

$$10 \log G = g = \beta_1 \cdot i^{\delta_1} - \gamma. \tag{1}$$

γ denotes the loss of the amplifier waveguide and the exponent δ_1 should be in the range of 1-3. Fig. 4 shows the measurement obtained. The gain g (in decibels) increases with the current according to a power law (1). Fig. 4 gives about $\delta_1 = 2.5$ for the exponent. The amplifier is driven into saturation by increasing the amplitude of the input signal. The detectable gain is then lower, but increases with the pump current by roughly the same exponent (Fig. 4).

A large gain bandwidth is to be expected in GaAs. The gain was measured as a function of the wavelength by adjusting the wavelength of the laser by way of the temperature. Since the wavelength of the laser shifts by about 0.34 nm/K, the wavelength of the laser could be shifted by about 24 nm by varying the laser temperature from -35 to +35°C. Fig. 5 shows the measurement. The amplification factor G remains much the same at this large wavelength range. The shape of the amplification band is somewhat asymmetrical. The wavelength of maximum gain coincides with that of the laser emission of the amplifier (arrow). Fig. 5 also shows the spontaneous optical power emission of the laser amplifier as a function of wavelength for three different pump currents. It will be noted that the bandwidth decreases with rising pump current, i.e., with increasing gain [15], and that the maximum of the spontaneous emission shifts relative to the maximum of the gain (for the same pump current) [14]. Since the spontaneous emission is responsible for the noise of the laser amplifier, the emission was first measured as a function of the pump current (Fig. 6). Theory [1] indicates that the amplified spontaneous optical power emission P at the amplifier output will increase with the gain according to the following relation:

$$P = P_s \cdot \frac{e^{g'} - 1}{g'}. \tag{2}$$

P_s denotes the (unamplified) spontaneous emission in all of

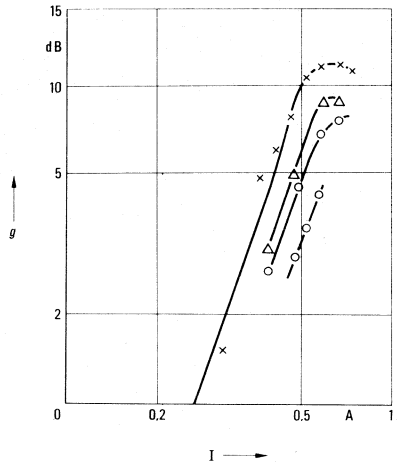

Fig. 4. Gain g as a function of the pump current i for input signals of various-size amplitude (saturation effect).

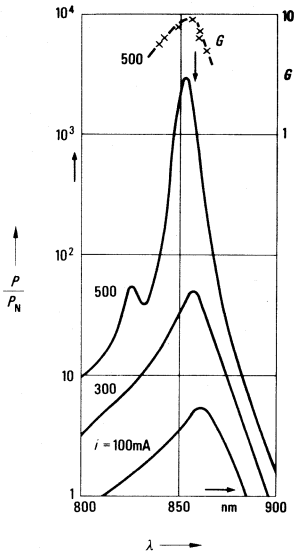

Fig. 5. Spontaneous optical power emission P/P_N for various pump currents i and power gain G as a function of wavelength. The arrow indicates the oscillation wavelength of the amplifier.

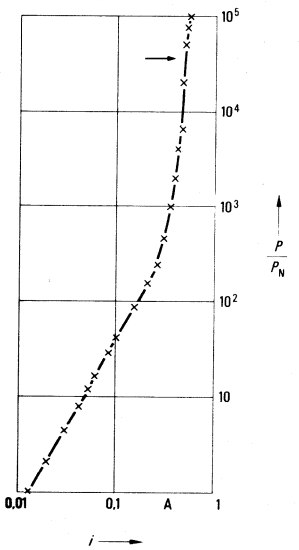

Fig. 6. Spontaneous optical power emission P/P_N as a function of the pump current i. The arrow indicates the threshold.

the modes covered by the measurements and g' the gain in Np ($g' = 0.1 \cdot g \cdot \ln 10$).

If the values calculated for g (or g') with (1) are substituted in (2) and compared with the measurement (Fig. 6) it will be noted that the abrupt rise in spontaneous emission is expressed well by the simple formulas (1) and (2). For small values of gain the relation (2) is reduced to $P \approx P_s$. For small amplifier pump currents it is accordingly possible to determine the dependence of P_s on the pump current i from Fig. 6. It may also be determined empirically from Fig. 6 that P_s likewise rises with the current according to a power law

$$P_s = \beta_2 \cdot i^{\delta_2}. \tag{3}$$

The measurements show the simple formulas (1)-(3) to describe with sufficient exactitude the performance of the amplifier as a function of the pump current. Since both power and exponential laws are effective, the pump current must be carefully regulated in order to assure stable parameters. Although the spontaneous emission is responsible for the amplifier noise, its mean value must not be confused with the noise power common to any communications system.

In a fiber optic communications system it is (especially with pulse code transmission) readily possible to slice off dc components at the photosensor so that the detector does not respond to the temporarily constant spontaneous emission. The noise added to the signal by the amplifier is then manifested by the increased amplitude fluctuations of the optical signal [3]. If the mean value is denoted n and the variance of the photon count during a scanning interval is denoted σ, the signal-to-noise ratio (SNR) will, assuming an ideal square-law photon counter, be given by

$$\frac{S}{N} = \left(\frac{n}{\sigma}\right)^2. \tag{4}$$

This relation can be measured with a real photon counter if the mean value and the variance of the signal are considerably larger than the intrinsic noise of the detector. For one measurement the laser was for this purpose run such that the generated optical pulses exhibited a fluctuating amplitude and lay considerably above the noise of the detector. By using a silicon photodiode it was possible to measure both the mean value and the amplitude fluctuation of these pulses. The results were used to determine the SNR with the amplifier on and off, and the noise figure was determined therefrom in the conventional manner. Fig. 7 shows the noise figure as a function of the gain. For the foregoing measurement the amplifier was driven harder towards saturation because, according to [16], a reduction in noise with nonlinear signal distortion is to be expected at saturation. This effect is clearly evident from the measurement curve. First the noise figure rises steadily with the gain [3], but falls off as saturation is reached. With this decreased noise figure, considerably more repeater sections can be cascaded as calculated in [2], [3] for a linear amplifier. Although the duration of the pulses used for this measurement was only of the order of nanoseconds, no serious pulse distortion was observed. The measurements show clearly that for pulse code modulation it is always recommendable to

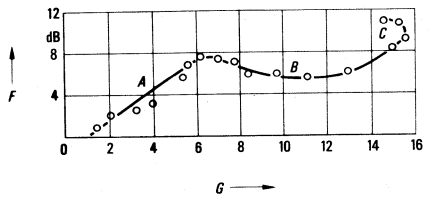

Fig. 7. Noise figure F as a function of the gain near to saturation. (a) Linear region. (b) Saturation. (c) Threshold.

drive the amplifier into saturation. The amplifier then exhibits, besides an improved noise figure, an overall efficiency which our measurements, as well as [7]-[9], show to approach that of the GaAs laser (about 0.2 W/A).

IV. Measurements on a Resonant Amplifier

When feedback is introduced into a laser amplifier, the traveling-wave amplifier becomes a resonant amplifier. Within the gain bandwidth of the laser material, the gain exhibits pronounced maxima and minima as a function of the frequency. The feedback can be produced by a periodic perturbation of the system [17] or by reflections at the unmatched end faces of the laser material [5]. In the latter case the power gain G_R of the resonant amplifier [18] is defined

$$G_R = \frac{T_1 \cdot T_2 \cdot G}{(1 - G \cdot \sqrt{R_1 R_2})^2 + 4G\sqrt{R_1 R_2} \cdot \sin^2 \phi} \tag{5}$$

where G denotes the amplification factor with which the optical power is amplified during a single passage through the laser material, R_1, R_2 denote the reflection coefficients, and T_1, T_2 denote the transmission factors for the optical power at the two end faces. $\phi = 2\pi L/\lambda = \omega L/c$ is the phase of a wave after passage through a laser material of the length L. The gain maxima are calculated with (5) for $\sin \phi = 0$, which may be ascribed to the known resonance condition of the Fabry-Perot cavity. The maximum gain approaches infinity when $G \cdot \sqrt{R_1 R_2}$ approaches unity, e.g., when the laser amplifier approaches its oscillation threshold. The periodic gain bands appearing due to (5) become steadily narrower.

A resonant amplifier offers the advantage that large gain is realized in what for optical frequencies is a narrow band (the noise filters added are of simpler design). It is, however, a drawback that even minor fluctuations may cause gain irregularities and that in a communication system the transmit frequency must coincide with one of the resonant frequencies of each amplifier.

For our measurements we brought the optical fibers close to the end faces of the GaAs laser material without immersion so that a thin layer of air provided sufficient reflectivity. Only laser and amplifier diodes of approximately equal length (and consequently approximately the same frequency separation between resonances) were chosen. The operating temperature was regulated such that the resonances in both the laser and the amplifier appeared at the same frequencies. This frequency matching was easily verifiable because the gain was at maximum. Fig. 8 shows the correspondingly adjusted maximum gain $G_{R\max}$ of the resonant amplifier as a function of the pump current. If the empirically determined gain for one

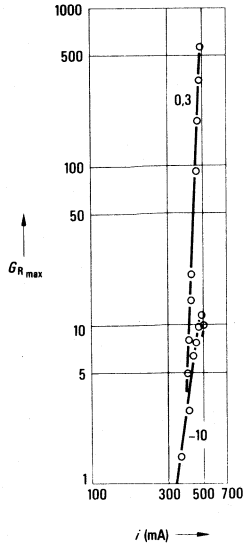

Fig. 8. Maximum amplification factor $G_{R\max}$ of resonant amplifier as a function of the pump current for 2 different input levels.

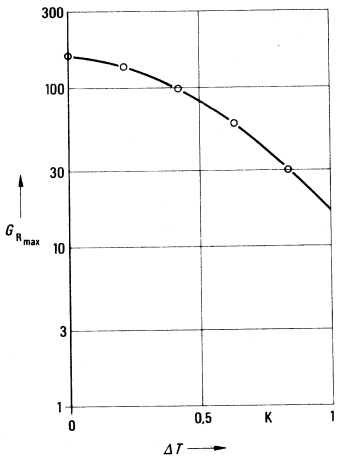

Fig. 9. Decrease in gain $G_{R\max}$ with temperature detuning T resonant amplifier.

passage through the amplifier is taken from Fig. 4 and substituted for G in (5), the maximum gain $G_{R\max}$ is found to agree well with the measurements in Fig. 8. Fig. 9 shows the described frequency matching by way of the temperature for a medium gain. If the temperature scale of Fig. 9 is converted with the aid of the length of the resonator into a frequency shift of the resonances, it is found that the frequency dependence so obtained approximately agrees with the shape of the amplification band which can be calculated with (5). It can further be determined from Fig. 9 that the temperature must be maintained constant at about ±0.4 K if the permissible fluctuation of the amplification factor is 30 percent. According to Fig. 7 the pump current must be maintained constant at ±0.4 percent for the same percentage fluctuation. Although it is essentially possible to realize amplification factors of over 1000 with a resonant amplifier, it is doubtless practical not to go beyond 100 in a communications system because the cost for the avoidance of instabilities would otherwise be excessive. Fig. 10 shows the performance of the resonant amplifier when

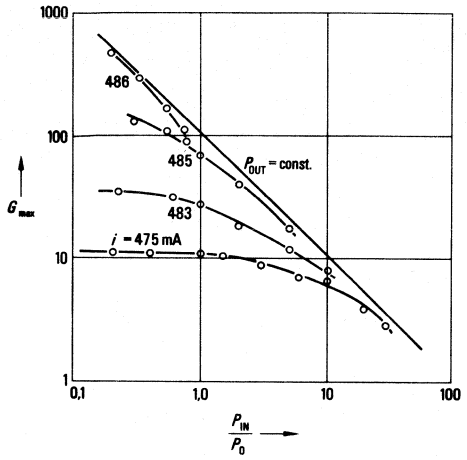

Fig. 10. Saturation of resonant amplifier. Gain G_{max} versus input power P_{in}/P_0 for various pump levels.

driven into saturation. The maximum gain is plotted as a function of the input power. The gain decreases at high input powers due to saturation. The limiting curve for various pump currents is shown as a curve of constant output power.

V. Conclusion

GaAs-DHS laser diodes can be used in fiber optic communications systems along with the coupling technique described. The laser diode can be run either in the traveling-wave or the resonant mode. In a communications system with pulse modulation techniques it is preferable to drive the laser line amplifier hard into saturation because of better noise performance and the higher efficiency. A combination of further accessories is required in order to allow the versatile use of this amplifier in fiber optic systems. Narrow-band filters, circulators, and nonlinear optical devices are here of special importance.

Acknowledgment

The authors wish to thank K. H. Zschauer, D. Pawlik, and H. Meixner for supplying the laser diodes; R. Khan and N. Douklias for supplying the optical fibers; M. O'Donnell for preparing the English version; and two unknown reviewers for valuable suggestions.

References

[1] K. Shimoda, H. Takahasi, and C. H. Townes, "Fluctuations in amplification of quanta with application to maser amplifiers," *J. Phys. Soc. Jap.*, vol. 12, pp. 686–700, 1957.

[2] S. D. Personick, "Applications for quantum amplifiers in simple digital optical communication systems," *Bell Syst. Tech. J.*, vol. 52, pp. 117–133, 1973.

[3] G. Zeidler and D. Schicketanz, "Use of laser amplifiers in a glass-fiber communications system," *Siemens Forsch. Entw.-Ber.*, vol. 2, pp. 227–234, 1973.

[4] G. Zeidler, "A pulse-regenerating optical transmission line," *Siemens Forsch. Entw.-Ber.*, vol. 2, pp. 235–238, 1973.

[5] J. E. Geusic and H. E. D. Scovil, "An unidirectional traveling wave optical maser," *Bell Syst. Tech. J.*, vol. 41, pp. 1371–1397, 1962.

[6] J. W. Klüver, "Laser amplifier noise at 3.5 microns in helium-xenon," *J. Appl. Phys.*, vol. 37, pp. 2987–2999, 1966.

[7] J. W. Crowe and W. E. Ahearne, "Semiconductor laser amplifiers," *IEEE J. Quantum Electron.*, vol. QE-2, pp. 283–289, Aug. 1966.

[8] R. Vuillenmier *et al.*, "Coherent amplification characteristics of a GaAs phased array," *Proc. IEEE (Special Issue on High-Power Semiconductor Devices)*, vol. 55, pp. 1420–1425, Aug. 1967.

[9] W. F. Kosonocky and R. H. Cornely, "Optical losses and efficiency in GaAs laser amplifiers," *IEEE J. Quantum Electron.*, vol. QE-4, pp. 125–131, Apr. 1968.

[10] D. Schicketanz and G. Zeidler, "Optical repeater for a wide-band fiber communication system," *IEEE J. Quantum Electron. (Digest of Technical Papers)*, vol. QE-9, p. 642, June 1973.

[11] F. K. Reinhart, J. Hayashi, and M. B. Panish, "Mode reflectivity and waveguide properties of double hetero-structure injection lasers," *J. Appl. Phys.*, vol. 42, pp. 4466–4479, 1971.

[12] G. A. Hockham and A. B. Sharpe, "Dielectric waveguide discontinuities," *Electron. Lett.*, vol. 8, pp. 230–231, 1972.

[13] F. Stern, "Semiconductor lasers: Theory," in *Laser Handbook*, F. F. Arecchi and E. O. Schulz-Dubois, Ed. Amsterdam, The Netherlands: North-Holland, 1972, pp. 425–440.

[14] C. J. Hwang, "Properties of spontaneous and stimulated emission in GaAs junction lasers," *Phys. Rev. B.*, vol. 2, no. 10, pp. 4126–4134, 1970.

[15] A. Yariv and J. P. Gordon, "Super radiant narrowing in fluorescence radiation," *J. Appl. Phys.*, vol. 34, no. 11, pp. 3410–3411, 1963.

[16] D. Marcuse, "Noise performance of an overloaded maser amplifier," *Proc. IEEE*, vol. 53, pp. 687–692, July 1965.

[17] a) S. R. Chuin and P. L. Kelley, "Analysis of the transmission, reflection, and noise properties of distributed feedback laser amplifiers," *Opt. Commun.*, vol. 10, no. 2, pp. 123–126, 1974.
b) A. Yariv and H. W. Yen, "Bragg amplification and oscillation in periodic optical media," *Opt. Commun.*, vol. 10, pp. 120–122, 1974.

[18] D. Röss, *Laser, Light Amplifiers and Oscillators*. New York–London: Academic, 1969, pp. 67–69.

Amplification and Excited State Absorption in Longitudinally Pumped Laser Dyes

ROBERT F. LEHENY, MEMBER, IEEE, AND JAGDEEP SHAH

Abstract—**Direct measurements of optical gain using a probe laser beam for the laser dye cresyl violet perchlorate (CVP) in methanol solution using longitudinal pumping at two different wavelengths are described. An analysis of these longitudinal pumping experiments is developed and analytical expressions relating measured gain to the measured pump laser transmission are presented. This analysis is developed in terms of relevant optical cross sections including the influence of excited state absorption. The results demonstrate the influence of excited state absorption at the pump wavelength on pumping efficiency and on the gain per pass at the probe laser wavelength.**

I. Introduction

THERE has been continued interest in the direct measurement of optical gain in dye systems since the original measurements of Huth on flashlamp pumped rhodamine 6G [1]. Since then, gain measurements have been extended to a number of other dye systems by the use of laser pumping [2]. Gillard *et al.* [3] have demonstrated saturation of small signal gain at high pumping intensities. In general, the detailed analysis of such measurements is complicated by inhomogeneous pumping of the dye and the possible effects of excited singlet state absorption (ESA), an effect that has not been widely discussed for laser dyes [4]. In this paper we demonstrate that these factors can be accounted for by coupling measurements of the saturable absorption parameters at the pump laser wavelength with measurements of small signal amplification. To illustrate the analysis we report measurements for cresyl violet perchlorate (CVP) in methanol solution, a dye which has been shown to be efficient for use in the 6500-6800-Å region [5]. We have previously described measurements of the ESA spectrum in the range 2-2.7 eV for this dye and demonstrate here how this phenomenon influences the efficiency for pumping the dye [4]. We also determine that ESA significantly reduces the effective cross section for stimulated emission.

In Section II we describe the measurements. We consider saturable absorption of the dye solution at two pump wavelengths, first, at the absorption peak for ground state absorption in CVP [Fig. 1(a)], and second, at a shorter wavelength for which significant excited state absorption [Fig. 1(b)] occurs. For these cases we describe separate measurement of small signal amplification of a probe laser tuned to the CVP fluorescence peak. In the presence of excited state absorption there are alternative absorption processes corresponding to transitions between excited states and higher energy states [Fig. 1(c)]. The importance of these processes depends on

Manuscript received July 31, 1974; revised October 3, 1974.
The authors are with Bell Laboratories, Holmdel, N.J. 07733.

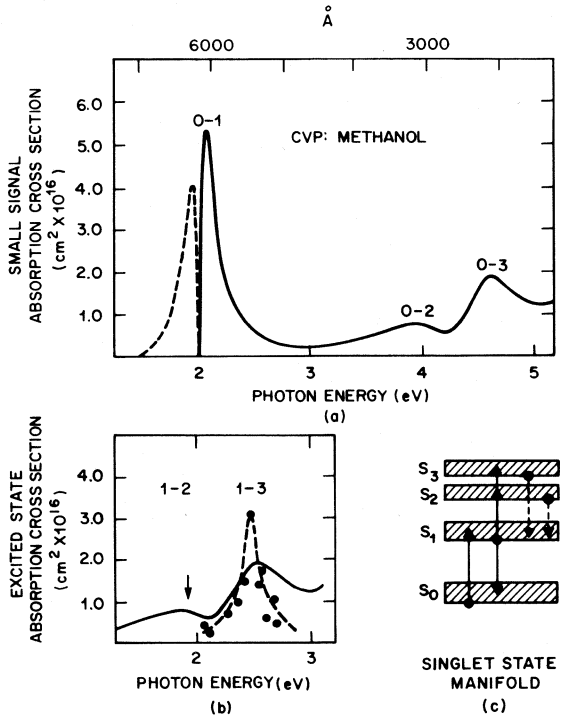

Fig. 1. (a) Low intensity absorption spectra for CVP in methanol solution. The dotted curve indicates the fluorescence spectra measured for the same solution. The index 0–*N* identifies initial and final singlet state electronic levels contributing to the observed absorption peak. (b) Excited state absorption spectra for CVP. The dotted curve indicates the measured variation in the range 2–2.7 eV while the solid curve was determined by assuming that the initial state for the ESA transitions corresponds to the peak of the 0–1 absorption of Fig. 1(a) and then translating the higher energy portion of that spectrum to lower energy. The arrow indicates the energy of the probe laser used to measure amplification. (c) Schematic representation of the assumed level structure for the singlet state manifold. Rapid internal conversion is assumed to leave the electron in the lowest vibrational level of the first singlet state, from which fluorescence occurs.

the wavelength dependent cross section for transitions between the excited states and the fraction of dye molecules that are excited. At the *pump* wavelength, excited state absorption competes with absorption from the ground state so as to reduce the effective pumping of the dye; at the *lasing* wavelength, excited state absorption competes directly with the stimulated emission process, reducing the effective cross section for stimulated emission.

At all pump levels the average small signal gain per pass through the pumped region is proportional to the number of molecules in the first excited state. For low input flux the dominant absorption process is described by Beer's law, for which the density of excited molecules varies exponentially along the pumping beam path. In this limit the calculation of net gain per pass $\bar{g} \equiv (1/L) \int_0^L g(x)\,dx$ is relatively straight-

forward. As the fraction of dye molecules in the excited state increases, deviations from Beer's law make determination of gain $g(x)$ at every point in the beam difficult. In Section III we demonstrate that, if only the net gain per pass $\bar{g}$ and not $g(x)$ is required, numerical computations can be avoided. The results of this analysis are general and we illustrate their utility by quantitatively determining the relevant absorption and stimulated emission cross sections for CVP.

II. Measurements

The CVP dye was obtained from Eastman Kodak and used without further purification. Fig. 1 summarizes the absorption spectrum for this dye. The gain measurements were made by exciting a 1-mm path of 2.5×10^{-4}-M/l methanol solution of CVP with a pump laser beam and probing this excited dye with a second collinear probe laser. Generation of these separately tunable lasers was accomplished using a single N_2 laser as illustrated in Fig. 2. With the 100-kW output of the N_2 laser divided evenly, ~ 5 kW was available from each dye laser in a > 5-ns pulse. Up to 10–15 kW was obtained when the entire 100-kW output of the N_2 laser was used to excite the pump beam laser.

We show in Section III that the amplification through a longitudinally pumped dye cell can be calculated analytically provided the variation in transmission of the pump beam through the dye is known. Therefore, in this section, we first describe the measurement of saturable transmission parameters for CVP. Typical results are shown in Fig. 3 for two pump wavelengths. At $\lambda = 5975$ Å the dye transmission exhibits typical response for a saturable absorber, the transmission through the cell increases with increasing pump intensity. However, for the pump laser set to $\lambda = 5145$ Å, a wavelength for which the ground state absorption cross section is approximately an order of magnitude smaller than at 5975 Å, we find the transmission decreases with increasing incident intensity. This decrease results directly from excited state absorption [4].

That the decrease in transmission does not contribute to an increase in the number of dye molecules in the first excited singlet state is dramatically demonstrated by observing the fluorescence from the S_1 level as the sample is moved through the focus of the input lens. The luminescence from the dye is observed to decrease by as much as an order of magnitude as the absorption *increases*. The additional absorption results from cycling the dye molecules between S_1 and higher levels with a net decrease in the number of molecules in the S_1 state [6].

We now consider the measurement of small signal amplification. The probe laser was generated by longitudinally pumping a separate CVP dye cell with the output of an untuned laser operated at $\lambda \sim 5700$ Å. In this way the available gain could be saturated so that the CVP laser operated close to the peak of the CVP fluorescence ($\lambda \sim 6375$ Å). The output of this laser was filtered and attenuated to a convenient level, then combined with the pump beam by means of a polarizing cube. The collinear beams were then focused onto the CVP sample cell and the transmitted light was collected with additional filtering to minimize the effect of fluorescence from the sample. The probe intensity was minimized to insure that saturation of the small signal amplification did not affect the measurements and care was taken to prevent the sample cell from lasing. The focused spot at the sample was ~ 50 μm in diameter for both beams and the intensity over this spot was relatively uniform. The output beams were apertured so that only the central overlapping portion was detected to minimize the possible effect of transverse intensity variations.

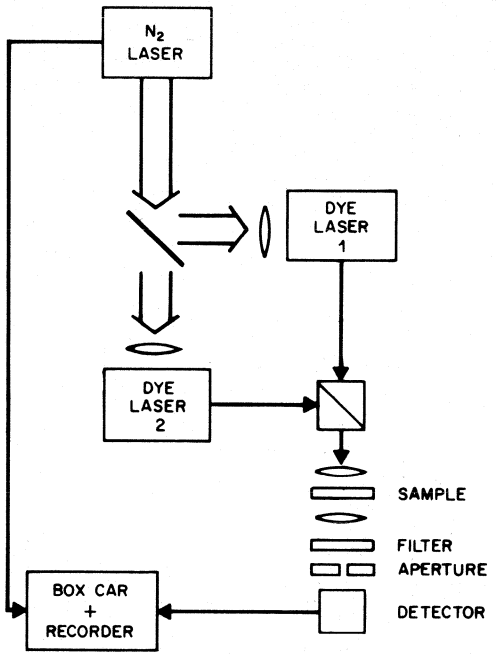

Fig. 2. Schematic of experiment. A polarizer in the pump laser cavity was set to polarize this laser's output to allow efficient beam combination in the polarizing cube. The output of the probe laser was filtered with a Kodak 2-60 filter, while the amplifier output was filtered with an Oriel f155 filter monochromator. A silicon cell detector was used.

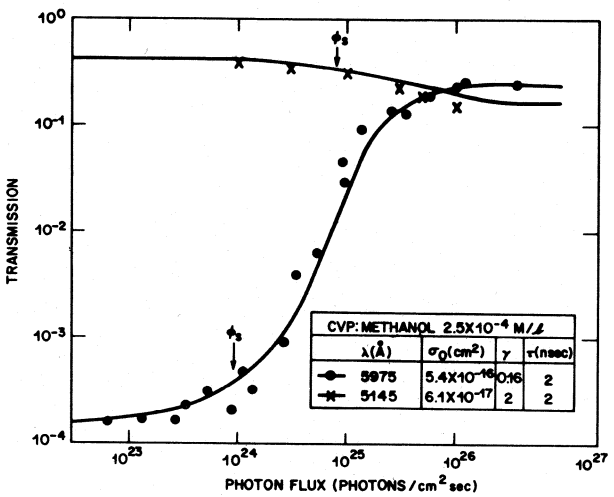

Fig. 3. Variation of transmission with input photon flux density through a 1-mm path length of 2.5×10^{-4}-M/l CVP for two wavelengths. The cross sections for small signal absorption were measured separately and are indicated on the figure. Values of γ and τ used in (4) of the text to compute the solid line are also indicated on the figure. The saturation photon flux density at each wavelength is indicated by an arrow.

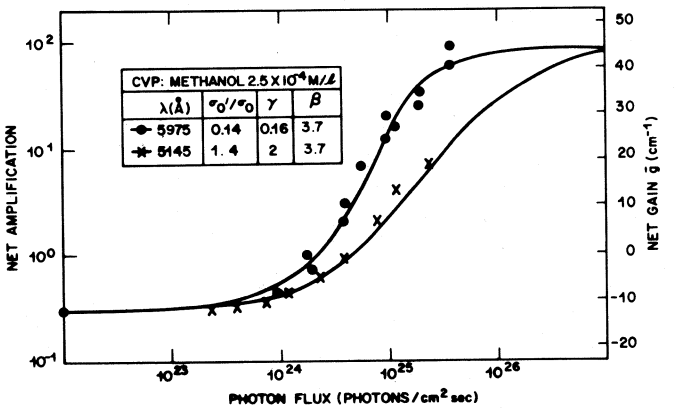

Fig. 4. Variation of net amplification with input photon flux density through a 1-mm path length of 2.5×10^{-4}-M/l CVP for a probe wavelength of 6357 Å and for two pump wavelengths. Values of β and σ_0'/σ_0 used in (8) of the text to compute the solid curves are indicated on the figure.

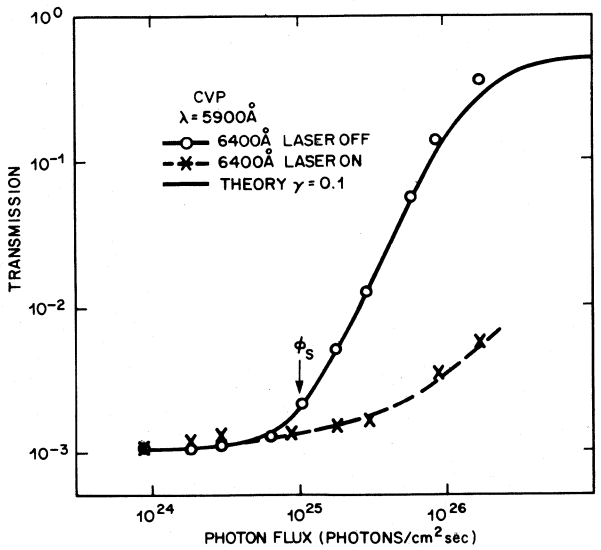

Fig. 5. Influence of an intense probe beam stimulating recombination on the saturation of transmission of a pump beam at 5900 Å. The solid line is a fit to the theory with $\tau = 2$ ns.

Typical results for the small signal amplification versus pump intensity are shown in Fig. 4. With a fraction of the N_2 laser diverted to pump the probe laser, the maximum available output from the pump beam was reduced somewhat over that available in the transmission measurement. The maximum net amplification measured for the 2.5×10^{-4}-M/l solution was $\sim 10^2$ ($\bar{g}l \sim 4.6$). Higher gains were observed for more highly concentrated solutions, but we experienced difficulty in maintaining linearity and in preventing the amplifier from oscillating.

The use of logarithmic scales in Fig. 4 tends to distort the apparent variation of gain with pump power. For low power the gain is found to increase linearly (a complete fit of the data to theory is described in Section III) reflecting the variation in absorbed power for small pump intensities. In this limit the small signal gain varies exponentially through the sample and this variation does not change with pump power. The principal effect of increasing pump power is a corresponding increase in the number of excited molecules. For the case of pumping at 5975 Å, saturation of the absorption at the input end of the cell results in more efficient pumping deeper into the sample with resultant continued increases of the gain until the entire sample is saturated. At 5145 Å, saturation of the input end results in less efficient pumping due to excited state absorption. While the presence of excited state absorption decreases the efficiency of pumping, it does not result in any net decrease in the S_1 population over the range of pump intensities available. The principal effect of excited state absorption is to reduce the differential efficiency for generating gain because of the additional absorption in the excited dye. For the conditions of our measurement we find at the highest pump intensity the available amplification at 5975 Å differs by an order of magnitude from that at 5145 Å, even though the absorbed powers are comparable.

As expected, increasing the probe laser intensity resulted in a decrease in the measured gain. This occurs when the signal flux is sufficient so that the rate of stimulated emission exceeds that of spontaneous emission. Then the relaxation of the excited state population is determined by the rate of stimulated emission, which results in a corresponding increase in the pump intensity required to saturate the absorption. The data shown in Fig. 5 for transmission versus pump intensity with and without the presence of a strong probe signal illustrate this effect.

III. Analysis and Discussion

In the limit of small signals the available amplification of a probe beam is proportional to the number of excited molecules it can interact with and the net cross section for stimulated emission. The analysis of amplification measurements therefore requires a determination of the distribution of excited molecules in the path of the probe laser beam which in turn is determined by the absorption of the pump beam. We analyze this interdependence by means of coupled equations governing the absorption of the pump beam and amplification of the probe beam.

Starting with the usual set of rate equations governing optical pumping for the level scheme illustrated in Fig. 1(c), and assuming the pump photon energy can excite an electron from S_1 to S_2, but that fast internal conversion occurs so that excitations from S_2 to higher states can be neglected, we have for the case of no transverse variation of the light beam:

$$\frac{dn_0}{dt} = \frac{n_1}{\tau} - n_0\sigma_0\phi$$

$$\frac{dn_1}{dt} = (n_0\sigma_0 - n_1\sigma_1)\phi - \frac{n_1}{\tau} + \frac{n_2}{\tau'}$$

$$\frac{dn_2}{dt} = -\frac{n_2}{\tau'} + n_1\sigma_1\phi, \qquad N = n_0 + n_1 + n_2 \tag{1}$$

with n_i the density of molecules in state i, N the total density, σ_i the cross section for absorption out of state i (at the pump wavelength), τ the time for relaxation between S_1 and S_0, and τ' the time for relaxation between S_2 and S_1. The incident

pump photon flux density is given by ϕ. For steady state,[1] and in the limit of $\tau' \ll \tau$ [7], these equations reduce to

$$n_1/n_0 = \phi/\phi_s$$
$$n_0/N = (1 + \phi/\phi_s)^{-1}. \quad (2)$$

For $\phi > \phi_s \equiv (\tau\sigma_0)^{-1}$, the saturation flux density, the number of molecules in the excited state, is greater than the number in the ground state, and absorption due to the ground state begins to decrease. The relative importance of excited state absorption depends on the magnitude of $n_1\sigma_1/n_0\sigma_0 \equiv \gamma\phi/\phi_s$ with $\gamma = \sigma_1/\sigma_0$. Writing for the pump beam absorption, $d\phi/dx = -(\sigma_0 n_0 + \sigma_1 n_1)\phi$ which from (2) can be written

$$\frac{dy}{dx} = -\alpha_0 y \frac{(1+\gamma y)}{1+y} \quad (3)$$

where $y = \phi/\phi_s$, $\alpha_0 = \sigma_0 N$, and x is distance into the cell. This relationship describes the saturable absorption in the dye as a function of the relative beam intensity y. For small y it reduces to the usual Beer's law expression $dy/dx = -\alpha_0 y$. At large y it again has this simple form with α_0 replaced by $N\sigma_1$, an absorption coefficient corresponding to the excited state absorption.

A number of investigators have discussed solutions to (3) with regard to saturable absorption in dyes [8]. The transmission (T) through a length of dye L, in terms of the normalized incident photon flux y_0, can be written

$$\left(\frac{1+\gamma y_0}{1+\gamma T y_0}\right)^{(1/\gamma)-1} = T/T_0 \quad (4)$$

with $T_0 = \exp -(N\sigma_0 L)$, the small signal transmission. This expression has been used to fit the data shown in Fig. 3 to obtain the solid curves shown in that figure. The data are fit with the choice of τ, γ indicated on the figure; σ_0 is determined from small signal absorption.

Analysis of the amplification measurement follows in a similar way. If we assume that Ψ, the probe beam photon flux, is small enough so that stimulated emission does not influence the relative population of excited and unexcited dye molecules, then (1)–(4) remain valid and the rate of increase of ψ with position is given by

$$\frac{d\psi}{dx} = (\sigma_s' n_1 - \sigma_0' n_0)\psi \equiv g(x)\psi(x) \quad (5)$$

with σ_s' the *net* cross section for stimulated emission ($\sigma_s' = \sigma_s - \sigma_1'$, the difference between the cross section for stimulated emission and that for excited state absorption at the *probe* wavelength) and σ_0' is the corresponding cross section for ground state absorption. Here n_1 and n_0 depend on the pump beam photon flux density according to (4). Expression (5) can be integrated to yield

$$\psi(L) = \psi(0) \exp \int_0^L g(x)\,dx = \psi(0) \exp \bar{g}L. \quad (6)$$

Direct evaluation of $\bar{g} = 1/L \int_0^L g(x)\,dx$ is quite complicated in general. Rewriting (5)

$$g(x) = \sigma_0'(\beta n_1 - n_0) = \sigma_0' N \left(\frac{\beta y - 1}{y+1}\right) \quad (7)$$

where $\beta = \sigma_s'/\sigma_0'$, and recognizing that the factor $(y+1)^{-1}$ also appears in (3), we can rewrite that expression to give

$$\frac{dy}{y}\left(\frac{1-\beta y}{1+\gamma y}\right) = \frac{\sigma_0}{\sigma_0'} g(x)\,dx. \quad (3')$$

Now this result can be directly integrated to give

$$\bar{g}L \equiv \int_0^L g(x)\,dx = \frac{\sigma_0'}{\sigma_0}\left[(1+\beta/\gamma)\ln\left(\frac{1+\gamma y_0}{1+T\gamma y_0}\right) + \ln T\right] \quad (8)$$

where T is given by (4). It is still necessary to solve (4) for T for each y_0 before $\bar{g}L$ can be determined from (8). However, the advantage of (8) is that it provides an analytic expression for the net amplification and eliminates the need for numerical integration of expression (5).

This result can be put in a more recognizable form if we assume $\gamma \to 0$ (no excited state absorption at the pump wavelength) then,

$$\bar{g}L = \frac{\sigma_s'}{\sigma_0}[(1-T)y_0 + (\ln T)/\beta] \quad (8a)$$

and in the limit that the pump beam absorption is not saturated, so that $T = \exp(-N\sigma_0 L)$.

$$\bar{g}L = \frac{\sigma_s'}{\sigma_0}(1-T)y_0 - \sigma_0' NL \quad (8b)$$

and finally, in the limit of small pump absorption, T becomes $1 - N\sigma_0 L$ giving

$$\bar{g}L = (\sigma_s' y_0 - \sigma_0')NL \quad (8c)$$

and the average gain is equal to the local gain.

The net amplification measurements shown in Fig. 4 were fitted to theory using (8) to obtain the solid curves shown on the figure. The procedure used was to first fit the transmission data shown in Fig. 3 to determine T versus ϕ and the parameters γ and ϕ_s. Using these parameters and T at each ϕ, (8) was used to determine $\bar{g}$. The only adjustable parameter in fitting the data in Fig. 4 is σ_s'. As indicated on the figure, the best fit is obtained with $\beta = 3.7$ which corresponds to a

[1] The principal conclusions concerning cross sections for various excited state processes obtained here result from determination of the properties of the dye when the density of excited molecules is saturated and do not depend on the details of how saturation is achieved. The rigorous use of steady state analysis in these pulsed experiments requires that the lifetime of the S_1 state be shorter than the pumping pulsewidth. We find our results can be fit with a 2-ns lifetime, while the laser pumping pulsewidth was > 5 ns. However, longer lifetimes (~ 4 ns) have been determined from fluorescence decay time measurements (E. P. Ippen, private communication). A detailed theory taking account of variations with time would be considerably more complicated than the analysis given here and we take the good agreement between our experimental results and the steady state theory in the range of pump intensities below saturation as evidence that the use of pumping pulsewidth comparable to the S_1 lifetime introduces no significant errors.

cross section $\sigma_s' \sim 2 \times 10^{-16}$ cm^2, a factor of 2 smaller than the cross section for absorption at 5975 Å.

Since the fluorescence spectrum mirrors the absorption spectrum for this dye, we expect that σ_s at the fluorescence peak should equal σ_0 at the absorption peak [9]. We attribute the measured difference to excited state absorption at the probe wavelength. Direct measurement of the ESA spectrum over the full range of photon energies for which stimulated emission can occur is not possible, since stimulated emission competes with this process [see (5)]. However, some estimate of excited state absorption in this energy range can be made from the high energy ground state absorption [Fig. 1(a)]; in particular, we can determine the energy difference between higher lying singlet states. In Fig. 1(a) we have labeled the various peaks in the absorption spectrum to indicate the index of the final electronic states involved. We have also previously described the measurement of the ESA spectrum in the range 2-2.7 eV, where we find a single peak at ~2.5 eV. If we take the peak of the 0-1 absorption as the initial energy for excited state absorption [10], then the peak at 2.5 eV in the ESA spectrum can be associated with transitions from the $n = 1 \rightarrow 3$ levels. With this assumption we have translated the high energy small signal absorption spectrum to lower energy and compared this translated spectrum to the measured ESA spectrum in Fig. 1(b). In this way we note that the contribution of the $n = 1 \rightarrow 2$ transitions should peak at ~1.9 eV or $\lambda = 6520$ Å (~600 meV below the $n = 1 \rightarrow 3$ peak) and therefore $n = 1 \rightarrow 2$ transitions can be expected to significantly reduce the net cross section for stimulated emission in CVP. While this procedure provides some information about the energies for which we expect ESA to be significant, our measurement of $\sigma's$ gives for the ESA cross section at 6375 Å, $\sigma' \sim 3 \times 10^{-16}$ cm^2 if we take $\sigma_s^{\text{theory}}(\lambda = 6375) = \sigma_0^{\text{mea}}(\lambda = 5975)$, and this value is a factor of 3 larger than the $n = 0 \rightarrow 2$ cross section. Since the initial states are different in each case some difference in absolute cross section is to be expected, and in fact we find the $n = 1 \rightarrow 3$ cross section is fifty percent larger than the $n = 0 \rightarrow 3$ [4]. More detailed measurements of the type described here would be required, over the entire gain spectrum, to provide complete data on the influence of ESA on the stimulated emission cross section.

IV. Summary and Conclusion

We have described the measurement and analysis of small signal gain measurements for the case of longitudinal pumping for the dye (CVP) in methanol solution. We have demonstrated that the influence of excited state absorption and absorption saturation effects can be accounted for by coupling measurements of saturable absorption parameters for the pump beam to the detailed measurements of optical gain. In this way we have demonstrated that excited state absorption at the pump can significantly influence the efficiency of stimulated emission. We have also shown how the influence of excited state absorption on stimulated emission can be determined from measurements of saturated gain. It is important to note that this last parameter affects not only the small signal gain coefficient, but also the losses in CW operation and thus the differential efficiency of the dye.

Acknowledgment

The authors wish to thank E. Beebe and A. DiGiovanni for technical assistance in making the measurements, A. Ashkin E. P. Ippen, and C. Lin for critical reading of the original manuscript, and K. H. Drexhage of Kodak Research Laboratories for helpful discussions.

References

[1] B. G. Huth, "Direct gain measurements of an organic dye amplifier," *Appl. Phys. Lett.*, vol. 16, pp. 185–188, 1970.
[2] C. V. Shank, A. Dienes, and W. T. Silfvast, "Single pass gain of exciplex 4-Mu and rodamine 6G dye laser amplifiers," *Appl. Phys. Lett.*, vol. 17, pp. 307–309, 1970.
[3] P. G. Gillard, N. D. Foltz, and C. W. Cho, "Gain in DTTC-methanol pollution as a function of pump power, wavelength and time," *Appl. Phys. Lett.*, vol. 23, pp. 325–327, 1973.
[4] a) J. Shah and R. F. Leheny, "Excited-state absorption spectrum of cresyl violet perchlorate," *Appl. Phys. Lett.*, vol. 24, pp. 562–564, 1974.
b) E. Sahar and I. Wieder, "Excited singlet state absorption spectrum with tunable dye lasers," *Chem. Phys. Lett.*, vol. 23, pp. 518–521, 1973.
[5] J. M. Yarborough, "CW dye laser emission spanning the visible spectrum," *Appl. Phys. Lett.*, vol. 24, pp. 629–631, 1974.
[6] I. Wieder, "Quenching of laser dye fluorence by absorption from excited singlet state," *Appl. Phys. Lett.*, vol. 21, pp. 318–320, 1972.
[7] C. Lin and A. Dienes, "Direct measurement of radiationless internal conversion rate from the second excited singlet to the first excited singlet state laser dye molecules," *Opt. Commun.*, vol. 9, p. 21, 1974.
[8] M. Hercher, W. Chu, and D. L. Stockman, "An experimental study of saturable absorbers for ruby lasers," *IEEE J. Quantum Electron. (Special Issue–1968 International Quantum Electronics Conference: Part II)*, vol. QE-4, pp, 954–968, Nov. 1968.
[9] F. P. Schafer, in *Dye Lasers: Topics in Applied Physics*, vol. 1, F. P. Schafer, Ed. New York: Springer, 1974, p. 35.
[10] K. H. Drexhage, private communication.

Analysis of Curved Optical Waveguides by Conformal Transformation

MORDEHAI HEIBLUM, STUDENT MEMBER, IEEE, AND JAY H. HARRIS, MEMBER, IEEE

Abstract—**The method of conformal transformations is applied to the analysis of waveguide bends. Equivalent structures are obtained that permit solution by traditional methods of optical waveguide analysis. Losses associated with both curvature and with the transition from straight to curved guides are discussed and simple first-order expressions that describe the dependence of the losses on waveguide parameters are derived.**

I. Introduction

CONFORMAL transformations provide a method for analyzing curved or otherwise varying waveguides that not only yields useful data concerning wave configurations and attenuation rates but also generates an equivalent structure whose properties may be readily appreciated on an intuitive level. Primary interest in this paper is centered on bend losses in curved waveguides. This determination is central to the design of integrated optical systems because switches and arrays of switches utilizing cylindrical waveguides require geometric displacements that are provided by bends.

The bend-loss problem has been previously investigated by Marcatili, Marcuse, and Lewin [1-a)-1-c)] using the established [2] technique of representing the field in the external region by a cylinder (Hankel) function of complex order and matching to fields in the guide that are assumed unperturbed from a straight guide. The transformations result in an analysis that differs from this previous work in that guides with a continuously varying refractive index such as diffused guides may be treated, in that radii of curvature need not be restricted to large values, and in that losses associated with a change in the direction of curvature required for a bend can be treated. Taylor [3] has also treated the bend problem using a computer-based analysis. Transformations not only provide an analytic approach but also avoid certain assumptions necessary for the efficient application of numerical methods.

Conformal transformations apply to solutions of the two-dimensional scalar wave equation

$$[\nabla_{x,y}^2 + k^2(x,y)]\psi = 0. \tag{1}$$

Solutions are obtained in a coordinate system u, v defined with respect to x and y by the relation

$$W = u + iv = f(Z) = f(x + iy) \tag{2}$$

where f is an analytic function. Expanding $\nabla_{x,y}^2$ in (1) with the aid of the Cauchy Riemann relations ($\partial u/\partial x = \partial v/\partial y$, $\partial u/\partial y = -\partial v/\partial x$), (1) may be expressed as

$$\left[\nabla_{u,v}^2 + \left|\frac{dZ}{dW}\right|^2 k^2(x(u,v), y(u,v))\right]\psi = 0 \tag{3}$$

where $|dW/dZ|^2 = (\partial u/\partial x)^2 + (\partial v/\partial x)^2$. Equation (3) is a well-known relation [4]. The objective of the transformation is to select an $f(Z)$ that converts curved boundaries in the x, y plane to straight ones in the u, v plane. Before discussing this matter further (see Section II) we wish to enumerate the kinds of integrated optical problems to which solutions to (1) are applicable.

1) TE mode on a planar guide. The guide is uniform in z with discrete or continuous index variation in x and y. The fields are constant in z and $\boldsymbol{E}$ has only a z component which we identify as ψ, i.e., $\boldsymbol{E} = \psi(x,y)\hat{z}$. Boundary conditions require continuity of ψ and $\nabla\psi$ and this continuity is maintained in the x, y plane if it is imposed in the u, v plane.

2) TM mode on a planar guide with discrete index variations and $\boldsymbol{H} = \psi(x,y)\hat{z}$. ψ is continuous and $(1/\epsilon)\nabla\psi$ is continuous.

3) TM mode on a planar guide with continuous index variation. In this case the wave equation for H_z is

$$[\nabla_{x,y}^2 + (\nabla_{x,y}\epsilon/\epsilon)\cdot\nabla_{x,y} + k^2(x,y)]H_z = 0 \tag{4}$$

and in the u, v coordinate system

$$[\nabla_{u,v}^2 + (\nabla_{u,v}\epsilon/\epsilon)\cdot\nabla_{u,v} + \left|\frac{dZ}{dW}\right|^2 k^2(x(u,v),y(u,v))]\psi = 0. \tag{5}$$

Although we concentrate on solutions to (1), the method of analysis is applicable to (4) or (5) as will be indicated.

4) Approximately applicable to cylindrical[1] waveguides that are uniform in the z direction. An example is a diffused waveguide [5] of rectangular cross section that undergoes a bend in the x, y plane. Using potential functions $A^{TE}(x,y,z)\hat{z}$ and $A^{TM}(x,y,z)\hat{z}$ that yield TE to z fields with $\boldsymbol{E} = \nabla \times A^{TE}\hat{z}$ and TM to z fields with $\boldsymbol{H} = \nabla \times A^{TM}\hat{z}$, approximate solutions to the wave equation can be expressed

$$A^{TM}(x,y,z) = g^{TM}(z)\psi(x,y). \tag{6}$$

For a guide centered about $y = 0$ and $z = 0$, $g(z)$ is a solution of

$$\left[\frac{\partial^2}{\partial z^2} + k^2(0,0,z)\right]g(z) = k_w^2 g(z) \tag{7}$$

where k_w is the wave-propagation constant for a planar guide. ψ is a solution of

Manuscript received August 13, 1974; revised October 8, 1974. This work was supported by NSF grant GK 38159.

M. Heiblum is with the Department of Electrical Engineering and Computer Sciences, University of California, Berkeley, Calif.

J. H. Harris is with the National Science Foundation, Washington, D.C.

[1] Also referred to as linear, two-dimensionally confined, and three-dimensional waveguides.

$$[\nabla^2_{x,y} + k^2(x, y, 0) - (k^2(0, 0, 0) - k_w^2)]\,\psi = 0. \quad (8)$$

We may identify (8) with (1) using a $k^2(x, y)$ in (1) that is modified by a constant. An equation of the form (5) results for A^{TE}. It is not our purpose to consider the approximation (6)–(8) in detail. This is a complex problem that has received only limited attention [6]. We wish merely to point out that within a customary approximation that derives from the field behavior in a rectangular waveguide with perfectly conducting walls, (1) may be employed to estimate the wave function in curved versions of such important integrated optical structures as diffused guides.

II. Equivalent Waveguide Structures

To illustrate the intuitive approach that conformal transformations provide, consider Fig. 1(a), which shows a circularly curved dielectric waveguide with a step discontinuity in refractive index at radii R_1 and R_2. Wave propagation along this structure is described by (1) in which $k^2(x, y)$ appears as a constant in each of the regions of the structure. Using the conformal transformation

$$W = R_2 \ln Z/R_2 \quad (9)$$

for which

$$\left|\frac{dZ}{dW}\right| = \exp(u/R_2) \quad (10)$$

(3) is found to describe the waveguide shown in Fig. 1(b). In the W plane the walls are straight and lie between $u = 0$ and $u = -R_2 \ln R_2/R_1$. The refractive index in the structure is the product of (10) and the refractive index in the appropriate region of the curved guide. Those familiar with optical waveguides will note that the index profile of the equivalent structure resembles that in a prism coupler [9]. It is clear that all of the modes of the equivalent structure will radiate to the right where the refractive index exceeds the maximum refractive index in the guide.

If the waveguide in Fig. 1 were a diffused guide in a substrate, as an important practical example, the process of lateral diffusion would result in an index profile of the kind illustrated in Fig. 2(a). The modes on the equivalent guide in Fig. 2(b) are radiative as before. Furthermore, unless the decay rate $n_3(\rho)$ of the lateral diffusion is sufficiently rapid the minimum on the right side of the curve in Fig. 2(b) will cease to appear and there will be no confined modes. This "critical decay" condition is readily found by setting $n_3(\rho) = |dZ/dW|^{-1}$ and results in the requirement

$$n_3(\rho) < n_2 \cdot (R_2/\rho) \qquad R_2 < \rho < (n_2/n_1)R_2. \quad (11)$$

When the equality of (11) is met, the right side of Fig. 2(b) is constant at value n_2 in the manner depicted in Fig. 3. If there are no guided waves in the equivalent structure, neither will there be any in the curved waveguide.

The circular structure with one boundary illustrated in Fig. 4 will also support guided, albeit lossy waves [12]. This is made apparent by the equivalent guide of Fig. 4(b). We have $n_2 < n_1$ in this case. The guided waves on this structure will have wave refractive indices n_w that lie in the range $n_1 > n_w > n_2$ and the waves themselves will be confined to the range $0 > u > R \ln n_2/n_1$. The latter limit is indicated in Fig. 5(a) as u_0. In the original structure this boundary appears at $\rho_0 = R \cdot (n_2/n_1)$. As illustrated in Fig. 5(b), a ray tangent to the circle of radius ρ_0 will strike the tangent to the boundary of

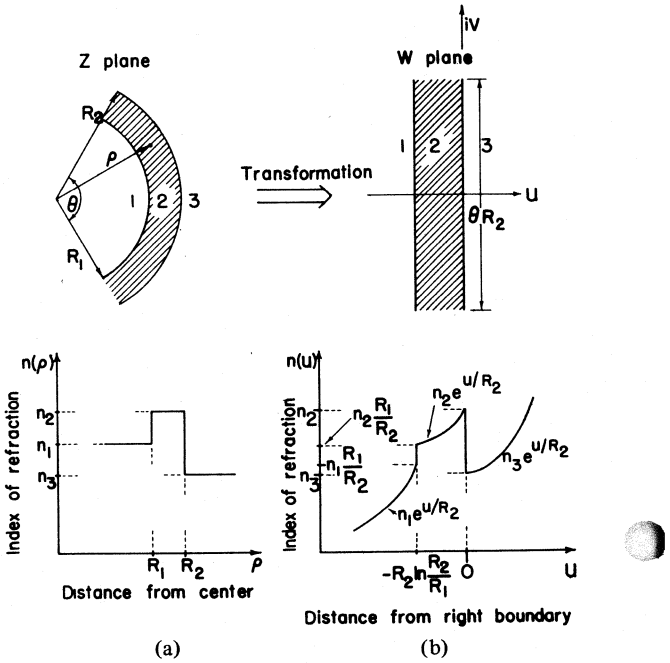

(a) (b)

Fig. 1. A two-dimensional bend with step index distribution (a) and its transformation (b).

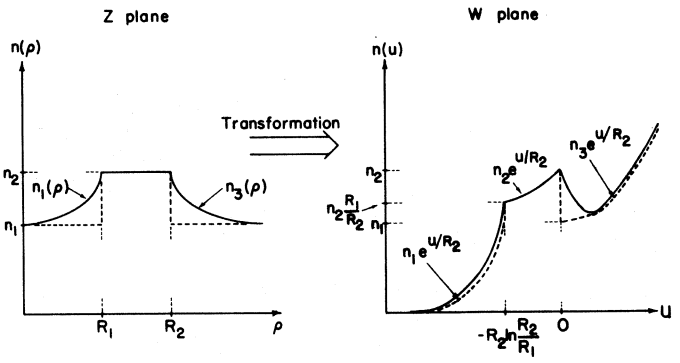

(a) (b)

Fig. 2. Index distribution of a diffused bend (a) and its transformation (b). (Dashed lines denote the transformed step distribution bend.)

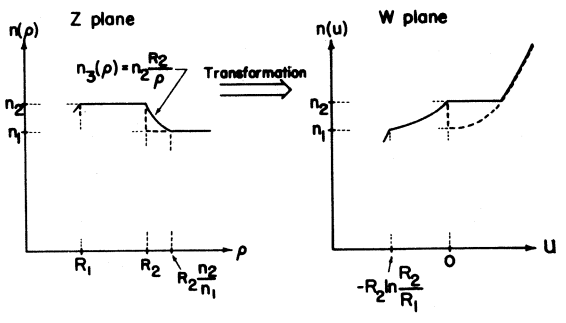

(a) (b)

Fig. 3. Index distribution of a diffused guide at "critical decay" for which waveguiding ceases.

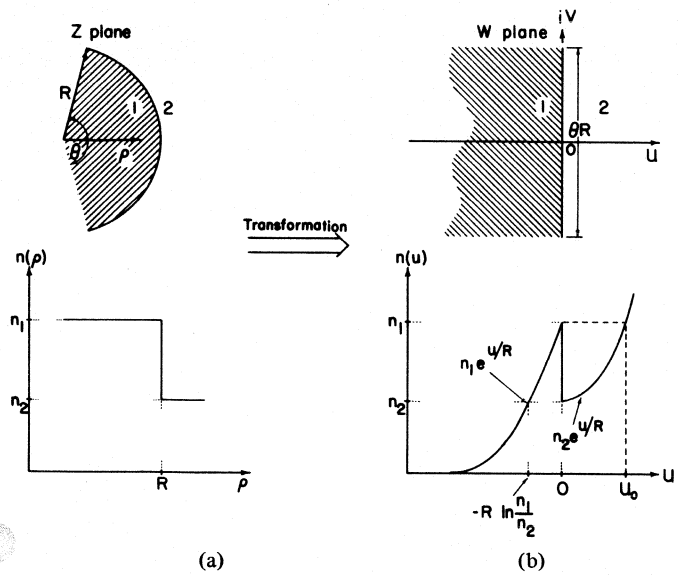

Fig. 4. A two-dimensional one-boundary bend with step index distribution (a) and its transformation (b).

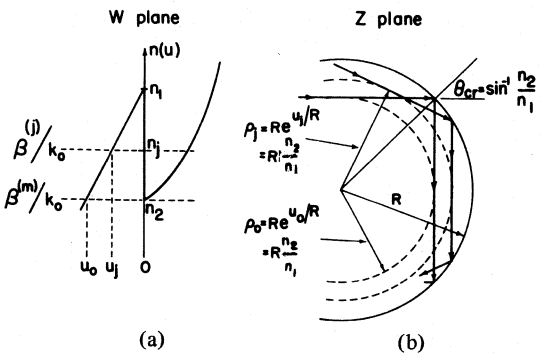

Fig. 5. Ray picture of modes j and m that propagate in the guide of Fig. 4.

he circular medium at the critical angle. Rays tangent to circles greater than ρ_0 are (nearly) totally reflected from the boundary while rays tangent to smaller circles are incident at angles less than the critical angle and pass through the boundary.

There are a number of transformations in addition to the logarithmic one (9) that are of potential interest in connection with integrated optics. One class of such transformations may be obtained from familiar equipotential surfaces and streamlines of electrostatics or laminar flow problems. Fig. 6, for example, shows the surfaces obtained when a conducting cylinder is placed in a uniform electric field. The transformation

$$W = Z + \frac{a^2}{Z} \tag{12}$$

applies to this situation with u equals constant defining the equipotential surfaces, and v equals constant defining the streamlines. If we have an optical waveguide with tapered walls (a horn-shaped structure [7] obtained by flaring a waveguide for coupling purposes, for example) that has the appearance of a segment of any two streamlines in Fig. 6, the transformation (12) will convert the waveguide into one with straight

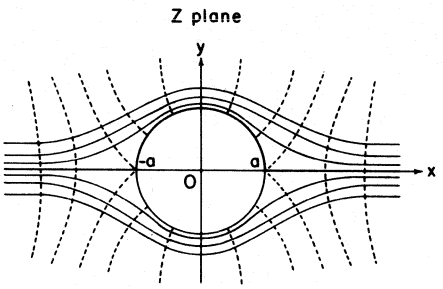

Fig. 6. Equipotential and streamlines of a conducting cylinder placed in a uniform electric field. The transformation $W = Z + a^2/Z$ converts curved guides whose shape is that of any two streamlines into waveguides with straight boundaries.

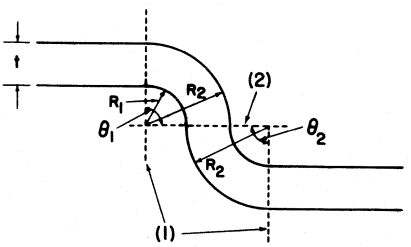

Fig. 7. Waveguide displacement produced by two circular bends. Dotted lines show transition regions.

walls. By varying a in (12), a wide variety of waveguide shapes can be generated. The refractive index in the equivalent structure varies along the guide as well as across it. This situation differs from the transformation (9) where the equivalent structure is uniform in the direction of propagation and necessitates a more complex analysis [8].

The waveguide bend illustrated in Fig. 7 represents an important passive integrated optical component. Under appropriate design the bend can consist of two sections of circular arcs connected to each other and to straight waveguide sections, as indicated by the dotted lines in Fig. 7. The arcs need not be 90° in length as in the figure. Loss mechanisms in this structure include the radiative loss due to modal attenuation along the bends and transition losses that occur between guides at the dotted lines. The remainder of the paper is devoted to an analysis of these effects that is based on the transformation (9).

III. Attenuation Along a Bend

Strictly speaking, the solution of (3) for structures with refractive index distributions of the kind shown in Figs. 1, 2, and 4 does not contain any guided waves because the refractive index at $u = \infty$ is greater than it is elsewhere. The region to the left of the minimum in refractive index can support a guided wave, however, and from a practical point of view, a field of the form

$$\psi(u, v) = F(u) \exp [i(\beta + i\alpha)v] = F(u) \exp [i(\beta + i\alpha)R_2\theta], \quad u < u_6 \tag{13}$$

can be used to represent the guided wave as in the prism coupler [9]. In this expression β and α are the respective propagation and attenuation constants of the wave, θ is the angular and $R_2\theta$ the actual length of the bend along the greater

arc, and $F(u)$ is the spatial characterization of the wave. Equation (13) can be used to the left of the turning point indicated as u_6 in Fig. 8 where $n(u_6) = \beta/k_0$.

$F(u)$, β, and α are functions of the radii of curvature of the bend. Characteristics of $F(u(x, y))$ determine transmission losses as the wave proceeds from one section to the next. This loss is discussed in Section IV. For the present we consider properties of β and α of a uniform bend. For the general structure shown in Fig. 8, β and α may be obtained as the solution of an eigenvalue equation that we express as

$$D_{1,6}(k_v)\big|_{k_v=\beta+i\alpha} = 0. \tag{14}$$

$D_{1,6}$, termed the "system function" for the structure, is a function of a wavenumber k_v. At certain values of k_v, $D_{1,6}$ is zero and these values are the complex propagation constants for waves on the structure.

The system function is the determinant obtained by matching boundary conditions for a multilayer structure when waves of arbitrary amplitude are assumed to exist in each layer. The system function for step index profiles is discussed in the Appendix. Our interest lies in the system function for continuously varying index profiles which can be obtained in the manner indicated in the Appendix. The method consists of subdividing the structure into thin slabs as indicated in Fig. 8, writing the expression for $D_{1,6}$ for a multilayer, and then taking the limit as the thickness of each slab reduces to differential dimensions. The limit procedure results in a series that must be expressed differently on each side of the turning points u_1, u_4, u_6 of Fig. 8 and in the vicinity of the turning points. The series expressions are presented in [11]. We will obtain approximate expressions by employing the first term of this series expression which involves Wentzel-Kramers-Brillouin (WKB) related approximations shown in the Appendix.

To present the equations to determine β and α we use the symbol k_u to represent the wavenumber

$$k_u(u) = [k_0^2 n^2(u) - k_v^2]^{1/2} \tag{15}$$

and define integrals over k_u as

$$h_{ij} = \int_{u_i}^{u_j} k_u(u)\, du. \tag{16}$$

The approximate eigenvalue equation for a wave propagating on the structure lying to the left of u_5 in Fig. 8 is found to be [see (A11)]

$$h_{2,3} + \left(h_{1^+,2} - \tan^{-1}\frac{K_{1^-}}{iK_{1^+}}\right) + \left(h_{3,4^-} - \tan^{-1}\frac{K_{4^+}}{iK_{4^-}}\right) = m\pi \tag{17}$$

where

$$K_{j^+,^-} = \begin{cases} k_u\big|_{u_{j^+,^-}}, & \text{for solutions of (3)} \\ \dfrac{k_u}{\epsilon}\Big|_{u_{j^+,^-}}, & \text{for solutions of (5).} \end{cases} \tag{18}$$

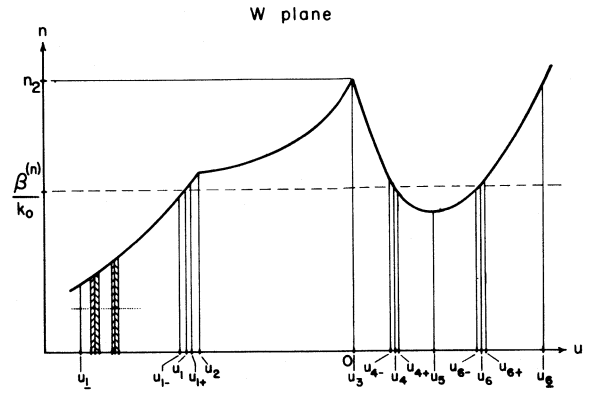

Fig. 8. Transformed index distribution of a bent guide with continuous index distribution. The turning points are u_1, u_4, and u_6. u_{1^+}, u_{1^-}, etc., define the positions at which the representation of the system function changes. The original straight guide has constant index between u_2 and u_3. u_1 and u_6 are arbitrary points beyond u_1 and u_6. To the right of u_1 some sublayers are shown that are used to reduce the system function for discrete layers to the system function of a continuously varying index distribution. (Characters with underbars in the figure appear boldface in text.)

Insight into (17) may be obtained by considering the simple uniform, straight-step index guide. For such a guide $n(u)$ is piecewise constant and the regions $u_{1^+} \rightarrow u_2$ and $u_3 \rightarrow u_{4^-}$ are of zero length. Equation (17) then reduces to

$$k_u t = m\pi + \tan^{-1}\frac{K_{1^-}}{iK_{1^+}} + \tan^{-1}\frac{K_{4^+}}{iK_{4^-}} \tag{19}$$

where t is the guide thickness and m is the mode order. This is the familiar eigenvalue equation for waveguides. The terms $\tan^{-1} K_j/iK_{j^+}$ are functions of k_v and take values between 0 and $\pi/2$ for a step discontinuity. At a continuous turning point, such as appears in Figs. 2 and 8, we may take $\tan^{-1} K_j/iK_{j^+}$ to be $\pi/4$ based on the assumption that u_{j^+} and u_{j^-} are selected to achieve this result. A more precise specification of the location of these points is discussed in Section IV. We will discuss examples of (17) for index distributions appropriate to waveguide bends following the discussion of α.

Using the same WKB-type approximation as is used to obtain (17), the change in propagation constant due to the presence of the high refractive index region on the right of Figs. 1, 2, 4 may be expressed

$$i\alpha = -\frac{1}{L}\left(\frac{K_{6^+} - K_{6^-}}{K_{6^+} + K_{6^-}}\right)\sin\left(2\tan^{-1}\frac{K_{4^-}}{iK_{4^+}}\right)\exp\left(2ih_{4^+,6^-}\right)$$
$$\simeq \frac{i}{L}\sin\left(2\tan^{-1}\frac{K_{4^-}}{iK_{4^+}}\right)\exp\left(2ih_{4^+,6^-}\right) \tag{20}$$

as obtained from (A12).

The terms in (20) are to be evaluated at β, the solution of (17). This renders $h_{4^+,6^-}$ positive imaginary in (20) and the exponential in (20), which may achieve small values, largely determines the behavior of α. The parameter L is the derivative of (17), viz.,

$$L = -\frac{\partial}{\partial k_v}\left[h_{2,3} + \left(h_{1^+,2} - \tan^{-1}\frac{K_{1^-}}{iK_{1^+}}\right) + \left(h_{3,4^-} - \tan^{-1}\frac{K_{4^+}}{iK_{4^-}}\right)\right]_{k_v=\beta} \tag{21}$$

and may be termed the *effective longitudinal ray length*. For TE modes in a uniform, straight guide ($h_{1^+,2} = h_{3,4^-} = 0$, $K_{i^\pm} = (k_u)_{u_{i^\pm}}$), for example, L is

$$L = \frac{\beta}{(k_u)_{u_3}}[t + 1/|k_u|_{u_{1^-}} + 1/|k_u|_{u_{4^+}}] = (\tan\phi)[t'] \tag{22}$$

where t' is the effective width of the waveguide, which includes the decay distances, and ϕ is the angle the wave normal in the guide makes with the surface of the guide (Fig. 9). The second equality in (20) follows from the assumption that u_{6^+} and u_{6^-} are selected so that $K_{6^+} = K_{6^-}/i$. For a continuous change in index at u_4 the sine function in (20) can be approximated by unity.

To further examine the equations for β and α we note that in regions in which the refractive index is constant in x, y, the equivalent index is $n(u) = n \exp u/R$. The resulting expression for $h_{i,j}$ can be integrated in closed form. As an example, for the single-boundary guide of Fig. 4, only $h_{1^+,2}$ of the h's is non-zero in (17). Taking $u_{1^+} = -R \ln (k_0 n_1/\beta)$ and $u_2 = 0$ we find the eigenvalue equation for β of a TE mode (3) to be

$$R\beta\left[\left(\frac{k_0^2 n_1^2}{\beta^2} - 1\right)^{1/2} - \cos^{-1}\frac{\beta}{k_0 n_1}\right] - \tan^{-1}\left(\frac{\beta^2 - k_0^2 n_2^2}{k_0^2 n_1^2 - \beta^2}\right)^{1/2} - \frac{\pi}{4} = m\pi. \tag{23}$$

Similarly, for the step index profile of Fig. 1, $u_2 = -R_2 \ln \cdot R_2/R_1$, $u_3 = 0$, $h_{1^+,2} = 0$, $h_{3,4^-} = 0$, and the eigenvalue equation is[2]

$$R_2\beta\left[\left(\frac{k_0^2 n_2^2}{\beta^2} - 1\right)^{1/2} - \left(\frac{k_0^2 n_2^2}{\beta^2}\frac{R_1^2}{R_2^2} - 1\right)^{1/2} - \cos^{-1}\left(\frac{\beta}{k_0 n_2}\right) + \cos^{-1}\left(\frac{\beta}{k_0 n_2}\frac{R_2}{R_1}\right)\right] - \tan^{-1}\left(\frac{\beta^2 - k_0^2 n_1^2\left(\frac{R_1}{R_2}\right)^2}{\left(\frac{R_1}{R_2}\right)^2 k_0^2 n_2^2 - \beta^2}\right)^{1/2} - \tan^{-1}\left(\frac{\beta^2 - k_0^2 n_3^2}{k_0^2 n_2^2 - \beta^2}\right)^{1/2} = m\pi. \tag{24}$$

For the diffused guide of Fig. 2, if the lateral diffusion results in an exponential-type decay of the form $n(\rho) = n_1 + (n_2 - n_1) \cdot \exp - [\zeta(\rho - R_2)/R_2]$ where ζ/R_2 is the decay rate of the index difference, the equivalent index profile is $n(u) = \exp \cdot [-\zeta \exp u/R_2 + \zeta + u/R_2]$. A closed form for $h_{3,4^-}$ is not known for such a profile. On the other hand, it is not difficult to generate approximations as is indicated in the next paragraph. Solutions of (23) and (24) can be obtained by graphical or numerical means.

The determination of α in closed form can be accomplished for index profiles exponential in the W plane. The results involve specification of $\sin(2\tan^{-1}K_{4^-}/iK_{4^+}), L$, and $\exp(2ih_{4^+,5})$. These results are presented in Table I. For the diffused guide of Fig. 2 with exponential lateral diffusion, we approximate $n(u) \sim n_1 \exp u/R_2 + (n_2 - n_1)\exp - bu/R_2$, where b/R_2 is the initial slope of $n(u)$ expressed in the previous paragraph; i.e., $b/R_2 = -[(1 - \zeta)/R_2] \exp \zeta$. An additional approximation for the diffused guide in Table I is made in the exponential term of α. We take

$$h_{4^+,6^-} \simeq 2[(\beta/k_0)^2 - n^2(u_5)]^{1/2}[u' - u_5] \tag{25}$$

where u_5 is the point at which $n(u)$ is a minimum (Fig. 8), viz., $u_5 = (R_2/1 + b) \ln [b(n_2 - n_1)/n_1]$, and u' is the point at which $k_u(u)$ decreases by $1/\sqrt{2}$, viz., $[(\beta/k_0)^2 - n^2(u')]^{1/2} = (2)^{-1/2} \cdot [(\beta/k_0)^2 - n^2(u_5)]^{1/2}$.

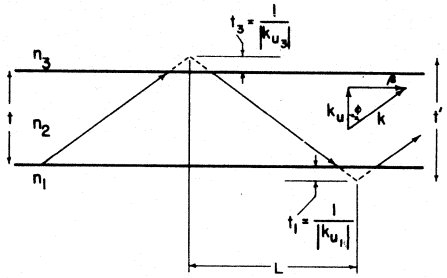

Fig. 9. The effective thickness t' and the effective longitudinal ray length L for a straight guide.

Turning to a consideration of the dependence of β and α on the radius of curvature, we note that as the radius of curvature decreases, the index profile of the guide is skewed increasingly upward on the right. Fig. 10 illustrates this point. The figure shows a waveguide of constant thickness at different radii of curvature. Note that when $n_2(R_1/R_2) < n_3$, the behavior of the step waveguide of Fig. 1 is similar to that of the single boundary guide of Fig. 4 since the inner boundary lies in the evanescent region of the wave. Furthermore, there is a minimum radius of curvature R below which the single-boundary and two-boundary guides cease to carry any mode. From (23), setting $\tan^{-1}$ and m to zero and $\beta = k_0 n_2$,

$$R_{\min} = (\lambda_0/8)/[((n_1^2/n_2^2) - 1)^{1/2} - \cos^{-1} n_2/n_1] \tag{26}$$

where λ_0 is the free-space wavelength. This same expression is obtained for the step index guide with n_1/n_2 replaced by n_2/n_3. When n_2 differs from n_1 by a small amount, $R_{\min}$ reduces to[3]

$$R_{\min} \simeq 0.1325\lambda_0/[(n_1 - n_2)/n_1]^{3/2}. \tag{27}$$

Using (26), $R_{\min} \simeq 0.45\lambda_0$ for $n_1/n_2 = 1.5$. Using (27), $R_{\min} \simeq 4200\lambda_0$ for $(n_1 - n_2)/n_1 = 10^{-3}$ and $R_{\min} \simeq 133\lambda_0$ for $(n_1 - n_2)/n_1 = 10^{-2}$.

When the radius of curvature is large compared to the wavelength, the value of β does not change radically from its value β_0 when the waveguide is straight. Using (24) to obtain a first-order expression for β in a step index guide, we find

$$\beta \simeq \beta_0 - \left(\frac{\partial[h_{1^+,4^-}]/\partial(1/R_2)}{-L}\right)\Bigg|_{1/R_2 = 0} \cdot 1/R_2 = \beta_0(1 - t/2R_2) \tag{28}$$

[2] For small t/R_2, (24) reduces to $[k_0^2 n_2^2 - (\beta R_2/R_1)^2]^{1/2} t - \psi_1 - \psi_2 = m\pi$.

[3] Defining $\cos^{-1} n_2/n_1 = y$ and $[(n_1/n_2)^2 - 1]^{1/2} = \tan y$, for small y $\tan y - y \simeq 1/3y^3$.

TABLE I

	$\sin(2\tan^{-1}\frac{K_{4+}}{iK_{4-}})$	L	$\exp(2i\,h_{4+,6-})$
Single Boundary (Fig. 4)	$\frac{2(k_1^2-\beta^2)^{1/2}(\beta^2-k_2^2)^{1/2}}{k_1^2-k_2^2}$	$\frac{\beta}{(k_1^2-\beta^2)^{1/2}(\beta^2-k_2^2)^{1/2}} + R\cos^{-1}\frac{\beta}{k_1}$	$\exp\{2R(\beta^2-k_2^2)^{1/2}-2\beta R \cdot \ln[\frac{\beta+(\beta^2-k_1^2)^{1/2}}{k_1}]\}$
Two Boundaries (Fig. 1)	$\frac{2(k_2^2-\beta^2)^{1/2}(\beta^2-k_3^2)^{1/2}}{k_2^2-k_3^2}$	$\frac{\beta}{[\beta^2-k_3^2(\frac{R_1}{R_2})^2]^{1/2}[k_2^2(\frac{R_1}{R_2})^2-\beta^2]^{1/2}} + \frac{\beta}{(\beta^2-k_3^2)^{1/2}(k_2^2-\beta^2)^{1/2}} + R_2[\cos^{-1}\frac{\beta}{k_2} - \cos^{-1}(\frac{\beta}{k_2}\cdot\frac{R_2}{R_1})]$	$\exp\{2R_2(\beta^2-k_1^2)^{1/2}-2\beta R_2 \cdot \ln[\frac{\beta+(\beta^2-k_3^2)^{1/2}}{k_3}]\}$
Diffused Guide (Fig. 2)	$\simeq 1$	$\frac{R_2}{a}\cos^{-1}\frac{\beta}{k_2}(\frac{R_1}{R_2})^{\frac{a-2}{2}} + \frac{R_2}{b}\cos^{-1}\frac{\beta}{k_2} + R_2[\cos^{-1}\frac{\beta}{k_2} - \cos^{-1}(\frac{\beta}{k_2}\frac{R_2}{R_1})]$	$\simeq \exp\{-4[\beta^2-k^2(u_5)]^{1/2}(u'-u_5)\}$

Note: The attenuation along a bend is given by α as expressed in (20). The three parameters L, sin, and exp that are given in (20) are given for single-boundary, two-boundary, and diffused curved guides. For diffused guide parameters see the paragraph containing (25) and note that a and b are related to the initial slopes of the refractive index profile on the inner and outer boundary, respectively, of the guide. Note also that $k_j = k_0 n_j$.

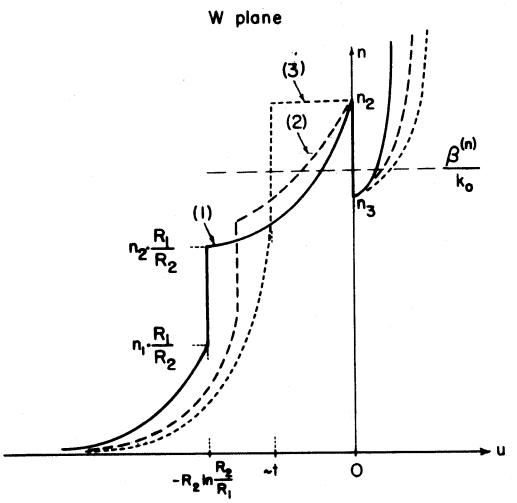

Fig. 10. Transformed index distribution of a step index guide of constant thickness at different radii of curvature. At small radius of curvature (1), i.e., when $R_1/R_2 < n_3/n_2$ the step index guide appears as a single-boundary guide. The dotted curve which corresponds to the largest radius of curvature should be labeled (3) and the dashed curve (2).

where $h_{1+,4-}$ is defined in (16), L is shown in (21), and t is the thickness of the guide $R_2 - R_1$. In (28) it is clear that a dramatic change in β occurs only when the radius of curvature approaches the guide thickness.

To consider the attenuation rate α expressed in (20), we note that the longitudinal ray path length has a simple geometric interpretation (Fig. 9) and is a number greater than the width of the equivalent guide. Unless $\exp(2ih_{4+,6-})$ is small, the attenuation is excessive. The exponential is small unless β approaches $k_0 n(u_5)$, where u_5 is the location of the index minimum (Fig. 8). For a prescribed αL we may specify a minimum β by solving equation (20) for β. Using the approximate expressions in Table I for a diffused waveguide and representing $n(u)$ near u_5 as $n(u_5) + (1/2)(\partial^2 n/\partial u^2)(u - u_5)^2$ we find

$$\beta_{\min} \simeq k_0 n(u_5) + \ln(\alpha L)^{-1}/8[n(u_5)/(\partial^2 n/\partial u^2)_{u_5}]^{1/2}$$

where

$$n(u_5) = n_1 b\left(\frac{n_2}{n_1} - 1\right)^{1/b+1} + (n_2 - n_1)b\left(\frac{n_2}{n_1} - 1\right)^{b/b+1}$$

$$[n(u_5)/\partial^2 n/\partial u^2]^{1/2} = R_2\left[\frac{1 + b(n_2 - n_1)}{1 + b^3(n_2 - n_1)}\right]^{1/2} \tag{29}$$

and b is related to the gradient of the lateral diffusion ζ/R_2 as discussed previous to (25). Using the value of L for a straight guide, (29) can provide a useful design relation for bends in diffused guides.

If we consider the attenuation rate of the step index guide (Fig. 1) for the situation in which $\beta = k_0 n_3(1 + \delta)$ differs by a small amount from the wavenumber of region 3, we find from Table I that the exponential term in α to first order in δ is

$$\alpha \propto \exp\left(-\frac{4\pi}{\lambda_0} R_2 n_3 \delta\right). \tag{30}$$

This simple expression shows that unless the radius of curvature approaches the value $\lambda_0/4\pi n_3\delta \sim \lambda_0/4\pi(n_2 - n_3)$ the attenuation will be small. Even when the index difference is 10^{-3}, a radius of curvature of several hundreds λ_0 can be tolerated.

It should be emphasized that the two-boundary guide (Fig. 1) behaves like a one-boundary guide (Fig. 4) not only when $n_2(R_1/R_2) < n_3$ (as was noted before) but also when $n_2(R_1/R_2) \geqslant n_3$ and $\beta > n_2(R_1/R_2)$. In both cases, the expressions for β and α for the one-boundary guide should be used.

As a point of reference, in the limit of large radii of curvature ($R_2 \gg \lambda_0, t$), the attenuation formula for a two-boundary guide (given in Table I) reduces to Marcuse's formula [2, eq. (32)] except for a factor of 2. This factor is the square of the transmission coefficient at the turning point and should be inserted in front of Marcuse's formula. The approximation for large radii can be shown easily by replacing the effective longitudinal ray length of the bend (L) by that of a straight guide (22) and by using $R_2 \gg t$.

IV. Transition Effects

The distortion in the index profile results in a displacement of the modes towards the outside of a bend and this effect results in transmission losses at the interfaces shown in Fig. 7. The WKB approximation of the spatial distribution of a mode in the region to the left of u_{6-} as obtained from (A6) is

$$F(u) = \begin{cases} (-1)^m [(|K_{4+}K_{4-}|)^{1/2}/|K_{4+} + K_{4-}|] (K_3/K)^{1/2} \exp i \displaystyle\int_{u_{4+}}^{u} k_u \, du, & u_{4+} < u < u_{6-} \\ (K_3/K)^{1/2} \cos \left(\displaystyle\int_{u_{1+}}^{u} k_u \, du - \tan^{-1} \frac{K_{1-}}{iK_{1+}} \right), & u_{1+} < u < u_{4-} \\ [(|K_{1+}K_{1-}|)^{1/2}/|K_{1+} + K_{1-}|](K_3/K)^{1/2} \exp i \displaystyle\int_{u}^{u_{1-}} k_u \, du, & u < u_{1-} \end{cases} \tag{31}$$

where K is the same as in (18) for an arbitrary point u. This expression holds outside the turning points. The positions u_{1-}, u_{1+}, etc., are determined by requiring

$$\left(\frac{\partial K/\partial u}{K} \frac{\pi}{k_u} \right)_{u_i^{\pm}} = \epsilon \tag{32}$$

where ϵ is a number much less than 1. Equation (32) is established by considering the second-order terms in the expansion of the system functions [11].[4]

Equation (31) indicates displacement of a mode because the argument of the cosine term contains an integral over $k_u = [k_0^2 n^2(u) - \beta^2]^{1/2}$ and the distortion in $n(u)$ results in a larger contribution from the right side of the guide than from the left. For the lowest order mode, the approximate peak occurs when the argument of the cosine is zero, i.e.,

$$\int_{u_{1+}}^{u} k_u \, du = \tan^{-1} \frac{K_{1-}}{iK_{1+}}. \tag{33}$$

Expressions for the integral in (33) may be obtained as in (23) and (24) using different representations in the regions $u_{1+} - u_2$, $u_2 - u_3$, $u_3 - u_{4-}$. The wave function within the guide region of a step index guide, for example, transformed back to the x, y plane is

$$F(\rho) = \left(\frac{k_2^2 - \beta^2}{k_2^2 \rho^2 / R_2^2 - \beta^2} \right)^{1/4} \cos \Big[(k_2^2 \rho^2 - \beta^2 R_2^2)^{1/2} - \beta R_2 \cos^{-1} (\beta R_2 / k_2 \rho) - (k_2^2 R_1^2 - \beta^2 R_2^2)^{1/2} + \beta R_2 \cos^{-1} (\beta R_2 / k_2 R_1) - \tan^{-1} \left(\frac{K_{1-}}{iK_{1+}} \right) \Big] \tag{34}$$

where $k_2 = k_0 n_2$ and

$$\tan^{-1} \frac{K_{1-}}{iK_{1+}} = \tan^{-1} \left[\frac{\beta^2 - k_0^2 n_1^2 (R_1/R_2)^2}{k_2^2 (R_1/R_2)^2 - \beta^2} \right]^{1/2}. \tag{35}$$

To provide a useful parameter we may determine the position of the peak ρ_0 of (34) in accordance with (33) to first order in $(\rho - R_1)/R_2$. The result is

$$\rho_0 \simeq R_1 + \left(\tan^{-1} \frac{K_{1-}}{iK_{1+}} \right) \Big/ [k_0^2 n_2^2 - (\beta R_2 / R_1)^2]^{1/2}. \tag{36}$$

Approximating β as in (28), with $\beta_0 = (1 - \delta') k_0 n_2$ where δ' is presumed small, and retaining first-order terms in $1/R_2$, ρ_0 reduces to

$$\rho_0 = \left(R_1 + \frac{t}{2} \right) + \frac{t}{2} \left\{ 1 - \frac{(2\delta')^{1/2} - 2t_3(\beta_0)/R_2}{[2\delta' + (t/R_2)^2]^{1/2}} \right\} \tag{37}$$

where $t = R_2 - R_1$ and $t_3(\beta_0)$ is the evanescent decay distance into region 3 of a straight guide (Fig. 9). The displacement ρ_0 is sensitive to the radius of curvature as presented by (t/R_2) only when β_0 differs from $k_0 n_2$ by an amount of the order $1/2(t/R_2)^2$.

The power transmitted at the transition between guides of different curvature, as appear in Fig. 7, can be estimated by the overlap integral

$$T^2 = 4 \frac{\left(\int F' F \, d\rho \right)^2 \Big/ \int F^2 \, d\rho \int F'^2 \, d\rho}{(1 + \beta'/\beta)^2} \tag{38}$$

where F' and F are the wave functions of connecting guides and β' and β are the propagation constants. T^2 can be evaluated numerically for any given configuration using (31), or as a specific example, (34). The overlap integral depends on the direction of the displacement (36). To provide an estimate of the power transmitted at intersection (2) of Fig. 7, consider the approximation $F(\rho) \sim \cos a(\rho - \rho_0)$ and $F'(\rho) \sim \cos \cdot$

[4] The second-order term in the expansion of the system function is

$$\frac{d}{du} \ln \frac{K(u_i)}{K(u)} \exp \left(i \int_u^{u_i} k_{u'} \, du' \right).$$

$a(\rho - \rho_0 + \Delta)$ where $a = \pi/2t$ and Δ represents the displacement between the two wave-function maxima in symmetric guides ($n_1 = n_3$), viz., $\Delta = 2(\rho_0 - R_1) - t$. We obtain

$$T^2 = \left(1 - \frac{\pi^2\Delta^2}{4t^2}\right)^2. \tag{39}$$

For small displacements the power loss is proportional to $(\Delta/t)^2$ and is a small percentage of the total. As Δ/t approaches unity there is, of course, substantial power loss. The overall power transmission of the structure shown in Fig. 7 may be approximated as a product of the form

$$T^2 = \left(1 - \frac{\pi^2\Delta_1^2}{4t^2}\right)^2 \cdot (1 - \exp(-2\alpha R_2\theta_1)) \cdot \left(1 - \frac{\pi^2\Delta^2}{4t^2}\right)^2 \cdot (1 - \exp(-2\alpha R_2\theta_2)) \cdot \left(1 - \frac{\pi^2\Delta_1^2}{4t^2}\right)^2 \tag{40}$$

where $\Delta_1 = \Delta/2$ is the displacement between guided-wave maxima at intersection (1) and θ_1 and θ_2 are the lengths of the arcs that make up a bend. Using (30) to approximate α and (37) to obtain Δ, (40) can provide a relatively simple approximation for the overall losses in a bend.

V. Conclusion

The method of conformal transformations has been shown to provide a useful qualitative as well as quantitative view of wave propagation in curved optical waveguides. The method requires no *a priori* limitations in radii of curvature or index differences. It has been shown how useful representations for the wave functions, eigenvalue equations, and attenuation constants can be obtained by analyzing equivalent structures in the transform plane. Using first-order approximations, simple expressions for the attenuation along a bend, the displacement of the wave from its position in a straight guide, the change in propagation constant due to bending of the guide, and the overall transmission loss in a practical bend have been presented.

Appendix

Solutions for the eigenfunctions and eigenvalue equations of continuously varying media may be obtained starting with solutions of a step discontinuous index profile containing constant index between steps. In such a profile, solutions to (3) or (5) are obtained by setting $\psi_j(u, v) = (1/K_j)(a_j^+ \exp ik_{u_j}u + a_j^- \exp -ik_{u_j}u) \exp ik_v v$ in layer j and matching boundary conditions at the interface between layers. The resulting equations in a_j^+ and a_j^- take the form

$$\left[\begin{array}{cc:cc} -K_1\exp(-ik_{u_1}u_1) & -K_2\exp(ik_{u_2}u_1) & K_2\exp(-ik_{u_2}u_1) & 0 \\ \exp(-ik_{u_1}u_1) & -\exp(ik_{u_2}u_1) & -\exp(-ik_{u_2}u_1) & 0 \\ \hdashline 0 & K_2\exp(ik_{u_2}u_2) & -K_2\exp(-ik_{u_2}u_2) & -K_3\exp(ik_{u_3}u_2) \\ 0 & \exp(ik_{u_2}u_2) & -\exp(-ik_{u_2}u_2) & -\exp(ik_{u_3}u_2) \end{array}\right] \left[\begin{array}{c} a_1^- \\ a_2^+ \\ a_2^- \\ a_3^+ \end{array}\right] = 0 \tag{A1}$$

where the k_u and K's are defined, respectively, in (15) and (18), the subscript refers to the layer, and u_1 and u_2 are two interfaces for a three-region problem.

The determinant of the matrix in (A1) is denoted $D_{1,3}$, while the determinants of the matrix within the dotted and dashed lines, respectively, are denoted $D_{1,2}$ and $D_{2,3}$. It is simple to show from (A1) that

$$D_{1,3} = D_{1,2}D_{2,3} - D'_{1,2}{}'D_{2,3} \tag{A2}$$

where the primes indicate

$$D'_{ij} = D_{ij}(k_{u_i}, \cdots, -k_{u_j}), \qquad {}'D_{ij} = D_{ij}(-k_{u_i}, \cdots, k_{u_j}). \tag{A3}$$

Furthermore, it may be shown that (A2) can be generalized to any number layers in the form

$$D_{1,N} = D_{1,p}D_{p,N} - D'_{1,p}{}'D_{p,N} \tag{A4}$$

where p is any layer between 1 and N.

The complex propagation constant for a guided wave is the value of k_v for which the determinant in (A1) is zero. The eigenvalue equation is thus

$$(D_{1,N})_{k_v=\beta+i\alpha} = 0. \tag{A5}$$

Furthermore, it may be shown that the eigenfunction can be expressed

$$F(u) = A\left[\frac{D_{1,p}}{2K_1 \cdots 2K_p}\exp(-ik_{u_p}u) - \frac{D'_{1,p}}{2K_1 \cdots 2K_p} \cdot \exp(ik_{u_p}u)\right], \qquad u_{p-1} < u < u_p \tag{A6}$$

where p refers to any layer in which (A6) is evaluated and A is a constant.

If the number of layers is permitted to become infinite and $n(u)$ becomes continuous, it is possible to represent the system functions in a series of the kind first described by Bremmer [10] and presented by Harris [11]. The first terms of the series are the WKB forms

$$D_{r,q}/(2K_r) \cdots (2K_{q-1}) \simeq (K_q/K_r)^{1/2}\exp\left[-i\int_{u_r}^{u_{q-1}} k_u\,du + i(k_{u_q}u_{q-1} - k_{u_r}u_r)\right]$$

$$'D'_{r,q}/(2K_r) \cdots (2K_{q-1}) \simeq -(K_q/K_r)^{1/2}\exp\left[i\int_{u_r}^{u_{q-1}} k_u\,du - i(k_{u_q}u_{q-1} - k_{u_r}u_r)\right]$$

$$D'_{r,q} = {}'D_{r,q} = 0. \tag{A7}$$

Near a turning point (A7) fails and we have

$$D_{r,q} \simeq (2K_r) \cdots (2K_{q-1})\left(\frac{K_r + K_q}{2K_q}\right)\exp i(k_{u_q}u_{q-1} - k_{u_r}u_r). \tag{A8}$$

The primes of (A8) are obtained as in (A3). The subscripts in (A7) and (A8) refer to sublayers as indicated in Fig. 8 and are described more fully in the next paragraph.

To express (A5) or (A6) for continuously varying media to the approximation (A7) and (A8) we employ (A4) sequentially stopping at each turning point (u_1, u_4, and u_6 of Fig. 8) and write, for example,

$$D_{1,6} = D_{1,1^-}\{[D_{1^-,1^+}D_{1^+,4^-}D_{4^-,4^+} + D'_{1^-,1^+}{}'D'_{1^+,4^-}{}'D_{4^-,4^+}] \cdot D_{4^+,6^-}D_{6^-,6^+} + [D_{1^-,1^+}D_{1^+,4^-}D'_{4^-,4^+} + D'_{1^-,1^+}{}'D'_{1^+,4^-}{}'D'_{4^-,4^+}] \cdot {}'D'_{4^+,6^-}{}'D_{6^-,6^+}\}D_{6^+,6}. \tag{A9}$$

The zero functions of the third equation in (A7) have been incorporated in (A9). Subscript **1** refers to the point u_1 located to the left of u_{1^-} as indicated in Fig. 8. Similarly, **6** refers to u_6 located to the right of u_{6^+}. Using the first equation in (A7) to describe the way the subscripts are used, we have

$$\frac{D_{1,1^-}}{2K_{u_1} \cdots 2K_{u_1}} = (K_{u_{1^-}}/K_{u_1})^{1/2} \exp\left\{-i\int_{u_1}^{u_{1^-}} k_u\, du + i[k_u(u_{1^-})u_{1^-} - k_u(u_1)u_1]\right\}. \tag{A10}$$

Note that to employ (A7) and (A8) conveniently, (A5) can also be written $D_{1,N}/2K_1 \cdots 2K_N = 0$.

The equation for β is obtained by neglecting the region to the right of u_{4^+} and can be expressed as

$$(D_{1,4^+}/2K_{u_1} \cdots 2K_{u_{4^+}})_{k_v=\beta} = 0. \tag{A11}$$

The equation for $i\alpha = (k_v - \beta)$ is obtained by setting $D_{1,6}$ to zero, expressing

$$(D_{1,4^+}/2K_{u_1} \cdots 2K_{u_{4^+}})_{k_v \simeq \beta} \simeq \left(\frac{\partial}{\partial k_v} D_{1,4^+}/2K_{u_1} \cdots 2K_{u_{4^+}}\right)_{\beta} \cdot (k_v - \beta)$$

and using (A4) with p at u_{4^+}. The result is

$$i\alpha = \left[\frac{(D'_{1,4^+}/2K_{u_1} \cdots 2K_{u_{4^+}})D_{4^+,6}}{\left(\frac{\partial}{\partial k_v} D_{1,4^+}/2K_{u_1} \cdots 2K_{u_{4^+}}\right)'D_{4^+,6}}\right]_{k_v=\beta}. \tag{A12}$$

In the text $K_{j^\pm}$ is used instead of $K_{u_j^\pm}$. Finally, the wave function is expressed using (A6) treating u_p as an arbitrary point u.

References

[1] a) E. A. Marcatili, "Bends in optical dielectric guides," *Bell Syst. Tech. J.*, vol. 48, pp. 2103–2132, Sept. 1969.
b) D. Marcuse, "Bending losses of the asymmetric slab waveguide," *Bell Syst. Tech. J.*, vol. 50, pp. 2551–2563, Oct. 1971.
c) L. Lewin, "Radiation from curved dielectric slabs and fibers," *IEEE Trans. Microwave Theory Tech.*, vol. MTT-22, pp. 718–727, July 1974.

[2] R. S. Elliott, "Azimuthal surface waves on circular cylinders," *J. Appl. Phys.*, vol. 26, pp. 368–376, Apr. 1955.

[3] H. F. Taylor, "Power loss at directional change in dielectric waveguides," *Appl. Opt.*, vol. 13, pp. 646–647, Mar. 1974.

[4] F. E. Borginis and C. H. Papas, "Electromagnetic waveguides and resonators," in *Handbuch der Physik*, vol. 16, S. Flügge, Ed., pp. 358–364.

[5] W. E. Martin, "Waveguide electro-optic modulation in II-VI compounds," *J. Appl. Phys.*, vol. 44, pp. 3703–3707, Sept. 1973.

[6] a) E. A. Marcatili, "Dielectric rectangular waveguide and directional coupler for integrated optics," *Bell Syst. Tech. J.*, vol. 48, pp. 2071–2102, Sept. 1969.
b) J. E. Goel, "A circular-harmonic computer analysis of rectangular dielectric waveguides," *Bell Syst. Tech. J.*, vol. 48, pp. 2133–2160, Sept. 1969.

[7] R. K. Winn and J. H. Harris, "Coupling from multimode to single-mode linear waveguides using horn-shaped structures," *IEEE Trans. Microwave Theory Tech.*, vol. MTT-23, pp. 93–97, Jan. 1975.

[8] a) D. Marcuse, "Mode conversion caused by slab imperfections of a dielectric slab waveguide," *Bell Syst. Tech. J.*, vol. 48, pp. 3187–3215, Dec. 1969.
b) J. H. Harris, R. K. Winn, and D. Dalgoutte, "Theory and design of periodic coupler," *Appl. Opt.*, vol. 11, pp. 2234–2241, Oct. 1972.

[9] a) L. V. Iogansen, "Theory of resonant electromagnetic systems with total internal reflection III," *Sov. Phys.–Tech. Phys.*, vol. 11, pp. 1529–1534, May 1967.
b) J. H. Harris, R. Shubert, and J. N. Polky, "Beam coupling to films," *J. Opt. Soc. Amer.*, vol. 60, pp. 1007–1016, Aug. 1970.

[10] H. Bremmer, "The WKB approximation as the first term of a geometrical optical series," *Commun. Pure Appl. Math.*, vol. 4, pp. 105–115, June 1951.

[11] J. H. Harris, "Analysis techniques for multilayer structures," *IEEE Trans. Microwave Theory Tech.*, vol. MTT-23, submitted.

[12] Lord Rayleigh, "The problem of the whispering gallery," in *Scientific Papers*, vol. 5. London: Cambridge, 1912, pp. 617–620.

[13] The following references contain material related to this article.
a) S. J. Maurer and L. B. Felsen, "Ray methods for trapped and slightly leaky modes in multilayered or multiwave regions," *IEEE Trans. Microwave Theory Tech.*, vol. MTT-18, pp. 584–595, Sept. 1970.
b) D. C. Chang and F. S. Barnes, "Reduction of radiation loss in a curved dielectric slab waveguide," Electromagnetic Lab., Dep. Elec. Eng., Univ. Colorado, Boulder, Sci. Rep. 2, July 1973.
c) D. Marcuse, "Bent optical waveguide with lossy jacket," *Bell Syst. Tech. J.*, vol. 53, pp. 1079–1101, July 1973.
d) S. Sheem and J. R. Whinnery, "Guiding by single curved boundaries in integrated optics," *Wave Electron.*, vol. 1, to be published.
e) —, "Modes of a curved surface waveguide for integrated optics," *Wave Electron.*, vol. 1, to be published.

The POPOP Dye Vapor Laser

PETER W. SMITH, MEMBER, IEEE, PAUL F. LIAO, CHARLES V. SHANK, C. LIN, AND PATRICK J. MALONEY, MEMBER, IEEE

Abstract—**We report a comprehensive study of the operation of a laser using the organic scintillator dye POPOP in the vapor phase. Laser operating parameters have been determined, and we describe tuning experiments which demonstrate an oscillation range of 25 nm. Gain measurements as a function of wavelength and time are reported for transverse pumping with the 337.1-nm output of a pulsed N_2 laser. The quantum efficiency has been measured as a function of temperature and pump wavelength, and a preliminary study has been made of the effect of buffer gases on the quantum efficiency and the gain. Spectral condensation measurements show 90 percent of the broad-band laser output can be obtained in a 1-nm band—indicating that even in a dilute vapor, the thermalization time of the laser levels is $<<1$ ns. We conclude by discussing the implications of these results for the achievement of an electrically pumped dye vapor laser.**

I. Introduction

RECENTLY, three groups have independently reported laser action in a new class of laser media—an organic dye vapor [1]-[3]. These lasers are of interest for a number of reasons. They operate at dye molecule densities comparable to those of liquid dye lasers, but their performance is not degraded by thermally induced refractive index changes. They are useful systems for the study of the dye molecules themselves, and are a source of new laser wavelengths. Perhaps the most important aspect of dye vapor lasers is that they offer the possibility of efficient operation under electrical excitation. If problems of decomposition of the dye molecules can be overcome, dye vapor lasers offer the promise of a high efficiency, tunable, broad-band visible laser.

Although a number of organic dye vapors have been studied [4], [5], the lowest threshold operation under optical pumping has been obtained with the organic scintillator dye POPOP (2, 2′-*p*-phenylenebis [5 phenyloxazole]).

In this paper we report on our studies of the POPOP vapor dye laser. In Section II we describe the experimental apparatus including the oven used to heat the dye. Section III contains measurements of the optical properties of POPOP vapor including measurements of quantum efficiency of fluorescence as a function of temperature, pump wavelength, and buffer gas. Measurements of gain under optical pumping with a pulsed N_2 laser are described in Section IV. The gain is measured as a function of wavelength and time, and the effect of helium buffer gas is studied. In Section V we present data on the operating characteristics of the POPOP laser, and conclude with a discussion of the implications of these results for the development of an electrically pumped dye laser.

II. Apparatus

The apparatus used for these experiments is shown schematically in Fig. 1. The dye vapor cell shown in Fig. 1(b) was constructed from fused quartz. The length of the cell was 4 cm, and its cross section 1 cm × 1 cm. The faces were of optical quality, and the quartz pieces used to make the cell had their inside edges beveled so that when the cell was assembled, the inside corners of the cell would not have any material extending into the path of the dye fluorescence. Crystals of POPOP dye were introduced into a section of quartz tubing attached to the arm of a quartz sample cell, and the entire system was pumped down to a vacuum of $\sim 10^{-7}$ torr. The dye was then melted under gentle heat so that the liquid dye flowed down into the main body of the sample cell, and the system was again pumped down to $\sim 10^{-7}$ torr. In this way any adsorbed gases are removed from the system. The cell was then sealed off under vacuum, or with the appropriate pressure of buffer gas.

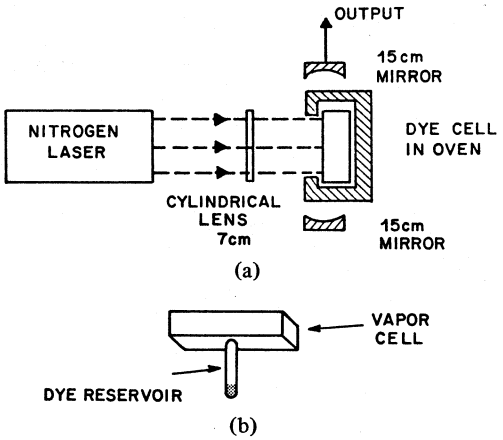

Fig. 1. Schematic view of dye vapor laser system. (a) As set up for laser experiments. (b) Sample cell.

The cell was placed in an oven, shown schematically in Fig. 1(a), which was designed to maintain the temperature of the dye reservoir at a lower temperature than the main body of the sample cell. This was accomplished by powering the two sections of the oven with two different temperature controllers. One governed the temperature of the dye reservoir (which determines the vapor pressure of the dye in the cell). The other was a differential controller which maintained the main body of the oven at a temperature somewhat higher than the dye reservoir (typically + 20°C). In this way "fogging" of the windows of the dye cell was avoided. The oven consisted of two aluminum chambers in which heating elements and temperature sensors were imbedded. The two chambers were separated by an insulator. Openings were made to permit entrance and exit of two light beams—one along the axis of the sample cell and the other perpendicular to it. It was verified that the temperature uniformity within the main body of the sample cell was within ∓5°C.

Optical pumping experiments were made using a pulsed N_2 laser giving output pulses of ~8-ns duration with a peak

Manuscript received September 11, 1974.
The authors are with the Bell Laboratories, Holmdel, N. J. 07733.

intensity of 400 kW. The beam was focused with a 7-cm focal length cylindrical quartz lens onto the entrance face of the sample cell. The beam cross section in the focal plane was 4 cm × ~300 μm.

III. The Optical Properties of POPOP Vapor

The organic dye POPOP is a crystalline solid at room temperature. Its melting point is approximately 245°C. Above this temperature the dye readily vaporizes and at temperatures ~350°C dye vapor densities which correspond closely to dye concentrations commonly found in liquid solution dye lasers are achieved. No thermal degradation has been observed at temperatures up to 350°C over periods of several days.

POPOP vapor absorption and emission spectra were obtained for several vapor densities. A Cary 14 Spectrometer was used to obtain the absorption data and a Perkin Elmer Model MPF-2A Fluorescence Spectrometer to obtain emission data. Fig. 2 shows the absorption and emission spectra of POPOP vapor at a dye reservoir temperature of 300°C. For comparison, the corresponding spectra for a liquid solution of POPOP in cyclohexane are also shown. The emission spectra are corrected for the response of the detection system and represent photon flux. Both vapor emission and absorption curves are broad almost featureless bands showing no clearly resolved vibrational structure. The vapor emission and absorption curves show nearly perfect mirror symmetry and both are shifted to shorter wavelengths by ~30 nm from the typical spectra for POPOP dissolved in liquid solutions [6]. The absorption and emission spectra of both the vapor and dye solutions occur over nearly identical 500-nm bandwidths. The large Stokes shift makes the dye vapor an excellent candidate for a laser material.

In Fig. 3 we show the temperature dependence of the absorption length at 337 nm (the wavelength of the nitrogen laser). The approximate dye concentrations indicated in Fig. 3 were computed by assuming that the absorption cross section of the molecules in the vapor is the same as for those in liquid solutions. Concentrations comparable to those found in liquid solution lasers can be readily obtained.

Vibrational relaxation plays an important role in the four level laser scheme of liquid solution dye lasers, and it is the interactions between the dye molecules and the solvent molecules which are thought to induce the vibrational relaxation. In the vapor phase, however, the collision rate can be extremely low, and the mean time between collisions longer than the excited state lifetime. The vibration relaxation which is so important for laser action might be expected to be slow in low-pressure dye vapors.

Information about the relaxation process can be obtained from the emission spectra, and the data indicates that collisions are in fact not required for the vibrational relaxation of the first excited singlet state of POPOP vapor. In the absence of vibrational relaxation, or if the relaxation time is comparable to or larger than the fluorescence lifetime of the excited singlet, the emission spectrum would depend critically on which vibrational state is excited and therefore would depend on the excitation wavelength. No such behavior was observed in our experiments. The emission data in Fig. 2 was taken with 340-nm excitation; however, no change in the position or shape of the

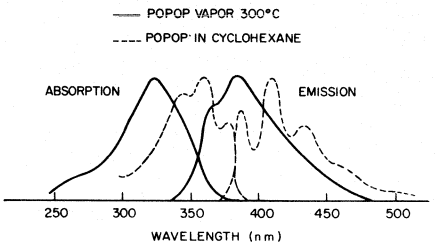

Fig. 2. Absorption and emission spectra for POPOP vapor at 300°C, and corresponding spectra for a liquid solution of POPOP in cyclohexane (from [6]).

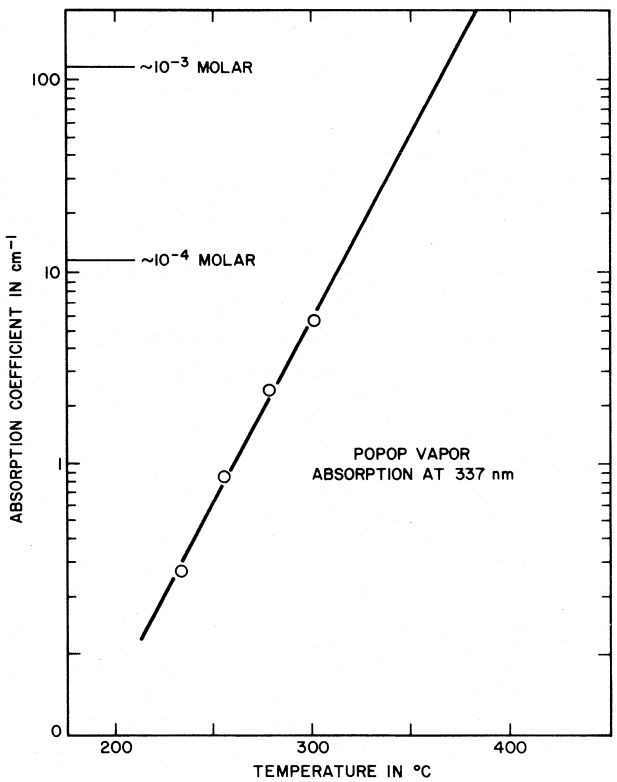

Fig. 3. POPOP vapor absorption at 337 nm as a function of dye reservoir temperature.

emission curve was found as the wavelength of the excitation was varied over the entire absorption band. This behavior was observed at all temperatures from 250°-325°C and is quite different from that which has been observed in rhodamine B (see [7]) where the vibrational relaxation rate appears to be small. The POPOP emission spectra also showed no dependence on collision frequency. Dye pressure (temperature) was varied and buffer gases were added (CO_2, He, SF_6) up to buffer gas pressures of 500 torr. The complete independence of the position and shape of the emission spectra on these two factors, excitation wavelength and collision frequency, implies an intramolecular relaxation process which is fast compared to the ~1.2 ns lifetime of the excited singlet state.

Fig. 4 shows a comparison of the excitation spectrum of POPOP vapor with the vapor's absorption spectrum. The excitation curve was obtained by monitoring the vapor fluorescence at a fixed wavelength, typically 380 nm, while sweeping the excitation wavelength and correcting for wavelength dependent variations in the excitation source intensity. If the fluorescence quantum efficiency of the vapor were con-

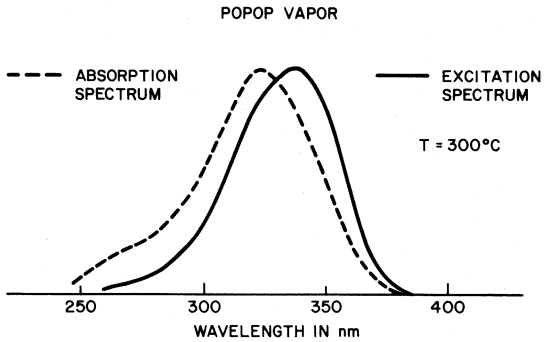

Fig. 4. A comparison of the absorption and excitation spectra for POPOP vapor at 300°C.

stant, the absorption and excitation curves would be identical. However, it is apparent from Fig. 4 that the quantum efficiency decreases with decreasing excitation wavelength (both curves are normalized at their peaks). Evidently, the higher energy photons have a greater probability of producing photodissociation, singlet-triplet conversion, or other photochemical processes. The effect of temperature on the excitation spectrum is shown in Fig. 5. Similar shifts of the absorption spectrum with temperature were not observed. The effect of higher temperatures is to decrease the quantum efficiency even more strongly at the shorter wavelengths.

Measurements of the absolute fluorescence quantum efficiency were made by comparing the peak fluorescence intensity of the vapor with the peak fluorescence intensity of POPOP dissolved in cyclohexane. In each case the fluorescence intensity was normalized to the number of absorbed photons as determined from absorption data. The quantum efficiency of the liquid solution was taken as unity.[1] With this technique we estimate an accuracy of 10 percent for relative values of the quantum efficiency and 20 percent for the absolute values. The results of these measurements are shown in Fig. 6. A falloff of quantum efficiency with temperature and decreasing pump wavelength is clearly shown.

Similar data were taken on the dye dimethyl POPOP. The main difference between the spectra of the two dyes is an approximately 10-nm shift of dimethyl POPOP vapor spectra to longer wavelengths. However, because of the dependence of the quantum efficiency on the location of the pump wavelength relative to the peak of the absorption curve, this shift results in a much lower quantum efficiency for excitation at 337 nm in dimethyl POPOP vapor than in POPOP (30 percent versus ~70 percent). Hence the laser threshold requirements of dimethyl POPOP for pumping with a pulsed nitrogen laser are significantly higher than for POPOP despite the fact that the 337-nm absorption of dimethyl POPOP vapor is stronger than that of POPOP vapor.

As a preliminary to the studies of the effects of buffer gases on gain reported in the next section, the effects of the buffer gases helium, CO_2, SF_6, and propane on the excitation and emission spectra of POPOP vapor were investigated. The buffer gas pressure in each case was 500 torr. As mentioned earlier, these buffer gases produced no marked changes in the fluorescence emission spectra. However, the fluorescence quantum efficiency was affected. These measurements are somewhat more uncertain than the quantum efficiency measurements made on POPOP vapor in a vacuum cell because the buffer gas slowed the approach of the POPOP vapor density to equilibrium and may have either enhanced the decomposition rate of the dye or chemically reacted with the dye. The preliminary results, however, showed that the addition of helium buffer gas had essentially no effect: the quantum efficiency was the same as that of the vacuum cell. The buffer gases CO_2, SF_6, and propane showed reduced fluorescence with estimated quantum efficiencies of 35 percent, 20 percent, and 5 percent, respectively. From this preliminary data we see that the quantum efficiency drops as the buffer gas molecule is made larger and more complex. Dye decomposition also appeared to be enhanced by the larger buffer gas molecules.

[1]The quantum efficiency of POPOP dissolved in cyclohexane is given as 0.93 by [1]. We have taken this to be unity for the purposes of this paper.

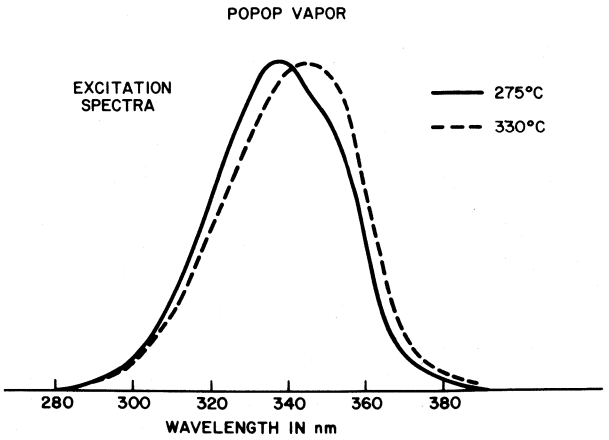

Fig. 5. Normalized excitation spectra for POPOP vapor at 275°C and 330°C.

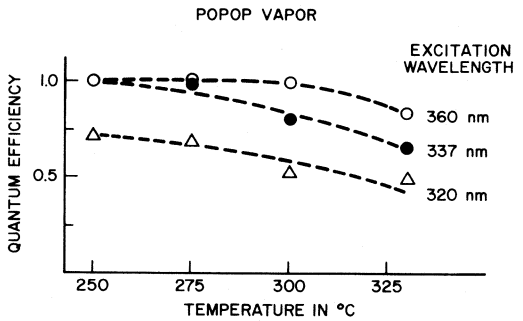

Fig. 6. Quantum efficiency of POPOP vapor as a function of temperature for several excitation wavelengths.

IV. Gain Data

The method that we used to measure the gain is a modification of the technique described by Silfvast and Deech [8] and later applied to dye lasers by Shank *et al.* [9]. The pumping configuration is as shown in Fig. 1(a), but no mirrors are used. Instead, the fluorescence along the axis of the pumped region is monitored by a detector. An aperture is placed in front of the detector to ensure that all of the collected light has passed through the pumped region, and the detector is placed far enough from the sample cell so that the detector-cell spacing is large compared to the length of the pumped region. A shutter arrangement between the pulsed N_2 laser and the sample

cell allows either one half, the other half, or the whole length of the sample cell to be pumped. Under these conditions we can determine both the gain coefficient α, and the ground state absorption coefficient β from measurements of the fluorescence intensity.

Let us define z as the coordinate along the axis of the pumped region and consider $z = 0$ as the end of the sample cell furthest from the detector. This geometry is illustrated in Fig. 7. If we consider the spontaneous fluorescence intensity from an elementary length dz to be Cdz, we can write I_1, the fluorescence intensity detected when the back 1/2 of the cell is pumped, as

$$I_1 = Ce^{-\beta l_2} \int_0^{l_1} \frac{e^{(\alpha-\beta)z}}{(d-z)^2}\, dz. \tag{1}$$

For our experiments $l_1 = l_2 = L/2$ where L is the length of the sample cell and we have $d >> L$. Under these conditions (1) becomes

$$I_1 = \frac{Ke^{-\beta L/2}}{\alpha - \beta}\left[e^{(\alpha-\beta)L/2} - 1\right] \tag{2}$$

where K is a constant proportional to the fluorescence power radiated per unit volume. We have assumed here that the gain is small enough so that the amplified spontaneous emission does not saturate the transition. This condition is well satisfied for the experiments reported in this paper. Similarly, the fluorescence intensity I_2 detected when the front 1/2 of the cell is pumped is given by

$$I_2 = \frac{K}{\alpha - \beta}\left[e^{(\alpha-\beta)L/2} - 1\right]. \tag{3}$$

When the entire cell is pumped

$$I_{1+2} = \frac{K}{\alpha - \beta}\left[e^{(\alpha-\beta)L} - 1\right]. \tag{4}$$

From (2) and (3), we find

$$\beta = \frac{2}{L}\ln\left(I_2/I_1\right) \tag{5}$$

and from (2), (3), and (4),

$$\alpha - \beta = \frac{2}{L}\ln\left[I_{1+2}/I_2 - 1\right]. \tag{6}$$

As shown in Fig. 7, a filter can be used in front of the detector in order to measure gain and absorption loss as a function of wavelength. For the experiments reported below, a monochromator with 3-nm bandwidth was used to select the wavelength of the detected fluorescence. The detector was a Sylvania Model 502 crossed field photomultiplier tube coupled to a Tektronix 7904 oscilloscope. The combined rise time of ~0.8 ns was fast enough to resolve the time dependence of the fluorescence. The pulsed N_2 laser pump pulse was also monitored and simultaneously displayed on the oscilloscope.

Fig. 8 shows the measured gain as a function of wavelength for POPOP vapor at 345°C in a vacuum. It can be seen that the gain (α) approximately follows the fluorescence curve

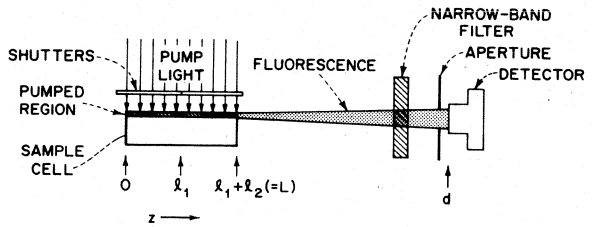

Fig. 7. Geometry of the apparatus used for gain measurements.

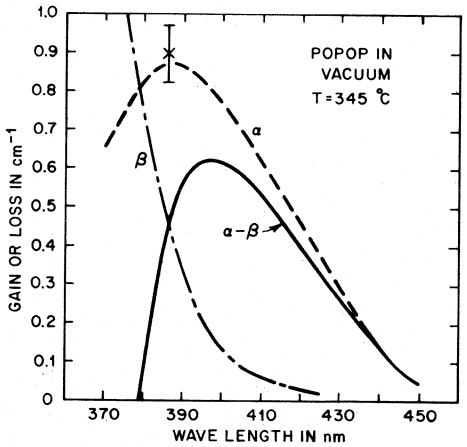

Fig. 8. Dependence of gain (α) and ground state absorption (β) on wavelength for POPOP vapor at 345°C in vacuum. For clarity only one experimental point has been shown with a bar to indicate the scatter of the data points.

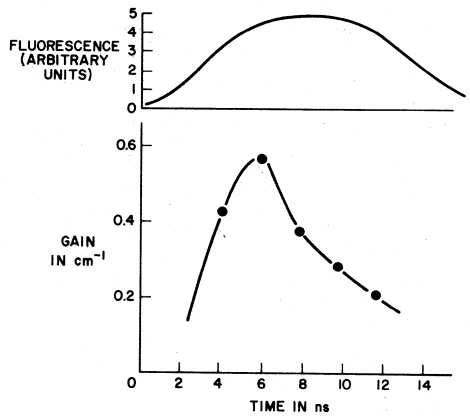

Fig. 9. The variation of POPOP vapor gain with time (no buffer gas). For comparison the off-axis fluorescence in arbitrary units is plotted on the same time scale. Data for $T = 330°C$ and $\lambda = 400$ nm.

(Fig. 2) while the net gain ($\alpha - \beta$) falls off rapidly at the shorter wavelengths due to the rapid increase in β.

The gain could be calculated as a function of time by using fluorescence data corresponding to given times after the initiation of the pump pulse. Fig. 9 shows the time variation of the POPOP vapor gain. For comparison, the off-axis fluorescence pulse in arbitrary units has been plotted on this figure with the same time scale. It can be seen that the gain falls off well before the end of the off-axis fluorescence pulse. This indicates that some mechanism such as triplet population buildup or poisoning by decomposition products is rapidly introducing loss.

We have investigated the effect of buffer gases on the time dependence of the gain. In the presence of a high pressure of He, the gain builds up more slowly, but does not fall off as

rapidly as the unbuffered POPOP vapor gain. A similar effect was observed with CO_2 buffer gas. A study of the effect of buffer gases on dye vapor gain and laser action is continuing and will be the subject of a subsequent publication.

V. Laser Experiments

By aligning laser mirrors at each end of the dye vapor cell as shown in Fig. 1, laser action could be obtained [3]. A well-collimated output beam could be seen using a fluorescent screen. Fig. 10 shows the relationship between the dye laser output power and the pump power, for POPOP vapor at 350°C in a vacuum. The slope efficiency is 10 percent.

A study was made of the spectral characteristics of the POPOP dye vapor laser with no buffer gas. Fig. 11 summarizes the results of these experiments. When broad-band laser mirrors were used, the laser output consisted of a broad featureless band of wavelengths of ~20 nm in width. When one of the laser mirrors was replaced with a diffraction grating, a ~1-nm-bandwidth output was obtained which could be tuned over a range of ~25 nm, as shown in Fig. 11. Fig. 12 shows a plot of laser output power versus wavelength for this experiment. It is not known why the output power drops off more rapidly at long wavelengths than we would expect from the gain measurements shown in Fig. 8.

Using a diffraction grating and an output mirror with 80-percent transmission, we found that the output power in a 1-nm band at the peak of the output versus frequency curve was 90 percent of the broad-band output power obtained by replacing the diffraction grating with a broad-band high reflectivity mirror. This high degree of spectral condensation implies an intraband thermalization time for the singlet ground state which is short compared to the upper state lifetime (~1 ns). If this relaxation time were long, a bottleneck would quickly occur in the lower laser level which would cause the laser to begin oscillating at another frequency or prematurely terminate the laser action. This is very direct evidence for rapid intraband thermalization in the absence of external influences (such as interactions with solvent molecules). Such behavior for the first excited singlet level was indicated by the study of the shape of the fluorescence spectrum as a function of pressure reported in Section III. A fast intraband relaxation for the first excited singlet level of dimethyl POPOP has recently been deduced from measurements of the onset of fluorescence after picosecond excitation pulses [10].

VI. Discussion and Conclusions

In Fig. 6, we show that the quantum efficiency of POPOP vapor increases at lower vapor pressures. This effect has also been observed with other dye vapors. In order to obtain a suitable pumping geometry for transverse pumped lasers, it is necessary to have the pump beam absorbed in a small distance—typically less than 1 mm—and thus high vapor densities corresponding to high temperatures must be used. If a longitudinal pumping geometry were used, however, much lower vapor densities, corresponding to absorption lengths of many centimeters, could be utilized. This would have the advantage of using the dye vapor in a regime where the quantum efficiency is close to unity, and result in more efficient laser operation. This would be particularly true for some dyes, such as the coumarins, that suffer severely from concentration quenching of fluorescence at vapor pressures above a few tenths of a torr.

Our experiments have shown that the optically pumped POPOP dye vapor laser has output power, efficiency, and tuning

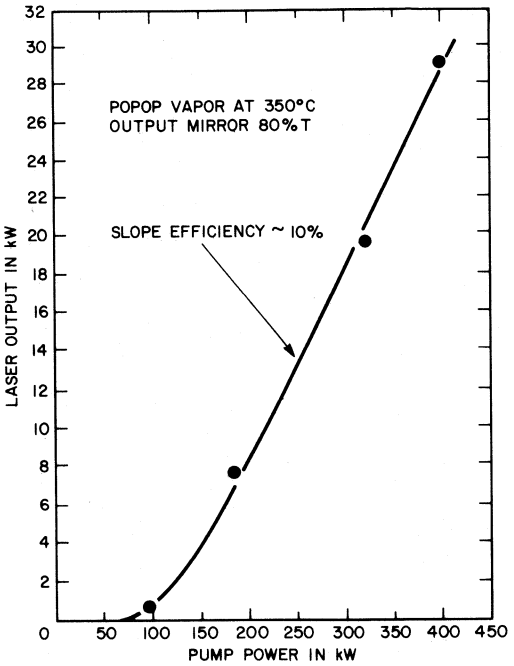

Fig. 10. Peak laser output power as a function of peak pump pulse power for POPOP vapor at 350°C using an 80-percent transmitting output mirror.

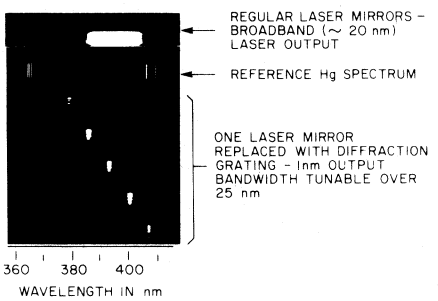

Fig. 11. POPOP vapor laser spectral output.

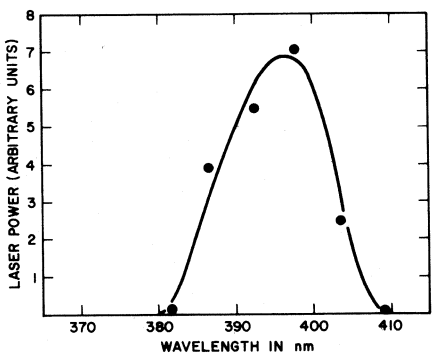

Fig. 12. POPOP vapor laser output power as a function of wavelength, when operated with one laser mirror replaced with a diffraction grating.

characteristics not too different from the average optically pumped liquid dye laser. What then is the interest in dye vapor systems? Some points have already been mentioned. A dye vapor laser provides freedom from pump-induced thermal gradient effects, a new range of laser wavelengths from a given dye, and a unique system in which to study the dye molecules themselves. Our main interest in the dye vapor laser, however, involves the development of an electrically excited dye vapor laser. In principle, such a laser could be an efficient, scalable source of tunable visible laser radiation. Even if efficient electronic excitation can be obtained, however, very high current densities will be required, and the problem of dye decomposition must be overcome. Our buffer gas studies show that relatively high helium buffer gas pressures have little effect on the quantum efficiency, but greatly increase the gain at times greater than ~5 ns after the initiation of the pump pulse. This may be due to the ability of the buffer gas to reduce dye decomposition by reducing the thermalization time for excited dye molecules. Further studies of the effects of buffer gases on dye vapor gain under both optical and discharge pumping are in progress.

In conclusion, we have reported a study of the operating characteristics of an optically pumped POPOP dye vapor laser, and have investigated in particular those properties of dye vapors whose understanding is important for the attainment of a discharge-excited dye vapor laser.

Acknowledgment

The authors wish to thank T. K. Gustafson and A. Dienes for several fruitful discussions relating to this work, and for their participation in some preliminary experimental studies.

References

[1] N. A. Borisevich, I. I. Kalosha, and V. A. Tolkachev, "Generation using complex organic molecules in gaseous phase," *Zh. Prikl. Spektrosk.*, vol. 19, pp. 1108–1109, 1973.

[2] B. Steyer and F. P. Schäfer, "A vapor-phase dye laser," *Opt. Commun.*, vol. 10, pp. 219–220, Mar. 1974.

[3] P. W. Smith *et al.*, "An optically-excited organic dye vapor laser," *Appl. Phys. Lett.*, vol. 25, pp. 144–146, Aug. 1974.

[4] B. Steyer and F. P. Schäfer, "A vapor-phase dye laser," presented at VIII Int. Quantum Electronics Conf., June 1974, Paper S3.

[5] P. W. Smith *et al.*, "Optical gain and laser action in organic dye vapors," presented at VIII Int. Quantum Electronics Conf., June 1974, Paper S4.

[6] I. B. Berlman, *Handbook of Fluorescence Spectra of Aromatic Molecules*, 2nd ed. New York: Academic, 1971.

[7] R. Pappalardo and S. Ahmed, "Emission from dyes in the vapor phase and the possibility of vapor-phase dye lasers," *J. Chem. Phys.*, vol. 10, pp. 5135–5155, 1972.

[8] W. T. Silfvast and J. S. Deech, "Six dB/cm single-pass gain at 7229Å in lead vapor," *Appl. Phys. Lett.*, vol. 11, pp. 97–99, Aug. 1967.

[9] C. V. Shank, A. Dienes, and W. T. Silfvast, "Single pass gain of exiplex 4-MU and rhodamine 6G dye laser amplifiers," *Appl. Phys. Lett.*, vol. 17, pp. 307–309, Oct. 1970.

[10] S. L. Shapiro, R. C. Hyer, and A. J. Campillo, "Polyatomic molecular relaxation in the absence of collisions," *Phys. Rev. Lett.*, vol. 33, pp. 513–515, Aug. 1974.

Correspondence

Physical Interpretation of Bistable Unidirectional Ring-Laser Operation

J. B. HAMBENNE AND M. SARGENT III

Abstract—**Oppositely directed running waves in a ring laser saturate themselves and one another by population depletion. In addition, as the Doppler broadening decreases, they saturate one another by scattering off induced Bragg gratings in the medium, i.e., off spatial holes burned into the population difference. This increased coupling results in bistable operation near the atomic line center for Doppler-broadened media and for any equal tuning for stationary atoms.**

Considerable interest has developed concerning the obtaining [1], [2] (and suppressing [3], [4]) of unidirectional operation in ring lasers; that is, operation for which the running waves travel in only one direction. The origins of the interest stem from both theoretical considerations (unidirectional operation is simpler to treat theoretically since spatial dependences drop out [5]) and practical considerations; for examples, in achieving optical isolation and increased efficiency [6]. On the other hand, unidirectional operation is a nuisance in gyro applications where two running waves traveling in opposite directions are required [3]. Bistable unidirectional operation is that for which either of two oppositely directed running waves oscillates alone, and for which one depends on past history. It has been predicted theoretically for stationary atoms by White [6] and on the basis of Lamb theory by Zeiger and Fradkin [7]. Both references also show that for Doppler-limited media, the mode coupling is reduced sufficiently to obtain monostable operation, except for central tunings. The bistability results from cross saturation of one running wave on the other in excess of the self-saturation of a wave on itself. The bistable operation has been observed experimentally in the argon-ion laser by Rigrod and Bridges [8] and in He–Ne near central tuning by Moss *et al.* [9] and Aronowitz [3].

In the present correspondence we explain the increased cross saturation in terms of backscattering off induced population-inversion gratings (spatial holes burned into the population difference) and examine the dependence on the Doppler-width parameter Ku (K is the wavenumber and u the average atomic speed). The existence of such gratings has been mentioned before (see, for example, Menogozzi and Lamb [10]), but the fact that the Lamb theories actually include the effect is new here. Note that we are not concerned here with frequency locking of the two running waves, a phenomenon that also yields a zero beat frequency. The beat note vanishes for unidirectional operation since one of the running waves is suppressed. Furthermore, the backscattering by population-inversion gratings does not contain the relative phase angle between the waves, whereas that due to mirrors, dust, etc., does contain this angle and thereby contributes to mode locking [11].

We consider a ring laser that might support two oppositely directed running waves of the electromagnetic field. Self-saturation is caused only by population depletion. This depletion also results in cross saturation to the extent that the two running waves interact with similar groups of atoms. In particular, in the Doppler-broadened medium with the laser tuned to line center, the waves interact with the same group of atoms, causing the self-saturation to equal the cross saturation that results from population depletion. Although the wave with higher linear gain can often suppress the other when the self-saturation is only slightly greater than the total cross saturation, bistable operation does not occur (see [5, ch. 9] for a detailed explanation).

As the Doppler broadening is reduced, however, an additional cross saturation comes into play. Specifically, the two waves add in the medium yielding a standing wave (for equal mode tuning) and burn spatial holes in the population inversion. This corrugated inversion pattern acts like a Bragg grating to reflect one running wave back into the other. Unlike scattering by the "principal" grating in the distributed feedback laser [12], the scattering here produces a net reflected wave that subtracts from the similarly directed wave (for stationary atoms, the gain grating is precisely out of phase with the standing-wave pattern). Such a population-inversion grating should also occur in the distributed-feedback laser. In any event, an additional cross saturation occurs. When the total cross saturation exceeds the self-saturation, either mode may suppress the other; which wins depends on the linear gains and initial intensities. In particular, we find that for the stationary-atom medium (straight homogeneous broadening), the Bragg-like contribution to the cross saturation actually equals the population-depletion contribution for any tuning. This might be called the van der Pol limit, inasmuch as his double-tank circuit [13] had twice the cross saturation that it had self-saturation, a result caused by analogous phenomena (see, for example, [5, ch. 4]). For the special case of the two-mirror standing-wave laser, the increased coupling yields an increased saturation resulting in an output only two thirds as large as the corresponding unidirectional ring configuration [6]. Here the third results from the three sources of saturation: 1) self-saturation of the running waves comprising the standing wave; 2) cross saturation from population depletion; and 3) cross saturation from Bragg reflection. The Bragg term is an example of atomic coherence induced by mode interference that shows up in analogous ways in other laser configurations (see, for example, [5]), such as population pulsations in multimode laser operation and electric quadrupole moments in the Zeeman laser. In these examples, the coherence term leads to a Ramanlike scattering of one mode into another, although for the bidirectional ring and Zeeman cases, no frequency shift occurs for equal tuning of the modes.

Our physical interpretation is based on third-order Lamb theory (see, for example, [5, ch. 11]), although other calculations [14] reveal that much of the same qualitative conclusions persist to strong-signal operation. Specifically, we describe the laser electric field by the superposition of two oppositely directed running waves

$$E(s,t) = \tfrac{1}{2} E_+(t) \exp\left[-i(\nu_+ t + \phi_+ - K_+ s)\right] + \tfrac{1}{2} E_-(t) \exp\left[-i(\nu_- t + \phi_- + K_- s)\right] + \text{c.c.} \quad (1)$$

Here s is the laser axis, the amplitudes $E_\pm(t)$ and phases $\phi_\pm(t)$ vary little in an optical-frequency period, $\nu_\pm$ are the mode-oscillation frequencies, and K is the mode's wavenumber (which we assume is the same for both waves in our current development). The mode intensity $I_+ = E_+^2$ is found to obey the

Manuscript received August 26, 1974. This work was supported in part by Kirtland Air Force Base (AFWL), Albuquerque, N. Mex.

J. B. Hambenne is with the Hughes Aircraft Corporation, Tucson, Ariz.

M. Sargent is with the Optical Sciences Center, University of Arizona, Tucson, Ariz. 85721.

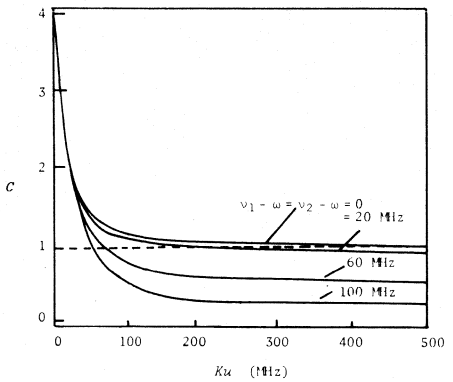

Fig. 1. Coupling parameter C of (3) plotted versus Doppler-width parameter Ku (in megahertz) for indicated detuning values. Upper and lower level decay rates are $2\pi \times 20.0$ and $2\pi \times 40.0$ MHz, respectively, and the dipole decay rate $(1/T_2)$ is $2\pi \times 100$ MHz. The dashed line gives $C = 1$, the dividing line between strong ($C > 1$) and weak coupling.

equation of motion

$$\dot{I}_+ = 2I_+(\alpha_+ - \beta_+ I_+ - \theta_{+-} I_-) \tag{2}$$

with a similar expression for I_-. Here α_+ is the net linear gain (that in excess of the loss) for I_+, β_+ is the self-saturation coefficient, and θ_{+-} is the cross-saturation coefficient. The phenomenon discussed above leads to values of θ_{+-} that are larger than those of β_+ (this result was noted in [4] and [10] for central tuning and Doppler-broadened media and in [7] and [10] for stationary atoms). In similar discussions in the past (see, for example, [15] or [5]), it has been convenient to use the coupling parameter defined by the ratio

$$C = \theta_{+-}\theta_{-+}/\beta_+\beta_-. \tag{3}$$

The bistable region is encountered for values of C greater than unity. For stationary atoms, the Bragg effect equals the population depletion yielding the value $C = 4$, considerably greater than unity. In the Doppler limit (the Doppler-width parameter Ku greatly exceeds the atomic decay rates), the coupling parameter has a squared Lorentzian dependence on detuning. The reduced coupling for nonzero detuning results from the fact that the running waves interact with different velocity ensembles, a phenomenon responsible for the Lamb dip in the standing-wave laser. In Fig. 1 we plot C as a function of Ku for several detuning values. We see that the coupling decreases as Ku increases. This is due to the facts that 1) moving atoms yield gain gratings reduced in peak-to-peak variation due to a tendency to see an average (i.e., not standing-wave) field, and 2) the gratings that do exist move out of phase with respect to one another leading to cancellation of the scattered waves. The decrease rate is characterized by the level decay rates (the Bragg contribution has Lorentzian dependence on these rates) inasmuch as the grating occurs in the population difference.

The dependence of grating shape on axial velocity is illustrated beautifully by [16, Fig. 8], a paper by Stenholm and Lamb, which treats the special case of the two-mirror standing-wave laser. In particular, that figure reveals that some velocity ensembles actually yield gratings that scatter in phase with the running waves (decrease the coupling). The grating effect vanishes completely in the Doppler limit due to combination of the cancellation and averaging. Other computations reveal that cavity rotation giving a symmetric tuning has little effect in the Doppler limit, but a pronounced effect for $Ku = 0$. Physically, this occurs since the Doppler-limit Bragg contribution is small and both waves interact with the same velocity ensemble (i.e., the population depletion contribution to the cross saturation is appreciable), while for small Ku, the grating contribution can be as large as that due to population depletion and has Lorentzian dependence on the splitting. The formulas that we have used for the coefficients are given (with appropriate specialization) by [15, eq. (61)], a paper by O'Bryan and Sargent (see also [7]).

We conclude that to achieve unidirectional operation, one should use stationary atoms with level decay rates exceeding any rotational splitting. Conversely, to obtain bidirectional operation, moving atoms with some detuning can be used. The standard mode of operation for ring gyros [3] involves two isotope media, for which this detuning condition is automatically satisfied. The coupling effects we have considered apply to any problem in which standing waves saturate the medium they interact with. In particular, lasers having two-mirror unstable-resonator configurations experience increased saturation of the nature discussed here to the extent that standing waves exist. Similarly, unstable ring resonators can be encouraged to oscillate in one direction through the use of homogeneously broadened media. Further discussion will be presented in a forthcoming paper [14] on strong-signal ring-laser operation.

ACKNOWLEDGMENT

The authors wish to thank F. A. Hopf and W. E. Lamb, Jr., for helpful conversations.

REFERENCES

[1] R. Ulrich and H. P. Weber, "Unidirectional thin-film ring laser," *Appl. Phys. Lett.*, vol. 20, pp. 38–40, Jan. 1972.
[2] F. R. Faxvog and A. D. Gara, "A traveling-wave laser," *Appl. Phys. Lett.*, vol. 25, pp. 306–308, Sept. 1974.
[3] F. Aronowitz, "Single isotope laser gyro," *Appl. Opt.*, vol. 11, pp. 405–412, Feb. 1972.
[4] —, "Effects of radiation trapping on mode competition and dispersion in the ring laser," *Appl. Opt.*, vol. 11, pp. 2146–2152, Oct. 1972.
[5] M. Sargent III, M. O. Scully, and W. E. Lamb, Jr., *Laser Physics*. Reading, Mass.: Addison-Wesley, 1974 (see especially ch. 11).
[6] J. A. White, "Stability of traveling waves in lasers," *Phys. Rev.*, vol. 137, pp. A1651–A1654, Mar. 1965; also —, "An implication for lasers of an aspect of interference at high field strengths," *Nature*, vol. 20, pp. 911–912, Feb. 1964.
[7] S. G. Zeiger and E. E. Fradkin, "Competition between two types of oscillation in a traveling wave laser (TWL)," *Opt. Spektrosk.*, vol. 21, pp. 386–390, Mar. 1966 (Transl.: *Opt. Spectrosc.*, vol. 21, pp. 217–219, Sept. 1966).
[8] W. W. Rigrod and T. J. Bridges, "Bistable traveling-wave oscillations of ion ring laser," *IEEE J. Quantum Electron.*, vol. QE-1, pp. 298–303, Oct. 1965.
[9] T. S. Moss, D. E. Killick, and E. T. de la Perrelle, "Unidirectional oscillation in travelling wave ring laser," *Infrared Phys.*, vol. 4, pp. 209–211, Oct. 1964.
[10] L. N. Menogozzi and W. E. Lamb, Jr., "Theory of a ring laser," *Phys. Rev.*, vol. A8, pp. 2103–2125, Oct. 1973 (population inversion gratings were also postulated on physical grounds by Yu. L. Klimontovich, V. N. Kuryatov, and P. S. Landa, "Wave synchronization in a gas laser with a ring resonator," *Zh. Eksp. Teor. Fiz.*, vol. 51, pp. 3–12, July 1966 (Transl.: *Sov. Phys.*–

JETP, vol. 24, pp. 1-7, Jan. 1967), who chose to neglect them in their analysis).
[11] F. Aronowitz and R. J. Collins, "Mode coupling due to back-scattering in a He-Ne traveling-wave ring laser," *Appl. Phys. Lett.*, vol. 9, pp. 55-58, July 1966.
[12] H. Kogelnik and C. V. Shank, "Stimulated emission in a periodic structure," *Appl. Phys. Lett.*, vol. 18, pp. 152-154, Feb. 1971.
[13] B. van der Pol, "The nonlinear theory of electric oscillations," *Proc. IRE*, vol. 22, pp. 1051-1085, Sept. 1934.
[14] J. B. Hambenne and M. Sargent III, to be published (the strong signal treatment is based on the continued fraction formulation of Menogozzi and Lamb [10]).
[15] C. L. O'Bryan, III, and M. Sargent III, "Theory of multimode laser operation," *Phys. Rev.*, vol. A8, pp. 3071-3092, Dec. 1973.
[16] S. Stenholm and W. E. Lamb, Jr., "Semiclassical theory of a high-intensity laser," *Phys. Rev.*, vol. 181, pp. 618-635, May. 1969.

New Laser Oscillation in the Oxygen Atom

D. G. SUTTON, L. GALVAN, AND S. N. SUCHARD

***Abstract*—A new laser oscillation has been observed in a pulsed discharge of He and O_2. This oscillation at 2.652 μm has been identified as belonging to the O(I) atom.**

A new laser oscillation in the O(I) atom has been observed. The laser emission was detected at a wavelength of 2.652 ± 0.003 μm. This wavelength can be assigned to the $4d\ ^5D^\circ \rightarrow 4p\ ^5P$ transition of the neutral O(I) atom when it is compared with the calculated wavelength obtained from known energy levels [1]. Other laser oscillations have previously been observed in the O(I) atom in the spectral region of 0.8–11.0 μm [2]: however, this is the first report of oscillation at this wavelength.

The laser apparatus used for these experiments has been described elsewhere [3]. Briefly, the laser tube consists of two 1.25-m (2.5-cm ID) Lucite pipes, which are fitted with 251 pairs of 470-Ω resistors in a double helical configuration coaxial with the optical axis. The gap between resistor pairs is 1.9 cm. One of these helices is connected to ground, which forms the cathode of the discharge circuit; the other is connected to a pulsed power supply triggered by a spark gap. The ends of the laser tube are sealed by CaF_2 windows at Brewster's angle. A stable optical cavity is formed about the laser tube by two silver-coated mirrors: a total reflector with a radius of curvature of 11.5 m and a flat output coupler with a 1-mm hole in its center. The entire length of the optical cavity is 3.2 m.

Manuscript received September 12, 1974. This work was supported by the Defense Advanced Research Projects Agency of the Department of Defense under U. S. Air Force Space and Missile Systems Organization (SAMSO) Contract F04701-74-C-0075.
The authors are with The Aerospace Corporation, El Segundo, Calif. 90245.

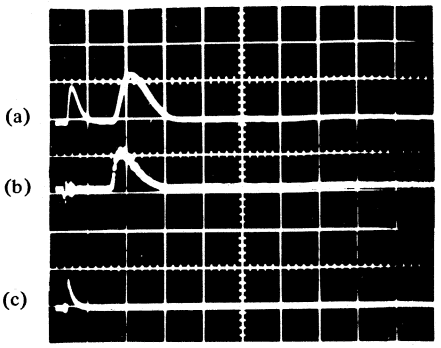

Fig. 1. Spectral output of the O(I) laser. (a) Total laser emission. (b) $^5D^\circ \rightarrow {}^5P$ emission at 2.652 μm. (c) Triplet emission at 0.8446 μm. (Time scale: 5 μs/div. Experimental conditions: 24-kV discharge through 80-torr He plus 2-torr O_2.)

Laser output is directed into a screen room where the beam is split into two parts by a sapphire flat. One of these beams is directed to an InSb detector to monitor the total laser emission; the other is directed through a 0.5-m monochromator to an identical InSb detector to monitor the spectrally resolved emission. Detector response is monitored with a fast oscilloscope.

The laser results are displayed in Fig. 1. Total laser emission is presented on the top oscilloscope trace and the spectrally resolved emission on the lower two traces: 2.652-μm emission in the middle and 0.8446-μm emission on the bottom. The time scale for all the traces is 5 μs/div. For a gas mixture of 80 torr He and 2 torr O_2 and a discharge voltage of 24 kV, both the 0.8446-μm triplet and 2.652-μm oscillations are seen. As the discharge voltage is lowered to 18 kV, the intensity of the 2.652-μm emission decreases to zero, while, as the voltage is increased to 30 kV, the 0.8446-μm emission decreases to zero.

Since the upper laser level of the transition is a $^5D^\circ$ state and the lower level a ^5P state, many separate laser components are possible. The resolution of our monochromator, however, would not allow us to separate the total emission into its separate components.

REFERENCES

[1] C. E. Moore, *Atomic Energy Levels* (Circular 467). Washington, D. C.: NBS, June 1949.
[2] R. J. Pressley, Ed., *Handbook of Lasers*, Chemical Rubber Co., Cleveland, Ohio, 1971.
[3] D. G. Sutton, L. Galvan, P. R. Valenzuela, and S. N. Suchard, "Atomic laser action in rare gas-SF_6 mixtures," The Aerospace Corp., El Segundo, Calif., TR-0074(4641)-7, 1974.

Contributors

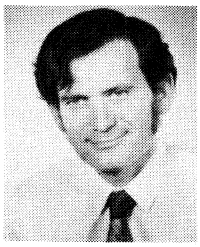

Jay H. Harris (S'57–M'66) was born in Newark, N. J., in 1936. He received the B.E.E. degree from the Polytechnic Institute of Brooklyn, Brooklyn, N. Y., in 1958, the M.S. degree from the California Institute of Technology, Pasadena, in 1959, and the Ph.D. degree from the University of California at Los Angeles in 1965.

From 1958 to 1965 he was a member of the Technical Staff of the Hughes Aircraft Company. His work there was concerned with various aspects of antenna design and electromagnetic-wave propagation. The academic year 1965–1966 was spent as a Fulbright Hayes Fellow at the Laboratoire d'Electronic of the University of Paris where he was engaged in research dealing with wave propagation in linear accelerators. In 1966 he went to the University of Washington, Seattle, where he was a Professor in the Department of Electrical Engineering. He was a Traveling Lecturer of the Optical Society of America from 1971 to 1972 and a Visiting Associate Professor at the University of California at San Diego (La Jolla) from 1972 to 1973. His research at Seattle dealt with wave propagation in plasmas, ultrasonic measurement of biological flow systems, and integrated optics and optical communications. He is currently at the National Science Foundation, Washington, D.C.

Dr. Harris is a member of the American Physical Society.

*

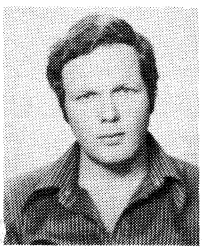

Mordehai Heiblum (S'74) was born in Holon, Israel, on May 25, 1947. He received the B.S. degree (honors) in electrical engineering from the Technion, Israel Institute of Technology, Haifa, in 1973, and the M.S. degree from Carnegie-Mellon University, Pittsburgh, Pa., in 1974. He spent the summer of 1974 in the Department of Electrical Engineering, University of Washington, Seattle. He is currently studying toward the Ph.D. degree in the Department of Electrical Engineering and Computer Sciences, University of California, Berkeley.

From 1967 to 1970 he served in the Israeli army. From 1970 to 1973 he was an Instructor in the Electronics Department at the Junior Technical High School, at the Technion.

Mr. Heiblum is a student member of the American Physical Society.

*



Robert F. Leheny (S'58–M'61) received the B.S. degree in electrical engineering from the University of Connecticut, Storrs, in 1960, and the Dr.Eng.Sc. in electrical engineering from Columbia University, New York, in 1967, where his dissertation topic was microwave interactions with plasmas.

From 1960 to 1961 he worked in the Systems Engineering Department of the Sperry Gyroscope Company. Between 1967 and 1968 he did postdoctoral work in the Plasma Laboratory at Columbia University. Since 1968 he has been a member of the Bell Laboratories, Holmdel, N.J. His current research interests are in semiconductor luminescence and laser physics.

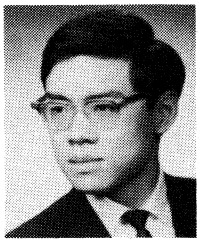

Paul F. Liao was born in Philadelphia, Pa., on November 10, 1944. He received the B.S. degree in physics from the Massachusetts Institute of Technology, Cambridge, in 1966, and the Ph.D. degree in physics from Columbia University, New York, N.Y., in 1973.

During 1973 he was a Research Associate at the Columbia Radiation Laboratory, Columbia University, and joined Bell Laboratories, Holmdel, N.J., in September 1973, where his interests lie in laser physics.

Dr. Liao is a member of the American Physical Society and Sigma Xi.

*

C. Lin was born in Taiwan, Republic of China, in 1945. He received the B.S.E.E. degree from the National Taiwan University, Taipei, Taiwan, in 1967, the M.S. degree in computer sciences from the University of Illinois, Urbana, in 1970, and the Ph.D. degree from the University of California, Berkeley, in 1973.

While at Berkeley he was a recipient of an IBM Graduate Fellowship and a Lankersheim Scholarship, as well as a Research Assistant in the Quantum Electronics Group of the Electronics Research Laboratory. He joined Bell Laboratories, Holmdel, N.J., in 1974. His current interest is in the field of picosecond pulses and dye lasers.

*

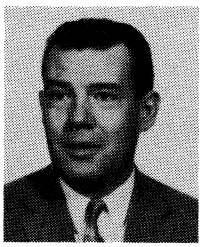

Patrick J. Maloney (S'71–M'71) was born in New York, N.Y., on November 11, 1925. He received the Associate degree in applied science (electrical technology) from New York Community College, New York, N.Y., in 1949.

From 1950 to 1951 he was assigned to the cesium beam clock project in the Microwave Standards Section of the National Bureau of Standards, Washington, D.C. From 1951 to 1953 he was engaged in experimental research with traveling-wave magnetrons at the Thermionics Branch of the Fort Monmouth Signal Corps Laboratory. From 1953 to 1961 he was employed at the IBM Thomas J. Watson Research Laboratory, New York, N.Y., where he worked in the fields of cryogenics, superconductivity, and thin films. He assisted Prof. C. H. Townes in the Michaelson-Morley experiment conducted at the Watson Laboratory using two ammonia masers. Since 1961 he has been assigned to the Department of Coherent Wave Physics, Bell Laboratories, Holmdel, N. J. He has been principally engaged in laser research ranging from the early ruby to the present gaseous devices.

*



D. Schicketanz was born in Puerto Montt, Chile, on October 5, 1943. He received the degree Ingeniero Civil Electricista from the University of Chile, Santiago de Chile, Chile, in 1969.

From 1969 to 1970 he was employed by the Electrical Engineering Research Laboratory, University of Chile. Since 1971 he has been with the Siemens Research Laboratories, Munich, Germany. His present work is on fiber optics.

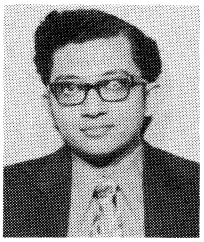

Jagdeep Shah was born in Surat, India. He received the B.Sc. degree in physics from Bombay University, Bombay, India, in 1962, and the Ph.D. degree in physics from the Massachusetts Institute of Technology, Cambridge, in 1967.

He has been with Bell Laboratories, Holmdel, N.J., since 1967, where he has been involved in studying optical properties of semiconductors, high-intensity effects in semiconductors, properties of organic dyes and dye lasers, and photoexcitation of superconductors.

Dr. Shah is a member of the American Physical Society.

*

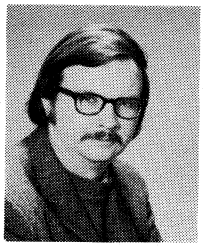

Charles V. Shank received the B.S., M.S., and Ph.D. degrees from the University of California, Berkeley, in 1965, 1966, and 1969, respectively.

Since 1969 he has been a member of the Coherent Optics Research Department at Bell Laboratories, Holmdel, N. J., where his present interests include dye lasers and waveguide devices.

*

Peter W. Smith (M'68) was born in London, England, on November 3, 1937. He received the B.Sc. degree in mathematics and physics in 1958 and the M.Sc. and Ph.D. degrees in physics in 1961 and 1964, all from McGill University, Montreal, P.Q., Canada. His thesis work was on the paramagnetic relaxation of iron group ions in dilute single crystals.

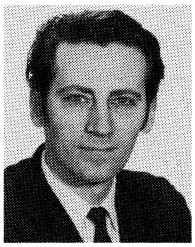

From 1958 to 1959 he was an Engineer at the Canadian Marconi Company, Montreal, Canada, where he worked on transistor circuitry. After obtaining the Ph.D. degree he joined the Bell Laboratories, Holmdel, N. J., where he has conducted research on the fundamental properties of gas lasers. In 1970 he spent nine months at the University of California, Berkeley, as Visiting McKay Lecturer in the Department of Electrical Engineering. His current interests include waveguide gas lasers and dye vapor lasers.

Dr. Smith is a member of the American Physical Society and the Optical Society of America.

*



G. Zeidler was born in Rosshaupt, Germany, in 1940. He studied at the Technical University of Munich, Munich, Germany.

Since 1975 he has been with the Siemens Research Laboratories, Munich, Germany. After working on solid-state lasers, optical range finders, and organic dye lasers, he is currently working on fiber optics and integrated optics.

MEMBERSHIP APPLICATION

IEEE MICROWAVE THEORY AND TECHNIQUES SOCIETY

Membership in the IEEE MICROWAVE THEORY AND TECHNIQUES Society entitles you to receive, for the low Society fee, the monthly IEEE Transactions on Microwave Theory and Techniques, and the quarterly Microwave Theory and Techniques Society Newsletter. You are kept informed of latest developments, meetings and conferences in your areas of interest, and are entitled to purchase informative conference records and other helpful educational aides at greatly reduced rates for members.

Use the convenient coupon to become a member of the IEEE MICROWAVE THEORY AND TECHNIQUES Society. If you are not a member of the IEEE, but would like to join, please check the appropriate box on the coupon. Descriptive materials and an IEEE membership application form will be sent to you immediately upon receipt.

*Society Fee: $7.00 for IEEE members of all grades except Student. Student Fee: $2.00. These rates apply to payments received September 1 through February. On payments received March 1 through August 31 remit one-half of the above rates. (Payments received September 1 through December 31 apply through December 31 of the following year.)



Membership Application/IEEE MICROWAVE THEORY AND TECHNIQUES Society
Send to: IEEE, Hadley Industrial Plaza, 3001 Hadley Rd - Unit #8,
So. Plainfield, N. J. 07080

☐ I am a _____ member of IEEE and hereby apply for membership in the MICRO-
(Grade) WAVE THEORY AND TECHNIQUES SOCIETY. I enclose a check for the Society fee* (made payable to IEEE).

☐ I am not now a member of the IEEE but would like to join. Please send information.

☐ I am interested in becoming a MICROWAVE THEORY AND TECHNIQUES Society Affiliate. Please send information.

Name _____ IEEE No. _____

Mailing Address _____

City _____ State/Country _____ Zip _____

Company _____

Field of Interest _____

MEMBERSHIP APPLICATION

IEEE ELECTRON DEVICES GROUP

Membership in the IEEE ELECTRON DEVICES Group entitles you to receive, for the low Group fee, the monthly IEEE Transactions on Electron Devices, and the bimonthly Electron Devices Group Newsletter. You are kept informed of latest developments, meetings and conferences in your areas of interest, and are entitled to purchase informative conference records and other helpful educational aids at greatly reduced rates for members.

Use the convenient coupon to become a member of the IEEE ELECTRON DEVICES Group or a Group Affiliate. If you are not a member of the IEEE, but would like to join, please check the appropriate box on the coupon. Descriptive materials and an IEEE membership application form will be sent to you immediately upon receipt.

*Group Fee: $7.00 for IEEE members of all grades except Student. Student Fee: $2.00. These rates apply to payments received September 1 through February. On payments received March 1 through August 31, remit one-half of the above rates. (Payments received September 1 through December 31 apply through December 31 of the following year.)



Membership Application/IEEE ELECTRON DEVICES GROUP
Send to: IEEE, Hadley Industrial Plaza, 3001 Hadley Rd - Unit #8,
So. Plainfield, N. J. 07080

☐ I am a _____ (Grade) member of IEEE and hereby apply for membership in the ELECTRON DEVICES Group. I enclose a check for the Group fee* (made payable to IEEE).

☐ I am not now a member of the IEEE but would like to join. Please send information.

☐ I am interested in becoming an ELECTRON DEVICES Group Affiliate. Please send information.

Name _____ IEEE No. _____

Mailing Address _____

City _____ State/Country _____ Zip ___

Company _____

Field of Interest _____

Analysis of Laser Emission in Ho^{3+}-Doped Materials

JOHN A. CAIRD AND LARRY G. DESHAZER

Abstract—**The oscillator strengths, transition rates, and branching ratios associated with known and potential laser transitions in trivalent holmium are discussed. Recently reported laser transitions between the $^5F_5$ and $^5I_5$ energy manifolds are found to have an abnormally low average oscillator strength, and an alternative explanation of the laser observation is suggested.**

I. Introduction

INDUCED electric dipole oscillator strengths and transition rates between energy levels of rare-earth ions in crystals can be calculated using a theory developed by Judd [1] and Ofelt [2]. In recent years the Judd-Ofelt (JO) model has been used in the analysis of rare-earth laser materials [3]-[6], and its use led to the discovery of the four-level Tm:Cr:$YA1O_3$ laser at 2.35 μm [7]. This paper reports the results of an application of the JO model to known and potential laser transitions in trivalent holmium.

II. Theoretical Background

According to the JO model, the oscillator strength f and spontaneous emission rate A of crystal field induced electric dipole fluorescence in a rare-earth ion are given by [8]

$$f_{JJ'} = \frac{8\pi^2 mc}{3h\bar{\lambda}(2J+1)}\left[\frac{(n^2+2)^2}{9n}\right] \cdot \sum_{t=2,4,6} \Omega_t |\langle 4f^n [S,L] J \| U^t \| 4f^n [S',L'] J' \rangle|^2 \quad (1)$$

and

$$A_{JJ'} = \frac{8\pi^2 e^2 n^2}{mc\bar{\lambda}^2} \cdot f_{JJ'} \quad (2)$$

where $\bar{\lambda}$ is the mean wavelength associated with the transition, n is the crystal's index of refraction at the mean wavelength, and $2J+1$ is the number of levels in the upper J-manifold. In (1) the $\langle \| U^{(t)} \| \rangle$ are doubly reduced matrix elements of unit tensor operators calculated in the intermediate coupling approximation [1], and the Ω_t are three empirical parameters. These empirical parameters can generally be determined for each ion-host combination by a least squares fit between calculated and measured oscillator strengths in the absorption spectrum. Equation (1) may then be used to calculate oscillator strengths in the fluorescence spectrum. It should be noted that (1) gives the oscillator strength summed over the Stark split components of the final energy manifold J' and averaged over the components of the initial energy manifold J.

The cross section for stimulated emission integrated over all Stark split components of the upper and lower J-manifolds is given by [5]

$$\int_{J \to J'} \sigma(\nu)\, d\nu = \frac{\bar{\lambda}^2}{8\pi c n^2} A_{JJ'} \quad (3)$$

where $\nu = 1/\lambda$. Using (2) this reduces to

$$\int_{J \to J'} \sigma(\nu)\, d\nu = \frac{\pi e^2}{mc^2} f_{JJ'} \quad (4)$$

which shows the significance of the oscillator strength in laser analysis. Without detailed line shape information (4) cannot be used to predict peak cross sections, but it is evident that transitions with larger oscillator strengths will generally have larger peak cross sections.

In the $4f^n$ ground configuration of rare-earth ions, electric dipole transitions become allowed only when the ion feels a perturbing field lacking inversion symmetry so that parity restrictions are broken. Magnetic dipole (md) transitions between levels with $|\Delta J \leqslant 1|$ are always allowed, however, and can on occasion be comparable in strength to the crystal field induced electric dipole (ed) transitions. A definition of the md oscillator strength consistent with (2) and (4) is given by [9]

$$f_{JJ'}(\text{md}) = \frac{h}{6\bar{\lambda}(2J+1)mc} \cdot n\, |\langle 4f^n [S,L]\, J \| L + 2S \| 4f^n [S',L']\, J' \rangle|^2 \quad (5)$$

where the matrix elements of $L + 2S$ can be evaluated using standard formulas given elsewhere [10].

A computer program was developed capable of calculating the unit tensor operator matrix elements in (1) between all J-manifolds in all rare-earth ions using previously published intermediate coupling wave functions [6]. The program was then used to calculate ed and md oscillator strengths, transition rates, and radiative branching ratios for a large number of ion-host combinations for which intensity parameters Ω_t had been published. The branching ratio for a transition $i \to j$ is simply given by

$$\beta_{i \to j} = \frac{A(i \longrightarrow j)}{\sum_{j'} A(i \longrightarrow j')} \quad (6)$$

Manuscript received June 7, 1974; revised October 16, 1974. This work was supported in part by the Air Force Systems Command, Air Force Avionics Laboratory, Wright-Patterson Air Force Base, Ohio, and in part by the U.S. Army ECOM under Contract DAABO7-74-C-0104.

J. A. Caird is with the Department of Physics, University of Southern California, Los Angeles, Calif. 90007, and with Hughes Aircraft Company, Culver City, Calif. 90230.

L. G. DeShazer is with the Departments of Electrical Engineering, Physics, and Materials Science, University of Southern California, Los Angeles, Calif. 90007.

where the sum in the denominator is over all states of lower energy. In these calculations emphasis was placed on transitions for which laser action and/or fluorescence has been reported, and those for which the radiative transition rates were large enough to exceed multiphonon emission rates. It was found that the vast majority of laser lines had oscillator strengths greater than 10^{-6}. In a few notable exceptions although the oscillator strengths were somewhat lower than 10^{-6}, the branching ratio associated with the laser transition was particularly high, and the upper level lifetime was long, allowing for the buildup of a large inversion density. The only other exceptions were found in cases where a trivalent rare-earth ion was placed on a divalent ion site in the laser material.

III. Application to Holmium

Laser emission from Ho^{3+} ions has been observed in many hosts on transitions between the $^5I_7$ and $^5I_8$ energy manifolds at wavelengths near 2 μm. Laser action in the green near 0.55 μm has also been reported on $[^5S_2, {}^5F_4] \rightarrow {}^5I_8$ transitions in CaF_2 [11] and BaY_2F_8 [12]. Recently stimulated emission in $Ho:BaY_2F_8$ near 2.4 μm has been attributed to transitions within the $^5F_5 \rightarrow {}^5I_5$ group [13]. Fluorescence originating in the $^5I_6$ state has also been observed in a number of crystals [9], [13], [14], but emission from other levels is often quenched by nonradiative processes.

The intensity parameters in the JO model for $Ho:YAlO_3$ were determined by Weber *et al.* [9] to be 1.82, 2.38, and 1.53 ($\times 10^{-20}$ cm^2) for Ω_2, Ω_4, and Ω_6, respectively. The electric dipole oscillator strengths and transition rates for fluorescence from low lying energy levels of Ho^{+3} in $YAlO_3$ can be easily derived from data given in [9] along with the indices of refraction of $YAlO_3$ given in [15]. These are tabulated for transitions from the $^5I_7$, $^5I_6$, $^5F_5$, and $[^5S_2, {}^5F_4]$ states in Table I. Calculation of the md contributions in Table I required the use of intermediate coupling wave functions for Ho^{3+} which were obtained from the authors of [9]. The branching ratios are in close agreement with those reported in [9], with the exception of the $^5F_5 \rightarrow {}^5I_4$ transition for which the ratio is found to be much smaller than previously reported.

Examination of Table I shows that the laser transitions $^5I_7 \rightarrow {}^5I_8$ and $[^5S_2, {}^5F_4] \rightarrow {}^5I_8$ have oscillator strengths greater than 10^{-6}, consistent with most other rare-earth lasers [6]. It is interesting to note that $^5F_4 \rightarrow {}^5I_8$ transitions may be more important than $^5S_2 \rightarrow {}^5I_8$ transitions for green laser emission, and therefore the relative positions of the $^5S_2$ and $^5F_4$ energy levels may have a large effect on laser performance. The $^5S_2 \rightarrow {}^5I_7$ transition at 0.76 μm also appears to have sufficient strength to support laser oscillation, but the $^5I_7$ lifetime is longer than the $^5S_2$, so that quenching of the $^5I_7$ level may be required. Conditions also appear to be favorable for laser emission on both the $^5I_6 \rightarrow {}^5I_7$ line at 2.9 μm and the $^5I_6 \rightarrow {}^5I_8$ line at 1.2 μm, particularly since the fluorescence lifetime of the $^5I_6$ level is reasonably long. At least one attempt to achieve laser action on the $^5I_6 \rightarrow {}^5I_7$ transition, however, was unsuccessful [13] even though the $^5I_7$ lifetime was significantly shortened by addition of Pr^{3+} and Eu^{3+} ions.

TABLE I

Oscillator Strengths, Transition Rates, and Branching Ratios for $Ho:YAlO_3$

Upper Level	Lower Level	Average frequency (cm^{-1}) [ref. 9]	Oscillator Strength ($\times 10^6$)		Transition Rate (sec^{-1})		Radiative Branching Ratio
			electric dipole	magnetic dipole	electric dipole	magnetic dipole	
$^5I_7$	$^5I_8$	5150	1.87	0.66	115	40	1.000
$^5I_6$	$^5I_7$	3500	0.98	0.74	30	22	.16
	$^5I_8$	8540	1.56	--	280	--	.84
$^5F_5$	$^5I_4$	2300	.008	.003	.11	.04	(.0001
	$^5I_5$	4350	.26	.02	12	1.0	.0032
	$^5I_6$	6910	1.36	.03	160	3.5	.039
	$^5I_7$	10410	2.86	--	770	--	.18
	$^5I_8$	15450	5.46	--	3270	--	.78
$^5S_2$	$^5F_5$	2740	0.04	--	0.6	--	.0002
	$^5I_4$	5030	1.00	--	63	--	.016
	$^5I_5$	7090	0.50	--	62	--	.015
	$^5I_6$	9650	1.12	--	260	--	.064
	$^5I_7$	13150	3.38	--	1450	--	.36
	$^5I_8$	18190	2.62	--	2190	--	.54
$^5F_4$	$^5F_5$	3090	0.41	0.29	9.6	6.8	.002
	$^5I_4$	5380	0.55	.001	39	.07	.005
	$^5I_5$	7440	1.73	.003	240	.41	.031
	$^5I_6$	10000	1.98	--	490	--	.064
	$^5I_7$	13500	1.61	--	730	--	.095
	$^5I_8$	18540	7.08	--	6160	--	.80

The oscillator strength of the $^5F_5 \rightarrow {}^5I_5$ emission is seen to be very small in comparison to other rare-earth lasers, and to the other holmium lasers in particular. The transition does not have mitigating advantages either. The upper level lifetime is not long, the lower level lifetime is long (predicted), and the radiative branching ratio is very small. It would seem that stimulated emission from the $^5F_5$ level and terminating on the $^5I_6$, $^5I_7$, and $^5I_8$ levels should have been observed first. One might ask if the intensity parameters for BaY_2F_8 could be much larger than in $YAlO_3$. The predicted radiative lifetimes for the $^5I_6$ and $^5I_7$ levels in $YAlO_3$ are 3 and 6 ms, respectively, while the measured lifetimes in BaY_2F_8 are 5 and 16 ms, respectively [13], indicating that the intensity parameters for BaY_2F_8 must in fact be smaller than for $YAlO_3$. In addition, examination of the unit tensor operator matrix elements involved [9] shows that changing the relative magnitudes of the three intensity parameters could not change the branching ratio appreciably. It could be that the stimulated emission cross section for this transition is sharply peaked, while the integral (4) remains small. However, laser oscillation was reported on three different lines: 2.362 μm, 2.375 μm, and 2.377 μm.

Our own work on the $Tm:YAlO_3$ laser at 2.3 μm [16] leads us to suggest that the emission seen by Johnson and Guggenheim may have been due to impurity thulium ions in their laser rod. It should be noted at the outset, however, that the authors of [13] indicate that the $Ho:BaY_2F_8$ laser

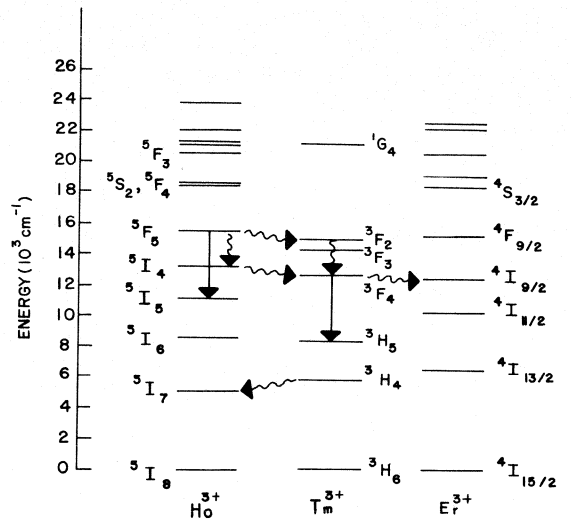

Fig. 1. Energy levels of Ho^{3+}, Tm^{3+}, and Er^{3+} indicating transitions in the 2.3–2.4-μm region.

material was of very high purity and that no fluorescence typical of thulium was observed [17].

Fig. 1 compares the energy levels and laser transitions of Ho^{3+} and Tm^{3+} in question. Er^{3+} is included for later discussion. The laser wavelengths which have been observed in $Tm:YAlO_3$ on $^3F_4 \rightarrow {}^3H_5$ transitions are 2.348 μm, 2.349 μm [18], and 2.272 μm [19], while the range of possible wavelengths in this group extends from 2.13 to 2.61 μm based on the energy levels given in [18]. Also indicated in Fig. 1 are possible mechanisms for nonradiative transfer from Ho^{3+} to Tm^{3+}. This excitation scheme is consistent with the observations of Johnson and Guggenheim since they indicate laser oscillation is initiated by pumping the $^5F_5$ level of Ho^{3+}. Nonradiative transfer from Ho^{3+} $^5I_4$ to Tm^{3+} $^3F_4$ is also possible, but direct excitation of the $^5I_4$ level of Ho^{3+} is ineffective because the absorption of the $^5I_4$ level is extremely weak. Cessation of oscillation early in the pump pulse attributed to terminal state population buildup was observed [13] and may be consistent with the Tm^{3+} $^3H_5$ level lifetime in BaY_2F_8 (though this is not observed in $YAlO_3$). The normal thulium $^3H_4 \rightarrow {}^3H_6$ fluorescence at 1.9 μm would be quenched by nonradiative energy transfer from the Tm^{3+} $^3H_4$ to the Ho^{3+} $^5I_7$ level, and would therefore be difficult to observe. Fluorescence from the $^3F_4 \rightarrow {}^3H_6$ transition at 0.8 μm might be expected, however, if thulium were responsible for the laser action. One might ask why the Tm^{3+} transition is not observed to lase in a large number of crystals in which Ho^{3+}, Er^{3+}, and Tm^{3+} are doped together to sensitize the 2-μm transition in holmium. Reference to Fig. 1 shows that the presence of erbium in these cases would quench fluorescence from the $^3F_4$ level of Tm^{3+} by nonradiative energy transfer to the $^4I_{9/2}$ level of Er^{3+}.

IV. Summary and Conclusion

An analysis of holmium laser transitions has been performed based primarily on the Judd-Ofelt theory of crystal field induced electric dipole oscillator strengths. The JO model appears to be useful in describing some of the actual and potential laser properties of Ho^{3+}, except in the case of the reported $^5F_5 \rightarrow {}^5I_5$ transitions. The observation of laser emission from holmium on these lines would not indicate a breakdown of the JO model, but would show that the applicability of the JO model to laser analysis is limited in its present form. If, however, the observed emission could be attributed to thulium impurities in the crystal, the JO model will have been a useful tool in the identification and prediction of the laser transitions.

References

[1] B. R. Judd, "Optical absorption intensities of rare-earth ions," *Phys. Rev.*, vol. 127, pp. 750–761, 1962.
[2] G. S. Ofelt, "Intensities of crystal spectra of rare-earth ions," *J. Chem. Phys.*, vol. 37, pp. 511–520, 1962.
[3] W. F. Krupke, "Radiative transition probabilities within the $4f^3$ ground configuration of Nd:YAG," *IEEE J. Quantum Electron.*, vol. QE-7, pp. 153–159, Apr. 1971.
[4] —, "Assessment of a promethium YAG laser," *IEEE J. Quantum Electron.* (Corresp.), vol. QE-8, pp. 725–726, Aug. 1972.
[5] —, "Induced-emission cross sections in neodymium laser glasses," *IEEE J. Quantum Electron.*, vol. QE-10, pp. 450–457, Apr. 1974.
[6] J. A. Caird, "Theoretical analysis of rare-earth laser materials," in the *Optical Society of America 1974 Spring Meeting Program* (Washington, D.C.), Apr. 21–25, p. 535.
[7] L. M. Hobrock *et al.*, "Four-level operation of Tm: Cr: $YAlO_3$ laser at 2.35 μm," in *Dig. Tech. Papers, VIII Int. Quantum Electronics Conf.* (Montreal, P. Q., Canada), May 8–11, 1972.
[8] W. F. Krupke, "Optical absorption and fluorescence intensities in several rare-earth doped Y_2O_3 and LaF_3 single crystals," *Phys. Rev.*, vol. 145, pp. 325–337, May 1966.
[9] M. J. Weber, B. H. Matsinger, V. L. Donlan, and G. T. Surratt, "Optical transition probabilities for trivalent holmium in LaF_3 and $YAlO_3$," *J. Chem. Phys.*, vol. 57, pp. 562–567, July 1972.
[10] B. G. Wybourne, *Spectroscopic Properties of Rare Earths.* New York: Interscience, 1965.
[11] Y. K. Voronko, A. A. Kaminsky, V. L. Osiko, and A. M. Prokhorov, "Stimulated emission of Ho^{3+} in CaF_2 at 5512Å," *Sov. Phys.–JETP Lett.*, vol. 1, pp. 3–5, Apr. 1965.
[12] L. F. Johnson and H. J. Guggenheim, "Infrared-pumped visible laser," *Appl. Phys. Lett.*, vol. 19, pp. 44–47, July 1971.
[13] —, "Electronic- and phonon-terminated laser emission from Ho^{3+} in BaY_2F_8," *IEEE J. Quantum Electron.*, vol. QE-10, pp. 442–449, Apr. 1974.
[14] G. H. Dieke, *Spectra and Energy Levels of Rare Earth Ions in Crystals.* New York: Interscience, 1968.
[15] K. W. Martin and L. G. DeShazer, "Indices of refraction of the biaxial crystal $YAlO_3$," *Appl. Opt.*, vol. 12, pp. 941–943, May 1973.
[16] J. A. Caird, J. Nella, and L. G. DeShazer, unpublished.
[17] L. F. Johnson, private communication.
[18] L. M. Hobrock, "Spectra of thulium in yttrium orthoaluminate crystals and its four-level laser operation in the middle infrared," Ph.D. dissertation, Univ. Southern California, Los Angeles, Jan. 1972.
[19] J. Nella, private communication.

Phase-Matched-Stimulated Four-Photon Mixing in Silica-Fiber Waveguides

ROGERS H. STOLEN

Abstract—**Stimulated four-photon mixing has been observed in silica-fiber waveguides. Phase matching is achieved by using the dispersion of the waveguide modes to compensate for bulk dispersion. The coherence lengths can be greater than 10 m and the gains more than double the usual Raman gain.**

I. Introduction

FIBER WAVEGUIDES provide a means for maintaining high optical intensities over long lengths. For self-phase-matched processes, such as stimulated Raman scattering in liquids and glasses, the interaction length is limited only by the linear absorption of the fiber which leads to a dramatic reduction of threshold power [1]. For processes such as four-photon mixing which are not automatically phase matched it is possible to use the dispersion of the waveguide modes to compensate for bulk dispersion in such a way as to achieve phase matching. This has been demonstrated by the observation of four-photon mixing (also called three-wave mixing) in a multimode fiber [2]. In that case, the effective coherence length was only 10 cm. This effective coherence length is reduced from the strictly infinite coherence length of perfect phase matching by imperfections in the guide. It will be shown here that for selected combinations of modes a relative insensitivity to imperfections will occur. Under these conditions effective coherence lengths increase from centimeters to meters in the same fiber and stimulated interactions are easily observed. The gain in this process is more than double the usual self-phase-matched Raman gain. The experimental results are presented first, followed by the explanation based on four-photon mixing.

II. Experimental Observations

The experimental arrangement is shown in Fig. 1. The output from a doubled Q-switched Nd:YAG laser is focused into a multimode guide. Peak powers were between 100 and 500 W. The output from the fiber is dispersed by a prism and displayed on a screen. The basic observation is that stimulated Stokes-anti-Stokes pairs are observed. This is in addition to the well-known stimulated Raman output which in fused silica occurs 460 cm^{-1} from the pump. The presence of the anti-Stokes shows that this is a four-photon process in which two pump photons are destroyed and Stokes and anti-Stokes photons created. Fig. 2 shows the results for two silica-core fibers [3]. A–C in Fig. 2 are from a 5-m fiber with a 5-μm core radius, and D is from 16 m of 2.5-μm core fiber. The pump at 532 nm is labeled P, and R is the self-phase-matched-stimulated Raman radiation. Stokes and anti-Stokes are designated S and A. A four-photon process requires phase matching and in all these cases this occurs with Stokes and anti-Stokes in different modes. The phase-matching frequency is different for different combinations of modes and for different fibers. The different pairs of modes were obtained by changing the coupling of the pump light into the fiber. Some of the pump propagates in the same mode as the Stokes and some in the same mode as the anti-Stokes: this doesn't show up in the photographs. The Stokes is always in the higher order mode. The anti-Stokes intensity is always less than the Stokes, with the strongest anti-Stokes observed close to the pump and no anti-Stokes seen at frequency shifts greater than 400 cm^{-1}. This is a consequence of the contribution of Raman gain to the four-photon intensities and will be discussed later. Neutral density filters were used to attenuate everything but the anti-Stokes in Fig. 2. From the photograph it is clear that the four-photon gain is larger than the Raman gain. This fact was used to estimate the coherence length. For a long fiber the self-phase-matched Raman process will dominate because the

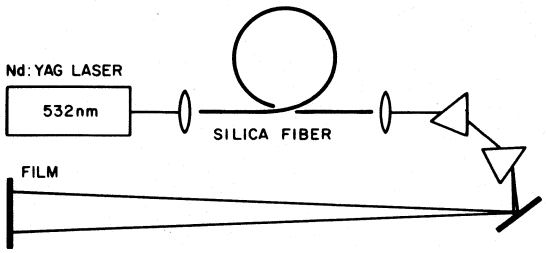

Fig. 1. Experimental arrangement.

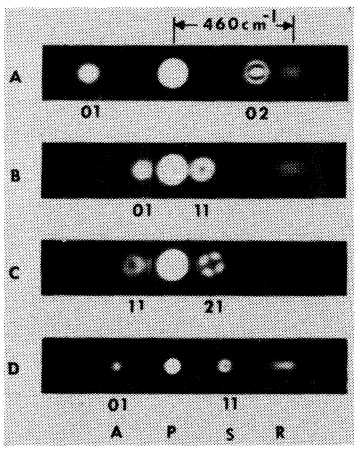

Fig. 2. Output from two silica fibers. A–C are from a 5-m length of 5-μm core radius fiber, and D is from 16 m of 2.5-μm core guide. Different Stokes (S) and anti-Stokes (A) pairs are obtained in A–C by adjusting the input coupling. P refers to the 532-nm pump and R is the non-phase-matched-stimulated Raman line. *ND* filters are used to attenuate everything but the anti-Stokes: 1.4 *ND* in A, 0.4 *ND* in B and C, and 1.0 *ND* in D. The modes are identified using the linearly polarized mode notation [5].

Manuscript received July 18, 1974.
The author is with Bell Laboratories, Holmdel, N.J. 07733.

coherence length for the four-photon process is less than the fiber length. Sections of fiber were then broken off until the four-photon process was the stronger. This length was taken to be the coherence length and was somewhere between 5 and 10 m. For shorter lengths of fiber the relative four-photon and Raman intensities remain about the same although more pump power is required to observe stimulated emission.

III. Phase Matching in Optical Fibers

It is precisely the fact that the pump is divided between two different modes and that Stokes appears in one of these modes while anti-Stokes appears in the other which leads to the long coherence lengths. In this section the method of calculating the phase-matching frequency for this process is illustrated. For comparison, the case where both pump photons are in the same mode is also treated. This latter type of process is characteristic of the phase-matched interactions observed in the previous mixing experiment [2]. These two cases will be referred to as "mixed-mode pump" and "single-mode pump" processes. The mixed-mode pump processes will have much longer coherence lengths than single-mode pump processes as will be shown in Section IV. The contribution of the guide modes to achieve phase matching can be understood by reference to Fig. 3 where the effective index of four fiber modes is plotted versus the characteristic number V which is proportional to frequency [5]. Linearly polarized mode [5] shapes are sketched alongside each branch. For the bulk material

$$k_A + k_S - 2k_P \equiv \Delta k(\Delta\bar{\nu}) > 0. \tag{1}$$

where k_A and k_S are the wave vectors of the high- and low-frequency waves and k_P refers to the pump. The bulk mismatch of the core material $\Delta k(\Delta\bar{\nu})$ is greater than zero. In Fig. 4, $\Delta k(\Delta\bar{\nu})$ is plotted versus $\Delta\bar{\nu}$ for fused silica [6]; $\Delta\bar{\nu}$ is the frequency shift in units of cm^{-1}. In the guide, each wave vector will be reduced slightly compared to the value in the bulk material. For example, the wave vector of the light in the 01 mode will be reduced by $2\pi(n_c - n)(1 - b_{01})\bar{\nu}$ where $\bar{\nu} = \nu/c$ and b is a normalized effective index which is defined in Fig. 3. In the approximation that the core-cladding index difference $(n_c - n)$ is independent of wavelength the result is to add to (1) another contribution to $k_A + k_S - 2k_P$ which we call $f(\Delta\bar{\nu})$

$$2\pi(n_c - n)(b_A\bar{\nu}_A + b_S\bar{\nu}_S - b_{P1}\bar{\nu}_P - b_{P2}\bar{\nu}_P) \equiv f(\Delta\bar{\nu}). \tag{2}$$

Consider the mixed-mode pump process illustrated in Fig. 3(a). Here the pump power is divided between the 01 and 02 modes. Stokes is in the 02 mode and anti-Stokes in the 01 which corresponds to observation. Expanding $b_A\bar{\nu}_A$ about $b_{P1}\bar{\nu}_P$ and $b_S\bar{\nu}_S$ about $b_{P2}\bar{\nu}_P$, using the definition of V in Fig. 3, and neglecting terms in $\Delta\bar{\nu}^2$, (2) reduces to

$$f(\Delta\bar{\nu}) = 2\pi(n_c - n)\left[\frac{d(b_{01}V)}{dV} - \frac{d(b_{02}V)}{dV}\right]\Delta\bar{\nu}. \tag{3}$$

The quantity $d(bV)/dV$ happens to be the normalized group delay and plots have been published for a simple waveguide structure [5]. At phase matching $f(\Delta\bar{\nu}) + \Delta k(\Delta\bar{\nu}) = 0$. In Fig. 4(a), $f(\Delta\bar{\nu})$ is plotted on the same scale as $\Delta k(\Delta\bar{\nu})$. The

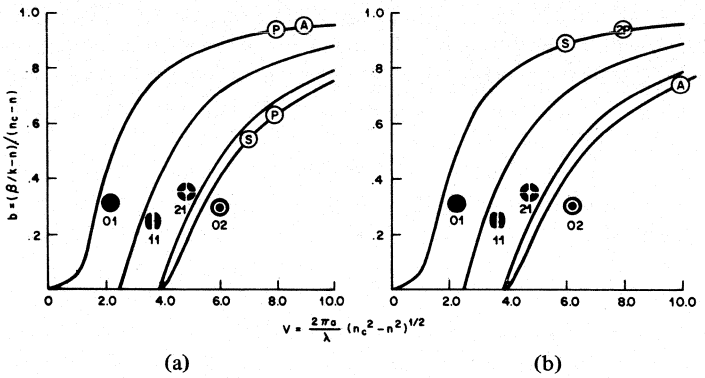

Fig. 3. Plots of the normalized effective index of refraction b for four-guide modes versus the characteristic number V. n_c and n are the core and cladding refractive indices, β is the propagation constant, k and λ the wave vector and wavelength in free space, and a is the core radius. Pump, Stokes, and anti-Stokes for a representative mixed-mode pump process is indicated in (a), and for a single-mode pump process in (b).

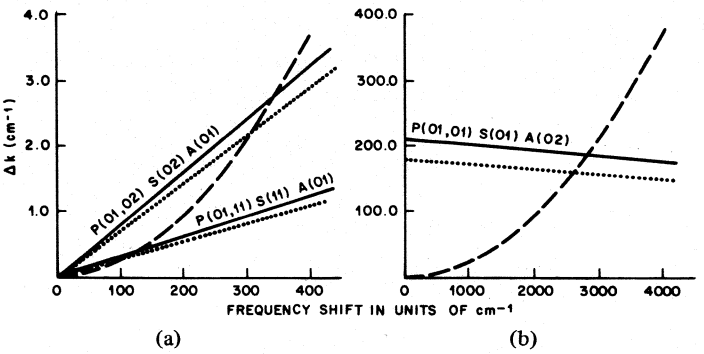

Fig. 4. Phase-matching diagrams for two mixed-mode pump processes (a), and a single-mode pump process (b). The dashed line is the bulk mismatch $\Delta k(\Delta\bar{\nu})$ plotted versus the frequency shift in units of cm^{-1}. The solid line is the contribution of the modes $f(\Delta\bar{\nu})$ for a guide with $a = 5.0$ μm and $n_c - n = 0.006$. The intersection of the curves is the phase-matching frequency. Note the difference in the horizontal axis. The dotted line illustrates the effect of an increase in core radius of 10 percent.

parameters used are taken from Fig. 3 which were calculated for a fiber of 5-μm core radius and $n_c - n = 0.006$. For comparison the similar process with Stokes 11, anti-Stokes 01 and pump 01 and 11, is also included. This process is phase matched at a smaller frequency shift. A single-mode pump process is illustrated in Fig. 3(b). Here pump light is only in the 01 mode, anti-Stokes in 02, and Stokes in 01. Symmetry considerations rule out combinations of 01 and 11 modes. Again using linear expansion

$$f(\Delta\bar{\nu}) = 2\pi(n_c - n) \cdot\left[(b_{02} - b_{01})\bar{\nu}_P + \left(\frac{d(b_{02}V)}{dV} - \frac{d(b_{01}V)}{dV}\right)\Delta\bar{\nu}\right]. \tag{4}$$

This curve is plotted in Fig. 4(b), again for the case of the 5-μm core fiber. For a fiber with several modes there will be many phase-matching combinations similar to those in Fig. 3. In general, single-mode pump processes will occur at much greater frequency shifts than mixed-mode pump processes. The mode labeled 11 in the photograph does not usually have the linearly polarized mode shape shown in Fig. 3. This mode is actually a combination of three almost degenerate modes,

each of which has a "doughnut" intensity profile [5]. Depending on the input coupling it seems to be possible to excite these in various combinations, and patterns have been observed ranging all the way from the two-lobe LP_{11} shape to a doughnut.

IV. Effective Coherence Length

The most interesting feature of the stimulated four-photon emission is the long coherence length. Previously, single-mode pump processes were studied in the 5-μm core fiber and a coherence length of only 10 cm was found [2]. This length depends on the fluctuations in diameter and $(n_c - n)$ which occur in any guide. Even if perfect phase matching were achieved at the beginning of a long guide there will be some point where conditions have changed. Changes in V will result in changes in $f(\Delta\bar{\nu})$ illustrated by the dotted line in Fig. 4. As a rough definition of the coherence length L_c we use the condition that

$$\delta k L_c \equiv \delta\,[f(\Delta\bar{\nu}) + \Delta k(\Delta\bar{\nu})]\,L_c \approx \pi. \tag{5}$$

The mixed-mode and single-mode pump processes described by (3) and (4) differ remarkably in their sensitivity to guide imperfections. If fluctuations in the core radius a are most important, then for the mixed-mode pump process

$$\delta k = 2\pi(n_c - n)\left[\frac{d^2(b_{01}V)}{dV^2} - \frac{d^2(b_{02}V)}{dV^2}\right]\Delta\bar{\nu}\,\frac{V}{a}\,\delta a \tag{6}$$

and for the single-mode pump process

$$\delta k = 2\pi(n_c - n)\left[\bar{\nu}_P\frac{d(b_{02} - b_{01})}{dV} + \Delta\bar{\nu}\left(\frac{d^2(b_{02}V)}{dV^2} - \frac{d^2(b_{01}V)}{dV^2}\right)\right]\frac{V}{a}\,\delta a. \tag{7}$$

Here $f(\Delta\bar{\nu})$ has been obtained from (3) and (4) and $(dV/da = V/a)$. The first term in (7) dominates primarily because of the difference between $\bar{\nu}_P$ and $\Delta\bar{\nu}$. The fiber used in [2] had $a = 5$ μm, $n_c - n = 0.006$, and $\delta a/a \simeq 0.2$ percent. The calculated coherence length for the single-mode pump process illustrated in Fig. 3(b) was 5 cm as compared to the measured 10 cm. In the mixed-mode pump processes the dominant term $\bar{\nu}_P d(b_{02} - b_{01})/dV$ drops out. For the same 5-μm core fiber the Stokes 02–anti-Stokes 01 combination should have $L_c = 5$ m and for S 11–A 01 $L_c = 29$ m. The long coherence length can be made even longer by a suitable choice of fiber parameters. From (6) it can be seen that if a phase-matched process occurs where $d[d(b_{01}V)/dV - d(b_{02}V)/dV]dV = 0$, then at least to first order this process would be insensitive to fluctuations in core diameter. In [5], $d(bV)dV$ is plotted versus V for different modes and it is apparent that this condition can be satisfied.

V. Comparison of Four-Photon and Raman Gain

The Stokes gain for the four-photon process is larger than the ordinary Raman gain, as is readily seen from the photographs in Fig. 2. The non-phase-matched Raman gain can be viewed as the imaginary part of a complex susceptibility, χ''. The real third-order susceptibility χ' makes possible the four-photon process. In the limits of pure real or pure imaginary susceptibilities Raman and four-photon gains are

$$g(\text{Raman}) = \alpha\,\frac{32\pi^2\omega_P}{n^2c^2}D_1\chi''\,\frac{P_p}{\pi\rho^2} \times 10^7\ \text{cm}^{-1} \tag{8a}$$

$$g(\text{four-photon}) = \beta\,\frac{32\pi^2\omega_p}{n^2c^2}D_2\chi'\,\frac{P_p}{\pi\rho^2} \times 10^7\ \text{cm}^{-1}. \tag{8b}$$

The intensity will increase as $\exp(gL)$, where L is the interaction length, P_p is pump power in watts, ω_p is the pump frequency, and n the refractive index. The effective radius ρ is to a good approximation the radius where the intensity of the lowest order fiber mode falls to $1/e$. The degeneracy factors D_1 and D_2 are 6 for Raman gain and 3 for four-photon gain for the case of a single-frequency pump [8]. The terms α and β appear because it is necessary to integrate over products of mode fields. For Raman gain with both pump and Stokes in the lowest order mode $\alpha \approx \frac{1}{2}$ [4]. With typical four-photon processes it can be shown that $\beta \approx \frac{1}{4}$. For fused silica the maximum value of χ'' at 460 cm^{-1}, as determined from the Raman-gain curve [4], is 0.5×10^{-15} ESU. The value of χ' has been reported to be about 5×10^{-15} ESU [7]. If these factors are combined, the four-photon gain is expected to be between two and three times the peak Raman gain for fused silica. This is consistent with the observations.

At frequencies less than 1000 cm^{-1} from the pump the four-photon gain is complicated somewhat by χ''. If χ'' were negligible, the Stokes and anti-Stokes intensities would be the same. The effect of χ'' is to increase the amplification of Stokes and to absorb anti-Stokes [9]. This explains the difference between the observed anti-Stokes and Stokes intensities. The real part of the susceptibility is also slightly frequency dependent in the frequency range of interest since χ' will be affected by χ'' through the Kramers–Kronig relations [9]. At low-frequency shifts χ' will be about 5 percent higher than the high-frequency value, while χ' will be depressed by about 5 percent around 500 cm^{-1}. In principle, the ratio of anti-Stokes and Stokes can be used to determine χ''/χ' at various frequency shifts. This is complicated by the need to calculate overlap integrals.

VI. Amplifier Gain and Bandwidth

To obtain some feeling for the amplification possible we choose a multimode fiber 10 m in length and with a 5-μm core radius. If we assume that the gain is 2.5 times the peak Raman gain, this means that a pump power of 50 W will result in a power amplification of e^3.

The amplifier bandwidth can be determined from the relative slopes of $f(\Delta\bar{\nu})$ and $\Delta k(\Delta\bar{\nu})$ in Fig. 4. We define the bandwidth $\delta\bar{\nu}$ by

$$\frac{d}{d(\Delta\bar{\nu})}[f(\Delta\bar{\nu}) + \Delta k(\Delta\bar{\nu})]\,\delta\bar{\nu}L = \pi. \tag{9}$$

For the single-mode pump processes the dominant term is $d(\Delta k)/d(\Delta\bar{\nu})$. For the mixed-mode pump processes the slopes of $f(\Delta\bar{\nu})$ and $\Delta k(\Delta\bar{\nu})$ are similar and the condition becomes

$$\frac{d(\Delta k)}{d(\Delta\bar{\nu})} - \frac{\Delta k}{\Delta\bar{\nu}}\,\delta\bar{\nu}L = \pi. \tag{10}$$

Again, using the index data for fused SiO_2 and choosing a length of 10 m, the bandwidth at a frequency 100 cm^{-1} from a 500-nm pump will be 1.4 cm^{-1}; at 500 cm^{-1} it will be 0.27 cm^{-1}. For a higher frequency shift process at 3000 cm^{-1}, $\delta\bar{\nu}$ is 2.2×10^{-3} cm^{-1}.

VII. Conclusion

In conclusion, the observation of stimulated four-photon mixing demonstrates that extremely long coherence lengths are possible for phase-matched nonlinear interactions in optical waveguides. The observed coherence lengths are two orders of magnitude larger than anything previously observed in solids. High amplification and broad bandwidths are possible using the four-photon interaction as an amplifier. The gain coefficient is more than double the self-phase-matched Raman gain. Other glasses might be expected to have even larger gains.

References

[1] E. P. Ippen, "Low-power quasi-cw Raman oscillator," *Appl. Phys. Lett.*, vol. 16, pp. 303–305, 1970; also R. H. Stolen, E. P. Ippen, and A. R. Tynes, "Raman oscillation in glass optical waveguide," *Appl. Phys. Lett.*, vol. 20, pp. 62–64, 1971.

[2] R. H. Stolen, J. E. Bjorkholm, and A. Ashkin, "Phase-matched three wave mixing in silica fiber optical waveguides," *Appl. Phys. Lett.*, vol. 24, pp. 308–310, 1974.

[3] W. G. French, A. D. Pearson, G. W. Tasker, and J. B. MacChesney, "Low-loss fused silica optical waveguide with borosilicate cladding," *Appl. Phys. Lett.*, vol. 23, pp. 338–339, 1973; also J. B. MacChesney *et al.*, "Low-loss silica core-borosilicate clad fiber optical waveguide," *Appl. Phys. Lett.*, vol. 23, pp. 340–341, 1973.

[4] R. H. Stolen and E. P. Ippen, "Raman gain in glass optical waveguides," *Appl. Phys. Lett.*, vol. 22, pp. 276–278, 1973.

[5] D. Gloge, "Weakly guiding fibers," *Appl. Opt.*, vol. 10, pp. 2252–2257, 1971.

[6] Index data for fused SiO_2 from, *American Institute of Physics Handbook*. New York: McGraw-Hill, 1963, p. 6: 25.

[7] A. Owyoung, R. W. Hellwarth, and N. George, "Intensity-induced changes in optical polarizations in glasses," *Phys. Rev.*, vol. 5B, pp. 628–633, 1972; also A. Owyoung, "Ellipse rotation studies in laser host materials," *IEEE J. Quantum Electron.*, vol. QE-9, pp. 1064–1069, Nov. 1973; also M. C. Levenson, "Feasibility of measuring the nonlinear index of refraction by third-order frequency mixing," *IEEE J. Quantum Electron. (Part I of Two Parts)*, vol. QE-10, pp. 110–115, Feb. 1974.

[8] P. D. Maker and R. W. Terhune, "Study of effects due to an induced polarization third order in the electric field strength," *Phys. Rev.*, vol. 137A, pp. 801–818, 1965.

[9] N. Bloembergen and Y. R. Shen, "Coupling between vibrations and light waves in Raman laser media," *Phys. Rev. Lett.*, vol. 12, pp. 504–507, 1964; also Y. R. Shen and N. Bloembergen, "Theory of stimulated Raman and Brillouin scattering," *Phys. Rev.*, vol. 137A, pp. 1787–1805, 1965.

The Mechanism of Single-Frequency Operation of the Hybrid-CO_2 Laser

A. GONDHALEKAR, N. R. HECKENBERG, AND E. HOLZHAUER

***Abstract*—The mechanism of a new method of obtaining high-power single-frequency pulses from a TEA-CO_2 laser is discussed. Measurements of the shape and monochromaticity of pulses from the hybrid laser which has both a TEA and a low-pressure gain section inside one resonator are presented. The mechanism of single-frequency operation of the hybrid laser is discussed with reference to numerical solutions of simplified rate equations. The low-pressure section provides gain only over a narrow range of frequencies so that a mode lying in that bandwidth builds up faster than neighboring modes to give a single-frequency pulse resembling in overall shape the normal TEA laser pulse. If the system is already lasing when the TEA discharge begins, the single-mode radiation already present rapidly grows to give a single-frequency pulse lacking a gain-switched peak.**

Manuscript received August 9, 1974; revised November 11, 1974. This work was undertaken as part of a collaboration between the Institut für Plasmaforschung and the Max-Planck-Institut für Plasmaphysik.

A. Gondhalekar and E. Holzhauer are with the Institut für Plasmaforschung, Universität Stuttgart, Pfaffenwaldring 31, 7 Stuttgart 80, Germany.

N. R. Heckenberg is with the Max-Planck-Institut für Plasmaphysik, Euratom Association, 8046 Garching, Germany.

I. Introduction

THE output pulse of a high-pressure CO_2 laser exhibits strong modulation resulting from beats between different cavity modes. Such modulation, usually appearing in the range 10–100 MHz, is highly undesirable for many applications. A high degree of modulation is observed because the modes making up the output pulse grow at essentially equal rates from spontaneous emission, which supplies nearly equal power to each. This occurs because the gain width in a high-pressure discharge is very large (~3 GHz at atmospheric pressure) compared to the mode spacing ($\leqslant$75 MHz for a 200-cm-long cavity), and the laser gain is effectively constant over a number of modes, as is the spontaneous emission rate.

It is possible to ensure operation on the lowest order transverse mode by taking advantage of the higher losses suffered by high-order modes when an aperture is introduced into the laser cavity. Attempts at longitudinal mode selection have centered on similarly causing the cavity losses to vary rapidly

with frequency so that one mode will grow more rapidly than any other during the pulse development. These methods have drawbacks; additional elements such as a grating and a gas cell [1] in the laser cavity reduce the output. On the other hand, the alignment of multimirror systems [2] is difficult to maintain.

By incorporating a low-pressure (total pressure 10 torr) gain section in the same laser cavity as the high-pressure (TEA) section, we can ensure a substantial increase in gain for the one longitudinal mode lying inside the narrow (~60-MHz-wide) gain profile of the low-pressure section. If the low-pressure section is already lasing when the electrical discharge in the high-pressure section begins, the single longitudinal-mode radiation already present in the cavity builds up to give a single-frequency pulse lacking a gain-switched peak [3].

In Section II we describe the hybrid laser and present measurements of electrical and other parameters for the low-pressure gain section and the TEA section. We then present measurements of the laser pulse shape and monochromaticity, pulse power, and total energy for the four different modes of operation of the hybrid laser. In Section III we present a simplified rate-equation description of the hybrid-laser operation. A semiquantitive agreement between this description and the experimental results is achieved.

II. The Hybrid-CO_2 Laser

A schematic diagram of the hybrid laser is given in Fig. 1. The active medium was divided into two sections, a pulsed TEA gain section partitioned off by a Brewster-angle NaCl window from a pulsed low-pressure gain section. The laser cavity was made up of a 600-cm-radius-of-curvature gold-coated 100-percent-reflecting concave mirror at one end and a plane 65-percent-reflecting germanium output mirror at the other. A 7-mm-diam aperture at the plain mirror restricted laser oscillation to the TEM_{00} mode. The cavity was 210 cm long, giving a longitudinal mode separation of about 71 MHz.

The low-pressure section was 100 cm long and was filled with a 1:3:18 mixture of CO_2:N_2:He at a total pressure of 10 torr. Fig. 2 shows the current pulse and the output laser pulse when an 8-nF capacitor charged to 15 kV was discharged longitudinally through this section. The current pulse was about 4 μs long and had a peak value of about 120 A. The laser pulse, which came after about 60 μs, started with a gain-switched peak of 60 W followed by a long lower power tail lasting for many tens of microseconds. The energy in this pulse was measured to be about 20 mJ. Using a CO_2 spectrum analyzer, the laser output was ascertained always to be on the $P(20)$ transition at 10.59 μ. Measurements with a fast GeAu detector (~1-ns rise time) showed that the laser output was single longitudinal mode.

The TEA section was of the type utilizing UV preionization of the active gas before the main electrical discharge is initiated [4]. This section was 60 cm long and was filled with a 1:2:3 mixture of CO_2:N_2:He at a total pressure of 720 torr. The two 60-cm-long Rogowski-profiled electrodes were 34 mm apart. The electrical discharge across the electrodes excited a total of 940 cm^3 of gas but the TEM_{00} mode used only 20 cm^3 of this volume. The main electrical discharge was

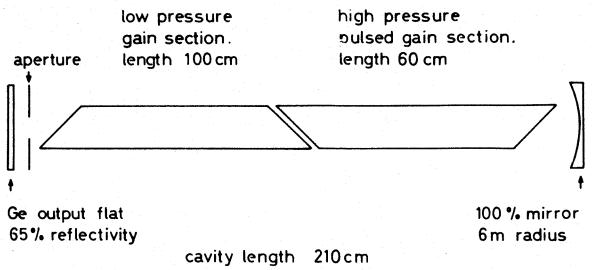

Fig. 1. Schematic diagram of the hybrid-CO_2 laser.

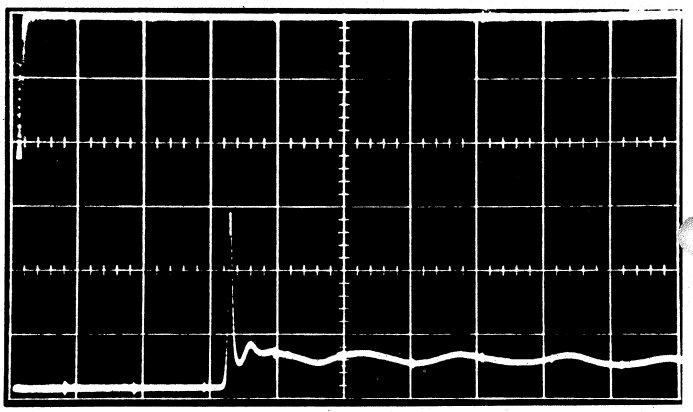

Fig. 2. Current pulse (upper trace: 50 A/div) and laser output (lower trace: 20 kW/div) for the low-pressure section. Time: 20 μs/div.

energized by the output of a two-stage Marx generator with total capacity of 37.5 nF and voltage of 64 kV. Fig. 3 shows the current through the discharge and the voltage across it. These two measurements show that the input power pulse to the laser gas has an approximately triangular shape of width (at half peak height) of about 350 ns. The peak electrical power dissipated in the gas was estimated to be 200 kW/cm^3. The output laser pulse obtained when this TEA section alone was excited is shown in Fig. 4(a), a pulse typical of TEA-CO_2 lasers. The oscilloscope was triggered at the start of the current pulse. The laser pulse came after a delay of abou 900 ns and had the familiar gain-switched peak followed by a long tail. The high-frequency modulation of the output is due to beating between several adjacent longitudinal modes. Again, the output was at 10.59 μ. The total energy in the pulse was approximately 140 mJ and the peak power about 300 kW.

When both sections were operated together, two different forms of behavior were observed, depending on the timing of the two pulses. In case 1 the electrical discharge in the TEA section was initiated 55 μs after the current pulse in the low-pressure section. At this time, the low-pressure section had an inverted population but the system was not yet lasing. The hybrid laser pulse is shown in Fig. 4(b). As before, the oscilloscope was triggered at the start of the current pulse in the TEA section. We notice that the output pulse resembles in overall shape the normal TEA laser pulse. However, the laser pulse started 200 ns earlier than the normal TEA laser pulse, and in addition no high-frequency modulation of the pulse occurred. The peak power in the laser pulse was about 250 kW and the total energy 140 mJ.

In case 2 the TEA section was energized 100 μs after the current pulse in the low-pressure section. At this time, the

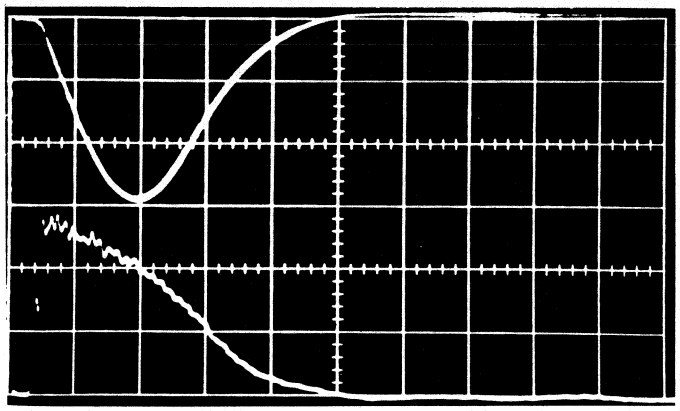

Fig. 3. Current (upper trace: 1.75 kA/div) and voltage (lower trace: 18.7 kV/div) for the TEA section. Time: 200 ns/div.

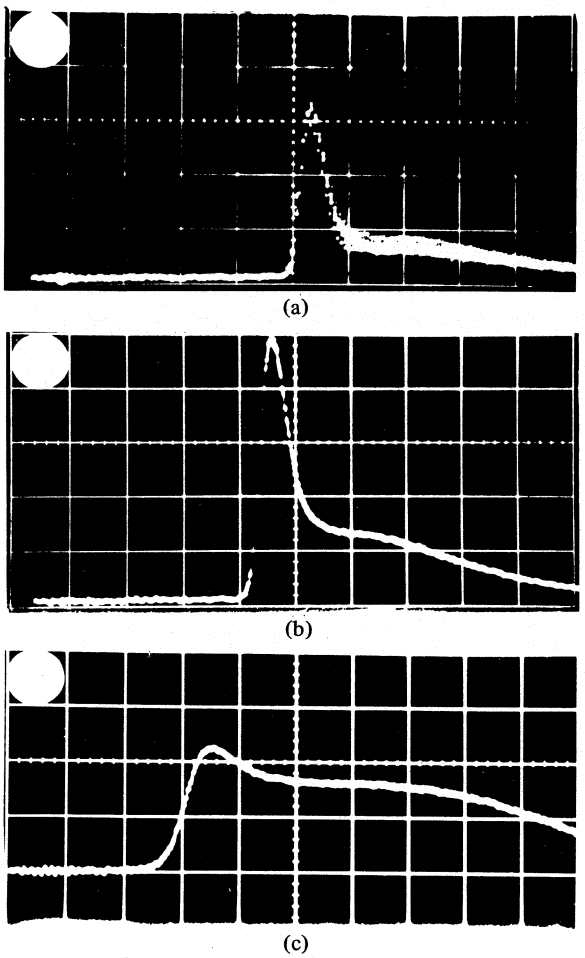

Fig. 4. Output pulses from the hybrid laser. Time: 200 ns/div. (a) Normal TEA-laser pulse (100 kW/div). (b) Hybrid-laser pulse with the low-pressure section operating below threshold (50 kW/div). (c) Hybrid-laser pulse with the low-pressure section operating above threshold (50 kW/div).

system was already lasing with an output power of 10–15 W. The type of hybrid laser pulse so obtained is shown in Fig. 4(c). The oscilloscope was triggered as before. The peak power in the laser pulse was now little more than 100 kW, and the total energy in the pulse remained unchanged at 140 mJ. We notice that unlike the normal TEA laser pulse, this one had no gain-switched peak, the pulse started about 400 ns earlier, and the mode beating was absent. The remaining modulation was measured to be smaller than 5×10^{-5} of the peak, the resolution being limited by detector noise. This represents a ratio of power in the main mode to the power in the unwanted neighboring modes of more than 10^9 [12].

III. Theory: A Rate-Equation Model

A simplified model of the hybrid laser has been developed which, since it produces many of the observed features of the system operation, throws light on the important operating mechanisms. The theoretical treatment is based on that used by Gilbert *et al.* [5] to describe the operation of a conventional TEA-CO_2 laser. They simplify the complicated level structure of the CO_2-N_2-He laser to a four-level structure, describing the time evolution of the population densities of the upper and lower laser levels and the excited nitrogen level (n_a, n_b, n_c, respectively) by the equations

$$\frac{dn_a}{dt} = I\sigma_e c(n_b - n_a) - \gamma_a n_a + \gamma_c(n_c - n_a) + W_a \tag{1}$$

$$\frac{dn_b}{dt} = I\sigma_e c(n_a - n_b) + \gamma_a n_a - \gamma_b n_b + W_b \tag{2}$$

$$\frac{dn_c}{dt} = \gamma_c(n_a - n_c) - \gamma_{c0} n_c + W_c \tag{3}$$

where I is the cavity radiation density, σ_e the cross section for stimulated emission, and c the velocity of light. γ_a, γ_b, and γ_{c0} are deactivation rate constants for the three levels while γ_c is the rate constant for transfer of energy from the excited nitrogen level to the upper CO_2 level. The rate equation for the density of radiation in the cavity is

$$\frac{dI}{dt} = -\gamma_0 I + I\sigma_e c(n_a - n_b) + n_a W_s \tag{4}$$

where γ_0 is the reciprocal of tne decay time of the photon density in the cavity and W_s is the rate of spontaneous emission into a mode. Having made estimates of the rate constants and pumping rates (W_a, W_b, W_c), they solve the differential equations numerically, obtaining reasonable agreement with measurements made on a small TEA laser.

In this treatment the radiation in the laser cavity is represented by a single radiation density integrated over all lasing modes so that no mode-beating structure appears in the calculated results.

We have used the same mathematical formalism and essentially the same rate constants, but have estimated the excitation rates for the upper laser level and the excited nitrogen from measurements of the discharge current and voltage [6]–[8]. According to these estimates, during the pumping pulse a peak power of some 120 kW/cm^3 goes into raising nitrogen molecules into the metastable state while some 16 kW/cm^3 of the total 200 kW/cm^3 dissipated in the discharge goes to raise CO_2 molecules to the upper lasing state. In the computer code the pumping pulse has been approximated by a triangular pulse of half-width 350 ns. The lower laser level is not pumped by electron collisions but is affected by the gas temperature which is difficult to estimate so that we have simply set this rate

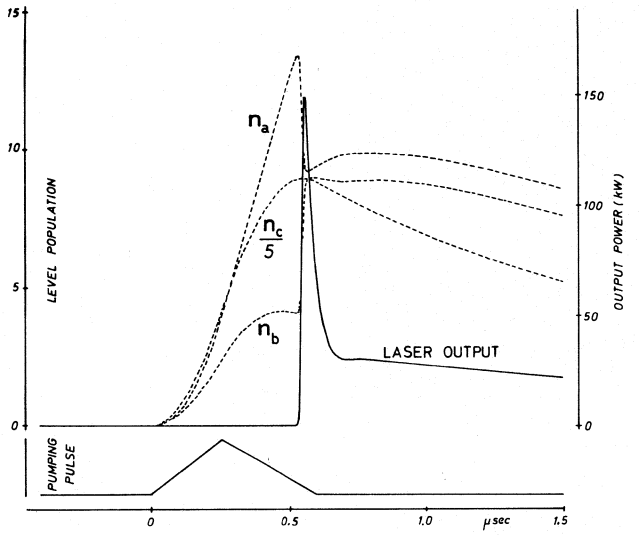

Fig. 5. Calculated output power and population densities for the normal TEA-laser pulse. The level population densities are expressed in units of the threshold inversion density ($\sim 1.5 \times 10^{16}/cm^3$).

equal to the electron collision excitation rate of the upper laser level [5].

With these parameters the model provides a substantially correct picture of the operation of the hybrid laser as a normal TEA laser, as can be seen from comparison of Fig. 4(a) and Fig. 5. The calculated output pulse energy of 70 mJ is within a factor of 2 of that observed; the calculated peak output power of 150 kW is to be compared with an observed value of 300 kW. Discrepancies such as the underestimation of the width of the gain-switched peak and pulse delay seem to be inherent deficiencies of the model [5]. Fig. 5 also shows that the population inversion in the TEA section grows rapidly to a value many times the threshold value before being suddenly depleted by the rapidly growing cavity radiation. During most of this rise, however, the population inversion is little affected by the modes present, which therefore grow with little competition. Several of the longitudinal modes near the center of the collision-broadened gain profile thus grow out of spontaneous emission with essentially equal rates to produce a heavily modulated pulse.

The low-pressure gain section of the hybrid laser has two effects on the pulse being built up by the TEA section. One is to considerably increase the round-trip cavity gain over a narrow-band of frequencies corresponding to the Doppler-broadened line profile. Since this width is about 60 MHz, whereas the longitudinal mode spacing of a 210-cm cavity is 71 MHz, only one longitudinal mode will experience substantial increase in gain. Secondly, when the low-pressure section is operated above threshold, there is, in addition, a substantial level of radiation of a single longitudinal mode present in the cavity before the TEA section is pulsed. The presence of this radiation can be handled directly in the computer code; the extra gain of the low-pressure section is simulated by adding small constant-excitation terms to the rate equations for the level populations, (1)–(3). Suitable values for these terms are determined empirically by seeking steady solutions of the equations which give either a continuous output of a few watts or a population inversion just below threshold.

The pulse shape calculated for the case where the gain of the low-pressure section is just below threshold (case 1) is shown in Fig. 6(a). Since threshold is reached much sooner after the pumping pulse than in the normal TEA laser [Fig. 6(b)], the pulse appears rather earlier in time but with essentially the same shape, i.e., a gain-switched peak followed by lower power "tail." Since the low-pressure section supplies gain but little energy, the peak power and total pulse energy are very little affected. All of these features agree with the experimental observations.

For the case where the low-pressure section is operated above threshold (case 2), a rather different pulse shape is obtained [Fig. 6(a)]. Fig. 6(b) shows how the presence of the high level of radiation in the cavity prevents the growth of a large population inversion, precluding the formation of a gain-switched peak. Thus the model predicts a longer pulse, lacking a pronounced gain-switched peak, and appearing earlier in time, just as is observed. The good qualitative agreement obtained in the two cases testifies to the importance of both of the two effects of the low-pressure section cited above.

In order to further examine the mechanism of the hybrid laser, another case was considered: the case where a continuous level of radiation is established in the cavity by external injection. Comparison with case 1 allows separation of the roles of the gain of the low-pressure section and the radiation in the cavity in case 2. In this case, the initial values for all of the population densities were taken as zero, as in the normal TEA case, but an additional steady source of radiation was included on the right-hand side of (4). This source rate was chosen so that an equilibrium intensity equal to that found in the cavity in case 2 was established before the TEA pump pulse was applied. Fig. 6(a) shows that the delay of the optical

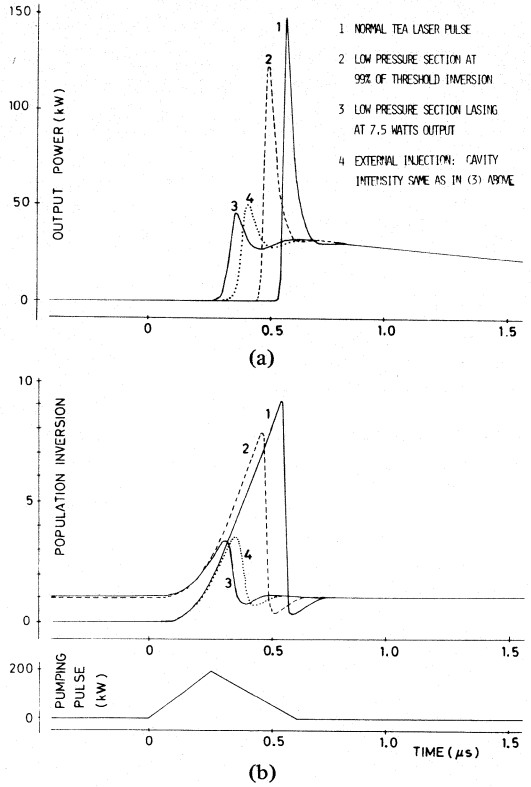

Fig. 6. Calculated output power and population densities for the hybrid laser. (a) Output laser pulses. (b) Population inversion in units of the threshold inversion density ($\sim 1.5 \times 10^{16}/cm^3$).

pulse was reduced compared to the normal TEA-laser case and the gain-switched peak greatly affected as in the above-threshold case (case 2). No comparable experiment could be performed because of the difficulty of matching the injected radiation to a mode of the TEA laser without the TEA laser affecting the injecting laser. The significance of the calculated result is, however, to indicate that the prior presence of radiation in the cavity has a significant effect on the laser pulse shape. Thus, when the low-pressure section of the hybrid laser is operated above threshold, both this factor and the increased gain due to the low-pressure section are important.

The early appearance of the pulse when the low-pressure section is excited is responsible for the observed lack of mode beating. The one mode inside the narrow-band gain profile builds up rather faster than others and can deplete the population inversion before other modes reach significant levels. As was pointed out earlier, until very shortly before the appearance of the gain-switched pulse, the various modes present grow independently so that comparison of the results shown in Fig. 6(a) can be used to make an estimate of the ratio of the dominant to other modes at the time of the gain-switched peak of the hybrid-laser pulse when the low-pressure section is operated just below threshold (case 1). This, in effect, makes the reasonable approximation that all modes experience the same gain in the high-pressure section, whereas only one is affected by the low-pressure section. In this case, a ratio of 10^7 in intensities is indicated. When the low-pressure section is operated above threshold (case 2) even better performance could be expected.

IV. Conclusion

We conclude that using the hybrid principle, very good frequency selection can be achieved without introducing losses in the TEA-CO_2 laser cavity. Such a laser could find application in plasma diagnostics [9], pulsed infrared radar, and optical pumping of submillimeter lasers which at present have low efficiencies due to the multimode output of the CO_2-laser pump pulse [10]. Pulses lacking a gain-switched peak may be useful in material studies. Study of nonlinear optical phenomena in gases and crystals (e.g., far-infrared generation by optical mixing), where interpretation is difficult due to fast modulation of the TEA-CO_2 laser pulse [2], may benefit from the availability of smooth high-power CO_2-laser pulses with well-defined power in the pulse. Further, a smooth high-power pulse is desirable for cutting and shaping a suitable short pulse for amplification and use in laser fusion research [11]. Lastly, the use of the hybrid configuration is not restricted to the CO_2 laser.

Acknowledgment

The authors wish to thank Dr. J. A. Beaulieu and Dr. O. R. Wood, II, for valuable comments and for drawing their attention to other work along these lines, including that mentioned in [1].

References

[1] T. A. DeTemple and A. Nurmikko, "The dynamics of single-mode operation of high-pressure CO_2 laser by means of saturable absorbers," *Opt. Commun.*, vol. 4, pp. 231–233, Nov. 1971.

[2] J. A. Weiss and L. S. Goldberg, "Single longitudinal mode operation of a transversely excited CO_2 laser," *IEEE J. Quantum Electron.* (Corresp.), vol. QE-8, pp. 757–758, Sept. 1972.

[3] A. Gondhalekar, E. Holzhauer, and N. R. Heckenberg, "Single longitudinal mode operation of high pressure pulsed CO_2 lasers," *Phys. Lett.*, vol. 46A, pp. 229–230, Dec. 1973.

[4] M. C. Richardson, K. Leopold, and A. J. Alcock, "Large aperture CO_2 laser discharges," *IEEE J. Quantum Electron.*, vol. QE-9, pp. 934–939, Sept. 1973.

[5] J. Gilbert, J. L. Lachambre, F. Rheault, and R. Fortin, "Dynamics of the CO_2 atmospheric pressure laser with transverse pulse excitation," *Can. J. Phys.*, vol. 50, pp. 2523–2535, Oct. 1972.

[6] W. L. Nighan, "Electron energy distributions and collision rates in electrically excited N_2, CO and CO_2," *Phys. Rev.*, vol. 2A, pp. 1989–2000, Nov. 1970.

[7] W. L. Nighan and J. H. Bennett, "Electron energy distribution functions and vibrational excitation rates in CO_2 laser mixtures," *Appl. Phys. Lett.*, vol. 14, pp. 240–243, Apr. 1969.

[8] S. J. Kast and C. Cason, "Performance comparison of pulsed discharge and E-beam controlled CO_2 lasers," *J. Appl. Phys.*, vol. 44, pp. 1631–1637, Apr. 1973.

[9] A. Gondhalekar and F. Keilmann, "Proposal of a new scheme using extreme forward light scattering for ion temperature measurement in stellarator and Tokamak plasmas," Max-Planck-Institut für Plasmaphysik, Garching, Germany, Rep. 2/202, Aug. 1971.

[10] F. Brown, E. Silver, C. E. Chase, K. J. Button, and B. Lax, "10-W methyl fluoride laser at 496 μm," *IEEE J. Quantum Electron.* (Corresp.), vol. QE-8, pp. 499–500, June 1972.

[11] C. Fenstermacher, Los Alamos Scientific Labs., private communication.

[12] A. Gondhalekar, N. R. Heckenberg, and E. Holzhauer, "Single longitudinal mode operation of the high pressure pulsed CO_2 laser," presented at the 8th Int. Quantum Electronics Conf., San Francisco, Calif., June 1974, Paper P11.

Correspondence

Mode-Dependent Retardation in (Ga,Al)P Waveguide Modulators

DAVID P. BORTFELD

Abstract—**Theoretically predicted mode-dependent modulation in (Ga,Al)P waveguide modulators for which the depletion region is small compared to the guide width is demonstrated experimentally. At 10 V the measured retardations of the three lowest order modes are 0.36, 0.78, and 1.13 rad, respectively.**

Manuscript received September 9, 1974; revised October 28, 1974.
The author was with the Laboratories RCA Ltd., Zurich, Switzerland. He is now with the David Sarnoff Research Center, Princeton, N.J. 08540.

In a recent theoretical treatment of p-n junction heterostructure waveguide modulators we discussed in detail the behavior of such devices when the depletion layer width t (corresponding to the modulated region) is less than the guide width [1]. If we assume that the waveguide is composed of three constant-index layers, then the intensity of the mth mode is proportional to $\cos^2(b_m X - \alpha_m)$ where b_m is the spatial frequency of the mth mode and x is the distance from one waveguide wall. Since it can be shown that the phase term α_m decreases with increasing mode number [1] the intensity for the higher order modes is higher at $x = 0$. If the p-n junction is highly asymmetric and located at $x = 0$ then the depletion layer penetrates only into the guide region. Assuming that the field is uniform over t we can write the change in the effective refractive index for the mth mode Δn_m as [1]

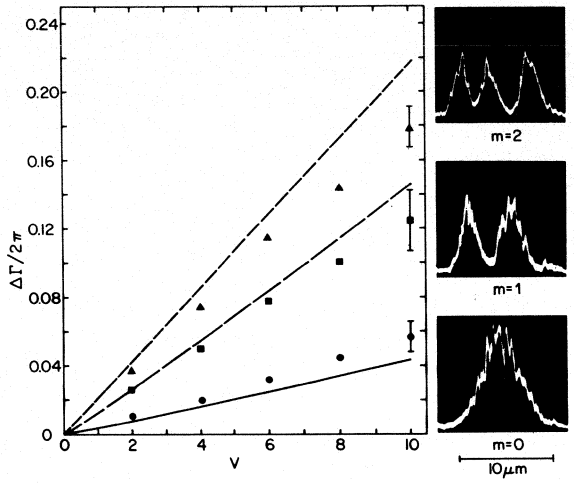

Fig. 1. Experimental points and theoretical curves for the modulation of the three lowest order modes. In order to eliminate strain effects we plot $\Delta\Gamma = \Gamma(V) - \Gamma(0)$. The photographs show the mode shapes. The scale is approximate.

$$\Delta n_m = \frac{\delta n}{b_m W} \left[b_m t + \sin b_m t \cos (b_m t - 2\alpha_m) \right] \tag{1}$$

where δn is the appropriate electrooptically induced index change and W is the effective guide width including the penetration into the cladding layers. The retardation Γ is then proportional to the difference between Δn_m for each TE, TM mode pair.

Note that for $b_m t \ll 1$, (1) becomes

$$\Delta n_m \approx \delta n \frac{t}{W} 2 \cos^2 \alpha_m \tag{2}$$

which clearly shows that the modulation is dependent upon the depletion layer width and the mode intensity at the waveguide wall. Thus, for very small t, higher order modes should be more strongly modulated.

In order to check the predictions of this simple model, we studied the performance of a number of (Ga,Al)P heterostructure modulators [2]. Laser light (6328 Å) polarized at 45° to the junction plane was focused on the input face of the guide using a 25X microscope objective. A high-power microscope was then used to project the image of the output face of the diode onto a vidicon which produced a picture on a monitor and an intensity profile on an oscilloscope. By carefully adjusting the input optics any one of the three lowest order modes could be generated in some single-heterostructure devices. The retardation was then measured by means of an Ehringhaus compensator and a photometric null detector. The averaged results for a number of measurements on one particular diode are shown as the points in Fig. 1. The error bars indicate the spread in the measurements which arise mainly from the difficulty in exciting pure modes by this technique. The accompanying photographs show the typical mode profiles obtained.

As a result of the difficulty in reproducing the mode profiles, consistent results could only be obtained on a few units. The mode-dependent behavior, however, was clearly seen on several devices so that the results are felt to be reasonably representative.

In order to apply (1) the exact layer width and refractive indices as well as the center-layer doping must be known. Since we lack detailed knowledge of these parameters we must develop a model on which to base our calculations. The model we use assumes a 7.5-μm GaP guiding layer ($n = 3.31$) doped n-type at about 10^{17} cm^{-3}. The lower waveguide wall is formed by the GaP–(Ga,Al)P heterojunction for which we estimate $n \approx 3.30$ on the basis of the expected Al concentration in the layer [2]. The upper waveguide boundary ($x = 0$) we take to be at the p-n junction. The diffused GaP p-layer is assumed to be 1.75 μm thick and with $n = 3.085$ and to be bounded on the upper side by air. (Because of the small index step and the proximity of the air–GaP interface, the thickness of the layer enters into the determination of b_m and α_m.)

Although the model appears to have several adjustable parameters, the choice was limited by requiring that the values be consistent with the measured layer thicknesses and the spatial frequencies of the modes. (No attempt was made to fit the mode shape *per se*.) The doping of the guiding n-region was directly measured by the capacitance–voltage method. The index step at the p-n junction was chosen to give the best match to the modulation data within the limits imposed in the preceding. The absolute magnitude $\Delta n = 0.0015$ lies considerably above the value predicted from a simple Drude model using the mid-10^{18}-cm^{-3} doping of the p-layer, but similar discrepancies have been found by other authors [3].

Note that, for 10^{17}-cm^{-3} doping, the maximum depletion layer thickness is about 0.6 μm at 10 V which is much smaller than the 7.5-μm guide width. Thus by (2), we would expect to see higher retardation for the higher order modes, which is clearly borne out in Fig. 1.

Since the junction is perpendicular to the [111] axis the appropriate values of δn needed for the application of (1) are

$$\delta n(\mathrm{TM}) \approx -2\,\delta n(\mathrm{TE}) = -n^3 r_{41} E/\sqrt{3} \tag{3}$$

where n is the refractive index (3.31 at 6328 Å) [4], r_{41} is the electrooptic constant (-0.98×10^{-10} cm/V) [4], and E is the average junction field. Using these values and assuming an abrupt, highly asymmetric junction together with (1) we obtain the continuous curves in Fig. 1. Considering the known limitations of the model [1], the agreement is excellent, which confirms the usefulness of (1) in predicting the behavior of such modulators on a semiquantitative basis.

ACKNOWLEDGMENT

The author wishes to acknowledge the help of H. Meier in the construction of the apparatus and of H. P. Kleinknecht and A. E. Widmer for providing the diodes.

REFERENCES

[1] D. P. Bortfeld, "Analysis of heterojunction optical waveguides with a modulated region smaller than the guide width," *IEEE J. Quantum Electron.*, vol. QE-10, pp. 551–556, July 1974.
[2] H. P. Kleinknecht and A. E. Widmer, "(Ga,Al)P optical waveguide modulators fabricated by liquid-phase epitaxy," *J. Appl. Phys.*, vol. 45, pp. 3453–3459, Aug. 1974.
[3] F. K. Reinhart, D. F. Nelson, and J. McKenna, "Electro-optic and waveguide properties of reverse-biased gallium phosphide p-n junctions," *Phys. Rev.*, vol. 177, pp. 1208–1221, Jan. 1969.
[4] D. H. Nelson and E. H. Nelson, "Electro-optic and piezoelectric coefficients and refractive index of gallium phosphide," *J. Appl. Phys.*, vol. 39, pp. 3337–3343, June 1969.

NaCl Surface Reaction in Chemical-Laser Devices

ALAN B. PETERSEN AND CURT WITTIG

Abstract—**Pronounced absorptions in the 8–17-μm region are observed on surfaces of NaCl that are used as Brewster windows in chemical lasers that derive their excitation from the CS_2/O_2 reaction. Surface reaction involves species that are formed during the chemical and photochemical processes that are active in the system. Implications regarding other reactive systems (using either chemical or electrical excitation) are also discussed.**

In this correspondence, we wish to communicate several observations regarding the reactivity of NaCl which is used as window material in pulsed chemical lasers. The implications of these observations are far-reaching and the principles involved may be applied to other materials and to a variety of situations in which these materials are used as an interface between the normal atmosphere and some active nonequilibrium gaseous system. There have been numerous investigations into the losses that are present in various materials (single and polycrystalline) that are suitable for devices that operate at infrared frequencies [1]–[3]. Most of this effort has been directed toward determining the intrinsic losses of these materials and preparing samples that are sufficiently free from impurity absorptions so that intrinsic losses dominate. One of the widespread uses of these materials is with high-power IR lasers, and in this application it is imperative that the material be free of even the smallest amount of absorption in order to avoid either serious damage to the component or undesirable thermally induced distortion of the laser beam.

On the other hand, the gaseous environment that exists in most high-power IR gas lasers is in a state of pronounced nonequilibrium with a variety of atomic, free radical, and metastable species present. Thus the inside surface of any material that acts as an interface (internal mirror, Brewster window, etc.) between the active laser medium and the outside world will be subjected to a rather harsh test of its inertness. Since it is difficult to physically remove the interface region to the extent that surface reaction is *entirely* suppressed, it is not obvious that a material with low intrinsic losses will be sufficiently chemically inert for use in situations where active species are present. In general, the reactions that take place at the surface of any candidate material deserve prime consideration in the evaluation of the material as a suitable candidate for use in infrared devices.

In our own work with infrared chemical lasers, we have observed that NaCl Brewster windows [4] that are used in pulsed chemical lasers are seriously affected after only short-term use. Details of the laser systems employed have been described elsewhere [5]. Briefly, mixtures containing CS_2 and O_2 as the chemically active species are photolyzed in the presence of a large enough excess of He to maintain approximately isothermal conditions ($\Delta T \leqslant 100$ K). In some experiments, CO_2 or N_2O is also present in the gas mix.

A most graphic display of the phenomenon is shown in Fig. 1. The spectrophotometer trace shows the presence of prominent absorptions in the 8–17-μm region of the IR. The transmission of the NaCl at visible wavelengths is almost unaffected and a casual observation of the NaCl shows no surface change at all. When the surface is viewed at nearly grazing incidence a bit of interference is observed indicating a surface layer of roughly 10–100-nm thickness. The general effect of absorption in the 8–17-μm range is quite repeatable. The details of the spectra change from one set of conditions to the next, but the effect is easily measured under nearly all experimental conditions [6]. In many cases, laser emission from CO_2 or N_2O was completely quenched by these absorptions, since strong broad absorptions often occurred near the characteristic laser frequencies of these molecules. In no instance were absorptions observed in the region 2.5–8.0 μm, where many powerful molecular lasers operate.

The surface changes that are observed are due to the interaction of the surface with the active species that are generated, either directly or indirectly, by the flash photolysis. There is no detectable surface reaction when the gases are stored in the cell without photolyzing the mixture or when the cell is evacuated and the photolysis flash is fired repeatedly. All experiments are carried out under approximately isothermal conditions since the concentration of buffer gas far exceeds the concentration of the reactive components. The transient ac-

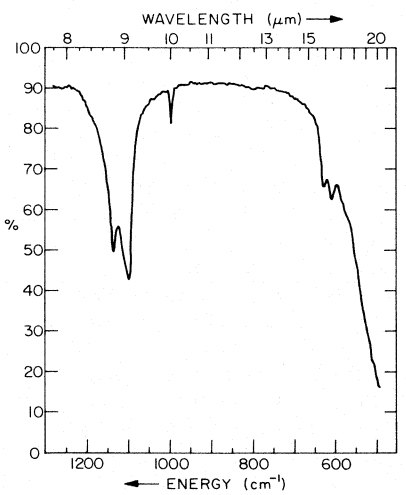

Fig. 1. IR spectrophotometer trace of a NaCl Brewster window taken from a pulsed chemical laser. The vertical scale represents percent transmission. The gas mix contained several torr of CS_2 and several tens of torr of O_2 + He. A photolysis pulse of nominally 10^3 J is used to initiate the chemical reaction. There are no detectable absorptions in the region: 2.5 μm $\leqslant \lambda \leqslant$ 8 μm.

Manuscript received October 1, 1974. This work was supported by the Joint Services Electronics Program, monitored by the Air Force Office of Scientific Research, under Grant Contract F44620-71-C-0067, and by the Research Corporation.

The authors are with the Department of Electrical Engineering, University of Southern California, University Park, Los Angeles, Calif. 90007.

tive species generated in these experiments are numerous and include O, S, SO, CS, S_2O, and many others. In addition, some of these species may be electronically and/or vibrationally excited. When one of the NaCl Brewster windows is replaced with BaF_2, we measure no change in the IR transmission of the BaF_2 window, although the NaCl window becomes badly contaminated in about two weeks time. Thus the surface change cannot be attributed to merely a deposit. No spontaneous cleanup is observed when samples are stored for several months in a dry atmosphere. If the absorbing species were physically adsorbed, some spontaneous cleanup should occur. We have made no attempt to heat the NaCl in vacuo to see if this restores its original transmission characteristics.

The observed spectra are in general rather complex and defy identification on the basis of the preliminary experiments that we have done to date. Various oxygen-containing cation impurities (CO_3, ClO_3, SO_4, etc.) are known to exist in alkali halide crystals and there are many reaction schemes that could satisfactorily account for the complex spectra that we have observed. Spectra obtained from samples that are doped even with only one impurity (e.g., CO_3) are often rather complex and the number, positions, and strengths of the characteristic absorptions change with concentration and other parameters [1]. The spectra shown in Fig. 1 are probably due to an anion of the form S_nO_m with SO_4 being the most likely suspect [7]. The possible superposition of absorptions due to several species and the complex conditions under which the surface reactions took place prevent us from making a positive identification of the absorbing species. Detailed kinetic experiments are currently underway in our laboratory aimed at sorting out some of the fundamental processes active in these systems. Many impurities such as carbon, alkaline earths, etc., that would not absorb radiation strongly of their own accord may be converted to cations via the introduction of atomic oxygen into the system (e.g., $C \rightarrow CO_3$). The large amount of atomic oxygen that is present in the chemical lasers under study in our laboratory is a prime suspect in this oxidation process. The large penetration depth manifest in our experiments is due either to the diffusion of atomic species into the bulk or the diffusion into the bulk of cations such as SO_4^{-2} which are formed initially at the surface. In two weeks time, the diffusion depth for SO_4^{-2} initially on the surface is 13 nm [9]. This rapid diffusion means that species introduced at the surface will quickly dissolve into the bulk leaving the surface free for further reaction.

Finally, we point out that this phenomenon is a general one and may be active and deserving of consideration in a variety of devices that are excited chemically and/or electrically. In the $CO^{\dagger}/CO_2$ [5] and $CO^{\dagger}/N_2O$ [8] chemical laser systems, absorptions are introduced that render NaCl useless as an interface material in these devices and the other alkali halides are expected to follow suit. Other IR materials and reactive systems deserve consideration in turn and experiments are currently underway toward this end in our laboratory.

ACKNOWLEDGMENT

The authors wish to thank Prof. D. A. Dows for the use of an infrared spectrophotometer during the course of this work.

REFERENCES

[1] C. A. Pitha and B. Bendow, in *Proc. 3rd Conf. High Power Infrared Laser Window Materials*, vol. 1, *Optical Properties* (1974), and references cited therein.
[2] T. F. Deutsch, "Absorption coefficient of infrared window materials," *J. Phys. Chem. Solids*, vol. 34, pp. 2091–2104, 1973.
[3] C. J. Duthler, "Infrared absorption in 10.6-μm-laser-window materials due to molecular-ion impurities," *J. Appl. Phys.*, vol. 45, pp. 2668–2671, 1974.
[4] The NaCl was supplied by the Harshaw Chemical Co.
[5] A. B. Petersen and C. Wittig, "A chemically pumped CO_2 laser from the CS_2/O_2 reaction," *Chem. Phys. Lett.*, vol. 27, pp. 442–444, 1974.
[6] Absorptions in this region have also been observed in a CW CO chemical laser: W. Q. Jeffers, private communication.
[7] a) F. A. Miller and C. H. Wilkins, "Infrared spectra and characteristic frequencies of inorganic ions," *Anal. Chem.*, vol. 24, pp. 1253–1298, 1952.
b) S. D. Ross, "Forbidden transitions in the I.R. spectra of some tetrahedral anions–II. Sulphates," *Spectrochim. Acta*, vol. 18, pp. 1575–1578, 1962.
c) R. A. Nyquist and R. O. Kagel, *Infrared Spectra of Inorganic Compounds.* New York: Academic, 1971. (The Sadtler Standard Spectra, Sadtler Res. Labs., Philadelphia, Pa.)
[8] A. B. Petersen and C. Wittig, "Chemically pumped N_2O laser," *Chem. Phys. Lett.*, to be published.
[9] M. Beniere, F. Beniere, and M. Chemla, "Diffusion and solubility of SO_4^{2-} in NaCl and KCl single crystals," *Solid State Commun.*, vol. 13, pp. 1339–1343, 1973.

Hollow-Cathode-Type CW White Light Laser

KAN-ICHI FUJII, TSUTOMU TAKAHASHI, AND YOSHIHIRO ASAMI

***Abstract*—A stable CW white laser light consisting of red (6360 Å, 6355 Å), green (5378 Å, 5338 Å), and blue (4416 Å) line spectra emitted from Cd ions has been obtained with an improved flute-type hollow-cathode He-Cd$^+$ laser tube and a broad-band optical cavity. The typical output-power level was about 10 mW, discharge conditions being 250 V and 0.6 A.**

Many visible as well as infrared laser line spectra have been obtained with the hollow-cathode-type He-Cd$^+$ laser tubes [1]–[4]. The authors have been trying to develop a single-gun CW white light laser due to the simultaneous oscillations of the three-color laser lines under fixed discharge conditions [5] because they have a special interest in visible laser lines for many engineering applications, such as color holography and color display [6]. Many studies on the improvements of the operating conditions as well as the tube structure have been made, and the ways to set the conditions for simultaneous oscillations have been clarified. A strong white laser light was successfully obtained with a pure dc power supply and two broad-band mirrors (made by Lambda Airton Company in the U.S.) which have a bandwidth of 2000 Å, a radius of 1 m, and a reflectivity of almost 100 percent.

A schematic diagram of the hollow-cathode-type He-Cd$^+$ laser tube used in our experiments is shown in Fig. 1. It is the characteristic of this laser tube to utilize the cathode region (consisting of a cathode dark space and a negative glow) of mixed He-Cd gases in the form of a hollow-cathode discharge. The hollow cathode was 4 mm in diameter and 80 cm in length, and was a perforated copper pipe covered with Pyrex glass. A thermocouple was made in contact with the hollow cathode to measure the cathode temperature. The partial pressure of the Cd vapor was estimated by the cathode temperature. A Cd metal was placed inside the cathode pipe. Ten anodes, made of tungsten rods 2 mm in diameter, were mounted with the intervals of 80 mm above each hole. The

Manuscript received October 22, 1974.
The authors are with the Department of Electrical Engineering, Faculty of Technology, Seikei University, Tokyo, Japan.

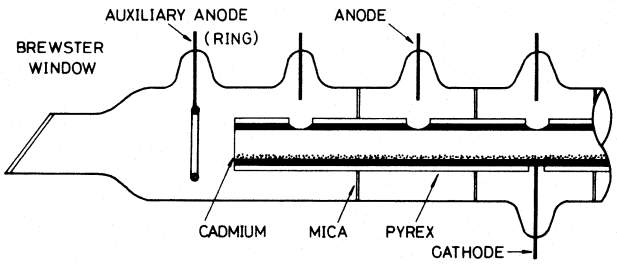

Fig. 1. Schematic diagram of the flute-type hollow-cathode laser tube.

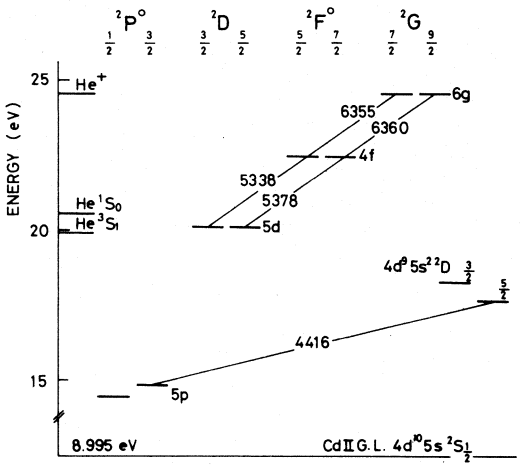

Fig. 2. Energy levels of Cd ion and visible laser transitions (wavelength in Å) which were obtained with the flute-type hollow-cathode He-Cd$^+$ laser tube.

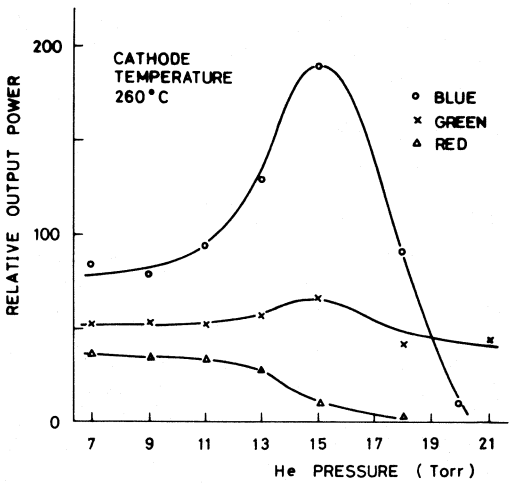

Fig. 3. Dependence of the laser output power on the He pressure.

distance of the anode from the cathode surface was 8 mm. Each anode was connected to the regulated dc power supply through a variable resistance of 1 kΩ. Mica spacers were inserted between the outer surface of the cathode and the inner surface of the glass envelope. A stable dc discharge was obtained at such a low pressure of He as 7 torr with these spacers. A liquid-nitrogen trap was set between the laser tube and the glass cock to eliminate the effect of impurities.

Fig. 2 shows the energy levels of a Cd ion and the laser transitions in the visible range which were obtained with our hollow-cathode-type He-Cd$^+$ laser tube. The red and the green laser line spectra have not been obtained with positive column-type He-Cd$^+$ laser tubes.

Fig. 3 shows the dependence of the laser output power on the He pressure for each of the three colors at a cathode temperature of 260°C. White laser light was obtained in the range of He pressure between 7 and 13 torr. At higher pressures above 13 torr it was difficult to obtain a balanced white laser light since the output power of red laser lines became weaker, while that of the blue laser line became much stronger. At lower pressures below 7 torr the discharge became unstable.

Fig. 4 shows the laser output power as a function of the

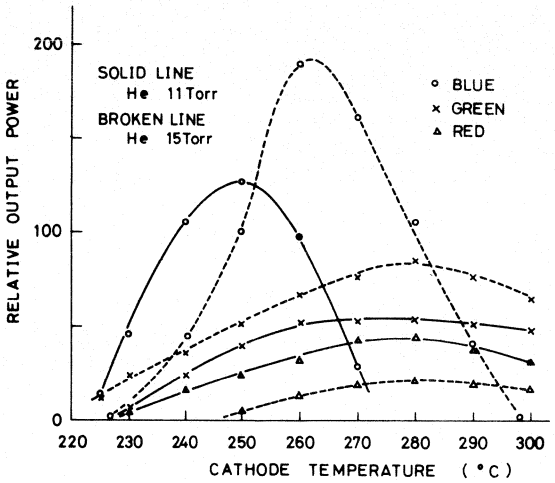

Fig. 4. Laser output power as a function of the cathode temperature (partial pressure of Cd vapor).

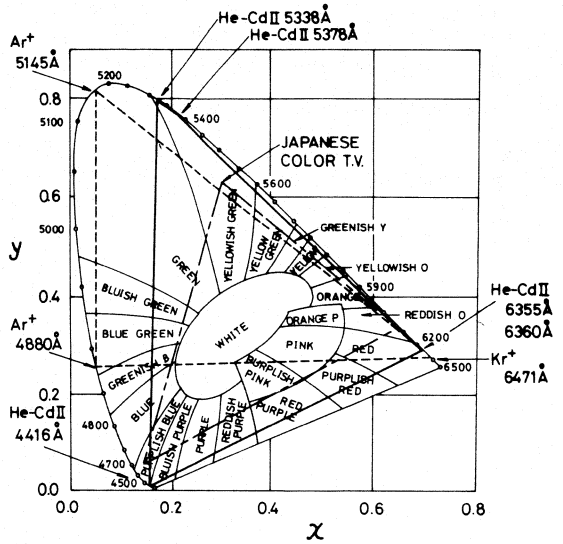

Fig. 5. CIE chromaticity diagram showing reproducing characteristics of He-Cd$^+$ laser (solid line), Ar-Kr$^+$ laser (broken line), and Japanese color TV (chain line).

cathode temperature (partial pressure of Cd vapor) at two different He pressures, 11 and 15 torr. A white laser light was obtained between 230 and 270°C at 11 torr (solid line), and between 250 and 290°C at 15 torr (broken line). The cathode temperature, which was adequate for an oscillation of the white laser light, slightly shifted toward higher regions with increasing He pressures. The laser outputs did not depend on the discharge currents since the laser tube operated on a constant current at steady-state conditions (the constant current value was about 0.6 A) [5].

Due to the characteristics of the cathode region, the hollow-cathode-type He-Cd$^+$ laser could result in three-color outputs with a single gun. In our experiments a flute-type He-Cd$^+$ laser tube was improved so as to operate at such a low pressure of He as to minimize the difference in laser outputs of the three colors.

Using the improved laser tube and a broad-band optical cavity, a pure and well-balanced CW white laser light was obtained. To show how close the dominant wavelengths of our He-Cd$^+$ laser are, the International Commission of Illumination (CIE) chromaticity diagram was drawn as in Fig. 5. It is clear from Fig. 5 that the He-Cd$^+$ laser has excellent characteristics in reproducing natural colors. In comparison, characteristics of the Ar-Kr$^+$ laser (broken line) and Japanese color TV (chain line) were also shown in Fig. 5. As may be seen, the characteristics of the He-Cd$^+$ laser are better than those of the Ar-Kr$^+$ laser and the color TV.

Since heavy atoms such as Cd are utilized, the Doppler width is narrower and therefore the axial mode numbers are fewer than other rare gas lasers [6]. Moreover, the angle of the polarization of the three colors was made coincident since a Brewster window having an almost constant refractive index in the range of the visible wavelength was used. The reason why the red and the green laser lines can be obtained only with the hollow-cathode-type He-Cd$^+$ laser tubes was reported a few years ago [5]. Other problems on the laser tube such as the discharge characteristic (constant-current characteristic [5]), the design principle [5], and the confining mechanism of the negative glow into the hollow cathode were also clarified [7].

In conclusion, we demonstrated that a stable CW single-gun

$He\text{-}Cd^+$ white light laser of the hollow-cathode type has excellent reproducing characteristics of the natural colors, as the contained wavelengths position properly in the chromaticity diagram. Stable CW oscillations are possible with low terminal voltages since the discharge may be sustained by the impressed voltage nearly equal to the cathode fall. These characteristics are considered to be very useful for practical applications.

ACKNOWLEDGMENT

The authors wish to thank Prof. Y. Sugawara of Seikei University and Prof. S. Hattori of Nagoya University for their useful discussions and advice. The authors also wish to thank Prof. I. Emori of Seikei University for his advice.

REFERENCES

[1] Y. Asami, Y. Sugawara, Y. Tokiwa, and T. Iijima, "Laser oscillation due to hollow cathode discharge" (in Japanese), Preprints of the Annu. Meeting Inst. Elec. Commun. Eng. Jap., Quantum Electron., no. 600, 1969.
[2] Y. Sugawara, Y. Tokiwa, and T. Iijima, "New CW laser oscillation in He-Cd and He-Zn hollow cathode lasers," *Japan. J. Appl. Phys.*, vol. 9, p. 1537, 1970.
[3] W. K. Schuebel, "New cw Cd vapor laser transitions in a hollow cathode structure," *Appl. Phys. Lett.*, vol. 16, pp. 470–472, 1970.
[4] É. K. Karabut, V. S. Mikhalevskii, V. F. Papakin, and M. F. Sém, "Continuous generation of coherent radiation in a discharge in Zn and Cd vapors," *Sov. Phys.—Tech. Phys.*, vol. 14, pp. 1447–1448, 1970.
[5] K. Fujii, "Characteristics of negative glow type He-CdII laser tube and fundamental studies on its designing" (in Japanese), *Trans. Inst. Elec. Eng. Jap.*, vol. 93-C, pp. 1–10, 1973.
[6] Y. Asami, K. Fujii, and T. Takahashi, "Hollow-cathode type He-Cd laser as a source of white light" (in Japanese), *Trans. Inst. Telev. Eng. Jap.*, vol. 27, pp. 617–623, 1973.
[7] K. Fujii, "Confining phenomena of negative glow observed in hollow cathode laser tube," *Japan. J. Appl. Phys.*, vol. 13, pp. 571–572, 1974.

Sixteen New IR Laser Dyes

J. PIERCE WEBB, F. GLENN WEBSTER, AND BERTRAND E. PLOURDE

Abstract—**Sixteen new IR laser dyes are reported. All lased successfully under excitation from a simple linear flashlamp of about 700-ns rise time. Untuned lasing wavelengths ranged from 810 to 972 nm. Laser output pulse energies from the four best of these dyes were 5–15 times greater than from diethylthiatricarbocyanine iodide (DTTC), with peak output of about 50 mJ obtained from 128-J excitation. Solvent effects with four selected laser dyes are also discussed.**

IR dye laser action under simple linear flashlamp excitation was obtained from 16 new laser dyes with untuned laser wavelengths spanning 810–972 nm. Whereas flashlamp-pumped dye lasers operating at wavelengths of up to 950 nm have been reported in the literature [1]–[4], these previous IR dye lasers have all been excited by ultrafast coaxial flashlamps with rise times of 80–150 ns. Our new dyes were all pumped with a flashlamp of ~700-ns rise time. Laser pulse durations (FWHM) from these new dyes ranged up to 800 ns. Output pulse energies from the four best of these new dyes were 5–15 times greater than from diethylthiatricarbocyanine iodide (DTTC). To our knowledge none of these 16 new dyes has been used in previous dye laser work.

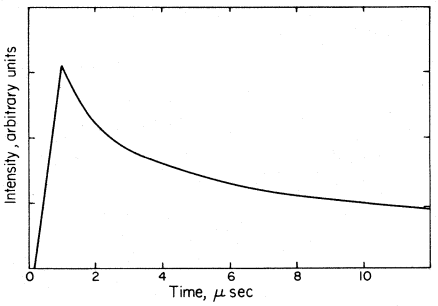

Fig. 1. Flashlamp excitation pulse shape. The curve is a drawing traced from an oscilloscope trace of the near-IR portion of our flashlamp output, measured by a fast silicon detector through a visible-blocking, IR-pass filter. Rise time of the infrared pumping pulse was approximately 700 ns.

Our source of excitation was a linear, air discharge flashlamp with a 3-mm bore and 15-cm arc length, located 1 mm from a 3-mm-bore dye cell of comparable length. The dye cell and flashlamp were enclosed in a 1.5-cm-diameter Plexiglas cylinder coated on the inside with high-reflectance white paint.

Prior to laser operation the flashlamp output was measured with a fast, small-area p-i-n photodiode after being filtered with an IR-passing filter that blocked wavelengths shorter than 700 nm. Rise time of the near IR pumping pulse from our air discharge flashlamp was about 700 ns, and the pulse-width was about 3.5 μs (FWHM), as shown in Fig. 1. Pumping bands of 5 of the best IR dyes are shown in Figs. 2–6.

We used a 36-cm-long, plane parallel resonant cavity with a 100-percent reflecting mirror and a 37-percent reflecting mirror both designed for uniform reflectance from 850–980 nm. Below 850 nm, the reflectance of the highly reflecting mirror dropped from 98-percent at 850 nm to 15-percent at 820 nm! Thus laser output from short wavelength dyes was discriminated against.

A 1-μF 20-kV capacitor is used for energy storage. The laser operates without any externally triggered electrical switch in the discharge circuit; it is actuated by evacuating the flashlamp to its breakdown pressure while full voltage is maintained across the lamp. An overdamped discharge current is observed with the air lamp in the circuit.

The laser output characteristics from 16 new near-IR dyes are shown in Table I. In these tests the dyes were dissolved to 10^{-4} M in dimethyl sulfoxide (DMSO), and the input energy to the lamp was 128 J. Recalling the low reflectance of the nominally high-reflectivity mirror at wavelengths shorter than 850 nm, the first four short wavelength dyes tagged with an (a) are certainly substantially better than this intercomparison indicates.

A 1.5-m grating spectrograph was used to record the laser wavelengths on KODAK High Speed Infrared Film 2481 (ESTAR Base). The absence of the two lasing wavelengths that are not reported results from our spectrograph having a cutoff at ~835 nm and from our not being able to borrow the instrument we used to measure IR-135 for IR-145 and 136. Their lasing wavelengths are certainly shorter than 835 nm, and we suspect based on dye structure that IR-145 is a little shorter than 810 nm and IR-136 a little longer than 810 nm.

Laser power was measured with a small-area p-i-n photodiode mounted 15 cm behind a 5-cm-diameter opal-glass diffuser. The fraction of light incident on the diffuser that reached the photodiode and the absolute spectral sensitivity of the

Manuscript received July 19, 1974; revised November 22, 1974. This work was supported in part by the Night Vision Laboratory, the U.S. Army Electronics Command, Ft. Belvoir, Va., under Contracts DAAK02-72-C0012 and DAAK02-73-C0185.

J. P. Webb and F. G. Webster are with the Research Laboratories, Eastman Kodak Company, Rochester, N.Y. 14650.

B. E. Plourde was with the Kodak Apparatus Division Research and Engineering, Eastman Kodak Company, Rochester, N.Y. 14650. He is now with the Avco Everett Research Laboratory, Inc., Everett, Mass. 02149.

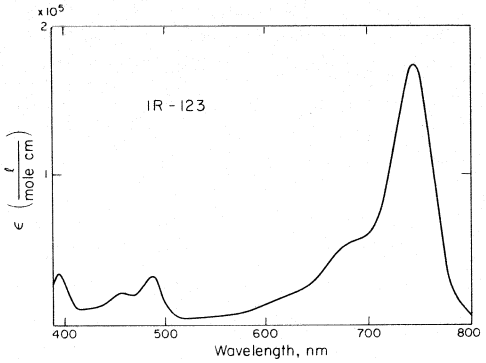

Fig. 2. Decadic molar extinction coefficient ϵ of IR-123.

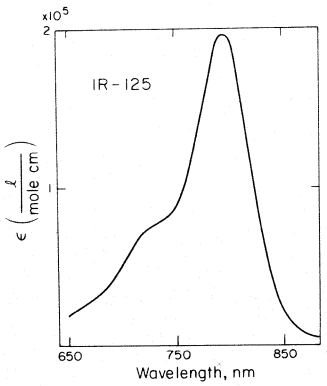

Fig. 3. Decadic molar extinction coefficient ϵ of IR-125.

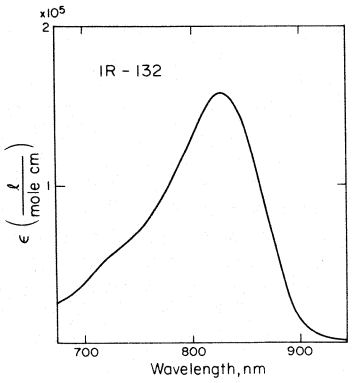

Fig. 4. Decadic molar extinction coefficient ϵ of IR-132.

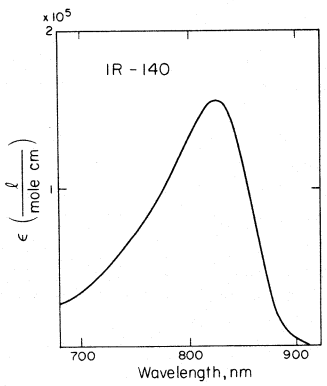

Fig. 5. Decadic molar extinction coefficient ϵ of IR-140.

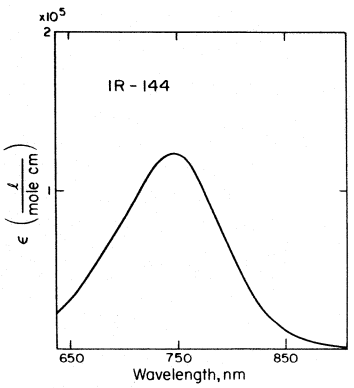

Fig. 6. Decadic molar extinction coefficient ϵ of IR-144.

TABLE I
FLASHLAMP-PUMPED INFRARED LASER DYES
(SEE APPENDIX I FOR DYE STRUCTURES)

Dye	Lasing Wavelength (nm)	Pulse Width (FWHM), τ 1/2 (μsec)	Peak Laser Power, P (kW)	P x τ 1/2 (mJ)
IR-135	810	0.32	6.5(a)	2.1(a)
145	UK(b)	0.55	7.3(a)	4.0(a)
136	UK(b)	0.25	6.0(a)	1.5(a)
123	835	0.33	13.3(a)	4.4(a)
109	875	0.50	17.0	8.6
139	883	0.56	17.0	9.3
116	885	0.30	6.5	2.0
134	888	0.26	6.7	1.7
144	880/945(c)	0.78	28/42(c)	22/33(c)
125	940	0.46	34.0	16.0
107	940	0.18	5.0	0.9
141	946	0.31	12.0	3.7
140	950	0.84	63.0	53.0
137	950	0.70	42.0	30.0
132	972	0.32	20.0	6.4
143	972	0.44	18.0	8.1
DTTC	872	0.38	9.4	3.6

(a) Short-wavelength laser dye: mirrors not optimized for λ<850 nm, so this dye is discriminated against.

(b) UK: unknown, less than the 835-nm cutoff of our spectrograph.

(c) Uncertainty in peak power and energy output is caused by uncertainty in lasing wavelength. First output corresponds to detector sensitivity at 880 nm; second output is for 940-nm sensitivity.

TABLE II
LASER OUTPUT IN AIR-EQUILIBRATED SOLVENTS
NORMALIZED PEAK OUTPUT POWER

Solvent	IR-123	IR-125	IR-132	IR-144
Pyridine	NT	ND	NT	4
Acetone	ND@10^{-4} M NT@4×10^{-5} M	ND	ND	ND
Methanol	NT	NT	NT	NT
Deuterated methanol	-	-	-	29
Ethanol	NT	NT	ND	NT
2-Methoxyethanol	NT	NT	NT	NT
Propanol	-	ND	ND	NT
Isopropanol	ND	ND	ND	ND
2,6-Lutidine	ND	ND	ND	ND
1,1,1-Trichloroethane	ND	ND	ND	ND
Dichloromethane	NT	ND	7	51
Acetonitrile	NT	ND	ND	ND
Benzonitrile	NT	ND	44	ND
N,N-Dimethylacetamide	NT	16	89	51
N,N-Dipropylacetamide	ND@10^{-4} M 32@4×10^{-5} M	ND	ND	-
N,N-Dimethylformamide	11	NT	61	29
1-Methyl-2-pyrrolidinone	6	11	ND	50
Propylene oxide	ND	ND	ND	ND
Dimethyl sulfoxide	100	100	100	100
Dipropyl sulfoxide	26	ND	ND	-
Tetramethylene sulfoxide	57	114	105	26
Hexamethyl phosphoric triamide	ND	ND	ND	ND
N-Formylpiperidine	37	-	-	-
1-Acetylpiperidine	11	-	-	-

NOTE: Outputs between dyes cannot be intercompared; measured output was arbitrarily normalized to the DMSO value.

- Not tried.

ND - Did not dissolve to 10^{-4} M

NT - Did not trigger scope at 10X sensitivity of DMSO recording. Thus, either did not lase or lased very poorly.

photodiode were measured separately. Our absolute power measurements should be correct to ±15 percent [5].

DTTC, a relatively well-known dye, is included in the table for comparison. One notes that the output pulse energy from IR-140 is about fifteen times greater than from DTTC, while IR-125, IR-137, and IR-144 are between five and ten times more energetic than DTTC. Pulse energies range up to ~50 mJ from IR-140.

The absolute laser pulse energies reported are characteristic of the laser configuration described in the preceding. We also tested dyes IR-125 and 144 in different laser configurations. In an Integrated Cell Resonant Cavity (ICRC) configuration, a cell with the same 37-percent R and 100-percent R mirrors coated directly on the outside of the cell windows was used with the air discharge lamp, and with a new laser head employing sealed linear flashlamps containing a variety of fill gases. Laser output from dyes IR-123, 125, 132, and 144 was also measured with a variety of output mirror reflectivities. Observations on results of these configuration changes are collected in Appendix II. Generally speaking, configuration-dependent results were completely consistent with well-understood principles of dye laser design. That is, results quoted in Tables I and II that appear to be configuration dependent can be generalized to other flashlamp-pumped laser systems so long as similarly fast rise time flashlamps are employed.

No tuning experiments employing a dispersive element in the cavity were performed. An attempt was made to optimize the dye concentration with four representative dyes: IR-123, 125, 132, and 144 [6]; measurements of lasing wavelength as a function of dye concentration provide some concentration tuning data. With mirrors that were spectrally flat from 850 nm to 980 nm, IR-125 lased from 924 nm (3×10^{-5} M in DMSO) to 952 nm (10^{-3} M in DMSO), IR-132 lased from 957 nm (3×10^{-5} M in DMSO) to 972 nm (10^{-4} M in DMSO), and IR-144 lased from 862 nm (10^{-5} M in DMSO) to 955 nm (10^{-3} M in DMSO). Untuned IR-144 solutions at 10^{-4} M in DMSO, tetrahydrothiophene oxide, 1-methyl-2-pyrrolidinone, and dimethylformamide all lased at 882 ± 8 nm and 950 ± 10 nm; frequently, both lasing wavelengths appeared during the same pulse. In this experimental configuration, incidentally, the optimum concentration was typically $1\text{–}2 \times 10^{-4}$ M in DMSO for these four dyes.

Our data show that no self-tuned laser output occurred between about 890 nm and 920 nm with any of the dyes and solvents used in our untuned laser configuration. We tentatively attribute this to a small solvent absorption peak from DMSO and other common solvents that occurs in this spectral region. DMSO and dichloromethane are hygroscopic solvents, of course, and the absorption observed in our spectro grade solvents could have resulted from water absorbed from the air rather than being intrinsic to the solvents. Tuning into this region with a dispersive tuning element in the cavity might be facilitated by careful dehydration of the solvent or by dye cells shorter than our 15-cm-long cuvettes.

Solvent effects are commonly important with dye lasers, and this is particularly true with IR laser dyes. We have investigated a variety of solvents for use with IR laser dyes. Lasability and laser output from four representative laser dyes dissolved in a variety of air-equilibrated solvents are listed in Table II.

The selection of solvents for the laser tests was based in part on a preliminary measurement of relative IR fluorescence yields from dye solutions excited by the air discharge flashlamp. These measurements were made on IR-107, 109, 116, 123, 125, 132, 134, and DTTC plus 25 other nonlasing IR dyes [7]. Although results varied somewhat from dye to dye, much higher fluorescence yields were consistently observed from highly polar solvents without OH groups such as dimethylformamide (DMF) and DMSO than from lower alcohols. Relative fluorescence yields from laser dyes dissolved in DMSO exceeded those from methanol solutions by 50–100 percent.

Hirth, Faure, and Lougnot [4] have shown that concentration of dissolved oxygen and the rate of collision between dye molecule and dissolved oxygen are important parameters influencing IR dye laser action in a system using fast (~100-ns rise time) excitation. Hirth *et al.* attribute their results to oxygen-enhanced intersystem crossing and triplet-state buildup, which would be more pronounced in methanol than in DMSO.

Our experiments all employed air-equilibrated solvents, and thus shed no light on the importance of dissolved oxygen in our long time (800-ns) domain. Our experiments do show that more is involved in these "solvent effects" in this long time domain than simple dissolved-oxygen effects. The most direct evidence for oxygen-independent effects in the host environment (solvent) came from substituting deuterated solvents for normal protonated solvents. The relative fluorescence yield of DTTC increased from 0.010 unit in CH_3OH to 0.020 unit in CD_3OD and from 0.019 in $(CH_3)_2SO$ to 0.023 in $(CD_3)_2SO$; the relative fluorescence of IR-132

increased from 4.9×10^{-3} in $(CH_3)_2SO$ to 8.2×10^{-3} unit in $(CD_3)_2SO$. (These relative fluorescence yields represent the peak fluorescence occurring at the flashlamp peak, not time-integrated fluorescence.) IR-144 did not lase at 10^{-4} M in CH_3OH, but did lase strongly at 10^{-4} M in CD_3OD in our flashlamp-pumped laser. These dramatic changes cannot be explained on the basis of oxygen effects, since oxygen solubility and solvent viscosity should be substantially independent of protonation versus deuteration of solvents.

These preliminary experiments with deuterated solvents were undertaken because we observed that the 800–950-nm (12 500 to 10 525 cm^{-1}) fluorescence region overlapped the third harmonic of the O–H stretch band and the fourth harmonic of the C–H stretch band. We speculated that this overlap might enhance nonradiative relaxation of excited-state dye molecules to the ground state. Since the deuteron is twice as heavy as the proton, the fundamental deuteron vibration frequencies are decreased by $\sim\sqrt{2}$, thus reducing the probability of resonant energy transfer from dye to solvent. At the very least, deuterated solvents provide alternative host solvents for IR laser dyes. These alternative solvents can be considered for IR laser dyes if the more common, highly polar, protonated solvents such as DMSO prove unsatisfactory for some reason, such as the small absorption peak around 900 nm, too high viscosity, etc.

In conclusion, we report 16 new IR laser dyes, all of which were successfully pumped with a simple linear flashlamp of 700-ns rise time. Untuned lasing wavelengths ranged from 810 nm to 972 nm. The four best of these dyes were from 5 to 15 times more energetic than DTTC.

Appendix I
Structures of New, Flashlamp-Pumped Infrared Dyes

IR-135

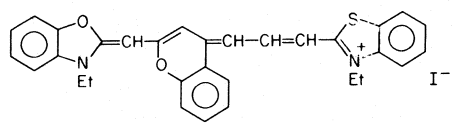

4-[3-(3-Ethyl-2-benzothiazolinylidene)propenyl]-2-[(3-ethyl-2-benzoxazolinylidene)methyl]-5,6-benzopyrylium iodide

IR-123

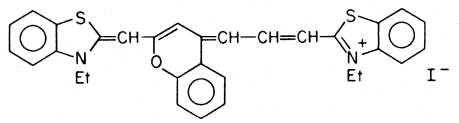

2-[3-(3-Ethyl-2-benzothiazolinylidene)methyl]-4-[3-(3-ethyl-2-benzothiazolinylidene)propenyl]-5,6-benzopyrylium iodide

IR-107

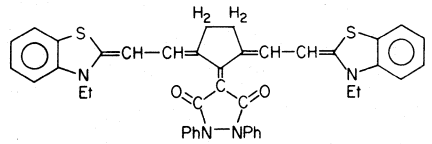

4-{2,5-Di[(3-ethyl-2-benzothiazolinylidene)ethylidene]cyclopentylidene}-1,2-diphenyl-3,5-pyrazolidinedione

IR-116

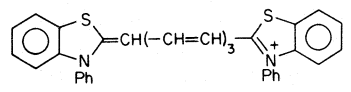

3,3'-Diphenylthiatricarbocyanine iodide

IR-136

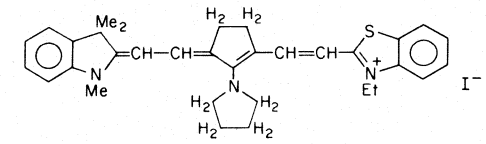

3'-Ethyl-10,12-ethylene-1,3,3-trimethyl-11-(1-pyrrolidinyl)indothiatricarbocyanine iodide

IR-137

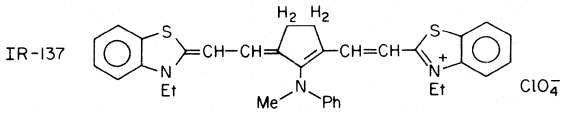

3,3'-Diethyl-10,12-ethylene-11-(N-methylanilino)-thiatricarbocyanine perchlorate

IR-140

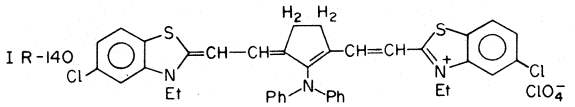

5,5'-Dichloro-11-diphenylamino-3,3'-diethyl-10,12-ethylenethiatricarbocyanine perchlorate

IR-134

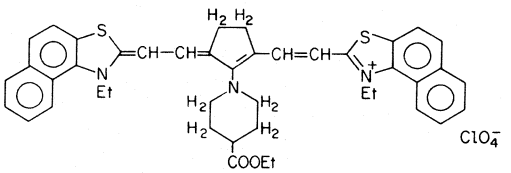

11-(4-Ethoxycarbonylpiperidino)-3,3'-diethyl-10,12-ethylene-4,5;4',5'-dibenzothiatricarbocyanine perchlorate

IR-143

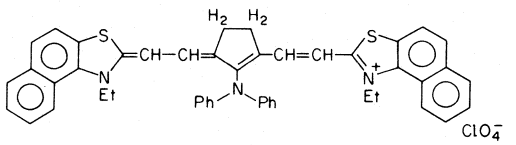

11-Diphenylamino-3,3'-diethyl-10,12-ethylene-4,5;4',5'-dibenzothiatricarbocyanine perchlorate

IR-144

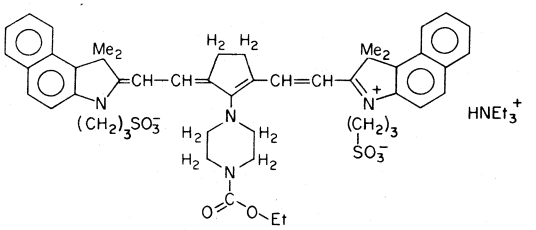

Anhydro-11-(4-ethoxycarbonyl-1-piperazinyl)-10,12-ethylene-3,3,3',3'-tetramethyl-1,1'-di(3-sulfopropyl)-4,5;4',5'-dibenzoindotricarbocyanine hydroxide, triethylammonium salt

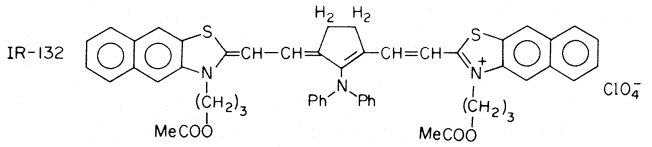

3, 3'-Di(3-acetoxypropyl)-11-diphenylamino-10, 12-ethylene-5, 6; 5', 6'-dibenzothiatricarbocyanine perchlorate

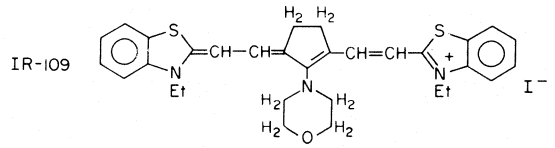

3, 3'-Diethyl-10, 12-ethylene-11-morpholinothiatricarbocyanine iodide

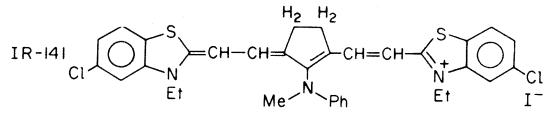

5, 5'-Dichloro-3, 3'-diethyl-10, 12-ethylene-11-(N-methylanilino)thiatricarbocyanine iodide

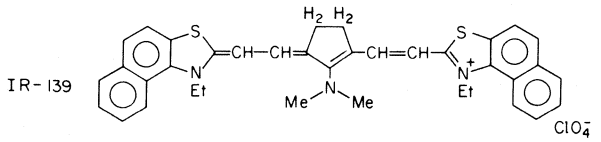

11-Dimethylamino-3, 3'-diethyl-10, 12-ethylene-4, 5; 4', 5'-dibenzothiatricarbocyanine perchlorate

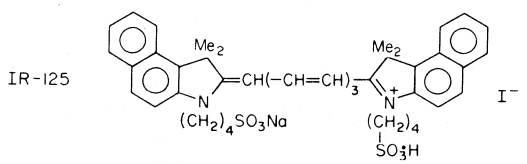

3, 3, 3', 3'-Tetramethyl-1, 1'-di(4-sulfobutyl)-4, 5; 4', 5'-dibenzoindotricarbocyanine iodide, monosodium salt

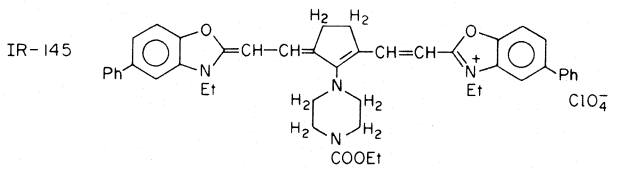

11-(4-Ethoxycarbonyl-1-piperazinyl)-3, 3'-diethyl-10, 12-ethylene-5, 5'-diphenyloxatricarbocyanine perchlorate

Appendix II
Different Laser Configurations

While all of the data reported in this paper were taken with the specific laser configuration (air discharge lamp, 37-percent R output mirror, etc.) described previously, experiments with several of these dyes were performed with different configuration lasers. Some general observations about IR laser dye performance under these different conditions are collected here in Appendix II.

Output Mirror Reflectivity

Good laser dyes IR-123, 125, 132, and 144 were tested in the air discharge lamp laser configuration with 93-percent R and 76-percent R output mirrors in addition to the 37-percent R mirror [6]. At 128-J discharge energy, the 37-percent R output mirror configuration yielded between 3X and 4X higher peak power outputs than the 76-percent R output mirror, and the 76-percent R output mirror yielded more than twice the output power of the 93-percent R output mirror for all four dyes.

ICRC

The Integrated Cell Resonant Cavity plus air discharge flashlamp configuration produced ~30-percent more energetic laser pulses with IR-125 and 144 than the separate cell and mirror configuration.

Flashlamp Pumping

A more standard laser head using interchangeable capacitors, a triggered spark gap, and interchangeable, sealed flashlamps containing a variety of fill gases was constructed and evaluated with dyes IR-125 and 144 [5]. These lamps were of the 3D6 configuration (3-mm bore by 6-in arc length) from ILC, and were filled with argon (20, 50, 150, and 350 torr), krypton (150 torr), xenon (20 and 150 torr), neon (20 torr), and nitrogen (20 torr). Capacitors of 0.3 μF, 0.5 μF, 1.0 μF, and 2.0 μF were coupled to the lamps through a spark gap and short length of coaxial cable. Compared to the air discharge lamp laser, the sealed lamp head had longer leads and a somewhat slower rise time . . . at least for capacitors larger than 0.3 μF. Also optical coupling between the sealed lamps and dye cell was poorer than with the air discharge lamp, because the enlarged ballast chambers on the 3D6 lamps forced a larger separation between lamp and dye cell and a larger (diffuse white painted) energy coupling cavity enclosing lamp and cell. The two effects led to a reduced laser output in the sealed lamp configuration; output pulse energies with IR-144 dropped to ~70 percent of the air discharge energies and IR-125 energies decreased to ~50 percent of air discharge energies. (A similar increase in spacing between dye cell and air discharge flashlamp in the original screening laser produced a similar decrease in laser power with IR-125.) Generally speaking, nitrogen at 20 torr had the fastest rise time of any of the gases we tested and was generally most satisfactory, though differences in performance among all of the low-pressure lamps was small. Incidentally, the lifetime of the air discharge lamp was much better than that of the sealed lamps.

Acknowledgment

The authors wish to thank P. R. Manzo of NVL for many valuable conversations. They also wish to thank Dr. O. Peterson (formerly with Kodak Research Laboratories) for technical assistance with the flashlamp, and Dr. B. B. Snavely (formerly with Kodak Research Laboratories) for helpful

suggestions. Dr. Peterson and Dr. Snavely are now with the Lawrence Livermore Laboratory.

REFERENCES

[1] G. Carboni and A. DiBene, "Flashlamp-excited dye laser emitting in the near infra-red," *Lett. al. Nuovo Cimento*, vol. 1, pp. 979–982, June 5, 1971.
[2] A. Hirth, J. Faure, and R. Schoenenberger, "Emission laser dans le proche infrarouge de colorants fluorescents pompés par éclair," *C.R. Acad. Sci.* (Paris), vol. 274B, pp. 747–750, Mar. 13, 1972.
[3] M. Maeda and Y. Miyazoe, "Flashlamp excited organic liquid laser in the range from 342 to 889 nm," *Japan J. Appl. Phys.*, vol. II, pp. 692–698, May 1972.
[4] A. Hirth, J. Faure, and D. Lougnot, "Quenching effects in flashlamp-excited polymethine dye lasers," *Opt. Commun.*, vol. 8, pp. 318–322, Aug. 1973.
[5] J. P. Webb, B. E. Plourde, and R. T. Janczak, "Infrared dye laser study," AD 769-939, Sept. 1973.
[6] J. P. Webb and B. E. Plourde, "Infrared dye laser study–Phase II," AD 762-354, Apr. 1973.
[7] ——, "Infrared dye laser study–Phase I," AD 748-863, Sept. 1972.

Contributors

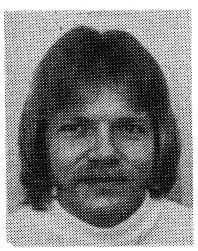

John A. Caird was born in Brooklyn, N.Y., on December 24, 1947. He received the B.S. degree in electrical engineering from Rutgers University, New Brunswick, N.J., and the M.S. degree in physics from the University of California, Los Angeles, in 1969 and 1971, respectively.

Since 1969 he has been a member of the Technical Staff in the Laser Division of the Hughes Aircraft Company, Culver City, Calif., and has continued his studies under the company's work-study fellowship program. He is currently working toward the Ph.D. degree in physics at the Center for Laser Studies, the University of Southern California, Los Angeles, where he was advanced to candidacy in December 1973.

Mr. Caird is a member of Eta Kappa Nu, Tau Beta Pi, and the Optical Society of America.

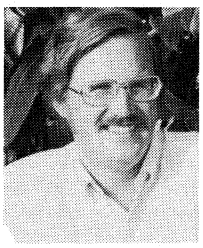

Larry G. DeShazer was born in Washington, D.C., on November 3, 1934. He received the B.S. degree in physics from the University of Maryland, College Park, in 1956 and the Ph.D. degree in physics from The Johns Hopkins University, Baltimore, Md., in 1963.

From 1963 to 1966 he was a Member of the Technical Staff of Hughes Aircraft Company, Culver City, Calif., engaged in research on energy transfer and fluorescence processes in solid-state laser materials, and later in studies of mode selection techniques for solid-state laser oscillators. In 1966 he joined the faculty of the Departments of Electrical Engineering and Materials Science at the University of Southern California, Los Angeles, Calif., as Assistant Professor. In addition, he joined the Department of Physics in 1970 and is currently Associate Professor. He has been mainly engaged in spectroscopy of rare-earth ions in laser glasses and

crystals, and saturated absorption of laser radiation by organic compounds. More recently he is studying laser-induced damage to thin-film coatings, and is concerned with generation and utilization of high-power optical beams. In 1973 he was appointed Director of the Center for Laser Studies at USC. He is consultant to Union Carbide Corporation, The Aerospace Corporation, and TRW Inc.

Dr. DeShazer is a member of the American Physical Society, the Optical Society of America, the American Association for the Advancement of Science, and Sigma Xi.

*



A. Gondhalekar was born in Uganda, Africa, in 1942. He received the B.Sc. (Honors) degree in physics from the University of Manchester, Manchester, England, in 1964, and continued his post-graduate studies at the Universities of Manchester and Oxford, Oxford, England, and Culham Laboratory, receiving the Ph.D. degree in 1968.

He is currently with the Institut für Plasmaforschung, University of Stuttgart, Stuttgart, Germany, where his research work has concentrated mainly on the study of plasma turbulence, various problems in laser scattering from plasmas, and, recently, laser development for application in plasma scattering.

*

N. R. Heckenberg was born in Sydney, Australia, in 1946. He received the B.Sc. (Honors) degree and the Ph.D. degree, both in physics, from the University of Sydney, Sydney, in 1967 and 1972, respectively.

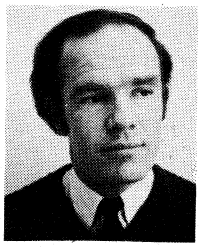

His research activities have centered on plasma diagnostics, and since 1972 he has worked on scattering of laser radiation from plasmas at the Max-Planck-Institut für Plasmaphysik, Garching, Germany.

*



E. Holtzhauer was born in Tuttlingen, Germany, on February 17, 1940. He received the Diplom in Electrical Engineering from the University of Stuttgart, Stuttgart, Germany, in 1967, and the Ph.D. degree for work on MED-flow in shock tubes in 1973.

Currently at the Institut für Plasmaforschung, University of Stuttgart, Stuttgart, he is working on plasma diagnostics with infrared lasers.

Dr. Holzhauer is a member of the Germa Physical Society.

*

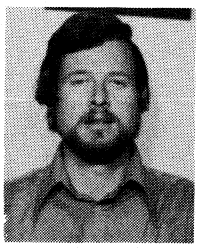

Rogers H. Stolen was born in Madison, Wis., in 1937. He received the B.S. degree from St. Olaf College, Northfield, Minn., in 1959, and the Ph.D. degree from the University of California, Berkeley, in 1965, and was a Post-Doctoral Fellow at the University of Toronto, Toronto, Ont., Canada.

He has been with Bell Laboratories, Holmdel, N.J., since 1966. His present research interests are nonlinear optics in optical waveguides and Raman scattering in glass.

Third-Order Susceptibility of Alkali Metal Vapors

HERMANN EICHER

Abstract—**This paper presents calculations of the third-order susceptibility in the alkali metal vapors involving spin-orbit coupling in the energy spectrum of the alkali atoms and some power transfer between the atoms in the ensemble and their surroundings, including the radiation field. The results are plotted as a function of wavelength in the vicinity of the neodymium and iodine laser lines, and their second, third, and fourth harmonics for each of the alkalies; i.e., 10 520 Å < (λ, 2λ, 3λ, 4λ) < 10 720 Å, and 13 070 Å < (λ, 2λ, 3λ, 4λ) < 13 230 Å, respectively.**

I. Introduction

A POSSIBLE approach to generate coherent radiation in the vacuum ultraviolet and soft X-ray region of the electromagnetic spectrum is to use third-harmonic generation in alkali metal vapors, which may follow sequential second-harmonic generation in nonlinear crystals, or frequency tripling in gas mixtures, to convert the high peak power of the neodymium or iodine lasers to a much shorter wavelength. Third-harmonic generation in the inert gases and in alkali metal vapors has been studied by Ward and New [1] and Miles and Harris [2], respectively. Obviously, third-harmonic power is proportional to the cube of the fundamental power and to the square of the third-order susceptibility $X^{(3)}$. This susceptibility has been calculated as a function of wavelength for each of the alkalies, neglecting spin-orbit coupling and relaxation effects in the electronic structure of the alkali atoms [2]. For that reason, the calculations are of limited accuracy if the driving frequency lies in the vicinity of resonances. Moreover, only the lowest four s, p, and d states are taken into account which makes the calculation invalid for certain regions of the driving frequency.

To obtain theoretical data of higher accuracy, the third-order susceptibility of the alkalies was reevaluated within the concept of quantum statistics. All exact energies of the s, p, and d states [3], split by spin-orbit coupling, for which the oscillator strengths $ns \rightarrow mp$ and $np \rightarrow md$ are tabulated [4], [5], were included in our calculations. A weak interaction of the atoms with their surroundings and with the radiation field which would provide some damping effects in the case of resonant third-harmonic generation is taken into consideration by introducing relaxation rates of the density-matrix elements.

In Section II, values for the dipole-matrix elements are derived, and the reduced matrix elements between the electronic states for each of the alkalies are tabulated. In Section III, the third-order susceptibility of an ensemble of alkali atoms is calculated by means of the density-matrix formalism. Computer results of the real part of $|X^{(3)}|$ are plotted versus incident wavelength in the vicinity of the neodymium and iodine lasers and their second, third, and fourth harmonics.

Manuscript received July 19, 1974; revised November 14, 1974.

The author is with the Physik-Department der Technischen Unisität, München, Germany.

II. Calculation of Dipole Matrix Elements

The bound eigenstates of the alkali atoms involving spin-orbit coupling are written in the form $|n, l, s = \frac{1}{2}, j, m\rangle$, where the radial part of the wave function depends only on the quantum numbers (n, l). The operator for the electric dipole moment $\boldsymbol{P} = -e \cdot \boldsymbol{r}$ is a tensor operator of rank one. Because of the spherical symmetry of our problem, we can assume the incident laser field to be linearly polarized in the z direction and thus take

$$\langle n, l, s, j, m | P_z | n', l', s, j', m' \rangle = -e \langle l, s, j, m, | T_0^{(1)} | l', s, j', m' \rangle \langle n, l \| r \| n', l' \rangle . \quad (1)$$

According to tensor techniques [6], the first factor is given in terms of 3-j and 6-j symbols [7]

$$\langle l, s, j, m | T_0^{(1)} | l', s, j', m' \rangle = (-1)^{j-m} \begin{pmatrix} j & 1 & j' \\ -m & 0 & m' \end{pmatrix} \cdot \langle l, s, j, \| T^{(1)} \| l', s, j' \rangle \quad (2a)$$

$$\langle l, s, j \| T^{(1)} \| l', s, j' \rangle = (-1)^{l+s+j'+1} (2j+1)^{1/2} \cdot (2j'+1)^{1/2} \cdot \begin{Bmatrix} j & 1 & j' \\ l' & s & l \end{Bmatrix} \cdot \langle l \| T^{(1)} \| l' \rangle \quad (2b)$$

$$\langle l \| T^{(1)} \| l' \rangle = (-1)^{l} (2l+1)^{1/2} (2l'+1)^{1/2} \cdot \begin{pmatrix} l & 1 & l' \\ 0 & 0 & 0 \end{pmatrix} . \quad (2c)$$

Table I gives the reduced matrix elements in (2b) between S, P, and D states of the alkalies. States with higher values of

TABLE I
REDUCED MATRIX ELEMENTS $\langle l, s, j \| T^{(1)} \| l', s, j' \rangle$ BETWEEN S, P, AND D STATES OF THE ALKALIES

	$^2S_{1/2}$	$^2P_{1/2}$	$^2P_{3/2}$	$^2D_{3/2}$	$^2D_{5/2}$
$^2S_{1/2}$	0	$-(2/3)^{1/2}$	$-(4/3)^{1/2}$	0	0
$^2P_{1/2}$	$-(2/3)^{1/2}$	0	0	$-(4/3)^{1/2}$	0
$^2P_{3/2}$	$(4/3)^{1/2}$	0	0	$-(4/15)^{1/2}$	$-(12/5)^{1/2}$
$^2D_{3/2}$	0	$(4/3)^{1/2}$	$-(4/15)^{1/2}$	0	0
$^2D_{5/2}$	0	0	$(12/5)^{1/2}$	0	0

TABLE II
DIPOLE, RADIAL-MATRIX ELEMENTS $\langle n, l, \|r\| n', l+1\rangle$ FOR LITHIUM (ATOMIC UNITS)

	2p	3p	4p	5p	6p	7p	8p	9p	10p	11p	12p	13p	14p	15p	16p
2s	−4.05	.213	.190	.142	.110	.088	.073	.060	.052	.052	.039	.035	.031	.031	.028
3s	2.96	−10.3	.036	.187	.166	.138	.117	.096	.084	.091	.063	.058	.051	.053	.047
4s	.787	7.33	−19.2	−.285	.133	.160	.150	.125	.113	.134	.084	.078	.069	.075	.067
5s	.423	1.86	13.5	−30.7	−.731	.032	.139	.134	.132	.181	.102	.097	.086	.099	.087
6s	.280	.981	3.30	21.3	−44.8	−1.31	−.088	.072	.123	.230	.111	.111	.100	.123	.108
7s	.205	.645	1.70	5.08	31.0	−61.4	−1.97	−.306	.017	.268	.097	.113	.105	.146	.129
8s	.160	.473	1.11	2.59	7.21	42.4	−80.6	−2.93	−.504	.238	.023	.086	.093	.169	.140
9s	.129	.369	.809	1.67	3.63	9.71	55.4	−102.	−3.80	−.129	−.223	−.007	.051	−.165	−.165
10s	.108	.300	.633	1.22	2.34	4.86	12.6	69.8	−128.	−2.66	−.860	.139	.029	.262	−.218
11s	.092	.249	.510	.939	1.68	3.07	6.20	15.8	87.5	−155.	−6.51	1.48	−.531	.018	.090

	3d	4d	5d	6d	7d	8d	9d	10d	11d	12d
2p	4.38	1.67	.971	.665	.497	.391	.319	.267	.226	.199
3p	−10.1	6.72	2.80	1.68	1.17	.885	.703	.578	.487	.419
4p	1.70	−20.9	9.60	4.05	2.45	1.71	1.30	1.04	.860	.723
5p	.609	3.90	−34.5	13.0	5.49	3.30	2.31	1.75	1.41	1.15
6p	.345	1.38	6.87	−51.0	16.9	7.10	4.25	2.96	2.27	1.78
7p	.233	.778	2.42	10.6	−70.6	21.5	8.91	5.30	3.74	2.77
8p	.174	.526	1.35	3.73	15.3	−93.1	26.4	10.9	6.55	4.42
9p	.136	.386	.901	2.05	5.25	20.3	−118.	32.2	13.4	7.65
10p	.111	.306	.668	1.38	2.91	7.06	26.5	−147.	39.5	15.3
11p	.101	.266	.557	1.07	2.04	4.10	9.66	36.1	−169.	40.4
12p	.080	.208	.424	.787	1.41	2.55	4.94	11.4	39.0	−213.
13p	.070	.180	.359	.644	1.11	1.87	3.28	6.22	13.6	50.2
14p	.061	.156	.307	.539	.897	1.45	2.39	4.08	7.36	17.0
15p	.057	.144	.278	.479	.774	1.23	1.90	3.07	4.98	9.47
16p	.051	.128	.245	.415	.663	1.01	1.55	2.35	3.61	6.14

the angular quantum numbers do not contribute to the third-order susceptibility because the ground state of the alkalies is a $^2S_{1/2}$ state, and it is assumed that this is the only populated level. The nonvanishing matrix elements in (2a) are therefore

$$\begin{aligned}
&\langle {}^2S_{1/2}, m=\pm\tfrac{1}{2}|T_0^{(1)}|{}^2P_{1/2}, m=\pm\tfrac{1}{2}\rangle = \mp\tfrac{1}{3}\\
&\langle {}^2S_{1/2}, m=\pm\tfrac{1}{2}|T_0^{(1)}|{}^2P_{3/2}, m=\pm\tfrac{1}{2}\rangle = (\tfrac{2}{9})^{1/2}\\
&\langle {}^2P_{1/2}, m=\pm\tfrac{1}{2}|T_0^{(1)}|{}^2D_{3/2}, m=\pm\tfrac{1}{2}\rangle = (\tfrac{2}{9})^{1/2}\\
&\langle {}^2P_{3/2}, m=\pm\tfrac{1}{2}|T_0^{(1)}|{}^2D_{3/2}, m=\pm\tfrac{1}{2}\rangle = \mp\tfrac{1}{15}\\
&\langle {}^2P_{3/2}, m=\pm\tfrac{1}{2}|T_0^{(1)}|{}^2D_{5/2}, m=\pm\tfrac{1}{2}\rangle = (\tfrac{6}{25})^{1/2}.
\end{aligned} \tag{3}$$

The absolute values of the radial-matrix elements in (1) are derived from oscillator strengths $f(n, l \to n', l+1)$ calculated by Anderson and Zilitis [4], [5]

$$\langle n, l\|r\|n', l+1\rangle^2 = f(n, l\to n', l+1) \cdot \frac{3(2l+1)}{2(l+1)\cdot|E_{n,l} - E_{n',l+1}|} \tag{4}$$

where the average energies $E_{n,l}$ are evaluated from the L–S split levels in Moore's tables [3]

$$\begin{aligned}
E_{n,p} &= \tfrac{1}{3}E(n\,{}^2P_{1/2}) + \tfrac{2}{3}E(n\,{}^2P_{3/2})\\
E_{n,d} &= \tfrac{2}{5}E(n\,{}^2D_{3/2}) + \tfrac{3}{5}E(n\,{}^2D_{5/2}).
\end{aligned} \tag{5}$$

In (4) and throughout the remainder of the paper all quantities are expressed in atomic units.

The sign of $\langle n, l\|r\|n', l+1\rangle$ may be found through the Bates and Damgaard [8] approach, corrected by Bebb [9],[1] which assumes a Coulombic radial potential field. Computer results of [9, eq. (A3)], giving the signs of the radial-matrix elements, are justified by yielding remarkably good agreement with (4). The dipole, radial-matrix elements for each of the alkalies are listed in Tables II-VI.[2]

III. THE THIRD-ORDER SUSCEPTIBILITY $X^{(3)}(3\omega)$

The coherent perturbation of the bound eigenstates $|E_n\rangle$ of the alkalies by an incident electric field

$$E(r,t) = \tfrac{1}{2}\,(E(r)e^{-i\omega t} + E^*(r)e^{i\omega t}) \tag{6}$$

is given by the Hamiltonian

$$H'(t) = e\,r\,E(r,t) = -\boldsymbol{P}\cdot E(r,t) \tag{7}$$

where the matrix elements of the dipole moment operator $\boldsymbol{P}$

[1] The correct expression of [9, eq. (A1d)] is given by $a_t = a_{t-1}(n^*/2t)\,[l(l+1) - (n^*-t)(n^*-t+1)]$.

[2] The definition of the radial-matrix elements differs from that of [2]. Note that the following $\langle z\rangle$ values in [2, table I] should be corrected to

Li $3s$–$4p$: $\langle z\rangle = +0.021$
K $7p$–$3d$: $\langle z\rangle = -0.209$
Cs $7s$–$8p$: $\langle z\rangle = -0.780$.

TABLE III
DIPOLE, RADIAL-MATRIX ELEMENTS $\langle n, l, \| r \| n', l+1 \rangle$ FOR SODIUM (ATOMIC UNITS)

	3p	4p	5p	6p	7p	8p	9p	10p	11p	12p	13p	14p	15p	16p	17p	18p
3s	−4.34	−.408	−.154	−.085	−.056	−.041	−.031	−.026	−.021	−.018	−.016	−.013	−.012	−.011	−.010	−.009
4s	4.34	−10.2	−1.17	−.471	−.270	−.192	−.134	−.105	−.085	−.071	−.061	−.052	−.046	−.041	−.037	−.034
5s	.914	10.3	−18.3	−2.23	−.922	−.534	−.361	−.269	−.210	−.171	−.144	−.122	−.106	−.094	−.085	−.076
6s	.471	1.94	[illegible]	−2.[illegible]	−3.59	−1.49	−.867	−.591	−.436	−.342	−.281	−.234	−.200	−.174	−.156	−.139
7s	.307	.965	3.25	28.6	−41.2	−5.23	−2.[illegible]	−1.27	−.859	−.639	−.503	−.407	−.341	−.292	−.258	−.228
8s	.224	.621	1.5[illegible]	4.36	41.1	−55.9	−7.14	−3.00	−1.74	−1.18	−.877	−.682	−.554	−.462	−.402	−.354
9s	.173	.449	1.00	2.31	6.75	55.7	−72.9	−9.40	−3.92	−2.28	−1.55	−1.14	−.893	−.730	−.617	−.509
10s	.139	.348	.720	1.45	3.16	8.94	72.6	−92.1	−11.9	−4.97	−2.89	−1.94	−1.43	−1.11	−.903	−.825
11s	.11[illegible]	.287	.56[illegible]	1.06	2.01	4.22	11.6	90.6	−115.	−14.2	−5.[illegible]	−3.36	−2.26	−1.66	−1.32	−.990
12s	.099	.236	.454	.804	1.41	2.57	5.27	14.3	112.	−138.	−17.6	−7.25	−4.16	−2.80	−2.05	−1.70
13s	.089	.210	.397	.684	1.14	1.92	3.42	6.83	18.1	132.	−168.	−19.3	−7.74	−4.38	−2.94	−2.09
14s	.080	.191	.357	.603	.975	1.56	2.56	4.44	[illegible].73	22.5	151.	−203.	−20.1	−7.70	−4.28	−2.84

	3d	4d	5d	6d	7d	8d	9d	10d	11d	12d	13d	14d	15d
3p	−5.88	−1.67	−.875	−.568	−.411	−.318	−.256	−.213	−.181	−.156	−.136	−.12[illegible]	−.090
4p	9.37	−10.5	−3.22	−1.73	−1.14	−.833	−.649	−.526	−.439	−.375	−.324	−.296	−.225
5p	−.153	19.6	−16.1	−5.05	−2.73	−1.[illegible]0	−1.32	−1.03	−.83[illegible]	−.701	−.599	−.535	−.420
6p	−.056	−.503	32.5	−23.0	−7.19	−3.88	−2.56	−1.[illegible]7	−1.46	−1.19	−.994	−.[illegible]69	−.690
7p	−.029	−.207	−1.07	48.3	−30.9	−9.63	−5.18	−3.41	−2.50	−1.94	−1.58	−1.34	−1.07
8p	−.018	−.116	−.458	−1.87	67.1	−40.1	−12.4	−6.63	−4.35	−3.17	−2.47	−2.02	−1.60
9p	−.012	−.077	−.264	−.[illegible]12	−2.90	88.7	−50.2	−15.5	−8.22	−5.39	−3.92	−3.06	−2.38
10p	−.009	−.055	−.174	−.466	−1.25	−4.16	113.	−61.6	−18.[illegible]	−10.0	−6.52	−4.75	−3.56
11p	−.007	−.043	−.129	−.317	−.734	−1.[illegible]3	−5.68	141.	−74.1	−22.5	−11.9	−7.74	−5.51
12p	−.006	−.034	−.100	−.232	−.495	−1.06	−2.48	−7.42	171.	−87.[illegible]	−26.6	−13.9	−8.99
13p	−.005	−.028	−.080	−.178	−.360	−.711	−1.43	−3.22	−9.26	204.	−103.	−30.4	−16.3
14p	−.004	−.024	−.068	−.148	−.285	−.534	−.981	−1.90	−4.12	−11.7	241.	−113.	−36.7
15p	−.004	−.021	−.058	−.123	−.234	−.412	−.728	−1.28	−2.40	−5.11	−13.9	283.	−151.
16p	−.003	−.019	−.050	−.105	−.197	−.331	−.575	−.935	−1.63	−2.98	−6.13	−20.7	313.
17p	−.003	−.016	−.043	−.089	−.163	−.270	−.467	−.705	−1.19	−1.97	−3.51	−8.63	−8.44
18p	−.002	−.014	−.038	−.079	−.138	−.261	−.315	−.658	−.837	−1.50	−2.32	−4.95	−1.24

are defined in (1). Using the density matrix ρ, the expectation value of the polarization $\boldsymbol{P}(t)$ is

$$\langle \boldsymbol{P}(t) \rangle = N \cdot Tr(\rho(t) \cdot \boldsymbol{P}) = N \cdot \sum_{m,n} \rho_{mn}(t) \cdot \boldsymbol{P}_{nm} \tag{8}$$

where N is the number of atoms per unit volume, and the summation is carried over the bound eigenstates. The density-matrix elements ρ_{mn} as functions of time can be obtained from the well-known von Neumann equation

$$i\hbar \frac{\partial \rho_{mn}}{\partial t} = [H, \rho]_{mn} \tag{9}$$

modified by introducing relaxation rates to take care of the fact that the atoms are interacting weakly with their surroundings and with the radiation field, an interaction which would provide some damping effects [10]. Thus we shall remedy (9) as follows: for the off-diagonal term ($n \neq m$) and for the diagonal term, the ρ_{mn} must satisfy the equations

$$i\hbar \left(\frac{\partial}{\partial t} + \Gamma_{mn} \right) \rho_{mn} = [H^{(0)} + H'(t), \rho]_{mn} \tag{10}$$

$$i\hbar \left(\frac{\partial \rho_{nn}}{\partial t} + \sum_k (\rho_{nn} W_{nk} - \rho_{kk} W_{kn}) \right) = [H^{(0)} + H'(t), \rho]_{nn} \tag{10'}$$

where the Γ_{mn} and W_{ij} are called the transverse and longitudinal relaxation rates, respectively. Since we are interested only in induced transitions between eigenstates, and not in transitions resulting from relaxation processes, the appropriate equation of motion for the diagonal elements of the density operator is obtained by setting W_{ij} equal to zero. $H^{(0)}$ is the Hamiltonian of the atom when the radiation field is absent; its matrix elements $\langle m | H^{(0)} | n \rangle = E_m \delta_{mn}$ are the energy eigenstates of the alkalies, tabulated by Moore [3]. Because the interaction term $H'(t)$ is much smaller than the unperturbed Hamiltonian $H^{(0)}$ of the medium, each matrix element of the density operator may be expanded in terms of powers of the perturbation

$$\rho_{mn} = \sum_p \rho_{mn}^{(p)}. \tag{11}$$

With the notation

$$\hbar \omega_{mn} = E_m - E_n \tag{12}$$

TABLE IV
DIPOLE, RADIAL-MATRIX ELEMENTS $\langle n, l, \| r \| n', l+1 \rangle$ FOR POTASSIUM (ATOMIC UNITS)

	4p	5p	6p	7p	8p	9p	10p	11p	12p	13p	14p	15p	16p	17p	18p
4s	−5.13	−.453	−.177	−.101	−.068	−.051	−.040	−.032	−.027	−.023	−.020	−.018	−.016	−.015	−.013
5s	4.65	−11.6	−1.14	−.444	−.250	−.167	−.123	−.096	−.078	−.065	−.056	−.049	−.043	−.039	−.035
6s	1.07	10.7	−20.3	−2.13	−.842	−.477	−.320	−.234	−.184	−.149	−.125	−.108	−.094	−.083	−.075
7s	.559	2.19	18.9	−31.3	−3.39	−1.36	−.770	−.516	−.380	−.297	−.242	−.203	−.174	−.152	−.136
8s	.368	1.10	3.61	29.1	−44.5	−4.94	−1.98	−1.13	−.757	−.557	−.435	−.354	−.298	−.254	−.224
9s	.269	.714	1.78	5.33	41.5	−60.0	−6.73	−2.71	−1.54	−1.03	−.760	−.596	−.484	−.409	−.353
10s	.209	.521	1.14	2.58	7.38	55.9	−77.9	−8.77	−3.53	−2.01	−1.35	−.986	−.771	−.616	−.517
11s	.169	.403	.817	1.62	3.50	9.71	72.7	−97.9	−11.2	−4.52	−2.57	−1.73	−1.27	−1.00	−.822
12s	.140	.322	.623	1.15	2.15	4.48	12.2	92.2	−119.	−14.2	−5.77	−3.30	−2.22	−1.61	−1.26
13s	.118	.264	.493	.862	1.50	2.71	5.52	14.9	115.	−142.	−17.7	−7.31	−4.21	−2.84	−2.10

	3d	4d	5d	6d	7d	8d	9d	10d	11d
4p	6.98	.204	−.217	−.244	−.218	−.188	−.163	−.140	−.124
5p	−6.03	14.8	.838	−.033	−.170	−.188	−.179	−.161	−.147
6p	−.853	−12.4	25.1	1.71	.272	−.021	−.104	−.123	−.129
7p	−.405	−2.09	−20.6	38.0	2.83	.671	.181	.025	−.045
8p	−.255	−1.01	−3.66	−30.7	53.1	4.18	1.16	.444	.174
9p	−.182	−.637	−1.76	−5.56	−42.8	70.7	5.74	1.74	.726
10p	−.140	−.458	−1.11	−2.66	−7.79	−57.0	90.8	7.57	2.36
11p	−.112	−.352	−.796	−1.67	−3.70	−10.3	−73.0	113.	9.51
12p	−.093	−.283	−.613	−1.19	−2.31	−4.89	−13.2	−91.3	138.
13p	−.079	−.236	−.494	−.916	−1.65	−3.04	−6.22	−16.5	−111.
14p	−.068	−.201	−.411	−.738	−1.26	−2.15	−3.85	−7.69	−20.0
15p	−.060	−.174	−.351	−.613	−1.01	−1.64	−2.72	−4.73	−9.32
16p	−.053	−.153	−.304	−.523	−.842	−1.32	−2.07	−3.33	−5.72
17p	−.048	−.136	−.268	−.454	−.717	−1.08	−1.67	−2.51	−4.02
18p	−.043	−.123	−.239	−.400	−.623	−.922	−1.39	−2.01	−3.04

TABLE V
DIPOLE, RADIAL-MATRIX ELEMENTS $\langle n, l, \| r \| n', l+1 \rangle$ FOR RUBIDIUM (ATOMIC UNITS)

	5p	6p	7p	8p	9p	10p	11p	12p	13p	14p	15p	16p	17p	18p	19p
5s	−5.31	−.580	−.251	−.152	−.106	−.080	−.063	−.052	−.043	−.037	−.032	−.028	−.025	−.023	−.020
6s	5.00	−11.8	−1.33	−.547	−.320	−.218	−.162	−.128	−.104	−.087	−.074	−.065	−.057	−.051	−.045
7s	1.13	11.4	−20.5	−2.39	−.984	−.572	−.388	−.289	−.226	−.184	−.154	−.132	−.114	−.101	−.089
8s	.589	2.25	19.8	−31.4	−3.74	−1.54	−.893	−.606	−.448	−.351	−.286	−.239	−.204	−.178	−.156
9s	.387	1.13	3.65	30.5	−44.6	−5.38	−2.22	−1.28	−.866	−.640	−.500	−.406	−.339	−.290	−.251
10s	.283	.727	1.78	5.36	43.3	−60.0	−7.30	−3.01	−1.73	−1.17	−.861	−.672	−.545	−.460	−.394
11s	.220	.528	1.14	2.56	7.35	58.2	−77.7	−9.49	−3.90	−2.24	−1.51	−1.11	−.863	−.695	−.573
12s	.178	.410	.818	1.61	3.46	9.65	75.2	−97.5	−11.9	−4.91	−2.82	−1.89	−1.39	−1.10	−.895

	4d	5d	6d	7d	8d	9d	10d	11d	12d	13d	14d	15d	16d	17d	18d
5p	6.66	−1.02	−.849	−.637	−.492	−.394	−.324	−.273	−.235	−.204	−.180	−.160	−.144	−.123	−.119
6p	−3.97	15.4	−1.35	−1.14	−.865	−.679	−.550	−.457	−.389	−.336	−.295	−.262	−.234	−.196	−.192
7p	−.817	−8.71	27.1	−1.58	−1.38	−1.06	−.838	−.683	−.573	−.491	−.426	−.376	−.332	−.273	−.273
8p	−.408	−2.05	−14.9	41.3	−1.74	−1.61	−1.25	−.987	−.812	−.683	−.585	−.512	−.449	−.360	−.364
9p	−.261	−1.04	−3.63	−22.6	58.3	−1.84	−1.82	−1.42	−1.14	−.935	−.787	−.680	−.590	−.461	−.472
10p	−.187	−.675	−1.85	−5.54	−32.0	77.9	−1.90	−2.01	−1.60	−1.28	−1.05	−.897	−.767	−.575	−.599
11p	−.144	−.489	−1.19	−2.81	−7.83	−42.7	100.	−1.87	−2.22	−1.77	−1.42	−1.18	−.978	−.740	−.760
12p	−.116	−.378	−.861	−1.80	−3.94	−10.4	−55.4	125.	−1.88	−2.43	−1.94	−1.58	−1.30	−.874	−.962
13p	−.096	−.306	−.667	−1.30	−2.52	−5.24	−13.4	−69.4	153.	−1.79	−2.60	−2.14	−1.69	−1.16	−1.21
14p	−.082	−.255	−.539	−1.01	−1.81	−3.33	−6.70	−16.8	−85.1	184.	−1.64	−2.84	−2.28	−1.38	−1.57
15p	−.071	−.217	−.449	−.813	−1.40	−2.39	−4.24	−8.33	−20.5	−102.	217.	−1.56	−2.93	−1.70	−2.02
16p	−.062	−.188	−.384	−.678	−1.13	−1.83	−3.03	−5.26	−10.1	−24.5	−121.	253.	−1.12	−1.63	−2.68
17p	−.055	−.166	−.332	−.579	−.937	−1.48	−2.33	−3.74	−6.37	−12.1	−29.0	−141.	291.	−2.98	−3.36
18p	−.049	−.147	−.293	−.502	−.799	−1.22	−1.88	−2.84	−4.53	−7.57	−14.2	−33.7	−164.	329.	−.841
19p	−.044	−.132	−.261	−.443	−.694	−1.04	−1.57	−2.27	−3.49	−5.34	−8.87	−16.5	−38.9	−195.	377.

TABLE VI
DIPOLE, RADIAL-MATRIX ELEMENTS $\langle n, l, \| r \| n', l+1 \rangle$ FOR CESIUM (ATOMIC UNITS)

	6p	7p	8p	9p	10p	11p	12p	13p	14p	15p	16p	17p	18p	19p	20p
6s	−5.68	−.637	−.284	−.174	−.122	−.093	−.075	−.061	−.052	−.045	−.039	−.034	−.031	−.028	−.025
7s	5.21	−12.5	−1.35	−.557	−.326	−.223	−.168	−.132	−.108	−.091	−.078	−.068	−.060	−.054	−.049
8s	1.21	11.8	−21.4	−2.39	−.976	−.564	−.385	−.285	−.224	−.183	−.154	−.132	−.115	−.102	−.092
9s	.636	2.37	20.3	−32.5	−3.71	−1.51	−.874	−.591	−.438	−.355	−.280	−.235	−.202	−.177	−.156
10s	.419	1.20	3.83	31.0	−46.0	−5.31	−2.16	−1.25	−.840	−.623	−.486	−.396	−.333	−.285	−.251
11s	.306	.772	1.87	5.55	44.0	−61.4	−7.29	−2.98	−1.71	−1.16	−.853	−.668	−.544	−.459	−.390
12s	.238	.557	1.18	2.65	7.56	59.3	−79.0	−9.58	−3.95	−2.28	−1.53	−1.13	−.887	−.714	−.622

	5d	6d	7d	8d	9d	10d	11d	12d	13d	14d	15d	16d	17d	18d	19d	20d
6p	5.69	−3.54	−1.75	−1.11	−.795	−.608	−.487	−.403	−.341	−.293	−.257	−.228	−.203	−.183	−.166	−.151
7p	−1.27	15.5	−5.79	−2.79	−1.76	−1.26	−.968	−.778	−.647	−.550	−.476	−.418	−.370	−.333	−.300	−.273
8p	−.354	−3.87	28.0	−8.28	−3.90	−2.45	−1.76	−1.35	−1.09	−.903	−.770	−.669	−.587	−.523	−.468	−.424
9p	−.179	−1.24	−7.29	43.4	−11.1	−5.14	−3.21	−2.29	−1.76	−1.41	−1.18	−1.01	−.872	−.768	−.682	−.613
10p	−.114	−.668	−2.36	−11.6	61.8	−14.2	−6.51	−4.04	−2.87	−2.19	−1.77	−1.48	−1.25	−1.09	−.955	−.854
11p	−.081	−.441	−1.28	−3.77	−16.9	83.3	−17.7	−8.02	−4.94	−3.49	−2.67	−2.16	−1.79	−1.52	−1.32	−1.15
12p	−.061	−.323	−.849	−2.04	−5.46	−23.1	108.	−21.7	−9.65	−5.92	−4.18	−3.21	−2.56	−2.13	−1.78	−1.59
13p	−.049	−.251	−.623	−1.35	−2.95	−7.45	−30.3	135.	−25.8	−11.5	−7.00	−4.93	−3.74	−2.99	−2.49	−2.03
14p	−.040	−.204	−.485	−.986	−1.94	−4.01	−9.72	−38.4	166.	−30.5	−13.5	−8.20	−5.70	−4.33	−3.39	−2.95
15p	−.034	−.170	−.394	−.768	−1.42	−2.63	−5.21	−12.3	−47.5	199.	−35.7	−15.7	−9.41	−6.54	−4.97	−3.81
16p	−.029	−.145	−.330	−.624	−1.10	−1.91	−3.40	−6.55	−15.2	−57.5	236.	−41.6	−17.9	−10.7	−7.36	−5.67
17p	−.026	−.126	−.282	−.521	−.893	−1.48	−2.47	−4.27	−8.06	−18.3	−68.2	276.	−47.2	−20.3	−12.1	−8.28
18p	−.023	−.111	−.245	−.445	−.747	−1.20	−1.91	−3.09	−5.23	−9.70	−21.6	−79.5	319.	−53.6	−22.7	−13.6
19p	−.020	−.099	−.216	−.388	−.638	−.997	−1.56	−2.36	−3.81	−6.26	−11.5	−25.2	−92.3	366.	−59.8	−25.5
20p	−.018	−.089	−.192	−.342	−.555	−.862	−1.26	−1.99	−2.82	−4.59	−7.35	−13.3	−29.2	−106.	415.	−67.1

we obtain from (10) and (10′)

$$i\hbar\left(\frac{\partial}{\partial t} + i\omega_{mn} + (1 - \delta_{mn})\,\Gamma_{mn}\right)\rho_{mn}^{(p)} = [H'(t), \rho^{(p-1)}]_{mn}. \tag{13}$$

It is assumed in our derivation that the spectral spread of the incident radiation is narrow compared to the transition linewidth $\hbar\Gamma_{mn}$ which must include contributions from the natural linewidth, pressure broadening, and self-broadening effects. This assumption would certainly be valid for a laser source. The effect of Γ_{mn} on the third-order susceptibility $X^{(3)}$ is significant only for the resonant case in which the driving frequency or its second or third harmonic lies in the vicinity of ω_{mn}

$$\omega, 2\omega, 3\omega \cong |\omega_{mn}|. \tag{14}$$

In that case, we can replace the relaxation rates Γ_{mn} in (13) by a single constant Γ, the transition linewidth of the two relevant eigenstates $|m\rangle$ and $|n\rangle$ in the resonant case. If the Hamiltonian $H^{(0)}$ of the medium is invariant under the parity transformation, the two eigenstates $|m\rangle$ and $|n\rangle$ must have opposite parity when resonant enhancement arises from odd harmonics of the incident frequency ω and vice versa. Assuming that the ground state $|g, {}^2S_{1/2}\rangle$ of the alkalies is the only populated level, the calculations which follow will give the resonance conditions for $X^{(3)}$:

$$\omega = \omega_{pg}$$

$$2\omega = \omega_{sg}, \omega_{dg}, \omega_{pp'}$$

$$3\omega = \omega_{pg}, \pm\omega_{sp}, \pm\omega_{pd} \tag{15}$$

where the energies of the ground state $|g\rangle$ and of the excited s, p, and d levels are indicated by indices. If the incident electric field is given by (6), then the third-order susceptibility $X^{(3)}(3\omega)$ is generally defined by the expectation value of the polarization at the third-harmonic frequency as

$$\langle P(3\omega t)\rangle = NX^{(3)}(3\omega)\cdot\left(\frac{E(r)}{2}\right)^3 e^{-3i\omega t} + \text{c.c.} \tag{16}$$

which can be evaluated from (8)

$$\langle \boldsymbol{P}(3\omega t)\rangle = N\sum_{mn}\rho_{mn}(3\omega t)\boldsymbol{P}_{nm}. \tag{17}$$

The required matrix elements of the density operator ρ are obtained in third-order perturbation theory by the method of successive approximation according to (13). Details of the calculation are given in the Appendix. Computer results of the real part of the third-order susceptibility for each of the alkalies are plotted in Figs. 1–10 as a function of wavelength in the vicinity of the neodymium and iodine laser lines, and their second, third, and fourth harmonics, respectively. Note that the wavelength scale corresponds to the fundamental laser frequency (curve *a*), and can be easily related to the incident second, third, or fourth harmonic of the laser radiation (curves *b*, *c*, and *d*). The calculated susceptibility for the 1.064-μm radiation in Rb vapor (1.072×10^{-32} ESU) agrees reasonably well with the reported generation of 0.3547-μm radiation by tripling the 1.064-μm radiation in a phase-matched mixture of

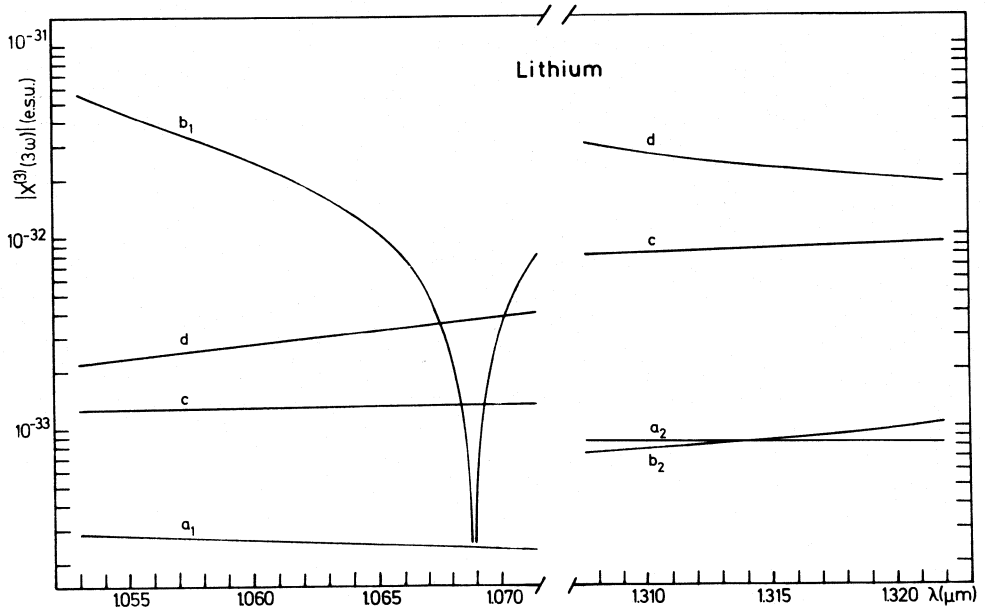

Fig. 1. Third-order susceptibility of lithium versus wavelength in the vicinity of the neodymium and iodine lasers. Curves a, b, c, and d are calculated for the first, second, third, and fourth harmonics of the incident laser radiation, respectively. For each curve, the logarithmic scale must be multiplied by a scaling factor: $a_1(1)$, $a_2(10^{-1})$, $b_1(10^{-3})$, $b_2(1)$, $c(10^{-3})$, and $d(10^{-4})$. The linewidth Γ is chosen to be 0.1 cm^{-1}.

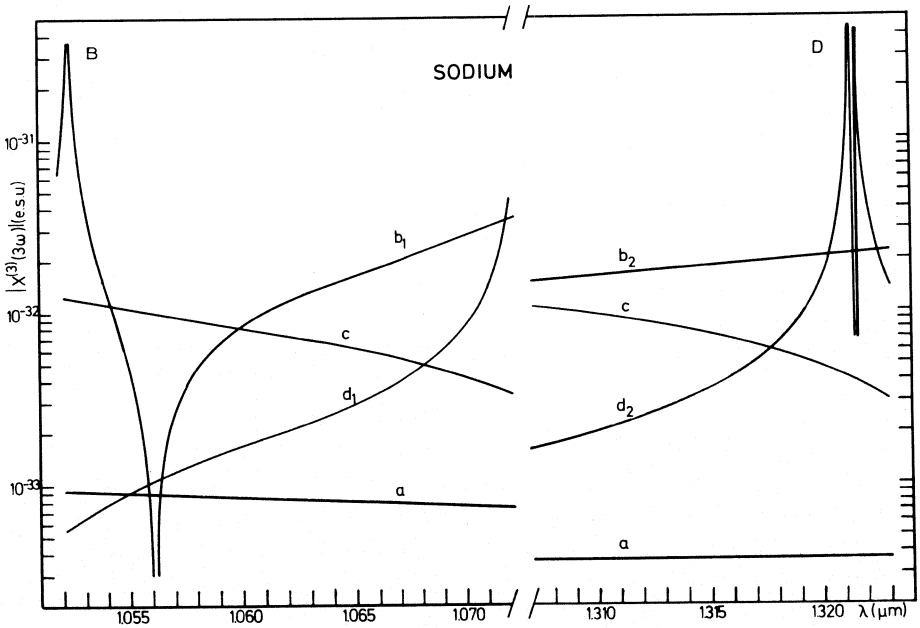

Fig. 2. Third-order susceptibility of sodium versus wavelength in the vicinity of the neodymium and iodine lasers. Curves a, b, c, and d are calculated for the first, second, third, and fourth harmonics of the incident laser radiation, respectively. For each curve, the logarithmic scale must be multiplied by a scaling factor: $a(1)$, $b_1(10^{-3})$, $b_2(10^{-2})$, $c(10^{-5})$, $d_1(10^{-4})$, and $d_2(10^{-3})$. The linewidth Γ is chosen to be 0.1 cm^{-1}. The resonances B and D are enlarged in Fig. 3.

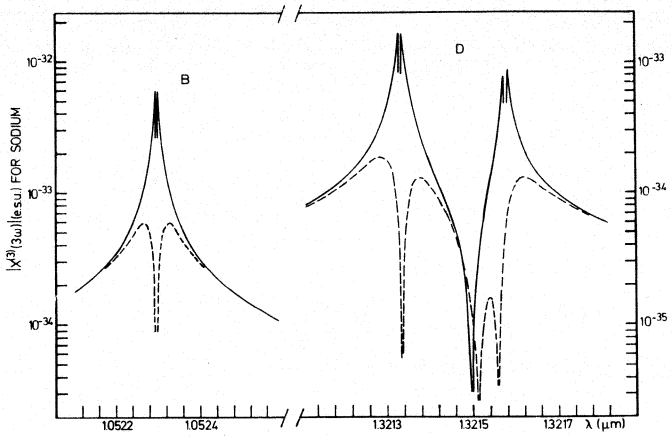

Fig. 3. Resonances of the third-order susceptibility of sodium for the second harmonic of the neodymium laser (*B*) and for the fourth harmonic of the iodine laser (*D*), enlarged from Fig. 2. Solid and dashed lines correspond to the linewidths $\Gamma = 0.1$ cm^{-1} and $\Gamma = 1$ cm^{-1}, respectively. The wavelengths of the three peaks ($\Gamma = 0.1$ cm^{-1}) are 0.5261485 μm (*B*), and 0.330333 μm, 0.330394 μm (*D*).

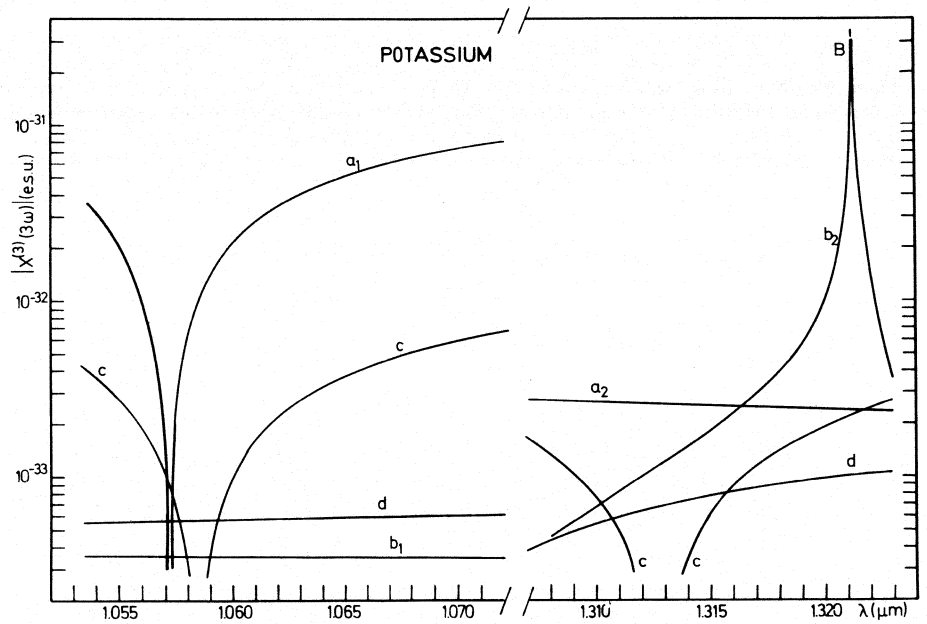

Fig. 4. Third-order susceptibility of potassium versus wavelength in the vicinity of the neodymium and iodine lasers. Curves *a*, *b*, *c*, and *d* are calculated for the first, second, third, and fourth harmonics of the incident laser radiation, respectively. For each curve, the logarithmic scale must be multiplied by a scaling factor: $a_1(10^{-2})$, $a_2(1)$, $b_1(10^{-2})$, $b_2(10^{-1})$, $c(10^{-4})$, and $d(10^{-3})$. The linewidth Γ is chosen to be 0.1 cm^{-1}. The resonance *B* is enlarged in Fig. 5.

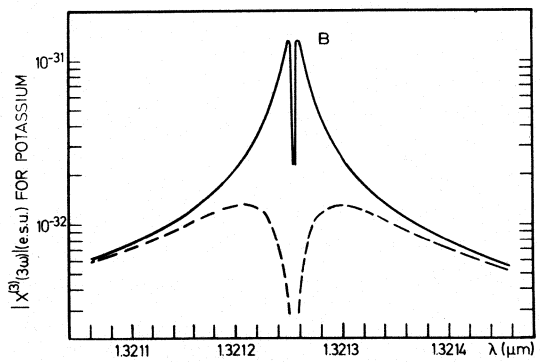

Fig. 5. Resonant third-order susceptibility of potassium for the second harmonic of the iodine laser, enlarged from Fig. 4. Solid and dashed lines correspond to the linewidths $\Gamma = 0.1$ cm^{-1} and $\Gamma = 1$ cm^{-1}, respectively. The resonant wavelength is 0.660627 μm.

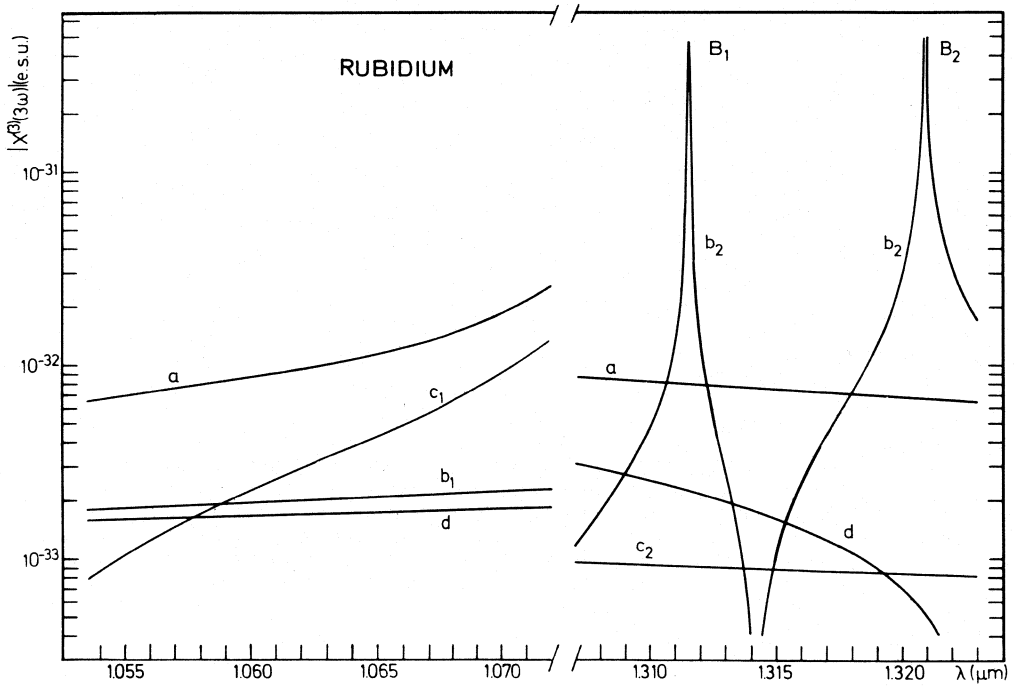

Fig. 6. Third-order susceptibility of rubidium versus wavelength in the vicinity of the neodymium and iodine lasers. Curves a, b, c, and d are calculated for the first, second, third, and fourth harmonics of the incident laser radiation, respectively. For each curve, the logarithmic scale must be multiplied by a scaling factor: $a(1)$, $b_1(10^{-2})$, $b_2(10^{-1})$, $c_1(10^{-3})$, $c_2(10^{-2})$, and $d(10^{-3})$. The linewidth Γ is chosen to be 0.1 cm^{-1}. The resonances B_1 and B_2 are enlarged in Fig. 7.

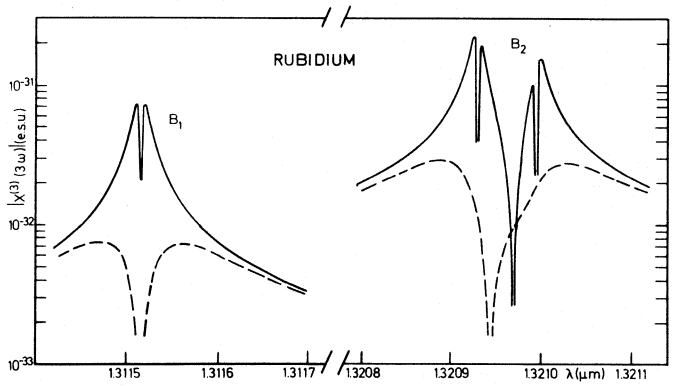

Fig. 7. Resonances of the third-order susceptibility of rubidium for the second harmonic of the iodine laser, enlarged from Fig. 6. Solid and dashed lines correspond to the linewidths $\Gamma = 0.1$ cm^{-1} and $\Gamma = 1$ cm^{-1}, respectively. The wavelengths of the three peaks ($\Gamma = 0.1$ cm^{-1}) are 0.655758 μm (B_1), and 0.660465 μm, 0.660498 μm (B_2).

rubidium and xenon [11], where the measured susceptibility is $X^{(3)}_{Rb}(\text{meas}) = 1.4 \times 10^{-32}$ ESU; the calculated value of Miles and Harris [2] is 6.15×10^{-33} ESU.[3]

Finally, it should be noticed that the resonances of $X^{(3)}$, seen in the figures, can be slightly shifted by an applied magnetic field according to the Zeeman-splittings of the atomic energy levels in order to enhance the susceptibility for a near-resonant laser radiation.

[3]Present calculations with the data of [2] yield the nonlinear susceptibility to be exactly a factor of 2 greater than that of Miles and Harris.

Appendix

In this Appendix, the third-order matrix elements of the density operator ρ are calculated by successive approximations according to (13). The starting point is the unperturbed system when the radiation field is absent. Therefore, if we consider that the unperturbed system is in the ground state $|g\rangle$, we get in the zeroth order

$$\rho^{(0)}_{mn} = \delta_{mg}\delta_{ng}. \tag{A1}$$

It is a systematic algebraic procedure to find the density-matrix elements as a power series in the perturbation $H'(t)$ of

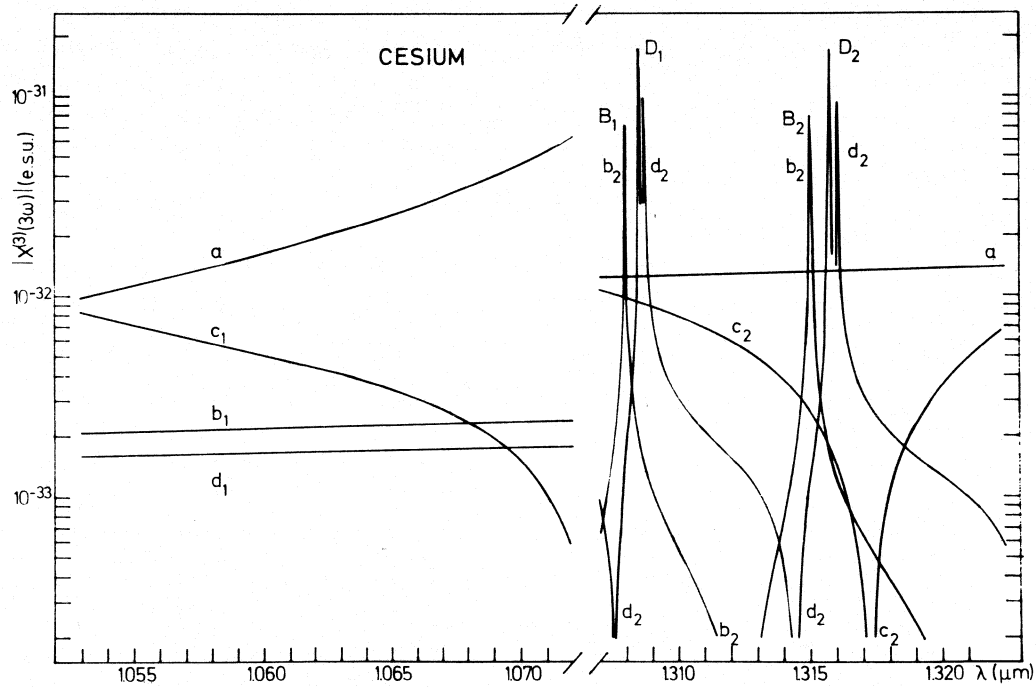

Fig. 8. Third-order susceptibility of cesium versus wavelength in the vicinity of the neodymium and iodine lasers. Curves a, b, c, and d are calculated for the first, second, third, and fourth harmonics of the incident laser radiation, respectively. For each curve, the logarithmic scale must be multiplied by a scaling factor: $a(1)$, $b_1(10^{-2})$, $b_2(1)$, $c_1(10^{-3})$, $c_2(10^{-4})$, $d_1(10^{-3})$, and $d_2(10^{-2})$. The linewidth Γ is chosen to be 0.1 cm^{-1}. The resonances B_1, B_2 and D_1, D_2 are enlarged in Figs. 9 and 10.

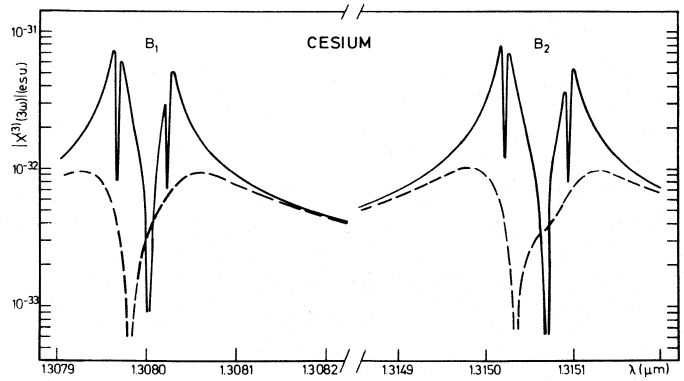

Fig. 9. Resonances of the third-order susceptibility of cesium for the second harmonic of the iodine laser, enlarged from Fig. 8. Solid and dashed lines correspond to the linewidths $\Gamma = 0.1$ cm^{-1} and $\Gamma = 1$ cm^{-1}, respectively. The wavelengths for the four peaks ($\Gamma = 0.1$ cm^{-1}) are 0.653984 μm, 0.654012 μm (B_1), and 0.657510 μm, 0.657547 μm (B_2).

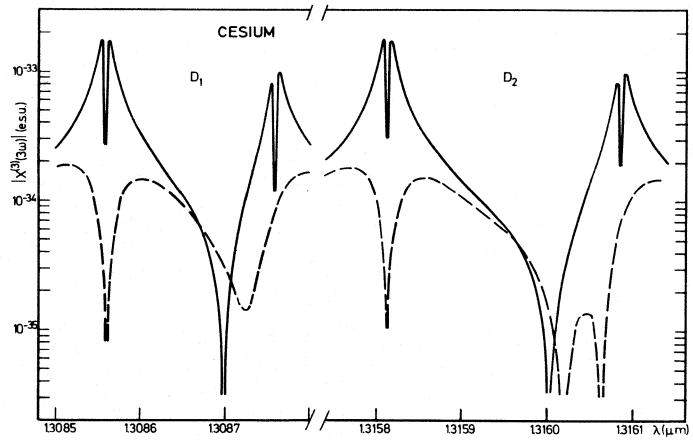

Fig. 10. Resonances of the third-order susceptibility of cesium for the fourth harmonic of the iodine laser, enlarged from Fig. 8. Solid and dashed lines correspond to the linewidths $\Gamma = 0.1$ cm^{-1} and $\Gamma = 1$ cm^{-1}, respectively. The wavelengths for the four peaks ($\Gamma = 0.1$ cm^{-1}) are 0.327140 μm, 0.327190 μm (D_1), and 0.328953 μm, 0.329021 μm (D_2).

(7). The terms will, in general, contain combination frequencies of the perturbation and may be written as

$$\rho_{mn}^{(1)} = A_{mn}^{(1)} e^{-i\omega t} + A_{nm}^{(1)*} e^{i\omega t}$$
$$\rho_{mn}^{(2)} = B_{mn}^{(2)} e^{-2i\omega t} + B_{mn}^{(0)} + B_{nm}^{(2)*} e^{2i\omega t}$$
$$\rho_{mn}^{(3)} = C_{mn}^{(3)} e^{-3i\omega t} + C_{mn}^{(1)} e^{-i\omega t} + C_{nm}^{(1)*} e^{i\omega t} + C_{nm}^{(3)*} e^{3i\omega t}. \quad \text{(A2)}$$

With the condition (A1) that the system is initially in state $|g\rangle$, we obtain from (13) the only nonvanishing coefficients

$$A_{pg}^{(1)} = -(E/2\hbar)P_{pg}/(\omega - \omega_{pg} + i\Gamma)$$
$$A_{gp}^{(1)} = (E/2\hbar)P_{pg}/(\omega + \omega_{pg} + i\Gamma) \quad \text{(A3)}$$

where the dipole-matrix elements and energy differences between the atomic eigenstates under consideration are indicated by the appropriate indices. Similarly, in second-order perturbation, we get

$$B_{pp}^{(2)} = (E/2\hbar)P_{pg}(A_{pg}^{(1)} - A_{gp}^{(1)})/2\omega$$

$$B_{gg}^{(2)} = -\sum_{p} B_{pp}^{(2)}$$

$$B_{pp'}^{(2)} = (E/2\hbar)(-P_{pg}A_{gp'}^{(1)} + P_{p'g}A_{pg}^{(1)})/(2\omega - \omega_{pp'} + i\Gamma)$$

$$B_{sg}^{(2)} = -(E/2\hbar)\sum_{p} P_{ps}A_{pg}^{(1)}/(2\omega - \omega_{sg} + i\Gamma)$$

$$B_{gs}^{(2)} = (E/2\hbar)\sum_{p} P_{ps}A_{gp}^{(1)}/(2\omega + \omega_{sg} + i\Gamma)$$

$$B_{dg}^{(2)} = -(E/2\hbar)\sum_{p} P_{dp}A_{pg}^{(1)}/(2\omega - \omega_{dg} + i\Gamma)$$

$$B_{gd}^{(2)} = (E/2\hbar)\sum_{p} P_{dp}A_{gp}^{(1)}/(2\omega + \omega_{dg} + i\Gamma). \quad \text{(A4)}$$

The coefficients $C_{mn}^{(3)}$ are obtained from the equation

$$C_{mn}^{(3)}(3\omega - \omega_{mn} + i\Gamma) = -(E/2\hbar)\sum_{k} \cdot (P_{mk}B_{kn}^{(2)} - P_{kn}B_{mk}^{(2)}) \quad \text{(A5)}$$

where the indices m and n are combinations of gp, pg, sp, ps, pd, and dp, respectively. Equation (17) may now be written as

$$\langle P(3\omega t)\rangle = N\sum_{mn} P_{nm}C_{mn}^{(3)}e^{-3i\omega t} + \text{c.c.} \quad \text{(A6)}$$

which determines directly the third-order susceptibility of (16).

Acknowledgment

The author wishes to thank Prof. W. Kaiser for stimulating this work, and Dr. H. Puell for discussions. The computational part of the work was carried out at the Leibniz-Rechenzentrum der Bayerischen Akademie der Wissenschaften.

References

[1] J. F. Ward and G. H. C. New, "Optical third-harmonic generation in gases by a focused laser beam," *Phys. Rev.*, vol. 185, pp. 57–72, 1969.
[2] R. B. Miles and S. E. Harris, "Optical third-harmonic generation in alkali metal vapors," *IEEE J. Quantum Electron.*, vol. QE-9, pp. 470–484, Apr. 1973.
[3] C. E. Moore, *Atomic Energy Levels*, vols. 1–3. Washington, D.C.: NBS, 1958.
[4] E. M. Anderson and V. A. Zilitis, "Oscillator strengths for sodium and potassium atoms calculated by a semiempirical method," *Opt. Spectrosc.*, vol. 16, pp. 99–101, 1964.
[5] —, "Semiempirical calculation of oscillator strengths for lithium, rubidium, and cesium atoms," *Opt. Spectrosc.*, vol. 16, pp. 211–214, 1964.
[6] B. R. Judd, *Operator Techniques in Atomic Spectroscopy*, (Advanced Physics Monograph Series), W. A. Nierenberg, Ed. New York: McGraw-Hill, 1963.
[7] M. Rotenberg, R. Bivins, N. Metropolis, and J. K. Wooten, Jr., *The Three-j and Six-j Symbols*. Cambridge, Mass.: M.I.T. Press, 1960.
[8] D. R. Bates and A. Damgaard, "The calculation of the absolute strengths of spectral lines," *Phil. Trans. Roy. Soc. London*, vol. A242, pp. 101–124, 1949.
[9] H. B. Bebb, "Quantitative theory of the two-photon ionization of the alkali atoms," *Phys. Rev.*, vol. 149, pp. 25–32, 1966.
[10] W. S. C. Chang, *Principles of Quantum Electronics*. Reading, Mass.: Addison-Wesley, 1969, p. 225.
[11] J. F. Young *et al.*, "Third-harmonic generation in phase-matched Rb vapor," *Phys. Rev. Lett.*, vol. 27, pp. 1551–1553, 1971.

Perturbation Theory of a Doubly Clad Optical Fiber with a Low-Index Inner Cladding

SHOJIRO KAWAKAMI, MEMBER, IEEE, AND SHIGEO NISHIDA, SENIOR MEMBER, IEEE

Abstract—**A doubly clad optical fiber which is composed of the core, inner cladding, and outer cladding is called a *W*-type fiber when the core has the largest index of refraction of the three and the inner cladding has the lowest. A *W*-type fiber is known to have several advantages over a conventional singly clad (SC) fiber. This paper presents simple, closed form approximations of a *W*-type fiber with respect to cutoff, the attenuation constant in the leaky wave region and a rapid change of the group velocity near cutoff, etc. In the approach to be described, a *W*-type fiber is thought of as a combined system of an SC fiber and an outer perturbing medium.**

Manuscript received September 9, 1974.
The authors are with the Research Institute of Electrical Communication, Tohoku University, Sendai, Japan.

I. Introduction

THIS paper presents a simple approximate theory of a doubly clad optical fiber shown in Fig. 1. The fiber consists of three portions: the core, inner cladding, and outer cladding. It is assumed that the outer cladding has a lower refractive index than the core, and the inner cladding has the lowest of the three. Such an optical fiber is referred to as a "*W*-type fiber" [1], [2]. It is known that a *W*-type fiber has several advantages over a conventional singly clad (hereafter abbreviated as SC) fiber: a *W*-type fiber has, as compared with an SC fiber, a tighter confinement property which minimizes the total waveguide dispersion and reduces absorption loss in

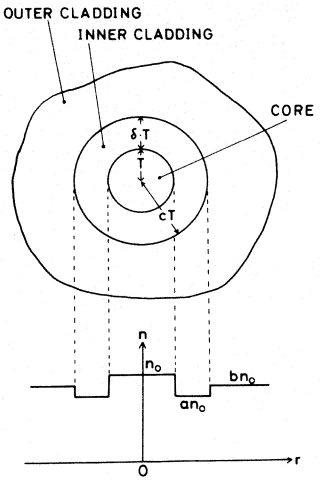

Fig. 1. Geometry and refractive index profile of a *W*-type fiber. The outer cladding is assumed to extend to infinity.

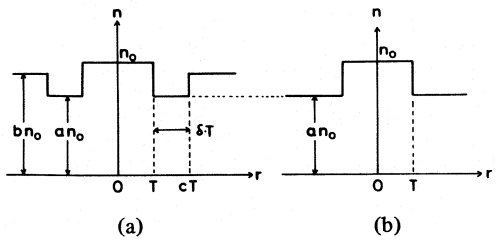

Fig. 2. Refractive index distribution of the following. (a) A *W*-type fiber. (b) The corresponding reference SC fiber. The reference SC fiber is obtained by letting $b = a$ in the *W*-type fiber.

the cladding. These characteristics have been predicted physically, and numerical solutions of the exact equations obtained are in excellent agreement with the prediction [2]. Though rigorous characteristic equations are derived in [2], they are very complicated. Numerical results are mainly presented concerning the propagating HE_{11} mode which is the lowest, and higher modes have not been investigated in detail. Numerical examples of general multimode doubly clad fibers have been reported [8].

This paper is intended to give a simple, though approximate, theory of a *W*-type fiber and to present formulas as a help for practical design work. The method of analysis is to regard a *W*-type fiber as a combined system of a reference SC fiber (the core and inner cladding) and a perturbing medium (the outer cladding) as shown in Fig. 2.

First, the characteristic equations are simplified for the case of weakly guiding fibers[1] and solved under the assumption of weak coupling: the latter approximation is valid when the inner cladding is sufficiently thick. Second, cutoff of each mode is approximately represented. Third, the attenuation constant of each mode below cutoff is derived through the perturbation theory. Finally, characteristics of each mode are treated in the frequency range above cutoff: the phase constant, group velocity, and power flow distribution among the three portions of the fiber are evaluated in a closed form.

[1]The words "weakly guiding" and "tightly confining" may sound contradictory. However, the former implies that the dielectric difference between the core and each surrounding medium is small, and the latter implies that a predominant portion of the electromagnetic power is confined within the core. Hence at a very high frequency, an optical fiber with a very small index difference is weakly guiding and tightly confining at the same time.

II. Derivation and Solution of the Characteristic Equations

The subject of this paper is a "*W*-type" optical fiber whose geometry and refractive index distribution are shown in Fig. 1. The core radius is denoted by T, and the thickness of the inner cladding is $\delta \cdot T$. The outer cladding is assumed to extend to infinity. All the three regions are assumed to be perfect insulators with the free-space permeability μ_0. Parameters a and b (see Fig. 1) are assumed to satisfy

$$1 > b > a. \tag{1}$$

The name of a *W*-type fiber comes from the shape of the index profile. In the following, we shall develop a theory of a weakly guiding *W*-type fiber: it is essential to assume

$$1 - b \ll 1, \quad 1 - a \ll 1. \tag{2}$$

At present, an index difference of the order of, or even significantly less than, 10^{-3} is common, and it is not difficult to have (2) satisfied. As in the case of an SC fiber [3], [4] the condition (2) makes the analysis much simpler. We further assume that

$$\delta \cdot T \gg \lambda/2\pi n_0 (b^2 - a^2)^{1/2} \tag{3}$$

where λ is the wavelength. This implies that the inner cladding should be "sufficiently" thick. The significance of the right-hand side will be clear later. The criterion (3) is, however, not rigorous. It should be replaced by (22) which requires $\hat{w}$ as a function of $\hat{v}$. In other words, the condition (3) is less rigorous but more convenient than (22). The two assumptions (weak guidance and sufficiently thick inner cladding) are fundamental ones of the following analysis.

We are interested in the electromagnetic field with the time and z dependence $\exp j(\omega t - \beta z)$. In order to have a guided mode, one must have

$$n_0 k_0 > \beta > b n_0 k_0 \tag{4}$$

where $k_0 = \omega(\epsilon_0 \mu_0)^{1/2}$. Guided modes are classified into hybrid modes (EH and HE modes), TE modes, and TM modes. First, we shall examine hybrid modes. It is assumed that the axial field components are expressed as

$$E_z = f(r) \cos n\theta \exp j(\omega t - \beta z) \tag{5}$$

$$H_z = \pm Y f(r) \sin n\theta \exp j(\omega t - \beta z) \tag{6}$$

where $Y = n_0(\epsilon_0/\mu_0)^{1/2}$ and $n \neq 0$. The hybrid modes are catalogued as HE_{nm} for the upper sign and EH_{nm} for the lower sign. Throughout this paper, when the double sign notation is used the upper sign is taken for the HE and the lower sign for EH modes [3], [5]. The radial function $f(r)$ is given by

$$f(r) = pJ_n(ur/T), \quad r < T$$

$$f(r) = qI_n(\hat{w}r/T) + sK_n(\hat{w}r/T), \qquad T < r < (\delta + 1)T$$
$$= hK_n(wr/T), \qquad T > (\delta + 1)T \tag{7}$$

where p, q, s, and h are constants to be determined. The quantities ju, $\hat{w}$, and w are normalized transverse propagation constants in the core, inner cladding, and outer cladding, respectively. They obey the relations

$$u^2 + \hat{w}^2 = (n_0k_0T)^2(1 - a^2) \equiv \hat{v}^2 \tag{8}$$

$$u^2 + w^2 = (n_0k_0T)^2(1 - b^2) \equiv v^2. \tag{9}$$

The quantities v and $\hat{v}$ are referred to as the normalized frequency of the W-type fiber and that of the reference SC fiber. When any one of u, $\hat{w}$, and w is known, the longitudinal phase constant β is given by

$$\beta^2 = (n_0k_0)^2 - (u/T)^2$$
$$= (an_0k_0)^2 + (\hat{w}/T)^2$$
$$= (bn_0k_0)^2 + (w/T)^2. \tag{10}$$

One can derive other field components from E_z and H_z using Maxwell's equations (see, for example, [2, (13)-(16)]). According to the assumption of weak guidance, $\epsilon(r)$ and β are approximated by $n_0^2\epsilon_0$ and n_0k_0 except where they appear in the combined form $\omega^2\epsilon\mu - \beta^2$. Equation (10) is used in the evaluation of $\omega^2\epsilon\mu - \beta^2$. Hence one obtains

$$\pm E_\theta = \mp H_r/Y = [jn_0k_0/(\omega^2\epsilon\mu - \beta^2)]$$
$$\cdot (f'(r) \pm nf(r)/r) \sin n\theta \exp j(\omega t - \beta z) \tag{11}$$

$$-E_r = -H_\theta/Y = [jn_0k_0/\omega^2\epsilon\mu - \beta^2)]$$
$$\cdot (f'(r) \pm nf(r)/r) \cos n\theta \exp j(\omega t - \beta z). \tag{12}$$

Using formulas of Bessel functions and modified Bessel functions, one can rewrite (11) and (12) as follows:

$$\begin{pmatrix} \pm E_\theta \\ -E_r \end{pmatrix} = \frac{1}{Y}\begin{pmatrix} \mp H_r \\ -H_\theta \end{pmatrix} = \begin{matrix} \sin n\theta \\ \cos n\theta \end{matrix} \exp j(\omega t - \beta z) \times \begin{cases} \pm(jn_0k_0T/u)pJ_{n\pm1}(ur/T), & r < T \\ (jn_0k_0T/\hat{w})(-qI_{n\mp1}(\hat{w}r/T) + sK_{n\mp1}(\hat{w}r/T)), & T < r < (\delta + 1)T \\ (jn_0k_0T/w) \cdot hK_{n\mp1}(wr/T), & r > (\delta + 1)T \end{cases} \tag{13}$$

where there are two choices, the upper ones go together and the lower ones go together. At dielectric discontinuities at $r = T$ or $r = (\delta + 1)T$, tangential field components must be continuous. One can easily represent p and h in terms of q and s from the continuity of E_z and H_z. Continuity of E_θ and H_θ leads to

$$\begin{bmatrix} K_n(\hat{w})\left(\frac{K_{n\mp1}}{\hat{w}K_n} \mp \frac{J_{n\mp1}}{uJ_n}\right) & I_n(\hat{w})\left(\frac{-I_{n\mp1}}{\hat{w}I_n} \mp \frac{J_{n\mp1}}{uJ_n}\right) \\ K_n(c\hat{w})\left(\frac{K_{n\mp1}}{c\hat{w}K_n} - \frac{K_{n\mp1}}{cwK_n}\right) & -I_n(c\hat{w})\left(\frac{I_{n\mp1}}{c\hat{w}I_n} + \frac{K_{n\mp1}}{cwK_n}\right) \end{bmatrix} \begin{pmatrix} s \\ q \end{pmatrix} = 0 \tag{14}$$

where $c = 1 + \delta$ and $K_{n\mp1}/c\hat{w}K_n$ is the abbreviation of $K_{n\mp1}(c\hat{w})/c\hat{w}K_n(c\hat{w})$, etc., throughout this paper. Existence of nontrivial solution to (14) leads to equating a second-order determinant to zero. Hence we have, for hybrid modes,

$$K_{n\mp1}/\hat{w}K_n \mp J_{n\mp1}/uJ_n = \frac{I_n(\hat{w})K_n(c\hat{w})}{K_n(\hat{w})I_n(c\hat{w})}$$
$$\cdot \left(\frac{I_{n\mp1}}{\hat{w}I_n} \pm \frac{J_{n\mp1}}{uJ_n}\right) \frac{K_{n\mp1}/c\hat{w}K_n - K_{n\mp1}/cwK_n}{I_{n\mp1}/c\hat{w}I_n + K_{n\mp1}/cwK_n}. \tag{15}$$

Simultaneous equations (8), (9), and (15) are the characteristic equations of a weakly guiding W-type fiber.

There are TE and TM mode families for $n = 0$, and the characteristic equation can be derived in a similar way. After some algebra, one finds that the TE_{0m} mode and TM_{0m} mode are degenerate. Their characteristic equations are the same as those of the HE_{2m} mode.

Similarly, there is some degeneracy relation between the HE and EH modes. We shall present the results without going into detail.

1) The $HE_{n+1,m}$ and $EH_{n-1,m}$ modes are degenerate for $n \geqq 2$.

2) The HE_{2m}, TE_{0m}, and TM_{0m} modes are degenerate.

Rigorously, the word "degenerate" used so far should be understood to imply "degenerate in the limit $a, b \to 1$." From the preceding degeneracy relations, we can concentrate on HE modes without loss of generality. We shall henceforth treat $HE_{n+1,m}$ mode ($n \geqq 0$). The characteristic equations for the $HE_{n+1,m}$ mode are listed again:

$$J_n/uJ_{n+1} - K_n/\hat{w}K_{n+1} = \frac{I_{n+1}(\hat{w})K_{n+1}(\hat{w})}{K_{n+1}(\hat{w})I_{n+1}(c\hat{w})}$$
$$\cdot \left(\frac{I_n}{\hat{w}I_{n+1}} + \frac{J_n}{uJ_{n+1}}\right) \frac{K_n/c\hat{w}K_{n+1} - K_n/cwK_{n+1}}{I_n/c\hat{w}I_{n+1} + K_n/cwK_{n+1}} \tag{16}$$

$$u^2 + \hat{w}^2 = (n_0k_0T)^2(1 - a^2) \equiv \hat{v}^2 \tag{17}$$

$$u^2 + w^2 = (n_0k_0T)^2(1 - b^2) \equiv v^2. \tag{18}$$

We shall hereafter denote by $F(u, \hat{w})$ and $\epsilon(u, \hat{w}, w)$ the left-hand side and right-hand side of (16), respectively.

We shall try to solve the preceding equations by regarding the W-type fiber as a combined system of the "reference SC fiber" surrounded by a perturbing outer medium. In Fig. 2 this interpretation is illustrated. This approach is justified when the following two conditions are satisfied.

1) The mode to be considered is above cutoff (i.e., propagating) along the reference SC fiber at the specified frequency.

2) The field strength at $r = (\delta + 1)T$ is much smaller than that at $r = T$.

When these two are satisfied, we proceed as follows: let the eigenvalue u and w of the reference SC fiber be denoted by U and $\hat{W}$. They are the solution of

$$J_n/UJ_{n+1} - K_n/\hat{W}K_{n+1} = 0 \tag{19}$$

$$U^2 + \hat{W}^2 = \hat{v}^2. \tag{20}$$

Equation (19) will be frequently utilized in the following analysis (e.g., in deriving (36), (40), (54), and (70)). These simultaneous equations are well known [3] and we assume that the eigenvalues U and $\hat{W}$ are already known. Substituting $u = U$ and $\hat{w} = \hat{W}$ into (17) and (18), one obtains

$$w^2 = \hat{W}^2(1 - b^2)/(1 - a^2) - U^2(b^2 - a^2)/(1 - a^2) \equiv W^2. \tag{21}$$

We look for the solution, close to U, $\hat{W}$, and W, of (16)-(18). The first factor $[I_{n+1}(\hat{w})K_{n+1}(c\hat{w})/I_{n+1}(c\hat{w})K_{n+1}(\hat{w})]$ in ϵ, given by (16), is of the order of $\exp(-2\delta\hat{W})$. From condition 2)

$$K_n((\delta + 1)\hat{W})/K_n(\hat{W}) \sim \exp(-\delta\hat{W}) \ll 1 \tag{22}$$

holds. Hence $\epsilon(u, \hat{w}, w)$ is very small. The solutions of (16)-(18) are expressed in the form

$$\begin{aligned} u &= U + \Delta u \\ \hat{w} &= \hat{W} + \Delta\hat{w} \\ w &= W + \Delta w. \end{aligned} \tag{23}$$

Substituting the preceding expressions into (16) and (17), and ignoring higher order terms, we obtain simultaneous linearized equations

$$\frac{d}{dU}\left(\frac{J_n}{UJ_{n+1}}\right)\Delta u - \frac{d}{d\hat{W}}\left(\frac{K_n}{\hat{W}K_{n+1}}\right)\Delta\hat{w} = \epsilon(U, \hat{W}, W) \tag{24}$$

$$U\Delta u + \hat{W}\Delta\hat{w} = 0. \tag{25}$$

Solving (24) and (25) for u, we have

$$U\Delta u = \frac{-\epsilon(U, \hat{W}, W)}{(1/U^2 + 1/\hat{W}^2)(1 - 2nK_n/\hat{W}K_{n+1})}. \tag{26}$$

Combining (10) and (26) leads to

$$\begin{aligned} \beta_0\Delta\beta &= -U\Delta u/T^2 \\ &= \frac{\epsilon(U, \hat{W}, W)/T^2}{(1/U^2 + 1/\hat{W}^2)(1 - 2nK_n/\hat{W}K_{n+1})} \end{aligned} \tag{27}$$

where $\beta_0^2 = (n_0k_0)^2 - (U/T)^2$. In (26) and (27), ϵ should be understood to represent

$$\epsilon = -\left(\frac{J_n}{UJ_{n+1}} + \frac{I_n}{\hat{W}I_{n+1}}\right)\frac{K_{n+1}(c\hat{W})I_{n+1}(\hat{W})}{K_{n+1}(\hat{W})I_{n+1}(c\hat{W})} \cdot \frac{K_n/c\hat{W}K_{n+1} - K_n/cWK_{n+1}}{I_n/c\hat{W}I_{n+1} + K_n/cWK_{n+1}}, \quad \text{for } W^2 > 0 \tag{28}$$

$$\epsilon = -\left(\frac{J_n}{UJ_{n+1}} + \frac{I_n}{\hat{W}I_{n+1}}\right)\frac{K_{n+1}(c\hat{W})I_{n+1}(\hat{W})}{K_{n+1}(\hat{W})I_{n+1}(c\hat{W})} \cdot \frac{K_n/c\hat{W}K_{n+1} - H_n^{(2)}/cBH_{n+1}^{(2)}}{I_n/c\hat{W}I_{n+1} + H_n^{(2)}/cBH_{n+1}^{(2)}}, \quad \text{for } W^2 = -B^2 < 0. \tag{29}$$

The nature of the solution depends on whether W^2 is positive or negative. When $W^2 > 0$, β_0 and $\Delta\beta$ are real, and one obtains a guided mode with the phase constant only slightly different from that of the reference SC fiber. When $W^2 < 0$, we have $\beta < bn_0k_0$ from (10). The perturbed mode has a larger phase velocity than the plane wave velocity in the outer medium and the mode loses its power in the form of radiation. Mathematically, $\Delta\beta$ becomes complex due to the presence of a Hankel function in (29). The perturbed mode is no longer a guided mode but a leaky wave which decays off exponentially as it propagates along the fiber.

III. Cutoff Characteristics

According to the results of Section II, the (first) approximation of the cutoff frequency $\hat{v}_{c1}$ is determined by the condition

$$F(U, \hat{W}) = 0 \tag{30}$$

$$U^2 + \hat{W}^2 = \hat{v}_{c1}^2 \tag{31}$$

and

$$U = v_{c1} = \hat{v}_{c1}[(1 - b^2)/(1 - a^2)]^{1/2} \tag{32}$$

which is equivalent to $W = 0$.

We shall examine the criterion of (3) for $\delta \cdot T$ being sufficiently large. Inequality (3) is equivalent to require that $\delta\hat{w} \gg 1$ at the first-order cutoff frequency: (8), (31), and (32) lead to (3).

Suppose that the simultaneous equations (19) and (20) are solved for U, and U is plotted versus $\hat{v}$ for each mode as in Fig. 3. The crossing of the $u - \hat{v}$ curve with the straight line $u = v$ corresponds to $\hat{v}_{c1}$. The portion between the $\hat{v}$ axis and

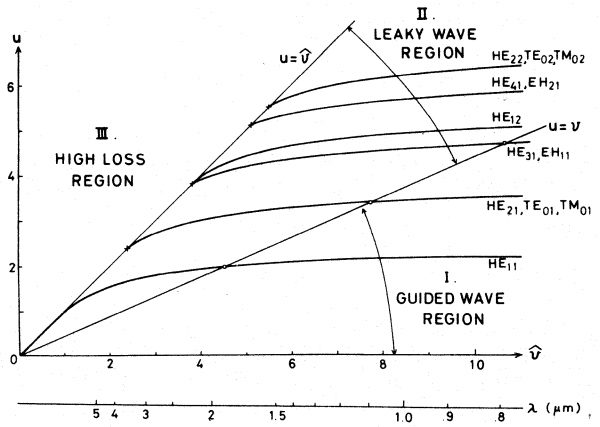

Fig. 3. Diagram indicating three regions of propagation. Each curve represents $u - \hat{v}$ characteristic of the specified mode of the reference SC fiber. In the W-type fiber, a specified mode is a guided mode in region I and leaky mode in region II. Region III is considered to be a high-loss region. A small circle on each curve denotes cutoff of the W-type fiber while a cross represents cutoff of the reference SC fiber.

the straight line $u = v$ corresponds to the guided wave region. In the portion between two straight lines $u = \hat{v}$ and $u = v$, each mode becomes a leaky wave. In the remaining part, namely between the u axis and the line $u = \hat{v}$, no mode propagates along the reference SC fiber and the perturbation theory is not applicable. An essentially the same situation is experienced in the analysis of a W-type slab waveguide. According to [6], this frequency region (denoted as region III in Fig. 3) corresponds to either a high-loss leaky mode or any low-loss improper mode which, however, it is not possible to excite efficiently.

The actual cutoff frequency of a W-type fiber is dependent on the value of δ. First-order cutoff defined by (30)-(32) does not, however, involve δ. To be more accurate, it is necessary to derive a second-order approximation for cutoff. Let us assume that we have the solution of the first-order cutoff conditions (30)-(32). The second-order cutoff frequency is denoted by $\hat{v}_{c2}$. The eigenvalues u and $\hat{w}$ for $\hat{v} = \hat{v}_{c2}$ are denoted by $U + \delta u$, $\hat{W} + \delta\hat{w}$. We have, from (16)-(18),

$$F(U + \delta u, \hat{W} + \delta\hat{w}) = \epsilon(U + \delta u, \hat{W} + \delta\hat{w}, W) \simeq \epsilon(U, \hat{W}, 0) \tag{33}$$

$$(U + \delta u)^2 + (\hat{W} + \delta\hat{w})^2 = \hat{v}_{c2}^2 \tag{34}$$

$$\delta u/U = \delta\hat{w}/\hat{W}. \tag{35}$$

The last equation results from

$$U + \delta u = [(1 - b^2)/(1 - a^2)]^{1/2}\hat{v}_{c2}.$$

Solving (33)-(35) for $\hat{v}_{c2}$, we have

$$\hat{v}_{c2} - \hat{v}_{c1} = (\hat{v}_{c1} \cdot \epsilon)/[U(\partial F/\partial U) + \hat{W}(\partial F/\partial\hat{W})] = -\frac{K_{n+1}(c\hat{W})I_{n+1}(\hat{W})}{K_{n+1}(\hat{W})I_{n+1}(c\hat{W})} \cdot \frac{(J_n/UJ_{n+1} + I_n/\hat{W}I_{n+1})\hat{v}_{c1}}{[(J_n(U)/J_{n+1}(U))^2 + (K_n(\hat{W})/K_{n+1}(\hat{W}))^2]}. \tag{36}$$

Example 1: We shall present a numerical example of a W-type fiber. In this example as well as throughout later examples, it is assumed that $a = 0.99821$, $b = 0.99966$, $n_0 = 1.5$, and $T = 15$ μm. However, the parameter δ is not fixed. In Fig. 3, the straight line $u = v = [(1 - b^2)/(1 - a^2)]^{1/2} \cdot \hat{v}$ is drawn for the case $a = 0.99821$, $b = 0.99966$. The first-order and second-order cutoff frequencies for the HE_{11} mode are

$$\hat{v}_{c1} = 4.4794 \tag{37}$$

$$\hat{v}_{c2} = 4.4411, \quad \text{for} \quad \delta = 0.5. \tag{38}$$

A computer program has been written by which the eigenvalue u of the exact equations for each mode is obtained when w is given [2]. It is found that the program operates normally when $w \geqq 10^{-4}$ but numerical errors begin to be observed when $w \leqq 10^{-5}$. We have determined cutoff (the value of u corresponding to $w = 0$) by the extrapolation procedure to be described in Section V as

$$\hat{v}_c = 4.4412 \tag{39}$$

with which (38) is in good agreement.

Let us consider the number of guided modes in a multimode W-type fiber, and assume that a number of modes propagate in the fiber. Roughly, a specified mode is above or below cutoff when v, defined by (9), is larger or smaller u_∞, where u_∞ represents the eigenvalue u in the limit $\hat{v} \to \infty$. Hence the number of guided modes mainly depends on b through the relation (9) but the number is not very sensitive to a. In other words, the number of guided modes depends mainly on the core and outer cladding while characteristics of guided modes are mainly determined by the core and inner cladding.

IV. Attenuation Constant of a Leaky Mode

The first-order attenuation constant of a leaky $HE_{n+1,m}$ mode is given by (-1) times the imaginary part of $\beta_0 + \Delta\beta$. By assumption β_0 is real, and we have, from (27)

$$\alpha = -\mathrm{Im}(\Delta\beta) = -\mathrm{Im}\left\{\frac{1}{\beta_0 T^2}\frac{\epsilon(U, \hat{W}, W)}{(1/U^2 + 1/\hat{W}^2)(1 - 2nK_n/\hat{W}K_{n+1})}\right\} \tag{40}$$

where ϵ is given by (29). When $\hat{W}$ and $B \gg 1$, we have

$$\alpha \sim \frac{1}{\beta_0 T^2}\frac{(2/\hat{W})\exp(-2\delta\hat{W})}{(1/U^2 + 1/\hat{W}^2)}\frac{2\hat{W}B}{\hat{W}^2 + B^2}. \tag{41}$$

The attenuation constant depends on the frequency and mode number. Consider a specified mode. As there is a guided mode when $\hat{v} > \hat{v}_{c1}$, the attenuation constant approaches zero as $\hat{v} \to \hat{v}_{c1} - 0$. Except very close to $\hat{v}_{c1}$ and the cutoff of the reference SC fiber, the dominant factor in (40) [where ϵ is given by (29)] is

$$I_{n+1}(\hat{W})K_{n+1}(c\hat{W})/I_{n+1}(c\hat{W})K_{n+1}(\hat{W}) \sim \exp(-2\delta\hat{W}).$$

Except close to the cutoff of the reference SC fiber, one obtains, roughly,

$$\hat{W} = (\hat{v}^2 - U^2)^{1/2} \sim \hat{v} - U^2/2\hat{v} \sim \hat{v} - u_\infty^2/2\hat{v} \tag{42}$$

where u_∞ is the mth zero of $J_n(u)$ for the $HE_{n+1,m}$ mode. Therefore, $\log \alpha$ is approximated by a linear expression with reference to $\hat{v}$ for the most part of region II in Fig. 3.

Example 2: The attenuation constants of a few lowest order modes in region II were calculated for parameters shown earlier, and plotted in Fig. 4. First, attenuation constants of a few modes for $\delta = 0.5$ ($\delta \cdot T = 7.5$ μm) are drawn in solid curves. The dashed ones correspond to $\delta = 0.9$ ($\delta \cdot T = 13.5$ μm). The leaky wave for $\delta = 0.9$ decays much more rapidly than that of the corresponding mode for $\delta = 0.5$. For example, at $v = 10$, the value of α for the HE_{31} mode is 3×10^{-4} dB/m for $\delta = 0.9$ and 3×10^{-1} dB/m for $\delta = 0.5$.

In the vicinity of cutoff of the reference SC fiber, the attenuation constant α becomes small when HE_{1m}, HE_{2m}, TE_{0m},

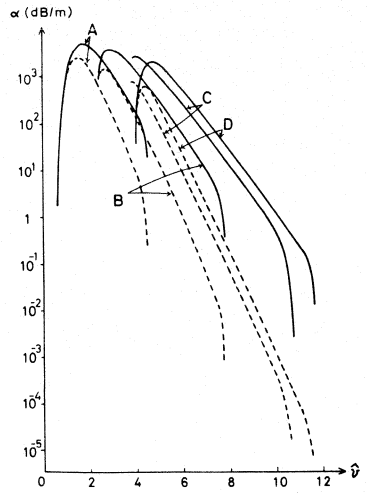

Fig. 4. Attenuation constant of each mode in the leaky wave region. Waveguide parameters are indicated in example 1. Solid lines are drawn for $\delta = 0.5$ and dashed ones for $\delta = 0.9$. Letters A, B, C, and D indicate HE_{11}, $HE_{21} + TE_{01} + TM_{01}$, $HE_{31} + EH_{11}$, and HE_{12}, respectively.

and TM_{0m} modes are considered. One can explain this behavior by considering the asymptotic form of the factor $(1 - 2nK_n/\hat{W}K_{n+1})$ in (40): when $\hat{W} \ll 1$, one obtains

$$1 - \frac{2nK_n}{\hat{W}K_{n+1}} = \begin{cases} 1, & n = 0 \\ -(\hat{W}^2/4)\ln(1.781\,\hat{W}/2), & n = 1 \\ \hat{W}^2/4n(n-1), & n \geqq 2. \end{cases} \quad (43)$$

Nevertheless, as stated earlier, the actual attenuation does not obey the first-order perturbation theory when $\hat{W}$ is small.

V. Group Velocity and Power Flow Distribution of a Propagating Mode

The phase constant of a propagating mode along a W-type fiber is given by (10) given any of the eigenvalues u, $\hat{w}$, and w. Usually, we have $\Delta\beta \ll \beta_0$. Above the cutoff frequency, the phase constant and field pattern are very close to those of the reference SC fiber. One must, however, examine the dependence of the phase constant on $\hat{v}$ at very close to the cutoff because in this region a large portion of the electromagnetic power of a certain mode is carried in the outer cladding.

A. Dispersion Relation Near the Cutoff Frequency

When we investigate the behavior of u, $\hat{w}$, and w at slightly higher than the cutoff frequency, we must use (15) instead of (26) because the presence of the outer cladding would significantly change the electromagnetic field of a certain mode. At the cutoff frequency $\hat{v}_c$ of the $HE_{n+1,m}$ mode, one obtains

$$F(u, \hat{w}) = \epsilon(u, \hat{w}, 0) \quad (44)$$

$$u^2 + \hat{w}^2 = \hat{v}_c^2 \quad (45)$$

$$u = [(1 - b^2)/(1 - a^2)]^{1/2}\,\hat{v}_c. \quad (46)$$

We shall obtain approximate functional dependence of w on $\Delta\hat{v} = \hat{v} - \hat{v}_c$. Let the value of eigenvalues be denoted by $u + \Delta u$, $\hat{w} + \Delta\hat{w}$, w at $v = v_c + \Delta\hat{v}$. We have

$$F(u + \Delta u, \hat{w} + \Delta\hat{w}) = \epsilon(u + \Delta u, \hat{w} + \Delta\hat{w}, w). \quad (47)$$

Subtracting (44) from (47), and ignoring higher order terms, we arrive at

$$\left(\frac{\partial F}{\partial u} - \frac{\partial \epsilon}{\partial u}\right)\Delta u + \left(\frac{\partial F}{\partial \hat{w}} - \frac{\partial \epsilon}{\partial \hat{w}}\right)\Delta\hat{w} = \epsilon(u, \hat{w}, w) - \epsilon(u, \hat{w}, 0). \quad (48)$$

We must adopt the difference expression in the right-hand side of (48) since in some cases $\partial\epsilon/\partial w$ does not exist in the limit $w \to 0$. We can approximate the left-hand side by $(\partial F/\partial u)\Delta u + (\partial F/\partial\hat{w})\Delta\hat{w}$ since $\epsilon/F = 0(\exp(-2\delta\hat{w}))$. We have, after some algebra,

$$(\partial F/\partial u)\Delta u + (\partial F/\partial\hat{w})\Delta\hat{w} = \left(\frac{J_n}{uJ_{n+1}} + \frac{I_n}{\hat{w}I_{n+1}}\right)\left(\frac{K_n}{c\hat{w}K_{n+1}} + \frac{I_n}{c\hat{w}I_n}\right)\frac{K_{n+1}(c\hat{w})I_{n+1}(\hat{w})}{K_{n+1}(\hat{w})I_{n+1}(c\hat{w})}$$
$$\times \begin{cases} 1/\ln(1.781\,cw/2), & n = 0 \\ (c^2w^2/4)\ln(1.781\,cw/2)/(1/2 + I_1/c\hat{w}I_2)^2, & n = 1 \\ -c^2w^2/[8n^2(n-1)(1/2n + I_n/c\hat{w}I_{n+1})^2], & n \geqq 2. \end{cases} \quad (49)$$

Similarly, we have

$$u\Delta u + \hat{w}\Delta\hat{w} = \hat{v}_c\Delta\hat{v} \quad (50)$$

$$2u\Delta u + w^2 = 2[(1 - b^2)/(1 - a^2)]\,\hat{v}_c\Delta\hat{v}. \quad (51)$$

The task is to solve simultaneous equations (49)–(51). When $n = 0$ or $n = 1$, we can show that $w^2/\Delta u$ and $w^2/\Delta\hat{w}$ approach zero in the limit $\Delta\hat{v} \to 0$. One obtains, then,

$$\Delta u = [(1 - b^2)/(1 - a^2)]^{1/2}\,\Delta\hat{v} \quad (52)$$

$$\Delta\hat{w} = [(b^2 - a^2)/(1 - a^2)]^{1/2}\,\Delta\hat{v} \quad (53)$$

from (50) and (51). Substituting these two into (49), one obtains

$$\ln\frac{1.781\,cw}{2} = -\frac{\hat{v}_c\left(\frac{J_0}{uJ_1} + \frac{K_0}{\hat{w}K_1}\right)\left(\frac{K_0}{c\hat{w}K_1} + \frac{I_0}{c\hat{w}I_1}\right)\frac{K_1(c\hat{w})I_1(\hat{w})}{K_1(\hat{w})I_1(c\hat{w})}}{\Delta\hat{v}\,[(J_0(u)/J_1(u))^2 + (K_0(\hat{w})/K_1(\hat{w}))^2]},$$

for $n = 0$

$$c^2w^2 \ln\frac{1.781\,cw}{2} - \left(1+\frac{2I_1}{c\hat{w}I_2}\right)^2 [(J_1(u)/J_2(u))^2 + (K_1(\hat{w})/K_2(\hat{w}))^2] = \frac{\left(\frac{J_1}{uJ_2}+\frac{K_1}{\hat{w}K_2}\right)\left(\frac{K_1}{c\hat{w}K_2}+\frac{I_1}{c\hat{w}I_2}\right)\frac{K_2(c\hat{w})I_2(\hat{w})}{K_2(\hat{w})I_2(c\hat{w})}}{\cdot\frac{\Delta\hat{v}}{\hat{v}_c}}, \quad \text{for } n=1. \tag{54}$$

When $n \geqq 2$, the expression (49) shows that the right-hand side of (49) is of the order w^2 in the limit $w \to 0$ and there is no singularity. We can accordingly ignore it since it is proportional to $\exp(-2\delta\hat{w})$. In other words, when $n \geqq 2$, the dependence of u and $\hat{w}$ on $\hat{v}$ is approximately the same as that of the reference SC fiber.

Example 3: The same parameters are assumed: $a = 0.99821$, $b = 0.99966$, $n_0 = 1.5$, and $T = 15$ μm. We further assume that $\delta = 0.5$. We wish to compare the approximation of (54) with the numerical solution of the exact equation. To calculate the right-hand side of (54), we substitute for u and $\hat{w}$ the first-order eigenvalues, given by (19) and (20), and obtain

$$w = (2/1.5 \times 1.781)\exp(-0.01276/\Delta\hat{v}). \tag{55}$$

Using the previously mentioned computer program, we calculated $\hat{v}$ versus w, where the minimum value of w is 10^{-4} as previously noted. Although explicit numerical evaluation of $\hat{v}_c$ is not feasible, it is expected from (54) and (55) that $1/\log(1.781\,cw/2)$ is approximated by a linear function of $\hat{v}$ for $w \to 0$. In Fig. 5, $1/\log(1.781 \times 1.5\,w/2) = 1/\log(1.3363\,w)$ is plotted versus $\hat{v}$. The straight line drawn in the figure has the tangent predicted by (55), and we find that (55) is a good approximation if Δv is appropriately redefined as $\Delta v = \hat{v} - \hat{v}_c$.

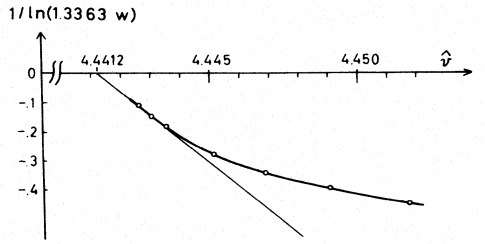

Fig. 5. Behavior of the eigenvalue w for the HE_{11} mode in the region close to the cutoff frequency. It should be observed that the quantity $1/\log(1.781\,cw/2)$ lies on a straight line when $w \to 0$. The cutoff frequency, obtained by extrapolation, is $v = 4.4412$. Small circles indicate sample points used.

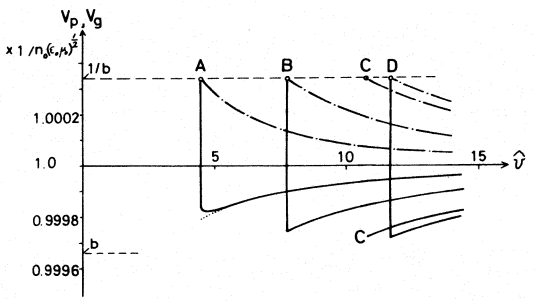

Fig. 6. Frequency dependence of the phase and group velocities of a few lowest modes. Letters A, B, C, and D represent HE_{11}, $HE_{21} + TE_{01} + TM_{01}$, $HE_{31} + EH_{11}$, and HE_{12}, respectively. The dotted-broken curves denote the phase velocities. The assumed parameters are: $a = 0.99821$, $b = 0.99966$, and $\delta = 0.5$. The dotted line is the plot of (57) for the HE_{11} mode. For other modes numerical solutions are in excellent agreement with (57).

B. Frequency Dependence of the Group Velocity

The frequency and mode number dependence of the group velocity plays an important role in the analysis of delay distortion. A general theory of a dielectric waveguide predicts, when applied to the analysis of a W-type fiber, that

$$\frac{1}{v_p v_g} = \frac{1}{n_0^2\epsilon_0\mu_0}\cdot\frac{P_{\text{core}} + a^2P_{ic} + b^2P_{oc}}{P_{\text{core}} + P_{ic} + P_{oc}} \tag{56}$$

where P_{core}, P_{ic}, and P_{oc} denote the power flow in the core, the inner cladding and in the outer cladding, respectively [7]. The phase and group velocities are denoted by v_p and v_g, respectively. The quantity v_p is equal to $1/bn_0(\epsilon_0\mu_0)^{1/2}$ at cutoff and decreases monotonically when the frequency increases. At $\omega = \infty$, v_p is equal to $1/n_0(\epsilon_0\mu_0)^{1/2}$. When any one of the HE_{1m}, HE_{2m}, TE_{0m}, and TM_{0m} modes is considered, nearly all the power flows in the outer cladding at very close to cutoff, and when the frequency becomes higher, the most part of power flows in the core. Using relation (56), one can predict the dependence of v_g of each mode on the frequency. The group velocity is equal to $1/bn_0(\epsilon_0\mu_0)^{1/2}$ at cutoff when any one of the HE_{1m}, HE_{2m}, TE_{0m}, and TM_{0m} modes is considered. Fig. 6 shows typical variation of v_g of each mode with the frequency. Note that

$$v_p = v_g = 1/bn_0(\epsilon_0\mu_0)^{1/2}$$

at cutoff for each of the HE_{11}, HE_{21}, TE_{01}, TM_{01}, and HE_{12} modes, and $v_g < 1/n_0(\epsilon_0\mu_0)^{1/2}$ at cutoff of the HE_{31} and EH_{11} modes. Far from cutoff, the group velocity of a mode along a W-type fiber is approximated by that of the reference SC fiber. In other words, one obtains

$$v_g n_0(\epsilon_0\mu_0)^{1/2} = 1 + (1 - 1/v_p^2)\cdot(1/2 - K_{n+1}(\hat{w})K_{n-1}(\hat{w})/K_n^2(w)) \tag{57}$$

for the $HE_{n+1,m}$ mode [3]. In order to analyze the rapid change of v_g, one should utilize (10) and (54). From (10) and (17), one derives

$$(\beta T)^2 = b^2\hat{v}^2/(1-a^2) + w^2 \tag{58}$$

and, after some algebra, one also obtains

$$\frac{1}{v_g} = n_0[(1-a^2)\epsilon_0\mu_0]^{1/2}\cdot\frac{b^2/(1-a^2) + (w/\hat{v})(dw/d\hat{v})}{[b^2/(1-a^2) + (w/\hat{v})^2]^{1/2}} \tag{59a}$$

$$\sim n_0(\epsilon_0\mu_0)^{1/2}b\{1 + (1-a^2)\cdot[(w/\hat{v})\,dw/d\hat{v} - (w/\hat{v})^2/2]/b^2\}. \tag{59b}$$

Combining (54) with (59a) or (59b), one obtains expressions for the group velocity of the HE_{1m} or HE_{2m} mode. For the HE_{11} mode, we may express (55) and (59a) in the form

$$w = A \exp(-B/\Delta\hat{v})$$

$$1/v_g \sim n_0(\epsilon_0\mu_0)^{1/2} b \{1 + [(1 - a^2)/b^2](A^2/\hat{v}_c) \cdot (B/\Delta\hat{v}^2 - 1/2\hat{v}_c) e^{-2B/\Delta\hat{v}}\}. \quad (60)$$

Example 4: The same parameters a, b, n_0, and T are assumed. The frequency response of the group velocity of the HE_{11} mode close to cutoff is plotted in Fig. 7(a). The dashed line shows the result of approximation (60) and the solid curve is based on the computer solutions of the exact equation. Observe that the two solutions are in good agreement when $\Delta\hat{v} < 3 \times 10^{-3}$.

In a multimode waveguide, a distortion of the signal is caused by the difference between the group delay of the fastest mode and that of the slowest mode. In the vicinity of cutoff of some higher mode (say the HE_{12} mode, see Fig. 6), the difference is large. It is advantageous not to use these frequency regions in order to have a low distortion. The same problem is known to exist also in the case of an SC fiber [4]. Comparing Fig. 6 with Fig. 4 of [4], one finds that the widths of the frequency regions to be avoided are much narrower when a *W*-type fiber is adopted. The widths have been found to be of the order $\Delta\hat{v} \lesssim \exp(-2\delta\hat{w})$ for the HE_{1m} mode and $\Delta\hat{v} \sim 1/\exp(\exp(2\delta\hat{w}))$ for the HE_{2m}, TE_{0m}, and TM_{0m} modes.

C. Power Flow Distribution Among the Three Portions

Usually, the most part of electromagnetic power is carried in the core. In the vicinity of cutoff, however, confinement becomes weaker. It is known [3] that, concerning an SC fiber, all the power is carried in the cladding at cutoff when the HE_{1m}, HE_{2m}, TE_{0m}, or TM_{0m} mode is considered. However, at cutoff of the $HE_{n+1,m}$ or $EH_{n-1,m}$ mode ($n \geqq 2$), $1/n$ times the total power of the mode is carried in the cladding. Likewise, in the case of a *W*-type fiber, at cutoff all the power is carried in the outer cladding when any one of the HE_{1m}, HE_{2m}, TE_{0m}, and TM_{0m} modes is considered. On the other hand, much less power than $1/n$ times the total power is carried in the outer cladding at cutoff of the $HE_{n+1,m}$ or $EH_{n-1,m}$ mode ($n \geqq 2$) due to the large transverse attenuation across the inner cladding. In this subsection, we shall derive closed form approximations of the power flow distribution. The electromagnetic power in the core, inner cladding, and outer cladding are, respectively, proportional to [see (7) and (13)]

$$P_{\text{core}} = (p/u)^2 \int_0^T J_n^2(ur/T)\, r\, dr \quad (61)$$

$$P_{ic} = (1/\hat{w})^2 \cdot \int_T^{cT} [qI_n(\hat{w}r/T) - sK_n(\hat{w}r/T)]^2\, r\, dr \quad (62)$$

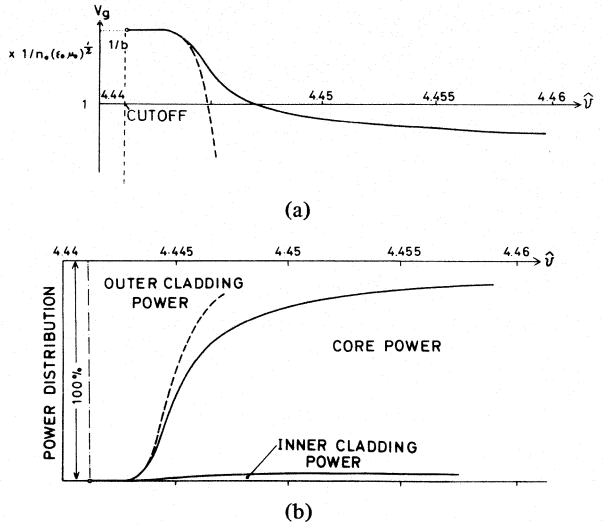

Fig. 7. (a) Frequency dependence of the group velocity of the HE_{11} mode near cutoff. (b) Power flow distribution among the core and the two claddings. In both figures solid curves and dashed lines correspond to computer solutions and closed form approximations based on (55), (59), (67)–(69).

$$P_{oc} = (h/w)^2 \int_{cT}^{\infty} K_n^2(wr/T)\, r\, dr \quad (63)$$

where the parameters p, q, s, and h satisfy

$$pJ_{n+1}(u) = qI_{n+1}(\hat{w}) + sK_{n+1}(\hat{w}) \quad (64)$$

$$hK_{n+1}(cw) = qI_{n+1}(\hat{w}) + sK_{n+1}(c\hat{w}) \quad (65)$$

$$sK_{n+1}(c\hat{w})\left(\frac{K_n}{c\hat{w}K_{n+1}} - \frac{K_n}{cwK_{n+1}}\right) = qI_{n+1}(c\hat{w})\left(\frac{I_n}{c\hat{w}I_{n+1}} - \frac{K_n}{cwK_{n+1}}\right). \quad (66)$$

Integrating (61)–(63), and ignoring insignificant terms of the order of $\exp(-2\delta\hat{w})$ with respect to unity, and eliminating a constant of proportionality, one arrives at

$$P_{\text{core}} \propto K_n^2(\hat{w})(J_n^2(u) - J_{n+1}(u)J_{n-1}(u)) \quad (67)$$

$$P_{ic} \propto K_n^2(\hat{w})(\xi_n(\hat{w}) - 1) - c^2K_n^2(c\hat{w})(\xi_n(c\hat{w}) - 1) \quad (68)$$

$$P_{oc} \propto c^2K_n^2(c\hat{w})(\xi_n(cw) - 1) \times \left[1 + \frac{I_n(c\hat{w})K_{n+1}(c\hat{w})}{I_{n+1}(c\hat{w})K_n(c\hat{w})} \cdot \frac{K_n/cwK_{n+1} - K_n/c\hat{w}K_{n+1}}{I_n/c\hat{w}I_{n+1} + K_n/cwK_{n+1}}\right]^2 \quad (69)$$

where $\xi_n(x)$ denotes $K_{n+1}(x)K_{n-1}(x)/K_n^2(x)$. P_{oc} should not be ignored near cutoff ($w \to 0$) when $n = 0$ or $n = 1$ because then $P_{oc} \to \infty$ in the limit $w \to 0$. For $n \geqq 2$, P_{oc} is of the order $\exp(-2\delta\hat{w})$ even at cutoff and can be ignored. Strictly, the second term in the right-hand side of (68) had better be omitted since it is of the order $\exp(-2\delta\hat{w})$ with respect to the first. However, we have retained the term in order to have exact formulas in the special case of $a = b$ and hence $w = \hat{w}$.

Far from cutoff ($w \gtrsim 1$), P_{oc} can be ignored when

$$\exp(-2\delta\hat{w}) \ll 1.$$

The fractional power in the core is given by

$$P_{\text{core}}/(P_{\text{core}} + P_{ic}) = (u/\hat{v})^2 [(\hat{w}/\hat{v})^2 + 1/\xi_n(\hat{w})] \quad (70a)$$

$$\sim 1 - u^2/\hat{v}^3 \quad (70b)$$

the last equation is valid when $\hat{v} \gg u$ and $\hat{w} \gg 1$.

Example 5: We assume the same parameters as before. In Fig. 7(b) are plotted the normalized power distribution near cutoff of the HE_{11} mode. Observe that the tendency of curves in Fig. 7(a) and 7(b) obeys the prediction of (56).

VI. Conclusion

A simple approximate method has been developed which is intended to analyze a *W*-type fiber. The method is based on the assumption of weak guidance and that of weak coupling between the outer cladding and the reference SC fiber.

The theory has been applied to the analysis of two remarkable properties of a *W*-type fiber: leaky mode characteristics below cutoff and the group velocity and power flow distribution anomalies at only slightly above cutoff. It is expected that the theory would be helpful in practical design work and in many cases the theory would eliminate the need for numerical solution of the exact equations.

Acknowledgment

The authors wish to thank Dr. M. Miyagi of Tohoku University and Dr. S. Onoda of Hitachi Ltd., for valuable discussions and advice.

References

[1] S. Kawakami and S. Nishida, "Anomalous dispersion of new doubly clad optical fibre," *Electron. Lett.*, vol. 10, pp. 38–40, Feb. 21, 1974.
[2] —, "Characteristics of a doubly clad optical fiber with a low-index inner cladding," *IEEE J. Quantum Electron.*, vol. QE-10, pp. 879–887, Dec. 1974.
[3] A. W. Snyder, "Asymptotic expressions for eigenfunctions and eigenvalues of a dielectric or optical waveguide," *IEEE Trans. Microwave Theory Tech. (1969 Symposium Issue)*, vol. MTT-17, pp. 1130–1138, Dec. 1969.
[4] D. Gloge, "Weakly guiding fibers," *Appl. Opt.*, vol. 10, pp. 2252–2258, Oct. 1971.
[5] E. Snitzer, "Cylindrical dielectric waveguide modes," *J. Opt. Soc. Amer.*, vol. 51, pp. 491–498, May 1961.
[6] S. Kawakami and S. Nishida, "Characteristics of cutoff modes in a symmetrical five layers slab optical waveguide with low index intermediate layers," *Trans. Inst. Electron. Comm. Eng. Jap.*, vol. 57-C, pp. 304–311, Sept. 1974.
[7] S. Kawakami, "On a relation between dispersion and power flow distribution in a dielectric waveguide," *J. Opt. Soc. Amer.*, to be published.
[8] R. Roberts, "Propagation characteristics of multimode dielectric waveguides at optical frequencies," presented at the IEE Trunk Telecommunication Conf., London, 1970.

High-Speed Electrooptic Waveguide Grating Modulator Using Epitaxial ZnO

JACOB M. HAMMER, SENIOR MEMBER, IEEE, D. J. CHANNIN, MICHAEL T. DUFFY, AND CLYDE C. NEIL

Abstract—**The results of a detailed study of electrooptic waveguide grating modulators are presented. Using low-loss epitaxial ZnO on sapphire waveguides with deposited interdigital electrodes diffraction percentages up to 80 percent at 80 V with rise times below 3 ns are observed. Capacitive power requirements on the order of 4 mW/MHz are predicted.**

A theoretical description which includes carrier and piezoelectric effects is given and is shown to be adequate for designing this type of modulator.

The grating waveguide modulator spatially separates the diffracted from the main beam and thus can be used for switching. In addition, the spatial separation allows a number of these to be cascaded on a common waveguide. These features make it probable that grating modulators will find a variety of uses in integrated optics.

Manuscript received September 9, 1974; revised November 21, 1974. This research was jointly sponsored by the Air Force Avionics Laboratory, Wright-Patterson AFB; the Office of Naval Research, Arlington, Va.; and the RCA Laboratories, Princeton, N.J.

The authors are with the RCA Laboratories, Princeton, N.J. 08540.

I. Introduction

In recent years, interest in the development of optical waveguides has been high. Optical waveguides have proved capable of being used to perform a variety of light-control functions analogous to those performed on electrons by integrated circuits. The advent of low-loss fiber optics as a promising transmission medium for light has heightened this interest.

Thus, in addition to the many papers on passive optical waveguides, there have been papers on switching [1], modulation [2], [10], [12], generation [3], frequency conversion [4], deflection [5], and electrically controlled guidance of light propagating in various optical waveguides [6]. In particular, bulk electrooptic grating modulators [2], [7], a Kerr liquid waveguide grating modulator [8], and an acoustooptic grating modulator have been reported earlier [5].

The electrooptic grating waveguide modulator described in

this report has the advantage of spatially separating the diffracted beam from the main beam and thus does not require a separate analyzer or strict control of the waveguide propagation characteristics as is required by the polarization and cutoff types of waveguide modulators [1], [9]. Also, because of the spatial separation, a number of grating modulators can be included on a single waveguide so that the output of one modulator can be used as the input to a second modulator. Thus it becomes possible to perform a variety of logic and switching functions on a single waveguide. The spatial separation also aids in obtaining high extinction ratios in the diffracted beam. Finally, our modulators are capable of extremely high-frequency response. As a result, the waveguide grating modulator promises to find a wide variety of uses in the field of integrated optics. A preliminary report on this work is given in [10]. Details of the growth and excellent waveguide properties of the single-crystal ZnO on Al_2O_3 films used in these experiments are described elsewhere [11]. The ZnO is grown by vapor phase deposition on $(01\bar{1}2)$-oriented Al_2O_3 so that the hexagonal c axis of the ZnO lies in the plane of the film. Waveguide losses, measured using a fiber-optic probe technique [11] below 1 dB/cm are observed in samples used for modulators. The as-grown single-crystal films are n-type with resistivities on the order of 1 $\Omega \cdot$ cm. These are polished after growth and Li compensated to resistivities greater than 10^5 $\Omega \cdot$ cm. The ZnO surface is then passivated by vapor depositing a 1000-Å-thick amorphous layer of Al_2O_3 which prevents long-term changes in surface resistivity.

An electrooptic waveguide grating modulator is based on the formation of an electrically induced phase diffraction grating in the guiding plane of an optical waveguide. For this purpose, the guide is made from material which exhibits the linear electrooptic (Pockels) effect.

Consider Fig. 1 in which interdigital metal electrodes are shown deposited on the surface of a transparent insulating layer (overlay) of amorphous Al_2O_3 on top of a single-crystal ZnO waveguide that has been epitaxially grown on a sapphire (Al_2O_3) substrate. When a voltage is applied between the interleaved fingers, electric fields fringe into the waveguide region. These fields vary periodically in the z direction.

The application of an electric field to a crystal such as ZnO, which exhibits the linear electrooptic effect, produces a change in index of refraction which is linearly proportional to the field and depends on the crystal orientation and light-polarization direction. In the particular case shown, an electric field parallel to the c-axis of the ZnO will change the index of refraction for either z- or y-polarized light traveling in the x direction.

Thus the z-component of the periodic electric field produced when a voltage is applied to the electrodes causes a periodic variation in index of refraction for light traveling as shown in the waveguide. The periodic index change acts as a diffraction grating and will cause some of the light to be diffracted through some angle in the waveguide plane.

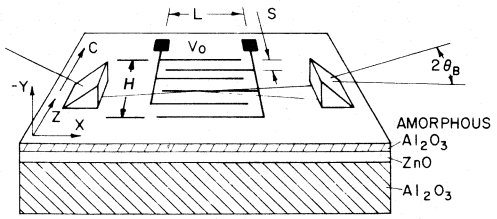

Fig. 1. Schematic diagram of electrooptic waveguide grating modulator.

II. Theory of Operation

In this section, theoretical relations which may be used to estimate the operating characteristics of the deflector modulator will be presented. We will first characterize the electrooptic effect in ZnO and give the relation between the electric field and the index of refraction. We then describe the rudiments of the operation of a thick (Bragg) periodic phase grating, relating the angles through which light is diffracted to the periodicity and relating the amount of light diffracted to the electrooptic index change. To make a quantitative estimate of the diffracted intensity, Engan's calculation of the fields produced by the electrodes is used. We then estimate power requirements. Finally, we consider some effects due to finite conductivity and piezoelectricity that may reduce the efficiency of the modulator.

A. Pockels Effect in ZnO

ZnO has 6-mm symmetry which implies that the electrooptic tensor has two important components, r_{13} and r_{33}. The subscripts 1, 2, and 3 are identified with the rectangular coordinates x, y, and z when z is taken parallel to the optic or c axis of the crystal. The following relations are obtained for the electrooptically induced index of refraction changes:

$$\Delta n_1 = -1/2\, r_{13} n_1^3 E_z$$
$$\Delta n_2 = -1/2\, r_{13} n_2^3 E_z$$
$$\Delta n_3 = -1/2\, r_{33} n_3^3 E_z \tag{1}$$

where n_1 and Δn_1 are the index and change in index, respectively, for x-polarized light traveling in the z or y direction; n_2 and Δn_2 designate y-polarized light traveling in the x or z direction; and n_3 and Δn_3 are for z-polarized light traveling in the x or y direction. E_z is the z component of the electric field in the crystal. For ZnO at $\lambda_0 = 6328$ Å, $n_1 = n_2 = 1.999$, and $n_3 = 2.015$, $r_{13} = -1.4 \times 10^{-12}$ m/V, and $r_{33} = +2.6 \times 10^{-12}$ m/V. Some of the physical constants of ZnO are listed in Table I.

For the geometry shown in Fig. 1, TE waveguide modes traveling in the x direction have z polarization, while TM modes traveling in the x direction have y polarization. Thus TE modes will experience an electrooptic effect characterized by r_{33}, the larger of the coefficients, while TM modes will see the smaller index changes characterized by r_{13}. The index changes shown in (1) will be used below to find the amplitude of the phase variation required to calculate the fraction of light diffracted by the electrooptic grating.

B. Bragg Phase Diffraction Gratings

We consider light traveling in the x direction through a medium with a z-periodic index of refraction variation. Expressing the index of refraction of the medium as the Fourier

TABLE I
CALCULATED VALUES

	Experimental Circuit (Theoretical)	Measured Values	Optimized Circuit (Theoretical)
S (cm)	7.6×10^{-4}	-	7.6×10^{-4}
d (cm)	1×10^{-4}	-	1×10^{-4}
W (cm)	S/4	-	S/2
L (cm)	0.3	-	0.5
H (cm)	0.04	-	0.01
E_z (m=1) (V/m)	$1.38 \times 10^{5} V_o$	-	$1.80 \times 10^{5} V_o$
E_z (m=2)	0	-	0
E_z (m=3)	$0.60 \times 10^{5} V_o$	-	0
$\Delta\phi/2$, m=1 (radians)	TE $2.15 \times 10^{-2} V_o$	-	$4.67 \times 10^{-2} V_o$
	TM $1.15 \times 10^{-2} V_o$	-	$2.51 \times 10^{-2} V_o$
V_o for I/I_o = 80%, m=1, TE (V)	52	80	24
V_o for I/I_o = 50%, m=1, TE (V)	37	55	17
C_o (F)	7.2×10^{-12}	6.0×10^{-12}	4.4×10^{-12}
Capacitive power at Eq.13(pulse)	30	60.3	4.0
I/I_o = 80% (mW/MHz) Eq.14(analog)	7.5	15.1	1.0
RC time constant, 50 ohm (sec)	3.6×10^{-10}	3.0×10^{-10}	2.2×10^{-10}
θ_B (deg)	1.19	1.19	1.19
$\Delta\theta$ (deg)	0.58	0.6 - 0.78	0.35

series $n_i(z) = (n_i)_m \cos(m\pi z/s)$, $n_i(z)$ thus varies periodically in z and is constant in x and y. The fundamental spatial period is $2s$. $(\Delta n_i)_m$ is the amplitude of the $(m-1)$ harmonic for light of polarization i. If we consider Fig. 1, we see that $2s$ is just the period of the fundamental of the electric field when the center-to-center spacing of adjacent fingers is s.

For the $(m-1)$ spatial harmonic we define a grating vector k_m which is normal to the plane of constant index—in our geometry parallel to the z direction—and has magnitude

$$|k_m| = m\frac{2\pi}{(2s)} = \frac{m\pi}{s}. \tag{2}$$

The propagation vector for a waveguide mode with effective index n_w lies in the waveguide plane, points in the direction of power flow, and has magnitude

$$|k_w| = 2\pi n_w/\lambda_0. \tag{3}$$

If such a mode is scattered by a periodic index variation into a new direction, then conservation of momentum would imply that

$$k_w - k_s = k_m. \tag{4}$$

Here k_s is the propagation vector of the scattered wave.

The scattering of a plane wave from a periodic potential conserves momentum in precisely this form [28]. It has also been shown [29] that a similar conservation law can be used for the scattering of a waveguide mode which has a well-defined momentum into another waveguide mode or a plane wave (radiation mode) which also has well-defined propagation constants. Thus we can use (4) to describe the scattering of a waveguide mode with propagation vector k_w into a second mode in a new direction with propagation vector k_s.

The Bragg condition may be stated as

$$|k_w| = |k_s|. \tag{5}$$

This means that the phase velocity of the scattered wave is unchanged and the vectors are aligned as illustrated in Fig. 2. From (2) and (5) and by simple geometry

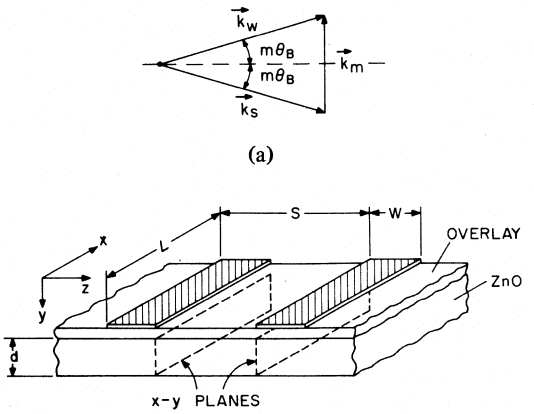

Fig. 2. (a) Vector diagram for calculation θ_B. (b) Section through waveguide and interdigital line showing x-y planes used in resistance calculation.

$$\sin(m\theta_B') = \frac{m\lambda_0}{2(2s)n_w} \tag{6}$$

where θ_B' is the Bragg angle for the fundamental period of the index variation and $m\theta_B'$ is the Bragg angle for the $(m-1)$ harmonic of the index variation. If, after scattering, the light passes from the medium of index n_w to a medium with index n_0, the Bragg angle measured in the medium n_0 is

$$\sin(m\theta_B) = \frac{m\lambda_0}{2(2s)n_0}. \tag{7}$$

Usually, the second medium is air or vacuum, $n_0 = 1$. In this case, θ_B is called the external Bragg angle and θ_B' is called the internal Bragg angle. Note that the angle between the undiffracted light and the diffracted light is $2\theta_B'$ internally and $2\theta_B$ externally.

The simple momentum conservation analysis assumes that the periodic medium extends an infinite distance along x so that the direction of k_m is precisely defined. In this case when θ is set to the Bragg angle, $(m\theta_B)$ for the $(m-1)$ harmonic, the ratio of the intensity of the diffracted light to the intensity of the light entering is given by [14]

$$\frac{I_m}{I_0} = \sin^2(\Delta\phi_m/2) \tag{8}$$

where I_m is the intensity diffracted at an angle $2m\theta_B$ to the direction of the entering light of intensity I_0, and $\Delta\phi_m$ is the amplitude of the phase change associated with the mth spatial period of the index variation. For infinite L the intensity of the diffracted light as θ departs from the Bragg angle is zero. Thus light is scattered into a solitary order at $m\theta_B$. When L is finite the direction of k_w is not precisely defined. Here, for angles θ other than $m\theta_B$, the intensity of the diffracted light is less than that given by (8). If a plot of I_m/I_0 is made as a function of $\theta - m\theta_B$, the width $\Delta\theta$ of the resulting "angular tuning" curve at I_m/I_0 equal to one-half its value at $\theta = \theta_B$ is given by [15]

$$\Delta\theta = \frac{n_w\lambda_0}{2L}\frac{\cos(m\theta_B')}{\sin(m\theta_B)\cos(m\theta_B)}.$$

For small values of $m\theta_B$ this becomes

$$\Delta\theta = \frac{2sn_w}{mL}. \tag{9}$$

As L approaches zero $\Delta\theta$ approaches infinity and momentum can be conserved for all values of θ giving rise to a thin grating type of diffraction in which multiple orders are observed as contrasted to the Bragg or "thick" case which allows only a single order. When $L >> (2s/m)^2/2\pi\lambda_0$, the diffraction is well characterized by (8) and only a single diffraction order need be considered [13].

To make use of (8) the amplitude of the phase change must be found as a function of the applied voltage and material properties. We now identify $(\Delta n_i)_m$ as the amplitude of the $m-1$ space harmonic of the electrooptic index change. $(\Delta n_i)_m$ will be found from (1) by setting E_z equal to $(E_z)_m$, the amplitude of the mth space harmonic of the field. The index $i = 1, 2, 3$ refers to the polarization direction which we have earlier identified with the TE and TM waveguide modes. We will drop this index and keep in mind that the calculation refers to a single polarization or waveguide mode.

The phase-change amplitude is related to the index-change amplitude by

$$(\Delta\phi)_m = \frac{2\pi(\Delta n)_m L}{\lambda_0}. \tag{10}$$

Using (1) and (10) we find

$$(\Delta\phi)_m = -\pi r_{33} n_3^3 \frac{L}{\lambda_0} (E_z)_m \tag{11}$$

for TE waveguide modes, and

$$(\Delta\phi)_m = -\pi r_{13} n_1^3 \frac{L}{\lambda_0} (E_z)_m \tag{12}$$

for TM waveguide modes.

Up to this point we have assumed both E_z and the light-intensity distribution to be constant in the y direction. Neither, however, is in fact constant. Thus, in order to make a rigorous calculation, we would have to average the applied field over the light-intensity distribution to find the correct value for use in (12).

The TE_0 and TM_0 modes of a symmetrical optical waveguide of the type we are studying has a symmetrical distribution of optical field centered in the waveguide film of form $\cos y$. (The origin of y is taken in the film center.) Engan [16] has analyzed the fields of interdigital surface electrodes and shows that $(E_z)_m$ falls off with distance from the surface as $\exp -(2m+1)(\pi/s)y$. For our waveguide thickness $y \sim 1$ μm and with $s \sim 8$ μm, the exponential may be expanded for $m = 0$ as $1 - (\pi/s)y$. Thus, with a roughly linear variation of E_z across the symmetric light distribution, a reasonable estimate might be considered to be obtained by using the value of E_z at the waveguide center in (12). This value of E_z may be expressed as a constant multiplied by the voltage applied between the electrodes by using Engan's calculation. Thus $(E_z)_m$ will be taken as equal to $A_m V_0$ and I_m/I_0 has the form $I_m/I_0 = \sin^2 BV_0$. For $m > 0$ the approximation will be much poorer than for $m = 0$.

Values of A_m for the two circuit geometries we consider are listed in Table I. Using these values in (11) the phase-change amplitudes as a function of V_0 for some of the space harmonics are also tabulated. With these amplitudes it is a simple matter to calculate the diffracted intensity ratio I_m/I_0 from (8). Values of V_0 required to obtain I_m/I_0 equal to 50 and 80 percent are included in Table I.

We note that I_m/I_0 increases almost as the square of V_0 and also as the square of the interaction length L.

C. Power Requirements

In general modulator applications it is conservative to assume that the power required to drive the modulator will be equal to the reactive power P_c. In our case, for a peak voltage V_0 this is given by [17]

$$P_c = \frac{\pi}{2} CV_0^2 \Delta f \tag{13}$$

where C is the capacitance of the interdigital circuit. Equation (13) is appropriate for pulse modulation.

For analog rather than pulse modulation the modulator will be biased with a dc voltage equal to $V_0/2$ so that as the applied signal swings positive and negative around the bias value direct frequency doubling due to the sine-squared response is not encountered. This also saves power. The bounding expression for the power here becomes

$$P_c = \frac{\pi}{8} CV_0^2 \Delta f. \tag{14}$$

In our experiments we measure V_0. The actual power dissipated in the modulator will, however, be given by

$$P = P_c \tan\delta \tag{15}$$

where $\tan\delta$ is the loss tangent associated with the materials which form the dielectric for the interdigital circuit. C may be found from a formula given by Engan [16]. Some typical values of C and of the capacitive power required in milliwatts per megahertz calculated from (13) and (14) are given in Table I.

Loss tangents of insulating crystals are in the range $1\text{-}2 \times 10^{-3}$. From Table I it can be seen that the power dissipated in the modulator is on the order 1-10 mW at frequencies in the gigahertz range.

We should observe that the frequency response of the electrooptic effect is in the region of 10^{14} Hz. The practical frequency limitation of electrooptic modulators is therefore set by circuit conditions. Since the interdigital line is basically a capacitive circuit we would expect that with simple connections the modulation rise times and frequency responses will be bounded by the RC time constant. Here R is the internal resistance of the supply, which will generally be 50 Ω and C is the capacitance of the interdigital line. For our values an RC time constant of about 0.5 ns is expected. Faster response than this can in principle be obtained by using appropriate networks.

D. Effects Due to Free Carriers

The resistivity of the epitaxial ZnO used in these experiments is controlled by compensation. It is of interest therefore to assess the effect that conductivity in the waveguide may have on the operation of the electrooptic grating.

There are two cases that may be distinguished and treated. These are a) electrodes in ohmic contact with the ZnO and b) electrodes fully insulated from the ZnO. Although the circuit in an actual modulator may be in poor contact or have slightly rectifying contacts, treatment of these two cases will provide bounds on the possible degradation that we would expect conductivity to cause in operating the modulator.

Case a) applies to gratings deposited directly on the ZnO. Case b) applies ideally to gratings deposited on a good insulating overlay. Finite conductivity can affect the operation either by carriers moving to alter or cancel the electric fields or by heating effects. In case a) we note that as long as ohmic contact is present the direct effect of free carriers on the electric field is zero. Current flows along the field lines which remain unaltered as long as V_0 is maintained. Here the heating effect will be the important one, and we will treat this case later.

In case b) the carriers will distribute on the insulating layer in a way that tends to cancel the electric field in the waveguide. We estimate the magnitude of the field cancellation as follows. The volume available in the ZnO to supply charge to each finger of the electrode structure is SLd where d is the waveguide thickness [see Fig. 2(b)]. The total available charge in this volume is

$$Q = SLd/\rho\mu \tag{16}$$

where ρ is the resistivity and μ the mobility. To get a worst case estimate imagine that Q is uniformly distributed on a plane surface of area dL (the waveguide thickness times the finger length), located midway between two adjacent fingers, and parallel to the x-y plane. The field of this "surface" charge will be parallel to E_z, of opposite sign, and will have magnitude

$$E = \frac{Q}{\epsilon\epsilon_0 Ld} = \frac{10^4 s}{\epsilon\epsilon_0 \rho d} \tag{17}$$

where s is in centimeters, ρ is in ohm centimeters, μ is in square centimeters per volt second, ϵ_0 is in farads per meter, and E is in volts per meter. The effective field $E_z' = E_z - E$. The mobility of epitaxial ZnO has been found to be on the order of 100 $cm^2/V \cdot s$. Using this value and taking the dielectric constant of ZnO to be 8, E_z' is plotted as a function of ρ with V_0 as a parameter in Fig. 3. As can be seen, for $\rho > 10^5\ \Omega \cdot$ cm, $E_z' \sim E_z$ for any appreciable V_0. For ρ below $10^3\ \Omega \cdot$ cm, the fields will be significantly reduced.

The calculation we have just made assumes that the only volume available to supply charge is that encompassed by the waveguide region under the interdigital circuit. Actually, the entire waveguide can act as a source of charge. The available waveguide volume is roughly 10^3 times larger than the volume under the circuit. Thus our calculation applies for times short compared to the time necessary for carriers to drift to regions under the circuit from remote waveguide regions. We may

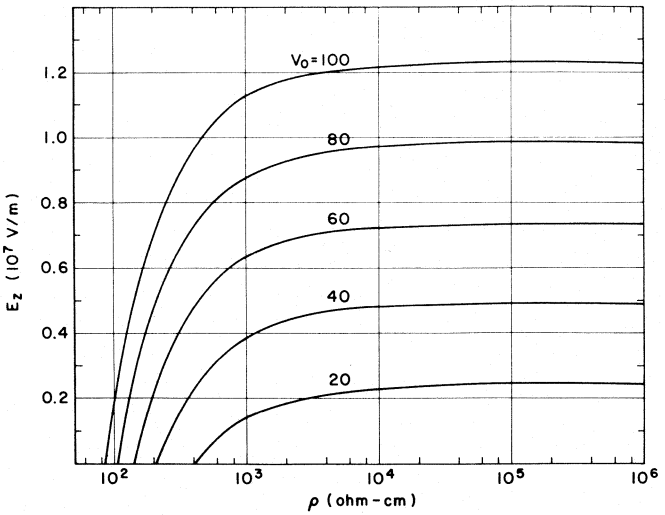

Fig. 3. Plot of z component of net electric field E_z' as a function of resistivity ρ. This plot shows how field is reduced by carriers when the electrodes are insulated from the waveguide.

crudely estimate this time as follows. Assume that a characteristic time is the time necessary for the carriers to drift from a median distance l_m in the waveguide to the circuit. The fields driving the carriers will be small and due to the fringing fields of the circuit edges. The edge field will be roughly in the ratio S/l_m to the fields in the circuit. Thus we can write the characteristic time as: $t_c = l_m/\mu E_{\text{fringing}}$, where $E_{\text{fringing}} = (S/l_m)E \sim (10^{-3} \times 10^3 V_0)$(V/cm). For $\mu = 100$ and $l_m = 1$ cm we have $t_c = 10^{-2}/V_0$. For $V_0 = 100$ V, $t_c = 10^{-4}$ s. Thus, very roughly, we can say that the calculation of field reduction can be used for frequencies well above 10 kHz or pulses much shorter than 10^{-4} s. At frequencies below these values we might expect much stronger reductions than predicted by (7) (see Fig. 3) and at dc we might expect almost complete cancellation for resistivities on the order of $10^5\ \Omega \cdot$ cm.

We now consider the effect finite resistivity will have because of ohmic heating and the resultant thermal changes in refractive index.

As an approximation assume that current flows uniformly in the z direction through the waveguide between x-y planes located at the near edges of two adjacent electrodes [see Fig. 2(b)]. In this approximation the resistance between two adjacent fingers is

$$R = \frac{\rho(s - w)}{Ld}. \tag{18}$$

Assuming the applied voltage is dropped across R, the ohmic power density P_0 is

$$P_0 = \frac{V_0^2}{\rho(s - w)^2}. \tag{19}$$

Mosekilde *et al.* [18] have calculated the temperature rise in an epitaxial layer with a uniformly distributed heat input. If we note that the main cooling takes place in the substrate and assume that heat flow parallel to the waveguide plane is negligible as compared with heat flow normal to the plane, we may

use their results. Doing this, the steady-state temperature rise ΔT is given by

$$(\Delta T)_{DC} = \frac{dbV_0^2}{K\rho(s-w)^2} \tag{20}$$

where K is the heat conductivity in watt centimeters per square centimeter in degrees Kelvin, b is the substrate thickness, 0.05 cm in our experiments, and all lengths are in centimeters. Equation (20) represents the temperature rise in the waveguide areas between adjacent fingers. In this approximation we assume that the waveguide area covered by a finger has no heat input and we also neglect heat flow into these regions.

The steady-state temperature will be reached in a time t_{DC} given by

$$t_{DC} = 2b^2/D \tag{21}$$

where $D = K/C_v$ and C_v is the heat capacity in joules per cubic centimeter in degrees Kelvin. For ZnO, $C_v = 2.75$, $K = 0.285$, $D = 0.103$, and for our experiment t_{DC} is approximately 50 ms.

We now briefly consider pulsed conditions. For pulses 50 ms or longer the dc temperature rise may be used. For pulses shorter than 50 ms the temperature rise will be less than $(\Delta T)_{DC}$ and may be found from a more complex formula given in [18]. We have plotted $\rho\Delta T/V_0^2$ as a function of pulse length t in Fig. 4. By use of this illustration the localized temperature rise can be found for any value of ρ, V_0, and t.

Our approximate calculation says that finite conductivity will result in localized heating between the finger pairs. This will occur when the electrodes are in ohmic contact with the ZnO. The temperature will be periodic with a spatial period equal to S.

Next we shall consider what this periodic temperature variation does to the index of refraction because a thermally induced index of refraction grating may interfere with the electrooptic grating.

A temperature change can affect the refractive index in three ways—by direct material expansion, through temperature dispersion of the index of refraction, and through the creation of stress birefringence. We expect the temperature dispersion to be the dominant effect and we will give an estimate of its magnitude.

Near room temperature the temperature dispersion in ZnO is approximated by [19]

$$(\Delta n)_T \sim 3 \times 10^{-7} T\Delta T. \tag{22}$$

By using (22) in conjunction with Fig. 4, $(\Delta n)_T$ can be found for a variety of voltages, resistivities, and pulse lengths.

For the purpose of evaluating the possible effect of $(\Delta n)_T$ on the operation of the electrooptic phase grating we make the arbitrary assumption that serious problems may arise when the thermal index change is 10 percent of the electrooptic index change or

$$(\Delta n)_T = 0.1(\Delta n) \text{ electrooptic.} \tag{23}$$

If we consider only the fundamental spatial frequency of the electrooptic effect, (23), in conjunction with (1) and the field

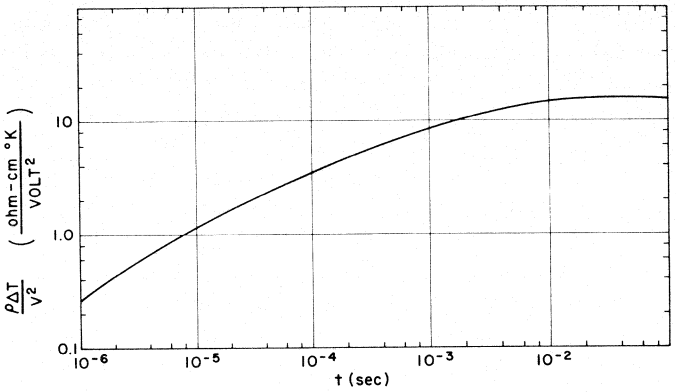

Fig. 4. Plot of $\rho\Delta T/V_0^2$ as a function of pulse length t. The space periodic-temperature rise ΔT can be found if the resistivity ρ and the pulse voltage V_0 are known.

harmonic values listed in Table I for the experimental circuit, gives

$$\Delta T = 0.14V_0 \tag{24}$$

as the limiting temperature rise. The constant is chosen so that with V_0 in volts ΔT is in degrees centigrade. In dc or long-pulse operation using (20), (24) will be satisfied when $\rho = 10^2 V_0$. The long-pulse heating effect is, of course, a problem only when the electrodes are in contact with the ZnO. For example, at $V_0 = 100$ V, ρ must be greater than $10^4\ \Omega \cdot$ cm. In the case of well-insulated contacts, the thermal effect will not be important.

We now may summarize our thoughts on the effect of finite conductivity on the operation of the electrooptic grating. In the case of electrodes in ohmic contact, carriers will cause localized heating which results in the production of a phase grating of period s (half the period of the electrooptic grating). The thermal grating will be seen at $\theta = 2v_B$ (first harmonic). We might also expect to see associated thermal lensing effects. This heating effect will be important if the resistivity is below about $10^4\ \Omega \cdot$ cm in long-pulse or CW operation.

In the case that electrodes are well insulated from the ZnO, the carriers will tend to cancel the fields. Here too it turns out that resistivities below $10^4\ \Omega \cdot$ cm will cause degradation.

We conclude, therefore, that it is important to ensure that material of the highest resistivity be used. Even with ρ on the order of $10^6\ \Omega \cdot$ cm we would expect low-frequency degradation although no high-frequency effects (frequency above 100 kHz) would be observed.

E. Acoustic Surface-Wave Generation

In general, linear electrooptic materials are also piezoelectric. The interdigital structure used to create the electrooptic phase grating is also capable of launching acoustic surface waves on piezoelectric materials at a resonant frequency determined by the electrode spacing and acoustic surface-wave velocity. We wish, therefore, to consider acoustic surface waves.

Coupling between the interdigital electrode structure and acoustic surface waves will take place at the resonant frequency

$$f_a = \frac{v_a}{2s} \tag{25}$$

where v_a is the surface acoustic-wave velocity. This has been determined empirically for the epitaxial ZnO on sapphire system by Pizzarello [20]. Using his results, for a nominal waveguide thickness of $d = 1$ μm and our spacing ($s = 7.6 \times 10^{-4}$ cm), $v_a = 5.4 \times 10^5$ cm/s and $f_a = 355$ MHz.

Pizzarello also gives the coupling factor k_a^2 as a function of the ZnO film thickness. For a 1-μm-thick layer, $k_a^2 = 2 \times 10^{-3}$. This value represents rather weak coupling. Thus, at frequencies near f_a, we would expect to couple energy into the acoustic surface wave but with rather low efficiency.

At frequencies below f_a the acoustic coupling would be expected to be negligible.

With very fast pulse rise times some of the energy will couple into the acoustic wave. The effect of this is uncertain.

III. Experimental Methods

A. Circuit Preparation

Several methods of forming the interdigital circuit on the waveguides were tried. The most successful was a photoresist lift-off technique. In this method the pattern is first contact-printed and developed onto a spun photoresist layer on the waveguide. Chromium films and then gold films are evaporated over the developed photoresist surface. Subsequent treatments in acetone removes the undeveloped photoresist along with its metal coating, leaving behind the pattern.

B. Measurement Procedures

A schematic diagram of the measuring setup is shown in Fig. 5. Laser light is focused on the input prism with a 20-cm lens. Provision is made to rotate the waveguide assembly around the z axis to reach the correct coupling angle for the mode to be studied. Small y- and z-translational motion of the lens allows the focused spot to be moved to optimize the coupling.

The waveguide is positioned so that the guided light passes beneath the modulator fingers. Provision is made to rotate the modulator around the y axis. Because the laser beam remains fixed in direction this rotation results in varying the angle between the guided light and the finger direction. This angle is

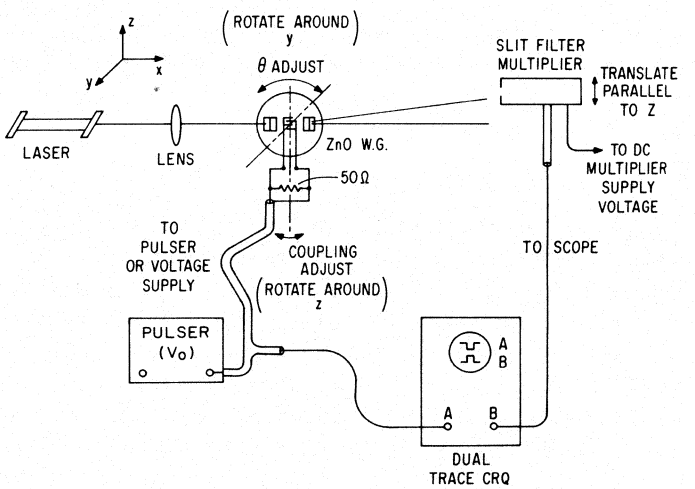

Fig. 5. Schematic diagram of experimental arrangement for measuring diffraction percentage and angular tuning range.

the θ of the theoretical description; it can be read to 30″ on the precision rotator used.

Light coupled out of the waveguide by the second prism passes through a slit and a filter into the window of an RCA 6199 photomultiplier. The slit-filter-multiplier assembly is located about 50 cm from the modulator and can be translated parallel to the z-direction. The motion allows the detector to be positioned to receive either the main beam or the diffracted beam.

With no voltage applied to the deflector it is possible to observe the Bragg diffraction due to the small increase in absorption for guided light traveling under a metal finger as compared with the guided light traveling under the gap between fingers. The effect is shown by the appearance of a second weak spot on a screen placed in front of the detector when θ is set at an angle which is twice θ_B for the electrooptic grating. This observation simplifies alignment. With θ set approximately to $m\theta_B$ for the desired harmonic, voltage from the pulser is applied and the signal produced by the modulated light can be seen on the scope when the detector is translated to the position of either the undiffracted or the diffracted beam. A 50-Ω matching termination is placed in parallel with the electrodes to avoid strong mismatch reflection and undue pulse distortion. The voltage measured is that across the termination. In an actual system a network or coaxial isolator would be employed to adsorb the reflected power. In the latter case, the power load on the source would be the capacitive power described earlier. The pulser is replaced by other voltage sources for certain measurements.

IV. Experimental Results and Discussion

In this section we will describe and discuss results of measurements made on three modulators. Samples A, B, and C have 1000-Å Al_2O_3 overlays and interdigital circuits deposited directly on the overlay. The samples are grown with different thicknesses such that sample A has seven TE and seven TM modes; sample B has five TE and five TM modes; and sample C has three TE and three TM modes.

A. Percentage Diffraction Measurements

Measurements of the percent output deflected as a function of voltage under a variety of operating conditions for the three samples are given in Figs. 6–8. Measurements on A and B are made under pulsed conditions with pulses approximately 0.5 μs long and pulse repetition rates of 20 kHz, giving a 1-percent duty cycle. Relatively short pulses are used to avoid arcing in the air above the interdigital circuits. The duty cycle is kept low to avoid overheating the 50-Ω load resistor at the higher pulse voltages. As mentioned earlier, proper isolation of source would be employed in systems use, and the duty cycle would not be restricted. Sample C was protected from arcing in the atmosphere by coating the top surface of the electrodes with a layer of polyester. The measurements on sample C were made under a variety of pulse lengths and frequency conditions and will be described in greater detail below. The data presented in Fig. 8 were, however, made under the same short-pulse conditions as the data presented for samples A and B.

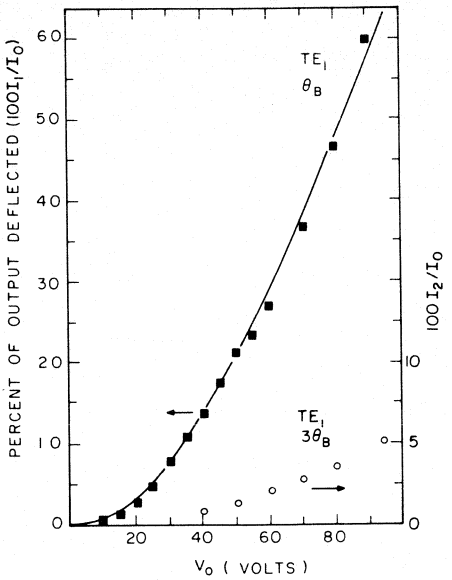

Fig. 6. Percent of light coupled out of the waveguide deflected (I/I_0) as a function of voltage for sample A. Squares are the data for the TE_1 mode with θ set to θ_B. Circles are for the TE_1 mode with θ set to $3\theta_B$ (second space harmonic). The scale factor is doubled for the $3\theta_B$ points. Solid curve is $\sin^2 BV_0$ normalized to θ_B data at V_0 = 50 V.

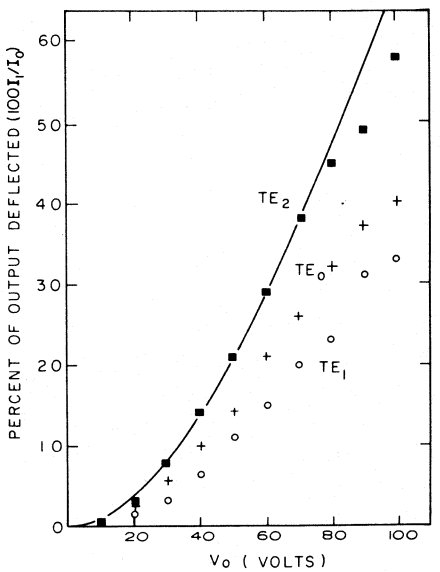

Fig. 7. Percent of light coupled out of the waveguide deflected (I/I_0 percent) as a function of voltage for sample B. All data taken with θ set to θ_B. Crosses TE_0, circles TE_1, squares TE_2. Solid curve is $\sin^2 BV_0$ normalized to TE_2 data at V_0 = 50 V.

The percent output ($100\, I_m/I_0$) deflected at the Bragg angle for the fundamental and for the second space harmonic of the grating in sample A is shown in Fig. 6. Here the TE_1 waveguide mode is used. The solid curve is a plot of $\sin^2 BV_0$, normalized to the data at V_0 = 50 V. The functional agreement is very good. The second space harmonic ($\theta = 3\theta_B$) data are plotted with a two times increase in scale factor. The second space harmonic results are in the expected ratio to the fundamental results.

In Fig. 7 the percentages deflected for the TE_0, TE_1, and TE_2 waveguide modes of sample B are plotted. All three sets of measurements are taken at $\theta = \theta_B$. As before, the solid curve $\sin^2 BV_0$ is normalized to the TE_2 result at V_0 = 50 V. We note that the TE_1 and TE_0 values are substantially less than the TE_2 values.

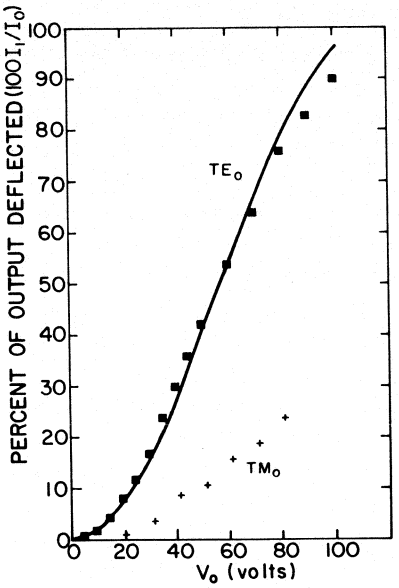

Fig. 8. Percent of light coupled out of the waveguide (I/I_0 percent) deflected for the TE_0 (squares) and TM_0 (crosses) waveguide modes of sample C as a function of voltage V_0. θ is set at θ_B. The solid curve is $\sin^2 BV_0$ normalized to TE_0 data at V_0 = 70 V.

In Fig. 8 the percent output deflected for the TE_0 and TM_0 waveguide modes of sample C is plotted. For these data θ is set to θ_B, the Bragg angle for the fundamental spatial period. The solid curve is a plot of $\sin^2 BV_0$ normalized to the TE_0 data at V_0 = 70 V. TE_0 data follow the sine-squared law reasonably well, showing some rolloff at the higher voltages. The ratio of TM_0 to TE_0 deflection percentage is in agreement with the theoretical expectation that this ratio should be as $(r_{13}/r_{33})^2$. The measured deflection is 80 percent at 80 V.

The data presented in Figs. 6-8 clearly show the correct functional form to be attributed to the action of an electrooptic phase grating of fundamental period $2s$.

The theoretical treatment accounts reasonably well for the observed differences between TE and TM waveguide modes and for the difference between the deflection at the fundamental spatial-frequency angle θ_B and that at the second-harmonic angle $3\theta_B$. The magnitude of the percentage deflection is less well accounted for. The theory predicts that 50-percent deflection should be obtained at V_0 = 41 V. Our best measured value (Fig. 8) is 50-percent deflection at 55 V. The mode-to-mode variation shown in Fig. 7 gives some indication of the sensitivity of the deflection to the exact field distribution and reinforces our recognition of the very approximate nature of the field and deflection-efficiency calculations. We observe no mode conversion in the modulated beams.

The total insertion loss including losses in the coupling prisms ranges between 85 and 95 percent. The variation apparently depends on the care with which the prisms are clamped in place.

B. Pulse Response and Carrier Effects

The high-frequency capabilities of the electrooptic waveguide grating modulators are illustrated by typical pulse-response measurements shown in Figs. 9 and 10.

Fig. 9 is a photograph of a dual oscilloscope trace of the pulse voltage and diffracted light. The light output follows the voltage with no apparent change in rise or fall time to within the 10-ns limitation of the Tektronix 547 oscilloscope and 1A1 dual-trace plug-in unit used. This pulse behavior, using longer pulses, however, is typical of the conditions observed when making the deflection percentage measurements described earlier.

To observe faster response times a delay-line pulser with 1-ns rise time was used. The multiplier output is observed with a 1S1 sampling plug-in unit installed in the 547 oscilloscope. The resultant oscilloscope trace of the diffracted light is shown in Fig. 10. Here we observe a rise time of less than 3 ns. This too is equipment-limited because the rise time of the RCA 6199 multiplier is on the order of 3 ns. Thus, to within our equipment limitations, we know that rise times of less than 3 ns are achieved. The actual limitation on the rise time, as has been pointed out earlier, is the RC time constant which is about 0.5 ns for the experimental circuit. At the other extreme we note that we cannot observe any diffraction with dc voltages applied.

At 60 Hz a fair amount of modulation is observed but is less than the short-pulse operation. This effect is shown in Fig. 11. Here the TE_0 data for sample C are plotted for two cases. The squares are for short-pulse operation, as in Fig. 8, while the crosses are for operation at 60 Hz. As might be expected at the higher voltages, where much charge is required for cancellation, little degradation is observed. At lower voltages a stronger degradation occurs. In general, this is in qualitative agreement with our analysis of the critical time.

To investigate the effect of free carriers further we make use

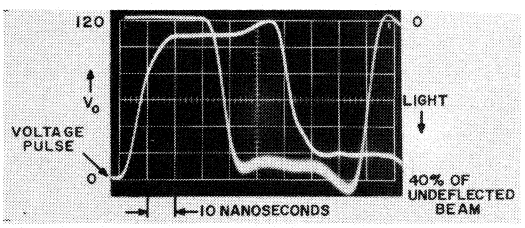

Fig. 9. Oscillogram of deflected output and applied voltage. Sample A. The delay between light and voltage pulse is due to the length of coaxial cable used. (10 ns/div.)

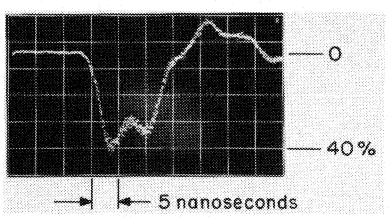

Fig. 10. Oscillogram of deflected output taken on sampling scope. The applied voltage from delay-line pulser has 1-ns rise time. The apparent response is limited by the 3-ns rise time of the photomultiplier. (5 ns/div.)

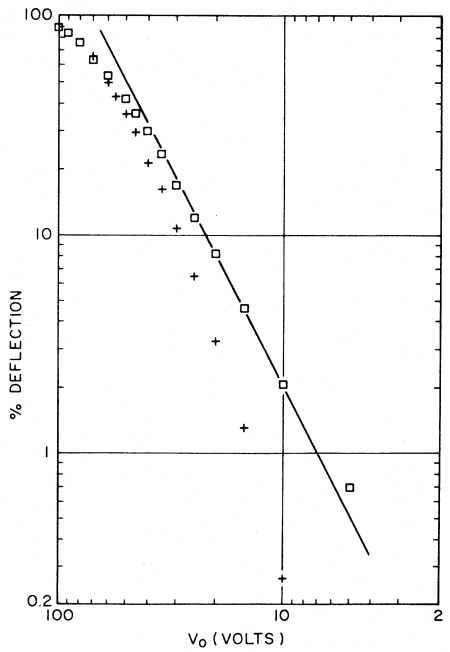

Fig. 11. Comparison between response to fast and slow voltage variation. Squares are deflected intensity for 0.5-μs pulses. Crosses are deflected intensity for 60 Hz.

of the photoconductive properties of the ZnO waveguide. We can create carriers by illuminating the waveguide with ultraviolet light and investigate how this affects the modulation. The relation between the density of carriers generated and the light intensity depends on the recombination mechanism. If we assume that radiative recombination between photoexcited electrons and holes dominates, then the carrier density will be proportional to the reciprocal square root of the light intensity [21].

The results of such a measurement on sample C are shown in Fig. 12. The closed circles are the experimental values at $V_0 = 60$ V. The intensity of the ultraviolet light is varied with a calibrated iris diaphragm and the observed reduction in the diffracted light is measured. The ordinate is the square root of the reduction in diffraction percentage which is proportional to the field. The abscissa is proportional to the resistivity which is lowered by increasing the incident ultraviolet radiation. Thus the theory (17) (see Fig. 3), may be used. The solid curve is the theoretical calculation normalized at high resistivity. There is some modest agreement. The practical implication of being able to control light with light in this type of waveguide should be noted.

C. Variation with θ

We note at this point that the average measured value of θ_B agrees to within our measurement error of $\pm 0.07^\circ$ (4′) with the theoretical value of 1.19°. To further demonstrate the thick-grating nature of these devices we measure the change in deflected output as θ is varied around θ_B. Results for sample B are given in Fig. 13.

The half-widths $\Delta\theta$ as measured from these curves show small variances around the calculated value. The calculation assumes a parallel beam. In the experiment the waveguided

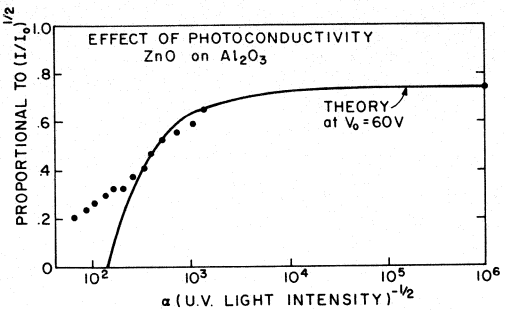

Fig. 12. Effect of photocarriers on deflected intensity. The ordinate is proportional to $(I/I_0)^{1/2}$ and hence is a measure of the net internal electric field. The abscissa is proportional to the density of photo-induced carriers.

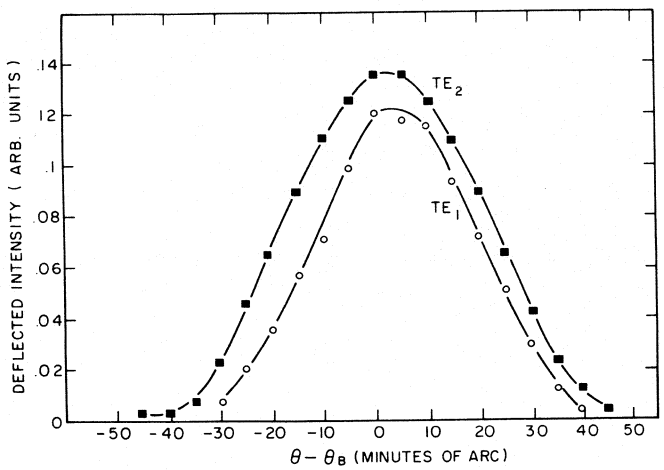

Fig. 13. Deflected intensity (arbitrary units) as θ is varied around θ_B. Sample *C*. Squares TE_2, $\Delta\theta = 0.73°$. Circles TE_1, $\Delta\theta = 0.60°$.

light has an angular spread that depends on the exact condition of focus and spatial position in the prism. These conditions are not closely controlled and will vary as one changes from mode to mode. Thus the measured spread is really a convolution of the spread of angles in the guided light with tuning of the Bragg effect.

The type of variation encountered is clearly shown in Fig. 13. The TE_2 data have $\Delta\theta = 0.73°$ while the TE_1 data have $\Delta\theta = 0.60°$ which is much closer to the theoretical value of 0.58°.

Despite these irregularities the general angular-tuning behavior of the modulators is in agreement with what would be expected for a Bragg phase grating and reinforces our identification of our observations as being due to electrooptically induced Bragg phase diffraction gratings.

D. Thermal Effects

The samples we have discussed thus far have had resistivities in the 10^6-$\Omega \cdot$ cm range. In this range we would not expect and indeed did not observe any thermal effects. In many early attempts we were unable to maintain the resistance of the ZnO layer and after circuit formation ended up with low-resistivity material. Under these conditions we measured ohmic resistances between the contacts on the order of 1000 Ω or less which indicated resistivities in the 10-100-$\Omega \cdot$ cm range. Here we did observe thermal-grating effects as would be expected from the analysis.

E. Use of Data and Theory to Design Interdigital Electrooptic Waveguide Modulators

On the basis of the measurements we have described in this section we may say with some confidence that the analysis in Section IV gives the correct functional relationships between the parameters of the interdigital electrooptic waveguide modulator. The analysis, however, underestimates the voltage required to obtain a given percentage deflection by 30 percent. This is not surprising and might even be considered gratifying in light of the rather coarse approximation made in taking the average value of the electric field produced by the grating. In general, the qualitative predictions of the theory as to pulse response and low-frequency operation are confirmed. We do not expect detailed quantitative predictions from this aspect of the analysis.

On the basis of our theoretical relations we have designed the parameters of an optimized interdigital modulator on ZnO. By increasing the interaction length to 0.5 cm and making the finger width equal to the finger separation ($w = s/2$), we find the parameters listed in Table I which may be compared with the experimental circuit. Voltages of around 25 V and powers on the order of a few milliwatts per megahertz would be expected.

Further improvement in this type of device can be achieved only by using superior materials such as the $LiNb_xTa_{1-x}O_3$ device recently reported [27].

V. Conclusion

Measurements on three epitaxial ZnO on Al_2O_3 waveguides with deposited interdigital electrode structures have been made. Behavior reasonably well characterized by the theory of electrooptic Bragg diffraction gratings is observed. Peak diffraction efficiencies as high as 80 percent at 80 V have been obtained. Diffraction by higher order space harmonics is observed and is in the ratio to the fundamental harmonic diffraction expected from theory. The ratio of diffraction between TE and TM modes is also in accord with the analysis. Our observations indicate that the theoretical description given here is adequate for design purposes.

We observe very high-frequency response and we predict even higher. We have little doubt that pulse response times of less than 1 ns can be achieved. Observations on low- and high-resistivity waveguides bear out our analysis of the thermal effects of carriers and indicate that this analysis can be used as a guide to resistivity requirements for the design of electrooptic grating modulators.

The research performed here confirms the feasibility of using electrooptical waveguides in a modulator-switching arrangement.

We have shown that our electrooptic grating waveguide modulator has the advantage of spatially separating the diffracted beam from the main beam and thus does not require a separate analyzer or strict control of the waveguide propagation characteristics as is the case for some other waveguide modulators. Furthermore, because of the spatial separation, a

number of grating modulators can be included on a single waveguide so that the output of one modulator can be used as the input to a second modulator, thus allowing a variety of logic and switching functions on a single waveguide. The spatial separation also aids in obtaining high extinction ratios in the diffracted beam. These features plus the extremely high-frequency response of our modulators leads us to conclude that they will find a wide variety of uses in the field of integrated optics.

References

[1] D. Hall, A. Yariv, and E. Garmire, "Observation of propagation cutoff and its control in thin optical waveguides," *Appl. Phys. Lett.*, vol. 17, pp. 127–129, Aug. 1970.

[2] J. M. Hammer, "Digital electro-optic grating deflector and modulator," *Appl. Phys. Lett.*, vol. 18, pp. 147–149, Feb. 1971.

[3] G. Zeidler, "Optical waveguide technique with organic dye lasers," *J. Appl. Phys.*, vol. 42, pp. 884–886, Feb. 1971.

[4] P. K. Tien, R. Ulrich, and R. J. Martin, "Optical second harmonic generation in form of coherent Cerenkov radiation from a thin-film waveguide," *Appl. Phys. Lett.*, vol. 17, pp. 447–450, Nov. 1970.

[5] L. Kuhn, M. L. Dakss, P. F. Heidrich, and B. A. Scott, "Deflection of an optical guided wave by a surface acoustic wave," *Appl. Phys. Lett.*, vol. 17, pp. 265–267, Sept. 1971.

[6] D. J. Channin, "Voltage-induced optical waveguide," *Appl. Phys. Lett.*, vol. 19, pp. 128–130, Sept. 1971.

[7] J. F. St. Ledger and E. A. Ash, "Laser beam modulation using grating diffraction effects," *Electron. Lett.*, vol. 4, pp. 99–100, Feb. 1968.

[8] J. N. Polky and J. H. Harris, "Interdigital electro-optic thin-film modulator," *Appl. Phys. Lett.*, vol. 21, pp. 307–309, Oct. 1972.

[9] P. K. Tien, R. J. Martin, R. Wolf, R. C. LeCraw, and S. L. Blank, "Switching and modulation of light in magneto-optic waveguides of garnet films," *Appl. Phys. Lett.*, vol. 21, pp. 394–396, Oct. 1972.

[10] J. M. Hammer, D. J. Channin, and M. T. Duffy, "Fast electro-optic waveguide deflectors modulator," *Appl. Phys. Lett.*, vol. 23, pp. 176–177, Aug. 1973.

[11] J. M. Hammer, D. J. Channin, M. T. Duffy, and J. P. Wittke, "Low-loss epitaxial ZnO optical waveguides," *Appl. Phys. Lett.*, vol. 21, pp. 358–360, Oct. 1972.

[12] D. J. Channin, "Optical waveguide modulation using nematic liquid crystal," *Appl. Phys. Lett.*, vol. 22, pp. 365–366, Apr. 1973.

[13] R. Adler, "Interaction between light and sound," *IEEE Spectrum*, vol. 4, pp. 42–54, May 1967.

[14] D. A. Pinnow, "Guide lines for the selection of acoustooptic materials," *IEEE J. Quantum Electron.*, vol. QE-6, pp. 223–238, Apr. 1970.

[15] H. M. Smith, *Principles of Holography*. New York: Wiley-Interscience, 1969, pp. 69–73.

[16] H. Engan, "Excitation of elastic surface waves by spatial harmonics of interdigital transducers," *IEEE Trans. Electron Devices*, vol. ED-16, pp. 1014–1017, Dec. 1969.

[17] I. P. Kaminow and E. H. Turner, "Electrooptic light modulators," *Proc. IEEE (Special Joint Issue on Optical Electronics with Applied Optics)*, vol. 54, pp. 1374–1390, Oct. 1966.

[18] E. Mosekilde, P. A. Lebwohl, and D. G. Carlson, "Transient heat flow from an epitaxial layer into the substrate," *Proc. IEEE* (Lett.), vol. 59, pp. 1030–1032, June 1971.

[19] Y. S. Park and J. R. Schneider, "Index of refraction on ZnO," *J. Appl. Phys.*, vol. 39, pp. 3049–3052, June 1968.

[20] F. Pizzarello, "Investigation of the surface acoustic wave properties of heteroepitaxial ZnO," *J. Appl. Phys.*, vol. 43, pp. 3627–3631, Sept. 1972.

[21] R. A. Smith, *Semi-Conductors*. New York: Cambridge, 1964, pp. 304–307.

[22] S. Ramo and J. R. Whinnery, *Fields and Waves in Modern Radio*, 2nd ed. New York: Wiley, 1960, pp. 135–138.

[23] *Handbook of Chemistry and Physics*, 50th ed., Chemical Rubber Co., 1969–1970.

[24] "Microwave acoustic and bulk device technique studies," Stanford Univ., Stanford, Calif., Tech. Rep. RADC-TR-70-46, 1970.

[25] M. Neuberger, "Zinc oxide data sheets," U.S. Dep. Commerce, AD425212, 1963.

[26] *Handbook of Lasers with Selected Data on Optical Technology*, 1st ed., Chemical Rubber Co., 1971.

[27] J. M. Hammer and W. Phillips, "Low-loss single-mode optical waveguides and efficient high-speed modulators of $LiNb_xTa_{1-x}O_3$ on $LiTaO_3$," *Appl. Phys. Lett.*, vol. 24, pp. 545–547, June 1974.

[28] E. I. Gordon, "A review of acoustooptical deflection and modulation devices," *Proc. IEEE (Special Joint Issue on Optical Electronics with Applied Optics)*, vol. 54, pp. 1391–1401, Oct. 1966.

[29] D. Marcuse, *Theory of Dielectric Optical Waveguides*. New York: Academic, 1974, ch. 4, pp. 132–172.

Near-Field Emission from GaAs Double-Heterostructure Laser Mirrors

B. W. HAKKI, MEMBER, IEEE

Abstract—The near fields of GaAs double-heterostructure (DH) laser mirrors are studied both in photoluminescent (PL) excitation and in lasing emission. The various liquid-phase-epitaxial (LPE) layers of the laser diode are optically delineated, with ∓ 0.1-μm resolution, in a wavelength-selective PL detection system. The near fields of the transverse lasing modes are correlated with the LPE layers that constitute the optical waveguide. With special emphasis on the large-cavity fundamental-mode Ppn'N laser, it is found that small changes in refractive index within the waveguide have pronounced effects on the distribution of stimulated power within the LPE layers. The fundamental mode is found to be contained within the slightly higher refractive-index gain region. This explains the previously observed localization of catastrophic mirror damage and the anomalously large angles of beam divergence. High-order modes are also excited in the gain region when its thickness and refractive-index step within the waveguide exceed some prescribed limits.

I. Introduction

THE potential practical importance of GaAs double-heterostructure (DH) injection lasers has led to increased interest in both CW and pulsed devices [1]-[5]. In addition to the basic operating characteristics such as power output, efficiency, and emission spectrum, the near-field emission from the laser mirror is of central importance in some applications where coupling to the laser is accomplished with optical fibers [6], [7]. The distribution of the stimulated near field within the waveguide is also important in determining the limits of catastrophic mirror damage, as well as the angle of divergence of the emitted beam. This paper describes the diagnostic techniques and gives results of measurements of stimulated near-field emission from GaAs DH lasers. Special emphasis is put on the study of the fundamental-mode Ppn'N laser in which mode control in a large cavity (2-3 μm) is achieved by restricting the gain region to $\approx\frac{2}{3}$ of the waveguide thickness [5]. The individual liquid-phase-epitaxial (LPE) layers of the laser mirror are delineated optically by photoexcitation. When the stimulated near-field distribution within the waveguide is related to the LPE layers, it is found that the shape of the lasing mode transverse to the junction plane is sensitive to the dopants added to the layers within the waveguide. In particular, the addition of a small amount (3.6 ∓ 1 percent) of aluminum to one of the layers in the waveguide, to achieve separate optical and carrier confinement, is found to lead not only to confinement of the fundamental mode to the gain region, but also to excitation of high-order modes in the gain region under certain conditions that have been predicted analytically [5]. As a result of this investigation it is possible to understand previous observations of localized catastrophic mirror damage [4] and apparent discrepancies (unreported) in beam divergence. This also has led to more detailed calculations of mode-intensity distribution that are in general agreement with experiment [8].

Manuscript received October 2, 1974; revised November 22, 1974.
The author is with Bell Laboratories, Murray Hill, N.J. 07974.

II. Emission from Laser Mirror

A. Measurement Technique

A schematic of the apparatus is shown in Fig. 1. Individual lasers are mounted in a fixture which allows a bias (dc or pulse) to be applied to the diode. The fixture is attached to (*X-Y-Z*) piezoelectric micrometers (PZM) that allow distance adjustment and calibration in the micron range. The laser mirror is imaged on a Si target of a vidicon camera tube by using a 100X oil-immersion metallurgical microscope lens. The high sensitivity of the Si diode array to the IR radiation is advantageous in this application. A beam splitter directs a 7993-Å-wavelength beam from a krypton laser onto the laser mirror through the objective lens.[1] The resultant photoluminescent (PL) emission from the laser is filtered through a slice of single-crystal CdTe, optically polished and antireflection coated with Al_2O_3. The bandgap absorption edge of CdTe situated at 8500 Å passes the GaAs PL emission but rejects the 7993-Å laser excitation. This arrangement also provides excellent contrast between the PL emission of GaAs which is longer than 8500 Å, and PL emission from $Ga_{0.7}Al_{0.3}As$ which is peaked at 6900 Å. This contrast delineates the laser LPE layers. The electron beam in the camera tube has the facility for electronic magnification ("zoom") of the image. The video signal is amplified and fed into a video monitor for display. In addition, to get a plot of local light intensity (linear scale) as a function of distance, the video signal is fed into an adjustable time-delay scope which is triggered by the horizontal-scan output from the scanner. The adjustable time delay allows any horizontal scan on the video monitor to be displayed as light intensity versus distance. A feedback loop from the scope gate to the video monitor causes local intensification of the particular horizontal line on the monitor. This method correlates the scope display with the video monitor image.

When distance measurements derived from this system are compared with those from a scanning electron microscope, agreement is obtained to within ∓ 0.1 μm. The Rayleigh resolution limit of $\lambda/2NA$ is 0.34 μm for the present optics, where λ is the free-space wavelength and NA is the numerical aper-

[1] Not shown in the schematic of Fig. 1 are means of directing light from a tungsten source to the laser mirror for ordinary viewing, as well as a defocusing lens for the krypton laser beam.

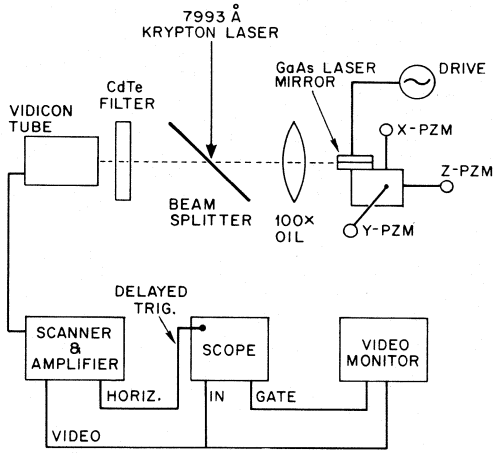

Fig. 1. Schematic of optical excitation and detection system used for studying the near-field emission from GaAs DH laser mirrors.

ture of the objective. The improved *distance* (not shape) resolution of 0.2 μm is due to two factors: 1) the increased contrast of photographic film; and 2) the use of well-defined inflection points in intensity scans to define boundaries between adjacent layers, as will be evident in later results.

To study the far-field radiation pattern of lasers, the IR laser beam is initially projected on the photosensitive surface of an image converter. The resulting visible image on the back surface is then focused on the camera tube. The use of the image converter is motivated by two reasons. First, the saturation level of the image converter at IR wavelengths is higher than that of the Si target. Second, the image converter eliminates the interference fringe lines seen in the Si target when the incident radiation is monochromatic.

B. Results

The Ppn'N lasers investigated are shown schematically in Fig. 2. Some devices have a final p-GaAs layer grown with heavy Ge doping to facilitate contacting, while others are terminated with the ternary P-$Ga_{0.7}Al_{0.3}As$ layer. Proton-beam bombardment is used to define stripes that are nominally 10 μm wide [9]. The main waveguide defined by the $Ga_{0.7}Al_{0.3}As$ layers is composed of a heavily Te-doped $Ga_{0.97}Al_{0.03}As$ layer which injects electrons into the Ge-doped GaAs layer. Hence the p-GaAs layer is the gain region, while the n'-$Ga_{0.97}Al_{0.02}As$ layer constitutes loss. When the thickness of the gain region is equal to or slightly larger than that of the loss region the electronic gain of the fundamental transverse mode is greater than that of higher order modes, and hence the fundamental mode is usually excited [5]. The choice of thicknesses for best mode discrimination depends on the degree of mode confinement within the gain region.

When such Ppn'N devices are studied in the system depicted in Fig. 1, the PL emission from the various LPE layers is shown in Fig. 3 for a particular laser diode. In this laser structure, a final 2.5-μm-thick p-GaAs layer is used for contacting, and the proton bombarded region in this layer has very low PL efficiency as evident from Fig. 3(a). This supports earlier measurements, in which proton bombardment had been shown to reduce the minority-carrier diffusion length as well as the radiative efficiency [10]. The stripe width, defined by

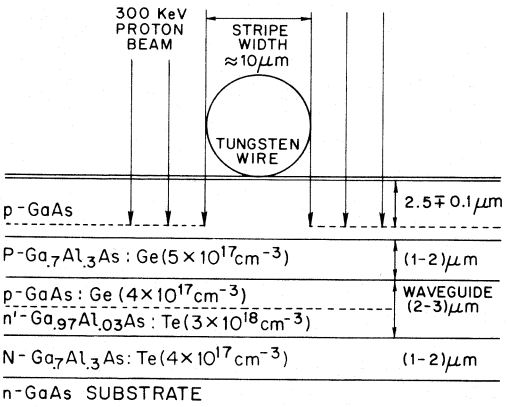

Fig. 2. The LPE layers that constitute the Ppn'N laser diode with a 10-μm-wide stripe geometry defined by proton bombardment.

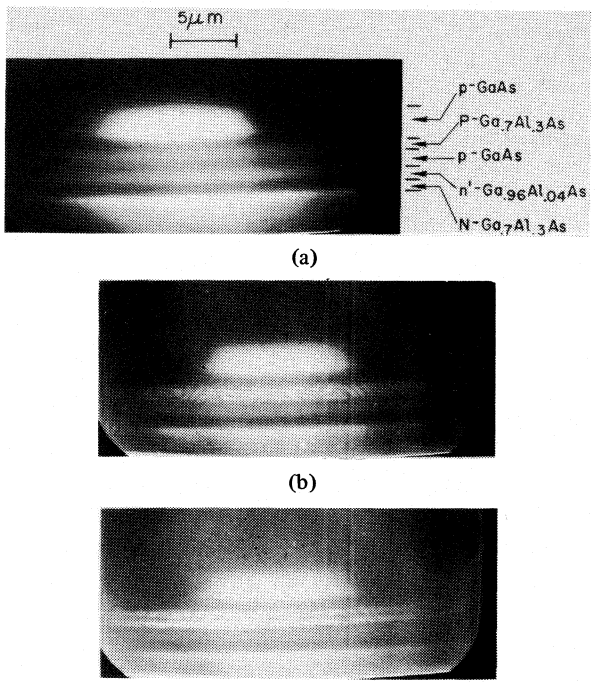

Fig. 3. Near-field emission from a Ppn'N laser. (a) The PL emission from the laser mirror. (b) PL emission and lasing fundamental mode. (c) PL emission and lasing first-order mode.

the unbombarded and hence bright region of the p-GaAs layer, is (9–12) μm wide. The boundary between the bombarded and unbombarded regions is tapered. The depth of penetration of the 300-keV proton beam in GaAs seems to be (2.5 ∓ 0.1) μm, as indicated by these PL measurements.

The waveguide region shown in PL emission in Fig. 3(a) contains a dark line separating the p-GaAs and n'-$Ga_{0.97}$-$Al_{0.03}As$ layers. This dark line is due to the space-charge region that exists in the unbiased diode. In this region photo-excited carriers are swept out by the field, and hence are unable to locally recombine radiatively.[2] Under conditions

[2]The level of PL intensity in the waveguide can be affected by whether the device is short circuited or open circuited. However, regardless of the circuit impedance, the space-charge region is always distinct as a dark line.

of PL excitation the influence of the space-charge region extends beyond its limited width due to the diffusion of the PL excited carriers. Hence the boundary between the n- and p-layers is difficult to locate with accuracy in this technique because of the width of the dark line in PL. If it is known *a priori* that the n-region is more heavily doped than the p-region, as is usually the case in Ppn′N structures, then most of the space-charge region occurs in the p-region. This can be checked experimentally by applying a reverse bias on the diode, and noting the direction of spread of the dark line.[3] Since the influence of the space-charge region on photo-excited carriers is greatest in the layer that contains the space-charge region, application of reverse bias usually provides an unambiguous determination of the p–n interface.

When a forward-bias pulse in excess of lasing threshold is applied to the diode, the resultant near field of the stimulated emission can be observed. For instance, Fig. 3(b) shows the stimulated fundamental mode excited in the same laser as that in Fig. 3(a). Here both PL and stimulated emission are depicted simultaneously. This method of observation provides a direct correlation between the near field of the stimulated emission and the various LPE layers. (The monochromatic emission gives rise to multiple reflections in the camera target and the resultant interference patterns associated with the stimulated emission make it easily distinguishable from the spontaneous PL emission.) It is evident, in Fig. 3(b), that the fundamental mode is well confined within the p-GaAs layer, which is the gain region. This is generally true of all Ppn′N laser structures operating in the fundamental transverse mode, and in which the Al concentrations in the P and N layers are the same.

When the same device of Fig. 3 is driven well above threshold, the first-order mode transverse to the junction plane is excited. In this case, the near field of the first-order mode is shown in Fig. 3(c), in relation to the various LPE layers. As in the case of the fundamental mode, the first-order mode is also confined within the gain region. This location of the first-order mode confirms theoretical predictions of excitation of a high-order mode within the gain region, in a structure with asymmetric refractive-index profile [5]. The conditions under which such a high-order mode is excited can be related to the width of the gain region relative to the refractive-index discontinuity at the p–n heteroboundary.

Although the results of Fig. 3 are qualitatively informative, insofar as the relative position of the stimulated near field with respect to the LPE layers, a quantitative evaluation is not simple. The difficulty in interpreting information contained in Fig. 3 is associated with the nonlinear sensitivity of photographic film. Hence the electronic scheme of Fig. 1 is employed to display on a scope the light intensity as a function of distance. An example of this is shown for another laser in Fig. 4. The PL emission from the laser mirror is given in Fig. 4(a), and the location of the intensity scan is marked by the intensified horizontal line. The various LPE layers of the Ppn′N laser are noted in Fig. 4(a). In Fig. 4(b), a plot is given of the PL emission intensity (on a linear scale) from the various layers as a function of distance. The low-intensity emission associated with the space-charge region is evident in Fig. 4(b). When the near field of the stimulated emission is displayed as a function of distance, without the PL emission, the result is given also in Fig. 4(b). This plot of the first-order-mode near field depicts several interesting features. In the first place, the null is quite deep, indicating good optical resolution. In the second place, the first-order mode is contained almost entirely in the gain region, as noted earlier. Finally, the depth of penetration into the P-$Ga_{0.7}Al_{0.3}As$ layer is very small ($\lesssim 0.3$ μm), whereas an appreciable tail in the intensity distribution extends into the passive n′-$Ga_{0.97}$-$Al_{0.03}As$ layer.

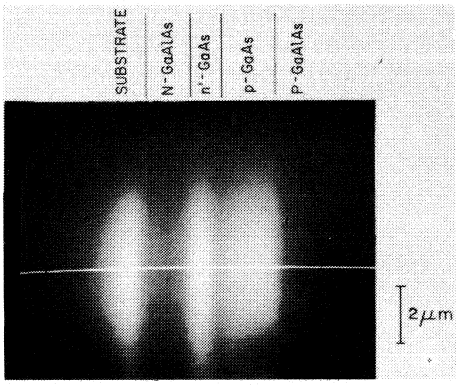

(a)

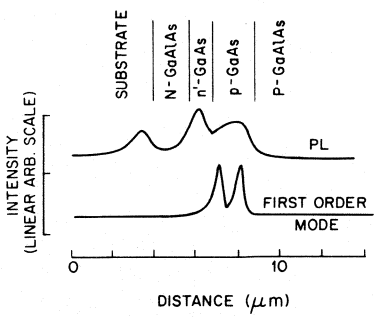

(b)

Fig. 4. Near-field emission from a Ppn′N laser. (a) PL emission from the laser mirror, with the white line designating the position of intensity scan in (b). The dark band in the N-layer is a spurious intensification in the video monitor. (b) PL intensity scan across laser mirror and scan of the near field of the lasing first-order mode.

Similar intensity scans show that the near fields of the fundamental and first-order modes subscribe to the same general behavior, namely, being predominantly confined to the P-GaAs gain region. In addition, the fundamental mode also has a tail in the intensity distribution that penetrates into the passive n′-region. However, the depth of penetration of the fundamental mode into the n′-region is less than that of the first-order mode.

Finally, it is found that the confinement of the high-order mode to the gain region is a strong indication of the presence of Al in the passive layer. Devices with no Al added to the n′-layer and operating in a high-order mode are distinguished by a near-field distribution which fills the whole waveguide,

[3] Application of reverse bias in excess of 10 V in an optical system utilizing 100× oil-immersion lenses is found to lead to gross optical distortion. This is suspected to be associated with the electrooptic coefficient of the oil. The use of 100× air lenses obviates this problem under high bias, but at a sacrifice in optical resolution.

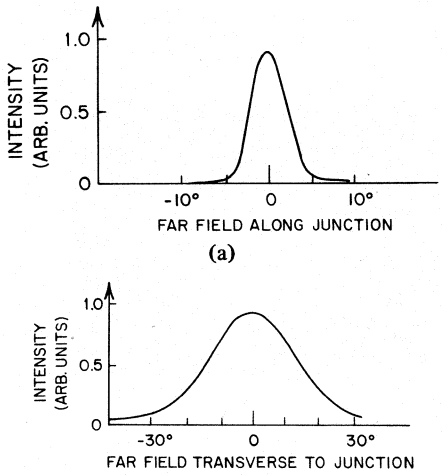

Fig. 5. Ppn'N stimulated emission projected on a planar surface. (a) Scan of intensity along junction plane. (b) Scan of intensity transverse to junction plane.

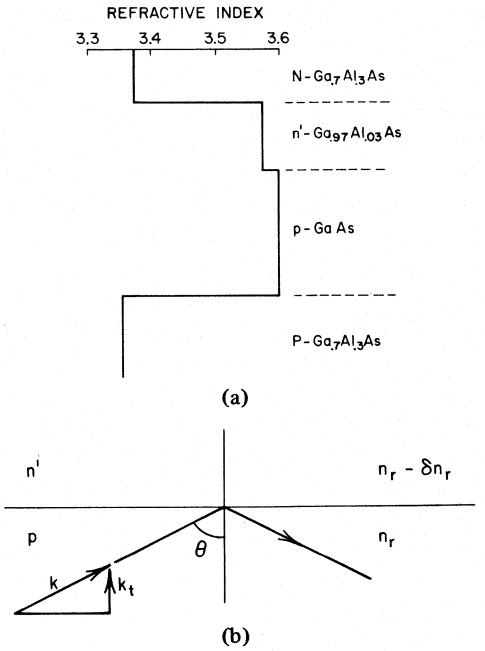

Fig. 6. Schematic representation of Ppn'N laser geometry. (a) Refractive-index variation across optical waveguide. (b) Reflection of rays at the p–n′ interface.

being nearly symmetric with respect to the center. Such devices may still operate in a fundamental mode very close to threshold, if the passive layer is doped with Te to a level of 3×10^{18} cm^{-3}. This Te doping level gives rise to an index discontinuity of $\approx 2 \times 10^{-2}$ at the p–n interface [11]. The near field of the fundamental mode shows some preference for the gain region. This may be attributable to the ease of confinement of the fundamental mode and its sensitivity to minor changes in refractive index caused either by doping or gain differences.

Fig. 5 shows the far-field radiation pattern of a laser in which the gain region is 1.2 μm thick and the unpumped n′-region is 0.9 μm, i.e., a total waveguide thickness of 2.1 μm. The full beamwidths, at the half-power points, transverse and along the junction plane are 34° and 6°, respectively. These angles are obtained after appropriate corrections are made on the intensity scans of Fig. 5 to account for the fact that the beam is being projected on a planar surface. (These corrections will be discussed in a later section.) It is evident that the results of Fig. 5 depict the far-field pattern of a laser operating in a fundamental mode both transverse and along the junction plane. The utility of this technique lies in the fact that even if the pattern were multifilamented, as is sometimes the case, the radiation pattern transverse to the junction plane can be measured for each filament separately by adjusting the scan position on the monitor.

III. Discussion

A qualitative understanding of the operation of the device can be acquired from the variation of the refractive index across the various layers shown schematically in Fig. 6(a). The refractive-index values of the layers that constitute the Ppn'N structure are consistent with recent measurements [12]. Therefore the optical containment characteristics of the transverse stimulated modes are a result of the small change in refractive index between the p- and n′-layers. Quantitatively, the degree of confinement within the gain region of a mode depends on whether its transverse propagation constant in the passive n′-region is real (propagation) or imaginary (attenuation). This, in turn, depends on whether the angle of incidence at the p–n′ heteroboundary, shown in Fig. 6(b), is less or greater than the critical angle [13], given by

$$\sin \theta_c = 1 - \delta n_r / n_r \tag{1}$$

where n_r and $n_r - \delta n_r$ are the refractive indices in the p- and n′-regions, respectively.

The angle of incidence at this heteroboundary of any mode is related to its transverse propagation constant by the relation

$$\sin \theta = (1 - k_t^2/k^2)^{1/2} \tag{2}$$

where k_t is the transverse propagation constant and k is propagation constant in the medium.

Suppose that a perturbation technique is applied to an initially symmetric GaAs/$Ga_{0.7}Al_{0.3}$As DH structure in which the active region is 2 μm thick. The unperturbed transverse propagation constants for the TE mode are obtained by solving the characteristic equation for the dielectric waveguide [14], [15]. For a lasing wavelength of 0.89 μm, the transverse propagation constants are 1.42×10^4, 2.84×10^4, and 4.26×10^4 cm^{-1} for the fundamental, first-, and second-order transverse modes, respectively. The structure is next perturbed by introducing a p–n′ heteroboundary within the 2-μm waveguide. For the doping levels shown in Fig. 2 and for 3-percent AlAs in the n′-region, the index discontinuity δn_r at the p–n′ heteroboundary is ≈ 0.03 [11]. Therefore, from (1), the sine of the critical angle is

$$\sin \theta_c = 1 - 8.3 \times 10^{-3}. \tag{3a}$$

Similarly, from (2) and the various propagation constants,

the angles of incidence of the modes are obtained from the relations

$$\sin \theta_0 = 1 - 1.5 \times 10^{-3} \tag{3b}$$

$$\sin \theta_1 = 1 - 6 \times 10^{-3} \tag{3c}$$

and

$$\sin \theta_2 = 1 - 14 \times 10^{-3}. \tag{3d}$$

It is obvious from (3a) to (3b) that the fundamental and first-order modes would be totally reflected at the p-n′ heteroboundary. Hence, in this perturbation approximation, the two lowest order modes would be confined to the gain region, and their fields in the unpumped n′-region would decay at an exponential rate k_t' given by

$$k_t' = k(\sin^2 \theta - \sin^2 \theta_c)^{1/2}. \tag{4}$$

Therefore, it is evident from (3b) to (4) that the first-order mode penetrates more deeply into the n′-region than the fundamental mode. These analytical deductions are entirely consistent with experimental observations, such as those given in Figs. 3 and 4, that show confinement of the low-order modes to the gain region.

The second-order mode, on the other hand, can propagate across the p-n′ heteroboundary with a real propagation constant in the n′-region. Such second-order modes are seldom observed experimentally in typical Ppn′N structures since their lasing thresholds are considerably higher than those of the fundamental and first-order modes. The confinement of the low-order modes to the gain region increases their coupling coefficient relative to the high-order modes, and at the same time reduces their mode loss. Hence the low-order modes tend to be the preferred modes.

The relevance of confinement of the fundamental mode within the gain region to far-field measurements of Fig. 6 is self-evident. But first, it should be appreciated that the projection of a divergent beam on a planar surface produces an intensity distribution which should be modified in order to get the angular distribution of the beam. Consider projection on the x-y plane and a source along the z axis at a distance D from the projection plane. If the surface intensity distribution along the x axis is $P(x)$, and the source has an angular distribution $I_s(\theta)$, where θ is measured in the x-z plane, then

$$\frac{P(x)}{P(0)} = \frac{I_s(\theta)}{I_s(0)} \cos^3 \theta \tag{5}$$

where $P(0)$ is the surface intensity at $x = 0$, and $I(0)$ is the source angular intensity along the z axis. Therefore the measured surface intensity distribution plots of Fig. 5 have to be corrected by the $\cos^3 \theta$ factor of (5) in order to get the angular distribution of the beam.

After having properly corrected the results of Fig. 5 to give the true beamwidth transverse to the junction plane, the results can be interpreted. If the fundamental mode were distributed symmetrically throughout the 2.1-μm waveguide, the beamwidth transverse to the junction plane would have been 28° [12]. On the other hand, if the fundamental mode were strongly confined to the 1.2-μm gain region, the beamwidth would have been 40° [12]. The measured beamwidth of 34° transverse to the junction plane therefore implies only partial confinement to the gain region, again consistent with the results of near-field measurements. There is evidently an appreciable contribution to the far field from that fraction of the field that penetrates into the unpumped n′-region.

The fact that the fundamental mode tends to be confined to the gain region more effectively than higher order modes changes the relative electronic gains of the various modes in the Ppn′N structure. If the index discontinuity at the p-n junction were absent, the fundamental mode would have the lowest relative threshold when the gain region is two-thirds of the waveguide thickness [4],[15]. In the Ppn′N structure, fundamental mode confinement to the gain region leads to best mode discrimination when the gain region is roughly half the waveguide width [8].

IV. Conclusion

The near-field emission from GaAs DH injection lasers is studied in an optical method that allows a correlation of the stimulated emission with the various LPE layers. The optical delineation of the LPE layers is accomplished by PL excitation of the laser mirror and the proper choice of optical filters. With a resolution of a few tenths of a micron, the location and shape of the stimulated near fields are related to the waveguide properties. It is found that in the Ppn′N laser where a heteroboundary is utilized to achieve separate optical and carrier confinement, the addition of aluminum in amounts as small as (1-3) percent has a marked influence on the distribution of power within the waveguide. It is found that the fundamental transverse mode is particularly sensitive to refractive-index variations within the waveguide, being contained preferentially in the higher refractive-index gain region.[4] The fringing field of the fundamental mode decays very rapidly in the large bandgap $Ga_{0.7}Al_{0.3}As$ layer, but penetrates more deeply into the passive n′-$Ga_{0.97}Al_{0.03}As$ layer. This containment of the fundamental mode within the gain region explains the experimental observation that catastrophic damage of Ppn′N laser mirrors tends to be most severe in the p-GaAs gain layer [4]. On the other hand, the higher order modes are more difficult to contain within the gain region, although the first-order mode can be excited in the gain region under some conditions that are consistent with analytical predictions. Qualitatively, the containment and symmetry of the high-order modes within the waveguide are used as a sensitive indication of the extent of refractive-index change within the waveguide.

Acknowledgment

The author wishes to thank D. C. Krupka for many useful discussions, and D. L. Van Haren and J. L. Statile for their able assistance in this work.

[4]The fundamental mode is the lowest threshold mode in Ppn′N structures with waveguide thicknesses of 2.5 μm, i.e., 1.5 and 1.0-μm-thick p- and n′-layers, respectively. This is a considerable improvement in fundamental-mode control over conventional symmetric DH lasers where the first-order mode tends to be excited when the thickness of the active region exceeds 0.5 μm.

REFERENCES

[1] Zh. I. Alferov, V. M. Andreev, E. L. Portnoi, and M. K. Trukan, "AlAs-GaAs heterojunction injection lasers with a low room-temperature threshold," *Sov. Phys.-Semicond.*, vol. 3, pp. 1107–1110, 1970.

[2] I. Hayashi, M. B. Panish, P. W. Foy, and S. Sumski, "Junction lasers which operate continuously at room temperature," *Appl. Phys. Lett.*, vol. 17, pp. 109–111, 1970.

[3] H. Kressel, H. F. Lockwood, and F. Z. Hawrylo, "Large-optical-cavity (AlGa) As-GaAs heterojunction laser diode: Threshold and efficiency," *J. Appl. Phys.*, vol. 43, pp. 561–567, 1972.

[4] T. L. Paoli, B. W. Hakki, and B. L. Miller, "Zero-order transverse mode operation of GaAs double-heterostructure lasers with thick waveguides," *J. Appl. Phys.*, vol. 44, pp. 1276–1280, 1973.

[5] B. W. Hakki and C. J. Hwang, "Mode control in GaAs large-cavity double-heterostructure lasers," *J. Appl. Phys.*, vol. 45, pp. 2168–2173, 1974.

[6] S. E. Miller, E. A. J. Marcatili, and T. Li, "Research toward optical-fiber transmission systems–Part I: The transmission medium," *Proc. IEEE*, vol. 61, pp. 1703–1726, Dec. 1973.

[7] S. E. Miller, T. Li, and E. A. J. Marcatili, "Research toward optical-fiber transmission systems–Part II: Devices and systems considerations," *Proc. IEEE*, vol. 61, pp. 1726–1751, Dec. 1973.

[8] D. C. Krupka, unpublished.

[9] J. C. Dyment, L. A. D'Asaro, J. C. North, B. I. Miller, and J. E. Ripper, "Proton-bombardment formation of stripe geometry heterostructure lasers for 300 K CW operation," *Proc. IEEE* (Lett.), vol. 60, pp. 726–728, June 1972.

[10] B. W. Hakki, "Carrier and gain spatial profiles in GaAs-stripe geometry lasers," *J. Appl. Phys.*, vol. 44, pp. 5021–5028, 1973.

[11] D. D. Sell, H. C. Casey, Jr., and K. W. Wecht, "Concentration dependence of the refractive index for n- and p-type GaAs between 1.2 and 1.8 eV," *J. Appl. Phys.*, vol. 45, pp. 2650–2657, 1974.

[12] H. C. Casey, Jr., D. D. Sell, and M. B. Panish, "Refractive index of $Al_xGa_{1-x}As$ between 1.2 and 1.8 eV," *Appl. Phys. Lett.*, vol. 24, pp. 63–65, 1974.

[13] E. I. Gordon, unpublished.

[14] F. K. Reinhart, I. Hayashi, and M. B. Panish, "Mode reflectivity and waveguide properties for double-heterostructure injection lasers," *J. Appl. Phys.*, vol. 42, pp. 4466–4479, 1971.

[15] B. W. Hakki, "Mode gain and junction current in GaAs under lasing conditions," *J. Appl. Phys.*, vol. 45, pp. 288–294, 1974.

[16] H. C. Casey, Jr., M. B. Panish, and J. L. Merz, "Beam divergence of the emission from double-heterostructure injection lasers," *J. Appl. Phys.*, vol. 44, pp. 5470–5475, 1973.

Effect of External Reflectors on Longitudinal Modes of Distributed Feedback Lasers

WILLIAM STREIFER, SENIOR MEMBER, IEEE, ROBERT D. BURNHAM, AND DONALD R. SCIFRES

Abstract–**The effect of external reflectors on longitudinal modes of distributed feedback (DFB) lasers is analyzed. The general case of dissimilar reflectors arbitrarily located relative to the phase of the DFB structure is considered. An eigenvalue equation for the propagation constants is derived and solved numerically for a variety of practical cases. Longitudinal mode thresholds, wavelengths, separations, and field distributions are obtained for GaAs lasers and for DFB lasers with a single reflector. It is shown that these quantities are very sensitive not only to the relative strength of the discrete and DFB, but also to the relative phases. Quite asymmetric transmitted powers are shown to occur under a variety of circumstances.**

I. INTRODUCTION

LONGITUDINAL modes in a distributed feedback (DFB) laser with external reflectors are studied in this paper. In such devices, internal reflections are caused by a periodic DFB structure. External, as opposed to internal, reflectors may be purposely produced in GaAs diode lasers by cleaving along a crystallographic plane to produce flat parallel surfaces. External reflectors on other DFB lasers can be implemented in obvious ways. Among the reasons for studying such devices is that the combined action of the internal and external reflectors sometimes reduces the laser threshold. Often too, other optical elements, such as couplers, guides, or modulators, within an integrated optic circuit may produce reflections which interact with the DFB structure. Finally, it is frequently convenient to cleave one or both end faces of a DFB diode laser to facilitate the experimental study.

The periodic feedback itself may be effected by variations in refractive index and/or gain or by a physical corrugation in the vicinity of the gain region. Since the latter structure is equivalent to a periodic variation in index and/or gain for most purposes, it suffices to consider

$$n(z) = n + (\Delta n)\cos(2\pi z/\Lambda + \Omega) \tag{1a}$$

and

$$\alpha(z) = \alpha + (\Delta\alpha)\cos(2\pi z/\Lambda + \Omega) \tag{1b}$$

where $n(z)$ is the refractive index, $\alpha(z)$ is the gain, and z is measured along the laser from $-L/2$ to $L/2$. Furthermore, n and α are constants and Δn and $\Delta\alpha$ are the amplitude variations with spatial period Λ and phase Ω. For nonsinusoidal variations (1a) and (1b) include only the constant and fundamental terms of the Fourier expansion. Equations (1a) and (1b) are appropriate only for analyzing first-order Bragg scat-

Manuscript received October 9, 1974.

The authors are with the Xerox Palo Alto Research Center, Palo Alto, Calif. 94304.

tering in the DFB structure. Often third-order Bragg scattering is employed in which case

$$n(z) = n + (\Delta n)\cos(6\pi z/\Lambda + \Omega) \tag{2a}$$

and

$$\alpha(z) = \alpha + (\Delta\alpha)\cos(6\pi z/\Lambda + \Omega) \tag{2b}$$

where Δn and $\Delta\alpha$ are the third-harmonic coefficients.

Previous analyses have considered the DFB structure without external reflectors (see Kogelnik and Shank [1]) and with identical external reflectors located exactly symmetric with respect to the grating (see Chinn [2]). The latter analysis is not general in that it does not cover most cases. Specifically, both the following requirements must be met if Chinn's derivation is to apply.

1) The reflectors must have identical reflectivity.

2) The reflectors must be located relative to the grating, such that $\Omega = 0$.

As will be shown, reflector position relative to the peaks and troughs of the grating greatly influences the longitudinal mode structure. Since physical control of the relative reflector-grating position is very difficult (because of the small physical period Λ for visible and near IR lasers), the general case must be considered.

In Section II of this paper the eigenvalue equation for longitudinal modes in a DFB laser with external reflectors is derived. Although the equation is generally applicable, it is solved numerically to yield net threshold gains and wavelengths for some important special cases in Section III, viz., GaAs DFB lasers with two cleaves and DFB lasers with one reflector. Longitudinal mode separations are also calculated and the variation of mode fields along the length of the laser are also determined in Section III. The latter computation yields the ratios of radiated power from each end of the device.

II. Derivation of the Equation

Following [1], [2] we seek solutions of

$$[\nabla^2 + k^2(z)]E(z) = 0 \tag{3}$$

where the time dependence of the electric field $E(z)$ is $e^{i\omega t}$ and

$$k^2(z) \approx \beta^2 + 2i\alpha\beta + 4\kappa\beta\cos(2\beta_0 z + \Omega). \tag{4}$$

Here

$$\beta_0 \triangleq \pi/\Lambda \tag{5a}$$

for first-order Bragg scattering ($3\pi/\Lambda$ for third order)

$$\beta \triangleq n\omega/c \tag{5b}[1]$$

and κ is the coupling coefficient ($\kappa \ll \beta$) given by

$$\kappa = \left(\frac{\beta}{2}\right)\left(\frac{\Delta n}{n}\right) + \frac{i\Delta\alpha}{2}. \tag{5c}$$

The assumptions $\Delta n \ll n$, $\alpha \ll \beta$, and $\Delta\alpha \ll \beta$, were employed in deriving (4). Both β and α are determined by the analysis which follows. Values of α specify net gain at threshold for laser oscillation and those of β specify the allowable values of ω and thereby the free-space wavelength λ_0.

Without loss of generality we seek solutions in the form

$$E(z) = R(z)\,e^{-i\beta_0 z} + S(z)\,e^{i\beta_0 z} \tag{6}$$

where $R(z)$ and $S(z)$ are opposite going waves with $R(z)$ propagating in the direction of increasing z. These functions are assumed to change slowly so that $R''(z)$ and $S''(z)$ can be neglected compared with $\beta_0 R'(z)$ and $\beta_0 S'(z)$. Then upon substitution in (3) we obtain

$$\begin{aligned}&[-2\beta_0 R' - \beta_0^2 R + \beta^2 R + 2i\alpha\beta R]\,e^{-i\beta_0 z}\\ &\quad + [2\beta_0 S' - \beta_0^2 S + \beta^2 S + 2i\alpha\beta S]\,e^{i\beta_0 z}\\ &\quad + 2\kappa\beta\left(e^{i2\beta_0 z}\,e^{i\Omega} + e^{-i2\beta_0 z}\,e^{-i\Omega}\right)\\ &\quad \cdot \left(Re^{-i\beta_0 z} + Se^{i\beta_0 z}\right) = 0\end{aligned} \tag{7}$$

and after isolating expressions with similar z dependence

$$-R' + (\alpha - i\delta)R = i\kappa e^{-i\Omega}S \tag{8a}$$

and

$$S' + (\alpha - i\delta)S = i\kappa e^{i\Omega}R \tag{8b}$$

where

$$\delta \triangleq \beta - \beta_0 \tag{9}$$

$|\delta| \ll \beta$ has been assumed, and terms which propagate as $e^{\pm i3\beta_0 z}$ have been dropped. Since (8a) and (8b) are constant coefficient linear differential equations they admit exponential solutions in the form

$$R(z) = r_1 e^{\gamma z} + r_2 e^{-\gamma z} \tag{10a}$$

and

$$S(z) = s_1 e^{\gamma z} + s_2 e^{-\gamma z} \tag{10b}$$

where r_1, r_2, s_1, and s_2 are constants. Without loss of generality $\mathrm{Re}(\gamma) > 0$, so that r_1 and s_2 grow as they propagate. The combined effects of gain and coupling from opposite going waves ($s_1 \rightarrow r_1$ and $r_2 \rightarrow s_2$) cause the growth. Growing waves have propagation constants given by $\beta_0 - \mathrm{Im}(\gamma)$ [cf. (6)]. The waves multiplied by r_2 and s_1 decay as they propagate with constant given by $\beta_0 + \mathrm{Im}(\gamma)$.

The substitution of (10a) and (10b) in (8a) and (8b) results in four equations when terms with identical z dependence are collected

$$\hat{\Gamma} r_1 = i\kappa e^{-i\Omega} s_1 \tag{11a}$$

$$\Gamma r_2 = i\kappa e^{-i\Omega} s_2 \tag{11b}$$

$$\Gamma s_1 = i\kappa e^{i\Omega} r_1 \tag{11c}$$

$$\hat{\Gamma} s_2 = i\kappa e^{i\Omega} r_2 \tag{11d}$$

where

$$\hat{\Gamma} = -\gamma + \alpha - i\delta \tag{12a}$$

and

$$\Gamma = \gamma + \alpha - i\delta. \tag{12b}$$

[1] A more complicated relation applies for waveguiding structures. In that case an equivalent index n_{eq} should be used in (5b).

These equations have nontrivial solutions if and only if γ satisfies the dispersion relation

$$\gamma^2 = (\alpha - i\delta)^2 + \kappa^2 \tag{13}$$

which, as expected, is independent of Ω.

The actual determination of γ, and thereafter α and δ, is achieved only after imposing the reflection conditions at $z = \pm L/2$. If the reflection coefficient at $z = -L/2$ is denoted by $\hat{\rho}_l$ and that at $z = L/2$ by $\hat{\rho}_r$, we obtain

$$(r_1 e^{-\gamma L/2} + r_2 e^{\gamma L/2})\, e^{i\beta_0 L/2} = \hat{\rho}_l (s_1 e^{-\gamma L/2} + s_2 e^{\gamma L/2})\, e^{-i\beta_0 L/2} \tag{14a}$$

and

$$(s_1 e^{\gamma L/2} + s_2 e^{-\gamma L/2})\, e^{i\beta_0 L/2} = \hat{\rho}_r (r_1 e^{\gamma L/2} + r_2 e^{-\gamma L/2})\, e^{-i\beta_0 L/2}. \tag{14b}$$

Next (11a) and (11d) are employed to eliminate r_2 and s_1 from (14a) and (14b). The latter equations are homogeneous in r_1 and s_2, so that nontrivial solutions exist only if

$$\frac{(1 - \rho_l \hat{\Gamma}/i\kappa)\, e^{-\gamma L}}{(\rho_l - \hat{\Gamma}/i\kappa)} = \frac{(\rho_r - \hat{\Gamma}/i\kappa)\, e^{\gamma L}}{(1 - \rho_r \hat{\Gamma}/i\kappa)} \tag{15}$$

where

$$\rho_l = \hat{\rho}_l e^{-i\beta_0 L}\, e^{i\Omega} \tag{16a}$$

and

$$\rho_r = \hat{\rho}_r e^{-i\beta_0 L}\, e^{-i\Omega}. \tag{16b}$$

Equation (15) can also be derived by setting the coefficient determinant of (11a), (11d), (14a), and (14b) equal to zero.

The phase functions in (16a) and (16b) are just those of the DFB structure at $z = \pm L/2$, i.e., at $z = -L/2$, which is the location of the left reflector, the index variation from (1a) is $\cos(-\beta_0 L + \Omega)$, where as in the preceding $\beta_0 = \pi/\Lambda$. Similarly, at the right reflector $z = L/2$ so that the index variation is $\cos(\beta_0 L + \Omega)$. Values of $-\beta_0 L + \Omega$ and $-\beta_0 L - \Omega$ are shown in Fig. 1(a) and (b), respectively, for various positions of the left and right reflectors in the case of a nonsinusoidal corrugation grating and first-order Bragg scattering. It should be noted that ρ_l and ρ_r also depend on the phase of $\hat{\rho}_l$ and $\hat{\rho}_r$, which are commonly π. In that case all phases in Fig. 1(a) and (b) are shifted by π to obtain those of ρ_l and ρ_r.

By solving (15) for $\hat{\Gamma}/i\kappa$ and employing the relation

$$\gamma = \frac{-i\kappa}{2}\left(\frac{\hat{\Gamma}}{ik} - \frac{ik}{\hat{\Gamma}}\right) \tag{17}$$

which follows from (11a), (11c), (12a), and (12b), we obtain (after substantial manipulation) the eigenvalue equation

$$\gamma L = \frac{-i\kappa L \sinh(\gamma L)}{\mathfrak{D}} \{(\rho_l + \rho_r)(1 - \rho^2)\cosh(\gamma L) \pm (1 + \rho^2)[(\rho_l - \rho_r)^2 \sinh^2 \gamma L + (1 - \rho^2)^2]^{1/2}\} \tag{18}$$

where

$$\mathfrak{D} = (1 + \rho^2)^2 - 4\rho^2 \cosh^2(\gamma L) \tag{19}$$

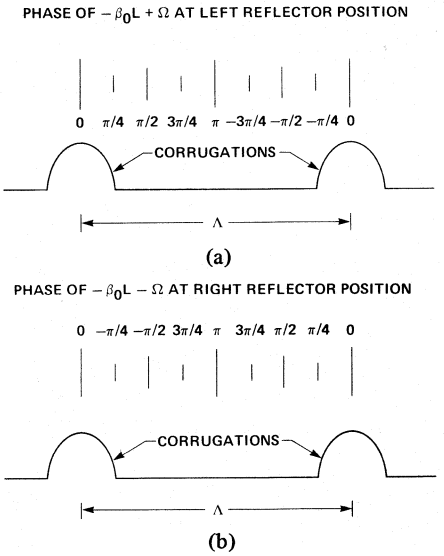

Fig. 1. Phases as a function of left- and right-reflector positions with first-order Bragg scattering.

and

$$\rho^2 = \rho_l \rho_r = \hat{\rho}_l \hat{\rho}_r e^{-2i\beta_0 L}. \tag{20}$$

Values of γ found by solving (18) determine the propagation constants for the longitudinal modes. For each γ, (13) is used to calculate α, which is the net gain required at threshold for that mode to lase and δ, which gives the laser frequency

$$\omega = \frac{c\beta}{n} = \frac{c}{n}(\beta_0 + \delta)$$

of that mode.

For the special case considered by Chinn [2], $\rho_l = \rho_r$, i.e., $\Omega = 0$, (18) reduces to (22). With $\rho_l = \rho_r = 0$ the equation derived by Kogelnik and Shank [1] is recovered.

Equation (18) is in an inconvenient form for solution since it contains a square root, two possible signs, and because the numerator and $\mathfrak{D}$ contain a common factor $\mathfrak{D}^{1/2}$. These difficulties are overcome by rewriting (18) in the form

$$\gamma L\, \mathfrak{D} + i\kappa L(\rho_l + \rho_r)(1 - \rho^2)\sinh(\gamma L)\cosh(\gamma L) = \mp i\kappa L(1 + \rho^2)\sinh(\gamma L)[(\rho_l - \rho_r)^2 \sinh^2(\gamma L) + (1 - \rho^2)^2]^{1/2} \tag{21}$$

squaring (21), and combining terms to obtain

$$(\gamma L)^2 \mathfrak{D} + (\kappa L)^2 \sinh^2(\gamma L)(1 - \rho_l^2)(1 - \rho_r^2) + 2i\kappa L(\rho_l + \rho_r)(1 - \rho^2)\gamma L \sinh(\gamma L)\cosh(\gamma L) = 0 \tag{22}$$

where the factor $\mathfrak{D}$ has been cancelled from the equation. No additional roots have been added by squaring (21) since both negative and positive signs precede the right-hand side.

Clearly, (22) and its solutions are unaffected by interchanging ρ_l and ρ_r. If $\rho_l \to -\rho_l^*$, $\rho_r \to -\rho_r^*$, and $\kappa \to \kappa^*$, then (22) is conjugated except for all functions depending on γL. Thus the solutions are conjugated; α is unchanged, but $\delta \to -\delta$. Conjugating κ is equivalent to shifting the gain variation by π; of

course if $\Delta\alpha = 0$, $\kappa = \kappa^*$. An interesting special case occurs when one reflectance (say ρ_r) is zero. Then $\rho^2 = 0$, $\mathfrak{D} = 1$, and (22) becomes

$$(\gamma L)^2 + (\kappa L)^2 \sinh^2(\gamma L)(1 - \rho_l^2) + 2i\kappa L\rho_l \gamma L \sinh(\gamma L)\cosh(\gamma L) = 0. \quad (23)$$

With $\rho_l = \pm 1$

$$\gamma L \pm 2i\kappa L \sinh(\gamma L)\cosh(\gamma L) = 0 \quad (24)$$

and

$$(2\gamma L) \pm i(2\kappa L)\sinh(2\gamma L) = 0 \quad (25)$$

which is the eigenvalue equation for a DFB laser of length $2L$ without reflectors.

In the limit $\kappa L \to 0$, solutions of (22) are given by

$$\mathfrak{D} = (1 + \rho^2)^2 - 4\rho^2 \cosh^2(\gamma L) = 0 \quad (26)$$

from which it follows that

$$\rho^2 e^{2\gamma L} = \rho_l \rho_r e^{2\gamma L} = 1. \quad (27)$$

Equation (27) expresses the threshold and resonance conditions for a laser with conventional reflectors. For any fixed κL and large values of Im (δL) (far from the Bragg condition) solutions of (22) also approach those given by (26) since $(\gamma L)^2$ has the largest magnitude in (22).

To obtain numerical solutions for the eigenvalues we rewrite (22) symbolically

$$W(\gamma L) = U(\gamma L) + iV(\gamma L) = 0 \quad (28)$$

where U and V are, respectively, the real and imaginary parts of the analytic function $W(\gamma L)$ and

$$\gamma L = x + iy. \quad (29)$$

Thus

$$U(x, y) = 0 \quad (30a)$$

and

$$V(x, y) = 0 \quad (30b)$$

are to be solved simultaneously. Let (x_r, y_r) denote a solution of (30a) and (30b), which is to be determined. Then at any point (x, y) we have

$$U(x_r, y_r) = U(x, y) + \partial U/\partial x|_{x,y}(x_r - x) + \partial U/\partial y|_{x,y}(y_r - y) = 0 \quad (31a)$$

and

$$V(x_r, y_r) = V(x, y) + \partial V/\partial x|_{x,y}(x_r - x) + \partial V/\partial y|_{x,y}(y_r - y) = 0 \quad (31b)$$

where only first-order terms in the expansion about (x, y) have been retained. Equations (31a) and (31b) are now solved for (x_r, y_r), viz.,

$$x_r = x + \frac{V(x,y)\partial U/\partial y - U(x,y)\partial V/\partial y}{D} \quad (32a)$$

and

$$y_r = y + \frac{U(x,y)\partial V/\partial x - V(x,y)\partial U/\partial x}{D} \quad (32b)$$

where

$$D = \frac{\partial U}{\partial x}\frac{\partial V}{\partial y} - \frac{\partial U}{\partial y}\frac{\partial V}{\partial x}. \quad (33)$$

Since (31a) and (31b) are only approximations, so too are (32a) and (32b). The new estimates are then used as (x, y) in (31a) and (31b) and the procedure is continued until U and V are, simultaneously, less than a specified tolerance. In applying this method we also required that (x, y) change less than a tolerance for a point to be accepted as a root. All numerical results in this paper were obtained by the preceding procedure. Usually, depending on the initial values of (x, y), less than nine iterations were required to achieve accuracies of better than 10^{-5}. The calculation was facilitated by the analytic character of $W(\gamma L)$, i.e.,

$$\frac{dW}{d(\gamma L)} = \frac{\partial U}{\partial x} + \frac{i\partial V}{\partial x}$$

and

$$\frac{\partial U}{\partial x} = \frac{\partial V}{\partial y}, \quad \frac{\partial U}{\partial y} = -\frac{\partial V}{\partial x}$$

so that

$$D = \left(\frac{\partial U}{\partial x}\right)^2 + \left(\frac{\partial V}{\partial x}\right)^2.$$

The derivative itself is given by

$$\frac{dW}{d(\gamma L)} = 2\gamma L\,\mathfrak{D} - 8(\gamma L)^2\rho^2 \sinh(\gamma L)\cosh(\gamma L) + 2(\kappa L)^2(1 - \rho_l^2)(1 - \rho_r^2)\sinh(\gamma L)\cosh(\gamma L) + 2i\kappa L(\rho_l + \rho_r)(1 - \rho^2)[\cosh(\gamma L)\sinh(\gamma L) + \gamma L \sinh^2(\gamma L) + \gamma L \cosh^2(\gamma L)]. \quad (34)$$

Occasionally, in applying the preceding method several starting points would converge to the same solution [say $x_r^{(1)}, y_r^{(1)}$]. To overcome this inconvenience $W(\gamma L)$ was divided by $\gamma L - x_r^{(1)} - iy_r^{(1)}$ to remove that root. Equation (34) for $dW/d(\gamma L)$ was then modified in an obvious fashion.

III. Thresholds, Wavelengths, and Mode Fields

The following subsection III-A contains results for longitudinal mode thresholds and frequencies of GaAs DFB lasers with two cleaved ends. In subsection III-B the case $\rho_r = 0.0$ is treated. Zero reflectivity can be achieved (or at least closely approximated) by antireflection coating a laser end surface or by matching an integrated laser to a guide. Various values of ρ_l are studied. Subsection III-C deals with longitudinal mode separation and III-D with fields and power distribution within the laser and transmitted through the end reflectors.

A. GaAs Lasers with Two Cleaved Faces

Since the refractive index ratio at the GaAs:air interface is 3.6, the electric field reflection coefficients are $(\hat{\rho}_l, \hat{\rho}_r) = (-0.565, -0.565)$. Consideration of all possible values of κL, $\beta_0 L$, and Ω is a virtual impossibility and so the discussion is restricted to real κL and values of $\beta_0 L$ which are multiples of $\pi/4$ in the range $-\pi < \beta_0 L \leqslant \pi$. With $-\pi < \Omega \leqslant \pi$ and increments of $\pi/4$ there are 64 possible geometries, but because the results are unchanged for $\rho_l \rightleftharpoons \rho_r$ and the eigenvalues are conjugated either if $(\rho_l, \rho_r) \rightarrow (-\rho_l^*, -\rho_r^*)$ or $(\rho_l, \rho_r) \rightarrow (-\rho_r^*, -\rho_l^*)$ only 13 cases need be treated. These are listed in Table I with their various equivalencies. In Table I the symbols † and †† denote $(-\rho_l^*, -\rho_r^*) = (\rho_l, \rho_r)$ and $(-\rho_l^*, -\rho_r^*) = (\rho_r, \rho_l)$, respectively, for these cases plots of αL versus δL are symmetric about $\delta L = 0$. Plots for $(\rho_l, \rho_r) = (0.565\, e^{i\pi/4}, 0.565\, e^{i\pi/4})$ and $(0.565, 0.565\, e^{i\pi})$ were presented in our earlier paper [3]. Here in Fig. 2, αL (the total net threshold gain) versus δL (which determines laser frequency) with κL (the coupling) as a parameter is shown for $(\rho_l, \rho_r) = (0.565\, e^{i\pi/2}, 0.565\, e^{i\pi/2})$, which is one of the geometries included in [2]. Six longitudinal modes are presented; it should be noted that high-threshold longitudinal modes exist near $\delta L = 0$, which are not shown in Fig. 3 of [2]. This mode, i.e., with minimum, positive δL, is plotted in Fig. 3 with $\hat{\rho}_l = \hat{\rho}_r = -0.565 = 0.565\, e^{i\pi}$, and $e^{-i\beta_0 L} = e^{-i\pi/2}$ for various values of Ω with κL as a parameter along each curve. Setting $e^{-i\beta_0 L} = e^{-i\pi/2}$ (or any other value) fixes the laser length. Then with $\Omega = 0$, the grating is symmetrically located. For first-order Bragg coupling, $\beta_0 = \pi/\Lambda$, and with $\Omega = +\pi/4$ the grating is shifted to the left relative to the reflectors by $\Lambda/8$ [cf. Fig. 1(a) and (b)]; with $\Omega = -\pi/4$ the grating is shifted to the right. Similarly, with $\Omega = \pm\pi/2$ it is shifted by $\Lambda/4$, etc. Note that shifts of $\Omega > \pi$ correspond to shifts of $\Omega < \pi$ and the plot depends only on $|\Omega|$ because of the eigenvalue equation symmetry properties. For third-order Bragg scattering, the third-harmonic refractive index variation is employed, i.e., $\beta_0 L = 3\pi/\Lambda$, and Ω is the phase of that harmonic. The situation for the third harmonic is illustrated in Fig. 4(a) and (b). Fig. 3 also gives values of αL and δL for the mode nearest $\delta L = 0$ with $\delta L < 0$, if every phase shown is changed according to the symmetry conditions discussed previously and listed in Table I. A plot similar to Fig. 2 is shown in Fig. 5 for $(\rho_l, \rho_r) = (0.565, 0.565\, e^{i\pi/2})$. From both figures it is evident, as noted in the previous section, that the thresholds approach those of a conventional cleaved mirror laser without DFB as $|\delta L|$ becomes large. The rate at which this occurs depends on κL.

TABLE I
COMBINATIONS OF $\beta_0 L$ AND Ω ENCOMPASSED BY THE SAME PHASES. THE † DENOTES $(-\rho_l^*, -\rho_r^*) = (\rho_l, \rho_r)$ AND †† DENOTES $(-\rho_l^*, -\rho_r^*) = (\rho_r, \rho_l)$

PHASE		EQUIVALENCE		CASES ENCOMPASSED	
ρ_l	ρ_r	$-\rho_l^*$	$-\rho_r^*$	Ω	$\beta_0 L$
0	0	π	π	$0, \pi$	$0, \pi$
$\pi/4$	$-\pi/4$	$3\pi/4$	$-3\pi/4$	$\pm\pi/4, \pm 3\pi/4$	$0, \pi$
$\pi/2$	$-\pi/2$	†	†	$\pm\pi/2$	$0, \pi$
$\pi/4$	$\pi/4$	$3\pi/4$	$3\pi/4$	0 π	$\pi/4, 3\pi/4$ $-\pi/4, -3\pi/4$
0	$\pi/2$	π	$\pi/2$	$\pm\pi/4$ $\pm 3\pi/4$	$\pi/4, 3\pi/4$ $-\pi 4, -3\pi/4$
$\pi/4$	$-3\pi/4$	$3\pi/4$	$-\pi/4$	$\pm\pi/2$	$\pm\pi/4, \pm 3\pi/4$
0	$-\pi/2$	π	$-\pi/2$	$\pm\pi/4$ $\pm 3\pi/4$	$-\pi/4, -3\pi/4$ $\pi/4, 3\pi/4$
$\pi/2$	$\pi/2$	†	†	0 π	$\pi/2$ $-\pi/2$
$\pi/4$	$3\pi/4$	††	††	$\pm\pi/4$ $\pm 3\pi/4$	$\pi/2$ $-\pi/2$
0	π	††	††	$\pm\pi/2$	$\pm\pi/2$
$-\pi/4$	$-3\pi/4$	††	††	$\pm\pi/4$ $\pm 3\pi/4$	$-\pi/2$ $\pi/2$
$-\pi/2$	$-\pi/2$	†	†	0 π	$-\pi/2$ $\pi/2$
$-\pi/4$	$-\pi/4$	$-3\pi/4$	$-3\pi/4$	0 π	$-\pi/4, -3\pi/4$ $\pi/4, 3\pi/4$

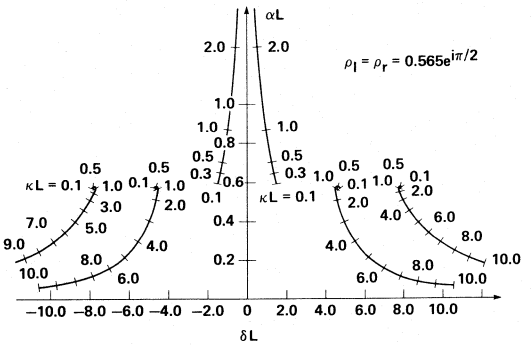

Fig. 2. Threshold and phase for longitudinal modes with κL as a parameter.

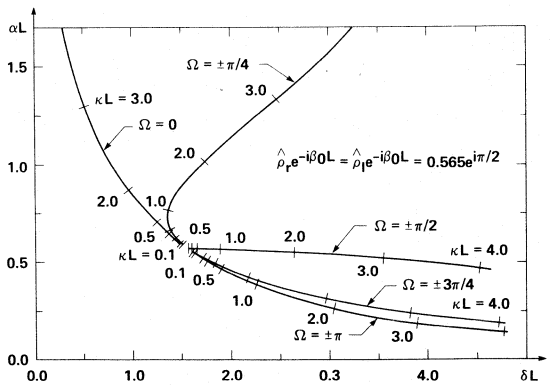

Fig. 3. Threshold and phase for one longitudinal mode with κL and Ω as parameters.

B. DFB Lasers with One Reflector ($\hat{\rho}_r = 0.0$)

Fig. 6 illustrates αL versus δL for $\delta L > 0$ near the Bragg condition $\delta L = 0$, with $\kappa L = 1.0$, $\rho_r \equiv 0.0$, and ρ_l taking on various values. Once again results for $\delta L < 0$ can be deduced from symmetry considerations. On the solid curves $|\rho_l| =$ constant, whereas phase $(\rho_l) =$ constant along the dashed curves. For $|\rho_l| = 0.0$, the phase is of no consequence and all dashed curves in Fig. 6 converge to $\alpha L = 1.75$, $\delta L = 2.67$, the point appropriate to a DFB laser without external reflectors [1]. For reflectivities $|\rho_l|$ greater than approximately 0.4 all thresholds regardless of phase are lower than $\alpha L = 1.75$. The phase (ρ_l), as noted after (16b), is just that of the grating structure at $z = -L/2$. For $\hat{\rho}_l = |\hat{\rho}_l|\, e^{i\pi}$ reflector positions relative to the grating are illustrated in Fig. 1(a) or Fig. 4(a) by adding π to the phases shown therein. Thus if $\rho_l = \pm 1.0$ the reflector images the grating such that it appears to be a DFB structure of length $2L$ without reflectors, a result which was derived analytically as (25) in the preceding. From Fig. 6, the solutions are $\alpha L = 0.429$, $\delta L = 1.69$ with $\rho_l = -1.0$ and $\alpha L = 0.885$, $\delta L = 3.15$ with $\rho_l = 1.0$. These values equal half those

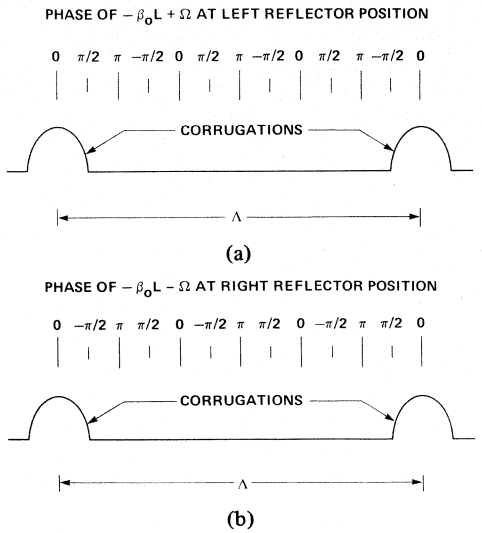

Fig. 4. Phases as a function of left- and right-reflector positions with third-order Bragg scattering.

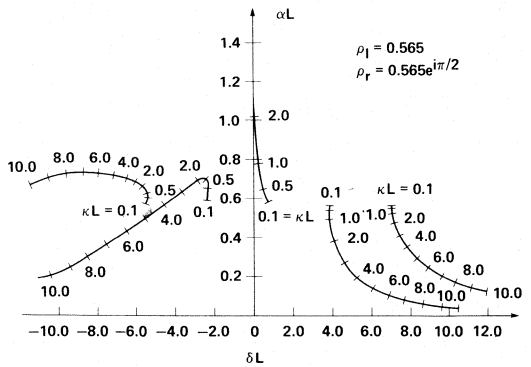

Fig. 5. Threshold and phase for longitudinal modes with κL as a parameter.

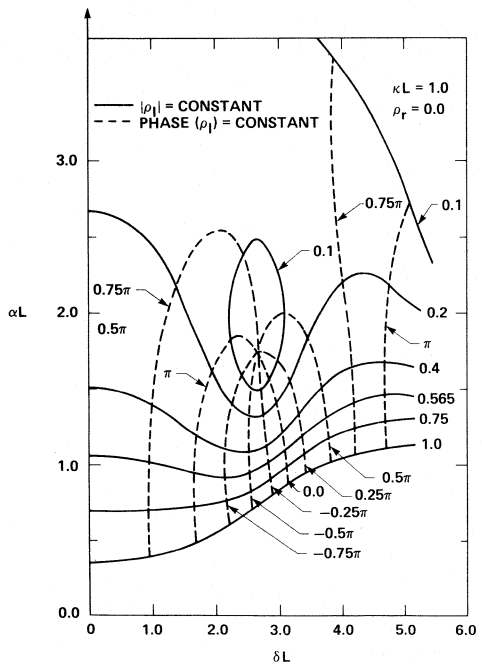

Fig. 6. Threshold and phase for longitudinal modes with $\rho_r = 0.0$ and $\kappa L = 1$. On the solid curves $|\rho_l|$ = constant and on the dashed curves phase (ρ_l) = constant.

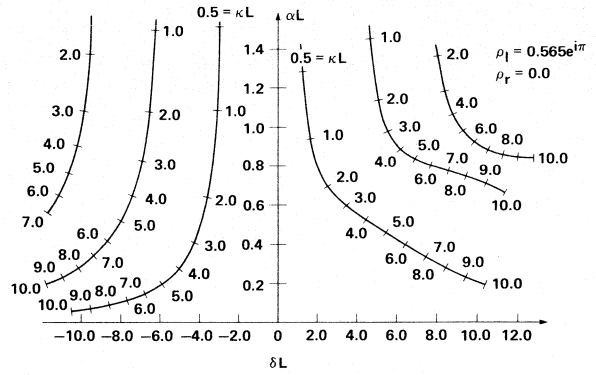

Fig. 7. Threshold and phase for longitudinal modes with κL as a parameter.

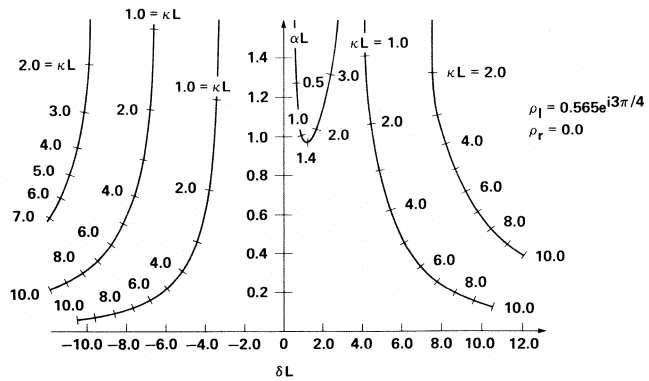

Fig. 8. Threshold and phase for longitudinal modes with κL as a parameter.

for the first and second longitudinal modes (numbering from $\delta L = 0$) of a DFB laser without reflectors and $\kappa L = 2.0$ (see [1]). The factor one-half occurs because (25) is for $2\gamma L$, whereas the equation for the single reflector geometry was solved for γL. Therefore κ, γ, α, and δ are identical in the two cases.

The minimum threshold as a function of phase occurs at $\pi/2$ for $|\rho_l|$ near 1.0 and quickly shifts to the vicinity of $-\pi/2$ as $|\rho_l|$ decreases. Perhaps this result is counterintuitive since placement at 0 or π may appear to optimally image the grating [see Fig. 1(a) and Fig. 4(a)]. It should be understood, however, that a grating length of $2L$ without reflectors and one of length L with one reflector are not identical even if $\rho_l = \pm 1.0$. This is the case because gratings continuously couple left and right going waves and the reflection interchanges directions and superimposes the wave differently. Furthermore, the threshold depends on the exact frequency of the waves (determined by δL) and their phases so that the preceding picture is overly simplistic.

Fig. 7 illustrates αL versus δL for six longitudinal modes with $\rho_r = 0.0$ and $\rho_l = 0.565\, e^{i\pi}$. For small κL, the reflector is relatively more important than the grating in determining device behavior, but as κL increases to overcoupled values the grating dominates. In fact, as shown in Fig. 8 for $\rho_l = 0.565\, e^{i3\pi/4}$, the mode with minimum $|\delta L|$, which does not exist in the pure DFB device, has an increasing threshold for $\kappa L \gtrsim 1.4$. For the other modes the threshold is generally lower with one reflector present rather than absent, although differences diminish with increasing κL.

C. Mode Separation

Longitudinal mode separation is obtained from differences in δL. If $\Delta(\delta L)$ is the difference between the ith and jth modes, then

$$\Delta(\delta L) = (\beta_i L - \beta_j L) = 2\pi L(n_{eq}^i/\lambda_i - n_{eq}^j/\lambda_j) \tag{35}$$

where λ_i, λ_j are the free-space wavelengths and n_{eq}^i, n_{eq}^j are the equivalent refractive indices, taking into account the laser waveguiding structure. As is customary we write

$$n_{eq}^j = n_{eq}^i + (dn_{eq}/d\lambda)_i(\lambda_j - \lambda_i)$$

substitute in (35) and solve for $\lambda_j - \lambda_i$ to obtain

$$\lambda_j - \lambda_i = \frac{\lambda_i\lambda_j\Delta(\delta L)}{2\pi n_{eq}^i L[1 - (dn_{eq}/d\lambda)_i(\lambda_i/n_{eq}^i)]}. \tag{36}$$

Often n_{eq} will approximate the active region index, $\lambda_i \approx \lambda_j$ (say λ), and $n_{eq}^i \approx n_{eq}^j$ (say n) so that

$$\lambda_j - \lambda_i = \frac{\lambda^2\Delta(\delta L)}{2\pi nL[1 - (dn/d\lambda)(\lambda/n)]}. \tag{37}$$

For $\Delta(\delta L) = \pi$, which is approximately correct for many of the longitudinal modes illustrated in this paper, this equation becomes

$$\lambda_j - \lambda_i = \frac{\lambda^2}{2nL[1 - (dn/d\lambda)(\lambda/n)]}. \tag{38}$$

This is the same result as for conventional lasers.

D. Mode Fields

Since saturation effects have not been considered the analysis applies only at threshold and absolute values of r_1, r_2, s_1, and s_2 in (10a) and (10b) cannot be determined. Instead, relative amplitudes, and thereby the energy distribution, within the DFB structure are computed as are the relative energies transmitted through the external reflectors.

From (11a) we have

$$r_1 = (i\kappa e^{-i\Omega}/\hat{\Gamma})s_1 \tag{39a}$$

and from (11d) and (14a)

$$r_2 = \frac{(1 - \rho_l\hat{\Gamma}/i\kappa)}{(\rho_l - \hat{\Gamma}/i\kappa)} e^{-i\Omega} e^{-\gamma L} s_1. \tag{39b}$$

In the special case $\rho_l = 0.0$

$$r_2 = -e^{-\gamma L} r_1 \tag{40}$$

so that

$$r_1 e^{\gamma z} + r_2 e^{-\gamma z} = 2r_1 e^{-\gamma L/2} \sinh[\gamma(z + L/2)] \tag{41}$$

in agreement with earlier results [1]. For $\rho_l = \pm 1.0$

$$r_2 = e^{-i\Omega} e^{-\gamma L} s_1. \tag{42}$$

From (39b) and (11d), we find

$$s_2 = \frac{i\kappa}{\hat{\Gamma}} \frac{(1 - \rho_l\hat{\Gamma}/i\kappa)}{(\rho_l - \hat{\Gamma}/i\kappa)} e^{-\gamma L} s_1 \tag{43}$$

which, by invoking (15), can be rewritten

$$s_2 = \frac{i\kappa}{\hat{\Gamma}} \frac{(\rho_r - \hat{\Gamma}/i\kappa)}{(1 - \rho_r\hat{\Gamma}/i\kappa)} e^{\gamma L} s_1. \tag{44}$$

Then with $\rho_r = 0.0$

$$s_2 = -e^{\gamma L} s_1 \tag{45}$$

so that

$$s_1 e^{\gamma z} + s_2 e^{-\gamma z} = 2s_1 e^{\gamma L/2} \sinh[\gamma(z - L/2)] \tag{46}$$

and with $\rho_r = \pm 1.0$

$$s_2 = \frac{i\kappa}{\hat{\Gamma}} e^{\gamma L} s_1 = e^{i\Omega} e^{\gamma L} r_1 \tag{47}$$

where (11a) has been employed.

The power in the wave $R(z)$ at any point in the DFB structure is

$$P_a(z) = c_1|r_1 e^{\gamma z} + r_2 e^{-\gamma z}|^2 \tag{48a}$$

that in $S(z)$ is

$$P_b(z) = c_1|s_1 e^{\gamma z} + s_2 e^{-\gamma z}|^2 \tag{48b}$$

where c_1 is a constant. The transmitted power through the right- and left-hand reflectors is

$$P_r = (1 - |\rho_r|^2)P_a(L/2) \tag{49a}$$

and

$$P_l = (1 - |\rho_l|^2)P_b(L/2) \tag{49b}$$

respectively. For $\rho_r = \rho_l$, $P_r = P_l$ for all modes as can be verified from the preceding formulas. Physically, this must be the case since the geometry is completely symmetric. However, if $\rho_l \neq \rho_r$, even if the magnitudes of the reflections are equal, $|\hat{\rho}_l| = |\hat{\rho}_r|$, P_r and P_l generally differ for each mode because of the phase difference. For the geometries marked † and †† in Table I, the modes and ratios P_r/P_l and P_l/P_r are symmetric about $\delta L = 0.0$. In Table II are listed values of αL, δL, and P_r/P_l for $(\rho_l, \rho_r) = (0.565, 0.565\, e^{i\pi/2})$ with $\kappa L = 1.0$. Note that the mode with maximum αL, i.e., minimum $|\delta L|$ also has the highest ratio $P_r/P_l = 5.0586$, all modes with $\delta L > 0$ have $P_r/P_l > 1.0$ and those with $\delta L < 0$ have $P_r/P_l < 1.0$. This is not a general characteristic, e.g., with $(\rho_l, \rho_r) = (0.565\, e^{-i\pi/4}, 0.565\, e^{i\pi/4})$, $P_r/P_l > 1.0$ for all modes. It is always true, however, that as $|\delta L|$ increases P_r/P_l approaches unity, since

TABLE II
VALUES OF αL, δL, AND P_r/P_l, THE RATIO OF TRANSMITTED POWER THROUGH THE LEFT REFLECTOR TO THAT TRANSMITTED THROUGH THE RIGHT REFLECTOR FOR NINE LONGITUDINAL MODES WITH $\rho_l = 0.565$, $\rho_r = 0.565e^{i\pi/2}$ AND $\kappa L = 1.0$

αL	δL	P_r/P_l
0.5969	-11.775	0.9023
0.6066	-8.632	0.8676
0.6278	-5.490	0.7956
0.7013	-2.378	0.5878
0.7805	0.270	5.0586
0.4945	3.897	1.3053
0.5288	7.054	1.1678
0.5417	10.200	1.1157
0.5486	13.345	1.0882

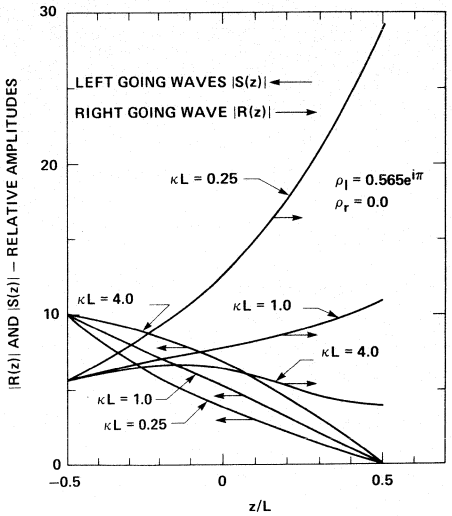

Fig. 9. Amplitudes of traveling waves for the first longitudinal mode (minimum $|\delta L|$) with $\delta L > 0$ and various κL.

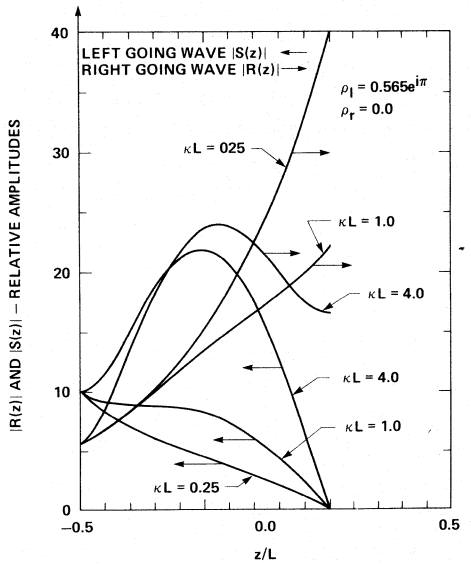

Fig. 10. Amplitudes of traveling waves for the first longitudinal mode (minimum $|\delta L|$) with $\delta L < 0$ and various κL.

then the longitudinal modes are primarily determined by the external reflectors and not the DFB structure.

In Figs. 9 and 10 are plotted $|R(z)|$ and $|S(z)|$ for the two longitudinal modes with minimum $|\delta L|$ and $\delta L > 0$, $\delta L < 0$, respectively. Here $(\rho_l, \rho_r) = (0.565\, e^{i\pi}, 0.0)$ and $\kappa L = 0.25$, 1.0, 4.0. In the undercoupled case ($\kappa L = 0.25$) the fields are approximately given by a single exponential, viz., $R(z) \sim r_1 e^{\gamma z}$, $S(z) \sim s_2 e^{-\gamma z}$. With increasing coupling ($\kappa L = 1.0$) both exponential terms in $R(z)$ and $S(z)$ are nonnegligible and in the overcoupled case Re (γL) is so small that the exponentials are more nearly oscillating functions. Power flows are proportional to the squares of the plotted fields and it is interesting to compute the ratio of transmitted power from (49a) and (49b). We find, for $\kappa L = 0.25$ and $\delta L > 0$, $P_r/P_l \approx 125$ whereas with $\delta L < 0$, $P_r/P_l \approx 245$.

IV. Remarks

The results presented in this paper provide insight into the longitudinal mode behavior of DFB lasers with external reflectors. We have shown that the relative positions of the reflectors and grating are of critical importance in determining laser thresholds, frequencies, and relative transmitted powers, which can differ markedly. The results were obtained under various assumptions, viz., the reflectors are aligned with the grating κ, the absorption, and the pumping are uniform along the laser length, all nonlinear effects of saturation, pumping, and spontaneous emission are neglected as is scattering from the grating other than into the desired Bragg order. No doubt these phenomena will affect comparisons with experimental results.

References

[1] H. Kogelnik and C. V. Shank, "Coupled-wave theory of distributed feedback lasers," *J. Appl. Phys.*, vol. 43, pp. 2327–2335, 1972.

[2] S. R. Chinn, "Effects of minor reflectivity in a distributed-feedback laser," *IEEE J. Quantum Electron.*, vol. QE-9, pp. 574–580, June 1973.

[3] W. Streifer, D. R. Scifres, and R. D. Burnham, *Appl. Phys. Lett.*, to be published.

Light Scattering from Periodic Refractive-Index Fluctuations in Asymmetric Slab Waveguides

D. MARCUSE, FELLOW, IEEE

Abstract—**We consider scattering of light out of the guiding layer into the substrate and the airspace of an asymmetric slab waveguide caused by periodic refractive-index fluctuations. Also discussed is the effect of backscattering of a guided wave into itself. The periodic index fluctuations may be caused by an acoustic surface wave. For this reason, we assume that the intensity of the index fluctuations decreases exponentially with increasing depth below the surface of the guide. However, our discussion is general, and the acoustic surface wave is used only as an example. Numerical results and graphic examples are given.**

INTRODUCTION

ACOUSTOOPTIC light deflectors using a surface acoustic wave and an optical wave that is guided by a thin-film waveguide have been discussed in the literature [1], [2]. However, a theoretical analysis of the asymmetric slab waveguide with periodic refractive-index fluctuation does not seem to have been published.

In this paper we are considering an asymmetric slab waveguide defined by the refractive-index distribution

$$n_0(x) = \begin{cases} n_3, & \text{for } x > 0 \\ n_1, & \text{for } 0 \geqslant x \geqslant -d \\ n_2, & \text{for } -d \geqslant x > -\infty. \end{cases} \tag{1}$$

The waveguide, its index distribution, and the coordinate system used to describe it are shown schematically in Fig. 1. The guided and radiation modes of this structure are well known [3]. The example of an asymmetric slab guide serves as a model for more general diffused waveguides.

The acoustic surface wave influences the refractive-index distribution. We ignore its time variation so that frequency-modulation effects caused by the interaction between the acoustic wave and the light wave are neglected. In the presence of the acoustic wave, we describe the refractive-index distribution by the equation

$$n(x) = \begin{cases} n_0(x), & \text{for } x > 0 \\ n_0(x) + \dfrac{(\Delta n_1^2)}{2n_1} e^{x/D} \cos \theta z, & \text{for } 0 \geqslant x > -d \\ n_0(x) + \dfrac{(\Delta n_2^2)}{2n_2} e^{x/D} \cos \theta z, & \text{for } -d \geqslant x > -\infty \end{cases} \tag{2}$$

with $n_0(x)$ given by (1). The form of these equations shows that we assume that the acoustic wave does not reach into the region $x > 0$, which is the airspace above film and substrate, so that $n_3 = 1$ in most cases of interest.

Manuscript received October 24, 1974.
The author is with Bell Laboratories, Crawford Hill Laboratory, Holmdel, N.J. 07733.

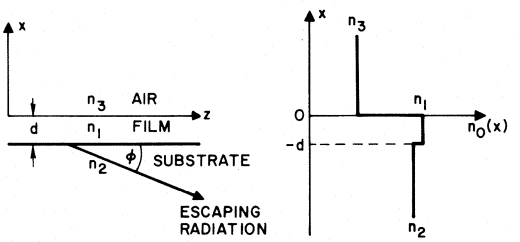

Fig. 1. Schematic of the asymmetric slab waveguide and its refractive-index distribution.

The acoustic wave decays in intensity with increasing distance below the surface of the asymmetric slab. Its intensity is assumed to have decayed to $1/e$ of its maximum value (at $x = 0$) at a depth of $x = D$. In the z direction, which coincides with the direction of propagation of the light wave, the acoustic wavelength is

$$\Lambda = \frac{2\pi}{\theta}. \tag{3}$$

The small factors (Δn_1^2) and (Δn_2^2) appearing in (2) depend on the power in the acoustic wave and on the acoustooptic coefficient of the materials. The form of (2) was chosen so that $n^2(x) \approx n_0^2(x) + (\Delta n^2)\, e^{x/D} \cos \theta$.

A general discussion of asymmetric slab waveguides with sinusoidal imperfections is given in [3]. It is well known that two light waves interact with each other via the acoustic wave, provided the phase-matching relation

$$|\beta_1 - \beta_2| = \theta \tag{4}$$

holds. The propagation constants β_1 and β_2 of the two optical modes may both belong to guided waves. In this case, the interaction converts power from one guided mode to another. In particular, it is possible to convert power from a given guided mode to its backward-traveling counterpart so that $\beta_2 = -\beta_1$. We shall discuss this case in detail. Another case of practical interest arises when β_2 is the z component of the propagation vector of a radiation mode. Of most interest is the case when the radiation escapes only into the substrate since it involves interaction with acoustic waves of relatively low frequency. The magnitude of the propagation vector of a plane wave in the substrate is $n_2 k$ ($k = 2\pi/\lambda$, free-space propagation constant). We thus have the relation

$$\beta_2 = n_2 k \cos \phi \tag{5}$$

where ϕ is the angle between the direction of the light beam and the film boundary. This angle is thus determined in terms of the propagation constant θ of the acoustic wave and the

propagation constant $\beta_1 = \beta_g$ of the guided optical mode by the relation

$$\phi = \arccos\left(\frac{\beta_g - \theta}{n_2 k}\right). \tag{6}$$

Since the frequency of the acoustic wave can be varied with a corresponding change of θ, the direction of the emerging optical beam can be changed, resulting in an optical-beam scanning device.

The efficiency of the beam scanner can be expressed in terms of the attenuation suffered by the guided wave. It is shown in [3] that light scattering by a sinusoidal imperfection of an optical waveguide causes the guided wave to decay exponentially in z direction according to the law

$$P(z) = P(0)\, e^{-2\alpha z}. \tag{7}$$

The form of the radiation field in the substrate of the guide is given by [3, eq. (4.2-39)]. The attenuation coefficient α appearing in (7) is sufficient to characterize the interaction between the guided mode and the acoustic wave, provided that the propagation constant of the acoustic wave is such that radiation, instead of coupling to other guided modes, results. In particular, we obtain only one radiated beam directed into the substrate if the relation

$$n_2 k > (\beta_g - \theta) > n_3 k \tag{8}$$

holds. For larger values of θ satisfying

$$n_3 k > (\beta_g - \theta) > -n_3 k \tag{9}$$

a second beam escapes into the airspace above the guiding layer. The total radiated power is now shared by the beam in the substrate and by the beam in air, but the attenuation coefficient α still indicates the total amount of power that is lost from the guided wave. This latter case is of less interest since it requires an acoustic wave of higher frequency which is highly attenuated in most materials.

As an example of guided-wave interaction, we limit ourselves to the case of scattering from a guided mode to its backward-traveling counterpart. This interaction takes place if

$$\theta = 2\beta_g. \tag{10}$$

This process requires very high acoustic frequencies, but it may be of practical interest because it is much more efficient than coupling from a guided mode to radiation. The interaction between two guided waves traveling in opposite directions is given by the equations [3]

$$c_1(z) = Ae^{-Rz} \tag{11}$$

and

$$c_2(z) = -Ae^{-Rz}. \tag{12}$$

The wave amplitude c_1 belongs to the wave traveling in the positive z direction, while c_2 is the amplitude of the wave traveling in the negative z direction. These equations apply to the special case that $c_1 = A$ at $z = 0$, and $c_2 = 0$ at $z = \infty$. It is apparent that wave 1 decays exponentially in its direction of propagation, while wave 2 grows as it advances in the guide.

The computation and discussion of the attenuation coefficient α and the coupling coefficient R will occupy the remainder of this paper.

Loss and Coupling Coefficient

Coupling between two modes (guided or radiation modes) is described by coupling coefficients of the approximate form [4], [3, p. 104, eq. (3.2-44), and p. 168, eq. (4.7-5)]

$$K_{\mu\nu} = \frac{\omega\epsilon_0}{4iP}\int_{-\infty}^{\infty} (n^2 - n_0^2)\, \mathfrak{E}_\mu^* \cdot \mathfrak{E}_\nu \, dx. \tag{13}$$

The radian frequency of the optical waves is designated as ω, and ϵ_0 is the dielectric permittivity of the vacuum. The expression is already simplified for the case of a slab waveguide by omitting integration in the y direction; consequently, P is the power-normalization coefficient of dimension watts/meter (unit length in the y direction, the direction in which no variation of any field quantities or waveguide irregularities occur). The refractive-index distribution $n = n(x)$ is given by (2), while $n_0 = n_0(x)$, the index distribution of the unperturbed waveguide, is given by (1). The script letters $\mathfrak{E}_\mu$ and $\mathfrak{E}_\nu$ indicate the electric-field vectors of the two coupled modes without their time and z variation. The asterisk stands for the complex conjugation. The subscripts μ and ν label the guided or radiation modes.

We substitute (1) and (2) into (13), neglect terms of the second order in (Δn^2), and omit the cosine factor obtaining

$$\hat{K}_{\mu\nu} = \frac{\omega\epsilon_0}{4iP}\int_{-\infty}^{0} (\Delta n^2)\, e^{x/D}\, \mathfrak{E}_\mu^* \cdot \mathfrak{E}_\nu \, dx. \tag{14}$$

The caret serves as a reminder that $\cos\theta z$ is absent from (14). The notation (Δn^2) indicates that either (Δn_1^2) or (Δn_2^2) must be used depending on whether the integration variable is in the range $0 \geqslant x \geqslant -d$ or $-d > x > -\infty$. The constant R appearing in (11) and (12) is related to $\hat{K}_{\mu\nu}$ by the equation [3]

$$R = \tfrac{1}{2}\,|\hat{K}_{\mu\nu}|. \tag{15}$$

Substitution of the fields for $\mathfrak{E}_\mu$ and $\mathfrak{E}_\nu$ results in the following explicit form of the coupling coefficient for a guided wave and its backward-traveling counterpart

$$R = \frac{k^2\kappa^2}{2\beta_g\left(d + \frac{1}{\gamma} + \frac{1}{\delta}\right)}\left\{(\Delta n_1^2)\left[\frac{D}{2\kappa^2}(1 - e^{-(d/D)}) + \frac{\left(\frac{1}{2D}\cos 2\psi + \kappa \sin 2\psi\right) - e^{-(d/D)}\left[\frac{1}{2D}\cos(2\kappa d - 2\psi) - \kappa \sin(2\kappa d - 2\psi)\right]}{\kappa^2\left(\frac{1}{D^2} + 4\kappa^2\right)}\right] + (\Delta n_2^2)\,\frac{e^{-(d/D)}}{(\kappa^2 + \gamma^2)\left(2\gamma + \frac{1}{D}\right)}\right\} \tag{16}$$

with

$$\tan \psi = \frac{\delta}{\kappa} \tag{17}$$

$$\kappa^2 = n_1^2 k^2 - \beta_g^2 \tag{18}$$

$$\gamma^2 = \beta_g^2 - n_2^2 k^2 \tag{19}$$

and

$$\delta^2 = \beta_g^2 - n_3^2 k^2. \tag{20}$$

$$\alpha = \frac{\pi}{4}\frac{\beta}{\rho}\sum_i |\hat{K}_{\mu\rho}^{(i)}|^2. \tag{25}$$

The form of the coefficient $\hat{K}_{\mu\rho}^{(i)}$ depends on the value of the propagation constant θ of the acoustic wave. If the inequality (8) applies, radiation is emitted only into the substrate because the guided mode interacts only with radiation modes that decay exponentially into the airspace of index n^3. This behavior is, of course, a consequence of total internal reflection at the air-film interface. In this case we obtain from (14), with the help of the guided and radiation modes listed in [3],

$$\hat{K}_{\mu\rho}^{(1)} = \frac{\kappa k^2}{\left[\pi\beta_g\left(d + \frac{1}{\gamma} + \frac{1}{\delta}\right)(\kappa^2 + \delta^2)\right]^{1/2}} \times \frac{\rho\sigma G_1}{\{\beta[\rho^2(\sigma\cos\sigma d + |\Delta|\sin\sigma d)^2 + \sigma^2(\sigma\sin\sigma d - |\Delta|\cos\sigma d)^2]\}^{1/2}} \tag{26}$$

Two special cases are of interest. For very small values of the penetration depth D of the acoustic wave, the index fluctuations are restricted to the immediate vicinity of the air-film interface so that the perturbation becomes equivalent to a sinusoidal distortion of that interface. The slab waveguide with sinusoidal interface distortion is described in [3]. If the interface distortion is given by the function

$$f(z) = b\cos\theta z \tag{21}$$

we find the equivalence

$$(\Delta n_1^2) = \frac{n_1^2 - n_2^2}{D} b \qquad \text{for } D \to 0 \tag{22}$$

and obtain from (16)

$$R = \frac{\kappa^2 b}{2\beta_g\left(d + \frac{1}{\gamma} + \frac{1}{\delta}\right)} \qquad \text{for } D \to 0 \tag{23}$$

in agreement with [3, eq. (4.2-3)] (specialized to the case of coupling between two waves traveling in opposite directions). In the other extreme, $D \to \infty$, we obtain from (16), for $(\Delta n_1^2) = (\Delta n_2^2) = (\Delta n^2)$,

$$R = \frac{(\Delta n^2) k^2}{4\beta_g\left(d + \frac{1}{\gamma} + \frac{1}{\delta}\right)}\left\{d + \frac{1}{\kappa^2 + \gamma^2} \times \left[\frac{\kappa^2}{\gamma} + \frac{(\gamma + \delta)(\kappa^2 + \gamma\delta)}{\kappa^2 + \delta^2}\right]\right\}. \tag{24}$$

The attenuation coefficient α, describing coupling between a guided mode and a very narrow band of radiation modes, is given by the expression[1]

with

$$G_1 = (\Delta n_1^2)\int_{-d}^{0} e^{x/D}\left(\cos\kappa x - \frac{\delta}{\kappa}\sin\kappa x\right) \times \left(\cos\sigma x - \frac{|\Delta|}{\sigma}\sin\sigma x\right) dx + (\Delta n_2^2)\left(\cos\kappa d + \frac{\delta}{\kappa}\sin\kappa d\right) e^{-(d/D)} \times \int_{-\infty}^{0}\left[\left(\cos\sigma d + \frac{|\Delta|}{\sigma}\sin\sigma d\right)\cos\rho x + \left(\frac{\sigma}{\rho}\sin\sigma d - \frac{|\Delta|}{\rho}\cos\sigma d\right)\sin\rho x\right] e^{[\gamma + (1/D)]x}\, dx. \tag{27}$$

In addition to the parameters that were already defined by (18)–(20), we have

$$\beta = \beta_g - \theta \tag{28}$$

$$\sigma^2 = n_1^2 k^2 - \beta^2 \tag{29}$$

$$\rho^2 = n_2^2 k^2 - \beta^2 \tag{30}$$

and

$$\Delta^2 = n_3^2 k^2 - \beta^2. \tag{31}$$

The integrals occurring in (27) have elementary solutions and can be found in [5]. We refrain from writing out their solutions to save space.

Finally, we need the coupling coefficient for the case (9). There are two types of radiation modes, and the sum in (25) must be extended over the contributions from both types of modes [3]. We indicate the two types with labels 2 and 3 and obtain ($i = 2, 3$)

[1] Equation (25) is obtained from [3, eqs. (3.4-19) and (4.2-24)].

$$\hat{K}_{\mu\rho}^{(i)} = \frac{\kappa k^2}{\left[\pi\beta_g\left(d + \frac{1}{\gamma} + \frac{1}{\delta}\right)(\kappa^2 + \delta^2)\right]^{1/2}} \times \frac{G_i}{\left\{\beta\left[(\cos \sigma d - F_i \sin \sigma d)^2 + \frac{\sigma^2}{\rho^2}(\sin \sigma d + F_i \cos \sigma d)^2 + \frac{\Delta}{\rho}\left(1 + \frac{\sigma^2}{\Delta^2} F_i^2\right)\right]\right\}^{1/2}} \tag{32}$$

with

$$F_i = \frac{1}{(\sigma^2 - \rho^2)\sin 2\sigma d}\left\{(\sigma^2 - \rho^2)\cos 2\sigma d + \frac{\rho}{\Delta}(\sigma^2 - \Delta^2) \pm \left[(\sigma^2 - \rho^2)^2 + 2\frac{\rho}{\Delta}(\sigma^2 - \rho^2)(\sigma^2 - \Delta^2)\cos 2\sigma d + \frac{\rho^2}{\Delta^2}(\sigma^2 - \Delta^2)^2\right]^{1/2}\right\} \tag{33}$$

and with

$$G_i = (\Delta n_1^2)\int_{-d}^{0}\left(\cos \kappa x - \frac{\delta}{\kappa}\sin \kappa x\right)(\cos \sigma x + F_i \sin \sigma x) \times e^{x/D}\, dx + (\Delta n_2^2)\left(\cos \kappa d + \frac{\delta}{\kappa}\sin \kappa d\right)e^{-(d/D)} \times \int_{-\infty}^{0}\left[(\cos \sigma d - F_i \sin \sigma d)\cos \rho x + \frac{\sigma}{\rho} \times (\sin \sigma d + F_i \cos \sigma d)\sin \rho x\right]e^{[\gamma + (1/D)]x}\, dx. \tag{34}$$

Discussion of Numerical Results

A natural application for an acoustooptic device of this type appears to be an asymmetric slab waveguide that consists of a thin guiding layer on top of a substrate of essentially the same material. The refractive index of the guiding layer may be increased by means of diffusion of a dopant or by outdiffusion of some component of the material. An example of the latter technique is given by the outdiffusion of Li from $LiNbO_3$ [6] or by the diffusion of metals into $LiNbO_3$ [7]. The advantage of this arrangement is the fact that $LiNbO_3$ is piezoelectric so that the acoustic wave can be excited simply by placing interdigital electrodes on the top of the material. Since the material of the guiding layer is practically identical with the material of the substrate, we use in this case

$$(\Delta n_1^2) = (\Delta n_2^2) = (\Delta n^2). \tag{35}$$

To calculate the effect of the wave interaction for this case we assume that the film thickness is $d = 1$ μm. For HeNe laser light with the wavelength of $\lambda = 0.6328$ μm, we have $kd = 9.9292$. The refractive index of the substrate is $n_2 = 2.2$, and for the film we use $n_1 = 2.21$. With $n_3 = 1$, we have, for the lowest order TE mode, $\kappa d = 1.899153$. Fig. 2 shows a plot of the attenuation constant that is obtained from (25)-(34). Instead of plotting α directly, we take the logarithm (to base 10) of the suitably normalized loss coefficient and divide it by 10. This method is necessary in order to plot the attenuation coefficient over a wide range of values of the independent variable θ/n_2k. Also shown is the angle ϕ of (6) at which the radiation escapes into the substrate. The curves extend symmetrically beyond $\phi = 90°$ so that $\alpha(180 - \phi) = \alpha(\phi)$. The various curves in Fig. 2 belong to different penetration depths D of the acoustic wave. Large values of D/d indicate that the acoustic wave reaches deep into the substrate; values of D/d less than unity indicate that the acoustic wave decreases in intensity even inside the guiding layer for the light wave.

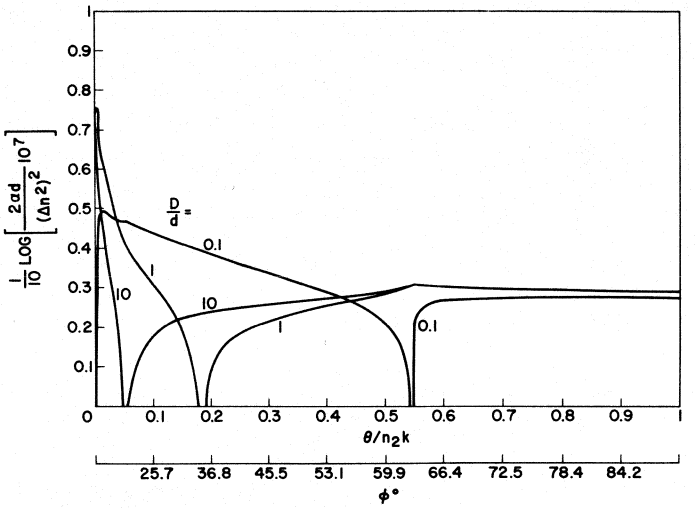

Fig. 2. Logarithmic plot of the normalized loss coefficient $2\alpha d/(\Delta n^2)^2$ as a function of the normalized propagation constant of the acoustic wave θ/n_2k or, equivalently, of the radiation angle ϕ in the substrate. Here, $n_1 = 2.21$, $n_2 = 2.2$, $n_3 = 1$, $kd = 9.9292$, and $\kappa d = 1.8992$.

The curves shown in Fig. 2 pass through zero at certain values of θ/n_2k or the corresponding angles ϕ. This vanishing of the coupling is an interference effect. According to Huygen's principle, we may assume that each element of the acoustic wave front acts as a point source of radiation. The magnitude of the resulting scattered light wave depends on the phase relationships of all the elementary waves to each other. At very small radiation angles, all contributions from one acoustic phase front add in phase, leading to the large peaks for small values of ϕ seen in Fig. 2. With increasing angle (the change in angle is accomplished by changing the propagation constant of the acoustic wave), the contributions from opposite ends of the acoustic phase front begin to cancel until, for certain radiation angles, complete cancellation results.

The slight kink in the curves at $\theta/n_2k = 0.545$ indicates the point at which radiation begins to escape, not only into the substrate, but also into the airspace above the guiding layer.

Since small radiation angles are of particular interest, the region $0 < \phi < 15°$ is shown stretched out in Fig. 3. The most striking features of these curves are the sharp peak values appearing at low radiation angles. The actual values of the radia-

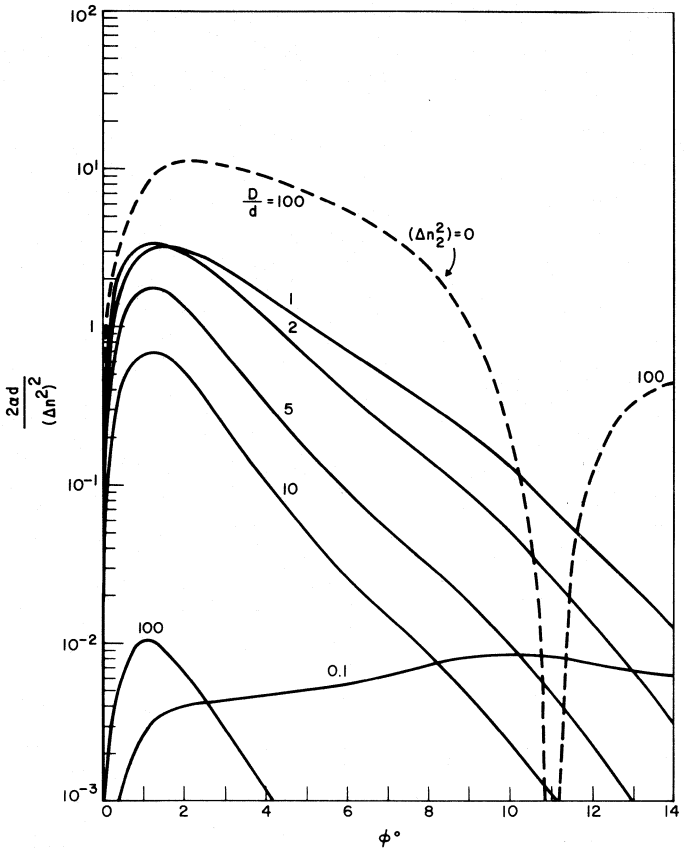

Fig. 3. An expansion of the loss coefficient shown in Fig. 2 for small angles ϕ.

tion peaks are determined by two competing effects. For a given value of (Δn^2) the volume of index fluctuations available for scattering increases with increasing penetration depth of the acoustic wave (increasing values of D/d). We would thus expect to see the radiation peak increase as D/d increases. This obvious effect is apparent only for the curve for $D/d = 0.1$ in comparison to the curves with $D/d = 1$ through 10. For all the other curves, the situation is reversed. This reversal is caused by mode orthogonality. If the acoustic wave would extend throughout all space with $D/d = \infty$, and the same value of (Δn^2) in all three regions, the integral in (14) would vanish because of mode orthogonality. The more uniform the acoustic wave becomes, the less contribution can be expected from the overlap integral in (14). In fact, it is because the acoustic wave does not extend into the airspace that we have a finite contribution to the scattering process even for $D/d = \infty$.

Mode orthogonality makes this type of acoustooptic coupler or beam scanner an inefficient device. It could work effectively only for small values of D/d. However, since the acoustic surface wave penetrates into the material to a depth that is comparable to its wavelength (which is much larger than that of the optical wave), small values of D/d cannot be obtained at low acoustical frequencies. The mode-orthogonality effect can be counteracted also by using materials for the guiding layer and substrate with different acoustooptic coefficients so that (Δn_1^2) and (Δn_2^2) become different. However, even in this case we may expect a poor coupling efficiency for large values of D/d and for tightly guided optical waves whose energy is contained almost exclusively inside the guiding layer. Good efficiency results only for waves close to cutoff that carry significant amounts of power in the substrate.

As an example, we consider the case of a slab waveguide whose acoustooptical coefficient is very small in the substrate by setting $(\Delta n_2^2) = 0$. Leaving the other waveguide parameters unchanged, we obtain the dotted curve shown in Fig. 3 for $D/d = 100$. Since mode orthogonality is less effective when the substrate no longer takes part in light scattering, the coupling efficiency is improved by three orders of magnitude. The same result is obtained with $(\Delta n_1^2) = 0$ and $(\Delta n_2^2) = (\Delta n^2)$. Even better results could be obtained for a wave that is closer to cutoff. In the present case we obtain from $n_1 = 2.21$, $n_2 = 2.2$, $n_3 = 1$, $kd = 9.9292$, and $\kappa d = 1.899153$, the value $\gamma d = 0.8608$. The parameter γ indicates the penetration depth of the light wave in the substrate. At a distance $1/\gamma$ the wave has decreased to $1/e$ of its field strength at the dielectric interface between the guiding layer and the substrate. In our example, the penetration depth is 1.16 times the width of the guiding layer. The wave is thus not very tightly bound to the guiding layer, but even weaker guidance would be possible.

In order to obtain a feeling for the required values of (Δn^2) let us consider specific numerical examples. In a typical case we may expect $D/d = 10$ so that we find from Fig. 3 the value

$$\frac{2\alpha d}{(\Delta n^2)^2} = 0.7 \tag{36}$$

at the peak of the loss curve at a substrate angle of $\phi = 1.2°$. To obtain a loss of $2\alpha L = 1$ Np = 4.34 dB in a waveguide of $L = 1$-cm length with a guide width of $d = 10^{-4}$ cm would require that $(\Delta n^2) = 1.2 \times 10^{-2}$. According to (2), we obtain the change of the refractive index from the equation

$$\Delta n = \frac{(\Delta n^2)}{2n} \tag{37}$$

so that $\Delta n = 2.7 \times 10^{-3}$. Such large values of Δn may be difficult to obtain by acoustical means. For a more realistic value of $\Delta n = 10^{-4}$ or $(\Delta n^2) = 4.4 \times 10^{-4}$, [8], we find instead

$$2\alpha L = 1.4 \times 10^{-3} \text{ Np} = 5.9 \times 10^{-3} \text{ dB}$$

for the conditions assumed earlier. Increasing the radiation angle from 1.2° to 10° reduces the coupling loss to $2\alpha L = 4.6 \times 10^{-6}$ Np $= 2 \times 10^{-5}$ dB. Figueroa [9] has measured values of $2\alpha L = 10^{-4}$ at a substrate angle of $\phi \approx 10°$. These values agree with our theory if we assume $D/d = 2$. These numbers show the inefficiency of an acoustical coupler whose guiding layer and substrate consist of essentially the same material. If the materials can be made substantially different so that either (Δn_1^2) or (Δn_2^2) is much larger than the index change in the rest of the waveguide structure, the conditions of the dotted curve in Fig. 3 prevail and we find

$$\frac{2\alpha d}{(\Delta n^2)^2} = 11$$

at the peak of the curve at $\phi = 2°$. For $\Delta n = 2.2 \times 10^{-4}$ we would have a coupling loss of $2\alpha L = 0.1$ Np = 0.43 dB. Coupling efficiencies of this order of magnitude have been re-

ported in the literature with a slab waveguide whose guiding layer and substrate consisted of different materials [2].

Fig. 4 corresponds to the same conditions that were assumed for Fig. 2, except that the value of kd is increased to $kd = 100$.

In order to include slabs with larger refractive-index differences between guiding layer and substrate we have drawn the coupling loss coefficient in Fig. 5 for the conditions $n_1 = 1.6$, $n_2 = 1.5$, $n_3 = 1$, and $kd = 12.572$ resulting in a value of $\kappa d = 2.59565$ for the lowest order TE mode. These conditions are similar to those used in [3, p. 139, fig. 4.2.2], except that there the next higher guided TE mode was considered. Fig. 5 shows pronounced maxima and minima. They are leaky wave resonances discussed in [3]. For small values of D/d, the curves of Fig. 5 are equivalent to scattering from a sinusoidally distorted air-film interface as was discussed earlier. For larger values of D/d, we see once more the deep minima of the loss curves caused by destructive interference of the wavelets originating along the acoustical phase front.

Finally, we turn to the case of backward scattering of a guided wave. Fig. 6 depicts three different cases labeled 1, 2, and 3. Case 1 corresponds to the conditions: $n_1 = 1.6$, $n_2 = 1.5$, $n_3 = 1$, $kd = 12.572371$, and $\kappa d = 2.59565$. Case 2 corresponds to $n_1 = 2.21$, $n_2 = 2.2$, $n_3 = 1$, $kd = 9.9292$, and $\kappa d = 1.899153$. Case 3 is similar to case 2 with the exception that $kd = 100$ and $\kappa d = 2.98388$. Backward scattering by means of an acoustic wave requires extremely high acoustic frequencies. However, our example is applicable to any kind of refractive-index fluctuation regardless of its cause. Backward scattering of a guided wave is not plagued by problems of mode orthogonality since a wave and its backward-traveling counterpart are not mutually orthogonal. It is thus advantageous to let the refractive-index disturbance extend as deeply into the substrate as possible. This trend is clearly apparent in Fig. 6 from the fact that all curves increase monotonically with increasing values of D/d reaching the asymptotic limit of (24). Consider again the example of $LiNbO_3$ with $n_1 = 2.21$ and $n_2 = 2.2$, case 2. We see from Fig. 6 that we obtain $RD/(\Delta n^2) = 1.1$ for large values of D/d. This gives $RL = 4.4$ for $L/d = 10^4$ and $(\Delta n^2) = 4.4 \times 10^4$. The incident wave is thus reduced in intensity to $e^{-8.8} = 1.5 \times 10^{-4}$ of its initial value. The slight index fluctuation of $\Delta n = 10^{-4}$ is thus very effective for backward scattering of a guided wave contrary to its ineffectiveness for coupling to radiation. This feature of backward scattering is useful for the design of distributed-feedback lasers [10], [11]. The other two cases depicted in Fig. 6 are even more efficient for the same value of (Δn^2).

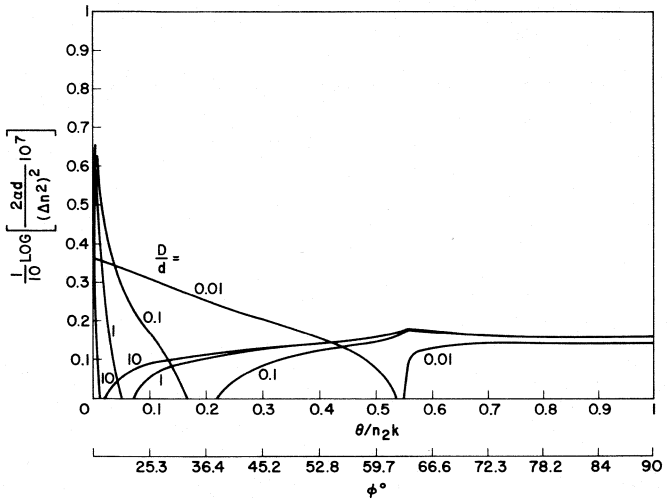

Fig. 4. This plot is similar to Fig. 2, except that $kd = 100$ and $\kappa d = 2.9839$.

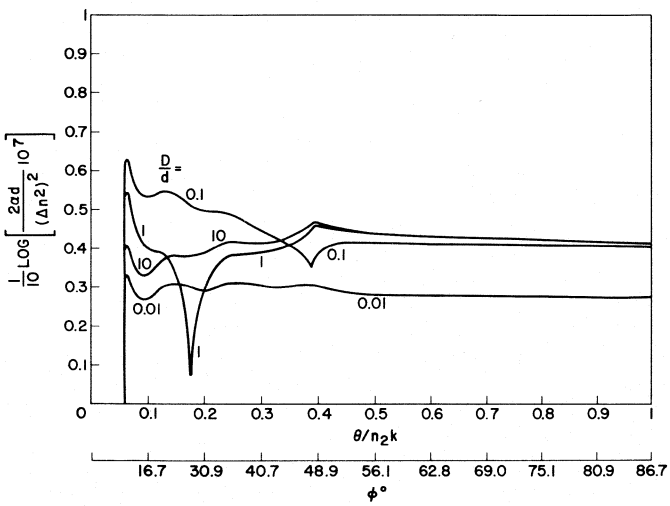

Fig. 5. This curve is similar to Fig. 2, except that $n_1 = 1.6$, $n_2 = 1.5$, $n_3 = 1$, $kd = 12.572$, and $\kappa d = 2.5956$. The curves show leaky wave resonances because of the large refractive-index difference between guiding region and substrate.

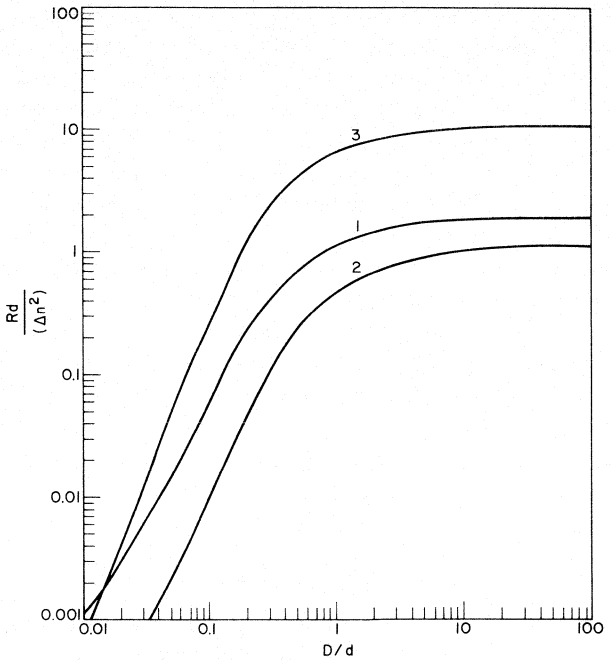

Fig. 6. Normalized coupling coefficient $Rd/(\Delta n^2)$ as a function of D/d. R describes coupling between a guided wave and its backward-traveling counterpart.

Conclusions

We have considered light scattering in asymmetric slab waveguides caused by periodic refractive-index perturbations whose intensity decreases exponentially with increasing depth in the substrate. Such an index fluctuation can be produced by an acoustical surface wave. We found that light scattering out of

the waveguide is very inefficient if the acoustical wave (or the index perturbation) reaches deep into the substrate, and if it affects the guiding region and the substrate in the same manner. This would happen if an acoustical wave were used in a waveguide formed by diffusion. Better efficiency can be achieved by several means. If the slab waveguide consists essentially of one single material, it would be necessary to restrict the penetration of the periodic index variations to a fraction of the guiding region so that mode orthogonality is prevented from cancelling the coupling effect. If the guide can be made of different materials, care should be taken to ensure that the acoustooptic coefficients of the guiding region and substrate are different. Very good results can be obtained for backward scattering of a guide wave into itself. In this case, mode orthogonality does not interfere with the coupling efficiency so that deep penetration of the periodic index fluctuations into the waveguide is desirable.

Acknowledgment

The author wishes to thank I. P. Kaminow for suggesting this problem and for several stimulating discussions.

References

[1] W. S. C. Chang, "Acoustooptical deflection in thin films," *IEEE J. Quantum Electron.* (Corresp.), vol. QE-7, pp. 167–170, Apr. 1971.
[2] F. R. Gfeller and C. W. Pitt, "Colinear acoustooptic deflection in thin films," *Electron. Lett.*, vol. 8, pp. 549–551, Nov. 1972.
[3] D. Marcuse, *Theory of Dielectric Optical Waveguides*. New York: Academic, 1974.
[4] A. W. Snyder, "Coupled-mode theory for optical fibers," *J. Opt. Soc. Amer.*, vol. 62, pp. 1267–1277, Nov. 1972.
[5] G. A. Korn and T. M. Korn, *Mathematical Handbook for Scientists and Engineers*. New York: McGraw-Hill, 1961.
[6] I. P. Kaminow and J. R. Carruthers, "Optical waveguiding layers in $LiNbO_3$ and $LiTaO_3$," *Appl. Phys. Lett.*, vol. 22, pp. 326–328, Apr. 1973.
[7] a) J. M. Hammer and W. Phillips, "Low-loss single-mode optical waveguides and efficient high-speed modulators of $LiNb_xTa_{1-x}O_3$ and $LiTaO_3$," *Appl. Phys. Lett.*, vol. 24, June 1974.
b) R. V. Schmidt and I. P. Kaminow, "Metal-diffused optical waveguides in $LiNbO_3$," *Appl. Opt.*, to be published.
[8] I. P. Kaminow, private communication.
[9] L. Figueroa, to be published.
[10] H. Kogelnik and C. V. Shank, "Stimulated emission in a periodic structure," *Appl. Phys. Lett.*, vol. 18, pp. 152–154, Feb. 1971.
[11] H. Kogelnik and C. V. Shank, "Coupled-wave theory of stimulated emission in a periodic structure," *J. Appl. Phys.*, vol. 43, pp. 2327–2335, May 1972.

Correspondence

Realization of a Mode-Selective Three-Mirror Reflector

H. EICHLER, G. SCHICK, AND W. WIESEMANN

***Abstract*—A simple new mode-selective mirror configuration is realized for obtaining single-mode operation of a six-mode He/Ne laser. Stable single-mode operation could be maintained without active stabilization methods over periods of more than 5 min.**

I. Introduction

Numerous approaches to obtain mode-selective laser resonators have been reported [1]. For a great number of applications the Fox–Smith interferometer turned out to be the most suitable device. However, as has been investigated theoretically [2], a configuration consisting of three parallel mirrors should have likewise remarkable selective properties. This paper describes experimental results of longitudinal mode selection in a He/Ne laser with such a three-mirror reflector.

II. Apparatus

The laser resonator including the three-mirror reflector is shown schematically in Fig. 1. The He/Ne discharge tube was 680 mm long and 2 mm in diameter. The mirrors were separated by Invar and quartz rods. The power reflection coefficients of all the mirrors were about 0.99. The mirror configuration did not obey the mode matching conditions due to a lack of long-radius mirrors (r_1 = 2 m, $r_2 = r_3 = \infty$, r_4 = 6 m, L_L = 0.78 m, and L_R = 0.08 m). The distance between mirrors 3 and 4 could be tuned piezoelectrically.

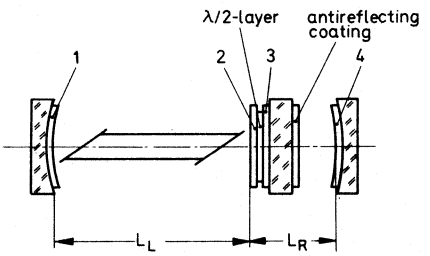

Fig. 1. He/Ne laser with three-mirror reflector consisting of mirrors 2, 3, and 4.

The reflection properties of the three-mirror reflector have been analyzed earlier. Fig. 2 shows the theoretical dependence of the power reflection coefficient R_{2*} of the three-mirror reflector on the phase shift between mirrors 3 and 4 for left-hand incidence. The parameters used for calculation are $R_1 = R_2 = R_3 = R_4 = 0.99$, $T_2 = T_3 = 7 \cdot 10^{-3}$ and $T_0 = 0.98$, where R_i, T_i are the power reflection and transmission coefficients of the ith mirror, respectively. T_0 is the power transmission of the λ/2-layer measured with a multiple reflection method [3]

Manuscript received October 29, 1974; revised December 18, 1974.
The authors are with the Optisches Institut, Technische Universität, Berlin, Germany.

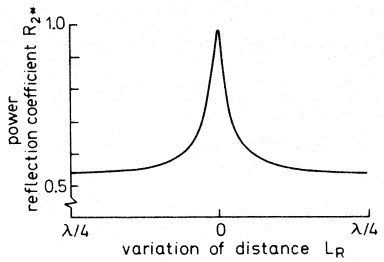

Fig. 2. Power reflection coefficient R_{2*} of the three-mirror reflector versus distance variation. Parameters are given in the text.

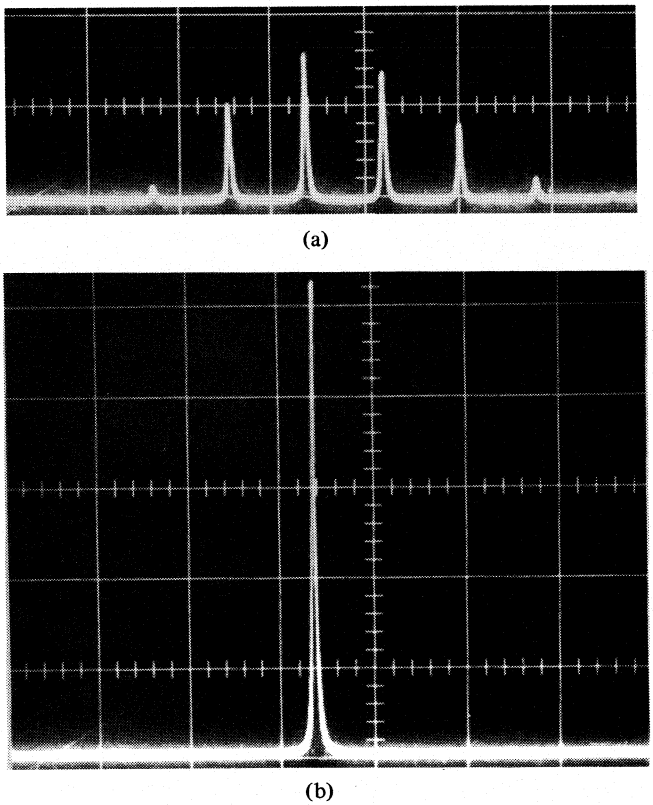

Fig. 3. Mode spectrum of the laser output as a function of frequency using (a) a flat mirror instead of the three-mirror reflector, and (b) the setup shown in Fig. 1.

using a test layer. The maximum power reflectivity of the three-mirror reflector amounts to 0.984. R_{2*} depends critically on the separation between mirrors 2 and 3. Therefore, mirrors 2 and 3 have been fabricated on a common substrate, separated by a λ/2-layer consisting of LaF_3. A power transmission coefficient of 0.1 and a halfwidth of 17 Å were measured for the interference filter consisting of mirrors 2 and 3 and the λ/2-layer (λ = 6328 Å).

III. Performance

In order to demonstrate the mode-selective properties of the three-mirror reflector the laser was first operated with a single flat mirror (R_2 = 0.99) instead of the three-mirror reflector. The mode spectrum [Fig. 3(a)] was monitored by a Spectra Physics scanning interferometer placed in front of mirror 1. Total power output (both sides) was 2.1 mW. After replacing the three-mirror reflector single-mode operation could be obtained [Fig. 3(b)] by tuning the distance L_R between mirrors 3 and 4 to an integer multiple of λ/2. Each of the six frequencies shown in Fig. 3(a) can be selected for single-mode operation by tuning the distance L_R. The total power of the single mode shown in Fig. 3(b) was 1 mW. No efforts were made for optimum output decoupling. Single-mode operation without mode jumping could be maintained without temperature stabilizing enclosures and servo loops for periods of 5–10 min after a warmup of half an hour.

The mirror configuration described here should be useful also for mode selection in other types of lasers.

Acknowledgment

The authors wish to thank Miss Ostwaldt for overcoming the difficulties of producing useful interference filters.

REFERENCES

[1] P. W. Smith, "Mode selection in lasers," *Proc. IEEE*, vol. 60, pp. 422–440, Apr. 1972.

[2] W. Wiesemann, "Longitudinal mode selection in lasers with three-mirror reflectors," *Appl. Opt.*, vol. 12, pp. 2909–2912, Dec. 1973.

[3] G. Koppelmann and K. Krebs, "Bestimmung schwacher Absorptionen in dünnen dielektrischen Schichten," *Z. Phys.*, vol. 156, pp. 38–54, May 1959.

Observations of Picosecond X-Ray Pulses

M. A. DUGUAY AND J. N. OLSEN

Abstract—**An upper limit on the duration of X-ray pulses emitted by a laser-produced plasma has been obtained using a picosecond optical-sampling system. When irradiating an iron target with 1-J 40-ps pulses from a Nd:glass laser, X-ray pulses were as short as 50 ps with a 0.5-percent conversion efficiency. The technique utilized direct excitation of a plastic scintillator and measurement of the scintillation light rise time. Time resolution was ≤50 ps.**

THE EXPERIMENT

Pulsed X-ray emissions in the nanosecond [1] and picosecond domains have many possible applications; pulsed radiography and X-ray laser excitation are two examples. In the laser-plasma context, picosecond-domain X-ray measurements are important diagnostics of the plasma time history. Recent advances in subnanosecond response X-ray detection have utilized fast vacuum photodiode [2] and ultrafast streak camera [3] techniques. In this work we report observation of 80-ps rise-time scintillation pulses excited by laser-plasma X-rays. Taking into account the scintillator characteristics, the X-ray pulse itself must be less than ~50 ps.

The apparatus used to create and observe ultrafast X-ray pulses is shown in Fig. 1. A 40-ps pulse of up to 1 J from a mode-locked Nd:YAG laser with glass amplifier [4] enters the system at a beam splitter; 75 percent of the energy is focused to an iron target. An NE 102 plastic scintillator,[1] placed 1 cm from the target behind a 10-μm-thick beryllium foil, converts the X-ray pulse into a fast-rising pulse of scintillation light which slowly decays. The subnanosecond rise time of the scintillation signal is monitored by a 5-channel optical sampler which is optically gated using the remaining 25 percent of the laser beam.

The optical-sampling technique has been described in detail previously [5], [6]. Briefly, optically induced birefringence in a CS_2 cell placed between crossed polarizers P_1 and P_2 provides signal transmission proportional to the square of the gating-beam intensity [7]. A 40-ps full width at half maximum (FWHM) infrared pulse thus allows transmission for 28 ps.

Manuscript received October 30, 1974; revised December 20, 1974. This work was performed with facilities at Sandia Laboratories, and was supported by the U.S. Atomic Energy Commission.

M. A. Duguay was with Bell Laboratories, Murray Hill, N.J. 07974. He is now with Sandia Laboratories, Albuquerque, N. Mex. 87115.

J. N. Olsen is with Sandia Laboratories, Albuquerque, N. Mex. 87115.

[1] Produced by Nuclear Enterprises Ltd., San Carlos, Calif. 94070.

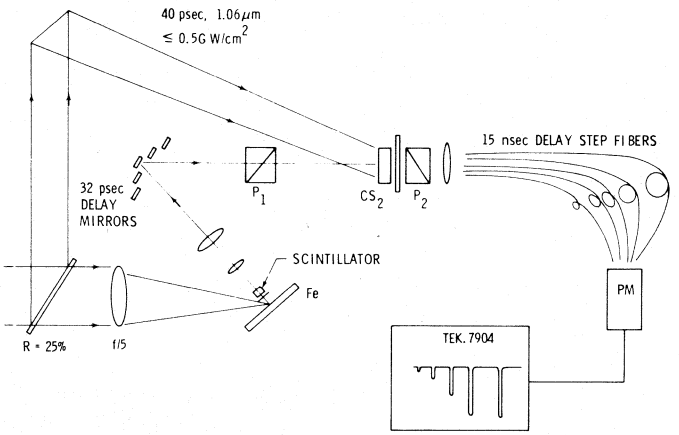

Fig. 1. Schematic of the picosecond X-ray apparatus. Not shown in the gating beam are a long focal-length lens and variable delay optics.

In the present application, the scintillation light is imaged from the scintillator surface onto an echelon array of mirrors. The five identical signals reflected from the mirrors enter the ultrafast gate at 33-ps intervals. When the gate opens for 28 ps, five samples are transmitted which span the scintillation rise time at 33-ps intervals for a total range of 132 ps. By varying the time at which the optical gate is opened on successive shots, a greater time range can be studied. The gated light in each of the five channels is imaged into an array of optical fibers, cut to delays of 5, 20, 35, 50, and 65 ns. Thus the samples can be conveniently detected and displayed at 15-ns intervals.

CALIBRATION AND RESULTS

The operation of the optical-gating array was tested as follows to assure picosecond gating and establish timing of the scintillation light relative to the laser input. A frequency-doubling crystal was inserted after the beam splitter and the foil was removed from the scintillator, thereby injecting a prompt 28-ps pulse of green light into the sampling array. Correct gating was demonstrated by single-channel response depending upon the gating-beam delay. Since the green signal is exactly synchronous with the infrared pulse, this enables one to establish an absolute time scale for the X-ray-induced scintillation light relative to the arrival time of the heating pulse. The relative sensitivities of the channels were obtained by removing the P_1 polarizer and displaying the green light in all channels.

A sampled display of the scintillation signal for 0.9 J on target is shown in Fig. 2(a). When the green-light calibration is used to normalize the observed samples, the sampled display of Fig. 2(b) is obtained. In this case, the scintillation is still rising in the fifth channel indicating a "long" X-ray pulse as discussed in the following. The X-ray yield is also monitored in a time-integrated mode using two p-i-n diodes behind beryllium foils (12 and 25 μm). Data from these detectors show $\langle h\nu \rangle \approx 1$ keV with up to 0.5-percent conversion efficiency for emission into 2π and correcting for absorption in the Be filters.

More reproducible and faster rise-time scintillation signals were obtained for slightly less energy on target, 0.5–0.7 J. In Fig. 3 a composite of several compatible shots with various gating delays is shown. The three middle time shots are normalized at their fourth channel; the earlier and later signals are normalized to agree with the middle shots. The longest delay measurements show that the scintillation does reach a

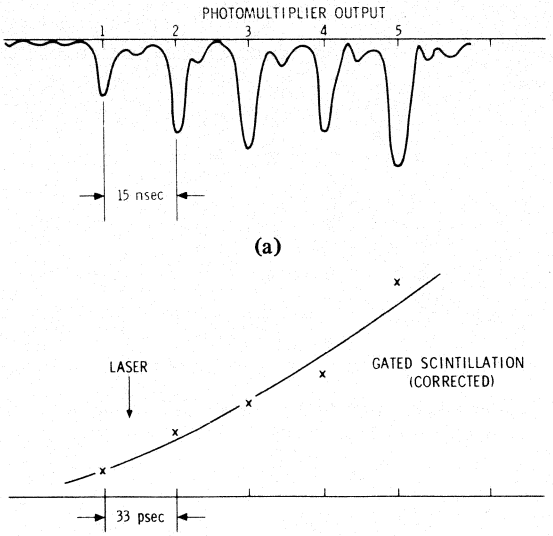

Fig. 2. Sampled scintillation signal for 0.9 J on target. The PM output is traced (a) from a 0.5-V/cm and 20-ns/cm oscilloscope display and corrected (b) for channel sensitivities.

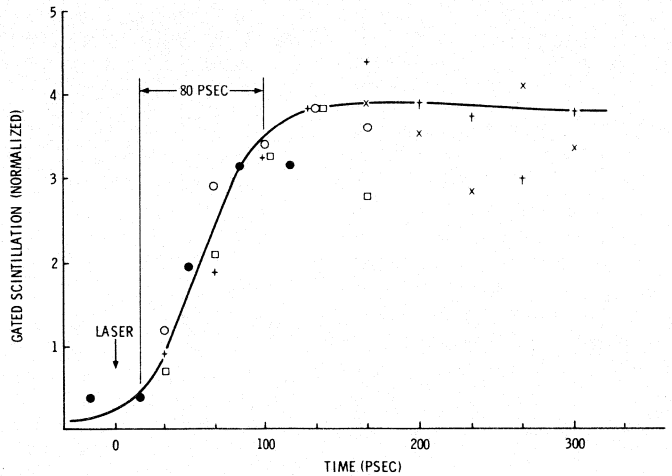

Fig. 3. Plot of the measured scintillation light as a function of time. The peak of the 1.06-μm heating laser pulse is taken as the origin of time. The curve is an eye-fit through points obtained on six separate laser shots.

plateau on the picosecond time scale, about 120 ps after the laser. The 10–90-percent rise time, $\tau_{10\text{-}90\%}$, is about 80 ps and the delay from the laser to 50-percent response, $\tau_{0\text{-}50\%}$, is 60–80 ps. Comparison of delay and rise time, as discussed below, set an upper limit of ~50 ps for the X-ray pulse duration.

The Scintillator Response

The role of the four-component plastic scintillator in detecting picosecond X-ray pulses is complicated by the absorption mechanism in the primary molecules and the several energy transfer times in converting absorbed energy to scintillation light [8]. In order to use a simple analytical model for the scintillator response, we assume a single time-independent excitation rate $1/\tau_R$, neglecting the time-dependent kinetics of intermolecular transfer mechanisms [9].

There are then four important times: τ_L, the Gaussian-laser half-width at the $1/e$ point (24 ps) which opens the CS_2 gate; τ_x, the X-ray pulse half-width; τ_R, the scintillator excitation time; and τ_D, the scintillator decay time (2.2 ns). Since τ_R has been reported to vary from less than 50 ps [10] to 900 ps [11], depending upon the exciting particle or wavelength, it appears that τ_R appropriate for excitation by 1-keV X-rays must be inferred from our data.

In a two-level model, the X-ray absorbing states decay to fluorescing states with $1/\tau_R$ rate and fluorescing states radiate with $1/\tau_D$ rate. Under these assumptions, the population of the fluorescing state N may be written as

$$N(t) \propto \int_{-\infty}^{t} dt' X(t') \left[\exp\left(-(t-t')/\tau_D\right) - \exp\left(-(t-t')/\tau_R\right)\right]$$

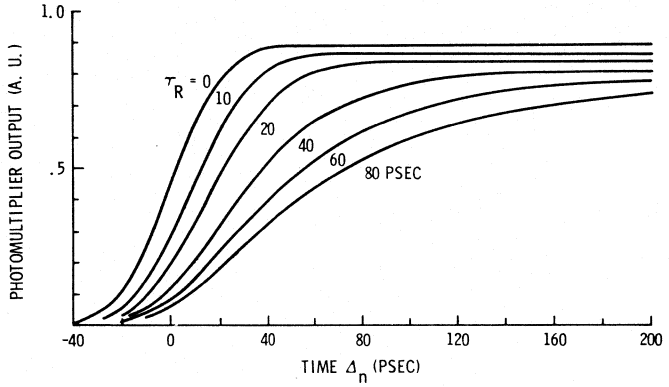

Fig. 4. Calculated photomultiplier output for various τ_R. Here both τ_X and τ_L have been chosen to be 24 ps, as an example.

where $X(t)$ is the X-ray pulse. The scintillation signal is simply $S(t) = N(t)/\tau_D$.

In the final measurement the fast photomultiplier records the integral of the scintillation light in each channel which was transmitted through the optical gate. Since the gate transmission depends upon the square of the gating intensity, the photomultiplier output in the nth channel, at time Δ_n, is

$$P(\Delta_n) \propto \int_{-\infty}^{\infty} dt \exp\left[-2(t - \Delta_n)^2/\tau_L^2\right] S(t).$$

For a Gaussian $X(t) = X_0 \exp\left[-t^2/\tau_X^2\right]$ the envelope of the $P(\Delta_n)$ is shown in Fig. 4 for various τ_R where τ_L, τ_X = 24 ps, as an example.

In the limit of $\tau_R \ll \tau_L, \tau_X$ the envelope of $P(\Delta_n)$ describes an error function with rise time $\tau_{10\text{-}90\%} \approx 2\,\tau_X$. For slower response times $\tau_{10\text{-}90\%} \approx \tau_R$ and the delay of the midpoint of the scintillator rise approaches $\tau_{50\%} = \tau_R \ln 2$. All three time scales τ_R, τ_X, and τ_L act to lengthen the rise time; however, only τ_R and any X-ray emission delay will cause a scintillation delay. Since X-ray emission delay is strongly limited by rapid plasma cooling, measurement of the scintillation delay allows an upper limit estimate of τ_R.

Discussion

By comparing the composite of results in Fig. 3 with the family of calculated responses in Fig. 4, we infer $\tau_R \leqslant 50$ ps from the observed 80-ps rise time after allowing for the effect of an assumed τ_X in the calculation. Such a τ_R is compatible with the observed delay time, within our accuracy, if the $X(t)$ is assumed to be somewhat delayed, say 10 ps. It is clear that for physically reasonable X-ray delays ($\leqslant \tau_L$) the observed combination of $\tau_{50\%}$ and $\tau_{10\text{-}90\%}$ can only be obtained for $2\tau_X \leqslant \tau_R \approx 50$ ps. We conclude that for modest energy inputs (0.5–0.7 J) the X-ray pulse duration was comparable or perhaps less than the scintillator response.

Acknowledgment

The authors wish to thank J. F. Cuderman for assistance in setting up the experiment and C. Martinex for highly competent technical support, particularly the operation of the laser. Special thanks are due to M. A. Palmer for lending laboratory space and equipment for this experiment. M. A. Duguay gratefully acknowledges discussions with P. J. Mallozzi of the Battelle Memorial Institute on the possibility of generating picosecond X-ray pulses.

References

[1] P. J. Mallozzi *et al.*, *Fundamental and Applied Laser Physics*. New York: Wiley, 1973, pp. 165–220.
[2] R. K. Bardin, D. Kohler, and L. F. Chase, Jr., "Fast time history measurement of plasma produced X-rays," *Bull. Amer. Phys. Soc.*, vol. 19, pp. 556–557, 1974.
[3] C. F. McConaghy and L. W. Coleman, "Picosecond X-ray streak camera," *Appl. Phys. Lett.*, vol. 25, pp. 268–270, 1974; also M. C. Richardson, private communication.
[4] J. N. Olsen, "Picosecond infrared holography on bismuth film," *Appl. Phys. Lett.*, vol. 24, pp. 220–222, 1974.
[5] M. A. Duguay and A. Savage, "Picosecond optical sampling oscilloscope," *Opt. Commun.*, vol. 9, pp. 212–215, 1973.
[6] G. C. Vogel, A. Savage, and M. A. Duguay, "Picosecond optical sampling," *IEEE J. Quantum Electron.*, vol. QE-10, pp. 642–646, Sept. 1974.
[7] M. A. Duguay and J. W. Hansen, "An ultrafast light gate," *Appl. Phys. Lett.*, vol. 15, pp. 192–194, 1969.
[8] J. B. Birks and R. W. Pringle, "Organic scintillators with improved timing characteristics," *Proc. Roy. Soc. Edinburgh*, vol. 70, pp. 233–244, 1972.
[9] J. B. Birks, "Energy transfer in organic systems VI. Fluorescence response functions and scintillation pulse shapes," *J. Phys. B*, vol. 1, pp. 946–957, 1968.
[10] S. L. Shapiro, R. C. Myer, and A. J. Campillo, "Rapid nonradiative transfer between dyes in the ternary scintillator NE102," *Appl. Opt.*, to be published.
[11] P. B. Lyons and J. Stevens, "Time response of plastic scintillators," *Nucl. Instrum. Methods*, vol. 114, pp. 313–320, 1974.

A Discharge Heated Copper Vapor Laser

R. S. ANDERSON, L. SPRINGER, B. G. BRICKS, AND T. W. KARRAS

Abstract—**A simple, reliable copper vapor laser is described with vapor produced by discharge heating. Average output power of 1.3 W has resulted at 6.8 kHz and a specific energy of 39 μJ/cm^3. Copper vapor density as high as 3 × 10^{16} cm^{-3} was achieved.**

Manuscript received November 14, 1974; revised December 3, 1974.
The authors are with the General Electric Company Space Sciences Laboratory, Valley Forge, Pa.

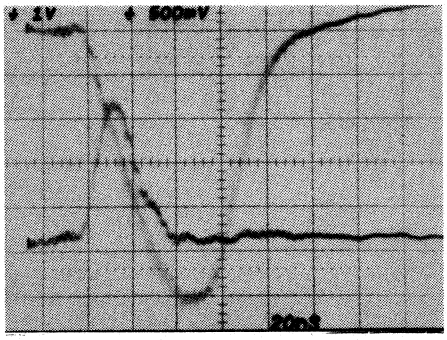

Fig. 1. Current and laser power. The laser discharge current as measured with a current transformer is shown on the upper trace and the laser power from a photodiode on the lower trace. Sweep was 20 ns/cm.

The copper vapor laser has shown potential as a high-power, high efficiency laser in the visible portion of the spectrum [1]-[3]. A key element in any such development must, of course, be the copper vapor source. Several different techniques for producing this vapor have been reported. As well as the original oven heated source [1], these have included heated expansion through a supersonic nozzle [4], explosion of copper wire and plasma gun acceleration [5], an evaporation-condensation cycle [6], and an efficient vaporizer producing a flowing medium [7]. Recently, low-temperature chemical production of copper vapor has also been reported [8], [9].

While several of these techniques promise high overall efficiency, at this time only Isaev *et al.* [2] have reported a practical copper vapor laser demonstrating both high power and high total system efficiency. In large part this was a result of the fact that no separate vapor source power was required. We report on the development of a self-heated copper laser similar in principle to that of Isaev and some preliminary results that were obtained.

In this laser the pulsed electrical discharge which pumps the inversion in the copper atom also serves to heat the tube and vaporize the copper. Thus no additional source of energy is required. The desired operating temperature is achieved through a proper balance of input power and radiation shielding. Normally, six minutes are required for the tube to heat up to a copper vapor pressure suitable for laser threshold; in nine minutes equilibrium and full power are reached.

The results from alumina tubes with two different gain regions are reported here, a small volume 0.28 $cm^2 \times 7$ cm and a larger volume 0.567 $cm^2 \times 8.5$ cm. In both cases long tantalum tube electrodes were inserted at each end, with a metal-ceramic seal at one end of each electrode and the discharge emerging from the other. As a result there was a hot bore region between the interior electrode ends and a cooler region external to them. This temperature gradient can produce diffusion of copper out of the hot zone. However, the discharge was carried by 10–30 torr of buffer gas (He, A, or Ne) which also limited the diffusion of copper.

During operation, the total input power was up to 1.5 kW as measured at the output of the power supply. The power supply inductively charged a 9-nF capacitor which was then discharged through the laser medium using an EG&G 1802 thyratron as a switch. Laser repetition rates between 1.8 and 10 kHz have been obtained with the thyratron and as high as 18 kHz using a quenching spark gap switch. Peak currents were the order of 10^3 A. Fig. 1 shows oscilloscope traces of the discharge current and the laser power.

Using the small gain region tube 0.27-W average power were obtained on both lines (5106 Å and 5782 Å) at a repetition rate of 4.2 kHz. This is equivalent to a specific energy of 33 $\mu J/cm^3$. With the large tube 1.3 W were obtained at a repetition rate of 6.8 kHz leading to a specific energy of 39 $\mu J/cm^3$.

All operation above about 0.100 W was strongly superradiant at both wavelengths. Optimum output mirror reflectivity was about 4 percent or lower. Removal of the output mirror entirely did not noticeably reduce the output power but did, of course, affect beam quality. Reduction of the rear mirror reflectivity from 99.9 percent to 50 percent and then to 4 percent, while holding the output mirror at 4 percent, also did not lead to substantial variation in the total output power.

These results are at least in part a result of the high copper vapor densities present. The tube temperature has been found to be as high as 1800°C–1850°C both by direct measurement with an optical pyrometer and observation of slight softening of the aluminum oxide. The copper vapor densities at this temperature are 3×10^{16} cm^{-3}, the highest thus far reported for a copper vapor laser.

With proper choice of materials, notwithstanding the slight softening of the aluminum oxide, the high temperatures within the device in no way limited operation. Lasing was maintained continuously for up to 12 h at a time without significant reductions in power. This demonstrates, as expected, that diffusion losses were greatly reduced by the presence of the buffer gas. The tube itself was generally valved off during operation implying negligible outgassing.

These results support the conclusions of Isaev [3] that the discharge heated copper vapor laser is a device of substantial practical significance.

ACKNOWLEDGMENT

The authors would like to thank B. Fox, T. E. Buczacki, and J. Nazar for their aid in laser construction and operation, and C. E. Anderson for useful technical discussions and his support.

REFERENCES

[1] W. T. Walter, M. Piltch, and G. Gould, "Efficient pulsed gas discharge lasers," *IEEE J. Quantum Electron.*, vol. QE-2, pp. 474–479, Sept. 1966.
[2] A. A. Isaev, M. A. Kazaryan, and G. G. Petrash, "Effective pulsed copper vapor laser with high average generation power," *JETP Lett.*, vol. 16, pp. 27–29, 1972.
[3] T. S. Fahlen, "Hollow cathode copper vapor laser," *J. Appl. Phys.*, vol. 45, pp. 4132–4133, 1974.
[4] G. R. Russell, N. M. Nerheim, and T. J. Pivirotto, "Supersonic electrical discharge copper vapor laser," *Appl. Phys. Lett.*, vol. 21, pp. 565–567, 1972.
[5] J. F. Asmus and N. K. Moncur, "Pulse broadening in a MHD copper vapor laser," *Appl. Phys. Lett.*, vol. 13, pp. 384–385, 1968.
[6] C. M. Ferrar, "Copper-vapor laser with closed cycle transverse vapor flow," *IEEE J. Quantum Electron.* (Corresp.), vol. QE-9, pp. 856–857, July 1973.

[7] T. W. Karras, R. S. Anderson, B. G. Bricks, "A spectroscopic study of high flow copper vapor lasers," *Bull. Amer. Phys. Soc.*, vol. 19, p. 153, 1974.
[8] C. J. Chen, N. M. Nerheim, and G. R. Russell, "Double-discharge copper vapor laser with copper chloride as a lasant," *Appl. Phys. Lett.*, vol. 23, pp. 514–515, 1973.
[9] C. S. Liu, E. W. Socov, and L. A. Weaver, "Copper superradiant emission from pulsed discharges in copper iodide vapor," *Appl. Phys. Lett.*, vol. 23, pp. 92–93, 1973.

Standing-Wave Effect in Laser-Saturation Experiments or When 2 is Less Than 1

H. J. GERRITSEN AND G. NIENHUIS

Abstract—**It is pointed out that, in order to obtain as large a population as possible in the upper state by laser pumping, the product of laser intensity and saturation parameter determines whether one gains or loses by reflecting the laser beam back into the saturated sample. Switching the polarization of the linearly polarized return beam by 90° eliminates this problem and is always advantageous.**

An amusing case of the previously stated paradox occurs when one attempts to saturate material by irradiating it with a resonant laser beam. Let the population of the ground-state level be denoted by N_1 and of the upper level by N_2, and let us consider the case that these levels are single and that they are the two lowest energy states.

Disregarding Doppler effects, either because the material is a solid, or because it is an atomic beam in which the atoms move perpendicularly to the laser beam, the rate equations for this case lead to the well-known stationary result

$$\frac{N_1 - N_2}{N_1 + N_2} = (1 + kI)^{-1} \tag{1}$$

where I is the laser intensity, and $k = \lambda^3(4\pi hc\Delta\nu)^{-1}$ is the saturation constant. Here λ is the wavelength of the radiation, h is Planck's constant, and $\Delta\nu$ is the linewidth of the absorption due to spontaneous decay. In many cases of practical interest, such as the pumping of a Na beam by a tunable CW dye laser, kI is of order unity. Furthermore, one often desires as large a value of N_2/N_1 as possible. Since usually the absorption experienced by the laser beam is not very large, one may be tempted to reflect the laser beam and have it traverse once more the volume to be pumped. The result is a standing wave, where some parts of space have a very large intensity which saturate easily, but where in the nodal planes saturation is not obtained at all. These nodal planes lay perpendicularly to the direction of the laser beams. The average population difference is then determined by

$$\frac{N_1 - N_2}{N_1 + N_2} = \frac{1}{\pi}\int_0^{\pi} dx\,(1 + 4kI\cos^2 x)^{-1} \tag{2}$$

where the integration is performed to obtain a volume average.

Manuscript received December 4, 1974.

H. J. Gerritsen is with the Department of Physics, Brown University, Providence, R.I. 02912. He is on leave at Fysisch Laboratorium, Rijksuniversiteit Utrecht, Utrecht, The Netherlands.

G. Nienhuis is with the Fysisch Laboratorium, Rijksuniversiteit Utrecht, Utrecht, The Netherlands.

The solution of (2) is

$$\frac{N_1 - N_2}{N_1 + N_2} = (1 + 4kI)^{-1/2}. \tag{3}$$

Comparison of (3) with (1) then leads to the intuitively acceptable result, that two-beam pumping is advantageous for low laser intensities. For if $kI < 2$, (3) is closer to zero than (1). At high intensities, one beam already pumps rather strongly, and the second beam does not add very much at the antinodal planes, since N_2/N_1 cannot exceed unity. But the two-beam situation suffers from the drop of intensity at the nodes. If $kI > 2$, (3) is farther from zero than (1). The break-even point occurs, as one sees, when $kI = 2$, in which case $N_2/N_1 = 0.5$. If the intensity of the laser is such that $kI > 2$, one better uses the beam once rather than twice.

A remedy to this situation is to switch the polarization of the reflected beam by 90° with a quarter-wave plate in front of the mirror. This generates a pattern of elliptical polarization without cancellation.

Photopreionization of the 3371-Å Pulsed N_2 Laser

N. A. KURNIT, S. J. TUBBS, K. BIDHICHAND, L. W. RYAN, JR., AND A. JAVAN

Abstract—**Photopreionization of the 3371-Å pulsed N_2 laser by use of a seed gas of low ionization threshold and flashlamp excitation is observed to result in increased laser output and reproducibility. Preionization also increases the range of permissible operating pressures, enabling operation with atmospheric-pressure mixtures of N_2 and He without reduced intensity.**

The 3371-Å pulsed N_2 laser [1] requires large current densities ($\gtrsim$1 kA/cm^2) and high electron temperature ($\gtrsim$5 eV) [2]. In order to operate with sufficiently high E/p to achieve these values, the N_2 laser is typically operated in a transverse discharge configuration with electric fields of ~10–30 kV/cm and pressure of 30–100 torr [3]. At higher pressures [4], where large amounts of energy could be stored and extracted, nonuniformities in the discharge leading to the formation of arcs tend to degrade the laser performance.

We have investigated the effect of volume photopreionization on the nitrogen-laser performance using a seed gas of low photoionization threshold and an external flashlamp [5]. The seed gas is used at sufficiently low partial pressure to ensure that the electron temperature is largely dominated by collisions with N_2 molecules. We observe significantly improved discharge uniformity and suppression of arcs over a wide pressure range, improved reproducibility of both the spatial distribution and intensity of the laser output, some increase in permissible operating pressures, including the ability to operate with atmospheric-pressure mixtures of N_2 and He, and an

Manuscript received December 13, 1974. This work was supported by the Office of Naval Research and the Air Force Cambridge Research Laboratories.

N. A. Kurnit, K. BidhiChand, L. W. Ryan, Jr., and A. Javan are with the Department of Physics, Massachusetts Institute of Technology, Cambridge, Mass. 02139.

S. J. Tubbs is with the Department of Meteorology, Massachusetts Institute of Technology, Cambridge, Mass. 02139.

increase in average laser power. The method also allows the use of a large-volume N_2 plasma (which requires excitation at correspondingly higher total current). This is of importance in possible realization of a high-energy N_2 laser.[1]

In the experiments, the nitrogen laser was similar to a design described by Small and Ashari [6] in which the current pulse is produced by a flat-plate Blumlein circuit consisting of two 25 X 25-cm capacitors etched on 18-mil-thick double-clad epoxy circuit board and charged to typically 16 kV. The electrodes are 10-mil-thick copper strips soldered along the length of the capacitors and edge opposed inside an evacuable lucite box. Electrode spacings of 1 cm and 0.2 cm have been tested. A single mirror was used at one end of the laser. Since the discharge is pressure confined in this laser, rather than confined by dielectric walls as in a number of designs, it is possible to place a standard Xe flashlamp inside the lucite box adjacent to the discharge region. We have utilized a 35-cm-long flashlamp placed 1.5 cm from the discharge and pulsed with typically 1.5 J (0.01 μF charged to 17 kV) in $\sim$5 μs. The volume preionization is produced by addition of trace amounts of triethylamine $[(C_2H_5)_3N]$ in a manner similar to that reported earlier for the production of large-volume high-density CO_2-laser plasmas [7]. The flashlamp current pulse is used to trigger a spark gap which initiates the laser discharge after a variable delay of 15–100 μs. The purpose of the photopreionization in this application is only to provide a sufficiently uniform initial electron distribution to ensure the creation of a uniform plasma when a voltage above avalanche breakdown is applied across the laser electrodes, and hence delay arc formation beyond the time during which laser oscillation occurs; thus only a small fraction of the total electron density need be supplied by the photoionization.

Before the introduction of triethylamine into the laser medium, it was observed that pulsing the flashlamp had little or no effect on the laser characteristics. For pure N_2 at low pressures ($\sim$100 torr), addition of small amounts of seedant by bubbling a small percentage of the laser gas through liquid triethylamine was, even without the flashlamp, sufficient to give a significant improvement in discharge uniformity and as much as a factor-of-2 increase in output power, to $\sim$50 kW in a 4-ns pulse.[2] The flashlamp gave a further small increase in laser power and reproducibility.[3] Fig. 1(a) shows a plot of relative laser output energy as a function of N_2 pressure both with and without preionization, for a 1-cm-wide discharge. The most significant visual differences occur on the high-pressure side of the curve, where the output without preionization becomes strongly arc limited.

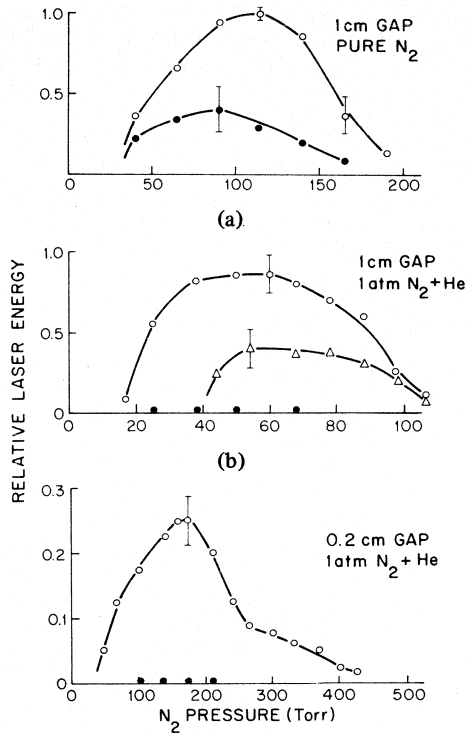

Fig. 1. Relative laser energy as a function of N_2 pressure for a) pure N_2 in 1-cm-gap laser, b) atmospheric-pressure mixture of N_2 and He with 1-cm gap, and c) atmospheric-pressure mixture of N_2 and He in 0.2-cm-gap laser. Open circles give output with flashlamp and optimized triethylamine flow; dots show output with no flashlamp and with triethylamine thoroughly purged from system. With atmospheric-pressure mixtures there is negligible output in the latter case. Triangles in (b) show output with triethylamine alone. Error bars indicate typical range of fluctuations during a series of 10 consecutive shots. (Magnitude of fluctuations is relatively constant along most curves, with corresponding decrease in percentage fluctuations near the peak of the curve; in the optimized curve in (a), a further decrease in fluctuations is observed near the peak of the curve.) Note the difference in pressure scales; in particular, (b) and (c) are scaled for the same ratio of field strength to nitrogen partial pressure.

A more dramatic behavior is illustrated in Fig. 1(b), which shows the laser output for an atmospheric-pressure mixture of N_2 and a He buffer[4] as a function of N_2 partial pressure, as determined from relative flow rates. Here, with no preionization the current is concentrated in a few arcs and there is negligible laser output, whereas with preionization the output is close to that obtained with pure N_2.

In this case again, triethylamine itself helps to produce a discharge which gives some laser action, but the laser performance is greatly improved when the flashlamp is fired shortly before the laser discharge. Delays of more than 50 μs between the flashlamp and laser reduce the effectiveness of the preionization. The discharge takes the form of a uniform distribution of closely spaced streamers as reported in [4], where atmospheric-pressure operation with pure N_2 was reported

[1] A publication which has just appeared in print discusses a different method in which a photostabilized discharge without the use of a seed gas is used to improve the performance of a UV N_2 laser; see V. Hasson, D. Preussler, J. Klimek, and H. M. von Bergmann, "Transverse double-discharge high-pressure glow excitation of UV lasing action in molecular nitrogen," *Appl. Phys. Lett.*, vol. 25, pp. 654–656, 1974.

[2] This effect may be attributable to the rapid rate of electron production from the low ionization threshold impurity. A similar effect has been reported in a CO_2–N_2–He laser mixture; see R. L. Schriever, "Uniform direct-current discharges in atmospheric-pressure He/N_2/CO_2 mixture using gas additives," *Appl. Phys. Lett.*, vol. 20, pp. 354–356, 1972. The laser power is strongly dependent on the fraction of volume utilized, the current density and rise time, and on whether the double-pass gain is high enough to saturate the transition.

[3] These experiments were performed at sufficiently low repetition rates ($\sim$2 pulses per second) so that the gas has time to be exchanged between shots. Some increase in reproducibility in such lasers can sometimes be observed at higher repetition rates, presumably due to some remaining background ionization, but for large energy deposition and high repetition rates arcing occurs if the gas is not exchanged quickly enough; see, for example, R. Targ, "Pulse nitrogen laser at high repetition rate," *IEEE J. Quantum Electron.* (Corresp.), vol. QE-8, pp. 726–728, Aug. 1972.

[4] T. Kobayasi, M. Takemura, H. Shimizu, and H. Inaba have reported such operation ("TEA UV nitrogen laser and its application to high sensitivity remote pulsed-Raman spectroscopy of atmospheric pollutants," presented at the IQEC 7th Int. Quantum Electronics Conf., Montreal, P. Q., Canada, May 1972, Paper M.9), but only at higher field strengths and with reduced intensity.

using higher field strengths and faster dielectric switches. It appears that photoionization should help to stabilize the discharge in such a TEA laser. The ability to operate at atmospheric-pressure mixtures of N_2 and He may in itself prove to be useful for some applications.

The maximum applied voltage of 16 kV was limited in these experiments by the breakdown potential of the epoxy board. In order to test the laser performance at higher E/p, a similar laser with a 2-mm gap was constructed. In this laser, with no photopreionization, the discharge was arc dominated at all but the lowest pressures, and laser performance was very poor. Photopreionization produces a discharge relatively free of arcs up to the highest pressure tested, and the laser gives an energy density comparable to that with the 1-cm gap, but in a smaller beam of smaller divergence (determined by the aspect ratio of the gap). Fig. 1(c) shows the pressure dependence of the output, again for an atmospheric-pressure mixture of N_2 and He. Some laser output was observed with as much as 400 torr of N_2. Since the discharge does not appear arc dominated even for high nitrogen pressure, the decrease of laser power at high pressure can presumably be attributed to the decrease of E/p.

We believe on the basis of these measurements that it should be possible by using preionization together with higher voltages and shaping of the electrodes to achieve atmospheric or higher pressure operation with pure N_2 or possibly with a mixture of N_2 and a buffer gas suitable for collisional quenching of the lower levels [8].

ACKNOWLEDGMENT

The authors wish to thank J. G. Small, J. Goldhar, and J. S. Levine for a number of helpful discussions. They also wish to thank J. Taller and J. Devir for their technical assistance.

REFERENCES

[1] H. G. Heard, "Ultra-violet gas laser at room temperature," *Nature*, vol. 200, p. 667, 1963.

[2] a) E. T. Gerry, "Pulsed-molecular-nitrogen laser theory," *Appl. Phys. Lett.*, vol. 7, pp. 6–8, 1965.
b) A. W. Ali, "A study of the nitrogen laser power density and some design considerations," *Appl. Opt.*, vol. 8, pp. 993–996, 1969.

[3] (a) D. A. Leonard, "Saturation of the molecular nitrogen second positive laser transition," *Appl. Phys. Lett.*, vol. 7, pp. 4–6, 1965.
b) J. D. Shipman, Jr., "Traveling wave excitation of high power gas lasers," *Appl. Phys. Lett.*, vol. 10, pp. 3–4, 1967. (For reference to a number of other designs, see E. E. Bergmann and E. Eberhardt, "A short high-power TE nitrogen laser," *IEEE J. Quantum Electron.* (Corresp.), vol. QE-9, pp. 853–854, Aug. 1973.)

[4] I. N. Knyazev, V. A. Letokhov, and V. G. Movshev, "TEA N_2 UV laser with reduced spectra," *Opt. Commun.*, vol. 6, pp. 250–252, 1972.

[5] A. Javan and J. S. Levine, "The feasibility of producing laser plasmas via photoionization," *IEEE J. Quantum Electron.*, vol. QE-8, pp. 827–832, Nov. 1972.

[6] J. G. Small and R. Ashari, "A simple pulsed nitrogen 3371 A laser with a modified Blumlein excitation method," *Rev. Sci. Instrum.*, vol. 43, pp. 1205–1206, 1972.

[7] a) J. S. Levine and A. Javan, "Observation of laser oscillation in a 1-atmosphere CO_2-H_2-He laser pumped by an electrically heated plasma generated via photoionization," *Appl. Phys. Lett.*, vol. 22, pp. 55–57, 1973.
b) H. J. J. Seguin, J. Tulip, and D. McKen, "Enhancement of photoelectron density in TEA lasers using additives," *Appl. Phys. Lett.*, vol. 23, pp. 527–529, 1973.

[8] L. Y. Nelson, G. J. Mullaney, and S. R. Byron, "Superfluorescence in N_2 and H_2 electron-beam-stabilized discharges," *Appl. Phys. Lett.*, vol. 22, pp. 79–80, 1973.

Notes and Lines

Generation of Second-Harmonic UV Radiation Using a Nonlinear Substrate Coated with a UV Absorbing Thin-Film Waveguide

BOR-UEI CHEN AND C. L. TANG

Abstract—**Second-harmonic Cerenkov radiation in the nonlinear substrate has been observed using a thin-film waveguide that is absorbing at the second harmonic but transparent at the fundamental wavelength.**

Second-harmonic generation using either a nonlinear thin-film waveguide or a thin-film waveguide deposited on a nonlinear substrate has been observed in the IR [1], [2], visible [3]–[6], and in the UV [7]. The second harmonic generated either propagates in the thin-film waveguide in the phase-matched case, or it is emitted in the nonlinear substrate in the form of Cerenkov radiation in the nonphase-matched case. In a previous publication [7], we reported on the observation of CW harmonic generation in the ultraviolet (λ_2 = 2850–3100 Å) using a thin-film waveguide on a nonlinear substrate. Both the phase-matched second harmonic in the thin-film and the nonlinear Cerenkov radiation in the substrate were observed. The thin-film structure consisted of an aluminum oxide waveguide deposited on a crystalline quartz substrate. Because of the difficulty in preparing good optical quality aluminum oxide film that was transparent in the UV region, the coherence length or the interaction length for the nonlinear process was relatively short (approximately 2 mm). The question that follows is whether the thin-film waveguide has to be transparent at the harmonic wavelength in the Cerenkov process in which the harmonic radiation propagates mainly in the nonlinear substrate. Since it is generally difficult to find high-index thin-film materials that are also transparent in the UV, if the latter requirement is not essential, a greater variety of materials that are easier to handle experimentally will also become usable in thin-film nonlinear optical experiments.

In this note, we report on an experiment in which a thin-film structure consisting of a Corning 7059 glass film on a nonlinear substrate was studied. The experimental setup is described in [7]. The CW dye laser was tunable from about 5650 Å to over 6100 Å with an output power on the order of 0.2 W. The laser light was coupled into the waveguide as a TE wave propagating along the z axis of the quartz substrate through a 14-cm focal length lens and a rutile prism. The Corning 7059 glass film was RF bias-sputtered onto the y-cut quartz substrate in an atmosphere of 3 μ oxygen and 7 μ argon. Both the refractive index and the thickness were measured by ellipsometry; the index at 6328 Å was found to be n(6328 Å) = 1.558 and the thickness 1.5 μ. The ordinary indices for the quartz substrate at the fundamental and the second-harmonic wavelengths were estimated to be n_0 (5900 Å) = 1.544, and n_0(2950 Å) = 1.580, respectively. The glass film was transparent at the fundamental wavelength but had an attenuation length shorter than 1 mm at the second-harmonic wavelength. Cerenkov radiation at the second-harmonic wavelength was observed in the substrate with an emission angle of ~11° relative to the film–substrate interface and found to vary linearly with the streak length far beyond 1 mm.

Fig. 1 shows the observed second-harmonic UV radiation as the streak length was varied from 3 mm to 15 mm at a fixed fundamental wavelength λ_1 = 5800 Å. The second-harmonic power detected varied approximately linearly with the streak length up to 10 mm. When the streak length was greater than 10 mm, part of the emitted Cerenkov radiation was intercepted by the quartz–air interface and was totally reflected internally at this surface due to the small Cerenkov angle. As a result, the second-harmonic light emerged at the end of the sample, became more divergent, and the collecting lens could not collect and focus all the signal into the monochromator; this accounted for the slight deviation from the straight line dependence shown in Fig. 1 for longer streak lengths. The measured absolute power of Cerenkov radiation was roughly 4×10^{-10} W at λ_1 = 5800 Å for a streak length of 15 mm, width of 60 μ, and a fundamental power of 0.2 W incident on the input focusing lens. This is comparable to the observed conversion efficiency when scaled to the same input power level reported in [7] for the aluminum oxide film.

Fig. 2 shows the typical spectral response of the second-harmonic output as the fundamental input wavelength was

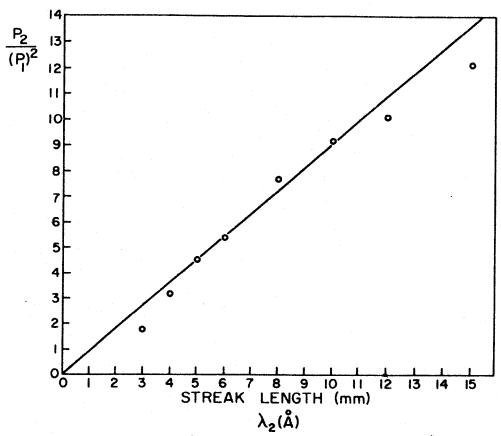

Fig. 1. Observed second-harmonic Cerenkov radiation versus streak length at λ_1 = 5800 Å. Each unit in the vertical scale corresponds to approximately 8×10^{-10} W^{-1}. P_2 is the emitted second-harmonic power collected by the collecting lens and P_1 is the total incident power on the focusing lens at the input.

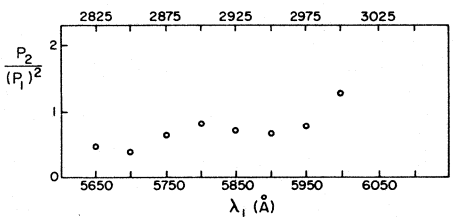

Fig. 2. Observed second-harmonic Cerenkov radiation versus input fundamental wavelength at streak length of L = 5 mm. The vertical scale is in relative units.

Manuscript received December 4, 1974. This work was supported in part by the National Science Foundation under Grant GK-33848 and in part by ARPA through the Materials Science Center of Cornell University.

The authors are with Cornell University, Ithaca, N.Y. 14853.

scanned from 5650 Å to 6100 Å for a fixed streak length $L = 5$ mm. The Cerenkov radiation was found again to be broadly and continuously tunable.

We have, therefore, demonstrated the possibility of using films that are absorbing at the generated wavelength for some nonlinear optical experiments.

References

[1] D. B. Anderson and J. T. Boyd, "Wideband CO_2 laser second harmonic generation phase matched in GaAs thin-film waveguides," *Appl. Phys. Lett.*, vol. 19, pp. 266–268, 1971.

[2] J. P. Van der Ziel, R. C. Miller, R. A. Logen, W. A. Nordland, Jr., and R. M. Mikulyak, "Phase-matched second-harmonic generation in GaAs optical waveguides by focused laser beams," *Appl. Phys. Lett.*, vol. 25, pp. 238–240, 1974.

[3] P. K. Tien, R. Ulrich, and R. J. Martin, "Optical second harmonic generation in form of coherent Cerenkov radiation from a thin-film waveguide," *Appl. Phys. Lett.*, vol. 17, pp. 447–450, 1970.

[4] Y. Suematsu, Y. Sasaki, and K. Shibata, "Second-harmonic generation due to a guided wave structure consisting of quartz coated with a glass film," *Appl. Phys. Lett.*, vol. 23, pp. 137–138, 1973.

[5] W. K. Burns and A. S. Lee, "Observation of noncritically phase-matched second-harmonic generation in an optical waveguide," *Appl. Phys. Lett.*, vol. 24, pp. 222–224, 1974.

[6] H. Ito, N. Uesugi, and H. Inaba, "Phase-matched guided optical second harmonic wave generation in oriented ZnS polycrystalline thin-film waveguides," *Appl. Phys. Lett.*, vol. 25, pp. 385–387, 1974.

[7] B.-U. Chen, C. L. Tang, and J. M. Telle, "CW harmonic generation in the uv using a thin-film waveguide on a nonlinear substrate," *Appl. Phys. Lett.*, vol. 25, pp. 495–498, 1974.

Contributors



Robert D. Burnham was born in Havre de Grace, Md., on March 21, 1944. He received the B.S., M.S., and Ph.D. degrees from the University of Illinois, Urbana, in 1966, 1968, and 1971, respectively. He held an NDEA Fellowship from 1966 to 1969 and a General Telephone and Electronics Fellowship from 1969 to 1971.

He has been a member of the Research Staff at the Xerox Palo Alto Research Center, Palo Alto, Calif., since 1971. His work has been centered on the growth and characterization of III-V compounds for device purposes.



D. J. Channin received the B.S. degree in physics from Case Institute of Technology, Cleveland, Ohio, in 1964, and the Ph.D. degree in physics from Cornell University, Ithaca, N.Y., in 1970. His dissertation and postdoctoral work at Cornell involved thermal and microwave phonon-pulse experiments at cryogenic temperatures.

From 1970 to the present he has been at the RCA Laboratories, Princeton, N.J. His work has included acoustooptic laser-beam modulators and deflectors, active and passive phenomena in optical waveguides, and the application of liquid crystals to optical waveguides and

to integrated-circuit testing.

Dr. Channin is a member of the American Physical Society, the Optical Society of America, Tau Beta Pi, and Sigma Xi.

*



Michael T. Duffy received the B.Sc. degree in physical chemistry in 1958, and the Ph.D. degree in solid-state chemistry in 1963, both from University College, Dublin, Ireland.

He was a Teaching Assistant at University College from 1961 to 1963. In 1964 he joined the University of Toronto as Research Associate and worked in molecular-beam research until July 1966, when he joined the staff of the RCA Laboratories, Princeton, N.J. Since then he has been engaged in materials research in the field of integrated electronics. He has worked on the synthesis and evaluation of thin-film dielectrics in MIS structures. His most recent work is synthesis and characterization of heteroepitaxial films on oxide substrates for application in surface-wave acoustic devices and integrated optics.

Dr. Duffy is a member of the Electrochemical Society. He received an RCA Laboratories Achievement Award in 1969 for work on the MNOS memory transistor, and again in 1973 for work on ZnO electrooptic modulator on sapphire.

*



Hermann Eicher was born in Munich, Germany, on September 6, 1934. He studied at the Technical University of Munich, Munich, and received the Ph.D. degree, under Prof. H. Maier-Leibnitz, in 1962.

From 1960 to 1968 he worked on the applications of the Mössbauer effect at the Technical University of Munich. In 1969 he turned to theoretical molecular physics and the interpretation of the electronic structure of the iron in biological molecules (ferredoxin, hemoglobin, and related compounds). In 1971 he became Privat Dozent (Habilitation) of theoretical physics at the Technical University of Munich. Since 1972 he has been dealing with quantum electronics, too. His publications include some 40 scientific papers.

*

B. W. Hakki (S'58–M'61), photograph and biography not available at the time of publication.

*

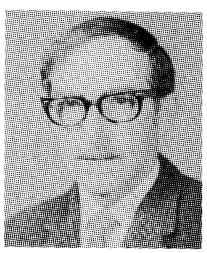

Jacob M. Hammer (SM'62) received the B.S. degree in engineering physics from New York University, New York, in 1950, the M.S. degree in physics from the University of Illinois, Urbana, in 1951, and the Ph.D. degree in physics from New York University, in 1956.

From 1956 to 1959 he worked at Bell Laboratories on microwave noise problems. In 1959 he joined the RCA Laboratories, Princeton, N.J., where he has worked on low-noise microwave research, electron interactions with atoms, and lasers. He spent the academic year 1968–1969 as a Senior Visitor at the Cavendish Laboratory, Cambridge, England. Since his return in August 1969, he has been studying problems in optical communication and waveguides.

Dr. Hammer is a member of the American Physical Society and Sigma Xi. He received the RCA Laboratories Outstanding Achievement Award in 1962, 1964, and 1973.

*



Shojiro Kawakami (S'60–M'69) was born in Gifu, Japan, on November 8, 1936. He received the B.E. degree in 1960, the M.E. degree in 1962, and the Ph.D. degree in 1965, all from the University of Tokyo, Tokyo, Japan.

In 1965 he was appointed a Research Associate at Tohoku University, Sendai, Japan, and since 1966 he has been an Assistant Professor. From 1960 to 1965 he was engaged in the research of millimeter waves and microwave switching circuits. Since 1965 his main interest has been in the field of optical communication.

Dr. Kawakami is a member of the Institute of Electronics and Communication Engineers of Japan and the Optical Society of America.

*



D. Marcuse (M'58–F'73) was born in Koenigsberg, East Prussia, Germany, on February 27, 1929. He received the degree of Diplom Physiker from the Freie Universitaet, Berlin, Germany, and the degree of Dr. Ing. from Technische Hochschule, Karlsruhe, Germany, in 1954 and 1962, respectively.

From 1954 to 1957 he worked at the Central Laboratory, Siemens and Halske, Berlin, Germany, on transmission-line problems and the development of the circular electric waveguide. In 1957 he became a member of the Technical Staff of the Bell Laboratories, Holmdel, N.J., and worked on the circular electric waveguide and masers. He is presently working on the transmission aspect of a light communications system. In addition, he is also an Adjunct Associate Professor at the University of Utah, Salt Lake City. He is the author of three books.

Dr. Marcuse is a member of the Optical Society of America.

*

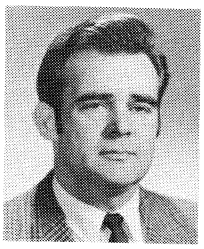

Clyde C. Neil was born in Belle Vernon, Pa., in 1932. He studied electronics at Trenton Technical Institute, Trenton, N.J., and graduated in 1956.

He was a civilian employee of the U.S. Government from 1956 to 1959, working in communications systems for the Army Security Agency, Arlington, Va. He joined the RCA Laboratories, Princeton, N.J., in 1959 and has worked in various areas of materials research, including chemical synthesis, low-temperature studies, and optical and far-infrared spectroscopy. For the last three years he has been involved with research and development of electro-optic waveguide materials and devices. He has several technical publications.



Shigeo Nishida (SM'59) graduated from Tohoku University, Sendai, Japan, in 1949, and received the Ph.D. degree in 1959 from the same university.

From 1949 to 1955 and 1955 to 1964 he was a Research Associate and an Assistant Professor at the Research Institute of Electrical Communication, Tohoku University, and since 1964 he has been a Professor there. For two years, from 1957 to 1959, he was a Research Associate at the Microwave Research Institute of the Polytechnic Institute of Brooklyn. His primary concerns in research are in the theoretical development of microwave and optical waveguides.

*

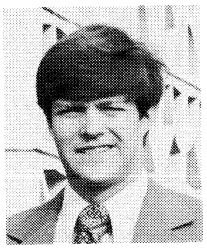

Donald R. Scifres was born in Lafayette, Ind., on September 10, 1946. He received the B.S. degree with honors in electrical engineering from Purdue University, West Lafayette, Ind., in 1968, and the M.S. and Ph.D. degrees in electrical engineering from the University of Illinois, Urbana, in 1970 and 1972. While at the University of Illinois he held a University of Illinois Doctoral Support Fellowship and a General Telephone and Electronics Fellowship.

In 1972 he joined the Xerox Palo Alto Research Center, Palo Alto, Calif., as a Research Scientist and is currently working on the optical properties of semiconductor materials and injection lasers.

Dr. Scifres is a member of the American Physical Society and the Optical Society of America.

*

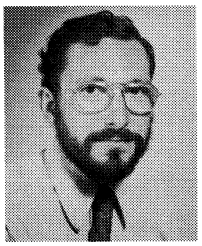

William Streifer (S'56–M'58–SM'73) was born in Poland, on September 13, 1936. He received the B.E.E. degree (magna cum laude) from the City College of New York, New York, in 1957, the M.S. degree in electrical engineering from Columbia University, New York, N.Y., in 1959, and the Ph.D. degree in 1962.

From 1957 to 1959 he was a Lecturer in the Department of Electrical Engineering, City College of New York, and from 1958 to 1959 he was a Research Engineer at the Heat and Mass Flow Analyzer Laboratory, Columbia University. In 1959 he accepted an NSF fellowship at Brown University, where he taught in the Division of Engineering and held a Bell Telephone Laboratories fellowship. From 1962 to 1972 he was a faculty member at the University of Rochester, where he held positions as Assistant Professor, Associate Professor, and Professor of Electrical Engineering. During the academic year 1969–1970, he was a Visiting Associate Professor at Stanford University. He is presently a Principal Scientist at the Xerox Palo Alto Research Center, Palo Alto, Calif. He has been a consultant to several corporations including Xerox from 1969 to 1972. He has published numerous papers in the fields of optics, electromagnetism, applied mathematics, and mathematical ecology.

Dr. Streifer is a fellow of the Optical Society of America.

Controlled Timewise Redistribution of Laser Energy

EMILIO PANARELLA AND LORNE L. T. BRADLEY

Abstract—An electronic feedback circuit is described which has been used in a Nd:glass high-power laser system for converting the spiky light emission into a smooth near-rectangular output of adjustable intensity and duration. The feedback circuit is also capable of converting the laser emission into a stroboscopic output of frequency of several hundreds of kilohertz or into a Q-switched high-intensity output. The attractive feature of the system is that the change from one type of laser operation into the other does not require any modification to the circuit, but only a simple readjustment of a few control knobs.

The feedback system incorporates a high-current fast photodiode, a Pockels-cell shutter, and a pulser. The main innovation of the present electronic feedback circuit over previously proposed systems is the ability to set the Pockels cell at any point of its transmission curve. This feature will be demonstrated to be of decisive importance in smoothing out the laser emission and in converting the spiky light output into a series of periodic light pulses.

I. Introduction

CURRENTLY, one of the important problems in high-power laser technology is to be able to control the power output from a laser in a preassigned way. It is well known that solid-state lasers, in their normal mode of operation, emit a series of irregular spikes, the nonregularity appearing in the spike amplitude, duration, and their time separation. It would be desirable to be able to redistribute the laser energy in such a way that the emission follows a regular intensity pattern. One of the early successes along this line was obtained with the Q-switching technique whereby the available stored energy in the laser system was delivered in a symmetrical pulse of a few tens of nanoseconds duration and several megawatts intensity [1]. A second success was achieved with the technique of mode locking whereby the laser energy was redistributed in a series of megawatt-intensity pulses of picosecond duration emitted at constant frequency in the gigahertz range [2].

Unfortunately, these two clear advances in laser technology have not been followed by others to fill the gap that the many other possible laser-energy redistribution patterns have left open. For instance, no decisive progress has been made in the generation of rectangular light pulses of microsecond duration or in the production of repetitive pulses in the megahertz frequency range. Some attempts have been made to reduce the spiky output from the laser to a rectangular output of tens of microseconds duration, but the success along this line has always been rather limited.

Marshall and Roberts [3] were first to introduce the idea of an electronic feedback system able to resist the buildup of radiation energy inside the laser cavity. Statz *et al.* [4] expanded this idea by developing the theory behind it. Marshall and Roberts [3] and Statz *et al.* [4] actually performed an experiment which showed that indeed spiking had been eliminated and a reasonably smooth pulse had been achieved. Thomas and Price [5] went a step further. They controlled the duration of the light output by adding a pulser to the feedback system. In this way, lasing action was prevented until the laser rod was fully pumped and was stopped again after a few microseconds. Unfortunately, the light output obtained in this way was far from rectangular and the onset of a high-frequency instability further deteriorated the initial part of the laser pulse. Pantell and Warszawski [6] used a nonlinear absorber (a benzene cell) within the laser cavity to stabilize the laser output. They showed that power stabilization had indeed been achieved and that the resultant laser emission followed the flashlamp output. However, the technique is of limited use in that it allows neither the shaping of the light pulse into rectangular form, nor the control over the light intensity and duration. Balashov *et al.* [7] were first to achieve a very good rectangular light pulse of 10-μs duration but their technique is not easily adapted to conventional lasers. In fact, it requires a spherical resonator for the laser cavity and the control of the light duration is obtained by changing the speed of rotation of the Q-switching prism. The light duration then ranges from 4 to 10 μs and no further stretching is possible.

During the course of our work on the problem of power stabilization of a Nd:glass laser by means of an electronic feedback system, we realized that the ideas of Marshall and Roberts [3], Statz *et al.* [4], and Thomas and Price [5] had validity as initial steps in the solution of the light-emission control problem. The theoretical analysis of [4] had indicated that complete spike elimination could only be achieved in the ideal situation of zero time delay between the laser momentary power output and the corrective action of the feedback system. In practical cases the delay is never zero and the power output oscillates around an average value, the oscillation frequency increasing with decreasing time delay. We initially thought that an improvement could be obtained by the insertion within the laser cavity of a lossy element capable of absorbing part of the electromagnetic energy flowing within the cavity. In fact, we thought, the rate of variation of laser power would be reduced in this way and the delayed feedback signal would be facilitated in its corrective action. On the other hand, we realized that the power absorption of the lossy element really had to depend on the average power output of the laser, the absorption being greater when larger power outputs were delivered by the laser. Then it came to mind that an element, the Pockels cell, which was part of our feedback system, could perform both functions indicated above. In fact, the only thing that it was necessary to do was to set a

Manuscript received July 8, 1974; revised December 11, 1974.

The authors are with the National Research Council, Ottawa, Ont., Canada K1A OR6.

bias voltage on the cell and the amount of electromagnetic energy flowing within the laser cavity would be thus reduced. As a consequence, we designed the electronic feedback system in such a way that the Pockels-cell biasing could be easily achieved on any point of the cell's transmission curve. We then found that good laser-output stabilization was achieved in this way and, as an added advantage, this also proved instrumental for the conversion of the spiky laser emission into a regular pulsed output.

In the following sections, we shall first describe in detail the electronic feedback circuit used to control the light emission from our high-power Nd:glass laser. Then we shall present the experimental results. From these, it will be apparent that indeed the feedback system is able to control the laser emission so as to have either a rectangular pulse of variable intensity and duration, or a single light pulse of megawatt intensity and nanosecond duration, or a series of pulses of kilowatt intensity and submicrosecond duration. It will be shown that the conversion from one type of laser operation into the other does not require any modification of the apparatus but is accomplished through a simple adjustment of control knobs in the electronic feedback circuit. This feature is surely attractive and will prove useful, especially in those laser applications (e.g., in plasma diagnostic) where either a long constant-intensity light pulse for streak photography or a series of laser pulses for frame photography are required and have to be quickly obtained.

II. Description of the Laser and Electronic Feedback System

The laser used in the experimentation consists of an 8-in long, $\frac{5}{8}$-in-diam Brewster-ended Nd:glass rod pumped by two linear flashlamps type EG&G FX-47C (Fig. 1). The optical cavity is formed by two wedged dielectric mirrors having reflectivities of 99 and 75 percent at the laser wavelength, respectively. The electronic feedback system is made up of a Pockels cell inserted in the laser optical cavity, a polarizer, a delayed pulse generator, a pulser, and a fast high-current photodiode. A splitter, made out of a fully reflecting mirror with a $\frac{5}{16}$-in-diam central hole, reflects the peripheral part of the beam, thus allowing the uniform intensity central zone to proceed unimpeded for further use. The reflected part, which is ~15 percent of the total beam, is detected by a fast photodiode type ITT F4000-S1 which drives the Pockels cell, the load resistance being chosen according to the type of laser operation required (rectangular emission, pulsed, or Q-switched).

In operation, lasing is prevented by properly biasing the Pockels cell with a positive voltage (= 3 kV). A trigger pulse simultaneously fires the flashlamps and activates the delayed pulse generator. The delayed signal triggers the pulser, which in turn controls the open time and sets a new bias voltage on the Pockels-cell shutter. The photodiode converts the laser light into an electrical current which develops a negative voltage across the variable resistor, thus varying the Pockels-cell light transmission.

The electronic circuit of the pulser (Fig. 2) is composed of an integrated circuit monostable multivibrator 74121, a television horizontal-beam power tube 6BG6, and two 200-V dc power supplies for the screen and grid bias voltages of the 6BG6 tube.

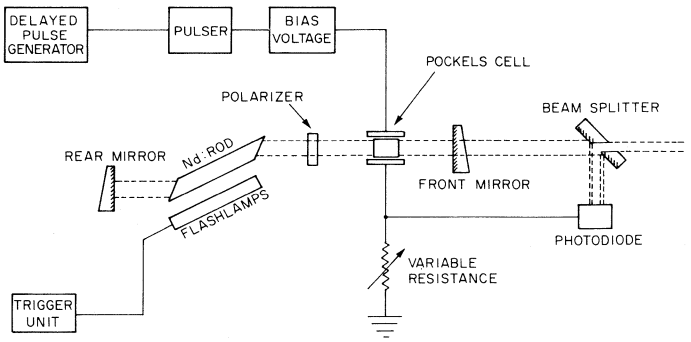

Fig. 1. Laser and electronic feedback system.

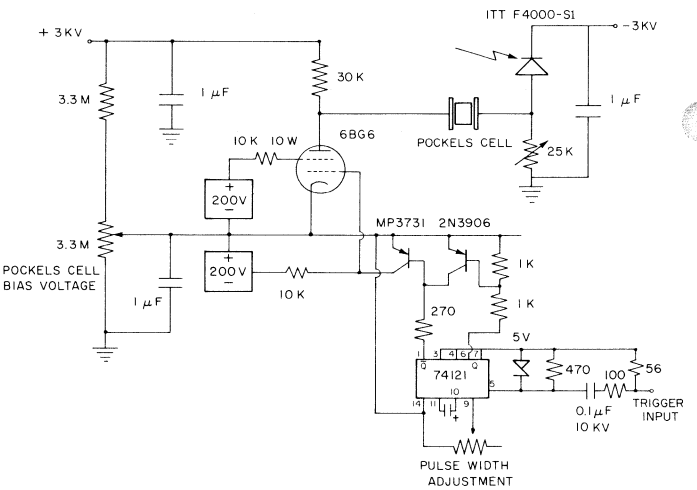

Fig. 2. Electronic circuit for control of intensity and duration of laser emission.

The trigger pulse from the delayed pulse generator turns the multivibrator 74121 on, which in turn switches on the tube 6BG6. Hence, the Pockels-cell voltage drops from +3 kV to a preset value at the cathode of the 6BG6 tube and the cell is then partially or fully open, according to the value of this bias voltage. After a period of time, which can be varied from 1 to 450 μs by means of a pulsewidth adjustment control, tube 6BG6 is turned off and the Pockels cell, restored to +3 kV, is effectively biased off.

The parameters of the feedback system that affect the laser operation are: 1) resistance across the photodiode; 2) Pockels-cell bias voltage; 3) Pockels-cell open time; and 4) delay time of the delay pulse generator.

In the following section we shall show the influence of these parameters on the laser operation.

III. Results

The familiar spiky output of the uncontrolled laser is shown in Fig. 3. The light emission begins after ≃240 μs from the initiation of the flashlamps discharge and proceeds undisturbed for ≃560 μs with large intensity fluctuations and spikes whose amplitude can reach the value of ≃315 kW.

We desire now to transform the irregular laser emission into

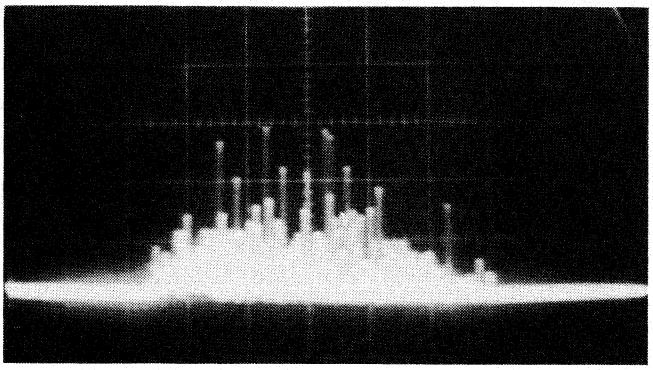

Fig. 3. Uncontrolled laser light output. Time: 100 μs/div. Intensity: 107 kW/div.

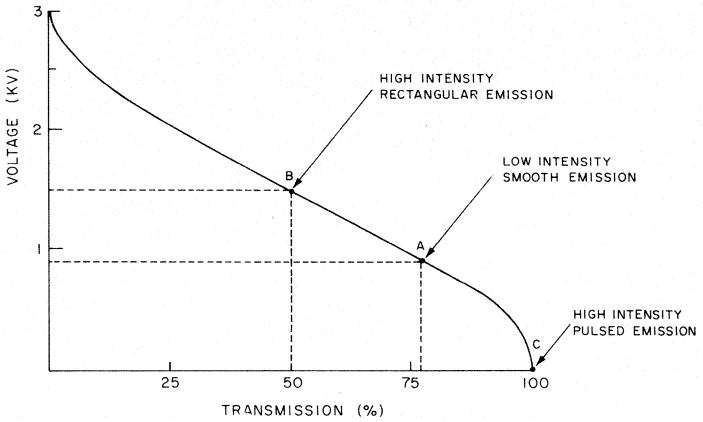

Fig. 4. Pockels-cell transmission curve.

either: a) a long spikeless output, or b) a rectangular pulse of adjustable intensity and duration, or c) a Q-switched high-intensity pulse, or d) a stroboscopic output.

In the following it will be shown that any one of the above results can be achieved by a proper setting of the feedback parameters.

A. Long Spikeless Output

If we want to stabilize the laser-power output without controlling its time duration, we have available two parameters, the Pockels-cell bias voltage and the photodiode resistance. The choice of the bias voltage is obviously dictated by the power level in which the laser has to operate. When the power is high, the bias voltage has to be set so as to reduce the Pockels-cell transmission. When the power is low the bias voltage can be set for cell's full transmission. In the particular case we are considering, the laser power to be extracted is the lowest of all, being just the normal output simply stabilized in amplitude. As a consequence, one would be inclined to set the bias voltage for full transparency of the Pockels cell. However, examination of the Pockels-cell transmission curve (Fig. 4) reveals that the curve is linear only in its central portion and that, if the cell operates at the full transmission point, the photodiode feedback voltage is virtually ineffective for corrective action. Hence, the operating point will be chosen at A, where the cell has the largest transmission still in the linear part of the curve. As for the photodiode resistance, we shall select the lowest possible value still capable of inducing a feedback voltage sufficient to stabilize the laser output. Fig. 5 shows three typical laser outputs obtained with (a) 200 Ω, (b) 500 Ω, and (c) 1000 Ω photodiode resistance. It can readily be seen that, although the values of the (a) and (b) resistances are appropriate for attaining a low circuit delay time, resistance (c) is the one necessary in order to obtain a good laser-power stabilization for most part of the laser emission. The output then lasts ≃400 μs with an average power of ≃23 kW and the power fluctuation is ≃20 percent, except in the initial part of the pulse, where it is higher. The cutoff of laser emission on the right side of the display is due to our pulser, which is not able to provide a pulse longer than 450 μs.

Unfortunately, the foregoing experimental results do not lend themselves to an easy comparison with the predictions

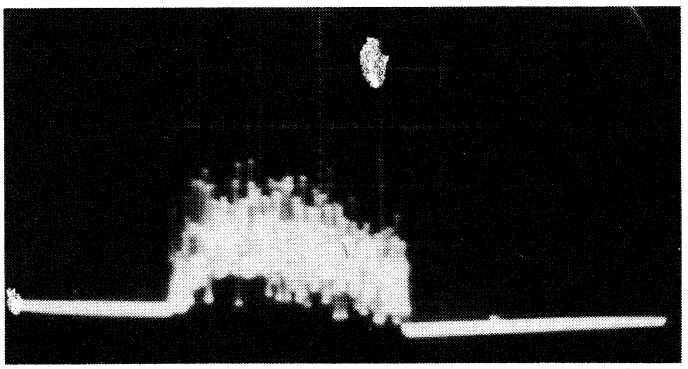

(a)

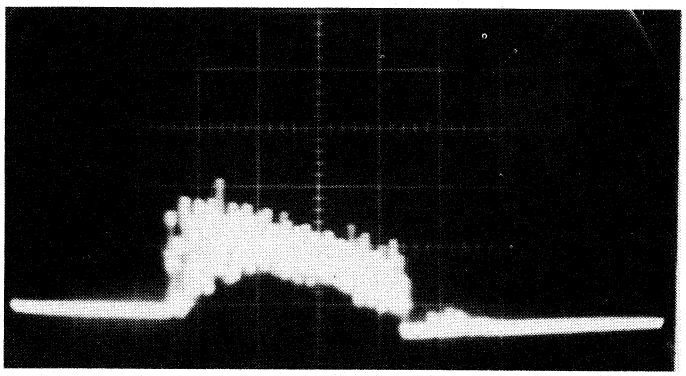

(b)

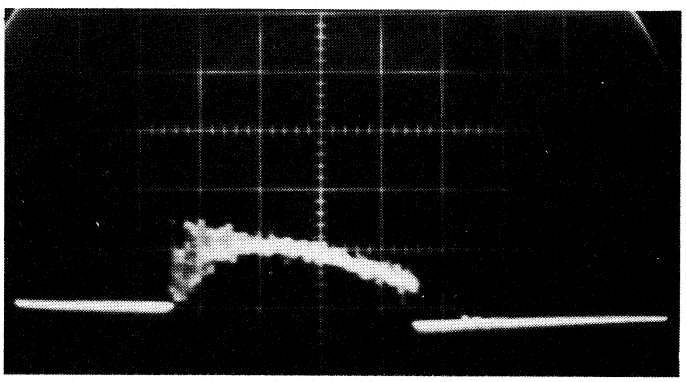

(c)

Fig. 5. Feedback-controlled light output. Pockels-cell bias voltage: 900 V. Undelayed lasing. Photodiode resistance: (a) 200 Ω; (b) 500 Ω; (c) 1000 Ω. Time: 100 μs/div. Intensity: 27 kW/div.

from the theoretical work of Statz *et al.* [4]. The reason is that the theory has been worked out for the particular case of insertion of a nonlinear absorber into the laser cavity, whereas in our case a Pockels cell has been inserted. The difference is that the calculations for the nonlinear absorber case have been done for constant losses in the system and variable time delays, whereas the Pockels-cell case involves simultaneous variation of time delays and system losses. However, we affirm that the loss term is more important than the time-delay parameter for a good stabilization of power output, as appears very clearly from the results of Fig. 5 and the results that will be shown in the next paragraph.

B. Rectangular Pulse of Adjustable Intensity and Duration

If it is required to control the time duration as well as the intensity of the light output, with the objective of obtaining rectangular emission, all four parameters in the system have to be adjusted. First, we shall set the pulse time duration for the value in which we are interested. Then, we shall delay lasing action until the stored energy is sufficient to yield a good rectangular output for the prescribed length of time. For instance, Fig. 6(c) shows the output when lasing action was started 300 μs after the initiation of the flashlamps discharge with the Pockels-cell bias voltage left at point *A* (Fig. 4) and the photodiode resistance set at 1000 Ω. It can be clearly seen that the light output, except for an initial overshoot, has near-rectangular form at power of $\simeq$27 kW for a time duration of $\simeq$50 μs. Fig. 6(a) and (b) show the effect of lower values photodiode resistances. It is readily seen that 200-Ω [Fig. 6(a)] and 500-Ω [Fig. 6(b)] resistances are insufficient for good power stabilization, which confirms what was found in the case of a long spikeless output.

If higher power for a shorter time is required, it is necessary to further delay lasing action and simultaneously reduce the duration of the light pulse. Clearly, now the Pockels-cell bias voltage has to be set for reduced cell's transmission. Fig. 7 shows the form of the laser emission when lasing has been delayed 650 μs after the initiation of the flashlamps discharge and the Pockels-cell bias voltage has been set at 1500 V (point *B* on the transmission curve, Fig. 4). The power stabilizing resistance has been found to be 2000 Ω in this case. As before, except for an initial overshoot, the laser emission is near-rectangular with intensity of $\simeq$150 kW for 14 μs.

If a much shorter light pulse at higher intensity is desired, it is simply necessary to reduce the photodiode resistance, in order to compensate for the light-intensity increase, leaving the Pockels-cell bias voltage at point *B* of Fig. 4. For instance, Fig. 8 shows the laser output when the photodiode resistance has been reduced to 100 Ω and lasing has been delayed 620 μs after the initiation of the flashlamps discharge. A pulse of $\simeq$2-MW intensity, 0.7-μs duration appears, as measured at half-power points.

C. Q-Switched High-Intensity Output

It is obvious that the feedback system used for the generation of rectangular light pulses does not impede the generation

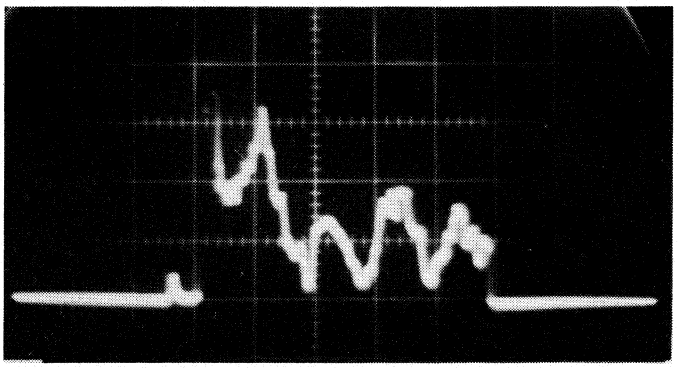

(a)

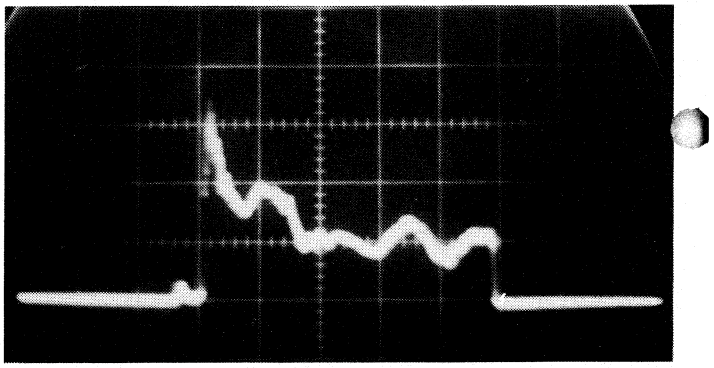

(b)

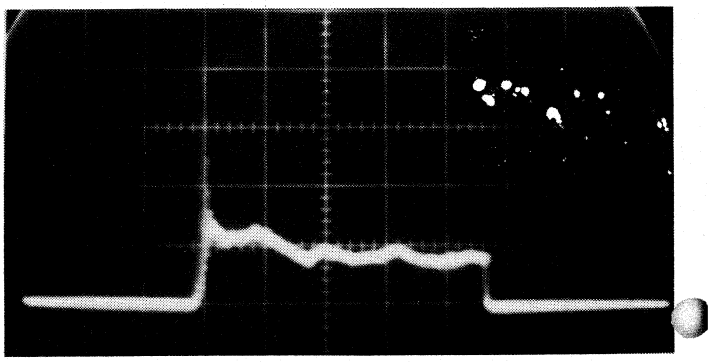

(c)

Fig. 6. Feedback-controlled light output. Pockels-cell bias voltage: 900 V. Delayed lasing. Photodiode resistance: (a) 200 Ω; (b) 500 Ω; (c) 1000 Ω. Time: 10 μs/div. Intensity: 27 kW/div.

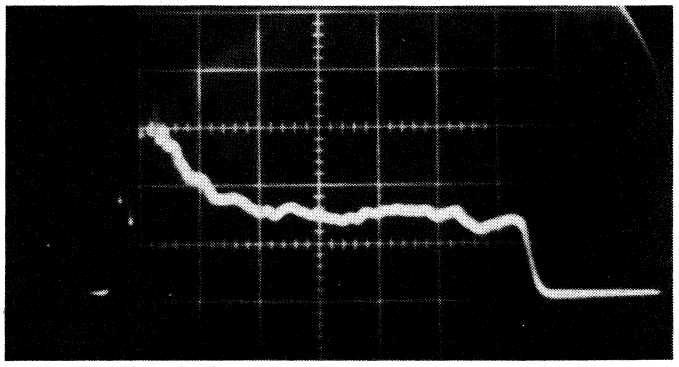

Fig. 7. Feedback-controlled light output. Pockels-cell bias voltage: 1500 V. Photodiode resistance: 2 kΩ. Delayed lasing. Time: 2 μs/div. Intensity: 107 kW/div.

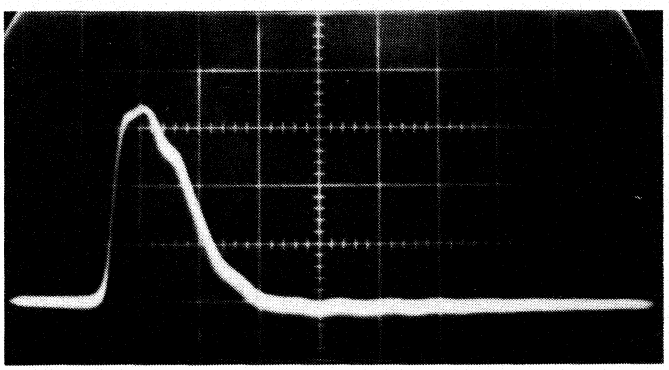

Fig. 8. Feedback-controlled light output. Pockels-cell bias voltage: 1500 V. Photodiode resistance: 100 Ω. Delayed lasing. Time: 0.5 μs/div. Intensity: 674 kW/div.

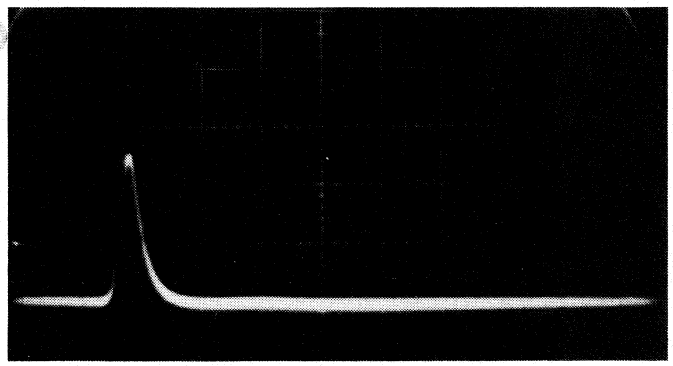

Fig. 9. *Q*-switched light output. Pockels-cell bias voltage: 0. Delayed lasing. Time: 0.5 μs/div. Intensity: 3.37 MW/div.

of *Q*-switched outputs. In fact, the only thing that is required to do is to set the Pockels cell for full transmission (point *C* of Fig. 4) and to eliminate the feedback light path. Then a *Q*-switched pulse will be obtained. Fig. 9 shows the laser emission when the Pockels cell is turned on 470 μs after the initiation of the flashlamps discharge. A 200-ns duration pulse appears with intensity of 8.5 MW.

D. Stroboscopic Output

Finally, if a series of light pulses are required, this can be obtained, as indicated in the work of [4], by providing a delay between the buildup of the electromagnetic energy within the laser cavity and the corrective action of the Pockels cell. In explicit terms, we simply need to increase the photodiode resistance. Fig. 10 shows the laser pulsed emission when the photodiode resistance has been increased to 15 kΩ, the Pockels cell set for full transmission, and lasing delayed 700 μs after the flashlamps discharge. Four pulses of submicrosecond duration and kilowatt intensity appear at a frequency of ≃1 MHz and many more pulses would be obtained by changing the duration of the Pockels-cell open time.

IV. Conclusions

In the present paper we have shown that the erratic emission from a high-power Nd:glass laser can be converted into a rectangular or pulsed emission of controlled intensity and duration. This result is achieved by the insertion into the laser cavity of a Pockels-cell shutter whose transmission is feedback controlled by a photodiode that monitors the laser output. An important feature of the present system is the ability to set the Pockels cell on any point of its transmission curve. This adjustment proved essential in obtaining either a rectangular emission of variable intensity and duration or a pulsed emission. We believe that the laser output in the rectangular mode can be smoothed further if a fraction larger than 15 percent of the available laser power (this is the value adopted by us) is deflected back to drive the Pockels cell. In fact, the photodiode resistance can have in this way a lower value, thus lowering the feedback delay time. Alternately, a nonlinear absorber can be added to the laser cavity, according to the ideas of Pantell and Warszawski [6] and Balashov *et al.* [7]. However, before proceeding along either one of these lines, it is important to consider very carefully if the advantage of obtaining a smoother pulse is offset by the disadvantage of a reduced light output.

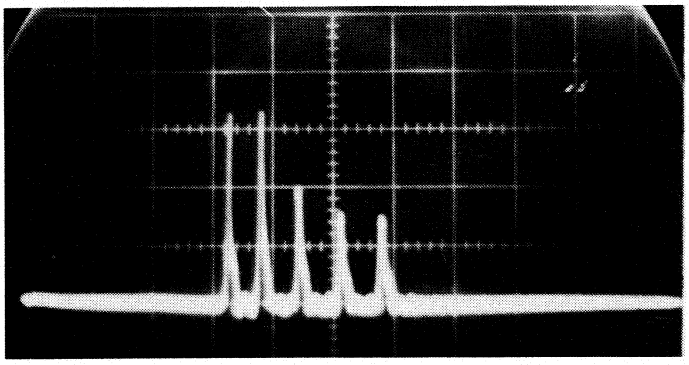

Fig. 10. Feedback-controlled light output. Pockels-cell bias voltage: 0. Photodiode resistance: 15 kΩ. Delayed lasing. Time: 2 μs/div. Intensity: 0.33 MW/div.

Acknowledgment

The authors would like to thank W. C. Michie and B. E. Moulton for the expert design and construction of the laser and V. Guty for the skilled technical assistance.

References

[1] F. J. McClung and R. W. Hellwarth, "Giant optical pulses from ruby," *J. Appl. Phys.*, vol. 33, pp. 828–829, Mar. 1962.

[2] A. J. DeMaria, D. A. Stetser, and H. Heynau, "Self-mode-locking of laser with saturable absorbers," *Appl. Phys. Lett.*, vol. 8, pp. 174–176, Apr. 1966.

[3] F. R. Marshall and D. L. Roberts, "Use of electro-optical shutters to stabilize ruby laser operation," *Proc. IRE* (Corresp.), vol. 50, p. 2108, Oct. 1962.

[4] H. Statz, G. A. DeMars, D. T. Wilson, and C. L. Tang, "Problem of spike elimination in lasers," *J. Appl. Phys.*, vol. 36, pp. 1510–1514, May 1965.

[5] C. H. Thomas and E. V. Price, "Feedback control of a *Q*-switched ruby laser," *IEEE J. Quantum Electron.*, vol. QE-2, pp. 617–623, Sept. 1966.

[6] R. H. Pantell and J. Warszawski, "Laser power stabilization by means of non-linear absorption," *Appl. Phys. Lett.*, vol. 11, pp. 213–215, Oct. 1967.

[7] I. F. Balashov, V. A. Berenberg, and B. A. Ermakov, "Generation of microsecond pulses in a ruby laser," *Sov. Phys.—Tech. Phys.*, vol. 13, pp. 699–700, Nov. 1968.

Fluctuations in Mode-Locking Threshold Due to Statistics of Spontaneous Emission

ROBERT WILBRANDT AND HORST WEBER

Abstract—A passively mode-locked Nd:YAG oscillator operating in TEM_{00} mode is investigated theoretically and experimentally. It is shown that a mode-locking threshold well above the normal lasing threshold exists and that this second threshold is of a probabilistic nature. This means that mode locking at a given pump rate in the region of threshold occurs only with a certain probability due to the Gaussian statistics of spontaneous emission. Experiments agree qualitatively with theory. Furthermore, thermal effects in the liquid absorber are shown to play an important role in mode-locking systems; they introduce an additional time-dependent loss or gain, depending on the experimental setup. This can either lead to increase of mode-locking threshold or to the appearance of higher order transverse modes and possible damage of laser components.

I. Introduction

A NUMBER of theories on Q switching and passive mode locking have been published in the literature. Some of them are [1], [2] based on rate equations for the laser medium, the absorber, and the photon density averaged over the round-trip time of the resonator, thus neglecting the statistical nature of spontaneous emission; in others the analysis is made by looking at the development of one or several ultrashort fluctuation pulses in a cavity with nonlinear absorber [3]-[13]. Both analytical and numerical computations were made. For a pulsed Nd:YAG mode-locked oscillator we wish to present the following: 1) a comparison between two theoretical approaches, the first being a system of rate equations similar to those used by Erickson and Szabo [1], the second being a somewhat refined model used by Caruso *et al.* [13]; 2) a statistical consideration of the mode-locking threshold; 3) a comparison of theory and experiments with respect to 1) and 2), which demonstrates the importance of considering the statistics of spontaneous emission in the theory; 4) experimental results of the influence of thermal blooming in the saturable absorber on mode-locking characteristics.

II. Theory

The two different systems of rate equations used to compute numerically the peak intensity (or energy, respectively) of a passively mode-locked laser as a function of pump rate are the following:

$$\frac{dn}{dk} = W \cdot t_L - (W+A) \cdot t_L \cdot n - \frac{\sigma_L \cdot t_L}{2\sigma_A \cdot t_A} \cdot n \cdot \varphi \qquad (1a)$$

$$\frac{d\varphi}{dk} = \left(\sigma_L \cdot l \cdot N_0 \cdot n - \gamma - \frac{\kappa_0}{1+\delta \cdot \varphi}\right) \cdot \varphi \qquad (1b)$$

and

$$\frac{dn}{dk} = W \cdot t_L - (W+A) \cdot t_L \cdot n - \frac{1}{\sigma_A \cdot l \cdot N_0} \left\{ \frac{1}{\delta} \ln \cdot [1 + T_0(e^{\delta \cdot E} - 1)] + M \cdot \langle E \rangle \cdot T_0 \right\} \cdot (G-1) \qquad (2a)$$

$$\frac{dE}{dk} = \frac{1}{\delta} \cdot \ln [1 + T_0(e^{\delta \cdot E} - 1)] \cdot R \cdot G - E \qquad (2b)$$

$$\frac{d\langle E \rangle}{dk} = (T_0 \cdot R \cdot G - 1) \cdot \langle E \rangle \qquad (2c)$$

where

- N_0 concentration of active Nd: atoms;
- n population in the upper laser level normalized to N_0;
- φ intensity (photons/square centimeter second) normalized to saturation intensity of the saturable dye;
- t_L round-trip time;
- k time normalized to round-trip time t_L;
- W pump rate;
- A Einstein coefficient of spontaneous emission;
- σ_L cross section for stimulated emission in the laser medium;
- l length of the laser medium;
- σ_A absorption cross section of the absorber at $\lambda = 1.06\ \mu$;
- t_A relaxation time of the absorber;
- δ ratio of beam cross section in the laser medium to beam cross section in the absorber;
- T_0 low-intensity transmission of the dye;
- κ_0 $= -\ln T_0$;
- R loss factor;
- γ $= -\ln R$;
- E energy density of the largest noise pulse within a round-trip time normalized to saturation energy density E_s of the absorber;
- $\langle E \rangle$ mean energy density of a noise pulse within a round-trip time normalized to saturation energy density E_s of the absorber;
- M number of oscillating longitudinal modes equal to number of noise pulses per round trip;
- G $= e^{\sigma_L \cdot l \cdot N_0 \cdot n}$ = single-pass gain in the laser rod;
- W_{th} $= A \cdot (\gamma + \kappa_0)/\sigma_L \cdot l \cdot N_0$ = threshold pump rate for stationary case.

The first set of equations is essentially the single-mode approach of Erickson and Szabo [1] with two modifications.

Manuscript received July 7, 1974; revised December 18, 1974. This work was sponsored by the Swiss National Foundation.

R. Wilbrandt is with the Atomic Energy Commission Risø Research Establishment, Roskilde, Denmark.

H. Weber is with the Institute of Applied Physics, University of Berne, Berne, Switzerland.

1) A pump term is included, which allows comparison with experiments.

2) Focusing of the beam into the absorber is considered by the introduction of the cross-section ratio δ.

The relaxation of the absorber is regarded as very fast compared to changes in intensity and intensity fluctuations are not taken into account.

The second set of equations is that used by Caruso *et al.* [13], where a single noise pulse with energy density E and short duration compared to the dye relaxation time propagates through the resonator. The model is somewhat refined compared to that of Caruso and somewhat simplified with respect to that of Fleck [10] in that background fluctuations are taken into account by a number M of noise pulses of mean energy $\langle E\rangle$. Thus (2a) describes the depletion of inversion by two terms: the energy E of the highest pulse and the energy $M \cdot \langle E\rangle$ of the M noise pulses. Equation (2b) characterizes the temporal behavior of the highest pulse which passes the nonlinear absorber and (2c) that of the background, where it is assumed that the mean energy $\langle E\rangle$ remains in the domain of linear absorption of the dye throughout the calculations. This approximation is confirmed by the numerical results.

We shall show that the single-mode approach does (as expected) not give a satisfying description of Q switching and mode-locking threshold, whereas the inclusion of background results is in much better correspondence with experiments.

Consider now the statistics of spontaneous emission in order to draw conclusions about the probabilistic nature of mode-locking threshold. If in the region of linear absorption the probability of a particular pulse having an energy greater than E is given by

$$f(E) = \frac{1}{\langle E\rangle}\int_E^\infty e^{-E/\langle E\rangle}\,dE \tag{3}$$

then the probability $p(E)$ of finding at least one such pulse among the number M of pulses per round trip is

$$p(E) = f(E)\sum_{n=0}^{M-1}[1-f(E)]^n = 1-[1-f(E)]^M. \tag{4}$$

With integration of (3) this results in

$$p(E) = 1-[1-e^{-E/\langle E\rangle}]^M. \tag{5}$$

In the following numerical integration of (2) $p(E)$ is varied by variation of the starting ratio $E/\langle E\rangle$. It should be noted that the background $M \cdot \langle E\rangle$ plays an important role in the depletion of inversion since it contains a considerable amount of energy. For example, with $M = 200$ and $p(E) = 0.6$ the ratio of background energy to maximum pulse energy is $M \cdot \langle E\rangle/E = 37$. We first show results for constant $p(E) = 0.63$ and compare the two sets of equations.

The integration was carried out starting at threshold with the following numerical values for Nd:YAG as laser medium and the absorber 9860 from Eastman Kodak: $E_s = 0.016$ J/cm^2 [13], $t_L = 10$ ns, $A = 5 \cdot 10^3$ s^{-1} [14], $\sigma_L = 3.5 \cdot 10^{-19}$ cm^2 [15], $l = 7.5$ cm, $\sigma_A = 3.7 \cdot 10^{-16}$ cm^2, $t_A = 9$ ps, $R = 0.5$, $M = 200$, $N_0 = 1.38 \cdot 10^{20}$ cm^{-3}, $E(0) = 10^{-14}$, $\varphi(0) = 10^{-14}$ (starting values at threshold). The resulting peak intensities and energies as a function of pump rate above threshold are shown for (1) in Fig. 1 and for (2) in Fig. 2. A comparison shows that without consideration of a fluctuation mechanism (Fig. 1) the "second threshold" W'_{th} [1], [13] lies above the considered pump rates even with focusing by a factor of 12 into the absorber. (We define as W'_{th} the value W at which the maximum values $\hat{\varphi}$ or $\hat{E} = 1$.) On the other hand, in the second model a mode-locking threshold is seen which depends on absorber transmission T_0 and focusing parameter δ. The time behavior of the largest pulse, the average pulse, and total gain in this latter case are shown in Fig. 3 at different pump rates for $T_0 = 0.6$, $p(E) = 0.6$, $\delta = 2$, whereby the maximum of E in this figure corresponds to $\hat{E}$ in Fig. 2. It is seen that the maximum of the pulse train is reached earlier at higher pump rates, but the height of the maximum pulse does not change considerably. Instead the higher inversion is mainly depleted into the background. Thus the system stabilizes itself. The importance of the background is also shown by the fact that its amount does not change significantly from a pump value ($W/W_{th} = 2.43$) just below mode-locking threshold to one ($W/W_{th} = 2.45$) just above.

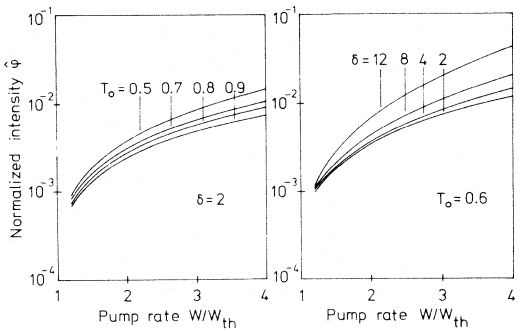

(a) (b)

Fig. 1. Intensity normalized to saturation intensity of the absorber as a function of pump rate normalized to threshold pump rate W_{th} [according to (1)]. (a) For different absorber transmissions. (b) For different beam cross-section ratios.

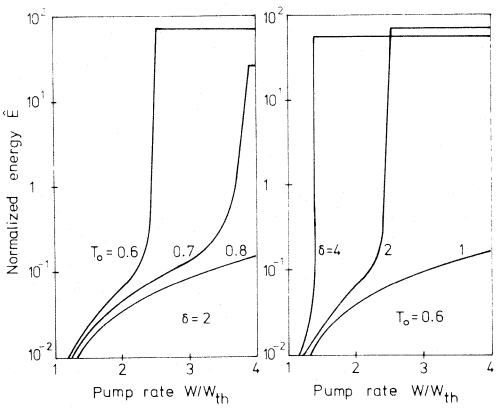

(a) (b)

Fig. 2. Energy of a picosecond-pulse at maximum of the pulse train normalized to saturation energy of the absorber as a function of pump rate normalized to threshold pump rate W_{th} [according to (2)]. (a) For different absorber transmissions. (b) Different beam cross-section ratios.

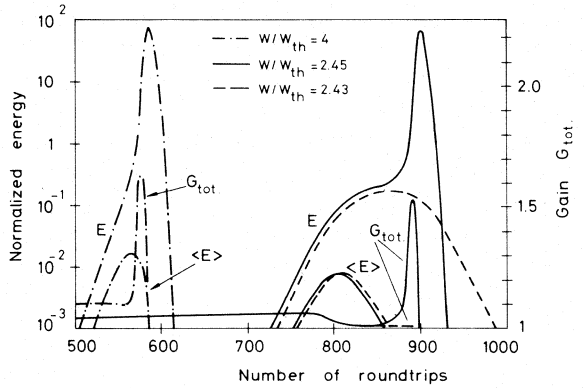

Fig. 3. Energy E of maximum pulse, energy $\langle E \rangle$ of mean pulse, and total single-pass gain G_{tot} as a function of number of round trips for different pump rates.

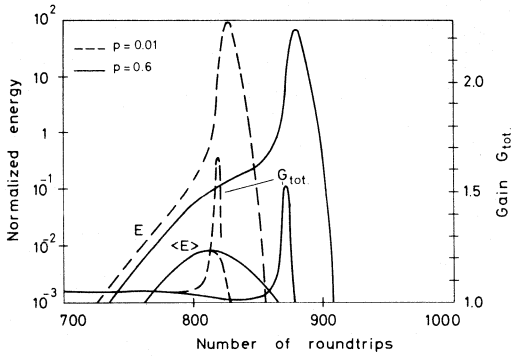

Fig. 4. Energy E of maximum pulse, energy $\langle E \rangle$ of mean pulse, and total single-pass gain G_{tot} as a function of number of round trips for different probabilities.

Very similar curves occur with Nd:glass instead of Nd:YAG, the difference being mainly that intensities in Nd:glass are generally higher by about a factor of 10 than in Nd:YAG, which leads to lower mode-locking threshold.

Next we show the influence of $p(E)$ on the calculations. In Fig. 4 the time behavior of the maximum pulse E, the mean pulse $\langle E \rangle$, and the total single-pass gain G_{tot} is shown for $p(E) = 0.6$ (solid lines) and $p(E) = 0.01$ (dashed lines) for $W/W_{th} = 2.45$, $T_0 = 0.6$, $\delta = 2$. It can be seen that for the smaller value of $p(E)$ the absorber is bleached earlier. Therefore, at the end of the linear phase the population is less depleted by the background, which leads to a higher gain. Correspondingly, the mode-locking threshold W'_{th} is decreased. The $p(E)$ corresponding to a certain W'_{th} can be regarded directly as the probability $p(W = W'_{th})$ to find this mode-locking threshold. Thus the probability $p(W = W'_{th})$ for bleaching the dye with pump rate W can be found as, for example, in Fig. 5 for $\delta = 2$.

III. Experiments

To compare the theoretical results with experiments, a resonator was set up, which exhibits very regular and reproducible spiking emission [16], [18] in the TEM_{00} mode. The reproducibility was the same as shown in [18]. The setup is seen in Fig. 6. It consisted of a 280-cm-long ring resonator with one curved mirror (radius of curvature 2 m). The laser

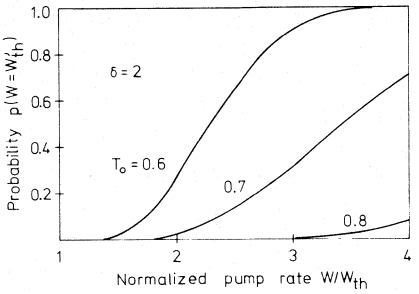

Fig. 5. Probability $p(W = W'_{th})$ that at a pump rate W mode locking occurs, as a function of normalized pump rate at different absorber transmissions for a beam cross-section ratio 2.

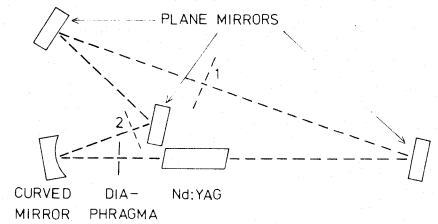

Fig. 6. Experimental setup of the mode-locking ring oscillator with the dye either in position 1 (beam waist) or position 2.

rod was a 3 in × 1/4 in Nd:YAG with ends cut at 6°. The TEM_{00} mode was selected by a diaphragm with 3.0-mm diameter. A 10-percent change in focal length of the thick lens produced by inhomogeneous heating of the laser rod leads only to a change of 10^{-3} in beam diameter. The largest beam diameter of the cavity is on the curved mirror, while the beam waist is found at position 1, which leads to a maximum value of $\delta = 4$. The experimentally resulting peak energies with the Kodak 9860 dye in position 2 are shown in Fig. 7. The pump rate W was obtained both by computer calculations and by a method described in [20]. From Fig. 7 it is seen that the experiments qualitatively follow the theory in that a "second threshold" W'_{th} is found, which depends on T_0 as predicted. However, mode locking occurs already for $\delta = 1$ which is not the case in the theory. One possible explanation for this discrepancy is thermal effects in the liquid, which shall be discussed in the following; another one is that while the pulse shortens in time, it is narrowed in space by the dye leading to higher energy densities and possibly to smaller losses at the diaphragm.

To obtain some statistics on the mode-locking threshold a series of 50 shots was investigated for each given pump rate and the number of mode-locking pulses counted. When no mode locking occurred, a spiking emission was found. The results are given in Fig. 8, where the probability for bleaching is plotted versus pump rate. They agree qualitatively with the theory. Again the experiments were carried out with $\delta = 1$. The mode-locking emission was quite reproducible as shown in Fig. 9. However, our experiments showed that while the qualitative behavior of the probability for mode locking is always of the indicated form in Fig. 8, the quantitative results depend on experimental conditions as, e.g., the size of the diaphragm. Closing the diaphragm by 10 percent led to considerably higher W'_{th} which supports the argument that beam

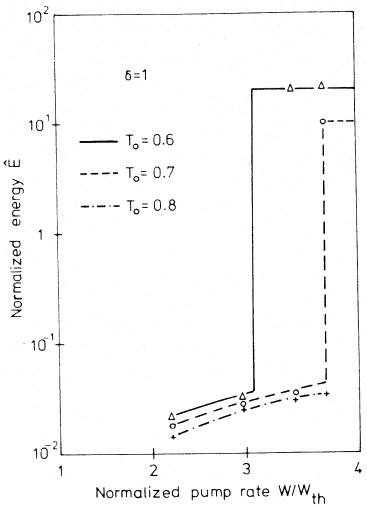

Fig. 7. Experimental results of the energy of a mode-locking pulse at maximum of the pulse train normalized to saturation energy of the absorber, as a function of normalized pump rate for different absorber transmissions.

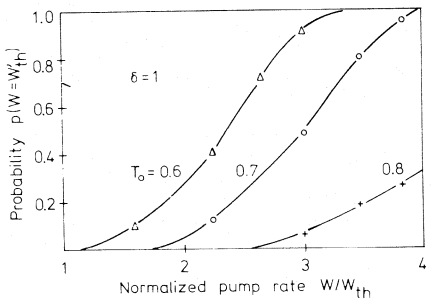

Fig. 8. Experimental results for the probability $p(W = W'_{th})$ that at a given pump rate W mode locking occurs as a function of normalized pump rate for a beam cross-section ratio 1.

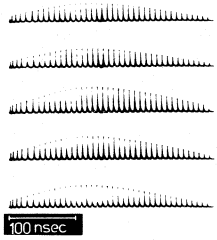

Fig. 9. Five subsequent mode-locking pulse trains.

narrowing effects as mentioned in the preceding are of considerable importance.

Regarding the influence of thermal effects in the absorber, it has been stated previously [19] that the liquid can be regarded as a time-dependent negative lens due to heating by a Gaussian intensity profile, which leads either to an additional time-dependent loss or gain mechanism. The position 2 (see Fig. 5) for the absorber is chosen such as to minimize the influence of a corresponding negative lens on the beam size at the diaphragm and in the laser rod. Putting the dye closer to the diaphragm leads to the appearance of higher order transverse modes, which can clearly be seen by the resulting mode patterns, and to damage of the mirror nearest to the beam

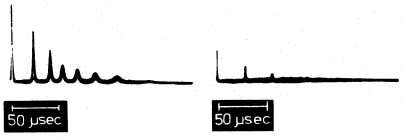

Fig. 10. Spiking emission with dye cell in position 1 (see Fig. 4) at $W/W_{th} = 2$. (a) With pure solvent (left). (b) With absorber of transmission $T_0 = 0.6$ (right).

waist. On the other hand, focusing into the absorber cell, as considered in the theory, by setting the dye in the beam waist at position 1 (corresponding to $\delta = 4$) augments time-dependent cutoff losses at the diaphragm due to thermal effects. Thus the intensity does not increase as expected from theory, but a reduction takes place. A picture of the emission with solvent and with absorber below mode-locking threshold ($T_0 = 0.6$) at position 1 for $W/W_{th} = 2$ is shown in Fig. 10. Thus it is clearly demonstrated that thermal effects play an important role in passive mode-locking systems. One reason that mode locking is much more reproducible with Nd:YAG than with Nd:glass is the higher cross section for stimulated emission in Nd:YAG, which leads to a lower spiking intensity [18] and reduces thermal effects compared to Nd:glass. Embedding the absorber in polymethylmetacrylate (PMMA) did not lead to significantly different behavior at least with Nd:glass, probably because the thermal gradient of index of refraction in PMMA is one of the highest of all solids. However, no experiments with PMMA were made with Nd:YAG.

IV. Conclusion

The theoretical and experimental investigation of a Nd:YAG mode-locking system has shown the following.

1) A distinct "second threshold" exists for mode locking above the normal lasing threshold.

2) This second threshold is characterized by a probability distribution, which means that mode locking in the region of threshold (which is the region of high selectivity [13] and therefore of interest) can only be expressed with a certain probability, the most favorable case being obtained with high absorber concentrations.

3) Thermal effects in the liquid absorber influence the mode-locking characteristics considerably and can as well lead to damage of the components of the laser as to a substantial increase or even suppression of mode-locking threshold.

Acknowledgment

The authors wish to thank Prof. K. P. Meyer for his interest in this work and Dr. W. Seka and Dr. H. J. Keller for many fruitful discussions.

References

[1] L. E. Erickson and A. Szabo, "Effects of saturable absorber lifetime on the performance of giant-pulse lasers," *J. Appl. Phys.*, vol. 37, pp. 4953-4961, 1966.

[2] E. Hofelich-Abate and F. Hofelich, "Time behaviour of a laser with saturable absorber as Q-switch," *J. Appl. Phys.*, vol. 39, pp. 4823-4827, 1968.

[3] V. S. Letokhov and V. N. Morozov, "Generation of ultrashort duration coherent light pulses," *Sov. Phys.–JETP*, vol. 25, pp. 862-866, 1967.

[4] V. S. Letokhov, "Dynamics of generation of a pulsed mode-locked laser," *Sov. Phys.–JETP*, vol. 27, pp. 746–751, 1968.
[5] ——, "Generation of ultrashort light pulses in a laser with a nonlinear absorber," *Sov. Phys.–JETP*, vol. 28, pp. 562–568, 1969.
[6] ——, "Ultrashort fluctuation pulses of light in laser," *Sov. Phys.–JETP*, vol. 28, pp. 1026–1027, 1969.
[7] T. I. Kuznetsova, "Statistics of appearance of ultrashort pulses in a laser with a bleachable filter," *Sov. Phys.–JETP*, vol. 30, pp. 904–909, 1970.
[8] P. G. Kryukov and V. S. Letokhov, "Propagation of a light pulse in a resonantly amplifying (absorbing) medium," *Sov. Phys.–Usp.*, vol. 12, pp. 641–672, 1970.
[9] B. Z. Zeldovich and T. I. Kuznetsova, "Generation of ultrashort light pulses by lasers," *IEEE J. Quantum Electron.*, to be published.
[10] J. A. Fleck, Jr., "Ultrashort pulse generation by Q-switched laser," *Phys. Rev. B.*, vol. 1, pp. 84–100, 1970.
[11] B. Hausherr, E. Mathieu, and H. Weber, "Influence of saturable-absorber transmission and optical pumping on the reproducibility of passive mode locking," *IEEE J. Quantum Electron.*, vol. QE-9, pp. 445–449, Apr. 1973.
[12] P. G. Kryukov and V. S. Letokhov, "Fluctuation mechanism of ultrashort pulse generation by laser with saturable absorber," *IEEE J. Quantum Electron.*, vol. QE-8, pp. 766–782, Oct. 1972.
[13] A. Caruso, R. Gratton, and W. Seka, "Mode-locked ring-laser and ring-amplifier characteristics," *IEEE J. Quantum Electron.*, vol. QE-9, pp. 1039–1043, Nov. 1973.
[14] J. E. Geusic, H. W. Marcos, and L. G. Van Uitert, "Laser oscillations in Nd-doped yttrium aluminum, yttrium gallium and gadolinium garnets," *Appl. Phys. Lett.*, vol. 4, pp. 182–184, 1964.
[15] J. K. Neeland and V. Evtuhov, "Measurements of laser transition cross-section in Nd:YAG," *Phys. Rev.*, vol. 156, pp. 244–246, 1967.
[16] J. Steffen, H. P. Lörtscher, and G. Herziger, "Fundamental mode radiation with solid-state lasers," *IEEE J. Quantum Electron. (Special Issue on 1971 IEEE/OSA Conference on Laser Engineering and Applications)*, vol. QE-8, pp. 239–245, Feb. 1972.
[17] G. Herziger, R. Stemme, and H. Weber, "Modulation technique to control laser material processing," *IEEE J. Quantum Electron. (Special Issue on 1973 IEEE/OSA Conference on Laser Engineering and Applications)*, vol. QE-10, pp. 175–178, Feb. 1974.
[18] R. Stemme, G. Herziger, and H. Weber, "Power and halfwidth of first laser spike," *Opt. Commun.*, vol. 10, pp. 221–223, 1974.
[19] R. Wilbrandt and H. Weber, "The effect of thermal blooming in a liquid filter on the emission of a Nd:glass laser," *Opt. Commun.*, vol. 9, pp. 231–233, 1973.
[20] ——, "Overshoot inversion of a Nd laser system," *Opt. Commun.* vol. 8, pp. 307–309, 1973.

Theory of Optical-Gain Measurements

PETER S. CROSS AND WILLIAM G. OLDHAM, MEMBER, IEEE

Abstract—**The widely used technique for determining optical gain and absorption from single-pass, amplified spontaneous emission (ASE) is analyzed with particular attention given to active-volume saturation and three-dimensional effects. The results for homogeneously broadened media show that the population inversion and hence the gain in the active region is diminished by high levels of spontaneous and ASE. The externally measured gain is further reduced for large output collection apertures that admit incompletely amplified off-axis rays. Criteria are given for the excitation and detection geometries required to ensure accurate (~10-percent) gain measurement. The simultaneous measurement of the equilibrium absorption coefficient can be made under less restrictive conditions.**

I. INTRODUCTION

THERE HAS BEEN considerable interest in recent years in the direct measurement of optical gain in various active media. In the usual technique using a pulsed-gas laser pump, the gain is found from the variation of the intensity of amplified spontaneous emission (ASE) with excitation geometry [1], [2]. Recently, Cross and Oldham have extended this technique to allow the measurement of the absorption coefficient of an umpumped region as well [3]. The combined measurement technique is illustrated in Fig. 1(a). The pumped region is a narrow stripe of length l translated a distance d from the sample edge with the output $I(l, d)$ collected along the stripe axis as shown. The ideal dependence of $I(l, d)$ is shown in Fig. 1(b). The optical gain is found from the variation of $I(l, d)$ with l, and the absorption coefficient is determined from the dependence of $I(l, d)$ on d. However, in order to accurately determine the optical gain or absorption from $I(l, d)$, the effects of active-region saturation and incomplete amplification of collected rays must be properly included.

This paper presents a detailed theoretical analysis of the gain-absorption measurement technique that explicitly investigates gain saturation and the effects of a nonzero collection aperture on the interpretation of experimental data. In Section II, the emission equations are derived that relate stimulated and spontaneous emission in homogeneously broadened media and include saturation. In Section III, the active-volume gain saturation is investigated for the geometry that is typically used in an ASE measurement. The effects of a nonzero collection aperture on the detected output are analyzed in Section IV. In Section V, the results are discussed and criteria are given for the measurement conditions necessary to accurately measure gain and absorption.

Manuscript received August 8, 1974; revised January 3, 1975. This work was supported in part by the Joint Services Electronics Program, Contract F44620-71-C-0087, and in part by Air Force Office of Scientific Research Grant 72-2385.

P. S. Cross was with the Department of Electrical Engineering and Computer Sciences and the Electronics Research Laboratory, University of California, Berkeley, Calif. 94720. He is now with the Institut für Angewandte Festkörperphysik, D-7800 Freiburg, Germany.

W. G. Oldham is with the Department of Electrical Engineering and Computer Sciences and the Electronics Research Laboratory, University of California, Berkeley, Calif. 94720.

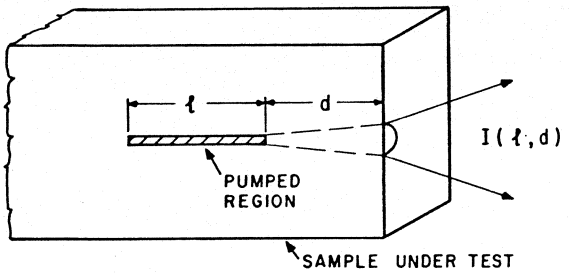

(a)

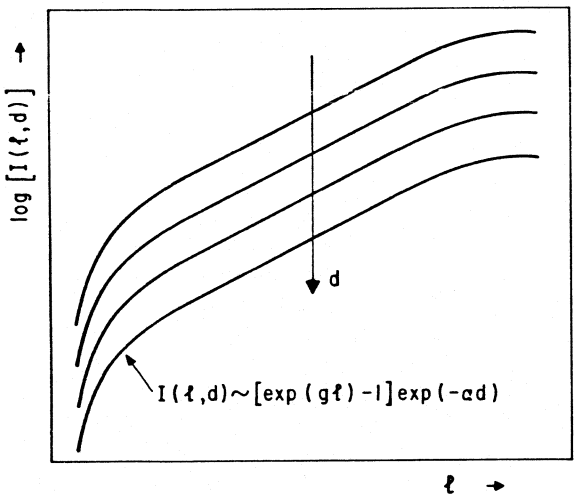

(b)

Fig. 1. (a) Schematic diagram of the measurement geometry in which light generated in the excitation stripe of length l propagates through an umpumped region of length d before being detected. (b) Ideal output-intensity characteristics.

II. Emission Equations with Saturation

An excited, optically active medium can be characterized by two parameters, r_{spon}, the spontaneous-emission rate per unit volume per unit energy, and g, the optical-gain coefficient. Both r_{spon} and g are functions of many parameters including excitation level, electromagnetic radiation intensity, absolute temperature T, and photon energy E. Under steady-state excitation, the total downward-transition rate must equal the pumping rate $\mathcal{P}$ as expressed by

$$\mathcal{P} = \mathcal{R}_{spon} + \mathcal{R}_{stim} + \mathcal{R}_{nr} \tag{1a}$$

$$\mathcal{P} = \int r_{spon}(E)\,dE + \int \Phi(E)\,g(E)\,dE + \mathcal{R}_{nr} \tag{1b}$$

where

$\Phi(E)\,dE$ the flux of photons with energy between E and $E + dE$;
$\mathcal{R}_{nr}$ the nonradiative transition rate;
$\mathcal{R}_{spon}$ the total spontaneous-emission rate per unit volume;
$\mathcal{R}_{stim}$ the total stimulated-emission rate per unit volume.

Equations (1a) and (1b) can often be applied as well to pulsed experiments, as discussed in Appendix I.

For many optical media used in laser applications, $\mathcal{R}_{spon}$ can be characterized by a lifetime τ_{spon}

$$\mathcal{R}_{spon} = n/\tau_{spon} \tag{2}$$

where n is the density of the excited species. Similarly, the nonradiative transition rate is given by

$$\mathcal{R}_{nr} = n/\tau_{nr} \tag{3}$$

where τ_{nr} is the nonradiative lifetime. Thus, (1a) can be written

$$\mathcal{P} = \mathcal{R}_{stim} + \mathcal{R}_{spon}(1 + \tau_{spon}/\tau_{nr}). \tag{4}$$

However, the relationship between $\mathcal{R}_{stim}$ and $\mathcal{R}_{spon}$ cannot, in general, be expressed in closed form. The amplitude and shape of the photon flux $\Phi(E)$ depend on the excitation level everywhere in the active volume, and therefore must be calculated from transcendental integral equations. In the present work, in order to reduce the computational complexity at minimum sacrifice, the photon-energy dependence is eliminated by approximating the emission characteristics with rectangular spectra of width ΔE. Thus the transition probabilities (spontaneous and stimulated) are independent of photon energy within the bandwidth ΔE, which tacitly requires very short energy-relaxation times (i.e., homogeneous broadening).[1]

In determining the onset of saturation in an ASE measurement, the use of the rectangular approximation is equivalent to assuming that the emission properties (r_{spon} and g) can be described by effective average values (over energy). In Appendix II it is verified for the illustrative cases of parabolic and triangular spectra that the effective average-gain coefficient is nearly constant for the conditions of interest in this analysis. The concomitant assumption that the spontaneous and stimulated spectra have the same width does in fact lead to an overestimation of the degree of saturation. In general, some portion of the spontaneous spectrum lies outside the gain spectrum and is consequently not amplified. Thus the results based on the rectangular approximation represent an upper bound on the degree of saturation. Carrying out the integral for $\mathcal{R}_{stim}$ in (1b)

$$\mathcal{R}_{stim} = \Phi \cdot g \cdot \Delta E = (I \cdot g)/E \tag{5}$$

which is expressed in terms of the integrated radiation intensity I. Following the usual Einstein treatment of induced transitions, $\mathcal{R}_{stim}$ is proportional to the product nI, where $\mathcal{R}_{spon}$ is proportional to n only. To find the proportionality constant relating $\mathcal{R}_{stim}$ to $\mathcal{R}_{spon}$ for the case of rectangular spectra, we define I_{sat} as the radiation intensity at which g (and consequently n and $\mathcal{R}_{spon}$) has dropped to one half its low-intensity value. Thus when I equals I_{sat}, from (4) and (5)

$$(\mathcal{R}_{spon,0}/2)(1 + \tau_{spon}/\tau_{nr}) = I_{sat}g_0/2E = \mathcal{P}/2 \tag{6}$$

where the subscript 0 denotes the low intensity value. Since g and $\mathcal{R}_{spon}$ are both proportional to n only and do not explicitly depend on I, the subscript 0 can be dropped in general, and for arbitrary intensity I, (6) is rearranged to give

$$g = [(E \cdot \mathcal{R}_{spon})/I_{sat}]\,(1 + \tau_{spon}/\tau_{nr}). \tag{7}$$

[1] To extend the analysis to provide spectral information and include inhomogeneously broadened systems would require specific density-of-states functions and accurate data or assumptions about energy-relaxation times. The additional scope of the results would not justify the greatly increased complexity.

For an interesting optical system in which the rectangular approximation is useful, I_{sat} is a constant of the system and independent of the excitation level. Examples include homogeneously broadened two- and three-level systems [4] and degenerate semiconductors [5]. Further, since g and $\mathcal{R}_{spon}$ depend only on radiative transitions, the proportionality constant in (7) $(1 + \tau_{spon}/\tau_{nr})/I_{sat}$ must be independent of τ_{nr}. Thus decreasing the nonradiative lifetime correspondingly increases the intensity at which gain saturation becomes important (I_{sat}).

From (4), (5), and (7), at arbitrary radiation intensity

$$\mathcal{G} = g\, I/E + g \cdot I_{sat}/E \tag{8}$$

and substituting for $\mathcal{G}$ from (6)

$$g = g_0/[1 + (I/I_{sat})]\,. \tag{9}$$

Equations (7) and (9), coupled with appropriate geometrical considerations, are used in Section III to calculate the gain and intensity everywhere in the active region.

III. Active-Volume Gain Saturation

To properly predict the manner in which gain saturation will manifest itself in an ASE experiment, a three-dimensional analysis is undertaken. Referring to Fig. 2, for the purposes of these calculations the active region is modeled as follows.

1) The cross section is approximated by a rectangle of dimensions $2t \times 2w$. The depth is a function of the combined effect of the nonzero absorption length of the pumping source and of the subsequent diffusion of the excited species. The effective width depends on the width of the stripe focused on the lateral diffusion.

2) To account for three-dimensional effects, the active volume is assumed to contain a collection of point sources emitting spontaneously, isotropically, and with random phases. The computed intensity at any point is the proper summation of spherical waves.

3) The stripe is assumed to be narrow (i.e., $l >> w, t$).

4) The quantities $\mathcal{R}_{spon}$ and g do not vary in the y and z directions.

5) In order to minimize the number of parameters in the computations which follow, τ_{nr} is taken as large compared to τ_{spon}. As a result, the effective saturation intensity I_{sat} is a minimum, and the computations represent the worst case for gain saturation. The crucial results involving active-region saturation are subsequently reexamined to include the effects of scaling due to nonradiative processes.

The manner in which the three-dimensional effects are handled is also illustrated in Fig. 2. The emitting element $dxdydz$ at position x emits a total power $E \cdot \mathcal{R}_{spon}(x)\, dxdydz$ into 4π sr. The receiving area at position x' presents a solid angle $\Omega(x - x')$ to the emitting volume, and as a result, only a fraction $\Omega(x - x')/4\pi$ of the rays emitted at x are collected at x'.[2] In addition, the rays that are collected at x' have experienced an amplification of $\exp\left(\int_{x'}^{x} g'(\xi)d\xi\right)$, where $g'(\xi)$ is the net gain $g - \alpha_e$, and α_e is the excess absorption due to parasitic processes such as free-carrier absorption and scattering. The amplification is expressed as an integral to allow for the variation of gain with position, owing to saturation. Thus the intensity at x' due to spontaneous emission at x, $I(x, x')$ is

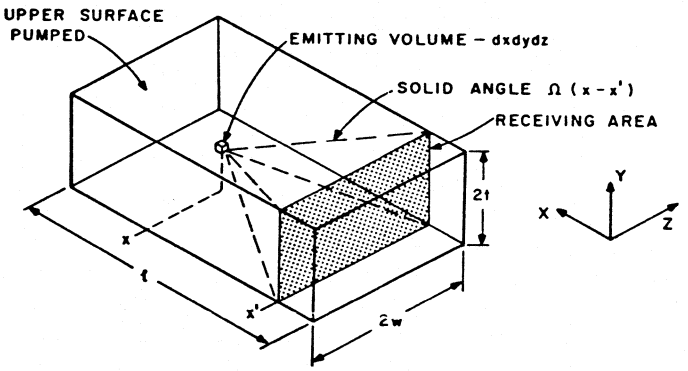

Fig. 2. Schematic diagram of the active volume illustrating the solid angle $\Omega(x - x')$.

$$I(x, x') = I_{spon}(x) \cdot \frac{\Omega(x - x')}{4\pi} \cdot \exp\left[\int_{x}^{x'} g'(\xi)\, d\xi\right] \tag{10}$$

where $I_{spon}(x) = E \cdot \mathcal{R}_{spon}(x)$. The complete solution at x' is the summation of all terms like (10). In deriving (10), the various waveguiding effects due to induced refractive-index variations have been neglected because of the following.

1) The temperature-induced change can be either positive or negative depending on the medium, but can usually be made negligible in the experiment.

2) The injected excess free-carrier concentration makes a negative contribution to the index that inhibits waveguiding.

3) The gain-induced index variation has an N-shaped dispersion [6] that can give a significant positive contribution for large gains, but only over a small fraction of the gain linewidth.[3]

Since the excited region is located near a sample edge, the intensity distribution in the active volume is in general asymmetric. Radiation incident on the sample edge undergoes a partial reflection due to the dielectric discontinuity, causing a fraction to make a second transit of the active region and be further amplified. Referring to Fig. 3(a), there are three components to the intensity at any point x'. The forward wave (FWD) is the cumulative effect of all emitting elements between l and x'; the reverse wave (REV) is the summation of the effects of the elements between x' and 0; and the reflected wave (REFL) is the contribution from those rays that have been generated in the active region, propagated to the front surface, and have been reflected back into the active region.

Integrating terms similar to (10), the following expressions are obtained:

$$I_{FWD}(x') = \frac{1}{4\pi}\int_{x'}^{l} I_{spon}(x) \cdot \Omega(x - x') \cdot \exp\left[\int_{x'}^{x} g'(\xi)\, d\xi\right] dx \tag{11}$$

[2] Due to the total internal reflection at the top surface, the effective receiving area is actually twice that shown in Fig. 2. The expression for $\Omega(x)$, derived in [5], is given by

$$\Omega(x) = 2\pi\left\{1 - \frac{2}{\pi}\cos^{-1}\left[\frac{2wt}{\sqrt{x^2 + w^2}\sqrt{x^2 + 4t^2}}\right]\right\}.$$

[3] Item 3 could become more significant in spectral, as opposed to wavelength-averaged measurements.

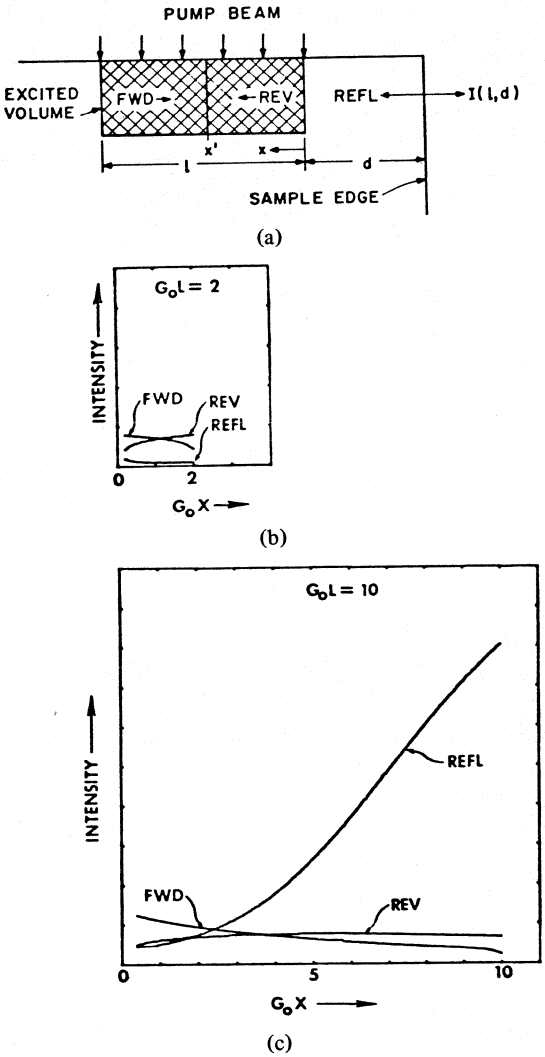

Fig. 3. (a) Cross-sectional view of the active region showing the three waves (forward, reverse, reflected) traveling in the sample. (b) The calculated variation of the intensity of the three waves with normalized position in the stripe for $G_0L = 2$. (c) The calculated variation of the intensity of the three waves for $G_0L = 10$. $G_0 = 0.03$: $R = 0.5$: $K = 0.025$: $D = 0$: $\rho = 6$.

$$I_{\mathrm{REV}}(x') = \frac{1}{4\pi}\int_0^{x'} I_{\mathrm{spon}}(x)\cdot\Omega(x'-x)\cdot\exp\left[\int_x^{x'} g'(\xi)\,d\xi\right]dx \tag{12}$$

$$I_{\mathrm{REFL}}(x') = \frac{1}{4\pi}R\cdot\exp(-2\alpha d)\cdot\exp\left[\int_0^{x'} g'(\xi)\,d\xi\right]\cdot\int_0^{l} I_{\mathrm{spon}}(x)\cdot\Omega(x+x'+2d)\cdot\exp\left[\int_0^{x} g'(\xi)\,d\xi\right]dx \tag{13}$$

where R equals the reflection coefficient at the front surface.

As a result of the intensity dependence of the gain in (9), equations (11)-(13) comprise a set of nonlinear integral equations that must be solved numerically. The parameters used in the numerical calculations are normalized to t, the half-depth of the active region, as shown in Table I.

TABLE I
PARAMETER NORMALIZATIONS

Parameter	Normalized Parameter	Value
Net Gain	G	$g'\cdot t$
Unsaturated Gain	G_o	$g_o'\cdot t$
Excess Absorption	K	$\alpha_e\cdot t$
Position	X	x/t
Stripe length	L	ℓ/t
Stripe width (aspect ratio)	ρ	w/t
Absorption path length	D	d/t
Collection half angle	θ	θ
Reflection coefficient	R	R

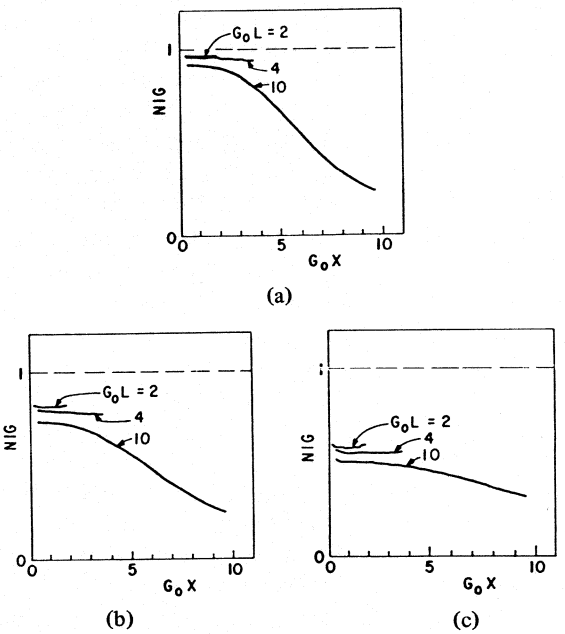

Fig. 4. The calculated variation of the NIG with normalized position in the stripe for three values of G_0L illustrating the saturation due to increasing ρ. $G_0 = 0.03$: $R = 0.5$: $K = 0.025$: $D = 0$. (a) $\rho = 1$. (b) $\rho = 6$. (c) $\rho = 20$.

Fig. 3(b) and (c) shows the calculated spatial variation of the three intensity components under laboratory conditions typical for a semiconductor medium at two values of the product G_0L. The reflected wave clearly dominates for large values of G_0L while the forward and reverse waves change relatively little with stripe length. The magnitude of the reflected wave can be significantly reduced by minimizing the reflection at the sample edge or translating the pumped region away from the sample edge.

A useful quantity for examining active-region saturation is the ratio G/G_0 defined as the normalized internal gain (NIG). Ideally, NIG equals 1 everywhere in the active volume, but nonzero values of radiation intensity cause NIG to be always less than 1. To further illustrate how saturation is manifested in an ASE experiment, Fig. 4 shows the NIG versus position for various values of G_0L, and explicitly demonstrates the effect of the aspect ratio ρ on the saturation: there is a higher degree of saturation for larger aspect ratios. Physically, the

ρ-dependence can be thought of as a purely geometrical effect where (referring to Fig. 2) each element of the receiving area at x' collects radiation from a source at x whose volume is proportional to ρ. Thus the intensity at x', and therefore the degree of saturation, rises as ρ is increased.

IV. Effects of a Nonzero Collection Aperture

In general, experimental conditions in an ASE measurement are such that the output is collected within a specific aperture. It is therefore desirable to be able to predict the angular dependence of the output. The calculations involved are best explained by referring to Fig. 5(a).

The fraction of the photons emitted by the indicated volume element that is collected by the external optics is the fraction within the cone of half-angle θ, where θ is related to the external collection angle by Snell's Law. In the example shown in Fig. 5(a), a significant fraction of the rays within the cone pass out of the active region (in the shaded area) before reaching the edge of the sample. Thus some of the rays within the cone are amplified over the entire distance from the emitting volume to the sample edge and some are not. The calculation is further complicated when the emitting element is positioned so that the cone intersects the top surface, where total internal reflection can occur due to dielectric discontinuity.

The complete solution involves numerical integrations over the five coordinates X, Y, Z, θ, and ϕ, and therefore converges exceedingly slowly. Thus suitable approximations are made here to simplify the computations.

To first order, the total intensity collected within half-angle θ can be approximated by the summation of only those rays that remain in the active region for the maximum distance. However, in reality, rays that leave the active region prematurely can contribute significantly to the total collected intensity, and a better estimate should be used. An improved approximation is made in the present work by counting as "effectively amplified" all those rays that receive at least $1/e$ of the available amplification and ignoring the remaining rays. In this approximation, the contribution $I(X, \theta)dX$ of the cross section at X to the total light in aperture θ can be expressed by

$$I(X,\theta)dX = \frac{\theta^2}{4} \cdot F(X,\theta) \cdot I_{\text{spon}}(X) \cdot \exp\left[\int_0^X G(\xi)\,d\xi\right] dX \tag{14}$$

where $F(X, \theta)$ is the fraction of the cone of rays of half-angle θ, emitted at position X, that is effectively amplified. The quantities $I_{\text{spon}}(x)$ and $G(X)$ are known from the saturation calculations in Section III, making the angular distribution calculation a straightforward numerical integration.

The calculations described in (14) are used to predict the detected output intensity as a function of the parameters L, θ, G_0, K, ρ, R, and D. Some typical results are presented below.

The variation of the collected output power is plotted versus excitation length in Fig. 5(b) for various values of collection angle. It can be seen that the deviation from the desired nominal slope becomes severe at large collection angles.

The slope of the log intensity versus the G_0L graph should be equal to unity in the ideal measurement. The actual slope,

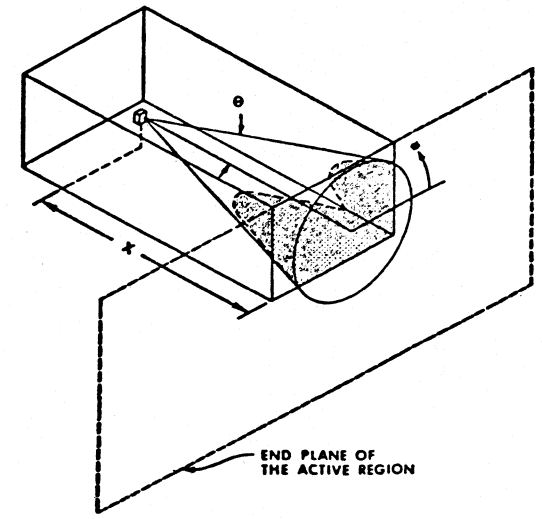

(a)

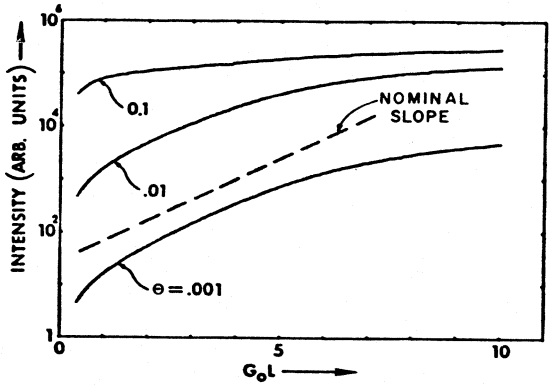

(b)

Fig. 5. (a) Diagram of the active volume showing the cone rays of the half-angle emitted by an element at position X. (b) The calculated variation of the output intensity for various collection half-angles θ. $G_0 = 0.03$: $R = 0.5$: $K = 0.025$; $D = 0$: $\rho = 6$.

defined as the normalized differential gain (NDG) is therefore a useful measure of gain saturation and other sources of error. Analytically, NDG is expressed by

$$\text{NDG} = \frac{1}{G_0}\frac{d\ln(I)}{dL} = \frac{1}{g_0'}\frac{d\ln(I)}{dl}. \tag{15}$$

Fig. 6 shows the dependence of NDG on the cross-sectional aspect ratio ρ (a) and on the nominal gain (b). The suppression of the curves below the nominal value does not have a monotonic variation with gain, and there seems to be an optimum condition, as will be discussed further in the next section.

Fig. 7 shows the calculated variation of the output intensity with translation distance D. The slope of all curves for large values of D is constant and exactly equal to the absorption coefficient in the unpumped region. Thus very accurate measurements of the equilibrium absorption coefficient can be made, as discussed in [3].

An interesting phenomenon that is encountered experimentally is observed in the theoretical results of Fig. 7. In absorption measurements where G_0L is large, as the excited region is translated away from the sample edge, the measured intensity remains nearly constant or actually increases for a distance, before falling into an exponential decay. The non-

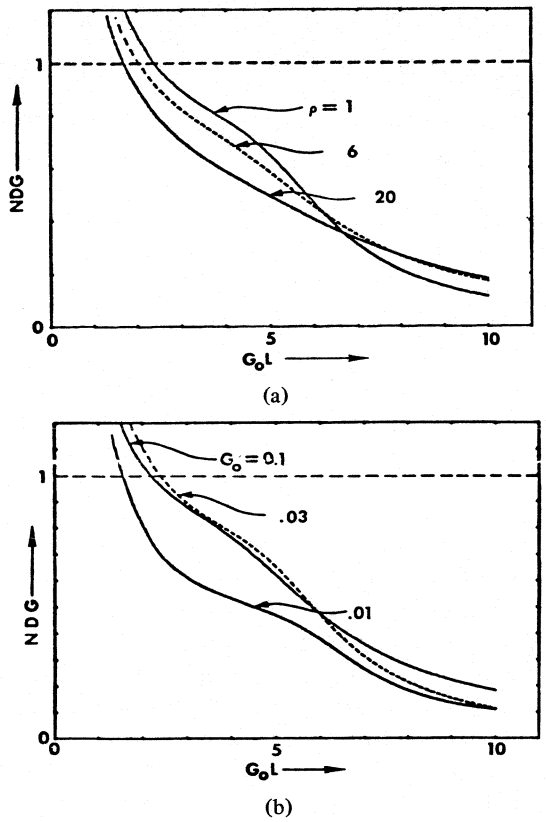

Fig. 6. The calculated NDG versus stripe length for various values of (a) cross-sectional aspect ratio ρ ($G_0 = 0.03$: $R = 0.5$: $K = 0.025$: $D = 0$: $\theta = 0.01$) and (b) low light-level gain G_0. $\rho = 1$.

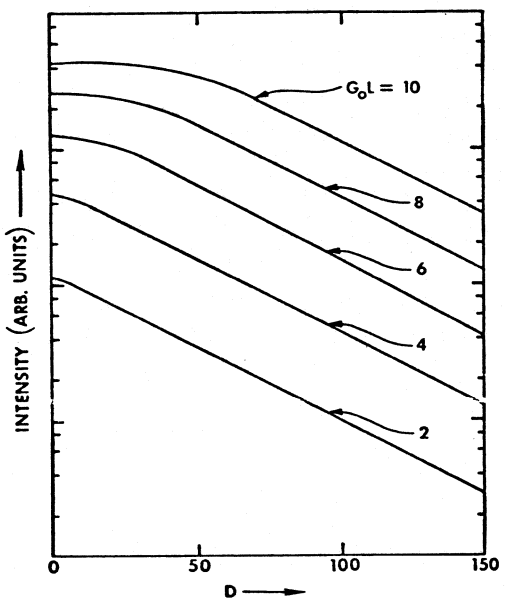

Fig. 7. The output intensity versus D (the normalized distance from the active region to the sample edge) for various values of the gain-length product. $G_0 = 0.1$: $\theta = 0.01$: $R = 0.5$: $\rho = 6$: $K = 0.025$.

exponential behavior for small D is a manifestation of the gain saturation exacerbated by the presence of the reflected wave. The output intensity leaving the active region increases due to the decreasing level of saturation as the active region is translated away from the sample edge. The increase is greater than the attenuation suffered while propagating through the unpumped region. When the reflected wave has been sufficiently attenuated, there is no further increase in emission to compensate the absorption, and the detected output then falls off exponentially. Although this appears to be a major source of error, the effect is easily discernable in the experiment, and the errors can therefore be avoided. It should be noted that saturation of the absorbing path near the excited volume due to high radiation intensity would cause further variations from the desired exponential behavior for small values of D. However, for large D the radiation intensity in the incremental absorption path (near the sample edge) becomes small.

V. Discussion

Figs. 6 and 7 illustrate that measured values of gain can be substantially below the true values, whereas the absorption coefficient can be very accurately determined. The errors in measured gain (NDG) stem from two major sources: 1) internal-gain saturation caused both by high levels of spontaneous emission and by stimulated emission primarily from the reflected wave; and 2) large collection apertures which allow undesired radiation to fall on the detector.

Errors in NDG can be minimized under the following "ideal" conditions.

1) The aspect ratio ρ approximately equals 1 to minimize the geometrical effect on saturation (see Fig. 4).

2) The reflection coefficient is small to minimize the contribution of the reflected wave to saturation. An alternative is to move the active region a long distance from the edge, but this has the attendant disadvantage that the collected output will be significantly attenuated.

3) The collection aperture is small so that only those rays that have traveled the maximum distance in the active region are detected.

The calculated results of an ideal gain measurement are shown in Fig. 8 for various values of G_0 and K. In Fig. 8(a), there is a low excess absorption, while in Fig. 8(b) the excess absorption is large. In both figures, there is an optimum range of G_0 over which the true gain is accurately measured. For gains that are too high, the corresponding high level of spontaneous emission causes internal-gain saturation, even in the absence of a reflection from the front surface. For gains too small, the stripe length becomes so long in the interesting region ($2 \lesssim G_0L \lesssim 6$) that the output collection aperture must be reduced.

Upon examination of a wide range of parameter values in the theoretical model, the limits of G_0 for accurate gain measurement are found to be

$$5\theta \lesssim G_0 \lesssim 0.06 - 2K. \tag{16}$$

The lower limit requires that a photon emitted at angle θ from the center of the active region at $X = L$ will remain in the active region for $G_0L = 5$. Thus (16) quantifies the requirement that all detected rays are effectively amplified. The physical origin of the upper limit in (16) is the high level of spontaneous emission that exists simultaneously with high gain (see Appendix III). The upper limit on measurable gain in (16) represents the worst case value (long nonradiative lifetime). For systems with short τ_{nr}, the gain-saturation limit is increased as discussed in Appendix III.

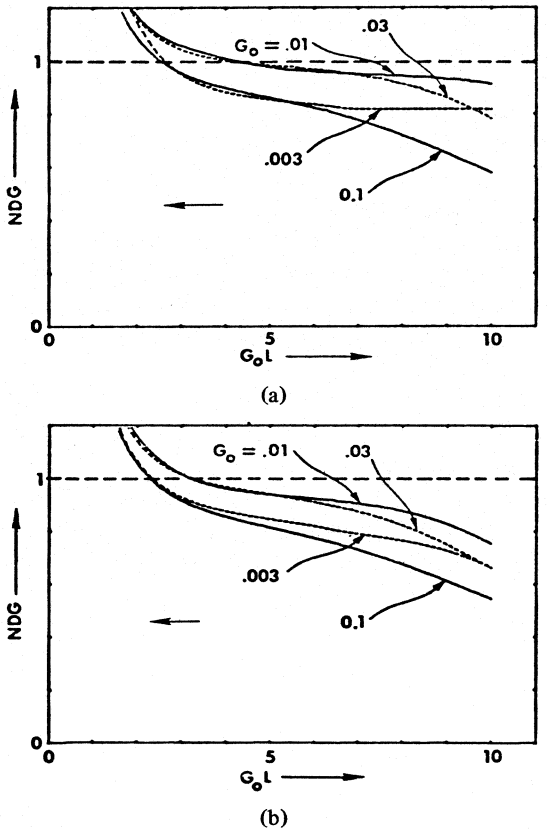

Fig. 8. (a) NDG versus excitation length under ideal conditions for various values of gain G_0. $R = 0$: $K = 0.0025$: $\theta = 0.001$: $\rho = 1$. (b) NDG versus excitation length under ideal conditions with large background absorption. $R = 0$: $K = 0.025$: $\theta = 0.001$: $\rho = 1$.

The major impact of (16) is that the dimensions of the experiment must be chosen according to the gain to be measured. As an example, using parameters typical of a semiconductor measurement, for $t = 2.5\ \mu$, $\alpha = 50\ \text{cm}^{-1}$, and $\theta = 0.001$, the ideal range of measurable gains is from 20 to 140 cm^{-1}.

In summary, for 10-percent accuracy (including the scaling due to nonradiative processes) the measurement conditions imposed are: R small, ρ near unity, and $5\theta \lesssim G_0 \lesssim 0.06\,(1 + \tau_{\text{spon}}/\tau_{\text{nr}}) - 2K$.

Due to low detector sensitivity or lack of dimensional control over the excited region, the conditions necessary for the ideal ASE experiment often cannot be met. As a result, the gain cannot be determined by the simple slope-measuring technique because there is no region of constant slope [see Fig. 5(b)]; a modification of the data-reduction process is required.

To first order, the cumulative effects of active-volume saturation and collection aperture can be included by approximating the NDG by

$$\text{NDG} = G_0 - aL + \text{higher order terms} \tag{17}$$

where the form of the first-order term is derived by noting that all effects tend to reduce the measured gain (hence the minus sign) and all effects reduce to zero at $L = 0$. In principle, G_0 can be determined from a plot of NDG versus L that is extrapolated back to $L = 0$.

For a wide range of parameter values (including large values of the reflection coefficient R), it is found that this method extends the measurement range with ~15-percent accuracy to

$$2\theta \lesssim G_0 \lesssim 0.1\,[1 + (4/\rho^2)]^{1/2} \cdot (1 + I_{\text{spon}}/\tau_{\text{nr}}) - 2K. \tag{18}$$

Outside these limits the first-order approximation fails and the error in the measurement becomes excessive.

Appendix I
Transient Pumping Effects

The theoretical results of Sections III, IV, and V are derived assuming a steady-state excitation, while most measurements of this type are made with pulsed sources [1], [2]. For example, with semiconductors and dyes, typical stripe lengths are $\lesssim$5 cm and double-pass photon transit times are therefore $\lesssim$200 ps. As a result, for pumping pulses longer than the excited-carrier lifetimes (a few nanoseconds) the system can be considered to be in an instantaneous equilibrium at all times. Hence the steady-state theory can be directly applied, even for an arbitrary pulse shape.

Experimentally, if the detector's frequency response is insufficient, the detected signal is actually the integral over the pulse duration and therefore depends on the pulse shape. Further analysis is required to extract the proper gain coefficient from the data of a pulsed measurement.

The mathematics of this computation are identical to that in Appendix II with the integration variable being time instead of photon energy. Thus only the results are discussed here. Fig. 9 displays the ratio of the differential gain g_{diff} for the specified pulse shapes to the differential gain for a rectangular pulse g_{rect} plotted versus the gain-length product. The curves are plotted with $Q = g_0'/\alpha_e$ as a parameter.

As examples, Fig. 9(a) shows the results for a parabolic pulse shape, and Fig. 9(b) shows the results for a triangular pulse shape. In general, the slope of the curves is small enough that a correction factor dependent only on pulse shape can be found.

Appendix II
Justification of the Rectangular-Spectrum Approximation

The assumption that the radiation in the sample has a rectangular spectrum is equivalent to assuming that the spontaneous and stimulated emission can be described by constant, average values. To verify the validity of the assumption, consider a cone of rays narrow enough to be essentially one-dimensional. From [2] we know that the intensity $I_E(l)$ at a particular photon energy E and stripe length l is given by

$$I_E(l) = K\,[I_{\text{spon}}(E)/g'(E)]\,\{\exp\,[g'(E)\,l] - 1\} \tag{19}$$

where K is a geometrical constant. The total intensity $I(l)$ is the integral of (19) with respect to E, and the differential gain g_{diff} is

$$g_{\text{diff}} = (d \ln\,[I(l)])/dl. \tag{20}$$

In the limit of high inversion in the active medium, the spontaneous and stimulated (gain) spectra have the same shape, thereby allowing the following simplification:

$$I_{\text{spon}}(E) = K'[g'(E) + \alpha_e] = K' \cdot g(E) \tag{21}$$

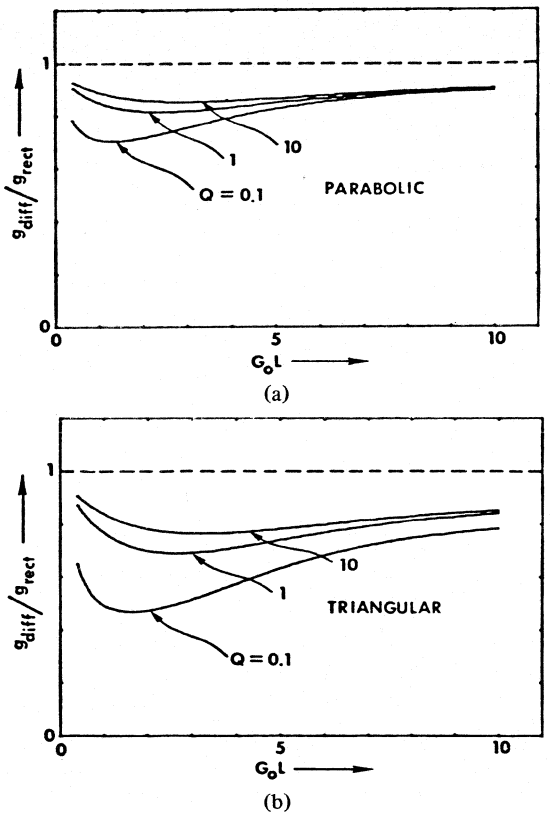

Fig. 9. The effect on the differential gain of a nonrectangular pumping pulse or nonrectangular gain line for (a) parabolic and (b) triangular shapes.

where K' is independent of photon energy. The absorption coefficient α_e is included to allow for any wavelength-independent absorption that must be overcome before net gain can be achieved. Thus the net internal gain $g'(E)$ varies from $-\alpha_e$ to g_0 as E is varied over the linewidth, and $I(l)$ is given by

$$I(l) = K'' \int_{\Delta E} \left[1 + \frac{\alpha_e}{g'(E)}\right] \cdot \{\exp [g'(E)l] - 1\}\, dE \qquad (22)$$

where ΔE is the emission linewidth and $K'' = K \cdot K'$.

Using (20) and (22), a comparison can be made between the case of a rectangular spectrum and the more physically appropriate case of a smoothly varying distribution. Specifically, parabolic[4] and triangular distributions are assumed here.

In Fig. 9(a), the ratio of g_{diff}, for a parabolic distribution, to g_{rect}, the differential gain for a rectangular distribution, is plotted versus $g_0 \cdot l$ with $Q(Q = g_0'/\alpha_e)$ as a parameter. The results for a triangular spectrum are shown in Fig. 9(b). The anticipated line-narrowing effects are evidenced by the slow variation of g_{diff} with gain-length product. However, in the region of primary interest in an ASE experiment ($2 < g_0'l < 6$), g_{diff} is fairly constant, especially for the frequently encountered situation where $Q > 1$. Thus the gain spectrum can be reasonably approximated by the constant, average value of 85 percent of the peak gain for the parabolic case, and 75 percent for the triangular.

[4]The results are not significantly different for other smoothly varying functions such as Gaussian or Lorentzian.

Appendix III

Saturation Due to Spontaneous Emission

The upper limit on G_0 is due to the high level of spontaneous emission that leads to high-intensity isotropic (undetected) stimulated emission. The upper limit in (16) is derived intuitively by finding the intensity that would exist in the active volume due to spontaneous emission alone, ignoring amplification (i.e., finding the lower limit on radiation intensity that can exist in the active volume under given excitation). Summing (11)–(13) for zero reflection coefficient

$$I(x')|_{g'=0} \simeq 2 \cdot I_{spon} \cdot \int_{\Delta l} \frac{\Omega(x)}{4\pi}\, dx \qquad (23)$$

where, for simplicity, $I_{spon}(x)$ is taken as constant. In [5] it is shown that the integral rapidly converges ($\Delta l \gtrsim 4t$) to $1.8\rho/(4 + \rho^2)^{1/2}$. Using (5) and (7) we get

$$\frac{I(x')|_{g'=0}}{I_{sat}} \simeq 3.6 \sqrt{\frac{\rho^2}{4 + \rho^2}} \cdot (G_0 + K)/(1 + \tau_{spon}/\tau_{nr}) \qquad (24)$$

when (9) is approximated in the limit $I \ll I_{sat}$

$$g'/g_0' \simeq 1 - (I/I_{sat})/(G_0 + K/G_0) \cong 1 - \epsilon \qquad (25)$$

where ϵ is the error in g' due to saturation. Finally, the upper limit on G_0 is

$$G_0 \lesssim 0.28\epsilon\, [(4 + \rho^2)^{1/2}/\rho^2]\, (1 + \tau_{spon}/\tau_{nr}) - 2K. \qquad (26)$$

Equation (16) follows for $\rho = 1$, $\epsilon = 10$ percent, and $\tau_{nr} \gg \tau_{spon}$.

References

[1] C. V. Shank, A. Dienes, and W. T. Silvast, "Single-pass gain of exciplex 4-mu and rhodamine 6G dye laser amplifiers," *Appl. Phys. Lett.*, vol. 17, pp. 307–309, 1970.
[2] K. L. Shaklee and R. F. Leheny, "Direct determination of optical gain in semiconductor crystals," *Appl. Phys. Lett.*, vol. 18, pp. 475–477, 1971.
[3] P. S. Cross and W. G. Oldham, "Monolithic measurement of optical gain and absorption in PbTe," *J. Appl. Phys.*, to be published.
[4] A. Yariv, *Quantum Electronics*. New York: Wiley, 1968, p. 266.
[5] P. S. Cross, Ph.D. dissertation, Univ. California, Berkeley.
[6] W. W. Anderson, "Mode confinement and gain in junction lasers," *IEEE J. Quantum Electron.*, vol. QE-1, pp. 228–236, Sept. 1965.

On the Saturation Effects and Start Jump of Gaussian Modes in Oscillators

W. J. WITTEMAN AND G. J. ERNST

Abstract—**The present paper deals with the interaction of a Gaussian mode with a homogeneous and an inhomogeneous laser transition. The interaction of the beam with the medium in a laser is treated by taking into account the spatial distribution of both radiation and gain. The intensity characteristics are very different from those obtained for a one-dimensional interaction of a plane wave with a saturating medium. In the presence of a small-signal gain profile the threshold condition requires much higher inversion densities along the optic axis than by ignoring this profile. For gas lasers, for instance, having a small-signal gain profile that is approximately described by a zero-order Bessel function, the threshold inversion density can be about 50 percent higher. For high-power systems the saturation of the medium by the Gaussian intensity distribution results in a considerable amount of radial radiation transport. For homogeneous transitions this amount is about equal to the stimulated emission and for inhomogeneous transitions it is about half of it, independent of the beamwidth. Further, it is found that if one slowly passes the threshold condition for laser action, the intensity jumps from zero to a certain value and vice versa. This effect has also been verified experimentally.**

I. Introduction

THE radiation intensities produced by steady-state lasers have been computed in the past by using one-dimensional interaction of a plane wave with a saturating medium [1], [2]. As far as the interaction is concerned, the resonator has been assumed to support plane electromagnetic waves with its outcoupling loss concentrated near the mirrors. By using this approximation, one calculates the intensity characteristics, maximum output flux densities, etc., as a function of gain and outcoupling loss for lines with homogeneous and inhomogeneous broadening. However, in any interaction phenomenon of an electromagnetic beam and an amplifying medium there is no plane wave and no uniform gain of the field due to the finite aperture, to the inhomogeneity of the medium, and/or to the intensity-induced saturation of the medium. This nonuniformity depends not only on the coordinate of the direction of propagation, but also on the coordinates perpendicular to the direction of propagation, i.e., the gain profile.

In search of maximum radiation production from an efficiently pumped optical system, it seems advisable to extend the intensity computations by removing the restrictions of only one-dimensional interaction. Usually, the spatial distribution of the radiation intensity is also computed without taking into account a nonuniform gain profile. But this turns out to be very reasonable, because as far as the radiation distribution is concerned it is found [3] that, at least for small laser systems, the geometry of the beam is practically unaltered by the inhomogeneity of the gain, so that the optical beam parameters such as beamwidth can be reasonably well predicted by neglecting the gain profile. This is found for a positive as well as a negative gain profile, because in both cases a change in amplitude distribution, which is expected by neglecting phase changes, is nearly canceled by the effect of phase changes. Therefore, it is found and in agreement with observations, that under normal experimental conditions of laser systems the effect of a gain profile, caused either by the small-signal gain or by the saturation, will leave the beam size practically unchanged. Thus there is no focusing or defocusing by the gain profile. However, we cannot neglect the gain profile for radiation-intensity studies. Here the gain profile, as we shall see, is an important parameter, even for small systems having low output power.

The analysis here treats homogeneous and inhomogeneous laser transitions. We restrict ourselves to a commonly used system of a single-mode Gaussian beam in a radially symmetric excited medium. The advantage of treating this system is its simplicity. The physics involved can be easily appreciated and the effects of various processes on the radiation intensity can be compared. It is found that the three-dimensional character of the gain has for any optimized laser system—high or low power, homogeneous or inhomogeneous transitions—a large bearing on the intensity characteristics and output powers. Furthermore, from the computation of the intensity characteristics a remarkable effect can be predicted: i.e., when a laser builds up the inversion and passes (slowly) the threshold condition for the Gaussian mode, the laser output does not start from zero, but jumps to a finite value. We verified this jump experimentally, which gives a direct proof of the so-called "radial radiation transport." Although the analysis is primarily set up to describe saturation effects and to compute laser characteristics, it is also seen that the threshold conditions are changed drastically by a small-signal gain profile.

II. The Incremental Gain

Since in the present analysis we are dealing with the propagation of a Gaussian beam in a normal resonator, the nonuniformity of the medium must be lenslike in order to preserve the Gaussian nature. This means that the medium is described by a quadratic profile. In fact, the appearance of high-power Gaussian laser beams supports the assumption that a quadratic description can be adequate. In practice, of course, no profile is quadratic, but it should be noted that for media having axial symmetry a series expansion of the propagation constant in terms of the radial distance from the axis

Manuscript received September 21, 1974; revised January 15, 1975.
The authors are with the Department of Physics, Twente University of Technology, Enschede, The Netherlands.

shows that the main terms near the axis (where the field is strongest) are the constant and quadratic ones.

The derivation [4] of the propagation laws for Gaussian beams in quite general lenslike media starts with the scalar wave equation

$$\nabla E + k^2 E = 0 \tag{1}$$

where the quadratic dependence of k^2 near the optic axis is given by

$$k^2(r,z) = k_0^2(z) + k_0(z)\, k_2(z)\, r^2 . \tag{2}$$

These medium constants are generally complex to allow for loss or gain. k_0 is the part of the propagation constant that does not depend on r, whereas k_2 describes the variation of the propagation constant with r and includes thermal effects, gain variations, and also the associated dispersive effects of the gain profile.

In solving (1), the main interest is in waves bouncing back and forth between two mirrors that propagate primarily in the z direction, or almost-plane waves. It can be shown that such waves with a Gaussian radial dependence satisfy (1). Accordingly, one writes

$$E(r,z) = E_1 \exp\{-i(\phi + T + \tfrac{1}{2} r^2 k_0/q)\} \tag{3}$$

in which the time-dependent part has been dropped, $d\phi/dz = k_0(z)$ is the complex propagation constant on the axis, T is a complex phase parameter, q is the complex beam parameter defined by

$$\frac{1}{q} = \frac{1}{R(z)} - i\,\frac{\lambda}{\pi\omega^2(z)} \tag{4}$$

where $R(z)$ is the radius of curvature of the wavefront, λ is the wavelength, and $\omega(z)$ is the beam waist. Substitution of (3) into (1) gives, after comparison of terms of equal powers of r, the following two differential equations:

$$T' = -i\left(\frac{1}{q} + \frac{k_0'}{2k_0}\right) \tag{5}$$

$$\frac{1}{q^2} + \left(\frac{1}{q}\right)' + \frac{k_0'}{k_0}\frac{1}{q} - \frac{k_2}{k_0} = 0 \tag{6}$$

where the prime means differentiation with respect to z. For laser systems, (2) can be approximated by

$$k = k_0 + \tfrac{1}{2} k_2 r^2 . \tag{7}$$

By separating real and imaginary parts, we write

$$k_0 = \beta_0 + i\alpha_0 \tag{8}$$

$$k_2 = \beta_2 + i\alpha_2 . \tag{9}$$

By differentiating (3) with respect to z and using (5), we find for E on the axis ($r = 0$)

$$\frac{1}{E}\frac{dE}{dz} = -i\left(k_0 - \frac{i}{q} - \frac{ik_0'}{2k_0}\right). \tag{10}$$

By adding the complex conjugates to both sides of (10), using (4), and assuming that the wavelength is constant along the axis, the incremental gain along the axis is found to be

$$\frac{1}{I}\frac{dI}{dz} = 2\left(\alpha_0 - \frac{1}{R(z)}\right). \tag{11}$$

By substituting (4), (8), and (9) into (6) and taking the imaginary part, we get

$$\frac{2}{R(z)} = \frac{d\ln\omega^2}{dz} - \tfrac{1}{2}\alpha_2\omega^2 . \tag{12}$$

By substituting (12) into (11), we finally get for the incremental gain on the optic axis

$$\frac{1}{I}\frac{dI}{dz} = 2\alpha_0 - \frac{d\ln\omega^2}{dz} + \tfrac{1}{2}\alpha_2\omega^2 . \tag{13}$$

The first term on the right-hand side of (13) describes the local conversion of inverted states into stimulating emission. This is the same term as found for a one-dimensional treatment with plane waves [5]. The last two terms on the right-hand side of (13), equal to $2/R(z)$, describe the part of the incremental gain due to convergence or divergence of the wavefront of a propagating wave [6]. One part of it, the second term of (13), is related to the continuity of propagating electromagnetic energy; in the absence of any interaction, the product of beam cross section and intensity at the optic axis of a Gaussian beam ($\omega^2 I$) is constant along the axis. Therefore this term simply describes focusing or defocusing of the beam. The last term on the right-hand side of (13) describes a contribution of the radial radiation transport to the incremental gain related to the parabolic gain profile. From (13) we obtain for the increase of energy flux

$$\frac{d\ln(I\omega^2)}{dz} = 2\alpha_0 + \tfrac{1}{2}\alpha\omega^2 . \tag{14}$$

It is seen that only the imaginary parts of the propagation constants, i.e., the gain and its profile, determine the increase of energy flux. Thermal and dispersive effects contribute in so far as they influence the beamwidth of the Gaussian mode [3]. But normally, the fractional change of beamwidth by thermal and dispersive effects is relatively small so that the incremental energy flux is practically given by the gain parameters.

In a laser system, the standing wave consists of a running wave in the $+z$ direction and one in the $-z$ direction. Although the beamwidths of the two running waves are not exactly equal, it turns out that in practice they can be taken equal at any place along the axis. If we write down (14) for both running waves, we then find because of bidirectional gain

$$\frac{d\ln(I\omega^2)_+}{dz} = -\frac{d\ln(I\omega^2)_-}{dz} \tag{15}$$

and we see that

$$(I\omega^2)_+ (I\omega^2)_- = \text{constant}. \tag{16}$$

Thus the product of the energy flux of the two running waves is constant along the axis.

III. Homogeneous Line Broadening

For homogeneous line broadening, the saturated amplitude gain coefficient α is related to the unsaturated or small-signal gain coefficient G, which depends on the line shape of the transition by

$$\alpha(r) = \frac{\frac{1}{2}G(r)}{1 + I_t(r)/I_0} \tag{17}$$

where I_0 is the saturation parameter and I_t the total intensity of the two running waves. Since we are interested in the constant and quadratic term of the gain profile, we substitute into (17) for the unsaturated gain profile

$$G(r) = G(1 + \tfrac{1}{2}\gamma r^2) \tag{18}$$

and for intensity

$$I_t(r) = I_t \exp(-2r^2/\omega^2). \tag{19}$$

For the constant term of the amplitude gain we obtain

$$\alpha_0 = \frac{\frac{1}{2}G}{1 + I_t/I_0}. \tag{20}$$

For the quadratic term we get

$$\alpha_2 = \frac{\frac{1}{2}G}{1 + I_t/I_0}\left(\gamma + \frac{4}{\omega^2}\frac{I_t/I_0}{1 + I_t/I_0}\right). \tag{21}$$

By substituting (20) and (21) into (14), we find for the incremental gain

$$\frac{d \ln (I\omega^2)}{dz} = \frac{G}{1 + I_t/I_0}\left(1 + \tfrac{1}{4}\gamma\omega^2 + \frac{I_t/I_0}{1 + I_t/I_0}\right). \tag{22}$$

It is seen that the contribution of radial radiation transport to the incremental gain comes from both the small-signal gain profile and the gain induced saturation. In general, the small-signal gain decreases with the distance from the axis (γ is negative). Such a profile broadens the wavefront and radiation energy is radially transported out of the center. This means that the threshold condition to start oscillations requires higher inversion densities along the axis than that predicted on the basis of one-dimensional plane-wave interaction.

This conclusion can also be reached more simply by stating that the integrated gain over the mode volume must be equal to the losses. Then one finds that the inversion along the axis is much higher than the average inversion needed to reach threshold. It is assumed, however, that the geometry of the beam is unchanged by the gain profile. In other words, it is assumed that if the effective diameter of the gain region has become smaller, the effective beam diameter does not become smaller. Only a more comprehensive analysis will show that the beamwidth is indeed practically unchanged by the gain profile [3].

In order to estimate the threshold condition, let us consider a small-signal gain profile proportional to the electron density of the discharge. In dealing with a positive column discharge, this gain profile can then be described by a zero-order Bessel function. The quadratic term of such a gain profile is

$$\gamma = -\frac{2.88}{\rho^2} \tag{23}$$

where ρ is the radius of the tube diameter.

The second term of (22) becomes $-0.72\ \omega^2/\rho^2$. In many single-mode oscillators the value of ω^2/ρ^2 is about $\frac{1}{2}$. Substituting this value into (23) makes the incremental gain for starting oscillations about 36 percent smaller than in the case where the small-signal gain profile is ignored.

The last term on the right-hand side of (22) describes the part of the radial radiation transport that comes from the change of the saturated gain profile by the Gaussian intensity distribution. For optimized laser systems, when $I_t/I_0 \gg 1$ the last term of (22) approaches one. Thus at high intensities the intensity profile itself leads to a radial radiation transport that contributes as much to the incremental gain as the stimulated emission from the local medium. It is interesting to note that the latter conclusion is independent of the beamwidth.

In order to find the intensity characteristics of an oscillator, we have to integrate (22) over a round trip through the resonator. In general, the beamwidth may vary considerably along the tube, so that the integration of (22) with the aid of (16) has to be worked out numerically. The integration becomes complicated because one also has to know the beamwidth at any place along the tube. The beamwidth in turn depends on α_2 and, in fact, on I_t. However, the general behavior of the obtained characteristics is similar to what will be obtained for the case where $\lambda L/\pi\omega^2 \ll 1$ (L is the length of the system), so that the beamwidth varies very little along the axis, and the outcoupling is not too large. In that case we find from (16) that the product of the intensities of the two running waves is constant. Let us consider a system having one totally reflecting mirror and one outcoupling mirror with reflectivity R. The maximum relative variation of the sum of the two intensities is equal to $\frac{1}{2}\sqrt{R}(1 + 1/R)$. It is seen that even for $R = 50$ percent the sum of the two intensities is constant to within 5 percent.

By integrating (22) over a round trip through the resonator and taking I_t as constant, we find

$$-\frac{\ln R}{2GL} = \frac{1}{1 + I_t/I_0}\left(1 + 0.25\ \gamma\omega^2 + \frac{I_t/I_0}{1 + I_t/I_0}\right). \tag{24}$$

The outcoupled intensity I_{out} is related to the total intensity within the laser by

$$I_{out} = \frac{1 - R}{1 + R} I_t. \tag{25}$$

Normalized values of the output intensity are plotted in Fig. 1 as a function of $-GL/\ln R$ for various values of $\epsilon = 1 + 0.25\ \gamma\omega^2$. In Fig. 2 we plotted the normalized output as a function of the reflectivity R for various values of GL and ϵ. It is seen that the threshold condition depends on the small-signal gain profile given by ϵ.

Furthermore, it can be seen that there are nonzero fields with smaller gain over loss ratios than at threshold. These

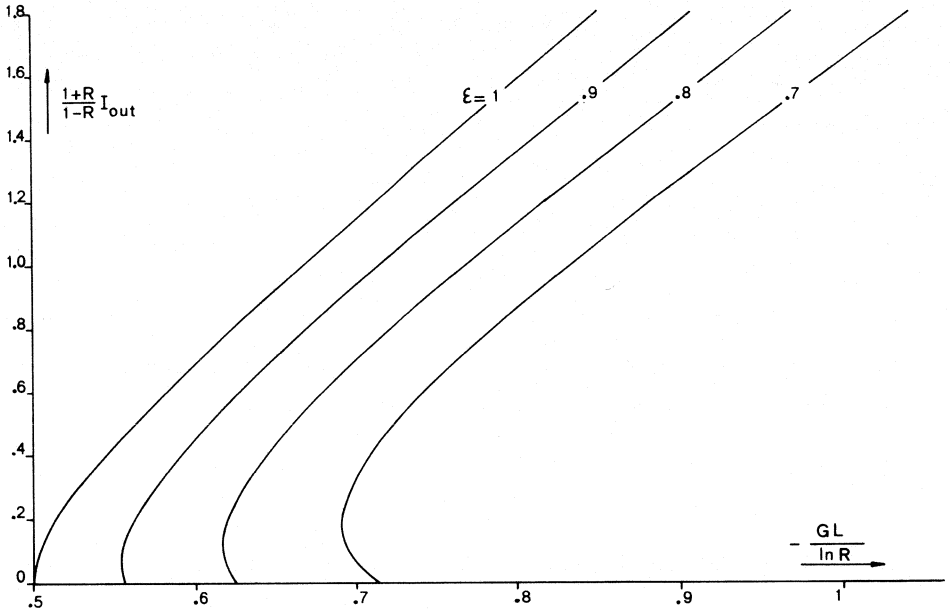

Fig. 1. The outcoupled intensity of homogeneous line broadening divided by the saturation-intensity parameter I_S is plotted versus the gain over loss ratio. The small-signal gain profile is indicated by $\epsilon = 1 + 0.25\,\gamma\omega^2$.

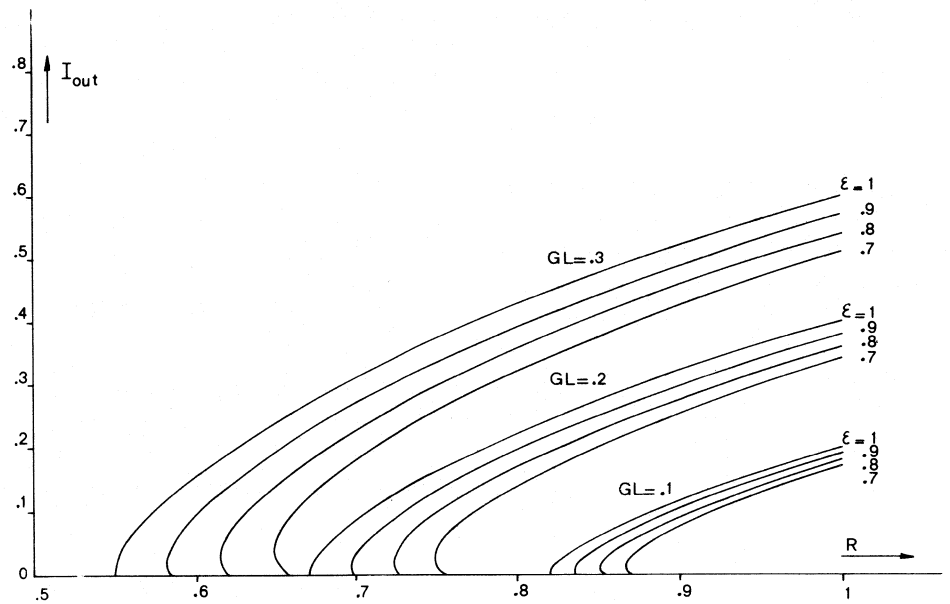

Fig. 2. The outcoupled intensity divided by I_S is plotted as a function of R for homogeneous line broadening. The characteristics indicate that near threshold the intensity is not continuously changeable, but jumps.

nonzero-field conditions can only be reached by a field that has already been built up within the resonator and therefore one first has to pass the zero-field threshold condition. By passing this point, the induced saturation levels the gain profile and, consequently, the divergence of the wavefront decreases, which means that less radiation is transported radially out of the center. Thus the apparent "loss factor" induced by the small-signal gain profile is reduced by the field itself and therefore, if for a Gaussian beam system the gain over loss ratio is slowly increased from below threshold, the intensity does not increase continuously from zero as one passes threshold but jumps to a certain value.

The jump depends on the small-signal gain profile. The stronger this profile, i.e., the smaller γ, the larger the start jump. For values of γ larger than or equal to zero there is no jump.

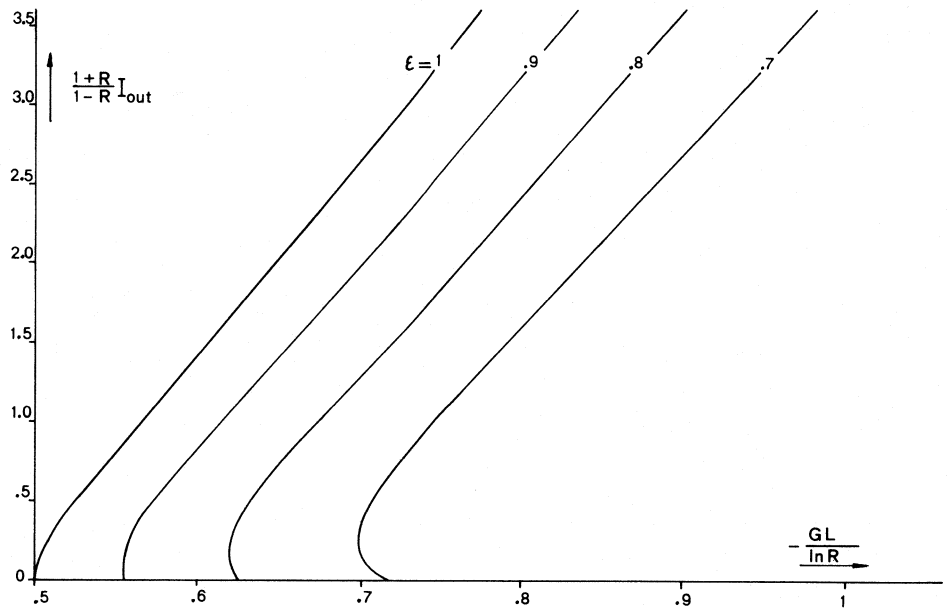

Fig. 3. The outcoupled intensity for inhomogeneous line broadening divided by the saturation parameter I_s is plotted versus the gain over loss ratio.

IV. Inhomogeneous Line Broadening

For inhomogeneous line broadening the saturated amplitude gain coefficient is known as

$$\alpha(r) = \frac{\frac{1}{2}G(r)}{\{1 + I_t(r)/I_0\}^{1/2}} \tag{26}$$

where $G(r)$ is again the small-signal intensity gain which depends on the line shape of the oscillating transition. Let us consider again that the small-signal gain profile and intensity distribution are given by (18) and (19), respectively. For the constant and quadratic term of the amplitude gain we find

$$\alpha_0 = \frac{\frac{1}{2}G}{\{1 + I_t/I_0\}^{1/2}} \tag{27}$$

$$\alpha_2 = \frac{\frac{1}{2}G}{\{1 + I_t/I_0\}^{1/2}} \left(\gamma + \frac{2}{\omega^2} \frac{I_t/I_0}{1 + I_t/I_0}\right). \tag{28}$$

By substituting (27) and (28) into (14), the incremental gain of an inhomogeneous transition becomes

$$\frac{d \ln (I\omega^2)}{dz} = \frac{G}{\{1 + I_t/I_0\}^{1/2}} \left(1 + \tfrac{1}{4}\gamma\omega^2 + \tfrac{1}{2} \frac{I_t/I_0}{1 + I_t/I_0}\right). \tag{29}$$

If the small-signal gain profile of gas lasers is again proportional to the electron density and therefore approximated by a zero-order Bessel function, we find, similar to the homogeneous case, that the threshold condition to start oscillation requires much higher inversion densities along the axis than by ignoring this gain profile. With ω^2/ρ^2 about 0.5, the threshold inversion density is about 50 percent higher. Further, we see that for $I_t/I_0 >> 1$ the contribution of radial radiation transport to the incremental gain due to the Gaussian intensity distribution is about equal to half the amount of stimulated emission given by the first term on the right-hand side of (29).

In order to find the intensity characteristics, we integrate (29) over a round trip through the resonator and consider again the case where the beamwidth varies little within the resonator, so that it can be approximated as constant. We find, similar to the homogeneous case,

$$-\frac{\ln R}{2GL} = \frac{1}{\{1 + I_t/I_0\}^{1/2}} \left(1 + 0.25\,\gamma\omega_+^2 \frac{0.5\, I_t/I_0}{1 + I_t/I_0}\right). \tag{30}$$

The normalized output intensities are plotted in Figs. 3 and 4. It is seen that the obtained characteristics also predict a start jump as one slowly increases the gain over loss ratio and passes threshold. Again, the jump only exists for negative values of γ and increases with decreasing γ. By comparing this result with the numerical evaluation of gain saturation as given by Fox and Li [8], it is seen that they did not find a start jump. The reason may be that they consider a homogeneous small-signal gain coefficient ($\gamma = 0$), which according to our results will indeed not lead to a start jump.

V. Start Jump of a Gaussian Mode

The aforementioned predicted start effect can be demonstrated experimentally. It can be found either by increasing the pumping power or by decreasing the outcoupling losses from below threshold. For continuously variable outcoupling losses we chose a Gaussian-mode CO_2 laser with an outcoupling cavity. The experimental setup is indicated in Fig. 5. The cavity has a length of 150 cm and an internal diameter of 9 mm. There is a totally reflecting gold mirror with a radius

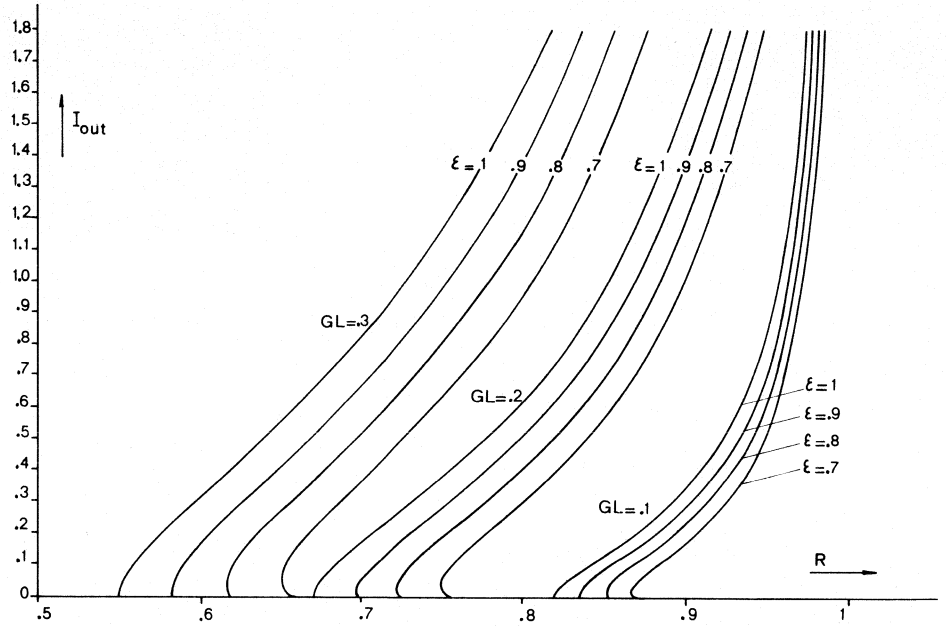

Fig. 4. The outcoupled intensity for inhomogeneous transitions is plotted versus reflectivity for various values of the small-signal gain and its profile parameter ϵ.

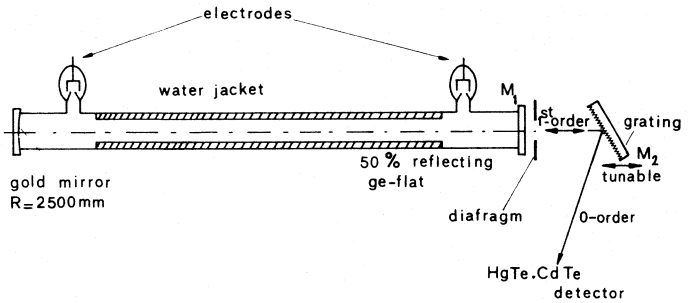

Fig. 5. Experimental arrangement of a Gaussian-mode laser with transition selective outcoupling cavity. The outcoupling is continuously variable. The grating is mounted on a tunable piezoelectric translator.

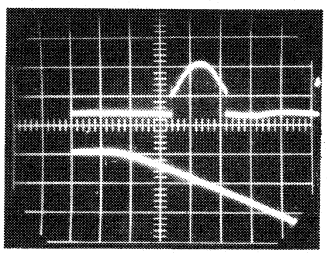

Fig. 6. The outcoupled intensity as a function of the position scanning of the piezoelectric translator. The reflectivity of the coupling cavity first increases and further on decreases with the translated position of the grating. The lower part shows the ramp voltage. The time scale is 5 ms/cm.

of curvature of 2500 mm on one side and a 50-percent reflecting germanium flat on the other side. The length of the discharge is about 130 cm. With a mixture of about 8 torr CO_2 and 6 torr He, the cavity is overcoupled and will not lase with a dc discharge current of about 10 mA. By placing a wavelength selective grating in front of the germanium flat, we use the first-order reflection on the grating for intracavity reflection and the zero-order reflection for outcoupling. The grating, mounted on a tunable piezoelectric translator for position scanning, together with the germanium flat, forms a Fabry-Perot (FP). This FP as an outcoupling cavity offers a variable narrow-band reflection [7]. In order to suppress higher order modes, a 4.2-mm diaphragm is placed between the grating and the germanium flat. The diffraction grating is gold coated, has 75 lines/mm, and is blazed for 10.6 μ. The outcoupled radiation is detected with a fast HgTe:CdTe photo diode having a time constant of a few nanoseconds.

Fig. 6 shows the output intensity as a function of the position scanning of the piezoelectric translator. The lower part shows the ramp voltage applied to the translator and the upper part shows the output as a function of time with 5 ms/division. The reflectivity is continuously varied by the applied ramp voltage from below threshold. At threshold the intensity does not increase continuously but clearly jumps. It also falls suddenly back to zero as the reflectivity is decreased by further scanning.

By using the laser system without the grating, varying gain is obtained by increasing the current suddenly from 1 to 40 mA. (In a dc experiment it will not lase at 40 mA.) After this change the inversion density grows and passes threshold and after some time the inversion drops again, probably due to thermal effects. The upper trace of Fig. 7 shows the change of current and the lower trace shows the radiation output. The time scale is 50 μs/division. Apparently, it takes some

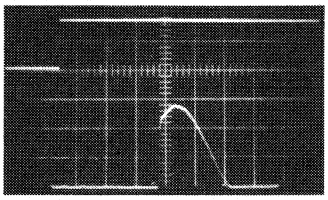

Fig. 7. The dc discharge current of about 1 mA is suddenly changed to 40 mA, as shown by the upper trace. The output of the laser without grating and diaphragm is shown by the lower trace. The time scale is 50 μs/cm.

time before the threshold inversion is built up, and then the oscillation jumps to a certain intensity. The extinction of the laser action is not sudden. It may be that, for the steady state of 40 mA due to thermal effects, the small-signal gain profile becomes flat or even reversed. If the same experiment is done by suddenly increasing the current from about 5 mA, where the steady-state oscillations exist, to 40 mA, it is found that the oscillating field increases continuously and finally drops to zero. This is shown in Fig. 8, where the time scale is 100 μs/division.

VI. Conclusions

A three-dimensional treatment of the interaction of a Gaussian mode and a saturated medium leads to conclusions that differ much from one-dimensional treatment. We wish to stress again that the gain parameters have practically no influence on the intensity distribution, i.e., there is no focusing owing to the gain parameters, but they have a large influence on the energy flux and output power. For both homogeneous and inhomogeneous transitions, the effect of the Gaussian distribution of the intensity on the saturation of the medium is a considerable increase of output power. Finally, it is found

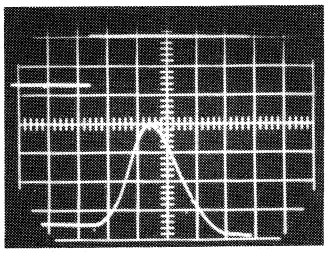

Fig. 8. A dc discharge of about 5 mA producing a weak laser field is suddenly changed to 40 mA, as shown by the upper trace. The Gaussian radiation intensity is shown to be continuous, and it finally goes to zero. The time scale is 100 μs/cm.

that near threshold the intensity is not continuously variable but jumps.

References

[1] W. W. Rigrod, "Saturation effects in high-gain lasers," *J. Appl Phys.*, vol. 36, pp. 2487–2490, Aug. 1965.
[2] P. W. Smith, "The output power of a 6328-Å He-Ne gas laser," *IEEE J. Quantum Electron.*, vol. QE-2, pp. 62–68, Mar. 1966.
[3] G. J. Ernst and W. J. Witteman, "Mode structure of active resonators," *IEEE J. Quantum Electron.*, vol. QE-9, pp. 911–918, Sept. 1973.
[4] H. Kogelnik, "On the propagation of Gaussian beams of light through lenslike media including those with loss or gain variation," *Appl. Opt.*, vol. 4, pp. 1562–1569, Dec. 1965.
[5] W. W. Rigrod, "Gain saturation and output power of optical masers," *J. Appl. Phys.*, vol. 34, pp. 2602–2609, Sept. 1963.
[6] G. J. Ernst and W. J. Witteman, "The effect of radial radiation transport on intensity characteristics and oscillation frequency of homogeneously broadened lasers," *IEEE J. Quantum Electron.*, vol. QE-10, pp. 37–44, Jan. 1974.
[7] —, "Transition selection with adjustable outcoupling for a laser device applied to CO_2," *IEEE J. Quantum Electron.*, vol. QE-7, pp. 484–488, Oct. 1971.
[8] A. G. Fox and T. Li, "Effect of gain saturation on the oscillating modes of optical masers," *IEEE J. Quantum Electron.*, vol. QE-2, pp. 774–783, Dec. 1966.

High-Resolution Spectral Measurements of SO_2 from 1176.0 to 1265.8 cm^{-1} Using a Single PbSe Laser with Magnetic and Current Tuning

FRANK ALLARIO, CLAYTON H. BAIR, AND JACK F. BUTLER, MEMBER, IEEE

Abstract—**A single magnetic- and current-tuned PbSe diode laser was used to measure completely resolved spectra of SO_2 at low pressures over a major portion (1176.0–1265.8 cm^{-1}) of the R branch of the ν_1 band for the first time. It is shown that the combination of magnetic and current tuning allows *complete* coverage of this 89.8-cm^{-1}-wide spectral region. Results generally show excellent agreement with theoretically generated spectra. Magnetic-tuning rates and, with magnetic field applied, current-tuning rates were observed to be significantly nonlinear. Precise spectroscopic data could be obtained with these nonlinearities taken into account. The current-tuning rate in zero magnetic field was essentially constant over the range investigated.**

I. Introduction

As a result of their narrow linewidths ($\leqslant 10^{-5}$ cm^{-1}) and wavelength tunability, Pb-salt semiconductor lasers have been used for ultrahigh-resolution spectral measurements in a variety of molecular gases, and have found application in atmospheric-pollution monitoring [1]. Semiconductor lasers also appear promising as high-resolution sensors of atmospheric pollutants from satellite or aircraft platforms [2]. Using several current-tuned $Pb_{1-x}Sn_xTe$ diode lasers of differing compositions, line intensities and positions in the ν_1 band of SO_2 have previously been measured in the P branch, from 1114.5 to 1167.8 cm^{-1} [3], [4]. Current-tunable semiconductor lasers of $Pb_{1-x}Sn_xTe$ have also been used to investigate the infrared spectrum of SO_2 at high resolution near 1130 cm^{-1} up to pressures of 1 atm [5]. In this paper we report on the use of a single magnetic- and current-tuned PbSe laser to generate individual absorption lines over a major portion (1176.0–1265.8 cm^{-1}) of the R branch of the ν_1 band of SO_2, a common atmospheric pollutant. The use of two separate tuning mechanisms allowed complete coverage of this region to be achieved. Pronounced tuning-rate nonlinearities were observed, and it is shown that precise spectroscopic information can be obtained in spite of such nonlinearities.

II. Experimental Apparatus

The diode laser used in this study was fabricated from single-crystalline PbSe grown by a method of recrystallization through the vapor phase. The growth temperature was approximately 800°C, with the temperature gradient maintained at a small value through the use of a Na heat-pipe furnace liner. Carrier concentration and type were controlled by adjustment of stoichiometry deviation without impurity doping. The homojunction diode was fabricated with a p-type skin on an n-type bulk and had cleaved end faces.

The diode was mounted on the cold finger of a liquid-helium Dewar and in the 1-in-diam bore of a superconducting solenoid. The temperature of the cold finger was not monitored but was believed to be below 10 K. The magnetic field was impressed parallel to the current flow along a ⟨100⟩ crystallographic axis and was variable to 50 kG. The output laser beam from the liquid-helium Dewar was collected by an $f/2$ spherical mirror and focused onto the entrance slit of an E-14 spectrograph whose bandpass was never larger than 0.14 cm^{-1}. The spectrograph provided mode isolation and gross frequency calibration. The laser beam was modulated at 520 Hz by a mechanical chopper and detected with a Cu:Ge detector. The electrical signal from the detector was processed by a lock-in amplifier and displayed on a strip-chart recorder. A current-regulated dc power supply with adjustable sweep capability (A. D. Little, Model SCPS-II) was used to excite the lasers. Oscilloscope displays of SO_2 absorption lines were also obtained by superimposing a small periodic-current ramp on the dc current. The absorption cell used for most of this work was 45.0 cm long and employed CaF_2 windows slightly wedged with respect to each other to eliminate interference fringes.

III. Tuning Mechanisms

The mechanism of magnetic tuning of PbSe semiconductor lasers has been described by Butler and Calawa [6], and Butler [7]. Shifting of the spontaneous-emission spectrum of PbSe lasers to wavelengths shorter than 8.5 μm is due to the magnetic-field dependence of the spin-split zero-order Landau levels of PbSe. Continuous tuning of individual laser modes with magnetic field is produced by the dependence of the index of refraction on the magnetic field given in [6]. Fig. 1 illustrates the frequency dependence of individual laser modes on magnetic field for the PbSe diode used in the present work, operated at a constant current of 0.750 A. This behavior is typical of other PbSe diodes we have studied. The inset in Fig. 1 is a schematic representation of the Landau-level structure; a discussion of these energy levels and transitions is

Manuscript received September 23, 1974; revised December 18, 1974.

F. Allario and C. H. Bair are with NASA Langley Research Center, Hampton, Va. 23665.

J. F. Butler is with Arthur D. Little, Inc., Cambridge, Mass. 02140.

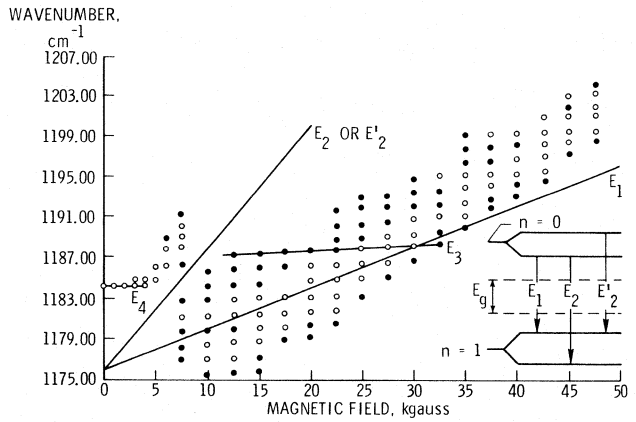

Fig. 1. Dependence of laser emission modes with magnetic field for 0.750 A. Inset is a schematic representation of zero-order spin-split Landau levels at band edges of PbSe. Curves E_2 and E_1 indicate theoretical mode shifting of energy levels due to Landau-level dependence of B from [6]. E_3 and E_4 are lines drawn through continuous laser modes as measured on the spectrograph, and indicate continuous mode tuning due to dependence of the index of refraction on B. PbSe: (TDL-11142-4); current: 0.750 A; bandpass: 0.14 cm^{-1}; ○ strong modes; • weak modes; $\Delta\nu = \pm 0.10$ cm^{-1}.

given in [7]. In the present work we were interested in exploiting magnetic tuning of PbSe to extend its useful tuning range for high-resolution spectral measurements on the SO_2 molecule in the region above 1176 cm^{-1}.

In Fig. 1, two regions of frequency tuning are observed: above and below 7.5 kG. For $B > 7.5$ kG, the modes are regularly spaced ($\Delta\nu = 1.4$ cm^{-1}) and numerous. Individual modes tune, on the average, approximately 0.1 cm^{-1} at an average tuning rate of approximately 4×10^{-5} cm^{-1}/G for a current of 0.750 A as indicated by curve E_3 in Fig. 1. Shifting of the emission wavelength with magnetic field as shown in Fig. 1 allowed the spectral range of PbSe to extend as high as 1205.0 cm^{-1} with a current of 0.750 A. At higher currents (1.2 A), laser modes at 50 kG had a wavenumber as high as 1266.0 cm^{-1}. The rated damage threshold for CW operation of the diode was 1.8 A, which should extend the frequency even higher, but in our work currents were maintained at values ≤ 1.2 A. To date, it has been estimated that this particular semiconductor laser has operated over 800 h without noticeable degradation in performance. The maximum power of individual laser modes was estimated to be > 75 μW/mode.

Current tuning of individual modes at constant magnetic field was also measured with the spectrograph to obtain approximate values of tuning rates and tuning ranges. Typically, tuning rates measured with the spectrograph appeared constant for currents below 0.800 A (due to low resolution), but with magnetic field applied, the tuning rates showed nonlinear behavior above 0.800 A. At $B = 20$ kG and $I = 0.750$ A, the tuning rate was estimated to be 4.0 cm^{-1}/A, and individual laser modes for these conditions were observed to tune as far as 2 cm^{-1}. This value is larger than the spacing between individual laser modes in Fig. 1, which shows that complete coverage of a broad spectral region can be achieved with the combination of current and magnetic tuning. In fact, complete coverage of the spectral region between 1175.0 and 1265.8 cm^{-1} was found to be possible with one PbSe diode.

For magnetic fields below 7.5 kG, the diode was not as well behaved in that it emitted fewer modes, with less maximum power per mode ($\simeq 25$ μW/mode). In general, operation below 7.5 kG was avoided since the smaller number of modes limited the spectral coverage, and the reduced power per mode limited the available signal. A more accurate measurement of tuning rates, using high spectral-resolution numerical results, is provided in the following sections.

IV. Spectral Measurements on SO_2

The high-purity sample gas was maintained at a pressure of 1 torr in the 45-cm cell, and was at room temperature. The general procedure was to hold the magnetic field fixed, while varying the diode current. The spectrograph setting was varied synchronously with diode current to continuously isolate a single mode as it was tuned over its range. For frequency calibration, a computer-generated spectrum from an SO_2 line compilation of R. F. Calfee[1] was used as reference. As will be discussed in the next section, significant tuning-rate nonlinearities were observed with magnetic field applied.

Fig. 2(a) is an example of raw data taken with a PbSe diode laser in the wavelength interval from 1176.70 to 1177.15 cm^{-1} using a magnetic field of 13.5 kG and a current ranging from 0.356 to 0.483 A. The length of the absorption cell was 375 cm, and the SO_2 pressure was 0.3 torr. The spectrometer bandpass was 0.14 cm^{-1}. Fig. 2(b) is a computer-generated spectrum of SO_2 over the same region. The spectrum was computed for $T = 300$ K, $p = 0.3$ torr, and $l = 375$ cm with a Voight profile assumed for the line shape. All lines on the computer-generated plot appear on the raw data. Weak lines not identified in the computer-generated scan are indicated with arrows on the scan of the raw data. These weak lines which appear frequently when long cell lengths are used are attributed to transitions of hot bands of SO_2. From knowledge of the spectrometer settings of wavelength and bandpass, and by visually comparing the raw data with computer-generated data, we were able to assign absolute wavelengths to absorption lines of the laser-generated scans. The complex spectra of the SO_2 molecule allowed unambiguous identification of SO_2 absorption lines throughout the region from 1176.0 to 1265.8 cm^{-1}. With the absolute wavelengths assigned, a tuning rate was then determined with knowledge of the current needed to generate individual portions of the scan. In this case, because the current is relatively low, the tuning rate is fairly linear; however, at higher currents, the nonlinearity can be observed on the scans of raw data.

Fig. 3(a) and (b) shows typical results of a comparison between a laser-generated absorption spectrum and a computer-generated spectrum over a wider region, from 1176.00 to 1178.00 cm^{-1}, for a shorter cell length (45.0 cm) and an SO_2 pressure of 1 torr. In this case, the laser-generated spectrum has been normalized to laser power variations and utilizes experimentally determined line intensities. Comparisons

[1] Theoretical absorption profiles for the ν_1 band of SO_2 were generated from a magnetic tape containing line-absorption parameters for SO_2. This work was performed at NOAA by R. F. Calfee. The magnetic tape is available at NASA Langley Research Center.

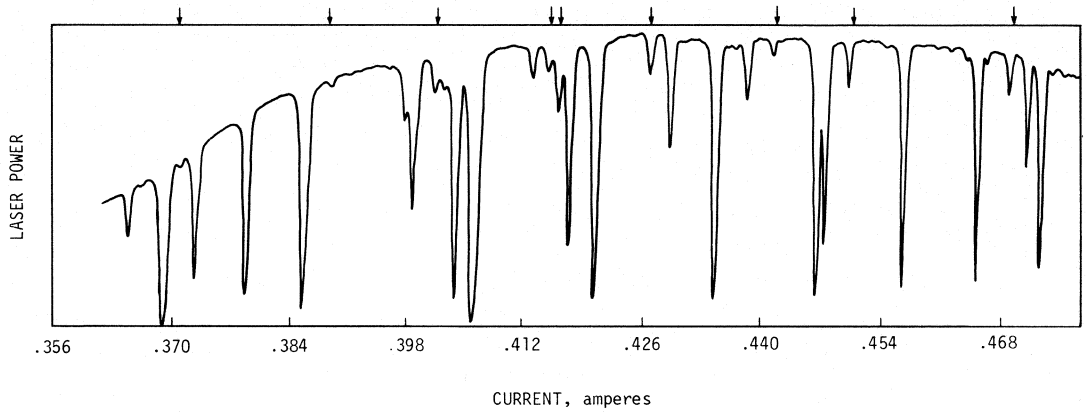

(a)

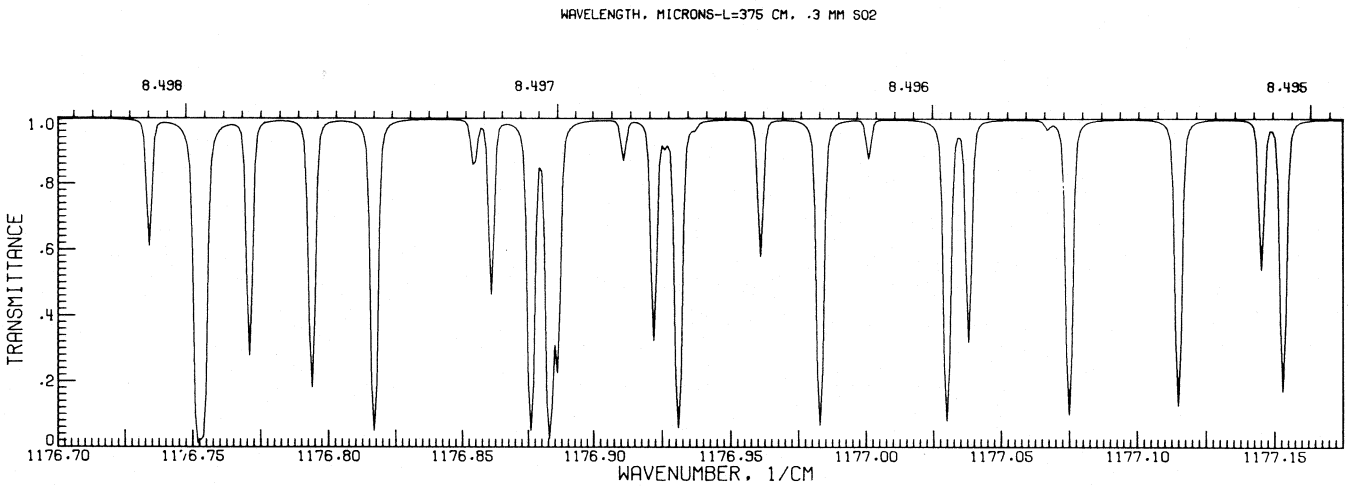

(b)

Fig. 2. (a) Raw data showing SO_2 absorption lines generated by a PbSe diode. B = 13.5 kG, the current range is from 0.356 to 0.483 A. Arrows indicate positions of SO_2 absorption lines not listed in computer-generated spectra. (b) Computer-generated spectra of the spectral region in 2(a). Cell length, 375 cm; pressure, 0.3 mm SO_2.

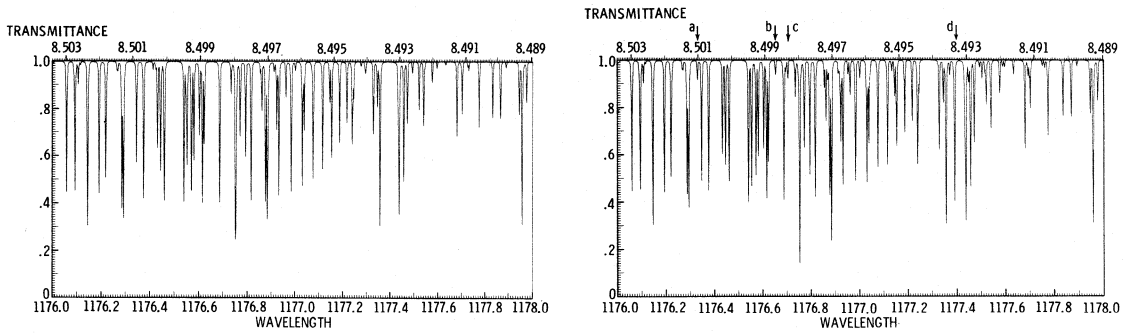

(a) (b)

Fig. 3. (a) Computer printout of ν_1-band spectrum of SO_2 between 1176.00 and 1178.00 cm^{-1} using a theoretical SO_2 line-parameter compilation developed by Calfee. Line shapes calculated with Voight profile: P = 1 torr, T = 300 K, and L = 45.0 cm. (b) Experimental diode laser scans with PbSe (TDL-11142-4). B = 15 kG; I = 0.770 to 0.950 A. *a*, *b*, *c*, *d* indicate lines not identified on theoretical computer scans.

similar to this were performed over the spectral region from 1176.0 to 1265.8 cm^{-1}, and complete coverage obtained [2], [8]. Again, it was observed that more lines appear on the experimental scan than on the computer-generated scan, although fewer lines appear here because of the shorter cell length (e.g., 1176.33 cm^{-1}, 1176.65 cm^{-1}, 1176.71 cm^{-1}, 1177.38 cm^{-1}). The additional weak lines are attributed to SO_2 hot bands, and the strong line at 1177.38 cm^{-1} is

attributed as an impurity NH_3 line. Absolute line intensities agreed to better than 10 percent.

V. Observations of Nonlinear Tuning Rates

This section describes an investigation into tuning-rate variations observed with PbSe diode lasers in magnetic fields. We have determined that magnetic-tuning rates and current-tuning rates (with magnetic field applied) for the PbSe laser used in our study are significantly nonlinear; tests with other PbSe diode lasers have confirmed this finding. Current tuning in zero magnetic field, on the other hand, was essentially constant over the range of currents investigated (0–1.2 A).

For accurate tuning-rate measurements, SO_2 absorption spectra were obtained by scanning the B-field or current, and calculating tuning rates from the theoretical line positions. These were substantiated by using a Fabry-Perot etalon to directly measure the tuning rates. The results are in excellent agreement, but the technique of measuring tuning rates with calculated absorption is believed to give higher precision.

Fig. 4 shows the dependence of the magnetic-tuning rate on the magnetic-field intensity with diode current maintained at 0.890 A. This figure was constructed by a curve fit of the form ae^{bx} to 21 data points. For 0.890 A, the tuning rate varied from 0.45 MHz/G at 11.0 kG, to approximately 3.4 MHz/G at 21.0 kG (1 MHz corresponds to 3.3×10^{-5} cm^{-1}).

Tuning rates were also observed to depend on current for a constant magnetic field. In Fig. 5, the measured dependence of tuning rate is shown as a function of current for three values of magnetic field. Again these curves were generated using theoretical separations of SO_2 absorption lines, measuring the current required to scan across them, and curve-fitting a function of the form ae^{bx} to the data points. For 35.0 kG, approximately 40 data points were generated. In this case, the current-tuning rate varied from 60 MHz/mA at 0.40 A, to a value greater than 700 MHz/mA at 1.0 A, representing more than an order-of-magnitude increase in tuning rate over this current range. For 15.0 kG, the tuning rate varied less, changing from 60 MHz/mA at 0.60 A to 450 MHz/mA at 1.0 A. At zero magnetic field, the current tuning was approximately 30 MHz/mA, and within the limits of a spectrograph measurement, was constant over the range of 0–1.2 A. It was observed for both magnetic and current tuning that adjacent modes shifted at the same rate, i.e., the mode spacings remained constant as mode positions were varied.

Tuning rates shown in Figs. 4 and 5 were obtained over a period of several days and the scatter in the tuning-rate data was approximately 10 percent. A check on the reproducibility of the tuning rates was performed by measuring the full width at half maximum (FWHM) of SO_2 absorption lines for self- and N_2 broadening with the same PbSe diode laser. The magnetic field was maintained constant at 20.0 kG, and the current scanned across six closely lying SO_2 absorption lines. The tuning rate was obtained from Fig. 5. Results are shown in Fig. 6 and are in excellent agreement with the earlier measurements made with PbSnTe diode lasers [3], [4].

Preliminary results in our laboratories obtained with several PbSSe diode lasers indicate that these ternary materials also

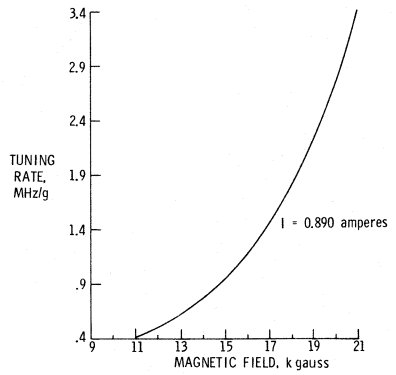

Fig. 4. Dependence of magnetic-tuning rate with magnetic field for fixed current (0.890 A). Curve fit to experimental points $y = ae^{bx}$ where [$a = 0.0398, b = 0.215$]. PbSe: (TDL-11142-4).

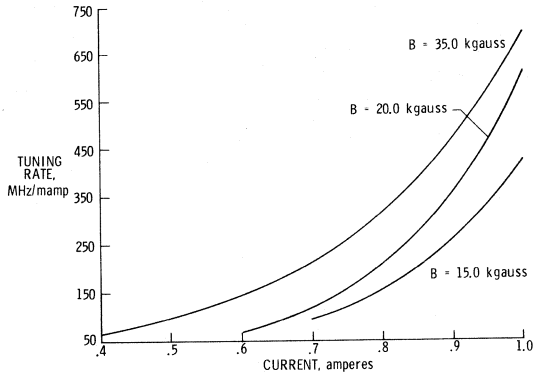

Fig. 5. Dependence of current-tuning rate versus current for three values of magnetic field. Curve fit to experimental points $y = ae^{bx}$ where [$a = 13.4, b = 3.96$] 35.0 kG, [$a = 2.65, b = 5.45$] 20.0 kG, [$a = 2.79, b = 5.04$] 15.0 kG. PbSe: (TDL-11142-4).

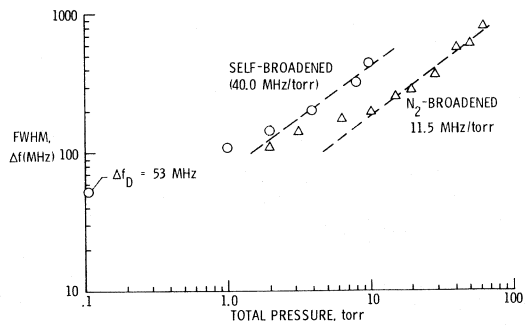

Fig. 6. Full width at half maximum (FWHM) of SO_2 for self- and N_2 broadening with PbSe diode (TDL-11142-4). Current tuning over six SO_2 absorption lines.

exhibit nonlinear tuning characteristics in the presence of a magnetic field. Nonlinear magnetic-field tuning rates in PbSSe have been previously observed [9], although a dependence of current-tuning rate on magnetic field was not reported.

Tuning of laser modes in semiconductor lasers is due to the dependence of the refractive index on the tuning parameter (current or magnetic field in this case). The observed constancy of mode spacing suggests that there is no significant mode pulling in our PbSe laser and hence the tuning rate is given simply by [6]

$$\frac{d\nu}{dX} = -\frac{\nu}{n}\left(\frac{\partial n}{\partial X}\right)_\nu \tag{1}$$

which may also be expressed as

$$\frac{d\nu}{dX} = -2\,l\nu\Delta\nu\left(\frac{\partial n}{\partial X}\right)_\nu.$$

In (1), ν is the emission frequency in wavenumbers, $\Delta\nu$ is the laser-mode spacing, l is the laser-cavity length, n is the laser refractive index, and X is the tuning parameter (B or I). Equation (1) may be used with tuning-rate data to obtain the dependence of the quantity $(\partial n/\partial X)_\nu$ on X. As an example, from (1) and Fig. 4, $(\partial n/\partial B)_\nu$ was found to have the values -0.85×10^{-7} $(G)^{-1}$ at 11 kG, and -6.8×10^{-7} $(G)^{-1}$ at 21 kG, at a current of 0.890 A. For comparison, [6] gives $(\partial n/\partial B)_\nu = -13 \times 10^{-7}$ $(G)^{-1}$ at a field of 20 kG and a current of approximately 0.4 A. A rapid change in refractive index with magnetic field is qualitatively expected from the sharply peaked nature of the density-of-states function of the spin-split Landau levels [10]. The details of the process would be expected to depend strongly on temperature, injection level, p-n-junction concentration profile, and other factors. Thus, on this basis, nonlinear tuning rates for both magnetic tuning and current tuning (in the presence of a magnetic field) can be qualitatively understood. We are presently investigating the theoretical aspects of these phenomena in greater detail.

VI. Summary

In this work, it has been shown that by using a combination of magnetic and current tuning with a single PbSe laser, it is possible to perform ultrahigh-resolution-absorption measurements with complete coverage from 1176.0 to 1265.8 cm^{-1}. Using this method, a major fraction of the R branch of the ν_1 band of SO_2 has been investigated, thus supplementing earlier measurements of the P branch made with several current-tuned PbSnTe lasers of differing compositions. In performing these measurements it was found necessary to account for pronounced tuning-rate nonlinearities to obtain quantitative spectroscopic information from laser-produced absorption spectra.

Acknowledgment

The authors wish to thank B. Williams for providing excellent technical support.

References

[1] E. D. Hinkley *et al.*, "Infrared spectroscopy with tunable lasers," *Topics in Applied Physics*, vol. 2, H. Walther, Ed. New York: Springer (in print).
[2] F. Allario *et al.*, "Tunable semiconductor lasers and their application to environmental sensing," presented at the 10th Anniv. Meet. Society of Engineering Science, Nov. 5–7, 1973.
[3] E. D. Hinkley *et al.*, "Tunable laser spectroscopy of the ν_1 band of SO_2," *J. Appl. Phys.*, vol. 43, p. 3222, July 1972.
[4] E. D. Hinkley, "Development and application of tunable diode lasers to the detection and quantitative evaluation of pollutant gases," Final Rep. to the Environmental Protection Agency, Contract F19628-70-C-0230, Sept. 30, 1971.
[5] G. A. Antcliffe and J. S. Wrobel, "Detection of the gaseous pollutant sulphur dioxide using current-tunable $Pb_{1-x}Sn_xTe$ diode lasers," *Appl. Opt.*, vol. 11, p. 1548, 1972.
[6] J. F. Butler and A. R. Calawa, "Magneto-emission studies of PbS, PbTe, and PbSe diode lasers," in *Physics of Quantum Electronics*, P. L. Kelley, B. Lax, and P. E. Tannewald, Ed. New York: McGraw-Hill, 1966, p. 458.
[7] J. F. Butler, "Magneto-emission experiments in $Pb_{1-x}Sn_xTe$," in *Solid State Communication*. New York: Pergamon.
[8] J. F. Butler *et al.*, "Infrared spectral measurements of SO_2 using PbSe diode lasers," *Bull. Amer. Phys. Soc.*, vol. 18, p. 1581, 1973.
[9] K. W. Nill *et al.*, "High-resolution spectroscopy using magnetic-field-tuned semiconductor lasers," *Appl. Phys. Lett.*, vol. 21, p. 132, 1972.
[10] L. M. Roth and P. N. Argyres, "Magnetic quantum effects," in *Physics of III-V Compounds*, A. C. Beer and R. K. Willardson, Ed. New York: Academic, 1967.

Spatial Hole Burning and Oligo-Mode Distance Control in CW Dye Lasers

INGOLF V. HERTEL AND ALEKSANDAR S. STAMATOVIĆ

Abstract—**Spatial hole burning at the position of the dye cell is identified to be responsible for stable double-, triple-, and higher oligo-mode action in a narrow-band CW dye laser. This may be exploited systematically to control the mode distances by arranging the positions of both resonator end mirrors. A total output power up to over 100 mW is obtainable for double- or triple-mode action. Special conditions are described to obtain stable double-mode action with 1772-MHz mode spacing, as needed for simultaneous optical pumping of the two sodium hyperfine ground states.**

I. Introduction

BY THE USE of dispersive elements and etalons, stable single-mode action may be achieved in CW dye lasers (see, e.g., [1], [2]).

However, when operating high above threshold as necessary for optical-pumping applications [3], stable oscillation on two modes, simultaneously, is frequently observed. This may be attributed to spatial hole burning [4], [5]. The spacing $\Delta\nu$ between these modes was usually a few times the FSR of the laser resonator $\Delta\nu_R$ as shown in Fig. 1, where a piezo-scanned Fabry-Perot interferometer (FPI 2) of 8-GHz FSR was used to display the mode structure. Pike [5] has avoided this effect by placing the dye cell in the center of the resonator.

One can systematically make use of the spatial hole burning in order to vary the mode distance and produce a well-defined double-mode distance. This can be of importance for optical pumping with dye lasers, when more than one hyperfine component is involved, as usual.

For example, with such a device the two hyperfine-structure ground states of sodium having a distance of 1772 MHz could be pumped simultaneously, allowing a higher equilibrium population of the excited states and pumping to any of the upper hyperfine levels, which was hitherto impossible [3]. Thus a systematic investigation will be presented here.

II. Experiment

The laser and analyzing system is shown in Fig. 2, and the data of the Fabry-Perot components used are given in Table I. We use essentially the folded cavity described by Kogelnik *et al.* [6] and Dienes *et al.* [7] in a modification recommended by Johnston and Runge [8].

In Fig. 2, two Brewster prisms 5 and 6 are used as dispersive elements. A 1-mm plane parallel, coated glass flat 7, is used as an FP etalon to limit the laser bandwidth. It can be tilted to change the frequency transmitted.

Manuscript received October 16, 1974; revised January 13, 1975.
The authors are with the Fachbereich Physik, Universität Trier-Kaiserslautern, Kaiserslautern, Germany.

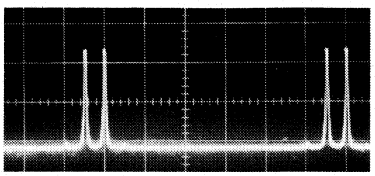

Fig. 1. Oscilloscope trace of double-mode action in a CW dye laser. Scale is 1.33 GHz/div. The mode distance is thus $\Delta\nu \approx 650$ MHz = $6 \times \Delta\nu_R$, the resonator FSR. The structure is repeated after the Fabry-Perot FSR = 8 GHz.

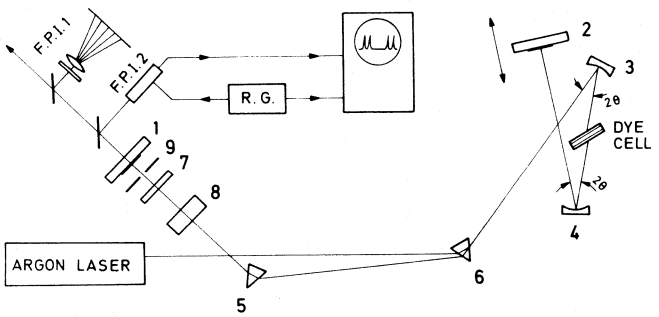

Fig. 2. Schematic of the laser and analyzing system. Items 1 and 2 are the resonator end mirrors with 96- and 99.9-percent reflectivity, respectively; 3 and 4 are curved mirrors with $r = 10$ cm, the total dye-cell thickness is 3 mm; 5 and 6 are Brewster prisms; 7 and 8 are Fabry-Perot etalons; and 9 is a slit, 1 mm wide.

TABLE I
Fabry-Perot Interferometer Components of the Experiment

COMPONENT	THICKNESS LENGTH (cm)	REFLECTIVITY R (%)	FSR (GHz)	FINESSE	PEAK WIDTH (GHz) AT TRANSMISSION 96%	50%
Laser Res.	115 to 180	96 and 99.9	.13 to .08			
No.8 a)	1	4	10	0.6	3	
glas flat b)	5.5	4	1.772	0.6	0.6	
No.7 a)	0.1	60	100	4.6	3	
glas flat b)	0.1	40	100	3.3	6	
FPI 1 glas flat	0.01	95	1000	50		20
FPI 2 spherical piezoscanned	3.75		8	150		0.05

An aperture stop 9, or, alternatively, a 10-mm glass flat 8, is used to prevent lasing at frequencies ±1 FSR of the 1-mm etalon.

The slit causes fewer losses but is more difficult to adjust. The angle Θ for compensation of the astigmatism is found to be not too critical and is chosen to be approximately $2\Theta \approx 12°$.

The two end mirrors are movable independently. The rela-

tively high (4-percent) transmission of the output mirror optimizes mirror losses to intracavity losses. The rhodamine 6-G solution in water is pumped with the 514.5-mm argon-ion laser line. The threshold pump power is less than 400 mW without and 525 mW with etalon and slit. The typical double-mode structure is observed with an FPI 2 on an oscilloscope screen. The mode distance $\Delta\nu$ is measured by comparing it to the FSR of FPI 2 (see Fig. 1). Alternatively, the number n of resonator FSR's $\Delta\nu_R$ between the two modes may be counted by twisting etalon 7 slowly. The mode distance is then $\Delta\nu = n \cdot \Delta\nu_R$, where $\Delta\nu_R$ is given by the resonator length. The $\Delta\nu$ values obtained in either way agree well. This is demonstrated in Fig. 3, where both modes can be seen before and after a mode hop on an expanded scale.

To make sure that really only near-neighboring laser modes occur, the 0.01-mm etalon FPI 1 was used to display the interference fringes which allow mode distances of >20 GHz to be distinguished. We have systematically varied the positions of the two laser end mirrors with respect to the dye cell for different combinations of etalons and slit. The mode distance and stability, as well as the output power, were measured for each mirror position.

III. Results and Interpretation

Let us denote by a and b the distances from the dye cell of end mirrors 1 and 2, respectively. Spatial hole burning of a mode with wavelength λ_1 affects a mode with λ_2 least, when

$$b = \beta \cdot (\lambda_1/2), \quad \text{with } \beta \text{ any large rational number}$$

and

$$b = \beta \cdot (\lambda_2/2) + m(\lambda_2/4), \quad \text{with } m = 1, 3, 5, \cdots, \text{odd}.$$

It follows that the conflict between two modes due to local hole burning is at a minimum when the mode distance is

$$\Delta\nu = (m/2) \cdot (c/2b), \quad m = 1, 3, 5, \cdots \tag{1}$$

where c is the velocity of light.

Of course, all mode spacings must be a multiple n of the resonator FSR

$$\Delta\nu = n \cdot \Delta\nu_R = n \cdot [c/2(a+b)], \quad n = 1, 2, 3, \cdots. \tag{2}$$

We may rewrite (1) and (2) dimensionless, measuring $\Delta\nu$ in units of $c/2a$

$$[\Delta\nu/(c/2a)] = (m/2)\,(a/b) \tag{1a}$$

$$[\Delta\nu/(c/2a)] = [n/(1 + b/a)]. \tag{2a}$$

While (2a) is a necessary condition for all mode distances in the laser resonator, (1a) gives desirable points for neighboring modes.

In Fig. 4, we plot, for convenience, the reciprocal equations that describe straight lines as a function of $x = b/a$

$$y = [(c/2a)/\Delta\nu] = (2/m)\,(b/a), \quad m = 1, 3, 5, \cdots \tag{1b}$$

$$y = [(c/2a)/\Delta\nu] = (1/n) + (1/n) \cdot (b/a), \quad n = 1, 2, 3, \cdots. \tag{2b}$$

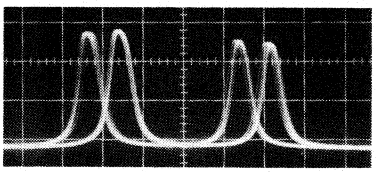

Fig. 3. FPI 2 trace; double exposure of double-mode action before and after one mode hop. Scale is 133 MHz/div; mode-hop distance, $\Delta\nu_R \approx 110$ MHz; mode distance $\Delta\nu = 5 \times \Delta\nu_R$.

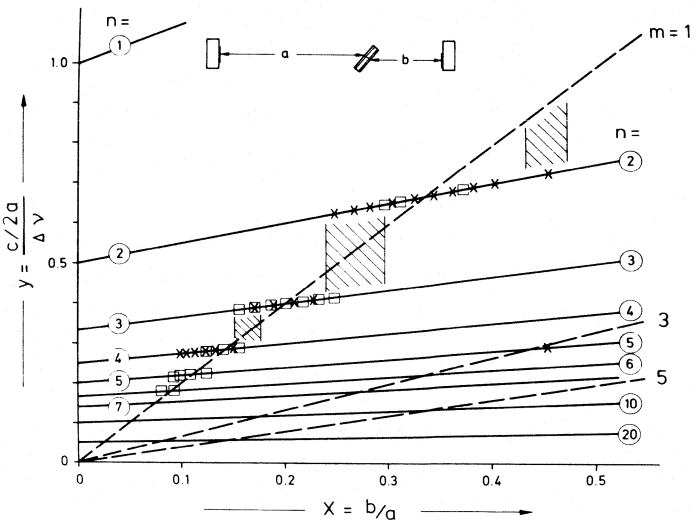

Fig. 4. Neighboring-mode conditions (1b) and (2b). All modes have to lie on the full n-lines, n being the mode distance, in units, of the resonator FSR. Antinodes coincide with nodes of the neighbor modes on the dashed m-lines, when m is the path difference in units of $\lambda/4$. Experimental points: × a = 105 cm, a = 129 cm. Shaded area represents unstable and difficult to adjust regions. Measurements were made with etalon 7a and slit or 7a and 8a (see Fig. 2).

Obviously, all observed modes have to fall on the full n-lines, and crossings between them and the dashed m-lines should be preferred, if spatial hole burning is responsible for double-mode action.

The experimental points are given for a = 105 cm, a = 129 cm, and varying b. The crossing points are definitely preferred; most stable actions usually are obtained at these points, and instability and difficulties in adjusting the laser occur where no crossing is near. Note the point near the $m = 3$, $n = 5$ crossing for large b, which is in competition with the more unstable modes on the $n = 2$ line for the same b/a.

A slight deviation from the preceding statement is occasionally found, especially in the region $n = 4$, $b/a \approx 0.1$, and a = 105 cm. The preferential $n = 5$ mode distance is obviously suppressed by etalon 7a (Fig. 2), limiting the bandwidth.

One important and somewhat surprising fact is that for larger b/a (fixed a), i.e., for smaller resonator FSR, triple- or multiple-mode action is observed with equal spacings, as shown in Fig. 5. The points in Fig. 3 always give the distance between next neighbors.

The pumping power in these experiments was 1.35 W, and up to 110-mW total output power was obtained with stable triple- or double-mode action, corresponding to 75 percent of the power obtained without etalon and slit.

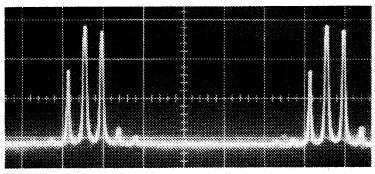

Fig. 5. FPI trace for triple-mode action: 1.33 GHz/div. Etalon 7*b* and slit were used.

The transit from double- to triple-mode action depends on the resonator losses and on the gain curve. Triple mode starts when the losses for the extreme modes become tolerable; e.g., the extreme-mode distance $2 \cdot \Delta\nu$ in Fig. 5 is $\approx$1 GHz. Etalon 7*b* (Fig. 2) (1 mm, $R = 40$ percent) was used here, while for the 7*a* (1 mm, $R = 60$ percent) etalon, triple modes appeared only, when $2 \cdot \Delta\nu \lesssim 600 \cdots 800$ MHz.

Still, the crossing rule for next neighbors holds. However, for the extreme mode's distance then, of course, node is on node in the cell.

Without a detailed study of the laser dynamics, this fact cannot be explained with the present knowledge about the homogeneous linewidth.

The stability of the mode structure near the *n–m* crossings is excellent, which means less than one or two mode hops per minute. The bandwidth of a single mode is better than 50 MHz, which is enough for all pumping applications, where saturation broadening determines the overall linewidth. The magnitude of the jitter is indicated in Fig. 3 (1-s exposure). Stability, bandwidth, and jitter could be greatly improved by avoiding thermal fluctuations, and using dust pipes, electronic stabilization, and great care.

Obviously, within the limits of the etalon bandwidth any mode distance $\Delta\nu$ can be chosen for stable double-, triple-, or higher oligo-mode action just by choosing the appropriate *a* and *b* according to (1) and (2). However, the number of modes occurring is not readily to be selected in the manner previously described. Especially for large mode spacing $\Delta\nu$ (e.g., 1772 MHz), it is not possible to obtain double-mode action without additional measures.

One may, however, insert another Fabry-Perot etalon in the cavity, having a free spectral range $\Delta\nu_{et}$ equal to the desired frequency difference, which would suppress intermediate modes. In addition to (1) and (2) the condition

$$\Delta\nu = \Delta\nu_{et} \tag{3}$$

must also hold. This, together with (1) and (2) leads finally to

$$a = n \cdot [c/(2 \cdot \Delta\nu_{et})] - b, \qquad n = 1, 2, 3, \cdots \tag{4}$$

$$b = (m/2)\,[c/(2 \cdot \Delta\nu_{et})], \qquad m = 1, 3, 5, \cdots. \tag{5}$$

Thus, for given n and m, the positions of *a* and *b* are fixed by the desired mode spacing $\Delta\nu_{et}$; n and m have to be chosen such that *a* and *b* are geometrically accessible.

We have used etalon 8*b* (5.5-cm glass flat, 1772-MHz FSR) to obtain two stable modes in 1772-MHz distance in the range of the Na-D lines.

Preselection was made with etalon 7*b* and the slit 9 (Fig. 2). Stable two-mode action is obtainable at a number of positions and has been investigated for $m = 3$, $n = 16$ corresponding to $a = 122.8$ cm and $b = 7.7$ cm; at $m = 4$, $n = 18$ ($a = 131.3$, $b = 21.2$); and finally, $m = 4$, $n = 17$ ($a = 122.8$, $b = 21.2$).

The adjustment of both *a* and *b* is not too critical; ±2 cm for *a* and ±1 cm for *b* may be tolerated without loss of stability. Care must be taken when adjusting the slit 9 (Fig. 2) and the tilt of the preselecting etalon 7 (Fig. 2).

The total output power for stable double modes spaced at 1772 MHz was up to 55 mW at 1.35-W pumping power, which is a fair result considering the high losses due to the long glass etalon. This could be improved by using an air-spaced etalon and a preselecting device with a higher FSR and flatter transmission curve (e.g., 0.5-mm 40-percent glass flat).

IV. Conclusion

Stable double-mode action with choosable mode distance is proved to be possible in CW dye lasers making use of spatial hole burning at the dye cell.

This allows simultaneous excitation from, or to, two different hyperfine states. More efficient optical pumping is thus possible on the one hand, and special hyperfine states become accessible to stationary pumping, which were hitherto emptied during the course of pumping.

Sodium-atom preparation in one of the $3^2P_{1/2}$ states for scattering processes may be one application, and in the growing field of laser-induced chemical reactions, and especially isotope separation (see, e.g., [9], [10]), new possibilities may emerge, especially when further improvement on the output power is obtained. Even spectroscopic applications of double-mode action may be thought of, e.g., in connection with light-beating techniques.

Acknowledgment

The authors wish to thank Prof. Demtröder for his valuable comments.

References

[1] W. Hartig and H. Walther, "High resolution spectroscopy with and frequency stabilization of a CW dye laser," *Appl. Phys.*, vol. 1, pp. 171–174, 1973.

[2] H. W. Schröder, H. Welling, and B. Wellegehausen, "A narrow-band single mode dye laser," *Appl. Phys.*, vol. 1, pp. 343–348, 1973.

[3] I. V. Hertel and W. Stoll, "Principles and theoretical interpretation of the electron scattering by laser excited atoms," *J. Phys. B: At. Mol. Phys.*, vol. 7, pp. 570–583, 1974.

[4] H. G. Danielmeyer, "Effects of drift and diffusion of excited states on spatial hole burning and laser oscillations," *J. Appl. Phys.*, vol. 42, pp. 3125–3132, 1971.

[5] C. T. Pike, "Spatial hole burning in CW dye lasers," *Opt. Commun.*, vol. 10, pp. 14–17, 1974.

[6] H. W. Kogelnik, E. P. Ippen, A. Dienes, and C. V. Shank, "Astigmatically compensated cavities for CW dye lasers," *IEEE J. Quantum Electron.*, vol. QE-8, pp. 373–379, Mar. 1972.

[7] A. Dienes, E. P. Ippen, and C. V. Shank, "High-effeciency tunable CW dye laser," *IEEE J. Quantum Electron.* (Corresp.), vol. QE-8, p. 388, Mar. 1972.

[8] W. D. Johnston, Jr., and P. K. Runge, "An improved astigmatically compensated resonator for CW dye laser," *IEEE J. Quantum Electron.* (Corresp.), vol. QE-8, pp. 724–725, Aug. 1972.

[9] K. L. Kompa, "Chemie mit Lasern," *Verh. Deut. Phys. Ges. (VI)*, vol. 9, p. 871, 1974.

[10] H. Stehle, "Physikalisch-technische Grundlagen einer Urananreicherung mit Lasern," *Verh. Deut. Phys. Ges. (VI)*, vol. 9, p. 872, 1974.

New CW Lines from a Submillimeter Waveguide Laser

HARRISON E. RADFORD

Abstract—**Sixty-one new CW laser lines with wavelengths between 0.1 and 1.5 mm have been observed with a waveguide laser optically pumped by a CO_2 laser.**

THE submillimeter optically pumped waveguide laser [1] is much smaller than its Fabry-Perot predecessor and holds promise as a compact, stable local oscillator for spectroscopy and radio astronomy. The pencil-thin waveguide resonator also offers a better match to the beam of a typical CO_2 pump laser than does the Fabry-Perot resonator, and thus allows more efficient excitation of the laser gas. To the extent that the number of available laser lines is increased, the frequency coverage of the waveguide laser, and hence its usefulness as a local oscillator, will increase as well. Using known laser gases, I have made an inventory of the CW oscillation wavelengths of a waveguide laser fabricated from half-inch copper tube, and find about 100, of which 61 are new.

The waveguide laser was patterned on that of Hodges and Hartwick [1], with minor changes dictated by convenience. The waveguide resonator was a 90-cm length of hard copper refrigeration tubing, 11 mm ID, internally polished with a carborundum-loaded swab. The mirrors were gold-coated Pyrex, one flat and one spherical (R = 10 m), positioned close to, but not in contact with, the ends of the waveguide. The grating-tuned CO_2 pump laser generated CW power in the lines $R(4)$ through $R(42)$ and $P(6)$ through $P(46)$ of both the 9.6 μm and 10.6 μm bands; the maximum output power, in lines near the middles of the R branches, was 25 W. The pump beam was focused into the waveguide resonator, through a 1-mm-diameter hole in the flat mirror, with 80 percent efficiency. The submillimeter power emerged from a 2-mm-diameter hole in the spherical mirror, and was focused by a polyethylene lens onto a quartz-windowed Golay detector, sensitive at wavelengths longer than 40 μm. Wavelengths were measured from voltage versus time recordings of the Golay detector output during linear translations of the spherical mirror.

CW laser emission was found in nine known laser gases: methanol (CH_3OH) [2]-[5], methyl fluoride (CH_3F) [2], vinyl chloride (CH_2CHCl) [2], vinyl cyanide (CH_2CHCN) [6], methylamine (CH_3NH_2) [5], [6], 1, 1 difluoroethylene ($C_2H_2F_2$) [3], [6], formic acid (HCOOH) [4], [5], [7], methyl cyanide (CH_3CN) [8], and ethyl fluoride (CH_3CH_2F) [4]. The last two gases have been studied previously only with pulsed CO_2 laser excitation, but were included in the search after several new high-threshold lines were found with the CW-pumped laser gases. Other pulse-pumped laser gases, ammonia [4], ethylene glycol [5], and methyl acetylene [8], failed to yield CW emission, as also did one CW-pumped laser gas, difluoroethane [3]. The line searches were carried out by first setting the gas pressure for maximum submillimeter signal on a known high-threshold line, and then testing each of the 82

TABLE I
NEW CW SUBMILLIMETER LASER LINES

Gas	Submillimeter Wavelength (μm)[a]	CO_2 Pump Line	Pump Wavelength (μm)	Threshold Power (W)	Threshold Pressure (mT)	Output Power (μW)
CH_3OH	96*	R(10)	9.329	2	150	600
	162	R(38)	10.136	<0.5	50	600
	232	R(10)	9.329	5	120	30
	249	R(34)	10.159	4	100	200
	254	R(38)	10.136	<0.5	50	600
	292	R(10)	10.318	7	150	30
	471	R(38)	10.136	1	120	200
$C_2H_2F_2$	523	P(16)	10.551	5	60	10
HCOOH	433*	R(22)	9.261	<0.5	20	500
	761	R(24)	9.250	3	30	0.5
	785	R(10)	9.174	<0.5	20	10
CH_3NH_2	180	P(46)	9.794	2	80	0.1
	288	R(4)	9.367	2	60	15
	314	R(4)	9.367	1	60	30
CH_3CH_2F	264*	P(18)	9.536	4	75	15
	336*	R(16)	9.294	6	75	3
	404*	R(30)	9.220	3	65	10
	405*	P(34)	9.676	6	60	0.3
	486	R(24)	9.250	3	75	5
	504*	R(24)	9.250	2	75	15
	519	R(4)	9.367	2	75	1
	595*	P(36)	9.695	1	60	2
	620*	P(22)	9.569	4	50	1
	853*	P(30)	9.639	2	75	2
	1013*	P(28)	9.621	2	75	0.1
	1069	R(10)	9.329	2	75	3
	1546	P(10)	9.473	3	100	0.3
CH_3CN	373*	P(20)	10.591	2	10	10
	392	R(12)	9.317	6	10	0.5
	456	R(16)	9.294	2	10	4
	496	P(6)	9.443	2	10	6
	653	P(30)	9.639	5	10	0.5
$CH_2CH\ CN$	489	P(8)	10.476	6	10	0.06
	503	R(12)	9.317	8	10	0.04
	578	R(14)	10.289	2	10	1
	623	R(12)	10.303	8	10	0.1
	631	R(6)	10.349	6	10	0.1
	722	P(42)	10.835	4	10	0.05
	738	P(16)	10.551	6	10	0.06
	775	R(42)	10.115	3	10	0.1
	793	R(40)	10.125	4	10	0.1
	828	R(18)	10.260	6	10	0.1
	910	R(12)	10.303	8	10	0.1
	940	P(28)	10.675	6	10	0.1
	1156	P(26)	10.653	5	10	0.06
	1184	R(38)	10.136	2	10	0.6
$CH_2CH\ Cl$	424	R(28)	10.195	4	35	3
	445	R(18)	10.260	5	40	1
	487	P(10)	9.473	7	40	0.06
	519	P(34)	10.741	4	30	0.4
	532	P(16)	9.520	6	30	1
	538	R(4)	10.365	6	20	0.1
	574	P(16)	10.551	3	20	15
	603	P(38)	10.787	1	30	25
	638	P(6)	10.458	3	20	3
	699	P(22)	9.569	6	20	0.6
	707	P(18)	9.536	4	35	10
	828	P(24)	9.586	2	30	2
	935	P(46)	10.885	1	20	0.5
	995	R(26)	10.207	2	35	2
	1041	R(36)	10.147	4	40	2

[a]Wavelengths marked with asterisks are equal, within experimental error, to wavelengths reported in previous pulse-pumping experiments on the same gas and with the same pump lines.

Manuscript received December 9, 1974.

The author is with the Center for Astrophysics, Harvard College Observatory and Smithsonian Astrophysical Observatory, Cambridge, Mass. 02138.

TABLE II
THE MOST POWERFUL CW LINES PRODUCED BY OPTICALLY PUMPED SUBMILLIMETER LASERS IN THE WAVELENGTH RANGE 0.1 TO 1 MM

Gas	Wavelength (μm)	Output Power (mW)	Ref.
CH_3OH	118.8	3	a
	162	0.6	b
	254	0.6	b
	570.5	1	a
	699.5	0.5	a
HCOOH	303.0	0.6	c
	394.2	3	c
	406.0	1	c
	420.0	1.5	c
	432.1	2	c
	433	0.5	b
	513.2	0.8	c
	743.0	0.5	c
$C_2H_2F_2$	554	1	a
	884	1	a

[a]See [3].
[b]Present work.
[c]See [7].

CO_2 pump wavelengths in turn for new submillimeter lines. This exhaustive search was not performed on the four gases mentioned above, which failed the initial tests on known lines.

Table I gives the inventory of new CW lines, arranged by molecule and submillimeter wavelength. The experimental uncertainty in these wavelengths, judged from measurements of standard lines that have been measured more precisely by others, is ±2 percent. Also tabulated are the threshold pump power and gas pressure for each line, and the submillimeter output power registered by the Golay detector at the highest power available in the pump line. Pump powers were measured with a calorimetric beam probe and corrected for the 80-percent transmission of the coupling optics. The Golay power readings are based on the manufacturer's calibration and are subject to an unknown wavelength-dependent error; they are tabulated for rough comparison purposes. Gas pressures were measured with thermocouple gauges, which were calibrated for air and located at the two ends of the waveguide resonator tube. The tabulated values are averages of the two pressure readings.

By judging from the pump power threshold values of Table I, a large number of the 61 new laser lines, perhaps as many as 40, can be credited to the improved pump efficiency of the waveguide laser. The remainder are low-threshold lines that should also oscillate in a CW-pumped Fabry-Perot resonator. Some are known pulse-pumped lines that have apparently not been tried until now in a CW-pumped laser; some are lines that appear to have slipped through the nets of previous searches.

Except for the strong lines of methanol and formic acid, the submillimeter output power in most of the new lines is low, a few microwatts being a typical value. This is enough for many applications of the waveguide laser to spectroscopy, but not for applications to heterodyne radiometry, where, typically, milliwatts of local oscillator drive are required to reach conditions of minimum mixer noise. Some increase in output power, particularly at long wavelengths, can be expected from waveguide resonators that are completely gold plated, have internal end mirrors [9], and are designed for critical output coupling and optimum pumping efficiency. With these improvements, a CW local oscillator for heterodyne radiometry could probably operate on at least the wavelengths listed in Table II, which are already at or near the milliwatt level of output.

REFERENCES

[1] D. T. Hodges and T. S. Hartwick, "A far-infrared waveguide laser," *Appl. Phys. Lett.*, vol. 23, pp. 252–253, 1973.
[2] T. Y. Chang, T. J. Bridges, and E. G. Burkhardt, "CW submillimeter laser action in optically pumped methyl fluoride, methyl alcohol, and vinyl chloride gas," *Appl. Phys. Lett.*, vol. 17, pp. 249–251, 1970.
[3] D. T. Hodges, R. D. Reel, and D. H. Barker, "Low-threshold CW submillimeter and millimeter-wave laser action in CO_2-laser pumped $C_2H_4F_2$, $C_2H_2F_2$, and CH_3OH," *IEEE J. Quantum Electron.* (Notes and Lines), vol. QE-9, pp. 1159–1160, Dec. 1973.
[4] R. J. Wagner, A. J. Zelano, and L. H. Ngai, "New submillimeter laser lines in optically pumped gas molecules," *Opt. Commun.*, vol. 8, pp. 46–47, 1973.
[5] T. K. Plant, P. D. Coleman, and T. A. Detemple, "New optically pumped far-infrared lasers," *IEEE J. Quantum Electron.* (Notes and Lines), vol. QE-9, pp. 962–963, Sept. 1973.
[6] S. F. Dyubko, V. A. Svich, and L. D. Fesenko, "Submillimeterband gas laser pumped by a CO_2 laser," *JETP Lett.*, vol. 16, pp. 418–419, 1972.
[7] S. F. Dyubko, V. A. Svich, and L. D. Fesenko, "Submillimeter laser using formic acid vapor pumped with carbon dioxide laser radiation," *Sov. J. Quantum Electron.*, vol. 3, p. 446, 1974.
[8] T. Y. Chang and J. D. McGee, "Millimeter and submillimeter wave-laser action in symmetric top molecules optically pumped via parallel absorption bands," *Appl. Phys. Lett.*, vol. 19, pp. 103–105, 1971.
[9] A. Tanaka, A. Tanimoto, N. Murata, M. Yamanaka, and H. Yoshinaga, "Optically pumped far-infrared and millimeter waveguide lasers," *Japan. J. Appl. Phys.*, vol. 13, pp. 1491–1492, 1974.

Correspondence

Stimulated-Emission Cross Section and Inversion Lifetime in a Three-Atmosphere Iodine Photodissociation Laser

F. T. ALDRIDGE

Abstract—**An iodine photodissociation laser has been operated at three atmospheres by adding an inert gas to the laser medium. With three atmospheres of helium added a stimulated-emission cross section of 2×10^{-19} cm^2 and an inversion half-life of 110 μs was observed.**

The iodine photodissociation laser uses the photodissociation of CF_3I or C_3F_7I to generate excited iodine atoms which can then give laser action by stimulated emission at 1.315 μ [1]

$$CF_3I + h\nu\,(2700\ \text{Å}) \rightarrow CF_3 + I^*\,(^2P_{1/2})$$

$$I^*\,(^2P_{1/2}) \rightarrow I\,(^2P_{3/2}) + h\nu\,(1.315\ \mu)\,.$$

The stimulated-emission cross section of I^* at low pressure is about 5×10^{-18} cm^2, too large for use in a large laser amplifier [2]. For this system to be useful as a high-energy short-pulse amplifier medium, the peak stimulated-emission cross section must be lowered without shortening the I^* lifetime excessively. One method of doing this is the addition of an inert gas to the system to pressure broaden the emission line, and this has been experimentally demonstrated at pressures up to 600 torr [3], [4]. In this work, the results are extended to three atmospheres and it is shown that under these conditions cross sections and lifetimes appropriate for large-pulsed laser systems are attained.

The laser setup is shown in Fig. 1. The quartz laser tube had an inside diameter of 4 mm and an illuminated length of 45 cm. The total cavity length was 1.7 m. Two rows of three flashlamps were mounted above and below the laser tube in an aluminum reflector. Each lamp had a 15-cm arc length, a 7-mm inside diameter, and was filled with 30 torr of xenon. A 1-μF capacitor, charged to 30 kV, was discharged through each row of flashlamps, giving a flash with a full-width half-maximum time of 5 μs. In order to keep all the pumped parts of the laser tube as evenly pumped as possible, the tube was covered with aluminum foil in sections where it was not next to a flashlamp arc. The Pockel's cell and glan prism were removed except when the laser was being Q switched. The laser output beam was split with an uncoated glass plate, with 92 percent of the beam going to a Hadron cone-type thermopile calorimeter and 8 percent to either an InSb detector or an S-1 photodiode detector for display on an oscilloscope. Argon and helium (Mathieson ultrahigh purity, 99.999 percent) were used without purification. n-C_3F_7I (Peninsular Chemresearch) was purified by distillation under vacuum from dry-ice–acetone temperature (−78°C) to liquid-nitrogen temperature (−190°C) with the middle 70 percent being used. The system was evacuated and filled with a fresh charge of gas mixture for each run.

At threshold, the following relation is true:

$$\frac{1}{\sqrt{R_1R_2}\,(1-L)} = \exp(\sigma \Delta N l) = G \qquad (1)$$

Manuscript received May 29, 1974; revised December 30, 1974. This research was performed under the auspices of the U.S. Atomic Energy Commission.

The author is with the University of California Lawrence Livermore Laboratory, Livermore, Calif. 94550.

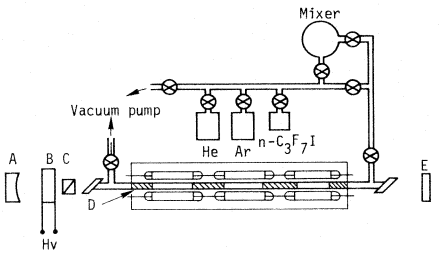

Fig. 1. Experimental apparatus. A—99-percent reflecting 10-m radius mirror; B—Pockel's cell; C—glan prism; D—aluminum-foil covering on laser tube; E—flat exit mirror, various reflectivities.

where σ is the stimulated-emission cross section, ΔN is the inversion population per unit volume, l is the length of the pumped laser medium, R_1 and R_2 are the reflectivities of the mirrors, and L is nonmirror cavity losses. Due to the differing multiplicities of excited- and ground-state iodine atoms, ΔN is equal to $(N_{I^*} - \frac{1}{2} N_I)$ and the total energy available from the inversion is equal to $\frac{2}{3} h\nu \Delta N$. R_1, R_2, and l are easily measured. If L and ΔN are determined, then σ can be calculated from threshold measurements. They were determined in the following way.

The laser tube was designed with a small diameter so that the laser medium was almost transparent to pumping radiation at all of the C_3F_7I concentrations used. Thus, since the pumping radiation is the same for each firing, the fraction of the C_3F_7I photolyzed is a constant. It was assumed that the ratio of excited- to ground-state iodine atoms formed was also a constant. It is known that photodissociation of C_3H_7I gives only excited iodine atoms [5]. When no inert gas was used threshold pressures of C_3F_7I ranged from 0.2 to 0.7 torr depending on the exit mirrors used. Thus, at pressures of 5–10 torr, the energy remaining in the inversion after laser action stopped was a small fraction of the energy originally available in I^* atoms. For a given set of mirror and other cavity losses, the laser output energy should thus be proportional to the total inversion or, in this case, to the C_3F_7I pressure. By measuring the output energy of the laser with several different exit mirrors, both the total energy stored in the inversion and the total cavity losses were determined.

Four series of runs were made with exit mirrors from 30- to 90-percent reflectivity to determine output energy as a function of C_3F_7I pressure. The results are shown in Fig. 2. Within experimental error the energy observed from the laser was proportional to the C_3F_7I pressure, showing that the assumptions made earlier are valid.

The total energy in the inversion and the nonmirror losses were calculated at C_3F_7I pressures of 5 and 10 torr using the data from Fig. 2. ΔN was calculated by dividing the total energy by $\frac{2}{3} h\nu$ and found to be 13.9 percent of $N_{C_3F_7I}$ at 5 torr and 13.8 percent at 10 torr. $N_{C_3F_7I}$ was calculated by assuming it to be a perfect gas.

The threshold pressure of C_3F_7I was then determined with up to three atmospheres of argon or helium added to the system. Threshold was determined for a given set of experimental conditions by reducing the concentration of C_3F_7I atoms until laser action was just detectable. Threshold pulses occurred about 20 μs after the flashlamps were triggered, when the flash intensity had fallen to 1 or 2 percent of maximum. Since the gain reached threshold while being pumped at only a few percent of the maximum rate, the rate of deactivation of I^* was

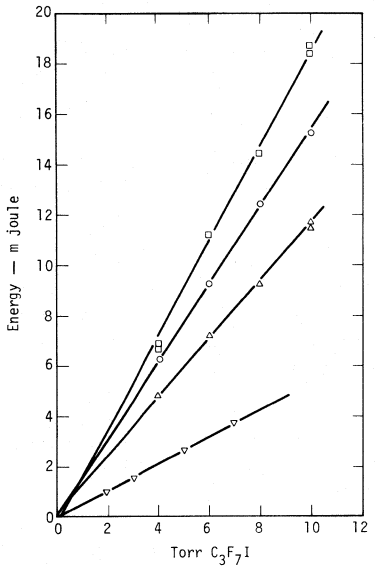

Fig. 2. Laser output energy without added inert gas. Exit-mirror reflectivity: □—30 percent; ○—50 percent; △—70 percent; ▽—90 percent.

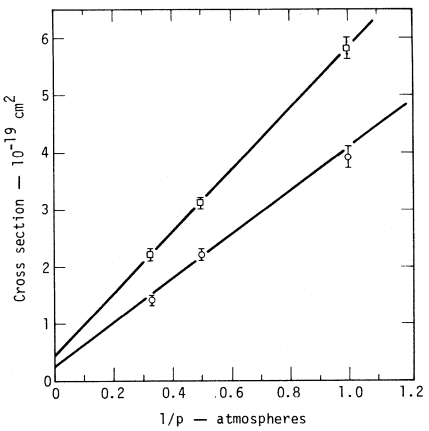

Fig. 3. Effect of pressure on stimulated-emission cross section. □—He added; ○—Ar added.

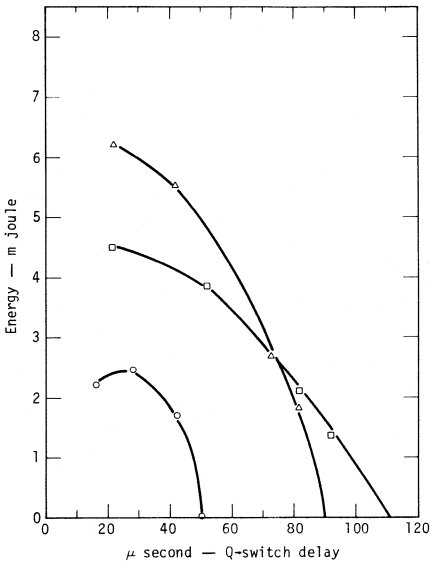

Fig. 4. Effect of Q-switch delay at three atmospheres. △—3-atm He at 29.5-torr C_3F_7I; □—3-atm He at 22.1-torr C_3F_7I; ○—3-atm Ar at 29.5-torr C_3F_7I.

low when threshold was reached. The stimulated-emission cross section of I^* was calculated with (1) using a ΔN value of 13.9 percent of $N_{C_3F_7I}$. The results are shown in Fig. 3, which shows the expected linear relationship between the cross section and the reciprocal of pressure. Argon is more effective as a pressure-broadening gas than helium.

The inversion lifetime at high pressure was measured using a Pockel's-cell Q switch. With the Q switch installed in the system and opened at the same time as the pumping flash, the threshold C_3F_7I pressure was determined for each set of operating conditions. The C_3F_7I pressure was then increased to twice the threshold value and laser action delayed by opening the Q switch after the flash.

The Q-switch delay time was lengthened until laser action was just detectable when it was opened. Since the peak inversion was initially twice the threshold level, it should have then fallen to half of its initial value, and this delay time was the inversion half-life. This method is approximate, but does show that the inversion lifetime is long enough at three atmospheres for the system to be useful.

The results are shown in Fig. 4. The 22.1-torr C_3F_7I data are twice threshold with three atmospheres of helium. The 29.5-torr C_3F_7I data with helium were run to show that the shorter lifetime with argon was not due to the higher C_3F_7I pressure needed to reach twice threshold with argon. It is clear that argon is a more effective deactivator of I^* than helium, and helium is probably a better choice for a pressurizing gas despite its lower efficiency as a line broadener.

The stimulated-emission cross section of 2.2×10^{-19} cm^2 and inversion half-life of 110 μs observed with three atmospheres of helium are both satisfactory for a large iodine laser system.

ACKNOWLEDGMENT

The author wishes to thank L. Wood, Y.-L. Pan, and D. Gregg for many helpful discussions and suggestions. He also wishes to thank E. Huss, L. Booth, and L. Kamppinen for assistance in constructing the apparatus.

REFERENCES

[1] J. V. V. Kasper and G. C. Pimentel, "Atomic iodine photodissociation laser," *Appl. Phys. Lett.*, vol. 5, pp. 231–233, Dec. 1964.
[2] P. Gensel, K. Hohla, and K. L. Kompa, "Energy storage of CF_3I photodissociation laser," *Appl. Phys. Lett.*, vol. 18, pp. 48–50, Jan. 1971.
[3] F. T. Aldridge, "High pressure iodine photodissociation laser," *Appl. Phys. Lett.*, vol. 22, pp. 130–132, Feb. 1973.
[4] V. S. Zuyev, V. A. Katulin, V. Yu. Nosach, and O. Yu. Nosach, "Investigations of the luminescence spectrum of atomic iodine," *Sov. Phys.–JETP*, vol. 35, pp. 870–873, Nov. 1972.
[5] S. J. Riley and K. R. Wilson, "Excited fragments from excited molecules: Energy partitioning in the photodissociation of alkyl iodides," *Discuss. Faraday Soc.*, vol. 53, pp. 132–146, Apr. 1972.

"Buried Modes" in Planar Media with Nonmonotonically Varying Index of Refraction

ESTHER M. CONWELL

Abstract—**When guiding is due to a continuously varying, rather than discontinuous, index of refraction, $n(z)$, and $n(z)$ peaks at some point inside the propagation medium, there may result "buried modes," i.e., modes whose exponential decay takes place inside the guiding medium rather than, as is usual, in an adjacent medium. The conditions for obtaining these modes are discussed in the Wentzel-Kramer-Brillouin (WKB) approximation and the mode equations given for both these modes and the usual ones for an illustrative case.**

Waveguiding in planar media with nonmonotonically varying index of refraction $n(z)$ has been reported by a number of researchers. The peaked index has been created by ion migration [1], [2] or impurity diffusion [3], [4]. Schematically, we may represent the resulting dielectric constant variation, $n^2(z)$, by the solid line in Fig. 1. This is similar to what was observed in [1], for example, in glass that had undergone electrically induced migration of Tl ions. For specificity we take $\epsilon = 1$ for $z < 0$. The guided modes will be assumed to propagate in the x-direction with propagation vector for the mth mode, $k_x^{(m)} \equiv (\omega/c)(\epsilon_{\text{eff}}^{(m)})^{1/2}$. For the situation of Fig. 1

$$\epsilon_b < \epsilon_{\text{eff}} < \epsilon_p. \tag{1}$$

It is readily seen that there is a difference between modes with $\epsilon_s < \epsilon_{\text{eff}} < \epsilon_p$, exemplified by $\epsilon_{\text{eff}}^{(1)}$, and those with $\epsilon_b < \epsilon_{\text{eff}} < \epsilon_s$, exemplified by $\epsilon_{\text{eff}}^{(2)}$. As can be deduced from the wave equation (see [5, (3)–(5)]) the E and H fields are oscillatory in character where $\epsilon(z) > \epsilon_{\text{eff}}$ and exponentially decaying where $\epsilon(z) < \epsilon_{\text{eff}}$. Thus the mode corresponding to $\epsilon_{\text{eff}}^{(2)}$ is oscillatory from the surface at $z = 0$ to $b^{(2)}$, while that corresponding to $\epsilon_{\text{eff}}^{(1)}$ is oscillatory only between $a^{(1)}$ and $b^{(1)}$. The latter therefore constitutes a buried mode. Evidence for such modes has been presented in [1] and [2], although the authors did not make a detailed comparison with theory. As pointed out in those references, the buried modes should have the advantage of lower attenuation since they are not subject to surface scattering.

Modes in a situation such as shown in Fig. 1 are most easily studied by the Wentzel–Kramer–Brillouin (WKB) approximation. The equation for determining the propagation vectors or ϵ_{eff}'s is conveniently stated [6], [7]

Manuscript received November 14, 1974.
The author is with the Xerox Webster Research Center, Webster, N.Y. 14580.

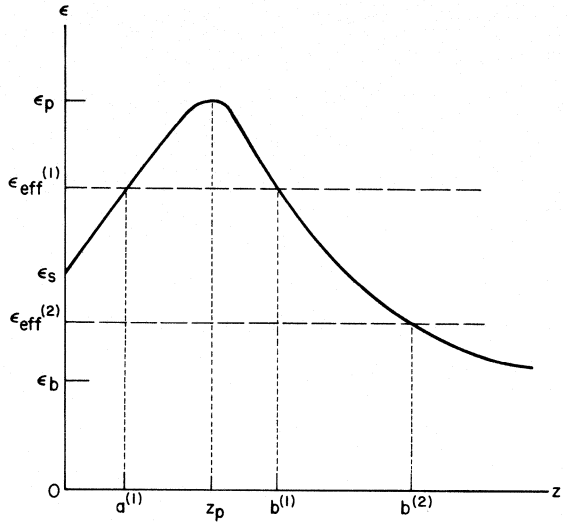

Fig. 1. ϵ versus z below the surface ($z = 0$) of the guiding medium. z_p is the coordinate of the peak value ϵ_p, and ϵ_s and ϵ_b the values of ϵ at the surface and in the interior, respectively. The a's and b's represent intersections of the horizontal lines labeled ϵ_{eff} with $\epsilon(z)$.

$$\int_a^b k_z(z)\,dz = \Phi_{10} + \Phi_{12} + m\pi, \qquad m = 0, 1, 2, \cdots \tag{2}$$

where

$$k_z = k[\epsilon(z) - \epsilon_{\text{eff}}]^{1/2} \tag{3}$$

k being ω/c, and a and b representing the extremes of the range in z for which the fields are oscillatory or, equivalently, for which k_z is real. (a and b are the WKB turning points.) The Φ's are related to the phase changes on reflection [6]. For reflection at the $z = 0$ interface, Φ is determined in the usual way for total internal reflection [8]. When the changes in $\epsilon(z)$ are small, i.e., $(\epsilon_p - \epsilon_b) \ll \epsilon_b$, as is generally the case, $\Phi \simeq \pi/2$ since k_z is quite small and the decay in air is rapid [6]. For reflection at points such as $a^{(1)}$, $b^{(1)}$, and $b^{(2)}$, $\Phi = \pi/4$, [6]. It is clear then that the equation for determining the modes is different for the buried ones and the ones oscillatory to the surface. Specifically, for the mth buried mode the mode equation is

$$\int_{a^{(m)}}^{b^{(m)}} k_z^{(m)}(z)\,dz = (m + \tfrac{1}{2})\pi, \qquad \epsilon_s < \epsilon_{\text{eff}}^{(m)} < \epsilon_p \tag{4}$$

while for modes that extend to the surface it is

$$\int_0^{b^{(m)}} k_z^{(m)}(z)\,dz = (m + \tfrac{3}{4})\pi, \qquad \epsilon_b < \epsilon_{\text{eff}}^{(m)} < \epsilon_s. \tag{5}$$

It should be noted that (4) will not describe the buried modes accurately unless $a^{(m)}$ is far enough from $z = 0$ so that the exponential decay is essentially complete there. If that is not the case, the additional boundary conditions at $z = 0$ will affect the modes substantially.

Although detailed experimental data with which to compare theory are not available, we present the results of a calculation for the two types of modes to illustrate the dependence on the relevant parameters. To simplify the integration we represent $\epsilon(z)$ by a straight line to the left of z_p, an exponential to the right. Specifically, we choose

$$\epsilon(z) = \epsilon_s + [(\epsilon_p - \epsilon_s)/z_p]z, \quad 0 \leqslant z \leqslant z_p \tag{6}$$

and

$$\epsilon(z) = \epsilon_b + (\epsilon_p - \epsilon_b)e^{(z_p - z)/d}, \quad z_p \leqslant z \leqslant \infty \tag{7}$$

where d is a constant determined by the diffusion or migration process. With (6) and (7) we obtain the mode equation for the buried modes

$$A(\epsilon_{\text{eff}}) = (m + \tfrac{1}{2})\pi, \quad \epsilon_s < \epsilon_{\text{eff}} < \epsilon_p \tag{8}$$

where

$$A(\epsilon_{\text{eff}}) = \frac{2kz_p}{3}\frac{(\epsilon_p - \epsilon_{\text{eff}})^{3/2}}{\epsilon_p - \epsilon_s} + 2kd\left\{(\epsilon_p - \epsilon_{\text{eff}})^{1/2} - (\epsilon_{\text{eff}} - \epsilon_b)^{1/2}\tan^{-1}\left(\frac{\epsilon_p - \epsilon_{\text{eff}}}{\epsilon_{\text{eff}} - \epsilon_b}\right)^{1/2}\right\}. \tag{9}$$

Accuracy of (8) requires, for the reason given earlier, that ϵ_{eff} not be too close to ϵ_s. For the other modes we find

$$A(\epsilon_{\text{eff}}) - \frac{2kz_p}{3}\frac{(\epsilon_s - \epsilon_{\text{eff}})^{3/2}}{\epsilon_p - \epsilon_s} = (m + \tfrac{3}{4})\pi, \quad \epsilon_b < \epsilon_{\text{eff}} < \epsilon_s. \tag{10}$$

We note that the possible number of buried modes may be increased by increasing z_p, d, or $(\epsilon_p - \epsilon_s)$. If ϵ_s were smaller than ϵ_b, all existing modes of the system would be buried ones.

References

[1] T. Izawa and H. Nakagome, "Optical waveguides formed by electrically induced migration of ions in glass plates," *Appl. Phys. Lett.*, vol. 21, pp. 584–587, Dec. 1972.

[2] T. G. Giallorenzi, E. J. West, R. Kirk, R. Ginther, and R. A. Andrews, "Optical waveguides formed by thermal migration of ions in glass," *Appl. Opt.*, vol. 12, pp. 1240–1245, June 1973.

[3] J. Noda, T. Saku, and N. Uchida, "Fabrication of optical waveguiding layer in $LiTaO_3$ by Cu diffusion," *Appl. Phys. Lett.*, vol. 25, pp. 308–310, Sept. 1974.

[4] L. Brillson and E. M. Conwell, "Optical guided waves in CdS_xSe_{1-x} layers," *J. Appl. Phys.*, vol. 45, pp. 5289–5293, Dec. 1974.

[5] E. M. Conwell, "Optical waveguiding in graded-index layers," *Appl. Phys. Lett.*, vol. 25, pp. 40–42, July 1974.

[6] P. K. Tien, S. Riva-Sanseverino, R. J. Martin, A. A. Ballman, and H. Brown, "Optical waveguide modes in single-crystalline $LiNbO_3$–$LiTaO_3$ solid-solution films," *Appl. Phys. Lett.*, vol. 24, pp. 503–505, May 1974.

[7] D. Marcuse, "TE modes of graded-index slab waveguides," *IEEE J. Quantum Electron.*, vol. QE-9, pp. 1000–1006, Oct. 1973.

[8] P. K. Tien and R. Ulrich, "Theory of prism-film coupler and thin-film light guides," *J. Opt. Soc. Amer.*, vol. 60, pp. 1325–1337, Oct. 1970.

On Saturation Mechanisms in PC He-Cd$^+$ Lasers

JERZY K. MIZERACZYK

Abstract—**The results of experimental studies on the saturation mechanisms in He-Cd laser discharge are presented. It is concluded that the saturation effects may be explained in terms of the influence of the discharge parameters on the helium triplet metastable density.**

Manuscript received November 27, 1974. This work was sponsored in part by the Institute of Quantum Electronics, WAT, Warsaw, Poland.

The author is with the Institute of Fluid-Flow Machines, Polish Academy of Sciences, Gdańsk, Poland. He is on leave at the Department of Electronics, Nagoya University, Nagoya, Japan.

Since the proposal of the He–Cd$^+$ laser [1] many papers have appeared which discuss the excitation mechanisms responsible for the population inversion on the $5s^2{}^2D_{5/2} - 5p^2{}^2P_{3/2}$ 4416-Å and $5s^2{}^2D_{3/2} - 5p^2{}^2P_{1/2}$ 3250-Å transitions of the Cd ion [2]–[8].

It is now accepted that Penning collisions between helium triplet metastable and cadmium ground-state atoms have importance as the process of population of the preceding upper Cd-ion levels in the positive column He–Cd laser discharge. But according to this excitation mechanism there are some troubles in explaining the effects of saturation of the He–Cd$^+$ laser power output, especially when at constant cadmium vapor pressure the discharge current is increased. A very interesting explanation of the behavior of He–Cd$^+$ laser output is given in [8] on the basis of the behavior of the He metastable densities measured in the He–Cd discharge.

This correspondence shows that the saturation mechanisms of the He–Cd$^+$ laser power output can be explained qualitatively in terms of the behavior of plasma parameters of the discharge and their influence on the He triplet metastable density in whole region of interest.

The cataphoresis-type discharge tube used in these studies was 3 mm in diameter and about 40 cm in active length. Cadmium of natural isotopic abundance was supplied from the side arm placed at $\frac{2}{3}$ of the active length, closer to the anode. The side-arm temperature was stabilized to better than $\pm\frac{1}{2}$°C. All parts of the tube except the small region of cadmium condensation were put in the oven at a temperature of 350 ± 7.5°C. The experiments were made over the following range of parameters: the discharge current, 15–155 mA; helium pressure, 1.5–6 torr; cadmium vapor pressure, 10^{-5}–$2 \cdot 10^{-3}$ torr. The cadmium pressure in the discharge was estimated from the temperature of the side arm. The plasma parameters: electric field, electron temperature, and density were obtained using the double-probe technique modified [9] to avoid the difficulty in getting the electron density in the He–Cd discharge from the conventional double-probe method [10].

Because of using the probes in the active region of the tube the behavior of the 4416-Å spontaneous-emission sidelight was observed instead of the laser power output. But fortunately, it is known from our experiments and those of the others [8], [11] that the spontaneous-emission sidelight at 4416 Å follows the same behavior as the laser output. It seems that the He–Cd$^+$ laser output depends on the pumping of the upper laser level rather than on the excitation and trapping effects of the lower laser level. This allows an explanation of the behavior of the He–Cd$^+$ laser power output at 4416 Å in terms of the spontaneous-emission sidelight following the power.

Typical results of the experiments are presented in Figs. 1 and 2. Fig. 1 shows the influence of increasing cadmium vapor density on the intensities of the spontaneous-emission sidelight of the Cd$^+$ at 4416 Å, Cd at 4799 Å, and He at 3889 Å and on the reduced electric field E/p, electron temperature V_e, and density n. These results were obtained for the fixed He pressure and discharge current optimal in the sense of the maximum of intensity of the 4416-Å laser line. The broken lines in Figs. 1 and 2 illustrate the variations of the He triplet metastable density M and normalized product of MN_{Cd}, where N_{Cd} is the density of the neutral cadmium atoms in the discharge. The plots of M and MN_{Cd} were obtained from the calculations based on the data of these experiments and on the rate equation for the He triplet metastable population in pure He discharge [8], modified by taking into account the destruction of the triplet metastables by Penning process in the He–Cd laser discharge. The final shape of the equation describing the He triplet metastable density in the He–Cd

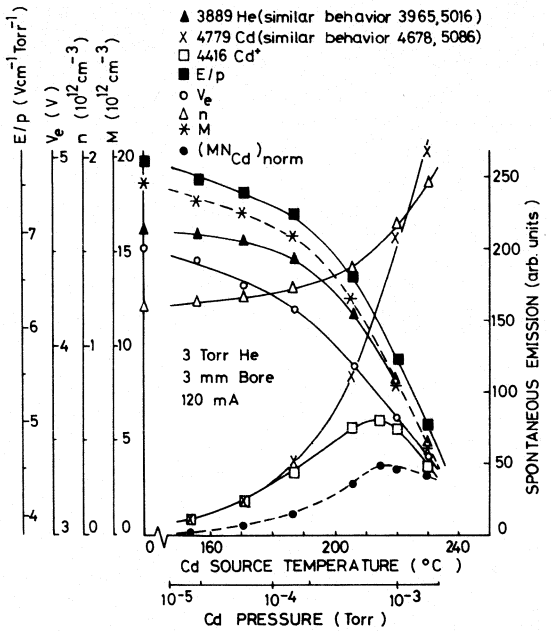

Fig. 1. Spontaneous emission of 3889-Å He, 4799-Å Cd, and 4416-Å Cd^+ lines, reduced electric field (E/p), electron temperature (V_e), and density (n), helium triplet metastable density (M), and normalized product MN_{Cd} (N_{Cd}-cadmium density) as functions of cadmium pressure in He–Cd laser discharge for fixed He pressure and discharge current. The broken lines show the results calculated.

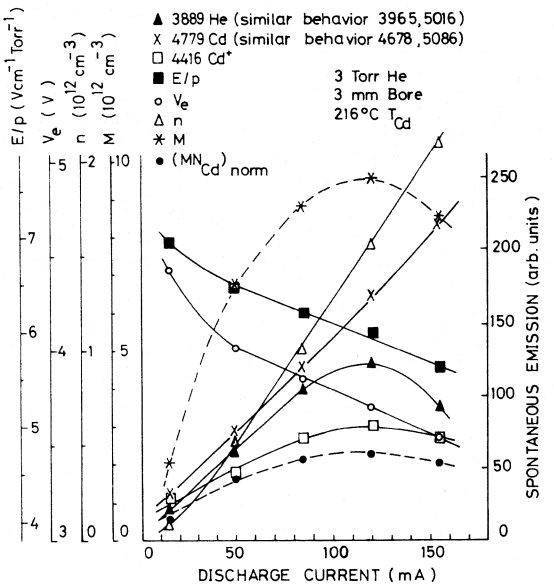

Fig. 2. Spontaneous emission of 3889-Å He, 4799-Å Cd, and 4416-Å Cd^+ lines, reduced electric field (E/p), electron temperature (V_e), and density (n), helium triplet metastable density (M), and normalized product MN_{Cd} (N_{Cd}-cadmium density) as functions of discharge current in He–Cd laser discharge for fixed He and Cd pressures. The broken lines show the results calculated.

discharge is as follows [12]

$$M = \frac{540n}{70n + N_{Cd} + 47}(E/p - 4) \quad (1)$$

where M and n are expressed in 10^{12} cm^{-3} and E/p in Vcm^{-1} $torr^{-1}$.

It is seen from Fig. 1 that the electron temperature and reduced electric field decrease with increasing cadmium density, contrary to the electron density. These are due to the inelastic collisions between electrons and neutral cadmium atoms. Also the metastable density decreases as cadmium density increases. It can be easily shown from (1) that the

decreasing of the metastable density is essentially determined by decreasing the reduced electric field rather than through the destruction of Penning process and electronic-collision effects in the region of interest. It is interesting to notice that the spontaneous emission of the 3889-Å line terminating on the triplet metastable level follows the metastable density plot. Spontaneous emission of the 4799-Å Cd indicates the increasing density of neutral cadmium atoms in the discharge.

According to the assumption that Penning collisions are the dominant source of the excitation of the upper level state the intensity of the 4416-Å emission sidelight would be proportional to the product of MN_{Cd} [2]. This was confirmed by these experiments. As is seen from Fig. 1 the normalized plot of MN_{Cd} follows the same behavior as the experimental values of sidelight intensity for the 4416-Å transition of Cd^+. Both these quantities saturate for the same value of cadmium vapor pressure of about $0.9 \cdot 10^{-3}$ torr. This means that the dependance of the spontaneous-emission sidelight at 4416 Å (and laser power output) on cadmium pressure can be understood in terms of the importance of Penning ionization in pumping processes of PC He–Cd^+ lasers.

Fig. 2 shows the behavior of the preceding quantities as the functions of discharge current for fixed He and Cd vapor pressures optimal in the sense of the maximum of the 4416-Å emission sidelight. According to (1), despite rapidly increasing electron density the He triplet metastable density saturates for the current of about 120 mA because of the decreasing reduced electric field when the discharge current increases. It means that the reducing of the mean electron energy and the E/p or V_e corresponding to it, due to the inelastic collisions of electrons in the He–Cd discharge, is important in the saturation mechanisms of the He triplet metastable density. As may be seen from Fig. 2 the 4416-Å emission sidelight follows the behavior of the metastable density and the plot of the product MN_{Cd}, and this is consistent with the generally accepted assumption that Penning ionization is important in the excitation mechanisms in the PC He–Cd^+ lasers.

It is worthwhile to notice that the plots of the triplet metastable density calculated herein is in a good agreement with those of measured values presented in [8].

It can be concluded that the saturation mechanisms in the PC He–Cd^+ lasers may be explained qualitatively by the behavior of the He triplet metastable density saturated due to the influence of the plasma parameters of the He–Cd discharge, the reduced electric field mainly.

ACKNOWLEDGMENT

The author wishes to thank Dr. Z. Zakrzewski, Prof. S. Hattori, and Dr. T. Goto of Nagoya University for helpful discussions, and J. Ziemann for technical assistance.

REFERENCES

[1] G. R. Fowles and B. D. Hopkins, "CW laser oscillation at 4416 Å in cadmium," *IEEE J. Quantum Electron.* (Notes and Lines), vol. QE-3, p. 419, Oct. 1967.

[2] W. T. Silfvast, "Penning ionization in a He-Cd discharge," *Phys. Rev. Lett.*, vol. 27, pp. 1489–1492, Nov. 1971.

[3] L. D. Shearer and F. A. Padovani, "De-excitation cross-section of metastable helium by Penning collisions with cadmium atoms," *J. Chem. Phys.*, vol. 52, pp. 1618–1619, Jan. 1970.

[4] C. E. Webb, A. R. Turner-Smith, and J. M. Green, "Optical excitation in charge transfer and Penning ionization," *J. Phys. B., At. Mol. Phys.*, vol. 3, pp. L134–L138, Nov. 1970.

[5] M. K. Djatlov, E. P. Ostapchenko, and V. A. Stepanov, "On the generation mechanism of the cadmium vapor laser," *Opt. Spectrosk.* (USSR), vol. 5, pp. 1014–1015, Nov. 1970; also *Opt. Spectrosc.*, vol. 29, pp. 539–540, Nov. 1970.

[6] G. J. Collins, R. C. Jensen, and W. R. Bennett, Jr., "Charge-exchange in the He–Cd laser," *Appl. Phys. Lett.*, vol. 19, pp. 125–128, Sept. 1971.

[7] M. Janossy, V. V. Itagi, and L. Csillag, "On the excitation mechanism and operation parameter of the 4416-Å He–Cd laser," *Acta Phys. Acad. Sci. Hung.*, vol. 32, pp. 149–163, Jan. 1972.

[8] P. G. Browne and M. H. Dunn, "Metastable densities and excitation process in the He–Cd laser discharge," *J. Phys. B., At. Mol. Phys.*, vol. 6, pp. 1103–1117, June 1973.

[9] J. K. Mizeraczyk, "A simple method of determination of electron density in PC He-metal laser discharges," *J. Appl. Phys.*, vol. 46, Apr. 1975.

[10] T. Goto, A. Kawahara, G. J. Collins, and S. Hattori, "Electron temperature and density in positive column He–Cd^+ lasers," *J. Appl. Phys.*, vol. 42, pp. 3815–3818, Sept. 1971.

[11] S. Hattori and T. Goto, private information.

[12] J. K. Mizeraczyk, "Studies of the plasma parameters and saturation effects in the positive column He–Cd^+ laser," in *Rep. Symp. Optics and Quantum Electronics* (Inst. Electron. Commun. Eng. Japan, Tokyo, Jan. 1975), pp. 9–22.

Contributors

Frank Allario was born in New York, N.Y., on December 10, 1940. He received the B.S. degree from Manhattan College, Riverdale, N.Y., in 1962, and the M.S. and Ph.D. degrees from the Polytechnic Institute of New York (PINY), Brooklyn, in 1965 and 1968, respectively.

At PINY he worked on diagnostics of high-energy plasmas. In November 1967 he joined NASA's Langley Research Center, Hampton, Va., and is currently Head of the Laser Physics and Applications Section, responsible for advanced laser and environmental sensor development programs.

Dr. Allario is a member of the American Physical Society, Sigma Pi Sigma, and the American Institute of Aeronautics and Astronautics.

*

Clayton H. Bair, photograph and biography not available at the time of publication.

*



Lorne L. T. Bradley was born in Trafalgar, Ont., Canada, on February 8, 1925. He graduated from Radio College of Canada, in 1944.

Immediately after graduation he went to work with RCA, Montreal, in the Inspection Department. In 1945 he joined the National Research Council of Canada, Ottawa, first with the Radio Engineering Division, then with the Applied Chemistry Division, and worked on electronic instrumentation for antenna pattern recorders, klystron and magnetron systems, nuclear magnetic resonance, and mass spectrometry. In 1963 he moved to the Physics Division to head the Electronics Section. Since then he has been involved with the designing of electronic instrumentation for laser digital-analog precision control systems, satellite communication, plasma physics, etc. He is actually interested in circuit design with microprocessing.

*

Jack F. Butler (S'60–M'63), photograph and biography not available at the time of publication.

Peter S. Cross, photograph and biography not available at the time of publication.

*



G. J. Ernst was born in Castricum, The Netherlands, on December 30, 1941. He received the doctor's degree from the University of Amsterdam, Amsterdam, The Netherlands, in 1966, where he participated in relaxation phenomena in silicon-iron alloys.

From 1966 to 1970 he was with Philips Research Laboratories, Eindhoven, The Netherlands, where he was engaged in technological applications of high-power laser systems. In 1970 he joined the Twente University of Technology, Enschede, The Netherlands, where he is now working in the field of nonlinear optics and high-power laser systems.

*

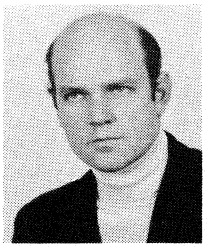

Ingolf V. Hertel was born in Dresden, Germany, on June 9, 1941. He graduated as Engineer for Technical Physics in Lübeck, Germany, in 1963. He received the Diplom in Physics from the University of Freiburg, Freiburg, Germany, in 1967. During 1967 and 1968 he worked as an Experimental Officer at the University of Southampton, Southampton, England, and received the Dr. rer.nat. from the University of Freiburg in 1969.

In 1969 and 1970 he was an Assistant in the Physics Department at the University of Mainz, Germany, and joined the University of Trier-Kaiserslautern, Kaiserslautern, Germany, in 1970 as a Professor of Physics. His main research interests are in atomic collision processes and lasers.

*

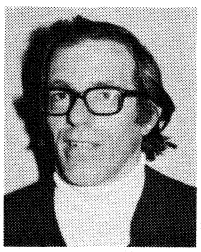

William G. Oldham (M'65) was born in Detroit, Mich., on May 5, 1938. He received the B.S. and Ph.D. degrees in electrical engineering from Carnegie Institute of Technology, Pittsburgh, Pa., in 1960 and 1963, respectively.

From 1963 to 1964 he worked for Siemens-Schuckertwerke, Erlangen, Germany, on vapor growth of III–V compounds. Since 1964 he has been on the faculty of the University of California, Berkeley. He is currently a Professor of Electrical Engineering and Computer Sciences,

and a member of the Electronics Research Laboratory. He spent a sabbatical year, 1970–1971, with the Technische Universität, Munich, Germany as an NSF Senior Postdoctoral Fellow, and is currently on an industrial leave (1974–1975) at Intel Corporation, Santa Clara, Calif.

*

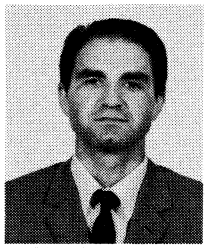

Emilio Panarella was born in Ferrandina, Italy, on January 3, 1933. He received the Doctoral Degree in navigational sciences from the University of Navigation, Naples, Italy, in 1956, presenting a thesis on the physics of polar aurorae.

In 1961 he was awarded a Postdoctorate Fellowship and went to the Polytechnic Institute of Brooklyn, N.Y., where he worked on microwave techniques for plasma diagnostics for one year. He then returned to Italy and worked on electron spin resonance with the Microwave Institute of the National Research Council of Italy, located in Florence. In 1964 he joined the Gas Dynamics Section, Division of Mechanical Engineering, National Research Council of Canada, Ottawa, and since then has been involved in the production, diagnosis, and theoretical analysis of hot plasmas, such as implosive and explosive discharges and laser-induced sparks.

Dr. Panarella is a member of the American Physical Society, the European Physical Society, and the Italian Physical Society.

*



Harrison E. Radford was born in Peterboro, N.H., on July 26, 1927. He received the B.S. degree in physics (*summa cum laude*) from the University of New Hampshire, Durham, in 1954, and the M.S. and Ph.D. degrees, both in physics, from Yale University, New Haven, Conn., in 1955 and 1959, respectively.

From October 1958 to May 1967 he was Project Leader in the Cryogenics Section of the Heat Division at the National Bureau of Standards. In May 1967 he became Project Leader in the High Voltage Section of the Electricity Division, also at the National Bureau of Standards, a position he held until July 1969. In August 1969 he went to the Smithsonian Astrophysical Observatory, Cambridge, Mass., where he is a Physicist (Microwave Spectroscopy) in the Radio Astronomy Laboratory. In September of that same year he became an Associate of the Harvard College Observatory, Harvard University, Cambridge, Mass.

Dr. Radford was awarded the Department of Commerce Silver Medal for Meritorious Service in 1963, and the Distinguished Alumni Award from the College of Technology, University of New Hampshire, in 1971.

*

Aleksandar S. Stamatović was born in Šabac, Yugoslavia, on December 26, 1940. He received the B.S. degree in physical chemistry, and the



M.S. and Ph.D. degrees in physics, all from the University of Belgrade, Belgrade, Yugoslavia, in 1963, 1966, and 1969, respectively.

In 1967 he joined the Department of Engineering and Applied Science at Yale University, New Haven, Conn., where he was involved in research on low-energy electron-molecule collisions. He is now at the University of Trier-Kaiserslautern, Kaiserslautern, Germany, on a leave of absence from the Institute of Physics, Belgrade, Yugoslavia. His research interests include electron-collision phenomena and lasers.

Dr. Stamatović is a member of the European Physical Society.

*



Horst Weber was born in Berlin, Germany, on March 28, 1935. He received the M.S. and Ph.D. degrees, both in physics, from the Technical University of Berlin, Berlin, in 1961 and 1965, respectively.

In 1967 he became an Assistant Professor at the Technical University of Berlin. In 1969 he joined the Institute of Applied Physics, University of Berne, Berne, Switzerland, and is now a Professor of Applied Physics and Head of the Laser Group. His research is related to ultrashort pulses, dye lasers, interaction of intense laser light with matter, and laser-induced plasmas.

*

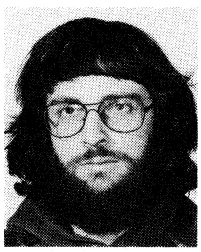

Robert Wilbrandt was born in Berne, Switzerland, on April 22, 1945. He received the M.S. degree in physics and the Ph.D. degree, both from the University of Berne, Berne, in 1971 and 1974, respectively.

He is now a Postdoctoral Fellow at the Atomic Energy Commission Risø Research Establishment, Roskilde, Denmark, where he is working on laser absorption and Raman spectroscopy.

*



W. J. Witteman was born in Monster, The Netherlands, on December 12, 1933. He received the degree of mechanical engineer from the Technical University of Delft, Delft, The Netherlands, in 1958, and the Ph.D. degree in physics from the Technical University of Eindhoven, Eindhoven, The Netherlands, in 1963.

He was a Postdoctoral Fellow from 1958 to 1959 and a Research Associate from 1959 to 1960 at the Institute for Fluid Dynamics and Applied Mathematics, University of Maryland, College Park, where he was engaged in shock tube work and molecular

relaxation phenomena. From 1961 until 1969 he was with Philips Research Laboratories, Eindhoven, The Netherlands, and participated from 1961 to 1963 in development work on high-pressure apparatus. Since 1963 he has been doing laser research and has published on continuous water-vapor lasers, mode competition in gas lasers, sealed-off high-power carbon-dioxide lasers, the behavior of water vapor added to a CO_2-laser mixture, and on relaxation phenomena in a CO_2 laser. Since September 1969 he has been a Professor at Twente University of Technology, Enschede, The Netherlands, where he is engaged in high-power systems and nonlinear optics.

ADVICE TO AUTHORS[1]

Abstract—**Suggestions are made about the preparation of papers to be submitted to IEEE Journals and Transactions including directions for writing equations compactly and some remarks about the form of references and about style.**

I. Preparation of Manuscripts

For general instructions about preparing manuscripts for this and other IEEE journals, see "Information for IEEE Authors," *IEEE Spectrum*, pp. 111–115, August 1965, and the inside back cover of this Transactions. In particular, the following points should be noted.

1) Manuscripts should be typed, and *everything* should be double-spaced.

2) The title page should carry the author's name, address, and zip code. There should be an abstract of no more than 200 words for a paper, no more than 50 for correspondence. Abstracts should contain only the simplest, one-line equations, and they should not refer to footnotes or to references.

3) It is preferred that references be given in footnotes, but they may be collected at the end if the author desires. Footnotes should be assembled on a separate page after the main text and any appendices.

4) Figure captions should be typed on a separate page at the end.

5) Glossy prints or india-ink copies of figures, suitable for engraving, must be supplied before publication.

6) Send three legible copies of your paper to the appropriate editor. See the inside back cover for the names of the editors and their areas of responsibility.

II. Writing of Equations

Every effort, consistent with clarity, must be made to write equations so that they take up as little space as possible. Some specific directions are the following.

1) Write equations as much on a single line of type as you can.

2) Use the diagonal (/) and negative exponents to avoid cumbersome fractional expressions. Use case fractions ($\frac{1}{2}$, $\frac{1}{4}$) for common fractions.

3) Although a bar, caret, tilde, or single dot can be set above a single letter, nothing should appear below a letter or above more than one letter, nor should a letter have more than one symbol above it. Use $\underset{\sim}{E}$ or angular brackets $\langle\rangle$ for expected values, not an overline.

4) Use fractional exponents instead of radical signs ($\sqrt{\ }$).

5) Use "exp" for the exponential function whenever the exponent takes more than a single line of type.

6) Matrices that have any simple symmetries should not be written out in full; they take too much space. Use a subscript notation instead, e.g., $\underset{\sim}{A} = ||a_{ij}||$.

7) Do not write out a column vector; display the transposed row vector instead.

8) Use boldface type, indicated by a wavy underline $\underset{\sim}{A}$, for vectors and matrices.

9) Introduce a new symbol for a complicated expression that is often repeated.

10) All mathematical symbols should be clearly identified, particularly if they are handwritten. Be sure that subscripts and superscripts are clearly designated.

11) Equations should be numbered consecutively throughout the text and referred to simply by number. The word "equation" should be used only at the beginning of a sentence.

"Equation (23) enables us to write (32) in the form ···."

12) Do not put complicated expressions in the limits of integrals or sums.

III. References

Use the standard IEEE form in references. For journal articles give names of all authors, full title, full name of journal, volume number, inclusive page numbers, month, and year. For books give the name of the publisher, his city, and the year of publication. References to books should always include page numbers. Reports and memoranda of limited circulation may be cited only by permission of the editor who is handling your paper.

IV. Usage

It is most important that your paper be correct, concise, and crystal clear. Attention to grammar fosters clarity. Here are some suggestions about usage.

1) Avoid jargon. Introduce new terminology only when it is indispensable.

2) Hyphenate complex modifiers to help the reader sort them out:
"capacity-equalized frequency-modulation channel."

3) Shun dangling participles.

4) Use "that" for defining relative clauses, "which" for nondefining relative clauses.
"The theorem that has just been proved permits us ···"
"This theorem, which was proved by Brown, permits us ···"

5) Avoid parenthetical expressions that interrupt the thought of a sentence or paragraph.

6) Avoid coy parentheses.
NO: "This (unique) solution of the (Fredholm) integral equation ···."
YES: "This unique solution of the Fredholm integral equation···"

7) Break up overlong paragraphs. Check whether a series of one-sentence paragraphs can be combined.

8) Do not overuse the word "case."
NO: "In the white-noise case···"
YES: "When the noise is white, ···"

9) Distinguish "can" and "may."
"According to (15), this expression can be written as ···"
"Interested readers may request copies of the report ···"

10) Do not use "too" to mean "very."
(What does "I cannot recommend this book too strongly" really mean?)

11) Do not use "essentially" to mean "approximately" or "effectively."
"Signal detection is essentially hypothesis testing."
"Outside the band the signal spectrum is nearly zero."
(*not* "essentially zero!")
"Under these conditions the noise is effectively white."
(*not* "essentially white!")

12) Use possessives.
"Jones's theorem" *not* "the theorem of Jones."

13) Distinguish "alternate" and "alternative."
"An alternative proof has been given by Smith."
"Alternate rows of the matrix contain only zeros."

14) "Based on" is adjectival; the adverbial phrase is "on the basis of."
"On the basis of these experiments we predict ···"
"Our prediction, based on incomplete data, was incorrect."

15) Capitalize adjectives and nouns derived from proper names, excepting names of units of measure, which are uncapitalized.
"Gaussian noise," "Cartesian coordinates,"
"The Hamiltonian of the system is ···"
"The inductance is 1 henry."

If you have difficulty in writing, a good book to study is *The Elements of Style*, by William Strunk, Jr. and E. B. White (New York: Macmillan 1959). It is now available in paperback. Reminiscing about his old teacher, E. B. White says in his introduction,

> "Will [Strunk] felt that the reader was in serious trouble most of the time, a man floundering in a swamp, and that it was the duty of anyone attempting to write English to drain this swamp quickly and get his man up on dry ground, or at least throw him a rope."

The reader is in trouble all of the time, the difficulties of the subject matter being what they are, and authors should strive to give him all the help they can.

[1] Reprinted from *IEEE Trans. Information Theory*, vol. IT-15, p. 338, March 1969, C. W. Helstrom, Editor.

Effect of Refractive-Index Nonlinearity on the Optical Quality of High-Power Laser Beams

B. R. SUYDAM, MEMBER, IEEE

Abstract—**Both small-scale and large-scale partial self-focusing produce phase distortions which result in loss of optical quality of the beam. Both effects are herein studied and both can result in significant power loss. Incipient fine-scale self-focusing losses can be mitigated by spatial filtering. Nonlinear lensing, i.e., partial large-scale self-focusing, is more or less serious depending on the size of the target onto which the beam is to be focused.**

I. Introduction

SELF-FOCUSING sets an upper limit [1] on the achievable intensity from a laser employing an optically dense host material such as glass or ruby. But even if very high intensity were achieved, the laser may well be useless unless the beam is of adequate optical quality. For example, for laser fusion experiments the light must be focused on a target of 100-μm radius, more or less. The question therefore arises whether the phase distortions introduced by the nonlinearity of the refractive index, which eventually would lead to self-focusing, may not spoil the optical quality of the beam long before self-focusing actually occurs. It is the purpose of this paper to investigate this question.

Self-focusing can occur in two quite distinct ways depending on the power level. At low power the beam tends to collapse more or less as a whole [2], [3]. At high-power levels there is also a tendency to collapse as a whole, but before this can proceed very far, the beam breaks up and self-focuses in a myriad of filaments [1], [4]. As we are interested primarily in very powerful beams we shall in this paper adopt the nomenclature that *self-focusing* means the unstable breakup of the beam into many filaments; for the general collapse of the beam as a whole we shall adopt the term *nonlinear lensing*. Both processes lead to optical loss.

Our analysis will be based on the quasi-optical equation

$$\frac{2i\omega}{v}\frac{\partial E}{\partial z} = \nabla^2 E + \gamma |E|^2 E \tag{1}$$

in which γ is proportional to n_2 and represents the nonlinear part of the refractive index, and v is phase velocity in the medium $v = c/n_0$. If we work in variables (x, y, z, τ) rather than (x, y, z, t), where

$$\tau = t - v/c \tag{2}$$

then (1) can represent the propagation of a pulse. In this case $\partial/\partial z$ is calculated with τ = const, i.e., in a frame moving with the pulse, and E depends on τ as a parameter only. In our work it will generally be more convenient to work in the real amplitude A and phase ϕ, given by

$$E = A \exp(i\phi) \tag{3}$$

rather than in E. We shall not, however, need to rewrite (1) in terms of A and ϕ.

We have been concerned mainly with the laser-induced fusion problem of focusing a very powerful laser beam onto a small target. It therefore seemed most natural to think of beam quality in terms of the smallest focal spot one can produce with an ideal lens. Accordingly, in this paper we measure beam quality in terms of achievable focal spot size.

II. Effect of Incipient Self-Focusing

At very high power levels small-scale perturbations grow to what are ultimately disastrous proportions. During this process, perturbations of the initially plane-wave front grow larger and progressively degrade the beam. To study the early phases of this growth it is sufficient to study initial perturbations of the amplitude and phase of the form [1], [4]

$$(\delta A)_{\text{initial}} = -A_0 \delta_A \sin(k_x x)\cos(k_y y)$$
$$(\delta\phi)_{\text{initial}} = \delta_\phi \sin(k_x x)\cos(k_y y). \tag{4}$$

Because it will soon outstrip all others, we confine our attention to the fastest growing mode; this grows as

$$(\delta A)_z = -A_0[\delta_A \cosh \alpha z + \delta_\phi \sinh \alpha z]\sin(k_x x)\cos(k_y y)$$
$$(\delta\phi)_z = [\delta_A \sinh \alpha z + \delta_\phi \cosh \alpha z]\sin(k_x x)\cos(k_y y). \tag{5}$$

Moreover, we may set $k_x = k_y$ as this mode ultimately grows fastest [1]. Thus after a few generations of growth the electric-field envelope will be

$$E = E_0[1 - \beta \sin kx \cos ky]\exp[i\beta \sin kx \cos ky] \tag{6}$$

where we have dropped indices on the k and have written $\beta = \frac{1}{2}(\delta_A + \delta_\phi)\exp(\alpha z)$ for short. In order for (6) to be a good approximation to the true perturbed field β should be small. We shall, however, wish to say something about finite perturbations and therefore shall *not* so restrict β, with the understanding that the use of our final formula with β not small requires justification.

The effect of incipient self-focusing is calculated by illuminating an aperture with the perturbed field (6) and examining the resultant Fraunhofer diffraction pattern. This simply amounts to a cross-ruled grating problem of the type discussed, for example, by Goodman [5]. The extra set of rulings and the amplitude modulation add nothing to the difficulty. At

Manuscript received May 20, 1974; revised October 14, 1974. This work was performed under the auspices of the U.S. Atomic Energy Commission.

The author is with the Los Alamos Scientific Laboratory, Los Alamos, N. Mex. 87544.

high-power levels $1/k$ is much smaller than the aperture, so the grating has many rulings each way. This has the result that the grating orders do not overlap. Thus the central spot has precisely the intensity and phase distribution which would have been produced by plane-wave illuminated aperture. Owing to diffraction into higher order spots, however, power is lost from the central spot; its intensity is reduced by the degradation factor

$$D = J_0^2(\beta/2)\,[J_0^2(\beta/2) + \beta^2 J_1^2(\beta/2)]\,/(1 + \beta^2/4). \tag{7}$$

The calculation of this result is outlined in the Appendix. Had there been an amplitude perturbation alone, it is clear that the degradation factor would have been

$$D^* = (1 + \beta^2/4)^{-1} \tag{8}$$

rather than (7). Table I gives numerical values of D^* and of D versus β. It is seen that, over the range of β tabulated, the amplitude and the phase perturbations account for approximately equal loss factors, that is to say D roughly equals $(D^*)^2$.

Actually, well before $\beta = 1$, higher harmonics of the normal mode (5) will develop [1], owing to nonlinear self-interaction of the perturbation. This results in a sharpening of the peaks and a broadening of the valleys of both δA and $\delta\phi$. When this happens, all of the energy in the amplitude perturbation is lost, as before, but as the phase peaks sharpen, the relative loss factor owing to phase modulation diminishes. In fact, it is easy to see that for a phase modulation, which is of the form of flat valleys and narrow spikes, the diffraction loss goes to zero as the spike width goes to zero *regardless* of spike height. Now it has been shown [6] that precisely one critical power goes into a self-focal spot. As each cell of our normal mode pattern contains 3.3735 critical powers [1], the quantity D^* goes to the asymptotic limit $1 - 1/3.3735 = 0.7036$. This corresponds with the last value $\beta = 1.298$ in Table I. It follows from our preceding discussion that the corresponding value of D, namely 0.5467, *is an overestimate of power loss at the self-focal limit*, because it does not allow for sharpening of the phase spikes.

TABLE I
DEGRADATION FACTORS D AND D^*

β	D, from Eq. (7)	D* from Eq. (8)
0.0	1.000	1.0000
0.1	0.9951	0.9975
0.2	0.9803	0.9901
0.3	0.9568	0.9780
0.4	0.9251	0.9615
0.5	0.8873	0.9412
0.6	0.8449	0.9174
0.7	0.7996	0.8909
0.8	0.7530	0.8621
0.9	0.7066	0.8316
1.0	0.6620	0.8000
1.298	0.5467	0.7036

Owing to the lack of a satisfactory mathematical theory of the later stages of self-focusing, we cannot compute the power loss as self-focus is approached. We have, however, shown that incipient self-focusing does not lead to enlargement of the main focal spot, but does lead to power loss in this (diffraction-limited) spot. As self-focus is approached the power-degradation factor monotonically approaches a limit lying somewhere between 0.55 and 0.70.

It follows that power on target (into the focus) increases monotonically as the amplifier output is raised, right up to the limit of self-focusing. Beyond the self-focusing limit all bets are off. If self-focusing occurs well inside the amplifier, scattered and diffracted light from the foci will interact nonlinearly with the remaining light. This automodulation of the beam will further degrade its optical quality in a way the author sees no way to estimate.

III. Nonlinear Lensing

Incipient self-focusing leads to diffraction of power out of the main focal spot, but to no loss of quality of the spot itself. Nonlinear lensing on the other hand leads to large-scale aberrations which smear the focal spot. Vlasov *et al.* [3] have developed a moment theory of (1) which seems particularly well suited to the problem of estimating focal spot size. The theory treats certain integrals evaluated over the full beam cross section Σ, namely

$$\begin{cases} W = \displaystyle\int_\Sigma A^2\, d\sigma \quad \rho^2 = \frac{1}{W}\int_\Sigma r^2 A^2 d\sigma \\ B = -\dfrac{v}{\omega W}\displaystyle\int_\Sigma A^2 \tilde{r}\cdot\nabla\phi\, d\sigma \\ C = \dfrac{v^2}{\omega^2 W}\displaystyle\int_\Sigma \left[(\nabla A)^2 + A^2(\nabla\phi)^2 - \frac{1}{2}\gamma A^4\right] d\sigma. \end{cases} \tag{9}$$

Clearly, they are all functions of z alone; the moment theory specifies the z dependence as

$$\begin{cases} W, C \text{ are constants} \\ B(z) = Cz + B_0 \\ [\rho(z)]^2 = Cz^2 + 2B_0 z + \rho_0^2 \end{cases} \tag{10}$$

where B_0 and ρ_0^2 are, respectively, B and ρ^2 evaluated at $z = 0$. From its definition it is apparent that ρ is the root-mean-square (rms) beam radius. Further noting that

$$\rho\frac{d\rho}{dz} = Cz + B_0 = B(z) \tag{11}$$

it is apparent that B measures the mean divergence of the

beam; precisely, B/ρ is the tangent of the mean divergence angle. From (10) we see that ρ^2 is a minimum when $z = z_m$

$$z_m = -B_0/C \tag{12}$$

and at this point $\rho = \rho_m$

$$\rho_m^2 = (\rho_0^2 C - B_0^2)/C. \tag{13}$$

The quantity z_m we shall call the focal distance, as modified by diffraction and by aberration and shall use ρ_m as our estimate of the aberrated focal spot size.

To make our computations we must know how the moments (9) transform on passage through a thin lens of focal length R. At the entrance to the lens let the moments and the field have the values

$$\rho = \rho_e \quad B = B_e \quad C = C_e \quad E = A \exp(i\phi_e). \tag{14}$$

At the exit ρ and A will not have changed, but the phase will be modified to

$$\phi = \phi_e + \omega r^2/(2cR). \tag{15}$$

Setting (15) into (9) we readily see that at the lens exit

$$\begin{cases} W = W_e \quad \rho^2 = \rho_e^2 \\ B = B_e - \rho_e^2/R \\ C = C_e - 2B_e/R + (\rho_e/R)^2. \end{cases} \tag{16}$$

By combining the lens transformation (16) with the translation transformation (10) we can compute the result of passing the beam through such an optical device as a telescope. In making such transformations it is useful to note that the quantity

$$\rho^2 C - B^2 \text{ is invariant both under translation (10) and under the lens transformation (16).} \tag{17}$$

As our first example, let us consider a beam which at $z = 0$ has a Gaussian profile and diverges with a radius of curvature R, so that

$$A = A_e \exp[-r^2/2a_e^2] \quad \phi = -\omega r^2/(2vR). \tag{18}$$

This beam is to be propagated a distance z through a nonlinear passive medium. We readily calculate

$$\begin{cases} W = \pi a_e^2 A_e^2 \quad \rho_0^2 = a_e^2 \\ B_0 = a_e^2/R \\ C = (v/\omega a_e)^2 [1 - \frac{1}{4}\gamma a_e^2 A_e^2 + (\omega a_e^2/vR)^2] \end{cases} \tag{19}$$

whence by (10) we have

$$[\rho(z)]^2 = a_e^2 [(1 + z/R)^2 - (N - 1)(vz/\omega a_e^2)^2], \qquad N \equiv \tfrac{1}{4}\gamma a_e^2 A_e^2. \tag{20}$$

For a parallel beam ($R = \infty$) ρ is constant if $N = 1$; for this reason we shall call N as defined in the preceding the number of critical powers in the beam. To be precise, because we used a Gaussian profile rather than a minimum critical power profile [3], N is 1.074 times the true number of critical powers as defined by Chiao *et al.* [7].

For a beam of many critical powers, self-focusing will occur in a distance z_f given by [1]

$$z_f = \frac{2\omega}{v\gamma A_e^2} \log(3/\delta) = \frac{\omega a_e^2}{2vN} \log(3/\delta) \tag{21}$$

where δ measures the initial perturbation. At $z = z_f$ (20) gives

$$[\rho(z_f)]^2 = a_e^2 \left\{ (1 + z_f/R)^2 - \frac{N - 1}{4N^2} [\log(3/\delta)]^2 \right\}. \tag{22}$$

Clearly, for any z in $0 \leqslant z \leqslant z_f$, $\rho^2 = a_e^2 (1 + z/R)^2$ is a very good approximation provided N is large. As we are interested only in $z \leqslant z_f$, propagation of a beam through a nonlinear medium can be treated by the simplest ray optics; the only effect of the nonlinear refractive index is a phase shift at the exit.

To show how we use the preceding ideas let us consider the divergent beam of Gaussian profile given by (18). Now, however, we pass it through an amplifying nonlinear medium of linear gain g Np/cm. The amplifier ends are at $z = 0$ and $z = l$. According to our preceding results, deduced from (22), the amplitude inside the amplifier can be expressed as

$$A(z) = (A_e/\zeta) \exp\left\{ -\frac{r^2}{2a_e^2\zeta^2} + \frac{1}{2} gz \right\}, \qquad \zeta \equiv 1 + z/R \tag{23}$$

provided only N is large. At the amplifier output the phase will consist of two parts, the term

$$\phi_L = -\omega r^2/(2vR\zeta_0), \qquad \zeta_0 \equiv 1 + l/R \tag{24}$$

which arises from the beam divergence, plus a nonlinear phase shift

$$\phi_{NL} = -\int_0^l \frac{v\gamma}{2\omega} [A(z)]^2 \, dz = -\frac{v\gamma}{2\omega} l_{\text{eff}} A_0^2 \exp(-r^2/a_0^2),$$

$$A_0 \equiv A_e/(1 + l/R) \quad a_0^2 \equiv a_e^2 (1 + l/R)^2 \tag{25}$$

where l_{eff} is an effective length. The integral is taken along the geometric optic rays on which $r/(a_e\zeta)$ is constant. Thus

$$l_{\text{eff}} = \exp(-gl) \int_0^l (\zeta_0/\zeta)^2 \exp(gz) \, dz. \tag{26}$$

At the exit we first collimate the beam as well as possible, i.e., reduce B_{exit} to zero, by means of a lens of focal length R_c. After this collimation we have

$$A = A_0 \exp(-r^2/2a_0^2) \quad \phi = \phi_L + \phi_{NL} + \omega r^2/2cR_c). \tag{27}$$

Setting these into (9) we first obtain

$$\rho_0^2 = a_0^2$$

$$B_0 = -\frac{ca_0^2}{\omega} \left\{ \frac{\omega}{c} \left(\frac{1}{R_c} - \frac{n_0}{R\zeta_0} \right) + \frac{vl_{\text{eff}}}{\omega a_0^4} N \right\} = 0$$

or

$$\frac{1}{R_c} = \frac{n_0}{R\zeta_0} - \left(\frac{v}{\omega a_0^2} \right)^2 n_0 l_{\text{eff}} N. \tag{28}$$

With this value of $1/R_c$ we calculate

$$C_0 = \frac{c^2}{\omega a_0^2}\left\{1 + \frac{7}{9}\left(\frac{vl_{\text{eff}}}{\omega a_0^2}N\right)^2\right\}. \tag{29}$$

In the last two equations N is the number of critical powers *in the exit* beam.

We now pass the beam through an ideal lens of focal length F. Under this transformation the quantity

$$\rho_0^2 C_0 - B_0^2 = \frac{c^2}{\omega^2}\left[1 + \frac{7}{9}\left(\frac{vl_{\text{eff}}}{\omega a_0^2}N\right)^2\right] \tag{30}$$

remains invariant, but C transforms to

$$C_F = \frac{a_0}{F}^2\left\{1 + \left(\frac{cF}{\omega a_0^2}\right)^2\left[1 + \frac{7}{9}\left(\frac{vl_{\text{eff}}}{\omega a_0^2}N\right)^2\right]\right\}. \tag{31}$$

Setting these values into (12) and (13), we obtain for the focal distance z_M and focal spot size ρ_M^2

$$z_m = F\Big/\left\{1 + \left(\frac{cF}{\omega a_0^2}\right)^2\left[1 + \frac{7}{9}\left(\frac{vl_{\text{eff}}}{\omega a_0^2}N\right)^2\right]\right\}$$

$$\rho_m^2 = \left(\frac{cF}{\omega a_0^2}\right)^2\left\{\frac{1 + \frac{7}{9}\left(\frac{vl_{\text{eff}}}{\omega a_0^2}N\right)^2}{1 + \left(\frac{cF}{\omega a_0^2}\right)^2\left[1 + \frac{7}{9}\left(\frac{vl_{\text{eff}}}{\omega a_0^2}N\right)^2\right]}\right\}. \tag{32}$$

Normally, the second term in the denominators of (32) will be much smaller than 1. If instead this term were unity, we would have $(\rho_m)^2 = a_0^2/2$. Thus, unless F is inordinately large, the beam quality becomes catastrophically bad long before the denominators differ appreciably from unity. Clearly, $(cF/\omega a_0)^2$, or more precisely, $(cF/\omega a_0)^2/[1 + (cF/\omega a_0^2)^2]$, is the mean-square radius of an ideal ($N = 0$) diffraction-limited spot. Thus we can define a degradation factor D by

$$\frac{1}{D} = \frac{(\rho_m)^2}{(\rho_{\text{ideal}})^2} = \frac{1 + \frac{7}{9}\left(\frac{vl_{\text{eff}}}{\omega a_0^2}N\right)^2}{1 + \left(\frac{cF}{\omega a_0^2}\right)^2\left[1 + \frac{7}{9}\left(\frac{vl_{\text{eff}}}{\omega a_0^2}N\right)^2\right]}$$

$$\doteq 1 + \frac{7}{9}\left(\frac{vl_{\text{eff}}}{\omega a_0^2}N\right)^2. \tag{33}$$

Everything has now been calculated except for l_{eff}. This quantity can be expressed exactly in terms of exponential integral functions, but it is more instructive to examine two limiting cases. First let us set $g = 0$. Then (26) gives

$$l_{\text{eff}} = l(1 + l/R), \quad \text{if } g = 0. \tag{34}$$

In the other limit consider an amplifier of sufficiently high gain and a beam of sufficiently weak divergence that $Rg \gg 1$. Then integrating (26) by parts gives

$$l_{\text{eff}} = \zeta_0^2 \exp(-g^l)\left\{\left[\frac{\exp(gz)}{g\zeta^2}\right]_0^l + \frac{2}{gR}\int_0^l \frac{1}{\zeta^3}\exp(gz)\,dz\right\}. \tag{35}$$

Continuing this process gives the asymptotic expansion

$$l_{\text{eff}} = \frac{1}{g}\left\{\left[1 + \frac{2}{g(R+l)} + \frac{2.3}{[g(R+l)]^2} + \cdots\right] - \zeta_0^2 \exp(-gl)\left[1 + \frac{2}{gR} + \frac{2.3}{(gR)^2} + \cdots\right]\right\}. \tag{36}$$

For a high-gain amplifier $\exp(-gl) \ll 1$ and

$$l_{\text{eff}} \doteq \frac{1}{g}\left\{1 + \frac{2}{g(R+l)}\right\}. \tag{37}$$

Clearly, the aberration is least when g is large and $R = \infty$.

For a parallel beam propagating through an amplifier of linear gain g it has been shown [1] that the critical intensity I_c, which just self-focuses at the exit, is given by

$$I_c = \frac{10^{-7} c\epsilon_0}{3\pi\epsilon_2}\left(\frac{gc/\omega}{4\Phi_M}\right)\log\left(\frac{3}{\delta}\right). \tag{38}$$

Rewriting this as the number of critical powers in the beam gives

$$N_c = \frac{\omega a_0^2 g n_0}{2c(4\Phi_M)}\log(3/\delta). \tag{39}$$

For an amplifier of power gain exceeding 6.43, $4\Phi_M = 0.7246$. Thus at the self-focusing limit the degradation factor owing to nonlinear lensing is

$$(1/D)_{\text{lim}} = 1 + 0.37\,[\log(3/\delta)]^2. \tag{40}$$

As $\log(3/\delta)$ could conceivably exceed 10 for an initially clean beam, ρ_m might be as large as five to ten times the ideal diffraction limit. For $\lambda = 1.06$ μm and $F/a_0 = 30$ the diffraction-limited rms radius is 5 μm. In this case the power loss starts to become serious for targets of 25–50-μm radius. For larger targets the nonlinear aberration will alter the intensity distribution over the target area, but will not lead to a serious loss of total power on target. It is easy to see from (33) that if ρ_m exceeds the target radius, power on target will be maximized by reducing the total output to the point where ρ_m matches the target size.

In the foregoing analysis we have tacitly assumed a steady beam, whereas normally the very high laser powers of which we have been thinking come as short pulses. But (1) describes pulses as well as continuous beams if we simply allow E to depend on the retarded time τ as a parameter. This in no way alters the moment theory; the only effect is that A, and hence N, in all our foregoing formulas now depend on τ. If we are interested only in peak power, we simply set this peak value of N into the appropriate formula, e.g., (32).

If instead we are interested in total energy on target, some sort of time averaging is required. As we wish to avoid a time-dependent collimating lens, the logical place to do this averaging is early in the problem. Hence we do our time averaging at the very beginning, that is we define time-averaged moments by simply extending the range of integration in (9) to cover all τ as well as the full beam cross section. This in no way modifies the basic equations (10) and (16). To illustrate let us return to our first example (18), but now we

allow A_e to depend on τ as

$$A_e = A_{e0} \exp(-\tau^2/2b^2). \tag{41}$$

The time-averaged quantities, which we write with a bar, become

$$\overline{W} = \tfrac{1}{2}\pi^{3/2} a_e^2 b A_{e0}^2 \quad \overline{\rho_0^2} = a_e^2$$
$$\overline{B}_0 = a_e^2/R$$
$$\overline{C} = (v/\omega a_e)^2 [1 - \gamma a_e^2 A_{e0}^2/(4\sqrt{2}) + (\omega a_e^2/vR)^2]. \tag{42}$$

Comparing with (19) we see that the sole result of this averaging is to replace N by $\overline{N}$, given by

$$\overline{N} = N_{\text{peak}}/\sqrt{2}. \tag{43}$$

With this simple substitution all our instantaneous results are transformed to time-averaged results.

IV. Conclusions

The most important result of Section II is intuitively obvious, namely that under the influence of incipient self-focusing alone, the central part of the far-field pattern is of high optical quality and the junk is all diffracted at large angle. Thus if incipient self-focusing were the only problem it could be solved by spatial filtering. An aperture in the focal plane of a lens could be several times the diffraction-limited spot size and yet filter the beam effectively. Moreover, from (7) it is very easily seen that such filtering would discard negligible total energy provided only it is done often enough.

The really serious problem is nonlinear lensing. In Section III we give a theory of this phenomenon which is mathematically sound, but it is based on the assumption that the rms spot radius is a good measure of optical quality. Fortunately, there is some experimental evidence on this point. Campillo *et al.* have recently measured the effect of nonlinear lensing in glass [8]. They report an experimental value of $2vlN/(\omega a_0^2)$ as 3.9. Thus from (33) $1/D = 13$ instantaneous peak and $1/\overline{D} = 7.0$ time averaged. Their optical system would have produced a diffraction-limited spot of 0.034-cm radius. Thus (32) predicts $\rho_m = 0.12$ cm, whereas they measured 0.10-cm peak value in their streak-camera record. We can make another comparison. Reference [8, fig. 1(a) and (b)] show, respectively, unaberrated and aberrated burn patterns. Measurement of these gives the aberrated to unaberrated radius ratio as approximately 2.1. Our theoretical prediction would be $(1/\overline{D})^{1/2} = 2.6$. Within experimental error our rms radius, both instantaneous peak and time averaged, seems to agree with what the eye aided by photography judges to be the focal-spot radius.

Appendix

The Far-Field Diffraction Pattern Produced by Incipient Self-Focusing

We wish to consider an aperture Σ, which for convenience we take to be a square $a \times a$, illuminated by the field (7). The far-field diffraction pattern is computed simply by following the prescription given by Goodman [5]. We expand the incident field (7) as a Fourier series and substitute the result as $E_0(\overline{x}, \overline{y})$ into the right-hand side of

$$E(x,y,z) = \frac{i\omega}{2\pi cz} \exp\left\{-\frac{i\omega}{2cz}(x^2+y^2)\right\} \cdot \int_\Sigma E_0(\overline{x},\overline{y}) \exp\left\{\frac{i\omega}{cz}(x\overline{x}+y\overline{y})\right\} d\overline{x}\,d\overline{y}. \tag{A1}$$

The expansion is perfectly straightforward and the series can be integrated term by term to give

$$E(x,y,z) = \frac{2i\omega E_0}{\pi cz} \exp\left[-\frac{i\omega}{2cz}(x^2+y^2)\right] \cdot [\Sigma_0 + \Sigma'] \tag{A2}$$

where Σ_0 is the zero-order term

$$\Sigma_0 = \frac{c^2z^2}{\omega^2 xy} J_{00}\left(\frac{\beta}{2}\right) \sin\left(\frac{\omega x a}{2cz}\right) \sin\left(\frac{\omega y a}{2cz}\right) \tag{A3}$$

and Σ' is the rest of the series, which we write as

$$\Sigma' = \frac{1}{a^2k^2} \sum_{m,n=-\infty}^{\infty}{}' a^2 J_{mn} \cdot \frac{\sin\frac{a}{2}\left[(m+n)k + \frac{\omega z}{cz}\right] \sin\frac{a}{2}\left[(m-n)k + \frac{\omega z}{cz}\right]}{[m+n+\omega x/kcz]\,[m-n+\omega y/kcz]}. \tag{A4}$$

The double sum $\Sigma\,\Sigma'$ extends over all m, n *except* $m = n = 0$. The coefficients J_{mn} are given by

$$J_{mn}\left(\frac{\beta}{2}\right) = J_m J_n + (i\beta/4) \cdot [J_m(J_{n-1} - J_{n+1}) + J_n(J_{m-1} - J_{m+1})] \tag{A5}$$

and every Bessel function has the argument $\beta/2$. Our equations (A3)–(A5) are an obvious generalization of Goodman's [5, eq. 4.23]. The double sum and product $J_m J_n$ arise because our phase modulation is two dimensional, and the terms in (A5) multiplied by $i\beta/4$ arise from the amplitude modulation.

As is well known, the grating orders all separate when the number of rulings, i.e., when $(ak)^2$, is large; thus the central (zero-order) spot pattern is given to good precision by (A2) with the term Σ' omitted. This is just the diffraction pattern of an $a \times a$ aperture illuminated by an initial field of intensity

$$I = |E_0|^2 |J_{00}|^2 = |E_0|^2 J_0^2 [J_0^2 + \beta^2 J_1^2] \tag{A6}$$

whereas our actual field had a mean intensity

$$\overline{I} = |E_0|^2 (1 + \beta^2/4) \tag{A7}$$

when averaged over the aperture. From this follows (7) of the main text.

Acknowledgment

The author wishes to thank the referees for their comments, which helped him improve the paper from its initial version.

REFERENCES

[1] B. R. Suydam, "Self-focusing of very powerful laser beams, Part I," in *Laser Induced Damage in Optical Materials: 1973* (NBS Special Publication 387), A. J. Glass and A. H. Guenther, Ed. Washington, D.C.: U.S. Government Printing Office, 1973.
——, "Self-focusing of very powerful laser beams II," *IEEE J. Quantum Electron.*, vol. QE-10, pp. 837–843, Nov. 1974.

[2] P. L. Kelley, "Self-focusing of optical beams," *Phys. Rev. Lett.*, vol. 15, pp. 1005–1008, Dec. 27, 1965.

[3] S. N. Vlasov, V. A. Petrishchev, and V. I. Talanov, "Averaged description of wave beams in linear and nonlinear media (The method of moments)," *Izv. Vyssh. Ucheb. Zaved. Radiofiz.*, vol. 14, pp. 1353–1363, Jan. 15, 1971 (English translation available from Consultants Bureau, a Division of Plenum Publishing Corporation, 227 West 17th St., New York, N.Y. 10011).

[4] V. I. Bespalov and V. I. Talanov, "Filamentary structure of light beams in nonlinear liquids," *Zh. Eksp. Teor. Fiz., Pis'ma Red.*, vol. 3, pp. 307–310, June 15, 1966.

[5] J. W. Goodman, *Introduction to Fourier Optics.* New York: McGraw-Hill, 1968, ch. 4.

[6] V. E. Zakharov, V. V. Sobolev, and V. S. Synakh, "Character of singularity and stochastic phenomena in self-focusing," *Zh. Eksp. Teor. Fiz., Pis'ma Red.*, vol. 14, pp. 390–393, Nov. 20, 1971.

[7] R. Y. Chiao, E. Garmire, and C. H. Townes, "Self-trapping of optical beams," *Phys. Rev. Lett.*, vol. 13, pp. 479–482, Oct. 12, 1964.

[8] A. J. Campillo, R. A. Fisher, R. C. Hyer, and S. L. Shapiro, "Streak camera investigation of self-focusing onset in glass," *Appl. Phys. Lett.*, vol. 25, pp. 408–411, Oct. 1, 1974.

Photon-Echo Behavior in the Presence of Extreme Inhomogeneous Broadening

NOBUO TAKEUCHI

Abstract—**Analysis of photon-echo behavior using single-mode excitation is given. It is shown that in the presence of extreme inhomogeneous broadening, the excitation with long pulses may display a complicated echo shape. Two typical cases are treated, one in which the pulses have equal length, and the other in which the pulses have equal electric-field strength. These show a large difference in echo behavior, especially for large excitation pulse areas.**

I. INTRODUCTION

COHERENT PHENOMENA in an inhomogeneously broadened system have recently attracted attention in optical transitions. In particular, the theory of superradiance has been closely investigated [1], [2]. The photon echo [3], [4] is a typical example of coherent phenomena and is developing as a powerful method of measuring the relaxation [5] and the interaction with the neighboring atoms in a system [6]. The inhomogeneous broadening must be much larger than the homogeneous broadening in order to avoid free induction decay; this is satisfied under usual conditions. Most photon-echo experiments have been done in systems where the inhomogeneous line broadening is much wider than the reciprocal of excitation pulsewidth [3]–[8] (we shall call this situation "long-pulse excitation"). However, these experiments have been analyzed on the assumption that the inhomogeneous width is much narrower than the reciprocal of pulsewidth; i.e., "short-pulse excitation." This assumption was enough to explain the echo behavior because the existence of many modes in the excitation pulses averaged out the fine structure in the echo shape generated by each mode.

With the advance of laser technology, a stable and single-frequency excitation source has been possible. Liao and Hartmann [7] demonstrated some of the peculiar features of photon echoes in ruby using single-frequency ruby-laser excitation. In electron spin echoes, Mims [9] has already demonstrated the existence of this peculiar behavior for the limited case of two equal excitation pulses. Yajima [10] calculated another limiting case (field strengths $E_1 = E_2$, pulsewidth $\tau_{p1} = \tau_{p2}/2$) in the photon echo in a semiconductor. In this paper we treat the more general case of two arbitrary square-wave excitation pulses. In the case of long-pulse excitation, off-resonant atoms also contribute to the echo formation. The rotation axis and angle for their pseudodipole moments (i.e., the Bloch vectors) [11] are different for a different combination of the excitation-field strength E and the pulsewidth τ_p even for a given pulse area θ, which leads to a different echo behavior. We treat two typical cases: 1) the excitation pulsewidth the same for both pulses (we shall call this "equal τ_p excitation"); and 2) the electric-field strength the same for both pulses ("equal E excitation").

II. FORMULA

We concentrate interest on an ordinary two-pulse echo and consider the simplest system consisting of atoms with two levels in the presence of extreme inhomogeneous broadening. The two relaxation times are taken equal ($T_1 = T_2 = T$). The

Manuscript received June 10, 1974; revised October 4, 1974.

The author was with the Radio and Electrical Engineering Division, National Research Council of Canada, Ottawa, Ont., Canada. He is now with the National Institute for Environment, P. O. Yatabe, Ibaraki 300-21, Japan.

system is optically thin and is irradiated by a circularly polarized plane wave with a frequency ω_0 coinciding with the center of the atomic distribution.

We express the state of a two-level atom by a pseudodipole moment [3] (i.e., the Bloch vector [11]) and follow Jaynes' semiclassical treatment of nuclear induction [12] and its application to spin echo by Bloom [13], taking into consideration the spatial distribution of atoms [3], [14]. When the time of travel of light through a sample is much shorter than the echo width, which is a usual situation, we can ignore the spatial distribution of atoms in a shape factor for the jth atom $S_j(\tau - \tau_j)$ [see (2)], which reduces $S_j(\tau - \tau_j)$ to $S(\tau - \tau_s)$ (where τ is the time after the second pulse and τ_s is the pulse separation). In the case of a large Fresnel number of the irradiated volume, the summation of a phase factor exp $[i(\boldsymbol{k} - 2\boldsymbol{k}_2 + \boldsymbol{k}_1)(\boldsymbol{R}_j - \boldsymbol{R}_{j'})]$ over all excited atoms yields an effective aperture of $\lambda^2/\epsilon A$ [3]. Then the echo intensity is given by

$$I(\boldsymbol{k}) = (N^2/4)(\lambda^2/\epsilon A) I_0(\boldsymbol{k}) \exp(-2t/T) S(\tau - \tau_s)^2 \quad (1)$$

with

$$S(\tau - \tau_s) = \theta_1 \theta_2^2/2 \int_{-\infty}^{\infty} d(\Delta\omega) g(\Delta\omega) [\cos(\Delta\omega(\tau - \tau_s)) \times \sin\phi_1/\phi_1 + \Delta\omega\tau_{p1} \sin(\Delta\omega(\tau - \tau_s)) \times (1 - \cos\phi_1)/\phi_1^2] (1 - \cos\phi_2)/\phi_2^2. \quad (2)$$

Here N is the total number of echo atoms, $I_0(\boldsymbol{k})$ is the spontaneous-emission intensity rate per unit time per mode from an individual atom, t is the time from the beginning of the first pulse, $\Delta\omega$ is the off-resonance frequency, $g(\Delta\omega)$ is the normalized atomic distribution function, ϕ_i is the rotation angle of the Bloch vector by the ith excitation pulse $(= \{(\gamma E_i)^2 + (\Delta\omega)^2\}^{1/2} \tau_{pi})$, and τ_{pi} is the width of the ith excitation pulse. The pulse separation τ_s is long enough compared with τ_{p1} to get rid of the overlapping with the induced free-induction decay [7].

As will be mentioned later, the echo shows a complicated shape for some situations. Hence the integrated echo energy $I_\tau(\boldsymbol{k})$ is more convenient to compare different experimental conditions, and is obtained integrating over τ

$$I_\tau(\boldsymbol{k}) = (N^2/4)(\lambda^2/\epsilon A) I_0(\boldsymbol{k}) \sqrt{2} \times \pi^{1/2} T_2^* F(E_1, \tau_{p1}; E_2, \tau_{p2}) \quad (3)$$

with

$$F(E_1, \tau_{p1}; E_2, \tau_{p2}) = \pi^{1/2} \theta_1^2 \theta_2^4/2\sqrt{2}\, T_2^* \times \int_{-\infty}^{\infty} d(\Delta\omega) [g(\Delta\omega)(1 - \cos\phi_2)/\phi_2^2]^2 \times [\sin^2\phi_1/\phi_1^2 + (\Delta\omega\tau_{p1})^2 (1 - \cos\phi_1)^2/\phi_1^4]. \quad (4)$$

III. Short-Pulse Excitation

In the case of short-pulse excitation, (2) is easily integrated and gives a Gaussian echo shape with the full width at half maximum (FWHM) of $2T_2^*(2 \ln 2)^{1/2}$. The echo peak position is determined only by the first pulse and for a small value of θ_1, it takes place at $\tau_s + \tau_{p1}/2$, [3], [13] after the termination of the second pulse, and for $\theta_1 = \pi/2$, it does so at $\tau_s + 2\tau_{p1}/\pi$.

IV. Short to Long-Pulse Excitation

It is necessary to investigate the transitional behavior from short-pulse to long-pulse excitation and to determine the range of the excitation parameter $\eta(= \tau_p/T_2^*)$ appropriate to each type of excitation. We select the case of equal pulsewidths, and the 90°-180° pulse sequence as typical values of θ_1 and θ_2.

The calculated echo shape $S(\tau - \tau_s)^2$ is plotted in Fig. 1 as a function of $(\tau - \tau_s)/T_2^*$ for a range of τ_p/T_2^* from 0.01 to 20. It is seen that as τ_p/T_2^* increases beyond unity, the echo intensity decreases, the width gradually increases, and the echo peak position shifts to the positive side. However, if we consider the peak position as a function of $(\tau - \tau_s)/\tau_p$ instead of $(\tau - \tau_s)/T_2^*$, as shown in Fig. 2(a), the echo peak stays very nearly at the position $(\tau - \tau_s)/\tau_p = 2/\pi$ for $\tau_p/T_2^* < 1$ and changes position for the region of $\tau_p/T_2^* > 1$. The situation of a stable feature for $\tau_p/T_2^* < 1$ and of a varying feature for $\tau_p/T_2^* > 1$ is seen also in the echo width, the integrated echo energy, and the ratio of the emitted energy to the absorbed energy [Fig. 2(b)]. The echo width stays constant at $2\Delta\tau(\text{FWHM}) = 2(2 \ln 2)^{1/2} T_2^* = 2.36\, T_2^*$ for $\tau_p/T_2^* \leqslant 0.7$ and gradually increases with τ_p/T_2^*, approaching $2\Delta\tau = \tau_p$ for $\tau_p/T_2^* \geqslant 5$. The normalized echo energy $F(\theta_1 = \pi/2, \theta_2 = \pi)$ takes the value of almost unity for $\tau_p/T_2^* \leqslant 0.7$ and gradually approaches $F(\theta_1 = \pi/2, \theta_2 = \pi) = 2.85\, T_2^*/\tau_p$ as τ_p/T_2^* in-

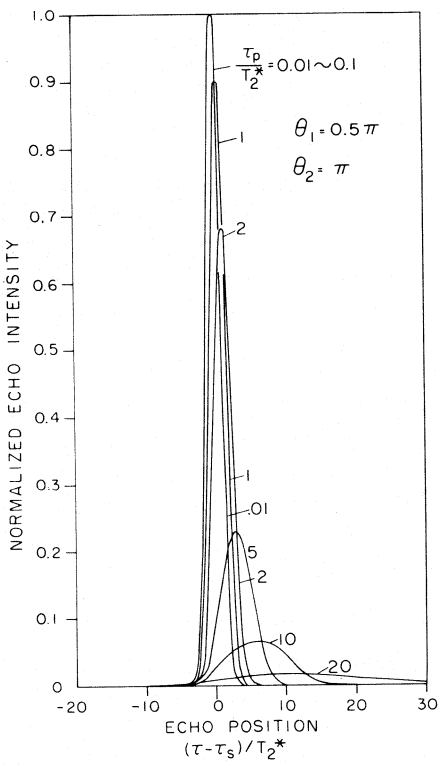

Fig. 1. The echo shape for excitation areas $\theta_1 = \pi/2$ and $\theta_2 = \pi$ with various values for the excitation parameter τ_p/T_2^*. The normalized echo intensity $(S(\tau - \tau_s))^2$ [see (2)] is shown on the vertical axis. The echo position on the horizontal axis is shown in the form $(\tau - \tau_s)/T_2^*$.

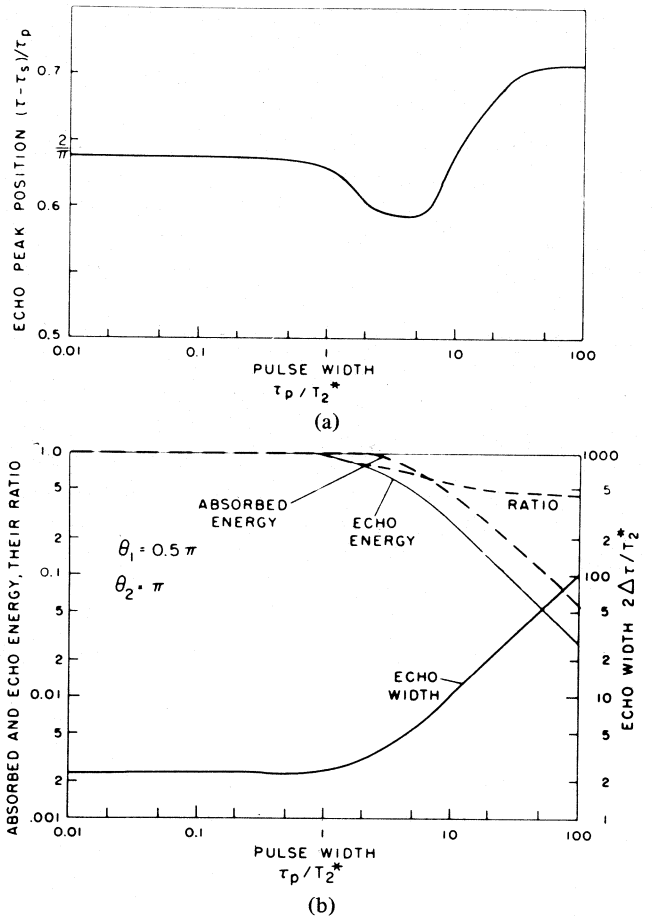

Fig. 2. Behavior of (a) the peak position in units of $\tau_p(=\tau_{p1}=\tau_{p2})$, and (b) the echo width (FWHM) in units of T_2^*. (b) Also shows the echo energy, the absorbed energy by a system, and their ratio, all of which are normalized to unity in the limit of short-pulse excitation. The calculation is done for $\theta_1 = \pi/2$ and $\theta_2 = \pi$ as a function of τ_p/T_2^*.

creases, which means that off-resonant atoms within the range of several times the resonant region $(1/\pi\tau_p)$ contribute to the echo formation. The ratio of the emitted energy in the photon echo to the absorbed energy in the system is also shown in Fig. 2(b), where the ratio at short-pulse excitation is normalized to be unity.

From the inspection of the case of 90°-180° sequence, it is found that the echo behavior is different on both sides of $\tau_p/T_2^* = 1$. In the range $0.2 \leqslant \tau_p/T_2^* \leqslant 5$, the transitional behavior can be seen, while outside this region the echo behavior is typical of short-pulse or long-pulse excitation. Similar features can be seen for different combinations of θ_1 and θ_2.

V. Long-Pulse Excitation with Equal Pulsewidth

We first treat the long-pulse excitation with an equal pulsewidth $(\tau_{p1} = \tau_{p2} = \tau_p)$. We choose the value of 100 as an excitation parameter $(\eta = \tau_p/T_2^*)$ because it corresponds to a parameter determined by a typical excitation pulsewidth of 30 ns [3] and the inhomogeneous broadening of 1.8 GHz (FWHM) in ruby.

The echo intensity was calculated as a function of $t_p = (\tau - \tau_s)/\tau_p$. Nonnegligible echo intensity ($>10^{-3}$ times the maximum) takes place in the range of $|(\tau - \tau_s)/\tau_p| \leqslant 2$. Since the second pulse has a function as a time-reversal pulse and a 180° pulse is typical in the short-pulse excitation, we first study the echo shape for a fixed $\theta_2(=\gamma E_2 \tau_p) = \pi$ while changing $\theta_1(=\gamma E_1 \tau_p)$ from 0.1π to 2π in 0.1π steps. The echo shapes are drawn in Fig. 3(a)-(d). We should notice that the maximum echo intensity expressed by $(S(\tau - \tau_s))^2$, which appears at $\theta_1 \approx 0.6\pi$, not at $\theta_1 = 0.5\pi$, is about 8×10^{-4}, and that this value is much smaller than unity (for the short-pulse excitation) but one order of magnitude larger than the square of the reciprocal excitation parameter $(T_2^*/\tau_p)^2$ of 10^{-4}, which roughly describes the square of the fraction of resonant atoms. The oscillatory shape for $\theta_1 > 1.5\pi$ partially depends on the

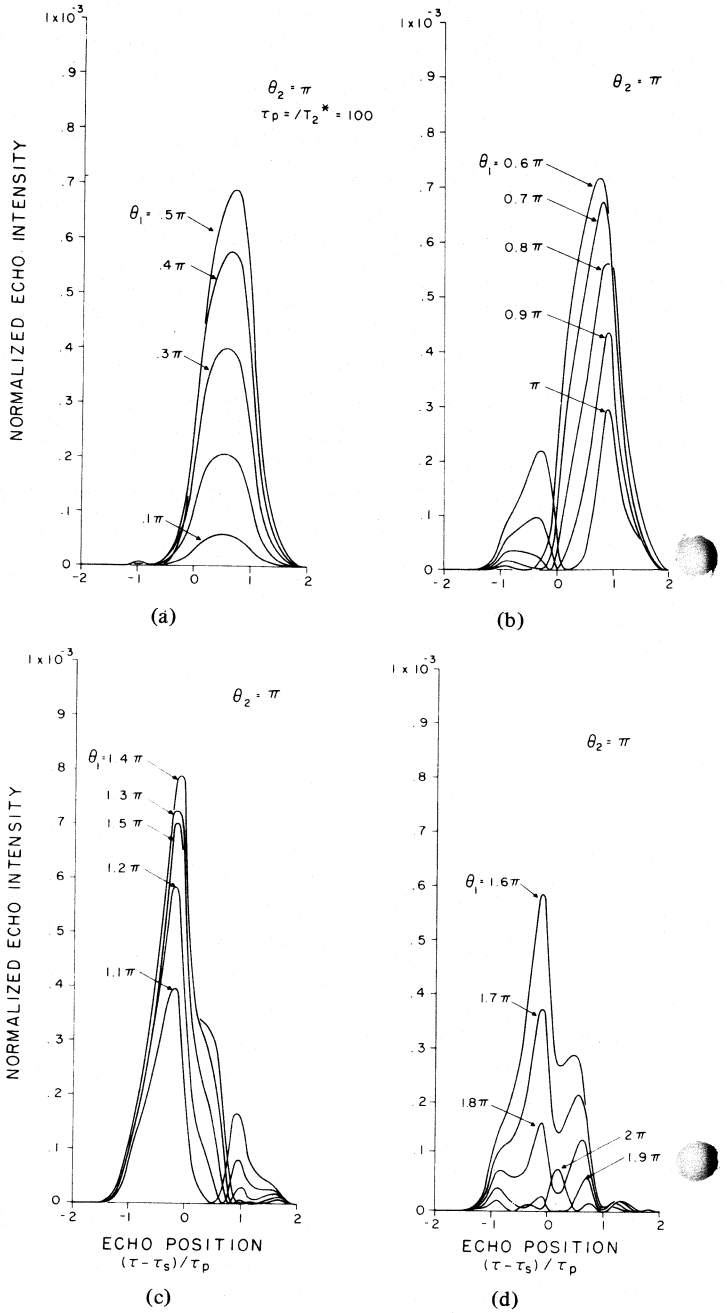

Fig. 3. The echo intensity $(S(\tau - \tau_s))^2$ in equal pulsewidth excitation as a function of the echo position $(\tau - \tau_s)/\tau_p$ for $\theta_2 = \pi$. (a) $\theta_1 = 0.1\pi$ to 0.5π. (b) 0.6π to π. (c) 1.1π to 1.5π. (d) 1.6π to 2π.

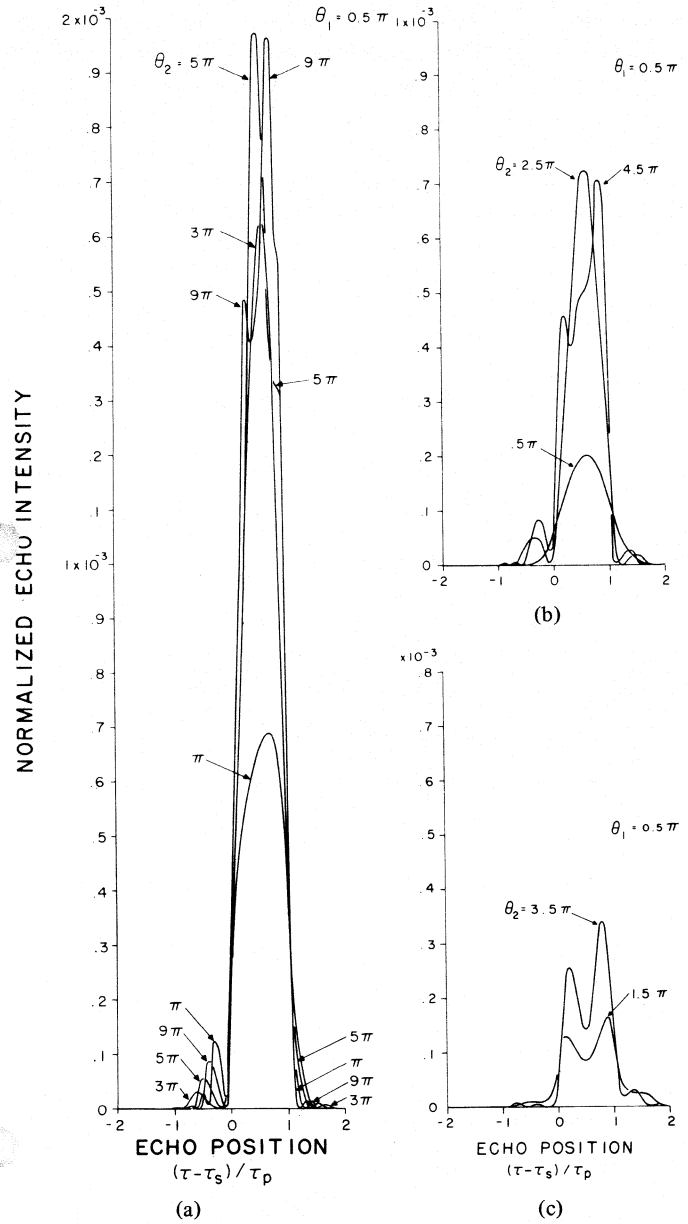

Fig. 4. The echo intensity $(S(\tau - \tau_s))^2$ in equal pulsewidth excitation for $\theta_1 = \pi/2$ and a large θ_2. (a) $\theta_2 = (2p + 1)\pi$. (b) $\theta_2 = (2p + \frac{1}{2})\pi$. (c) $\theta_2 = (2p + \frac{3}{2})\pi$ (p is an integer). It should be noticed that a shallow "notch" is seen in (c).

fact that the condition $\theta_2 > \theta_1$,[1] which gives an efficient time-reversal effect, is not satisfied. Further calculations for $\theta_2 = \pi$ with larger values of θ_1 show only slight enhancement of the peak intensity since θ_2 is smaller than θ_1. The (main) peak is on the positive side of $\tau - \tau_s$ for $\theta_1 = (2p + \frac{1}{2})\pi$ and on the negative side for $\theta_1 = (2p + \frac{3}{2})\pi$. For $\theta_1 = (2p + 1)\pi$, we can see the notched echo where the minimum is centered on the echo signal.

The echo shapes for $\theta_1 = \pi/2$ are shown in Fig. 4(a)-(c). For $\theta_1 = \pi/2$ the echo peak is always located on the positive side of $\tau - \tau_s$. Since θ_2 is larger than $\theta_1 = \pi/2$, the echo intensity is enhanced with an increase in θ_2.

In equal τ_p excitation, the periodicity in θ_1 and θ_2, which is seen in short-pulse excitation, still remains. The extremum of echo intensity takes place around a multiple of $\pi/2$ in θ_1 and $\theta_2/2$. The echo with θ_1 and $\theta_2/2$ off from the multiple of $\pi/2$ shows an intermediate behavior of neighboring multiples of $\pi/2$.

VI. Long-Pulse Excitation with Equal Field Strength

In long-pulse excitation with equal field strength E, we also choose a value 100 as the excitation parameter $\eta = 1/\gamma E T_2^*$ referring to Liao and Hartmann's paper [7], ($\theta = \pi/2$ for τ_p = 80 ns). The change of the echo shape for $\theta_1 (0.1\pi \sim 2\pi)$ with a fixed $\theta_2 = \pi$ is shown in Fig. 5(a)-(d). General features seen in equal τ_p excitation can also be seen here. We should notice that the echo width is determined by the excitation pulsewidth.

A "notched echo" with $\theta_1 = 3\pi$ and $\theta_2 = 0.5\pi$ in [7] is reproduced in Fig. 6, also with $\theta_1 = 2\pi$ and $\theta_2 = 0.5\pi$.

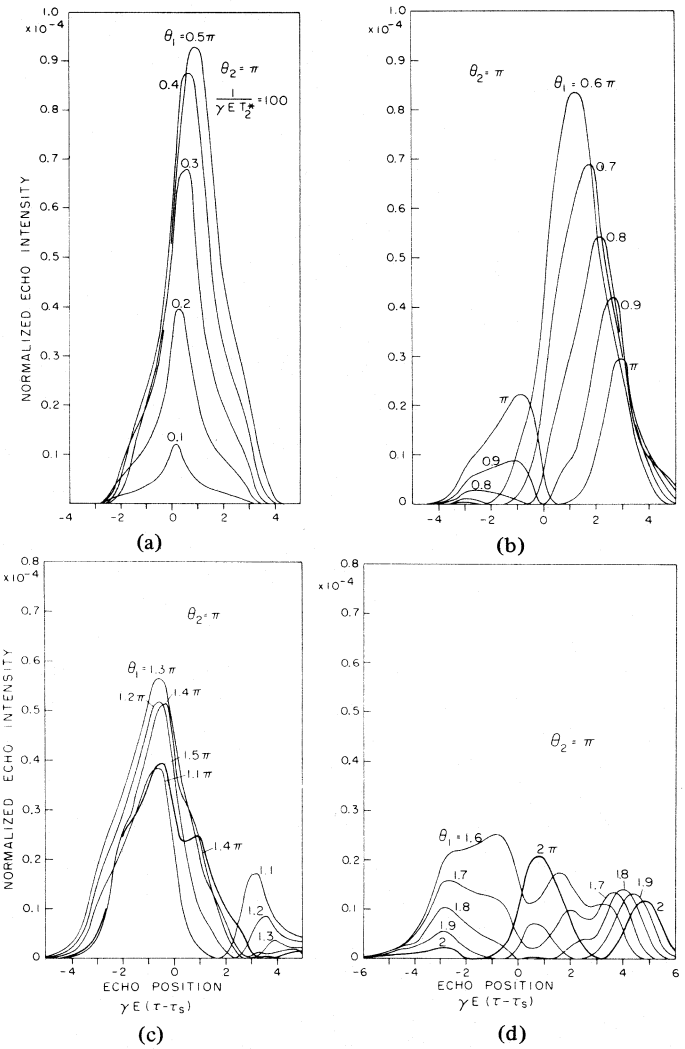

Fig. 5. The echo intensity $(S(\tau - \tau_s))^2$ in equal electric-field excitation as a function of the echo position $\gamma E(\tau - \tau_s)$ for $\theta_2 = \pi$. (a) $\theta_1 = 0.1\pi$ to 0.5π. (b) 0.6π to π. (c) 1.1π to 1.5π. (d) 1.6π to 2π.

[1] For equal τ_p excitation, a larger area θ, i.e., a larger field strength E, orients the rotation axis of each Bloch vector nearer to the applied electric-field direction. This leads to more efficient time reversal by the second pulse for $\theta_2 > \theta_1$ under long-pulse excitation.

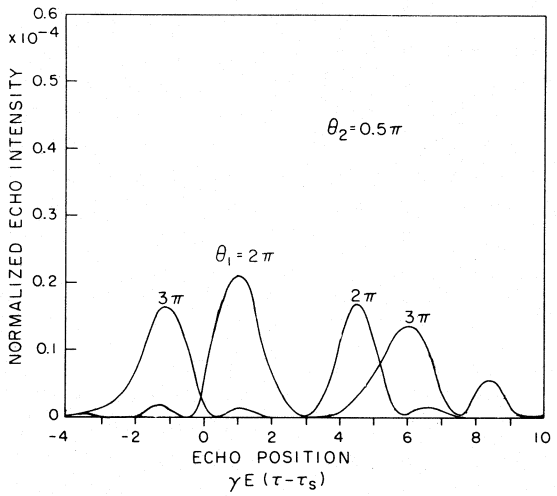

Fig. 6. The echo intensity $(S(\tau - \tau_s))^2$ in equal electric-field excitation for $\theta_2 = 0.5\pi$ and $\theta_1 = 2\pi$ and 3π with respect to the echo position $\gamma E(\tau - \tau_s)$.

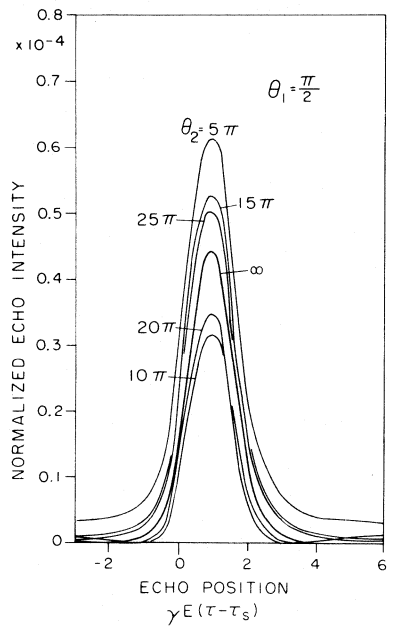

Fig. 7. The echo intensity $(S(\tau - \tau_s))^2$ in equal electric-field excitation for $\theta_1 = \pi/2$ and a large θ_2. The echo intensity gradually converges to an asymptotic shape.

For a large value of θ_2, the averaging effect of the second pulse can be seen. With an increase of θ_2 the Bloch vectors excited by the first pulse are averaged and the contribution from off-resonant atoms is washed away. The echo shape tends to take an asymptotic shape determined by θ_1 without the enhancement of echo intensity. In Fig. 7, an example for $\theta_1 = \pi/2$ is shown. This explains the stable echo at $\theta_1 = \pi/2$ and $\theta_2 = 25\pi$ mentioned in [7]. The averaging effect is different from the narrow spectrum excitation by the long second pulse, which should show a longer echo pulsewidth.

VII. Discussion

We now discuss the relation of the resonance frequency region with the excitation condition. When the echo is excited by two pulses with $\theta_1, \theta_2 \leqslant \pi$, and with $\tau_{p1} \approx \tau_{p2}$, the atom with $\Delta\omega \leqslant 2\pi/\tau_{p1}$ mainly contributes to the echo formation. In equal τ_p excitation, the resonant frequency region is fixed to $1/\pi\tau_p$ because of a fixed (arbitrary) value of excitation parameter $\eta = \tau_p/T_2^*$. With an increase of θ_2 (i.e., an increase of E_2) from $\theta_2 \simeq \pi$ to a large value, the frequency region of atoms contributing to echo formation is widened several times. Consequently, the echo intensity for θ_2 with $(2p + 1)\pi$ (p is an integer) is also enhanced several times. When θ_1 increases in addition to θ_2, the frequency region approaches the whole inhomogeneous broadening as in short-pulse excitation. On the contrary, in equal E excitation, the constant electric field determined by a given parameter $\eta = 1/\gamma E T_2^*$ does not expand the frequency region contributing to echo formation. With an increase of θ_2 (i.e., an increase of τ_{p2}), the averaging of the rapidly oscillating Bloch vector for an off-resonant atom leads to a stable width of echo, instead of widening the echo width (i.e., narrowing the resonance frequency region), and does not bring an enhancement of echo intensity.

In this paper the complex echo behavior in long-pulse excitation was analyzed, based on the simplest model of a two-level atomic system excited by two square-wave pulses. For a case of Gaussian pulse excitation with an amplitude $E_i \exp[-(t - t_i)^2/\tau_{gi}^2]/\pi^{1/2}$, which is nearer to an actual situation by pulse laser excitation, the treatment in this paper gives a good approximation by substituting the pulse area $\theta_i = \gamma E_i \tau_{pi}$ by $\theta_i = \gamma E_i \tau_{gi}$.

Acknowledgment

The author wishes to thank Dr. A. Szabo, Prof. S. R. Hartmann, and Prof. T. Yajima for valuable discussions and comments.

References

[1] R. Jodoin and L. Mandel, "Superradiance in an inhomogeneously broadened atomic system," *Phys. Rev. A*, vol. 9, pp. 873-884, Feb. 1974.

[2] S. M. Zakharov and E. A. Manykin, "Superradiance and photon echo effects in the interaction of coherent optical pulses with inhomogeneously broadened systems," *Sov. J. Quantum Electron.*, vol. 3, pp. 104-107, Sept.-Oct. 1973.

[3] I. D. Abella, N. A. Kurnit, and S. R. Hartmann, "Photon echoes," *Phys. Rev.*, vol. 141, pp. 391-406, Jan. 1966.

[4] J. P. Gordon, C. H. Wang, C. K. N. Patel, R. E. Slusher, and W. J. Tomlinson, "Photon echoes in gases," *Phys. Rev.*, vol. 179, pp. 294-309, Mar. 1969.

[5] a) P. F. Liao and S. R. Hartmann, "Magnetic field- and concentration-dependent photon echo relaxation in ruby with simple exponential decay," *Opt. Commun.*, vol. 8, pp. 310-311, Aug. 19, 1973.
b) A. Compaan, "Concentration-dependent photon-echo decay in ruby," *Phys. Rev. B.*, vol. 5, pp. 4450-4465, June 1972.

[6] a) P. F. Liao, P. Hu, R. Leigh, and S. R. Hartmann," Photon-echo nuclear double resonance and its application in ruby," *Phys. Rev. A.*, vol. 9, pp. 332-340, Jan. 1974.
b) A. Compaan, L. Q. Lambert, and I. D. Abella, "Level crossing effects and spin-dependent decay of circularly polarized photon echoes in ruby," *Opt. Commun.*, vol. 3, pp. 236-239, June 1971.
c) L. Q. Lambert, "Effects of superhyperfine interactions on photon-echo behavior in dilute ruby," *Phys. Rev. B*, vol. 7, pp. 1834-1846, Mar. 1973.

[7] P. F. Liao and S. R. Hartmann, "Radiation locked photon echoes and optical free induction in ruby," *Phys. Lett.*, vol. 44A, pp. 361-362, July 1973.

[8] N. Takeuchi, S. Chandra, Y. C. Chen, and S. R. Hartmann, "Photon echoes in $LaF_3:Nd^{3+}$ and YAG:Nd^{3+}," *Phys. Lett.*, vol. 46A, pp. 97-98, Dec. 1973.
[9] W. B. Mims, "Electron spin echo," in *Electron Paramagnetic Resonance*, S. Geschwind, Ed. New York: Plenum Press, 1972, pp. 263-351; also "Electron echo methods in spin resonance spectroscopy," *Rev. Sci. Instrum.*, vol. 36, pp. 1472-1479, Oct. 1965; also "Spin echoes from broad resonance lines with high turning angles," *Phys. Rev.*, vol. 141, pp. 499-502, Jan. 1966.
[10] T. Yajima, "Photon echo in an interband transition," presented at the Physical Society of Japan Spring Meet., 1972.
[11] R. P. Feynman, F. L. Vernon, Jr., and R. W. Hellwarth, "Geometrical representation of the Schrödinger equation for solving maser problems," *J. Appl. Phys.*, vol. 28, pp. 49-52, Jan. 1957.
[12] E. T. Jaynes, "Matrix treatment of nuclear induction," *Phys. Rev.*, vol. 98, pp. 1099-1105, May 1955.
[13] A. L. Bloom, "Nuclear induction in inhomogeneous fields," *Phys. Rev.*, vol. 98, pp. 1105-1111, May 1955.
[14] S. M. Zakharov, E. A. Manykin, and E. V. Onishchenko, "Contribution to the theory of nonstationary process of the photon-echo type in crystals with ferromagnetic impurities," *Sov. Phys.—JETP*, vol. 32, pp. 714-719, Apr. 1971.

Scaling Generalizations for a CO Electric Laser

WILLIAM B. LACINA AND GARY L. McALLISTER

Abstract—**Several scaling generalizations for a high-pressure CO electric-discharge laser (EDL) are presented and compared with experimental data from a pulsed e^--beam-stabilized device. It is shown that the transient evolution of the CO laser medium is mainly dependent only upon the total energy deposition per CO molecule as a function of time. Results of theoretical calculations for CO/Ar mixtures are presented which show that, for temperatures 100-300 K, laser threshold occurs after $E/p_{CO} \sim 0.5 - 1.0$ J/l/torr (CO) has been deposited, and that steady state is attained after $E/p_{CO} \sim 1.7 - 2.6$ J/l/torr (CO) has been deposited. Experimental results for a variety of CO/Ar and CO/N_2 mixtures confirm these predictions for a range of excitation rates. These generalizations make it possible to predict the temporal power characteristics of a large class of both pulsed and flowing CW CO lasers without resort to extensive computer calculations. Characterization of the gain saturation as a function of total radiation intensity was also investigated. Results indicate that, after attainment of steady state, the CO EDL saturates with threshold level like a simple two-level system, with a scaled saturation intensity of $I_{sat}\xi/p_{CO}^2 \sim 0.6 = 6.4$ W/cm^2/torr^2 (CO) over the range of temperatures from 60 to 300 K (ξ is the fraction of CO self-broadening to total broadening).**

I. Introduction

A MOLECULAR-KINETIC model for an electrically excited (CO, N_2, Ar, He, $\cdots$) gas mixture has been constructed for the calculation of the radiative characteristics of a CO laser oscillator or amplifier. A computer program for the numerical solution of the steady state or transient master equation for the diatomic species has been developed to predict vibrational population distributions, gain and saturation parameters, energy transfer and extraction rates, conversion efficiencies, output intensities, and spectral distributions. The radiative calculations are self-consistent with the saturated gain on all oscillating transitions equal to the losses. The plasma kinetics are described by a Boltzmann energy distribution, with electron density and temperature adjusted self-consistently in the calculation as a function of time to produce a specified temporal input power. A more complete discussion of the assumptions upon which this model is based has been given elsewhere [1], [2], where numerical results for a variety of operating conditions were presented and compared with experimental data from a pulsed high-pressure e^--beam-stabilized CO electric-discharge laser (EDL) oscillator. Similar analytical work on the CO EDL has been presented by numerous other authors [3]-[8].

It is possible to make several reasonable approximations that allow certain general scaling laws for a CO EDL to be formulated [9]. These generalizations, which depend only upon a few basic parameters, make it possible to predict the temporal output characteristics of a large class of both pulsed and flowing CW CO laser systems. Although the present theoretical results are limited to gas mixtures containing CO and monatomic diluents only, comparisons with experimental data for both CO/Ar and CO/N_2 are included. It is found experimentally that the excitation times required to attain threshold and steady state agree with the scaling results predicted for CO/Ar. Uncertainties in the CO-N_2 and N_2-N_2 VV rates make theoretical analysis for CO/N_2 mixtures less reliable. However, the experimental results indicate that CO/N_2 systems can be scaled similarly. Except for the spectral details,

Manuscript received August 2, 1974; revised January 10, 1975. This research was supported in part by the Advanced Research Projects Agency of the Department of Defense and monitored by the Office of Naval Research under Contract N00014-72-C-0043.

W. B. Lacina is with the Northrop Research and Technology Center, Laser Technology Laboratories, Hawthorne, Calif. 90250.
G. L. McAllister was with the Northrop Research and Technology Center, Laser Technology Laboratories, Hawthorne, Calif. 90250. He is now with the Exxon Corporation, Richland, Wash.

it is possible to design general CO/X systems to a very good approximation without resort to extensive computer calculations.

II. Theoretical Model

The present theoretical model consists of four basic systems of equations that couple the CO vibrational-state population densities, the radiation intensities, the gas kinetic temperature, and the plasma-kinetic parameters (electron density and temperature) as a function of time. Since the general formulation of these equations and the assumptions made have been described previously [2], they will be summarized only briefly here. Certain approximations (most of which are not required for the complete computer analysis) make it possible to obtain a variety of general results in terms of a very small set of scale parameters [8], [9]. In fact, one basic parameter related to pumping is all that is required to present a reasonably simple description of the CO EDL under the set of approximations to be discussed later.

The molecular-kinetic processes are described by the master equation for the vibrational population densities n_v of the CO molecule

$$dn_v/dt = R_v^e + \sum_X R_v^{\mathrm{VT}}(\mathrm{CO}, X) + R_v^{\mathrm{VVT}}(\mathrm{CO}, \mathrm{CO}) + R_v^{\mathrm{VVT}}(\mathrm{CO}, \mathrm{N_2}) + R_v^{\mathrm{spon}} + R_v^{\mathrm{stim}} \quad (1)$$

with pumping and relaxation processes which include: 1) electron-impact excitation of the vibrational states; 2) vibration-to-translation (VT) deactivation processes; 3) near-resonant vibration-to-vibration (VVT) single-quantum-exchange collisions; 4) spontaneous radiative decay; and 5) stimulated-emission and absorption processes. Sources for rates have been summarized previously [2].

Radiation intensities are calculated by requiring that the gain coefficients for all oscillating transitions be equal to the loss coefficient at all times. The rotational levels are assumed to be in thermal equilibrium with the molecular-kinetic temperature, and rotational cross relaxation is assumed to be sufficiently fast that only one rotational line can oscillate in any given vibrational band. Losses such as mirror absorption, output coupling, window losses, or intracavity line-selection losses are all assumed to be uniformly distributed throughout the laser gain medium. These cavity losses are assumed to be small enough that the approximation of a spatially uniform intensity distribution over the length of the active medium is adequate for describing the molecular and radiative characteristics of the medium. The optical resonator is assumed to be formed by two plane-parallel mirrors (one totally reflecting, the other with reflectivity R) separated by a distance L. From the oscillator gain conditions, $R \exp[2(\alpha - \beta)L] = 1$, the gain coefficient α for an oscillating line (for $R \sim 1$) must be equal to the threshold loss $\gamma = \beta + (1 - R)/2L$, where β is the loss coefficient for the cavity exclusive of the output coupling.

The analysis assumes that the plasma kinetics can be treated with a Boltzmann electron energy distribution, with a self-consistent adjustment of the electron density and effective temperature as a function of time to produce a prescribed temporal input excitation power characterized by a rise and fall time. Physically, the choice of that form for the electrical-excitation power is appropriate for an e^--beam-sustained CO device with the rise time related to the approach to steady state of the electron density and the fall time to the decay of the sustainer voltage due to the discharge of a capacitor bank. Calculations have shown that, for a specified electrical input power, the molecular-kinetics predictions are quite insensitive to the detailed plasma parameters chosen to produce that power (e.g., trading off n_e and T_e, or modifying the assumed Boltzmann distribution).

It is, of course, important that reverse ("superelastic") electron-molecule collisions be included in the molecular kinetics. Then the analysis will reflect the physical phenomenon that, as the vibrational levels become excited, the effective electron temperature T_e rises to maintain the specified input power. A tacit assumption is made that for low values of E/N, all of the electrical power is transferred directly to vibrational excitation.

Effects of gas heating from VV and VT kinetic processes, as well as from rotational equilibration accompanying stimulated emission, are included in the analysis.

In order to derive a useful set of generalized results that can easily be scaled, it is first necessary to simplify the equations by introducing approximations that will reduce the number of scale parameters required to a reasonable minimum value. Although the additional approximations to be discussed here are neither required nor invoked in the complete computer analysis, they will be useful for summarizing the results of the computer calculations in a coherent way. The objective here is to show that a rather general class of pulsed CO oscillators can be described quite accurately in terms of only one basic scale parameter that defines the electrical pumping per CO molecule.

For a high-pressure oscillator operating at temperatures in the range 60–300 K, the spontaneous radiative and VT decay terms in the master equation can be neglected. (Spontaneous terms contribute typically $\lesssim 0.1$ percent to total power balance at CO pressures $\lesssim 10$ torr, and (CO, X) VT deactivation $\sim 10^{-2} - 10^{-6}$ percent for $X = \mathrm{CO}$, Ar, He, $\mathrm{N_2}$.) It is convenient to classify the results of calculations to be presented here by referring to initial values of the temperature T_{mol} and the pressures p_{CO}, p_X. A theoretical prediction that only a small percentage of electrical power is converted to kinetic heating (typically <10 percent), even after steady state has been attained, has been experimentally verified [10]. Thus, for reasonably dilute CO gas mixtures, it is a good approximation to neglect the temperature rise for pulse times that are comparable to the time required to reach steady state (although heating effects have been retained in the analysis). The calculations correspond to fixed-number densities, and because of the small temperature rises, the pressures will change from their initial values by only a small fraction during that time scale. All of the calculations to be presented here correspond to cases for which the electrical excitation was

kept constant as a function of time during the pulse, with temporal evolution of the electron temperature T_e to maintain the given power loading.

The coupled set of equations of [2] with the approximation discussed previously can be written in dimensionless form by introducing the following quantities:

$$\begin{aligned} x_v &= n_v/N_{CO} \\ x_e &= n_e/N_{CO} \\ \tau &= p_{CO}t \\ f &= 1 + (3/2)p_{tot}/p_{CO} \\ \xi &= \Delta\nu_{CO}/\Delta\nu_{tot} \\ &= \frac{p_{CO} < v_{rel}(CO, CO) > \sigma^{opt}(CO, CO)}{\sum_X p_X < v_{rel}(CO, X) > \sigma^{opt}(CO, X)} \\ \tilde{\gamma} &= \gamma/\xi \\ \tilde{W}_e &= W_e/p_{CO}^2 \\ \tilde{I} &= I\xi/p_{CO}^2 \\ \tilde{E} &= E/p_{CO} \end{aligned} \tag{2}$$

where x_v are the relative populations, x_e is a measure of the degree of ionization, f is related to the number of thermal degrees of freedom, and ξ is the fractional percentage of total optical line broadening caused by CO. $\tilde{\gamma}$, $\tilde{W}_e$, $\tilde{I}$, and $\tilde{E}$ are scaled threshold loss (cm^{-1}), power density (watts/cubic centimeter/torr squared (CO)), intensity (watts/square centimeter/torr squared (CO)), and energy density (joules/cubic centimeter/torr (CO)). The definition of the parameter ξ given here applies to a situation in which pressures are high enough ($\gtrsim 20$ torr) that optical lines are predominantly pressure broadened.

If these scale parameters are introduced, the master equation expresses the evolution of the relative populations x_v as a function of scale time $\tau = p_{CO}t$. This is to be expected, since the electrical excitation is kept constant, and the dominant kinetic processes are (two-body) VV collisions. Thus the physics of the molecular vibration states depends explicitly only upon the kinetic temperature and the scaled electrical excitation $\tilde{W}_e = W_e/p_{CO}^2$. Implicitly, however, it depends also upon the scaled threshold-loss coefficient $\tilde{\gamma}$ for the cavity due to the oscillation condition, and upon the parameter f due to the kinetic heating.

It is apparent that the set of parameters (T_{mol}, $\tilde{W}_e$, $\tilde{\gamma}$, f) completely characterizes the CO EDL under these approximations; all other inputs to the mathematical model consist only of fundamental physical constants. In the following section, a variety of numerical results based on the complete computer analysis for this model will be presented and discussed to show the relative sensitivity of these parameters.

III. Theoretical Results

Computer calculations were carried out for a fixed value $f = 16$ (corresponding to a dilute, 10-percent CO mixture). The kinetic temperatures T_{mol} included (60, 100, 150, 200, 300) K, the scaled electrical pumping rates (0.2, 0.5, 1.0, 2.0, 5.0, 10, 20, 50, 100, 200) $W/cm^3/torr^2$, and the scaled threshold-loss coefficients (0.1, 0.2, 0.5, 1.0, 3.0, 7.0, 10, 20) percent/cm. From the results of any given case specified completely by the set of four parameters (T_{mol}, $\tilde{W}_e$, $\tilde{\gamma}$, f), the general class of problems that can be scaled exactly from those results is quite restrictive; it allows only the variation of the CO partial pressure, provided that the electrical excitation W_e is scaled by p_{CO}^2, and that the threshold level and gas-mixture ratio are held constant. However, except for the scaled excitation power $\tilde{W}_e$, most of these parameters do not have a sensitive effect on the power response of the system as a function of time (although detailed spectral predictions may have a more critical dependence). Thus the class of problems that can be analyzed from a given case is often more extensive than that just described. The reasons for this are the following. 1) The most important parameter, the scaled excitation $\tilde{W}_e$, is a measure of the electrical pumping per molecule relative to the rate of VV cross relaxation, and thus specifies the ratio of the two dominant kinetic processes in the CO EDL. 2) A pulsed high-pressure CO EDL typically operates in a regime where oscillation is high above threshold, and thus results for optical power extraction will usually be insensitive to the scaled cavity-loss coefficient $\tilde{\gamma}$. Unless the ratio $\tilde{W}_e/\tilde{\gamma}$ becomes very small the medium intensity will be high above the saturation intensity, and the optical output will be independent of $\tilde{\gamma}$. 3) The temperature rise for pulse times comparable to the time required to reach steady state is small, so the results do not depend critically upon f, providing it is large. This parameter is mainly important for detailed predictions of spectral distribution. 4) Results of calculations for systems operating with parameters in the ranges previously noted do not show a significant sensitivity to dependence on T_{mol}.

Fig. 1 shows plots of the quantum power efficiency (for the total optical conversion of electrical input) for a variety of different values of $\tilde{W}_e$ as a function of $p_{CO}t$, for $T_{mol} = 100$ K. Results of calculations show that the most important parameter for small values of $\tilde{\gamma}$ is the scaled excitation power $\tilde{W}_e$, and that the optical output is relatively insensitive to $\tilde{\gamma}$ for small values of $\tilde{\gamma}$. It is apparent from Fig. 1 (and from similar results for other values of $\tilde{\gamma}$ and T_{mol}) that the optical output efficiency displays a remarkably similar behavior over a wide range of the parameter $\tilde{W}_e$. In fact, these results can be used

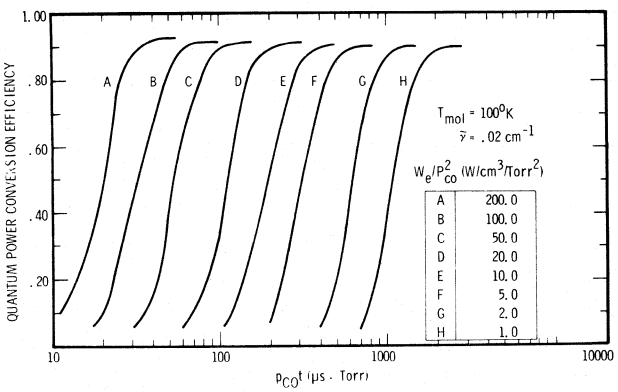

Fig. 1. Quantum power-conversion efficiency versus a function of scale time $p_{CO}t$, for several values of scaled excitation power W_e/p_{CO}^2, at 100 K.

to show that, for a given temperature T_{mol} and a fixed value of quantum efficiency η/η_∞ (where η_∞ is the steady-state value), a log-log plot of $p_{CO}t$ versus the scaled power $\tilde{W}_e$ is approximately linear. For example, Fig. 2 shows such a plot for the turn-on time $p_{CO}t_0$ (obtained by tangentially extrapolating the curves of Fig. 1 to the origin and neglecting a small initial bump that often occurs in the calculations) versus $\tilde{W}_e$. The slope of the linear curves of Fig. 2 is approximately $-\frac{5}{6}$ and was found to be independent of T_{mol} and $\tilde{\gamma}$; the variation in the magnitude of the curves is less than a factor of 2 within the range of temperatures chosen. The turn-on time corresponds to the point where $\eta = 0$; however, it is apparent that the curves of Fig. 1 remain similar as time evolves. Thus, for a fixed temperature T_{mol}, the time t required to attain any specified value η/η_∞ for the optical extraction efficiency satisifies

$$\tilde{e} = p_{CO}t\tilde{W}_e^{5/6} = \text{constant} \tag{3}$$

which implies that, within a range of values for $\tilde{\gamma}$, which are suitably small, a "universal" plot of efficiency versus the parameter $\tilde{e} = p_{CO}t\tilde{W}_e^{5/6}$ can be constructed. As an example, all of the plots for the conditions of Fig. 1 can be summarized as shown in Fig. 3. (The value of the steady-state efficiency η_∞ depends only slightly upon $\tilde{W}_e$, T_{mol}, and $\tilde{\gamma}$.) The significance of the parameter $\tilde{e}$ can be seen by noting that if the exponent of $\tilde{W}_e$ in (3) were unity instead of $\frac{5}{6}$, $\tilde{e}$ would represent the total electrical energy $\tilde{E} = W_e t/p_{CO}$ (J/l/torr(CO)) which has been deposited into CO vibrational energy up to time t. Therefore, the response of the system is approximately a function only of the specific input energy $\tilde{E}$ (which is, of course, a function of time and the excitation rate). The power efficiency can be integrated to give a universal curve for the energy efficiency ϵ/η_∞ as a function of the parameter $\tilde{e}$, and this result is also presented in Fig. 3.

Among the important conclusions to be drawn from the previous remarks are the following. Characteristic times required to attain any specified efficiency satisfy a condition given by (3); a special case of this relation, which has been discussed by Rockwood and Hunter [11], is that the time required to attain threshold (i.e., $\eta = 0^+$) requires a fixed energy deposition into CO. For the range of temperatures (100–300 K) and for the reasonably small values of $\tilde{\gamma}$ discussed here, turn-on occurs after a specific electrical energy $E_0 \sim 0.5 - 1.0$ J/l/torr (CO) has been deposited, and steady state is attained after an energy $E_{ss} \sim 1.7 - 2.6$ J/l/torr (CO) has been deposited. (These numbers correspond to a specific pumping rate $\tilde{W}_e = 1.0$ W/cm^3/torr (CO)^2; for other values of $\tilde{W}_e$, (3) shows that these deposition energies increase as $\tilde{W}_e^{1/6}$.) The typical range of values for $\tilde{W}_e$ in the data to be presented later is sufficiently small that the $\tilde{W}_e^{1/6}$ variation is not significant, and thus experimental results will be plotted in terms of the more physically significant quantity $\tilde{E} = W_e t/p_{CO}$. However, the theoretical results correspond to a range of values for $\tilde{W}_e$ that vary by a factor ~200, and $\tilde{W}_e^{1/6}$ can therefore vary by a factor ~2.5, showing that the exponent 5/6 can be significant for higher pumping.

It is interesting to characterize the CO medium by a saturation intensity. Although the full kinetic model contains

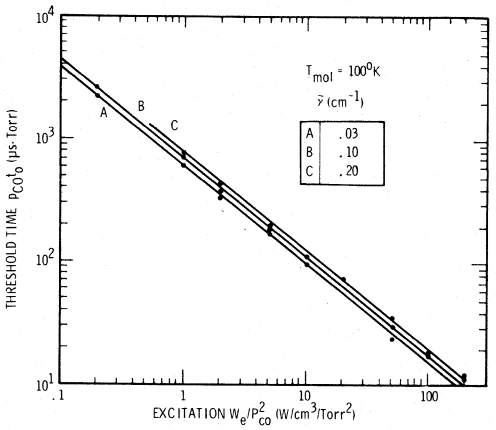

Fig. 2. Scaled threshold time $p_{CO}t_0$ as a function of scaled excitation W_e/p_{CO}^2 for several values of loss $\tilde{\gamma}$ at 100 K.

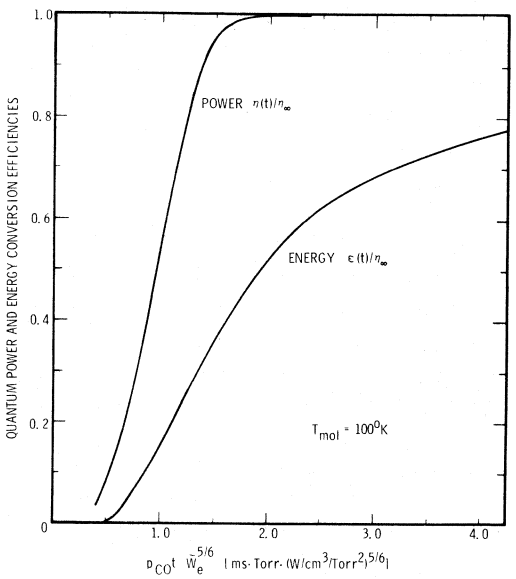

Fig. 3. Generalized power and energy-conversion efficiencies as a function of $p_{CO}t(W_e/p_{CO}^2)^{5/6}$ at 100 K. (Note that without the 5/6 exponent the units of the horizontal axis would correspond to energy deposition in joules/liter/torr (CO).)

simultaneous oscillation on several lines, we now neglect this feature and investigate how the gain saturates as a function of threshold level and total intensity in the medium. From the analysis of a simple two-level model, it can be shown that the saturated gain $\alpha(I)$ satisfies

$$\alpha(I) = \alpha_0(1 + I/I_s)^{-1} \tag{4}$$

where the saturation intensity I_s is independent of the electrical pumping. We shall show that, at steady state, the CO EDL follows a simple dependence of this form, and an estimate of the scaled saturation intensity as a function of T_{mol} will be derived. In terms of scaled quantities, (4) becomes, upon setting $\alpha(I) = \gamma$,

$$\tilde{\gamma} + \eta_\infty \tilde{W}_e/\tilde{I}_s = \tilde{\alpha}_0 \tag{5}$$

where the steady-state condition $\tilde{\gamma}\tilde{I} = \eta_\infty \tilde{W}_e$ has been used. Thus, for a fixed value $\tilde{W}_e$, the steady-state oscillator power efficiency η_∞ and the cavity threshold $\tilde{\gamma}$ are linearly related

if the laser gain medium saturates according to the relation of (4). That is, if $\eta_\infty(0)$ is the limiting value of the steady-state efficiency for $\tilde{\gamma} \to 0$ (lossless cavity), then

$$\tilde{\gamma} = -[\eta_\infty - \eta_\infty(0)]\, \tilde{W}_e/\tilde{I}_s. \tag{6}$$

Fig. 4 shows η_∞ plotted versus $\tilde{\gamma}$ for $T_{mol} = 100$ K for two different values of $\tilde{W}_e$, and as (6) shows, the slope $|d\tilde{\gamma}/d\eta_\infty|$ of these curves is proportional to $\tilde{W}_e$. Furthermore, the proportionality constant determines the scaled saturation intensity, which is determined from Fig. 4 to be $\tilde{I}_s \sim 0.8$ W/cm^2/torr^2. Similar plots for a fixed value of $\tilde{W}_e$ and variable temperature T_{mol} are shown in Fig. 5. All of these curves are linear to a very good approximation, and the saturation intensities obtained from their slopes are summarized in the following table. During the transient evolution, the relation between the quantum efficiency and the cavity threshold does not seem to follow a linear relationship:

T_{mol}(K)	60	100	150	200	300
I_s(W/cm^2/torr^2)	0.6	0.8	1.6	2.5	6.4

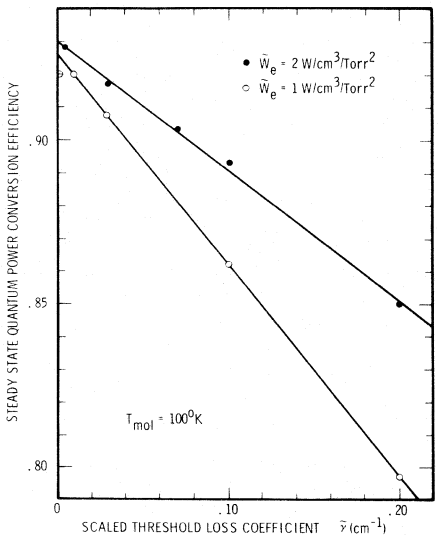

Fig. 4. Steady-state power efficiency as a function of scaled threshold loss coefficient $\tilde{\gamma}$ for an oscillator, for two values of scaled excitation $\tilde{W}_e = We/p_{CO}^2$. Note that the slopes of these curves are proportional to $\tilde{I}_s/\tilde{W}_e$, where $\tilde{I}_s$ is the scaled saturation intensity.

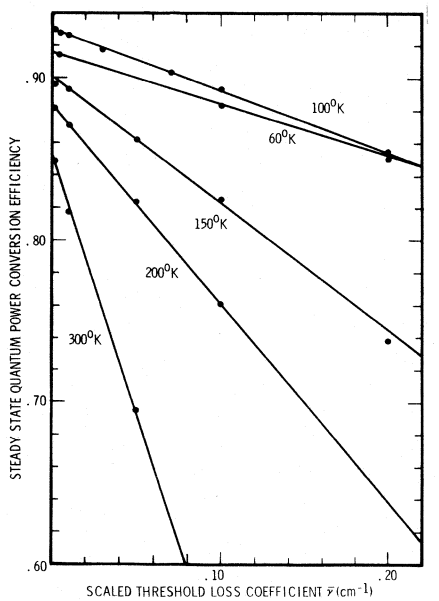

Fig. 5. Steady-state power efficiency as a function of scaled threshold loss coefficient $\tilde{\gamma}$ for several different temperatures, for $\tilde{W}_e$ = 2 W/cm^3/torr(CO)^2.

Small-signal gain characteristics can be obtained from (5) with $\tilde{\gamma} = 0$. For values of pumping and cavity threshold considered here, it is apparent that the small-signal gain is proportional to $\tilde{W}_e$

$$\tilde{\alpha}_0 = \eta_\infty(0)\, \tilde{W}_e/\tilde{I}_s. \tag{7}$$

For efficient operation of the oscillator (high above threshold), the necessary condition is $\tilde{\alpha}_0 >> \tilde{\gamma}$, and therefore (since $\eta_\infty \sim 1$)

$$\tilde{W}_e/\tilde{\gamma} >> \tilde{I}_s. \tag{8}$$

IV. Experimental Comparisons and Conclusions

The electrical-excitation times required to reach laser threshold and steady state have been measured for CO/Ar and CO/N_2 gas mixtures and are compared in the following to the scaling generalizations described in Section III. The laser used for these measurements was an e^--beam-stabilized electric-discharge CO laser with a 10 × 10 × 100-cm discharge region. The operating temperature was 80 K with gas pressures typically in the range from 50 to 200 torr. The nominal operating parameters were $E/N = 1.1 \times 10^{-16}$ V · cm^2, sustainer current density $I_s = 2$ A/cm^2, and e^--beam current density $I_b = 25$ mA/cm^2. Output energies exceeding 500 J/pulse have been obtained. The electrical-excitation pulse length was 75 μs and the optical pulse length varied between 20–100 μs depending on the electrical-excitation rate and the gas mixture used.

The laser output energy was measured with a ballistic thermopile calorimeter (Hadron Series 117) and the temporal pulse shape was monitored with a Ge:Au detector. Fig. 6 illustrates a typical pulse shape for CO/N_2 with a nearly constant electrical-excitation rate for 75 μs. In this example, laser threshold is reached 38 μs after the electrical excitation

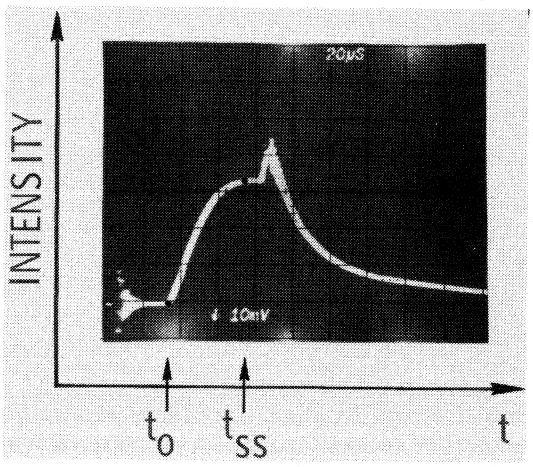

Fig. 6. Scope trace of total optical output power as a function of time for a typical e^--beam laser pulse.

is initiated and the output lasts considerably longer than the excitation pulse length. This long decay is typical of CO/N_2 gas mixes due to the time required for energy stored in the vibrational levels of nitrogen to be transferred back to the CO molecules. The pulse shapes for CO/Ar mixtures look similar except that the pulse decay time is shorter, since no energy is stored in the argon.

The laser threshold time t_0 is taken to be that time from initiation of the sustainer current to the point where the laser intensity is about 3-5 percent of the maximum intensity as indicated by the arrow in Fig. 6. This threshold is generally sharp and the time is therefore well defined. The steady-state time t_{ss} is defined as the time required to reach ~95 percent of the maximum value, also indicated by an arrow in Fig. 6. This value is not as sharply defined as t_0 and considerable spread in the data may occur for the determination of steady state.

It was shown in Section III that the inverse of the threshold and steady-state times for CO/Ar laser-gas mixtures should scale as $p_{CO}\tilde{W}_e^{5/6}$, where $\tilde{W}_e$ is the electrical-excitation rate (watts/cubic centimeter/torr squared (CO)). For the range of experimental variables considered ($\tilde{W}_e \sim 1$), the exponent $(\frac{5}{6})$ can be taken to be unity with the resulting physical interpretation that, regardless of the excitation rate, fixed specific energies (joules/liter/torr (CO)) must be deposited to attain threshold and steady state. Experimental values of threshold and steady-state times were measured for CO/Ar gas mixtures from 75 to 150 torr. The inverse times are plotted in Fig. 7 and, as predicted by the scaling generalizations, are proportional to W_e/p_{CO}. From Fig. 7 it is concluded that approximately 0.9 J/l/torr (CO) must be deposited in order to reach threshold, which is in good agreement with the scaling generalizations which predict that 0.5 - 1.0 J/l/torr (CO) is necessary. The experimental value for the deposited energy required to attain steady state, ~2.0 J/l/torr (CO), is also in good agreement with the scaling predictions of 1.7 - 2.6 J/l/torr (CO).

The calculations discussed in Section III are valid only for gas mixtures of CO and monatomic diluents. However, the scaling generalizations appear to be valid for CO/diatomic systems, provided that only the fractional energy into the CO system is used for scaling. Experimental measurements of the threshold and steady-state times for a fixed CO/N_2 (1:6) mixture are shown in Fig. 8. It is apparent from this graph that the inverses of these times scale with W_e just as they do for CO/Ar mixtures although the required total energy deposited is different. This is to be expected because the deposited energy is split between the CO and N_2. It would seem, in fact, that the required energy deposited in the CO vibrational system should be the same regardless of the diluent and that the fractional amount deposited into nitrogen can be determined from the experimental data; i.e., a specific energy $E(CO)/p_{CO}$ must be deposited into vibrational excitation of CO in order to attain any given efficiency.

Additional evidence is provided for the previous supposition by measurements of the threshold time dependence on the fractional content of CO, $f_{CO} = p_{CO}/p_{tot}$. These data, shown in Fig. 9, indicate that the total specific energy required to achieve threshold increases linearly with f_{CO} which, when

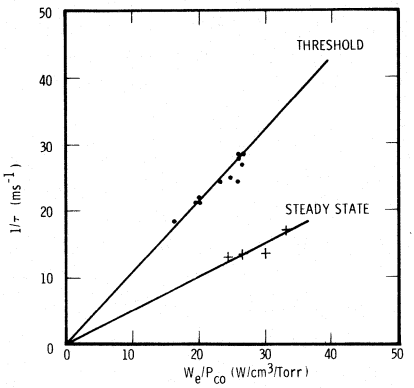

Fig. 7. Inverse of experimentally observed times required for attainment of threshold and steady state for a CO/Ar gas mixture, as a function of W_e/p_{CO}.

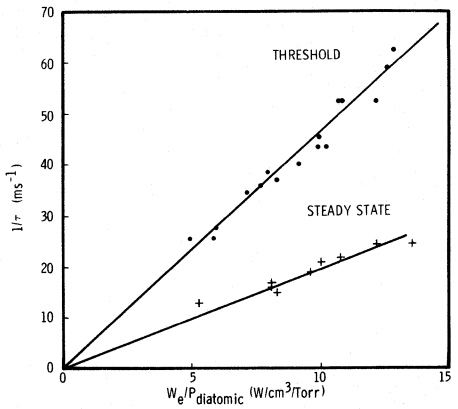

Fig. 8. Inverse of experimentally observed times required for attainment of threshold and steady state for a 1:6 CO/N_2 gas mixture.

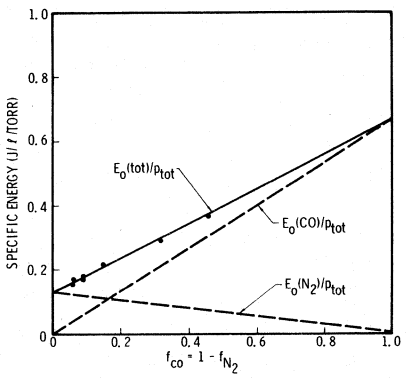

Fig. 9. Experimental specific energies as a function of fractional CO content required for attainment of laser threshold for CO/N_2 gas mixtures.

extrapolated to $f_{CO} = 1$, gives ~0.7 J/l/torr (CO), which agrees approximately with the previous results for CO/Ar mixtures. If it is assumed that the required threshold energy deposited in CO is always 0.7 J/l/torr (CO), the remaining fraction into nitrogen increases linearly with $f_{N_2} = 1 - f_{CO}$, as is also shown in Fig. 9. That is

$$E_0(\text{tot})/p_{\text{tot}} = f_{CO}E_0(CO)/p_{CO} + f_{N_2}E_0(N_2)/p_{N_2}. \quad (9)$$

From the experimental value for $E_0(CO)/p_{CO}$, it is determined that $E_0(N_2)/p_{N_2} = 0.13$ J/l/torr(N_2). The physical

interpretation of the experimental data presented in Fig. 9 is that the energy deposition per molecule is six times higher than CO than for N_2. Thus it appears that the scaling generalizations derived for CO/Ar mixtures can also be applied to systems with diatomic diluents, and that accurate knowledge of the large number of kinetic rates required for a complete analysis of the CO/N_2 system is not essential for prediction of approximate laser performance.

References

[1] W. B. Lacina, "Kinetic model and theoretical calculations for steady state analysis of an electrically excited CO laser amplifier system," Northrop Rep. NCL 71-32R, Aug. 1971.

[2] W. B. Lacina, M. M. Mann, and G. L. McAllister, "Transient oscillator analysis of a high-pressure electrically excited CO laser," *IEEE J. Quantum Electron.*, vol. QE-9, pp. 588–593, June 1973.

[3] W. Q. Jeffers and C. E. Wiswall, "Analysis of pulsed CO lasers," *J. Appl. Phys.*, vol. 42, pp. 5059–5065, Nov. 1971.

[4] R. E. Center and G. E. Caledonia, "Theoretical description of the electrical CO laser," *Appl. Phys. Lett.*, vol. 19, pp. 211–213, Oct. 1971; also —, "Vibrational distribution functions in anharmonic oscillators," *J. Chem. Phys.*, vol. 55, pp. 552–561, July 1971.

[5] J. W. Rich, "Kinetic modeling of the high power carbon monoxide laser," *J. Appl. Phys.*, vol. 42, pp. 2719–2730, June 1971.

[6] R. L. McKenzie, "Vibrational relaxation and radiative gain in expanding flows of anharmonic oscillators," NASA Tech. Note NASA TN D-7050, Mar. 1971.

[7] S. D. Rockwood, J. E. Brau, W. A. Proctor, and G. H. Canavan, "Time-dependent calculations of carbon monoxide laser kinetics," *IEEE J. Quantum Electron. (Part II of Two Parts. 3rd Conference on Chemical and Molecular Lasers)*, vol. QE-9, pp. 120–129, Jan. 1973.

[8] R. J. Hall and A. C. Eckbreth, "Kinetic modeling of CW CO electric-discharge lasers," *IEEE J. Quantum Electron.*, vol. QE-10, pp. 580–590, Aug. 1974.

[9] W. B. Lacina, "Scaling generalizations for a pulsed CO EDL," Northrop Rep. NRTC 73-43R, Oct. 1973.

[10] F. E. C. Culick, P. I. Shen, and W. S. Griffin, "Studies of the acoustic waves formed in an electric discharge CO laser cavity," presented at the AIAA ASME Thermophysics and Heat Transfer Conf., Boston, Mass., July 15–17, 1974.

[11] S. D. Rockwood and R. O. Hunter, "An efficiency threshold for CO laser operation," presented at the 25th Gaseous Electronics Conf., London, Ont., Canada, Oct. 1972.

Experiments and Theory on Energy Extraction in an Atmospheric-Pressure CO_2 Amplifier with 60 ns-1 μs Pulses

G. GIRARD, J. C. FARCY, M. MICHON, AND P. VINCENT

Abstract—**We measured the energy extraction for 60-ns pulses and compared our experimental and theoretical results. The theoretical curve is in agreement with the experimental results. We plotted the theoretical evolution of α, N_{001}/N_A, N_{100}/N_A, and T in an amplifying stage. We finally compared the different energy extraction versus the pulse duration.**

I. Introduction

THE ability of a CO_2 laser pulse with 60 ns-1 μs duration to extract energy from an atmospheric-pressure CO_2 amplifier was studied. We have measured the energy extraction from an amplifying stage for 60-ns pulses by varying the input energy, and have compared these results with a rate equation theory. The theory presented here is an extension of a method employed by Schwartz *et al.* [1]. Basov *et al.* [2] and Brunet [3] have obtained similar equations for CO_2 mixtures. Experimental results are in good agreement with the theoretical ones. We also deduced the theoretical evolution of the gain, the translational temperature, and the population of the upper and lower levels in an amplifying stage. A comparison is made between the maximum extractable energies for 1.5-ns (single and multiline), 60-ns, 100-μs, 0.5-μs, and 1-μs pulses.

Manuscript received September 19, 1974; revised January 22, 1975. This work was supported by the Commissariat à l'Energie Atomique, Centre d'Etude de Limeil, Limeil, France.

The authors are with the Laboratoires de Marcoussis, Centre de Recherches de la Compagnie Générale d'Electricité, Marcoussis, France.

II. Experiment

The experimental apparatus was arranged as shown in Fig. 1. Single-longitudinal and transversal-mode operation of a pulsed atmospheric-pressure CO_2 laser is obtained through the use of an intracavity SF_6 cell [4], [5]. The cavity is about 2 m long and is composed of a grating and a germanium reflector. A diaphragm, 8 mm in diameter, is used to restrict oscillations to a single transverse mode. The absorber cell is 1 cm thick with parallel Brewster-angle windows. Operation on a single longitudinal mode is obtained with about 2 torr of SF_6 in the cell. The output pulses are 60-ns full width at half maxi-

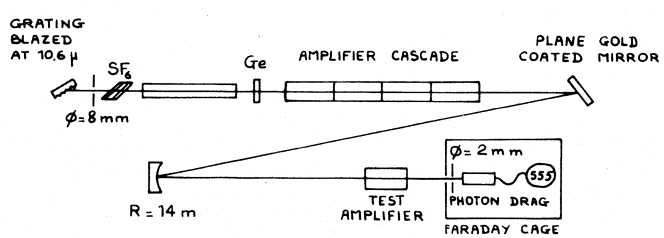

Fig. 1. Experimental setup for measuring energy gain.

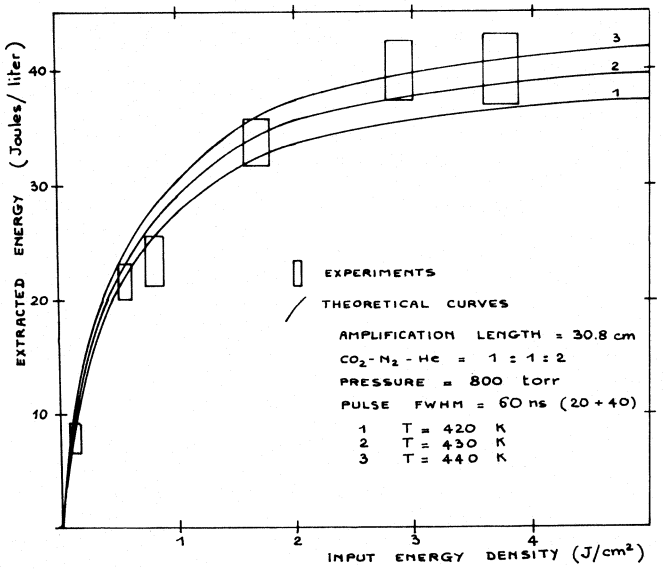

Fig. 2. Comparison between experimental and computed energy extractions for a medium of length 30 cm with small-signal gain $\alpha_0 = 0.0435\ \text{cm}^{-1}$.

mum (FWHM) (20-ns rise time and 40-ns decay time). This oscillator is followed by 4 m of amplification with an overall small-signal gain of about 10^4. At the output of the amplifier chain the beam is focused into the test amplifier to reach a high level of energy density. The test amplifier, 30 cm long, has been described elsewhere [6]. Eventually, the beam reaches the photon-drag detector. Attenuators are set in front of the photon drag in order to be in its linear response range [7]. Because of radial intensity variations, a Gaussian-shaped beam does not experience the same degree of saturation over its cross section. In order to overcome this effect, a diaphragm 2 mm in diameter is set in front of the detector so that the photon drag intercepts a small but radially uniform portion of the beam.

The experiment is performed as follows. Various levels of energy density at the output of the chain are obtained by firing an appropriate number of amplifiers and by adjusting the pump energy. For all these levels of energy, the shape of the pulse was not modified. The photon-drag detector output is displayed on an oscilloscope. Photographic records are taken with the test amplifier alternately on and off. We have operated our test amplifier with a CO_2-N_2-He mixture of 1:1:2, for an input energy corresponding to $\alpha_0 = 0.0435\ \text{cm}^{-1}$, $T = 430$ K, and $T_3 = 2550$ K, where T is the translational temperature of the mixture and T_3 is the vibrational temperature of the ν_3 mode. The results of the energy-gain measurements are shown in Fig. 2. Each datum point is the average of ten measures. Rectangles represent the magnitude of the experimental error.

III. Theory

At atmospheric pressure the transfer times between vibrational levels of a mode are of the order of 10 ns and the transfer times between rotational levels are of the order of 0.1 ns [8]. As a consequence, whenever the laser pulse duration is long compared to these transfer times, a Boltzmann distribution is maintained during the pulse between the vibrational levels of a mode and between rotational levels. The vibrational temperature of the ν_1 and ν_2 modes of the CO_2 molecule and the rotational temperature are equal to the temperature of translation T.

The variables introduced in the rate equations are the photon density ϕ and the mean numbers A of quanta per vibrational mode. We have to consider three sets of equations: 1) the relaxation equations; 2) the relations between the populations of the levels 001, 100, and the mean numbers of quanta per mode; and 3) the rate equations.

A. Relaxation Equations [3]

1) The relaxation of the vibrational energy of N_2 occurs via the following process:

$$N_2(v=1) + N_2(v=0) \xrightarrow{k_{10}(B,B)} 2N_2(v=0) \tag{1a}$$

$$N_2(v=1) + CO_2(00^\circ 0) \xrightarrow{k_{10}(B,A)} N_2(v=0) + CO_2(00^\circ 0) \tag{1b}$$

$$N_2(v=1) + M \xrightarrow{k_{10}(B,C)} N_2(v=0) + M \tag{1c}$$

$$N_2(v=1) + CO_2(00^\circ 0) \xrightarrow{k_{10}^{01}(B,A)} N_2(v=0) + CO_2(00^\circ 1). \tag{1d}$$

$k_{10}(B,B)$, $k_{10}(B,A)$, $k_{10}(B,C)$ are the constants of vibration-translation (VT) deexcitation (A for CO_2, B for nitrogen, C for helium). $k_{10}^{01}(B,A)$ is a constant of vibration-vibration (VV) transfer.

2) The relaxation of the vibrational energy of the ν_1 mode of the CO_2 is due to VV transfers between the ν_1 and ν_2 modes.

$$CO_2(10^\circ 0) + CO_2(00^\circ 0) \xrightarrow{k_{02}^{10}} \begin{bmatrix} CO_2(01^1 0) + CO_2(01^1 0) \\ CO_2(02^\circ 0) + CO_2(00^\circ 0). \end{bmatrix} \tag{2}$$

3) The relaxation of the vibrational energy of the ν_2 mode is due to the following VT process:

$$CO_2(01^1 0) + CO_2(00^\circ 0) \xrightarrow{k^{10}(A,A)} 2CO_2(00^\circ 0) \tag{3a}$$

$$CO_2(01^1 0) + N_2(v=0) \xrightarrow{k^{10}(A,B)} CO_2(00^\circ 0) + N_2(v=0) \tag{3b}$$

$$CO_2(01^1 0) + M \xrightarrow{k^{10}(A,C)} CO_2(00^\circ 0) + M. \tag{3c}$$

4) The relaxation of the vibrational energy of the ν_3 mode is due to VV transfers to the ν_1 and ν_2 modes.

$$CO_2(00^\circ 1) + CO_2(00^\circ 0) \xrightarrow{k_{03}^{10}(A,A)} \begin{bmatrix} CO_2(3\nu_2) + CO_2(00^\circ 0) \\ CO_2(2\nu_2) + CO_2(\nu_2) \end{bmatrix} \tag{4a}$$

$$CO_2(00^\circ 1) + N_2(v=0) \xrightarrow{k_{03}^{10}(A,B)} CO_2(3\nu_2) + N_2(v=0) \tag{4b}$$

$$CO_2(00°1) + M \xrightarrow{k_{03}^{10}(A,C)} CO_2(3\nu_2) + M. \quad (4c)$$

The rate constants k are taken principally from Taylor and Bitterman [9]. The actual rate constants employed are tabulated in Table I for $T = 430$ K [10].

5) In the following relaxation equations, a, b, and c are the molar concentrations of CO_2, N_2, and He; N_A, N_B are the numbers of CO_2 and N_2 molecules and

$$A_1 = \frac{E_1}{N_A h\nu_1} \quad A_2 = \frac{E_2}{N_A h\nu_2} \quad A_3 = \frac{E_3}{N_A h\nu_3} \quad B = \frac{E_B}{N_B h\nu_B}$$

are the average number of quanta per vibrational mode.

$$\frac{dA_1}{dt} = -k_{02}^{10}(A,A)\,[A_1(A_2+1)^2 - \epsilon_{12}(A_1+1)A_2^2] \quad (5a)$$

where

$$\epsilon_{12} = \exp\,[-h(\nu_1 - 2\nu_2)/kT] \quad (5b)$$

$$\frac{dA_2}{dt} = k_{02}^{10}(A,A)\,[A_1(A_2+1)^2 - \epsilon_{12}(A_1+1)A_2^2] + \tfrac{3}{2}[ak_{03}^{10}(A,A) + bk_{03}^{10}(A,B) + ck_{03}^{10}(A,C)] \cdot [A_3(A_2+1)^3 - \epsilon_{32}(A_3+1)A_2^3] - [ak^{10}(A,A) + bk^{10}(A,B) + ck^{10}(A,C)] \cdot [A_2 - A_2(T)] \quad (6a)$$

where

$$\epsilon_{32} = \exp\,[-h(\nu_3 - 2\nu_2)/kT] \quad (6b)$$

$$A_2(T) = 1/[\exp(h\nu_2/kT) - 1] \quad (6c)$$

$$\frac{dA_3}{dt} = -[ak_{03}^{10}(A,A) + bk_{03}^{10}(A,B) + ck_{03}^{10}(A,C)] \cdot [1 + A_2(T)]^3\,[A_3 - A_3(T)] - bk_{01}^{10}(A,B)\,[B(T)+1]\left[A_3 - \frac{A_3(T)}{B(T)}B\right] \quad (7a)$$

where

$$A_3(T) = 1/[\exp(h\nu_3/kT) - 1] \quad (7b)$$

$$\frac{dB}{dt} = -ak_{01}^{10}(A,B)\,[\epsilon_{3B}B(A_3+1) - A_3(B+1)] - [ak_{10}(B,A) + bk_{10}(B,B) + ck_{10}(B,C)]\,[B - B(T)] \quad (8a)$$

where

$$\epsilon_{3B} = \exp\,[-h(\nu_3 - \nu_B)/kT] \quad (8b)$$

$$B(T) = 1/[\exp(h\nu_B/kT) - 1]. \quad (8c)$$

B. Relations Between the Populations of the Levels 001, 100, and the Mean Numbers of Quanta per Mode

The populations of the upper and lower levels of the laser transition are, respectively,

TABLE I
DIFFERENT RATE CONSTANTS FOR $T = 430$ K

Rate Constants	$cm^3\ s^{-1}$ ($T = 430$ K)
$k_{10}(B,B)/N$	5.46×10^{-18}
$k_{10}(B,A)/N$	5.46×10^{-18}
$k_{10}(B,C)/N$	1.43×10^{-15}
k_{02}^{10}/N	4.68×10^{-13}
$k^{10}(A,A)/N$	1.65×10^{-14}
$k^{10}(A,B)/N$	2.82×10^{-15}
$k^{10}(A,C)/N$	2.03×10^{-13}
$k_{03}^{10}(A,A)/N$	1.53×10^{-14}
$k_{03}^{10}(A,B)/N$	5.74×10^{-15}
$k_{03}^{10}(A,C)/N$	4.15×10^{-15}

$$N_{100} = N_A \exp\left(-\frac{h\nu_1}{kT}\right) Q_v^{-1} \quad (9a)$$

$$N_{001} = N_A \exp\left(-\frac{h\nu_3}{kT_3}\right) Q_v^{-1} \quad (9b)$$

where

$$Q_v^{-1} = \left[1 - \exp\left(-\frac{h\nu_1}{kT}\right)\right]\left[1 - \exp\left(-\frac{h\nu_2}{kT}\right)\right]^2 \cdot \left[1 - \exp\left(-\frac{h\nu_3}{kT_3}\right)\right]. \quad (9c)$$

The mean numbers of quanta per vibrational mode are

$$A_1 = \frac{\exp\left(-\frac{h\nu_1}{kT}\right)}{1 - \exp\left(-\frac{h\nu_1}{kT}\right)} \quad (10a)$$

$$A_2 = \frac{\exp\left(-\frac{h\nu_2}{kT}\right)}{1 - \exp\left(-\frac{h\nu_2}{kT}\right)} \quad (10b)$$

$$A_3 = \frac{\exp\left(-\frac{h\nu_3}{kT_3}\right)}{1 - \exp\left(-\frac{h\nu_3}{kT_3}\right)}. \quad (10c)$$

The following relations are deduced from (9) and (10):

$$N_{100} = N_A \frac{A_1}{(1+A_1)^2\left(1+\frac{A_2}{2}\right)^2(1+A_3)} \quad (11a)$$

$$N_{001} = N_A \frac{A_3}{(1+A_1)\left(1+\frac{A_2}{2}\right)^2(1+A_3)^2}. \quad (11b)$$

C. Rate Equations

Equation (11) is introduced into the classical equation

$$\frac{\partial \phi}{\partial t} + c\frac{\partial \phi}{\partial x} = \phi \frac{8\pi^2 \nu}{3h\delta\nu} |\mu_{vv'}|^2 \frac{J}{2J+1} \cdot \left(N_{001} f_{J-1} \frac{2J+1}{2J-1} - N_{100} f_J\right) \tag{12a}$$

and the rate equations are

$$\frac{\partial \phi}{\partial t} + c\frac{\partial \phi}{\partial x} = \phi \frac{8\pi^2 \nu}{3h\delta\nu} |\mu_{vv'}|^2 \frac{J}{2J+1} N_A \cdot \left[f_{J-1} \frac{2J+1}{2J-1} \frac{A_3}{(1+A_1)\left(1+\frac{A_2}{2}\right)^2 (1+A_3)^2} - f_J \frac{A_1}{(1+A_1)^2\left(1+\frac{A_2}{2}\right)^2 (1+A_3)}\right] \tag{12b}$$

$$\frac{\partial A_3}{\partial t} = -\phi \frac{8\pi^2 \nu}{3h\delta\nu} |\mu_{vv'}|^2 \frac{J}{2J+1} \left[f_{J-1} \frac{2J+1}{2J-1} \cdot \frac{A_3}{(1+A_1)\left(1+\frac{A_2}{2}\right)^2 (1+A_3)^2} - f_J \frac{A_1}{(1+A_1)^2\left(1+\frac{A_2}{2}\right)^2 (1+A_3)}\right] - [ak_{03}^{10}(A,A) + bk_{03}^{10}(A,B) + ck_{03}^{10}(A,C)] \cdot [1+A_2(T)]^3 [A_3 - A_3(T)] - bk_{01}^{10} \cdot [B(T)+1]\left[A_3 - \frac{A_3(T)}{B(T)} B\right] \tag{13}$$

$$\frac{\partial A_1}{\partial t} = \phi \frac{8\pi^2 \nu}{3h\delta\nu} |\mu_{vv'}|^2 \frac{J}{2J+1} \left[f_{J-1} \frac{2J+1}{2J-1} \cdot \frac{A_3}{(1+A_1)\left(1+\frac{A_2}{2}\right)^2 (1+A_3)^2} - f_J \frac{A_1}{(1+A_1)^2\left(1+\frac{A_2}{2}\right)^2 (1+A_3)}\right] - k_{02}^{10}[A_1(A_2+1)^2 - \epsilon_{12} A_2^2 (A_1+1)]. \tag{14}$$

Equations (13), (14), (6a), and (8a) describe the amplification process.

The initial conditions are determined by T_{3i} and T_i (initial values of T and T_3). The initial vibrational temperature of N_2 is assumed to be equal to T_{3i} (see Section V).

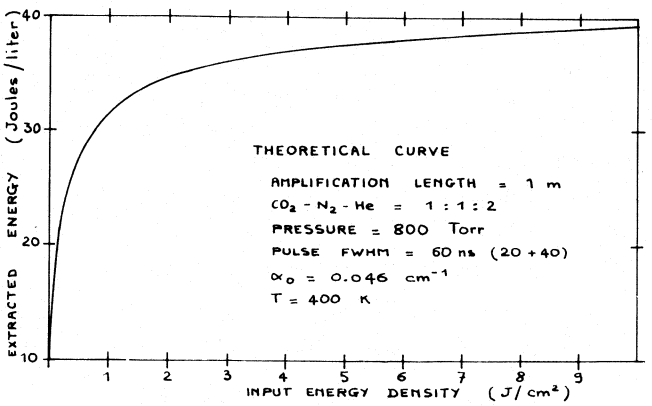

Fig. 3. Theoretical energy extraction versus incident-pulse energy density for a 60-ns FWHM pulse (20 + 40 ns) from an amplifier state 1 m long with a small-signal gain $\alpha_0 = 0.046$ cm^{-1}.

D. Comparison between Experimental Results and Theoretical Ones

The pulse shape is represented for convenience by the function $\phi(t) = \phi_0/\cosh^3(a(t - t_0))$ which corresponds to an exponential function during the buildup time and during the decay time; t_0 is the time of the pulse peak intensity. However, the a value is different for $t < t_0$ and $t > t_0$. The calculations were carried out for an N_2-CO_2-He mixture of 1:1:2, $T = 430$ K, a small-signal gain $\alpha_0 = 0.0435$ cm^{-1} corresponding to $T_3 = 2550$ K, an input-pulse 60-ns FWHM (20-ns rise time, 40-ns decay time), an amplification length 1 = 30 cm, and a pressure $p = 800$ torr. The initial vibrational temperature of N_2 is assumed to be equal to the vibrational temperature T_3. The experimental and theoretical curves are in good agreement (Fig. 2).

In Fig. 3 the same type of curve for a 1-m amplifier is plotted. The small-signal gain is $\alpha_0 = 0.046$ cm^{-1} (value for α_0 usually appearing in the literature). The CO_2-N_2-He mixture is 1:1:2 and the pressure is 800 torr. The pulse FWHM is 60 ns (20 + 40 ns).

IV. Theoretical Evolution of the Pulse Shape Versus Power and of the Functions $\alpha, N_{001}/N_A, N_{110}/N_A$, and T Versus Time

In Fig. 4 the theoretical evolution versus power of the FWHM of a pulse in an amplifier cascade is plotted. The characteristics of the pulse entering the amplifier cascade are the following. Its FWHM is 60 ns (20 + 40 ns) and its peak power is 10^6 W/cm^2. Each amplifier of the cascade is identical to the one previously described. The theoretical evolution of the pulse FWHM versus power is negligible until an input power density is equal to 5×10^7 W/cm^2. This was previously verified in the experiment described in Section II.

In Fig. 5 the evolution of the functions α, N_{001}/N_A, N_{100}/N_A, and T versus time in such an amplifier is plotted. The increase of N_{001} after the pulse is due to the $N_2 \rightarrow CO_2$ energy transfer. During the pulse, the energy transfer $N_2 \rightarrow CO_2$ is weak and the maximum available energy is equal to about 35 percent of the initial energy of the ν_3 mode (i.e.,

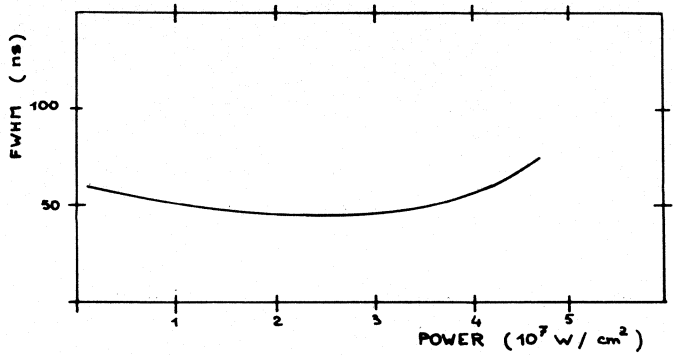

Fig. 4. Theoretical evolution versus power of the FWHM of a 60-ns (20 + 40) pulse in an amplifier cascade. The original peak power of the pulse is 10^6 W/cm^2. Each amplifier of the cascade is identical to the one described in Fig. 3.

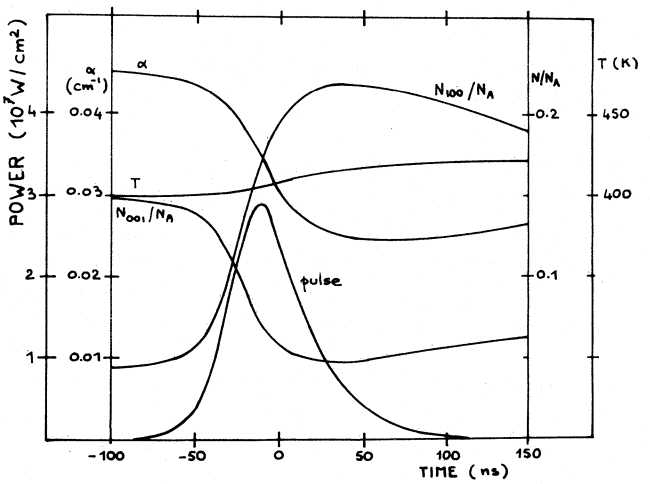

Fig. 5. Theoretical evolution of α, N_{001}/N_A, N_{100}/N_A, and T versus time in an amplifying stage.

taking account of the quantum efficiency of the laser emission of 0.41, only 90 percent of the extractable energy of the ν_3 mode can be extracted). The temperature of translation increases during and after the pulse. This is due to an increase of the ν_1 mode energy followed by a transfer to the translation via the ν_2 mode.

V. Theoretical Evolution of the Energy Extraction versus the Pulse Duration: 1.5 ns-60 ns-100 ns-0.5 μs-1 μs

In Fig. 6 the energy extraction versus input energy from an amplifier stage for input pulses with different FWHM is plotted. The calculations were carried out for a CO_2-N_2-He mixture of 1:1:2, p = 800 torr, T = 400 K, α_0 = 0.046 cm^{-1} corresponding to T_3 = 2370 K, and for input-pulse FWHM of 60 ns ②, 100 ns ③, 0.5 μs ④, and 1 μs ⑤ with a 20-ns rise time. We have added the results of energy extraction, as obtained previously [11], for a 1.5-ns FWHM pulse, ①. In Fig. 7 are plotted typical energies versus T_3, the vibrational temperature ν_3 mode, and the corresponding small-signal gain for a CO_2-N_2-He mixture 1:1:2, at p = 800 torr and

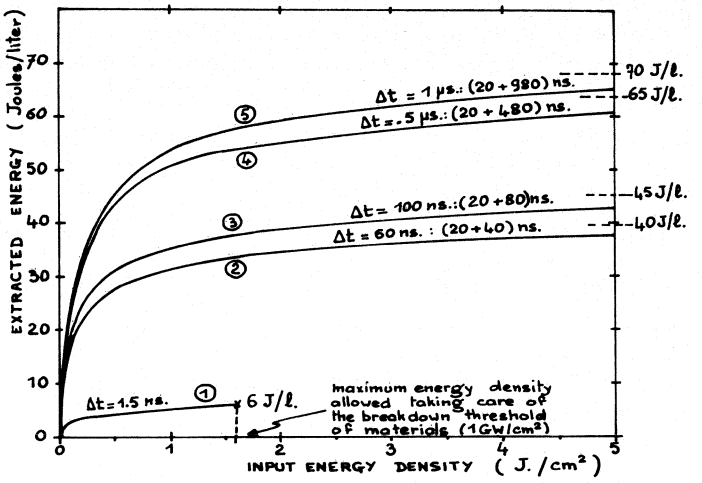

Fig. 6. Theoretical energy extraction versus incident-pulse energy density for different FWHM pulse: 1.5 ns, 60 ns, 100 ns, 0.5 μs, and 1 μs. The values given by the asymptotes are the energies extracted by a 10-J/cm^2 input-pulse energy density.

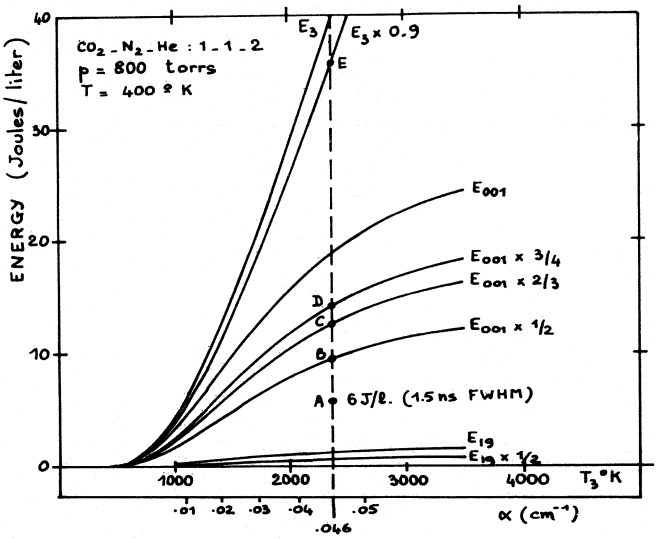

Fig. 7. Typical energies in CO_2 molecules versus T_3.

T = 400 K. E_3 is the energy stored on the ν_3 vibrational mode and E_{001} is the energy stored on the rotational level J' = 19. These energies are multiplied by the factor 0.41 corresponding to the quantum efficiency, i.e.,

$$E_3 = 0.41\,\mathfrak{N}(CO_2)\,k\theta_3\,\frac{\exp(-\theta_3/T_3)}{1-\exp(-\theta_3/T_3)} \tag{15}$$

$$E_{001} = 0.41\,\mathfrak{N}(CO_2)\,k\theta_3\exp\left(-\frac{\theta_3}{T_3}\right)\left[1-\exp\left(-\frac{\theta_1}{T}\right)\right] \cdot\left[1-\exp\left(-\frac{\theta_2}{T}\right)\right]^2\left[1-\exp\left(-\frac{\theta_3}{T_3}\right)\right] \tag{16}$$

$$E_{19} = E_{001}\,\frac{2hB'}{kT}(2J-1)\exp\left[-\frac{hB'}{kT}J(J-1)\right]. \tag{17}$$

A 1.5-ns pulse consisting of a single vibrational-rotational

TABLE II
EXTRACTABLE ENERGY AS A FUNCTION OF THE PULSE LENGTH

Pulse Length	Index	Maximum Extractable Energy for $\alpha_0 = 0.046$ cm^{-1}
1.5 ns (single line)	A	6 J/l
1.5 ns (multiline at 10.6 μ)	B	9.5 J/l
1.5 ns (multiline at 9.6 and 10.6 μ)	C D	12.5 J/l 14 J/l
60 ns (→ the whole energy stored in CO_2)	E	40 J/l
100 ns (→ the whole energy stored in CO_2 + a part of the energy stored in N_2)		45 J/l
0.5 μs (→ nearly the whole energy stored in $CO_2 + N_2$)		65 J/l
1 μ (→ the whole energy stored in $CO_2 + N_2$)		70 J/l

transition will extract 6 J/l for α_0 equal to 0.046 cm^{-1}. The maximum energy density extractable by a 1.5-ns pulse consisting of multiline transitions within the 10.6-μ band will be $1/2\,E_{001}$ [12]; the factor 1/2 is due to the bottleneck of the lower level. If the 1.5-ns pulse consists of multiline transitions within the 9.6- and 10.6-μ bands, the maximum energy density extractable will be $2/3\,E_{001}$; the factor 2/3 is due to the fact that there are now two lower levels, 100 and 020. If the transitions between the two sublevels $02^{0}0$ and $02^{2}0$ are fast enough, the maximum energy density extractable will be $3/4\,E_{001}$. The values corresponding to $\alpha_0 = 0.046$ cm^{-1} (T_3 = 2370 K) are indicated by a vertical line in Fig. 7. Taking into account the theoretical results, the energy extractable from the ν_3 mode by a 60-ns pulse is about 90-percent E_3. The energy extractable by a 1-μs pulse is about double than the energy extractable by a 60-ns pulse. In fact, for the same number of N_2 and CO_2 molecules, nearly the same amount of energy is extractable from N_2 as from CO_2. We summarize in Table II the different extractable energy as a function of the pulse length.

VI. CONCLUSIONS

To describe the gain saturation in a CO_2 atmospheric-pressure amplifier, we used a theoretical model taking account of the various vibrational energy exchange mechanisms between species, between vibrational modes, and between levels of a mode. This model was confirmed experimentally with 60-ns pulse durations. It appears that at atmospheric pressure, nearly all the extractable energy of the medium will be extracted in a 0.5-μs pulse with 20 MW/cm^2 pulse power density.

APPENDIX
DETERMINATION OF T AND T_3

The method used to determine T and T_3 has been described elsewhere [6]. We would like to describe some improvements on our method and purpose some corrections. Once the peak small-signal gain α_0 is plotted versus the quantum number of the line (Fig. 8), it is somewhat inaccurate to determine T by combining the experimental values of α_0 in groups of two by two, because of the fluctuations of α_0 due to other transitions than those considered (001 → 100). It is more appropriate to determine T and T_3 simultaneously by comparing all the experimental values of α_0 to a set of theoretical curves. This is what we did in Fig. 8. These curves were plotted for a CO_2-N_2-He mixture of 1:1:2, a pressure of 800 torr, and different pairs of values for T and T_3. In Fig. 9 there is a set of extreme theoretical curves, and in Fig. 8 is the set of the average theoretical curves. From these curves we can deduce the values of α_0, T, and T_3 in this experiment: $\alpha_0 = 0.0435$ cm^{-1} ± 10 percent; T = 430 K ± 10 percent; T_3 = 2550 K ± 20 percent.

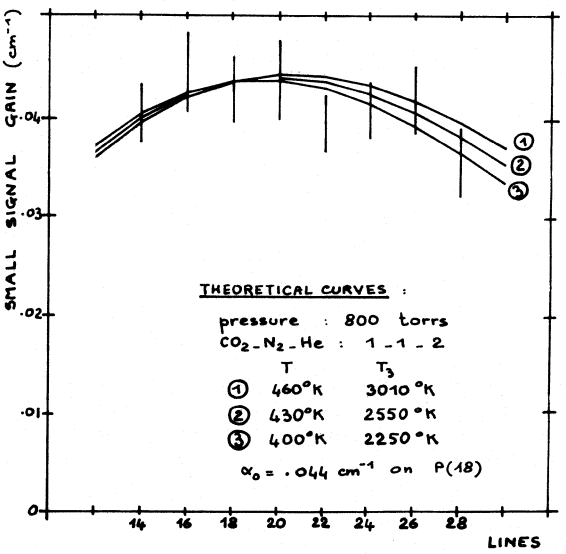

Fig. 8. Comparison between experimental and theoretical gain variations versus the quantum number of the line.

The errors are rather significant, especially for T_3; this error is inherent to the method for high values of the small-signal gain.

The dependence of the small-signal gain on T_3 is not linear. In our experiments, α_0 may come close to its maximum value. Near this maximum the error on T_3 is high. A small variation of α_0 corresponds to a high variation of T_3. These errors are now evaluated.

For a given T and a given mixture

$$\alpha = Ax(1 - x) \tag{A1}$$

where

$$x = \exp(-\theta_3/T_3) \tag{A2}$$

and A is a constant.

$$\frac{d\alpha}{dx} = A(1 - 2x)$$

$$\frac{d\alpha}{\alpha} = \frac{1 - 2x}{1 - x}\,\frac{dx}{x}. \tag{A3}$$

The gain is maximum for $x = \frac{1}{2}$

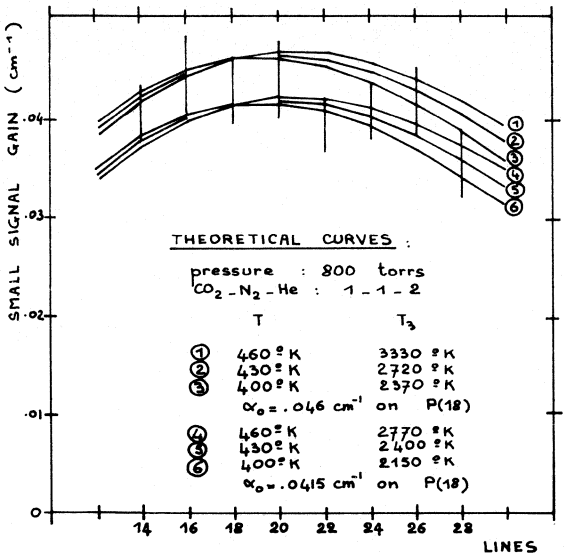

Fig. 9. Comparison between experimental and theoretical gain variations versus the quantum number of the line.

$$\alpha_M = A/4.$$

From (A1) we obtain

$$\alpha = 4\alpha_M x(1 - x)$$

$$4\alpha_M x^2 - 4\alpha_M x + \alpha = 0$$

$$x = 1/2 - 1/2(1 - \alpha/\alpha_M)^{1/2}. \tag{A4}$$

From (A2) we obtain

$$\left|\frac{dx}{x}\right| = \frac{dT_3}{T_3}\,\frac{\theta_3}{T_3}. \tag{A5}$$

Adding (A5) and (A3), we obtain

$$\frac{dT_3}{T_3} = \frac{1 - x}{1 - 2x}\,\frac{d\alpha}{\alpha}. \tag{A6}$$

Adding (A5) and (A4), we obtain

$$\frac{dT_3/T_3}{d\alpha/\alpha} = \frac{1}{2(1 - \alpha/\alpha_M)^{1/2}} + \frac{1}{2}. \tag{A7}$$

In Fig. 10 we have plotted the function (A7). The value corresponding to our experiment is indicated by point E. The error on T_3 is nearly twice the error on α as suggested in the preceding.

Thus this method to determine T and T_3 is valid only for low excitation of the mixture. But, as indicated in this paper, the determination of T_3 is considerably more accurate if one studies long-pulse amplification.

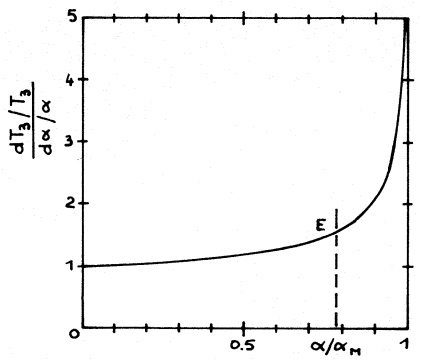

Fig. 10. Evolution of dT_3/T_3 versus $d\alpha/\alpha$.

ACKNOWLEDGMENT

The authors wish to thank H. Brunet for helpful discussions and P. Cottin and M. Huguet for technical assistance. They also wish to thank A. Fertal for his help in the determination of T and T_3.

REFERENCES

[1] R. N. Schwartz, Z. I. Slawsky, and K. F. Herzfeld, "Calculation of vibrational relaxation times in gases," *J. Chem. Phys.*, vol. 20, pp. 1591-1599, Oct. 1952.

[2] N. G. Basov, V. G. Mikhailov, A. N. Oraevskii, and V. A. Shcheglov, "Molecular population inversion in the supersonic flow of a binary gas in a laval nozzle," *Sov. Phys.–Tech. Phys.*, vol. 13, pp. 1630-1636, June 1969.

[3] H. Brunet, "Remarques sur les constantes de transfert d'énergie vibrationnelle du mélange CO_2-N_2-He," *C. R. Acad. Sci.* (Paris), vol. 274, pp. 619-622, Feb. 28, 1972; also Erratums, *C. R. Acad. Sci.* (Paris), vol. 274, p. 1257, May 29, 1972.

[4] A. Nurmikko, T. de Temple, and S. E. Schwarz, "Single-mode operation and mode locking of high-pressure CO_2 lasers by means of saturable absorbers," *Appl. Phys. Lett.*, vol. 18, pp. 130-132, Feb. 15, 1971.

[5] T. de Temple and A. Nurmikko, "The dynamics of single-mode operation of high-pressure CO_2 laser by means of saturable absorbers," *Opt. Commun.*, vol. 4, pp. 231-233, Nov. 1971.

[6] G. Girard, M. Huguet, and M. Michon, "High-power double-discharge TEA laser medium diagnostic," *IEEE J. Quantum Electron.* (Corresp.), vol. QE-9, pp. 426-428, Mar. 1973.

[7] P. J. Bishop, A. F. Gibson, and M. F. Kimmitt, "The performance of photon-drag detectors at high laser intensities," *IEEE J. Quantum Electron.*, vol. QE-9, pp. 1007-1011, Oct. 1973.

[8] P. K. Cheo and R. L. Abrams, "Rotational relaxation rate of CO_2 laser levels," *Appl. Phys. Lett.*, vol. 14, pp. 47-49, Jan. 15, 1969.

[9] R. L. Taylor and S. Bitterman, "Survey of vibrational relaxation data for processes important in the CO_2-N_2 laser system," *Rev. Mod. Phys.*, vol. 41, pp. 26-47, Jan. 1969.

[10] H. Brunet, private communication.

[11] G. Girard, J. C. Farcy, A. Fertal, and M. Michon, "Experiments and theory of nanosecond pulse extraction in an atmospheric pressure CO_2 amplifier," *IEEE J. Quantum Electron.* (Corresp.), vol. QE-10, pp. 901-902, Dec. 1974.

[12] B. J. Feldman, "Short-pulse multiline and multiband energy extraction in high-pressure CO_2-laser amplifiers," *IEEE J. Quantum Electron.*, vol. QE-9, pp. 1070-1078, Nov. 1973.

The Optically Pumped Far-Infrared Laser: Rate Equations and Diagnostic Experiments

J. O. HENNINGSEN AND H. G. JENSEN

Abstract—A four-level rate-equation model for an optically pumped far-infrared (FIR) laser is presented, and an expression is derived for the output power as a function of pump power and gas pressure. The theory is compared with measurements on the 570.5-μm line of CH_3OH, pumped by a CO_2 laser. The width of the gain curve is measured and is shown to go below the Doppler width of the laser transition at low pressure. This indicates that the use of a monochromatic pump source leads to a velocity selective pumping process.

I. Introduction

IN THE SEARCH for stable monochromatic radiation sources bridging the gap between the infrared (IR) range and the millimeter-wave range, the optically pumped far-infrared (FIR) lasers attract considerable interest. The first observation of laser action in the FIR by optical pumping was reported in 1970 by Chang and Bridges [1], and an extensive survey of the subsequent rapid development of this field is found in a review article by Chang [2].

Until now, the interest has been mainly focused on increasing the number of lines and extending the spectral coverage. In contrast, with a few exceptions [3]-[5], relatively little attention has been paid to the study of the laser as such. The aim of this paper is to present a four-level rate-equation model and to correlate this model with experiments. Section II contains the theory and leads up to an expression giving the FIR output power as a function of pump power and gas pressure. We compare this expression with measurements on the 570.5-μm line emitted when CH_3OH is pumped by the 9.52-μm $P(16)$ line of a CO_2 laser [6] and Section III contains the experimental details together with some observations concerning this particular line. The analysis of the results follows in Section IV, and we show that by studying the gain width as a function of pressure, information can be obtained concerning the particular nature of monochromatic pumping.

II. Theoretical Model

Rate Equations

We describe the laser by a four-level system as shown in Fig. 1 where 0 is some rotational level in the vibrational ground state, 1 and 2 are adjacent rotational levels in a low-lying excited vibrational state, sufficiently above the ground state to be thermally unpopulated, and 3 represents the lumped effect of those rotational levels in the upper vibrational manifold, which are not directly involved in the laser transition $2 \rightarrow 1$.

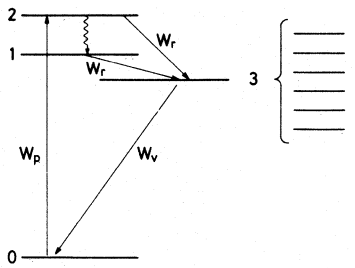

Fig. 1. Four-level model for the optically pumped FIR laser.

In the pumping process, which is assumed to take place uniformly over the mode volume of the laser, molecules are excited from 0 to 2 at a rate w_p by a CO_2 laser tuned to the $0 \rightarrow 2$ absorption line. Collisions between the molecules, occurring at a rate w_r, are very efficient in establishing thermal equilibrium among the rotational levels of a given vibrational state. w_r can therefore be assumed to be much larger than the rate w_v of relaxation back to the vibrational ground state. To be precise, the return back to 0 takes place via other rotational levels in the vibrational ground state. In addition, as will be demonstrated in Section IV, the pumping is effective for molecules inside a narrow velocity range only, and a complete cycle for the molecules will therefore also involve relaxation across the velocity profile inside a given rotational level. The quantity w_v represents the combined effect of all of these processes, and it must therefore be regarded as a phenomenological quantity.

In equilibrium, the net production of photons by stimulated emission from 2 to 1 must equal the losses, and neglecting spatial variations, the rate equations governing the total occupation numbers per unit volume N_i of the various molecular levels, and the number n of FIR photons, are the following:

$$\frac{dN_0}{dt} = w_v N_3 - w_p N_0 \tag{1}$$

$$\frac{dN_1}{dt} = B_{21} n \left(N_2 - \frac{g_2}{g_1} N_1 \right) - w_r N_1 \tag{2}$$

$$\frac{dN_2}{dt} = w_p N_0 - w_r N_2 - B_{21} n \left(N_2 - \frac{g_2}{g_1} N_1 \right) \tag{3}$$

$$N = N_0 + N_1 + N_2 + N_3 \tag{4}$$

Manuscript received September 20, 1974; revised January 27, 1975. This work was supported by Statens Naturvidenskabelige Forskningsråd. A preliminary version of this work was presented at the International Conference on Submillimeter Waves and Their Applications, Atlanta, Ga., June 5-7, 1974.

The authors are with the H. C. Ørsted Institute, the University of Copenhagen, Copenhagen, Denmark.

$$\frac{dn}{dt} = -2\pi\gamma n + B_{21} n \left(N_2 - \frac{g_2}{g_1} N_1\right) \tag{5}$$

where N is the total number of molecules in the 0 state in the absence of pumping, g_1 and g_2 denote the degeneracy of the levels 1 and 2, γ is the cavity half-width [full width at half maximum (FWHM)] and measures the FIR losses, including coupling losses, and B_{21} is the Einstein coefficient for stimulated emission.

In the rate equations we have neglected terms arising from spontaneous emission since the spontaneous lifetime at FIR frequencies is of the order of seconds. Further, we have assumed that w_v, albeit smaller than the rotational relaxation rate w_r, is still so large that we can neglect the collisional population of 1 and 2. In quantitative terms this corresponds to the requirement $w_v >> (w_r/\mu)$, where μ is the effective number of levels represented by the level 3. Presumably, this assumption is too restrictive, since collisions will to a first approximation populate 1 and 2 equally, and hence leave the inversion unchanged. However, it does lead to a substantial simplification of the model.

Solving (1)-(5) for the equilibrium situation, where all time derivatives are zero, we arrive at an equilibrium FIR photon density

$$n = \frac{g_1}{g_1 + g_2} \frac{w_r}{B_{21}} \left(\frac{N B_{21} w_p}{2\pi\gamma w_r (1 + w_p/w_v)} - 1\right) \tag{6}$$

and the FIR output power is given by

$$P_{\mathrm{FIR}} = \tfrac{1}{2} ncAh\nu \tag{7}$$

where A is the effective area of the coupling hole, c is the velocity of light, and ν the FIR frequency. This result may be written in the form

$$P_{\mathrm{FIR}} = \frac{1}{2} t P_s \left(\frac{2Lg}{t + a} - 1\right) \tag{8}$$

where t is the relative coupling loss per double pass, a is the loss from other mechanisms, g is the small signal gain per unit length, L is the active length of the laser, and P_s is the saturation power [7]. Relating the losses to the cavity half-width and introducing the active volume V of the laser, we can then make the identifications

$$g = \frac{B_{21}}{c w_r} \frac{N w_p}{1 + w_p/w_v} \tag{9}$$

$$P_s = h\nu \frac{Vc}{L} \frac{g_1}{g_1 + g_2} \frac{w_r}{B_{21}} . \tag{10}$$

Pressure and Pump-Power Dependence

The step needed in order to make contact with experiments, is to derive the dependence of the various quantities in (6) on pressure p and pump power U. Assuming homogeneous broadening, the Einstein coefficient $B_{21}(\nu)$ is given by

$$B_{21}(\nu) = \frac{c^3}{4\pi^2 \nu^2 t_{\mathrm{sp}} \Delta\nu_N} f(\nu) \tag{11}$$

where ν is the frequency, t_{sp} is the spontaneous lifetime of the 2 state, $\Delta\nu_N$ is the homogeneous linewidth (FWHM) of the $1 \rightarrow 2$ transition, and $f(\nu)$ is a normalized Lorentzian of width $\Delta\nu_N$. The rotational relaxation rate w_r is related to the homogeneous linewidth, so that we have

$$w_r = \pi \Delta\nu_N = \pi C p \tag{12}$$

where C is a constant.

The loss parameter a contains a constant contribution from diffraction losses, scattering losses at the mirrors, etc. In addition, self-absorption of the FIR radiation may give rise to pressure-dependent terms, varying as p if the laser line is coincident with the FIR absorption line, and as p^2 if this is not the case, the width of the absorption line then accounting for the second factor of p.

The pump rate w_p depends on pressure and pump power in a fairly complicated way. It is proportional to the intensity I of pump radiation in the cavity, but I in turn depends on the power absorbed in the gas, and therefore on w_p. A further complication is added by the fact that the absorption must be allowed to saturate. Denoting the power absorbed in the gas by U_{abs}, and assuming that a fraction ξ of this power goes into the $0 \rightarrow 2$ transition, we have

$$\xi U_{\mathrm{abs}} = h\nu_p V \frac{N w_p}{1 + w_p/w_v} \tag{13}$$

where ν_p is the pump frequency. The rate equation for the pump intensity in the cavity is

$$\frac{dI}{dt} = U - 2\pi\Gamma I - U_{\mathrm{abs}} \tag{14}$$

where Γ measures the loss rate of the pump radiation at zero pressure. w_p is obtained by solving (13), (14) for $dI/dt = 0$, and for the expression entering in (6) we then find

$$\frac{N w_p}{1 + w_p/w_v} = \frac{\xi}{V h\nu_p} \frac{p/p_s}{1 + p/p_s} \frac{U}{1 + U/U_s} \tag{15}$$

where

$$p_s = 2\pi k T \xi\Gamma / h\nu_p f_0 \zeta V \tag{16}$$

$$\zeta = w_p / I \tag{17}$$

$$U_s = (1 + p/p_s) \cdot 2\pi\Gamma w_v / \zeta \tag{18}$$

and where k is the Boltzmann constant and f_0 the fraction of the total number of molecules being in the 0 state in the absence of pumping. U_s is a parameter determining the saturation of the pump transition with increasing pump power, and in the limit $U << U_s$, p_s is the pressure at which the absorption in the gas equals the pressure-independent losses. The expression (15) is valid provided just one of the conditions

$$p << p_s, \quad U << U_s, \quad U >> U_s \tag{19}$$

is satisfied. We have not introduced any explicit pressure dependence of w_v since the precise nature of the rate-limiting process in the decay back to the 0 state is not known.

The qualitative behavior of g, P_s, and P_{FIR} is found by com-

bining (8)–(10) with (11), (12), (15)

$$g(\nu) = \frac{G}{2Lp^2} \frac{p/p_s}{1+p/p_s} \frac{U}{1+U/U_s} \tag{20}$$

$$P_s = \frac{2Q}{G} \frac{\nu}{\nu_p} p^2 \tag{21}$$

$$P_{\mathrm{FIR}} = tQ \frac{\nu}{\nu_p} \left(\frac{1}{t+a} \frac{p/p_s}{1+p/p_s} \frac{U}{1+U/U_s} - \frac{p^2}{G} \right) \tag{22}$$

where

$$G = \frac{Lc^2 \xi}{2\pi^3 \nu^2 t_{\mathrm{sp}} C^2 V h \nu_p} f(\nu) \tag{23}$$

$$Q = \xi \frac{g_1}{g_1 + g_2}. \tag{24}$$

Inspection of (22) shows that P_{FIR} increases linearly with U for $U \ll U_s$, and saturates for $U \gg U_s$. When the pressure is increased at constant U, P_{FIR} will start out proportional to p, go through a maximum, and eventually go to zero again. Neglecting FIR self-absorption and assuming $U \ll U_s$, all the p dependence is explicit in (22), and for the optimum pressure we then find

$$p_{\mathrm{opt}} \propto U, \qquad p \ll p_s \tag{25}$$

$$p_{\mathrm{opt}} \propto U^{1/3}, \qquad p \gg p_s. \tag{26}$$

III. Experiments

To check the theoretical results derived in the preceding section, we studied the 570.5-μm line of CH_3OH, using the experimental arrangement shown in Fig. 2. The resonator and beamsplitter construction is in principle similar to that described by Chang [1]. The resonator length is 110 cm and its diameter 10 cm. One mirror is flat; the other is concave, with a 3.5-m radius of curvature, and is provided with a central 5-mm coupling hole. The length of the resonator is stabilized by 3 Invar rods. This is very important since at low pressure the gain width may drop to about 0.3 MHz, corresponding to less than 1-μm variation in resonator length.

The single mode CO_2 radiation is focused at a 1-mm hole in the beamsplitter by a 58-cm focal-length NaCl lens, and it enters the FIR cavity with a divergence half-angle of 10 mrad. A tungsten bolometer, constructed from the filament of a small light bulb, can be inserted in the cavity as shown in Fig. 2 and is used for checking the pump intensity. The CO_2 power level is adjusted by a gas attenuator of length 10 cm, based on CH_3OH. An axial blower circulates the gas in order to prevent distortion of the beam profile due to local heating. The power level is monitored by a disk calorimeter which can be inserted after the attenuator. It is calibrated against a cone calorimeter onto which the beam could be directed by an auxiliary mirror placed immediately in front of the entrance window of the FIR cavity. A separate measurement ascertained that by proper focusing all the power could be passed through the beamsplitter.

The FIR signal is chopped at 10 Hz and detected by a He-cooled Ge bolometer. The pressure in the FIR cell is measured by a Pirani gauge which has an appropriate sensitivity down to a few meter torr. Since its response is different for different gases, we calibrated it for CH_3OH against an absolute gauge of the Bourdon type, manufactured by Texas Instruments. Measurements were made by adjusting the pressure, sealing off the FIR cell, closing all pumps to avoid vibrations, and then scanning the cavity length slowly at a number of different CO_2 power levels. At regular intervals the setting of the CO_2 laser was checked, but very little adjustment was usually needed.

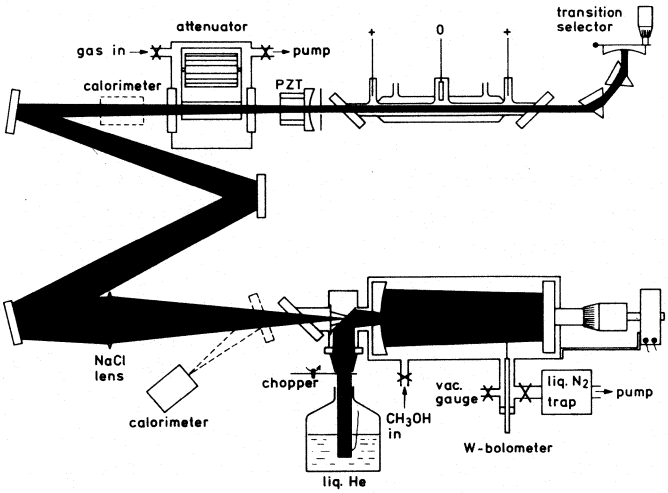

Fig. 2. Schematic diagram of the experimental arrangement.

Although the 570.5-μm line is listed in the literature as a single line [4], [6], [8], our experiments show that it consists of three components. The two strongest ones are of about equal strength, and separated by 1.3 MHz. The third, situated 0.4 MHz outside the doublet, is much weaker and could only be observed at a pressure of 6.5 mtorr. FIR output was observed over a CO_2 tuning range of about ±20 MHz, centered at an offset of +25 MHz relative to the CO_2 line center. Inside this range, the frequency separation between the two components as well as their relative amplitude, was essentially independent of pump frequency, pump power, and gas pressure, and also unaffected by various asymmetric perturbations of the cavity. We therefore conclude that the doublet arises from transitions between two sets of nearly degenerate molecular energy levels, the degeneracy presumably being produced by the internal rotation of the molecule.

The cavity scans indicate that usually only one transition will oscillate at a time if the cavity is tuned to the corresponding line center. However, both transitions are pumped, and the main effect of the degeneracy is therefore to introduce a source of dissipation for the pump power. This can be accounted for through the factor ξ [see (13)], while the p and U dependences are left unchanged. At the highest values of pressure and pump power the overlap of the lines is substantial, and they tend to be pulled together. For this reason the measurement of gain width could not be extended beyond 50 mtorr.

Saturation Effects

The variation of P_{FIR} with pump power at different pressures is shown in Fig. 3. The nonlinear behavior below 20 mtorr shows that in this range saturation effects are impor-

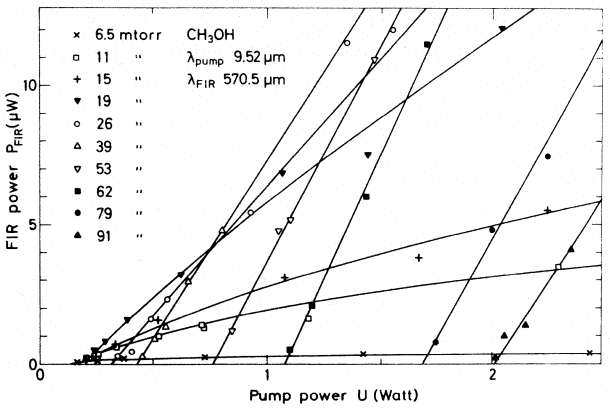

Fig. 3. FIR output as a function of pump power for various pressures. Solid lines are fitted to the theoretical expression.

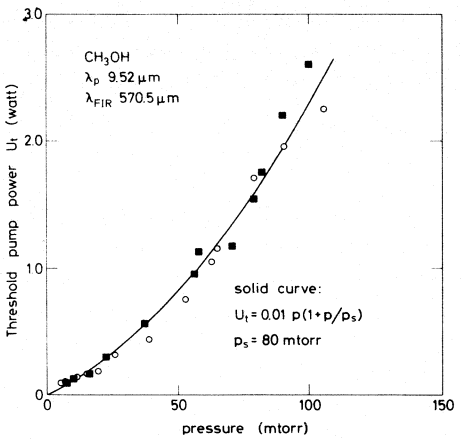

Fig. 4. Threshold pump power U_t as a function of pressure, different symbols denoting different runs. Solid curve is the theoretical prediction.

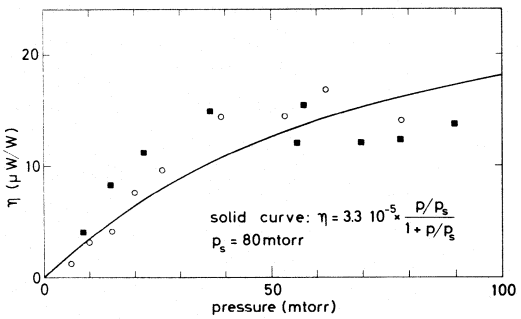

Fig. 5. Experimental values for conversion efficiency, different symbols denoting different runs. Solid curve is the theoretical prediction.

tant. Such effects have not previously been observed in this type of laser. A fit to (22) results in the solid lines of Fig. 3, yielding U_s values ranging from about 0.5 W at the lowest pressures to more than 5 W at 19 mtorr. These values are associated with a quite large uncertainty, particularly at the higher pressures where the deviation from linear behavior of P_{FIR} is small. From (18) it follows that the variation of U_s reflects that of w_v since, as will be shown in the following, we are in the limit $p \ll p_s$. The increase of U_s with pressure therefore indicates that w_v is determined by collisions, even though the large uncertainty precludes a reliable determination of its functional dependence on p.

Threshold Pump Power

A quantity of practical importance is the threshold pump power U_t, whose experimentally determined variation with pressure is shown in Fig. 4. Disregarding an insignificant correction from saturation effects at the lowest pressures, we find from (22)

$$U_t = \frac{p_s\, p}{G}(1 + p/p_s)\,(t + a). \tag{27}$$

In order to determine the possible pressure dependence of the loss parameter a, the absorption of FIR radiation in CH_3OH was measured in an external cell. It was found to have a weak p^2 dependence, the loss at 100 mtorr corresponding to only 0.01 percent per double pass of the cavity. This experiment would not give information about losses due to absorption of the FIR radiation by molecules in those levels, which are nearly degenerate with the lower laser level, since these are only populated under pumping conditions. However, such a loss term would depend on the pump power and hence change the U dependence of (22), and there is no experimental evidence for such a term. We may consequently take a to be independent of pressure.

The solid line in Fig. 4 represents the expression (27), using the parameters p_s = 80 mtorr and $p_s(t + a)/G$ = 0.01 W/mtorr. The overall agreement is good, but considering the two sets of data points independently, there are discrepancies which appear to be of a systematic nature. Due to the nonuniform pumping the pressure dependence of the pump intensity will vary from point to point in the resonator. A change in pressure then leads not only to a change in the total power absorbed, but also to a redistribution, and consequently the exact pressure dependence of U_t may be more complicated than predicted by (27).

According to (27) U_t should tend to zero in the limit $p \to 0$, but this is true only as long as the homogeneous linewidth $\Delta\nu_N$ is proportional to p [see (12)]. As p is reduced, $\Delta\nu_N$ will eventually reach a constant value, and this will lead to a finite lower limit for U_t. Our lowest measured threshold power is 0.1 W but the data are not sufficiently precise to decide whether this represents the limiting value.

Differential Conversion Efficiency

The differential conversion efficienty η is defined as the slope of $P_{\mathrm{FIR}}(U)$ in the unsaturated limit. We find from (22)

$$\eta = Q\frac{\nu}{\nu_p}\cdot\frac{t}{a+t}\cdot\frac{p/p_s}{1+p/p_s}. \tag{28}$$

Fig. 5 shows the measured values for η compared with the expression (28), using p_s = 80 mtorr as before, and adjusting the constant factor to yield a reasonable overall agreement. As for U_t, we expect the main source of the deviations to be the nonuniform pumping.

Frequency Dependence of the Small Signal Gain

Experimentally, we can determine the variation of the small signal gain with frequency by making use of its known dependence on pump power. At the threshold for oscillation the small signal gain always equals the total losses. Thus compar-

ing the two threshold pump-power levels U_t and $U > U_t$, corresponding to the center frequency ν_0 and a detuned frequency ν, respectively, we find by using (20)

$$\frac{g(\nu(U))}{g(\nu_0)} = \frac{U_t}{U}\frac{1 + U/U_s}{1 + U_t/U_s}. \tag{29}$$

The desired variation can be derived from this expression by measuring, as a function of pump power, the range of cavity tuning over which oscillations can be sustained. Fig. 6 shows the result of such a procedure, plotted so as to reveal Lorentzians as straight lines. The gain width (FWHM) is shown as a function of pressure in Fig. 7, and it follows the expression (12) with C = 38 MHz/torr, down to about 20 mtorr. This confirms our *ab initio* assumption of homogeneous broadening of the $1 \rightarrow 2$ transition.

The Doppler width of the transition is 1.15 MHz, using a temperature of 300 K. Fig. 7 clearly shows that the gain width goes below this value at low pressure, and the excited molecules can therefore not have a Maxwellian velocity distribution. We see this as a consequence of the monochromatic pumping. The Doppler width of the $0 \rightarrow 2$ transition is of the order of 70 MHz, so that the pump radiation interacts with molecules inside a very narrow velocity range only. Consequently, the Doppler width of the $2 \rightarrow 1$ transition will be suppressed. Two effects counteract this velocity selective pumping. Power broadening may lead to a broader velocity distribution if the pump transition is saturated [9]. However, since all the data points of Fig. 7, possibly excluding the one at 6.5 mtorr, can be derived by considering the unsaturated limit $U \ll U_s$, this appears to play a minor role. Further, velocity cross relaxation inside the excited level will tend to restore the Maxwellian velocity distribution [10]. The rate at which this takes place in CH_3OH is not known, but we may take as a guideline the value 12 MHz/torr obtained for CO_2 in [10]. From (7), (11) the rate $B_{21}n$ of stimulated emission is estimated to be about 20 MHz at a FIR output of 10 μW, and this indicates that the Doppler profile cannot be restored before the molecules have left the 2 level.

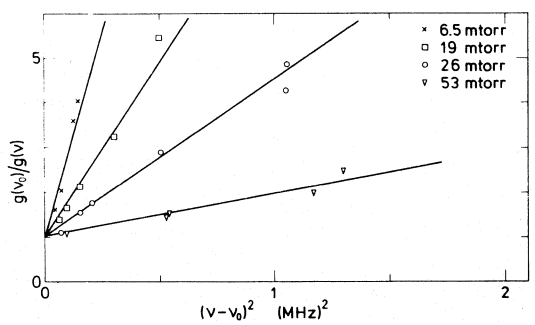

Fig. 6. Determination of the gain-curve line shape, straight lines corresponding to Lorentzians.

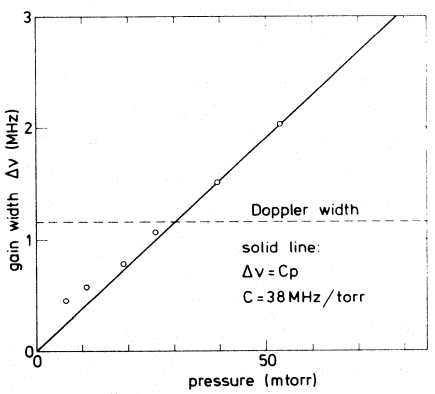

Fig. 7. Gain width (FWHM) as a function of pressure.

Below 20 mtorr the gain width levels off and approaches a constant value of 0.4 MHz. An estimate shows that time-of-flight effects lead to a much smaller linewidth, but the effect could be caused by velocity cross relaxation. Most likely, however, it arises from the finite cavity half-width which is estimated to be about 0.3 MHz, and which limits the experimental resolution.

IV. Conclusion

The four-level model described in this paper accounts reasonably well for pressure and pump-power dependences observed in a study of the 570.5-μm line of CH_3OH, the main discrepancies being attributed to nonuniform pumping. By studying the pressure dependence of the gain width, it is shown that the laser is homogeneously broadened down to at least 20 mtorr. In this range the gain width is smaller than the Doppler width of the laser transition due to the monochromatic pumping process.

Acknowledgment

The authors wish to thank A. Hermansen for helpful discussions and the Central Workshop of the H. C. Ørsted Institute which manufactured whatever was asked for with never-failing ability.

References

[1] T. Y. Chang and T. J. Bridges, "Laser action at 452, 496 and 541 μm in optically pumped CH_3F," *Opt. Commun.*, vol. 1, pp. 423–426, Apr. 1970.

[2] T. Y. Chang, "Optically pumped submillimeter-wave sources," in *Proc. Int. Conf. Submillimeter Waves and Their Applications* (Atlanta, Ga.), June 5–7, 1974, pp. 13–14; also *IEEE Trans. Microwave Theory Tech. (Part I of Two Parts: Special Issue on the First International Conference on Submillimeter Waves and Their Applications)*, vol. MTT-22, pp. 983–988, Dec. 1974.

[3] J. R. Tucker, "Theory of an FIR gas laser," in *Proc. Int. Conf. Submillimeter Waves and Their Applications* (Atlanta, Ga.), June 5–7, 1974, pp. 17–18; also *IEEE Trans. Microwave Theory Tech.* (Abstracts), vol. MTT-22, p. 1117, Dec. 1974.

[4] M. Yamanaka and H. Yoshinaga, "Compact waveguide lasers in the submillimeter and millimeter wave regions," in *Proc. Int. Conf. Submillimeter Waves and Their Applications* (Atlanta, Ga.), June 5–7, 1974, pp. 26–27; also *IEEE Trans. Microwave Theory Tech.* (Abstracts), vol. MTT-22, pp. 1117, Dec. 1974.

[5] M. Yamanaka *et al.*, "On the transverse mode in an optically pumped far-infrared NH_3 laser," *Japan. J. Appl. Phys.*, vol. 13, pp. 843–850, May 1974.

[6] T. Y. Chang, T. J. Bridges, and E. G. Burkhardt, "CW submillimeter laser action in optically pumped methyl fluoride, methyl alcohol, and vinyl chloride gases," *Appl. Phys. Lett.*, vol. 17, pp. 249–251, Sept. 1970.

[7] W. W. Rigrod, "Gain saturation and output power of optical masers," *J. Appl. Phys.*, vol. 34, pp. 2602–2609, Sept. 1963.

[8] D. T. Hodges, R. D. Reel, and D. H. Barker, "Low-threshold CW submillimeter- and millimeter-wave laser action in CO_2-laser-pumped $C_2H_4F_2$, $C_2H_2F_2$, and CH_3OH, *IEEE J. Quantum Electron.* (Corresp.), vol. QE-9, pp. 1159–1160, Dec. 1973.

[9] C. H. Townes and A. L. Schalow, *Microwave Spectroscopy*. New York: McGraw-Hill, 1955, pp. 371–373.

[10] H. Granek, C. Freed, and H. Haus, "Experiment on cross relaxation in CO_2," *IEEE J. Quantum Electron.*, vol. QE-8, pp. 404–414, Apr. 1972.

Near Single-Line Operation of a Free-Burning $CS_2/O_2/N_2O$ Flame Laser with a Nondispersive Optical Cavity

KENNETH D. FOSTER, GEORGE H. KIMBELL, AND DAVID R. SNELLING

Abstract—The $CS_2/O_2/N_2O$ flame laser has been operated for the first time under conditions in which the spectral output is nearly single line. This transition is the $P_{10\text{-}9}(17)$ of CO at 5.4265 μm, the same transition which was observed to oscillate in single-line fashion by Hirose *et al.* in an electrically initiated CO chemical laser. It is suggested that the unique behavior of this line may be due to its close proximity to a P branch transition in an adjacent band, namely the $P_{9\text{-}8}(23)$ line, such that the gain profiles of the two lines overlap. Calculations suggest that at the conditions of these experiments, the separation of the line centers for this pair is about 0.3 Å or less.

The $P_{10\text{-}9}(17)$ transition was also found to be totally absent under certain conditions of high multiline power, particulary at low O_2 and N_2O flows. This may be due to absorption by a high-band R branch transition at 5.4266 μm, namely the $R_{15\text{-}16}(32)$ line.

I. Introduction

INTEREST in the efficient conversion of chemical energy into laser energy led to a great deal of research into the hydrogen halide, hydrogen halide-CO_2 transfer, and CO chemical lasers. Most of these lasers rely on initiation of the important chemical reactions by injection of electrical energy into the system.

The first purely chemical continuous-wave (CW) laser was the DF-CO_2 transfer laser [1], where the F atoms required for initiation were formed by the reaction of NO with F_2.

A particularly interesting avenue of research for a chemical CW laser is the study of flame excitation processes. In 1970 Foster and Kimbell [2] reported intense infrared radiation (IR) from flames of carbon disulfide and oxygen. This radiation was identified as emission from vibrationally excited CO formed in the flame. The observation of radiation from high vibrational levels of CO indicated that the vibrational temperature of the CO far exceeded the flame temperature. Under certain conditions vibrational population inversions were found to exist in the flame.

Later studies of the electrically assisted CS_2/O_2 chemical laser [3], [4] (the O atoms were produced in an electrical discharge) showed that the chemical mechanism responsible for the laser action near 5 μm was the following:

$$O + CS_2 \longrightarrow CS + SO \tag{1}$$

$$S + O_2 \longrightarrow SO + O \tag{2}$$

$$O + CS \longrightarrow CO^{\dagger} + S. \tag{3}$$

The pumping reaction (3) was shown to produce vibrationally excited CO with almost 90 percent of the reaction exothermicity going into CO vibration [5]-[8]. This rather simple mechanism is obviously not adequate at the elevated temperatures present in a free-burning flame of CS_2 and O_2. At temperatures of about 1000 K reactions such as

$$SO + O_2 \longrightarrow SO_2 + O \tag{4}$$

$$SO + SO \longrightarrow SO_2 + S$$

$$\longrightarrow S_2O_2 \longrightarrow S_2O + O \tag{5}$$

become important.

Pilloff *et al.* measured gain [9] and later achieved laser action [10] in CS_2/O_2 flames. Addition of N_2O was found to increase the output power up to 0.6 W [11].

Improvement of the efficiency and total power of the $CS_2/O_2/N_2O$ laser has been reported by Linevsky and Carabetta [12]. These authors found N_2O to have an even more striking effect than did Searles and Djeu [11]. A thirty-fifty-fold increase in output power was observed when N_2O was added. In electrically assisted CS_2/O_2 chemical lasers, the role of N_2O is believed to be principally one of depopulating the lower vibrational levels of CO due to vibrational-vibrational (V-V) energy transfer [13]. At the elevated temperatures present in flames, it has also been suggested [12] that N_2O may participate in the flame chemistry. In a footnote of [12] the authors report output powers of some 25 W and chemical efficiencies of 2.5 percent. Spectroscopic studies of the laser output spectrum showed lasing to occur from the $v = 12 \longrightarrow 11$ band near 1790 cm^{-1} to $v = 5 \longrightarrow 4$ band near 1980 cm^{-1}.

We describe here what is believed to be the first observation of a nearly single-line operation in the $CS_2/O_2/N_2O$ flame laser under certain conditions of gas mix. No dispersive elements were used in the optical cavity. Laser output spectra having somewhat higher resolution than those reported previously [12] are also given.

II. Experimental

The burner which was used in this study was 43 cm long and was constructed primarily of aluminum. A schematic representation of the essential features of the burner is shown in Fig. 1. The O_2 and N_2O flows were premixed and liquid carbon disulfide was injected into a vaporizer by using a suction feed through a fine control needle valve. The vaporizer consisted of an aluminum cylinder about 15 cm long and 10-cm radius half-filled with solid copper chunks. The outside of the cylinder was wrapped with heating tape. A 12-l ballast volume was inserted immediately downstream of the vaporizer to

Manuscript received September 26, 1974; revised January 29, 1975.

The authors are with the Defence Research Establishment Valcartier (DREV), Valcartier, P.Q., Canada.

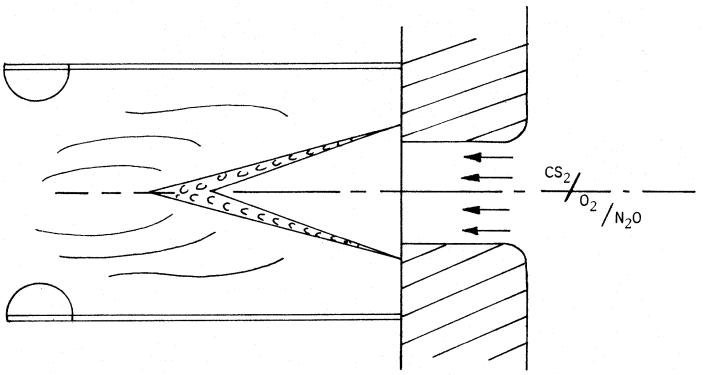

Fig. 1. $CS_2/O_2/N_2O$ flame and burner shows unburned-gas, flame-front, and burned-gas regions. The laser axis is just upstream from the apex of the flame front.

minimize pressure fluctuations. The CS_2 vapor then passed through a sonic orifice of known dimensions into the premixed O_2/N_2O stream at a pressure of about 70 torr. After allowing enough flow time to ensure complete mixing this $CS_2/O_2/N_2O$ stream was spread the length of the burner and underwent a pressure drop across some 200 small channels down to the ambient pressure in the flame region of about 30 torr. At the exit of these channels, the flow was allowed to "settle" through a 3-cm × 40-cm channel extending some 10 cm in the flow direction. Finally, the flow was narrowed to a 1-cm × 40-cm slot giving a linear velocity of 10–15 ms^{-1} to the unburned gas as it entered the flame region. The flame shape relative to the burner is shown as the shaded area in Fig. 1. The side walls were found to render the flame more stable. A small auxiliary flow of N_2 was added through the window supports to prevent sulfur deposition and a larger flow (about five to ten times the total combustible flow) of ballast N_2 which was added downstream of the combustion chamber in order to dilute and cool the hot product gases.

Representative flows for the experiments described here were $CS_2 \sim 2.5$ mmoles/s; $O_2 \sim 30$ mmoles/s; $N_2O \sim 7$ mmoles/s. The total pressure in the combustion chamber was kept between 25 and 35 torr for most experiments.

The optical cavity consisted of a 10-m radius of curvature total reflector of the protected metal type and a 98-percent reflectivity germanium partial reflector of 10-m radius of curvature. The optical axis was centered slightly upstream of the apex of the flame front.

Total power measurements were performed with a coherent radiation power meter.

Some spectroscopic measurements were conducted with a CO spectrum analyzer (Optical Engineering Inc.) having a nominal resolution of 0.0024 μm, determined largely by the thermosensitive display screen. For these experiments the laser beam was focused on the entrance slit. The slit was then used to control the radiant flux on the display screen. The display screen was photographed using a Polaroid camera mounted on the instrument.

For higher resolution measurements, a 1-m McPherson instrument (Model 2051) was used with 50-μm slits and a 150-1/mm grating blazed for 4 μm. The laser beam was chopped at 680 Hz and detected with a Mullard Labyrinth InSb detector whose output was connected to a lock-in amplifier (PAR-HR8). Rapid recording (2000 A/min) was accomplished by use of a visicorder (Honeywell Model 906B). The wavelength was calibrated with a HeNe laser in the 8th, 9th, and 10th orders.

III. Results

The maximum output power that has been observed in the present flame laser is 15.5 W at a CS_2 flow rate of 2.5 mmoles/s. The flows of N_2O and O_2 were 6.3 mmoles/s and 31.5 mmoles/s, respectively, and the total pressure was 31.5 torr. This corresponds to a chemical efficiency based on the reaction $O + CS \longrightarrow CO + S + 80$ kcal/mole, of about 2 percent.

Thermocouple measurements of the flame temperature, under conditions of lower CS_2 flow rates than those used in the preceding, indicated the temperature reached a maximum of about 1000 K. Linevsky and Carabetta [12] have measured maximum temperatures of approximately 1300 K for flow rate and total pressure conditions similar to those described here. They have found that the gain region is slightly upstream of the flame in the front in the unburned gas region and estimate the temperature in this region to be (800 ± 200)K.

Preliminary laser output spectra were taken using a CO spectrum analyzer. This proved to be a very convenient instrument since the whole spectrum was displayed at one time on a thermosensitive screen having wavelength and frequency scales. Experiments involving the effects of gas mix on the laser output spectrum could be performed in a short period of time. The effect of N_2O on the laser output spectrum was as follows. With a flow of N_2O of 6.31 mmoles $\cdot s^{-1}$ there were approximately 32 lasing lines. An increase in N_2O flow to 11.1 mmoles $\cdot s^{-1}$ resulted in the appearance of only about 20 lines. Of these lines the most dominant appeared at 5.423 μm. This line was absent from the spectrum at the lower N_2O flow. A further increase of the N_2O flow to 12.7 mmoles $\cdot s^{-1}$ showed approximately ten weak lines and one intense line again at 5.423 μm.

The dependence of the laser output spectrum on O_2 flow was found to behave in a manner similar to that of N_2O. With an oxygen flow of 32 mmoles/s and 13.2 mmoles/s of N_2O the spectrum was nearly single line. As the O_2 flow was reduced to 25 mmoles/s more lines appeared and the 5.423-μm line became very weak. With a further reduction in oxygen to 20 mmoles/s the spectrum was multiline but again with no line at 5.423 μm. This line, at 5.423 μm on the display screen, corresponds to the $P_{10\text{-}9}$ (17) line.

On the basis of the preceding results, it was decided to examine the CO flame laser output spectrum at higher resolution.

The 1-m McPherson was used with both entrance and exit slits set at 50 μm. Measurements of a single line indicated that the resolution of the instrument (by the Rayleigh criterion) was approximately 0.16 cm^{-1}. Linevsky and Carabetta's [12] flame-laser spectra using an interferometer have a stated resolution of approximately 0.5 cm^{-1}.

The output spectra are shown in Fig. 2. The upper multiline spectrum was taken under the following flow conditions $CS_2 = 2.15$ mmoles/s, $O_2 = 28.6$ mmoles/s, $N_2O = 5.41$ mmoles/s. The total pressure was 35.8 torr and the total multiline laser power was about 11 W. Even with the present resolution some lines are not resolved so that assignment is somewhat ambiguous. However, certain closely spaced lines

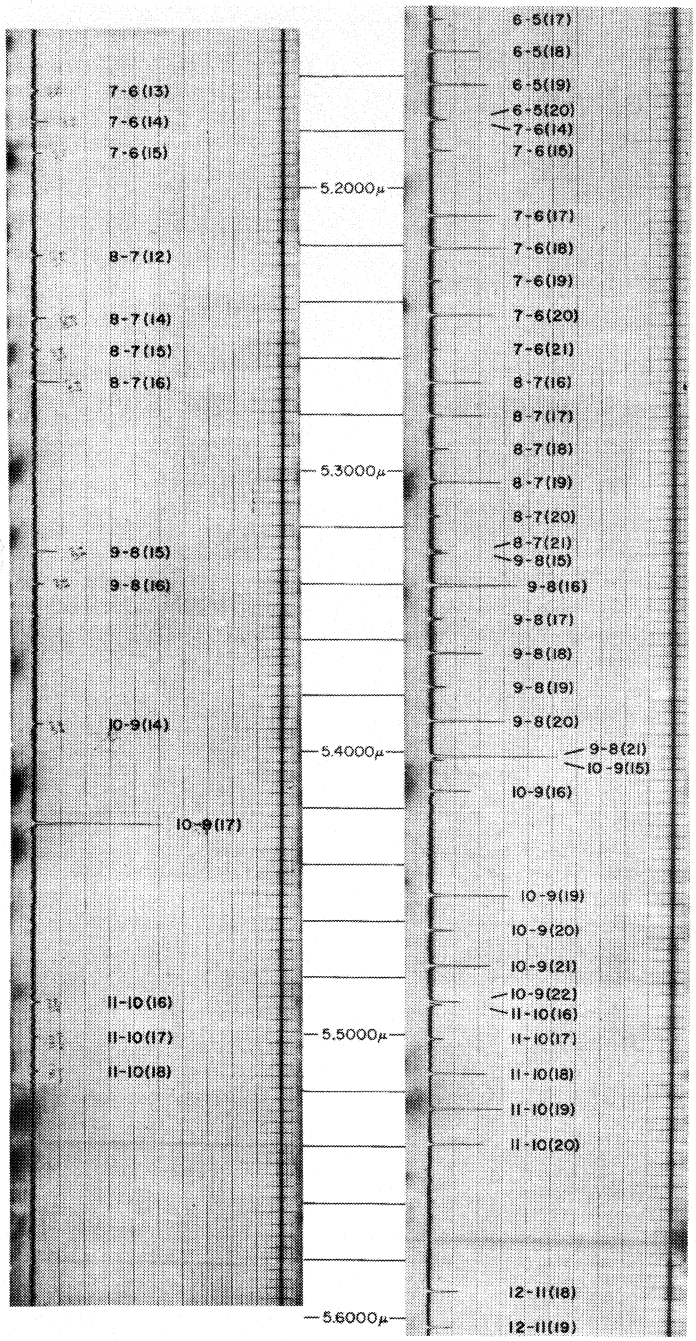

Fig. 2. Photos of high resolution spectra (RN 0.16 cm^{-1}) for multiline and near single-line conditions. $P_{v-v^1}(J^1) \equiv v\text{-}v^1(J^1)$.

are resolved which were not resolved with the CO spectrum analyzer. Three lines are notable by their absence: $P_{7\text{-}6}$ (16), $P_{10\text{-}9}$ (17), and $P_{10\text{-}9}$ (18). The $P_{10\text{-}9}$ (17) line is the line which was found to behave in a peculiar fashion during the experiments using the spectrum analyzer so that its absence under these conditions was not unexpected. The other two lines, however, i.e., $P_{7\text{-}6}$ (16) and $P_{10\text{-}9}$ (18), were seldom observed in any of our spectra. It should be pointed out that these two lines were also absent from Linevsky and Carabetta's spectra.

The lower spectrum shown in Fig. 2 was obtained under conditions which were previously shown to give a near single-line output, i.e., at higher N_2O and O_2 flows than for the multiline spectrum. The $P_{10\text{-}9}$ (17) line indeed predominates and represents about 65 percent of the output power at these conditions. The following flows were used for the near single-line operation: $CS_2 = 2.2$ mmoles/s, $O_2 = 32.6$ mmoles/s, $N_2O = 10.1$ mmoles/s. The total pressure was 31.8 torr and the laser output power was 1-1.5 W.

IV. Discussion

Single-line operation of an electrically excited CS_2/O_2 chemical laser has been observed previously [14]. This was a longitudinal flow system employing a diluent helium flow and a total pressure of 10.5 torr. Single-line output was observed on the $P_{10\text{-}9}$ (17) line at 5.426 μm, the same line which was found to dominate in the present flame laser. This single-line operation was attributed [14] to V-V coupling sufficiently rapid that CO vibrational level populations equilibrate faster than the stimulated emission rate. Laser oscillation was then supposed to occur on only the highest gain line with the other lines kept below threshold. It was suggested that the conditions of temperature and pressure employed in their experiment thus resulted in single-line operation.

The fact that near single-line operation on the same line has been obtained in the present $CS_2/O_2/N_2O$ flame laser, which operates at very different conditions than the preceding longitudinal laser, suggests that the preceding explanation of rapid V-V coupling may not be sufficient to explain the preceding effect. The question which may be raised then is: "Why should the $P_{10\text{-}9}$ (17) line have the highest gain in both systems?"

It is therefore suggested that besides the previously mentioned rapid V-V coupling, the tendency for single-line operation is due to something unique about the $P_{10\text{-}9}$ (17) line itself. Tabulated values of the various wavelengths for CO fundamental transitions reveal a near coincidence between the $P_{10\text{-}9}$ (17) line (1842.818 cm^{-1}) and the $P_{9\text{-}8}$ (23) line (1842.824 cm^{-1}). The CO line positions were calculated from a recent determination of the molecular constants given by Roh and Rao [15].

These molecular constants reproduce most of the observed CO line positions within ±0.005 cm^{-1} for CO P branch lines. If the separation of the $P_{10\text{-}9}$ (17) and $P_{9\text{-}8}$ (23) line centers is of the same order as the isolated linewidth, then the gain profiles for the two lines will overlap, i.e., a photon emitted in the process $v = 10, J = 16 \longrightarrow v = 9, J = 17$ can be amplified in part by the inversion between $v = 9, J = 22$ and $v = 8, J = 23$. Unfortunately, sufficiently accurate wavelengths of these transitions are not available.

One experiment which would help explain the behavior of this line would be to scan the cavity length with one mirror mounted on a piezoelectric translator. This would entail operation on the axial transverse mode and a cavity length such that the longitudinal mode separation was greater than the linewidth. For geometrical reasons, such an experiment was not performed with the apparatus described herein.

In order to examine the effect of the line center separation on the gain profile, approximate CO linewidths have been calculated using an empirical expression for the Voight profile [16]. For the purposes of this calculation, the gas in the active region of the flame laser was assumed to consist of CO, O_2, and N_2O. The mole fractions of the components were set

at 0.053, 0.631, and 0.316, respectively, and the total pressure was put at 30 torr. These conditions coincide approximately with the near single-line conditions which were observed. The self-broadening cross section for CO was computed from data by Williams *et al.* [17]. The broadening cross section for N_2O was assumed to equal that for CO_2 which was obtained from the same source. The broadening cross section for O_2 was estimated from the formula

$$\sigma_{opt}(CO\text{-}O_2) = \sigma_{opt}(CO\text{-}X) \cdot \frac{\sigma_{coll}(CO\text{-}O_2)}{\sigma_{coll}(CO\text{-}X)}$$

where

$\sigma_{opt}(CO\text{-}O_2) \equiv$ broadening cross section of O_2

$\sigma_{opt}(CO\text{-}X) \equiv$ broadening cross section of species X

$\sigma_{coll}(CO\text{-}O_2)$, $\sigma_{coll}(CO\text{-}X) \equiv$ hard sphere collision cross sections for $CO\text{-}O_2$ and $CO\text{-}X$ collisions, respectively.

Values of $\sigma_{opt}(CO\text{-}X)$ were taken from the data of Williams *et al.* for $X \equiv$ Ar, N_2, and H_2. The resultant values of $\sigma_{opt} \cdot (CO\text{-}O_2)$ were 55.2 A^2, 59.1 A^2, and 55.3 A^2, respectively. The average value of 56.5 A^2 was then used in subsequent calculations. In view of the slight J dependence of the cross section [16], the preceding cross sections were computed for $J = 20$ to be

$$\sigma_{opt}(CO\text{-}CO) \simeq 70.3\ A^2$$

$$\sigma_{opt}(CO\text{-}N_2O) \simeq 65\ A^2$$

$$\sigma_{opt}(CO\text{-}O_2) \simeq 56.5\ A^2.$$

The Doppler width was taken to correspond to a temperature of 800 K.

Lorentzian and Doppler widths, determined from the preceding data to be 64 MHz and 211 MHz, respectively, were then employed in the empirical approximation to the Voight profile of Whiting [16] in order to obtain a normalized gain profile. Fig. 3 shows the extent of overlap for two equally intense lines at various line center separations. It will be noted, for instance, that at a line center separation of three Voight widths (i.e., 0.723 Å for the conditions used here) and a Lorentzian to Voight width ratio of 0.261 the central valley is about 5 percent of the two isolated peak heights. The fractional increase in peak gain as a function of line center separation is shown in Fig. 4, again assuming equally intense lines. The peak gain is seen to be 10 percent greater than that for the isolated lines at a line center separation of about 1.2 Voight widths or about 0.29 Å. If the proposed explanation for the tendency to operate on a single line is correct, and the peak gain for the line at 5.4265 μm is augmented because of an overlap between the $P_{10\text{-}9}$ (17) and $P_{9\text{-}8}$ (23) profiles, then the line centers must be within about 0.3 Å (or 0.01 cm^{-1}) of each other.

The absence of the line at 5.4265 μm under conditions where the overall multiline power is high is difficult to explain by the preceding argument. In view of the dependence of the gain on J as shown in [18], it is difficult to envisage a situation where gain on $P_{10\text{-}9}$ (17) would be offset by a loss on

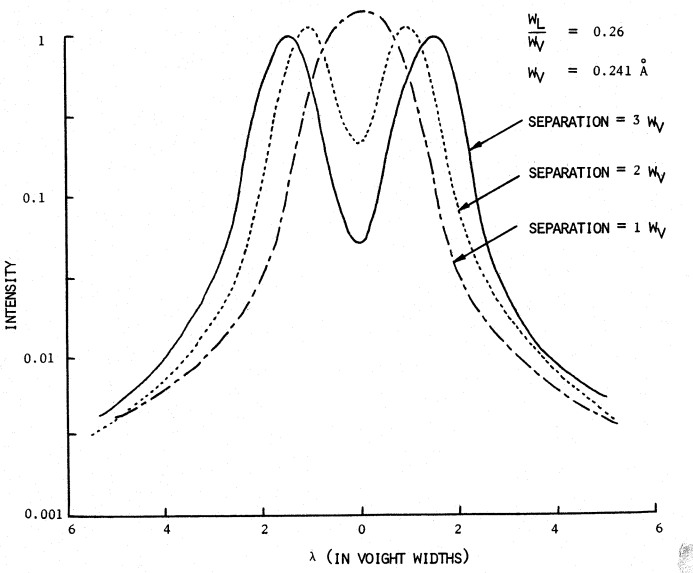

Fig. 3. Dependence of the extent of overlap on the line center separation assuming equal intensities for isolated lines, $W_1 \equiv$ Lorentzian width full width at half maximum (FWHM), $W_v \equiv$ Voight width (FWHM).

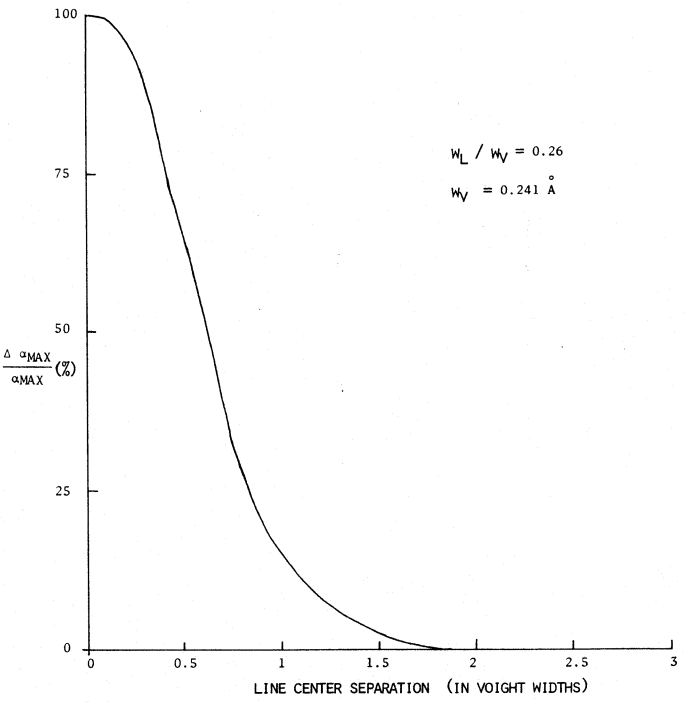

Fig. 4. Fractional increase in peak gain coefficient as a function of line center separation.

$P_{9\text{-}8}$ (23) or vice versa such that the line did not lase since they are both P branch lines of adjacent bands. Only if there was a sharp difference in the N_{10}/N_9 and N_9/N_8 inversion ratios could this circumstance prevail. It is possible, however, that if an R branch line of high J number overlapped with $P_{10\text{-}9}$ (17), then $P_{10\text{-}9}$ (17) radiation would tend to be absorbed. Examination of the wavelengths of the CO R branch transitions indicates the existence of a line at 1842.819 cm^{-1} in the 16-15 band, namely, the $R_{15\text{-}16}$ (32) transition. Although the existence of these high v CO molecules was not confirmed directly in the present experiments, they have been

found to be present in previous CS_2/O_2 experiments (see, for example, [8]).

The molecular constants for CO (15) give the following line positions: $P_{10\text{-}9}$ (17) 1842.818 cm^{-1}, $P_{9\text{-}8}$ (23) 1842.824 cm^{-1}, and $R_{15\text{-}16}$ (32) 1842.819 cm^{-1} [14]. It can be seen that, within the experimental error of ± 0.005 cm^{-1}, the three lines are coincident.

The absence of $P_{10\text{-}9}$ (17) under conditions of low O_2 and N_2O flows, as well as the predominance of $P_{10\text{-}9}$ (17) with high O_2 and N_2O flows does lend some support to this explanation of R branch absorption. If the absence of $P_{10\text{-}9}$ (17) is indeed due to R branch absorption in the 16-15 band then the addition of O_2 will preferentially lower the populations in high v levels and hence remove absorbers from the system by the V-V transfer process

$$CO_{v=15} + O_2 \longrightarrow CO_{v=14} + O_{2\,v=1} + 222\ cm^{-1}.$$

The peak at $P_{10\text{-}9}$ (17) will therefore increase in intensity with increasing O_2. The rate constant increases, for example, from 2.1×10^{-14} $cm^3 s^{-1}$ for $CO_{v=12}$ to 4.4×10^{-14} $cm^3 s^{-1}$ for $v = 13$ [19].

It is noteworthy that this unique behavior of the $P_{10\text{-}9}$ (17) line has manifested itself in pulsed chemical CO lasers. In the first report by Pollack [20] of chemical laser action in the CS_2/O_2 system using a flash, the highest J number P branch line for any of the bands was P (14) except for the 10-9 band which showed lasing lines at $P(10)$, $P(11)$, $P(12)$, $P(13)$, and $P(17)$. Jacobson and Kimbell [21] observed a similar effect in their TEA-style CS_2/O_2 laser, i.e., the anomalous presence of the $P_{10\text{-}9}$ (17) line.

The possibility of vibrational-rotational cascades caused by the radiation field should be considered. The fact that it is possible to achieve a condition of near single-line operation indicates that cascade pumping of other lines by the $P_{10\text{-}9}$ (17) line apparently does not occur. Cascade pumping of vibrational-rotational lines should be most important under conditions where the rate of stimulated emission exceeds the rate of rotational relaxation, thereby allowing individual rotational levels to have nonequilibrium populations. In the present system, the $P_{10\text{-}9}$ (17) line would cascade pump the $P_{9\text{-}8}$ (18) line only if the population of the $v = 9, J = 17$ level were significantly increased by the $P_{10\text{-}9}$ (17) radiation. Similar considerations apply to cascade pumping of the $P_{11\text{-}10}$ (16) line. Calculations by Coleman *et al.* [14] suggest that the rate of V-V coupling may exceed the rate of stimulated emission in the longitudinal flow system. This would likely apply to the present flame system as well which operated at a higher temperature and pressure than the longitudinal system. Hence the rate of rotational relaxation will also exceed the stimulated emission rate. Under these conditions radiation from the $P_{10\text{-}9}$ (17) line should have the effect of slightly raising the populations of all accessible J levels in the $v = 9$ level. Also one would expect a concomitant decrease of populations of J levels in the $v = 10$ level. As pointed out in [14], however, vibrational relaxation itself is very rapid. This will greatly reduce the buildup in population in $v = 9$. To sum up, the absence of cascade pumping by the $P_{10\text{-}9}$ (17) transition is probably a reflection of the very rapid rotational and vibrational relaxation processes in relation to the rate of stimulated emission. Perturbations in populations caused by the $P_{10\text{-}9}$ (17) line are rapidly spread over many rotational and vibrational levels. Moreover, other potential transitions do not have the benefit of an augmented gain due to overlap of the gain profiles. Apparently, the resultant change in any single v, J level population is insufficient to result in cascade pumping.

In view of the possible importance of overlap of line profiles a search was made of CO transitions to determine whether other overlaps occurred. Vibrational levels up to 20 and J values up to 35 were considered. Since the molecular constants in [15] are believed to predict the frequencies to ± 0.005 cm^{-1}, coincident transition pairs whose line positions differ by ± 0.01 cm^{-1} or less were found.

In the P branch, of 350 pairs of transitions considered, there were seven coincidences found within the limits indicated in the preceding. Of these, only one pair involved a transition within the lasing region in the present system (i.e., $v \sim 5$-12 and $J \sim 12$-25). This coincidence was between $P_{10\text{-}9}$ (17) and $P_{9\text{-}8}$ (23) with frequency difference of 0.006 cm^{-1}.

To examine possible absorption effects, a search was made for coincidences between P and R branch lines. Some 16 coincidences between line pairs were found according to the preceding limit of 0.01 cm^{-1}. Of these, six involved a P branch transition within the lasting region of the present system. Both the P-P and P-R coincidences are shown in Table I. Two of the P-R pairs reflect the three-way coincidence namely, $P_{10\text{-}9}$ (17), $P_{9\text{-}8}$ (23), and $R_{15\text{-}16}$ (32). The adjacent

TABLE I

CO TRANSITION COINCIDENCES				$\Delta\nu$ (cm^{-1})[a] (calc'd)
P-P				
$P_{20\text{-}19}$	(3)	$P_{18\text{-}17}$	(17)	0.004
$P_{19\text{-}18}$	(10)	$P_{17\text{-}16}$	(23)	0.008
$P_{17\text{-}16}$	(5)	$P_{16\text{-}15}$	(12)	0.004
$P_{17\text{-}16}$	(21)	$P_{16\text{-}15}$	(27)	0.003
$P_{16\text{-}15}$	(2)	$P_{13\text{-}12}$	(22)	0.006
$P_{11\text{-}10}$	(9)	$P_{12\text{-}11}$	(2)	0.005
*$P_{10\text{-}9}$	(17)	$P_{9\text{-}8}$	(23)	0.006
P-R				
$P_{17\text{-}16}$	(1)	$R_{19\text{-}20}$	(26)	0.005
$P_{17\text{-}16}$	(3)	$R_{19\text{-}20}$	(23)	0.007
$P_{16\text{-}15}$	(1)	$R_{16\text{-}17}$	(6)	0.004
$P_{16\text{-}15}$	(7)	$R_{18\text{-}19}$	(17)	0.005
*$P_{12\text{-}11}$	(16)	$R_{16\text{-}17}$	(23)	0.003
*$P_{12\text{-}11}$	(21)	$R_{16\text{-}17}$	(15)	0.006
*$P_{11\text{-}10}$	(21)	$R_{16\text{-}17}$	(25)	0.008
$P_{10\text{-}9}$	(6)	$R_{12\text{-}13}$	(17)	0.000
$P_{10\text{-}9}$	(9)	$R_{12\text{-}13}$	(13)	0.007
*$P_{10\text{-}9}$	(17)	$R_{15\text{-}16}$	(32)	0.001
*$P_{10\text{-}9}$	(18)	$R_{14\text{-}15}$	(19)	0.007
*$P_{9\text{-}8}$	(23)	$R_{15\text{-}16}$	(32)	0.005
$P_{6\text{-}5}$	(6)	$R_{6\text{-}7}$	(0)	0.006
$P_{6\text{-}5}$	(10)	$R_{9\text{-}10}$	(20)	0.000
$P_{3\text{-}2}$	(6)	$R_{6\text{-}7}$	(25)	0.009
$P_{3\text{-}2}$	(16)	$R_{5\text{-}6}$	(3)	0.001

[a] Computed using molecular constants from [15].
[b] Denotes coincidences having P branch transition in the range $v = 5$-4, $J \sim 12$-25 up to $v = 12$-11, $J = 12$-25.

line P_{10-9} (18) is noted with its coincidence with R_{14-15} (19). The absence of the lines P_{12-11} (21), P_{12-11} (16), and P_{11-10} (21) from the laser output spectrum may also be partly attributable to R branch absorption through the coincidences indicated in Table I. However, the absence of one other line, the P_{7-6} (16) is not explainable by R branch absorption.

V. Summary and Conclusions

Laser output spectra for the $CS_2/O_2/N_2O$ flame laser revealed that the laser line at 5.4265 μm, namely, the P_{10-9} (17) line was very sensitive to the O_2 and N_2O flow rates in the system. Under conditions of high O_2 and N_2O flow a nearly single-line condition was found where the line at P_{10-9} (17) accounted for about 65 percent of the total laser power.

It is suggested that the behavior of this line can be explained by invoking an overlapping line profile argument. The proximity of a nearby line, the P_{9-8} (23), may be such as to permit significant overlap of their gain profiles. Linewidth calculations suggest that for the conditions of these experiments the line centers would have to be within about 0.3 Å (0.01 cm^{-1}) of each other to significantly affect the peak gain of this line pair.

The absence of the P_{10-9} (17) line under certain high multiline power conditions and the dependence of this line intensity on the O_2 partial pressures may be due to absorption by the R branch line R_{15-16} (32). Similarly, the absence of other P branch lines under most conditions may be attributable to R branch absorption.

References

[1] T. A. Cool and R. R. Stephens, "Chemical laser by fluid mixing," *J. Chem. Phys.*, vol. 51, pp. 5175-5176, 1969.

[2] K. D. Foster and G. H. Kimbell, "Vibrational population inversion of CO in a free-burning CS_2/O_2 flame," *J. Chem. Phys.*, vol. 53, pp. 2539-2540, 1970.

[3] C. Wittig, J. C. Hassler, and P. D. Coleman, "Continuous-wave carbon monoxide chemical laser," *J. Chem. Phys.*, vol. 55, pp. 5523-5532, 1971.

[4] R. D. Suart, P. H. Dawson, and G. H. Kimbell, "CS_2/O_2 chemical lasers: Chemistry and performance characteristics," *J. Appl. Phys.*, vol. 43, pp. 1022-1032, 1972.

[5] G. Hancock, C. Morley, and I. W. M. Smith, "Vibrational excitation of CO in the reaction: O + CS → CO + S," *Chem. Phys. Lett.*, vol. 12, pp. 193-196, 1971.

[6] K. D. Foster, "Initial distribution of $CO^\dagger$ from the reaction O + CS → $CO^\dagger$ + S," *J. Chem. Phys.*, vol. 57, pp. 2451-2455, 1972.

[7] S. Tsuchiya, N. Nielsen, and S. H. Bauer, "Lasing action and relative populations of vibrationally excited carbon monoxide in pulsed-discharged carbon disulphide-oxygen-helium mixture," *J. Phys. Chem.*, vol. 77, pp. 2455-2464, 1973.

[8] H. T. Powell and J. D. Kelley, "Vibrational distribution of carbon monoxide from O + CS → S + CO (v)," *J. Chem. Phys.*, vol. 60, pp. 2191-2192, 1974.

[9] N. Djeu, H. S. Pilloff, and S. K. Searles, "Determination of optical gain for CO transitions in a CS_2-O_2 flame by oscillation-range measurements," *Appl. Phys. Lett.*, vol. 18, pp. 538-540, 1971.

[10] H. S. Pilloff, S. K. Searles, and N. Djeu, "CW CO laser from the CS_2-O_2 flame," *Appl. Phys. Lett.*, vol. 19, pp. 9-11, 1971.

[11] S. K. Searles and N. Djeu, "Characteristics of a CW CO laser resulting from a CS_2-O_2 additive flame," *Chem. Phys. Lett.*, vol. 12, pp. 53-56, 1971.

[12] M. J. Linevsky and R. A. Carabetta, "CW laser power from carbon disulfide flames," *Appl. Phys. Lett.*, vol. 22, pp. 288-291, 1973.

[13] R. D. Suart, S. J. Arnold, and G. H. Kimbell, "Power enhancement of a CO chemical laser by the addition of vibrationally cool gases," *Chem. Phys. Lett.*, vol. 7, pp. 337-340, 1970.

[14] Y. Hirose, Y. Nachshon, T. A. DeTemple, and P. D. Coleman, "Single line operation of a 2-W longitudinal CW CO chemical laser with no frequency-selective element in the optical cavity," *Appl. Phys. Lett.*, vol. 23, pp. 195-197, 1973.

[15] W. B. Roh and K. N. Rao, "CO laser spectra," *J. Mol. Spectrosc.*, vol. 49, pp 317-321, 1974.

[16] E. E. Whiting, "An empirical approximation to the Voight profile," *J. Quant. Spectrosc. Radiat. Transfer*, vol. 7, pp. 61-88, 1967.

[17] D. Williams, D. C. Winstrand, R. J. Brockman, and B. Curnutte, "Collisional broadening of infrared absorption lines," *Mol. Phys.*, vol. 20, pp. 769-785, 1971.

[18] C. K. N. Patel, "Vibrational-rotational laser action in carbon monoxide," *Phys. Rev.*, vol. 141, pp. 71-83, 1966.

[19] G. Hancock and I. W. M. Smith, "Quenching of infrared chemiluminescence. 1: The rates of de-excitation of CO ($4 \leqslant v \leqslant 13$) by He, CO, NO, N_2, O_2, OCS, N_2O and CO_2," *Appl. Opt.*, vol. 10, pp. 1827-1842, 1971.

[20] M. A. Pollack, "Laser oscillation in chemically formed CO," *Appl. Phys. Lett.*, vol. 8, pp. 237-238, 1966.

[21] T. V. Jacobson and G. H. Kimbell, "Transversely spark-initiated chemical laser with high pulse energies," *J. Appl. Phys.*, vol. 41, pp. 5210-5212, 1970.

Interferometric Measurements of the Nonlinear Refractive-Index Coefficient Relative to CS_2 in Laser-System-Related Materials

MICHAEL J. MORAN, CHIAO-YAO SHE, MEMBER, IEEE, AND ROBERT L. CARMAN

Abstract—**Using time-resolved interferometry, we have compared the nonlinear wavefront distortion induced by the simultaneous propagation of an intense light beam in pertinent sample materials relative to the known reference material. Utilizing several normalization techniques, these measurements have led to precise values for the nonlinear coefficient n_2 good to 10 percent.**

I. Introduction

BEAM PROPAGATION effects associated with an intensity-dependent index of refraction

$$n = n_0 + n_2 \langle E^2 \rangle \equiv n_0 + \Delta n \tag{1}$$

where $E(t) = \epsilon(t) \cos \{\omega_0 t - k_0 z - \delta\phi(z, t)\}$, have been an important consideration in the development of short-pulse high-peak-intensity laser systems. This is especially true for solid-state lasers. The radial dependence of the laser-beam intensity distribution leads to both gross spatial beam distortions [1] and small-scale fluctuation instabilities [2], while the time dependence of the intensity distribution leads to self-phase modulation [3] and optical shocks [4] (particularly when linear chromatic dispersion is important) [5]. For pulse durations near T_2 (the transition dephasing time) of the system, the presence of an intensity-dependent refractive index can further complicate the coherent pulse-propagation problem [6].

Because the small-signal or perturbation analysis of these effects involves exponentially growing Fourier components, the magnitude of n_2 must be accurately determined in order to characterize the propagation problem. Furthermore, the illumination of the mechanisms responsible for n_2 may provide avenues for further optimization of the laser materials.

Many methods [7] have been employed to measure n_2 or, more generally, the full tensor [8] $\chi^{(3)}_{ijkl}(-\omega, \omega, \omega, -\omega)$. A particularly attractive technique for performing this class of measurements is to use a Mach-Zehnder interferometer. The interferometric technique was first proposed [9] in 1968 in a form where the output fringe pattern was time integrated. The time-resolved output fringe pattern yields both much more information and better precision [10], [11] than previously used methods. However, elimination of systematic errors and the establishment of the actual peak laser intensity still limit the experimental accuracy of [10] and [11]. In this paper we describe some experiments performed with time-resolved interferometry and a 1-ns pulsed laser system. The experiments used a Mach-Zehnder interferometer, where one arm of the interferometer contained the sample of unknown nonlinearity and the reference arm contained a compensating CS_2 cell with the same linear optical path length and a known nonlinear response [12]. Thus n_2 was measured relative to CS_2 under conditions where systematic errors were removed and high precision was possible. Relative numbers were believed to be good to ±10-percent absolute accuracy.

Manuscript received October 30, 1974; revised February 10, 1975. This work was performed under the auspices of the U.S. Atomic Energy Commission.

M. J. Moran is with the Lawrence Livermore Laboratory, University of California, Livermore, Calif. 94550.

C.-Y. She is with Colorado State University, Fort Collins, Colo. 80521.

R. L. Carman is with the Los Alamos Scientific Laboratory, University of California, Los Alamos, N. Mex. 87544.

II. Discussion of Experiment

In Fig. 1 we present a schematic of the basic experiment. The output beams from the interferometer were carefully overlapped spatially and temporally at the slit of an LLL ultrafast streak camera [13] (resolution ~10 ps). The camera was used to establish that the two interferometer arms had an equal path length to within 1.5 mm. This was further checked by obtaining interferometer fringes with a simple image-converter camera when a 20-ps-duration ruby-laser pulse was used to illuminate the interferometer. The interferometer beam splitters were uncoated and wedged glass substrates while the reflectors were 50-percent reflectivity mirrors, thus necessitating the preceding technique for linear path-length adjustment. Although the n_2 of CS_2 was typically 10–100 times that of the samples, the nonlinear phase delay was approximately the same in the reference and sample because of the different intensities in the two arms. By varying the relative

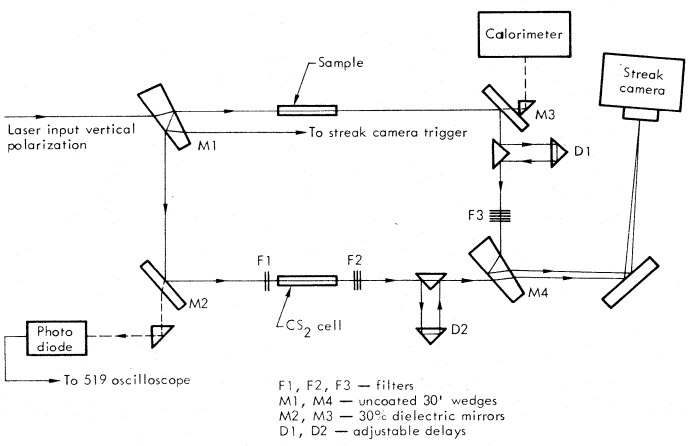

Fig. 1. Schematic of experimental arrangement.

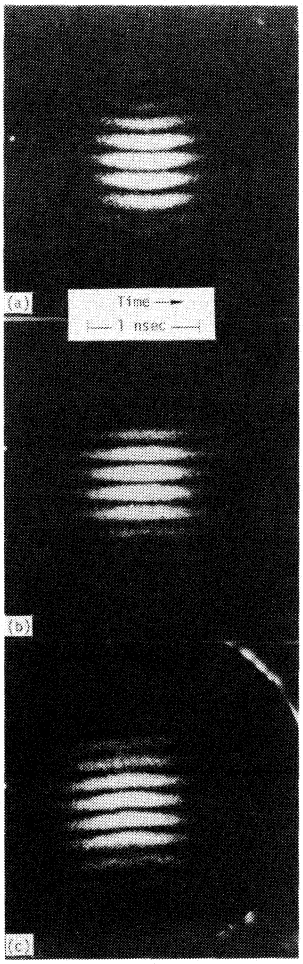

Fig. 2. Time-resolved fringe patterns. (a) Nonlinear delay greatest in ED-2 arm. (b) Nonlinear delay same in both arms. (c) Nonlinear delay greatest in CS_2 arm.

intensity between the two arms (using identical filters before the sample and after the CS_2 or vice versa), the relative phase delay in the arms was similarly varied. This was established using the streak camera to determine the interferometer fringe distortion as a function of time (and, consequently, intensity). When the fringe pattern is independent of intensity, both the nonlinear path length increases and the linear path lengths are the same for both arms. Under these conditions, the intensity ratio between the two arms is inversely proportional to the n_2 ratio of the samples. Fig. 2(a)-(c) illustrates the time-resolved fringe patterns used to determine the n_2 ratio.

For our measurements we used a Nd:YAG-Nd:glass laser system [14] capable of output energies as high as 1 J. The output pulse was spectrally bandwidth limited and spatially within 50 percent of the minimum uncertainty angle for our finite beam. The beam quality was important because amplitude or phase-modulated beams would have caused numerous experimental difficulties.

The experimental operating conditions were designed to allow the maximum possible phase delay in the samples without the presence of small-scale instabilities. The onset of self-focusing in the samples was accompanied by a "washing out" of the Mach-Zehnder fringes, as shown in Fig. 3. In order to obtain the required intensities for the experiment, but at the same time avoid nonlinear processes in the final laser amplifiers, the laser output beam was telescoped down to an approximate 2-mm full width at half maximum (FWHM) intensity diameter. The washing out of the interferometer fringes, together with the 2-mm beam diameter, limited the useful nonlinear optional path delay to $\frac{1}{2}$ wavelength. When no sample was present we further checked that a thin-lens analysis of the phase distortion in the CS_2 approximately predicted the magnitude of the time-resolved interference patterns. Here

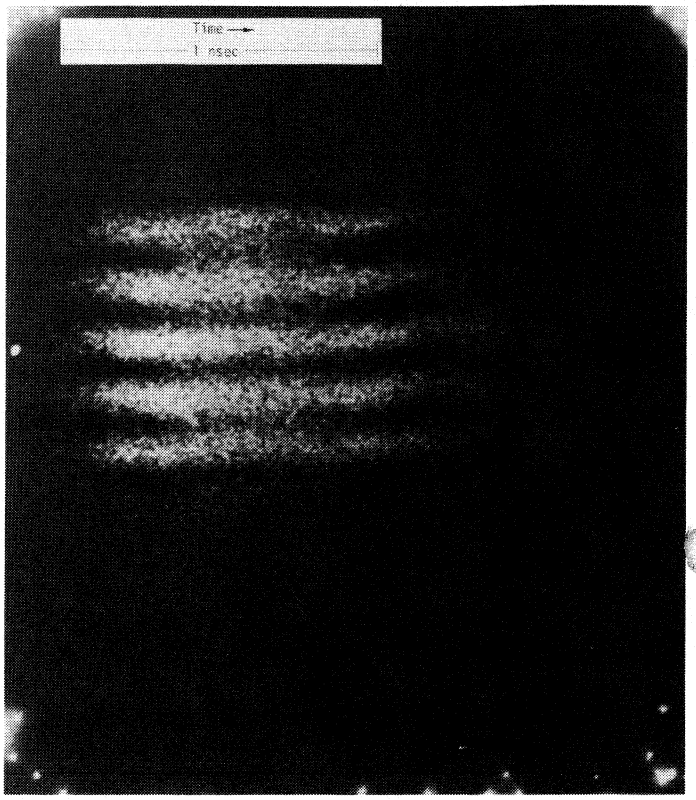

Fig. 3. Fringe pattern at self-focusing threshold intensity.

$$f_{\text{equivalent}} \approx \frac{a^2}{4\Delta n l} \simeq \frac{Z_{sf}^2}{n_0 l} \tag{2}$$

where a is the beam radius, l the cell length, Δn the nonlinear path increase, and Z_{sf} the self-focusing length for a semi-infinite medium.

Under certain experimental conditions the onset of this lensing was accompanied by a temporal breakup of the laser pulse. This effect was different from the washing out of fringes previously mentioned. It was most often observed when the beam waist was at or in front of the CS_2-cell entrance window. Fig. 4(a) shows streak pictures of the input and output laser pulses from a CS_2 cell. The output shows a mild lensing during the intense portion of the pulse with a random time structure imposed on the pulse envelope. The missing energy in this case was reflected back toward the laser with no dramatic frequency change. At roughly ten times the input energy, as in the previous case, the output beam self-focuses, and Fig. 4(b) shows the input and output pulses from the CS_2 cell under these conditions. The relative filtering be-

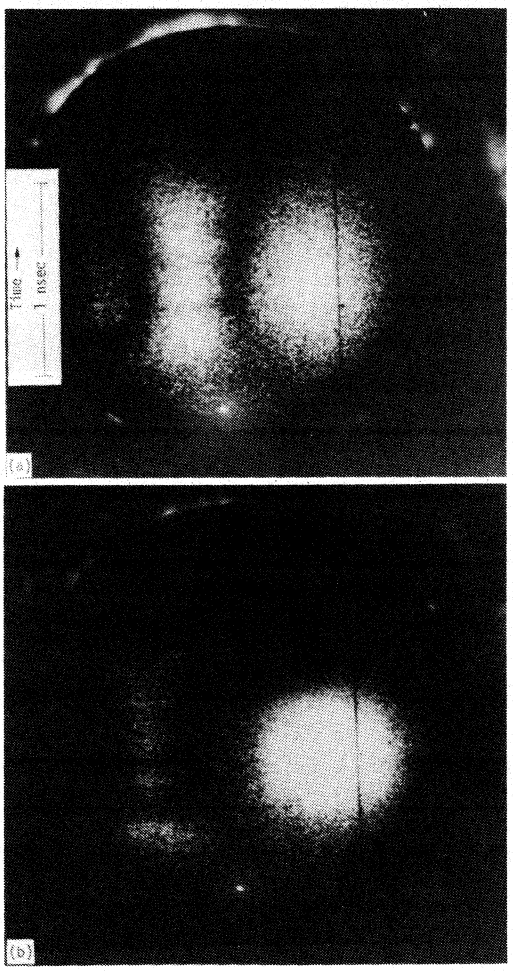

Fig. 4. Pulse time breakup. (a) Pulse intensity below self-focusing threshold. (b) Pulse intensity above self-focusing threshold. The dark line in these photographs is a small wire on the camera slit used to determine the streak direction.

tween the two output beams of Fig. 4(a) and (b) was the same, and it is interesting that roughly the same laser intensity was transmitted through the CS_2 cell in both situations. The unexpected temporal breakup was also observed with an SF_6 Schott glass rod at an intensity higher roughly by the ratio of the n_2. The mechanism for reflecting the light just prior to self-focusing has not been unequivocally established in our situation, but Owyoung [15] has attributed similar behavior to Brillouin scattering. When n_2 data were being taken we always avoided the conditions shown in Fig. 4(a) and (b). This was possible because the laser intensity was routinely reproducible to 20 percent.

By plotting and least squares fitting the relative fringe shift versus the relative pulse intensity, it was possible to obtain precise values for the ratio of the index change Δn for the sample to that for CS_2. It was not necessary to measure the absolute laser intensity to determine n_2 since the time history of the laser pulse in both arms of the interferometer is always the same, and both nonlinear elements have an instantaneous response. Therefore, only the relative pulse energies need be determined. The pulse energy ratios were determined using two LLL Gunn-type calorimeters [16] (good to ±1 percent) and previously calibrated neutral density filters (good to ~5

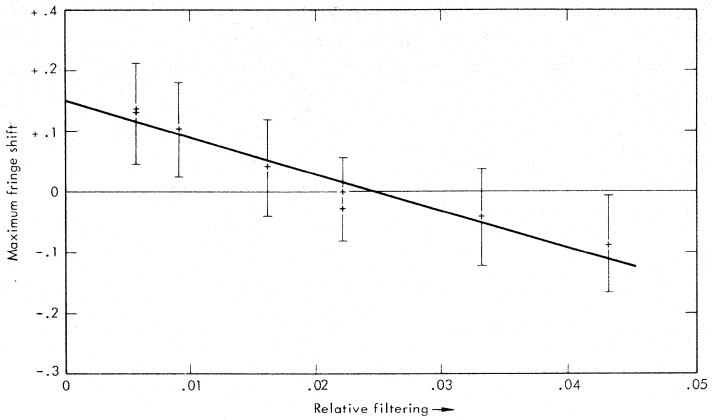

Fig. 5. Fringe shift versus relative filtering.

percent). The filters were calibrated at 1.06 mm with a Cary spectrophotometer[1] and were used at a position in the laser beam where they responded as linear attenuators, as was verified with calorimetry. A typical plot of the fringe distortion versus relative intensity including error bars is shown in Fig. 5. In order to compare data on different laser shots, as in Fig. 5, it was necessary to normalize all the plotted data to the same relative peak laser intensity, since the fringe shift is a function of both the relative and absolute laser intensity. We found that Tektronix 519 oscillograms[1] (system response 0.4 ns) were sufficiently accurate for this purpose.

III. Results

The results of the data taken on numerous materials are summarized in Table I. Since our data are in the form of a ratio, column 4 represents our output. In the absence of an absolute measurement of n_2 for CS_2 at 1.06 μm, we have used an absolute measure of n_2 in ED-2 by Speck and Bliss [11] together with our relative measurement of n_2 $(CS_2)/n_2$ (ED-2) to provide the absolute numbers quoted in column 5. This procedure allows estimation of absolute n_2 values with ±30-percent accuracy. For n_2 ratios measured here, the ~10-percent precision quoted is due to the normalization to the same laser peak intensity and the spatial resolution of the streak camera. With ~5-lines/mm resolution, a 25-mm slit, and six fringes on the slit, we are limited to ~25 resolution points between fringes. Using microdensitometry, we are able to measure $\frac{1}{30}$ of a fringe shift (with a total of $\frac{1}{3}$ fringe distortion) by enhancing the signal to noise somewhat through scanning several neighboring positions along the slit and taking advantage of the expected fringe symmetry. Another source of error was the absolute calibration of our filters. These errors can be reduced somewhat by performing the least squares fit to the data, as in Fig. 5, in the determination of the null condition from which n_2 is established. Practical limitations on alignment accuracy at the camera slit provided further limits on the overall accuracy of determinating n_2, but was not an important contribution here.

[1] Reference to company or product name does not imply approval or recommendation of the product by the University of California or the U.S. Atomic Energy Commission to the exclusion of others that may be suitable.

TABLE I
RESULTS OF n_2 MEASUREMENTS

Sample	Laser Polarization [a]	n_0	$\frac{n_2(\text{Sample})}{n_2(CS_2)}$	$n_2(\text{Sample}) \times 10^{13}$ [b] (Estimated)
CS_2 [b]		1.62	1.0	110. ± 33
ED-2 [c]	V	1.55	.0139 ± .0017	1.53
C835 [d]	V	1.50	.0166 ± .0017	1.83
C1020 [d]	V	1.50	.0016 ± .0018	1.83
C2828 [d]	V	1.53	.0184 ± .0018	2.08
YAG [e]	V	1.83	.0315 ± .003	3.47
YAG	C	1.83	.0253 ± .0035	2.78
SF_6 [f]	V	1.77	.032 ± .009	9.0
SF_6 [f]	C	1.77	.051 ± .005	5.6
RUBY	V	1.76	.0135 ± .0013	1.48
Lucite	V	1.49	.025 ± .0045	2.74

[a] V = vertical, linear. C = circular.
[b] n_2 of CS_2 determined by using independent measurement of n_2 of ED-2 glass by Speck and Bliss [11] with our ED-2 measurement with a resulting uncertainty of ±30 percent.
[c] Manufactured by Owens Illinois.
[d] Manufactured by American Optical.
[e] Measurement performed with beam propagating along (111) axis with optical electric-field vector 45 from (01-1) axis.
[f] Manufactured by Schott Optical.

The data in Table I are not raw data, but have been corrected for several effects. We have taken into account Fresnel losses and beam cross-sectional changes associated with the tilted end faces of the sample rods. Furthermore, in relating the nonlinear phase change to the increase in the refractive index, we have used the k vector and optical field internal to the materials leading to the usual definition of n_2 internal $= n_0 n_2^{\text{vac}}$. For the Lucite measurement we have also corrected for the linear absorption at 1.06 μm.

The full third-order nonlinear susceptibility in question is, in general, a fourth-rank tensor, but for isotropic materials such as CS_2 or glass, there are only three independent elements of this tensor [15], [17]. When we further assume a monochromatic laser there are only two independent terms. It has been shown [15], [18] that n_2 for circularly polarized light versus linearly polarized light, a ratio of 2/3 for an electronic response is expected, while other ratios are to be expected when nuclear contributions are present. Table I shows for Nd:YAG and Schott SF_6 glass, where the two polarization measurements were made, the ratio is 2/3 to well within experimental error for SF_6 glass, while the ratio is 13 percent higher than 2/3 for Nd:YAG which is still within experimental error. Using a simple Stark-effect model including local field effects and only one judiciously chosen ultraviolet absorption (harmonic oscillator) frequency [19], the magnitudes and ratios of n_2 for the solids listed in Table I can be fairly well predicted. Also we note, as expected, that changing the Nd concentration for a given host-glass composition does not produce a measurable change in n_2, while changing the host glass can lead to significant differences in n_2. Our measurement found the n_2 of ED-2 to be lower than the n_2 of the American Optical glasses, but other measurements at 6943 Å [15], [20] have found the opposite result for similar glass compositions. This difference probably indicates that n_2 is a function of excitation frequency, as expected from the Stark-effect model [19].

IV. CONCLUSIONS

In rating materials as candidates for lasers or laser systems, it is important to recognize that the absolute magnitude of n_2 is not the only important consideration. Inhomogenieties in the linear refractive properties of the materials will broaden the spatial Fourier spectrum, enhancing the growth of small-scale instabilities and ultimate beam breakup [2]. When considering the third-order nonlinear refractive-index effects, the significant parameter is the minimization of the nonlinear phase change, which is an integral over the optical path length to be propagated. In unsaturated gain but amplifying media, a more meaningful comparison of materials is obtained if values of n_2/g are used, where l/g is referred to as the gain length obtained in the amplifier in question.

There are other kinds of materials used in laser amplifier chains in addition to amplifiers, and they have nonlinear figures of merit which also are not generally just the magnitude of n_2. It is important to include the expected length l required of Faraday rotator glass, for example, leading to $n_2 l$ as the nonlinear figure of merit for candidate materials for this application. In the case of electrooptic materials, we must integrate the polarization decomposition effects over the path length, properly taking account of the difference in n_2 for linear and circular polarized light, leading to an even more complicated relationship.

As a final comment, with this interferometric method of determining n_2, assessment of the magnitude of higher order terms in the expansion of the refractive index with optical electric-field strength is possible [21]. If, for example, the $n_4 E^4$ term were comparable to the magnitude of the minimum fringe distortion in our experiments, in either the CS_2 or any of the samples, the plot of fringe shift versus relative intensity would not have been linear. There would also appear to be a bulge in the high-intensity fringes near the maximum-intensity part of the fringe pattern, due to the $n_4 E^4$ term. The lack of any evidence for such effects establishes an upper limit for the magnitude of n_4 which, for example, in ED-2 glass was $n_4 \sim 6 \times 10^{-21}$ (ESU^4), [21].

ACKNOWLEDGMENT

The authors wish to thank E. Snitzer of the American Optical Company for his cooperation in supplying some of the glass samples used in this set of experiments. They also wish to thank L. Coleman, S. Thomas, and G. Tripp for their assistance with the LLL ultrafast streak cameras used, and D. Speck for the loan of one of the same.

REFERENCES

[1] a) For a theoretical discussion, see, for example, the following: P. L. Kelley, "Self-focusing of optical beams," *Phys. Rev. Lett.*, vol. 15, pp. 1005-1008, Nov. 1965.
b) V. N. Lugovoi and A. M. Prokhorov, "A possible explanation of the small-scale self-focusing filaments," *Pis'ma Zh. Eksp. Teor.*

Fiz., vol. 7, pp. 153–155, Mar. 1968; also *JETP Lett.*, vol. 7, pp. 117–119, Mar. 1968.
c) For a discussion of an experimental verification, see, for example, the following: C. C. Wang and G. W. Racette, "Effect of linear absorption on self-focusing of laser beam in CS_2," *Appl. Phys. Lett.*, vol. 8, pp. 256–257, May 1966.
d) A. V. Butenin, V. V. Korobkin, A. A. Malyutin, and M. Ya. Shchelev, "Investigation of the kinetics of self-focusing in liquids," *Pis'ma Zh. Eksp. Teor. Fiz.*, vol. 6, pp. 687–690, Sept. 1967; also *JETP Lett.*, vol. 6, pp. 173–176, Sept. 1967.
e) M. M. T. Loy and T. R. Shen, "Study of self-focusing and small-scale filaments of light in nonlinear media," *IEEE J. Quantum Electron.*, vol. QE-9, pp. 409–422, Mar. 1973.

[2] a) R. Y. Chiao, P. L. Kelley, and E. Garmire, "Stimulated four-photon interaction and its influence on stimulated Rayleigh-Wing scattering," *Phys. Rev. Lett.*, vol. 17, pp. 1158–1161, Nov. 1966.
b) R. L. Carman, R. Y. Chiao, and P. L. Kelley, "Observation of degenerate stimulated four-photon interaction and four-wave parametric amplification," *Phys. Rev. Lett.*, vol. 17, pp. 1281–1283, Dec. 1966.
c) A. J. Campillo, S. L. Shapiro, and B. R. Suydam, "Periodic breakup of optical beams due to self-focusing," *Appl. Phys. Lett.*, vol. 23, pp. 628–630, Dec. 1973.
d) —, "Relationship of self-focusing to spatial instability modes," *Appl. Phys. Lett.*, vol. 24, pp. 178–180, Feb. 1974.

[3] a) F. Shimizu, "Frequency broadening in liquids by a short light pulse," *Phys. Rev. Lett.*, vol. 19, pp. 1097–1100, Nov. 1967.
b) R. R. Alfano and S. L. Shapiro, "Observation of self-phase modulation and small scale filaments in crystals and glasses," *Phys. Rev. Lett.*, vol. 24, pp. 592–594, Mar. 1970.

[4] F. DeMartini, C. H. Townes, T. K. Gustafson, and P. L. Kelley, "Self-steepening of light pulses," *Phys. Rev.*, vol. 164, pp. 312–323, Dec. 1967.

[5] R. A. Fisher and W. K. Bischel, "Pulse compression for more efficient operation of solid state laser amplifier chains," *Appl. Phys. Lett.*, vol. 24, pp. 468–470, May 1974.

[6] J. A. Fleck, Jr., and R. L. Carman, "Laser pulse shaping due to self-phase modulation in amplifying media," *Appl. Phys. Lett.*, vol. 22, pp. 546–548, May 1973.

[7] a) P. D. Maker, R. W. Terhune, and C. M. Savage, "Intensity dependent changes in the refractive index in liquids," *Phys. Rev. Lett.*, vol. 12, pp. 507–509, May 1964.
b) G. Mayer and F. Gires, "Action d'une onde lumineuse intense sur l'indes de refraction des liquides," *Compt. Rend.*, vol. 258, pp. 2039–2042, Feb. 1964.
c) M. A. Duguay, J. W. Hansen, and S. L. Shapiro, "Nd:glass laser radiation," *IEEE J. Quantum Electron.*, vol. QE-6, pp. 725–743, Nov. 1970.
d) M. D. Levenson, "Feasibility of measuring the nonlinear index of refraction by third-order frequency mixing," *IEEE J. Quantum Electron. (Part I of Two Parts)*, vol. QE-10, pp. 110–115, Feb. 1974.

[8] C. C. Wang, "Nonlinear susceptibility constants and self-focusing of optical beams in liquids," *Phys. Rev.*, vol. 152, pp. 149–156, 1966.

[9] A. P. Veduta and B. P. Kirsanov, "Variation of the refractive index of liquids and glasses in a high intensity field of a ruby laser," *Sov. Phys.–JETP*, vol. 27, pp. 736–738, Nov. 1968.

[10] E. A. McLean, L. Sica, and A. J. Glass, "Interferometric observation of absorption induced index change associated with thermal blooming," *Appl. Phys. Lett.*, vol. 13, pp. 369–371, Dec. 1968.

[11] E. S. Bliss, D. R. Speck, and W. W. Simmons, "Direct interferometric measurements of the nonlinear index coefficient n_2 in laser materials," *Appl. Phys. Lett.*, vol. 25, pp. 728–730, Dec. 1974.

[12] R. W. Hellwarth and N. George, "Nonlinear refractive indices of CS_2-CCl_4 mixtures," *Opto-Electron.*, vol. 1, pp. 213–217, 1969.

[13] L. W. Coleman and S. W. Thomas, "New 10-ps streak camera for laser pulse diagnostics," presented at the Conf. Laser Engineering and Applications, Washington, D.C., 1973, Paper 19.9.

[14] B. C. Johnson, L. L. Steinmetz, R. L. Carman, and W. H. Lowdermilk, "A laser oscillator that directly produces bandwidth limited pulses in the 1-ns region and an amplifier chain that maintains the single-pulse coherence," presented at the Conf. Laser Engineering and Applications, Washington, D.C., 1973, Paper 2.10.

[15] A. Owyoung, "Ellipse rotation studies in laser host materials," *IEEE J. Quantum Electron.*, vol. QE-9, pp. 1064–1069, Nov. 1973.

[16] S. R. Gunn, paper in preparation.

[17] P. D. Maker and R. W. Terhune, "Study of optical effects due to an induced polarization third order in the electric field strength," *Phys. Rev.*, vol. 137, pp. A801–A818, Feb. 1965.

[18] a) R. W. Hellwarth, A. Owyoung, and N. George, "Origin of the nonlinear refractive index in liquid CCl_4," *Phys. Rev. A*, vol. 4, pp. 2342–2347, Dec. 1971.
b) A. Owyoung, R. W. Hellwarth, and N. George, "Intensity induced changes in optical polarizations in glasses," *Phys. Rev. B*, vol. 5, pp. 628–633, Jan. 1972.

[19] a) N. L. Boling, A. J. Glass, and A. Owyoung, paper in preparation.
b) M. D. Levenson and N. Bloembergen, "Dispersion of the nonlinear susceptibilities of cubic and isotropic media," presented at the 8th Int. Quantum Electronics Conf., San Francisco, Calif., June 1974, Paper F.6.

[20] R. W. Hellwarth, J. Cherlow, and T.-T. Yang, unpublished.

[21] T. K. Gustafson, P. L. Kelley, R. Y. Chiao, and R. G. Brewer, "Self-trapping in media with saturation of the nonlinear index," *Appl. Phys. Lett.*, vol. 12, pp. 165–168, Mar. 1968.

Studies of the Inversion and Lower Level Relaxation in Pulsed TE CO_2 Discharges

BRIAN K. GARSIDE, JOHN REID, AND EDWARD A. BALLIK, MEMBER, IEEE

Abstract—**It has generally been supposed that the rise and fall times of the gain in pulsed CO_2 laser discharges reflect the effective lifetimes of the lower and upper laser levels. Consequently, the ratio of the upper to lower level populations N_u/N_l should change during the evolution of the gain, and should be a relatively large number at the gain peak. The problems associated with the determination of this ratio using conventional direct gain measurements are discussed, and a new in-cavity technique is described that has sufficient precision to determine the ratio N_u/N_l as a function of time. The results obtained unambiguously demonstrate that the lower laser level empties rapidly during the rise time of the gain. This conclusion is further reinforced by some measurements concerning the time variation of the gain in the hot band ($01^11 \rightarrow 11^10$).**

I. Introduction

IT HAS generally been supposed that the rise and fall times of the gain in pulsed CO_2 laser discharges reflect the effective lifetimes of the lower and upper laser levels [1]. Furthermore, the symmetric stretching vibrational mode of CO_2 (including the lower laser level, 10^00) is thought to be very strongly coupled to the bending mode. Consequently, the relaxation of the lower laser level is controlled by the energy decay in the bending mode, in particular the vibration-translation (V-T) relaxation of the 01^10 level. As thermal equilibrium is very rapidly established between the bending and symmetric stretching vibrational modes, they can be assumed to have a common temperature (T_1) [2]. This temperature rises during the discharge current pulse, but relaxes quickly at the V-T rate after the current pulse. Therefore, T_1 attains a value close to the gas translational temperature within a few V-T decay times. As a particular consequence of this model, no more than 5 percent of the total CO_2 molecules can be excited into the lower laser level, whatever the value of T_1, and this population will have fallen to less than 1 percent after a few V-T decay times. The inversion in pulsed CO_2 lasers is typically several percent of the available CO_2 molecules. In both double-discharge and resistive-pin systems, the gain peak occurs several V-T decay times after the current pulse. Consequently, in these lasers, the ratio of the upper (N_u) to lower (N_l) laser level populations should be a relatively large number (>6) at the gain peak.

Manuscript received November 13, 1974; revised January 29, 1975. This work was supported in part by the National Research Council and in part by the Defence Research Board of Canada.

B. K. Garside and E. A. Ballik are with the Departments of Engineering Physics and Physics, McMaster University, Hamilton, Ont., Canada.

J. Reid was with the Departments of Engineering Physics and Physics, McMaster University, Hamilton, Ont., Canada. He is now with the Division of Physics, National Research Council of Canada, Ottawa, Ont., Canada.

Several measurements have been reported recently which cast doubt on the above interpretation of the gain dynamics. In the first place, some measurements of the lower level relaxation indicate that the coupling between the Fermi-resonance levels (10^00, 02^00) and the rest of the bending mode may be much weaker than hitherto supposed [3], [4]. Secondly, measurements of the gain on different rotational lines for the ($00^01 \rightarrow 10^00$) transition in pulsed discharges have been employed to show that the population in the lower laser level exceeds 10 percent of the total number of CO_2 molecules [5]. Several investigators have reported low values for the ratio of the upper to the lower laser level populations at the peak of the gain [5], [6]. These results are clearly not consistent with the conventional model of the pulsed gain dynamics, but they can be accounted for if the following alternate model is postulated. Suppose that, at the end of the current pulse, an inversion is produced between the laser levels, and considerable energy is stored in the bending mode. The rise time of the gain now simply corresponds to the emptying of the energy from the bending mode and the consequent decrease in the value of the partition function. During this time, the lower laser level is supposed to be more or less decoupled from the bending mode, and so suffers little decay. The fall time of the gain corresponds, as before, to the decay of the upper laser level, but there may now also be a contribution from the lower level (presumably somewhat similar) decay time.

It is important to establish which of these two models correctly describes the laser gain dynamics. The pumping efficiencies into the upper level and the associated laser dynamical calculations are very different in the two models. Consequently, the approach to the problem of extracting more output energy/unit volume from CO_2 lasers depends greatly on which model is correct. The work described in this paper is aimed at discriminating unambiguously between these two possible dynamical models. The strategy employed is described briefly in what follows.

Gain measurements of the conventional type allow the difference between N_u and N_l to be monitored. This alone cannot distinguish between the two models. What is required is a means of measuring the *ratio* of the upper to the lower laser level populations during the dynamical changes in the gain. This can be done, in principle, by measuring the gain as a function of time on many lines in the P and R branches of the 10.4-μ band. The ratio of the maximum gain obtained in the R branch to the maximum gain in the P branch (R/P hereafter) is a measure of the ratio N_u/N_l at the instant of time chosen, provided that the rotational temperature is known [7]-[9]. Measurements of gain, made in the conventional fashion employing a CW probe laser, are reported in Section II. These

results are analyzed to determine a rotational temperature, and the accuracy with which a value for N_u/N_l can be extracted is studied. It is concluded that this technique lacks sufficient precision for the task at hand. A new technique, having a much higher precision, is described in Section III. This method employs an improved version of a previously reported [10] in-cavity laser technique for measuring gain, using observations of the time delay between the peak of the excitation current pulse and the onset of lasing action. This approach permits the ratio N_u/N_l to be monitored from the end of the current pulse to the peak of the gain. The decay of the lower laser level during this time is clearly demonstrated. This behavior is consistent with the model in which the bending and symmetric stretching modes are in thermal equilibrium, and the energy decay is controlled by the V-T relaxation of the 01^10 level. The alternate model, in which the 10^00 population decays much more slowly than the rise time of the gain, is ruled out. Finally, in Section IV, this issue is settled beyond doubt by some studies of the dynamics of lasing action on the hot-band transition ($01^11 \rightarrow 11^10$) at 11 μ.

II. Direct Laser Amplifier Gain Measurements

A. Experimental Arrangement

Fig. 1 is a schematic diagram of the apparatus used for small-signal gain measurements. A stable CW CO_2 laser was operated in the fundamental TEM_{00} mode. An internal grating allowed the output to be tuned over several lines in the P and R branches of the 10.4-μ band. The output beam had a power of approximately 1 W, and an amplitude stability of 2 percent. This beam was chopped by a spinning disk at the common focus of two Ge lenses, passed through the test amplifier, and then focused onto a Ge:Au detector (rise time 300 ns). The effective beam diameter in the discharge region was kept as small as possible, and the maximum spot size was generally less than 2 mm ($1/e$ intensity) throughout the discharge region. The amplifier [11] employs a resistor-pin discharge to excite the gas mixture. Although this type of discharge has been superceded by double-discharge and electron-beam systems in most applications, it is nevertheless an effective method of obtaining stable discharges in small volumes. Measured gains remained constant when the probe signal was reduced by a factor of 10, confirming that the gain was measured in the small-signal region.

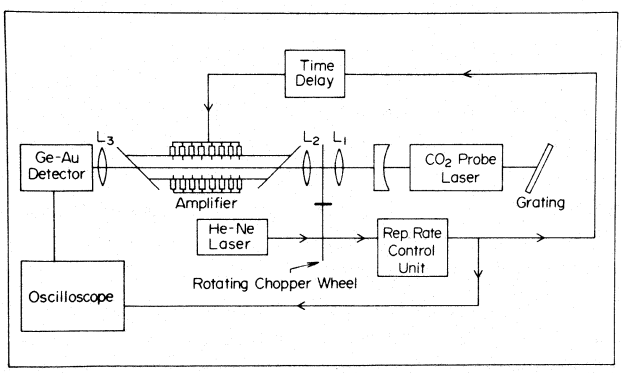

Fig. 1. Schematic diagram of apparatus used for direct measurements of gain.

The method used to trigger the amplifier discharge circuit is similar to the one employed by Jacobs [12], modified to permit electronic control of the repetition rate of the amplifier. The rotating chopper wheel periodically admits both the 10.6-μ CW probe beam and a 6328-Å He-Ne laser "trigger" beam through two small slots located 180° apart. The "trigger" beam falls upon a photodiode and the resulting train of pulses is fed to a repetition rate control unit. This reduces the pulse repetition rate to 2 or 3 pulses per second (pps) while maintaining the time synchronization. These pulses, with a suitable time delay, are used to trigger both the discharge and the monitoring oscilloscope. This scheme yields a single oscilloscope trace of the probe beam amplitude prior to, during, and after amplification. The time delay to the amplifier can be adjusted to locate the gain pulse anywhere on the probe signal. This enables the time base to be expanded to determine rise times, or compressed to examine the absorption after the amplifier pulse. Further advantages of this technique are described by Jacobs [12].

B. Results

Fig. 2 shows the measured peak gains obtained on the P and R branches of the 10.4-μ band for all the wavelengths at which the CW laser probe could be operated. A moderately low total gas pressure of 80 torr was employed in the laser amplifier to ensure excellent stability and repeatability of the discharge. This is reflected in the small errors shown for the gain measurements. The gas mixture was 10 percent CO_2, 6 percent N_2, and 84 percent He, and the energy input to the discharge was approximately 100 J/l · atm. The measured gain on $P(18)$ was 2 percent/cm. It is well known that the J dependence of the gain on the P branch is given, in the case of pressure broadening, by [6]-[8]

$$\alpha_P = \frac{(\text{const}) N_l B_l \cdot J F_J}{\Delta\nu(J)\lambda(J)} \cdot \left[\frac{N_u B_u}{N_l B_l} \exp\left(-\frac{E_u(J-1)}{kT}\right) - \exp\left(-\frac{E_l(J)}{kT}\right)\right]. \quad (1)$$

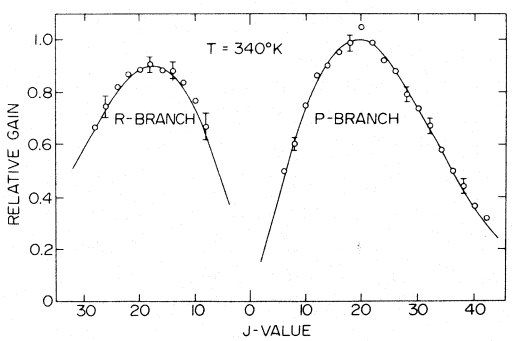

Fig. 2. Measured peak gain for several R- and P-branch transitions in the 10.4-μ band. The fitted curve [using (1) and (2)] corresponds to $T = 340$ K and $N_u/N_l = 10$. A 10 percent CO_2: 6 percent N_2: 84 percent He mixture at 80-torr total pressure was used, with an input energy of ~100 J/l · atm. The $P(18)$ peak gain was 2 percent/cm. Some typical error bars are also indicated.

A similar expression holds for the R branch, viz.,

$$\alpha_R = \frac{(\text{const})N_l B_l \cdot (J+1)F_J}{\lambda(J)\Delta\nu(J)} \cdot \left[\frac{N_u B_u}{N_l B_l}\exp\left(-\frac{E_u(J+1)}{kT}\right) - \exp\left(-\frac{E_l(J)}{kT}\right)\right] \cdot \quad (2)$$

In these two expressions, the constant contains all the factors which are not J dependent (J is the rotational number of the lower laser level). F_J accounts for the interaction between vibration and rotation, giving a small J dependence to the total transition moment [13]. B_u and B_l are the rotational constants for the upper and lower vibrational levels, and $E_u(J)$ and $E_l(J)$ are the respective rotational energies of the Jth level. $\lambda(J)$ is the wavelength of the transition, and $\Delta\nu(J)$ is the linewidth. In the work described here, we are only interested in relative values of gain on different transitions. Hence, it is not necessary to separate the line strength into contributions from the transition moment and linewidth. The absorption data of Cousin *et al.* [13] is used in a self-consistent fashion, and rotational constants and wavelengths are taken from [14].

Careful examination of (1) and (2) shows that the variation of gain with J depends strongly upon the value of the rotational temperature T. Observe that in Fig. 2 the measured ratio of the gain maximum of the R branch to that on the P branch is 0.90. As we shall see, for a value as high as this, the variation in gain with J is insensitive to N_u/N_l, and depends almost entirely on the rotational temperature. The lines fitted to the experimental points correspond to a value for T of 340 K to within a precision of ±15 K. This rather moderate increase above room temperature is in agreement with measurements reported elsewhere [7]. Observe that the gain on the $P(20)$ line is anomalously high. Such an effect has been reported previously, and ascribed to the presence of a hot-band gain line which overlaps $P(20)$ [15], [16]. Fig. 3 shows results obtained with the same gas mixture and total pressure as employed previously, but with a considerably larger discharge input energy (~250 J/l · atm). The rotational temperature which best fits the observations in this case is 410 K with an estimated precision of ±20 K. Observe that, once again, the gain on the $P(20)$ line is anomalously high. In this figure, we have only shown the P branch for convenience. The maximum gain on the R branch, on the same arbitrary scale as the P branch, is 0.90 ± 0.02.

The fit obtained between theory and experiment for the J dependence of the gain in the above experiments is excellent, and the precision of the data points is very high. The question now is, given this precision, how well can we determine N_u/N_l? Fig. 4 displays the results of a calculation of the ratio (R/P) as a function of N_u/N_l, for two rather different rotational temperatures. Evidently, R/P is extremely insensitive to the value of N_u/N_l when $R/P \gtrsim 0.85$.

It should be emphasized that when considering relative gains, the value of (R/P) is the only factor which is sensitive to N_u/N_l. Patel [8] gives a further demonstration of this for values of N_u/N_l very close to 1.0.

The experimental implications of this behavior are illustrated by the error bar shown in the figure, which represents a precision of ±5 percent in the ratio (R/P). Evidently, either the precision of the gain measurements must be made much better than 5 percent, or this method of determining N_u/N_l must be abandoned for values greater than two. A precision of 5 percent is typical of results obtained with direct gain measurements and so the only recourse is to find a more accurate method. It is fortunate that it is only the ratio of the gains on the P and R branches, not the absolute values, which is required. In this case, a high-precision technique for comparing the relative gains will do the trick. One approach to this problem is described in the next section.

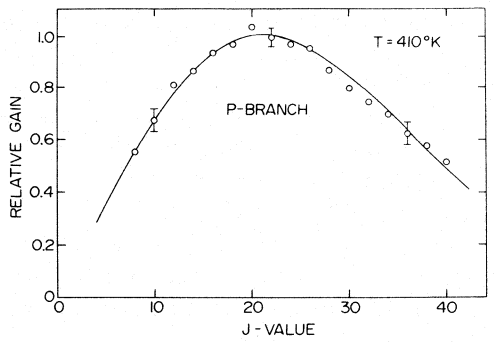

Fig. 3. Measured peak gain for several P-branch transitions in the 10.4-μ band. The fitted curve corresponds to $T = 410$ K and $N_u/N_l = 10$. Gas mixture and pressure were the same as for Fig. 2, but the discharge energy was increased to ~250 J/l · atm. This gave a peak gain of 1.5 percent/cm on $P(18)$.

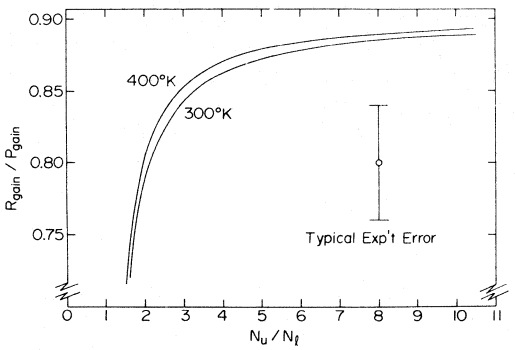

Fig. 4. The ratio of the maximum gain in the R branch to the maximum gain in the P branch (R/P) plotted as a function of N_u/N_l, for two different rotational temperatures. Also displayed is a typical experimental error bar of ±5 percent in the value of R/P.

III. In-Cavity Laser Gain Measurements

We have previously reported an experimental method for studying the time-dependent gain in TEA CO_2 lasers [10]. The technique involves an investigation of the time delay from the current pulse to the onset of lasing. In the present work, investigations of a similar type are made, but the measurements obtained are treated in a somewhat different fashion. The use of a diffraction grating within the laser cavity permits operation on a wide variety of P- and R-branch lines in the 10.4-μ band. It is this expanded capability that is the key to a new method of data analysis. The raw data required for subsequent analysis are acquired in the following way. At a given discharge input energy, the time delay to the onset of lasing is measured over a wide range of P- and R-

branch gain lines. Now, the relative variation of the gain over the P- and R-branch lines is well known [see (1) and (2)]; it depends on the rotational temperature and the J value for the particular line. Consequently, for an *assumed* value of the rotational temperature, the gain on each rotational line relative to that on $P(18)$ can be predicted. The time delay data are now treated as follows. Assume a value for the rotational temperature, and calculate the gains on all the relevant P- and R-branch lines relative to $P(18)$, which is assigned an arbitrary value of 1.0. For each rotational line, plot the *calculated* relative gain against the *observed* time delay. Now, increasing the rotational temperature has the effect of increasing the relative gain on high J-value lines and reducing that on the low J-value lines (see Fig. 5). Accordingly, only if we made the correct choice of initial temperature will the high J and low J-value points lie on the same curve. This is illustrated in Fig. 6. The high and low J-value points are indicated by crosses and circles, respectively. The anomalous point indicated by a square corresponds to the $P(20)$ line. (It is of interest to note that anomalous gain is found on $P(20)$ at discharge pressures as low as 25 torr. This suggests either a very close coincidence between $P(20)$ in the $00^01 \rightarrow 10^00$ band and $P(23)$ in the $01^11 \rightarrow 11^10$ band, or an unexpectedly narrow linewidth for the $P(20)$ transition [14], [15].) Two choices of rotational temperature are shown. The value of 360 K is obviously a wrong choice in that the low and high J-value points are clearly separated. A reduction of only 30 K is sufficient to bring the two sets of points into agreement. This serves to indicate the precision with which the rotational temperature can be determined. The gas mixture and other relevant experimental parameters are given in the figure caption. There is a complication which has been ignored thus far. From Section II it is known that the relative gain variation among the rotational levels depends on N_u/N_l. Consequently, it follows that to fit a rotational temperature requires a value for N_u/N_l. Although this is certainly true, the value chosen is of little consequence provided that it is greater than four. Furthermore, the values of T and N_u/N_l can, if necessary, be simultaneously determined. Variations in N_u/N_l serve mainly to change the ratio of the peak gain in the R branch to that in the P branch. The following strategy can now be applied. Select a value of N_u/N_l and separately fit a rotational temperature to the P-branch and R-branch data, employing the method indicated in Fig. 6. Repeat for different values of N_u/N_l. In general, the rotational temperatures obtained for the P and R branches will be different. Only when N_u/N_l has the right value will the two temperatures agree. Typical results are displayed in Fig. 7. Evidently, for the experimental situation analyzed (which is the same as for Fig. 6) the value of $N_u/N_l \gtrsim 6$ and T is 330 K. As indicated earlier, it is actually only necessary to carry out this procedure when N_u/N_l is less than four. In making measurements over the wide wavelength range required for this method, it is important to take precautions that the resonator loss is not significantly wavelength dependent.

When an appropriate determination of the values of T and N_u/N_l has been made according to the above prescription, the resulting time delay curve is an accurate plot of laser pulse time delay against *relative gain*. This is all we need to compare the gain on the P and R branches of the 10.4-μ band. It is of interest to observe that we can employ the technique described in [10] to determine the temporal variation of the gain once the plot of relative gain against time delay is known. Furthermore, if the cavity loss is known to fair precision, the actual magnitude of the peak gain (on $P(18)$ say) can be determined. Reference should be made to the original paper for details. Fig. 8 shows the time variation and magnitude of the gain in $P(18)$ deduced in this way for a 10 percent CO_2:90 percent He gas mixture at 75-torr total pressure.

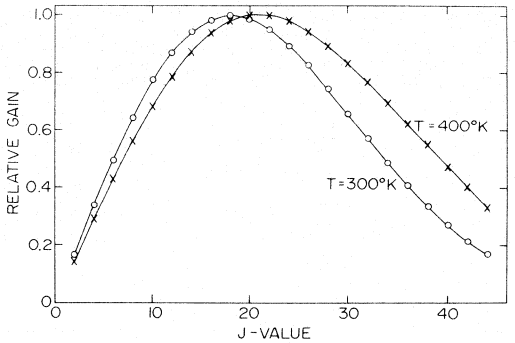

Fig. 5. Relative gains on the P-branch transitions of the 10.4-μ band for two different rotational temperatures calculated using (1).

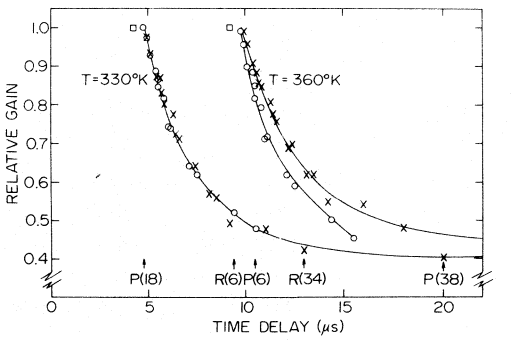

Fig. 6. Time delay to lasing as a function of relative gain for transitions $P(6)$ to $P(38)$ and $R(6)$ to $R(34)$. Transitions with J values greater than 20 are represented by X, those with J values less than 20 by 0. $P(20)$ is represented by □. The time delay curve is plotted for two different rotational temperatures, 330 K and 360 K. (N_u/N_l was taken as 10 in each case.) The data for 360 K have been shifted 5 μs to the right. Discharge mixture is 10 percent CO_2: 90 percent He at 75-torr total pressure, with an input energy ~90 J/l · atm.

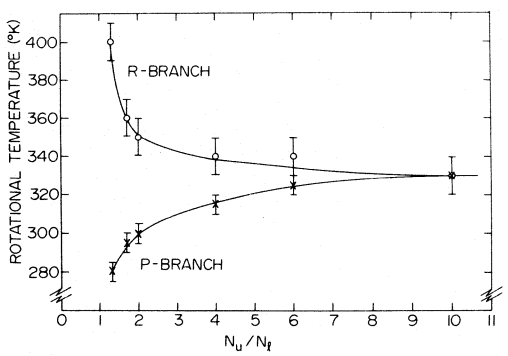

Fig. 7. Determination of N_u/N_l using the data of Fig. 6. As N_u/N_l is varied, the P- and R-branch temperatures are fitted separately, using (1) and (2). The error bars represent fitting errors.

Also shown is the result of a direct measurement of the gain on the same line using a probe laser. The small discrepancies between the two curves are well within the range of experimental error.

A method has now been established for determining an accurate plot of relative gain against observed time delay in the laser resonator. Clearly, the maximum gain on the R branch will correspond to that line which lases with the shortest time delay. It is only necessary to locate this time delay on the curve of relative gain against time delay in order to establish the R/P ratio. This technique can be employed to measure the R/P ratio as a function of time, by changing either the laser cavity loss or gain on $P(18)$. As a matter of fact, this R/P ratio is an average over the time to the onset of lasing from the instant the gain exceeds the loss. Operation at relatively low pressure ensures that this time is short compared with the rise time of the gain. Fig. 9 shows the results of such an experiment carried out with a 10 percent CO_2 : 90 percent He gas mixture at a total pressure of 35 torr. The different curves were generated by changing the gain and loss in the laser resonator. The horizontal error bar displayed on each curve represents the maximum variation in the time delay of that R-branch line with the highest gain. As a measure of the precision of the technique, the data points employed in obtaining one of the time delay curves are also displayed. The values of the N_u/N_l ratios appropriate to each of the error bars are shown in the figure. Since the value of N_u is falling during this time, these observations can only be accounted for if the lower laser level itself is emptying during the rise time of the gain. In the next section, we present further independent evidence that this indeed must be the case.

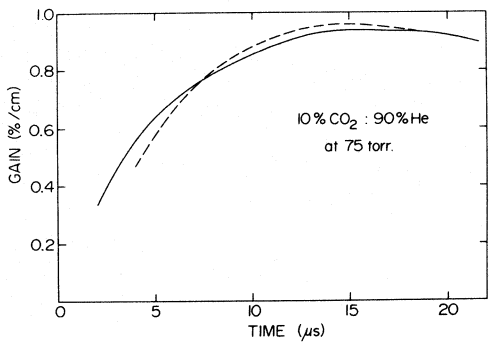

Fig. 8. Time variation of the gain on $P(18)$ as measured directly with a CW probe laser (solid line) and as deduced from the time delay data of Fig. 6 (dashed line). Discharge conditions are given in the caption of Fig. 6. Zero time corresponds to the peak of the discharge current pulse.

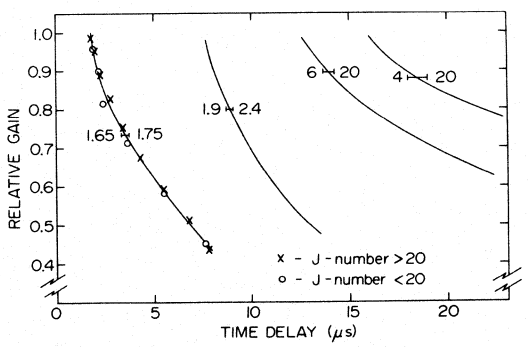

Fig. 9. Variation of the ratio N_u/N_l during the rise time of the gain. The four time delay curves are generated by varying the excitation conditions and cavity loss for a 10 percent CO_2:90 percent He mixture at 35-torr total pressure. The horizontal bars on each curve represent the maximum variation in the time delay of the R-branch line with the highest gain. Also indicated is the corresponding range of N_u/N_l. The gain peak occurs approximately 27 μs after the peak of the current pulse (0 μs).

IV. Hot-Band Lasing Observations

It is known that there is a hot-band transition ($01^1 1 \rightarrow 11^1 0$) which has maximum gain in the region of 11 μ [17]. The inversion which is obtained for this band is related to that of the 10.4-μ band by the ratio of the $01^1 0$ to the $00^0 0$ populations. Evidently, the ratio of the gain in the hot band to that of $P(18)$ in the 10.4-μ band is a measure of the bending mode temperature. Consequently, provided that the relative line strengths are known [13], time delay measurements of the type described in Section III can be employed to determine the bending mode temperature. Fig. 10 shows plots of relative gain against time delay obtained in the fashion described in Section III. The gas mixture was 10 percent CO_2: 90 percent He at a total pressure of 35 torr. The limits of the time delay obtained for the peak of the hot band is indicated by the horizontal error bars on the time delay curves. The two different curves were obtained by varying the resonator loss. By this method, it was determined that the gain on the hot band was 26 percent of that on $P(18)$ during the initial portion of the gain rise time. This determination was checked by measuring the time delay obtained on $P(18)$ for one fourth of the gain (see arrow in the figure). The measured gain ratio corresponds to a bending mode temperature of 700 K. At the later time, the measured gain ratio of 0.155 corresponds to a bending mode temperature of 515 K. This confirms that the bending mode does not attain very high vibrational temperatures (~1300 K) such as would be required if the rise of the gain corresponded only to the change in partition function as the bending mode cools. The time delay measurements on

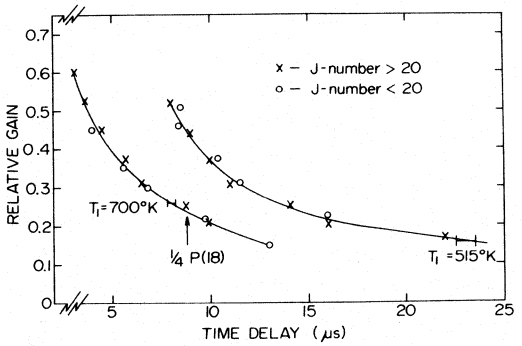

Fig. 10. Variation of the bending mode temperature T_1 during the rise time of the gain. The two time delay curves are generated by varying the cavity loss for a 10 percent CO_2: 90 percent He mixture at 35-torr total pressure. The horizontal bars on each curve represent the maximum variation in the time delay of the $P(20)$ transition of the hot band. The arrow indicates the time delay obtained on $P(18)$ of the 10.4-μ band when the total gain in the amplifier has been reduced by a factor of 4. The gain peak occurs approximately 27 μs after the peak of the current pulse (0 μs).

the hot band were made using the $P(20)$ line at 10.99 μ. There is a stronger transition at 11.02 μ, corresponding to the overlap of the $P(56)$ line in the 10.4-μ band with the $P(23)$ line in the hot band [18]. This transition was avoided in the present work.

V. Discussion and Conclusions

In the Introduction, two models are presented that can account for the gross features of the gain evolution in pulsed CO_2 lasers. In one model, the rise time of the gain is a reflection of the decay of the population of the lower laser level. This is the generally accepted model of CO_2 laser gain dynamics. However, several measurements have been reported recently which cast doubt on this interpretation. To account for these measurements, we have postulated an alternative model in which the gain rise time corresponds only to the cooling of the bending mode, and both upper and lower laser level populations remain relatively unchanged. The key difference between these two models from an observational point of view lies in the behavior of the ratio N_u/N_l. For the former model, this ratio will be large at the gain peak, regardless of initial conditions, and will be monotonically increasing in value during the buildup of the gain. For the latter model, however, the ratio will be constant during the evolution of the gain. In this paper, we have reported experiments aimed at the determination of N_u/N_l at the peak of the gain, and for selected times during the gain buildup.

The conclusion reached as a result of these measurements, namely that the lower laser level undoubtedly empties during the rise time of the gain, is reinforced by some measurements concerning the gain on the hot band ($01^1 1 \rightarrow 11^1 0$).

In Section II, results are reported of the direct measurement of the peak gain on a number of rotational lines in the P and R branches of the 10.4-μ band. It is shown that these results can be analyzed to obtain values for both the rotational temperature and the ratio N_u/N_l. This ratio is found to be large at the peak of the gain for several discharge input energies. The precision with which values of N_u/N_l can be obtained from experimental data is analyzed.

It is shown that, although some indication of the size of N_u/N_l can be obtained, it is too inaccurate in general to be employed for a study of changes in this ratio as the gain evolves. Accordingly, we have devised an alternative scheme which has the necessary accuracy.

A technique is described in Section III for *comparing* the gains on the P and R branches of the 10.4-μ band to a high precision. This is basically all that is required to obtain a value for N_u/N_l. This method involves a comparison of the time delays to the onset of lasing from the current pulse for a number of P- and R-branch gain lines. This approach is used to determine the value of N_u/N_l and the rotational temperature for selected times during the onset of the gain. It is clearly demonstrated that N_u/N_l changes from a value less than two at a time shortly after the end of the current pulse to a value greater than six near the peak of the gain pulse. This constitutes clear evidence that the model of the gain dynamics in which the bending and symmetric stretching vibrational modes of CO_2 are strongly coupled is correct. The energy in these modes decays at a rate equal to the V-T relaxation rate of the $01^1 0$ level. The coupling between the bending and symmetric stretching modes must be faster than this rate, which is determined by the partial pressure of the He in the gas mixture. For sufficiently high CO_2 content mixtures, the coupling between the $10^\circ 0$ level and the bending mode is determined by the effectiveness of CO_2-CO_2 collisions [19]. In the particular case of a 10-percent CO_2: 90-percent He mixture, it follows that the relaxation rate of the $10^\circ 0$ level into the bending mode must be greater than 3×10^4 torr^{-1}s^{-1}. This value is in good agreement with the calculations of Seeber [20] and Sharma [21], and the experimental results of Stark [19]. However, it exceeds the rate deduced in [4] by an order of magnitude, and is significantly faster than that observed in [3].

Section IV gives a brief account of some measurements made on the lasing behavior of the hot-band transition ($01^1 1 \rightarrow 11^1 0$). The important characteristic of this transition is that the ratio of the hot-band gain to the gain in the 10.4-μ band is a measure of the $01^1 0$ population. We have applied this, using an experimental method much like that employed in Section III, to show that the bending mode temperatures during the rise time of the gain are much too small to permit the gain increase after the current pulse to be accounted for in terms of a decrease in the partition function of the bending mode. This provides an independent confirmation of the above conclusions concerning the two postulated models of the gain dynamics.

All the data presented in this report were taken at gas pressures below 100 torr. However, relaxation rates in CO_2 lasers are collisionally controlled, and the results can be scaled directly to higher pressures. The duration of the gain pulse will, of course, be inversely proportional to the gas pressure. Even at atmospheric pressure, the lower laser level will be almost empty at the time of the gain peak, providing that short excitation current pulses are used.

It is also pertinent to observe that, although the conditions in low-pressure dc-excited CO_2 lasers are very different from those existing in pulsed lasers, several recent measurements [22] have determined that the population of the lower laser level is close to equilibrium with the gas temperature. Once again, this confirms the existence of very strong coupling between the bending and symmetric stretching modes.

References

[1] P. K. Cheo, "Relaxation of CO_2 laser levels by collisions with foreign gases," *IEEE J. Quantum Electron. (Special Issue on 1968 Int. Quantum Electron. Conf.: Part I)*, vol. QE-4, pp. 587–593, Oct. 1968.
— "Effects of CO_2, He and N_2 on the lifetimes of the $00^\circ 1$ and $10^\circ 0$ CO_2 laser levels and on pulsed gain at 10.6 μ," *J. Appl. Phys.*, vol. 38, pp. 3563–3568, Aug. 1967.

[2] M. C. Fowler, "Influence of plasma kinetic processes on electrically excited CO_2 laser performance," *J. Appl. Phys.*, vol. 43, pp. 3480–3487, Aug. 1972 (and cited references).

[3] K. Bulthuis, "Laser power and vibrational energy transfer in CO_2 lasers," *J. Chem. Phys.*, vol. 58, pp. 5786–5794, June 1973.

[4] W. A. Rosser, Jr., E. Hoag, and E. T. Gerry, "Relaxation of excess populations in the lower laser level CO_2 (100)," *J. Chem. Phys.*, vol. 57, pp. 4153–4164, Nov. 1972.

[5] L. J. Denes and L. A. Weaver, "Laser gain characterization of near-atmospheric CO_2:N_2:He glows in a planar electrode geometry," *J. Appl. Phys.*, vol. 44, pp. 4125–4136, Sept. 1973.

[6] H. Brinkschulte and R. Lang, "Gain measurements in a TEA CO_2 laser," *Phys. Lett.*, vol. 47A, pp. 455-456, May 1974.
[7] A. M. Robinson, "Gain distribution in a CO_2 TEA laser," *Can. J. Phys.*, vol. 50, pp. 2471-2474, 1972.
[8] C. K. N. Patel, "Interpretation of CO_2 optical maser experiments," *Phys. Rev. Lett.*, vol. 12, pp. 588-590, May 1964.
[9] J. Y. Coester and Ph. Vautier, "Realisation d'un amplificateur a grand gain sans circulation de gaz fonctionnant entre 9 et 11 μ," *Infrared Phys.*, vol. 7, pp. 173-180, 1967.
[10] B. K. Garside, E. A. Ballik, and J. Reid, "Pulse delays in TEA CO_2 lasers," *J. Appl. Phys.*, vol. 43, pp. 2387-2390, May 1972.
[11] J. Reid, E. A. Ballik, and B. K. Garside, "Saturation of the net electron excitation of the CO_2 (00°1) laser level as a function of discharge input energy," *Opt. Commun.*, vol. 12, pp. 354-359, Dec. 1974.
[12] R. R. Jacobs, "Technique for gain determinations in pulsed CO_2 TEA lasers," *Rev. Sci. Instrum.*, vol. 44, pp. 1146-1147, Aug. 1973.
[13] C. Cousin, C. Rossetti, and C. Meyer, "Spectroscopie avec source laser. Étude des transitions de vibration-rotation $\nu_3 - \nu_1$, $\nu_3 - 2\nu_2$, et $(\nu_3 + \nu_2) - (\nu_1 + \nu_2)$ de l'anhydride carbonique," *C. R. Acad. Sci.* (Paris), vol. 268, pp. 1640-1643, June 1969.
[14] T. Y. Chang, "Accurate frequencies and wavelengths of CO_2 laser lines," *Opt. Commun.*, vol. 2, pp. 77-80, July 1970.
[15] R. Ely and T. K. McCubbin, Jr., "The temperature dependence of the self-broadened half-width of the *P*-20 line in the 001-100 band of CO_2," *Appl. Opt.*, vol. 9, pp. 1230-1231, May 1970.
[16] S. Singer, "Observations of anomalous gain coefficients in TEA double-discharge CO_2 lasers," *IEEE J. Quantum Electron.*, vol. QE-10, pp. 829-831, Nov. 1974.
[17] J. A. Howe and R. A. McFarlane, "New emission systems in CO_2," *J. Mol. Spectrosc.*, vol. 19, pp. 224-226, 1966.
B. Hartmann and B. Kleman, "Laser lines from CO_2 in the 11-18 micron region," *Can. J. Phys.*, vol. 44, pp. 1609-1612, 1966.
[18] C. Meyer, C. Rossetti, and P. Barchewitz, "Development and spectroscopic application of monochromatic and single mode CO_2 lasers," *IEEE J. Quantum Electron. (2nd Conf. on Chemical and Molecular Lasers)*, vol. QE-6, pp. 179-180, Mar. 1970.
[19] E. E. Stark, Jr., "Measurement of the 10°0-02°0 relaxation rate in CO_2," *Appl. Phys. Lett.*, vol. 23, pp. 335-337, Sept. 1973.
[20] K. N. Seeber, "Radiative and collisional transitions between coupled vibrational modes of CO_2," *J. Chem. Phys.*, vol. 55, pp. 5077-5081, Nov. 1971.
[21] R. D. Sharma, "Kinetics of equilibration of 1388-cm^{-1} vibrational level of CO_2," *J. Chem. Phys.*, vol. 49, pp. 5195-5197, Dec. 1968.
[22] A. A. Mikaberidze, V. N. Ochkin, and N. N. Sobolev, "Population of the lower active level in a carbon dioxide laser," *Sov. J. Quantum Electron.*, vol. 3, pp. 21-23, July 1973.
D. Gaultier, D. Bailly, E. Arie, and C. Rossetti, "Détermination dans CO_2 excité des populations des niveaux vibrationnels ν_3 et ν_1 et de la température rotationelle," *C. R. Acad. Sci.* (Paris), vol. B272, pp. 269-271, Jan. 1971.
D. Bailly, D. Gaultier, C. Rossetti and P. Barchewitz, "Etat stationnaire dans des plasmas CO_2-N_2, CO_2-He et CO_2-N_2-He produits par décharge electrique," *Can. J. Phys.*, vol. 50, pp. 2605-2613, 1972.

Modes in Diffused Optical Waveguides of Arbitrary Index Profile

G. BENJAMIN HOCKER, MEMBER, IEEE, AND WILLIAM K. BURNS

Abstract—**A method is presented for numerical calculation of the phase constants of the modes of diffused optical waveguides of arbitrary index profile. For a given bulk and surface index, the phase constants can be plotted against diffusion depth. Graphs giving the number of modes supported by a guide with a particular diffusion depth and index change can also be calculated. Examples are given for complementary error function, Gaussian, and exponential profiles, with indices representative of metal-diffused $LiNbO_3$ guides. It is also shown that, by making certain approximations, the modes of a diffused waveguide may be described by just two quantities, a normalized diffusion depth and a normalized mode index. A single universal chart of these two quantities can be made for any diffusion shape, and all diffused guides with this diffusion shape are described by this chart. Charts are given for complementary error function, Gaussian, and exponential shapes. Careful measurement of effective mode indices of Ni-diffused $LiNbO_3$ guides fit the universal chart for a complementary error-function shape. A second type of universal chart for each shape relates the number of modes to the diffusion depth and indices of refraction.**

Manuscript received December 2, 1974. The work of G. B. Hocker was supported in part by the University of Minnesota Graduate School and the University Computer Center. The work of W. K. Burns was supported by the Advanced Research Projects Agency.

G. B. Hocker was on leave with the Naval Research Laboratory, Washington, D.C. 20375. He is with the Department of Electrical Engineering, the University of Minnesota, Minneapolis, Minn. 55455.
W. K. Burns is with the Naval Research Laboratory, Washington, D.C. 20375.

I. Introduction

Optical waveguides having a graded index have been formed in lithium niobate by outdiffusion [1] and by indiffusion [2], by diffusion in II-VI semiconductors [3], in glass [4], and in other materials [5]. In such waveguides the index of refraction is a smoothly varying function of depth and is higher at or near the surface than in the bulk material. The variation in index with depth may be of the form of a complementary error function, a Gaussian, a simple exponential, or may be of a shape not described by any simple mathematical function [1], [2], [4], [6].

To use such waveguides in integrated optics devices, it is useful to know the number of modes and their phase constants for any given diffusion profile. Calculations have been made analytically for only two possible profiles: one in which the dielectric constant is assumed to vary exponentially with depth [7] and one where the dielectric constant varies linearly with depth [8]. In both cases, exact solutions involving Bessel functions are obtained, but only for TE modes.

In Section II we describe a simple numerical method for calculating the phase constants of the modes of diffused waveguides of arbitrary index of refraction profile using a digital

computer. The method is based on wave optics considerations, and includes the phase shifts on reflection from the waveguide surfaces. Sample calculations are given plotting the effective indices of the various waveguide modes versus diffusion depth for exponential, Gaussian, and complementary error-function index profiles representative of diffused lithium niobate waveguides. Also given are plots for each of these three index profiles showing the diffusion depths and index changes necessary to produce a given number of waveguide modes in lithium niobate.

In Section III it is shown that, by making certain approximations, the diffused waveguide modes may be described by just two quantities, a normalized diffusion depth and a normalized mode index. A single universal chart of these two quantities can be made for any diffusion shape. Such a chart describes any guide having this diffusion shape, and examples are given for complementary error function, Gaussian, and exponential. Another universal chart is given for each of these shapes relating the number of modes supported by the waveguide to the diffusion depth and indices of refraction.

II. Numerical Calculations

Let the dielectric waveguide material occupy the half-space $y > 0$. The index of refraction profile may be written as

$$n(y) = n_b + \Delta n\, f(y/D) \tag{1}$$

where the maximum value of $n(y)$ is denoted $n_s = n_b + \Delta n$. The function $f(y/D)$ describes the variation in the index due to diffusion and takes on values between 0 and 1. For example, $f(x) = \text{erfc}\,(x)$ or $\exp(-x^2)$ or $\exp(-x)$. $f(x)$ will be referred to as the diffusion shape, and D as the diffusion depth. When the diffusion depth is given in units of the free-space wavelength, it is denoted $Y_0 = D/\lambda$. We shall assume here that $f(x)$ has its maximum value at $x = 0$ and decreases with increasing x, although the method is easily adapted to other situations. Thus n_b represents the index in the bulk undiffused material, while n_s is the index at the surface after diffusion.

With each allowed waveguide mode is associated a phase constant β. The limits on β are

$$n_s k_0 > \beta > n_b k_0 \tag{2}$$

where $k_0 = 2\pi/\lambda$ is the free-space phase constant. An effective index of refraction n_{eff} can be defined for each mode by

$$\beta = n_{\text{eff}} k_0 \tag{3}$$

where the limits on n_{eff} are

$$n_s > n_{\text{eff}} > n_b. \tag{2'}$$

As shown in Fig. 1(a) for a mode propagating in the x direction with a propagation vector $\beta(\hat{x}) = n_{\text{eff}} k_0 \hat{x}$, a wave at a depth y_i has a propagation vector $n(y_i) k_0 \hat{r}$, where $\hat{r}$ makes an angle θ_i with the x axis. θ_i is given by

$$\theta_i = \cos^{-1}\left(\frac{n_{\text{eff}}}{n(y_i)}\right). \tag{4}$$

At this depth y_i, the y component of the propagation vector of the wave is $n(y_i) k_0 \sin\theta_i$. For an incremental propagation distance Δx along x, the wave penetrates a depth Δy_i as in

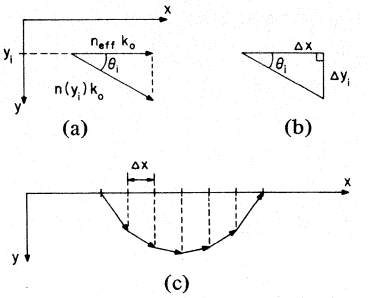

Fig. 1. (a) Wave-vector diagram for a mode with phase constant $n_{\text{eff}} k_0$ and a wave depth y_i with phase constant $n(y_i) k_0$. (b) Incremental propagation of mode by Δx increases depth of wave by $\Delta y_i = \Delta x \tan\theta_i$. (c) Piecewise-linear path of wave corresponding to waveguide mode as used in computer calculations.

Fig. 1(b)

$$\Delta y_i = \Delta x \tan\theta_i. \tag{5}$$

Across Δy_i the incremental transverse phase variation is

$$\phi_i = n(y_i) k_0 \sin\theta_i \Delta y_i. \tag{6}$$

Beginning at the surface with a given n_{eff}, then θ_i, Δy_i, and ϕ_i can be calculated by computer for each small increment Δx, following the wave as it dips into the diffused waveguide and returns to the surface as shown in Fig. 1(c). Typically, several hundred straight-line segments are used to approximate the wave's path.

When a wave in a material of index n_a undergoes total internal reflection at an interface with material of index n_b ($n_b < n_a$), then there is a phase shift on reflection given by [9]

$$2\Phi_{ab} = -2\tan^{-1}\left[(n_a^2 \sin^2\alpha - n_b^2)^{1/2}/n_a \cos\alpha\right] \tag{7a}$$

for a wave polarized perpendicular to the plane of incidence and

$$2\Phi_{ab} = -2\tan^{-1}\left[n_a^2(n_a^2 \sin^2\alpha - n_b^2)^{1/2}/n_b^2 n_a \cos\alpha\right] \tag{7b}$$

for a wave polarized in the plane of incidence. α is the angle between the incident wave vector and the normal to the interface.

Such a reflection takes place at the top surface of the diffused waveguide, at the interface between the diffused guide material and air. For this reflection $n_a = n_s$, $n_b = 1$, $\alpha = (\pi/2) - \theta_0$, and $n_a \sin\alpha = n_s \cos\theta_0 = n_{\text{eff}}$. Hence the phase shift at this surface is given by

$$2\Phi_1 = -2\tan^{-1}\left[(n_{\text{eff}}^2 - 1)^{1/2}/(n_s^2 - n_{\text{eff}}^2)^{1/2}\right] \tag{8a}$$

for TE modes, and by

$$2\Phi_1 = -2\tan^{-1}\left[n_s^2(n_{\text{eff}}^2 - 1)^{1/2}/(n_s^2 - n_{\text{eff}}^2)^{1/2}\right] \tag{8b}$$

for TM modes. Since for diffused guides produced to date $\Delta n \ll n_b$, then n_{eff}^2 is close to n_s^2 and both are $\gg 1$. Thus $2\Phi_1$ is close to $-\pi$, typically, between -0.8π and -0.95π for guide parameters so far reported in the literature.

The wave which dips into the diffused guide also undergoes a phase shift at the point of maximum penetration y_t where it turns back toward the surface. This point is defined by $n(y_t) = n_{\text{eff}}$. The phase shift at this reflection is a limiting case of (7) with a wave approaching grazing incidence and an

index discontinuity approaching zero. To show that the phase shift has a limiting value, let the wave traveling in the x direction with effective index n_{eff} be incident on an interface at $y = y_t$ between material for index $n(y_t - \delta)$ and $n(y_t + \delta)$. The slope of the index profile at $y = y_t$ is $(dn/dy)(y_t)$, so

$$n(y_t - \delta) = n(y_t) - \delta \frac{dn}{dy}(y_t) = n_{\text{eff}} - \delta \frac{dn}{dy}(y_t) \tag{9a}$$

$$n(y_t + \delta) = n_{\text{eff}} + \delta \frac{dn}{dy}(y_t). \tag{9b}$$

Substituting (9a) and (9b) into (7) and taking the limit as $\delta \to 0$, gives

$$2\Phi_2 = -2 \lim_{\delta \to 0} \tan^{-1} \cdot [(n_{\text{eff}}^2 - n(y_t + \delta)^2)^{1/2}/(n(y_t - \delta)^2 - n_{\text{eff}}^2)^{1/2}]$$

$$= -2 \tan^{-1}(1) = -\frac{\pi}{2} \tag{10a}$$

for TE modes [10]. Similarly, for TM modes

$$2\Phi_2 = -\frac{\pi}{2}. \tag{10b}$$

The fundamental requirements for the existence of a waveguide mode is that the total transverse phase shift for one round trip across the guide must be an integral multiple of 2π. This is expressed in the eigenvalue or mode dispersion equation

$$\sum \phi_i + 2\Phi_1 + 2\Phi_2 = 2m\pi \tag{11}$$

with $m = 0, 1, 2, \cdots$ and where the summation can be carried out numerically as previously described. A computer routine can easily search out the value of n_{eff} satisfying (11) for each m and for any given diffusion profile $n(y)$. The diffusion shape $f(x)$ can be a mathematical function, or could be numerically defined by experimental measurements.

Calculations have been made using $n_b = 2.20$ and $\Delta n = 0.010$. This is typical for extraordinary polarized modes in metal-diffused lithium niobate waveguides. Choices for $f(x)$ include a complementary error function, a Gaussian function, and a simple exponential. The complementary error function is expected to best describe metal-diffused $LiNbO_3$, at least up to the time when all of the metal has just been diffused into the substrate [2]. A Gaussian profile would be expected for diffusion times much longer than this. Fig. 2(a)-(c) gives the allowed values of n_{eff} for TE modes versus diffusion depth $Y_0 = D/\lambda$ in units of the free-space wavelength, for these three choices of $f(x)$. Calculations were also made for TM modes, but these are not shown here since they are very close to the corresponding TE modes. Calculations have also been made for $n_b = 2.29$ and $\Delta n = 0.010$, representing ordinary polarized waves in $LiNbO_3$. The resulting curves are virtually indistinguishable from Fig. 2(a)-(c) if the ordinates of Fig. 2(a)-(c) are simply relabeled to run from 2.29 to 2.30 (n_b to n_s) with the scale remaining the same. With suitable relabeling of the ordinates, Fig. 2(a)-(c) can be used as good representations of any guides with $\Delta n = 0.010$ and n_b in the range of 2.1-2.3.

To check the accuracy of our method, we have compared our

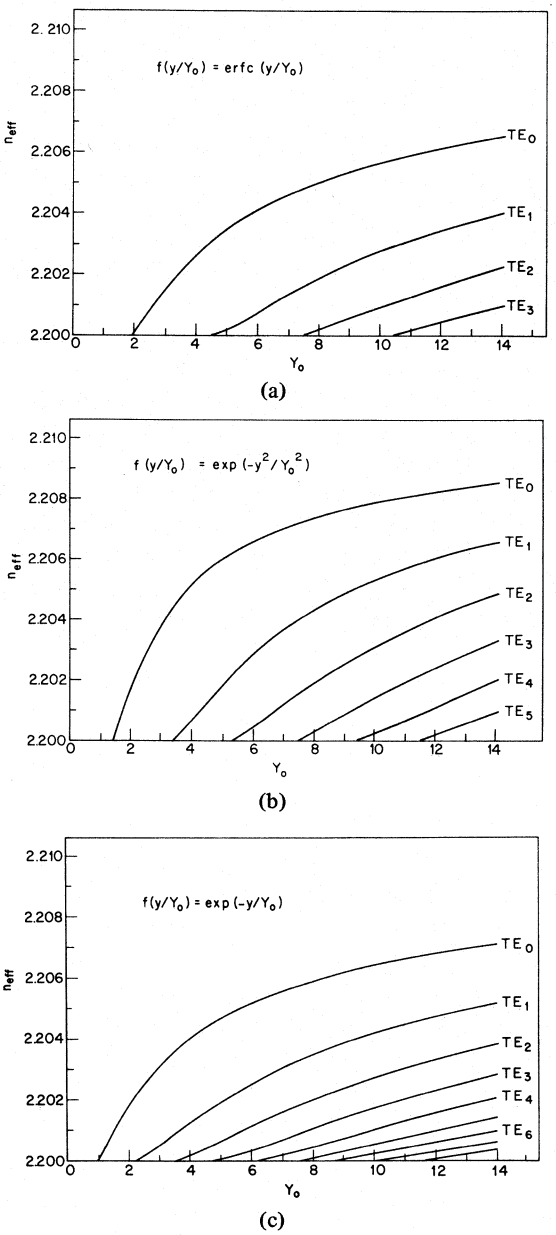

Fig. 2. Allowed values of n_{eff} for TE modes in diffused waveguide plotted against diffusion depth $Y_0 = D/\lambda$ in units of free-space wavelength, with indices typical of metal-diffused $LiNbO_3$. The index profile is as follows. (a) A complementary error function. (b) A Gaussian. (c) An exponential.

calculations with the exact solutions obtained by Conwell for an exponential dielectric constant profile [7]. For a dielectric constant of 6.1 in the bulk material and 6.4 at the surface, we choose the diffusion depth to give $\xi = 27.0$ and solve [7, eq. (8)]. The values of n_{eff} obtained agree to 10^{-4} in n or 0.17 percent of Δn as shown in Table I. This accuracy is believed to be maintained in calculations for other $f(x)$, and confirms our calculations of $\Sigma \phi_i$, $2\Phi_1$, and $2\Phi_2$.

Curves such as Fig. 2(a)-(c) have several uses. If the diffusion shape is already known, Y_0 can be determined from the set of n_{eff} observed experimentally or the diffusion depth and/or index change needed to produce a given set of n_{eff} can be obtained. Sets of curves such as these should also be useful for determining what diffusion shape best describes an observed set of n_{eff}. However, these applications may require

TABLE I
n_{eff} FOR EXPONENTIAL DIELECTRIC CONSTANT

m	Our Calculations	Exact Solution of [7]
0	2.5083	2.5082
1	2.4952	2.4951
2	2.4865	2.4866
3	2.4804	2.4805
4	2.4761	2.4760
5	2.4731	2.4731
6	2.4711	2.4711
7	2.4701	2.4701

Note: $\epsilon_b = 6.1$, $\epsilon_s = 6.4$ ($n_b = \sqrt{6.1}$, $n_s = \sqrt{6.4}$, $Y_0 = 3.949447$).

that many such curves be plotted for various n_b and Δn. In Section III, several approximations will be made which allow all diffused guides having the same diffusion shape to be described by a single universal chart relating a normalized mode index to a normalized diffusion depth.

It is desirable to know for a given diffusion shape $f(x)$, what combinations of diffusion depth and index change Δn produce waveguides which support a given number of modes. For a particular n_b and Δn, the values of $Y_0 = D/\lambda$ corresponding to cutoff for the various modes can be found from (11) by a simple computer search routine. To restrict the penetration of the wave to a finite depth, we define cutoff as $n_{eff} = n_b + 10^{-3}\Delta n$. Using $n_b = 2.20$, we plot the values of Δn and Y_0 obtained in this way for $f(x)$ given by a complementary error function, a Gaussian, and an exponential, shown here as Fig. 3(a)-(c), respectively. The curves for cutoff of the various modes divide each of these figures into regions of Δn and Y_0 where waveguides would support no modes, one mode, two modes, etc., and so should be particularly useful when designing single-mode waveguides. The bottom two curves in Fig. 3(c) agree with the analytical expressions given by Conwell [13]. Calculations for n_b from about 2.1 to 2.3 give nearly identical curves, so Fig. 3(a)-(c) are applicable to a number of materials with bulk index in this range.

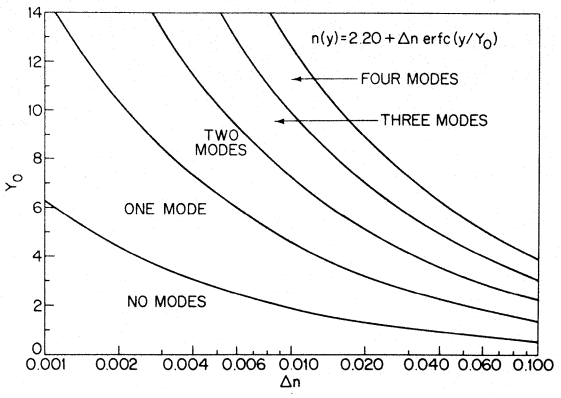

Fig. 3. Index change $\Delta n = n_s - n_b$ versus diffusion depth $Y_0 = D/\lambda$ in units of free-space wavelength, showing the number of waveguide modes. $n_b = 2.20$, and the index profile is as follows. (a) A complementary error function. (b) A Gaussian. (c) An exponential.

III. UNIVERSAL CURVES FOR DIFFUSED WAVEGUIDE MODES

Kogelnik and Ramaswamy have recently shown that, by defining a set of three normalized parameters describing thin-film optical waveguides, the modes of any thin-film waveguide can be determined from a universal chart [12]. The parameters include: a normalized film thickness V; a normalized effective mode index b; and a measure of the asymmetry between substrate and superstrate indices a. The mode dispersion equation normally gives β or n_{eff} for each mode in terms of five independent quantities: the index of refraction of guide, substrate, and superstrate; the guide width; and optical wavelength. This can be reduced to an equation for the normalized guide index b, in terms of only the two normalized parameters V and a. A universal chart of b versus V is obtained, with a as a parameter, which describes any thin-film waveguide. Since b is weakly dependent on a, curves of b versus V for only a few values of a are sufficient. In this section, we show that (11) can, with certain approximations, be written in a normalized form, giving a universal chart of normalized mode index versus normalized diffusion depth for each diffusion shape.

From the definition of θ_i in (4), $\sin\theta_i$ can be written as

$$\sin\theta_i = (1 - \cos^2\theta_i)^{1/2} = \left[\frac{n(y_i)^2 - n_{eff}^2}{n(y_i)^2}\right]^{1/2} \tag{12}$$

so that (6) becomes

$$\sum \phi_i = k_0 (n(y_i)^2 - n_{eff}^2)^{1/2} \Delta y_i. \tag{13}$$

As $\Delta y_i \to 0$, this becomes an integral

$$\sum \phi_i \to 2k_0 \int_0^{y_t} (n(y)^2 - n_{\text{eff}}^2)^{1/2}\, dy \tag{14}$$

where

$$n(y_t) = n_{\text{eff}}.$$

Equation (11) can therefore be written as

$$2k_0 \int_0^{y_t} (n(y)^2 - n_{\text{eff}}^2)^{1/2}\, dy + 2\Phi_1 + 2\Phi_2 = 2m\pi. \tag{15}$$

Let us now make the approximation

$$n(y)^2 \cong n_b^2 + (n_s^2 - n_b^2) f(y/D). \tag{16'}$$

We can now introduce the normalized diffusion depth V

$$V = k_0 D(n_s^2 - n_b^2)^{1/2} \tag{17}$$

and normalized mode index b

$$b = \frac{n_{\text{eff}}^2 - n_b^2}{n_s^2 - n_b^2} \tag{18}$$

where D is the diffusion depth given in the same system of units as k_0. V and b are the same parameters used in [12], with diffusion depth D replacing the guide width.

Using the approximation of (16) along with the definitions of (17) and (18), the integral in (15) becomes

$$2k_0 \int_0^{y_t} (n(y)^2 - n_{\text{eff}}^2)^{1/2}\, dy = 2V \int_0^{x_t} (f(x) - b)^{1/2}\, dx \tag{19}$$

where $x = y/D$ and $f(x_t) = b$. Since we are considering diffused waveguides bounded above by air, and since n_s is appreciably larger than 1 and $\Delta n \ll n_s$, calculations are simplified and the introduction of a third parameter is avoided by approximating

$$2\Phi_1 \cong -\pi. \tag{20}$$

Note that this removes the distinction between TE and TM modes in isotropic materials. In anisotropic materials they will of course see different n_b and Δn depending on crystal orientation. The mode dispersion (11) becomes

$$2V \int_0^{x_t} (f(x) - b)^{1/2}\, dx = (2m + \tfrac{3}{2})\pi \tag{21}$$

for $m = 0, 1, 2, \cdots$. Equation (21) is a more general form of the equation obtained in [11] by use of the Wentzel-Kramers-Brillouin (WKB) approximation.

For a particular diffusion shape $f(x)$, the values of V satisfying (21) for a given value of b are easily obtained. Universal charts of b versus V for $f(x)$ given by a complementary error function, a Gaussian function, and an exponential are given as Fig. 4(a)-(c). Each of these universal charts describes *all* diffused waveguides having the specified $f(x)$ shape, within the approximations of (16) and (20). While they are not as accurate as the type of calculation shown in Fig. 2, these universal charts should be much more useful, since repeated calculations for each specific case are not necessary. Instead, a single universal chart may be used to find the values of n_s and diffusion depth which best fit an experimentally observed n_b and set of n_{eff} for a given $f(x)$. As a check on the accuracy of these results, we use the values of n_{eff} for $Y_0 = 12.0$ from Fig. 2(a)-(c) to calculate the corresponding b and V. Comparing these with Fig. 4(a)-(c), they agree to within 2 percent of b, indicating that the approximations we have made do not introduce any serious errors.

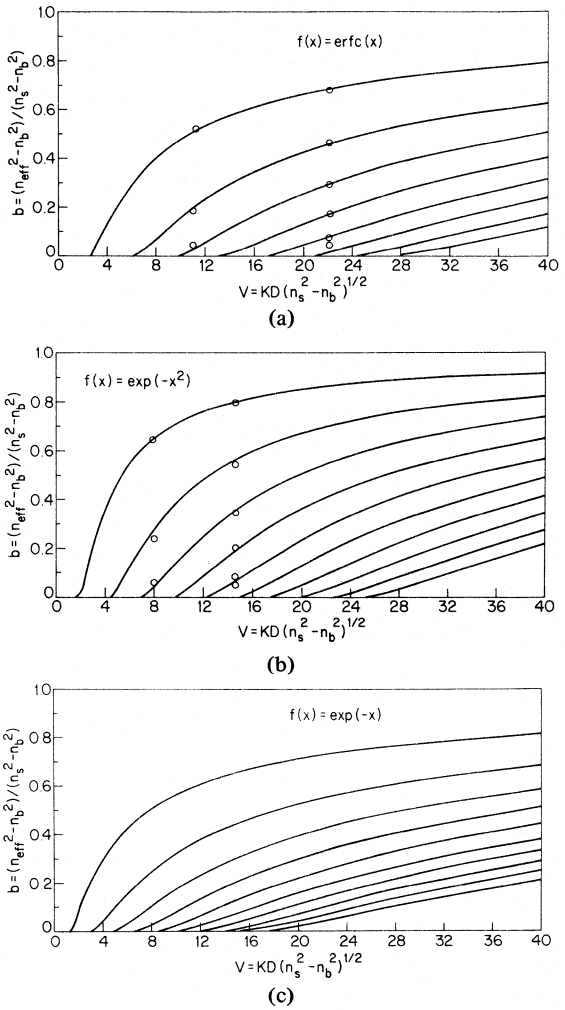

Fig. 4. Universal chart of normalized mode index $b = (n_{\text{eff}}^2 - n_b^2)/(n_s^2 - n_b^2)$ versus normalized diffusion depth $V = k_0 D(n_s^2 - n_b^2)^{1/2}$ for a diffusion shape of the following. (a) A complementary error function. (b) A Gaussian. (c) An exponential. Experimental measurements of TM-mode effective indices in two Ni-diffused $LiNbO_3$ guides are fitted to charts (a) and (b). Measurement uncertainties are indicated by the size of the data points, except for the sixth mode of the six-mode guide, which was detectable but not resolvable. The better fit to theory in (a) indicates that the experimental diffusion profiles are nearly complementary error function.

As an example of the use of the universal charts in Fig. 4, we have plotted the experimental results of mode effective index measurements of two metal-diffused $LiNbO_3$ guides. The waveguides were made by diffusing 500 Å of Ni into Y-X $LiNbO_3$ plates at temperatures near 900°C, as reported in

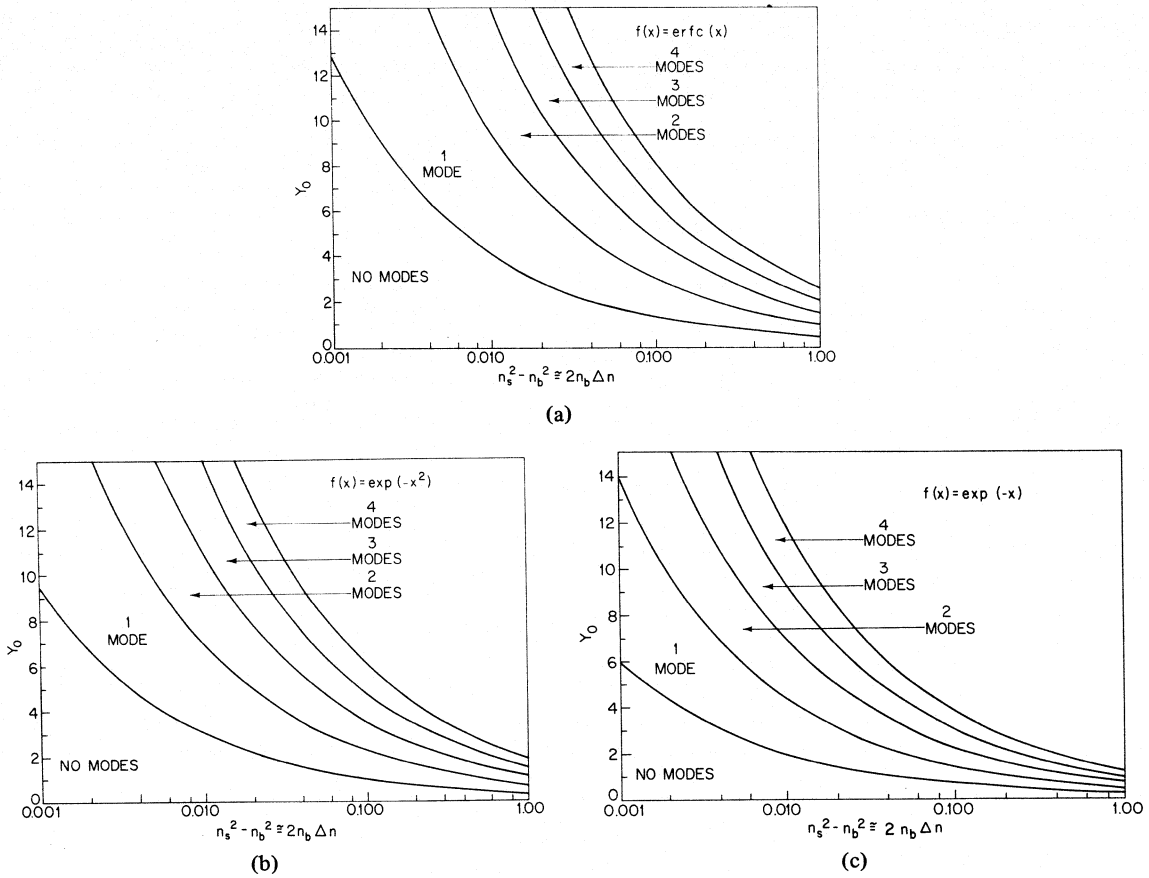

Fig. 5. Universal chart of diffusion depth $Y_0 = D/\lambda$ versus $n_s^2 - n_b^2 \cong 2n_b\,\Delta n$ showing the number of waveguide modes for a diffusion shape of the following. (a) A complementary error function. (b) A Gaussian. (c) An exponential.

[2]. Measurements of TM coupling angles were made on a Gaertner L123 Precision Spectrometer which allowed angular readings to 5″. Resetability errors then predominate and correspond to experimental uncertainties in effective index of $\pm 2\text{-}3 \times 10^{-3}$ percent. A best fit of the experimental data is plotted on both the Gaussian and complementary error function universal charts in Fig. 4 [2]. Comparison of these plots implies that diffusion profiles which closely approximate a complementary error function were obtained, particularly so for the six-mode waveguide. The three- and six-mode waveguides had values for Δn and D of 0.016 and 4.24 μm, and 0.0051 and 14.9 μm, respectively, based on the complementary error-function profile [14].[1]

The cutoff of the mth mode is easily found from (21), since for cutoff $b \to 0$ and $x_t \to \infty$. Thus cutoff of the mth mode is given by

$$V \int_0^\infty \sqrt{f(x)}\,dx = (m + \tfrac{3}{4})\,\pi \tag{22}$$

or, in terms of the (unnormalized) diffusion depth and indices of refraction

$$Y_0 = D/\lambda = \frac{(m + 3/4)}{2\sqrt{n_s^2 - n_b^2}\displaystyle\int_0^\infty \sqrt{f(x)}\,dx}. \tag{23}$$

Curves of Y_0 versus the parameter $(n_s^2 - n_b^2)$ $(\cong 2n_b\,\Delta n)$ for cutoff of the first five modes are shown in Fig. 5(a)-(c) for $f(x)$ given by a complementary error function, a Gaussian, and an exponential, respectively. These are universal charts similar to the form of Fig. 3, relating the diffusion depth and parameter $(n_s^2 - n_b^2)$ to the number of modes supported by the guide.

IV. Conclusions

Both the numerical method of Section II and the generalized method of Section III can be used to describe the modes of diffused optical waveguides of a variety of index profiles. The calculations of Section II are capable of high accuracy in finding the allowed set of n_{eff} from n_b, Δn, and Y_0 for a given shape $f(x)$. However, these calculations must be repeated for each change in the parameters. The methods of Section III are a less accurate but more practical alternative. The charts given in that section suffice, within the approximations made to describe all diffused waveguides having complementary error function, Gaussian, and exponential profiles.

[1] *Note Added in Proof:* Better data have improved the fit to the erfc profile for the sixth mode of the six-mode guide.

REFERENCES

[1] I. P. Kaminow and J. A. Carruthers, "Optical waveguiding layers in $LiNbO_3$ and $LiTaO_3$," *Appl. Phys. Lett.*, vol. 22, pp. 326–328, 1973.

[2] R. V. Schmidt and I. P. Kaminow, "Metal-diffused optical waveguides in $LiNbO_3$," *Appl. Phys. Lett.*, vol. 25, pp. 458–460, 1974.

[3] H. F. Taylor, W. E. Martin, D. B. Hall, and V. N. Smiley, "Fabrication of single-crystal semiconductor optical waveguides by solid-state diffusion," *Appl. Phys. Lett.*, vol. 21, pp. 95–98, 1972.

[4] T. G. Giallorenzi *et al.*, "Optical waveguides formed by thermal migration of ions in glass," *Appl. Opt.*, vol. 12, pp. 1240–1245, 1973.

[5] J. Noda, T. Saku, and N. Uchida, "Fabrication of optical waveguiding layer in $LiTaO_3$ by Cu diffusion," *Appl. Phys. Lett.*, vol. 25, pp. 308–310, 1974.

[6] a) J. Crank, *The Mathematics of Diffusion.* New York: Oxford, 1956.
b) H. H. Woodbury and R. B. Hall, "Diffusion of the chalcogens in the II-VI compounds," *Phys. Rev.*, vol. 157, pp. 641–655, 1967.

[7] E. M. Conwell, "Modes in optical waveguides formed by diffusion," *Appl. Phys. Lett.*, vol. 26, pp. 328–329, 1973.

[8] D. Marcuse, "TE modes of graded-index slab waveguides," *IEEE J. Quantum Electron.*, vol. QE-9, pp. 1000–1006, Oct. 1973.

[9] M. Born and E. Wolf, *Principles of Optics.* New York: Pergamon, 1965.

[10] The limit in (10) can be found more rigorously by use of l'Hospital's Rule, which also gives $2\Phi_2 = -\pi/2$.

[11] P. K. Tien *et al.*, "Optical waveguide modes in single-crystalline $LiNbO_3$–$LiTaO_3$ solid-solution films," *Appl. Phys. Lett.*, vol. 24, pp. 503–506, 1974.

[12] H. Kogelnik and V. Ramaswamy, "Scaling rules for thin-film optical waveguides," *Appl. Opt.*, vol. 13, pp. 1857–1862, 1974.

[13] E. M. Conwell, "Modes in anisotropic optical waveguides formed by diffusion," *IEEE J. Quantum Electron.*, vol. QE-10, pp. 608–612, Aug. 1974.

[14] A TM mode in the geometry used here (x-propagating y-diffused, c axis in the z direction) sees only the ordinary index of refraction. However, in general, a TM mode in an anisotropic material sees both indices of refraction, and the first term in (15) would be multiplied by the ratio of two indices. See, for example, W. K. Burns and J. Warner, "Mode dispersion in uniaxial optical waveguides," *J. Opt. Soc. Amer.*, vol. 64, pp. 441–446, 1974.

Noise Characteristics of Stripe-Geometry Double-Heterostructure Junction Lasers Operating Continuously—I. Intensity Noise at Room Temperature

THOMAS L. PAOLI, MEMBER, IEEE

Abstract—**Measurements of the noise fluctuations present in the output intensity from stripe-geometry double-heterostructure junction lasers operating continuously at room temperature are reported. In some but not all the lasers studied, the low-frequency (50-MHz) fluctuations exhibit the quieting expected of an amplitude-stabilized oscillator operating above threshold. The intensity noise in these lasers becomes shot noise limited at currents about 10 percent above threshold, even when many longitudinal modes are oscillating. Additional measurements demonstrate explicitly the effective elimination of the wave-interaction, or excess, noise during the transit of the threshold region. However, in other lasers which are nominally similar, only a partial reduction of the excess noise occurs above threshold, resulting in a noise level which can be more than ten times the shot-noise limit. In addition, we find in all lasers studied thus far no quieting at high frequencies (4 GHz), in apparent contradiction to the behavior expected of a well-stabilized oscillator.**

Manuscript received December 2, 1974. Preliminary results of this paper were presented at the 8th International Quantum Electronics Conference, San Francisco, Calif., June 10–13, 1974.

The author is with Bell Laboratories, Murray Hill, N.J. 07974.

I. INTRODUCTION

SINCE the pioneering work of Armstrong and Smith [1] in 1964, the statistical properties of the light emitted by a junction laser have received very little attention. However, the utilization of this laser as a source in an optical communication system necessitates a thorough evaluation of its noise characteristics. Furthermore, a detailed investigation of the statistical fluctuations of its emission and junction current can provide much information about the fundamental properties of this laser.

Intrinsic fluctuations in the output intensity of junction lasers were theoretically studied first by McCumber [2], then by Haug and Haken [3], [4], and most recently by Morgan and Adams [5]. In addition to the early experimental work of [1], the fluctuations in the neighborhood of the spiking resonance were observed by Paoli and Ripper [6], while the intensity noise in multifilament lasers has been

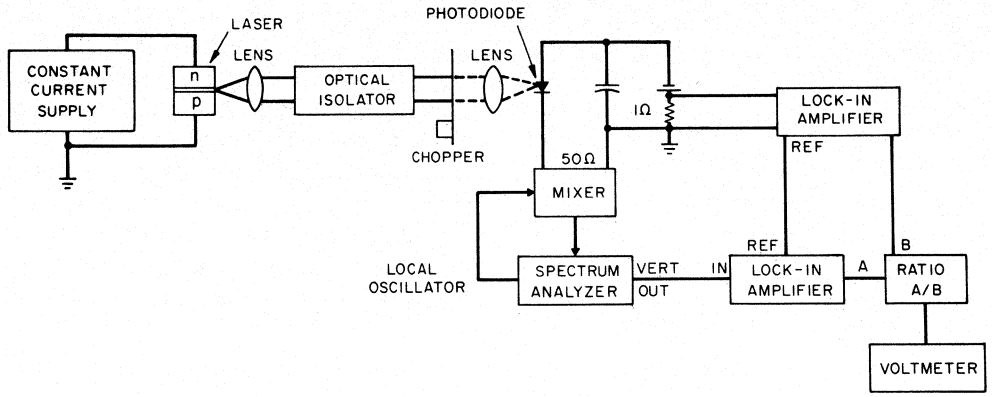

Fig. 1. Schematic diagram of the system used to measure the relative noise fluctuations of the light intensity from stripe-geometry double-heterostructure junction lasers.

studied by Guekos and Strutt [7]. The latter work indicates the complications inherent in attempting to measure the intrinsic intensity fluctuations in the presence of random filaments.

In this paper, we present experimental observations of the intensity-noise characteristics of present-day stripe-geometry junction lasers operating continuously at room temperature. Some initial results of this work were briefly reported previously [8]. In general, we find that some but not all of our lasers exhibit the quieting expected of an amplitude-stabilized oscillator operating above threshold. Low-frequency (50-MHz) intensity fluctuations in these lasers are shot-noise limited at currents greater than about 10 percent above threshold, even when many longitudinal modes are oscillating. However, other lasers which are nominally similar exhibit intensity noise which is many times higher than the shot-noise limit. In addition, we find in all lasers studied thus far no quieting at frequencies above the spiking resonance.

II. Experimental Details

A. Measurement System

Fluctuations in the light intensity from CW junction lasers were measured with the single-detector system shown schematically in Fig. 1. Because of the low level of the signal generated by the intensity fluctuations, phase-sensitive detection was utilized to improve the overall signal-to-noise ratio. Consequently, the laser light was collected and chopped before being focused onto a coaxially mounted Si p-n avalanche photodiode or a Si p-i-n photodiode. An optical isolator, consisting of a polarizer and a quarter-wave plate, was inserted between the laser and the photodiode to avoid interaction of the laser with reflections from the detector. The photodiode was biased at constant voltage with a coaxial capacitive coupling.

The ac output of the photodiode was coupled through the capacitor to a double-balanced mixer (Relcom M1F) which was used[1] in place of the internal input mixer of a conventional spectrum analyzer (Hewlett-Packard, 851B/8551B). In this way, the sensitivity of the receiver was increased by more than 10 dB. With this improvement plus the gain provided by the avalanching photodiode, the sensitivity of the system was more than 20 dB greater than that of the receiver used previously [6]. Consequently, the shot-noise level was within the system sensitivity, even at laser currents well below threshold.

The vertical output of the analyzer was directed to a lock-in amplifier whose output provided the A input for a ratio unit (PAR model 230). The B input was obtained from the output of a second lock-in whose input was the average photocurrent as measured by the chopped voltage produced across a 1-Ω standard resistor located at the output of the bias supply. The output of the second lock-in was also taken as indicative of the average light intensity.

The output at frequency $f = \omega/2\pi$ of the system described previously is [2]

$$S_{\mathrm{REL}}(f) = \frac{2\Delta f|b(\omega)|^2}{|b(0)|} \cdot \frac{[\eta\langle N\rangle_t F + \eta^2 P(\omega)]}{\eta\langle N\rangle_t} \tag{1}$$

where $\langle N\rangle_t$ is the time-average light intensity in photons/second, η is the quantum efficiency of the detector, F is the noise factor for the photodiode [9], $b(\omega)$ is the frequency-response function for the complete system including the gain and carrier-transport factors for the photodiode [9], Δf is the analyzer bandwidth, and $P(\omega)$ is the power spectrum of the fluctuating intensity. We call $S_{\mathrm{REL}}(f)$ the relative noise power since it is a measure of the intensity noise relative to the shot noise expected for the same average photocurrent. The first term on the right of (1) arises from shot-noise fluctuations of the signal. The factor F accounts for the enhancement of the shot noise by the gain process within the photodiode and increases with the carrier multiplication [9]. The second term, which is called the excess noise, arises from the time variation of the intensity. The power spectrum $P(\omega)$ is directly related to the intensity-correlation function of the incident light. For the later discussion, we rewrite (1) in normalized form as

$$S_{\mathrm{REL}}(f) = \alpha F + \eta\alpha \frac{P(\omega)}{\langle N\rangle_t} \tag{2}$$

where $\alpha \equiv 2\Delta f|b(\omega)|^2/|b(0)|$. For comparison, we note that the relative noise power $S_{\mathrm{REL}}(f)$ is αF times the factor

[1] Spectrum-analyzer modification kit A (Relcom p/n 7001-0689).

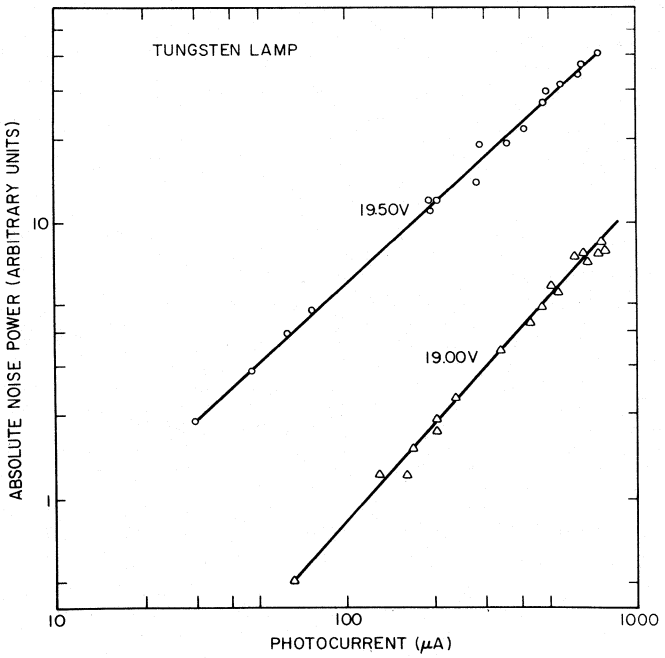

Fig. 2. The absolute noise power at 50 MHz produced by a tungsten lamp as a function of the photocurrent. The photocurrent is varied by attenuating the lamp intensity with neutral-density filters. Note the substantial gain in signal, i.e., absolute noise power, obtained by increasing the bias voltage on the avalanching photodiode from 19.00 to 19.50 V.

$(1 + S_e/S_s)$ used by Freed and Haus [10] to characterize the noise of He-Ne lasers.

For a broad-band optical source, such as an incandescent lamp, the spectral brightness is too low to produce detectable excess noise in comparison with the shot noise. Consequently, the sensitivity and linearity of the system were determined by measuring the noise produced by a tungsten lamp as a function of the photocurrent. The photocurrent produced by the lamp was varied over the same range as that obtained with the lasers by attenuating the lamp output with neutral-density filters. The experimental results shown in Fig. 2 indicate that the system response is reasonably linear and that a substantial gain in signal, i.e., the absolute noise, is obtained with the avalanching photodiode. Since the noise level of the overall receiver is determined primarily by noise intrinsic to the spectrum analyzer, the signal gain obtained from the photodiode leads directly to improvement of the signal-to-noise ratio of the system. For the measurements described in the following, the bias voltage was held constant at 19.50 V.

B. Lasers

Lasers used in the present work were fabricated from conventional double-heterostructure material grown by liquid-phase epitaxy [11] under near-equilibrium conditions [12]. The four-layered wafers were composed of a thin layer of p-type GaAs (the active layer) sandwiched between p- and n-type layers of $Al_xGa_{1-x}As$. The $Al_xGa_{1-x}As$ layers contained between 24 and 36-percent Al, depending on the wafer. The active layers were 0.2–0.3 μm thick and doped with Ge to provide a hole concentration in the low 10^{17}-cm^{-3} range.

Stripe-geometry lasers were fabricated from the epitaxial wafers by proton bombardment [13]. The use of the stripe-geometry eliminates the complications inherent in broadly contacted diodes which oscillate in random filaments. All lasers had stripe widths nominally equal to 13 μm. In most cases, thick Au pads were plated on the p-side before cleaving. For efficient heatsinking, each laser was bonded to a metallized high-thermal-conductivity diamond mounted on a copper stud.

Laser current was provided either by a 6-V storage battery or by a commercial constant-current source. Within the experimental accuracy, both sources gave identical results.

III. Experimental Results

A. Amplitude-Stabilized Lasers

As reported previously [8], the frequency spectrum of the fluctuating light intensity from a GaAs junction laser operating above threshold contains a pronounced peak due to the excitation of the "spiking" resonance of the laser by quantum shot noise. At currents just above threshold, the frequency of this resonance is typically 200–500 MHz for 380-μm-long lasers. At frequencies below about 100 MHz, the spectrum has been observed [8] to be essentially flat, as expected theoretically [2], [4], [5]. Consequently, we can take measurements of the noise at a convenient frequency, such as 50 MHz, to be indicative of the behavior of the low-frequency plateau.

In some GaAs double-heterostructure lasers, a pronounced reduction in the low-frequency intensity noise occurs above threshold as predicted [2], [4], [5]. Such behavior was reported previously [8] for Si-doped lasers and is shown in Fig. 3 for one of the Ge-doped lasers studied in the present work. At currents below 75 mA, the relative intensity noise in the light polarized parallel to the junction plane (TE) is essentially independent of the current, or equivalently, the light intensity. This behavior indicates that the intensity fluctuations have the character of pure shot noise in this current range. As the current is increased above 75 mA, stimulated emission becomes an appreciable fraction of the TE intensity as indicated by the superlinear increase of the intensity shown in Fig. 3. Consequently, the relative noise increases abruptly with current until the threshold (91 mA) for amplitude-stabilized oscillation is reached. Further increases in current produce a rapid decrease of the relative noise back to its low-current value as the dynamic saturation of the gain effectively stabilizes the intensity fluctuations. The existence of regenerative oscillations in this diode was also confirmed by the existence of a sharp "knee" (at 88.5 mA) in the variation of the TE intensity with current (also shown in Fig. 3) and by observation of the longitudinal-mode spectrum. The spectrum of the total emission at a current well above threshold, as shown in Fig. 4, indicates that regenerative oscillation occurs in many longitudinal modes. As reported previously [8], the spectral observations do not define a precise value for the threshold current, since on the scale of 1-mA changes in the current there is no abrupt change in the spectrum.

On the other hand, over the entire current range, the relative noise in the intensity of the light polarized perpendicular to the junction plane (TM) remained approximately constant and

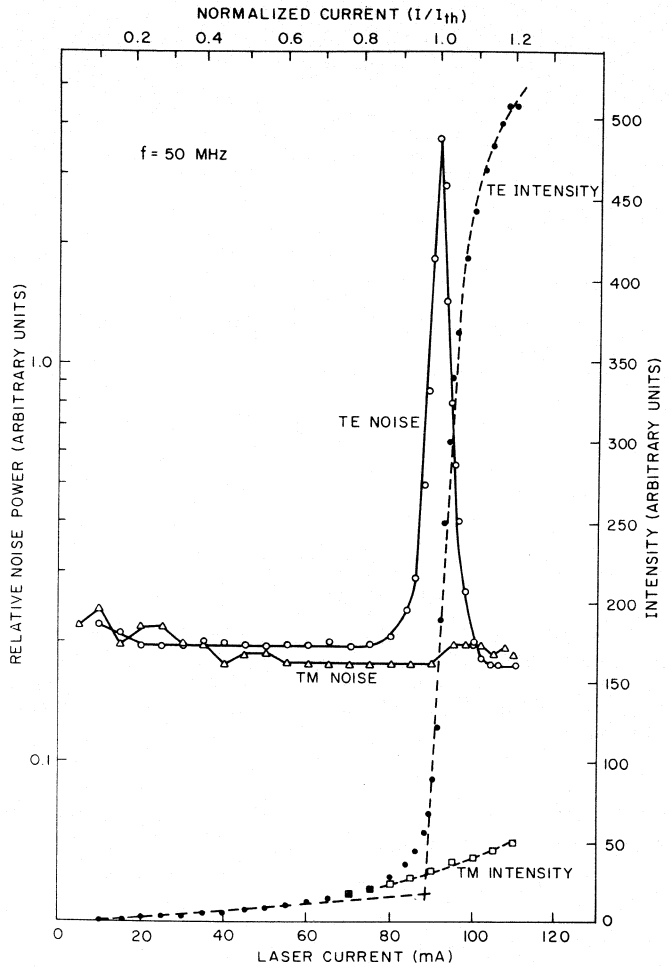

Fig. 3. Variation of the relative intensity noise for both TE and TM polarized light as a function of laser current. The noise power is measured in a 1-MHz interval centered at 50 MHz. Also shown are the variation of the intensities of the TE and TM light as a function of laser current.

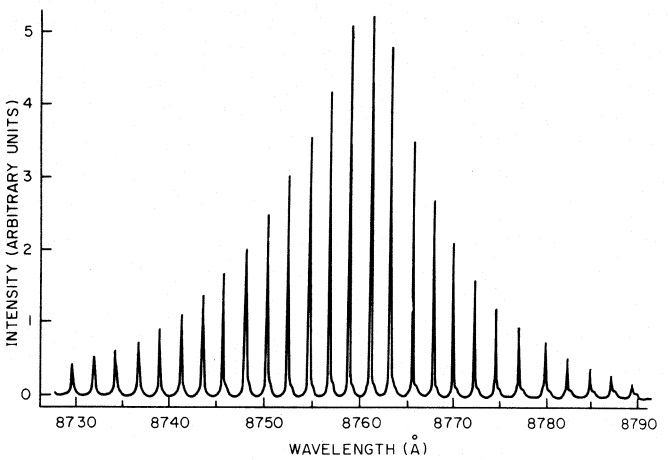

Fig. 4. The spectra of the total light intensity emitted by the same laser as used in Fig. 3. The operating current is 110 mA and corresponds to a point 20 percent above threshold where there is no observable excess noise in the TE intensity.

equal to the noise in the TE emission at low currents. This behavior indicates that the TM modes do not oscillate and, in fact, experience little gain narrowing of their linewidth. The subthreshold nature of these modes was confirmed by 1) the

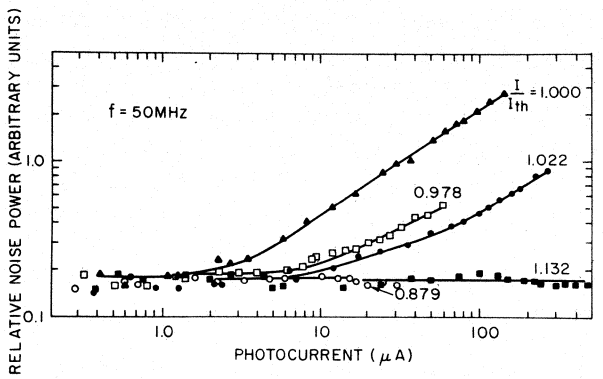

Fig. 5. Variation of the relative intensity noise at 50 MHz for TE polarized light as a function of laser intensity incident on the photodiode. For each curve the laser current is maintained constant equal to the value indicated by the respective label. The threshold current is taken as the current at which the relative noise is maximum in Fig. 3.

absence of a knee in the variation of their intensity with current, as shown in Fig. 3, and 2) the absence of deep nulls in their spectrum.

In the vicinity of threshold, the pronounced change in the character of the noise is readily observed in the variation of the relative noise power with photocurrent for different laser currents. By attenuating the laser intensity with neutral density filters, the experimental results shown in Fig. 5 were obtained for the laser of Fig. 3. At laser currents well below ($0.879\ I_{th}$) and well above ($1.132\ I_{th}$) threshold, the relative noise at 50 MHz is independent of the average light intensity which is incident on the detector. This behavior indicates that the intensity fluctuations at this frequency are pure shot noise. On the other hand, at threshold, just below ($0.978\ I_{th}$), and just above ($1.022\ I_{th}$), the relative noise decreases with decreasing incident intensity, indicating the presence of appreciable intensity-dependent excess noise. However, as the intensity is decreased to values where the excess noise becomes negligible, the relative noise becomes independent of photocurrent and equal to the value $(\alpha F)_{50\ \mathrm{MHz}} = 0.175 \pm 0.025$ established by the system response to pure shot noise. In principle, the shot-noise level αF can also be determined from the measurements made with the tungsten lamp as described in Section II-A. However, in practice the value obtained with the lamp was only about 65 percent of the value obtained with the lasers. This difference may be due to the larger detector area seen by the focused image of the lamp as compared to the laser. This conclusion is suggested by the agreement of the values for αF found with the junction lasers, spontaneously emitting diodes, and a He-Ne laser.

At laser currents where the excess noise is appreciable, the linearity of the behavior at high photocurrents shown in Fig. 5 suggests that the power spectrum of the intensity fluctuations is proportional to a power of the average intensity. The value of this exponent is obtained from the slope of a log-log plot of the excess noise, i.e., $S_{\mathrm{REL}}(f) - \alpha F = \eta\alpha P(\omega)/\langle N\rangle_t$ versus photocurrent. For the measurements at $I = 0.978\ I_{th}$, we find that $P(\omega)$ varies very nearly as $\langle N\rangle_{t,cc}^2$,[2] in agreement with

[2]The subscript *cc* indicates laser current is held constant.

the behavior expected for a noise amplifier operating with fixed gain [1]. For $I = 1.000\ I_{th}$, i.e., the current at which $S_{REL}(f)$ reaches its maximum value in Fig. 3, we find $P(\omega) \sim \langle N \rangle_{t,cc}^{1.85}$ which is close to the expected quadratic behavior.

A similar analysis of the excess noise as a function of increasing laser current indicates that below threshold $P(\omega)$ in this laser varies as $\langle N \rangle_t^{5.5}$.[3] However, at currents in the vicinity but below threshold where many identical modes are excited, $P(\omega)$ is expected [2] to increase as $\langle N \rangle_t^3$. This discrepancy suggests that the linearized theory as applied to many identical modes may not adequately describe the detailed variation of the noise in the subthreshold region. Above threshold, we find that the dependence of $P(\omega)$ on $\langle N \rangle_t$ cannot even be represented by a simple power, indicating clearly that quantitatively a single-mode theory of the intensity noise does not apply to the multimode laser intensity. However, a detailed comparison with the multimode theory [2] has not been undertaken due to our lack of knowledge of the modal parameters.

Although the intensity noise at 50 MHz shows the pronounced reduction expected of an amplitude-stabilized oscillator above threshold, the excess noise at frequencies above the resonance exhibits no such quieting. For example, Fig. 6 shows the variation of the relative noise $S_{REL}(f)$ in a 1-MHz bandwidth centered 200 MHz above and below 4 GHz[4] (a convenient frequency) as a function of laser current. At currents below threshold the behavior of the noise in the TE light near 4 GHz is similar to that at 50 MHz, i.e., the relative noise remains constant for currents up to 75 mA and then increases rapidly as the pump current approaches threshold. However, in marked contrast to the low-frequency fluctuations, the 4-GHz noise shows only a very small reduction as the current is increased just above threshold before continuing to increase anomalously with further increases in current. This anomalous increase in the high-frequency noise is qualitatively similar to that observed previously [8] with Si-doped double-heterostructure lasers. However, in the latter case, no evidence of any reduction was observed at threshold.

As shown in Fig. 6, the relative noise in the TM modes, which do not experience appreciable gain, remains approximately constant over the entire range of currents. The value of this constant 5.5 ± 0.5 coincides within the experimental accuracy with the value for the noise in the TE emission at low pumping. Additional measurements described in the next paragraph and others performed with LED's and a He-Ne laser indicate that the constant 5.5 ± 0.5 is the response of the detection system to shot noise, i.e., $(\alpha F)_{4\ GHz}$. However, as with the measurements at 50 MHz, $(\alpha F)_{4\ GHz}$ obtained this way is slightly greater than the value obtained with a tungsten lamp.

The characteristics of the noise near 4 GHz were also studied by varying with neutral-density filters the intensity of the TE emission incident on the detector. The resulting dependence

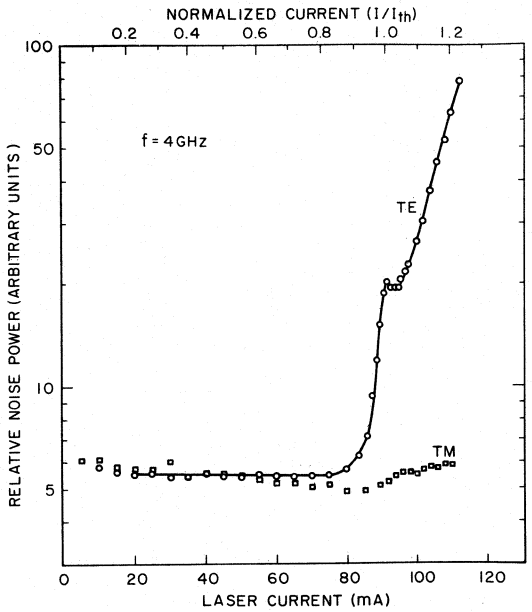

Fig. 6. Variation of the relative intensity noise in 1-MHz intervals centered 200 MHz above and below 4 GHz as a function of the laser current for the same laser as Figs. 3 and 4. For current normalization, threshold is taken as the current at which the relative noise is maximum in Fig. 3.

of the relative noise power on the photocurrent $\propto \langle N \rangle_{t,cc}$ is shown in Fig. 7 for several laser currents. At a current well below threshold ($0.879\ I_{th}$), the relative noise at 4 GHz remains constant $(\alpha F)_{4\ GHz} = 5.5 \pm 0.5$ with changes in the photocurrent, indicating pure shot noise. At higher laser currents, the relative noise decreases with decreasing incident intensity, indicating the presence of appreciable intensity-dependent excess noise. At low intensities where the excess noise is negligible, the relative noise again approaches the shot-noise value $(\alpha F)_{4\ GHz} = 5.5 \pm 0.5$ for each laser current.

Analysis of the excess noise at 4 GHz as a function of the incident intensity indicates that at constant laser current $P(\omega)$ varies as $\langle N \rangle_{t,cc}^m$. The exponent m is 1.90, 1.91, 1.93, and 1.84 at I/I_{th} equal to 1.000, 1.044, 1.132, and 1.209, respectively. The proximity of the values for m to 2 suggests that the excess noise even at a laser current where it is anomalously high is not substantially different from the noise obtained with an amplifier operating with unsaturated gain.

Further analysis of the excess noise as a function of increasing laser current suggests that $P(\omega)$ at 4 GHz in this laser varies as $\langle N \rangle_t^{4.85}$ over a limited range of currents below threshold. Above threshold, and especially in the range of anomalous excess noise, no simple dependence on $\langle N \rangle_t$ could be found for $P(\omega)$.

B. Unstabilized Lasers

Not all of the double-heterostructure lasers studied in this work show the characteristic quieting described in the previous section. In some lasers, the excess intensity noise at low frequencies is only partially reduced above threshold, as shown in Fig. 8. At best, the light intensity from this device is nearly twice as noisy when oscillating regeneratively as when operated as a purely spontaneous emitter. As indicated in

[3] Note that laser current is varied to obtain this dependence, hence the absence of the subscript *cc*.

[4] Signals at both 3.8 and 4.2 GHz are detected simultaneously when the local oscillator frequency is 4 GHz, since the IF frequency is 200 MHz.

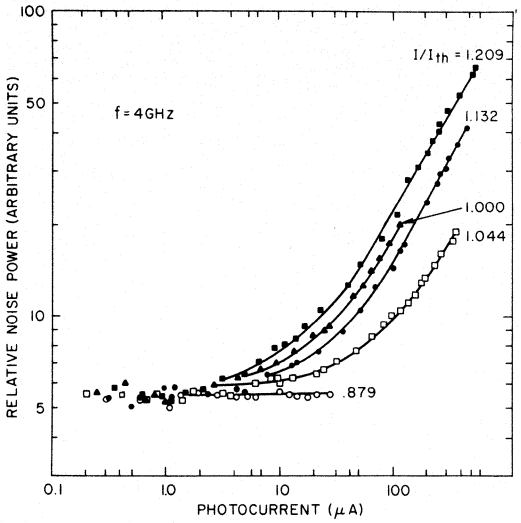

Fig. 7. Variation of the relative intensity noise near 4 GHz for TE polarized light as a function of laser intensity incident on the photodiode. For each curve the laser current is maintained constant.

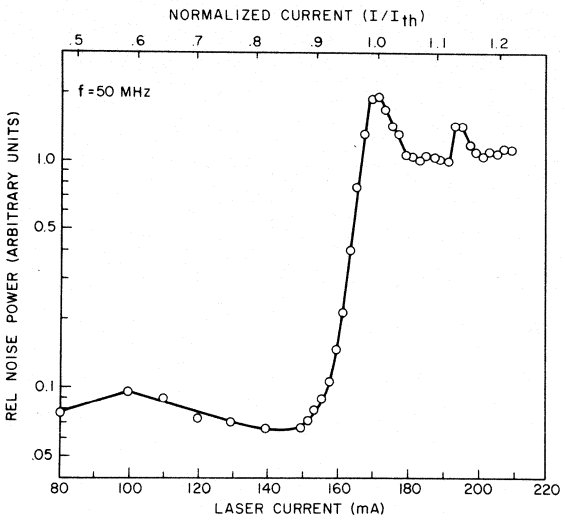

Fig. 9. Variation of the relative noise at 50 MHz for the TE emission as a function of laser current for another unstabilized laser.

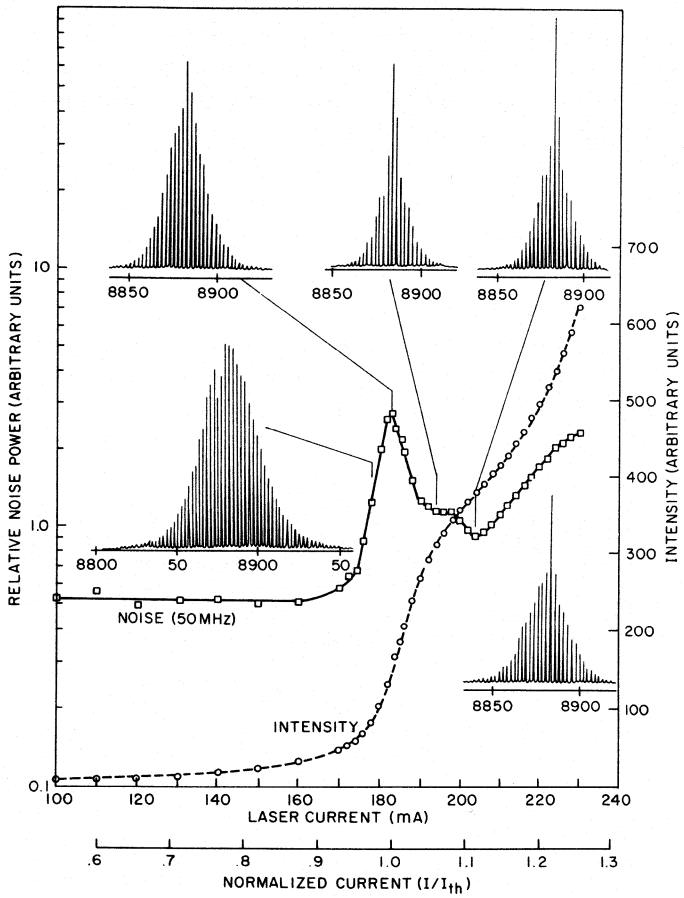

Fig. 8. Variation of the relative intensity noise at 50 MHz and the total intensity of the TE emission as a function of laser current for an unstabilized laser. The longitudinal mode spectra obtained at selected currents are also shown.

Fig. 8, the total intensity also departs from a linear dependence on pump current at the current where the relative noise stops decreasing. Similar "kinks" in the intensity-current relation have been reported previously [14], especially for lasers with stripe widths greater than 20 μm. At the present time, the exact cause of this nonlinear behavior is not known for certain and the number of diodes studied thus far is insufficient to determine whether it is always accompanied by incomplete stabilization of the intensity fluctuations.

In addition, as the current in this laser is increased more than 11 percent above threshold, the relative intensity noise also increases. This increase in the noise seems to be accompanied by a slight broadening of the overall spectrum on the short wavelength side, as indicated by the spectra shown in Fig. 8. Furthermore, high-resolution scans of each longitudinal mode show a loss of the fine structure associated with transverse modes of different spatial distribution along the junction plane [15]. The disappearance of the spectral fine structure on each longitudinal mode may indicate either a spectral broadening of the linewidth of the fundamental transverse mode or a decrease of the frequency interval between the transverse modes. The high-resolution spectra as well as visual observation of the far field also show no evidence for the onset of oscillation in a second filament.

The behavior of another laser for which only a partial reduction of the excess noise occurs is shown in Fig. 9. The fluctuations in the emission from this laser are of particular interest since regenerative oscillation occurred primarily in a single longitudinal mode, as indicated by the spectra of Fig. 10. Although single-mode lasers might be expected from earlier work [16] done at 4.2 K to be at least as quiet as multimode devices, this particular device is more than 10 times noisier above threshold than below. However, the high level of noise in this case is probably not a result of oscillation in a single mode. Another laser from the same wafer also showed a high level of excess noise above threshold but oscillated in many (7-10) longitudinal modes. Unfortunately, the small number of lasers available for testing has precluded determining whether this type of instability is symptomatic of a wafer or only of individual lasers. In addition, both lasers were about 8 mils long and the dependence of stabilization on laser length, if any, has not been determined. Finally, it is interesting to note that the slight perturbation in the noise level which

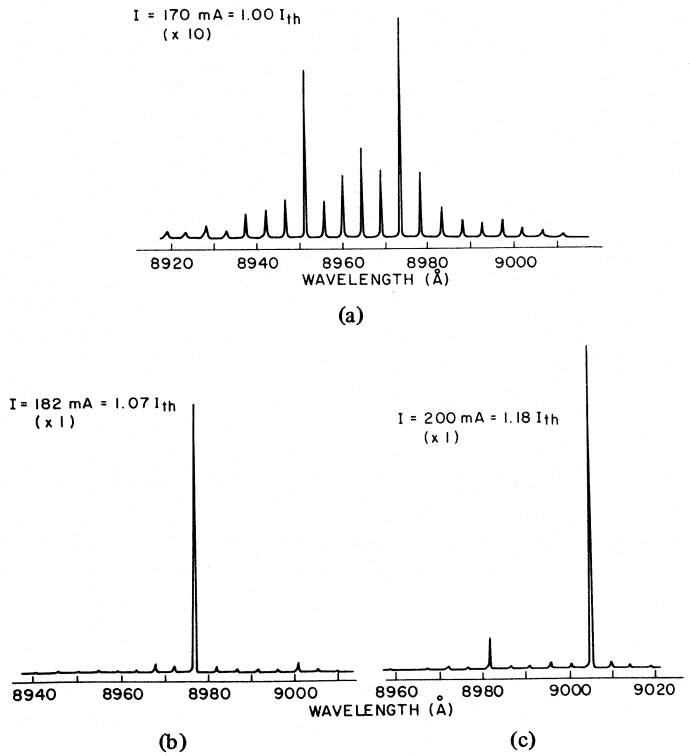

Fig. 10. Longitudinal mode spectra for the same laser as Fig. 9.

occurs between 190 mA and 200 mA was accompanied by a change in the oscillating longitudinal mode as shown in parts (b) and (c) of Fig. 10. However, further study is required to determine if this relation is significant or only coincidental.

IV. Conclusion

In this work we have investigated the noise fluctuations present in the total intensity of stripe-geometry GaAs-$Al_xGa_{1-x}As$ double-heterostructure junction lasers operating continuously at room temperature. The experimental results show that in some lasers stabilization of the low-frequency (50-MHz) fluctuations occurs at threshold. As predicted by McCumber [2], this stabilization of the total intensity occurs even when many longitudinal modes are oscillating regeneratively. In a well-stabilized laser, we have shown that the intensity fluctuations can be reduced to pure shot noise at pump levels as low as 10 percent above threshold. With additional measurements we have also demonstrated the effective elimination of the intensity-dependent excess noise during the transit of the threshold region.

In the same lasers, however, stabilization of high-frequency (4-GHz) fluctuations does not accompany the quieting observed at low frequencies. Although a slight reduction of the excess noise at 4 GHz is observed to occur at threshold, further increases in the level of the laser current above threshold cause the high-frequency noise to increase anomalously. At 20 percent above threshold, the noise level can be more than an order of magnitude greater than pure shot noise. At present, the precise source of this high noise level is not known. However, it is clear that such noise does not originate in a high-frequency disturbance of the population inversion, since nonlasing emission in the orthogonal polarization shows no increased noise. The lack of stabilization may indicate that for times shorter than about 0.5 ns the population inversion does not respond to the fluctuating intensity rapidly enough to provide effective quieting. Such an ineffective response could result from an unexpectedly long energy or spatial relaxation time. In addition, interactions between the fundamental and first-order transverse modes (along the junction plane) with the same longitudinal mode number may be important in determining the observed noise at 4 GHz, since the intermode spacing is about 5.5-6 GHz in these lasers. However, these and other possibilities require further study for clarification.

This initial investigation of the noise characteristics of room-temperature junction lasers has also demonstrated that many stripe-geometry lasers exhibit only a partial reduction of the low-frequency excess noise above threshold, resulting in a noise level which can be more than 10 times pure shot noise. Lasers with this behavior have been observed to oscillate in either many or primarily one longitudinal mode. No evidence was found to indicate that this type of instability was a result of competitive interactions between filaments. The exact cause of the ineffective stabilization has not been determined but is presently under investigation. In particular, the possibility that this instability is symptomatic of certain laser batches needs to be given serious consideration. The reproducibility of low-noise lasers remains an open but important question.

Acknowledgment

The author wishes to thank H. Melchior for useful discussions, C. J. Hwang, J. C. Dyment, and R. L. Hartman for providing the lasers, and B. C. De Loach, Jr., and L. A. D'Asaro for helpful comments on the manuscript.

References

[1] For a review of this early work, see J. A. Armstrong and A. W. Smith in *Progress in Optics*, vol. VI, E. Wolf, Ed. New York: Wiley, pp. 211–257, and references contained therein.
[2] D. E. McCumber, "Intensity fluctuations in the output of CW laser oscillators," *Phys. Rev.*, vol. 141, pp. 306–322, Jan. 1966.
[3] H. Haug and H. Haken, "Theory of noise in semiconductor laser emission," *Z. Phys.*, vol. 204, pp. 262–275, 1967.
[4] H. Haug, "Quantum-mechanical rate equations for semiconductor lasers," *Phys. Rev.*, vol. 184, pp. 338–348, Aug. 1969.
[5] D. J. Morgan and M. J. Adams, "Quantum noise in semiconductor lasers," *Phys. Status Solidi*, vol. 11, pp. 243–253, 1972.
[6] T. L. Paoli and J. E. Ripper, "Observation of intrinsic quantum fluctuations in semiconductor lasers," *Phys. Rev. A*, vol. 2, pp. 2551–2555, Dec. 1970.
[7] G. Guekos and M. J. O. Strutt, "Laser-light noise and current noise of GaAs CW laser diodes," *IEEE J. Quantum Electron.*, vol. QE-6, pp. 423–428, July 1970.
[8] T. L. Paoli, "Intrinsic fluctuations in the output intensity of double-heterostructure junction lasers operating continuously at 300°K," *Appl. Phys. Lett.*, vol. 24, pp. 187–190, Feb. 1974.
[9] For an excellent discussion of noise in photodiode, see H. Melchior, "Demodulation and photodetection techniques," in *Laser Handbook*, vol. I, F. T. Arecchi and E. O. Schulz-du Bois, Ed. Amsterdam, The Netherlands: North-Holland, 1972, pp. 725–835.
[10] C. Freed and H. A. Haus, "Photocurrent spectrum and photoelectron counts produced by a gas laser," *Phys. Rev.*, vol. 141, pp. 287–298, Jan. 1966.
[11] I. Hayashi, M. B. Panish, P. W. Foy, and S. Sumski, "Junction

lasers which operate continuously at room temperature," *Appl. Phys. Lett.*, vol. 17, pp. 109–111, Aug. 1970.
[12] L. R. Dawson, unpublished.
[13] J. C. Dyment *et al.*, "Proton-bombardment formation of stripe-geometry heterostructure lasers for 300 K CW operation," *Proc. IEEE* (Lett.), vol. 60, pp. 726–728, June 1972.
[14] J. C. Dyment, C. J. Hwang, and A. R. Hartman, "Dependence of threshold current density and differential quantum efficiency of the stripe width of proton-bombarded double heterostructure lasers," unpublished.
[15] T. H. Zachos and J. E. Ripper, "Resonant modes of GaAs junction lasers," *IEEE J. Quantum Electron.*, vol. QE-5, pp. 29–37, Jan. 1969.
[16] A. W. Smith and J. A. Armstrong, "Intensity noise in multimode GaAs laser emission," *IBM Syst. J.*, vol. 10, pp. 225–232, May 1966.

Microwave Switching by Picosecond Photoconductivity

A. M. JOHNSON AND D. H. AUSTON

Abstract—**Bulk photoconductivity produced by the absorption of picosecond optical pulses in silicon transmission-line structures has been used to switch and gate microwave signals. The technique permits the generation of microwave and millimeter-wave pulses as short as a single cycle, and requires only a few microjoules of optical energy. The basic features of the device are illustrated with switching experiments at 1 GHz and 10 GHz, and the results are discussed with reference to the physical properties of the high-density plasma responsible for the switching.**

I. Introduction

IN MANY CASES, both for experimental purposes and for applications, it is desirable to have a capability for generating very short bursts of microwave and millimeter-wave signals of relatively high power. The current state of the art, however, is limited to switching speeds of approximately 1 ns [1]. Furthermore, at these speeds, the semiconductor p-i-n diodes which are used for this purpose are limited to powers of a few tens of watts. In this paper, we describe a simple optical technique for switching microwave signals which offers a significant improvement of both speed and power handling.

Although bulk semiconductor plasmas have received considerable attention as microwave switching devices [2], the use of high-density, optically generated plasmas has not been given serious consideration. Aside from the obvious speed capability, picosecond optical pulses have the additional advantage of enabling the generation of extremely high-density plasmas without damaging the material. Longer optical pulses are less efficient since they tend to produce more heating, and consequently are more likely to cause damage. It has recently been demonstrated [3] that plasma densities in excess of 10^{20} cm^{-3} can be readily generated by the absorption of single-picosecond optical pulses in semiconductors. Plasmas such as these are highly degenerate and have quasi-metallic properties. Their high conductivities make them ideal for bulk switching applications. The research reported in this paper is an extension of related work [4] in which switching and gating of dc signals was achieved with solid-state plasmas produced by picosecond pulses.

Manuscript received December 9, 1974.

A. M. Johnson was with Bell Laboratories, Murray Hill, N.J. 07974. He is now at the Polytechnic Institute of New York, Brooklyn, N.Y. 11201.
D. H. Auston is with Bell Laboratories, Murray Hill, N.J. 07974.

II. Optoelectronic Microwave Switching

An example of a microwave switch which utilizes the photoconductivity produced by picosecond optical pulses is illustrated in Fig. 1. It consists of a 50-Ω microstrip transmission-line [5] structure fabricated on a high-resistivity silicon substrate. The microstrip line consists of a uniform aluminum ground plane on the bottom and a narrow strip for an upper conductor in which there is a gap. Input and output microwave signals are coupled to the silicon chip by 3-mm coaxial-to-microstrip launchers. In a typical application, one side of the device would be connected to a microwave-signal source and the other to a load or test instrument. The switching action is produced by two optical pulses; one in the green region of the spectrum at $\lambda = 0.53$ μm, which is used to turn on the switch, and the other in the infrared at $\lambda = 1.06$ μm, which turns it off. The absorption constant at $\lambda = 0.53$ μm in silicon is 8×10^3 cm^{-1}, and consequently the effect of absorbing a green pulse in the microstrip gap is to produce a thin surface

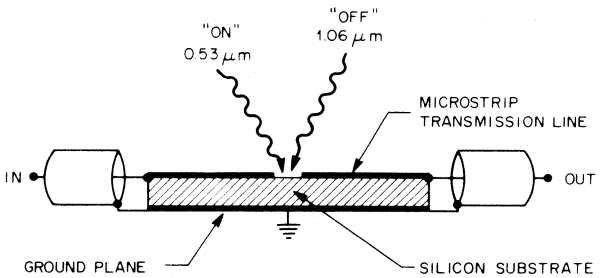

Fig. 1. An optoelectronic switch. The transmission of the switch is turned on by a surface layer of photoconductivity produced by the green pulse, and is turned off by volume photoconductivity produced by the infrared pulse, which shorts the device.

layer of conductivity across the gap. If it is sufficiently intense, the green pulse can close the gap by producing a net resistance which is much less than the characteristic impedance of the microstrip line, thus permitting efficient transmission of the microwave signal across the device.

To turn off the switch the infrared pulse is absorbed at the gap. In this case, however, the absorption depth is 1.4 mm, and consequently the pulse penetrates through the substrate to the ground plane, producing a region of high conductivity between the upper and lower conductors. This shorts the transmission line, preventing further transmission by totally reflecting the incident microwave signal. Unlike conventional semiconductor junction devices, this switch does not depend on recombination or carrier sweepout to turn off. The optically generated electrons and holes remain; the volume conductivity of the second pulse has merely annulled the effect of the surface layer of conductivity produced by the first pulse. Consequently, the switching speed can be extremely fast, being primarily limited by the durations of the optical pulses. Also the device is capable of handling moderately high microwave powers unlike conventional semiconductor switches which are limited by junction breakdown and thermal dissipation. Since the controlling signals are optical pulses, near-perfect isolation exists between the gated microwave signals and the gating signals. A disadvantage of this technique is the repetition rate, since carriers must recombine or be swept out before the switch can be used again. This aspect of the device is discussed in detail in Section VI.

The specific device illustrated in Fig. 1 consisted of a silicon slab of resistivity, $\rho = 10^4\ \Omega \cdot$ cm, measuring 1.5 X 1.5 X 0.043 cm, which was syton polished on both faces. The microstrip conductors were formed by evaporating 5000 Å of aluminum through a shadow mask, followed by a heat treatment of 10 min at 550°C in flowing N_2. The strip width was chosen to be 0.034 cm for a characteristic impedance Z_0 of 50 Ω. The size of the gap in a typical case was equal to the strip width.

The microstrip geometry is particularly suitable for the device since it is capable of supporting a quasi-TEM mode of low dispersion over very large bandwidths. This feature permits a single device to be used over a wide range of carrier frequencies and, more important, it enables it to handle extremely fast transients which may have bandwidths almost as large as the carrier frequency (e.g., when gating a single cycle, $\Delta f \simeq f_0$).

The optical pulse at 1.06 μm was generated by extracting a single pulse with a laser-triggered spark gap and Kerr cell from a train produced by a mode-locked Nd:glass laser (see Fig. 2). The 0.53-μm pulse was produced by second-harmonic generation in a 1-cm KDP crystal. These two pulses were then separated in a dichroic beamsplitter, the infrared pulse was delayed relative to the green pulse, and both pulses were focused onto the microstrip gap. From previous measurements the widths of the infrared and green pulses were estimated to be approximately 8 and 5 ps, respectively.

III. Experimental Results

To evaluate the performance of the switch, measurements were made at two microwave frequencies, 1 GHz and 10 GHz. The reason for using the low 1-GHz carrier frequency was simply to permit the direct observation of the gated waveshape on a high-speed oscilloscope without using a microwave detector. The low repetition rate of 3 pulses per minute of the Nd:glass laser prevented the use of a sampling oscilloscope. The input cable was connected directly to a 1-GHz oscillator of approximately 100-mW output power, and the gated output was connected directly to a fast oscilloscope of 1-GHz bandwidth (rise time was 0.3 ns). Green and infrared pulses of approximately 10 μJ each were used for switching. Typical results are shown in Fig. 3. In Fig. 3(a) a burst of approximately 8 cycles was generated by first turning on the switch with a green pulse and then turning it off with an infrared pulse delayed 8 ns. In Fig. 3(b), a delay of only 1 ns was used to produce a microwave pulse of a single cycle. The peak transmission through the gate was at least 95 percent, and no appreciable signal level was observed on the oscilloscope when the switch was in the off state both before and after the gating pulses.

To measure the response at 10 GHz a high-speed back-diode microwave detector in a 3-mm coaxial mount was used to rectify the output signal. The detector output was amplified in a pulse amplifier with a gain of 35 and displayed on the oscilloscope. The overall system time response of the detector-amplifier-oscilloscope combination was estimated to be 2.0 ns. Typical results are illustrated in Fig. 4. In Fig. 4(a) the effect of the green pulse is observed (the detector output signal was negative), showing a clean step with a rise time limited by the detection system. Fig. 4(b) shows the effect of the infrared pulse, which terminates the signal transmission in an equally

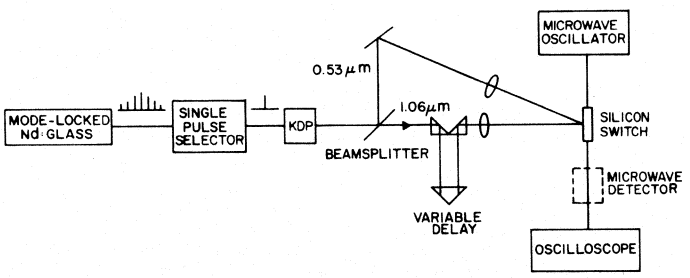

Fig. 2. Schematic diagram of the experiment. The silicon switch is the device illustrated in Fig. 1.

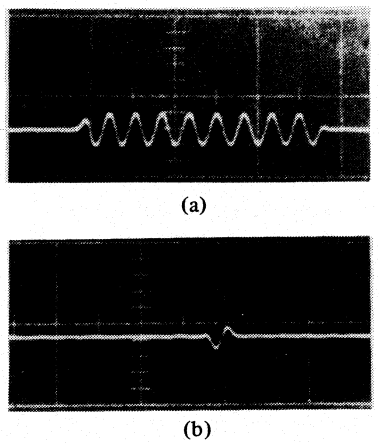

Fig. 3. Gating of a 1-GHz signal. The delay between the infrared and green pulses was approximately 8 ns in (a) and 1 ns in (b). (3 ns/div.)

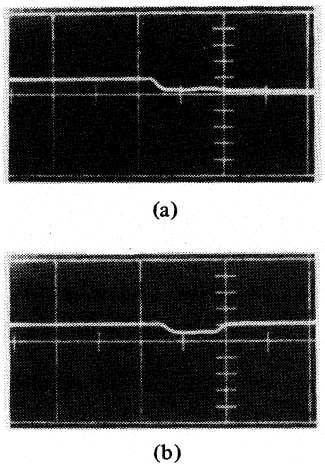

(a)

(b)

Fig. 4. Optoelectronic gating of a 10-GHz signal. The transmitted microwave signal was detected, amplified, and displayed on a fast oscilloscope (negative signal). In (a) the effect of the green pulse is seen to turn on the transmission, and in (b) the infrared turns it off. (10 ns/div.)

fast time. In this case, the delay between the infrared and green pulses was approximately 6 ns. The peak microwave power was approximately 25mW. These results are very reproducible, and no damage was observed to either the metallization or the silicon after many hundreds of shots.

At the time these experiments were performed, a high-power source of microwaves was not available, and consequently it was not possible to make a complete evaluation of the power-handling capabilities of the switch. The extreme broad-band feature of the device, however, permits us to obtain an estimate from dc power ratings. Constant voltages as large as 100 V have been applied without breakdown or excess heating. For a 50-Ω characteristic impedance this is equivalent to a microwave rating of 200-W CW. If the input signal is pulsed rather than continuous, even greater power ratings should be possible, perhaps as large as 1 kW.

While these preliminary results do not demonstrate the full speed capability of the switch, they do serve to adequately illustrate the basic features of the device. Related measurements [4] in which the switch was used to gate a dc signal clearly demonstrate that the ultimate switching speed can be comparable to the durations of the optical pulses, i.e., as short as 10 ps.

IV. Picosecond Photoconductivity

The response of the switch to the two optical pulses can be analyzed in the following straightforward manner. If recombination and trapping are neglected, the total number of electrons and holes produced in the crystal are each simply equal to the number of absorbed photons. For the case of the surface layer of conductivity produced by the green pulse, we find that the total conductance G_1 across a gap of length l is

$$G_1 = \frac{4n_r}{(n_r+1)^2}\left(\frac{e}{\hbar\omega}\right)(\mu_n+\mu_p)\frac{\mathcal{E}_1}{l^2} \tag{1}$$

where

n_r refractive index of the substrate;
$\hbar\omega/e$ photon energy in volts;
$\mu_n+\mu_p$ sum of electron and hole mobilities;
$\mathcal{E}_1$ energy of green pulse incident on the gap.

Expression (1) was obtained by integrating the conductivity over the exponential profile induced by the absorbed optical intensity. Typical plasma densities and conductivities can be as large as 10^{19}-10^{20} cm^{-3} and a few thousand $(\Omega\cdot\text{cm})^{-1}$, respectively. Collision frequencies of the degenerate solid-state plasma are typically in excess of 10^{12} Hz, and consequently the plasma is highly damped even in the millimeter-wave region. In spite of the high conductivities, the skin depth is greater than the thickness of the plasma layer in most cases of interest.

As an example, we consider a typical case, with the following choice of parameters: $n_r = 3.6$, $\hbar\omega/e = 2.34$ V, $(\mu_n+\mu_p) = 2000$ cm^{2}V^{-1}s^{-1}, $l = 0.034$ cm, and $Z_0 = 50\ \Omega$. The total conductance normalized to the characteristic admittance Z_0^{-1} of the transmission line is

$$G_1 Z_0 = 24/\mu\text{J}. \tag{2}$$

Hence 1 μJ or less should be adequate to provide efficient switching. Notice that the required optical energy for a fixed $G_1 Z_0$ varies as the square of the gap length.

The effect of the infrared pulse can be similarly analyzed. In this case, however, the longer absorption depth necessitates the inclusion of multiple optical reflections between the substrate surfaces. Summing these and integrating over the substrate thickness, the conductance G_2 connecting upper and lower conductors is

$$G_2 = \frac{2\alpha_2^2 n_r}{(n_r+1)^2}\,\frac{e^{-\alpha_2 h}}{\tan^{-1}(\sin h\alpha_2 h)}\left[1-\left(\frac{n_r-1}{n_r+1}\right)^2 e^{-2\alpha_2 h}\right]^{-1} \cdot \frac{e}{\hbar\omega}(\mu_n+\mu_p)\mathcal{E}_2 \tag{3}$$

where

α_2 absorption constant of the infrared pulse;
h substrate thickness;
$\mathcal{E}_2$ infrared pulse energy incident on the gap.

If the absorption depth is considerably larger than the substrate thickness, (3) reduces to the following simpler form:

$$G_2 \simeq \frac{2\alpha_2}{h}\frac{e}{\hbar\omega}(\mu_n+\mu_p)\mathcal{E}_2, \qquad \alpha_2 h \ll 1. \tag{4}$$

For example, with $\alpha_2 = 7$ cm^{-1}, $h = 0.043$ cm, and $\hbar\omega/e = 1.17$ V we find

$$GZ_0 = 8.7/\mu\text{J}. \tag{5}$$

Since the photoconductivity produced by the infrared pulse occupies a larger volume, the plasma density and conductivity are usually considerably less than in the case of the green pulse. Typical densities are 10^{16}-10^{17} cm^{-3} and conductivities 1-10 $(\Omega\cdot\text{cm})^{-1}$. At frequencies up to 10 GHz the skin depth corresponding to the conductivities is still greater than a fraction of a millimeter, and consequently the use of a lumped conductance to describe the infrared photoconductivity is justified. At higher frequencies and larger gap lengths, the detailed transmission properties of the plasma must be

considered. In both the infrared and green-produced plasmas, the conductivities are sufficiently large that the dielectric relaxation time, ϵ/σ, is 1 ps or less, and consequently does not affect the switching speed. Although the infrared pulse is somewhat less efficient than the green pulse in this specific example, it is clear that a few microjoules of infrared should produce an adequate shorting conductance.

The results of the experiments are generally in fair agreement with the theoretical estimates of the photoconductivity. Expressions (1) and (3) tend to underestimate the energy requirements somewhat, particularly in the case of the green pulses. The reason for this may in part be due to a reduction in carrier mobilities at high densities by degeneracy and electron-hole scattering. A more detailed study of photoconductivity at high excitation levels is in progress to determine the importance of these effects.

V. Microwave Transmission

The overall transmission coefficient of the device can be estimated by a simple model which characterizes the photoconductivity by series and parallel lumped-circuit elements in the microstrip transmission line. In addition to the conductances G_1 and G_2, derived in Section IV, it is necessary to account for the small displacement current across the gap due to the finite capacitance of the gap C_g, [6]. The following expressions determine the power-transmission coefficients in the three separate states of the switch:

$$\text{OFF: } T_0 = \frac{4[(G_g Z_0)^2 + (\omega Z_0 C_g)^2]}{(1 + 2Z_0 G_g)^2 + (2\omega Z_0 C_g)^2}, \qquad t < t_1 \quad (6)$$

$$\text{ON: } T_1 = \left| \frac{2G_1 Z_0}{1 + 2G_1 Z_0} \right|^2, \qquad t_1 < t < t_2 \quad (7)$$

$$\text{OFF: } T_2 = \left| \frac{2G_1 Z_0}{1 + 2G_1 Z_0 + G_2 Z_0 + G_1 G_2 Z_0^2} \right|^2, \qquad t_2 < t \quad (8)$$

where t_1 and t_2 are the times at which the green and infrared pulses are absorbed in the microstrip gap and G_g is the conductance of the gap in the absence of any optical pulses. For simplicity, we have assumed that the durations of the optical pulses are negligible compared to the gating period. As an example, we consider a typical case with $\mathcal{E}_1 = \mathcal{E}_2 = 10\ \mu\text{J}$, $C_g = 1.5 \times 10^{-14}$ F, $G_g = 10^{-5}\ \Omega^{-1}$. Using (2), (5), and (6)-(8), we find

$$\text{OFF: } T_0 = 8.9 \times 10^{-3} \text{ @ } 10 \text{ GHz } (-21 \text{ dB}), \qquad t < t_1$$

$$\text{ON: } T_1 = 0.996\ (-0.02 \text{ dB}), \qquad t_1 < t < t_2$$

$$\text{OFF: } T_2 = 5 \times 10^{-4}\ (-33 \text{ dB}), \qquad t_2 < t\,.$$

The use of a larger infrared energy would clearly further reduce the transmission T_2. To improve T_0, it is necessary to either reduce the overall geometry of the switch or increase the gap length, or both. The latter case, of course, will increase the optical-energy requirements.

VI. Recombination

Recombination of the optically generated electrons and holes is clearly an important feature of the device, since the photoconductivity must decay before the device can be used again. Preliminary measurements indicate that the principal recombination mechanism is band-to-band Auger [7] recombination. This is a nonradiative process whereby an electron and a hole recombine and give their energy to a third particle, which can be either an electron or a hole, instead of emitting a photon. In an intrinsic plasma the Auger recombination rate is proportional to the cube of the density, and consequently is expected to be dominant in high-density plasmas such as those produced by picosecond pulses. Radiative recombination in silicon is insignificant. For the case of the surface photoconductivity produced by the green pulse, integration of the Auger rate equation, neglecting diffusion, predicts the following time decay of the conductance G_1:

$$G_1(t) = G_1(0) \frac{1}{\sqrt{t/\tau}} \log\left[\sqrt{t/\tau} + \sqrt{1 + t/\tau}\right] \quad (9)$$

where $\tau = (2n_0^2 \gamma_3)^{-1}$, n_0 is the initial plasma density, and γ_3 is the rate constant in the Auger equation $\partial n/\partial t = -\gamma_3 n^3$. Preliminary measurements of the decay of G_1 show reasonably good agreement with the general features of (9), particularly in the initial stages of the decay. Depending on the excitation level, the conductance decayed to one-half its initial value in anywhere from 10 to 100 ns, in typical cases, depending on the excitation level. At longer times, however, recombination appeared to proceed somewhat faster than (9) would predict, probably due to the influence of traps which were too few in number to appreciably affect the decay at higher densities. Diffusion and sweepout can also affect the decay rate. The overall time for the transmission due to G_2 alone to decay to a percent was approximately 1 μs.

The repetition rate imposed by the rather slow recombination is a distinct disadvantage for a practical device. Fortunately, there are a number of relatively straightforward measures that can be taken to greatly improve the rate. For example, the addition of gold to silicon is known [8] to reduce carrier lifetimes to a few nanoseconds. Also the use of other substrate materials, such as GaAs, which have much faster intrinsic recombination rates could potentially increase the repetition rate to 1 GHz.

VII. Summary

We have described a simple optoelectronic switch for microwave applications in which the switching action is controlled by picosecond optical pulses. The device has a potential for switching relatively high-power microwave and millimeter signals with an ultimate time precision limited by the optical pulse durations. The basic features of the device were illustrated by switching 1-GHz and 10-GHz signals. In both cases, the observed response times were limited by the resolution of available microwave detection techniques. The physical properties of the plasma generation and recombination are reason-

ably well understood, although further study is needed to elucidate the details of the conduction process at very high carrier densities, and the dynamics of the recombination.

ACKNOWLEDGMENT

The authors wish to thank P. LeFur for his technical assistance.

REFERENCES

[1] M. C. Young, H. N. Prinson, R. J. Blum, and B. R. Tripp, "A nanosecond *X*-band switch," *Proc. IEEE* (Lett.), vol. 55, pp. 2185–2187, Dec. 1967.
[2] K. E. Mortenson, A. L. Armstrong, J. M. Borrego, and J. F. White, "A review of bulk semiconductor microwave control components," *Proc. IEEE* (*Special Issue on Microwave Semiconductors*), vol. 59, pp. 1191–1200, Aug. 1971.
[3] D. H. Auston and C. V. Shank, "Picosecond ellipsometry of transient electron-hole plasmas in germanium," *Phys. Rev. Lett.*, vol. 32, pp. 1120–1123, 1974.
[4] D. H. Auston, "Picosecond optoelectronic switching and gating in silicon," *Appl. Phys. Lett.*, vol. 26, pp. 101–103, 1975.
[5] See, for example, M. V. Schneider, "Microstrip lines for microwave integrated circuits," *Bell Syst. Tech. J.*, vol. 48, pp. 1421–1444, 1969.
[6] V. Rahmat-Samii, T. Itoh, and R. Mittra, "A spectral domain analysis for solving microstrip discontinuity problems," *IEEE Trans. Microwave Theory Tech.*, vol. MTT-22, pp. 372–378, Apr. 1974.
[7] L. Huldt, "Band to band Auger recombination in indirect gap semiconductors," *Phys. Status Solidi*, vol. 8, pp. 173–187, 1971.
[8] W. M. Ballis, "Properties of gold in silicon," *Solid-State Electron.*, vol. 9, pp. 143–168, 1966.

Effects of Focusing on Third-Order Nonlinear Processes in Isotropic Media

GARY C. BJORKLUND, MEMBER, IEEE

Abstract—**A theoretical analysis of third-order nonlinear interactions of focused laser beams is performed for the processes $\omega_1 + \omega_2 + \omega_3 \rightarrow \omega_4$, $\omega_1 + \omega_2 - \omega_3 \rightarrow \omega_4$, and $\omega_1 - \omega_2 - \omega_3 \rightarrow \omega_4$. The total power and far-field beam profile of the generated radiation is related to the total powers of the fundamental beams, to the tightness and location of the focus, and to the value of the difference between the wave vectors of the generated radiation and driving polarization. The optimum degree of wave-vector mismatch as a function of tightness and location of focus is determined for each of the three processes. The process $\omega_1 + \omega_2 - \omega_3 \rightarrow \omega_4$ is found to be unique in that it is always optimized by focusing as tightly as possible. Experimental results, which verify the theory for the processes $\omega_1 + \omega_2 + \omega_3 \rightarrow \omega_4$ and $\omega_1 + \omega_2 - \omega_3 \rightarrow \omega_4$, are presented.**

I. INTRODUCTION

THIRD-ORDER nonlinear processes in isotropic media have recently been utilized for efficient frequency tripling of high-power laser radiation [1], [2], for the production of tunable [3], [4] and fixed-frequency [5], [6] coherent vacuum ultraviolet (VUV) radiation, for up-conversion of infrared (IR) radiation [7], [8], for the production of tunable IR radiation [9], and for coherent anti-Stokes Raman spectroscopy [10]–[13]. These processes involve frequency sum and/or difference mixing between as many as three different fundamental frequencies. In order to achieve the high-power densities required by these processes without damaging the windows of the cell containing the nonlinear medium, it is often necessary to focus the fundamental beams tightly enough to produce a depth of focus small in comparison to the cell length. Focusing in this manner dramatically alters the form of the functional dependence of the efficiencies on the mismatch between the wave vectors of the generated radiation and driving polarization.

This paper presents a theoretical and experimental investigation of the effects of focusing on the processes $\omega_1 + \omega_2 + \omega_3 \rightarrow \omega_4$, $\omega_1 + \omega_2 - \omega_3 \rightarrow \omega_4$, and $\omega_1 - \omega_2 - \omega_3 \rightarrow \omega_4$. The optimum values of the wave-vector mismatch Δk (defined as the wave vector of the generated radiation minus the wave vector of the driving polarization) are found to depend on the tightness and location of the focus. In the case of very tight focusing with the fundamental beam-waist region entirely contained within the cell, efficient generation can be achieved only for restricted values of Δk. It is shown that Δk must be nonzero and negative for the process $\omega_1 + \omega_2 + \omega_3 \rightarrow \omega_4$ and that Δk must be nonzero and positive for the process $\omega_1 - \omega_2 - \omega_3 \rightarrow \omega_4$. Given a nonlinear medium with dispersion characteristics proper to produce the correct sign for Δk, each of these processes can be optimized by varying the tightness of focus. The process $\omega_1 + \omega_2 - \omega_3 \rightarrow \omega_4$ is found to be unique in that it can always be optimized by varying the tightness of

Manuscript received December 11, 1974. This research was supported by the Advanced Research Projects Agency, U.S. Department of Defense (monitored by the ONR under Contract N00014-67-A-0112-0086) and by the National Aeronautics and Space Administration.

The author was with the Microwave Laboratory, Stanford University, Stanford, Calif. 94305. He is now with Bell Laboratories, Holmdel, N.J. 07733.

focus, regardless of the dispersion characteristics of the nonlinear medium.

These focusing effects arise from the well-known phase shift of π rad which occurs as a beam traverses the region of the focus. This phase shift also affects the driving polarization and, except for the process $\omega_1 + \omega_2 - \omega_3 \rightarrow \omega_4$, introduces a slip in phase between the driving polarization and the generated radiation. Destructive interference between portions of the generated radiation arising from different locations in the cell will result unless this slip in phase is compensated by a wave-vector mismatch of the proper sign.

In the following sections, a rigorous theoretical analysis is used to derive expressions which relate the total power and far-field beam profile of the generated radiation to the total powers of the fundamental beams, to the tightness and location of focus of these beams relative to the dimensions of the cell, and to the value of the wave-vector mismatch. Numerical evaluations of these expressions are presented for a wide variety of cases. Procedures for the optimization of the total generated power are discussed. Experimental results, which verify some aspects of the theory, are presented.

It should be noted that the effects of focusing in the case of third-harmonic generation in isotropic media have been previously considered by Miles and Harris [1] and by Ward and New [14]. The rigorous theoretical analysis of this paper is an extension of the work of Ward and New and of Kleinman *et al.* [15].

II. Theory

In this section expressions are developed for the total output power and beam shape of the generated radiation produced by the four-wave mixing processes $\omega_1 + \omega_2 + \omega_3 \rightarrow \omega_4$, $\omega_1 + \omega_2 - \omega_3 \rightarrow \omega_4$, and $\omega_1 - \omega_2 - \omega_3 \rightarrow \omega_4$. The basic approach is to specify the spatial variation of the driving polarization, perform a Fourier decomposition of the driving polarization into plane-wave components, calculate the generated radiation field arising from each such component, and then to determine the total generated field by summing the contributions of all of these components.

The fundamental beams at ω_1, ω_2, and ω_3 are assumed to be lowest order Gaussian modes which propagate concentrically along the z axis with identical waist locations and identical confocal beam parameters. If the wave vectors of these beams in the nonlinear medium are taken as k_1, k_2, and k_3, respectively, and if the electric-field amplitudes are taken as $\boldsymbol{E}_{10}$, $\boldsymbol{E}_{20}$, and $\boldsymbol{E}_{30}$, respectively, then the fundamental electric field is given by

$$\boldsymbol{E}(r, t) = \text{Re}\,[\boldsymbol{E}_1(r)\exp(-i\omega_1 t) + \boldsymbol{E}_2(r)\exp(-i\omega_2 t) + \boldsymbol{E}_3(r)\exp(-i\omega_3 t)] \quad (1)$$

with $\boldsymbol{E}_n$, where $n = 1, 2$, or 3, given by the theory of Boyd and Gordon [16] as

$$\boldsymbol{E}_n(r) = \boldsymbol{E}_{n0}\exp(ik_n z)(1 + i\&)^{-1} \cdot \exp[-k_n(x^2 + y^2)/b(1 + i\&)]. \quad (2)$$

In (2), b is the confocal parameter, defined by

$$b = \frac{2\pi\omega_0^2}{\lambda} = \frac{2\pi\omega_0^2 n}{\lambda_0} = \frac{2\lambda_0}{n\theta^2} = k\omega_0^2 \quad (3)$$

where ω_0 is the beam-waist radius, n is the index of refraction, λ_0 is the vacuum wavelength, and θ is the far-field diffraction half-angle. & is a normalized coordinate along the z axis, defined as

$$\& = \frac{2(z - f)}{b} \quad (4)$$

where f is the position of the focus (beam waist) along the z axis.

If the fundamental and generated beams are all assumed to be linearly polarized in the same direction, the vector nature of the electric fields as well as the tensor nature of the nonlinear susceptibility may be neglected, and the driving polarization at ω_4 is given by

$$P_4(r, t) = \text{Re}\,[P_4(r)\exp(-i\omega_4 t)] \quad (5)$$

where

$$P_4(r) = \begin{cases} \frac{3}{2}N\chi(-\omega_4;\omega_1,\omega_2,\omega_3)E_1(r)E_2(r)E_3(r), \\ \qquad (\text{for } \omega_1 + \omega_2 + \omega_3 \rightarrow \omega_4) \\ \frac{3}{2}N\chi(-\omega_4;\omega_1,\omega_2,-\omega_3)E_1(r)E_2(r)E_3^*(r), \\ \qquad (\text{for } \omega_1 + \omega_2 - \omega_3 \rightarrow \omega_4) \\ \frac{3}{2}N\chi(-\omega_4;\omega_1,-\omega_2,-\omega_3)E_1(r)E_2^*(r)E_3^*(r), \\ \qquad (\text{for } \omega_1 - \omega_2 - \omega_3 \rightarrow \omega_4) \end{cases} \quad (6)$$

with χ the nonlinear susceptibility per atom and N the number density of atoms of the nonlinear medium. (When two or three of the input frequencies are degenerate, the factor of $\frac{3}{2}$ in (6) must be changed to $\frac{3}{4}$ or $\frac{1}{4}$, respectively.)

The nonlinear medium is considered to occupy the semi-infinite space $z > 0$, with the space $z < 0$ considered to be a vacuum. Then from (2) and (6), for the process $\omega_1 + \omega_2 + \omega_3 \rightarrow \omega_4$, the driving polarization at ω_4 is given by

$$P_4(r) = \frac{3}{2}N\chi(-\omega_4;\omega_1,\omega_2,\omega_3)E_{10}E_{20}E_{30} \times \exp(ik'z)(1 + i\&)^{-3}\exp\left[\frac{-k'(x^2 + y^2)}{b(1 + i\&)}\right]B(z) \quad (7)$$

where k', the wave vector of the driving polarization, is given by

$$k' = k_1 + k_2 + k_3 = k'' \quad (8)$$

and where

$$B(z) = \begin{cases} 1, & z > 0 \\ 0, & z < 0. \end{cases} \quad (9)$$

Similarly, for the process $\omega_1 + \omega_2 - \omega_3 \rightarrow \omega_4$,

$$P_4(r) = \frac{3}{2} N\chi(-\omega_4; \omega_1, \omega_2, -\omega_3) E_{10} E_{20} E_{30} B(z) \times \exp(ik'z)(1 + i\xi)^{-2}(1 - i\xi)^{-1} \times \exp\left[\frac{(-k'' + i\xi k')(x^2 + y^2)}{b(1 + \xi^2)}\right] \quad (10)$$

where k' is now defined as

$$k' = k_1 + k_2 - k_3 \quad (11)$$

and k'' is defined as before.

Finally, for the process $\omega_1 - \omega_2 - \omega_3 \rightarrow \omega_4$

$$P_4(r) = \frac{3}{2} N\chi(-\omega_4; \omega_1, -\omega_2, -\omega_3) E_{10} E_{20} E_{30} B(z) \times \exp(ik'z)(1 + i\xi)^{-1}(1 - i\xi)^{-2} \times \exp\left[\frac{(-k'' + i\xi k')(x^2 + y^2)}{b(1 + \xi^2)}\right] \quad (12)$$

where k' is now defined as

$$k' = k_1 - k_2 - k_3 \quad (13)$$

and k'' is defined as before.

The next step is to perform a Fourier decomposition of $P_4(r)$ to determine the amplitudes of the plane-wave components of the driving polarization. $P_{4(K)}$, the amplitude of the plane-wave component with wave vector K, is defined by

$$P_{4(K)} = (2\pi)^{-3} \int_{-\infty}^{\infty} dx'' \int_{-\infty}^{\infty} dy'' \int_{-\infty}^{\infty} dz'' P_4(r'') \times \exp(-iK \cdot r''). \quad (14)$$

$E_{4(K)}(r)$ the generated radiation field arising from the plane-wave component of the driving polarization with wave vector K, and $P_{4(K)}$ can be shown by Maxwell's equations to be related by

$$\nabla \times \nabla \times E_{4(K)}(r) - k_4^2 E_{(K)}(r) = 4\pi k_0^2 P_{4(K)} \exp(iK \cdot r) \quad (15)$$

where k_4 and k_0 are the wave vectors of the generated radiation in the nonlinear medium and in vacuum, respectively. Equation (15) may be solved subject to the boundary condition that the tangential component of $E_{4(K)}$ vanish at the vacuum-medium interface. For $K_x, K_y \ll K_z$ and $|K| - k_4 \ll |K|, k_4$ Kleinman [17] has shown that

$$E_{4(K)}(r) = i[2\pi k_0^2 z/k_4]\, g(U_K) \exp(iK \cdot r) P_{4(K)} \quad (16)$$

with

$$U_K = iz[K_z - k_4 + (K_x^2 + K_y^2)/2k_4] \quad (17)$$

and

$$g(x) = [1 - \exp(-x)]/x = \int_0^1 \exp(-xp)\, dp. \quad (18)$$

The wave-vector mismatch Δk is defined by the relation

$$\Delta k = k_4 - k'. \quad (19)$$

This choice of sign for Δk is opposite from that of Ward and New [14] but consistent with Miles and Harris [1].

The substitutions $k_4 = k' + \Delta k$ and $p = -\frac{1}{2} b(\xi' - \xi)/z$ may be performed in (17) and (18) to yield (assuming $\Delta k \ll k_4, k'$)

$$g(U_K) = \left(\frac{b}{2z}\right) \int_{-\zeta}^{\xi} d\xi' \times \exp\{ib[K_z - k' + (K_x^2 + K_y^2)/2k' - \Delta k] \times (\xi' - \xi)/2\} \quad (20)$$

where $\xi = 2(z - f)/b$ and $\zeta = 2f/b$.

The total generated electric field $E_4(r)$ is derived by combining the $E_{4(K)}(r)$

$$E_4(r) = \int_{-\infty}^{\infty} dK_x \int_{-\infty}^{\infty} dK_y \int_{-\infty}^{\infty} dK_z E_{4(K)}(r) \quad (21)$$

where $E_{4(K)}(r)$ is defined by (16), (20), and (14).

These integrals may be evaluated by first integrating over K_z to yield the factor $\delta(z'' - z)$, then integrating over z'', and finally integrating over x'', y'', K_x, and K_y by means of the formula [15]

$$\int_{-\infty}^{\infty} \exp[-iqx - isx^2]\, dx = (\pi/is)^{1/2} \exp(iq^2/4s), \quad \mathrm{Im}(s) < 0. \quad (22)$$

For $\omega_1 + \omega_2 + \omega_3 \rightarrow \omega_4$, the result is

$$E_4(r) = i\frac{3N}{2k_4} \pi k_0^2 b\chi(-\omega_4; \omega_1, \omega_2, \omega_3) E_{10} E_{20} E_{30} \times \exp(ik'z)(1 + i\xi)^{-1} \times \exp\left[\frac{-k'(x^2 + y^2)}{b(1 + i\xi)}\right] \times \int_{-\zeta}^{\xi} \frac{\exp[-(ib/2)\Delta k(\xi' - \xi)]}{(1 + i\xi')^2} d\xi' \quad (23)$$

while for $\omega_1 + \omega_2 - \omega_3 \rightarrow \omega_4$

$$E_4(r) = i\frac{3N}{2k_4} \pi k_0^2 b\chi(-\omega_4; \omega_1, \omega_2, -\omega_3) E_{10} E_{20} E_{30} \times \exp(ik'z) \times \int_{-\zeta}^{\xi} d\xi' \times \frac{\exp[-(ib/2)\Delta k(\xi' - \xi)]}{(1 + i\xi')(k'' - ik'\xi')H} \exp\left[\frac{-(x^2 + y^2)}{bH}\right] \quad (24)$$

and for $\omega_1 - \omega_2 - \omega_3 \rightarrow \omega_4$

$$E_4(r) = i\frac{3N}{2k_4}\pi k_0^2 b\chi(-\omega_4;\omega_1,-\omega_2,-\omega_3)E_{10}E_{20}E_{30} \times \exp(ik'z) \times \int_{-\xi}^{\xi} d\xi' \times \frac{\exp[-(ib/2)\Delta k(\xi'-\xi)]}{(1-i\xi')(k''-ik'\xi')H} \exp\left[\frac{-(x^2+y^2)}{bH}\right]. \quad (25)$$

k' is defined by (8), (11), and (13) in (23)-(25), respectively. k'' is always given by (8) and the function H is defined by

$$H = H(\xi,\xi') = \frac{(1+\xi'^2)}{(k''-ik'\xi')} - i\frac{(\xi'-\xi)}{k'}. \quad (26)$$

If the nonlinear medium is contained in a cell of length L with input window located at $z = 0$ and with the location of the focus at $z = f$, then (23)-(25), with $\xi = 2(L-f)/b$, $z = L$, and $\zeta = 2f/b$, completely describe the amplitude of the generated field at the plane of the output window. The functional dependence of the field distribution upon the transverse coordinates x and y scales with the value of k', b, and ξ.

It can be seen from (23) that for the process $\omega_1 + \omega_2 + \omega_3 \rightarrow \omega_4$, $E_4(r)$ is always a lowest order Gaussian mode with the same confocal parameter and waist location as the input beams. However, (24) and (25) show that for the processes $\omega_1 + \omega_2 - \omega_3 \rightarrow \omega_4$ and $\omega_1 - \omega_2 - \omega_3 \rightarrow \omega_4$, $E_4(r)$ is not in general a single Gaussian mode except when $k'' = k'$. The multimode output of the difference-mixing processes may be explained as resulting from a mismatch between the size of the driving polarization beam waist and the size of the generated radiation beam waist which would correspond to the confocal parameter of the input beams. This mismatch may be represented by the ratio k''/k'. When $k''/k' = 1$, these beam waists are of the same size, and a lowest order Gaussian beam with the same confocal parameter and waist location as the input beams can be produced. The sum-mixing process $\omega_1 + \omega_2 + \omega_3 \rightarrow \omega_4$ always has $k''/k' = 1$ and thus always produces a lowest order Gaussian beam output.

For all three mixing processes it may be seen that $E_4(r)$ is circularly symmetrical about the z axis and that the total generated power at ω_4 is thus obtained by performing integrals of the form

$$\int_0^\infty 2\pi R\,|E_4(R)|^2\,dR \quad (27)$$

where $R = (x^2+y^2)^{1/2}$ and $z = L$. It is convenient to define the dimensionless functions $F_j(b\Delta k, b/L, f/L, k''/k')$ by the relations

$$F_j\left(b\Delta k, \frac{b}{L}, \frac{f}{L}, \frac{k''}{k'}\right) = \frac{8}{9}\frac{k_4^2 k'}{\pi^3 k_0^4}\frac{1}{b^3\chi^2|E_{10}E_{20}E_{30}|^2} \times \int 2\pi R|E_4(R)|^2\,dR \quad (28)$$

where $j = 1$, 2, or 3 implies $\omega_1 + \omega_2 + \omega_3 \rightarrow \omega_4$, $\omega_1 + \omega_2 - \omega_3 \rightarrow \omega_4$, or $\omega_1 - \omega_2 - \omega_3 \rightarrow \omega_4$. Although the spatial distribution of $E_4(r)$ depends upon the value and units of k' and b, the integrated intensity represented by the F_j depends only on the dimensionless parameters $b\Delta k$, b/L, f/L, and k''/k'.

With all wave vectors expressed in units of cm^{-1}, b in centimeters, N in atoms/cubic centimeters, χ in ESU per atom, and with total power in watts, the total generated power $\mathcal{P}_4$ is given by

$$\mathcal{P}_4 = (6.318\times10^{-4})\frac{k_0^4 k_1 k_2 k_3}{k_4^2 k'}N^2\chi^2\,\mathcal{P}_1\,\mathcal{P}_2\,\mathcal{P}_3 \times F_j\left(b\Delta k, \frac{b}{L}, \frac{f}{L}, \frac{k''}{k'}\right) \quad (29)$$

where $\mathcal{P}_1$, $\mathcal{P}_2$, and $\mathcal{P}_3$ are the total powers of each of the fundamental beams. (When two or three of the input frequencies are degenerate, the factor of 6.318×10^{-4} in (29) must be changed to 1.580×10^{-4} or 1.755×10^{-5}, respectively.)

For the process $\omega_1 + \omega_2 + \omega_3 \rightarrow \omega_4$

$$F_1\left(b\Delta k, \frac{b}{L}, \frac{f}{L}, \frac{k''}{k'}\right) = \left|\int_{-\xi}^{\xi} d\xi \frac{\exp[-(ib/2)\Delta k\xi']}{(1+i\xi')^2}\right|^2. \quad (30)$$

Thus $F_1(b\Delta k, b/L, f/L, 1)$ is equivalent to the quantity $|I(3,\Delta k,\xi,\zeta)|^2$ as defined by Ward and New [14] (who define Δk with the opposite sign). In the tight-focusing limit where b is short compared to the cell, and the entire focal region is contained within the cell ($\xi, \zeta \rightarrow \infty$), the integral may be solved in closed form to yield

$$F_1(b\Delta k, 0, 0.5, 1) = \begin{cases} \pi^2(b\Delta k)^2\exp[b\Delta k/2), & \text{for } \Delta k < 0 \\ 0, & \text{for } \Delta k \geqslant 0. \end{cases} \quad (31)$$

For the process $\omega_1 + \omega_2 - \omega_3 \rightarrow \omega_4$

$$F_2\left(b\Delta k, \frac{b}{L}, \frac{f}{L}, \frac{k''}{k'}\right) = \frac{2k'}{\pi b}\int_0^\infty 2\pi R\,dR \times \left|\int_{-\xi}^{\xi} d\xi' \frac{\exp[-(ib/2)\Delta k\xi']}{(1+i\xi')(k''-ik'\xi')H} \times \exp\left[\frac{-R^2}{bH}\right]\right|^2 \quad (32)$$

with H defined by (26) and k' and k'' defined by (8) and (11). In the tight-focusing limit and in the case $k'' = k'$

$$F_2(b\Delta k, 0, 0.5, 1) = \pi^2\exp[-b|\Delta k|]. \quad (33)$$

For the process $\omega_1 - \omega_2 - \omega_3 \rightarrow \omega_4$

$$F_3\left(b\Delta k, \frac{b}{L}, \frac{f}{L}, \frac{k''}{k'}\right) = \frac{2k'}{\pi b}\int_0^\infty 2\pi R\, dR \times \left|\int_{-\xi}^{\xi} d\xi' \frac{\exp\left[-(ib/2)\,\Delta k\xi'\right]}{(1 - i\xi')(k'' - ik'\xi')H} \times \exp\left[\frac{-R^2}{bH}\right]\right|^2 \quad (34)$$

with H defined by (26) and k' and k'' defined by (8) and (13). In the tight-focusing limit and in the case $k'' = k'$

$$F_3(b\Delta k, 0, 0.5, 1) = \begin{cases} 0, & \text{for } \Delta k \leq 0 \\ \pi^2(b\Delta k)^2 \exp\left[b\Delta k/2\right], & \text{for } \Delta k > 0. \end{cases} \quad (35)$$

III. Evaluation of the F_j

The functions F_j were numerically evaluated as continuous functions of $b\Delta k$ for various sets of discrete values of b/L, f/L, and k''/k'. From (30), (32), and (34) it is evident that the evaluation of each F_j involves an integration over ξ' which may be put in the form of a Fourier transformation. An efficient discrete fast Fourier transform (FFT) routine [18] was employed to numerically evaluate the F_j on an IBM computer. This routine is capable of performing a 4096-element complex discrete Fourier transform in less than 4 s of computer time. One such transformation is sufficient to completely specify F_1 as a function of $b\Delta k$ for one set of values of b/L and f/L, or to evaluate $|E_4(R)|^2$ as a function of $b\Delta k$ for one set of values of $b/L, f/L, k''/k'$, and R. F_2 and F_3 were calculated as functions of $b\Delta k$ for one set of values of $b/L, f/L$, and k''/k' by evaluating $|E_4(R)|^2$ for 40 discrete values of R and then integrating over R by means of the trapezoidal rule. Thus the determination of F_2 or F_3 as a function of $b\Delta k$ for a single set of values of $b/L, f/L$, and k''/k' required the FFT routine to be run 40 times and required approximately 3 min of computer time.

The behavior of the F_j near the tight-focusing limit was studied in detail. It was determined that, when $b/L \leq 0.1$ and when $b \leq f \leq L - b$, the F_j as functions of $b\Delta k$ may, to a good approximation, be represented by the curve for F_j versus $b\Delta k$ corresponding to the infinitely tight-focusing limit where $b/L = 0.0$ and $f/L = 0.5$. For instance, the maximum deviation of the numerically computed $F_1(b\Delta k, 0.1, 0.5, 1)$ from the analytically derived $F_1(b\Delta k, 0, 0.5, 1)$ of (31) is less than 0.1 for all values of $b\Delta k$.

F_1 for $b/L \leq 0.1$ and $f/L = 0.5$ are plotted in Fig. 1; F_2 for $b/L \leq 0.1$, $f/L = 0.5$, and $k''/k' = 1$, 1.1, 1.5, 2.0, and 3.0 are plotted in Fig. 2; and F_3 for $b/L \leq 0.1$, $f/L = 0.5$, and $k''/k' = 1$, 1.1, 1.5, 2.0, and 3.0 are plotted in Fig. 3. The analytical results of (31), (33), and (35) were used to supply the curves for $b/L = 0$, while the numerical results were used for $b/L \neq 0$.

In the case of tight focusing, the F_j, when viewed as functions of $b\Delta k$, have the mutual characteristic of possessing a single large peak. As the value of $b\Delta k$ departs from the optimum value, the F_j approach zero in a nearly asymptotic manner. In the case of b/L slightly more than zero, some sidelobe structure appears far in the wings. However, as long as the fundamental beam-waist region is contained entirely in the cell, these sidelobes are always less than 0.1 percent of the magnitude of the peak value of F_j. (This is in distinct contrast to the plane-wave case, where sidelobes to the main peak occur with magnitudes as high as 4 percent of the maximum value.)

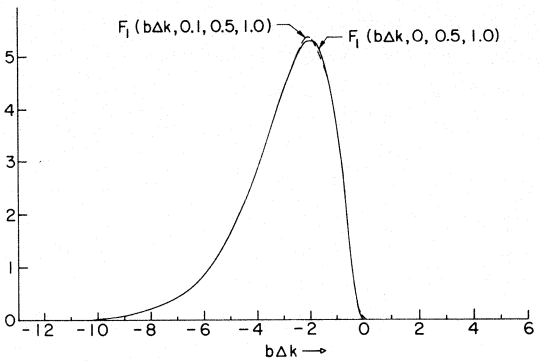

Fig. 1. F_1 versus $b\Delta k$ for $b/L \leq 0.1$ and $f/L = 0.5$.

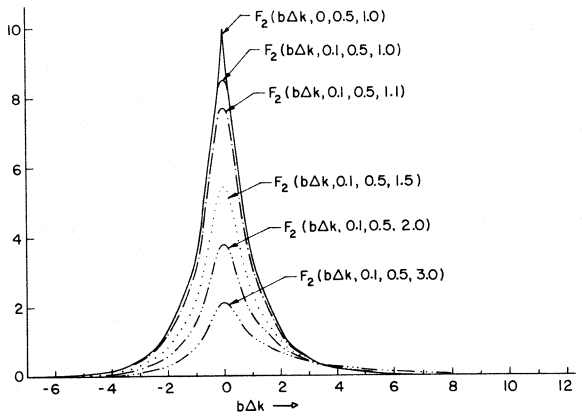

Fig. 2. F_2 versus $b\Delta k$ for $b/L \leq 0.1$; $f/L = 0.5$; and $k''/k' = 1.0$, 1.1, 1.5, 2.0, and 3.0.

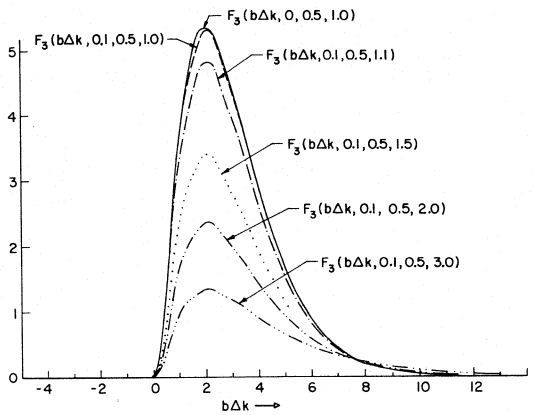

Fig. 3. F_3 versus $b\Delta k$ for $b/L \leq 0.1$; $f/L = 0.5$; and $k''/k' = 1.0$, 1.1, 1.5, 2.0, and 3.0.

In the case of very loose focusing, the F_j approach the plane-wave limit, as given by Miles and Harris [1], of

$$\lim_{b/L \to \infty} F_j\left(b\Delta k, \frac{b}{L}, 0.5, \frac{k''}{k'}\right) = \frac{4L^2}{b^2}\,\mathrm{sinc}^2\left(\frac{\Delta kL}{2}\right). \tag{36}$$

The value of k''/k' is irrelevant to the behavior of the F_j in the plane-wave case. The peak of this sinc^2 function is offset from zero by $\Delta k = -4/b$ for F_1 and by $\Delta k = 4/b$ for F_3, while for F_2 the peak is always at zero.

The complete evolution of the form of the F_j from the tight focusing limit to the plane-wave limit is demonstrated in Figs. 4 and 5 for the case of F_1. Families of curves of F_1 versus $b\Delta k$ for various locations of the focus (various values of f/L) are plotted in Figs. 6–10, where each figure corresponds to a different, constant value of b/L. Fig. 6 shows that, for tight focusing, F_j versus $b\Delta k$ is relatively unchanged as long as the fundamental beam-waist region is entirely contained within the cell. Fig. 10 illustrates that, for b much larger than L, F_j versus $b\Delta k$ is relatively unchanged as long as the cell is located close to the beam-waist location. Figs. 7–9 show the more complicated behavior of the intermediate cases. In every case, however, when the beam-waist location is far outside of the cell, the location of the peak of the F_j lies very near to $b\Delta k = 0$.

The dependence of the mode structure of the generated radiation upon $b\Delta k$ may be determined by monitoring $|E_4(R)|^2$ as a function of the transverse coordinate R for each value of $b\Delta k$. For the processes $\omega_1 + \omega_2 - \omega_3 \rightarrow \omega_4$ and $\omega_1 - \omega_2 - \omega_3 \rightarrow \omega_4$, when $k''/k' \neq 1$, the far-field intensity distribution evolves from a nearly Gaussian shape for $b\Delta k \leqslant 0$, to a circularly symmetric ring pattern as $b\Delta k$ becomes large and positive. This nearly Gaussian shape is in close agreement with the far-field intensity distribution which would arise from a lowest order Gaussian mode with the same wavelength as the generated radiation and with the same confocal parameter and waist location as the fundamental beams. The circularly symmetric ring pattern is of the type which has been observed by Terhune [19] and others for anti-Stokes radiation produced by three-wave mixing. The results of this section thus indicate that this ring pattern will appear only when $b\Delta k$ is positive. A typical evolution of the far-field pattern as Δk is changed is presented in Fig. 11 for the process $\omega_1 + \omega_2 - \omega_3 \rightarrow \omega_4$ with $k''/k' = 3$.

IV. A Physical Basis for the Behavior of the F_j

Several aspects of the behavior of the F_j, including the optimum values of $b\Delta k$ and the invariance with respect to the exact location of the focus in the tight-focusing case, may be explained by a simple model which takes into account the additional phase shift caused by focusing.

From (2) and (6), it can be seen that the amplitude of the driving polarization strongly peaks in the region of the fundamental beam waists. A region of significant generation may somewhat arbitrarily be defined as bounded by the z values at which the driving polarization falls to 10 percent of its peak value. In the case of tight focusing, when b is much less than L and the fundamental beam-waist region is located entirely within the cell, the boundaries of the generating region are

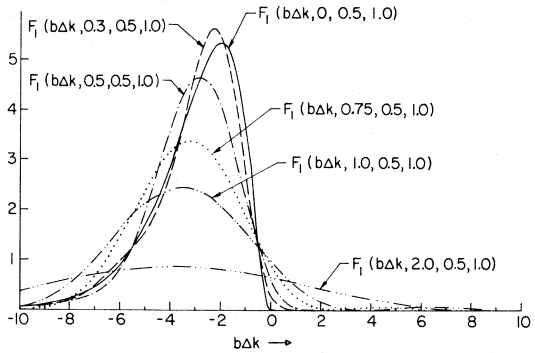

Fig. 4. F_1 versus $b\Delta k$ for f/L = 0.5 and b/L = 0, 0.3, 0.5, 0.75, 1.0, and 2.0.

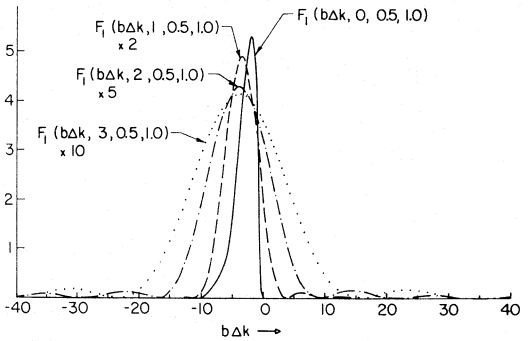

Fig. 5. F_1 versus $b\Delta k$ for f/L = 0.5 and b/L = 0, 1, 2, and 3.

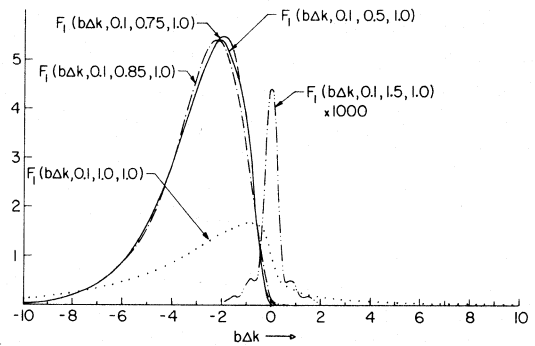

Fig. 6. F_1 versus $b\Delta k$ for b/L = 0.1 and f/L = 0.5, 0.75, 0.85, 1.0, and 1.5.

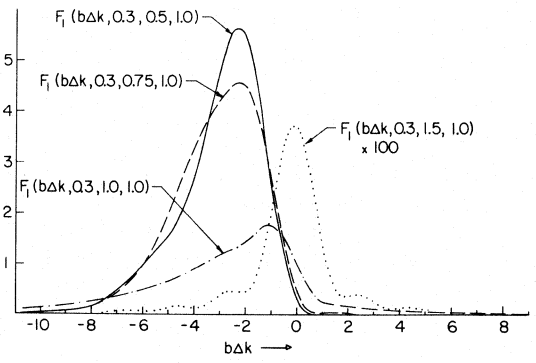

Fig. 7. F_1 versus $b\Delta k$ for b/L = 0.3 and f/L = 0.5, 0.75, 1.0, and 1.5.

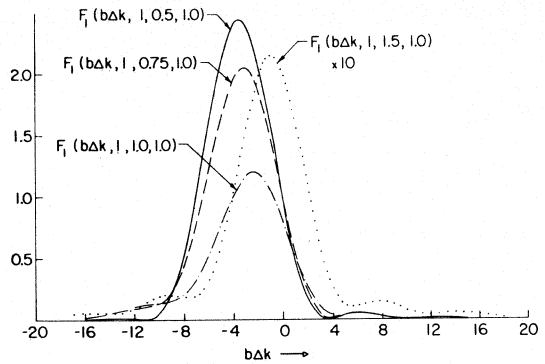

Fig. 8. F_1 versus $b\Delta k$ for $b/L = 1$ and $f/L = 0.5$, 0.75, 1.0, and 1.5.

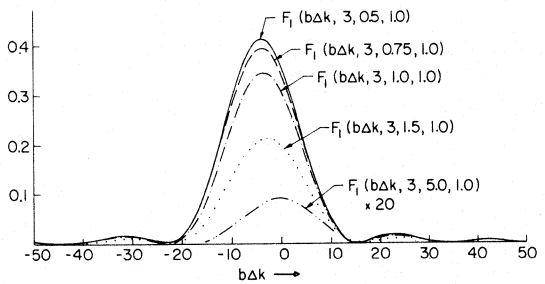

Fig. 9. F_1 versus $b\Delta k$ for $b/L = 3$ and $f/L = 0.5$, 0.75, 1.0, 1.5, and 5.0.

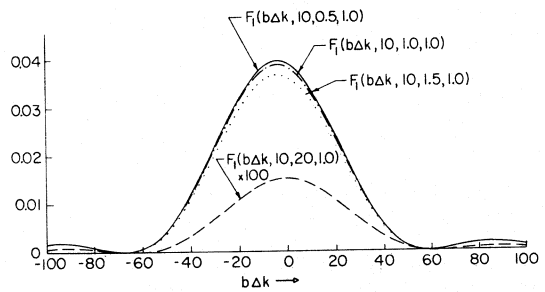

Fig. 10. F_1 versus $b\Delta k$ for $b/L = 10$ and $f/L = 0.5$, 1.0, 1.5, and 20.0.

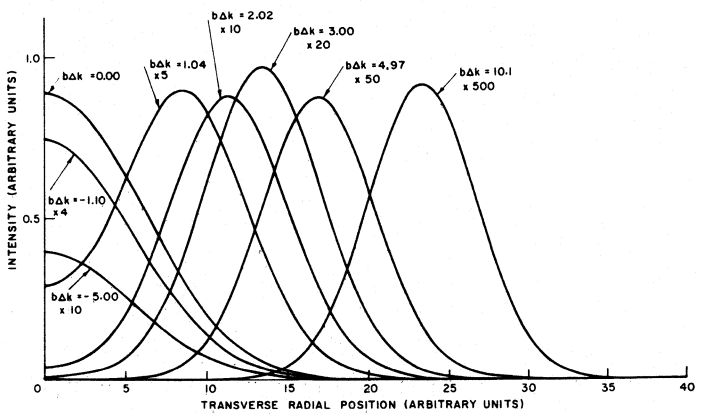

Fig. 11. Far-field intensity distribution for several values of $b\Delta k$ for the process $\omega_1 + \omega_2 - \omega_3 \rightarrow \omega_4$ with $k''/k' = 3.0$. The distribution in each case is calculated at the position of the output window of a cell with $b/L = 0.1$ and $f/L = 0.5$.

located at $\xi = -2$ and $\xi = +2$ (or $z = f - b$ and $z = f + b$). In the case of loose focusing, when b is much larger than L, the boundaries are located at the input and output windows of the cell.

From (2), it can be seen from the term

$$(1 + i\xi)^{-1} = (1 + \xi^2)^{-1/2} \exp(-i \tan^{-1} \xi)$$

that a focused lowest order Gaussian beam undergoes a shift in phase given by $\tan^{-1} \xi$ as it propagates through the waist region. The driving polarization given by (6) then experiences a phase shift of $3 \tan^{-1} \xi$ for $\omega_1 + \omega_2 + \omega_3 \rightarrow \omega_4$, $\tan^{-1} \xi$ for $\omega_1 + \omega_2 - \omega_3 \rightarrow \omega_4$, and $-\tan^{-1} \xi$ for $\omega_1 - \omega_2 - \omega_3 \rightarrow \omega_4$. If it is assumed that the optimum conversion efficiency occurs when the generated radiation is nearly a lowest order Gaussian mode with the same confocal parameter as the fundamental beams, then the generated radiation may be considered to experience a phase shift of $\tan^{-1} \xi$. Thus a slip in phase between the driving polarization and the generated radiation of $2 \tan^{-1} \xi$ for $\omega_1 + \omega_2 + \omega_3 \rightarrow \omega_4$ and of $-2 \tan^{-1} \xi$ for $\omega_1 - \omega_2 - \omega_3 \rightarrow \omega_4$ occurs, while no slip in phase occurs for $\omega_1 + \omega_2 - \omega_3 \rightarrow \omega_4$. This slip in phase causes destructive interference between radiation generated in different portions of the generating region.

The slip in phase due to focusing may be compensated to some degree by the wave-vector mismatch Δk introduced by the dispersion of the nonlinear medium. The optimum value of Δk, Δk_{opt}, is that value which exactly cancels the total slip in phase which occurs as the generating region is traversed.

In the case of tight focusing, when the entire generating region is contained within the cell, this requirement yields

$$\Delta k_{opt} \cong \begin{cases} -2.2/b, & \text{for } \omega_1 + \omega_2 + \omega_3 \rightarrow \omega_4 \\ 0, & \text{for } \omega_1 + \omega_2 - \omega_3 \rightarrow \omega_4 \\ +2.2/b, & \text{for } \omega_1 - \omega_2 - \omega_3 \rightarrow \omega_4 \end{cases} \tag{37}$$

in good agreement with the exact results. Since significant generation occurs only in the generating region, it follows that this behavior should be independent of the exact location of the focus so long as the entire generating region is contained within the cell.

In the case of loose focusing, when the entire cell is located in the beam waist, these arguments yield

$$\Delta k_{opt} = \begin{cases} -\dfrac{4}{b}, & \text{for } \omega_1 + \omega_2 + \omega_3 \rightarrow \omega_4 \\ 0, & \text{for } \omega_1 + \omega_2 - \omega_3 \rightarrow \omega_4 \\ \dfrac{4}{b}, & \text{for } \omega_1 - \omega_2 - \omega_3 \rightarrow \omega_4 \end{cases} \tag{38}$$

again in good agreement with the exact results.

V. Optimization of the Tight-Focusing Case

In this section, procedures for the optimization of the total generated power are developed for the case of tight focusing ($b/L \leqslant 0.1$) with the fundamental beam-waist region entirely contained within the cell. If limiting processes [1] such as

pump depletion, absorption, breakdown, saturation, thermal defocusing, and the quadratic Kerr effect are neglected, then the total generated power at ω_4 is always given by (29) and thus obeys the proportionality relation

$$\mathcal{P}_4 \propto \mathcal{P}_1 \mathcal{P}_2 \mathcal{P}_3 N^2 \chi^2 F_j(b\Delta k, b/L, f/L, k''/k'). \tag{39}$$

The parameters $\mathcal{P}_1 \mathcal{P}_2 \mathcal{P}_3$, χ, and k''/k' are considered to be constant and thus the optimization procedure reduces to maximizing the quantity $N^2 F_j(b\Delta k, b/L, f/L, k''/k')$ by varying the parameters N, $b\Delta k$, b/L, and f/L.

When N is a parameter which is independent of $b\Delta k$, b/L, and f/L, the optimization procedure further simplifies to increasing N to the highest possible value while independently maximizing F_j. By the results of Section III, the maximization conditions for the F_j under these tight-focusing conditions are then simply to set $b\Delta k$ to $b\Delta k_{\text{opt}}$ given by

$$b\Delta k_{\text{opt}} = \begin{cases} -2, & \text{for } \omega_1 + \omega_2 + \omega_3 \rightarrow \omega_4 \\ 0, & \text{for } \omega_1 + \omega_2 - \omega_3 \rightarrow \omega_4 \\ +2, & \text{for } \omega_1 - \omega_2 - \omega_3 \rightarrow \omega_4 \end{cases} \tag{40}$$

regardless of the exact values of b/L and f/L (so long as $b/L \leqslant 0.1$ and $b \leqslant f \leqslant L - b$).

The parameter $b\Delta k$ may be adjusted to its optimum value by means of altering b or by altering Δk. The value of b may be straightforwardly altered by varying the tightness of focus, but in order for the tight-focusing approximation of this section to remain valid, b/L must remain less than 0.1. In order to make Δk a parameter which is independent of N, another medium with negligible nonlinearity but appreciable dispersion may be mixed with the nonlinear medium [1]. Δk could then be controlled by varying the concentration of the added medium. The process $\omega_1 + \omega_2 - \omega_3 \rightarrow \omega_4$ is unique in that the optimum value of b is always zero, regardless of the value of Δk. It should be noted that the procedure of optimizing by adjusting b is valid only if the nonlinear medium can tolerate the high-power densities introduced by very tight focusing. If this is not possible, the best compromise is to reduce b to the smallest permissible value and then to adjust Δk to reach $b\Delta k_{\text{opt}}$.

The value of F_j is severely reduced if $b\Delta k$ deviates from its optimum value. The tolerances on the value of $b\Delta k$ which correspond to F_j maintaining a desired fraction of its peak value may be determined from Fig. 1, Fig. 2, or Fig. 3. It is particularly important to note that the process $\omega_1 + \omega_2 + \omega_3 \rightarrow \omega_4$ requires that $b\Delta k$ be nonzero and positive while the process $\omega_1 - \omega_2 - \omega_3 \rightarrow \omega_4$ requires that $b\Delta k$ be nonzero and negative. The generated total power at ω_4 under these optimized conditions is given by (29) with F_j set to its peak value from Fig. 1, Fig. 2, or Fig. 3.

Different optimization procedures are required when N is a parameter which is not independent of $b\Delta k$. One particularly important case occurs when Δk is constrained to be proportional to N while b is constrained to be constant and N is a free parameter. In this case, the quantity which must be maximized in the optimization procedure is $\Delta k^2 F_j(b\Delta k, b/L, f/L, k''/k')$. This quantity is not dimensionless, and depends on the absolute value of b. Therefore it is appropriate to define the dimensionless quantity

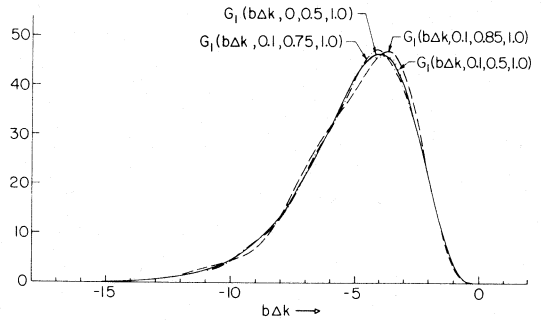

Fig. 12. G_1 versus $b\Delta k$ for $b/L \leqslant 0.1$ and $f/L = 0.5$, 0.75, and 0.85.

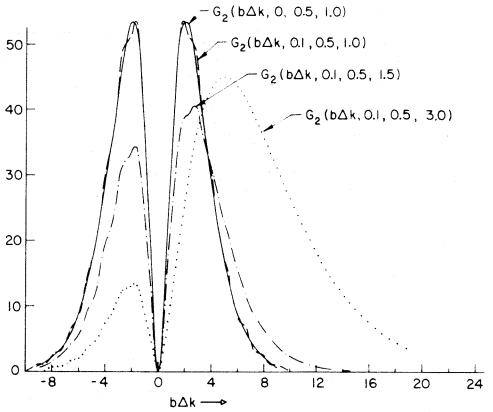

Fig. 13. G_2 versus $b\Delta k$ for $b/L \leqslant 0.1$; $f/L = 0.5$; and $k''/k' = 1.0$, 1.5, and 3.0.

$$G_j(b\Delta k, b/L, f/L, k''/k') = (\Delta k b)^2 F_j(b\Delta k, b/L, f/L, k''/k') \tag{41}$$

and to realize that the quantity which must be maximized is then $(1/b)^2 G_j(b\Delta k, b/L, f/L, k''/k')$.

G_1 is plotted for $b/L = 0$ and $b/L = 1$ with $f/L = 0.5$, 0.75, and 0.85 in Fig. 12. Here it is apparent that, as in the case of the F_j, the value of b/L in the G_j may to a good approximation be replaced by zero for b/L less than 0.1. In addition, for tight focusing, the G_j are independent of the value of f/L as long as the entire input beam-waist region is contained within the cell. G_2 is plotted for $f/L = 0.5$, $b/L = 0.1$ in Figs. 13 and 14. G_3 is plotted for $f/L = 0.5$, $b/L = 0.1$ in Fig. 15.

Since N is the only free parameter, the optimization procedure is to adjust $b\Delta k$ to maximize G_j by adjusting N. Let $(b\Delta k)_{\text{opt}}$ be the value of $b\Delta k$ which corresponds to the peak of G_j. Define the coefficient of proportionality α by the relation $\Delta k = \alpha N$. Then the optimization procedure reduces to adjusting N to the value $N_{\text{opt}} = (b\Delta k)_{\text{opt}}/\alpha b$.

From (29) and (41), the total generated power in this optimized case is

$$\mathcal{P}_4 = (6.318 \times 10^{-4}) \frac{k_0^4 k_1 k_2 k_3}{k_4^2 k'} \frac{\chi^2 \mathcal{P}_1 \mathcal{P}_2 \mathcal{P}_3 G_j}{\alpha^2 b^2} \tag{42}$$

where G_j is given its peak value from Fig. 12, Fig. 13, Fig. 14, or Fig. 15.

It may be noted that in order to reach this optimized condition, α must be negative for the process $\omega_1 + \omega_2 + \omega_3 \rightarrow \omega_4$, while α must be positive for the process $\omega_1 - \omega_2 - \omega_3 \rightarrow \omega_4$. The process $\omega_1 + \omega_2 - \omega_3 \rightarrow \omega_4$ is unique in that G_2 possesses

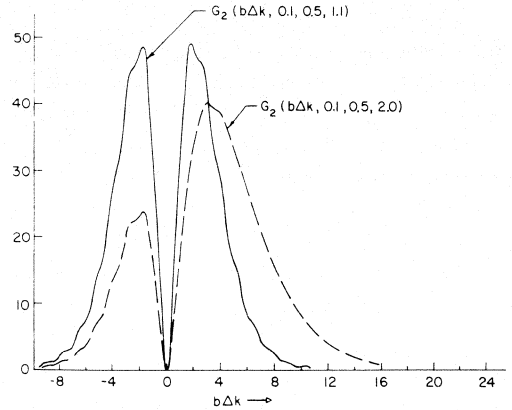

Fig. 14. G_2 versus $b\Delta k$ for $b/L \leqslant 0.1$; $f/L = 0.5$; and $k''/k' = 1.1$ and 2.0.

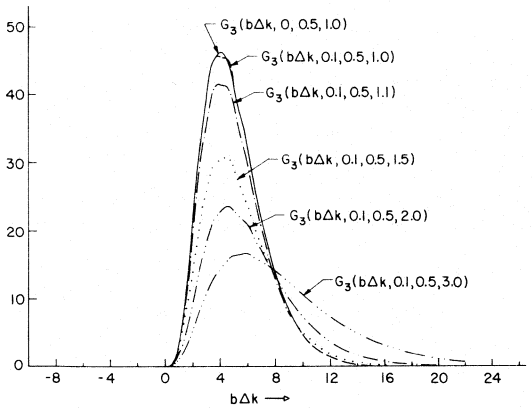

Fig. 15. G_3 versus $b\Delta k$ for $b/L \leqslant 0.1$; $f/L = 0.5$; and $k''/k' = 1.0$, 1.1, 1.5, 2.0, and 3.0.

peaks for positive and negative $b\Delta k$ and thus α may be either negative or positive.

VI. Experimental Results

An experiment has been conducted which verifies the theory of this paper for the process $\omega_1 + \omega_1 + \omega_1 \rightarrow 3\omega_1$ (third-harmonic generation) in the case of very tight focusing near the center of the cell. In these experiments the nonlinear medium was Xe gas, the fundamental beam had a wavelength of 3547 Å, and the generated radiation had a wavelength of 1182 Å. For this process, Xe possesses both a high nonlinear susceptibility and the proper dispersion characteristics to produce a negative value for Δk.

The experimental setup was identical with that of Kung *et al.* [6], except that the 3547-Å beam was passed through a lens-diamond pinhole-shearing aperture spatial filter in order to produce a very high-quality diffraction-limited beam with well-known parameters.

In this experiment, approximately 0.1 percent of the 3547-Å radiation was converted to 1182-Å radiation. The fundamental beam was focused at the center of the cell and b/L was 0.025. Fig. 16 shows the relative power output at 1182 Å versus Xe pressure with no Ar in the cell. The agreement of the triangular data points to the theoretical function $G_1(b\Delta k, 0, 0.5, 1)$ is excellent. The departure of the circular data points from theory is caused by the multimode character of the fundamental beam which results from an incorrect shearing aperture diameter. The process of fitting G_1 to the data

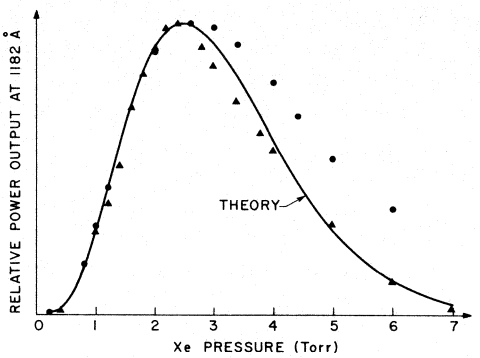

Fig. 16. Relative power output at 1182 Å versus Xe pressure. (The triangular points represent data from a run in which the shearing aperture was set to the proper diameter. The circular points represent data from a run in which the shearing aperture was open too far. The solid curve represents the best fit to the function $G_1(b\Delta k, 0, 0.5, 1)$ to the triangular points.)

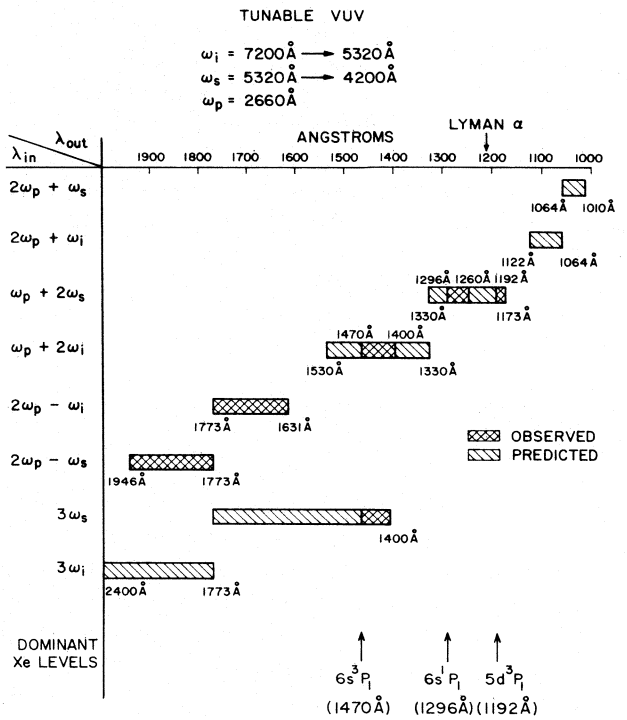

Fig. 17. Summary of the tunable VUV output achieved by Kung [4]. ω_p is pump frequency at 2660 Å, ω_s is signal frequency tunable from 5320 Å to 4200 Å, and ω_i is idler frequency tunable from 7200 Å to 5320 Å.

yields the coefficient of proportionality between Δk and the atomic-number density of the nonlinear medium, and thus provides an alternative method of determining the dispersion between the fundamental and generated wavelengths. The fit in Fig. 16 yielded $\Delta k = (-5.99 \times 10^{-17}) N_{Xe}$ (CGS units).

Some aspects of the theory of this paper for the processes $\omega_1 + \omega_1 - \omega_3 \rightarrow \omega_4$ and $\omega_1 + \omega_1 + \omega_3 \rightarrow \omega_4$ have been verified in a series of experiments performed by Kung [4]. These experiments concerned the mixing of a fixed-frequency pump at 2660 Å ($\omega_p = \omega_1$) with a variable-frequency signal or idler ($\omega_s, \omega_i = \omega_3$) in Xe gas to produce tunable coherent VUV radiation. Kung's experimental configuration involved very tight focusing of the fundamental beams. Fig. 17 shows the maximum possible spectral range which would be predicted for each process on the basis of simple addition or subtraction of the available fundamental photon energies. Fig.

17 also shows the range of tunable VUV output actually observed by Kung. The process $\omega_1 + \omega_1 + \omega_3 \rightarrow \omega_4$ produced a detectable signal at ω_4 only when ω_4 was near to, and on the short wavelength side of a strong Xe line. This is a necessary condition to produce anomalous dispersion and thus the negative values for Δk necessary to optimize G_1. The process $\omega_1 + \omega_1 - \omega_3 \rightarrow \omega_4$, however, produced a detectable signal over the entire maximum possible spectral range. This result would be expected since G_2 may be optimized for either negative or positive Δk. Thus the theory qualitatively explains the results of these experiments.

VII. Conclusions

This paper has presented a theoretical and experimental investigation of the effects of focusing on third-order nonlinear processes in isotropic media. A rigorous theory which relates the total power and far-field beam profile of the generated radiation to the various parameters of the fundamental beams and to the wave-vector mismatch has been developed. In the case of tight focusing with the fundamental beam-waist region entirely contained within the cell, it has been shown that the process $\omega_1 + \omega_2 + \omega_3 \rightarrow \omega_4$ can be efficient only in media whose dispersion characteristics produce a negative wave-vector mismatch and that the process $\omega_1 - \omega_2 - \omega_3 \rightarrow \omega_4$ can be efficient only in media whose dispersion characteristics produce a positive wave-vector mismatch. The process $\omega_1 + \omega_2 - \omega_3 \rightarrow \omega_4$ can be efficient in media with all types of dispersion characteristics and is always optimized by focusing as tightly as possible.

The improved understanding contributed by this paper of the far-field beam profile of the generated radiation for the process $\omega_1 + \omega_2 - \omega_3 \rightarrow \omega_4$ has important applications for coherent anti-Stokes Raman spectroscopy. By controlling the value of $b\Delta k$, the mode of the output radiation may be varied from near Gaussian to a ring-shaped pattern of variable cone angle. The cone angle of this ring pattern may be increased to the point where the generated radiation and the Gaussian fundamental beams become completely spatially separated in the far field. The advantages in detectivity which accrue from spatial separation between the generated radiation and fundamental beams may thus be secured for geometries which involve collinear propagation of the fundamental beams.

In the VUV and soft X-ray spectral regions, index of refraction data are often completely lacking and even the sign of the wave-vector mismatch produced by various media may be unknown. In this case, if Δk is of the wrong sign and/or if b is of the wrong value, the efficiencies of the processes $\omega_1 + \omega_2 + \omega_3 \rightarrow \omega_4$ and $\omega_1 - \omega_2 - \omega_3 \rightarrow \omega_4$ may be reduced by several orders of magnitude. Thus the process $\omega_1 + \omega_2 - \omega_3 \rightarrow \omega_4$ with very tight focusing has the highest probability of successfully producing a sufficient output for detection.

Acknowledgment

The author wishes to thank S. E. Harris, R. L. Byer, D. M. Bloom, A. H. Kung, E. A. Stappaerts, D. W. Phillion, and especially J. F. Young for many stimulating and helpful conversations. The author also wishes to thank C. M. Bjorklund for help in preparing the figures and B. Yoshizumi for help in constructing the apparatus.

References

[1] R. B. Miles and S. E. Harris, "Optical third-harmonic generation in alkali metal vapors," *IEEE J. Quantum Electron.*, vol. QE-9, pp. 470–484, Apr. 1973.
[2] D. M. Bloom, G. W. Bekkers, J. F. Young, and S. E. Harris, "Third harmonic generation in phase matched alkali metal vapors," *Appl. Phys. Lett.*, submitted for publication.
[3] R. T. Hodgson, P. P. Sorokin, and J. J. Wynne, "Tunable coherent vacuum-ultraviolet generation in atomic vapors," *Phys. Rev. Lett.*, vol. 32, pp. 343–346, 1974.
[4] A. H. Kung, "Generation of tunable picosecond VUV radiation," *Appl. Phys. Lett.*, vol. 25, pp. 653–654, 1974.
[5] A. H. Kung, J. F. Young, G. C. Bjorklund, and S. E. Harris, "Generation of vacuum ultraviolet radiation in phase-matched Cd vapor," *Phys. Rev. Lett.*, vol. 29, pp. 985–988, 1972.
[6] A. H. Kung, J. F. Young, and S. E. Harris, "Generation of 1182 Å radiation in phase-matched mixtures of inert gases," *Appl. Phys. Lett.*, vol. 22, pp. 301–302, 1973.
[7] S. E. Harris and D. M. Bloom, "Resonantly two-photon pumped frequency converter," *Appl. Phys. Lett.*, vol. 24, pp. 229–230, 1974.
[8] D. M. Bloom, J. T. Yardley, J. F. Young, and S. E. Harris, "Infrared up-conversion with reasonantly two-photon pumped metal vapors," *Appl. Phys. Lett.*, vol. 24, pp. 427–428, 1974.
[9] P. P. Sorokin, J. J. Wynne, and J. R. Lankard, "Tunable coherent IR source based upon four-wave parametric conversion in alkali metal vapors," *Appl. Phys. Lett.*, vol. 22, pp. 342–344, 1973.
[10] P. D. Maker and R. W. Terhune, "Study of optical effects due to an induced polarization third order in the electric field strength," *Phys. Rev.*, vol. 137, pp. 801–818, 1965.
[11] P. R. Regnier and J. P. Taron, "On the possibility of measuring gas concentrations by stimulated anti-Stokes scattering," *Appl. Phys. Lett.*, vol. 23, pp. 240–242, 1973.
[12] M. D. Levenson, "Feasibility of measuring the nonlinear index of refraction by third-order frequency mixing," *IEEE J. Quantum Electron. (Part I of Two Parts)*, vol. QE-10, pp. 110–115, Feb. 1974.
[13] R. F. Begley, A. B. Harvey, and R. L. Byer, "Coherent anti-Stokes Raman spectroscopy," *Appl. Phys. Lett.*, vol. 25, pp. 387–390, 1974.
[14] J. F. Ward and G. H. C. New, "Optical third harmonic generation in gases by a focused laser beam," *Phys. Rev.*, vol. 185, pp. 57–72, 1966.
[15] D. A. Kleinman, A. Ashkin, and G. D. Boyd, "Second-harmonic generation of light by focused laser beams," *Phys. Rev.*, vol. 145, pp. 338–379, 1966.
[16] G. D. Boyd and J. P. Gordon, "Confocal multimode resonator for millimeter through optical wavelength masers," *Bell Syst. Tech. J.*, vol. 40, pp. 489–508, 1961.
[17] D. A. Kleinman, "Theory of second harmonic generation of light," *Phys. Rev.*, vol. 128, pp. 1761–1775, 1962.
[18] O. Buneman, private communication.
[19] a) R. W. Terhune, "Nonlinear optics," *Solid State Design*, vol. 4, pp. 38–46, 1963.
b) B. P. Stoicheff, "Characteristics of stimulated Raman radiation generated by coherent light," *Phys. Lett.*, vol. 7, pp. 186–188, 1963.

Effects of Near-Resonance Self-Absorption on CO Laser Kinetic Modeling

WILLIAM B. LACINA

Abstract—**Resonance self-absorption from overlapping lines is an important pressure-dependent mechanism for theoretical analysis of a high-pressure CO laser. Although the effect on total optical output efficiency, kinetic heating rate, and transient time scales is small, predicted output spectral distributions can change significantly. Results of calculations will be presented which show that output power is redistributed to higher vibrational bands with more unique $P(J)$ characteristics. Previous analytical work on CO laser kinetics produced distributions that lay one or two v bands lower than what is observed, and was incapable of explaining anomalous spectra which often show certain transitions missing. Qualitative comparisons with experiment indicate that these effects occur at much lower pressures than theoretically predicted by this analysis. This suggests that further work will be required to correctly describe the mechanism of optical broadening in a CO laser medium.**

Introduction

In recent years, several theoretical analyses of CO laser kinetics have been reported [1]-[8]. In general, the results of calculations have agreed reasonably well with experimental comparisons at cryogenic temperatures, although there remain certain theoretical discrepancies that still need to be resolved to obtain a realistic and reliable model. These include, for example, 1) anomalies in output spectral distribution, 2) differences in predicted time scales, 3) degraded optical extraction efficiency with kinetic heating, and 4) sensitive dependence on molecular temperature. With varying levels of approximation and differences of approach, present theoretical models for a CO electric-discharge laser (EDL) consist of numerical computer solutions to the coupled set of equations that describe the molecular kinetics, plasma kinetics, gas dynamics, and optical fields (with gain equal to loss) in a simple plane parallel resonator. In addition to the approximations and simplifying assumptions, the model predictions are subject to uncertainties in the knowledge of various rate constants and to the possibility of the omission of important fundamental physical mechanisms. In regard to the latter possibility, we have proposed [9] that resonance self-absorption in the CO medium itself can be an important pressure-dependent effect that must be included for correct theoretical modeling of the CO laser.

At total pressures approaching atmospheric, line broadening in the CO laser is dominated by collisions, with a half-width ~0.05-0.1 cm^{-1}. (Doppler broadening is much less, and is important only at low temperatures, with total pressures $\lesssim$ 20 torr.) Therefore, at high pressures, the collision broadening of lines results in several significant spectral overlaps for almost every CO transition, so that laser oscillation on one vibrational-rotational line can be absorbed (or have enhanced gain) due to near-resonant transitions of other bands. Of particular importance is the fact that the $P(J)$ transitions (which are the ones which oscillate) most frequently have overlaps with $R(J)$ transitions of *higher* vibrational bands, and thus absorptive pumping to higher v levels results.

Results of calculations to be reported here show that, for high pressures, this mechanism can produce output spectral distributions that are significantly different from those predicted on the basis of previous theoretical models. A variety of experimental evidence is available which indicates the presence of this effect. For example, some transitions are never observed in high-pressure laser devices, and spectral distributions generally lie in vibrational bands higher than predicted. Results of transient small-signal gain measurements recently reported by Boness and Center [10] also show anomalous holes for certain transitions. They find that, in a CO/N_2 ~ 20/80-torr mixture at 130 K, the gains for $6 \rightarrow 5$ $P(10)$ and $7 \rightarrow 6$ $P(10)$ are degraded by overlaps with $8 \rightarrow 7$ $R(3)$ and $9 \rightarrow 8$ $R(3)$, respectively, and that coincidence of the $5 \rightarrow 4$ $P(13)$ transition with the $8 \rightarrow 7$ $R(7)$ line results in total absence of gain. Their kinetic calculations of small-signal gain with the inclusion of resonance absorption produce a reasonable qualitative explanation of their experimental data. Fig. 1 shows experimental data [11] of integrated spectral output energy from a CO/Ar = 50/150-torr pulsed CO laser oscillator, pumped at 20 kW/cm^3 for 50 μs at 80 K. The spectrum is not time resolved, and thus contains several $P(J)$ components which probably occur as the pulse evolves in time; note, however, that the $6 \rightarrow 5$ $P(10)$, $7 \rightarrow 6$ $P(10)$, and $8 \rightarrow 7$ $P(11)$ transitions never appear. Although definitive comparisons of the theory with experimental spectra are not yet available, it will be shown

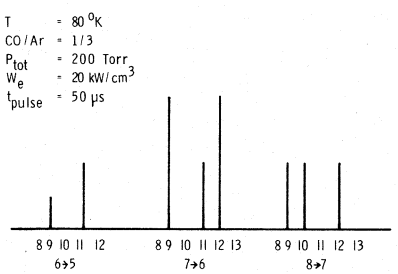

Fig. 1. Experimental integrated output spectrum from an e^--beam-sustained pulsed CO laser oscillator, with a CO/Ar = 50/150-torr gas mixture at 80 K, pumped at 20 kW/cm^3 for 50 μs, showing spectral anomalies.

Manuscript received December 13, 1974. This work was supported in part by the Air Force Weapons Laboratory, Air Force Systems Command, United States Air Force, Kirtland Air Force Base, Albuquerque, N. Mex., under Contract 75-C-0018, and the Defense Advance Research Projects Agency (ARPA), Arlington, Va.

The author is with the Northrop Research and Technology Center, Laser Technology Laboratories, Hawthorne, Calif. 90250.

that the mechanism of near-resonant absorption based on currently accepted optical-broadening constants alters the analytical predictions at high pressures. Based upon this fact and the strong qualitative experimental evidence available that supports it, resonance absorption must be included in the theoretical model for high-pressure CO lasers. However, as the calculations to be presented show, further work is required to improve the understanding of optical wing broadening to correctly describe its pressure dependence quantitatively.

The existence of resonances can lead to either of two possibilities: 1) the absorptions are so strong that laser oscillation is permanently inhibited from certain transitions; or 2) oscillation occurs, but relative spectral output as a function of vibrational band shifts upward because higher v levels are absorptively pumped. Both of these effects can have important consequences for line selection. It is possible that certain lines with favorable atmospheric transmission may never be attainable from high-pressure devices. (For example, $6 \rightarrow 5$ $P(10)$ has never been observed from the pulsed e^--beam-sustained CO EDL even at total pressures ~ 85 torr at 100 K with an intracavity water-vapor line-selection cell.) Furthermore, the upward shift of the spectrum makes it more difficult to obtain output in vibrational bands $6 \rightarrow 5$ and below, where almost all of the good atmospheric lines ($>$ 10-km e-folding range) are found. Finally, there is a small frequency shift from line center for oscillating transitions that is associated with the frequency dependence of the gains when resonance absorption is included. These shifts, which will be discussed in the following, are not expected to favorably alter any of the atmospheric transmission properties predicted for the CO laser.

Basic Theory

In this section, the theoretical formulation of the radiation calculations for a self-consistent oscillator analysis with resonance absorption will be outlined. It will be shown how this set of equations simplifies considerably when the mechanism of resonance absorption is neglected. For the optical analysis of the CO laser, stimulated emission processes are described by requiring that radiation intensities be instantaneously adjusted to maintain the (saturated) gain coefficients for all oscillating transitions equal to the threshold loss. Without resonance absorption the threshold condition is determined from the line-center gain on the laser transition alone.

However, with the inclusion of near-resonance absorption (or enhanced gain), the optical output intensities for all of the levels become coupled. The threshold condition must then be defined by the *net* gain coefficient for an oscillating transition, determined from line-center gain offset by wing absorption of all the near-resonant transitions of other bands. Furthermore, the calculations must be consistent kinetically, with all of the resulting optical emissions and absorptions included in the master equation for the population densities of the vibrational levels. Basically, these are the only generalizations required for extension of the previous analysis, and all of the prior assumptions can be retained. For example, we shall continue to assume a simple oscillator model with gain equal to loss in a spatially uniform plane parallel resonator. Furthermore, rotational levels are assumed to be in thermal equilibrium with the molecular temperature, with rotational cross relaxation taken to be sufficiently fast that only one rotational line can oscillate in any given vibrational band. Optical losses such as mirror absorption, output coupling, internal windows, or intracavity line selection are assumed to be uniformly distributed throughout the laser gain medium.

Emission and absorption for all transitions will be described by homogeneous collision broadening, with a normalized Lorentzian line shape

$$S(\tilde{\nu}, \tilde{\nu}_0) = (\Delta\tilde{\nu}/\pi c)\,[(\tilde{\nu} - \tilde{\nu}_0 - \delta\tilde{\nu})^2 + \Delta\tilde{\nu}^2\,]^{-1} \tag{1}$$

where frequencies $\tilde{\nu} = \nu/c$ are expressed in cm^{-1}. $\delta\tilde{\nu}$ is a pressure-induced shift of the center frequency $\tilde{\nu}_0$ of the transition, and will be neglected, although it is likely to be important at very high pressures ($>$ several atmospheres). The optical-broadened half-width is taken to be

$$\Delta\tilde{\nu} = \sum_X N_X \langle v(\text{CO}, X)\rangle\, \sigma^{\text{opt}}(\text{CO}, X)/(2\pi c) \tag{2}$$

where the sum is over the components X of the gas mixture. N_X are the total population densities, $\langle v(\text{CO}, X)\rangle$ are relative thermal velocities, and $\sigma^{\text{opt}}(\text{CO}, X)$ are the optical-broadening cross sections for the (CO, X) dephasing collisions. For the calculations to be reported here, we have taken average cross sections reported by Williams *et al.* [12] for the $1 \rightarrow 0$ CO fundamental band: $\sigma^{\text{opt}}(\text{CO}, \text{CO}) = 80 \times 10^{-16}$ cm^2 and $\sigma^{\text{opt}}(\text{CO}, \text{Ar}) = 60 \times 10^{-16}$ cm^2. The line-broadening assumptions will be discussed further in the following.

It is most convenient to label the complete set of vibrational-rotational transitions by (v, J, K), where $K = 1$ corresponds to $v \rightarrow v - 1$ $P(J)$ and $K = -1$ to $v \rightarrow v - 1$ $R(J - 1)$. (Then both P and R transitions appear symetrically in sums over $J = 1$ to $J = J_{\max}$, which is here taken to be 25.) With infinitely fast rotational cross relaxation, the frequency-dependent gain or absorption coefficients for all transitions are given by

$$\alpha_{vJK}(\tilde{\nu}) = n_v(t)\sigma^{21}_{vJK}(\tilde{\nu}) - n_{v-1}(t)\sigma^{12}_{vJK}(\tilde{\nu}) \tag{3}$$

in terms of the vibrational level population densities $n_v(t)$ and the stimulated emission cross sections, which are defined by

$$\begin{aligned}
\sigma^{21}_{vJK}(\tilde{\nu}) &= C_{vJK}\, B_v \exp\,[-B_v J(J - K)/kT] \\
\sigma^{12}_{vJK}(\tilde{\nu}) &= C_{vJK}\, B_{v-1} \exp\,[-B_{v-1} J(J + K)/kT] \\
C_{vJK} &= S(\tilde{\nu}, \tilde{\nu}_{vJK})\,\tilde{\nu}_{vJK} J \\
&\quad \cdot A_{10} |R_{v,v-1}/R_{10}|^2/(8\pi k T \tilde{\nu}^{\,3}_{10}).
\end{aligned} \tag{4}$$

Here, $A_{10} = 30.3$ s^{-1} is the $1 \rightarrow 0$ spontaneous radiative rate, $\tilde{\nu}_{10} = 2143$ cm^{-1} is the fundamental $1 \rightarrow 0$ frequency, $k = 0.69$ cm^{-1}/K is the Boltzmann constant, $|R_{v,v-1}/R_{10}|^2$ is the ratio of dipole moments, B_v is the rotational constant for level v, and T is the molecular temperature. The ratio of dipole moments $|R_{v,v-1}/R_{10}|^2$ is taken to be that given by Penner [13] for a Morse oscillator, and is approximately $|R_{v,v-1}/R_{10}|^2 \approx v$. (Note that C_{vJK} contains the factor J which applies for either $P(J)$ or $R(J - 1)$ transitions.) The gains α_{vJK} are a function of time, and because of kinetic heating, so are the stimulated emission cross sections σ^{21}_{vJK} and σ^{12}_{vJK} as a result of their dependence on T. However, for simplicity of notation the t dependence has been suppressed.

In general, the total gain coefficient for any frequency $\tilde{\nu}$ can be expressed as a sum of gains and absorptions over all of the transitions of the medium

$$\alpha(\tilde{\nu}) = \sum_{vJK} \alpha_{vJK}(\tilde{\nu}). \tag{5}$$

For a self-consistent oscillator analysis, the spectrum at time t is defined by the condition that $\alpha_L(t) \equiv \alpha(\tilde{\nu}_L) = \gamma_L$, where γ_L are the loss coefficients and $\tilde{\nu}_L$ are the frequencies for the set of lasing transitions $(v_L, J_L, 1)$, $L = 1, 2, \cdots, N$. (Except for calculations involving intracavity line selection, the loss coefficients γ_L are constant, independent of L.) The set of transitions L is restricted to one $P(J)$ line for any given v band, and as the transient evolution proceeds, this set can change. The intensities $I_L(t)$ of the set of N transitions which have attained threshold at time t satisfy a linear set of N equations of the form $d\alpha_L(t)/dt = 0$

$$(d/dt) \sum_{vJK} [n_v(t)\sigma^{21}_{vJK}(\tilde{\nu}_L) - n_{v-1}(t)\sigma^{12}_{vJK}(\tilde{\nu}_L)] = 0 \tag{6}$$

which become

$$\sum_{vJK} [\dot{n}_v(t)\sigma^{21}_{vJK}(\tilde{\nu}_L) - \dot{n}_{v-1}(t)\sigma^{12}_{vJK}(\tilde{\nu}_L)]$$

$$= - \sum_{vJK} [n_v(t) d\sigma^{21}_{vJK}/dT - n_{v-1}(t) d\sigma^{12}_{vJK}/dT]\, \dot{T} \tag{7}$$

for $L = 1, 2, \cdots, N$. $\dot{T}$ is determined by the instantaneous heating rate as a function of time. The time derivatives of the population densities are defined by the molecular kinetics master equation

$$\dot{n}_v(t) = R_v(t) + \sum_{JKL} [\beta_{v+1,JK}(\tilde{\nu}_L) - \beta_{vJK}(\tilde{\nu}_L)]\, I_L(t) \tag{8}$$

which is shown here explicitly separated into the kinetic terms $R_v(t)$ (e.g., electrical excitation, VV and VT relaxation, spontaneous emission, etc.) and the stimulated emission and absorption terms

$$I_L(t)\beta_{vJK}(\tilde{\nu}_L) = \alpha_{vJK}(\tilde{\nu}_L)\, I_L(t)/hc\tilde{\nu}_{vJK}. \tag{9}$$

Thus the set of linear equations for the intensities $I_L(t)$ becomes

$$\sum_{L'} \Phi_{LL'}(t)\, I_{L'}(t) = \phi_L(t) \tag{10}$$

where

$$\Phi_{LL'}(t) = \sum_{\substack{vJK \\ J'K'}} \{\sigma^{21}_{vJK}(\tilde{\nu}_L)\, [\beta_{v+1,J'K'}(\tilde{\nu}_{L'}) - \beta_{vJ'K'}(\tilde{\nu}_{L'})]$$

$$+ \sigma^{12}_{vJK}(\tilde{\nu}_L)\, [\beta_{v-1,J'K'}(\tilde{\nu}_{L'}) - \beta_{vJ'K'}(\tilde{\nu}_{L'})]\,\} \tag{11}$$

and

$$\phi_L(t) = - \sum_{vJK} [\sigma^{21}_{vJK}(\tilde{\nu}_L)\, R_v(t) - \sigma^{12}_{vJK}(\tilde{\nu}_L)\, R_{v-1}(t)]$$

$$- \sum_{vJK} [n_v(t)\, d\sigma^{21}_{vJK}/dT - n_{v-1}(t)\, d\sigma^{12}_{vJK}/dT]\, \dot{T}. \tag{12}$$

Thus all of the vibrational levels of the medium become optically coupled whenever there are resonant transitions with sufficient overlap. Without the mechanism of resonance self-absorption, the set of linear equations for the intensities $I_L(t)$ is considerably simplified; in that case, it reduces to a tridiagonal system since only line-center terms occur. If perfect resonance is implicitly assumed, it is convenient to suppress the frequency dependence and to simplify the subscript notation; without resonance absorption, all of the sums collapse, and (11) becomes

$$\Phi_{L,L+1} = \sigma^{21}(v_L, J_L)\, \beta(v_L + 1, J_{L+1})\, \delta(v_L + 1, v_{L+1})$$

$$\Phi_{L,L} = - \beta(v_L, J_L)\, [\sigma^{21}(v_L, J_L) + \sigma^{12}(v_L, J_L)]$$

$$\Phi_{L,L-1} = \sigma^{12}(v_L, J_L)\, \beta(v_L - 1, J_{L-1})\, \delta(v_L - 1, v_{L-1}) \tag{13}$$

where $K = 1$, specifying that all terms in (13) correspond to $P(J)$ transitions, has been suppressed for simplicity. It is also tacitly assumed in (13) that the upper laser vibrational levels v_L increase monotonically with the index L (i.e., that the transitions are labeled sequentially).

Equation (13) forms the basis of the radiation calculations reported previously [7]. The more general formulation expressed by (11) consists of sums which couple any two transitions L, L' for which there exist overlapping wings. In the numerical calculations based on (11) to be reported here, the sums are truncated beyond a specified number of collision half-widths $\Delta\tilde{\nu}$, which is taken to be a variable input parameter. After the radiation intensities $I_L(t)$ have been determined by inversion of (10), the resulting stimulated emission and absorption terms that occur in the master equation (8) can be obtained and the integration continued.

Numerical Results and Conclusions

Calculations based on the old and new radiation models were compared for a variety of pressures, electrical pumping rates, and molecular temperature. Contrary to some of the initial speculations [9], the results indicate that resonance absorption does not have a significant effect on predictions of total optical output efficiency, kinetic heating rates, or transient evolution. Changes are typically less than 10 percent, and therefore the parameter scaling generalizations reported recently [14] are not immediately invalidated. However, the predicted output spectral distribution does change significantly, with the output power redistributed to the higher vibrational bands.

Previous calculations produced distributions that lay about one or two v bands lower than what is observed, and were incapable of explaining anomalous experimental spectra which often show certain transitions always missing. The envelope of intensities calculated on the basis of (13) is usually peaked at the lowest vibrational band (or next to it) with a monotonic decrease for increasing v, while calculations with resonance absorption based on (11) produce more distinctive distributions. Furthermore, the predicted $P(J)$ characteristics become more unique, both as a function of time for any given v band, and relative to each other for several v bands at any fixed time.

To assess the sensitivity to resonance, the distance (in frequency) from line center, beyond which terms in the sums of

(11) were truncated, was treated as a variable input parameter. This parameter was increased until further terms made no significant contribution to the accuracy of the final results, and it was found that resonances as far away as 50–100 $\times \Delta\tilde{\nu}$ had to be included. Thus the assumption of Lorentzian wing absorption itself becomes important and must be examined and evaluated. Furthermore, there are open questions that remain about the optical-broadening cross sections σ^{opt} (CO, X; v, J, T). The dependence on rotational level [12] and molecular temperature [15] for different species X has been the object of limited experimental investigations for the $1 \rightarrow 0$ infrared absorption band. However, since the mechanism of optical broadening for CO probably originates from dipole-dipole collisional interactions, the possibility also exists that the cross sections for all the levels may not be constant, but an increasing function of the vibrational level v. Further experimental work to determine the vibrational-level dependence (if any) for these cross sections would be important, since there are presently no available data.

Although definitive time-resolved spectral data are not presently available, semiquantitative comparisons with experiment indicate that the important spectral effects occur at much lower pressures (~0.1 atm) than predicted by this analysis ($\lesssim$0.5 atm). This suggests the possibility of uncertainty in present knowledge of the CO optical pressure-broadening mechanism, since an increase in wing absorption (either by non-Lorentzian wings or increased broadening cross sections) would cause the predicted effects to appear at correspondingly lower pressures.

Comparison of calculations with and without absorption for CO/Ar = 20/80 torr at 80 K, pumped at 500 W/cm^3, showed no significant changes in either spectral distribution or magnitude of predicted intensities (< 1-percent change). Further calculations were carried out for CO/Ar mixtures of 100/200 and 100/600 torr at 100 and 300 K, with (constant) electrical pumping rates of 10, 20, and 50 kW/cm^3. (The optical resonator was assumed to be formed by two plane parallel mirrors with 80- and 100-percent reflectivities, separated by 50 cm, with a 6-percent/pass intracavity optical loss.) Fig. 2 shows a comparison of the predicted transient evolution of the optical output for CO/Ar = 100/600 torr at 300 K, pumped at a constant rate of 20 kW/cm^3 for 20 μs. Fig. 3 shows the predicted intensity distribution near the end of the pulse (18 μs) with and without resonance effects, and Fig. 4 shows a comparison of the $P(J)$ spectral designations as a function of time. Note that the intensity envelope, as well as the $P(J)$ characteristics, are considerably different. The significant differences originate completely from the resonance absorption mechanism, and not from differences in heating (temperature rise was ~40 K, with a change less than 1 percent for the two calculations). Fig. 5 shows predicted intensity distributions at the end of the pulse (20 μs) for the same case, but with initial temperature T = 100 K. Similar results were obtained for the other cases analyzed, and thus the presentation of further spectral plots would neither be necessary nor useful here. The intention has been to demonstrate that this mechanism is important for theoretical modeling of a high-pressure CO laser.

However, to show the effects of pressure and pumping in a

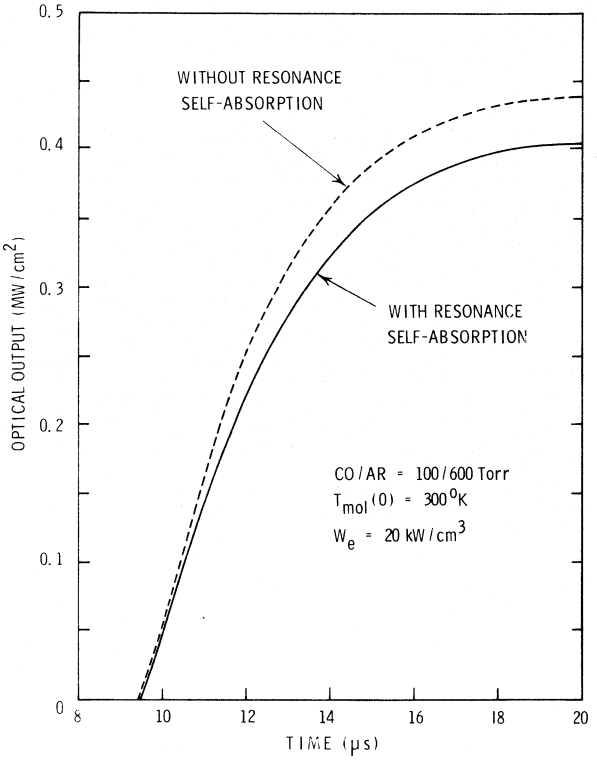

Fig. 2. Total optical output intensity as a function of time, with (solid) and without (dashed) resonance self-absorption included.

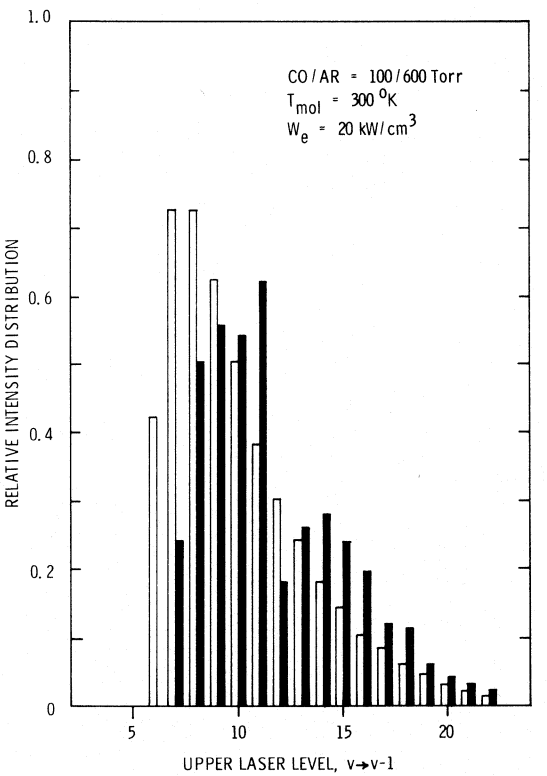

Fig. 3. Relative intensity distribution (full scale = 100 kW/cm^2) predicted at pulse end, with (solid) and without (open) resonance absorption.

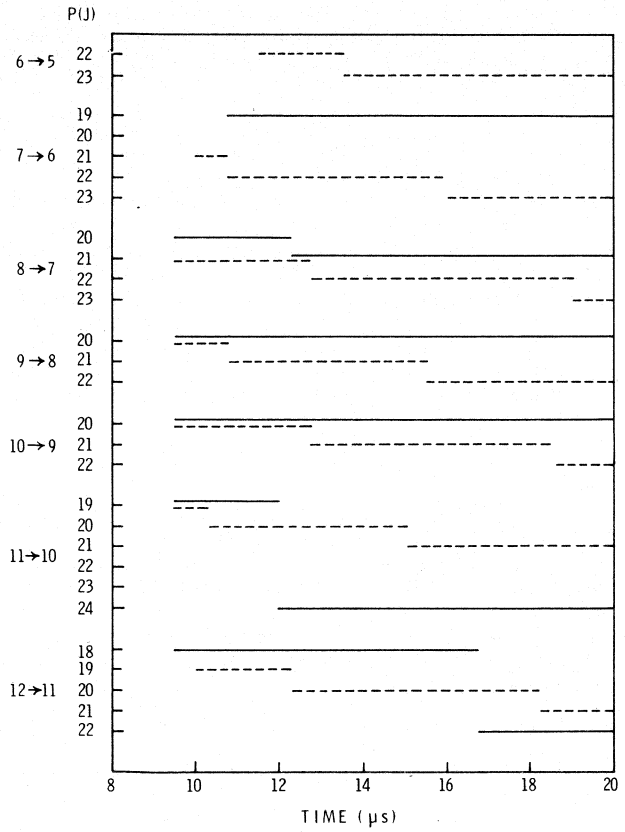

Fig. 4. $P(J)$ spectral characteristics as a function of time, with (solid) and without (dashed) resonance self-absorption.

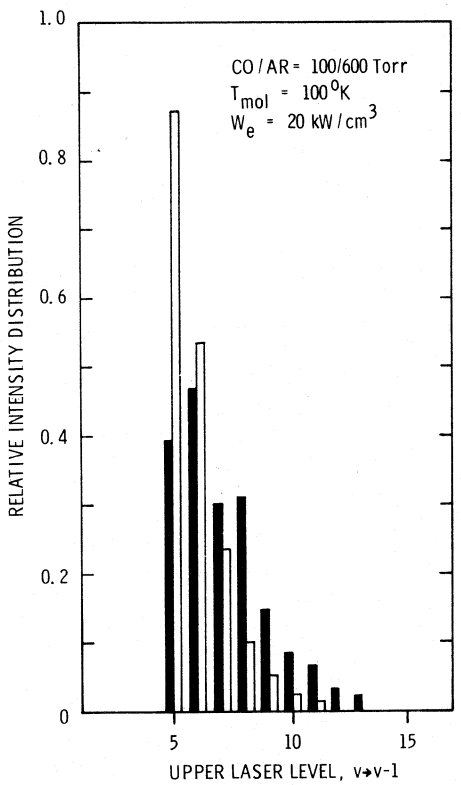

Fig. 5. Relative intensity distribution (full scale = 300 kW/cm^2) predicted at pulse end, with (solid) and without (open) resonance absorption.

brief quantitative way, it is convenient to summarize for several cases the percentage η of electrical power W_e (W/cm^3) that is distributed to different bands by the absorption mechanism (at steady state, for example). This is defined by

$$\eta = \sum_L [\alpha(v_L, J_L) - \gamma_L] I_L / W_e \tag{14}$$

where $\alpha(v_L, J_L)$ denotes the line-center gain for transition L as in (13). Results are presented in Table I. It was found that, for the case presented in Figs. 2-4, $\eta \sim 0.13$, and that resonances as far as $\sim 50 \times \Delta\tilde{\nu}$ (corresponding to ~ 2.4 cm^{-1}) were required for the calculation. (Typically, the net gain for each oscillating transition contained contributions from ~ 10 overlapping lines.)

The gain coefficient for any CO transition is a sum of Lorentzians (5) over all of the resonant lines, and thus the frequency dependence will be distorted. Therefore, oscillation frequencies will be shifted slightly from the line centers. Calculations show that the magnitude of these shifts is not significant; predicted changes for the frequencies of the lines of Fig. 4 were < 0.005 cm^{-1}, which is comparable to typical cavity mode separations. Frequency shifts of this magnitude do not result in significantly improved atmospheric transmission predictions. Calculations for atmospheric transmission, based on molecular absorption through a horizontal path at sea level in a midlatitude winter model using McClatchey AFCRL atmospheric constituent data, were carried out for all the CO lines in the first ten vibrational bands with the line-center frequencies shifted by as much as ± 0.02 cm^{-1}. This did not produce any significant changes, so frequency shifts anticipated from resonance absorption should not be considered important.

It is clear from this analysis that, if present values for optical cross sections and assumptions of Lorentzian broadening are valid, then resonance absorption is important for theoretical modeling of CO lasers at pressures approaching atmospheric. However, experimental evidence strongly suggests that the effects occur at much lower pressures ($\lesssim 0.1$ atm). This may be explained if wing absorptions are a factor of ~ 10 greater than assumed. It has been the purpose of this paper to assess quantitatively the effect of resonance absorption as a function of gas pressures, temperature, and pumping rates, and to show that it is *necessary* (although perhaps not sufficient) to modify

TABLE I
PERCENTAGE η OF ELECTRICAL INPUT POWER W_e THAT IS REDISTRIBUTED TO DIFFERENT VIBRATIONAL LEVELS BY ABSORPTIVE PUMPING FOR SEVERAL DIFFERENT CASES AT STEADY STATE

Case W_e (kW/cm^3)	10	20	50
CO/Ar = 100/600 T(0) = 100 K	.20	.30	.49
CO/Ar = 100/200 T(0) = 100 K	.15	.17	.34
CO/Ar = 100/600 T(0) = 300 K		.14	

Note: Results correspond to $t = 20$ μs except for $W_e = 10$ kW/cm^3, for which $t = 40$ μs.

contemporary theoretical models of CO-laser kinetics to include this mechanism. It will be necessary in future work to resolve this as well as remaining discrepancies (such as rotational equilibration) to achieve a more complete understanding of the CO laser.

References

[1] a) R. E. Center and G. E. Caledonia, "Theoretical description of electrical CO laser," *Appl. Phys. Lett.*, vol. 19, pp. 211–213, Oct. 1971.
b) —, "Vibrational distribution functions in anharmonic oscillators," *J. Chem. Phys.*, vol. 55, pp. 552–561, July 1971.

[2] J. W. Rich, "Kinetic modeling of the high power carbon monoxide laser," *J. Appl. Phys.*, vol. 42, pp. 2719–2730, June 1971.

[3] a) R. L. McKenzie, "Vibrational relaxation and radiative gain in expanding flows of anharmonic oscillators," NASA TN D-7050, Mar. 1971.
b) —, "Diatomic gasdynamic lasers," *Phys. Fluids*, vol. 15, pp. 2163–2173, Dec. 1972.

[4] W. B. Lacina, "Kinetic model and theoretical calculations for steady state analysis of an electrically excited CO laser amplifier system," Northrop Res. Technol. Ctr., Hawthorne, Calif., Northrop Rep. NCL 71-32R, Aug. 1971.

[5] W. Q. Jeffers and C. E. Wiswall, "Analysis of pulsed CO lasers," *J. Appl. Phys.*, vol. 42, pp. 5059–5065, Nov. 1971.

[6] S. D. Rockwood, J. E. Brau, W. A. Proctor, and G. H. Canavan, "Time-dependent calculations of carbon monoxide laser kinetics," *IEEE J. Quantum Electron. (Part II of Two Parts. 3rd Conference on Chemical and Molecular Lasers)*, vol. QE-9, pp. 120–129, Jan. 1973.

[7] W. B. Lacina, M. M. Mann, and G. L. McAllister, "Transient oscillator analysis of a high-pressure electrically excited CO laser," *IEEE J. Quantum Electron.*, vol. QE-9, pp. 588–593, June 1973.

[8] R. J. Hall and A. C. Eckbreth, "Kinetic modeling of CW CO electric-discharge lasers," *IEEE J. Quantum Electron.*, vol. QE-10, pp. 580–590, Aug. 1974.

[9] W. B. Lacina and G. L. McAllister, "Resonance self-absorption in CO lasers," *Appl. Phys. Lett.*, vol. 26, pp. 86–89, Feb. 1975.

[10] M. J. W. Boness and R. E. Center, "Observations of small signal gain in a high pressure pulsed CO electric discharge laser," presented at the 27th Gaseous Electronics Conf., Houston, Tex., Oct. 1974, Paper CA-1; also *Appl. Phys. Lett.*, to be published.

[11] V. G. Draggoo, private communication.

[12] D. Williams, D. C. Wenstrand, R. J. Brockman, and B. Curnutte, "Collisional broadening of infrared absorption lines," *Mol. Phys.*, vol. 20, pp. 769–785, 1971.

[13] S. S. Penner, *Quantitative Molecular Spectroscopy and Gas Emissivities*. Reading, Mass.: Addison-Wesley, 1959, p. 141, eq. (7-93).

[14] a) W. B. Lacina and G. L. McAllister, "Scaling generalizations for a CO electric laser," this issue, pp. 235–241.
b) —, "Scaling generalizations for a pulsed CO EDL," Northrop Res. Technol. Ctr., Hawthorne, Calif., Northrop Rep. NRTC 73-43R, Oct. 1973.

[15] G. M. Hoover and D. Williams, "Infrared absorptance of carbon monoxide at low temperatures," *J. Opt. Soc. Amer.*, vol. 59, pp. 28–33, Jan 1969.

Correspondence

On the Mechanism of the $N(^4S) + CS_2$ Reaction: N_2–CO_2 Laser Pumping from the Products of the $N(^4S) + CS_2$ Reaction

T. J. McGEE AND F. X. POWELL

Abstract—**The reaction of N atoms with CS_2 has been studied and a mechanism for the reaction proposed. It has been demonstrated that the N + NS reaction produces vibrationally excited N_2. Evidence has been presented which indicates that the rate of the N + CS_2 reaction is substantially slower than first indicated. The analogous reaction N + OCS ⟶ NS + CO has also been studied and a mechanism proposed.**

Introduction

In 1973 Hirose *et al.* [1] reported the achievement of a CO laser from the reaction of discharged nitrogen with O_2 and CS_2. The authors presented evidence leading to the following proposed mechanism:

$$N + CS_2 \longrightarrow CS + NS \quad (1)$$

Manuscript received February 25, 1975. This research was supported by the Office of Naval Research.

T. J. McGee was with the Department of Chemistry, The Catholic University of America, Washington, D.C. 20017. He is now with the Department of Chemistry, the University of Maryland, College Park, Md. 20742.

F. X. Powell is with the Department of Chemistry, The Catholic University of America, Washington, D.C. 20017.

$$N + NS \longrightarrow N_2 + S \quad (2)$$

$$S + O_2 \longrightarrow SO + O \quad (3)$$

$$O + CS_2 \longrightarrow CS + SO \quad (4)$$

$$O + CS \longrightarrow CO^* + S. \quad (5)$$

In their work Hirose *et al.* assumed rate constants on the order of 10^{14} $cm^3/mole \cdot s$ for reactions (1) and (2), largely because the power levels achieved by this reaction were very close to those achieved when O_2 was discharged and reacted directly with CS_2. The work reported herein confirms that the reaction of N + CS_2 reaction is rapid enough to participate in the laser-pumping mechanism but it does not appear to be as rapid as suggested by Hirose.

In a previous paper [2] we have reported the technique of CO_2 laser pumping by species born of a chemical reaction, notably vibrationally excited N_2. Using this technique with the N + CS_2 system has shown that the N + NS reaction, like the analogous N + NO reaction, produces vibrationally excited N_2.

Experimental

The apparatus has been previously described in [2] and only slight modifications were made for these experiments. The reaction zone/optical path was increased to 2 m which resulted in a more stable laser system for the reactions studied, and laser power was measured from reflection off the Brewster's angle rather than by hole coupling. 10 torr of nitrogen was discharged using a condensed discharge of 5 kV and

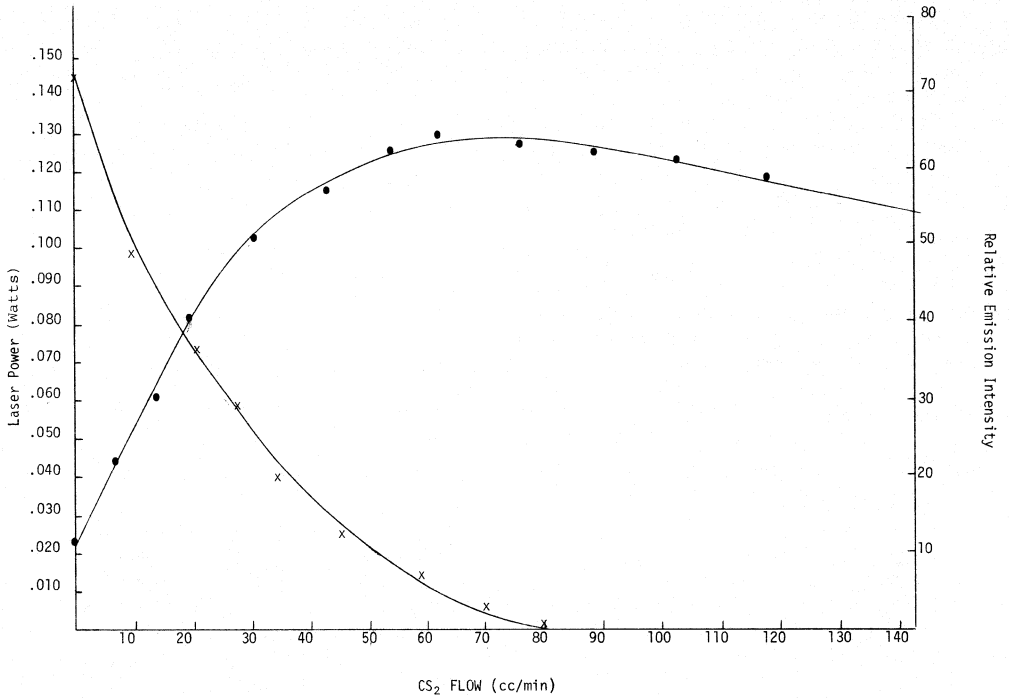

Fig. 1. Titration of N atoms with CS_2. X–N_2 first positive series versus CS_2 flow. •–Laser power versus CS_2 flow.

200 mA, yielding approximately 0.4-percent N atoms. The pressure of CO_2 was kept constant in the experiments at 1.5 torr. Both a chemical trap and a liquid-N_2 trap were used to prevent explosions from CS and unreacted CS_2.

Results and Discussion

When CO_2 was introduced to the flowing nitrogen afterglow, a low-power CO_2 laser was generated from the near-resonant transfer of energy from vibrationally excited N_2. The addition of CS_2 resulted in a linear increase in laser power, as shown in Fig. 1. As in the work with NO this curved into a maximum and decreased beyond the endpoint due to collisional deactivation of the CO_2 by the excess of CS_2. Spectral analysis of the lasing radiation on a Perkin-Elmer 112 G IR spectrophotometer showed that all lasing occurred at 10.6 μ. Radiation at 11.5 μ, corresponding to the CS_2 transitions observed by Patel [3], was not observed in any of the experiments described herein.

Fig. 1 also shows a plot of the decay of the N_2 first-positive series measured at 5804 Å. It can be seen that the laser-power maximum and the endpoint of the N + CS_2 reaction as measured by zero intensity of the N_2 first-positive emission closely coincide, indicating that the N atoms were directly responsible for producing the species pumping the CO_2 laser. It is also possible that a small fraction of the CO_2 inversion is due to vibrational energy transfer from the NS and CS produced in reaction (1). Transfer of any vibrational energy released into NS or CS to CO_2 would necessarily be slow compared to the near-resonant transfer from N_2^*, (ω_e for NS and CS are 1220 and 1285 wavenumbers, respectively [4]).

Although equipment for the determination of accurate kinetic data was not available, it was possible to make a rough estimate of the reaction rate by comparison of the reaction with the N + NO reaction. The N + NO reaction has been well studied and has a reported rate constant of 1.8×10^{13} cm^3/mole · s [5]. In our previous work, this reaction was studied using a 16-in optical path which was sufficiently long for the reaction to proceed while still in the optical path. Experiments with CS_2 using the 16-in optical path resulted in a laser-power maximum long before the first-positive bands went to zero. In order to react all the N atoms in the 16-in zone, it was necessary to add such a large excess of CS_2 that the CO_2 was collisionally deactivated and no laser power was observed. Increasing the length of the reaction zone/optical path to 2 m, which increased the residence time in the optical path from 5 to 27 ms, enabled the N atoms and CS_2 to react in more nearly stoichiometric concentrations and the laser-power maximum then agreed with zero intensity of the N_2 first-positive series. This necessary increase in residence time thus indicates that the N + CS_2 reaction is substantially slower than the N + NO reaction, perhaps by as much as an order of magnitude.

This estimate of a rate constant on the order of 10^{12} cm^3/mole · s, is approximately equal to the rate constant reported for the O + CS_2 reaction [6] and thus would be sufficiently rapid to produce the relatively high laser-power levels reported by Hirose.

The reaction mechanism does not appear to be as simple as indicated by reactions (1) and (2). Evidence has been presented [7]–[9] indicating that the CS formed in the reaction is in the singlet state which makes reaction (1) doubly spin-forbidden. We therefore suggest the following mechanism, using the reaction intermediate advanced by Westbury and Winkler [7], which takes into account the spin-forbidden nature of the reaction:

$$N(^4S) + CS_2 \longrightarrow N \cdot CS_2(111) \quad (6)$$

$$N \cdot CS_2(111) \longrightarrow N \cdot CS_2(1\downarrow 1) \quad (7)$$

$$N \cdot CS_2(1) \longrightarrow NS(1) + CS \quad (8)$$

$$N + NS \longrightarrow N_2^* + S. \quad (9)$$

This mechanism proposes a rapid equilibrium with the intermediate being formed in a quartet state. The second step of the reaction would appear to be the rate-determining step as it involves a radiationless isomerization to the doublet state. The increase in exothermicity from this step can then cause the decomposition of the intermediate to doublet NS and singlet CS, whereupon the NS further reacts with an N atom to yield vibrationally excited N_2 and the S necessary to

Hirose's laser-pumping mechanism. Reactions (6)–(9) followed by reactions (3)–(5) would then appear to be the mechanism for Hirose's laser. It can be seen that in this sequence of reactions, CS molecules have two sources: The N + CS_2 reaction scheme and the O + CS_2 mechanism. This fact doubtless contributes to the relatively high laser-power levels observed.

Because of its chemical similarities, OCS was also reacted with N atoms. In spite of the fact that the N + OCS reaction is thermodynamically more favorable than the N + CS reaction, it is apparently much slower. It was possible to generate a slight increase in laser power followed by a deactivation of the laser by excess OCS long before the reaction consumed the available N atoms. Extension of the reaction zone to 10 ft (the maximum length at our disposal) failed to alter these experimental results appreciably, indicating that the reaction is considerably slower than the N + CS_2 reaction. The slight increase in laser power did, however, show that this reaction as well ultimately results in vibrationally excited N_2. Thus a mechanism similar to that for the N + CS reaction can be proposed

$$N(^4S) + OCS \longrightarrow N \cdot OCS(111) \quad (10)$$

$$N \cdot OCS(111) \longrightarrow NOCS(1\downarrow 1) \quad (11)$$

$$NOCS(1) \longrightarrow NS + CO \quad (12)$$

$$N + NS \longrightarrow N_2^* + S. \quad (13)$$

Conclusion

In this work, we have reported the achievement of a CO_2 laser by means of the reaction of N atoms with CS_2 to form, after a series of subsequent steps, vibrationally excited N_2 which can transfer energy by a near-resonant V–V transfer with CO_2. It has been demonstrated that the N + CS_2 reaction sequence is sufficiently rapid to be involved in the laser-pumping mechanism proposed by Hirose *et al.*, although it appears that the reaction is not as fast as they had assumed in their work. A more detailed mechanism for the reaction of N atoms with CS_2 has been advanced, utilizing the reaction intermediate first proposed by Westbury and Winkler [7]. This mechanism takes into account the spin-forbidden nature of reaction (1).

Additionally, the apparently slow reaction of N + OCS ⟶ NS + CO has been studied. The increase in laser power at low flow rates of OCS gives further evidence that the reaction

$$N + NS \longrightarrow N_2 + S$$

produces N_2 in a vibrationally excited state. A mechanism similar to that of the N + CS_2 reaction has been proposed.

References

[1] Y. Hirose, J. C. Hassler, and P. D. Coleman, "A CW-CO chemical laser from the reaction of active nitrogen with O_2 and CS_2," *IEEE J. Quantum Electron. (Part II of Two Parts. 3rd Conference on Chemical and Molecular Lasers)*, vol. QE-9, pp. 114–117, Jan. 1973.

[2] T. J. McGee and F. X. Powell, "CO_2-laser pumping via transfer from N_2 species produced from the reaction of NO with discharged nitrogen," *IEEE J. Quantum Electron.*, vol. QE-10, pp. 853–860, Dec. 1974.

[3] C. K. N. Patel, "CW laser oscillations in an N_2-CS_2 system," *Appl. Phys. Lett.*, vol. 7, pp. 273–274, 1965.

[4] G. Herzberg, *Molecular Spectra and Molecular Structure*, vol. 1: *Spectra of Diatomic Molecules*, 2nd ed. Princeton, N.J.: Van Nostrand, 1950.

[5] L. F. Phillips and H. I. Schiff, "Reactions in the atomic nitrogen-ozone system," *J. Chem. Phys.*, vol. 36, pp. 1509–1517, 1962.

[6] R. D. Suart, P. H. Dawson, and G. H. Kimbell, "CS_2/O_2 chemical lasers: Chemistry and performance characteristics," *J. Appl. Phys.*, vol. 43, p. 1022, 1972.

[7] R. A. Westbury and C. A. Winkler, "The reactions of active nitrogen with hydrogen sulfide and carbon disulfide," *Can. J. Chem.*, vol. 38, pp. 334–342, 1960.

[8] G. Parker, "Flash photolysis spectroscopy: A new method for the study of free radical reactions," *Proc. Roy. Soc., Ser. A*, vol. 200, p. 284, 1950.

[9] P. J. Dyne and D. A. Ramsay, "Some observations on the CS 'radical,'" *J. Chem. Phys.*, vol. 20, pp. 1055–1056, 1952.

Multimode Bragg Diffractions in an Ion-Exchanged Optical Waveguide with a Sputter-Etched Periodic Surface Corrugation

K. ASAKAWA, M. KONDO, Y. OHTA, F. SAITO, AND T. YAMAZAKI

Abstract—**An optical diffraction phenomenon in an ion-exchanged planar optical waveguide with a sputter-etched periodic surface corrugation was experimentally investigated in detail. A single-mode incident beam simultaneously gave rise to several diffracted beams of different mode indices in different directions. This phenomenon was interpreted on the basis of the phase-matching diagram for the multimode Bragg diffraction by using measured wave vectors of the propagation modes and of the surface corrugation.**

In recent years, work on several planar optical waveguides with periodic structures for integrated optics has been reported [1], [2]. The collinear Bragg diffraction for the phase-grating structure in the deposited thin-film optical waveguide have been both experimentally and theoretically investigated to a great extent, in connection with grating couplers [3] and DFB lasers [4]. Very little was mentioned, however, about noncollinear Bragg diffractions in the multimode optical waveguide [2].

An ion-exchanged planar optical waveguide on a glass substrate has been reported to have many advantages, such as extremely low propagation loss and easy fabrication of buried or undulating waveguide structures by electromigration technique [5]. Such a waveguide can propagate many modes, since its high refractive index layer is generally thicker than the deposited thin-film optical waveguide.

This correspondence reports experimental results on the noncollinear Bragg diffraction phenomenon in the above-mentioned ion-exchanged planar optical waveguide, whose surface is periodically corrugated by sputter-etching technique.

A planar optical waveguide was formed on the surface of an approximately 30- by 10- by 3-mm F-2 glass substrate by ion-exchange technique. The refractive index profile normal to the surface was measured by the interference microscope and was found to be nearly parabolic. The waveguide is 50 μm thick and optical propagation loss is less than 0.1 dB/cm.

A periodic surface corrugation was fabricated on the waveguide by an RF sputter-etching technique. Prior to the sputtering, a 12-μm pitch grating pattern was formed with AZ-1350 photoresist in a 3- by 3-mm area on the waveguide surface. The surface grating obtained in this way had a 12-μm pitch with 250 grooves in the 3- by 3-mm area. Its depth was about 0.5 μm.

Configuration of the optical diffraction experiment is shown in Fig. 1. An He–Ne laser beam (6328 Å) was coupled into

Manuscript received January 16, 1975.

K. Asakawa, M. Kondo, Y. Ohta, and F. Saito are with Central Research Laboratories, Nippon Electric Company, Ltd., Kawasaki, Japan.

T. Yamazaki is with the Research Laboratory, Nippon Sheet Glass Company, Ltd., Itami, Japan.

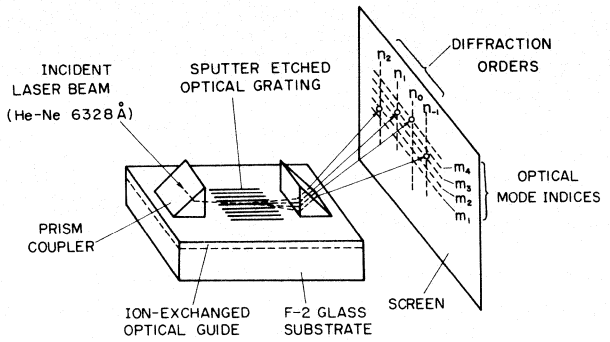

Fig. 1. Experimental configuration on multimode Bragg diffraction by sputter-etched surface corrugation.

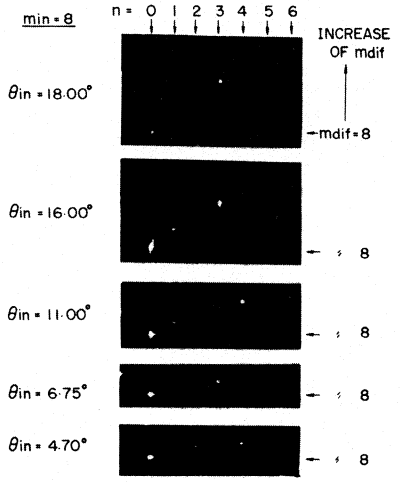

Fig. 2. Photographs of diffracted beam spots on the screen. The diffraction order n changes in the horizontal direction, and the diffracted mode index m_{dif} in the vertical direction.

and out of the planar optical waveguide through prism couplers. Excitation of a particular TE mode was accomplished by adjusting the angle incident to the input prism coupler.

When a single-mode incident beam in the waveguide (hereinafter referred to simply as an incident beam) impinged on the grating, many diffracted beam spots appeared simultaneously on both sides of the transmitted beam spot on the screen behind the output prism coupler. A diffracted beam spot always lay on one of the m lines, as shown in Fig. 1.

Fig. 2 shows photographs of typical diffraction patterns. The m lines mentioned above are too faint to be recorded in the photographs. In Fig. 2, the diffraction order is indicated by n and the incident and the diffracted mode indices are indicated by m_{in} and m_{dif}, respectively. Incident angle θ_{in} is the angle between the incident beam and the grating groove direction. Diffraction patterns changed definitely, even for small incident angle change, say, 0.15°.

The typical relationship between n and m_{dif} for $m_{in} = 11$ is diagramed in Fig. 3. In this diagram, filled circles show observed diffracted beam spots. Dashed line curves were obtained by connecting the circles corresponding to the simultaneously observed diffracted beam spots for given θ_{in} values. It is noted that the maximum mode index change from the incident mode to the diffracted mode becomes as high as 11 and a diffracted beam of as high as the sixth order is observed at $\theta_{in} = -8.43°$.

Diffracted beam intensity incident angle dependence is measured for $m_{in} = 11$ and the results are shown in Fig. 4. The diffracted mode index m_{dif} is indicated at the top of each

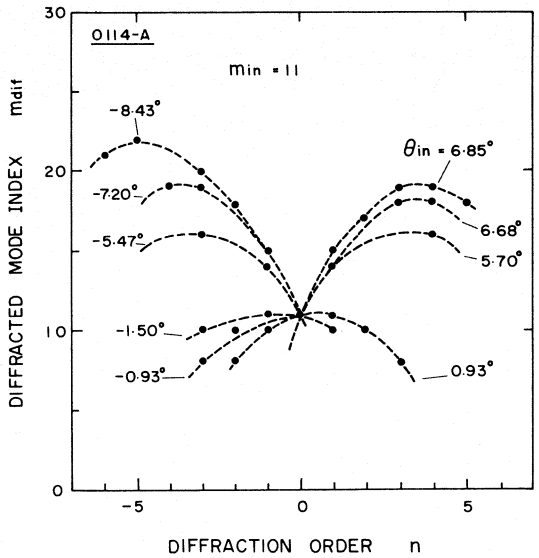

Fig. 3. Relationship between the diffracted mode index m_{dif} and the diffraction order n for $m_{in} = 11$.

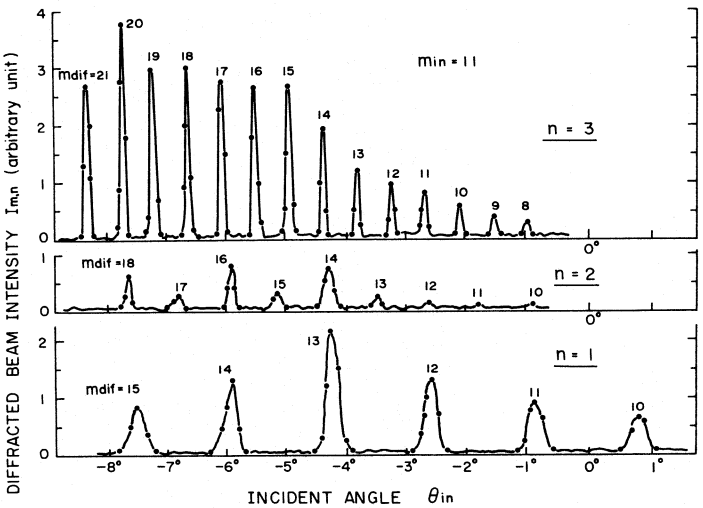

Fig. 4. Measurement of diffracted beam intensity versus incident angle θ_{in} for $m_{in} = 11$.

peak. For $n = 1$, angular width $\delta\phi_{in}$ of each peak is about 0.3°, which is nearly one-fifth of the angular interval $\Delta\theta_{in}$ between two adjacent peaks. Even if n increases, the ratio $\delta\theta_{in}/\Delta\theta_{in}$ is almost invariant. For $\theta_{in} = 2.6°$ and 4.3°, diffractions of several orders were simultaneously observed. Since vertical scales for different n's in Fig. 4 are the same, it is of interest that the maximum diffracted beam intensity for $n = 3$ is larger than that for $n = 1$.

These experimental results can be interpreted in terms of a multimode Bragg diffraction phase-matching diagram by using the measured relationship between wavenumbers, β's for the propagation mode, and mode indices. Fig. 5 shows effective refractive index β/k values for the TE mode, measured by the conventional prism-coupler technique. Here, $k = 2\pi/\lambda_0$ and λ_0 is vacuum light wavelength.

Fig. 6 shows translation of the observed relationships between n, m_{dif}, and θ_{in} given in Fig. 4, into a phase-matching diagram with the aid of measured β/k values. Magnitudes of concentric circle radii indicate β/k's for $m_{in} = 8$ to 14, shown in Fig. 5. Here, the abscissa is parallel to the grating grooves and the arrows show grating wave vectors. Solid, dotted, and

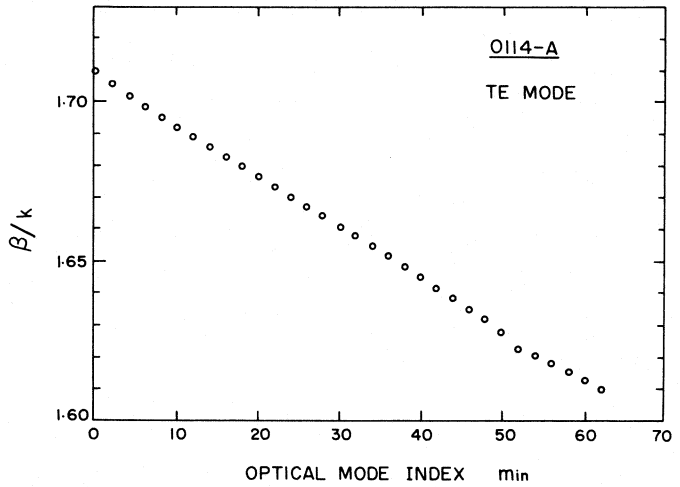

Fig. 5. Effective refractive index β/k for propagation mode in optical waveguide used in the experiment.

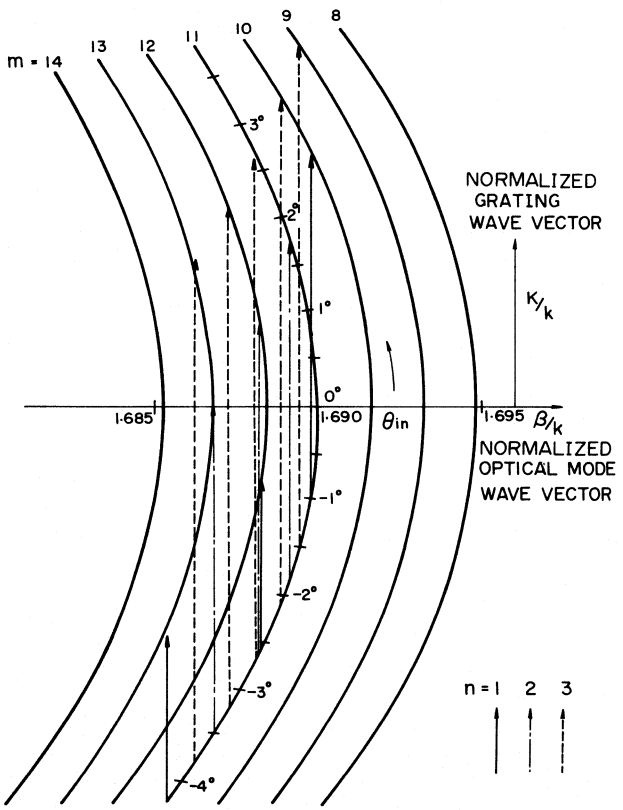

Fig. 6. Translation of observed n, m_{dif}, and θ_{in} relationships into the phase-matching diagram for multimode Bragg diffraction. Concentric circle radii β_m/k's were derived from the values in Fig. 5. The value of K/k is calculated from a 12-μm grating pitch. Solid, dotted, and dashed arrows represent diffractions of n = 1, 2, and 3, respectively.

dashed line arrows, whose lengths are equal to K/k, $2K/k$, and $3K/k$, respectively, distinguish diffractions of n = 1, 2, and 3 in Fig. 4, respectively. Since the 11th mode is excited in the experiment, incident angle θ_{in} is indicated on the circumference where m_{in} = 11, and each arrow starts from a point corresponding to θ_{in} giving the diffracted beam-intensity peak shown in Fig. 4.

As a result of such translation, most of the arrow vertices always come close to, or appear on some one of the circumferences, as shown in Fig. 6. Those circumferences give mode indices of the diffracted beams, which exactly agree with the mode indices obtained in the experiment. Thus, the phase-matching diagram for the multimode Bragg diffraction successfully explains the observed behavior of the diffracted beams in the experiment.

ACKNOWLEDGMENT

The authors wish to thank Dr. T. Uchida and Dr. K. Koizumi for their continuous encouragement and M. Sakaguchi and K. Nishikawa for their helpful suggestions.

REFERENCES

[1] A. Yariv, "Coupled-mode theory for guided-wave optics," *IEEE J. Quantum Electron.*, vol. QE-9, pp. 919–933, Sept. 1973.
[2] W. S. C. Chang, "Periodic structures and their application in integrated optics," *IEEE Trans. Microwave Theory Tech.*, vol. MTT-21, pp. 775–785, Dec. 1973.
[3] K. Ogawa and W. S. C. Chang, "Analysis of holographic thin film grating coupler," *Appl. Opt.*, vol. 12, pp. 2167–2171, Sept. 1973.
[4] H. Kogelnik and C. V. Shank, "Coupled-wave theory of distributed feedback lasers," *J. Appl. Phys.*, vol. 43, pp. 2327–2335, May 1972.
[5] T. Izawa and H. Nakagome, "Optical waveguide formed by electrically induced migration of ions in glass plates," *Appl. Phys. Lett.*, vol. 21, pp. 584–586, Dec. 1972.

Nd:$LiNbO_3$ Laser

I. P. KAMINOW AND L. W. STULZ

Abstract—**Laser action at 1.0845 μm is demonstrated in a neodymium-doped $LiNbO_3$ crystal pumped by 0.7525-μm krypton laser, which happens to coincide with a Nd absorption line. Although $LiNbO_3$ is a good laser host, with good electrooptic and acoustooptic properties, laser damage limits its applicability at present unless one is willing to maintain the crystal at 165°C.**

INTRODUCTION

Laser action in Nd-doped $LiNbO_3$ has been studied on several occasions [1] with the object of employing the excellent piezoelectric, electrooptic, acoustooptic, or nonlinear optic properties of the crystal within the laser medium. Laser emission at 1.0845 μm was first reported in 1967 [2] and 1969 [3] in flashlamp-pumped crystals of relatively poor quality.

At room temperature, strong pumping bands, containing sharp peaks, were noted [3] in the near infrared at 0.75, 0.81, and 0.88 μm, where semiconductor diode lasers or light-emitting diodes might serve as pump sources. We have found a close coincidence between the 0.7525-μm krypton laser line and one of these absorption peaks. With this pump, laser action was observed in a high-quality crystal placed inside a resonator formed by external mirrors. It was found, however, that even with the long wavelengths involved, optical index damage limits the laser life to a few minutes. Past experience indicates that this problem can be alleviated by warming the crystal or by reducing the Fe content in the $LiNbO_3$ crystal [4]. Our ultimate objective was to fabricate optical waveguide laser devices in these crystals.

EXPERIMENTAL

An a-axis boule of Nd:$LiNbO_3$ was pulled from a melt containing 0.5 percent of Nd_2O_3 by weight by Crystal Technology, Inc. The optical quality of the crystal was excellent.

Manuscript received February 10, 1975.
The authors are with Bell Laboratories, Crawford Hill Laboratory, Holmdel, N.J. 07733.

The measured absorption coefficients for the 0.7525-μm Kr laser line were $\alpha_{\parallel} = 1.2\ cm^{-1}$ (5.4 dB/cm) and $\alpha_{\perp} = 2.0\ cm^{-1}$ (8.7 dB/cm) for polarizations parallel and perpendicular to the c axis, respectively. The peak of the absorption line is within 0.5 Å of 0.7525 μm and the linewidth (full width at half maximum [FWHM]) is 25 Å for both polarizations. The fluorescent decay time τ was found to be 100±5 μs for either polarization when excited by chopped 0.7525-μm radiation.

A polished rod having dimensions 10 mm × 3 mm × 3 mm in the a, b, and c directions, respectively, was inserted in the resonator illustrated schematically in Fig. 1(a). Matching liquids with negligible absorption loss at 0.75 and 1.08 μm were employed to reduce the Fresnel reflection losses at the crystal faces. For CCl_4 ($n = 1.46$ at 1 μm) and $LiNbO_3$ ($n_{\perp} = 2.24$, $n_{\parallel} = 2.16$), the reflection coefficients are $r_{\perp} = 4.4$ percent and $r_{\parallel} = 3.7$ percent. The coatings on the flat and 2-cm-radius mirrors are identical and transmit 82 percent at 0.7525 μm and ~0.3 percent at 1.08 μm in air.

The resonator is designed so that the crystal length L is half the confocal length $b = (2\pi w_0^2 n)/\lambda$ at the laser wavelength where n is the appropriate refractive index and w_0 is the Gaussian beam-waist radius at the flat mirror. Then the mirror spacing d is 2.05 cm. The confocal requirement ensures minimum beam divergence over the crystal length; the beam diameter at the far end of the crystal is $\sqrt{2}$ times the value at the waist. At 1.08 μm, $w_0 = 40$ μm; at 0.75 μm, $w_0 = 33$ μm. A 14.6-cm focal-length lens was employed to match the pump and laser mode volumes, approximately, as indicated in Fig. 1(b); the pump-waist radius is estimated to be 40 μm. The pump beam is chopped at a 60-Hz rate with a duty cycle of $\frac{1}{34}$ (0.5-ms pulses) in order to inhibit laser damage.

Laser oscillation is observed with input pump powers as low as 280 mW. The Nd:$LiNbO_3$ laser power is detected with a silicon pin photodetector and oscilloscope. Pump laser damage causes the 1.08-μm output power to decrease as soon as it is observed; laser output disappears completely after about 10 min for 300 mW of 0.75-μm input. Taking the input mirror transmission and the absorption coefficient of the crystal into account gives an absorbed pump power that is 0.6 times the input power for parallel polarization and 0.7 times the input power for perpendicular polarization. Thus, with a duty cycle of $\frac{1}{34}$, approximately 3 J of absorbed pump energy over an effective cross-sectional area $\pi w_0^2 = 5 \times 10^{-5}\ cm^2$ terminates laser action due to damage effects.

The laser output is polarized parallel to the c axis irrespective of pump polarization. Plotting laser output versus pump input for parallel input polarization yields an incident pump threshold of 250 mW, or an absorbed power threshold of 150 mW, or an absorbed intensity at threshold of $3 \times 10^3\ W/cm^2$. The uncertainity in threshold measurements is estimated to be about ±20 percent because of the damage problem. For perpendicular input polarization, the incident threshold power is somewhat higher (about 275 mW) than for parallel input polarization.

Laser damage was studied as a function of temperature in an undoped and a Nd-doped $LiNbO_3$ crystal for 0.7525-μm light polarized parallel or perpendicular to the c axis. The 14.6-cm lens was used to focus the light into the crystals. The transmitted spot was observed on a screen. At room temperature, the spot became distorted and, after a time, reached an equilibrium shape which was elongated parallel to the c axis. Above a critical temperature, the equilibrium spot became identical with the unperturbed spot. This critical temperature was about the same for both crystals and for both polarizations. Moreover, the critical temperature was a weak function of input power, varying between 130°C at 60 mW and 160°C at 370 mW. Thus, if the Nd:$LiNbO_3$ crystal were maintained at 165°C, we would expect that laser action would not be limited by damage. These temperatures are close to those found [4] for annealing damage in $LiNbO_3$ at 0.5145 μm. Crystals damaged in the present laser experiments were routinely rehabilitated by heating them in an oven at about 200°C for a few hours.

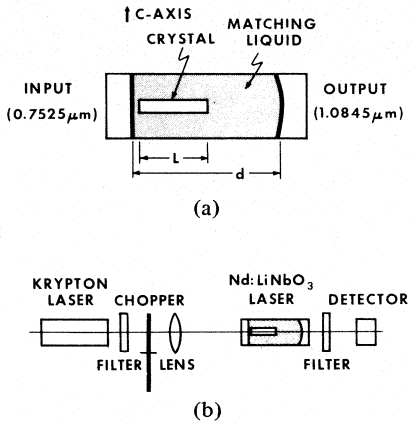

Fig. 1. (a) Nd:$LiNbO_3$ laser resonator. (b) Experimental arrangement.

CALCULATIONS

The cross section for laser emission in Nd:$LiNbO_3$ cannot be estimated without measurements of the Nd concentration in the crystal and of certain other spectroscopic quantities. However, the laser gain, which is an important parameter for laser-device design, can be estimated from the observed threshold power.

The threshold-power measurements given previously should be regarded only as upper limits because the rapid optical damage does not allow optimization of pump and cavity orientations. Further, the pump-beam volume probably does not match the laser resonator-mode volume very well. Thus we obtain only a *lower limit* on the laser gain using the measured quantities. The pump intensity varies exponentially as

$$I(z) = I_0 \exp(-\alpha_{\parallel} z) \tag{1}$$

along the crystal length z, for parallel polarization. Here I_0 is the pump power per unit area, $A \approx \pi w_0^2$, of the Gaussian beam at threshold. The overall gain, exp (gL), is obtained by integrating the gain per unit length $\gamma I(z)$ along the crystal length

$$gL = \int_0^L \gamma I(z)\, dz = \gamma I_0 (1 - \exp(-\alpha_{\parallel} L))\alpha_{\parallel}^{-1}\ \text{Np}. \tag{2}$$

Then equating the gain to the sum of the Fresnel reflection losses, the mirror loss, and an estimated 0.03-dB/cm bulk crystal loss, we find the gain per unit pump intensity

$$\gamma = 4.3 \times 10^{-5}\ cm/W. \tag{3}$$

If γ is calculated (rather than measured) for Nd:YAG using known values of cross section and other parameters [5] one obtains an *upper limiting* value which is about seven times this measured Nd:$LiNbO_3$ value.

Consider now a Nd:$LiNbO_3$ waveguide laser of length $L = 1$ cm and 4 × 4-μm cross section with dielectric mirrors coated on the ends. Such a waveguide might be formed by etching a ridge in a planar guide [6] or by diffusing metal through a mask [7]. Assume that the mirrors pass the pump completely and that the output mirror reflects 99 percent (10^{-2} Np, 4×10^{-2} dB) while the input mirror reflects 100 percent (0 Np, 0 dB) at 1.08 μm. Typical waveguide loss (scattering and absorption) for a good guide at 1.08 μm might be 20 percent (0.22 Np, 1 dB). Then the pump power required

at 0.7525 μm would be 1.5 mW. The power required in the 0.81- or 0.88-μm bands, where a GaAlAs semiconductor laser might serve as the pump, should be comparable.

Conclusions

Lithium niobate is a reasonably good host for a Nd laser; i.e., the gain is not markedly smaller than for Nd:YAG. However, optical index damage limits its utility at present. Heating the crystal to 165°C, though inconvenient, should eliminate the damage problem. Since $LiTaO_3$ is ordinarily less susceptible to damage than $LiNbO_3$, it might prove to be a better host.

The combination of laser gain and electrooptic or acousto-optic effect in the same medium offer some interesting device possibilities, particularly in optical waveguide configurations. A threshold pump power as low as 1.5 mW may be expected when the laser mode is confined within a 4-μm × 4-μm guide by a ridge or diffused strip guide. The resonator can be formed by mirrors on the ends of the guide or by a distributed feedback grating on the guide. The laser can be quenched or the power can be dumped from the cavity by an acoustic wave.

Alternatively, an electric field applied to the guide will change the phase length of the cavity electrooptically. Then if the resonator is sufficiently short that only one longitudinal mode receives gain, that mode can be shifted from the peak to the wings of the gain curve in order to switch the laser on or off. The required resonator length and modulating voltage are approximately 1 mm and 10 V, respectively. If a distributed feedback grating is used instead of mirrors, its resonant wavelength can be tuned electrooptically to turn the laser on or off.

References

[1] A. A. Kaminskii, "Laser and spectroscopic properties of activated ferroelectrics," *Sov. Phys.–Crystallog.*, vol. 17, p. 198, 1972.

[2] N. F. Evlanova, A. S. Kovalev, V. A. Koptsik, L. S. Kornienko, and A. M. Prokhorov, "Stimulated emission of $LiNbO_3$ crystals with neodymium impurity," *JETP Lett.*, vol. 5, p. 291, 1967.

[3] L. F. Johnson and A. A. Ballman, "Coherent emission from rare earth ions in electrooptic crystals," *J. Appl. Phys.*, vol. 40, p. 297, 1969.

[4] A. M. Glass, G. F. Peterson, and T. J. Negran, "Optical index damage in electrooptic crystals," in *An Introduction to Electrooptic Devices*, I. P. Kaminow Ed. New York: Academic, 1974.

[5] R. B. Chesler and J. E. Geusic, "Solid-state ionic lasers," in *Laser Handbook*, F. T. Arecchi and E. O. Schulz-DuBois, Ed. Amsterdam, The Netherlands: North-Holland, 1972.

[6] I. P. Kaminow, V. Ramaswamy, R. V. Schmidt, and E. H. Turner, "Lithium niobate ridge waveguide modulator," *Appl. Phys. Lett.*, vol. 24, p. 622, 1974.

[7] R. D. Standley and V. Ramaswamy, "Niobium diffused $LiTaO_3$ optical waveguides–Planar and embedded strip guides," *Appl. Phys. Lett.*, vol. 25, p. 711, 1974.

10.6-μm FM-Chirp Radar Using Narrow-Band Correlation Detection

W. E. BICKNELL, L. R. TOMASETTA, AND R. H. KINGSTON

Abstract–**We report the demonstration of high-resolution 10.6-μm radar-range resolution using a broad-band FM-chirp signal, but requiring only narrow-band performance in a heterodyne detector.**

Manuscript received February 17, 1975. This work was sponsored by the Advanced Research Projects Agency of the Department of Defense.

The authors are with the Massachusetts Institute of Technology Lincoln Laboratory, Lexington, Mass. 02173.

Introduction

Pulse-compression or FM-chirp waveforms have been utilized extensively for range-Doppler radar systems at microwave frequencies [1], [2]. Previously reported work on the use of FM waveforms at 10.6 μm has been concerned with short pulses having a relatively low time–bandwidth product and with a CW technique [3]–[5]. We wish to report the demonstration of high-resolution radar ranging using a broad-band chirped signal but requiring only narrow-band performance in the heterodyne photodetector. The waveform, a 500-MHz linear FM pulse of 10-μs duration, is generated as an optical sideband of the main laser frequency in a broad-band traveling-wave electrooptic modulator. By performing correlation detection at the optical frequency, using a chirped local oscillator, the required detector output bandwidth is markedly reduced and is determined by the desired range interval rather than the waveform bandwidth.

Experimental Setup

A diagram of the experimental arrangement is shown in Fig. 1. The FM-chirp generator employed to drive a traveling-wave electrooptic modulator had a total excursion of 500 MHz, a center frequency of 14.85 GHz, and a PRF of 10 kHz. A *Ku*-band traveling-wave tube amplified the peak-chirp drive power to 150 W. A stable, single-mode CO_2 laser provided 15 W in a beam that was focused through the modulator [6]. The modulator employed a 12-cm-length section of reduced-height waveguide containing two 6-cm-long AR-coated GaAs rods placed in tandem [7], [8]. To achieve phase-velocity matching, the rods only partially filled the waveguide in the transverse *H*-plane dimension [9]. Microwave impedance matching was achieved by use of waveguide input and output irises [10]. The crystal orientation of the rods was chosen to provide polarization modulation of the output beam. A polarizer comprised of a pair of Brewster-angle Ge plates was used following the modulator to extinguish the carrier component of the modulator output while transmitting the orthogonally polarized sideband components. The carrier power was further suppressed by a Fabry–Perot interference filter that was tuned to a single FM-chirped sideband center frequency. Just prior to entering the Fabry–Perot, the beam was transformed into a 0.5-cm-diam collimated mode.

The measured 10.6-μm throughput loss of the modulator was 2.7 dB. This was primarily attributed to the diffraction losses at the entrance and exit ports of the modulator, the small safety factor exhibited by the crystal cross section, and the end-face reflections of the two GaAs rods employed. The microwave throughput loss of approximately 3 dB was found to be primarily due to wall and metal-to-metal contact losses in the brass waveguide structure. The structure was water cooled. The beam exiting from the polarizer was com-

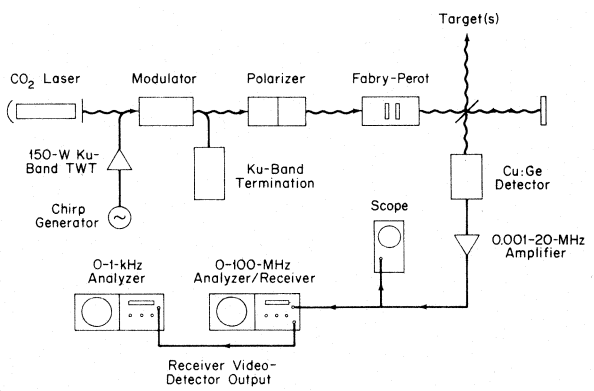

Fig. 1. Schematic of experimental apparatus.

prised of about 212 mW of unsuppressed carrier power along with 6.3 mW of power in each sideband. Throughput loss of the polarizer was 1.3 dB. The Fabry–Perot had a finesse of 30 and a FSR slightly in excess of 30 GHz. Its peak transmission throughput loss was measured to be 3.2 dB. The beam exiting from the Fabry–Perot was comprised of a single FM-chirped sideband of 3 mW and a residual unsuppressed carrier of 2 mW.

A Michelson interferometer transceiver system employing a nominal 3-dB beam splitter and a Cu:Ge detector was utilized. A 10X beam expander was used in the transmit/receive path to facilitate illumination of two retroreflector targets. The detector has an F60 FOV and a 4.2 K, 10-percent bandwidth filter centered at 10.6 μm. With the approximately 0.5-mW local-oscillator power incident upon the detector from the reference arm of the interferometer, its noise performance was determined by the noise figure of the post-detector video amplifier [11]. Use of HgCdTe detectors offers the possibility of a g–r noise-limited sensitivity with this local-oscillator power [12].

Stationary Targets

Fig. 2 shows the amplitude-versus-time and the frequency-versus-time characteristics of a transmit and receive waveform. The received wave was delayed by Δt due to the round trip to and from the target. Here Δt was less than or equal to 0.267 μs, which accrued from using a maximum range of 40 m. When the transmit and receive waveforms were correlated with the Cu:Ge detector, a difference frequency Δf appeared at the output of the detector. It is seen from Fig. 2 that for the case here

$$\Delta f\,(\text{MHz}) = 50 \cdot \Delta t\,(\mu\text{s}) = \tfrac{1}{3} R\,(\text{m})$$

where R is the range in meters.

Fig. 3 shows the return from a mirror spaced 1.7 m further from the detector than the reference or local-oscillator-arm mirror of Fig. 1. The 570-kHz difference frequency is evident. The oscillation is superimposed on a dc pulse that is due to the local-oscillator signal.

Fig. 4 shows the spectrum of a pulse train due to a retroreflector target at 40 m. This was observed on the 0–100-MHz spectrum analyzer of Fig. 1. The center frequency of the spectrum was 13.3 MHz, and the spectrum's amplitude envelope exhibits close to the expected sinc-function dependence on frequency.

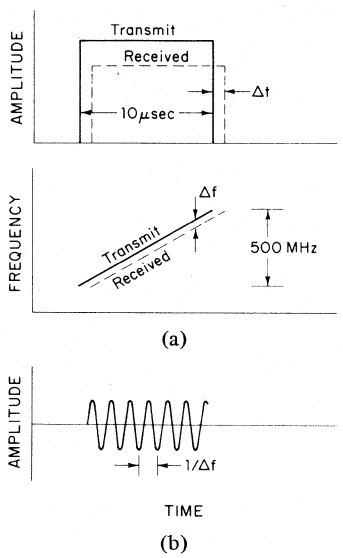

Fig. 2. (a) Amplitude versus time and frequency versus time of the transmit and receive waveforms. (b) Amplitude versus time of the correlated waveform.

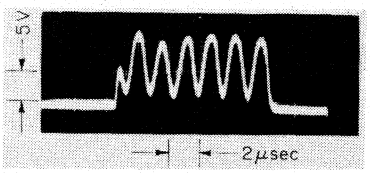

Fig. 3. Correlated return from a mirror with a 1.7-m path-length difference.

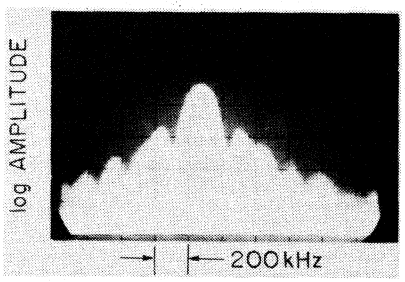

Fig. 4. Power spectrum of a retroreflector at a 40-m range.

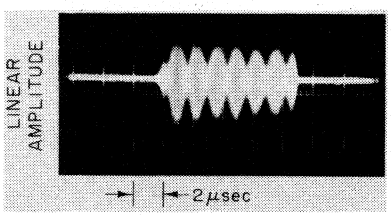

Fig. 5. Correlated return from two retroreflectors at 40-m range, separated by 2 m.

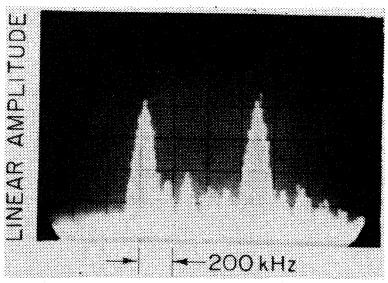

Fig. 6. Power spectrum of the correlated return shown in Fig. 5.

Figs. 5 and 6 show the time and frequency-domain display of the correlated return from two retroflectors at a nominal 40-m range, but separated by 2 m. The time-domain oscilloscope display of Fig. 5 shows the envelope-modulated waveform of the sum of two individual 13-MHz bursts separated in frequency by 333 kHz. The envelope modulation frequency f_m is given by

$$f_m\,(\text{MHz}) = \tfrac{1}{6} \Delta R\,(\text{m})$$

where ΔR is the target's separation. In the frequency domain two distinct spectral peaks are evident in Fig. 6. Resolution of two returns could be readily discerned on the 0–100-MHz analyzer for separations as close as 0.6 m. Below about 0.6-m separation, the spectral peaks observed on the analyzer became separated less than the reciprocal of the correlation-waveform duration, and the ability to distinguish the separate spectral peaks tended to diminish.

By use of an FM-chirp waveform and correlation-detection

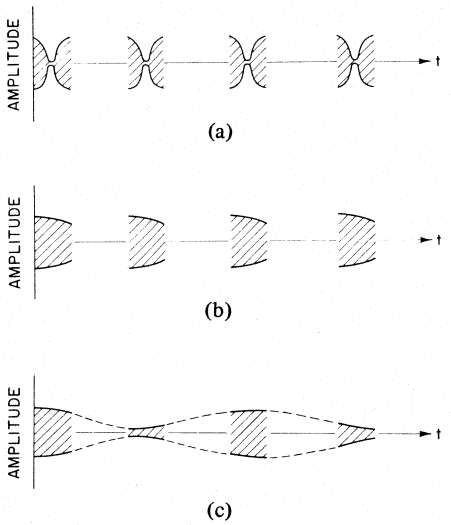

Fig. 7. Envelope of the correlated waveforms for the following. (a) Two targets that are marginally resolved in range. (b) Two stationary targets that cannot be resolved in range. (c) Two targets that cannot be resolved in range but one target moving with respect to the other.

range resolution appropriate for a 500-MHz bandwidth waveform can clearly be obtained with a detector and analyzing system that has a considerably smaller bandwidth.

Moving Targets

The waveform employed could be used to distinguish moving targets from stationary targets within a range-resolution cell. In radar terminology this is known as moving-target-indicator (MTI) capability [1]. This capability results from the effect of target motion on the detected, correlation waveform shown in Fig. 2(b). Target motion causes the phase of the correlation beat signal to change from pulse to pulse. The effect of target motion could thus be discerned by monitoring the phase of the correlation pulse that passes through a given spectrum-range window. Such monitoring was not possible with the instrumentation at hand, and therefore a method utilizing the effect of target motion on the envelope of the return from two targets was utilized instead. The utilized technique is analogous with "non-coherent MTI" [1].

Fig. 7(a) shows the envelope of the correlated waveform for two targets that are marginally resolvable in range. The difference frequency of the returns causes approximately one cycle of envelope modulation. As the targets are moved closer together their correlated return frequencies become sufficiently close such that only a small fraction of an envelope cycle occurs over the duration of a correlation pulse. Because of the targets' stationary position the envelope is repeated for each pulse. This case is illustrated in Fig. 7(b). If one target moves with respect to the other, however, the phase of the envelope modulation progresses from pulse to pulse, as shown in Fig. 7(c). The progressing envelope of the pulses then gives, in effect, a sampling of the Doppler beat.

To verify this MTI capability the 0–100-MHz analyzer was tuned to the nominal 13-MHz-range frequency for two retroreflector targets placed at 40 m but separated by a few centimeters. One retroreflector was moved to give a 500-Hz Doppler. The output of the tuned analyzer was, after being envelope detected and low-pass filtered, fed into a second 0–1-kHz spectrum analyzer. Fig. 8 shows the output spectrum of the 0–1-kHz analyzer. The 500-Hz peak vanished when

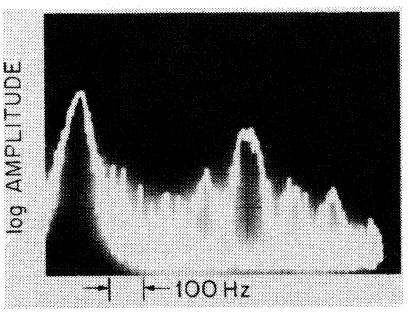

Fig. 8. Power spectrum of envelope waveform showing the relative Doppler of two targets unresolved in range.

the return from either the moving or stationary retro was blocked.

The performance of large time–bandwidth exchange waveforms can be realized at laser-carrier frequencies because of the phase coherence of the microwave FM-chirp generator and the use of correlation detection. With this technique range resolution is limited by only the bandwidth of the transmit waveform, and not by the bandwidth of the detector.

Acknowledgment

The authors wish to thank J. Margolin for helpful discussions, and D. Bromaghim for the loan of a microwave FM-chirp generator.

References

[1] M. I. Skolnik, *Introduction to Radar Systems*. New York: McGraw-Hill, 1962, secs. 3.3 and 10.9.
[2] A. W. Rihaczek, *Principles of High-Resolution Radar*. New York: McGraw-Hill, 1969, ch. 7.
[3] E. T. Treacy, "Generation of chirped pulses at 10.6 microns wavelength," *Proc. IEEE* (Lett.), vol. 56, pp. 2053–2054, Nov. 1968.
[4] R. L. Abrams, "Characteristics of 10.6-μ chirped pulses, *IEEE J. Quantum Electron.* (Corresp.), vol. QE-5, pp. 522–523, Oct. 1969.

[5] T. E. Honeycutt and W. F. Otto, "FM-CW radar range measurement with a CO_2 laser," *IEEE J. Quantum Electron.* (Corresp.), vol. QE-8, pp. 91–92, Feb. 1972.
[6] C. Freed, "Design and short-term stability of single-frequency CO_2 lasers," *IEEE J. Quantum Electron.*, vol. QE-4, pp. 404–408, June 1968.
[7] F. -S. Chen, "Modulators for optical communication," *Proc. IEEE (Special Issue on Optical Communication)*, vol. 58, pp. 1440–1457, Oct. 1970.
[8] M. E. El-Shandwily and S. M. El-Dinary, "Traveling-wave coherent light-phase modulator," *IEEE Trans. Microwave Theory Tech.*, vol. MTT-20, pp. 132–137, Feb. 1972.
[9] P. H. Vartanian, W. P. Ayres, and A. L. Helgesson, "Propagation in dielectric slab loaded rectangular waveguide," *IRE Trans. Microwave Theory Tech.*, vol. MTT-6, pp. 215–222, Apr. 1958.
[10] C. T. M. Chang, "Equivalent circuit for partially dielectric-filled rectangular-waveguide junctions," *IEEE Trans. Microwave Theory Tech.*, vol. MTT-21, pp. 403–411, June 1973.
[11] R. J. Keyes and T. M. Quist, "Low-level coherent and incoherent detection in the infrared," in *Semiconductors and Semimetals*, vol. 5. New York: Academic, 1970, pp. 321–359.
[12] D. L. Spears, I. Melngailis, T. C. Harman, and C. Freed, "High-speed 10.6 μm HgCdTe photodiodes," *Solid State Res.*, no. 2, M.I.T. Lincoln Lab., Lexington, pp. 2–6, 1973.

Correction to "Experiments and Theory of Nanosecond Pulse Extraction in an Atmospheric Pressure CO_2 Amplifier"

G. GIRARD

In the above correspondence,[1] the last sentence in the second paragraph of Section III which reads: "Experimental results are expected to fall between these curves." should be deleted.

The experimental results do fall between the two curves of Fig. 4 (as shown when comparing Figs. 2 and 4). The two curves on Fig. 4 should not, however, be considered as upper and lower limits for experimental values as could be inferred from the last sentence as given in the second paragraph of Section III in the original correspondence.

Manuscript received February 15, 1975.

The author is with the Section Sources d'Ondes Cohérentes, Département Recherches Physiques de Base, Laboratoires de Marcoussis, Centre de Recherches de la Compagnie Générale d'Electricité (CGE), Marcoussis, France.

[1] G. Girard, J. C. Farcy, A. Fertal, and M. Michon, *IEEE J. Quantum Electron.* (Corresp.), vol. QE-10, pp. 901–902, Dec. 1974.

Notes and Lines

Two-Electron Laser Transition in SN(I)?

D. G. SUTTON, L. GALVAN, AND S. N. SUCHARD

Abstract—**A new laser oscillation has been observed in a pulsed discharge of He and $SnCl_4$. This oscillation at 1.061 μm corresponds to the $5s5p^3\ {}^3D_1^\circ \longrightarrow 5s^2 5p6p\ {}^3P_2$ transition in Sn(I).**

The purpose of this note is to report a new laser transition obtained in mixtures of $SnCl_4$ and He. The discharge tube and cavity are identical to those described in earlier publications [1], [2]. The laser tube consists of two 1.25-m (2.5-cm ID) Lucite pipes, each fitted with 251 pin-pairs of 470-Ω resistors mounted transverse to the optical axis in a double-helical configuration. The gap between resistor pairs is 1.9 cm. One of these helices is connected to ground, which forms the cathode of the discharge circuit; the other is connected to a pulsed power supply triggered by a spark gap. The resultant discharge has a duration of 2 μs. The ends of the laser tube are sealed by suprasil windows at Brewster's angle. A stable optical cavity is formed about the laser tube by two silver-coated mirrors: a total reflector with a radius of curvature of 11.5 m and a flat output coupler with a 1-mm hole in its center. The entire length of the optical cavity is 3.2 m.

Laser output is directed into a screen room where the beam is split into two parts by a sapphire flat. One of these beams is directed to an InSb detector to monitor the total laser emission; the other is directed through a 0.5-m monochromator to an identical InSb detector to monitor the spectrally resolved emission. Detector response is monitored with a fast oscilloscope.

Manuscript received January 3, 1975. This work reflects research supported by the Defense Advanced Research Projects Agency of the Department of Defense under USAF Space and Missile Systems Organization (SAMSO) Contract F04701-74-C-0075.

The authors are with The Aerospace Corporation, El Segundo, Calif. 90245.

When small amounts of $SnCl_4$ (0.05–3 torr) are discharged in a bath of He (85–250 torr) at 65 kV, a single pulse of 1.061-μm laser radiation is detected. The pulse initiates 3 μs after the termination of the discharge, has a 3 μs half-width [full width at half maximum (FWHM)], and has a total duration of 8 μs.

When Moore's tables [3] are gleaned for transitions that occur at this wavelength, the only possibility that satisfies the electronic dipole selection rules is the $5s5p^3\ {}^3D_1^\circ \longrightarrow 5s^2 5p6p\ {}^3P_2$ transition in the Sn(I) spectrum. Helium, chlorine, and their positive ions have no dipole-allowed transitions at this wavelength.

In Meggers' 1940 analysis of the Sn(I) spectrum [4], the upper laser state with a term value of 56658 cm^{-1} was designated as the ${}^1P_1^\circ$ state of the $5p({}^2P_{3/2})6d$ configuration. In Shenstone's reinterpretation, which appears in Moore [3, vol. III, pp. 74–79], the state at 56658 cm^{-1} is reassigned to be $5s5p^3\ {}^3D_1^\circ$. If Shenstone's analysis is correct, the 1.061-μm laser oscillation arises from stimulated emission on a two-electron transition.

It may be noted that the energy required for the atomization of $SnCl_4$ plus the term value of $Sn({}^3D_1^\circ)$

$$SnCl_4 \longrightarrow Sn({}^3D_1^\circ) + 4Cl$$

is 446 kcal, nearly equal to the 455 kcal carried by the $He({}^3S_1)$ metastable. This may indicate that metastable helium plays an important role in the excitation mechanism, especially since the laser action occurs in the afterglow of the discharge.

References

[1] D. G. Sutton, L. Galvan, P. R. Valenzuela, and S. N. Suchard, "Atomic laser action in rare gas-SF_6 mixtures," The Aerospace Corp., El Segundo, Calif., Tr-0074(4641)-7, 1974.

[2] D. G. Sutton, L. Galvan, and S. N. Suchard, "New laser oscillation in the oxygen atom," to be published.

[3] C. E. Moore, *Atomic Energy Levels* (Circular no. 467), vol. I and vol. III. Washington, D.C.: NBS, June 1949 and May 1958.

[4] W. F. Meggers, "First spectrum of tin," *J. Res. Nat. Bur. Stand.*, vol. 24, p. 153, 1940.

Contributors

D. H. Auston, photograph and biography not available at the time of publication.

*



Edward A. Ballik (S'56–M'60) was born in Toronto, Ont., Canada, on June 28, 1931. He received the B.Sc. degree in engineering physics from Queen's University, Kingston, Ont., Canada, in 1959, and the D.Phil. degree in physics from the University of Oxford, Oxford, England, in 1964.

Since 1960 he has been active in the laser field. He is currently with the Department of Engineering Physics at McMaster University, Hamilton, Ont., Canada.

*



Gary C. Bjorklund (M'75) was born in Passaic, N.J., on November 17, 1946. He received the B.S. degree in physics from the Massachusetts Institute of Technology, Cambridge, and the M.S. and Ph.D. degrees in applied physics from Stanford University, Stanford, Calif., in 1968, 1969, and 1974, respectively. His thesis work was on nonlinear optics in gases and on vacuum–ultraviolet holography.

From 1969 to 1971 he served in the U.S. Army. In October 1974 he joined Bell Laboratories, Holmdel, N.J. His current interests are in nonlinear optics and laser physics.

*

William K. Burns, for a photograph and biography please see page 62 of the January 1975 issue of this JOURNAL.

*



Robert L. Carman was born in Bay Shore, N.Y., on January 15, 1941. He received the A.B. degree in physics, mathematics, and chemistry from Adelphi University, Garden City, N.Y., and the Ph.D. degree in physics from Harvard University, Cambridge, Mass., in 1958 and 1968, respectively.

In 1957 he was a National Science Foundation Research Fellow working in solid-state physics. From 1958 through 1964 he worked in high-energy physics at the Brookhaven National Laboratories cosmotron and sychrotron, as well as at the Cambridge Electron Accelerator as a Member of the Cambridge Bubble Chamber Group. From 1964 to 1968 he was a Staff Member of the Lincoln Laboratory, Massachusetts Institute of Technology, where his work on lasers and high-intensity light propagation began. During this period he consulted for the National Aeronautics and Space Administration, the Institute for Defense Analysis, and several commercial firms. From 1968 through 1970 he was a Postdoctorate Research Fellow with the Department of Engineering and Applied Physics, Harvard University, where work was begun on ultrahigh brightness lasers and nonlinear optics utilizing picosecond pulses. During this period he remained a consultant at the Lincoln Laboratory and carried out some joint work with United Aircraft's Research Laboratory. From 1970 to 1974 he was employed by the Lawrence Livermore Laboratory, University of California, Livermore, where for the latter three years he was a Group Leader in charge of the development of advanced solid-state laser oscillators, advanced research in solid-state laser-system design and diagnostics, and basic research in nonlinear optics. In 1974 he transferred to the Staff of the Los Alamos Scientific Laboratory, University of California, Los Alamos, N. Mex., where he is currently concerned with experimental aspects of high-energy lasers, the nonlinear optics of laser-produced plasmas, and advanced concepts in high-energy laser systems.

*

J. C. Farcy, photograph and biography not available at the time of publication.

*

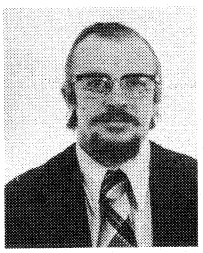

Kenneth D. Foster was born in Ontario, Canada, on January 11, 1941. He received the B.Sc. degree in chemistry and the Ph.D. degree in physical chemistry, both from the University of Alberta, Edmonton, Alta., Canada, in 1961 and 1967, respectively.

In 1967 he was engaged in postdoctoral studies at the University of Florida, Gainesville, which involved the investigation of Penning ionization reactions using beams of metastable helium atoms. Since 1969 he has been with the Defence Research Establishment Valcartier (DREV), Valcartier, P.Q., Canada, where he is working on chemical lasers.

*



Brian K. Garside was born in Ashton, Lancs., England, on January 29, 1940. He received the B.A. and Ph.D. degrees in physics from the University of Oxford, Oxford, England, in 1962 and 1966, respectively.

In 1966 he became a member of the Technical Staff of Bell Laboratories, Holmdel, N.J., where he was engaged in investigations of gas lasers. Since 1968 he has been with the Department of Engineering Physics at McMaster University, Hamilton, Ont., Canada, where he has continued to work on laser systems.

G. Girard, photograph and biography not available at the time of publication.

*

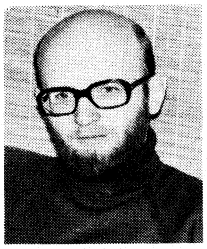

J. O. Henningsen was born in Sønderborg, Denmark, on February 11, 1939. He received the M.S. degree in electrical engineering and the technical licentiate degree, both from the Technical University of Denmark, Lyngby, in 1963 and 1967, respectively. His dissertation was on cyclotron resonance in metals.

He was a staff member at Physics Laboratory I, at the Technical University of Denmark until 1970, working with resonances and electromagnetic-wave propagation in solids at microwave frequencies. He continued this work at far-infrared frequencies at the University of Maryland, College Park, until 1972. Since then he has been a member of Physics Laboratory I, H. C. Ørsted Institute, University of Copenhagen, Copenhagen, Denmark, working with far-infrared lasers and their application in solid-state physics.

*



G. Benjamin Hocker (S'69–M'69) was born in Harrisburg, Pa., in September 1942. He received the B.E.P degree and the Ph.D. degree in applied physics, both from Cornell University, Ithaca, N.Y., in 1965 and 1970, respectively.

Since 1970 he has been an Assistant Professor in the Department of Electrical Engineering at the University of Minnesota, Minneapolis. He has done research on mass-spectroscopic studies of molecular-gas lasers, and on materials and devices for integrated optics.

Dr. Hocker is a member of the Optical Society of America and the American Society for Engineering Education.

*



H. G. Jensen was born in Vojens, Denmark, on August 7, 1926. He received the B.Sc. degree from the Technical University of Denmark, Copenhagen, in 1948, and the Ph.D. degree from Copenhagen University, Copenhagen, in 1951.

He joined the H. C. Ørsted Institute, University of Copenhagen, in 1963. During 1965 and 1966 he was a Visiting Scientist at the Center for Materials Science, Cambridge, Mass., working with nonlinear optics. His research interests include electromagnetic-field theory, quantum optics, and laser physics.

Dr. Jensen is a member of the Danish Physical Society and the European Physical Society.

*

A. M. Johnson, photograph and biography not available at the time of publication.

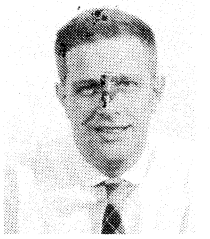

George H. Kimbell received the B.A. (Hons.), M.A., and Ph.D. degrees in physical chemistry from the University of Toronto, Toronto, Ont., Canada, in 1961.

For two years he worked as a Research Assistant at the Imperial College of Science and Technology, London, England, and in 1963 he joined the Canadian Defence Research Estabment Valcartier (DREV), Valcartier, P.Q., Canada. As leader of the Combustion Group since 1967, he became Head of the Chemistry Section, Propulsion Division in 1971.

*

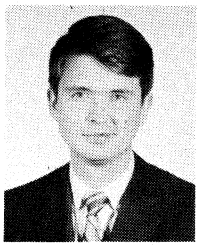

William B. Lacina received the B.S. degree in 1962 from Rensselaer Polytechnic Institute, Troy, N.Y., where he was a Union Carbide Scholar. He received the M.S. and Ph.D. degrees in physics from Harvard University, Cambridge, Mass., in 1963 and 1969, respectively, where he held a National Science Foundation Predoctoral Fellowship. His doctoral research involved an experimental and theoretical study of the effects of disordering on the phonon optical properties of mixed crystal systems.

He has held summer research appointments at the Oak Ridge National Laboratory, Oak Ridge, Tenn., and the Lawrence Radiation Laboratory, Livermore, Calif. In 1969 he joined the Northrop Research and Technology Center, Hawthorne, Calif., where he has been involved with the study of molecular gas lasers, nonlinear optical effects in the infrared, and pulsing and modulation techniques for the CO_2 laser. Current work is directed toward an understanding of the molecular and plasma kinetic processes in the electrically excited CO laser, with emphasis on design of high-power and high-efficiency pulsed and CW laser systems.

*



Gary L. McAllister was born in Quincy, Ill., on November 4, 1939. He received the B.S. degree in electrical engineering from Iowa State University, Ames, in 1961, the M.S. degree in electrical engineering from Purdue University, West Lafayette, Ind., in 1965, and the Ph.D. degree in electrical engineering from the University of Southern California, Los Angeles, in 1969.

From 1961 to 1963 he served as Instructor in the U.S. Army Signal School, Fort Monmouth, N.J. From 1965 to 1966 he was a member of the Technical Staff of Hughes Aircraft Company, Culver City, Calif., engaged in research on saturated absorption of laser radiation and solid-state laser amplifiers. From 1969 to 1971 he was an Assistant Professor in the Department of Electrical Engineering, Colorado State University, Fort Collins. In 1971 he joined the Northrop Research and Technology Center, Hawthorne, Calif., where he was involved with the study of high-power molecular gas lasers. In 1974 he joined the Exxon Corporation in Richland, Wash., where he is now working on laser techniques for isotope separation.

*

M. Michon, photograph and biography not available at the time of publication.

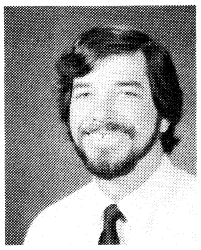

Michael J. Moran was born in Oakland, Calif., on June 4, 1946. He received the B.S. degree in engineering physics from the University of California at Berkeley, and the M.S. degree in physics from the University of New Hampshire, Durham, in 1968 and 1970, respectively.

He is currently employed at the Lawrence Livermore Laboratory, University of California, Livermore, and is a doctoral candidate at the University of California at Davis.

*

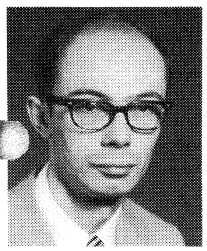

Thomas L. Paoli (S'59-M'73) was born in Springfield, Ill., on May 27, 1940. He received the B.S. degree in electrical engineering and the B.A. degree (magna cum laude), both from Brown University, Providence, R. I., in 1962, and the Ph.D. degree in applied physics from Stanford Univeristy, Stanford, Calif., in 1967. During the summer of 1964 he attended the Summer School of Theoretical Physics of the University of Grenoble, Les Houches, France.

He was a Research Assistant and a National Science Foundation Fellow (1962-1967) at Stanford University, working on optical coherence theory. He has also held summer positions with the Applied Research Laboratory of Sylvania Electronic Systems, where he worked on communication theory, and with the Electronic Defense Laboratory of Sylvania, where he worked on laser theory. In 1967 he joined Bell Telephone Laboratories, Inc., Murray Hill, N.J., where his research has been concentrated on GaAs injection lasers.

Dr. Paoli is a member of Phi Beta Kappa, Tau Beta Pi, Sigma Xi, and the American Physical Society.

*



John Reid was born in Littleborough, Lancs., England, on December 14, 1948. He received the B.A. degree in physics from the University of Oxford, Oxford, England, in 1970, and the M.Sc. and Ph.D. degrees from McMaster University, Hamilton, Ont., Canada, in 1972 and 1975, respectively.

From 1970 to 1974 he was engaged in the investigation of CO_2 lasers. He is currently working on laser spectroscopy in the Division of Physics of the National Research Council of Canada, Ottawa, Ont., Canada.

*

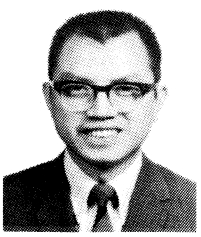

Chiao-Yao She (S'61-M'65) was born in Fukien, China, on August 4, 1936. He received the B.S. degree from the National Taiwan University, Taipei, Taiwan, the M.S. degree from the North Dakota State University of Agriculture and Applied Sciences, Fargo, and the Ph.D. degree from Stanford University, Stanford, Calif., all in electrical engineering, in 1957, 1961, and 1964, respectively.

He was a Research Assistant from 1961 to 1964 and then a Research Associate for the following summer at the Stanford Electronics Laboratories. From 1964 to 1968 he was an Assistant Professor of Electrical Engineering at the University of Minnesota, Minneapolis. He joined the Colorado State University, Fort Collins, in September 1968 where he is now an Associate Professor of Physics. His research interests include both theoretical and experimental aspects of light-scattering spectroscopy and quantum electronics.

Dr. She is a member of the American Physical Society, the Optical Society of America, Eta Kappa Nu, and Sigma Xi.

*



David R. Snelling was born in Bognor Regis, England, on September 14, 1937. He received the B.Sc. and Ph.D. degrees in chemistry, both from Birmingham University, Birmingham, England, in 1959 and 1962, respectively.

From 1962 to 1964 he was engaged in postdoctoral studies at the University of Toronto, Toronto, Ont., Canada, with Dr. J. C. Polanyi, and from 1964 to 1966 he worked with Dr. E. J. Bair at Indiana University, Bloomington. On joining the Defence Research Establishment Valcartier (DREV), Valcartier, P.Q., Canada, in 1966, he was engaged in research into upper atmospheric photochemistry. Since 1971 he has headed a Chemical Laser Research Group at DREV.

*



B. R. Suydam (M'72) was born in New Jersey on October 12, 1916. He received the B.S. degree from Pennsylvania State University, University Park, and the Sc.D. degree in physics from the Massachusetts Institute of Technology, Cambridge, in 1937 and 1940, respectively.

From 1940 to 1947 he worked on design of electronic instruments for the U.S. Naval Proving Ground, Dahlren, Va. Since 1947 he has been a Staff Member at the Los Alamos Scientific Laboratory, Los Alamos, N. Mex., where he has worked first on effects of nuclear weapons, and later in theoretical plasma physics as applied to the controlled thermonuclear reaction research. Recently, remaining in the broad field of CTR research, he has switched to the field of nonlinear optics.

Dr. Suydam is a fellow of the American Physical Society.

*

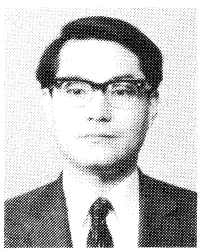

Nobuo Takeuchi was born in Tokyo, Japan, in 1941. He received the B.Sc., M.Sc., and Ph.D. degrees, all from the University of Tokyo, Tokyo, in 1963, 1965, and 1969, respectively.

His research fields are laser spectroscopy, nonlinear optics, and atomic coherent phenomena. He joined the Institute for Solid State Physics at the University of Tokyo in 1968, was at Columbia University from 1971 to 1973, and received a postdoctoral fellowship from the National Research Council of Canada, where he was from 1973 to 1975. In 1975 he joined the National Institute for Environment, Ibaraki, Japan, as a Senior Research Staff member.

Dr. Takeuchi is a member of the American Physical Society, the Physical Society of Japan, and the Japan Society of Applied Physics.

*

P. Vincent, photograph and biography not available at the time of publication.

SECOND SUMMER COLLOQUIUM on ELECTRONIC TRANSITION LASERS

Marine Biology Laboratory Conference Center
Woods Hole, Mass.

SEPT. 17-19, 1975



Contributed papers are solicited on the following subjects:

- Chemically pumped, electronic transition lasers
- Electrically, collision, or optically pumped electronic transition lasers
- Branching ratios and quantum yields for chemiluminescent systems
- Deactivation and quenching rates for electronically excited systems
- Spectroscopic analysis and potential curves for laser candidate molecules

Proceedings to be published by M.I.T. Press



For Information & Applications Write to:
J. Steinfeld, 2-221 M.I.T., Cambridge, Massachusetts 02139
Applications Due June 1st / Summaries of Papers Due August 1st



Sponsored by:
Chemistry Department
and Spectroscopy Laboratory, M.I.T.
Air Force Weapons Laboratory
Aerospace Corporation
Joint Council on Quantum Electronics

Financial Support Provided by
Air Force Office of Scientific Research

Influence of Contaminants on the CO_2 Electric-Discharge Laser

PETER BLETZINGER, SENIOR MEMBER, IEEE, DAVID A. LABORDE, WILLIAM F. BAILEY, WILLIAM H. LONG, JR., PETER D. TANNEN, AND ALAN GARSCADDEN, SENIOR MEMBER, IEEE

Abstract—In CO_2-N_2-He electric-discharge lasers, small concentrations of impurities may be present in the original gases, or new species may be generated by the discharge. In order to determine the effects of such impurities, controlled amounts of possible contaminants were introduced into the amplifier of a CO_2 probe-amplifier system. Small-signal gain was reduced in all cases when CO, O_2, NO, N_2O, or NO_2 molecules were added. It was found that less than 0.1 percent of NO_2 or N_2O markedly reduces the laser gain and alters the discharge impedance. A discharge model which describes a three-component positive-column plasma (electrons, positive ions, and negative ions) yields results consistent with the observations. The influence of attachment and detachment rates on molecular gas discharge characteristics and stability are studied.

INTRODUCTION

THE CO_2 dc discharge laser operates at high efficiency in the glow discharge mode with an optimum mixture of CO_2, N_2, and He which depends on the total pressure, flow rate, current density, and discharge geometry [1]. The operating conditions for a given geometry of this weakly ionized plasma ($n^+/N = 10^{-7}$) are determined by a self-consistent balance of charged-particle production and loss. The discharge properties are controlled by collisional kinetics, plasma chemistry, laser operation, and boundary conditions.

In those papers dealing with mass-spectrometric measurements of CO_2 laser discharges [2]-[6] the main emphasis has been on the rate of dissociation of CO_2 into CO and O_2 and how this dissociation is changed by operating conditions or gas additives. However, the possible effects on laser performance of the other minor species that are known to exist [7] have not been measured. Therefore, the purpose of the present study was to determine the influence of nitrogen oxides and other candidate dissociation products on the discharge properties and optical gain characteristics of a CO_2 laser.

EXPERIMENT

Calibrated amounts of contaminant gases were added to an open-cycle flowing CO_2-N_2-He laser discharge. Discharge voltage and small-signal gain were monitored as functions of current. The discharges studied were at total pressures of 5, 10, and 15 torr. The amplifier-tube active length was approximately 57 cm between hollow Kovar electrodes in a water-cooled Pyrex tube, with a 22-mm internal diameter (ID). The gas flow rates of CO_2-N_2-He were in the ratio 5:10:85, and the gas residence time in the discharge was approximately 20 ms.

A frequency stable laser,[1] operating on the $P20$ line of the 10.6-μ transitions, was used to measure small-signal gain. The intensities of the reference and amplified beam were measured simultaneously using thermocouples with digital readouts. To compensate for any fluctuations in the probe oscillator output power, the ratio of these two intensities was evaluated. The discharge current was swept linearly from 5 to 75 mA in a period of approximately 5 min. The probe beam from the oscillator was 1.57-mm diameter at its 6-dB points at the input window and 4.6-mm diameter at the exit window, the distance between windows being 110 cm. The total power in the probe beam was typically 100 mW.

RESULTS

The principal results are shown in Figs. 1-5. The upper half of each figure shows the amplifier gain as a function of the discharge current for selected amounts of added contaminant. The lower half shows the discharge voltage (measured simultaneously with the gain data) as a function of the same parameters. The abrupt transition in the discharge characteristics, apparent on some of the diagrams, corresponds to the glow-to-arc transition. Extremely noisy current-voltage curves correspond to the presence of large-amplitude low-frequency striations. For comparison with theoretical modeling, our primary interest will be in the glow regime at low currents with small amounts of contaminants.

Figs. 1 and 2 show the effects of adding CO and O_2, respectively, to a discharge operating at 15-torr pressure in CO_2-N_2-He. Similar results were obtained at 10 and 5 torr. The discharge impedance and the amplifier gain were relatively insensitive to the presence of added CO or O_2. The impedance was increased by CO but decreased by O_2.

Fig. 3 shows the results of adding NO to a discharge at 15 torr. The discharge impedance increases at low current and decreases at high current, while the small-signal gain decreases at all currents. Significant effects were observable at less than

Manuscript received March 7, 1973; revised February 20, 1975.

P. Bletzinger, D. A. LaBorde, W. F. Bailey, W. H. Long, Jr., and A. Garscadden are with the Aerospace Research Laboratories, Wright-Patterson Air Force Base, Ohio 45433.

P. D. Tannen was with the Aerospace Research Laboratories, Wright-Patterson Air Force Base, Ohio 45433. He is now with the Air Force Weapons Laboratory, Kirtland Air Force Base, N. Mex.

[1] This probe laser was a prototype stable laser developed by Sylvania, Inc., for the Avionics Laboratory, Wright-Patterson Air Force Base, Ohio.

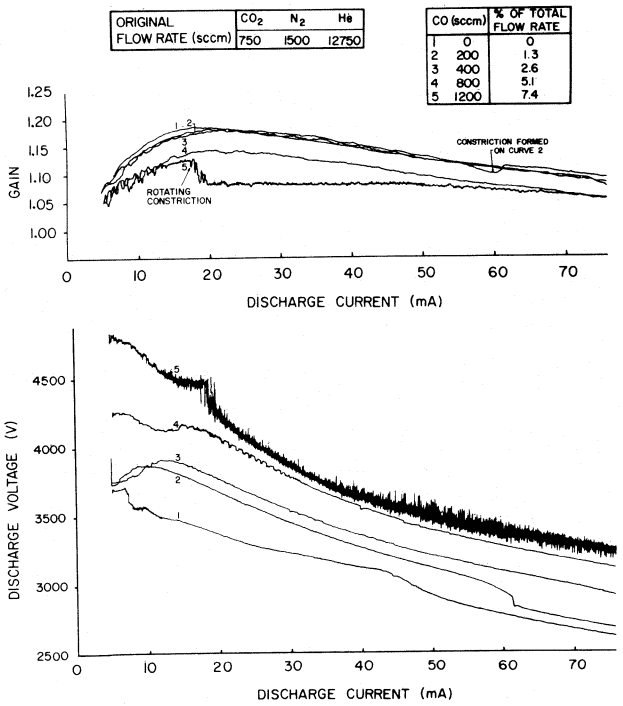

Fig. 1. Influence of carbon monoxide on CO_2–N_2–He laser at a total pressure of 15 torr. Upper: Laser gain versus discharge current and amount of added CO. Lower: Discharge voltage versus discharge current and amount of added CO.

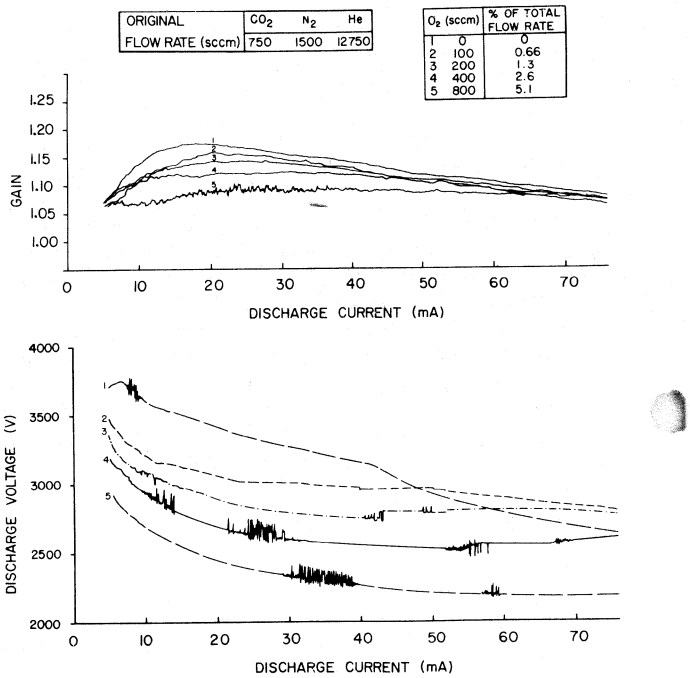

Fig. 2. Influence of oxygen at 15-torr total pressure on laser gain and discharge impedance.

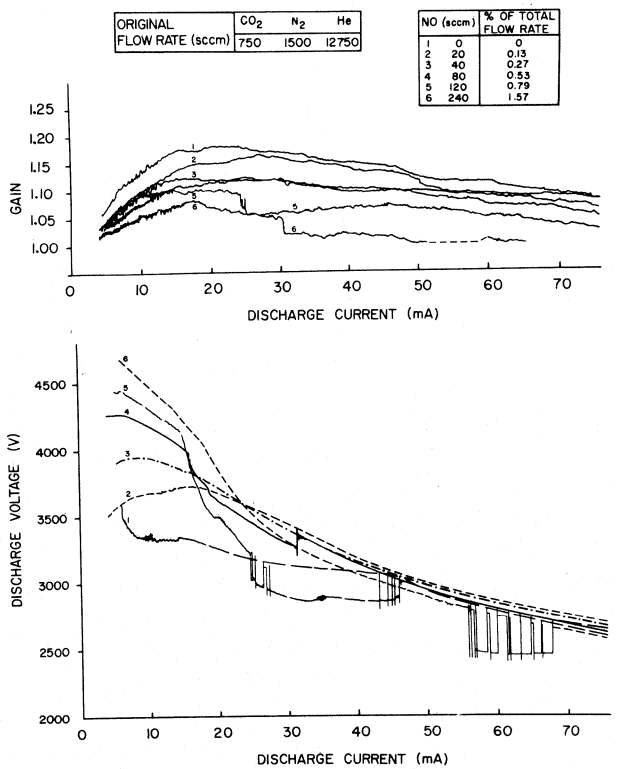

Fig. 3. Influence of nitric oxide at 15-torr total pressure.

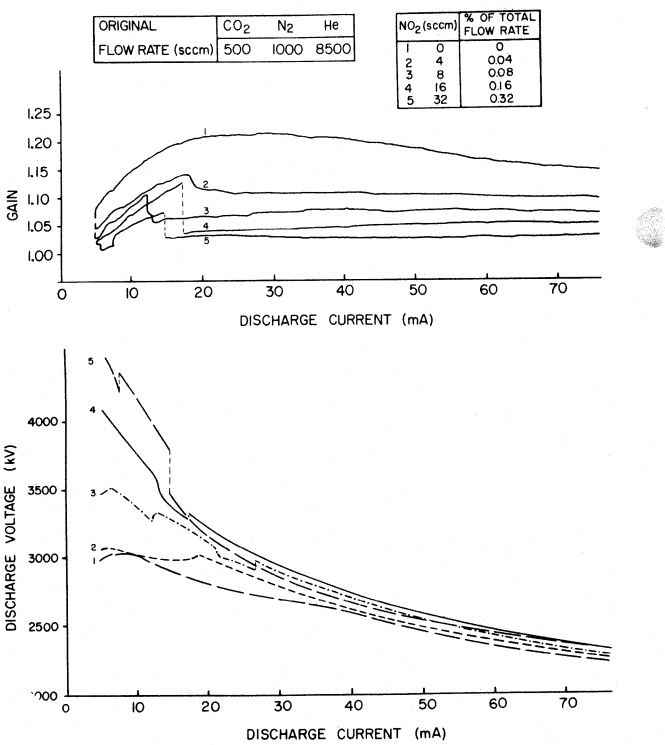

Fig. 4. Influence of nitrogen dioxide at 10-torr total pressure.

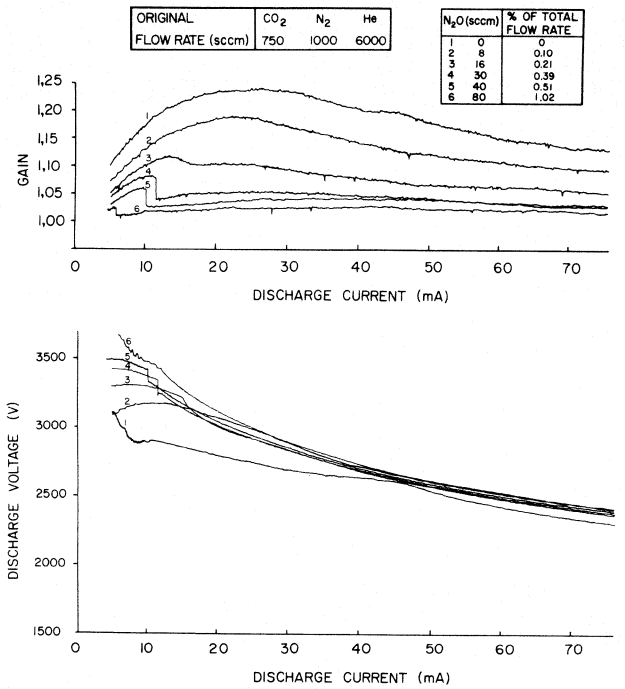

Fig. 5. Influence of nitrous oxide at 10-torr total pressure.

0.1-percent addition (relative to the total gas flow rate) of NO. At higher currents the gain was extinguished by NO concentrations of approximately 1.5 percent. With 120 Standard cubic centimeters per minute of NO added, the discharge was unstable between high-voltage and low-voltage modes and the laser gain was essentially zero above 30 mA. Similar effects were recorded at pressures of 10 and 5 torr. The discharges at higher total pressures, however, were more sensitive to the presence of NO.

Nitrogen dioxide, NO_2, was very effective in modifying the laser plasma properties at 10 torr (Fig. 4). At the lowest current, there was an increased impedance of about 50 percent with 0.3-percent NO_2. The discharge became unstable at approximately 18 mA for addition of NO_2 of only 0.04 percent. Constriction occurred at lower currents as the contaminant level was increased. Even in the constricted mode, the impedance of the discharge with NO_2 was slightly higher than without contaminants. At 15 torr the addition of only 0.1 percent caused the plasma to become violently unstable with almost complete loss of gain.

Nitrous oxide, N_2O gave results that are very similar to those for NO_2. However, the amounts required to cause the equivalent loss of gain were about a factor of 2 higher. At 10-torr pressure (Fig. 5) the discharge impedance increased about 30 percent at low currents. The amplifier gain was significantly reduced at N_2O levels above about 0.05 percent. There was zero gain at higher current densities and N_2O concentrations above approximately 0.5 percent. The N_2O will dissociate into other compounds including NO. However, the effects of added N_2O were found to be more severe at higher flow velocities and to be more serious than an equivalent concentration of NO.

Discussion

The addition of contaminants to the CO_2 electric-discharge laser alters the discharge impedance, affects plasma stability, and degrades the small-signal gain. These parameters are all interrelated and dependent on the microscopic processes taking place in the plasma. The discharge impedance is determined by the balance achieved between charged-particle production and loss. The neutral-gas temperature is determined by the power input to the discharge and is therefore a function of discharge impedance. The small-signal gain has been shown to be extremely sensitive to changes in the gas temperature [8]. Introduction of gases with large attachment or detachment rates modifies the positive-negative ion balance. A large negative ion concentration and the presence of species with attachment rates which vary rapidly with E/N (the ratio of applied electric field to neutral number density) can seriously affect discharge stability [10].

To interpret the observations presented here, a theoretical model has been constructed employing a three-component plasma (positive ions, negative ions, and electrons) in a background neutral-gas mixture. The relationships between discharge current, impedance, gas pressure, and gas composition are considered using the particle-conservation equations for the charged species

$$zn_e - \frac{D_a^+}{\Lambda_+^2} - r_i n_- n_+ - r_e n_e n_+ = 0 \tag{1}$$

$$an_e - \frac{D_a^-}{\Lambda_-^2} - r_i n_- n_+ - dn_- = 0 \tag{2}$$

and

$$n_e = n_+ - n_- \tag{3}$$

where the ion densities are evaluated on axis. The conservation equation for electrons has been replaced by the assumption of quasi-neutrality. The positive- and negative-ion temperatures are equal to the neutral-gas temperature which is assumed to be independent of radial position.

In the preceding equations, z is the rate for electron impact ionization in the mixture, including processes such as $CO_2 + e^- \rightarrow CO_2^+ + 2e^-$, and a is the rate for dissociative attachment, e.g., $O_2 + e^- \rightarrow O + O^-$. These rates and the electron mean energy and drift velocity were evaluated using a numerical solution of the collisional Boltzmann equation with the cross sections of Phelps *et al.* for momentum transfer and vibrational excitation, and the cross sections of Rapp *et al.* [12] for ionization and attachment (Figs. 6 and 7). The rate constants for ion-ion recombination r_i and electron-ion recombination r_e were taken to be constant. The rate for associative detachment d for the reaction $X + O^- \rightarrow XO + e^-$ is proportional to the density of detaching gas X, where X is either CO or NO.

The ambipolar diffusion coefficients D_a^+ and D_a^- were evaluated by Thompson [11] in a three-component plasma and are functions only of n_-/n_e when $T_e/T_g \gg 1$ (Fig. 8). The diffu-

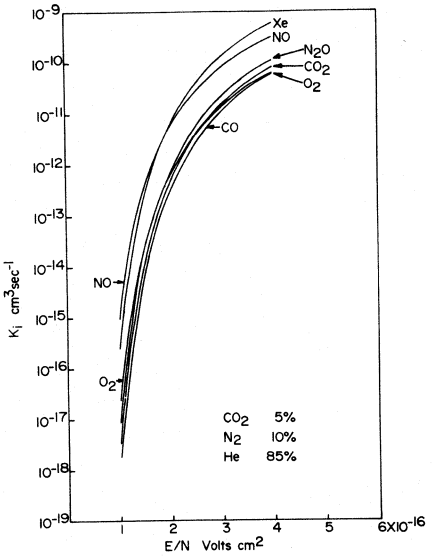

Fig. 6. Ionization rates in a CO_2–N_2–He discharge laser calculated using an electron energy distribution function derived from the numerical solution of the collisional Boltzmann equation.

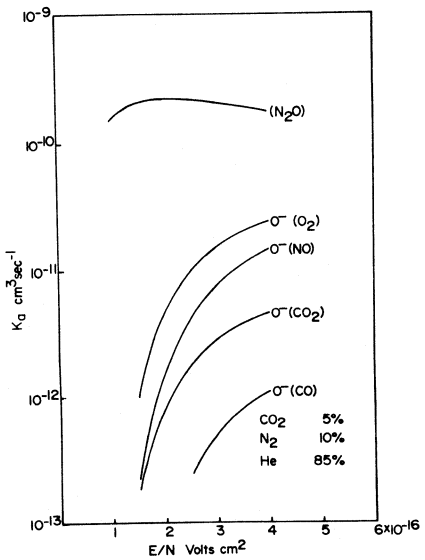

Fig. 7. Electron-molecule attachment rates in a CO_2–N_2–He discharge laser.

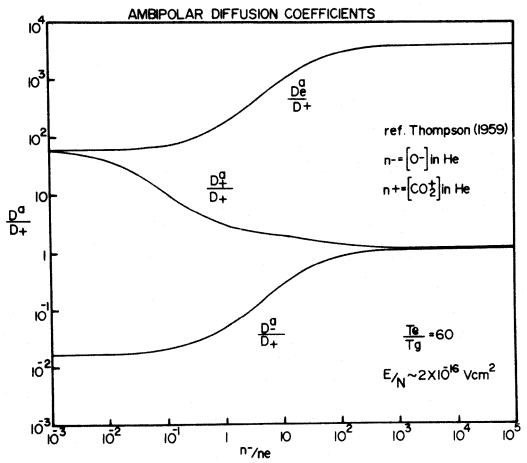

Fig. 8. Dependence of ambipolar diffusion coefficients D_a^+ and D_a^- on (n_-/n_e) in a three-component plasma.

sion lengths for positive and negative ions defined by

$$\Lambda_\pm = \left[\frac{1}{rn_\pm}\frac{\partial}{\partial r}\left(r\frac{\partial n_\pm}{\partial r}\right)\right]^{-1/2}$$

are approximately equal to $R/2.4$. The loss of negative ions to diffusion is in general negligible compared to that for positive ions, because the ambipolar field retards the radial flow of negative charges. The diffusion of electrons, with their higher temperature and mobility, is sufficient to balance the positive-ion loss. The transition to free diffusion, when the radial field goes to zero, occurs for n_-/n_e greater than 100.

Using (1) and (3), we can express the ionization rate z required to balance positive-ion loss as a function of n_-/n_e for a given neutral-gas density. This function is plotted in Fig. 9, with the corresponding E/N on the right ordinate, for a CO_2–N_2–He mixture in the ratio 5:10:85, at 300 K and 10 torr. The steady-state operating point of the discharge is then defined by the intersection of this curve with the curve representing (2). At low currents, where recombination is negligible, this point is given by $n_-/n_e = a/d$. Movement along this steady-state curve can be achieved by varying either the attachment or detachment rate. As will be seen later, the region to the right of the dashed line in Fig. 9 is unstable, and the parameters E/N and n_-/n_e are no longer confined to the solid curve.

With no contaminants added except those naturally occurring in the discharge, the operating point occurs at $n_-/n_e = 0.3$, near the minimum value of E/N. Adding small quantities of CO, which has a large cross section for electron detachment from O^- [23], moves the operating point to the left, resulting in a small increase in impedance. Adding quantities of CO sufficient to reduce the ionization rate by lowering the tail of the electron energy distribution further increases the imped-

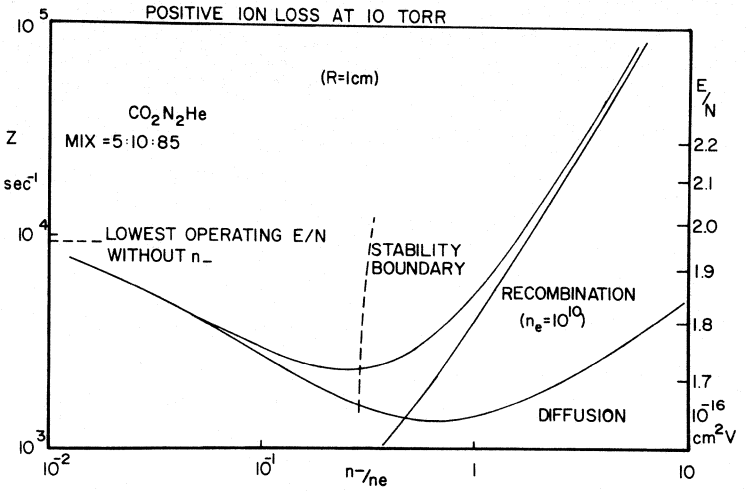

Fig. 9. E/N, ionization rate, diffusion, and recombination losses in a low-pressure CO_2–N_2–He (5:10:85) discharge as a function of negative-ion density and electron density (total pressure 10 torr, discharge current 10 mA).

ance. A gas with a large attachment cross section, such as NO_2 or N_2O (Fig. 7), moves the steady-state point to the right and results in a higher electric field if the discharge remains stable.

The addition of NO has competing effects on impedance. Its low ionization potential provides an easy source of electrons which allows the discharge to operate at a lower E/N. This effect is most evident at high currents where the fields are lower and the electron energy distribution is falling more rapidly in the vicinity of the ionization thresholds. At low currents, the more important process is detachment by NO, which tends to increase the discharge impedance, moving the operating point in Fig. 9 to the left of the minimum.

Changes in impedance and small-signal gain may also be brought about by plasma instabilities, which manifest themselves in two forms. The first form involves moving striations in the positive column, which do not alter the glow character of the discharge, but cause fluctuations in the sidelight emmission. These fluctuations were not observed in the small-signal gain due to spatial and temporal averaging. The striations have the effect of allowing the discharge to operate at a lower average electric field than in their absence [14]. The second form of instability is the sudden constriction of the glow into a bright filament. This is accompanied experimentally by a drop in impedance and degradation of the small-signal gain.

In order to explain these effects in the context of the foregoing model, the stability of the solution was analyzed by examining the time development of a small-amplitude plane-wave perturbation, keeping the gas temperature constant. This technique predicts the onset condition and early growth of moving striations, but cannot follow large deviations from the steady state. Due to the constant-temperature assumption, the model does not include the transition to a constricted discharge, which is believed to be a thermal instability [21]. Following a procedure similar to that used in [10], the criterion for the growth of long wavelength fluctuations in the plasma is found to be

$$z(K(z, v_d)-1)-a(K(a, v_d)-1)+\frac{D_a^+}{\Lambda_+^2}+d+r_i(n_-+n_+)<0 \tag{4}$$

where $K(x,y)=(x/y)(\partial y/\partial x)$ and v_d is the electron drift velocity. The rates and number densities occurring in this expression are evaluated at steady-state conditions. Since $K(z, v_d)$ is generally greater than 1, the only term which can give rise to moving striations is the attachment rate when $K(a, v_d)$ is greater than 1. All the other terms tend to damp the oscillations.

As we can see in Fig. 7, O_2 has a large attachment rate which exhibits a strong E/N dependence. The value of $K(a, v_d)$ for O_2 is approximately 4. Hence moving striations can be induced by the addition of O_2. They can be quenched by the addition of a sufficient amount of a detaching gas, such as CO. Both of these results have been confirmed experimentally [14]. Although NO_2 and N_2O have large attachment rates, they do not give rise to moving striations because of the weak dependence of those rates on E/N (Fig. 7). In fact, since $K(a, v_d)$ is less than 1 for these gases, they can also be used to quench moving striations.

We now consider the behavior of the small-signal gain at low currents before the onset of constriction. It has been shown [22] that the gain in a CO_2 laser amplifier is an increasing function of n_e and a strongly decreasing function of T_g. In the present device, the higher electric fields caused by contaminants increase the electron drift velocity. To maintain a constant total current, then, the average electron density must be reduced. In addition, at these elevated E/N values the efficiency of pumping the vibrational levels is diminished. Both of these effects reduce the population inversion of the CO_2 (001) level and hence the small-signal gain. An even more important process is thought to be thermal bottlenecking brought on by increased gas temperature. Once again the higher electric fields increase the ohmic heating, which is

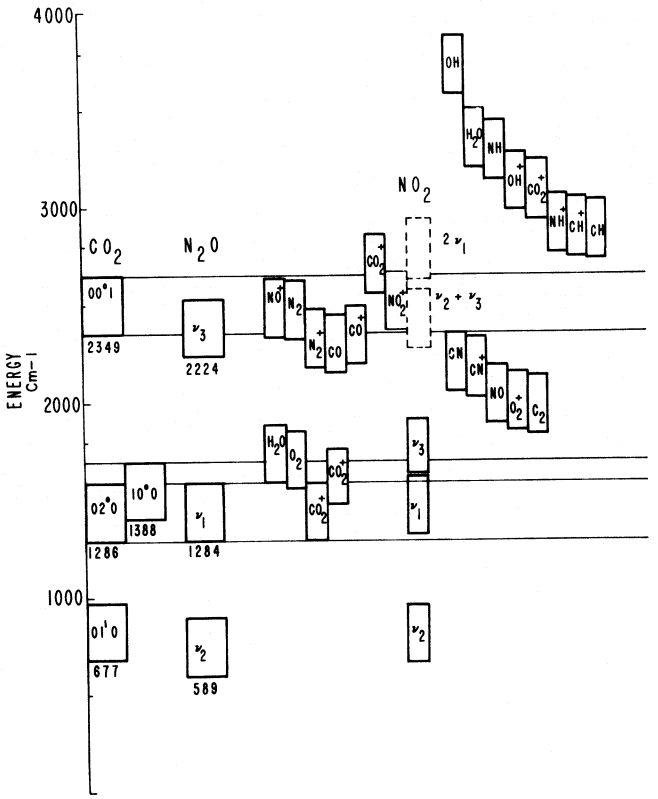

Fig. 10. Energy resonance between vibrational levels of molecular species in CO_2-N_2-He discharge lasers. Each level is broadened by about 300 cm^{-1}, equivalent to a gas temperature of approximately 400 K. This figure is adapted from [9].

coupled into the gas through elastic collisions with electrons and VT relaxation. The hot gas is then more efficient in exciting the lower laser level through the CO_2 bending mode.

The addition or creation of vibrational species nearly resonant with the upper laser level provides new channels for energy transfer which can also degrade the small-signal gain characteristics [9] (Fig. 10). This effect, however, is believed to be negligible in the present experiment. The VV rates between $N_2(v = 1)$ and the contaminants considered in the preceding are less than the resonant energy exchange rate between $N_2(v = 1)$ and $CO_2(000)$. Therefore, the quantities of contaminant required to compete with CO_2 would have to be comparable to the CO_2 concentration. For the small quantities of nitrogen oxides added in the present experiment, this process is insignificant.

Conclusions

The observed variations of discharge and laser properties can be explained adequately by a three-component modeling of the discharge operation. The impedance variations are due principally to alteration of the negative-ion density due to contaminant addition. Instabilities generated by contaminant addition arise from the strong E/N dependence of their attachment rates. Gas temperature increases, resulting from the increase in discharge impedance, reduce the normalized laser gain. The influence of the additives, especially NO_2, on the laser output and discharge stability becomes more severe at higher pressures and current densities.

In a previous paper [7], we reported the mass-spectrometric measurement of the buildup of nitrogen oxides in CO_2-N_2-He sealed-off positive-column discharges at pressures of a few torr. Under these conditions the preceding results show that the contaminant most adverse to laser efficiency is NO_2. The mass-spectrometer investigation showed that at 80 mA in a 1:2:5 mix at 5 torr, NO_2 attains an equilibrium concentration of 0.23 percent. Our results show that this will quench laser operation. At lower currents, e.g., 10 mA, the NO_2 equilibrium concentration is 0.04 percent. The contaminant concentration versus gain studies show that this will reduce the gain of the laser by approximately one-half. These characteristics have been observed in sealed-off lasers. Thus the generation of nitrogen oxides, especially NO_2, is considered to be the reason that efficient sealed-off high-power CO_2 lasers require the methods outlined in the following.

If one flows the laser gases sufficiently fast, it is possible to avoid the effects of contaminants and postpone the onset of the discharge instability if the gases are exhausted. This is not always feasible or economical. The results of this study can be applied to nonflowing or recycled gas laser systems. However, operation of nonflowing and recycled CO_2 gas laser systems will suffer some degradation due to the self-generation of impurities. Methods to overcome the loss in laser gain are as follows: 1) devising a method of selective scrubbing of the nitrogen oxides; 2) avoiding their generation by the use of a low ionization potential gas; 3) utilizing catalysts to change the chemical kinetics; or 4) eliminating nitrogen from the discharge. This last method seems to be the most practical for sealed-off lasers. When nitrogen is replaced by an approximately equal quantity of CO, it has been shown to pump the $CO_2(001)$ level in both sealed-off and gas-mixing lasers [16]. Earlier papers [17], [18], on the influence of xenon on CO_2 lasers showed not only the benefits of the xenon additive, but also that it was possible to run the laser without nitrogen. Improved long-life performance at reasonable output powers resulted. This success can be attributed to the stabilizing effects of the CO detachment, and the minimization of the nitrogen oxides. Efficient resonant energy transfer from CO to CO_2 establishes the population inversion [19], [20].

References

[1] P. K. Cheo, "CO_2 lasers," in *Lasers: A Series of Advances*, vol. 3, A. K. Levine and A. J. DeMaria, Ed. New York: Dekker, 1971, ch. 2, pp. 11-267.

[2] E. S. Gasilevich *et al.*, "Dissociation of CO_2 in plasma of CO_2 laser," *Sov. Phys.–Tech. Phys.*, vol. 14, pp. 86-91, July 1969.

[3] J. A. Macken, E. Matovich, and R. A. Brandewie, "Chemical equilibria in the CO_2 laser," *Bull. Amer. Phys. Soc.*, vol. 12, p. 669, May 1967.

[4] N. Karube and E. Yamaka, "Mass spectrometric studies of a sealed CO_2 laser," *J. Appl. Phys.*, vol. 41, pp. 2031-2042, Apr. 1970.

[5] F. Freudenthal, "Collision processes in a CO_2 laser plasma," *J. Appl. Phys.*, vol. 41, pp. 2447-2453, May 1970.

[6] J. M. Austin and A. L. S. Smith, "Analysis of positive ions in CO_2 gas laser systems," *J. Phys. D.*, vol. 5, pp. 468-475, Mar. 1972.

[7] P. D. Tannen, P. Bletzinger, and A. Garscadden, "Species composition in the CO_2 discharge laser," *IEEE J. Quantum Electron.*, vol. QE-10, pp. 6-11, Jan. 1974.

[8] R. H. Bullis, W. L. Nighan, M. C. Fowler, and W. J. Wiegand, "Physics of CO_2 electric discharge lasers," *AIAA J.*, vol. 10, pp. 407–414, Apr. 1972.
[9] R. W. Nicholls, "Energy resonance between molecular species in CO_2 gas lasers," *Nature*, vol. 226, pp. 353–354, Apr. 1970.
[10] R. Haas, "Plasma stability of laser discharges in molecular gases," *Phys. Rev. A.*, vol. 8, pp. 1017–1043, Aug. 1973.
[11] J. B. Thompson, "The ion balance of the oxygen D.C. glow discharge," *Proc. Roy. Soc., Ser. A*, vol. A262, p. 519, 1961.
[12] D. Rapp and D. Briglia, "Total cross sections for ionization and attachment in gases by electron impact, II: Negative ion formation," *J. Chem. Phys.*, vol. 43, pp. 1480–1489, Sept. 1, 1965.
[13] L. Pekarek and M. Sicha, "The connection between low-gradient form of the positive column in oxygen and moving striation," *Czech. J. Phys.*, vol. B 10, p. 740, 1960.
[14] W. L. Nighan and W. J. Wiegand, "Influence of negative-ion processes on steady-state properties and striations in molecular gas discharges," *Phys. Rev. A.*, vol. 10, pp. 922–945, Sept. 1974.
[15] G. Ecker, W. Kroll, and O. Zoller, "Thermal instability of the positive column," *Phys. Fluids*, vol. 7, pp. 2001–2006, Dec. 1964.
[16] D. H. Douglas-Hamilton and S. Mani, "An electron attachment plasma instability," *Appl. Phys. Lett.*, vol. 23, pp. 508–510, 1973.
[17] P. Bletzinger and A. Garscadden, "Influence of xenon on sealed-off CO_2 lasers," *Appl. Phys. Lett.*, vol. 12, pp. 289–291, May 1968.
[18] P. O. Clark and J. Y. Wada, "The influence of xenon on sealed-off CO_2 lasers," *IEEE J. Quantum Electron.*, vol. QE-4, pp. 263–266, May 1968.
[19] H. W. Brinkschultz, "The influence of CO on CO_2 laser performance," *IEEE J. Quantum Electron. (Special Issue on 1968 International Quantum Electronics Conference: Part II)*, vol. QE-4, pp. 948–953, Nov. 1968.
[20] E. N. Lotkova, V. N. Ochkin, and N. N. Sobolev, "Dissociation of carbon dioxide and inversion in CO_2 lasers," *IEEE J. Quantum Electron.*, vol. QE-7, pp. 396–402, Aug. 1971.
[21] W. L. Nighan and W. J. Wiegand, "Causes of arcing in CO_2 convection laser discharges," *Appl. Phys. Lett.*, vol. 25, pp. 633–636, Dec. 1974.
[22] M. C. Fowler, "Influence of plasma kinetic processes on electrically excited CO_2 laser performance," *J. Appl. Phys.*, vol. 43, pp. 3480–3487, Aug. 1972.
[23] J. L. Mauer and G. L. Schulz, "Associative detachment of O^- with CO, H_2, and O_2," *Phys. Rev. A*, vol. 7, pp. 593–605, Feb. 1973.

A Theory of Forced Mode Locking

HERMANN A. HAUS, FELLOW, IEEE

Abstract—**Differential equations are derived for forced mode locking of a homogeneously broadened laser in the frequency domain and time domain. Simple methods are presented for the analysis of pulse shapes for other than sinusoidal modulation. The higher order Hermite-Gaussian solutions of the synchronous sinusoidal modulation are shown to be unstable and hence unrealizable in the steady state.**

I. Introduction

THE THEORETICAL investigations of mode locking may be roughly divided into two groups (see [1] for a large list of references): 1) those which treat the mode-locking process in the time domain, e.g., the paper by Kuizenga and Siegman [2]; and 2) those which treat the phenomenon in the frequency domain as injection locking of cavity modes (notably the paper by McDuff and Harris [3]). In this paper we unify these two approaches and show when one or the other is preferable.

The introduction of yet another theory of mode locking needs justification. The presentation here serves the following purposes.

1) Some problems of mode locking are more conveniently analyzed in terms of injection locking of cavity modes, others in terms of the propagation of pulses through the laser cavity. A unified theory which establishes a simple correspondence between the two approaches facilitates the proper choice of description.

2) As an example of the injection-locking approach, a stability analysis of the mode-locked supermodes is carried out. The stability analysis of injection locking recently discussed lucidly by Kurokawa [4] can be adapted easily for this purpose.

3) The differential equations of mode locking in the time domain derived here are shown to be in one-to-one correspondence with the one-dimensional Schroedinger equation of a particle in a potential well. Hence known solutions of the Schroedinger equation can be applied to the mode-locking problem.

In Section II we give a brief derivation of the equation governing the spectrum of mode-locked pulses. The approach is in close correspondence with that of [5]. In Section III we apply the equation to the case of strong sinusoidal mode locking of the homogeneously broadened laser and obtain the well-known Hermite-Gaussian solutions. In Section IV we Fourier transform the fundamental equation and show how the result may be interpreted in terms of pulse propagation through the system. New results are presented in the remaining sections. In Section V we derive a quantum mechanical analog for the solution of the mode-locking problem with other than sinusoidal modulation. This analog facilitates the

Manuscript received April 29, 1974; revised February 18, 1975. This work was done at M.I.T., and was supported in part by the Joint Services Electronics Program under Contract DAAB07-71-C-0300 and in part by the U.S. Army Research Office, Durham, N.C., under Contract DAHC04-72-C-0044.

The author is with Bell Laboratories, Holmdel, N.J. 07733, on leave from the Department of Electrical Engineering and the Research Laboratory of Electronics, Massachusetts Institute of Technology, Cambridge, Mass. 02139.

solution of mode locking by a general periodic modulation. In Section VI we present the stability analysis of the steady-state solutions. It is shown that, for synchronous sinusoidal modulation, all Hermite-Gaussian solutions, except the lowest order one, are unstable.

II. Mode Locking as Injection Locking

In this section we develop an equation for the Fourier components of the optical-field amplitude in a cavity containing a mode-locking element. This equation can be reduced to a difference equation when the modulation is sinusoidal. We use as the starting point the injection-locking model of high-Q resonators containing an active medium. The analysis will use equivalent admittances, which can be related to the geometry and the parameters of the media inside the cavity in the usual way [5]. Identification of the admittances with the gain per pass, loss per pass, etc., is made in Section IV, where we rederive the basic equations in the time domain.

Injection locking of a single mode of a cavity containing an active medium may be analyzed with the aid of the equivalent circuit of Fig. 1. Here the admittance $Y_L(|V|)$ represents the admittance produced by the active medium; it is, in general, complex and a function of the "voltage" V, and Y_C is the cavity admittance, a function of ω. If a current source I_S of frequency ω is applied across the circuit as indicated, then the equation for this injection-locked oscillator is given by [4]

$$I_S = [Y_C(\omega) + Y_L(\omega, |V|)]\, V. \tag{1}$$

Equation (1) can be adapted to the case of a mode-locked optical cavity involving the interaction among many axial modes. The identification of equivalent-circuit elements of each resonance circuit (representing one axial laser mode) with laser and optical cavity parameters has been treated in the literature [5].

The electric field in the cavity is expanded in the set of axial modes $\bar{e}_k(\bar{r})$ of the lossless cavity. The mode patterns $\bar{e}_k(\bar{r})$ are standing waves with nodes at the mirrors, and with transverse dependences that are functions of the geometry and the parameters of the media within the cavity. Within a distance z_0 from the end mirrors, the $\bar{e}_k$ are approximately equal over a band of k values obeying the inequality $\Delta k \ll L/z_0$, where L is the cavity length.

One assumes at the outset that mode locking is successful and that the Fourier components of the electric field have frequencies that are spaced evenly, separated by the modulation frequency of the mode-locking element ω_M. In general, any mode $\bar{e}_k(\bar{r})$ has a time dependence with many Fourier components. If the Q of the cavity modes is high, then only the Fourier component nearest to the cavity-mode resonance frequency is appreciably excited. In this case, the expansion of the time-dependent electric-field distribution in the cavity

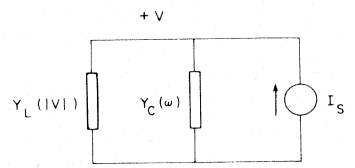

Fig. 1. Equivalent circuit for single-mode injection-locked oscillator.

$\bar{E}(\bar{r}, t)$ is

$$\bar{E}(\bar{r}, t) = \exp(j\omega_0 t) \sum_k V_k \exp(jk\omega_M t)\, \bar{e}_k(\bar{r}) + \text{c.c.} \tag{2}$$

where the kth mode has the frequency

$$\omega_k = k\omega_M + \omega_0. \tag{3}$$

The fast time dependence $\exp j\omega_0 t$ has been explicitly extracted where ω_0 is to be identified with the frequency of oscillation of the central mode ($k = 0$), the mode nearest to the peak of the laser gain profile (peak of the negative conductance Re Y_L).

Each complex amplitude V_k obeys a set of equations that can be represented by a parallel resonant circuit [5]. The equivalent circuits describing different modes are coupled by the sideband generation of the mode-locking element, i.e., the driving current for the kth cavity mode I_{Sk} contains contributions of $V_i (i \neq k)$. We shall disregard couplings as caused by other effects. Thus, in particular, we shall assume that the gain of the laser medium (represented by Y_L) is time independent and therefore no sidebands are produced on frequency components amplified by the laser medium. This in turn implies that the relaxation time of the population inversion is long compared with the cavity transit time so that the laser medium, while affected by the time average optical power in the cavity, does not respond to instantaneous power variations. (This assumption was also made in [2] and [6].) Generalizing (1) to the kth cavity mode with amplitude V_k one has

$$[Y_{Ck}(\omega_k) + Y_L(\omega_k)]\, V_k = I_{Sk}. \tag{4}$$

Consider first the dependence of $Y_{Ck}(\omega_k)$ upon ω_k. The kth cavity mode has a quality factor Q (assumed to be the same for all modes) and a resonance frequency

$$\omega_{k0} = k\Delta\omega + \omega_0 - \delta\omega_0 \tag{5}$$

where $\Delta\omega$ is the separation between the resonances of the (empty-axial) cavity modes and $\delta\omega_0$ is the detuning of the oscillation frequency of the central mode. Since the frequency of excitation is given by (3), one has

$$Y_{Ck} = G_C \left[1 + jb + kj2Q \frac{\omega_M - \Delta\omega}{\omega_0}\right] \tag{6}$$

where $G_C(1 + jb)$ is the admittance of the mode with $k = 0$; $b = (2Q/\omega_0)\,\delta\omega_0$. Next consider I_{Sk} of (4). If the cavity is mode locked by the time-dependent loss of a mode-locking element, then

$$I_{Sk} = -G_C \left[m(t) \sum_l V_l \exp(jl\omega_M t)\right]_{k\text{th Fourier component}} \tag{7}$$

where $m(t)$ has the time dependence of the loss modulation with period $2\pi/\omega_M$ and its magnitude is a measure of the "loading" of the cavity by the mode-locking element.[1] In (7) all modes l affect the mode k equally ($m(t)$ is l and k

[1] A time-modulated loss element causes a time dependence of the inverse Q. If the contribution to the inverse Q of the time-dependent loss element is denoted by $1/Q_M(t)$, then $m(t) = Q/Q_M(t)$.

independent), an assumption justified if the mode-locking element is near one of the mirrors.

Finally, consider the equivalent admittance $Y_L(\omega_k)$ of the laser medium. The laser gain is frequency dependent, and a Lorentzian line shape will be assumed. The admittance may be normalized to G_C so that

$$Y_L(\omega_k) = -G_C \frac{g}{1 + j\dfrac{\omega_k - \omega_0}{\omega_L}} \tag{8}$$

where ω_L is the laser medium linewidth, and g is the magnitude of the negative conductance at line center normalized to G_C.[2] We have assumed that the center frequency of the laser line coincides with the oscillation frequency of the cavity mode $k = 0$. We shall show later that this approximation is always a satisfactory one.

Next we assume [6] that (8) can be expanded in $(\omega_k - \omega_0)/\omega_L$ and only terms up to second order are retained

$$Y_L(\omega_k) \simeq -G_C g \left\{1 - \left(\frac{\omega_k - \omega_0}{\omega_L}\right)^2 - j\frac{\omega_k - \omega_0}{\omega_L}\right\}. \tag{9}$$

This assumption implies that the pulsewidths predicted by the ensuing analysis must be long compared with $1/\omega_L$, a situation usually encountered in practice. A further consequence of this assumption is the disregard of nonuniformity of mode spacing in the wings of the mode-locked spectrum.

Combining (4) and (6)-(8) one obtains the basic equation of mode locking expressed in the frequency domain.

$$\left\{1 + jb + \frac{jk\omega_M}{\omega_L}(\delta + g) - g\left[1 - \left(\frac{k\omega_M}{\omega_L}\right)^2\right]\right\} V_k = -\left[m(t)\sum_l V_l \exp(jl\omega_M t)\right]_{k\text{th Fourier component}} \tag{10}$$

where the "detuning" parameter δ is

$$\delta \equiv \frac{\omega_M - \Delta\omega}{\omega_M} 2Q \frac{\omega_L}{\omega_0}. \tag{11}$$

The equivalent negative conductance g decreases monotonically with increasing laser intensity. If the laser medium is near one of the end mirrors, and the $\bar{e}_k$ of all modes of interest are approximately the same, the saturation is a function of the sum of the intensities $\Sigma_k |V_k|^2$. Through proper normalization of the $\bar{e}_k$ in (2), the summation of the field intensities can be made equal to the net power P traveling towards the end mirror, $\Sigma_k |V_k|^2 = P$. If the equivalent negative conductance g is produced by inversion of a two-level medium of relaxation time T_L, then g obeys the following differential equation:

$$\dot{g} = -\frac{g - g_0}{T_L} - g\frac{P}{T_L P_L} \tag{12}$$

where g_0 is the small signal value of g and P_L is the saturation power. For the steady state one obtains

$$g = \frac{g_0}{1 + \dfrac{P}{P_L}} \tag{13}$$

where the assumption is made that $T_L >> T_R$, the round-trip time of the pulses, so that g does not possess an appreciable time-varying component [2]. Further, (13) assumes that all axial modes have the same saturation power, i.e., $1/P_L$ is a constant in the time domain, not an operator. This assumption is valid if the spectrum of the pulse solutions is narrow compared with the laser linewidth. Finally, (13) disregards spatial hole-burning effects. This is rigorous if the laser medium is short and near one of the mirrors but is an approximation otherwise.

III. Solution for Sinusoidal Modulation

In this section we shall solve the basic equation (10) for the special case of sinusoidal modulation. This is done, in part, to relate the present formalism to the literature, and, in part, to obtain the relations necessary for the stability analysis of the solutions carried out in Section VI.

For a (co-)sinusoidal modulation

$$m(t) = 2M(1 - \cos \omega_M t). \tag{14}$$

The injection current of (7) is

$$I_{Sk} = G_C M(V_{k-1} - 2V_k + V_{k+1}). \tag{15}$$

Introducing (15) into (10) we obtain the second-order difference equation

$$\left\{1 + jb - g\left[1 - \left(\frac{k\omega_M}{\omega_L}\right)^2\right] + j\frac{k\omega_M}{\omega_L}(\delta + g)\right\} V_k = M[V_{k-1} - 2V_k + V_{k+1}]. \tag{16}$$

If many modes are to be locked, and if the variation of the gain over a frequency range corresponding to the mode spacing is small, then the difference equation can be replaced by a second-order differential equation [6], [7].[3] One has

$$[V_{k+1} - 2V_k + V_{k-1}] \longrightarrow \omega_M^2 \frac{d^2V}{d\omega^2}$$

where V_k is now replaced by a continuous function of the variable ω, the frequency deviation from ω_0, and ω_M is the frequency separation of the spectral lines. The modes are identified by the continuous variable

$$\omega = \lim_{\substack{k\to\infty \\ \omega_M \to 0}} k\omega_M$$

where k is the mode number, which assumes both positive and negative values. One obtains for (16), [6]

$$\left[1 + jb - g\left(1 - \frac{\omega^2}{\omega_L^2}\right) + j\frac{\omega}{\omega_L}(\delta + g)\right] V = M\omega_M^2 \frac{d^2V}{d\omega^2}. \tag{17}$$

$\delta + g$ is identical to the detuning parameter d of [8]. Equation

[2] The normalized negative conductance g may be expressed in terms of the (negative) Q_L of the laser medium and the cavity mode Q, $g = Q/|Q_L|$.

[3] Letokhov has replaced the discrete frequency spectrum of the cavity modes by a continuum. He did not take into account the laser gain profile and hence did not get the same steady-state solutions.

(14) is particularly simple, if we require that

$$\delta + g = 0. \tag{18}$$

This implies that the modulation frequency is adjusted to equal the cavity-mode frequency separation as modified by the laser medium. With (18) satisfied, (17) is identical with the harmonic oscillator equation of quantum mechanics, where V plays the role of the wave function and ω the role of the spatial variable.

$$M\omega_M^2 \frac{d^2V}{d\omega^2} - g\frac{\omega^2}{\omega_L^2} V = (1 + jb - g)V. \tag{19}$$

The solutions are the well-known Hermite-Gaussians [6]

$$V(\omega) = H_n(\omega/\omega_P) \exp - \tfrac{1}{2}(\omega/\omega_P)^2 \tag{20}$$

where [2], [6]

$$\omega_P = \sqrt[4]{(M/g)}\,\sqrt{\omega_L\,\omega_M}. \tag{21}$$

Equation (20) defines "supermodes" or "mode-locking modes" of the mode-locked oscillator. The lowest order supermode was obtained by Kuizenga and Siegman [2], and the higher order supermodes by Haken and Pauthier [6] and others [9], [10]. We shall show in Section VI that all higher order supermodes ($n > 0$) cannot be excited in the steady state because they are unstable.

The role of the energy eigenvalues E_n of the harmonic oscillator is played by the parameter $g - (1 + jb)$ in (20). We find for the quantization of this parameter

$$E_n = g - 1 = \frac{2\sqrt{Mg}\;\omega_M(n + 1/2)}{\omega_L} \tag{22}$$

and

$$b = 0. \tag{23}$$

The central mode is found to oscillate at line center.

Equation (22) determines the power in the mode-locked cavity. Indeed, by using the dependence of g upon power P, (13), we find the following relationship for P:

$$\frac{P}{P_L} = \frac{g_0}{1 + \mu + \sqrt{2\mu + \mu^2}} - 1 \tag{24}$$

where $\mu = \frac{1}{2}(2n + 1)^2\, M(\omega_M/\omega_L)^2$. If a saturation formula different from (13) is assumed, the power is still determined from (22) and still decreases monotonically with μ.

Let us now return to an interpretation of the present solution in terms of the physical model used as a starting point of the investigation, the injection-locking model. We must remember that the differential equation was used as a mathematical approximation to the difference equation, and that the solution obtained must be interpreted as an approximate solution of the difference equation if the replacement is made: $V(\omega) \to V_k$ and the solution (20) are assigned values only at discrete frequencies ω_k. Mode locking has led to simultaneous oscillation of many modes in a homogeneously broadened system, even though the unmodulated system would have oscillated only in a single mode. The simultaneous oscillation in many modes is allowed because of injection locking. The

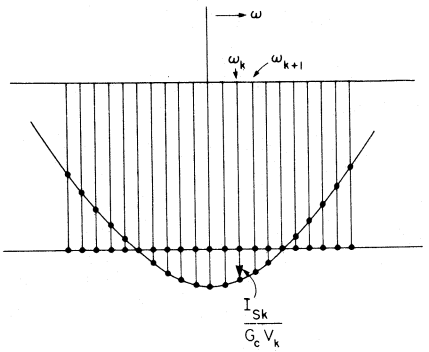

Fig. 2. The balancing of admittance discrepancy by injected currents produced by mode-locking modulation.

injection currents are given by (15). Fig. 2 shows a plot of the real part of the two sides of (16) versus ω_k (the imaginary part vanishes because of assumed synchronous modulation), showing explicitly the discrepancies $\mathrm{Re}[Y_C(\omega_k) + Y_L(\omega_k)]$ which are balanced by the modulation-produced "source" current normalized to the oscillation voltage I_{Sk}/V_k.

Suppose, now, we had not made the assumption that the center frequency of the laser line coincides with the oscillation frequency ω_0 of the mode $k = 0$. The actual deviation cannot be greater than $\omega_M/2$. The laser medium contributes a susceptance to this mode of magnitude equal to or less than

$$\frac{\omega_M}{2}\,\mathrm{Im}\left.\frac{dY_L}{d\omega}\right|_{\omega=0} = \frac{\omega_M}{2\omega_L}\, gG_C.$$

The mode then oscillates not at its (empty-cavity) resonance frequency, but a frequency away from it

$$|\delta\omega| = \frac{1}{4}\,\frac{\omega_M}{\omega_L}\, g\Delta\omega_C$$

where $\Delta\omega_C = \omega_0/Q$ is the cavity-mode bandwidth. Along with it, all other oscillation frequencies are shifted by this same amount, which is very small because $\omega_M g/\omega_L \ll 1$.

The results obtained thus far are well known. They have been checked experimentally by Kuizenga and Siegman [11], and Smith *et al.* [12]. One can extend the analysis to cover phase (reactive) rather than loss (resistive) modulation by replacing M by an imaginary quantity, again arriving at results derived previously [2], [8]. We shall not go into details, but concentrate instead on problems that have not received adequate treatment.

IV. The Mode-Locking Equation in the Time Domain

Forced mode locking with a modulation function $m(t)$ of arbitrary (periodic) time dependence is analyzed most conveniently in the time domain. Also the time-domain description permits an alternate interpretation of the mode-locking equation and of the assumptions that were made in its derivation. For this purpose, we study the Fourier transform of (10). We define the time function $v(t)$ as the Fourier transform of V_k

$$v(t) = \sum_k V_k \exp(j\omega_k t). \tag{25}$$

Since the mode amplitudes $\bar{e}_k(\bar{r})$ are equal to each other at one of the end mirrors, where all $\bar{e}_k$ have a common node, (25) may be interpreted as the time-dependent amplitude of the standing-wave field near one of the mirrors. Alternately, it is proportional to the time-dependent amplitude of the electric-field pulse traveling towards the end mirror.

With the definition (25), the Fourier transform of (10) is

$$\left\{1 + jb - g\left[1 + \frac{1}{\omega_L^2}\frac{d^2}{dt^2}\right] + \frac{g+\delta}{\omega_L}\frac{d}{dt}\right\} v(t) = -m(t)v(t). \tag{26}$$

Equation (25) may be interpreted in terms of the time-domain approach of mode locking. A pulse of electric field, $E(t) = v(t) \exp j\omega_0 t$ of complex time-dependent amplitude $v(t)$, experiences changes in one round-trip time T_R due to each of the components of the system. The cavity causes a decay and also a phase shift of the amplitude $v(t)$ if all frequency components of $E(t)$ are shifted by a constant $\delta\omega_0$ from the cavity resonance frequencies

$$v(t) \longrightarrow v(t) \exp - \frac{\omega_0 T_R}{2Q} \exp - j\delta\omega_0 T_R. \tag{27}$$

The laser medium amplifies and disperses the pulse. If an expansion like (9) is made of the frequency-dependent gain $G(\omega)$, then

$$v(t) \longrightarrow \exp\left\{G(\omega_0)\left[1 + \frac{1}{\omega_L^2}\frac{d^2}{dt^2} - \frac{1}{\omega_L}\frac{d}{dt}\right]\right\} v(t). \tag{28}$$

Here the exponential operator is to be interpreted in terms of its Taylor expansion. Finally, the passage through the mode-locking element of time-dependent loss $L(t)$ changes the pulse by

$$v(t) \longrightarrow v(t) \exp - L(t). \tag{29}$$

The existence of a steady state requires that the pulse experience no more than a time advance δT (or delay, $\delta T < 0$) upon one round trip. Expanding all exponentials to first order, a step that is legitimate if the changes wrought on the pulse on one passage by the elements of the system are small, one obtains

$$v(t - T_R) - \frac{\omega_0 T_R}{2Q}\left\{1 + jb - g\left[1 + \frac{1}{\omega_L^2}\frac{d^2}{dt^2} - \frac{1}{\omega_L}\frac{d}{dt}\right] + m(t)\right\} v(t - T_R) = v(t - T_R + \delta T) \tag{30}$$

where we have introduced the parameters b, g, and $m(t)$ which may be expressed in terms of $\delta\omega_0, L(t)$, and $G(\omega_0)$

$$b = 2Q\frac{\delta\omega_0}{\omega_0} \tag{31}$$

$$m(t) = \frac{2Q}{\omega_0 T_R} L(t) \tag{32}$$

$$g = \frac{2Q}{\omega_0 T_R} G(\omega_0). \tag{33}$$

An expansion of $v(t - T_R + \delta T)$ to first order in δT reproduces (26) with δ identified with

$$\delta = \frac{2Q\omega_L \delta T}{\omega_0 T_R}. \tag{34}$$

Thus we have fully interpreted the Fourier transform of (10) in terms of the steady-state requirement upon a pulse shaped by the components of the laser system.

V. General Time-Dependent Loss Modulation

With the aid of the mode-locking equation in the time domain, (26), it is possible to study mode locking by an arbitrary periodic loss modulation $m(t)$. Equation (26) can be reduced to a standard equation of quantum mechanics by the change of variable

$$v(t) = V(t) \exp\left[\tfrac{1}{2}(g + \delta)\omega_L t/g\right]. \tag{35}$$

Introducing (35) into (26), one obtains the differential equation for $V(t)$

$$\frac{g}{\omega_L^2}\frac{d^2V}{dt^2} - m(t)V(t) = -EV(t) \tag{36}$$

with

$$E = g\left[1 - \left(\frac{g+\delta}{2g}\right)^2\right] - (1 + jb). \tag{37}$$

This is a well-known equation of quantum mechanics. A particle with the mass $2m/\hbar^2 = \omega_L^2/g$ moves in the potential well $m(t)$ where the role of the spatial variable x of quantum mechanics is now played by the *time*.

Because the eigenvalues E of this problem are real, we find $b = 0$, the mode at laser line center oscillates at its resonance frequency also for this form of modulation.

The sinusoidal modulation problem of the homogeneously broadened laser could have been solved in the time domain, with $1 - \cos\omega_M t \to \frac{1}{2}(\omega_M t)^2$ and the Hermite-Gaussian solutions would have been obtained, another way of observing the invariance of Hermite-Gaussians with regard to Fourier transformation. Consider as another example a very deep modulation of the mode-locking crystal which shuts off transmission entirely outside an interval of length τ. This is shown in Fig. 3. Equation (32) for the square potential well is the quantum mechanical problem of an electron in a perfectly reflecting box. The eigenfunctions and eigenvalues of

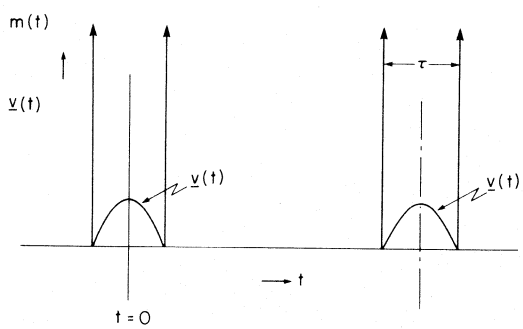

Fig. 3. "Deep" modulation and the quantum mechanical wave function analog.

this problem are [13]

$$V(t) = \cos \frac{n\pi}{\tau} t \tag{38}$$

in the time domain. The eigenvalue equation yields

$$g\left[1 - \left(\frac{g+\delta}{2g}\right)^2\right] - 1 = \frac{g}{\omega_L^2}\left(\frac{n\pi}{\tau}\right)^2. \tag{39}$$

In the time domain the mode-locked pulse is confined to the time interval τ. Equation (39) shows that excessive detuning of the modulation quenches the laser; no solution is found for $g + \delta > 2\sqrt{g(g-1)}$.

If the square-wave modulation is modified to one of lesser depth, one has the problem of a particle in an open-square well with well-known eigenfunctions [13].

One may think of other modulation functions $m(t)$ for which either quantum mechanical solutions exist, or for which one may arrive at qualitative conclusions as to the shape of the mode-locking pulse. Consider, for example, the approximations made when the discrete spectrum of the cavity-mode oscillations was replaced by a continuum, and the modulation of loss was represented by the operator $d^2/d\omega^2$. In the time domain, this operator is replaced by the multiplier $-\frac{1}{2}t^2$. The analog of the full cosinusoidal modulator is the particle in a cosinusoidal potential. When the modulation is strong enough so that the eigenvalue levels are near the bottoms of the wells, one obtains a set of solutions in each of the well bottoms, which are the Hermite-Gaussians. When the modulation is decreased, the height of the wells is decreased and solutions are found with overlap between the (wave) functions within each of the periodic wells. The mode locking is not strong enough to suppress the field amplitude between the pulses.

VI. Stability of Solutions

The existence of a solution of the mode-locking equation does not imply physical realizability. In particular, a whole set of Hermite-Gaussian solutions is found in the case of sinusoidal modulation. Which of these solutions is realized in the steady state? In order to answer this question one must resort to a stability analysis.

In this section we study the stability of the supermodes with respect to arbitrary perturbations for synchronous modulation. We shall follow the analysis of stability of injection locking of a single oscillator of Kurokawa [4]. In this analysis, the assumed steady state is perturbed, and the perturbation is taken to be a slow function of time (compared with the time variation of the unperturbed oscillation). An instantaneous frequency and growth or decay rate is obtained for the perturbation. If it can be shown that there is no net growth the injection locking is stable. We shall extend this analysis to the study of the stability of "steady-state" mode-locking solutions. Here all oscillations are coupled to each other through the mode-locking process. Study of transients implies the replacement of the frequencies ω_k of the modes by $\omega_k + \Omega_k$ where Ω_k is complex: $-\text{Im}(\Omega_k) > 0$ implies growth of excitation. Further the "instantaneous" perturbation frequency Ω_k itself is a function of time. Thus even temporary growth may be offset by eventual decay.

The objective then is to obtain an equation for a complex perturbation δV_k of the steady state V_k of the kth axial mode. The frequency Ω_k of the perturbation is, in general, a function of the phase ϕ_k between δV_k and V_k. The perturbation obeys the same difference equation (16) as V_k, except that ω_k must be replaced everywhere by $\omega_k + \Omega_k$ and g may be perturbed because an amplitude perturbation changes P and thus changes g. All ω_k dependent parameters may be expanded to first order in the Ω_k if the Ω_k are assumed small (small growth or decay and phase deviations within one transit time T_R). We shall disregard all derivatives of the parameters of (4) with respect to Ω_k, except that of $\text{Im}\, Y_{Ck}(\omega_k)$. This is an approximation which disregards energy storages other than the electromagnetic energy storage of the cavity modes. If the oscillation of the perturbation δV_k of the kth axial mode occurs with the frequency $\omega_k + \Omega_k$, then the admittance to be associated with δV_k is

$$Y_{Ck}(\omega_k + \Omega_k) = Y_{Ck}(\omega_k) + j\Omega_k \frac{2Q}{\omega_k}$$

or in the continuum limit

$$Y_C(\omega + \Omega) \cong Y_C(\omega) + j\Omega \frac{2Q}{\omega_0}. \tag{40}$$

If we assume that the unperturbed solution is the nth supermode $V_n(\omega)$ excited at synchronism (i.e., $g + \delta = 0$) expand the difference equation as indicated and go to the continuum limit, we obtain the equation [compare (17)]

$$\left[M\omega_M^2 \frac{d^2}{d\omega^2} + g\left(1 - \frac{\omega^2}{\omega_L^2}\right) - 1\right]\delta V + (\delta g)\left(1 - \frac{\omega^2}{\omega_L^2} - j\frac{\omega}{\omega_L}\right)V_n = \frac{2Q}{\omega_0} j\Omega\, \delta V. \tag{41}$$

Because the change of the pulse per transit time T_R has been assumed small, $j\Omega T_R \delta V$ is the change of δV within one transit time T_R

$$j\Omega\, T_R \delta V = \Delta \delta V.$$

One may define the slow-time variable $T = NT_R$, where N is the number of transits. In terms of T, the rate of change of the pulse spectrum as a function of the time parameter T is

$$j\Omega \delta V = \frac{\Delta \delta V}{T_R} = \frac{\Delta \delta V}{\Delta T} = \frac{\partial \delta V}{\partial T} \tag{42}$$

where we use a partial derivative to emphasize that δV is a function of T and ω.

Next consider the perturbation δg. In general, δg obeys a differential equation in time. Thus if one adheres to the two-level model of (12), then δg obeys the differential function

$$\frac{\partial}{\partial T}\delta g = -\frac{\delta g}{\tau} - \frac{g}{T_L}\frac{\delta P}{T_L} \tag{43}$$

where

$$\frac{1}{\tau} = \frac{1}{T_L}\left(1 + \frac{P}{P_L}\right). \tag{44}$$

Suppose that the mode spectrum $V_n(\omega)$ is so normalized that $\int |V_n(\omega)|^2 d\omega$ is equal to the power P. Then

$$\delta P = 2 \int V_n(\omega) \operatorname{Re} \delta V \, d\omega \tag{45}$$

where the phase of the perturbation is measured with respect to the steady state. Equation (45) suggests the expediency of an expansion of the perturbation δV in terms of orthonormal eigenfunctions which, except for one, are orthogonal to V_n. The obvious set is the one defined by the differential equation

$$M\omega_M^2 \frac{d^2}{d\omega^2} u_p - g \frac{\omega^2}{\omega_L^2} u_p = -E_p u_p \tag{46}$$

with eigenvalues E_p given by (22). The steady-state solution V_n is a member of the set. We put

$$V_n = A_n u_n(\omega). \tag{47}$$

The perturbation is expanded in terms of the complete set

$$\delta V(T, \omega) = \sum_p a_p(T) u_p(\omega). \tag{48}$$

Introducing (48) in (41), with $j\Omega$ replaced by d/dT, multiplying the result by $u_q(\omega)$, and integrating over all m, we obtain

$$\frac{2Q}{\omega_0} \frac{da_q}{dT} = -(E_q - E_n) a_q + \delta g \, A_n C_{qn} \tag{49}$$

where

$$C_{qn} = \int_{-\infty}^{\infty} \left[1 - \frac{\omega^2}{\omega_L^2} - j \frac{\omega}{\omega_L} \right] u_q u_n \, d\omega. \tag{50}$$

Equation (43) for the gain perturbation becomes

$$\frac{d}{dT} \delta g = -\frac{\delta g}{\tau} - \frac{2g}{T_L} \frac{A_n \operatorname{Re} a_n}{P_L}. \tag{51}$$

For $n \neq q$ the perturbation of gain δg vanishes and one finds

$$\frac{2Q}{\omega_0} \frac{d}{dT} a_q = -(E_q - E_n) a_q. \tag{52}$$

The amplitude a_q is uncoupled from all the others. Growth of a_q occurs for $q < n$. This finding is the consequence of the fact that a mode $q < n$ requires less gain in the steady state, according to (22), than the mode n. If the two modes are orthogonal, then the power does not change to first order due to addition of a perturbation $a_q u_q$ to the steady-state $A_n u_n(\omega)$. Hence no gain change occurs. As the gain is higher already than the one required for the steady state of the qth mode, the perturbation grows.

Next consider the equations for the perturbation of the lowest order mode $n = 0$. The equations for a_0 are uncoupled from all the other amplitudes $a_q, q \neq 0$. Separating a_0 into phase and amplitude

$$a_0 = r \exp(j\phi_0)$$

introducing this expresison into (49) and (51), eliminating the gain variation δg, one obtains a second-order differential equation. Dividing by the phase factor $\exp j\phi_0$ and separating the equation into its real and imaginary parts, one obtains

$$\ddot{r} - \dot{\phi}_0^2 r + \frac{1}{\tau} \dot{r} = -\left(\frac{\omega_0}{2Q} \frac{g}{T_L} \frac{P}{P_L} \right) C_{00} r (1 + \cos 2\phi_0) \tag{53}$$

$$r\ddot{\phi}_0 + 2\dot{r}\dot{\phi}_0 + \frac{1}{\tau} r\dot{\phi} = \left(\frac{\omega_0}{2Q} \frac{g}{T_L} \frac{P}{P_L} \right) C_{00} r \sin 2\phi_0. \tag{54}$$

The coefficient C_{00} is equal to

$$C_{00} = 1 - \frac{1}{2} \frac{\omega_P^2}{\omega_L}.$$

Note that C_{00} is positive for all values of ω_P permitted by our original assumption of narrow pulse-bandwidth. Equations (53) and (54) are the equations of motion of a particle of inverse mass equal to $C_{00}\omega_0 gP/(2QT_L P_L)$ in a force field

$$f_r = -(1 + \cos 2\phi_0) r$$

$$f_\phi = \sin 2\phi_0 \, r.$$

This force field is conservative (its curl vanishes) and hence is properly represented by a potential $\Phi(r, \phi_0)$ which is found to be

$$\Phi = \frac{r^2}{2} (1 + \cos 2\phi_0).$$

This potential is a parabolic trough, with the bottom of the trough aligned along the $\phi_0 = (\pi/2)$ axis. A particle launched at any point with a certain velocity (the analog of a perturbation of given initial phase, amplitude, and time rate of change) will experience a damped oscillatory motion until finally it lands at the bottom of the trough, in general, at a finite distance from the origin. Translated into the language of the perturbation evolution, we find that an arbitrary initial perturbation of given initial phase, amplitude, and time rate of change experiences damped oscillations running through various phases, but always ending up with $\phi_0 = \pm 90°$, in quadrature with the steady state. This final phase indicates a quadrature component to the steady state, or a phase change of the factor $\exp j\omega_0 t$. The behavior is analogous with that of the simple van der Pol oscillator for which one also finds that random noise perturbations cause a random walk of the phase of the oscillation [16].

Next consider the equations obtained for the perturbation amplitudes a_1 and a_2 from (49). The amplitudes a_q for $q > 2$ are all uncoupled because $C_{q0} = 0$ for $q > 2$ and they all decay. On the other hand, $\operatorname{Re} a_0$ acts as a source of a_1 and a_2. Since the natural "frequencies" of a_1 and a_2 have positive imaginary parts, the amplitudes a_1 and a_2 in turn vanish along with $\operatorname{Re} a_0$. Hence we have shown that for synchronous modulation the $n = 0$ supermode is stable with respect to arbitrary perturbations.

VII. Conclusions

An analysis of forced mode locking has been presented in both the time domain and the frequency domain. For deep sinusoidal modulation, the well-known Hermite-Gaussian supermode solutions have been obtained. Transformation

of the equations into the time domain for a general periodic modulation led to a simple quantum analog of a particle in a periodic potential well. This analog permitted the observation that a shallow sinusoidal modulation was the analog of a particle motion in a sinusoidally spatially varying potential. When the modulation is deep, and the pulses (wave functions) are well separated, the potential can be approximated by a parabola within the range occupied by any one of the wave functions. In this limit the Hermite-Gaussian solutions are obtained.

Maybe the most important new result of this paper is the conclusion that all Hermite-Gaussian steady-state solutions for synchronous modulation are unstable except the lowest order one. We have determined the response of the fundamental (Gaussian) mode to an initial perturbation and found, in general, that all such perturbations die down, resulting in a phase perturbation of the carrier.

ACKNOWLEDGMENT

The author wishes to thank C. P. Ausschnitt for many useful discussions.

REFERENCES

[1] P. W. Smith, M. A. Duguay, and E. P. Ippen, "Mode-locking of lasers," in *Progress in Quantum Optics*, J. H. Sanders and S. Stenholm, Ed. New York: Pergamon, 1974.
[2] D. J. Kuizenga and A. E. Siegman, "FM and AM mode locking of the homogeneous laser–Part I: Theory," *IEEE J. Quantum Electron.*, vol. QE-6, pp. 694–708, Nov. 1970.
[3] O. P. McDuff and S. E. Harris, "Nonlinear theory of the internally loss-modulated laser," *IEEE J. Quantum Electron.*, vol. QE-3, pp. 101–111, Mar. 1967.
[4] K. Kurokawa, "Injection locking of microwave solid-state oscillators," *Proc. IEEE*, vol. 61, pp. 1386–1410, Oct. 1973.
[5] J. R. Fontana, "Theory of spontaneous mode locking in lasers using a circuit model," *IEEE J. Quantum Electron.*, vol. QE-8, pp. 699–703, Aug. 1972.
[6] H. Haken and M. Pauthier, "Nonlinear theory of multimode action in loss modulated lasers," *IEEE J. Quantum Electron.*, vol. QE-4, pp. 454–459, July 1968.
[7] V. S. Letokhov, "Dynamics of generation of a pulsed mode locking laser," *Sov. Phys.–JETP*, vol. 27, pp. 746–751, Nov. 1968.
[8] A. E. Siegman and D. J. Kuizenga, "Modulator frequency detuning effects in the FM mode-locked laser," *IEEE J. Quantum Electron.*, vol. QE-6, pp. 803–808, Dec. 1970.
[9] T. J. Nelson, "A coupled-mode analysis of mode locking in homogeneously broadened lasers," *IEEE J. Quantum Electron. (Part I of Two Parts)*, vol. QE-8, pp. 29–33, Feb. 1972.
[10] D. M. Kim, S. Marathe, and T. A. Rabson, "Eigenfunction analysis of mode-locking process," *J. Appl. Phys.*, vol. 44, pp. 1673–1675, Apr. 1973.
[11] D. J. Kuizenga and A. E. Siegman, "FM and AM mode locking of the homogeneous laser–Part II: Experimental results in a Nd:YAG laser with FM modulation," *IEEE J. Quantum Electron.*, vol. QE-6, pp. 709–715, Nov. 1970.
[12] P. W. Smith, T. J. Bridges, E. G. Burkhardth, and O. R. Wood, "Mode-locked high-pressure waveguide CO_2 laser," *Appl. Phys. Lett.*, vol. 21, pp. 470–472, Nov. 1972.
[13] L. D. Landau and E. M. Lifshitz, "Nonrelativistic theory," in *Quantum Mechanics*, A. S. Davydov, Ed. Reading, Mass: Addison-Wesley, 1958, pp. 64–67.
[14] W. A. Edson, "Noise in oscillators," *Proc. IRE*, vol. 48, pp. 1454–1466, Aug. 1960.

Spectroscopy and Laser Oscillation Properties of Lithium Neodymium Tetraphosphate

KENJU OTSUKA, ASSOCIATE MEMBER, IEEE, TOMOAKI YAMADA, MASATOSHI SARUWATARI, AND TATSUYA KIMURA, MEMBER, IEEE

Abstract–**Optical absorption, fluorescence, and laser characteristics of lithium neodymium tetraphosphate ($LiNdP_4O_{12}$, abbreviated as LNP) were examined. The crystal belongs to the monoclinic system (pseudoorthorhombic system) and the Nd content is $4.37 \times 10^{21}\,cm^{-3}$. The lifetime of the $^4F_{3/2}$ level is 120 μs, which is one-half of 230 μs observed in Nd:YAG. The largest effective emission cross section at the line peak (1.047$_7$ μm) was spectroscopically determined as $3.2 \times 10^{-19}\,cm^2$ for the electric vector parallel to the pseudoorthorhombic c axis and quantum efficiency was estimated as 0.48.**

Quasi-continuous laser oscillation pumped by a chopped Ar-ion laser was achieved with a 1.85-mm-long crystal. The output light was linearly polarized along the pseudoorthorhombic c axis of the crystal, which does not depend on the polarization direction of the pump light.

The measured threshold and round-trip loss yield the value of $3.1 \times 10^{-19}\,cm^2$ for the effective emission cross section of LNP, which is in good agreement with the value obtained from the spectroscopic data.

Manuscript received August 22, 1974; revised February 10, 1975.
The authors are with the Musashino Electrical Communication Laboratories, Nippon Telegraph and Telephone Public Corporation, Tokyo, Japan.

I. INTRODUCTION

AS AN EFFICIENT laser material, in which active ions are an essential component of the chemical compound, neodymium pentaphosphate (NdP_5O_{14}) was proposed by Danielmeyer and Weber [1]. Although the Nd content of $4 \times 10^{21}\,cm^{-3}$ is about 30 times higher than that of Nd:YAG, the crystal has little concentration quenching and the lifetime of $^4F_{3/2}$ state is 66 μs. Moreover, the lifetime of NdPP was recently reported to increase up to 120 μs by annealing

the crystal [2]. Quasi-continuous and continuous laser oscillations with very low threshold were also reported in (Nd, La) and (Nd, Sc) pentaphosphate, respectively [3], [4].

Recently, we reported the fluorescence in lithium neodymium tetraphosphate ($LiNdP_4O_{12}$, abbreviated as LNP) as another material with little concentration quenching [5]. Single crystals of LNP up to about 3 X 3 X 3 mm in size were obtained by the top-seeded Kyropoulos method from a melt of composition different from LNP. Fundamental crystallographic properties of LNP are summarized.

Stoichiometry	$LiNdP_4O_{12}$.
System	Monoclinic (pseudoorthorhombic).
Space group	$C2/c - C_{2h}^6$.
Lattice constants	a = 16.45 Å, b = 7.07 Å, c = 13.25 Å, $\beta = 143°37'$ (a = 9.76 Å, b = 13.25 Å, c = 7.07 Å).
Density (calculated)	3.39 g/cm^3.
Z	4 molecules/unit cell.
Nd concentration	4.37×10^{21} cm^{-3}.
Refractive index (6328 Å)	1.58.

The present paper reports the spectroscopic properties such as absorption, fluorescence, and laser transition cross section, and the examination of quasi-continuous oscillation of LNP laser.

II. Spectroscopy and Laser Transition Cross Sections

Several plates normal to the crystallographic axes cut out from the boules of LNP were polished to a uniform thickness and their absorption spectra were examined, using a Cary 14R recording spectrometer. The absorption spectra of an a plate which correspond to the most intense absorption band ($^4I_{9/2} \rightarrow {}^4F_{5/2}, {}^2H_{9/2}$) are shown in Fig. 1. The peak absorption cross section of the line at 8009 Å ($^4I_{9/2}(2) \rightarrow {}^4F_{5/2}(2)$) was $\sigma_a = 1.25 \times 10^{-19}$ cm^2. This is very much in line with the cross section for Nd:YAG at 8100 Å (1.20×10^{-19} cm^2) [6]. Since the Nd concentration is about 30 times higher in LNP than in Nd:YAG and the absorption cross sections are nearly the same for both materials, the absorption coefficient of LNP is about 30 times larger than that of Nd:YAG at the most intense absorption band.

The room-temperature lifetime of the $^4F_{3/2}$ state was determined by measuring the spontaneous decay on an oscilloscope. The sample was excited by Xe flashlamp of 0.6-μs pulse duration or a dye laser (5965 Å) of 1-μs pulse duration. The decay was exponential with a $1/e$ lifetime τ_f of 120 μs.

The emission cross sections were determined at room temperature, using the method reported by Neeland and Evtuhov [7] and recently refined by Singh *et al.* [8] in the case of Nd:YAG. The method consists of the following two processes: 1) the direct determination of the transition cross sections from the ground-state manifold ($^4I_{9/2}$) to the laser state manifold ($^4F_{3/2}$) by the absorption measurement; and 2) the comparison of fluorescence-emission intensities from the laser state manifold to the lower manifold with those of $^4F_{3/2} \rightarrow {}^4I_{9/2}$.

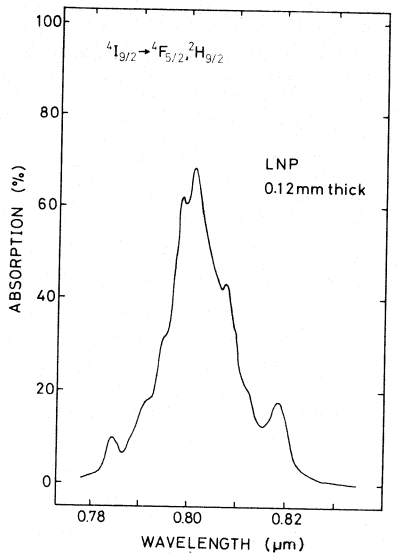

Fig. 1. Absorption spectra of an a plate LNP of 0.12-mm thickness at the most intense absorption band.

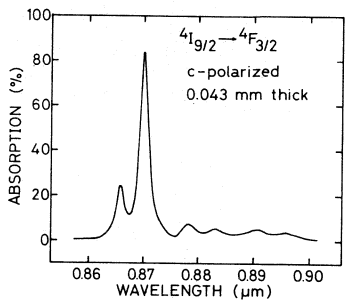

Fig. 2. Absorption spectra of LNP 43 μm thick, which correspond to the transitions from the ground state to the $^4F_{3/2}$ state for the light polarized along the pseudoorthorhombic c axis of the crystal.

Since the laser emission is linearly polarized along the pseudoorthorhombic c axis, as described in the next section, the measurements were made for the electric vector parallel to the c axis.

Fig. 2 shows the absorption spectra of the $^4I_{9/2} \rightarrow {}^4F_{3/2}$ transitions measured on a 43-μm-thick plate of LNP. From the absorption coefficients determined by the figure, the peak absorption cross sections $\sigma_{R_1} = 2.3 \times 10^{-19}$ cm^2 and $\sigma_{R_2} = 0.31 \times 10^{-19}$ cm^2 were obtained for the R_1 (0.870_8 μm) and R_2 (0.866_6 μm) lines which correspond to the transitions from the ground state $^4I_{9/2}(1)$ to the lower and upper levels of the $^4F_{3/2}$ state, respectively. The population of the $^4I_{9/2}(1)$ level is $0.40N_0$ at room temperature, where N_0 is the total Nd-ion density.

The fluorescence spectra were examined as follows. The sample was excited by a high-pressure Hg lamp and the fluorescence from LNP was detected with a cooled S-1 photomultiplier and a lock-in amplifier after it had been passed through a polarizer. The relative spectral sensitivity of the detection system was calibrated with a NBS standard lamp.

The Nd^{3+} ion has four fluorescence groups that originate from the two $^4F_{3/2}$ levels. The transitions into the $^4I_{15/2}$ levels around 1.9 μm and the $^4I_{13/2}$ levels around 1.3 μm were weak in LNP. The shortest wavelength transitions near 0.9 μm

which terminate in the five $^4I_{9/2}$ levels are shown in Fig. 3. The sample thickness was 25 μm to make corrections due to reabsorption small; however, the peak value of the R_1 line was corrected to be consistent with the absorption spectra and the relative population between the two $^4F_{3/2}$ levels. The fluorescence from the $^4F_{3/2} \rightarrow {}^4I_{11/2}$ levels was shown in Fig. 4, which was measured in exactly the same experimental arrangement. The intensity scale in Fig. 4 is the same as in Fig. 3. The splitting of the two $^4F_{3/2}$ levels could be found by looking for pairs with equal spacing in the spectra. The I-level energies could be determined by ordering the pairs according to their wavenumber, where spectra measured for the electric vector parallel to the pseudoorthorhombic a and b axes were also taken into consideration. The results of this procedure are shown in Fig. 5.

As seen in Fig. 6, the 1.0647-μm laser line of LNP consists of two Lorentzian lines at room temperature. The l_1 line located at 1.0647 μm has a peak value of about 0.88 times the total peak value with 17-Å full width between half-intensity points. The l_2 line located at about 13 Å longer from the l_1 line has a peak value of about 0.24 times the peak value of the l_1 line with 25-Å full width. We shall define the effective emission cross section for the ion in the $^4F_{3/2}$ manifold as follows:

$$\sigma_l = \frac{\sigma_{l_1} + \sigma_{l_2} a}{1 + a} \tag{1}$$

where σ_{l_1} and σ_{l_2} are the cross sections of the two transitions at the laser line peak (1.0647 μm), and a is the Boltzmann factor between the R_1 and R_2 levels at room temperature (0.76).

If we assume that the peak emission cross sections of the R_1 ($^4F_{3/2}(1) \rightarrow {}^4I_{9/2}(1)$) and R_2 ($^4F_{3/2}(2) \rightarrow {}^4I_{9/2}(1)$) lines are equal to the peak absorption cross sections σ_{R_1} and σ_{R_2}, respectively, the ratio of the peak emission intensities to the R_1 and R_2 lines to those of the laser lines are given as

$$(dI_{R_1}/d\lambda)/(dI_{l_1}/d\lambda) = (\nu_{R_1}/\nu_{l_1})^5 (\sigma_{R_1}/\sigma_{l_1})$$
$$(dI_{R_2}/d\lambda)/(dI_{l_2 p}/d\lambda) = (\nu_{R_2}/\nu_{l_2})^5 (\sigma_{R_2}/\sigma_{l_2 p}) \tag{2}$$

where $\sigma_{l_2 p}$ is the emission cross section at the l_2-line peak and ν represents the transition frequency. From Figs. 3, 4, and 6 $\sigma_{l_1}/\sigma_{R_1} = 2.2$ and $\sigma_{l_2 p}/\sigma_{R_2} = 5.1$ were obtained. Using the values for σ_{R_1} and σ_{R_2}, determined by the absorption measurement and (1), we obtained the laser transition cross section $\sigma_l = 3.2 \times 10^{-19}\,\mathrm{cm}^2$ ($\sigma_{l_1} = 5.1 \times 10^{-19}\,\mathrm{cm}^2$, $\sigma_{l_2 p} = 1.6 \times 10^{-19}\,\mathrm{cm}^2$, $\sigma_{l_2} = 0.8 \times 10^{-19}\,\mathrm{cm}^2$ at 1.0647 μm).

Integrating the curves of Figs. 3 and 4 and then converting from intensity into number of photons, the branching ratios were obtained as $\beta_{9/2} = 0.36$ and $\beta_{11/2} = 0.64$, where $\beta_{13/2}$ and $\beta_{15/2}$ were assumed to be negligibly small. The branching ratio of the l_1 line was calculated as 0.20.

The same measurements were made for the electric vector parallel to the a and b axes. The results are summarized in Table I.

The total radiative lifetime τ_r could be calculated by using

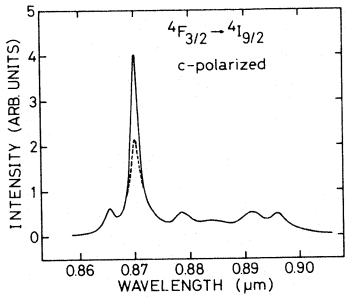

Fig. 3. Fluorescence of the shortest wavelength band of LNP 25 μm thick for the electric vector parallel to the c axis. The dashed curve shows the measured fluorescence spectra and the solid curve shows the corrected one, taking into account reabsorption.

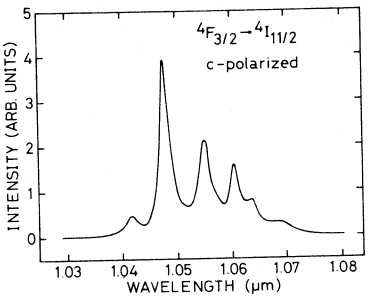

Fig. 4. Fluorescence of the strongest band of LNP 25 μm thick for the electric vector parallel to the c axis. The intensity scale in Fig. 4 is the same as Fig. 3.

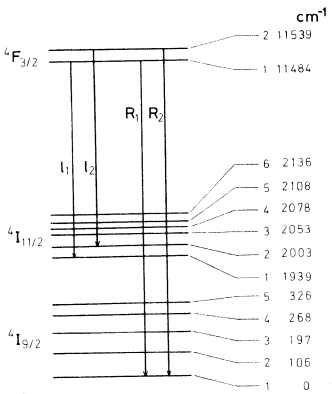

Fig. 5. Energy levels and main transitions in LNP at 300 K. R_1 and R_2 lines are also presented.

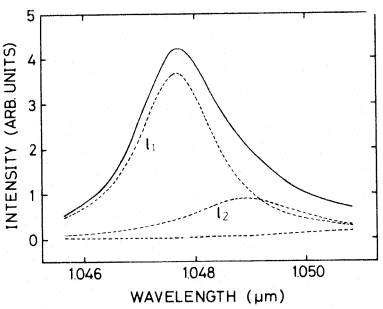

Fig. 6. Emission spectrum of the 1.0647-μm laser lines at 300 K. Two Lorentzian lines contributing to the laser transition are shown by dashed curves.

TABLE I

	β_{l_1}	$\Delta\lambda_{l_1}$	σ_{l_1}	β_{l_2}	$\Delta\lambda_{l_2}$	σ_{l_2}	σ_l
a	0.19	20Å	2.1×10^{-19}cm^2	0.12	24Å	1.5×10^{-19}cm^2	1.5×10^{-19}cm^2
b	0.16	19	1.7	0.11	23	1.3	1.3
c	0.20	17	5.1	0.07	25	1.6	3.2

Note: Branching ratios, linewidths, and peak emission cross sections for the two transitions in the 1.047_7-μm laser line in LNP for the electric vectors parallel to the pseudoorthorhombic *a*, *b*, and *c* axes. The effective emission cross sections at the laser line are also shown.

the relation

$$\tau_r^{-1} = (4\pi^2 cn^2 F_{l_1}/\lambda_{l_1}^4)\left(\sum\sigma_{l_1}\Delta\lambda_{l_1}/\beta_{l_1}\right)\Big/3 \qquad (3)$$

where c is the velocity of light, n is the refractive index, F_{l_1} is the fraction of ions in the $^4F_{3/2}(1)$ level (0.57) and the summation was made over the values for the electric vector along the *a*, *b*, and *c* axes. From the values listed in Table I, τ_r was obtained as 250 μs. This total radiative lifetime is much longer than the measured fluorescent lifetime τ_f of 120 μs, and therefore the radiative quantum efficiency is estimated as $\eta = \tau_f/\tau_r = 0.48$. For a comparison, the fluorescent lifetime in the limit of zero concentration was measured. In $Li(Nd_xR_{1-x})P$ (R = Y, La, Gd) the lifetime increases from 120-320 μs with the concentration (N) dependence of $\tau_f = \tau_0(1 + QN^2)^{-1}$, where the cross relaxation rate Q was obtained as about 0.5×10^{-43}cm^6. Although LNP has a little concentration quenching, the quenching is much less than other host materials, i.e., the value of Q is about 20 times smaller than that of Nd:YAG [9].

III. Laser Characteristics

We report in this section quasi-continuous laser action in LNP. The experimental arrangement is shown in Fig. 7. A chopped Ar-ion laser (5145 Å) served as a pump. The Ar-ion laser pulses had a duration of 300 μs-2 ms, a duty factor of 2-50 percent, and was linearly polarized. The following results were obtained with a crystal 1.85 mm long (pseudo-orthorhombic *a* axis) and 1 mm wide (*c* axis) cemented on a copper heat sink. The thickness of the crystal was 0.7 mm (*b* axis). The resonator is of a nearly semiconcentric type with mirrors M_1 (radius of curvature R_1 = 9 cm, transmittance at 1.047_7 μm, T_1 = 0.1, 1.2, 2, 3 percent) and M_2 ($R_2 = \infty$, T_2 = 0.1 percent) separated by about 9 cm. The crystal was placed just in front of M_2. The focal length of the lens L focusing the pump beam was 5 cm and adjusted to minimize the pumped volume in the crystal.

The power absorbed by the crystal was measured with a silicon photocell as the difference between input and output power. The absorption coefficient depends on the polarization direction of the pump light. The maximum absorption was obtained when the polarization direction of the pump light was adjusted along the *c* axis of the LNP, and the crystal of 1.85-mm length absorbed about 100 percent of the pump light.

The output power through the mirror M_1 is shown in Fig. 8

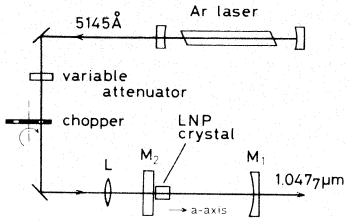

Fig. 7. Experimental arrangement of the quasi-continuous LNP laser.

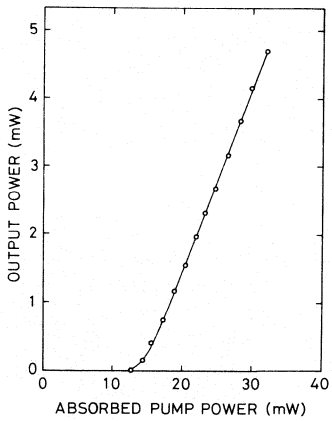

Fig. 8. The output power through the mirror M_1 (T_1 = 1.2 percent) as a function of the absorbed pump power at 5145 Å.

as a function of the absorbed pump power at 5145 Å, where T_1 and T_2 were fixed as 1.2 and 0.1 percent, respectively. The threshold was P_{th} = 12.7 mW and the slope efficiency was 27 percent.

The LNP laser emission was linearly polarized along the *c* axis of the crystal, which does not depend on the polarization direction of the pump light.

The output waveform shows the relaxation oscillation in the onset of laser oscillation, as shown in Fig. 9.

The round-trip loss of the resonator L_c was directly measured by the change of threshold with $\ln(r_1 r_2)$, where r_1 and r_2 were the mirror reflectivities. The measured threshold was plotted as a function of $-\ln(r_1 r_2)$ in Fig. 10. From Fig. 10, the round-trip loss, except the transmission losses of the mirrors, is found to be 0.03.

The output-beam spot size of the LNP-laser radiation was measured as a function of the distance from the mirror M_1, as shown in Fig. 11(a), and we estimated the spot size at the mirror M_1 as w_m = 2.2 mm. With w_m = 2.2 mm and R_1 = 9 cm, the oscillating beam spot size in the 1.85-mm-long LNP crystal was calculated in Fig. 11(b), using the propagation laws for the fundamental mode [10, eqs. (20) and (23)], and considering the effect of refractive index. From Fig. 11(b), the beam spot size averaged over the crystal length is found to be w_a = 43 μm.

The effective emission cross section for the ion in the $^4F_{3/2}$ manifold can be calculated from

$$\sigma_l = \frac{L_c h\nu\pi w_a^2}{2P_{th}\tau_f} \qquad (4)$$

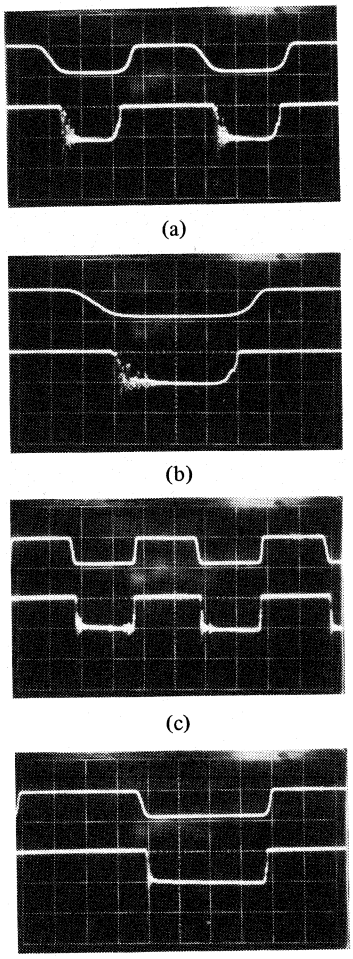

Fig. 9. Quasi-continuous output observed with an S-1 photomultiplier. The upper and lower traces represent the pump light and the output of the LNP laser, respectively. Absorbed pump power: 32 mW. (a) 200 μs/div. (b) 100 μs/div. (c) 1 ms/div. (d) 500 μs/div.

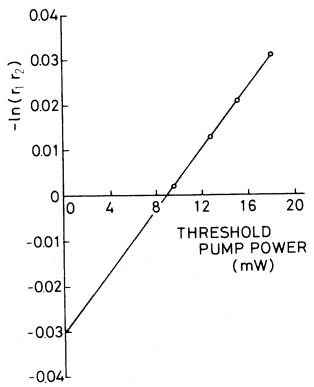

Fig. 10. The laser threshold as a function of $-\ln(r_1 r_2)$, where r_1 and r_2 are the mirror reflectivities.

where ν is the pump frequency. With $\nu = 5.83 \times 10^{14}$ Hz, $w_a = 43$ μm, and $\tau_f = 120$ μs, the effective emission cross section σ_l is determined as 3.1×10^{-19} cm^2 assuming $L_c = 0.043$ and $P_{th} = 12.7$ mW from Figs. 8 and 10. This is in good agreement with the value of 3.2×10^{-19} cm^2 obtained from the spectroscopic data.

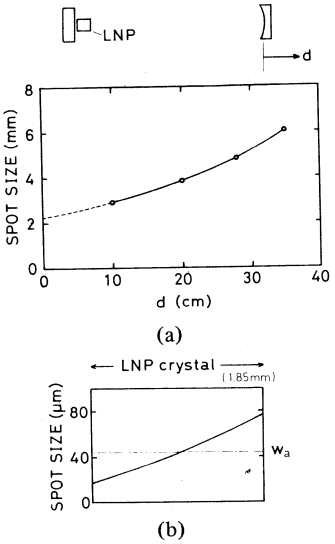

Fig. 11. The oscillating beam spot size of the LNP laser. (a) The output-beam spot size as a function of the distance from the mirror M_1 ($R_1 = 9$ cm). (b) The oscillating beam spot size in the LNP crystal. The mirror spacing is about 9 cm and the crystal is located about 0.2 mm apart from the mirror M_2.

The output spectra of the laser were analyzed with a JASCO single grating monochrometer with a resolution of 0.1 Å. The output spectrum was 2 Å wide for TEM_{00} mode.

IV. Conclusion

Optical absorption, fluorescence, and laser characteristics of $LiNdP_4O_{12}$ were examined. The laser transition cross section of 3.2×10^{-19} cm^2 obtained from the spectroscopic data was in good agreement with that obtained from the measured threshold, round-trip loss, and beam spot size of quasi-continuous laser operation.

With 5145-Å pump, observed threshold was 12.7 mW and the slope efficiency was 27 percent when the spot size of the cavity mode was 43 μm.

Since the largest laser transition cross section, for the electric vector parallel to the pseudoorthorhombic c axis, is 1.8 times that of Nd:YAG [8], the ground-state population density of 4.37×10^{21} cm^{-3} is 33 times higher than 1-percent doped Nd:YAG and the lifetime of $^4F_{3/2}$ state is as long as 120 μs despite the high Nd concentration, LNP may be useful as a high gain material especially for transverse pumping by luminescent diodes if large crystals with high quality could be grown.

Acknowledgment

The authors wish to thank J. Nakano for support in growing the LNP laser crystal. They also wish to thank Miss H. Suzuki for her excellent technical assistance, and Dr. N. Niizeki and Dr. Y. Furukawa for encouraging this work and offering valuable criticism.

REFERENCES

[1] H. G. Danielmeyer and H. P. Weber, "Fluorescence in neodymium ultraphosphate," *IEEE J. Quantum Electron.*, vol. QE-8, pp. 805–808, Oct. 1972.

[2] B. C. Tofield, H. P. Weber, T. C. Damen, and G. A. Pasteur, "On the growth of neodymium pentaphosphate crystals for laser action," *Mater. Res. Bull.*, vol. 9, pp. 435–448, Apr. 1974.

[3] T. C. Damen, H. P. Weber, and B. C. Tofield, "NdLa pentaphosphate laser performance," *Appl. Phys. Lett.*, vol. 23, pp. 519–520, Nov. 1973.

[4] H. G. Danielmeyer, G. Huber, W. W. Krühler, and J. P. Jeser, "Continuous oscillation of a (Sc, Nd)pentaphosphate laser with 4 milliwatt pump threshold," *Appl. Phys.*, vol. 2, pp. 335–338, Dec. 1973.

[5] T. Yamada, K. Otsuka, and J. Nakano, "Fluorescence in lithium neodymium ultraphosphate single crystals," *J. Appl. Phys.*, vol. 45, pp. 5096–5097, Nov. 1974.

[6] T. Kushida, H. M. Marcos, and J. E. Geusic, "Laser transition cross section and fluorescence branching ratio for Nd^{3+} in yttrium aluminum garnet," *Phys. Rev.*, vol. 168, pp. 289–291, Mar. 1968.

[7] J. K. Neeland and V. Evtuhov, "Measurement of the laser transition cross section for Nd^{3+} in yttrium aluminum garnet," *Phys. Rev.*, vol. 156, pp. 244–246, Apr. 1967.

[8] S. Singh, R. G. Smith, and L. G. Van Uitert, "Stimulated-emission cross section and fluorescent quantum efficiency of Nd^{3+} in yttrium aluminum garnet at room temperature," *Phys. Rev. B.*, vol. 10, pp. 2566–2572, Sept. 1974.

[9] H. G. Danielmeyer and M. Blätte, "Fluorescence quenching in Nd:YAG," *Appl. Phys.*, vol. 1, pp. 269–274, May 1973.

[10] H. Kogelnik and T. Li, "Laser beams and resonators," *Proc. IEEE (A Special Joint Issue on Optical Electronics)*, vol. 54, pp. 1312–1329, Oct. 1966.

The Effects of Gas Additives on TEA CO_2 Lasers

A. L. S. SMITH, T. H. BETT, AND P. G. BROWNE

Abstract—**The effects of the selective addition of the gases H_2, CO, O_2, NO, NO_2, and N_2O on the output peak power and stability of a flowing-gas TEA laser operating with a basic mixture of CO_2, N_2, and He are examined. These additive gases are possible products of reactions which occur in the discharge region of the laser and have considerable bearing on the operation of a sealed TEA laser.**

The power output is increased with the limited addition of H_2 (~5 percent) or NO (~0.2 percent), whereas N_2O, NO_2, O_2, and CO reduce the power output when present in any amount; 50-percent reduction being obtained with ~0.23-percent N_2O, ~0.15-percent NO_2, ~4-percent O_2, and ~22-percent CO.

H_2 (and possible NO) limits the transition from a diffuse glow to arc discharge by allowing a larger range of operating conditions, whereas CO reduces the range of operating conditions for stable operation. O_2 does not affect the discharge, whereas N_2O and NO_2 both encourage the transition to arcing.

I. INTRODUCTION

In a typical flowing-gas TEA laser the gas is completely replaced between discharge pulses. Thus the plasma chemistry is dependent on the species introduced by the gas flow and any species produced by the electrical-discharge pulse which can affect the discharge characteristics within the discharge period (~0.1 μs), or can collisionally affect the molecular species in the time up to the appearance of the infrared (IR) laser-emission pulse (0.5–1.5 μs). These will include electrons, primary positive ions, and other ions formed by very rapid charged-particle reactions such as charge transfer and electron attachment. The quantities of neutral particles, atomic or molecular, formed on this time scale will be too small to affect the laser excitation or relaxation.

In a sealed TEA laser, however, the reaction products of many discharge pulses may build up considerable concentrations of other molecular species, which lead to changes in the operating characteristics and possible device failure. The possible effects of these reaction products on a preionized TEA laser can be categorized under five headings.

A. Photon Production and Absorption

If the preionization is produced by a photon flux from a subsidiary discharge between a trigger wire and the anode [1] or by trigger sparks [2], then the reaction products may affect these preliminary discharges and hence the photon emission and resonant absorption processes. The photon flux is necessary to produce an initial electron density (by photoionization or photoelectric emission from the electrodes) sufficient to prevent the main diffuse discharge constricting into an arclike channel, by ensuring that the individual avalanches in the main discharge are sufficiently close together that the local electric field is not affected by the presence of individual streamers [3]. This condition is apparently met if there is sufficient bulk photoionization in the discharge region to produce an electron density $\geq 10^4$ cm^{-3}.

It has also been observed [4] that the breakdown potential

Manuscript received October 1, 1974; revised March 3, 1975.

A. L. S. Smith is with the Department of Physics, University of St. Andrews, St. Andrews, Fife, Scotland.

T. H. Bett was with the University of St. Andrews, St. Andrews, Fife, Scotland. He is now with AWRE, Aldermaston, England.

P. G. Browne was with the University of St. Andrews, St. Andrews, Fife, Scotland. He is now with the Department of Electrical Engineering and Electronics, University of Liverpool, Liverpool, England.

V_s of the main discharge decreases considerably with an increase in the preionization photon flux.

B. Main Discharge Equilibrium

The main discharge reduced field, E/N (electric field E, particle number density N) for atmospheric-pressure discharges with current densities less than 1000 A cm^{-2} is controlled by a balance between the following bulk processes: ionization (rate coefficient k_i), attachment (rate coefficient k_a), recombination (rate coefficient k_r), and detachment (rate coefficient k_d). Thus the balance equation for electrons may be written as

$$n_e n k_i + n_n n k_d = n_e n_p k_r + n_e n k_a \quad (1)$$

where n, n_e, n_p, n_n are the number densities of neutrals, electrons, positive ions, and negative ions, respectively, and all the rate coefficients are appropriately weighted for the gas mixture [5]-[7]. The reaction products can affect some or all of these bulk processes, so that a change in the E/N value of the discharge results.

C. Main Discharge Stability

Although an initial electron density of $\sim 10^4$ cm^{-3} is adequate to ensure uniformity of the main pulsed discharge it is not adequate to sustain this main discharge, which requires an electron density of 10^{10}-10^{12} cm^{-3}. To achieve this electron density necessitates a main discharge E/N value which is so great that the diffuse discharge can rapidly undergo a transition into a single arclike channel. This is more likely to happen either when the main discharge pulse is long and the arc formative time lag is small [over voltage $(V - V_s)$ large, where V is the applied potential] [8] or when it is possible for all the stored energy to be guided into the one arc channel or when the attachment coefficient exceeds the ionization coefficient and has a positive dependence on the electron temperature [9].

D. Electron Excitation

If the breakdown potential V_s and running reduced field E/N are changed, for instance, by Sections I-A and B in the preceding, then the energy distribution and density of the electrons will change and the excitation rates to the upper and lower laser levels will be altered. Likewise, the rate of gas heating will vary, and changes in the optical gain will result.

E. Vibrational Excitation and Deexcitation

The lifetimes of the laser levels are controlled by collisional processes. The maximum rate constants for such processes are about 10^5 $torr^{-1}s^{-1}$, so that any gas species must have a partial pressure of at least 10 torr for effective collisional interaction within ~ 1 μs; i.e., the concentration of any reaction species must be at least ~ 1 percent of an atmospheric-pressure mixture to have an effect on the lifetimes of excited states in the discharge.

In a sealed-device dissociation products of CO_2, such as CO,O, and O_2, are found together with oxides of nitrogen and various positive and negative ions. There are also small amounts of H_2 and H_2O desorbed from the laser walls and electrodes. Since so many species are present it is not easy to identify their individual effects in a sealed device, but if they are selectively added to a flowing gas device, then their individual effects can be isolated.

We report here on the effects of the addition of the gases H_2, CO, O_2, N_2O, NO, and NO_2 on the output power and discharge stability of a flowing-gas TEA laser operating with a basic mixture of CO_2, N_2, and He. These additive gases can be expected to have considerable bearing on the operation of a sealed TEA laser in view of the previously mentioned effects, Sections I-A-E.

We have used a TEA laser similar to that described by Pearson and Lamberton [1]. The Rogowski profile electrodes are 20 cm long, 2 cm wide, and 1 cm apart. Electrical pulses were obtained from a 7.5-nF low-inductance capacitor discharged at about 1 pulse per second (pps) through a spark gap. The main discharge was initiated by photon emission from a predischarge between two trigger wires and the anode, the energy being supplied by two 180-pF capacitors charged to the same potential as the main capacitor. The flow rate of the $CO_2/N_2/He$-additive-gas mixture through the device was sufficient to completely change the gas between consecutive pulses. The individual gas flow rates were measured with calibrated flow meters. The resonant cavity consisted of a 100-percent plane reflector and a 20-percent transmitting germanium plane reflector separated by 30 cm. The output power was measured with a photon drag monitor together with a 100-MHz oscilloscope and camera. The pulse output was found to have a shape very similar to that obtained by Pearson and Lamberton [1], with a sharp initial spike followed by a long tail. The maximum peak power observed was 1.6 MW and the pulse energy was found to be linearly proportional to the peak power. The results in the following should be directly scalable to devices with larger excitation volumes.

II. Addition of Hydrogen

Both hydrogen and helium are known to be desirable additive gases in CO_2 lasers. In CW low-pressure devices (10-30 torr) helium lowers the gas temperature and relaxes the lower laser level, while in atmospheric-pressure devices the helium is found to be essential to stop the discharge developing in the arc mode. Normally, $CO_2/N_2/He$ TEA devices are operated with the minimum amount of helium necessary to avoid arc formation since this gives maximum power output, as the amount of CO_2 and N_2 is then a maximum. As mentioned in Section I-C, too large a discharge potential leads to arc formation. Deutsch [10] found that a TE laser at 50-250 torr can be operated at higher discharge potentials (and hence higher output powers) without the formation of arcs if 3-10 percent of hydrogen is added to the gas mixture.

We have studied the effects on the peak laser power output (W) of adding hydrogen to several different $CO_2/N_2/He$ mixtures (Fig. 1). The hydrogen has little effect when present up to 9 percent of the total gas pressure, but with greater amounts the output power drops. These results are replotted in Fig. 2 with the power output W, normalized to the power output with no added hydrogen W_0 and the added hydrogen expressed

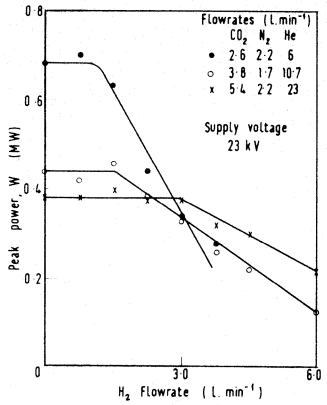

Fig. 1. Variation of laser peak power with flow rate of added hydrogen for three $CO_2/N_2/He$ mixtures.

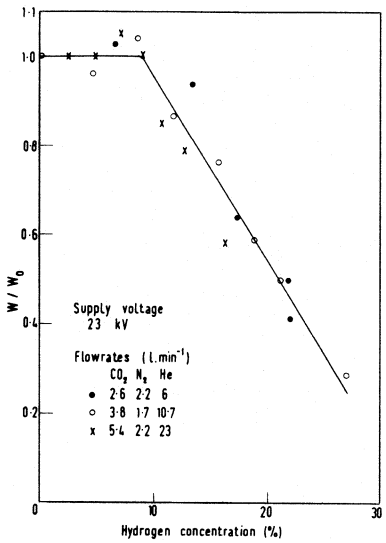

Fig. 2. Effect of addition of hydrogen on the normalized power output W/W_0 of a TEA laser.

as a percentage of the total gas mixture. One curve is seen to describe all three sets of results.

The total gas pressure in the laser was kept at 1 atm at all times and the flow rates of the CO_2, N_2, and He kept constant as the hydrogen was added. So as the hydrogen was added the other gases passed through the laser cavity faster and their partial pressures decreased. This could become significant for the carbon dioxide and nitrogen when a considerable quantity of the additive was used, but the composition change was small compared with that between the three sets of results of Figs. 1 and 2.

The general form of the curve can be understood in the following way. The ν_3 mode of CO_2 is collisionally excited by the $\nu = 1$ vibration of nitrogen with a time constant τ_1 of 400-700 ns (this is the major parameter causing the delay between the current pulse and the laser pulse). The ν_3 mode of CO_2 is deexcited by collisions with hydrogen. When the deexcitation time constant for the process is less than τ_1 the population of the ν_3 mode is significantly reduced, i.e., the laser power is reduced when

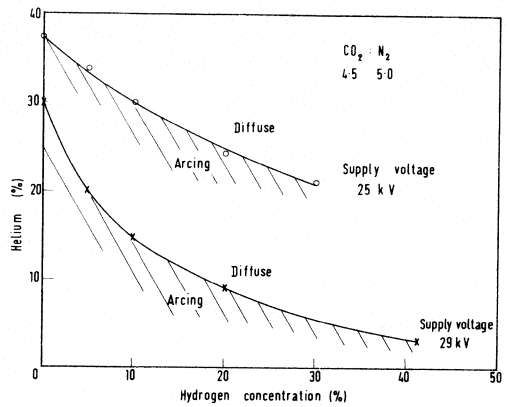

Fig. 3. Dependence of arcing limit in a $CO_2/N_2/He/H_2$ mixture at 25 and 29 kV on concentrations of He and H_2.

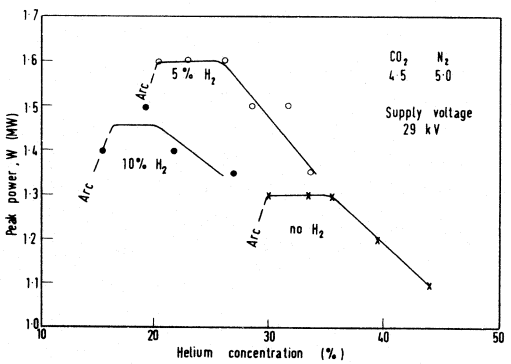

Fig. 4. Effect of the addition of hydrogen on the peak power output of a $CO_2/N_2/He$ TEA laser with varying amounts of helium.

$$\frac{1}{k_{H_2} P_{H_2}} \leqslant \tau_1$$

where k_{H_2} is the deexcitation rate constant of the ν_3 mode by collisions with molecular hydrogen [11] and P_{H_2} is the partial pressure of hydrogen. Taking the values $\tau_1 = 600 \times 10^{-9}$ s and $k_{H_2} = 5 \times 10^3$ torr^{-1} s^{-1} shows that the laser power should be reduced for $P_{H_2} \geqslant 300$ torr. This compares reasonably well with the experimental range of 70 torr for initial observation of power falloff and 250 torr for cessation of oscillation.

It is seen that up to 70 torr of hydrogen (9 percent) may be added without any loss of peak power. This allows the laser to be operated at higher voltages [10] (and hence higher energy input) and also allows the helium content in the gas mixture to be reduced. Fig. 3 shows this latter point for potentials of 25 and 29 kV. As the hydrogen percentage is increased, the helium percentage can be reduced without arcing. Further, Fig. 4 shows the peak power plotted against the percentage of added helium, for no added hydrogen, for 5-percent added hydrogen, and for 10-percent added hydrogen. With about 5-percent added hydrogen the peak power output can be at least 20 percent greater than without the hydrogen.

One of the functions of the hydrogen is to suppress the onset of the arc discharge, probably by enhancing the initial preionization, rather than altering the main discharge E/N. If the latter was so, one would expect a power increase with an other-

wise constant mixture as the hydrogen was added (see Section IV).

III. Addition of Oxygen and Carbon Monoxide

The carbon dioxide in a Pearson-type TEA laser is dissociated by 0.1-0.3 percent per discharge pulse [12]. The dissociation products are carbon monoxide and atomic oxygen. At atmospheric pressure the atomic oxygen is converted to molecular oxygen within a few milliseconds [13] by three-body collision processes and within this time it will have negligible effect on the vibrational excitation or relaxation of the carbon dioxide [14], [15].

We have selectively added molecular oxygen to several different $CO_2/N_2/He$ laser mixtures, and typical results are shown in Fig. 5. There is a slow decrease in power output with increasing amounts of oxygen added, the rate of decrease is the same for the different $CO_2/N_2/He$ mixtures at a given discharge voltage V, but varies with the value of V. No arcing was observed under any conditions.

The molecular oxygen is not present in sufficient quantity to alter the collisional lifetimes of the upper or lower laser states [16]-[18], nor is there any reason to think that oxygen will alter the photon preexcitation. Thus the most likely cause of the power decrease with added oxygen is that it has altered the E/N of the main discharge slightly, which in turn affects the laser excitation rate. The variation in E/N is brought about as follows. Oxygen has a similar rate of ionization in the discharge to carbon dioxide, but its electron attachment rate is an order of magnitude higher than that of CO_2 [9]. Consequently, to overcome this additional electron loss mechanism, the E/N value of the discharge must increase.

The effect on the laser power of the addition of carbon monoxide to several different $CO_2/N_2/He$ mixtures is shown in Fig. 6. As for oxygen there is a slow decrease in power output with an increasing amount of the additive gas, but in this case the rate of decrease depends slightly on the gas mixture. Arcing was easily obtained, occurring more readily at low values of $V - V_s$ and with mixtures low in helium content.

There is no reason to expect the carbon monoxide to affect the preionization, and in the quantities involved it will not significantly alter the lifetimes of the upper and lower laser levels [11]. However, the carbon monoxide may be expected to alter considerably the discharge E/N for the following reasons. As was discussed in Section I-B the E/N of the discharge is determined by a balance of the bulk charge collision processes. In the $CO_2/N_2/He$ laser the major dissociation process is via a neutral excited-state path [19] described by the reaction

$$CO_2 + e \longrightarrow CO_2^* + e \longrightarrow CO + O + e \tag{2}$$

but there will also be a small amount of dissociative attachment [20] according to the reaction

$$CO_2 + e \xrightarrow{k_a} CO + O^-. \tag{3}$$

The oxygen ion will rapidly form clusters with the carbon dioxide [21] rather than detach by collisions with other heavy particles. The resulting CO_3^- ions are relatively stable and it

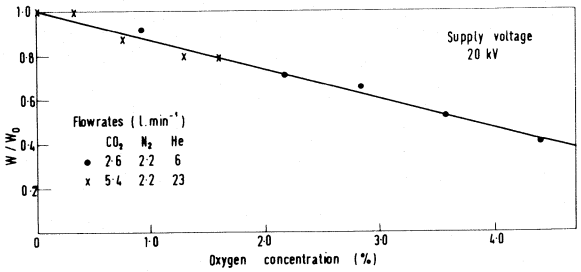

Fig. 5. Effect of the addition of oxygen on the normalized power output W/W_0 of a TEA laser.

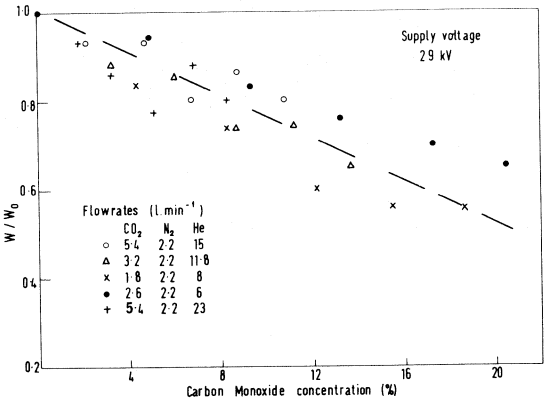

Fig. 6. Effect of the addition of carbon monoxide on the normalized power output W/W_0 of a TEA laser.

has been shown that [9] when the detachment rate is small (1) reduces to $k_i \approx k_a$. However, if carbon monoxide is present the extra detaching reaction

$$CO_3^- + CO \xrightarrow{k_d} 2CO_2 + e \tag{4}$$

occurs with a rate constant [21] (k_d) of 5×10^{-13} $cm^3 s^{-1}$. Although this is fairly slow, if sufficient carbon monoxide is added the effect is the same as if there were no negative-ion processes involved and the discharge can run at a lower value of E/N. The rate limiting process in the formation of the CO_3^- is the attachment reaction (3), so that in equilibrium this must balance the detachment reaction (4), i.e.,

$$n_e k_a [CO_2] = k_d [CO] [CO_3^-].$$

The ratio of concentration of negative ions to electrons is given by

$$\frac{[CO_3^-]}{n_e} = \frac{[CO_2]}{[CO]} \frac{k_a}{k_d} \tag{5}$$

assuming that the dominant negative ion is CO_3^-.

The value of k_a will of course depend on the gas mixture and exact discharge conditions, but in the TEA laser it will be $\sim 10^{-12}$ $cm^3 s^{-1}$, so that the negative-ion population is small compared with the electron population only when the carbon monoxide concentration is the same or greater than the carbon dioxide concentration. In our case the CO_2 concentration is 15-25 percent and the power decrease is ~20 percent with 9-percent added CO and 50 percent with 22-percent added

CO. The power is falling when the amount of added CO would be expected to lower the discharge E/N and hence increase the power output. Even if the reverse of reaction (3) is faster than expected this discrepancy would not be explained. An alternate hypothesis is that the added carbon monoxide used came from iron cylinders and may have formed iron carbonyls, which form negative ions and hence as the "carbon monoxide" is added so the discharge E/N would be raised [22].

IV. Addition of Oxides of Nitrogen

Tannen *et al.* [23] have measured both neutral species and positive ions in a dc electrical discharge in flowing $CO_2/N_2/He$ mixtures at low pressures (1-5 torr) and have found a considerable amount (100-1000 ppm) of the oxides of nitrogen. Bletzinger *et al.* [24] have suggested that the oxides of nitrogen, especially NO_2 and N_2O, may affect the discharge stability because of their high attachment rates. We have failed (using low-sensitivity mass spectrometry) to find any oxides of nitrogen (detection limit ~100 ppm) in atmospheric pressure TEA devices, but we have found some evidence at lower pressures (1-20 torr). Recently, NO and NO_2 have been observed [25] in concentrations of the order of parts per million in a flowing-gas TEA laser.

To determine the effects of NO, NO_2, and N_2O on the power output and discharge stability of the TEA laser we have added these gases to different $CO_2/N_2/He$ mixtures. Fig. 7 shows the effect on the peak power output of increasing the amount of N_2O and NO_2 in the gas mixture. The output power decreases by 50 percent with the addition of 0.23-percent N_2O or 0.15-percent NO_2. At a discharge potential of 20 kV arcing occurs with 0.42-percent N_2O or 0.26-percent NO_2, but at higher voltages arcing occurs with less of the additive gas.

Since such small amounts of NO_2 and N_2O cause a decrease in power output the effect cannot be due to any alteration of the lifetimes of the laser vibrational levels, nor is there any reason to expect that these gases alter the preexcitation photon processes. However, both N_2O and NO_2 are known to strongly attach electrons with attachment rates one to two orders of magnitude greater than CO_2 [9], [20], [26]. The ionization rate of N_2O is similar to that of CO_2 and that of NO_2 is probably also similar since its ionization potential is nearly the same. Thus the effect of adding both gases should be to raise the E/N of the discharge.

Fig. 8 shows the effect on the laser power of adding NO to three different $CO_2/N_2/He$ mixtures. There is a small increase (~15 percent in peak power output with about 0.2-percent added NO, and then a decrease with 50 percent of the original power being reached with about 2-percent added NO (but varying with the different $CO_2/N_2/He$ mixtures). No arcing was observed when adding these amounts of NO.

The initial power increase with added NO can be explained by its low ionization potential (9.2 eV) compared with CO_2 (13.79 eV). This gives NO an ionization-rate constant in a typical laser system nearly an order of magnitude greater than CO_2 or any of the other species, whereas its attachment rate is very similar to that of CO_2 [9]. Alternatively, it has been

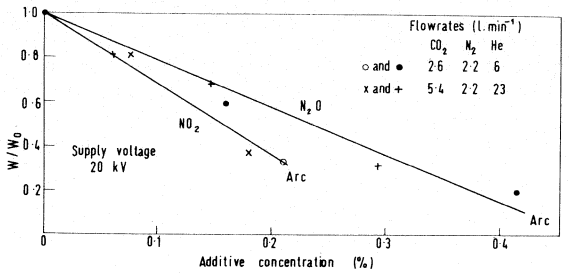

Fig. 7. Effects of the addition of nitrous oxide and nitrogen dioxide on the normalized power output W/W_0 of a TEA laser.

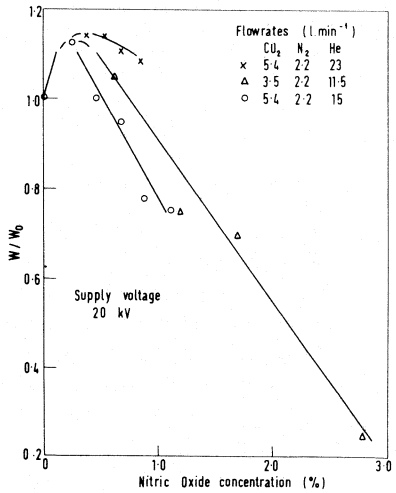

Fig. 8. Effect of the addition of nitric oxide on the normalized power output W/W_0 of a TEA laser for three $CO_2/N_2/He$ mixtures.

suggested that NO might increase the preionization because its ionization potential is low enough (9.25 eV corresponds to a photon of wavelength of 1340 Å) for the ~1200-Å photons thought to be responsible for the preionization to ionize it [27]. In either case the E/N value necessary to sustain the discharge is lower. The subsequent decrease in power is more difficult to explain: the collisional relaxation of the 001 laser level is not fast enough [28].

V. Conclusions

The method of selectively adding individual gases to the flowing-gas TEA laser has shown that the different gases have widely different effects on the laser power. Carbon monoxide and hydrogen have little effect until they are present in concentrations similar to those of the original gas constituents, whereas NO_2 and N_2O affect the laser power when present with a concentration about two orders of magnitude smaller.

N_2O, NO_2, O_2, and CO when present in any amount reduce the peak power output of the laser. However, small amounts of H_2 (~5 percent) and NO (~0.2 percent) can increase the peak output power, but larger amounts decrease it. H_2 (and possibly NO) limit the transition to arcing while O_2 does not seem to affect it. On the other hand, N_2O and NO_2 encourage the transition to arcing, but only after the power has been very greatly reduced. Carbon monoxide seems to affect the arcing in a more complicated manner. It limits the range of operation of the TEA laser, but within that range does not

affect the glow to arc transition until the power has been greatly reduced.

The increase in power output with the limited addition of hydrogen appears to be due to the ability of the laser to operate under better excitation conditions without arcing due to a change in the preionization process. Likewise, the initial increase in laser power with NO may be due to enhanced preexcitation. The only significant collisional effect with the laser vibrational levels is that of hydrogen in large concentrations when the upper laser level is deexcited. All the other effects appear to be due to changes in the main discharge processes which give rise to variations in the E/N value of the discharge and hence to variations in the rate of excitation of the upper laser level. It is clear from (1) that for a full analysis of the main discharge one needs a knowledge of all the ionization, recombination, attachment and detachment rates for each species, and how these rates vary with electron energy. Much of this information is not available. Both Nighan and Wiegand [9] and Bletzinger *et al.* [24] have attempted to determine theoretically the effects of additive gases on the discharge of a low-pressure gas laser by mainly considering the effects of the additives on the ionization and attachment rates. From this one would expect a lowering of the discharge E/N value with the addition of NO, large increases with the addition of N_2O and NO_2, a small increase with the addition of oxygen, and little effect with the addition of CO. If a lowering of the E/N value of the discharge is linked with improved laser excitation and an increase with poorer excitation, then the relative behavior of the power output with the addition of NO, NO_2, N_2O, and O_2, which we have observed, is clear. As we have seen and as Nighan and Wiegand [9] pointed out the situation with carbon monoxide may be more complicated because of the formation of fairly stable cluster ions. Also in the case of carbon monoxide such a large quantity of the gas is being added that it is not adequate to just consider a modification of the E/N of the discharge, the value of the optimum E/N for laser excitation may change [29].

The theoretical analyses should be extended to cover the potentially useful additive gases H_2 and NO and also CO because of its complicated effects. It would seem less necessary to investigate NO_2 and N_2O further because they do not become harmful until they reach a concentration of greater than 100 ppm, whereas they are almost certainly generated in sealed devices in concentrations considerably less than this.

Acknowledgment

The authors wish to thank H. Foster of the Services Electronics Research Laboratory, Baldock, for arranging the loan of some of the equipment used.

References

[1] P. R. Pearson and N. M. Lamberton, "Atmospheric pressure CO_2 lasers giving high output energy per unit volume," *IEEE J. Quantum Electron. (Part II of Two Parts: Special Issue on 1971 IEEE/OSA Conference on Laser Engineering and Applications)*, vol. QE-8, pp. 145–149, Feb. 1972.

[2] M. C. Richardson, "Multiline mode-locked uv preionised CO_2 laser," *Appl. Phys. Lett.*, vol. 25, pp. 31–33, 1974.

[3] A. J. Palmer, "A physical model on the initiation of atmospheric pressure glow discharges," *Appl. Phys. Lett.*, vol. 25, pp. 138–140, 1974.

[4] G. A. Kachickas and L. H. Fisher, "Formative time lags of uniform field breakdown in N_2," *Phys. Rev.*, vol. 88, pp. 878–883, 1952.

[5] L. J. Denes and J. J. Lowke, "V-1 characteristics of pulsed CO_2 laser discharges," *Appl. Phys. Lett.*, vol. 23, pp. 130–132, 1973.

[6] O. P. Judd and J. Y. Wada, "Investigations of a UV preionized electrical discharge and CO_2 laser," *IEEE J. Quantum Electron.*, vol. QE-10, pp. 12–20, Jan. 1974.

[7] R. Geballe and M. L. Reeves, "A condition on uniform field breakdown in electron-attaching gases," *Phys. Rev.*, vol. 92, pp. 867–868, 1953.

[8] G. V. Livey, I. D. Chambers, and O. Farish, "Transient glow discharges in N_2-CO_2-He mixtures," in *Proc. 3rd Int. Conf. Gas Discharges* (London, England, 1974), pp. 348–352.

[9] W. L. Nighan and W. J. Wiegand, "The influence of negative ion processes on the stability of molecular gas discharges," preprint.

[10] T. F. Deutsch, "Effect of hydrogen on CO_2 TEA lasers," *Appl. Phys. Lett.*, vol. 20, pp. 315–316, 1972.

[11] P. K. Cheo, "CO_2 lasers," in *Lasers: A Series of Advances*, vol. 3, A. K. Levine and A. J. DeMaria, Ed. New York: Dekker, 1971.

[12] J. M. Austin, A. L. S. Smith, and P. G. Browne, "Dissociation in TEA CO_2 lasers," *Phys. Lett.*, vol. 46A, pp. 427–428, 1974.

[13] A. L. S. Smith and J. M. Austin, "Atomic oxygen recombination in carbon dioxide laser gases," *J. Phys. B.*, vol. 7, pp. L191–L192, 1974.

[14] R. E. Center, "Vibrational relaxation of CO_2 by O atoms," *J. Chem. Phys.*, vol. 59, pp. 3523–3527, 1973.

[15] J. H. W. Cramp and J. D. Lambert, "Vibrational relaxation of CO_2 (v_3) by O atoms," *J. Chem. Phys. Lett.*, vol. 22, pp. 146–149, 1973.

[16] J. A. F. Alexander, J. T. Houghton, and W. B. McKnight, "Collisional relaxation from the v_3 vibration of CO_2," *J. Phys. B.*, ser. 2, vol. 1, pp. 1225–1226, 1968.

[17] K. M. Merrill and R. C. Amme, "Deactivation of the CO_2 bending mode by collisions with N_2 and O_2^*," *J. Chem. Phys.*, vol. 51, pp. 844–846, 1969.

[18] F. Cannemeyer and A. E. de Vries, "Vibrational relaxation of CO_2 in CO_2-N_2 and CO_2-O_2 mixtures," *Physica* (Utrecht), vol. 74, pp. 196–204, 1974.

[19] A. L. S. Smith and J. M. Austin, "Dissociation mechanism in pulsed and continuous CO_2 lasers," *J. Phys. D.*, vol. 7, pp. 314–322, 1974.

[20] D. Rapp and D. D. Briglia, "Total cross sections for ionisation and attachment in gases by electron impact. II Negative ion formation," *J. Chem. Phys.*, vol. 43, pp. 1480–1489, 1965.

[21] D. A. Price, "Ion-molecule reaction rates in carbon dioxide, carbon monoxide mixtures at elevated temperatures and pressures," preprint.

[22] J. E. Parr and J. L. Moruzzi, "Negative ions in carbon monoxide," in *Proc. 10th Int. Conf. Phenomena in Ionized Gases* (Oxford, England, 1971), p. 8.

[23] P. D. Tannen, P. Bletzinger, and A. Garscadden, "Species composition in the CO_2 discharge laser," *IEEE J. Quantum Electron.*, vol. QE-10, pp. 6–11, Jan. 1974.

[24] P. Bletzinger *et al.*, "Influence of contaminants on the CO_2 electric-discharge laser," this issue, pp. 317–323.

[25] H. J. Schotzau *et al.*, "Mass spectroscopy of the plasma of cw and TEA CO_2 laser discharges," *Phys. Lett.*, vol. 48A, pp. 205–206, 1974.

[26] B. H. Mahan and I. C. Walker, "Rate of attachment of gaseous electrons to nitrogen dioxide," *J. Chem. Phys.*, vol. 47, pp. 3780–3782, 1967.

[27] "Investigation of UV photoionisation sustained discharge for gas lasers," Hughes Res. Labs., Contract Rep. NOOO14-73-EOL87, Jan.-June 1973.

[28] W. A. Rosser and E. T. Gerry, "De-excitation of vibrationally excited CO_2 (001) by collisions with CO_2, H_2, NO, and Cl_2*," *J. Chem. Phys.*, vol. 54, pp. 4131–4132, 1971.

[29] J. J. Lowke, A. V. Phelps, and B. W. Irwin, "Predicted electron transport coefficients and operating characteristics of CO_2-N_2-He laser mixtures," *J. Appl. Phys.*, vol. 44, pp. 4664–4671, 1973.

Pulsed Operation of an Optically Pumped Far-Infrared Molecular Laser

H. J. A. BLUYSSEN, ROBERT E. McINTOSH, SENIOR MEMBER, IEEE, A. F. VAN ETTEGER, AND PETER WYDER

Abstract—**An investigation of the far-infrared (FIR) response of an optically pumped molecular laser to an infrared (IR) pulse source is presented. It is shown that a three-level laser model explains the observed amplitude and delay of FIR output pulses when a reduction factor for participating molecules is included in the model. A discussion of those physical mechanisms that might be responsible for the reduction factor is given along with a description of how the FIR laser's performance depends on various physical parameters.**

I. INTRODUCTION

SINCE Chang and Bridges reported the first optically pumped far-infrared (FIR) molecular laser in 1970 [1], this promising method of generating submillimeter waves has been studied extensively. Investigators have discovered over 250 lasing transitions at wavelengths ranging between 40 and 2000 μm using at least 18 different molecules. Although CW operation is possible for approximately 25 percent of these transitions, most experimental studies have utilized pulsed infrared (IR) pump sources owing to the large amounts of FIR output which can be achieved. TEA lasers have been used, for example, to generate FIR pulses of several kilowatts [2]. An excellent review of FIR molecular laser development has been recently given by Chang [3].

In their first paper, Chang and Bridges described the pressure dependence of the peak amplitude of a 496-μm FIR pulse which was generated in CH_3F by a 1.5-kW CO_2 laser pulse. They measured this amplitude to increase with pressure up to approximately 0.08 torr and, after being constant to approximately 0.400 torr, to drop off rapidly to zero at 1 torr. They observed the pulse duration to be approximately one-half of a microsecond. More interestingly, they observed a noticeable delay between the start of their Q-switch CO_2 pump pulse and the peak of the FIR output. This delay increases with decreasing pressure to 1.5 μs at a few millitorr.

Although the qualitative behavior of a molecular laser has also been discussed by other authors, we are unaware of literature in which the dynamics of the FIR lasing mechanism during transient pumping is analyzed. In particular, it is felt that there is a strong need to develop appropriate models that adequately predict the dependence of FIR output pulse characteristics from the IR pump excitation and the physical properties of the lasing molecules. In addition to giving a better understanding of the physical mechanisms themselves, such models are essential to the further development of these devices for application. The results reported in this paper follow from our effort to contribute to these objectives.

In this paper we present experimental measurements of FIR pulses generated in an optically pumped molecular laser similar to that described by Chang and Bridges and we compare these results with calculations made using the three-level maser model of Bloembergen [4].

In Section II we describe the experimental apparatus which is used to measure those FIR pulse parameters indicated in Fig. 1 as follows: 1) peak amplitude; 2) delay between start of pump pulse and peak of FIR pulse; and 3) pulse half-width. Details are given related to the test apparatus and measurement procedure. Of particular interest are the precautions used to eliminate the effect of the fluctuations of the pump source on the measurements. We complete this section by presenting typical amplitude and delay measurements of FIR pulses generated in $C_2H_2F_2$.

The time-dependent three-level maser model of Bloembergen [4] is used in Section III to describe the transient behavior of the molecular laser. Rate equations for the population of the participating laser levels are given along with the equation governing FIR radiation resulting from the stimulated emission occurring in the cavity. The coefficients for these nonlinear

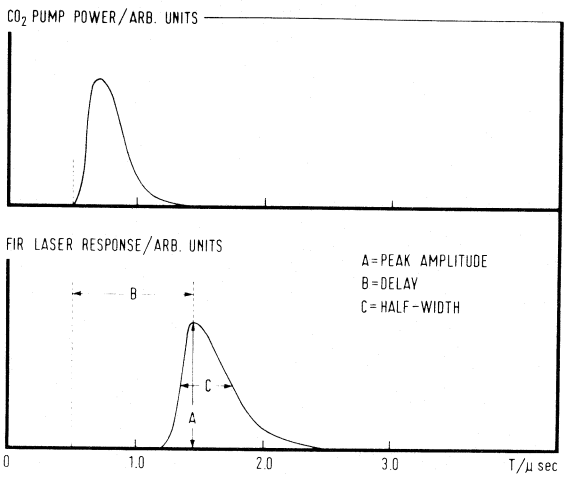

Fig. 1. Diagram showing the CO_2 laser pump pulse and the FIR laser pulse response.

Manuscript received October 16, 1974.

H. J. A. Bluyssen, A. F. van Etteger, and P. Wyder are with the Fysisch Laboratory, University of Nijmegen, Nijmegen, The Netherlands.

R. E. McIntosh was on leave at the Fysisch Laboratory, University of Nijmegen, Nijmegen, The Netherlands. He is now with the Department of Electrical and Computer Engineering, University of Massachusetts, Amherst, Mass. 01002.

equations can be specified for the case of a CH_3F laser because the rotational-vibrational laser transitions for 496-μm FIR radiation have been completely specified [1]. Consequently, we have been able to numerically compute the temporal behavior of the population levels and the FIR output as a function of pressure. Comparing calculations of FIR pulse amplitude and delay with measurements, we obtain qualitative agreement over the entire pressure range. However, in order to achieve quantitative agreement, we must introduce a phenomenological pressure-dependent factor in our model. The pressure dependence of this factor suggests that collisional-dependent effects play a role in FIR molecular lasers at lower operational pressures.

The dependence of our solution on parameters such as the cavity decay time, the frequency of collisional deexcitation, and pulse pump power and shape are also discussed in Section IV. This discussion is of interest because it sheds light on the performance of optically pumped FIR laser systems (including those where the precise levels of the lasing transitions have not been identified) which are to be designed.

II. Pulse Measurements

The experimental test system used to measure the FIR pulse characteristics is shown in Fig. 2. The major components of this system include: 1) the FIR molecular laser; 2) the Q-switched IR pump laser; 3) the IR and FIR detection systems; and 4) the video recording system (to facilitate the data gathering). Each of these subsystems is described briefly.

FIR Molecular Laser

The FIR laser under test is similar to that originally described by Chang and Bridges [1]. The laser cavity is formed from one concave (2.5-m radius of curvature) gold-coated aluminum mirror located approximately 1 m from a gold-coated flat mirror. Both mirrors are 10 cm in diameter and the spherical mirror is mounted on a micrometer stage for tuning purposes. A 1.6-mm hole is located at the center of the flat mirror in order to allow the transmission of the pump and FIR radiation in and out of the cavity. The FIR output is deflected by a 45° gold-coated mirror and leaves the vacuum vessel through a TPX lens as a parallel beam. Absolute pressure measurements of the test gas were provided by a McLeod manometer.

IR Pump Laser

The pump radiation is provided by a CO_2 laser consisting of a gold-coated (4.0-m radius of curvature) spherical mirror and a gold-coated grating having 72 lines per millimeter. The grating is mounted on a piezoelectric translator so that each CO_2 laser transition may be tuned over approximately 100 MHz. Q switching is achieved by means of an air-driven rotating mirror which is situated within the laser cavity. The CO_2 laser beam is focused into the FIR cavity by means of a Ge lens after reflecting off of a beam splitter (80-percent reflecting Ge plate). We have determined that the CO_2 pulses entering the FIR cavity region have peak powers of several hundred watts and durations ranging from 300 to 400 ns when the Q switch is rotating between 40 and 100 Hz.

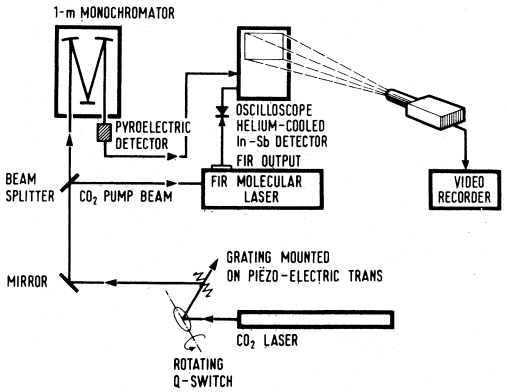

Fig. 2. The experimental test system used to measure FIR pulse characteristics.

IR and FIR Detection Systems

The beam splitter transmits approximately 20 percent of the CO_2 pulse to a 1-m monochromator which has a pyroelectric detector at its output. With the entrance and exit slits nearly closed, this system is used to resolve the CO_2 pump transition to well within the desired accuracy. With the slits wide open, the system is a sensitive detector having a rise time of approximately 5 ns. The FIR radiation pulse is detected by means of a helium-cooled InSb element placed in an external magnetic field. The sensitivity of this device is specified as 200 V/W and the rise time is less than 100 ns at 500-μm wavelengths. The outputs of the IR and FIR are both fed to a double-beam oscilloscope having 20-MHz bandwidth. Both channels of this oscilloscope are triggered by the output of a photodetector that monitors a He-Ne laser beam reflected off the rotating mirror which Q switches the CO_2 laser.

Video Recording System

As the Q switching of the CO_2 laser results in some fluctuations in the pump pulse amplitude and frequency, it is useful to obtain records of the pulse shape of each FIR output pulse and its corresponding excitation pulse. Since the output pulses are observed to depend on peak pump power, these records are used to insure that data presented in our experimental curves represent a constant pump power. (This precaution is particularly important near the high- and low-pressure cutoffs where the FIR signal is strongly affected by small pump fluctuations.) We have recorded the shapes of the CO_2 pump pulse and the FIR output pulse using a television camera and a video recording unit during the performance of the experiment. Consequently, the experimental data presented in this paper were obtained by viewing each pair of pulse images when replaying the tape afterwards. Although each pair of images represents an average of three consecutive pulses (due to the finite scan time of the camera), this technique is successful in removing fluctuations having a frequency of less than 20 Hz.

Measurements of the pump and FIR pulse were obtained for pressures of the test gas inside the molecular laser between 0.004 and 0.3 torr. A video tape of these measurements at each pressure was made over a 1-min interval with the result

that each ensemble contained approximately 3000 pairs of pulse images. In playing back the tapes, we used those ensemble images which corresponded to the larger FIR pulses in obtaining measured values of the signal characteristics shown in Fig. 1. This was done to eliminate effects due to frequency variations that may occur in the pump signal. By choosing the maximum output signals corresponding to a given CO_2 pump power, we maintain that all measurements presented were obtained while the pump frequency was optimally tuned to the FIR transition. Although these precautions seem unnecessary in the case of the CH_3F laser, which is discussed in detail in the next section, they are clearly necessary in the case of the $C_2H_2F_2$ laser. In the latter case, we found fluctuations in the pump signal to cause standard deviations in the FIR pulse amplitude, delay, and half-width of up to 10 percent of the mean values.

We note here that experimental errors in determining the peak CO_2 and FIR pulse amplitudes and the pressure of the molecular test gas are estimated to be less than 10 percent for most of our measurements. The errors in our pressure measurements may be greater than 10 percent at pressures below 10 mtorr, but only one experimental data point is presented in this paper (see Fig. 6) in this pressure range.

Typical experimental results are shown in Fig. 3 that show the peak amplitude and time delay for the $C_2H_2F_2$ molecule as a function of pressure. Shown is the 554-μm wavelength which is pumped by the 10.53-μm CO_2 laser line. Since the nature of the lasing transitions is not known for $C_2H_2F_2$ as far as we know, we were unable to calculate theoretical curves for comparison with these measurements. However, it is useful to examine these results before proceeding because such an examination is helpful in understanding the theoretical results given for the CH_3F molecule in the next section.

The behavior of the peak amplitude and delay for $C_2H_2F_2$ are similar to that for CH_3F as previously described by Chang and Bridges. The most significant differences are that $C_2H_2F_2$ exhibits a larger low-pressure cutoff than CH_3F and the flat portion of the peak amplitude-pressure curve which is so noticeable for CH_3F is absent in the case of $C_2H_2F_2$. A comparison of the high-pressure cutoff is not meaningful because our measurements were performed using a lower pump field. We also observe that the delay between the excitation and FIR response pulses is minimum at the maximum of the peak amplitude curve. In addition to observing the increase of delay with decreasing pressures noted earlier at low pressures in CH_3F [1], we measure the pulse delay to increase at high pressures in $C_2H_2F_2$. This last effect has also been observed by us in other gases at other frequencies but we, like Chang and Bridges, have not observed this behavior in CH_3F.

Summarizing, we state that in those cases measured by us, substantial delays are always observed at low pressures when the peak amplitude is small. We have also observed increased delay at higher pressures when the peak amplitude begins to drop off in various gases. We show that the observed relationship between amplitude and delay results directly from the role which the number of participating molecules plays in the rate equations given in the next section.

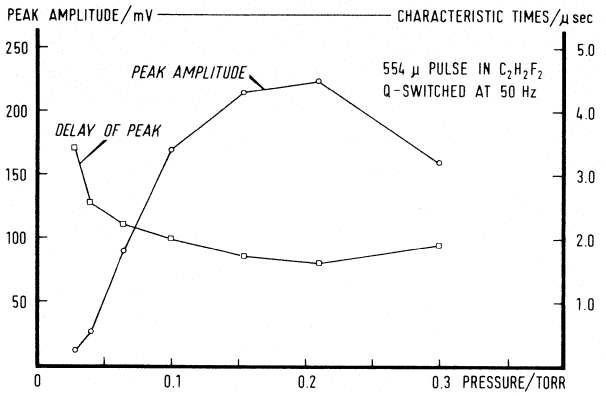

Fig. 3. Experimental results showing the peak amplitude and time delay for the $C_2H_2F_2$ molecule as a function of pressure. A 10.53-μm CO_2 laser line was used as a pump to generate a 554-μm FIR output.

III. Solution of Three-Level Model

To better understand the generation of FIR pulses in CH_3F we have used a three-level system for our theoretical model similar to that proposed by Bloembergen [4] for an RF pumped solid-state maser. Although the system of energy levels for methyl fluoride is known to be more complicated than the system assumed here, we justify the use of a simplified model as a first approximation by the following remarks.

1) Pumping may occur simultaneously for two transitions (see Fig. 4(a)), while six transitions may give rise to laser action. In the three-level model shown in Fig. 4(b) we consider only the pumping transition $(\nu, J, K) = (0, 12, 1) \rightarrow (1, 12, 1)$ and the laser transition $(1, 12, 1) \rightarrow (1, 11, 1)$. In our experiments, we tune the FIR cavity so that only the $(1, 12, 1) \rightarrow (1, 11, 1)$ transition lases. In that case, the stimulated emission rate for the $(0, 13, 1) \rightarrow (0, 12, 1)$ transition must be small during the pump pulse owing to the long delay times observed for this transition [1]. The replenishment of the $J = 12$ level by this transition can be neglected, therefore, during the pump pulse. The effect of the stimulated emission of the cascade transition $(1, 11, 1) \rightarrow (1, 10, 1)$ on the population level of the $J = 11$ level may be included in the rate equations and does not influence the total number of molecules in our three-level model.

2) The $\nu = 0$ state has a number of rotational levels which have energies that differ from the lower pump level (0, 12, 1) by less than κT. Participation of these levels in the pump dynamics is limited below pressures of 0.1 torr, because the duration of the pump pulse (approximately 0.3 μs) is equal to or less than the characteristic time for reaching thermal equilibrium by collisional relaxation (greater than about 0.3 μs at pressures below 0.1 torr).

3) CO_2 power simultaneously pumps the desired pump transition and the $(0, 12, 2) \rightarrow (1, 12, 2)$ transition. However, we estimate that only 10-15 percent of the CO_2 power pumps the $K = 2$-band transition when the pump power is tuned such that optimum output power from the $(1, 12, 1) \rightarrow (1, 11, 1)$ lasing transition occurs. This is within the experimental error of our pump power measurements.

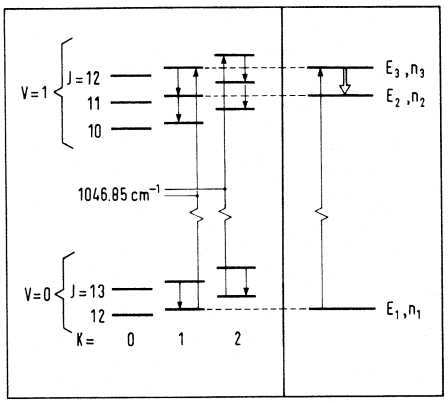

Fig. 4. Energy-level diagrams for CH_3F. (a) Laser transitions observed by Chang and Bridges [1]. (b) Three-level model used in present calculations.

4) Finally, energy transfer between the pumped levels of the $K = 1$ and $K = 2$ bands may have an effect on the number of molecules assumed in our three-level model. This effect is neglected in our initial calculations but we later acknowledge that the transfer of energy between K levels may provide some of the justification needed to introduce a phenomenological factor into subsequent calculations. This factor modifies the number of molecules in the system that participate in FIR lasing.

A three-level model yields the following set of rate equations which relate n_3 and n_2, the populations of the upper and lower laser levels, to the FIR laser radiation $\rho_1(t)$, which builds up in the cavity due to stimulated emission.

$$\begin{aligned}\partial n_3/\partial t = {} & n_3[-(g_3/g_1+1)B_{31}\rho_p(t) - w(1.008+A)] \\ & + n_2[-(g_3/g_1)B_{31}\rho_p(t) - w(0.008-0.91A)] \\ & + B_{32}\rho_1(t)[(g_3/g_2)n_2 - n_3] \\ & + n_0[(g_3/g_1)B_{31}\rho_p(t) + 0.008w] \qquad (1)\end{aligned}$$

$$\begin{aligned}\partial n_2/\partial t = {} & n_3[A-0.008]w - n_2[0.91A+1.008]w \\ & + B_{32}\rho_1(t)[n_3 - (g_3/g_2)n_2] + 0.008n_0w \qquad (2)\end{aligned}$$

$$\begin{aligned}\partial\rho_1/\partial t &= B_{32}h\nu_{32}[n_3 - (g_3/g_2)n_2]\rho_1 - \rho_1(t)/\tau \\ &= G_T\rho_1(t) - \rho_1(t)/\tau. \qquad (3)\end{aligned}$$

The statistical weights for the various rotational levels involved are given by $g_i = 2J_i + 1$, and n_0 is the total number of molecules present in the three levels. In our model we assume that the collisional deexcitations from the two lasing levels to the ground state are the same; i.e., the deexcitation rates w_{31} and w_{21} are expressed by the quantity w, which is given by $w = \pi\Delta\nu_p$, where $\Delta\nu_p$ is the pressure-broadened linewidth. The collisional deexcitation rate from the upper level to the intermediate level is, in general, not the same as w and we take account of this by defining the ratio $A = w_{32}/w$. The constant τ accounts for FIR cavity losses and is given by $(L/c\gamma)$ where L is the cavity length, c is the speed of light, and γ is the cavity attenuation factor. Furthermore, the numerical constants in (1) and (2) follow from the evaluation of the quantities; $\exp[-h\nu_{13}/\kappa T]$, $\exp[-h\nu_{12}/\kappa T]$, and $\exp[-h\nu_{23}/\kappa T]$ at room temperature and the respective transition frequencies.

In the preceding equation, $B_{31}\rho_p(t)$ and $B_{32}\rho_p(t)$ are the induced transition rates for the pump and laser transitions, respectively. Their theoretical values are computed from

$$B_{3j} = 2\pi_2|\mu_{3j}|^2 g(0)/3h^2\epsilon_0 \qquad (4)$$

at resonance where $|\mu_{31}|^2$ and $|\mu_{32}|^2$ are the electric dipole moment matrix elements. In the case of the pump transitions the linewidth $\Delta\nu_D$ is Doppler broadened[1] and $g_D(0) = 0.939/\Delta\nu_D$. The FIR laser transition is assumed to be partly pressure broadened and in this case we take $g(0) = [(\Delta\nu_D/0.939)^2 + (\Delta\nu_p/0.637)^2]^{-1/2}$. Thus, at high pressures, $g(0) = 0.637/\Delta\nu_p = g_p(0)$ and at low pressure, $g(0) = g_D(0)$.

It is widely known that the theoretical FIR radiation gain of optically pumped molecular lasers [$G_T = B_{32}h\nu_{23}[n_3 - (g_3/g_2)n_2]$ in (3)] is greater than that achieved in practice. This discrepancy may be caused by a host of physical mechanisms; however, our present thinking is that one of the two mechanisms given in the following is responsible for the output power limits of the FIR laser.

1) Hole-Burning: The linewidth of the pump transition is Doppler broadened and is much larger than that of the pump radiation (30 MHz versus 3 MHz). The pump radiation therefore excites only a portion of the molecules occupying the lower pump level (1). Collisions tend to restore the equilibrium velocity distribution within that pumped rotational sublevel and the rate of this velocity cross relaxation depends on pressure. Consequently, the number of molecules assumed to participate in the lasing process is both high and pressure dependent.

2) Population Diffusion to Other States: Above 0.25 torr some of the molecules may be pumped to levels other than the upper level of the assumed three-level model. Also some mole-

[1] In Section IV we note that pressure-broadening effects might also play a role in FIR generation.

TABLE I
PHYSICAL PARAMETERS FOR CH_3F FIR LASER

Physical parameter	Symbol	Value	Units
1. Electric dipole moments	μ	6.17×10^{-30}	Coul.m
	$\lvert\mu_{31}\rvert^2 = \frac{\mu^2 K^2}{J(J+1)}$	2.44×10^{-61}	$[\text{Coul.m}]^2$
	$\lvert\mu_{32}\rvert^2 = \frac{\mu^2(J^2-K^2)}{J(2J+1)}$	1.815×10^{-59}	$[\text{Coul.m}]^2$
2. Doppler line-widths	$\Delta\nu_D$	1.3×10^6 (for $\nu_{32}=6\times10^{11}$ sec^{-1})	sec^{-1}
		6.8×10^7 (for $\nu_{31}=3\times10^{13}$ sec^{-1})	
3. Pressure broadened line width FIR line.	$\Delta\nu_p$	$5. \times 10^6$ (at .1 Torr)	sec^{-1}
4. Total number of molecules per meter^3	n_0	1.6794×10^{19} (at .1 Torr)	m^{-3}
5. Initial number of molecules in upper levels	$n_3(0)$	$.00730\ n_0$	m^{-3}
	$n_2(0)$	$.00868\ n_0$	
6. Initial FIR energy [note: solution nearly independent of this quantity]	$\rho_1(0)$	3.182×10^{-25}	Watt.sec.m^{-3}
7. FIR cavity decay constant	τ	$7. \times 10^{-8}$	sec
8. Deexcitation ratio	A	1	dimensionless

cules on the upper level may be transferred by means of collisions to levels not included in our model. An indication of the levels involved has been given by Weitz *et al.* [6], [7], who have made fluorescence measurements. These effects should also cause the effective number of molecules in our model to be lower and pressure dependent.

To account for these effects in our model, we introduce a pressure-dependent reduction factor $F(P)$, such that the population n_j at each level is replaced by an effective population $F(P)n_j$. Replacing n_j by $F(P)n_j$ in (1)-(3), we obtain three new system equations. The first two equations are identical to (1) and (2) after they have been divided by $F(P)$, but the third equation takes the form

$$\partial\rho_1/\partial t = F(P)G_T\rho_1 - \rho_1/\tau. \tag{5}$$

From the resulting equations, we note that the reduction factor $F(P)$ has the effect of modifying the gain G_T in (5).

For reference purposes, the values of the various physical parameters used in this paper are summarized in Table I. In this table $n_2(0)$, $n_3(0)$, and $\rho_1(0)$ are the initial values of the three independent variables.

Computed Results

Equations (1)-(3) have been solved on an IBM 370/158 computer using Hamming's modified predictor-corrector method for the pump transitions $(\nu, J, K) = (0, 12, 1) \rightarrow (1, 12, 1)$ and the lasing transition $(1, 12, 1) \rightarrow (1, 11, 1)$ in CH_3F. Here the usual symbols ν, J, and K are used to indicate the vibrational (ν) and rotational (J and K) quantum numbers of the symmetric top molecule under study. The time dependence of the pump energy in our program was chosen to be

$$\begin{aligned}
\rho_p(t) &= 0, && t < 0.4 \\
&= \rho_{p0} \exp\left[-(t-1)^2/\sigma_1^2\right], && 0.4 < t < 1 \\
&= \rho_{p0}\left[(1-K)\exp\left[-(t-1)^2/\sigma_2^2\right] - K(t-3)/2\right], && 1 < t\ 3 \\
&= 0, && 3 < t
\end{aligned} \tag{6}$$

where t is given in microseconds. By varying the peak pump energy ρ_{p0}, the variances σ_1 and σ_2, and the parameter K (which accounts for the tail which is occasionally observed on the excitation pulse), the IR pump signal can be simulated rather accurately for various Q-switch repetition rates. For the calculations presented here we use the values: $\rho_{p0} = 1.5 \times 10^{-4}$ W · s/m^3; $\sigma_1 = 0.1$ μs; $\sigma_2 = 0.25$ μs; and $K = 0.001$ to represent the CO_2 pulse Q switched at 100 Hz. In the fourth section we discuss the effects that alterations in the pump pulse shape have on FIR pulses.

Fig. 5 shows the solution of the rate equations for the CH_3F molecule lasing at 496 μm at pressures of 0.125 and 0.3 torr. These curves correspond to a pump pulse (see hashed curve) having 300-W peak power and a duration of 320 ns. In both cases, the population inversion reaches its maximum value at the peak of the pumping pulse. At 0.125 torr, a rapid increase in FIR stimulated emission quickly depletes the population inversion level to about 18 percent of its maximum value. This rapid switching may account for the steepened front edge of the FIR response which is observed experimentally. At the 0.3-torr pressure, this switching phenomenon is no longer present and the FIR peak output is delayed more than at 0.125 torr. Although this last result is consistent with

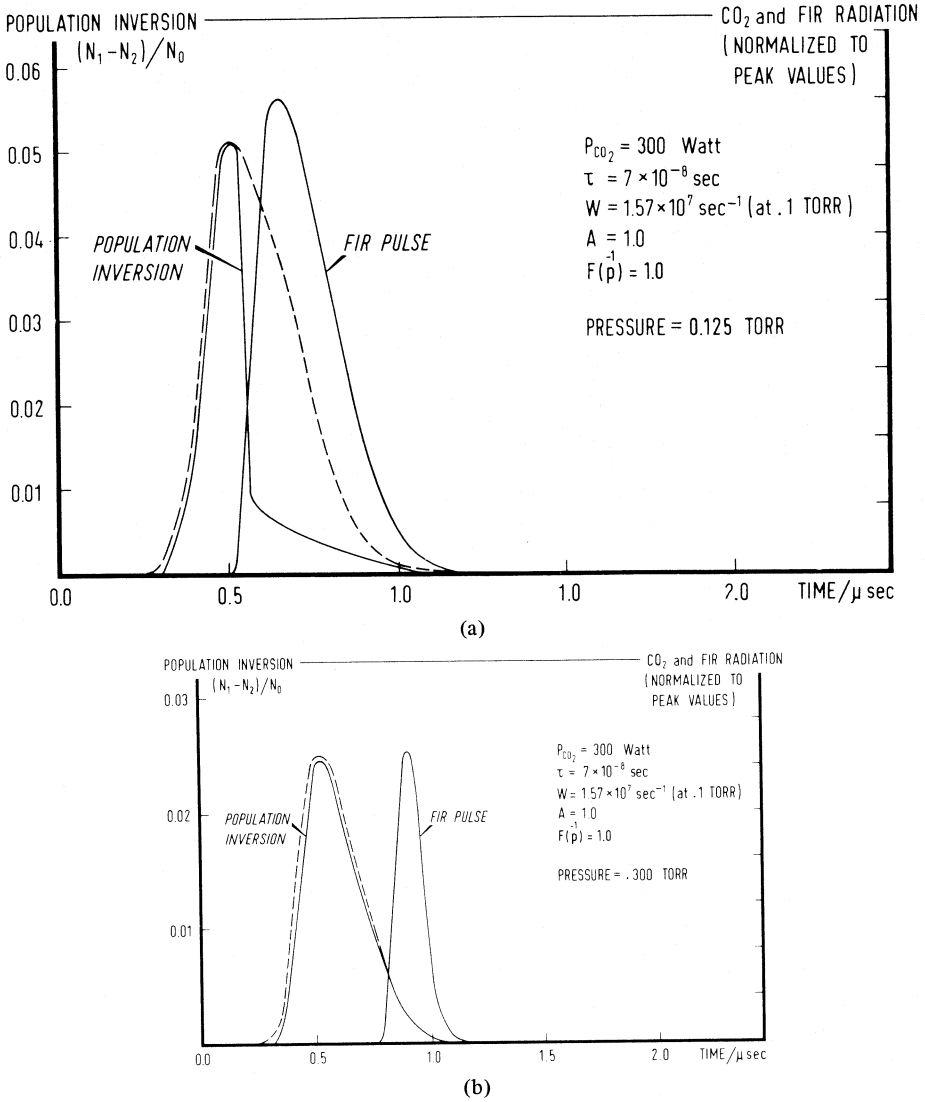

Fig. 5. Solution of the rate equations for the CH_3F molecule lasing at 496 μm at a pressure of 0.125 and 0.3 torr. These curves correspond to a pump pulse of the 9.55-μm CO_2 line (hashed curves) having 300-W peak power and a duration of 320 ns.

measurements made in other gases, it does not agree with experimental measurements of CH_3F radiation at 496 μm.

The experimentally and theoretically determined values of the peak pulse power and delay between the start of the pump pulse and the peak of the FIR pulse are shown in Fig. 6(a) as a function of pressure. Although these results are in qualitative agreement, there are quantitative disagreements which need resolution. The salient difference between the theoretically computed results and the measurements lies in the magnitude of the computed gain in the pressure range of maximum output. Besides yielding peak amplitudes which are larger than those experimentally observed, the calculated amplitude response with pressure is not flat in the 0.05–0.19-torr pressure range. Further, the measured increase in delay that occurs at pressures below 0.04 starts at pressures below 0.01 in our model.

Both of these differences have been traced to the strong dependence that the peak amplitude and delay of the FIR pulse have on the number of molecules in our three-level system. Consequently, we have carried out a numerical search for the phenomenological function $F(P)$ in (5) which causes the experimental and computed amplitude curves to agree. We found that the values of $F(P)$, which give agreement between measured and computed amplitudes, also result in agreement between measured and calculated pulse delays [see Fig. 6(b)]. It is our feeling that the computation of a single function $F(P)$, which causes both signal characteristics to agree with measurement over the entire pressure range, is evidence that the observed amplitude and delay behavior results from the effective reduction of participating molecules. A plot of the obtained phenomenological factor $F(P)$ is shown in Fig. 7. It is seen that this function increases nearly linearly with pressure.

Computed responses of the population inversion and FIR output after inclusion of the factor $F(P)$ are shown in Fig. 8 for two pressures. We observe larger FIR pulse rise times than for our previous calculations. The calculated pulse half-widths for both sets of calculations do not vary significantly with pressure. However, the computed pulse durations are less (ap-

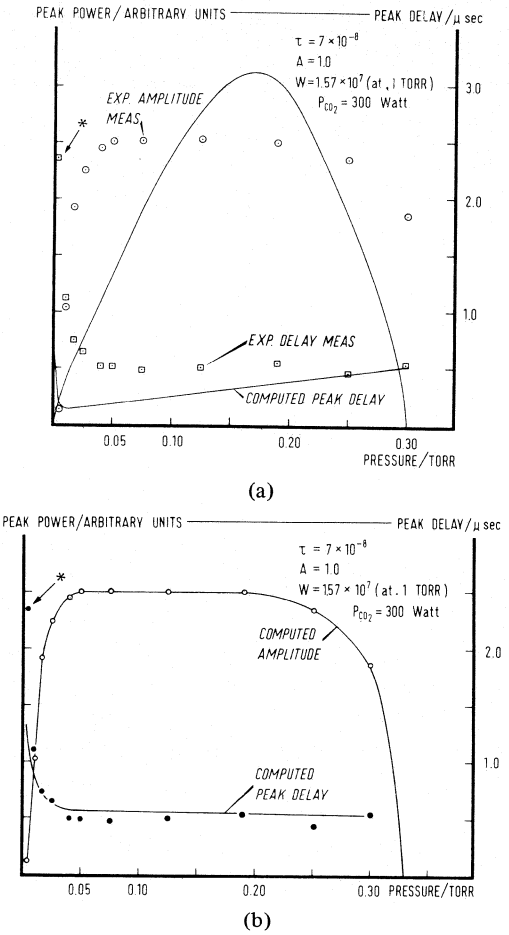

Fig. 6. Experimentally and theoretically determined values of the FIR pulse power and delay between start of the pump pulse and peak of the FIR pulse as a function of pressure for the CH_3F molecule lasing at 496 μm and pumped by the 9.55-μm CO_2 line. (a) The calculations made with the theoretical FIR radiation gain G_T. (b) The calculations made with the phenomenological value $G_p = F(P)G_T$. (* indicates data point where pressure resolution is less than 10 percent.)

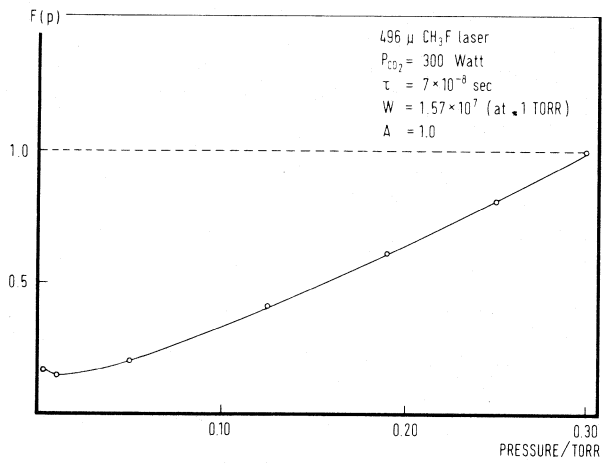

Fig. 7. Plot of the obtained phenomenological gain factor $F(P)$ as a function of pressure.

proximately 0.3 μs) than those observed experimentally by us and Chang and Bridges (approximately 0.500 μs). We believe that this inconsistency may be explained by the rise time of the InSb detector (less than 0.100 μs) which was used to obtain the measurements.

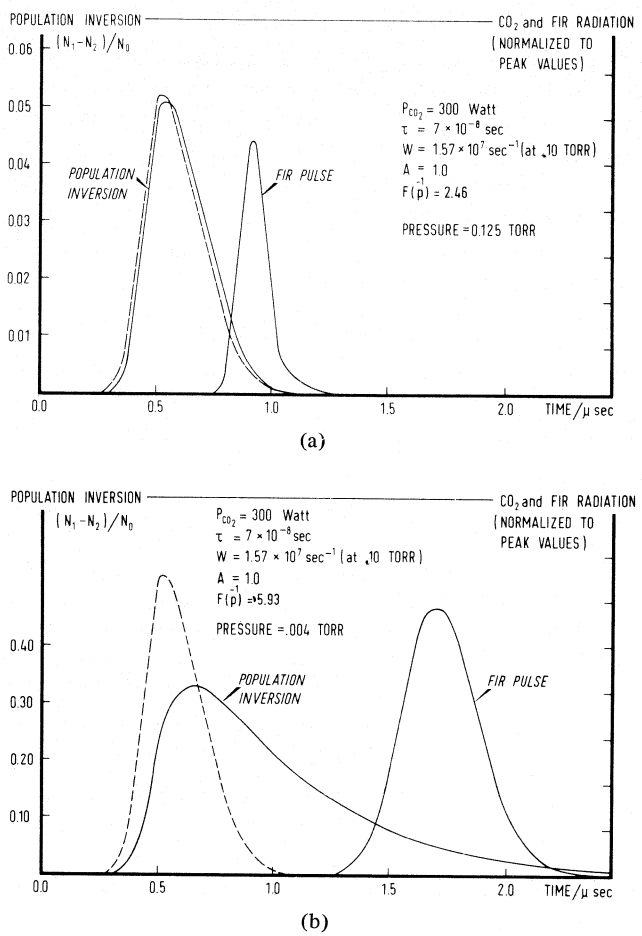

Fig. 8. Solutions of the rate equations for the CH_3F molecule lasing at 496 μm at a pressure of 0.125 and 0.004 torr. These curves correspond to a pump pulse (hashed curves) of the 9.55-μm CO_2 line having 300-W peak power and a duration of 320 ns. Calculations were made using the phenomenological FIR radiation gain $G_p = F(P)\,G_T$ shown in Fig. 6.

IV. Discussion

The results of the previous section indicate that the observed pressure-dependent time delays are explained by the effective number of molecules participating in lasing in the optically pumped medium. In the following, we elaborate on how the pressure dependence of $F(P)$ may be caused by the CO_2 pump radiation "burning a hole" in the Doppler distribution of the molecular transitions. We then note the effects that other physical parameters may have on the pulsed operation of the optically pumped FIR laser.

The dependence of the gain factor for FIR radiation [G_T in (3)] is proportional to both the population inversion density Δn and the line-shape factor at resonance $g_D(0)$. In addition to depending on the intensity of the pump radiation, Δn is directly proportional to the number of molecules in the gas that actually participate in the lasing process. We have already noted that the linewidth of the pump transition (approximately 30 MHz owing to Doppler broadening) is much larger than the linewidth of the pump radiation (approximately 3 MHz for a CO_2 pump pulse of 320-ns duration). Consequently, the pump radiation excites only those molecules occupying a 3-MHz portion of the pump transition distribution. This means that the number of molecules assumed to

participate in the lasing process in our calculations [where $F(P) = 1$] is high, and therefore the observed gain should be less than the theoretical gain. In fact, a reasonable first estimate of the reduction factor $F(P)$ from this mechanism might be to take the ratio of the CO_2 radiation linewidth to the IR pump transition linewidth. However, at high enough power the CO_2 beam will "burn a hole" into the distribution of the pump transition. In this case the width of the hole, and therefore $F(P)$, may be related to the pressure-broadened component of the pump transition and to velocity cross relaxation [5] in addition to the half-width of the pump radiation. The former two factors are of interest because they indicate the rate at which molecules having transition energies outside the hole region can contribute to the supply of molecules participating in the FIR lasing process. This rate of contribution should be greater for high pressures than for low pressures owing to collision effects. It may be expected, therefore, that the effective value of n_0 increases with pressure in agreement with the computed results shown in Fig. 7.

It is reasonable to expect that in addition to the mechanism described in the preceding, there may be other effects which decrease the actual number of molecules taking part in the FIR laser action. We have already mentioned that some of the molecules may be pumped to levels other than the upper level of the three-level model assumed. Also some molecules in the upper level may be transferred to levels not included in our model. We have not conjectured how these mechanisms yield the observed pressure dependence of $F(P)$, however, because the transfer process is not clearly understood at this time.

Gain reduction through changes in the line-shape factor at low pressures implies that the laser transition linewidth does not increase with pressure as rapidly as assumed in our model. Diffusion effects may account for some of this discrepancy in a qualitative way. However, it can be shown quantitatively that this mechanism only accounts for a small fraction of the gain modification needed to explain the observed amplitude and delay curves.

In comparing theory with measurements for CH_3F, we have used known physical quantities in the calculation of the three-level model. In addition, we have varied these parameters in our computations to gain insight into the relationship that these quantities have with the peak pulse amplitude and delay of the FIR pulse. We summarize our conclusions in the following.

1) Dependence on Pump Power Radiation Level ρ_p: The peak FIR pulse energy is dependent on the level of pump radiation. Although this dependence is less important at low pressures, owing to saturation effects, we find the upper pressure limit (where lasing ceases) to be strongly dependent on the pump level. Thus our theoretical model predicts the experimentally known fact that increased output is achieved when both the CO_2 pump radiation and molecular gas pressure are increased. Our model also suggests that the delay is related to the level of pump radiation.

2) Dependence on CO_2 Pump Pulse Shape: We have varied the pulse-shape parameters appearing in (6) and have determined that the FIR pulse characteristics depend primarily on the integrated pump radiation (i.e., $\int \rho_p(t)\,dt$) in our model. Thus we predict that the shape of the pump pulse is of little importance in designing pulsed optically pumped molecular lasers.

3) Dependence on Collisional Deexcitation Rates w and Aw: Collisional deexcitation is unimportant at low pressures, according to our calculations. However, we find the pressure range over which lasing occurs to depend strongly on w. This range is extended considerably, for example, when the collisional deexcitation rate is reduced. By reducing w, we find that the computed peak pulse amplitude is substantially increased, whereas the delay is hardly affected. The dependence of pulse characteristics on A has been found to be small, confirming that the choice of this parameter is not critical in calculations.

4) Dependence of Cavity Decay Time τ: We find that increasing τ leads to enhanced FIR output power levels but has no appreciable effect on pulse delay. For example, an increase in τ from 70 to 100 ns results in approximately twice as much peak FIR pulse energy. Further increases in τ, however, will not result in additional power out for a practical system because these increases can be achieved only by reducing the size of the hole through which FIR radiation is coupled out of the laser.

Acknowledgment

The authors wish to thank H. Fetterman and T. Y. Chang for useful discussions related to this work. They also wish to thank P. Groen for his assistance with the computer program and H. Salemink for his assistance with the experimental measurements.

References

[1] T. Y. Chang and T. J. Bridges, "Laser action at 452, 496, and 541 μm in optically pumped CH_3F," *Opt. Commun.*, vol. 1, pp. 423–426, Apr. 1970.

[2] F. Brown, S. R. Horman, A. Palevsky, and K. J. Button, "Characteristics of a 30-kW peak, 496 μm, methylfluoride laser," *Opt. Commun.*, vol. 9, pp. 28–30, Sept. 1973.

[3] T. Y. Chang, "Optically pumped submillimeter wave sources," in *Proc. Int. Conf. Submillimeter Waves and Their Applications.*

[4] N. Bloembergen, "Proposal for a solid state maser," *Phys. Rev.*, vol. 104, p. 324, 1956.

[5] J. R. Tucker, "Theory of an FIR gas laser," in *1974 Int. Conf. Submillimeter Waves and Their Applications, Dig. Tech. Papers* (Atlanta, Ga., June 1974), pp. 17–18.

[6] E. Weitz, G. Flynn, and A. Ronn, "Laser excitation and equilibration of excited vibrational states in CH_3F," *J. Chem. Phys.*, vol. 56, p. 6060, 1972.

[7] E. Weitz and G. Flynn, "Partial vibration energy map for methyl fluoride: A laser fluorescence study," *J. Chem. Phys.*, vol. 58, p. 2781, 1973.

Effect of Rotational and Intramode Vibrational Coupling on Short-Pulse Amplification in CO_2

ROBERT J. HARRACH

Abstract—**The extraction of stored energy from a CO_2-laser amplifier by a short-duration input pulse is described using a rate-equation theory. The influence of rotational and intramode vibrational energy-transfer processes is studied as a function of the energy density E_{in} and width τ_p of the input pulse. By a suitable choice of normalized variables δ and E_{in}/E_{sat} for the extracted-energy and input-energy density, it is found that the results for different values of τ_p are interrelated by simple translations in a δ versus E_{in}/E_{sat} diagram. The characteristic curves in this diagram are nearly independent of the amplifier gain factor exp ($\alpha_0 L$) for high-gain systems. A comparison of the theory with experimental results of Figueira *et al.* shows satisfactory agreement and leads to an estimate of (1.0-3.5) 10^6 $s^{-1}torr^{-1}$ for the rate of intramode vibrational-vibrational (VV) energy transfer in CO_2.**

I. Introduction

PREVIOUS STUDIES have shown that the saturation characteristics of high-pressure molecular-laser amplifiers are significantly affected by rotational energy transfer [1]-[6]. In particular, the rotational relaxation rate [4] of about 10^7 s · torr in carbon dioxide gas accounts for a substantial increase in the energy gain experienced by a nanosecond-duration pulse in an atmospheric-pressure CO_2 amplifier [1]. Beyond this, we show that intramode vibrational-vibrational (VV) energy transfer is rapid enough to influence amplification on a time scale of about 50 ns. The analysis is based on a reservoir model [1] to describe rotational coupling and a vibrational-temperature model [7], [8] to calculate the effect of vibrational relaxation. The theory is applied to interpret some recent experiments by Figueira *et al.* [5] on energy extraction by short-duration pulses in a heavily saturated CO_2 amplifier.

The range of effects one can expect is gauged by the parameters τ_p/τ_r, τ_p/τ_{vv}, and E_{in}/E_{sat}, where τ_p is the duration of the input pulse and E_{in} is its energy density. τ_r and τ_{vv} represent characteristic times for rotational and intramode VV energy transfer. E_{sat}, which is inversely proportional to the product of the absorption cross section σ and the energy gain factor exp ($\alpha_0 L$) of the amplifier, is a characteristic saturation level for the input-energy density. By including the influence of intramode VV as well as rotational interactions, we are able to analyze the properties of pulse amplification over a wide range of these parameter values, covering four orders of magnitude variation in τ_p/τ_r and six orders in E_{in}/E_{sat}.

When the pulse duration is so short that $\tau_p/\tau_r \ll 1$, the rotational and vibrational energy transfers do not have time to occur during the pulse-molecule interaction. The amplifying medium then acts like a two-level system, as described in the rate-equation approximation[1] by Frantz and Nodvik [9]. The amount of energy the pulse can extract from the medium in this case is governed by the initial value of the population-inversion density $(n^u - n^l)$ of the upper (u) and lower (l) vibrational-rotational levels directly involved in the laser transition.

In the opposite extreme, when the input pulse duration is quite large relative to τ_r, the field-induced changes in n^u and n^l can be countered by rotational and vibrational energy exchange. We find that the extractable energy in this limit is determined by the appreciably larger population-inversion density $\gamma(M+1)[n^u(0) - n^l(0)]$. The factor M arises from rotational energy transfer while the factor γ is contributed by the intramode VV process (slower types of vibrational relaxation are neglected). In a typical case, M is about 15 and γ about 3.

The effect of rotational coupling in the case of arbitrary τ_p/τ_r value is analyzed in Section II and Appendix A; intramode VV coupling is described in Section III and Appendix B. A comparison of the theory with published experimental results [5] is made in Section IV, where it is shown that the inclusion of vibrational energy transfer is essential to the interpretation of the data. A fit of the theory to the data leads to an estimate of (1.0-3.5) $10^6 P_{CO_2}$ s^{-1} for the rate of intramode VV energy transfer, where P_{CO_2} is the partial pressure of CO_2 in torr.

II. Effect of Rotational Coupling

We consider a homogeneously broadened laser transition between a pair of molecular-energy levels u and l, each of which is part of a band of rotational levels strongly coupled by collisional interactions (Fig. 1). Since the quantum mechanical selection rules for collision-induced transitions among the various rotational levels of most molecules are not well understood [3], [10], we will use a reservoir model. In this model the particular laser level u (or l) in the rotational band is singled out, while the rest of the levels in the band are treated collectively. The totality of these other rotational levels constitute the rotational reservoir for level u (or l).

The details of the model are developed in Appendix A, where it is shown that the basic equations relating the flux

Manuscript received November 21, 1974; revised February 24, 1975. This work was performed under the auspices of the U.S. Energy Research and Development Administration.

The author is with the University of California, Lawrence Livermore Laboratory, Livermore, Calif. 94550.

[1] A semiclassical (rather than rate-equation) theory is needed to treat most aspects of electromagnetic-pulse amplification in the very short pulse regime where $\tau_p/\tau_r \lesssim 1$. However, as noted in [1b)], the amount of energy extracted from the medium by the pulse in this regime is apparently satisfactorily described using rate equations.

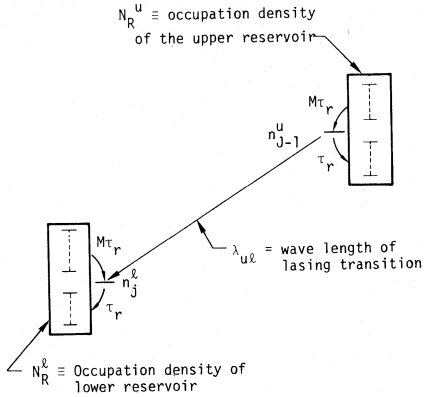

Fig. 1. Rotational reservoir model.

density I of the radiation pulse and the population densities n^u and n^l of the laser levels and N_R^u and N_R^l of the rotational reservoirs are (A-11)-(A-15). This rotational-reservoir (RR) model is essentially the same as the model first analyzed by Schappert [1].

In Appendix A the RR model is solved analytically in the two limiting cases where the input pulse duration τ_p is either very long or very short compared to the rotational relaxation time τ_r. Despite the limitations of the RR model, stemming from the neglect of vibrational energy transfer when $\tau_p \gg \tau_r$ and the neglect of phase-dependent effects[1] when $\tau_p \lesssim \tau_r$, these analytical solutions provide useful benchmarks for the amount of rotational-band energy extractable from the amplifier as a function of the ratio τ_p/τ_r. In the remainder of this section we introduce convenient normalization factors for the extracted-energy and input-energy density and discuss the RR model results for arbitrary τ_p/τ_r value. The role of vibrational energy transfer is explored later in Section III.

Extracted Energy and Energy Gain

The major focus of our attention is the energy gain G_E of the amplifier, defined as the ratio of the output-energy density (in, say, joules/square centimeters) to the input-energy density

$$G_E \equiv E_{out}/E_{in} = \int_{-\infty}^{\infty} I(x = L, t')\, dt' \Big/ \int_{-\infty}^{\infty} I(x = 0, t')\, dt'. \tag{1}$$

The extracted-energy density, or amount of energy per unit area extracted from the amplifier by the pulse, is given in terms of G_E by $(E_{out} - E_{in}) = (G_E - 1)E_{in}$.

In the limiting cases $\tau_p/\tau_r \gg 1$ and $\tau_p/\tau_r \ll 1$ the RR-model energy-gain relation can be integrated analytically for an arbitrary input pulse shape to give G_E as a function of the input-energy density

$$E_{in} = h\nu_{ul} \int_{-\infty}^{\infty} I_0(t')\, dt'.$$

For relatively long-duration pulses the energy gain is, using (A-21)-(A-25),

$$\lim_{\tau_p/\tau_r \gg 1} G_E = [(M+1)E_{sat} \exp(\alpha_0 L)/E_{in}] \cdot \ln\{1 + \exp(\alpha_0 L)[\exp(E_{in}/(M+1)E_{sat} \cdot \exp(\alpha_0 L)) - 1]\}. \tag{2}$$

Similarly, when the input pulse duration is very short, the energy gain is given by this same equation with M set equal to zero

$$\lim_{\tau_p/\tau_r \ll 1} G_E = (E_{sat} \exp(\alpha_0 L)/E_{in}) \ln \cdot \{1 + \exp(\alpha_0 L)[\exp(E_{in}/E_{sat} \exp(\alpha_0 L)) - 1]\}. \tag{3}$$

Here E_{sat} is a characteristic saturation level for E_{in} defined by

$$E_{sat} \equiv (h\nu_{ul}/2\sigma) \exp(-\alpha_0 L). \tag{4}$$

Inspection of (3) shows that for very short-duration pulses the regime of linear amplification (i.e., where E_{out} is linearly proportional to E_{in}) occurs for $E_{in} \ll E_{sat}$. The extracted-energy density in this case is

$$(E_{out} - E_{in}) = (G_E - 1)E_{in} = (\exp(\alpha_0 L) - 1)E_{in}. \tag{5}$$

Nonlinear (saturation) effects are significant whenever E_{in} is comparable to or greater than E_{sat}. Similarly, in the limit of large τ_p/τ_r value the regime of linear amplification is given by $E_{in} \ll (M+1)E_{sat}$, and, in general, the input-energy density required to produce a given degree of saturation in this limit is larger by a factor $(M+1)$.

The parameter E_{sat} and the extracted-energy density given by (5) provide very convenient reference values for E_{in} and $(E_{out} - E_{in})$ in the general case of arbitrary τ_p/τ_r. Throughout the remainder of this paper the energy saturation characteristics will be discussed in terms of the variation with E_{in}/E_{sat} of the normalized extracted energy δ defined by

$$\delta = (E_{out} - E_{in})/E_{in}(\exp(\alpha_0 L) - 1) = (G_E - 1)/(\exp(\alpha_0 L) - 1). \tag{6}$$

Results for Arbitrary τ_p/τ_r

The reservoir-model equations (A-11)-(A-15) or (A-15)-(A-17) require numerical solution when the duration τ_p of the input pulse is neither very large nor very small compared to the rotational relaxation time τ_r. This entails that specific numerical values be assigned for the amplifier parameters σ, M^u, M^l, τ_r, $n_{j-1}^u(0)$, $n_j^l(0)$, $N_R^u(0)$, and $N_R^l(0)$. Once the time- and space-dependent population densities and radiation flux density are found for a given problem, the normalized extracted energy δ can be calculated as a function of E_{in}/E_{sat} by means of (A-25), (1), (4), and (6).

Fig. 2, obtained by solving (A-11)-(A-15) on a CDC 7600 computer, illustrates the variation of δ versus E_{in}/E_{sat} for the case of a Gaussian input pulse. Each curve in the figure corresponds to a given value of the ratio $\tau_p/\tau_r = 0.1, 1.0, 10, 100$, or 1000. (Recall that τ_p refers to the duration of the *input* pulse; as the pulse propagates through the amplifier its shape

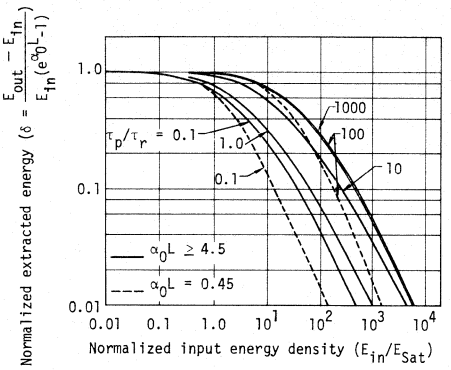

Fig. 2. Curves of normalized extracted-energy versus normalized input-energy density for Gaussian input pulses. Solid lines correspond to ratios of pulsewidth to rotational relaxation time τ_p/τ_r = 0.1, 1.0, 10, 100, and 1000 for $\alpha_0 L \gtrsim 4.5$ Dashed lines correspond to τ_p/τ_r = 0.1 and 100 for $\alpha_0 L$ = 0.45.

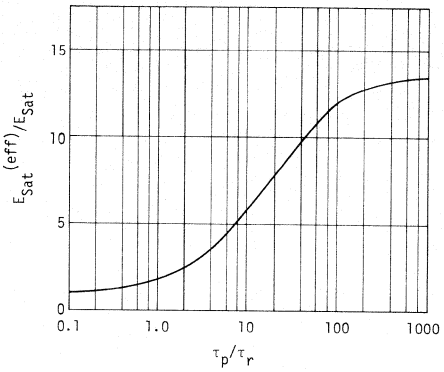

Fig. 3. Effective saturation-energy density for a multilevel system, relative to saturation-energy density for a two-level system, versus τ_p/τ_r.

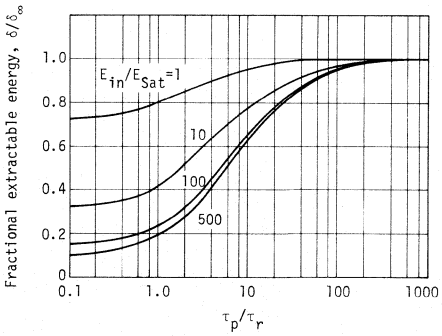

Fig. 4. Fractional extracted energy versus τ_p/τ_r for Gaussian input pulses and E_{in}/E_{sat} = 1, 10, 100, and 500. The fractional extracted energy is defined as $\delta/\delta_\infty = (E_{out} - E_{in}) / \lim_{\tau_p/\tau_r \to \infty} (E_{out} - E_{in})$.

and effective duration can change.) Owing to the choice of normalization factors for the plotted variables, the results are practically independent of the gain-length product $\alpha_0 L$ so long as it is above a value of about 4.5. The solid lines in Fig. 2 apply for this high-gain regime $\alpha_0 L \gtrsim 4.5$; the dashed lines represent the smaller value $\alpha_0 L = 0.45$. A corresponding set of curves constructed for the case of rectangular input pulses is only slightly different from Fig. 2, indicating that the extracted energy for arbitrary τ_p/τ_r value is not very sensitive to the input pulse shape.

The particular numerical problem on which Fig. 2 is based corresponds to pulse amplification on a $P(16)$ transition in a $He/N_2/CO_2$ = 3/1/1 laser gas mixture at temperature T = 325 K and pressure P = 0.85 atm. The small-signal gain of the system is $\alpha_0 = 0.045$ cm^{-1} and other relevant parameters are [8] $\sigma = (1.97)\ 10^{-18}$ cm^2, $n^u_{J-1}(0) = n^u_{15}(0) = (2.33)\ 10^{16}$ cm^{-3}, $n^l_J(0) = n^l_{16}(0) = (7.68)\ 10^{14}$ cm^{-3}, $N^u_R(0) = (3.06)\ 10^{17}$ cm^{-3}, $N^l_R(0) = (1.00)\ 10^{16}$ cm^{-3}, and $\tau_r = (1.72)\ 10^{-10}$ s. The amplifier length was taken to be L = 10 cm for the small-gain results, and $L \geq 100$ cm for the high-gain examples.

The curve labeled $\tau_p/\tau_r = 0.1$ is indistinguishable from the analytical result given by (3). Likewise, the curve labeled $\tau_p/\tau_r = 1000$ is virtually indistinguishable from the analytical result using the value $M \cong M^l \cong M^u = N^u_R(0)/n^u_{15}(0) \cong 13$ in (2).

To a good approximation any pair of curves labeled by different τ_p/τ_r values in Fig. 2 are related to one another by a simple translation property. This property is exact for the extreme cases $\tau_p/\tau_r << 1$ and $\tau_p/\tau_r >> 1$ as seen by comparing (2) and (3): If the abscissa value $E_{in}/E_{sat} = a$ corresponds to the ordinate value $\delta = b$ for $\tau_p/\tau_r << 1$, then the abscissa value $E_{in}/E_{sat} = (M+1)a$ corresponds to $\delta = b$ for the $\tau_p/\tau_r >> 1$ curve. This feature can be used to define an effective saturation-energy density $E^{(eff)}_{sat}$ for arbitrary τ_p/τ_r value. We define $E^{(eff)}_{sat}$ as the E_{in} value that gives rise to the same degree of saturation (same δ value) for a given ratio τ_p/τ_r as does the value $E_{in} = E_{sat}$ for $\tau_p/\tau_r << 1$. Fig. 3, which is derived from Fig. 2, shows $E^{(eff)}_{sat}/E_{sat}$ as a function of τ_p/τ_r. As τ_p/τ_r tends to infinity, $E^{(eff)}_{sat}/E_{sat}$ asymptotically approaches the value $(M+1) \cong 14$. As stated earlier, vibrational energy transfer becomes important when $\tau_p/\tau_r >> 1$, so this asymptotic limit would never be realized in practice.

A second quantity of interest that we can obtain from Fig. 2 is the dependence of the extracted energy on input pulse duration for a given input energy density E_{in}. As shown in Fig. 4, the reservoir model predicts that the extracted energy is monotonically increased by increasing τ_p and correspondingly decreasing I_{in} (to maintain fixed E_{in}). The ordinate in this figure is the ratio of extracted energy for a given τ_p/τ_r value to the maximum extracted energy as τ_p/τ_r is made very large while keeping E_{in} fixed

$$\delta/\delta_\infty = (E_{out} - E_{in}) \Big/ \lim_{\tau_p/\tau_r >> 1} (E_{out} - E_{in}).$$

Fig. 4 shows that the effects of varying τ_p are considerably more pronounced for larger input-energy densities.

III. Effect of Vibrational Energy Transfer

When the input pulse duration is long compared to the rotational relaxation time, it may be inadequate to consider only the influence of the rotational energy reservoirs. Other secondary reservoirs of stored energy can come into play on this longer time scale. In this section we estimate the effect of the most rapid type of vibrational energy transfer for the important example of a CO_2 amplifier. The basis of the cal-

culation is a vibrational-temperature model [7], [8] and the relevant process is intramode VV energy transfer. The basic physics of the model and necessary preliminaries to the calculation are discussed in Appendix B.

We begin with the expression [(B-4) in the Appendix] for the total vibrational energy $\mathcal{E}_T^{(\mathrm{vib})}$ per unit volume in the excited CO_2 gas mixture. Just before the pulse enters the amplifier the initial value of this quantity is

$$\mathcal{E}_T^{(\mathrm{vib})}(r_0, s_0) = N_c\left\{\hbar\omega_{\nu 1}\left[\frac{s_0}{(1-s_0)} + \frac{s_0^2}{(1-s_0)^2}\right] + \hbar\omega_{\nu 3}\frac{r_0}{(1-r_0)}\right\}. \tag{7}$$

The symbols in this equation are explained in Appendix B. The initial values r_0, s_0 for the Boltzmann factors are determined by the particular method used to pump the amplifier and by the relatively slow gas kinetic processes [8]. The connection of the Boltzmann factors to quantities we have used up to this point is that they determine the initial population densities $n_{J-1}^u(0)$, $N_R^u(0)$, etc., for a CO_2 problem. In particular, the factors n_T^u and n_T^l in (A-2) and (A-3) are given by $n_T^u = N_c r_0/Q(r_0, s_0)$ and $n_T^l = N_c s_0^2/Q(r_0, s_0)$, where Q is the partition function defined in (B-3). The initial population-inversion density on the u-l transition is then, from (A-3) with $(J \pm 1)$, approximated by J

$$\Delta n(0) \cong (2J/J_{\mathrm{opt}}^2)\exp\left[-J^2/2J_{\mathrm{opt}}^2\right] N_c(r_0 - s_0^2)/Q(r_0, s_0) \tag{8}$$

with J_{opt} given by (A-4). The numerical example treated earlier in Section II corresponds to the values $r_0 = 0.11$, $s_0 = 0.06$, $N_c \cong (3.8)\ 10^{18}\ \mathrm{cm}^{-3}$, $J = 16$, and $J_{\mathrm{opt}} \cong 17$.

Now in order to get an upper bound on the reservoir-model results for energy extraction, we suppose that the amplifier input pulse has a duration τ_p that is long compared to both the rotational relaxation time τ_r and the intramode VV relaxation time τ_{vv}, but short compared to any other vibrational relaxation times. The pulse causes energy to be transferred from the $\nu 3$ mode of a CO_2 molecule to the $\nu 1$ mode via stimulated emission between the energy levels $u = (J-1; 0, 0, 1)$ and $l = (J; 1, 0, 0)$. This occurs gradually enough that the intramode VV relaxation process adjusts the equilibrium population distributions in the modes (i.e., adjusts the values of r and s). Immediately following the passage of the pulse through the amplifier, the modes are characterized by final Boltzmann-factor values r_f, s_f. The total vibrational energy per unit volume in this post-pulse state is given by (7) with r_f and s_f replacing r_0 and s_0.

We can determine r_f and s_f in the following way. First it is noted that the driving force of stimulated emission can only change the Boltzmann factors to the point where

$$r_f = s_f^2 \tag{9}$$

since upon reaching this value the population-inversion density on the transition is zero by (8). Secondly, by conservation of energy the decrease in vibrational energy per unit volume must equal the energy $(\Delta\mathcal{E})_{\mathrm{VV}}$ per unit volume added to the radiation pulse

$$\mathcal{E}_T^{(\mathrm{vib})}(r_0, s_0) - \mathcal{E}_T^{(\mathrm{vib})}(r_f, s_f) = (\Delta\mathcal{E})_{\mathrm{VV}}. \tag{10}$$

The energy added to the pulse is itself a fraction $(\omega_{\nu 3} - \omega_{\nu 1})/\omega_{\nu 3}$ of the energy lost from the $\nu 3$ mode

$$(\Delta\mathcal{E})_{\mathrm{VV}} = (\omega_{\nu 3} - \omega_{\nu 1})\,\Delta\mathcal{E}_{\nu 3}/\omega_{\nu 3} = \frac{(\omega_{\nu 3} - \omega_{\nu 1})}{\omega_{\nu 3}}\left\{\frac{r_0}{1-r_0} - \frac{r_f}{1-r_f}\right\}\hbar\omega_{\nu 3} N_c. \tag{11}$$

By solving (10) and (11) simultaneously and using (9) to eliminate r_f, we find that s_f satisfies a quadratic equation. The solution is

$$\sqrt{r_f} = s_f = \{[4(c_0+3)c_0 + 1]^{1/2} - 1\}/2(c_0+3) \tag{12}$$

with

$$c_0 = \frac{s_0}{(1-s_0)}\left[1 + \frac{s_0}{1+s_0}\right] + \frac{r_0}{(1-r_0)}. \tag{13}$$

The maximum amount of energy that can be extracted by the pulse when the intramode VV processes have time to occur is then given by $(\Delta\mathcal{E})_{\mathrm{VV}}$ in (11) using the r_f value from (12). This can be compared to the maximum extractable energy per unit volume due to rotational relaxation alone, namely $(\Delta\mathcal{E})_{\mathrm{RR}} = h\nu_{ul} \cdot \Delta N/2 = (h\nu_{ul}/2) N_c(r_0 - s_0^2)/Q(r_0, s_0)$.

This comparison gives

$$(\Delta\mathcal{E})_{\mathrm{VV}}/(\Delta\mathcal{E})_{\mathrm{RR}} = \gamma \tag{14}$$

where the constant γ is

$$\gamma = [2Q(r_0, s_0)(\omega_{\nu 3} - \omega_{\nu 1})/2\pi\nu_{ul}] \cdot \left\{\frac{r_0}{(1-r_0)} - \frac{r_f}{(1-r_f)}\right\}\Big/(r_0 - s_0^2). \tag{15}$$

Thus the effect of intramode VV processes is to enlarge the size of the reservoir population-inversion density from the value $\Delta N = (\Delta N_R + \Delta n)$ to a value γ times greater. For the numerical example treated in Section II we find that $r_f = 0.0179 = s_f^2$, which gives $\gamma = 2.72$ for this problem. The result for the normalized extracted energy δ is shown in Fig. 5. The curve labeled 2LS in the figure refers to the $\tau_p/\tau_r \ll 1$ limit, and is accurately given by (3) for any single-peaked input pulse shape. The curve RR represents the $\tau_p/\tau_r \gg 1$ limit with only rotational relaxation taken into account. The RR curve can be constructed using (2), which amounts to simply translating the 2LS curve to the right by a factor $(M+1) \cong 14$. The curve labeled VV applies when τ_p is large compared to the intramode VV relaxation time. It can be constructed by translating the 2LS curve to the right by a factor $(M+1)\gamma \cong 38$, or by solving the detailed pulse-propagation problem using a computer code based on a vibrational-temperature model [8]. We have made computer runs of this type and find precise agreement with the result using the translation factor $(M+1)\gamma$.

The three curves 2LS, RR, and VV in Fig. 5 can readily be drawn for any given CO_2 laser amplifier since they are determined by an analytical expression (3) and two translation factors involving easily calculable quantities M and γ [from

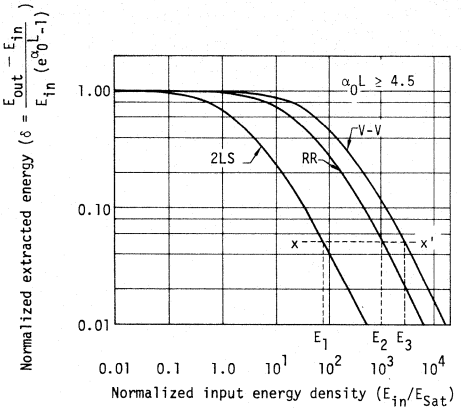

Fig. 5. Limiting curves for a CO_2 amplifier. The curves 2LS, RR, and VV refer, respectively, to the limits $\tau_p/\tau_r \ll 1$, $\tau_p/\tau_r \gg 1$ with only rotational coupling included, and $\tau_p/\tau_r \gg 1$ with both rotational and intramode VV energy transfer included. The indicated abscissa points have values in the ratio $E_3:E_2:E_1 = \gamma(M+1):(M+1):1$, as explained in the text.

(A-10) and (15), respectively]. The curves for intermediate τ_p/τ_r values can be interpolated reasonably accurately by using the same relative positions as shown in Fig. 2.

IV. Comparison with Experiment

The amplification of nanosecond-duration CO_2 pulses in the heavily saturated regime has been studied experimentally by Figueira *et al.* [5]. Using a two-stage electron-beam-controlled amplifier, they obtained data on output energy q_{out} as a function of input energy q_{in} for three different pulse durations corresponding to the values $\tau_p/\tau_r \cong 25$, 100, and 350.

The foregoing theory deals with energy densities E rather than energies q. To compare the experimental results to the theory we will transform all data points q_{out} versus q_{in} to a δ versus E_{in}/E_{sat} diagram by using

$$\delta = \left(\frac{q_{out}A_{in}}{q_{in}A_{out}} - 1\right) \Big/ (\exp(\alpha_0 L) - 1) \tag{16}$$

and

$$E_{in}/E_{sat} = (q_{in} 2\sigma / h\nu_{ul} A_{in}) \exp(\alpha_0 L) \tag{17}$$

in which A_{in} and A_{out} are the effective cross-sectional areas of the input pulse and the output pulse, respectively.

In calculating the effective areas it is necessary to take into account that the input pulse used by Figueira *et al.* is a diverging Gaussian beam and that A_{out} exceeds A_{in} due to the effects of both diffraction and saturation. The transverse spot size of the input pulse is specified by w_0, the radius from the pulse center to the point where the intensity has declined by a factor $1/e$. By diffraction the corresponding spot size of the output pulse is $w = w_0 + \theta L$, where θ is the divergence angle and L is the propagation distance through the amplifier. Thus diffraction effects alone give

$$(A_{out}/A_{in})_{diffr} = (w/w_0)^2. \tag{18}$$

Using the quoted [5] values $w_0 = 0.89$ cm, $\theta = 0.7$ mrad, and $L = 200$ cm we get $(w/w_0)^2 \cong 1.3$.

The effect of saturation is to increase the off-axis energy relative to the on-axis energy. The Gaussian transverse distribution of intensity in the input plane is converted into a more nearly uniform distribution over the spot size in the output plane. The compound effect of saturation and diffraction acting simultaneously is thus to give an area ratio

$$(A_{out}/A_{in}) \cong \int_0^w 2\pi r\, dr \Big/ \int_0^{w_0} \exp(-r^2/w_0^2)\, 2\pi r\, dr$$

$$= (w/w_0)^2/[1 - \exp(-1)]. \tag{19}$$

This gives the estimate $(A_{out}/A_{in}) \cong 2$ to be used in (16).

The cross section $\sigma = \lambda_{ul}^2/(4\pi^2 \tau_{ul} \Delta\nu)$ in (17) is evaluated using $\lambda_{ul} = 10.6$ μm, $\tau_{ul} = 4.2$ s, and the expression [8] for the pressure-broadened linewidth in a $He/N_2/CO_2$ gas mixture

$$\Delta\nu(\text{Hz}) = (1.29)\, 10^{-11} N T^{1/2} [(0.695)\, \psi_{He} + (0.755)\, \psi_{N_2} + \psi_{CO_2}] \tag{20}$$

where N is the total number of molecules per unit volume and the ψ's represent the mole fractions of different species. For the $He/N_2/CO_2 = 3/(1/4)/1$ system at 450 K used by Figueira *et al.*, we find

$$\sigma = (1.67)\, 10^{-18}\ \text{cm}^2. \tag{21}$$

Combining this result with the quoted gain-length factor $\alpha_0 L = (0.051\ \text{cm}^{-1})\ (200\ \text{cm}) = 10.2$, we have the saturation-energy density

$$E_{sat} = (h\nu_{ul}/2\sigma) \exp(-\alpha_0 L) = (5.62\ \text{mJ/cm}^2) \exp(-10.2) \tag{22}$$

or $E_{sat} = (2.09)\, 10^{-4}\ \text{mJ/cm}^2$.

The remaining quantities needed for the theory-experiment comparison can be inferred from the small-signal gain value α_0 and the system temperature and pressure. In particular, the translation factors $(M+1)$ and γ in (A-10) and (15) are found to be

$$(M^u + 1) \cong (M^l + 1) \cong \Delta N(0)/\Delta n(0) = 16.5 \tag{23}$$

and

$$\gamma \cong 3.49 \tag{24}$$

Fig. 6 shows the distribution of data points for the three cases $\tau_p/\tau_r = 25$, 100, and 350 relative to the theoretical curves. It is seen that the data for $\tau_p/\tau_r = 100$ are closely approximated by the corresponding RR curve. This indicates that transfer of vibrational energy is fairly negligible on this time scale of $\tau_p \cong 20$ ns at about one-quarter atmosphere partial pressure of CO_2.

The significant role played by the intramode VV process is clearly evident, however, in the data for $\tau_p/\tau_r = 350$. As the depth of saturation is increased the experimental data points increasingly deviate from the RR 350 curve until they closely approach the upper bound VV curve representing full extraction of energy from both the RR's and the intramode vibrational reservoirs. The RR's alone can account for less

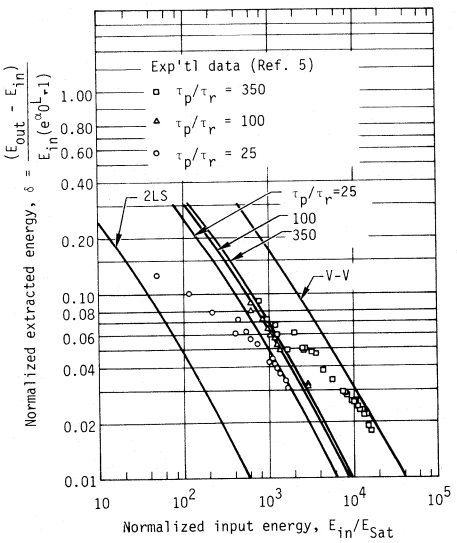

Fig. 6. Comparison of theory with experimental data adapted from [5].

than half of the observed extracted energy at high E_{in}/E_{sat} values for this case.

These results allow us to estimate the imprecisely known rate of intramode VV transfer in CO_2. The fact that the influence of this process is fairly negligible at $\tau_p = 100\tau_r$ but is very pronounced at $350\tau_r$ implies that the intramode VV relaxation time τ_{vv} lies in the range $10\tau_r < \tau_{vv} < 35\tau_r$ for this system. Since the partial pressure of CO_2 in this case is $P_{CO_2} = \psi_{CO_2} P = (0.235)P$ and the rate of rotational energy transfer is [4]

$$(1/\tau_r P) \cong [(1.1)\,\psi_{CO_2} + (0.7)\,\psi_{He} + (1.0)\,\psi_{N_2}] \cdot 10^7\ s^{-1}torr^{-1} \cong (0.81)\ 10^7\ s^{-1}torr^{-1} \quad (25)$$

we obtain the result [11][2]

$$(1/\tau_{vv}P_{CO_2}) \cong (1.0\text{-}3.5)\ 10^6\ s^{-1}torr^{-1}. \quad (26)$$

The data points for $\tau_p/\tau_r = 25$ agree with the expectations based on the RR model for E_{in}/E_{sat} values greater than about 10^3, but fall significantly below these expectations for lower input-energy densities. We have not satisfactorily accounted for this discrepancy. It may be due in part to the double-peaked input pulse used in the experiments [5], which would make the effective input pulse duration an increasing function of the degree of saturation for low to moderate E_{in}/E_{sat} values.

In summary, a relatively simple rate-equation theory has been used to describe the complicated effects of rotational and vibrational coupling on the energy-saturation characteristics of a short-pulse CO_2-laser amplifier. By analyzing the problem in terms of suitably normalized variables, the theoretical results for different pulse durations were found to be interrelated by simple translations in a δ versus E_{in}/E_{sat} diagram. Over a very broad range of E_{in}/E_{sat} values the curves in this diagram are practically independent of the amplifier gain factor $\exp(\alpha_0 L)$, so long as $\exp(\alpha_0 L) \gtrsim 90$. Since vibrational as well as rotational coupling is taken into account, the theory can be usefully applied to situations where the pulse duration is up to several thousand times longer than the rotational relaxation time in a CO_2 system. For still longer pulse durations, extending into the domain of microseconds or more, a vibrational-temperature model, such as that in [8], can be used to describe the amplification process. Finally, a comparison of the short-pulse theory to published experimental results has led to an estimate of the imprecisely known rate of intramode VV transfer in CO_2.

Appendix A
Rotational-Reservoir Model

In a gas comprised of linear polyatomic molecules the number density $\bar{n}_J$ of molecules occupying the Jth rotational level of a given vibrational state in thermal equilibrium is approximately given by [12]

$$\bar{n}_J = (2J+1)\,(Bhc/kT)\,(1/\kappa_0)\,n_T \exp[-(Bhc/kT)J(J+1)] \quad (A\text{-}1)$$

where T is the gas temperature in degrees Kelvin, $B = h/8\pi^2 c\,\mathcal{I}$ is the rotational constant in cm^{-1}, $\mathcal{I}$ is the moment of inertia of the molecule, and h, c, and k are Planck's constant, the speed of light in vacuum, and Boltzmann's constant, respectively. The parameter κ_0 takes the value one or one-half, depending on the symmetry of the molecules; e.g., for a gas of $CO^{16}O^{16}$ molecules $\kappa_0 = \frac{1}{2}$, while for $CO^{16}O^{18}$ $\kappa_0 = 1$. The rotational quantum number J assumes any integer value from 0 to ∞ when $\kappa_0 = 1$, but every other J value is missing when $\kappa_0 = \frac{1}{2}$. The quantity n_T is the total number of molecules per cubic centimeter in all rotational levels corresponding to a given vibrational state

$$n_T = \sum_J^{\infty} \bar{n}_J \cong \kappa_0 \int_0^{\infty} \bar{n}_J\, dJ. \quad (A\text{-}2)$$

Now, if $\bar{n}_J^u$ and $\bar{n}_J^l$ represent the number density of molecules in the Jth rotational levels of the upper and lower vibrational states between which a laser transition occurs, then the initial population-inversion density for the transition is

$$\Delta n(0) = \bar{n}_{J+\Delta J}^u - \bar{n}_J^l = (2J-1)\,(\beta/\kappa_0)\,n_T^u \exp[-\beta J(J-1)] - (2J+1)\,(\beta/\kappa_0)\,n_T^l \exp[-\beta J(J+1)] \quad (A\text{-}3)$$

[2]This result (26) represents an average rate that is influenced by all types of intramode VV processes for the $\nu 1$, $\nu 2$, and $\nu 3$ modes [see the discussion accompanying (B-1) in Appendix B]. The value (26) is consistent with the only measured CO_2 intramode VV rates of which we are aware. These are the rate $(5.3 \pm 1)\ 10^6\ s^{-1}torr^{-1}$ for the process

$$CO_2(01^11) + CO_2(00^00) \rightleftarrows CO_2(01^10) + CO_2(00^01)$$

determined by Burak *et al.* in [11a)], and the rates $(1.6 \pm 0.2)\ 10^6\ s^{-1}torr^{-1}$ and $(4 \pm 0.4)\ 10^6\ s^{-1}torr^{-1}$ for the processes

$$CO_2(00^01) + C^{13}O_2(00^00) \rightleftarrows CO_2(00^00) + C^{13}O_2(00^01)$$

and

$$CO_2(00^01) + CO^{18}O^{16}(00^00) \rightleftarrows CO_2(00^00) + CO^{18}O^{16}(00^01)$$

respectively, determined by Stephenson *et al.* in [11b)].

where $\beta \equiv Bhc/kT$, and we have taken $\Delta J = -1$ for a P-branch vibrational-rotational transition.

The particular J value for which $\Delta n(0)$ is maximum is the nearest allowed integer to the value

$$J_{\text{opt}} = (kT/2Bhc)^{1/2}. \tag{A-4}$$

This result follows most simply by making the approximations $J - 1$ and $J + 1 \cong J$ in (A-3) and then solving for the J value that makes $\partial \Delta n(0)/\partial J = 0$.

For a given $P(J)$ transition between the levels u and l, neighboring rotational levels provide a fairly tightly coupled reservoir of stored energy. To describe this coupling it is convenient to separate out the particular laser level u (or l) in the rotational band, and treat the rest of the levels in each band collectively as indicated in Fig. 1. To find the effective relaxation times for transfer of rotational energy between the laser levels and the reservoirs, we invoke the principle of overall microscopic reversibility for population exchanges between levels in a rotational band. Denoting the thermal-equilibrium population densities of any pair of levels by $\bar{n}_J$ and $\bar{n}_k$, and denoting the transition-rate probabilities (number of transitions per second) for $J \to k$ and $k \to J$ processes by w_{Jk} and w_{kJ}, respectively, this principle is expressed as

$$\bar{n}_J \sum_{k=0}^{\infty}{}' w_{Jk} = \sum_{k=0}^{\infty}{}' \bar{n}_k w_{kJ}. \tag{A-5}$$

The sum in (A-5) goes over all levels in the band except $k = J$, and the prime on the sum is a reminder that $k \neq J$. The overall rotational relaxation time τ_r for transfer out of level J to all other rotational levels in the band is defined by

$$1/\tau_r = \sum_{k=0}^{\infty}{}' w_{Jk}. \tag{A-6}$$

We define a collective relaxation time $M \cdot \tau_r$ for transitions from all levels of the reservoir to the level J by the relation

$$\bar{N}_R/(M\tau_r) = \sum_{k=0}^{\infty}{}' \bar{n}_k w_{kJ} \tag{A-7}$$

where

$$\bar{N}_R = \sum_{k=0}^{\infty}{}' \bar{n}_k \tag{A-8}$$

is the thermal-equilibrium population density of the reservoir. Using the definitions (A-6)-(A-8) in (A-5), we find that M is the thermal-equilibrium ratio of the reservoir and level J populations

$$M = \bar{N}_R/\bar{n}_J = \left(\sum_{k=0}^{\infty} \bar{n}_k - \bar{n}_J \right) \Big/ \bar{n}_J. \tag{A-9}$$

Using (A-1) for $\bar{n}_k$, and approximating the sum by integral, as in (A-2), it follows easily that

$$M = M(J) = (kT/Bhc)\,[\kappa_0/(2J+1)] \cdot \exp\,[(Bhc/kT)\,J(J+1)] - 1. \tag{A-10}$$

Rate Equations

From the foregoing discussion and definitions, we can immediately write down the rate equations for the reservoir model indicated schematically in Fig. 1. The variation in time of the population densities n^u_{J-1} and n^l_J of the laser levels and of the collective population densities N^u_R and N^l_R of the other levels in the two rotational bands is described by

$$\partial n^u_{J-1}/\partial t = -\sigma I(x,t)\,(n^u_{J-1} - n^l_J) - n^u_{J-1}/\tau_r + N^u_R/(\tau_r \cdot M^u) \tag{A-11}$$

$$\partial N^u_R/\partial t = -N^u_R/(\tau_r M^u) + n^u_{J-1}/\tau_r \tag{A-12}$$

$$\partial n^l_J/\partial t = \sigma I(x,t)\,(n^u_{J-1} - n^l_J) - n^l_J/\tau_r + N^l_R/(\tau_r \cdot M^l) \tag{A-13}$$

$$\partial N^l_R/\partial t = -N^l_R/(\tau_r M^l) + n^l_J/\tau_r \tag{A-14}$$

where M^l is given directly by (A-10), and M^u is given by the same expression with $(J - 1)$ replacing J. The space- and time-dependent radiation flux density I (photons/s $\cdot$ cm^2) is assumed to satisfy the familiar transport equation

$$\partial I/\partial t + c\partial I/\partial x = c\sigma(n^u_{J-1} - n^l_J) \cdot I \tag{A-15}$$

where $\sigma = \lambda^2_{ul}/(4\pi^2 \tau_{ul} \Delta\nu)$ is the cross section for stimulated emission and λ_{ul}, τ_{ul}, and $\Delta\nu$ are, respectively, the wavelength, spontaneous lifetime, and linewidth of the u to l transition.

In the event that $M^u \cong M^l$ (i.e., $\bar{N}^u_R/\bar{n}^u_{J-1} \cong \bar{N}^l_R/\bar{n}^l_J$) the four population-density equations (A-11)-(A-14) can be reduced to a pair of equations [1] for the population-inversion densities $\Delta n = (n^u_{J-1} - n^l_J)$ and $\Delta N_R = (N^u_R - N^l_R)$

$$\partial(\Delta n)/\partial t = -2\sigma I \cdot \Delta n - \Delta n/\tau_r + \Delta N_R/(\tau_r M) \tag{A-16}$$

$$\partial(\Delta N_R)/\partial t = \Delta n/\tau_r - \Delta N_R/(\tau_r \cdot M). \tag{A-17}$$

The problem is completely determined by specifying the initial conditions on the population densities, e.g., $\Delta n(0)$ and $\Delta N_R(0)$ for (A-16) and (A-17), and by specifying the boundary condition $I(0,t)$ and initial condition $I(x,0)$ for the incident pulse. Whether the set of (A-11)-(A-15) or (A-15)-(A-17) is used, the solution is expedited by the customary transformation to independent variables $\tau = t - x/c$ and $\zeta = x/c$, which gives the simple operator relationships $\partial/\partial t + c\partial/\partial x = \partial/\partial\zeta$ and $\partial/\partial t = \partial/\partial\tau$.

Limiting Cases

A very useful feature of the reservoir model is that it admits analytical solutions [1] in both the limits $\tau_p/\tau_r \ll 1$ and $\tau_p/\tau_r \gg 1$. To demonstrate this we will consider the slightly simplified set of (A-15)-(A-17), which apply when the population-density ratios $N^l_R(0)/n^l_J(0)$ and $N^u_R(0)/n^u_{J-1}(0)$ for the lower and upper rotational bands are approximately equal.

$\tau_p/\tau_r \gg 1$: When the envelope of the input radiation pulse changes slowly compared to the rotational relaxation time, the population of the reservoirs can continually adjust to any changes in n^u_{J-1} and n^l_J caused by the pulse. Mathematically,

this situation is expressed in (A-17) by writing

$$\partial \Delta N_R/\partial t = (\Delta n(t) - \Delta N_R(t)/M)/\tau_r \cong 0$$

for all t. Thus the population-inversion density of the reservoirs remains continuously in steady state[3] with the population-inversion density of the laser levels

$$\Delta N_R(t) = M\Delta n(t), \quad (\tau_p/\tau_r \gg 1). \tag{A-18}$$

If we now add together (A-16) and (A-17) and use this result we have

$$\partial(\Delta N_R + \Delta n)/\partial t = (M+1)\,\partial(\Delta n)/\partial t = -2\sigma I \Delta n.$$

The reservoir-model equations in the limit $\tau_p/\tau_r \gg 1$ therefore reduce to the pair

$$\partial(\Delta n)/\partial t = -2\sigma I \Delta n/(M+1) \tag{A-19}$$

$$\partial I/\partial t + c\partial I/\partial x = c\sigma I \Delta n. \tag{A-20}$$

Apart from the factor $(M+1)$ in (A-19), this is the pair of coupled equations solved by Frantz and Nodvik [9]. The general solution obtained by their method is

$$\Delta n(x,t) = \Delta n(x,0)/\{1 + \exp[C_1(x)] \cdot [\exp[C_2(x,t)] - 1]\} \tag{A-21}$$

$$I(x,t) = I_0(t - x/c)/\{1 + \exp[-C_2(x,t)] \cdot [\exp[-C_1(x)] - 1]\} \tag{A-22}$$

in which

$$C_1(x) = \sigma \int_0^x \Delta n(x',0)\,dx' \tag{A-23}$$

and

$$C_2(x,t) = [2\sigma/(M+1)] \int_{-\infty}^{t-x/c} I_0(\tau')\,d\tau'. \tag{A-24}$$

The function $\Delta n(x,0)$ is the initial population-inversion density and $I_0(t) = I(x = -\infty, t)$ is the input pulse shape. Specifically, we will deal with cases where the initial inversion density is spatially uniform: $\Delta n(x,0) = \Delta n(0)$ for $0 \leqslant x \leqslant L$, so that $C_1(x) = \alpha_0 x$, where α_0 is the small-signal incremental gain given by

$$\alpha_0 = \sigma \Delta n(0). \tag{A-25}$$

Also the input pulse shapes we will consider are the rectangular: $I_0(t - x/c) = I_0 =$ constant for $0 \leqslant (t - x/c) \leqslant \tau_p$, and the Gaussian: $I_0(t - x/c) = I_0 \exp[-(t - x/c)^2/(\tau_p/2\sqrt{\ln 2})^2]$ for $-\infty \leqslant (t - x/c) \leqslant \infty$.

$\tau_p/\tau_r \ll 1$: There is insufficient time for the reservoirs to influence pulse amplification if the pulse duration is short[1] in comparison with τ_r. In this limit we put $(1/\tau_r) = 0$ in the reservoir-model rate equations (A-11)-(A-14) or (A-16)-(A-17) and obtain a pair of equations like (A-19) and (A-20), but with $M = 0$. The general solution in this case is obtained from (A-21)-(A-24) by setting $M = 0$ wherever it occurs.

[3] This steady-state relation cannot be maintained if the field is too intense, however. By examining the implicit steady-state condition $|\Delta N_R/M\tau_r| \gg |\partial \Delta N_R/\partial t|$, it is found that the flux density I must satisfy $I \ll (1/(2\sigma M\tau_r))$. In terms of energy density this translates to $(E_{in}/E_{sat}) \ll (\tau_p/M\tau_r) \exp(\alpha_0 L)$, where E_{sat} is defined by (4) in the text.

Appendix B

Vibrational-Temperature Concept for CO_2

Detailed descriptions of the vibrational and rotational energy levels of the carbon dioxide molecule are readily available [12]. In this appendix we briefly review some of this information, and sketch the vibrational-temperature concept [7], [8] that is used in Section III of the text to derive upper bound results on our reservoir model.

The linear triatomic CO_2 molecule can vibrate in three linearly independent normal modes designated as $\nu 1$ (symmetric stretching), $\nu 2$ (bending), and $\nu 3$ (asymmetric stretching). The vibrational energy state of a given CO_2 molecule can be expressed by giving the number of excitation quanta in each of these modes. The number of CO_2 molecules per cubic centimeter which have i quanta each of size $\hbar\omega_{\nu 1}$ in the $\nu 1$ mode, and $(j + j')$ quanta of size $\hbar\omega_{\nu 2}$ in the doubly degenerate $\nu 2$ mode, and k quanta of size $\hbar\omega_{\nu 3}$ in $\nu 3$ is written $N_c(i, j + j', k)$. Each of the quantum numbers i, j, j', k can take any integer value from 0 to ∞, and the spacings of adjacent levels in the modes are approximately given by $\hbar\omega_{\nu 1} \cong (2.76)10^{-13}$ ergs, $\hbar\omega_{\nu 2} \cong (1.33)10^{-13}$, and $\hbar\omega_{\nu 3} \cong (4.67)10^{-13}$.

An infinite set of rotational energy levels is associated with each vibrational level. The rotational energy is approximately $BhcJ(J+1)$, where B is the rotational constant (inversely proportional to the molecule's moment of inertia) and J is the integer rotational quantum number. A given vibrational-rotational energy level of the CO_2 molecule is then determined by the values of J, i, $(j + j')$, and k. For example, the familiar 10.6-μm band of CO_2 transitions occurs between the lower level $(J; 1, 0, 0)$ and the upper level $(J \pm 1; 0, 0, 1)$.

Transfers of vibrational, rotational, and translational energy occur in collisions between a CO_2 molecule and a molecule A, which may be another CO_2 molecule or a molecule of some other species present in the gaseous mixture. The vibrational-temperature concept exploits the wide disparity in the rates of different types of these elementary energy-transfer processes. The two most rapid and efficient processes are those between the rotational and translational degrees of freedom (i.e., the RT processes proceeding at a rate $1/\tau_r \cong 10^7 P\ s^{-1}$ where P is the total pressure in torr) and the intermolecular vibrational energy exchanges within a given vibrational normal mode (intramode VV processes with an imprecisely known rate which we estimate in Section IV to be $1.0\text{-}3.5\ 10^6 P_{CO_2}\ s^{-1}$ where P_{CO_2} is the partial pressure of CO_2 in torr). An example of an intramode VV process is

$$CO_2[\nu 3(k)] + CO_2[\nu 3(k')] \rightleftarrows CO_2[\nu 3(k-1)] + CO_2[\nu 3(k'+1)]. \tag{B-1}$$

The notation $CO_2[\nu 3(k)]$ refers to a CO_2 molecule with k quanta in the $\nu 3$ mode and arbitrary numbers of quanta in modes $\nu 1$ and $\nu 2$. The process (B-1), and its counterparts for

the $\nu 1$ and $\nu 2$ modes, involves an almost lossless redistribution of vibrational energy in the mode.

The basic assumption of a vibrational-temperature model is that the RT and intramode VV processes occur so rapidly on the time scale of interest that the population distributions they lead to are continually in equilibrium. Thus the population distribution of the rotational levels associated with any vibrational level v is a Boltzmann distribution at the gas translational temperature T; i.e., $n(J; v)$ is proportional to $(2J+1)$ $\exp[-hcBJ(J+1)/kT]$ as in (A-1). Similarly, the population distribution in each of the vibrational normal modes is continuously a Boltzmann distribution at a (vibrational) temperature θ_α, where $\alpha = \nu 1$, $\nu 2$, or $\nu 3$. For example, the number density of CO_2 molecules which have $(n+1)$ quanta in the $\nu 3$ mode is smaller than the number density with n quanta in this mode by the Boltzmann factor $r \equiv \exp[-\hbar\omega_{\nu 3}/k\theta_{\nu 3}]$. The occupation of the $\nu 2$ mode is similarly characterized by a Boltzmann factor $s \equiv \exp[-\hbar\omega_{\nu 2}/k\theta_{\nu 2}]$, where $\theta_{\nu 2}$ can be made to differ greatly from $\theta_{\nu 3}$ under a selective excitation (pumping) process. The $\nu 1$-mode Boltzmann factor is approximately given by $\exp[-\hbar\omega_{\nu 1}/k\theta_{\nu 1}] \cong s^2$ since $\omega_{\nu 1} \cong 2\omega_{\nu 2}$ and $\theta_{\nu 1} \cong \theta_{\nu 2}$ due to a strong (Fermi resonance) coupling between the $\nu 1$ and $\nu 2$ modes. The population density of CO_2 molecules in the mixed vibrational state $(i, j+j', k)$ is then expressible [8] as

$$N_c(i, j+j', k) = N_c r^k s^{2i+j+j'}/Q(r, s) \tag{B-2}$$

where N_c is the total number of CO_2 molecules per unit volume and Q is the partition function given by

$$1/Q(r, s) = (1-r)(1-s^2)(1-s)^2. \tag{B-3}$$

The total vibrational energy $\mathcal{E}_T^{(\mathrm{vib})}$ per unit volume in a CO_2 gas laser mixture is simply given in terms of the Boltzmann factors

$$\begin{aligned}\mathcal{E}_T^{(\mathrm{vib})} &= \sum_{i,j,j',k=0}^{\infty} N_c(i, j+j', k) \\ &\quad \cdot (i\hbar\omega_{\nu 1} + (j+j')\hbar\omega_{\nu 2} + k\hbar\omega_{\nu 3}) \\ &= N_c \left\{ \hbar\omega_{\nu 1} \left[\frac{s}{(1-s)} + \frac{s^2}{(1-s^2)} \right] + \hbar\omega_{\nu 3} \frac{r}{(1-r)} \right\}.\end{aligned} \tag{B-4}$$

Thus $\mathcal{E}_T^{(\mathrm{vib})}$ is the sum of the energies per unit volume $(\mathcal{E}_{\nu 1} + \mathcal{E}_{\nu 2} + \mathcal{E}_{\nu 3})$ in each of the vibrational normal modes, where $\mathcal{E}_{\nu 3} = N_c\hbar\omega_{\nu 3} r/(1-r)$, etc.

The kinetic equations of the vibrational-temperature model [8] describe the evolution of T and the θ_α (or r and s) in time, taking explicit account of slower energy-transfer processes. These include vibrational-translational (VT) and VV types (other than intramode VV) as well as electron-molecule collisions, etc. This sort of model is appropriate to describe gain generation in a high-pressure ($\sim$ 1-atm) CO_2 laser on a microsecond time scale and can be used to study the amplification of moderate-intensity pulses with durations $\gtrsim 1$ μs.

Acknowledgment

The author wishes to thank D. K. Miller for the significant contributions he made to this paper through his efforts in computer programming, running of problems, and analysis of the results.

References

[1] a) G. T. Schappert, "Rotational relaxation effects in short-pulse CO_2 amplifiers," *Appl. Phys. Lett.*, vol. 23, pp. 319–321, Sept. 1973.
b) E. E. Stark, Jr., W. H. Reichelt, G. T. Schappert, and T. F. Stratton, "Comparison of theory and experiment for nanosecond-pulse amplification in high-gain CO_2 amplifier systems," *Appl. Phys. Lett.*, vol. 23, pp. 322–324, Sept. 1973.

[2] C. P. Christensen, C. Freed, and H. A. Haus, "Gain saturation and diffusion in CO_2 lasers," *IEEE J. Quantum Electron.*, vol. QE-5, pp. 276–283, June 1969.

[3] P. K. Cheo, "CO_2 lasers," in *Lasers*, A. K. Levine and A. J. DeMaria, Ed. New York: Dekker, 1971, ch. 2, pp. 111–267.

[4] a) P. K. Cheo and R. L. Abrams, "Rotational relaxation rate of CO_2 laser levels," *Appl. Phys. Lett.*, vol. 14, pp. 47–49, Jan. 1969.
b) R. L. Abrams and P. K. Cheo, "Collisional relaxation of CO_2 rotational levels by N_2 and He," *Appl. Phys. Lett.*, vol. 15, pp. 177–178, Sept. 1969.
c) R. R. Jacobs, K. J. Pettipiece, and S. J. Thomas, "Rotational relaxation rate constants for CO_2," *Appl. Phys. Lett.*, vol. 24, pp. 375–377, Apr. 1974.

[5] J. F. Figueira, W. H. Reichelt, G. T. Schappert, T. F. Stratton, and C. A. Fenstermacher, "Nanosecond pulse amplification in electron-beam-pumped CO_2 amplifiers," *Appl. Phys. Lett.*, vol. 22, pp. 216–218, Mar. 1973.

[6] F. A. Hopf and C. K. Rhodes, "Influence of vibrational, rotational, and reorientational relaxation on pulse amplification in molecular amplifiers," *Phys. Rev. A*, vol. 8, pp. 912–929, Aug. 1973.

[7] a) R. N. Schwartz, Z. I. Slawsky, and K. F. Herzfeld, "Calculation of vibrational relaxation times in gases," *J. Chem. Phys.*, vol. 20, pp. 1591–1599, Oct. 1952.
b) W. J. Witteman, "On vibrational relaxations in carbon dioxide," Phillips Res. Rep. Suppl. 2, 1963.
c) B. F. Gordietz, N. N. Sobolev, V. V. Sokovikov, and L. A. Shelepin, "Vibrational level population inversion of polyatomic molecules," *Phys. Lett.*, vol. 25A, pp. 173–175, July 1967.

[8] R. J. Harrach and T. H. Einwohner, "Four-temperature kinetic model for a CO_2 laser amplifier," Lawrence Livermore Lab. Rep. UCRL-51399, May 1973 (the computer code described in this report was generalized by D. K. Miller to include pulse propagation).

[9] L. M. Frantz and J. S. Nodvik, "Theory of pulse propagation in a laser amplifier," *J. Appl. Phys.*, vol. 34, pp. 2346–2349, Aug. 1963.

[10] R. R. Jacobs, S. J. Thomas, and K. J. Pettipiece, "J-Dependence of rotational relaxation in the CO_2 00°1 vibrational level," *IEEE J. Quantum Electron.*, vol. QE-10, pp. 480–486, May 1974.

[11] a) I. Burak, Y. Noter, and A. Szöke, "Vibration-vibration energy transfer in the ν_3 mode of CO_2," *IEEE J. Quantum Electron.*, vol. QE-9, pp. 541–544, May 1973.
b) J. C. Stephenson, R. E. Wood, and C. B. Moore, "Near-resonant energy transfer between infrared-active vibrations," *J. Chem. Phys.*, vol. 48, pp. 4790–4791, May 1968.

[12] G. Herzberg, *Molecular Spectra and Molecular Structure II: Infrared and Raman Spectra of Polyatomic Molecules*. New York: Van Nostrand, 1945.

The Optically Gated Dye Cell—A High-Speed Shutter and Pulse Shaper

G. A. MASSEY, MEMBER, IEEE, AND R. A. ELLIOTT

Abstract—This paper discusses characteristics of a class of devices that use a saturable absorber irradiated by an optical control pulse, or gating pulse, to alter the shape of a transmitted optical signal. We consider two device geometries: a longitudinally gated cell, in which signal and gate beams are nearly parallel, and a transverse cell, in which the medium is bleached by a gating pulse applied at right angles to the signal beam. The longitudinal device permits synthesis of rising exponential signal pulses with arbitrary, subnanosecond time constants. The transverse geometry can provide pulses of complex shape and permits independent optimization of several device parameters. The dynamics of the saturable absorber (with particular emphasis on liquid dye systems) is analyzed in detail, and a pulse-shape synthesis procedure is outlined. Spurious nonlinear effects are considered, and an example of pulse shaping for laser-driven fusion is given.

INTRODUCTION

IN APPLICATIONS that require shuttering or shaping of light pulses with time constants and synchronism well below 1 ns, increasing difficulty in generating the electronic-gating signal is encountered if electrooptic or magnetooptic devices are used, and acoustooptic devices suffer from transit-time limitations that become severe in this time regime. For these reasons optically grated Kerr cells [1] have been used for this purpose. The principal advantage of the Kerr cell is that it can be gated by picosecond optical pulses generated by mode-locked lasers. This paper presents an analysis of a type of device which shares this advantage and offers additional versatility for pulse shaping.

Saturable absorbers have been used extensively to mode lock lasers [2] and as an optical shutter in a type of streak camera [3], but they have not yet been widely exploited in their possible role as a modulating element which allows one optical signal to interact with another. The relaxation times of these materials, particularly the bleachable dye solutions, can be widely varied and offer interesting possibilities for modulating optical pulses over time intervals from picoseconds to nanoseconds. In the devices we are considering, a cell filled with saturable absorber is irradiated with a strong "gating" pulse at the absorption frequency. Depending on the shape, intensity, and polarization of the gating pulse (which may, in fact, consist of several optical pulses) the transmission of the cell for an incident "signal" pulse will be altered. The exponential dependence of the cell transmission on such factors as cell length and population difference between the ground state and excited state of the absorber permits a wide range of transmission functions to be synthesized using only a few gating pulse shapes. In this paper we restrict our attention to liquid solutions of bleachable dyes, although many of the considerations apply to gaseous or solid media as well. In the following sections we describe two types of cell geometry that offer particular advantages in specific pulse-shaping applications and present an analysis of the absorption dynamics that applies even when the ground-state population is substantially depleted. We also estimate the magnitude of spurious nonlinear effects such as phase modulation, beam steering, and focusing, and finally we apply the previously stated theory to the shaping of 1.06-μm pulses for laser-induced fusion.

Manuscript received January 2, 1975; revised March 3, 1975. This work was performed under the auspices of the U.S. Atomic Energy Commission.

The authors are with the Oregon Graduate Center, Beaverton, Oreg. 97005.

CELL GEOMETRY

We have considered two different types of dye cell configurations in the course of this work. The first type, the longitudinal cell or cell array, can produce signal pulse shapes that are exponentially rising functions of time. The exponential time constants that can be achieved in this way are shorter than can be obtained using conventional pulsed laser oscillator techniques. By combining several cells of different absorber concentrations and lengths in a longitudinal array, as in Fig. 1, a variety of rising pulse shapes can be generated. In these systems a very short, intense gating pulse is applied to one end of a sequence of dye cells of different lengths and concentrations. A signal pulse to be shaped is applied to the opposite end. By selecting a dye with relaxation long compared to the time required for light to propagate through the cell and by utilizing a gating energy density high enough to produce substantial bleaching with the leading edge of the gating pulse, one can achieve the effect of an attenuator cell whose length shortens linearly with time. The gating energy required for this case is

$$E_g > -\frac{Ah\nu \ln T_0}{2\sigma} \tag{1}$$

where $h\nu$ is the photon energy, A is the beam cross-sectional area, T_0 is the unbleached cell transmission for the signal, and σ is the absorption cross section per molecule of the dye. As an example, if we consider a value of T_0 of 10 percent and a dye for which $\sigma \approx 10^{-16}$ cm^2 at 1.06 μm, we find that E_g/A must be greater than 2.2 mJ/cm^2 which, for a 50-ps pulse, corresponds to about 43 MW/cm^2.

The signal envelope observed at the output of a cell of length L with N_0 dye molecules per unit volume is easily shown to be approximated by

$$P_s(t) \approx P_{so}\left(t - \frac{nL}{c}\right) \exp\left(-\sigma N_0 L\right) \exp\left(\frac{\sigma N_0 ct}{2n}\right) \tag{2}$$

where c/n is the pulse velocity in the dye cell and $P_{so}(t)$ is the envelope of the signal applied to the cell input. Clearly, if P_{so} has exponential form, one can alter the growth coefficient

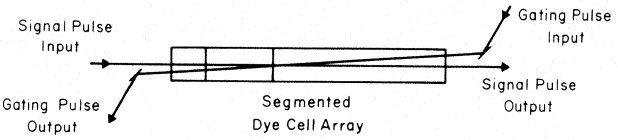

Fig. 1. Longitudinal dye cell configuration. Dye concentration and cell length are different for each segment, with higher concentrations in the shorter cells.

in the exponent by the additive constant ($\sigma N_0 c/2n$), which may be different for each cell in the array through selection of the concentration N_0. Each cell produces its effect during a time segment $2nL/c$ in duration.

Because the intensities required for this system are considerable and the optical paths traversed by the signal can be many centimeters for shaping long pulses, undesirable, nonlinear effects may be present in this geometry; however, it still may be a very convenient way to generate synchronized *gating* pulses with the correct shape for use with the transversely gated cell geometry discussed below.

The second type of dye cell system is the transverse geometry, which we have considered as a means of overcoming the long optical path (for signal) and high gating intensities inherent in the longitudinal system. In the transverse system, shown schematically in Fig. 2, the gating pulse is introduced approximately at right angles to the signal beam. The length of the cell along the signal axis is a short length (e.g., of the order of a centimeter) for which the signal-beam diameter is to be optimized to achieve the least possible depletion of the gating pulse across the aperture. We start our analysis by letting L_s be the signal length and L_g be the gate length (cell width) through the dye. For a dye concentration of N_0 molecules per unit volume, the unsaturated transmissions for signal (T_s) and gate (T_g) are

$$T_s = \exp(-\sigma N_0 L_s) \tag{3}$$

and

$$T_g = \exp(-\sigma N_0 L_g). \tag{4}$$

Taking the ratio of the logarithms of the previous equations we obtain

$$L_s/L_g = \ln T_s/\ln T_g. \tag{5}$$

Now it is desirable to have the most uniform possible gating intensity across L_g subject to the constraint that L_s be reasonably small. We therefore must specify the values of T_g and T_s allowable in our system, thus determining L_s/L_g from (5), and then we seek the minimum L_s and L_g which satisfy this aspect ratio. For a Gaussian signal beam with an intensity profile versus radius r of the form

$$I(r) = I_0 \exp\left(-\frac{2r^2}{w^2}\right) \tag{6}$$

propagating along the Z axis ($Z = 0$ at the center of the system), the spot radius $w(Z)$ varies according to the relation [4]

$$w^2(Z) = w_0^2\left[1 + \left(\frac{\lambda_0 Z}{\pi n w_0^2}\right)^2\right] \tag{7}$$

where λ_0 is the signal wavelength in air, n is the refractive index of the dye solvent, and w_0 is the spot radius at the beam waist, which we take to be centered in the cell. In this case, the largest aspect ratio for any central spot radius w_0 is obtained when L_s is set equal to the confocal parameter $b = (2\pi n w_0^2/\lambda_0)$. A reasonable choice for L_g is four times the spot radius at the ends of the system; thus we take

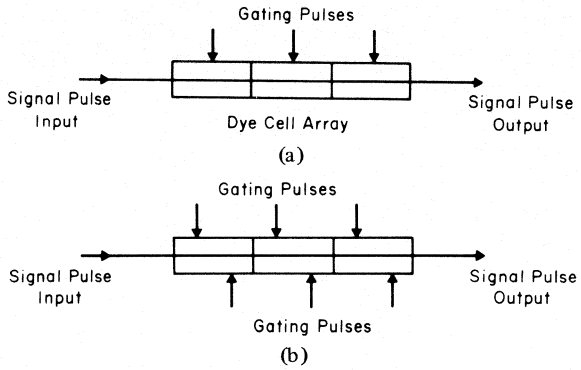

Fig. 2. Transverse dye cell configurations. Gating pulses of different durations are applied to each cell segment, either from one side (a), or symmetrically (b) to avoid a gradient of bleaching across the signal aperture. (a) Single-sided gating configuration. (b) Symmetrical gating.

$$L_g = 4\sqrt{2}\, w_0 \tag{8}$$

or

$$L_s/L_g = \frac{\pi n w_0}{2\sqrt{2}\,\lambda_0}. \tag{9}$$

This choice directly yields the desired results

$$w_0 = \frac{2\sqrt{2}\,\lambda_0}{\pi n}\frac{\ln T_s}{\ln T_g} \tag{10}$$

$$L_g = \frac{16\lambda_0}{\pi n}\frac{\ln T_s}{\ln T_g} \tag{11}$$

$$L_s = \frac{16\lambda_0}{\pi n}\left(\frac{\ln T_s}{\ln T_g}\right)^2. \tag{12}$$

From (3) we also obtain the concentration

$$N_0 = \frac{1}{\sigma L_s}\ln(1/T_s). \tag{13}$$

The previous equations completely specify the static characteristics of the optimized transverse system. As an indication of the results forthcoming from this analysis, consider a complete cell system for which $\lambda_0 = 1.064\ \mu$m, $n = 1.4$, $T_g = 0.9$ (90-percent transverse uniformity with the gating pulse incident from one side only), and $T_s = 10^{-4}$ (providing at least 10^3 of dynamic range for signal shaping). In this case

$$w_0 = 59.8\ \mu\text{m}$$

$$L_g = 0.338\ \text{mm}$$

$$L_s = 2.958\ \text{cm}$$

and

$$N_0 = 3.114 \times 10^{16}\ \text{cm}^{-3}$$

for $\sigma = 10^{-16}$ cm^2. The beam area in this case would be about πw_0^2, or 1.12×10^{-4} cm^2, which is sufficiently small to imply the use of signal powers less than about 1 kW to avoid signal-induced interactions.

It is immediately apparent that the tolerance of T_g can be reduced somewhat from the previous example if the gating pulse is reflected back through the dye cell by a mirror, or if the pulse is split and applied to opposite sides of the cell simultaneously, so that the first-order gradient of gating intensity over the signal aperture is nulled out. Such a geometry would have to be designed very carefully to avoid problems of standing waves and spatial inhomogeneities which might affect the bleaching dynamics and might even diffract a portion of the signal beam.

We now discuss the temporal behavior of the transverse dye cells under bleaching excitation and present a synthesis procedure for pulse shaping.

Dynamics of Saturable Absorber Dyes

We consider a system of dye molecules which can be approximated by a randomly oriented array of absorbing dipoles. The action of linearly polarized light on such a system is to create anisotropies in both the ground- and excited-state populations. The degree of anistropy varies with time depending on the intensity of the exciting light pulse, the excited-state lifetime, and rotational Brownian motion [5], if the orientation of the molecules is not fixed. Earlier studies of such systems have either neglected molecular reorientation [6], considered relaxation from a prepared initial distribution without subsequent excitation [7], [8], or ignored the depletion of the ground-state population by the exciting light pulse [9]. If the system is to be considered as an ultrafast modulator, none of these effects can be ignored in general. The analysis presented here takes account of each of these effects, but is somewhat simplified in that the molecules are assumed to be spherically symmetric rotors with a single relaxation time, τ_{0r}, rather than asymmetric rotors which may have as many as six relaxation times [7], [8]. In addition we consider only thin dye cells so that attenuation of the gating pulse can be ignored.

We define $n_1(\theta, \phi; t)$ to be the population of ground-state molecules whose absorption dipoles are oriented in the direction (θ, ϕ) at time t and $n_2(\theta, \phi; t)$ to be the same quantity for the excited state. The rate equations controlling these populations are more conveniently written in terms of the sum and difference of n_1 and n_2, i.e.,

$$n(\theta, \phi; t) = n_1(\theta, \phi; t) - n_2(\theta, \phi; t)$$

and

$$N(\theta, \phi; t) = n_1(\theta, \phi; t) + n_2(\theta, \phi; t).$$

The exciting light pulse is taken to be linearly polarized and the direction of polarization defines the polar axis $\theta = 0$. The excitation rate for molecules in the ground state whose absorption dipoles lie at an angle θ to this direction is proportional to $3\sigma \cos^2 \theta$ with σ being the usual absorption cross section for random dipole orientation. Using these definitions, we obtain for the rate equations

$$\frac{dn}{dt} = -6\sigma \cos^2 \theta I_g(t)\, n(\theta, \phi; t) + \frac{1}{\tau}\,[N(\theta, \phi; t) - n(\theta, \phi; t)] + \frac{1}{6\tau_{0r} \sin \theta} \frac{\partial}{\partial \theta}\left[\sin \theta \frac{\partial n(\theta, \phi; t)}{\partial \theta}\right] \tag{14}$$

$$\frac{dN}{dt} = \frac{1}{6\tau_{0r} \sin \theta} \frac{\partial}{\partial \theta}\left[\sin \theta \frac{\partial N(\theta, \phi; t)}{\partial \theta}\right] \tag{15}$$

with $I_g(t)$ being the light intensity and τ the natural lifetime of the excited state. Assuming that at $t = 0$ all are in the ground state and isotropically distributed, i.e., $N(\theta, \phi; 0) = n(\theta, \phi; 0) = (N_0/4\pi)$, then solution of the second equation is trivial

$$N(\theta, \phi; t) = N(\theta, \phi; 0) = \frac{N_0}{4\pi}. \tag{16}$$

Noting that there is no ϕ dependence in the rate equations we drop it from the arguments and expand $n(\theta, t)$ in Legendre polynomials

$$n(\theta, t) = \frac{N_0}{4\pi} \sum_{k=0}^{\infty} a_k(t) P_k(\cos \theta). \tag{17}$$

Substituting in the rate equation and using the orthogonality of the P_k we get

$$\frac{da_k}{dt} = -3\sigma(2k+1) I_g(t) \sum_{k'=0}^{\infty} a_{k'}(t) \cdot \int_0^{\pi} P_{k'}(\cos \theta) P_k(\cos \theta) \cos^2 \theta \sin \theta \, d\theta + \frac{1}{\tau} \delta_{k,0} - \frac{a_k(t)}{\tau} - \frac{k(k+1)}{6\tau_{0r}} a_k(t). \tag{18}$$

The first term in (18) couples the coefficients of different orders, resulting in two hierarchies of equations, one for the odd orders and one for the even orders. The coefficients of the odd-order polynomials are identically zero because of the initial condition $n(\theta, 0) = (N_0/4\pi)$. The even-order equations are

$$\frac{da_0}{dt} = \frac{1}{\tau} - \frac{1}{\tau} a_0(t) - 2\sigma I_g(t)\left[a_0(t) + \frac{2}{5} a_2(t)\right] \tag{19a}$$

and

$$\frac{da_{2k}}{dt} = -\left(\frac{1}{\tau} + \frac{k(2k+1)}{3\tau_{0r}}\right) a_{2k}(t) - 6\sigma I_g(t) \cdot \left[\frac{4k^2 + 6k + 2}{16k^2 + 32k + 15} a_{2k+2}(t) + \frac{8k^2 + 4k - 1}{16k^2 + 8k - 3} a_{2k}(t) + \frac{2k(2k-1)}{16k^2 - 16k + 3} a_{2k-2}(t)\right] \tag{19b}$$

for $k \geq 1$.

These equations present some difficulty: they are coupled, the coefficients in the differential equations are not constant,

and the system is infinite. However, the first term in (19b) is $0(k^2)$ while all the other terms are 0(1). This indicates that for a given set of parameters the system can be truncated at an order M which makes

$$6\sigma(I_g)_{\max} \ll \frac{1}{\tau} + \frac{M(2M+1)}{3\tau_{0r}}. \tag{20}$$

The resulting finite system of equations can then be solved numerically.

Let us assume that the system of equations has been solved and we have an expression for the difference in the population of the ground and excited states

$$n(\theta) = \frac{N_0}{4\pi}\left[a_0 + a_2 P_2(\cos\theta) + a_4 P_4(\cos\theta) + \cdots\right]. \tag{21}$$

What then is the effect of this collection of dye molecules on the intensity of an independent light beam (we assume it to be too weak to perturb the system) propagating at any arbitrary direction and with arbitrary linear polarization? In traversing a distance Δx the intensity will be diminished by

$$\Delta I_s = -3\sigma\Delta x \int_0^{2\pi}\int_0^{\pi} n(\theta)\cos^2\gamma \sin\theta\, d\theta\, d\phi \tag{22}$$

where γ is the angle between the direction of polarization of the light and the direction defined by (θ, ϕ). If θ_0 is the angle between the direction of polarization and the polar axis of the distribution of molecular orientations, then

$$\cos\gamma = \cos\theta\cos\theta_0 + \sin\theta\sin\theta_0\cos\phi. \tag{23}$$

When (21) and (23) are substituted into (22), and use is made of the orthogonality properties of the Legendre polynomials, we find that

$$\frac{\Delta I_s}{\Delta x} = -3\sigma\frac{N_0}{4\pi}\left[\frac{4\pi}{3}a_0 + \frac{8\pi}{15}a_2 P_2(\cos\theta_0)\right]. \tag{24}$$

For simplicity consider $\theta_0 = 0$ and assume that $n(\theta)$ does not vary along the path of light. The transmittance of the dye as a function of time is then

$$T_s(t) = \frac{I_s(t)}{I_0} = \exp\left\{-N_0\sigma L_s\left[a_0(t) + \frac{2}{5}a_2(t)\right]\right\} \tag{25}$$

with L_s being the length of the path, and $a_0(t)$ and $a_2(t)$ being obtained by solving (19).

The problem is now to determine if it is possible to produce a reasonable approximation to the desired signal-pulse intensity using a system of dye cells bleached by a few pulses which can be readily produced. The parameters of the system which must be specified are: the absorption cross section σ; the dye concentration N_0; the length of the dye cells L_s; the natural lifetime of the excited state τ; and the rotational relaxation time τ_{0r}. For the recently developed nickel-complex dyes useful at 1.06 μm, and assuming a solvent such as chloroform, $\tau \approx 5$ ns and $\sigma \approx 10^{-16}$ cm^2 [10]-[13]. Much shorter τ values are obtained with the same dye in solvents such as iodoethane.

The rotational relaxation time can be estimated from the Debye-Stokes-Einstein hydrodynamic model [5]: $\tau_{0r} = (3\eta V/kT)$, where η is the shear viscosity of the solvent and V is the "volume" of the molecule. The volume to be used can be found by estimating the molecular radius a from the bond lengths in the complex and setting $V = (4\pi/3)a^3$. Alternatively, one might take the measured value of τ_{0r} for a molecule such as rhodamine 6G in the same solvent and scale this value according to the ratio of the molecular weights of the two dyes. Since viscosity is strongly temperature dependent, it is not unreasonable to consider τ_{0r} a parameter which can be controlled almost arbitrarily in any real system. As a limiting case τ_{0r} might be infinite if the dye is suspended in a transparent solid.

The dye concentration N_0 and cell length L_s are constrained by requirements on the unbleached transmittance T_s and the cell-geometry considerations as discussed previously. T_s for an individual cell is in turn determined by the total dynamic range required and the number of cells and gating pulses needed to obtain the desired light-intensity curve $I_s(t)$ with the desired accuracy.

Given an input signal $I_{s0}(t)$, the synthesis problem is to determine what gating-pulse intensity $I_g(t)$ must be inserted into (19) to produce the required $a_0(t)$ and $a_2(t)$ to be used in (25) to give the transmission $T(t)$ for a particular cell in the array. This problem cannot be solved in closed form. However, an approximate expression for $I_g(t)$ which may be used as a starting point for the trial and error solution of (19) and (25) can be obtained if it is assumed that $a_2 \ll a_0$ and that terms in $1/\tau_{0r}$ can be neglected in (19). This procedure yields

$$\frac{d}{dt}\left(a_0 + \frac{2}{5}a_2\right) \approx \frac{1}{\tau} - \frac{1}{\tau}\left(a_0 + \frac{2}{5}a_2\right) - \frac{18\sigma}{5}I_g\left(a_0 + \frac{2}{5}a_2\right)$$

or using (25)

$$I_g = \frac{5}{18\sigma \ln T}\left(\frac{\sigma N_0 L_s}{\tau} - \frac{1}{\tau}\ln T - \frac{1}{T}\frac{dT}{dt}\right). \tag{26}$$

The numerical solution of (19) truncated at some convenient order, say $k = 3$, can be effected for the trial gating pulse $I_g(t)$ obtained from (26). The values of $a_0(t)$ and $a_2(t)$ so obtained are used in (25) to determine the transmittance $T_1(t)$ of the first dye cell. This is compared with the desired $T(t)$ and $I_g(t)$ is modified in a way intended to improve the agreement. Once the optimum conditions for the first dye cell have been effected and the time interval over which a good fit is obtained is determined, the procedure is repeated for the next dye cell in the array. Equation (26) can again be used with $T_i(t)$ instead of $T(t)$ to obtain an approximate gating pulse for the ith cell in the array.

Nonlinear Optical Effects

If the intensities and optical path lengths are sufficiently large, nonlinear changes in refractive index of the dye solutions under exposure to the intense gating pulses (or possibly even the signal pulses) used in these systems can produce beam focusing and steering as well as spurious phase modulation

which might ultimately distort the spatial and temporal form of the transmitted signal. We have separated these effects into refractive-index changes induced in the solvent and index changes which accompany bleaching of the dye molecules. Since the signal-beam intensity can be independently adjusted to any reasonable value in the systems we are considering, it is principally the gating-pulse powers and power densities which are of concern here. At high optical electrical-field strengths E, the change in refractive index of the solvent is simply n_2E^2, where n_2 is the effective nonlinear coefficient for the particular liquid used and E^2 is the mean square value of the field. Hellwarth [14] has listed n_2 values for a large number of useful common solvents; the values vary from 1.1×10^{-19} $(m/V)^2$ for CS_2 to 7.5×10^{-21} $(m/V)^2$ for acetone.

The differential phase shift induced on a signal of free-space wavelength λ_0 in passing through a path length L_s in a nonlinear solvent of refractive index n_0 is

$$\Delta\phi = \frac{2\pi}{\lambda_0}\Delta n L_s = \frac{2\pi}{\lambda_0} n_2 E^2 L_s = \frac{2\pi n_2}{\lambda_0 n_0}\sqrt{\mu_0/\epsilon_0}\, I L_s \tag{27}$$

where $\sqrt{\mu_0/\epsilon_0} \approx 377\ \Omega$ and I is the gating intensity. A typical maximum value of I in a gated dye cell should be of the order of 10 MW/cm^2, and the total length for a system of three cells might be $L_s \approx 3$ cm. For a solvent such as chloroform, with $n_2 = 2.11 \times 10^{-20}$ $(m/V)^2$ and $n_0 = 1.4$ at 1.06 μm, we obtain $\Delta\phi = 0.101$ rad, or $\Delta\phi/L_s = 33.7$ mrad/cm of path. Because this $\Delta\phi$ is small compared to a radian, we see that beam steering of the signal due to the largest possible monotonic gradient in I across the aperture will be small compared to the diffraction spread of the signal beam. In addition, the result implies that temporal variations in I will not phase modulate the signal by an amount comparable to the Fourier transform spectral spread inherent in the signal-envelope variations, since $\Delta\phi/\Delta t < 1/\Delta t$, while $\Delta\omega\Delta t \approx 2\pi$ for a transform-limited pulse.

Another effect to be considered is self-focusing of the gating signal, which might result in the breakup of the gating beam into self-trapped filaments if the gating power and path length are large enough and if there are significant gradients in the gating-beam intensity across the cell. From the paraxial theory for self-trapping of Gaussian beams [15], the critical power P_c to produce self-focusing is

$$P_c = \frac{\lambda_0^2}{8\pi n_2\sqrt{\mu_0/\epsilon_0}}. \tag{28}$$

Evaluating this expression for chloroform at 1.06 μm we obtain a value of 5.6 kW for P_c. Since the dye cell geometry we are considering requires a gating beam area L_sL_g of roughly 0.1 cm^2, and an intensity as high as 10 MW/cm^2 might be needed, a total power as high as about 1 MW may be present, exceeding the previous critical power by a factor of nearly 200. To determine how serious the problem of gating-beam self-focusing will be in a thin dye cell ($L_g \approx 3 \times 10^{-4}$ m) we evaluated the paraxial wavefront curvature $1/R$ that would result when a Gaussian plane-wave beam of average intensity I and spot radius w_0 refracts through a thin cell of nonlinear liquid of thickness δ. If we then approximate, as a worst case, a geometry for which $w_0 \approx \delta \approx L_g$, and evaluate the induced parabolic phase shift, we obtain the curvature

$$\frac{1}{R} \approx \frac{4n_2}{n_0^2}\sqrt{\frac{\mu_0}{\epsilon_0}}\frac{I}{L_g}. \tag{29}$$

From this we find that an I of 10 MW/cm^2, $L_g = 3 \times 10^{-4}$ m, $n_2 = 2 \times 10^{-20}$ $(m/V)^2$, and $n_0^2 = 2$ give us $R \approx 200$ m. We therefore conclude that if reasonably uniform gating intensity is maintained over the cell area, significant gating-beam breakup can be avoided along the very short path L_g, since it will be much less than R. This should permit the use of gating-pulse powers much higher than the corresponding critical power indicated by (28).

Changes in refractive index due to dye bleaching are also present because of the Kronig–Kramers relation connecting the real and imaginary parts of the dielectric constant of the dye. If we write the total dielectric constant of the dye molecules in a loss-free solvent as

$$\epsilon = \epsilon_0(\epsilon_r' - i\epsilon_r'') \tag{30}$$

it is readily shown that for cases of practical interest here that $\epsilon_r''/\epsilon_r' \ll 1$. Under this approximation we obtain

$$\alpha \approx \frac{2\pi\epsilon_r''}{n\lambda} \tag{31}$$

for the exponential attenuation coefficient for intensity, where n is the solvent refractive index. We note that ϵ_r'' results from the dye molecules alone and not from the solvent. The loss ϵ_r'' of α is accompanied by a reactive susceptibility of the dye alone which we designate as $\epsilon_{rd}' - 1$. Since this is much smaller than the susceptibility of the solvent, we obtain an approximate refractive-index contribution from the dye

$$\Delta n \approx \frac{\epsilon_{rd}' - 1}{2n}. \tag{32}$$

Finally, we have the Kronig–Kramers relation [16]

$$\epsilon_{rd}'(\omega) - 1 = \frac{2}{\pi}\int_0^\infty \frac{x\epsilon_r''(x)\,dx}{x^2 - \omega^2}. \tag{33}$$

By substitution of (31) and (32) we obtain

$$\Delta n(\lambda) = \frac{\lambda}{2\pi^2}\int_{y=0}^\infty \frac{\alpha(y)\,dy}{1 - y^2} \tag{34}$$

in which the loss exponent $\alpha(y)$ is evaluated at a wavelength λ' such that $\lambda'/\lambda = y$. Equation (34) can be written in a more useful form by evaluating the signal phase shift $\Delta\phi(\lambda)$ corresponding to $\Delta n(\lambda)$

TABLE I
GATING PULSE INTENSITIES FOR THREE-CELL SYSTEMS

Cell Number	$I_i(t)$ (τ_{or} = 1/3 nsec)	$I_i(t)$ (τ_{or} = 2 nsec)	$I_i(t)$ (τ_{or} = ∞)
i = 1	$2.44 \times 10^{-4} \exp(1.08\,t)$	$1.74 \times 10^{-4} \exp(1.1\,t)$	$1.71 \times 10^{-4} \exp(1.08\,t)$
i = 2	$0.0253 \exp[4.43(t - 8)]$	$0.0241 \exp[4.37(t - 8)]$	$0.0268 \exp[4.2(t - 8)]$
i = 3	$13.1 \exp\left(\frac{t - 9.542}{.170}\right)^2$	$12.46 \exp\left[\left(\frac{t - 9.544}{.173}\right)^2\right]$	$12.15 \exp\left[\left(\frac{t - 9.548}{.178}\right)^2\right]$
$I_i(t)$ in MW/cm^2; t in nanoseconds			

$$\Delta\phi_s(\lambda) = \frac{2\pi\Delta n(\lambda) L_s}{\lambda}$$

$$= \frac{L_s}{\pi}\int_{y=0}^{\infty} \frac{\alpha(y)\,dy}{1 - y^2}. \tag{35}$$

Since at any wavelength $\alpha L_s = \ln(1/T_s)$, we actually require only the total cell transmission at some wavelength and the relative spectral distribution of α to evaluate (35) for a cell of any length.

We obtained numerical data for the α values of the nickel-complex dye from [11] over the spectral range 0.8–1.3 μm and evaluated (34) and (35) for the special case $T_s = 10^{-4}$ at 1.064 μm. This work yielded

$$\Delta n(1.064\ \mu\text{m}) = 8.57 \times 10^{-6} \quad (L_s = 1 \text{ cm is assumed})$$

and $\Delta\phi_s$ (1.064 μm) = 0.506 rad (any length cell). These numbers of course imply that a change of dye transmission from 10^{-4} to unity could result in a phase change of about $\frac{1}{2}$ rad at 1.064 μm. If this change occurs over a time Δt the corresponding frequency spread would be

$$\Delta\omega \approx |\Delta\phi/\Delta t|$$

and we see that for these numbers the signal should remain essentially transform limited. However, since $\Delta\phi_s$ is comparable to 1 rad, beam steering and nonlinear focusing can approach the diffraction limit for this effect if there are significant variations in gating-beam intensity over the cell. This is the justification for our constraints on signal-beam diameter and dye concentration discussed earlier.

APPLICATION TO LASER FUSION

A possible application of the pulse-shaping techniques we have been describing is to the creation of pulses with the proper time behavior for use in laser-fusion experiments. One intensity function that has been considered for this application is the expression [17]

$$I(t) = I_0(1 - t/T)^{-15/8} \tag{36}$$

where $I(t)$ is of interest over the time interval $0 \leqslant t \leqslant 9.4$ ns and T is 9.45 ns. This function increases faster than an exponential and does not seem to be approximated by any "naturally produced" laser-pulse envelope. For this reason some type of active shaping is necessary.

We have applied our shaping synthesis procedure to approximate the $I(t)$ of (36). We selected as a signal input a growing exponential of the form $\exp(t/4)$ with t in nanoseconds, and considered an array of three transversely gated dye cells filled with a dye of cross section 10^{-16} cm^2 and an excited-state lifetime of 5 ns. The three gating pulses were assumed to be either exponential or Gaussian because it was expected that these could be readily produced. The entire calculation was carried out for three different orientational relaxation times τ_{0r}: $\frac{1}{3}$ ns, 2 ns, and infinity. In each case τ_{0r} was assumed to be the same in all of the cells. The unbleached transmissions of the three cells were taken to be 0.1, 0.05, and 0.01. The best fit to (36) was found for a slower exponential gating pulse applied to the first cell, a faster exponential to the second, and a subnanosecond Gaussian pulse to the third.

Computer runs were made for the three values of the orientational relaxation time, with (19) truncated at various orders to ensure that negligible errors were being introduced by truncating the hierarchy. This was particularly important for infinite τ_{0r} because the criterion given in (20) does not hold. It was found that it was necessary to include up to the 6th-order Legendre coefficients for $\tau_{0r} = \frac{1}{3}$ and 2 ns and up to the 10th-order for infinite τ_{0r}.

Table I gives the gating pulses calculated for the three cells for these values of τ_{0r}. The transmittance of the array varies from 5×10^{-5} at the beginning to ≈ 0.084 at the end of the 9.4-ns interval. In each case, the calculated transmittance was made to fit $I(t)$ in (36) within 10 percent over a range of output-signal intensity covering about four orders of magnitude. The agreement between the 3-cell transmission and the ideal function, for τ_{0r} = 2 ns, is shown in Fig. 3. Clearly, this system is capable of generating a rather complicated pulse waveform with an accuracy that probably exceeds that of the input signal and gating pulses that could be realized in practice.

CONCLUSION

We have presented a preliminary analysis of the characteristics of saturable absorber systems in which a signal pulse is intensity modulated by one or more gating pulses. A synthesis procedure useful for numerical calculation of the necessary

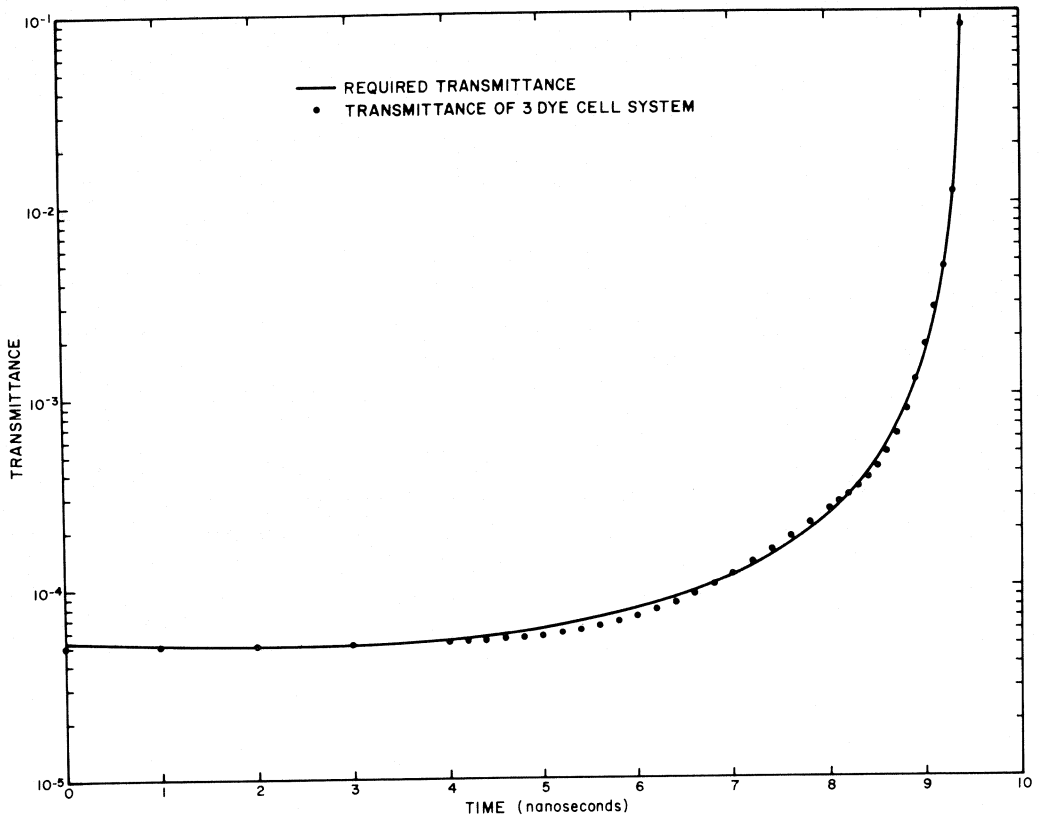

Fig. 3. Synthesized transmittance function for a 3-cell transversely gated system. Required transmittance corresponds to generation of a pulse for laser fusion.

gating intensities has been discussed. Limitations imposed by undesirable nonlinear properties of liquid dye systems have been estimated, and the performance of a 3-cell dye system of potential use in shaping master oscillator pulses for laser-fusion experiments has been calculated to illustrate the possibilities offered by this technique. We believe devices of this type may also prove useful in optical radar and in a variety of experiments in which short laser pulses are made to interact with physical systems.

References

[1] M. A. Duguay and J. W. Hansen, "An ultrafast light gate," *Appl. Phys. Lett.*, vol. 15, pp. 192–194, Sept. 1969.

[2] See, for example, P. W. Smith, "Mode-locking of lasers," *Proc. IEEE*, vol. 58, pp. 1342–1357, Sept. 1970.

[3] G. Mourou and B. Drouin, "Réalisation d'un nouvel obturateur ultra rapide. Application a la mesure directe de la durée des impulsions d'un laser rubis modes couplés," *Opt. Commun.*, vol. 4, pp. 48–49, Sept. 1971.

[4] H. Kogelnik and T. Li, "Laser beams and resonators," *Appl. Opt.*, vol. 5, pp. 1550–1567, Oct. 1966.

[5] P. Debye, *Polar Molecules*. London: Dover, 1929.

[6] G. Mourou and M. M. Denariez-Roberge, "Polarization of fluorescence and bleaching of dyes in a high-viscosity solvent," *IEEE J. Quantum Electron.*, vol. QE-9, pp. 787–790, Aug. 1973.

[7] T. J. Chuang and K. B. Eisenthal, "Theory of fluorescence depolarization by anisotropic rotational diffusion," *J. Chem. Phys.*, vol. 57, pp. 5094–5097, Dec. 1972; also "Studies of effects of hydrogen bonding on orientational relaxation using picosecond light pulses," *Chem. Phys. Lett.*, vol. 11, pp. 368–370, Oct. 1971.

[8] G. G. Belford, R. L. Belford, and G. Weber, "Dynamics of fluorescence polarization in macromolecules," *Proc. Nat. Acad. Sci. U.S.*, vol. 69, pp. 1392–1393, June 1972.

[9] D. W. Phillion, D. J. Kuizenga, and A. E. Siegman, "Rotational diffusion and triplet state processes in dye laser solutions," *J. Chem. Phys.*, vol. 61, pp. 3828–3839, Nov. 1974.

[10] K. H. Drexhage and U. T. Müller-Westerhoff, "New *Q*-switch compounds for infrared lasers," *IEEE J. Quantum Electron.* (Notes and Lines), vol. QE-8, p. 759, Sept. 1972.

[11] K. H. Drexhage and G. A. Reynolds, "New dye solutions for mode-locking infrared lasers," *Opt. Commun.*, vol. 10, pp. 18–20, Jan. 1974.

[12] D. Magde, B. A. Bushaw, and M. W. Windsor, "*Q*-switching and mode-locking the Nd^{3+}-glass laser with the nickel dithienes," *IEEE J. Quantum Electron.* (Notes and Lines), vol. QE-10, p. 394, Mar. 1974.

[13] D. Magde, B. A. Bushaw, and M. W. Windsor, "Picosecond flash photolysis and spectroscopy: Bis-4-dimethylaminodithiobenzil)-Ni(II), BDN," *Chem. Phys. Lett.*, vol. 28, pp. 263–269, Sept. 1974.

[14] R. W. Hellwarth, "Effect of molecular redistribution on the nonlinear refractive index of liquids," *Phys. Rev.*, vol. 152, pp. 156–165, Dec. 1966.

[15] W. G. Wagner, H. A. Haus, and J. H. Marburger, "Large-scale self-trapping of optical beams in the paraxial ray approximation," *Phys. Rev.*, vol. 175, pp. 256–266, Nov. 1968.

[16] See, for example, L. D. Landau, and E. M. Lifshitz, *Electrodynamics of Continuous Media*. Oxford: Pergamon, 1960, p. 260.

[17] J. Nuckolls *et al.*, Lawrence Livermore Lab. Rep. UCRL-50021-73-1, pp. 83–87, 1973.

Pulsewidth of the Mode-Locked, Internally Frequency-Doubled Laser

JOEL FALK, MEMBER, IEEE, AND C. BRECK HITZ, MEMBER, IEEE

Abstract—**The variation in the output pulse duration of a mode-locked internally frequency-doubled (MLFD) laser was experimentally studied. The dependence of pulse duration on second-harmonic conversion rate and modulation index in a Nd:YAG laser is reported. The laser was frequency doubled by a barium sodium niobate crystal located inside the laser cavity and was mode locked by a quartz acousto-optic loss modulator.**

The observed variation of pulse duration with modulation depth and second-harmonic conversion rate is in good agreement with theory. The techniques reported should allow continuous variation of 1.06-μm pulse duration from about 50 ps to greater than 900 ps to be obtained.

THE MODE-LOCKED, internally frequency-doubled (MLFD) Nd:YAG laser is an attractive source for optical communications systems. Its wavelength, 532 nm, falls near the optimum response of many optical detectors. The laser is capable of a high pulse-repetition-rate short-pulse output that is useful for pulse-code modulation formats. The large fundamental-wavelength optical fields available within the Nd:YAG optical cavity make efficient conversion to the second harmonic possible and permit generation of useful output powers at relatively high system efficiency.

The primary difficulty encountered in the use of the MLFD Nd:YAG laser as a high-data-rate communications transmitter occurs because of the difficulty of maintaining the short-pulse duration available from a fundamental-wavelength Nd:YAG laser during the second-harmonic generation (SHG) process. This difficulty arises because the intracavity SHG tends to increase the fundamental-wavelength laser pulse duration which in turn increases the pulse duration of the harmonic pulse. Losses caused by SHG are directly proportional to the instantaneous power present at the fundamental wavelength and hence are greatest at the peak of the pulse and smallest at its extremes. This greater loss inflicted on the center of the pulse increases the measured pulse duration [1].

Although these increased pulse durations are detrimental to optical communications the variable-pulse-duration output that is achievable by changing the rate of conversion of fundamental-wavelength power to second harmonic is useful for other applications. The operation of a subnanosecond, variable-pulse-duration optical source has uses in laser fusion and nonlinear optics experiments [2], [3]. Other authors have used internal frequency doubling in a similar manner to that reported here to control the durations of the submicrosecond pulses available from Q-switched lasers [3], [4].

Falk [5] has theoretically analyzed the AM mode-locked, internally doubled laser and has found that the laser's pulse duration is determined by a competition among three mechanisms. These are the following: 1) the amplitude modulation which imposes a loss on the pulse, 2) the gain of the active laser medium, and 3) the frequency-doubling process. The amplitude modulator shortens the pulse duration, and the frequency-doubling process increases it. Because the gain medium has a finite bandwidth, it increases the pulse duration and places a lower limit on the pulse duration achievable.

The purposes of the present paper are the following: 1) to present results that substantiate some of the theoretical predictions of the earlier paper, and 2) to demonstrate the operation of a mode-locked laser whose pulse duration is easily controllable.

Falk has shown that the effect of SHG on the pulsewidth of a MLFD laser is describable in terms of a parameter α_{SHG} defined as the average single-pass power loss due to the frequency-doubling process [5], that is

$$\alpha_{SHG} = \frac{1}{2}\frac{P_{SHG}}{P_c} \tag{1}$$

where P_{SHG} is the total (two-direction), time-average, second-harmonic power produced if P_c is the average fundamental power passing through the nonlinear crystal in each direction. He showed that if the effect of the gain medium's linewidth is negligible, and if the modulator drive frequency is chosen so that the pulse suffers minimum loss in the modulator, then pulse duration is given by

$$\tau = 2[\sqrt{2}\ln 10]^{1/2}\frac{1}{\omega_m}\left[\frac{\alpha_{SHG}}{\delta_L}\right]^{1/2}. \tag{2}$$

The strength of the amplitude modulation is measured by the value of δ_L. This modulation index is defined so that the time-average single-pass modulator power transmission is $(\exp - \delta_L)$. The other parameters in (2) are defined as follows: ω_m is the circular frequency of the amplitude modulation; and τ is the laser pulse duration measured between the 10-percent points of the second-harmonic output. Equation (2) applies when the pulse duration is determined only by the amplitude modulator and frequency doubler and is not influenced by the laser gain linewidth. This occurs for sufficiently large values of single-pass second-harmonic power loss so that [5]

$$\alpha_{SHG}^2 >> 8g\delta_L(\omega_m^2/\Delta\omega_a^2) \tag{3}$$

Manuscript received January 7, 1975. This work was supported in part by the Advanced Development Program 405B, Air Force Avionics Laboratory, Wright-Patterson Air Force Base, Ohio.

J. Falk is with GTE Sylvania Inc., Electro-Optics Organization, Mountain View, Calif. 94042.

C. B. Hitz was with GTE Sylvania Inc., Electro-Optics Organization, Mountain View, Calif. 94042. He is now with the General Photonics Corporation, Santa Clara, Calif. 95051.

where

$\Delta\omega_a$ the laser fluorescent linewidth;
g single-pass *saturated* electric-field laser gain.

The pulse duration predicted by (2) is radically different from that expected from a fundamental-wavelength mode-locked laser where [6]

$$\tau \sim (\omega_m)^{-1/2}(\delta_L)^{-1/4}. \quad (4)$$

The present paper reports the results of an experimental effort designed to verify the accuracy of the functional dependence given in (2). Fig. 1 is a diagram of the laser investigated. The active laser medium is Nd:YAG and frequency doubling is accomplished using a 5-mm cube of barium sodium niobate. The laser is limited by an aperture to fundamental transverse mode (TEM_{00}) operation. The optical resonator, which consists of three mirrors, is designed so that the second-harmonic power generated in each direction can be measured separately. Since mirror M_3 is partially reflecting at the harmonic wavelength, there are interference effects between the two beams which, in general, prevent them from containing equal power [7]. Mirror M_3 has a calibrated transmission at 1.06-μm of 0.5 percent so that the average fundamental circulating power can be determined from a measurement of the power output through M_3.

The laser was mode locked by a quartz loss modulator driven at 250 MHz, approximately one-half of the axial mode spacing of the 30-cm optical-length cavity. This modulator was a low-Q, acoustically resonant device whose modulation index varied with both the temperature of the quartz substrate and the RF drive frequency to the $LiNbO_3$ transducer [8]. Fig. 2 shows the measured variation in modulation index caused by a change in temperature of the quartz substrate. The variation of modulation index with change in modulator drive frequency follows a curve similar in shape to Fig. 2 and has a frequency spacing between acoustic resonances of ~250 kHz.

Thus, if the modulation index is to be maintained at a constant level during mode-locking experiments, accurate control of both the temperature of the quartz substrate and of the drive frequency to the modulator must be maintained. In the experiments reported here the quartz block was maintained at a constant temperature to within ±0.2°C by a thermistor-control-feedback circuit and the modulator drive frequency was manually held constant to within ±3 kHz. In addition, heating of the modulator substrate due to RF and acoustic losses in the modulator resulted in a frequency shift of the acoustic resonance of 110 kHz/W of RF input power to the modulator. This required that the average power input to the modulator be held nearly constant (±5 percent) to avoid changes in modulation index.

The approximate modulation depth δ_L at 1.06 μm was inferred from a measurement of the modulator's time-average diffraction efficiency at 632.8 nm [9]. The values of δ_L at 1.06 μm used in the experimental results shown in Fig. 3 were several times 10^{-3} so that the inequality given by (3) was well satisfied. Variation in the value of δ_L was accomplished by varying the duty cycle of the pulsed input drive to the modulator, while maintaining an average power input of 0.5 W. In a typical experimental run the modulator duty cycle was 0.18 and the modulator "on" time was 10 ms. Constant input power was necessary to avoid shifting the frequency of the acoustic resonance and thereby changing the diffraction ef-

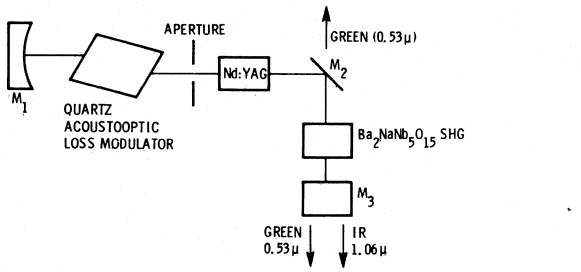

Fig. 1. Diagram of experimental laser. Mirror M_1 has a radius of curvature of 27 cm. Mirrors M_2 and M_3 are flat. Thermal focusing in the Nd:YAG rod makes the optical cavity stable.

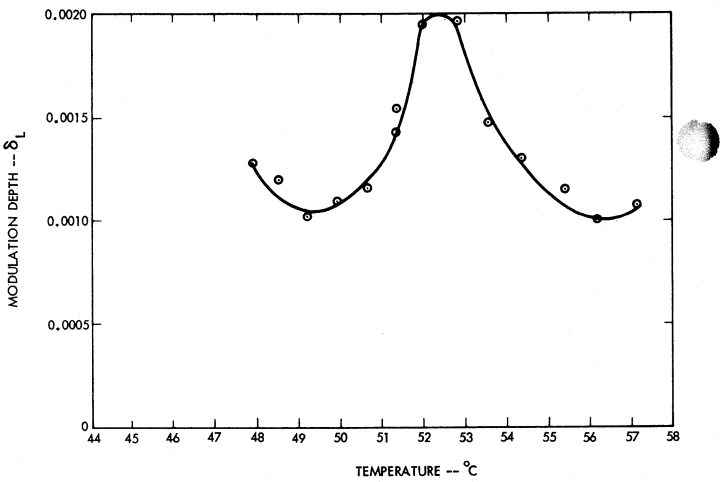

Fig. 2. Modulation depth of modulator as a function of the substrate temperature.

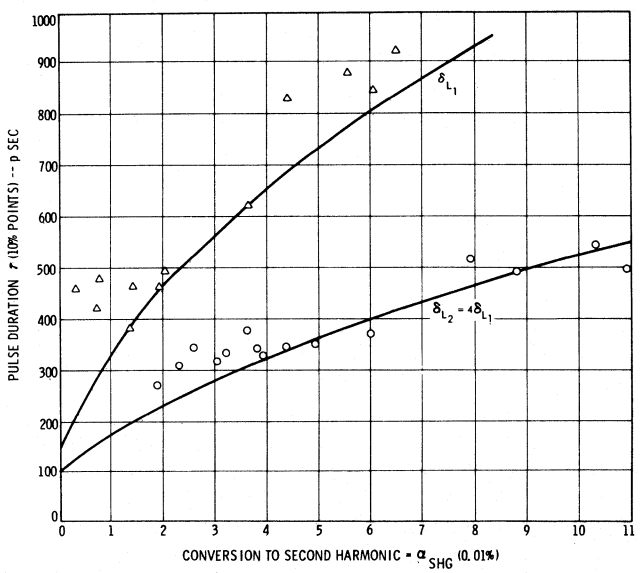

Fig. 3. Experimental data for two different modulation depths. The modulation depth (δ_L) used for the lower data points is four times as large as those used for the upper data points. The solid lines are drawn to show the theoretical $(\alpha_{SHG})^{1/2}$ dependence of pulse duration on second-harmonic conversion rate.

ficiency. An observed linear variation of modulation depth at 632.8 nm with drive power allowed a calibration of the relative modulation index in terms of the modulator duty cycle.

Operation of the modulator in a pulsed mode also permitted an indirect measurement of the laser's pulsewidth without requiring the use of fast photodiodes [10] or sophisticated beam overlap techniques [11]. Pulsewidth was inferred from the enhancement in green output power and decrease in infrared (IR) circulating power which were observed when the drive power was switched "on" to the loss modulator. Since the harmonic output from the laser is proportional to the square of the fundamental-wavelength circulating power and inversely proportional to the pulse duration [12] the enhancement E of the second-harmonic output power due to mode locking can be written

$$E = \frac{K}{\tau}\left(\frac{P_{c1}}{P_{c2}}\right)^2. \tag{5}$$

In (5) P_{c1} is the fundamental-wavelength circulating power with the modulator on and P_{c2} is its value with the modulator off. This method of determining pulse duration requires one direct measurement of pulse duration in order to determine the constant of proportionality K. A pulse duration of 1000 ps (10-percent power points) was measured directly along with the corresponding values of P_{c1}, P_{c2}, and E. The pulsewidths reported in this paper were then calculated from (5).

The value of the laser's saturated gain, determined from an independent measurement of total cavity losses, was 0.02.

Fig. 3 shows the principal result of this paper, the experimentally observed variation of laser pulse duration as a function of α_{SHG}. The efficiency of the SHG process (i.e., α_{SHG} itself) was controlled by selecting various temperatures for the nonlinear crystal in the vicinity of the phase-matching temperature [13]. The numerical values of α_{SHG} were determined from (1).

Several difficulties were encountered in performing the experiments described in the preceding.

1) At low-α_{SHG} severe relaxation oscillations were often observed when the laser was mode locked. This made precise evaluation of the low-α_{SHG} pulse duration difficult. When the loss modulation was removed, the relaxation oscillations usually disappeared. The appearance of relaxation oscillations in a loss-modulated laser has been previously noted and briefly discussed by Kinsel [14].

2) At modulation depths greater than about 0.05 the modulator introduced a noticeable CW loss. This loss is probably caused by the presence of an acoustic traveling wave in addition to the acoustic standing wave responsible for the laser mode locking. This traveling wave would result from any effect which makes the oppositely directed acoustic waves in the quartz substrate of unequal amplitude or not completely overlapping. Effects that might be responsible for the CW modulator loss thus include acoustic attenuation in quartz, acoustic diffraction, and the use of a substrate with nonparallel ends. The observed CW loss for the modulator used cannot be completely explained in terms of any of these three mechanisms.

In spite of the difficulties outlined in the preceding, the agreement between theory and experiment in Fig. 3 is good (especially at higher values of α_{SHG}), i.e., the pulse durations experimentally observed agree with the $(\alpha_{SHG})^{1/2}$ and the $(\delta_L)^{-1/2}$ dependence predicted by (2) [15].[1] Unfortunately, verification of the theory in the low-conversion-efficiency short-pulse region was hampered by the difficulties outlined previously.

Thus the technique of intracavity SHG has been shown to be useful in generating an optical pulse train with pulses whose duration can be changed in a predictable way. In a Nd:YAG laser pulse durations from 50 ps [6] to at least as long as the 900-ps durations reported here should be possible.

Acknowledgment

The authors wish to thank J. D. Barry, C. J. Kennedy, and R. S. Reynolds for their helpful comments on this paper.

References

[1] C. B. Hitz and L. M. Osterink, "Simultaneous intracavity frequency doubling and mode locking in a Nd:YAG laser," *Appl. Phys. Lett.*, vol. 18, pp. 378–380, May 1, 1971.

[2] J. Nuckolls, J. Emmett, and L. Wood, "Laser-induced thermonuclear fusion," *Phys. Today*, vol. 26, pp. 46–53, Aug. 1973.

[3] J. E. Murray and S. E. Harris, "Pulse lengthening via overcoupled internal second-harmonic generation," *J. Appl. Phys.*, vol. 41, pp. 609–613, Feb. 1970.

[4] J. F. Young, J. E. Murray, R. B. Miles, and S. E. Harris, "Q-switched laser with controllable pulse length," *Appl. Phys. Lett.*, vol. 18, pp. 129–130, Feb. 15, 1971.

[5] J. Falk, "A theory of the mode-locked, internally frequency-doubled laser," *IEEE J. Quantum Electron.*, vol. QE-11, pp. 21–31, Jan. 1975.

[6] D. J. Kuizenga and A. E. Siegman, "FM and AM mode locking of the homogeneous laser–Part I: Theory," *IEEE J. Quantum Electron.*, vol. QE-6, pp. 694–708, Nov. 1970.

[7] J. M Yarborough, J. Falk, and C. B. Hitz, "Enhancement of optical second harmonic generation by utilizing the dispersion of air," *Appl. Phys. Lett.*, vol. 18, p. 70, Feb. 1, 1971.

[8] L. E. Hargrove, R. L. Fork, and M. A. Pollack, "Locking of He-Ne laser modes induced by synchronous intracavity modulation," *Appl. Phys. Lett.*, vol. 5, pp. 4–5, July 1, 1964.

[9] D. A. Pinnow, "Guide lines for the selection of acoustooptic materials," *IEEE J. Quantum Electron.*, vol. QE-6, pp. 223–238, Apr. 1970.

[10] J.-P. Hazan, J. Haisma, G. Marie, and J. Nussli, "Real-time oscilloscope observation of an ultrafast photodiode response to mode-locked laser pulses," *IEEE J. Quantum Electron.* (Corresp.), vol. QE-6, pp. 744–745, Nov. 1970.

[11] D. J. Bradley and G. H. C. New, "Ultrashort pulse measurements," *Proc. IEEE*, vol. 62, pp. 313–345, Mar. 1974.

[12] A. A. Grutter, H. P. Weber, and R. Dandliker, "Imperfectly mode-locked laser emission and its effects on nonlinear optics," *Phys. Rev.*, vol. 185, p. 629, Sept. 10, 1969.

[13] F. R. Nash, G. D. Boyd, M. Sargent, III, and P. M. Brindenbaugh, "Effect of optical inhomogeneities on phase matching in nonlinear crystals," *J. Appl. Phys.*, vol. 41, pp. 2564–2575, May 1970.

[14] T. S. Kinsel, "A stabilized mode-locked Nd:YAlG laser using electronic feedback," *IEEE J. Quantum Electron. (Part I of Two Parts)*, vol. QE-9, pp. 3–8, Jan. 1973.

[15] a) C. J. Kennedy, "Mode domain analysis of the mode locked and frequency-doubled laser," *J. Quantum Electron.*, to be published. b) O. Bernecker, "Limitations for mode-locking enhancement of internal SHG in a laser," *IEEE J. Quantum Electron.*, vol. QE-9, pp. 897–900, Sept. 1973.

[1] It should be noted that other treatments of mode-locked internally frequency-doubled lasers implicitly predict the functional behavior described by (2).

Heating in a CW Nd-Pentaphosphate Laser

HEINZ P. WEBER, MEMBER, IEEE, AND B. C. TOFIELD

Abstract—**In a Kr-laser pumped CW Nd-pentaphosphate (NdP_5O_{14}) laser, with a threshold of 1.6 mW, an internal quantum efficiency of 63 percent is measured using a novel method. Bistable operation between oscillating and nonoscillating regimes is observed, resulting from the thermal lens created in the pumped zone. If stimulated emission is initially absent, this lensing effect is strong, making the resonator unstable and stimulated emission cannot build up. With stimulated emission initially present, heat development is reduced by the stimulated process itself and the resonator remains in the stable regime. For both situations, temperatures in the pumped area are determined using Raman spectroscopy. For the nonlasing situation, a fluorescence quenching rate of 68 percent, originating from Nd-Nd interactions is deduced, in close agreement with an earlier finding.**

A TEMPERATURE RISE in a Nd laser material increases the pump threshold owing to linewidth broadening and also because of the greater reabsorption of laser radiation resulting from the increased thermal population of the terminal laser state. Heat is developed by the optical pumping process itself, and the undesired rise in temperature can be kept at a minimum by adequate heatsinking and by pumping at the longest possible wavelength.

We report here measurements of the temperature rise due to pumping in a CW NdP_5O_{14} (NdPP) laser [1]. In a laser with 63-percent internal quantum efficiency heat development results in thermal lensing, leading to a reproducible bistable laser operation. Temperature in the pumped area is measured using Raman spectroscopy. The results provide quantitative agreement with previous measurements of the degree of fluorescence quenching caused by Nd-Nd interactions, based on lifetime investigations.

Crystals of NdP_5O_{14} were grown [2] in a H_2O-saturated N_2 atmosphere at a temperature of 550°C. Twin free crystals [3], with fluorescent lifetime [2] $\tau = 120$ μs and 1-mm length, were clamped on a brass block. A thin film of contact grease ensured good heat transfer. The laser resonator (see Fig. 1) consisted of two mirrors with reflectivities $R \approx 99.8$ percent at 1.05 μm and radii of curvature of 2.5 cm, arranged in close to concentric resonator configuration with the crystal at the center of the cavity. A Kr^+-ion-laser pump beam was focused to a spot of approximately 20-μm diameter in the crystal, and CW laser action was achieved using any of the three IR pump wavelengths 676.4 nm, 752.5 nm, and 799.3 nm. The threshold was similar with the resonator axis along either the [100] or [011] crystal directions, and the lowest threshold was 1.6-mW absorbed pump power at 752.5 nm, which is close to the value achieved elsewhere [4]. Above threshold, output increased linearly with input up to the maximum available pump power of 80 mW. Significant internal scattering of laser light could be easily detected with an infrared-sensitive phosphor card.

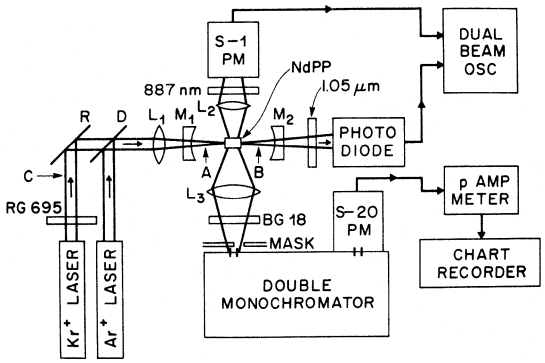

Fig. 1. Experimental arrangement. The Kr^+-ion-laser beam, redirected by reflector R, and focused with lens L_1 onto the NdPP crystal, longitudinally pumps the Nd laser. Mirrors M_1, M_2 with radii of curvature 2.5 cm and reflectivities of 99.8 percent at 1.05 μm form a close to concentric resonator. The laser output passes through a 1.05-μm transmitting filter and is detected by a Si photodiode. The spontaneous fluorescence is collected by lens L_2, passes through an 887-nm transmitting filter ($\Delta\lambda = 10$ nm), and is detected with a dry-ice-cooled S-1 photomultiplier and recorded on the lower traces of the oscilloscope. The Ar^+-ion-laser beam at 488.0 nm is made collinear with the pump beam by the dichroic beamsplitter D and generates the Raman spectrum. The IR transmitting filter RG 695 eliminates blue fluorescence from the Kr discharge. Raman-scattered light is collected by lens L_3 and imaged onto the entrance slit of the double monochromator. The mask shadows light from the second half of the NdPP crystal. Filter BG 18 blocks IR light from entering the monochromator. The gratings, blazed at 1 μm, are used in second order. Gas from boiling liquid N_2 cools the S-20 photomultiplier at the exit slit of the spectrometer. The output signal is processed by a p-Amp meter and recorded with a chart recorder.

The measured external quantum efficiency of the laser of 5 percent is of marginal value because mirror transmission was not optimized for optimum efficiency. A meaningful and precise value for the internal efficiency of the laser, however, is gained by using a novel method employing monitoring of the intensity of the fluorescence light into the Nd ground manifold. In Fig. 2 the complete optical cycle is shown. The pump light of 752.5 nm pumps the $^4S_{3/2}$ and $^4F_{7/2}$ manifolds that decay nonradiatively (with thermalization energy D_1) into the $^4F_{3/2}$ manifold. This thermalization efficiency is approximately unity, as will be verified later on. The $^4F_{3/2}$ manifold has three decay routes: a) fluorescence quenching Q; b) laser emission L into the $^4I_{11/2}$ manifold; and c) spontaneous fluorescence F into any of the ^4I manifolds. We denote the branching ratio for these decays as q, l, and f. The distribution of fluorescence F into the four manifolds are for Nd systems such that the average photon energy is almost equivalent to that of the F_2 decay. For the energy considerations in the later part of this paper we will simplify our analysis by assuming that all the fluorescence F is of energy F_2.

The decay of the $^4F_{3/2}$ levels for the nonlasing (N) and lasing

Manuscript received January 21, 1975.

H. P. Weber is with Bell Laboratories, Holmdel, N.J. 07733.

B. C. Tofield was with Bell Laboratories, Holmdel, N.J. 07733. He is now with the Materials Physics Division, Atomic Energy Research Establishment, Harwell Didcot, Oxon., England.

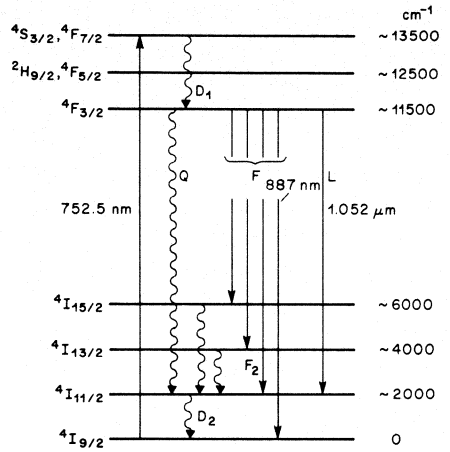

Fig. 2. Energy-level diagram of NdPP. Level assignments and energies are given at the left- and right-hand sides, respectively. Straight vertical lines represent radiative and wavy vertical lines nonradiative transitions. The 752.5-nm pump light populates the $^4S_{3/2}$ and $^4F_{7/2}$ manifolds which decay nonradiatively with thermalization energy D_1 into the $^4F_{3/2}$ manifold with efficiency ≈ 1. The three decay routes from $^4F_{3/2}$ are a) fluorescence quenching Q, b) laser emission L, and c) spontaneous fluorescence F, into any of the ^4I manifolds. The average energy of a fluorescence photon is F_2. The thermalization energy from $^4I_{11/2}$-$^4I_{9/2}$ is denoted by D_2.

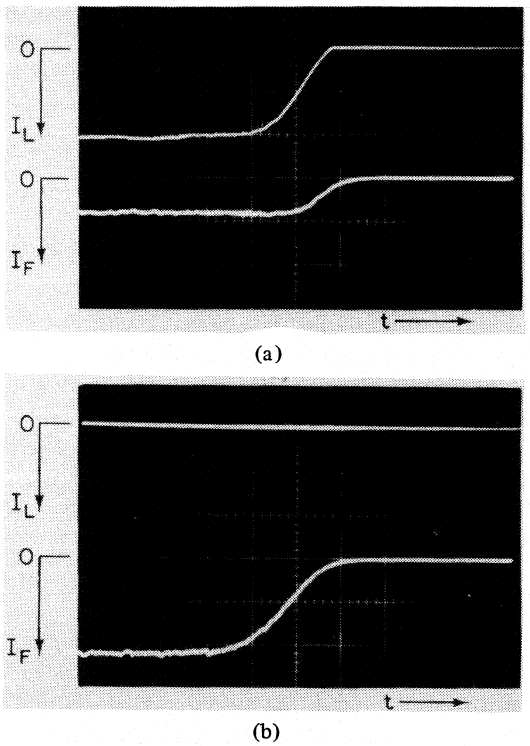

Fig. 3. Light intensities of NdPP laser. Laser output intensity I_L recorded by the photodiode (upper trace) and $^4F_{3/2}$-$^4I_{9/2}$ fluorescence light intensity I_F at 887 nm monitored by an S-1 photomultiplier (lower trace). The time scale is 0.5 ms/cm. For the second half of the time periods the pump beam is blocked. (a) For ideal mirror alignment. (b) Same conditions as for (a) but with mirror M_2 (Fig. 1) slightly misaligned, to curtain laser action.

(L) situation is described by (1a) and (1b), respectively

$$1 = q_N + f_N \tag{1a}$$

$$1 = l + q_L + f_L = l + p(q_N + f_N) \tag{1b}$$

where p is the directly measurable reduction of fluorescence intensity if laser action takes place. The internal quantum efficiency for stimulated emission from the $^4F_{3/2}$ manifold is given by $r = (1 - p)$. (Note that the measurement of r is independent of the degree of quenching q.) By monitoring the reduction in fluorescence intensity into any of the ^4I manifolds after onset of laser action, p may be measured. It is experimentally convenient to measure the fluorescence intensity into the ground $^4I_{9/2}$ manifold at 887 nm. In Fig. 3 the intensity of the laser output at 1.052 μm measured with a Si photodiode is shown together with the fluorescence monitored at 887 nm with a dry-ice-cooled S-1 photomultiplier. Fig. 3(a) shows the intensities for ideally aligned mirrors, and Fig. 3(b) shows them for a slightly misaligned mirror M_2. For the second half of the time period the pump beam was blocked. A reduction factor $p = 0.37$ for the fluorescence was observed corresponding to an internal quantum efficiency for laser action of $r = 63 \pm 2$ percent.

Upon pumping at 752.5 nm (see Fig. 2) the thermalization decay paths D_1 and D_2 convert 30 percent of the pump energy into heat. The nonradiative quenching process Q produces additional heat. Due to the temperature increase in the absorbing focal spot a thermal lens is formed, converting the nearly concentric resonator into an unstable resonator. A stable resonator can be obtained again by slightly shortening the mirror spacing. Observable modifications of the resonator characteristics will be used in the following to directly demonstrate that a sizable fraction of the population of the $^4F_{3/2}$ manifold decays via the quenching process Q.

When the NdPP laser was oscillating, pumped with 80 mW of pump power, and a mirror separation close to critical, we blocked feedback at position B with a cardboard. After removal of the cardboard, oscillation did not build up again. After inserting and removing the cardboard at position A laser oscillation always restarted. A reproducible, truly bistable operation was observed. The insertion time found necessary at A or B to switch from one mode to the other was found to be $\sim\frac{1}{10}$ s. By adjusting mirror M_2 we were also able to switch between two finite, well-defined intensity levels. This behavior results from the generation of a thermal lens. Different amounts of heat are developed for the two situations. By blocking feedback at B (Fig. 1) the crystal was allowed to heat in a nonlasing condition. The thermal lens formed converted the previously concentric resonator into an unstable resonator and lasing did not recommence after removal of the screen. By blocking at A (Fig. 1), on the other hand, heating could not occur and laser oscillation always recommenced after the screen was removed. The difference in contribution of heat generation for the two situations is $r \cdot q_N \cdot F_2$ per excited ion. The stimulated emission effectively carries heat out of the laser and thus has a cooling effect. Obviously, this effect can only be strong if q_N is large and the internal efficiency $r = (1 - p)$ is high. It is practically impossible, however, to obtain precise results about the temperature in the lasing area from a difference of resonator adjustments.

A quantitative measure of the temperature rises under lasing and nonlasing conditions, and hence of the quenching efficiency q may be obtained by monitoring the pumped area of the crystal by Raman spectroscopy. The intensity of an anti-Stokes Raman line with energy shift E is directly proportional

to the occupation number $\bar{n}$ of the phonon state with energy E, and

$$\bar{n} = 1/[\exp(E/kT) - 1] \tag{2}$$

is strongly dependent on temperature T, especially for $E >> kT$. Due to an overlap with a weak Nd fluorescence, the Kr^+-ion-laser pump beam itself could not be used as the Raman source. Instead we used the 488.0-nm line of an Ar^+-ion laser, and with the dichroic beamsplitter D the Ar laser beam was made collinear with the Kr-laser pump beam, in order to occupy the same focal spot. The light-scattering area was imaged onto the entrance slit of a double monochromator, with a mask used to block all but the image of the more strongly pumped front half of the NdPP crystal. The grating, blazed at 1 μm, was used in second order and a Schott BG 18 filter blocked any IR light from the spectrometer. An S-20 photomultiplier, cooled with gas from boiling liquid N_2, served as detector. Spectra were recorded covering the whole Stokes and anti-Stokes range of the 488.0-nm Ar line. The Raman spectra look all very similar to the spectrum published elsewhere [2], and no superimposed structure due to excited-state absorption seemed to be present when Kr and Ar laser beams were simultaneously present in the crystal. The highest energy anti-Stokes line observable corresponds to an energy $E = 672$ cm^{-1}, and the wavelength selector of the double monochromator was locked onto this line (at 472.5 nm). We measured the scattered intensity when the Kr^+-laser beam pumped the NdPP crystal and when it was blocked (at position C in Fig. 1). With an aligned resonator (lasing condition) we measured a ratio $V_L = 1.14:1$, and for a misaligned resonator (nonlasing condition) we measured a ratio $V_N = 1.23:1$.

The ratios correspond to temperature increases of $\Delta T_L = (11 \pm 1)^\circ$C and $\Delta T_N = (18 \pm 1)^\circ$C above the temperature when the nonabsorbed-Ar-laser beam alone transversed the crystal. These temperatures are averages over the spot size, which was not necessarily perfectly overlapping with that of the pump beam, so that the absolute temperature increases may have been higher. From their ratio significant conclusions with respect to the amount of quenching can be drawn. The observed temperature increases ΔT_L and ΔT_N are directly proportional to the amounts of heat H_L and H_N, generated per absorbed pump photon, in the lasing and nonlasing condition, respectively. From Fig. 2 we obtain, for the two situations, the relations

$$H_N = D_1 + D_2 + q_N \cdot F_2 \tag{3a}$$

$$H_L = D_1 + D_2 + p \cdot q_N \cdot F_2. \tag{3b}$$

With $H_N:H_L = 18:11$, $p = 0.37$, and $D_1 + D_2 = 4000$ cm^{-1}, we find $q_N = 0.68 \pm 0.1$. This quenching rate q_N of the $^4F_{3/2}$ level can also be obtained by comparing lifetimes for different x in $Nd_xLa_{1-x}P_5O_{14}$ [2], [5], [6]. With $\tau(x = 1) = 120$ μs and $\tau(x = 0.01) = 320$ μs, a quenching ratio

$$q_N = 1 - \tau(x = 1)/\tau(x = 0.01) \tag{4}$$

of 0.625 is obtained, in close agreement with the value previously found. The agreement supports the result that the emission cross section is independent of Nd concentration [6]. The suggestion that the lifetime shortening for higher Nd concentration is the result of a larger emission cross section at a high concentration [4] cannot explain our observed temperature effects. The agreement between the two values of q_N also supports the result [5] that for dilute crystals the fluorescence efficiency is unity and the efficiency for multiphonon decay of the $^4F_{3/2}$ levels is negligibly small. A significant multiphonon decay would result in a far smaller value of q_N determined by the lifetime measurement, and the same would hold if the efficiency of the nonradiative decay D_1 (Fig. 2) were far smaller than unity.

In conclusion, we have found, in a CW NdPP laser with a 1.6-mW threshold, an internal quantum efficiency of 63 percent. Due to heat developed by the optical pumping, thermal lensing in the laser crystal was found which led, under critical adjustment, to a bistable mode of laser operation. By measuring the intensities of a Raman anti-Stokes line, the temperature of the laser medium was measured for an aligned and misaligned resonator. The "cooling" effect of stimulated emission was clearly observed. Qualitative analysis shows that under the nonlasing condition the fluorescence is quenched by $\frac{2}{3}$ as a result of nearest neighbor Nd–Nd interactions. Although the temperature increase due to CW pumping is in the range of 20°C in our experimental arrangement, this does not severely modify the laser properties, but does demonstrate the need for adequate heatsinking. Use of $Nd_{0.5}La_{0.5}P_5O_{14}$ instead of NdP_5O_{14} would reduce the heat generated per unit volume by $\frac{2}{3}$, due to the reduced Nd^{3+} concentration and the 50-percent reduction in q, which will also result in an expected lower threshold [6]. The suggested [7] advantageous rapid electronic-energy migration in NdP_5O_{14} was recently shown to be far too small to influence the laser properties [8]. These results, therefore, render the less concentrated material more attractive for device applications than undiluted NdP_5O_{14}.

Acknowledgment

The authors wish to thank J. M. Worlock and P. F. Liao for helpful discussions and suggestions.

References

[1] For a review and a list of references, see, B. C. Tofield, H. P. Weber, T. C. Damen, and P. F. Liao, "Optical properties of Nd pentaphosphate–A high Nd-concentration laser material," *J. Solid State Chem.*, vol. 12, pp. 207–212, Jan. 1975.

[2] B. C. Tofield, H. P. Weber, T. C. Damen, and G. A. Pasteur, "On the growth of Nd pentaphosphate crystals for laser action," *Mater. Res. Bull.*, vol. 9, pp. 435–448, Apr. 1974.

[3] H. P. Weber, B. C. Tofield, and P. F. Liao, "Ferroelastic behavior and the monoclinic to orthorhombic phase transition in MP_5O_{14}(M = La-Tb)," *Phys. Rev. B*, vol. 11, pp. 1152–1159, Feb. 1975.

[4] G. Huber, J. P. Jeser, W. W. Krühler, and H. G. Danielmeyer, "Laser action in pentaphosphate crystals," *IEEE J. Quantum Electron. (1974 International Quantum Electronics Conference: Digest of Technical Papers)*, vol. QE-10, p. 766, Sept. 1974.

[5] H. P. Weber, P. F. Liao, and B. C. Tofield, "Emission cross section and fluorescence efficiency of Nd-pentaphosphate," *J. Quantum Electron.*, vol. QE-10, pp. 563–567, July 1974.

[6] S. Singh, D. C. Miller, J. R. Potopowics, and L. K. Shick, "Emission cross section and fluorescence quenching of Nd^{3+} in La pentaphosphate," *J. Appl. Phys.*, vol. 46, pp. 1191–1196, Mar. 1975.

[7] M. Blätte, H. G. Danielmeyer, and R. Ulrich, "Energy transfer and the complete level system of NdUP," *Appl. Phys.*, vol. 1, pp. 275–278, 1973.

[8] P. F. Liao, H. P. Weber, and B. C. Tofield, "Electronic excitation migration in Nd pentaphosphate," *Solid State Commun.*, vol. 16, pp. 881–883, Apr. 1975.

Correspondence

Amplification of the 1.32-μm Line in Nd:YAG

T. R. LOREE, L. M. SHERMAN, AND J. M. THORNE

Abstract—**Single-pass amplifier gains at 1.32 μm have been measured in an 80-mm Nd:YAG rod, achieving a saturated gain of 3.1. Small-signal gain comparisons imply a stimulated-emission cross-section ratio (1.32/1.06 μm) of 0.19.**

In addition to the normal 1.06-μm wavelength, the Nd:YAG laser can produce a number of other lines ranging from 0.95 to 1.84 μm [1]–[4]. The 1.32-μm line has application in optical parametric oscillators (OPO's). When doubled to 0.66 μm, this line is a pumping wavelength for a 90°-cut temperature-tuned $LiNbO_3$ OPO. Pumping with 0.66 μm allows tuning of the OPO crystal through the degeneracy wavelength within the temperature range in which the $LiNbO_3$ is chemically stable [5].

The desire to scale up such an OPO system led us to investigate the problem of amplifying the 1.32-μm line in Nd:YAG. The amplifier units used 9.5-mm-diam 80-mm-long Nd:YAG rods with uncoated 12°-cut ends. About 70 mm of the rod was pumped by two linear flashlamps in a double elliptical cavity filled with circulating water.

As these amplifiers produce a maximum energy gain of about 30 for 1.06-μm radiation, it was expected that a saturated gain of 2–4 could be obtained at 1.32 μm. These rough predictions were made on the assumption that the ratio of the cross sections for these two transitions would be the same as the ratio of the natural logarithms of the saturated gains. Cross-section values were obtained from two sources.

1) Deserno *et al.* [3] measured the single-pass gains for a number of lines in an oscillator. Gain slopes taken from their data imply the ratio

$$\sigma_{1.32}/\sigma_{1.06} = 0.4$$

giving a predicted saturated gain of 3.9 for 1.32 μm.

2) Stimulated-emission cross sections for Nd:YAG have been most recently measured by Singh *et al.* [6]. Assuming that the "1.06" line is a combination of $R_2 \rightarrow Y_3$ and $R_1 \rightarrow Y_2$ and that the "1.32" line is both $R_2 \rightarrow X_1$ and $R_2 \rightarrow X_2$, one obtains a cross-section ratio of 0.2. This value gives a saturated-gain prediction of 2.0 for the 1.32-μm radiation.

The experimental gain measurements were made in a straightforward manner by ratioing the signals from reference and signal calorimeters. The original beam of about 1 mJ was generated by a tunable Chromatrix 1000 Nd:YAG oscillator, split to provide the reference signal, amplified, and detected by a calorimeter. The measured single-pass gains for both 1.06 and 1.32 μm are plotted in Fig. 1 as a function of total flashlamp pumping energy. The maximum gain at 1.06 μm was not quite 30 at saturation, and the saturated gain for the 1.32-μm line was about 3.

A number of experimental strategies were employed to lend credence to this result. The input beam was apertured, spatially filtered, and carefully matched to the rod diameter. The timing of the input pulse relative to the firing of the amplifier flashlamps was varied. The temperature of the amplifier rod was varied throughout the range 5–30°C. No combination of variables resulted in appreciably different results.

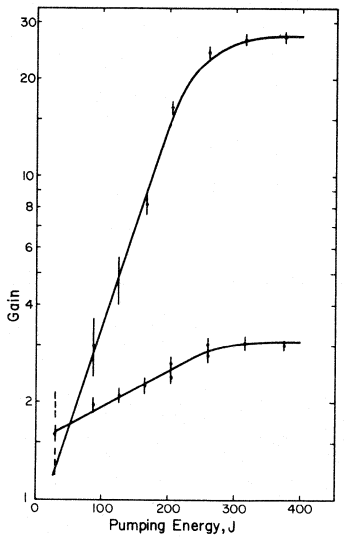

Fig. 1. Experimental single-pass gains for millijoule-level pulses in an 80-mm Nd:YAG rod for 1.06 and 1.32-μm wavelengths.

The low-energy portions of the exponential gain curves may be reasonably fit with straight lines, as shown in Fig. 1. The failure of either curve to intersect the origin is indicative of the imperfections in the rod (residual losses) and/or experimental procedures. The most valid method of estimating the 1.32/1.06 cross-section ratio from these data is to compare the slopes of the straight-line sections of the experimental curves. The single-pass unsaturated gain is given by

$$G_i = \exp(N\sigma_i L)$$

where N is the population inversion density, σ_i is the stimulated-emission cross section for wavelength i, and L is the pumped length of the rod. As both transitions of interest share a common upper $^4F_{3/2}$ state, one may approximate that N is proportional to the flashlamp energy and the same for both transitions at a given lamp input energy. It follows that a ratio of the straight-line slopes will also be the ratio of the cross sections. In this way we obtain

$$\sigma_{1.32}/\sigma_{1.06} = 0.19 \pm 0.05$$

where the limits are determined by the extremes of straight-line fits to the data. This result is in excellent agreement with the ratio obtained from the data of Singh *et al.*

Manuscript received December 19, 1974; revised March 17, 1975. This work was performed under the auspices of the U.S. Atomic Energy Commission.

T. R. Loree and L. M. Sherman are with the Los Alamos Scientific Laboratory, University of California, Los Alamos, N. Mex. 87544.

J. M. Thorne is with the Department of Chemistry, Brigham Young University, Provo, Utah 84601.

References

[1] R. W. Wallace and S. E. Harris, "Oscillation and doubling of the 0.946 μ line in Nd^{3+}:YAG," *Appl. Phys. Lett.*, vol. 15, pp. 111–112, Aug. 15, 1969.

[2] R. G. Smith, "New room temperature CW laser transitions in YAlG:Nd," *IEEE J. Quantum Electron.* (Corresp.), vol. QE-4, pp. 505–506, Aug. 1968.

[3] U. Deserno, D. Röss, and G. Zeidler, "Quasicontinuous giant pulse emission of $^4F_{3/2} \rightarrow {}^4I_{13/2}$ transitions at 1.32 μm in YAG:Nd^{3+}," *Phys. Lett.*, vol. 28A, pp. 422–423, Dec. 30, 1968.

[4] R. W. Wallace, "Oscillation of the 1.833-μ line in Nd^{3+}:YAG," *IEEE J. Quantum Electron.* (Corresp.), vol. QE-7, pp. 203–204, May 1971.

[5] R. L. Byer, "Optical parametric oscillators," in *Treatise in Quan-*

tum Electronics, H. Rabin and C. L. Tang, Ed. New York: Academic, to be published.
[6] S. Singh, R. G. Smith, and L. G. Van Uitert, "Stimulated-emission cross section and fluorescent quantum efficiency of Nd^{3+} in yttrium aluminum garnet at room temperature," *Phys. Rev. B.*, vol. 10, pp. 2566–2572, Sept. 15, 1974.

Pumping of Red Continuous-Wave Laser Dyes

F. A. BEISSER AND D. J. EILENBERGER

Abstract—**Two methods of operating red CW dye lasers are examined. A single laser with a mixture of rhodamine 6G and cresyl violet perchlorate (CVP) is compared with a tandem system in which a rhodamine 6G laser is used to pump a CVP laser. At high pumping levels the tandem system is shown to be superior.**

The wavelength range of CW dye lasers has recently been extended to cover the spectrum from 4150 to 7900 Å [1]. Over most of this range, excitation of the dyes is achieved by optical pumping with one or more lines from a CW argon laser. When using dyes in the far-red portion of the spectrum the absorption of available wavelengths is small and excitation becomes inefficient. In this correspondence, we compare two possible ways of surmounting this problem. The first is to utilize a mixture of dyes and use energy transfer between the dye molecules to excite a laser dye. In particular, we have investigated the cresyl violet laser using a mixture of rhodamine 6G with cresyl violet to provide excitation energy transfer [1], [2]. Secondly, we have constructed a separate rhodamine 6G laser as an optical pump for a cresyl violet laser.

The optical configuration used in the experiments to be discussed here was a folded three-mirror cavity described previously [3]. In the first set of experiments dye mixtures were investigated. Rhodamine 6G was added to the ethylene glycol solvent until approximately 90 percent of the 5145-Å pump power was absorbed. Cresyl violet perchlorate (CVP) was then added to the solution and measurements of power and gain were made for different concentrations of CVP. The gain was measured by observing threshold with a calibrated variable-loss device internal to the laser resonator. The measured gain is therefore gain in excess of dye and resonator losses. All three mirrors were high reflectivity.

The results of the gain versus input pump power for the optimum CVP concentration are plotted in Fig. 1. Note that the gain increases linearly up to about 3-W input power at which point it begins to roll off. Above 3 W thermal effects begin to induce loss, which is apparently responsible for the curve rolling off.

In order to compare the efficiency of energy transfer with direct excitation, the rhodamine 6G laser (without CVP) was used for direct optical pumping of a CVP laser with the same cavity configuration. The concentration of CVP was adjusted to absorb 85 percent of the 5825-Å pumping power from the rhodamine 6G laser. Again the measurements of the CVP laser were taken as a function of 5145-Å pump power into the rhodamine 6G laser. These results are also plotted in Fig. 1. Note that the gain increased linearly with 5145-Å power over the range of measurement. A maximum output power of 585 mW at $\lambda = 6900$ Å was achieved. With the tandem pumping system one would expect reduced thermal effects since the heating is distributed into two streams.

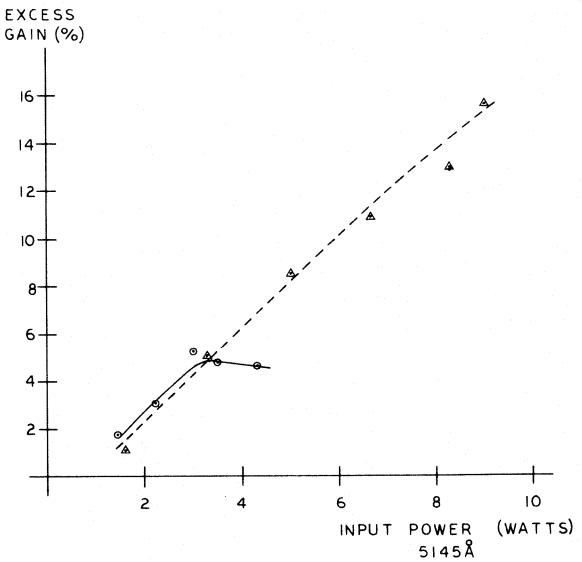

Fig. 1. Excess gain for CVP laser versus argon laser input power. Circles indicate data for the dye mixture. Triangles are data for tandem system.

It was noted that a decrease in overall gain and output power occurred over a period of several days due to a deterioration of the CVP. The CVP was observed to recover somewhat by bubbling nitrogen through the solution for a period of about 16 h. The decay of the CVP occurred in both systems. Operating in a nitrogen atmosphere may help to stabilize the CVP laser output in either system.

Nile blue perchlorate (NBP) was also investigated. A peak output of 200 mW at 7200 Å was observed using a rhodamine 6G pump with 9 W of 5145-Å pumping power. The output of the NBP was also observed to deteriorate over a period of days. Nitrogen had no apparent effect on this system.

In conclusion we have compared a dye mixture system and a tandem pumping arrangement for the CVP laser. At pumping powers below 3 W both the mixture and the tandem scheme produced nearly equal results. Since the rhodamine 6G laser operated with an efficiency of about 30 percent one deduces an approximately equal efficiency for energy transfer in the mixed solution. The basic limitation of the mixture scheme appears to be large thermal effects from the combined Stokes loss of both dyes.

ACKNOWLEDGMENT

The authors wish to thank A. Bergman, C. V. Shank, and E. P. Ippen for helpful discussions and advice.

REFERENCES

[1] J. M. Yarborough, "CW dye laser emission spanning the visible spectrum," *Appl. Phys. Lett.*, vol. 24, pp. 629–630, 1974.
[2] C. Lin and A. Dienes, "Study of excitation transfer in laser dye mixtures by direct measurement of fluorescence lifetime," *J. Appl. Phys.*, vol. 44, pp. 5050–5052, 1973.
[3] A. Dienes, E. P. Ippen, and C. V. Shank, "High-efficiency tunable CW dye laser," *J. Quantum Electron.* (Corresp.), vol. QE-8, p. 388, Mar. 1972.

Manuscript received January 3, 1975; revised March 13, 1975.
The authors are with Bell Laboratories, Holmdel, N. J. 07733.

3547-Å Pumped High-Power Dye Laser in the Blue and Violet

K. KATO

Abstract—**Efficient generation of high-power dye-laser radiation in the blue and violet has been achieved by pumping longitudinally with the third harmonic of a Nd:YAG laser. A peak power as high as 2.4 MW at 4890 Å and peak powers in excess of 1.3 MW from 4300 to 5100 Å have been obtained.**

With the development of a high-power Nd:YAG laser system, it has been possible to obtain a high-repetition-rate high-power visible dye laser using the second-harmonic radiation as a pump source [1]. However, an optical pump by the 5321-Å radiation does not allow lasing of dyes at wavelengths shorter than approximately 5400 Å. The third-harmonic radiation of a Nd:YAG laser could be an attractive pump source to extend this wavelength limit, and can offer the important advantage of higher repetition rates than the dyes pumped by the second harmonic of a ruby laser. In this correspondence we wish to report the efficient generation of a 3547-Å pumped high-power dye laser that is capable of high average power in the blue and violet region of the spectrum. A high-repetition-rate visible dye laser pumped by the third harmonic of a Nd:YAG laser has previously been reported by Okada *et al.* [2], but they have used very low pump powers and have consequently obtained much lower output powers and conversion efficiencies than the values reported in this correspondence. The dye laser reported here has produced a peak power as high as 2.4 MW with an average power of 390 mW at 4890 Å at a pulse repetition rate of 20 pulses per second (pps) and peak powers in excess of 1.3 MW from 4300 to 5100 Å.

Fig. 1 is a schematic diagram of the experimental setup. The basic pump source was a repetitively Q-switched Nd:YAG oscillator–amplifier system working in the TEM_{00} transverse mode and in 2–4 axial modes with a peak power of 50 MW and 12-ns pulse duration. The 10-ns 22-MW second-harmonic radiation at 5321 Å generated from a temperature-tuned deuterated cesium dihydrogen arsenate (CD*A) crystal [3] was frequency mixed with the transmitted fundamental radiation in a phase-matched rubidium dihydrogen phosphate (RDP) crystal [4]. The third-harmonic radiation at 3547 Å was characterized by a peak power of 10.5 MW and 8-ns pulse duration. The measured angular divergence of the 5-mm-diam third-harmonic beam was 0.95 mrad. As shown in Fig. 1, the third-harmonic beam was physically separated from the fundamental and second harmonic by a high-quality Glan polarizer, and was used to pump a dye laser in an on-axis longitudinal configuration. The 40-cm-long dye-laser cavity was a folded three-mirror configuration consisting of a flat dichroic mirror, a 50-percent-reflectivity broad-band flat output mirror, and a 1200-lines/mm diffraction grating for wavelength tuning. By inserting a telescope having an angular magnification of 5 between the dichroic mirror and the diffraction grating, the linewidth of the dye-laser spectrum was reduced to less than 2 Å with a corresponding decrease in the output power by a factor of 1.2. The dichroic mirror had approximately 92-percent transmission at 3547 Å and 98–99-percent reflectivity from 4300 to 5250 Å. The 1-cm-thick dye cell consisted of two 2.5-cm-diam uncoated fused silica windows wedged by approximately 8° to prevent internal coupling. The dye flow was transverse to the optical axis of the dye-laser cavity. All the dye compounds used in this experiment were purchased from Eastman Kodak and New England Nuclear Company in dye-laser quality and used without further recrystallization, though the solutions were purified through 0.7-μ filters. The dye concentration was approximately 7×10^{-4} mole/l with some adjustment made to minimize the threshold.

Manuscript received February 4, 1975; revised March 5, 1975.

The author is with the First Research Center, Japan Defence Agency, Nakameguro 2-2-1, Meguro, Tokyo, Japan.

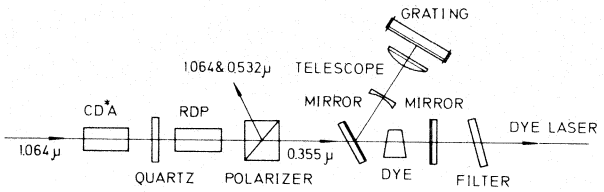

Fig. 1. Schematic diagram of experimental setup.

TABLE I
DYE-LASER PERFORMANCE PUMPED BY THIRD HARMONIC OF ND:YAG LASER

dye compound	solvent	central lasing wavelength	average output power
dimethyl POPOP	p-dioxane	4320 Å	250 mW
coumarin 120	ethanol	4410	220
coumarin 2	methanol	4540	330
7-diethylamino-4-methylcoumarin	ethanol	4570	380
coumarin 102	methanol	4850	270
7-diethylamino-4-trifluoromethylcoumarin	p-dioxane	4890	390

Note: The pump power at 3547 Å is 10.5 MW at a pulse repetition rate of 20 pps.

The detection of the dye-laser pulses was made through an UV cutoff glass filter and a high-speed photodiode–oscilloscope system having an overall rise time of less than 1 ns. With this system we have observed that the pulse shape and pulse duration of the dye laser closely followed the pump pulse in the high-gain region of the tunability range. For the low-gain region near the limits of the tunability range the pulse duration dropped to 50–60 percent of the pump pulse. The spectral linewidth of the dye-laser output analyzed with a 1-m grating spectrograph was well under 2 Å, but a frequency jitter of up to 5 Å was often observed. This instability is probably due to the mechanical vibrations of the dye-laser cavity.

Table I represents the central lasing wavelength and the average output power achieved with different combinations of dye compounds and solvents. The tunability range of the dye-laser output for individual dye solutions was around 500 Å, which could probably be somewhat extended by optimizing the output-mirror reflectivity. We note that in excess of 20-percent energy conversion efficiency from the 3547-Å pump power to the dye-laser output has been obtained with three different dyes. The best conversion efficiency obtained was 23 percent for a p-dioxane solution of 7-diethylamino-4-trifluoromethylcoumarin [5]. The excellent conversion efficiencies observed were due to the near optimum matching of the pump wavelength to the absorption bands of the dye compounds utilized, and to the perfect overlap between the dye-laser mode and the pump beam in the on-axis longitudinal pumping scheme. With a p-dioxane solution of 7-diethylamino-4-trifluoromethylcoumarin, we have obtained a peak output power of 2.4 MW with an average power of 390 mW around 4890 Å at a pump power of 10.5 MW and a pulse rep-

etition rate of 20 pps. The short wavelength limit for which the dyes could be lased was determined by the rapid fall in the reflectivity of the dichroic mirror rather than by the relatively low quantum efficiency of the organic scintillators. For instance, BBE dissolved in p-dioxane lased very efficiently around 4000 Å in an off-axis longitudinal pumping scheme.

The fine adjustment of the intracavity telescope for a minimum angular divergence of the dye-laser beam was made by observation of the far-field pattern with a high-magnification camera, and the result obtained was 1.15 ± 0.15 mrad irrespective of the wavelength. The spatial profile of the 5-mm-diam dye-laser beam was close to Gaussian and no inhomogeneous structure was observed.

The system described in the preceding has been operated many hours without noticeable deterioration in the dye-laser output power, although the dichroic mirror exhibited some surface damage after 1 h of operation due to the UV pump power.

When the dye-laser output was focused by a 3.5-cm-long focal-length lens, breakdown in air was observed with all the dye solutions listed in Table I. A preliminary measurement of the breakdown threshold in air at atmospheric pressure showed a monotonic increase of breakdown threshold with increasing wavelength from 4300 to 5100 Å, in qualitative agreement with previous measurements [6] made with a similar dye-laser system pumped by a frequency-doubled single-mode ruby laser [7].

In summary, we have reported the efficient operation of a high peak power and high average power dye-laser system in the blue and violet using the third harmonic of a Nd:YAG laser as a pump source.

References

[1] E. O. Ammann, C. D. Decker, and J. Falk, "High-peak-power 532-nm pumped dye laser," *IEEE J. Quantum Electron.* (Corresp.), vol. QE-10, pp. 463-465, Apr. 1974.

[2] M. Okada, S. Shimizu, and S. Ieiri, "Dye laser pumped by the third harmonic of Nd:YAG laser," *Japan. J. Appl. Phys.*, vol. 12, pp. 1284-1285, 1973.

[3] K. Kato, "Second-harmonic generation in CDA and CD*A," *IEEE J. Quantum Electron.* (Corresp.), vol. QE-10, pp. 616-618, Aug. 1974.

[4] K. Kato, "Efficient uv generation at 3547 Å in RDP," *Appl. Phys. Lett.*, vol. 25, pp. 342-343, 1974.

[5] E. J. Schimitschek, J. A. Trias, M. Taylor, and J. E. Celto, "New improved laser dye for the blue-green spectral regions," *IEEE J. Quantum Electron.* (Corresp.), vol. QE-9, pp. 781-782, July 1973.

[6] A. J. Alcock, K. Kato, and M. C. Richardson, unpublished.

[7] K. Kato, A. J. Alcock, and M. C. Richardson, "Conversion of high power ruby laser radiation to the uv in RDP," *Opt. Commun.*, vol. 11, pp. 5-7, 1974.

Five-Year Operation of a He-Ne Laser

W. P. KOLB

Abstract—**A metal ceramic He-Ne laser has been operating on lifetest for over five years (> 47 000 h). During this period there has been no appreciable change in either the output power or the voltage-current characteristics of the unit. These results indicate the possibility of extremely long-life He-Ne lasers.**

Manuscript received March 14, 1975; revised March 24, 1975.

The author is with the Electron Dynamics Division, Hughes Aircraft Company, Torrance, Calif. 90509.

Some of the many possible life-limiting mechanisms in He-Ne lasers have been discussed by several different authors [1]-[5]. This correspondence reports the construction and continuous operation of a cold-cathode metal-ceramic He-Ne laser for over five years (> 47 000 h). The operating characteristics for this laser have remained essentially unchanged over this period, and the lifetest is continuing.

Background

The laser being lifetested was built around the basic design that Bridges and Kolb described in previous articles [6]-[8]. The device was built in June 1969 and placed on lifetest in September of that year.

Construction

The construction details of the laser are shown in Fig. 1. The laser package, not including the output window, is a cylinder 13.5 in long and 2.5 in in diameter. The plasma tube envelope is made of stainless steel, Kovar, and alumina ceramic. The alumina ceramic bore is 8.5 in long with a 1.5-mm inside diameter. The mirrors, a 2-m radius output and total reflecting flat, are supported by the outer cylinder which is made of aluminum. The cold cathode is made of 2024 aluminum alloy and the snout on the stainless-steel mirror/window holder serves as the anode. The gas volume is 350 cm^3. The dielectric mirrors, which are coated on fused silica substrates, are internal to the vacuum envelope. The output beam is transmitted through a Corning 7056 glass window which is sealed to the vacuum jacket using a P.R. Mallory electrostatic sealing technique. No organic materials were used anywhere in the vacuum tube.

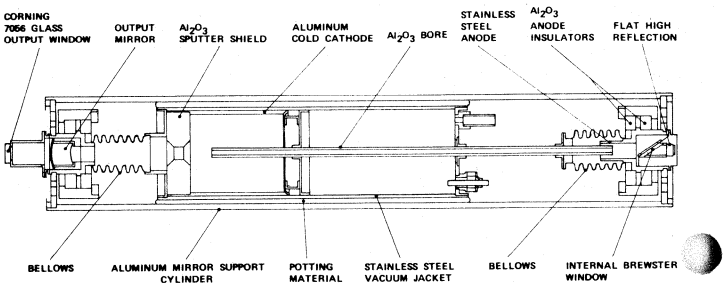

Fig. 1. A section view of the laser showing the construction details.

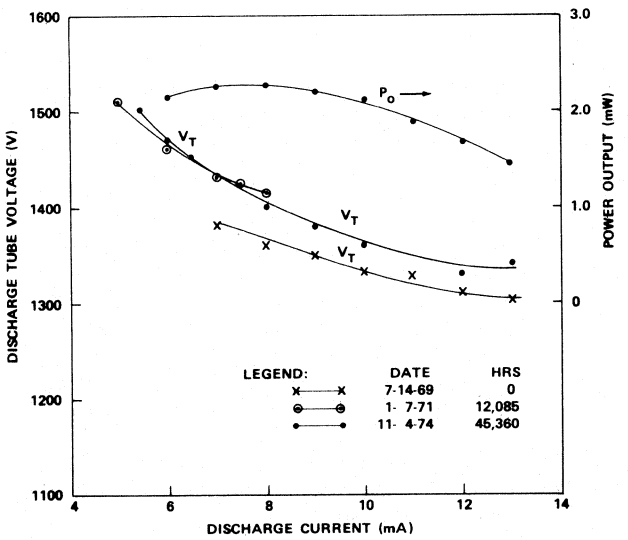

Fig. 2. The voltage-current characteristics of the discharge tube taken at different times during test. The power-output-current characteristics after 45 360 h of operation.

Processing and Packaging

The discharge tube was assembled using high-temperature brazing and heli-arc welding techniques. It was given a normal vacuum bakeout at 325°C for 20 h. The cathode was then oxidized in 3 torr of O_2 using a discharge current of ≈50 mA. The tube was filled to 2.0 torr with a 6:1 ratio of He to Ne. The maximum power output seen prior to pinchoff was 3.25 mW.

The laser discharge tube was then packaged in the aluminum mirror support cylinder. The maximum power obtained in the final package configuration was 2.25 mW.

Lifetesting

The lifetest started September 2, 1969. The laser has been operating continuously at a discharge current of 7.5 mA since that time except for infrequent shutdown when data were taken. Fig. 2 is a plot of the voltage-current characteristic taken initially and at subsequent times during test. A plot of the output power versus discharge current after the five-year period is also shown. Although no initial power data were taken at various currents, the initial pressure was selected to optimize the power in the 7–8-mA region.

Conclusions

The results obtained to date indicate the possibility of building He–Ne lasers with operating lifetimes in excess of five years. The relative importance of the many unique construction features of the metal ceramic discharge tube is not totally understood. However, large gas volume, low cathode current density, cathode geometry, large area anode design, high sputter-resistant ceramic bore, electrostatically shielded mirrors, ultraclean construction, high-temperature bakeout, and low activity of getter, especially with regard to oxygen, are all important. The ranking of importance of these design considerations would require considerable investigation. It is, however, safe to say that the results of this lifetest prove the possibility of building He–Ne lasers with lifetimes in excess of five years when all of the preceding factors are considered.

References

[1] R. Turner, K. M. Baird, M. J. Taylor, and C. J. Van der Hoeven, "Lifetime of helium-neon lasers," *Rev. Sci. Instrum.*, vol. 35, pp. 996–1001, Aug. 1964.

[2] U. Hochuli and P. Haldemann, "Cold cathodes for possible use in 6328 Å single mode He–Ne gas lasers," *Rev. Sci. Instrum.*, vol. 36, pp. 1493–1494, Oct. 1965.

[3] U. Hochuli, P. Haldemann, and D. Hardwick, "Cold cathodes for He–Ne gas lasers," *IEEE J. Quantum Electron. (1967 Conference on Laser Engineering and Applications)*, vol. QE-3, pp. 612–614, Nov. 1967.

[4] U. Hochuli and P. Haldemann, "Gas laser," U.S. Patent 3 614 642.

[5] W. P. Kolb, "Cold cathode gas laser discharge tube," U.S. Patent RE 27 282.

[6] W. B. Bridges and W. P. Kolb, "First space-qualified laser," *Laser Focus*, vol. 5, pp. 39–42, Oct. 1969.

[7] W. B. Bridges, "Design of a space qualified laser," NASA Contractor Rep., NASA CR-1663, Oct. 1970.

[8] W. B. Kolb, "Research directed toward perfecting a design for a space qualified He–Ne laser," NASA Contractor Rep., NASA CR-1664, Sept. 1970.

Correction to "Theory of Optical Gain and Threshold Properties of Semiconductor Lasers"

A. G. ALEKSANIAN

In the above paper,[1] on page 299, formula (9) should read

$$g(\omega) = 4\pi e^2 \Delta \bar{f} m^{3/2} \delta (\epsilon_e^v)^{3/2} / m_0 c \epsilon_0^{1/2} \hbar^3 \gamma \times \frac{[X(\beta) + 2\beta]^{3/2} \sinh(\Gamma_0 - \beta/\theta) \exp\{-X^2(\beta)/4\delta^2\}}{[\delta^2 + (X(\beta) + 2\beta)^2]^{3/2} \left[\cosh\frac{\Gamma_0 - \beta}{\theta} + \cosh\left(\frac{X(\beta) - \beta}{\theta} - Z_0\right)\right]}. \quad (9)$$

Formula (11), on page 300, should read

$$g(\omega) = B_0 \frac{\gamma^{3/2}\pi^{1/2}}{2^{11/4}} \cdot \frac{\exp\{-X_0^2/2\} \sinh[(F - \hbar\omega)/2kT] D_{-3/2}(-2^{1/2}X_0)}{\sinh^2[(F - \hbar\omega)/4kT] + \cosh^2[\zeta(X^m - X_m)]} \quad (11)$$

where

$$B_0 = 32 e^2 m_e^{1/2} \Delta_0 \pi^{1/2} N_A a_v^3 / 3\epsilon_0^{1/2} c\hbar^3 \omega\gamma (1 + a_v^2 K_e^2)^4.$$

Manuscript received March 21, 1975.

The author is with the Radio Physics and Electronics Institute, Academy of Science of Armenian SSR, Ashtarek, USSR.

[1] A. G. Aleksanian, I. A. Poluektov, and Yu. M. Popov, *IEEE J. Quantum Electron.*, vol. QE-10, pp. 297–305, Mar. 1974.

Contributors



William F. Bailey was born in Cleveland, Ohio, in 1942. He received the B.S. degree from the United States Military Academy, West Point, N.Y., and the M.S. degree in physics from Ohio State University, Columbus, in 1964 and 1966, respectively.

From 1966 to 1970 he was assigned as a Theoretical Physicist to the Air Force Weapons Laboratory, Kirtland Air Force Base, N. Mex. In 1970 he was reassigned to the Aerospace Research Laboratories, Wright-Patterson Air Force Base, Ohio, where he headed a theoretical group analyzing nonequilibrium laser discharges. He is currently enrolled in the doctoral program at the Air Force Institute of Technology, Wright-Patterson Air Force Base.

*

T. H. Bett, photograph and biography not available at the time of publication.

*



Peter Bletzinger (M'58-SM'71) was born in Stuttgart, Germany, on September 3, 1929. He received the Dipl. Ing. degree and the Dr. Ing. degree, the latter in 1966, both from the Technical University of Stuttgart, Stuttgart.

In 1955 he joined the Standard Electronic Division of International Telephone and Telegraph, Stuttgard, and in 1956 he went to the Communications and Navigation Laboratory, Wright-Patterson Air Force Base, Ohio, where he worked on navigational systems. In 1961 he joined the Aerospace Research Laboratories, where he has been working in the fields of high-speed photography, electrooptics, plasma diagnostics, and gas lasers.

*



H. J. A. Bluyssen received the doctorandus degree in physics and mathematics from the University of Utrecht, Utrecht, The Netherlands, in 1962. He joined the Physics Department of the University of Nijmegen, Nijmegen, The Netherlands, where he worked under Prof. A. Dymanus on molecular-beam microwave spectroscopy and received the doctorate degree in physics in 1968.

He is currently working on far-infrared lasers and is interested in their application to solid-state physics.

Dr. Bluyssen is a member of the American Physical Society.

P. G. Browne, photograph and biography not available at the time of publication.

*

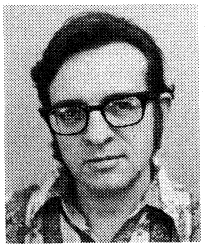

R. A. Elliott was born in Canada in 1937. He received the B.A. degree in 1960, the B.Sc. degree in physics in 1961, and the M.Sc. degree in physics in 1963, all from Queen's University Kingston, Ont., Canada. He received the Ph.D. degree in 1966 from the University of British Columbia, Vancouver, where he specialized in kinetic theory and nonequilibrium statistical mechanics.

He was a research associate of Prof. E. W. Montroll at the Institute for Fundamental Studies, University of Rochester, from 1966 to 1969. While there he worked on random-walk theory and its application to exciton conduction in macromolecules and molecular crystals. Since 1969 he has been at the Oregon Graduate Center, Beaverton. His research interests have expanded to include laser propagation through turbulent media, statistical models of small-scale turbulence, high-gain optical-parametric interactions, and laser pulse shaping.

Dr. Elliott is a member of the Canadian Association of Physicists.

*

Joel Falk (S'64-M'70), for a photograph and biography please see page 62 of the January 1975 issue of this JOURNAL.

*

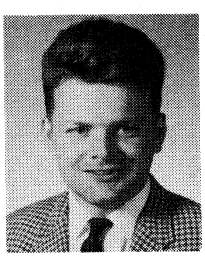

Alan Garscadden (M'69-SM'71) was born in Glasgow, Scotland, on June 10, 1937. He received the B.Sc. (Hons.) and Ph.D. degrees from Queen's University, Belfast, Northern Ireland, in 1958 and 1962, respectively.

In 1962 he joined the Aerospace Research Laboratories, Wright-Patterson Air Force Base, Ohio, where he is currently working on instabilities in plasmas and on discharge processes in gas lasers. In 1972 he was appointed Director of the Plasma Research Laboratory.

Dr. Garscadden is a member of the American Physical Society.



Robert J. Harrach was born in Colorado on March 30, 1937. He received the A.B. degree in physics from Dartmouth College, Hanover, N.H., in 1960, and the M.S. and Ph.D. degrees in physics from the University of Colorado, Boulder, in 1962 and 1965, respectively.

As a graduate student and one year thereafter he worked in the Atomic Frequency and Quantum Electronics Sections of the National Bureau of Standards, Boulder. In 1966 he joined the University of California, Lawrence Livermore Laboratory, Livermore, Calif., where he is currently a member of the Theoretical Division. His research has dealt primarily with high-power lasers and nonlinear optics. Since 1970 he has concurrently held a position as Lecturer in the Department of Applied Science, University of California, Davis-Livermore.

*



Hermann A. Haus (S'50–A'55–SM'58–F'62) attended the Technische Hochschule, Graz, Austria, from 1946 to 1948, and the Technische Hochschule, Vienna, Austria, in 1948. He received the B.S. degree from Union College, Schenectady, N.Y., the M.S. degree from Rensselaer Polytechnic Institute, Troy, N.Y., and the Sc.D. degree from Massachusetts Institute of Technology, Cambridge, Mass., all in electrical engineering, in 1949, 1951, and 1954, respectively.

He is Elihu J. Thomson Professor of Electrical Engineering and a Research Staff Member of the Research Laboratory of Electronics, Massachusetts Institute of Technology. He also serves as a Consultant to the Raytheon Company. From 1959 to 1960 he was a Visiting Professor and Guggenheim Fellow at the Technische Hochschule, Vienna. He is coeditor of the recent book *Noise in Electron Devices*, coauthor of the monographs *Circuit Theory of Linear Noise Networks* and *Electrodynamics of Moving Media*, and coauthor of the book *Case Studies in Electromagnetism*. He is currently on leave at Bell Laboratories, Holmdel, N.J.

Dr. Haus is a member of Sigma Xi.

*

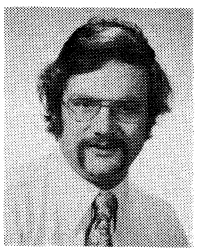

C. Breck Hitz (M'70) was born in Palm Springs, Calif., on January 1, 1944. He received the B.S. degree in physics from the Pennsylvania State University, University Park, and the M.S. degree in physics from the University of Massachusetts, Amherst, where he was an N.D.E.A. Fellow in 1966 and 1969, respectively.

After joining GTE Sylvania Inc., Mountain View, Calif., in 1969 he was involved in optical communication system components and nonlinear optics development. He has been active in several nonlinear optics projects including a study of the techniques of frequency doubling the CO_2 laser, and has assisted in the development of a mode-locked space-qualified Nd:YAG laser. His present interests include novel modulation techniques and vapor-phase nonlinear optics. He is now with the General Photonics Corporation, Santa Clara, Calif.

Mr. Hitz is a member of the American Physical Society.



Tatsuya Kimura (S'66–M'71) was born in Osaka, Japan, on February 20, 1940. He received the B.S. degree in electrical engineering, the M.S. degree in electronic engineering, and the Ph.D. degree in the field of quantum electronics, all from the University of Tokyo, Tokyo, Japan, in 1962, 1964, and 1967, respectively.

In 1967 he joined the Musashino Electrical Communication Laboratories, Nippon Telegraph and Telephone Public Corporation, Tokyo, Japan. He has been engaged in work on equipment for optical communications, such as light modulators, detectors, PM–AM converters, optical FDM filters and laser oscillators, and guided millimeter-wave transmission systems and equipment.

Dr. Kimura is a member of the Institute of Electronics and Communication Engineers of Japan, the Japan Society of Applied Physics, the Physical Society of Japan, and the American Physical Society.

*



David A. LaBorde received the B.S. degree from Northeast Louisiana State University, Monroe, and the M.S. degree in engineering physics from the Air Force Institute of Technology, Wright-Patterson Air Force Base, Ohio, in 1960 and 1972, respectively. He attended the Armed Forces Staff College in 1974.

He entered the Air Force in 1960 and after attending Officer Training School, he received a commission in the United States Air Force in 1961. Upon completion of flying schools, he served as an Electronic Warfare Officer in the Strategic Air Command until 1970. He served four tours in Southeast Asia as a crew member on B-52 and AC-130 aircraft between the years 1965 and 1973. He is currently assigned to the Aeronautical Systems Division (AFSC), Wright-Patterson Air Force Base, as an Electronic Warfare Engineer.

*

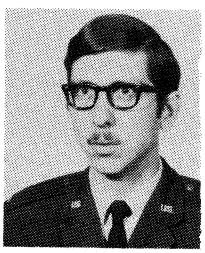

William H. Long, Jr., was born in San Francisco, Calif., on May 11, 1947. He received the B.S. degree in physics from the California Institute of Technology, Pasadena, and the M.S. degree in plasma physics from the University of Wisconsin at Madison in 1969 and 1970, respectively.

Since joining the Air Force in May 1971, he has been assigned to the Aerospace Research Laboratories, Wright-Patterson Air Force Base, Ohio. His research has included theoretical and experimental studies of the electric-discharge laser, low-energy electron kinetics, and positive-column modeling in molecular gases.



G. A. Massey (M'67) received the B.S.E.E. degree from the California Institute of Technology, Pasadena, in 1959, and the M.S. and Ph.D. degrees from Stanford University, Stanford, Calif., in 1967 and 1970, respectively.

From 1959 to 1963 he was a member of the Engineering Staff of the Raytheon Company, Santa Barbara, Calif., where he worked in the areas of optical communications, modulator device development, and laser range-finders. In 1963 he joined the Electro-Optics Group of GTE Sylvania, Mountain View, Calif., where, as Senior Engineering Specialist, his activities included development of laser vibration sensors and acoustooptical devices, research in acoustical holography and acoustical imaging systems, laser mode locking, and development of high-power lasers, new materials for solid-state lasers, and nonlinear optical devices. He joined the Faculty of the Oregon Graduate Center, Beaverton, in 1972, and currently holds the position of Professor in the Applied Physics Department. His current research activities include nonlinear optical devices, dye lasers, and laser remote-sensing techniques.

Dr. Massey is a member of the Optical Society of America and the Acoustical Society of America.

*

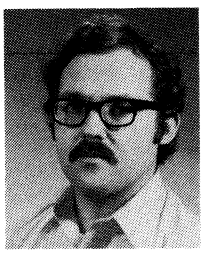

Robert E. McIntosh (S'66-M'67-SM'72) was born in Hartford, Conn., on January 19, 1940. He received the B.S. degree in electrical engineering from Worcester Polytechnic Institute, Worcester, Mass., in 1962, the S.M. degree in applied physics from Harvard University, Cambridge, Mass., in 1964, and the Ph.D. degree from the University of Iowa, Iowa City, in 1967. His Ph.D. dissertation was in the area of nonlinear behavior of plasmas.

He was a member of the Technical Staff at Bell Laboratories, North Andover, Mass., from 1962 until 1965, where he worked in a microwave networks group. In 1967 he joined the Department of Electrical and Computer Engineering, University of Massachusetts, Amherst, where he is now a Professor. He spent the 1973-1974 academic year as Guest Professor of Physics at the Fysisch Laboratorium Katholieke Universiteit, The Netherlands. His teaching and research interests are in electromagnetic field theory, microwaves, plasmas, and communication engineering.

Dr. McIntosh is a member of the International Scientific Radio Union, the American Physical Society, Sigma Xi, Tau Beta Pi, Phi Kappa Phi, and Eta Kappa Nu. He is a Past Chairman of the Springfield section of the IEEE, and was a member of the National Membership and Transfers Committee of the IEEE. He is also the Chairman of the Steering Committee of the IEEE International Symposium on Antennas and Propagation, which is to be held at the University of Massachusetts in 1976.

*

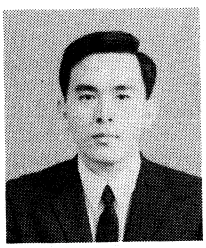

Kenju Otsuka (A'73) was born in Anto, Manchuria, on January 2, 1946. He received the B.S. degree in communication engineering from Tohoku University, Sendai, Japan, in 1968.

In 1968 he joined the Musashino Electrical Communication Laboratories, Nippon Telegraph and Telephone Public Corporation, Tokyo, Japan. He has been engaged in the research of the technique of mode locking in solid-state lasers and more recently in the investigation of Nd-ultraphosphate lasers for high bit-rate optical transmission systems.

Mr. Otsuka is a member of the Institute of Electronics and Communication Engineers of Japan and the Japan Society of Applied Physics.

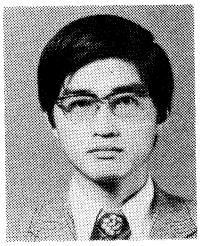

Masatoshi Saruwatari was born in Miyazaki, Japan, on April 3, 1945. He received the B.S. degree in pure and applied science, and the M.S. degree in coordinated sciences, both from the University of Tokyo, Tokyo, Japan, in 1968 and 1970, respectively.

In 1970 he joined the Musashino Electrical Communication Laboratories, Nippon Telegraph and Telephone Public Corporation, Tokyo. He has been engaged in research on optical communication equipment such as optical frequency multiplexers and solid-state laser oscillators.

Mr. Saruwatari is a member of the Institute of Electronics and Communication Engineers of Japan and the Japan Society of Applied Physics.

*

A. L. S. Smith, photograph and biography not available at the time of publication.

*



Peter D. Tannen was born in the Bronx, N.Y., on February 17, 1936. He received the B. Aero. Engr. degree from Rensselaer Polytechnic Institute, Troy, N.Y., and the M.S. degree in astronautical engineering from the Air Force Institute of Technology, Wright-Patterson Air Force Base, Ohio, in 1957 and 1962, respectively. He is a doctoral candidate for the Ph.D. degree from the Air Force Institute of Technology.

From 1962 to 1967 he was a Project Engineer at the Air Force Special Weapons Center, Kirtland Air Force Base, N. Mex. From 1969 to 1973 he was a Research Physicist with the Plasma Physics Laboratory, Aerospace Research Laboratories, Wright-Patterson Air Force Base. He is currently at the Air Force Weapons Laboratory, Kirtland Air Force Base.

Major Tannen is an associate fellow of the American Institute of Aeronautics and Astronautics, and a member of the American Association for the Advancement of Science, Tau Beta Pi, and Sigma Gamma Tau.

*

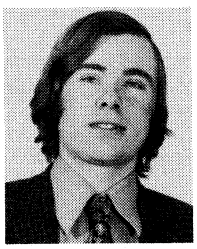

B. C. Tofield received the B.A. degree in chemistry and the D.Phil. degree in inorganic chemistry, both from Oxford University, Oxford, England, in 1966 and 1969, respectively.

From 1969 to 1972 he was a Turner and Newall Research Fellow at the Inorganic Chemistry Laboratory, Oxford University. While there, he worked on the preparation and magnetic and structural properties of high-oxidation-state rare-earth and transition-metal oxides, structural details of nonstoichiometry in oxide perovskites by neutron and electron diffraction, and bonding in rare-earth and transition metal systems by neutron scattering. He was with Bell Laboratories, Holmdel, N.J., from 1972, where he has been involved in the development and conception of new rare-earth laser crystals and nonlinear optical properties of inorganic crystals. He is currently with the Materials Physics Division, Atomic Energy Research Establishment, Harwell Didcot, Oxon., England.



A. F. van Etteger was born in Nijmegen, The Netherlands, in 1943. He completed his engineering training in 1965.

In 1965 he joined the Instrumentation Group of the Faculty of Science at the University of Nijmegen. After a period of six years he accepted the position of Research Associate in the Physics Department at the same University, where, ever since, he has actively participated in the development, design, and other problematics in relation to molecular lasers operating in the far-infrared region of the electromagnetic spectrum.

*

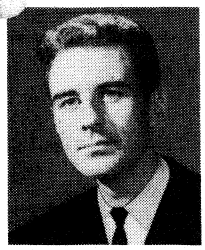

Heinz P. Weber (M'72) was born in Winterthur, Switzerland, on April 18, 1939. He received the Diploma in physics from the Swiss Federal Institute of Technology, Zürich, Switzerland, in 1964, and the Ph.D. degree from the University of Berne, Berne, Switzerland, in 1968.

From 1964 he has been a Graduate Research Assistant at the Institute of Applied Physics, University of Berne, engaged in problems in the field of nonlinear optics and the generation and measurement of ultrashort light pulses. Since joining Bell Laboratories, Holmdel, N.J., in 1969, he has been involved in research on integrated optics. He has explored ways to form optical waveguides and integrated-optics structures using photosensitive organic compounds. He has also investigated new rare-earth laser crystals with high Nd concentration and small concentration quenching, as well as concepts for miniaturized lasers using such materials.

Dr. Weber is a member of the American Optical Society.

*



Peter Wyder was born in Burgdorf, Switzerland, in 1934. He received the diploma in physics and the Dr. sc. nat. degree from the Swiss Federal Institute of Technology, Zurich, Switzerland.

His main research interest is experimental solid-state physics. From 1964 to 1966 he was a Fellow of the Miller Institute for Basic Research in Science at the University of California at Berkeley, and from 1966 to 1967 he was a Research Fellow at Harvard University. Since 1967 he has been a Professor of Physics at the University of Nijmegen, Nijmegen, The Netherlands.

*

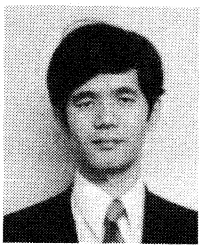

Tomoaki Yamada was born in Tokyo, Japan, on November 1, 1942. He received the B.S. degree from the University of Tokyo, Tokyo, in 1965.

He joined the Musashino Electrical Communication Laboratories, Nippon Telegraph and Telephone Public Corporation, Tokyo, in 1965 where he is currently a Deputy Director of the Sixth Section. He has been working on ferroelectrics and solid-state laser crystals.

He is a member of the Physical Society of Japan and the Japan Society of Applied Physics.

MEMBERSHIP APPLICATION

IEEE ELECTRON DEVICES GROUP

Membership in the IEEE ELECTRON DEVICES Group entitles you to receive, for the low Group fee, the monthly IEEE Transactions on Electron Devices, and the bimonthly Electron Devices Group Newsletter. You are kept informed of latest developments, meetings and conferences in your areas of interest, and are entitled to purchase informative conference records and other helpful educational aids at greatly reduced rates for members.

Use the convenient coupon to become a member of the IEEE ELECTRON DEVICES Group or a Group Affiliate. If you are not a member of the IEEE, but would like to join, please check the appropriate box on the coupon. Descriptive materials and an IEEE membership application form will be sent to you immediately upon receipt.

*Group Fee: $7.00 for IEEE members of all grades except Student. Student Fee: $2.00. These rates apply to payments received September 1 through February. On payments received March 1 through August 31, remit one-half of the above rates. (Payments received September 1 through December 31 apply through December 31 of the following year.)

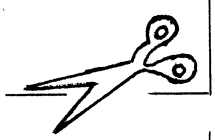

Membership Application/IEEE ELECTRON DEVICES GROUP
Send to: IEEE Service Center, 445 Hoes Lane, Piscataway, NJ 00854

☐ I am a _____ (Grade) member of IEEE and hereby apply for membership in the ELECTRON DEVICES Group. I enclose a check for the Group fee* (made payable to IEEE).

☐ I am not now a member of the IEEE but would like to join. Please send information.

☐ I am interested in becoming an ELECTRON DEVICES Group Affiliate. Please send information.

Name _____ IEEE No. _____

Mailing Address _____

City _____ State/Country _____ Zip ____

Company _____

Field of Interest _____

Introduction

Semiconductor Lasers—1975

THIS ISSUE of the IEEE JOURNAL OF QUANTUM ELECTRONICS marks the fourth special issue of this journal devoted to semiconductor lasers. It comes at a time when the active effort on semiconductor lasers around the world is the largest it has ever been. For the increasing number of specialists in this field, this issue provides a convenient collection of current papers for future reference. For interested workers in other fields, this volume presents a snapshot view of topics under current investigation by researchers in the field.

The issue is sponsored by the 1974 IEEE International Semiconductor Laser Conference, which was held on November 18–20, 1974, in Atlanta, Ga. The conference was attended by 160 specialists from the United States, Japan, England, Germany, Canada, France, The Netherlands, the Soviet Union, Switzerland, Brazil, and Italy. This record number of participants clearly demonstrated the high level of attention which semiconductor lasers presently enjoy.

Although the program committee led by A. R. Calawa was faced with many more papers than could possibly be accommodated, they successfully arranged 46 papers into 6 formal sessions and 2 evening sessions. In spite of the full and taxing program, there was ample time and energy for lively discussion during and after each session. Topics of discussion ranged over most aspects of semiconductor lasers from the very practical problem of device reliability to the exciting possibilities of distributed-feedback structures. Corrugations in the laser waveguide were used as an output coupler to obtain a well-collimated beam or as a mode selector to achieve tunable single-frequency operation, while theoretical and experimental studies of degradation by dark-line formation were presented in attempts to understand more clearly the nature and origin of this perverse mechanism. Although the reliability of junction lasers remained a primary concern of most workers, the nervous fear that such devices might be limited to relatively short CW lives was somewhat alleviated by the informal report by Bell Laboratories of a continuous lifetime in excess of 14 000 h for at least one junction laser.[1] Reproducibility remains the most vexing problem. Hopefully, by the time of the next semiconductor laser conference, solution of this problem will have led to the commercial availability of CW junction lasers.

Theoretical and experimental characteristics of $Ga_xAl_{1-x}As$ double-heterostructure lasers with thin active regions received considerable attention, with discussions centering on waveguide modes, optical-scattering loss, depolarization of the lasing emission, and saturation effects. Heterostructures in other materials were not neglected with current interest focused on lead-salt and $GaAs_{1-y}P_y$ lasers. New laser structures as well as new methods of making old structures were examined. Notable were the use of a two-dimensional waveguide to obtain lasing in a small active region at a low input current and the monolithic integration of a junction laser phase coupled to a passive waveguide as a means for directly obtaining a guided output beam. Other attractive coupling schemes are also described in this issue. Oxygen implantation and selective heterojunction growth were presented as two new ways to form stripe-geometry lasers. With the second technique, continuous lasing at wavelengths as short as 7610 Å was obtained. Continuous operation at temperatures as high as 9°C was also reported for stripe-geometry lasers fabricated from material growth by molecular-beam epitaxy.

Mode interactions, always a popular subject for discussion, encompassed stimulated scattering at high power levels, longitudinal mode locking, and self-induced intensity pulsations. Externally imposed diffractive coupling was used to induce coherence of separate lasers, while an optical fiber was incorporated into a laser cavity to achieve transverse mode control.

The eternal subjects of time delays, Q switching, and related transient effects still provided ground for active debate. Hopefully, a final chapter in this elusive story is emerging with the recognition of the role played by a loss of the optical confinement. Other topics included another persistent phenomenon in semiconductor lasers, namely filament formation, as well as semiconductors excited by electron beams and electric fields.

In conclusion, I hope that this issue will be not only a useful reference and stimulus for those actively working on semiconductor lasers but also interesting to those engaged in other fields of quantum electronics. I thank the authors and referees without whose contributions this issue would not exist. In addition, all of us who profited by attending the conference or by reading the papers of this issue are grateful to J. E. Ripper for his enthusiastic initiation of the 1974 Conference and to N. Holonyak, Jr., for accepting the responsibility for its success. A very special note of thanks goes to J. A. Rossi for his persistent attention to the myriad arrangements so necessary to a smoothly running conference and to the JOURNAL OF QUANTUM ELECTRONICS, the IEEE Group on Electron Devices, IBM, and Bell Laboratories for their financial support of this issue.

The program of the IV IEEE International Semiconductor Laser Conference was as follows.

[1] See R. L. Hartman and R. W. Dixon, *Appl. Phys. Lett.*, vol. 26, pp. 239–242, Mar. 1, 1975.

SESSION I: Theory and Device Physics
M. J. Adams, *Chairman*

1) "Self-consistent calculations of the electrical and optical characteristics of the double heterostructure GaAs laser," *K. A. Shore and M. J. Adams.*
2) *"The analysis of optical scattering loss in double-heterostructure injection lasers with narrow active layers," *G. H. B. Thompson, J. E. A. Whiteaway, and P. A. Kirkby.*
3) *"Modal properties of very thin heterojunction structures," *J. K. Butler, I. Ladany, and H. Kressel.*
4) *"DH lasers in the limit of thin active regions," *W. P. Dumke.*
5) "Transverse modes in semiconductor injection lasers with thin active layer," *K. Kurokawa.*
6) "Energy-dependent rate equations for semiconductor lasers," *B. A. Rogers.*

SESSION II: Mode Properties of Lasers
M. Balkanski, *Chairman*

1) "Pressure induced mode conversion in homostructure GaAs junction lasers," *N. B. Patel, T. J. B. Serra, and M. B. Zakias.*
2) *"Transverse mode control of stripe-geometry large-cavity GaAs lasers optically coupled to single-mode fibers," *D. C. Krupka and T. L. Paoli.*
3) "Critical power in narrow stripe and wide sawed lasers," *H. S. Sommers, Jr.*
4) "Formation of spatially coherent beam from a GaAs laser diode array," *E. M. Phillip-Rutz.*
5) *"GaAs-GaAlAs double heterostructure injection lasers with distributed feedback," *M. Nakamura, K. Aiki, J. Umeda, A. Katzir, A. Yariv, and H. W. Yen.*
6) *"Coupling coefficients, thresholds, and propagation constants for modes in distributed feedback laser diodes," *D. R. Scifres, W. Streifer, and R. D. Burnham.*
7) "Electron beam excited distributed feedback laser in CdS," *Y. Aoyagi and S. Namba.*

SESSION III: New Laser Structures and Processes
M. Pilkuhn, *Chairman*

1) *"Optical and thermal properties of buried-heterostructure injection lasers," *T. Tsukada and Y. Shima.*
2) *"Integrated twin-guide AlGaAs laser with multi-hetero structure," *Y. Suematsu, M. Yamada, K. Hayashi, K. Furuya, and S. Ibukuro.*
3) *"Oxygen implanted double heterojunction GaAs/GaAlAs injection lasers," *J. M. Blum, J. C. McGroddy, P. G. McMullin, K. K. Shih, A. W. Smith, and J. F. Ziegler.*
4) *"Visible light-emitting lasers of new hetero-isolation stripe-geometry," *K. Itoh, M. Inoue, and I. Teramoto.*
5) *"Monolithic $Ga_{1-x}In_xAs$ mesa lasers with grown optical facets," *F. A. Blum, K. L. Lawley, F. H. Doerbeck, and W. C. Holton.*
6) *"Semiconductor lasers with the light output through the diffraction grating on the surface of the waveguide layer," *Zh. I. Alferov, V. M. Andreyev, S. A. Gurevich, R. F. Kazarinov, V. R. Larionov, M. N. Mizerov, and E. L. Portnoy.*
7) *"Application of molecular beam epitaxial layers to heterostructure lasers," *H. C. Casey, Jr., A. Y. Cho, and P. A. Barnes.*

SESSION IV: Degradation
Y. Nannichi, *Chairman*

1) *"Degradation in injection lasers," *G. R. Woolhouse.*
2) *"Degradation sources in GaAs-AlGaAs double heterostructure lasers," *R. Ito, H. Nakashima, S. Kishino, and O. Nakada.*
3) "X-ray observation of DH laser crystals," *K. Ishida, J. Matsui, I. Sakuma, Y. Nannichi, and I. Hayashi.*
4) *"Degradation and intensity fluctuation in CW AlGaAs double-heterostructure junction lasers," *S. Gonda, S. Mukai, and Y. Makita.*
5) *"Dislocation pinning in GaAs by the deliberate introduction of impurities," *P. A. Kirkby.*
6) "Deformation behavior of pulsed double-heterostructure diode lasers," *R. Keller and Ch. Risch.*
7) "Characterization of GaAs-AlGaAs double-heterojunction laser structures using optical excitation," *G. A. Acket, W. Nijman, R. P. Tijburg, and P. J. de Waard.*

SESSION V: Transient Effects
T. L. Paoli, *Chairman*

1) *"Anomalous interaction of spectral modes in semiconductor laser," *A. P. Bogatov, P. G. Eliseev, and B. N. Sverdlov.*
2) *"The gain profile and time delay effects in GaAs/$Ga_{1-x}Al_xAs$ heterostructure lasers," *J. A. Rossi, J. J. Hsieh, and H. Heckscher.*
3) *"Suppression of intensity self-pulsations in CW junction lasers by frequency-selective optical feedback," *T. L. Paoli and J. E. Ripper.*
4) *"Multimode operation and mode-locking effect in injection lasers," *H. Bachert, P. G. Eliseev, M. A. Manko, V. P. Strahov, S. Raab, and C. M. Thay.*
5) *"*H*-pulsing: A transient effect in GaAs/$Ga_xAl_{1-x}As$ injection lasers," *S. Grundorfer, M. J. Adams, and B. Thomas.*
6) *"A comprehensive model for *Q* switching in semiconductor lasers," *B. Thomas, M. J. Adams, and S. Grundorfer.*
7) "Filament formation in GaAs lasers," *F. D. Nunes, J. E. Ripper, N. B. Patel, and M. D. Campos.*
8) "Single heterostructure lasers: The effect of injected carriers on optical guiding and its role in critical temperature behavior, *Q* switching, and delays," *P. R. Selway, G. H. B. Thompson, G. D. Henshall, and J. E. A. Whiteway.*

SESSION VI: Lasers of IV-VI and Other Compounds
I. Melngailis, *Chairman*

1) "Optical mode confinement in diffused PbSe diode lasers," *P. M. Asbeck and G. W. Pratt.*
2) "$Pb_{1-x}Sn_xTe$ epitaxial heterostructure lasers and waveguides," *J. N. Walpole, R. W. Ralston, A. R. Calawa, T. C. Harman, and J. P. McVittie.*
3) *"Lead-tin telluride double heterojunction laser diodes," *L. R. Tomasetta and C. G. Fonstad.*
4) "$PbS_{(1-x)}Se_x$ double heterostructure diode lasers," *K. J.*

*Paper printed in this issue.

Steger, G. F. McLane, and U. Strom.

5) *"Liquid phase epitaxial $In_{1-x}Ga_xP_{1-z}As_z/GaAs_{1-y}P_y$ quaternary-ternary heterojunction lasers (77°K, $x = 0.70$, $z \sim 0.01$, $y = 0.38$)," *J. J. Coleman, W. R. Hitchens, N. Holonyak, Jr., M. J. Ludowise, W. O. Groves, and D. L. Keune.*

6) "Room-temperature heterojunction laser diodes from vapor-grown $In_{1-x}Ga_xP/GaAs$ structures," *C. J. Nuese, M. Ettenberg, and G. H. Olsen.*

EVENING SESSION I: Short Additional Papers
H. C. Casey, Jr., *Chairman*

1) "Electronically scannable semiconductor laser device," *J. R. Packard, J. M. Magnusson, H. U. Brueckner, and W. H. Strehlow.*

2) *"Depolarization of the lasing emission from CW double-heterostructure junction lasers," *T. L. Paoli.*

EVENING SESSION II: Short Additional Papers
J. C. Dyment, *Chairman*

1) "Distributed feedback double-heterostructure GaAs injection lasers with fundamental grating," *D. B. Anderson, R. R. August, and J. E. Coker.*

2) *"Grating-coupled AlGaAs double-heterostructure diode lasers," *P. Zory and L. D. Comerford.*

3) "Investigation of laser action in semiconductors excited by an electric field," *A. Molchanov, A. S. Nasiboy, A. Z. Obidin, A. N. Pechenov, and Yu. M. Popov.*

Although the following paper was also accepted by the program committee, the authors were unable to present it at the conference.

1) "Radiation noise in injection lasers," *V. P. Gribkovskii, V. K. Kononenko, G. I. Ryabtsev, and V. A. Samoilyukovich.*

Conference Chairman: N. HOLONYAK, JR.
Vice-Chairman: J.E. RIPPER
Treasurer and Arrangements Chairman: J.A. ROSSI
Technical Program Committee: A.R. CALAWA (*Chairman*), J.F. BUTLER, J.C. DYMENT, H. KRESSEL, M.B. PANISH, J.I. PANKOVE, A.W. SMITH

THOMAS L. PAOLI, *Guest Editor*
Bell Laboratories
Murray Hill, N.J. 07974

Lead–Tin Telluride Double-Heterojunction Laser Diodes: Theory and Experiment

L. R. TOMASETTA AND C. G. FONSTAD, MEMBER, IEEE

Abstract—Calculations of threshold current densities for lead-tin telluride double-heterojunction (DH) laser diodes are presented, in which the spatial distribution of the injected minority carriers and the critical level of minority carrier injection necessary for population inversion are considered. Excellent agreement between the predictions of this model and experimental data is obtained, which suggests that credible predictions of high-temperature performance can be made. The need to inject a critical level of minority carriers is shown to be the principal contribution to the threshold current density except at very low temperature and to lead to a rapid increase in threshold with increasing temperature. It is found experimentally that below 40 K the threshold no longer decreases with temperature; two possible explanations for this behavior are suggested.

INTRODUCTION

THE IMPORTANCE of the double-heterojunction (DH) device geometry, see Fig. 1, in reducing semiconductor diode laser threshold current densities has been well documented in the (Ga, Al)As alloy system [1]. Heterojunction geometries have also very recently been used in Pb-salt diode lasers, specifically in the Pb(S, Se) [2] and (Pb, Sn)Te [3]-[5] alloy systems. Significant systematic reduction of threshold current densities in DH (Pb, Sn)Te laser diodes has recently been demonstrated by Tomasetta and Fonstad [3] and continuous operation of (Pb, Sn)Te laser diodes at 77 K has been achieved by Groves *et al.* with the aid of the DH geometry and careful heat sinking [5].

While experimental progress in Pb-salt laser diodes has been dramatic, theoretical calculations of threshold currents have been less successful. Published calculations [6] predict threshold current densities much lower than those observed, and furthermore predict a much more gradual increase of threshold with temperature than one in fact observes. These discrepancies are important to resolve because without a credible model it is impossible to understand the limiting device and materials parameters, or to predict ultimate device performance, i.e., threshold current density and efficiency.

In this paper we will first look at the limitations of the simple model and point out where it is invalid for DH (Pb, Sn)Te laser diodes. We will then present a more detailed model which is in agreement with the experimental results measured in this program [3] and by others [4], [5]. From this model we can begin to identify the parameters that will be important to further reduce threshold current densities, and can make more realistic predictions concerning high-temperature operation of $Pb_{1-x}Sn_xTe$ laser diodes.

Manuscript received December 19, 1974; revised February 3, 1975. This work was supported in part by the National Science Foundation. This paper is based in part on a dissertation submitted to the Department of Electrical Engineering, Massachusetts Institute of Technology, by L. R. Tomasetta, in partial fulfillment of the requirements for the Ph.D. degree.

L. R. Tomasetta was with the Department of Electrical Engineering and Center for Materials Science and Engineering, Massachusetts Institute of Technology, Cambridge, Mass. 02139. He is now with the Massachusetts Institute of Technology Lincoln Laboratory, Lexington, Mass. 02173.

C. G. Fonstad is with the Department of Electrical Engineering and Center for Materials Science and Engineering, Massachusetts Institute of Technology, Cambridge, Mass. 02139.

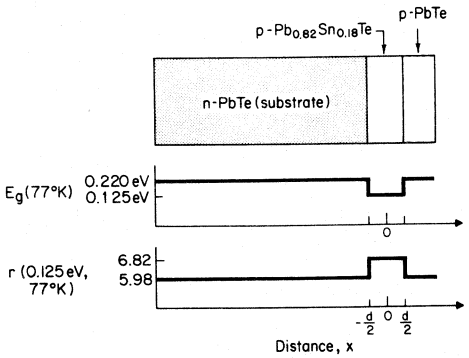

Fig. 1. An ideal, symmetrical DH lead-tin telluride laser diode and the variation of energy gap and refractive index perpendicular to the junction plane. The numbers indicated are for 77 K and typical of those used in this work. The improvement in performance of the DH geometry in comparison with the simple p-n junction device is a result of optical and minority carrier confinement that occurs at the heterojunctions. The three-layer dielectric waveguide structure helps to keep the optical field confined to the higher index active region where the optical field aids stimulated emission. The p-p heterojunction creates an electrical barrier to minority carriers thereby requiring their recombination in the center higher index active region where the optical field and minority carrier concentration are greatest, rather than in the passive regions where their recombination does not aid stimulated emission.

GAIN IN SEMICONDUCTOR LASERS, $T = 0$ MODEL

Lasher and Stern [7] have shown that the net gain in the active region of a semiconductor laser is

$$G = \frac{\int_{-d/2}^{d/2} g[n_p(x)]\, E^2(x)\, dx}{\int_{-d/2}^{d/2} E^2(x)\, dx} \tag{1}$$

where $g[n_p(x)]$ is the gain distribution across the active region as a function of the injected minority carrier concentration, and $E(x)$ is the optical field. At $T = 0$, for the case where the minority carrier diffusion length L_D is much greater than the width of the active region d, the following approximations are valid [6]:

$$g[n_p(x)] = An_p(x) \tag{2a}$$

$$n_p(x) = n_p(-d/2). \tag{2b}$$

By relating G in the active region to the internal losses α, and the end face losses $(1/L)\ln(1/R)$, the threshold current density J_T of the laser diode is found to be [7]

$$J_T = \frac{8\pi q d r^2 \Delta\nu(\alpha + 1/L \ln 1/R)}{\eta_{\text{int}} \lambda_0^2} \tag{3}$$

where λ_0 is the free-space wavelength, η_{int} is the internal quantum efficiency, $\Delta\lambda$ is the spontaneous linewidth, d is the active region width, r is the index of refraction in the active region, L is the length of the cavity, and R is the mirror reflectivity. The absorption coefficient α is the sum of two terms, α_0 the absorption loss in the high-index region, and α_D the diffraction loss [8].

Because the end losses $(1/L)\ln(1/R)$ typically dominate the loss mechanisms until

$$d < \frac{\lambda_0}{2r} \tag{4}$$

when diffraction losses become significant, decreasing d results in a nearly linear decrease in J_T. Fig. 2 shows results of threshold current calculations for (Pb, Sn)Te DH laser diodes at 8, 77, and 195 K based on the $T = 0$ model given by (3) and the analysis of the optical fields provided by Anderson [8]. They are identical to results obtained using the technique of Sleger *et al.* [6].

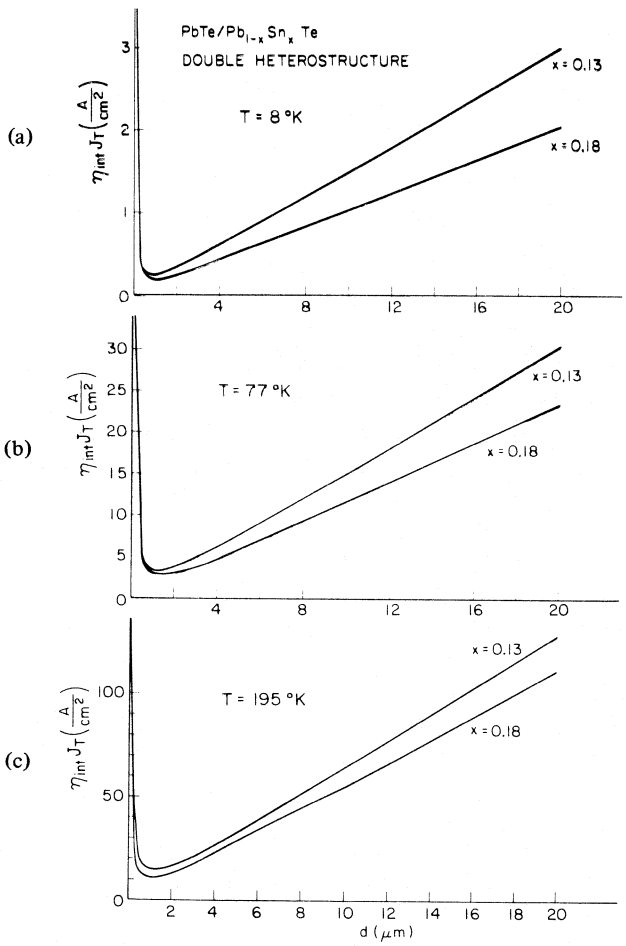

Fig. 2. (a) Threshold current density of $Pb_{1-x}Sn_xTe$ DH laser diodes at 8 K calculated using the $T = 0$ constant gain model. The horizontal scale is the active region, i.e., $Pb_{1-x}Sn_xTe$ layer, width. Two alloy compositions, $x = 0.13$ and $x = 0.18$, are presented. $L = 0.05$ cm. (b) Same with $T = 77$ K. (c) Same with $T = 195$ K.

Limitations of $T = 0$ Model

A closer examination of the two assumptions implicit in deriving (3) clearly indicates that great care must be exercised when using it to predict threshold currents of semiconductor lasers. The first assumption (2a) is valid only at $T = 0$. For any other temperature the well-known condition for internal optical gain must be used [9]

$$|\psi_n - \psi_p| \geq h\nu \tag{5}$$

where ψ_n, ψ_p are the quasi-Fermi levels of the electrons and holes, respectively, and $h\nu$ is the lasing energy.

The significant implication of (5) is that there is a certain minority carrier density that must be built up before there is any gain at all. The gain variation with injected minority carriers is given by [10]

$$g[n_p(x)] = A(n_p(x) - n_t) \tag{6}$$

where n_t is the threshold value of injected minority carriers needed to satisfy the equality condition in (5). Of course, if n_t is very much less than $n_p(x)$, then (6) is only an insignificant variation of (2a). This is what occurs at $T = 0$ where $n_t = 1\ \text{cm}^{-3}$ if the majority carrier population is degenerate. But if the required gain is a result of the small difference between two large quantities $n_p(x)$ and n_t, then the effect of the minimum injection level for gain n_t is significant and must be considered.

The behavior of the quasi-Fermi levels with doping, temperature, and injection level for an ideal semiconductor is provided by Blakemore [11]. Details of the band structure and quasi-Fermi-level movement peculiar to $Pb_{1-x}Sn_xTe$ are provided by Adler *et al.* [12]. The results of this calculation are illustrated in Fig. 3. From this figure we find that for a majority carrier concentration of $5 \times 10^{17}\ \text{cm}^{-3}$, n_t is $1.6 \times 10^{16}\ \text{cm}^{-3}$ at 77 K and increases to $8 \times 10^{17}\ \text{cm}^{-3}$ at 195 K. If the majority carrier concentration is increased to $1 \times 10^{18}\ \text{cm}^{-3}$, n_t decreases to $3 \times 10^{15}\ \text{cm}^{-3}$ at 77 K and $4 \times 10^{17}\ \text{cm}^{-3}$ at 195 K. Note that the decrease in n_t for a doubling of the majority carrier concentration is fivefold at 77 K, but is only twofold at 195 K.

The second assumption that the minority carrier distribution is constant across the active region and equal to the value at the point of injection, (2b), is valid only when the diffusion

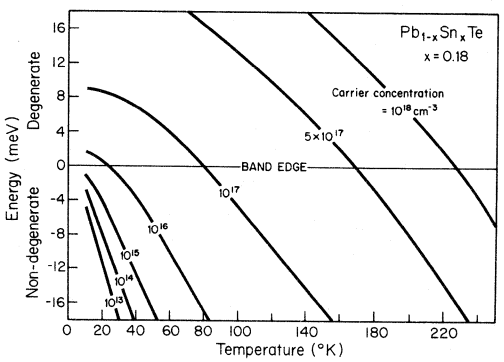

Fig. 3. Position of quasi-Fermi level in $Pb_{0.82}Sn_{0.18}Te$ for various carrier concentrations as a function of temperature. Because the bands are symmetrical, these curves can be used for both electrons and holes (after [12]).

length of the injected minority carriers L_D is much greater than the active region width d. When L_D is not much greater than d this assumption has the effect of overestimating the optical gain of the laser. The seriousness of the miscalculation depends on the magnitudes of L_D, d, and n_t. Another result of assuming a constant gain across the active region is that the zeroth-order mode is always the highest gain mode. The validity of this result will be discussed shortly.

$T \neq 0$ Model

We now proceed to recalculate threshold current densities for DH lasers in a more general way than (3), accounting for both the minimum injection level for gain and the spatial distribution of the injected minority carriers. The carrier distribution in the active region of a DH laser like that shown in Fig. 1 can be approximated by the solution to

$$\frac{\partial^2 n_p}{\partial x^2} - \frac{n_p - n_{p0}}{D_n \tau_n} = 0 \tag{7}$$

where n_p is the total minority carrier density; n_{p0} is the equilibrium minority carrier density; and D_n and τ_n are the minority carrier diffusion coefficient and lifetime, respectively. The diffusion length L_D is

$$L_D = \sqrt{D_n \tau_n}. \tag{8}$$

We are assuming that the minority carrier lifetime τ_n is not a function of position. In fact, the lifetime depends on the amount of stimulated recombination at each point which is in turn proportional to $E^2(x)$. Hakki [13] has considered this problem for GaAs heterostructure lasers. The difference between his more complex result and our simpler result is significant only well above threshold, and should therefore not be important for our calculations of threshold current density. The boundary conditions on the DH laser are: 1) one-way injection of minority carriers from the n-PbTe into the p-$Pb_{1-x}Sn_xTe$; and 2) no electron flow from the p-$Pb_{1-x}Sn_xTe$ to the p-PbTe, i.e., $(\partial n_p/\partial x)_{d/2} = 0$.

Solution of (7) with these boundary conditions yields

$$n_p(x) = \frac{n_p(-d/2)\cosh\left[(d - 2x)/2L_D\right]}{\cosh\left(\frac{d}{L_D}\right)}. \tag{9}$$

The gain coefficient A in (6) can be determined from Pilkuhn [14]

$$g[n_p(x)] = \frac{\eta_{\text{int}} c^2}{8\pi r^2 \nu^2 \Delta\nu \tau_n}(n_p(x) - n_t). \tag{10}$$

The net gain in the active region can then be calculated using (1), (9), and (10), and optical-field results from Anderson [8]

$$G = \frac{\eta_{\text{int}} c^2}{8\pi r^2 \nu^2 \Delta\nu \tau_n}\left[f(a, d, L_D) n_p(-d/2) - n_t\right] \tag{11}$$

where

$$f(a, d, L_D) = \left\{\frac{2}{L_D} \cdot \cos^2(ad/2)\sinh(d/L_D) + 4L_D a^2 \sinh(d/L_D) + 4a \sin(ad/2) \cdot \cos(ad/2) \cdot [1 + \cosh(d/L_D)]\right\} \Big/ \cdot [(d/2) + (1/2a)\sin(ad)] \cdot [8a^2 + (2/L_D^2)] \cdot \cosh(d/L_D)$$

where a is the transverse propagation constant of the optical field in the active region.

The threshold current is found by equating (11) with the total losses of laser. The gain at threshold G_T is

$$G_T = \alpha_D + \alpha_0 + \frac{1}{L}\ln\frac{1}{R}. \tag{12}$$

The diffraction losses α_D were calculated using the technique of Anderson [8], [16]. The absorption losses are dominated by free-carrier absorption, and are given by

$$\alpha_0 \simeq \alpha_{fc} = \frac{p_p q^3 \lambda_0^2}{4\pi^2 r c^3 \epsilon_0 \mu_h m_c^{*2}} \tag{13}$$

where p_p is the majority carrier (hole) concentration, c is the speed of light, ϵ_0 is the permittivity of free space, μ_h is the hole mobility, and m_c^* is the valence band conductivity effective mass.

Threshold Current Density Calculations

Using (11) and (12), and

$$J = qD_n\left(\frac{\partial n_p}{\partial x}\right)\Big|_{-d/2} \tag{14}$$

we can calculate the threshold current density for DH (Pb, Sn)Te lasers like those shown in Fig. 1.

$$J_T = \frac{qD_n}{L_D}\frac{\tanh(d/L_D)}{f(a, d, L_D)}\left[\frac{8\pi r^2 \nu^2 \Delta\nu \tau_n}{\eta_{\text{int}} c^2} G_T + n_t\right]. \tag{15}$$

Figs. 4–7 present the results of such calculations for p-PbTe/p-$Pb_{0.82}Sn_{0.18}Te$/n-PbTe devices. Figs. 4, 5, and 7 correspond to an active region majority carrier concentration N_A of 5×10^{17} cm^{-3} at 8, 77, and 195 K, respectively. Fig. 6 repeats the 77 K calculation with $N_A = 1 \times 10^{18}$ cm^{-3}. The vertical scale in these figures is J_{th}, while the horizontal scale is the active region width. In each figure a set of curves is presented with minority carrier diffusion length as the parameter; it is varied from 2–20 μm. The spontaneous emission linewidth was taken at 2 kT. To calculate τ_n from L_n (8), D_n was taken to be 100 cm^2/s at 77 K and to vary inversely with temperature [16]. η_{int} was set equal to 1 (this point is discussed further in the following).

At 8 K, Fig. 4, the results are nearly identical to those of the $T = 0$ model, but at 77 K, Figs. 5 and 6, the threshold currents are nearly two orders of magnitude higher. At 195 K the results differ by more than three orders of magnitude.

Looking at Figs. 4–7, and the previous discussions, we can

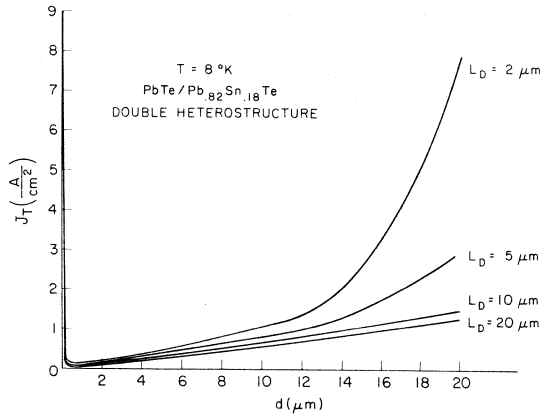

Fig. 4. Threshold current density for $Pb_{0.82}Sn_{0.18}Te$ DH laser diodes at 8 K calculated using the $T \neq 0$ model presented in this work. Minority carrier diffusion length is used as a parameter and the horizontal scale is the active region, i.e., (Pb, Sn)Te layer, width. The vertical scale is J_T. The active region doping is 5×10^{17} cm^{-3}, p-type. η_{int} was taken to be 1 (see text). $L = 0.05$ cm.

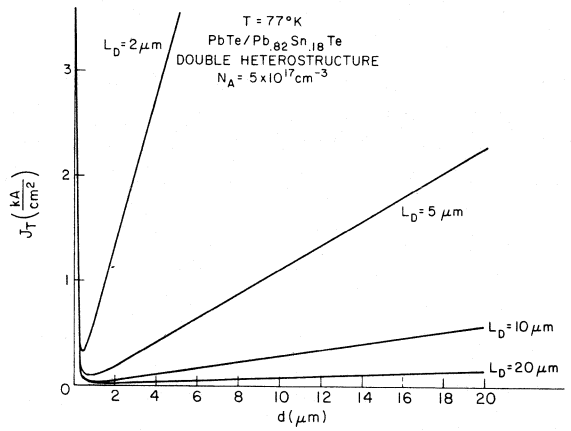

Fig. 5. Same as Fig. 4 for 77 K.

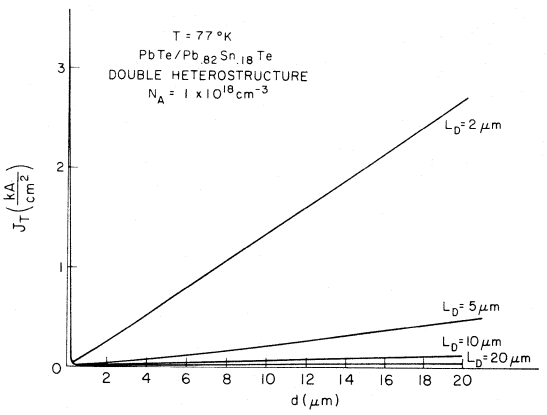

Fig. 6. Same as Fig. 5 with an active region doping of 10^{18} cm^{-3}, p-type.

point out some important features and results of these calculations as follows.

A. Temperature

The main variation of threshold with temperature is not a variation in the coefficients of (15), but rather the change in n_t. At $T = 8$ K, n_t is essentially zero because the majority quasi-Fermi level is so far into the band that a small current will move the minority carrier quasi-Fermi level close enough to the band edge to satisfy (5) for gain. At 77 K the majority quasi-Fermi level is not as far into the band and an injection level of 1.6×10^{16} cm^{-3} is needed for gain to occur. This already represents a substantial current and, in fact, represents the dominant contribution to threshold current. As temperature is increased, the majority carrier quasi-Fermi level becomes less degenerate and finally nondegenerate, and the bandgap increases. As a result, n_t increases rapidly with temperature and the current needed to provide a specific gain increases with n_t.

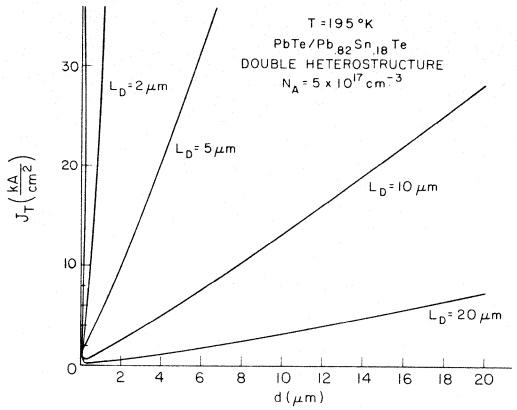

Fig. 7. Same as Fig. 4 for 195 K.

B. Carrier Concentration

As the majority carrier concentration increases, n_t decreases, reducing the current needed for a given value of gain. Thus the threshold can be reduced by increasing the active region doping until end face and free-carrier absorption losses become dominant. For example, as the majority carrier concentration is increased from 5×10^{17}–10^{18} cm^{-3}, the increased free-carrier absorption losses are still insignificant and at 77 K the threshold is reduced by a factor of 5, Figs. 5 and 6. The effect is smaller at higher temperatures, however, and the same change in doping level only leads to a twofold reduction in J_T at 195 K.

C. Optical Mode

One result of the spatial variation of the gain and the asymmetry of the minority carrier injection with respect to the active region is that maximum gain occurs at $x = -d/2$ rather than $x = 0$, the center of the optical-field pattern. Consequently, greater gain is possible for higher order optical modes than for the $m = 0$ mode under certain circumstances. Consider the case where $L_D \ll d$. The gain coefficient $g(x)$ is a maximum at $x = -d/2$ and rapidly decays as x increases. Since the net gain G is a result of the integration of $g(x)E^2(x)$, it is desirable to have $E(x)$ large where $g(x)$ is large. The $m = 1$ and $m = 2$ modes have large optical-field densities near $x = -d/2$ and can have significantly higher gain. For the case $d \leqslant L_D$, however,

the case corresponding to thin DH, which is the one of most interest, the difference in gain for different modes is insignificant. The diffraction losses for higher order modes are larger and thus threshold current densities for these modes are larger. We have restricted ourselves to consideration of only the lowest order mode in Figs. 4-7; inclusion of higher order modes would keep the predicted threshold current from increasing indefinitely with increasing d.

D. Spontaneous Lifetime and Efficiency

In the calculations we have assumed 100-percent internal efficiency, $\eta_{int} = 1$. This, of course, can only be true for the one situation for which the minority carrier lifetime τ_n is equal to the spontaneous radiative recombination lifetime τ_r. The other curves should be adjusted for the proper $\eta_{int} = \tau_n/\tau_r = L_D^2/\tau_r D_n$ by increasing the contribution to J_T from the term in (15) involving G_T by a factor of η_{int}^{-1}. This contribution is essentially the J_T obtained in the $T = 0$ model, so making the adjustment is straightforward. In many cases where the n_t term is the dominant factor in J_T, this correction is small and can be neglected, particularly in light of the uncertainties in the parameter values used in the calculations. This is the situation in the 77 and 195 K cases considered here, Figs. 5-7. In all cases neglecting the adjustment will lead to conservative (lower limit) estimates of L_D, τ_n, and ultimately η_{int} when the calculated threshold current densities are compared to experimental results.

Recent calculations [17][1] indicate that at 77 K τ_r is approximately 20 ns. Using this value at 77 K, η_{int} ranges from 2 percent for the $L_D = 2$ μm, $\tau_n = 0.4$-ns curve, to >100 percent for the $L_D = 20$ μm, $\tau_n = 40$-ns curve (which, of course, simply means that for the values of D and τ_r used, L_D is never as large as 20 μm at 77 K). For $\tau_n = \tau_r$, i.e., $\eta_{int} = 100$ percent at 77 K, $L_D \simeq 14$ μm. At 8 K the diffusion length corresponding to $\tau_n = 20$ ns is 45 μm; at 195 K it is 9 μm.

Experimental Results

To examine the effects of active region thickness and temperature on threshold current in (Pb, Sn)Te DH laser diodes, a series of heterostructure laser diodes was fabricated which were identical in all controllable respects except that the active region thickness varied from 4-20 μm. Growth, fabrication, and testing details as well as threshold current density dependence on active region thickness have previously been reported [3] for these devices without an attempt to compare the experimental results with theory.

In Fig. 8 experimental threshold data [3] have been plotted on the same graph with the curves from Fig. 5 which were theoretical calculations for a similar device. A minority carrier diffusion length $L_D \simeq 3$ μm, a minority carrier lifetime $\tau_n \simeq 1$ ns, and a $\eta_{int} \simeq 5$ percent are indicated. We point out that

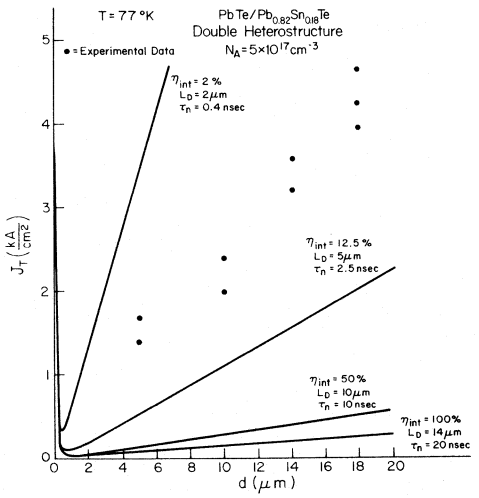

Fig. 8. Comparison of experimental pulsed threshold current densities with theoretical curves: $T = 77$ K. The solid curves are the same as those in Fig. 5 except that η_{int} has been calculated for each curve assuming $\tau_r = 20$ ns and $D = 100$ cm^2/s; the vertical scale is J_T.

many parameter values are assumed in arriving at these quantitative conclusions; experiments are currently in progress to obtain direct measurement of L_D, τ_n, and η_{int}, and to carefully confirm the theoretical predictions. It is felt, however, that the parameter values used in the calculations are reasonable and that the conclusions will be substantially unchanged once more exact values for each device are known.

There is experimental evidence that a minority carrier lifetime of 1 ns and an efficiency of 5 percent are not unreasonable. In particular, Asbeck [17] has recently measured a lifetime of 2.3 ns in PbSe laser diodes at 77 K and he infers an efficiency of 10 percent. Walpole *et al.* [4] see evidence of large internal quantum efficiencies in some of their diodes. These results had been irreconcilable with the earlier $T = 0$ theory which predicts very low thresholds for efficient devices.

Further support for the model can be obtained by comparing the experimentally observed temperature variation of threshold with the predicted variation. This is done for a 10-μm, $Pb_{0.82}Sn_{0.18}Te$/PbTe DH laser in Fig. 9. The theoretical curves correspond to $\tau_r = 20$ ns and $\eta_{int} = 5$ percent and 100 percent, respectively. (The η_{int} adjustment has been made in the $\eta_{int} = 5$ percent curve.) For contrast, the $T = 0$ model prediction, $\eta_{int} = 100$ percent is plotted also. The much more rapid increase of threshold with temperature predicted by the present model is dramatically evident. Good agreement in this respect with the data is also seen above 40 K.

Below 40 K neither model predicts the observed threshold plateau. The existence of such a plateau is not unusual and similar plateaus have been seen in GaAs laser diodes[2] and in

[1] Asbeck shows that the spontaneous lifetime is inversely proportional to the bandgap, the index of refraction, and an interband matrix element, and calculates a spontaneous lifetime for degenerate PbSe of 9.3 ns at 77 K. Using this value, and the bandgap and index of refraction of (Pb, Sn)Te, the lifetime of $Pb_{0.82}Sn_{0.18}Te$ is found to be 16.5 ns at 77 K if the value of the matrix element is assumed to be the same.

[2] With this reference to GaAs laser diode work it is appropriate to mention that the shortcomings of a $T = 0$ model and the importance of a critical minority carrier injection level n_t have been appreciated in GaAs DH laser research for some time. It is interesting to note that because of the larger density of states effective masses and narrower bandgap in $Pb_{1-x}Sn_xTe$, n_t is an even more important factor in $Pb_{1-x}Sn_xTe$ than in GaAs.

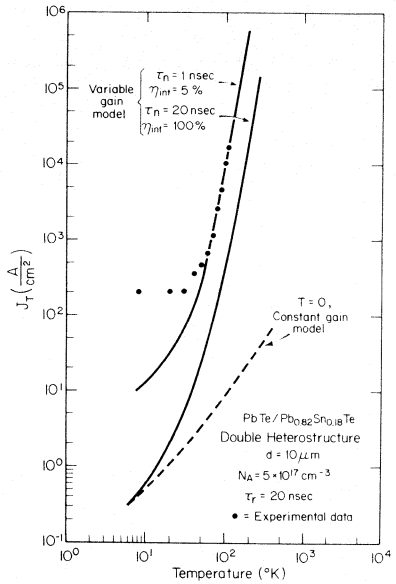

Fig. 9. Comparison of the temperature variation of J_T measured experimentally for a $Pb_{0.82}Sn_{0.18}Te$ DH diode with active region width 10 μm, and the theoretical prediction. τ_r was again taken to be 20 ns and D was assumed to vary inversely with temperature.

other IV-VI laser diodes [4], [5], [18]. The important point, however, is that only now that we have a model which accurately predicts the threshold current densities above 40 K can we identify this as an anomalous region in DH (Pb, Sn)Te laser diodes. Two possible explanations for this plateau might be the following.

1) The spontaneous linewidth will not continue to decrease indefinitely with temperature and will ultimately be limited by scattering mechanisms to some finite value. This might contribute a factor of 2 or 3 to the threshold but does not seem sufficient to make up the entire difference.

2) There may be a leakage current across the junction due to one or more of a number of sources such as surface leakage, traps, or interface states (caused perhaps by the heterojunction lattice mismatch). This current would have to be of the order of 100-200 A/cm^2 in this device.

Summary and Conclusions

From the experimental and theoretical threshold results presented and the comparisons made between them we can draw the following important general conclusions.

1) The $T = 0$ threshold model is inappropriate at temperatures much above 10 K and leads to ever increasing errors as temperature increases. It cannot be used to make predictions concerning high-temperature operation.

2) A model which accounts for the spatial variation of the gain and for the critical injection level necessary for inversion is seen to work very well for temperatures greater than 40 K. As temperature increases, the critical minority carrier injection level n_t becomes the dominant factor determining threshold current density and causing its rapid increase with increasing temperature.

3) It appears from the model that the reductions in threshold current density achievable by using the DH structure will ultimately allow routine continuous wave (CW) operation at 77 K; but at higher temperatures, greater than 150 K, for example, the increasing critical minority carrier injection level and the decreasing diffusion length indicate that CW operation will be difficult to achieve even in DH lasers.

4) Some improvement in threshold at high temperatures can be obtained by increasing the majority carrier density in the active region. Above 5×10^{18} cm^{-3} it is likely that increased free-carrier absorption losses will negate the gains from reducing the critical injection level.

5) The plateau in the threshold-temperature relation for $T < 40$ K is not explained by either model. Two possible explanations for it in these DH lasers have been proposed but the exact mechanism is unknown.

Acknowledgment

The authors wish to thank A. Colozzi for his technical assistance in the experimental portion of this work. Dr. J. N. Walpole's contributions through discussions of the theoretical threshold predictions, the low-temperature plateau, and his experimental observations are gratefully acknowledged. We also would like to acknowledge many helpful discussions with Dr. P. Asbeck and Dr. J. R. Lowney and with Prof. S. D. Senturia and Prof. A. L. McWhorter.

References

[1] M. B. Panish and I. Hayashi, "Heterostructure injection lasers," in *Applied Solid State Science*, vol. 4, R. Wolfe, Ed. New York: Academic, 1974, pp. 235-238.

[2] K. J. Sleger *et al.*, "Single heterostructure $PbS_{1-x}Se_x$ diode lasers," *J. Appl. Phys.*, vol. 45, pp. 5069-5071, Nov. 1974.

[3] a) L. R. Tomasetta and C. G. Fonstad, "Threshold reduction in $Pb_{1-x}Sn_xTe$ laser diodes through the use of double heterojunction geometries," *Appl. Phys. Lett.*, vol. 25, pp. 440-442, Oct. 1974.
b) —, "Thallium and indium doped $Pb_{1-x}Sn_xTe$ by liquid phase epitaxy," *Mater. Res. Bull.*, vol. 9, pp. 799-802, June 1974.
c) —, "Liquid phase epitaxial growth of laser heterostructures in $Pb_{1-x}Sn_xTe$," *Appl. Phys. Lett.*, vol. 24, pp. 567-570, June 1974.

[4] J. N. Walpole *et al.*, "Single heterojunction $Pb_{1-x}Sn_xTe$ diode lasers," *Appl. Phys. Lett.*, vol. 23, pp. 620-622, Dec. 1973.

[5] S. H. Groves, K. W. Nill, and A. J. Strauss, "Double heterostructure $Pb_{1-x}Sn_xTe$-PbTe lasers with CW operation at 77 K," *Appl. Phys. Lett.*, vol. 25, pp. 331-333, Sept. 1974.

[6] a) K. J. Sleger, G. F. McLane, and D. Mitchell, "Calculation of the optical confinement in $PbS_{1-x}Se_x$ double heterojunction laser," *J. Nonmetals*, vol. 1, pp. 297-310, 1973.
b) —, "Performance potential of $PbS_{1-x}Se_x$ and $Pb_{1-x}Sn_xTe$ double heterostructures," presented at the Narrow Bandgap Semiconductor Conf., Nice, France, Sept. 1973.

[7] G. Lasher and F. Stern, "Spontaneous and stimulated recombination radiation in semiconductors," *Phys. Rev.*, vol. 133, pp. A553-A563, Jan. 1964.

[8] W. W. Anderson, "Mode confinement and gain in junction lasers," *IEEE J. Quantum Electron.*, vol. QE-1, pp. 228-236, Sept. 1965.

[9] M. G. A. Bernard and G. Duroffourg, "Laser conditions in semiconductors," *Phys. Status Solidi*, vol. 1, pp. 699-703, 1961.

[10] S. M. Sze, *Physics of Semiconductor Devices*. New York: Wiley, 1969, p. 695.

[11] J. S. Blakemore, *Semiconductor Statistics* (International Series of Monographs on Semiconductors), vol. 3. New York: Pergamon, 1962.

[12] a) M. S. Adler, C. R. Hewes, and S. D. Senturia, "$\vec{k} \cdot \vec{p}$ model for the magnetic energy levels in PbTe and $Pb_{1-x}Sn_xTe$," *Phys. Rev. B.*, vol. 7, pp. 5186-5195.

b) S. D. Senturia, M. S. Adler, C. R. Hewes, and A. C. Smith, "A $\vec{k} \cdot \vec{p}$ band model for PbTe and $Pb_{1-x}Sn_xTe$ based on Knight shift studies," *J. Nonmetals*, vol. 1, pp. 195–205, 1973.
[13] B. W. Hakki, "Mode gain and junction current in GaAs under lasing conditions," *J. Appl. Phys.*, vol. 25, pp. 288–294, Jan. 1974.
[14] M. H. Pilkuhn, "The injection laser," *Phys. Status Solidi*, vol. 25, pp. 9–62, Jan. 1968.
[15] T. C. Harman, "Narrow-gap semiconductor lasers," in *The Physics of Semimetals and Narrow-Gap Semiconductors*, D. L. Carter and R. T. Bate, Ed. New York: Pergamon, 1971, pp. 363–382.
[16] L. R. Tomasetta, Ph.D. dissertation, Massachusetts Institute of Technology, Cambridge, Sept. 1974, unpublished.
[17] P. Asbeck, Ph.D. dissertation, Massachusetts Institute of Technology, Cambridge, Dec. 1974.
[18] T. C. Harman and I. Melngailis, "Narrow gap semiconductors," in *Applied Solid State Science*, vol. 4, R. Wolfe, Ed. New York: Academic, p. 69.

Selection of Modes Perpendicular to the Junction Plane in GaAs Large-Cavity Double-Heterostructure Lasers

D. C. KRUPKA, MEMBER, IEEE

Abstract—**The gains and reflectivities of the transverse-electric (TE) modes of GaAs large-cavity double-heterostructure (DH) (P-p-n′-N) lasers have been calculated in order to study mode selection perpendicular to the junction plane. The GaAs laser is modeled as a passive dielectric-slab waveguide composed of four layers whose optical constants are taken from recent literature. In lasers having a cavity thickness of a few microns, a small difference in refractive index between the p- and n′-region leads to the fundamental mode being confined to the p-region. Discrimination in favor of this mode without significant penalty in threshold gain may be achieved by utilizing the mode-dependent loss in the n′-layer. It is found that optimum mode discrimination in favor of the fundamental mode is governed by a suitable combination of the p-layer thickness, loss in the n′-region, and the difference of refractive indices of the p- and n′-layers. This analysis contrasts with an earlier analysis of the case of uniform refractive index in which it was found that the p-layer should be twice as thick as the n-layer for optimum mode discrimination. The calculated mode shapes in P-p-n′-N lasers are found to be in qualitative agreement with those observed recently by Hakki, and also with earlier observations that catastrophic mirror damage in P-p-n′-N lasers is confined to the p-region. Contrary to experimental observation, the model predicts that lasers having cavity thicknesses as large as 3 μm should operate stably in the fundamental mode. Possible reasons for this discrepancy are advanced. A simplification of the P-p-n′-N laser, which consists of omitting the N-layer thus yielding an asymmetric double-heterostructure laser, is suggested, and the merits and drawbacks of such a design are discussed.**

I. Introduction

THE possibility of obtaining pulsed powers of the order of 0.5 W from a GaAs stripe geometry laser, coupled with the ease of modulation and prospects for low ultimate cost, make this device an attractive candidate for a variety of applications. For many of these, it is required that the laser operate in the fundamental transverse mode, with its inherent beam ellipticity minimized. Reduction of beam ellipticity is particularly important in systems which employ a single-mode optical fiber to act either as a mode filter for the GaAs radiation or as a mode-selecting element [1]. Although ellipticity may be reduced by recourse to some narrow mesa structure, such a technique would entail reducing the mirror area to the point of risking mirror damage. It is important, therefore, to investigate laser designs which lead to stable operation in a fundamental transverse mode having low ellipticity and which provide output powers of at least 40 W/mm of stripe width.

One answer to the present problem has been to fabricate lasers with provision for the separate confinement of carriers and of the optical field [2], [3]. Another approach is the P-p-n-N or P-p-n′-N laser, shown in Fig. 1, with a cavity thickness of about 2 μm. This second class of structures is capable of supporting several transverse modes perpendicular to the junction plane which are typically transverse electric (TE) [5]. Since the effective angle of incidence at the mirror facets increases for higher order modes [5], these will possess a lower lasing threshold by virtue of their lower mirror transmission loss unless means are found for discriminating against them. This discrimination has been achieved by confining the gain to a selected portion of the cavity [4]. Calculations by Ripper[1] had shown that optimum mode discrimination favoring the fundamental mode in a laser with a uniform refractive index across the cavity would be achieved by inverting the population over a region extending from one side over approximately two-thirds of the optical waveguide. Successful operation of a thick-cavity zero-order-mode laser utilizing these ideas was first reported by Paoli *et al.* [4].

In order to appreciate the need for position selective inversion, it is helpful to consult Fig. 2, showing the fundamental and first-order TE modes perpendicular to the junction plane (TE_0 and TE_1) of a P-p-n-N laser with a cavity width of 2 μm and an index discontinuity between the ternary and binary regions of 0.14. The electronic gain of the mth-order TE mode

Manuscript received January 3, 1975; revised January 29, 1975.
The author is with Bell Laboratories, Murray Hill, N.J. 07974.

[1] J. E. Ripper, unpublished calculation. The author is grateful to L. A. D'Asaro for allowing him to study Ripper's results.

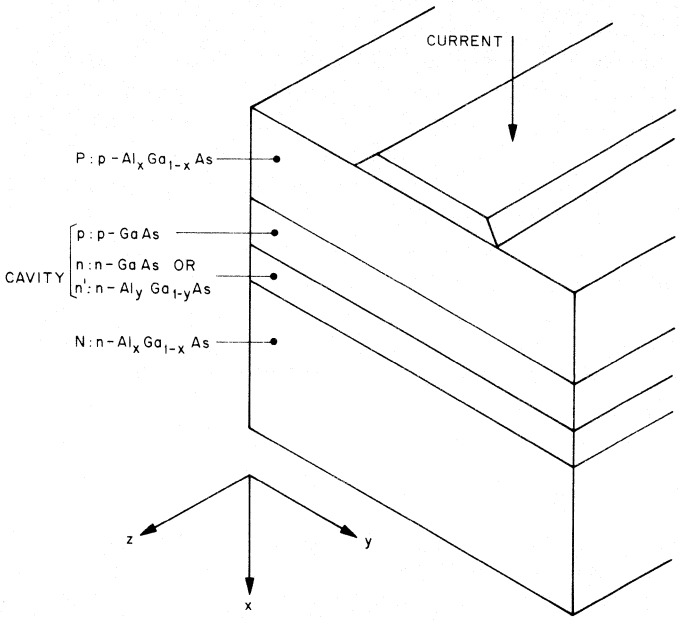

Fig. 1. Physical structure of a P-p-n-N or P-p-n'-N laser. The distinction between the two types lies in the introduction of a small amount of Al to the n-GaAs to produce a P-p-n'-N laser. The stripe contact which is 12 μm wide and the coordinate system employed in the present work are also shown. The two inner layers are referred to as the cavity.

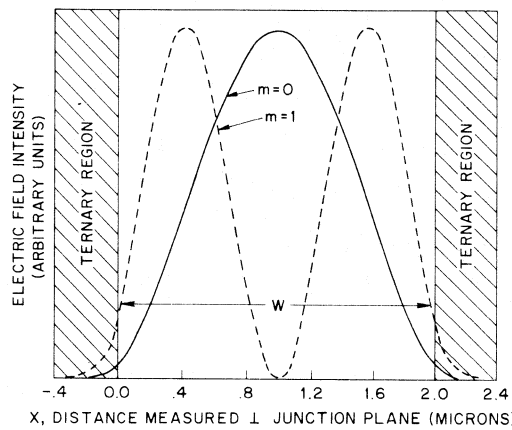

Fig. 2. The fundamental ($m = 0$) and first-order ($m = 1$) mode intensities (not normalized) or a P-p-n-N laser with a cavity width of 2 μm and a symmetric index profile with refractive indices of 3.48 and 3.62 are shown.

G_m is given by [6], [7]

$$G_m = \frac{k_0}{\beta} \int_{-\infty}^{\infty} n(x) g(x) \mathcal{E}_m^2(x)\, dx \tag{1}$$

where $\mathcal{E}_m(x)$ is the normalized electric field of the mth mode, $g(x)$ is the spatial distribution of gain or loss, $n(x)$ is the refractive index profile, and β/k_0 is the effective refractive index seen by the mode. If $g(x)$ is uniform over the cavity region ($0 \leqslant x \leqslant W$), the electronic gains of the two modes are almost identical, and the first-order mode may oscillate by virtue of its lower mirror loss [5], [8]. Inverting the population over exactly half of the guide, say, from $x = 0$ to $x = W/2$, would likewise provide little mode discrimination. On the other hand, confining the gain to two-thirds of the cavity from $x = 0$ to $x = \frac{2}{3}W$ clearly does result in mode discrimination since the inversion now exists over about 70 percent of the fundamental mode and over 55 percent of the first-order mode volume. This simple intuitive idea is stressed here since it will be important in understanding much of the material to follow.

While theory and experiment [4] indicated that mode discrimination could be achieved by appropriate definition of the region of inverted population, it remained for Hakki and Hwang [9] to explain and demonstrate improved control of the dimensions of the gain region. They concluded that in order to restrict gain to the p-region, hole injection from that region to the n-region had to be eliminated or greatly reduced. As the laser approaches threshold, the electron concentration in the p-region is estimated to be 1.8×10^{18} cm^{-3} [10], and this causes the electron quasi-Fermi level to rise into the conduction band by an amount approximately given by

$$\Delta E = \frac{\hbar^2}{2m_e} (3\pi^2 n_e)^{2/3} \approx 70 \text{ meV}. \tag{2}$$

In the above expression n_e is the electron concentration and the other symbols have their usual meaning with $m_e/m_0 = 0.068$ for GaAs. As pointed out in [9], (2) neglects a number of possible complicating effects such as nonparabolicity of the bands and band shrinkage at high concentration. For a lightly doped n-region, it is found that a potential drop of about 25 meV from the p- to the n-region, favorable for hole flow, will result [11]. Thus, unless appropriate steps are taken, gain will not be confined to the p-layer. Doping of the n-region by an amount in excess of 2×10^{18} cm^{-3} will produce a barrier for hole flow as will the addition of Al. (For low Al concentrations the shift is approximately 12.5 meV/mole percent [12].) It was recognized [9] that the presence of Al would modify the refractive index profile of the laser, and could lead to excitation of higher order modes effectively confined to the gain region when sufficiently large cavity thicknesses were employed. In such extreme cases, mode discrimination favoring the fundamental mode could be lost.

It is the purpose of this work to examine in more detail how the addition of the n-dopant and Al to the unpumped region, essential to the proper operation of this laser, affects the transverse-mode structure and mode selection in GaAs P-p-n'-N lasers. The change in the refractive index profile caused by these additions alters the mode structure sufficiently to force one to reexamine design parameters based on the assumption that the refractive index is uniform across the optical cavity. This work further suggests modifications of the laser design which result in a simpler structure.

It should be pointed out that calculations of the type to be described here have been carried out by Anderson [6] and by Butler and Kressel [13], [14]. The present analysis differs in that it includes calculations of mode reflectivities and considers specific geometries and doping levels. The work has been greatly aided by recent measurements [15]-[17] of the optical properties of GaAs and $Ga_xAl_{1-x}As$ over a useful range of energies and for a variety of doping levels.

Section II contains a description of the model to be used in the calculations and outlines the method. It also includes a summary of the optical properties of the various layers deemed

useful for this discussion. In Section III the results of numerical calculations of mode shapes, gains, and reflectivities are presented for a number of possible laser designs. These calculations demonstrate the importance of accurately taking into account the refractive index profile when calculating mode gains. In Section IV the calculations are compared with experimental data and conclusions are drawn concerning the factors governing mode selection. These lead directly to a suggested modification of the P-p-n′-N structure. A summary of the findings is given in Section V.

II. Calculations

A. Waveguide Modes

The GaAs laser is modeled as a dielectric slab, infinite in the plane of the junction and composed of the following four layers: ternary P; binary p of width W_p; an n′ or "unpumped" region of width W_n; and ternary N (c.f. Fig. 3). The ternary layers are assumed to be infinitely thick. Doping leads to a difference between the refractive indices n_p and $n_{n'}$ of the binary p- and the n′-regions, and the difference $n_p - n_{n'}$ is defined as δn. It is assumed that the modes propagate along the z direction and that the fields are independent of the y coordinate, taken to be in the plane of the junction, so that one may speak of TE_m and TM_m modes. Only TE modes will be considered here, since when lasing occurs in higher order modes, they are generally observed to be TE [14].

In this geometry only E_y, H_x, and H_z components are nonvanishing, and the magnetic components may be obtained from a knowledge of E_y which, in regions under consideration, takes the form

$$E_y = \mathcal{E}(x)\, e^{i(\omega t - \beta z)}$$

$\mathcal{E}(x)$ being the normalized field distribution along the x axis. The four-layer slab has been treated by Smith [18].

It will be assumed that the solutions for the modes are determined from the knowledge of the waveguide dimensions and the real part of the dielectric constant. For the absorption losses encountered in the devices to be discussed, it is entirely reasonable to neglect the imaginary part of the dielectric constant when discussing guidance perpendicular to the junction plane [8].

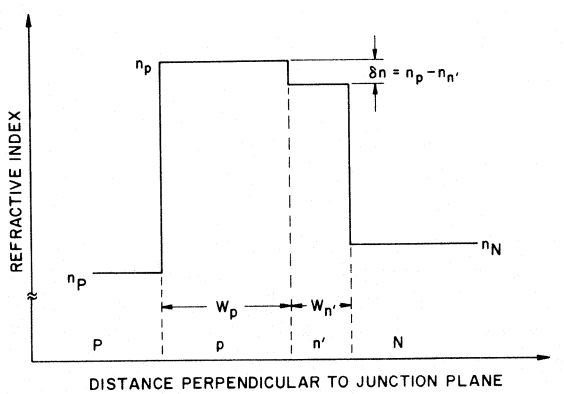

Fig. 3. Refractive index profile employed in the calculations. The refractive indices have subscripts which identify them as belonging to the ternary p-region; n_p, etc. The quantity δn is defined as $n_p - n_{n'}$, and the widths of the p- and n′-regions are W_p and $W_{n'}$.

B. Mode Gains

The chief aim of this work is to determine the electronic gain at threshold of all the modes for a given laser geometry and to determine parameters which optimize mode discrimination in favor of the fundamental mode at threshold. No attempt has been made to consider the influence of the presence of a lasing mode upon the gain profile.

Fig. 4 shows the gain profile which will be used throughout. Absorption and interface scattering give rise to the loss. Strictly speaking, the gain is not uniform over the p-region as indicated, but the departure from that assumption may not be sufficiently large for the majority of the designs to be considered if one assumes a typical diffusion length for electrons in the p-layer of 4–5 μm [19], [20].

C. Device Parameters

For the sake of consistency, all parameters necessary for mode-gain calculations have been taken from [15]–[17]. All data are based on a wavelength of 0.8875 μm (1.397 eV) since this corresponds to a typical lasing energy observed for this type of laser [21]. The refractive index data are summarized in Tables I and II, while Table III contains relevant information on absorption coefficients. The absorption coefficients for $Al_xGa_{1-x}As$ were estimated from the GaAs data at an energy of $1.4 - \Delta(x)$ eV, where $\Delta(x)$ is the change in the bandgap for a fraction x of Al [12]. Since the values of x do not exceed 0.05, such a procedure should give reasonable values.

To determine the refractive index of the active region at threshold, the following approach was adopted. The lasers currently fabricated have a p-doping in the active layer of approximately 4×10^{17} cm^{-3} which, using Table II, yields a refractive index of 3.62. At threshold, this refractive index will be altered by the increase in free carrier concentration and also as a result of inversion. In order to estimate these effects

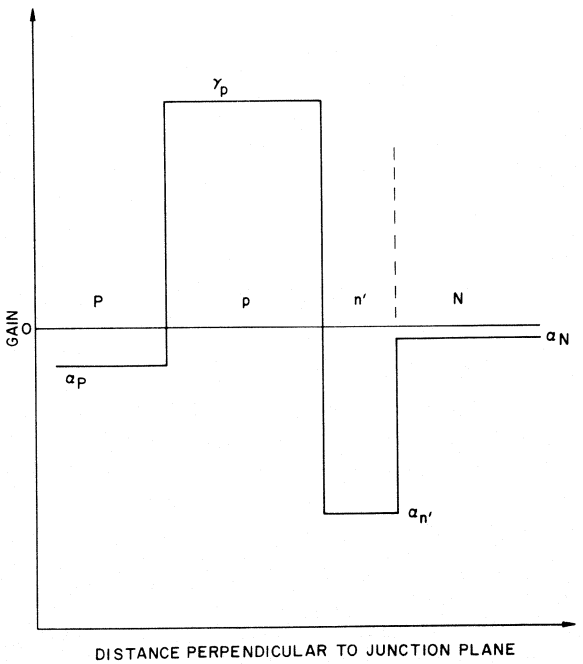

Fig. 4. Assumed gain profile perpendicular to the junction plane. The absorption coefficients α are subscripted in an obvious manner. The gain in the p-region necessary to attain fundamental mode threshold is designated γ_p.

TABLE I
REFRACTIVE INDICES OF GaAs AND $Al_xGa_{1-x}As$ AT 0.8875 μm*

Composition, x	Refractive Index
0.0, undoped	3.605
0.035	3.585†
0.05	3.565†
0.07	3.555
0.10	3.522
0.15	3.480
0.20	3.452
0.24	3.430
0.29	3.390

*[15]. The technique used there had an uncertainty in n of ±0.005.
†Interpolated from the data of [15].

TABLE II
EFFECT OF DOPING ON THE REFRATIVE INDEX OF n- AND p-TYPE GaAs AT 0.8875 μm*

	Doping (cm^{-3})	Refractive Index
n	5.9×10^{17}	3.620
	2.0×10^{18}	3.605
	3.3×10^{18}	3.593
	4.5×10^{18}	3.585†
	6.7×10^{18}	3.575
p	4.9×10^{17}	3.620
	1.2×10^{18}	3.620
	5×10^{18}	3.610
	1×10^{19}	3.590
	1.6×10^{19}	3.585

*[17].
†Interpolated from data presented in [17].

TABLE III
ABSORPTION COEFFICIENTS FOR n-GaAs AND n-$Al_xGa_{1-x}As$ AT 0.8875 μm*

	Doping (cm^{-3})	α(cm^{-1})
GaAs	2.0×10^{18}	80
	3.3×10^{18}	40
	4.5×10^{18}	30†
	6.7×10^{18}	35
$Al_{.035}Ga_{.965}As$	2.0×10^{18}	13
	3.3×10^{18}	11
	6.7×10^{18}	20
$Al_{.05}Ga_{.95}As$	2.0×10^{18}	11
	3.3×10^{18}	9†
	6.7×10^{18}	20

*From [16] and estimated as described in the text.
†Interpolated from [16].

for the present analysis, use will be made of the results of Selway *et al.* [22] on single-heterostructure (SH) lasers. These authors give

$$\Delta n \approx -(5\text{-}11)\times 10^{-21}\, n_{inj} \qquad (3)$$

where n_{inj} is the injected carrier concentration at threshold. Equation (3) is not expected to represent accurately the refractive index shift for our lasers, which, in contrast to the SH devices, have a lightly doped active region, and, consequently, a different "inversion" contribution to the change in refractive index. In the absence of more appropriate data, however, we shall assume the validity of (3). Thus, using $n_{inj} = 2\times10^{18}$ cm^{-3} [10],

$$-0.02 \lesssim \Delta n \leqslant -0.01$$

and we shall take $\Delta n = -0.015$, making $n_p = 3.605$.

In the calculations that follow, the most important material parameters are actually $\delta n = n_p - n_{n'}$, and, to a somewhat lesser extent, $\alpha_{n'}$, the loss in the n'-region (cf. Fig. 4). Thus, even if the absolute value chosen for n_p is not quite accurate, the results plotted in Figs. 6 and 7 will remain useful since one can adjust the doping levels in the n'-region, and thus the value of $n_{n'}$, to keep δ_n at the value used in these figures while also maintaining $\alpha_{n'}$ sufficiently close to the values used in the plots.

III. RESULTS

A. Mode Shapes

Before launching into a discussion of mode discrimination, it will be helpful to consider the appearance of some low-order modes in order to obtain further physical understanding of the effects of mode shape on discrimination. Fig. 5(a) shows the $m = 0$ and the $m = 1$ modes for a laser with a 2-μm cavity having the p-n junction located to yield $W_p/W_n = 2.3$. The refractive index step, δn of 0.02, is sufficiently large to confine over 90 percent of the $m = 0$ mode to the p-region while confining about 70 percent of the $m = 1$ mode. Fig. 5(b) shows the effect of reducing the width of the p-region for the same value of δn. The fundamental mode spills out of the gain region with only about 70 percent of the power now being carried in that region. However, the $m = 1$ mode has but 20 percent of its power in the p-layer, with the bulk concentrated in the n-region. Clearly, mode discrimination favoring the fundamental mode is improved in the situation shown in Fig. 5(b) at the price of increased threshold gain.

Fig. 5(c) illustrates yet another effect to be encountered. The sole difference between Fig. 5(a) and (c) is the doubling of δn in the profile shown in Fig. 5(c). Increasing the refractive index step results in compression of the $m = 1$ mode into the active region with a resulting loss in discrimination. For the case shown in Fig. 5(c), there are 96 and 83 percent of the $m = 0$ and $m = 1$ modes, respectively, in the active region.

B. Mode Gains

The calculation of mode gain is carried out as follows. The index profile shown in Fig. 3 is used to calculate the modes $\mathcal{E}_m(x)$, using Smith's expressions [18], and these in turn are employed in determining mode reflectivities as described in the Appendix. For a laser whose length L is 375 μm, which is the standard used in these calculations, and for cavity thicknesses in excess of 2 μm, the fundamental mode reflectivity is such as to yield a total mirror loss α_0 of approximately 30 cm^{-1} when the mirrors are merely cleaved surfaces. (The mirror loss for the mth mode is obtained from the relation

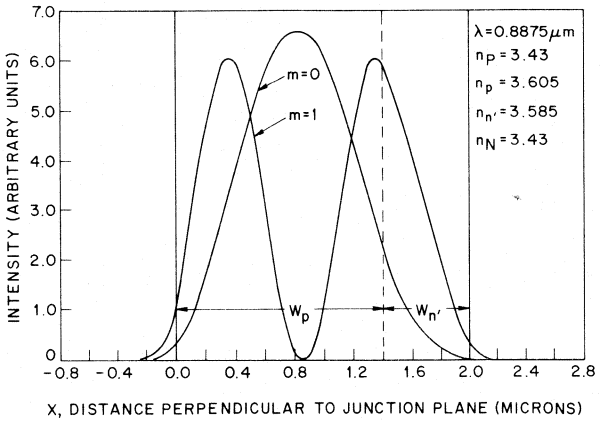

(a)

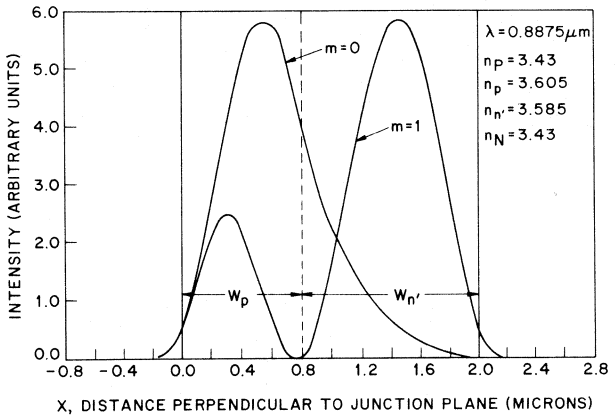

(b)

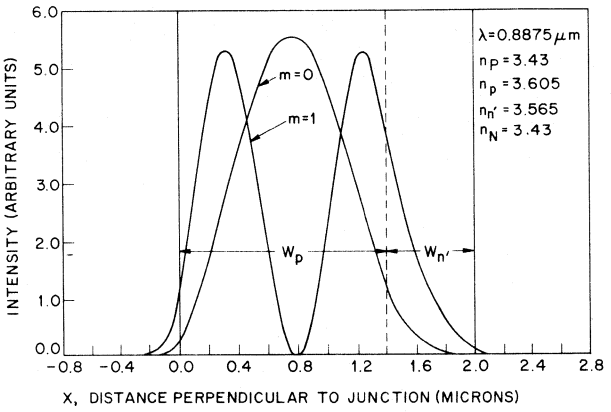

(c)

Fig. 5. Illustrating the effects of layer thickness and index profile on the shapes of the fundamental and first-order modes (not normalized for power). In all cases $n_p = n_N = 3.43$ and $n_p = 3.605$. (a) 2-μm cavity with $W_p = 1.4$ μm and $n_{n'} = 3.585$. (b) Same as (a) except that $W_p = 0.8$ μm. (c) Same as (a) except that $n_{n'} = 3.565$.

$\alpha_m = -(1/L) \ln R_m$, where R_m is the mode reflectivity of the mth mode.) For these lasers to attain fundamental mode threshold it is required that

$$\alpha_0 = G_0 = \frac{k_0}{\beta}\left(-n_P\alpha_P \int_{\text{P-region}} \mathcal{E}_0^2(x)\,dx + n_p\gamma_p \int_{\text{p-region}} \mathcal{E}_0^2(x)\,dx - n_{n'}\alpha_{n'} \int_{\text{n'-region}} \mathcal{E}_0^2(x)\,dx - n_N\alpha_N \int_{\text{N-region}} \mathcal{E}_0^2(x)\,dx\right). \quad (4)$$

Equation (4) is used to solve for the quantity γ_p (cf. Fig. 4) which is the gain in the p-region required to attain fundamental mode threshold. Knowledge of γ_p together with the absorption coefficients now determines the gain profile $g(x)$ as in Fig. 4 and permits calculation of the gains G_m of all higher order modes. Thus the present calculations determine the gains for all higher order modes *given that there exists sufficient gain for the fundamental mode* to oscillate.

C. Specific Examples

1) 2-μm Cavity: In Fig. 6(a)–(c) are plots of mode gain G_m, mirror loss α_m, and γ_p, the gain in the p-region required to attain fundamental mode threshold as a function of the position of the p-n junction in a 2-μm cavity which supports a total of five modes. The left-hand scale refers to G_m and α_m, while the scale on the right applies to γ_p. All the data presented have been calculated for the case of ternary layers possessing 24-mole percent of AlAs.

Since the plot of γ_p is simpler to treat, it is considered first. The physical reasons underlying its appearance have been presented in Section III-A. The increase of γ_p as the width of the active region is reduced reflects the fact that a smaller fraction of the fundamental mode volume occupies the active layer and thus gain must be increased to attain threshold. When the gain region is wide, the fundamental mode is contained almost entirely within the gain region and suffers little loss. Under such conditions $\gamma_p \approx \alpha_0$.

The mirror losses α_m have been drawn as straight lines although these quantities change as the position of the p-n junction is varied. For the 2-μm cavity the difference between the α_m values for the case when the junction is at the midpoint of the cavity and the case when the entire cavity is made of p-material is less than 5 percent. For present purposes this difference is considered negligible. Naturally, the lower order modes which are more tightly bound will be less sensitive to changes in the index profile than the highest order modes. For a given position of the p-n junction, the curves of α_m and G_m

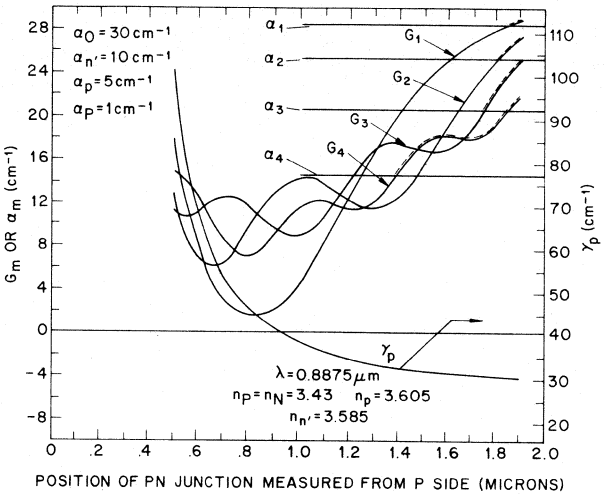

(a)

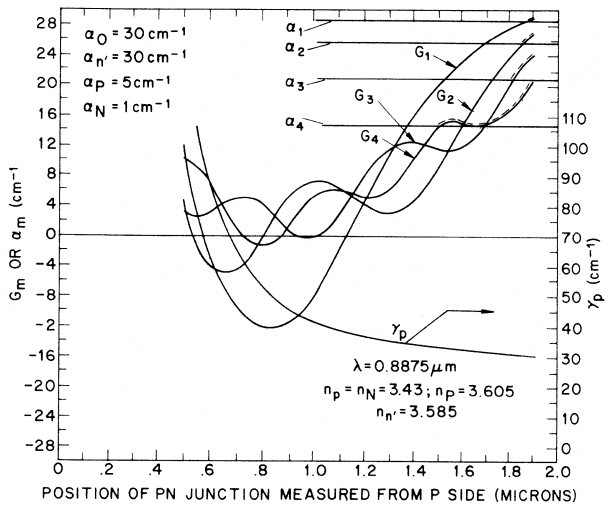

(b)

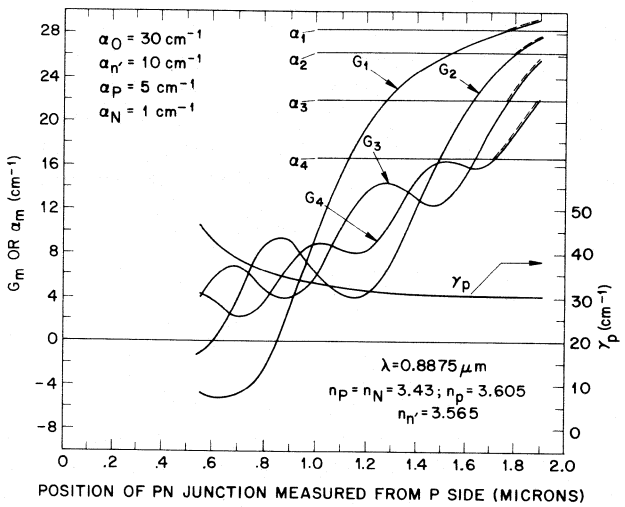

(c)

Fig. 6. Mode properties of a 2-μm cavity. The following quantities are plotted as a function of the position of the p-n junction measured from the p-P boundary: G_m—the mode gain of the mth mode; α_m—effective mirror loss for the mth mode. If $G_m > \alpha_m$, the fundamental mode will not reach threshold before the mth mode, and G_m is shown with broken lines. γ_p—gain in the gain region required to attain fundamental ($m = 0$) mode threshold assuming an effective mirror loss, $\alpha_0 = 30\ cm^{-1}$. It is assumed that operation is at 0.8875 μm with the following properties held constant: $\alpha_P = 5\ cm^{-1}$; $\alpha_N = 1\ cm^{-1}$; $n_N = n_P = 3.43$; $n_p = 3.605$. (a) $\alpha_{n'} = 10\ cm^{-1}$, $n_{n'} = 3.585$. (b) $\alpha_{n'} = 30\ cm^{-1}$, $n_{n'} = 3.585$. (c) $\alpha_{n'} = 10\ cm^{-1}$, $n_{n'} = 3.565$.

may be used to determine whether or not the mode will attain threshold before the fundamental. As long as $\alpha_m > G_m$ for $m > 0$, the fundamental has the lowest threshold. Note that there are, of course, no curves for α_0 and G_0. The reason for this is that both α_0 and G_0 are taken to be equal to 30 cm^{-1} for all positions of the p-n junction and the value of γ_p is adjusted to satisfy (4).

As the p-region is broadened, the electronic gain G_m tends to increase in an oscillatory fashion that results from the detailed shapes of the modes and the distribution of mode volume between the two regions. When the p-region is made very narrow, the curves of G_m begin to rise again, reflecting the rise in γ_p due to the reduced coupling of the fundamental mode to the gain region.

The chief aim of Fig. 6(a)-(c) is to demonstrate how mode discrimination as measured by the difference ($\alpha_m - G_m$) is affected by loss in the n'-region and by the size of the refractive index step δn. It must be kept in mind that the two effects are *not* separable in general. The effects of loss are considered first. Fig. 6(a) and (b) shows the mode gains for structures having $\delta n = 0.02$ and differing only in loss in the n'-region. From Tables I-III it may be seen that Fig. 6(a) with an absorption coefficient in the n'-region, $\alpha_{n'} = 10\ cm^{-1}$, would correspond to a structure with 3.5-percent Al and an electron concentration somewhat in excess of $3.3 \times 10^{18}\ cm^{-3}$. The parameters in Fig. 6(b) are appropriate for a laser with an unpumped region with no Al and $n \approx 4.5 \times 10^{18}\ cm^{-3}$. The key point is illustrated by considering the gain curves for a gain-region thickness of approximately 1.2 μm. In the case of $\alpha_{n'} = 10\ cm^{-1}$, the mode gains for all higher order modes lie

between 12 and 16 cm^{-1}. For $\alpha_{n'} = 30\ cm^{-1}$, mode gains are between 4 and 8 cm^{-1}, and γ_p is not greatly increased thereby. Thus, in this case, higher loss in the n'-region considerably improves mode selection without significantly raising the threshold gain.

For a 2-μm cavity, the effects of changes in δn at fixed loss are shown in Fig. 6(a) and (c). The parameters given in Fig. 6(c) are representative of a laser with a 3.5-percent Al concentration in the n'-layer and an electron concentration of about 4×10^{18} cm^{-3}, producing $\delta n = 0.04$. Qualitatively, the effect of a larger δn is to degrade the mode discrimination between the $m = 0$ and the $m = 1$ modes if one restricts one's attention to the practical region where $W_p/W_{n'} \geq 1$. The physical explanation for this effect was discussed earlier in connection with Fig. 5(c). The larger value of δn leads, however, to an improved discrimination between the $m = 0$ and $m = 4$ modes. With $W_p/W_{n'} = 2$, the laser in Fig. 6(c) would have a stable fundamental mode, whereas the laser in Fig. 6(a) would have both fundamental and fourth-order modes. The best approach for a 2-μm cavity P-p-n'-N laser thus appears to be to dope heavily the unpumped region to an electron concentration between 4.5×10^{18} and 5.5×10^{18} cm^{-3} to provide both loss as well as δn. Using the ideas of [11], such designs give rise to potential barriers against hole flow of 110 and 130 meV, respectively.

It remains to determine the location of the p-n junction which will lead to oscillation in a fundamental mode having the greatest width. If one arbitrarily stipulates that $\alpha_m - G_m \geq 4\ cm^{-1}$ for $m \neq 0$, then one finds from Fig. 6(b) that a gain region in a 2-μm cavity can be about 1.4 μm wide. Further reduction of the p-layer width gives better mode discrimination but leads to an undesirably smaller mode width. Optimum mode discrimination, as measured by a maximum in $(\alpha_m - G_m)$ for $m > 0$, appears to be attained at a W_p of about 0.9 μm. This conclusion differs considerably from Ripper's[1] simple model where a uniform index across the cavity was assumed. His model, applied to a 2-μm cavity, would predict optimum mode discrimination for a p-layer 1.3 μm thick.

2) 3-μm Cavity: The results for the 3-μm cavity are shown in Fig. 7(a)-(c). In each case the structure will support a total of eight modes but only four are plotted for clarity's sake, and also because the highest order modes are very rarely observed. As with Fig. 6(a)-(c), the local gain γ_p is adjusted to give a fundamental mode gain G_0 of 30 cm^{-1}.

The improved mode discrimination realized by loss in the n'-region is once again apparent by comparing the mode gains for structures differing only in $\alpha_{n'}$ [e.g., Fig. 7(a) and (b)]. Increasing δn from 0.02 to 0.04 [Fig. 7(a) and (c)] has a strong effect on mode discrimination between the $m = 0$ and $m = 1$ modes. For the larger δn, both modes are essentially confined to the gain region, and there is very little discrimination for values of W_p/W_n, of interest.

Since Fig. 7(a)-(c) shows only four curves rather than the full seven supported by these 3-μm cavities, Table IV has been prepared to show the effects of δn and loss for all modes in 3-μm cavities having $W_p/W_{n'} = 2$. This ratio has been chosen as it leads to reasonable mode discrimination as well as a fundamental mode whose width is not too much smaller than

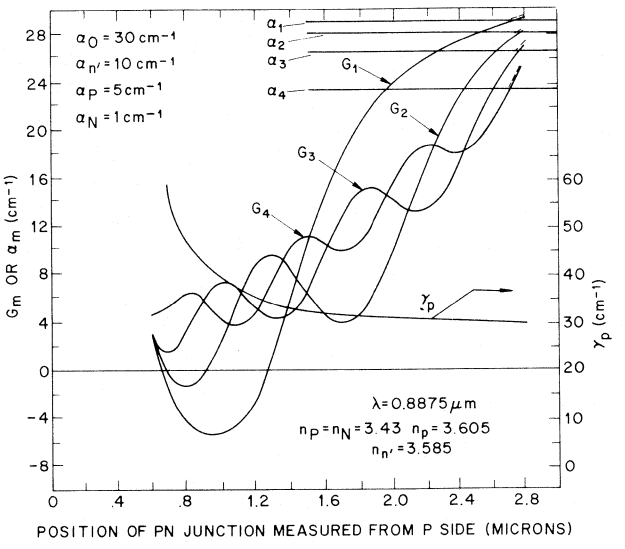

(a)

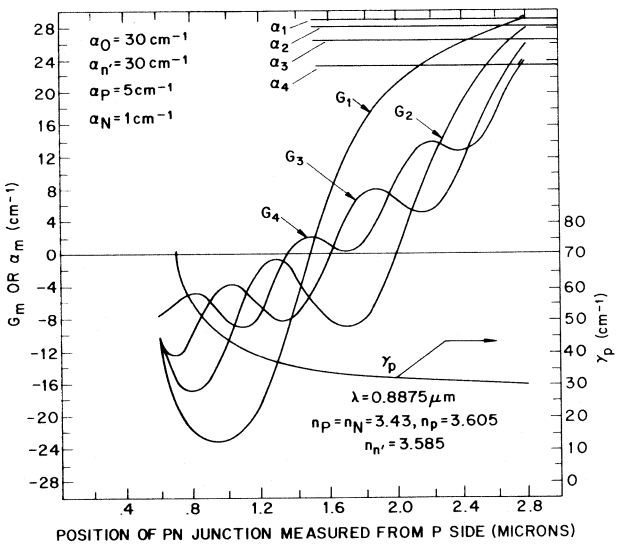

(b)

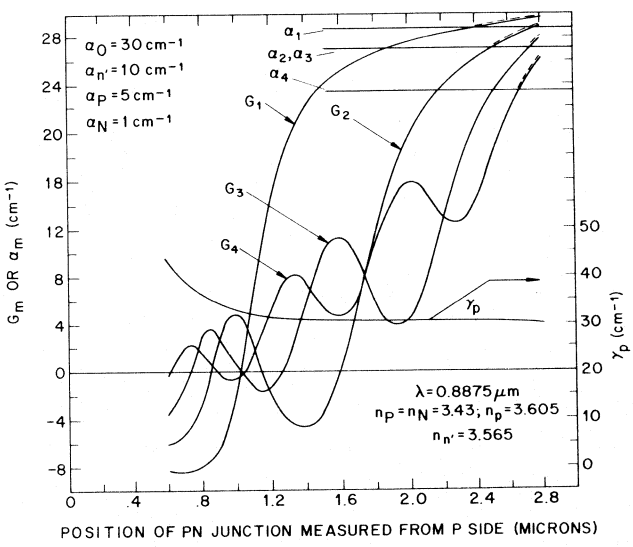

(c)

Fig. 7. Mode properties of a 3-μm cavity. Only four of seven possible modes are shown for clarity. For quantities plotted as a function of the position of the p-n junction measured from the p-P boundary, see caption of Fig. 6.

TABLE IV
MODE GAINS AND REFLECTIVITIES FOR THREE DIFFERENT DESIGNS FOR A 3-μm CAVITY P-p-n′-N LASER OPERATING AT 0.8875 μm

	Mode No. (m)	Mirror Loss, α_m (cm^{-1})	Mode Gain, G_m (cm^{-1}) With $\alpha_{n'}$ = 30 cm^{-1}	Mode Gain, G_m (cm^{-1}) With $\alpha_{n'}$ = 10 cm^{-1}
(a) $n_{n'}$ = 3.585				
	1	29.0	21.2	24.1
	2	28.1	0.56	10.3
	3	26.4	6.8	14.3
δn = 0.02	4	23.6	9.3	15.8
	5	20.2	6.2	13.5
	6	14.6	10.1	15.5
	7	11.9	6.0	11.2
(b) $n_{n'}$ = 3.565				
	1	28.7		27.7
	2	27.2	At 0.8875 μm the combination of $n_{n'}$ = 3.565 and $\alpha_{n'}$ = 30 cm^{-1} is not physically realizable.	20.2
	3	27.1		4.6
δn = 0.04	4	23.5		15.9
	5	20.4		11.4
	6	15.2		13.3
	7	14.4		9.2

Note: α_P = 5 cm^{-1}; α_N = 1 cm^{-1}; α_0 = 30 cm^{-1}. (Laser length = 375 μm.) $n_P = n_N$ = 3.43; n_p = 3.605; $W_p/W_{n'}$ = 2 in all cases.

the cavity width. The important quantity to consider is $\alpha_m - G_m$, and it is seen that the design with $\delta n = 0.02$ and $\alpha_{n'} = 30$ cm^{-1} leads to better mode discrimination than the other two designs listed. For a 3-μm cavity of this general design, however, optimum mode discrimination in favor of the fundamental occurs when $W_p \approx 1$ μm ($W_p/W_{n'} \approx \frac{1}{2}$) but this leads to a fundamental mode with a width so much smaller than the cavity that it is not considered to be a useful design for high-power lasers.

Throughout this section, results have been presented for a model in which there is 24-percent Al in the ternary layers. Some calculations have been carried out for the case of 18-percent Al. It was found that with the exception of the highest order modes, where small differences appear, the results differ negligibly from those presented here.

IV. DISCUSSION

The aforementioned calculations are based on a simple threshold model and emphasize two aspects of P-p-n′-N laser design important for good mode discrimination: 1) a relatively small value for δn, one sufficient to confine primarily the fundamental mode to the gain region; and 2) loss outside the gain region to ensure lower gain for higher order modes. It has been shown that a model which includes a nonzero δn predicts values of W_p which optimize mode discrimination very different from those predicted for $\delta n = 0$.

Our lasers are currently designed with p = 4×10^{17} cm^{-3} for the gain region and n = 4×10^{18} cm^{-3} and approximately 3.5-percent Al in the n′-region. Based on the figures summarized in Tables I–III, such designs lead to a δn of approximately 0.04. Thus lasers having cavities about 2 μm thick would be expected to display a pronounced shift of the $m = 0$ and $m = 1$ modes into the gain region. This has been observed recently by Hakki [23], who studied the near field emission of P-p-n′-N lasers superposed on the photoluminescence of the laser mirrors excited by a krypton laser. In other studies, Paoli *et al.* [4] have noted that when mirrors failed catastrophically in their P-p-n′-N lasers, operating in the fundamental mode, damage was confined essentially to the p-layer. Although no Al was deliberately introduced into the n-region of these lasers, it was deduced from other observations that there was some inadvertent "drag-over" of Al from the N-layer during growth. A gradient in Al concentration from the ternary region towards the p-P boundary would be expected to yield effects on mode shape qualitatively similar to those produced by a step in index.

While there exists qualitative agreement between the present calculations and the observed mode shapes, no P-p-n′-N lasers have been fabricated which have a 3-μm cavity with a 2-μm active region and operate at threshold in the $m = 0$ mode [24]. For the current design parameters, however, the model does predict fundamental mode operation. In light of this discrepancy, there must be other factors affecting operation that have not been fully accounted for in the analysis. As stated previously, such lasers have been designed with doping profiles leading to $\delta n = 0.04$ and $\alpha_{n'} \approx 10$ cm^{-1}. According to Fig. 7(c), there is thus very little discrimination in favor of the fundamental mode expected for 3-μm cavity lasers at the design value of $W_p/W_{n'} = 2$, and it is possible that rather small departures from the model assumptions can account for the observations. One possibility is discussed in the following.

Shurtz [25] has recently carried out self-consistent calculations of the lasing behavior of the modes perpendicular to the junction plane and finds that for lasers of the type discussed here, with a 1-μm active region, the carrier profile in this region is fairly uniform at threshold, but becomes peaked at the P-p heteroboundary above threshold. For wider active regions these effects, due to finite diffusion lengths, are expected to be more pronounced and will be reflected in a gain profile more favorable for the $m = 1$ mode than that assumed. The effect of such a mode profile on higher order modes is more difficult to assess.

A notable result of the present calculations is that there is really no optimum ratio of $W_p/W_{n'}$ for P-p-n′-N lasers in general; the mode-selection behavior is governed largely by W_p and δn. The relation of W_p and δn in determining the Al doping in the n′-region had been considered earlier by Hakki and Hwang [9]. Such considerations lead one, therefore, to a simplification of the laser structure in which the N-layer is simply omitted, producing an asymmetric double-heterostructure (ADH) laser. It is clear from Fig. 5(a)–(c) that the fundamental mode in P-p-n′-N lasers with typical values of δn should be little affected by the presence of the ternary N-region since the optical field virtually vanishes at the n′-N heteroboundary. The main effect on the mode properties resulting from the omission of the N-layer will be a reduction of the mode content, and a tendency for the modes to penetrate a little more deeply into the lossy unpumped region, leading to mode discrimination in favor of the fundamental mode. The absence of high-order modes would be particularly helpful in designing antireflective layers in a system such as discussed in [1].

Table V is a summary of calculated mode gains and mode reflectivities of ADH lasers with gain regions 1.4 and 2.0 μm thick. For comparison, the results on related P-p-n′-N structures have been included. The refractive indices and absorption coefficients used are the same as those employed in calculating

TABLE V
SUMMARY OF CALCULATED PROPERTIES OF P-p-n′-N AND ADH LASERS AT 0.8875 μm

Ppn′N				ADH			
width of p region = 1.4 μm width of n′ region = 0.6 μm				width of p region = 1.4 μm			
Mode Order m	γ_p (cm^{-1})	G_m (cm^{-1})	α_m (cm^{-1})	Mode Order m	γ_p (cm^{-1})	G_m (cm^{-1})	α_m (cm^{-1})
0	31.5	30.0	30.0	0	31.6	30.0	30.0
1	"	24.5	28.6	1	"	22.1	28.5
2	"	12.2	26.5				
3	"	13.0	22.7				
4	"	14.7	17.1				
width of p region = 2 μm width of n′ region = 1 μm				width of p region = 2 μm			
0	30.6	30.0	30.0	0	30.6	30.0	30.0
1	"	27.7	28.7	1	"	27.7	28.9
2	"	20.2	27.2	2	"	12.3	28.4
3	"	4.6	27.1				
4	"	15.9	23.5				
5	"	11.4	20.4				
6	"	13.3	15.2				
7	"	9.2	14.4				

Note: The following parameters are assumed: $n_P = 3.430$; $n_p = 3.605$; $n_{n'} = 3.565$; $n_N = 3.430$; $\alpha_P = 5$ cm^{-1}; $\alpha_{n'} = 10$ cm^{-1}; $\alpha_N = 1$ cm^{-1}; $\alpha_0 = 30$ cm^{-1}. (Laser length = 375 μm.)

the data contained in Figs. 6(c) and 7(c). As anticipated in the preceding, these ADH lasers support fewer modes and possess threshold gains γ_p equal to or only marginally greater than those of P-p-n′-N lasers. Furthermore, mode discrimination in favor of the fundamental mode is at least as good as that in P-p-n′-N lasers. Thus, since the fabrication of ADH lasers is simpler than that of P-p-n′-N lasers, they would appear to be an attractive approach to large-optical-activity high-power lasers. Although these lasers are related to SH lasers, which are known in some cases to exhibit Q-switching behavior, this is not expected to be a problem for values of δn of interest [26].

While these lasers appear to have useful mode properties, they have no n′-N heteroboundary and thus lack a high barrier to hole flow. An excess hole current density, J'_p, may, therefore, result. This point is considered in the following. For the ADH lasers, the upper limit for the excess hole current density $(J'_p)_{max}$, is proportional to the product of hole concentration in the n′-region and the thermal velocity [11]. For the lasers considered in Table V, one finds $(J'_p)_{max} \approx 36$ kA/cm^2. This is clearly a large overestimate since SH lasers possess lower thresholds than this. Some estimate of the factor by which $(J'_p)_{max}$ should be reduced to provide a more realistic estimate of J'_p may be obtained by considering results on SH lasers.

For SH lasers we may express the threshold current density J_{th} as

$$J_{th} = (J_{th})_0 + J'_p \tag{5}$$

where $(J_{th})_0$ is the threshold current density which would be observed for a double-heterostructure (DH) laser having the same active layer width d and a doping level in the ternary layers leading to full confinement of optical field and charge carriers. For such DH lasers $(J_{th})_0/d \approx 5$ kA/cm^2 μm [27].

Selway *et al.* [22] report on SH lasers having $d = 2$ μm, with room-temperature thresholds estimated[2] to be 17 kA/cm^2, $\delta n = 0.01$, and a doping in the n substrate of $3 - 4 \times 10^{18}$ cm^{-3}. Using (5) and a carrier concentration at threshold of 2×10^{18} cm^{-3}, one estimates $J'_p \approx 7$ kA/cm^2. Using the same data as the preceding, one obtains, following [11], $(J'_p)_{max} \approx 180$ kA/cm^2. This suggests that a reduction factor no greater than 0.04 be used in estimating the real excess hole current density from the upper limit calculated. Reduction factors ranging between 0.01 and 0.08 have been determined in an analogous manner using data on SH lasers reported by Hayashi and Panish [28] and Minden and Premo [29]. With a reduction factor of 0.04, one obtains $J'_p \approx 1.5$ kA/cm^2 for the ADH lasers considered in Table V. This represents a 15-percent increase in threshold current density for the laser having a 2-μm-wide active layer.

Provided the excess hole current density can be kept to the levels estimated here, appropriately designed ADH lasers may represent a useful simplification of the P-p-n′-N design.

V. SUMMARY

Using recent data on the optical properties of GaAs and $Al_xGa_{1-x}As$, calculations have been made of the mode-selection properties perpendicular to the junction plane of P-p-n′-N lasers. These calculations lead to the design principle of confining the fundamental mode to the gain region and letting the higher order modes spill out into the unpumped n′-region. It has been demonstrated that loss in the n′-region is important in mode selection and that in appropriately designed structures such loss does not significantly raise the threshold of the fundamental mode. Earlier design rules for the ratio $W_p/W_{n'}$ which were based on the assumption of a uniform refractive index across the cavity, break down for practical doping levels in the n′-region, and the governing parameters become instead W_p and δn. These findings have led to the suggestion that P-p-n′-N lasers be simplified by omitting the N-layer to produce an ADH laser. The potential usefulness of such a laser hinges on the ability to achieve low excess hole currents while maintaining a stable fundamental mode with low ellipticity.

APPENDIX
CALCULATION OF MODE REFLECTIVITY

A method suggested by McKenna[3] and employed by Reinhart *et al.* [8] and Gordon [30] is outlined in order to show more directly what approximations are being made.

For a region characterized by a real refractive index n, the reduced wave equation [31] for TE modes is written

$$\frac{\partial^2 E_y}{\partial z^2} + \frac{\partial^2 E_y}{\partial x^2} + k^2 n^2 E_y = 0 \tag{A1}$$

where k is the propagation constant in free space. Solutions for the modes are assumed to take the form $E_y = \mathcal{E}(x)e^{-i\beta z}$ and the modes for the four-layer slab are obtained by solving (A1) in each region and matching at the boundaries.

For a uniform dielectric medium with refractive index n, there exists a complete set of plane-wave solutions of (A1), which takes the form

[2] This was done by linearly interpolating the threshold values between 20 and 40°C.

[3] J. McKenna, quoted in [8]. The author is grateful to him for explaining the method outlined here.

$$\Psi = Ae^{-ikn(z\cos\theta + x\sin\theta)}.$$

Here A is a normalization constant and θ is the angle which the propagation vector k makes with the z axis. For calculation of mode reflectivity, it would be convenient to expand the guided modes in terms of the plane waves since the reflectivity of the latter may be calculated readily. Strictly speaking, this method is permissible if the mode is contained entirely within a single medium. This is never exactly true, but since the fractional difference between refractive indices of interest is small ($\leqslant$5 percent), the approximation may be a reasonable one, especially for the lower order modes when a large number of modes is present. Thus one may write for the mth mode when it reaches the mirror at $z = 0$

$$\mathcal{E}_m(x) = \int_{-\infty}^{\infty} F_m(l)e^{-iknlx}\,dl \tag{A2}$$

where $l = \sin\theta$, and $F_m(l)$ is the Fourier coefficient at l for the mth mode. An appropriate choice for the value of the refractive index n will be discussed in the following. When the mth mode is reflected at the mirror ($z = 0$) a reflected *wave* $\mathcal{E}(x)$ results which may be expressed as

$$\mathcal{E}(x) = \int_{-\infty}^{\infty} R(l)F_m(l)e^{-iknlx}\,dl \tag{A3}$$

where $R(l)$ is the Fresnel (field strength) reflection coefficient. One may expand $\mathcal{E}(x)$ in terms of the complete set of guided and continuum modes of the laser, the mth coefficient of this expansion being identified as the reflection amplitude of the mth mode. The guided TE modes have the normalization condition [31, p. 324]

$$\int_{-\infty}^{\infty} \mathcal{E}_m \mathcal{E}_k^*\,dx = \frac{2P\omega\mu}{\beta_m}\delta_{mk} \tag{A4}$$

where P is the power carried by the mode, ω is the angular frequency, μ is the permeability of the medium, and β_m is the propagation constant of the mth mode. The subscripts m and k label the modes. Using orthogonality of the slab modes, one finds that the coefficient of the mth mode is given by

$$C_m = \frac{\beta_m}{2P\omega\mu}\int_{-\infty}^{\infty} \mathcal{E}_m^* \int_{-\infty}^{\infty} F_m(l)R(l)e^{-iknlx}\,dl\,dx$$

$$= \frac{\beta_m}{4\pi P\omega\mu}\int_{-\infty}^{\infty} |F_m(l)|^2 R(l)\,dl. \tag{A5}$$

The second step in the preceding equation follows from interchange of the order of integration and the definition of the inverse Fourier transform. The mode reflectivity is simply

$$R_m = |C_m|^2. \tag{A6}$$

The problem of the choice of n in (A5) has been resolved by replacing n by β_m/k for all modes. This is in keeping with the spirit of the picture of a wave traveling in a medium of effective index β_m/k. Since the equivalent mirror loss α_m has a logarithmic dependence on mode reflectivity, viz.

$$\alpha_m = -\frac{1}{L}\ln R_m$$

α_m will not depend critically on the details of the approximation. For a symmetric three-layer slab 2 μm thick with refractive indices of 3.43 and 3.565, the aforementioned method for determining mirror reflectivity has been checked against Ikegami's [5] more elaborate calculation. The results are shown in the following table:

	$\ln(1/R_m)$	
Mode Number m	Present Method	Ikegami
0	1.16	1.14
1	1.08	1.07
2	0.97	0.97
3	0.84	0.78
4	0.71	0.66

As expected, good agreement is obtained for low-order modes, and the agreement is better than 8 percent for the higher order ones. Apart from its simplicity, the present method has the virtue of being capable of treating cases where antireflection layers are evaporated on the mirror surfaces.

Acknowledgment

The author wishes to thank B. W. Hakki for stimulating discussions during the course of this work, particularly concerning aspects of P-p-n-N laser design and performance, and for his careful reading of an early version of the manuscript. He also wishes to thank H. C. Casey, Jr., who has been most helpful with advice concerning the optical properties of GaAs and $Al_xGa_{1-x}As$, and D. Cook, L. A. D'Asaro, J. McKenna, R. C. Miller, T. L. Paoli, M. B. Panish, F. K. Reinhart, and D. L. Rode for fruitful discussions.

References

[1] D. C. Krupka and T. L. Paoli, "Transverse-mode control of junction lasers optically coupled to single-mode fibers," *IEEE J. Quantum Electron.*, this issue, pp. 503–507.
[2] G. H. B. Thompson and P. A. Kirkby, "Low threshold-current in 5-layer-heterostructure (GaAl)As/GaAs localized-gain-region injection lasers," *Electron. Lett.*, vol. 9, pp. 295–296, June 1973.
[3] H. C. Casey, Jr., M. B. Panish, W. O. Schlosser, and T. L. Paoli, "GaAs-$Al_xGa_{1-x}As$ heterostructure laser with separate optical and carrier confinement," *J. Appl. Phys.*, vol. 45, pp. 322–333, Jan. 1974.
[4] T. L. Paoli, B. W. Hakki, and B. I. Miller, "Zero-order transverse mode operation of GaAs double-heterostructure lasers with thick waveguides," *J. Appl. Phys.*, vol. 44, pp. 1276–1280, Mar. 1973.
[5] T. Ikegami, "Reflectivity of mode at facet and oscillation mode in double-heterostructure injection lasers," *IEEE J. Quantum Electron.*, vol. QE-8, pp. 470–476, June 1972.
[6] W. W. Anderson, "Mode confinement and gain in junction lasers," *IEEE J. Quantum Electron.*, vol. QE-1, pp. 228–236, Sept. 1965.
[7] Zh. I. Alferov, S. A. Gurevich, A. G. Zabrodskii, and E. L. Portnoi, "Polarization of the radiation emitted from injection-type heterostructure lasers," *Fiz. Tekh. Poluprov.*, vol. 7, pp. 1638–1641, Aug. 1973 (English transl.: *Sov. Phys.–Semicond.*, vol. 7, pp. 1095–1096, Feb. 1974).
[8] F. K. Reinhart, I. Hayashi, and M. B. Panish, "Mode reflectivity and waveguide properties of double-heterostructure injection lasers," *J. Appl. Phys.*, vol. 42, pp. 4466–4479, Oct. 1971.
[9] B. W. Hakki and C. J. Hwang, "Mode control in GaAs large-

cavity double-heterostructure lasers," *J. Appl. Phys.*, vol. 45, pp. 2168–2173, May 1974.
[10] C. J. Hwang and J. C. Dyment, "Dependence of threshold and electron lifetime on acceptor concentration in GaAs–$Ga_{1-x}Al_xAs$ lasers," *J. Appl. Phys.*, vol. 44, pp. 3240–3244, July 1973.
[11] D. L. Rode, "How much Al in the AlGaAs–GaAs laser?" *J. Appl. Phys.*, vol. 45, pp. 3887–3891, Sept. 1974.
[12] O. Berolo and J. C. Wooley, "Electroreflectance spectra of $Al_xGa_{1-x}As$ alloys," *Can. J. Phys.*, vol. 49, pp. 1335–1339, May 1971.
[13] J. K. Butler, "Theory of transverse cavity mode selection in homojunction and heterojunction semiconductor laser diodes," *J. Appl. Phys.*, vol. 42, pp. 4447–4457, Oct. 1971.
[14] J. K. Butler and H. Kressel, "Transverse mode selection in injection lasers with widely spaced heterojunctions," *J. Appl. Phys.*, vol. 43, pp. 3404–3411, Aug. 1972.
[15] H. C. Casey, Jr., D. D. Sell, and M. B. Panish, "Refractive index of $Al_xGa_{1-x}As$ between 1.2 and 1.8 eV," *Appl. Phys. Lett.*, vol. 24, pp. 63–65, Jan. 1974.
[16] H. C. Casey, Jr., D. D. Sell, and K. W. Wecht, "Concentration dependence of the absorption coefficient for n- and p-type GaAs between 1.3 and 1.6 eV," *J. Appl. Phys.*, to be published.
[17] D. D. Sell, H. C. Casey, Jr., and K. W. Wecht, "Concentration dependence of the refractive index for n- and p-type GaAs between 1.2 and 1.8 eV," *J. Appl. Phys.*, vol. 45, pp. 2650–2657, June 1974.
[18] G. E. Smith, "Phase matching in four-layer optical waveguides," *IEEE J. Quantum Electron.* (Corresp.), vol. QE-4, pp. 288–289, May 1968.
[19] H. C. Casey, Jr., B. I. Miller, and E. Pinkas, "Variation of minority-carrier diffusion length with carrier concentration in GaAs liquid-phase epitaxial layers," *J. Appl. Phys.*, vol. 44, pp. 1281–1287, Mar. 1973.
[20] B. W. Hakki, "Mode gain and junction current in GaAs under lasing conditions," *J. Appl. Phys.*, vol. 45, pp. 288–294, Jan. 1974.
[21] T. L. Paoli, private communication.
[22] P. R. Selway, G. H. B. Thompson, G. D. Henshall, and J. E. A. Whiteaway, "Measurement of the effect of injected carriers on the p-n refractive-index step in single heterostructure diode lasers," *Electron. Lett.*, vol. 10, pp. 453–455, Oct. 1974.
[23] B. W. Hakki, "Near-field emission from GaAs double-heterostructure laser mirrors," *IEEE J. Quantum Electron.*, vol. QE-11, pp. 149–154, Apr. 1975.
[24] —, private communication.
[25] R. Shurtz, Night Vision Lab., Ft. Belvoir, Va., private communication.
[26] G. H. B. Thompson, P. R. Selway, G. D. Henshall, and J. E. A. Whiteaway, "Role of optical guiding in critical-temperature behavior, delays and Q-switching in single heterostructure GaAs/(GaAl)As lasers," *Electron. Lett.*, vol. 10, pp. 456–457, Oct. 1974.
[27] E. Pinkas, B. I. Miller, I. Hayashi, and P. W. Foy, "GaAs–$Al_xGa_{1-x}As$ double heterostructure lasers–Effect of doping on lasing characteristics of GaAs," *J. Appl. Phys.*, vol. 43, pp. 2827–2835, June 1972.
[28] I. Hayashi and M. B. Panish, "GaAs–$Ga_xAl_{1-x}As$ heterostructure injection lasers which exhibit low thresholds at room temperature," *J. Appl. Phys.*, vol. 41, pp. 150–163, Jan. 1970.
[29] H. T. Minden and R. Premo, "High-temperature GaAs single heterostructure laser diodes," *J. Appl. Phys.*, vol. 45, pp. 4520–4527, Oct. 1974.
[30] E. I. Gordon, "Mode selection in GaAs injection lasers resulting from Fresnel reflection," *IEEE J. Quantum Electron.*, vol. QE-9, pp. 772–776, July 1973.
[31] D. Marcuse, *Light Transmission Optics*. New York: Van Nostrand-Reinhold, 1972, p. 306.

The Angular Beam Divergence in Double-Heterojunction Lasers with Very Thin Active Regions

W. P. DUMKE

Abstract—**An analytical expression is found for the angular beam divergence from a double-heterojunction (DH) laser in the limit of an infinitely thin active region. In this limit the beam divergence is proportional to the thickness of the active region and to the index of refraction difference between the active and confining layers. A simple expression combining the limiting expressions for thin and thick active regions gives a very accurate fit to the numerical calculations of the beam divergence for intermediate active region thicknesses.**

IT HAS BEEN SHOWN by Kressel *et al.* [1] and by Selway and Goodwin [2] that double-heterojunction (DH) GaAs injection lasers may be made with thin active regions without having a large angular spread of the coherent light in the plane perpendicular to the active region. Besides having thin active regions, such lasers also had a smaller index of refraction step at the interface between the active and confining layers which allowed the light to penetrate some distance into the $Ga_{1-X}Al_XAs$ layers. In spite of this penetration and because of the superlinear dependence of gain with current in room-temperature injection lasers, the current thresholds were low, reflecting the thinness of the active layers.

Casey *et al.* [3] have numerically calculated the beam divergence at half-intensity $\theta_\perp$ as a function of active region thickness d for several values of X ($Ga_{1-X}Al_XAs$ composition). In this paper we wish to show that there is a simple expression for $\theta_\perp$ in the limit as $d \to 0$ which yields the values of $\theta_\perp$ attainable for small d and X. In calculating the limiting value of $\theta_\perp$ we will use the latest data on index of refraction for $Ga_{1-X}Al_XAs$. For intermediate values of d we shall present an expression for $\theta_\perp$ having the correct limiting behavior for thin or very thick active regions and which agrees extremely well with the detailed numerical calculations of Casey *et al.* [3].

In a symmetrical three-layer optical waveguide, the solution for the vector potential of the lowest order confined TE mode

Manuscript received December 6, 1974; revised January 30, 1975.
The author is with the IBM Thomas J. Watson Research Center, Yorktown Heights, N.Y. 10598.

is of the form [4] $A_0 \cos qx$ in the active region $|x| < d/2$ with index of refraction N_1, and $A_0 \cos(qd/2) \exp(-p|x|)$ in the confining layers $|x| > d/2$ where the index of refraction is $N_2 < N_1$. The requirements on the continuity of the tangential electric- and magnetic-field components at $x = \pm d/2$ yield a matching condition [4]

$$\tan qd = \frac{2p/q}{1 - (p/q)^2}$$

which is further constrained by the wave equation that

$$q^2 + p^2 = \frac{(N_1^2 - N_2^2)\omega^2}{c^2}.$$

As $d \to 0$, $\tan qd \to qd$ and $p/q \to 0$. The matching condition simplifies to

$$p \cong \frac{dq^2}{2} \cong \frac{d(N_1^2 - N_2^2)\omega^2}{2c^2}.$$

The far-field pattern as $d \to 0$ is due to a source field at the end face of the form

$$E(x) = E_0 \exp(-p|x|).$$

If θ is the angle between the active region plane and a line from the end face to a point a distance R from the laser (R large compared to laser dimensions) and $k_0 = 2\pi/\lambda$, then we may approximately write the field at R as

$$E(\theta) = \frac{\exp(ik_0R)}{R} \int_{-\infty}^{\infty} E(x) \exp(-ik_0 x \sin\theta)\, dx.$$

If we substitute the preceding form for $E(x)$, we obtain

$$E(\theta) = \frac{E_0 \exp(ik_0R)}{R} \frac{2p}{p^2 + k_0^2 \sin^2\theta}$$

which yields a far-field dependence of intensity on θ of

$$I(\theta) \propto |E(\theta)|^2 \propto \frac{p^2}{(p^2 + k_0^2 \sin^2\theta)^2}.$$

The half-intensity angle is determined by the condition

$$\frac{I(\theta_{1/2})}{I(0)} = \frac{p^4}{(p^2 + k_0^2 \sin^2\theta)^2} = \frac{1}{[1 + (k_0/p)^2 \sin^2\theta]^2} = \frac{1}{2}$$

which requires $\sin\theta_{1/2} = (\sqrt{2} - 1)^{1/2} p/k_0$. If $\theta_{1/2}$ is small, we may write

$$\theta_\perp = 2\theta_{1/2} \cong \frac{(\sqrt{2} - 1)^{1/2}}{\pi} p\lambda = 0.205 p\lambda.$$

In a laser with a thick active region the transverse dependence for the lowest order mode is approximately $E \propto \cos(\pi x/d)$, which can be shown to yield $\theta_\perp = 1.2\,\lambda/d$. If in the case of a penetrating mode we relate the total energy in the mode $\mathscr{E}_t$, to the average energy density in the active region $\mathscr{E}_d$, we may introduce an effective width $d^* = (\mathscr{E}_t/\mathscr{E}_d)d$ characterizing the width of the photon distribution. In the notation of Casey *et al.* [3], $d^* = d/\Gamma$. For lasers with very thin active regions it is easy to show that $d^* = 1/p$. Therefore we may write

$$\theta_\perp = 0.205\,\lambda/d^*.$$

This is to be compared with the preceding expression $\theta_\perp = 1.2\,\lambda/d = 1.2\,\lambda/d^*$ for the limit $d \to \infty$, that is for a mode which is perfectly confined. Obviously, the smooth variation of the exponential components of the mode in the confining layers contributes less to the beam divergence than if the energy were contained in an active region of width $d = 1/p$.

From the expression for p we may relate $\theta_\perp$ to the layer properties

$$\theta_\perp = 0.41\,\pi^2(N_1^2 - N_2^2)d/\lambda.$$

For $Ga_{1-X}Al_XAs$ the variation of N_2 with X is fairly linear for $X < 0.3$. For small X we may write $N_1^2 - N_2^2 \cong -2N_1 (\partial N_2/\partial X)_0 X$.

From the measurements of Casey *et al.* [5], we obtain $-N_1(\partial N_2/\partial X)_0 \cong 2.5$. Substituting this value gives a limiting beam divergence in radians for GaAs-$Ga_{1-X}Al_XAs$ injection lasers as $d \to 0$ of

$$\theta_\perp = 20 \frac{dX}{\lambda}.$$

For $d = 0.1\ \mu$m, $X = 0.1$, and $\lambda = 0.88\ \mu$m, we obtain

$$\theta_\perp = 13°.$$

Thus by having a thin active region and a small compositional difference (small $N_1 - N_2$), both of which result in a mode which penetrates deep into the confining layers, we are able to obtain a small beam divergence. The difference between the preceding value of $\theta_\perp$ and that calculated by Casey *et al.* of $\sim 11°$ for the $d = 0.1\ \mu$m and $X = 0.1$ case reflects the fact that even for these parameters we are not quite close enough to the limiting case for the preceding expression for the divergence to be perfectly accurate.

We may combine the expressions for $\theta_\perp$ in the two limits $d \to 0$ and $d \to \infty$ in a single expression of the form

$$\theta_\perp = \frac{a\,d/\lambda}{1 + a(d/\lambda)^2/1.2}$$

where $a = 0.41\,\pi^2(N_1^2 - N_2^2) = 20X$.

This expression yields the correct values for $\theta_\perp$ in the two limits, but it is a somewhat arbitrary choice of those functions having the proper limiting behavior. For intermediate values of d, however, this expression yields reasonably good agreement with the values calculated by Casey *et al.* [3], and provides a convenient formula for predicting the divergence of a given DH laser.

Having a simple expression to describe $\theta_\perp(d, X)$ we may perform some elementary analysis to see at what values of d, $\theta_\perp$ will be maximum and how this maximum varies with X. Setting $(d\theta_\perp/dd) = 0$ yields a maximum value of $\theta_{\perp\max} = \frac{1}{2}\sqrt{1.2a}$ at a value of $d = \lambda\sqrt{1.2/a}$. For a "typical" GaAs-$Ga_{1-X}Al_XAs$ DH laser with $X = 0.3$ and $\lambda = 0.88\ \mu$m, $\theta_{\perp\max} = 1.33$ rad $= 76°$ at $d = 0.39\ \mu$m. From these results, as from the earlier calculations of Casey *et al.* [3], it can be seen that many of our DH injection lasers are actually made having values of d and X close to the values which result in the largest amount of beam di-

vergence. By using a lower Al composition and active region thickness the divergence can be significantly reduced.

There is one precaution one must take, however, if reduced values of X and d are to be used. If the mode penetrates far into the confining layers, it is important that these layers be thick enough so that the intensity is sufficiently attenuated through the thickness of the layers. If the layers are too thin some of the light will leak through resulting in an increased loss and higher thresholds. From calculations which will be published elsewhere [6] this required thickness may exceed that commonly used for the top $Ga_{1-X}Al_XAs$ layer when X and d are small. For a laser with $X = 0.1$ and $d = 0.1$ μm, a confining layer thickness of ~ 3 μm is needed to prevent such leakage.

References

[1] H. Kressel *et al.*, "Mode guiding in symmetrical (AlGa)As–GaAs heterojunction lasers with very narrow active regions," *RCA Rev.*, vol. 32, pp. 393–401, Sept. 1971.
[2] P. R. Selway and A. R. Goodwin, "The properties of double heterostructure lasers with very narrow active regions," *J. Phys. D.*, vol. 5, pp. 904–914, May 1972.
[3] H. C. Casey, Jr., M. B. Panish, and J. L. Merz, "Beam divergence of the emission from double-heterostructure injection lasers," *J. Appl. Phys.*, vol. 44, pp. 5470–5475, Dec. 1973.
[4] W. W. Anderson, "Mode confinement and gain in injection lasers," *J. Quantum Electron.*, vol. 1, pp. 228–236, Sept. 1965.
[5] H. C. Casey, Jr., D. D. Sell, and M. B. Panish, "Refractive index of $Al_xGa_{1-x}As$ between 1.2 and 1.8 eV," *Appl. Phys. Lett.*, vol. 24, pp. 63–65, Jan. 1974.
[6] W. P. Dumke, to be published.

Internal Optical Losses in Very Thin CW Heterojunction Laser Diodes

J. K. BUTLER, MEMBER, IEEE, H. KRESSEL, FELLOW, IEEE, AND I. LADANY, MEMBER, IEEE

Abstract—**Theoretical calculations are presented showing the relationship between the internal laser absorption and structural parameters appropriate for CW room-temperature lasers. These diodes have submicron-thick recombination regions, and very small spacings between the heat sink and the recombination region to minimize the thermal resistance. The optical loss is shown to be strongly dependent on the degree of radiation confinement to the active region. In particular, absorption in the surface GaAs layer providing the ohmic contact becomes very significant when the intermediate (AlGa)As layer is reduced below about 1 μm. It is further shown that excessive penetration into the GaAs regions gives rise to anomalies in the far-field radiation profiles in the direction perpendicular to the junction plane. Proper design of the internal structure of the laser avoids large increases of the threshold current density as well as large decreases in the external differential quantum efficiency from interaction with the contact layer. The design curves presented can be used to predict the gain required at threshold for a broad range of structural parameters of interest in low-threshold laser design.**

Manuscript received December 26, 1974; revised January 24, 1975. This work was supported in part by the Office of Naval Research, Arlington, Va., under Contract N00014-73-C-0335, and in part by NASA, Langley Research Center, Hampton, Va., under Contract NAS1-11421.

J. K. Butler is with Southern Methodist University, Dallas, Tex. 75275.
H. Kressel and I. Ladany are with RCA Laboratories, Princeton, N.J. 08540.

Introduction

LASER DIODES designed for CW operation require the recombination region to be located in the proximity of the heat sink in order to minimize their thermal and electrical resistance. Previous work [1]–[3] has shown that an optimum combination of low threshold current density and moderate radiation-pattern beamwidth is best obtained from double-heterojunction lasers with submicron-wide active regions with strong electron-hole pair confinement but weak field confinement to the recombination region. Because the optical field may extend outside the recombination region into high-loss regions, the diode geometry and material parameters must be selected for optimum distance between the active region and the heat sink. Extreme reduction in certain layer dimensions increases the threshold current density, while excessive thickness increases the thermal resistance. This paper presents the results of theoretical calculations on the effect of structural parameters on the laser threshold. We also show both theoretically and experimentally that anomalies in the far-field radiation patterns result from complex interactions between the radiation field and highly absorbing regions in the vicinity of the recombination region.

Device Model and Radiation Distribution

The diodes selected for the present analysis are (AlGa)As double-heterojunction diodes emitting at ~8000 Å of the type which has demonstrated long-term reliability [4]. The schematic cross section of the double-heterojunction diode is shown in Fig. 1(a). Beginning at the mounting surface of the diode, region 1 is a GaAs surface layer ($p \approx 10^{19}$ cm^{-3}) about 1 μm thick for ohmic contact; region 2 is of p-type $Al_xGa_{1-x}As$ ($\sim 10^{18}$ cm^{-3}); region 3 is the $Al_yGa_{1-y}As$ recombination region ($y < x$); region 4 is the n-type ($\sim 10^{18}$ cm^{-3}) $Al_zGa_{1-z}As$ ($z > x$); region 5 is the n-type ($\sim 10^{18}$ cm^{-3}) GaAs substrate. Fig. 1(b) shows the refractive-index distribution at the lasing wavelength. Other relevant numerical parameters used in the numerical calculations presented will be discussed later. Such structures are prepared by liquid-phase epitaxy. The recombination region, not deliberately doped, has an electron concentration of 5×10^{16} cm^{-3}.

For low thermal and electrical resistance of the diode it is essential to keep regions 1 and 2 thin. Region 2 is a particularly strong contributor to the thermal resistance because of the low thermal conductivity of (AlGa)As compared to that of GaAs [5]. However, because of the spread of the optical field outside the recombination region into the surrounding ones, the structural design must be chosen to prevent excessive optical loss.

The solution of Maxwell's equations in a five-layer laser structure has been effected previously [6], [7]; we applied the results to the five-layer geometry in Fig. 2. The computer program used for the calculations uses the complex dielectric constant $\kappa = \kappa' - j\kappa''$ of each region. The real part $\kappa' = n^2$, where n is the index of refraction, while $\kappa'' = n\alpha/k_0$, where α is the absorption coefficient and k_0 is the free-space wavenumber. The structure studied here has indices of refraction n_1, n_5 (in regions 1 and 5, respectively), which are larger than the index n_3 of the optical cavity, while for the structure in [6], $n_1, n_5 < n_3$. However, the mathematical solution of the fields for both structures is identical. The reason for the similarity is due to the condition placed on the fields in regions 1 and 5, i.e., the fields must decay exponentially to zero as $|x| \to \infty$. This condition is satisfied here because the material is lossy. (The field exponential decay factor in regions 1 and 5 is strongly related to the absorption constants α_1 and α_5, as will be illustrated.) On the other hand, if regions 1 and 5 are reactive, the fields would not tend to zero as $|x| \to \infty$.

A simple intuitive understanding of the transverse-field distribution can be obtained from knowledge of the value of the complex propagation constant. Aside from their x-dependence, the propagating fields have the form $\exp(j\omega t - \gamma z)$, where $\gamma = \alpha + j\beta$; $-\alpha$ represents the modal gain; and β determines the wave characteristics along z. In normalized form, we write $\beta = k_0 B$, where B must satisfy the condition that $n_2, n_4 < B < n_3$ for energy trapped predominately in region 3. In region 3 the field has largely a sinusoidal dependence which can be represented to a good approximation by two plane waves propagating at angles $\pm\theta_1$, with respect to the z axis. These two waves combine to give a wave component along the z direction carrying a majority of the optical energy (see Fig. 2). However, since the material in all regions is lossy, a characteristic associated with the complex dielectric constant, there is an additional wave component in the $\pm x$ directions which supplies power to regions 1, 2, 4, and 5. In regions 2 and 4 the field distributions have a predominant exponential or hyperbolic dependence along the x direction because the normalized propagation constant $B > n_2, n_4$. The propagating components of the fields in regions 2 and 4 carry a majority of the energy along the z direction as indicated in Fig. 2. However, we stress the fact that since the material is lossy there will be a wave component in regions 2 and 4 supplying power to regions 1 and 5. The magnitude of the x component of the Poynting vector P_x, compared to its z component P_z, is a function of the optical properties and widths of the various regions of the five-layer structure; however, for the geometries discussed in this paper the ratio $P_x/P_z \ll 1$. In regions 1 and 5, where $B < n_1, n_5$, the transverse-field dependence consists of damped traveling waves propagating away from the active region; i.e., positive x direction in region 1 and the negative x direction in

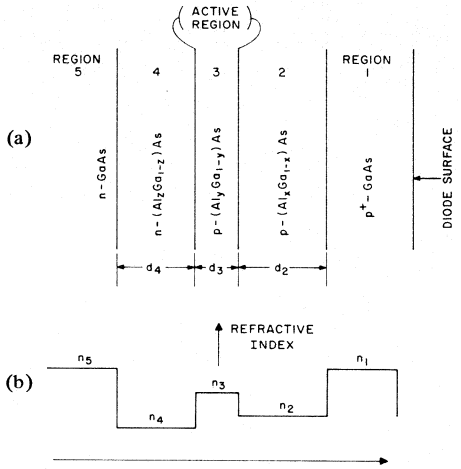

Fig. 1. Schematic of double-heterojunction diode showing the five regions relevant to the present work and the distribution of the refractive index at the lasing photon energy.

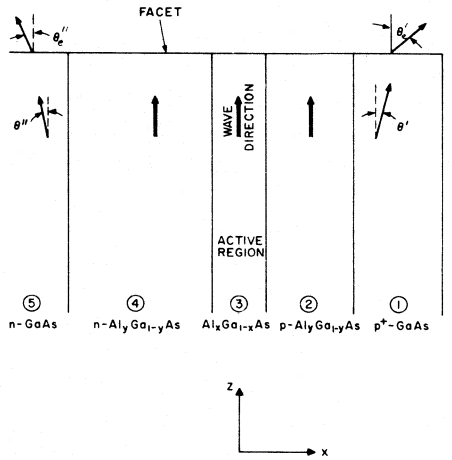

Fig. 2. Wave propagation in the five layers of the diode showing the effect of transmission through the highly absorbing GaAs regions 1 and 5 on the radiation emitted at the facet at those regions. (Not shown are the relatively small wave components in the transverse direction which carry energy from the active region into the lossy passive regions.)

region 5. Consequently, the fields in regions 1 and 5 are composed of plane waves propagating in both the x and z directions with a resultant wave propagating at angles θ' and θ'' with respect to the z axis as shown in Fig. 2.

The decrease of the fields along the x direction in the two outer GaAs regions is dependent upon the absorption coefficient of these layers. To illustrate this effect, we show in Fig. 3(a) the near-field intensity pattern for a symmetrical structure ($n_2 = n_4$ in Fig. 1) with the parameters given in Table I and two different values for the absorption coefficient in regions 1 and 5; Case 1, $\alpha_1 = \alpha_5 = 10\ \text{cm}^{-1}$; and Case 2, $\alpha_1 = \alpha_5 = 15\,000\ \text{cm}^{-1}$, which is appropriate to above-bandgap energy radiation [8].

Case 1: The optical field penetrates through the 1-μm-thick (AlGa)As layer (region 2) and deep into the GaAs region 1. Since $n_1 > n_2$, the field does not "see" an optical barrier and propagates in region 1, and has little dependence on x because α_1 is small.

Case 2: The penetration depth within layer 1 is small because of large α_1. The higher the absorption coefficient, the shallower the penetration in a manner analogous to the "skin-depth" effect in metallic layers.

A particularly interesting fact is that the strong attenuation of the radiation by the surface layer affects the far-field radiation pattern in the direction perpencidular to the junction. This is illustrated in Fig. 3(b) which shows the far field calculated [7] for the near-field distribution of Fig. 3(a). Note the extra peak at $\theta = 60°$, the magnitude of which depends on the fraction of the power propagating in region 1. The plane wave inside the GaAs region 1, propagating at the slight angle θ' with respect to the z axis, exits the laser facet at an angle $\theta_e' = \sin^{-1}(n_1 \sin\theta')$. Fig. 3(b) shows no similar peak due to field propagating through the n-type GaAs region, because, as shown in Fig. 3(a), only an insignificant fraction of the power is now propagating in the n-type GaAs region. A strong penetration to region 5 would have resulted in an additional peak on the left-hand side of the far-field radiation pattern of Fig. 3(b).

The focus of this paper is on structures with equal refractive-index steps at the two heterojunctions. However, we illustrate the previously predicted effect of additional features in far-field radiation pattern structure due to the presence of the p-type GaAs surface layer, using an experimental asymmetrical double-heterojunction structure where the radiation spreads preferentially toward one diode surface. Fig. 4 shows the cross section of such a diode together with the near-field radiation pattern calculated for the specific device parameters ($Al_{0.3}Ga_{0.7}As$-$Al_{0.09}Ga_{0.91}As$-$Al_{0.18}Ga_{0.82}As$) with appropriate Δn values [9]. It is evident from Fig. 4 that the field penetrates through the 1.4-μm-thick p-type (AlGa)As layer into the GaAs surface layer at the right. The far-field radiation pattern was calculated from the near-field curve of Fig. 4 and compared to the measured far field in Fig. 5. Both the experimental and theoretical far-field curves show the small additional peak expected when appreciable radiation propagates in the p-type GaAs surface layer. While an analysis of asymmetrical structures is outside the scope of this paper, we note that the room-temperature threshold current density of the above laser was 18 000 A/cm^2 and its total differential quantum efficiency was 7 percent (400-μm cavity length, broad area contact). The high threshold current density compared to typical (AlGa)As double-heterojunction lasers with submicron active regions [4] is due to both poorer radiation confinement and stronger absorption in the p-GaAs surface layer. The low differential quantum efficiency (compared to typical 40-percent values in good quality lasers) is directly related to excessive absorption in the previously described laser consistent with the radiation spread into the p-GaAs region.

TABLE I
MATERIAL PARAMETERS FOR FIG. 3

Layer #	n	$\alpha(\text{cm}^{-1})$	Region Thickness (μm)
1	3.59	–	≥ 4
2	3.46	10	1
3	3.54	-40 [a]	0.25
4	3.46	10	2
5	3.59	–	> 1

[a] Choice of value is not critical in determining the radiation pattern.

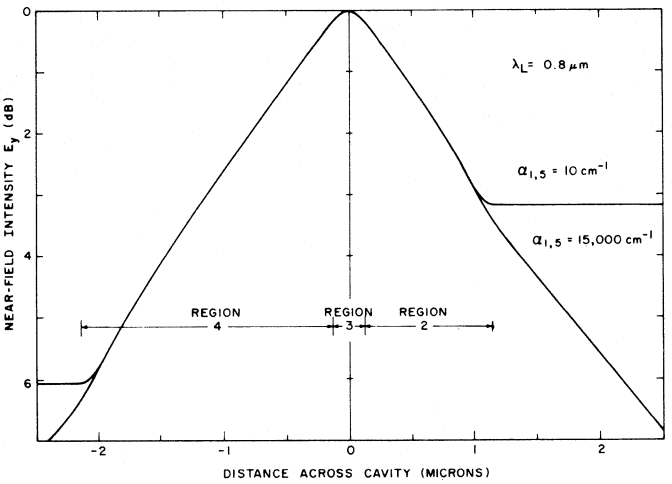

(a)

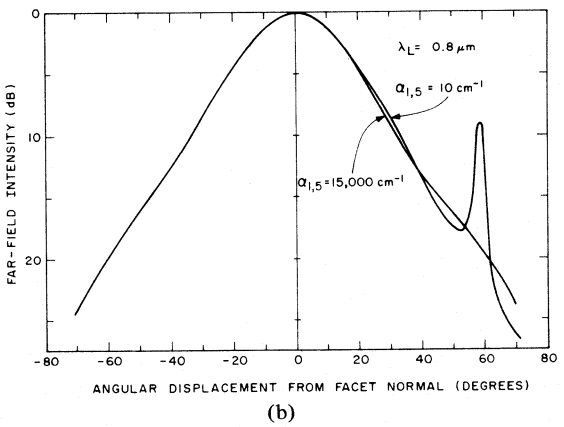

(b)

Fig. 3. (a) Near field for a structure with parameters given in Table I for two values of the absorption coefficient in the GaAs regions 1 and 5. The lasing wavelength is taken as 0.8 μm. (b) Far field calculated from the near field shown in (a) for the two assumed absorption-coefficient values.

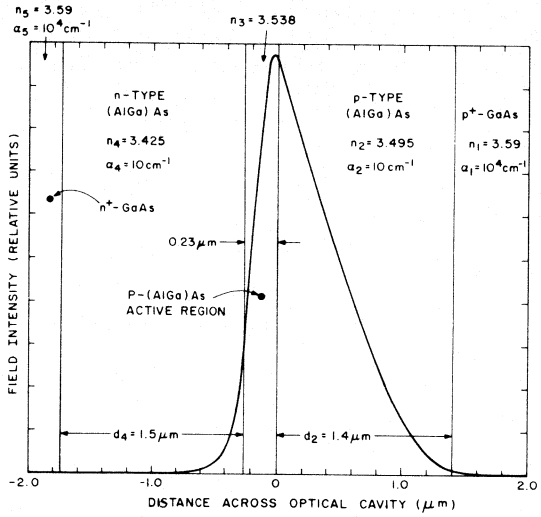

Fig. 4. Near field calculated for an asymmetrical laser in which the radiation is preferentially spreading toward the surface of the structure. The index values are indicated as well as the thickness of each relevant region. The index values were first estimated from the (AlGa)As compositions in each region and then "fine tuned" to match the experimental far-field pattern. The thicknesses were measured on the actual laser.

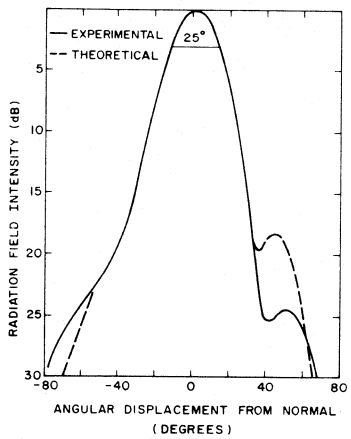

Fig. 5. Far field calculated from the near field of Fig. 4 compared to the experimentally measured pattern for the same laser to show the additional peak at the right due to radiation propagation in the highly absorbing p-type GaAs region 1.

Design Curves

The material in each of the five regions is characterized by its relative complex dielectric constant κ. The imaginary part of κ is related to the absorption coefficient while the real part is related to the index of refraction. The contributions to the effective absorption coefficient include free-carrier absorption within the recombination region, a weighted coefficient value $\bar{\alpha}$ from the other laser regions which takes into account the fraction of the radiation in each region, and the cavity-end loss α_{end}. We define the quantity Γ in the conventional sense as the fraction of the propagating power that lies within the recombination region 3. We define a quantity G_{th} in terms of $\bar{\alpha}$ and Γ

$$G_{th} = \frac{\bar{\alpha}}{\Gamma}. \tag{1}$$

Therefore, G_{th} represents the recombination-region gain coefficient at lasing threshold for a laser with no free-carrier absorption within the recombination region ($\alpha_{fc} = 0$) and no cavity-end losses ($\alpha_{end} = 0$).

For a laser of finite length and finite α_{fc}, the recombination-region gain coefficient at threshold g_{th} is

$$\Gamma(g_{th} - \alpha_{fc}) = \Gamma G_{th} + \alpha_{end}$$

or

$$g_{th} = G_{th} + \alpha_{fc} + \frac{1}{\Gamma}\alpha_{end}. \tag{2}$$

In terms of the above quantities, the external differential quantum efficiency η_{ext} is

$$\eta_{ext} = \eta_i \frac{\alpha_{end}}{\alpha_{end} + (\alpha_{fc} + G_{th})\Gamma} \tag{3}$$

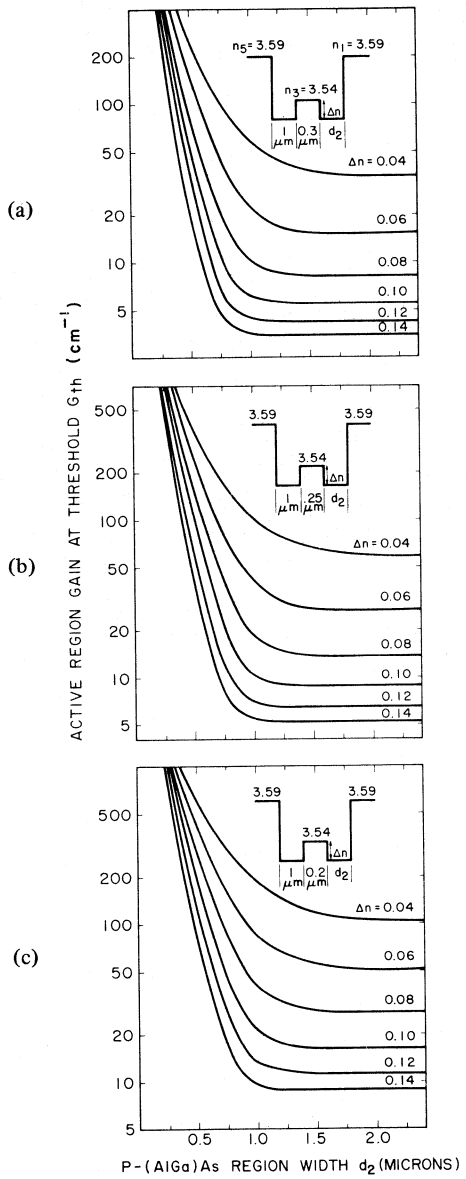

Fig. 6. The active-region gain coefficient ($\lambda_L = 0.8$ μm) at threshold G_{th} calculated for various device parameters with quantities noted in the insert sketch held constant. Both the refractive-index step Δn and the width d_2 of the p-type (AlGa)As region 2 are varied.

where η_i is the customary internal quantum efficiency. In the region where the linear theory of lasing is adequate, a cavity of length L and facet reflectivity R has $\alpha_{end} = (1/L) \ln (1/R)$; typically $\alpha_{fc} = 10\ cm^{-1}$.

Once g_{th} is known, the threshold current density J_{th} is determined by the thickness d_3 of the recombination region, the internal quantum efficiency, and the relationship between gain and injected carrier density. In the simplest case, the gain near threshold is assumed to be linearly related to the injected carrier density and

$$J_{th} \propto \frac{d_3}{\eta_i} g_{th}. \tag{4}$$

The theoretical curves presented in this section concern G_{th} for thin structures of particular interest to low-threshold cavities required for CW operation; for example, the diode structure with a recombination region of $Al_{0.1}Ga_{0.9}As$ (lasing wavelength ≈ 8000 Å), although the results have wider applicability. The parameters are: $n_3 = 3.54$; $n_1 = n_5 = 3.59$, and $\alpha_1 = \alpha_5 = 15\,000\ cm^{-1}$. In regions 2 and 4 the loss is due to free-carrier absorption and is relatively low: $\alpha_2 = \alpha_4 = 10\ cm^{-1}$. The calculations are presented in terms of the index difference $\Delta n \equiv n_3 - n_2$ between the recombination region and the adjacent layers, and the thickness of the adjacent layers.

Figs. 6-9 present analytical curves which are useful in predicting g_{th} for known parameter values. The first set of curves (Fig. 6) shows the effect on G_{th} of changes in the width of region 2 and of Δn for three different recombination-region thickness values: 0.2, 0.25, and 0.3 μm. For a given Δn, the narrower the recombination region, the greater the radiation spread, and hence the greater the effect of the absorption in

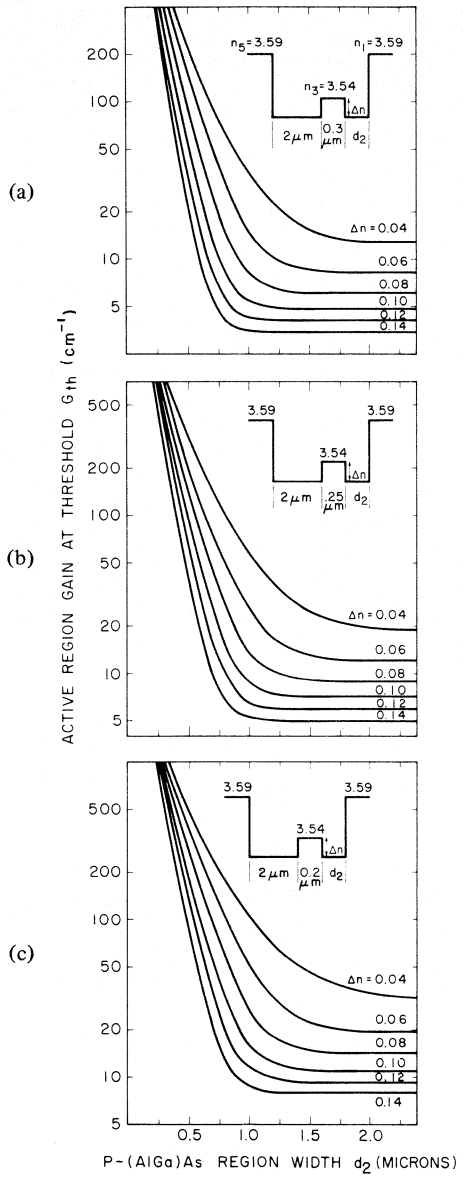

Fig. 7. The active-region gain coefficient (λ_L = 0.8 μm) at threshold G_{th} calculated for various device parameters with quantities noted in the insert sketch held constant. This figure differs from Fig. 6 in that the thickness of region 4, d_4, is 2 μm instead of 1 μm.

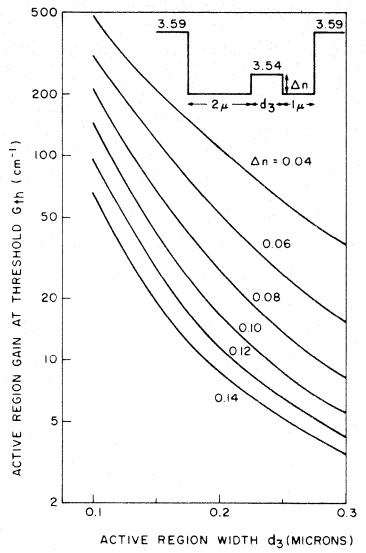

Fig. 8. The active-region gain coefficient (λ_L = 0.8 μm) at threshold as a function of the active-region width d_3 for various Δn values.

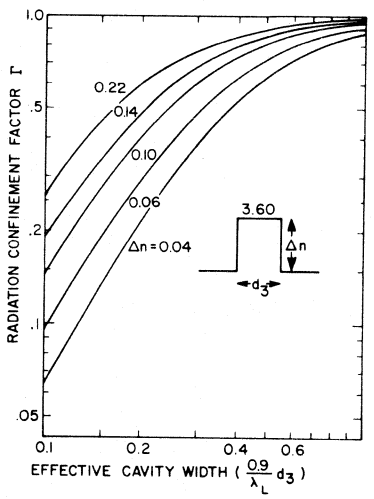

Fig. 9. The radiation-confinement factor Γ as a function the width of the recombination region d_3 for various Δn values. Note that the d_3 axis can be adjusted for different lasing wavelengths (in micrometers) by normalization.

the GaAs regions on G_{th}. Note the general result that the thickness of p-type (AlGa)As region no longer affects G_{th} when it exceeds ~1 μm. The curves in Fig. 7 show similar calculations with the thickness of the (AlGa)As-n-type region (d_4) assumed to be 2-μm thickness instead of 1 μm as in Fig. 6. Since the thermal resistance of the diodes when mounted with the p-side on the heat sink is not affected by the thickness of region 4, it is of interest to determine whether increasing its thickness has a significant effect on G_{th} with other factors being constant. Fig. 7 shows that G_{th} is indeed reduced by widening region 4 with the improvement being dependent on the design details. Fig. 8 shows comprehensive plots of G_{th} with the active-region width as a variable for a set of Δn values, keeping the thickness of regions 2 and 4 fixed at 1 and 2 μm, respectively.

Finally, we show in Fig. 9 the dependence of Γ on various structural parameters. The confinement to the thin recombination regions is seen to change rapidly with small changes in the refractive-index step Δn. However, as the recombination-region width approaches 1 μm, Γ is nearly unity for the broad range of parameters shown.

Conclusion

Theoretical calculations have been presented showing the relationship between the internal laser absorption and structural parameters appropriate for CW room-temperature lasers. These diodes have submicron-thick recombination regions, and very small spacings between the heat sink and the recombination region to minimize the thermal resistance. The optical loss is shown to be strongly dependent on the degree of radiation confinement to the active region. In particular, absorption in the surface GaAs layer providing the ohmic contact becomes

very significant when the intermediate (AlGa)As layer is reduced below about 1 μm. It has been further shown that excessive penetration into the GaAs regions gives rise to anomalies in the far-field radiation profiles in the direction perpendicular to the junction plane. Proper design of the internal structure of the laser avoids large increases of the threshold current density as well as large decreases in the external differential quantum efficiency from interaction with the contact layer. The design curves presented can be used to predict the gain required at threshold for a broad range of structural parameters of interest in low-threshold laser design.

Acknowledgment

The authors wish to thank Dr. H. S. Sommers, Jr., and Dr. J. I. Pankove for discussions and comments on the manuscript.

References

[1] H. Kressel *et al.*, "Mode guiding in symmetrical (AlGa)As–GaAs heterojunction lasers with very narrow active regions," *RCA Rev.*, vol. 32, pp. 393–401, Sept. 1971.
[2] a) G. H. B. Thompson and P. A. Kirkby, "(GaAl)As lasers with a heterostructure for optical confinement and additional heterojunctions for extreme carrier confinement," *IEEE J. Quantum Electron. (Part II of Two Parts. Special Issue on 1972 IEEE Semiconductor Laser Conference)*, vol. QE-9, pp. 311–318, Feb. 1973. b) P. A. Kirkby and G. H. B. Thompson, "High peak power from (GaAl)As–GaAs double-heterostructure injection lasers," *Appl. Phys. Lett.*, vol. 22, p. 638, June 1973.
[3] H. C. Casey, M. P. Panish, and J. L. Merz, "Beam divergence of the emission from double-heterostructure injection lasers," *J. Appl. Phys.*, vol. 44, pp. 5470–5475, Dec. 1973.
[4] I. Ladany and H. Kressel, "The influence of device fabrication parameters on the gradual degradation of (AlGa)As CW laser diodes," *Appl. Phys. Lett.*, vol. 25, pp. 708–711, Dec. 15, 1974.
[5] M. A. Afromowitz, "Thermal conductivity of $Ga_{1-x}Al_xAs$ alloys," *J. Appl. Phys.*, vol. 44, pp. 1292–1294, Mar. 1973.
[6] J. K. Butler, "Theory of transverse cavity mode selection in homojunction and heterojunction semiconductor diode lasers," *J. Appl. Phys.*, vol. 42, pp. 4447–4457, Oct. 1971.
[7] J. K. Butler and J. Zoroofchi, "Radiation fields of GaAs–(AlGa)As injection lasers," *IEEE J. Quantum Electron.*, vol. QE-10, pp. 809–815, Oct. 1974.
[8] I. Kudman and T. Seidel, "Absorption edge in degenerate p-type GaAs," *J. Appl. Phys.*, vol. 33, pp. 771–773, Mar. 1962.
[9] H. Kressel, H. F. Lockwood, and J. K. Butler, "Measurements of the refractive index step and of carrier confinement at (AlGa)As–GaAs heterojunctions," *J. Appl. Phys.*, vol. 44, pp. 4095–4097, Sept. 1973.

Calculations of the Continuous-Wave Lasing Range and Light-Output Power for Double-Heterostructure Lasers

P. GAREL-JONES AND JOHN C. DYMENT

Abstract—**Procedures for calculating the range of currents and heat-sink temperatures in which continuous-wave (CW) operation is possible and the light-output power levels within this range are presented for double-heterostructure (DH) lasers with an oxide-insulated stripe geometry. A one-dimensional heat-flow model has been assumed within the device followed by two-dimensional heat flow into the heat sink. It is shown that a laser with stripe dimensions (13 μm × 400 μm) and typical thicknesses can achieve CW operation at heat-sink temperatures up to about 431 K. At 300 K, the theoretical power output is in the 40–50-mW range for $J = 2J_{th}$. The effects of varying thicknesses and the aluminum content in the GaAlAs confining layer are considered. The limitations of the calculation are discussed as well as its applicability to other stripe-geometry devices.**

Nomenclature

T_j Junction temperature.
$\Delta T(i)$ Temperature rise across layer (i).
$T(i)$ Temperature at boundary between layers (i) and $(i+1)$.
$D(i)$ Thickness of layer (i).
$K(i)$ Thermal conductivity of layer (i).
T_{HS} Heat-sink temperature.
L Length of stripe contact.
S Width of stripe contact.
A Area of stripe contact ($A = LS$).
x Fraction of Al in layer (2), $Ga_{1-x}Al_xAs$.
α Reduction in thermal conductivity due to presence of Al from [13]. For $x = (0,0.1,0.2,0.3,0.4)$, $\alpha = (1.00,2.33,3.06,3.76,4.45)$.
J Current density.
I Total current ($I = JA$).
V Total voltage ($V = V_0 + IR_s$).
V_0 Approximate junction voltage

$$V_0 = 1.49 - [0.00058\, T_j^2/(T_j + 300)].$$

R_s Series resistance.
$J_{th}(T_j)$ Threshold current density at junction temperature T_j.
$\eta(T_j)$ External differential quantum efficiency at junction temperature T_j.
P_L CW light output at current density $J > J_{th}$ ($P = \eta V A[J - J_{th}]$).
P_H Power dissipated as heat in the junction region.
$R_T(T_j)$ Thermal resistance from junction at T_j to the heat sink.

Manuscript received December 23, 1974; revised February 13, 1975.
The authors are with Bell-Northern Research, Ottawa, Ont., Canada.

INTRODUCTION

IN THIS PAPER our purpose is twofold. In Part I, a set of procedures is developed for calculating the allowable range of currents and heat-sink temperatures in which continuous-wave (CW) operation is possible for double-heterostructure (DH) lasers with an oxide-insulated stripe-geometry contact [1]. In Part II, the permissable CW light-output power is calculated for any current within the CW lasing range. In stripe-geometry devices, the current through the junction is confined which thus creates a narrow source of heat. Because the oxide acts as a thermal barrier, the flow of heat can be considered as one-dimensional from the junction region to the stripe and then two-dimensional as the heat flows into the heat sink. The thermal resistances obtained from this model will be applicable to oxide stripe geometries [1], to buried layer heterostructures [2], which have an oxide barrier, and to etched mesa structures [3]. However, this model will overestimate the thermal resistance of devices in which current confinement is achieved by means of proton bombardment [4], various diffusion techniques [5]-[7], lateral injection techniques [8], or heteroisolation techniques [9]. In all of these latter devices, there is no oxide barrier and the heat flow from the junction region should be considered as two-dimensional [6], [10]. For these cases, the present calculation would overestimate the junction temperature and underestimate the light-output power. Further discussion on these points follows in Part II.

The concept of a CW lasing region boundary has been used by Dyment *et al.* [11] for a homostructure laser. These same concepts have been used in Part I, but the problem is now somewhat more complicated because of the multiple layers contained in a DH laser. In the present calculations, the experimentally known temperature dependences for threshold current density (J_{th}) are used along with estimates of the temperature dependences of the voltage (V) and thermal conductivities of GaAs and GaAlAs. Calculations of the light-output power within the CW lasing region boundary were not previously performed in [11], but become increasingly important in view of the current efforts to improve the reliability of DH lasers. The light-output powers calculated in Part II depend critically on the value of the junction temperature (T_j) and the associated values of $J_{th}(T_j)$ and external differential quantum efficiency $\eta(T_j)$. These temperature dependences were both obtained experimentally as described in the next section.

TEMPERATURE DEPENDENCES OF THRESHOLD CURRENT DENSITY AND EFFICIENCY

The temperature dependences of both J_{th} and η have been obtained from experimental measurements of light output as a function of pulsed current density using DH laser structures as shown in Fig. 1. A low duty cycle was used so that T_j was approximately equal to the heat-sink temperature (T_{HS}) which was increased in steps from 295-415 K.

From the sharp increases in light output which occur where $J = J_{th}$, we established that the typical temperature dependence has the form

$$J_{th}(T_j) = J_0 \exp(T_j/T_0) = 232 \exp(T_j/125). \quad (1)$$

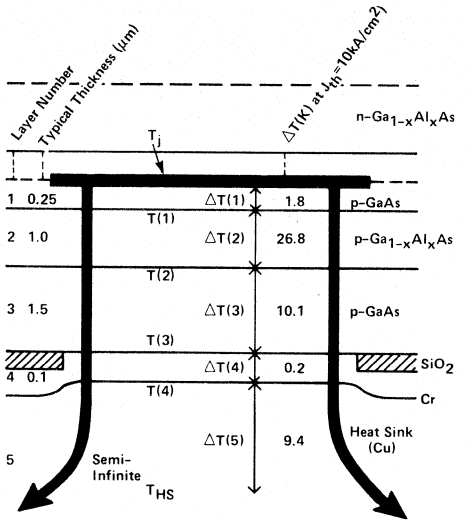

Fig. 1. Heat-flow model for a continuously operating DH laser with an oxide-insulated stripe geometry. Heavy lines represent the flow of heat from the center of the active region to the heat sink which is assumed to be Cu for the calculations. Assuming typical thicknesses as indicated and $x = 0.3$, $R_s = 1\ \Omega$, $S = 13\ \mu$m, and $L = 400\ \mu$m, the temperature rises for $J_{th} = 10$ kA/cm² are given. In experimental lasers, the heat sink actually has a layer of Au between the device and the Cu. This is neglected in the calculation due to the similar thermal conductivities of Au and Cu.

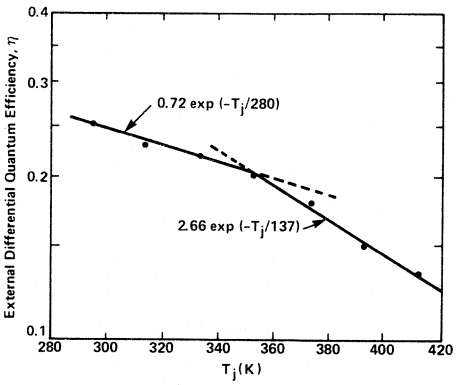

Fig. 2. Variation of external differential quantum efficiency (η) with junction temperature (T_j) for a typical DH laser with a stripe geometry.

By setting $J_0 = 232$ A/cm², we ensure that $J_{th} \simeq 2500$ A/cm² at room temperature, a value usually obtained in our CW lasers. The magnitude of $T_0 = 125$ K is the average of the measured values which ranged from 115 to 140 K.

The magnitudes of $\eta(T_j)$ were obtained from the slopes of the total light-output power from both mirrors for $J > J_{th}$. A typical set of data has been plotted in Fig. 2. It can be seen that η decreases from about 0.25 at $T_j \simeq 300$ K to about 0.13 at $T_j = 415$ K; however, the decrease is not linear but is slightly concave downward. To a reasonable degree of accuracy, the data can be approximated by two exponential regions as follows:

$$\eta(T_j) = 0.72 \exp(-T_j/280), \quad T_j < 350\ \text{K}$$
$$\eta(T_j) = 2.66 \exp(-T_j/137), \quad T_j > 350\ \text{K}. \quad (2)$$

The analytical expressions in (1) and (2) have been used in the computer calculations.

PART I—CALCULATION OF THE BOUNDARY OF THE CW LASING REGION ($J = J_{th}$)

Fig. 1 illustrates the heat-flow model for a DH laser with an oxide-insulated stripe contact. A source of heat power P_H of width (S) and length (L) is assumed localized at the center of the p-type GaAs active region although its exact location and extent is somewhat uncertain. Further discussion concerning this point is presented in the following. Heat flows linearly through successive layers of p-GaAs, p-GaAlAs, p-GaAs, and Cr before spreading into a semi-infinite Cu heat sink. In experimental devices, there is usually a thick layer of Au ($\simeq$15 μm) and a bond metal In ($\simeq$1 μm) between the Cr and the Cu heat sink but, since the thermal conductivities of Au and Cu are similar and the In is thin, little error is made by assuming that Au and Cu act together as a semi-infinite half-space (assumed to have the thermal conductivity of pure Cu). The heat flowing through these layers produces corresponding temperature rises $\Delta T(i)$ which have been calculated using the parameters and formulas given in the Nomenclature and Table I. Layers (1)-(5) are assumed to be at the constant temperatures T_j, $T(1)$, $T(2)$, $T(3)$, and $T(4)$, respectively, for the purposes of determining their thermal conductivities. The total temperature decrease from the junction to the heat sink is

$$T_j - T_{HS} = \sum_{i=1}^{5} \Delta T(i). \tag{3}$$

We now briefly discuss some of the differences between the present calculation for a DH laser and the calculation cited previously for the homostructure device [11]. The thermal conductivities $K(1)$ and $K(3)$ for the p-GaAs layers are required at temperatures above 300 K in contrast to the previous work in which temperatures far below 300 K were used. For this purpose we have plotted the data of Amith *et al.* [12], and have obtained the temperature dependences given in Table I. Unfortunately, the temperature dependence for the thermal conductivity of the p-$Ga_{1-x}Al_xAs$ layer (2) is not known. We have assumed that the temperature dependence will be the same as for p-GaAs [12], but we have reduced the overall magnitude by the term α (see Table I) since values of α are known from the recently published data of Afromowitz [13]. The Nomenclature lists values of α for Al contents ranging from $x = 0$ to $x = 0.4$, the range of interest to us. It is realized that the assumption of the same temperature dependence for GaAlAs will probably overestimate the temperature rise in layer (2). This can be inferred from data for another alloy ($GaAs_{1-x}P_x$) given by Carlson *et al.* [14], which suggests that the temperature dependence of thermal conductivity in an alloy will be less than in the pure material and indeed will also be different for different values of x. In view of the lack of experimental data on this parameter, the assumption of the same temperature dependence serves as a worst case calculation by overestimating $\Delta T(2)$.

For each given value of J_{th}, a ΔT value is calculated as in (3) assuming that all of the input electrical power $P_H = VAJ_{th}$ is dissipated as heat in the device where

$$V = V_0 + AJ_{th}R_s \tag{4}$$

TABLE I
FORMULAS FOR CALCULATING TEMPERATURE RISES IN A DH LASER WITH AN OXIDE STRIPE-GEOMETRY CONTACT OF WIDTH S (13 μM) AND LENGTH L (400 μM)

Layer	Material	Thickness (cm)	Thermal Conductivity [a] (W cm^{-1} K^{-1})	ΔT (K)
(1)	p-GaAs	$D(1) = 0.25 \times 10^{-4}$	$K(1) = 0.91 \exp\left(\frac{-T_j}{367}\right)$	$\Delta T(1) = \frac{P_H}{LS} \frac{D(1)}{K(1)}$
(2)	p-$Ga_{1-x}Al_xAs$	$D(2) = 1.0 \times 10^{-4}$	$K(2) = \frac{0.91}{\alpha} \exp\left(\frac{-T(1)}{367}\right)$	$\Delta T(2) = \frac{P_H}{LS} \frac{D(2)}{K(2)}$
(3)	p-GaAs	$D(3) = 1.5 \times 10^{-4}$	$K(3) = 0.91 \exp\left(\frac{-T(2)}{367}\right)$	$\Delta T(3) = \frac{P_H}{LS} \frac{D(3)}{K(3)}$
(4)	Cr	$D(4) = 0.10 \times 10^{-4}$	$K(4) = 0.86$	$\Delta T(4) = \frac{P_H}{LS} \frac{D(4)}{K(4)}$
(5)	Cu	Semi-Infinite	$K(5) = 3.90$	$\Delta T(5) = \frac{P_H \ln(4L/S)}{K(5)\pi L}$

[a] Thermal conductivities for Cr and Cu are assumed to be independent of temperature for these calculations. For the GaAs layers the temperature dependences $K(1)$ and $K(3)$ have been obtained from the data of [12] and are valid for temperatures $\geq$ 300 K. For the GaAlAs layer the same temperature dependence for $K(2)$ has been assumed but the magnitude has been reduced by the factor α (from [13]).

and

$$V_0 = 1.49 - \frac{0.00058T_j^2}{(T_j + 300)}. \tag{5}$$

In (4), V_0 and $AJ_{th}R_s$ represent the voltage contributions from junction and series resistance, respectively. In DH lasers, typical values of R_s (obtained from the slopes of I-V plots at high currents) are about 1 Ω. Such values are significantly higher than the 0.14-Ω values used for homostructures [11]. Higher R_s values mean that a much larger portion of the power is dissipated at contacts and throughout the bulk material outside the junction region. This creates a distributed heat source. In addition, a distributed source of heat will also arise from those photons which are created and subsequently absorbed in the device. Since the center of the active region is located within both of these distributed heat sources, there is reasonable justification for locating the entire source of heat within the active region itself.

In (5), the explicit form for V_0 assumes that the junction voltage will vary with the same temperature dependence as the GaAs bandgap. This variation, which is believed to be more accurate than the expression used in [11], has been taken from Panish and Casey [15] with the value of the constant term reduced by 0.030 eV since the recombination is assumed to occur through an acceptor level in p-type GaAs.

For each selected value of J_{th}, the ΔT values calculated from (3) to (5) are subtracted from the corresponding junction temperatures obtained from (1) to form the boundary of the CW lasing region. Fig. 3 shows the result of a typical computer calculation in which 80 values of J_{th} were used ranging from 0 to 40 kA/cm^2. For the typical parameters listed in the caption, the predicted maximum heat-sink temperature for CW operation is 431 K with the corresponding value of J_{th} being 14 000 A/cm^2. It is of interest to compare these numbers with the best experimental numbers in the literature. To date, the highest heat-sink temperature reported for CW

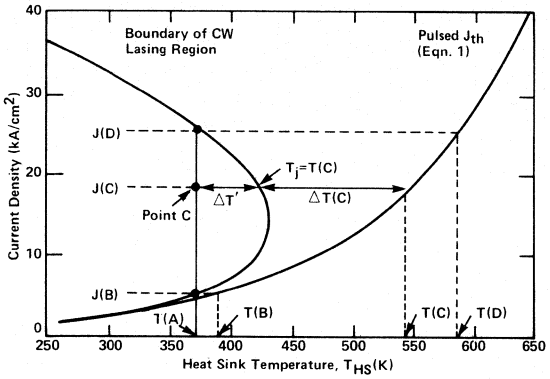

Fig. 3. Computer calculation of the CW lasing region for a DH laser with an oxide-insulated stripe geometry. Assuming parameter values as in Fig. 1, the highest heat-sink temperature for CW operation is 431 K. Superimposed on the calculation are some currents and heat-sink temperatures which will aid in the discussion of Fig. 4.

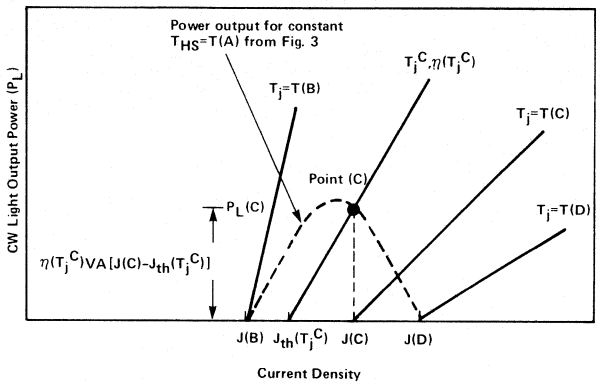

Fig. 4. Schematic illustrating how the light-output power P_L is derived for a general current density $J(C)$ within the CW lasing region. $J(C)$ lies between the turn-on current $J(B)$ and turn-off current $J(D)$. The dashed line is a schematic representation of how P_L would vary along the constant heat-sink temperature $T(A)$ of Fig. 3. Spontaneous light-output power is assumed to be zero in this figure. Typical computer results are presented in Figs. 5 and 6.

operation is 110°C (383 K) which occurred at J_{th} = 12 500 A/cm² [4]. This comparison should be reasonably valid since the layer thicknesses in the experimental device are nearly identical to those used in the calculation. The agreement is quite close with respect to current density; however, the calculated maximum CW operating temperature is considerably higher than the experimental value. In principle, since the experimental device has no oxide barrier, two-dimensional heat flow should be applicable and its maximum CW operating temperature should exceed the value calculated in Fig. 3. One possible explanation for the discrepancy is the fact that the experimental device could contain some voids between the bond metal and the heat sink.

Finally, in order to get some idea as to which layers contribute the largest temperature rises, values of $\Delta T(1)$-$\Delta T(5)$ have been given in Fig. 1 for a selected value of J_{th} = 10 kA/cm². Clearly, the p-GaAlAs layer (2) gives by far the largest temperature rise. In practice, it is unlikely that its thickness can be reduced very much below the 1 μm assumed here before an increase of optical loss occurs because of penetration of some of the guided light through the p-GaAlAs to the p-GaAs layer. The thickness of layer (3) might be reduced somewhat below 1.5 μm, but it should not be thinner than about 1 μm in order to ensure low thresholds and long lifetimes. Concerning the heat sink, replacement of the Au-Cu combination by a Au-diamond combination will provide only a small reduction in the overall temperature rise. This is due to the fact that the heat has to pass through about 15 μm of Au before reaching the diamond.

Part II—Calculation of the Light-Output Power Within the CW Lasing Region ($J > J_{th}$)

Suppose a line of constant heat-sink temperature labeled $T(A)$ in Fig. 3 is selected and the dc current is increased from zero. The laser will turn on at $J(B)$ where $T_j = T(B)$ and will continue to lase throughout the CW lasing region before turning off at $J(D)$ at which point $T_j = T(D)$. Turn-off is due to internal heating in the device at high-current densities. For a current density of $J(C)$ at point C, between $J(B)$ and $J(D)$, the emitted light-output power depends on both the junction temperature T_j^C and the corresponding external differential quantum efficiency $\eta(T_j^C)$. Suppose that these values are known so that $J_{th}(T_j^C)$ can be calculated from (1). Then, with reference to Fig. 4, which shows schematically the relationship between the various currents and temperatures noted in Fig. 3, the output light power $P_L(T_j^C)$ at point C [where $T_{HS} = T(A)$] is

$$P_L(T_j^C) = \eta(T_j^C)\, VA\, [J(C) - J_{th}(T_j^C)]. \tag{6}$$

For self-consistency, P_L must also satisfy the condition

$$T_j^C = T(A) + R_{th}(T_j^C)[VAJ(C) - P_L(T_j^C)] \tag{7}$$

where $R_{th}(T_j^C)$ is the thermal resistance for a junction temperature T_j^C which is already known from Part I. Equation (7) takes into account that the junction temperature is cooled because of the escape of the optical power from the device. Rapid convergence of (7) is achieved by assuming, as a first approximation, that T_j^C will be cooler than $T(C)$ by the amount which $T(A)$ is less than the heat-sink value at $J_{th} = J(C)$. That is

$$T_j^C = T(C) - \Delta T' \quad \text{(first approximation)} \tag{8}$$

where $\Delta T'$ is as indicated in Fig. 3. When the trial value of T_j^C and the calculated value from (7) agree to within 1 percent, the final value of P_L is calculated from (6).

In Fig. 5 the preceding procedures were used to calculate values of P_L for five different heat-sink temperatures (300, 325, 350, 375, 400 K). The parameters used in Fig. 3 were retained. At T_{HS} = 300 K, the laser must operate about 30 percent above J_{th} in order to have a power output of 10-20 mW; this prediction is in good agreement with our own experimental results and with those of Hartman *et al.* [16]. The locus of points at constant junction temperatures of T_j = 400 K and T_j = 450 K are also indicated in Fig. 5. Since the junction temperature can rise to over 600 K within the CW lasing region at T_{HS} = 300 K, the expressions used for J_{th} and η from (1) and (2) may no longer hold. It is known that these expressions are valid up to T_j = 415 K (the extent of our data) and probably it would be safe to extrapolate them to T_j = 450 K. Thus, in Fig. 5, all of the calculated values to

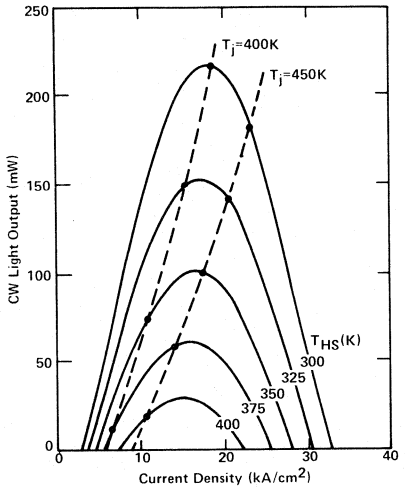

Fig. 5. Computer calculations of the CW light-output power as a function of current density for five selected values of heat-sink temperature (T_{HS}). Device parameters as in Fig. 1. Dashed lines join points of constant junction temperature for T_j = 400 K and T_j = 450 K.

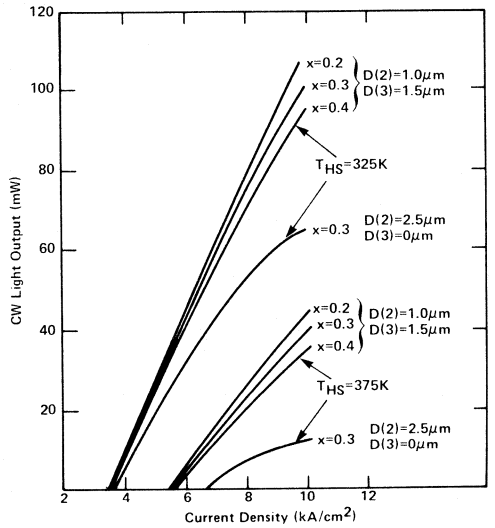

Fig. 6. Computer calculations of output for heat-sink temperatures of 325 K and 375 K. Effect of variations in Al content (x) and layer thicknesses [$D(2)$ and $D(3)$] are shown.

the left side of the T_j = 450 K line are based on known data and should closely correspond to the experimental situation. Those values to the right side of the T_j = 450 K line will be accurate only to the extent to which the extrapolations are valid.

Although light-output powers in excess of 200 mW are predicted by this calculation, these would not likely be achieved in practice because they are in the 10^6 W/cm^2 range where catastrophic degradation of the laser mirrors can occur [17]. In addition, it is unlikely that CW lasers will be operated at current densities above 10 kA/cm^2 under reliable conditions. For these two reasons, in Fig. 6 we have selected two heat-sink temperatures of 325 and 375 K and current densities less than 10 kA/cm^2 to ensure that light-output power levels are about 100 mW or less. Here we see what happens when the Al content is varied from $x = 0.2$ to $x = 0.4$. Note that there is relatively little effect on the power output when the layer thickness of p-GaAlAs is thin (i.e., $D(2) = 1.0$ μm). A much larger reduction in power output is obtained by making the p-GaAlAs thicker (i.e., $D(2) = 2.5$ μm, $D(3) = 0$ μm). This is particularly true at the higher heat-sink temperatures which would be appropriate for accelerated life testing.

Discussion and Conclusions

Procedures for calculating the CW lasing region and light-output power within the CW region have been presented for DH lasers with an oxide-insulated stripe-geometry contact [1]. One-dimensional heat flow has been assumed within the device followed by two-dimensional heat flow into the semi-infinite heat sink. The methods employed should be valid for other lasers such as the buried-layer heterostructure [2] which is also oxide insulated and the mesa structures [3]. In these devices, the one-dimensional heat-flow model may slightly overestimate the junction-temperature rise because it neglects sideways flow heat out through the oxide and heat loss through the sides or top. In addition, our assumption that the thermal conductivity for the p-GaAlAs alloy has the same temperature dependence as GaAs probably causes a further overestimate of the junction temperature. Thus our calculations will predict a CW lasing region which is too small and light-output power levels which are also too small.

For other structures in which current confinement is achieved by proton bombardment [4], diffusion techniques [5]-[7], lateral injection [8], or heteroisolation [9], a two-dimensional heat-flow model should be employed beginning at the junction. This will further lower the overall thermal resistance [6], [10] and will lead to even larger CW lasing regions and light-output power levels.

The calculations have pointed out two areas in which further work is required before more precise analyses of DH lasers are attempted at temperatures above 300 K. The first area concerns the unknown temperature dependence of the thermal conductivity of GaAlAs alloys. At present, our knowledge is limited to the room-temperature values measured by Afromowitz [13]. Since a large portion of the overall thermal resistance occurs in the GaAlAs layer, there is a definite need for measurements of thermal conductivity in such layers above 300 K. The second area of concern is the rather large values of the series resistance (≃1 Ω) in DH devices. From (4), we can estimate that at $J \simeq 25$ kA/cm^2, there is as much heat generated in the series resistance as at the junction. This reduces overall device efficiency and probably means that our assumption of a localized source of heat power in the center of the active region is less valid at high currents. One possible source of the high resistance could be high-resistivity interfacial layers introduced during crystal growth.

For oxide-stripe DH lasers with typical thicknesses and a heat-sink temperature of 300 K, the maximum predicted light-output power is in excess of 200 mW for a stripe width of 13 μm; these power levels are close to the catastrophic limit [17] and would require current densities about seven times higher than threshold. A more reliable operating current level for CW lasers would be below two times threshold in which case about 40–50 mW of light-output power would be expected for a heat sink at 300 K.

REFERENCES

[1] J. E. Ripper, J. C. Dyment, L. A. D'Asaro, and T. L. Paoli, "Stripe-geometry double heterostructure junction lasers: Mode structure and CW operation above room temperature," *Appl. Phys. Lett.*, vol. 18, pp. 155–157, Feb. 1971.

[2] T. Tsukada, "GaAs-$Ga_{1-x}Al_xAs$ buried-heterostructure injection lasers," *J. Appl. Phys.*, vol. 45, pp. 4899–4906, Nov. 1974.

[3] T. Tsukada *et al.*, "Very low current operation of mesa-stripe-geometry double heterostructure injection lasers," *Appl. Phys. Lett.*, vol. 20, pp. 344–345, May 1, 1972.

[4] J. C. Dyment *et al.*, "Proton bombardment formation of stripe-geometry heterostructure lasers for 300 K CW operation," *Proc. IEEE* (Lett.), vol. 60, pp. 726–728, June 1972.

[5] W. Susaki, H. Namizaki, H. Kan, and A. Ito, "A new geometry double heterostructure injection laser for room-temperature continuous operation: Junction-stripe-geometry DH lasers," *J. Appl. Phys.*, vol. 44, pp. 2893–2894, June 1973.

[6] H. Yonezu *et al.*, "A GaAs-$Al_xGa_{1-x}As$ double heterostructure planar stripe laser," *Japan. J. Appl. Phys.*, vol. 12, pp. 1585–1592, Oct. 1973.

[7] M. Takusagawa *et al.*, "An internally striped planar laser with 3-μm stripe width oscillating in transverse single mode," *Proc. IEEE* (Lett.), vol. 61, pp. 1758–1759, Dec. 1973.

[8] H. Namizaki, H. Kan, M. Ishii, and A. Ito, "Transverse-junction-stripe-geometry double-heterostructure lasers with very low threshold current," *J. Appl. Phys.*, vol. 45, pp. 2785–2786, June 1974.

[9] K. Itoh, M. Inoue, and I. Teramoto, "New heteroisolation stripe-geometry visible-light-emitting lasers," this issue, pp. 421–426.

[10] W. B. Joyce and R. W. Dixon, "Thermal resistance of heterostructure lasers," *J. Appl. Phys.*, vol. 46, pp. 855–862, Feb. 1975.

[11] J. C. Dyment, J. E. Ripper, and T. H. Zachos, "Optimum stripe width for continuous operation of GaAs junction lasers," *J. Appl. Phys.*, vol. 40, pp. 1802–1808, Mar. 1969.

[12] A. Amith, I. Kudman, and E. F. Steigmeier, "Electron and phonon scattering in GaAs at high temperatures," *Phys. Rev.*, vol. 4A, pp. A1270–A1276, May 1965.

[13] M. A. Afromowitz, "Thermal conductivity of $Ga_{1-x}Al_xAs$ alloys," *J. Appl. Phys.*, vol. 44, pp. 1292–1294, Mar. 1973.

[14] R. O. Carlson, G. A. Slack, and S. J. Silverman, "Thermal conductivity of GaAs and $GaAs_{1-x}P_x$ laser semiconductors," *J. Appl. Phys.*, vol. 36, pp. 505–507, Feb. 1965.

[15] M. B. Panish and H. C. Casey, Jr., "Temperature dependence of the energy gap in GaAs and GaP," *J. Appl. Phys.*, vol. 40, pp. 163–167, Jan. 1969.

[16] R. L. Hartman, J. C. Dyment, C. J. Hwang, and M. Kuhn, "Continuous operation of GaAs-$Ga_{1-x}Al_xAs$ double heterostructure lasers with 30°C half-lives exceeding 1000 h," *Appl. Phys. Lett.*, vol. 23, pp. 181–183, Aug. 1973.

[17] B. W. Hakki and F. R. Nash, "Catastrophic failure in GaAs double-heterostructure injection lasers," *J. Appl. Phys.*, vol. 45, pp. 3907–3912, Sept. 1974.

Oxygen-Implanted Double-Heterojunction GaAs/GaAlAs Injection Lasers

JOSEPH M. BLUM, MEMBER, IEEE, J. C. McGRODDY, MEMBER, IEEE, PAUL G. McMULLIN, MEMBER, IEEE, K. K. SHIH, MEMBER, IEEE, ARCHIBALD W. SMITH, SENIOR MEMBER, IEEE, AND J. F. ZIEGLER

Abstract—**We describe a new process for stripe formation in double-heterostructure GaAs/GaAlAs injection lasers. This process, which uses oxygen-ion implantation to form the stripe through a chemical doping effect, has several advantages over alternative methods, both with respect to device processing and device properties and has produced high yields of CW room-temperature lasers. We present the details of the device structure and fabrication processes. The results of annealing studies, optical measurements, and lifetesting are described.**

INTRODUCTION

A NEW PROCESS for the formation of stripe-geometry double-heterojunction GaAs/GaAlAs injection lasers has been developed and has the capability of producing high yields of CW room-temperature devices. These lasers utilize the doping effects of oxygen implantation first reported by Favennec *et al.* [1] to form high-resistance areas in the GaAs, thus providing the isolation necessary to pump only a narrow stripe laser region.

The use of a stripe geometry greatly facilitates the continuous operation of lasers at room temperature. There are, however, many different types of stripe-forming methods. The oxygen-implanted stripe devices have the advantage of requiring less critical processing than the other methods. For example, they do not require the diffusion [2], etching [3], or annealing [4], [5] control required for the diffused, mesa etch, or proton-bombarded stripe-geometry lasers, respectively.

The oxygen-induced damage is sufficiently annealed during a subsequent diffusion step that no special annealing process is required. Annealing and aging studies have shown that any residual damage due to the implantation does not cause detrimental effects on the lifetime of the oxygen-implanted lasers. It has also been found that oxygen-implanted devices offer the potential advantage of better lateral confinement than other structures due to the special nature of the edges of the oxygen-implanted regions.

Manuscript received December 12, 1974; revised February 5, 1975.
The authors are with the IBM Thomas J. Watson Research Center, Yorktown Heights, N. Y. 10598.

This paper will describe the fabrication processes used to make these devices as well as their optical characteristics which appear to be unique. The CW room-temperature aging characteristics will also be presented.

Fabrication

Fig. 1 is a sketch of an oxygen-implanted laser chip. The effects of the oxygen implantation are indicated as buried high-resistivity regions.

The material used for this device is a four-layer liquid-phase-epitaxy double heterostructure grown on an n-type silicon-doped ⟨100⟩ oriented GaAs substrate with a carrier concentration of 1-2 × 10^{18} cm^{-3}. An 8-μm buffer layer (not shown on the figure) of tin- or tellurium-doped GaAs with a carrier concentration of 1 × 10^{18} cm^{-3} is first grown on the substrate in order to smooth out irregularities sometimes seen at the interface between the substrate and the subsequent layer. The next four layers are grown as shown in the figure using state-of-the-art liquid-phase-epitaxial techniques [6]. The two GaAlAs layers above and below the silicon-doped active layer contain 30-percent aluminum. The active layer contains up to 10-percent aluminum.

A graphical representation of the oxygen distribution, calculated using LSS range theory [7] with modifications [8]-[10] due to the high energy of implantation (> 1 MeV), after it has been implanted into a typical laser wafer, is shown in Fig. 2. The Gaussian-like distribution of oxygen atoms is superimposed on the doping levels that would be found in such a four-layer laser structure. The typical carrier concentrations in each layer, starting from the surface of the wafer, are 1 × 10^{18}, 5 × 10^{17}, 5 × 10^{17}, and 1 × 10^{17} cm^{-3}. Isolation is provided in the regions where the oxygen-implanted level is higher than the background doping. According to Favennec *et al.* [1], these semi-insulating properties are due to the chemical doping effects of oxygen where each oxygen ion can remove two carriers. The chemical doping effect, as opposed to the implantation-induced damage, has been verified in our laboratory. A dose of 10^{14} ions/cm^2 was found to be an optimum level, i.e., sufficient to form the necessary isolation barrier but not so much as to produce damage which could not be annealed out conveniently. The energy used on each wafer was determined by the actual thickness of the upper two layers. In the case shown in this figure an energy of 2.5 MeV was found to be adequate for an upper-two-layer total thickness of 2.0 μm.

In order to form oxygen-implanted stripe-geometry laser devices from the liquid-phase-epitaxial wafer a number of processes are required. These processes are indicated in Fig. 3.

Fiducial lines are first formed by the chemical etching of a sputtered Al_2O_3 film [11] through a photoresist mask using a 1:1 H_3PO_4:H_2O solution (70-75°C). The lines are 25 μm wide on 200-μm centers and are parallel to the ⟨110⟩ direction. The middle drawing shows the wafer during and after oxygen implantation. Materials which have been successfully used to mask against oxygen ions with energy in the range 2-3 MeV include gold and nickel electroformed masks, and AZ 1350

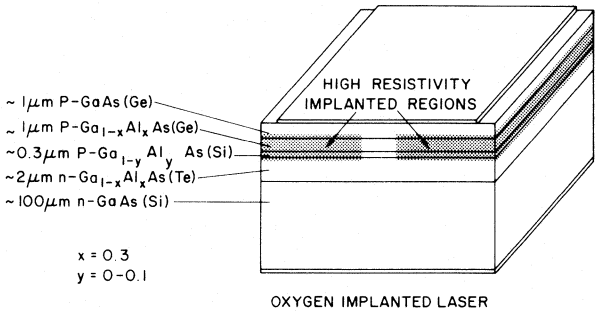

Fig. 1. Schematic drawing of completed oxygen-implanted laser chip.

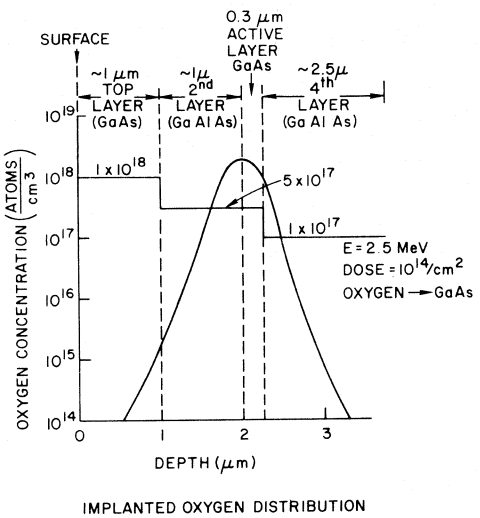

Fig. 2. Graphical representation of a typical oxygen-implanted distribution superimposed on the background impurity levels of a typical four-layer laser structure.

photoresist (~ 5 μm thick). These masks are aligned parallel and centered with respect to the Al_2O_3 marker lines.

The experimental arrangement for ion implantation consisted of a 3-MeV ion accelerator, a magnetic energy-analysis system, a 5-kG double-quadrupole focusing system, and a 5-keV sawtooth beam-sweep plate. The beam was raster scanned over the wafer at a repetition rate of 80 sweeps/s. The implant dose accuracy was estimated to be ±30 percent and the uniformity accuracy was ±10 percent. The broad band below the surface in the middle diagram represents the high-resistivity region due to the presence of both damage and oxygen atoms immediately after completion of the implantation step.

In the lower diagram the completed wafer can be seen. To get to this stage after the implantation process, zinc is diffused into the wafer to a depth of 0.4 μm at 600°C for 30 min using a $ZnAs_2$ source. The diffusion process not only provides low-resistance contacts but also conveniently serves as an annealing step to remove most of the defects produced by the implantation. Evaporated chromium-gold contacts are used for the p-contacts. The original Al_2O_3 marker lines are used once again to locate the p-metal photoetch mask and are etched away after the metal is removed in order to delineate each laser

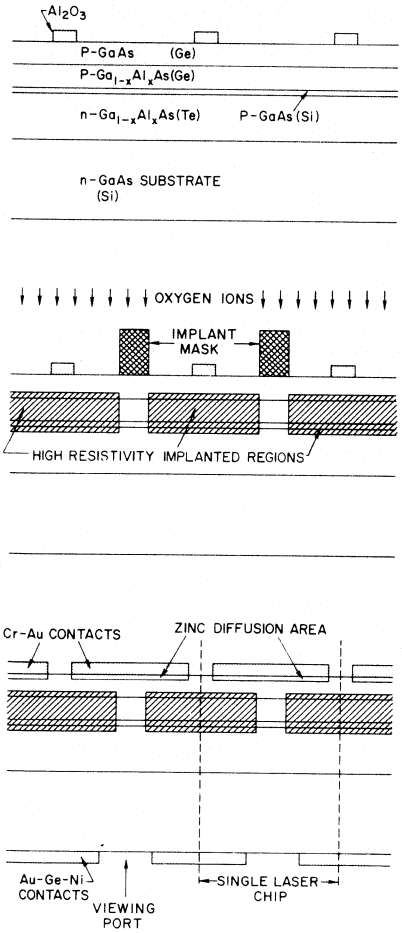

Fig. 3. Schematic drawing of wafer after various fabrication processing steps. Top—after photoetching aluminum oxide fiducial lines. Middle—during and after oxygen implantation. Bottom—completed wafer.

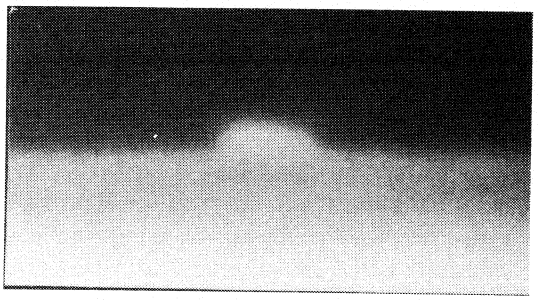

Fig. 4. Photomicrograph of cleaved oxygen-implanted laser chip after annealing taken by scanning electron microscope in the cathodoluminescent mode. Width of nonimplanted (masked) region is 25 μm.

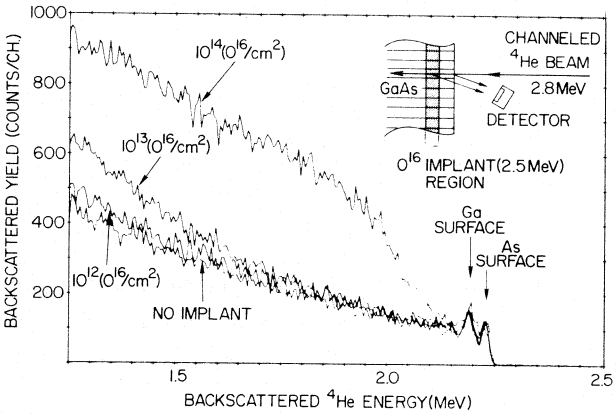

Fig. 5. Backscattered yield versus backscattered energy of ^{4}He ions.

contact. The 500 Å:5000 Å Cr:Au films are etched by first removing the gold layer using a KI-I_2 solution and then removing the chromium layer by etching in a 1:1:1 HCl:H_3PO_4:H_2O solution (65–70°C) after the surface has been activated by touching it with zinc. After lapping and polishing the substrate side to a total thickness of 100 μm, a 5000-Å evaporated gold-germanium-nickel alloy is used for the n-contact [12]. If required, viewing ports are also etched using the KI-I_2 solution into the n-type metal contacts prior to a 2-min 485°C alloying heat treatment in nitrogen. Isolated laser-array strips or individual laser chips are then cleaved and mounted on indium-plated copper heat sinks.

Implantation Damage and Annealing Studies

The oxygen-implanted regions can be seen on a cleaved laser chip using a scanning electron microscope in the cathodoluminescent mode as shown in Fig. 4. Here the effects of the oxygen implantation after annealing reduce the cathodoluminescent efficiency in the implanted region revealing the nonimplanted region which is 25 μm wide.

Fig. 5 shows the degree of damage produced by various oxygen-implant doses as measured by channeling and backscattering of 2.8-MeV He^+ ions. Data are shown for GaAs samples that have been implanted with 2.5-MeV oxygen ions with doses of 10^{14} cm^{-2}, 10^{13} cm^{-2}, and 10^{12} cm^{-2} as well as an unimplanted sample. These results indicate that about 15 percent, 5 percent, and 2 percent of the bonds in the GaAs have been damaged, respectively [13]. After annealing for 30 min at 600°C (the zinc-diffusion cycle) all of the backscattering data resulted in curves similar to the nonimplanted GaAs indicating that the crystal damage had been removed to a value of less than 2 percent. Preliminary data obtained from photoluminescence measurements have indicated that there is still some residual optical damage left after normal annealing during the diffusion cycle. This residual damage appears to be of little consequence since aging data show that no obvious detrimental effects have occurred, and measurements of the thermal resistance of packaged devices indicate that the thermal conductivity of the materials has not been adversely affected by implantation.

Continuous room-temperature operation has been achieved from devices both with and without annealing. In the unannealed devices the 30-min 600°C diffusion step was performed before the implantation process so that the only heat treatment those devices received was for 2 min at 485°C which removes very little damage. However, the yield of CW room-temperature devices is significantly higher from the annealed group than the unannealed group made from the same wafer.

This could be due to a higher thermal resistance of unannealed implanted material.

With oxygen implantation it is the presence of the chemical-dopant oxygen which causes the implanted regions to have high resistivity. This is in contrast to the proton-bombardment method where the damage causes the high resistivity. In the oxygen case the damage is (ideally) annealed out, while in the proton case some residual damage is essential and the subsequent annealing cycle [5] required to eliminate excessive optical loss is rather critical. The annealing of the oxygen bombardment-induced damage could be adequately performed by any temperature above the 600°C temperature used for the diffusion. However, by selecting the diffusion cycle, which must be done anyway to form low-resistance contacts, a special annealing cycle is conveniently avoided.

Optical Measurements

Spatial-intensity profiles of the spontaneous emission were measured on oxygen stripe-geometry devices for comparison with two other stripe-contact technologies: proton implantation and diffusion. In Fig. 6 is shown an oxygen-implanted test device which was fabricated as described before with a 50-μm-wide viewing port etched in the n-type contact metallurgy on the polished GaAs substrate. The spontaneous emission from the laser stripe was observed perpendicular to the ⟨100⟩ surface of the laser through the etched openings. The intensity profile of the spontaneous emission across the stripe (i.e., perpendicular to the lasing direction) was obtained by scanning an enlarged image of the stripe with a slit. A magnification of 20X was obtained with a NA 0.4 microscope objective. This gives a resolution of about 1 μm at 8500 Å. A slit width of 20 μm was used which gave an overall resolution of about 2 μm. The lasers were driven about 20 percent below threshold with 2-μs current pulses. The light passing through the scanning slit was detected with an S-1 photomultiplier and a boxcar integrator. The focusing and alignment of the stripe image of the slit were performed with the aid of an infrared (IR) TV system.

A range of profile shapes for a nominal implant mask width of 25 μm was observed in oxygen-implanted lasers made from different wafers which can be seen in Fig. 7. The shapes varied from sharp to diffuse and can be attributed to different degrees of oxygen doping or penetration into the active layer. If oxygen does not penetrate the active layer the stripe profile should be determined by the diffusion length of electrons into the p-type active layer. Using the theory derived by Hakki [14], this diffuse profile approximates a profile calculated from a diffusion length of 6 μm for carriers both in and out of the laser stripe. This is in good agreement with the value obtained by Hakki [14] for the case of proton-bombarded stripes without penetration. The unexpected sharp profile is believed to occur when the implanted oxygen penetrates into the active layer or deeper into the p-GaAlAs layer. In this case the oxygen doping has a significant effect on the diffusion of carriers out of the stripe.

The relationship between the stripe width and the threshold

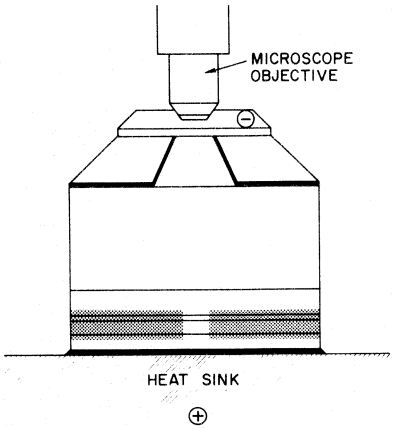

Fig. 6. Schematic view of specially prepared oxygen-implanted laser chip with viewing port for measurement of spatial intensity profiles of the spontaneous emission across the stripe (perpendicular to lasing direction).

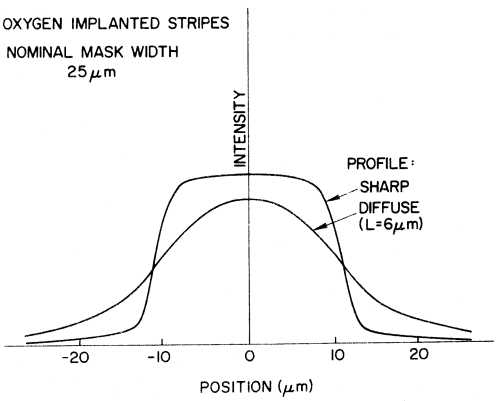

Fig. 7. Range of spatial-intensity profile shapes from sharp to diffuse as measured across the stripe. Nominal mask widths—25 μm.

current is also of interest. In order to investigate this, stripes of nominal widths of 12.5, 25, and 50 μm were fabricated on the same wafer using photoresist for the oxygen-implantation masks. Sharp profiles were obtained as shown in Fig. 8. The edges of the 50-μm profile trace were more tapered because the opening in the contact on the back of the wafer was too small for this case. The relative change in the threshold with stripe width is plotted in Fig. 9, along with data taken from published results for proton-bombarded [14] and diffused stripes [3]. The threshold current-density ratio increase is only 1.25 for the 12.5-μm oxygen-implanted stripes, compared to 1.9 for the other techniques. This result indicates that the sharp profile is not due to an increase in the nonradiative recombination rate in the implanted region. It should be noted that the oxygen-implanted ratio data were obtained from adjacent units on three bars which exhibited unusually uniform characteristics. It is unlikely that as reliable a result would have been obtained with individual chips. It should also be noted that the small change in threshold with stripe width was produced only from devices that had sharp profiles. The diffuse profiles produced results similar to the proton-bombarded and diffused stripe technologies. The sharp pro-

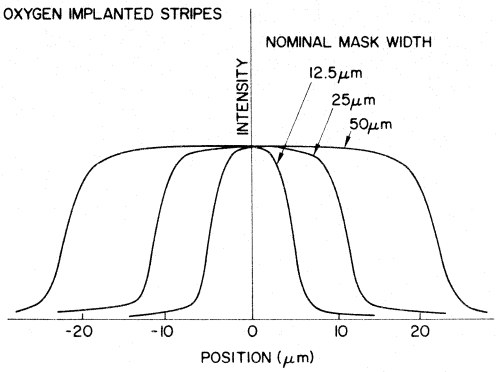

Fig. 8. Spatial-intensity profiles measured on different nominal mask widths 12.5 μm, 25 μm, and 50 μm from same wafer (adjacent devices on bars containing many lasers).

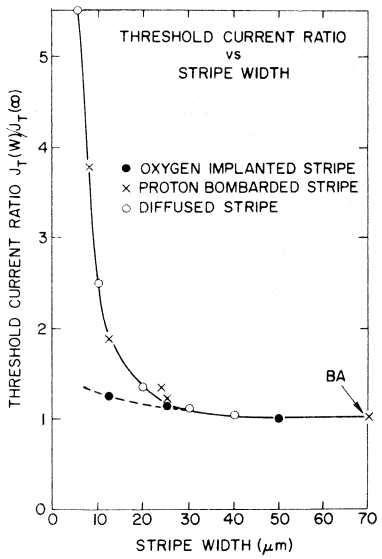

Fig. 9. Relative change in threshold [threshold current ratio $J_T(W)/J_T(\infty)$] versus stripe width. BA is broad area device.

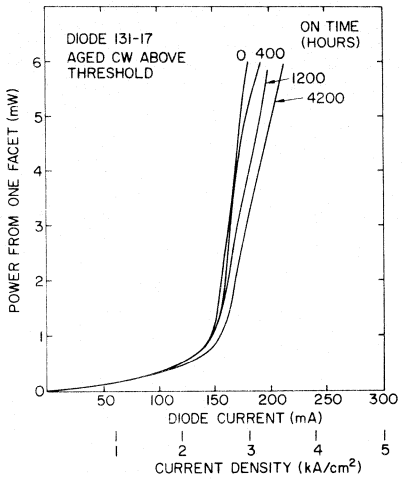

Fig. 10. Power output (from one facet) versus dc diode current measured after various times of CW aging. 10 percent above threshold at 15°C (water-cooled heat-sink temperature).

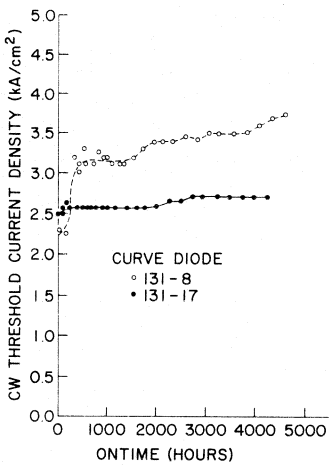

Fig. 11. CW threshold current density versus on-time of CW aging. 10 percent above threshold at 15°C (water-cooled heat-sink temperature).

files are not always formed when the oxygen implantation extends into the active region and it is not known why the sharp lateral confinement is not found in all such cases. Once this phenomenon is better understood it should permit the fabrication of stripe contacts less than 10 μm wide without excessively high threshold current densities.

Aging Studies

From aging studies it is clear that oxygen-implanted devices are capable of stable operation above threshold. The thermal resistance of packaged units is typically 0.8°C cm²/kW indicating a substantial heat flow through the implanted regions. Fig. 10 shows the change in laser characteristics of a device which has been aged for more than 4000 h in a dry nitrogen atmosphere at 15°C (which was the temperature of the water-cooled heat sink). The current was adjusted to be about 10 percent above the CW threshold. The time dependence of the CW threshold for this device is shown in Fig. 11, together with data for another laser. It can be seen that after some initial increase the thresholds of both lasers are stable for long periods of time.

Oxygen-implanted devices have also exhibited a maximum CW power output at room temperature of as high as 1 mW/μm of junction width from a device with an active region thickness of 0.3 μm. Continuous operation has also been obtained at a maximum heat-sink temperature of 80°C.

Conclusions

In summary, we have developed a new stripe-geometry technology which utilizes high-resistivity regions produced by oxygen implantation to isolate the stripe region. This technology offers simplified processing insofar as it does not require any critical annealing to remove radiation damage. Whatever residual damage remains is not sufficiently detrimental to prevent long-lived room-temperature CW lasers from being fabricated.

In addition, the oxygen-implantation process apparently offers the possibility of a unique barrier to be formed along

the edges of the laser stripe which seems to affect carrier outdiffusion. With further understanding of this phenomenon it should be possible to fabricate practical lasers with stripe widths of less than 10 μm.

Acknowledgment

The authors wish to thank C. Burstell for skillful assistance with most of the device processing; J. DeGelormo for the wafer preparation; H. Ifill, F. Feigel, and A. Landon for the device testing; C. Bremer for his work on the SEM; G. Hutchins for packaging the devices; and V. Garrison, R. Potemski, and W. Hammer for their special assistance in the processing of the devices. They also wish to thank B. Monemar for the photoluminescence measurements, and B. Crowder, W. P. Dumke, and F. Morehead for helpful discussions.

References

[1] P. N. Favennec, G. P. Pelous, M. Binet, and P. Baudet, "Compensation of GaAs by oxygen implantation," in *Ion Implantation in Semiconductors and Other Materials* (IBM Research Symposia Series), B. L. Crowder, Ed. New York: Plenum, 1973, pp. 621–630.

[2] H. Yonezu *et al.*, "A GaAs-$Al_xGa_{1-x}As$ double heterostructure planar stripe laser," *Japan. J. Appl. Phys.*, vol. 12, pp. 1585–1592, Oct. 1973.

[3] T. Tsukada *et al.*, "Very low current operation of mesa-stripe-geometry double-heterostructure injection lasers," *Appl. Phys. Lett.*, vol. 20, pp. 344–345, May 1972.

[4] J. C. Dyment *et al.*, "Proton-bombardment formation of stripe-geometry heterostructure lasers for 300 K CW operation," *Proc. IEEE* (Lett.), vol. 60, pp. 726–728, June 1972.

[5] J. C. Dyment, J. C. North, and L. A. D'Asaro, "Optical and electrical properties proton bombarded p-type GaAs," *J. Appl. Phys.*, vol. 44, pp. 207–213, Jan. 1973.

[6] K. K. Shih, G. R. Woolhouse, A. E. Blakeslee, and J. M. Blum, "Surface imperfections in GaAs-$Al_xGa_{1-x}As$ DH LPE layers," in *Proc. 1974 5th Int. Symp. Gallium Arsenide: Inst. Phys. Soc. Conf. Ser.*, to be published.

[7] J. Lindhard, M. Scharff, and H. Schiott, "Range concepts and heavy ion ranges," *Kgl. Dan. Vidensk., Mat. Fys. Medd.*, no. 14, pp. 1–42, Oct. 1963.

[8] H. Nakata, "Ranges of nitrogen ion in Al, Ni, Ag, and Au," *Can. J. Phys.*, vol. 46, pp. 2765–2769, Oct. 1968.

[9] A. Kostka and S. Kalbitzer, "Electrical properties of silicon implanted with boron ion on MeV energy," *Radiat. Eff. Phys. Chem. Biol.*, vol. 19, pp. 77–82, 1973.

[10] J. Zieger *et al.*, "High energy ion implantation in silicon," in *International Conference on Ion Implantation–1974*. New York: Plenum, to be published.

[11] J. M. Blum and K. K. Shih, "The liquid phase epitaxy of $Al_xGa_{1-x}As$ for monolithic planar structures," *Proc. IEEE (Special Issue on Thick and Thin Films for Electronic Applications)*, vol. 59, pp. 1498–1502, Oct. 1971.

[12] K. K. Shih and J. M. Blum, "Contact resistances of AuGeNi, AuZn and Al to III-V compounds," *Solid-State Electron.*, vol. 15, pp. 1177–1180, 1972.

[13] J. F. Ziegler, "Determination of lattice disorder profiles in crystals by nuclear backscattering," *J. Appl. Phys.*, vol. 43, pp. 2973–2981, July 1972.

[14] B. W. Hakki, "Carrier and gain spatial profiles in GaAs stripe geometry lasers," *J. Appl. Phys.*, vol. 44, pp. 5021–5028, Nov. 1973.

Striped-Substrate Double-Heterostructure Lasers

R. D. BURNHAM, D. R. SCIFRES, MEMBER, IEEE, J. C. TRAMONTANA, AND A. S. ALIMONDA

Abstract—**A different type of stripe-geometry laser is demonstrated in which current confinement is achieved by selective diffusion of the n-type substrate prior to growth of the GaAs/GaAlAs heterostructure layers. This structure exhibits low room-temperature threshold currents resulting from the small lateral-current spreading from the edges of the stripe. Lowest order transverse-mode operation is achieved for stripe widths of 10 μm.**

Introduction

IN ORDER to achieve low-threshold room-temperature laser operation in double-heterostructure (DH) GaAs/$Ga_{1-x}Al_xAs$ injection lasers current must be restricted to flow across a small area of the device. Several methods have been developed which laterally confine the current by the use of selective diffusion techniques. These include the internal-stripe [1] and planar-stripe [2] geometries. In these devices the process of fabricating the current-confining stripe is performed after growth of the heterostructure layers.

The striped-substrate device which is shown schematically in Fig. 1 has a current-confining channel which is formed prior to growth of the heterostructure layers. When the diode is forward biased the p-n junction between the selectively diffused region in the substrate and the first n-type $Ga_{1-x}Al_xAs$ layer is reverse biased leading to current flow only through the narrow n-type channel in the substrate. Control of the depth of the diffusion defining the channel has little effect on current confinement leading to increased simplicity of fabrication and uniformity of devices. The width of the current-carrying stripe can be controlled quite easily and accurately by monitoring the time of diffusion. These stripes can also be made much narrower than those obtained with other diffused-stripe techniques [1], [2]. This is because with the striped-substrate technique the current-carrying channel is n-type and the

Manuscript received December 16, 1974; revised January 27, 1975.

The authors are with the Xerox Palo Alto Research Center, Palo Alto, Calif. 94304.

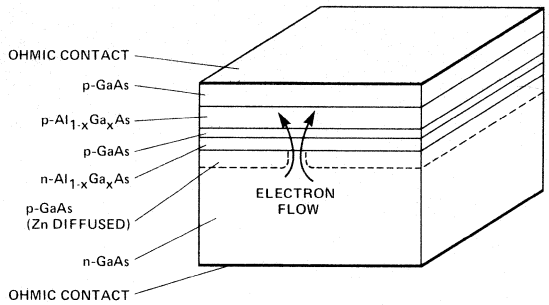

Fig. 1. Schematic diagram of the striped-substrate laser.

TABLE I
PARAMETERS FOR GROWTH, COMPOSITION, AND GEOMETRY OF A STRIPED-SUBSTRATE LASER

Layer	X	Ga (g)	Al (mg)	Doping (mg)	Initial Growth Temp. (°c)	Growth Time (min)	Thickness (μm)
1st n-$Ga_{1-x}Al_xAs$	.40	4	5	Te/0.05	780	3	0.65
2nd p-GaAs	—	4	—	Ge/15	778.5	1/2	0.45
3rd p-$Ga_{1-x}Al_xAs$	.40	4	5	Ge/25	778	5	1.4
4th p-GaAs	—	4	—	Zn/40	776.5	30	15

Note: (Cooling rate–0.5°C/min. Substrate doping–$N_D - N_A = 2 \times 10^{18}/cm^3$.

n-type channel narrows as the Zn-diffused p-type region widens. In contrast, for internal- [1] and planar-stripe [2] geometries, the current-carrying channel is p-type and therefore this channel widens as the diffusion of Zn proceeds. Finally, free-carrier absorption losses due to the absorption of the light wave which spreads into the n-$Ga_{1-x}Al_xAs$ layer should be lower than that of the internally striped laser [1] since the high p-type carrier concentration defining the channel is in close proximity to the unpumped region of the laser rather than the active region.

FABRICATION

The device consists of an n-type substrate which is selectively made p-type prior to growth. The n-type channel is formed by masking the top surface of the substrate with Si_3N_4 stripes (~18 μm wide) and then diffusing Zn from a Zn_3As_2 source at 700°C for 10 min. This results in a diffusion depth of ~5 μm and leaves an n-type channel width of 8 μm at the substrate surface. This channel width may be varied by changing either the diffusion time or the nitride stripe width. The nitride is then removed and ~1 μm of material is lapped from the top of the substrate in order to eliminate any surface damage caused by the diffusion. This leaves a final stripe width of ~10 μm. (No growths were made on unpolished substrates and therefore it is not known whether this step is necessary to insure good device performance.)

GaAs/$Ga_{1-x}Al_xAs$ layers are then grown on the selectively diffused substrate using conventional liquid-phase-epitaxy (LPE) techniques [3]. A chart of compositions, layer thicknesses, and growth conditions for a typical wafer are given in Table I. An SEM cross section of the device is shown in Fig. 2. No chemical etching is needed to delineate the various layers. The first n-$Ga_{1-x}Al_xAs$ grown layer is kept fairly thin (~0.7 μm) and slightly lower doped than in conventional DH lasers in order to increase the spreading resistance across this layer. This spreading resistance is further increased by a slight back diffusion of Zn into the first grown layer during LPE growth of the subsequent layers. For the growth conditions shown

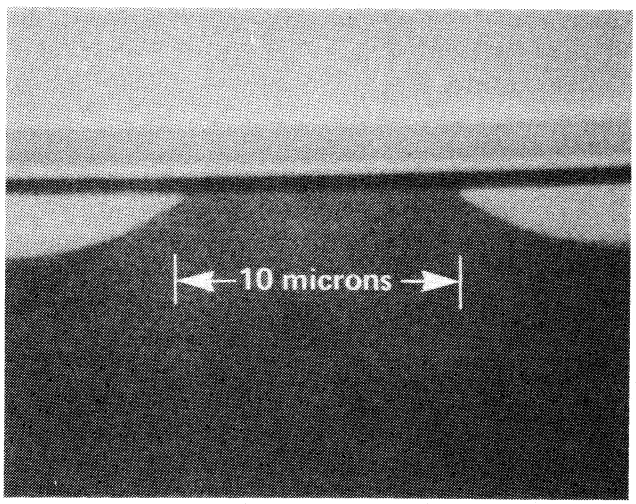

Fig. 2. SEM photograph of a cleaved cross section of the striped-substrate laser. The lower region is the n-type substrate, and the curved region is the p-type diffusion which defines the current-carrying n-type channel. The normal heterostructure layers are grown on top of the selectively diffused substrate. These are, from top to bottom, p-GaAs, p-$Ga_{0.6}Al_{0.4}As$, p-GaAs active layer, and n-$Ga_{0.6}Al_{0.4}As$.

above the Zn back-diffused ~0.1 μm into the first grown layer. The final p-GaAs layer was grown quite thick for ease in contacting. Since this layer was thick no attempt was made to heat sink the diodes for CW operation.

In order to saw the diodes into chips it was necessary to accurately position the saw wire between the buried channels. This registration was accomplished by scribing a shallow groove with a diamond scribe at the edge of the substrate parallel to a cleave plane prior to photoresist masking. The Zn diffusion mask was then positioned relative to this scribe line. After LPE growth this scribe line was still clearly visible on the top of the wafer and the saw wire was positioned relative to this registration mark.

Experimental Results

Pulsed threshold currents as low as 150 mA at room temperature were measured for diodes with diffused stripe widths of ~10 μm. This corresponded to a threshold current density of ~8000 A/cm^2 when measured by dividing the total current by the stripe width times the length of the diode. A "control" substrate with no selective diffusion was also grown simultaneously with the striped substrate in order to measure the increase in threshold current density in the stripe-geometry diodes. Large-area diodes from this control wafer exhibited threshold current densities of ~5000 A/cm^2. Thus the striped-substrate geometry showed a 60-percent increase in threshold current density as compared to large-area diodes from the same wafer. This increase is similar to that observed in the planar-stripe- [2] geometry diodes for 10-μm stripe widths.

An estimate of the dependence of this increase in threshold current density on current spreading in the first n-GaAlAs layer can be made based on a calculation by Dumke [4]. The assumptions made for this calculation are: 1) the n-GaAlAs layer is thin and can be characterized by a sheet resistivity R_s; 2) the junction has an exponential current-voltage characteristic; and 3) the final two p-layers of the device have very high conductivity so that the potential is uniform across them. If W is the actual stripe width in the laser, an effective stripe width (W_{eff}) can be found which is the sum of the actual stripe width (W) and the current-spreading term. That is

$$W_{\text{eff}} = W + 2^{3/2}\left(\frac{2kT}{R_s j_0 e}\right)^{1/2} \tag{1}$$

where j_0 is the threshold current density of a broad-contact laser, k is Boltzmann's constant, T is temperature, and e is electronic charge. For a laser with the first grown layer having a carrier concentration of $n \sim 10^{17}/\text{cm}^3$, a mobility of 150 cm^2/V · s, and a layer thickness of 0.6 μm, R_s is ~6700 Ω/□. If the threshold current density for a large-area diode is 5000 A/cm^2, then the effective stripe width assuming an actual channel width of 10 μm is 11 μm. Thus the current spread in the thin n-GaAlAs layer accounts for only 10 percent of the observed increase in threshold current density. The additional current spread may be accounted for by ambipolar diffusion of the injected carriers in the active layer. Such an effect has been observed experimentally in proton-implanted stripe-geometry lasers [5]. The limiting factor governing thresholds for narrow substrate stripes is therefore not current spreading in the n-GaAlAs layer. However, if this layer has a direct gap, the electron mobility can be substantially higher than that used for the indirect gap layer leading to appreciable current spreading in this layer. For example, an electron mobility of 4000 cm^2/V · s in direct GaAlAs leads to $R_s \sim 260$ Ω/□ and an effective stripe width of 16 μm disregarding the additional spread due to ambipolar diffusion in the active layer. Therefore, care should be taken to make the first layer indirect.

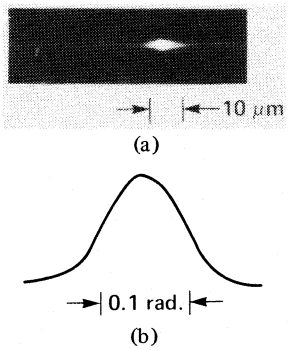

Fig. 3. Near- and far-field radiation patterns from a laser with a 10-μm stripe width. (a) Near-field pattern. (b) Far-field pattern.

Lowest order transverse-mode operation in the junction plane can also be readily achieved in striped-substrate lasers with stripe widths of 10 μm or less. Fig. 3 shows the near- and far-field pattern of a laser with a 10-μm stripe width. These data were taken at a current level 1.05 times threshold and confirm lowest order transverse-mode operation. At slightly higher currents (5-10 percent above threshold) first-order transverse modes are excited. Also, as larger stripe widths are used, higher order transverse modes are observed. The dependence of mode order on stripe width appears to be similar to that observed for the planar-stripe laser [2].

In conclusion, the striped-substrate planar laser can exhibit low room-temperature threshold current levels and fundamental transverse-mode operation. It is easy to fabricate since stripe width can be accurately controlled and the number of processes which must be performed after LPE growth are minimized.

Acknowledgment

The authors wish to thank R. Ewing and G. McKinley for SEM and microprobe measurements.

References

[1] M. Takusagawa *et al.*, "An internally striped planar laser with 3-μm stripe width oscillating in transverse single mode," *Proc. IEEE* (Lett.), vol. 61, pp. 1758-1759, Dec. 1973.

[2] H. Yonezu *et al.*, "A GaAs-$Al_xGa_{1-x}As$ double heterostructure planar stripe laser," *Japan. J. Appl. Phys.*, vol. 12, pp. 1585-1592, Oct. 1973.

[3] B. I. Miller, E. Pinkas, I. Hayaski, and R. J. Capik, "Reproducible liquid-phase-epitaxial growth of double heterostructure GaAs-Al_xGa_{1-x} laser diodes," *J. Appl. Phys.*, vol. 43, pp. 2817-2825, June 1972.

[4] W. P. Dumke, "Current thresholds in stripe contact lasers," *Solid-State Electron.*, vol. 16, pp. 1279-1281, 1973.

[5] B. W. Hakki, "Carrier and gain spatial profiles in GaAs stripe geometry lasers," *J. Appl. Phys.*, vol. 44, pp. 5021-5028, Nov. 1973.

New Heteroisolation Stripe-Geometry Visible-Light-Emitting Lasers

KUNIO ITOH, MORIO INOUE, AND IWAO TERAMOTO

Abstract—**Visible-light-emitting lasers were fabricated, using a new stripe-geometry double heterostructure. The distinct feature of the geometry is the isolation of the contact stripe electrode to p-GaAs by the use of a layer of n-$Ga_{1-z}Al_zAs$ epitaxially grown on top of p-GaAs. This geometry results in small internal strain, few crystal imperfections, and low thermal resistance in diodes so that high laser performance can be obtained. Lasing wavelengths as short as 7610 Å and 6680 Å have been attained in CW and pulsed operation, respectively, at room temperature. Various characteristic features of the lasers are described with regard to optical spectra, lasing thresholds, and external quantum efficiencies.**

I. Introduction

THE mixed compound $Ga_{1-y}Al_yAs$ has been the subject of recent investigations into visible-light-emitting lasers. Many types of lasers have been reported, and the shortest wavelengths reported for pulsed operation are 6380 Å at 77 K in p-n homojunction lasers [1]; 6280 Å and 7180 Å at 77 K and 300 K, respectively, in single-heterostructure lasers [2]; and 6190 Å and 6930 Å at 77 K and 300 K, respectively, in double-heterostructure lasers [3]-[5]. CW operation at room temperature at a wavelength of 7730 Å has been obtained using a double-heterostructure stripe geometry [6]. However, difficulty has been encountered in obtaining CW operation in the visible region because of poor thermal dissipation of an oxide-stripe geometry.

The present paper proposes a new type of stripe-geometry laser, here named the heteroisolation stripe (HIS) laser, in which thermal dissipation is improved, permitting room-temperature CW operation in the "visible" region. Also described are the properties of visible-light-emitting lasers using the HIS geometry covering the emission wavelength from 9000 Å to 7610 Å in CW operation and to 6680 Å in pulsed operation. Some properties are analyzed using the band model of $Ga_{1-y}Al_yAs$.

II. HIS Laser

Many kinds of stripe geometry have been proposed and developed up to the present, such as the oxide stripe [7], proton-bombardment stripe [8], planar stripe [9], mesa stripe [10], and internal stripe [11]. Most of these conventional stripe lasers can be classified into the following three types:

1) stripe lasers whose stripes are isolated with an insulator such as silicon dioxide, silicon nitride, or aluminum oxide;
2) stripe lasers which are isolated with zinc-diffused p-n junctions;
3) stripe lasers which are isolated with the bombarded high-resistivity regions.

When an insulator is used for isolation, a boundary strain occurs between GaAs and the insulator film because of the difference in their thermal-expansion coefficients. Furthermore, the resistance to heat flow is considerably high because of the low thermal conductivity of the insulator.

On the other hand, into stripe lasers isolated with zinc-diffused p-n junctions may be introduced crystal imperfections, such as dislocations and lattice defects in the vicinity of the active region. These crystal imperfections near the active region cause an increase of the threshold current density [11] and of the degradation rate [12].

Though the problems previously mentioned are almost negligible in the bombardment-stripe lasers, a proper annealing procedure is required to reduce the high optical absorption in the bombarded region [8].

The structure of the HIS laser is shown schematically in Fig. 1. The uppermost fifth layer of n-$Ga_{1-z}Al_zAs$ is epitaxially grown on the fourth p-GaAs layer, and this n-$Ga_{1-z}Al_zAs$ layer is partly etched in a stripe until the surface of the fourth layer is revealed. When a positive voltage is applied to the upper electrode in Fig. 1, current flows through the stripe. No current flows through other parts because the p-n junction of p-GaAs and n-$Ga_{1-z}Al_zAs$ is reverse biased. In other words, the contact stripe of p-GaAs is isolated by the n-$Ga_{1-z}Al_zAs$ layer epitaxially grown on top of p-GaAs.

The characteristics of the HIS laser are as follows.

1) Because of the close matching of the lattice constants between GaAs and $Ga_{1-z}Al_zAs$, much less boundary strain occurs than in other stripe lasers using insulator films. Fig. 2 shows the experimental and theoretical results of stresses in GaAs under a silicon dioxide film and a $Ga_{1-z}Al_zAs$ layer. GaAs wafers 100 μm thick were used as substrates on which silicon dioxide was deposited at 400°C. The $Ga_{1-z}Al_zAs$ layers were liquid-phase epitaxially grown at 850°C. The stress which occurs in GaAs just under the deposited silicon dioxide film was obtained from the observed deflected curvature of the substrate and the thickness of the silicon dioxide film [13].

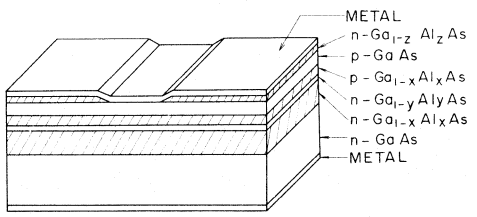

Fig. 1. Structure of the HIS laser.

Manuscript received December 2, 1974; revised January 15, 1975.

The authors are with the Research Laboratory, Matsushita Electronics Corporation, Takatsuki, Osaka, Japan.

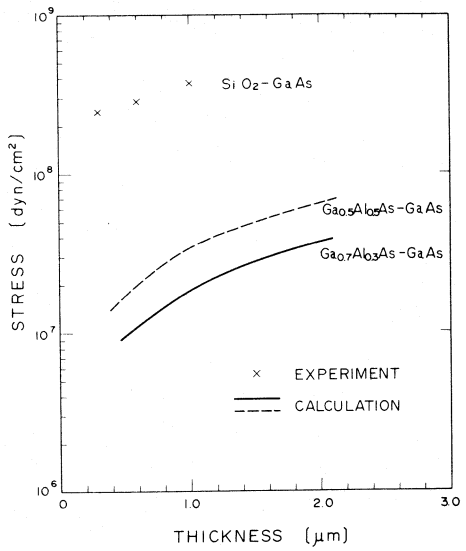

Fig. 2. Experimental and theoretical results of stresses in GaAs under a silica film and under a $Ga_{1-z}Al_zAs$ layer (see text).

The stress in GaAs just under the $Ga_{1-z}Al_zAs$ layer was estimated from the thermal-expansion-coefficient difference, because no detectable substrate deflection was found when the thickness of the epitaxial $Ga_{1-z}Al_zAs$ was less than 2 μm. From Fig. 2, it can be seen that the stress in GaAs under the $Ga_{1-z}Al_zAs$ layer is approximately one order of magnitude smaller than that under the silicon dioxide film. Therefore, it is possible to reduce the internal stress by using a $Ga_{1-z}Al_zAs$ layer instead of a silicon dioxide film.

2) The heat-flow resistance can be much lowered in comparison with that in the oxide-stripe geometry because the heat generated in the active region can be dissipated not only through the stripe window but also through the uppermost $Ga_{1-z}Al_zAs$ layer.[1]

3) The deep zinc-diffusion or proton-bombardment process, which may introduce crystal imperfections, is not required in this HIS laser.

III. Experiment and Measurement

A. Fabrication Method of the HIS Lasers

Five successive layers, as shown in Fig. 1, were grown on an n-GaAs substrate by the conventional liquid-phase-epitaxial method [14]. Table I shows the composition of each solution and the aluminum composition ratio of each layer. The active layer, which is practically undoped n-$Ga_{1-y}Al_yAs$, was grown from the second melt. The value of y was changed from 0 to 0.36 to make infrared and visible-light-emitting lasers. For infrared lasers, the value of x in the first and third $Ga_{1-x}Al_xAs$ layers was fixed to 0.3, while in the case of visible-light-emitting lasers, it was chosen to be 0.5–0.8 to assure the efficient confinement of the injected carriers. The thicknesses of the third and fourth layers were made as thin as 0.5 μm and 1 μm, respectively, to minimize the current spread in the active region. The aluminum fraction z of the isolating n-$Ga_{1-z}Al_zAs$ layer was 0.4–0.6 to facilitate the selective etching, and its thickness was 0.5–1 μm.

For the selective etching of $Ga_{1-z}Al_zAs$, hot phosphoric acid was used, since it dissolves only $Ga_{1-z}Al_zAs$ and not GaAs. Fig. 3 shows a photograph of the cross section after the selective etching. The etched surface is very smooth as shown in this photograph. For ohmic contact, a gold-tin alloy was deposited on both sides. The diode was finally mounted either on a copper block or on a diamond heat sink.

TABLE I
Composition of Each Solution and the Aluminum Composition Ratio of Each Layer

Layer	Ga [g]	GaAs [mg]	Al [mg]	Dopant [mg]	Values of x,y,z
1st n-$Ga_{1-x}Al_xAs$	1	50	2.3 - 6.4	120 (Sn)	0.3 - 0.8
2nd n-$Ga_{1-y}Al_yAs$	1	80	0 - 2.7	-	0 - 0.36
3rd p-$Ga_{1-x}Al_xAs$	1	50	2.3 - 6.4	50 (Zn)	0.3 - 0.8
4th p-GaAs	1	80	-	50 (Ge)	-
5th n-$Ga_{1-z}Al_zAs$	1	50	3.3 - 4.8	30 (Sn)	0.4 - 0.6

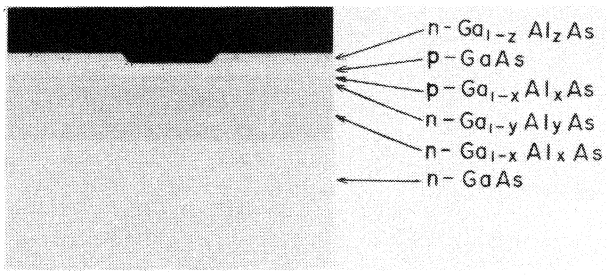

Fig. 3. Photograph of the cross section of the HIS laser. Stripe width is about 10 μm.

B. Measurement

The thickness of each layer was measured by means of an optical microscope or a scanning electron microscope. The solid compositions x and z were estimated by X-ray microanalysis, and the value of y was estimated from the lasing peak emission [2]. The near-field pattern was depicted on a Si vidicon. The optical power was measured by an integrating sphere or a calibrated p-i-n photodiode.

The pulsed operation measurements were made at a repetition rate of 100 Hz with a pulsewidth of 100 ns.

IV. Experimental Results

A. Threshold Current Density Versus Lasing Wavelength

Fig. 4 shows the relationship between the lasing wavelength and the threshold current density J_{th} of the HIS laser at room temperature. The black circles and white circles indicate the results for CW operation and pulsed operation, respectively. The stripe widths of these lasers are 20–30 μm, the cavity

[1] Quantitative analysis of the thermal resistance in the HIS geometry has not been performed yet. We observed, however, that the CW light output from the HIS lasers with 30-μm-wide stripes on copper heat sinks thermally saturates at the current density of about 7000 A/cm^2 which is approximately 1.3 times the saturation current density of the oxide-stripe lasers with 5000-Å-thick oxide films. This result may suggest that the thermal resistance is considerably lower in the HIS lasers than in the oxide-stripe lasers.

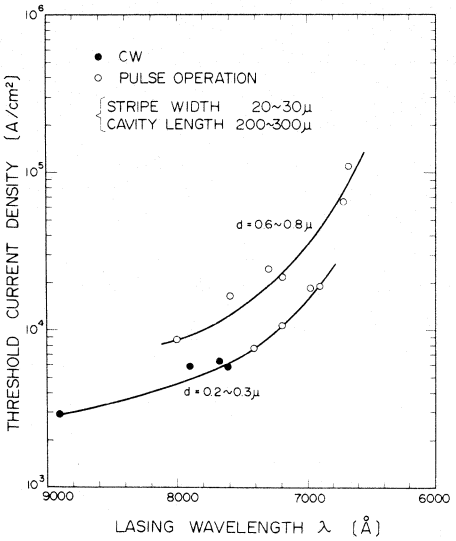

Fig. 4. Relationship between the lasing wavelength and the threshold current density. The black circles and white circles indicate the results of CW operation and pulsed operation, respectively.

lengths are 200–300 μm, and the active region thicknesses are 0.2–0.3 μm and 0.6–0.8 μm.

Fig. 4 indicates that J_{th} increases as the lasing wavelengths becomes shorter, especially in the range of wavelengths shorter than 7500 Å. Further discussion is presented in Section V.

The shortest lasing wavelength attained at room temperature was 6680 Å with J_{th} of 1.1×10^5 A/cm^2. As far as we know, this is the shortest lasing wavelength ever attained in any injection-type semiconductor lasers at room temperature. The shortest lasing wavelength obtained in CW operation was 7610 Å, i.e., the "visible" wavelength, which is also the shortest wavelength ever attained in CW operation at room temperature. It is possible to see the near-field pattern of these lasers with the unaided eye and also the far-field pattern can be seen on a white screen in a darkened room.

B. Transverse and Axial Modes

The operating modes of these visible-light-emitting lasers can be observed at the junction plane through a microscope. In the HIS geometry it is easy to obtain single transverse modes, not only in the infrared region, but also in the visible region. In Fig. 5, the optical near-field patterns of the lower order modes are shown for lasers emitting visible light. Fig. 5(a) shows the fundamental transverse mode TE_{00}, which was obtained in CW operation at a wavelength of 7620 Å. Fig. 5(b) shows a first-order transverse mode TE_{01} at a lasing wavelength of 7200 Å. The lasing spectra of the laser in Fig. 5(a) are shown in Fig. 6. Fig. 6(a) shows the spectrum at a current level of 550 mA, which is 20 percent higher than the threshold (460 mA). The expected longitudinal mode spacing in this laser is 4.2 Å, assuming that the refractive index is 3.4. The oscillation in Fig. 5(a) is almost in a single axial mode of 7619 Å. Some of the HIS lasers operated not only in a single transverse mode, but also in a single axial mode. Fig. 6(b) shows the spectrum at a current level as high as 600 mA for the same laser, where two axial modes of 7609 Å and 7633 Å

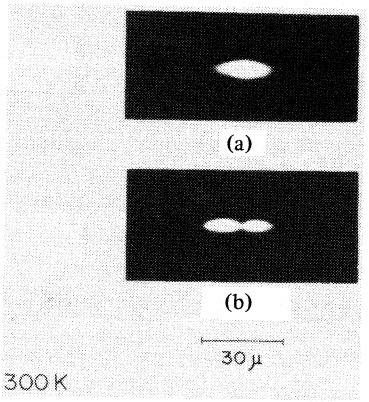

Fig. 5. Lower order modes of the optical near-field pattern of the visible-light-emitting lasers. (a) TE_{00} mode (H97 – 12). λ = 7620 Å: I = 550 mA: I_{th} = 460 mA. (b) TE_{01} mode (H104 – 14). λ = 7200 Å: I = 800 mA: I_{th} = 700 mA.

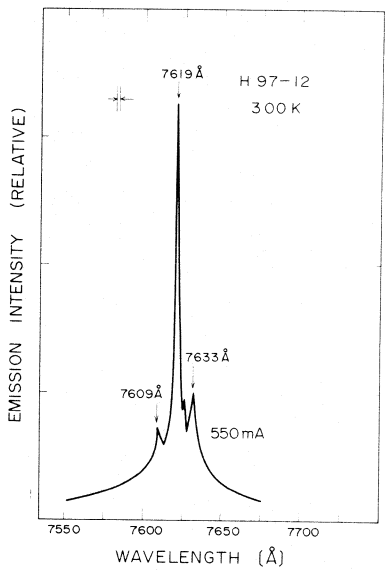

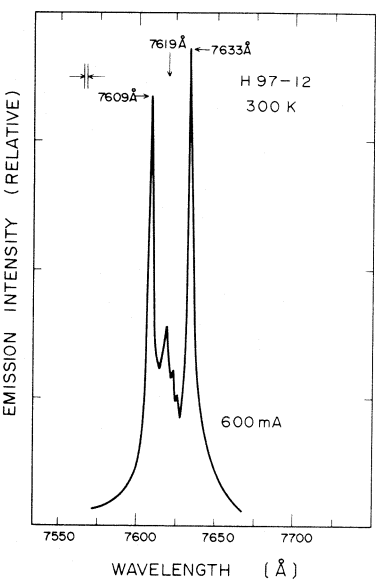

Fig. 6. Lasing spectra of lasers operating continuously at room temperature. (a) Spectrum at a current of 550 mA. (b) Spectrum at a current of 600 mA.

are dominant. At this current level, however, the transverse mode was still TE_{00}. As the current is further increased, more axial modes appear.

On the other hand, the pulsed lasing spectrum of Fig. 5(b) showed about ten axial modes, even just above the threshold.

Generally speaking, it is rather easy to fabricate lasers which operate in a single transverse mode, while it becomes increasingly difficult to obtain a single axial mode as the wavelength is decreased. This may be due to the poor homogeneity of the active region at relatively high aluminum fractions.

C. Temperature Dependence of Threshold Current Density

Temperature dependence of J_{th} of HIS lasers with the Al composition in the active region as a parameter is shown in Fig. 7. The active-region thickness of 1 μm is used as the normalizing value, assuming that J_{th} is proportional to the thickness. It is seen that the temperature dependence of J_{th} increases with increasing Al composition in the active region. A detailed discussion concerning this characteristic is presented in Section V.

D. External Differential Quantum Efficiency

External differential quantum efficiency $\Delta\eta$ decreases as the lasing wavelength becomes shorter. In the infrared region, the typical value of $\Delta\eta$ of HIS lasers is 30–40 percent, while $\Delta\eta$ is 10–20 percent at 7600 Å and 3 percent at 6900 Å. The main cause of the decrease of $\Delta\eta$ in the short-wavelength region is the decrease in the internal quantum efficiency due to the thermal transfer of electrons from the [000] conduction-band minimum into the ⟨100⟩ minima. The typical value of $\Delta\eta$ of infrared HIS lasers is relatively high among various kinds of stripe lasers. This could be, in the HIS geometry, attributed to the good current confinement just under the stripe contact obtained by making the third and fourth layers as thin as possible.

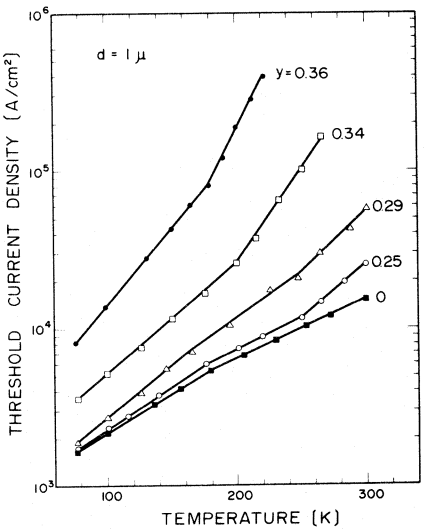

Fig. 7. Temperature dependence of the J_{th} of HIS lasers with a parameter of Al composition in the active region. The active-region thickness is normalized to 1 μm.

V. Discussion

A. Gain and Loss of Visible-Light-Emitting Lasers

The experimental relation obtained between the threshold current density and the lasing wavelength can be discussed in terms of the gain and loss of broad contact geometry lasers of double heterostructure. It has been empirically known that the gain per unit length g of GaAs double-heterostructure lasers is proportional to the mth power of the current density J, where m takes a constant value between 1 and 3 [15]. Since the gain is equal to the total loss at the threshold

$$g_{th} = \alpha + \frac{1}{L} \ln \frac{1}{R} \tag{1}$$

and

$$g_{th} = \beta J_{th}^{m} \tag{2}$$

where L is the cavity length, R is the reflectivity at the mirror, α is the internal loss, and β is the gain constant. For our lasers whose lasing wavelength and active-layer thickness are 9000 Å and 0.6 μm, respectively, the most appropriate value of m is found to be 2 as shown in Fig. 8. Provided $m = 2$ is valid throughout the wavelength range under consideration, the values of β and α can be estimated as a function of the lasing wavelength.

The results are given in Table II where, for comparison, the normalized gain constants βd^2 are also listed, assuming perfect carrier and optical confinement in the double heterostructure. It is seen that the normalized gain constant decreases as the

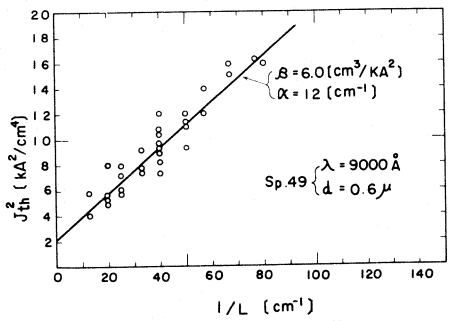

Fig. 8. Relation between the J_{th} and $1/L$, where L is the cavity length. The lasing wavelength is 9000 Å and the active-region thickness is 0.6 μm.

TABLE II
GAIN CONSTANT AND INTERNAL LOSS

Diode No.	49	80	102	101	35
λ (300K) [Å]	9000	8000	7500	7200	6900
d [μ]	0.6	0.8	0.4	0.15	0.2
β [cm³/kA²]	6.0	2.2	3.6	2.6	0.21
α [cm⁻¹]	12	15	20	20	25
βd^2 [cm³·μ^2/kA²]	2.2	1.4	0.58	0.059	0.0084

wavelength becomes shorter, probably resulting from the decrease of internal quantum efficiency.

On the other hand, the internal loss α increases only a little as the wavelength becomes shorter. This is presumably due to the slight increase of free-carrier absorption. It is known that the free-carrier-absorption constant is inversely proportional to the effective mass of an electron [16]. In $Ga_{1-y}Al_yAs$, the effective mass of an electron in the ⟨100⟩ minima is five to ten times larger than that in the [000] minimum. This heavy mass suppresses the increase of free-carrier absorption at the short wavelength in spite of the sharp increase of injected electrons in the ⟨100⟩ minima.

It follows that the increase of J_{th} of HIS lasers at short lasing wavelengths, as shown in Fig. 4, is predominantly due to the decrease of the gain constant rather than to the slight increase of the internal loss.

B. Temperature Dependence of the Threshold Current Density

As mentioned in Section IV-C, the temperature dependence of J_{th} increases with increasing aluminum composition. The most probable reason for this is the decrease of internal quantum efficiency η_i with increasing temperature due to thermal depopulation of the [000] minimum.

A simple calculation for η_i is carried out based on the following assumptions.

1) Both bands are parabolic.

2) The internal loss is independent of y of $Ga_{1-y}Al_yAs$.

3) The energy difference between the [000] and six ⟨100⟩ minima is independent of temperature.

4) All the carriers in the [000] minimum radiatively recombine, while those in the ⟨100⟩ minima recombine nonradiatively.

5) All the injected carriers are in the [000] minimum when $y = 0$.

6) J_{th} is inversely proportional to η_i.

From assumption 4), $\eta_i(y, T)$ is given by

$$\eta_i(y, T) = N_1(y, T)/[N_1(y, T) + N_2(y, T)] \tag{3}$$

where N_1 and N_2 are the injected electron concentrations in the [000] minimum and in the six ⟨100⟩ minima, respectively. From assumptions 2) and 4), N_1 is independent of y, i.e., $N_1(y, T) = N_1(0, T)$. From assumption 5) we can estimate $N_1(0, T)$ using the following relation [15]:

$$N_1(0, T) \approx J_{th}\bar{\tau}/ed \tag{4}$$

where e is the electron charge and $\bar{\tau}$ is the average spontaneous lifetime of the injected carriers. The value of $\bar{\tau}$ can be assumed independent of temperature and estimated by measuring the lasing delay time [17]. We obtained 10 ns for the value of $\bar{\tau}$ at room temperature. The injected electron concentrations N_1 and N_2 are described as follows [18]:

$$N_1 = 6.55 \times 10^{21} \int_0^{\infty} \frac{(m_1^*)^{3/2} E^{1/2} dE}{1 + \exp[(E - E_F)/kT]} \tag{5}$$

$$N_2 = 6.55 \times 10^{21} \int_{f(y)}^{\infty} \frac{6(m_2^*)^{3/2} [E - f(y)]^{1/2} dE}{1 + \exp[(E - E_F)/kT)} \tag{6}$$

where E_F is the Fermi level, $f(y)$ is the energy difference between the [000] and ⟨100⟩ minima, m_1^* and m_2^* are the effective electron masses in the [000] minimum and in the ⟨100⟩ minima, respectively. The effective masses m_1^* and m_2^* were assumed to be 0.072 and 0.35, respectively [2]. Since N_1 is given by (4), we can estimate N_2 from (6) using E_F determined by combination of (4) and (5).

From the assumption 5), the normalized threshold current density $J_{th}^*(y, T)$ is given by

$$J_{th}^*(y, T) \equiv \frac{J_{th}(y, T)}{J_{th}(0, T)} = \left(\frac{\eta_i(y, T)}{\eta_i(0, T)}\right)^{-1} = (\eta_i(y, T))^{-1}. \tag{7}$$

The calculated results of $J_{th}^*(y, T)$ with a parameter y of $Ga_{1-y}Al_yAs$ are shown by the solid curves in Fig. 9, where the experimental results are also plotted for comparison. The most reasonable conclusion to be drawn from Fig. 9 is that the temperature dependence of J_{th} can presumably be explained in terms of the temperature dependence of η_i, although quantitative agreement between the calculated and experimental results is not so excellent because of the over-simplified assumption. For a more precise calculation, it would be necessary to take the temperature dependence of $f(y)$, α, and $\bar{\tau}$ into account. In addition, the values of y should be estimated in a more appropriate way.

C. Laser Series Resistance

As mentioned in Section III, the value of x for the first and third layers in the present visible-light-emitting lasers was chosen to be 0.5–0.8, where $Ga_{1-x}Al_xAs$ has an indirect band gap. This might result in a laser series resistance much higher than that in the direct band-gap range. However, the product of the series resistance and the stripe area in HIS lasers was found to be in the range of 3×10^{-4}–6×10^{-4} $\Omega \cdot cm^2$, typically 4.5×10^{-4} $\Omega \cdot cm^2$, regardless of the values of x and y. This series resistance observed is one order of magnitude higher than the calculated value 3.1×10^{-5} $\Omega \cdot cm^2$, as shown in Table III. Therefore, it is suggested that the series resistance is determined predominantly by the contact resistance at the interface between the crystal and the heat sink rather than by

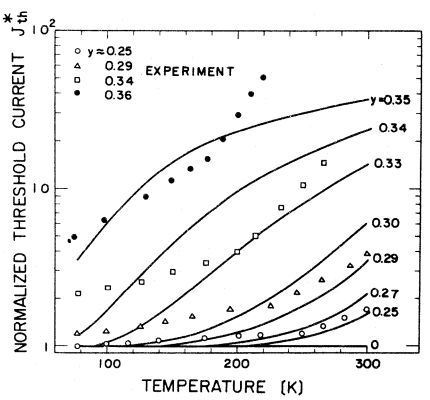

Fig. 9. Temperature dependence of the normalized J_{th} with a parameter y of $Ga_{1-y}Al_yAs$. The theoretical curve was calculated as described in the text.

TABLE III
CALCULATED SERIES RESISTANCE OF THE HIS LASER

Layer	Carrier concentration (cm^{-3})	Resistivity Rs (Ω.cm)	Thickness t (μm)	Rs X t ($\Omega.cm^2$)
n-GaAs	1.0×10^{18}	2.0×10^{-3}	100	2.0×10^{-5}
n-$Ga_{0.7}Al_{0.3}As$	1.0×10^{18}	7.0×10^{-3}	8.0	5.6×10^{-5}
n-GaAs	3.0×10^{16}	6.0×10^{-2}	0.3	1.8×10^{-6}
p-$Ga_{0.7}Al_{0.3}As$	5.0×10^{18}	2.5×10^{-2}	0.5	1.3×10^{-6}
p-GaAs	2.0×10^{18}	2.0×10^{-2}	1.0	2.0×10^{-6}
			Total	3.1×10^{-5}

Composition of the active region is GaAs.

the bulk resistance of the diode. As a result, the laser power-conversion efficiency should be little affected by the value of x even in the indirect band-gap range.

VI. SUMMARY AND CONCLUSION

A new stripe-geometry double-heterostructure laser, in which a contact stripe electrode to p-GaAs is isolated with an overgrown n-$Ga_{1-z}Al_zAs$ layer, is reported. This device has the practical advantages in low internal strain and low heat-flow resistance.

With this structure we obtained CW laser operation at a wavelength as short as 7610 Å at room temperature, which is the shortest "visible" wavelength ever attained.

In pulsed operation at room temperature, we observed the emission down to 6680 Å, also the shortest ever attained.

A single optical mode was often obtained in the axial mode as well as in the transverse mode.

The observed increase in threshold current density at short wavelength is ascribed mainly to the steep decrease in gain constant with increasing aluminum composition.

The temperature dependence of the threshold current density is discussed in terms of the internal quantum efficiency.

The external differential quantum efficiency at room temperature typically obtained in the infrared HIS lasers is as high as 40 percent. This high efficiency results from the reduced current spreading in the HIS geometry with the very thin third and fourth layers.

ACKNOWLEDGMENT

The authors wish to thank Dr. M. Takeshima and S. Fujiwara for helpful discussions and comments, and T. Matsuda for assistance in the photoetching process.

REFERENCES

[1] W. Susaki, T. Sogo, and T. Oku, "Stimulated emission from $(Ga_{1-x}Al_x)As$ junctions," in *1968 Proc. Int. Symp. GaAs*, (Inst. of Phys. and the Physical Soc., London, England, 1969), pp. 116–120.

[2] H. Kressel, H. F. Lockwood, and H. Nelson, "Low-threshold $Al_xGa_{1-x}As$ visible and IR-light-emitting diode lasers," *IEEE J. Quantum Electronics* (*Special Issue on Semiconductor Lasers*), vol. QE-6, pp. 278–284, June 1970.

[3] H. Kressel and F. Z. Hawrylo, "Red-light-emitting $Al_xGa_{1-x}As$ heterojunction laser diodes," *J. Appl. Phys.*, vol. 44, pp. 4222–4223, Sept. 1973.

[4] K. Itoh, "Visible light-emitting semiconductor lasers of double heterostructure," in *1973 Proc. Int. Conf. Solid State Devices*, (Japan Soc. Appl. Phys., Tokyo, Japan, 1974), pp. 49–53.

[5] —, "6190 Å emission at 77 K of $Ga_{1-x}Al_xAs$ double heterostructure," *Appl. Phys. Lett.*, vol. 24, pp. 127–129, Feb. 1974.

[6] B. I. Miller *et al.*, "Semiconductor lasers operating continuously in the 'visible' at room temperature," *Appl. Phys. Lett.*, vol. 18, pp. 403–405, May 1971.

[7] J. E. Ripper, J. C. Dyment, L. A. D'Asaro, and T. L. Paoli, "Stripe-geometry double heterostructure junction lasers: Mode structure and cw operation above room temperature," *Appl. Phys. Lett.*, vol. 18, pp. 155–157, Feb. 1971.

[8] J. C. Dyment *et al.*, "Proton-bombardment formation of stripe-geometry heterostructure lasers for 300 K CW operation," *Proc. IEEE* (Lett.), vol. 60, pp. 726–728, June 1972.

[9] H. Yonezu *et al.*, "A GaAs-$Al_xGa_{1-x}As$ double heterostructure planar stripe laser," *Japan. J. Appl. Phys.*, vol. 12, pp. 1585–1592, Oct. 1973.

[10] T. Tsukada *et al.*, "Very-low-current operation of mesa-stripe-geometry double-heterostructure injection lasers," *Appl. Phys. Lett.*, vol. 20, pp. 344–345, May 1972.

[11] M. Takusagawa *et al.*, "An internally striped planar laser with 3-μm stripe width oscillating in transverse single mode," *Proc. IEEE* (Lett.), vol. 61, pp. 1758–1759, Dec. 1973.

[12] I. Ladany and H. Kressel, "The influence of device fabrication parameters on the gradual degradation of (AlGa)As CW laser diodes," *Appl. Phys. Lett.*, vol. 25, pp. 708–710, Dec. 1974.

[13] F. K. Reinhart and R. A. Logan, "Interface stress of $Al_xGa_{1-x}As$-GaAs layer structure," *J. Appl. Phys.*, vol. 44, pp. 3171–3175, July 1973.

[14] I. Hayashi, M. B. Panish, P. W. Foy, and S. Sumski, "Junction lasers which operate continuously at room temperature," *Appl. Phys. Lett.*, vol. 17, pp. 109–111, Aug. 1970.

[15] E. Pinkas, B. I. Miller, I. Hayashi, and P. W. Foy, "GaAs-$Al_xGa_{1-x}As$ double heterostructure lasers–Effect of doping on lasing characteristics of GaAs," *J. Appl. Phys.*, vol. 43, pp. 2827–2835, June 1972.

[16] T. S. Moss, *Optical Properties of Semiconductors*. London, 1959, pp. 29–33.

[17] J. C. Dyment, J. E. Ripper, and T. P. Lee, "Measurement and interpretation of long spontaneous lifetimes in double heterostructure lasers," *J. Appl. Phys.*, vol. 43, pp. 452–457, Feb. 1972.

[18] H. P. Maruska and J. I. Pankove, "Efficiency of $GaAs_{1-x}P_x$ electroluminescent diodes," *Solid-State Electron.*, vol. 10, pp. 917–925, Sept. 1967.

Transverse-Junction-Stripe Lasers with a GaAs p-n Homojunction

H. NAMIZAKI

Abstract—A new semiconductor laser structure named the transverse-junction-stripe (TJS) laser, in which the active region is a GaAs p-n homojunction sandwiched between GaAlAs layers, has been developed. It is possible to operate the laser continuously at room temperature below 100 mA. The minimum threshold current is 34 and 50 mA in pulsed and continuous operation, respectively. Relatively high efficiencies have been obtained, comparable to those of conventional double-heterostructure (DH) lasers. The transverse mode is fundamental in both directions and is almost independent of input current up to three times the threshold current. The longitudinal mode stays nearly single over a wide range of input current. The TE/TM power ratio exceeds 100 at 1.5 times the threshold current.

I. Introduction

In conventional homojunction lasers, a large amount of heat generation raises the temperature of the p-n junction, which increases the threshold current density further and prevents continuous lasing at room temperature. With double-heterostructure (DH) lasers, the threshold current density is reduced through carrier and optical confinement, allowing them to operate continuously [1]. It is also possible to operate homojunction lasers continuously without raising the threshold current density, if the heat produced at the p-n junction can be removed effectively. The transverse-junction-stripe (TJS) laser has a very small active region made of a GaAs p-n junction sandwiched between GaAlAs layers [2]. The generated heat is effectively removed through one of the GaAlAs layers, enabling this laser to operate continuously under 100 mA at room temperature.

In addition, the TJS-laser has the structure of a two-dimensional waveguide. It is well known that in most stripe-geometry DH lasers the active region has little guiding effect in the direction parallel to the junction so that when the stripe width becomes narrow, the optical field spreads into the adjacent absorbing region, and the threshold current increases rapidly [3]. To obtain a smaller active region and lower threshold currents, it is desirable that the active region be constructed into a two-dimensional waveguide. The TJS-laser presents a new structure to realize this idea, utilizing the automatic formation of a refractive index difference across the p-n junction.

II. Device Structure and Fabrication

A schematic diagram of the TJS-laser is shown in Fig. 1. The epitaxial wafers used in the experiment have layers of n-GaAlAs, n-GaAs, n-GaAlAs, p-GaAlAs, and p- or undoped-GaAs on n-GaAs substrates, being different from the usual DH wafers only in the location of the p-n junction. The typical

Manuscript received November 28, 1974; revised December 30, 1974.
The author is with the Central Research Laboratories, Mitsubishi Electric Corporation, Itami, Hyogo, Japan.

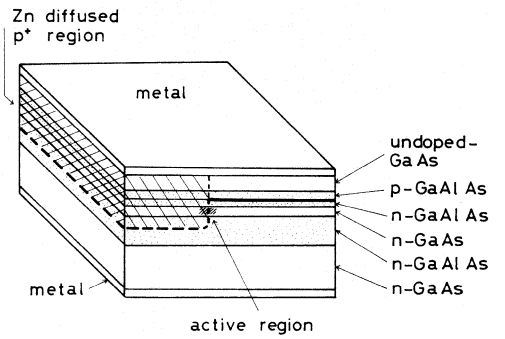

Fig. 1. Schematic diagram of the TJS-laser. P-n junctions are indicated by thick solid and dashed lines.

TABLE I
Parameters of Each Grown Layer of a TJS-Laser Wafer

layer	material	thickness (um)	Al content	carrier concentration (/cm^3)	dopant
1st	n-GaAlAs	12	0.42	1 x 10^{18}	Te
2nd	n-GaAs	0.35	---	1.5 x 10^{18}	Te
3rd	n-GaAlAs	0.8	0.42	1 x 10^{18}	Te
4th	p-GaAlAs	1.4	0.42	1 x 10^{18}	Ge
5th	undoped-GaAs	3	---	1 x 10^{16}	--

parameters of each grown layer are tabulated in Table I. Layer thicknesses were measured with an optical and scanning electron microscope. Carrier concentration and Al content were estimated from other wafers grown under similar conditions. TJS-lasers were fabricated from the wafers as follows. Zn was diffused selectively at 650°C into the second n-GaAlAs layer from the surface of the epitaxial layers using Si_3N_4 stripe films as a diffusion mask. Heat treatment was subsequently performed at 950°C for 2 h. During the heat treatment, diffusion fronts moved about 2 μm deeper and the carrier concentration in this rediffused region was about $1 \times 10^{19}/cm^3$, while that inside the formerly diffused region was about $1 \times 10^{20}/cm^3$. Metallic contact was made by evaporating Cr and Au. When the fifth GaAs layer was undoped, Si_3N_4 films were removed, marking the Zn-diffused region with shallow etched lines on the surface before the evaporation. The dimensions of chips were about 300 μm long, 150 μm wide, and 90 μm high. The width of the Zn-diffused region was 50 μm and the depth about 10 μm. For continuous operation, the chips were bonded upside down on Cu or type-2A diamond heat sinks with In solder.

In Fig. 1 thick solid and dashed lines show the p-n junctions, formed by epitaxial growth and Zn diffusion, respectively. The p-n junction consists of GaAs and GaAlAs homojunctions.

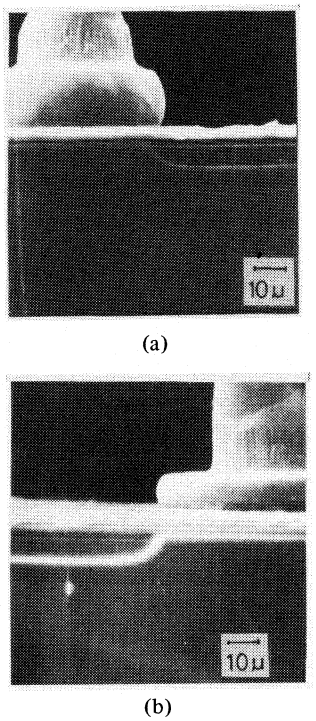

(a)

(b)

Fig. 2. Slightly etched mirror surfaces (a) without and (b) with an image of induced current, which shows the location of the p-n junctions.

As the diffusion potential of the GaAs junction is lower than that of the GaAlAs junction, current is concentrated towards the GaAs junction. Then lasing occurs near the GaAs p-n junction plane which lies across the second GaAs layer. The fifth p- or undoped-GaAs layer was introduced to obtain good ohmic contact. And, consequently, a fourth p-GaAlAs layer was added so as to prevent the shunt current, which would flow through the GaAs–GaAlAs heterojunction formed between the third GaAlAs and fifth GaAs layers. As can be seen from Fig. 1, the TJS-laser has an active region like a homojunction laser and like a DH laser in the directions parallel and transverse to the grown layers, respectively. The heat generated in the active region is removed through the third to the fifth layers into the heat sink, and these layers must be thin enough, especially the third and fourth GaAlAs layers, which have a lower thermal conductivity than GaAs. Fig. 2 shows a photograph made by a scanning electron microscope of a slightly etched mirror surface with and without an image of induced current, to show the location of the p-n junction.

III. Properties of the TJS-Lasers

A. Threshold Current

The development of the TJS-laser was intended to obtain low threshold current. It is possible to reduce the threshold current if a smaller cross-sectional area of the active region is obtained. In the usual DH lasers, the thickness of the active region is already reduced as much as possible, but it seems difficult to reduce the width. This difficulty arises mainly because precise control of dimensions near 1 μm can be achieved more easily by epitaxial growth than by etching or other macroscopic fabrication processes. In TJS-lasers, the width of the active region is automatically controlled by making a p-n junction transverse to the thin GaAs layer sandwiched between GaAlAs layers. This structure can be made by the usual fabrication processes.

If the threshold current density is assumed to be 40 000 A/cm^2 [4], one can expect the threshold current of the TJS-laser to be 36 mA when the cavity length is 300 μm and the active-region thickness is 0.3 μm. Fig. 3 shows typical current–light intensity characteristics of a TJS-laser in pulsed and continuous operation at room temperature. The threshold current is typically 40 mA and 50 mA in pulsed and continuous operation, respectively. Threshold currents of some representative diodes are tabulated in Table II with external quantum efficiencies and cavity lengths.

The temperature dependence of the threshold current has also been measured. An example is shown in Fig. 4. At low temperatures the threshold current increases in proportion to the cube of the absolute temperature T. Above a certain temperature, which is very close to room temperature, the threshold increases more rapidly. The relatively large difference in threshold current between pulsed and continuous operation is attributed to this behavior. The temperature rise at the active region in continuous operation is roughly estimated to be about 10°C, which corresponds to a thermal resistance of about 120°C/W. The relation $I_{th} \propto T^3$ is similar to that obtained with a conventional homojunction laser [5] and seems to be reasonable since the TJS-laser has an active region consisting of a p-n homojunction. On the other hand, the rapid increase of threshold current at a higher temperature may be attributed to an increase in the shunt current flowing through the GaAlAs homojunction outside the active region. An increase in the shunt current was suggested by an observed increase of spontaneous emission near 6600 Å. A rough estimation can be made with a method similar to that used to calculate the threshold current of the junction-stripe-geometry DH lasers [6]. Current densities J_1 and J_2, which flow through the GaAs and GaAlAs homojunction, respectively, have the following relation:

$$\Delta E_g - (kT/q) \ln (J_2/J_1) = J_2 R_2 - J_1 R_1 \quad (1)$$

where ΔE_g is the difference between the bandgap energies of GaAs and GaAlAs, k is Boltzmann's constant, and q is the electronic charge. R_1 and R_2 are the series resistances between the electrodes for the unit area of the junctions. The threshold current I_{th} is given with current densities at the threshold, J_{1th} and J_{2th}, as

$$I_{th} = J_{1th} S_1 + J_{2th} S_2 \quad (2)$$

where S_1 and S_2 are the areas of the junctions. To calculate the solid curves in Fig. 4, the following assumptions were made: 1) the shunt current through the epitaxially grown junction can be neglected because of high resistivity of the thin p-layer; 2) J_{1th} is proportional to T^3, and the proportionality constant was chosen to match the experimental threshold current at a low temperature; 3) ΔE_g is chosen to be 0.50 eV, which was estimated from the wavelength difference of two emission peaks corresponding to the GaAs and GaAlAs p-n junctions, and R_2 to be $1 \times 10^{-4}\ \Omega \cdot \text{cm}^2$, which is experi-

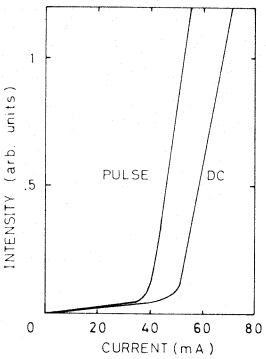

Fig. 3. Typical current-light intensity characteristics of the TJS-laser in pulsed and continuous operations.

TABLE II
SOME CHARACTERISTICS OF TJS-LASERS

operation	diode No.	L (um)	I_{th} (mA)	η_d (%)
pulse	A-3-0	217	40	11
	A-1-1	270	63	20
	B-1-9	282	43	42
	B-2-6	571	110	29
	B-2-11	232	34	49
cw	A-3-0	217	50	8
	A-3-1	230	80	18
	B-3-2	282	52	24
	B-3-6	316	51	13

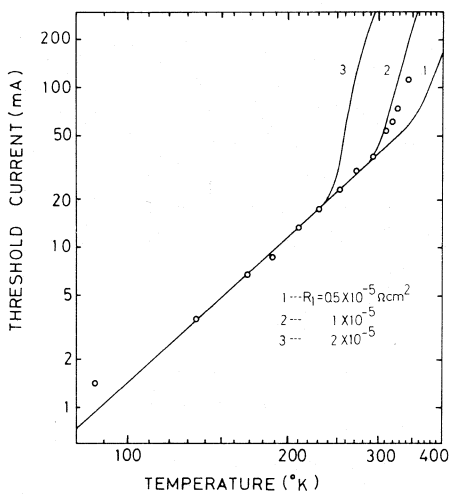

Fig. 4. Temperature dependence of threshold current. Experimental values are shown in open circles and the solid lines are calculated with (1) and (2). Relatively abrupt increase above room temperature can be attributed to the shunt current which flows through the GaAlAs homojunctions.

mentally obtained in broad-contact lasers with Cr and Au metallic contact. On setting the value of R_2 it is assumed that the current flowing through the GaAlAs junction does not spread in the lateral direction. However, the current flowing

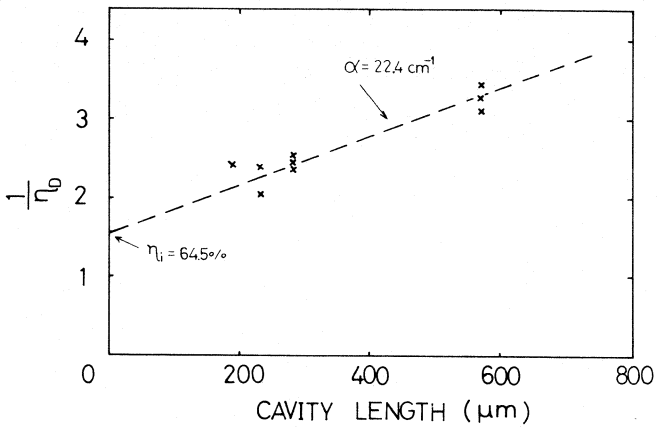

Fig. 5. Reciprocal of the external quantum efficiencies versus the cavity lengths.

through the GaAs junction seems to spread widely in both the p- and n-regions because of the very narrow width of the junction. The spreading of the current causes a reduction of the apparent resistance R_1, and some reasonable values for R_1 are used in the calculation. Although some discrepancies exist between the experimental and calculated slope of the curve, qualitative agreement, which is all that can be expected from these rough assumptions, is obtained. It is of interest to note that a reduction of R_1 allows the current to be confined in the active region even when J_1 is higher than a few tens of thousand amperes/square centimeter, which is not expected in the junction-stripe-geometry DH lasers [6].

B. External Quantum Efficiency and Light Output

External quantum efficiencies of some diodes are listed in Table II. The values seem to be somewhat scattered among wafers and locations in a wafer. However, some of the values are comparable with those obtained in conventional DH lasers [7]. And, especially, some values in continuous operation are higher than those of DH lasers. In Fig. 5 the reciprocal of the external quantum efficiency η_d for a series of diodes fabricated from a single wafer is plotted as a function of the cavity length L. These are related as

$$1/\eta_d = (1 + \alpha L/\ln R^{-1})/\eta_i \tag{3}$$

where η_i is the internal quantum efficiency, α the attenuation constant, and R the reflectivity of the mirror surface. From the dashed line in Fig. 5, α of 22.4 cm^{-1} and η_i of 64.5 percent are obtained. These values are close to those of the DH laser and differ from those obtained with conventional homojunction lasers [8]. The reason is not evident, but it may be supposed that the ratio of absorbed power in the p-region to the total power is smaller than in the conventional homojunction lasers. Fig. 6 shows an example of the temperature dependence of η_d. The slope of the curve below room temperature is relatively gentle, which seems to be an intrinsic characteristic of this structure. The abrupt decrease above room temperature, which also can be attributed to the shunt current, corresponds to the abrupt increase of the threshold current.

The maximum output power was measured using 500-ns pulses at low duty cycle. Fig. 7 shows an example of light out-

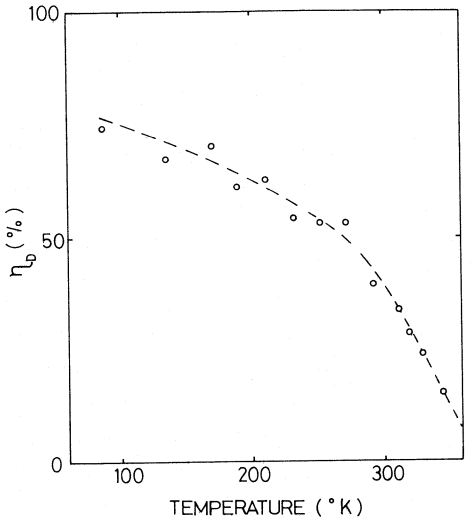

Fig. 6. Temperature dependence of the external quantum efficiency.

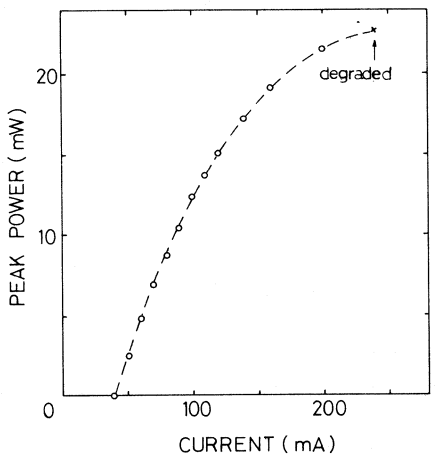

Fig. 7. Optical output power against input current. At an output power of about 23 mW from one mirror surface, the diode degraded. The value corresponds to the power density of about 3×10^6 W/cm^2 or 11 W/mm.

put in relation to the input current. At an output of 23 mW from one mirror surface, the diode degraded but still continued lasing. After the degradation, damage was observed near the active region on the mirror surfaces. As is described in Part C, the area on the mirror surface from which light is emitted is about 0.35×2.0 μm^2. The highest power of 23 mW corresponds to a power density of 3×10^6 W/cm^2, or 11-W/mm width of output face, which can be compared to the value of 16 W/mm in a usual DH laser with 0.45-μm active-region width [7].

C. Lasing Modes

In the TJS-laser optical confinement occurs due to the differences in refractive index in both the directions parallel and perpendicular to the grown layers. That is, the active region of the TJS-laser forms a two-dimensional dielectric waveguide. Transverse modes which are determined by the differences of refractive index are stable and can be well controlled by the dimensions of the waveguide. Experimentally, the fundamental transverse mode was observed in both directions when the

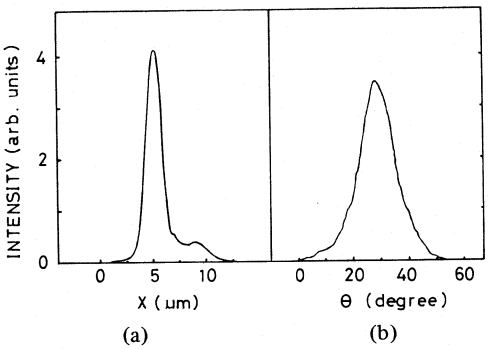

Fig. 8. An example of (a) near- and (b) far-field pattern in the direction parallel to the grown layers.

active region was thinner than 0.5 μm. The mode structure in the direction perpendicular to the grown layers is expected to be similar to that of usual DH lasers [3], [9] and this was confirmed experimentally. As for the direction parallel to the grown layers, the near- and far-field patterns are shown in Fig. 8. The distance between the half-power points in the near field is 1.5-2.0 μm, and the full beamwidth at the half-power points in the far field is 12-14°. These values are similar to those of homojunction lasers. Also, like conventional homojunction lasers, there often exists a subpeak in the near-field pattern, which always appears on the n-side of the p-n junction [10]. The subpeak appearing in the near-field pattern, which causes a perturbation in the far-field pattern, seems to be due to reflection by some small irregularities of the p-n junction plane. The location and the intensity of the subpeak is widely scattered among diodes, and sometimes the subpeak is separated from the main peak by more than 20 μm on the mirror surface where no gain can be expected. The near-field patterns stay unchanged when the input current increases even up to about three times the threshold current. In Fig. 9 two examples are shown in which the half-width of the near-field intensity is related to the input current. The transverse modes in TJS-lasers resemble TE and TM modes, because the confinement in the direction parallel to the grown layers is much weaker than in the perpendicular direction. The power ratio of TE/TM was measured with a Polaroid HR polarizer whose extinction coefficient was not certain but seemed to exceed 150. Fig. 10 shows an example. The ratio increases rapidly from the threshold and exceeds 100 at 1.5 I_{th} and 120 at twice I_{th}.

In most of the TJS-lasers from the two wafers ever fabricated, the longitudinal mode is almost single, as shown in Fig. 11, when driven continuously. Typically, as the input current increases to about twice I_{th}, the lasing wavelength jumps successively to longer values separated by an amount determined by the cavity length, due to the temperature rise of the active region with increasing input power. However, the range of input current in which two longitudinal modes are stable is very narrow compared to that of single-mode operation, which suggests that single-mode operation is more stable in TJS-lasers. The reason is not evident, but it may be supposed that in uniformly fabricated lasers some relation exists between longitudinal and transverse modes and that a single transverse mode leads to a single longitudinal mode. When diodes degrade

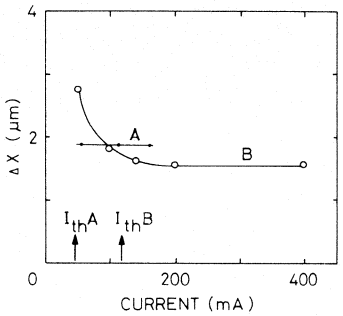

Fig. 9. The distance between the half-power points in the near field against input current. Two examples are shown, of which the threshold currents are indicated in the figure.

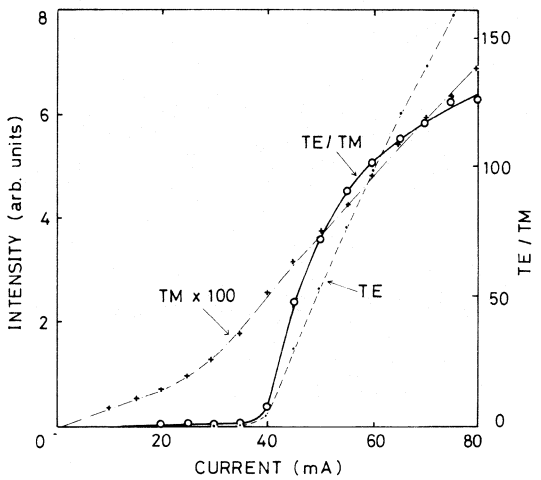

Fig. 10. The power ratio TE/TM in relation to input current. Intensities of TE and TM modes are also shown.

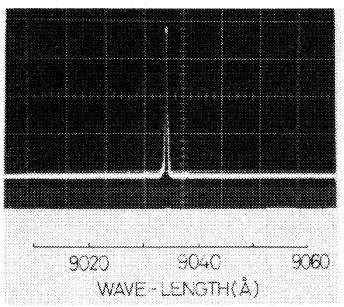

Fig. 11. Typical spectrum of the TJS-laser.

gradually through continuous operation, typically during several to several tens of hours, longitudinal modes tend to increase in number, which may be due to inhomogeneity arising in the active region during the operation.

IV. Summary

TJS-lasers with an active region consisting of a p-n homojunction have been developed. It is shown that it is possible to operate the homojunction laser continuously at room temperature if heat can be removed effectively. The TJS-laser has many distinct characteristics different from the conventional DH or homojunction lasers. It can have a low threshold current of about 50 mA and relatively high efficiency. The lasing mode is almost single in both the transverse and longitudinal directions.

TJS-lasers can be fabricated relatively easily, for they only need the usual fabrication techniques. A precise control of dimension is not required except for the thickness of the grown layers. For all these reasons, the TJS-laser has promise for application in integrated optics.

Acknowledgment

The author wishes to thank A. Ito and M. Ishii for their encouragement, and H. Kan for the preparation of the epitaxial wafers and helpful discussions. He also wishes to thank W. Susaki and Dr. K. Ikeda for useful discussions.

References

[1] I. Hayashi, M. B. Panish, and F. K. Reinhalt, "GaAs-$Al_xGa_{1-x}As$ double heterostructure injection lasers," *J. Appl. Phys.*, vol. 42, pp. 1929–1941, Apr. 1971.

[2] H. Namizaki, H. Kan, M. Ishii, and A. Ito, "Transverse-junction-stripe-geometry double-heterostructure lasers with very low threshold current," *J. Appl. Phys.*, vol. 45, pp. 2785–2786, June 1974.

[3] J. E. Ripper, J. C. Dyment, L. A. D'Asaro, and T. L. Paoli, "Stripe-geometry double heterostructure junction lasers: Mode structure and CW operation above room temperature," *Appl. Phys. Lett.*, vol. 18, pp. 155–157, Feb. 1971.

[4] W. Susaki, T. Oku, and T. Sogo, "Threshold current density in solution-grown GaAs laser diodes," *IEEE J. Quantum Electron.* (Corresp.), vol. QE-3, pp. 332–333, July 1967.

[5] G. Burns, F. H. Dill, Jr., and M. I. Nathan, "The effect of temperature on the properties of GaAs laser," *Proc. IEEE* (Corresp.), vol. 51, pp. 947–948, June 1963.

[6] H. Namizaki, H. Kan, M. Ishii, and A. Ito, "Characteristics of the junction-stripe-geometry double heterostructure lasers," *Japan. J. Appl. Phys.*, vol. 13, pp. 1618–1623, Oct. 1974.

[7] B. I. Miller, E. Pinkas, I. Hayashi, P. W. Foy, and R. Capik, "Highly uniform $Al_xGa_{1-x}As$ double-heterostructure lasers and their characteristics at room temperature," *Appl. Phys. Lett.*, vol. 19, pp. 340–343, Nov. 1971.

[8] M. H. Pilkuhn and H. Rupprecht, "Optical and electrical properties of epitaxial and diffused GaAs injection lasers," *J. Appl. Phys.*, vol. 38, pp. 5–10, Jan. 1967.

[9] H. Yonezu, K. Kobayashi, and I. Sakuma, "Threshold current density and lasing transverse mode in a GaAs-$Al_xGa_{1-x}As$ double heterostructure laser," *Japan. J. Appl. Phys.*, vol. 12, pp. 1593–1599, Oct. 1973.

[10] T. H. Zachos, "Gaussian beams from GaAs junction lasers," *Appl. Phys. Lett.*, vol. 12, pp. 318–320, May 1968.

$Al_xGa_{1-x}As$ Double-Heterostructure Rib-Waveguide Injection Laser

T. P. LEE, MEMBER, IEEE, C. A. BURRUS, FELLOW, IEEE,
B. I. MILLER, AND R. A. LOGAN, SENIOR MEMBER, IEEE

Abstract—A "rib-guide" optical-waveguide structure proposed as a means of injection-laser transverse-mode control, independent of current distribution, has been demonstrated in an AlGaAs double-heterostructure (DH) diode laser. The new structure showed stable single-transverse-mode operation at currents to twice threshold with small rib dimensions, and the observed higher order modes in large structures are in reasonable agreement with theory.

TRANSVERSE-MODE control in an injection laser, particularly the suppression of higher order modes, is an extremely important factor in achieving efficient coupling of the light output into low-loss single-mode optical fibers. Stripe-contact [1]-[3], mesa-structure [4], and diffusion-isolation [5] geometries have all been used to effect some control of the spatial distribution of the current and, thus, to obtain a spatial-gain distribution in the junction plane that is conducive to single-mode operation. Recently, Miller [6] has proposed a "rib-guide" optical-waveguiding structure to restrict the number of propagating modes independent of the current distribution. This rib-guide configuration is one form of the slab-coupled waveguides which have been analyzed in connection with integrated optical circuits and optical-fiber transmission lines [7], and experimental passive single-heterostructures of this type have demonstrated good mode characteristics [8]. We report here an experimental demonstration of *active* rib-guide $Al_xGa_{1-x}As$ devices: double-heterostructure (DH) injection lasers which showed stable single-transverse-mode operation at currents up to twice threshold.

Fig. 1(a) is a schematic representation of the rib waveguide. The structure is comprised of a rectangular dielectric waveguide "rib" of refractive index n_1 resting on a slab having the same index. The slab and rib are sandwiched between dielectric layers of lower index n_2. In a waveguide separated from the slab, waveguide modes which have the same propagation constant k_z as modes in the slab couple strongly to each other when the waveguide and slab are in contact. Since the slab-guide modes can propagate in any direction, waveguide modes coupled to them leak away from the rib and are dissipated through radiation at the slab edges. Thus only modes with longitudinal propagation constants k_z *larger* than the slab fundamental propagation constant $[k^2n_1^2 - (\pi/t)^2]^{1/2}$ travel with low loss along the ribbed section. By adjusting the rib-guide dimensions and the slab thickness, the number of propagating modes can be selected. For the example illustrated in Fig. 1(b), the number of such modes is three.

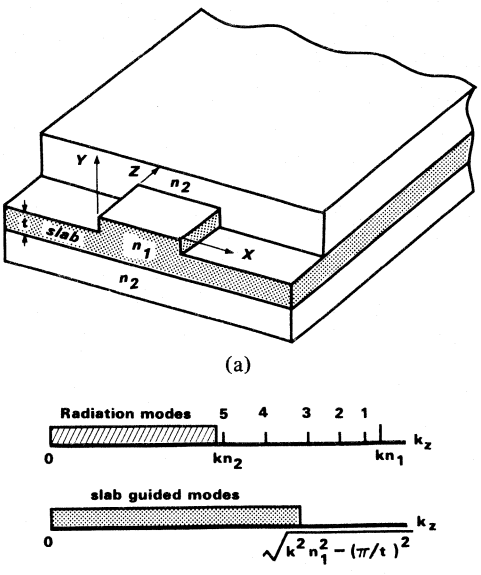

Fig. 1. (a) A schematic representation of the rib-guide structure. (b) A mode spectrum representation. The upper line is for the isolated rectangular optical waveguide and the lower line for the isolated slab guide, kn_1 and kn_2 are plane-wave propagation constants in medium n_1 and n_2, and $\sqrt{k^2n_1^2 - (\pi/t)^2}$ is the propagation constant of the fundamental mode in a uniform slab of thickness t.

Approximate formulas for characterization of the slab-coupled waveguide have been derived in [7]. The particular characteristics of interest to the design of a rib-guide laser are the number of propagating modes and the guide dimensions for single-mode operation. Using the notation of [7], the maximum number of field peaks P in the x direction and Q in the y direction of the highest order propagating mode E_{pq}^x (TE-like mode) or E_{pq}^y (TM-like mode) are given by

$$P = \frac{W}{T}\left[\sqrt{1 - (T/H)^2} + \frac{2}{\pi}\frac{T^2}{WH}\right] \tag{1}$$

and

$$Q = \frac{H}{T}\left[1 - \left(\frac{T}{W}\right)^2\left(1 - \frac{2T}{\pi H}\right)^2\right]^{1/2} \tag{2}$$

where W, H, and T are, respectively, normalized rib-guide width and height and normalized thickness of the slab guide.

Manuscript received December 9, 1974; revised January 9, 1975.

T. P. Lee and C. A. Burrus are with the Crawford Hill Laboratory, Bell Laboratories, Holmdel, N.J. 07733.

B. I. Miller and R. A. Logan are with the Murray Hill Laboratory, Bell Laboratories, Murray Hill, N.J. 07974.

In particular, for a symmetrical rib guide as shown in Fig. 1(a),

$$W = w\left[1 + \frac{n_1^2}{n_2^2}\frac{2}{v}\left(\frac{h}{w}\right)\right] \tag{3}$$

$$H = h\left[1 + \frac{2}{v}\right] \quad \text{for } E_{pq}^x \text{ modes} \tag{4}$$

$$T = t\left[1 + \frac{2}{v}\left(\frac{h}{t}\right)\right] \tag{5}$$

and

$$W = w\left[1 + \frac{2}{v}\left(\frac{h}{w}\right)\right] \tag{6}$$

$$H = h\left[1 + \frac{n_1^2}{n_2^2}\frac{2}{v}\right] \quad \text{for } E_{pq}^y \text{ modes} \tag{7}$$

$$T = t\left[1 + \frac{n_1^2}{n_2^2}\frac{2}{v}\left(\frac{h}{t}\right)\right] \tag{8}$$

where

$$v = kt(n_1^2 - n_2^2)^{1/2} \tag{9}$$

and w and h are the actual dimensions of the rib, and t is the actual thickness of the slab as noted in Fig. 1(a).

If $T/H \ll 1$, [(1) and (2)], the rib guide is multimoded. Single-mode operation dictates $Q = 1$ and $P \leqslant 2$ (i.e., E_{21}^x is cut off), which yields the maximum rib-guide width for a given slab-guide thickness

$$\frac{W}{H} \leqslant \frac{2\left(\frac{T}{H}\right)}{\sqrt{1 - \left(\frac{T}{H}\right)^2}}\left(1 - \frac{1}{\pi}\frac{T}{H}\right). \tag{10}$$

In Fig. 2 we have plotted the geometry of the rib guide for single-mode operation (E_{11}^x mode only) in GaAs-$Al_xGa_{1-x}As$ DH structures using the values of indices shown in the insert. The two curves are for two GaAs-layer thicknesses chosen as examples of the rib-guide lasers.

Rib-guide lasers were fabricated in three steps by liquid-phase-epitaxy processes. First, two layers, n-AlGaAs followed by p-GaAs, were grown on a GaAs substrate. Second, controlled step-height ribs were formed on the GaAs layer by anodization etching procedures [8], [9] and standard photolithographic processes. Finally, the top confinement layer of p-AlGaAs and the p-GaAs layer for contacting purposes were grown [10].

Formation of the rib structure involves at least two difficulties not encountered in conventional multilayer liquid-phase epitaxy. First, regrowth takes place on surfaces which have been subjected to wet chemical processing; and second, etch-back at the start of regrowth should be controlled if rib heights of 0.02–0.1 μm are to be maintained.

An adequately clean surface for regrowth was prepared by removing the oxide remaining after the final anodization with HCl and a deionized water rinse, and a subsequent 2–3-min

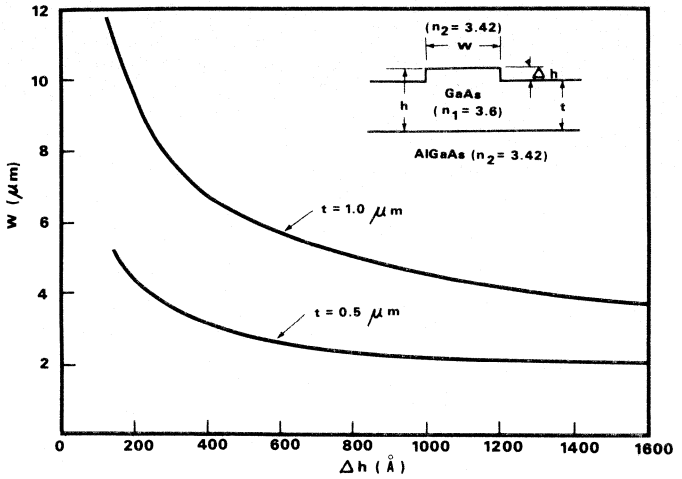

Fig. 2. Dimensions of rib guide in GaAs-AlGaAs DH's for single-mode operations.

etch in 0.01-percent Br-methanol to remove the thin oxide created by the water rinse. The oxide problem is greatly increased by the presence of aluminum in the GaAs layer, and thus drag-over of Al to the second grown layer (GaAs) should be minimized (we believe the Al content of the active GaAs layer should be less than 0.008). This problem was overcome by growing this layer in two steps from separate melts so that any Al drag-over was diluted in the melt from which the second portion of the GaAs layer was grown. With an initial growth of about 0.3 μm and a second layer of about 0.7 μm, the final GaAs layer was almost free of AlAs, with x, the mole fraction of aluminum, typically in the range of 0.003–0.005.

Immediate regrowth with minimal rounding of the rib-guide edges from etch-back was achieved by careful equilibration of the AlGaAs melt. The solution was maintained at 800°C for 2 h before a source seed [11] was slid under it for 15–30 min. Then, with the bottom of the melt (where growth occurs) at equilibrium, the furnace was cooled at 0.25°C/min through 3–4°C to start the growth on the source seed. Finally, the source seed was quickly replaced by the rib-guide substrate and growth was continued to the desired thickness.

It should be noted that the active layer was p-type and that the p-n junction was grown into the second layer at the n-AlGaAs/p-GaAs interface. Thus subsequent processing and regrowth did not affect the junction. However, n-type active regions also have been prepared successfully with the p-n junction at the regrowth interface.

Samples were grown with the GaAs active-layer thickness ranging from 0.3 to 0.8 μm, and the rib-guide step height varying from 250 to 2500 Å. Rib-guide widths of 5, 10, and 20 μm were made on the same sample so that mode properties could be compared. Ohmic contact stripes were aligned with the rib guides and applied to the top layer by conventional SiO_2 and photolithographic techniques. About six diodes of each width were measured, and the results for the better units are tabulated in Table I. The threshold currents were generally higher than those obtained with more conventional oxide-masked stripe-geometry layers, probably due to defects intro-

TABLE I
EXPERIMENTAL RESULTS OF DH STRUCTURE RIB-GUIDE LASERS

DIODE NO.	STRIPE WIDTH (μm)	RIB WIDTH (μm)	STEP HEIGHT Δh(Å)	t (μm)	I_{th} (A)	η_{ext} (%)	NO. OF MODES OBSERVED	NO. OF MODES CALCULATED
CGL-511	10	5	1000	0.3	.480	18	3	4
CGL-902	10	5	1000	0.8	1.080	30	2	2
CGL-1001	10	5	500	0.6	.860	18.4	1	2
CGL-1706	5	5	500	0.6	1.00	-	1	2
CGL-521	15	10	1000	0.55	.690	15.2	4	4
CGL-700	15	10	460	0.6	.550	22	3	4
CGL-1023	15	10	500	0.6	1.29	17	3	4
CGL-1223	15	10	1700	0.8	1.18	16.6	4	4
CGL-542	25	20	1000	0.55	.64	21.2	8	8
CGL-721	25	20	460	0.6	.79	30.6	8	9
CGL-940	25	20	1000	0.8	1.13	29	7	8
CGL-1040	25	20	500	0.6	1.06	18.9	8	9

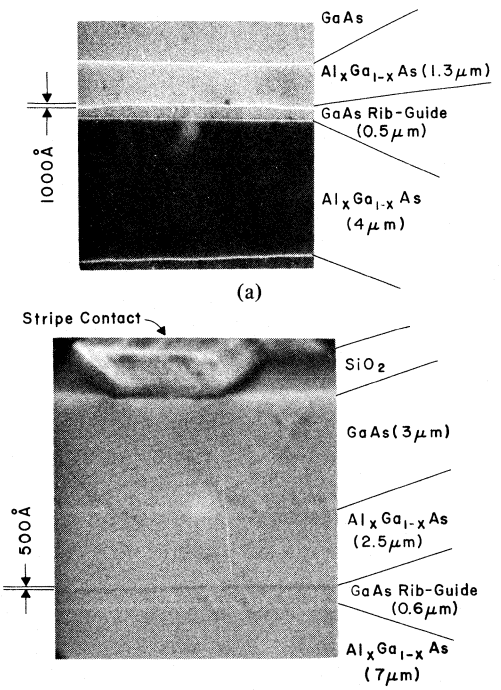

Fig. 3. Scanning-electron-beam microscope pictures of rib-guide cross sections. (a) For E_{21}^x mode. (b) For E_{11}^x fundamental mode.

duced in the regrowth, although the best unit had a threshold current density (~3 kA/cm^2) comparable to typical values for the oxide-masked stripe-geometry devices of 25-μm stripe width.

All diodes operated in TE-like modes with a single field peak along the y direction (perpendicular to the junction plane) and several peaks along the x direction (in the junction plane). The maximum number of peaks increased with the rib-guide width. For Δh = 1000 Å and t = 0.6-0.8 μm, P = 2-3, 3-4, and 7-8 for w = 5 μm, 10 μm, and 20 μm, respectively. Values calculated from (1)-(5) rounded to the nearest lower integer would be P = 2, 4, and 9, respectively, in fairly good agreement with the observed modes. The modes were fairly stable with increasing current, in contrast to conventional stripe-geometry lasers in which the modes are usually unstable at high currents. A scanning-electron-microscope picture of a 5-μm-wide guide capable of supporting a second-order mode is shown in Fig. 3(a).

For a reasonably well-defined rib edge, a step height of about 500 Å is needed. With $\Delta h \approx$ 500 Å, the maximum rib-guide width for single-mode operation according to Fig. 2 is 3 μm for t = 0.5 μm, and 6 μm for t = 1.0 μm. Because the 500 Å ribs were not observable after the regrowth, an indexing method was employed to align the contact stripes to the rib guides. This method and the roughness of the regrown surface limited our alignment ability to 5 μm or larger rib-guide widths.

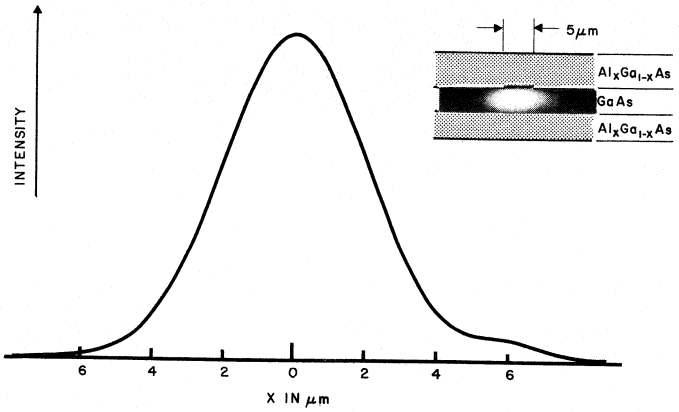

Fig. 4. Near-field radiation scan of the output from a laser producing single transverse mode.

Thus we were not able to realize the calculated single-mode structures.

However, single-mode operation was observed in more than half a dozen diodes from one wafer with rib-guide parameters $t = 0.6$ μm, $\Delta h \cong 500$ Å, and $w = 5$ μm, dimensions somewhat larger than those shown in Fig. 2. The discrepancy (fewer modes than calculated) may be due to the fact that the actual difference of the index of refraction between GaAs and $Al_xGa_{1-x}As$ layers is less than 5 percent, which is assumed in the calculation. A scanning-electron-microscope picture of the rib-guide cross section is shown in Fig. 3(b), and the near-field radiation patterns as scanned by a photodiode and seen with an infrared microscope are shown in Fig. 4. The mode was fairly pure and stable up to twice the threshold current.

The number of modes observed in the rib-guide lasers was higher than that of conventional stripe-geometry lasers of comparable width, which indicates that the modes were indeed strongly guided by the effective index differences at the rib edges. Stronger guidance rather generally implies smaller waveguide dimensions for single-mode operation. However, with the rib-guide structure there are several parameters for mode control in addition to stripe width. Thus, for example, all the dimensions could be increased proportionally without changing, in principle, the mode characteristics. Undoubtedly, threshold would increase for large thickness H, but reasonably low thresholds might be maintained by providing separate confinement of carriers by use of the large-optical-cavity structure.

We conclude that control of transverse laser modes in injection lasers by use of a rib-waveguide structure is feasible, and that stable single-mode operation at current densities several times threshold is possible. However, the requirements of uniform layer growth, smooth interfaces, reduced etch-back, and good regrowth on surfaces subjected to wet chemical processing are not easily met by present liquid-phase-epitaxial processes. Molecular-beam epitaxy [12] may offer an attractive alternative for making such sophisticated laser structures.

Acknowledgment

The authors wish to thank E. A. J. Marcatili for many helpful discussions, R. D. Standley for many SEM photographs of the waveguide structure, F. Favire for fabricating devices, and R. M. Derosier for testing.

References

[1] J. C. Dyment, "Hermite-Gaussian mode pattern in GaAs junction lasers," *Appl. Phys. Lett.*, vol. 10, pp. 84–86, 1967.
[2] J. E. Ripper, J. C. Dyment, L. A. D'Asaro, and T. L. Paoli, "Stripe geometry DH junction lasers: Mode structure and cw operation above room temperature," *Appl. Phys. Lett.*, vol. 18, pp. 155–157, 1971.
[3] J. C. Dyment *et al.*, "Proton-bombardment formation of stripe-geometry heterostructure laser for 300 K CW operation," *Proc. IEEE* (Lett.), vol. 60, pp. 726–728, June 1972.
[4] T. Tsukada *et al.*, "Very low current operation of mesa stripe geometry double heterostructure injection lasers," *Appl. Phys. Lett.*, vol. 20, p. 344, 1972.
[5] H. Yonezu *et al.*, "A GaAs-$Al_xGa_{1-x}As$ double heterostructure planar stripe laser," *Japan. J. Appl. Phys.*, vol. 12, pp. 1585–1592, 1973.
[6] S. E. Miller, unpublished work.
[7] E. A. J. Marcatili, "Slab-coupled waveguides," *Bell Syst. Tech. J.*, vol. 53, pp. 645–674, 1974.
[8] F. K. Reinhart, R. A. Logan, and T. P. Lee, "Transmission properties of rib waveguide formed by anodization of epitaxial GaAs and $Al_xGa_{1-x}As$ layers," *Appl. Phys. Lett.*, vol. 24, pp. 270–272, 1974.
[9] R. A. Logan, B. Schwartz, and W. J. Sunburg, "The anodic oxidation of GaAs in aqueous H_2O_2 solution," *J. Electrochem. Soc.*, vol. 120, p. 1385, 1973.
[10] C. V. Shank, R. V. Schmidt, and B. I. Miller, "Double heterostructure GaAs distributed-feedback laser," *Appl. Phys. Lett.*, vol. 25, pp. 200–201, 1974.
[11] D. L. Rode, "Isothermal diffusion theory of LPE: GaAs, GaP, bubble garnet," *J. Cryst. Growth*, vol. 20, pp. 13–23, 1973.
[12] A. Y. Cho, "Film deposition of molecular beam technique," *J. Vac. Sci. Technol.*, vol. 8, pp. S31–S38, 1971.

GaAs–GaAlAs Double-Heterostructure Injection Lasers with Distributed Feedback

MICHIHARU NAKAMURA, K. AIKI, J. UMEDA, A. KATZIR, A. YARIV, MEMBER, IEEE, AND H. W. YEN

Abstract—**GaAs-GaAlAs double-heterostructure distributed-feedback injection lasers are investigated at temperatures between 80 and 150 K under pulsed operation. The optical feedback for laser oscillation is provided by a corrugated interface between the p-GaAs active layer and the p-GaAlAs layer. The corrugation is made by two methods, ion milling and chemical etching, and the latter method is found to give the lower threshold. The laser oscillation occurs in a single longitudinal mode, whose wavelength is stable against the change of the excitation level. The temperature dependence of the wavelength of the distributed-feedback laser is shown to be 0.5 A/deg, which is about $\frac{1}{3}$ to $\frac{1}{4}$ that of the conventional Fabry-Perot (FP) laser.**

I. INTRODUCTION

SHORTLY after the demonstration of the laser oscillation in distributed-feedback dye lasers [1]-[4] and the subsequent theoretical analysis [5], the feasibility of distributed-feedback GaAs lasers was investigated at 77 K by optical pumping [6]-[9]. Following this the effort shifted toward the realization of injection-type distributed-feedback lasers, and laser oscillation has recently been demonstrated in homojunction [10], single-heterostructure [11], and double-heterostructure [12], [13] lasers.

In a previous paper [12] we have reported briefly the observation of laser oscillation in GaAs-GaAlAs double-heterostructure distributed-feedback lasers. The optical feedback for the laser oscillation was provided by a corrugated interface between the p-GaAs active layer and the p-GaAlAs layer. In this paper we describe a detailed study of the properties of these distributed-feedback lasers in the temperature range of 80–150 K.

II. EXPERIMENTAL METHOD

Fig. 1 shows a typical cleaved cross section of the distributed-feedback lasers described in the following. The corrugation period is 3470 Å and the depth is 1800 Å. In the fabrication of such a structure, an n-$Ga_{0.7}Al_{0.3}As$ layer doped with Sn and a p-GaAs (active) layer doped with Ge were first grown on an n-GaAs substrate by conventional liquid phase epitaxy. The thickness of these layers was ~3 μm and ~1 μm, respectively.

The corrugation of the p-GaAs layer was achieved by ion milling [14] or by chemical etching [15]. In the case of ion milling, 5-keV Ar ions were incident on the p-GaAs layer

Manuscript received December 5, 1974; revised February 27, 1975. The work of A. Katzir and A. Yariv was supported by the Office of Naval Research and by the Advanced Projects Research Agency through the Naval Electronics Laboratory Center.

M. Nakamura, K. Aiki, and J. Umeda are with the Central Research Laboratory, Hitachi Ltd., Kokubunji, Tokyo, Japan.

A. Katzir, A. Yariv, and H. W. Yen are with the California Institute of Technology, Pasadena, Calif. 91109.

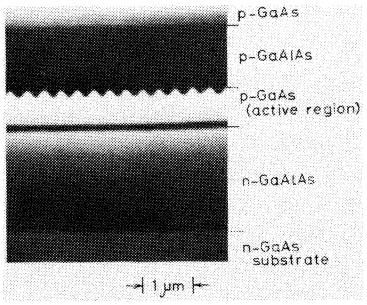

Fig. 1. A scanning electron microscope (SEM) photograph of the cross section of a distributed-feedback laser along the direction of light propagation. The corrugation period is 3470 Å.

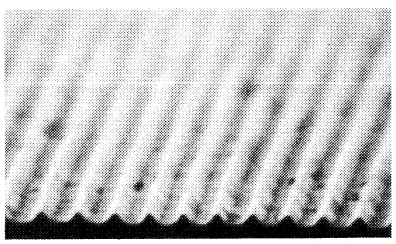

Fig. 2. A GaAs grating made by chemical etching. The period is 3470 Å.

through a photoresist mask produced by holographic photolithography. Fig. 2 shows the surface corrugation made by the chemical etching, where the grooves are composed of {111} *A*-side surfaces and a (100) bottom surface. The depth was 1500–1800 Å for the period of ~0.34 μm.

Next a p-$Ga_{0.7}Al_{0.3}As$ layer (~2 μm thick) and a p-GaAs layer (~1 μm thick), both doped with Ge, were grown on the corrugated surface of the p-GaAs layer by liquid phase epitaxy. The meltback of the corrugated surface during the epitaxial growth was avoided by growing the layers at relatively low temperatures (~700°C) with a cooling rate of 5°C/min as reported in [16].

Fig. 3 shows the schematic structure of the distributed-feedback laser. The laser has a mesa-stripe geometry [17] in order to limit the injection to a rectangular area. The width of the stripe is 50 μm. The metallic contacts of the laser were made by evaporating Cr and Au on the p-side, and Au-Ge-Ni on the n-side. The length of the Cr-Au contact in different lasers varied between 150 and 1100 μm. A lossy unexcited waveguide with a length of 2.5–3 mm was continuous to the current-excited section. This eliminated optical feedback from the end surface. The output was obtained through the front surface as shown in Fig. 3. The laser was pumped by applying current pulses with a duration of 50 ns and a repetition rate of 100 Hz.

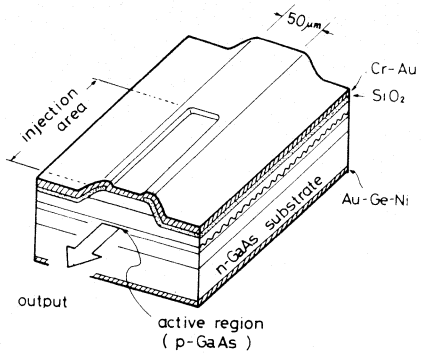

Fig. 3. The schematic structure of the distributed-feedback laser.

III. Results and Discussion

A. Spectral Characteristics

The emission spectra of a typical injection laser is shown in Fig. 4, where the period of the corrugation is 3470 Å, the length of the active region is 1050 μm, and the threshold current density is 750 A/cm^2. In this figure the spontaneous emission has a broad peak centered at 8255 Å. Just above the threshold (390 mA), a narrow peak of stimulated emission appears at 8225 Å. The linewidth of the stimulated emission is 0.5 Å. The diode lased in a single longitudinal mode, whose wavelength was stable with respect to changes of excitation level from threshold to over four times the threshold. The lasing light was polarized with the electric-field vector parallel to the junction plane.

Lasers in which the length of the unexcited waveguide was less than 1 mm exhibited the coexistence of two oscillations: one due to the grating and the other to feedback involving the end surface. The oscillation by grating feedback was identified by the small temperature dependence of the lasing wavelength. When the unexcited waveguide is longer than 2 mm, which is the case in the following experiments, the influence of the end surface is not observed in the emission spectrum.

Fig. 5 shows the spectrum of a typical laser as a function of temperature. The laser, whose length was 630 μm, required a threshold current density of 1.8 kA/cm^2 at 80 K and of 8.6 kA/cm^2 at 145 K. The current was chosen to be about 1.05 times the threshold at each temperature. In this figure, the peak wavelength of the spontaneous emission at 80 K is shorter by 78 Å than that of the stimulated emission. As the temperature increases, the peak of the spontaneous emission shifts more rapidly than the peak of the stimulated emission does. At 145 K, the peak wavelength of the spontaneous emission is longer by 17 Å than that of the stimulated emission.

A small auxiliary peak is seen in the spectrum of Fig. 5. We have no satisfactory explanation as to its origin, since its temperature dependence is inconsistent with either that of a normal Fabry-Perot (FP) mode or higher order DFB modes. It could, possibly, represent some hybrid combination. This peak is absent in lasers possessing longer unpumped corrugated end sections. Typical of the latter category is the laser whose spectrum is shown in Fig. 4.

Fig. 6 shows the wavelength of the stimulated-emission peak

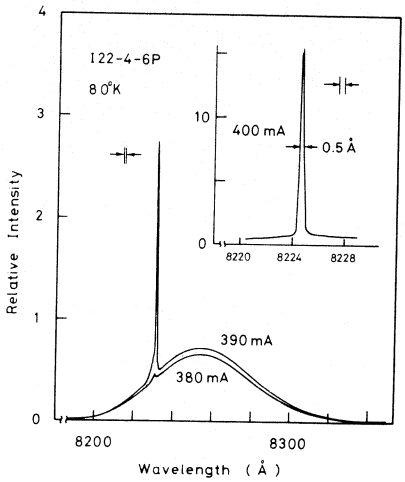

Fig. 4. The emission spectra of a typical laser. The period and the depth of the corrugation are 3470 Å and 1800 Å, respectively. The threshold current density is 750 A/cm^2 at 80 K.

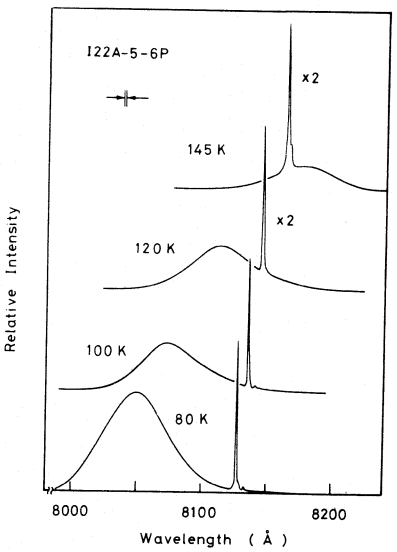

Fig. 5. Temperature dependence of the emission spectrum. The current is chosen to be ~1.05 times the threshold for each temperature.

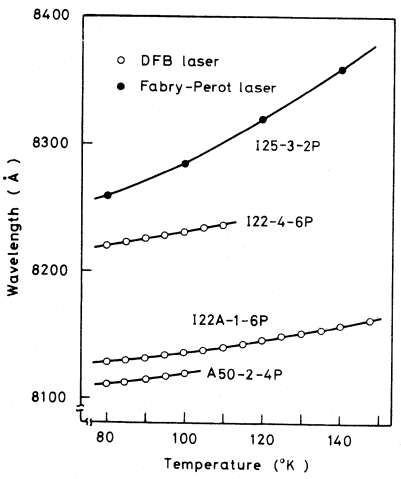

Fig. 6. The lasing wavelength as a function of temperature.

as a function of temperature. The temperature dependence of the main peak of a typical FP laser is also shown in this figure. It is seen from this figure that the wavelength of the distributed-feedback laser shifts at a rate of 0.5 Å/deg. Theoretically, the wavelength of the distributed feedback laser λ is given approximately by [5]

$$\lambda \simeq \frac{2n_g\Lambda}{l} \tag{1}$$

where n_g is the effective refractive index of the waveguide, Λ is the period of the corrugation, and $l = 3$. By differentiating (1) with respect to the temperature T, one gets the relation

$$\frac{d\lambda}{dT} = \frac{\lambda}{\bar{n}_g}\frac{\partial n_g}{\partial T} \tag{2}$$

where

$$\bar{n}_g = n_g - \frac{\partial n_g}{\partial \lambda}\lambda. \tag{3}$$

With $\bar{n}_g \simeq 4.5$ and $\partial n_g/\partial T \simeq 3 \times 10^{-4}$/deg [18], we have $d\lambda/dT \simeq 0.57$ Å/deg, which agrees with the experimental result in Fig. 6.

On the other hand, the peak wavelength of the FP laser changes at a rate of 1.5-2 Å/deg, reflecting the shift of the band-gap energy with temperature.

B. The Threshold Current Density

The threshold of the laser oscillation is a function of such structure parameters as the length and the thickness of the active region, and the depth of the corrugation. The dependence of the threshold current density on the length of the active region L is shown in Fig. 7. The lasers were made from two wafers with chemically etched corrugations, I18 and I22. The thickness of the active region and the depth of the corrugation are 0.9 μm and 1600 Å in I18, and 0.8 μm and 1800 Å in I22, respectively. The period of the corrugation is 3470 Å and the lasing wavelength is 8249 ± 5 Å for all the lasers. In Fig. 7 the threshold current density j_{th} decreases with the increase of L as $j_{th} \propto L^{-0.8}$.

For $L = 400$ μm and $T = 80$ K, the threshold current density was typically 10 kA/cm^2 in the laser with the ion-milled grating, and 2 kA/cm^2 in the laser with the chemically etched grating. The lowest threshold current density of 750 A/cm^2 was obtained in a chemically etched laser with $L = 1050$ μm whose emission spectrum is shown in Fig. 4.

The higher threshold current density in the ion-milled lasers was found to be due to the nonradiative recombination of injected carriers near the interface. This is clearly demonstrated by the photoluminescence measurement as shown in Fig. 8. In this measurement, a part of the p-GaAs layer was ion milled by ~1000 Å, and then a p-$Ga_{0.4}Al_{0.6}As$ layer was grown by liquid phase epitaxy at 700-670°C. The p-GaAs layer was excited by a Kr laser (6471 Å) through the top p-$Ga_{0.4}Al_{0.6}As$ layer at room temperature, and the photoluminescence from the p-GaAs layer was monitored by a TV camera. In this figure, the intensity of the photoluminescence is about two orders of magnitude weaker in the ion-milled GaAs layer than in the original GaAs layer. This fact demonstrates that ion milling produces nonradiative recombination centers thus increasing the threshold current density.

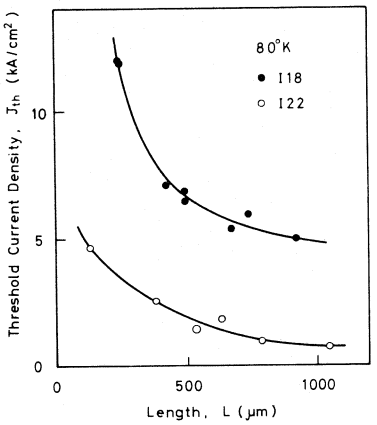

Fig. 7. The threshold current density as a function of the length of the active region.

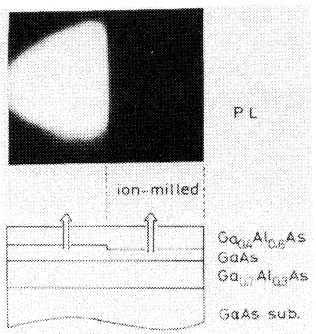

Fig. 8. Photoluminescence from a GaAs epitaxial layer. A part of the GaAs epitaxial layer was ion milled.

In the laser with the chemically etched grating, the number of nonradiative recombination centers was much reduced, and the lower threshold operation became possible. Further reduction of the threshold current density may be achieved by adopting the separate-confinement heterostructure with a corrugated interface as was proposed elsewhere [19]. In this structure, the effect of the nonradiative centers should be greatly reduced since the corrugated interface is separated from the active layer. The use of the fundamental grating with a period of 0.12 μm should lead to further reduction in the threshold current density.

IV. Conclusion

GaAs-GaAlAs double-heterostructure distributed-feedback injection lasers were investigated at temperatures between 80 and 150 K under pulsed operation. The grating was made by ion milling or by chemical etching. The laser oscillation occurred in a single longitudinal mode even at high current densities. The lasing wavelength was stable against the change of the excitation level. The temperature dependence of the lasing wavelength was found to be about 0.5 Å/deg and was explained by the temperature dependence of the refractive index of the waveguide. The lowest threshold current density of

750 A/cm^2 was obtained in a laser with a chemically etched grating. The threshold current densities of lasers with ion-milled gratings were found to be higher than those of chemically etched lasers because of the surface damage caused by the ion bombardment. Further reduction of the threshold current density is expected to result from the use of the separate-confinement heterostructure and a fundamental grating.

Acknowledgment

The authors wish to thank Dr. Y. Otomo and Dr. O. Nakada of the Central Research Laboratory, Hitachi Ltd., for their support of this work. They also wish to thank S. Yamashita for his assistance in the experiment.

References

[1] H. Kogelnik and C. V. Shank, "Stimulated emission in a periodic structure," *Appl. Phys. Lett.*, vol. 18, p. 152, 1971.
[2] C. V. Shank, J. E. Bjorkholm, and H. Kogelnik, "Tunable distributed-feedback dye laser," *Appl. Phys. Lett.*, vol. 18, p. 395, 1971.
[3] D. P. Schinke, R. G. Smith, E. G. Spencer, and M. F. Galvin, "Thin-film distributed-feedback laser fabricated by ion milling," *Appl. Phys. Lett.*, vol. 21, p. 494, 1972.
[4] P. Zory, "Laser oscillation in leaky corrugated optical waveguides," *Appl. Phys. Lett.*, vol. 22, p. 125, 1973.
[5] H. Kogelnik and C. V. Shank, "Coupled-wave theory of distributed feedback lasers," *J. Appl. Phys.*, vol. 43, p. 2327, 1972.
[6] M. Nakamura *et al.*, "Optically pumped GaAs surface laser with corrugation feedback," *Appl. Phys. Lett.*, vol. 22, p. 515, 1973.
[7] M. Nakamura *et al.*, "Laser oscillation in epitaxial GaAs waveguide with corrugation feedback," *Appl. Phys. Lett.*, vol. 23, p. 224, 1973.
[8] H. W. Yen *et al.*, "Optically pumped GaAs waveguide lasers with a fundamental 0.1 μ corrugation feedback," *Opt. Commun.*, vol. 9, p. 35, 1973.
[9] C. V. Shank, R. V. Schmidt, and B. I. Miller, "Double-heterostructure GaAs distributed feedback laser," *Appl. Phys. Lett.*, vol. 25, p. 200, 1974.
[10] H. M. Stoll and D. H. Seib, "Distributed feedback GaAs homojunction injection laser," *Appl. Opt.*, vol. 13, p. 1981, 1974.
[11] D. R. Scifres, R. D. Burnham, and W. Streifer, "Distributed-feedback single heterojunction GaAs diode laser," *Appl. Phys. Lett.*, vol. 25, p. 203, 1974.
[12] M. Nakamura *et al.*, "GaAs–$Ga_{1-x}Al_xAs$ double heterostructure distributed feedback diode lasers," *Appl. Phys. Lett.*, vol. 25, p. 487, 1974.
[13] D. B. Anderson, R. R. August, and J. E. Coker, "Distributed-feedback double-heterostructure GaAs injection laser with fundamental grating," to be published.
[14] H. L. Garvin *et al.*, "Ion beam micromachining of integrated optics components," *Appl. Opt.*, vol. 12, p. 455, 1973.
[15] L. Comerford and P. Zory, "Selectively etched diffraction gratings in GaAs," *Appl. Phys. Lett.*, vol. 25, p. 208, 1974.
[16] M. Nakamura *et al.*, "Liquid phase epitaxy of GaAlAs on GaAs substrate with fine surface corrugations," *Appl. Phys. Lett.*, vol. 24, p. 466, 1974.
[17] T. Tsukada *et al.*, "Very-low-current operation mesa-stripe-geometry double-heterostructure injection lasers," *Appl. Phys. Lett.*, vol. 20, p. 344, 1972.
[18] J. Zoroofchi and J. K. Butler, "Refractive index of n-type gallium arsenide," *J. Appl. Phys.*, vol. 44, p. 3697, 1973.
[19] M. Nakamura and A. Yariv, "Theoretical analysis of low threshold GaAs–GaAlAs injection lasers with corrugation feedback," in *Dig. 1974 Topical Meeting on Integrated Optics*, Jan. 1974.

Single-Heterostructure Distributed-Feedback GaAs-Diode Lasers

ROBERT D. BURNHAM, DONALD R. SCIFRES, MEMBER, IEEE, AND WILLIAM STREIFER, SENIOR MEMBER, IEEE

Abstract—**This paper reports the fabrication, testing, and analysis of distributed-feedback (DFB) single-heterostructure (SH) electrically pumped GaAs lasers. The techniques of fabricating the DFB grating and diode using interferometric exposure of photoresist, development, ion milling, liquid-phase-epitaxial growth, and diffusion are described in detail. Next, experimental results on a variety of diodes operating at 77 K are presented. It is shown that narrow laser linewidth (< 0.15 Å) and low threshold operation (775 A/cm^2) can be obtained. Also reported is output coupling from the grating which results in highly collimated laser beams with divergence of approximately 0.35°. Coupling coefficients, which determine laser threshold, are computed as a function of device parameters including physical dimensions, refractive indices, grating size and shape, and Bragg order for single- and double-heterostructure geometries. Calculated and measured thresholds are shown to be in good agreement.**

Manuscript received November 18, 1974; revised February 7, 1975.
The authors are with the Xerox Palo Alto Research Center, Palo Alto, Calif. 94304.

I. Introduction

IN A RECENT LETTER we reported the first observation of laser operation in an electrically pumped distributed-feedback (DFB) diode [1]. Since this laser requires no discrete end mirrors as is the case with a conventional diode laser it is potentially useful as a source for integrated optical circuits. In addition, DFB injection lasers have several other unique features which make them potentially useful even as discrete devices. First, the feedback is frequency selective so that various laser wavelengths within the gain line may be obtained. Second, DFB lasers enhance the possibility of mode control [2]–[4] and, finally, the periodic DFB structure may be used as an output coupler to obtain a polarized low-divergence laser beam [5]. These attributes may make DFB injection lasers useful in point-to-point communications as well as enhancing their utility in fiber optic systems.

As described previously [6], the feedback mechanism in DFB lasers is that of backward Bragg scattering from a periodic perturbation of either the refractive index or gain in the laser waveguide. In our devices such feedback is provided by a periodic corrugation which is distributed along and integrated with the gain region in a GaAs/GaAlAs single-heterostructure (SH) diode. A schematic diagram of such a device is shown in Fig. 1. It consists of a GaAs n-type substrate (refractive index n_3), a GaAs p-type active region (index n_2), and a GaAlAs p-type grown layer (index n_1). Since n_2, the refractive index of the GaAs p-type layer, is greater than n_1 and n_3, light generated by minority-carrier injection across the p-n junction is guided in this layer. The thickness (t) of this active layer is, of course, critical in determining laser threshold of the device since it affects not only the current and wave confinement as in conventional SH diodes [7] but also the feedback from the grating. In Fig. 1 the grating period is Λ, w denotes the width of a rectangular tooth, and g is the peak-to-valley height of the grating. To satisfy the Bragg condition for DFB operation the periodic corrugations at the interface between the GaAs substrate and the GaAlAs layer must be spaced a multiple of a half wavelength of light in the medium. For a free-space wavelength of 8500 Å and $n_2 \simeq 3.6$

$$\Lambda \simeq 1180\, m \text{ Å}, \qquad m = 1, 2, 3, \cdots .$$

The diodes described herein have grating periods corresponding to $m = 3$ and $m = 4$.

This paper is divided into three main sections. In Section II, techniques used in fabrication of the grating and subsequent epitaxial growth are described. Next, in Section III experimental results are discussed. In particular, we point out that care must be taken to insure that DFB rather than unwanted discrete feedback from diode faces is the dominant feedback mechanism. For this reason diodes with both saw-cut- and antireflection- (AR) coated faces were used to minimize the discrete feedback. Thresholds of these diodes were compared with control diodes of similar geometry but with no DFB structure. Another quite conclusive test for DFB is correlation of grating spacing with the laser wavelength. Again, the use of control diodes for comparison is advantageous to insure that the observed wavelength shifts are not a function of diode geometry or doping concentrations. Finally, in Section IV we describe some analytic and numerical results relating to coupling coefficients and thresholds of DFB devices. These are found to be in good agreement with experimentally obtained values.

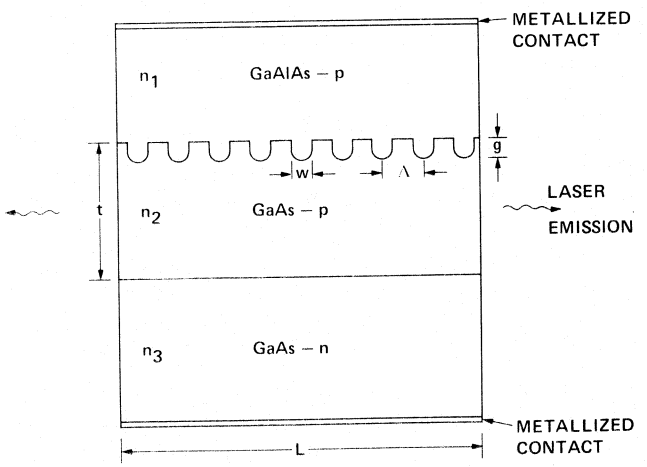

Fig. 1. The geometry of the SH DFB diode laser.

II. Device Fabrication

In this section steps for fabricating SH DFB lasers are described. These consist of 1) exposure of photoresist by two interfering laser beams [8], 2) development of photoresist, 3) ion-beam etching the pattern into the substrate [9], and 4) liquid-phase-epitaxial growth of GaAlAs over the corrugated substrate surface. We begin step 1) by spin coating photoresist (AZ 1350) onto a well-cleaned and dried Si-doped (N_d-N_a $\sim 2\text{-}4 \times 10^{18}$ cm^{-3}) GaAs substrate at 6000 r/min to achieve a film thickness of ~3000 Å. These films were further processed by baking at 125°C for 2.5 min to activate the resist.

To expose the film, a single-frequency Ar^+ laser (4579 Å) is split into equal-intensity beams by a variable-density beam splitter. This light is deflected by mirrors through a 10-μm spatial filter and interferes at an angle Θ on the photoresist film. To generate a 3600-Å spacing ($m = 3$) in the photoresist $\Theta \simeq 40°$. With a power density of ~2.5 mW/cm^2 in each beam a 15-s exposure followed by a 1-2-min development in undiluted AZ developer solution is used. A usable grating mask over approximately 1 in^2 of the substrate is produced.

The masked substrate is then ion-beam machined for ~1 h with a Commonwealth Scientific IMMI-IV ion miller set at ~100-μA beam current. The wafer is positioned so that the Ar beam is parallel to the grooves in the mask. The ion beam is also directed at an angle of 10-15° with the wafer plane to yield a smooth and unpitted grating. A scanning-electron-microscope (SEM) photograph of such a grating is shown in Fig. 2. Groove spacing is ~3500 Å and the groove depth is ~1700 Å. The smoothness of the groove is directly attributable to the grazing incidence of the ion beam which actually acts to correct defects created during the exposure and development processes. Milling at normal incidence results in a badly pitted surface. Various groove profiles result when the milling time is varied. For example, a flat-topped groove results if all photoresist is not removed during the milling process or if the photoresist is developed down to the substrate before milling. This groove shape may be advantageous during subsequent liquid-phase-epitaxy growth where meltback must be

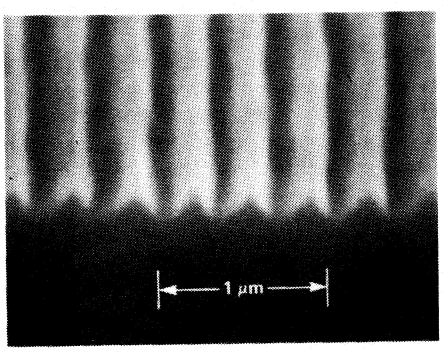

Fig. 2. SEM photograph of a grating.

avoided [10]. The diffraction efficiency of the gratings was measured for evaluation purposes prior to completing the fabrication process. The intensity of a He-Ne laser (6328 Å) beam diffracted at an angle of ~70° from the grating was compared to the intensity of the same beam reflected at near-normal incidence from an unmilled GaAs wafer. The efficiencies of these gratings are in the range of 30–40 percent.

After ion milling the remaining photoresist is removed with both acetone and plasma etching in an oxygen atmosphere. The wafer is then etched lightly with HCL and HF. Zn-doped GaAlAs layers are then grown on the corrugated GaAs substrates by conventional liquid-phase-epitaxy techniques. The mole fraction of Al is 0.3–0.7 at the interface between the substrate and the grown layer. After prebaking for ~1 h at 770°C the furnace is cooled at a rate of 1 deg/min. Then 15 min later the controllers are set 10°C cooler. 3 min after that the substrate, which is recessed as much as 1.5 mm, is then slid under the first melt which contains 4-g Ga, 6-mg Al, and 40-mg Zn, and also contains a polished undoped wafer of GaAs wetted to the top surface of the melt. The presence of this wafer is crucial since it guarantees that the entire melt is saturated with GaAs and thus prevents meltback of the corrugations on the substrate. It also results in the growth of layers which are more uniform in thickness and composition. The initial contact temperature is kept low (~750°C) to also reduce the effect of meltback [10]. The substrate remains beneath the first melt for 10 min and is then pulled into a melt containing 4-g Ga, 100-mg Zn, and a GaAs wafer for source material. From this melt a final layer of p-type GaAs is then grown for ease in making ohmic contact to the p-side of the wafer. The resulting layer thicknesses are ~6 μm of GaAlAs and 15–20 μm of GaAs. During growth of the two epitaxial layers the Zn diffuses $\sim\frac{1}{2}$ μm into the substrate. Following growth and cleaning of the Ga from the wafer a Zn_3As_2 diffusion is performed in an evacuated ampoule at ~800°C for 10 min to produce a p-n junction 1.5–2 μm from the GaAlAs grown layer. Previous reports [7] indicate that this is the optimum distance from the GaAlAs layer for low-threshold laser operation in cleaved-mirror SH diodes.

Next metallization of the entire wafer surface is performed. Ti, Pt, and Au are used for the p-alloy, whereas Au-Sn is used to make ohmic contact to the n-type substrate. In several cases the entire surface is not metallized. Instead a small ball of a p-type or n-type metal alloy (~5-mils diameter) is wetted to one side of the device in a hydrogen atmosphere while the other side is alloyed to a TO-5 Au-plated header. Since the spreading resistance is low, the devices appear to be uniformly pumped when viewed with an IR up-converting microscope. The wafer is next cleaved and/or sawed into chips which are mounted on headers. In some cases all four sides of a chip are saw cut to reduce reflections back into the active region of the laser and thus allow the grating to provide the dominant feedback mechanism. Also in order to isolate the effects of the grating "control" wafers are fabricated. A portion of the GaAs substrate is cleaved and cleaned before ion milling. All subsequent steps including LPE are simultaneously performed on this wafer. Therefore, the control and DFB diodes are identical except for the presence of the grating. These diodes are then compared as part of the experimental study reported in the next section.

III. Experimental Results

This section is divided into three subsections. First we discuss laser thresholds for DFB diodes of various geometries including those with saw-cut and AR-coated end reflectors. Second, spectral results obtained for DFB lasers are presented. Finally, the observation of radiation modes which lead to very low-divergence laser beams radiating normal to the plane of the p-n junction are discussed.

All experimental measurements were performed at liquid-nitrogen temperature. The diodes were excited with 0.5-μs pulses at a repetition rate of 1 kHz. Laser spectra were analyzed with a Spex 1-m spectrometer operating in first order and detected with an RCA C31034B photomultiplier. The near- and far-field patterns were observed with an IR up-converting microscope and the far-field patterns were also scanned by rotating a fiber light pipe angularly around the axis of the diode. The light output from this fiber was detected with a photomultiplier and plotted on a recorder.

Laser Thresholds

Threshold current densities for DFB diodes were measured for various geometries and cavity configurations. Three end-mirror configurations were used. First the end faces of the diodes were saw cut rather than cleaved in order to reduce the light reflected directly back into the active region. SEM photographs of the saw cut show that the surface is extremely rough when viewed on a scale comparable to a wavelength of light in the crystal (~1200 Å). Thus it should provide diffuse reflections when struck at normal incidence. This, of course, is not the case when struck at shallow angles as noted in the literature [11]. Control diodes (those with no grating near the junction) which are ~2 mm long showed an increase of 3–4 times in threshold current densities when their cleaved end faces were damaged by saw cuts. In these cases the diodes sometimes lased across the short diode dimension directly beneath the alloyed contact since this area was more highly and uniformly pumped. The mode spectra in the case of saw-cut control diodes consisted of a broad band of mostly unresolvable longitudinal modes with no strongly apparent mode spacing. In comparison, DFB diodes whose cleaved ends were saw cut showed only a 1.1 to ~2 times increase in threshold and lased over a narrower wavelength range. An example of this is shown in Fig. 3. As shown, a saw-cut diode 1.9 mm long and 0.46 mm wide lased at 8 A corresponding to a threshold current density of 775 A/cm^2. This threshold current density was as low as that obtained for any cleaved-mirror control diode.

Although saw cutting the diode end mirrors can be used to qualitatively look for the effects of DFB, it is difficult to characterize these devices quantitatively. Therefore, two other cavity configurations were tested. First, vacuum grease was applied to both cleaved faces of the diode and second an AR $\lambda/4$ coating was deposited on one cleaved end. In the case of vacuum grease with a refractive index of ~1.5 the power reflection at normal incidence was reduced from 33 to

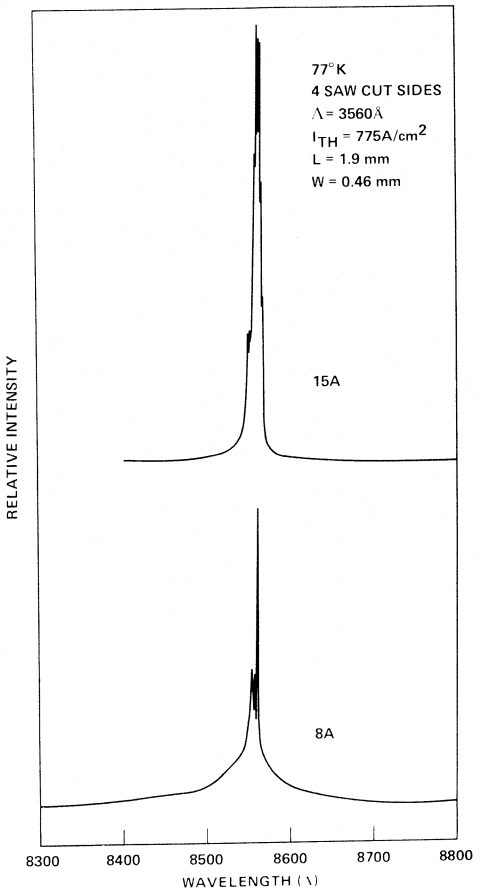

Fig. 3. Spectra of a low-threshold DFB diode laser.

~17 percent at the cleaved surface. The AR coating has a 0.2-percent power reflection at 8500 Å. Results of threshold current-density measurements for one set of diodes with these configurations are shown in Table I. For the control diode

$$\exp(2\alpha L) = (R_1 R_2)^{-1} \quad (1)$$

where α is the net threshold gain and R_1, R_2 are the power reflectivities at the mirrors. The numerical values listed for that diode in Table I agree almost exactly with those computed from (1) when an absorption of $\alpha_{abs} = 10$ cm^{-1} is taken into account. With that absorption the listed DFB diodes all exhibit smaller increases in measured threshold current than the control diode as the reflectivity was changed.

Spectral Results

In Fig. 4 spectra are shown for two DFB lasers with different grating spacings. For a spacing of $\Lambda = 3480$ Å [Fig. 4(a)] the spontaneous emission peaks at ~8470 Å, but the diode lases at ~8440 Å, on the high-energy side of the spontaneous-emission line. This diode was 825 μm long and had one end cleaved and the other saw cut. Since at 8440 Å there is significant absorption the threshold current density for this diode is quite high (6000 A/cm^2). Control diodes with cleaved ends lased between 8465 and 8500 Å (dependent on diode length) on the long-wavelength side of the spontaneous peak. The spectra shown in Fig. 4(b) are for a diode with $\Lambda = 3550$ Å. In this case laser emission occurs on the low-energy side of the spontaneous peak at 8550 Å. This diode was 1.5 mm long and

TABLE I
PUMPING THRESHOLDS OF FOUR DIODES WITH CLEAVED ENDS, INDEX-MATCHED ENDS, AND ONE CLEAVED-ONE AR-COATED END

Diode ID	J_{TH} (A/cm^2)			Diode Length (mm)
	Cleaves	Index Matching Fluid	AR Coating	
Control	1.73 x 10^3	2.36 x 10^3	3.82 x 10^3	0.85
DFB	1.42 x 10^3	1.79 x 10^3	1.86 x 10^3	1.47
DFB	1.49 x 10^3	1.79 x 10^3	2.55 x 10^3	1.32
DFB	1.36 x 10^3	1.61 x 10^3	2.01 x 10^3	2.58

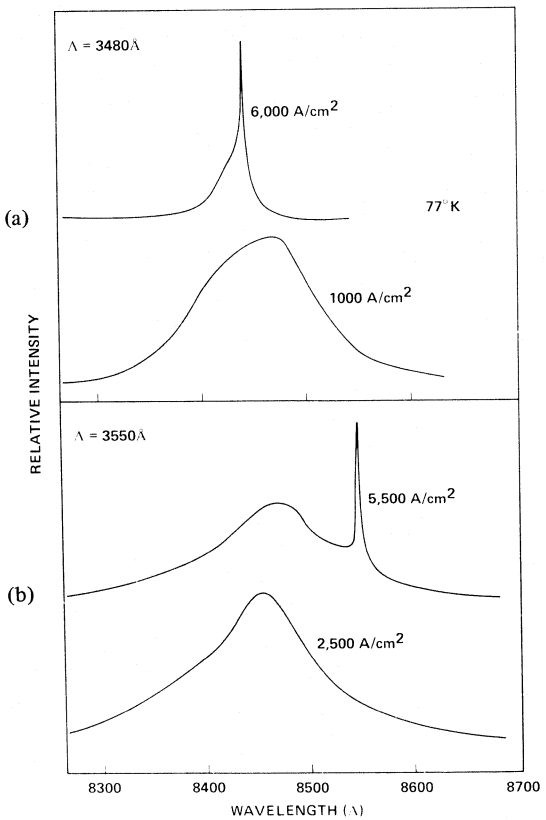

Fig. 4. Two spectra of DFB diode lasers oscillating far from line center.

saw cut on both ends. The threshold current density is again high because of the lower gain at wavelengths far from line center.

A plot of laser wavelength versus corrugation spacing for several diodes is shown in Fig. 5. The corrugation spacing is measured directly by observation in a calibrated high-power optical microscope and also indirectly by observation of the angle of diffracted light from the substrate surface. We estimate the measurement accuracy as ±4 Å. As indicated in the figure, the laser wavelength increases as the grating spacing is increased. However, no single straight line representing a particular refractive index can be drawn through the points because of dispersion at wavelengths near the band gap of the crystal. In fact, the Bragg formula yields $n_2 \simeq 3.59$ at 8583 Å and $n_2 \simeq 3.63$ at 8460 Å. The higher refractive index near the band edge has been observed by other workers for GaAs [12]. Some of the scatter in the points may result from the effects of nonuniform pumping which causes the index to vary along the crystal or because different longitudinal modes

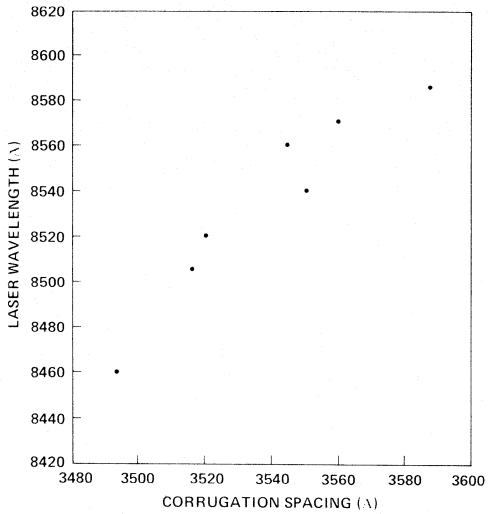

Fig. 5. Laser free-space wavelength versus corrugation spacing for several DFB diodes.

oscillate. Also, some shift in wavelength might be expected for diodes at different pumping levels.

Another important spectral property which theoretically should be achieved more readily in DFB than in cleaved-mirror lasers is that of single-mode operation. We have obtained narrow-linewidth single-mode operation in a DFB laser with one cleaved and one AR-coated face. These results are shown in the spectra of Fig. 6 for a diode of ~475-μm length and 200-μm width. At laser threshold of 3.3 A, the linewidth was measured to be a maximum of 0.15 Å which is the limiting spectrometer resolution at this wavelength. Therefore, the laser line might well be considerably narrower than this measurement indicates. Such narrow-linewidth single-mode laser operation is not normally achieved with SH diode lasers because of the lack of uniform excitation both in the direction perpendicular to the junction and in the junction plane [23]. At a current of 3.5 A, multimode oscillations were observed. Either other longitudinal modes attained threshold or other laser filaments formed along the junction plane. At ~3.7 A another filament was clearly visible when the cleaved face was viewed with the IR up-converting microscope.

The mode spectrum of another DFB laser near threshold with a 2.1-mm cavity length and one cleaved and one saw-cut end mirror is shown in Fig. 7. Several longitudinal modes are clearly resolvable and have a mode spacing of ~0.35 Å. This mode separation agrees well with that predicted by the equation

$$\Delta\lambda = \frac{\lambda^2}{2nL\,[1 - (\lambda/n)\,(dn/d\lambda)]} \tag{2}$$

which approximately holds for SH DFB lasers with small coupling as well as conventional lasers [2].

We have found analytically [2] that the physical position of the cleaved mirrors, relative to the grating peaks, greatly affects the longitudinal mode structure. Often the mode nearest the Bragg frequency has a substantially higher threshold than the other longitudinal modes and is not present in the measured spectra. As expected, other longitudinal modes nearest the Bragg frequency are most strongly affected by the

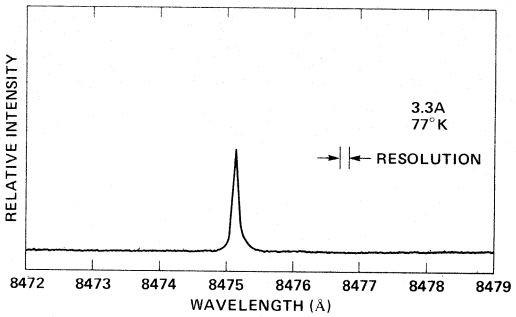

Fig. 6. Spectrum of a narrow linewidth DFB diode laser.

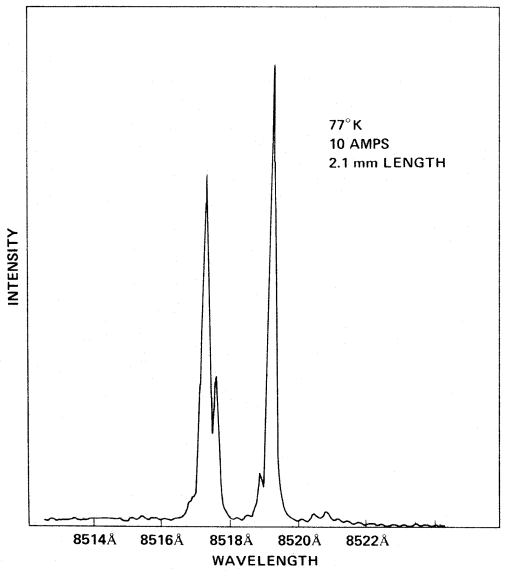

Fig. 7. Spectrum illustrating longitudinal modes of a DFB diode laser.

grating and their thresholds may be either increased or decreased relative to those determined by cleaves alone. However, mirror reflectivity determines threshold a few modes away from the Bragg frequency for small and moderate values of κL (κ is the coupling coefficient). In the spectrum shown in Fig. 7 the two modes nearest the apparent Bragg frequency do not oscillate. Such behavior is consistent with theoretical predictions [2], [19].

In the direction perpendicular to the p-n junction only the TE_0 and TM_0 modes are confined because of the small refractive-index difference of the p-n junction at one boundary of the 2.0-μm-thick waveguide. The existence of only lowest order transverse modes has been previously observed in cleaved-mirror SH lasers [13]. The transverse-mode structure in the plane of the p-n junction is not similarly constrained because no method for limiting the pumped junction area was used.

Radiation Modes

The last experimental results to be discussed involve the launching of radiation modes at angles to the plane of the p-n junction. Such modes have been observed in both optically pumped dye lasers [14], [15] and in optically pumped GaAs platelet lasers [16]. They occur because gratings diffract in several orders. For example, in Fig. 8 is shown a wave traveling

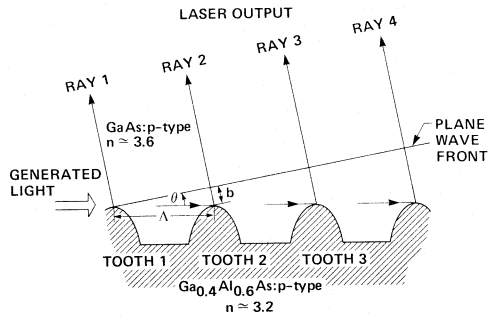

Fig. 8. Geometric representation of radiating modes in a DFB diode laser.

in the plane of the p-n junction which is diffracted out of this plane. The wavefront radiates at an angle Θ with the interface between the GaAs and GaAlAs p-type layers. An elementary view of this situation based on geometrical considerations follows. Ray 1 is in phase with ray 2 if Θ is such that

$$\sin \Theta = \frac{m\lambda_0}{n\Lambda} - 1 \tag{3}$$

where m is an integrer, λ_0 is the free-space laser wavelength, n is the equivalent refractive index of the waveguiding layer, and Λ is the corrugation spacing. For SH GaAs lasers $n \simeq n_2$. This equation is obtained by requiring that

$$\Lambda + b = \frac{m\lambda_0}{n} \tag{4}$$

in order for the wave to be in phase. When the radiation mode escapes the crystal the beam undergoes refraction so that the angle the wavefront makes with the top surface of the crystal (ϕ) is given by

$$\sin \phi = \frac{m\lambda_0}{\Lambda} - n\,. \tag{5}$$

In the case of a DFB laser (3) can be satisfied by $m = 0, 1, 2$ when $\lambda_0/n = \Lambda$, which is the condition for second-order Bragg scattering. Other grating spacings can be used to couple a beam out normal to the plane of the p-n junction. In general, if

$$\frac{\Lambda n}{\lambda_0} = p, \qquad p = 1, 2, 3, \cdots \tag{6}$$

there exists at least one solution of (3) such that $\phi = 0$ and the beam is radiated normal to the junction. This corresponds to Bragg scattering of order $2p$ in the DFB structure. In particular, if $p = 1$ only the radiation mode normal to the plane of the grating exists. This is not true for larger values of p.

A schematic of the DFB laser in which light is coupled out of the diode normal to the plane of the p-n junction is shown in Fig. 9. The diode is identical to the DFB structures described previously except that a grating period of 4693 Å (corresponding to fourth-order DFB) is fabricated between the p-GaAs and GaAlAs layers. This grating provides both DFB and output coupling of the guided wave in the cavity. As indicated in the figure a collimated beam is coupled out at 90° from the entire top surface of the n-GaAs layer. Two other beams, not shown, are also coupled into the GaAs n-layer at

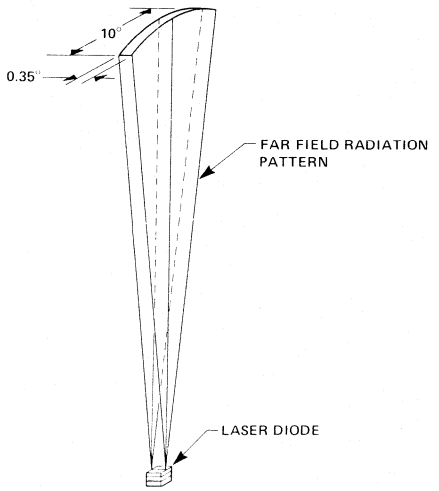

Fig. 9. Near- and far-field radiation pattern of a radiating DFB diode laser.

$\theta = +30°$ and 150°; the latter is produced by the left-going wave (see Fig. 8). However, these are totally internally reflected as are those coupled into the GaAlAs layer. A spacing of $\Lambda = 2400$ Å would not produce these beams.

In contrast to the DFB lasers described previously the cleaved end faces of these diodes are coated with a gold film of approximately 98-percent reflectivity. Thus most of the power output is scattered from the grating rather than being transmitted through the cleaves. The crystal faces orthogonal to the grating are saw cut. The diode is bonded with the p-side down on the header. A top contact (~1.25-μm diameter) is alloyed to one end of the device leaving a clear-surface emitting area over $\frac{2}{3}$ of the diode. The n-type GaAs substrate is sufficiently thick and heavily doped ($N_d - N_a \sim 2 \times 10^{18}$ Si) that current spreads nearly uniformly over the emitting area.

Laser threshold current densities were ~1.2 kA/cm^2 for a typical device of length 750 μm. The laser wavelength of this device was 8480 Å, which is both the expected laser wavelength for cleaved-mirror diodes without DFB and also the wavelength selected by this particular grating spacing. In general, thresholds and lasing wavelengths are determined by the combined effects of the distributed and discrete feedback. It is clear that the diode is lasing near the Bragg condition for DFB operation since the far-field pattern has only a single narrow lobe normal to the plane of the p-n junction.

A scan of the far-field pattern obtained by angularly rotating a light pipe connected to a photomultiplier about an axis centered on the diode is shown in Fig. 10. A 500-μm slit which gave an angular resolution of ~0.1° was employed before the light pipe. At a current of 7.2 A, which is ~1.7 times threshold, the bandwidth of the laser emission was 7 Å. By scanning across the diode axis the divergence of the beam in the direction determined by the grating along the length of the diode was measured to be only 0.35°. This is close to the predicted value of $\Delta\phi$, the angular divergence of the beam. By differentiating (5) we find

$$\Delta\phi = \frac{1}{\cos\phi}\left[\frac{m\lambda_0}{n\Lambda} - \frac{\lambda_0}{n}\frac{dn}{d\lambda}\right]\frac{\Delta\lambda}{\lambda_0}\,n. \tag{7}$$

For a grating spacing of 4693 Å (taking the dispersion term

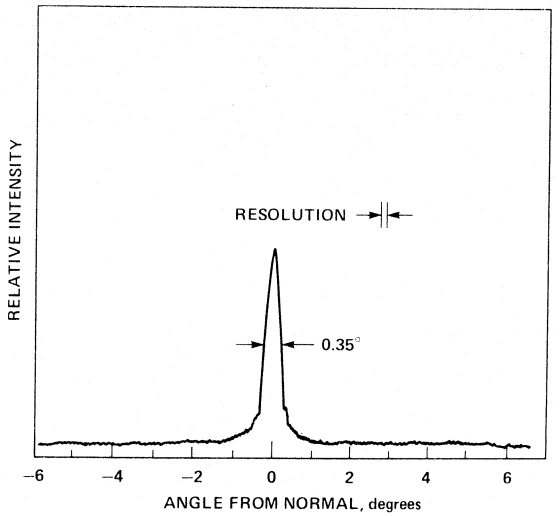

Fig. 10. Angular divergence of the far-field radiation parallel to the grating.

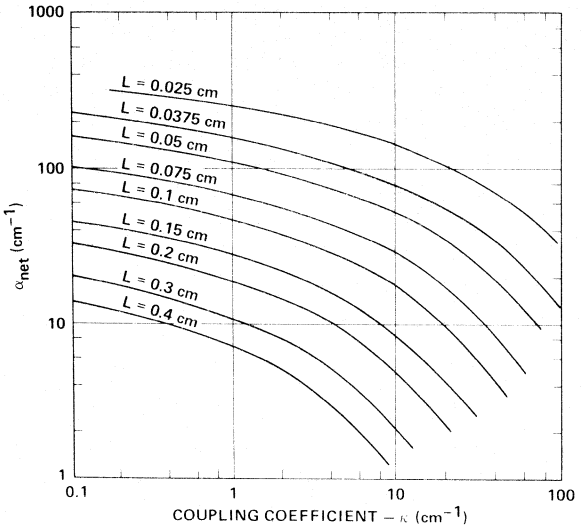

Fig. 11. Net gain at threshold versus coupling coefficient with length as a parameter.

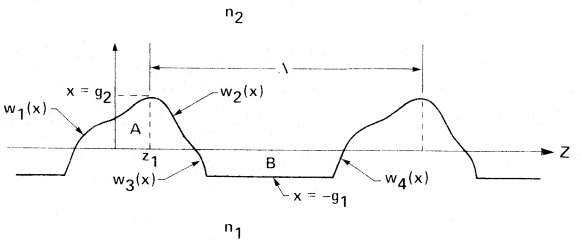

Fig. 12. Two arbitrarily shaped teeth of a corrugation grating.

$(\lambda_0/n)/(dn/d\lambda) = -0.25$), (7) yields an angular divergence of 3.7×10^{-3} rad or 0.21°. The slight discrepancy probably occurs because of the finite length of the diode. A uniform radiator 500 μm long would produce an angular divergence of ~0.1° with 8500-Å light. This enhancement of beam collimation occurs because the divergence is roughly inversely proportional to the size of the radiator and this diode radiates over its entire length rather than across the ~2-μm junction thickness.

Both the near- and far-field patterns were also examined through an infrared up-converting microscope. In the near field a single filament is observed across the entire length of the diode (except where covered by the contact). The far-field pattern showed a single sharp vertical stripe whose vertical divergence is typical of that determined by the width of a lasing filament. The output beam was found to be virtually 100-percent polarized with the E-field parallel to the grating grooves. This observation is in agreement with previous theoretical analysis [17]. Linear polarization is of course an added advantage to output coupling orthogonal to the junction.

IV. Analytic Results

The pumping thresholds and laser frequencies of DFB devices depend greatly on the strength of coupling between the left- and right-going traveling waves. The case of pure DFB (no external reflectors) was treated by Kogelnik and Shank [18] and their results are presented in a slightly different form as Fig. 11. Here is plotted net threshold gain versus coupling coefficient with device length as a parameter. Using this figure one can determine minimum necessary device length L given κ and available α or given α and L the plot specifies minimum values of κ. Chinn [19] studied DFB lasers with identical symmetrically located external reflectors and the present authors [2] have considered the general case of any external-reflector geometry. In all geometries device behavior depends critically on the coupling coefficient κ, but κ is usually defined in terms of a continuous variation in refractive index and/or gain along the length of the device. Many lasers, such as the one described earlier in this paper, have discrete periodic corrugations rather than continuous variations. Thus the coupling coefficient must be computed from the geometry of the corrugations.

Many authors [20]–[22] approach this problem by utilizing a perturbation technique. They consider a three-layer structure without corrugations which can model both single- and double-heterojunction GaAs lasers as well as thin-film dye lasers. Transverse modes are computed for the unperturbed geometry and the coupling of identical oppositely traveling modes via the corrugations is calculated. To carry out this procedure with greater accuracy, the boundary for the unperturbed mode calculation must be chosen at the area average of the corrugations (the areas labeled A and B in Fig. 12 are equal) and not at their base as in [3] and [22]. Thus in computing the unperturbed modes the thickness of the center layer is taken to be the distance from the n_2–n_3 interface to the z axis shown in Fig. 12, i.e., $\bar{t}$, and not t, the active-layer thickness prior to milling (cf. Fig. 1).

The coupling coefficient for TE modes is then given by [22]

$$\kappa = \frac{\omega^2 \mu_0 \epsilon_0 N_e^2}{2\beta_e} \int_{-\infty}^{\infty} \Delta\,[n^2(x,z)]\, \mathcal{E}_e^2(x)\, dx \tag{8}$$

where

$$\mathcal{E}_e(\chi) = \begin{cases} \exp(qx), & x \leqslant 0 \\ \cos(hx) + (q/h)\sin(hx), & 0 \leqslant x \leqslant t \\ [\cos(ht) + (q/h)\sin(ht)] & \\ \quad \cdot \exp[-p(x-t)], & t \leqslant x \end{cases} \tag{9}$$

$$N_e^2 = \frac{2h^2}{(h^2+q^2)(t+q^{-1}+p^{-1})} \tag{10}$$

$$q = \sqrt{\beta_e^2 - n_1^2 k^2}$$

$$h = \sqrt{n_2^2 k^2 - \beta_e^2}$$

$$p = \sqrt{\beta_e^2 - n_3^2 k^2} \tag{11}$$

and β_e is the propagation constant found by solving

$$\tan(h\bar{t}) = \frac{h(q+p)}{h^2 - pq}. \tag{12}$$

In (8), only the spatial harmonic of $\Delta[n^2(x,z)]$ appropriate to the Bragg-scattering order is to be retained, κ is defined by comparison with the equation connecting the opposite-going waves (cf. [18] and [22]), and

$$\Delta[n^2(x,z)] = \begin{cases} n_1^2 - n_2^2 & \text{in area } A \\ n_2^2 - n_1^2 & \text{in area } B \end{cases} \tag{13}$$

of Fig. 12. Since the corrugations are periodic so too is $\Delta[n^2(x,z)]$.

Consider now a single corrugation as shown in Fig. 12. Here $w_i(x)$, $i = 1, 2, 3, 4$ describe the tooth boundary. If any of these functions are not single valued, the tooth shape can be decomposed into two or more curves with single-valued boundaries. Then the results are superimposed by summing the contributions to κ. In the event the situation is as illustrated in Fig. 12 we have

$$\Delta[n^2(x,z)] = \begin{cases} (n_1^2 - n_2^2) \sum_{p=-\infty}^{\infty} \{u[w_2(x) - z + p\Lambda] \\ \quad - u[w_1(x) - z + p\Lambda]\}, \quad x > 0 \\ (n_2^2 - n_1^2) \sum_{p=-\infty}^{\infty} \{u[w_4(x) - z + p\Lambda] \\ \quad - u[w_3(x) - z + p\Lambda]\}, \quad x < 0 \end{cases} \tag{14}$$

where $u(z) = 1$ for $z > 0$ and 0, $z < 0$. Since (14) is periodic in z it can be expanded in a Fourier series whose coefficients depend on x. After some manipulation we obtain

$$\Delta[n^2(x,z)] = \begin{cases} (n_1^2 - n_2^2)\left[\frac{w_2(x) - w_1(x)}{\Lambda} - \frac{i}{2\pi}\sum_{m=-\infty}^{\infty}\frac{1}{m}\right. \\ \quad \cdot \{\exp[i2\pi m w_2(x)/\Lambda] \\ \quad - \exp[i2\pi m w_1(x)/\Lambda]\} \\ \quad \left.\cdot \exp(-i2\pi m z/\Lambda)\right], \quad x > 0 \\ (n_2^2 - n_1^2)\left[\frac{w_4(x) - w_3(x)}{\Lambda} - \frac{i}{2\pi}\sum_{m=-\infty}^{\infty}\frac{1}{m}\right. \\ \quad \cdot \{\exp[i2\pi m w_4(x)/\Lambda] \\ \quad - \exp[i2\pi m w_3(x)/\Lambda]\} \\ \quad \left.\cdot \exp(-i2\pi m z/\Lambda)\right], \quad x < 0. \end{cases} \tag{15}$$

Since the mth spatial harmonic acts to couple energy from the left- to right-going waves

$$\kappa_e = \frac{-i\omega^2\mu_0\epsilon_0(n_1^2 - n_2^2)N_e^2}{4\pi\beta_e m}\left\{\int_0^{g_2}\{\exp[i2\pi m w_2(x)/\Lambda] - \exp[i2\pi m w_1(x)/\Lambda]\}\,\mathcal{E}_e^2(x)\,dx - \int_{-g_1}^{0}\{\exp[i2\pi m w_4(x)/\Lambda] - \exp[i2\pi m w_3(x)/\Lambda]\}\,\mathcal{E}_e^2(x)\,dx\right\} \tag{16}$$

where, as shown in Fig. 12, g_1 and g_2 are the maximum tooth heights in media 1 and 2, respectively, and m is the Bragg-scattering order. An expression similar to (16) holds for TM modes.

For rectangular teeth $w_2(x) = -w_1(x) = w/2$, $w_3(x) = w/2$, $w_4 = \Lambda - w/2$, and the area averaging condition yields

$$g_1 = wg/\Lambda \tag{17a}$$

and

$$g_2 = (1 - w/\Lambda)g \tag{17b}$$

where g is the total tooth height. After integration (16) becomes

$$\kappa_e = \frac{\omega^2\mu_0\epsilon_0(n_1^2 - n_2^2)N_e^2}{4\pi\beta_e m}\sin\left(\frac{\pi m w}{\Lambda}\right) \cdot \left\{g_2 + \frac{\sin(2g_2h)}{2h} + \frac{q}{h^2}[1 - \cos(2g_2h)] + \frac{q^2}{h^2}\left[g_2 - \frac{\sin(2g_2h)}{2h}\right] - \frac{1}{q}[1 - \exp(-2qg_1)]\right\}. \tag{18}$$

It should be recalled that this equation is valid only for small values of $|\kappa|$ which result when $|n_1^2 - n_2^2|$ and/or the ratio $g/\bar{t}$ are small.

The coupling coefficients for both TE and TM modes appear to be proportional to $n_1^2 - n_2^2 \simeq (n_1 - n_2)(n_1 + n_2)$, but this is only approximately true since h, g, β, and N depend on n_1 and n_2. Dependence on the Bragg-scattering order m is completely described by the term

$$\frac{\sin(\pi m w/\Lambda)}{m} \tag{19}$$

and for integral values of mw/Λ, κ is zero, e.g., w/Λ, = 0.5, and $m = 2, 4, 6, \cdots$. The variation of κ with $n_2 - n_3$, t (the central-layer thickness), w/Λ, and the transverse-mode number are not evident from a superficial examination of (18) since they influence g, h, β, and N, and therefore are best displayed by means of plots. Also although the variation of $|\kappa|$ with tooth height g is completely contained in the bracketed expression in (18) that dependence is rather complex and best exhibited graphically. In Fig. 13 we show the variation of κ with g for a SH GaAs laser at $\lambda_0 = 8500$ Å, $t = 2.0$ μm, $m = 3$, and various values of w/Λ. Actually, as noted above, t is measured from the tooth base and $\bar{t}$ used for the unperturbed modes is

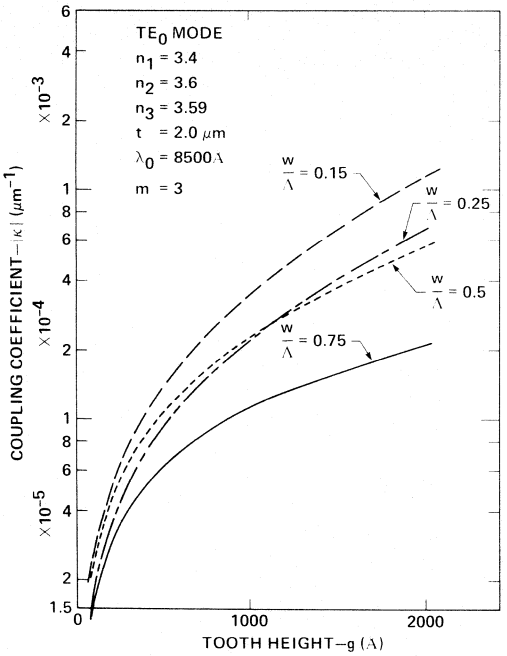

Fig. 13. Coupling coefficient versus tooth height for the TE_0 mode and rectangular teeth in a SH DFB diode laser.

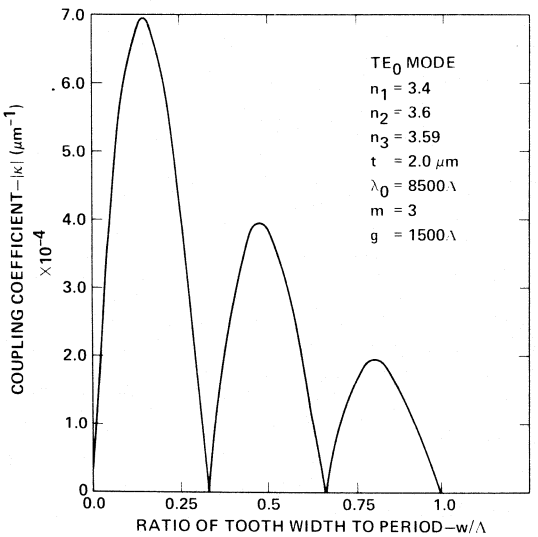

Fig. 14. Coupling coefficient versus the ratio of the tooth width to the period for a rectangular grating in a SH DFB diode laser operating in the TE_0 mode.

$$\bar{t} = t - g_1 = t - wg/\Lambda.$$

In this geometry only the TE_0 and TM_0[1] modes propagate and the latter coupling coefficient is approximately 0.9 of the former. For very small g the variation is linear, but this is not easy to detect on the semilog plot employed. Of the four values of w/Λ plotted, $w/\Lambda = 0.15$ yields the largest coupling coefficient, but actually the dependence of $|\kappa|$ on w/Λ is more complex. In Fig. 14 we plot $|\kappa|$ versus w/Λ for the same geometry with $g = 1500$ Å. The features exhibited by this plot depend on several factors. First, as w/Λ increases the boundary of the unperturbed modes and the teeth interact more and more with the evanescent part of the mode in region

[1] These were numbered as the first mode in our earlier papers.

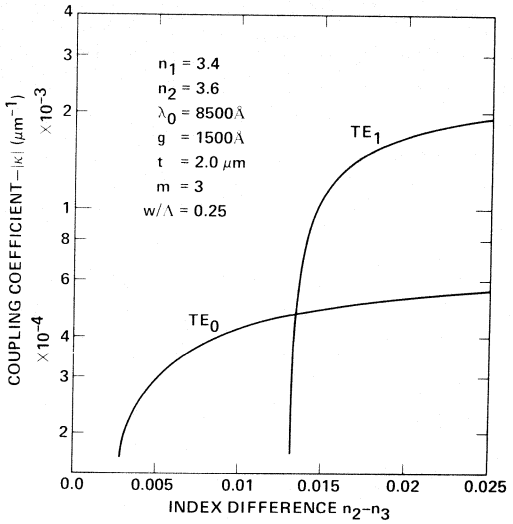

Fig. 15. Coupling coefficient versus index difference for the TE_0 and TE_1 modes and rectangular teeth in a SH DFB diode laser.

1 rather than the more intense oscillatory part of the mode in the center layer. This accounts for the general decrease in $|\kappa|$ with w/Λ. Second, as w/Λ changes there exist differing degrees of interference from various parts of the tooth along the z direction. This phenomenon accounts for the zeros in $|\kappa|$ [cf. (19)]. Finally, as w/Λ varies so too does $\bar{t}$, which changes the mode distribution. For $t = 2.0$ μm, the effect is to increase $|\kappa|$ for all w/Λ.

Fig. 15 is a plot of $|\kappa|$ versus $n_2 - n_3$ for TE modes in a SH diode laser. According to published results [13] the n-type GaAs index should be ~3.59 so that only the lowest mode will propagate. Note too that $|\kappa|$ becomes relatively independent of $n_2 - n_3$ once that index difference exceeds rather small values. Also as soon as the index difference becomes large enough to support two modes the second coupling coefficient exceeds the first. That this is generally the case is illustrated in Fig. 16 for a double-heterostructure geometry where κ is plotted versus t. The increase in coupling coefficient with transverse mode numbers occurs because well-confined higher order transverse modes have a greater fraction of their total energy in the vicinity of the corrugations. To take advantage of this fact the corrugation period should be selected to resonate these higher order transverse modes and thus achieve lower thresholds or use shorter lengths [3], [24].

Consider next a sinusoidal grating located symmetrically about the x and z axes. The integrals which result from substituting $w_i(x)$, $i = 1, 2, 3, 4$ in (16) can be evaluated either analytically after expanding $\mathcal{E}_e^2(x)$ in a power series or numerically. By employing the former procedure we obtain rapidly converging series for κ and plot $|\kappa|$ versus g for the TE_0 mode of a SH GaAs laser in Fig. 17. Also shown are plots of $|\kappa|$ versus g for rectangular teeth with $m = 1$ and 3. The coupling coefficients for $m = 1$ are of the same order of magnitude for rectangular and sinusoidal teeth; however, for $m = 3$, $|\kappa|$ is dramatically reduced with sinusoidal teeth in contrast to $|\kappa|$ for rectangular teeth. If, because of fabrication limitations, one can only produce teeth with a maximum aspect ratio g/Λ of say 0.5, then a third-order rectangular grating will yield a higher κ than its first-order counterpart, i.e., for $\Lambda = 3500$ Å, $g = 1750$ Å, $\kappa \simeq 5.6 \times 10^{-4}$ μm^{-1}, whereas with $\Lambda = 1167$ Å,

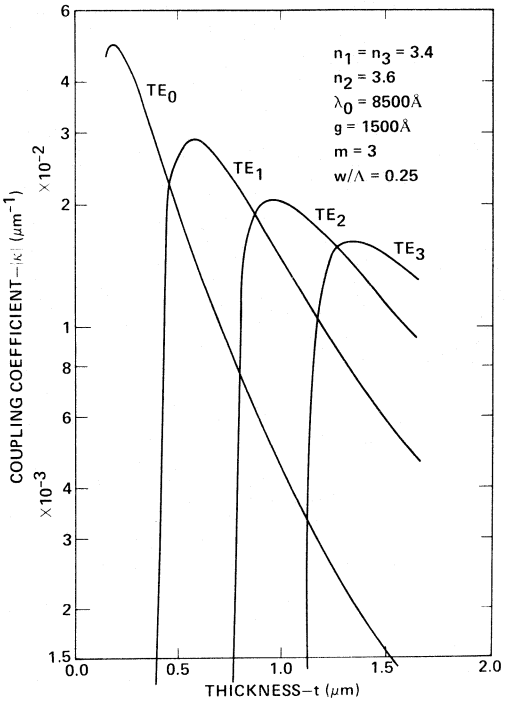

Fig. 16. Coupling coefficient versus active-region thickness for TE modes and rectangular teeth in a DH DFB diode laser.

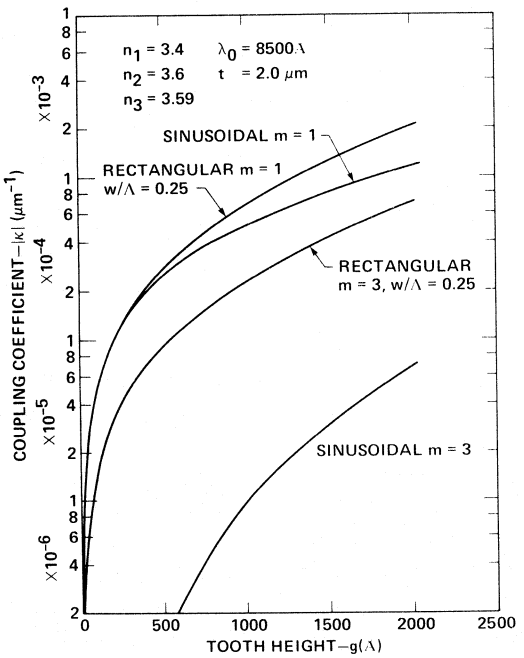

Fig. 17. Coupling coefficient versus tooth height for the TE_0 mode in a SH DFB diode laser with sinusoidal or rectangular teeth and first- or third-order Bragg scattering.

$g = 583$ Å, $\kappa \simeq 3.4 \times 10^{-4}\ \mu m^{-1}$. Of course the same is not true for other teeth shapes and the additional radiation losses which occur when higher order Bragg scattering is employed should also be taken into account.

According to Fig. 17 our rectangular grating with $m = 3$ and $g \simeq 1500$ Å, has $\kappa \simeq 4 \times 10^{-4}\ \mu m^{-1} = 4\ cm^{-1}$. Then from Fig. 11, for the 0.19-cm laser described in Section III (cf. Fig. 4) we require $\alpha_{th} \simeq 11\ cm^{-1}$. If the absorption and radiation losses are approximately $\alpha_{abs} \simeq 10\ cm^{-1}$ and $\alpha_{rad} \simeq 5\ cm^{-1}$ the gain at threshold is $g_{th} \simeq 26\ cm^{-1}$. Since for SH GaAs lasers [13]

$$g_{th} \simeq 30 \frac{cm}{kA} \times J_{th}$$

we obtain

$$J_{th} \simeq \frac{26}{30} \frac{kA}{cm^2} = 866 \frac{A}{cm^2}$$

which agrees well with the experimentally measured threshold value of 775 A/cm^2 reported earlier in this paper.

V. Conclusion

We have presented and discussed our fabrication technique's experimental results, and calculations of coupling coefficients for SH DFB lasers.

Acknowledgment

The authors wish to thank J. Tramontana and A. Alimonda for their assistance in crystal growth and diode fabrication. They also wish to thank R. Ewing, G. McKinley, and F. Walton for SEM and TEM measurements.

References

[1] D. R. Scifres, R. D. Burnham, and W. Streifer, "Distributed-feedback single heterojunction GaAs diode laser," *Appl. Phys. Lett.*, vol. 25, pp. 203–206, 1974.

[2] a) W. Streifer, D. R. Scifres, and R. D. Burnham, "Longitudinal modes in distributed feedback lasers with external reflectors," *J. Appl. Phys.*, vol. 46, pp. 247–249, Jan. 1975.
b) W. Streifer, R. D. Burnham, and D. R. Scifres, "Effect of external reflectors on longitudinal modes of distributed feedback lasers," *IEEE J. Quantum Electron.*, vol. QE-11, pp. 154–161, Apr. 1975.

[3] W. Streifer, R. D. Burnham, and D. R. Scifres, "Coupling coefficients and propagation constants in guided wave distributed feedback lasers," *J. Appl. Phys.*, vol. 46, pp. 946–948, Feb. 1975.

[4] S. Somekh, "Transverse mode control in a distributed feedback semiconductor laser," *Proc. IEEE* (Lett.), vol. 62, pp. 277–278, Feb. 1974.

[5] D. R. Scifres, R. D. Burnham, and W. Streifer, "Highly collimated laser beams from electrically pumped SH GaAs/GaAlAs distributed feedback lasers," *Appl. Phys. Lett.*, vol. 26, p. 48, 1975.

[6] H. Kogelnik and C. V. Shank, "Stimulated emission in a periodic structure," *Appl. Phys. Lett.*, vol. 18, pp. 152–154, 1971.

[7] I. Hayashi and M. B. Panish, "GaAs-$Ga_xAl_{1-x}As$ heterostructure injection lasers which exhibit low thresholds at room temperature," *J. Appl. Phys.*, vol. 41, pp. 150–163, 1970.

[8] M. J. Beesley and J. G. Castledine, "The use of photoresist as a holographic recoding medium," *Appl. Opt.*, vol. 9, pp. 2720–2724, 1970.

[9] D. P. Schinke, R. G. Smith, E. G. Spencer, and M. F. Galvin, "Thin-film distributed-feedback laser fabricated by ion milling," *Appl. Phys. Lett.*, vol. 21, pp. 494–496, 1972.

[10] M. Nakamura *et al.*, "Liquid phase epitaxy of GaAlAs on GaAs substrates with fine surface corrugations," *Appl. Phys. Lett.*, vol. 24, pp. 466–468, 1974.

[11] M. Ettenberg, H. F. Lockwood, and H. S. Sommers, Jr., "Radiation trapping in laser diodes," *J. Appl. Phys.*, vol. 43, pp. 5047–5051, 1972.

[12] H. C. Casey, D. D. Sell, and M. B. Panish, "Refractive index of $Al_xGa_{1-x}As$ between 1.2 and 1.8 eV," *J. Appl. Phys.*, vol. 24, pp. 63–65, 1974.

[13] H. Kressel, H. Nelson, and F. Z. Hawrylo, "Control of optical losses in p-n junction lasers by use of a heterojunction: Theory

and experiment," *J. Appl. Phys.*, vol. 41, pp. 2019–2031, 1970.
[14] P. Zory, "Laser oscillation in leaky corrugated optical waveguides," *Appl. Phys. Lett.*, vol. 22, pp. 125–128, 1973.
[15] K. O. Hill and A. Watanabe, "Passive-core corrugated-waveguide laser," *Appl. Opt.*, vol. 12, pp. 430–433, 1973.
[16] Zh. I. Alferov *et al.*, "Semiconductor laser with extremely low divergence of radiation," *Sov. Phys.–Semicond.*, vol. 4, pp. 541–542, 1974.
[17] H. Kogelnik, "Coupled wave theory for thick hologram gratings," *Bell Syst. Tech. J.*, vol. 48, pp. 2909–2947, 1969.
[18] H. Kogelnik and C. V. Shank, "Coupled-wave theory of distributed feedback lasers," *J. Appl. Phys.*, vol. 43, pp. 2327–2335, 1972.
[19] S. R. Chinn, "Effects of mirror reflectivity in a distributed-feedback laser," *IEEE J. Quantum Electron.*, vol. QE-9, pp. 574–580, June 1973.
[20] D. Marcuse, "Mode conversion caused by surface imperfections of a dielectric slab waveguide," *Bell Syst. Tech. J.*, vol. 48, pp. 3187–3215, 1969.
[21] S. Wang, "Proposal of periodic layered waveguide structures for distributed lasers," *J. Appl. Phys.*, vol. 44, pp. 767–780, 1972.
[22] A. Yariv, "Coupled-mode theory for guided-wave optics," *IEEE J. Quantum Electron.*, vol. QE-9, pp. 919–933, Sept. 1973.
[23] S. Iida, K. Takata, and Y. Unno, "Spectra behavior and linewidth of (GaAl)As–GaAs double-heterostructure lasers at room temperature with stripe geometry configuration," *IEEE J. Quantum Electron. (Part II of Two Parts. Special Issue on 1972 IEEE Semiconductor Laser Conference)*, vol. QE-9, pp. 361–366, Feb. 1973.
[24] J. E. Bjorkholm and C. V. Shank, "Distributed-feedback lasers in thin-film optical waveguides," *IEEE J. Quantum Electron.*, vol. QE-8, pp. 833–838, Nov. 1972.

Semiconductor Lasers with the Light Output Through the Diffraction Grating on the Surface of the Waveguide Layer

ZH. I. ALFEROV, V. M. ANDREYEV, S. A. GUREVICH, R. F. KAZARINOV, V. R. LARIONOV, M. N. MIZEROV, AND E. L. PORTNOY

Abstract—In AlAs–GaAs semiconductor heterojunction lasers, due to the interaction of the waveguide modes with a diffraction grating on the surface of the waveguide layer, output of coherent radiation has been obtained through the plane parallel to the layer.

The angle of divergence of the radiation in this case was equal to 0.5° both with optical and injection pumping. The possibility of fabricating a new type of semiconductor laser with small radiation divergence has been proven experimentally.

COHERENT radiation in semiconductor lasers is usually generated in a thin active layer and is emitted through its cleaved facets. Diffraction divergence as large as several tens of degrees has been measured because of the extremely small radiating aperture. In order to reduce the diffraction divergence of radiation, it is necessary to increase the area of the radiating aperture. This can be achieved by coupling the radiation out through a surface parallel to the waveguide layer. With this aim, the diffraction grating was imbedded at the waveguide surface and radiation was coupled out due to the interaction between the waveguide modes and the grating [1].

Manuscript received December 16, 1974.
The authors are with the A. F. Ioffee Physico-Technical Institute, Leningrad, USSR.

This report concerns the experimental investigation of the possibility of coupling out coherent radiation at an angle to the waveguide surface, both by optical and injection pumping.

For the case of optical pumping two layers were grown in succession on a GaAs substrate oriented in the (100) plane, the first layer was an 80-μm-thick layer of n-$Al_{0.3}Ga_{0.7}As$ and the second layer was a 2-μm-thick layer of n-GaAs ($N_d = 10^{17}$ cm^{-3}). After growth the substrate was removed with a selective etch in order to observe the radiation coupled out through the n-$Al_{0.3}Ga_{0.7}As$ layer. The diffraction grating was made on the waveguide layer surface by using an interference photoetching technique [2]. The period of the grating is given by

$$|\sin \alpha| = n - \frac{\lambda_0}{a} \tag{1}$$

where α is the angle of radiation coupled out into the air, n is the refractive index of GaAs, λ_0 is the oscillation wavelength in a vacuum, and a is the grating period. Feedback is achieved by using the cleaved facets of the platelet as the Fabry–Perot resonator (Fig. 1).

The radiation spectra in the plane, perpendicular to the cleaved facets and the diffraction grating, represent two narrow peaks symmetrical, with respect to the normal, to the

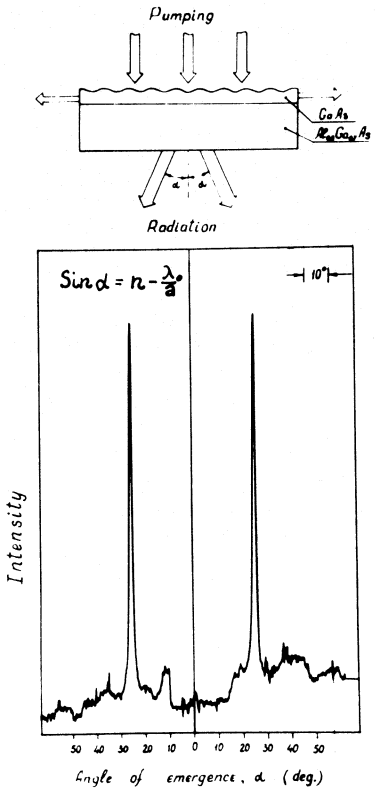

Fig. 1. A spectrum of distributed space radiation in a plane perpendicular to the cleaved facets and the diffraction grating by optical pumping.

waveguide surface (Fig. 1). The half-width of each of these peaks $\Delta\alpha$ is equal to 0.01 rad [3]. This value of divergence is determined by the multimode character of oscillation

$$\Delta\alpha = \frac{\Delta\lambda_0}{a \cdot \cos\alpha} \cdot \tag{2}$$

Measurements were performed at 77 K and 300 K and the samples were pumped by a pulse laser with a radiation wavelength of 3300 Å.

For injection pumping of the waveguide layer, specimens of low-threshold DH lasers with an undoped n-GaAs active layer were used [4]. In the central part of the laser on the side of the p-emitter, a window was etched right to the waveguide layer (Fig. 2). Then a diffraction grating with a period of $a = 0.22$ μm was etched at the waveguide surface (Fig. 3). As in the case of optical pumping, cleaved facets of the specimen parallel to grating lines served as a resonator, whereas the other two facets were saw cut. Current pulses were 100 ns at 300 K.

The radiation emitted through the window from the grating region were two pairs of narrow visible beams symmetrical with respect to the normal of the radiating surface. Their angular position is determined by the value of the longitudinal wave-vector components in the passive region of the waveguide K_m, and also by the grating period and the oscillation wavelength λ_0

$$\sin\alpha = \left| \frac{K_m - \beta}{K_0} \right| \tag{3}$$

where $\beta = 2\pi/a$, $K_m = 2\pi n_m/\lambda_0$, and $K_0 = 2\pi/\lambda_0$. Here n_m is

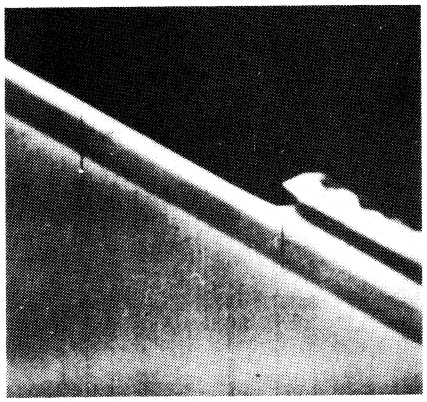

Fig. 2. A photograph of a four-layer heterolaser-structure cleaved facet locally etched down to the narrow-gap active layer 2 μm thick.

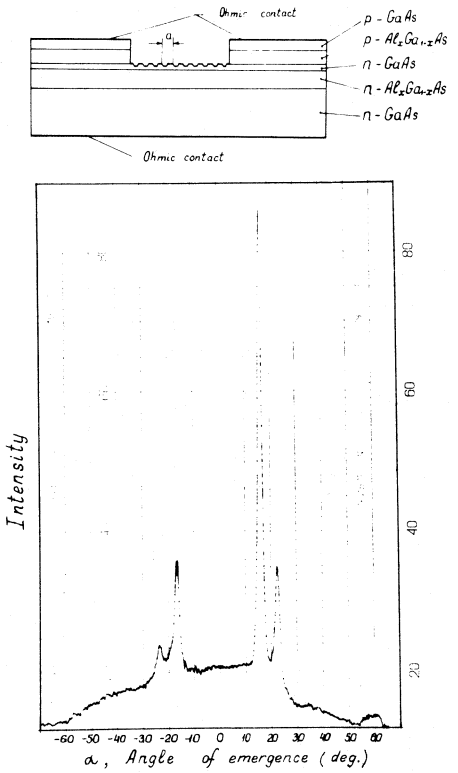

Fig. 3. An injection-laser spectrum with the diffraction grating on the surface of the waveguide layer and the diagram of distributed space radiation in a plane perpendicular to the cleaved facets and the diffraction grating.

the effective refractive index for the mode with transverse index m. Angular divergence for each beam was ~0.5° and was determined by the width of the oscillation line, corresponding to the case of optical pumping.

In spite of the resonator having a passive region, the threshold current of the structure in Fig. 3 was not significantly higher than that of conventional DH lasers without the passive region. The reason for this is due to the forbidden gap-width-narrowing effect [5] in regions of a high injection level. This allows the oscillation line to shift into the region of energies less than the forbidden gap width of the material in the passive region of the waveguide.

The forbidden gap-narrowing effect is easily observed in

lasers with constant composition in the undoped active layer. When we use the ordinary "sliding" boat construction for obtaining heterolaser structures there occurs a partial transferrence of Al into the melt from which the crystallization of the narrow-band active layer is grown. This leads to an inhomogeneity of the active-layer composition and to the shift of the generated radiation energy to a shorter wavelength region. To avoid this peculiarity we developed a boat construction in which the substitution of melts onto the substrate is not performed by shifting the substrate under melts of different composition, but by a compulsory displacement of one melt by another. By way of multiple melt substitution we manage to obtain a nearly complete homogeneity of the active-region composition with the generation energy equal to 1.39 eV when the undoped n-GaAs is grown. In this case, the energy of the coherent radiation is less than that of the absorption edge [6]. The corrugated passive region in this case does not yield absorption losses.

The proposed combination of an active region of the heterolaser structure occurring under ohmic contact and a corrugated passive region of the waveguide may be of use when fabricating injection distributed-feedback heterolasers. If the grating period is a multiple of half-wavelengths of light in the waveguide, the passive region of the heterolaser structure will serve as mirrors.

References

[1] R. F. Kazarinov and R. A. Suris, *Phys. Technol. Semicond.*, vol. 6, p. 1359, 1972.
[2] L. V. Beljakov, D. N. Gorjachev, M. N. Mizerov, and E. L. Portnoy, *J. Tech. Phys.*, vol. 44, p. 1331, 1974.
[3] Zh. I. Alferov *et al.*, *Phys. Technol. Semicond.*, vol. 8, p. 832, 1974.
[4] Zh. I. Alferov *et al.*, *Phys. Technol. Semicond.*, vol. 8, p. 2031, 1974.
[5] V. M. Asnin and A. A. Rogachev., *Solid State Phys.*, vol. 5, p. 1730, 1963.
[6] Zh. I. Alferov *et al.*, *Phys. Technol. Semicond.*, vol. 8, p. 1270, 1974.

Grating-Coupled Double-Heterostructure AlGaAs Diode Lasers

P. ZORY, MEMBER, IEEE, AND L. D. COMERFORD, ASSOCIATE MEMBER, IEEE

Abstract—**Corrugated AlGaAs waveguide devices have been fabricated which emit low-divergence (~1° by 15°) laser beams nearly normal to the waveguide plane when pulsed electrically at room temperature. The devices are fabricated from material which is essentially the same as that used to fabricate CW room-temperature lasers, differing only in that the two top layers of AlGaAs and GaAs are very thin (~0.4 μm and 0.1 μm, respectively). Threshold current densities of 3000–4000 A/cm^2 are typical in these devices even though ~20 percent of the resonator length is unpumped. The far-field pattern produced by the TE polarized leaky-wave laser beams emanating from the unpumped region is usually composed of two mode lines. A theory is outlined which describes how these mode lines are generated. The possibility of obtaining distributed-feedback (DFB) oscillation in devices of this type is also discussed.**

I. Introduction

SOME of the basic properties of spatially periodic, grating-like structures utilized to couple light into and out of optical waveguides have been discussed recently by Ulrich [1]. There are basically two types: one which utilizes a corrugated grating-type structure [2]; and the other which utilizes a thick Bragg-grating-type structure [3]. The grating-coupler section(s) of a waveguide can also be utilized to couple light between guided modes in both the forward and backward directions. In addition, this guided mode coupling can occur simultaneously with input–output coupling. These coupling processes can be operative in various combinations in a grating-coupled (GC) waveguide laser, that is, a waveguide laser with a built-in grating(s), and can greatly influence its behavior.

In the first experiments with GC lasers [4], gratings of the thick Bragg type were integrated into the light-amplifying medium and were utilized to provide the feedback necessary for oscillation. Devices of this type are known as distributed-feedback (DFB) lasers. In subsequent experiments [5], gratings of the corrugated type were utilized to provide both DFB lasing and leaky-wave output coupling in optical waveguides. Grating structures which provide both DFB and leaky-wave output coupling are limited primarily to the corrugated types since it is difficult to fabricate high-quality "interleaved" Bragg gratings (two or more sets of diffracting planes) into potentially practical light-amplifying waveguides.

The possibility of corrugating double-heterostructure (DH) AlGaAs diode lasers in order to obtain low-divergence output beams has been a subject of considerable speculation over the last few years and has been discussed in some detail by Kazarinov and Suris [6]. If the device is designed so that first-order diffraction gives rise to a leaky-wave output beam(s) nearly normal to the plane of the waveguide, then the possibility exists that the DFB due to second-order backward diffraction within the waveguide [7] will be an important factor in determining the operational characteristics of the device even though the dominant feedback for oscillation is derived from

Manuscript received January 3, 1975; revised February 4, 1975.
The authors are with the IBM Thomas J. Watson Research Center, Yorktown Heights, N.Y. 10598.

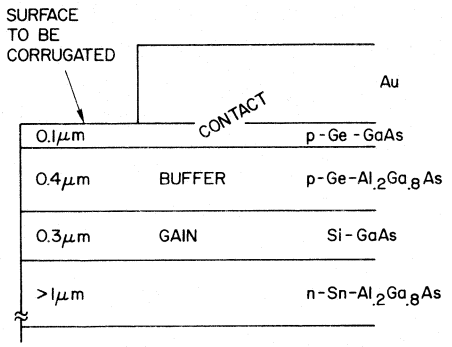

Fig. 1. Structure of the double-heterojunction material used to fabricate the GC diode lasers.

the mirror-like end facets [8]. AlGaAs devices which utilize third-order DFB for oscillation cannot generally emit output beams across the plane of the waveguide since the first- and second-order diffracted waves are trapped by total internal reflection within the planar structure. Such nonleaky DFB diode devices have been fabricated in single-heterojunction [9], homojunction [10], and DH configurations [11] and made operational in the vicinity of 100 K.

In this paper we report on the theory and observed behavior of corrugated DH-AlGaAs diode lasers which emit low-divergence (in one dimension) leaky-wave laser beams nearly normal to the waveguide plane when pulsed electrically at room temperature. The behavorial characteristics of other similar devices are also reported on in this journal (Alferov *et al.*). A recent publication [12] has reported the observation of a low-divergence output beam from a corrugated single-heterojunction diode laser cooled to 77 K. This device apparently behaves in a fashion similar to the corrugated fourth-order DFB dye-laser devices described in [5], although the presence of high-reflectivity coatings on the cleaved end facets tends to make it difficult to prove that the DFB mechanism is operable.

In Section II of this paper, the behavior of the TE_0-mode gain coefficient in thin buffer-layer DH material (see Fig. 1) is considered and the mode-coupling processes which can occur when material of this type is corrugated are described. In Section III, the device fabrication techniques utilized are briefly outlined and the operational characteristics of typical devices discussed. These are summarized as follows: 1) the leaky-wave laser beams are usually two in number and are emitted in directions nearly normal to the waveguide plane; 2) each beam has a rectangular divergence of about 1° by 15°; and 3) threshold current densities usually fall in the 3000–4000-A/cm^2 range even though the central region of the laser resonator (~70 μm long by 60 μm wide) is unpumped.

II. Theory

The main problem in fabricating low-threshold GC diode lasers is that of fabricating a diffraction grating sufficiently close to the gain layer to be functional without disrupting the injection and radiative recombination processes taking place in that layer. Since function in the case discussed here refers mainly to leaky-wave output coupling rather than DFB oscillation, the problem can be solved simply by fabricating the grating far from the gain layer as depicted in Fig. 1. The structural design shown is essentially the same as is used to make CW room-temperature diode lasers except that the p-AlGaAs buffer layer and the p-GaAs part of the contact are both much thinner than their usual values of about 1 μm [13]. Before discussing the details of the grating coupling processes, it is instructive to demonstrate that prior to grating fabrication, this configuration is not substantially lossy. This is accomplished using the upper curve in Fig. 2 which is a plot of the dependence of the TE_0-mode gain coefficient on buffer-layer thickness for the case where the contact layer is gold[1] (see the Appendix for details of the calculation). If it is assumed that the 0.3-μm-thick layer of silicon-doped GaAs has a gain coefficient of 25 cm^{-1}, then the gain available to the TE_0 mode of the structure for large buffer thickness is about 17 cm^{-1}. The 17/25 ratio is just a measure of how well the TE_0-mode field distribution overlaps the gain layer when the aluminum-gallium ratio in the layers above and below the gain layer is 0.25. If the contact layer is gold, it is seen that the TE_0-mode gain coefficient does not begin to drop substantially until the buffer thickness is less than 0.2 μm. In fact, the TE_0-mode gain coefficient reaches a maximum value when the buffer thickness is about 0.7 μm. This peaking behavior occurs because the absorptive loss introduced by bringing the gold contact closer to the gain layer is more than offset by the increase in mode overlap with the gain layer. The very thin layer (0.1 μm) of p-GaAs shown in Fig. 1 is incorporated into the design primarily for contacting purposes. It is expected that the loss factor associated with this thin layer is negligible in comparison to the loss factor introduced by the diffraction grating (see Section III). The addition of a layer of optical-quality gold on top of the grating should not, according to the data of Fig. 2, add any additional loss other than that due to the increased diffraction efficiency of the corrugated interface. If the contact layer is thick GaAs, as is the case in typical DH diode lasers, then the TE_0-mode gain coefficient begins to drop rapidly when the buffer-layer thickness approaches 0.7 μm (lower curve in Fig. 2). This phenomenon, commonly observed in internal reflection spectroscopy [14], is due primarily to leaky-wave excitation [15] rather than absorptive loss and is the basis for explaining the operation of prism couplers [16], [17].

If it is assumed that a grating of sinusoidal cross section is fabricated into the surface of an AlGaAs buffer layer, and that the grating is of amplitude a and period $d = \lambda/n_0$ (where n_0 is the effective refractive index of the TE_0 mode at vacuum wavelength λ), then an approximate expression for the power-loss coefficient due to first-order (−1) leaky-wave excitation normal to the waveguide plane is [18]

$$\alpha_0^{(-1)} \cong (ka)^2 \frac{n_g^2 - n_0^2}{2n_0 w_0} (n_b - \delta_c) \exp(-2p_0 t_b). \quad (1)$$

In this expression k is equal to $2\pi/\lambda$, n_g and n_b are the refractive indices (real parts) of the gain and buffer layers, δ_c is equal to 1 or 0 depending on whether the contact layer is air

[1] In the calculation, it is assumed that the 0.1-μm-thick GaAs layer shown in Fig. 1 is nonexistent.

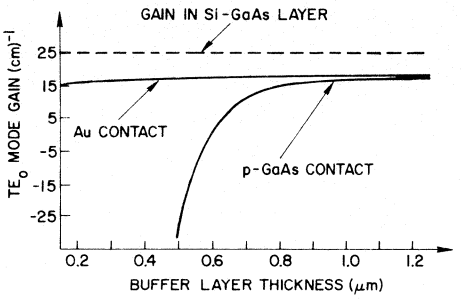

Fig. 2; Dependence of the TE_0-mode gain coefficient on buffer-layer thickness for the cases where the contact (defined in Fig. 1) is either gold or thick GaAs.

or gold, p_0 is the exponential decay factor of the TE_0 mode in the buffer layer, t_b is the buffer-layer thickness, and w_0 is the effective waveguide thickness or mode width $\equiv(2/p_0) + t_g$ (gain-layer thickness).

If $\delta_c = 1$ in (1), implying an AlGaAs-air corrugated interface, then two oppositely directed leaky waves are generated from unidirectional TE_0 light propagating in the waveguide. The wave which appears on the air side of the interface is called the transmitted leaky wave and the one which appears on the AlGaAs side of the interface is called the reflected leaky wave. The sum of the loss coefficients due to the transmitted leaky wave $\alpha_0^{(-1T)}$ and the reflected leaky wave $\alpha_0^{(-1R)}$ is equal to the expression for $\alpha_0^{(-1)}$ given in (1). They are related by the equation [18]

$$\alpha_0^{(-1R)} = n_b \alpha_0^{(-1T)}. \tag{2}$$

If it is assumed that $ka = 0.31$ (about one-half the maximum value which can be achieved if selective etching is used to make the grating [19]) and that t_b is 415 nm, then $\alpha_0^{(-1T)}$ is about 1 cm^{-1} (see the Appendix for other values used in the computation). This implies that in this configuration it takes a distance of 100 μm to convert about 1 percent of the power in a unidirectional TE_0 mode into transmitted leaky-wave power traveling normal to the waveguide plane. Although the loss coefficient associated with the reflected leaky wave is about 3.5 times larger than that associated with the transmitted leaky wave, the reflected wave is not easily utilized since its emission direction is into the relatively thick (~100-μm) lossy GaAs substrate normally present in these devices. If $\delta_c = 0$ in (1), implying an AlGaAs-gold corrugated interface, then only one leaky wave is generated, the reflected leaky wave. In this case, the associated loss coefficient $\alpha_0^{(-1R)} = \alpha_0^{(-1)}$ is equal to about 6 cm^{-1}. Since its direction is the same as the reflected leaky wave generated at the AlGaAs-air corrugated interface, the power in the beam cannot be fully utilized unless a window is opened for its exit through the lossy GaAs substrate. The evanescent wave interaction giving rise to these leaky waves is depicted in Fig. 3 for the case where two counter-running TE_0 waves, R_0 and S_0, are propagating in the waveguide. In drawing Fig. 3, it has been assumed that λ is not quite equal to $n_0 d$, as was previously assumed. In this case, the leaky waves associated with R_0 and S_0, viz., $R_0^{(-1)}$ and $S_0^{(-1)}$, are not emitted normal to the waveguide plane, and consequently are distinguishable from each other. The emis-

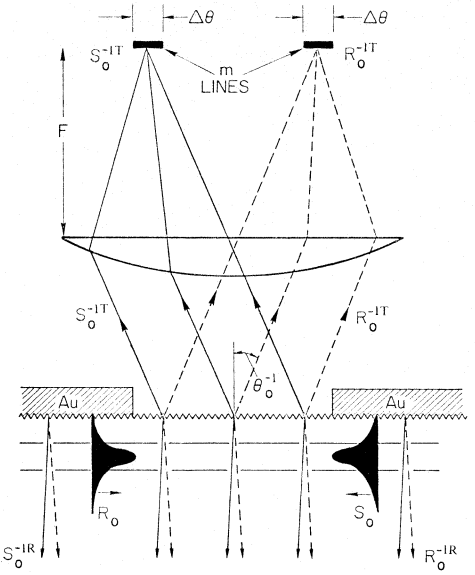

Fig. 3. Leaky waves $R_0^{(-1)}$ and $S_0^{(-1)}$ generated by the evanescent wave interaction of the counter-propagating waves R_0 and S_0 with the corrugated interface. $R_0^{(-1T)}$ and $S_0^{(-1T)}$ have spot sizes in the focal plane of the lens equal to the product of the lens focal length F and the beam divergence $\Delta\theta$. Aperture A mentioned in text is the opening between the gold contact pads.

sion angle $\theta_0^{(-1)}$ for first-order leaky waves which escape into the air (in this case, the transmitted leaky waves emitted through aperture A, viz., $R_0^{(-1T)}$ and $S_0^{(-1T)}$), is given by [5]

$$\sin\theta_0^{(-1)} = n_0 - \frac{\lambda}{d}. \tag{3}$$

For the case shown it is assumed that $n_0 \gtrsim \lambda/d$, so that the leaky waves are forward waves rather than backward waves. A forward leaky wave is one whose component in the plane of the waveguide has the same direction as the guided wave from which it is generated [15].

Since each leaky wave has a well-defined emission direction, they can be focused to different locations in the back focal plane of a lens as shown in Fig. 3. The spot size ΔX, or equivalently the beam divergence, $\Delta\theta \equiv \Delta X/F$, depends on a superposition of two divergence functions: $\Delta\theta(A)$—the divergence due to the finite spatial width A of the output aperture A; and $\Delta\theta(\Delta\lambda)$—the divergence due basically to the finite spectral width $\Delta\lambda$ of the laser oscillation.[2] An approximate expression for $\Delta\theta(A)$ is [20]

$$\Delta\theta(A) \cong \lambda/A \tag{4}$$

and an approximate expression for $\Delta\theta(\Delta\lambda)$, obtained from (3), is

$$\Delta\theta(\Delta\lambda) \cong |\Delta n(\Delta\lambda)| + |\Delta\lambda/d|. \tag{5}$$

In writing (5), it has been assumed that the mode dispersion is normal, i.e., n increases as λ decreases, so that the two terms on the right-hand side of (5) always add. In typical AlGaAs lasers, the dispersion term $\Delta n(\Delta\lambda)$ is dominated by the $\Delta\lambda/d$

[2] In computing $\Delta\theta(\Delta\lambda)$ for a given laser, it will be assumed that $\Delta\lambda$ is equal to the full width at half height of the laser-power spectral-envelope function.

term. If the output aperture is large and the laser bandwidth is small, output beams with very low divergence will be obtained. For example, the leaky waves generated in the corrugated DFB dye-laser devices described in [5] had measured divergences of less than 0.002°. If beam width in the lateral dimension of the waveguide is narrow (due, for example, to filamentary lasing), then the two focused spots of width $\Delta\theta$ shown in Fig. 3 will appear as two lines of width $\Delta\theta$ when viewed along the waveguide normal. Lines of this type, usually called mode lines or ***m*** lines [21] can be utilized to provide a great deal of information about the nature and behavior of such devices, especially those that support two or more transverse modes.

If $n_0 = \lambda/d$, then $\sin\theta_0^{(-1)}$ is equal to zero and all $R_0^{(-1)}$ and $S_0^{(-1)}$ leaky waves are directed precisely normal to the waveguide plane. In this situation, the two ***m*** lines in Fig. 3 coalesce into one ***m*** line in the center of the field and the second-order diffracted wave $R_0^{(-2)}$ feeds energy into S_0 while $S_0^{(-2)}$ feeds energy into R_0. Using the same assumptions and symbol definitions as those used in deriving (1), an expression can be derived for the backward-coupling coefficient specifying this second-order DFB process [18]

$$\kappa_{00}^{(-2)} \cong (ka)^2 \frac{n_g^2 - n_0^2}{2n_0 w_0} \sqrt{0.5(n_b^2 - \Delta_c)} \exp(-p_0 t_b). \qquad (6)$$

The new symbol Δ_c is equal to $+n_b$ or $-2(5.3)^2$ depending on whether the corrugated interface is AlGaAs-air or AlGaAs-gold, respectively. The argument of the exponential decay term has the value $(-p_0 t_b)$ rather than the value $(-2p_0 t_b)$ used in (1) since $\kappa_{00}^{(-2)}$ describes a coupling between mode amplitudes [22]. Using the same values as used in evaluating (1), we obtain $\kappa_{00}^{(-2)} \cong 26\ \text{cm}^{-1}$ for an AlGaAs-air corrugated interface and $\kappa_{00}^{(-2)} \cong 73\ \text{cm}^{-1}$ for an AlGaAs-gold corrugated interface. Although these values are fairly large, it is the product of $\kappa_{00}^{(-2)}$ with L, the device length, that determines to a large extent the degree to which the DFB mechanism influences device behavior. For example, it can be shown using the theory of Kogelnik and Shank [22] that the threshold for DFB oscillation is equal to the threshold for cleaved-facet mirror-feedback (MFB) oscillation in GaAs lasers when $\kappa L \cong 3.5$. Consequently, if the value of $\kappa_{00}^{(-2)}$ is less than $100\ \text{cm}^{-1}$ and device lengths are less than 350 μm, as is true for the devices in our experiments, cleaved-facet MFB oscillation will occur at lower pump currents than DFB oscillation. Of course, what actually happens in devices where the DFB and MFB mechanisms are comparable in strength can be quite varied depending on such factors as the differences between the frequency of peak gain and the resonant DFB frequency and the longitudinal mode frequencies [8], [23], [24], gain saturation [25], etc. For example, if we assume that $n_0 d$ is not equal to the peak-power MFB oscillation wavelength but is within a few nanometers of this value, then both DFB and MFB oscillation might be obtained separately. In this case, one would observe two ***m*** lines due to MFB oscillation as shown in Fig. 3 and one ***m*** line in the center of the field due to DFB oscillation. Some of the GC lasers studied in our experiments satisfied this "few nanometer" criterion, but none of them showed a single ***m*** line in the center of the far field even at high-current drive levels. These results are discussed in more detail in the next section. The reader will be able to follow the flow of the presentation in Section III more easily if he keeps in mind that the experimental approach was to attempt to fabricate GC TE_0 diode lasers which emit transmitted leaky waves normal to the waveguide plane—single ***m*** line devices. The longitudinal modes of such devices will normally give rise to unresolved fine structure within the ***m*** line.

III. Device Fabrication and Experimental Results

As discussed in Section II, GC lasers which emit leaky waves normal to the waveguide plane satisfy the relation $\lambda = n_0 d$. Consequently, in order to determine the corrugation period d to be fabricated into the DH material used to make these devices (see Fig. 1), one must know the wavelength λ that the material prefers to lase at and the effective refractive index n_0 of the TE_0 mode of the DH waveguide. The TM_0 mode is not considered since material of this type almost invariably lases on the TE_0 mode of the waveguide. The procedure then is to measure the output λ of some conventionally fabricated diodes and to estimate n_0 using calculation techniques described in the previous section. A grating with period $d = \lambda/n_0$ is then fabricated onto a piece of the DH material using the selective etching techniques described in [19]. In our case, the measured λ was in the vicinity of 865 nm and n_0 was the calculated value 3.532 for the model shown in Fig. 1. Consequently, a grating with $d = 244.9 \pm 0.1$ nm was fabricated.

The next procedure is to spin photoresist onto the corrugated wafer and open up a periodic array of holes into which 500-nm-thick gold contact pads are electroplated. It is important, of course, that the surface be properly cleaned and that a high-quality gold electroplating solution be used if good contacts are to be obtained. After plating and cleaning, a new layer of photoresist is spun onto the material and a parallel array of slots is opened between the contact pads. An etchant is then utilized to remove sufficient material at the bottom of the slots so that the resulting grooves electrically isolate the individual lasers on bars cleaved from this material. An operating GC diode laser on one such bar is shown in Fig. 4. The photograph was obtained from a TV monitor screen connected to an infrared-sensitive camera which views the laser through magnifying optics. The 70-μm dimension is the width of the output aperture A described in Section II and shown in a side view in Fig. 3. The bright-dark striations observed across the output aperture are due to interference effects in the glass plate covering the photocathode of the TV camera.

The main features of device operation which can be observed in Fig. 4 are: 1) the device lases in filaments; and 2) the strongest filaments tend to lase along the edges of the electroplated gold pads. These features were characteristic of almost all the GC lasers studied in the experiments. The particular device shown is lasing with a pulsed drive current twice its threshold drive current of 250 mA/pad. This corresponds to a threshold current density of about 3300 A/cm^2 since the dimensions of both contact pads are about 60 μm by 125 μm. The threshold current density for single-pad pumping was about 14 500 A/cm^2. On the other hand, uncorrugated de-

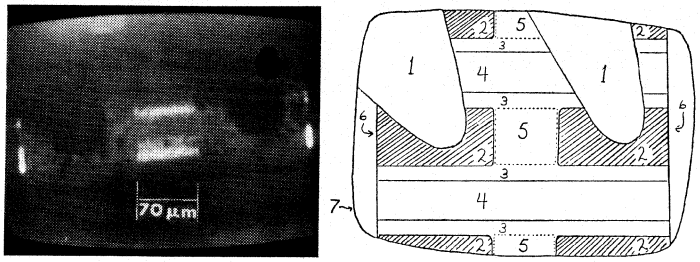

Fig. 4. Left: top view of an operating GC diode laser. It is located on a cleaved bar with several similar devices. The various features are numbered in the diagram on the right. 1) Contacting pins. 2) Gold contact pads. 3) Corrugated mesa surface. 4) Electrical isolation grooves. 5) Output aperture for transmitted leaky waves. Brightness distribution in corresponding area in photo at left indicates that lasing filaments along edges of contact pads are strongest. 6) Cleaved facets. Bright spots along cleaved facets in photo at left are due to scattered light coupled out from lasing filaments. 7) Edge of TV monitor screen.

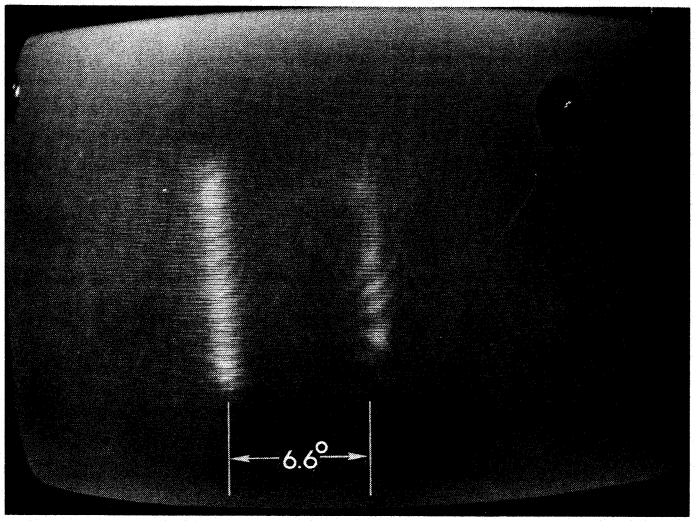

Fig. 5. Far-field pattern of the GC diode laser shown in Fig. 4. The two mode lines (*m* lines) are 6.6° apart and the beam divergence obtained from the left *m* line is about 1.2° by 11°.

vices with about the same cavity length and no openings in the contact layer had typical threshold current densities in the vicinity of 2000 A/cm^2. The current pulses used in all these experiments were bell shaped with a full width at half current of 450 ns. By changing the magnifying optics appropriately, the far field of the laser shown in Fig. 4 could be imaged onto the photocathode of the TV camera. A photograph of the TV screen in this case is shown in Fig. 5. As can be observed, the far field consists basically of two *m* lines of the type described in Section II. The bright–dark striations are due to the same interference effects as occur in the near-field photograph in Fig. 4. The angular scale is determined with good accuracy by replacing the laser with a photolithographically fabricated double slit which, when illuminated by a He–Ne laser, produces the well-known Young's double-slit interference pattern on the TV screen.

Before proceeding to discuss the fact that two *m* lines rather than one are observed and that they have different relative intensities, it is instructive first to compare the linewidth of the well-resolved *m* line on the left in Fig. 5 with the values calculated using (4) and (5). From (4), $\Delta\theta(A) \cong 0.7°$, and from (5), $\Delta\theta(\Delta\lambda) \cong 0.9°$. In evaluating (5), it was assumed that the $\Delta\lambda/d$ term was 4 times larger than the dispersion term and that $\Delta\lambda$ was approximately equal to 3 nm, the measured value. The theoretical value of $\Delta\theta$ to be compared with the measured $\Delta\theta$ is expected to be somewhat greater than 0.9° although its exact value is not easy to predict. The relatively large value obtained from Fig. 5, $\Delta\theta \cong 1.2°$, is easily accounted for if several filaments are lasing and the dispersion term is effectively larger due to mode-pushing effects. This view is supported by the fact that the higher threshold GC devices which tended to run in one or two well-separated filaments had *m* lines usually about 1° in width. The *m* line length of about 11° in Fig. 5 indicates, using (4), that the lasing filaments are about 4.5 μm wide. Most of the higher threshold devices measured had *m* line lengths in the vicinity of 15°, implying filament widths of about 3.3 μm.

Assuming that the two *m* lines of Fig. 5 are derived from $R_0^{(-1T)}$ and $S_0^{(-1T)}$ leaky waves, as shown in Fig. 3, then the fact that one line is weaker implies that R_0 is stronger than S_0 or vice versa. This was verified by noting that when one of the contacting pins shown in Fig. 4 was removed and the current through the other pad increased sufficiently to get strong lasing, the weak line disappeared almost completely. When the removed contacting pin was cleaned and replaced, both *m* lines were observed and were almost equally bright. The new threshold current in this case was only slightly lower than that previously stated. The fact that one *m* line disappears when one pad is pumped implies that the unpumped waveguide in this material is quite lossy since the wave traveling through the unpumped region is apparently reduced in intensity by at least an order of magnitude rather than the factor of 4 or so that would be expected from the cleaved facet and leaky-wave losses.

The question as to why two *m* lines are observed rather than one *m* line as predicted by the design criterion, $\lambda = n_0 d$, is best answered by assuming that the value of n_0 used in the design was incorrect. This assumption implies that the DH waveguide in the laser of Fig. 4 is not the same as the theoretical model shown in Fig. 1. Detailed scanning electron microscope (SEM) measurements on the cleaved facet of the laser in Fig. 4 showed in fact that the gain-layer thickness was very close to 0.2 μm rather than the 0.3 μm expected. The buffer-layer thickness, somewhat difficult to measure due to edge noise, was about the expected thickness of 0.42 μm. In addition, photoluminescence measurements on a beveled piece of the DH material indicated that more aluminum was present than assumed in the model—about 30 percent in the n-AlGaAs layer and about 25 percent in the buffer layer. Making the appropriate changes in the resonance equation parameters listed in the Appendix, and using the observed peak-power wavelength of 867 nm, a new value of the effective refractive index of the mode was obtained, $n_0 = 3.487$. Using these values in (3), one obtains $\theta_0^{(-1)} = -3.0°$, in good agreement with the measured value of 3.3° obtained from Fig. 5. The negative sign in front of the theoretical value of $\theta_0^{(-1)}$ arises because $n_0 < \lambda/d$ and, as mentioned in Section II, implies the existence of backward leaky waves. This was verified in the

single-pad pumping experiment previously described by relating the position of the single ***m*** line in the far field to the known direction of propagation within the waveguide of the strong component of the lasing mode giving rise to this ***m*** line.

Since the peak-power wavelength in the previously mentioned device was 867 nm, one would not expect the DFB mechanism to be operable since the DFB resonant wavelength of $n_0 d = 854$ nm would be too far removed from the peak gain region. However, other GC lasers fabricated from the same corrugated material had peak-power wavelengths and ***m*** line separations in the vicinity of 859 nm and 2°, respectively, consistent with the same $n_0 d$ previously given. As discussed at the end of Section II, one might expect that an 859 nm-2° device driven at high current would exhibit a single DFB ***m*** line between the two MFB ***m*** lines since there should be some gain available at 854 nm. Since such behavior was not observed and since the spectral width (full width at half laser power) for all devices was in the vicinity of 3 nm, it was concluded that the DFB mechanism was not operable in any of these devices.[3] This conclusion does not prove that the DFB mechanism could not be operable in devices with the theoretical coupling coefficients calculated in Section II since the detailed leaky-wave output power and corrugation-depth measurements needed to verify the existence of the coupling coefficients in our devices were not performed in this series of experiments.

IV. Conclusions

Corrugated DH-AlGaAs diode lasers were fabricated and low-divergence (in one dimension) leaky-wave output beams were observed when the devices were electrically pulsed at room temperature. It was concluded from ***m*** line and wavelength measurements that the DFB mechanism was not operable in the devices examined. From a practical point of view, it would be desirable to have a sufficiently strong DFB mechanism so that only one low-divergence narrow-bandwidth leaky laser beam would be emitted precisely normal to the plane of the waveguide. In addition, it would be desirable to cover aperture A with a gold contact (Fig. 3), cover the cleaved facets with a high-reflectivity protective coating, and exit the reflected leaky wave through a hole in the GaAs substrate. Based on these experiments, it appears that it may be possible to fabricate CW room-temperature devices of this type. Such devices would prove useful in optical communications and other applications where low-divergence laser beams are of importance.

Appendix

The two TE_0-mode gain-coefficient dependences on buffer-layer thickness (t_b) shown in Fig. 2 are obtained from exact solutions of the four-layer waveguide resonance equation [26] under the following assumptions:

1) the two contact layers and the lower n-AlGaAs layer are very thick;
2) the gain layer is 0.3 μm thick, as shown in Fig. 1;
3) the complex refractive indices of the layers at vacuum wavelength $\lambda = 865$ nm are [27], [28]: GaAs contact layer $n_c = 3.60 - (0.001)i$; gold contact layer $n_c = 0.16 - (5.3)i$; buffer layer and n-$Al_{0.2}Ga_{0.8}As$ layer $n_b = 3.47$; gain layer $n_g = 3.60 + (0.0017)i$.

The values of the parameters listed below can be utilized to evaluate (1) and (6) in the text. These values are roughly the same for all values of t_b in both curves of Fig. 2. The parameters are: 1) effective refractive index $\equiv n_0 = 3.532$; 2) real part of transverse wave vector in buffer layer $\equiv p_0 = 4.76$ μm^{-1}; and 3) effective waveguide thickness ≡ mode width $w_0 = 718$ nm. The values of the coupling coefficients calculated from (1) and (6) are reliable only if the corrugation is sinusoidal, $ka < 0.1$, $n_b \lesssim n_g$ and the gold contact is a good reflector, i.e., $n(\text{gold}) \cong -5.3i$.

Acknowledgment

The authors wish to thank the IBM Injection Laser Group, particularly J. Blum and K. K. Shih, for providing them with the DH material used in these experiments and for helpful advice. They also wish to thank V. Maniscalco, J. Marinace, B. Monemar, and A. Tuttle for useful technical assistance and advice, and L. Kuhn, E. Lean, A. Reisinger, E. Spiller, and J. White for many helpful discussions.

References

[1] R. Ulrich, "Efficiency of optical grating couplers," *J. Opt. Soc. Amer.*, vol. 63, pp. 1419-1431, 1973.
[2] M. L. Dakss, L. Kuhn, P. F. Heidrich, and B. A. Scott, "Grating couplers for efficient excitation of optical guided waves in thin films," *Appl. Phys. Lett.*, vol. 16, pp. 523-525, 1970.
[3] H. Kogelnik and T. P. Sosnowsky, "Holographic thin film couplers," *Bell Syst. Tech. J.*, vol. 49, pp. 1602-1608, 1970.
[4] H. Kogelnik and C. V. Shank, "Stimulated emission in a periodic structure," *Appl. Phys. Lett.*, vol. 18, pp. 152-154, 1971.
[5] P. Zory, "Laser oscillation in leaky corrugated optical waveguides," *Appl. Phys. Lett.*, vol. 22, pp. 125-128, 1973.
[6] R. F. Kazarinov and R. A. Suris, "Injection heterojunction laser with a diffraction grating on its contact surface," *Sov. Phys.–Semicond.*, vol. 6, pp. 1184-1189, 1973.
[7] K. O. Hill and A. Watanabe, "Passive-core corrugated-waveguide laser," *Appl. Opt.*, vol. 12, pp. 430-433, 1973.
[8] S. R. Chinn, "Effects of mirror reflectivity in a distributed-feedback laser," *J. Quantum Electron.*, vol. QE-9, pp. 574-580, June 1973.
[9] D. R. Scifres, R. D. Burnham, and W. Streifer, "Distributed feedback single heterojunction GaAs diode laser," *Appl. Phys. Lett.*, vol. 25, pp. 203-206, 1974.
[10] H. M. Stoll and D. H. Seib, "Distributed feedback GaAs homojunction injection laser," *Appl. Opt.*, vol. 13, pp. 1981-1982, 1974.
[11] M. Nakamura, K. Aiki, J. Umeda, A. Yariv, H. W. Yen, and T. Morikawa, "GaAs-$Ga_{1-x}Al_xAs$ double heterojunction distributed feedback diode lasers," *Appl. Phys. Lett.*, vol. 25, pp. 487-488, 1974.
[12] D. R. Scifres, R. D. Burnham, and W. Streifer, "Highly collimated laser beams from electrically pumped SH GaAs/GaAlAs distributed feedback lasers," *Appl. Phys. Lett.*, vol. 26, pp. 48-50, 1975.
[13] P. G. McMullin, J. Blum, K. K. Shih, A. W. Smith, and G. R. Woolhouse, "Effect of doping on degradation of GaAs-$Al_xGa_{1-x}As$ injection lasers," *Appl. Phys. Lett.*, vol. 24, pp. 595-597, 1974.

[3] It should be pointed out that the nonobservation of a single ***m*** line in the center of the far field is not in itself proof that the DFB mechanism is inoperative since the two leaky waves contributing to this ***m*** line may destructively interfere.

[14] N. J. Harrick, *Internal Reflection Spectroscopy.* New York: Interscience, 1967.
[15] T. Tamir, "Inhomogeneous wave types at planar interfaces: III–Leaky waves," *Optik*, vol. 38, pp. 269–297, 1973.
[16] J. H. Harris, R. Shubert, and J. N. Polky, "Beam coupling to films," *J. Opt. Soc. Amer.*, vol. 60, pp. 1007–1016, 1970.
[17] P. K. Tien and R. Ulrich, "Theory of prism-film coupler and thin-film light guides," *J. Opt. Soc. Amer.*, vol. 60, pp. 1325–1337, 1970.
[18] P. Zory, *Semiconductors and Semimetals.* New York: Academic, to be published.
[19] L. Comerford and P. Zory, "Selectively etched diffraction gratings in GaAs," *Appl. Phys. Lett.*, vol. 25, pp. 208–210, 1974.
[20] J. W. Goodman, *Introduction to Fourier Optics.* San Francisco: McGraw-Hill, 1968, p. 63.
[21] P. K. Tien, R. Ulrich, and R. J. Martin, "Modes of propagating light waves in thin deposited semiconductor films," *Appl. Phys. Lett.*, vol. 14, pp. 291–294, 1969.
[22] H. Kogelnik and C. V. Shank, "Coupled-wave theory of distributed feedback lasers," *J. Appl. Phys.*, vol. 43, pp. 2327–2335, 1972.
[23] S. Wang, "Principles of distributed feedback and distributed Bragg-reflector lasers," *IEEE J. Quantum Electron.*, vol. QE-10, pp. 413–427, Apr. 1974.
[24] W. Streifer, D. R. Scifres, and R. D. Burnham, "Longitudinal modes in distributed feedback lasers with external reflectors," *J. Appl. Phys.*, to be published.
[25] K. O. Hill and A. Watanabe, "Envelope gain saturation in distributed-feedback lasers," *Appl. Opt.*, to be published.
[26] A. Reisinger, "Characteristics of optical guided modes in lossy waveguides," *Appl. Opt.*, vol. 12, pp. 1015–1025, 1973.
[27] H. C. Casey, D. D. Sell, and M. B. Panish, "Refractive index of $Al_xGa_{1-x}As$ between 1.2 and 1.8 eV," *Appl. Phys. Lett.*, vol. 24, pp. 63–65, 1974.
[28] *American Institute of Physics Handbook*, 3rd ed. New York: McGraw-Hill, 1972.

Integrated Twin-Guide AlGaAs Laser with Multiheterostructure

Y. SUEMATSU, MEMBER, IEEE, M. YAMADA, AND K. HAYASHI

Abstract—**An integrated twin-guide (ITG) laser which has an active waveguide for laser oscillation and an external waveguide for the light output is proposed as an integrated-optics laser or as a new semiconductor laser, and its properties are investigated theoretically and experimentally. ITG lasers were constructed in the form of an AlGaAs multiheterostructure, and their preliminary characteristics were obtained with both optical pumping and current injection at room temperature. The end mirrors of the active waveguide were fabricated by a back-sputtering method. The axial mode selectivity was predicted by the analysis and observed experimentally.**

I. INTRODUCTION

ONE OF THE MOST important problems for the realization of monolithic integrated-optical circuits is the formation of an integrated-optics laser with an optical output circuit. Semiconductor lasers, especially AlGaAs double-heterostructure (DH) lasers, are expected to be the most feasible candidates for integrated-optics lasers. A conventional semiconductor laser has already included many functions in itself, such as the current-injection pumping, the direct modulation, and the cavity constructions. However, the problem of the connection to the external waveguide in a monolithic way has not been fully investigated because the conventional semiconductor lasers utilize cleaved faces as the reflecting mirrors. The distributed-feedback laser might be considered along this direction of research [1]–[3]. The vapor-grown GaAs laser, whose mirrors are constructed at the walls of the mask, was also suggested [4].[1]

As another approach, we proposed an integrated twin-guide (ITG) laser [5] which integrates an external waveguide and an optically coupled active waveguide. In this paper we give a summary of the basic experimental characteristics of ITG AlGaAs lasers. This laser consists of an active waveguide (I) for the laser oscillation and an external waveguide (II) through which the laser beam is taken. The oscillating guided waves were coupled between the two waveguides in a way similar to that of a directional coupler. These waveguides were constructed in the form of a multiheterostructure by successive liquid-phase epitaxial growth. The mirror surfaces of the active waveguide were fabricated by RF backsputtering.

Manuscript received November 25, 1974; revised January 20, 1975. This work was supported in part by research foundations of the Monbusho and Electrical Communication Laboratories of the Nippon Telegraph and Telephone Public Corporation.

The authors are with the Department of Electrical and Electronic Engineering, Tokyo Institute of Technology, O-okayama, Meguro-ku, Tokyo, 152 Japan.

[1] During the preparation of this publication, a method for the connection between optical components by a monolithically prepared thick waveguide was also reported in AlGaAs-laser structures [9].

II. Theoretical Behavior of ITG Lasers

An analytical model for the ITG laser is shown in Fig. 1. Dielectric guides form a system of coupled waveguides consisting of guides (I) and (II). Mirrors are located at both ends of each waveguide, so that the resonator consists of a double-cavity type between guides (I) and (II). If mirrors at guide (II) are removed, the resonator becomes a single-cavity type. The coupling between the two waveguides is most effective when the guide system is degenerate [6], i.e., when the propagation constants of each guide are equal at the well-separated condition.[2] The coupled wave is expressed as a combination of the characteristic even and odd modes [7], with propagation constants β_e and β_o, respectively, which are determined by conventional methods [8]. The lengths of the active waveguide (I) and the arm of the external one (II) are l and l_s, respectively. The gains of the coupled waves are calculated by a perturbation term in the wave equation. The resonant and threshold conditions can be obtained from the calculations of the net gain and the phase shift of the coupled waves after one round trip in the resonator. Only typical results are mentioned here assuming the guide system is degenerate. The calculations and detailed discussion will be published later.

Assume the oscillation wavelength is λ, the effective refractive index of guide (I) is n, the reflection coefficients of the ends of active and external waveguides are unity and R, respectively, the net threshold mode gain $2(g - \alpha)l$ for the laser oscillation is shown in Fig. 2(a) with the horizontal axis, the normalized wavenumber. If the external waveguide (II) is lossless, the net mode gain $2(g - \alpha)l$ is expressed using the medium gain factor $\bar{g}$ and loss $\bar{\alpha}$ of guide (I),

$$2(g - \alpha)l \simeq 2(\bar{g} - \bar{\alpha})\,\xi_4 l \tag{1}$$

where ξ_4 is the fractional power of a normalized characteristic mode at guide (I) and becomes $\xi_4 \lesssim \frac{1}{2}$ in the degenerate guide system. The parameter C is the coupling coefficient between two waveguides and is expressed by

$$C = \sin^2\,[(\beta_e - \beta_o)l/2]. \tag{2}$$

The threshold gain shows minimum value $(g - \alpha)_{\min}$ at $1/\lambda = (2m + 1)\pi/(4\pi n l_s)$ and increases for other values of λ, thereby providing axial mode selection in the ITG laser, particularly for the range of $C < 0.5$. The increasing rate of threshold gain is shown in Fig. 2(a) by dashed lines.

To consider this complicated system as a conventional single-guide laser, we define an equivalent reflection coefficient R_{eq} which shows overall power reflectivity at the end planes of the guide (I), as shown in Fig. 1. The relation between R_{eq} and the reflection coefficient R at the output end is shown in Fig. 2(b), for the minimum threshold gains, $2(g - \alpha)_{\min}l$. If there are no reflections at the output ends, namely $R = 0$ or nonresonant operation of the external guide, then $R_{eq} = 1 - C$. Using this R_{eq}, the threshold equation is written by

$$(\bar{g} - \bar{\alpha})\,\xi_4 = \ln\,(1/R_{eq})/l. \tag{3}$$

[2]The coupling problem between a slab laser and a slab waveguide was also treated at a weakly coupled condition by [10].

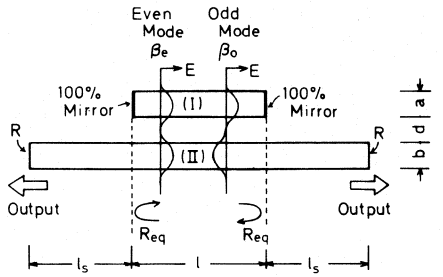

Fig. 1. Analytical model of the ITG laser.

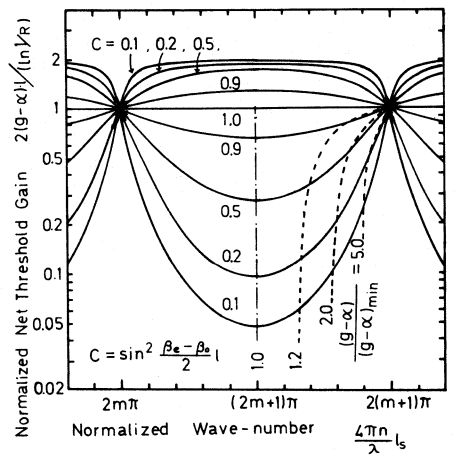

(a)

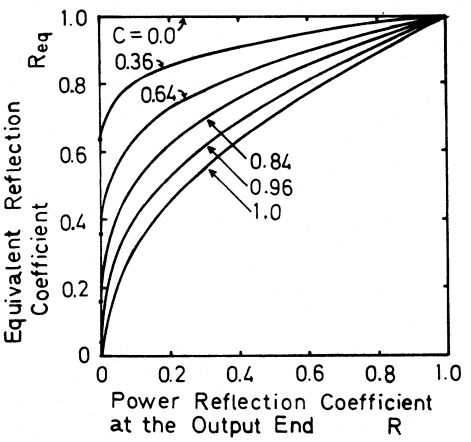

(b)

Fig. 2. (a) Threshold gain versus oscillating wavelength. (b) Equivalent reflection coefficient R_{eq} versus reflection coefficient R at the output ends.

The total power efficiency is also expressed analogous to that of the conventional single-guide laser using R_{eq}.

Experimentally, the assumption of degeneracy of waveguides is not always satisfied. In the case of weak coupling, the coupling is severely reduced by a small parameter deviation from the degenerate condition, and the effect decreases with increasing the coupling, or decreasing the separation d [6]. In the case of strong coupling, the situation is a little different and complicated. In this case, coupling does not increase with decreasing d for very small d, and it is not so severely affected by the parameter deviations.

III. Fabrication of an ITG AlGaAs Laser

A. Determination of the Guide Parameters

The thicknesses of two waveguides a and b and refractive indices of each layer were chosen to give identical propagation constants β_I and β_{II} when the two waveguides are well separated. Efficient coupling is not obtained for $\beta_I \neq \beta_{II}$, as is likely to be the case in the experiment. However, this mismatching becomes more tolerable if the distance between the guides d is decreased. Therefore d was chosen as small as the limitation of the fabrication technique would permit.

B. Fabrication Process of an ITG AlGaAs Laser

$Al_xGa_{1-x}As$ multilayers were grown on the (100) face of the GaAs substrate using successive liquid-phase epitaxial growth. The layer thicknesses and Al contents of an actual ITG AlGaAs laser are shown in Fig. 3. These device parameters are almost identical to the ones required analytically. Since the Al content of the external waveguide was larger than that of the active waveguide, the absorption loss of the external waveguide was small at the oscillating wavelength. The p-n junction for the current injection was the lower boundary of the active waveguide. The p-type and n-type layers were doped with Ge and Sn, respectively.

Subsequently, we put a mask on the (100) surface of the aforementioned AlGaAs wafer for backsputtering, as shown in Fig. 4(a). The mask was a cleaved GaAs strip approximately 300 μm wide. The (110) surfaces of the mask were arranged to be parallel to (110) surfaces of the wafer within a few degrees. The exposed parts of wafer were etched off by the RF backsputtering, as shown in Fig. 4(b). The Ar gas pressure was 8×10^{-3} torr, the supplied field intensity was 100 V/cm, and the current density was 0.8 mA/cm^2. These conditions gave an etching rate of about 1 μm/h. The newly formed (110) walls were used as the mirror surfaces of the active waveguide, as indicated in Fig. 4(c). As shown in Fig. 5, the flatness of these (110) surfaces was not so inferior to that of the cleaved ones.

In the case of current-injection ITG lasers, all of the back-sputtered surfaces were coated with a RF sputtered glass film (Corning 7059) to prevent the flow of current. Metal electrodes were applied after the glass coating. The mirror surfaces of the active waveguide were also coated with metal (Au) to increase the reflectivity and to prevent completely the direct output through these surfaces. The end surfaces of the external waveguide for the output were prepared by cleaving.

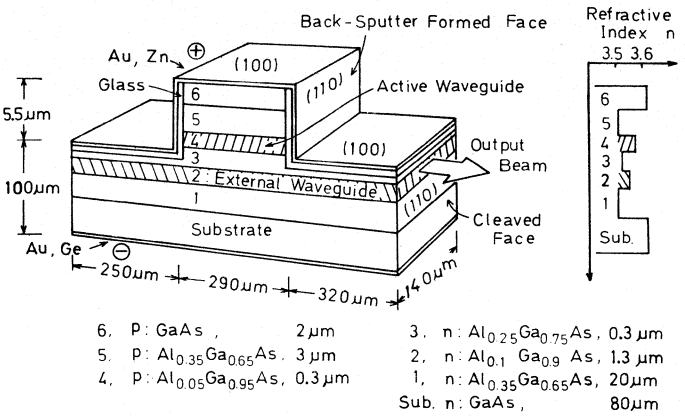

Fig. 3. Construction of the ITG laser.

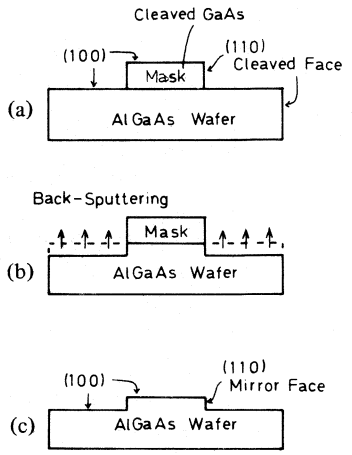

Fig. 4. Mirror fabrication by the back-sputtering method.

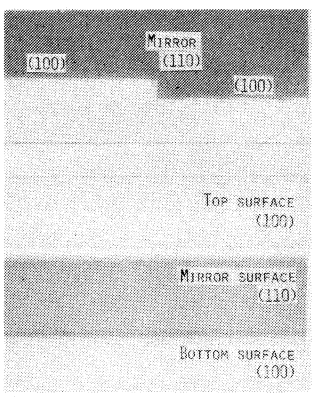

Fig. 5. Photographs of the back-sputter faces.

C. Experimental Results

Firstly, we examined the applicability of the back-sputter mirrors. Several DH lasers were constructed with three-layer AlGaAs prepared by epitaxial growth. All of the layers were n-type for the convenience of optical pumping. The end mirrors of the active waveguide were fabricated by back-sputtering. This DH laser was optically pumped by the second harmonics (λ - 0.53 μm) of a Q-switched YAG laser at liquid-nitrogen temperature. The pumping beam was focused to a stripe shape of 30×300 μm^2 with maximum peak-power density of 1.5×10^4 W/cm^2. The pulse rate was 400 Hz with a pulsewidth of 100 ns. The pumping power is considered to be absorbed in the top layer, namely the cladding of the active layer. Thus excited free carriers are believed to be diffused into the active layer. The oscillating beam was taken out directly from the back-sputter mirror. The output spectrum at the maximum pumping power is shown in Fig. 6. The threshold density of pumping power was 1×10^4 W/cm^2, which was about two times higher than that of the conventionally cleaved

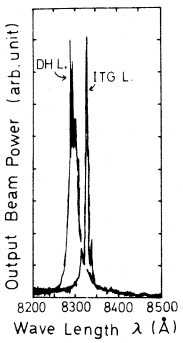

Fig. 6. Output spectra of AlGaAs DH laser with back-sputter mirrors and AlGaAs ITG laser. Both lasers were optically pumped at liquid-nitrogen temperature.

DH lasers prepared from the same wafer due, probably, to the incompleteness of mirrors.

Secondly, several optically pumped ITG lasers with an external waveguide were fabricated [5]. These lasers were constructed from five AlGaAs layers. All layers were n-type. The back-sputter mirrors were coated with Al. The pumping method was the same as that mentioned previously. A typical spectrum for those lasers at 77 K is shown in Fig. 6. The wavelength corresponds to the energy gap of the material of the active waveguide. The spectral width was about 5 Å which was about $\frac{1}{3}$ of the aforementioned DH laser. This spectral narrowing is considered to be due to the twin-guide-resonator structure, as expected from the aforementioned analysis.

Finally, ITG lasers were prepared as shown in Fig. 3, and these were operated by current pulses at room temperature. The pulse rate of the injection current was 500 Hz with the pulsewidth of 10 ns. The central wavelength of the output spectrum was 8420 Å, which corresponds to the energy gap of the material of the active waveguide. The spectra are not yet good enough. The threshold current density was about 1×10^4 A/cm^2. The output light from the external waveguide was observed by an infrared video camera.

IV. Conclusion

An ITG laser was fabricated in the form of an AlGaAs multiheterostructure. The mirrors for the active waveguide were successfully fabricated using the back-sputtering method. The laser operation was examined by both optical pumping at liquid-nitrogen temperature and the pulse current at room temperature. A tendency toward axial mode selectivity was observed experimentally as predicted by the theory outlined in this paper.

The independent choice of laser parameters is possible. For example, the thickness of the active waveguide can be selected thin enough for lower threshold, while that of the external waveguide can be thick enough for reduced beam angle of the output. The absorption loss of the external waveguide may be small at the laser wavelength.

Acknowledgment

The authors wish to thank K. Sugiyama, S. Ibukuro, and S. Akiba for experimental help. They also wish to thank K. Furuya and K. Kishino for their helpful theoretical discussions.

References

[1] H. Kogelnik and C. V. Shank, "Stimulated emission in a periodic structure," *Appl. Phys. Lett.*, vol. 18, pp. 152–154, Feb. 1971.
[2] M. Nakamura *et al.*, "Laser oscillation in epitaxial GaAs waveguides with corrugation feedback," *Appl. Phys. Lett.*, vol. 23, pp. 224–225, Sept. 1973.
[3] D. R. Scifres, R. D. Burnham, and W. Streifer, "Distributed-feedback single heterojunction GaAs diode laser," *Appl. Phys. Lett.*, vol. 25, pp. 203–206, Aug. 1974.
[4] F. A. Blum, K. L. Lawley, W. C. Scott, and W. C. Holton, "Optically pumped grown GaAs mesa surface laser," *Appl. Phys. Lett.*, vol. 24, pp. 430–432, May 1974.
[5] Y. Suematsu, M. Yamada, and K. Hayashi, "A multi-hetero-AlGaAs laser with integrated twin guide," *Proc. IEEE* (Lett.), vol. 63, p. 208, Jan. 1975.
[6] L. O. Wilson and F. K. Reinhart, "Coupling of nearly degenerate modes in parallel asymmetric dielectric waveguides," *Bell Syst. Tech. J.*, vol. 53, pp. 717–739, Apr. 1974.
[7] E. A. J. Marcatili, "Dielectric rectangular waveguide and directional coupler for integrated optics," *Bell Syst. Tech. J.*, vol. 48, pp. 2071–2102, Sept. 1969.
[8] Y. Suematsu and K. Furuya, "Characteristic modes and scattering loss of asymmetric slab optical waveguides," *Trans. Inst. Electron. Eng. Jap.*, vol. 56, pp. 277–284, May 1973.
[9] F. K. Reinhart and R. A. Logan, "Monolithically integrated AlGaAs double heterostructure optical components," *Appl. Phys. Lett.*, vol. 25, pp. 622–624, Nov. 1974.
[10] R. K. Watts, "Evanescent field coupling of thin-film laser and passive waveguide," *Appl. Phys. Lett.*, vol. 44, pp. 5635–5636, Dec. 1973.

Integrated GaAs–$Al_xGa_{1-x}As$ Double-Heterostructure Laser with Independently Controlled Optical Output Divergence

R. A. LOGAN, MEMBER, IEEE, AND F. K. REINHART, MEMBER, IEEE

Abstract—Liquid-phase-epitaxial growth procedures have been used to form a double-heterostructure (DH) laser in which the radiation is taper coupled from the active layer into a passive waveguide. The taper extends smoothly over distances ~100 μm and efficiently couples the radiation from the electrically pumped section into a low-loss adjacent waveguide of comparable dimension (0.5 μm). The passive-waveguide dimension beyond the taper coupler is widened to any desired dimension by inserting a cooling fin (or spacer) into the growth melt, permitting control of the laser output divergence without mode conversion. These structures have been made with the following properties: threshold current density 2.6 kA/cm^2; differential quantum efficiency 28 percent; taper coupling efficiency ~90 percent; and half-power radiation field angles of 48 and 29° from the active (0.5 μm thick) and passive (1.5 μm thick) regions, respectively. Using similar growth procedures, devices have been constructed where the laser radiation is taper coupled into passive waveguides permitting both laser mirrors to be formed in passive regions.

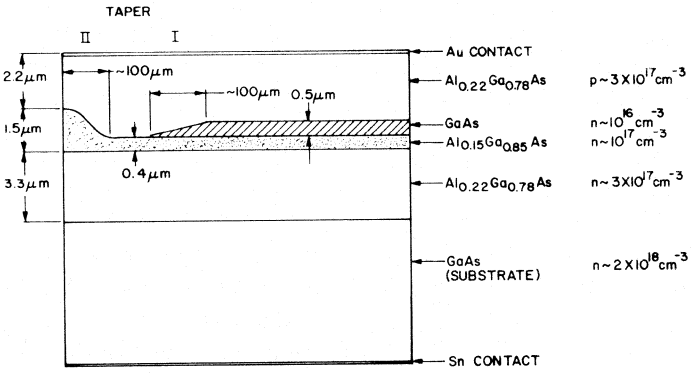

Fig. 1. Schematic cross section of a TCL. Coupling between active- and passive-waveguide sections occurs at taper I. Also shown is a thickness transition of the passive-waveguide section II for control of the radiation pattern.

I. INTRODUCTION

MONOLITHIC integration of double-heterostructure (DH) lasers with passive-single-heterostructure (SH) or DH waveguide elements has been achieved recently using modifications of liquid-phase-epitaxy (LPE) growth procedures to form GaAs–$Al_xGa_{1-x}As$ heterostructures [1]–[3]. The modifications described thus far can be characterized by the method of optical coupling between the active- (pumped) and passive-waveguide sections: 1) the composition coupled laser [1] (CCL) consists of a passive waveguide of increased band gap (and width) contiguous to the active layer in the laser; 2) the phase coupled laser [2] (PCL) is basically a simple sandwich structure of two waveguide layers of differing Al composition that should ideally carry a pair of degenerate modes; 3) the taper coupled laser [3] (TCL), like the PCL, is a simple sandwich structure in which the layer with the low Al concentration (active layer) tapers to zero thickness within the structure, causing the radiation to couple into an adjacent passive-waveguide layer. Continuous-wave integrated lasers could be constructed using any of these coupling methods with greatly varying degrees of difficulty. In this paper we shall restrict our discussion to the CCL and TCL. The growth of CCL structures is very simple in principle and exhibits mode coupling efficiencies from the active to the passive section near unity. These attractive features are, however, restricted by the dramatic increase of the growth rate of the waveguide layer under the melt divider used to grow the bicompositional layer. The increased growth rate makes precise thickness control difficult, particularly for the growth conditions of small melt spacer-to-substrate clearance, used when a sharp composition transition from the active- to the passive-waveguide-layer section is desired. This contrasts with the TCL structure fabrication where a sharp separation between active- and passive-waveguide sections is achieved but where the mode coupling efficiency is not *a priori* expected to be unity. For control of the radiation patterns and the power densities at the mirror of DH lasers, it becomes highly desirable to develop wide passive regions. A combination of the growth techniques for the CCL and TCL adds more flexibility in the fabrication of novel structures permitting construction of devices such as shown in Fig. 1. This structure is basically a TCL with a passive-waveguide thickness variation characteristic of the CCL. Thin active- and passive-waveguide layers provide for a very high taper coupling efficiency and a low-threshold current density. The wide passive waveguide at the mirror reduces the power density at the mirror and the angular width of the radiation field. The thin passive guide also acts as a mode filter if it is sufficiently narrow, thereby ensuring the stability of the transverse mode. The device construction does not preclude any of the techniques of lateral mode stabilization employed in standard DH lasers [4]. In Section II the novel growth procedures are discussed. The measurements and results are presented in Section III.

Manuscript received December 23, 1974; revised February 10, 1975.
The authors are with Bell Laboratories, Murray Hill, N.J. 07974.

II. PROCEDURE

The device of Fig. 1 was grown with conventional LPE procedures [5] modified 1) to produce a layer with a rib of enhanced local growth by insertion of a spacer (or cooling fin) into the melt, and 2) to grow partial layers terminated by smooth tapers using a thin sapphire mask under a portion

of the growth melt. A schematic cross section of the growth boat is shown in Fig. 2(a). The boat was machined from dense carbon[1] and was contained in a pure H_2 ambient in a quartz furnace liner. The layers were grown by successively sliding a (100) oriented rectangular substrate with (110) edges, under saturated melts while cooling the furnace from 850°C at a rate of 0.2°C/min. Dopants and excess GaAs were added to the Ga melts after a preliminary bake out at 800°C for 16 h with access through a porthole in the quartz furnace liner so as not to reoxidize the baked-out Ga. Saturation at the bottom of the melt was insured by use of a saturation seed[2] which preceded the sample to the growth region.

The boat design differs from conventional ones in that each melt is contained in thin-walled (0.5-mm) modules that fit snugly into recesses in the main boat. This design[3] permits great flexibility in layer growth since individual modules can be modified to grow layers of varying complexity without disturbing the growth conditions of adjacent layers. For example, module 2 of Fig. 2(b) contains a thin partition that has permitted growth of a single bicompositional layer from two different adjacent melts in the module [1]. The use of a thin insulating mask at the bottom of module 3 of Fig. 2(b) causes layer growth to occur in two predetermined areas, with layer segments terminating in smooth tapers, decreasing to zero thickness in distances ~100 μm [3], [6].

The construction of the device of Fig. 1 requires the successive growth of four layers with modules 2 and 3 of Fig. 2(b) used to provide the enhanced local growth and tapered segments, respectively. The initial layer was grown using a melt composition [7] to grow $Al_{0.22}Ga_{0.78}As$ at 850°C by sliding the saturating seed and then the substrate under the first module, while cooling the furnace at a rate of 0.2°C/min. The furnace temperature profile was adjusted so that the exposed push rod [on the left side in Fig. 2(a)] extended into a zone about 3°C higher in temperature than the uniform zone of the boat. Thus, on the first movement of the push rod bringing the substrate to module 1, the boat temperature, monitored with a thermocouple as shown in Fig. 2(a), increased about 0.5°C causing melt back into the substrate. This procedure, which is similar to that developed by Hayashi *et al.* [5], causes improved wetting of the first layer to the substrate and improves the quality of the subsequent grown layers as well. As the slider is pushed to subsequent wells, no perceptible temperature rises were observed ($\Delta T \lesssim 0.1$°C).

Identical melt compositions were used on either side of the spacer in module 2 to grow $Al_{0.15}Ga_{0.85}As$. Since the carbon spacer acts as a cooling fin, the growth rate directly under the spacer is greater than that in the adjacent areas, so that layer 2 consists of two flat regions joined by a thicker region whose width is approximately that of the spacer. Using a given spacer, the growth rate under the spacer varies primarily with the spacer to substrate clearance. For a 100-μm-wide spacer

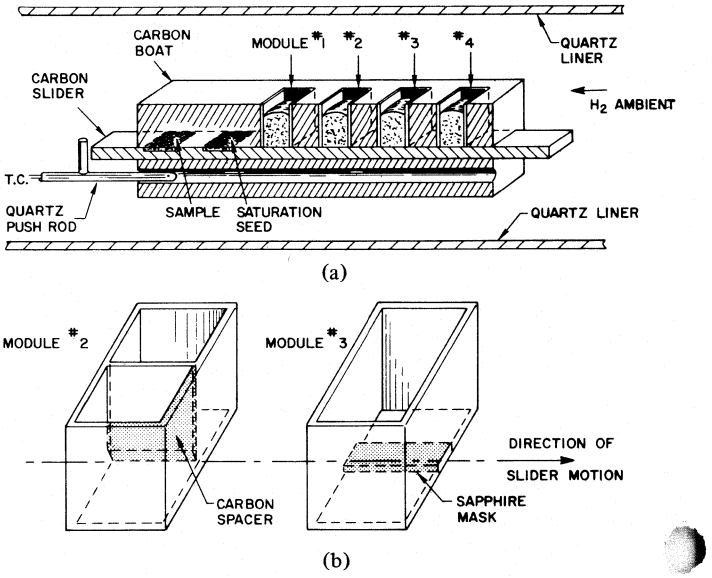

Fig. 2. (a) Schematic cross section of the growth apparatus. (b) Module inserts for obtaining tapers and enhanced local growth. The sample and saturation seed dimensions are ~1 × 1.5 × 0.025 cm^3.

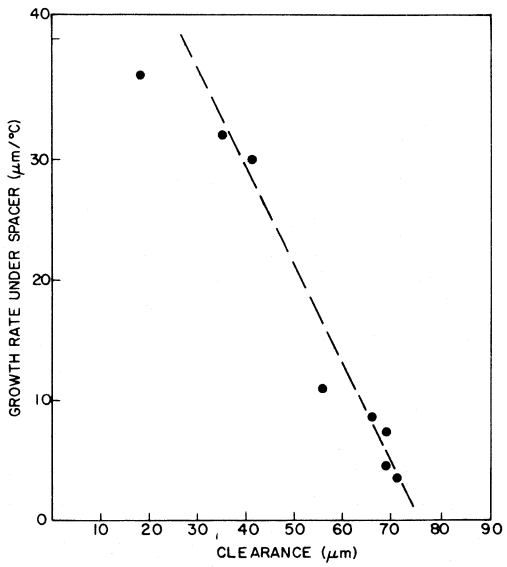

Fig. 3. Growth-rate dependence on the spacer-to-substrate clearance of module 2.

with a lower edge tapered to a width of 25 μm, the growth rate under the spacer is plotted against the spacer-to-substrate clearance in Fig. 3. The growth rates were determined from the observed growth obtained with a furnace cooling of 0.4°C, where the growth rate away from the spacer is ~1.25 μm/°C. The growth rate depends markedly on spacer-to-substrate clearance, as would the thermal gradient at the substrate; however, at the lowest clearance (18 μm) the replenishment of solute to the growth interface became a limiting factor, as evidenced by a small depression in the central region of the layer bulge directly under the spacer.

The growth of the GaAs layer segments with tapered edges was accomplished using the well containing module 3, which contains a 1.1-mm-wide sapphire mask, 0.25 mm thick centered on the same axis as the carbon spacer as shown in Fig. 2(b).

[1] Poco Graphite, Inc., Decatur, Tex., Carbon grade DFP-32.

[2] A procedure developed by L. R. Dawson and described by D. L. Rode, "Isothermal diffusion theory of LPE: GaAs, GaP, bubble garnet," *J. Cryst. Growth*, vol. 20, pp. 13–23, 1973.

[3] This modular boat was designed by B. I. Miller.

The sample-to-sapphire mask clearance was 70 μm, and the separation between tapered layer segments was 1.1 mm, approximately the width of the mask. The layer edges taper smoothly to zero thickness over distances of 100–150 μm. The use of a carbon mask instead of sapphire enhances growth at the layer edge, causing the layer to terminate in an abrupt mound.

The top cladding of $Al_{0.22}Ga_{0.78}$ was grown from a conventional module. Cleaving the sample through the (110) plane centered on the maximum of the bulge in layer 2 produced two sets of devices shown in Fig. 1, all with nearly identical properties. In addition, test pieces were cleaved out of the uniform areas away from the tapers for evaluation. Prior to cleaving, conventional contacts were applied: a 0.1-μm-Zn diffused layer with subsequent evaporation and alloying of Au to the p-layer and Sn to the substrate.

III. Results and Discussion

All measurements were made at room temperature with excitation by 100-ns current pulses. Typical control section lasers cut from the uniform areas of the wafer had active-layer thicknesses, $d \simeq 0.5$ μm. For typical control laser cavity lengths, $l = 0.5$ mm, the threshold current density $j_{th} \simeq 2.6$ kA/cm^2, and the differential quantum efficiencies $\eta_d \simeq 38$ percent with approximately 80 percent of the mirror illuminated when lasing. The corresponding values for short control lasers with $l = 0.25$ mm were $j_{th} = 3$ kA/cm^2 and $\eta_d \simeq 43$ percent with 60 percent of the mirror illuminated when lasing. From these data one deduces an internal quantum efficiency $\eta_i \simeq 80 \pm 20$ percent with a typical loss constant $\alpha \simeq 16$ cm^{-1}.

Taper coupled lasers such as shown in Fig. 1 were cleaved from the wafers with typical active-region length $l_a \simeq 0.6$ mm and $d = 0.5$ μm. This resulted in $j_{th} \simeq 2.6$ kA/cm^2 and $\eta_d \simeq 28$ percent with typically 60 percent of the mirror illuminated in the lasing state. Using the methods described in [3], a taper coupling efficiency t was found to be ≈ 90 percent. In all of the TCL's measured, there was no indication of lasing perpendicular to the taper gradient. Furthermore, the tapers terminated cleanly without any evidence of ribbons of overgrowth beyond the taper section as sometimes previously encountered [3], [6].

All of the TCL's did show a very high degree of polarization of the lasing radiation in TE modes except near the edges of the device. The presence of the tapers only slightly modified the degree of polarization as compared with that in the control units. The polarization observation together with the preceding characterization experiments clearly demonstrate an adequate taper growth control, which permits small-scale integration of optical waveguide components. This coupling method also allows isolation of the active region entirely away from outside surfaces such as cleaved mirrors. A TCL with two active-layer tapers coupling the radiation into a passive waveguide of uniform thickness ($d \sim 0.5$ μm) was constructed and lased with $j_{th} \sim 5$ kA/cm^2 and $\eta_d \sim 14$ percent. In Fig. 4 the far field patterns are shown for a TCL such as shown in Fig. 1. From the narrow active region ($d \approx 0.5$ μm) the full half-power angle for the radiation field was $\approx 48°$, whereas the corresponding value from the wide passive guide ($d \simeq 1.5$ μm) was $\approx 29°$. These values agree quite well with the estimated ones based on the guide dimensions and indices of refraction [8]. The far field patterns were tested at several pumping levels up to currents corresponding to $2j_{th}$. No change in the shape of the patterns was observed over this large current-density range. The mode selection mechanisms, due to the narrow active- and passive-waveguide sections, are therefore very effective. This experiment also demonstrates that mode conversion in the thickness transition in the passive section is negligible, as evidenced by the narrow half-power radiation angle.

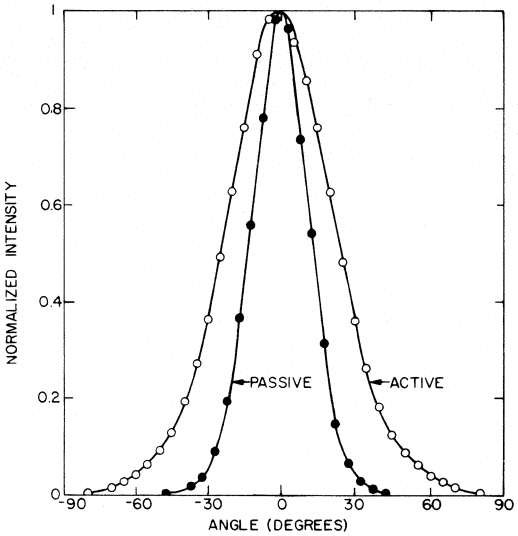

Fig. 4. Far field radiation patterns normalized to peak intensity. Radiation from active side ($d \approx 0.5$ μm)—open circles, and passive side ($d \approx 1.5$ μm)—solid dots.

The modular approach used in the layer growth thus permits a large variation of growth procedures that are required for growing integrated optical devices without constructing an entirely new growth boat for each desired sequence of epitaxial layers. Moreover, the variation of the properties of one layer, obtained by using an appropriately designed module, does not influence the growth conditions of the adjacent layers. While the use of a mask permits growth of layer segments with tapered edges, this technique may also be used to leave an area of the waveguide exposed. The passive-SH-waveguide section thus formed provides electrical isolation between adjacent devices, and on the exposed waveguide one may construct distributed Bragg reflectors [9], [10] or transmission filters [11], or rib waveguides [12] to enhance lateral passive-waveguide mode control and other devices whose operation does not require a regrowth of cladding layers. The ability to independently control the divergence angle permits optimization of the coupling of the laser to optical fibers.

Acknowledgment

The authors wish to thank H. G. White for growing the LPE layers and J. J. Schott for his assistance in device preparation and measurements. They also wish to thank B. I. Miller for generously providing the basic design of the growth boat with modular growth wells, and J. L. Merz, R. C. Miller, and C. H. Henry for many helpful discussions.

REFERENCES

[1] F. K. Reinhart and R. A. Logan, "Monolithically integrated AlGaAs double heterostructure optical components," *Appl. Phys. Lett.*, vol. 25, pp. 622–624, 1974.

[2] Y. Suematsu, M. Yamada, and K. Hayashi, "Integrated twin-guide AlGaAs laser with multiheterostructure," this issue, pp. 457–460.

[3] F. K. Reinhart and R. A. Logan, "GaAs-AlGaAs double heterostructure lasers with taper coupled passive waveguides," *Appl. Phys. Lett.*, vol. 26, pp. 516–518, 1975.

[4] T. P. Lee, C. A. Burrus, B. I. Miller, and R. A. Logan, "$Al_xGa_{1-x}As$ double-heterostructure rib-waveguide injection laser," this issue, pp. 432–435.

[5] I. Hayashi, M. B. Panish, and F. K. Reinhart, "GaAs-$Al_xGa_{1-x}As$ double heterostructure injection lasers," *J. Appl. Phys.*, vol. 42, pp. 1929–1941, 1971.

[6] J. L. Merz, R. A. Logan, W. Wiegmann, and A. C. Gossard, "Taper couplers for GaAs-$Al_xGa_{1-x}As$ waveguide layers produced by liquid phase and molecular beam epitaxy," *Appl. Phys. Lett.*, vol. 26, pp. 337–340, 1975.

[7] M. B. Panish and M. Ilegems, *Progress in Solid State Chemistry*, H. Reiss and J. O. McCaldin, Ed. New York: Pergamon, 1972, vol. 7, pp. 39–83.

[8] H. C. Casey, D. D. Sell, and M. B. Panish, "Refractive index of $Al_xGa_{1-x}As$ between 1.2 and 1.8 eV," *Appl. Phys. Lett.*, vol. 24, pp. 63–65, 1974.

[9] S. Wang, "Principles of distributed feedback and distributed Bragg-reflector lasers," *IEEE J. Quantum Electron.*, vol. QE-10, pp. 413–427, Apr. 1974.

[10] C. V. Shank and R. V. Schmidt, "Optical technique for producing 0.1 μ periodic surface structures," *Appl. Phys. Lett.*, vol. 23, pp. 154–155, 1973.

[11] D. C. Flanders, H. Kogelnik, R. V. Schmidt, and C. V. Shank, "Grating filters for thin film optical waveguides," *Appl. Phys. Lett.*, vol. 24, pp. 194–196, 1974.

[12] F. K. Reinhart, R. A. Logan, and T. P. Lee, "Transmission properties of rib waveguides formed by anodization of epitaxial GaAs on $Al_xGa_{1-x}As$ layers," *Appl. Phys. Lett.*, vol. 24, pp. 270–272, 1974.

Monolithic $Ga_{1-x}In_xAs$ Diode Lasers

F. H. DOERBECK, K. L. LAWLEY, F. A. BLUM, MEMBER, IEEE, AND J. C. CAMPBELL, MEMBER, IEEE

Abstract—**Monolithic homojunction diode lasers have been fabricated from vapor-grown $Ga_{1-x}In_xAs$ ($0 \leq x \geq 0.06$) mesa structures with grown optical facets. The $Ga_{1-x}In_xAs$ lasers have been operated at 77 K, and similar GaAs mesa devices have lased between 77 K and 300 K. Monolithic arrays of up to six mesa lasers on a single substrate have been operated with all lasers oscillating simultaneously.**

I. INTRODUCTION

IN a preliminary letter [1], we reported the fabrication of monolithic GaAs injection mesa lasers with grown optical facets. The present work is based on previous experiments with optically pumped $Ga_{1-x}In_xAs$ mesa lasers [2], [3]. We have now fabricated $Ga_{1-x}In_xAs$ ($0 \leqslant x \leqslant 0.06$) mesa-laser diodes, demonstrating wavelength tunability in a monolithic laser. Also we have successfully operated monolithic arrays of up to six GaAs lasers on a single substrate with all devices oscillating simultaneously. Further details concerning the fabrication and properties of these diode mesa lasers are given in this article.

Manuscript received December 2, 1974; revised February 18, 1975. This work was supported in part by the U.S. Office of Naval Research.

The authors are with Texas Instruments Incorporated, Dallas, Tex. 75222.

Important to the development of integrated optical circuits (IOC's) is the need for a monolithic nondiscrete injection-laser source. Wavelength tunability of the laser is needed for matching regions of low loss for the dielectric waveguides of an IOC and for optical fiber links. Discrete wavelength tunability is achievable with the $Ga_{1-x}In_xAs$ lasers reported here since the laser emission shifts toward longer wavelengths with increasing InAs content. GaAs waveguides then become transparent to the emitted radiation. Only a few percent InAs is needed to achieve low-loss propagation. Thus the $Ga_{1-x}In_xAs$-GaAs system is a good candidate for IOC development.

Another advantage of the diode lasers described here lies in the elimination of cleaving or polishing the optical facets used in conventional discrete-diode laser fabrication. The cleaving process is a major factor in laser yield and may even play a role in limiting laser lifetimes. Growing the optical facets as described here obviates the necessity of cleaving. Also arrays of lasers are readily made using the monolithic techniques described below.

Section II of this article describes the material's growth and fabrication techniques for making the laser. It is particularly noteworthy that all the fabrication steps involve conventional semiconductor processing and photolithography. Measure-

ments of the laser-emission characteristics are described in Section III and conclusions are given in Section IV.

II. Materials and Fabrication

The $Ga_{1-x}In_xAs$ mesas are grown by the selective vapor-epitaxy technique described previously [2], [3] in which growth was restricted to diamond-shaped holes in the SiO_2 mask. The vapor-phase system uses AsH_3, HCl, H_2, and gallium and indium sources. The background doping level for as-grown n-type mesas is approximately 10^{16} cm^{-3}. Higher doping levels ($\sim 10^{18}$ cm^{-3}) are obtained by introducing sulfur into the hydrogen flow. Carrier concentrations are measured by point-contact breakdown on the mesas and Hall measurements on full-surface semi-insulating pilot slices grown with the mesas. The mesas are diamond-shaped pedestals with vertical {111} sides grown on n-type {110} GaAs substrates ($n \sim 10^{18}$ cm^{-3}). The {111} growth planes form the optical cavity. The molar percent of InAs is readily changed by altering the Ga-to-In ratio in the reactor source boats. No grading of the InAs content during growth has been attempted. The InAs content of the mesas is determined by room-temperature photoluminescence measurements.

A p-n junction is formed in the mesas by converting the top part of the mesa to p-type. The technique chosen to accomplish this is diffusion of Zn from Zn-doped SiO_2 layers positioned on the tops of the mesas only. Two techniques are used for making these layers. One is RF discharge deposition of a sandwich structure described previously [2]. Using conventional photolithographic masking, we remove the oxide sandwich from all portions of the slice except the tops of the mesas. A second technique is to implant Zn into a 500-Å-thick layer of SiO_2. This technique eliminates the necessity of photomasking and patterning the doped oxide since the Zn is not implanted in the oxide on the sides of the mesas. The Zn ions are implanted with an energy of 20 keV with a total dose of 10^{16} cm^{-2}. The entire slice is then coated with 2000 Å of undoped SiO_2 to protect the mesa walls during diffusion. The junction-formation steps are shown in Fig. 1. Diffusion of Zn into the slice is accomplished by heating the slice in a nitrogen atmosphere at 800–850°C for periods of 10–40 min. Junction depths of 1–6 μm are obtained with a surface Zn concentration of $\sim 10^{20}$ cm^{-3}. A plot of Zn concentration versus depth for a GaAs device is shown in Fig. 2. These data are taken using a calibrated spreading resistance probe on an angle-lapped device. Some of the devices have been diffused without patterning the Zn-doped oxide so that Zn enters both the sides and the tops of the devices. While this does produce a narrow lossy region at the edges of the optical cavity, low-threshold lasers have been successfully fabricated in this manner.

After removal of the SiO_2 layers, electrical contacts are formed by alloying selectively electroplated gold to the mesa tops and to the back of the slice. Photomasking is used to prevent plating on other parts of the slice. Both full-surface and 2.5-mil stripe contacts are used. Diced chips containing two-six mesa devices each are then soldered to a gold-plated header (mesa up).

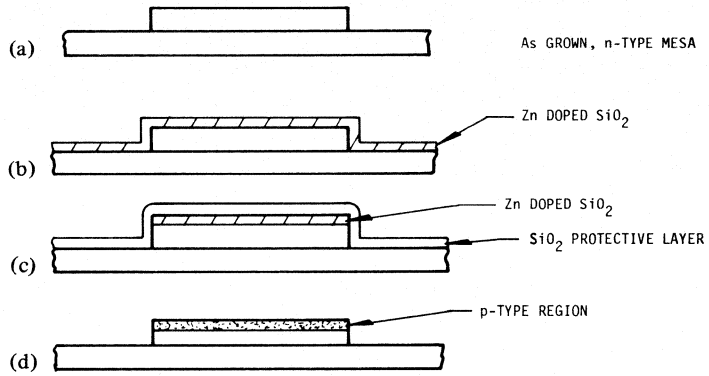

Fig. 1. Injections mesa-laser junction-formation steps. (a) As-grown n-type mesa. (b) Slice fully coated with Zn-doped SiO_2. (c) Slice after photolithography and SiO_2 coating. (d) Slice after diffusion and oxide removal.

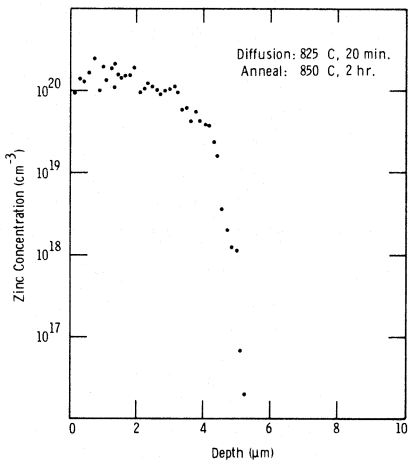

Fig. 2. Zn concentration versus depth for a mesa junction.

III. Laser Characteristics

After the mesa diodes have been fabricated and mounted on headers, the devices are attached to a copper cold finger in a Dewar and cooled (usually to 77 K). The diodes are excited with a 100–200-ns pulse at a repetition rate of 100–500 Hz. The laser-emission spectra are obtained with a 3/4-μm monochrometer and an ITT FW118 photomultiplier which has an S-1 photocathode. The peak output power of the lasers is measured with an ITT F-4000 biplanar photodiode.

Injection lasers have been fabricated from mesas with n-type carrier concentrations between 10^{16} cm^{-3} and 3×10^{18} cm^{-3}. The threshold current densities (at 77 K) of the GaAs lasers are strongly dependent on the carrier concentrations, ranging from ~ 2 kA/cm^2 for the best heavily doped devices to ~ 100 kA/cm^2 for lightly doped ones. The high thresholds for the lightly doped diodes are a result of the difficulty of achieving population inversion in these devices. Selected Zn-implant GaAs devices have been operated at dry-ice (200 K) and ambient (300 K) temperatures with threshold current densities of ~ 30 kA/cm^2 and ~ 100 kA/cm^2, respectively. Typical values for the total peak output power from heavily doped GaAs lasers are several tenths of a watt; however, a peak output in excess of 3 W with a drive current of 40 A has been

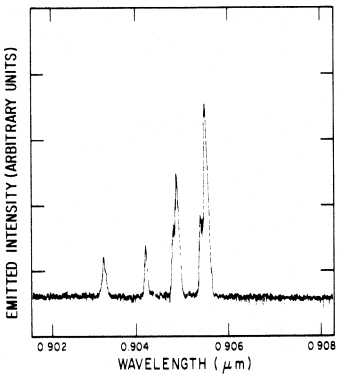

Fig. 3. Emission spectrum of a $Ga_{0.95}In_{0.05}As$ mesa laser driven with a bias current of 11 A at 77 K.

measured. In contrast, the peak power output of lightly doped lasers are usually a few milliwatts.

The lowest threshold observed for heavily doped $Ga_{1-x}In_xAs$ mesa lasers is 24 kA/cm^2 at 77 K, independent of the InAs content. Lower threshold currents have been reported recently by Nuese *et al.* [5] for discrete $Ga_{1-x}In_xAs$ lasers. The active layer of their lasers was grown by vapor phase and was separated from the GaAs substrate by a graded buffer layer. The higher threshold currents of our devices may be caused by lattice strain. We observe that the top surface of the $Ga_{1-x}In_xAs$ mesas appears pitted in comparison with the mirror-smooth surface of GaAs mesas.

An emission spectrum of a $Ga_{0.95}In_{0.05}As$ mesa laser is shown in Fig. 3. The laser emission is shifted almost 700 Å with respect to the GaAs mesas, thus making these $Ga_{1-x}In_xAs$ lasers compatible with GaAs waveguides. The spacing of these modes is approximately 6.3 Å, yielding $n_{eff} \simeq 3.7$. This value is consistent with a previous report for conventional discrete $Ga_{1-x}In_xAs$ laser diodes [4]. The highest peak power output observed for a $Ga_{1-x}In_xAs$ laser was 0.8 W at approximately 40 A.

The mesa laser readily lends itself to fabrication into arrays since several hundred lasers are grown adjacent to one another on a single chip. To make a linear array of mesa lasers we simply cut a strip containing the desired number of devices from a batch-processed slice and mount it on a header as shown in Fig. 4. This particular array contains six stripe-geometry GaAs mesa lasers. By connecting the diodes in parallel with an appropriate series resistance for each device, it is possible to obtain the rather uniform laser emission illustrated in Fig. 5. In this figure the radiation from the array has been focused on an infrared vidicon and displayed on a CRT. To obtain this picture, a 1-Ω resistor was placed in series with two of the lasers. This method of mounting lasers also allows us to check variations of the laser thresholds from one device to another along the chip. The laser threshold currents for the individual diodes in the array of Fig. 5 ranged from 1.2–2.6 A. A peak power output of 3 W was obtained from the six-laser array when driven by a total current of 50 A. Present mesa-laser arrays have higher threshold currents and lower efficiencies than conventionally fabricated laser arrays [5]. The observation that adjacent mesa lasers have similar parameters is, however, encouraging for future IOC development.

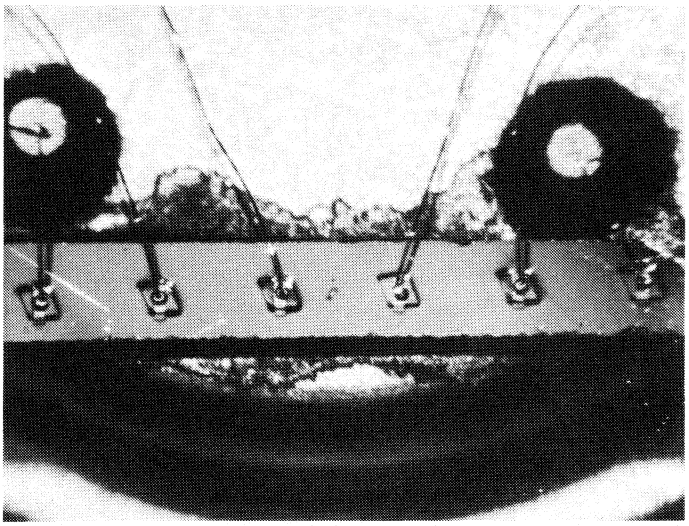

Fig. 4. Photograph of an array of six stripe-geometry GaAs-diode mesa lasers cut from a batch-processed slice.

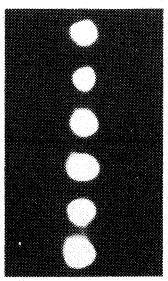

Fig. 5. Infrared-vidicon display of the emission from a six-element monolithic array of Zn-implanted GaAs mesa lasers.

IV. Conclusion

We have demonstrated the feasibility of growing the optical facets of $Ga_{1-x}In_xAs$ semiconductor diode lasers. We have fabricated monolithic $Ga_{1-x}In_xAs$ ($0 \leqslant x \leqslant 0.06$) mesa diodes which operate as lasers at wavelengths between 8300 Å and 9100 Å at 77 K, demonstrating the wavelength tunability in a monolithic-mesa semiconductor laser. These devices have the potential of matching low-loss regions of optical fibers and GaAs dielectric waveguides for communications applications. They also readily lend themselves to the fabrication of laser arrays.

Acknowledgment

The authors wish to thank H. Hendricks and his colleagues of NASA, Langley Field, for preparing the Zn-ion-implanted samples. They also wish to thank D. W. Shaw for discussion of mesa growth; K. C. Wiemer, for advice on the Zn-doped SiO_2; A. R. Reinberg, for oxide deposition; and G. Pollack, for the spreading-resistance probe measurements. Also, they are indebted to W. Abercrombie, S. H. Howison, F. D. Sinclair, and W. A. Dillon for their expert technical assistance.

REFERENCES

[1] F. A. Blum, K. L. Lawley, F. H. Doerbeck, and W. C. Holton, "Monolithic GaAs injection lasers with grown optical facets," *Appl. Phys. Lett.*, vol. 25, pp. 620-621, 1974.

[2] F. A. Blum, K. L. Lawley, W. C. Scott, and W. C. Holton, "Optically-pumped grown GaAs mesa surface laser," *Appl. Phys. Lett.*, vol. 24, pp. 430-432, 1974.

[3] F. A. Blum, K. L. Lawley, and W. C. Holton, "Monolithic $Ga_{1-x}In_xAs$ mesa lasers with grown optical facets," to be published.

[4] H. M. Macksey, J. C. Campbell, G. W. Zack, and N. Holonyak, "Zn-diffused laser junctions in $In_xGa_{1-x}As$ and $InAs_xP_{1-x}$ grown from In solution at constant temperature," *J. Appl. Phys.*, vol. 43, pp. 3534-3537, 1974.

[5] C. J. Nuese, M. Ettenberg, R. E. Enstrom, and H. Kressel, "CW laser diodes and high power arrays of $In_xGa_{1-x}As$ for 1.06-μm emission," *Appl. Phys. Lett.*, vol. 24, pp. 224-227, 1974.

Application of Molecular-Beam Epitaxial Layers to Heterostructure Lasers

H. C. CASEY, JR., MEMBER, IEEE, A. Y. CHO, AND P. A. BARNES

Abstract—**GaAs-$Al_xGa_{1-x}As$ double-heterostructure (DH) lasers with Si-doped n-type active layers have been prepared by molecular-beam epitaxy (MBE) and the laser properties evaluated. With 0.2-μm-thick active layers and 300-μm cavity lengths, typical room-temperature threshold current densities J_{th} of 5.0×10^3 A/cm^2 and best values of 2.5×10^3 A/cm^2 have been obtained. Stripe-geometry devices were run CW up to 9°C. Photoluminescence (PL) studies of single layers grown with the donors Si, Ge, and Sn show that the luminescent intensity for MBE n-type layers depends on the substrate temperature during growth. The PL intensity for Sn-doped MBE layers was greater than for high-quality Sn-doped liquid-phase-epitaxial layers.**

I. INTRODUCTION

WITHIN the last year, sufficient results have been achieved to permit description of GaAs-$Al_xGa_{1-x}As$ double-heterostructure (DH) lasers prepared by molecular-beam epitaxy (MBE). Although MBE for this application is still in an early stage of investigation, threshold current densities are presently within about a factor of 2 of the values obtained for similar-geometry DH lasers prepared by liquid-phase epitaxy (LPE). If comparable-performance DH lasers can be prepared by MBE, then the improved-layer reproducibility and large-area growth would make MBE a reasonable alternative to consider. In addition to this immediate problem of GaAs-$Al_xGa_{1-x}As$ DH lasers, it is the structures, compounds, and devices that cannot be prepared by LPE that will require a new thin-film technology. Double heterostructures have been prepared by MBE to permit us to learn the techniques necessary for the preparation of layers and heterostructure interfaces that have the required optical and electrical properties. The results described in this paper are part of a continuing investigation to apply MBE to these requirements for new optoelectronic and integrated optics structures.

Manuscript received December 12, 1974; revised January 27, 1975.
The authors are with Bell Laboratories, Murray Hill, N.J. 07974.

The results for GaAs-$Al_xGa_{1-x}As$ DH lasers prepared by MBE with Mg-doped p-type active layers have been described previously [1]. For structures with 0.5-μm-thick active layers and 350-μm cavity length, pulsed-threshold current densities J_{th} at room temperature were 3.5×10^4 A/cm^2 for as-grown wafers. Annealing reduced J_{th} to 4.0×10^3 A/cm^3 [1]. It should be pointed out that the usual acceptors such as Zn or Cd are not useful acceptors for MBE. These impurities have a high vapor pressure and tend to reevaporate from the growing-layer surface rather than be incorporated in the growing layer. For MBE, Ge is an acceptor only for growth under the excess-Ga condition [2]. Since smoother layers are generally obtained for excess-As conditions, it may not be desirable to utilize Ge as a p-type dopant. Hole concentrations only up to $\sim 5 \times 10^{16}$ cm^{-3} can be achieved by Mg while retaining smooth layer growth at 650°C. Hole concentrations of $\sim 1 \times 10^{18}$ cm^{-3} may be obtained with Mn [3a)], and $\sim 4 \times 10^{19}$ cm^{-3} with Be [3b)]. Manganese has an acceptor ionization energy [3] near 0.1 eV and Be can diffuse rapidly. At the present time, DH lasers with Mn- or Be-doped active layers have not been prepared.

Because of these properties of acceptor impurities in GaAs MBE layers, DH lasers with n-type active layers have been investigated. The preparation of MBE lasers with Si-doped n-type active layers are described in Section II and the laser properties are summarized in Section III. Studies were also made of the influence of substrate temperature on the layer

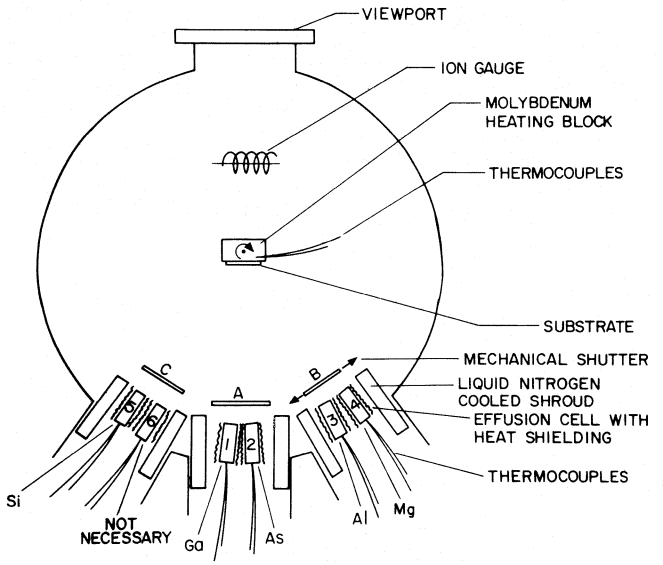

Fig. 1. Schematic representation of the MBE growth system.

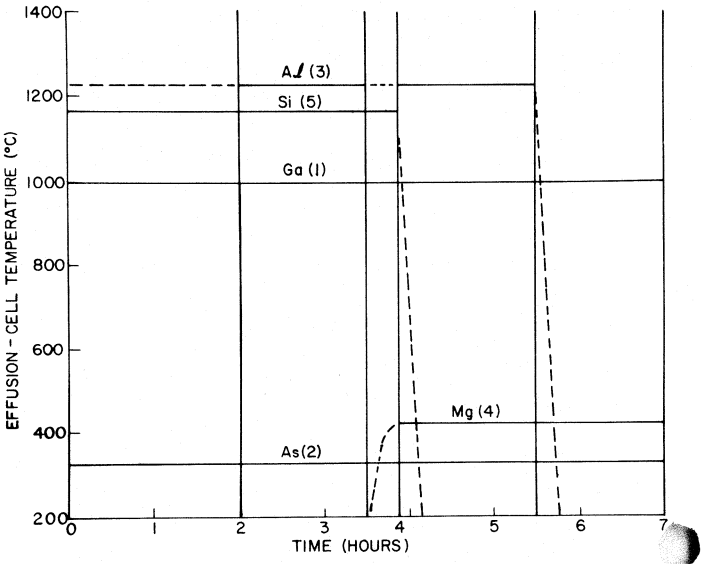

Fig. 2. Temperature–time cycles used to grow the five-layered DH lasers. Solid lines indicate an open shutter, while the dashed line indicates that the shutter is closed.

luminescence for layers doped with the donors Si, Ge, and Sn. These photoluminescence measurements on single layers are described in Section IV. The single-layer photoluminescence was found to be better for Sn-doped MBE layers than for Sn-doped LPE layers.

II. Layer Growth

A schematic representation of the growth apparatus is shown in Fig. 1. The layer growth takes place within a high-vacuum chamber. The pressure is $\sim 10^{-9}$ torr before heating the effusion cells. The substrate is 2 X 2 cm and is heated to between 600 and 650°C. For the heterostructure lasers with an n-type active layer, five effusion cells and three shutters are used. As described previously [1], six effusion cells are used for p-type active layers. The effusion cells are made of pyrolytic BN and are essentially a heated cylinder with one end open. The contents of each effusion cell are shown in Fig. 1. Silicon is the n-type impurity and Mg is the p-type impurity. Aluminum is very reactive, and therefore it tends to attack the effusion cell. The shutters permit instantaneous change from one layer composition to another.

The temperature-time cycles used to grow the DH lasers with the Si-doped n-type active layer are shown in Fig. 2. During growth the background pressure is in excess of 2×10^{-7} torr. The first layer to be grown is a Si-doped buffer layer and becomes an n-type $Al_xGa_{1-x}As$ layer by opening shutter *B*. It simplifies the arrangement of effusion cells to use the same donor for the n-type GaAs and $Al_xGa_{1-x}As$ layers. The remaining layers are then grown by opening and closing the shutters and heating the effusion cells to the temperatures indicated in Fig. 2. For MBE, the layer thickness varies linearly with growth time, and the growth rate used for this work is approximately 1 μm/h. The growth rate is determined by the Ga flux (or Ga and Al) for the excess As growth condition. Further description of MBE-layer growth has been given elsewhere [4], [5].

III. Laser Properties

Both broad-area and stripe-geometry DH lasers were prepared. The as-grown wafers with n-type active layers had much lower threshold current densities than the wafers with p-type active layers. For broad-area DH lasers with 0.2-μm active layers, 150-μm width, and 300-μm cavity lengths, typical pulsed values of J_{th} at 297 K were 5.0×10^3 A/cm^2 and best values were 2.5×10^3 A/cm^2. The electron concentration in the Si-doped n-type active layers was $\sim 1.5 \times 10^{18}$ cm^{-3}. Although annealing did not always reduce J_{th}, the best value was obtained for an annealed wafer. Differential quantum efficiencies were typically 30–40 percent. For an active-layer thickness of 0.2 μm, J_{th} for comparable geometry LPE DH lasers should be $\sim 1.5 \times 10^3$ A/cm^2.

Stripe-geometry DH lasers were fabricated in the same manner as for LPE wafers [6]. A scanning electron photomicrograph of the structure used is shown in Fig. 3(a). Some irregularity may be seen at the p-GaAs/P-$Al_{0.23}Ga_{0.77}As$ interface and is due to doping $Al_xGa_{1-x}As$ with Mg which has a low sticking coefficient and requires a high flux that interferes with smooth growth. The P-$Al_{0.23}Ga_{0.77}As$ layer was kept sufficiently thick to prevent this interface from affecting the optical field. The device properties for a 13-μm-wide stripe that was mounted p-side down on a Cu heat sink are summarized in Fig. 3(b). The current-voltage behavior appears completely normal and very good uniformity among the devices was observed. As indicated, CW operation has only been achieved up to 9°C with the stripe geometry. For CW operation, $J_{th} \approx 1.2 \times 10^3$ A/cm^2.

Continuous operation was limited to 9°C (282 K) due to a steep temperature dependence of the threshold current. A fit of experimental data to the empirical formula, $J_{th} \propto \exp(T/T_0)$, leads to an experimental value of $T_0 = 40 \pm 2$ K for several devices with 0.22-μm active layers. This value differs from the

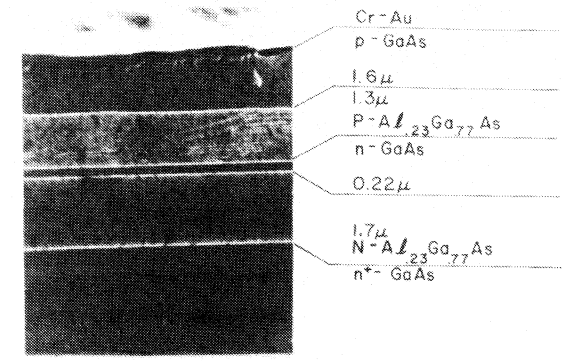

(a)

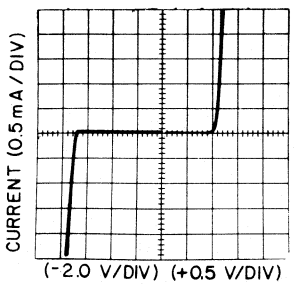

CW BELOW 9 °C (48°F)
λ = 8781 ± 20 Å
C_0 = 18 ± 1 pF
V_f (100 mA) = 1.47 ± .04 V
R_f = 1.2 ± 0.2 Ω
I_{th} ≈ 410 mA (PULSED)

(b)

Fig. 3. (a) Scanning electron photomicrograph of the etched surface of the MBE DH laser. The layer thickness, Al composition, and conductivity type are indicated for each layer. (b) Summary of the 13-μm-wide stripe-geometry DH laser properties.

values for LPE-DH lasers [7] of T_0 = 120 K for 1-μm active layers and T_0 = 165 K for 0.5-μm active layers. Further, at 9°C the CW current through the diode was 630 mA (~1.28 W) which would raise the temperature of the laser active layer approximately 50 K above the heat-sink temperature. This rise in junction temperature was observed from the wavelength shift of the spontaneous emission.

IV. Single-Layer Photoluminescence

It has been our experience that the heterostructure spontaneous-emission efficiency is directly related to J_{th}, and this variation in efficiency is related to the photoluminescence (PL) of single layers. A recent example is the behavior observed for the as-grown and annealed p-type MBE layers [1], [8]. Therefore the PL for single GaAs MBE layers was compared to Sn-doped LPE layers. No quantitative data can be extracted from this type of measurement alone, but PL serves as a useful guide to the luminescent behavior of layers prepared under various conditions and with designated impurities. As for acceptors, the high vapor-pressure donors such as S and Se are not incorporated into the growing layer. However, electron concentrations greater than 1×10^{18} cm^{-3} may readily be achieved with the group IV impurities. The results for Si, Ge, and Sn are shown in Figs. 4-6, respectively.

In Fig. 4, room-temperature PL (excitation λ = 5145 Å) intensities of single layers doped with Si are compared to the PL of Sn-doped LPE layers. The carrier concentrations were determined by Hall measurements. The Sn-doped LPE samples

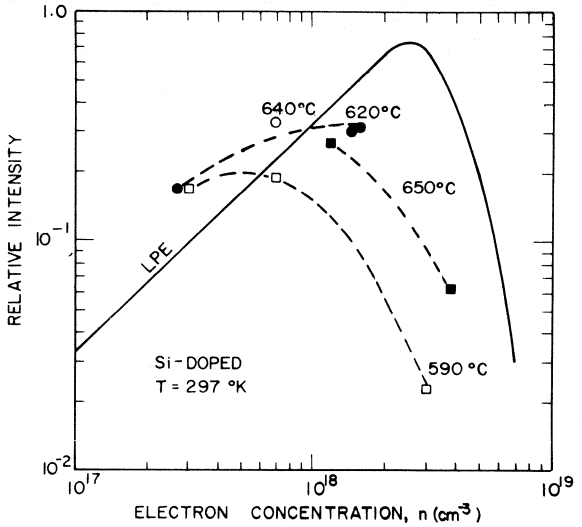

Fig. 4. Relative PL peak intensity. The LPE sample is Sn-doped. The numbers on the figure were the substrate temperature during growth of the Si-doped n-type MBE layers.

were previously studied [9] and have been found to be representative of the highest PL intensity n-type LPE layers. The data points for the LPE layers are not shown, but are the samples illustrated in [9, fig. 5]. The numbers in Figs. 4-6 are the MBE substrate temperature during growth. A detailed discussion of the interpretation of the PL intensity is beyond the scope of this paper [10]. At low excitation, the radiative recombination rate is proportional to the reciprocal of the radiative lifetime τ_r, and the total recombination rate is proportional to $(1/\tau_{nr} + 1/\tau_r)$, where τ_{nr} is the nonradiative lifetime. Therefore, the PL intensity at a given carrier concentration is proportional to the ratio of the nonradiative lifetime to the radiative lifetime for $\tau_r > \tau_{nr}$. When the sample is not closely compensated, the radiative lifetime depends only on the carrier concentration [11], and the PL intensity is a measure of the relative τ_{nr}. Hence, MBE data above the LPE curve represent less nonradiative recombination in the MBE layer than for the LPE layer, while data below the LPE curve represent greater nonradiative recombination.

For the Si-doped samples, a higher substrate temperature during growth improves the PL intensity for samples with electron concentrations n near 7×10^{17} cm^{-3}. At electron concentrations greater than ~1×10^{18} cm^{-3}, the PL intensity for a substrate temperature of 590°C is less than for higher substrate temperature; however, an increase from 620 to 650°C slightly reduces the PL intensity. This reversal is also observed in Fig. 5 for the data points near 2×10^{18} cm^{-3}. Since the electron concentration in this region does not increase with effusion-cell temperature as much as expected from the low-concentration behavior, the impurity concentration probably exceeds n, and the electrically inactive impurity may lead to an increase in nonradiative recombination. The active layers for the DH lasers described in Section III had $n \approx 1.5 \times 10^{18}$ cm^{-3}, and Fig. 4 indicates a PL intensity that is about a factor of 2 less than the LPE curve. This substrate temperature de-

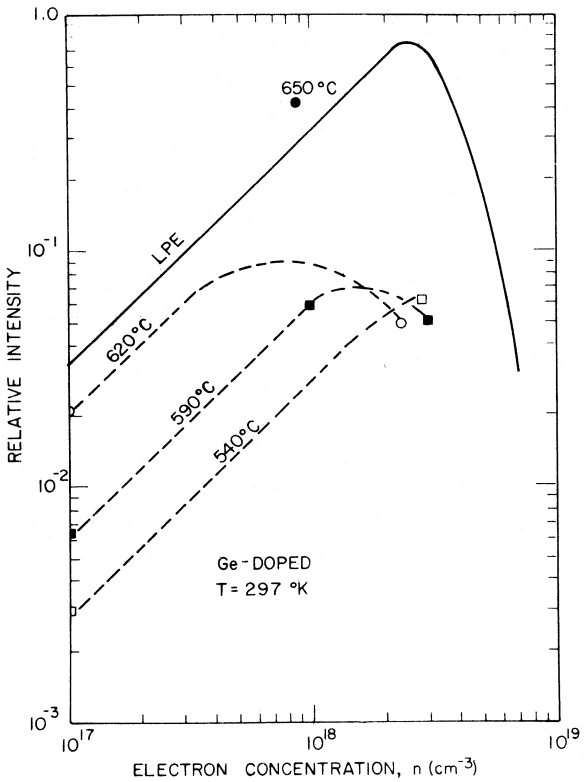

Fig. 5. Relative PL peak intensity. The LPE sample is Sn-doped. The numbers on the figure were the substrate temperature during growth of the Ge-doped n-type MBE layers.

pendence is in general agreement with the observation that the lower threshold DH lasers were grown at temperatures between 620 and 650°C. The substrate temperature is limited to about 650°C because higher temperatures result in poor surface morphology.

The PL intensities for the Ge-doped n-type layers are given in Fig. 5. The substrate temperature has a larger influence with Ge than for Si, and only for temperatures near 650°C does the PL intensity approach and exceed the LPE curve. Because of this result, Ge does not appear to be a favorable MBE donor for luminescent applications.

In Fig. 6, the PL intensity for Sn-doped n-type layers is shown. For the 640°C substrate temperature, the MBE PL intensity exceeds the LPE value. Although not shown in Fig. 6, a decrease by a factor of 10 in the electron concentration to 2.5×10^{16} cm^{-3} decreases the PL intensity by the same amount. The 570°C point shows that the Sn case does not have a strong substrate temperature dependence. This result of greater PL intensity for the MBE Sn-doped layers suggests that Sn is a good choice to consider for DH active layers.

V. Conclusions

Studies of GaAs-$Al_xGa_{1-x}As$ DH lasers prepared by MBE with Si-doped n-type active layers resulted in J_{th} within about a factor of 2 of the values obtained for comparable geometry LPE structures. Although annealing was required for MBE p-type active layers, low J_{th} was obtained for as-grown MBE wafers with n-type active layers. However, the best J_{th} was obtained for an annealed wafer. Preparation of stripe-geometry devices confirmed the uniformity of DH lasers expected for MBE wafers. Measurement of single-layer PL demonstrated

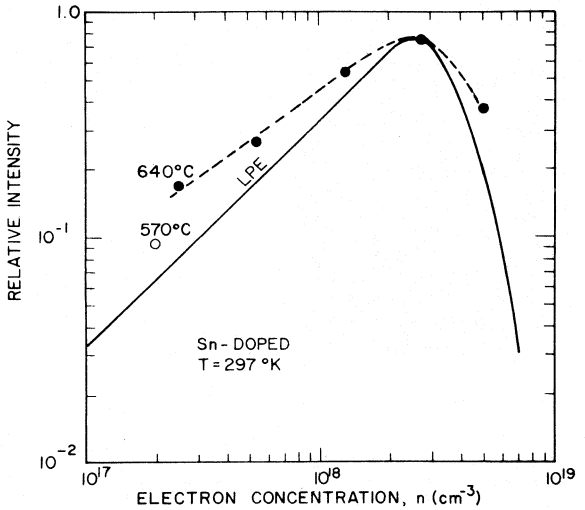

Fig. 6. Relative PL peak intensity. The LPE sample is Sn-doped. Th numbers on the figure were the substrate temperature during grow of the Sn-doped n-type MBE layers.

the influence of substrate growth temperature on the layer luminescence. Tin-doped MBE layers gave greater PL intensity than similarly doped LPE layers and appear promising for luminescent applications.

Acknowledgment

The authors wish to thank M. B. Panish for useful discussions during this study. They also wish to thank C. Radice for aid in preparation of the MBE samples and P. W. Foy for fabrication of the broad-area DH lasers.

References

[1] A. Y. Cho and H. C. Casey, Jr., "GaAs-$Al_xGa_{1-x}As$ double-heterostructure lasers prepared by molecular-beam epitaxy," *Appl. Phys. Lett.*, vol. 25, pp. 288–290, Sept. 1974.

[2] A. Y. Cho and I. Hayashi, "P-N junction formation during molecular-beam epitaxy of Ge-doped GaAs," *J. Appl. Phys.*, vol. 4[illegible] pp. 4422–4425, Oct. 1971.

[3] a) M. Ilegems and R. Dingle, "Acceptor incorporation in beam-epitaxial GaAs," presented at the 5th Int. Symp. GaAs and Related Compounds, Deauville, France, Sept. 24–26, 1974.
b) M. Ilegems, private communication.

[4] A. Y. Cho, "Film deposition by molecular-beam techniques," *J. Vac. Sci. Technol.*, vol. 8, pp. S31–S38, Sept./Oct. 1971.

[5] A. Y. Cho and H. C. Casey, Jr., "Properties of Schottky barriers and p-n junctions prepared with GaAs and $Al_xGa_{1-x}As$ molecular beam epitaxial layers," *J. Appl. Phys.*, vol. 45, pp. 1258–1263, Mar. 1974.

[6] J. C. Dyment, L. A. D'Asaro, J. C. North, B. I. Miller, and J. E. Ripper, "Proton-bombardment formation of stripe-geometry heterostructure lasers for 300 K CW operation," *Proc. IEEE* (Lett.), vol. 60, pp. 726–728, June 1972.

[7] I. Hayashi, M. B. Panish, and F. K. Reinhart, "GaAs-$Al_xGa_{1-x}As$ double heterostructure injection lasers," *J. Appl. Phys.*, vol. 42, pp. 1929–1941, Apr. 1971.

[8] A. Y. Cho and H. C. Casey, Jr., "GaAs-$Al_xGa_{1-x}As$ double heterostructure lasers prepared by molecular-beam epitaxy," presented at the Device Research Conf., Santa Barbara, Calif., June 1974.

[9] H. C. Casey, Jr., B. I. Miller, and E. Pinkas, "Variation of minority-carrier diffusion length with carrier concentration in GaAs liquid phase epitaxial layers," *J. Appl. Phys.*, vol. 44, pp. 1281–1287, Mar. 1973.

[10] C. J. Hwang, "Quantum efficiency and radiative lifetime of the band-to-band recombination in heavily doped n-type GaAs," *Phys. Rev. B*, vol. 6, pp. 1355–1359, Aug. 1972.

[11] H. C. Casey, Jr., and F. Stern, to be published.

Liquid Phase Epitaxial $In_{1-x}Ga_xP_{1-z}As_z/GaAs_{1-y}P_y$ Heterojunction Lasers

J. J. COLEMAN, STUDENT MEMBER, IEEE, N. HOLONYAK, JR., FELLOW, IEEE, M. J. LUDOWISE, P. D. WRIGHT, STUDENT MEMBER, IEEE, W. O. GROVES, AND D. L. KEUNE

Abstract—The growth and laser properties of $In_{1-x}Ga_xP_{1-z}As_z/GaAs_{1-y}P_y$ single heterojunction laser diodes are described. High-quality p-type $In_{1-x}Ga_xP_{1-z}As_z$ layers are grown by liquid phase epitaxy (LPE) on n-type VPE $GaAs_{1-y}P_y$ substrates of composition $y = 0.32 - 0.40$. Laser operation (77 K) of these quaternary-ternary heterojunctions is demonstrated at shorter wavelengths (<6300 Å) and lower thresholds ($J_{th} \lesssim 6.2 \times 10^4$ A/cm^2) than comparable $GaAs_{1-y}P_y$ homojunctions. The increase observed in threshold current ($5x$) between $y = 0.38$ and $y = 0.40$ $GaAs_{1-y}P_y$ substrates is attributed to the usual effect of E_X approaching E_Γ near the direct-indirect transition. From the well-defined cavity mode structure observed on these heterojunctions, data are obtained at relatively high energy on the index dispersion quantity $\{n - \lambda(dn/d\lambda)\}$, which increases monotonically with photon energy and provides a reference for the distinctly different behavior observed on N-doped $GaAs_{1-y}P_y$ ($h\nu \sim E_\Gamma \sim E_N$).

INTRODUCTION

FROM earlier work it is known that by means of liquid phase epitaxy (LPE) the quaternary AlGaAsP can be grown on the ternary GaAsP, thus permitting the formation of single and double heterojunction lasers [1], [2]. Unfortunately this method of forming a heterojunction on $GaAs_{1-y}P_y$ is difficult if the GaP percentage y in the ternary is appreciable ($y \gtrsim 0.10$), higher compositions y leading to relatively high (inconvenient) growth temperatures [3]. A different approach to the problem of growing a wide-gap emitter on $GaAs_{1-y}P_y$ is to utilize $In_{1-x}Ga_xP$, which can be grown of laser quality on $GaAs_{1-y}P_y$ or GaAs ($x = 0.52 + 0.48y$, $0 \leqslant y \leqslant 1$) by means of constant-temperature LPE [4]-[7]. The only problem relative to heterojunction fabrication via the approach of growing a second epitaxial layer (LPE) on a previously grown first layer (VPE) is that of defect formation at the metallurgical junction (not necessarily in the LPE layer itself) if a good lattice match is not accomplished. Achieving a good lattice match turns out to be a difficult procedure. That is, it is quite difficult to control all of the LPE growth parameters so that the $In_{1-x}Ga_xP$ layer is well lattice matched on the $GaAs_{1-y}P_y$ substrate in the sense that the metallurgical junction is adequately free of boundary ("surface") defects, and likewise the LPE layer itself (etch pit density $\lesssim 10^4/cm^2$).

We find that the problem of lattice matching $In_{1-x}Ga_xP$ on a $GaAs_{1-y}P_y$ substrate is eased if the ternary is rendered a quaternary by the incorporation of a small amount ($z \sim 0.01$) of As in the LPE layer changing it to $In_{1-x}Ga_xP_{1-z}As_z$ [8]. Small deviations Δx in the Ga composition x of $In_{1-x}Ga_xP_{1-z}As_z$ from the lattice-match condition on $GaAs_{1-y}P_y$ then are capable of being balanced by compensating small deviations Δz in As composition z that hardly change the electrical and optical behavior of the quaternary LPE layer, which itself ($z \sim 0.01$) is not much different in electrical and optical behavior from the ternary $In_{1-x}Ga_xP$ that lattice matches the $GaAs_{1-y}P_y$ substrate. If an increase (decrease) Δx in Ga percentage occurs in the $In_{1-x}Ga_xP_{1-z}As_z$ LPE layer from the proper composition for a lattice match on $GaAs_{1-y}P_y$, the lattice constant decreases (increases; see Fig. 1). This change in lattice constant is compensated by a corresponding increase (decrease) Δz of As in the crystal, which increases (decreases) the lattice constant sufficiently to keep it constant. The net

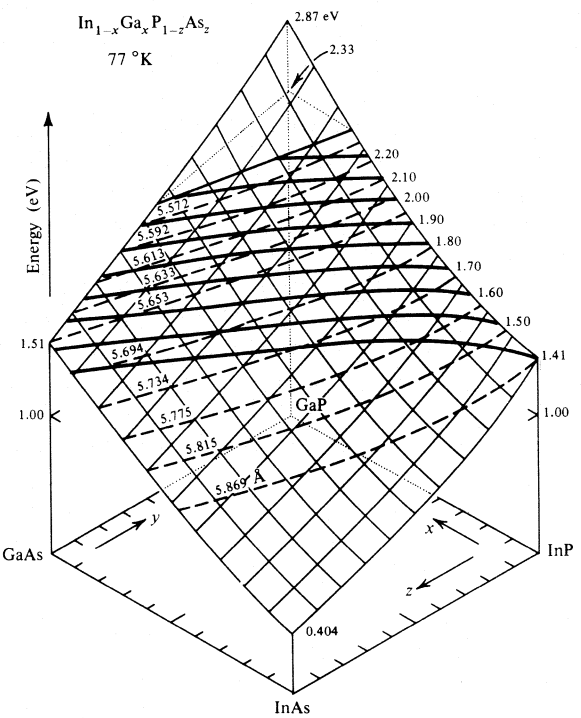

Fig. 1. Energy-gap surface (77 K) as a function of crystal composition for the quaternary alloy system $In_{1-x}Ga_xP_{1-z}As_z$. The edges are divided into mole fractions of the individual binary constituents. Plotted also on the surface are isolattice-constant lines (dashed, 5.869-5.572 Å) and isoenergy-gap lines (solid, 1.41-2.20 eV). From the fact that the isolattice-constant and isoenergy-gap lines intersect, it is apparent that a wide range of compositions of $In_{1-x}Ga_xP_{1-z}As_z$ of higher energy gap can be grown along an isolattice-constant line on $GaAs_{1-y}P_y$ of lower energy gap, making possible also the growth of $In_{1-x}Ga_xP_{1-z}As_z/In_{1-x'}Ga_{x'}P_{1-z'}As_{z'}$ ($x \neq x'$, $z \neq z'$) homoheterojunctions.

Manuscript received November 18, 1974; revised January 20, 1975. This work was supported in part by the National Science Foundation under Grant DMR 72-03045-A01 and in part by the Advanced Research Projects Agency under Contract DAHC-15-73-G-10.

J. J. Coleman, N. Holonyak, Jr., M. J. Ludowise, and P. D. Wright are with the Department of Electrical Engineering and Materials Research Laboratory, University of Illinois at Urbana-Champaign, Urbana, Ill. 61801.

W. O. Groves and D. L. Keune are with the Monsanto Company, St. Louis, Mo. 63166.

effect is a small overall decrease (increase) in the energy gap in the resulting $In_{1-x}Ga_xP_{1-z}As_z$, as is evident from Fig. 1 and the fact that the isoenergy-gap lines (solid) cross the isolattice-constant lines (dotted, 5.572-5.869 Å). Compared to homojunctions, the quality of the heterojunctions we have been able to construct on $GaAs_{1-y}P_y$ suggests that latching (one lattice locking on the other) [9] occurs when $In_{1-x}Ga_x \cdot P_{1-z}As_z$ is grown by LPE on $GaAs_{1-y}P_y$.

It is evident that the quaternary $In_{1-x}Ga_xP_{1-z}As_z$ ($z \sim 0.01$ or even larger) affords greater freedom and leeway than the ternary ($z = 0$) in fulfilling the basic lattice-match requirement of $GaAs_{1-y}P_y$ [1], [2], [8], [10] permitting in turn the LPE growth of high-quality heterojunctions on VPE $GaAs_{1-y}P_y$. In this paper we describe the growth of these heterojunctions and their laser operation in the crystal composition range $y = 0.32$-0.40, including at significantly shorter wavelengths and lower thresholds than comparable homojunctions [11].

Heterojunction Growth

By means of constant temperature LPE (~800°C, open-tube furnace) [4]-[8] we grow laser-quality (etch pit density $\lesssim 10^4/cm^2$)[1] p-type $In_{1-x}Ga_xP_{1-z}As_z$ layers lattice matched on n-type VPE $GaAs_{1-y}P_y$ substrates, where $x \approx 0.52 + 0.48y$ if $z = 0$ and is larger if $z > 0$. Heterojunctions are formed by dilute Zn diffusion from the melt into the $GaAs_{1-y}P_y$ substrate during the growth cycle. In the present work we have employed laser-quality $GaAs_{1-y}P_y$ substrates varying in composition from $y = 0.32$ to beyond $y = 0.40$ and have grown $In_{1-x}Ga_xP_{1-z}As_z$ epitaxial layers that are adjusted in composition x [4]-[8] to match each substrate composition y. Electron microprobe measurements indicate that the As fraction in the quaternary LPE layer is $z \sim 0.01$ but in some cases has been adjusted deliberately to be higher ($z \sim 0.10$) since there is much freedom in this variable and in x as long as the quaternary energy gap is maintained higher than that of the ternary substrate (see Fig. 1).

To grow the p-type quaternary layer, a cylindrical graphite boat with removable end caps is employed that contains an In-rich solution, the substrate crystal, and a source crystal of GaP which prevents Ga depletion from the solution [4]-[7]. Because of the large lattice mismatch between InP (5.869 Å) and GaP (5.451 Å) and the large Ga distribution coefficient [12], the choice of melt composition, and thus the crystal composition x, is sensitive to the composition y of the $GaAs_{1-y}P_y$ substrate. For $y \approx 0.40$ $GaAs_{1-y}P_y$, a typical melt consists of 10.5 g In, 0.20 g of InP, 0.13 g of GaP, 15 mg of InAs, and 75 mg of Zn.

Melt compositions, such as above, that will grow a lattice-matched quaternary epitaxial layer on a $GaAs_{1-y}P_y$ substrate are determined experimentally. First, from $In_{1-x}Ga_xP$ thermodynamic phase data [13] and experience [4], [7], an In-rich melt containing an approximately correct amount of InP and a purposefully insufficient amount of GaP is prepared which is intended to yield "lattice-matched" $In_{1-x}Ga_xP$ on the $GaAs_{1-y}P_y$ substrate. Then the amount of InAs necessary to grow a $z \sim 0.01$ quaternary layer is determined by trial and error, and is held constant in subsequent growth runs. Finally, the additional GaP necessary for saturation is provided by a GaP source wafer that is rotated into the melt during the saturation cycle (described below). After this procedure has been carried out once or twice, in later growths "fine tuning" of the composition is accomplished by varying slightly the amount of InP and GaP in the melt and correlating these values to crystal quality (etch pit density $< 10^4/cm^2$).

The LPE crystal growth procedure itself is carried out in two steps, with first the melt (once determined) being saturated at ~810°C for approximately 1 h. After the boat has cooled, a $GaAs_{1-y}P_y$ substrate crystal is placed off-center at one end, and a GaP source wafer is placed similarly off-center at the other end. The boat is reheated long enough to insure complete dissolution of the melt and the simultaneous incorporation of the Zn dopant, which is added to the boat after the saturation step because of the high Zn vapor pressure. After a 5-10°C cool-down to effect supersaturation, the boat is rotated to allow the melt to contact the substrate and permit the growth of a p-type quaternary layer. During the reheat cycle and growth of the p-type layer, Zn diffuses 1-2 μ into the n-type $GaAs_{1-y}P_y$ substrate, creating a thin compensated active region between the electrical junction and the metallurgical barrier.

A cleaved and etched cross section of a typical final structure ($y \approx 0.38$) is shown in Fig. 2. It is not a simple matter to determine directly the perfection of the ternary-quaternary heterojunction boundary, except by comparing heterojunction laser performance with that of homojunctions of the same composition y. The perfection of the LPE quaternary layer, however, is evident from its appearance after polishing and etching, and its behavior in photoluminescence. If the etch pit density is relatively low ($\lesssim 10^4/cm^2$; see [7, fig. 3]), as in the present work, the photoluminescence is strong and photopumped laser operation of thin samples of the $In_{1-x}Ga_xP_{1-z}As_z$ LPE layer is possible (5500 Å, $x \sim 0.70$, $z \sim 0.01$, 77 K). We infer that the ternary-quaternary heterojunction boundary itself is reasonably free of defects based on the energy range and quality of the diode laser performance that is described in what follows.

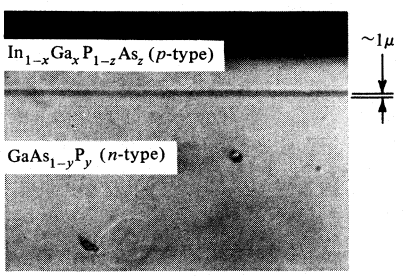

$In_{1-x}Ga_xP_{1-z}As_z/GaAs_{1-y}P_y$ Heterojunction
$x \sim 0.70, y \approx 0.38, z \sim 0.01$

Fig. 2. Cleaved and etched face of an $In_{1-x}Ga_xP_{1-z}As_z/GaAs_{1-y}P_y$ heterojunction grown by LPE. Both the metallurgical junction and a thin (~1 μ) compensated active layer in the VPE $GaAs_{1-y}P_y$ substrate are clearly distinguishable. The circular mottled areas are due to the etching process and cannot be correlated with any crystal imperfections.

[1]Thin photopumped samples of LPE $In_{1-x}Ga_xP_{1-z}As_z$ ($x \sim 0.70$, $z \sim 0.01$) operate as lasers at $\lambda \sim 5500$ Å (77 K), just as do similar $In_{1-x}Ga_xP$ ($x \sim 0.70$) samples [4] when the LPE layer is grown with a good lattice match on the substrate (i.e., when possessing less than 10^4 etch pits/cm^2, see [4] and [7]).

Threshold and Spectral Data

Although the entire $GaAs_{1-y}P_y$ crystal composition range $y < 0.40$ is of interest for various studies, in the work reported here we have been concerned mainly with $y \approx 0.32$ to 0.40 crystals. This is an interesting crystal composition range because, for example, in N-doped $GaAs_{1-y}P_y$ the isoelectronic trap state lies just above the Γ band edge ($E_N > E_\Gamma$) for $y \approx 0.38$ and just below ($E_N < E_\Gamma$) for $y \approx 0.40$. We mention that these heterojunctions are the first diodes in which the N isoelectronic trap has been involved in stimulated recombination. That is, the effect of the N trap (A-line) can be observed in $In_{1-x}Ga_xP_{1-z}As_z/GaAs_{1-y}P_y$:N heterojunctions but not in comparable homojunctions [14], [15]. Also, $y = 0.38$–0.40 crystals are of fundamental interest because of the proximity of the X-band minima to the Γ minimum in the composition range approaching the direct-indirect transition ($E_\Gamma = E_X$ at $y \equiv y_c \approx 0.46$, 77 K [16]). That is, as $y \to y_c \approx 0.46$, the direct band edge E_Γ approaches the indirect edge E_X and direct-gap band-to-band recombination weakens [17]. Moreover, donor states associated with the indirect band minima approach and become degenerate with E_Γ before the indirect band edge itself, and thus cause a premature weakening of the direct-gap band-to-band recombination. This is evident from the following energy estimates (77 K):

$$\begin{aligned} E_X - E_\Gamma \text{ [16]} &\approx 80 \text{ meV} && y = 0.38 \\ &\approx 60 \text{ meV} && = 0.40 \\ &\approx 39 \text{ meV} \sim E_D(X) = E_D(\text{Te}) \text{ [18]} && = 0.42. \end{aligned} \tag{1}$$

Depending upon the donor species and its depth, it is clear that the indirect behavior of $GaAs_{1-y}P_y$ intrudes rapidly in the range $y \sim 0.40$, and should be observable in laser thresholds as, in fact, is the case.

Heterojunction laser data on $y = 0.38$ $GaAs_{1-y}P_y$ (see Fig.) are shown in Figs. 3-5. At low-current levels (17.6 A/cm^2, Fig. 3), the emission is fairly broad and because of small filling of the donor band tail, peaks ~50 meV below the region of laser emission. As the current is increased, band filling causes the emission to shift (~50 meV) to higher energy but not as much (~100 meV) as in conventional Zn-diffused $GaAs_{1-y}P_y$ homojunctions of comparable donor doping ($n_d \sim 10^{18}$/cm^3) [19], which, incidentally, do not operate at these high energies and low thresholds. The small band-filling shift observed here may be an indication that during the LPE heterojunction growth process donors out-diffuse from the substrate while Zn in-diffuses.

For the $y = 0.38$ laser diode of Fig. 3, the spectral width is ~22 meV just below laser threshold and, as expected, narrows abruptly to ~3 meV at threshold ($J_{th} = 1.4 \times 10^4$ A/cm^2). As Fig. 4 shows, owing to the Zn acceptor, the heterojunction laser operates at considerably lower energy than the same n-type substrate $GaAs_{1-y}P_y$ when photopumped. When the heterojunction diode of Figs. 3-5 is driven harder (Fig. 5), a slight increase occurs in the range of laser operation on the shorter wavelength side of the emission spectrum and a much larger increase on the longer wavelength side. On the shorter wavelength side, laser modes exist to within about kT of

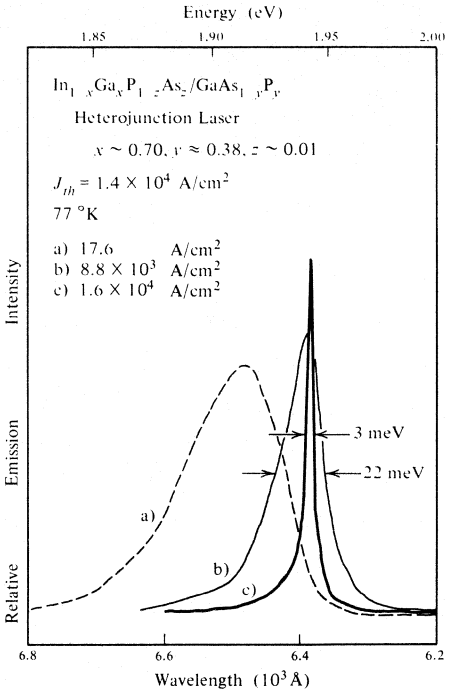

Fig. 3. Emission spectra (77 K) of an $In_{1-x}Ga_xP_{1-z}As_z/GaAs_{1-y}P_y$ ($x \sim 0.70$, $y \approx 0.38$, $z \sim 0.01$) heterojunction laser diode fabricated by the LPE growth of the quaternary on the VPE ternary substrate. At low excitation levels (17.6 A/cm^2) the emission spectrum (dashed) is fairly broad and occurs at low energy. At higher excitation, band filling occurs, the emission shifts (~50 meV), abrupt narrowing is observed, and laser operation is achieved at a current density of ~1.4×10^4 A/cm^2, or almost 20× smaller than for comparable homojunctions.

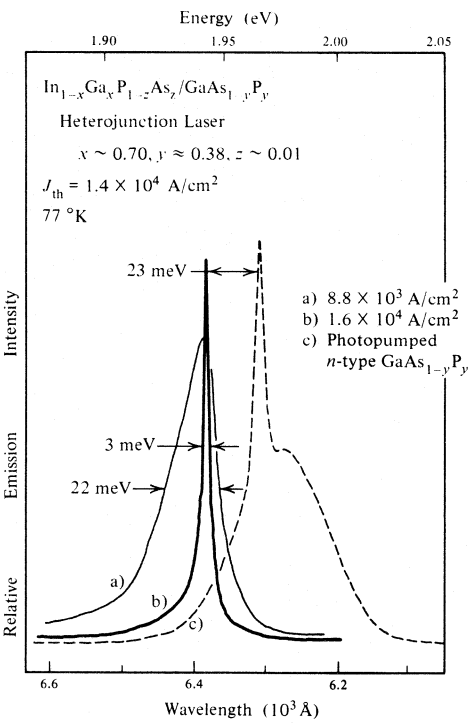

Fig. 4. Emission spectra (77 K) obtained on the $In_{1-x}Ga_xP_{1-z}As_z/GaAs_{1-y}P_y$ heterojunction laser diode of Fig. 3 just below and above laser threshold. At threshold, the spectrum narrows abruptly to a half-width of ~3 meV. Shown as a dashed curve for comparison are data obtained on a thin photopumped n-type $GaAs_{1-y}P_y$ platelet taken from the same substrate. The 23 meV downward energy shift is due to the Zn acceptor in the active region of the heterojunction.

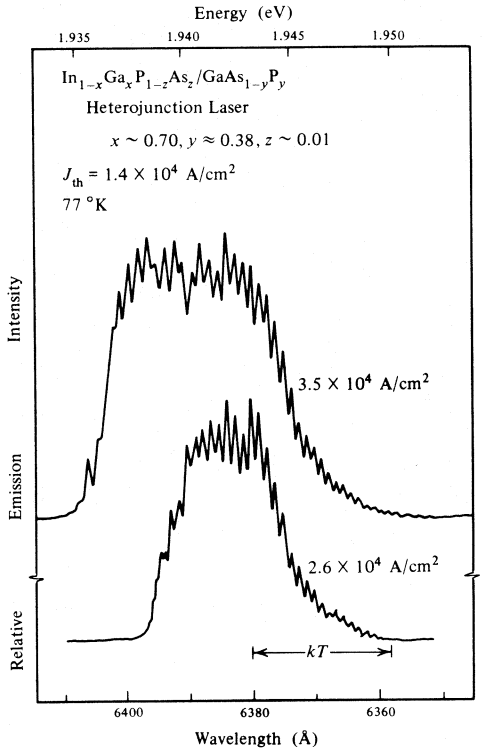

Fig. 5. Emission spectra (77 K) obtained at higher excitation levels on the $In_{1-x}Ga_xP_{1-z}As_z/GaAs_{1-y}P_y$ heterojunction laser diode of Figs. 3 and 4. Cavity modes are evident at wavelengths shorter than 6360 Å and at current densities well below (10×) those of comparable homojunctions. As the diode is driven harder, there is a large increase in the range of laser operation on the longer wavelength side of the emission spectrum and a smaller increase on the shorter wavelength side, which extends to within $\sim kT$ of $E_\Gamma - E_{Zn}$.

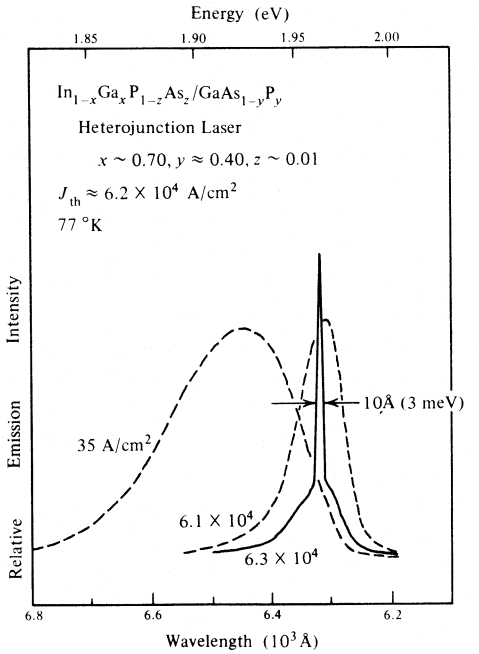

Fig. 6. Emission spectra (77 K) obtained on $y \approx 0.40$ $In_{1-x}Ga_x \cdot P_{1-z}As_z/GaAs_{1-y}P_y$ ($x \sim 0.70, z \sim 0.01$) heterojunction laser diode. At low excitation levels (35 A/cm^2) the emission is broad and is centered significantly below the stimulated emission peak. At higher excitation levels band filling occurs (~50 meV), abrupt spectral narrowing is observed, and laser operation is achieved at a current density of $\sim 6.2 \times 10^4$ A/cm^2. This higher threshold current density (5×) than for the diode of Figs. 2–5 is expected as the composition y of the $GaAs_{1-y}P_y$ substrate approaches the direct-indirect crossover y_c ($E_\Gamma = E_X$ at $y \equiv y_c \approx 0.46$, 77 K), and E_X approaches E_Γ ($E_X - E_\Gamma \approx 60$ meV at $y = 0.40$).

$E_\Gamma - E_{Zn} = 1.952$ eV. In this region a high-energy Boltzmann tail is observed because of the low optical losses of these diodes. As expected, band filling does not play much of a role beyond the point of threshold because of the increased (stimulated) recombination rate. We mention that the higher energy modes of Fig. 5 are comparable to the highest energies observed previously on $GaAs_{1-y}P_y$ homojunctions [11], but occur here at *10× lower* excitation levels, thus giving some indication of the quality of these heterojunctions.

Higher energy heterojunction laser operation has been obtained on $y \approx 0.40$ $GaAs_{1-y}P_y$ substrates as shown in Fig. 6 [8]. Although not shown in Fig. 6, the highest energy modes extend to well below 6300 Å, which is considerably shorter than for all previous $GaAs_{1-y}P_y$ diodes. We mention also that significantly lower excitation levels have been employed in the work reported here than for comparable $GaAs_{1-y}P_y$ homojunctions.

For the laser diodes of Fig. 6, the threshold currents ($J_{th} \approx 6.2 \times 10^4$ A/cm^2) are significantly higher (5×) than for $y = 0.38$ $GaAs_{1-y}P_y$, which in turn exhibits higher threshold currents than $y = 0.32$ crystal (see Figs. 3 and 7). As already mentioned, this behavior is expected as $y \to y_c$ and indirect donor states, as in (1), approach E_Γ. It is not clear, however, that the limit for $In_{1-x}Ga_xP_{1-z}As_z/GaAs_{1-y}P_y$ heterojunction laser operation occurs at $y = 0.40$. Rather, it is more likely that the limit is higher, perhaps as high as $y = 0.42$ according to the estimates of (1). This is suggested by two other observations. 1) The heterojunctions of this work have not been optimized in terms of doping, active layer thickness, or heat treatment effects, and probably can be extended in operation to higher limits, particularly if sophisticated stripe geometries are employed. 2) The heterojunction *I–V* characteristics of this work give no hint of "freeze-out" at 77 K to higher impedances, even for crystal compositions near $y_c \approx 0.46$ (77 K). On the other hand, homojunctions in this composition range generally exhibit a pronounced lean in the *I–V* characteristics at 77 K.

Index Dispersion

One of the desirable properties of the heterojunctions described here is that somewhat above laser threshold the emission is essentially all stimulated due to the relatively good carrier and optical energy confinement. This permits well-defined cavity modes to develop with little spontaneous background radiation as is shown for the $y = 0.32$ crystal of Fig. 7. We mention that this is not the case, however, for N-doped $GaAs_{1-y}P_y$ substrates, where the effect of the N trap is to introduce strong non-$k = 0$ recombination components and a relatively strong spontaneous radiation background [14]. This behavior is likely to occur also as $y \to y_c$ and, according to the estimate of (1), indirect-gap behavior begins to intrude due to the proximity of the *X*-band edge rather than the effect of the N trap.

From the usual laser-mode spacing formula

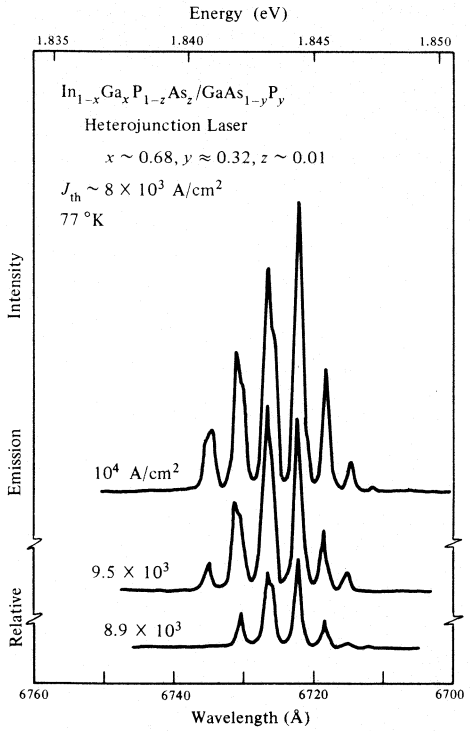

Fig. 7. Laser modes (77 K) of an $In_{1-x}Ga_xP_{1-z}As_z/GaAs_{1-y}P_y$ ($x \sim 0.68$, $y \approx 0.32$, $z \sim 0.01$) heterojunction just above threshold ($J_{th} \sim 8 \times 10^3$ A/cm^2). The emission is essentially all stimulated with well-developed cavity modes (and low spontaneous emission background) due to the relatively good carrier and optical energy confinement of the heterojunction.

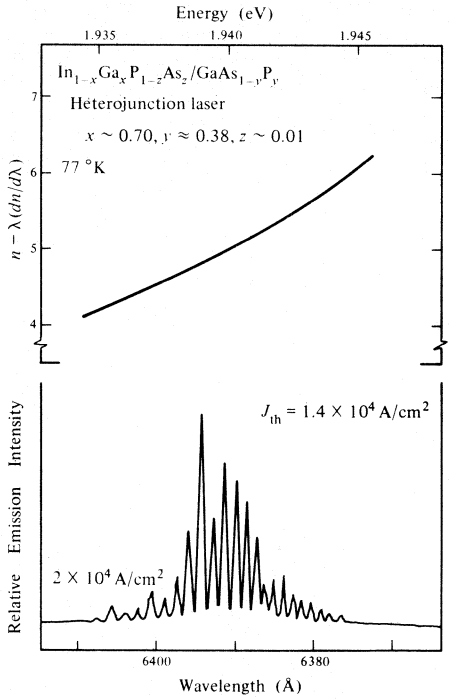

Fig. 8. Emission spectra (77 K) at high excitation level and index of refraction dispersion data $\{n - \lambda(dn/d\lambda)\}$ for an $In_{1-x}Ga_xP_{1-z}As_z/GaAs_{1-y}P_y$ heterojunction laser diode. The index expression increases monotonically with energy, indicating an increase in absorption at higher energy as expected. This device exhibits the typical mode structure of a Fabry–Perot structure operated well above laser threshold.

$$\Delta\lambda = (\lambda^2/2L)\,\{n - \lambda(dn/d\lambda)\}^{-1} \qquad (2)$$

where L is the diode length and n the index of refraction, the dispersion quantity $\{n - \lambda(dn/d\lambda)\}$ can be determined at various wavelengths if well-defined modes are observed, as in the present work. For example, for the diode of Figs. 2–5, we obtain the data of Fig. 8. To obtain the index dispersion quantity plotted in the upper part of Fig. 8, an expanded plot of the laser-mode spectrum has been employed to insure accuracy. The monotonically increasing character of the upper curve of Fig. 8 displays the classic behavior expected of direct-gap band-to-band laser diodes [20]. For example, a similar plot (4.2 K) for the $y \approx 0.40$ diode of Fig. 6 is shown in Fig. 9 and is almost identical to the curve of Fig. 8 except for the expected shift to shorter wavelength (6255 Å $< \lambda <$ 6270 Å). In N-doped $GaAs_{1-y}P_y$, however, more complicated behavior is observed, which also depends upon whether the N trap lies above or below the Γ band edge as is reported elsewhere [15]. Finally, we mention that only in these heterojunctions has the effect of the N trap in stimulated emission been observed in a current-driven structure [14], [15].

Conclusions

In comparison to LPE $In_{1-x}Ga_xP$ layers grown on $GaAs_{1-y}P_y$ substrates, which yield rather poor heterojunctions unless an excellent lattice match is realized accidentally, we find that a small addition of As to the LPE growth process leads to uniformly good $In_{1-x}Ga_xP_{1-z}As_z/GaAs_{1-y}P_y$ heterojunctions. Because the isolattice-constant lines of Fig. 1 *cross* the isoenergy-gap lines, it is possible to grow, along an isolattice-constant line, a wide range of compositions of $In_{1-x}Ga_x \cdot P_{1-z}As_z$ of higher energy gap on $GaAs_{1-y}P_y$ of lower energy gap. In the present work the As composition has been restricted to the range $z \sim 0.01$, but this is not necessary and it is possible to grow $In_{1-x}Ga_xP_{1-z}As_z/In_{1-x'}Ga_{x'}P_{1-z'} \cdot As_{z'}$ ($x \neq x'$, $z \neq z'$) homoheterojunctions on $GaAs_{1-y}P_y$ substrates.

In the present work, i.e., the simpler case of $In_{1-x}Ga_x \cdot P_{1-z}As_z/GaAs_{1-y}P_y$ single heterojunctions grown on $y =$ 0.32–0.40 substrates, we observe much lower laser threshold currents than for comparable $GaAs_{1-y}P_y$ homojunctions. In addition, laser operation has been achieved at considerably shorter wavelengths (<6300 Å) than for $y \approx 0.40$ $GaAs_{1-y}P_y$ homojunctions. Because of the relatively good carrier and optical energy confinement of these quaternary-ternary heterojunctions, above laser threshold the spontaneous radiation background is low and, as is typical of heterojunctions, very good cavity modes can be resolved. This permits measurement of the index expression $\{n - \lambda(dn/d\lambda)\}$ in an energy range not previously examined in $GaAs_{1-y}P_y$. These results turn out to be useful in comparison with those on N-doped $GaAs_{1-y}P_y$ in studying the peculiarities of the N isoelectronic trap in a ternary system in the range $E_N \sim E_\Gamma$.

Finally, we remark that because no attempt has been made to optimize the various geometrical and doping parameters of the heterojunctions of this work, it is almost certain that threshold currents can be reduced and the wavelength range be extended still further.

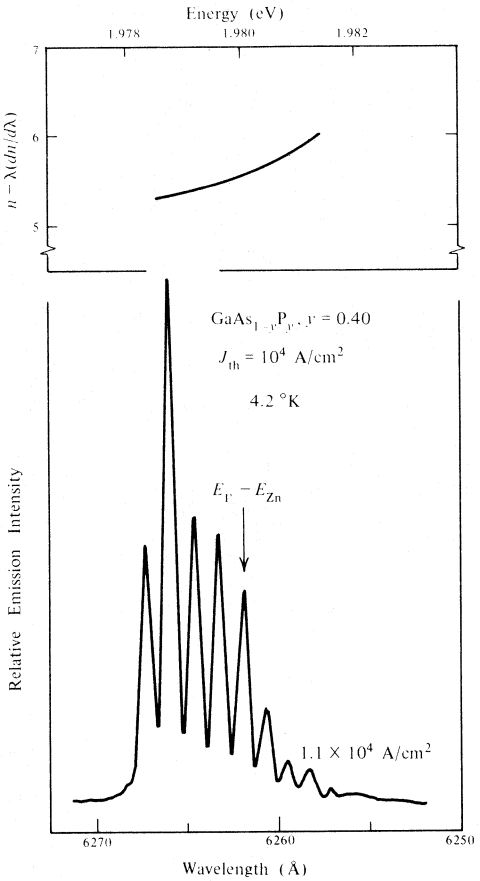

Fig. 9. Laser spectra (4.2 K) and index of refraction dispersion data $\{n - \lambda(dn/d\lambda)\}$ for an $In_{1-x}Ga_xP_{1-z}As_z/GaAs_{1-y}P_y$ heterojunction ($x \sim 0.70, y \approx 0.40, z \sim 0.01$) operated just above threshold. As expected, the index expression increases monotonically with energy through the donor band-tail region and into the band edge. Unlike these data, the first recorded for $y \sim 0.40$ $GaAs_{1-y}P_y$, structure is observed in the index data if N traps are introduced into the region (energy) of laser operation [15].

Acknowledgment

The authors wish to thank W. R. Hitchens, M. H. Lee, and R. J. Nelson for helpful discussions and assistance and M. G. Craford (Monsanto) for a long series of helpful discussions on $GaAs_{1-y}P_y$. They also wish to thank R. I. Gladin, K. A. Kuehl, B. L. Marshall, Y. S. Moroz, J. T. Romweber, and R. C. Arndt for their technical assistance.

References

[1] R. D. Burnham, N. Holonyak, Jr., and D. R. Scifres, "$Al_xGa_{1-x} \cdot As_{1-y'}P_{y'}$-$GaAs_{1-y}P_y$ heterostructure laser and lamp junctions," *Appl. Phys. Lett.*, vol. 17, pp. 455–457, Nov. 1970.

[2] R. D. Burnham, N. Holonyak, Jr., H. W. Korb, H. M. Macksey, D. R. Scifres, J. B. Woodhouse, and Zh. I. Alfërov, "Double heterojunction AlGaAsP quaternary lasers," *Appl. Phys. Lett.*, vol. 19, pp. 25–28, July 15, 1971.

[3] —, "Tverdie rastvori AlGaAsP i inzhektsionnie lazeri s dvumya geteroperekhodami na ih osnove," *Phys. Tekhn. Poluprovod.*, vol. 6, pp. 97–102, Jan. 1972 (*Sov. Phys.–Semicond.*, vol. 6, pp. 77–81, July 1972).

[4] H. M. Macksey, M. H. Lee, N. Holonyak, Jr., W. R. Hitchens, R. D. Dupuis, and J. C. Campbell, "Crystal and luminescence properties of constant-temperature liquid-phase-epitaxial $In_{1-x} \cdot Ga_xP$ ($x \sim 0.7$) grown on (100) $GaAs_{1-x}P_x$ ($x \sim 0.04$)," *J. Appl. Phys.*, vol. 44, pp. 5035–5040, Nov. 1973.

[5] J. C. Campbell, W. R. Hitchens, N. Holonyak, Jr., M. H. Lee, M. J. Ludowise, and J. J. Coleman, "Luminescence, laser and carrier-lifetime behavior of constant-temperature LPE $In_{1-x} \cdot Ga_xP$ ($x = 0.52$) grown on (100) GaAs," *Appl. Phys. Lett.*, vol. 24, pp. 327–330, Apr. 1, 1974.

[6] W. R. Hitchens, N. Holonyak, Jr., M. H. Lee, J. C. Campbell, J. J. Coleman, W. O. Groves, and D. L. Keune, "Liquid phase epitaxial (LPE) grown-junction $In_{1-x}Ga_xP$ ($x \sim 0.63$) laser of wavelength $\lambda \sim 5900$ Å (2.10 eV, 77°K)," *Appl. Phys. Lett.*, vol. 25, pp. 352–354, Sept. 15, 1974.

[7] W. R. Hitchens, N. Holonyak, Jr., M. H. Lee, and J. C. Campbell, "Liquid phase epitaxial growth and photoluminescence characterization of laser-quality (100) $In_{1-x}Ga_xP$," *J. Cryst. Growth*, vol. 27, pp. 154–165, Dec. 1974.

[8] J. J. Coleman, W. R. Hitchens, N. Holonyak, Jr., M. J. Ludowise, W. O. Groves, and D. L. Keune, "Liquid phase epitaxial $In_{1-x} \cdot Ga_xP_{1-z}As_z/GaAs_{1-y}P_y$ quaternary (LPE)-ternary (VPE) heterojunction lasers," *Appl. Phys. Lett.*, vol. 25, pp. 725–727, Dec. 15, 1974.

[9] G. B. Stringfellow, "The importance of lattice mismatch in the growth of $Ga_xIn_{1-x}P$ epitaxial crystals," *J. Appl. Phys.*, vol. 43, pp. 3455–3460, Aug. 1972.

[10] G. A. Antypas and R. L. Moon, "Growth and characterization of InP-InGaAsP lattice-matched heterojunctions," *J. Electrochem. Soc.*, vol. 120, pp. 1574–1577, Nov. 1973.

[11a] J. J. Tietjen, J. I. Pankove, I. J. Hegyi, and H. Nelson, "Vapor-phase growth of $GaAs_{1-x}P_x$ room-temperature injection lasers," *Trans. AIME*, vol. 239, pp. 385–387, Mar. 1967.

[11b] C. J. Nuese, A. G. Sigai, and J. J. Gannon, "Orange laser emission and bright electroluminescence from $In_{1-x}Ga_xP$ vapor-grown p-n junctions," *Appl. Phys. Lett.*, vol. 20, pp. 431–434, June 1, 1972.

[12] H. M. Macksey, N. Holonyak, Jr., R. D. Dupuis, J. C. Campbell, and G. W. Zack, "Crystal synthesis, electrical properties, and spontaneous and stimulated photoluminescence of $In_{1-x} \cdot Ga_xP$:N grown from solution," *J. Appl. Phys.*, vol. 44, pp. 1333–1341, Mar. 1973.

[13] G. B. Stringfellow, P. F. Lindquist, and R. A. Burmeister, "Liquid phase epitaxial growth in $Ga_xIn_{1-x}P$," *J. Electron. Mat.*, vol. 1, pp. 437–457, 1972.

[14] J. J. Coleman, N. Holonyak, Jr., A. B. Kunz, W. O. Groves, D. L. Keune, and M. G. Craford, "Resonant enhancement (?) of the recombination probability at the nitrogen-trap, Γ-band edge crossover in $GaAs_{1-x}P_x$:N ($E_N = E_\Gamma$, $x \equiv x_N$)," *Solid State Commun.*, vol. 16, pp. 319–322, Feb. 1975.

[15] J. J. Coleman, N. Holonyak, Jr., M. J. Ludowise, A. B. Kunz, M. Altarelli, W. O. Groves, and D. L. Keune, "Index dispersion above the fundamental band edge in nitrogen-doped $GaAs_{1-y}P_y$ ($y = 0.38$, $E_N > E_\Gamma$)," *Phys. Rev. Lett.*, vol. 33, pp. 1566–1569, Dec. 23, 1974.

[16] M. G. Craford, R. W. Shaw, A. H. Herzog, and W. O. Groves, "Radiative recombination mechanisms in GaAsP diodes with and without nitrogen doping," *J. Appl. Phys.*, vol. 43, pp. 4075–4083, Oct. 1972.

[17] J. C. Campbell, N. Holonyak, Jr., M. G. Craford, and D. L. Keune, "Band structure enhancement and optimization of radiative recombination in $GaAs_{1-x}P_x$:N (and $In_{1-x}Ga_xP$:N)," *J. Appl. Phys.*, vol. 45, pp. 4543–4553, Oct. 1974.

[18] M. G. Craford, G. E. Stillman, J. A. Rossi, and N. Holonyak, Jr., "Effect of Te and S donor levels on the properties of $GaAs_{1-x}P_x$ near the direct-indirect transition," *Phys. Rev.*, vol. 168, pp. 867–882, Apr. 1968.

[19] C. J. Nuese, G. E. Stillman, M. D. Sirkis, and N. Holonyak, Jr., "Gallium arsenide-phosphide: Crystal, diffusion, and laser properties," *Solid-State Electron.*, vol. 9, pp. 735–749, Aug. 1966.

[20] M. I. Nathan, G. Burns, and A. B. Fowler, "Dispersion and loss in GaAs injection lasers," in *Radiative Recombination in Semiconductors*. New York: Academic, 1965, pp. 205–208.

Efficient InSb Laser with Resonant Longitudinal Optical Pumping

N. MENYUK, A. S. PINE, AND A. MOORADIAN

Abstract—External quantum efficiency of > 20 percent has been achieved from tunable CW InSb lasers resonantly pumped with a CO laser. Thin InSb platelets at < 10 K were pumped in a longitudinal geometry with the InSb recombination emission parallel to the CO radiation. Single-longitudinal-mode operation with power up to 10 mW has been achieved with a 0.1-0.3-cm^{-1} linewidth, mechanically or thermally tunable over several cm^{-1}. Magnetic-field effects on the threshold and emission frequency have also been studied.

Introduction

OPTICAL PUMPING of semiconductor lasers provides a convenient means of excitation and investigation of those materials which are not readily available as injection lasers. The semiconductor laser can act as a tunable frequency converter for the usual fixed-wavelength pump. Several years ago, Phelan optically pumped InSb at ~10 K with pulsed GaAs diode lasers [1], [2] and flashlamps [3] in a transverse geometry where the 5.3-μm InSb laser radiation was emitted from cleaved edges perpendicular to the pumped face. This same geometry was used more recently to pressure tune InSb at 77 K with Q-switched Nd:YAG excitation [4], and to temperature and magnetic-field tune InSb at 10 K pumped with CW GaAs, Nd:YAG, and CO lasers [5]. The CW GaAs pumping led to a convenient tunable infrared source capable of Doppler-limited spectroscopy [5] of nitric oxide, ethylene, and water vapor in the 5.3-μm region. The transverse-pumped InSb typically yielded 1-10-μW output power for an incident power of 20-200 mW.

Much more efficient optical conversion has now been achieved by near-resonant excitation in a longitudinal geometry where the parallel incident radiation and stimulated emission are normal to the polished InSb platelet faces. A single-ended CW output of up to 10 mW has been obtained in a single-longitudinal Fabry-Perot mode with an incident CO laser power of 160 mW. This is almost a thousand times more output power than for the transverse geometry. An external quantum efficiency of ~ 21 percent is calculated from the double-ended output power divided by the absorbed incident power $(2P_{out}/(1-R)P_{in})$ where the reflectivity $R \simeq 44$ percent. Thresholds for the two geometries are comparable (10-20 mW) and the emission frequencies are 20-30 cm^{-1} higher for longitudinal pumping. Magnetic-field effects on the threshold and emission frequencies are similar for the two pumping schemes.

Longitudinal bulk pumping of semiconductor lasers was first accomplished by Stillman *et al.* [6] and Johnson and Holonyak [7] for Cd(SeS) and Ga(AsP) crystals in the red spectral region. They established that the platelet thickness L should be less than the carrier diffusion length or the pump light absorption depth. At the same time the Fabry-Perot mode spacing $\Delta\nu_L = 1/2\eta^* L$ should not be larger than the spontaneous-emission gain bandwidth. For InSb at liquid-helium temperatures the spontaneous bandwidth is on the order of $kT/hc \sim 5$ cm^{-1}; so for an effective refractive index $\eta^* = \eta - \lambda(\partial\eta/\partial\lambda) \sim 5$, the minimum thickness should be ~ 200 μm. Since this thickness is several times the carrier diffusion length, it is necessary to resonantly pump near the absorption edge of the crystal. The number of longitudinal cavity modes that can oscillate is roughly the gain bandwidth divided by $\Delta\nu_L$; so single-mode operation is easily achieved for platelets near the minimum thickness.

Manuscript received January 16, 1975; revised February 18, 1975. This work was supported by the National Science Foundation.

The authors are with the Lincoln Laboratory, Massachusetts Institute of Technology, Lexington, Mass. 02173.

Experiment

The InSb platelet samples were prepared from ~ 1-cm^2 wafers cut from low-carrier-concentration (n or p ~ 10^{14} cm^{-3}) ingots grown by Cominco. The laser-cavity faces were etch-polished (2-percent Br in CH_3OH) to a high luster at the desired thickness with a parallelism better than 1 mrad. The platelets were spring clamped and thermal-compound greased to a helium-Dewar copper cold finger having a 3-mm optical aperture. The optical excitation was provided by a stable CW grating-tunable CO laser focused onto the sample with a spherical 10-cm-focal-length BaF_2 lens. The sample was tilted a few degrees from normal incidence to avoid feedback into the CO laser. Forward InSb laser emission was measured directly by a calibrated Eppley thermopile or with a Barnes InSb photovoltaic detector through a Spex $\frac{3}{4}$-m grating spectrometer and chopper. Forward, rather than backward, emission was monitored since the InSb provided partial filtering of the CO radiation, and since no beamsplitter would be required. The InSb could be probed spatially and wedge tuned by simple lateral motion of the sample. The magnetic field could be applied in the plane of the platelet normal to the optical propagation.

Thresholds, conversion efficiencies, and spectral properties were measured on a number of samples of varying carrier concentration and type, crystal orientation, and thickness. These variables had little systematic effect on the results, except for the thickness dependence of the number of Fabry-Perot modes. Also ⟨111⟩-face orientation was avoided because of poor surface polish. The data presented here (except where indicated) are for a Cominco (ingot #W501) p-type = 4×10^{13}-cm^{-3} ⟨110⟩-face crystal of thickness $L = 180$ μm operating in a single dominant longitudinal mode.

The CW thresholds of both longitudinal- and transverse-pumped InSb lasers are compared in Fig. 1 as a function of the near-resonant incident CO frequency. The threshold of the transverse-surface-pumped sample described earlier [5]

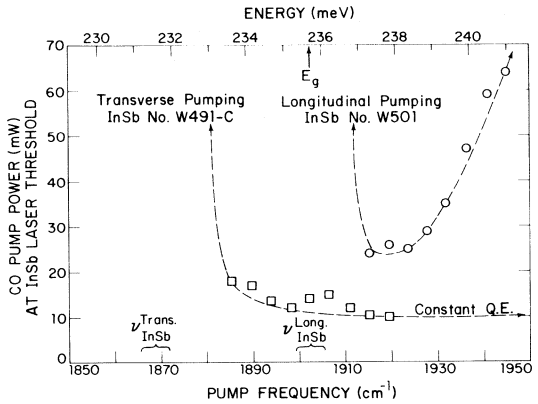

Fig. 1. Threshold power of InSb laser versus CO-pump laser frequency for transverse □ and longitudinal ○ geometry. InSb-laser-emission range and energy gap is indicated; extrapolated constant quantum efficiency (QE) curve is also shown.

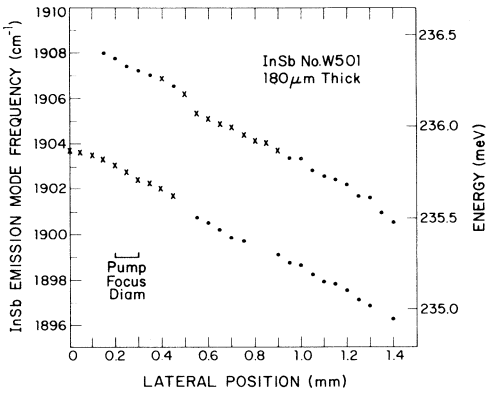

Fig. 2. Wedge tuning of longitudinal InSb laser modes by lateral displacement. Principal modes indicated by × and subsidiary modes by ·

(Cominco #W491-C, n ~ 1.4×10^{14} cm^{-3}, ⟨111⟩-face, ⟨110⟩ cleaved edges spaced by 300 μm, thickness ~ 30 μm) decreases just above the absorption edge to a shallow minimum and then increases slowly along a curve of roughly constant quantum efficiency all the way up to a near-IR Nd:YAG pump (65-mW threshold). The threshold of the longitudinal-bulk-pumped sample drops precipitously above the absorption edge to a sharper minimum and then rises steeply due to a decreasing absorption depth for the higher pump frequency. CW longitudinal laser emission could not be achieved with the Nd:YAG laser pump. Also indicated in Fig. 1 is the range of laser frequencies emitted by the two samples and the published band gap [8] E_g of the material.

There are several noteworthy points illustrated in Fig. 1. First, the shapes of the two threshold curves are characteristic of the pumping geometries and are qualitatively explained on the basis of surface and volume excitation. Second, the comparable magnitudes of the thresholds at minimum are probably due to the similar excitation volumes and population-inversion densities for the two schemes. The transverse pump is focused with a 10-cm cylindrical lens for a beam waist of ~ 100 μm and an excited volume of ~ 0.9×10^6 μm^3 assuming carrier diffusion to the rear surface and subsequent confinement. The longitudinally pumped volume is ~ 2×10^6 μm^3. The threshold-density agreement is fortuitous since thresholds varied by factors of 3–5 due to sample inhomogeneity.

The frequency shift exhibited by both the absorption edge and laser emission of the InSb in the two geometries is unexplained. It has been noted that sample inhomogeneity [5] and dopant variation [2] create frequency discrepancies of this magnitude. However, in these experiments a systematic trend toward higher frequencies for longitudinally pumped samples has been observed; the data shown are for typical samples. A similar pumping shift was observed on samples prepared from the same wafer and no overlap occurred for the highest frequency transverse and lowest frequency longitudinal samples tested.

Band-gap shifts could arise from temperature or stress variations or from the dynamic Burstein shift (band filling). However, the same cold-finger mounting techniques were used for all CO-pumped samples, so that stress and temperature shifts were not expected. In addition, since the incident power density was comparable for the two pumping cases, band filling should also have been comparable. The dynamic Burstein shift was directly observed in the longitudinal geometry as a highly nonlinear transmission (bleaching or saturable absorption) of the InSb platelet to the CO radiation above the band gap.

The longitudinally pumped InSb sample could be mechanically tuned continuously over several cm^{-1} by lateral displacement of the sample, as shown in Fig. 2. Here the lack of parallelism of the polished cavity surfaces (~ 0.5 mrad) results in wedge tuning of the Fabry–Perot modes. Principal modes are indicated by crosses; subsidiary modes, by dots; a single dominant mode was achieved over much of the range. Some sample inhomogeneity may also contribute to this tuning, particularly where the weaker modes are displaced beyond the original spontaneous gain bandwidth.

Spectral traces of the wedge-tuned InSb laser emission and transmitted CO-pump radiation are shown in Fig. 3. Here the resolution of the spectrometer (~ 0.1 cm^{-1}) is sufficient to observe a broadening of the InSb mode width over the CO linewidth. This broadening of from 0.1 to 0.3 cm^{-1} is attributed to a number of closely spaced transverse cavity modes associated with each longitudinal mode. The number of transverse modes allowed is roughly $\eta^* a^2/\lambda L$, the Fresnel number, where a is the aperture, or beam, radius. In the case of Figs. 2 and 3, $a \sim 50$ μm, $L \sim 180$ μm, so ~ 13 modes are supportable and are probably launched by the surface roughness and lack of parallelism. The wedge effect over the beam spot size is seen in Fig. 2 to correspond to the observed width. The surface roughness for etch-polished and $\frac{1}{4}$-μm-diam diamond-paste-polished InSb has also been probed with a 2.5-μm-radius Dektak stylus and is shown in Fig. 4. These surface irregularities, if accurately depicted, are less severe than the wedge effect for causing transverse modes. More refined polishing techniques could sharpen the InSb linewidth, but the Fresnel number is still unfavorably large. A longer cavity decreases the Fresnel number, but increases the possible number of longitudinal modes. Surface aperturing using photoresist etch-roughening could reduce a, but this would eliminate the possibility of wedge tuning or surface probing.

The forward InSb emission corresponding to the spectra of

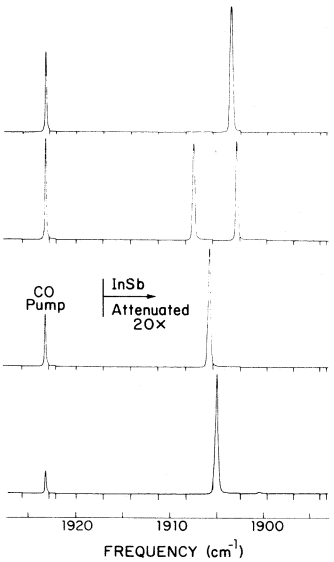

Fig. 3. Wedge-tuned InSb laser spectra. InSb #W501 corresponding to Fig. 2. The InSb emission is attenuated by a factor of 20 with a mica filter to avoid detector saturation for linewidth comparison to residual CO-pump line at 1923.5 cm^{-1}.

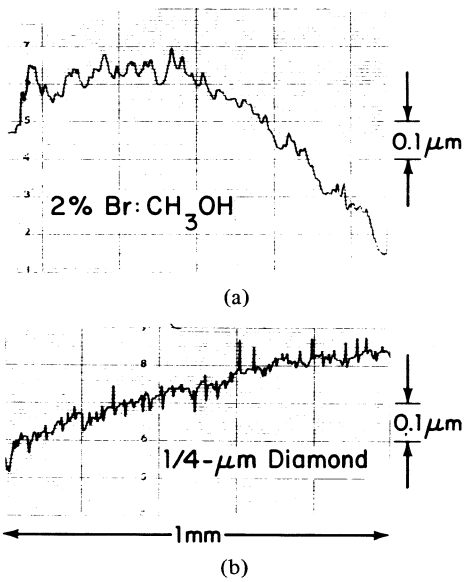

Fig. 4. Surface roughness of polished InSb samples. (a) 2-percent Br in CH_3OH etch-polish. (b) $\frac{1}{4}$-μm diamond-paste polish.

Fig. 3 was about 7.5 mW in the dominant mode for about 160 mW of incident CO radiation at 1923.5 cm^{-1} and a reflectivity of 44 percent. The double-ended efficiency was therefore ~ 17 percent which could be increased slightly with magnetic field.

Magnetic-Field Effects

The effects of magnetic field on the threshold, conversion efficiency, and emission frequency of InSb lasers have been the subject of a number of interesting studies for both optical [2], [5] and injection pumping [9]-[14]. It has been found previously [2], [5], [9], [11], [12] that magnetic fields decrease threshold and increase efficiency. This has been attributed [12] to a field-dependent condensation of the Landau-level density-of-states. Similar effects in InAs diode lasers [15] have been interpreted as magnetic deflection confinement of diffusing and drifting carriers. The magnetic-field dependence of the CW threshold of the longitudinal optically pumped InSb is given in Fig. 5. These results resemble previous optically pumped cases [2], [5] but are less dramatic than for InSb diode lasers [9], [11]. Here there are no drift fields and the illuminated region is already larger than the carrier diffusion length, so the confinement interpretation is not appropriate. The Landau condensation mechanism seems to be applicable and may explain the Fig. 5 threshold variations in correspondence with the mode shifts shown in Fig. 6(b).

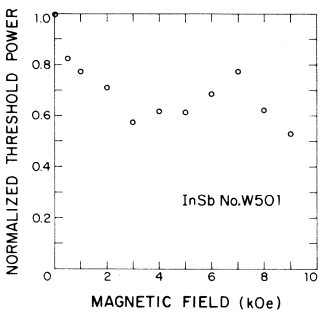

Fig. 5. Magnetic-field dependence of CW InSb threshold.

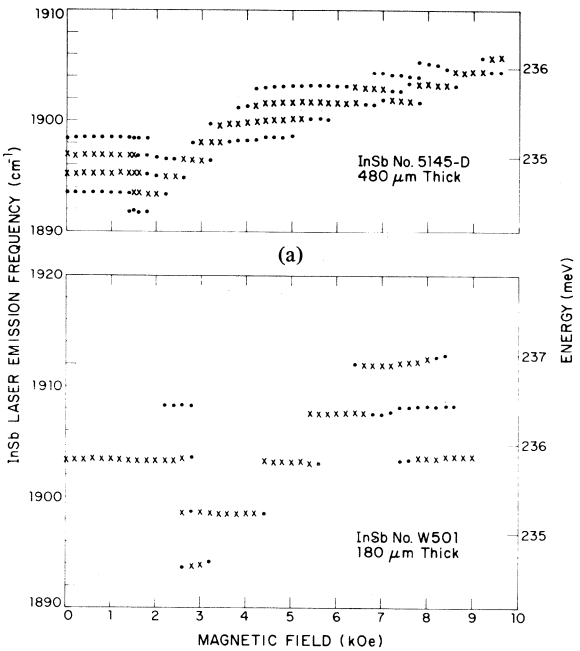

Fig. 6. Magnetic-field dependence of InSb laser mode frequencies for two sample thicknesses. Principal modes indicated by × and subsidiary modes by ·

The double-ended conversion efficiency in this case increases irregularly to ~ 21 percent at 8.5 kOe with 10-mW forward output for a 160-mW pump at 1923.5 cm^{-1} and $R = 44$ percent.

There is less universal experimental accord on the magnetic-field dependence of the emission frequency of InSb lasers. Phelan *et al.* [9] and Bell and Rogers [13] observed a strong

linear increase of frequency at moderate fields (20-30 kOe) followed by a sudden frequency drop and smaller linear increase at higher fields. These two segments were attributed to up and down spin states of the lowest Landau level. A different ordering was observed by Shotov *et al.* [14] with the large-slope segment at lower fields (4-10 kOe) at lower frequency than the high-field segment. This was explained by transitions of electrons to light and heavy hole bands, respectively. None of these studies gave zero field results because of the higher thresholds required.

For CW transverse optically pumped InSb [5], a low-field (1.5-2 kOe) minimum in the emission frequency was observed. Fig. 6 shows similar results for samples of two different thicknesses optically pumped in a longitudinal geometry. Though there are minor differences in the magnetic-field tuning between these samples and the transverse-pumped case [5], the presence of the low-field minimum seems to be independent of pumping geometry, field or crystal orientation, and sample concentration or type.

Prior to the CW transverse pumped case [5], no data on the emission frequency between 0 and 2 kOe had been reported. We speculated there [5] that the low-field minimum may be caused by a magnetic-field-induced increase in the exciton binding energy which allows the exciton peak to emerge from the continuum density-of-states at moderately low fields. The bound exciton is relatively stable in position for low fields since it tunes according to a quadratic Zeeman effect. The linear Landau-level tuning of the free carriers in the band therefore lifts the continuum away from the exciton. At zero field the band states and exciton (with finite linewidth due to lifetime effects) are not resolved, and the density-of-states may peak above the exciton level. As the field is raised the exciton becomes discrete and its peak defines the laser frequency. At still higher fields, when the cyclotron energy greatly exceeds the zero-field binding energy, the exciton level approaches the field dependence of the free-electron Landau level [16]. Such an effect has been advanced by Johnson [17] to interpret structure in the low-temperature magnetoabsorption spectrum of InSb.

Application to Spectroscopy

Doppler-limited spectroscopy at 5.3 μm has been demonstrated with CW InSb lasers optically pumped in the transverse geometry [5]. The longitudinally pumped lasers with tunable single-mode output of much higher power have an even greater potential for spectroscopy. At present the resolution of the device is limited by the broad linewidth (0.1-0.3 cm^{-1}) arising from the spurious transverse-cavity modes associated with the longitudinal peak. This linewidth, which is barely adequate for atmospheric-broadened spectroscopy, may be improvable with refined fabrication techniques.

The mechanical- and magnetic-field-tuning techniques are useful to obtain quasi-continuous coverage over tens of cm^{-1}. Mode hopping is prevalent with magnetic tuning as seen in Fig. 6 where each mode pulls very little with field. Significant mode pulling as a function of magnetic field has been observed in the InSb spin-flip Raman laser, where the spontaneous linewidth can be comparable to, or narrower than, the cavity linewidth [18], [19]. In the present case, the broader gain profile and small H-field dependence of η^* results in very small continuous tuning.

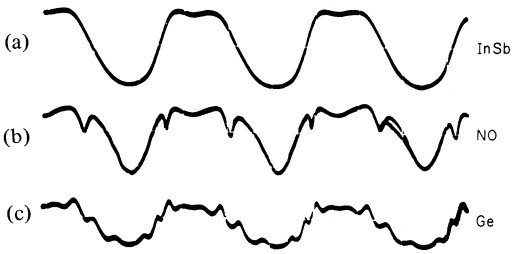

Fig. 7. Oscilloscope traces of real-time temperature tuning of longitudinal InSb laser by 60-Hz modulation of CO-pump intensity. (a) Direct frequency- and amplitude-modulated InSb emission at 1903.1 cm^{-1}. (b) Transmission through a 10-cm 10-torr cell of NO exhibiting $R_{1/2}(15/2)$ absorption dips upon heating and cooling. (c) Transmission through a Ge etalon with 0.13-cm^{-1} fringe spacing.

Wedge tuning provides potentially continuous coverage between modes as exhibited in Fig. 2. However, at present wedge tuning creates annoying amplitude fluctuations due to the stochastic nature of the transverse modes supported by the poorly polished surfaces. For these reasons, mechanical and magnetic-field tuning are most useful for biasing the emission in the spectral range of interest, where temperature tuning can be used for fast smooth scanning. Such thermal scanning can be achieved by simply modulating the incident pump intensity. An example of real-time temperature tuning is shown in Fig. 7 where the CO laser power is 20 percent modulated with a 60-Hz sine wave applied to the discharge voltage. The upper trace (a) is the resultant frequency- (and amplitude-) modulated output of the InSb at 1903.1 cm^{-1}; the middle trace (b) is a spectral absorption of the $R_{1/2}(15/2)$ line of nitric oxide at 10 torr in a 10-cm cell; the bottom trace (c) shows the interference fringes of a 0.96-cm-thick Ge etalon. The traces are poorly resolved because the laser linewidth is broader than the spectral features examined.

Conclusions

The high-power tunable single-mode operation of the longitudinal optically pumped InSb laser makes it a potentially attractive device for infrared spectroscopy and communications. The principal drawback is its broad linewidth which may be amenable to improvement. Some important features of this laser relative to the transverse pumped device are not understood. Foremost among these are: 1) the hundred-fold increase in conversion efficiency where the excitation density and thresholds are comparable, and 2) the shift to higher frequencies of the pump absorption and output emission of the longitudinal device. In addition, while the much broader mode width of the longitudinal-pumped device may be due to surface roughness and lack of parallelism, the mode purity of the transverse-pumped laser is surprising in view of its comparably large Fresnel number. The magnetic-field effects on the threshold and efficiency are similar to earlier results and are apparently related to magnetic condensation of the density-of-states and resultant mode shifts. Exciton effects are thought to be responsible for the low-field minimum in the emission frequency of InSb.

ACKNOWLEDGMENT

The authors wish to thank S. R. J. Brueck and C. Hurwitz for their invaluable help. They also wish to thank S. Palmacci, H. Favreau, and S. Duda for technical assistance.

REFERENCES

[1] R. J. Phelan and R. H. Rediker, "Optically pumped semiconductor laser," *Appl. Phys. Lett.*, vol. 6, pp. 70–71, 1965.
[2] R. J. Phelan, Jr., "Laser emission by optical pumping of semiconductors," in *Physics of Quantum Electronics*, P. L. Kelley, B. Lax, and P. E. Tannenwald, Ed. New York: McGraw-Hill, 1966, pp. 435–441.
[3] —, "Incoherent source optical pumping of visible and infrared semiconductor lasers," *Proc. IEEE* (Lett.), vol. 54, pp. 1119–1120, Aug. 1966.
[4] N. Menyuk, A. S. Pine, J. A. Kafalas, and A. J. Strauss, "Effects of pressure on optically pumped GaSb, InAs and InSb lasers," *J. Appl. Phys.*, vol. 45, pp. 3477–3484, 1974.
[5] A. S. Pine and N. Menyuk, "Optically pumped cw InSb lasers for NO spectroscopy," *Appl. Phys. Lett.*, vol. 26, pp. 231–233, 1975.
[6] G. E. Stillman *et al.*, "Volume excitation of an ultrathin single-mode CdSe laser," *Appl. Phys. Lett.*, vol. 9, pp. 268–269, 1966.
[7] M. R. Johnson and N. Holonyak, "Optically pumped thin-platelet semiconductor lasers," *J. Appl. Phys.*, vol. 39, pp. 3977–3985, 1968.
[8] S. Zwerdling, W. H. Kleiner, and J. P. Theriault, "Oscillating magnetoabsorption in InSb under high resolution," *J. Appl. Phys.* (suppl. to vol. 32), pp. 2118–2123, 1961.
[9] R. J. Phelan *et al.*, "Infrared InSb laser diode in high magnetic fields," *Appl. Phys. Lett.*, vol. 3, pp. 143–145, 1963.
[10] I. Melngailis, R. J. Phelan, and R. H. Rediker, "Luminescence and coherent emission in a large-volume injection plasma in InSb," *Appl. Phys. Lett.*, vol. 5, pp. 99–100, 1964.
[11] A. P. Shotov, S. P. Grishechkina, and R. A. Muminov, "Generation of coherent radiation in electron-hole plasmas in indium antimonide," *Sov. Phys.–Solid State*, vol. 8, pp. 1998–1999, 1967.
[12] A. P. Shotov, M. S. Mirgalovskaya, R. A. Muminov, and M. R. Raukhman, "Coherent emission of indium antimonide crystals with pulled p-n junctions," *Sov. Phys.–Semicond.*, vol. 1, pp. 1193–1194, 1967.
[13] R. L. Bell and K. T. Rogers, "The mechanism of band-gap laser action in InSb diodes," *Appl. Phys. Lett.*, vol. 5, pp. 9–11, 1964.
[14] a) A. P. Shotov, "Tunable semiconductor infrared lasers," *J. Japan Soc. Appl. Phys.* (suppl. to vol. 42), pp. 282–288, 1972.
b) I. I. Zasavitskii, B. N. Matsionashvili, and A. P. Shotov, "Tuning the coherent radiation frequency of indium antimonide by a magnetic field," *Sov. Phys.–Semicond.*, vol. 4, pp. 274–276, 1970.
[15] I. Melngailis and R. H. Rediker, "Properties of InAs lasers," *J. Appl. Phys.*, vol. 37, pp. 899–911, 1966.
[16] J. O. Dimmock, "Introduction to the theory of exciton states in semiconductors," in *Semiconductors and Semimetals*, R. K. Willardson and A. C. Beer, Ed. New York: Academic, 1967.
[17] E. J. Johnson, "Observation of exciton fine structure in the interband magnetoabsorption of InSb and germanium," *Phys. Rev. Lett.*, vol. 19, pp. 352–355, 1967.
[18] S. R. J. Brueck and A. Mooradian, "Efficient, single-mode, cw, tunable spin-flip Raman laser," *Appl. Phys. Lett.*, vol. 18, pp. 229–230, 1971.
[19] C. K. N. Patel, "Spin flip Raman laser and applications," in *Laser Spectroscopy*, R. G. Brewer and A. Mooradian, Ed. New York: Plenum, pp. 471–491, 1974.

The Analysis of Optical Scattering in Double-Heterostructure and Five-Layer Heterostructure (GaAl)As/GaAs Injection Lasers

G. H. B. THOMPSON, P. A. KIRKBY, AND J. E. A. WHITEAWAY

Abstract—**The optical-absorption loss in (GaAl)As/GaAs heterostructure lasers with narrow active layers and passive layers doped below 5×10^{17} cm^{-3} should be less than 5 cm^{-1}. Measurements which have been made on a variety of three- and five-layer lasers have seldom shown such low figures. Optical-scattering loss at imperfections in the heterostructure interface could account for the discrepancy. An analysis of the scattering in both three- and five-layer heterostructures is presented. Curves are derived relating the absorption coefficient with the dielectric-constant step at the waveguide wall, the active-layer thickness, and the magnitude of the roughness. Measured losses as high as 12 cm^{-1} can be accounted for by a roughness amplitude of only 0.01 μm.**

Manuscript received January 8, 1975; revised February 10, 1975. This work was carried out with the support of the Procurement Executive, United Kingdom Ministry of Defence and sponsored by CVD.

The authors are with the Standard Telecommunication Laboratories Ltd., London Road, Harlow, Essex, England.

I. INTRODUCTION

In a semiconductor laser optical absorption and dissipation processes decrease the external quantum efficiency and increase the threshold current density. Pinkas *et al.* [1] investigated these characteristics in double-heterostructure lasers with a variety of n- and p-type doping levels in the active layer. By measuring the dependence of incremental quantum efficiency on laser length they deduced values of the absorption coefficient α. The absorption coefficient was found to lie in the range 10 cm^{-1} and upwards. Pinkas *et al.* were satisfied that they could ascribe it to free-carrier absorption, either by the free carriers introduced by the doping or, when the doping was low, by the free carriers injected into the active layer to produce inversion.

We have investigated (GaAl)As/GaAs heterostructure lasers

in which the free-carrier absorption should be considerably reduced. In these layers the active layer was made particularly narrow so that the light was not strongly confined and could spread into the surrounding layers, which were deliberately doped at a low level ($< 5 \times 10^{17} cm^{-3}$) to reduce the free-carrier concentration. Some of these lasers were normal double heterostructures in which a wide spread of the optical distribution was desired for high peak power [2] and some were five-layer structures in which additional optical confinement barriers were provided by enclosing the first three layers between two additional layers of higher AlAs content [3]. Free-carrier losses should have been less than 5 cm^{-1}.

Only in one case have we measured a total optical-absorption loss low enough (4.8 cm^{-1}) to be accounted for by free carriers alone. In general, the absorption loss has been considerably greater than this. Although reasonably consistent for lasers from a given slice, it has varied apparently randomly from slice to slice. We believe that the additional loss can be attributed to optical scattering from roughness at the heterojunction interfaces and present here a theoretical analysis of the magnitude of the effects which may be expected. The analysis is based on the methods described by Marcuse [4] for determining the scattering from a slab dielectric guide, which we have extended to cover the range of dimensions and refractive-index steps appropriate to laser structures.

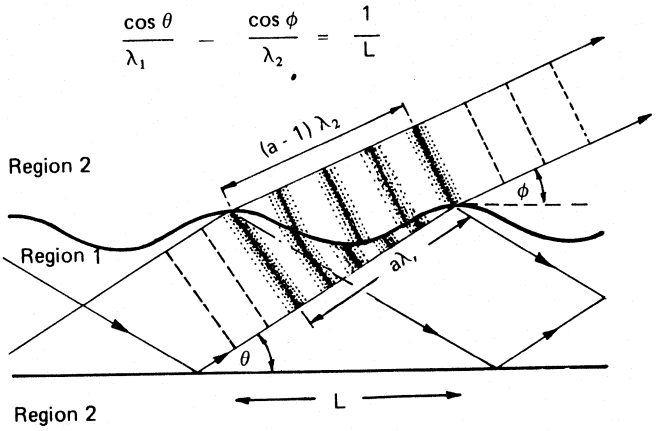

Fig. 1. Beam radiated from the corrugated interface of a dielectric-slab waveguide.

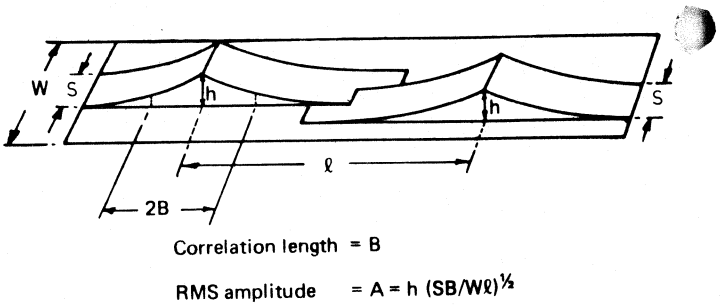

Fig. 2. Representation of roughness of heterojunction interface.

II. Analysis of Optical Scattering

A. Periodic and Statistical Roughness

A systematic sinusoidal undulation of the interface of a dielectric-slab guide scatters a guided wave into a directional beam of radiation. This makes an angle with the guide direction determined by the periodicity of the undulation, the relative dielectric constants of the inner and outer media of the waveguide, and the effective angle of incidence of the guided wave. The angle is given by an equation analogous to the equation for an optical grating. The general behavior is illustrated in Fig. 1.

The form of scattering produced by less regular imperfections in the interfaces of the dielectric guide depends on the Fourier spectrum of the roughness. Marcuse, in his analysis, defined the roughness in terms of an rms deviation of the interface from perfect planarity, given by an amplitude A, and described the particular form of the irregularity in terms of a correlation length B. The latter quantity, which roughly determines the extent of any given irregularity, is difficult to characterize precisely. In Marcuse's definition the correlation function of the roughness is assumed to decay exponentially with distance from any given point along the direction of the waveguide with a characteristic length B. Such an assumption still allows a wide range of irregularities to be included. Amongst these is one particularly simple example whose cross section is itself represented by an exponential shape, as illustrated in Fig. 2. It consists of a V-shaped groove, or ridge, with a width to the $1/e$ points of $2B$. Alternatively, a sawtooth groove or ridge would equally well satisfy the condition. Either of these are reasonably characteristic of the actual defects observed at the interface.

Fig. 3 shows the form of optical scattering induced by a guided wave at a rough interface with the previously stated characteristics, calculated according to the methods to be described. The dielectric guide illustrated is typical of that in a double-heterostructure laser with a thin active layer (the guide thickness is 0.12 μm and the dielectric-constant step is 1.3 at both guide interfaces). The polar diagram of the scattered intensity is shown for two values of the correlation length B. The scattered light emerges from the guide over a finite range of angles but is still fairly directional. The direction of peak intensity depends on $2\pi B$ in the case of a rough interface in a similar way to its dependence on the wavelength of the corrugation in the case of a sinusoidal interface. The angle ϕ indicates the direction of the scattered beam in the latter case. (Note, however, that for sinusoidal roughness ϕ becomes zero and then ceases to exist for long enough corrugation wavelength, in which case second-order effects should be taken into account.) The general tendency is for the polar diagram of the scattered intensity from the rough surface to rotate with ϕ, as B is increased, towards a more glancing angle of emergence, although it never drops to zero even for very large B.

Calculation of the total absorption loss of the fundamental guided mode due to scattering involves firstly obtaining the scattered intensity at any given angle of emergence, secondly

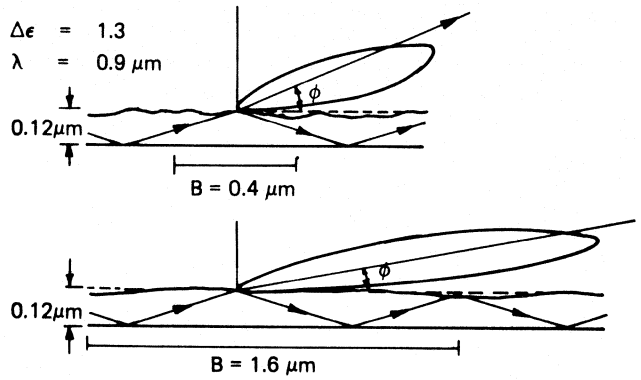

Fig. 3. Examples of beam radiated from dielectric-slab waveguide with rough interface.

integrating over all angles of emergence, and thirdly relating the total scattered intensity to the power carried by the fundamental mode. When additional modes can propagate in the guide it is necessary also to include in the scattering loss the power coupled to these modes. Although this power is not lost from the guide it is no longer coherent with the lasing mode and hence should not be included in determining the conditions which apply at threshold.

B. Scattering Theory for Three-Layer Guides

Marcuse gives an integral expression from which the absorption coefficient α, due to scattering from the fundamental mode into unguided waves, can be obtained in terms of the roughness amplitude A and the correlation length B. The variable parameters are the dielectric constants of the inner layer and the outer layers (a symmetrical guide is treated in which both outer layers have the same dielectric constant), the thickness of the center layer, and the wavelength. We will take the outer layers as having a dielectric constant of ϵ and the center layer as having a dielectric constant of $\epsilon(1 + \Delta)$ and a thickness of d. By judicious normalization it is possible to reduce the number of variable parameters and provide a more general expression better suited to numerical computation. We will define a normalized attenuation coefficient due to scattering α_0 such that

$$\alpha_0 = 2\pi\alpha/\Delta^2\beta_\epsilon^3 A^2 \tag{1}$$

where β_ϵ is the propagation constant of TEM waves in the outer layers of the dielectric guide ($= 2\pi\epsilon^{1/2}/\lambda$). We will also define a normalized correlation length B_n given by

$$B_n = \beta_\epsilon \Delta B. \tag{2}$$

The normalized absorption coefficient is then given, according to the Marcuse expression, by

$$\alpha_0 = \frac{2P_0\Delta Q_0^2}{x_0 B_n (P_0 D + 1)} \int_{-1}^{1} \frac{P}{(x_0 - x)^2 + (A/B_n)^2} \cdot \left\{ \frac{\cos^2 QD}{Q^2 - \cos^2 QD} + \frac{\sin^2 QD}{Q^2 - \sin^2 QD} \right\} dx \tag{3}$$

where

$$\begin{aligned} D &= \beta_\epsilon \Delta^{1/2} d/2 \\ Q_0 &\text{ satisfies } \cos(Q_0 D) = Q_0 \\ P_0^2 &= 1 - Q_0^2 \\ x_0^2 &= 1 + P_0^2 \Delta \\ P^2 &= (1 - x^2)/\Delta \\ Q^2 &= 1 + P^2 \end{aligned}$$

and we assume that both sides of the waveguiding layer are equally rough and described by the same parameters A and B. There are now only three variable parameters in the expression, namely Δ, D, and B_n.

Marcuse also gives an expression from which the absorption coefficient due to scattering from the fundamental mode into the mth-order mode can be obtained in terms of A and B. Using similar units to those in (3) above the normalized contribution α_m to the scattering loss is given by

$$\alpha_m = \frac{2\pi}{x_1 x_2 B_n} \cdot \left[\frac{Q_0^2 Q_m^2}{\{(x_0 - x_m)^2/\Delta^2 + (1/B_n)^2\}\{D + 1/P_0\}\{D + 1/P_m\}} \right] \tag{4}$$

where

$$\begin{aligned} Q_m &\text{ satisfies } \cos(Q_m D - m\pi/2) = Q_m \\ P_m^2 &= 1 - Q_m^2 \\ x_m^2 &= 1 + P_m^2 \Delta. \end{aligned}$$

We have computed the scattering coefficient from the fundamental mode into unguided radiation, and where relevant, into the higher order guided modes for two different values of Δ over a range of values of B_n and D. The results for the total scattering loss $(\alpha_0 + \Sigma\alpha_m)$ and the scattering into guided modes are shown for the two values of Δ in Figs. 4 and 5, respectively. The first point to be observed is that although the values used for Δ in the two figures differ by more than a factor of 5 (0.1115 compared with 0.0201) the two sets of curves are very similar and lie within 10 percent of one another over the major part of the range of interest. This is particularly convenient for interpolation of Δ, using a relatively small number of computed results, and indicates that Δ has been introduced in the most appropriate manner in the normalization of the quantities in (1) and (2).

The second point to be observed is that all the curves of scattering coefficient $(\alpha_0 + \Sigma\alpha_m)$ versus correlation length B_n for a given value of the guide thickness $2D$ show a relatively flat maximum. There is little variation in $(\alpha_0 + \Sigma\alpha_m)$ over an order of magnitude variation in B_n centered on the maximum. The results are therefore not very dependent on the particular type of surface roughness, which suggests that they should be reasonably reliable for predicting the actual behavior in practice. The value of B_n for which the maximum occurs lies close to unity ($B \simeq 0.5\ \mu$m) over the range of D from 0.6 to 1.3 (approximate range of guide widths 0.15-0.35 μm) becoming larger for narrower guides and also, as a result of coupling to higher order guided modes, for wider guides.

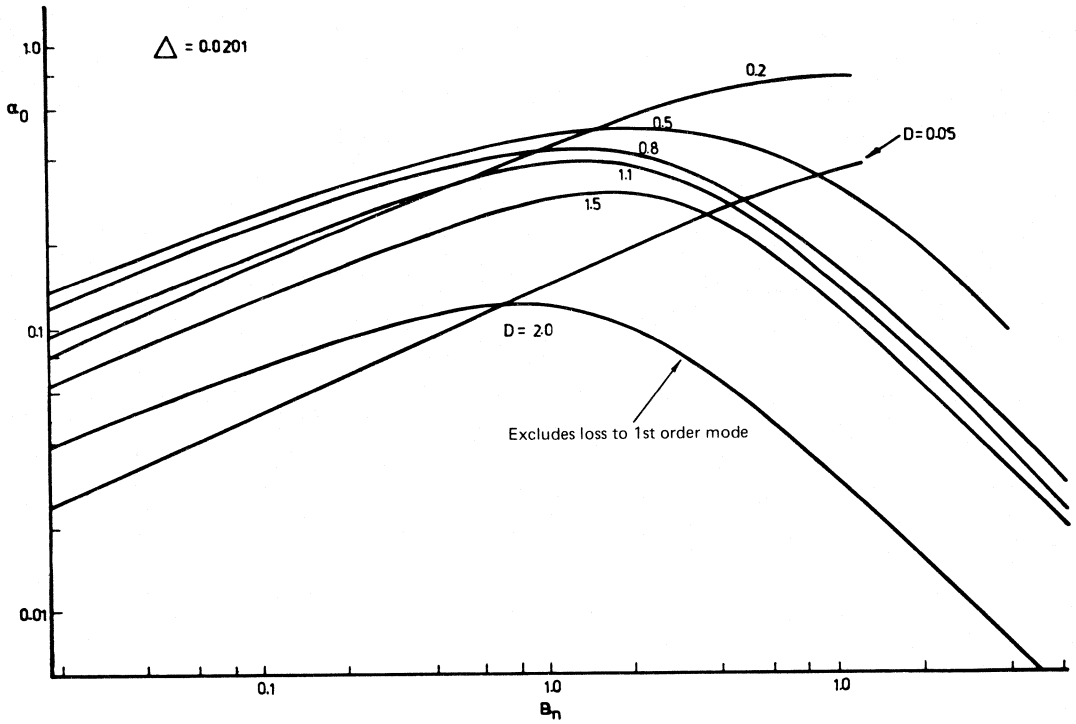

Fig. 4. Normalized absorption coefficient due to scattering as a function of correlation length with D as a parameter for a proportional step in ϵ of 0.0201.

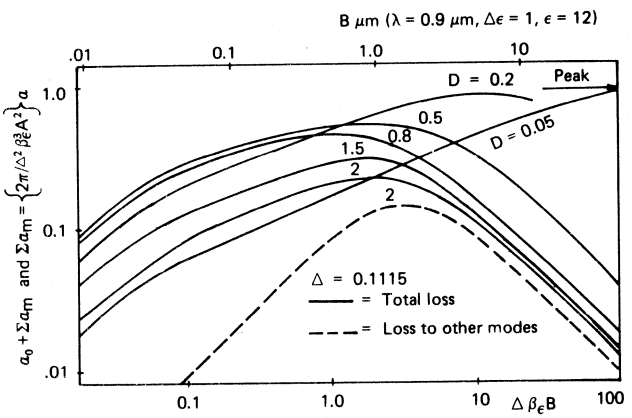

Fig. 5. Normalized absorption coefficient due to scattering as a function of correlation length with D as a parameter for a proportional step in ϵ of 0.1115.

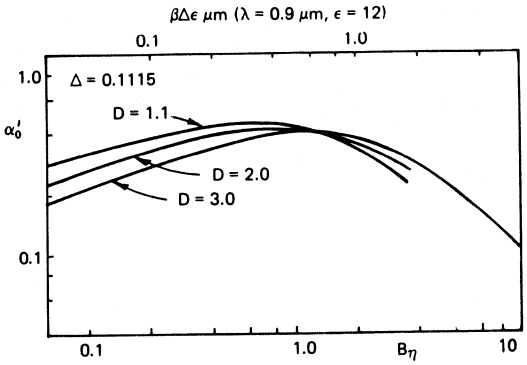

Fig. 6. Normalized absorption coefficient due to scattering from center layer of five-layer structure as a function of correlation length with D as a parameter.

C. Scattering Theory for Five-Layer Guides

In the five-layer laser it is necessary to take into consideration the additional scattering that occurs at the interfaces which bound the thin central layer. If the center layer is considered to be sufficiently narrow to avoid perturbing the overall optical distribution to any appreciable extent, then it is possible to modify Marcuse's expression quite simply to describe the new scattering situation. The expression contains the product of the fields due to the fundamental mode with the fields of the unguided continuum modes at the perturbing boundary, which is taken to be the outer boundary of the guided layer. If instead we take the product of the fields on the center line, we obtain an expression which would apply to roughness in the thin center layer of a five-layer structure. The new expression is

$$\alpha_0' = \frac{2\Delta}{(D + 1/P_0)x_0 B_n} \int_{-1}^{1} \frac{(Q^2 - 1)^{1/2}}{(x_0 - x)^2 + (\Delta/B_n)^2} \cdot \left\{ \frac{dx}{Q^2 - \cos^2 QD} \right\}. \tag{5}$$

The value of α'_0 is plotted in Fig. 6 against B_n for various values of D. It appears that over the range of values of D of interest the curves are very similar to each other and all peak at a value of α'_0 of around 0.42.

III. Application of Scattering Theory

We will use the results previously described as a basis for optimizing the dielectric waveguide structure for minimum scattering loss, in the presence of whatever unavoidable roughness may remain on the interfaces of the dielectric guide. The important variable parameters in the case of the three-layer

guide are the thickness of the center layer and the dielectric-constant step at the interfaces. In the case of the five-layer guide the effect of the dielectric-constant steps which bound the thin central layer must also be considered. We will not take the correlation length of the roughness into account but simply assume, in the numerical computations, that its value is such as to maximize scattering for given rms roughness amplitude in each particular situation. This will result in a slight overestimate of scattering loss in some cases although errors are unlikely to exceed a factor of 2.

A. Effect of Thickness of Dielectric Guide

We will first consider the direct effect of the thickness of the center layer of the dielectric guide on the scattering loss from the fundamental mode. This is plotted in Fig. 7, with α_0 as the ordinate and d as the abscissa. α_0, as previously described, is maximized with respect to B_n. The scale on the x axis for d applies to the situation where the center layer is bounded by a dielectric-constant step $\Delta\epsilon$ of unity, corresponding to steps in AlAs content at the boundary interfaces of about 23 at %. It may be adjusted to apply to other dielectric-constant steps by dividing by $(\Delta\epsilon)^{1/2}$. The curve shows that the peak scattering loss decreases monotonically, as the layer width is increased, by approximately an order of magnitude between $d(\Delta\epsilon)^{1/2} = 0.1$ μm and 0.9 μm. At a value of $d(\Delta\epsilon)^{1/2}$ of 0.44 μm the first-order mode becomes capable of propagating. There is a marked additional drop in scattering to unguided modes for widths greater than this value. This effect is compensated by the increased scattering to the first-order mode and the curve for the total scattering passes smoothly through the first-order mode cutoff. In practice, in a simple three-layer laser, operation switches to the first-order mode for center-layer thickness greater than about 0.6 μm. In such a case, it is necessary to consider the scattering out of the first-order mode and the curve of Fig. 7 is no longer applicable.

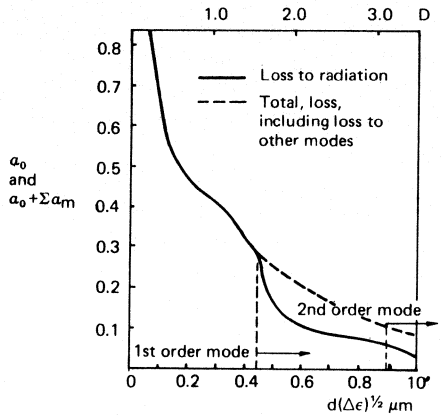

Fig. 7. Effect of thickness of center layer on absorption coefficient due to scattering. Loss to unguided modes and total loss, including loss to guided modes, is shown.

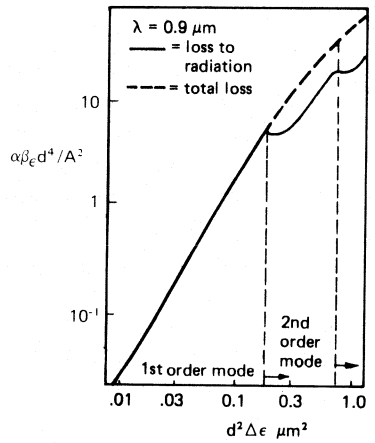

Fig. 8. Effect of step in dielectric constant on absorption coefficient due to scattering.

B. Effect of Step in Dielectric Constant

The second parameter available for adjustment is the dielectric-constant step $\Delta\epsilon$. The normalized scattering coefficient, as given by (1), contains the square of Δ and hence we must expect Δ to be an important factor. The effect on the scattering loss of varying $\Delta\epsilon$ for a fixed value of the layer thickness d and the roughness amplitude A is illustrated in Fig. 8. The quantity $\alpha\beta_\epsilon d^4/A^2$, proportional to the scattering coefficient, is plotted against $d^2\Delta\epsilon$. The scattering increases rapidly as $\Delta\epsilon$ is increased, showing an approximate square-law dependence on $\Delta\epsilon$ up to the point where the first-order mode starts to propagate. Beyond this point the increase is slower and a considerable proportion of the total scattering goes to exciting higher order guided modes. The dielectric-constant step is evidently the dominating factor in determining the scattering loss.

C. Optimized Structure

The general conclusion from the previous two sets of curves is that, in order to minimize scattering, the dielectric step should be reduced as much as possible and the guiding layer should be made as wide as possible. However, these two conclusions are not necessarily compatible with the other design requirements of a laser. The first requirement is that the composition step at the boundary of the active layer should be sufficient, in the case of the three-layer laser, to give carrier confinement. This requires a minimum dielectric-constant step, in most cases, of the order of 0.5. The second requirement is that the dielectric-constant step should be large enough, in conjunction with the value of d used, to confine the light to the width S required for the application. In the three-layer laser the interdependence of optical and carrier confinement imposes limitations. Increasing the width of the optical guiding layer increases the threshold current density directly, and this must be taken into account when considering how much the scattering can be reduced. In the five-layer laser there is scope for reduction of scattering losses without affecting threshold current density. The characteristics of the optical cavity affect threshold only via the effective optical width S and an optical coupling constant k [5]. Provided the thin layer of injected carriers lies centrally within the optical cavity, variations of k can be neglected. Hence combined changes of Δ and d (applying here to the total width of the three center layers) which keep S constant cause no appreciable change in threshold. It then becomes a useful exercise to optimize Δ and

d for given S to obtain minimum scattering from the outer boundaries of the three-layer resonator. It will, of course, also be necessary to consider what scattering is introduced by the presence of the additional thin active layer, lying close to the center of the resonator.

In Fig. 9 we plot the scattering loss for a range of dielectric guides, in all of which the optical distribution has the same effective width. The effective width S is defined in terms of the optical-intensity distribution $I(x)$ and the peak optical intensity I_0 by

$$S = \int_{-\infty}^{\infty} I(x)\,dx/I_0. \tag{6}$$

In a structure where d is adjusted to give maximum optical confinement for a given dielectric-constant step the width of the optical distribution is given by [5]

$$S = 0.391\lambda/(\Delta\epsilon)^{1/2}. \tag{7}$$

If d is adjusted up or down from the value required for this condition, then the dielectric-constant step must be increased. Hence we will label the dielectric-constant step which appears in (7) $\Delta\epsilon_{\min}$. Fig. 9 shows the relative change in the scattering coefficient α_0 as d is varied, the quantity plotted on the horizontal scale being $d(\Delta\epsilon_{\min})^{1/2}$, the wavelength being 0.9 μm, and the effective width of the optical distribution being $0.352/(\Delta\epsilon_{\min})^{1/2}$ μm. Minimum scattering, in fact, occurs in the region where the dielectric-constant step lies close to $\Delta\epsilon_{\min}$. There is a reasonably wide and flat minimum over the range of d given by

$$0.2/(\Delta\epsilon_{\min})^{1/2} < d < 0.45/(\Delta\epsilon_{\min})^{1/2}\ \mu\text{m}. \tag{8}$$

Because the dielectric constant has to be significantly increased at the extremes, the scattering loss rises, and it does so more markedly for small rather than large d. The limit for large d arises from scattering into the first-order mode, which can propagate for values of d greater than $0.38/(\Delta\epsilon_{\min})^{1/2}$. Optimum operation of the five-layer laser should therefore be obtained for values of d in the vicinity of $0.25/(\Delta\epsilon_{\min})^{1/2}$ where the minimum value of dielectric-constant step $\Delta\epsilon_{\min}$ applies.

On the assumption that the construction has been optimized for the optical width concerned let us see how the scattering loss actually depends on the width. Since operation is always at the same value of D of approximately 0.95, the normalized scattering coefficient has a value for all widths of $\alpha_0 = 0.42$ (maximized with respect to the correlation length), see Fig. 5. Using (1) in conjunction with the expression for D in (3) and the value of S in (7), gives the following relation for the optimized scattering coefficient in terms of the optical width, the amplitude of the roughness, and the free-space wavelength:

$$\alpha_{\min} = 0.388\,\frac{\lambda}{\epsilon^{1/2}}\,\frac{A^2}{S^4}. \tag{9}$$

Taking $\epsilon^{1/2} = 3.5$ and $\lambda = 0.9$ μm gives

$$\alpha_{\min} \simeq 10^3 A^2/S^4 \tag{10}$$

where $\alpha_{\min}$ is measured in cm^{-1} and A and S are measured in micrometers. The important thing to notice about (10) is the extreme sensitivity to the width S. The dependence is in proportion to the inverse fourth power. This is reminiscent of the Rayleigh scattering law where the scattering loss depends on the inverse fourth power of wavelength. In the present case S is related to the transverse component of wavelength, and so the analogy between the two relationships is close.

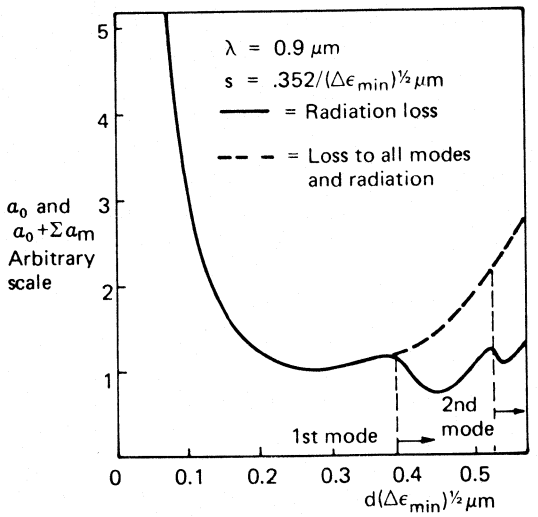

Fig. 9. Effect of thickness of center layer on absorption coefficient due to scattering under conditions where Δ is adjusted to keep width of optical distribution constant.

The minimum value of S which would normally be encountered in practice would be about 0.3 μm (corresponding to a difference in AlAs content between the center and outer layers of 30 at %. An rms roughness amplitude of 0.01 μm would, according to (10), give an attenuation coefficient of approximately 12 cm^{-1}.

The optical scattering from the center layer of a five-layer structure, according to the results in Fig. 6, is almost independent of d. Using the peak value of the normalized attenuation coefficient of 0.42, in conjunction with the normalization relation of (1), gives the following expression for the actual attenuation coefficient:

$$\alpha = 16.5\,\frac{(\Delta\epsilon)^2 A^2}{\epsilon^{1/2}\lambda^3}. \tag{11}$$

Taking $\epsilon^{1/2} = 3.5$ and $\lambda = 0.9$ μm then gives

$$\alpha = 6.5\,A^2(\Delta\epsilon)^2 \tag{12}$$

where α is measured in cm^{-1} and A is measured in micrometers. The minimum value of $\Delta\epsilon$ associated with good carrier confinement in the center layer is 0.5 (11 at % step in AlAs content). Inserting this in (12) and taking the rms roughness as 0.01 μm produces a scattering loss of 1.6 cm^{-1}. This is similar to the loss which would be produced by scattering from the outer boundaries of an optimized optical-confinement layer 0.5 μm thick. Hence, although the loss is not excessive, it does put an appreciable limitation on the effective improvement which can be obtained in the overall loss by widening S. Efforts at improving the smoothness of the interface should therefore be particularly applied to the active layer of a five-layer structure.

IV. Measurement and Interpretation of Optical-Absorption Coefficient

A. Theory

For currents up to about 50 percent above threshold the incremental quantum efficiency of a laser η is related to the laser length L, the end-face reflection coefficient R (assumed symmetrical at both ends), and the optical-absorption coefficient by [6]

$$\frac{1}{\eta} = \frac{1}{\eta_0}\left\{1 + \frac{\alpha L}{\log(1/R)}\right\} \tag{13}$$

where η_0 is the internal quantum efficiency. α is made up of various contributions, of which we are particularly concerned with the scattering contribution α_s and the free-carrier contribution α_{fc}. The free-carrier loss should be further subdivided into the contribution due to the original doping α_{fc0} and the contribution due to the injected carriers α_{fc1}. The latter has to be separated because it is the only contribution which varies with laser length, as a result of variations in gain and hence injected carrier concentration. To allow for this effect we use the following relation for laser gain g at threshold:

$$g = \alpha_s + \alpha_{fc0} + \alpha_{fc1} + \log(1/R)/L. \tag{14}$$

In addition we also need the relation between gain g and injected carrier concentration n. For values of n sufficiently greater than a fixed concentration n_0 we have found that for initial doping levels of 5×10^{17} cm^{-3} or less we can represent g by an expression of the form

$$g = \rho B(n - n_0) \tag{15}$$

where the factor B determines the gain if all the light is contained within the active layer, and ρ is a loading factor < 1 which depends on the proportion of the optical distribution which lies within the active layer. The free-carrier loss due to injected carriers is represented by

$$\alpha_{fc1} = \rho C n \tag{16}$$

where ρ is the same loading factor. We take the effect of the electrons and holes to be equal, which gives C a value of 10^{-17} cm^2, twice that quoted by Pinkas *et al.* [1] for electrons only. Eliminating g and n between (14)-(16) gives the following relation for the absorption loss due to the injected free carriers:

$$\alpha_{fc1} = \frac{C}{B - C}\{\alpha_s + \alpha_{fc0} + \rho B n_0 + \log(1/R)/L\}. \tag{17}$$

Inserting this into (13) gives the following relation between quantum efficiency and laser length:

$$\frac{1}{\eta} = \frac{B}{B - C}\frac{1}{\eta_0}\left\{1 + \frac{(\alpha_s + \alpha_{fc0} + \rho C n_0)L}{\log(1/R)}\right\}. \tag{18}$$

Comparing this expression with (13) we see that the effect of the injected free carriers is to contribute a length-independent attenuation of $\rho C n_0$ (corresponding to a free-carrier concentration of n_0) and to reduce the apparent internal efficiency by a factor of $(1 - C/B)$. Hence, by plotting the measured values of $1/\eta$ against $L/(\log(1/R))$, we obtain $(\alpha_s + \alpha_{fc0} + \rho C n_0)$ as the negative intercept on the axis of $L/(\log(1/R))$. If α_{fc0} and $\rho C n_0$ are known, the absorption coefficient α_s due to optical scattering may be found.

B. Results

We have evaluated optical-absorption coefficients for a range of double-heterostructure lasers and some five-layer lasers. These were obtained from $1/\eta$ versus $L/(\log(1/R))$ plots varying either L or R or varying both quantities. The total measured absorption coefficients lay mostly in the range 10–18 cm^{-1} with occasional lower or higher values. In general the estimated absorption due to free carriers lay in the approximate range 5–10 cm^{-1}. This leaves a margin of between 5 and 10 cm^{-1} which can be attributed to optical scattering. According to (10) this can be explained by an rms amplitude of roughness at the guide interfaces of around 0.01 μm. This is in reasonable agreement with observation.

In Figs. 10 and 11 we show the precise results obtained for a set of five-layer lasers and for a particularly low-loss double-heterostructure laser. In the case of the five-layer lasers the thickness of the center layer was 0.07 μm and the thickness of the center three layers was 0.35 μm. The step in AlAs content was 12 at % between the center and intermediate layers and was a further 27 percent between the intermediate and outer layers. The effective width of the optical distribution, as deduced from the far-field polar diagram, was 0.37 μm. In conjunction with the 0.07-μm center layer this gives a loading

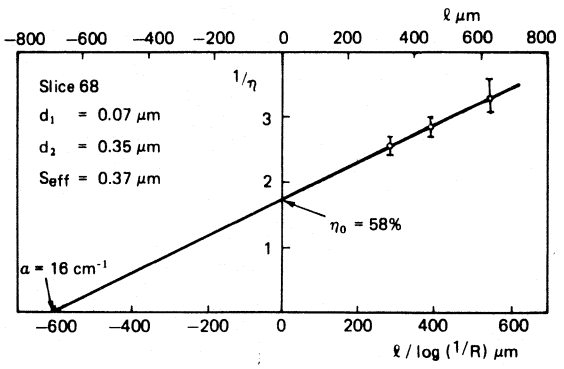

Fig. 10. Plot of measured reciprocal efficiency against length for five-layer lasers.

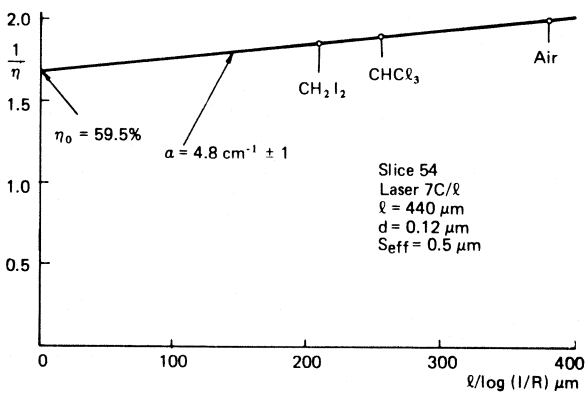

Fig. 11. Efficiency/reflection measurements in three-layer laser. Reflection coefficient varied by immersion of laser in various liquids.

factor ρ of 0.19. The doping level throughout the center three layers was $5 \times 10^{17}\,cm^{-3}$ and the injected carrier concentration n_0 was approximately $1.5 \times 10^{18}\,cm^{-3}$ as deduced from the threshold current variation with laser length and the measured spontaneous recombination time (derived from laser switch-on delay). Taking the effect of holes as being equal to that of electrons this combination should give a free-carrier absorption coefficient of approximately 5.5 cm^{-1}. The experimental plot in Fig. 10, which was obtained by measuring the efficiency of sets of lasers of three different lengths with five lasers in each set, gives an absorption coefficient of $16 \pm 3\ cm^{-1}$, which is about 10 cm^{-1} greater than the anticipated free-carrier loss, and corresponds to an rms roughness at the guide interfaces of about 0.015 μm.

In Fig. 11 we show the experimental results for an asymmetrical double-heterostructure laser with a 0.12-μm-thick active layer. The AlAs content of the p- and n-type (GaAl)As layers bounding the active layer were, respectively, 18 at % and 24 at %. This asymmetry produced a relatively wide optical distribution of 0.5 μm, displaced mainly towards the p-side of the structure. The doping level of all three layers was $5 \times 10^{17}\,cm^{-3}$ and the injected carrier concentration n_0 in the active layer was approximately $10^{18}\,cm^{-3}$. If we again take the holes as giving a loss equal to that of the electrons, we estimate a free-carrier absorption of 4.5 cm^{-1}. The measured results were obtained on a single laser. The reflection coefficient of the end faces was varied by immersing the laser in liquids of different refractive index. The measured optical-absorption coefficient was $4.8 \pm 1\ cm^{-1}$. Hence in this case the total optical absorption was little greater than the anticipated free-carrier absorption. The measurement accuracy was barely adequate to estimate the contribution of optical scattering, but it was of the order of 0.5 $cm^{-1} \pm 1\ cm^{-1}$. This corresponds approximately to an rms surface roughness of 0.004 ± 0.004 μm.

V. Conclusion

We have extended Marcuse's original analysis of scattering losses suffered by zero-order modes in symmetrical dielectric waveguides at imperfections in the boundary walls to cover the dimensions and the range of dielectric-constant steps applicable to double-heterostructure lasers. We have also analyzed the scattering losses from the thin center layer of five-layer lasers. In both cases the analysis was hampered by the difficulty of precise definition of the roughness. However, a reasonable estimate of the maximum expected losses can be made which is probably correct within a factor of 2. The important factors which determine the losses are the rms amplitude of the roughness and the magnitude of the dielectric-constant step. The losses vary as the square of both these quantities. In average double-heterostructure devices the dividing line between acceptable and unacceptable scattering loss ($\sim 5\ cm^{-1}$) occurs for a roughness amplitude of about 0.01 μm. Conditions are much alleviated in devices with wider than normal center layers, particularly if the dielectric-constant step is reduced to retain single-mode operation.

The total absorption loss has been measured in a variety of lasers. When the estimated free-carrier loss of around 5 cm^{-1} is subtracted the residual loss varies between about 1 and 10 cm^{-1}. According to our analysis this corresponds to a range in roughness amplitude of between 0.004 and 0.015 μm.

References

[1] E. Pinkas, B. I. Miller, I. Hayashi, and P. W. Foy, "GaAs-$Al_xGa_{1-x}As$ double heterostructure lasers–Effects of doping on lasing characteristics of GaAs," *J. Appl. Phys.*, vol. 43, pp. 2827–2835, June 1972.

[2] P. A. Kirkby and G. H. B. Thompson, "High peak power from (GaAl)As-GaAs double heterostructure injection lasers," *Appl. Phys. Lett.*, vol. 8, pp. 638–640, June 1973.

[3] G. H. B. Thompson and P. A. Kirkby, "Low threshold-current density in 5-layer heterostructure (GaAl)As/GaAs localized-gain-region injection lasers," *Electron. Lett.*, vol. 9, pp. 904–906, June 1973.

[4] D. Marcuse, "Mode conversion caused by surface imperfections of a dielectric slab waveguide," *Bell Syst. Tech. J.*, vol. 48, pp. 3187–3215, Dec. 1969.

[5] G. H. B. Thompson and P. A. Kirkby, "(GaAl)As lasers with a heterostructure for optical confinement and additional heterojunctions for extreme carrier confinement," *IEEE J. Quantum Electron. (Part II of Two Parts: Special Issue on 1972 IEEE Semiconductor Laser Conference)*, vol. QE-9, pp. 311–318, Feb. 1973.

[6] J. R. Biard, W. M. Carr, and B. S. Reed, "Analysis of a GaAs laser," *Trans. AIME*, vol. 230, pp. 286–290, 1964.

Depolarization of the Lasing Emission from CW Double-Heterostructure Junction Lasers

THOMAS L. PAOLI, MEMBER, IEEE

Abstract—Measurements of the polarization characteristics of the optical emission from CW $Al_zGa_{1-z}As$-$Al_xGa_{1-x}As$ double-heterostructure (DH) junction lasers are reported. Spectral observations demonstrate that in many lasers the lasing emission is not linearly polarized as expected from the conventional electromagnetic (EM) theory of the laser. A small but measurable field component is observed orthogonal to the main emission. In some lasers, the optical field is shown to be elliptically polarized, while in other devices the polarization state is more complex. The observed depolarization of the lasing modes is attributed to a strain-induced anisotropy in the dielectric properties of the laser waveguide. The anisotropic configuration which leads to elliptically polarized light is analyzed in detail and is shown to be equal to a pure shear in a plane parallel to the junction.

I. Introduction

WITHIN the conventional electromagnetic (EM) theory of the double-heterostructure (DH) junction laser, two classes of transverse modes can propagate in the laser waveguide [1]. For one class of waves, called transverse electric (TE), the electric field is transverse to the direction of propagation and linearly polarized parallel to the junction plane. For the other class, termed transverse magnetic (TM), it is the magnetic field which is normal to the axial direction and polarized parallel to the junction. However, since the Fresnel reflectivity of the semiconductor-air interface is largest for waves with an electric field perpendicular to the plane of incidence [2]-[4] the optical loss at a cleaved, uncoated mirror is greater for TM modes than for TE modes. Because other losses are normally low in the DH laser, the relative mirror losses for the bound waveguide modes usually determine which mode has the lowest threshold. Consequently, above the lasing threshold, the output power from DH lasers is most commonly observed to be highly polarized with the optical electric field parallel to the junction plane [4]-[8].

In the present paper, measurements of the polarization state of the spectrally resolved lasing emission from $Al_zGa_{1-z}As$-$Al_xGa_{1-x}As$ DH lasers are reported. In general, we find that when spectrally resolved the lasing emission is depolarized, i.e., the lasing emission is not linearly polarized as expected from the conventional EM theory of the laser. A small but measurable field component is observed orthogonal to the main emission. The external introduction of an optical phase difference between the orthogonal components demonstrates that the two polarizations are synchronous and consequently that the waves are not pure TE modes. With some lasers appropriate choice of the phase difference produces a linearly polarized field, indicating that the oscillating mode is in fact elliptically polarized. However, in other lasers, the polarization state is more complex. This observation differs from the previous work of Bogatov *et al.* [7], in which no synchronism between the orthogonally polarized modes was found.

As a possible cause for the depolarization of the lasing modes, anisotropies in the dielectric properties of the laser waveguide are proposed. The anisotropy which leads to an elliptically polarized wave is obtained from the analysis of McKenna and Morrison [9]. Additional experiments suggest that the observed mode distortion arises from strains, most probably induced by a nearby bonding surface. Consequently, an analysis of the strain configuration which produces the appropriate anisotropy is also presented.

Manuscript received January 3, 1975; revised February 13, 1975.
The author is with Bell Laboratories, Murray Hill, N.J. 07974.

II. Experimental Details

A. Lasers

In general, the DH lasers used in the present study were composed of a thin ($\leqslant$0.4-μm) active layer sandwiched between two layers of $Ga_{1-x}Al_xAs$ or $Ga_{1-x}Al_xP_yAs_{1-y}$ [10]. While all wafers were grown on {100} substrates, a wide variety of different combinations of waveguiding and active layers were used, including active layers with and without Al. Stripe-geometry lasers were fabricated from the epitaxial wafers by proton bombardment [11]. All lasers had stripe widths nominally equal to 13 μm and were 380 μm long. All mirrors were formed by uncoated facets cleaved on {110} planes. In most cases thick (~12-μm) gold pads were plated on the p-side before cleaving. For efficient heat sinking in continuous operation, each laser was bonded either to a metallized diamond mounted on a copper stud or directly to the copper stud.

B. Experimental Setup and Results

The polarization characteristics of the laser modes were studied with the system shown schematically in Fig. 1. In order to obtain optimum performance from optics used in the analysis, the laser emission was collimated by adjusting the

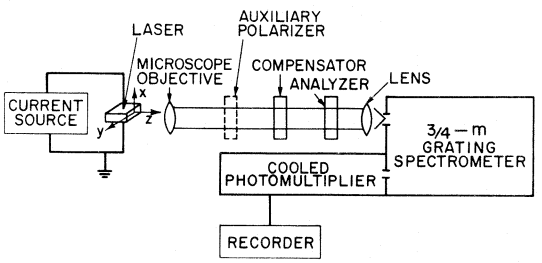

Fig. 1. Schematic diagram of the system used to observe and analyze polarization characteristics of optical spectra from CW stripe-geometry DH lasers.

axial position of the microscope objective to focus the emitted light at infinity as established by a telescope. A calcite prism, the analyzer, was then employed in the primary analysis of the polarization state of the optical beam before it was focused into the grating spectrometer. The spectrometer was used to resolve spectrally the TE and TM modes which in general are not degenerate in GaAs DH lasers [7].

A typical example of such an analysis performed on a laser which oscillated in a pure TE mode is shown in Fig. 2. Fig. 2(a) shows the spectrum of the oscillating TE modes, i.e., the analyzer was set to transmit light with an optical electric field parallel to the junction plane. Furthermore, amplification of this spectrum reveals that no additional weak modes with this polarization are present. With the analyzer rotated by 89.6° the combined spectra of the TE and TM modes displayed in Fig. 2(b) were obtained to show the lack of degeneracy between the two classes of modes. An additional rotation of the analyzer by 0.4° produced the spectrum of Fig. 2(c) in which the signals at frequencies corresponding to the TE modes have been eliminated, leaving only the nonlasing TM modes. This behavior demonstrates that the lasing TE modes (and equally well the nonlasing TM modes) are in fact linearly polarized to better than 1 part in 10^4. Furthermore, it establishes that there is essentially no depolarization of the beam by the optics.

With other DH lasers studied in the same way, the light emitted at the lasing wavelengths was not linearly polarized. For example, optical spectra obtained from another diode are shown in Fig. 3. The oscillating modes are shown in Fig. 3(a) and the spectrum of the orthogonally polarized light is shown in Fig. 3(b). While the signals at the wavelengths of the lasing modes showed a definite minimum as the polarizer was rotated, there was no angle at which they were zero. Furthermore, these signals were not due to leakage by the analyzer since insertion of a crossed polarizer between the analyzer and the spectrometer produced no detectable signal. The angle (θ) of the analyzer at which the intensities of the lasing wavelengths are minimal we take to be the most accurate measure of the nominal TM direction and define this angle[1] to be zero ($\theta = 0°$). We conclude then that the emission at wavelengths corresponding to the lasing modes in this device were not pure linearly polarized.

In order to identify the actual state of polarization of the emission at the lasing frequencies the standard analysis, as outlined, for example, by Jenkins and White [12], was performed. For this analysis an optical phase compensator was used in conjunction with the analyzer as shown in Fig. 1. The procedure consisted of aligning the optic axis of the compensator parallel to the direction of maximum optical intensity, in this case $\theta = 90°$, and then adjusting the phase difference produced by the compensator to give a minimum in the signal transmitted by the analyzer. If the minimum produced in this way is zero, the incident beam is uniquely determined to be in a pure state of elliptical polarization. If the minimum is not zero, but occurs at the initial analyzer angle, the incident beam is a mixture of linearly polarized and unpolarized light. On the other hand, if the angle at which the nonzero minimum occurs is changed, the incident beam is composed of linearly and elliptically polarized light.

[1]However, it should be noted that this direction is not necessarily perpendicular to the junction plane. From laser to laser the actual polarizer angle varied within a degree of its nominal value.

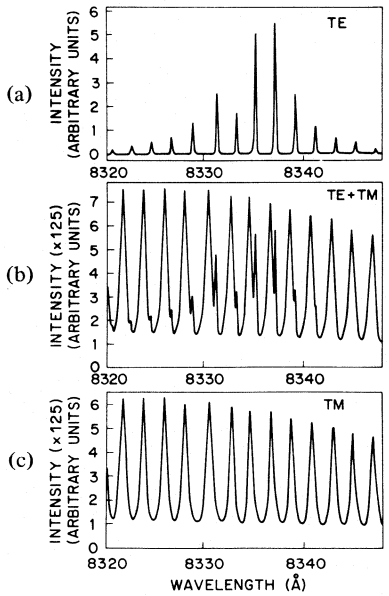

Fig. 2. CW spectra of a DH laser operating at 1.1 times threshold which does not show depolarization of the lasing emission. In (a) the polarizer angle is set to transmit the TE lasing emission while in (c) the angle corresponds to transmission of the subthreshold TM emission. Note the absence of the TE frequencies in (c) indicating the lasing emission is linearly polarized. In (b) the polarizer angle is rotated by +36′ [from (c)] to allow transmission of both TE and TM modes and thereby show the lack of degeneracy between their frequencies. In (a) the spectrometer slit width is 2 μm while in (b) and (c) it is 10 μm.

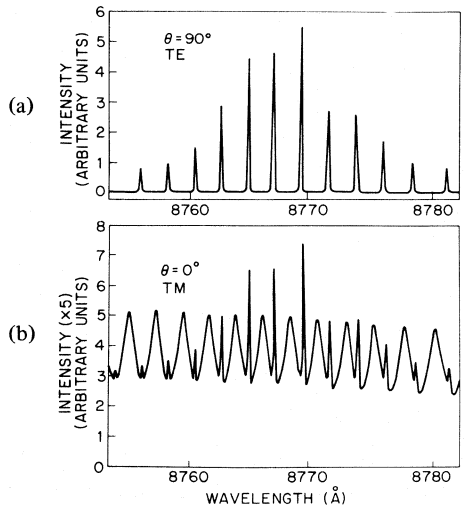

Fig. 3. Optical spectra from a CW DH laser operating at 1.05 times threshold. In (a) the analyzer angle θ is set at 90° corresponding to transmission of the TE polarized emission. In (b), $\theta = 0°$ corresponding to the minimum of the signals at the lasing wavelengths. Note the lack of degeneracy between the modes at the lasing wavelengths and the TM modes. The units of the vertical scales in (a) and (b) are the same.

To analyze the optical emission from the DH lasers in this way, we began by accurately aligning the optic axis of the compensator with the TE direction. This was accomplished by defining the TM direction as the angle at which the amplitudes of the lasing modes were a minimum and then crossing the auxiliary polarizer shown in Fig. 1 with the analyzer such that no signal was detected at the spectrometer output. The polarizer was then transmitting the TE polarized emission. An Ehringhaus compensator was next inserted between the polarizer and the analyzer and oriented with its optic axis parallel to the TE direction by minimizing the signal transmitted by the analyzer. For this orientation with incident linearly polarized light as established by the auxiliary polarizer, changes in the phase difference produced by the compensator had very little effect on the magnitude of the light transmitted by the analyzer, confirming that its optic axis was parallel to the TE direction.

With the auxiliary polarizer removed from the beam and the orientation of the compensator fixed, the phase compensation of the beam was adjusted to minimize the amplitude of the lasing modes as detected with the analyzer set at $\theta = 0°$. Then the analyzer orientation was adjusted if necessary to minimize further these amplitudes and thereby complete the polarization analysis procedure previously outlined.

An example of one class of results achieved with this procedure is shown in Fig. 4. Fig. 4(a) is the spectrum of the emitted light after passing through the compensator and analyzer set at 0°. Qualitatively, this spectrum is similar to one obtained without the compensator. However, rotation of the analyzer by only 1° produced the spectrum displayed in Fig. 4(b) in which signals at the wavelengths of the lasing modes [indicated by arrows in Fig. 4(a)] can no longer be detected. Furthermore, the suppression of the lasing modes in this way occurred only for the specific phase difference of approximately 0.6 π in this case. For other settings of the compensator, the signal amplitude at each lasing frequency was not fully suppressed for any angle of the analyzer. Similarly, with the compensator set at 0.6 π, the signals were zero only for $\theta = +1°$ so that this combination of compensator and analyzer settings was unique. For future reference we define this null angle to be θ_0. In view of the standard procedure for polarization analysis, we conclude that the polarization of the lasing emission from this diode was pure elliptical with a phase difference of approximately 0.6 π between the orthogonal components of the field.

With the phase compensation at 0.6 π, the direction of the maximum field was changed from the TE direction $\theta = 90°$ to $\theta = 90° + \theta_0$. The tilt results because when the orthogonal field components are in phase, as they are at the compensator output, the resulting linearly polarized field vector is given by their vector sum. Consequently, the tilt angle θ_0 should also be given by the ratio of the orthogonal field components themselves, as

$$\tan \theta_0 = \sqrt{\frac{I(0°)}{I(90°)}} \tag{1}$$

where $I(\theta)$ is the modal intensity corresponding to the analyzer set at θ. Thus, by measuring[2] the intensity of a mode with $\theta = 90°$ and the intensity of the orthogonal component at $\theta = 0°$, θ_0 can be independently estimated. For the laser used for Fig. 4, we found experimentally that $\theta_0 = 42'$. This value is in good agreement with the directly measured value of 1°.

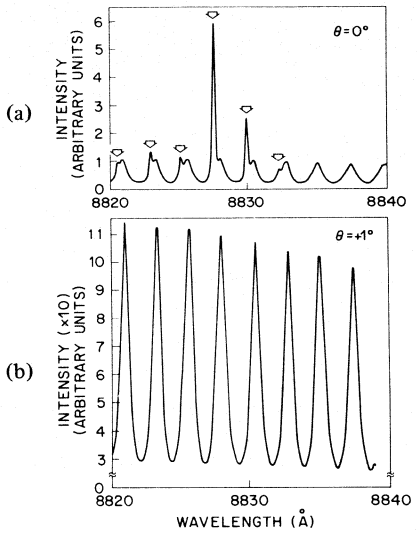

Fig. 4. CW spectra of emission from a second DH laser after passing through phase compensator set for a phase compensation of 0.6π and the analyzer. In (a) the analyzer angle θ is 0° while in (b) the analyzer angle is +1°. The absence of signals in (b) at the wavelengths corresponding to the TE-like modes [indicated by arrows in (a)] show that the lasing light after passing through the compensator is linearly polarized.

III. Discussion

In this section, we consider possible sources for the observed depolarization of the lasing modes. The existence of pure linear polarization in some lasers suggests that the depolarization of the field is not a result of the two-dimensional nature of the stripe-geometry waveguide [13]. On the other hand, the observed coherence between the orthogonally polarized field components makes optical scattering from randomly distributed centers or waveguide nonuniformities an unlikely source. Consequently, we turn our attention to mode-coupling processes which in general maintain coherence between the coupled waves.

It is well known that the propagating modes in anisotropic thin-film waveguides are in general neither pure TE nor TM [9], [14]. In view of the experimental results, the most likely source of the anisotropy is strain in the laser waveguide. Consequently, we shall discuss the effect of an anisotropic waveguide as if it were strain induced although much of the discussion is independent of the precise cause.

The lowest order perturbed modes of a dielectric waveguide in the presence of a small uniform strain have been calculated in detail by McKenna and Morrison [9]. In the presence of strain, the dielectric matrix for the waveguide is no longer

[2] By using the unpolarized spontaneous emission from a GaAs diode, the transmissivity of the spectrometer plus analyzer was observed to be essentially the same (within 10 percent) for $\theta = 0°$ and $\theta = 90°$.

diagonal in the coordinate system shown in Fig. 1. Following [9], we write the dielectric matrix elements as

$$K_{\alpha\beta}(x) = K_{\alpha}^{(0)}(x)\,\delta_{\alpha\beta} + \eta S_{\alpha\beta}, \qquad \alpha, \beta = 1, 2, 3$$
$$\delta_{\alpha\beta} = \begin{cases} 0, & \alpha \neq \beta \\ 1, & \alpha = \beta \end{cases} \tag{2}$$

where α, β are the coordinate indices, $K_{\alpha}^{(0)}(x)$ defines the waveguide in the absence of strain, and $\eta S_{\alpha\beta}$ is the matrix element arising from the photoelastic effect with η a small parameter used in the perturbation analysis. As a result of the off-diagonal elements in the dielectric matrix, the propagating fields are in general no longer pure TE or TM modes. An exception to this rule occurs when all off-diagonal elements except S_{13} are zero, in which case pure TE and TM modes are still allowed.

For the case in which S_{12} is the only nonzero off-diagonal element, analysis [9] shows that the x and y components of the electric field in the perturbed TE mode are in phase. Consequently, the perturbed TE mode is linearly polarized but at an angle with respect to the y axis, i.e., the direction of the polarization for the unperturbed TE mode. Because the x and y components of the field have slightly different shapes in the x direction, the angle of tilt varies slightly as a function of position x in the waveguide.

The final case to be considered is one in which the only off-diagonal element not taken equal to zero is S_{23}. From the analysis [9], it is straightforward to show that the x component of the perturbed TE mode is pure imaginary, indicating that the two orthogonal components are 90° out of phase with respect to each other. This phase shift corresponds to an elliptically polarized wave. However, the analysis also indicates that the ellipticity of the polarization varies with the transverse coordinate x due again to the different spatial distributions of the x and y components of the field.

Although the strain field actually obtained in a bonded DH laser is by no means as ideal as assumed in the analysis, nevertheless the calculations show that the observed elliptically polarized mode can be understood qualitatively in terms of a strain-induced anisotropy in the waveguide. Furthermore, elliptical polarization arises only for a particular anisotropy, namely, one in which $S_{23} \neq 0$. This element of the dielectric matrix can be related [15] to the stress field $\sigma_{\mu\nu}$ by the piezooptical coefficients $\pi_{\alpha\beta\mu\nu}$ as

$$\eta S_{23} = -n^4 \sum_{\mu,\nu=1}^{3} \pi_{23\mu\nu}\sigma_{\mu\nu} \tag{3}$$

where n is the index of refraction. GaAs or $Ga_{1-x}Al_xAs$ which are crystals of class $\bar{4}3m$ have only three different piezooptical coefficients when referred to the crystal axes. However, the coordinate system chosen for the modal analysis of the waveguide (shown in Fig. 1) does not in general correspond to the coordinate system defined by the crystal axes. For lasers grown on {100} substrates with mirrors cleaved on {100} planes, the coordinate system defined by the crystal axes is related to the system of Fig. 1 by a 45° rotation about the x axis. With the appropriate transformation of the piezooptical coefficients, it is straightforward to show that the important element of the dielectric matrix is generated as

$$\eta S_{23} = -n^4 \tfrac{1}{2} (\pi_{11} - \pi_{12})(\sigma_{32} + \sigma_{23}) \tag{4}$$

where the piezooptical coefficients have been expressed in standard contracted notation [15] and the stress components are in the waveguide coordinate system. Thus the ηS_{23} arises from a pure shear in the y-z plane. In terms of the stresses along the crystal axes, the shear can be written as

$$\sigma_{32} + \sigma_{23} = \sigma'_{22} - \sigma'_{33} \tag{5}$$

where σ'_{22} and σ'_{33} are the stresses along the (010) and (001) axes, respectively. Thus the shear is generated by unequal stresses along two crystal axes.

Within the perturbation theory of McKenna and Morrison [9], we can estimate the magnitude of ηS_{23} for the experimental lasers which in turn can be used to estimate the shear stress. As an example, we use the laser of Fig. 4 for which the undoped (n-type) active region was 0.4 μm thick and was bounded by layers of $Ga_{0.77}Al_{0.23}As_{0.994}P_{0.006}$. From the results of [9], we estimate a value $\eta S_{23} = 0.1$ for a tilt angle $\theta_0 = 1°$. Although this corresponds to a change of less than 0.08 percent in the dielectric constant of the active region, it is large enough to place some doubt on the applicability of the perturbation calculation in a quantitative estimate of the stress level.

With the inadequacy of the calculation in mind, we now use the value of ηS_{23} to estimate the stress level from (4). In addition, to obtain a room-temperature value for the piezooptical coefficient $\pi_{11} - \pi_{12}$ it is necessary to extrapolate the available experimental results [16]. Unfortunately, this is not straightforward in GaAs because of the large dispersion shown by $\pi_{11} - \pi_{12}$ near the bandedge. Nevertheless, we obtain a lower bound of 20×10^{-14} cm^2/dyn on $\pi_{11} - \pi_{12}$ by linearly extrapolating the data of [16] from 1.38 to 1.404 eV (8830 Å). From (4), we obtain an estimated stress level of approximately 6×10^9 dyn/cm^2. This value is certainly an upper limit on the stress level needed to produce the observed effect since our extrapolated value of $\pi_{11} - \pi_{12}$ may considerably underestimate the actual value.

Recent analysis [17] has indicated that the intrinsic stress in DH lasers due to the lattice mismatch of AlAs and GaAs is equivalent to a hydrostatic tension superimposed over a uniaxial pressure perpendicular to the {100} heteroboundary planes. Since for this stress distribution $\sigma'_{22} - \sigma'_{33} = 0$ it is unlikely that the shear necessary to induce depolarization originates in the interfacial strain inherent to the epitaxial growth. This conclusion is also supported by the experimental observation that depolarization also occurred in lasers with phosphorus added to the $Ga_{1-x}Al_xAs$ layers in order to relieve this interfacial strain [18].

On the other hand, it is certainly reasonable to expect that the necessary shear strains could develop during bonding of a laser to its heat sink and perhaps even be intensified as a result of the heating incurred during continuous operation. In

addition, high stress concentrations can develop [19] at the edges of thin films deposited on semiconductors. Consequently, the plated gold pad and its interaction with the heat sinking bond are also potential sources of a shear strain. Experimentally, the importance of the bonding situation was suggested, although not proved, in a comparison of the depolarization observed in a group of 20 lasers from the same wafer, half of which were bonded in the conventional manner with the p-side adjacent to the heat sink, while the remainder were bonded with the n-side adjacent to the heat sink. In the former case the waveguide was within a few microns of the bond, while with n-side bonding the waveguide was approximately 4 mils from the bond due to the substrate. Experimentally, *all* lasers with p-sided bonds showed oscillation in a mode which was not linearly polarized while only *half* of the devices with n-sided bonds showed this depolarization. A possible source of strain in lasers with n-side bonds is the top wire-bonded contact.

The presence of some strain was also detected in all these devices by observing transmitted infrared (IR) light with crossed polarizers [20]. In general, the strain appeared to be more intense in lasers with p-side than with n-side bonds. However, the observed strain was located primarily near the edges of the chip in most cases, suggesting that it was a result of the cleaving operation rather than bonding. In most lasers very little if any strain was detected with this technique near the active region defined by the stripe. In addition, there appeared to be no correlation between the strength of the depolarization in a single laser and the intensity of the strain detected with the crossed polarizers. We conclude that the depolarization of the lasing mode may be a more sensitive probe of at least the shear strain in the vicinity of the active region.

One further point which deserves some discussion is the observed mode coupling in the presence of the lack of degeneracy between the TE and TM modes, for example, as shown in Fig. 3. From a coupled-mode point of view [14], when it is applicable, it can be shown that the frequency splitting between the perturbed TE and perturbed TM modes is always larger than the frequency difference between the unperturbed modes. Consequently, it is not possible to conclude from a spectrum of the perturbed modes how far the uncoupled modes are from degeneracy.

In conclusion, we note that it was not possible to obtain the full compensation demonstrated in Fig. 4 with all lasers in which depolarization was observed. In most cases, adjustment of the compensator produced a nonzero minimum in the signal transmitted by the analyzer at an analyzer angle $1^\circ > \theta > 0^\circ$. From the polarization analysis described in Section II-B, this result suggests that the lasing emission is a mixture of linearly and elliptically polarized light such as is expected when both S_{12} and S_{23} are not zero. The lack of full compensation may also be due to the spatially varying ellipticity of the mode mentioned previously or to a strain field which is too strong or too spatially nonuniform to maintain the validity of the analytic model. A study of the polarization state as a function of position in the mirror illumination may help to distinguish these effects.

IV. Conclusion

In this work we have investigated the polarization characteristics of some stripe-geometry $Al_zGa_{1-z}As$-$Al_xGa_{1-x}As$ DH junction lasers operating continuously at room temperature. The experimental results demonstrate that many of these devices do not oscillate in a linearly polarized mode as predicted by the conventional EM theory of this laser. In some cases the field can be shown to be elliptically polarized, while in other devices the polarization state is more complex.

The observed depolarization of the lasing modes can be explained by an anisotropy in the dielectric properties of the laser waveguide. In particular, elliptically polarized modes are possible for one configuration of the anisotropy. The anisotropy itself is attributed to strains produced during the bonding of the laser to its heat sink. In such a case it is a shear strain which leads directly to the elliptical polarization. Consequently, the observation of depolarization in the lasing emission can serve as a sensitive test for the presence of undesirable strain in bonded lasers.

Acknowledgment

The author wishes to thank F. K. Reinhart, J. McKenna, and J. A. Morrison for many helpful discussions. He also wishes to thank L. A. D'Asaro and B. C. DeLoach for their critical reading of the manuscript, and J. F. Svacek for his technical assistance.

References

[1] See, for example, M. J. Adams and M. Cross, "Electromagnetic theory of heterostructure injection lasers," *Solid-State Electron.*, vol. 14, pp. 865–883, 1971.

[2] I. Hayashi, M. B. Panish, and F. K. Reinhart, "GaAs-$Al_xGa_{1-x}As$ double heterostructure injection lasers," *J. Appl. Phys.*, vol. 42, pp. 1929–1941, Apr. 1971.

[3] T. Ikegami, "Reflectivity of mode at facet and oscillation mode in double-heterostructure injection lasers," *IEEE J. Quantum Electron.*, vol. QE-8, pp. 470–476, June 1972.

[4] F. K. Reinhart, I. Hayashi, and M. B. Panish, "Mode reflectivity and waveguide properties of double-heterostructure injection lasers," *J. Appl. Phys.*, vol. 42, pp. 4466–4479, Oct. 1971.

[5] J. E. Ripper, J. C. Dyment, L. A. D'Asaro, and T. L. Paoli, "Stripe-geometry double heterostructure junction lasers: Mode structure and CW operation above room temperature," *Appl. Phys. Lett.*, vol. 18, pp. 155–157, Feb. 1971.

[6] I. Sakuma *et al.*, "Continuous operation of junction lasers at room temperature," *Japan. J. Appl. Phys.*, vol. 10, pp. 282–283, 1971.

[7] A. P. Bogatov *et al.*, "Pulsed and continuous output characteristics of stripe-geometry symmetrical heterojunction lasers at 300°K," *Sov. Phys.–Semicond.*, vol. 6, pp. 34–38, July 1972.

[8] H. S. Sommers, Jr., "Experimental properties of injection lasers. V. Strong polarization," *J. Appl. Phys.*, vol. 45, pp. 237–242, Jan. 1974.

[9] J. McKenna and J. A. Morrison, "The effects of strain on electromagnetic modes of anisotropic dielectric waveguides at p-n junctions," *Bell Syst. Tech. J.*, vol. 47, pp. 1933–1956, Nov. 1968.

[10] J. C. Dyment *et al.*, "Threshold reduction by the addition of phosphorous to the ternary layers of double-heterostructure GaAs lasers," *Appl. Phys. Lett.*, vol. 24, pp. 481–484, May 1974.

[11] J. C. Dyment *et al.*, "Proton-bombardment formation of stripe-geometry heterostructure lasers for 300 K CW operation," *Proc. IEEE* (Lett.), vol. 60, pp. 726–728, June 1972.

[12] F. A. Jenkins and H. E. White, *Fundamentals of Optics*, 3rd ed. New York: McGraw-Hill, 1957, p. 562.

[13] E. I. Gordon, "Mode selection in GaAs injection lasers resulting from Fresnel reflection," *IEEE J. Quantum Electron.*, vol. QE-9, pp. 772–776, July 1973.

[14] S. Yamamoto, Y. Koyamada, and T. Makimoto, "Normal-mode analysis of anisotropic and gyrotropic thin-film waveguides for integrated optics," *J. Appl. Phys.*, vol. 43, pp. 5090–5097, Dec. 1972.
[15] J. F. Nye, *Physical Properties of Crystals: Their Representation by Tensors and Matrices*. London, England: Oxford, 1957, pp. 243–254.
[16] A. Feldman and D. Horowitz, "Dispersion of the piezobirefringence of GaAs," *J. Appl. Phys.*, vol. 39, pp. 5597–5599, Nov. 1968.
[17] F. K. Reinhart and R. A. Logan, "Interface stress of $Al_xGa_{1-x}As$-GaAs layer structures," *J. Appl. Phys.*, vol. 44, pp. 3171–3175, July 1973.
[18] G. A. Rozgonyi, C. J. Hwang, and T. J. Ciesielka, "Determination of lattice curvature, relative lattice parameter differences, and the origin of stresses in LPE layers of $Ga_{1-x}Al_xAs$ on GaAs," *J. Electrochem. Soc.*, vol. 120, p 333, 1973.
[19] J. H. Serebrinsky, "Stress concentration in silicon-insulator interfaces," *Solid-State Electron.*, vol. 13, pp. 1435–1444, 1970.
[20] R. L. Hartman and A. R. Hartman, "Strain-induced degradation of GaAs injection lasers," *Appl. Phys. Lett.*, vol. 23, pp. 147–149, Aug. 1973.

Thermal Characteristics of Buried-Heterostructure Injection Lasers

TOSHIHISA TSUKADA, MEMBER, IEEE, AND YASUJI SHIMA

Abstract—**The thermal characteristics and CW operation of buried-heterostructure (BH) injection lasers, in which the GaAs active regions are completely buried in $Ga_{1-x}Al_xAs$, are described. The narrow active regions of these diodes facilitate effective heat dissipation. Thus, the CW operation of these lasers has been achieved without the p-GaAs layers usually grown in double-heterostructure (DH) lasers for electrical contacting purposes and with the heat dissipation through n-GaAs substrates. Even in this disadvantageous configuration, the temperature rise in the active regions of BH lasers at threshold is much smaller than that of p-side-down DH lasers. The calculation using an approximate formula can explain these low experimental values fairly well. Due to low operating current and effective heat dissipation, BH lasers can be operated continuously at room temperature on very small heat sinks such as TO-5 transistor headers.**

I. Introduction

HETEROSTRUCTURE lasers have been studied extensively in recent years. Double-heterostructure (DH) injection lasers [1], [2] have especially attracted the interest of many workers, because of their low threshold current density and their capability of continuous operation at room temperature. In order to achieve low thresholds, the active layer thicknesses of DH lasers need to be smaller than 0.5 μm. However, the widths of the active layers are in the order of several tens of microns. Therefore, the widths are larger than the thicknesses by about two orders of magnitude. This large discrepancy between the width and the thickness has produced a detrimental effect on the electrical and optical characteristics of these lasers. The excitation of higher order modes, the instability of modes against the change in current, and the anisotropic beam divergence are some examples of undesirable properties.

We have developed buried-heterostructure (BH) lasers [3] which have narrow active regions in contrast to the slab-like active layers of conventional semiconductor lasers. In BH lasers, the cross sections of the active regions have their widths approximately equal to their thicknesses. Cross-sectional areas as small as 1 μm^2 or less have been realized. In [3], we described the fabrication and characteristics of BH lasers and some of the unique properties of these lasers, such as the low-current operation, the reproducible realization of the lowest order transverse mode (TE_{00}), the stability of mode patterns against changes in current, the isotropic beam divergence, etc. Moreover, BH lasers have superior thermal characteristics because of the filamentary nature of the active or heat-generating region. In this paper, we describe in some detail the thermal characteristics of these lasers and their CW operation on small heat sinks.

II. Thermal Properties

The heat removal from the active region of a laser diode as well as the threshold current density is of great importance for the CW operation of the diode [4]. Generally, the thermal resistance expressed in units of degree/watt represents the temperature rise for input power of 1 W into the active region. However, in the case of semiconductor devices such as injection lasers of various geometries, the thermal resistance multiplied by the area is a more meaningful and convenient quantity in representing their facility to remove the heat generated per unit area of the junction. Using this quantity we obtain the temperature rise ΔT in the active region at threshold

$$\Delta T = R_T (J_{th} V) \quad (1)$$

Manuscript received November 25, 1974; revised January 20, 1975.
The authors are with the Central Research Laboratory, Hitachi Ltd., Kokubunji, Tokyo, Japan.

where R_T is the thermal resistance multiplied by the area expressed in units of degree cm^2/watt, J_{th} is the threshold current density, and V is the junction voltage. Because the product of J_{th} and V is nearly constant in laser diodes of various geometries, R_T can be used as a measure in comparing the thermal properties of semiconductor lasers.

The rigorous calculation of the R_T for a laser diode is not always easy. However, it is possible to calculate the R_T of a BH laser approximately by using the formula given in the literature [5] when it is mounted with its p side up as shown in Fig. 1. The formula is given for the case of an isothermal rectangular parallelepiped buried in a semi-infinite medium having an isothermal surface, and is expressed as follows:

$$R_T = \frac{W}{1.685\kappa}\left[\log\left(1+\frac{h}{W}\right)\right]^{0.59}\left(\frac{h}{d}\right)^{0.078} \times 10^{-4} \qquad (2)$$

where κ (W/deg · cm) is the thermal conductivity of the medium, h (μm) is the distance from the active region to the heat sink which is nearly equal to the thickness of the n-GaAs substrate, W(μm) is the width, and d(μm) is the thickness of the active region. The value of κ used in the following calculation is the thermal conductivity of GaAs. The active region is surrounded by a thin layer of GaAlAs of which the thermal conductivity is about one-fourth that of GaAs. This GaAlAs region will increase the R_T to some degree. However, this effect will be partially at least canceled out by the transparency of the GaAlAs region to spontaneous emission below threshold. The high internal efficiency of the spontaneous emission in the active region and the transparency of the surrounding medium mean that heat is not localized at the active region but rather at interfaces between the GaAlAs region and the GaAs substrate where the absorption of the emission occurs. Thus, a substantial part of heat is transferred through the GaAlAs region without feeling its low thermal conductivity. This justifies the use of the approximate formula given in (2). The range of validity of this formula is not quite certain. However, as will be shown later, the calculated R_T represents fairly well the actual R_T in the range involved.

Fig. 2 shows a plot of R_T as a function of W. The R_T becomes very small as the width of the active region gets narrower. For $W = 1$ μm, which is realizable in BH lasers, the R_T is as low as 0.27×10^{-3} deg · cm^2/W. This value of the R_T corresponds to the temperature rise in the active region of 1°C [$J_{th} = 2$ kA/cm^2 and $V = 2$ V were substituted into (1)]. This low value of the R_T stems from the geometry of the BH laser where the heat-generating region is completely buried in a medium with a reasonable thermal conductivity. A curve of R_T versus W, when W is wide, is shown in Fig. 3 again for the case of the p-side-up bonding. Even if the width of the active region is as wide as 50 μm, the R_T is not so large, i.e., 5.80×10^{-3} deg · cm^2/W, and corresponds to the temperature rise of 23°C (again $J_{th} = 2$ kA/cm^2 and $V = 2$ V were used). This result suggests the possibility of continuous operation of ordinary DH lasers, bonded to heat sinks with their p sides up provided the active region is embedded in a proper medium.

We can also calculate the thermal resistance from these figures. The thermal resistance of a p-side-up diode of which the active region is 1 μm in its width, becomes 67.5 deg/W (the assumed cavity length is 400 μm). For a 50-μm-wide diode it becomes 29 deg/W. Thus, the thermal resistance of a 1-μm BH laser is higher than that of broader (50-μm) lasers by 2.3 times. However, this by no means implies poor thermal characteristics of BH lasers. The meaning of this description is

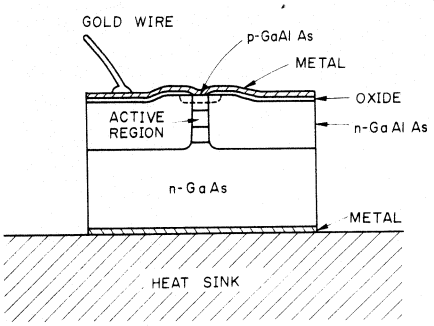

Fig. 1. BH injection laser mounted on a heat sink with its p side up. The lasers are typically 400 μm long, 300 μm wide, and 100 μm thick. The active regions are 1 μm^2 or less.

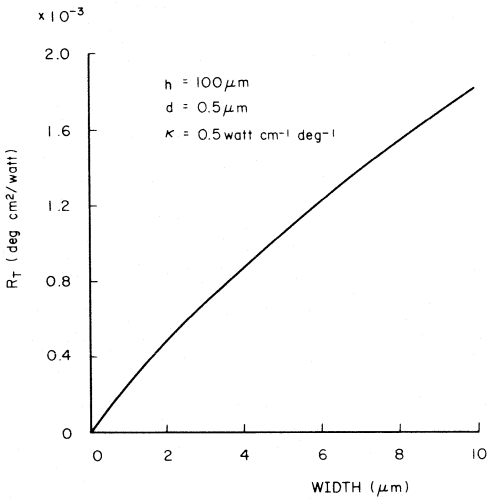

Fig. 2. R_T versus W for p-side-up lasers with narrow active region widths. The assumed thicknesses of the active region and the substrate are 0.5 μm and 100 μm, respectively. The thermal conductivity of GaAs was substituted into κ.

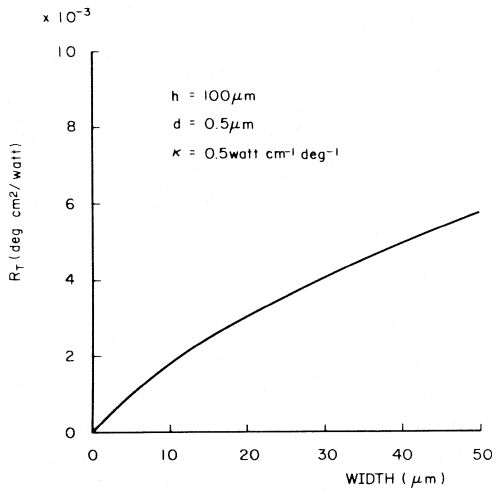

Fig. 3. R_T versus W for p-side-up lasers with wider active region widths. The assumed values of parameters are the same as in Fig. 2.

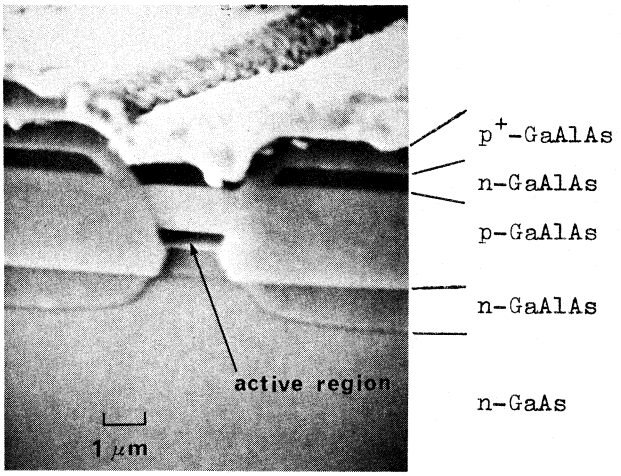

Fig. 4. Scanning electron photomicrograph of stain-etched facet of a BH laser. The thickness, the base, and the upside of the active region are 0.4, 1.1, and 1.3-μm, respectively. In this wafer, the n-p-n structure was grown in the secondary LPE and the p^+ layer was formed on top of the wafer by a Zn diffusion.

that the temperature rise of a BH laser is 2.3 times higher than that of a broad laser when the *same input power* was fed into these lasers. In reality, however, a BH laser at threshold needs a smaller input power than a broad laser by one order of magnitude or more. Therefore, the temperature rise of a BH laser at threshold is much smaller than that of a broad laser. This is due to the good heat dissipation of this laser.

In conclusion, the use of the R_T is appropriate in discussing thermal characteristics of semiconductor lasers of various geometries.

III. Experimental Procedures

BH lasers were fabricated using two-step liquid-phase-epitaxial (LPE) growth as described previously [3]. The first step in LPE is the consecutive growth of the four layers on an n-GaAs substrate. These layers are n-GaAs (~3 μm), n-$Ga_{1-x}Al_xAs$ (~1 μm), GaAs (~0.5 μm), and p-$Ga_{1-x}Al_xAs$ (~1 μm). The n and p layers were doped with Sn and Ge, respectively. The aluminum content x was chosen to be 0.2-0.4. The p-GaAs layer usually included for electrical contacting purposes in the double-heterostructure wafer was not grown in our experiments. This layer is not always necessary for the CW operation of BH lasers. The next step in the fabrication is the mesa etching of the epitaxial layers to define the narrow active region. The mesa etching must be deep enough to reach the n-GaAs epitaxial layer. Then the secondary LPE growth of $Ga_{1-z}Al_zAs$ ($z \geqslant x$) was performed completing the burying of the active region in the GaAlAs. This burying layer was usually undoped or lightly doped with n-type impurities. Controlling the growth time interval, we can adjust the thickness of this layer to the level of the crystal surface before etching. Then Zn was diffused through the oxide window 2 μm wide to form a shallow p^+ layer on top of the active region. Fig. 4 shows the stain-etched cleaved surface of a BH laser. In this wafer, the p-n-p-n structure was adopted to confine the current to the active region.

After thinning the wafer by polishing off the n-GaAs substrate to a thickness about 100 μm, Cr and Au was evaporated onto the p side of GaAlAs, and Au-Ge-Ni onto the n-GaAs substrate. BH lasers were bonded onto metallized diamonds mounted on copper heat sinks. Some of the BH lasers were bonded with their p sides down onto heat sinks as was described for DH lasers. However, most of the BH lasers were bonded with their p sides up. In this case, the contact to the p side of the laser was made with bonded gold wires. Several other lasers selected for low threshold were bonded with their p sides up on copper disks 0.4 mm in thickness and 1.8 mm in diameter which were mounted on TO-5 transistor headers.

The thermal resistance was calculated from the spectral peak shift of the spontaneous emission. The spectrum of the spontaneous emission of laser diodes operated with low-duty cycle pulses of a particular current level less than I_{th} was first recorded. Then these diodes were operated with dc current (or with high-duty cycle pulses) at the same current level. From the shift of the spectral peak between these two operations, the temperature rise in the active region was estimated. The wavelength shift of the spontaneous emission by a temperature increase of 1 deg was measured independently to be 3 Å.

IV. Results

Although p-GaAs layers for electrical contacting purposes were not used in our BH lasers, these lasers have operated continuously at room temperature due to their superior thermal characteristics. For diodes mounted with their p sides down onto heat sinks, the spectral shift from pulsed-to-dc operation was unmeasurable so far as our method is concerned. This means a very small temperature rise in the active region. A temperature rise of several degrees has been observed in diodes mounted with their p sides up onto heat sinks. The smallest value of R_T obtained in p-side-up diodes is 0.5×10^{-3} deg · cm^2/W. The active region width of this diode is 2 μm. Therefore, the measured R_T is in close agreement with the calculated value shown in Fig. 2. The temperature rise in the active region may be estimated to be about 2 deg, in contrast

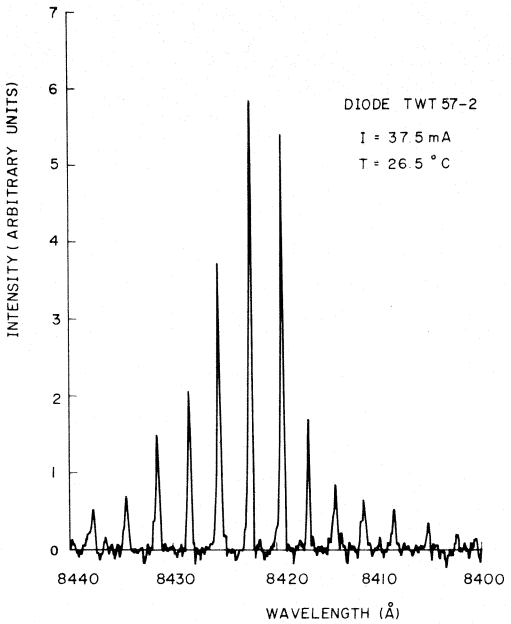

Fig. 5. Lasing spectrum of a continuously operating BH laser mounted on a TO-5 header.

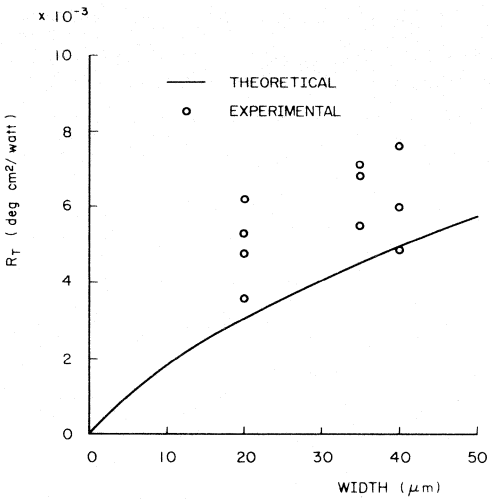

Fig. 6. Comparison of the experimental values of R_T with the calculated values. Experimental data were obtained in VLMS DH lasers operating continuously at room temperature. Although these data are somewhat scattered, the R_T nearly equal to the calculated value will be obtained reproducibly once the bonding conditions are determined.

to a temperature rise of 5-10°C usually observed in well-bonded DH lasers mounted with their p sides down onto heat sinks. Thus, the temperature rise of p-side-up BH lasers is several times lower than that of p-side-down DH lasers. The lowest dc threshold current so far obtained is 17 mA in a diode with 0.7 X 1 X 390-μm^3 active region. This diode was bonded with its p side up and its pulsed threshold current was 15 mA. The threshold current density of this diode was 3.8 kA/cm^2 which is rather high compared with the threshold of the wider (44 μm) laser fabricated from the same wafer, i.e., 1.6 kA/cm^2. This apparent high-current density of the narrow laser comes from the leakage of current through the GaAlAs p-n junction. The p^+ layer above the active region is wider than the 2-μm-wide oxide window due to the lateral diffusion of Zn, and is about 4 μm wide. Therefore, if the width of the active region is narrower than 4 μm, the apparent J_{th} becomes higher than the actual current density. In reality, a J_{th} as low as 1.6 kA/cm^2 has been obtained in a diode with an active region 4 μm wide.

Low threshold current and good heat dissipation have made it possible to realize the continuous operation of BH lasers with small heat sinks. A BH laser bonded with its p side up onto a copper disk mounted on a TO-5 transistor header has operated continuously at room temperature. The pulsed I_{th} of this diode was 18 mA and dc I_{th} was 37 mA. Because the heat capacity of a TO-5 header is small, the operating current level became higher compared with a diode mounted on a more bulky heat sink. Nevertheless, the temperature rise in the active region was estimated to be about 30°C, which is comparable to the values obtained in the usual mesa-stripe-geometry DH lasers [4]. Fig. 5 shows the lasing spectrum of a continuously operating BH laser mounted on a TO-5 header.

As was described in Section II, Fig. 3 implies that conventional DH lasers bonded with their p sides up can also be operated continuously at room temperature. This prediction has been confirmed experimentally. Fig. 6 shows the experimental and calculated values of the R_T of VLMS DH lasers [6]. Although the experimental values are somewhat scattered, there exist experimental values almost equal to the calculated values. This means that if optimized conditions are adopted in the bonding, an R_T equal to the calculated values is reproducibly obtainable.

V. Discussion

The bonding of injection lasers with their p sides up onto heat sinks has the following advantages over that of lasers with their p sides down. Firstly, stress-reduced bonding and stress-reduced operation are possible. The p-side-down lasers cannot be bonded without impressing stresses onto the active regions. Such stress tends to induce the multiplication of defects or dislocations along the active layer. However, the p-side-up lasers can be bonded and operated with minimal stress on the active regions. Another advantage of p-side-up bonding is the small scatter among the values of the R_T of bonded lasers. In p-side-down bonding, the bonding condition directly influences the value of the R_T. However, in p-side-up bonding, the contribution to the R_T mainly comes from the substrate. Therefore, the influence of the bonding conditions is small. Thus, the smaller scatter in the value of the R_T and the reproducibility of bonding can be obtained. In the third place, the degradation process in the active region may be observed by directly scanning the surface of the laser by SEM. This observation has been the main difficulty in observing the degradation processes of p-side-down lasers. The existence of defects and dislocations in the active region can be checked before operation or after limited operation of laser diodes. In this way, the selection of good diodes becomes possible. This inspection is rather important in the application of diodes as coherent sources in many fields.

In the bonding process of p-side-down lasers, delicate care must be taken not to short the p-n junctions of these diodes.

Moreover, the diodes must be bonded just at the edges of or overhanging heat sinks in order to avoid interference of the laser beam with the reflected beam from the heat sink. In p-side-up bonding, these restrictions can be slackened because the active regions are apart from the heat sinks.

VI. Conclusion

BH lasers have been shown to have superior thermal characteristics over conventional lasers. The narrow nature of the heat-generating region facilitates good heat dissipation from the active region. For this reason, the CW operation of BH lasers has been shown to be possible 1) without p-GaAs layers for electrical contacting purposes; 2) with heat dissipation through the n-GaAs substrate; 3) without diamond heat sinks; and 4) with very small heat sinks.

The CW operation on a TO-5 header is a typical demonstration of superior thermal characteristics of these lasers. The product of the thermal resistance and the area was calculated and was shown to decrease as the width of the active region decreases. This decrease means a small temperature rise in the active region with the same current density. The calculated value of this product has been shown to explain the experimental results fairly well. The extension of this calculation towards the broader active region has suggested the possibility of the continuous operation of stripe-geometry lasers with p-side-up bonding. This prediction was verified experimentally in VLMS DH lasers with their stripe widths ranging from 20 to 40 μm.

The reliability of p-side-up BH lasers has not been studied extensively in this work. However, highly reliable diodes are expected because of the stress-reduced bonding and operation, the low probability of including defects in the small active region, and the good heat dissipation from the narrow active region.

Acknowledgment

The authors would like to thank Dr. O. Nakada for his encouragement throughout the course of this work. They are also grateful to N. Chinone for his useful discussion and to S. Yamashita for his help in the bonding of diodes and for measurements of the thermal resistance.

References

[1] Zh. I. Alferov, V. M. Andreev, E. L. Portnoi, and M. K. Trukan, "AlAs-GaAs heterojunction injection lasers with a low room-temperature threshold," *Fiz. Tekh. Poluprov.*, vol. 3, pp. 1328-1332, Sept. 1969.

[2] I. Hayashi, M. B. Panish, P. W. Foy, and S. Sumski, "Junction lasers which operate continuously at room temperature," *Appl. Phys. Lett.*, vol. 17, pp. 109-111, Aug. 1970.

[3] T. Tsukada, "GaAs-$Ga_{1-x}Al_xAs$ buried-heterostructure injection lasers," *J. Appl. Phys.*, vol. 45, pp. 4899-4906, Nov. 1974.

[4] T. Tsukada, R. Ito, H. Nakashima, and O. Nakada, "Mesa-stripe-geometry double-heterostructure injection lasers," *IEEE J. Quantum Electron. (Special Issue on 1972 IEEE Semiconductor Laser Conference)*, vol. QE-9, pp. 356-361, Feb. 1973.

[5] J. P. Holman, *Heat Transfer.* New York: McGraw-Hill, 1972, p. 59.

[6] O. Nakada, N. Chinone, S. Nakamura, H. Nakashima, and R. Ito, "Continuous operation over 2500 h of double-heterostructure laser diodes with output powers more than 80 mW," *Japan. J. Appl. Phys.*, vol. 13, pp. 1485-1486, Sept. 1974.

A New Technique for Measuring the Thermal Impedance of Junction Lasers

THOMAS L. PAOLI, MEMBER, IEEE

Abstract—**A new method is presented to measure the temperature of the optical cavity of a junction laser as a function of the average electrical power supplied to the device. The technique relies upon a null measurement of the exact wavelength of a single Fabry-Perot mode and therefore does not require a preliminary calibration measurement. Because of the small linewidth of the mode, very small (<0.2°C) temperature differences are easily measured. The method is utilized to obtain the thermal impedance for several different types of bonded stripe-geometry junction lasers.**

Manuscript received December 2, 1974; revised January 20, 1975.
The author is with Bell Laboratories, Murray Hill, N.J. 07974.

I. Introduction

THE THERMAL impedance of a junction laser is an important parameter for achieving optimum performance in continuous or rapidly pulsed operation. For example, the useful lifetime of laser diodes is known to depend on their operating temperature [1]. Furthermore, a large temperature rise in a rapidly pulsed device during periods of heavy usage can produce temporary but undesirable changes in threshold or operating wavelength. Consequently, it is important to have an accurate but simple measure of the temperature, and hence the thermal impedance, of a bonded laser.

Any measurement of the thermal impedance of a diode involves determining the temperature change produced by a known variation of the input power. In the past, temperature shifts have usually been deduced from the observed changes in laser threshold or the total spectrum of spontaneous or stimulated emission [2], [3]. However, both methods are unsatisfactory for several reasons. First, they require a "calibration" measurement of the temperature dependence of the observed quantity. For maximum reliability the calibration should be performed on the actual device under study and so the complete measurement for each laser can be very time-consuming Secondly, neither the threshold nor the overall optical spectrum of present-day junction lasers is very sensitive to temperature. For example, in low-power double-heterostructure (DH) lasers where the temperature rise due to continuous operation is typically 5°C, the corresponding change in threshold may be 5 to 10 percent and the spectral shift is only 10 to 15 Å. On the other hand, a measurement of laser threshold involves a large uncertainty since the threshold is usually not well defined when measured by observing the far field or the spectrum [4]. Similarly, spectral shifts are difficult to measure accurately, due to the large radiative linewidth.

In this paper, we present a new method for measuring the temperature rise of a laser diode as a function of average electrical power supplied to the device. The method utilizes the temperature dependence of the refractive index within the laser waveguide and is therefore sensitive to the temperature within the optical cavity itself. The use of the refractive index differs from previously reported techniques which depend on the temperature variation of the bandgap energy [2], [3]. Furthermore, the present technique relies upon a null measurement of the exact wavelength of a single Fabry-Perot mode of the laser cavity and therefore does not require a preliminary calibration measurement. Consequently, a complete measurement on each laser can be performed very rapidly but accurately. In addition, because of the small linewidth of each mode, very small (<0.2°C) temperature differences are easily measured. In Section II, the method and its instrumentation are described in detail. Experimental results including some measured values of thermal impedance for several different types of stripe-geometry junction lasers are reported in Section III. Conclusions of the present work are presented in Section IV.

II. Experimental Technique

A. Principle of Null Measurement

Since the refractive index of a semiconductor is temperature dependent, the resonant frequency of each Fabry-Perot mode in a junction laser varies with the temperature of the laser resonator. At room temperature, this shift is more than 1 Å/deg [5]. Since the width of a Fabry-Perot mode near threshold can be less than 0.2 Å, the wavelength of a single longitudinal mode is a sensitive indicator of the temperature of the laser cavity.

In the present work, we determine the temperature rise associated with operating a laser continuously by measuring the drop in heat-sink temperature ΔT_{HS} which is required to maintain an individual Fabry-Perot mode at a preselected wavelength as the operational duty cycle is increased at constant current from near 0 to 100 percent. Since the laser current is a constant, nulling of the wavelength shift means that the optical cavity is at the same temperature in continuous operation as it was at very low duty cycle. Consequently, we can identify ΔT_{HS} as the temperature rise ΔT_{CW} for CW operation provided that the preselected wavelength corresponds to the optical cavity at the initial heat-sink temperature. This latter requirement is satisfied by operating the laser at a very low-duty cycle ($<10^{-3}$) where the average heating is negligible and selecting the wavelength for the designated mode at a time early within the current pulse in order to minimize the transient heating. However, as with all techniques which in some way utilize a pulsed measurement to avoid heating, the initial transient temperature rise leads to a systematic error in the measurement which will be discussed further in Section IV.

After the temperature rise ΔT_{CW} is determined, the thermal impedance R_{th} of the laser is calculated from the definition

$$\Delta T_{CW} = R_{th} P_{CW} \tag{1}$$

where P_{CW} is the average externally supplied electrical power given by the current I times the device voltage V. In order that P_{CW} actually represents the heat dissipated in the device, it is important that the current be chosen near and preferably below the laser threshold so that the radiative power is a small fraction of the input power.

With lasers for which continuous operation is not possible or undesirable, a variation of the above method can be used to determine the thermal impedance. In this case, the temperature of the laser cavity is measured as a function of the average electrical power P_{AV} supplied to the laser. P_{AV} is varied by changing the repetition frequency of the applied current pulses while the pulsewidth and amplitude are held constant. As a result of the increased heating, the wavelength of a Fabry-Perot mode observed at a fixed time during the pulse increases. The temperature rise is then measured directly by reducing the heat-sink temperature enough to compensate for the wavelength shift. In this way, a calibration of wavelength shift versus temperature is avoided. The thermal impedance is obtained from the slope of the temperature versus P_{AV} relation, and a pulsed measurement of the voltage, thereby eliminating the necessity of continuous operation.

B. Measurement System

The temperature rise associated with operating a laser continuously was measured with the system shown schematically in Fig. 1. In order to select a Fabry-Perot mode for use in the null measurement, each laser was pulsed on for typically 500 ns at 2000 pulses/s. The amplitude of the pulse current was chosen as near to threshold as allowed by the system sensitivity. The laser light was focused into a $\frac{3}{4}$-m Spex Spectrometer whose optical output was detected by a cooled photomultiplier. The output of the photomultiplier was amplified and displayed on a real-time oscilloscope for observation of the light pulse for the wavelength interval (≈0.2 Å) selected by the spectrometer. Typically, the light pulse observed at a fixed wavelength was much shorter than the total current

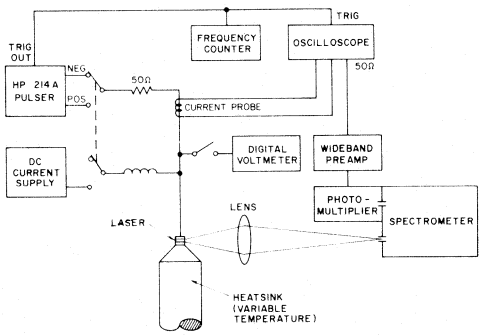

Fig. 1. Schematic diagram of the system used to measure the thermal impedance of stripe-geometry junction lasers. For duty cycles less than 50 percent, the pulser was used alone to pulse the laser on. For duty cycles greater than 50 percent, the pulser was used in conjunction with the dc supply to pulse the laser off.

pulse since the wavelength of each mode is shifted during the current pulse due to transient heating. To minimize the transient temperature difference between the laser and the heat sink, the initial wavelength for the mode was selected within the first 50 ns of the pulse and after initial transient oscillations had ceased. In addition, the rise time of the current pulse was adjusted to be a few nanoseconds less than the sample time to decrease further the initial heat input. After the wavelength had been set on the spectrometer in this way, no further adjustments to the spectrometer were made during the measurement. By convention, the heat-sink temperature for this initial setup was 25°C.

In practice the selected mode was tracked from low-duty cycle to continuous operation by reducing the heat-sink temperature slowly while simultaneously increasing the duty cycle at which constant current pulses were applied to the laser. In this way increases in the average input power were used to compensate for the cooling and thereby maintain the wavelength of the longitudinal mode at its preselected time-resolved value. Because of the unavailability of a pulser tunable from low to 100 percent duty cycle, it was necessary to make the transition in two stages. For duty cycles less than 50 percent, the limit of the pulser, the pulser was used alone and increases in the duty cycle were produced by increasing the pulse rate with a fixed pulsewidth. For operation at duty cycles greater than 50 percent, laser excitation was supplied by a pulser with reversed polarity in conjunction with a dc supply as shown in Fig. 1. In this stage, the effective duty cycle was increased by decreasing the pulsewidth. When the width had been reduced to its minimum value, the pulse amplitude was decreased to zero and the laser was operated continuously. The temperature rise ΔT_{CW} of the laser resonator was then determined by adjusting the heat-sink temperature at which the peak of the mode occurred at the preselected wavelength.

For determination of the thermal impedance, the laser voltage was measured with the digital voltmeter shown in Fig. 1. The heat-sink temperature for this measurement was always set at 25°C - ΔT_{CW}. Consequently, the measured values correspond to the laser resonator at approximately 25°C.

C. Lasers

Lasers used in the present study were either conventional DH devices intended for continuous operation with relatively low optical power output of P-p-n-N lasers intended for high-power pulsed operation in a fundamental mode [6]. The multilayered structure of the DH laser consists of a thin ($\lesssim 0.4$ μm) active layer of p-type GaAs sandwiched between p- and n-type layers of AlGaAs. The P-p-n-N laser is also a multilayered heterostructure device with the difference that the p-n junction is located within a relatively thick (2 to 3 μm) optical waveguide as described previously [6]. All lasers were fabricated into stripe-geometry devices by proton bombardment [7]. Stripe widths were nominally 13 μm. All lasers were bonded with indium on to diamonds bonded to Cu studs or directly to the Cu studs. A detailed description of the heat sinks and bonds is given in [8].

III. Experimental Results

The temperature rise associated with CW operation and the corresponding thermal impedance are summarized in Table I for the several different lasers studied in this work. The values for ΔT_{CW} listed in this table were all obtained by nulling the wavelength shift of an individual Fabry-Perot mode from low-duty cycle to continuous operation. The temperature rise ΔT_{CW} corresponds to an operating current near threshold.

To confirm the tabular value for L-734HA-2.3, the shift of the total spectrum of spontaneous emission at 50 mA was also measured as shown in Fig. 2. The current is chosen to be well below threshold in order to avoid modulation of the spectra by Fabry-Perot modes, which tend to obscure the spectral peak. As usual, the experimental points show considerable scatter, but their average value gives R_{th} = 22.1°C/W which is consistent with the value given in Table I. The scatter and uncertainty shown in Fig. 2 demonstrate the difficulty encountered when measuring R_{th} by this method in lasers where the temperature rise is only a few degrees.

In some devices such as P-p-n-N lasers intended for high-power pulsed operation, continuous operation may be undesirable due to the high level of input power required. With such devices, the temperature rise ΔT as a function of average input power can be used to estimate the thermal impedance. As an evaluation of this technique, R_{th} for L-734HA-2.3 was also measured in this way. As shown in Fig. 3 the temperature rise ΔT measured by the null technique is proportional to the duty cycle from 0 to 100 percent, indicating that the measurement is sensitive to the average dissipated power. From the slope of the line determined by the points below 50 percent and the measured voltage for continuous operation, we calculate R_{th} for this laser to be 20.9°C/W, which also is in good agreement with the value obtained by taking the laser to CW conditions. However, it should be noted that many points must be taken to determine the slope accurately.

Also shown in Fig. 3 is the rise in temperature with duty cycle for another laser from the same batch, L734HA-4.2. Again the dependence is linear to 100 percent and gives R_{th} = 56.4°C/W in close agreement with the tabled value.

The experimental points of ΔT versus duty cycle for a short P-p-n-N laser L714-6-3 are shown in Fig. 4 for different sample times t_s within the current pulse. From the slope of the line, we calculate R_{th} for this laser to be 94°C/W which is the value given in Table I. Also it is clear from the figure that at least for times less than 400 ns the measured value of ΔT is not sensitive to the exact time t_s at which the modal wavelength shift is nulled.

TABLE I

LASER No.	TYPE	LENGTH	HEATSINK	ΔT_{CW} (°C)	R_{th} (°C/watt)
L734HA-2.3	DH	380 μm	p side down on copper	8.1 (160 mA)	22.2
L734HA-4.2	DH	380 μm	p side down on copper	21.5 (150 mA)	57.8
L714-6-3	PpnN	102 μm	p side down on diamond	not operated continuously	94 (260 mA)
L714-6-2	PpnN	127 μm	p side down on diamond	not operated continuously	75 (380 mA)
L684S-00	DH	152 μm	n side down on copper	21.2 (80 mA)	146.8
L736HA-1.3	DH	380 μm	p side down on copper	6.6 (180 mA)	22.1

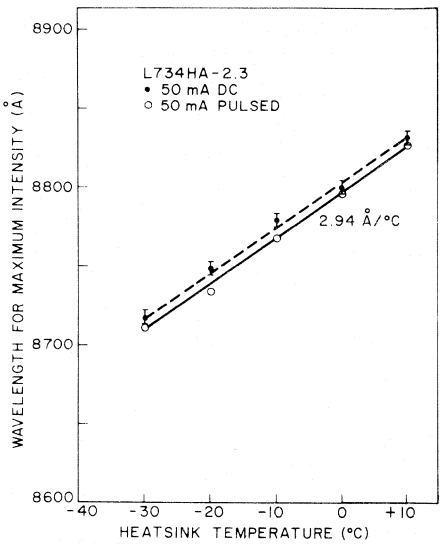

Fig. 2. Spectral shift of the spontaneous emission peak as a function of heat-sink temperature for L734HA-2.3 operated pulsed and continuously. The points obtained with pulsed operation are used to calibrate the temperature dependence of the spectral peak for this laser. The temperature rise obtained from the wavelength shift between the dc and pulsed points at a constant heat-sink temperature is used to calculate the thermal impedance.

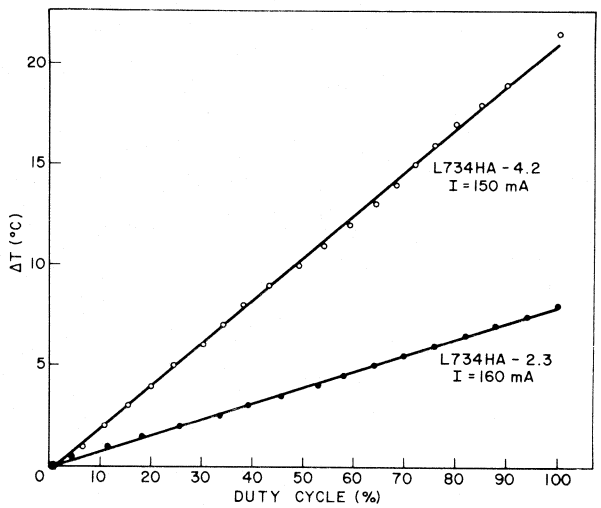

Fig. 3. Temperature rise measured by the null technique as a function of duty cycle for a DH laser, L734HA-2.3. Note that the dependence is quite linear from 0 to 100 percent and that the ΔT_{CW} obtained this way is the value given in Table I.

As a check on the measured value, the thermal impedance for L714-6-3 was also estimated from the shift of the total spectrum of spontaneous emission produced by changing from low-duty-cycle operation to continuous operation. Although the experimental data obtained at 100 mA show considerable scatter as indicated in Fig. 5, the average of the values obtained this way, R_{th} = 90°C/W, is consistent with the value obtained by the null measurement.

The variation of ΔT with duty cycle for the last three diodes listed in Table I is shown in Fig. 6. From these measurements, we find R_{th} = 75°C/W for L714-6-2, R_{th} = 142°C/W for L684S-00, and R_{th} = 23.1°C/W for L736HA-1.3. The latter two values also agree quite well with the values in Table I.

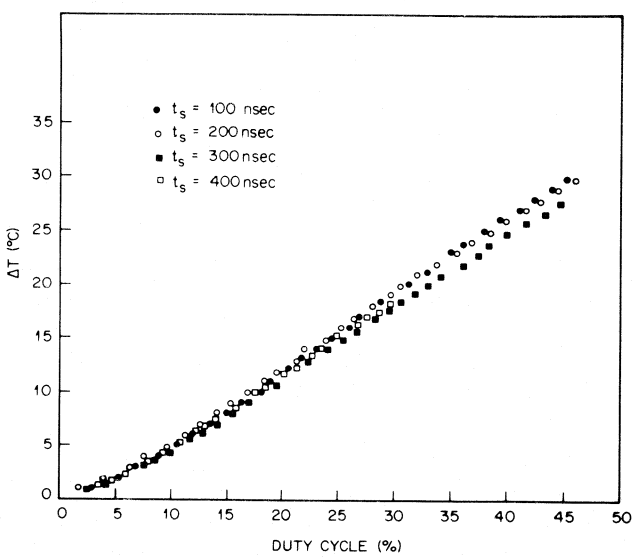

Fig. 4. Temperature rise as a function of duty cycle for a P-p-n-N laser L714-6-3. The parameter t_s is the time between the start of the current pulse and the point at which the wavelength shift of the Fabry-Perot mode is nulled. Note that the slope of the line is relatively insensitive to this time.

IV. Conclusion

In this work, we have shown that the thermal impedance of stripe-geometry junction lasers can easily be determined with a null measurement of the wavelength of an individual Fabry-

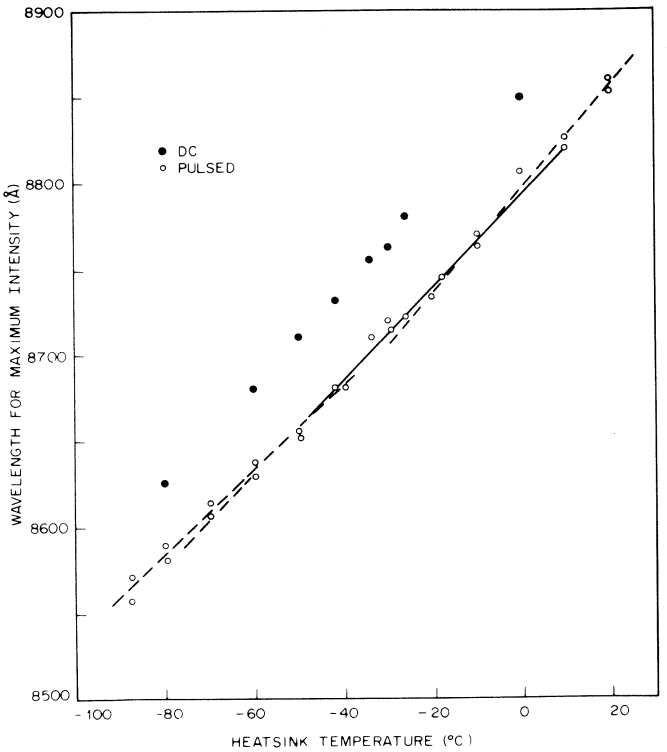

Fig. 5. Spectral shift of the spontaneous emission peak at 100 mA as a function of heat-sink temperature for a P-p-n-N laser, L714-6-3. These data are used to calculate the thermal impedance of this laser for comparison with the value obtained with the null measurement.

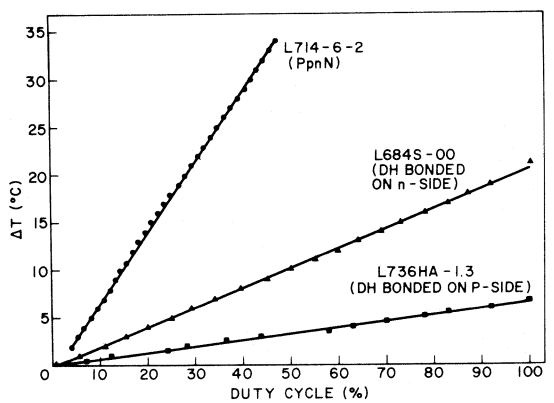

Fig. 6. Temperature rise as a function of duty cycle for a short P-p-n-N laser, a DH laser bonded on its p side, and a short DH laser bonded on its n side.

Perot mode of the laser cavity. The technique does not require a preliminary calibration and can be performed quickly and accurately. Because of the relative ease with which the measurement is performed, studies of the thermal impedance as a function of current level or absolute laser temperature are feasible. The technique should also be useful in an assessment of the relative importance of heat transfer by spontaneous emission.

Since the modal wavelength is used as the temperature indicator, the technique acutally is sensitive to the temperature within the optical resonator rather than the temperature at the p-n junction. Furthermore, the measured value is in some way an average over the transverse spatial distribution of temperatures which may exist in the stripe-geometry device [8], as well as over local hot spots which may exist along the laser axis. Consequently, the technique has the distinct advantage of measuring an average internal temperature for the laser as compared to the local temperature indicated by observation of the spontaneous emission generated near a laser mirror.

We have also demonstrated in this work that a null measurement of the modal wavelength can be used to measure the average temperature of a pulsed laser as a function of its duty cycle. From such a measurement, the thermal impedance of the laser can be estimated without operating the device continuously. However, since the measurement technique is somewhat more involved and involves an extrapolation to CW conditions, this method is considered to be less reliable than the direct measurement of the temperature associated with continuous operation.

The measurement technique has been illustrated with measurements on several stripe-geometry lasers including P-p-n-N and conventional DH lasers. The values obtained are consistent with those obtained by using the spectral shift of the spontaneous emission. Since R_{th} is expected to be inversely proportional to the device length L, comparison of different devices is facilitated by use of the coefficient $R_{th}L$. For two P-p-n-N lasers, $R_{th}L$ was measured to be approximately 375 deg mil/W which is consistent with the nominal value calculated [8] recently for this type of structure. For a conventional DH laser with good thermal characteristics, $R_{th}L$ was measured to be approximately 331 deg mil/W which is somewhat lower than the minimum value expected [8] for this structure. The difference may be due to the systematic error introduced by the initial transient temperature rise described in Section II. For a nominal DH laser, an initial rise of about 2 to 3°C might be expected from simple thermal considerations [9]. In terms of the small ΔT_{CW} being measured with DH lasers, this systematic error may be appreciable. Consequently, a further assessment of its actual magnitude is necessary before a detailed comparison with the theoretical values is justified. In addition, the discrepancy may also be partly due to incomplete confinement of the current to the assumed stripe width and/or to some heat generation between the active region and the heat sink. In the latter case, the generated heat would have a minimal effect on the temperature of the optical cavity. On the other hand, for another DH laser from the same wafer, $R_{th}L \approx 867$ deg mil/W was obtained, indicating some of the variability obtained with these devices. Finally, with a conventional DH laser bonded n-side down, a value of approximately 881 deg mil/W was obtained for $R_{th}L$. This relatively high value of thermal impedance reflects the effect of the thick substrate layer which is between the junction and the heat sink. As with the other DH laser, the measured value is somewhat lower than calculated [8] for this bonding geometry.

Acknowledgment

The author wishes to thank L. A. D'Asaro for helpful comments on the manuscript and J. F. Svacek for his technical assistance.

References

[1] R. L. Hartman and R. W. Dixon, *Appl. Phys. Lett.*, vol 26, pp. 239-242, Mar. 1, 1975.

[2] C. H. Gooch, "The thermal properties of gallium arsenide laser structures," *IEEE J. Quantum Electron.*, vol. QE-4, pp. 140-143, Apr. 1968.

[3] H. Meixner and R. Unger, "Optical method for determination of the thermal resistivity of laser diodes," *Siemens Z.*, vol. 3, pp. 190–194, 1974.
[4] T. L. Paoli, unpublished.
[5] Yu. A. Bykovskii *et al.*, "Heating of semiconductor injection pulse lasers," *Instrum. Exp. Tech.* (USSR), vol. 15, pt. 2, pp. 864–866, 1972.
[6] T. L. Paoli, B. W. Hakki, and B. I. Miller, "Zero-order transverse mode operation of GaAs double-heterostructure lasers with thick waveguides," *J. Appl. Phys.*, vol. 44, pp. 1276–1280, Mar. 1973.
[7] J. C. Dyment, L. A. D'Asaro, J. C. North, B. I. Miller, and J. E. Ripper, "Proton-bombardment formation of stripe-geometry heterostructure lasers for 300 K CW operation," *Proc. IEEE* (Lett.), vol. 60, pp. 726–728, June 1972.
[8] W. B. Joyce and R. W. Dixon, *J. Appl. Phys.*, vol. 46, pp. 855–862, Feb. 1975.
[9] W. Engeler and M. Garfinkel, "Thermal characteristics of GaAs laser junctions under high power pulsed conditions," *Solid-State Electron.*, vol. 8, pp. 585–604, July 1965.

Transverse Mode Control of Junction Lasers Optically Coupled to Single-Mode Fibers

D. C. KRUPKA, MEMBER, IEEE, AND THOMAS L. PAOLI, MEMBER, IEEE

Abstract—**Preliminary experimental results are reported to demonstrate that fundamental transverse mode operation can be obtained from a multimode double-heterostructure (DH) junction laser while simultaneously coupling its output into a single-mode optical fiber. Mode selection has been achieved by three different methods: 1) incorporating the fiber into the resonant cavity; 2) using the reflections off the diode-fiber interface; and 3) by a combination of the aforementioned methods. In all approaches the diode-fiber interface effectively becomes a mirror with a reflectivity which is higher for the fundamental mode than for all other modes of the DH waveguide. By using the reflections off the diode-fiber interface, a peak pulsed power of 80 mW has been obtained from the uncoated end of a single-mode fiber butted against a P-p-n-N junction laser. This laser radiated a peak power of 165 mW in a first-order mode when operated without coupling to the fiber.**

I. Introduction

IN THIS WORK, we present preliminary results to show that a single-mode optical fiber can be effectively used to obtain transverse mode control in a multimode double-heterostructure (DH) junction laser while simultaneously coupling its output into the fiber. In principle, mode selection may be achieved either by incorporating the fiber into the resonant cavity (intracavity selection) or by using reflections off the diode-fiber interface (reflective selection). In both approaches the diode-fiber interface can be considered as a mirror which preferentially excites the fundamental mode of the DH waveguide.

In Section II, calculations are presented for the efficiency of optical coupling between a stripe-geometry junction laser with a thick waveguide and available low-loss optical fibers. The calculations indicate the conditions required for efficient coupling. In Section III, experiments are described which demonstrate the use of a fiber as a mode-selecting element. The results indicate that the intracavity and reflectivity effects may be present simultaneously with varying relative contributions. In the conclusions presented in Section IV, it is argued that the intracavity effect is to be preferred and that it may help in suppressing filamentation in lasers operated well above threshold.

Manuscript received January 3, 1975; revised January 27, 1975.
The authors are with Bell Laboratories, Murray Hill, N.J. 07974.

II. Diode-Fiber Coupling

Coupling from a stripe-geometry DH laser operating in the fundamental mode to an optical fiber with a round core is inherently inefficient because of the ellipticity and astigmatism [1] of the GaAs laser beam. An estimate of the coupling efficiency κ may be obtained by approximating the modes of the laser and fiber by equivalent Gaussian modes and using expressions derived by Kogelnik [2] for the coupling coefficient. If the beam astigmatism is neglected, it is found that optimum coupling is achieved when the mode cross-sectional areas are equal. For a laser having a 12-μm stripe width, and for typical laser and fiber refractive index profiles, this criterion leads most often to the requirement that the fiber be single mode. More accurate formulas for coupling have been derived by Cook [3] who represented the fundamental mode of the GaAs laser by a product of two Gaussian functions but used an exact expression for the fiber's fundamental (HE_{11}) mode.

Using the formulas given in [3], the coupling coefficient as a function of fiber core diameter, for the case of a fiber butted against the laser, has been calculated for a Gaussian laser mode with a $2w_{0x} = 9$ μm parallel to the junction plane and different waists $2w_{0y}$ perpendicular to the junction plane. The choice of $2w_{0x}$ is a nominal value taken from previous measurements [1]. The beam's astigmatism has been taken into account by assuming that the "perpendicular waist" is located at the mirror while the "parallel waist" has been placed 35.5 μm inside the laser [1]. The fiber core index is $n_1 = 1.458$ and the cladding index is $n_2 = 1.454$. These indices are

appropriate for the fibers available to us at the time of the experiment and, as outlined in the following, do not represent an optimum choice of $n_1 - n_2$. The results are plotted in Fig. 1.

The calculations show that for a given fiber core diameter, the coupling coefficient is a strong function of ellipticity $\epsilon = 2w_{0x}/2w_{0y}$, and that, as predicted on the basis of the simple Gaussian model, optimum coupling for typical values of ϵ is attained with single-mode fibers. Furthermore, it is found that the fiber core which optimizes κ is a very weak function of the core diameter for $\epsilon \gtrsim 2$. This may be appreciated on the basis of the simple model [2] which dictated equal mode areas for optimum coupling.

As ϵ is increased, the laser mode area is decreased (since $2w_{0x}$ is kept fixed), and the fiber mode diameter must be reduced to maintain optimum coupling. However, the fiber mode area may not be reduced indefinitely. As the core diameter is reduced a minimum value of mode diameter is attained, after which, further reduction of the core diameter leads to a growth of the mode area with an increasingly larger fraction of the mode power being carried in the cladding [4]. For the fiber used in the calculations, the minimum mode diameter, measured between $1/e^2$ points of intensity, is approximately 5.8 μm at a core diameter of 4.2 μm [4]. This is in reasonable agreement with the more rigorous calculations presented in Fig. 1 which suggest that the minimum effective mode diameter occurs at a core diameter of approximately 4.5 μm. Thus, in order to improve the coupling to the lasers with $\epsilon \geqslant 2$, one requires fibers having larger values of $n_1 - n_2$ which lead to smaller minimum mode diameters.

From Fig. 1 it is noted that in order to exceed $\kappa \approx 0.5$, one is forced to use a laser with $2w_{0y} \gtrsim 2$ μm. With a cavity thickness giving rise to such mode dimensions, it becomes increasingly difficult to maintain operation of a GaAs laser in the fundamental mode perpendicular to the junction plane. However, as will be shown in Section III, a short section of single-mode fiber butted against the laser mirror face, with a mirror at its remote end, can be used to force the laser to switch to fundamental mode operation.

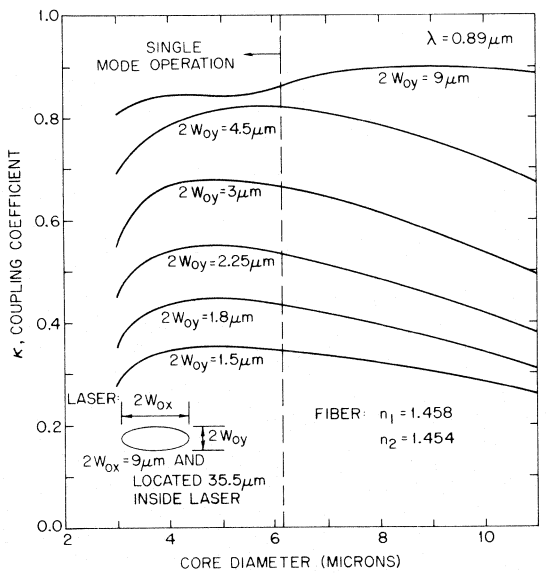

Fig. 1. Coupling coefficient κ as a function of fiber core diameter for lasers assumed to have Gaussian modes. In all cases the field at the laser mirror is assumed to have a width $2w_{0x} = 9$ μm and to be located 35.5 μm inside the laser face. The fiber has a core index $n_1 = 1.458$ and a cladding index $n_2 = 1.454$. Each curve is characterized by a different value of $2w_{0y}$. The calculations are carried out for a wavelength of 0.89 μm.

The mode selection can be understood as follows. Each mode transmitted through the diode-fiber interface may be expanded in terms of the single guided mode (HE_{11}) and the continuum (or cladding) modes of the fiber. However, the largest coupling efficiency occurs between the fiber mode and the fundamental mode of the DH waveguide because of the similarity of their spatial distributions. Immersion of the fiber in an index matching fluid strips or eliminates the cladding modes with the result that the power reaching the remote end of the fiber is entirely in the HE_{11} mode. A mirror is placed at the end of the fiber in order to return a portion of this power to the diode-fiber interface where it is again preferentially coupled to the fundamental mode of the DH waveguide. This output mirror effectively increases the reflectivity of the laser mirror for the fundamental mode by an amount

$$\Delta R_0 = \kappa^2 R_f \tag{1}$$

where R_f is the reflectivity of the HE_{11} mode at the fiber's remote end and κ appears squared because the wave passes through the coupling plane twice. It is assumed that the fiber is much longer than the laser. If ΔR_0 is sufficient to overcome the difference between the net gain of the fundamental mode and that of the oscillating mode, the laser will be forced to switch to fundamental mode operation. For lower values of ΔR, it is also possible to have the fundamental mode coexist with a higher order mode.

The use of a passive section in tandem with a laser has been advanced by Snitzer and LaMarre [5] and also by Miller [6]. The first two proposed a single-mode fiber in series with a laser, while the latter suggested the use of an intracavity dielectric guide with a cross section "substantially congruent with the shape of the cross section of the active region" of a solid state laser.

Mode selection can also result from positioning the laser and fiber such that the reflectivity of the fundamental mode is made higher than that of the other mode. An analysis of transverse mode selection by means of a distant mirror in a more controlled situation has been carried out by Hakki [7].

III. Experimental Results

To demonstrate the feasibility of the mode selection technique in a case where the intracavity effect is dominant, an experiment was set up as indicated schematically in Fig. 2. The laser selected was an $Al_xGa_{1-x}As$-GaAs heterostructure of the P-p-n-N type [8] with a waveguide thickness of 3 μm which lased in the first-order mode perpendicular to the junction plane ($m = 1$). Along the junction plane the contact current was confined to 12 μm by proton bombardment [9]. A quarter-wave layer of ZnS was coated [10] on one face of the diode to serve as an antireflective coating between the DH waveguide and the optical fiber [$n_{ZnS} \approx (n_{fiber} \cdot n_{GaAs})^{1/2}$]. This AR coating is useful to reduce the reflections from the diode-fiber interface which tend to preferentially excite modes other than the fundamental in the DH waveguide. A single-

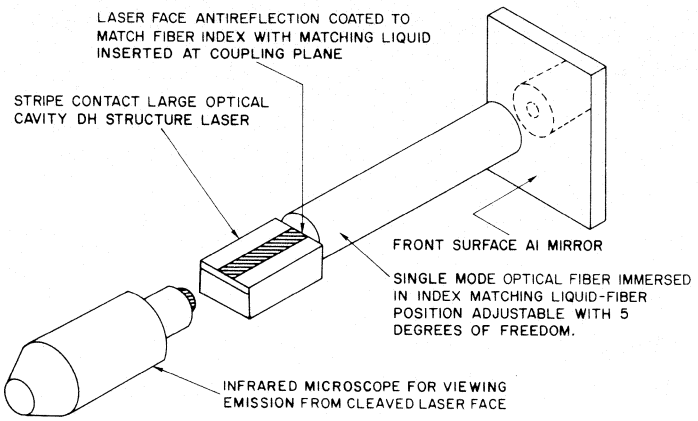

Fig. 2. Experimental setup. The fiber, approximately 10 cm long and immersed in index matching fluid to strip the cladding modes, may be positioned to have its end accurately parallel to the laser face and its core aligned with the laser waveguide. One face of the laser is AR coated to minimize reflections from the fiber-laser interface while the other is simply as cleaved. Changes in the radiation from the cleaved face induced by motion of the mirror are monitored by an infrared microscope.

mode fiber, approximately 10 cm long, with a core diameter of 5.7 μm (HE_{11} mode diameter ≈ 6.3 μm) was nestled in a trough containing index matching fluid. The index of refraction of the core was 1.458 while that of the fiber cladding was 1.454. A drop of index fluid was also placed on the fiber's tip before butting it against the coated face of the diode.

The position of the fiber was then adjusted with a micromanipulator having 5° of freedom to yield maximum transmitted power. During this phase the far-field radiation pattern from the uncoated diode face showed little change indicating minimal reflection from either end of the fiber. However, as a front surface Al mirror with its plane accurately adjusted to be perpendicular to the fiber's axis was advanced toward the free end of the fiber, notable changes occurred in the far field.

When the mirror was approximately 100 μm from the fiber's end, the laser mode was observed to begin a transition from the $m = 1$ to the $m = 0$ mode. The change appeared to be complete when the fiber-mirror separation was approximately 13 μm. When the mirror was pulled back, the laser reverted to $m = 1$ mode operation. First-order-mode operation was likewise obtained by keeping one end of the fiber butted against the laser and the other against the mirror, but displacing the fiber in a random manner by distances of a few microns. In all cases there was a unique position of the fiber which led to $m = 0$ operation. It was possible to break the index matching fluid seal between the laser and the fiber and then to remake it and obtain behavior identical to that described previously. There was no observable difference in threshold between the $m = 0$ obtained with the fiber and the $m = 1$ mode obtained without the fiber.

Fig. 3(a) shows a photograph of the far-field radiation pattern taken through the infrared microscope with the mirror removed, while Fig. 3(b) is a similar photograph taken with the Al mirror butted against the fiber's free end. The fiber's position relative to the laser is the same for both figures. The change from $m = 1$ to $m = 0$ operation is clearly seen. A scan of the far-field radiation pattern perpendicular to the junction

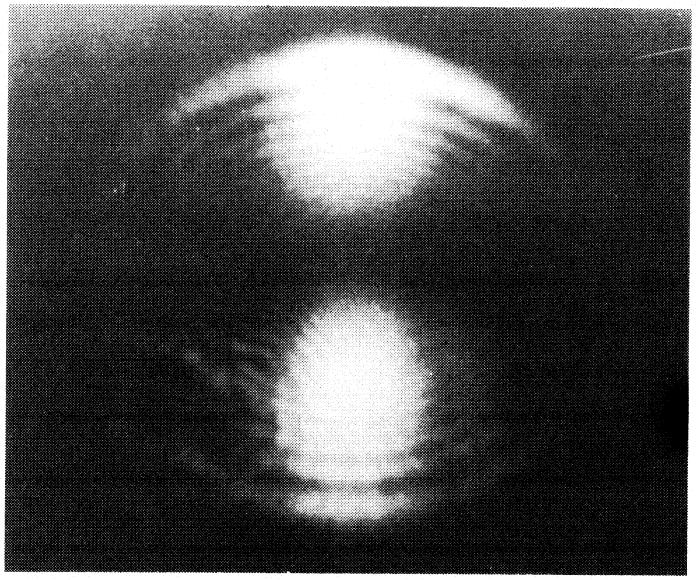

(a)



(b)

Fig. 3. Photographs of far-field patterns. (a) The $m = 1$ mode radiating from the cleaved face of the laser when the fiber is butted against its other face and the Al mirror is removed. $I = 1.4$ A. Exposure time in 2 s. The ring pattern is caused by the lens. (b) The $m = 0$ mode induced by butting the Al mirror against the fiber's remote end. The current is the same as in (a) but the exposure time is 0.5 s.

plane is shown in Fig. 4 and yields a full width at half-power of 19.4°. The refractive index profile obtained from the nominal doping levels [11], [12] may be used to calculate a far-field pattern [13] yielding a full width at half-power of 21° in reasonable agreement with observation. A far-field scan parallel to the junction plane gave a full width at half-power of approximately 10° implying operation in a filament with $2w_{0x} = 4$ μm.

Spectra were also observed for this laser in order to assess the degree of coupling achieved between the DH waveguide and the optical fiber. Fig. 5(a) shows the spectrum of the $m = 1$ mode obtained without the Al mirror, while Fig. 5(b) is the spectrum of the fundamental mode as selected by the external cavity. The shift of the oscillation spectrum to longer

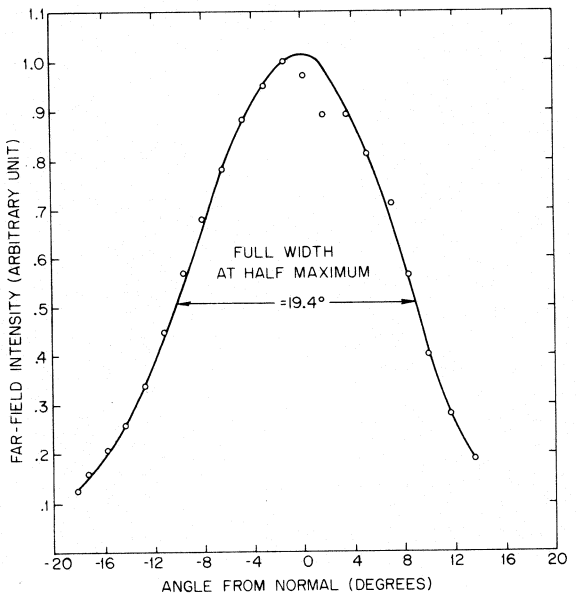

Fig. 4. Far-field scan perpendicular to junction plane when Al mirror is butted against the fiber's remote end. I = 1.4 A. For the laser used, the calculated full width at half maximum is 21°.

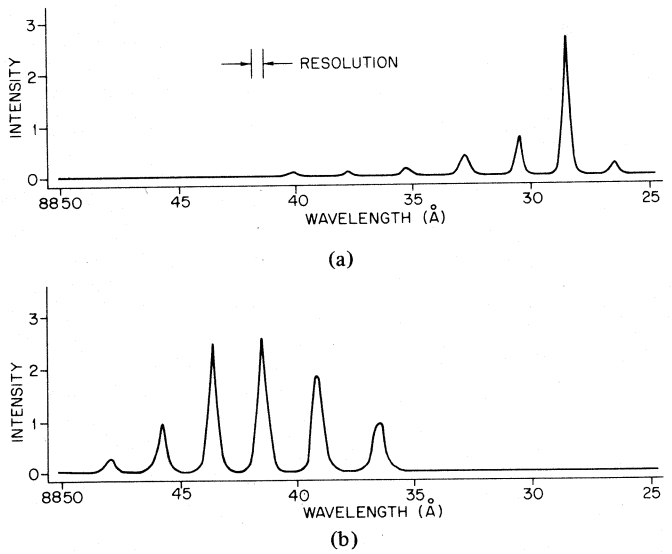

Fig. 5. Lasing spectra of the laser whose optical output is coupled into a single-mode optical fiber. (a) Mirror out. The output of the remote end of the fiber is not reflected back into the fiber and the laser oscillated in an m = 1 mode perpendicular to the junction. (b) Mirror in. An Al mirror is used to return the fiber output to the laser, thereby switching the oscillation to a fundamental mode perpendicular to the junction plane.

wavelengths achieved with the external feedback is consistent with the improved cavity Q demonstrated by the mode selection shown in Fig. 3(b). In addition, there is no evidence in the spectrum of Fig. 5(b) of the m = 1 modes indicating that oscillation is occurring predominantly in the fundamental mode. However, the spacing of the modes obtained with the external feedback corresponds to the longitudinal mode separation of the 375-μm diode alone (≈2 Å). Since the spacing of longitudinal resonances in the diode plus fiber cavity is much smaller than 2 Å, it is clear that oscillation in the external cavity occurs only at frequencies within the linewidth of the diode resonances. This observation indicates that there is a significant reflection for the fundamental mode at the diode-fiber interface, although it is not sufficient by itself to produce oscillation.

The absence of oscillation between the resonances of the short cavity can be attributed to either weak coupling between the fiber and DH waveguide or to a high reflectivity at the diode-fiber interface. For the laser used in the experiment with $2w_{0y}$ estimated to be 2 μm[1] and $2w_{0x}$ taken to be 4 μm, a value for κ of approximately 0.5 is expected on the basis of Gaussian approximations and the Kogelnik formulas [2]. With no reflectivity at the diode-fiber interface and an R_f near 100 percent, κ = 0.5 should provide a ΔR_0 of approximately 30 percent which should be sufficient to produce oscillation at frequencies between the resonances of the diode cavity. This conclusion suggests the possibility that it is primarily the reflectivity of the diode-fiber interface which is substantially reducing the "effective" coupling between the DH waveguide and fiber, and thereby preventing oscillation at these off-resonance frequencies.

In another experiment using a different laser and fiber, we realized the situation in which reflectivity selection dominated. In this case the laser's oscillating mode was changed from m = 1 to m = 0 by judicious positioning of the fiber (with no mirror on its free end) in relation to the laser's waveguide. In this case it was also possible to locate the fiber to produce m = 0 operation without maximizing the power coupled into the fiber mode, indicating that the interface reflectivity was dominant. However, it was possible to maintain mode selectivity while simultaneously maximizing the power transmitted through the fiber. Under optimal conditions, a peak power of 80 mW (100 ns pulses, 100 pulses per second) arising from the HE_{11} mode was radiated from the remote end of the fiber. Without the fiber in place, the laser operating at the same current, radiated a peak power of 165 mW in the m = 1 mode.

It was also possible to obtain an intermediate situation where neither the intracavity nor the reflectivity effects dominated. Using yet another laser-fiber combination, it was found that butting a fiber with its end coated with index matching oil against the laser switched its operation from pure m = 1 to a mixture of m = 0 modes. However, when a mirror was brought up against the fiber's remote end, the conversion to m = 0 was completed.

IV. Conclusion

In this work, we have demonstrated the possibility of obtaining fundamental transverse mode operation from a multimode DH junction laser while simultaneously coupling its output into a single-mode optical fiber. One way of achieving this result is to utilize the reflections from the diode-fiber interface to select the fundamental mode of the diode waveguide. Although this was successfully accomplished, it is at best difficult and unreliable, depending to a large extent on the details of the fiber surface.

The alternate and preferred method of incorporating the single-mode fiber into the resonant cavity has been successfully used to obtain fundamental mode operation from a large-cavity DH laser which otherwise oscillated in a first-order

[1] This estimate is based on the thickness of the epitaxial layer thicknesses measured using a scanning electron microscope.

mode perpendicular to the junction plane. This result was achieved with a net coupling efficiency of much less than 50 percent due to a substantial reflectivity at the diode-fiber interface. In principle, it should be possible to reduce the mode reflectivities at the laser-fiber interface to less than 1 percent by tailoring the AR layer.

Another potential benefit of intracavity selection, for which there exists but meager evidence at present, concerns filamentation. If the laser-fiber coupling can be increased sufficiently so that the region of the diode in which lasing occurs is determined primarily by the optical fiber, then the deleterious effects of filamentation such as beam steering and erratic light pulses, which are so common in junction lasers operated at high levels above threshold and at high duty cycles, may be eliminated. In this situation, the optical properties of the output beam will be independent of the pumping current since the fiber mode is independent of the internal dynamics of the laser diode.

Acknowledgment

The authors wish to thank B. W. Hakki for many useful discussions and suggestions, and for providing the AR-coated lasers used in this work. They also wish to thank D. D. Cook for making available his computer program for the evaluation of laser-fiber coupling coefficients, W. G. French for providing the single-mode fibers, and L. A. D'Asaro and R. C. Miller for their helpful comments on the manuscript.

References

[1] T. H. Zachos and J. C. Dyment, "Resonant modes of GaAs junction lasers—III: Propagation characteristics of laser beams with rectangular symmetry," *IEEE J. Quantum Electron.* (*Special Issue on Semiconductor Lasers*), vol. QE-6, pp. 317–324, June 1970.
[2] H. Kogelnik, "Coupling and conversion coefficients for optical modes," in *Proc. Symp. Quasi-Optics*, J. Fox, Ed. Brooklyn, N.Y.: Polytechnic Press, 1964, pp. 333–347.
[3] D. D. Cook, private communication.
[4] D. Gloge, "Weakly guiding fibers," *Appl. Opt.*, vol. 10, pp. 2252–2258, Oct. 1971.
[5] E. Snitzer and D. A. LaMarre, U.S. Patent 3 395 366, July 30, 1968.
[6] S. E. Miller, U.S. Patent 3 790 902, Feb. 5, 1974.
[7] B. W. Hakki, U.S. Patent 3 824 493, July 6, 1974.
[8] T. L. Paoli, B. W. Hakki, and B. I. Miller, "Zero-order transverse mode operation of GaAs double-heterostructure lasers with thick waveguides," *J. Appl. Phys.*, vol. 44, pp. 1276–1280, Mar. 1973.
[9] J. C. Dyment, L. A. D'Asaro, J. C. North, B. I. Miller, and J. E. Ripper, "Proton-bombardment formation of stripe-geometry heterostructure lasers for 300 K CW operation," *Proc. IEEE* (Lett.), vol. 60, pp. 726–728, June 1972.
[10] B. W. Hakki and C. J. Hwang, "Mode control in large-cavity double-heterostructure laser," *J. Appl. Phys.*, vol. 45, pp. 2168–2173, May 1974.
[11] H. C. Casey, Jr., D. D. Sell, and M. B. Panish, "Refractive index of $Al_xGa_{1-x}As$ between 1.2 and 1.8 eV," *Appl. Phys. Lett.*, vol. 24, pp. 63–65, Jan. 1974.
[12] D. D. Sell, H. C. Casey, Jr., and K. W. Wecht, "Concentration dependence of the refractive index for n- and p-type GaAs between 1.2 and 1.8 eV," *J. Appl. Phys.*, vol. 45, pp. 2650–2657, June 1974.
[13] G. A. Hockham, "Radiation from a solid-state laser," *Electron. Lett.*, vol. 9, pp. 389–391, Aug. 1973.

Multimode Operation and Mode-Locking Effect in Injection Lasers

H. BACHERT, P. G. ELISEEV, M. A. MANKO, V. P. STRAHOV, S. RAAB, AND CHAN MIN THAY

Abstract—**The oscillation regime of GaAs injection lasers has been investigated by methods of time-resolved spectroscopy and nonlinear interferometry. The relative roles of random and correlated process were studied. Spectroscopic data and interferometric investigations of laser samples in CW as well as in pulse regimes show that in most cases multimode operation occurs with random phase fluctuations. However, in some cases signs of mode locking of longitudinal modes were observed with ultrashort pulsation. The duration time of the pulsation is estimated to be about 3 ps.**

Manuscript received November 20, 1974; revised February 19, 1975.

H. Bachert and S. Raab are with the Central Institute of Optics and Spectroscopy, Academy of Science of the GDR, Berlin, Germany.

P. G. Eliseev, M. A. Manko, V. P. Strahov, and C. M. Thay are with the P. N. Lebedev Physical Institute, Academy of Science of the USSR, Moscow, USSR.

I. Introduction

AS IS WELL KNOWN, GaAs injection lasers operating well above threshold emit radiation distributed over a large number of spectral modes. Previous time-resolved spectroscopic studies [1]–[4] have shown a connection between the multimode regime of emission and nonstationary phenomena such as self-induced pulsation. Most informative investigations were performed with stripe-geometry double-heterostructure lasers providing single-filament operation [2], [3]. It was shown that there is a tendency to single-frequency operation when steady-state emission takes place. However, the behavior of lasers is quite different when self-induced pulsation appears. Probability of excitation of several other

spectral modes has increased. We shall discuss a difference of spectral output of laser emission for a nonstationary and stationary oscillation and consider the number of spectral modes excited versus pumping current (Section II). Then we will consider autocorrelation data on laser emission to single out the phase-locking effects which can also influence the multimode regime of oscillation in semiconductor lasers (Section III).

II. Spectroscopic Data on Injection-Laser Emission for Nonstationary and Stationary Conditions of Operation

Previous experiments on time-resolved spectroscopy of laser emission from injection lasers have included a comparison of the averaged and instantaneous spectral distribution of the laser emission [1] and classification of the regimes of operation of semiconductor lasers [2], [3]. The influence of an external high-frequency modulation of the pumping current on the spectral distribution of laser emission was also investigated [4]. It is worthwhile to review results of these investigations.

1) Steady-state oscillation is mostly single-frequency oscillation, while interruption of the oscillation leads to excitation of several new spectral modes, at least for a short duration of time. Such an interruption may be produced by external modulation or may happen due to self-induced pulsation.

2) Oscillation regimes of injection lasers appear when current grows above the threshold as follows: stationary (single-frequency) regime; similar regime interrupted by switching of dominant mode; regular self-induced pulsation (multifrequency) regime; irregular self-induced pulsation regime.

3) Laser-emission spectrum averaged over time coincides with instantaneous spectrum only in the stationary regime. When self-induced pulsation takes place, the spectral distribution of laser emission changes randomly from one spike to another. The latter statement is valid if intensity falls down to the spontaneous level after every spike.

Fluctuations of the spontaneous level of radiation intensity have been suggested to be responsible for such a random variation of the spectral distribution of laser emission [1]. Recently, Morozov [5] has treated the physical model of nonstationary operation of injection lasers taking into account the fluctuation of the spontaneous emission.

On the basis of this approach the number of longitudinal modes involved in laser oscillation can be predicted as a function of the pumping level. This number M_q is determined by the following expression which is valid in the case of regular pulsation:

$$M_q \simeq 0.84 \left(\tan \frac{\tau_p}{\tau_e} \cdot \frac{1}{C} \cdot \frac{I - I_{th}}{I_{th}} \right)^{0.25} \left(\frac{\delta\alpha}{\alpha} \right)^{-0.5} \quad (1)$$

where τ_p and τ_e are the lifetimes of photons and electrons, respectively, C is the parameter of pulsation [5], I is the pumping current, I_{th} is the threshold current, $\delta\alpha/\alpha$ is the relative deficit of the optical gain at the neighboring longitudinal mode at threshold. The top of the gain spectral contour is assumed to be of parabolic form. Parameter C is slowly dependent on the pumping level. Therefore, the number M_q would follow approximately a power dependence on relative overdrive $Y = (I - I_{th})/I_{th}$ with an exponent $\frac{1}{4}$. Calculated curves are shown in Fig. 1 for two values of $\delta\alpha/\alpha$, 1) 10^{-4} and 2) 10^{-3}. In the figure we have plotted the experimental points corresponding to various injection lasers, having cavities of the Fabry-Perot type. Obviously, there is a tendency for these experimental points to follow in the same manner as the calculated curve, when $Y > 0.1$. Another manner of dependency M_q on Y is seen at smaller Y and also in Fig. 2, where $M_q(Y)$ is plotted for an injection laser with a selective cavity [6]. Such a laser operates at $M_q = 1$ up to some value of Y, and M_q grows rapidly above this value and approaches the calculated curve 4 corresponding to curve 2 in Fig. 1. It is found that the self-induced pulsation can be suppressed by the mode-selection operation in a certain range of Y. Thus there is an extended range of Y, where the laser operates in a stationary manner with $M_q = 1$. At higher Y spiking appears and M_q increases. These results are in good agreement with the preceding discussed representation.

In essence, the number of excited spectral modes M_q at a definite pumping level may be equal to 1, if stationary oscillation takes place, or follows expression (1), if self-induced regular pulsation takes place. We see that there is serious evidence of the strong influence of spontaneous emission on the appearance of the laser spectrum in the nonstationary condition. Further investigation and discussion in the paper will concern the problem of the phase-locking phenomena in semiconductor lasers in multimode operation.

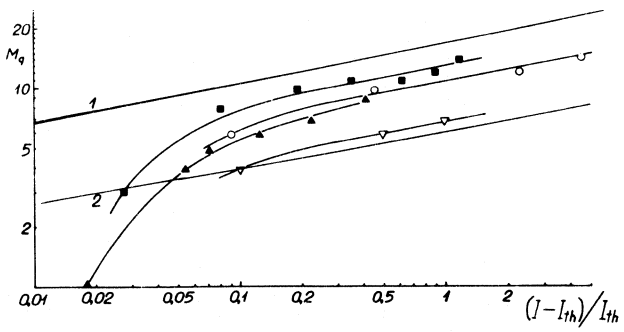

Fig. 1. Theoretical (1,2) and experimental dependence on the number of excited longitudinal modes M_q at a normalized current at 77 K. (■—InP laser; ○—GaAs laser; ▲—$InP_{1-x}As_x$ laser; ▽—$Ga_{1-x}Al_xAs$ stripe laser.)

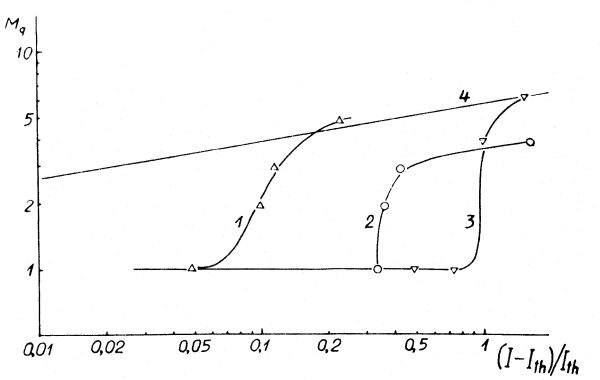

Fig. 2. Influence of mode-selective elements on the number of excited longitudinal modes $M_q(Y)$. (1,3—GaAs laser with grating; 2—$GaP_x \cdot As_{1-x}$ laser with composite cavity; 4—theoretical values for nonstationary states.) Operating temperature was 77 K.

III. Interferometric Measurements

For the investigation of the temporal-emission structure of the injection lasers a typical scanning Michelson interferometer was used [7] with a delay of 0.8 m. Linear and nonlinear registration methods for the output of the scanning Michelson interferometer [8] have been applied for these investigations in the time range of 10^{-13}-10^{-9} s.

The linear registration method of the output measures the temporal autocorrelation function of the pulse amplitude $G_\omega(\tau)$, and the detector output signal is

$$S_\omega(\tau) = I_\omega [1 + G_\omega(\tau)] \tag{2}$$

where τ means the variable delay time introduced to one part of the split beam and I_ω is the pulse energy.

Principally, the linear interferometer can only measure the power-density spectrum. But it is also possible to measure the coherence time τ_c, because this parameter is related to the spectral bandwidth. In any case, $S_\omega(0) = 2I_\omega$ and the highest contrast of the signal $S_\omega(\tau)$ cannot be more than 2. The injection lasers which have been investigated were excited at 77 K continuously or with 0.5-μs current pulses at a 50-kHz repetition rate.

A typical linear interferogram is shown in Fig. 3. In this way it is possible to obtain information about the coherence time τ_c of the stimulated emission, about the spectral modes half-width, and about the time τ_1 of one round trip in the cavity (the influence of different mode frequencies can be seen).

It can be seen that the position of these peaks is not influenced by different excitations of the injection laser. In the case of the nonlinear registration method of $LiIO_3$ crystal was used and the temporal autocorrelation function of the pulse intensity $G_{2\omega}(\tau)$ can give information about the real pulse length $\Delta\tau_\omega$ of the ultrashort pulses. The output signal of the detector is given by

$$S_{2\omega}(\tau) = \chi\eta_{2\omega} I_\omega^2 [1 + 2G_{2\omega}(\tau)] \tag{3}$$

where χ is the efficiency of the nonlinear effect and $\eta_{2\omega}$ is the efficiency of the applied photodetector for the frequency 2ω. If the stimulated radiation of the injection laser after a temporal period $(2n^*l/c)$ (where n^* is the effective refractive index, l is the length of the resonator, and c is light velocity) have pulses and the nonlinear detection of the output signal $S_{2\omega}(\tau)$ shows a contrast ratio of 3 that means phase synchronization occurred. For this case, $G_{2\omega}(0) = 1$, and for $\tau > \Delta\tau_{2\omega}$ the received value of $G_{2\omega}(\tau) = 0$. In this way it is possible to decide if mode locking takes place or not.

In the nonlinear interferogram shown in Fig. 4, near zero for several pulses, a contrast ratio of nearly 3:1 can be observed. Similar interferograms are seen in Fig. 5. Figs. 4 and 5 show that the picosecond pulses are limited to 5-10 round-trip times because of the simultaneous spiking with a pulse duration of 0.1 ns. Within the spiking pulse, random phase fluctuation is observed. The half-widths $\Delta\tau_{2\omega}$ of these



Fig. 4. Nonlinear interferogram of a GaAs injection laser at a current of 1.36 A and at a operating temperature of 77 K (I_{th} = 0.65 A).

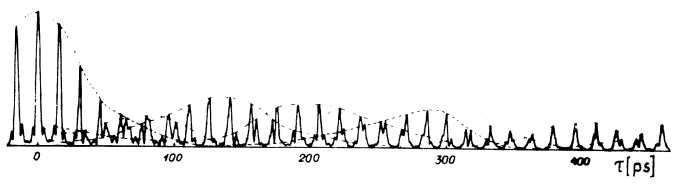

(a)

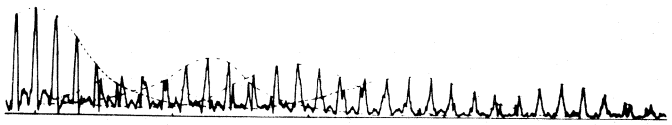

(b)

Fig. 3. Linear interferograms of GaAs epitaxial laser diodes at the excitation currents. (a) 1.5 A. (b) 1.08 A at 77 K (I_{th} = 0.82 A). (On the ordinate is shown the autocorrelation function of the pulse amplitudes.)

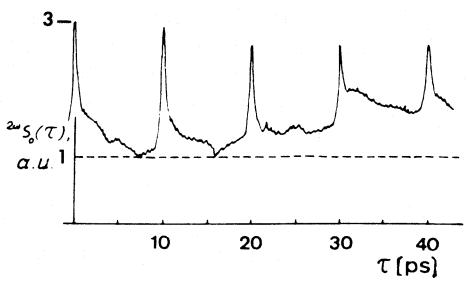

(a)

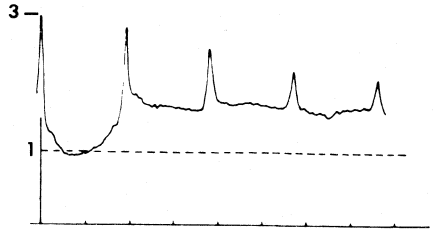

(b)

Fig. 5. Nonlinear interferograms of a GaAs injection laser at a current of 1.04 A (a) and 0.75 A (b) at 77 K (I_{th} = 0.65 A).

picosecond pulses from Fig. 5 are less than 1 ps. An estimation by the method of Kuznetsova [9] gives values of 3 ps in accordance with the measured 1-ps pulses.

IV. Conclusion

Thus we have evidence of the mode locking of the longitudinal modes in injection lasers with a rather short cavity. This effect may originate from an internal optical nonlinearity of the semiconductor medium favoring the ultrashort pulses in the picosecond range. Hypothetically, a nonlinearity was found recently in GaAs. This is a self-induced transparency for two-photon absorption [10] which was observed when ultrashort pulses of a neodymium-glass laser passed through GaAs samples at a low temperature. It was found that at high radiation intensity the two-photon absorption coefficient decreases for very short pulses in comparison with its value for pulses of nanosecond duration. If two-photon absorption occurs within the active region of a semiconductor laser, the ultrashort pulsing operation will have lower optical losses than random phase operation.

Because the mode-locking effect takes place simultaneously with a self-induced pulsation of the laser emission its regularity is strongly limited by interruption of oscillation. Thus the deep nanosecond pulsation restricts the regularity of the ultrashort pulsation.

References

[1] A. P. Bogatov, P. G. Eliseev, V. I. Panteleev, and E. G. Shevchenko, "A comparison of the instantaneous and averaged spectra of the injection laser operating with a self-induced pulse" (in Russian), *Kvantovaya Elektron.*; also *Sov. Radiophys.*, p. 93, 1971.

[2] A. P. Bogatov *et al.*, "Study of the single-mode injection laser," *IEEE J. Quantum Electron. (Part II of Two Parts)*, vol. QE-9, pp. 392–394, Feb. 1973.

[3] A. P. Bogatov *et al.*, "About the kinetic of the injection laser spectrum and the effect of suppressing single-mode generation" (in Russian), *Kvantovaya Elektron.*, vol. 1, pp. 14–20, May 1973.

[4] P. G. Eliseev, L. P. Ivanov, A. S. Logginov, and K. Ya. Senatorov, "The influence of microwave modulation on the injection laser spectrum" (in Russian), *Kvantovaya Elektron.*, vol. 1 pp. 151–154, Jan. 1974.

[5] V. N. Morozov, "On the theory of multimode excitation in semiconductor lasers" (in Russian), *Kvantovaya Elektron.*, vol. 1, pp. 634–644, Mar. 1974.

[6] D. Ackerman *et al.*, "Methods for mode selection in injection lasers," *Sov. J. Quantum Electron.*, vol. 1, pp. 60–65, 1971.

[7] D. Gloge and T. P. Lee, "Signal structure of continuously self-pulsing GaAs lasers," *IEEE J. Quantum Electron.*, vol. QE-7, pp. 43–45, Jan. 1971.

[8] A. J. DeMaria, W. H. Glenn, Jr., M. J. Brienza, and M. E. Mack, "Picosecond laser pulses," *Proc. IEEE*, vol. 57, pp. 2–25, Jan. 1969.

[9] T. I. Kuznetsova, "On the problem of recording ultrashort light pulses" (in Russian), *Zh. Eksp. Teor. Fiz.*, vol. 55, pp. 2453–2458, 1968.

[10] A. Z. Grasjuk *et al.*, "The dependence of two-photon absorption in GaAs on the light pulse duration" (in Russian), *Pis'ma Zh. Eksp. Teor. Fiz.*, vol. 17, pp. 584–587, May 1973.

Anomalous Interaction of Spectral Modes in a Semiconductor Laser

A. P. BOGATOV, P. G. ELISEEV, AND B. N. SVERDLOV

Abstract—**Anomalous asymmetric interaction of the closely spaced spectral modes of a semiconductor laser is found experimentally in lasers with selective external cavities. The stimulated scattering of the laser radiation by dynamic inhomogeneities of the electron density is considered to be responsible for the anomalous mode interaction.**

I. Introduction

SEMICONDUCTOR media are optical materials of significant nonlinearity. Self-induced modulation of the intensity and frequency of oscillation in semiconductor lasers [1]-[5] can be pointed out as examples of the nonlinear effects on laser oscillation dynamics. A nonlinear part of the complex dielectric constant $\tilde{\epsilon}$ was taken into account when laser spiking in semiconductor lasers was treated theoretically [6], [7].

Manuscript received November 20, 1974; revised January 29, 1975.

The authors are with the P. N. Lebedev Physical Institute, Academy of Science of the USSR, Moscow, USSR.

In this paper a new nonlinear effect is considered which leads to an anomalous mode interaction in laser spectra. The effect differs from the usual competition of modes appearing due to homogeneous broadening. The new effect is asymmetric: the longer wavelength spectral mode of two neighboring modes dominates. Such an interaction occurs at small spectral distances (not greater than about 10^{11} Hz) which is smaller than the homogeneous bandwidth (10^{12}-10^{13} Hz). The physical model of the effect is a stimulated scattering of the laser radiation inside the laser medium by dynamic inhomogeneities of $\tilde{\epsilon}$ appearing due to variation of the electron density. Such variation in electron density depends upon the radiation intensity which determines the rate of stimulated transitions. As is well known, the real part of $\tilde{\epsilon}$ of a semiconductor depends on the electron concentration n because the plasma resonance frequency and absorption edge are dependent on n. An estimation of the value of Re $(\partial\tilde{\epsilon}/\partial n)$ for GaAs at its own laser wavelength near the absorption edge gives about 10^{-20} cm^3. Thus variation of the electron density n

produces a variation of the dielectric constant (real part, due to the previously mentioned reasons; imaginary part, due to the inversion of the population).

An asymmetric spectral-mode interaction occurs due to the radiation scattering by a dynamic variation of electron density. These variations are a kind of "recombination wave" appearing due to deviations of the pumping-emission balance, but not due to a virtual displacement of the plasma. Therefore, scattering processes can occur without limitation from the momentum-conservation rule (no dispersion law for these "waves").

In Section II the experimental observation is presented which suggests the anomalous mode interaction. In Section III a theoretical treatment is given of the perturbation of the spectral-gain curve in the vicinity of the laser frequency ω_0. The change of the gain is described by an odd function of the frequency difference $\Omega = \omega_0 - \omega$, which can provide the asymmetric mode interaction.

II. Experimental Results

Our experiments were performed with room-termperature single-heterostructure GaAs-AlGaAs lasers with an antireflective coating operated with an external cavity containing spectrally selective elements (Fig. 1). The laser action has been obtained with a linear and with a ring cavity including a reflective diffraction grating [Fig. 1(a) and (b)], and with the cavity containing two independently controlled gratings [Fig. 1(c)]. Single-grating cavities [8]-[11] allowed a narrow-line laser output tunable within a certain spectral range. The largest output power up to 5 W has been obtained with the bandwidth less than 0.1 nm, whereas at lower power level (0.5 W) the bandwidth may be less than 0.01 mm [11]. Such a spectral line is called nominally "spectral mode" even if it contains several longitudinal modes of the external cavity. The reason is that their spatial distribution inside the active medium coincides closely until their spectral bandwidth is much less than the intermode spacing of the diode resonator. At a high level of pumping, the internal-mode lasing appears, sometimes simultaneously with the external narrow-line lasing. It has been noticed that a strong external spectral mode suppresses weak internal modes more effectively on the shorter wavelength side than on the longer wavelength side.

To investigate this mode-interaction phenomenon, the double-grating cavity has been arranged. Operation in two spectral modes has been observed. Mode interaction was found to be dependent on the spectral distance between them and on the position of one relative to the other. Two experiments were performed. The first involved a measurement of the intensity of a tunable mode as a function of wavelength at fixed pumping current. Results are presented in Fig. 2. Value Φ_λ^0 was measured when only one tunable mode was excited (the second grating was blocked by a black screen). When the fixed spectral mode at λ_0 was excited simultaneously with the tunable mode, the dependency Φ_λ was modified [Fig. 2(b)], the range of tuning was decreased from 4 nm to 3 nm, and a discontinuity appeared at λ_0. Notice a nonmonotonic dependence of Φ_λ at the left side of λ_0. Value Φ_{λ_0} is the intensity of the fixed mode at λ_0 as a function of the wave-

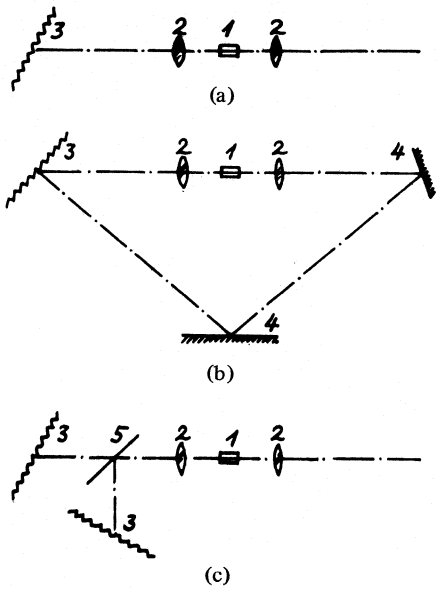

Fig. 1. Schemes of the external selective cavities used in this study. (a) A linear autocollimation scheme. (b) A ring scheme. (c) A double-grating autocollimation scheme. 1: laser diode; 2: lens; 3: reflecting diffraction grating; 4: mirror; 5: beam splitter.

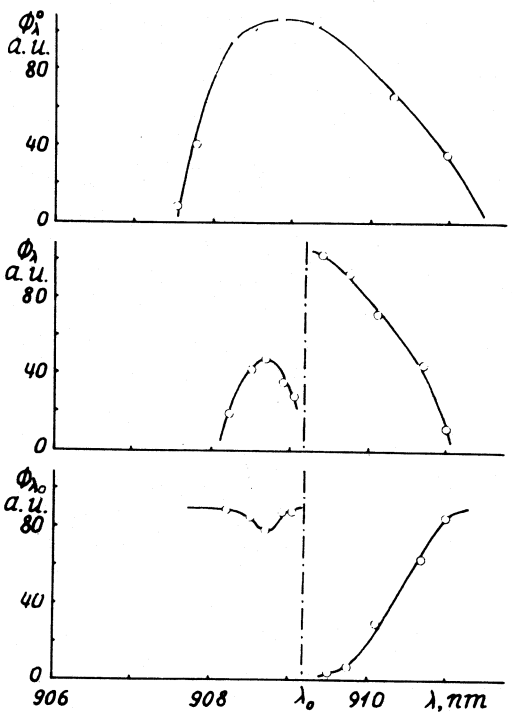

Fig. 2. Dependences of values Φ_λ^0, Φ_λ, and Φ_{λ_0} on the wavelength of the tunable spectral mode when optical scheme of Fig. 1(c) is used. Φ_λ^0 is the intensity of the tunable spectral mode when only one diffraction grating is open. Φ_λ is the intensity of the tunable mode when both gratings are open and lasing at λ_0 occurs. Φ_{λ_0} is the intensity of the fixed spectral mode which lases at λ_0. A single-heterostructure diode is used with the antireflection-coated Fabry-Perot cavity of length 1 mm at 300 K driven by 80-A current pulses of duration time 0.25 μs and of repetition-frequency rate 200 Hz. Thickness of the active layer is about 2 μm.

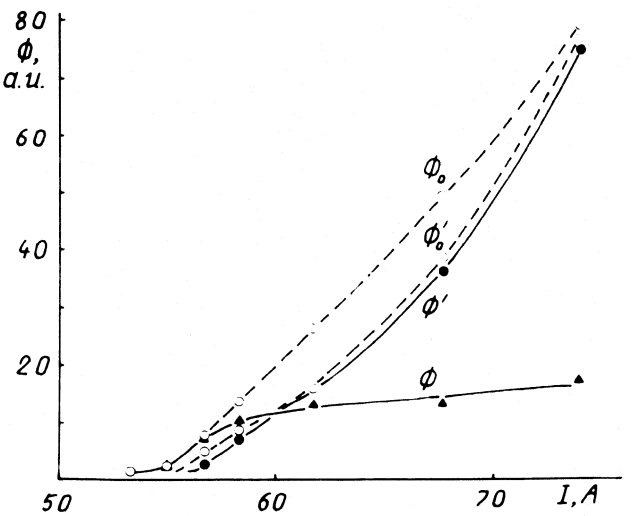

Fig. 3. Current dependence of intensities of two spectral modes, operating at 908.9 nm (Φ), and at 909.2 nm (Φ′) with the same scheme, diode, and pulsing regime as in Fig. 2. Index 0 corresponds to measurements when only one diffraction grating is open.

length of a tunable mode when both modes are excited simultaneously. Thus the tunable mode was quenched effectively when it approached the fixed mode at the shorter wavelength side.

In the second experiment, the intensities of two spectral modes spaced 0.3 nm apart were measured as a function of pumping current (see Fig. 3). It has been found that the intensity of the shorter wavelength mode saturated at a high pumping current whereas that of the longer wavelength mode grew with increasing current.

These results show that the mode interaction at small spectral distances ($\leqslant 10^{11}$ Hz) becomes asymmetric in favor of the longer wavelength mode when the intensity of laser radiation is high enough ($\geqslant 10^4$ W/cm^2). Electron concentration in these experiments is as large as about 10^{18} cm^{-3}, which corresponds to the highest pump-current density up to 4×10^4 A/cm^2.

III. Analysis of the Mechanism of Anomalous Spectral-Mode Interaction

Asymmetric perturbation of the spectral-gain profile may be provided by a nonlinear stimulated scattering of laser radiation at frequency ω_0 by dynamic inhomogeneities of the electron density. The analysis will be limited to the case of a weak signal at a probe frequency $\omega_1 = \omega_0 - \Omega$; it will also be assumed that the relaxation time of the polarization of the medium is small in comparison with $1/\Omega$, thus the amplitude of polarization P follows closely the field amplitude. The effect under investigation is a nonlinear addition of P_{NL} to a linear polarization

$$P = \tilde{\epsilon}_0 \mathcal{E} + 4\pi P_{NL} \tag{1}$$

where P is the polarization vector of the medium, $\mathcal{E}$ is the electric-field vector, and $\tilde{\epsilon}_0 \equiv \epsilon + i\epsilon'$ is the complex dielectric constant which involves a linear real part and an imaginary part.

Our physical model is based on two equations, one of them is for the electromagnetic field [12], [13], another is for the electron density n, which includes the effects of diffusion, and spontaneous and stimulated recombination [14]

$$(\tilde{\epsilon}_0/c^2)(\partial^2 \mathcal{E}/\partial t^2) - \nabla^2 \mathcal{E} = -(4\pi/c^2)(\partial^2 P_{NL}/\partial t^2) \tag{2}$$

$$\partial n/\partial t - D\nabla^2 n + n/\tau + \alpha n|\mathcal{E}|^2 = G \tag{3}$$

where D is a diffusion constant, τ is the electron lifetime in the absence of the electromagnetic field, G is the pumping rate, and α is a proportionality coefficient for the rate of stimulated recombination.

Let us present the electromagnetic field as a series over modes of an ideal resonator [15]

$$\mathcal{E}(r, t) = \sum_j [E_j(t) + \text{c.c.}]\ \varphi_j(r). \tag{4}$$

The orthogonal normalized functions $\varphi_j(r)$ are solutions of the wave equation

$$\nabla^2 \varphi_j(r) + k_j^2 \varphi_j(r) = 0 \tag{5}$$

where k_j is the wave vector. Our analysis will be limited to a case when strong oscillation exists in the only mode

$$\mathcal{E}_0(r, t) = [E_0(t) + \text{c.c.}]\ \varphi_0(r) \tag{6}$$

whereas in other modes oscillations are very weak (single-mode laser operation)

$$|E_0(t)| >> |E_j(t)|, \quad j \neq 0. \tag{7}$$

Now we would like to investigate the behavior of the field in one of the nonlasing modes $\mathcal{E}_1(r, t)$ in the presence of the strong field $\mathcal{E}_0(r, t)$. We substitute (4) into (2), multiply both sides of the equation obtained by $\varphi_j(r)$, and then integrate over the volume of the resonator V. This procedure leads to a following equation:

$$(\partial^2 E_1/\partial t^2) + \tilde{\omega}_1^2 E_1 = -(4\pi/\tilde{\epsilon}_0) \int_V (\partial^2 P_{NL}/\partial t^2)\, \varphi_1(r)\, dV \tag{8}$$

where $\tilde{\omega}_1 = \omega_1 - i\gamma_1$, γ_1 is a damping parameter of a corresponding mode of oscillation. To calculate the right side of (8), it is necessary to find the form of the inhomogeneity of a nonlinear polarization, which can be approximated by a linearization as

$$P_{NL} = (\mathcal{E}_0/4\pi)\, \delta\tilde{\epsilon} = (\mathcal{E}_0/4\pi)(\partial\tilde{\epsilon}/\partial n)\, \delta n \tag{9}$$

where $\delta\tilde{\epsilon}$ is the variation of dielectric constant, and δn is the variation of electron density. Both variations appear due to the superimposing of two fields $\mathcal{E}_0$ and $\mathcal{E}_1$, and they are oscillating values with frequency Ω. Such a variation of electron density does not influence the oscillation regime at ω_0 until E_1 is small enough and Ω is larger than the oscillation bandwidth. Threshold level of the optical gain is supplied by the value of the electron density averaged over time, whereas the instantaneous deviation δn is quite usual for the multimode oscillator.

The deviation produces a dynamic phase lattice

$$\delta\tilde{\epsilon}(r, t) \approx (\partial\tilde{\epsilon}/\partial n)\, \delta n(r, t)$$

which scatters laser radiation ω_0 in the same direction, with a Stoke's shift by Ω. This nonlinear contribution to the polarization of the medium at frequency $\omega_1 = \omega_0 - \Omega$ is presented by the right side of (8). Oscillations E_1 would have an increasing amplitude if this contribution could compensate a damping term in the left side of the equation. As to scattering into the back direction, it seems to be less important because the small distance variations of n are smoothed effectively due to electron diffusion. We shall deal with variations δn which are averaged over distances as large as $(\lambda/2)(\epsilon)^{-1/2}$, and this approach corresponds to neglect of the backscattering. To obtain $\delta n(r, t)$, one has to consider (3). In the Appendix it is shown that the right side of (8) may be approximately expressed by a combination of averaged values of electron density $\bar{n}_0$, recombination probability Γ, and intensity $|E_0|^2$. Now the equation for E_1 may be expressed as follows:

$$(\partial^2 E_1/\partial t^2) + \tilde{\omega}_1^2 E_1 = -(\omega_1^2/\tilde{\epsilon}_0)(\partial\tilde{\epsilon}/\partial n) \cdot (\alpha\bar{n}_0 K E_1 |E_0|^2)/(i\Omega + \Gamma) \tag{10}$$

where K is an "overlap coefficient" also explained in the Appendix. This equation has an unstable solution if the following expression is valid:

$$(\omega_1/2)(\alpha\bar{n}_0 K|E_0|^2)\,\mathrm{Im}\,[(1/\tilde{\epsilon}_0)(\partial\tilde{\epsilon}/\partial n)/(i\Omega + \Gamma)] > \gamma_1 . \tag{11}$$

It is possible to use the following expression:

$$\mathrm{Im}\left(\frac{1}{\tilde{\epsilon}_0}\cdot\frac{\partial\tilde{\epsilon}}{\partial n}\cdot\frac{1}{i\Omega+\Gamma}\right) \approx -\frac{1}{\epsilon}\left(\frac{\Omega}{\Omega^2+\Gamma^2}\,\mathrm{Re}\,\frac{\partial\tilde{\epsilon}}{\partial n} - \frac{\Gamma}{\Omega^2+\Gamma^2}\cdot\mathrm{Im}\,\frac{\partial\tilde{\epsilon}}{\partial n}\right) = -\frac{1}{\epsilon}\,\mathrm{Re}\,\frac{\partial\tilde{\epsilon}}{\partial n}\cdot\frac{\Omega-\Gamma\xi}{\Omega^2+\Gamma^2}$$

$$= -\frac{1}{\epsilon\Gamma}\cdot\mathrm{Re}\,\frac{\partial\tilde{\epsilon}}{\partial n}\cdot F(\Omega,\xi) \tag{12}$$

where

$$\xi \equiv [\mathrm{Im}\,(\partial\tilde{\epsilon}/\partial n)]/[\mathrm{Re}\,(\partial\tilde{\epsilon}/\partial n)]$$

and function F is

$$F(\Omega,\xi) = \frac{\Gamma(\Omega-\Gamma\xi)}{(\Omega^2+\Gamma^2)} . \tag{13}$$

From the result it is seen that the spectral-mode interaction which is treated here gives an additional gain (or absorption) in the weak mode due to the parametric influence of strong mode. Spectral shape of this additional gain is determined by the function $F(\Omega)$ presented in Fig. 4 for the particular value of $\xi = 0.3$ (approximate estimation). This additional gain

$$\delta g = -\frac{\omega_1}{c(\epsilon)^{1/2}}\left(\mathrm{Re}\,\frac{\partial\tilde{\epsilon}}{\partial n}\right)\alpha\bar{n}_0|E_0|^2 KF(\Omega)/\Gamma \tag{14}$$

superimposes two effects: namely, laser radiation scattering by variation of Re $\tilde{\epsilon}$ with an odd contour $\Omega/(\Omega^2+\Gamma^2)$, and laser radiation scattering by variation of Im $\tilde{\epsilon}$ with an even contour $\xi\Gamma/(\Omega^2+\Gamma^2)$. The former type of stimulated scattering is an important explanation of the asymmetric mode interaction. The value δg is positive at $\Omega > \Gamma\xi$ and is negative for the shorter wavelength side where $\Omega < \Gamma\xi$. The latter type of scattering gives a negative addition which does not influence the qualitative results; however, it shifts the asymmetric curve from the zero point $\Omega = 0$. Extrema of δg are at the following points:

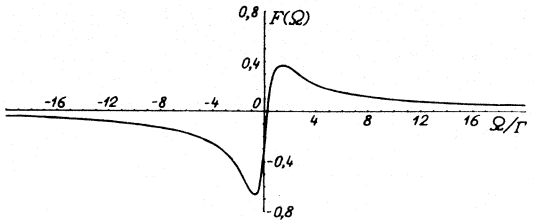

Fig. 4. Computed shape of $F(\Omega)$ spectral distribution of additional gain produced by the nonlinear scattering process analyzed in this paper. Notice that Γ is a rather small value, and experimentally it is possible to follow only peripheral parts of the curve $F(\Omega)$.

$$\Omega_{1,2} = \Gamma[\xi \pm (1+\xi^2)^{1/2}] . \tag{15}$$

The maximal value of δg saturates at $\alpha|E_0|^2 >> 1/\tau$ and it shifts to the longer wavelength side if the intensity $|E_0|^2$ grows. This maximal value can be expressed as follows:

$$\delta g_m \approx -\frac{\bar{n}_0\omega_1}{4c\sqrt{\epsilon}}\left(\mathrm{Re}\,\frac{\partial\tilde{\epsilon}}{\partial n}\right)\frac{\sqrt{1+\xi^2}}{1+\xi+(1+\xi^2)^{1/2}} \tag{16}$$

where the estimation of K performed in the Appendix is used. The limiting value of the additional gain for the GaAs laser from expression (16) is dependent on the mean electron density and is equal to about

$$\delta g_m \approx (2 \times 10^{-16}\ \mathrm{cm}^2)\,\bar{n}_0 . \tag{17}$$

Expression (17) is valid for estimation of additional gain due to stimulated scattering only in order of value. Because of the finite bandwidth of the laser radiation at ω_0 such a value on the additional gain may not be observed. At larger Ω, additional gain decreases approximately as $1/\Omega$. Its value at the neighboring longitudinal mode of a typical diode cavity appears to be about 10^{-1} cm^{-1}, which is quite comparable with the gain deficit. Therefore, this mechanism can provide an instability of single-frequency oscillation at a high level of optical flux.

IV. Discussion and Conclusion

We believe that the experimental observation presented gives evidence for a new type of mode interaction. It cannot be understood as a result of producing a simple dip of optical gain near the laser frequency because of the asymmetric nature of the experimental curve. Furthermore, the usual asymmetry of the gain contour in a semiconductor laser is not enough for fitting of the experimental data. It is obvious from Fig. 2(b) that the efficiency of the asymmetric interaction of spectral modes is larger at small distances between them and decreases at large spectral distances. It was found recently [16], [17] that the delay time of the lasing, relative to beginning of current pulse, could be spectrally dependent. But near the optimal spectral point there is a wide range where this delay, as well as the threshold current, is quite constant. All our

observations were obtained for this range. We have also shown that there was no significant difference in temporal behavior of the two interacting modes by additional experiments mentioned in [18].

The intensity dependence of the interaction presented in Fig. 3 appears to be similar to that for various mechanisms of stimulated scattering (see, for example, such dependences for Mandelshtam-Brillouin backscattering [19]). The saturation is typical for the shorter wavelength component which is a pumping wave.

The experimental conditions described here are favorable for the observation of the anomalous mode interaction because they avoid masking effects due to space inhomogeneity of the diode and due to the broadening of laser-output spectrum. Also it is important to perform these measurements at a high level of electron density, as high as 10^{18} cm^{-3}, which corresponds to our experiments. We could observe the asymmetric spectral-distance-dependent mode competition which was found to be in qualitative agreement with the theoretical model of stimulated scattering of laser radiation by dynamic inhomogeneities of electron density. This new mechanism is quite specific only for an inverted medium where the real dielectric constant is dependent on inversion of population.

We believe that the mechanism can act in a much wider range of experimental conditions where its direct observation is difficult. Let us remember that in semiconductor lasers there are many spectral modes which have approximately the same net gain above the threshold. Small perturbation of the gain curve due to the anomalous mode interaction can produce a significant change of the laser output like switching of the dominant mode and failure of the single-frequency oscillation observed in [4]. On the basis of this model one can explain why introduction of the spectrally selective element into the laser cavity leads to suppression of self-induced pulsation [4]. Unfortunately, very interesting problems concerning the multimode laser dynamics are too complicated to be solved taking into account this new mechanism of mode interaction. We have restricted the theoretical treatment to the case of a small signal in the probe mode for this reason. Similarly, we have estimated the contribution of other types of stimulated scattering in semiconductor lasers due to temperature variations ("temperature" scattering) and due to repulsion of electrons from the regions of strong radiation intensity. The contribution appears to be less important than that from the previously described mechanism.

Appendix
Calculation of the Nonlinear Polarization

The electron density $n(r, t)$ may be presented in the following form:

$$n(r, t) = n_0(r) + \delta n(r, t) \tag{18}$$

where $n_0(r)$ is the stationary part of the local electron density and $\delta n(r, t)$ is the time-dependent part, the mean value of which is equal to zero. Substitution of (18) into (3) leads to its separation into equations where only terms linear in $\delta n(r, t)$ and $\mathcal{E}_1$ are kept. The first equation relates to coordinate variation of $n_0(r)$

$$-D\nabla^2 n_0(r) + [n_0(r)/\tau] + \alpha n_0(r)\,|\mathcal{E}_0(r, t)|^2 = G \tag{19}$$

and the second equation relates to $\delta n(r, t)$

$$(\partial \delta n/\partial t) + (\delta n/\tau) - D\nabla^2 \delta n + \alpha \delta n\,|\mathcal{E}_0|^2 = -\alpha n_0 \mathcal{E}_0^* \mathcal{E}_1 + \text{c.c.} \tag{20}$$

where the asterisk labels the complex-conjugate value. A reasonable simplification of (20) may be obtained if one performs averaging of δn over small distances along the resonator axis z. Because of fast electron diffusion, periodic variation of δn due to a standing wave can be neglected. Therefore it is not necessary to deal with small scale variation of values $|\mathcal{E}_0|^2$ and $\mathcal{E}_0^* \mathcal{E}_1$. Smoothing action of the diffusion will be effective when the following expression is valid:

$$(4D\epsilon/\lambda^2) > \Omega. \tag{21}$$

On the other hand, a longer scale variation of δn is not influenced by electron diffusion because the expression

$$[c/(\epsilon D\tau)^{1/2}] > \Omega \tag{22}$$

is valid. With these assumptions one may drop out a diffusion term and perform averaging

$$\overline{|\varphi_0|^2} = [2(\epsilon)^{1/2}/\lambda] \int_z^{z+\lambda/2(\epsilon)^{1/2}} |\varphi_0|^2\, dz' \tag{23}$$

$$\overline{\varphi_0 \varphi_1} = [2(\epsilon)^{1/2}/\lambda] \int_z^{z+\lambda/2(\epsilon)^{1/2}} \varphi_0 \varphi_1\, dz'. \tag{24}$$

Thus (20) can be rewritten in the following way:

$$(\partial \delta n/\partial t) + (\delta n/\tau) + \alpha \delta n\,|E_0|^2\,\overline{|\varphi_0|^2} = -\alpha n_0 E_0^* E_1 \overline{\varphi_0 \varphi_1} + \text{c.c.} \tag{25}$$

Solution of this equation is

$$\delta n = -\frac{\alpha n_0 E_0^* E_1 \overline{\varphi_0 \varphi_1}}{i\Omega + (1/\tau) + \alpha |E_0|^2 \overline{|\varphi_0|^2}} + \text{c.c.} \tag{26}$$

Now we use expressions (9) and (26) to rewrite (8) for E_1

$$\frac{\partial^2 E_1}{\partial t^2} + \tilde{\omega}_1^2 E_1 = \frac{1}{\tilde{\epsilon}} \frac{\partial \tilde{\epsilon}}{\partial n} \cdot \int \frac{\alpha n_0 \varphi_0(r)\, \varphi_1(r) \overline{\varphi_0 \varphi_1}\, [\partial^2 (E_0 E_0^* E_1)/\partial t^2]}{i\Omega + (1/\tau) + \alpha |E_0|^2 \overline{|\varphi_0|^2}} dV$$

$$= -\frac{\omega_1^2}{\tilde{\epsilon}} \frac{\partial \tilde{\epsilon}}{\partial n} |E_0|^2 E_1 \int \frac{\alpha n_0 \varphi_0(r)\, \varphi_1(r)\, \overline{\varphi_0 \varphi_1}\, dV}{i\Omega + (1/\tau) + \alpha |E_0|^2 \overline{|\varphi_0|^2}}. \tag{27}$$

Further analysis needs accurate calculation of the distributions of n_0 and mode configurations. If the Q-factor of the cavity is high enough, these distributions are not too significant for estimation of the effect under investigation. Assume the following approximation:

$$\int \frac{\alpha n_0 \varphi_0 \varphi_1 \overline{\varphi_0 \varphi_1}\, dV}{i\Omega + 1/\tau + \alpha |E_0|^2 |\varphi_0|^2} \approx \frac{\alpha \bar{n}_0}{i\Omega + \Gamma} K \tag{28}$$

where $\bar{n}_0$ and Γ are mean values of the stationary electron density and effective recombination probability, correspondingly, and K is an "overlap" coefficient of inversion and combinated mode configurations. For example, in the case of the ideal resonator and in approximation of plane waves, this coefficient is equal to about $0.5/V$, where V is the volume of the cavity.

References

[1] N. G. Basov, "Dynamics of injection lasers," *IEEE J. Quantum Electron. (Special Issue, 1968 International Quantum Electronics Conference: Part II)*, vol. QE-4, pp. 855–864, Nov. 1968.

[2] V. I. Magalyas *et al.*, "Modulation and synchronization of the emission of a semiconductor injection laser," *Sov. Phys.–JETP Lett.*, vol. 6, p. 68, 1967.

[3] N. G. Basov, V. N. Morozov, V. V. Nikitin, and A. S. Semenov, "A study of pulsation regime of GaAs lasers" (in Russian), *FTP*, vol. 1, p. 1570, 1967.

[4] A. P. Bogatov *et al.*, "Study of the single-mode injection laser," *IEEE J. Quantum Electron. (Part II of Two Parts, Special Issue on 1972 IEEE Semiconductor Laser Conference)*, vol. QE-9, p. 392–394, Feb. 1973.

[5] P. G. Eliseev, L. P. Ivanov, A. S. Logginov, and K. Ya. Senatorov, "Influence of high frequency modulation on spectrum of radiation emission of injection laser" (in Russian), *Kratkie Soobshch. Fisike*, FIAN, vol. 6, p. 55, 1972.

[6] R. G. Allakhverdian *et al.*, "Influence of the refractive index nonlinearity on the radiation dynamics of semiconductor laser" (in Russian), *Kvantovaya Elektron., Sov. Radio*, p. 53, 1971.

[7] R. G. Allakhverdian, A. N. Oraevsky, and A. F. Suchkov, "Influence of the waveguiding property of the p-n junction on the oscillation regime of the GaAs diode lasers" (in Russian), *FTP*, vol. 4, p. 341, 1970.

[8] H. D. Edmonds and A. W. Smith, "Second-harmonic generation with the GaAs laser," *IEEE J. Quantum Electron. (Special Issue on Semiconductor Lasers)*, vol. QE-6, pp. 356–360, June 1970.

[9] R. Ludeke and E. P. Harris, "Tunable GaAs laser in an external dispersive cavity," *Appl. Phys. Lett.*, vol. 20, p. 499, 1972.

[10] D. Akerman *et al.*, "Spectral selection in injection lasers with the help of diffraction gratings" (in Russian), *Kratkie Soobshch. Fizike*, p. 9, 1973.

[11] D. Akerman *et al.*, "Injection laser with diffraction grating in the resonator" (in Russian), *Kvatovaya Elektron.*, vol. 1, p. 1145, 1974.

[12] V. S. Starunov and I. L. Fabelinski, "Mandelshtam–Brillouin scattering and entropy (temperature) scattering of light" (in Russian), *Progr. Phys. Sci.*, vol. 98, p. 441, 1969.

[13] B. Ya. Zeldovich and I. I. Sobelman, "Stimulated scattering of light provided by absorbtion" (in Russian), *Progr. Phys. Sci.*, vol. 101, p. 3, 1970.

[14] H. Statz, C. L. Tang, and J. M. Lavine, "Spectral output of semiconductor lasers," *J. Appl. Phys.*, vol. 35, p. 2581, 1964.

[15] E. M. Belenov, V. N. Morozov, and A. N. Oraevsky, "Problems in the dynamics of lasers and masers," in *Quantum Electronics in Lasers and Masers*, D. V. Skobel'tsyn, Ed. New York: Plenum, 1972, p. 202.

[16] J. A. Rossi, H. Heckscher, G. E. Stillman, and S. R. Chinn, "Time delay in external-cavity-controlled GaAs/$Ga_xAl_{1-x}As$ single-heterostructure diode lasers," *Appl. Phys. Lett.*, vol. 23, p. 254, 1973.

[17] J. A. Rossi, H. Heckscher, and S. R. Chinn, "Threshold, spectral and output characteristics of GaAs/$Ga_{1-x}Al_xAs$ single-heterostructure diode lasers," *Appl. Phys. Lett.*, vol. 23, p. 257, 1973.

[18] A. P. Bogatov, P. G. Eliseev, and B. N. Sverdlov, "Anomalous interaction of spectral types of oscillation in semiconductor laser" (in Russian), *Kvantovaya Elektron.*, vol. 1, p. 2286, 1974.

[19] M. Maier, W. Rother, and W. Kaiser, "Penetration and strong reflection of laser light in CS_2," *Phys. Lett.*, vol. 23, p. 83, 1966.

Injection-Induced Modulation of Laser Light by the Interaction of Laser Diodes

JUN-ICHI NISHIZAWA, FELLOW, IEEE, AND KATSUHIKO ISHIDA

Abstract—**The experimental investigation of laser-light modulation by injecting laser light of a frequency, which is slightly different from the cavity resonant frequency, into a laser-diode cavity is reported. For this investigation, the interaction of two laser diodes was used and the relation between the oscillation frequency spectra and the lasing frequency difference of the two diodes was measured where the frequency difference was greater than the locking frequency range. The sidebands generated by the injection of laser light were measured to judge an appearance of the injection-induced modulation of light intensity. Modulation in the frequencies from 10 to 90 GHz was achieved by using laser diodes of 60–130-μm length. It was experimentally shown that the upper frequency limit of the injection-induced modulation was related to the Q value of the laser-diode cavity.**

Manuscript received November 28, 1974; revised February 25, 1975.

The authors are with the Research Institute of Electrical Communication, Tohoku University, Sendai, Japan.

I. Introduction

NISHIZAWA showed that when a laser beam whose frequency is slightly different from the cavity resonant frequency is injected into a laser diode, the electromagnetic field of the injected laser light starts to oscillate in the active region of the laser diode [1]–[3]. The electromagnetic field of the injected laser light is coupled with the oscillating cavity modes through the injected carriers [2], [4], so that the electromagnetic fields of the cavity modes are also forced to oscillate. This results in an injection-induced modulation of the laser output intensity and oscillation spectra consisting of equally spaced frequencies separated by the frequency of the injection-induced modulation.

In order to realize highly efficient modulation of laser-light intensity, the length of laser diodes must be taken into con-

sideration [1]. Nishizawa *et al.* [5] succeeded in modulating the light intensity of laser diodes at 46 GHz using laser diodes whose longitudinal-mode separations were nearly equal to the modulation frequency. And it was also reported that the degree of modulation becomes largest when the modulation frequency is a multiple of the fundamental frequency of the cavity [6]. On the other hand, it is possible to realize efficient high-frequency modulation by using a laser diode whose cavity bandwidth is large enough for the sidebands generated due to modulation. In other words, higher frequency modulation is possible in the laser diodes with a lower Q value. First-order mode locking, in spite of the appreciable dispersion of the refractive index, has been obtained in a very long (4–20-mm) electron-beam-pumped laser [7] due to the low Q value of the semiconductor laser cavity.

In this report, it is experimentally demonstrated that the modulated laser-light beam can be obtained from a laser-diode cavity by injecting a laser beam whose frequency is different by more than the locking frequency range from the cavity resonant frequency, and that the upper limit of the modulation frequency is related to the Q value of the laser-diode cavity. Our experimental results show that injection-induced modulation up to frequencies as high as 90 GHz can be obtained through the interaction of laser diodes in this way.

II. Experimental Procedure

The experimental arrangement is shown in Fig. 1. Two laser diodes A and B, whose lasing wavelengths differ by less than about 5 Å, were aligned end to end to be optically coupled to each other with a separation d. For improvements of optical coupling between the two laser diodes, it is most important to align the active regions of the two diodes in the same plane. In the present study, the two diodes were aligned as follows: one diode was set to lase itself and the other to exhibit a maximum photovoltage. The separation d was controlled with high accuracy by the use of a micrometric screw and a piezoelectric element and was held rigidly to obtain stable coupling [8]. Then the currents above their thresholds were supplied to diodes A and B.

The relation between the frequency spectra of the output light from diode B and the lasing frequency of diode A was measured with the lasing frequency of diode B kept constant while that of diode A was varied. It was not possible to directly observe the time variation of light intensity in the millimeter-wave region for lack of such a high-speed photodetector. Instead, the appearance of the sidebands due to the injection of laser light from A was used as a measure of the injection-induced modulation. That is, sidebands were detected and their intensities relative to the main peak were measured. This method was previously used to detect 46-GHz modulation of a laser diode [5].

There are two methods to achieve high-frequency modulation. In one, the diode length is chosen so that the modulation frequency f is nearly equal to the fundamental frequency of the cavity [5] expressed as

$$f = \frac{c}{2L\left(n + \omega \dfrac{dn}{d\omega}\right)}.$$

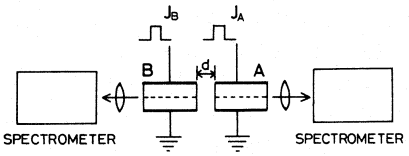

Fig. 1. The experimental arrangement for the interaction of laser diodes A and B.

Here L is the diode length, n is the refractive index, c is the velocity of light in the vacuum, and ω is optical angular frequency. In the other method, the Q value of a laser-diode cavity is made very small so that at least one of the sidebands generated by the modulation is included within the bandwidth of the cavity resonance [3]. The latter method was used in our present experiments. The Q value was lowered by reducing the length of the laser diodes (60–130 μm).

When laser diodes lasing at many longitudinal modes are optically coupled to each other, lasing frequencies easily hop to other frequencies, at least some of which are common to the two diodes when the lasing frequency difference is small [8]. But this hopping of lasing frequency was found to be experimentally difficult to obtain in the optical coupling of two laser diodes which lase at a single longitudinal mode when operated alone. Therefore, laser diodes which lased in a single longitudinal mode were describable in our experiments. The laser diodes having lengths less than 100 μm lase very easily in a single frequency. So it is most convenient to use shorter laser diodes not only for reducing the Q value but also for a single-frequency operation. The enhanced mode selectivity [8] is difficult to obtain due to the large longitudinal-mode separation in laser diodes shorter than 90 μm, and the lasing wavelengths do not jump from the self-oscillation frequencies to other frequencies by the optical coupling of the two diodes. The diodes used were GaAs–GaAlAs stripe-geometry double-heterostructure laser diodes whose stripe width was 20 μm. These diodes were operated at room temperature and pulsed at 500 Hz with 100-ns pulses. The lasing frequency of A was shifted due to the change of the active-region temperature by varying the dc current supplied to A. For a shift of the lasing frequency by as much as 9.8×10^{11} rad/s, which corresponds to the shift of the wavelength of 4 Å, the output intensity of A changed by less than 10 percent.

III. Experimental Results and Considerations

The change of the output spectra of B was measured as the lasing frequencies of A were varied. ω_A, ω_B represent the lasing angular frequency self-oscillation, $\delta\omega_A, \delta\omega_B$ the fundamental frequency separation of the laser cavity, J_A, J_B the current supplied to A and B, respectively.

When the lasing frequency difference between ω_A and ω_B satisfies the condition $\Delta\omega_m < |\omega_A - \omega_B| < \delta\omega_B/2$, the peaks of the output frequency spectra were given by only ω_A and ω_B, and new oscillation peaks other than ω_A and ω_B were not observed. Here $\Delta\omega_m$ is the largest difference between ω_A and ω_B at which new oscillation peaks other than ω_A and ω_B were observed. New oscillation peaks appeared when the lasing frequency difference became less than some value $\Delta\omega_m$. Thus, when $|\omega_B - \omega_A| \leqslant \Delta\omega_m$, diode B was operated at ω_A, ω_B and the induced frequency ω_i, but when $|\omega_A -$

$\omega_B| > \Delta\omega_m$, diode B operated only at ω_A and ω_B. Various pairs of optically coupled laser diodes were used and the new oscillation peak ω_i was never observed when the oscillation frequencies of two diodes satisfied the condition of $|\omega_B - \omega_A| > \Delta\omega_m$, whether $\omega_A < \omega_B$ or $\omega_A > \omega_B$. The frequency of the induced oscillation peak ω_i generated when $|\omega_B - \omega_A| < \Delta\omega_m$ was changed by varying the lasing frequency ω_A. These experimental results show that the induced oscillation peaks are not due to the growth of new lasing spots, which might occur due to optical coupling of diodes A and B, but that the generation of the new oscillation peaks is a fundamental phenomenon induced by the coexistence of the two electromagnetic fields having very close frequencies.

Although J_B was variously changed, the induced oscillation peaks other than ω_A and ω_B were not generated when J_B was below the threshold current (J_{Bth}) of B, but were observed only when $J_B > 1.07\ J_{Bth}$. Thus, one of the required conditions for the appearance of the induced signal at ω_i is that diode B have some high gain or that a signal exists at ω_B.

Fig. 2 shows the change of the output spectra of B as ω_A was varied. As the fundamental cavity frequency A is 2.7×10^{12} rad/s, which corresponds to 11 Å, there is only one mode of A included in the output spectra of B. P_A is the output power from A when $J_B = 0$, and P_B is for B when $J_A = 0$. For d equal to 30 μm, the optical coupling coefficient between A and B is about 0.04 [8]. Therefore the actually injected laser power into B from A is about 0.8 mW in this case. The output spectra consist of only two peaks at ω_A and ω_B in the case of $\omega_A - \omega_B = 8.1 \times 10^{11}$ rad/s, which corresponds to $\lambda_B - \lambda_A = 3.3$ Å, as shown in Fig. 2(a) (1). But a new oscillation peak ω_i appears on the low-frequency side of ω_B when $|\omega_A - \omega_B| \leqslant 5.4 \times 10^{11}$ rad/s, which corresponds to $|\lambda_B - \lambda_A| \leqslant 2.2$ Å. The frequency of this induced oscillation ω_i was changed by varying the lasing frequency of A, but always $\omega_A - \omega_B = \omega_B - \omega_i$; i.e., the induced oscillation is generated at the frequency of $2\omega_B - \omega_A$. The induced oscillation appears either at $2\omega_B - \omega_A$ [e.g., Fig. 2(a)] or at $2\omega_A - \omega_B$ [e.g., Fig. 2(b)] or at both frequencies of $2\omega_B - \omega_A$ and $2\omega_A - \omega_B$. These experimental results show that sidebands at $\omega_B \pm (\omega_B - \omega_A)$ and $\omega_A \pm (\omega_B - \omega_A)$ are generated by injecting laser light of frequency ω_A into B oscillating at ω_B; thus the output intensity of B can be modulated at the frequency of $|\omega_B - \omega_A|$ by the injection of laser light.

These experimental results can be explained by the mechanism which was proposed by Nishizawa [1]-[3]. When the laser beam frequency ω_A is injected into B oscillating at ω_B for $|\omega_A - \omega_B| < \Delta\omega_m$, the electromagnetic field corresponding to ω_A in the active cavity of B is modulated at frequency f given by [1]-[3]

$$f = \frac{c}{2\sqrt{\epsilon}\, l_B} \cdot \frac{|\lambda_B - \lambda_A|}{\delta\lambda_B} = \frac{|\omega_A - \omega_B|}{2\pi}$$

where l_B is the length of B; c is the velocity of light in the vacuum; ϵ is the dielectric constant of the active region of B; λ_A and λ_B are the lasing wavelengths corresponding to ω_A and ω_B, respectively; and $\delta\lambda_B$ is the longitudinal-mode separation corresponding to $\delta\omega_B$.

The electromagnetic field of the cavity resonant mode corresponding to ω_B is forced to oscillate due to the oscillation of

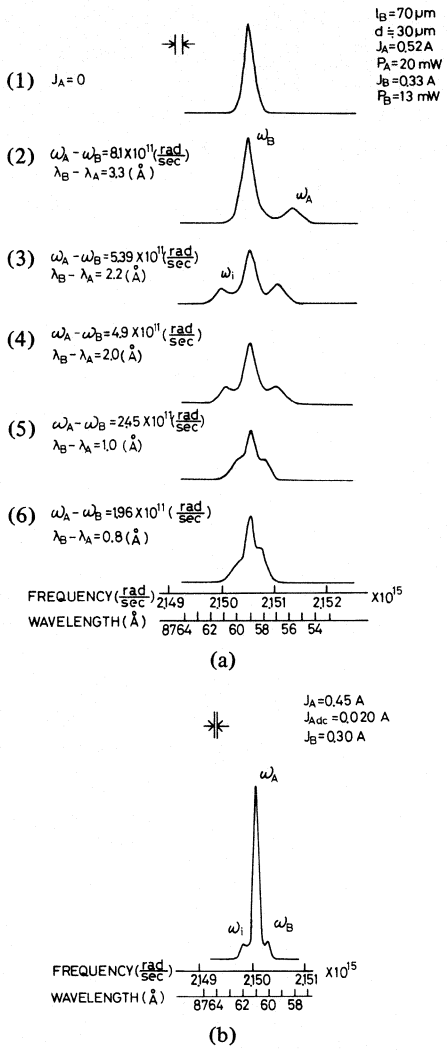

Fig. 2. The change of the output spectra of B as the lasing frequency of A was varied. The length of B is 70 μm and its fundamental cavity frequency $\delta\omega_B$ is 3.18×10^{12} rad/s, which corresponds to 13 Å. ω_A and ω_B are the lasing frequency of A and B, respectively. ω_i is the frequency of the induced oscillation. J_{Ath} is 0.37 A and J_{Bth} is 0.29 A.

the amplitude of the injected laser-light field and the coupling between the laser modes through the population inversion [2], [4]. As the light-field amplitude of the injected mode becomes larger, the partition ratio of population inversion for the cavity resonant mode becomes smaller due to the interaction between laser modes through the population inversion [2], [4]. Therefore, the amplification factor for the injected mode becomes higher, and that for the cavity resonant mode becomes smaller. When the light-field amplitude of the injected mode is smaller, the cavity resonant mode strongly lases. This phenomenon is similar to super regenerative detection [1]-[3]. As the amplitudes of the electromagnetic fields of the laser modes in the active region oscillate in this way, oscillation spectra consist of equally spaced frequency with the separation corresponding to $|\omega_A - \omega_B|$. In the example shown in Fig. 2(a), ω_A and $\omega_i (= 2\omega_B - \omega_A)$ are sidebands of ω_B. The degree of modulation, which is obtained from the ratio of the intensity of sidebands to that of carrier wave, is about 98 percent in the case of $\omega_A - \omega_B = 4.9 \times 10^{11}$ rad/s, which corresponds to $\lambda_B - \lambda_A = 2$ Å. Thus the

output intensity is considered to be modulated in the degree of 98 percent at 83 GHz. As ω_A approaches ω_B, then the ratio of the oscillation intensity at sidebands to that of main peak (ω_B) becomes larger and thereby overmodulation occurs. The degree of modulation can be changed by varying the current supplied to A and B. Fig. 2(b) shows the results for the same diode pair as Fig. 2(a) when ω_A was made lower than ω_B by increasing the dc current supplied to A, and J_A and J_B were changed. The degree of modulation is about 60 percent in this case.

Now the slight asymmetry of the sideband peaks, which is observed in Fig. 2(a), may be due to the additional laser power from A injected into B.

In the normal injection-locking experiments when the frequency difference is greater than the locking range, the frequency of the oscillator shifts toward the frequency of the locking signal [9]. The same phenomenon occurs also in the injection locking of lasers [10]. But this shift of the lasing frequency could not be observed in our experiments, since the shift is too small to be resolved by the spectrometer used in our experiments.

The frequency range for injection-induced modulation is shown in Fig. 3, where δ shows the frequency separation between the lowest frequency and the highest frequency of the oscillation spectra of B. That is, $\delta = (\omega_A - \omega_i)/2\pi$, corresponding to Fig. 2(a). But δ can be represented as $\delta = P|\omega_A - \omega_B|/2\pi$, where P is an integer. $P = 1$ indicates that the frequencies of the oscillation spectra are only at ω_A and ω_B, and that injection-induced modulation does not occur [e.g., Fig. 2(a) (1)]. The induced signal appears at the frequency of $2\omega_B - \omega_A$ or $2\omega_A - \omega_B$ for $P = 2$, but for $P = 3$ the induced signal appears at both frequencies of $2\omega_B - \omega_A$ and $2\omega_A - \omega_B$. Fig. 3(a) shows the results in the case of $l_B = 90$ and 70 μm. The data points satisfy the relation $\delta = 2 \cdot |\omega_A - \omega_B|/2\pi$ in the frequency range of $|\omega_A - \omega_B|/2\pi \leqslant \Delta\omega_m/2\pi = 87$ GHz, but the relation $\delta = |\omega_A - \omega_B|/2\pi$ holds well in the range of $|\omega_A - \omega_B|/2\pi > 97$ GHz. As the maximum frequency of the injection-induced modulation is obtained from $\Delta\omega_m/2\pi$, the maximum modulation frequency of the diode having $l_B = 70$ μm is about 90 GHz. Fig. 3(b) shows the results for the diode having $l_B = 130$ μm, where the maximum modulation frequency is about 50 GHz.

Fig. 4 shows the relation between the longitudinal-mode separation $\delta\omega_B$ of B and the maximum frequency difference $|\omega_B - \omega_A|_{\max}/2\pi = \Delta\omega_m/2\pi$ at which modulation occurs. The $\delta\omega_B$ is expressed as

$$\delta\omega_B \doteqdot \pi c/\sqrt{\epsilon}\, l_B.$$

Therefore, higher frequency modulation is possible in the shorter laser diodes. The Q value of a laser-diode cavity is given (11) as

$$Q = \omega_c \tau_c = \frac{\omega_c}{\Delta\omega_c}$$

where the cavity lifetime τ_c is

$$\frac{1}{\tau_c} = \frac{1}{\tau_m} + \frac{1}{\tau_s}.$$

τ_m is the contribution to the cavity lifetime, resulting from

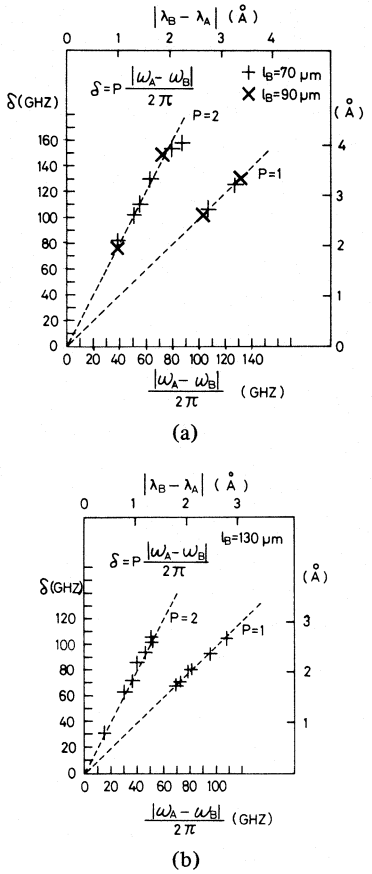

Fig. 3. The frequency range for modulation. δ is the difference between the lowest and the highest frequency in the output of B. $P = 1$ indicates that injection-induced modulation does not occur and $P = 2$ indicates the occurrence of modulation. (a) For $l_B = 90$ μm and $l_B = 70$ μm. (b) For $l_B = 130$ μm.

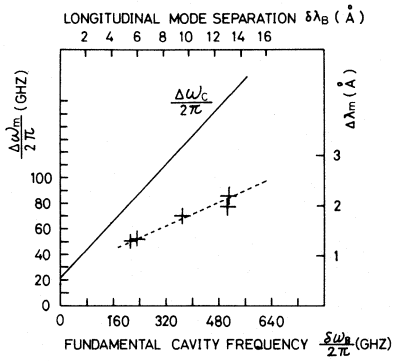

Fig. 4. The relation between the fundamental cavity frequency of B and the maximum frequency difference at which injection-induced modulation occurs, i.e., the maximum modulation frequency. The solid line shows the bandwidth of the laser-diode cavity. Here, $\Delta\lambda_m = (2\pi c/\omega_m^2) \cdot \Delta\omega_m$.

the loss of radiation through the mirrors alone, and is given as $\tau_m = -2\sqrt{\epsilon}\, l/c \ln(\rho_1 \cdot \rho_2)$, where ρ_1, ρ_2 are reflectivities, and τ_s corresponds to the scattering and absorption losses. $\Delta\omega_c$ is the bandwidth of the cavity. So $\Delta\omega_c$ can be expressed as

$$\Delta\omega_c = \frac{1}{2\pi}\left\{\ln\left(\frac{1}{\rho_1 \cdot \rho_2}\right)\right\} \delta\omega_B + \frac{\alpha c}{\sqrt{\epsilon}}.$$

Here, $\alpha c/\sqrt{\epsilon} = 1/\tau_s$. α is experimentally determined from the

relation of

$$J_{th} = \frac{1}{\beta}\left\{\alpha - \frac{1}{l}\ln(\rho_1 \cdot \rho_2)\right\}.$$

The calculated bandwidth of the laser cavity is shown in Fig. 4. It can be seen that the higher frequency modulation is realized in the laser diode with lower Q value. The appearance of sidebands indicates that the modulation of population inversion induced by the injection of laser light reacts back on the oscillating laser modes. This reaction is effective when the sidebands generated to the oscillating laser frequencies are included within the bandwidth of the cavity. Therefore the frequency range of the injection-induced modulation is reasonably considered to be related to the Q value of the laser cavity.

References

[1] J.-I. Nishizawa, "Recombination lifetime in a semiconductor laser diode," *IEEE J. Quantum Electron.*, vol. QE-4, pp. 143-147, Apr. 1968.

[2] —, "Interaction of light beam in semiconductor laser diode," presented at the 1973 Int. Conf. Solid State Devices, Tokyo, Japan, Aug. 1973.

[3] —, *Image Technol. Eng.* (in Japanese), vol. 2, pp. 29-45, Oct. 1971.

[4] J. Nishizawa and K. Ishida, "Integrated optics through the population of injected carriers," presented at the 2nd Int. Topical Meet. Integrated Optics, New Orleans, La., Jan. 1974.

[5] S. Takamiya, F. Kitasawa, and J.-I. Nishizawa, "Amplitude modulation of diode laser light in millimeter-wave region," *Proc. IEEE* (Lett.), vol. 56, pp. 135-136, Jan. 1968.

[6] R. F. Broom and E. Mohn, "Modulation of gallium arsenide diode lasers in an external resonator," *J. Appl. Phys.*, vol. 39, pp. 4851-4852, Sept. 1968.

[7] O. V. Bogdankevich, A. N. Mestvirshvili, A. N. Pectronov, and A. F. Scuhkov, "Mode locking in a semiconductor laser with electronic excitation on an internal nonlinear active medium," *Zh. Eksp. Teor. Fiz., Pis'ma Red.*, vol. 12, Aug. 1970.

[8] J. Nishizawa, K. Ishida, and M. Suzuki, "Optical interaction of GaAs-GaAlAs double-heterostructure laser diodes through the population of injected carrier," in preparation.

[9] K. Kurokawa, "Injection locking of microwave solid-state oscillators," *Proc. IEEE*, vol. 61, pp. 1386-1410, Oct. 1973.

[10] K. Shimoda and T. Yazima, *Quantum Electronics* (in Japanese), vol. 1. Tokyo, Japan: Shokabo, 1972, pp. 127-149.

[11] R. H. Pantel and H. E. Puthoff, *Fundamentals of Quantum Electronics.* New York: Wiley, pp. 111-112.

Direct Modulation of a Double-Heterostructure Laser Using a Schottky-Barrier-Gate Gunn-Effect Digital Device

HISAYOSHI YANAI, SENIOR MEMBER, IEEE, MITSUHIRO YANO, STUDENT MEMBER, IEEE, AND TAKESHI KAMIYA

Abstract—**By using a Schottky-barrier-gate Gunn-effect digital device the direct modulation of a GaAs-$Al_xGa_{1-x}As$ double-heterostructure laser was achieved with a rise time of 250 ps. The dependence of the optical waveforms on the bias-current levels was investigated in detail. The results are compared with a rate-equation analysis. A discrepancy between the present theory and the experiment indicates the existence of an additional relaxation mechanism.**

Introduction

THE CAPABILITY of high-speed direct modulation is one of the most attractive features of GaAs injection lasers, and a number of modulation schemes have been proposed and investigated in the range between 200 Mbit/s and 2.3 Gbit/s [1]-[8]. Among them, Thim *et al.* utilized a two-terminal Gunn-effect digital device and successfully obtained subnanosecond pulses [8], [9]. One of the authors (H. Y.) has been developing a three-terminal Gunn-effect digital device (a Schottky-barrier-gate Gunn-effect digital device [10], hereafter denoted as SBG-GEDD), which generates constant current pulses of very fast rise time and has the capability of handling fairly high current levels. It is expected therefore that this type of device is also useful for the pulse modulation of an injection laser.

The advantage of using a Gunn-effect digital device may lie principally in the fact that it can supply fast current pulses of constant waveforms without any shaping. Due to the simplicity of the circuit, it is easy to minimize the parasitic impedance effect. On the other hand, in combining the laser and the SBG-GEDD, we must choose a suitable bias-current level considering both the threshold current of the laser and the SBG-GEDD. As the dynamic behavior of the laser changes strongly as a function of injection current, it seems important to investigate the time-response characteristics of this modulation scheme as a function of bias current.

In this report experimental investigation of direct modulation of a double-heterostructure (DH) laser diode using a SBG-GEDD is described, with special emphasis on the bias-current dependence of the time-response characteristics. By attaching a parallel resistor to the SBG-GEDD, we were able to operate a variety of combinations of laser and SBG-GEDD's, with different threshold levels.

Manuscript received November 25, 1974; revised January 20, 1975. This work was supported by the Toray Science Foundation, Japan. Part of this work was presented at the 4th European Solid State Device Research Conference, Nottingham, England, September 1974.

H. Yanai and M. Yano are with the Department of Electronic Engineering, University of Tokyo, Tokyo, Japan.

T. Kamiya is with the University of Tokyo, Tokyo, Japan. He is on leave at the Max-Planck-Institut für Festkörperforschung, Stuttgart, Germany.

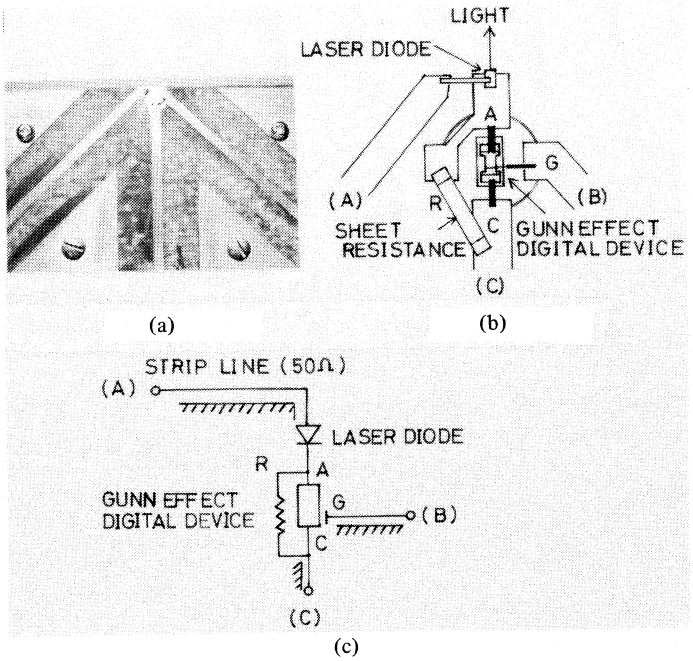

Fig. 1. Circuit diagram of a laser-modulation scheme using a SBG-GEDD. (A) is connected to a bias-pulse generator (pulsewidth of 100 ns), (B) is connected to a word generator, and (C) is grounded or connected to a current waveform monitor. A, G, C, and R denote the anode, gate, cathode of the SBG-GEDD, and the sheet resistor, respectively. (a) Photograph. (b) Construction of circuit. (c) Equivalent circuit.

It should be noted that by connecting the two devices in series we obtain negative optical pulses, where the transient behaviors are somewhat different from positive pulse modulation. In both cases the occurrence of spiking oscillations is an important problem.

After examining the time response of the photodiode, we will compare the experimental results with the analysis using rate equations. The observed changes of rise time and of ringing frequency are reasonably explained by the conventional model, but the observed damping-time constant associated with the ringing phenomenon is found to be shorter than the calculated value. It is also observed that an exponentially decaying component is superimposed on the oscillatory transient. The possible cause of these discrepancies is also discussed.

Experiments

The modulation circuit consists of a laser diode, a SBG-GEDD, and a sheet resistor. These elements are connected as depicted in Fig. 1. The bias-current level is chosen slightly below the Gunn oscillation threshold and simultaneously above the laser threshold by a certain amount. Without a triggering pulse, the laser operates continuously. When a triggering pulse is applied at the gate, the SBG-GEDD generates a single negative current pulse, causing a reduction of the lasing output, i.e., a negative optical pulse.

By properly choosing the value of resistance R of the sheet resistor, we can operate various combinations of laser and SBG-GEDD's with different threshold currents. Through a simple circuit-theoretical consideration the formula for determining R is found as

$$R = V_{\text{th}}^{G}/(I^{L} - I_{\text{th}}^{G}) \tag{1}$$

where V_{th}^{G}, I_{th}^{G}, and I^{L} are the threshold voltage of the SBG-GEDD, the threshold current of the SBG-GEDD, and the bias-current level of the laser, respectively. The relation between the current drop of the laser ΔI^{L} and that of the SBG-GEDD ΔI^{G} is

$$\Delta I^{L} = \frac{R}{R + R_i + R^{L}} \cdot \Delta I^{G} \tag{2}$$

where R_i and R^{L} denote the output impedance of the bias source and the internal resistance of the laser, respectively.

Only pulsed operation is used with a pulsewidth of 100 ns in order to avoid heating and possible degradation of the laser or of the SBG-GEDD. A 1-Gbit/s word generator (Iwatsu WG-101) is used as a trigger source and modulation up to 500 Mbit/s was successfully made. In this paper, however, we shall confine ourselves to the single pulse-response characteristics. The studies of the word effects will be reported later.

The upper trace of Fig. 2 shows the current waveform of the SBG-GEDD and the lower trace shows the triggering pulse waveform. It is seen from the figure that the pulsewidth is 1.1 ns according to an active length of 90 μm, the rise time is less than 100 ps, and the current drop ΔI^{G} is 40 mA.

Fig. 3 shows the relation between the injection current I^{L} and the output light intensity I_L of the laser used. The laser has a threshold current I_{th}^{L} of 225 mA, a cavity length l^{L} of 210 μm, a stripe width w^{L} of 15 μm (fabricated by the proton-bombardment technique), and an active-region thickness t^{L} of 0.5 μm (measured by SEM observation of the cleaved surface).

A silicon avalanche photodiode (a product of Nippon Electric Co.) is used to detect the output signal. Although the specification by the manufacturer ensured the frequency re-

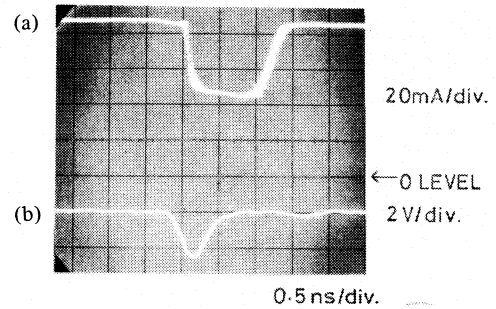

Fig. 2. Current waveform of the SBG-GEDD. (a) The upper trace is the current pulse. (b) The lower trace is the trigger pulse. Time scale: 1 div = 0.5 ns.

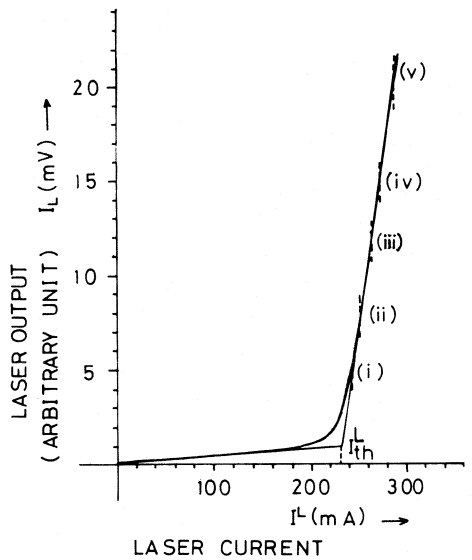

Fig. 3. Output characteristics of a stripe-geometry DH laser. Threshold current is 225 mA. The bias points used in observations of modulated waveforms (Fig. 4) are indicated by roman numbers.

sponse only up to 1 GHz at $\lambda = 0.6328\ \mu m$, our diode showed better response, as will be discussed later (see Fig. 5).

We have observed the output-pulse waveforms under various bias-current levels. In Fig. 4 the upper traces show the current waveforms and the lower traces show the output signals of the avalanche photodiode. Fig. 4 (i)-(v) correspond to the normalized bias-current levels (I^L/I^L_{th}) of 1.09, 1.13, 1.18, 1.22, and 1.29, respectively. As shown in this figure, the rise time shortens from 800 ps to 240 ps as the bias level is increased from 1.09 to 1.29. The fall time remains constant at 240 ps. It is probably limited by the fall time of the current pulse.

The optical signal of our device also shows a relaxation oscillation. This behavior is qualitatively in agreement with previous observations on positive optical pulse modulation. Examining the traces in detail, however, we find that an exponentially decaying component is presented in addition to the damped oscillatory transient

$$A_1 e^{-(t/\tau_d)} \cos(2\pi f_r t) + A_2 e^{-(t/\tau')}. \tag{3}$$

The determination of f_r, τ_d, and τ' is performed as follows. First we determine f_r from the interval between the maxima in the damped oscillations. Next, by plotting the light intensity for the times $t = (2N-1)/4f_r$, where N is an integer, we obtain A_2 and τ'. Subtracting then the second term from the total curve we determine τ_d. The results are tabulated in Table I(a).

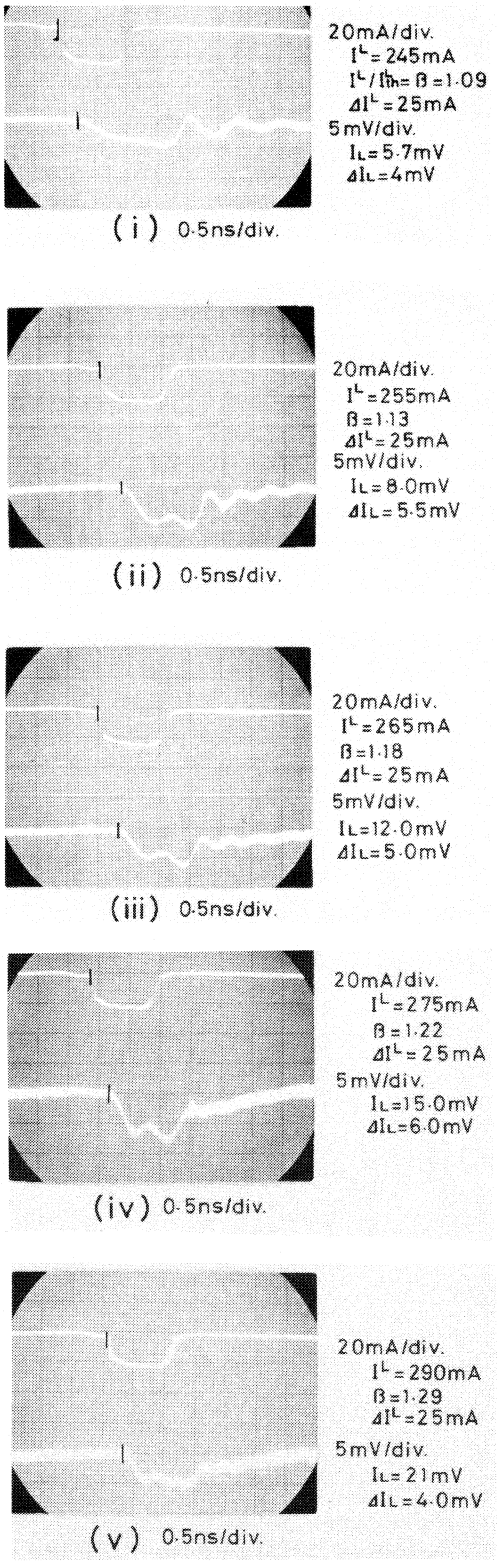

Fig. 4. Dependence of the observed optical-pulse waveforms on current-bias level. The upper traces give the current pulse; the lower traces show the optical pulses.

In order to check the effect of the time-response characteristics of the avalanche photodiode on the observed waveforms in Fig. 4, the following additional experiment was performed. The light pulse of an identical pulse-modulated laser with in-

TABLE I
BIAS-CURRENT-LEVEL DEPENDENCE OF RISE TIME, RELAXATION FREQUENCY, ITS DECAY-TIME CONSTANT, AND DECAY-TIME CONSTANT FOR THE ADDITIONAL EXPONENTIAL DECAY TERM

(a) Results for the laser corresponding to Fig. 4.

I^L/I^L_{th}	$(I^L-\Delta I^L)/I^L_{th}$	t_r(ns) meas.	t_r(ns) calc.*	f_r(GHz) meas.	f_r(GHz) calc.	τ_d(ns) meas.	τ_d(ns) calc.	τ'(ns) meas.
1.09	0.98	0.80		1.4	1.57	0.80	8.5	0.47
1.13	1.02	0.50	0.69	2.1	1.89	0.53	7.9	0.70
1.18	1.07	0.30	0.36	2.2	2.22	0.44	7.4	0.83
1.22	1.11	0.25	0.29	2.3	2.45	**	6.9	**
1.29	1.18	0.24	0.23	2.8	2.81	**	6.3	**

(b) Results for the other laser (w^L=12μm, L^L=200μm, I^L_{th}=96mA, τ_e=3ns, τ_{ph}=2ps, b=2.4)

I^L/I^L_{th}	$(I^L-\Delta I^L)/I^L_{th}$	t_r(ns) meas.	t_r(ns) calc.*	f_r(GHz) meas.	f_r(GHz) calc.	τ_d(ns) meas.	τ_d(ns) calc.	τ'(ns) meas.
1.13	1.02	0.70	1.12	1.1	1.12	0.90	6.1	0.90
1.19	1.08	0.50	0.56	1.4	1.40	0.75	5.5	0.80
1.22	1.11	0.45	0.47	**	1.50	**	5.2	0.55
1.25	1.14	0.35	0.42	1.6	1.60	0.55	5.0	0.60
1.27	1.16	0.30	0.39	1.8	1.66	0.50	4.9	0.45

*$1/(2f'_r)$ is listed, where f'_r is calculated by (5), substituting $(I^L - \Delta I^L)$ instead of I^L.

**Not determined due to the insufficient quality of the experimental data.

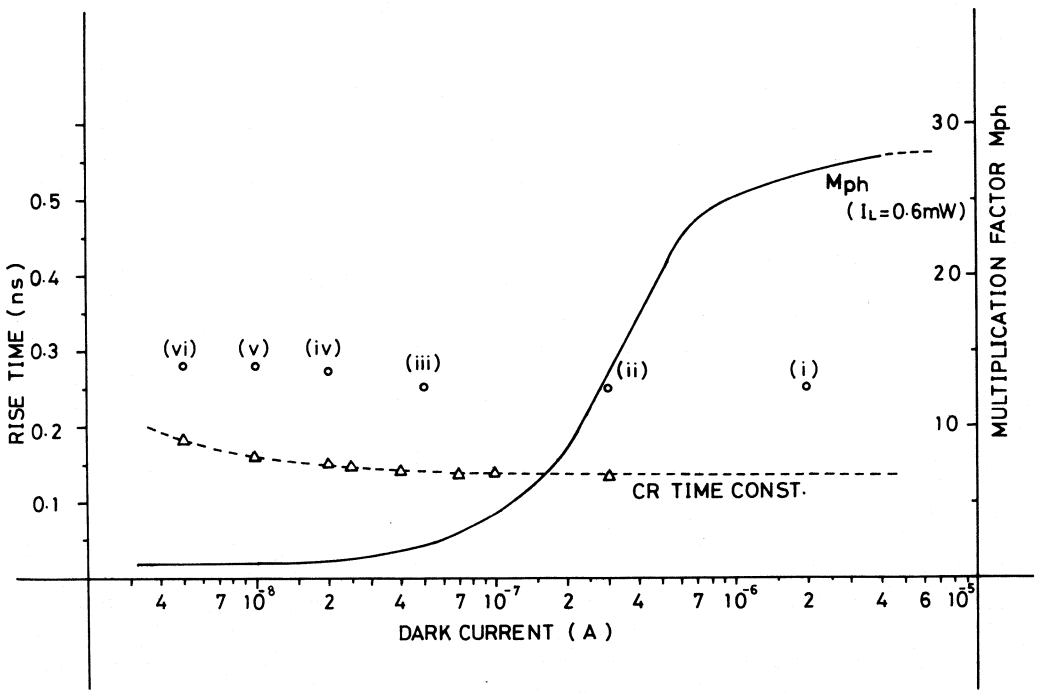

Fig. 5. Reverse-bias dependence of the time-response characteristics of a silicon avalanche photodiode. The bias conditions are expressed by the dark current. The solid curve is the multiplication factor *Mph*, the broken curve gives the *RC* time constant, and the circles with roman numbers indicate the rise time observed with an identical laser-light pulse. The scale for the rise time and for the *RC* time constant is common.

tensity I_L of 0.6 mW is detected by the avalanche photodiode under various reverse-bias conditions. As the reverse voltage is changed from 10 V to 72 V, the dark current increases from 5×10^{-8} A to 7×10^{-6} A, and at the same time the multiplication factor changes from 1 to 28. In contrast to this large change of sensitivity, the observed waveforms show only little change. The observed rise time is indicated in Fig. 5 as a function of the dark current by circle marks accompanied by roman numbers. The change of the multiplication factor is plotted by the solid curve. It is clear that the observed rise time is scarcely affected by the avalanche phenomenon in the photodiode. The junction capacitance of the avalanche photodiode was also measured as a function of the reverse-bias condition and the result is displayed in Fig. 5 with triangle marks connected smoothly with a dashed curve, representing the *RC* time constant. Here the value of the resistance means the load resistance of the photodiode, in our case equal to 50Ω. As the *RC* time constant is less than half of the observed rise time, it can be said that the effect of the *RC* time constant on the rise time is also small.

We have also measured the turn-on delay time. For the case of strong excitation, a narrow-pulse emission is observed at the onset of the laser oscillation. The narrowest pulse observed by our avalanche photodiode has a width of 250 ps. This observation also indicates the speed of the avalanche photodiode.

Discussions

From the experimental observations (Figs. 2, 4, and 5) we conclude that the time response of the modulation scheme investigated here is mainly limited by the dynamics of the laser itself, rather than by the SBG-GEDD or by the avalanche photodiode.

It is interesting to compare the observed damped oscillatory behavior with the rate-equation analysis of transient response of lasers due to Adams [11], although his model of analysis does not give the second term of (3). In his analysis, the current dependence of the gain is assumed as follows:

$$g = g_0 (I^L/I^L_{\text{th}})^b. \tag{4}$$

A small-signal analysis gives the damped harmonic oscillation with relaxation frequency f_r and a damping time constant τ_d as

$$f_r = \{b(I^L/I^L_{\text{th}} - 1)/\tau_e \cdot \tau_{\text{ph}}\}^{1/2} \cdot \frac{1}{2\pi} \tag{5}$$

and

$$\tau_d = 2\tau_e \{b(I^L/I^L_{\text{th}} - 1) + 1\}^{-1} \tag{6}$$

where τ_e and τ_{ph} are the electron lifetime and photon lifetime, respectively.

The electron lifetime τ_e at threshold in our experiment can be estimated from the measurement of the excitation current dependence of the turn-on delay time t_d [12]:

$$\tau_e = td \left(\ln \frac{I^L}{I^L - I^L_{\text{th}}}\right)^{-1}. \tag{7}$$

For the laser used in the observations of Fig. 4, τ_e is thus estimated as $\tau_e = 5.0$ ns.

The photon lifetime τ_{ph} is defined by the following expression [13]:

$$\tau_{\text{ph}} = \frac{n}{c}\left(\alpha - \frac{\ln r}{L^L}\right)^{-1} \tag{8}$$

where n, c, and r are refractive index of the active region of the laser, the light velocity in the vacuum, and the reflection coefficient at the cleaved surfaces of the laser, respectively. α is the internal optical loss coefficient (cm^{-1}), and the length of the cavity is expressed by L^L.

Furthermore, because it has been shown by Pinkas *et al.* that in DH lasers the injected electrons are nearly perfectly confined to the active region, the gain is expressed as a function of current density divided by the thickness of the active region t^L [14]. The threshold condition for laser oscillation is given by the following equation, assuming the bth power dependence of gain on current, (4):

$$B(J_{\text{th}}/t^L)^b = \left(\alpha - \frac{\ln r}{L^L}\right). \tag{9}$$

Here J_{th} is the threshold current density of the laser and B is the proportionality constant.

For an active region, as was used in the present experiment ($\text{Na} \approx 10^{18}$ cm^{-3}), it has been reported that a typical value of the normalized threshold current density (J_{th}/t^L) is about 5 $\text{kA/cm}^2 \cdot \mu\text{m}$ [13], [14] for a cavity length of 380 μm, with an internal loss coefficient $\alpha \fallingdotseq 10\ \text{cm}^{-1}$, which corresponds to a photon lifetime of 3 ps. For the laser in the experiment of Fig. 4, the normalized threshold current density is 14.3 $\text{kA/cm}^2 \cdot \mu\text{m}$.

Using these values and (5), (8), and (9), the relaxation frequency is calculated with b as a fitting parameter. The best fit is obtained when $b = 2.0$, and the result is tabulated in Table I(a). As a reference, the results for the other laser are also shown in Table I(b). The value of b is roughly in agreement with previous reports [13], [14]. The agreement between the calculated relaxation frequency is rather good. The observed rise time is also in rough agreement with $1/2f_r'$, where f_r' is calculated by (5), substituting $(I^L - \Delta I^L)$ instead of I^L. On the other hand, the damping-time constant calculated by using (6) shows a remarkable disagreement with the experimental value. This fact suggests that some other relaxation mechanism beyond Adams' model exists in our lasers and should be incorporated in the model. An improvement of the model is required also from the existence of the additional decaying component as expressed by the second term of (3).

Russer *et al.* have performed a computer simulation of positive optical pulse modulation using a set of multimode rate equations [15], in which the contribution of spontaneous emission is retained in the rate equation of the photon density of each mode. They found a decreased damping-time constant due to the spontaneous-emission term. The laser used by us has a relatively thick active region and it is possible that the transient interaction of different transverse modes provides an additional path of energy flow. Another possibility is the thermalization process inside the conduction band. Recently, Brosson *et al.* showed experimentally that the intraconduction-band thermalization time in semiconductor lasers is much longer than had been expected for heavily doped ($\text{Na} \simeq 10^{18} \sim 10^{19}$ cm^{-3}) samples [16].

In the present stage it is difficult to identify which mechanism is playing an important role in our experimental situation. We expect that a measurement of the time response as a function of the doping and of the size of the active region may provide the necessary information.

Conclusion

We find the following characteristic features in the time response of a DH laser using a Schottky-barrier-gate Gunn-effect digital device: 1) the combination of lasers with SBG-GEDD's with different threshold current can be achieved by attaching a parallel resistor to the SBG-GEDD; 2) by increasing the bias current up to 1.29 times the threshold current, the rise time shortens monotonically down to 240 ps; 3) the dependence of the rise time and of the observed ringing frequency on the bias current can well be fitted to the theoretical expression for the relaxation frequency of the laser based on a rate-equation analysis; 4) in the fitting procedure, the power factor of the

current dependence of the gain $b \equiv [\log (g/g_0)]/[\log (I^L/I^L_{th})]$ is estimated to be 2.0; 5) the observed damping-time constant associated with the ringing is substantially shorter than the calculated value, which suggests the existence of an additional relaxation mechanism; 6) an additional exponentially decaying component in the damped oscillatory transient is observed. Typically, the time constant ranged between 0.5 ns and 0.8 ns. Through these observations the feasibility of subnanosecond pulse modulation of a DH laser using a SBG-GEDD, and the importance of selecting the proper bias-current level have been indicated.

Acknowledgment

The authors wish to thank Dr. K. Maeda and Dr. Y. Unno of Toshiba Central Research Center for supplying the lasers. They also wish to thank Dr. K. Sekido of the Central Research Laboratory of Nippon Electric Co. for fabricating the SBG-GEDD, Dr. P. Russer of the Forschungsinstitut of AEG-Telefunken for information on the theoretical treatment of pulse modulation prior to publication.

References

[1] P. Russer and S. Schulz, "Direkte Modulation eines Doppelheterostrukturlasers mit einer Bitrate von 2,3 Gbit/s," *Arch. Elek. Übertragung*, vol. 27, pp. 193–195, Apr. 1973.

[2] M. Chown *et al.*, "Direct modulation of double-heterostructure lasers at rates up to 1 Gbit/s," *Electron. Lett.*, vol. 9, pp. 34–36, Jan. 1973.

[3] D. Schicketanz, "Modulation von Gallium Arsenid Laserdioden," *Siemens Forsch. Entwicklung.*, vol. 2, pp. 218–221, Aug. 1973.

[4] T. Ozeki and T. Ito, "Pulse modulation of DH-(GaAl)As lasers," *IEEE J. Quantum Electron. (Part II of Two Parts: Special Issue on 1972 IEEE Semiconductor Laser Conference)*, vol. QE-9, pp. 388–391, Feb. 1973.

[5] —, "A 200 Mbit/s PCM DH-GaAlAs laser communication experiment," presented at the 1973 Conf. Laser Engineering and Applications, Washington, D.C., May 30–June 1, 1973; also *IEEE J. Quantum Electron. (1973 IEEE/OSA Conf. on Laser Engineering and Applications, Dig. Tech. Papers)*, vol. QE-9, p. 692, June 1973.

[6] J. E. Carroll and J. G. Farrington, "Short-pulse modulation of gallium arsenide lasers with Trapatt diodes," *Electron. Lett.*, vol. 9, pp. 166–167, Apr. 1973.

[7] I. Hayashi, "Recent progress in semiconductor lasers–CW GaAs lasers are now ready for new applications," *Appl. Phys.*, vol. 5, pp. 25–36, July 1974.

[8] H. W. Thim *et al.*, "Subnanosecond pulse code modulation of GaAs lasers by Gunn effect switches," presented at the 1973 IEEE Int. Solid-State Circuits Conf., Philadelphia, Pa., Feb. 1973; also abstract in *Dig. Tech. Papers.*

[9] H. W. Thim *et al.*, "Bistable switching in high quality GaAs Gunn diodes with overcritical nl product," in *Proc. 4th Int. Conf. GaAs and Related Compounds* (Sept. 1972), pp. 267–274.

[10] T. Sugeta, M. Tanimoto, T. Ikoma, and H. Yanai, "Characteristics and applications of a Schottky-barrier-gate Gunn-effect digital-device," *IEEE Trans. Electron Devices*, vol. ED-21, pp. 504–515, Aug. 1974.

[11] M. J. Adams, "Rate equations and transient phenomena in semiconductor lasers," *Opt. Electron.*, vol. 5, pp. 201–215, Mar. 1973.

[12] K. Konnerth and C. Lanza, "Delay between current pulses and light emission of a gallium arsenide injection laser," *Appl. Phys. Lett.*, vol. 4, pp. 120–121, 1964.

[13] P. R. Selway, A. R. Goodwin, and G. H. B. Thompson, "Heterostructure injection lasers," in *Festkörperproblems*, vol. 14, H. J. Queisser, Ed. Vienna, Austria: Braunschweig, 1974, pp. 119–152.

[14] E. Pinkas, B. I. Miller, I. Hayashi, and P. W. Foy, "GaAs-$Al_xGa_{1-x}As$ double heterostructure lasers–Effect of doping on lasing characteristics of GaAs," *J. Appl. Phys.*, vol. 43, pp. 2827–2835, June 1972.

[15] P. Russer and H. Hillbrand, private communication.

[16] P. Brosson, E. S. Pinheiro, N. B. Patel, and J. E. Ripper, "Dynamics of electrons in heavily doped GaAs," in *Proc. 12th Int. Conf. Physics of Semiconductors* (Stuttgart, Germany, 1974), pp. 1104–1108.

Suppression of Intensity Self-Pulsations in CW Junction Lasers by Frequency-Selective Optical Feedback

THOMAS L. PAOLI, MEMBER, IEEE, JOSÉ E. RIPPER,
A. C. MOROSINI, AND N. B. PATEL, MEMBER, IEEE

Abstract—**Suppression of the self-induced intensity pulsations from CW junction lasers has been achieved by operating the laser with frequency-selective optical feedback. The feedback is achieved by optically coupling a diffraction grating to a laser mirror. The feedback suppresses all longitudinal modes except one or two and thereby eliminates the mode interactions necessary for sustained optical pulsing. The experimental results directly support the previously proposed model for self-induced optical pulsing in semiconductor lasers.**

SELF-INDUCED pulsations in the output intensity have been reported for both homostructure junction lasers operating continuously at liquid-nitrogen temperatures [1] and double-heterostructure (DH) lasers operating continuously at room temperature [2]. Such optical pulsations have been attributed [3] to the excitation of the relaxation oscillations of the laser through the nonlinear mixing of three or more longitudinal modes in the active medium. Consequently, self-pulsations by this mechanism can occur only in the presence of several longitudinal modes. In this paper, we experimentally confirm this conclusion by demonstrating that suppression of all but one or two modes in a self-pulsing junction laser leads directly to elimination of the intensity pulsations. Mode suppression is achieved by optically coupling a diffraction grating to the laser.

The lasers used in the present work were all stripe-geometry diodes fabricated from either GaAs-AlGaAs DH material grown by liquid-phase epitaxy or GaAs homostructure material with shallow junctions made by Zn diffusion. For the DH lasers, the current-confining stripes were formed with the technique of proton bombardment [4], while stripes in the homostructure diodes were defined by the metallic contacts [5]. All stripes were nominally 12 μm wide. Lasers were 380 μm long and had cleaved uncoated facets. Each laser was bonded to a metallized copper stud for continuous operation at room or liquid-nitrogen temperature. The copper studs were beveled on each side to allow unobstructed emission of light from both mirrors of the laser.

Frequency-selective optical feedback was applied to a laser by optically coupling one mirror of the diode to a diffraction grating through a microscope objective (numerical aperture = 0.8, focal length ≈ 4 mm) as shown schematically in Fig. 1.

Manuscript received December 9, 1974; revised January 27, 1975. This work was accomplished while one of the authors (TLP) was visiting the Instituto de Fisica, Universidade Estadual de Campinas, Campinas, Brazil.

T. L. Paoli is with Bell Laboratories, Murray Hill, N.J. 07974.

J. E. Ripper, A. C. Morosini, and N. B. Patel are with the Instituto de Fisica, "Gleb Wataghin," Universidade Estadual de Campinas, Campinas, Brazil.

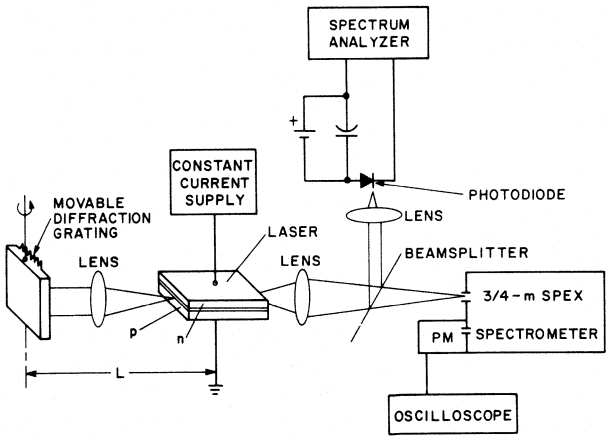

Fig. 1. Schematic diagram of system used to provide frequency-selective optical feedback to a self-pulsing junction laser and to observe simultaneously the optical spectrum and time variation of the light intensity. The spectrometer is equipped with a rotating diffraction plate synchronized with the oscilloscope.

The grating was ruled with 590 lines/mm, blazed for 7500 Å, and positioned at a variable distance L from the laser. With the laser and grating properly aligned, only light in a narrow band of optical frequencies was reflected back into the active region. For the DH lasers the orientation of the grating and laser was as shown in Fig. 1, where the ruling is perpendicular to the junction. This orientation avoided the critical alignment required in the customary arrangement [6] where the rulings are parallel to the junction plane. The frequency selectivity obtained with this type of optical feedback applied to nonpulsing DH lasers has been demonstrated previously [7]. However, the alignment is not so critical with homostructure lasers because of their wider waveguide perpendicular to the junction plane. Consequently, for these lasers the parallel orientation of grating and laser was utilized to achieve a narrower bandwidth for the reflectivity. The center wavelength of the grating reflectivity was reproducibly tuned by rotating the grating angle about an axis perpendicular to the junction plane of the DH lasers and about an axis parallel to the junction of the homostructure diodes.

The time variation of the laser intensity was monitored by focusing a portion of the light emitted from the second laser mirror into a fast photodiode coupled to a microwave spectrum analyzer. Simultaneously, the remainder of the output was used to observe the optical spectrum of the light with a grating spectrometer equipped with a rotating diffraction plate [8]. In this way, the effect of the grating on the optical spectrum and the intensity pulsations were observed in real time.

A typical example of the effect produced by coupling the grating to a self-pulsing DH junction laser is shown in Fig. 2. The top portion of part (a) of this figure is the optical spectrum of the laser light obtained without the grating and shows the multimode emission characteristic [2], [3] of lasers undergoing self-induced intensity pulsations. The fundamental (630 MHz) and first harmonic (1260 MHz) of the intensity pulsations, as observed with the photodiode and spectrum analyzer, are shown in the top half of Fig. 2(b).

With the grating optically coupled to the laser and properly aligned, the dispersion of the grating produced an optical feedback which was frequency selective. As a result, the optical spectrum was narrowed as indicated in the lower portion of Fig. 2(a). The width of this spectrum corresponds to at most two longitudinal modes and was determined primarily by the grating. In this case, the grating was positioned at $L \approx 28$ cm, but the experimental results were not critically dependent on this distance. Simultaneous with the reduction of the number of oscillating modes, the intensity pulsations were eliminated, as shown by the lower microwave spectrum in Fig. 2(b). The weak signal in this spectrum has a frequency (1040 MHz) corresponding to twice the frequency separation ($c/2L$) of cavity resonances formed by the grating and the diode face and probably originates in beats between modes of the external cavity.

Similar results were obtained with homostructure lasers. As shown in Fig. 3, the intensity pulsations were completely suppressed when the optical feedback from the grating induced oscillation in a single longitudinal mode of the laser. As is evident from a comparison of Figs. 2 and 3, the optical spectra obtained with the homostructure lasers were somewhat narrower than those obtained with the DH lasers. This result is probably due to the narrower bandwidth of the reflectivity obtained with the parallel orientation of grating and homostructure laser as compared to that obtained with the perpendicular arrangement used with the DH laser.

Results similar to those shown in Figs. 2 and 3 were also obtained as the bandwidth selected by the grating was tuned from one side of the optical spectrum to the other. However, as the suppression of the majority of the modes was reduced as a result of tuning to the wings of the optical spectrum, the amplitude of the pulsation was increased. In addition, the observed suppression was not dependent on the distance L between the laser and grating.

The suppression of the pulsations obtained with frequency-selective feedback contrasts markedly with the enhancement and locking produced by feeding back all frequencies in the laser output. The nonselective feedback reinforces all lasing modes of the internal cavity and thereby enhances the mode interactions producing the self-pulsations [3]. Furthermore, modes of the external cavity are phase locked (with a frequency spacing equal to the pulse rate) in groups centered about the internal cavity mode frequencies [9]. As previously reported [10], nonselective optical feedback narrows the pulses and pulls the pulse rate to a frequency greater than the self-induced rate. The pulling is always to frequencies higher than the self-induced rate because the feedback signal is actually a trigger pulse which must arrive before the laser spontaneously emits a pulse in order to be effective. This behavior

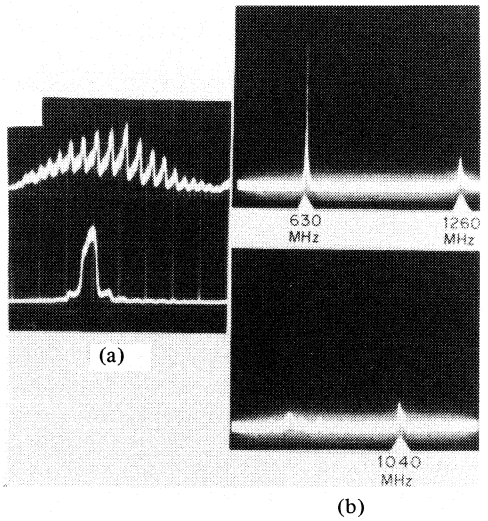

Fig. 2. (a) Optical spectra and (b) intensity-modulation spectra obtained from a continuously operating stripe-geometry DH junction laser. For the upper half of (a), the laser is operated *without* external feedback and exhibits self-induced intensity pulsations as indicated by the intensity spectrum shown in the top half of (b). For the lower traces in (a) and (b), the laser is operated *with* a diffraction grating optically coupled to the laser.

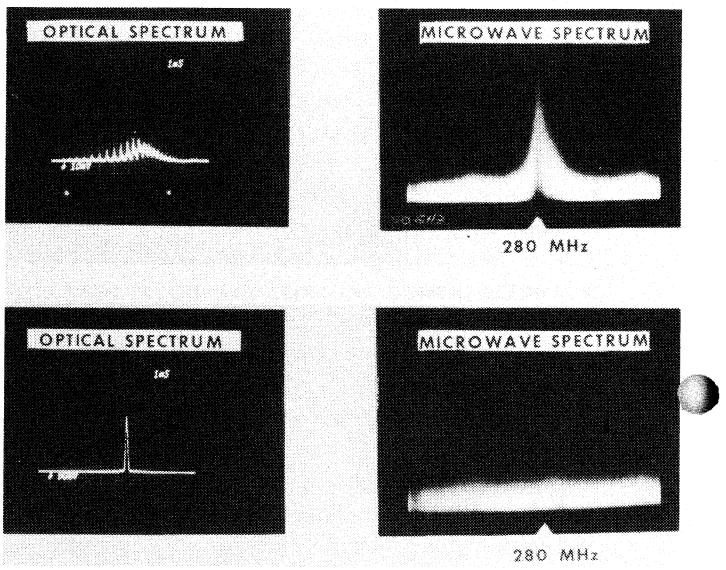

Fig. 3. Optical spectra and intensity-modulation (microwave) spectra obtained for a stripe-geometry homostructure junction laser operating continuously at 77 K. For the upper half of the figure, the laser is operated *without* feedback and exhibits self-induced intensity pulsations at 280 MHz as indicated by the microwave spectrum. For the lower traces, the laser is operated in a single longitudinal mode selected by optically coupling the diffraction grating to the laser. The microwave spectrum shows no evidence of any modulation of the laser intensity. The laser current is 1.3 times threshold.

is illustrated in Fig. 4 by the spectral display of the pulse rate obtained with optical feedback from a mirror positioned at various distances L from the laser. As the distance L is decreased from L_0 + 9.7 cm to L_0 + 0.9 cm ($L_0 \approx 75$ cm), the pulse rate ν_P moves continuously higher according to the relation $\nu_P = N(c/2L)$, where N is an integer and c is the speed of light. However, when the optical-feedback signal becomes less than the minimum required for locking (at $L \approx L_0$), the

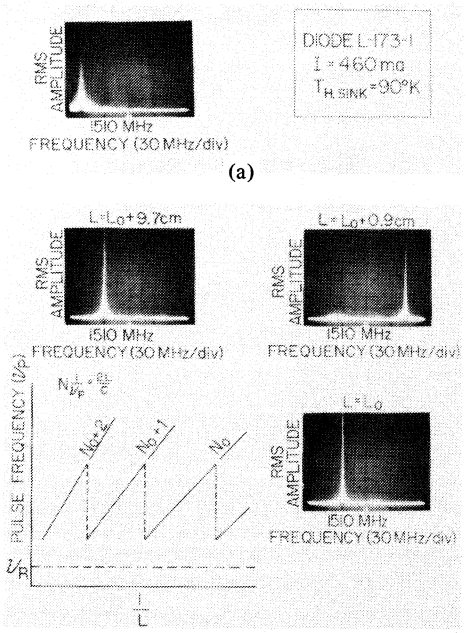

Fig. 4. Experimentally observed frequency pulling produced by the optical feedback of self-induced intensity pulsations from a continuously operating GaAs homostructure junction laser. (a) Without feedback. The pulses were spontaneously generated at a rate of 1390 MHz. (b) With feedback. The laser was operated with the reflection of the pulsing light from an external mirror focused back into the laser. The mirror was placed a distance L away from the laser diode with the distance L_0 approximately equal to 75 cm.

pulse rate changes discontinuously to a lower frequency corresponding to $(N-1)(c/2L)$. With further decreases in L, the process repeats itself as illustrated in Fig. 4.

The experimental results demonstrate that self-induced pulsations of the intensity from a CW junction laser are eliminated when the number of oscillating longitudinal modes is reduced to one or two. Consequently, the present experiments suggest that frequency-selective feedback may be a useful technique to eliminate self-pulsations when an unmodulated optical beam is desired. In addition, these observations support the previous proposal [3] that the interaction of several longitudinal modes is required to establish self-induced pulsations in some semiconductor lasers.

Acknowledgment

The authors wish to thank the GaAs Laser Department at Bell Laboratories, Murray Hill, N.J., for providing some of the lasers used in this work, L. A. D'Asaro for a critical reading of the manuscript, and Telecomunicacões Brasileiras S.A. for their support.

References

[1] T. L. Paoli and J. E. Ripper, "Optical pulses from CW GaAs injection lasers," *Appl. Phys. Lett.*, vol. 15, pp. 105–107, Aug. 1969.

[2] J. E. Ripper and T. L. Paoli, "Optical self-pulsing of junction lasers operating continuously at room temperature," *Appl. Phys. Lett.*, vol. 18, pp. 466–468, May 1971.

[3] T. L. Paoli and J. E. Ripper, "Coupled longitudinal mode pulsing in semiconductor lasers," *Phys. Rev. Lett.*, vol. 22, pp. 1085–1088, May 1969.

[4] J. C. Dyment, L. A. D'Asaro, J. C. North, B. I. Miller, and J. E. Ripper, "Proton-bombardment formation of stripe-geometry heterostructure lasers for 300 K CW operation," *Proc. IEEE* (Lett.), vol. 60, pp. 726–728, June 1972.

[5] J. C. Dyment, "Hermite-Gaussian mode patterns in GaAs junction lasers," *Appl. Phys. Lett.*, vol. 10, pp. 84–86, Feb. 1967.

[6] J. A. Rossi, S. R. Chinn, and H. Heckscher, "High-power narrow linewidth operation of GaAs diode lasers," *Appl. Phys. Lett.*, vol. 23, pp. 25–27, July 1973, and references contained therein.

[7] T. L. Paoli and J. E. Ripper, "Single longitudinal mode operation of CW junction lasers by frequency-selective optical feedback," *Appl. Phys. Lett.*, vol. 25, pp. 744–746, Dec. 1974.

[8] R. H. Roldan, "Rapid-scan spectroscopy with a refractor plate as the scanning device," *J. Sci. Instrum.*, vol. 40, p. 1388, 1969.

[9] J. E. Ripper and T. L. Paoli, "Mode configurations in second-order mode-locked lasers," *IEEE J. Quantum Electron. (Part I of Two Parts)*, vol. QE-8, pp. 74–79, Feb. 1972.

[10] T. L. Paoli and J. E. Ripper, "Frequency stabilization and narrowing of optical pulses from CW GaAs junction lasers," *IEEE J. Quantum Electron. (Special Issue on Semiconductor Lasers)*, vol. QE-6, pp. 335–339, June 1970.

A Comprehensive Model for Q Switching in Semiconductor Lasers

BEN THOMAS, M. J. ADAMS, AND STEPHAN GRÜNDORFER

Abstract—**By combining a carrier concentration-dependent loss term with our earlier time-dependent saturable absorption loss term we have produced a comprehensive theory for Q switching which successfully accounts for the results so far reported. The concentration-dependent loss term shows a superlinear dependence with current due to the decrease of real guiding at the p-n junction. This increase in loss, however, reaches a maximum and shows a slight decrease at higher concentrations due to the onset of weak imaginary guiding.**

I. Introduction

THE transient effects of long time delays and internal Q switching in semiconductor lasers are by now well documented [1]-[8], [12]. Since our ideas on long time delays have already been reported [5]-[7], this paper will be concerned with the Q-switching mechanism. The effect is observed in lasers which also show long time delays, and previous theories have attributed Q switching to the saturable absorption process involved in the time delays. A recent review [8] highlighted the unsatisfactory state of the theories for Q switching, and in this paper we will show that the additional effects of optical confinement are necessary for a satisfactory account.

Our theory of long time delays [5], [6] involved saturable absorption via energy states in an impurity band tail not in thermal equilibrium with the main part of the conduction band. This theory was successful in providing an explanation for both the current and temperature dependence of long time delays and was also used to predict certain spectral changes in the light output. A subsequent experimental search for and successful observation of these spectral changes provided further confirmation of the model [7]. During the setting up of the model it became apparent that the different current and temperature dependences of long time delays and Q switching indicated the presence of two distinct processes and also that our saturable absorption model as it stood could not provide a satisfactory explanation for Q switching. We therefore considered in detail the current and temperature dependence of the loss and gain necessary to explain Q switching and concluded that a superlinear dependence of loss with current was required and that such a dependence was provided by a consideration of optical confinement [9], [10], [16]. Combining the saturable absorption process with the mechanism resulting from the effects of optical confinement produces a comprehensive model which provides an explanation for long time delays [7], [8], H-pulsing (discussed in detail in this issue) [9], and Q switching [16].

Manuscript received November 25, 1974; revised February 6, 1975. This research was supported by the Science Research Council. This paper incorporates work done under a CVD contract, and is published by permission of the Ministry of Defence (Procurement Executive). The original ideas for this theory were presented at ESSDERC 1973, Munich, Germany, September 18-21, 1973. This paper was presented at the IEEE Semiconductor Conference, Atlanta, Ga., November 18-20, 1974.

B. Thomas is with the Department of Applied Physics and Electronics, University of Wales Institute of Science and Technology, Cardiff, Wales.

M. J. Adams is with the Electro-Optics Group, Plessey Radar, Cowes, Isle of Wight, England.

S. Gründorfer is with the Institut für Angewandte Physik und Ludwig Boltzmann Institut für Festkörperphysik, Universität Wien, Strudlhofg 4, A-1090, Wien, Austria.

II. Experimental Details and Results

The laser diode driving and light-recording system described previously [5], [7] was used for these measurements and in order to avoid appreciable heating effects pulse lengths between 20 and 180 ns were used at low duty cycles. To minimize transient effects from irregularities in the current the 50-Ω line producing the rectangular current pulse (rise time <1 ns) was carefully matched to the laser mounted in the familiar pill-type package. Various injection lasers for this study were kindly selected and provided by P. R. Selway and A. R. Goodwin, Standard Telecommunications Laboratories, Harlow, England; we shall illustrate the agreement between experimental and theoretical results by showing the characteristics for laser type H139.

This is a GaAs-$Ga_xAl_{1-x}As$ single-heterostructure laser fabricated in the usual way by liquid-phase epitaxy on a Si-doped substrate having an electron concentration of 3.2×10^{18} cm^{-3}. This laser had an active-region width of $d = 1.3$ μm and showed a characteristic critical temperature $T_c = 220$ K marking the onset of saturable absorption and long time delays. It is necessary at this stage to stress the importance of distinguishing between the various time delays. Thus the intrinsic time delay (ITD) is required to produce population inversion at temperatures $T < T_c$; the long time delays (LTD's) are introduced by the saturable absorption mechanism at temperatures $T > T_c$ (both ITD and LTD decrease with increasing current), and abnormal time delays (ATD) increase with increasing current leading to the effect of Q switching. For temperatures below and above T_c, single-heterostructure laser H139 had a difference between ITD and LTD at $I/I_{th} = 1.2$ of the order of 4 ns, and because this could easily be masked by uncertainties in I_{th}, a method of determining I_{th} from the onset of a single mode on the spontaneous background was used [7].

The increasing time delay due to the ATD at higher currents and temperatures characteristic of Q-switching lasers is easily seen in Fig. 1. These data are summarized in Fig. 2(a) for ratios of $I/I_{th} = 1.2$ and 1.5, and Fig. 2(b) shows the threshold-current curves for lasing and Q switching. Incidentally, this curve is very similar to the threshold-current curves produced

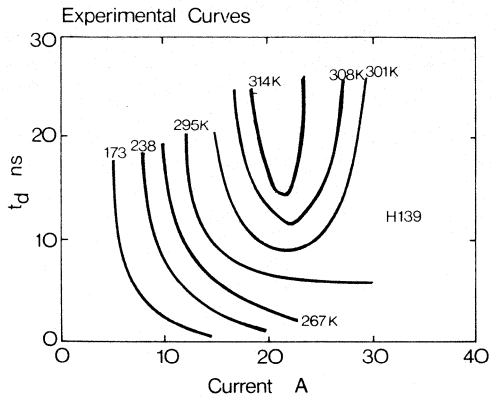

Fig. 1. Time delay t_d versus current I measured at various temperatures.

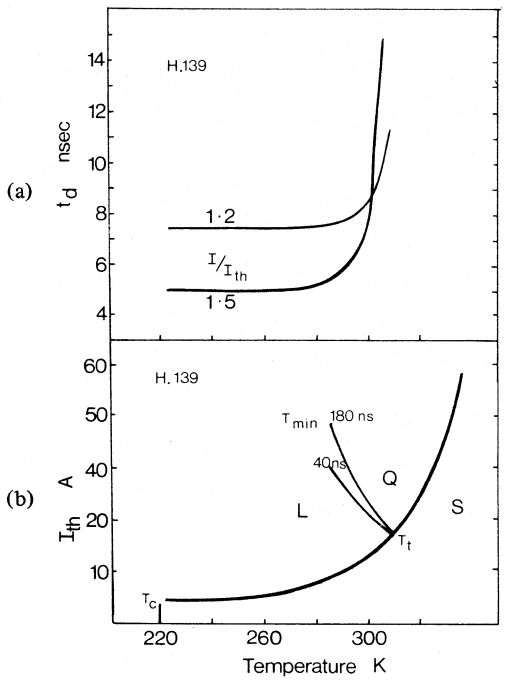

Fig. 2. (a) Time delay t_d versus temperature T curves for ratios of I/I_{th} (1) 1.2, (2) 1.5 showing rapid increase in t_d due to the ATD. (b) Characteristic threshold-current curve separating the spontaneous, lasing, and Q-switching regions. T_t = 320 K, the triple-point temperature where the three regions meets. $T_{min} \simeq 270$ K, the minimum temperature at which Q switching can occur. The difference between the effect of 40 and 180-ns pulses is indicated.

for H-pulsing lasers [9]. To characterize the Q switching we have considered two temperatures: T_t the triple-point temperature at the point where the spontaneous, lasing, and Q-switching regions meet (320 K for H139), and T_{min} the minimum temperature at which Q switching can occur (about 270 K for H139). Both these temperatures, however, are slightly affected by the length of the current pulse and show a decrease for shorter pulses. The critical temperature T_c is in general distinct from T_t and T_{min}.

III. The Comprehensive Model

Our theory of saturable absorption for LTD's has been discussed in considerable detail previously [5], [6], and we have presented a detailed consideration of optical confinement and waveguiding efficiency elsewhere in this issue [9]. To combine the two processes we construct a total laser loss term as the sum of a time-dependent loss plus a carrier concentration-dependent loss. The expression becomes

$$\text{total loss} \propto \frac{bN_t}{An + 1/\tau_t}\left\{\frac{1}{\tau_t} + An \exp\left(-\left(An + \frac{1}{\tau_t}\right)t\right)\right\} + (u + vn^2) \quad (1)$$

where the meaning of the symbols and the numerical values for a typical GaAs-$Ga_xAl_{1-x}As$ single-heterostructure laser used in the calculations are given in Table I.

The variation of this total loss coefficient with increasing carrier concentration n is shown by the curved traces in Fig. 3 where the temporal variation of the total loss is indicated by the curve sequence a, b, c. Curve a shows loss versus n for time $t = 0$, i.e., when the laser is switched on, curve b shows the loss versus n after a time t = 100 ns into the current pulse, and curve c shows the loss versus n after infinite time, i.e., CW operation. The straight lines T_1, T_2, and T_3 show the gain as

TABLE I

Symbol	Meaning	Value
τ_e	lifetime for conduction-band electrons	1 ns
τ_t	lifetime for tail electrons in deep tail-states	100 ns
u	current-independent optical loss	2×10^{11} s^{-1} (24 cm^{-1})
v	effect of electron concentration on the loss	2×10^{-24} cm^6 s^{-1}
A	rate coefficient for conduction band to tail states transitions	2×10^{-11} cm^3 s^{-1}
bN_t	rate coefficient for absorbing transitions into tail states	10^{12} s^{-1}
c	coefficient in gain expression	65 cm^3 s^{-1} K^3
d	active-region width	1.6 μm

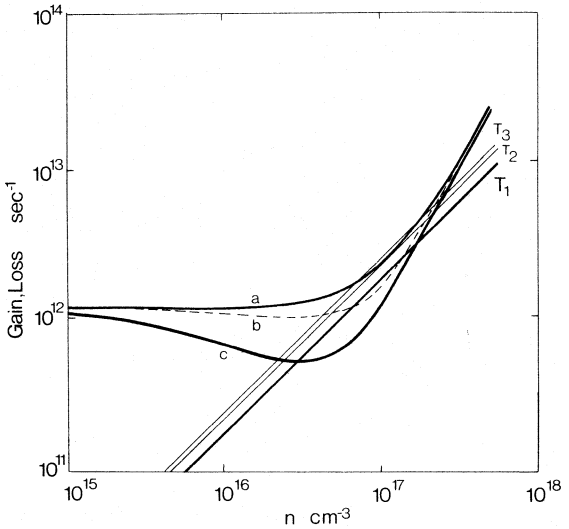

Fig. 3. Theoretical total loss coefficient a, b, and c, and laser gain T_1, T_2, and T_3 as functions of carrier concentration. Curves a, b, and c show the total loss after times $t = 0$, $t = 100$ ns, and $t = \infty$ into the current pulse, respectively. Straight lines T_1, T_2, and T_3 show the gain for different temperatures with $T_1 > T_2 > T_3$. The small time dependence of the gain due to heating effects is not shown.

a linear function of carrier concentration n for three different temperatures with $T_1 > T_2 > T_3$. The gain is independent of time except for a small heating effect not shown here.

The bold gain line T_1 does not intersect curve a and it is clear there is always a delay time for this temperature; the delay is represented in this picture by the lowering of the loss curve with time. For the $t = 100$-ns loss curve we have two intersections with the gain line T_1 indicating the two carrier concentrations at which a delay of 100 ns will appear on the time delay versus current curves. For the two intersections between curve c ($t = \infty$) and line T_1, the lower point gives the lasing threshold for CW operation and the upper the Q-switching threshold for this situation.

More detailed results, however, were obtained using the three rate equations for $T > T_c$ in [6, eqs. (8)-(10)] by assuming a specific temperature dependence for the gain and replacing the photon lifetime term $(1/\tau_p)$ by the concentration-dependent loss term $(u + vn^2)$. Solving the equations as outlined in [6] gave the following expression for time delay as a function of carrier concentration n and temperature T:

$$t_d = \frac{1}{\left(An + \frac{1}{\tau_t}\right)} \ln \left\{ \frac{bN_t An}{\left(An + \frac{1}{\tau_t}\right)\left(\frac{cn}{T^3} - u - vn^2 - \frac{bN_t}{(An\tau_t + 1)}\right)} \right\}. \tag{2}$$

A threshold value for the electron concentration in this case was also obtained by solving the equation

$$\frac{cn}{T^3} = u + vn^2 + \frac{bN_t}{(An\tau_t + 1)}. \tag{3}$$

Solutions of (2) for time delay t_d versus carrier concentration n at various temperatures and using again the typical values for the single-heterostructure laser (Table I) are shown in Fig. 4. The striking resemblance of these curves to the experimentally recorded curves in Fig. 1 is immediately apparent, including the ATD leading to Q switching. Furthermore, solutions for (2) and (3), Fig. 5(a) and (b), show good agreement with the curves of Fig. 2(a) and (b) recorded for the single-heterostructure laser H139 which has a triple-point temperature $T_t = 320$ K. The overall form of the threshold current versus temperature characteristic including the boundary between lasing and Q switching is also in good agreement with other experimental observations published for single-heterostructures [4], [11], homostructures [3], [12], and for electron-beam-pumped lasers [13]. Although the curves of Fig. 5(b) were calculated assuming an infinitely long pulse, further calculations for a 20-ns pulse showed a movement of T_t and the boundary between lasing and Q switching towards lower temperatures. This is in agreement with the results for 40 and 180-ns pulses in Fig. 2(b) and with the results reported in [3].

In spite of the excellent agreement between theory and experiments over the current densities so far considered, our theory has not covered the experimental results reported for very high current densities in single heterostructures [4] and in stripe-geometry GaAs lasers [3], [12]. These results show

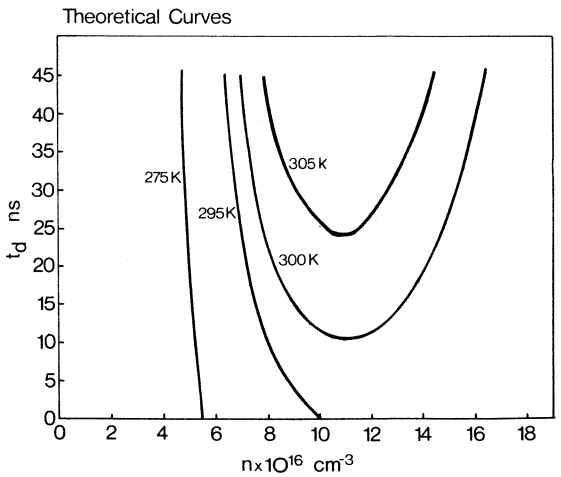

Fig. 4. Theoretical curves for time delay t_d versus carrier concentration n at various temperatures obtained as solutions to (2) using the parameters from Table I.

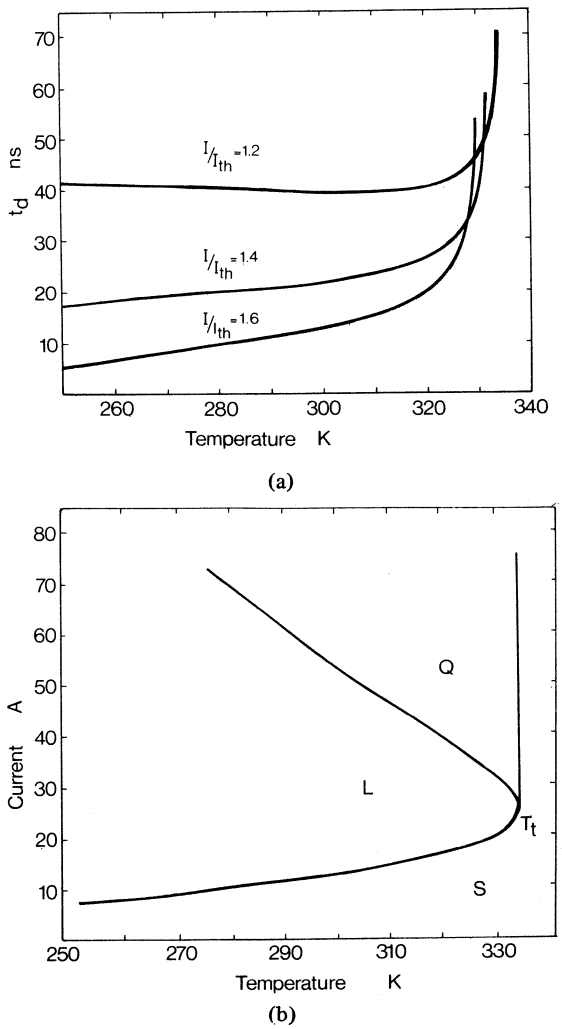

Fig. 5. (a) Theoretical curves obtained from computation of (2) giving time delay as a function of temperature for various ratios of I/I_{th}. (b) Equation (3) giving the threshold- and boundary-current curves versus temperature for the spontaneous, lasing, and Q-switching regions. $T_t \simeq 335$ K.

that the *Q*-switching region is bounded from the lasing region by a further curve on the high-current side of the *Q* region on the current-temperature plots. This produces a characteristic S loop of the boundary between *Q* switching and normal lasing.

Extending our theory into this regime is relatively simple if we consider the complete concentration-dependent loss curve in the high carrier-concentration region [10]. The superlinearity of the loss curve with current arises due to a decrease in the efficiency of real guiding on the n-side of the active lasing region. This superlinear increase, however, reaches a maximum and the loss decreases to a constant relatively high level at high current densities. Taking into account the complex dielectric-constant change which should be used [10] shows that the breakdown of real guiding is now replaced by a weaker, but nevertheless important imaginary guiding due to high absorption losses in the n-type region.

A qualitative consideration of the theory and of the intersection of the complete loss-gain curves at higher current densities, Fig. 6(a), results in a threshold-current characteristic with temperature shown schematically in Fig. 6(b). The boundary between lasing and *Q* switching does indeed map out an S-shaped curve in agreement with experimental observations [3], [4], [12]. This S shape provides a further characteristic parameter for the *Q* switching, namely the minimum temperature $T_{\min}$ representing the low-temperature limit of the *Q*-switching region. A simple analysis reveals that this temperature is given by

$$T_{\min} = \left[\frac{c^2}{4v(u + bN_t)}\right]^{1/6}. \tag{4}$$

$T_{\min}$ is also dependent to a certain extent on pulse length, but for an infinite pulse and the values from Table I, $T_{\min} = 276$ K was obtained.

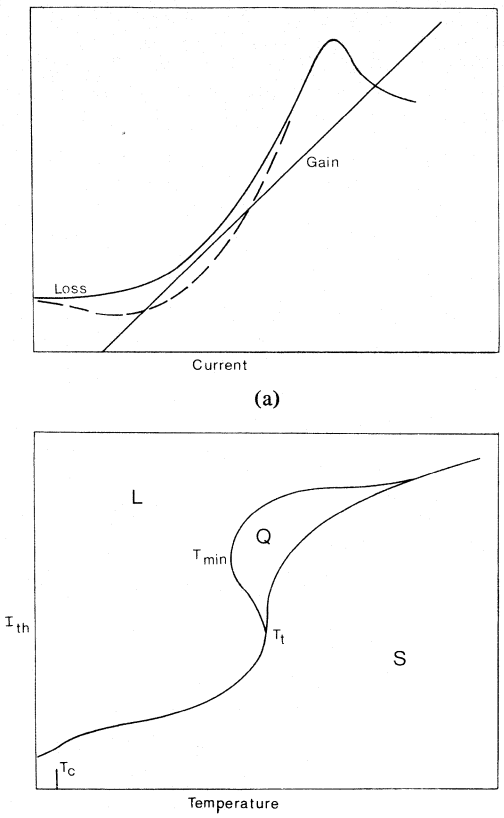

Fig. 6. Schematic diagrams showing (a) the concentration-dependent loss versus *n* curve obtained by taking into account both the real and imaginary waveguiding for a 3-layer dielectric slab; and (b) the characteristic S curve obtained for the boundaries separating the spontaneous, lasing, and *Q*-switching regions in the threshold current versus temperature plot from a qualitative consideration of the gain–loss curves in (a).

IV. Conclusions

The good agreement between the theory and published experimental results, together with its comprehensive nature, makes this model for transient effects particularly attractive. Further support for confidence in the model was provided by solving the full rate equations using a Runge-Kutta numerical procedure and integration in the time domain. The results of these detailed calculations were in good agreement with the simplified calculations and showed the complicated processes occurring during LTD's and *Q* switching. On switching off the current for laser action the solutions showed that the photon density depletes with a lifetime of the order of picoseconds, the electron concentration in the conduction band decreases with a lifetime of nanoseconds, whilst the electron concentration in band tails has a long lifetime of the order of microseconds. For the *Q*-switching region, on the other hand, although n and n_t decrease as before, the photon density shows a peak of half-width ~100 ps occurring after a period of less than 200 ps from the switchoff. The width of the pulse is in agreement with experimental estimates of the width from observations.

It is clear that an explanation for the spectral emission for *Q* pulses [5] will now be provided by a consideration of band filling and the detailed wavelength variation of the concentration-dependent loss curve. It is also clear to us that the theory could provide an explanation for the interesting wavelength-dependent time delays [14], [15] reported for lasers operated with an external grating cavity. This explanation would rely upon the wavelength variation of the concentration-dependent loss term. What is certain is that the theory has an important rôle in the design of lasers for low thresholds, high-temperature operation, minimal time delays, and with no *Q* switching [17]. In the event of *Q* switching not being entirely undesirable for an optical-communication application, the theory may indicate that in order to achieve extremely short pulses *H*-pulsing lasers [9] modulated at high repetition rates should be used at currents which minimize the initial pulse during switchon.

Acknowledgment

The authors wish to thank P. R. Selway, A. R. Goodwin, and G. H. B. Thompson both for supplying the lasers used in this work and for many stimulating and valuable discussions.

References

[1] G. E. Fenner, "Delay of the stimulated emission in GaAs laser diodes near room temperature," *Solid-State Electron.*, vol. 10, pp. 753–764, Aug. 1967.

[2] J. E. Ripper, "Time delays and *Q* switching in junction lasers: I–Theory," *IEEE J. Quantum Electron. (Part I of 2 Parts)*, vol. QE-5, pp. 391–395, Aug. 1969.

[3] J. E. Ripper and J. C. Dyment, "Time delays and *Q* switching in

junction lasers: II–Computer calculations and comparison with experiment," *ibid.*, pp. 396–403, Aug. 1969.
[4] E. A. Ulmer, Jr., and I. Hayashi, "Internal Q switching in GaAs–$Ga_xAl_{1-x}As$ heterostructure lasers," *IEEE J. Quantum Electron. (Special Issue on Semiconductor Lasers)*, vol. QE-6, pp. 297–299, June 1970.
[5] M. J. Adams *et al.*, "Time delays and Q switching in homostructure and heterostructure injection lasers," *IEEE J. Quantum Electron. (Part II of Two Parts: Special Issue on 1972 IEEE Semiconductor Laser Conference)*, vol. QE-9, pp. 328–337, Feb. 1973.
[6] S. G. Gründorfer and M. J. Adams, "Theoretical considerations of time delays in semiconductor lasers," *IEEE J. Quantum Electron.*, vol. QE-9, pp. 814–819, Aug. 1973.
[7] B. Thomas, D. Mistry, and C. F. L. Davies, "The temperature dependence of spectral emission from semiconductor lasers showing long time delays," *IEEE J. Quantum Electron.*, vol. QE-10, pp. 401–405, Apr. 1974.
[8] J. E. Ripper and J. A. Rossi, "Delays and Q switching in semiconductor lasers–Still an open question," *IEEE J. Quantum Electron.*, vol. QE-10, pp. 435–441, Apr. 1974.
[9] S. Gründorfer, M. J. Adams, and B. Thomas, "H-pulsing: A transient effect in GaAs/$Ga_xAl_{1-x}As$ injection lasers," this issue, pp. 532–537.
[10] M. Cross and M. J. Adams, "Effects of doping and free carriers on the refractive index of direct-gap semiconductors," *Opto-Electron.*, vol. 6, pp. 199–216, 1974.
[11] Y. Unno, M. Yamamoto, and S. Iida, "Internal Q switching in $Ga_{1-x}Al_xAs$–GaAs heterostructure lasers," *Japan. J. Appl. Phys.*, vol. 9, pp. 1181–1182, Sept. 1970.
[12] J. E. Ripper and J. C. Dyment, "Internal Q switching in GaAs junction lasers," *Appl. Phys. Lett.*, vol. 12, pp. 365–367, June 1968.
[13] A. Masuyama, M. Kawabe, K. Masuda, and S. Namba, "Internal Q switching in n-type GaAs lasers under electron beam excitation," *Japan. J. Appl. Phys.*, vol. 10, pp. 1281–1282, Sept. 1971.
[14] J. A. Rossi, H. Heckscher, G. E. Stillman, and S. R. Chinn, "Time delays in external-cavity-controlled GaAs/$Ga_xAl_{1-x}As$ single-heterostructure diode lasers," *Appl. Phys. Lett.*, vol. 23, pp. 254–256, Sept. 1973.
[15] J. A. Rossi, H. Heckscher, and S. R. Chinn, "Threshold, spectral and output power characteristics of GaAs/$Ga_xAl_{1-x}As$ single-heterostructure diode lasers," *Appl. Phys. Lett.*, vol. 23, pp. 257–259, Sept. 1973.
[16] S. Gründorfer, M. J. Adams, and B. Thomas, "New theory of internal Q switching in semiconductor lasers," *Electron. Lett.*, vol. 10, pp. 354–356, Aug. 1974.
[17] H. T. Minden and R. Premo, "High temperature GaAs sing heterojunction laser diodes," *J. Appl. Phys.*, vol. 45, pp. 4520–4527, Oct. 1974.

H-Pulsing: A Transient Effect in GaAs/$Ga_xAl_{1-x}As$ Injection Lasers

STEPHAN GRÜNDORFER, M. J. ADAMS, AND BEN THOMAS

***Abstract*—"H-shape" light pulses, i.e., short light pulses superimposed on the beginning and end of a steady laser emission, are observed from pulsed single-heterostructure lasers operated at particular temperatures and currents. At a slightly higher current the steady laser emission is extinguished leaving the two peaks. The effect, observed in single-heterostructure lasers fabricated on low doped n-type substrates, was studied for various driving currents and laser temperatures.**

A theoretical study involving computations with standard laser parameters has resulted in light-output curves having a similar form. The rate equations computed contained a superlinear carrier-concentration-dependent loss term as well as the term for the emission of spontaneous photons into the laser mode. Loss of optical confinement due to carrier-induced changes in refractive index is proposed as an explanation for the superlinear carrier-dependent loss.

Manuscript received November 25, 1974; revised February 6, 1975. This work was supported in part by the Science Research Council and in part by a CVD contract, and is published by permission of the Ministry of Defence (Procurement Executive). The original idea for the model was first presented at ESSDERC 1973, Munich, Germany, September 18–21, 1973. This paper was presented at the IEEE International Semiconductor Laser Conference, Atlanta, Ga., November 18–20, 1974.

S. Gründorfer is with the Institut für Angewandte Physik und Ludwig Boltzmann Institut für Festkörperphysik, Universität Wien, Strudlhofg 4, A-1090, Wien, Austria.

M. J. Adams is with the Electro-Optics Group, Plessey Radar, Cowes, Isle of Wight, England.

B. Thomas is with the Department of Applied Physics and Electronics, University of Wales Institute of Science and Technology, Cardiff, Wales.

I. Introduction

THE suggested application of semiconductor lasers in, for example, optical-communication systems, makes a thorough study of their time-dependent behavior a necessity [1]–[3]. Indeed, for any kind of pulse modulation, long time delays between the beginning of the current pulse and the onset of stimulated light emission or a Q-switching effect at the end of the current pulse are both undesirable in an uncontrolled form. In order to prevent these effects or, on the other hand, to make use of them, it is necessary to develop a comprehensive theory for them [4]–[7]. In the process of investigating the transient effects of GaAs/$Ga_xAl_{1-x}As$ single-heterostructure injection lasers we have observed a further effect which has to be considered in addition to long time delays and Q switching. The effect consists essentially of two sharp short light pulses, one occurring immediately after the beginning of the current pulse and the other one immediately after the end of the current pulse [20] and has been termed "H-pulsing" by us. The light spikes are superimposed on a steady laser-emission pulse. Since the second light pulse looks very much like the familiar Q-switching pulse, the first light pulse was initially thought to be due to distortions at the beginning of the current pulse, e.g., overshooting. Careful examination of current rise and decay characteristics has

revealed, however, that irregularity in the driving-current pulse can be excluded as being the source of the initial light pulse. An explanation of *H*-pulsing, therefore, must be sought in terms of the properties of the injection lasers showing the effect, rather than by an external agency.

The behavior of the effect was studied over a range of temperatures and injected currents for a variety of lasers. The effect was easily observed in single-heterostructure lasers fabricated on relatively low doped ($\simeq 2.5 \times 10^{18}$ cm^{-3}) n-type substrates with active-region thickness d, less than the optimum active-region thickness $d \simeq 2$ μm, i.e., in lasers for which the optical confinement of the electromagnetic wave is poor [8], [9]. It was not observed, however, in double-heterostructure lasers, where the optical confinement is always good [8]. In the lasers investigated, *H*-pulsing occurred over a narrow range of temperatures and injected current levels. The minimum current I_H for the effect to show was always greater than the threshold value I_{th}, and I_H/I_{th} showed a slight increase with decreasing temperature.

II. Experimental Details and Results

This effect was brought to our attention by P. R. Selway and A. R. Goodwin of the Standard Telecommunications Laboratories, Harlow, England, who also supplied the lasers used in this study. Although we initially considered that the peak at the beginning of the light-output pulse could be due to an overshoot effect of the driving current into the laser, an examination of the current rise and decay characteristics, together with careful matching of the laser into the 50-Ω line, dispelled this idea. In addition, *H*-pulsing was observed over a narrow temperature range in lasers fabricated on a relatively low doped n-type substrate with a narrow active-region width d.

Typical examples of lasers showing the effect are the following: Type H34 Te-doped substrate electron concentration 2.7×10^{18} cm^{-3}, $d = 1.9$ μm and Type H64 Si-doped substrate electron concentration 2.6×10^{18} cm^{-3}, $d = 1.8$ μm. The *H*-pulse form, together with the extinction of the steady output for a slightly higher value of the 40-ns current pulse, is shown in Fig. 1 for laser H34. A light-output pulse having

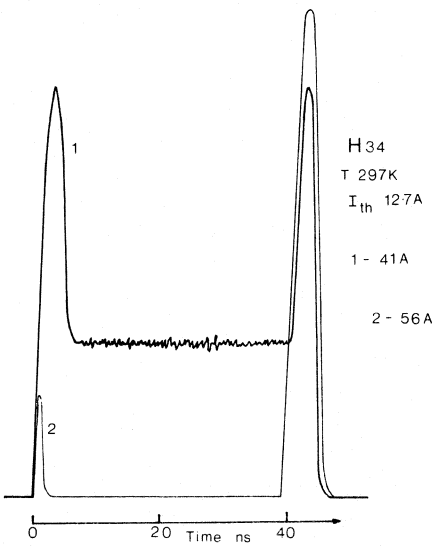

Fig. 1. Recording of the light-output pulse versus time showing the *H*-pulse effect 1) and the extinguishing of the steady laser output 2) at a slightly higher current.

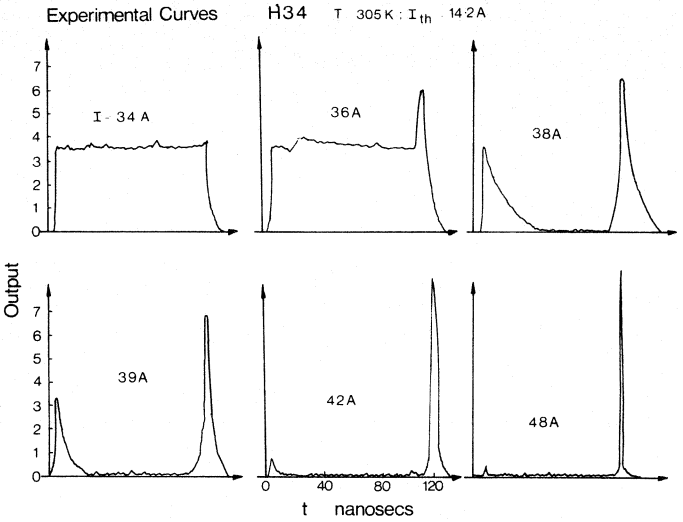

Fig. 2. High output pulses versus time recorded for a series of increasing current pulse values.

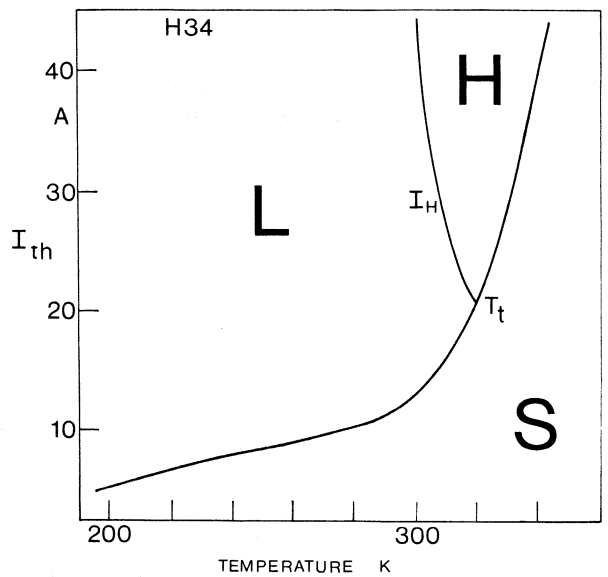

Fig. 3. Threshold current versus temperature characteristic showing the lasing, *H*-pulsing, and spontaneous regions. The I_H boundary between lasing and *H*-pulsing gives the minimum current at which *H*-pulsing will occur at a particular temperature.

similarities to those shown in Fig. 1 has also been reported by Kressel [20]. The complicated variation in form of the pulse with increasing current is shown in Fig. 2, whilst the measurement of the variation of lasing threshold current (I_{th}) with temperature resulted in a characteristic curve (Fig. 3) very similar to those recorded for internal Q switching [4], [7]. A triple-point temperature (T_t) as well as I_H the boundary current separating the lasing and *H*-pulsing regions are also seen in the figure. The laser did not show a temperature T_c characteristic of the onset of long time delays. All the measurements on the lasers previously reported were carried out using driving and detection equipment described previously [4].

III. Mathematical Development of the Model

The appropriate way to investigate time-dependent behavior in semiconductor lasers is a rate-equation approach [1]-[5]. For a single-mode approximation, these rate equations for the

electron concentration in emitting states n, and the photon density in the lasing mode N, can be written as

$$\frac{dn}{dt} = P - \frac{n}{\tau_e} - g(n)N \tag{1}$$

$$\frac{dN}{dt} = g(n)N - L(n)N + r_{\text{spon}} \tag{2}$$

where P is the pumping rate for the electrons associated with the injected current, τ_e is the electron lifetime in the emitting states, and $g(n)$ is proportional to the peak of the gain-frequency curve for the laser. $L(n)$ is the optical loss of the laser, under normal conditions taken constant, and r_{spon} is the spontaneous emission of photons into the lasing mode. The normal transient behavior of this system is the buildup of n to the threshold value n_{th}, found as usual by neglecting the spontaneous emission and equating the gain and the loss under steady-state conditions

$$g(n_{\text{th}}) = L(n_{\text{th}}). \tag{3}$$

This threshold is reached in a short time delay (t_d), necessary to build up the population inversion, which is found by integrating (1) whilst neglecting the last term, since the photon concentration is considered negligible before the onset of lasing. The time delay is given by [10]

$$t_d = \tau_e \ln\left[\frac{P}{P - P_{\text{th}}}\right] \tag{4}$$

where $P_{\text{th}} = (n_{\text{th}}/\tau_e)$. When lasing commences, the electron concentration n saturates at n_{th}, and all further pumping power goes into output by increasing the photon density N. In order to achieve a light spike instead of a continuous light output, however, the optical loss must become bigger than the gain shortly after threshold is reached and lasing starts.

It is easily seen that one way to achieve such a system is by assuming a loss which is not constant but varies with a higher power of n than the gain. Fig. 4(a) shows such a situation, where the gain is assumed to be linear in n, i.e., $g(n) = an$, while the loss is assumed to be quadratic in n, i.e., $L(n) = u + vn^2$. Here a contains the square of the matrix element for the stimulated emission, u is the optical loss before onset of the current pulse (i.e., for $n \simeq 0$), and v is a small factor taking the influence of the electron concentration on the loss into account.

Assuming a rectangular current pulse the electron concentration builds up with a time constant essentially given by τ_e. From Fig. 4(a) and (b) it can be seen that as the electron concentration increases with time, n_1 is reached, and lasing can commence. But the electron concentration "overshoots" due to the fact that in (1) the third term on the right-hand side becomes big only after some time when the photon density has increased enough. If n_1 and n_2 are not too far apart, and the pumping rate P is big enough, the electron concentration will increase beyond n_2, the loss therefore will again be higher than the gain, and the photon concentration will decrease forming the short initial light pulse.

After the end of the current pulse, on the other hand, when the electron concentration is decaying, one again passes through the region where the gain is bigger than the loss,

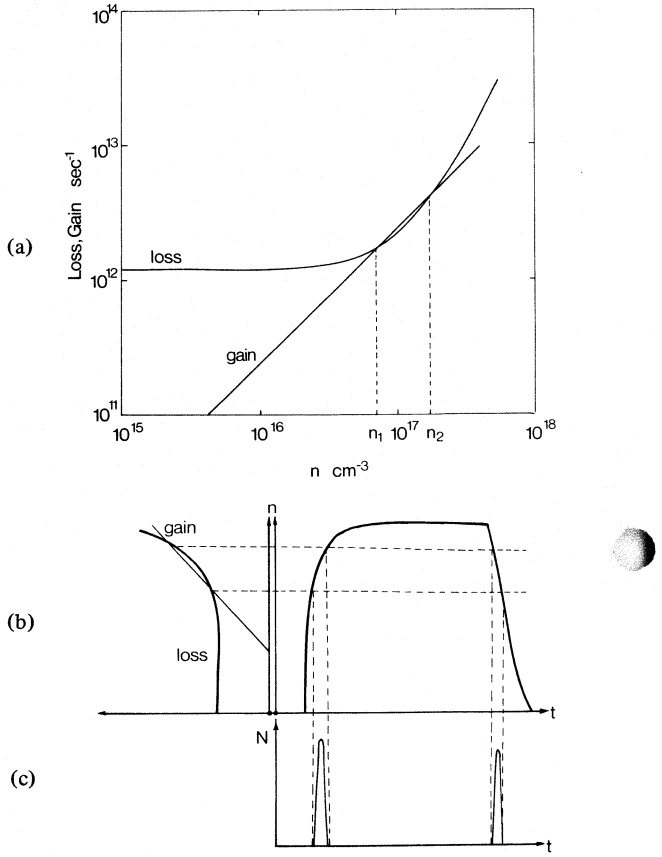

Fig. 4. (a) Curves showing linear gain and superlinear loss dependence with electron concentration. (b) Combination of the loss and gain curves from (a) and the variation of electron concentration with time for a rectangular current input pulse. (c) Light-output pulses produced as the electron concentration passes through regions with gain > loss.

producing a short light pulse as shown schematically in Fig. 4(c).

The two spikes are dependent on the rise and fall time of the electron concentration, as can be seen from Fig. 4(b) and (c). The bigger the current, the steeper will be the rise in the region between n_1 and n_2, i.e., the shorter and smaller the first light pulse will be in comparison with the second one, as can also be seen from the experimental results. Also, if the current pulse cannot be assumed rectangular, this will have an influence on the width and rise time of the light spikes, since it alters the rate of rise and decay of the electron concentration.

In the numerical integration of (1) and (2), the spontaneous emission r_{spon} is not neglected (as is normally the case), since it seems to be essential to introduce the right boundary conditions. If the photon density were assumed to be zero (as is done by neglecting the spontaneous emission), then it cannot build up in the very short time available when the electron concentration is between n_1 and n_2. Due to the spontaneous emission, however, there is always a finite concentration of photons present, which facilitates buildup of the photon population in a very short time.

IV. Discussion of the Superlinear Loss

Various forms for the gain function $g(n)$ have been proposed in the literature, including a linear variation with carrier concentration n [11]-[13], logarithmic variation with n [1], and more complicated forms of functional dependence on n [14],

[2], [15]. In the present instance we will choose for simplicity a linear dependence, as was used in previous rate-equation calculations [5]. It remains to discuss the assumption of the superlinear dependence of the laser loss on the carrier concentration. It should be emphasized that any superlinear dependence will produce similar results for a linearly dependent gain function; our assumption of a quadratic dependence was used for simplicity and merely served to illustrate the behavior. The crucial point is that the loss should vary with a higher power of n than the gain, so that two points of intersection are possible, as is illustrated in Fig. 4(a). The physical reason for this superlinear loss function can be found in the reduced waveguiding, and hence higher diffraction losses which occur with increasing carrier concentration, i.e., injected current density, in single-heterostructure lasers [6], [9].

The effect occurs only in single-heterostructure lasers with low substrate doping and an active-layer thickness of less than some optimum value, $d \lesssim 2\ \mu$m. Fig. 5 illustrates schematically the electromagnetic-confinement features of the single-heterostructure laser at (a) low and (b) high current levels. For low currents, the refractive-index distribution is modeled by a 3-layer dielectric slab with the index of the active layer at about 3.6, that of the passive p^+-AlGaAs layer at about 3.4, and that of the passive n-layer at about 3.59. These figures are typical for single-heterostructure lasers and have been calculated for typical doping levels and have been successfully used in previous waveguiding studies of these devices [8]. The corresponding distribution of electromagnetic-field intensity in the device is also shown in Fig. 5(a) and is seen to be slightly asymmetric, as one would expect, showing a deeper penetration of the light into the n-type layer than into the p^+-side.

For high currents [Fig. 5(b)], we must allow for the effect of increased electron concentration on the refractive index of the semiconductor. In the passive regions, the effect of current density will be negligible, since the carrier densities are determined principally by the doping levels via the requirement of charge neutrality. For the active region, however, at high current densities the electron concentration will increase and produce a consequent decrease in the refractive index. The index change occurs in two ways: 1) by the plasma interaction, and 2) by the Kramers-Kronig relationship from the change in absorption edge with increasing carrier concentration [9]. It has been shown [15] that the second of these mechanisms is dominant and that the refractive-index variation depends linearly on carrier concentration to a good approximation, as

$$\Delta\mu \simeq -k\Delta n \tag{5}$$

where $\Delta\mu$ is the change in refractive index due to a change Δn in electron concentration in the active region, as is shown in Fig. 6(a). The coefficient k can be found from the following:

1) experimental measurements of wavelength shift below threshold [16];
2) the Kramers-Kronig analysis of Thompson [15];
3) a series expansion of the expression for refractive index deduced by Adams and Cross [8], [9];
4) the far-field measurements of Selway *et al.* [23].

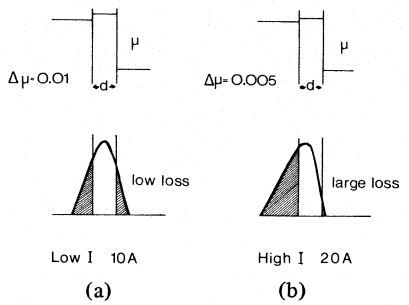

Fig. 5. Refractive index μ and optical losses for a single heterostructure. Diagram indicates the refractive-index levels of a 3-layer-slab dielectric waveguide of n-type passive region, p-type active-region thickness d, and $Ga_xAl_{1-x}As$ region. $\Delta\mu$ gives the refractive-index step between n-type and p-type regions. The penetration of the electromagnetic-field intensity into the passive regions is also indicated. (a) Low current, $\Delta\mu = 0.01$. (b) High current, $\Delta\mu = 0.005$.

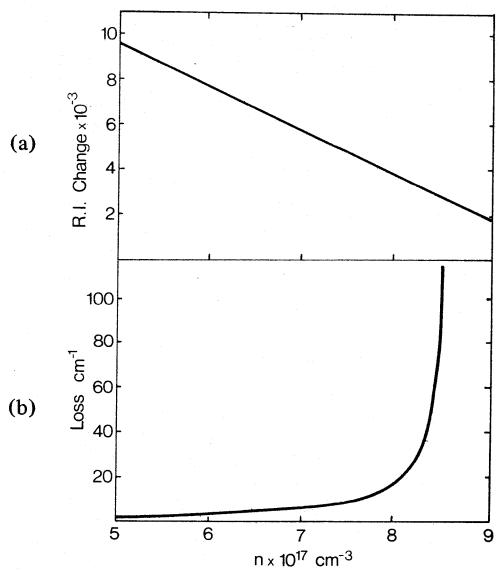

Fig. 6. (a) Variation of refractive index with electron concentration $\Delta\mu = -k\Delta n$. (b) Variation of diffraction loss with electron concentration for the 3-layer-slab dielectric waveguide (Fig. 5).

The values found from 1)-4) for GaAs differ by, at most, a factor of 2, and the value to be used here is that calculated as in 3), viz., $k = 2 \times 10^{-20}$ cm^3.

Returning to Fig. 5, we see that the reduction of refractive index in the active region as a result of increased current density leads to much worse confinement of the electromagnetic field than for low currents. This is manifested by the penetration of the light into the n-region, with an associated large increase of diffraction loss. $\Delta\mu$ follows the form given by (5), and this has been used in waveguiding calculations for the 3-layer dielectric slab of the type described in [17] to compute the variation of diffraction loss α with n. The result shown in Fig. 6(b) is a steep rise in α as the electron concentration reaches the critical value corresponding to equality of the refractive indices in the n-type passive and p-type active regions.

This provides the mechanism for our assumed superlinear variation of laser loss with injected-electron concentration or, equivalently, current density.

The current-dependent loss mechanism discussed here is

clearly only important when the refractive-index values in the n-type passive and p-type active regions are fairly close, say less than 0.01 of each other. Since n-type index decreases for increasing doping levels, very high current density would be needed for the effect to occur for medium or highly doped substrates. It is therefore clear that the mechanism is only important for low substrate doping levels, especially near the critical value of $1\text{-}2 \times 10^{18}$ cm^{-3}, where waveguiding can break down completely in single-heterostructure lasers. This is entirely in agreement with the experimental fact that H-pulsing only occurs in single-heterostructure lasers whose substrate doping level is low.

V. Theoretical Results and Comparison with Experiment

For the comparison of the experimental results given in Section II with our model, a numerical integration of the rate equations (1) and (2) was performed. For the computation the gain and loss functions were assumed as indicated: $g(n) = an$ and $L(n) = u + vn^2$. Using (3) one finds the threshold value of n as being the lower one of the two possible solutions

$$n_{th} = n_1 = \frac{a - \sqrt{a^2 - 4uv}}{2v} \tag{6}$$

while

$$n_H = n_2 = \frac{a + \sqrt{a^2 - 4uv}}{2v} \tag{7}$$

is the minimum electron concentration to be reached if H-pulsing is to occur. The temperature dependence of both n_{th} and n_H (associated with I_{th} and I_H, respectively, and shown for laser H34 in Fig. 3) is easily understood when one takes the temperature dependence of the gain function $g(n)$ into account. In this case a cannot be assumed constant anymore but is a function of temperature. From a theoretical treatment of threshold-current temperature dependence [18], [19] or from empirical expressions for this dependence, one can find a specific temperature dependence for $g(n)$. Since a simple T^{-3} dependence is frequently observed at higher temperatures, it seems to be appropriate to assume

$$g(n) = an = \frac{cn}{T^3}. \tag{8}$$

In Fig. 4(a) an increase in temperature is resembled by a bodily shift of the $g(n)$ line to lower values. It can now easily be seen that as the temperature increases n_{th} increases, while n_H decreases, as was also observed experimentally (Fig. 3).

For the computer calculation of the current dependence we used for simplicity a fixed temperature (represented by a = constant) and the following parameters for gain and loss: $a = 2.01 \times 10^{-5}$ cm^3 s^{-1}, $u = 10^{12}$ s^{-1}, and $v = 1.01 \times 10^{-22}$ cm^6 s^{-1}. The other parameter values in (1) and (2) were: $\tau_e = 10^{-9}$ s and $r_{spon} = 5 \times 10^4\, n(\text{cm}^{-3}\ \text{s}^{-1})$.

Fig. 7(a)-(d) show computed solutions for a rectangular current pulse with a 7-ns pulsewidth and different pumping rates P/P_{th} or I/I_{th}, respectively, as indicated in the figure.

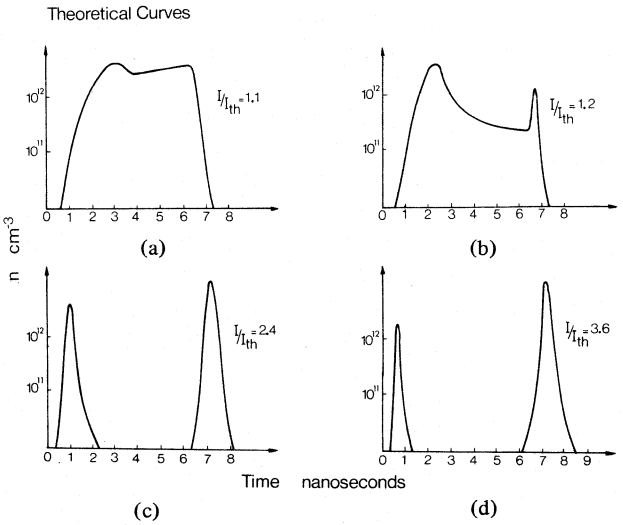

Fig. 7. Theoretical light-output pulses versus time calculated for increasing ratios of I/I_{th} using parameters indicated in the text.

For increasing pumping rates the sequence of Fig. 7(a)-(d) illustrates the following:

1) the shortening of the delay before the first light spike, in accordance with the behavior anticipated from (4);
2) an increase of the delay between the end of the current pulse and the onset of the second light spike;
3) the constant-decay rate of the electrons, and consequently similar width and height of the second light pulse;
4) the decrease of both height and width of the first pulse, as discussed in Section IV.

All of points 2)-4) are in good agreement with the experimental observations of H-pulsing, Fig. 2.

VI. Conclusion

The excellent agreement between the results of our theoretical model and the results of our observations of H-pulsing is indisputable. On the other hand, the value of our explanation lies in its use in laser design for avoiding the effect or alternatively utilizing it to the best advantage. Thus the H-pulsing effect is obviously avoided in the excellent optical confinement achieved in double-heterostructure lasers and in high-power single-heterostructure lasers fabricated on n-doped substrates doped to higher electron concentrations, e.g., laser-type AGA 251/1, [21]. Single-heterostructure lasers with n$^+$-doped regions grown by liquid-phase epitaxy also show superior optical confinement [22]. It appears to us, however, that it may be possible to use the model in designing a laser with superior high-frequency characteristics, since 1) the photon lifetime involved with the loss of optical confinement is measured in picoseconds and 2) the long time delays due to saturable absorption are not present in H-pulsing lasers. The light pulse at the beginning of the current pulse is easily suppressed by rapid current rise time.

A further value of the model is described in [7], where it has been combined with our earlier saturable absorption model to produce a comprehensive theory of long time delays, H-pulsing, and Q switching. Saturable absorption is considered

to be absent from *H*-pulsing lasers since lasing occurs immediately from the conduction band and there are insufficient states in the band tail of the low doped n-type substrate to produce appreciable saturable absorption.

ACKNOWLEDGMENT

The authors wish to thank P. R. Selway, A. R. Goodwin, and G. H. B. Thompson of Standard Telecommunication Laboratories for supplying lasers and for many useful discussions. They also wish to thank W. Kleinert of the Institut für Mathematik, Technische Hochschule, Vienna, Austria, for useful discussions and Prof. E. Bukovics for the use of a hybrid computing system.

REFERENCES

[1] N. G. Basov, "Dynamics of injection lasers," *IEEE J. Quantum Electron. (Special Issue: 1968 International Quantum Electronics Conference: Part II)*, vol. QE-4, pp. 855–864, Nov. 1968.

[2] T. L. Paoli and J. E. Ripper, "Direct modulation of semiconductor lasers," *Proc. IEEE (Special Issue on Optical Communication)*, vol. 58, pp. 1457–1465, Oct. 1970.

[3] M. J. Adams, "Rate equations and transient phenomena in semiconductor lasers," *Opto-Electron.*, vol. 5, pp. 201–215, Nov. 1973.

[4] M. J. Adams *et al.*, "Time delays and *Q* switching in homostructure and heterostructure injection lasers," *IEEE J. Quantum Electron. (Part II of Two Parts: Special Issue on 1972 IEEE Semiconductor Laser Conference)*, vol. QE-9, pp. 328–337, Feb. 1973.

[5] S. Gründorfer and M. J. Adams, "Theoretical considerations of time delays in semiconductor lasers," *IEEE J. Quantum Electron.*, vol. QE-9, pp. 814–819, Aug. 1973.

[6] S. Gründorfer, M. J. Adams, and B. Thomas, "New theory of internal *Q*-switching in semiconductor lasers," *Electron. Lett.*, vol. 10, pp. 354–356, Aug. 1974.

[7] B. Thomas, M. J. Adams, and S. Gründorfer, "A comprehensive model for *Q* switching in semiconductor lasers," this issue, pp. 528–532.

[8] M. J. Adams and M. Cross, "Electromagnetic theory of heterostructure injection lasers," *Solid-State Electron.*, vol. 14, pp. 865–883, Sept. 1971.

[9] M. Cross and M. J. Adams, "Effects of doping and free carriers on the refractive index of direct-gap semiconductors," *Opto-Electron.*, vol. 6, pp. 199–216, 1974.

[10] K. Konnerth and C. Lanza, "Delay between current pulse and light emission of a gallium arsenide injection laser," *Appl. Phys. Lett.*, vol. 4, pp. 120–121, Apr. 1964.

[11] G. J. Lasher, "Analysis of a proposed bistable injection laser," *Solid-State Electron.*, vol. 7, pp. 707–716, Oct. 1964.

[12] H. Statz, C. L. Tang, and J. M. Lavine, "Spectral output of semiconductor lasers," *J. Appl. Phys.*, vol. 35, pp. 2581–2585, Sept. 1964.

[13] H. Haug, "Quantum-mechanical rate equations for semiconductor lasers," *Phys. Rev.*, vol. 184, pp. 338–348, Aug. 1969.

[14] M. J. Adams, "A theory of oscillations in the output of GaAs junction lasers," *Phys. Status Solidi*, vol. 1, pp. 143–152, Dec. 1970.

[15] G. H. B. Thompson, "A theory of filamentation in semiconductor lasers including the dependence of dielectric constant on injected carrier density," *Opto-Electron.*, vol. 4, pp. 257–310, Aug. 1972.

[16] M. R. Matthews, R. B. Dyott, and W. P. Carling, "Filaments as optical waveguides in GaAs lasers," *Electron. Lett.*, vol. 8, pp. 570–572, Nov. 1972.

[17] W. W. Anderson, "Mode confinement and gain in junction lasers," *IEEE J. Quantum Electron.*, vol. 1, pp. 228–236, Sept. 1965.

[18] G. Lasher and F. Stern, "Spontaneous and stimulated recombination radiation in semiconductors," *Phys. Rev.*, vol. 133, pp. A553–A563, Jan. 1964.

[19] M. J. Adams, "A simple approximation for high temperature properties of the injection laser," *Brit. J. Appl. Phys.*, vol. 2, pp. 1549–1553, Nov. 1969.

[20] H. Kressel, "Semiconductor lasers," in *Lasers*, vol. 3, A. K. Levine and A. J. DeMaria, Ed. New York: Marcel Decker, 1971, p. 72.

[21] B. Thomas, D. Mistry, and C. F. L. Davies, "The temperature dependence of spectral emission from semiconductor lasers showing long time delays," *IEEE J. Quantum Electron.*, vol. QE-10, pp. 401–405, Apr. 1974.

[22] H. T. Minden and R. Premo, "High-temperature GaAs single heterojunction laser diodes," *J. Appl. Phys.*, vol. 45, pp. 4520–4527, Oct. 1974.

[23] P. R. Selway, G. H. B. Thompson, G. D. Henshall, and J. E. A. Whiteaway, "Measurement of the effect of injected barriers on the p-n refractive index step in single heterostructure diode lasers," *Electron. Lett.*, vol. 10, pp. 453–455, Oct. 1974.

The Gain Profile and Time-Delay Effects in External-Cavity-Controlled GaAs Lasers

J. A. ROSSI, J. J. HSIEH, AND H. HECKSCHER

Abstract—**An external dispersive cavity is used to map out the gain profile of single-heterostructure (SH), double-heterostructure (DH), and large-optical-cavity (LOC) lasers. The variations in gain profile with dopant and device operating conditions are reported. With certain cavity arrangements, long time delays in DH devices are observed; this shows that saturable absorption can be present in these as well as in all other types of GaAs diodes. A model combining saturable absorption with a breakdown in optical guiding makes it possible to consistently interpret all reported time-delay data for GaAs diffused-junction (DJ) and SH diode lasers, including Q-switching and abnormal-delay effects. Finally, experiments where two gratings are used to oscillate a diode simultaneously at two different, independently variable frequencies are described.**

I. Introduction

TO REDUCE the large emission bandwidth and the large divergence found in most III-V compound diode lasers, several workers have utilized the operation of diodes in an external cavity (EC). By this method, some control over the longitudinal [1]-[4] or transverse [5] (or both) mode patterns is obtained; this has already proved useful for some applications [6]. This paper describes results obtained by operating GaAs heterostructure lasers in an EC. Specifically, the gain profile has been measured for single, double, and large-optical-cavity heterostructures with different active-region dopants and under different device operating conditions. We find that double-heterostructure (DH) diodes have a flat symmetric gain profile which can yield >300-Å tunable output from a single diode. In contrast, the single-heterostructure (SH) gain profile is quite asymmetric and is generally about 200 Å wide. In addition to these spectral data, we present new experimental results which show that long time delays can occur in DH and large-optical-cavity (LOC) lasers in which one of the diode end faces is antireflection (AR) coated. Since the coating lowers the intensity of the electromagnetic wave in the active region, the observation of delays in these structures is consistent with the saturable absorption model used to account for the long time delays observed in conventional (i.e., cleaved uncoated faces) SH and diffused-junction (DJ) lasers. We hypothesize that the delays in the conventional lasers occur because the intensity of the electromagnetic wave in the active region is lower in these structures than in uncoated DH lasers. We show that this reduced-intensity model is also consistent with other data, including the abnormal delay and Q-switching effects, reported for SH and DJ diodes. Finally, we briefly describe the operation of diodes in a double-grating cavity in which a diode can be forced to oscillate at two different, independently variable frequencies.

Manuscript received January 10, 1975; revised February 27, 1975. This work was supported by the Department of the Air Force.

The authors are with the Lincoln Laboratory, Massachusetts Institute of Technology, Lexington, Mass. 02173.

II. Previous Work on Time-Delay Effects

Because the EC gain-profile results which we will discuss also involve important time-delay effects, we will first briefly review the delay effects reported for conventional lasers with cleaved uncoated faces. Several workers [7]-[9] have shown that the time dependence of the laser emission from SH or DJ devices depends strongly on the operating temperature. When operated at temperatures below a critical temperature T_c, the time delay τ_d, between the application of the current pulse I and the onset of lasing follows the relation [10]

$$\tau_d = \tau_s \ln \frac{I}{I - I_{\text{th}}} \tag{1}$$

where τ_s is the injected carrier spontaneous lifetime and I_{th} is the threshold current. If we assume that the smallest controllable value of I/I_{th} is ~ 1.02, then for spontaneous lifetimes on the order of 1-2 ns, the observed value of τ_d should never be more than 4-8 ns. According to the literature, this is in fact the case, and (1) adequately describes the time dependence for SH [11] and DJ [7] diodes for $T < T_c$, and for DH and LOC diodes at all operating temperatures since no T_c has yet been reported for these structures [12], [13]. For temperatures above T_c, SH and DJ diodes show long time delays, typically $\tau_d \sim 20$-100 ns, and hence (1) was presumed to be invalid. The long delays were attributed to an absorption process which saturates at some time during the pulse [7], [14]. Fig. 1 summarizes these reported effects.

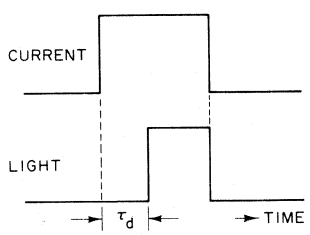

	$T < T_c$	$T > T_c$
DJ, SH	$\tau_d = \tau_s \ln I/I-I_{th} \lesssim 8$ nsec	$\tau_d \sim 50$-100 nsec
DH, LOC	$\tau_d = \tau_s \ln I/I-I_{th} \lesssim 15$ nsec	

Fig. 1. Summary of reported time-delay phenomena for DJ, SH, DH, and LOC laser diodes. The maximum values of τ_d for $T < T_c$ are computed by multiplying the spontaneous lifetime τ_s by the current overdrive factor, assuming $I = 1.02 I_{\text{th}}$.

There are four additional effects which are important for SH and DJ devices. First, for some diodes at or near T_c, the time delay increases when the current amplitude is increased [14], [15]. This effect has been called "abnormal delay" and typically exists over a small temperature or current interval. Second, for some diodes there is no emission during the current pulse, but a "Q-switched" light pulse occurs after the end of the pulse [9], [16]. Third, as T approaches T_c, I_{th} increases very rapidly [7], [9]. Fourth, as T approaches T_c, there is a considerable change in the temperature dependence of the lasing energy. For $T \ll T_c$, the rate of change of the lasing energy is ~ -0.4 me V/°C; but for temperatures near T_c, the rate is much smaller and, in some cases, may even be positive over a small temperature range before again returning to a negative rate [17]. (This spectral behavior is nicely illustrated in [17, fig. 2].) The significance of these four points will become evident in the discussion of EC results below.

III. Experimental Results

A. SH Devices

To map the gain profile for a device, a single-ended dispersive external cavity was used. In this arrangement described previously [3] and shown here schematically in Fig. 2, light emitted from a cleaved AR-coated face is collimated by a lens and dispersed by a diffraction grating. The diode light is reimaged in the focal plane of the lens, but spatially dispersed so that only a small wavelength interval is reincident on the diode active region for amplification and lasing. By rotating the grating, the feedback wavelength and hence the lasing wavelength can be changed. For measuring the time dependence of the emitted light, we used a wide-bandwidth oscilloscope in conjunction with either a silicon avalanche photodiode or a calibrated vacuum phototube; in either case the response time of the detection system was <1 ns. For spectral measurements, the emitted light was analyzed by a 1-m spectrometer (resolution ~ 0.2 Å). The infrared microscope shown in Fig. 2 was used for cavity alignment as well as for observations of the lasing pattern on the diode facet. Throughout this work, the diodes were operated at or above room temperature and were driven by a low duty cycle ($f \sim 100$ Hz) rectangular current pulse 100 ns long with a rise time of less than 1 ns.

Fig. 3 shows the curve of threshold current versus lasing energy, or gain profile, for an SH device operated at room temperature. The data were obtained by aligning the grating for operation at a certain photon energy $h\nu$ and increasing the current until lasing occurred. The grating was then rotated and the procedure repeated. For $h\nu < 1.365$ eV, the curve is double valued. For example, if the grating is lined up to operate at $h\nu = 1.360$ eV and the current is increased, lasing begins at ~ 6 A and stops at ~ 13.5 A. This feature is characteristic of all SH diodes we have examined.

Fig. 4 shows schematically the time dependence of the laser emission from these SH diodes. With the grating set to provide feedback at energy $h\nu_2$, the light-output pulse for three rectangular current pulses of different amplitudes ($I_A < I_B < I_C$) is shown by the right-hand portion of the figure. In this case, the light output follows the current according to (1), and little or no delay is observed. The amplitude of the light output increases as the current amplitude is increased (this is not indicated in the figure). If the grating is lined up to operate at $h\nu_1$, then as the current amplitude is increased a significant delay develops between the current pulse and the light-output pulse, until at I_C the light pulse is delayed almost to the end of the current pulse. For $I > I_C$, only spontaneous emission is observed. Thus, the gain profile is composed of two portions: a lower energy portion, characterized by a delay that increases

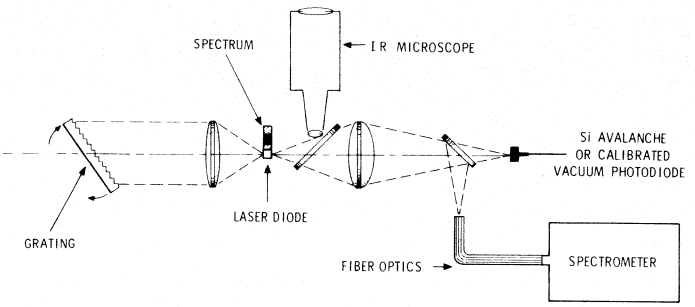

Fig. 2. Schematic illustration of the EC and associated detection apparatus used in this work.

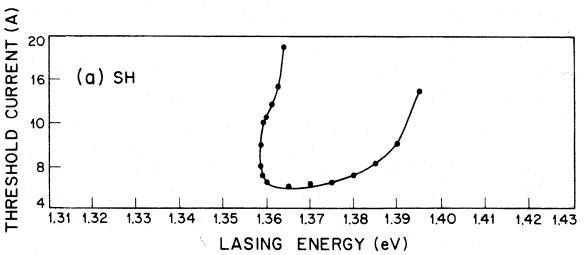

Fig. 3. Threshold current versus lasing energy for a typical SH diode operated pulsed (100 ns) at room temperature. (If the current pulse is only 50 ns, the left-hand branch of the curve is rotated clockwise.)

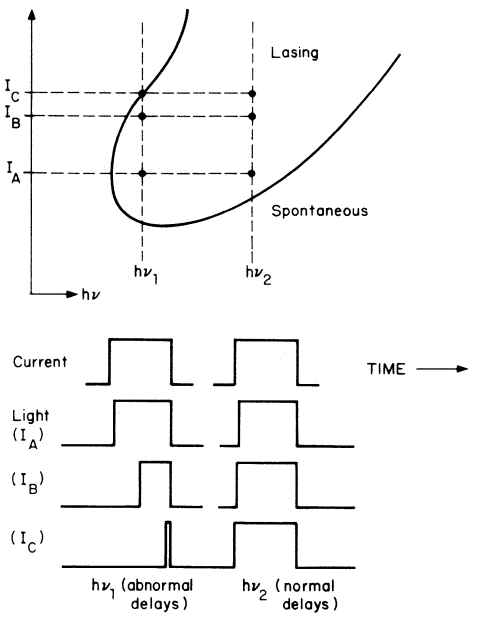

Fig. 4. Schematic of the SH gain profile showing the light output versus current ($I_A < I_B < I_C$) when the diode is lased at $h\nu_1$ or $h\nu_2$. For lasing at $h\nu_1$, the delay increases with increasing current (abnormal-delay effect), whereas at $h\nu_2$ the time-delay behavior is normal [described by (1)]. The change in amplitude of the light output is not indicated.

with increasing current, i.e., an abnormal-delay region; and a higher energy portion characterized by normal time behavior. At high injection levels the abnormal region monotonically moves into the higher energy portion.[1]

Fig. 5 shows the gain profiles for another SH at several different operating temperatures. At 20°C, the profile is similar to that shown in Fig. 3, having a "toe" region with abnormal delays and a region without these effects at higher energies. When the temperature is increased to 52°C, the entire curve shifts to higher currents and lower energy, as expected, but the low-energy portion moves only slightly, while the high-energy portion moves faster. The net effect is a significant decrease in the tuning width. Increasing the temperature to 60°C continues this trend, and in addition, causes the toe region to disappear. At this temperature a significant delay between the current pulse and the light output (20-30 ns at $I \simeq 1.5I_{th}$) is observed over the entire profile; however, this delay is "normal," since it does not increase with increasing current. In fact, in this temperature range the behavior of these diodes is typical of uncoated SH diodes as their temperature of operation approaches the transition temperature [9], [11]. A further increase in the temperature to 64°C results in a more symmetric gain profile and in an increase in the delay to about 40-50 ns measured at $1.5I_{th}$. In summary, as the temperature is increased, the gain profile moves to lower energy, the abnormal-delay region disappears, and a long delay is observed over the entire profile.

By examining the EC data it is possible to predict the behavior of an uncoated diode. For example, in Fig. 5 there is a minimum threshold current $(I_{th})_{min}$ at each temperature. If we plot $(I_{th})_{min}$ versus T for these and several other temperatures, we obtain the data shown in the inset. These data are obviously similar to reported data [9], [11] for the variation of I_{th} with temperature for SH and DJ devices: $(I_{th})_{min}$ increases sharply as T_c is approached. As another example, if we assume that an uncoated diode would lase at the energy for which $(I_{th})_{min}$ occurs, it follows that the rate of change of the lasing energy with temperature will first be negative, then approach zero, and perhaps even become positive, and finally be increasingly negative as $T \rightarrow T_c$, in qualitative agreement with the data in [17] discussed above.

B. LOC and DH Devices

In Fig. 6 we show the gain profiles for LOC and DH devices operated at room temperature. For these structures the gain profiles are fairly symmetric around a center energy which depends on the active-region dopant. Diodes from two different LOC wafers were measured. The gain profile centered at 1.375 eV was obtained for diodes made from a wafer whose active region was doped with both Zn and Si. The profile centered at ~ 1.355 eV was obtained for diodes with only Si doping in the active region. For DH diodes, changing from Zn and Si doping of the active region to heavy Si doping (1.5-

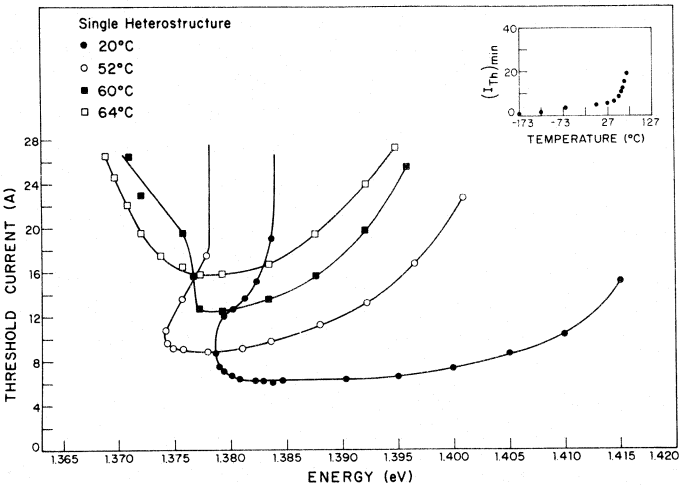

Fig. 5. The variation in the SH gain profile with temperature. Note that the abnormal-delay region (where lasing stops at sufficiently high currents) is eliminated at higher temperatures. The inset shows a plot of the minimum threshold current $(I_{th})_{min}$ needed for lasing at several different temperatures.

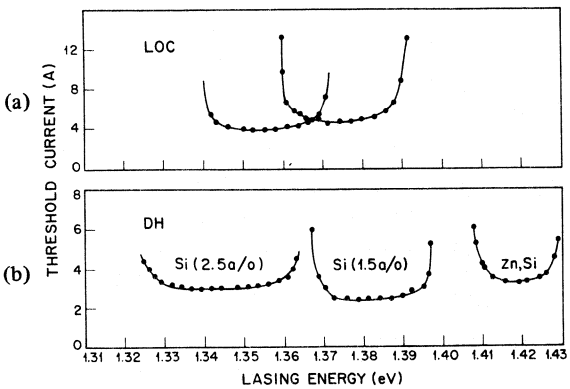

Fig. 6. Gain profiles for (a) LOC and (b) DH devices. Note the more symmetric appearance when compared to the SH gain profile (Fig.3). The different gain profiles were obtained by changing the active-region dopant.

atomic-percent Si in the solution used to grow the active layer) both broadens the tuning curve and shifts the centroid of the curve to a lower energy. Even heavier Si doping (2.5-atomic-percent Si in the solution) continues this trend, yielding diodes which may be continuously tuned over a 40-meV (300 Å) range.

For LOC or DH lasers there are no regions of the gain profile where the diode stops lasing as the current is increased. Also, for these structures, as the temperature is increased the whole tuning curve shifts to lower energy at a rate of ~ -0.4 meV/°C, as shown in Fig. 7. This rate is in good agreement with the reported shift of the bandgap with temperature [18].

In this section we report the observation of long time delays in DH and LOC devices. No such delays in devices of these types were observed in the studies discussed in Section II and summarized in Fig. 1. In Fig. 8 we have plotted the delay time τ_d versus current overdrive factor $\ln I/(I - I_{th})$ for two DH diodes made from the same wafer. The triangular points were taken on a conventional diode with cleaved uncoated faces ($R_1 = R_2 \simeq 0.3$). The variation is linear and the parameter τ_s

[1]According to the discussion in Section II, this means that the whole emission line is subject to a breakdown in guiding as $T \rightarrow T_c$. However, below T_c the portion of the gain profile subject to abnormal delays depends on the current density.

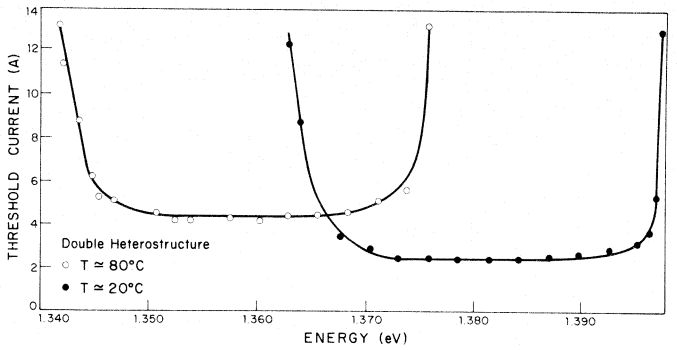

Fig. 7. The variation in the DH gain profile with temperature. The whole profile shifts to lower energy with increasing temperature at a rate ~−0.4 meV/°C.

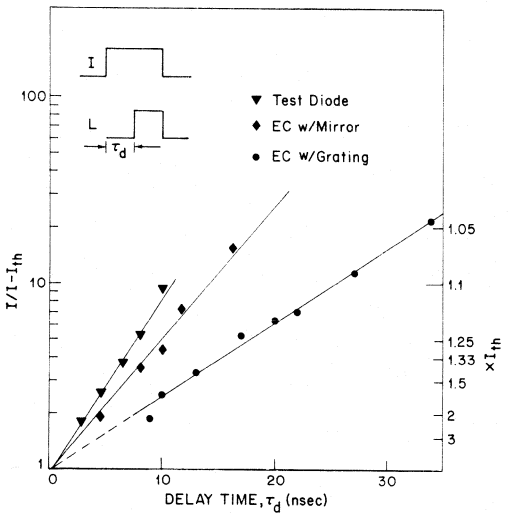

Fig. 8. The measured time delay between the current pulse and light-output pulse τ_d versus $I/(I - I_{th})$ for three different cavity configurations of a DH diode.

in (1) is 4.5 ns. All the uncoated diodes made from this wafer yield the same results to within experimental error, ± 1 ns. The rectangular points were taken on a diode with one face AR coated which was operated in an EC with a flat Au mirror as the back resonator face. Note that the data are shifted toward longer τ_d for the same value of $I/(I - I_{th})$, but the variation is still linear, with $\tau_s \sim 6$ ns. This trend continued when the Au mirror was replaced by a diffraction grating; for this case the data are represented by the circular points which again vary linearly, but with τ_s increased to ~ 11 ns.

Fig. 9 shows the same type of data for two LOC diodes. The square points were obtained from an uncoated diode (both faces cleaved, $R_1 = R_2 \simeq 0.3$). The data are linear with $\tau_s \simeq 3$ ns. The circular data points were obtained from a diode with one uncoated face and one coated face ($R_1 \simeq 0.3, R_2 \sim 0.01$). In this case the value of τ_s is increased to about 60 ns, well beyond the estimates of the injected carrier lifetime [12].

C. Double-Grating and Composite-Resonator Experiments

In this section we will briefly describe some experiments made in a double-gravity cavity. The experimental arrangement is exactly the same as before, except that we introduce a 50-50 beam splitter into the collimated beam path and add a

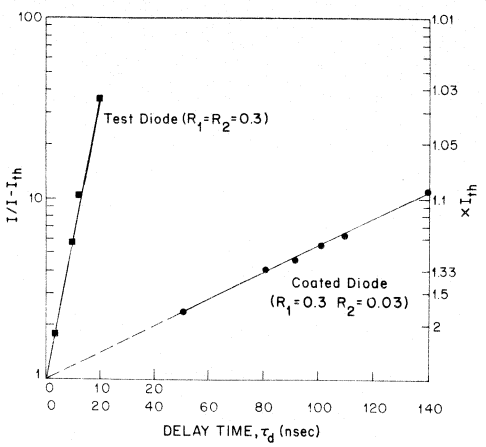

Fig. 9. Time delay versus current overdrive for two LOC devices.

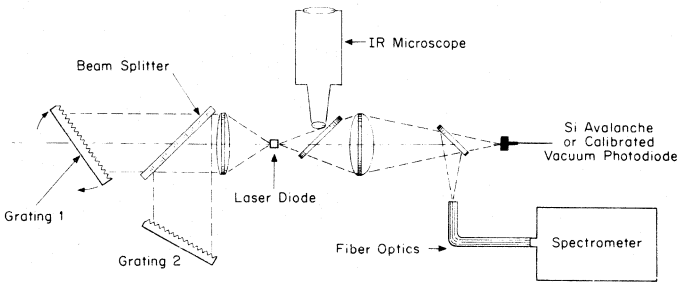

Fig. 10. Schematic illustration of a double-grating cavity which allows the diode to be lased at either the frequency controlled by grating 1, the frequency of grating 2, or at both frequencies simultaneously.

second grating to the cavity, as shown in Fig. 10. Now the diode can oscillate at two different frequencies depending on the setting of the gratings, as illustrated by the spectra for a DH diode shown in Fig. 11. The upper spectrum [Fig. 11 (a)] was obtained by blocking off the feedback from one grating so that the diode lases only in one narrow line. The lower spectrum [Fig. 11 (b)] was obtained by introducing feedback from the second grating, causing a second line to oscillate simultaneously with the first. We feel this technique may be useful in studying the dynamics of the gain profile for any semiconductor laser. We have also done double-grating experiments on an SH diode, with results similar to those in Fig. 11 in that two lines will oscillate. However, because of the abnormal delay region,[2] the results are very complicated and will not be discussed here [19].

Finally, we have also operated uncoated diodes in an external cavity with a grating. In this case the situation is very similar to that discussed by Bjorkholm *et al.* [20] for dye lasers. The spectra obtained for an SH diode are shown in Fig. 12. In the uppermost spectrum the diode is lasing in several longitudinal Fabry-Perot modes without any grating feedback. In Fig. 12 (b)-(f), the grating feedback is added and tuned through the modes. When the grating is tuned close to the modes, all the power is pulled into the grating line, so that an

[2]The time-delay data are affected because a high-energy line (with normal delay) can saturate the absorbers, thereby allowing a low-energy line to oscillate.

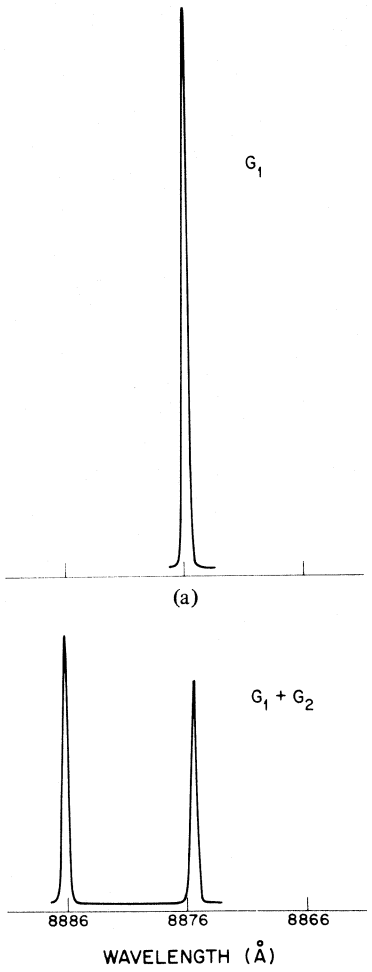

Fig. 11. The spectral output from a DH diode operated in a double-grating cavity. (a) Upper trace–grating G_1 feeds back radiation at 8876 Å. (b) Lower trace–both gratings feed back: G_1, at 8876 Å; G_2, at 8886 Å. The amplitude scale is not the same for both traces.

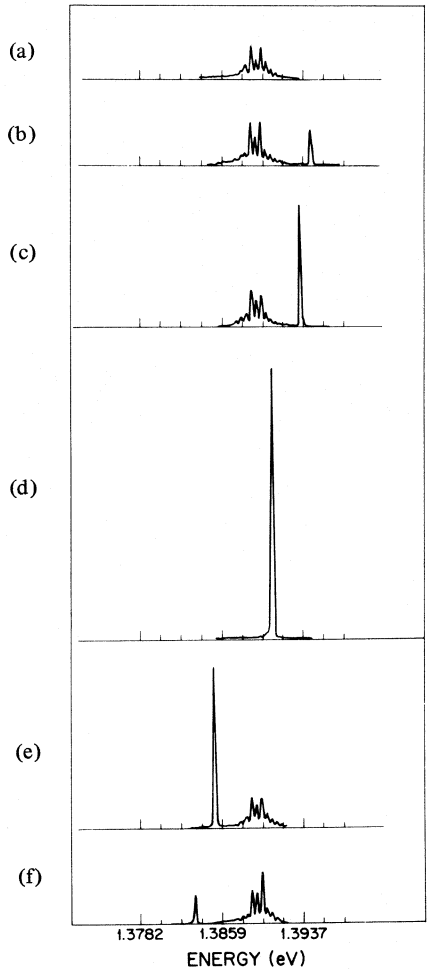

Fig. 12. The spectral output from an uncoated SH diode operated in an external cavity. In spectrum (a) the diode is lasing with the grating feedback blocked. In (b)–(f) the grating feedback is unblocked and the grating-controlled line is tuned through the diode's own self-lasing spectrum.

AR coating is clearly not necessary for all applications. We note, however, that the tuning range over which the diode radiates all its power in a single narrow line is only ~ 5 meV (30 Å), which is greatly reduced from the AR-coated case. Furthermore, Paoli and Ripper [21], who have operated uncoated CW diodes in this way, found that this tuning is only quasi-continuous.

IV. Discussion

The data of Figs. 8 and 9 show that long delays can be observed in DH and LOC devices, but only under certain operating conditions. The common feature of these conditions is that they cause a reduction in the electromagnetic wave intensity inside the active region. Thus, for the AR-coated diode of Fig. 8, I_{th} is increased by ~ 5 percent when the Au mirror is replaced by the diffraction grating. However, the photon density inside the cavity is greatly lowered because the grating is highly dispersive and returns only a very small portion of the emission to the active region. In contrast, the mirror returns all the emission (except for small reflection losses), since in this case the junction is reimaged in the lens focal plane. Thus, for the grating, the small increase in photon density due to a higher I_{th} is more than offset by the loss of photons due to dispersion. There is a similar difference between the conventional diode and the AR-coated diode with the Au mirror. In this case, the addition of external optics causes a loss which is not quite offset by the decrease in the transmission loss of the resonator. This must be the case because I_{th} is essentially unchanged for the two configurations, but the calculated transmission losses are cut in half (~ 47 to 23 cm^{-1}). Hence for Fig. 8 we expect the highest wave intensity inside the cavity for the cleaved uncoated diode; a lower intensity is expected for the coated diode-mirror combination, and an even lower intensity for the coated diode-grating combination.

On the basis of this analysis, we believe that the long time delays in the AR-coated DH and LOC devices are fundamentally due to a saturable absorption process, just as in DJ and SH diodes. Although this process is also operative in uncoated DH and LOC devices, because of their superior optical confinement the photon density in these devices is high enough to saturate the absorption so rapidly that long delays do not occur. By applying an AR coating we can reduce

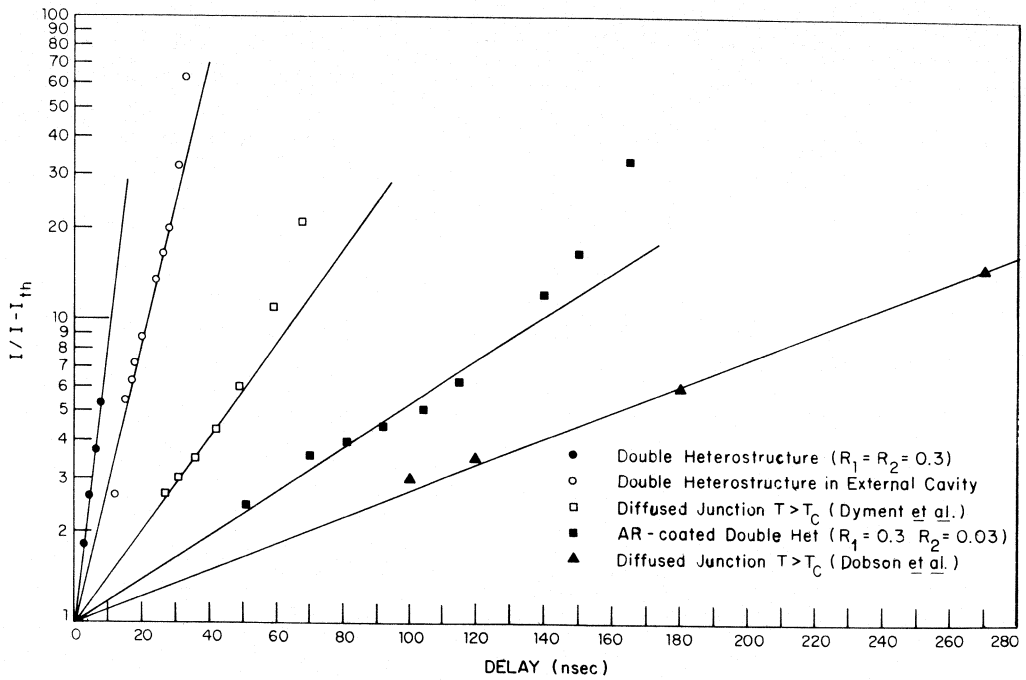

Fig. 13. Time delay versus current overdrive curves illustrating the similarity between our results for coated DH or LOC devices and the results for DJ devices operated above T_c reported by Dyment and Ripper [7] and Dobson *et al.* [22].

the photon density to the point where the time required to saturated the absorption becomes appreciable, and long delays can be observed.

This explanation of long delays in DH and LOC devices suggests that the long-delay effects in SH and DJ diodes at $T > T_c$ are also due to a reduction in the electromagnetic wave intensity in the active region. This proposal is strongly supported by the data shown in Fig. 13, which include curves of τ_d versus $\ln I/(I - I_{th})$ for a DH device, a DH device in an EC, and a coated DH device lased without an EC, together with data taken from Dyment and Ripper [7] and from Dobson *et al.* [22] for DJ diodes operated above T_c. The data for DJ diodes below T_c, which would lie on a nearly vertical line located near our DH data, have been omitted from Fig. 13 for clarity. The straight lines drawn in Fig. 13 are not intended to compare the data with (1), but are used to emphasize the trend in the variation of the time delay for different diodes [23]. Thus, as discussed above, the data for the DH devices show a decreasing slope for a decreasing photon density in the active region, and the data for the DJ diodes go from nearly vertical at $T < T_c$ to a greatly decreased slope at $T > T_c$. We propose that in a SH or DJ diode, at the current levels necessary to drive the device, as $T \to T_c$ there is a breakdown in waveguiding which reduces the intensity of the wave in the active region sufficiently for the saturable absorption to cause a long time delay. This model, which combines a breakdown in waveguiding with a saturable absorption, is also consistent with all other reported time-delay effects, as we will now show [24].

First, we consider the case of abnormal delays, in which the time delay between the current pulse and the diode light output *increases* with increasing current, exactly opposite to what is predicted by (1). In this case we assume that the increase in current amplitude decreases the waveguiding of the structure, causing the intensity of the wave in the active region to decrease. It therefore takes longer to eliminate the saturable absorption, and the time delay is increased. For a diode operated in an EC where the lasing wavelength is fixed, the diode will eventually be shut off, as reported previously [25] (see Figs. 3 and 4). A conventional diode will try to oscillate at a shorter wavelength which still can "fit" into the guide or which has the gain needed to overcome the additional diffraction loss; this has also been observed [11], [17] as discussed above. There are at least two ways [26]-[28] in which the refractive index (and therefore the waveguiding) of the active region can change with drive level: 1) by the negative contribution to the index from injected minority carriers (plasma effect), and 2) through the Kramers-Kronig integral which relates the absorption coefficient α, or changes in α, to the index of refraction. These changes in the index with current are probably small ($\sim$ 0.1-1 percent) but are important in a SH or DJ diode because the waveguide is asymmetric and is, in fact, established by small index variations. Therefore, the losses can be increased greatly by a small index change at one of the waveguide boundaries. Thus abnormal time delays may be attributed to a breakdown in guiding coupled with saturable absorption. This explanation is also consistent with the fact that no abnormal delays have ever been reported for DH or LOC devices; in these devices, because of the large index of refraction discontinuities ($\sim$ 5-10 percent), a breakdown in guiding with current is not likely to occur.

By using the same model, Q-switching effects can be qualitatively explained as follows. Immediately after the application of the current pulse, the saturable absorption losses dominate and prevent lasing. Although the saturable losses decrease with time during the current pulse, the diffraction loss

from a breakdown in guiding still prevents the diode from lasing. If, following the current pulse, the guiding is restored faster than the injected carriers are lost, a Q-switched output pulse can result. Since the guiding is expected to change rapidly with carrier density, this assumption is not unreasonable.

Additional features of the waveguide-breakdown model make it consistent with other reported data. A breakdown in guiding should first affect the longest wavelengths because these no longer fit into the guide or, alternately, they do not have the gain needed to overcome the additional diffraction loss. EC data [25] showing that the time delay increased as the lasing wavelength increased are thus in agreement with the model. According to Thomas *et al.* [29], the model can also account for H-pulsing [30]. The model is also consistent with all previous data on the dependence of delay effects on active-region doping and width. For example, for a fixed lasing frequency in the p-side of a DJ or SH diode, increasing the substrate doping (n-side) leads to a decrease in the index of refraction on the n-side of the junction [31], [32] which results in an improved guiding in the unexcited structure. Hence, a higher T_c would be expected for devices with a higher substrate doping; this is in agreement with the experimental results for these structures [7], [24c)]. Similarly, a smaller active-region width should lead to a decrease in guiding resulting in a lower T_c, as observed experimentally [9], [24c)]. Changes in the near-field pattern showing a spreading of the light emission as $T \rightarrow T_c$ [33], and changes in the far-field pattern showing a narrowing of the beamwidth as $T \rightarrow T_c$ [34] are also consistent with the model.

V. Conclusions

We have shown how the dispersive EC can be used to study the gain profile types of heterostructures, for differently doped active regions and different device operating conditions. We have also shown that long time delays can be observed in DH and LOC diodes, which indicates that saturable absorption can occur in these as well as in all other types of GaAs diodes. Although saturable absorption has recently been attributed to a nonequilibrium process [23], this model conflicts with some experimental results. For example, according to the nonequilibrium model, diodes with heavily Si-doped active regions should show long time delays, but we did not observe such delays in Si-doped diodes lasing near 9250 Å. Further, we doubt that the saturable absorption occurs in the n-type passive layer of a SH diode because in that case, uncoated LOC structures should show long delays, and of course the highest energy transitions should be affected first, contrary to EC data. Thus the conclusive identification of this absorption mechanism, in our opinion, still remains open. More important, the removal (if possible) of this absorption from the active region may yield improved lasers and light-emitting diodes. The existence of H-pulsing indicates that there is material available without significant saturable absorption.

To test the breakdown-in-guiding model a quantitative treatment should be developed. The observed variation of the cutoff energy with injected carrier density (cf. Figs. 3, 4, upper branch) could then be compared to that expected from theory. Finally, we note that the photon density in the active region may be reduced in structures that do not utilize a Fabry-Perot cavity with uncoated faces. Such a structure—for example, a laser physically coupled to a fiber through an index matching medium—might therefore show time delays that would be detrimental for wide-band applications in integrated optical circuits or optical communication systems.

Acknowledgment

The authors wish to thank T. A. Lind and M. J. Button for expert technical assistance throughout this work, and S. R. Chinn for several helpful discussions.

References

[1] H. D. Edmonds and A. W. Smith, "Second-harmonic generation with the GaAs laser," *IEEE J. Quantum Electron. (Special Issue on Semiconductor Lasers)*, vol. QE-6, pp. 356-360, June 1970.

[2] R. Ludeke and E. P. Harris, "Tunable GaAs laser in an external dispersive cavity," *Appl. Phys. Lett.*, vol. 20, pp. 499-510, June 1972.

[3] J. A. Rossi, S. R. Chinn, and H. Heckscher, "High-power narrow-linewidth operation of GaAs diode lasers," *Appl. Phys. Lett.*, vol. 23, pp. 25-27, July 1973.

[4] P. G. Eliseev and N. N. Shuiken, "Single mode and single frequency injection lasers," *Sov. J. Quantum Electron.*, vol. 3, pp. 181-192, Nov.-Dec. 1973.

[5] E. M. Philipp-Rutz, "High-radiance room-temperature GaAs laser with controlled radiation in a single transverse mode," *IEEE J. Quantum Electron.*, vol. QE-8, pp. 632-641, July 1972.

[6] T. Flom and D. Coombes, "Multiple target tracking and target attitude determination with a scanning laser radar," presented at the National Aerospace Meeting, Mar. 1974.

[7] J. C. Dyment and J. E. Ripper, "Temperature behavior of stimulated emission delays in GaAs diodes and a proposed trapping model," *IEEE J. Quantum Electron.*, vol. QE-4, pp. 155-160, Apr. 1968.

[8] G. Guekos and M. J. O. Strutt, "Temperature dependence of the delay time between the current pulse and the laser emission of GaAs laser diodes," *Electron. Lett.*, vol. 3, pp. 533-534, Dec. 1967.

[9] E. A. Ulmer, Jr., and I. Hayashi, "Internal Q switching in GaAs-$Ga_XAl_{1-X}As$ heterostructure lasers," *IEEE J. Quantum Electron. (Special Issue on Semiconductor Lasers)*, vol. QE-6, pp. 297-299, June 1970.

[10] K. Konnerth, "Turn-on delay in GaAs lasers operated at room temperature," presented at the Solid State Device Research Conf., Princeton, N. J., June 21-23, 1965.

[11] M. J. Adams *et al.*, "Time delays and Q switching in homostructure and heterostructure injection lasers," *IEEE J. Quantum Electron. (Part II of Two Parts, Special Issue on 1972 IEEE Semiconductor Laser Conference)*, vol. QE-9, pp. 328-337, Feb. 1973.

[12] J. C. Dyment, J. E. Ripper, and T. P. Lee, "Measurement and interpretation of long spontaneous lifetimes in double heterostructure lasers," *J. Appl. Phys.*, vol. 43, pp. 452-457, Feb. 1972.

[13] C. J. Hwang and J. C. Dyment, "Dependence of threshold and electron lifetime on acceptor concentration in GaAs-$Ga_{1-X}Al_XAs$ lasers," *J. Appl. Phys.*, vol. 44, pp. 3240-3244, July 1973.

[14] G. E. Fenner, "Delay of stimulated emission in GaAs laser diodes near room temperature," *Solid-State Electron.*, vol. 10, pp. 753-764, Aug. 1967.

[15] J. E. Ripper and J. C. Dyment, "Time delays and Q switching in junction lasers: II—Computer calculations and comparison with experiment," *IEEE J. Quantum Electron. (Part I of 2 Parts)*, vol. QE-5, pp. 396-403, Aug. 1969.

[16] ——, "Internal Q-switching in GaAs junction lasers," *Appl. Phys. Lett.*, vol. 12, pp. 365-367, June 1968.

[17] B. Thomas, D. Mistry, and C. F. L. Davies, "The temperature dependence of spectral emission from semiconductor lasers showing long time delays," *IEEE J. Quantum Electron.*, vol. QE-10, pp. 401-405, Apr. 1974.

[18] M. B. Panish and H. C. Casey, Jr., "Temperature dependence of the energy gap in GaAs and GaP," *J. Appl. Phys.*, vol. 40, pp. 163-167, Jan. 1969.

[19] A. P. Bogatov, P. G. Eliseev, and B. N. Sverdlov, "Anomalous interaction of spectral modes in a semiconductor laser," this issue, pp. 510–515.
[20] J. E. Bjorkholm, T. C. Damen, and J. Shah, "Improved use of gratings in tunable lasers," *Opt. Commun.*, vol. 4, pp. 283–284, Dec. 1971.
[21] T. L. Paoli, J. E. Ripper, A. C. Morosini, and N. B. Patel, "Suppression of intensity self-pulsations in CW junction lasers by frequency-selective optical feedback," this issue, pp. 525–527.
[22] C. D. Dobson, J. Franks, and F. S. Keeble, "Characteristics of GaAs lasers near room temperature," *IEEE J. Quantum Electron.*, vol. QE-4, pp. 151–154, Apr. 1968.
[23] The nonlinear variation of τ_d in Fig. 13 is similar to that calculated by S. Gründorfer and M. Adams, in "Theoretical considerations of time delays in semicondictor lasers," *IEEE J. Quantum Electron.*, vol. QE-9, pp. 814–819, Aug. 1973.
[24] We wish to point out that several other workers also seem to agree (for the present) on this model. The interested reader is referred to several papers in this issue and to:
a) S. Gründorfer, M. J. Adams, and B. Thomas, "New theory of internal Q-switching in semiconductor lasers," *Electron. Lett.*, vol. 10, pp. 354–357, Aug. 1974.
b) G. H. B. Thompson, P. R. Selway, G. D. Henshall, and J. E. A. Whiteaway, "Role of optical guiding in critical temperature behavior, delays and Q-switching in single heterostructure GaAs/(GaAl)As lasers," *Electron. Lett.*, vol. 10, pp. 456–457, Oct. 1974.
c) H. Minden and R. Premo, "High temperature GaAs single heterostructure laser diodes," *J. Appl. Phys.*, vol. 45, pp. 4520–4527, Oct. 1974.
[25] J. A. Rossi, H. Heckscher, G. E. Stillman, and S. R. Chinn, "Time delays in external cavity controlled GaAs/$Ga_{1-x}Al_xAs$ single heterostructure diode lasers," *Appl. Phys. Lett.*, vol. 23, pp. 254–256, Sept. 1973.
[26] F. Stern, "Dispersion of the index of refraction near the absorption edge of semiconductors," *Phys. Rev.*, vol. 133, pp. A1653–A1664, Mar. 1964.
[27] a) J. K. Butler, "Index of refraction changes in semiconductors with population inversion" (Abstract), *IEEE J. Quantum Electron. (Special Issue on Semiconductor Lasers)*, vol. QE-6, p. 316, June 1970.
b) G. H. B. Thompson, "Theory for filamentation in semiconductor lasers including the dependence of dielectric constant on injected carrier density," *Opto-Electron.*, vol. 4, pp. 257–310, Sept. 1972.
[28] M. Cross and M. J. Adams, "Effects of doping and free carriers on the refraction index of direct gap semiconductors," *Opto-Electron.*, vol. 6, pp. 199–216, Aug. 1974.
[29] B. Thomas, M. J. Adams, and S. Gründorfer, "A comprehensive model for Q switching in semiconductor lasers," this issue, pp. 528–532.
[30] a) B. Thomas *et al.*, "Time delays, Q-switching and H-pulsing in homostructure and heterostructure injection lasers," presented at the 3rd European Solid State Device Research Conf., Munich, Germany, Sept. 1973.
b) S. Gründorfer, M. J. Adams, and B. Thomas, "H-pulsing: A transient effect in GaAs/$Ga_xAl_{1-x}As$ injection lasers," this issue, pp. 532–537.
c) G. D. Henshall, "Achievement of high peak power in GaAs injection lasers," presented at the 3rd European Solid State Device Research Conf., Munich, Germany, Sept. 1973.
[31] D. D. Sell, H. C. Casey, Jr., and K. Wecht, "Concentration dependence of the refractive index for n- and p-type GaAs between 1.2 and 1.8 eV," *J. Appl. Phys.*, vol. 45, pp. 2650–2657, June 1974.
[32] J. Zoroofchi and J. K. Butler, "Refractive index of n-type gallium arsenide," *J. Appl. Phys.*, vol. 44, pp. 3697–3699, Aug. 1973.
[33] I. Hayashi and M. B. Panish, "GaAs-$Ga_{1-x}Al_xAs$ heterostructure injection lasers which exhibit low thresholds at room temperature," *J. Appl. Phys.*, vol. 41, pp. 150–163, Jan. 1970.
[34] P. R. Selway, G. H. B. Thompson, G. D. Henshall, and J. E. A. Whiteaway, "Measurement of the effect of injected carriers on the p-n refractive index step in single heterostructure diode lasers," *Electron. Lett.*, vol. 10, pp. 453–455, Oct. 1974.

Degradation and Intensity Fluctuations in CW AlGaAs Double-Heterostructure Junction Lasers

SHUN-ICHI GONDA AND SEIJI MUKAI

Abstract—**The intensity fluctuations in the output of CW AlGaAs semiconductor lasers were measured as functions of pumping current and operating time. The magnitude of fluctuation decreases with increasing aging time. The shift after degradation in the resonant-peak frequency for the normalized pumping rate is small. An increase of the half-width of the resonance peak is also observed, together with an increase of the threshold current and a decrease of the external differential quantum efficiency. The fluctuation spectra due to the quantum shot noise were calculated using rate equations with parametric variation of the pumping rate and the internal quantum efficiency. From the qualitative agreement between calculated and experimental results, changes in the intensity fluctuations after degradation are considered to be partly due to a decrease of the internal quantum efficiency or gain.**

Manuscript received November 18, 1974; revised February 7, 1975.
The authors are with the Optoelectronics Section, Electrotechnical Laboratory, Tokyo, Japan.

I. Introduction

DEGRADATION of CW AlGaAs double-heterostructure lasers is characterized by a decrease of the emission intensity, an increase of the threshold current, and a decrease of the external differential quantum efficiency. This behavior can be explained by the formation of "dark lines" [1]–[3] which are nonradiative recombination regions and crystalline defects observed in degraded lasers.

Another characteristic of interest is the intrinsic intensity fluctuations in the output of semiconductor lasers. Armstrong and Smith [4] investigated the intensity fluctuations in the light emitted by a GaAs laser operated continuously near 10 K in the frequency range between 2 kHz and 10 MHz as a function of pumping current, and observed the fluctuation

maximum near the threshold current. McCumber [5] calculated the intensity fluctuations due to the quantum shot noise, expected in the output of four-level CW laser oscillators, using linearized rate equations, and Haug [6] made similar calculations for semiconductor lasers. They found that above threshold there is a sharp resonance in the gigahertz region. The existence of a sharp peak in the fluctuation spectrum was shown indirectly by Ikegami and Suematsu [7] investigating the resonance frequency by using a modulated driving current. On the other hand, D'Asaro *et al.* [8] observed a peak in the gigahertz region of the fluctuation spectrum of semiconductor lasers. They concluded that this peak was not due to the quantum shot noise, because the dependence of the fluctuations on the pumping current was not correct. Paoli [9], [10] observed directly the peak due to the excitation of the natural resonance by the quantum shot noise in the above-threshold frequency spectrum of the output of AlGaAs junction lasers operated CW at 77 K and room temperature.

The internal change of the lasing process after degradation is reflected in the intensity fluctuations. For example, Yang *et al.* [11] reported that self-pulsation was observed in the output after degradation. The present paper presents experimental results on the rms intensity fluctuations in the frequency region below 10 MHz and the fluctuation spectra in the region 0.1~2 GHz as a function of pumping current in the output of AlGaAs junction lasers operated continuously at room temperature. The change in the intensity fluctuations was measured after an appropriate aging time. The relation between the degradation and the intensity fluctuations will be discussed using simple rate equations.

II. Experimental

Samples used in the present work were fabricated from double-heterostructure material grown by liquid-phase epitaxy. The active layer of this material was less than 1 μm thick and contained a small amount of Al. As for the stripe geometry, two types were used. One type was native-oxide stripe-geometry (NOS) lasers [12] fabricated by Toshiba. The active layer of this type was doped with Si. Lasers were about 150 μm long with stripe width nominally equal to 20 μm. The other was planar stripe-geometry (PS) lasers [13] fabricated by the Nippon Electric Co. The active layer was doped with Ge. Lasers were about 240 μm long with a stripe width of 15 μm. For CW operation at room temperature, each laser was bonded to a copper heat sink.

The rms intensity fluctuations for the low-frequency part between 2 kHz and 10 MHz were measured with a single-detector arrangement similar to that used by Armstrong and Smith [4]. The fluctuations in the output current of a p-i-n photodiode (UDT PIN-10) were measured with an rms voltmeter (HP 3400A). The dc photocurrent was determined simultaneously by using an RC divider network. The low-frequency cutoff of 2 kHz was fixed by the divider, the high-frequency cutoff of 10 MHz by the voltmeter. The rise time of the photodiode was about 15 ns.

The frequency spectrum of the intensity fluctuations was measured with a single-detector system similar to that used by Paoli and Ripper [9]. The laser light was passed through a chopper and focused onto a coaxially mounted p-n avalanche photodiode whose rise time was about 0.1 ns. The output of the photodiode was coupled to a spectrum analyzer (HP 851B/8551B) whose output was directed to a lock-in amplifier for phase-sensitive detection. For optical isolation a lens with a small diameter and focal distance was placed near the laser and away from the photodiode. The output from the system $P(\omega)$ was corrected using the frequency-response function of the system which was measured by observing the spectrum generated by white light. The relative photon noise $S(\omega)$ is related to the calibrated output by the following equation:

$$S(\omega) \equiv \int \langle \Delta N_p(t) \Delta N_p(t+\tau) \rangle e^{i\omega\tau}\, d\tau / \langle N_p \rangle^2 = (P(\omega)/2\,\Delta_f)/P_{\mathrm{dc}} \quad (1)$$

where Δ_f is the bandwidth of the spectrum analyzer and $N_p(t)$ the photon number.

Some of the lasers measured show sharp peaks and narrow half-width in the frequency spectra. Modulation of this type can be observed in the time domain with a sampling oscilloscope. The modulation was observed using a delay line and the modulation itself as a trigger, with care to reducing the trace jitter due to incomplete periodicity of the signal.

III. Experimental Results

The frequency spectra of the intensity fluctuations for various lasers are shown in Figs. 1 and 2 as a function of pump level. The ordinate shows the relative noise power $S(\omega)$ defined by (1). No appreciable difference in the fluctuation characteristics was found between the NOS and PS lasers. The relative noise spectra observed in a laser, $L1$, which has an intermediate external differential quantum efficiency (about 10 percent) is shown in Fig. 1. After 98 h and 260 h of continuous operation at 100 mA (the output was about 1 mW) at 22°C, the threshold current of this laser increased from 83.8 mA to 92.9 mA and 102.1 mA, respectively. Solid lines and dashed lines in Fig. 1 are the spectra before and after the operation.

The above-threshold spectra show the resonant peaks. The relative noise increases with increasing pumping current. As pointed out before [10], this absence of stabilization at room temperature may be due to an ineffective response to the fluctuating intensity because of longer thermalization times. After long-term operation the magnitude of the resonant peak decreases, as shown in Fig. 1. The tendency of the absence of stabilization is unchanged. The relative noise spectra observed in a laser, $L2$, which has a rather high external differential quantum efficiency (more than 20 percent), and in a laser, $L3$, which has a rather low efficiency (about 5 percent), are shown in Fig. 2 with solid lines and broken lines, respectively. In laser $L2$, at currents a little above threshold, the fluctuations increase abruptly and show anomalous peaks, and the peaks due to higher harmonics grow at the high-noise power level. The fluctuations with these sharp peaks may be incipient self-pulsation due to second-order mode locking [14]. After

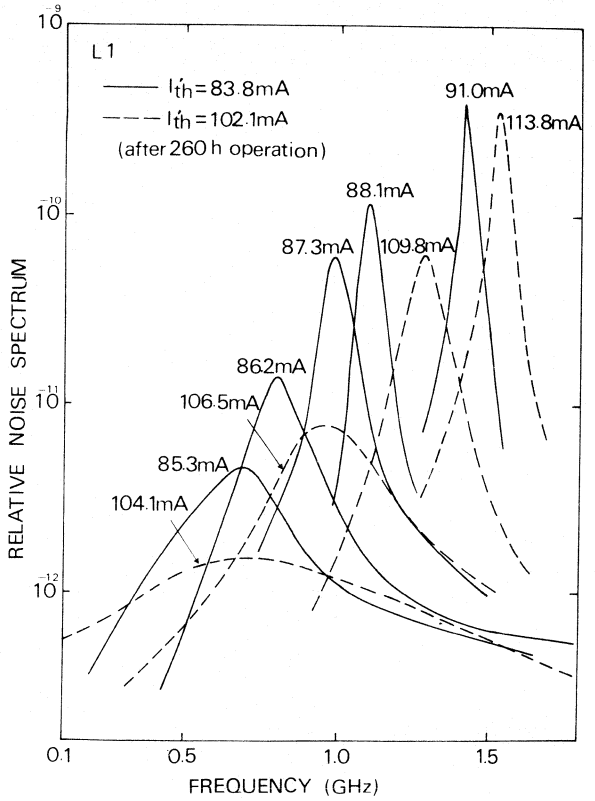

Fig. 1. Intensity-fluctuation spectra obtained from a semiconductor laser, $L1$, with an intermediate quantum efficiency before operation, and after operating continuously for about 260 h.

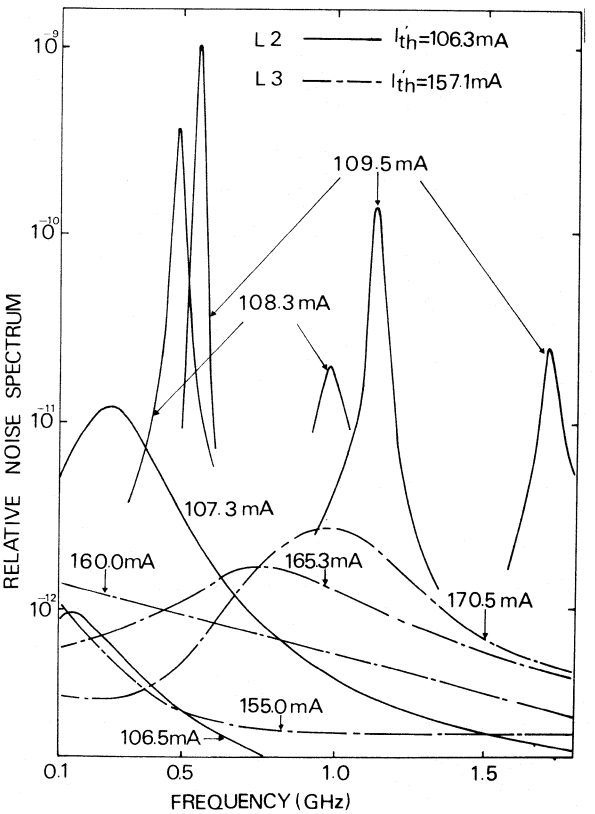

Fig. 2. Intensity-fluctuation spectra from a semiconductor laser, $L2$, with high quantum efficiency and a laser, $L3$, with low quantum efficiency.

operation there are no drastic changes in these spectra. In laser $L3$ with low efficiency, the peak of the fluctuation does not grow so rapidly and the half-width of the peak does not decrease greatly with increasing pumping current.

The relation between the peak frequency ν_R and the current I expected for the small-signal fluctuations excited by the quantum shot noise is given by [5]

$$\nu_R^2 = \alpha^2(I/I'_{th} - 1) \tag{2}$$

where I'_{th} is the threshold current when $\nu_R = 0$, and this is almost coincident with the threshold current I_{th} obtained from the current-output power characteristics. The dependence of the peak frequency on the pumping current for laser $L1$ is shown in Fig. 3 together with that for another laser $L2'$ which shows fluctuation spectra similar to $L2$ in Fig. 2. Equation (2) holds for laser $L1$. This dependence indicates that the fluctuations in laser $L1$ are caused by a resonant mechanism excited by the quantum shot noise. The coefficients α in (2) have nearly the same values, 4.7 GHz, for each stage of operation. The fluctuations after degradation, therefore, are also due to the quantum shot noise. The relation $\nu_R^2 = \alpha^2(I/I'_{th} - 1)$ also holds for laser $L3$. At first sight, the shift of the peak frequency seems to be small for laser $L3$, but the dependence of the peak frequency on the current normalized by the threshold current is of the same order as in the case of Fig. 1. On the other hand, (2) does not hold for laser $L2'$, as shown in Fig. 3. This deviation, abrupt increase, large values of peak height, and the existence of higher harmonics indicate that the fluctuations make a transition from small-signal fluctuation to incipient pulsation with in-

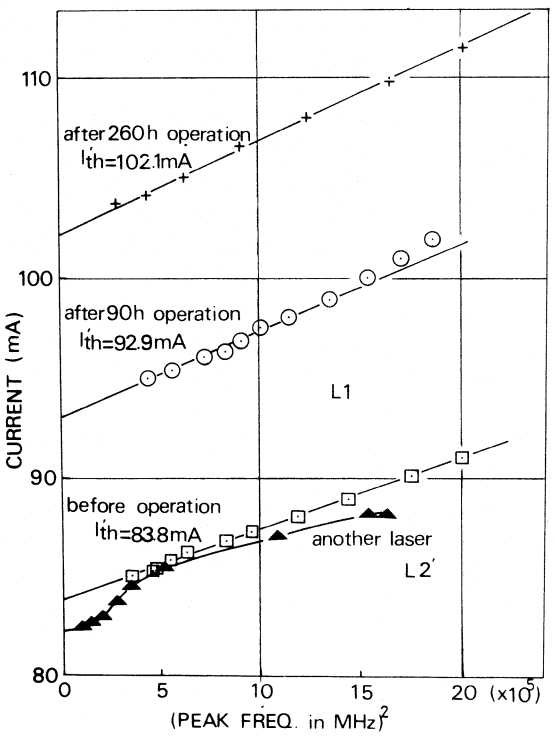

Fig. 3. The relations between the pumping current and the peak frequency of intensity-fluctuation spectra ν_R after various periods of continuous operation for laser $L1$ and the relation for laser $L2'$, showing deviations from the formula $\nu_R^2 = \alpha^2(I/I_{th} - 1)$.

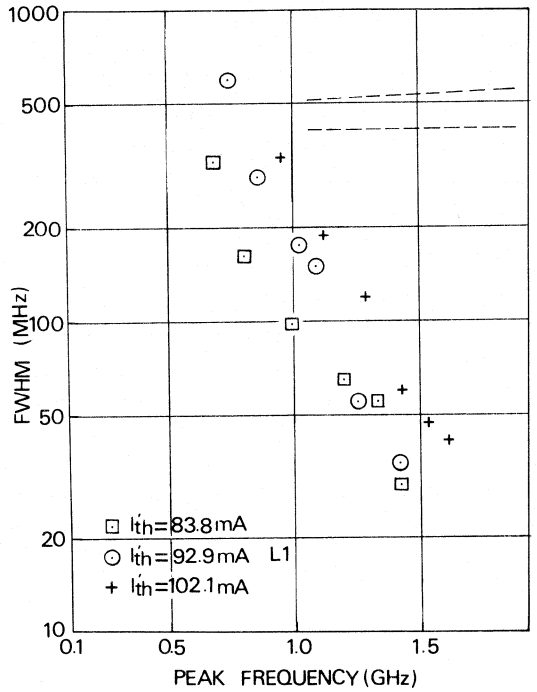

Fig. 4. The relations between the FWHM and the peak frequency in the intensity-fluctuation spectra after various periods of continuous operation for laser $L1$. The dashed line is a relation calculated from the quantum shot-noise model.

creasing pumping current. Abrupt decrease of the full width at half maximum (FWHM) of the peak shows that the noise becomes nearly periodic when the pulsation occurs.

Fig. 4 shows the FWHM of the fluctuation spectra of laser $L1$. The FWHM of spectra decreases rapidly with increasing pumping current. This is not consistent with a tendency expected from the quantum shot-noise model, which is shown with dashed lines.

In some cases, after degradation, very sharp and large peaks were observed in the frequency spectrum of intensity fluctuations, together with their high harmonics. This phenomenon appears to be the self-pulsation and may be caused by repetitive Q switching, with dark-line regions in the degraded lasers acting as saturable absorbers, as reported previously [11].

The absolute rms values of the low-frequency part (<10 MHz) of the intensity fluctuations for lasers $L2$ and $L3$ are shown in Fig. 5 as a function of pumping current. The dashed curves are output-current characteristics. The rise and fall of the rms fluctuations for laser $L2$ having higher external differential quantum efficiency near threshold are very sharp. The rise of the fluctuations for laser $L3$ having low efficiency is gradual and the magnitude of the peak is small. Although not shown here, the rise and fall of the fluctuation for laser $L2$ are intermediate. As the degradation proceeds, the rise and fall become gradual and the magnitude of the peak becomes small. The fall after the rise is due to the saturation of the gain [4]. The tendency for the peak to broaden after degradation is thought to be caused by the decrease of the gain.

Fig. 6 shows the sampling-oscilloscope traces of the fluctuations in the output of laser $L2$ with high external differential quantum efficiency. When the pumping current is 116.1 mA, the period (about 1 ns) of the fluctuations in Fig. 6 corresponds to the peak frequency (955 MHz) in the frequency spectrum. With decreasing pumping current the period becomes longer, corresponding to the shift of the peak to lower frequency. When the pumping current is 116.1 mA, the ratio of the rms fluctuations of the output current of the photodiode obtained from Fig. 6 to the dc component of the current is about 17 percent. The depth of the modulation again indicates that this fluctuation is self-pulsation.

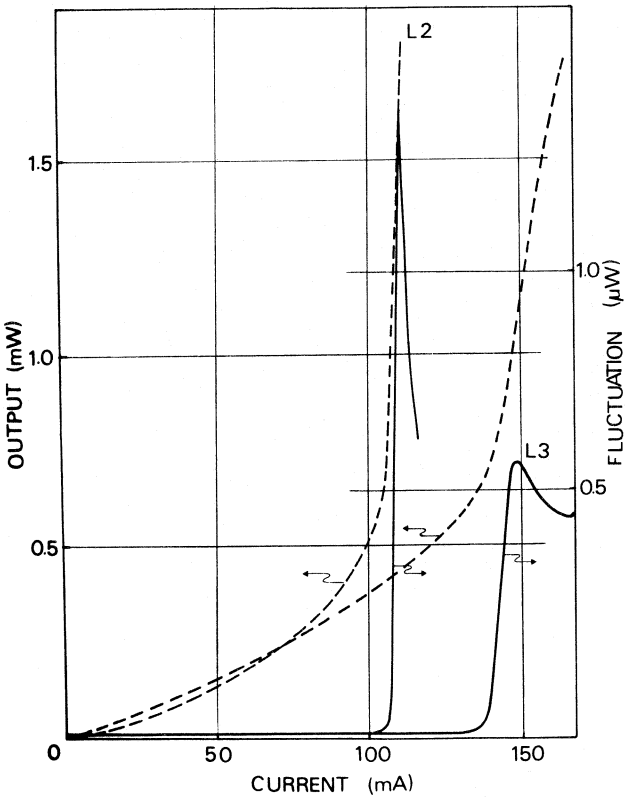

Fig. 5. Low-frequency intensity fluctuations in the output of lasers $L2$ and $L3$ as a function of pumping current. The dashed curves give the total output power.

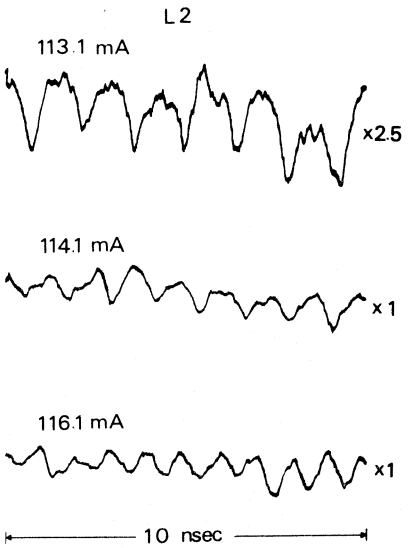

Fig. 6. Sampling-oscilloscope traces of intensity fluctuations in the output of a laser with high quantum efficiency.

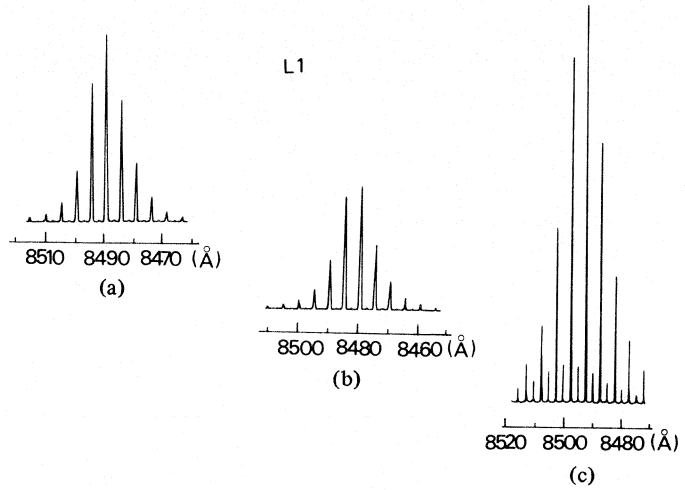

Fig. 7. The emission spectra of laser $L1$ with intermediate external differential quantum efficiency after various periods of continuous operation. (a) Before operation. (b) After 187-h operation. (c) After 497-h operation.

Fig. 7 shows the emission spectra of laser $L1$. The spectrum (a) was observed before long-term operation and (b) was observed after operating continuously for 187 h, showing no significant change in spite of the change in the fluctuation spectra. In the emission spectrum (c) after 497-h operation, another longitudinal mode family appeared. However, no drastic change in the intensity fluctuations was found at this stage of degradation. This may indicate that there is no large correlation between the change of the intensity fluctuations and the emission spectra within the limits of this experiment.

IV. Discussion and Conclusion

The change in the intensity fluctuations after degradation is the decrease of the relative noise due to the quantum shot noise, and in some cases self-pulsation occurs due to the formation of the absorption region. Since the occurrence of self-pulsation has already been discussed, let us discuss the change in the relative noise due to the quantum shot noise in this section.

Yonezu *et al.* [3] considered the dark line in a degraded laser as a fast nonradiative recombination center, and investigated the quantitative relation between the number of dark lines in a laser cavity and degraded lasing characteristics such as threshold current and external differential quantum efficiency. Little or noninverted population of the minority carriers is achieved in the dark line due to the fast dissipative nonradiative process in the degraded region, which makes the gain of the region low or even absorptive.

Morgan and Adams [15] calculated the noise spectrum of single-mode junction lasers generated by the quantum shot noise by assuming homogeneous gain and photon distribution in the cavity. We have examined the effect of degradation on the fluctuation spectra on the basis of their calculation by changing the parameter, internal quantum efficiency η, as a most fundamental result of dark line formation [16]. Values of the parameters used in this calculation are [15]: temperature 320 K; rate coefficient containing the matrix element for

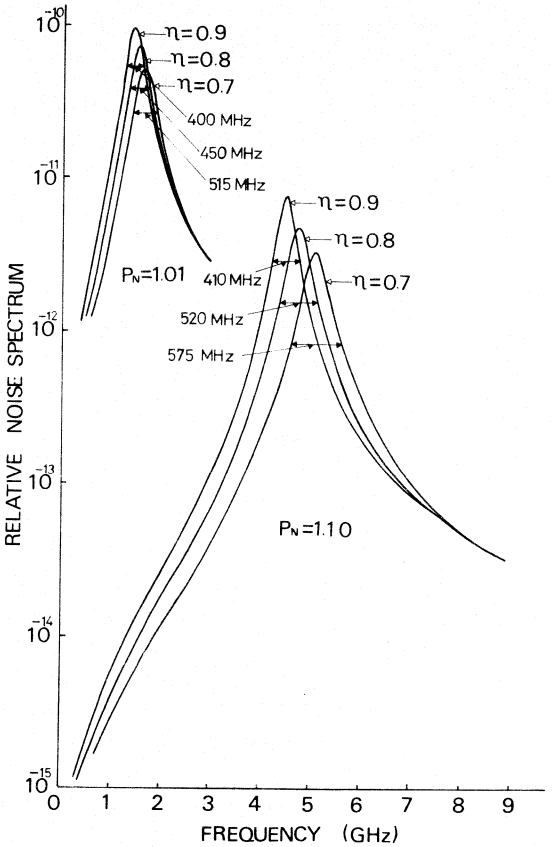

Fig. 8. Calculated intensity-fluctuation spectra of a semiconductor laser for the normalized pumping rates $P_N = 1.01$ and $P_N = 1.10$ with the parametric variation of internal quantum efficiency η.

lasing process 7.5×10^{-11} cm^3 s^{-1}; number of modes per unit energy per unit volume 9×10^{26} erg^{-1} cm^{-3}; volume of the active region 10^{-9} cm^3; effective mass for electrons in the conduction band 6.37×10^{-29} g; effective mass for holes in the valence band 4.55×10^{-28} g; and photon lifetime 10^{-12} s. Photon lifetime used here is the reciprocal of the rate of all the photon-annihilating processes except the process in which an electron-hole pair is created by photon absorption. This is already taken into account in the gain term of a basic rate equation. The lifetime is therefore assumed to be constant throughout the aging process.

Fig. 8 shows the dependence of the fluctuation spectra on the pumping current $P_N = I/I_{th}$ and the internal quantum efficiency η. With the same value of the internal quantum efficiency the current dependence of the fluctuations is as follows: 1) the peak frequency ν_R increases following the relation $\nu_R^2 = \alpha^2(I/I_{th} - 1)$; 2) the relative magnitude of the fluctuation decreases with increasing pumping current; and 3) the FWHM of the peak increases slightly with increasing pumping current. Let us compare these features with experimental results before degradation. Feature 1) is consistent with the experiment qualitatively, but the absolute value of ν_R in the calculation is larger than that of the experiment. This may depend on the selection of values of parameters. Feature 2) is contrary to the experiment. As discussed before [10], this may be due to long thermalization times. Feature 3) is also contrary to the experiment. With decreasing internal

quantum efficiency η from 0.9 to 0.7, the resonance peak shifts to higher frequency, the magnitude of the peak decreases, and the FWHM increases. For comparison, the change in the threshold current might be taken as a measure of degradation. The calculated threshold currents which correspond to $\eta = 0.9$, 0.8, and 0.7 are $I_{th} = 119.8$, 134.7, and 153.5 mA, respectively. The ratio is 1:1.12:1.28. The stages of degradation in the experiment are considered to be the stage of $\eta = 0.9$, $\eta = 0.8$, and between $\eta = 0.8$ and $\eta = 0.7$. As for the magnitude of the peak, there are some ambiguities in the experimental results and it is difficult to make a quantitative comparison, but qualitatively both calculated and observed magnitude decrease with increasing aging time. The value in (2) changes from $\alpha(\eta = 0.9) = 14.3$ in the first stage to $\alpha = 15.6$ GHz in the third stage. The relative change is larger than the experimental results, but the descrepancy is not so large. The FWHM increases by 20 ~ 30 percent in the calculation and increases by 100 ~ 200 percent in the experiment. Taking into account the roughness of the model, qualitatively the calculated results are thought to be in reasonable agreement with experimental results.

In conclusion, experimental results observed after degradation: 1) a decrease of the magnitude of the fluctuations; 2) no appreciable shift in the resonant peak frequency for the normalized pumping current; and 3) an increase of the FWHM of the resonant peak, can be qualitatively explained from a decrease of internal quantum efficiency after degradation in the quantum shot-noise model.

Acknowledgment

The authors wish to thank Dr. Y. Makita for his cooperation and discussion, and Dr. J. Shimada and Dr. G. Matsumoto for stimulating discussions, and Dr. K. Sakurai for his continual interest, and Dr. T. L. Paoli for his helpful comments on the manuscript. They also wish to thank the members of the semiconductor laser groups of the Nippon Electric Co. Ltd. and Toshiba Co. Ltd. for their cooperation.

References

[1] B. C. De Loach, Jr., B. W. Hakki, R. L. Hartman, and L. A. D'Asaro, "Degradation of CW GaAs double-heterostructure lasers at 300 K," *Proc. IEEE* (Lett.), vol. 61, pp. 1042–1044, July 1973.

[2] H. Yonezu *et al.*, "Degradation mechanism of (Al · Ga) As double-heterostructure laser diodes," *Appl. Phys. Lett.*, vol. 24, pp. 18–19, Jan. 1974.

[3] H. Yonezu, M. Ueno, T. Kamejima, and I. Sakuma, "Lasing characteristics in a degraded GaAs-$Al_xGa_{1-x}As$ double heterostructure laser," *Japan. J. Appl. Phys.*, vol. 13, pp. 835–842, May 1974.

[4] J. A. Armstrong and A. W. Smith, "Intensity fluctuations in GaAs laser emission," *Phys. Rev.*, vol. 140, pp. A155–A164, Oct. 1965.

[5] D. E. McCumber, "Intensity fluctuation in the output of CW laser oscillators I," *Phys. Rev.*, vol. 141, pp. 306–322, Jan. 1966.

[6] H. Haug, "Quantum-mechanical rate equations for semiconductor lasers," *Phys. Rev.*, vol. 184, pp. 338–348, Aug. 1969.

[7] T. Ikegami and Y. Suematsu, "Carrier lifetime measurement of a junction laser using direct modulation," *IEEE J. Quantum Electron.*, vol. QE-4, pp. 148–151, Apr. 1968.

[8] L. A. D'Asaro, Sr., J. M. Cherlow, and T. L. Paoli, "Continuous microwave oscillations in GaAs junction lasers," *IEEE J. Quantum Electron.*, vol. QE-4, pp. 164–167, Apr. 1968.

[9] T. L. Paoli and J. E. Ripper, "Observation of intrinsic quantum fluctuations in semiconductor lasers," *Phys. Rev. A*, vol. 2, pp. 2551–2555, Dec. 1970.

[10] T. L. Paoli, "Intrinsic fluctuations in the output intensity of double-heterostructure junction lasers operating continuously at 300°K," *Appl. Phys. Lett.*, vol. 24, pp. 187–190, Feb. 1974.

[11] E. S. Yang *et al.*, "Degradation-induced microwave oscillations in double-heterostructure injection lasers," *Appl. Phys. Lett.*, vol. 24, pp. 324–327, Apr. 1974.

[12] Y. Unno, M. Yamamoto, and H. Kurihara, "N.O. stripe semiconductor lasers," in *Abstr. 34th Applied Physics Meet.* (Japan, 1973), pt. 1, p. 243.

[13] H. Yonezu *et al.*, "A GaAs-$Al_xGa_{1-x}As$ double heterostructure planar stripe laser," *Japan. J. Appl. Phys.*, vol. 12, pp. 1585–1592, Oct. 1973.

[14] T. L. Paoli and J. E. Ripper, "Coupled longitudinal mode pulsing in semiconductor lasers," *Phys. Rev. Lett.*, vol. 22, pp. 1085–1089, May 1969.

[15] D. J. Morgan and M. J. Adams, "Quantum noise in semiconductor lasers," *Phys. Status Solidi*, vol. 11, pp. 243–253, 1972.

[16] N. Chinone, R. Ito, and O. Nakada, "Measurement of minority carrier lifetime during gradual degradation of GaAs-$Ga_{1-x}Al_xAs$ double-heterostructure lasers," *IEEE J. Quantum Electron.* (Corresp.), vol. QE-10, pp. 81–84, Jan. 1974.

Degradation Sources in GaAs–AlGaAs Double-Heterostructure Lasers

RYOICHI ITO, HISAO NAKASHIMA, MEMBER, IEEE, SEIGO KISHINO, AND OSAMU NAKADA

Abstract—Several sources of the dark-line defect (DLD) that causes rapid degradation of GaAs–AlGaAs double-heterostructure (DH) lasers have been identified by means of photoluminescence (PL) topography and a laser-induced degradation technique. All the sources that have been identified correspond to crystal defects, among which dark-spot defects (DSD) that are native to as-grown wafers are found to be most important. The growth and propagation processes of DLD's and DSD's have also been investigated. These defects are found to be highly mobile under high-intensity laser pumping. The correlation between the substrate dislocations and the DSD's has been examined by etching and X-ray topography. Although most DSD's correspond to etch-pits in epilayers, they are not always correlated with substrate dislocations.

I. Introduction

IT IS NOW well established that rapid degradation of GaAs-$Al_xGa_{1-x}As$ double-heterostructure (DH) lasers is caused by the development of local regions of low luminescence efficiency, or dark-line defects (hereafter denoted as DLD) in the active layer during device operation [1]-[3]. Furthermore, DLD's have been identified as dislocation networks by a transmission-electron-microscope observation [4]. Dislocations threading through the active layer have been proposed to generate DLD's.

Experimentally, however, little has been reported on the sources and growth processes of DLD's. A remarkable feature of the DLD is that the ease with which it is generated is very sensitive to the location on the wafer. We have attempted to clarify the factors leading to the growth of DLD's, or more practically, which part of a wafer is susceptible to degradation. If this objective can be achieved, the yield of degradation-resistant devices should be significantly increased.

The purpose of this paper is to show that the majority of DLD's originate at crystal defects, both gross and microscopic, that can be identified by spatially resolved photoluminescence (PL) observation, or PL topography. Some new features will also be reported on the growth processes of DLD's, which may provide a new insight on the nature of DLD's.

II. Experimental

The growth processes of DLD's in DH crystals have been investigated by means of PL topography and a laser-induced degradation technique. PL topography, which has been developed independently by us [5] and Johnston and Miller [6], provides a simple, rapid, and nondestructive means of assessing the overall quality of DH wafers. The only requirement is that the pumping laser power reach the active layer: the p^+-GaAs layer normally grown to reduce the contact resistance has to be removed, and the p-$Al_xGa_{1-x}As$ layer has to be transparent to the pumping beam. The latter requirement leads to $x \gtrsim 0.5$ for the 6471-Å line of the krypton-ion laser. DH wafers employed in our experiments were composed of a Te-doped n-GaAs substrate (300-500 μm thick), a Sn-doped n-$Al_xGa_{1-x}As$ layer ($x \cong 0.5$, 5 μm thick), an undoped $Al_yGa_{1-y}As$ active layer ($y \cong 0.05$, 0.3-1 μm thick), and a Ge-doped p-$Al_xGa_{1-x}As$ cap layer ($x \cong 0.5$, 2-11 μm thick).

A variety of growth imperfections have been revealed by PL topography; an example is shown in Fig. 1 which compares

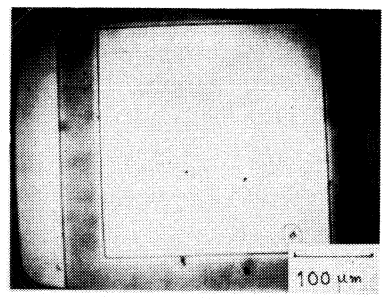

(a)

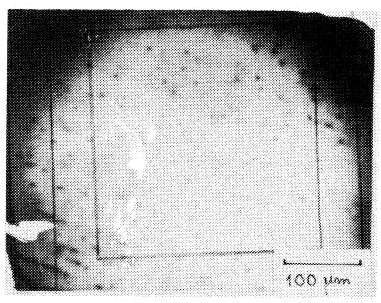

(b)

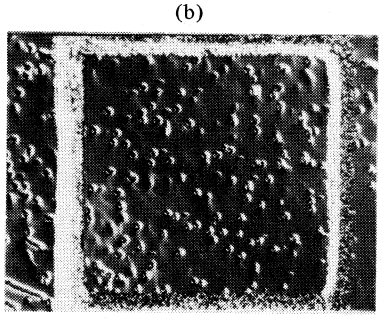

(c)

Fig. 1. Growth imperfections in the active layer of a DH crystal revealed by PL topography. (a) Photomicrograph of the surface of a three-layer DH crystal. The square pattern is an oxide deposited to identify the location. (b) PL pattern of the active layer. (c) Photomicrograph of the surface of the active layer after removal of the top ternary layer.

Manuscript received November 27, 1974; revised January 20, 1975. This work was supported in part by the Ministry of International Trade and Industry.

The authors are with the Central Research Laboratory, Hitachi, Ltd., Kokubunji, Tokyo 185, Japan.

the surface of the top ternary layer, the PL pattern of the active layer, and the surface of the active layer that has been exposed by removing the ternary layer. Dark spots apparent in the PL pattern coincide precisely with physical defects localized in the active layer [5]. These physical or morphological defects can also be observed by IR transmission image and should be distinguished from microscopic defects which are more subtle in nature and more important in generating DLD's, as will be discussed later.

When the pump intensity is increased to several kilowatts/square centimeter, DLD's are often observed to grow, whether the sample is lasing or not [7], [8]. In fact, most of our experiments were done on as-grown wafers. If the carrier lifetime is assumed to be 5 ns [3], the concentration of excited electron-hole pairs is estimated to be $3.3 \times 10^{18}/cm^3$ for $d = 0.5$ μm and a pump power of 10 kW/cm^2. The temperature rise at the pumped region has been estimated to be at most 80°C at an intensity of 10 kW/cm^2. This estimate was based on the measurement of the spectral shift in homoepitaxial wafers. In the case of DH crystals, large spectral distortions, or even the peak shift to higher energies with an increase of pump power, negated any attempt to estimate the temperature rise.

The features of optically induced DLD's are so similar to those of electrically induced DLD's that there is little doubt about the identity of both the defects. This has been recently confirmed by Petroff *et al.* by TEM observation [9].

III. Results and Discussions

A. Sources of Dark-Line Defects

We have found that DLD's originate at particular sites in wafers where crystal defects exist. Dark-line sources, which we have identified, include various kinds of surface damages induced by scratches, indentations, nonuniform bonding, etc., crystal edges, stacking faults, and small dark spots observed in PL patterns of undegraded wafers. Areas free from these dark-line sources have been found to suffer little, if any, degradation. Once a DLD is generated, however, it can be propagated into any part of the wafer by moving the laser beam.

Any surface damage is almost certainly lethal with respect to long-life device operation. Relatively deep surface damage, irrespective of whether it reaches the active layer or not, causes darkening in the PL pattern instantly [10], [11]. More slight or shallow damage does not cause darkening unless the sample is highly pumped. With high-intensity laser pumping, however, DLD's are developed in the damaged area.

In order to gain more quantitative information, we have damaged a wafer with a Knoop indenter. In Fig. 2 are shown (a) the photomicrograph of a surface indented with a load of 4 ~ 7 g, (b) the undegraded PL pattern, and (c) the PL pattern after 10-min laser pumping. The top ternary layer is 11 μm thick. The longer diagonal of the indentation under a load of 8.6 g was found to be 12.9 μm. This yields a Knoop hardness value of 740 kg/mm^2. The depth of the indentation is roughly an order of magnitude smaller than the longer diagonal. As seen in Fig. 2(c), DLD's show up as doublets at every indented site. The relation between the thickness of the ternary layer and the separation of the doublet DLD suggests

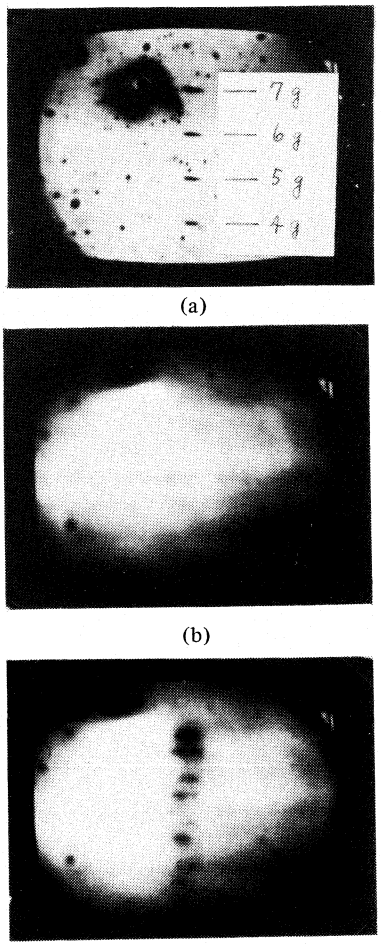

(a)

(b)

(c)

Fig. 2. DLD generation from surface indentations. (a) Photomicrograph of a surface indented with a Knoop indenter under a load of 4 ~ 7 g. (b) PL pattern before degradation. (c) PL pattern after 10-min laser pumping.

that the defects, presumably dislocations, have penetrated from the surface with an angle of 50 ~ 60°.

The fact that the ternary layer is extremely susceptible to damage is also evidenced by the observation that an Ar 4880-Å beam, which is almost totally absorbed in the ternary layer, burns holes in the surface at a power density exceeding ~10 kW/cm^2, as shown in Fig. 3. DLD's are naturally developed in the active layer, as seen in Fig. 3(b). This and other surface-damage effects could probably be explained by penetration of dislocations from the surface which is highly strained owing to the binary-ternary lattice mismatching. Obviously, we should avoid any processes that might exert local stresses at the surface [10], [11].

We have checked the effect of temperature rise on the development of DLD's in scratched wafers. In Fig. 4 are shown PL patterns of (a) an undegraded part scratched with tweezers, (b) the same region after being heated at 180°C for 10 min and then cooled to room temperature, and (c) the same region after a 5-kW/cm^2 pumping for 2 min at room temperature. The heat treatment had no effect, while the laser pumping produced DLD's rapidly. This observation indicates that high pump intensity is far more effective in generating DLD's than

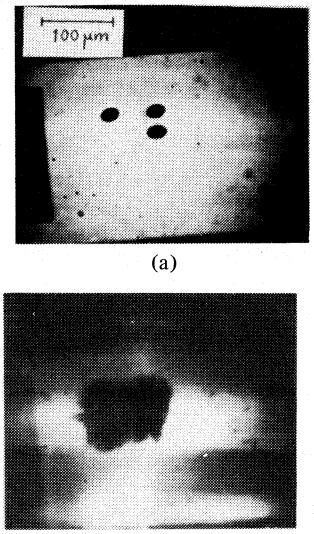

(a)

(b)

Fig. 3. Holes burnt in the surface of a DH crystal by irradiation with an Ar 4880-Å beam at an intensity of 10 kW/cm^2. (a) Photomicrograph of the surface. (b) PL pattern of the active layer.

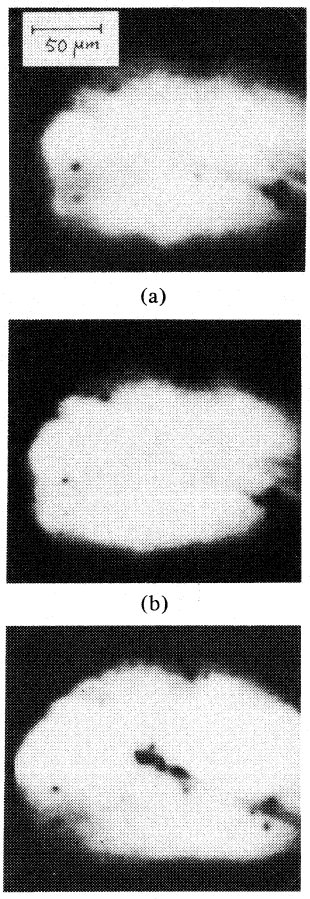

(a)

(b)

(c)

Fig. 4. Effect of a temperature rise on the DLD generation from a surface damage. (a) PL pattern of an undegraded wafer scratched with tweezers. (b) PL pattern taken after the wafer was heated at 180°C for 10 min and then cooled to room temperature. (c) PL pattern taken after a 5-kW/cm^2 pumping for 2 min at room temperature.

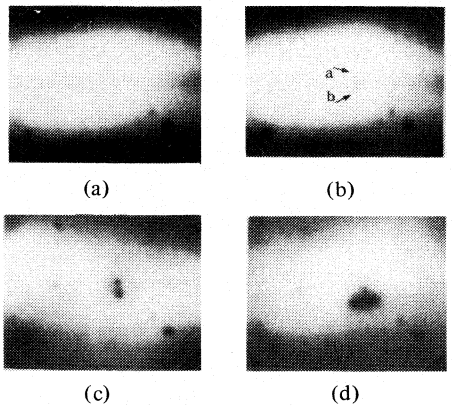

(a) (b)

(c) (d)

Fig. 5. PL patterns showing a DLD generation from a stacking fault. Pumping: 5 kW/cm^2. (a) Initial. (b) 12 min. (c) 28 min. (d) 120 min.

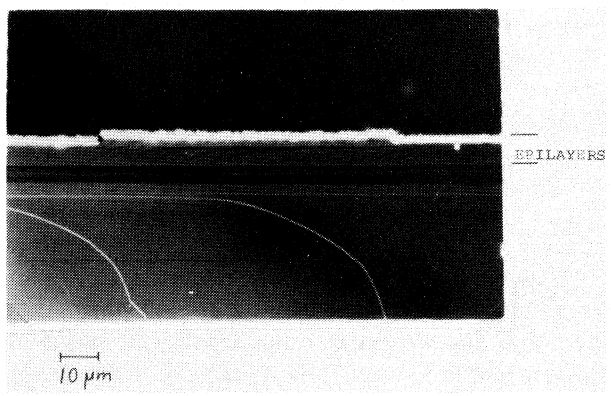

Fig. 6. Microsteps in a cleaved mirror-facet of a mesa-stripe-geometry DH laser revealed by differential-interference-contrast microscopy.

is temperature rise. It is to be noted that the temperature rise of the active layer of laser diodes operated CW is normally $10 \sim 20$°C.

Stacking faults, which are observed as short-line defects oriented along ⟨110⟩ directions on (100) wafers, have been found to nucleate DLD's. A sequence of photographs shown in Fig. 5 show how a DLD is developed from a stacking fault. Under high-intensity pumping, dark spots appear at the end points, marked by the arrows *a* and *b*, of a stacking fault. They grow darker, and eventually a DLD is grown from one of the dark spots. Presumably DLD's originate at partial dislocations threading through the active layer.

We have found that some crystal edges, both cleaved and scribed, give rise to DLD's. Dislocation generation from the crystal edge is well known in silicon technology. Stress concentration as well as microdefects produced in the process of cleaving and scribing are probably responsible for the generation of DLD's. In fact, differential-interference-contrast microscopy reveals in a number of cases the existence of microsteps in the cleaved facet, particularly in epilayers, as illustrated in Fig. 6. Although the correlation between these microsteps and degradation is yet to be established, more attention should be paid to the process of preparing mirror facets.

DLD's have also been found to originate at those defects

that appear as dark spots, several micrometers in extent, observed in PL patterns of undegraded samples. A typical example is illustrated in Fig. 7, where PL patterns before and after high-intensity laser pumping are shown. In this case, DLD's in Fig. 7(b) were grown from several dark spots marked as *a–h* in Fig. 7(a). Under laser pumping, dark spots become darker, and eventually DLD's develop from these spots. Since almost all dark spots give rise to DLD's, they are considered to be the most important sources of rapid degradation, at least in our DH wafers, at the present stage.

Several attempts have been made to identify the nature of these defects. First of all, the dark-spot defects (hereafter denoted as DSD) in question are different from the dark spots as shown in Fig. 1. The latter are morphological defects caused by the imperfect epitaxial growth and can be eliminated by addition of a small amount of aluminum ($x \cong 0.01 \sim 0.05$) in the active layer [10]. It seems that a small but finite amount of thermodynamic activity of aluminum in the melt facilitates the smooth growth of the active layer on the n-type ternary layer.

A comparison was made between the PL pattern of the active layer and that of the underlying substrate. In a number of cases a good correspondence was obtained as regards the position of DSD's [8]. An etching study showed that while the majority of etch-pits correspond to DSD's, as illustrated in Fig. 8, the contrary is not always true. Furthermore, an X-ray topographic examination indicates that dislocations inherited from the substrate do not always give rise to DSD's and therefore DLD's.

These observations suggest that DSD's have several origins. Although the substrate dislocation is certainly one candidate, it is not always active. Segregated impurities and macroscopic foreign particles such as carbon powder are other possibilities. More detailed study is needed to clarify the nature of DSD's. It seems obvious, however, that the use of good substrates with low dislocation-densities and a careful control of crystal-growth processes are highly beneficial in obtaining good diodes.

B. Some Features of Dark-Line-Defect Propagation

The growth velocity of DLD's is typically $10^{-6} \sim 10^{-5}$ cm/s at a power density $\sim$10 kW/cm^2, and somewhat increases at elevated temperatures. In certain cases, fast-growing ⟨110⟩-oriented DLD's, with a velocity as high as $10^{-3} \sim 10^{-2}$ cm/s, have been observed. In such cases, minute step-lines, quite similar to slip bands observed in plastically deformed metals, can be seen on the surface of the wafer with differential-interference-contrast microscopy, as illustrated in Fig. 9. DLD's exactly corresponding to the surface step-lines are developed in the active layer.

Some DSD's have been observed to move along ⟨110⟩ directions under high-intensity laser pumping. Fig. 10 illustrates an example. DSD's marked as $a \sim d$ have changed their position and contrast as a result of a short-period (several seconds) pumping. The velocity is very fast, on the order of $10^{-3} \sim 10^{-2}$ cm/s. This observation clearly indicates that dislocations are involved in these DSD's.

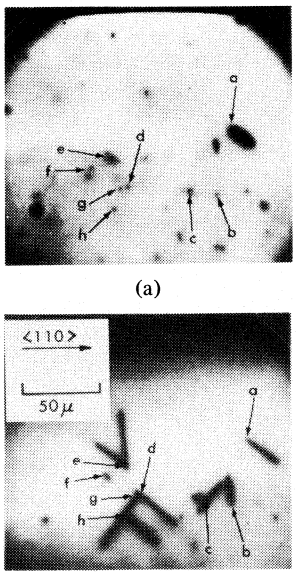

Fig. 7. DLD generation from DSD's that are native in as-grown wafers. (a) PL pattern before degradation. (b) PL pattern after laser pumping.

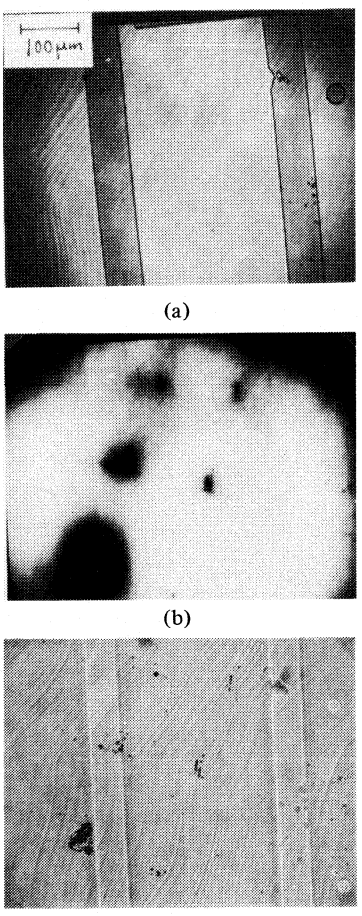

Fig. 8. DSD's and etch-pits. (a) Surface of a DH crystal. The stripes are oxide overlays. (b) PL pattern of the active layer. (c) Etch-pits in the epilayer revealed by the *AB*-etchant [17].



(a)

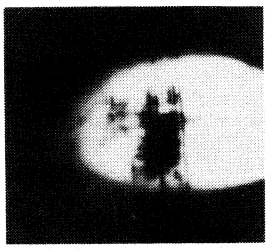

(b)

Fig. 9. Step-lines associated with fast-growing DLD's. (a) Differential-interference-contrast photomicrograph of the surface of a degraded wafer. (b) PL pattern of the active layer.

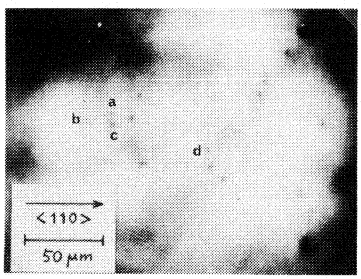

(a)

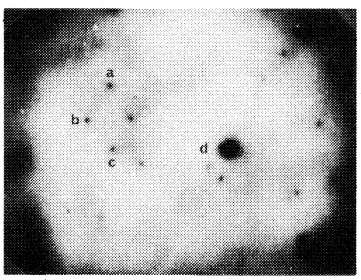

(b)

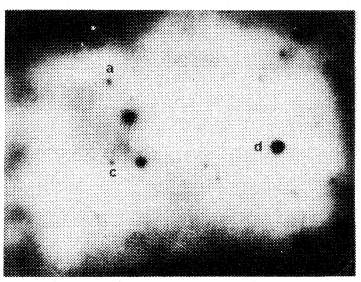

(c)

Fig. 10. Movement of DSD's under high-intensity laser pumping. (a) Initial PL pattern. (b), (c) PL patterns after pumping for several successive seconds.

The contrast of a DLD depends on the pump intensity and pump time. The observation that the DLD becomes darker as the pumping is continued suggests that the DLD has an internal structure, consistent with the three-dimensional dislocation-network structure as revealed by TEM study [4].

The previous observations indicate that both climb and, possibly, glide processes of dislocations are responsible for the DLD propagation. The remarkably high velocity of the DLD propagation and the motion of DSD's is puzzling [12], even if account is taken of the misfit-induced stresses [13].

Quite recently, DLD's and DSD's similar to those in the DH crystal were observed in electrically pumped single-heterostructure and homoepitaxial crystals [14]; also in optically pumped GaP crystals [15]. In view of these facts, we are inclined to regard the DLD generation as a rather prevailing phenomenon in III-V semiconductors. The unusually high mobility of dislocations and the very rapid climb in the presence of high-density carriers should be studied in more detail not only from the viewpoint of device physics but also from that of dislocation theory.

IV. Conclusions

Various sources of DLD's in GaAs-AlGaAs DH lasers have been identified by means of PL topography and a laser-induced degradation technique. Degradation sources that have been identified include various kinds of surface damages, crystal edges, stacking faults, and DSD's observed in PL patterns of undegraded wafers. All these sources are considered to involve dislocations [18]. Some DSD's are dislocations inherited from the substrate, while others are created only in the epilayers. Although not all the substrate dislocations are active as degradation sources, the use of low-dislocation-density substrates tends to provide a higher yield of long-life devices.

Under high-intensity pumping, some DSD's move with unusually high velocities, and DLD's grow with unexpected rapidity. The mechanisms of the dynamical behaviors of these defects are not yet understood.

Although PL topography has proved to be very useful in evaluating three-layer DH crystals, it cannot be applied straightforwardly to the four-layer structure that is normally employed in CW lasers. However, the improved mesa-stripe geometry that we have developed [16] is amenable to PL inspection, since in this geometry mesa-etching is stopped halfway in the p-type ternary layer and thus the active layer beneath the etched region can be inspected by PL topography.

This selection method and other improvements in fabrication processes have resulted in the increased yield of obtaining devices that have a CW life exceeding 1000 h. In order to obtain a CW life exceeding, say, 10 000-h reproducibly, it is felt that degradation mechanisms other than the DLD should be intensively investigated.

Acknowledgment

The authors wish to thank N. Chinone for assistance in the measurements, and S. Nakamura, Y. Sasaki, H. Matsuda, and Y. Suzuki for preparation of the samples.

REFERENCES

[1] B. C. De Loach, Jr., B. W. Hakki, R. L. Hartman, and L. A. D'Asaro, "Degradation of CW GaAs double-heterojunction lasers at 300 K," *Proc. IEEE* (Lett.), vol. 61, pp. 1042–1044, July 1973.

[2] H. Yonezu *et al.*, "Degradation mechanism of (Al · Ga)As double-heterostructure laser diodes," *Appl. Phys. Lett.*, vol. 24, pp. 18–19, Jan. 1974.

[3] N. Chinone, R. Ito, and O. Nakada, "Measurement of minority carrier lifetime during gradual degradation of GaAs-$Ga_{1-x}Al_xAs$ double-heterostructure lasers," *IEEE J. Quantum Electron.* (Corresp.), vol. QE-10, pp. 81–84, Jan. 1974.

[4] P. Petroff and R. L. Hartman, "Defect structure induced during operation of heterojunction GaAs lasers," *Appl. Phys. Lett.*, vol. 23, pp. 469–471, Oct. 1973.

[5] R. Ito, H. Nakashima, and O. Nakada, "A simple method for obtaining luminescent pattern of double heterostructure crystals," *Japan. J. Appl. Phys.*, vol. 12, pp. 1272–1274, Aug. 1973.

[6] W. D. Johnston, Jr., and B. I. Miller, "Degradation characteristics of CW optically pumped $Al_xGa_{1-x}As$ heterostructure lasers," *Appl. Phys. Lett.*, vol. 23, pp. 192–194, Aug. 1973.

[7] W. D. Johnston, Jr., W. M. Callahan, and B. I. Miller, "Observation of dark-line degradation sites in AlGaAs/GaAs DH laser material by etching and phase-contrast microscopy," *J. Appl. Phys.*, vol. 45, pp. 505–507, Feb. 1974.

[8] R. Ito, H. Nakashima, and O. Nakada, "Growth of dark lines from crystal defects in GaAs-GaAlAs double heterostructure crystals," *Japan. J. Appl. Phys.*, vol. 13, pp. 1321–1322, Aug. 1974.

[9] P. Petroff, W. D. Johnston, Jr., and R. L. Hartman, "Nature of optically induced defects in $Ga_{1-x}Al_xAs$-GaAs double heterojunction laser structures," *Appl. Phys. Lett.*, vol. 25, pp. 226–228, Aug. 1974.

[10] O. Nakada, R. Ito, H. Nakashima, and N. Chinone, "Spectral and spatial behavior of luminescence from the active layer of GaAs-$Ga_{1-x}Al_xAs$ double heterostructure laser diodes," in *Proc. 5th Conf. Solid State Devices* (Tokyo, Aug. 1973), pp. 43–48.

[11] W. D. Johnston, Jr., "Macroscopic deterioration of fluorescence from $Al_xGa_{1-x}As$-GaAs DH material following microscopic physical damage," *Appl. Phys. Lett.*, vol. 24, pp. 494–496, May 1974.

[12] V. B. Osvenskii, L. P. Kholodnyi, and M. G. Mil'vidskii, "Influence of dopants on the velocity of dislocations in GaAs single crystals," *Sov. Phys.–Solid State*, vol. 15, pp. 661–662, Sept. 1973.

[13] F. K. Reinhart and R. A. Logan, "Interface stress of $Al_xGa_{1-x}As$-GaAs layer structures," *J. Appl. Phys.*, vol. 44, pp. 3171–3175, July 1973.

[14] H. Yonezu, T. Kamejima, M. Ueno, and I. Sakuma, paper presented at the Autumn Meet. Japan Society of Applied Physics, Fukui, Oct. 1974.

[15] K. Aiki, private communication.

[16] O. Nakada, N. Chinone, S. Nakamura, H. Nakashima, and R. Ito, "Continuous operation over 2500 h of double heterostructure laser diodes with output powers more than 80 mW," *Japan. J. Appl. Phys.*, vol. 13, pp. 1485–1486, Sept. 1974.

[17] M. S. Abrahams and C. J. Buiocchi, "Etching of dislocations on the low-index faces of GaAs," *J. Appl. Phys.*, vol. 36, pp. 2855–2863, Sept. 1965.

[18] P. Petroff and R. L. Hartman, "Rapid degradation phenomenon in heterojunction GaAlAs-GaAs lasers," *J. Appl. Phys.*, vol. 45, pp. 3899–3903, Sept. 1974.

Degradation in Injection Lasers

G. R. WOOLHOUSE

Abstract—**The climb networks to be expected in an injection laser through 1) electromigration and 2) thermomigration are considered. It is shown that a model involving electromigration and dislocation pipe diffusion can explain the experimental results [1], [2], [7]. It is predicted that thermomigration may be important in optically pumped devices. It is further shown that elastic strain, *per se*, cannot be responsible for the degradation.**

Where numerical reduction is appropriate, parameters of the GaAs-$Ga_{1-x}Al_xAs$ system are used. The activation energy for pipe diffusion in GaAs is estimated to be 0.75 eV and the process is believed to be controlled by the diffusion of arsenic vacancies.

I. INTRODUCTION

THE short lifetime of CW-operated GaAs-$Al_xGa_{1-x}As$ injection lasers is a problem that has stimulated much recent interest [1]-[5]. The degradation is associated with the appearance of dark-line defects (DLD's) in electroluminescent patterns of the operating device. Despite much speculation, the nature of the DLD remained a mystery until Petroff and Hartman [1] showed by transmission electron microscopy that it was due to the development of a densely packed dislocation network extending through the active region of the device and into the neighboring Al-rich regions. It was apparent that the network originated from a single threading dislocation (one passing through all the epitaxial layers from the substrate to the epilayer surface). In addition, Petroff and Hartman [7] reported that the loops present within the network were of the *vacancy* type, i.e., formed by the precipitation of vacancies on the threading dislocation. However, more recent results due to Hutchinson *et al.* [2] indicate that the networks are basically of the *interstitial* type although some vacancy loops were found due to a pinching-off process within the body of the network. These apparently divergent results can be brought into concordance by assuming that the loops examined by Petroff and Hartman were formed by a pinching-off process within the body of an otherwise interstitial-type network as proposed by Hutchinson *et al.* In any event, both sets of observations rule out the possibility that the dislocations in the network are generated solely by

Manuscript received December 26, 1974; revised January 29, 1975.

The author is with the IBM Thomas J. Watson Research Center, Yorktown Heights, N.Y. 10598.

the action of a stress (glide) and indicate that climb is operative. In the absence of large stresses this process necessitates diffusion (a very slow process in GaAs at room temperature [6]). It is therefore, at first sight, surprising that the networks develop so rapidly (typically, within a few hours).

The purpose of this paper is to show how the development of dislocation networks such as those observed by Petroff and Hartman [1] and Hutchinson *et al.* [2] can be accounted for semiquantitatively. The model presented invokes the mechanism of *pipe diffusion* and the phenomenon of *electromigration* (EM). Effects of *thermomigration* (TM) are also considered. Unfortunately, certain parameters for these processes in GaAs are not known accurately. The theory can therefore only be shown to be plausible at this stage.

II. Point-Defect Sources and Migration Forces

To account for the extensive climb of a threading dislocation it is necessary to understand the source of the point defects (whether vacancies or interstitials). Petroff and Hartman [7] invoke the existence of a quenched-in vacancy supersaturation associated with the epilayer interfaces, whereas Hutchinson *et al.* [2] believe that there exists a quenched-in supersaturation of free interstitials in doped GaAs. It is the central theme of this paper that a dislocation is induced to climb at points along its length where *divergences* of the *atomic flux due to pipe diffusion* exist. There are two cases to consider.

Case 1: The divergence is such that a *supersaturation* of vacancies arises at some point in the dislocation pipe. The dislocation is forced to climb at that point to return the vacancy concentration to its equilibrium value thus creating a *vacancy*-type network, i.e., the excess vacancies are *absorbed* by the dislocation.

Case 2: The divergence is such that a local *undersaturation* of vacancies arises at some point in the dislocation pipe. It is then forced to climb creating an *interstitial*-type network, i.e., vacancies are *emitted* by the dislocation in an attempt to bring the local concentration back up to equilibrium. These processes are shown schematically in Fig. 1 for a threading dislocation (taken to be pure edge for the sake of simplicity).

Friedel [18, p. 107] has an expression for the *climb force* which for a pure-edge dislocation reduces to

$$F_c = \frac{kT}{b^2} \ln\left(\frac{c}{c_0}\right) \tag{1}$$

where

- b Burgers vector of the dislocation;
- c actual vacancy concentration in the neighborhood of the dislocation;
- c_0 equilibrium vacancy concentration in the neighborhood of the dislocation.

Case 1 corresponds to $c \gg c_0$: the climb force is large and positive and acts to decrease the area of extra half-plane. This is consistent with Thompson and Balluffi's [41] definition of *positive climb*.

Case 2 corresponds to $c \ll c_0$: the climb force is large and negative and acts to increase the area of extra half-plane. This is consistent with Thompson and Balluffi's definition of *negative climb*.

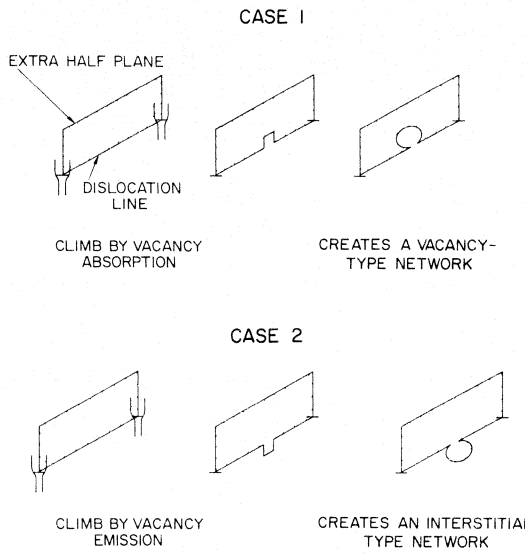

Fig. 1. Dislocation climb due to vacancy supersaturation (Case 1) and vacancy undersaturation (Case 2). See text for further explanation.

In this paper the existence of such divergences is sought and found to be an *intrinsic* function of the operation of the device rather than being dependent upon the *thermal history* of the epitaxially grown material [2], [7]. It is not hereby claimed that point-defect supersaturations do not preexist in laser material, but merely that their preexistence is not required for the development of climb networks.

III. Electromigration (EM)

Whenever an electric current flows in a material it is accompanied by a flow of atoms. This phenomenon, EM [8], [9] is due to two driving forces.

1) Electrostatic Drive: This is the force acting on the ions due to the electric field analogously to the force acting on the ions in an electrolytic cell. This always acts to drive the positive ions in the direction of the electric field and has the same sense on a given ion in p-type as in n-type material.

2) Carrier-Wind Force: This is a frictional force acting on the atoms of a solid due to the motion of the charge carriers. For the sake of simplicity we will consider the forces acting on vacancies. An analogous argument could easily be constructed for interstitials. In n-type material the carriers (electrons) flow opposite to the applied electric field and hence the atoms are also forced in this direction. Thus vacancies are forced parallel to the electric field. In p-type material, on the other hand, the carriers (holes) flow parallel to the electric field, forcing vacancies opposite to the applied electric field. This argument was apparently first given by Fiks [11] and extensive experimental confirmation of it has been reported in the Soviet literature on Si, Ge, and InAs [34]-[40]. In addition, this reversal effect, which is summarized in Fig. 2, has been observed for Cu and Li impurities in GaAs by Boltaks and Dzhafarov [10]. Carrier-wind effects are expected to become important in semiconductors when the carrier concentration reaches the 10^{17}-10^{19}/cm^3 range [11]. Laser material for electrically pumped de-

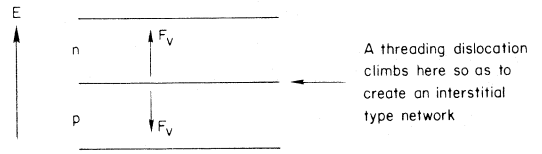

Fig. 2. Vacancy driving forces due to carrier-wind effects (electromigration) at a p-n junction operated in forward bias.

vices is usually doped to these levels so that we anticipate that carrier-wind effects will be important. In the case of a forward-biased p-n junction illustrated in Fig. 2, carrier-wind effects lead to a net flux of vacancies away from the junction and thus to the development of an *interstitial-type network* (Case 2). This is consistent with the experimental results as discussed in Section I.

It is usual to combine both electrostatic drive and carrier-wind effects by writing the complete force for EM as

$$F_{EM} = Z^* e \rho j \tag{2}$$

where

Z^* effective atomic number of a moving ion;
e electronic charge;
ρ the resistivity of the material in question;
j the current density.

All these parameters are known in the GaAs-$Ga_{1-x}Al_xAs$ system except for Z^* which has not been measured for vacancies as far as the author is aware. However, to predict the rate of climb of the dislocation we need ΔZ^*, the change in Z^* across the p-n junction. In general this will be a function of the carrier concentrations in the p- and n-regions and also possibly the temperature. According to the data of Boltaks and Dzhafarov for Cu in GaAs, its value lies in the neighborhood of 0.47 at 820-830°C, which, fortuitously, is identical to the value obtained by Rembeza [40] for Au in InAs at 520-670°C with $1.6 \times 10^{17}/cm^3$ carriers in the n-region and $3 \times 10^{19}/cm^3$ carriers in the p-region. Although the data of Sterkhov and Pavlov [38] indicate that ΔZ^* for self-diffusion may be larger than this, we will take $\Delta Z^* \simeq 0.5$. Typical values for some of the other parameters in (1) are: $\rho = 0.2\ \Omega \cdot$ cm (Ge-doped $Ga_{0.7}Al_{0.3}As$, $n = 5 \times 10^{17}/cm^3$) [12] and $j = 2 \times 10^3$ A/cm^2 (typical threshold current density) [13]. Thus $\Delta F_{EM} \simeq 1.2 \times 10^2$ eV/cm, where ΔF_{EM} is the change in driving force across the junction. This result will be used later to evaluate the rate of climb.

IV. Thermomigration (TM)

The active region of a laser is hotter than anywhere else since this is where electron-hole recombination takes place, and a substantial fraction of this recombination is nonradiative. Because of the need to conduct this heat away, temperature gradients exist in the device which can give rise to vacancy driving forces. The force for TM [9], [14] is

$$F_{TM} = -\frac{Q^*}{T}\frac{dT}{dZ}. \tag{3}$$

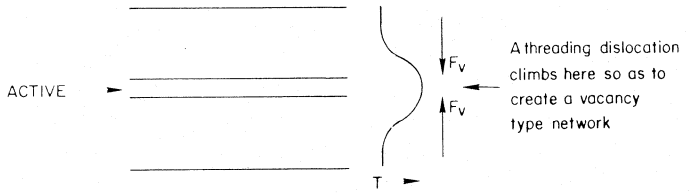

Fig. 3. Schematic temperature distribution and vacancy driving forces due to thermomigration in an injection laser. Q^* is assumed to be positive (see text).

Here, dT/dZ is the temperature gradient, T the temperature, and Q^* is the heat of transport.

The sense of F_{TM} is such that if Q^* is positive (which it is in most materials for which data exist [30]), matter is driven down the temperature gradient, and vacancies are driven into the active region from both sides. This is shown schematically in Fig. 3. It should be emphasized, however, that the vacancies are not merely driven in order to reestablish the equilibrium vacancy concentration in the active region—the driving force persists as long as the heat flow exists.

In order to evaluate (3) numerically we need to know the active-region temperature rise. The literature values for this are somewhat variable, running from 5°C to 50°C [3], [13], [15]. The average figure of 30°C is still unreasonably high by present standards for a well-heat-sunk electrically pumped device, but it is not believed to be an overestimate for optically pumped material. Using this figure we can calculate the temperature gradients in the device using values for the thermal conductivity of GaAs and $Ga_{0.7}Al_{0.3}As$ measured by Afromowitz [16]. Taking 0.7 μ and 1.0 μ for the thicknesses of the p-$Ga_{0.7}Al_{0.3}As$ and p-GaAs layers, respectively, we find the temperature gradient across the p-$Ga_{0.7}Al_{0.3}As$ layer to be a maximum because its thermal conductivity is a minimum. It has the value 3×10^5°C/cm under these conditions. If in addition we take Q^* for GaAs to be 1 eV (this has not been measured, but is a reasonable guess based on the values measured for other materials [30]), we obtain

$$\Delta F_{TM} \simeq 2 \times 10^3 \text{ eV/cm}$$

where ΔF_{TM} is the change in driving force across the active region. It is likely that TM will give rise to the development of *vacancy-type* networks (Case 1) although this depends on the assumption of a positive Q^*. It is anticipated that it will be important in optically pumped devices. It should be pointed out that the thermal gradients in an optically pumped heterojunction device arise from the fact that the absorption coefficient for the pumping light is much higher in the active region than in the bounding Al-rich layers. As the optical absorption is roughly uniform throughout a homojunction laser we would not expect it to degrade rapidly. Petroff *et al.* [31] have reported that optical pumping does not result in network formation in *homo*junctions while it does in *hetero*junctions. In addition, they reported that the networks developed are of the vacancy type consistent with the reasoning just presented, although they did not appear to determine this directly. Lastly, it should be mentioned that homojunction devices

are expected to degrade by DLD formation when electrically pumped as has been observed [29].

V. Elastic Strain

Another factor which has been invoked to explain the development of climb networks is elastic strain. This arises during the epitaxial growth of a layer on a substrate when there is misfit between the lattice parameters of overgrowth and substrate. The misfit can be accommodated in two ways: coherently or incoherently. In coherent accommodation there is perfect continuity between lattice planes of overgrowth and substrate and the misfit manifests itself in a bowing of the resultant wafer. In incoherent accommodation the misfit is taken up by regular arrays of misfit dislocations at each interface. For an up-to-date review of the subject of misfit dislocations see Matthews [43]. In both coherent and incoherent cases elastic strains exist in the wafer, and it is instructive to examine whether these strains can give rise to point-defect driving forces. To do this we have recourse to elasticity theory and write for the interaction energy between a vacancy and an elastic stress field σ_{ij}

$$E_{\text{int}} = - V_v \delta \sigma_{mm}. \tag{4}$$

Here V_v is the volume of a vacancy, δ is a parameter describing the relaxation around a vacancy (equal to one-third of the change of volume associated with it), and σ_{mm} is the trace of the stress tensor σ_{ij}. Thus the force on a vacancy is

$$F_{el} = - \frac{\partial E_{\text{int}}}{\partial z} \tag{5}$$

where z is taken normal to the epitaxial layers. The stress gradient can be estimated from the bowing of the wafer

$$\frac{\partial \sigma_{mm}}{\partial z} = \frac{6K}{R} \left(\frac{1 - 2\nu}{1 - \nu} \right). \tag{6}$$

Here K is the bulk modulus, ν is the Poisson's ratio, and R is the radius of curvature of the wafer; we have ignored local inhomogeneities in wafer composition. Taking

$V_v = 3.3 \times 10^{-23}$ cm^3 (estimated from [17])
$\delta \simeq 0.03$ (a typical value—see Friedel [18, p. 80])
$K = 7.5 \times 10^{11}$ dyn/cm^2 (from Brantley [19])
$\nu = 0.31$ (from Brantley [19])
$R = 7$ m (Rozgonyi *et al.* [20])

we find $F_{el} \simeq 2 \times 10^{-3}$ eV/cm.

There are two points to make about this result. The first is that it is a uniform force driving vacancies from the epilayer surface to the substrate—there are no divergences associated with it. Secondly, its magnitude is at least five orders of magnitude less than the migration forces discussed earlier.

Although with the epilayer thickness usually chosen, GaAs-$Ga_{1-x}Al_xAs$ lasers almost certainly have coherent interfaces, the case of incoherent interfaces will also be discussed here for the sake of completeness. A practical example is that of devices prepared from $In_xGa_{1-x}As$ on GaAs substrates which apparently do have incoherent interfaces [21]. One can say the following: the elastic stresses vanish at points farther from the interfaces than the misfit-dislocation spacing. Making certain simplifying assumptions about the nature of the misfit dislocations and using the known stress fields around them, one can evaluate the vacancy driving forces. We find that the forces are significant only very close to (within about 50 Å of) the misfit-dislocation core. Moreover, they fall off very rapidly (with the reciprocal of the square of the distance) in and away from the interface. Compared with the migration forces discussed earlier they can safely be neglected.

VI. Mode of Point-Defect Transport

It is possible to estimate the actual rate of accumulation of point defects in a degrading laser from Petroff and Hartman's published pictures [1]. They found that the dislocations in the network lay in the (001) plane. Thus the number of point defects in the network can be found by dividing the total area of the loops and dipoles by the cross-sectional area of a point defect. Taking 10^{-15} cm^2 for this [17], and 100 h for the degradation time, we arrive at a point-defect accumulation rate $\simeq 3 \times 10^3$/s, a value which cannot be accounted for by bulk diffusion alone: a simple calculation using the most recent values for the self-diffusion coefficient for Ga vacancies [6] predicts a point-defect accumulation rate which is 19 orders of magnitude too small.

The most likely explanation for the observed dislocation network development is that it is due to *pipe diffusion* along the threading dislocation. This is a phenomenon which has been fairly well studied in metals [22] and has also been observed in semiconductors [23]-[25]. Briefly, what happens in pipe diffusion is that the disordered material in the neighborhood of a dislocation permits much faster diffusion than in the bulk. Activation energies much smaller than in the bulk are found. To estimate the effect of this, it is usual to assume that the vacancies move in a "pipe" typically one or two atomic spacings in diameter.

We can calculate the activation energy for pipe diffusion (U_p) necessary to explain the observed point-defect accumulation rate (PDAR) as follows:

$$\text{PDAR} = D_0^p \exp\left(- \frac{U_p}{kT} \right) \cdot \frac{A_D}{V_v} \cdot \frac{\Delta F}{kT}. \tag{7}$$

In (7), PDAR is the point-defect arrival (or departure, in Case 2) rate at the point of divergence of the flux, and is obtained from the Einstein relationship for the drift velocity of a diffusing species due to a driving force. The velocity is multiplied by the cross-sectional area of the dislocation pipe A_D, and the concentration of vacancies in the pipe to give PDAR. The vacancy formation energy in the pipe is combined with the vacancy motion energy in the diffusion coefficient of a single defect in the pipe to give U_p, the activation energy for self-diffusion in the pipe. D_0^p is the preexponential factor in the pipe diffusion coefficient, ΔF is the change in driving force at the point of divergence, and the other quantities have their usual meanings.

We now assume that D_0^p is equal to the bulk value (examination of Balluffi's data for fcc metals shows that on the average this is a reasonable approximation). However, we are in a dilemma as to which species controls the diffusion rate: Ga or As vacancies. Examination of the data of Chiang and Pearson [6] indicates that the diffusivity of As vacancies is 31 orders of magnitude smaller than the diffusivity of Ga vacancies at room temperature. Since the process will be controlled by the slower diffusing species, it seems logical to take D_0^p equal to the preexponential factor for the diffusivity of As vacancies.

We can equate PDAR to the observed value (3×10^3/s) and set

$$\Delta F = 1.2 \times 10^2 \text{ eV/cm } (\Delta F_{EM})$$

$$A_D = 5.5 \times 10^{-15} \text{ cm}^2$$

$$D_0^p = 7.9 \times 10^3 \text{ cm}^2/\text{s for As vacancies [6]}.$$

We find $U_p = 0.75$ eV.

The activation energy for pipe diffusion is about one-fifth of the corresponding bulk value [6]. This ratio is low, but not totally unreasonable (Balluffi [22] reports values for this ratio between 0.4 and 0.7, and a value as low as 0.3 has also been reported [26], although these data relate only to fcc metals. There appears to be a shortage of equivalent data for semiconductors). In addition, the value of 0.75 eV is in good agreement with the value of the activation energy for degradation of GaAs light-emitting diodes (LED's) [32] (0.8 eV). Such precise agreement must be considered fortuitous at this stage, in view of the uncertainty about some of the parameters of the theory. Furthermore Hartman *et al.* [33] have obtained a value of 0.93 eV for the activation energy for degradation of GaP LED's. Thus it seems that the rate of DLD growth can be explained with this model, assuming reasonable values for the parameters. However, it is instructive to determine how sensitive the derived value of U_p is to some of these parameters. The DLD growth time was taken to be 100 h which seems to be a reasonable average figure for the lifetime of a laser failing by DLD formation. In fact, the derived value of U_p is relatively insensitive to the assumed value of the DLD growth time: it is 0.69 eV if the growth time is 10 h and 0.81 eV if it is 100 h. U_p varies with the assumed value of D_0^p in a similar manner.

Additional support for an EM model of the kind developed here lies in the experiments of Newman and Ritchie [27]. They found that the rate of degradation of heterojunction devices increased with the current density at the same rate, independent of whether the current was below or above the threshold value for lasing action, indicating that the degradation may be a purely electrical effect in this case, independent of the optical density in the device.

This model provides an alternative rationalization of the experimental data of McMullin *et al.* [13]. They found that lasers whose active regions were doped with Sn and Te degraded very much faster than those with active regions doped with Si and Ge. Kirkby [42] has argued on the basis of strain energy considerations that the tendency for dopant segregation to a dislocation would be greater in the case of Sn and Te than in the case of Si and Ge. Thus, in the former case, carrier-wind effects would be enhanced and ΔZ^* would be bigger, causing more rapid degradation.

This model also offers a possible explanation for the degradation of homojunction lasers [28] and LED's [29].

VII. Conclusions

1) EM and TM both can give rise to point-defect driving forces which are adequate to explain the observed development rates of climb networks.

2) EM probably predominates in well-heat-sunk electrically driven devices, and is predicted to give rise to interstitial-type networks consistent with the experimental evidence [1], [2], [7], as discussed in Section I.

3) TM is probably important in optically pumped devices, and is predicted to give rise to vacancy-type networks, consistent with a reported experimental observation [31]. This conclusion depends upon the assumption that Q^* is positive.

4) Elastic strain gives rise to driving forces many orders of magnitude less than migration effects.

5) The activation energy for pipe diffusion of vacancies in GaAs is estimated to be about 0.75 eV.

Acknowledgment

The author wishes to thank Dr. P. S. Ho and also various members of the IBM CW injection-laser group for useful discussions. Thanks are also due to Dr. P. W. Hutchinson, Dr. P. S. Dobson, and Dr. D. H. Newman for useful discussions and for access to their paper prior to publication. Particular thanks are due to Dr. A. W. Smith and Dr. J. C. McGroddy for advice and encouragement. The reviewers are to be thanked for pointing out some errors and numerous obscurities.

References

[1] P. Petroff and R. L. Hartman, "Defect structure introduced during operation of heterojunction GaAs lasers," *Appl. Phys. Lett.*, vol. 23, p. 469, 1973.

[2] P. W. Hutchinson, P. S. Dobson, S. O'Hara, and D. H. Newman, "The defect structure of degraded heterojunction GaAlAs-GaAs lasers," *Appl. Phys. Lett.*, vol. 26, p. 250, 1975.

[3] T. L. Paoli and B. W. Hakki, "CW degradation at 300°K of GaAs double heterostructure junction lasers. I. Emission spectra," *J. Appl. Phys.*, vol. 44, p. 4108, 1973.

[4] B. C. De Loach, Jr., B. W. Hakki, R. L. Hartman, and L. A. D'Asaro, "Degradation of CW GaAs double-heterojunction lasers at 300 K," *Proc. IEEE* (Lett.), vol. 61, pp. 1042-1044, July 1973.

[5] H. Yonezu *et al.*, "Degradation mechanism of (ALGa)As double heterostructure laser diodes," *Appl. Phys. Lett.*, vol. 24, p. 18, 1974.

[6] S. Y. Chiang and G. L. Pearson, "Lattice defects in annealed GaAs single crystals," *Bull. Amer. Phys. Soc.*, vol. 18, p. 1578, 1973.

[7] P. Petroff and R. L. Hartman, "Rapid degradation phenomenon in heterojunction GaAlAs-GaAs lasers," *J. Appl. Phys.*, vol. 45, p. 3899, 1974.

[8] H. B. Huntington, "Electromigration," in *Encyclopedia of Chemical Technology*, R. E. Kirk and D. F. Othner, Ed. New York: Wiley, 1971, p. 278.

[9] T. Hehenkamp, "Study of point defects in metals by electro- and thermo-transport," in *Vacancies and Intersititial in Metals*, A. Seeger *et al.*, Ed. New York: Elsevier, 1970, p. 91.

[10] B. I. Boltaks and T. D. Dzhafarov, "The effect of applied electric field on diffusion of impurities in gallium arsenide," *Phys. Status*

Solidi, vol. 19, p. 705, 1967.
[11] V. B. Fiks, "Entrainment of ions by electrons in semiconductors," *Soviet Phys.–Solid State*, vol. 1, p. 1212, 1959.
[12] K. K. Shih and G. D. Pettit, "Properties of Ge-doped GaAs and $Al_xGa_{1-x}As$, Sn-doped $Al_xGa_{1-x}As$ and Si-Te-doped GaAs," *J. Electron. Mater.*, vol. 3, p. 391, 1974.
[13] P. G. McMullin *et al.*, "Effect of doping on degradation of GaAs-$Al_xGa_{1-x}As$ injection lasers," *Appl. Phys. Lett.*, vol. 24, p. 595, 1974.
[14] H. B. Huntington, "Driving forces for thermal mass transport," *J. Phys. Chem. Solids*, vol. 29, p. 1641, 1968.
[15] D. H. Newman, S. Ritchie, and S. O'Hara, "Experimental tests of proposed mechanisms for gradual degradation of GaAs double-heterostructure injection lasers," *IEEE J. Quantum Electron.* (Corresp.), QE-8, pp. 379-382, Mar. 1972.
[16] M. A. Afromowitz, "Thermal conductivity of $Ga_{1-x}Al_xAs$ alloys," *J. Appl. Phys.*, vol. 44, p. 1292, 1973.
[17] M. E. Straumanis and C. D. Kim, "Phase extent of gallium arsenide determined by the lattice constant and density method," *Acta Crystallogr.*, vol. 19, p. 256, 1965.
[18] J. Friedel, *Dislocations.* New York: Pergamon, 1964.
[19] W. A. Brantley, "Calculated elastic constants for stress problems associated with semiconductor devices," *J. Appl. Phys.*, vol. 44, p. 534, 1973.
[20] G. A. Rozgonyi, P. M. Petroff, and M. B. Panish, "Elimination of dislocations in heteroepitaxial layers by the controlled introduction of interfacial misfit dislocations," *Appl. Phys. Lett.*, vol. 24, p. 251, 1974.
[21] M. Ettenberg *et al.*, "Metallurgical and electroluminescent characteristics of vapor-phase and liquid-phase epitaxial junction structures of $In_xGa_{1-x}As$," presented at the Conf. Preparation and Properties Electronic Materials, Boston, Mass., Sept. 1974.
[22] R. W. Balluffi, "On measurements of self-diffusion rates along dislocations in f.c.c. metals," *Phys. Status Solidi*, vol. 42, p. 11, 1970.
[23] D. A. Grenning and A. H. Herzog, "Dislocations and their relation to irregularities in zinc-diffused GaAsP p-n junctions," *J. Appl. Phys.*, vol. 39, p. 2783, 1968.
[24] H. Widmer, "Effect of dislocations on self-diffusion in germanium," *Phys. Rev.*, vol. 125, p. 30, 1962.
[25] H. J. Queisser, K. Hubner, and W. Shockley, "Diffusion along small-angle grain boundaries in silicon," *Phys. Rev.*, vol. 123, p. 1245, 1961.
[26] N. A. Gjostein, "Short circuit diffusion," *Diffusion* (American Society for Metals, 1973), p. 262.
[27] D. H. Newman and S. Ritchie "Gradual degradation of GaAs double-heterostructure lasers," *IEEE J. Quantum Electron.* (*Part II of Two Parts, Special Issue on 1972 IEEE Semiconductor Laser Conference*), vol. QE-9, pp. 300–305, Feb. 1973.
[28] H. Kressel and N. E. Byer, "Physical basis of noncatastrophic degradation in GaAs injection lasers," *Proc. IEEE*, vol. 57, pp. 25–33, Jan. 1969.
[29] J. R. Biard, G. E. Pittman, and J. F. Leezer, "Degradation of quantum efficiency in gallium arsenide light emitters," in 1966 Proc. Int. Symp. Gallium Arsenide, Reading, England, Sept. 1966; also in *Proc. Inst. Phys. and Phys. Soc.* (London, England, 1967), p. 113.
[30] P. S. Ho, "Electromigration and Soret effect in cobalt," *J. Phys. Chem. Solids*, vol. 27, p. 1331, 1966.
[31] P. Petroff, W. D. Johnston, Jr., and R. L. Hartman, "Nature of optically induced defects in $Ga_{1-x}Al_xAs$-GaAs double-heterojunction laser structures," *Appl. Phys. Lett.*, vol. 25, p. 226, 1974.
[32] H. Okamoto, S. Nakaya, and Y. Arai, in *Proc. 1973 IEEE 11th Annu. Reliability Physics Conf.*, p. 261.
[33] R. L. Hartman, B. Schwartz, and M. Kuhn, "Degradation and passivation of GaP light-emitting diodes," *Appl. Phys. Lett.*, vol. 18, p. 304, 1971.
[34] Yu. I. Kozlov, "Electrotransport of gold in heavily doped silicon," *Soviet Phys.–Semicond.*, vol. 5, p. 1074, 1971.
[35] M. K. Bakhadyrkhanov, B. I. Boltaks, and G. S. Kulikov, "Diffusion electrotransport and solubility of manganese impurities in silicon," *Soviet Phys.–Solid State*, vol. 14, p. 1441, 1972.
[36] B. I. Boltaks, G. S. Kulikov, and R. Sh. Malkovich, "Electrical transport of gold in silicon," *Soviet Phys.–Solid State*, vol. 2, p. 2134, 1961.
[37] B. I. Boltaks and S. I. Rembeza, "Diffusion and electrical transport of zinc in indium arsenide," *Soviet Phys.–Solid State*, vol. 8, p. 2117, 1967.
[38] V. A. Sterkhov and P. V. Pavlov, "Self diffusion of germanium along intrinsic dislocations in an external electric field," *Soviet Phys.–Solid State*, vol. 9, p. 495, 1967.
[39] V. A. Sterkhov, V. A. Panteleev, and P. V. Pavlov, "Diffusion and electrotransport of indium and silver along dislocations in silicon," *Soviet Phys.–Solid State*, vol. 9, p. 533, 1967.
[40] S. I. Rembeza, "Diffusion of gold in indium arsenide," *Soviet Phys.–Semicond.*, vol. 1, p. 516, 1967.
[41] R. M. Thompson and R. W. Balluffi, "Kinetic theory of dislocation climb," *J. Appl. Phys.*, vol. 33, p. 803, 1962.
[42] P. A. Kirkby, "Dislocation pinning in GaAs by the deliberate introduction of impurities," presented at the 4th IEEE Int. Semiconductor Laser Conf., Atlanta, Ga., Nov. 1974, Paper D5.
[43] J. W. Matthews, in *Dislocation Theory: An Encyclopaedic Handbook*, F. R. N. Nabarro, Ed. New York: Marcel Dekker, to be published, 1976.

Dislocation Pinning in GaAs by the Deliberate Introduction of Impurities

P. A. KIRKBY

Abstract—Recent work has shown that the primary cause of rapid degradation in GaAs-(GaAl)As lasers is the propagation of dark-line defects which originate at threading dislocations present in the as-grown material.

This paper considers the effect of first-order elastic interactions between dislocations and deliberately added impurities, such as the commonly used dopants and group III or V impurities. Strongly interacting impurities tend to concentrate preferentially around dislocations in positions where they relieve stress, thus forming an impurity cloud. Subsequent movement of the dislocation then becomes energetically unfavorable. For impurities such as In, Sb, and N the pinning forces can be as large as 10^{10} dynes/cm^2.

It seems likely that this type of dislocation pinning can be used to eliminate or greatly reduce the probability of a threading dislocation initiating a dark-line defect.

Introduction

RECENT WORK on [1]-[3] degradation in GaAs-(GaAl)As double-heterostructure lasers has shown that one of the primary degradation mechanisms results from the rapid movement and elongation of dislocations that thread the active layer of the device. The dislocations involved move at velocities of at least 10^{-7} cm/s, despite the fact that the average temperature of the active region is below 50°C. Dislocations are not normally mobile in GaAs at such a low temperature because of the high Peierls stresses resulting from the covalent bonding of GaAs. A temperature of over 200°C and stresses of over 10^8 dynes/cm^2 are needed to produce glide velocities greater than 10^{-7} cm/s [4], [5], the velocity being strongly dependent on dopant type. The dislocations have been found to move predominantly by climb rather than glide. Thus point defects must be intimately related to this process.

In many metals dislocations can be immobilized by the deliberate introduction of impurities. For instance, the hardness of aluminium is greatly increased by the introduction of impurities such as Si, Fe, Cu, and others [6]. This paper discusses the possibility of pinning dislocations in double-heterostructure lasers by the use of similar interactions. This would then eliminate the rapid degradation of lasers containing threading dislocations. The magnitude of the pinning force that results from the addition of various impurities at concentrations which will not deleteriously affect laser performance is calculated. It appears that certain group III or V impurities such as In, Sb, and Tl are the most suitable for this purpose. The pinning force resulting from their elastic-misfit interaction with dislocations will resist stresses approaching 10^{10} dynes/cm^2.

Manuscript received January 13, 1975; revised February 26, 1975. This work was sponsored by CVD, and was carried out with the support of the Procurement Executive, United Kingdom Ministry of Defence.

The author is with the Standard Telecommunication Laboratories Ltd., London Road, Harlow, Essex, England.

Dislocation-Impurity Interactions

Any interaction between an impurity and a defect such as a dislocation will alter the equilibrium impurity concentration c around the dislocation with respect to its concentration c_0 at a large distance from the dislocation. If the total interaction energy at any point is E_t, then the equilibrium concentration c of the impurity at that point, provided the solid solution is dilute, is given by the Boltzmann equation

$$c = c_0 \exp(-E_t/kT). \tag{1}$$

There are many contributions to the total interaction energy E_t between an impurity and a dislocation. Fiore and Bauer [6] describe the components of the total interaction that result from elastic misfit, elastic modulus, electrical, chemical, and other forces. Bullough and Newman [7] show that in silicon and germanium the elastic-misfit interaction is by far the most significant in all cases except when the impurity atom is of very similar radius to the host lattice atom for which it substitutes. Electrical interactions [6], [7], which result from interaction between a charged impurity atom and the electrical field of a dislocation may be significant for dopant impurities at a low temperature. However, when considering the uncharged group III or V impurities in GaAs we can ignore the electrical interaction. Let us therefore consider the elastic-misfit interaction between an impurity and the common 60° dislocation in GaAs.

Impurity Distribution Around 60° Dislocation

The energy of the elastic-misfit interaction between a 60° dislocation in GaAs and an impurity atom of radius R is given by [8, pp. 462–465]

$$E_i = \frac{\beta \sin\theta}{r} \tag{2}$$

where

$$\beta = \frac{4}{3}\frac{(1+\nu)}{(1-\nu)}\mu b_e R_0^3 \epsilon$$

where r and θ define the position of the impurity atom;

- ν Poisson's ratio is 0.3;
- μ Voight average shear modulus [8, pp. 398–405] is 4.9×10^{11} dynes/cm^2;
- b_e edge component of Burger's vector is 3.5 Å;

R_0 radius of host-lattice atom for which impurity substitutes;
ϵ $= (R - R_0)/R_0$.

Thus, assuming that the elastic-misfit interaction is dominant, the impurity concentration around the dislocation is given by

$$c \simeq c_0 \exp(-\beta \sin\theta / rkT). \tag{3}$$

These equations, which assume linear elasticity theory, break down very close to the core of the dislocation where the stresses are so large that the atomic displacements are an appreciable fraction of the interatomic distances. It is usual to assume that the interaction energy limits at a maximum value $E_{i\max} \simeq |\beta/b|$. The value of the interaction coefficient β, which is directly proportional to the impurity misfit parameter ϵ, indicates the strength of the interaction between any given impurity and a dislocation of a particular Burger's vector. As would be expected, small impurity atoms have increased concentration on the side of the dislocation containing the extra half-plane and reduced concentration on the opposite side. This is illustrated in Fig. 1. For weak interactions ($\beta/b < kT$), the increase of impurity concentration on one side of the dislocation is equal to the decrease on the opposite side so that, averaged around the dislocation, there is no net effect on impurity incorporation. For strong interactions, however, there is a net increase in the concentration of impurity atoms around the dislocation. This region of local accumulation is referred to as an impurity cloud. For strong interactions at sufficiently low temperatures the impurity concentration can reach the atomic density of the host lattice and precipitation occurs. Under these conditions it is necessary to use the Fermi-Dirac distribution to obtain the impurity concentration [8, pp. 465-468]. The linear impurity concentration along the dislocation core c_d is then given to a better approximation by

$$c_d \simeq \left(a + \frac{na}{c_0} \times \exp(-E_{t\max}/kT)\right)^{-1} \tag{4}$$

where

a separation of atoms along core of dislocation (= 4 Å);

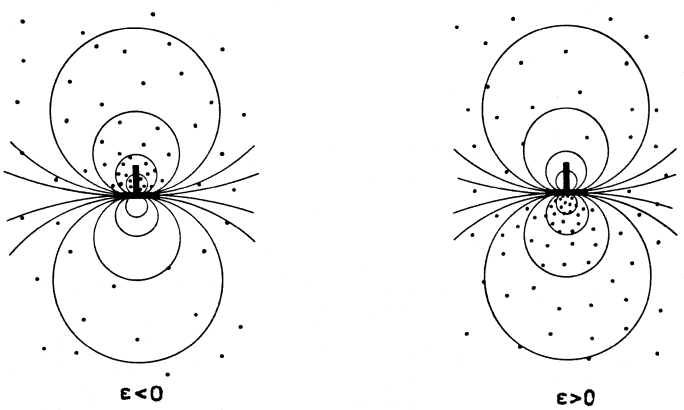

Fig. 1. The impurity distribution around an edge dislocation. The circles represent contours of constant hydrostatic pressure. Small impurity atoms ($\epsilon < 0$) concentrate on the side of the dislocation containing the extra half-plane; large atoms ($\epsilon > 0$) opposite.

n density of possible impurity sites;
$E_{t\max}$ maximum total interaction energy.

The equilibrium impurity distribution given in (3) is a strong function of temperature. Thus the impurity distribution will alter during the cool-down after growth and become "frozen in" when the diffusion coefficient of the impurity becomes low enough. Bullough and Newman [7] show that the equilibrium distribution around a dislocation is reached in a time such that $\sqrt{Dt} = 10^{-6}$ cm. For a typical impurity atom such as Sn the temperature at which the impurity concentration freezes in is 700-750°C for postgrowth cooling rates between 0.1 and 2.0°C/s. The freeze-in temperature will increase as the diffusion constant of the impurity concerned decreases or as the postgrowth cooling rate increases.

Dislocation Climb in an Impurity Atmosphere

The effect of an impurity cloud on dislocation climb involves interaction between impurities and the dislocation, and interaction between the impurities and the point defects which are absorbed or generated by the climbing dislocation. The interaction between a climbing dislocation and an impurity cloud does not appear to have been discussed in the literature, probably because climb usually occurs only at high temperatures where the impurities themselves have a high mobility. This results in an impurity drag on the dislocation but not a definite pinning action. During the rapid degradation of double-heterostructure lasers the average active-region temperature does not exceed about 50°C. Thermal calculations indicate that the actual temperature of the dislocation is unlikely to exceed 400°C at the very most [9]. Thus, under normal circumstances, group III or V impurities, which seem most appropriate for dislocation pinning, will have an extremely low diffusion coefficient. An immobile cloud formed by such impurities can produce large pinning forces against dislocation climb and glide. Let us investigate the strength of this pinning interaction.

The impurity cloud around the dislocation partially relieves its stress energy. If the dislocation is displaced by a distance y, while the impurity cloud remains fixed, then the total interaction energy per unit length increases by $W(y)$. This results in a restoring force per unit length, $F = dW/dy$, acting on the dislocation and pinning it to its initial position. This pinning force has been calculated rigorously for the case of weak impurity interactions on dislocation glide by Hirth and Lothe [8, pp. 619-620]. The maximum restoring force is given by $c_0\beta^2/b_e kT$. The pinning force has not previously been calculated for the case of dislocation climb. We present here a treatment of dislocation climb which uses a method directly analogous to that used by Hirth and Lothe for dislocation glide. The increase in interaction energy per unit length of the displaced dislocation is given by (Fig. 2)

$$W = \int_{r=b}^{\infty} \int_{\theta=0}^{2\pi} (c - c_0)\{E_T(r,\theta) - E_T(r',\theta')\}\, r \cdot dr \cdot d\theta \tag{5}$$

where the origin of the polar coordinates r and θ is the original

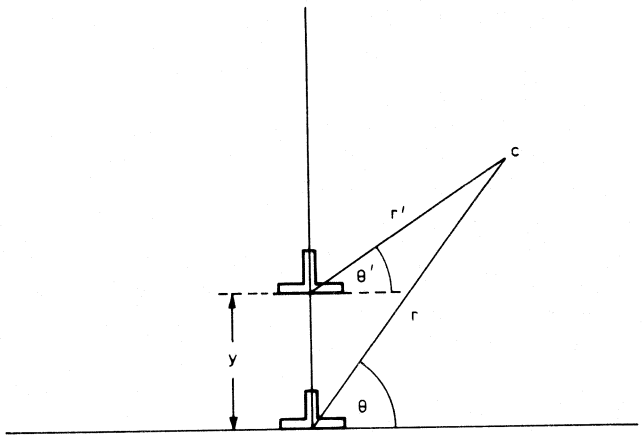

Fig. 2. Dislocation climbing in a fixed-impurity atmosphere.

position of the dislocation and the origin of r' and θ' is the new position of the dislocation, displaced by a distance y.

If the elastic-misfit interaction is dominant, then substitution from (2) and (3) gives

$$W = \int_{r=b}^{\infty} \int_{\theta=0}^{2\pi} c_0 \left(\exp \frac{\beta \sin \theta}{rkT} - 1\right) \left(\frac{\beta \sin \theta'}{r'} - \frac{\beta \sin \theta}{r}\right) \cdot r \cdot dr \cdot d\theta. \tag{6}$$

This expression cannot be evaluated analytically for the case of climb. In the case of dislocation glide, Hirth and Lothe show that a good result can be obtained by considering only the row of atoms closest to the core of the dislocation. For strong interactions the approximation is even better because $c - c_0$ decreases more rapidly with r than for weak interactions. It therefore seems reasonable to make this approximation for the calculation of the effect of strongly interacting impurities upon dislocation climb.

Consider, for example, a 60° dislocation moving by pure climb, as shown in Fig. 3(a). The dislocation illustrated is an α dislocation of the shuffle set [10]. For clarity the lattice is shown undistorted and is drawn with all the bonds in the missing half-plane stretched. The absorption of a Ga and an As interstitial, or the capture of a Ga and an As atom from the adjacent lattice with the resultant generation of a Ga and an As vacancy, moves the dislocation downwards a distance $S = a_0/\sqrt{3} = 3.2$ Å to position 1 (extrinsic). The reverse process moves the dislocation upwards to position 2 (intrinsic). The positions of the first four atoms that would be added in extrinsic climb are also shown, with their atomic bonds missing. The lattice is shown in Fig. 3(b), with the atomic bonds distorted in a more realistic manner. For strongly interacting impurities with a large atomic radius ($\beta > 0$), the row of atoms labeled A will be nearly saturated with impurity atoms at a linear density c_d. For strongly interacting impurities with a small atomic radius ($\beta < 0$), row B will be nearly saturated. The approximate coordinates of these respective rows of impurity atoms are $y = \pm S/2 \simeq \pm 1.6$ Å positive for $\beta < 0$ and negative for $\beta > 0$. Equation (6) now reduces to

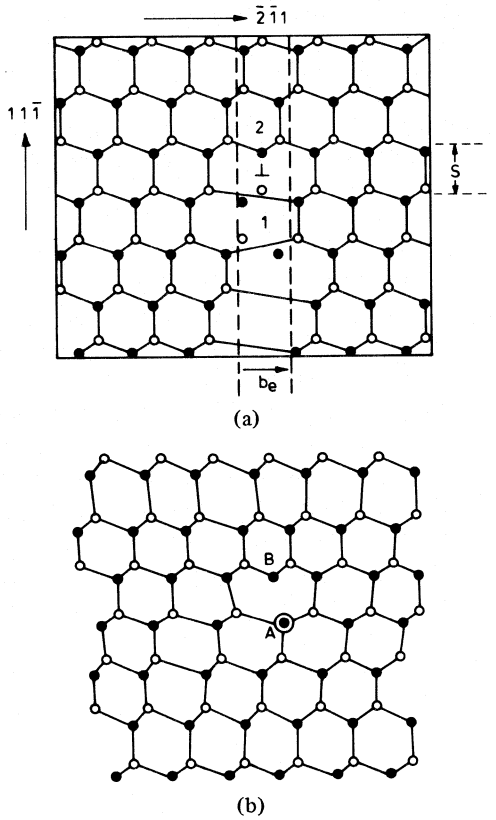

Fig. 3. (a) Pure climb of a 60° α dislocation of the shuffle type viewed along its length (011 direction). The Burger's vector is 101, hence pure climb is in the $11\bar{1}$ or $\bar{1}\bar{1}1$ direction to position 1 extrinsic or position 2 intrinsic. (b) A more realistic view of the same dislocation illustrating pinning by row A (large impurity atoms) or row B (small impurity atoms).

$$W = c_d(E_i(p) + E_{i\max}) \tag{7}$$

where $E_{i\max} = |\beta/S| \simeq |\beta/b|$, and $E_i(p)$ is the interaction energy of an impurity atom with the dislocation when they ar separated by a distance p given by $p = (S/2 - y)$ for $\beta < 0$ and $p = -(S/2 + y)$ for $\beta > 0$. $E_i(p)$ is found by substitution into (2) with $\theta = 90°$. For $|p| < S$ we will assume that the interaction limits at $\pm E_{i\max}$. The interaction changes from positive to negative between the rows of atoms on either side of the dislocation. A physically reasonable approximation to $E_i(p)$ is given by

$$\begin{aligned} E_i(p) &= \beta/p, && |p| > S \\ &= \pm E_{i\max}, && S/2 < |p| < S \\ &= 2\beta p/S^2, && |p| < S/2. \end{aligned} \tag{8}$$

Substitution of (8) into (7) then gives the distribution of W as plotted in Fig. 4(a) ($\beta < 0$, in this case). The potential distribution in the direction of climb is noticeably different from that in the direction of glide [8, pp. 619-620]. For glide the dislocation simply has to move out of a potential well. For climb, however, the dislocation not only has to climb out of a potential well, but also, in the direction of the pinning-

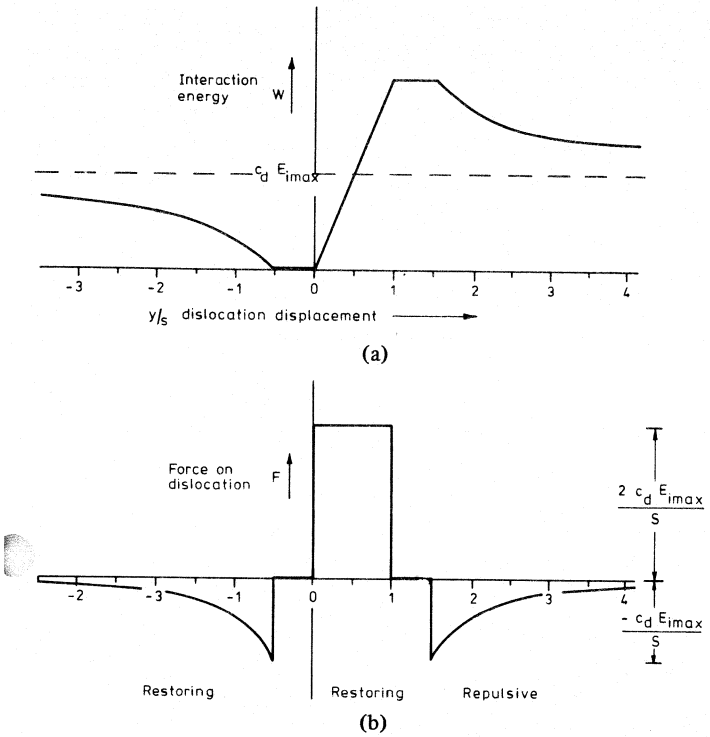

Fig. 4. Interaction between a row of pinning atoms at position $y/S = \frac{1}{2}$ and a dislocation displaced in the y direction. (a) Total interaction energy. (b) Force on dislocation.

impurity row, it has to climb over a potential barrier of equal height to the depth of the well. Until the top of this barrier is reached ($0 < y < S$), the restoring force per unit length pinning the dislocation is very large and given by

$$\frac{dW}{dy} = \frac{2c_d E_{imax}}{S}. \tag{9}$$

Once over this barrier, however, ($y > 3S/2$), there is a repulsive force per unit length given by

$$F = -c_d \beta (y - S/2)^{-2}. \tag{10}$$

For dislocation displacement away from the pinning-impurity row ($y < -S/2$) there is a restoring force per unit length again given by (10). This has a maximum value at $y = -S/2$ of

$$F_{max} = \frac{c_d \beta}{S^2} = \frac{c_d E_{imax}}{S}. \tag{11}$$

These pinning forces are very similar to those found for strongly interacting impurities in dislocation glide where the maximum pinning force is given by $F = c_d E_{imax}/b$, [8, pp. 619-620].

This reasoning assumes that the dislocation is reasonably straight. In reality the situation is more complex since the dislocation climbs by the motion of jogs [8, pp. 519-526]. Hence the forces that have been derived are only approximate.

This treatment of the pinning force will not, of course, be applicable if the point defects involved in the climb process enhance the mobility of the impurities to such an extent that the impurities move with the dislocation, despite the low temperature at which the climb is occurring. Vacancies could enhance the impurity mobility, whereas interstitials could not. It is, however, still controversial whether interstitials or vacancies [1], [2] are involved in the climb process; but even if it were vacancies, it is doubtful if the mobility of the impurity cloud would be sufficiently enhanced to destroy the pinning action.

Force on the Climbing Dislocation

Equations (9) and (11) give the maximum force resulting from impurity interaction which is capable of pinning the climbing dislocation. Peierls stresses will also contribute to the pinning of the dislocation. These result from periodic changes in potential energy as the dislocation moves between the atomic planes forming the crystal. The magnitude of the Peierls stress can be very high in covalent crystals, up to $10^{-2}\ \mu = 5 \times 10^9$ dynes/cm^2. However, this stress reduces exponentially with temperature and also reduces greatly if the dislocation is not exactly aligned with a low-index crystallographic direction [8, pp. 506-510]. It therefore may not produce significant dislocation pinning and will be neglected in this treatment. Let us assume therefore that if the impurity-pinning force alone is exceeded, then the dislocation will break away from its impurity cloud. Comparison of the pinning force with the actual force on the dislocation will determine the significance of the pinning force.

For the dislocation climb in the y direction this force per unit length is given by

$$F_y = F_{yel} + F_{yos} \tag{12}$$

where F_{yel} is the total elastic force on the dislocation in the y direction, and F_{yos} is the osmotic force on the dislocation resulting from point-defect supersaturation.

The elastic force on the dislocation includes a contribution from both the edge b_e and screw b_s components of the dislocation Burger's vector.

$$F_{yel} = \sigma_{xx} b_e + \sigma_{xz} b_s \tag{13}$$

where

σ_{xx} normal stress;
σ_{xz} shear stress.

Reinhart and Logan [10] have estimated the residual elastic stresses in the epitaxial layers of a double-heterostructure laser to be in the range $1\text{-}5 \times 10^8$ dynes/cm^2 as a result of the thermal-expansion differences between GaAs and GaAlAs. Ishida *et al.* [9] have estimated that thermal stresses resulting from local heating at the dislocation could reach 10^9 dynes/cm^2. This stress could result in a maximum force per unit length on the dislocation (13) of 35 dynes/cm.

The osmotic force on a dislocation in GaAs is a complex function of the defect distribution, as GaAs is a binary compound and there are four native point defects. Hirth and Lothe [8, pp. 201-249] treat the case of dislocation climb

by vacancy absorption in an elemental material. This can be extended to the case of GaAs as follows.

If the dislocation climbs from the origin to position y (see Fig. 2), then the number of point defects absorbed is related to the distance y that the dislocation has climbed by

$$\frac{yb_eL}{v} = n(\mathrm{As}_v) - n(\mathrm{As}_I) = n(\mathrm{Ga}_v) - n(\mathrm{Ga}_I) \tag{14}$$

where

L	length of dislocation;
v	volume of Ga + As atom;
$n(PD)$	number of point defects absorbed, a negative value corresponds to point-defect generation;
subscript v	vacancies;
subscript I	interstitials.

It is implicit in this expression that one type of point defect from each sublattice of the GaAs crystal must be involved in the climb process. The free energy liberated when a point defect is absorbed is given by the chemical potential $G(PD)$ of the point defect concerned which can be expressed as

$$G(PD) = kT \ln \frac{c(PD)}{c_0(PD)} \tag{15}$$

where $c(PD)$ is the concentration of the point defect and $c_0(PD)$ is the equilibrium concentration of the defect. Thus the total energy δG liberated as the dislocation climbs in the y direction is given by

$$\delta G = G(\mathrm{As}_v) \cdot n(\mathrm{As}_v) + G(\mathrm{Ga}_v) \cdot n(\mathrm{Ga}_v) - G(\mathrm{As}_I) \cdot n(\mathrm{As}_I) - G(\mathrm{Ga}_I) \cdot n(\mathrm{Ga}_I). \tag{16}$$

The osmotic force per unit length on the dislocation is

$$F_{yos} = \frac{\delta G}{Ly}. \tag{17}$$

Substitution of (14)-(16) into (17) gives the osmotic force on the dislocation in terms of the proportional supersaturation $c(PD)/c_0(PD)$ of the point defects concerned. For instance, if Ga_v and As_v only are involved then

$$F_{yos} = \frac{kTb_e}{v} \ln \left(\frac{c(\mathrm{As}_v) \times c(\mathrm{Ga}_v)}{c_0(\mathrm{As}_v) \times c_0(\mathrm{Ga}_v)} \right). \tag{18}$$

A similar expression can be written for any pair of point defects which might produce climb. The coefficient of the logarithm in this expresison, kTb_e/v (= 30 dynes/cm at room temperature), is the osmotic force produced in the presence of a point-defect supersaturation of e. The actual point-defect supersaturation in the vicinity of a dislocation in a laser under operating conditions is not known. Both Petroff and Hartman [1] and Woolhouse [12] have discussed the behavior. Factors of importance in determining the point-defect concentration are the thermal quenching history of the GaAs, the point-defect mobility, the elastic stresses, the electrical effects on charged point defects, and possibly the concentration of impurities. This last possibility has been discussed by McMullin *et al.* [13] who suggested that interactions between point defects and dopants might explain variations of rapid degradation rate with dopant type. The quasi-equilibrium point-defect concentration in the vicinity of the dislocation is also not known and will depend on thermal and other effects. Hence it is clearly impossible to estimate the magnitude of the osmotic force with any accuracy. We can, however, adopt the inverse procedure and estimate the maximum amount of point-defect supersaturation which, in conjunction with the elastic forces, would be just insufficient to overcome the pinning force of the impurity cloud.

It will be noticed from the previous treatment that the osmotic force on the dislocation is comparable with the estimated elastic forces at a point-defect supersaturation of e, and that these correspond to stresses of about 10^9 dynes/cm^2. At higher supersaturation the osmotic force becomes dominant, but on account of the logarithmic term in (18) the equivalent stress does not increase by an order of magnitude (to 10^{10} dynes/cm^2) until the supersaturation has increased by 10^4. Let us therefore consider the pinning forces produced by impurities in GaAs in terms of equivalent breakaway stress σ_{By} and attribute significance to values of σ_{By} lying within or above the range 10^9-10^{10} dynes/cm^2.

Impurities Suitable for Dislocation Pinning in Double-Heterostructure Lasers

The most suitable impurities for dislocation pinning are the group III or V impurities which have a large misfit parameter ϵ. These impurities usually form complete solid solutions with GaAs [e.g., Ga(AsP); (GaIn)As; Ga(AsSb)]. The maximum concentration at which they can be incorporated into practical double-heterostructure devices is at least as high as 1 at % being only limited by lattice-mismatch problems [14]. Since they have the same valence as the atom for which they substitute, they have a negligible electrical effect at this concentration, even at low temperature; thus their effect on dislocation motion can be considered entirely in terms of the elastic-interaction model.

The size-effect elastic interactions of various group III or V impurities are shown in Table I, with the most strongly interacting of these at the top and the weakest at the bottom. The radius of the impurity atom [15], its misfit parameter ϵ, interaction coefficient β, and maximum elastic-interaction energy $E_{i\max}$ are given. The strongest interactions are with B and N. The author is not, however, aware of experimental evidence of their easy incorporation into GaAs. The more commonly used elements In, Sb, and Tl have strong interactions, and P can just be classed as a strong interaction. Al has virtually no size-effect interaction whatsoever.[1] Consider, for example, the case of the addition of indium to GaAs at a low level of say 1 at %. Substitution into (4) gives $c_d = 6 \times 10^6$ cm^{-1} assuming a freeze-in temperature of 700°C. This corresponds to about 25-percent substitution of In atoms for Ga atoms at the core of the dislocation. The elastic or osmotic

[1] Second-order interactions, such as elastic-modulus interactions, may be important for the case of Al which can be added at high concentration ≃ 10 at % to the active layer, see [6]-[8, p. 469].

TABLE I
DISLOCATION PINNING RESULTING FROM THE ADDITION OF VARIOUS GROUP III OR V IMPURITIES TO GaAs

Dislocation Pinning in GaAs using group III or V impurities

	Dopant (site)	R_{imp} Å	ϵ %	β x 10^{-22} cgs	$E_{i\ max}$ eV	σ_{BY} dynes/cm^2
Strong interaction	N (As)	0.7	−40	−500	0.90	2×10^{10}
	Tl (Ga)	1.47	17	210	0.38	5×10^{9}
	Sb (As)	1.36	15	190	0.34	5×10^{9}
	In (Ga)	1.44	14	175	0.31	3×10^{9}
	P (As)	1.10	−7	−90	0.16	6×10^{8}
Weak interaction	Al (Ga)	~ 1.26	10^{-2}	0.1	0.00	~ 10^{4}

stress σ_{By} required to cause the dislocation to break away from such an impurity cloud is given by (9) or (11) as 3 or 6×10^9 dynes/cm^2. Table I gives the lower of these values of σ_{By} for all the impurities considered based on the same assumptions. The upper value, appropriate when the dislocation is trying to climb towards, rather than away from the pinning impurity row is given by multiplying these values by 2. Several of these impurities such as In, Sb, Tl, and N produce pinning forces appreciably greater than the likely elastic and osmotic forces with values of σ_{By} approaching or greater than 10^{10} dynes/cm^2. Such a pinning force could also pin against osmotic forces resulting from proportional point-defect supersaturations of $e^{10} = 2 \times 10^4$ at room temperature.

It seems unlikely that any of the commonly used dopant impurities would be suitable for dislocation pinning. This is because the maximum concentration c_0 at which they can be added to the double heterostructure without deleterious side effects is usually about 3×10^{18} atoms/cm^3. The elastic interactions for such impurities are given in Table II. Even for the more strongly interacting of these impurities (Cd, for example) the linear density of the impurity at the dislocation core $c_d = 2.5 \times 10^5$ cm^{-1}, assuming a 700°C freeze-in temperature. The resultant maximum pinning force, (9) or (11), is 5 or 10 dynes/cm and $\sigma_{By} = 1.5$ or 3.0×10^8 dynes/cm^2. This is unlikely to pin the dislocation effectively. It is possible, of course, that electrical interactions may be significant with charged impurities such as these. However, it seems unlikely that this will affect c_d because the freeze-in temperature is about 700°C where the electrical effect of charged impurities is likely to be screened by the high intrinsic free-carrier density.

EXPERIMENTAL EVIDENCE

There is no information in the literature relating to the degradation properties of double-heterostructure lasers with suitable group III or V impurities included in the active region. Perhaps the only relevant information comes from Ettenberg *et al.* [16] who have recently reported results of the degradation of (GaIn)As double-heterostructure light-emitting diodes. Despite the fact that these diodes contained

TABLE II
ELASTIC INTERACTION BETWEEN A 60° DISLOCATION AND VARIOUS DOPANTS IN GaAs

Interactions of dopants in GaAs with dislocation stress fields at 700°C

	Dopant (site)	R_{imp} Å	ϵ %	β x 10^{-22} cgs	$E_{i\ max}$ eV
Strong interaction	Sn (As)	1.40	18.6	220	0.40
	Cd (Ga)	1.48	17.4	210	0.40
	S (As)	1.04	−11.8	−150	0.27
	Te (As)	1.32	11.8	100	0.27
	Sn (Ga)	1.40	11.1	140	0.24
	Si (Ga)	1.17	−7.1	−90	0.16
	Zn (Ga)	1.31	3.1	45	0.08
	Se (As)	1.14	−3.4	−40	0.07
	Ge (As)	1.22	3.4	40	0.07
	Ge (Ga)	1.22	−3.4	−40	0.02
	Mg (Ga)	1.30	3.1	35	0.06
Weak interaction	Si (As)	1.17	−0.85	10	0.02

a high density of dislocations, when the indium content of the active layer was 20 percent, the degradation rate was found to be independent of dislocation density in the range 10^6–10^9 dislocations/cm^2. Furthermore, the diodes were reported to be very resistant, from the point of view of degradation, to mechanical stresses resulting from device mounting. This is in marked contrast to GaAs/GaAlAs double-heterostructure lasers which are extremely sensitive to device mounting stresses [17]. These results are consistent with the assumption that the dislocations are strongly pinned when the active region contains an appreciable fraction of In.

CONCLUSIONS

The addition of certain group III or V impurities to GaAs is likely to produce dislocation pinning against stresses approaching 10^{10} dynes/cm^2 without deleteriously affecting double-heterostructure laser performance. Such pinning forces will almost certainly overcome the likely elastic stresses on the dislocation, although it remains to be determined experimentally whether they will overcome the osmotic forces which also contribute to the force on a climbing dislocation. It is therefore possible that the addition of these impurities to the active layer of double-heterostructure lasers will eliminate or inhibit the type of rapid degradation which results from dislocation motion. Experimental evidence relating to this suggestion is sparse at present; however, degradation results of GaInAs/(GaAs) LED's is consistent with the assumption that the dislocations are strongly pinned in GaInAs.

REFERENCES

[1] P. Petroff and R. L. Hartman, "Rapid degradation phenomenon in heterojunction Ga(AlAs)-GaAs lasers," *J. Appl. Phys.*, vol. 45, pp. 3899–3906, Sept. 1974.
[2] P. W. Hutchinson, P. S. Dobson, S. O'Hara, and D. H. Newman, "The defect structure of degraded heterojunction GaAlAs-GaAs lasers," *Appl. Phys. Lett.*, Nov. 1974.
[3] H. Yonezu *et al.*, "Degradation mechanism of (AlGa)As double

heterostructure laser diodes," *Appl. Phys. Lett.*, vol. 24, pp. 18–19, Jan. 1974.

[4] D. Laister and G. M. Jenkins, "Deformation of single crystals of gallium arsenide," *J. Mater. Sci.*, vol. 8, pp. 1218–1232, Sept. 1973.

[5] S. K. Choi and M. Mihara, "Impurity effects on the dislocation velocity in GaAs," *J. Phys. Soc. Japan*, vol. 32, p. 1154, 1972.

[6] N. F. Fiore and C. L. Bauer, "Binding of solute atoms to dislocations," *Progr. Mater. Sci.*, vol. 13, pp. 85–133, 1967.

[7] R. Bullough and R. C. Newman, "The interaction of impurities with dislocations in silicon and germanium," in *Progress in Semiconductors*, vol. 7, A. F. Gibson and R. E. Burgess, Ed. London: Heywood, 1963, pp. 99–136.

[8] J. P. Hirth and J. Lothe, *Theory of Dislocations.* New York: McGraw-Hill, 1968.

[9] K. Ishida *et al.*, "X ray observation of DH laser crystals," presented at the IEEE Int. Semiconductor Laser Conf., Atlanta, Ga., Nov. 1974, Paper IV-3.

[10] F. K. Reinhart and R. A. Logan, "Interface stress of $Al_xGa_{1-x}As$-GaAs layer structures," *J. Appl. Phys.*, vol. 44, pp. 3171–3179, July 1973.

[11] G. H. Olsen, M. S. Abrahams, and T. J. Zamerowski, "Asymmetric cracking in III-V compounds," *J. Electrochem. Soc., Solid State Technol.*, vol. 121, pp. 1650–1656, Dec. 1974.

[12] G. R. Woolhouse, "Degradation in injection lasers," presented at the IEEE Int. Semiconductor Laser Conf., Atlanta, Ga., Nov. 1974, Paper IV-1.

[13] P. G. McMullin *et al.*, "Effect of doping on degradation of GaAs-$Al_xGa_{1-x}As$ injection lasers," *Appl. Phys. Lett.*, vol. 24, pp. 595–597, June 1974.

[14] G. A. Rozgonyi, P. M. Petroff, and M. B. Panish, "Control of lattice parameters and dislocations in the system $Ga_{1-x}Al_xAs_{1-y}P_y$/GaAs," to be published.

[15] A. F. Wells, *Structural Inorganic Chemistry*, 2nd ed. London: Oxford, 1950, p. 50.

[16] M. Ettenburg and C. J. Nuese, "Degradation of $In_xGa_{1-x}As$ LED's and phonon-kick," presented at the Specialist Conf. Technology of Electroluminescent Diodes, Atlanta, Ga., 1974, Paper 12.

[17] R. L. Hartman and A. R. Hartman, "Strain-induced degradation of GaAs injection lasers," *Appl. Phys. Lett.*, vol. 23, pp. 147–149, Mar. 1973.

An Infrared Heterodyne Radiometer for High-Resolution Measurements of Solar Radiation and Atmospheric Transmission

BERNARD J. PEYTON, SENIOR MEMBER, IEEE, ANTHONY J. DiNARDO, STEVEN C. COHEN, JOHN H. McELROY, SENIOR MEMBER, IEEE, AND ROBERT J. COATES, FELLOW, IEEE

Abstract—A tunable, Dicke-switched, infrared heterodyne radiometer (IHR) has been designed, fabricated, tested, and used to observe solar radiation and determine the atmospheric transmissivity in the 9-11-μm spectral band. The IHR provides a spectral resolution of 6.7×10^{-3} cm^{-1}, a minimum detectable power level of 2.9×10^{-23} W/Hz, and a temperature resolution of less than 1 K for a source temperature of 1000 K, an IF predetection bandwidth of 100 MHz, and an integration time of 30 s. Detailed design equations and measured IHR performance are presented. The IHR was used to make solar and atmospheric transmission measurements and a vertical path atmospheric attenuation of 2.3 dB has been established under favorable weather conditions. The attenuation of solar radiation due to cloud cover and haze have also been investigated.

I. Introduction

DIRECT detection-type infrared radiometers have been widely used for a variety of astrophysical and atmospheric propagation measurements [1], [2]. The recent development of high-resolution infrared heterodyne receivers now permits similar measurements with an instrument which exhibits nearly quantum-noise-limited receiver sensitivity and previously unattainable spectral resolution [3]-[5]. Potential applications of IHR have been described [6]-[11] and solar measurements using an infrared heterodyne radiometer (IHR) have been reported [12]-[17].

II. Overview of IHR

In an IHR, the incident infrared radiation collected at the input aperture and a coherent laser local oscillator (LO) beam simultaneously illuminate a photomixer forming a heterodyne band-limited signal. The collected infrared signal energy spans the frequency intervals $\nu_{LO} + \nu_{IF} - B/2 < \Delta\nu < \nu_{LO} + \nu_{IF} + B/2$ (sum band) and $\nu_{LO} - \nu_{IF} - B/2 < \Delta\nu < \nu_{LO} - \nu_{IF} + B/2$ (difference band), where ν_{LO} is the laser local oscillator frequency of the IHR. The IF signal is amplified, synchronously detected, and integrated, providing a dc voltage proportional to the incident infrared radiation intensity. The predetection electronic bandwidth (B) of 100 MHz establishes the instantaneous infrared bandwidth of the IHR (6.7×10^{-3} cm^{-1}) while even finer resolution (1.33×10^{-4} cm^{-1}) has been achieved by inserting a 2-MHz IF filter. The spectral resolution of the IHR is ultimately limited to several kilohertz by the short-term frequency stability of the laser LO [18]. The resultant spectral resolution of the IHR is 2 to 4 orders of magnitude finer than that presently obtainable with conventional passive spectroscopic measurement techniques.

Manuscript received October 23, 1974; revised April 8, 1975. This work was supported by NASA, Goddard Space Flight Center, Greenbelt, Md.

B. J. Peyton and A. J. DiNardo are with AIL, Division of Cutler-Hammer, Melville, N.Y. 11746.

S. C. Cohen, J. H. McElroy, and R. J. Coates are with NASA, Goddard Space Flight Center, Greenbelt, Md.

III. IHR Minimum Detectable Power and Signal-to-Noise Ratio

The heterodyne receiver sensitivity as a function of IF frequency, noise equivalent power (NEP) (f), for a reverse biased photovoltaic photomixer is given [3] by

$$\mathrm{NEP}(f) = \frac{h\nu}{\eta}\left\{1 + \frac{2k(T_m + T'_{IF})G_D}{qI_0}\left[1 + (f/f_c)^2\right]\right\} = \frac{h\nu}{\eta'} \quad (1)$$

where $h\nu$ is the photon energy, T_m is the photomixer temperature, T'_{IF} is the effective input noise temperature of the IF preamplifier, G_D is the reverse shunt conductance of the photomixer, I_0 is the LO induced photocurrent, q is the electronic charge, and f_c is the 3-dB cutoff frequency of the photomixer. For convenience these latter terms are grouped into an effective receiver quantum efficient η'. For the case where the operating instantaneous IF bandwidth B is less than f_c, the receiver sensitivity, NEP, is given by

$$\mathrm{NEP} = \frac{h\nu}{\eta'}B. \quad (2)$$

The IHR postdetection signal-to-noise ratio (SNR) for an extended thermal source is given by

$$\mathrm{SNR} = \frac{P_s\alpha(B\tau)^{1/2}}{\mathrm{NEP}\,\mathcal{K}} = \frac{P_s\eta'\alpha(B\tau)^{1/2}}{h\nu B\mathcal{K}} \quad (3)$$

where P_s is the power received from the thermal source within the diffraction limited IHR field of view, contained in a spectral window of extent $2B$, and of correct polarization for heterodyne detection, $\mathcal{K}$ is the sensitivity constant = 2 for a 50-percent Dicke-type radiometer, τ is the postdetection integration time of an ideal integrator, and α is the transmittance of the media and optics between the thermal source and the infrared photomixer.

When observing a thermal source of temperature T_s, the IHR SNR is given by

$$\mathrm{SNR} = \frac{\eta'\alpha(B\tau)^{1/2}}{e^{h\nu/kT_s} - 1}, \qquad f_c > B \quad (4)$$

where k is the Boltzmann's constant. For the case of solar

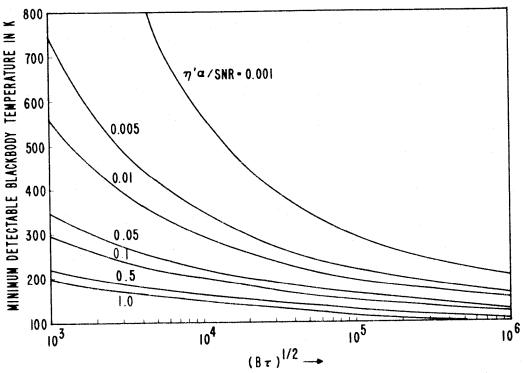

Fig. 1. Calculated minimum detected blackbody temperature versus $(B\tau)^{1/2}$ at $\lambda = 10.6$ μm with $\eta'\alpha$/SNR as a parameter.

measurements at $\lambda = 10.6$ μm and the conditions of $T_s = 5000$ K, $B = 10^8$ Hz, $\tau = 3$ s, $\alpha = 0.25$, and $\eta' = 0.1$, the calculated post-detection SNR is approximately 32 dB.

Using (3) and (4), the IHR minimum detectable source power and temperature can be determined for the effective receiver quantum efficiency η' and $(B\tau)^{1/2}$ product. The calculated $T_{s\min}$ is given in Fig. 1 as a function of $(B\tau)^{1/2}$ with $\eta'\alpha$/SNR as a parameter. For the measured IHR NEP of 2×10^{-19} W/Hz ($\eta' = 9.35$ percent), $B = 100$ MHz, $\tau = 30$ s, and an approximate optical transmittance of $\alpha = 0.25$, the calculated IHR minimum detectable thermal source power for $\text{SNR}_p = 1$ is, $P_{s\min} = 3 \times 10^{-15}$ W and the corresponding source temperature is $T_{s\min} = 190$ K.

IV. IHR Temperature Resolution

For the case of a thermal source, the IHR temperature resolution, $\Delta T_s/T_s$, defined as the normalized change in source temperature for which a change in the IHR output level can be observed is given (Appendix A) by

$$\frac{\Delta T_s}{T_s} = \frac{k^2 T_s}{2h^2\nu^2} \cdot \frac{[\exp(h\nu/kT_s) - 1]^2}{\alpha \exp(h\nu/kT_s)} \cdot \frac{K}{(B\tau)^{1/2}} \cdot \left[\frac{2h\nu\alpha}{k[\exp(h\nu/kT_s) - 1]} + \int_{f_1}^{f_2} \frac{\text{NEP}(f)\, df}{kB} \right]. \quad (5)$$

For $\alpha = 1$, $\eta' = 0.1$, $B\tau = 10^8$ ($B = 100$ MHz and $\tau = 1$ s, for example), $T_s = 100$ K, the IHR resolution is 8.6×10^{-4}, while for $B\tau = 10^{10}$, the resolution improves to 8.6×10^{-5}. For solar measurements, $T_s \approx 5000$ K [19], the calculated IHR temperature resolution is approximately 7×10^{-5} for $B\tau = 10^9$ and degrades to approximately 2.3×10^{-4} for $B\tau = 10^8$.

V. IHR Instrumentation

A. Equipment Description

The infrared heterodyne radiometer is made up of a diffraction limited collecting telescope, an optical Dicke switch, a wide-band heterodyne receiver, a discretely tunable laser LO, a variable temperature blackbody reference source, and radiometric processing electronics (see Fig. 2). In operation, the infrared energy from the source is collected by a 6-in off-axis

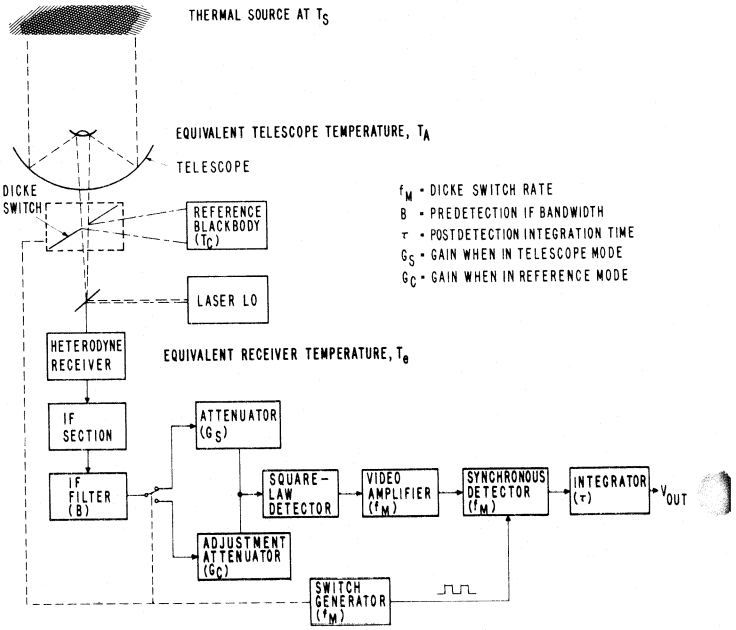

Fig. 2. Block diagram of infrared heterodyne radiometer (IHR).

telescope and compared to the output of a variable temperature (300-1500 K) reference blackbody by means of an optical Dicke switch that alternately switches the receiver field of view (FOV) between the collecting telescope and the reference blackbody. The heterodyne radiometer output voltage is proportional to the difference between the collected source energy and the reference blackbody energy within the IF bandwidth; therefore, when the reference temperature is made equal to the source temperature, their respective energies at the photomixer are equal and the radiometer output voltage is zero (null-balanced).

A liquid nitrogen cooled PV-HgCdTe photodiode is employed as the photomixer and has a measured quantum efficiency of 13 percent and a 3-dB cutoff frequency of greater than 125 MHz at $\lambda = 10.6$ μm and $T_m = 77$ K. The measured receiver sensitivity (NEP) is less than 2×10^{-19} W/Hz at 10.6 μm. The IF and video portion of the IHR provides flexibility in the choice of IF predetection bandwidth, postdetection integration time, and electronic gain.

B. Null-Balanced Operation with Gain Modulation

The calculated temperature resolution for a null-balanced Dicke-switched IHR assumes a balanced receiver in which the source temperature T_s and blackbody reference temperature T_c are equal. When the source temperature exceeds the maximum available reference temperature as for the case of solar measurements, the employment of gain modulation is a useful technique for obtaining a null-balanced output. Gain modulation is achieved by providing different IF gains during the observation times of the source and reference temperatures. In practice, two stable, precise IF attenuators are switched alternately in synchronism with the Dicke switch. The IF gain is G_s when the receiver is observing the telescope and G_c when the receiver observes the radiation from the reference (see Fig. 2). The radiometer will be null-balanced for the condition

$$G_s(\text{NEP} + P_s) = G_c(\text{NEP} + P_c) \tag{6}$$

where P_s is the net source power received at the IHR of IF bandwidth B. The heterodyne receiver NEP defines the receiver noise level equation (1)[1] and the blackbody reference power at the IHR is given by

$$P_c = \frac{2h\nu B}{\exp(h\nu/kT_c) - 1} \tag{7}$$

under coherent diffraction limited constraints (see Appendix A), unity transmissivity, $\alpha = 1$, and where T_c is the actual reference temperature. The reference blackbody used in the IHR has a maximum temperature of 1300 K, and therefore direct null-balanced radiometer operation is not possible when observing very hot sources such as the sun.

The temperature resolution with which the IHR can measure the source temperature for a gain-modulated IHR is given by

$$\frac{\Delta T_s}{T_s} = \Delta T_c \frac{T_s}{T_c^2}\left\{\frac{2h\nu B}{\exp(h\nu/kT_c) - 1}\right\}^2 \frac{G_c \exp(h\nu/kT_c)}{\left[\text{NEP}(G_c - 1) + \dfrac{G_c h\nu B}{\exp(h\nu/kT_c) - 1}\right]\left[\text{NEP}(G_c - 1) + h\nu B + \dfrac{G_c h\nu B}{\exp(h\nu/kT_c) - 1}\right]}. \tag{8}$$

Therefore, a measurement of the reference temperature resolution $(\Delta T_c/T_c)$, the infrared wavelength, the reference temperature, the transmissivity, the gain modulation, the receiver sensitivity, and the IF bandwidth can be used to calculate the temperature resolution for a source temperature which is larger than the reference temperature.

For the case of zero gain modulation ($G_c = G_s = 1$ and $\Delta G = 0$), (8) reduces to $\Delta T_s = \Delta T_c\,(T_s/T_c)^2$ and for the null-balanced case where $T_s = T_c$, then $\Delta T_s = \Delta T_c$. The calculated 10.6-μm IHR temperature resolution with gain modulation is identical to that obtained when the IHR is null-balanced by means of a reference source whose temperature is equal to the source temperature; therefore, no degradation in temperature resolution is incurred when gain modulation is employed.

C. Solar Resolution Elements

The diffraction-limited IHR field of view is

$$\theta_{DL} = 2.44\frac{\lambda}{D} \approx 1.7 \times 10^{-4} \text{ rad} \tag{9}$$

where $\lambda = 10.6$ μm and D is the telescope diameter (6 in). When the photomixer area matches the diffraction limited spot size, the number of resolution elements across the solar disk is approximately given by

$$N \approx \left(\frac{\theta_s}{\theta_{DL}}\right)^2 \approx 3025 \tag{10}$$

where θ_s is the solar angle $= 9.3 \times 10^{-3}$ rad.

[1]For this discussion it is assumed that the laser LO power is much larger than the reference and the source power. Therefore, the NEP is fixed near the quantum limit condition and does not vary with source or reference power.

VI. IHR Laboratory Measurements

A. Measured Temperature Resolution

The IHR temperature resolution was measured using a calibrated blackbody source for the experimental conditions of: $\lambda_{LO} = 10.6$ μm, NEP $= 2 \times 10^{-19}$ W/Hz at the photomixer input, $B = 100$ MHz, and $\tau = 3$ s. The calculated and measured values of the IHR temperature resolution for several values of media transmittance α are given in Fig. 3. The measured data indicate that the IHR media transmissivity is approximately $\alpha = 0.25$. The nonideal transmissivity is due to the optic losses, the nonsquare Dicke switch, the 25-percent obscuration caused by the laser LO injection mirror, and the fact that the diffraction limited spot size of the IHR is slightly smaller than the active area of the photomixer.

The measured resolution was $\Delta T_s/T_s = 3 \times 10^{-3}$ for $T_s = 1000$ K and increased to $\Delta T_s/T_s = 5.3 \times 10^{-2}$ for $T_s = 300$ K. The calculated and measured values of IHR temperature resolution are in reasonably good agreement and it appears that the effects of fast laser LO amplitude fluctuations which were excluded from the calculations (Appendix A) do not significantly degrade the IHR temperature resolution. The discrepancy between the calculated and measured values of IHR temperature resolution near $T_s = 300$ K may be due to the nonzero emissivity of the optical surfaces which are expected to be most significant for nearly ambient sources.

For comparison the calculated temperature resolution of an IHR with $\alpha = 1$, and $B\tau = 10^{10}$ is also shown in Fig. 3. This improved performance represents an IHR with an integration time of 10 s and a presently achievable [5] heterodyne receiver IF bandwidth of $B = 1$ GHz.

The null-balanced IHR output data distribution given in Fig. 4, is nearly Gaussian; a condition which indicates random

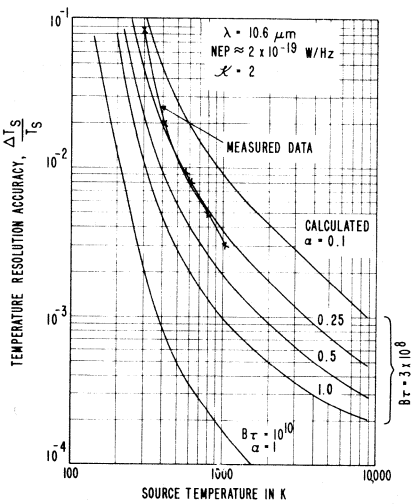

Fig. 3. Calculated and measured temperature resolution of a null-balanced Dicke-switched IHR.

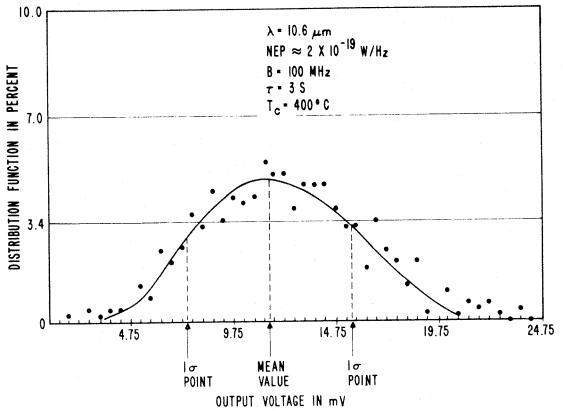

Fig. 4. Measured IHR output voltage distribution for null-balanced condition.

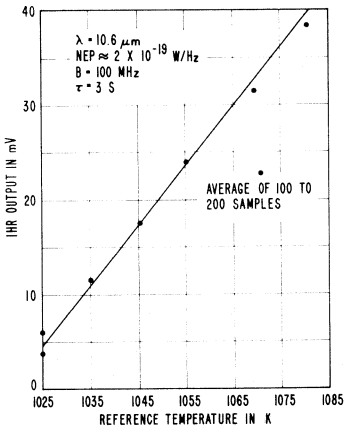

Fig. 5. Measured IHR output voltage as a function of reference temperature.

noise fluctuations. The IHR temperature resolution can be determined from the output data distribution since the 1σ points of a Gaussian distribution are the rms data error of the IHR [2]. Translation of this voltage distribution to a temperature distribution can be accomplished when the variation of the IHR output voltage with source temperature is known.

B. Measured Linearity

The IHR output voltage was sampled once per second with a digital millivoltmeter. The average values of data samples measured for the condition of a fixed source temperature and a variable reference temperature are given in Fig. 5. The IHR was null-balanced at a reference temperature T_c = 1085 K, and the measurement data were taken over a 23-min test period as T_c was lowered in 10-K steps to a value of 1025 K. Each measurement point shown in Fig. 5 represents the average value of about 150 data samples and the measured output voltage was found to be nearly linear with changing reference temperature.

VII. Solar and Atmospheric Transmittance Measurements

A. Solar Disk

The IHR has been installed at the Goddard Space Flight Center's Optical Research Facility at 76° west longitude and 39° north latitude where it has been used to make solar disk

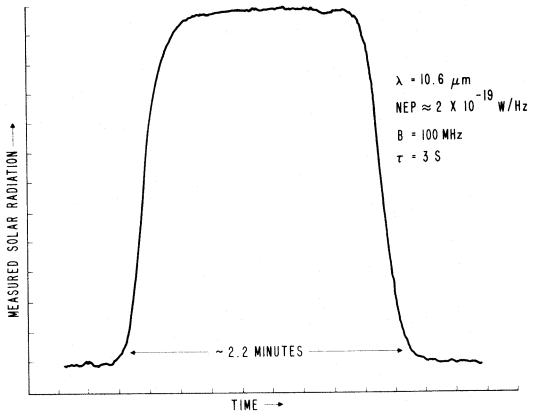

Fig. 6. Solar scan measured with an IHR.

and atmospheric transmission measurements at selected CO_2 laser wavelengths. A coelostat mounted on concrete piers was used to track the sun and direct the incoming radiation onto the collecting telescope. The scan of the solar disk, shown in Fig. 6, was obtained by interrupting the coelostat drive and allowing the sun to traverse the field of view of the IHR telescope. During some of the solar measurements, SNR's in excess of 25 dB were obtained compared to a calculated SNR of 28 dB.

The amplitude fluctuations in the scan shown in Fig. 6 indicate temperature variations of less than 3 percent across the solar disk and represent an upper limit on the measured solar uniformity.

B. Atmospheric Transmission

The solar radiation $P(\nu)$ collected at the IHR is the product of the incident unattenuated solar radiation P_0 and an exponential attenuation term due to the intervening atmospheric losses. Thus

$$P(\nu) = P_0 \exp(-\alpha_a(\nu)\, h \sec\theta) \tag{11}$$

where $\alpha_a(\nu)$ is the atmospheric attenuation coefficient at the laser LO frequency, h is the vertical height of the atmosphere, θ is the zenith angle of the sun, and $h \sec\theta$ is the path length of the sunlight through the atmosphere. When the IHR is operated in an unbalanced mode ($T_s >> T_c$), the output voltage is proportional to the collected source energy. The slope of the logarithm of $P(\nu)$ plotted against sec θ is $-\alpha_a(\nu)\, h$ and $\exp(-\alpha_a(\nu)\, h)$ is the vertical path attenuation. The decrease in the IHR output voltage as the sunlight propagates through longer atmospheric paths was measured under reasonably clear atmospheric conditions. The data are plotted in Fig. 7. The vertical path attenuation was 2.3 dB and is principally due to the line absorption of atmospheric CO_2.

In addition to making clear sky measurements, the effects of cloud cover on direct path propagation were examined and it was found that even small changes in light cloud cover can produce significant changes in the collected solar energy. IHR measurements have demonstrated that summer haze can produce 6-dB additional attenuation fluctuations in the infrared sunlight signal, while heavier cloud covers may produce attenuations in excess of 25 dB. A portion of one observation during a period of light cloud cover is shown in Fig. 8. Peak to valley

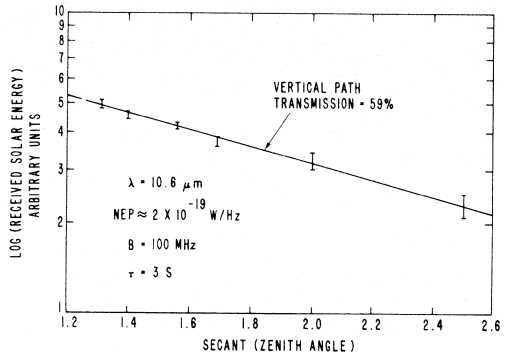

Fig. 7. Variation of solar energy collected at IHR versus secant of solar zenith angle. Measurements were made on March 28, 1973 for a temperature of 56°F and relative humidity of 35 percent.

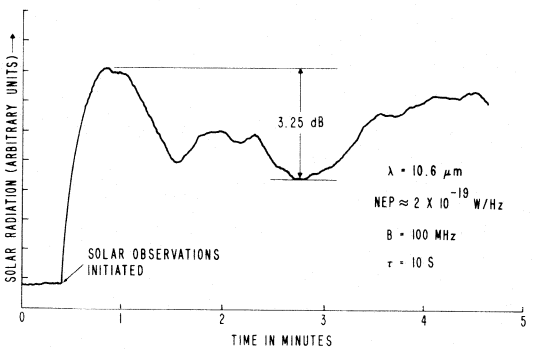

Fig. 8. Measured solar radiation through light patchy clouds using an IHR.

variations of 3.25 dB were observed over the 4-min measurement interval.

VIII. Conclusions

An IHR having a spectral bandwidth of 6.7×10^{-3} cm^{-1} ($2B = 2 \times 100$ MHz) has been developed and used to measure solar radiation near 10.6 μm. Using the solar measurement data, the vertical path atmospheric transmissivity and the effects of cloud cover have been determined. The atmospheric attenuation has been measured over the narrow spectral interval of the IHR rather than the wider spectral bandwidths realized with conventional receivers and the improved spectral resolution is significant since the absorption linewidths of atmospheric constituents are about 10^{-1} cm^{-1} while the separation between absorption lines is about 1.7 cm^{-1} [2]. In a related measurement program, the IHR has been modified to operate with a cooled 8.5-μm diode laser LO and used to measure the infrared emissions of Mars and the moon [22].

It has been proposed that the IHR can be used for the determination and vertical profiling of atmospheric gases by setting the laser LO to overlap the spectral signature line of a selected molecular constituent [9], [23], [24]. IHR spectral bandwidths of up to 10^{-1} cm ($2B = 2 \times 1.5$ GHz) are achievable near 10.6 μm [25] and therefore the spectral profiles of molecular signature lines can be precisely examined. Cooled diode lasers [26], [27] which exhibit low power and wide tunability, may be particularly useful as LO's in heterodyne receivers which are specially designed to overlap the signature lines of specific atmospheric constituents.

Appendix A
Temperature Resolution Accuracy of an Infrared Heterodyne Radiometer

The IHR temperature resolution ΔT_s defined as the maximum change in source temperature for which no change in output SNR is observable at the radiometer output can be obtained by employing the classical definition of temperature resolution ΔT for an RF-microwave radiometer [28], [29] which is given by

$$\Delta T = \frac{K T_{sys}}{(B\tau)^{1/2}}. \tag{12}$$

where T_{sys} is the equivalent system temperature = $T_a + T_e$, T_a is the equivalent source temperature at the receiver telescope, and T_e is the equivalent receiver noise temperature[2] (see Fig. 2), B is the IF bandwidth, τ is the integration time, and $K = 2$ for a Dicke-switched radiometer.

A. Receiver Noise Temperature

The equivalent heterodyne receiver noise power of the IHR is given by

$$P_n = \int_{f_1}^{f_2} \mathrm{NEP}(f)\, df = kT_e B \tag{13}$$

where P_n is the receiver noise power and the receiver noise equivalent power [NEP (f)] is given by (2) for a reverse biased photovoltaic photomixer.

B. Equivalent Source Temperature

The total power emitted into a hemisphere, within a spectral interval $\Delta\nu$ from a small area, ΔA, due to a thermal source at temperature T_s is given [30] by

$$\Delta P_s = \frac{2\pi}{\lambda^2} \cdot \frac{h\nu\, \Delta\nu\, \Delta A}{\exp(h\nu/kT_s) - 1}. \tag{14}$$

Since the power per steradian emitted normal to the surface is $\Delta P_s/\pi$ and only one-half of the emitted power on average is of the correct polarization for heterodyne detection, the net power received by a diffraction limited heterodyne receiver having a captured area A and subtending a solid angle Ω is

$$P_s = \frac{h\nu\, d\nu\, \alpha}{\exp(h\nu/kT_s) - 1} = kT_a B \tag{15}$$

where $A\Omega = \lambda^2$ for diffraction limited heterodyne operation [30] and α is the media transmittance. The frequency interval $d\nu$ of a heterodyne receiver is fixed by the IF bandwidth and is equal to $2B$ for spectrally broad-band sources since there is both a sum and difference frequency band.

C. IHR Temperature Resolution Accuracy

The temperature resolution with which the IHR can measure a thermal source of temperature T_s is obtained by recognizing that the total power in the IHR is given by

[2] T_a and T_e are not physical temperatures.

$$P = P_s + P_n. \tag{16}$$

Taking the first derivative of P with respect to the source temperature and letting $dP/dT_s = \Delta P/\Delta T_s$, one obtains

$$\Delta T_s = \Delta P \frac{dT_s}{dP_s} = kB\Delta T \frac{dT_s}{dP_s}. \tag{17}$$

Using (15)

$$\frac{dT_s}{dP_s} = \frac{kT_s^2}{h^2\nu^2} \cdot \frac{[\exp(h\nu/kT_s) - 1]^2}{2\alpha \exp(h\nu/kT_s) B}. \tag{18}$$

Combining (13), (15), (17), and (18) the IHR temperature resolution is given by

$$\frac{\Delta T_s}{T_s} = \frac{k^2 T_s}{2h^2\nu^2} \cdot \frac{[\exp(h\nu/kT_s) - 1]^2}{\alpha \exp(h\nu/kT_s)} \cdot \frac{K}{B\tau} \cdot \left\{ \frac{2h\nu\alpha}{k\{\exp(h\nu/kT_s) - 1\}} + \int_{f_1}^{f_2} \frac{\text{NEP}(f)\, df}{kB} \right\}. \tag{19}$$

The IHR temperature resolution can be degraded by laser amplitude fluctuations which occur faster than the Dicke-switch rate. Optic losses are included in the media transmittance term α as a general loss of efficiency.

References

[1] R. A. Hanel *et al.*, "The Nimbus 4 infrared spectroscopic experiment," *J. Geophys. Res.*, vol. 77, p. 2629, May 1972.

[2] A. R. Barringer, "Optical correlation spectrometry for remote sensing of air pollution," *J. Opt. Soc. Amer.*, vol. 60, pp. 729–730, May 1970.

[3] B. J. Peyton *et al.*, "High-sensitivity receiver for infrared laser communication," *IEEE J. Quantum Electron. (Part II of Two Parts. Special Issue on 1971 IEEE/OSA Conf. Laser Engineering and Applications)*, vol. QE-8, pp. 252–263, Feb. 1972.

[4] M. C. Teich, "Infrared heterodyne detection," *Proc. IEEE*, vol. 56, pp. 37–46, Jan. 1968.

[5] F. R. Arams, E. W. Sard, B. J. Peyton, and F. P. Pace, "Infrared 10.6-micron heterodyne detection with gigahertz IF capability," *IEEE J. Quantum Electron.*, vol. QE-3, pp. 484–492, Nov. 1967.

[6] J. H. McElroy, "Infrared heterodyne solar radiometry," *Appl. Opt.*, vol. 11, p. 1619, July 1972.

[7] R. J. Menzies and M. S. Shumate, "Usefulness of the infrared heterodyne radiometer in remote sensing of atmospheric pollutants," AIAA Paper 71-1083, 1971.

[8] I. Melngailis, "The use of lasers in pollution monitoring," *IEEE Trans. Geosci. Electron. (Special Issue–Third Annual International Geoscience Electronics Symposium)*, vol. GE-10, pp. 7–17, Jan. 1972.

[9] B. J. Peyton, "Atmospheric monitoring using infrared heterodyne radiometry," in *Proc. Int. Telemetering Conf.* (Los Angeles, Calif., Oct. 1974).

[10] P. Brockman and R. K. Seals, "Laser measurements of high altitude aircraft emissions," presented at AIAA 6th Fluid and Plasma Dynamics Conf., Palm Springs, Calif., July 1973. Paper AIAA-73-704.

[11] R. T. Menzies, "Remote detection of SO_2 and CO_2 with a heterodyne radiometer," *Appl. Phys. Lett.*, vol. 22, June 1973.

[12] S. R. King, D. T. Hodges, T. S. Hartwick, and D. H. Baker, "High resolution atmospheric-transmission measurement using a laser heterodyne radiometer," *Appl. Opt.*, vol. 112, p. 1106, June 1973.

[13] J. Gay and A. Journet, "Infrared interferometer," *Nature (Phys. Sci.)*, vol. 241, p. 32, 1973.

[14] Th. deGraauw and H. Van deStadt, "Infrared heterodyne detection of the moon, planets and stars at 10 μm," *Nature (Phys. Sci.)*, vol. 246, p. 73, Dec. 3, 1973.

[15] D. W. Peterson, M. A. Johnson, and A. L. Betz, "Infrared heterodyne spectroscopy of CO_2 on Mars," *Nature*, vol. 250, p. 128, July 12, 1974; also M. A. Johnson, A. L. Betz, and C. H. Townes, "10 μm heterodyne stellar interferometer," *Phys. Rev. Lett.*, vol. 33, pp. 1617–1620, Dec. 1974.

[16] A. J. DiNardo, B. J. Peyton, S. C. Cohen, J. H. McElroy, and R. J. Coates, "An infrared heterodyne radiometer for high-resolution measurements of solar radiation," *IEEE J. Quantum Electron. (1973 IEEE/OSA Conf. Laser Engineering and Applications: Dig. Tech. Papers)*, vol. QE-9, p. 662, June 1973.

[17] S. C. Cohen, "Field operational performance of an infrared heterodyne radiometer," presented at 2nd Joint Conf. on Remote Detection of Atmospheric Pollutants, Washington, D.C., Dec. 1973.

[18] C. Freed, "Designs and experiments relating to stable lasers," in *Proc. Freq. Stand. Meteorology Seminar* (Quebec, Canada, Sept. 1971), pp. 226–261.

[19] F. H. Murcray, D. G. Murcray, and W. J. Williams, *Appl. Opt.*, vol. 3, p. 1373, 1964.

[20] E. Parzen, *Modern Probability Theory and Its Applications*. New York: Wiley, 1960.

[21] R. A. McClatchey *et al.*, "AFCRL atmospheric absorption line parameters compilation," AF Cambridge Res. Lab., Tech. Rep. AFCRL-TR-73-0096, Jan. 1973.

[22] M. Mumma, T. Kostiuk, S. C. Cohen, D. Buhl, and P. C. Von Thuna, "Infrared heterodyne spectroscopy of astronomical and laboratory sources at 8.5 μm," *Nature*, vol. 253, p. 514, Feb. 1975.

[23] R. K. Seals, "Theoretical analysis of improvements in remote sensing of atmospheric and pollutant gases through high resolution detection of individual infrared emission lines," presented at AIAAA 6th Fluid and Plasma Dynamics Conf., Palm Springs, Calif., July 16–18, 1973, AIAA Paper 73-703.

[24] W. L. Smith, "Interative solution of the radiative transfer equation for the temperature and absorbing gas profile of an atmosphere," *Appl. Opt.*, vol. 9, p. 1993, Sept. 1970.

[25] R. A. Lange, P. Kalisiak, I. Rubinstein, and F. P. Pace, "10.6-μm heterodyne monopulse receiver with Doppler tracking capability," *IEEE J. Quantum Electron. (1973 IEEE/OSA Conf. Laser Engineering and Applications: Dig. Tech. Papers)*, vol. QE-9, pp. 669–670, June 1973.

[26] E. D. Hinkley, "Development and application of tunable diode lasers to the detection and quantitative evaluation of pollutant gases," Lincoln Lab., Tech. Rep. F19628-70-C-0230, Sept. 1971.

[27] E. D. Hinkley, T. C. Harman, and C. Freed, "Optical heterodyne detection at 10.6 μm of the beat frequency between a tunable $Pb_{0.88}Sn_{0.12}Te$ diode laser and a CO_2 gas laser," *Appl. Phys. Lett.*, vol. 13, p. 49, 1968.

[28] M. E. Tiuri, "Radio astronomy receivers," *IEEE Trans. Mil. Electron. (Radio and Radar Astronomy)*, vol. MIL-8, pp. 264–272, July–Oct. 1964.

[29] J. D. Kraus, *Radio Astronomy*. New York: McGraw-Hill, 1966.

[30] A. E. Siegman, "The antenna properties of optical heterodyne receivers," *Proc. IEEE (Special Joint Issue on Optical Electronics)*, vol. 54, pp. 1350–1356, Oct. 1966.

Thermooptical Effects of Intracavity $Ba_2Na(NbO_3)_5$ on a Frequency-Doubled Nd:YAG Laser

JAMES D. BARRY, MEMBER, IEEE, AND CHANDLER J. KENNEDY

Abstract—**The two major thermooptical influences on a frequency-doubled Nd:YAG laser by an intracavity $Ba_2Na(NbO_3)_5$ crystal are discussed and theoretically examined. The absorption of λ106- and λ0.53-μm power by the crystal is shown to lead to the formulation of a thermally induced lens and diffraction loss due to the aspherical distortion. Equations for each are formulated. The effects of the lens and diffraction loss to the performance of the laser are illustrated. The modification to the laser resonator due to the inclusion of these effects is discussed.**

I. Introduction

THE internally frequency-doubled Nd:YAG laser has received considerable attention for use in space laser communications. The use of this laser in space demands the most efficient utilization of the second-harmonic conversion process and pump light due to power limitations on board any spacecraft. Since it is at least possible in theory to convert 100 percent of the optimally coupled fundamental power to second-harmonic power using an intracavity frequency doubler [1], we have chosen this design for space use. However, the introduction of the doubling element in the laser cavity introduces additional losses which were not present in the fundamental wavelength laser, so that 100-percent conversion is not possible in practice. We report on our investigation of what we believe to be the most fundamental causes of the deoptimization of the laser due to the presence of the doubling crystal.

The perturbation to the laser system by the doubling crystal is caused by its absorption of λ1.06- and λ0.53-μm radiation. This influence has been recognized as a thermal distortion but the importance, especially for an optimized space laser, has not been previously studied. The general thermooptical influence to the laser occurs in a twofold manner [2]. The first is due to the added power-dependent cavity loss due to the aspherical components of the thermal lens and the second is due to the modification of the laser resonator by the thermal lens.

These effective losses are not generally recognized and must be included in any effort to optimize the laser resonator. Additionally, the induced thermal profile can disrupt the frequency-doubling process and lead to degraded λ0.53 output power. The basic influences of the absorption of optical power have been previously recognized [3], [4] and the distortion of uniform frequency doubling in the $Ba_2Na(NbO_3)_5$ crystal reported [5]. These effects are dependent upon crystal quality and impurities. A summary of present $Ba_2Na(NbO_3)_5$ crystal properties is listed in Table I.

Manuscript received November 26, 1974; revised March 27, 1975.

The authors are with the Air Force Avionics Laboratory, Space Laser Communications Program 405B, Wright-Patterson Air Force Base, Ohio 45433.

TABLE I
SUMMARY OF THE IMPORTANT PROPERTIES OF THE PRESENTLY AVAILABLE FREQUENCY-DOUBLING CRYSTAL $Ba_2Na(NbO_3)_5$

	Structure	Orthorhombic (T<300°C)
ρ	Density	5.42 gm cm^{-3}
T_c	Curie Temperature	560°C
T_m	Melt Temperature	1450°C
T_s	Storage Temperature	150°C
T_p	Phase Match Temperature	85.0°C
ΔT_p	Phase Match Temperature, FWHM	1°C
α	Thermal Coefficient Expansion	1 x 10^{-5} $°C^{-1}$
n	Index of Refraction (λ1.06u, o-ray, z axis)	2.26
$\frac{\partial n}{\partial T}$	Thermal Coefficient of Index of Refraction (e-ray)	8 x 10^{-5} $°C^{-1}$
	(o-ray)	-2.5 x 10^{-5} $°C^{-1}$
K	Thermal Conductivity	0.035 w $cm^{-1}°C^{-1}$
d	(λ1.06/λ0.53) Conversion Coefficient	1.1 x 10^{-22} mV^{-1}
α_1	λ1.06 Absorption Coefficient	2.0 x 10^{-3} cm^{-1}
α_2	λ0.53 Absorption Coefficient	40 x 10^{-3} cm^{-1}
L_B	Crystal Dimensions, Commercial	0.5 cm (cube)

II. Approach

The intracavity frequency-doubled laser considered here is being developed for the Air Force Space Laser Communications Program 405B. The ferroelectric crystal $Ba_2Na(NbO_3)_5$ has been chosen for use as the intracavity frequency-doubling element. The crystal is an optimum choice for Nd:YAG laser systems where damage problems may be ignored and high-conversion efficiency is required.

The arrangement of the intracavity frequency-doubled Nd:YAG laser is illustrated in Fig. 1. An intracavity lens is used to collimate the beam within the laser rod and to place the beam waist at a position where the proper value of the beam diameter in the frequency-doubling crystal may be achieved. The position of the crystal is fixed due to its use as an acoustooptical mode-locking element and the spatial limitations of the acoustical column. The position and focal length of the lens is varied to achieve the desired results. The design of the laser is specifically orientated towards a confocal arrangement for insensitivity to misalignment and thermal changes [6].

The theoretical analysis of the laser proceeded by first determining the thermal profile within the $Ba_2Na(NbO_3)_5$ crystal due to the absorption of the incident radiation. The thermal profile is related to the induced lens focal length. The induced

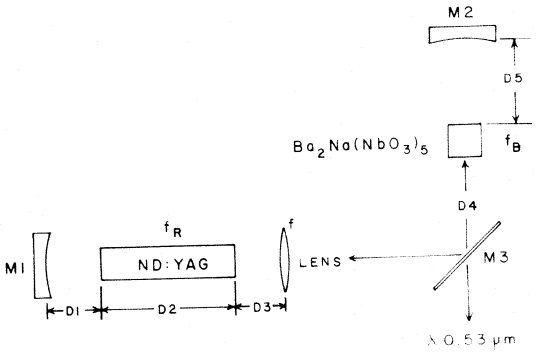

Fig. 1. Schematic of the configuration of the intracavity frequency-doubled Nd:YAG laser under development for space use. The intracavity lens is used to obtain a collimated beam through the rod and to focus the beam into the $Ba_2Na(NbO_3)_5$ crystal. The λ0.53-μm light generated exits the laser through mirror $M3$.

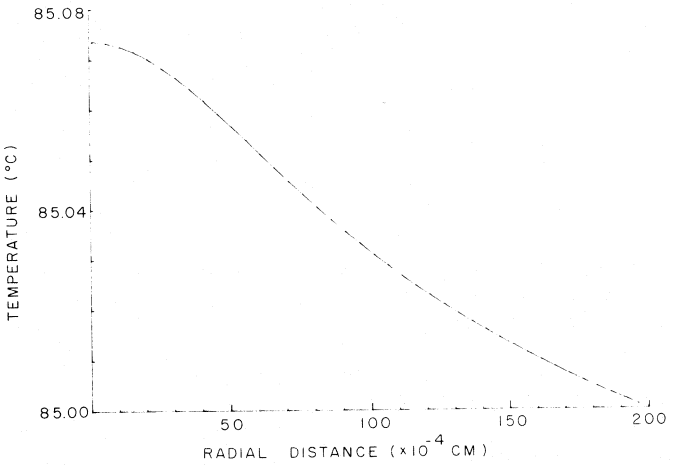

Fig. 2. The radial temperature profile in the $Ba_2Na(NbO_3)_5$ crystal due to the absorption of λ1.06-μm power. The values $W_B = 75 \times 10^{-4}$, $\alpha_1 = 0.002\ cm^{-1}$, and $2I = 20$ W are used.

lens modifies the laser optical cavity parameters and alters the original resonator design. Calculations show that the modifications lead to deleterious effects to the laser. The theoretical resonator analysis of the intracavity frequency-doubled laser proceeded by a closed-form self-consistent computer technique using the *ABCD* matrix representation of optical elements for Gaussian beam propagation [7].

III. Thermal Profile

The radial temperature distribution in the anisotropic $Ba_2Na(NbO_3)_5$ crystal due to the heat generated by the absorption of λ1.06- and λ0.53-μm radiation is assumed to be described in the steady state by the approximate relation

$$\frac{1}{r}\frac{\partial}{\partial r}\left(Kr\frac{\partial T}{\partial r}\right) + W(r) = 0 \tag{1}$$

where cylindrical symmetry has been assumed for mathematical simplicity, K is the thermal conductivity of $Ba_2Na(NbO_3)_5$, $K = 0.035$ W $cm^{-1}/°C^{-1}$ [8], and the heat source term is related to the assumed TEM_{00} Gaussian mode by

$$W(r) = Q_0 \exp(-2r^2/w_B^2) \tag{2}$$

where w_B is the $\exp(-2)$ power point of the laser in the $Ba_2Na(NbO_3)_5$ crystal.

The heat quantity Q_T is determined by spatial integration over $W(r)$ and is the total heat resulting from the absorbed laser radiation, so that $Q_T = Q\pi w_B^2 L\,[1 - \exp(-2R_0^2/w^2)]/2$ where R_0 is the radius at which the boundary is practically established. The exponential is negligible for $R_0 > w_B$ but should be retained for configurations where the crystal and beam dimensions are not too dissimilar. The total heat deposited is also given by the bidirectional incident λ1.06-μm power and the total λ0.53-μm power times their respective absorption factor $[1 - \exp(-\alpha_i L_B)]$ where α_1 is the λ1.06-μm absorption coefficient, α_2 is the λ0.53-μm absorption coefficient, and L_B is the crystal length, so that $Q_T = (2\alpha_1 I + \alpha_2 P_{2\omega})L_B$. The λ1.06-μm absorption dominates since the λ1.06-μm power is at least fifty times greater than that due to λ0.53 μm.

We are presently using $Ba_2Na(NbO_3)_5$ crystals which have relatively low absorption coefficients at λ1.06 and λ0.53 μm. A normal value for α_1 is $<0.002\ cm^{-1}$ and for α_2 is $\simeq 0.04\ cm^{-1}$ [9].[1] These crystals were specifically developed for low iron content for the space laser and may not be commercially available at this time. The circulating λ1.06-μm power of the space Nd:YAG laser is about 10 W with frequency doubling and about 30 W without. The λ0.53-μm power is of order 200 mW. The heat absorbed Q_T in the crystal is then of order 24 mW · cm^{-1} with frequency doubling and 60 mW · cm^{-1} without.

The solution of (1) is achieved by placing the physically satisfying boundary conditions of $\partial T/\partial r = 0$ at $r = 0$ and $T(r) = T_0$ at $r = R_0$ of the $Ba_2Na(NbO_3)_5$ crystal. The thermal profile is effectively given by

$$T(r) = T_0 + \frac{2\alpha_1 I}{4\pi K}\left\{\sum_1 \frac{(-2r^2/w_B^2)^n}{n\cdot n!} - \sum_1 \frac{(-2R_0^2/w_B^2)^n}{n\cdot n!}\right\} \tag{3}$$

which differs somewhat from previous forms for $T(r)$ in that (3) reduces to the isothermal condition when the heat input is zero and is valid beyond $r = w_B$ due to the retention of the R_0 and $n > 1$ terms. We presently use $R_0 = 0.025$ cm and w_B is of the order 75×10^{-4} cm. The series is numerically caused to converge using a CDC 3600 computer; several hundred terms are required [10].[2] The thermal difference $\Delta T = T(r = 0) - T(r = w_B)$ is essentially equal to

$$\frac{I\alpha_1}{2\pi K}(-1)\sum_1 \frac{(-2)^n}{n\cdot n!}$$

where the series converges with $n = 15$ to ~1.32 and $\Delta T \simeq 6.2 \times 10^{-3} \times I$ °C when $\alpha_1 = 0.002\ cm^{-1}$. The change in temperature ΔT will be used to define the thermally induced focal length. An example of the form of $T(r)$ from (2) is shown in Fig. 2 for $w_B = 75 \times 10^{-4}$ cm, $\alpha_1 = 0.002$, and $2I = 20$ W. The form will remain similar for other I and w_B, but the absolute value of $T(r)$ will vary.

[1] The absorption coefficients of $Ba_2Na(NbO_3)_5$ crystals have been measured at λ0.488, λ0.53, and λ1.06 μm using the pyroelectric signal method induced by absorbed laser radiation, Air Force Avionics Laboratory, Wright-Patterson Air Force Base, Ohio.

[2] A unique computer program subroutine was generated to solve the summation involving large integers raised to large powers and divided by large number factorials.

IV. Thermal Lens

The focal length f_B of the induced lens in the $Ba_2Na(NbO_3)_5$ is found from the relation of the lens power of a thick lens formed by a radial thermal gradient [11]. The radius of curvature of the deformed plane surfaces of the crystal faces perpendicular to the laser axis is $R = a^2/2\Delta nL$, where a is the effective radial range of the thermal influence and ΔnL is the optical path length change induced by the thermal effect. We set $a = w_B$, and the focal length is given by

$$f_B = \frac{w_B^2}{4(n-1)L_B(\alpha n + \partial n/\partial T)\,\Delta T - \dfrac{4L_B(n-1)}{n}\{L_B(\alpha n + \partial n/\partial T)\,\Delta T\}^2/w_B^2} \tag{4}$$

where n is the index of refraction of $Ba_2Na(NbO_3)_5$, α is the coefficient of linear expansion, $\partial n/\partial T$ is the thermal coefficient of the ordinary ray index of refraction, and L_B is the crystal length. The form of f_B can be simplified greatly since $L_B(n-1)^2/nR^2 \ll 1$ thereby eliminating the second term of the denominator, and the resulting form of f_B is that familiar to most [6]. The focal length, using the previously noted ΔT, is equivalent to $f_B = -1.5 \times 10^7 w_B^2/I$, and negative due to the negative value of the $\partial n/\partial T$.

We use the value for the induced focal length to modify the $ABCD$ matrix for the $Ba_2Na(NbO_3)_5$ crystal. The crystal is treated as a lenslike medium [7]. The radial index parameter n_{2B} is related to the index n by $n = n_0 - n_{2B}r^2/2$ and to f_B by

$$f_B = \frac{\sqrt{n_0/n_{2B}}}{n_0 \sin\left(L_B\sqrt{n_{2B}/n_0}\right)} \tag{5}$$

which is interpreted as a negative focal length for use in the matrix. The 2×2 $ABCD$ matrix C element is subsequently positive due to the negative values of f_B. Using the preceding relations, $f_B = -84.4$ cm when $w_B = 75 \times 10^{-4}$ cm and $2I = 20$ W and $f_B = -28.1$ cm when $w_B = 75 \times 10^{-4}$ cm and $2I = 60$ W. The associated n_{2B} values are 2.4×10^{-2} and 7.2×10^{-2}, respectively.

A similar concept holds for the laser rod which also has a thermally induced focal length [2], [4]. The relation is somewhat modified by the equation for ΔT when nonuniform heating occurs, as is the case with KRb lamps, and evidently with Kr lamps of the 6-mm bore design.

V. Wavefront Aberration Losses

Even though we use the induced lens as a simple lens effect, we also recognize that the $n > 1$ terms on $T(R)$ include aspherical effect and give rise to diffraction losses due to the thermal profile in the $Ba_2Na(NbO_3)_5$ crystal.

Let $\Phi(r)$ be the purely radial aberration function introduced by the thermally distorted crystal. Then the far-field intensity as a function of angle from the beam axis is [12]

$$I(\beta\Theta) = \frac{8\pi}{R^2\lambda^2 w^2} \cdot \left| \int_0^\infty r \exp\left[i\Phi(r)\right] \exp\left(-r^2/w^2\right) J_0(\beta\Theta r)\, dr \right|^2 \tag{6}$$

where $\beta = 2\pi/\lambda$, λ is the wavelength, and R is the range of the image plane. For small aberrations, we approximate the exponent by $1 + i\,\Phi(r)$ and we use the lowest order thermally induced aberration, letting $\Phi(r) = p(r/w)^4$. In this analysis, the integral form

$$\int_0^\infty x^{\mu-1} \exp\left(-x^2\right) J_0(bx)\, dx$$

occurs and has the value [13],

$$\tfrac{1}{2}\,\Gamma(\mu/2)\, M(-\mu/2 + 1, 1, b^2/4) \exp\left(-b^2/4\right) \tag{7}$$

where M is the confluent hypergeometric function. The first term in (7) has $\mu = 2$ and $b = \beta\Theta w$, the second integral has $\mu = 6$ and the same b. Therefore, we obtain

$$I(\beta\Theta) = \frac{8\pi}{R^2\lambda^2 w^2} \left| \frac{w^2}{2} \exp\left(-(\beta\Theta w)^2/4\right) M(0, 1, (\beta\Theta w)^2/4) + ipw^2 \exp\left(-(\beta\Theta w)^2/4\right) M(-2, 1, (\beta\Theta w)^2/4) \right|^2. \tag{8}$$

Since $M(0, 1, z) = 1$ and $M(-2, 1, z) = z^2 - 4z + 2$, we have

$$I(\beta\Theta) = \frac{2\pi w^2}{R^2\lambda^2} \left[1 + 4p^2 \left(\frac{(\beta\Theta w)^4}{16} - (\beta\Theta w)^2 + 2 \right)^2 \right] \cdot \exp\left[-(\beta\Theta w)^2/4\right]. \tag{9}$$

Integrating the power in the far field at a range R, we have

$$P = \frac{2\pi R^2}{w^2\beta^2} \int_0^\infty I(\beta\Theta w) \cdot \beta\Theta w \cdot d(\beta\Theta w) \tag{10}$$

and evaluating the integral, and normalizing to unity relative to the unaberrated condition $p = 0$, we have for the far-field power

$$P = \frac{1}{1 + 6p^2} \simeq 1 - 6p^2. \tag{11}$$

Since P increases as the aberration increases, the aberrated beam has a smaller total power in the TEM_{00} mode than the nonaberrated beam. The power loss must be

$$\alpha_d = 6p^2. \tag{12}$$

The diffraction loss is related to the thermal distortion by realizing the definition for aberration function $\Phi = \Delta(nL)^{(4)}(2\pi/\lambda) = p(r/w)^4$, where the fourth-order factor is assumed, as noted before.

We compute α_d by using $\Delta(nL)^{(4)}$ as defined by

$$\Delta(nL)^{(4)} = L_B(\alpha n + \partial n/\partial T)\,\Delta T^{(4)}$$
$$\Delta T^{(4)} = \frac{\alpha_1 I}{2\pi K}\left(\frac{2r^2/w_B^2}{2 \cdot 2!}\right)^2 \tag{13}$$

and with $\alpha_1 = 0.001$, we have that

$$\alpha_d = 5 \times 10^{-6} I^2. \tag{14}$$

When $\alpha_d = 0.001$, $I = 14.1$ W.

VI. Laser Power Influence

The frequency-doubled laser power is related to the circulating power at phase match by [14]

$$P_{2w} = 2\epsilon I^2 \tag{15}$$

where the temperature phase match condition for ϵ is assumed, $\epsilon = 5.65 \times 10^{-8} L/w_B^2$, and L is the conversion length within the crystal, normally assumed to be 0.3 cm. The circulating power with the influence of frequency was shown to be [8]

$$I = \frac{\alpha\beta + \epsilon}{2\epsilon\beta} \left\{ \sqrt{1 + \frac{4\epsilon\beta(g_0 - \alpha)}{(\alpha\beta + \epsilon)^2}} - 1 \right\} \tag{16}$$

where the single direction properties are used; α is the passive cavity losses, β is the saturation parameter for the Nd:YAG medium, and $\beta = k/w_R^2$ with $k = 2.89 \times 10^{-4}$, and g_0 is the unsaturated gain. This equation reduces to the familiar expression, $P_w = (g_0/\alpha - 1)/\beta$ when $\epsilon = 0$. Optimum coupling occurs when $\epsilon = \alpha\beta$. The beam diameter in the laser rod is denoted by w_R and the waist diameter in the resonator by w_0.

We analytically illustrate in Fig. 3 the effect to the laser resonator by inclusion of the $Ba_2Na(NbO_3)_5$ lens. We plot the variation of the three important beam diameters in the laser cavity, $2w_R$, $2w_B$, and $2w_0$, as the intracavity lens-to-rod separation is varied. The resonator configuration is $R = -300$ cm, $R = +2.5$ cm, $f = 11$ cm, and the rod thermally induced focal length is 140 cm. The dashed curves represent the relationship when $I = 30$ W, $\epsilon = 0$, and only $\lambda 1.06$-μm absorption occurs, so that $f_B = -28.1$ cm. The solid curves represent the relationship when $I = 10$ W, $\epsilon > 0$, and both $\lambda 1.06$- and $\lambda 0.53$-μm absorption occurs, so that $f_B = -84.4$ cm. It is clear that the beam diameters change as the $Ba_2Na(NbO_3)_5$ lens focal length varies. The difference between the curves increases as the lens position is moved from the confocal position. Since the $\lambda 0.53$-μm laser power is proportional to w_R^4 and w_B^{-2}, by (15), the effect of f_B has an influence upon the laser operation. The laser should be optimized when $\epsilon > 0$ rather than when $\epsilon = 0$ due to the resonator variations. We have found that the resulting $\lambda 0.53$-μm power obtained can be different by 10-20 percent.

The curves of Fig. 3 are not general in nature but are particular to the resonator configuration used. Each individual resonator design must be examined relative to its parameters, and the appropriate $Ba_2Na(NbO_3)_5$ thermally induced focal length included so that an optimum configuration may be achieved.

The influence of the diffraction loss $\alpha_d = \gamma I^2$ is to reduce the available $\lambda 1.06$-μm circulating power and degrade the $\lambda 0.53$-μm performance. The effect of an additional 0.001 loss due to diffraction effects in the space laser would be to decrease the $\lambda 0.53$-μm power by about 10 percent. This value

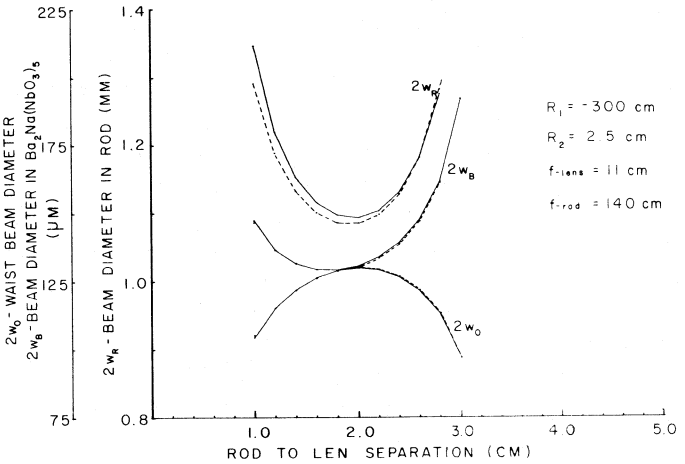

Fig. 3. The effect of the $Ba_2Na(NbO_3)_5$ thermally induced lens to the laser resonator is illustrated by the variation of $2w_R$, $2w_B$, and $2w_0$ as the lens-to-rod separation is varied. The solid curve represents the relationship when $I = 10$ W, $\epsilon > 0$, and $f_B = -84.4$ cm. The dashed curve represents that when $I = 30$ W, $\epsilon = 0$, and $f_B = -28.1$ cm.

is, of course, dependent upon the values α, β, and g_0, and may increase or decrease for other values of the laser parameters.

We have found that the inclusion of the diffraction loss term allows greater agreement between experiment and theory. For example, ambiguities arose after an experiment was performed with an end-pumped ND:YAG laser operating CW, TEM_{00}, and with an intracavity frequency-doubling crystal [15]. The $\lambda 1.06$-μm leakage power through an end mirror and the $\lambda 0.53$-μm power generated were monitored as the $Ba_2Na(NbO_3)_5$ crystal temperature was varied through phase match. The ratio of the circulating power, as measured by the leakage power, when $\epsilon = 0$ to that at phase match was determined. The ratio of the calculated circulating powers using (16) was much different until the diffraction loss was included. The results were then consistent with the experiment. The circulating power was calculated by numerical iteration since the equation for I which results from the inclusion of the diffraction loss in the rate equations is cubic and does not have a simple solution.

It is important to note that the diffraction loss is real and cannot be removed by resonator optimization as can the apparent loss due to the $Ba_2Na(NbO_3)_5$ thermal lens. Losses of order 0.001 are of significant consequence to the space laser and great effort is being made here to minimize all losses.

VII. Conclusion

It is clear that the $Ba_2Na(NbO_3)_5$ losses, whether by diffraction or apparent losses from the thermal lens, must absolutely be considered in the design of a laser of this type. Such losses and effects should be considered in other lasers with intracavity elements. We expect similar losses to be present due to acoustical absorption in the $Ba_2Na(NbO_3)_5$ as well, when the acoustooptical mode locking is included. The losses and effects are more or less small effects for the low-power lasers of the type we are presently developing. However, the addition of 10 percent in frequency-doubled power represents a large benefit to the space laser due to required conservation of energy. The added losses will have a greater effect upon

more powerful lasers due to the circulating power dependence of the loss.

ACKNOWLEDGMENT

We wish to acknowledge the suggestions and advice of two unknown referees.

REFERENCES

[1] R. G. Smith, "Theory of intracavity second-harmonic generation," *IEEE J. Quantum Electron.*, vol. QE-6, pp. 215-223, Apr. 1970.

[2] A. Stein, "Thermooptically perturbed resonators," *IEEE J. Quantum Electron.*, vol. QE-10, pp. 427-434, Apr. 1974.

[3] M. Okada and S. Ieiri, "Influence of self-induced thermal effects on second-harmonic generation," *IEEE J. Quantum Electron.*, vol. QE-7, pp. 469-471, Sept. 1971.

[4] J. D. Foster and L. M. Osterink, "Thermal effects in a Nd:YAG laser," *Appl. Phys.*, vol. 41, pp. 3656-3663, 1970.

[5] A. R. Clobes and A. Stein, "Thermal effects in intracavity frequency doubling crystals," presented at the 1973 Spring Meeting of the Optical Society, Denver, Colo., Paper C15.

[6] J. Steffen, J. P. Lortscher, and G. Herziger, "Fundamental mode radiation with solid-state lasers," *IEEE J. Quantum Electron. (Part II of Two Parts)*, vol. QE-8, pp. 239-245, Feb. 1972.

[7] H. Kogelnik, "Imaging of optical mode-resonators with internal lenses," *Bell Syst. Tech. J.*, vol. 24, pp. 455-494, 1965.

[8] B. Rice, personal communications, McDonnell Douglas Astronautics Company-East, St. Louis, Mo., 1974.

[9] W. Knecht, personal communication, Air Force Avionics Laboratory, Wright-Patterson Air Force Base, Ohio.

[10] C. Whited, personal communication, Air Force Avionics Laboratory, Wright-Patterson Air Force Base, Ohio.

[11] F. A. Levine, "TEM enhancement in cw Nd:YAG by thermal lensing compensation," Perkin-Elmer Corporation, unpublished.

[12] M. Born and W. Wolf, *Principles of Optics.* New York: Pergamon, 1964, pp. 384-395.

[13] M. Abramowitz and I. A. Stegun, Ed., *Handbook of Mathematical Functions with Formulas, Graphs and Mathematical Tables.* New York: Dover, 1965, p. 509.

[14] A. Yariv, *Introduction to Optical Electronics.* New York: Holt, Rinehart and Winston, Inc., 1971, pp. 194-199.

[15] L. Huff, "Sun pumped laser," Air Force Avionics Laboratory, AFAL-TR-73-368, 1973, pp. 104-108.

Theory of Porous Wall Capillary Tubes for Flowing Gas Lasers

ARISTOTLE PAPAYOANOU AND AKIRA FUJISAWA

Abstract—**Flowing gas capillary lasers exhibit high optical gains. However, as a result of the linear axial pressure variation in the tube bore, gain and saturation intensities are not axially uniform. This pressure variation can be reduced by introducing the gas into the tube bore through the walls of a porous capillary tube. Analysis of the gas flow shows that the axial pressure variation in the porous wall tubes is more gradual than for dense wall tubes leading to more uniform gain conditions. The saturation intensity is more uniform not only due to the reduced pressure anisotropy but also, at higher flow rates, because of axially varying particle dwell times in the discharge region.**

I. INTRODUCTION

WAVEGUIDE capillary lasers exhibit high optical gains and saturation intensities for flowing gas CO_2 systems [1]-[3]. However, axial flow systems give rise to a linearly varying pressure distribution which can cause highly variable gains and saturation intensities along the tube axis [1]-[2]. For narrow bore tubes, fast flow or long capillaries this axial pressure differential can become large thereby limiting the optimum pressure, for gain, to a relatively short length of the tube axis. As previously discussed [4] this establishes realistic limits in scaling such amplifier tubes to long lengths. A method introduced to reduce the pressure anisotropy is to use porous walled capillary tubing. The gas enters the capillary bore discharge region by being pumped from a high-pressure chamber, surrounding the tube, through the pores of the tube wall as shown in Fig. 1. An earlier paper [4] cited experimental and analytical results indicating that more uniform gain conditions are attainable in porous walled capillary tubes for flowing CO_2 laser amplifiers. This paper analyzes the applicable flow conditions and determines the pressure and fluid velocity distributions. It also considers the effect of such flow on the saturation intensity. Finally, experimental data on an improved porous wall capillary tube system are presented.

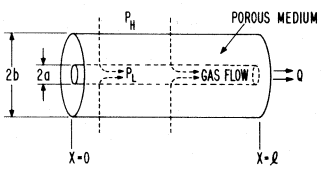

Fig. 1. Representation of gas flowing through porous wall of capillary tube. Gas enters bore along tube length from a high-pressure chamber and is pumped, at volume rate Q, through capillary. The pressure P_H is uniform while P_L, a function of x, varies along the bore.

Manuscript received December 3, 1974; revised March 27, 1975.

A. Papayoanou is with the U.S. Army Electronics Command Laboratories, Fort Monmouth, N.J. 07703.

A. Fujisawa is with the 1st Research Center, Japanese Defense Agency, Tokyo, Japan, and was on leave with the U.S. Army Electronics Command Laboratories, Fort Monmouth, N.J. 07703.

II. Theory

To analyze the flow situation and determine the pressure distribution we first discuss certain basic viscous flow characteristics.[1]

A gas flowing axially in a dense walled capillary tube of length ℓ and bore radius a obeys the Hagen-Poiseuille viscous flow equations. In this case a pressure gradient is established between the ends of the capillary to overcome gas viscosity η and maintain the flow. In the following discussion the gas temperature is taken to be T, k is the Boltzmann constant, and the pressure difference ΔP is equal to $P_1 - P_2$ where P_1 is the input pressure at $x = 0$ and P_2 is the lower exit pressure at $x = \ell$. $\bar{P}$ represents the average pressure $(P_1 + P_2)/2$. The flow $\mathcal{F}$ in particles per second is given by [5], [6]

$$\mathcal{F} = \frac{\pi a^4 \bar{P}}{8\eta k T} \frac{1}{\ell} \Delta P. \tag{1}$$

Hence, for given capillary bore radius a, and gas properties η and T, the particle current $\mathcal{F}$ depends on $\Delta P/\ell$. In analogy with electrical flow [7] we associate $\mathcal{F}$ with the current i, ΔP with the potential difference and the axial flow resistance $\mathcal{R}$ with the ohmic resistance. Then

$$\mathcal{R} = \frac{8\eta k T}{\pi a^4 \bar{P}} \ell. \tag{2}$$

For viscous flow of fluids through porous media Darcy's law states [6]-[8]

$$v_0 = \frac{\kappa}{\eta} \nabla P \tag{3}$$

where ∇P is the pressure gradient across the porous medium having a "permeability" κ and η is the fluid viscosity. The fluid velocity v_0 is considered to be averaged over a region of space small with respect to macroscopic dimensions in the flow system but large with respect to pore size. For steady-state isothermal flow of an ideal gas, as assumed here, it can be shown [6] that the radial flow through a cylindrical shell of length ℓ, inner radius a, and outer radius b, has a volume flow rate Q given by

$$Q = \frac{\pi \kappa \ell \rho_0 (P_H^2 - P_L^2)}{\eta \ln (b/a)} \tag{4}$$

where ρ_0 is the gas density at unit pressure (equation of state $\rho = \rho_0 P$ assumed), P_H represents the high pressure at the outer tube walls and P_L the lower bore pressure as in Fig. 1. The mass current is $\rho Q = \mathcal{F}_P$. As in the case of Hagen-Poiseuille flow the term analogous to the electrical potential difference is the pressure differential $P_H - P_L$ and the radial flow resistance $\mathcal{R}_P$ is given by

$$\mathcal{R}_P = \frac{\eta \ln (b/a)}{\pi \kappa \rho \rho_0 (P_H + P_L)} \frac{1}{\ell}. \tag{5}$$

[1] Viscous flow occurs at pressures, applicable here, in which the particle mean free path is much less than the bore or pore dimensions. In this case the transport rates of the gaseous components are equalized as a result of collisions between unlike particles and the gas flows as a fluid.

It is the form of (5) which is of interest in further calculations. One notes that $\mathcal{R}_P$ is proportional to $1/\ell$. This allows us to represent the radial flow through the walls of the porous tube, by electrical analogy, as current flow in an equivalent parallel circuit.

Axial flow resistance in a dense wall capillary, see (2), is proportional to tube length ℓ so that the applicable equivalent circuit in this case is that of a series resistance. This is represented in Fig. 2(a) where the tube is divided into N equal length sections each having resistance r. Voltages V_1' and V_N' are the respective analogs of P_1 and P_2 as defined in (1). Fig. 2(b) represents the circuit analog for flow in the porous wall capillary tube having the same bore radius and length as the dense wall capillary. V and V_N are the respective analogs of the uniform high-pressure P_H at the outer tube walls and the exit pressure at the capillary end, $x = \ell$. For purposes of this analysis flow is taken to be in the $+x$ direction.

We have calculated the current distribution appropriate to Fig. 2(b) in terms of ϵ, where $\epsilon = r/R$, and find

$$i_1 = i_2 \frac{1}{1+\epsilon}$$

$$i_2 = i_3 \frac{1}{(1+\epsilon) + \dfrac{\epsilon}{1+\epsilon}}$$

$$i_3 = i_4 \frac{1}{(1+\epsilon) + \dfrac{\epsilon}{(1+\epsilon) + \dfrac{\epsilon}{1+\epsilon}} + \dfrac{1}{1+\epsilon} \dfrac{\epsilon}{(1+\epsilon) + \dfrac{\epsilon}{(1+\epsilon)}}} \tag{6}$$

etc.

Assuming that terms in ϵ^2 can be neglected one finds to first order that, for $n = 1, 2, 3, \cdots, N$

$$i_{n+1} = i_n(1 + n\epsilon) \tag{7}$$

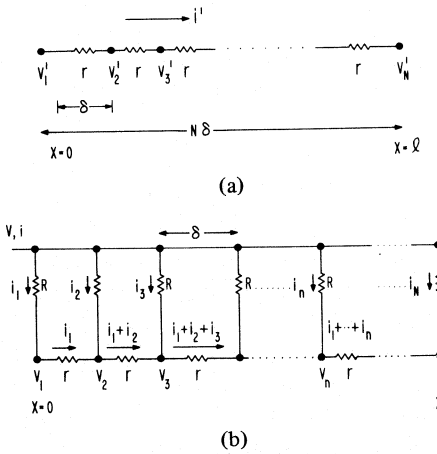

Fig. 2. (a) Electrical circuit analog of flow through capillary of dense walled tube. The resistance to flow over a length segment δ is taken to be r and the particle current remains fixed along the tube axis. (b) Electrical circuit analog for flow in porous wall capillary tube with same bore and length as dense wall tube represented in (a). For length segments δ the radial resistance to flow through the porous wall is R and axial resistance to flow is r. The particle current is no longer uniform along the tube axis.

or in terms of i_1 on the right-hand side

$$i_n = i_1 \left(1 + \epsilon \frac{n(n-1)}{2}\right). \tag{8}$$

Using the preceding one compares the total voltage (i.e., pressure) drop in the bores of the porous and dense walled tubes.

$$\frac{\Delta V_{1-N}^{\text{porous}}}{\Delta V_{1-N}^{\text{dense}}} = \frac{r[i_1 + (i_1 + i_2) + (i_1 + i_2 + i_3) + \cdots + (i_1 + i_2 + \cdots + i_N)]}{i'Nr}. \tag{9}$$

If it is assumed that $i_1 \simeq i_2 \simeq i_3 \simeq \cdots \simeq i_N$, so that $i_1 \simeq i/N$, the numerator in (9) is simplified and one need only use the summation formula for the arithmetic progression, i.e., $1 + 2 + 3 + \cdots + N = N(N+1)/2$. The assumption made in the preceding is discussed in the Appendix. From (9) it now follows that

$$\frac{\Delta V_{1-N}^{\text{porous}}}{\Delta V_{1-N}^{\text{dense}}} = \frac{(i/N)\left(\frac{N(N+1)}{2}\right)}{i'N} = \frac{1}{2}\frac{i}{i'}, \quad \text{for } N \gg 1. \tag{10}$$

Now i and i' can be described by the system standard flows so that for identical system standard flow rates, i.e., $i = i'$

$$\Delta V_{1-N}^{\text{porous}} = \tfrac{1}{2}\,\Delta V_{1-N}^{\text{dense}}. \tag{11}$$

Next we determine the pressure distribution in the bore of the porous wall tube. For $n \leqslant N$ one can write

$$\frac{V_1 - V_n}{V_1 - V_N} = \frac{r[i_1 + (i_1 + i_2) + \cdots + (i_1 + i_2 + \cdots + i_n)]}{r[i_1 + (i_1 + i_2) + \cdots + (i_1 + i_2 + \cdots + i_N)]} \tag{12}$$

and again assuming that $i_1 \simeq i/N$ one can write

$$\frac{V_1 - V_n}{V_1 - V_N} = \frac{(i/N)\left(\frac{n(n+1)}{2}\right)}{(i/N)\left(\frac{N(N+1)}{2}\right)} \approx \frac{n^2}{N^2} \tag{13}$$

for $n, N \gg 1$.

Since the tube is divided into sections of length δ such that $n\delta = x$ and $N\delta = \ell$, it follows that

$$\frac{V_1 - V_n}{V_1 - V_N} = \frac{x^2}{\ell^2}. \tag{14}$$

Since $V_1 = P_A$ is the high pressure at $x = 0$ of the porous capillary bore, V_n is the pressure $P(x)$ at position x along the capillary axis, and $V_N = P_B$ is the exit low pressure one can write

$$P(x) = P_A - (P_A - P_B)(x/\ell)^2. \tag{15}$$

From (11) it is noted that for identical system standard flow rates in the dense and porous wall systems that

$$(P_A - P_B)^{\text{porous}} = \tfrac{1}{2}(P_1 - P_2)^{\text{dense}}. \tag{16}$$

Hence for identical system standard flow rates the total pressure drop in the porous wall system is half that in the dense wall system and, furthermore, the pressure drop from the high- to the low-pressure side is considerably more gradual in the porous wall tube since it declines according to $(x/\ell)^2$ rather than (x/ℓ).

It can also be shown using assumptions previously made that the mass current distribution in the porous wall capillary is given by

$$i(x) = i\frac{x}{\ell}. \tag{17}$$

Since the pressure distribution in the bore falls from some initial pressure P_A to a lower exit pressure P_B it follows, because $i(x) = \pi a^2 \bar{m} n(x) \cdot v(x)$ and $P(x) = n(x) \cdot kT$, that the fluid velocity v increases along the tube axis. Assuming an axially constant gas temperature T one can write

$$v(x) = i\frac{kT}{P_A \bar{m}\pi a^2}\frac{x/\ell}{[1 - (1 - P_B/P_A)(x/\ell)^2]} \tag{18}$$

where $\bar{m}$ is the average particle mass.

III. Saturation Intensity

The saturation intensity I_s can be written as [9]

$$I_s = \frac{8\pi^2 hc\Delta\nu}{\lambda^3(\tau_u + \tau_\ell)} t_{\text{sp}} \tag{19}$$

where τ_u, τ_ℓ are the lifetimes of the upper and lower laser states, respectively, neglecting degeneracies of levels, λ is the wavelength, t_{sp} is the lifetime for spontaneous radiative transition between upper and lower laser levels, h is Planck's constant, c is the speed of light, and $\Delta\nu$ is the Lorentzian half-width of the transition. For fast flowing systems the upper and lower lifetimes are reduced by the rapid introduction of unexcited gas molecules, i.e., CO_2, into and excited molecules out of the discharge region. Then [10]

$$\tau_u = \frac{\tau_2 \tau_F}{\tau_2 + \tau_F}; \quad \tau_\ell = \frac{\tau_1 \tau_F}{\tau_1 + \tau_F} \tag{20}$$

where τ_F is the dwell time of the flowing gas in the discharge region and τ_2, τ_1 are the upper and lower level collisional lifetimes which are inversely dependent on the pressure. Typically, $\tau_1 \ll \tau_2$ and $\tau_1 \ll \tau_F$ so (19) can be written

$$I_s = \frac{8\pi^2 hct_{\text{sp}}}{\lambda^3}\frac{\Delta\nu}{\tau_2}\frac{\tau_2 + \tau_F}{\tau_F}. \tag{21}$$

In the limit of zero flow, i.e., $\tau_F \to \infty$, the right-hand side depends on the ratio $\Delta\nu/\tau_2$. Since $\Delta\nu \propto P$ and $\tau_2 \propto 1/P$ one obtains the familiar result [11], [12] that $I_s \propto P^2$. However, in the case of flow where τ_F becomes comparable to τ_2 the saturation intensity increases beyond the values established by collisional effects. The value applicable to our CO_2 mixture [4] was estimated from published data of relaxation time constants [13] and compared with average values of τ_F applicable to the flow rates used in our experiments. At moderate to high standard flow rates, 15-30 sccm/s in our 1-mm bore tubes, we have found that the average τ_F becomes

comparable to τ_2 and thus must contribute to increasing I_s.

The more interesting aspect is the effect that this flow has on the axial dependence of the saturation intensity. One notes that

$$\tau_F = \frac{\ell - x}{v(x)}. \tag{22}$$

Hence for particles introduced through the pores, into the bore, near the tube ends τ_F becomes very small not only because the numerator in (22) decreases but also because $v(x)$ increases as x increases as seen from (18). Thus the flow acts to increase I_s near the end of the capillary tube thereby countering the effect of the axially decreasing pressure. The net effect is a tendency to maintain I_s axially constant over the capillary length.

IV. Experimental Results

Experimental data for flowing CO_2 gas mixtures using an improved porous wall gain system have been obtained. The basic system configuration was similar to that previously reported [4]. However, the active gain length was increased to 15 cm, an improved cooling block was used, overall system purity was considerably improved, and antireflection coated ZnSe windows were used.

Fig. 3 shows measured small signal gains, on the $P(22)$ line, at a near optimum, 1.8-mA discharge current, using tapwater cooling. Gains up to 21 dB/m were measured. Subsequent measurements made with the probe laser stabilized on the $P(20)$ line center indicates gains approximately 6 percent higher than shown in Fig. 3. Somewhat higher values could be obtained, especially at lower pressures, with higher discharge currents. The largest value measured, on the $P(20)$ line, was 24.3 dB/m at 2.2 mA, a mean pressure of 62 torr, and a flow rate of 12.8 sccm/s. The gain characteristics found appear consistent with the experimental data obtained with conventional CO_2 lasers [10, pp. 739-742]. Included in Fig. 3 are the E/N values for the three flow rates investigated. E

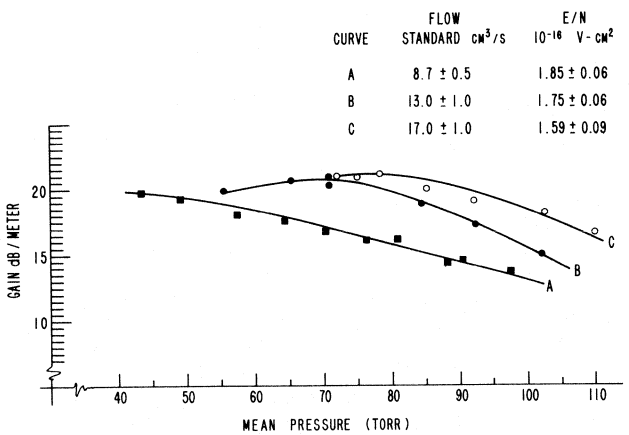

Fig. 3. Small signal gain characteristics of 15-cm-long porous wall capillary tube having a 1-cm bore diameter. Discharge current was 1.8 mA and the gas mixture ratio was $He:CO_2:N_2 = 5:3:2$. Measurements made on $P(22)$ line. Tube wall temperatures were in range 17-23°C. Gas was pumped equally out both tube ends. Total system flow rate is double value given in figure.

is the axial electric field and N is the mean particle number density. Neglecting differences between our mixture ratio and that used in the quantitative analysis of Nighan and Bennett [14] one sees that our experimental E/N values correspond to discharge conditions in which electronic collisions efficiently populate the upper laser vibrational level of CO_2 as well as the first eight vibrational levels of N_2. The gain tube thus operates at near optimum pumping conditions.

The gain tube was also used as part of an oscillator. Dielectric coated cavity mirrors with a 12.5-cm radius of curvature but different reflectivities were used. Optimum spacing of the mirrors from the tube ends was found to be 11.5 ± 0.3 cm. Operating at a mean pressure of 103 torr, a flow rate of 13 sccm/s a current of 1.8 mA, and a tube voltage of 9.4 kV we have measured the output power as a function of mirror transmissivity. For mirror transmissivities of 10, 22, and 34 percent the laser power was 0.36, 0.66, and 1.0 W. Higher transmissivity mirrors are required, but were not available, to experimentally determine the optimum transmission. Peak output was on the $P(20)$ line. Higher powers could be attained at higher discharge currents but this was not systematically investigated. The beam cross section, as observed on a thermal image plate, was a well-defined circle with no visible outer ring.

Appendix

On proceeding from (9) to (10) and (12) to (13) in the text it has been assumed that $i_1 \simeq i_2 \simeq i_3 \simeq \cdots \simeq i_N$ so that $i_1 \simeq i/N$. The following discussion reveals the conditions under which $i_1 \simeq i/N$. Such conditions are similar to those necessary in assuming that $i_1 \simeq i_2 \simeq i_3 \simeq \cdots \simeq i_N$. From Fig. 2(b) one notes that $i = i_1 + i_2 + i_3 + \cdots + i_N$. Using (8) from the text one can write

$$i = i_1 \left[N + \epsilon \sum_1^N \frac{n(n-1)}{2} \right]. \tag{A1}$$

From the summation formulas, $\Sigma n^2 = N(N+1)(2N+1)/6$ and $\Sigma n = N(N+1)/2$ with the sums going from 1 to N, it follows that

$$i = i_1 N \left[1 + \epsilon \frac{(N-1)(N+1)}{6} \right] \tag{A2}$$

and for $N >> 1$

$$i_1 = \frac{i}{N} \frac{1}{(1 + \epsilon N^2/6)}. \tag{A3}$$

But $\epsilon = r/R$ and from the definitions of r and R, i.e., $r = \mathcal{R}/N$ and $R = N\mathcal{R}_P$, one sees that $\epsilon = (1/N^2)(\mathcal{R}/\mathcal{R}_P)$. Thus

$$i_1 = \frac{i}{N} \frac{1}{(1 + \mathcal{R}/6\mathcal{R}_P)}. \tag{A4}$$

The simplification introduced in deriving (10) and (13) that $i_1 = i/N$, is justified when the total capillary flow resistance is less than the total radial flow resistance of the porous shell.

The ratio $\mathcal{R}/\mathcal{R}_P$ depends on various known tube dimensions such as bore diameter, capillary length, shell thickness, average pressures, etc., as well as terms less susceptible to direct deter-

mination such as the permeability κ and the effective viscosity η for gas flow through the pores. Our experimental measurements indicate that $\mathcal{R}/\mathcal{R}_P$ is considerably less than 1 for the porous capillary used. Furthermore, unless tubes of higher porosity or thinner shells (our wall thickness was 3 mm) are used the simplifications used in the text seem reasonable for most experimental setups.

References

[1] T. J. Bridges, E. G. Burkhardt, and P. W. Smith, "CO_2 waveguide lasers," *Appl. Phys. Lett.*, vol. 20, pp. 403–405, May 15, 1972.

[2] E. G. Burkhardt, T. J. Bridges, and P. W. Smith, "BeO capillary CO_2 waveguide laser," *Opt. Commun.*, vol. 6, pp. 193–195, Oct. 1972.

[3] J. J. Degnan, H. E. Walker, J. H. McElroy, and N. McAvoy, "Gain and saturation intensity measurements in a waveguide CO_2 laser," *IEEE J. Quantum Electron.*, vol. QE-9, pp. 489–491, Apr. 1973.

[4] A. Papayoanou and A. Fujisawa, "Porous wall BeO capillary waveguide laser," *Appl. Phys. Lett.*, vol. 26, pp. 158–160, Feb. 15, 1975.

[5] R. D. Present, *Kinetic Theory of Gases*. New York: McGraw-Hill, 1958.

[6] R. B. Bird, W. E. Stewart, and E. N. Lightfoot, *Transport Phenomena*. New York: Wiley, 1960.

[7] M. Muskat, *The Flow of Homogeneous Fluids Through Porous Media*. Ann Arbor, Mich.: Edwards, 1946.

[8] P. C. Carman, *Flow of Gases Through Porous Media*. London, England: Butterworth, 1956.

[9] C. P. Christensen, C. Freed, and H. A. Haus, "Gain saturation and diffusion in CO_2 lasers," *IEEE J. Quantum Electron.*, vol. QE-5, pp. 276–283, June 1969.

[10] A. J. DeMaria, "Review of CW high-power CO_2 laser," *Proc. IEEE*, vol. 61, pp. 731–748, June 1973.

[11] Y. Nachson and U. P. Oppenheim, "Gain saturation in the CO_2 laser," *Appl. Opt.*, vol. 12, pp. 1934–1939, Aug. 1973.

[12] R. L. Abrams and W. B. Bridges, "Characteristics of sealed-off waveguide CO_2 lasers," *IEEE J. Quantum Electron.*, vol. QE-9, pp. 940–946, Sept. 1973.

[13] D. C. Tyte, "Carbon dioxide lasers," in *Advances in Quantum Electronics*, vol. 1, D. W. Goodwin, Ed. New York: Academic, 1970.

[14] W. L. Nighan and J. H. Bennett, "Electron energy distribution functions and vibrational excitation rates in CO_2 laser mixtures," *Appl. Phys. Lett.*, vol. 14, pp. 240–243, Apr. 15, 1969.

TE CO_2 Laser Pulse Decay and Molecular Relaxation Rates

BRIAN K. GARSIDE, JOHN REID, AND EDWARD A. BALLIK, MEMBER, IEEE

Abstract—**A theoretical model for TE CO_2 laser dynamics is presented, incorporating the effects of coupling between the rotational sublevels of the laser vibrational states associated with the 10.4-μm transition. It is shown that proper incorporation of this coupling is extremely important for modeling both the initial gain-switched output peak and the subsequent rate at which the radiation energy decays away. In particular, it is demonstrated that the latter rate is a measure of the rate at which energy is removed from the lower laser level.**

The lower laser level is coupled to the bending mode by several relatively rapid vibrational energy exchange processes. The coupled bending and asymmetric stretching modes then lose energy at a much slower rate, controlled by the conversion of vibrational energy to translational energy. A proper choice of initial laser level populations allows the decay rate of the pulse tail to be controlled by either one of these. A novel experimental technique is described which allows the two ranges of operation to be explored. A comparison between theory and experiment produces excellent agreement, and the results are employed to determine values for the relevant rates.

Manuscript received January 6, 1975; revised March 27, 1975. This work was supported in part by the National Research Council and the Defence Research Board of Canada.

B. K. Garside and E. A. Ballik are with the Department of Engineering Physics and the Department of Physics, McMaster University, Hamilton, Ont., Canada.

J. Reid was with the Department of Engineering Physics and the Department of Physics, McMaster University, Hamilton, Ont., Canada. He is now with the Division of Physics, National Research Council of Canada, Ottawa, Ont., Canada.

I. Introduction

IT HAS BEEN demonstrated elsewhere that, to generate theoretical laser output pulses in agreement with experiment, it is essential to allow explicitly for the coupling between the rotational sublevels of the vibrational states associated with the 10.4-μm laser transition in CO_2 [1]. The importance of allowing for this coupling is self-evident for nanosecond pulses, but is less apparent for pulses two orders of magnitude longer than the rotational level coupling time. Nevertheless, proper allowance for this coupling makes a great difference to the predicted temporal shape of the gain-switched laser output, particularly for discharges at moderate gas pressures. Furthermore, the proper incorporation of rotational level coupling has a considerable impact on the modeling of the rate at which the laser energy decays away following the initial gain-switched peak. In this case, the impact of the rotational coupling rate is less direct; its importance lies mainly in the fact that the appropriate conditions of inversion and radiation density in the output pulse "tail" can be reproduced.

In what follows, it will be shown that the behavior of the laser pulse tail is sensitive to the various molecular vibrational energy relaxation rates controlling the decay of the lower laser level population. A comparison between observations

of the laser energy decay and a laser model properly incorporating rotational level coupling permits determination of the rates controlling deactivation of the lower level.

Fig. 1 shows the relevant energy levels of the CO_2 molecule. The lower laser level ($10^0 0$) is coupled to the bending mode by several decay mechanisms [2], [3]. These are represented by 1(*a*), 1(*b*), and 1(*c*), and the resultant overall (fast) equilibrium rate is called Rate 1 with a relaxation time τ_1. On a longer time scale, it is known that the decay of the $10^0 0$ population is controlled by the emptying of the bending mode via collisionally induced transfer of vibrational energy from the $01^1 0$ level to translational energy (*V-T* collisions) [4], [5]. This *V-T* rate will be represented by a time constant τ_{VT}, and is generally supposed to be much slower than Rate 1. In the present work, we have employed a laser technique which permits the decay of the laser energy to be controlled by either τ_1 or τ_{VT}. The experimental approach involves the use of a *Q* switch in a TE CO_2 laser resonator. This switch permits the time at which the laser pulse appears, relative to the discharge current pulse, to be varied at will. A proper choice of this time allows either τ_1 or τ_{VT} to dominate the laser decay. This facility has been employed to determine both relaxation rates under conditions appropriate to laser operation.

Several authors have reported experiments aimed at determining CO_2 ($10^0 0$) decay rates employing conventional longitudinal discharge CO_2 lasers at low pressure [6], [7]. The techniques involve the use of pulsed discharges, in which the decay of the laser radiation, after discharge deactivation, was studied. In particular, the results obtained by Bulthuis [7] indicate that the $10^0 0$ level is apparently weakly coupled to the bending mode, a result also obtained by Rosser *et al.* [8]. These results are at variance with calculations of the coupling rates 1(*a*), 1(*b*), and 1(*c*) [2], [3]. Furthermore, using the most direct measurement technique reported to date, Stark has shown that rate 1(*b*) alone is an order of magnitude faster than the *V-T* rate [9]. We have demonstrated previously, from studies of the small-signal gain in TE CO_2 lasers, that Rate 1 is at least as fast as the *V-T* rate [10]. It is apparent that the relaxation behavior of the $10^0 0$ level in CO_2 is still the subject of much uncertainty. In the present work, we exploit the experimental capability of adjusting the timing of the laser output pulse relative to the discharge pulse to investigate the impact of the various lower laser level deactivation mechanisms. The approach has the twofold advantage that it permits the rate coefficients to be observed under actual lasing conditions, and that the output pulse can, if necessary, be far removed from the influence of the discharge. The previously described techniques lack this capability in that the decay of the laser energy commences during, or very shortly after, the discharge.

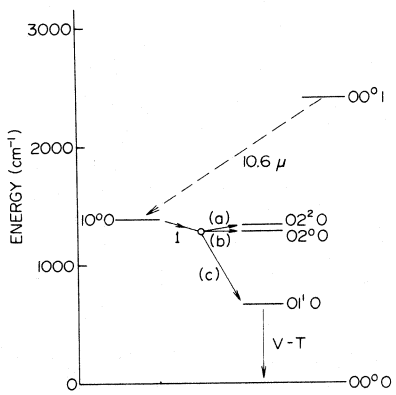

Fig. 1. Energy levels of the CO_2 molecule, and relaxation mechanisms of the lower laser level.

In the following sections, the relevant theoretical model of the laser system will be discussed, and the importance of incorporating rotational coupling into the model will be demonstrated. The experimental system will be described, and it will be demonstrated that the tail of the laser output pulse is controlled by the *V-T* rate when the laser pulse appears well before the occurrence of the gain peak. On the other hand, for operation at times beyond the occurrence of the gain maximum, the pulse tail is controlled by Rate 1. Values are thus determined for the relevant molecular relaxation rates. In particular, it is found that the vibrational coupling of the $10^0 0$ level to the bending mode is much faster than the $01^1 0$ *V-T* deactivation rate. The value obtained for this vibrational energy transfer rate is consistent with the calculations of Seeber [3] and Sharma [2], and the experiments of Stark [9]. It is not in agreement with the results of Bulthuis [7] and Rosser *et al.* [8].

II. Theoretical Model

The laser model employed here is similar to that used by Manes and Seguin [11]; but with the major difference that it has been extended to allow explicitly for the effects of rotational level coupling. The excess population in the lower laser level relaxes to the combined bending and symmetric stretching mode (BS mode) with a time constant τ_1. The BS mode thereafter loses energy at the *V-T* rate. We have simplified the model by considering all relaxation rates as constant throughout the laser pulse. This assumption is reasonable when, as in the case here, all mode temperatures remain small during the pulse [11], [12].

The differential equations governing the system, after completion of the electrical discharge pulse, are as follows:

$$\frac{dN_u}{dt} = -g_\alpha c(n^u_{J-1} - n^l_J)\rho - \frac{N_u}{\tau_u} \tag{1}$$

$$\frac{dN_l}{dt} = +g_\alpha c(n^u_{J-1} - n^l_J)\rho - \frac{N_l - N^e_l(T_1)}{\tau_1} \tag{2}$$

$$\frac{d(n^u_{J-1} - n^l_J)}{dt} = -2g_\alpha c(n^u_{J-1} - n^l_J)\rho - \frac{(n^u_{J-1} - n^l_J) - K(J)\Delta N}{\tau_R} \tag{3}$$

$$\frac{d\rho}{dt} = g_\alpha c(n^u_{J-1} - n^l_J)\rho - \frac{\rho}{\tau_c} \tag{4}$$

$$\frac{dE_{bs}}{dt} = \frac{E_u}{\tau_u} + \frac{E_l - E^e_l(T_1)}{\tau_1} - \frac{E_{bs} - E^e_{bs}(T)}{\tau_{VT}} \tag{5}$$

where $N_u(E_u)$, $N_l(E_l)$ are the populations (energies) in the upper and lower laser levels, $\Delta N = N_u - N_l$, n^u_{J-1} and n^l_J are the populations of the particular rotational sublevels on which lasing occurs, and $K(J)\Delta N$ is the equilibrium value of the rotational inversion ($\sim\frac{1}{15}$ of the total inversion for $P(18)$). ρ is the in-cavity photon density and τ_c is the cavity decay time. The parameter E_{bs} is the energy in the combined BS mode, excluding the lower laser level, which is treated separately. When a parameter is written with the superscript e, e.g., $E^e_{bs}(T)$, it represents the equilibrium value of that parameter at a temperature T. The coefficient, g_α (gain per unit length for unit inversion), is easily determined for any gas mixture and pressure using the data of Robinson [13]. In general, g_α and $K(J)$ have slightly different values for the upper and lower levels, but the average values can be used without any significant loss of accuracy. The other parameters occurring in these equations are the relaxation times; τ_R is the rotational relaxation time and τ_u is the upper laser level decay time.

Observe that, provided the small-signal gain (which is a function of time) and the cavity decay time are known, the major unknown parameters are the relaxation times τ_R, τ_1, and τ_{VT}. The appropriate values of τ_R have been determined previously from a study of the gain-switched output pulse, for the experimental conditions employed in the present work [1]. (For the 10-percent CO_2:90-percent He mixture, this rotational relaxation rate is $3.6 \times 10^6\ s^{-1}\ torr^{-1}$.) Accordingly, for our present purposes, τ_R will be treated as a known parameter, and we concentrate on the importance of the parameters τ_1 and τ_{VT} in determining the behavior of the output pulse. A term was incorporated into the set of (1)-(5) representing the pumping of the $00^\circ1$ level from combination levels such as 01^10. The rate constant determined by Burak *et al.* [14] was used for this purpose, but it turned out that this term made very little difference to the computed pulses. The same result was found for other similar pumping terms such as $CO_2(00^\circ2) + CO_2(00^\circ0) \rightarrow 2CO_2(00^\circ1)$. Starting conditions for numerical calculation employ a small initial value of ρ at the instant of Q switching.

In the following sections, we shall discuss experimental observations of the laser pulse tails and employ the above theory in their interpretation. Prior to proceeding with this plan, the predictions of the above theory for typical experimental circumstances are compared with those deduced by taking $\tau_R = 0$. That is, a comparison is made between the present and previously employed theories describing TE CO_2 lasers [11], [15]-[17]. Parameters typical of a 10-percent CO_2:90-percent He gas mixture, at a total pressure of 27 torr, were employed for the calculations. This gas pressure is typical of those employed in the subsequent experiments. Similar differences between the two theories also occur at higher pressures. Fig. 2 shows the predicted behavior of the laser pulse and the gain in the $P(18)$ transition as a function of time, obtained when the rotational levels maintain thermal equilibrium throughout the laser pulse. Observe that the laser pulse has a main peak which decays away rapidly, and is followed by a subsidiary peak. This reflects the behavior of the inversion. The main laser pulse depletes the inversion almost to zero, and so (provided the cavity decay time is much faster than τ_1) the pulse decays away at a rate close to the cavity decay rate. The inversion then recovers as the excess population is removed from the lower laser level on a time scale commensurate with τ_1. If this recovery produces a sufficiently large inversion, the radiation density will build up to another smaller peak. This order of events may occur several times; a third pulse is in fact produced 3 μs after the main peak in this case. Such behavior has been predicted previously using similar laser models, but has not usually been observed for gas mixtures without N_2 [17]. Fig. 3 shows the behavior of the laser pulse and gain predicted when the finite rotational level coupling time is taken into account. For purposes of

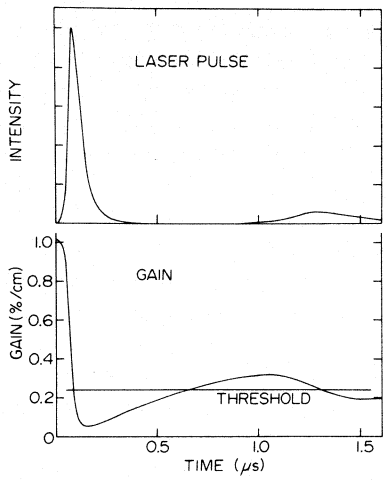

Fig. 2. Laser pulse and gain, calculated employing a model which does not include rotational coupling. The cavity length is 200 cm, with a cavity decay time of 33 ns, and the amplifier length is 92 cm. All vibrational relaxation rates used in the calculations are chosen to correspond to a 10-percent CO_2:90-percent He mixture at 27 torr total pressure; the values of Rate 1 and the V-T rate used are those determined in Section III. Lasing takes place at the peak of the time-dependent gain.

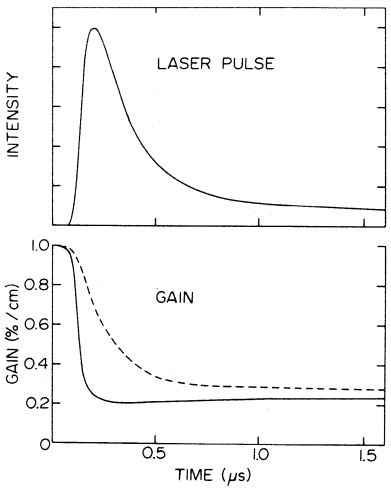

Fig. 3. Laser pulse and gain calculated employing a model including the finite rotational level coupling time ($\tau_R = 10$ ns). All other parameters are the same as for Fig. 2. The dashed line indicates the time dependence of $g_\alpha K(J)\Delta N$. Note the large departure from rotational equilibrium at the time of the laser pulse peak. The threshold gain is 0.24 percent/cm, the same as in Fig. 2.

comparison, the gain corresponding to the thermal equilibrium inversion is also plotted for the same transition (dashed line). Observe that the laser output pulse now decays away monotonically and that the $P(18)$ inversion is reduced to a value considerably less than the equilibrium value. In this case, the transfer of energy from other rotational lines at a finite rate prevents the main peak of the pulse from depleting the entire inversion, and serves to hold the gain close to threshold at the start of the pulse tail. The tail then subsequently decays at a rate determined by the emptying of the lower laser level. For the situation shown, the lower laser level emptying is controlled by τ_1. In the next section, we shall show that observed output pulses are of the general form given in Fig. 3. Furthermore, experimental conditions can be chosen so that *either* τ_1 *or* τ_{VT} determines the rate at which the pulse tail decays.

III. Experimental Methods and Observations

Fig. 4 is a schematic diagram of the apparatus used to observe the laser pulse decay. The laser cavity contains a resistor-pin discharge tube [18] and two 1-in focal length antireflection-coated Ge lenses. A diffraction grating acts as one mirror of the resonator, and permits the laser wavelength to be selected from a range of rotational lines. The cavity can be Q switched by means of a rapidly rotating slotted disk, which is positioned to intersect the cavity at the common focus of the two lenses. The activation time of the Q switch is considerably faster than the buildup time of the laser pulse, and introduces no additional losses into the cavity during lasing. The timing of the Q switching relative to the firing of the gain tube is controlled using a 6328-Å He-Ne laser "trigger" beam. This beam passes through a second slot in the rotating disk and is incident on a photodiode. This arrangement produces a train of output pulses from the photodiode synchronized with the laser resonator switching times. The pulse train is fed to a repetition rate control unit, which counts down the repetition rate to 2 or 3 pulses per second (pps) while maintaining time synchronization. These pulses, suitably delayed, are employed to trigger both the gain tube and the monitoring oscilloscope. The time delay controlling the firing of the laser discharge can be adjusted so that the laser pulse is located at any interval during the time-dependent gain. Two apertures were positioned in the cavity to ensure that lasing occurred in the TEM_{00} mode, and that no higher order transverse modes were present. Lasing generally occurred on several longitudinal modes, as evidenced by nanosecond spiking structure in the pulse. It was experimentally determined that the laser pulse envelope did not depend upon the details of this structure. Consequently, the detector system response time was adjusted to display only the pulse envelope.

The shape of the laser output pulse was studied at various stages during the time development of the laser gain. Fig. 5 illustrates the laser pulses observed prior to, and just after, the peak of the gain. Notice particularly the relatively large and very long pulse tails which occur for laser operation at times well before the gain maximum. The pulse tails which occur for times at, and beyond, the gain peak are well defined but relatively smaller in magnitude. Furthermore, the tails in this region decay away at a rate roughly an order of magnitude faster than those observed during the rise time of the gain.

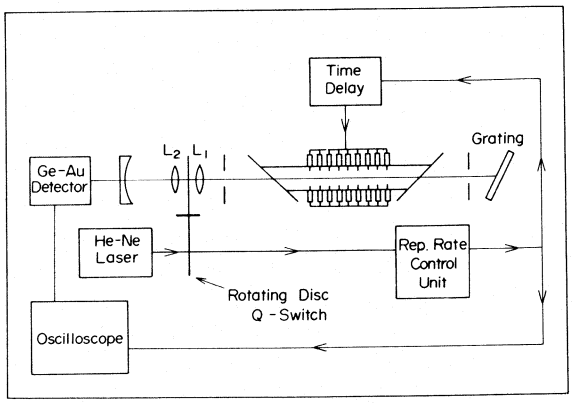

Fig. 4. Schematic diagram of apparatus. The total cavity length is 200 cm, with a decay time of 33 ns, and the length of the active medium is 92 cm.

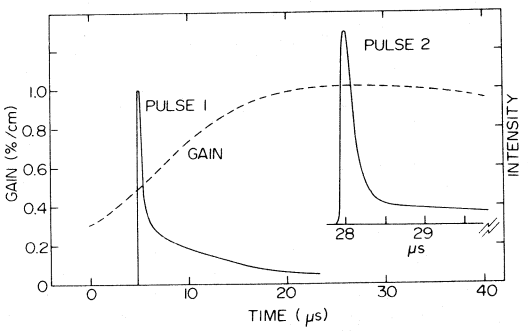

Fig. 5. Two experimentally observed laser pulses together with the small-signal gain profile. A 10-percent CO_2:90-percent He gas mixture was employed, at a total pressure of 36 torr. Pulse 1 is obtained when no Q switch is used; lasing occurs early in the rise time of the gain. Pulse 2 is typical of the pulses obtained when lasing is arranged to take place at, or just beyond, the peak of the gain. Note that an expanded time scale is employed in plotting Pulse 2. The peak intensity of Pulse 2 is 5 times that of Pulse 1.

The great differences observed in the pulses which occu before or after the gain peak arise in the following manner. During the early part of the gain rise time, there is a large population in both the upper and lower laser levels. The gain increases as the population decays away from the lower laser level. The BS modes are in thermal equilibrium during this decay, which arises through V-T transitions of the 01^10 level. If lasing occurs during the early part of this decay, there is a large population remaining in the lower laser level after the peak of the laser pulse. This population is near equilibrium with the rest of the BS modes. It decays away at the V-T rate and so serves to pump the inversion on this time scale. This pumping thereby controls the decay time of the laser pulse tail. When lasing occurs after the peak of the gain pulse, the situation is very different. In this case, the initial energy pumped into the BS modes has decayed away, and these modes are near equilibrium with the translational degree of freedom. As a consequence, the lower level is almost empty just prior to the onset of lasing. The population transferred to the lower laser level during the main laser pulse can now relax to the rest of the BS mode with the time constant τ_1. Again, this produces a pumping of the inversion which serves to control the decay rate of the laser pulse tail. The time scale is naturally much shorter in this case than when the decay is controlled by the V-T rate.

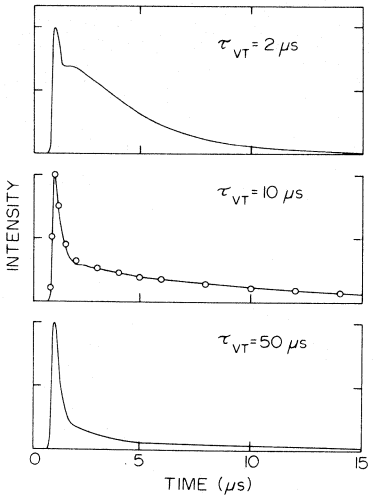

Fig. 6. Computed laser pulses (solid lines) for a range of τ_{VT} values. All other parameters correspond to the experimental conditions appropriate to Pulse 1 in Fig. 5; this pulse is indicated on the central plot as a series of experimental points.

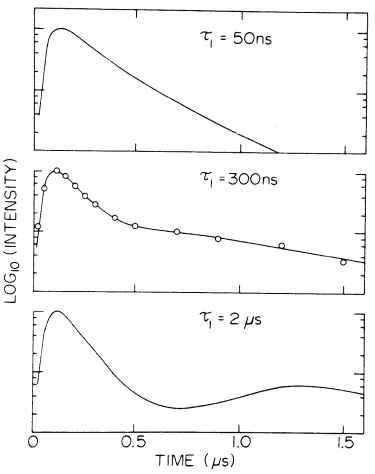

Fig. 7. Computed laser pulses (solid lines) for a range of τ_1 values. All other relaxation rates are chosen to correspond to a 10-percent CO_2:90-percent He mixture at the experimental pressure of 72 torr. The experimental pulse indicated in the central plot was obtained by Q switching the cavity to give lasing at the gain peak (1-percent/cm). To better demonstrate the behavior in the laser pulse tails, the laser intensities have been plotted on a logarithmic scale.

The behavior of the pulse in the two different operating regimes can now be compared with the theory presented in Section II. Furthermore, if sufficiently good agreement is obtained between the laser model predictions and the experimental observations, then values for the relevant molecular relaxation rates can be determined. In what follows, it will be shown that the agreement between theory and observation is excellent. This is particularly satisfying because it has not required the use of a many variable-parameter fit. Applying methods described elsewhere, all the relevant laser parameters, such as values of the gain and laser resonator losses, are experimentally measured [10], [18]. In essence, the fit to the gain-switched peak is a zero parameter fit, and only either τ_1 or τ_{VT}, whichever is appropriate, is varied to obtain the correct behavior of the laser pulse tail.

Fig. 6 shows a typical example of an output pulse obtained for lasing during the rise time of the gain. The output pulse was displayed on an oscilloscope and then photographed. Experimental points, taken from such a photograph, are shown in the figure. Also indicated are pulses predicted from the theory for different values of τ_{VT}. In order to provide a stringent test of the theory, τ_{VT} was not arbitrarily chosen to give the best fit. Instead, the value of τ_{VT} deduced from the data of Taylor and Bitterman [5] was used. For the gas mixture employed (10-percent CO_2:90-percent He at 36 torr), τ_{VT} is 10 μs. This value of τ_{VT} not only gives the excellent fit to the experimental laser pulse seen in Fig. 6, but also accurately models the time dependence of the experimental small-signal gain, when the lasing terms are removed from (1)-(5). (The value of τ_1 employed is of little consequence provided that it is less than τ_{VT}.)

Fig. 7 shows an example of an output pulse, observed at a time just beyond the small-signal gain peak. Little change is observed in the general shape of the experimental pulse for

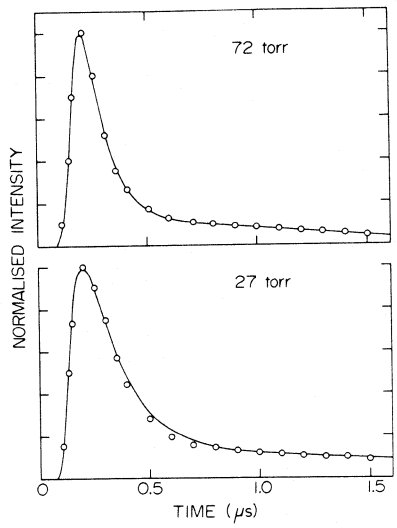

Fig. 8. Comparison of computed (solid lines) and observed laser pulses for two widely different gas pressures in a 10-percent CO_2:90-percent He mixture. In each case, lasing took place just after the peak of the time-dependent gain (1 percent/cm). Rate 1 is set at 4.6×10^4 s^{-1} $torr^{-1}$ in each calculation, and all other relaxation rates are similarly scaled with pressure.

later and later times during the decay of the gain. This indicates that once the gain has attained its peak value, all influence of extraneous discharge products has disappeared. In Fig. 7, the experimental pulse is compared with pulses generated by employing several different values of τ_1 in the theoretical model. To better demonstrate the behavior of the laser pulse tails, the laser intensities have been plotted on a logarithmic scale. Evidently, the pulse tail is very sensitive to the value of this parameter. The present apparatus could not be operated above 150 torr, since this marked the onset of intermittent air breakdown at the common focus of the two lenses employed in the Q switch. However, this is no real disadvantage, because at high pressures Rate 1 is so fast that the laser tails cannot be distinguished from the falling edge of the main peak. Over the range of pressure studied, the output pulse tail is sensitive to the value of τ_1 to the extent that it can be employed as a measure of the effective relaxation rate. This rate was found to scale with pressure and had a value of 4.6×10^4 s^{-1} $torr^{-1}$ for a 10-percent CO_2:90-percent He mixture. Fig. 8 shows the fits obtained, using this value, for two widely different gas pressures. It is a source of satisfaction that such excellent fits can be obtained by simply scaling all relaxation rates with pressure. It is noteworthy that the experimental change in the relative intensity of the laser pulse is also reproduced closely by the theory. In the following section, the significance of these observations is discussed, and the results are related to the work of others.

IV. Discussion and Conclusions

Previous models of gain-switched TE CO_2 lasers have not taken account of the finite coupling time between rotational sublevels of the 10.4-μm band [11], [15]-[17]. We have demonstrated here and elsewhere [1] that, in order to obtain good fits with experimentally observed laser pulses, it is necessary to include the effects of rotational coupling. The laser model described in Section II not only fits the observed rise and fall times of the main laser pulse, but also reproduces the appropriate conditions of inversion and radiation density in the initial part of the laser pulse tail. These correct starting conditions are essential for subsequent comparisons between the theoretical and experimental behavior of the laser pulse tails.

It is shown that the behavior of the laser pulse tail is controlled by the emptying of the lower laser level. The relaxation of the lower laser level takes place in two stages: 1) A fast relaxation into the bending mode levels (Rate 1), and 2) a subsequent slower relaxation of the bending mode (V-T). By carefully controlling the experimental parameters, we have measured both these rates under actual lasing conditions. The results obtained for the V-T rate are in agreement with the data given by Taylor and Bitterman [5]. We have measured Rate 1 over a wide range of pressure for a 10-percent CO_2:90-percent He mixture. The rate constant for the mixture is 4.6×10^4 s^{-1} $torr^{-1}$. Assuming that CO_2 is twenty times more effective than He for this relaxation [9], the effective relaxation rate for CO_2 is $\sim 3 \times 10^5$ s^{-1} $torr^{-1}$. This value is in good agreement with the calculations of Seeber [3] and Sharma [2], and with the experimental results of Stark [9]. Seeber calculates an effective value for Rate 1 of $\sim 2 \times 10^5$ s^{-1} $torr^{-1}$, while Sharma gives an estimate of $\sim 6 \times 10^5$ s^{-1} $torr^{-1}$. Stark has directly measured the $10^0 0 \rightarrow 02^0 0$ relaxation rate and obtains a value of 1.4×10^5 in CO_2. Manes and Seguin [11] have used a technique somewhat akin to the method reported here to estimate the coupling rate between the symmetric stretching mode and the bending mode in CO_2. By comparing experimental laser pulses at atmospheric pressure with a theoretical model, they determined that the intermode coupling rate was $\sim 1.4 \times 10^6$ s^{-1} $torr^{-1}$. However, their theoretical model did not explicitly include rotational relaxation, with the result that their estimated coupling rate is probably too fast.

It follows from the above that the lower laser level in CO_2 is very strongly coupled to the bending mode levels, with a coupling rate certainly greater than 10^5 s^{-1} $torr^{-1}$. This is much greater than the results reported by Bulthuis [7] and Rosser *et al.* [8], who obtain coupling rates of 1.5×10^4 and 10^3 s^{-1} $torr^{-1}$, respectively. Undoubtedly, these rates are incorrect for the lasing conditions reported here. The source of the very large disagreement is not clear and merits further investigation.

We have chosen to determine relaxation rates by fitting to the shape of the experimental pulses. In principle, the rates can be determined by fitting to the absolute intensity of the pulses, but this requires a calibrated detector and an accurate knowledge of cavity mode and active medium volumes. These additional complications make intensity comparisons inherently less accurate than pulse-shape comparisons. This is particularly true in the pulse tails, which contain only a small fraction of the total energy of the pulse.

Although relaxation rates reported here were measured in a 10-percent CO_2:90-percent He mixture, the technique can easily be extended to measure rates in other He:CO_2 mixtures. Preliminary observations using other mixtures indicate that the

V-T is helium controlled, as is expected from the data of Taylor and Bitterman [5]. Preliminary results on the variation of Rate 1 with mixture indicate that CO_2 is an order of magnitude more effective than He at relaxing the lower laser level into the bending mode. The addition of N_2 to the laser gas mixture produces laser pulses with very long tails which obscure the CO_2 relaxation rates. Nevertheless, by extending the theoretical model to include a nitrogen ($v = 1$) pump term, the CO_2-N_2 coupling rate can, in principle, be determined.

The in-cavity laser technique described in this paper is an extremely versatile method of measuring relaxation rates. We have employed it to measure relaxation times in CO_2 which differ by more than three orders of magnitude; from *V-T* times of tens of microseconds to rotational coupling times of nanoseconds. The method has the additional advantage that it measures directly relaxation rates which are relevant to the laser dynamics.

References

[1] E. A. Ballik, B. K. Garside, and J. Reid, "Rotational coupling and laser dynamics in TE CO_2 lasers," *Appl. Phys. Lett.*, vol. 26, pp. 380-382, Apr. 1975.

[2] R. D. Sharma, "Kinetics of equilibration of 1388-cm^{-1} vibrational level of CO_2," *J. Chem. Phys.*, vol. 49, pp. 5195-5197, Dec. 1968.

[3] K. N. Seeber, "Radiative and collisional transitions between coupled vibrational modes of CO_2," *J. Chem. Phys.*, vol. 55, pp. 5077-5081, Nov. 1971.

[4] a) P. K. Cheo, "Relaxation of CO_2 laser levels by collisions with foreign gases," *IEEE J. Quantum Electron. (Special Issue: 1968 Int. Quantum Electronics Conf.: Part I)*, vol. QE-4, pp. 587-593, Oct. 1968.
b) ——, "Effects of CO_2, He and N_2 on the lifetimes of the $00^\circ 1$ and $10^\circ 0$ CO_2 laser levels and on pulsed gain at 10.6 μ," *J. Appl. Phys.*, vol. 38, pp. 3563-3568, Aug. 1967.

[5] R. L. Taylor and S. Bitterman, "Survey of vibrational relaxation data for processes important in the CO_2-N_2 laser system," *Rev. Mod. Phys.*, vol. 41, pp. 26-47, Jan. 1969.

[6] T. A. DeTemple, D. R. Suhre, and P. D. Coleman, "Relaxation rates of lower laser levels in CO_2," *Appl. Phys. Lett.*, vol. 22, pp. 349-350, Apr. 1973.

[7] K. Bulthuis, "Laser power and vibrational energy transfer in CO_2 lasers," *J. Chem. Phys.*, vol. 58, pp. 5786-5794, June 1973.

[8] W. A. Rosser, Jr., E. Hoag, and E. T. Gerry, "Relaxation of excess populations in the lower laser levels $CO_2(100)$," *J. Chem. Phys.*, vol. 57, pp. 4153-4164, Nov. 1972.

[9] E. E. Stark, Jr., "Measurement of the $10^\circ 0$-$02^\circ 0$ relaxation rate in CO_2," *Appl. Phys. Lett.*, vol. 23, pp. 335-337, Sept. 1973.

[10] B. K. Garside, J. Reid, and E. A. Ballik, "Studies of the inversion and lower level relaxation in pulsed TE CO_2 discharges," *IEEE J. Quantum Electron.*, vol. QE-11, pp. 264-270, June 1975.

[11] K. R. Manes and H. J. Seguin, "Analysis of the CO_2 TEA laser," *J. Appl. Phys.*, vol. 43, pp. 5073-5078, Dec. 1972.

[12] W. J. Witteman, "Vibrational relaxation in carbon dioxide," *J. Chem. Phys.*, vol. 35, pp. 1-9, July 1961.

[13] A. M. Robinson, "Gain distribution in a CO_2 TEA laser," *Can. J. Phys.*, vol. 50, pp. 2471-2474, 1972.

[14] I. Burak, Y. Noter, and A. Szöke, "Vibration-vibration energy transfer in the ν_3 mode of CO_2," *IEEE J. Quantum Electron.*, vol. QE-9, pp. 541-544, May 1973.

[15] G. C. Vlases and W. M. Moeny, "Numerical modelling of pulsed electric CO_2 lasers," *J. Appl. Phys.*, vol. 43, pp. 1840-1844, Apr. 1972.

[16] D. L. Lyon, "Comparison of theory and experiment for a transversely excited high-pressure CO_2 laser," *IEEE J. Quantum Electron. (Part II of Two Parts: 3rd Conf. on Chemical and Molecular Lasers)*, vol. QE-9, pp. 139-153, Jan. 1973.

[17] J. Gilbert, J. L. Lachambre, F. Rheault, and R. Fortin, "Dynamics of the CO_2 atmospheric pressure laser with transverse pulse excitation," *Can. J. Phys.*, vol. 50, pp. 2523-2535, 1972.

[18] J. Reid, E. A. Ballik, and B. K. Garside, "Saturation of the net electron excitation of the CO_2 ($00^\circ 1$) laser level as a function of discharge input energy," *Opt. Commun.*, vol. 12, pp. 354-359, Dec. 1974.

The Influence of Oxygen on CO-Laser Performance

H. KEREN, P. AVIVI, AND F. DOTHAN

Abstract—**Additions of a few parts per thousand of oxygen to a CO-He mixture change drastically the laser output power, the axial field in the positive column, and the slope of the *E-I* curve of the discharge. The intensity of the spectrum of vibrational transitions of the CO molecule increases when oxygen is added; the increase is especially pronounced for transitions from higher ($v > 7$) levels. The most prominent feature in the visible spectrum is the disappearance of the C_2-Swan bands with the addition of oxygen. The populations of CO vibrational levels were derived from the IR spectra; they increase by more than an order of magnitude for $v > 7$. The electron energy distribution was derived from measured E/N and the Boltzmann equation. Oxygen affects the Boltzmann equation (and thus the electron energy-distribution function) through the change in E/N, which is in turn determined by ionization and deionization processes. The fractional power transfer from electrons increases to vibrational levels and decreases to electronic levels.**

I. Introduction

THE strong influence of the addition of small quantities of oxygen on the output power of a CO laser is well known. Osgood *et al.* [1], who investigated a mixture of He-N_2-CO-O_2, believe that oxygen prevents the dissociation of CO and the subsequent formation of CN, a relaxant of CO vibrational levels. Taieb and Legay [2] excited N_2 vibrationally and mixed it with neutral CO. They found that increasing additions of O_2 to the CO-N_2 mixture produced first an *increase* of CN and of the laser power, and then a decrease of both. Jöeckle and Peyron [3] investigated the infrared fluorescence of CO excited by active nitrogen. They found that small additions of oxygen lead to an increase of radiation from vibrational levels of CO in the ground state. Larger quantities of O_2 produce a decrease of the infrared radiation. Bhaumik *et al.* [4] maintained that in the presence of oxygen the reaction

$$CO \rightleftarrows C + O$$

is driven preferentially to the left. Larger additions of oxygen change the discharge properties and inhibit lasing. Hartwick and Walder [5] observe that the influence of O_2 cannot be explained solely by the prevention of CO dissociation. They point out that changes of the electron energy distribution and electron density have to be considered.

The purpose of this research is to contribute to the understanding of the effect of oxygen on electronic and vibrational excitation, on ionization, and on macroscopical discharge properties. For this purpose, we recorded and studied the visible and infrared spectra and obtained populations of CO vibrational levels with and without oxygen. We calculated the fractional power transfer from electrons to electronic excitation and to vibrational levels with the help of the Boltzmann equation and from experimental data. In the following we postulate and discuss possible physical mechanisms to explain the influence of oxygen.

Manuscript received January 23, 1975; revised March 20, 1975.

The authors are with The Racah Institute of Physics, The Hebrew University of Jerusalem, Jerusalem, Israel.

II. Experimental Arrangement

A schematic drawing of the experimental arrangement is given in Fig. 1.

The gases used were Matheson research grade. All experiments were performed at room temperature and the partial pressures were CO, 1.4 torr and He, 18 torr. The axial field strength was measured by means of probes and an electrostatic voltmeter.

The infrared radiation was measured by means of a Perkin-Elmer Model 210-B grating monochromator and a PbS (Type B Infratron Products) uncooled detector. In front of the PbS detector a germanium lens was placed to prevent high orders of visible lines entering the detector.

The near UV and the visible spectrum were obtained by means of a $\frac{3}{4}$-m Spex grating spectrometer.

Phase-sensitive detection was used for the UV, visible, and IR spectroscopy.

III. Results

A. Discharge Properties

Fig. 2(a) shows the lasing power at a discharge current of 17 mA as a function of the partial pressure of oxygen. Without oxygen there was no lasing at any current and at any CO or He pressure. The lasing threshold is obtained with the addition of 20-m · torr oxygen, and the maximum laser power (3.8 W) with 50-m · torr oxygen. Further addition of oxygen results in a gradual decrease of laser power, until it becomes zero at oxygen pressures above about 230 m · torr.

Fig. 2(b) shows the axial field in the positive column of the discharge (current 17 mA) as a function of oxygen pressure. Between oxygen pressures of 10 and 25 m · torr there is a drop in the axial field strength from 136 to 88 V/cm. Laser action appears just before the axial field reaches its minimum value. Further additions of oxygen up to 400 m · torr do not change the axial field.

Moving striations at a frequency of about 9 kHz were observed in the He-CO discharge. Upon addition of O_2 these striations disappear gradually and are not observed at all in the partial pressure range from 20- to 400-m · torr oxygen. This indicates that the measured decrease in E/N is the true dc value and not an average of an oscillatory *E*-field.

Fig. 3 shows *E-I* curves (axial field in the positive column as a function of the discharge current) without oxygen (curve 1) and with 50-m · torr oxygen (curve 2). Without oxygen the *E-I* curve has a positive slope; above 17 mA an abrupt change in the discharge characteristics occurs: it becomes unstable in the form of moving "snakelike" patterns. With addition of

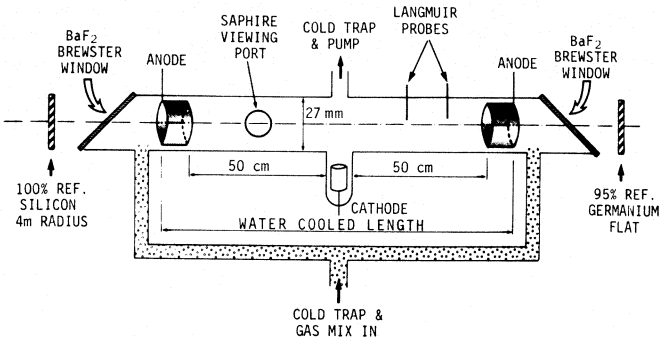

Fig. 1. Schematic of experimental setup.

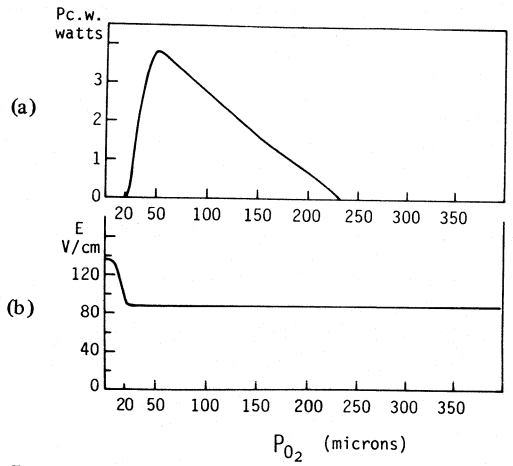

Fig. 2. Influence of partial pressure of O_2 on (a) lasing power and (b) axial electric field in discharge.

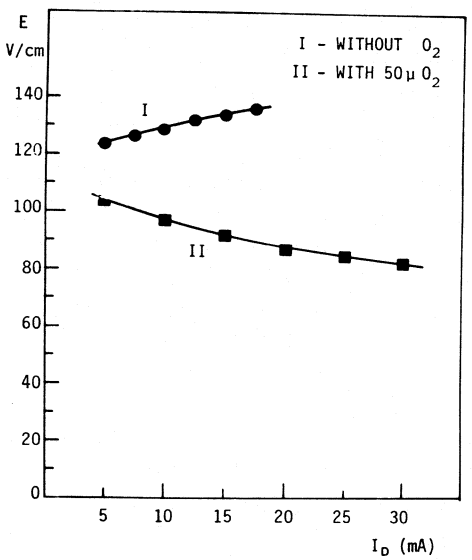

Fig. 3. Influence of partial pressure of O_2 on *E-I* curves of the discharge.

50-m · torr oxygen the slope of the *E-I* curve becomes negative and the discharge is stable at any current value.

B. Spectroscopical Properties of the Discharge

The near UV and visible spectra are given in Fig. 4(a)-(d) (bottom—without oxygen; top—with 50-m · torr oxygen; current strength in both cases, 10 mA). Without oxygen the following bands are detected (see Figs. 5 and 6 for the relevant

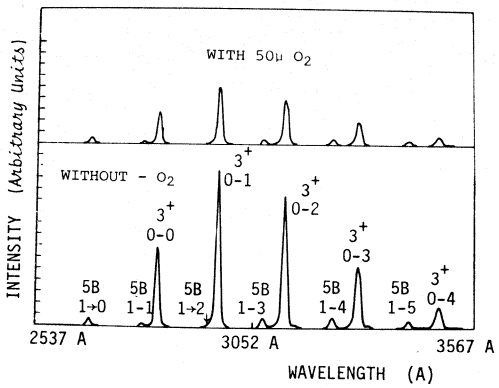

(a)

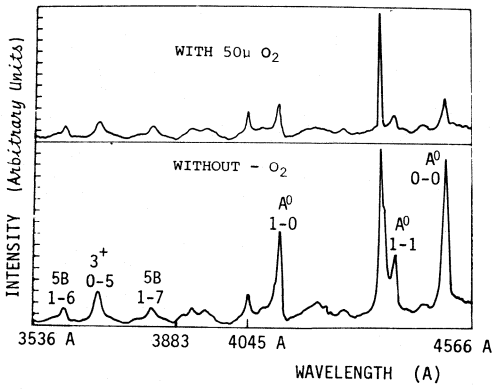

(b)

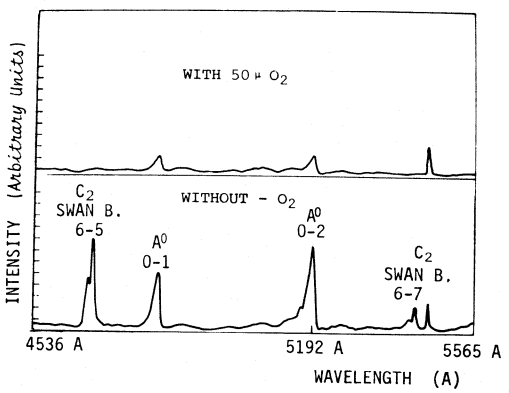

(c)

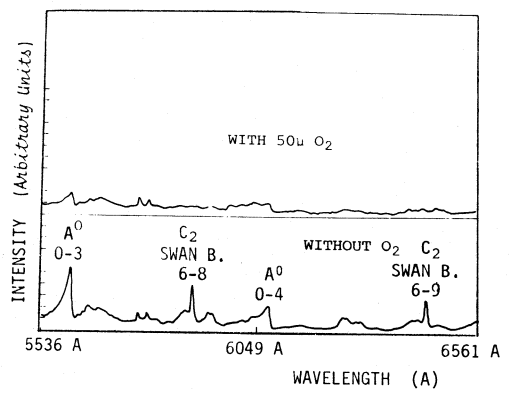

(d)

Fig. 4. (a) Influence of 50 m · torr of oxygen on the emission spectrum in the near UV. (b) Influence of 50 m · torr of oxygen on the emission spectrum between 3536 and 4566 Å. (c) Influence of 50 m · torr of oxygen on the emission spectrum between 4536 and 5564 Å. (d) Influence of 50 m · torr of oxygen on the emission spectrum between 5536 and 6561 Å.

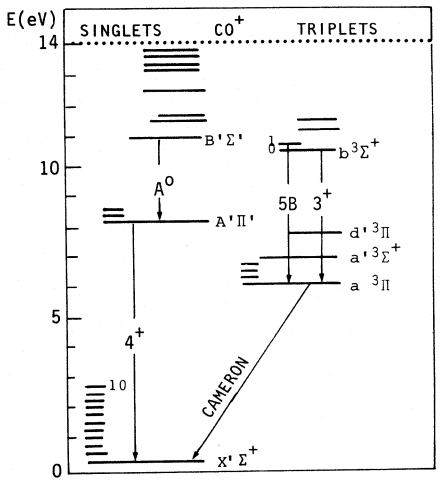

Fig. 5. Simplified energy-level diagram of CO molecule.

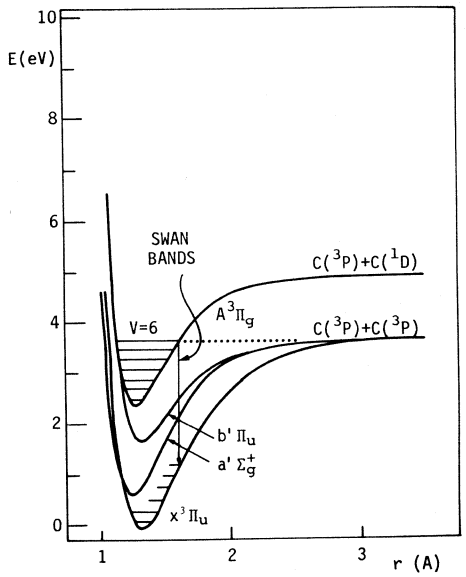

Fig. 6. Potential curves of the low electronic states of the C_2 molecule.

transitions): CO-3$^+$, 5B, A°, C_2-Swan bands. The lines of the 3$^+$ band have the highest intensity. The Swan bands are due to transitions from $v' = 6$ of the $A^3\Pi_g$ electronic level to $v'' = 5, 7, 8, 9$ of the electronic ground state.

The addition of 50-m · torr oxygen results in a decrease of the intensity of the 3$^+$ and A° bands of CO by a factor of 3, and of the 5B band by a factor of 2. The C_2 bands disappear entirely.

In the infrared region, the first overtone (transitions between vibrational levels $n + 2$ and n) of CO were recorded. The relative response of the instrument train as a function of wavelength was determined by scanning a blackbody source. Fig. 7 shows the results, corrected for system sensitivity. The slit width of the spectrometer was 400 μm (low-resolution measurement). The lower curve is the IR spectrum of the discharge without oxygen. The current was 12 mA and the axial field 132 V/cm. The upper curve shows the spectrum with 50-m · torr oxygen, at a current of 18 mA and an axial field of 88 V/cm. The power input, and thus the gas temperature of

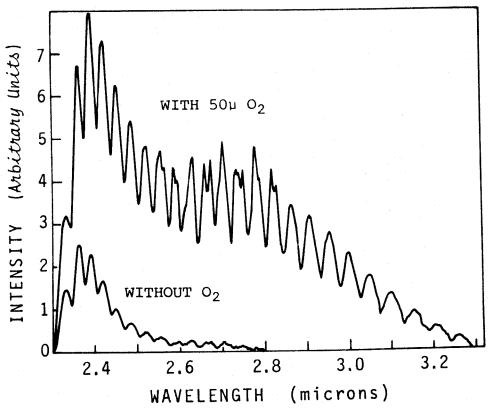

Fig. 7. Influence of the partial pressure of O_2 on the IR first-overtone emission spectrum of the CO–He mixture.

the discharge, was the same in both cases. It can be seen that the ratio of intensities, with and without oxygen, becomes greater for transitions involving high vibrational levels.

C. Distribution of Vibrational-Level Population

The procedure for the calculation of the distribution of CO molecules within vibrational levels (unfolding) was similar to that used by Horn and Oettinger [6]. To perform the unfolding of the low-resolution spectrum, the instrumental linewidth was found ($\Delta\lambda_{1/2}$ = 67 Å) by means of calibration with the sixth order of the 4358-Å Hg line. The rotational temperature was determined from the high-resolution spectrum (slit width, 25 μm). The R rotational transitions of the vibrational $2 \rightarrow 0$ transition do not overlap with higher vibrational-rotational transitions; from the relative line intensities the rotational temperature was found to be T_R = 460 K.

The populations of the vibrational levels are determined by finding the best fit of a synthetic spectrum to the measured spectrum. The synthetic spectrum is calculated from assumed vibrational populations, taking into account the rotational temperature and instrumental width. For the purpose of the calculation, 40 rotational lines of each of the P and R branches were considered. The synthetic spectrum (not shown here) is nearly identical with the measured one.

Fig. 8 shows the population distribution of vibrational levels which results from the unfolding procedure. The increase of the population of higher vibrational levels with the addition of 50-m · torr oxygen to the CO–He mixture is striking. While the populations for the $v = 1$ level are approximately equal with and without oxygen, they are different by a factor of 10 for $v = 7$, and by a factor of 20 for $v = 13$; the difference is presumably much greater for $v > 15$ (see Fig. 7).

IV. Electron Energy Distribution and Fractional Energy Transfer

The fraction of energy transferred by electrons to CO vibrational levels and to CO electronic levels was determined by solving numerically the Boltzmann equation for our experimental conditions. The form of the Boltzmann equation was that used by Nighan [7]. Cross sections for vibrational excitation were taken from Schulz [8] and for electronic excita-

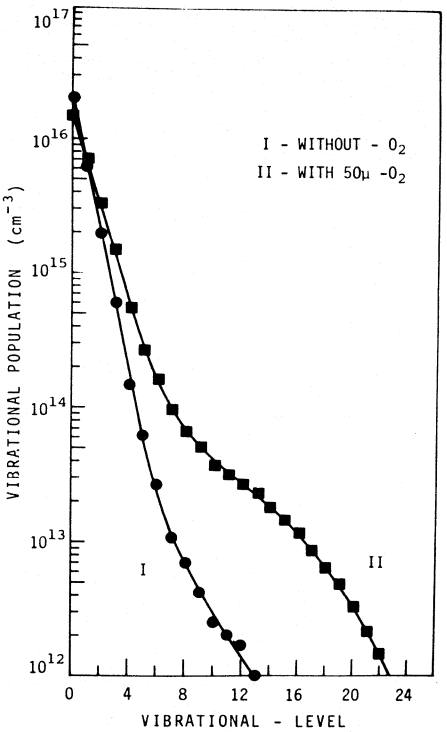

Fig. 8. Calculated vibrational population distribution as derived from Fig. 7.

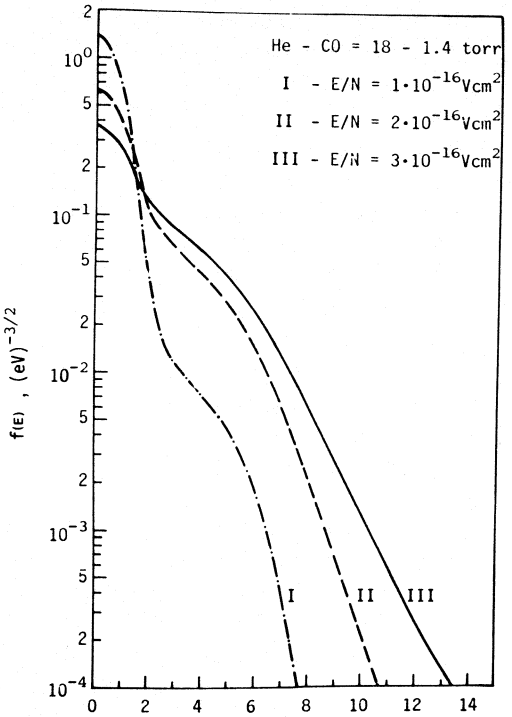

Fig. 9. Calculated electron energy distribution for different values of E/N.

tion from Chung and Lin [9]. Momentum-transfer cross sections for He and CO were used, as given by Massey *et al.* [10] and Hake and Phelps [11], respectively. Superelastic collisions between electrons and CO vibrational levels were not considered. The influence of the small quantities of oxygen on the energy transfer from electrons was neglected because the loss of electron energy is predominantly determined by CO. This is so because the relative gas densities are $\delta[O_2]:\delta[CO] = 1:30$; moreover, the relative cross sections for O_2 are smaller than for CO, [11].

Oxygen affects the Boltzmann equation (and thus the electron energy-distribution function) through the change in E/N, which is in turn determined by ionization and deionization processes.

Fig. 9 shows the calculated electron energy-distribution function for three different values of E/N. Two of the curves are for E/N values used in our experiments: $E/N = 3 \times 10^{-16}$ V/cm^2, without oxygen, and $E/N = 2 \times 10^{-16}$ V/cm^2, with 50-m · torr oxygen. The non-Maxwellian form of the distribution is pronounced. The similarity of the distributions to those obtained by Nighan [12] should be noted.

The reduction of E/N in the positive column caused by the addition of O_2 produces a change in the electron energy distribution, leading to a depletion of high-energy electrons and an overall shift of the distribution to lower energies. As a consequence, there is less excitation of electronic levels and more of vibrational levels.

Fig. 10 shows the fractional energy transfer from electrons as a function of E/N. In our experimental conditions *without oxygen* 63 percent of the energy is expended for electronic excitation and 37 percent for vibrational excitation. With the addition of 50-m · torr oxygen the figures are: 36-percent electronic, 64-percent vibrational. This means the energy transfer into vibrational levels was increased by 75 percent, and the transfer into electronic levels decreased by 45 percent.

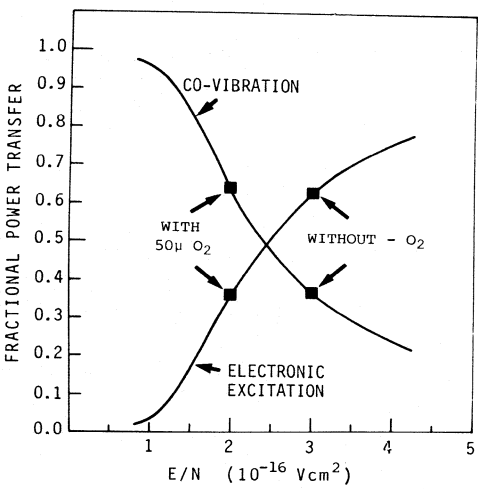

Fig. 10. Fractional electron–molecule power transfer as computed for experimental conditions.

V. Discussion and Conclusion

The axial field is drastically reduced when about 1 percent of oxygen is added to the CO-He mixture [Fig. 2(b)]; from this we conclude that the oxygen strongly influences the ionization process. A further indication in the same direction is the change of the slope of the *E-I* curve (Fig. 3) from a positive slope (without oxygen) to a negative one (with

oxygen). This can be explained by stage processes such as excitation and subsequent ionization of metastable states, probably of the oxygen molecule. More direct evidence for this mechanism should be provided by the identification of the dominant ion in the discharge. Without oxygen the ionization is probably from the ground state of the CO molecule, and not from the metastable $a^3\Pi$ level, as this level is efficiently relaxed by collisions with CO in the ground state (rate constant 1.1×10^{-10} cm^{3}s^{-1}), [13]. An interesting feature in the visible spectrum is the disappearence of C_2-Swan bands when oxygen is added. As mentioned before, only the transitions from $v' = 6$ of the $A^3\Pi_g$ electronic level to $v'' = 5, 7, 8, 9$ levels of the ground state are involved. This indicates that the origin of the radiation from the C_2 molecule is due to the recombination of the C atom into the excited C_2 molecule.

The intensity of A°, $5B$, and 3^+ bands of CO decrease when oxygen is added (see diagram of CO levels given in Fig. 5). There is also indirect evidence for the decrease of the population of the metastable $a^3\Pi$ level of the CO molecule, which is populated either by direct electronic excitation or by radiative transitions $5B$ and 3^+ from the upper levels. The disappearance of the C_2 bands can be explained by the decrease of the $a^3\Pi$ population, as most of the carbon is produced by the reaction

$$CO(a^3\Pi) + CO(v \geqq 0) \rightarrow CO_2 + C + KE.$$

The energy levels of the O_2 molecule (see Fig. 11) include metastable levels at 1 eV, 1.5 eV, 5 eV, 6 eV, and possibly also at higher levels. The relaxation of the $CO(a^3\Pi)$ level by the reaction

$$CO(a^3\Pi) + O_2 \rightarrow CO + O_2 + KE$$

is very efficient (relaxation constant 2×10^{-10}cm^{3}s^{-1}), [13]. In this process the energy of the $CO(a^3\Pi)$ levels is not converted to kinetic energy, but is stored in a long-lived metastable level of the oxygen molecule.

In conclusion, it seems from our experiments and calculations that small additions of O_2 to CO-He laser mixtures cause primarily a change in the electron energy distribution. This change reveals itself by an increase of the relative fraction of energy transferred by electrons to vibrational levels in the ground state of CO at the expense of energy transferred to electronic levels. This results in an increase of lasing power, as has indeed been observed.

We suggest here that O_2 depopulates, very efficiently, the $a^3\Pi$ level of CO, which is a sink of wasted electron energy in the absence of O_2. In addition, the striking evidence for stepwise excitation in the presence of O_2 leads us to believe that the following processes occur: electrons excite CO molecules to the $a^3\Pi$ level, which is then efficiently quenched by O_2 molecules and its energy transferred to a metastable level of O_2. The ionization proceeds from such a metastable level. This mechanism implies that the main positive-charge carrier in a lasing mixture with small additions of O_2 should be oxygen-molecular ions. This implication is currently being investigated, and the results will be reported in due course.

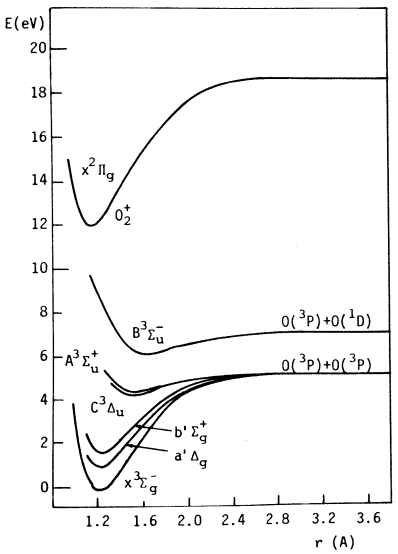

Fig. 11. Potential energy curves for some states of O_2 and O_2^+.

References

[1] R. M. Osgood, Jr., W. C. Eppers, Jr., and E. R. Nichols, "An investigation of the high-power CO laser," *IEEE J. Quantum Electron.*, vol. QE-6, pp. 145–154, Mar. 1970.

[2] G. Taieb and F. Legay, "Mechanism of a CO-N_2 laser," *Can. J. Phys.*, vol. 48, pp. 1956–1983, Sept. 1970.

[3] R. Jöeckle and M. Peyron, "Chimiluminiscence infrarouge de l'oxyde de carbone excité par l'azote active'," *C.R. Acad. Sci.*, vol. 261, pp. 1819–1822, Aug. 1965.

[4] M. L. Bhaumik, W. B. Lacina, and M. M. Mann, "Characteristics of a CO laser," *IEEE J. Quantum Electron. (Part II of Two Parts. Special Issue on 1971 IEEE/OSA Conference on Laser Engineering and Applications)*, vol. QE-8, pp. 150–160, Feb. 1972.

[5] T. S. Hartwick and J. Walder, "Effect of O_2 on CO laser performance," *IEEE J. Quantum Electron.* (Corresp.), vol. QE-8, pp. 455–456, May 1972.

[6] K. P. Horn and P. E. Oettinger, "Vibrational energy transfer in diatomic gas mixtures," *J. Chem. Phys.*, vol. 54, pp. 3040–3046, Apr. 1971.

[7] W. L. Nighan, "Electron energy distributions and collision rates in electrically excited N_2, CO and CO_2," *Phys. Rev. A*, vol. 2, pp. 1989–2000, Nov. 1970.

[8] G. J. Schulz, "Vibrational excitation of N_2, CO and H_2 by electron impact," *Phys. Rev. A*, vol. 135, pp. A988–A994, Aug. 1964.

[9] S. Chung and C. C. Lin, "Electron excitation of electronic states of the CO molecule," *Phys. Rev. A*, vol. 9, pp. 1954–1964, May 1974.

[10] H. S. W. Massey, E. H. S. Burhop, and H. B. Gilbody, *Electronic and Ionic Impact Phenomena*, vol. 1. Oxford: Clarendon Press, 1969, p. 26.

[11] R. D. Hake, Jr., and A. V. Phelps, "Momentum-transfer and inelastic collision cross sections for electrons in O_2, CO and CO_2," *Phys. Rev.*, vol. 158, pp. 70–84, June 1967.

[12] W. L. Nighan, "Electron kinetic processes in CO laser," *Appl. Phys. Lett.*, vol. 20, pp. 96–99, Jan. 1972.

[13] G. W. Taylor and D. W. Setser, "Quenching rate constants for $CO(a^3\Pi)$," *J. Chem. Phys.*, vol. 58, pp. 4840–4851, June 1973.

Multiphoton Optical Heterodyne Detection

MALVIN CARL TEICH, SENIOR MEMBER, IEEE

Abstract—**After reviewing recent work on multiphoton direct detection and single-photon heterodyne detection, we examine the behavior of a multiphoton absorption heterodyne receiver. Expressions are obtained for the detector response, signal-to-noise ratio (SNR), and minimum detectable power for a number of cases of interest. Receiver performance is found to depend on the higher order correlation functions of the radiation field and on the local oscillator (LO) irradiance. Although performance similar to that of the single-photon heterodyne receiver can theoretically be achieved, practical problems would appear to make this difficult. A physical interpretation of the process in terms of the absorption of monochromatic and nonmonochromatic photons is given. The double-quantum case is treated in particular detail; the results of a preliminary experiment are presented and suggestions for future experiments are provided.**

I. Introduction

Inasmuch as single-quantum optical heterodyne detection and multiple-quantum optical direct detection are by now well-understood processes, it seems natural to investigate the properties of a detection scheme in which both are performed simultaneously. In this paper, we obtain the response and the signal-to-noise power ratio for a multiple-quantum absorption heterodyne receiver, with particular attention devoted to the simplest case, i.e., the mixing of two waves in a double-quantum infrared or optical device.

After briefly considering the relevant results pertinent to each of the processes individually (Section I), we derive the combination device response for the general multiple-quantum photomixing process in Section II. In Section III, the response for the important two-quantum case is obtained and given a physical interpretation. In Section IV, we obtain the signal-to-noise ratio (SNR) for a receiver using a multiphoton optical heterodyne device, and compare it with the SNR for conventional optical heterodyne detection. The results of a two-photon experiment are presented in Section V, while a suggested setup for future experiments, as well as the applicability of the scheme in general, is reserved for Section VI.

A. Multiphoton Direct Detection

The ordinary photoeffect was discovered by Hertz in 1887 and explained in terms of the absorption of a single quantum of light by Einstein in his now famous work published in 1905 [1]. It was not until 1959, however, that the relationship between the statistics of an arbitrary incident radiation field and the emitted photoelectrons was firmly established by Mandel [2]. Consideration of the general photodetection process in terms of quantum-electrodynamic coherent states of the radiation field was undertaken by Glauber [3] in 1963, and by Kelley and Kleiner [4] in 1964, and provides a convenient starting point for calculations involving multiple-photon as well as single-photon absorptions.

Multiple-quantum photoemission, being a higher order effect, is most easily observed in the absence of ordinary (first-order) photoemission. For the two-quantum case, it becomes important when

$$\tfrac{1}{2}\, e\phi < h\nu < e\phi \tag{1}$$

where $h\nu$ is the photon energy of the incident radiation and $e\phi$ is the work function of the material under consideration. (Even when (1) is satisfied, however, it should be kept in mind that small amounts of single-quantum photoemission can arise from excited electrons in the Fermi tail [5].) The two-quantum photoeffect was first experimentally observed in 1964. Using a GaAs laser, Teich *et al.* [6] observed the effect in sodium metal, while Sonnenberg *et al.* [7] induced it in Cs_3Sb with a Nd-doped glass laser. Since that time, there have been a number of experimental measurements of second- and higher order photoelectric yields in a variety of materials [8]-[12].

Theoretical work has focused on two aspects of the problem: perturbation theory and other calculations of the transition probabilities in the material, and the effect on the transition probability of the statistical nature of the radiation field. Makinson and Buckingham [13] were the first to predict the second-order effect and calculate its magnitude based on a surface model of photoemission; this work was expanded by Smith [14], Bowers [15], and Adawi [16]. The analogous volume calculation was performed by Bloch [17] and later corrected by Teich [8], and Teich and Wolga [9].

All of the models predict a two-quantum dc photocurrent $W_{dc}^{(2)}$ (expressed in amperes) proportional to the square of the incident radiation power P and inversely proportional to the irradiated area A. Using the results of a number of authors [8], [9], [14]-[17], we can therefore write the double-quantum dc photocurrent as

$$W_{dc}^{(2)} = \Lambda^{(2)}(\lambda, T)\, P \propto IP. \tag{2}$$

Here $\Lambda^{(2)}$ is the two-quantum yield expressed in amperes per watt [9], λ is the radiation wavelength, T is the sample temperature, P is the radiation power expressed in watts, and I is the irradiance at the detector expressed in watts per square centimeter. The two-quantum efficiency (electrons/photon) is denoted by η_2, and is related to the two-quantum yield by the relationship

$$\Lambda^{(2)} = (e/h\nu)\, \eta_2 \propto I. \tag{3}$$

Here, the quantity $(h\nu/e)$ is the incident photon energy expressed in electronvolts and is of order unity. For the k-photon process, defining $W_{dc}^{(k)}$, $\Lambda^{(k)}$, and η_k as the k-photon analogs of the quantities defined above, the following generalized results

Manuscript received January 27, 1975. This work was supported in part by the National Science Foundation, and in part by the John Simon Guggenheim Memorial Foundation.

The author is with the Department of Electrical Engineering and Computer Science, Columbia University, New York, N.Y. 10027, and is a Fellow of the John Simon Guggenheim Memorial Foundation, New York, N.Y.

are obtained:

$$W_{dc}^{(k)} = \Lambda^{(k)}(\lambda, T)\, P \propto I^{k-1} P \tag{4}$$

and

$$\Lambda^{(k)} = (e/h\nu)\, \eta_k \propto I^{k-1}. \tag{5}$$

Typical numerical values for the two-quantum yield are [9] $\Lambda_{Na}^{(2)}(8450\ \text{Å}, 300\ \text{K}) \sim 8 \times 10^{-16} I$ and $\Lambda_{Cs_3Sb}^{(2)}(10\,600\ \text{Å}, 300\ \text{K}) \sim 5 \times 10^{-11} I$ A/W. Again I represents the irradiance at the detector in watts per square centimeter. These values, even when precisely measured, can vary by a factor (usually $\leqslant 2$) depending on the coherence properties of the inducing radiation, as we now consider.

Theoretical work relating to multiple-quantum statistical effects began in 1966 with an examination of the higher order field correlation functions by Teich and Wolga [18] and by Lambropoulos *et al.* [19]. This was followed by more detailed calculations by Mollow [20] and by Agarwal [21]. All of these studies predicted a factor of $k!$ enhancement for the magnitude of certain k-quantum processes induced by chaotic (rather than coherent) sources. This enhancement was later observed in the two-quantum photoeffect by Shiga and Imamura [10], and in second-harmonic generation (SHG) by Teich *et al.* [22]. The theoretical relationship between two-quantum photocurrent spectra and the incident radiation statistics was then obtained by Diament and Teich [23], and compared with the analogous single-quantum results previously given by Freed and Haus [24]. In 1969 two-quantum photocounting distributions were calculated for amplitude-stabilized, chaotic, and generalized laser sources by Teich and Diament [25]. This work was extended to higher order photocounting distributions by Barashev in 1970 [26], who also wrote an excellent and comprehensive review article on multiple-quantum photoemission and photostatistics in 1972 [27].

B. Single-Photon Heterodyne Detection

Being a first-order effect, ordinary optical and infrared heterodyne detection has received far more attention than has multiple-quantum detection. The usefulness of the technique in applications ranging from spectroscopy to radiometry has been well documented. The effect was first observed by Forrester *et al.* [28] in a classic experiment using two Zeeman components of a visible (incoherent) spectral line. With the development of the laser, photomixing became relatively easy to observe and was studied by Javan *et al.* [29] at 1.15 μm using a He-Ne laser, and by Siegman *et al.* [30b)] at 6943 Å with a ruby laser. Extending this work into the middle infrared, Teich *et al.* used a CO_2 laser at 10.6 μm in conjunction with a copper-doped germanium photoconductive detector operated at 4 K [31], and with a lead-tin selenide photovoltaic detector operated at 77 K [32].

The observed signal-to-noise power ratio for these experiments was found to behave in accordance with the theoretical expression obtained for parallel plane-polarized beams under ideal conditions [31]-[34], i.e.,

$$\text{SNR}^{(1)} = \eta_1 P_1 / h\nu \Delta f. \tag{6}$$

Here, η_1 is the detector quantum efficiency (electrons per photon), P_1 is the received signal radiation power, $h\nu$ is the photon energy, and Δf is the receiver bandwidth. For radiation beams which are not parallel to within an angle $\theta = \lambda/d$, with d the detector aperture, the SNR is reduced below the value given in (6) by spatial averaging of the mixing signal over the detector aperture. This effect was studied in detail by Siegman and by Mandel and Wolf [34], and is frequently referred to as "wash-boarding." Similar calculations have been effected for focused radiation beams, as first considered by Read and Fried [35].

Shortly thereafter, this work was extended to experimental and theoretical studies of the statistical nature of the heterodyne signal resulting from the beating of a coherent wave with a Gaussian scattered wave [36], [37]. Although the stochastic nature of this signal depends in detail on the irradiance statistics, the SNR is found to be essentially independent of the higher order correlation functions of the field [36], [37]. Furthermore, using the first-order coherent field results of Titulaer and Glauber [38] for absorption detectors, an explicit calculation for the case of two-beam photomixing has shown that sum- and double-frequency components do not appear in the detected current, and that the heterodyne process can be interpreted in terms of the annihilation of a single (nonmonochromatic) photon [39], [40], as was qualitatively appreciated by Forrester *et al.* [28]. Finally, a concise review of the basic theoretical and experimental aspects of heterodyne detection in the infrared and optical, as well as a partial review of the literature, was prepared by Teich in 1970 [41]. Another such review, emphasizing nonlinear heterodyne detection, will appear shortly [42].

II. Multiphoton Photomixing

We begin this section by considering a two-quantum absorption detector initially in the ground state. The detector response $W^{(2)}$ at the space-time point $x_a = \vec{r}_a, t_a$ may be written in terms of the second-order correlation function $G^{(2)}$ [3], [18], [20], [25], and is given by

$$W^{(2)} \propto \text{tr}\,\{\rho E^-(x_a) E^-(x_a) E^+(x_a) E^+(x_a)\} \equiv G^{(2)}(x_a x_a x_a x_a). \tag{7}$$

Here, ρ is the density operator for the field, and E^- and E^+ represent the negative- and positive-frequency portions of the electric field operator E, respectively. We assume that the final state of the detector is much broader than the bandwidth of the incident radiation, and that a broad band of final states is accessible [20], [21].

If we specifically consider the mixing of two single-mode, amplitude-stabilized, first-order coherent waves, both of which are well collimated, parallel, plane polarized along a common unit vector, and normally incident onto a photosensitive material, we may write the positive portion of the electric field operator E^+ as the superposition of two scalar fields

$$E^+ = \mathscr{E}_1^0\, e^{-i\omega_1 t} + \mathscr{E}_2^0\, e^{-i\omega_2 t} \tag{8}$$

with angular frequencies ω_1 and ω_2. This is equivalent to assuming a semiclassical approach which makes use of the analytic signal [43]. The complex wave amplitude $\mathscr{E}_i^0$ can be expressed in terms of its absolute magnitude $|\mathscr{E}_i^0|$ and a phase

factor $e^{i\alpha_i}$ such that

$$\mathcal{E}_1^0 = |\mathcal{E}_1^0| e^{i\alpha}$$
$$\mathcal{E}_2^0 = |\mathcal{E}_2^0| e^{i\beta}. \tag{9}$$

Under these conditions, the quantum-statistical detector responses can be written in terms of the fields as

$$\text{tr}\{\rho E^- E^+\} \Rightarrow |\mathcal{E}_1^0|^2 + |\mathcal{E}_2^0|^2 + 2|\mathcal{E}_1^0||\mathcal{E}_2^0| \cos[(\omega_1 - \omega_2)t + (\beta - \alpha)] \tag{10}$$

and

$$\text{tr}\{\rho E^- E^- E^+ E^+\} \Rightarrow (|\mathcal{E}_1^0|^2 + |\mathcal{E}_2^0|^2 + 2|\mathcal{E}_1^0||\mathcal{E}_2^0| \cos[(\omega_1 - \omega_2)t + (\beta - \alpha)])^2. \tag{11}$$

These expressions are scalar quantities and contain no spatial dependence because of the assumptions of plane polarization, parallel beams, and normal incidence.

Generalizing these results to sinusoidal beam photomixing in which the k-photon detector response is the normally ordered product [3]

$$W^{(k)} \propto \text{tr}\{\rho[E^-(x_a)]^k [E^+(x_a)]^k\} \tag{12}$$

and using the binomial theorem leads to a heterodyne signal given by

$$\begin{aligned} W^{(k)} = \zeta_k(&\{|\mathcal{E}_1^0|^2 + |\mathcal{E}_2^0|^2\}^k \\ &+ \binom{k}{1}\{|\mathcal{E}_1^0|^2 + |\mathcal{E}_2^0|^2\}^{k-1}\{2|\mathcal{E}_1^0||\mathcal{E}_2^0| \\ &\cdot \cos[(\omega_1 - \omega_2)t + (\beta - \alpha)]\} \\ &+ \binom{k}{2}\{|\mathcal{E}_1^0|^2 + |\mathcal{E}_2^0|^2\}^{k-2}\{2|\mathcal{E}_1^0||\mathcal{E}_2^0| \\ &\cdot \cos[(\omega_1 - \omega_2)t + (\beta - \alpha)]\}^2 + \cdots \\ &+ \binom{k}{r}\{|\mathcal{E}_1^0|^2 + |\mathcal{E}_2^0|^2\}^{k-r}\{2|\mathcal{E}_1^0||\mathcal{E}_2^0| \\ &\cdot \cos[(\omega_1 - \omega_2)t + (\beta - \alpha)]\}^r + \cdots \\ &+ \{2|\mathcal{E}_1^0||\mathcal{E}_2^0| \cos[(\omega_1 - \omega_2)t + (\beta - \alpha)]\}^k). \end{aligned} \tag{13}$$

Here ζ_k represents a proportionality constant for the k-photon process. The leading dc terms are proportional to $|\mathcal{E}_1^0|^{2k}$ and $|\mathcal{E}_2^0|^{2k}$, and may be associated with the absorption of k monochromatic photons, each of which arises from a given beam (1 and 2, respectively). The highest frequency current component is proportional to

$$|\mathcal{E}_1^0|^k |\mathcal{E}_2^0|^k \cos[k(\omega_1 - \omega_2)t + \phi]$$

and corresponds to the absorption of k nonmonochromatic photons, each of which must be associated with both of the beams. It is evident from the above that multiple- and sum-frequency terms do not appear in the k-photon absorption heterodyne detector output, in analogy with the result for the one-quantum case [39]-[41].

III. Two-Photon Photomixing

Inserting the constants ζ for the one- and two-quantum cases in (13), the detector responses for coherent signal mixing are, respectively,

$$W^{(1)} = \zeta_1(|\mathcal{E}_1^0|^2 + |\mathcal{E}_2^0|^2 + 2|\mathcal{E}_1^0||\mathcal{E}_2^0| \cos[(\omega_1 - \omega_2)t + (\beta - \alpha)]) \tag{14}$$

and

$$\begin{aligned} W^{(2)} = \zeta_2(&|\mathcal{E}_1^0|^4 + |\mathcal{E}_2^0|^4 + 2|\mathcal{E}_1^0|^2 |\mathcal{E}_2^0|^2 \\ &+ 4|\mathcal{E}_1^0|^3 |\mathcal{E}_2^0| \cos[(\omega_1 - \omega_2)t + (\beta - \alpha)] \\ &+ 4|\mathcal{E}_1^0||\mathcal{E}_2^0|^3 \cos[(\omega_1 - \omega_2)t + (\beta - \alpha)] \\ &+ 4|\mathcal{E}_1^0|^2 |\mathcal{E}_2^0|^2 \cos^2[(\omega_1 - \omega_2)t + (\beta - \alpha)]). \end{aligned} \tag{15}$$

Using the double-angle formula for the last term in (15), $W^{(2)}$ may also be written as

$$\begin{aligned} W^{(2)} = \zeta_2(&|\mathcal{E}_1^0|^4 + |\mathcal{E}_2^0|^4 + 4|\mathcal{E}_1^0|^2 |\mathcal{E}_2^0|^2 \\ &+ 4|\mathcal{E}_1^0|^3 |\mathcal{E}_2^0| \cos[(\omega_1 - \omega_2)t + (\beta - \alpha)] \\ &+ 4|\mathcal{E}_1^0||\mathcal{E}_2^0|^3 \cos[(\omega_1 - \omega_2)t + (\beta - \alpha)] \\ &+ 2|\mathcal{E}_1^0|^2 |\mathcal{E}_2^0|^2 \cos[2(\omega_1 - \omega_2)t + 2(\beta - \alpha)]) \end{aligned} \tag{16}$$

when this $\cos^2$ term is present. As noted previously, double- and sum-frequency terms are absent.

It is not difficult to associate various second-order correlation functions $G^{(2)}(x_a x_b x_c x_d) \equiv [abcd]$ with (15). (When two beams are present, we must consider a space-time point for each of the beams so that the index in $G^{(2)}$ takes on two values [18].) Thus the first term, $|\mathcal{E}_1^0|^4$, may be associated with [1111], the second with [2222], the third with [1221] and [2112], the fourth with the four permutations of [1112], the fifth with the four permutations of [2221], and the sixth with the four permutations of [1212], with $b \neq c$. The coefficient of each term in (15) is therefore equal to the number of permutations in the appropriate form of the correlation function for that term. The physical interpretation follows immediately: the first two dc terms in (15) arise from the absorption of two monochromatic photons, both from the same beam. The third dc term, which exists in two permutations with $b = c$, arises from the two ways in which two single monochromatic photons can be absorbed, one from each beam. The fourth and fifth terms correspond to the absorption of a single monochromatic photon from one of the beams plus a single nonmonochromatic photon which must be associated with both beams. These terms therefore contribute currents at the difference frequency $(\omega_1 - \omega_2)$, in analogy with the single-quantum heterodyne interference term [39]-[41]. The final term corresponds to the absorption of two nonmonochromatic photons, and therefore varies at double the difference frequency, i.e., at $2(\omega_1 - \omega_2)$; clearly there is no analogous process possible in the one-quantum case.

We note that the absorption of two nonmonochromatic photons imparts an additional dc value to the double-difference-frequency term, as may be seen by comparing (15) and (16). This additional term, of magnitude $2|\mathcal{E}_1^0|^2 |\mathcal{E}_2^0|^2$, appears in the presence of double-quantum photomixing; in the absence of such photomixing, we must obtain $W^{(2)}$ from (15) and *not* from (16). In this latter case, the detector response reduces to the previously obtained result [18]

$$\begin{aligned} W^{(2)}[\text{mixing absent}] &= \zeta_2(|\mathcal{E}_1^0|^4 + |\mathcal{E}_2^0|^4 + 2|\mathcal{E}_1^0|^2 |\mathcal{E}_2^0|^2) \\ &= \zeta_2'(I_1 + I_2)^2 \end{aligned} \tag{17}$$

where I_i represents the intensity of the ith beam and ζ_2' is a new proportionality constant.

The results presented above can be expanded to modulated, noncoherent, and nonparallel beam mixing. As an example, we consider two ideal amplitude-stabilized nonparallel ($\theta > \lambda/d$) plane traveling waves impinging on a two-quantum detector, so that washboarding can occur. In contrast to the one-quantum case, the detector responds to the *square* of the spatial intensity variation across the detector aperture at every instant of time, resulting in a factor of 2 enhancement in the dc cross term, as obtained with pure temporal mixing. Thus the two-quantum dc photocurrent will in general be enhanced due to spatiotemporal intensity variations (interference fringes); the magnitude of this enchancement depends on the system configuration. Experimental evidence for two-quantum enhancement due to spatial variations has, in fact, been provided by Shiga and Imamura [10] and by Teich *et al.* [22].

As a final example, we consider mixing due to radiation which is nonsinusoidal (i.e., not coherent to all orders). We consider two parallel, plane-polarized, normally incident superimposed beams of radiation from the same chaotic source, one of which is a time-delayed version of the other (delay τ_δ) entering one double-quantum detector. This was previously shown to be equivalent to a self-integrating Hanbury-Brown-Twiss device [18]. For a thermal source in the absence of a beat signal, we find

$$W^{(2)}[\text{mixing absent}] = 2\zeta_2'(I_1^2 + 2I_1 I_2 + I_2^2), \qquad \tau_\delta < \tau_c \quad (18)$$

and

$$W^{(2)}[\text{mixing absent}] = 2\zeta_2'(I_1^2 + I_1 I_2 + I_2^2), \qquad \tau_\delta > \tau_c \quad (19)$$

where τ_c is the coherence time of the source. For $\tau_\delta < \tau_c$, (18) represents the enhancement of both the single-beam and the mixed-beam counting rates, arising from the tendency of these photons to arrive in correlated pairs (assuming that the detector intermediate state lifetime $\tau_l \ll \tau_c$). For $\tau_\delta > \tau_c$, however, there is no correlation between the arrival time of a photon from one beam and the arrival time of a photon from the other. Thus the absorption of two photons from a single beam is enhanced by a factor of 2 relative to the absorption of one photon from each beam, leading to a cross term of 1. This can also be qualitatively understood from the point of view of additive Gaussian fields; the sum of two fully correlated Gaussian random processes ($\tau_\delta < \tau_c$) has a greater variance than that of two independent Gaussian random processes ($\tau_\delta > \tau_c$) leading to an enhanced value for the cross term when $\tau_\delta < \tau_c$.

From the foregoing, it is clear that the double-quantum current can be calculated for a variety of configurations involving different relative time scales, angular separations, polarization properties, and statistical characteristics. Some additional examples are treated in [18]. Clearly, the second-order correlation functions of the field play an important role in determining the magnitude of the signal, in distinction to the one-quantum case.

IV. Signal-to-Noise Ratio

We now follow the usual procedure used for the single-quantum case [31]-[33], [37] to calculate the approximate SNR for k-photon sinusoidal heterodyne detection. We begin with two-quantum photomixing, neglecting the double-difference-frequency component and assuming that the ac signal is at the fundamental-difference-frequency (IF) between the two waves. Thus, considering the mixing of two parallel coherent waves as described in Section II, (16) yields

$$W_{\text{IF}}^{(2)} = 4\zeta_2(|\mathcal{E}_1^0|^3\,|\mathcal{E}_2^0| + |\mathcal{E}_1^0|\,|\mathcal{E}_2^0|^3) \cdot \cos[(\omega_1 - \omega_2)t + (\beta - \alpha)] \quad (20)$$

and

$$W_{\text{dc}}^{(2)} = \zeta_2(|\mathcal{E}_1^0|^4 + |\mathcal{E}_2^0|^4 + 4|\mathcal{E}_1^0|^2\,|\mathcal{E}_2^0|^2) \quad (21)$$

so that

$$W^{(2)} = \left\{1 + \frac{4(|\mathcal{E}_1^0|^3\,|\mathcal{E}_2^0| + |\mathcal{E}_1^0|\,|\mathcal{E}_2^0|^3)\cos[(\omega_1 - \omega_2)t + (\beta - \alpha)]}{|\mathcal{E}_1^0|^4 + |\mathcal{E}_2^0|^4 + 4|\mathcal{E}_1^0|^2\,|\mathcal{E}_2^0|^2}\right\} W_{\text{dc}}^{(2)}. \quad (22)$$

We now assume that one of the waves (which we call the local oscillator or LO) is strong, i.e., $E_2 \gg E_1$, in which case

$$W_{\text{IF}}^{(2)} \simeq 4(|\mathcal{E}_1^0|/|\mathcal{E}_2^0|)\,W_{\text{dc}}^{(2)} \cos[(\omega_1 - \omega_2)t + (\beta - \alpha)] \quad (23)$$

and

$$\langle[W_{\text{IF}}^{(2)}]^2\rangle \simeq 8(|\mathcal{E}_1^0|^2/|\mathcal{E}_2^0|^2)\,[W_{\text{dc}}^{(2)}]^2. \quad (24)$$

The noise power can be obtained from the two-quantum photocurrent spectrum [23] which, in turn, is related to the stochastic nature of the radiation source. For a coherent and strong LO, however, the k-quantum counting statistics will be Poisson [25], [26], and the two-quantum (shot) noise power is then

$$\langle[W_n^{(2)}]^2\rangle = 2e[W_{\text{dc}}^{(2)}]\Delta f. \quad (25)$$

Thus using (2), (24), and (25), the two-quantum SNR can be written as

$$\text{SNR}^{(2)} \simeq \frac{4P_1}{e\Delta f}\left(\frac{W_{\text{dc}}^{(2)}}{P_2}\right) = \frac{4P_1}{e\Delta f}\Lambda^{(2)}. \quad (26)$$

Using the relationship between the two-quantum yield $\Lambda^{(2)}$ and the two-quantum efficiency η_2 given in (3), we finally obtain

$$\text{SNR}^{(2)} \simeq 4\eta_2 P_1/h\nu\Delta f. \quad (27)$$

We recall from (3) that η_2 is itself proportional to the irradiance of the LO, and we must have $4\eta_2 < 1$. The result is therefore similar to that for the single-quantum heterodyne detector given in (6); in that case, however, η_1 is independent of the LO. The two-quantum minimum detectable power (MDP) [31], [32] therefore becomes

$$\text{MDP}^{(2)} \simeq h\nu\Delta f/4\eta_2. \quad (28)$$

This corresponds to a minimum number of photons $\mathfrak{N}_{\text{min}}^{(2)}$, detectable in the resolution time of the receiver [$\tau_r \sim (\Delta f)^{-1}$],

given by

$$\mathfrak{N}_{\min}^{(2)} \simeq (4\eta_2)^{-1}. \tag{29}$$

We note that SNR at the double-difference frequency, corresponding to the absorption of two nonmonochromatic photons, is reduced by the factor (P_1/P_2). Clearly, using methods similar to those presented above and in [18] and [37], we can obtain analogous SNR expressions for photomixing with nonsinusoidal beams.

The SNR at the fundamental-difference frequency $(\omega_1 - \omega_2)$ may also be obtained for coherent beam mixing in the k-photon absorption heterodyne detector. Following a series of steps similar to those given above, we find

$$\mathrm{SNR}^{(k)} \simeq c_k \eta_k P_1/h\nu\Delta f \tag{30}$$

$$\mathrm{MDP}^{(k)} \simeq h\nu\Delta f/c_k\eta_k \tag{31}$$

and

$$\mathfrak{N}_{\min}^{(k)} \simeq (c_k\eta_k)^{-1} \tag{32}$$

where c_k is a constant (dependent on k), and η_k is proportional to I^{k-1}, where I is the LO irradiance [see (5)]. Here $c_k\eta_k < 1$.

V. Experiment

In this section we describe a preliminary set of experiments in which double-quantum photoemission was observed from a sodium surface simultaneously illuminated by two superimposed beams of laser radiation. While ac photomixing terms were not observed in these experiments, the measurements are consistent with the theoretical calculations given in Section III.

A. Configuration

The apparatus used for the experimental measurement of two-quantum photomixing is shown in the block diagram of Fig. 1. The radiation source was a pulsed GaAs multimode semiconductor injection laser operated at 77 K and emitting a peak radiation power of 400 mW at about 8450 Å. Mode shifts due to laser heating occurred during the pulse duration, which was about 35 μs. The radiation was collimated by a 10-cm focal length lens, passed through an iris, and then through a configuration of dielectric beam splitters and antireflection coated prisms resembling a Mach-Zender interferometer. The beam splitters were approximately $\frac{2}{3}$ transmitting and were flat only to about 1 wavelength; the optical phase across the beam could therefore be considered to vary. The purpose of the interferometer configuration was to allow the irradiance of each beam (denoted as 1 and 2) to be independently controlled by means of calibrated attenuating filters. Beam 1 could also be time-delayed with respect to beam 2 by means of a sliding prism (see Fig. 1), but this capability was not important in these experiments where τ_δ was always greater than τ_c due to the very small value of τ_c. After passing through a second iris and a (6-cm focal length) focusing lens, the radiation was allowed to impinge on a specially constructed Na-surface photomultiplier tube, which has been described previously [6], [8], [9]. A Polaroid type HN-7 sheet polarizer was almost always placed at the front face of the photomultiplier as shown in Fig. 1 (the one exception will be noted later). The electron-multiplied current was passed through a 1-MΩ load resistor which fed a Princeton Applied Research (PAR) low-noise preamplifier followed by a PAR lock-in amplifier. Phase-sensitive detection was performed at 2.2 kHz, which is the fundamental repetition frequency of the pulsed laser output. Large integration times were used so that only the dc or average value of this current component was measured. The reference signal for the lock-in amplifier was obtained directly from the silicon-controlled-rectifier power supply [44] used to drive the laser.

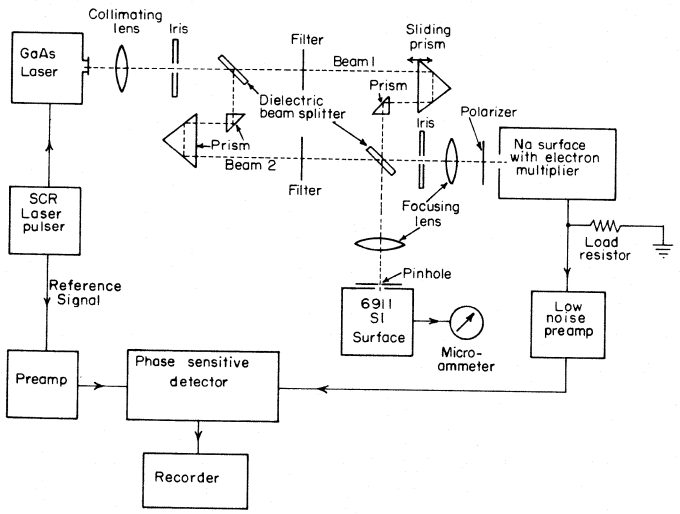

Fig. 1. Block diagram of the double-quantum photomixing experimental arrangement.

Radiation from the other leg of the interferometer was focused onto a 25-μm diameter pinhole which acted as an aperture stop at the face of a standard Dumont 6911 type S-1 photomultiplier. This provided a relatively accurate method for superimposing the two beams [8]. This is critical since the double-quantum response is inversely proportional to the illuminated area A. The beams were adjusted to achieve maximum output from the 6911 photomultiplier tube, a procedure which was often difficult and required a great deal of care.

B. Method

The following procedure was used in making a measurement. 1) The beams were aligned to provide maximum current from the 6911 photomultiplier. 2) Beam 1 was blocked and the double-quantum current $\overline{W_2^{(2)}}$ from beam 2 was maximized by imaging the laser junction on the sodium surface, and then recorded. Using a calibrated attenuating filter, it was ascertained that pure two-quantum emission was occurring, i.e., that $\overline{W_2^{(2)}} \propto I_2^2$, where I_2 represents the irradiance of beam 2. 3) Beam 2 was blocked and the double-quantum current from beam 1 was recorded, after verifying that it was $\propto I_1^2$. (The constant of proportionality was taken to be the same in both cases.) 4) Both beams were then unblocked and, after once again verifying that pure double-quantum emission was occurring, the total average double-quantum current $\overline{W^{(2)}}$ (at the fundamental repetition frequency of 2.2 kHz) was recorded.

Experiments were performed with different value of I_1/I_2,

obtained by attenuating one of the beams relative to the other by means of thin gelatin (Kodak Wratten) filters. Ordinary glass filters could not be used to provide the decrements of light intensity because refraction in the glass caused the imaged spot size and position to change thus altering the two-quantum current in an unpredictable way.

C. Results

The total average fundamental-repetition-frequency two-quantum photoelectric current $\overline{W^{(2)}}$, for different intensity ratios of the two constituent beams (I_1/I_2), is presented in Fig. 2. The solid curve represents the equation $W^{(2)} \propto (I_1 + I_2)^2$ which is simply the parabola $(1 + I_1/I_2)^2$ when the intensity I_2 is normalized to unity. This represents a cross term of $2I_1I_2$, and is so labeled. The cross term of $4I_1I_2$, on the other hand, is shown by the dashed line in Fig. 2. Only the highest observed values of $\overline{W^{(2)}}$ are plotted in Fig. 2, many more points having been found to lie below the curves. This has been attributed to the difficulty in obtaining precise alignment of the two radiation beams, and therefore superposition of the focused spots on the sodium surface.

The triangles in Fig. 2 represent data for linearly or partially polarized radiation, while the circle is for cross-polarized radiation (this is the one exception mentioned previously). The experimental measurements are consistent with the following interpretation. The laser output consists of a number of more-or-less independent Fabry–Perot modes which are changing during the pulsewidth due to heating of the laser junction [8]. The radiation may therefore be considered to behave as a Gaussian source with a coherence time $\tau_c \sim (\Delta\nu)^{-1} \sim 10^{-13}$ s. Since the intermediate-state lifetime for the double-quantum sodium photodetector is much shorter than the radiation coherence time, the irradiance fluctuations result in a factor of 2 enhancement of the single-beam photocurrents. As far as the irradiance cross term is concerned, the two-quantum current will also be enhanced by a factor of 2 owing to the random spatial irradiance fluctuations across the detector for the superimposed beams. Thus we obtain a relative cross terms of 2, i.e., $\overline{W^{(2)}} \propto I_1^2 + 2I_1I_2 + I_2^2$, in agreement with the data.

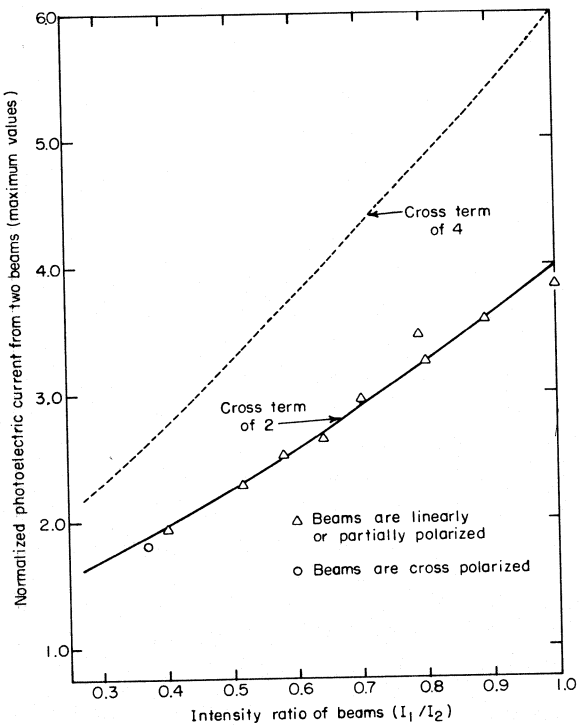

Fig. 2. The average double-quantum photocurrent from two beams (maximum values) versus the intensity ratio of the beams.

VI. Discussion

From the foregoing, it is clear that multiple-quantum heterodyne detection is somewhat more complex than the analogous single-quantum process. In particular, the average detector response and the SNR are found to depend on the higher order correlation functions of the radiation field and on the LO irradiance. From a physical point of view, it has been possible to associate various terms in the detected current with specific kinds of photon absorptions. Calculations of the SNR and MDP for a number of cases have been carried out. The results of a preliminary two-quantum photomixing experiment are in agreement with the theory.

Although it appears that the k-photon heterodyne detector can be made to perform as well as the single-photon heterodyne detector by simply increasing the LO intensity, a number of practical problems would likely make this difficult. Inasmuch as the transition probabilities decrease rapidly as k is increased, and are furthermore proportional to A^{1-k}, it appears that very high LO intensities would be required to place η_k anywhere in the vicinity of 0.1 for $k > 2$. Aside from alignment problems, these high intensities could result in thermionic emission from cathode heating, or possibly cathode damage.

The two-quantum case is therefore likely to be the most interesting, and also the easiest to examine experimentally. A possible arrangement for studying the effect in a more detailed and controlled fashion is the following. The radiation from a 0.5-mW He–Ne laser, operating at a wavelength of 1.15 μm, is passed through an acoustooptic modulator (which splits it into two frequencies) and a focusing lens. A 5-μm focused spot size, corresponding to an area of 2.5×10^{-7} cm^2, would then provide an incident irradiance $I \sim 2 \times 10^3$ W/cm^2. Using a Cs_3Sb photocathode with a work function ~2.05 eV and a yield [7] $\sim 5 \times 10^{-11}\, I$ A/W, a two-quantum current $\sim 5 \times 10^{-11}$ A may then be obtained. An experiment of this nature would allow the validity of (15), (16), and (27) to be examined. A YAG:Nd laser could be substituted for the He–Ne laser for an even simpler experimental configuration, since focusing would not then be required.

We observe that the use of a two-quantum photomixer in a three-frequency nonlinear heterodyne detection receiver [45] would result in a reduction of the SNR by the factor (P_1/P_2), corresponding to the absorption of 2 nonmonochromatic photons as discussed earlier. It therefore does not appear to be suitable for this application. We also note that information relating to the intermediate-state lifetime of the detector (τ_I) can be obtained by measuring the two-quantum detector output for various values of τ_c.

Although the emphasis in this paper has been on linearly polarized incident radiation, considerable enhancement of

the k-quantum photocurrent may occur for circularly (or elliptically) polarized radiation, as recently discussed by a number of authors [46].

Acknowledgment

The author wishes to thank Prof. G. J. Wolga of Cornell University for many valuable discussions in connection with the experiments reported here.

References

[1] A. Einstein, "Concerning a heuristic point of view toward the emission and transformation of light," *Ann. Physik.*, vol. 17, p. 132, 1905 (transl.: *Amer. J. Phys.*, vol. 33, pp. 367–374, May 1965).

[2] a) L. Mandel, "Fluctuations of photon beams: The distribution of the photo-electrons," *Proc. Phys. Soc.* (London), vol. 74, pp. 233–243, Sept. 1959.
b) See also E. M. Purcell, "The question of the correlation between photons in coherent rays," *Nature*, vol. 178, pp. 1449–1450, Dec. 1956.
c) L. Mandel, "Fluctuations of photon beams and their correlations," *Proc. Phys. Soc.* (London), vol. 72, pp. 1037–1048, Dec. 1958.

[3] a) R. J. Glauber, "The quantum theory of optical coherence," *Phys. Rev.*, vol. 130, pp. 2529–2539, June 1963.
b) —, "Coherent and incoherent states of the radiation field," *Phys. Rev.*, vol. 131, pp. 2766–2788, Sept. 1963.

[4] P. L. Kelley and W. H. Kleiner, "Theory of electromagnetic field measurement and photoelectron counting," *Phys. Rev.*, vol. 136, pp. A316–A334, Oct. 1964.

[5] M. C. Teich and G. J. Wolga, "Work-function estimation with a single yield measurement," *J. Opt. Soc. Amer.*, vol. 57, pp. 542–543, Apr. 1967.

[6] M. C. Teich, J. M. Schroeer, and G. J. Wolga, "Double-quantum photoelectric emission from sodium metal," *Phys. Rev. Lett.*, vol. 13, pp. 611–614, Nov. 1964.

[7] H. Sonnenberg, H. Heffner, and W. Spicer, "Two-photon photoelectric effect in Cs_3Sb," *Appl. Phys. Lett.*, vol. 5, pp. 95–96, Sept. 1964.

[8] M. C. Teich, "Two quantum photoemission and dc photomixing in sodium," Ph.D. dissertation, Cornell University, Ithaca, N.Y., Feb. 1966, unpublished (also Tech. Rep. 453, Materials Science Center, Cornell University, Ithaca, N.Y., Feb. 1966).

[9] M. C. Teich and G. J. Wolga, "Two-quantum volume photoelectric effect in sodium," *Phys. Rev.*, vol. 171, pp. 809–814, July 1968.

[10] F. Shiga and S. Imamura, "Experiment on relation between two-photon absorption and coherence of light," *Phys. Lett.*, vol. 25A, pp. 706–707, Nov. 1967.

[11] E. M. Logothetis and P. L. Hartman, "Three-photon photoelectric effect in gold," *Phys. Rev. Lett.*, vol. 18, pp. 581–583, Apr. 1967.

[12] —, "Laser-induced electron emission from solids: Many-photon photoelectric effects and thermionic emission," *Phys. Rev.*, vol. 187, pp. 460–474, Nov. 1969.

[13] R. E. B. Makinson and M. J. Buckingham, "The second order photoelectric effect at a metal surface," *Proc. Phys. Soc. A* (London), vol. 64, pp. 135–139, Feb. 1951.

[14] R. L. Smith, "Two-photon photoelectric effect," *Phys. Rev.*, vol. 128, pp. 2225–2229, Dec. 1962.

[15] H. C. Bowers, "Theoretical and experimental considerations of the double-quantum photoelectric effect," M. S. thesis, Cornell University, Ithaca, N.Y., Feb. 1964, unpublished.

[16] I. Adawi, "Theory of the surface photoelectric effect for one and two photons," *Phys. Rev.*, vol. 134, pp. A788–A798, May 1964.

[17] P. Bloch, "Preliminary investigation of the two-photon photoelectric effect," *J. Appl. Phys.*, vol. 35, pp. 2052–2054, July 1964.

[18] M. C. Teich and G. J. Wolga, "Multiple-photon processes and higher order correlation functions," *Phys. Rev. Lett.*, vol. 16, pp. 625–628, Apr. 1966.

[19] P. Lambropoulos, C. Kikuchi, and R. K. Osborn, "Coherence and two-photon absorption," *Phys. Rev.*, vol. 144, pp. 1081–1086, Apr. 1966.

[20] B. R. Mollow, "Two-photon absorption and field correlation functions," *Phys. Rev.*, vol. 175, pp. 1555–1563, Nov. 1968.

[21] G. S. Agarwal, "Field-correlation effects in multiphoton absorption processes," *Phys. Rev. A*, vol. 1, pp. 1445–1459, May 1970.

[22] M. C. Teich, R. L. Abrams, and W. B. Gandrud, "Photon-correlation enhancement of SHG at 10.6 μm," *Opt. Commun.*, vol. 2, pp. 206–208, Oct. 1970.

[23] P. Diament and M. C. Teich, "Relation between radiation statistics and two-quantum photocurrent spectra," *J. Opt. Soc. Amer.*, vol. 59, p. 661, May 1969.

[24] a) C. Freed and H. A. Haus, "Photocurrent spectrum and photoelectron counts produced by a gas laser," *Phys. Rev.*, vol. 141, pp. 287–298, Jan. 1966.
b) G. Lachs, "Effects of photon bunching on shot noise in photoelectric detection," *J. Appl. Phys.*, vol. 39, pp. 4193–4199, Aug. 1968.

[25] M. C. Teich and P. Diament, "Two-photon counting statistics for laser and chaotic radiation," *J. Appl. Phys.*, vol. 40, pp. 625–633, Feb. 1969.

[26] P. P. Barashev, "Statistical characteristics of a multiphoton photocurrent," *Zh. Eksp. Teor. Fiz.*, vol. 59, pp. 1318–1326, Oct. 1970 (transl.: *Sov. Phys.-JETP*, vol. 32, pp. 720–723, Apr. 1971).

[27] —, "The multiquantum photoemissive effect in condensed media and statistical characteristics of the multiquantum photocurrent," *Phys. Status Solidi (a)*, vol. 9, pp. 9–43 (pt. I) and pp. 387–414 (pt. II), Jan. and Feb. 1972.

[28] A. T. Forrester, R. A. Gudmundsen, and P. O. Johnson, "Photoelectric mixing of incoherent light," *Phys. Rev.*, vol. 99, pp. 1691–1700, Sept. 1955.

[29] A. Javan, E. A. Ballik, and W. L. Bond, "Frequency characteristics of a continuous-wave He–Ne optical maser," *J. Opt. Soc. Amer.*, vol. 52, pp. 96–98, Jan. 1962.

[30] a) B. J. McMurtry and A. E. Siegman, "Photomixing experiments with ruby optical maser and traveling wave microwave phototubes," *Appl. Opt.*, vol. 1, pp. 51–53, Jan. 1962.
b) A. E. Siegman, S. E. Harris, and B. J. McMurtry, "Optical heterodyning and optical demodulation at microwave frequencies," in *Optical Masers*, J. Fox, Ed. New York: Wiley, 1963, pp. 511–527.

[31] M. C. Teich, R. J. Keyes, and R. H. Kingston, "Optimum heterodyne detection at 10.6 μm in photoconductive Ge:Cu," *Appl. Phys. Lett.*, vol. 9, pp. 357–360, Nov. 1966.

[32] M. C. Teich, "Infrared heterodyne detection," *Proc. IEEE*, vol. 56, pp. 37–46, Jan. 1968 (Reprinted in *Infrared Detectors*, R. D. Hudson, Jr. and J. W. Hudson, Ed. Stroudsburg: Dowden, Hutchinson and Ross, 1975).

[33] a) B. M. Oliver, "Signal-to-noise ratios in photoelectric mixing," *Proc. IRE* (Corresp.), vol. 49, pp. 1960–1961, Dec. 1961.
b) H. A. Haus, C. H. Townes, and B. M. Oliver, "Comments on 'Noise in photoelectric mixing'," *Proc. IRE* (Corresp.), vol. 50, pp. 1544–1546, June 1962.

[34] a) A. E. Siegman, "The antenna properties of optical heterodyne receivers," *Proc. IEEE (Special Joint Issue on Optical Electronics)*, vol. 54, pp. 1350–1356, Oct. 1966.
b) L. Mandel and E. Wolf, "Optimum conditions for heterodyne detection of light," *J. Opt. Soc. Amer.*, vol. 65, pp. 413–420, Apr. 1975.

[35] W. S. Read and D. L. Fried, "Optical heterodyning with noncritical angular alignment," *Proc. IEEE* (Corresp.), vol. 51, p. 1787, Dec. 1963.

[36] M. C. Teich, "Homodyne detection of infrared radiation from a moving diffuse target," *Proc. IEEE*, vol. 57, pp. 786–792, May 1969.

[37] M. C. Teich and R. Y. Yen, "On the signal-to-noise ratio for optical heterodyne detection," *J. Appl. Phys.*, vol. 43, pp. 2480–2481, May 1972.

[38] a) U. M. Titulaer and R. J. Glauber, "Correlation functions for coherent fields," *Phys. Rev.*, vol. 140, pp. B676–B682, Nov. 1965.
b) —, "Density operators for coherent fields," *Phys. Rev.*, vol. 145, pp. 1041–1050, May 1966.

[39] M. C. Teich, "Field-theoretical treatment of photomixing," *Appl. Phys. Lett.*, vol. 14, pp. 201–203, Mar. 1969.

[40] —, "Quantum theory of heterodyne detection," in *Proc. 3rd Photoconductivity Conf.*, E. M. Pell, Ed. New York: Pergamon, 1971, pp. 1–5.

[41] —, "Coherent detection in the infrared," in *Semiconductors and*

Semimetals, R. K. Willardson and A. C. Beer, Ed. New York: Academic, 1970, vol. 5, *Infrared Detectors*, ch. 9, pp. 361-407.
[42] —, "Nonlinear heterodyne detection," in *Topics in Applied Physics*, R. J. Keyes, Ed. New York: Springer, 1976, *Optical and Infrared Detectors*, to be published.
[43] a) L. Mandel, "Complex representation of optical fields in coherence theory," *J. Opt. Soc. Amer.*, vol. 57, pp. 613-617, May 1967.
b) L. Mandel and E. Wolf, "Coherence properties of optical fields," *Rev. Mod. Phys.*, vol. 37, pp. 231-287, Apr. 1965.
[44] M. C. Teich, D. A. Berkley, and G. J. Wolga, "Silicon-controlled-rectifier long-pulse driver for injection lasers," *Rev. Sci. Instr.*, vol. 36, pp. 973-974, July 1965.
[45] a) M. C. Teich, "Three-frequency heterodyne system for acquisition and tracking of radar and communications signals," *Appl. Phys. Lett.*, vol. 15, pp. 420-423, Dec. 1969.
b) M. C. Teich and R. Y. Yen, "Three-frequency nonlinear heterodyne detection. 1: cw radar and analog communications," *Appl. Opt.*, vol. 14, pp. 666-679, Mar. 1975.
c) —, "Three-frequency nonlinear heterodyne detection. 2: Digital communications and pulsed radar," *Appl. Opt.*, vol. 14, pp. 680-688, Mar. 1975.
[46] a) R. A. Fox, R. M. Kogan, and E. J. Robinson, "Laser triple-quantum photoionization of cesium," *Phys. Rev. Lett.*, vol. 26, pp. 1416-1417, June 1971.
b) S. Klarsfeld and A. Maquet, "Circular versus linear polarization in multiphoton ionization," *Phys. Rev. Lett.*, vol. 29, pp. 79-81, July 1972.

Studies of Relaxation Oscillations in Organic Dye Lasers

CHINLON LIN

Abstract—**The transient phenomena of relaxation oscillations and "initial spikes" in organic dye lasers are studied experimentally and theoretically. Both damped relaxation oscillations and initial spikes are clearly observed in N_2 laser-pumped dye lasers under appropriate conditions which are furthermore shown to agree with theoretical considerations. Linearized rate equations obtained with small-signal approximation are used to describe the initial-spiking phenomenon; for the more general phenomenon of relaxation oscillations computer solutions of the coupled rate equations are obtained. Comparisons with experimental observations show excellent qualitative agreement. Based on the results of these studies, a general technique using the idea of controlled resonator transients is described for tunable subnanosecond pulse generation from laser-pumped dye lasers in the near UV and the visible region of the spectrum.**

I. Introduction

THE PHENOMENON of relaxation oscillations or "spiking" has been observed and studied extensively in solid-state lasers under pulsed excitation [1], [2]. Although in most cases random spiking with pulses of irregular spacings and amplitudes were observed, there were observations of perfectly regular damped relaxation oscillations [2], [3]. Such regular damped relaxation oscillations are expected from theoretical analyses using the coupled rate equations [4]-[6]. It is generally recognized to be a phenomenon due to the interaction between the excess population inversion of the active medium and the photon energy of the electromagnetic field inside the resonator. The characteristics of the relaxation oscillations depend on the rate of change of the population inversion due to pumping, spontaneous decay and stimulated emission, and the rate of buildup and decay of photons in the resonator due to stimulated emission and various loss mechanisms such as output coupling, scattering, diffraction, and absorption.

In addition to being a common phenomenon in solid-state lasers, relaxation oscillations have also been observed and studied in gas lasers [7]. In the case of dye-solution lasers, relaxation oscillations have not been previously reported. However, in the first organic dye laser, Sorokin *et al.* [8] noticed that under certain conditions a Q-switched ruby laser-pumped dye laser had an "initial spike" in the output, which otherwise displayed the time variation similar to that of the pumping pulse. The observation was shown to agree qualitatively with the expected transient response of the dye laser under the corresponding experimental conditions. Miyazoe and Maeda [9] have further applied small-signal analysis to study the conditions for the appearance of such initial spikes. They pointed out that dye lasers are generally operated close to the border region between spiking and nonspiking. This is in contrast to solid-state lasers for which the spiking phenomenon is almost ubiquitous.

In this paper we report the observation and investigation of regular damped relaxation oscillations in N_2 laser-pumped dye lasers. Pulses with an initial spike are also observed; it is shown to be a special case of the more general phenomenon of relaxation oscillations. The characteristics of these transient responses are studied experimentally and compared with theoretical considerations. Excellent qualitative agreement is obtained. Because of the relative ease and large workable range in choosing desired dye-laser parameters (e.g., dye-laser medium and resonator length, resonator mirror reflectivities, dye-solution concentration, dye-fluorescence lifetime, etc.) laser-

Manuscript received February 7, 1975.
The author is with Bell Laboratories, Holmdel, N.J. 07733.

pumped organic dye lasers provide a new, convenient laser system for studies of relaxation oscillations, an important phenomenon manifesting the transient interaction of radiation with matter through stimulated emission.

We also describe a general technique for short-pulse generation from laser-pumped dye lasers. The technique makes use of the dye-laser resonator transients which are in the form of damped relaxation oscillations. From the result of our studies on these relaxation oscillations we show that dye-laser pulses much shorter than the pumping pulse can be obtained by proper choices of parameters such as photon-cavity decay time, the level of pumping, etc. Based on this general technique of controlled-resonator transients high repetition-rate subnanosecond pulses tunable in the near UV and the visible region have been obtained from N_2 laser-pumped dye lasers.

In the following sections previous studies of the initial spikes in both ruby laser-pumped and flashlamp-pumped dye lasers [8], [9] are first reviewed and then compared with our observations and studies of the more general phenomenon of damped relaxation oscillations. The technique of short-pulse generation by means of controlled resonator transients is then briefly described.

II. Rate Equations

To facilitate our later discussions let us first write down the well-known rate equations [5], [6]. Assuming a dye laser can be represented by an ideal four-level system, neglecting the triplet states for short-pulse excitation [10], the rate equations describing the population inversion and the photons are

$$\frac{dn}{dt} = W - Bnq - \frac{n}{\tau} \tag{1}$$

$$\frac{dq}{dt} = Bnq - \frac{q}{t_c} \tag{2}$$

where n is the inversion and is nearly equal to the upper state population; q is the number of photon quanta in the resonator; B is the Einstein coefficient for stimulated emission; W is the pumping rate; τ is the fluorescence lifetime; and t_c is the photon-cavity decay time. If the cavity losses are assumed to be primarily transmissive ones, then

$$t_c = \frac{T_c}{1-R} = \frac{\eta l + (L-l)}{C(1-R)} \tag{3}$$

where R is the geometric mean, $R = (R_1R_2)^{1/2}$, of the cavity mirror reflectivities, and T_c is the cavity transit time; $T_c = [\eta l + (L-l)]/C$, where L is the cavity spacing, l and η are the length and the refractive index of the active medium, respectively, and C is the speed of light. In equilibrium $(dn/dt) = (dq/dt) = 0$ and we have

$$n = n_0 = \frac{1}{Bt_c} \tag{4}$$

$$q = q_0 = \frac{W - \frac{n_0}{\tau}}{Bn_0}. \tag{5}$$

Note n_0 is the threshold inversion above which $(dq/dt) > 0$. The threshold pumping rate W_t is defined as

$$W_t = \frac{n_0}{\tau} = \frac{1}{Bt_c\tau}. \tag{6}$$

Using (4), rate equations (1) and (2) can be written as

$$\frac{dn}{dt} = W - \frac{n}{n_0}\frac{q}{t_c} - \frac{n}{\tau} \tag{7}$$

$$\frac{dq}{dt} = \frac{q}{t_c}\left(\frac{n}{n_0} - 1\right). \tag{8}$$

III. Initial Spikes

In this section we first review the observation and studies of initial spikes in ruby laser-pumped dye lasers by Sorokin *et al.* [8], and in flashlamp-pumped dye lasers by Miyazoe and Maeda [9]. Both the results of a small-signal analysis and the computer solutions are examined and compared with experimental observations in various dye lasers. The study of this special case of spiking behavior provides the basis for a better understanding of the more general phenomenon of relaxation oscillations.

A. Experimental Observations of Initial Spikes

In the study of the output characteristics of their first dye laser, Sorokin *et al.* [8] noticed the presence of a fast rise-time initial peak in the laser pulse which otherwise had a time variation roughly similar to the shape of the ruby laser-pumping pulse. They observed that this CAP (chroloaluminum phthalocyanine) dye laser had an initial peak, which became a sharper spike for a more lossy cavity; on the other hand, the output of another dye laser, DTTC (3,3′-diethylthiatricarbocyanine iodide), operated in a different cavity configuration, displayed no such initial spike. They obtained computer solutions of the coupled rate equations using parameters of the CAP dye laser and found good resemblance with experimental results. The DTTC dye laser was not studied in detail; they suggested that the presence of self-absorption might account for the absence of the initial peak.

Subsequently, Miyazoe and Maeda [9], noting that spiking behavior is in general seldom observed in dye lasers, applied the standard small-signal analysis to obtain the conditions for the appearance of initial spikes. It was pointed out that dye lasers are generally operated close to the border region between spiking and nonspiking. By using a special flashlamp-pumped rhodamine 6G dye laser with a 25-mm-long dye cell and a resonator length of 5 cm, they observed an initial spike; the spike disappeared when a 18-cm resonator length was used. Similar experiments were attempted under various resonator conditions by using several kinds of ruby laser-pumped polymethine dyes, but they could not observe such a distinct initial spike. Comparing their observation with that of the CAP dye laser they stated that although the reason for the absence of spiking is not obvious, one important reason seems to be the fact that the fluorescence lifetime of CAP or rhodamine 6G dye is about 6-10 ns while that of polymethine dyes is smaller than 3 ns.

In our experiments with N_2 laser-pumped dye lasers we have observed not only the initial spikes but also the more general

phenomenon of damped relaxation oscillations. A typical pulse with an initial spike is shown in Fig. 1(c). The theoretical considerations and the comparisons with various experiments for the initial-spike case are discussed in the following; the physical picture of spiking is more readily visualized in this case.

B. Small-Signal Analysis

Small-signal analysis has commonly been applied to study the relaxation oscillations in solid-state lasers. It is better suited for studying initial spikes because of the small-signal approximation. Coupled rate equations (1) and (2) can be linearized to be

$$\frac{d^2 n_1}{dt^2} + W_0 B t_c \frac{dn_1}{dt} + \left(W_0 B - \frac{1}{\tau t_c}\right) n_1 = 0 \tag{9}$$

$$\frac{d^2 q_1}{dt^2} + W_0 B t_c \frac{dq_1}{dt} + \left(W_0 B - \frac{1}{\tau t_c}\right) q_1 = 0 \tag{10}$$

where n_1 and q_1 are the small-signal perturbations and W_0 is the assumed constant excitation. The equations are identical in form and have solutions of the form of an exponentially damped sinusoid, with the damping time constant t_d and oscillation frequency ω given by

$$t_d = \frac{W_0 B t_c}{2} \tag{11}$$

$$\omega = \frac{1}{2}\sqrt{\frac{4\left(W_0 B t_c - \frac{1}{\tau}\right)}{t_c} - (W_0 B t_c)^2}. \tag{12}$$

The solution is truly oscillatory only if ω is real. Regarding a single damped oscillation as the initial spike, Miyazoe and Maeda [9] obtained the following condition for spiking as, for ω to be real:

$$\frac{4\left(W_0 B t_c - \frac{1}{\tau}\right)}{t_c} - (W_0 B t_c)^2 > 0. \tag{13}$$

We can rewrite this condition as

$$\frac{4\left(\frac{1}{t_c} - \frac{1}{\tau}\right)}{t_c} - \left(W_0 B t_c - \frac{2}{t_c}\right)^2 > 0 \tag{14}$$

from which we can see $\tau > t_c$ is a necessary but not sufficient condition for spiking. Defining $m = (W_0/W_t) = W_0 B t_c \tau$ as the ratio of the actual pumping level to the threshold pumping rate we obtain from (14) the necessary and sufficient condition required for the initial spike to appear

$$\frac{\tau}{t_c} > \frac{m^2}{4(m-1)}. \tag{15}$$

For $m = 2$, $\tau > t_c$ is required; for $m \gg 1$ the condition becomes $\tau > (m/4)\, t_c$.

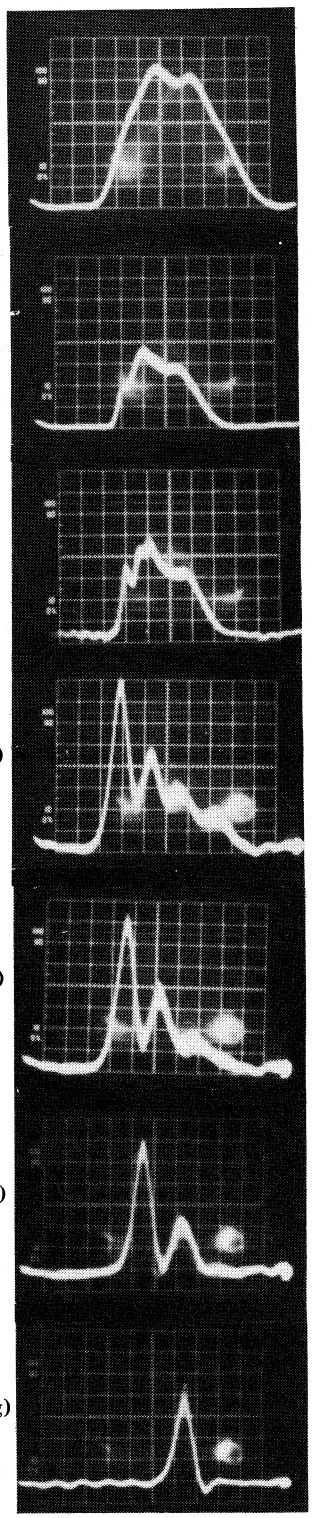

Fig. 1. (a) N_2 laser pulse. (b)–(g): Output pulse from a 7D4MC dye laser ($t_c \sim 50$ ps) as the pump power is decreased. Time scale: 2ns/cm for (a)–(c); 1 ns/cm for (d)–(g). Vertical scale arbitrary.

C. Computer Solutions

Without making use of the small-signal approximation and assuming a more realistic time-varying excitation (Gaussian for a Q-switched ruby laser pulse) Sorokin *et al.* [8] obtained

numerical solutions to the coupled rate equations (7) and (8), using parameters appropriate for their dye-laser experiments. The computer plots strongly resembled the observed pulse characteristics. In particular, the computer solutions indicated 1) that for higher mirror reflectivities (or larger t_c) the initial peak is either less prominent or absent; 2) that in the case when an initial spike is seen the initial peak becomes less sharp and smaller in amplitude (e.g., becomes a small step) as the pumping level is increased; and 3) that in a certain range of pumping levels the time variation of the pulse subsequent to the initial peak is similar to that of the pumping pulse.

We have also obtained computer solutions for the case of our N_2 laser-pumped dye lasers. Assuming a trapezoidal excitation pulse [see Fig. 1(a)] and using parameters of our experiments, we have found essentially the same qualitative behavior for the initial spikes. Our computer solutions are to be described in Section IV where the initial spike is shown to be a special case of the more well-known phenomenon of damped relaxation oscillations.

Note that a close comparison will show that the results of the small-signal analysis are well consistent with the computer solutions for the initial spike case.

D. Comparisons and Discussions

The results of the theoretical considerations previously described can explain a number of experimental observations. 1) The more lossy cavity (higher output coupling) [8] and the shorter cavity length [9] favor the appearance of a more distinct initial peak because of shorter t_c. 2) The absence of the initial spike in the polymethine dye lasers reported in [9] is due to the small values of the fluorescence lifetime. 3) The absence of the initial spike in the DTTC iodide laser reported in [8] can also be explained as due to a small τ/t_c ratio. Not only does DTTC iodide, also a polymethine dye, have a shorter τ, but also the length of the cavity used (22 cm) was much larger than that (5 cm) used for the CAP dye laser, with mirror reflectivities being about the same. 4) Our experimental observations of the initial spike in a N_2 laser-pumped dye laser, as shown in Fig. 1(b) and (c), agree very well with the computer results. That is, in the range when an initial spike is observed, the spike becomes less distinct and smaller in amplitude as the pumping power is increased. 5) For most dye lasers t_c is usually of the same order as τ in the nanosecond range; hence, spiking or nonspiking are observed depending upon the laser parameters. In solid-state lasers τ is usually (microsecond or millisecond) much larger than t_c; hence, strong spiking behavior is often seen. An exceptional case is the $CaF_2:Sm^{2+}$ laser [3], in which the spiking was not observed. This is probably also due to its shorter excited-state lifetime ($\tau \approx 1\,\mu s$) as compared with the large value of t_c for the very high mirror reflectivities used.

Thus it is seen that the physical picture as well as the conditions of the initial spike could be well described by the small-signal analysis, which is in turn consistent with the computer results for the case of the initial spike. For the studies of damped, strongly modulated relaxation oscillations, however, the small-signal approximation is not applicable and computer solutions have to be used.

IV. Relaxation Oscillations in Dye Lasers

A. Experimental

We have observed regular, damped relaxation oscillations in a N_2 laser-pumped dye laser. The N_2 laser pulse (~10 ns, 100 kW, 100 pulses per second (pps), λ = 337 nm) is focused with a quartz cylindrical lens (f = 7.5 cm) in a standard transverse pumping geometry. Different dye-cell lengths and cavity spacings are used. For cavity reflectors we used various combinations of dielectric mirrors, uncoated cell windows, and diffraction gratings. For clear observation of damped relaxation oscillations a photon-cavity decay time t_c much shorter than the dye-fluorescence lifetime τ is needed. This is easily obtained in the N_2 laser-pumped dye lasers where short cavity length and high output coupling (cavity loss) can be conveniently used.

For detection of the laser pulse-time characteristics a Korad KD-1 vacuum photodiode and a Tektronix 7904 oscilloscope are used. The system response time is ~800 ps.

In the following we use the experimental results from 7D4MC (7-diethylamino-4-methylcoumarin) and rhodamine 6G dye lasers as our examples. Qualitatively similar results have also been obtained from several other dyes in the near UV and the visible region. The concentration of the dye solutions used was in the 5×10^{-3}-5×10^{-4}-M range.

Fig. 1(b)-(g) show typical pulse developments observed from a 7D4MC dye laser (1-cm dye cell with uncoated windows aligned; $t_c \sim 50$ ps) as the N_2 laser-pumping power is decreased from high values to low values. The level of pumping can be varied either by changing the N_2 laser power-supply discharge voltage, or by inserting UV absorbing attenuators before the lens. The N_2 laser pulses from AVCO C950 systems are approximately trapezoidal, typically as shown in Fig. 1(a). Fig. 1(b) and (c) show that, when the pumping level is much higher than threshold, the dye laser pulse displays roughly the time variation of that of the N_2 laser pulse, though shortened by the intensity dependence. An initial peak of much faster rise time is seen; and, as previously mentioned, the initial peak is sharp and large, or is less distinct and small in amplitude, depending on the pumping level. As the level of pumping is decreased enough the damped relaxation oscillations begin to appear, as shown in Fig. 1(d)-(g). The number of oscillations is reduced when the pumping power is decreased; eventually only a single spike remains. This functional dependence on the pumping power of the damped relaxation oscillations, as well as other experimental observations to be described in the following, will be shown to have excellent qualitative agreement with computer solutions pertaining to our experimental conditions.

Fig. 2(a)-(c) are the damped relaxation oscillations observed in a rhodamine 6G dye laser with $t_c \sim 60$ ps (1-cm dye cell, ~1.3-cm-long cavity formed by a diffraction grating and one uncoated cell window). The general characteristics are almost identical to those of the 7D4MC dye laser. Similar damped re-

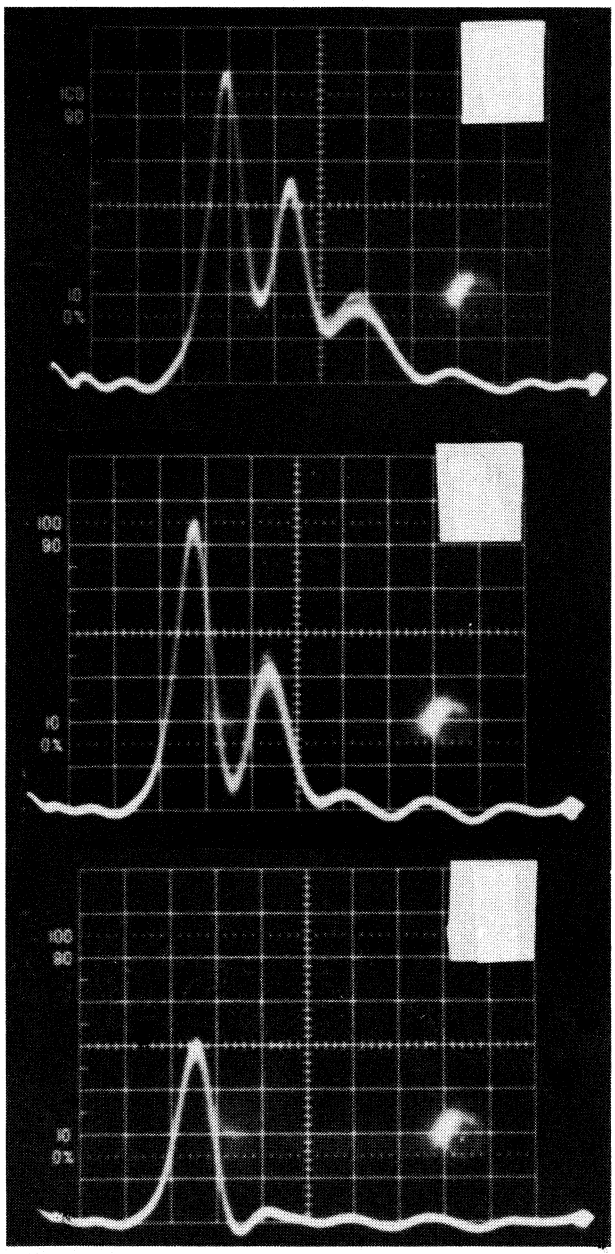

Fig. 2. (a)-(c): Damped relaxation oscillations observed in a rhodamine 6G dye laser ($t_c \sim 60$ ps) as a function of decreasing pump power. Time scale: 1 ns/cm.

laxation oscillations are observed in the following dyes (for $t_c \sim 50$ ps): rhodamine B, fluorescein disodium salt, coumarin 120, butyl-PBD, and Pilot Chemical Co.'s dye #386. We have also noticed that, for UV dyes which have shorter excited-state lifetimes [11], the oscillation peaks are often less regular or less distinct. Nevertheless, from these experimental observations it can be stated that damped relaxation oscillations is a general transient behavior readily observed in N_2 laser-pumped dye lasers with short t_c. This provides a new, convenient laser system to study the basic transient interaction between the excess population inversion and the cavity photons, and to compare it with that in solid-state lasers.

B. Computer Analyses

Our experimental conditions differ from those of [8], primarily in that we have a much shorter cavity length and much lower cavity reflectivities. Secondly, the N_2 laser pulse in our case is more of a trapezoidal than a Gaussian time variation, although this turns out to be of minor significance for the observation of damped relaxation oscillations, as our computer results show.

In our computer analyses the notations of [8] are used: $x = t/t_c$ is the normalized time; $y_1(x)$ is the normalized photon quanta ($y_1(0) = 10^{-7}$ assumed); $y_2(x)$ is the normalized population inversion ($y_2(0) = 0$); α is the level of pumping above threshold ($\alpha = 1$ at threshold); $\beta = \tau/t_c$ is the ratio of fluorescence lifetime over photon-cavity decay time; and γ is a measure of the pumping pulse duration normalized to t_c. Because of the much smaller values of t_c in our dye lasers the parameters β and γ of our computer solutions are much larger than those of [8]. We have assumed three different excitation pulses: Gaussian, square wave, and trapezoidal, of comparable full width at half maximum (FWHM) pulsewidths. Although the rise time of the population inversion ($y_2(x)$ or $n(t)$) is dependent on the pumping pulse waveform, as is expected from the rate equation (7), the general characteristics of the photon intensity ($y_1(x)$ or $q(t)$) in the region of damped, strongly modulated relaxation oscillations are not appreciably different for the three excitations assumed.

Using a GE Mark III time-sharing system and the mathematical subroutine RKPB/DRKPB (Runge-Kutta method) for solving coupled differential equations, we obtained computer plots typically as shown in Figs. 3 and 4. From our computer plots using various values of t_c, α, β, and γ, the results of our computer analyses can be summarized as follows.

1) The initial spike is a special case of damped relaxation oscillations.

2) In the case when relaxation oscillations are present, larger α (higher pumping level) increases the number of oscillations and decreases the spacings between oscillation peaks, eventually leading to the case of the initial spike.

3) Although each "spike" in the damped relaxation oscillations has a different duration (increasing with time and decreasing with α), which is also smaller than the spike spacing, there is indeed a fairly constant (slightly decreasing with time) spacing between peaks which can be designated as the period of oscillation.

4) The damping of the well-defined relaxation oscillations, such as shown in Figs. 3 and 4, can be roughly approximated by an exponential decay. For example, the semilog plot for the oscillation peaks of Fig. 3(h) is roughly a straight line from which $t_d \approx 1.3$ ns is obtained.

5) Smaller values of t_c (corresponding to larger values of β and γ) favor the development of more distinct relaxation-oscillation peaks.

C. Comparisons with Experiments and Discussions

There is excellent qualitative agreement between our experimental observations and the results of the computer analyses previously summarized. Notably, the functional dependence of the relaxation oscillations on the pumping power is clearly observed (as Figs. 1 and 2 indicate), the number of oscillations is reduced, and the spacing between oscillation peaks increased as the level of pumping is gradually decreased. Furthermore, a close examination of these figures shows that indeed each spike in the damped relaxation oscillations has a different

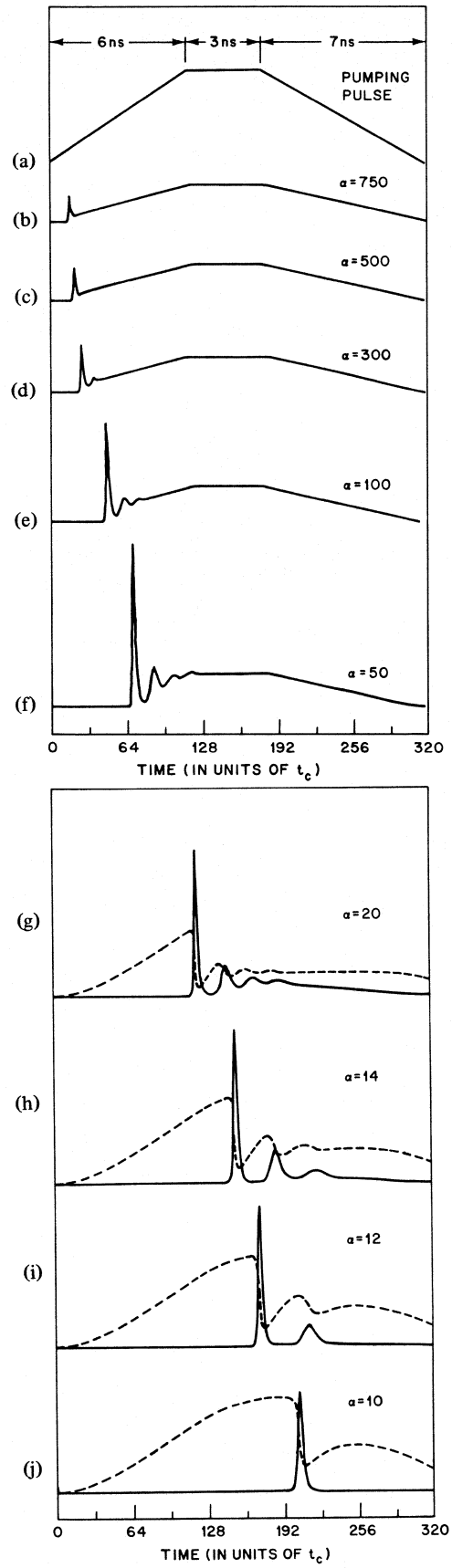

Fig. 3. Computer plots of the solutions of coupled rate equations. t_c = 50 ps, β = 40 (τ = 2 ns), and γ = 1 ns/t_c = 20. Parameter α (level of pumping above threshold) is varied from (b) to (j) as indicated. (a) The approximated N_2 laser pumping pulse. The solid curve represents normalized photon intensity; the dashed curve corresponds to normalized inversion.

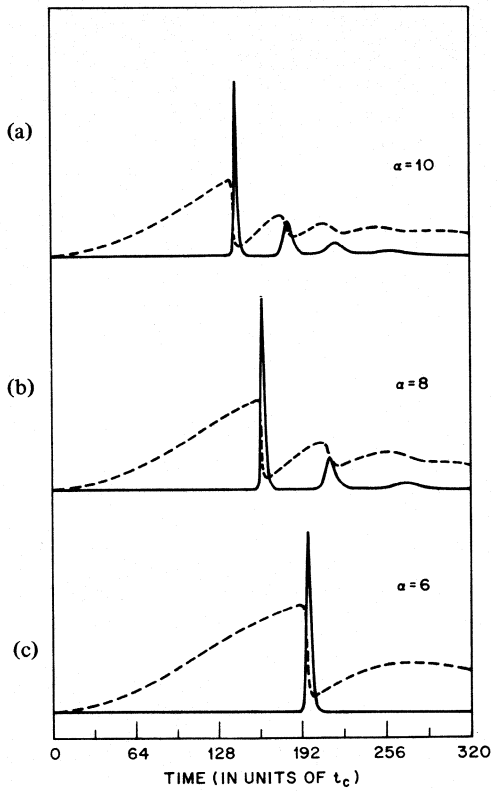

Fig. 4. Same as Fig. 3(h)–(j), except β = 120 (τ = 6 ns) and different α as indicated.

duration which increases with the oscillation number and decreases with pumping level, and that there is a fairly constant oscillation period which is larger than the duration of the spikes. It is also found that semilog plots of the oscillation peaks versus time, of the damped relaxation oscillations, such as shown in Fig. 1(e) and Fig. 2(a), do not deviate much from straight lines, so that the damping for these cases is approximately exponential. Finally, concerning t_c, it is observed that, in a 7D4MC dye laser for which t_c is increased to about 300 ps (a 4-cm dye cell, with an external 99-percent reflector aligned with one uncoated cell window) we found that, although initial spikes can clearly be seen, no well-defined damped relaxation oscillations developed. Undoubtedly, the required ratio of τ/t_c for the observation of regular damped relaxation oscillations is larger than that for the appearance of an initial spike, which is consistent with our computer analyses.

Thus we have shown that there is excellent qualitative agreement between theoretical considerations and experimental results. Quantitatively, the agreement is satisfactory though not as impressive. For example, from Fig. 3(h) the approximated decay-time constant $t_d \simeq 1.3$ ns; the corresponding decay-time constant from Fig. 1(e) is $\simeq 2.3$ ns. The spacing between oscillation peaks is 1.6 ns from the computer plot, which compares well with the experimental result of 1.5 ns. In general, the experimentally observed damping rate is slower, and the obtained spike durations larger than would be predicted from the computer solutions using the appropriate parameters.

Note that in flashlamp-pumped solid-state lasers the parameters γ (pumping pulse duration) and β (fluorescence lifetime τ over t_c) are usually much larger than in the case of dye lasers. As a consequence, many periods of distinct relaxation oscillations, with a slow damping rate (of the order of τ), are ob-

served in contrast to just a few cycles observed in our experiments. Except for this time-scale difference the general behavior of the damped relaxation oscillations should be the same for both laser systems. It is particularly interesting to compare the observations in a four-level, $CaF_2:U^{+3}$ laser [3] with ours in dye lasers. In this flashlamp-pumped solid-state laser it was observed that, when the pump power was reduced in a range close to threshold, the oscillatory output showed a gradual decrease in the number of spikes and an increase in the spike spacing. Such behavior is qualitatively identical to our experimental observations, which have been shown to agree well with theoretical expectations. It may thus be stated that with appropriately selected cavity and pumping parameters the phenomenon of damped relaxation oscillations, with initial spiking as a special case, is a general one observable in all lasers which can be described by the coupled rate equations [1], [2], [5]. This is so simply because it is a consequence of the transient interaction between population inversions and cavity photons, a consequence of the very process of the stimulated emission in lasers.

V. Short-Pulse Generation by Controlled Transients

The previous experimental and theoretical studies of the transient response of dye lasers show that it is possible to generate dye-laser pulses much shorter than the pumping pulse by careful control of dye-laser and pumping parameters. Normally, the laser-pumped dye lasers are operated with large values of t_c and at such a high pumping level that dye-laser pulses largely similar to those of the pumping pulse are obtained. From Figs. 1-4 it is obvious that one can choose a small t_c dye-laser cavity and obtain a single spike of a duration considerably shorter than that of the pumping pulse by carefully controlling the pumping power. Computer plots (Figs. 5 and 6) also show that similar short-duration single pulses can be obtained with a Gaussian excitation pulse; therefore, a Q-switched ruby laser, Nd^{3+} lasers, or their harmonics can similarly be used as the pumping source.

We have applied this general technique of controlled resonator transients to N_2 laser-pumped dye lasers and obtained high repetition-rate subnanosecond pulses tunable in the near UV and the visible region of the spectrum. The detail of the experiment is described elsewhere [12]. We would like to mention that while computer analyses indicate a single pulse of less than 250 ps should be obtained in our N_2 laser-pumped dye lasers [Figs. 3(j) or 4(c)] our experimental results are in the 600–900-ps range. Just how short a pulse can one obtain depends on the particular parameters; computer solutions show that the pulse obtainable in general is at least greater than a few t_c. Since a dye laser is a high-gain medium for which very small values of t_c can be used, one can in principle expect to obtain pulses less than 100 ps with carefully chosen parameters. Tunable pulses of controlled duration in the nanosecond range can also be obtained with the same technique.[1]

[1] An interesting finding is that in 1966 D. Röss proposed a method for "giant pulse shortening" for solid-state lasers, which turns out to be a special case of our general technique. See D. Röss, "Giant pulse shortening by resonator transients," *J. Appl. Phys.*, vol. 37, pp. 2004–2006, Apr. 1966.

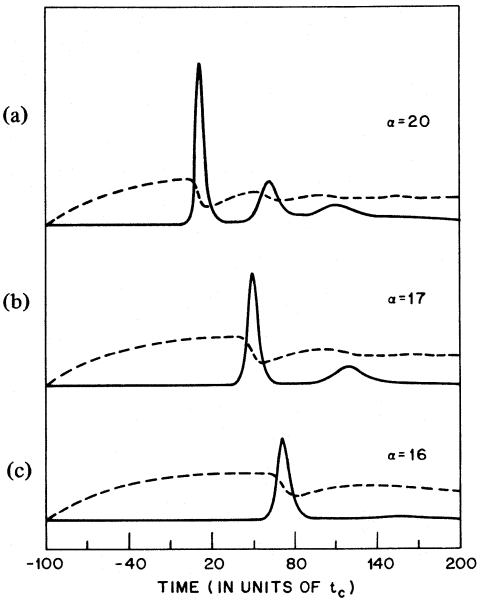

Fig. 5. Computer plots assuming a Gaussian pumping pulse of 20-ns duration (FWHM). $t_c = 50$ ps, $\beta = 40$.

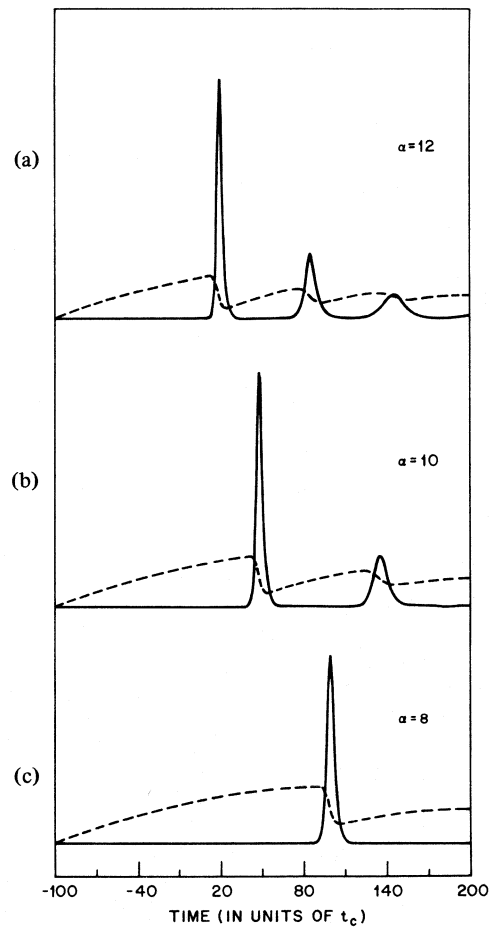

Fig. 6. Same as Fig. 5, except $\beta = 120$ and different α as indicated.

VI. Conclusion

In this paper we have studied and compared, experimentally and theoretically, the phenomena of initial spikes and regular damped relaxation oscillations in laser-pumped dye lasers. We have shown excellent qualitative agreement between experimental observations and theoretical considerations. We have

also pointed out the idea of controlled resonator transients as a general technique for short-pulse generation.

ACKNOWLEDGMENT

The author wishes to thank C. V. Shank for helpful discussions and W. J. Tomlinson for assistance with the time-sharing system. He also wishes to thank A. Ashkin for reading and commenting on the manuscript.

REFERENCES

[1] G. Birnbaum, *Optical Masers*. New York: Academic, 1964, pp. 51–56 and pp. 191–195.
[2] a) V. Evtuhov and J. K. Neeland, "Pulsed ruby lasers," in *Lasers*, A. K. Levine, Ed. New York: Dekker, 1966, pp. 81–109.
b) L. F. Johnson, "Optically pumped pulsed crystal lasers other than ruby," in *Lasers*, A. K. Levine, Ed. New York: Dekker, 1966, pp. 174–176.
[3] P. P. Sorokin and M. J. Stevenson, "Stimulated emission from $CaF_2:U^{+3}$ and $CaF_2:Sm^{+2}$," in *Advances in Quantum Electronics*, J. R. Singer, Ed. New York: Columbia Univ. Press, 1961, pp. 65–76.
[4] H. Statz and G. deMars, "Transients and oscillation pulses in masers," in *Quantum Electronics*, C. H. Townes, Ed. New York: Columbia Univ. Press, 1960, pp. 531–537.
[5] C. L. Tang, "On maser rate equations and transient oscillations," *J. Appl. Phys.*, vol. 34, pp. 2935–2940, Oct. 1963.
[6] R. Dunsmuir, "Theory of relaxation oscillations in optical masers," *J. Electron. Contr.*, vol. 10, pp. 453–458, June 1961.
[7] L. W. Casperson and A. Yariv, "The time behavior and spectra of relaxation oscillations in a high-gain laser," *IEEE J. Quantum Electron. (Part I of Two Parts)*, vol. QE-8, pp. 69–73, Feb. 1972.
[8] P. P. Sorokin, J. R. Lankard, E. C. Hammond, and V. L. Moruzzi, "Laser-pumped stimulated emission from organic dyes: Experimental studies and analytical comparisons," *IBM J. Res. Develop.*, vol. 11, pp. 130–147, Mar. 1967.
[9] Y. Miyazoe and M. Maeda, "On the spiking phenomenon in organic dye lasers," *IEEE J. Quantum Electron.* (Corresp.), vol. QE-7, pp. 36–37, Jan. 1971.
[10] F. P. Schäfer, "Principles of dye laser operation," in *Dye Lasers*, F. P. Schäfer, Ed. New York: Springer-Verlag, 1973, pp. 1–90.
[11] I. B. Berlman, Ed., *Handbook of Fluorescence Spectra of Aromatic Molecules*, 2nd ed. New York: Academic, 1971.
[12] C. Lin and C. V. Shank, "Subnanosecond tunable dye laser pulse generation by controlled resonator transients," *Appl. Phys. Lett.*, vol. 26, pp. 389–391, Apr. 1975.

10.6-μm Waveguide Laser Power Amplifier

MARVIN B. KLEIN AND RICHARD L. ABRAMS, MEMBER, IEEE

Abstract—**The results of a study intended to characterize the properties of CW 10.6-μm waveguide power amplifiers are reported. The analysis considers both single- and double-pass devices, and includes the effects of gain narrowing and power broadening. Experiments on a 1.65-mm-bore device with an active length of 77 cm have been performed. Gains as high as 17 dB/m have been measured at room temperature.**

I. INTRODUCTION

THE DEVELOPMENT of the waveguide gas laser concept [1]–[3] and its extension to small high-pressure sealed-off waveguide CO_2 lasers [4] has led to the consideration of other CO_2 laser devices in capillary bores. Among the devices of interest are tunable lasers for use as Doppler tracking local oscillators [5] and high-gain wide-band power amplifiers for laser radar systems. Conventional CO_2 laser devices are inadequate for these applications because their gain bandwidth is limited to a Doppler broadened value of $\approx$50 MHz. However, in a waveguide device, the high operating pressure ($\approx$150 torr) results in a pressure-broadened gain linewidth in excess of 750 MHz. Furthermore, the efficient guiding properties of waveguide devices insure low optical losses for long active lengths.

Manuscript received February 10, 1975; revised March 31, 1975. The research reported in this paper was sponsored by the Advanced Research Projects Agency, monitored by the Office of Naval Research.

The authors are with Hughes Research Laboratories, Malibu, Calif. 90265.

In this paper we report the results of a study intended to characterize the properties of wide-band high-power CW laser amplifiers. This study includes the analysis of amplifier performance in terms of independent design parameters and experiments on a prototype 1-m device. The results obtained permit the confident design of larger devices to meet specific performance goals.

II. WAVEGUIDE AMPLIFIER THEORY

A. Basic Equations

In this section we will derive expressions relating independent amplifier parameters such as overall length, small-signal gain coefficient, and linewidth to system design requirements such as overall gain, output power, and output linewidth. The solutions will include the effects of distributed loss as well as gain saturation. The application of the theory to a double-pass configuration also will be considered.

For a monochromatic input beam at frequency ν, the frequency-dependent saturation of small-signal gain in a homogeneously broadened amplifier is described by

$$\alpha(\nu) = \frac{\alpha_0}{\left[1 + \frac{I(\nu)}{I_s(\nu)}\right][1 + \delta^2]}. \tag{1}$$

In this equation $\alpha(\nu)$ is the saturated gain at frequency ν, α_0 is the small-signal gain at line center, $I(\nu)$ and $I_s(\nu)$ are the beam intensity and saturation intensity at frequency ν, and δ

is the normalized frequency detuning given by

$$\delta = \frac{2(\nu - \nu_0)}{\Delta\nu} \tag{2}$$

where $\Delta\nu$ is the unsaturated gain linewidth and ν_0 is the line center frequency. The saturation intensity $I_s(\nu)$ may be related to the saturation intensity at line center by

$$I_s(\nu) = (1 + \delta^2) I_s(\nu_0). \tag{3}$$

Substituting this expression into (1) and writing $\gamma(\nu) = I(\nu)/I_s(\nu_0)$, we obtain

$$\alpha(\nu) = \frac{\alpha_0}{1 + \delta^2 + \gamma(\nu)}. \tag{4}$$

The incremental gain may be written as

$$\frac{1}{I(\nu)} \frac{dI(\nu)}{dz} = \alpha(\nu) - \beta \tag{5}$$

where β is the distributed loss. Combining (4) and (5) and solving by separation of variables, we obtain

$$\frac{\alpha_0 L}{1 + \delta^2} - \beta L = \ln \frac{\gamma_2(\nu)}{\gamma_1} - \frac{\alpha_0}{\beta(1 + \delta^2)} \cdot \ln \frac{\alpha_0 - \beta(1 + \delta^2) - \beta\gamma_2(\nu)}{\alpha_0 - \beta(1 + \delta^2) - \beta\gamma_1} \tag{6}$$

where γ_1 is the normalized input intensity (assumed constant with frequency), $\gamma_2(\nu)$ is the normalized output intensity, and L is the amplifier length.

For a given set of required amplifier conditions, (6) may be used to study design tradeoffs in small-signal gain, linewidth, and overall length. In the device under study here, the distributed loss is much less than the line center gain coefficient, so that except in the far wings of the gain profile, the relationship $\beta(1 + \delta^2) << \alpha_0$ is satisfied. In this case, (6) reduces to

$$\alpha_0 L = (1 + \delta^2) \ln \frac{\gamma_2(\nu)}{\gamma_1} + [\gamma_2(\nu) - \gamma_1]. \tag{7}$$

For large gains ($\gamma_1 << \gamma_2$) at line center ($\delta = 0$), (7) becomes

$$\gamma_2(\nu_0) = \alpha_0 L - \ln \frac{\gamma_2(\nu_0)}{\gamma_1}. \tag{8}$$

The last term in (8) is related to G, the saturated gain (at line center) in decibels, by

$$G = 4.34 \ln \frac{\gamma_2(\nu_0)}{\gamma_1}. \tag{9}$$

Combining (7)-(9) and solving for δ, we obtain

$$\delta = \frac{2(\nu - \nu_0)}{\Delta\nu} = \left(\frac{\gamma_2(\nu_0) - \gamma_2(\nu) - \ln \dfrac{\gamma_2(\nu)}{\gamma_2(\nu_0)}}{\ln \dfrac{\gamma_2(\nu)}{\gamma_2(\nu_0)} + 0.23G} \right)^{1/2}. \tag{10}$$

Equation (10) may be used to obtain the frequency dependence of $\gamma_2(\nu)$ for various values of the system gain G and the output intensity at line center $\gamma_2(\nu_0)$. The variation of the half-power linewidth $\Delta\nu_{3\ \mathrm{dB}}$ of $\gamma_2(\nu)$ may be obtained (for large gain) from (10) using $\gamma_2(\nu) = 1/2\ \gamma_2(\nu_0)$. Thus we find

$$\Delta\nu_{3\ \mathrm{dB}} = \Delta\nu \left(\frac{\gamma_2(\nu_0)/2 + \ln 2}{0.23G - \ln 2} \right)^{1/2}. \tag{11}$$

The effects of gain saturation on the output linewidth are clearly evident in (11). At low levels of saturation ($\gamma_2(\nu_0) << 1$), the output linewidth is reduced (gain narrowing) by a factor approximately proportional to $G^{-1/2}$, or $(\alpha_0 L)^{-1/2}$. As saturation becomes important, the output is broadened again (power broadening), and the linewidth may even exceed the small-signal gain linewidth $\Delta\nu$. This variation is displayed in Fig. 1, which is a plot of the normalized output linewidth as a function of the normalized line center intensity for various values of the overall gain. In Fig. 2 we have also plotted complete line profiles for several typical sets of amplifier parameters (using (10)). Power broadening is effective throughout the line profile. This is not true when distributed loss is present; in this case, the amplifier line shape is truncated at the frequencies where the unsaturated gain equals the distributed loss.

B. Double-Pass Amplifier

The extension of the above approach to a double-pass configuration is straightforward. We consider the experimental arrangement shown in Fig. 3. The intensities of waves traveling the $+z$ and $-z$ directions are now labeled $I_+(\nu)$ and $I_-(\nu)$, respectively. The gain saturation equation may now be written as

$$\alpha(\nu) = \frac{\alpha_0}{1 + \delta^2 + \dfrac{I_+(\nu) + I_-(\nu)}{I_s(\nu_0)}}. \tag{12}$$

By definition, the incremental gain may also be written as

$$\alpha(\nu) = \frac{1}{I_+} \frac{dI_+}{dz} \tag{13}$$

$$\alpha(\nu) = \frac{1}{I_-} \frac{dI_-}{dz}. \tag{14}$$

If we now substitute $\gamma_+(\nu) = I_+(\nu)/I_s(\nu_0)$ and $\gamma_-(\nu) = I_-(\nu)/I_s(\nu_0)$ into (13) and (14) and then combine the two equations, we obtain

$$\frac{d\gamma_+(\nu)}{\gamma_+(\nu)} = -\frac{d\gamma_-(\nu)}{\gamma_-(\nu)}. \tag{15}$$

The solution to this equation is

$$\gamma_+(\nu)\gamma_-(\nu) = C \tag{16}$$

where C is a constant. Combining (12), (13), and (16), we obtain

$$\frac{1}{\gamma_+(\nu)} \frac{d\gamma_+(\nu)}{dz} = \frac{\alpha_0}{1 + \delta^2 + \gamma_+(\nu) + \dfrac{C}{\gamma_+(\nu)}}. \tag{17}$$

By separation of variables and integration from 0 to L, we

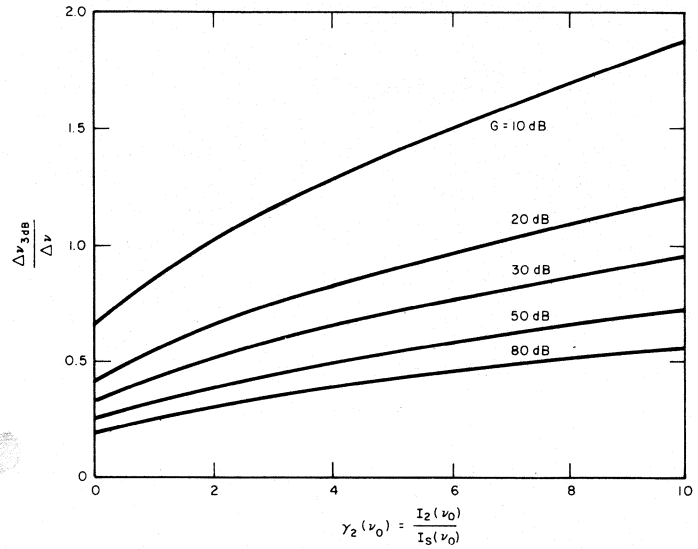

Fig. 1. Normalized output linewidth versus normalized output intensity for several values of overall gain.

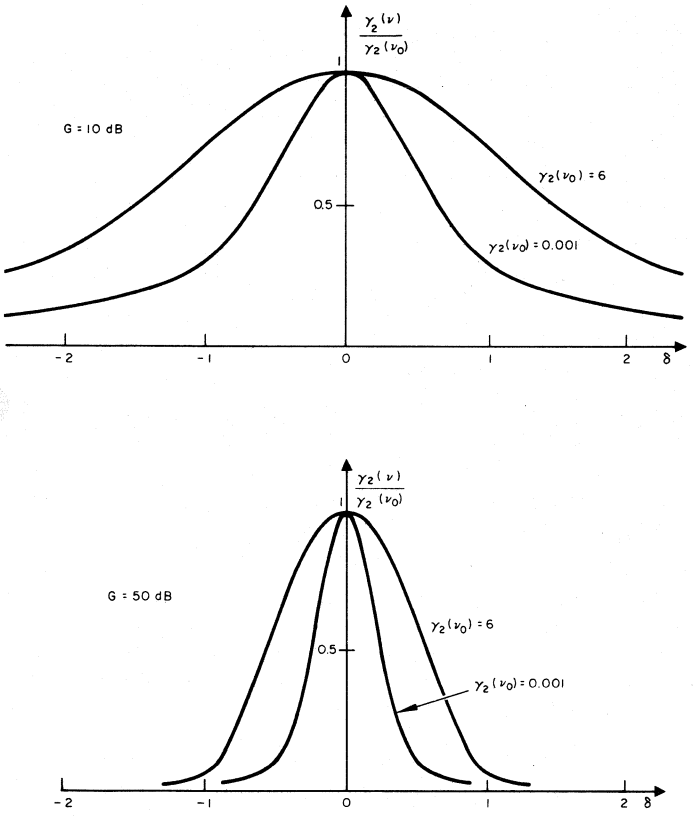

Fig. 2. Normalized line profiles for $G = 10$ dB (upper) and $G = 50$ dB (lower).

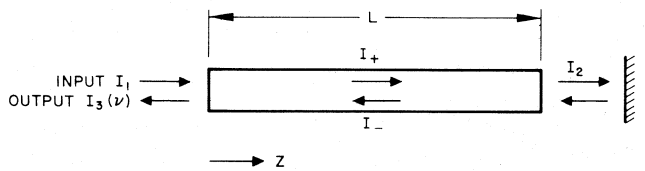

Fig. 3. Double-pass amplifier configuration.

obtain

$$(1+\delta^2)\ln\frac{\gamma_2(\nu)}{\gamma_1}+[\gamma_2(\nu)-\gamma_1]+\frac{C}{\gamma_1}-\frac{C}{\gamma_2(\nu)}=\alpha_0 L. \quad (18)$$

To eliminate γ_2, we make use of (16), applied at each end of the amplifier:

$$\gamma_1\gamma_3(\nu)=[\gamma_2(\nu)]^2=C \quad (19)$$

where γ_1, $\gamma_2(\nu)$, and $\gamma_3(\nu)$ are defined in Fig. 3. By combining (18) and (19) we obtain

$$(1+\delta^2)\ln\frac{\gamma_3(\nu)}{\gamma_1}+2[\gamma_3(\nu)-\gamma_1]=2\alpha_0 L. \quad (20)$$

By comparison, a single pass through the length L yields the relation (see (8))

$$(1+\delta^2)\ln\frac{\gamma_3(\nu)}{\gamma_1}+[\gamma_3(\nu)-\gamma_1]=\alpha_0 L. \quad (21)$$

A more convenient comparison between the single-pass and double-pass configurations may be obtained (using the preceding equations) by writing expressions for the device length required to produce a given line center output $\gamma_3(\nu_0)$ and saturated gain G, for a given incremental gain α_0 (we also assume $\gamma_3 \gg \gamma_1$).

$$\text{Single Pass:}\quad L=\frac{1}{\alpha_0}[\gamma_3(\nu_0)+0.23G] \quad (22)$$

$$\text{Double Pass:}\quad L=\frac{1}{\alpha_0}\left[\gamma_3(\nu_0)+\frac{0.23G}{2}\right]. \quad (23)$$

Thus the potential length decrease in going to a double-pass configuration (assuming 100-percent reflectivity at the end mirror) can be as much as 50 percent, depending on the relative magnitudes of $\gamma_3(\nu_0)$ and G.

Another parameter of interest is the half-power bandwidth; this may be obtained from (20) by setting $\gamma_3(\nu)=\gamma_3(\nu_0)/2$ with the result

$$\Delta\nu_{3\,dB}=\Delta\nu\left(\frac{\gamma_3(\nu_0)+\ln 2}{0.23G-\ln 2}\right)^{1/2}. \quad (24)$$

By comparison, a single pass through the same amplifier yields

$$\Delta\nu_{3\,dB}=\Delta\nu\left(\frac{\gamma_3(\nu_0)/2+\ln 2}{0.23G-\ln 2}\right)^{1/2}. \quad (25)$$

Thus in addition to the increased small-signal gain, the double-pass configuration yields a considerably larger linewidth, due to the increased saturation produced at the input (and output) end of the device.

C. Amplifier Design Procedure

In order to design a laser amplifier with given performance characteristics, we require knowledge of the small-signal gain coefficient α_0, the line center saturation intensity $I_s(\nu_0)$, and the linewidth $\Delta\nu$, as functions of pressure, current, and tube diameter. By making use of these parameters in the analytical relationships derived in the previous section, we can calculate the minimum active device length required to achieve given design goals. This calculation can be repeated for a

variety of experimental conditions, so that optimum conditions requiring the shortest amplifier length may be found. This approach will be followed in the device design procedure given in Section VII.

III. Test-Bed Description

In designing a waveguide amplifier of 1-m nominal length, several problems are met. As a first consideration, it should be noted that ceramic sections with 1- to 2-mm drilled holes cannot be obtained in lengths greater than 12 to 15 cm. Thus in our device we have made use of a segmented design which incorporates seven separate ceramic (BeO) sections and connecting Kovar flanges. Each section is 12.5 cm long, with a 1.65-mm bore. The use of separate ceramic segments suggests a parallel connection of electrical power and gas flow, as represented schematically in Fig. 4 and shown in more detail in Fig. 5. The electrical connections are arranged so that all of the connecting flanges are grounded (for safety reasons) and the center electrodes serve as cathodes (to eliminate sputtering near the windows at each end). The 2-mm spacing between sections is large enough to allow adequate gas flow, but small enough to maintain a low theoretical value of optical loss (0.09 percent). The individual segments are attached to separate heat sink mounts which are in turn fastened to an I-beam support. Each discharge region is 5.5 cm in length so that the overall length of the active region (with 14 discharges) is 77 cm.

An important consideration in the amplifier construction is

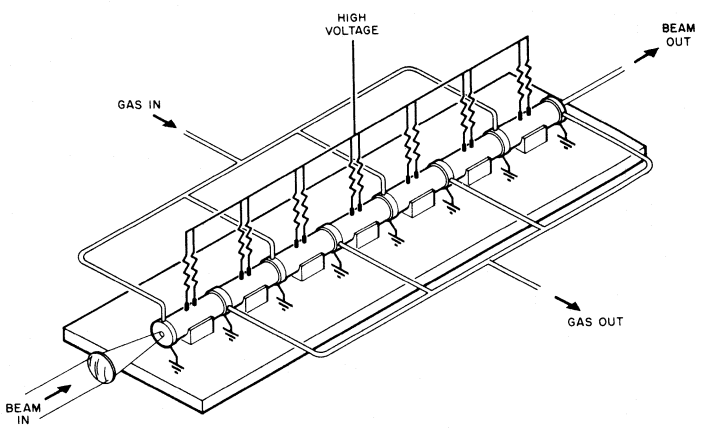

Fig. 4. Amplifier assembly.

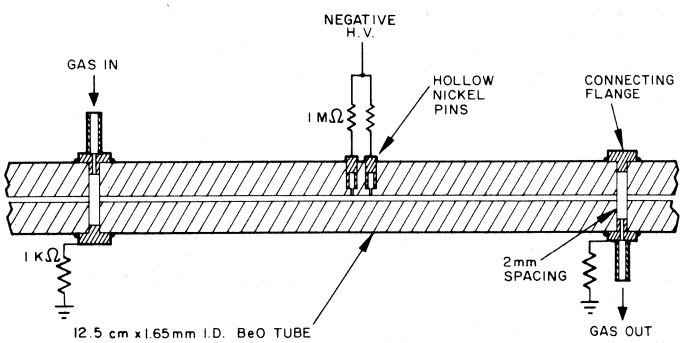

Fig. 5. Detail of electrical and gas flow connections.

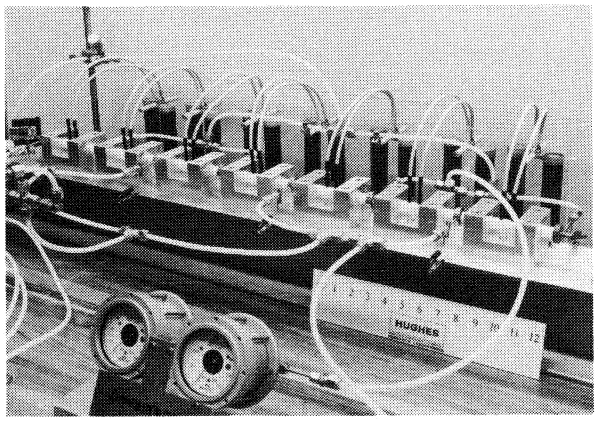

Fig. 6. Completed amplifier.

the mechanical alignment of the separate ceramic sections. For the device under consideration here, two optical techniques were used for achieving optimum alignment. First, an unfocused 6328-Å laser beam was passed down the amplifier bore. As each ceramic section was added, its lateral position at the new joint was adjusted for minimum scattering of the He-Ne beam at the joint (as observed in a darkened room). The angular alignment of each section was optimized by minimizing the scattered light within the bore itself, and by optimizing the symmetry of the output beam. After each section was aligned in this fashion, it was fastened securely to the I-beam.

After all sections had been aligned and fastened in the above manner, the overall transmission at 10.6 μm was measured. This was accomplished by first passing the beam from a 1-W CO_2 laser through a telescope adjusted to provide optimum coupling into the low loss EH_{11} waveguide mode. After several alignment attempts, we were able to achieve an overall 10.6-μm transmission of 92 percent. The theoretical transmission, accounting for both coupling and guiding losses, is approximately 97 percent. We believe that the additional loss in this case is due to residual misalignment at the joints between sections. As the final step in the assembly, the connecting flanges were epoxied to the ceramic; the Brewster window material was CdTe. A photograph of the completed device is shown in Fig. 6.

IV. Gas Flow Considerations

As discussed earlier, the seven ceramic sections have parallel gas flow connections to minimize the pressure drop across the total device length. A schematic diagram of the gas flow system is given in Fig. 7. Helium, nitrogen, and carbon dioxide in ultra-pure form (99.999-percent purity) are fed from separate tanks through individual flowmeters and needle valves to a mixing manifold, and then into the discharge region. The flow then passes through a throttle valve (for control of the amplifier pressure) and is exhausted through a (Welch 1402) 5.6-ft^3/min mechanical pump.

The gas flowmeters can be connected and calibrated to read mass flow (e.g., torr-liters per second) or volumetric flow (e.g., liters per second). Greater accuracy and ease in calibration is obtained by maintaining the flow tubes at constant pressure

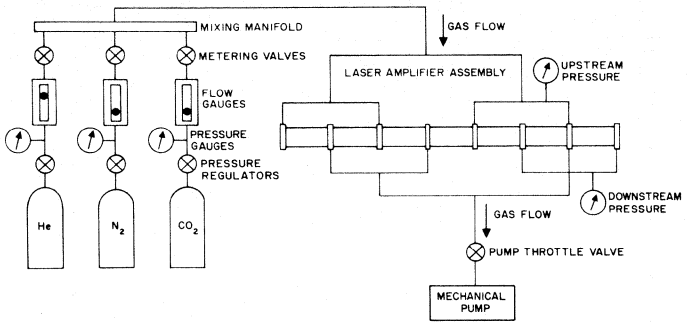

Fig. 7. Schematic diagram of gas flow system.

and regulating the flow with downstream needle valves (as shown in Fig. 7). In this mode of operation the flowmeter reading is proportional to mass flow. For the purpose of relating amplifier parameters to flow rates, the flow is best specified by the number of gas fill changes per second for each separate flow length. This quantity may then be compared directly to the rates of other relevant processes in the discharge. For the geometry of our flow system, we have

$$N = 5.33 \times 10^2 \frac{Q_T}{P_0} \text{ changes/s} \tag{26}$$

where Q_T is the total mass flow in torr-liters per second, and P_0 is the average pressure in torr.

V. Electrical Circuitry

As mentioned earlier, the separate ceramic sections each contain two centrally located hollow nickel cathodes. The Kovar connecting flanges serve as common anodes for adjacent discharges. The high-voltage power supply (with positive ground) provides negative high voltage to the cathodes through separate 1-MΩ ballast resistors. The anodes are connected to ground through separate 1-kΩ resistors. The voltage drop across these resistors is a convenient measure of the discharge current.

Although the high-voltage power supply has an option which provides rapid application of a preset voltage to the 14 amplifier discharges, simultaneous ignition of all discharges is very difficult to achieve except at low pressures, or in helium-rich mixtures. In order to avoid this problem, we inject a high-voltage pulse (60 kV) into the negative high-voltage lead from the dc power supply at the same time that this supply is switched on. The combination of these two fast rising voltage sources produces reliable ignition of all discharges in most cases.

VI. Experimental Results

In this section we report the results of measurements of small-signal gain coefficient and saturation intensity for a variety of experimental conditions. The experimental arrangement for all optical experiments is identical. The source oscillator is a 1-W conventional bore CO_2 laser tuned to line center of the $P(20)$ transition. The output from this laser is focused onto the entrance aperture of the first amplifier section by passing through a telescope adjusted for optimum coupling to the EH_{11} mode. A variable attenuator is also

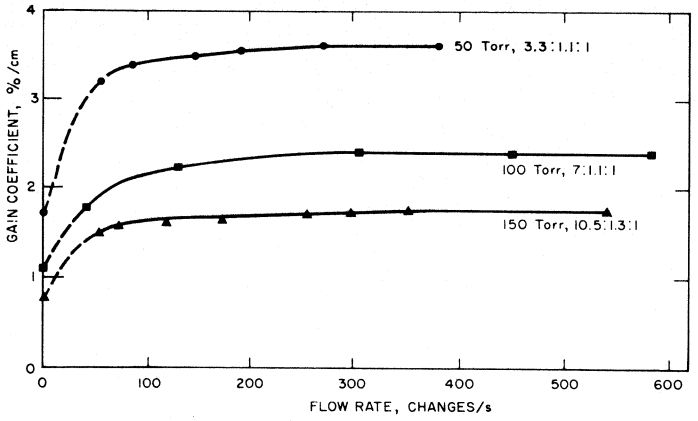

Fig. 8. Gain versus flow rate for 50-, 100-, and 150-torr pressure. The gas mixtures are presented in the ratios He:Ne:CO_2. The discharge current was 3 mA.

provided at the input to the amplifier. A power meter at the amplifier exit is used to measure transmitted power. In order to obtain the input power to the amplifier, the transmitted power through the passive amplifier (with 8-percent transmission loss) was multiplied by 1.08. The amplifier gain was then given by the ratio of the transmitted power through the active amplifier divided by input power as given above. In general, our gain measurements were performed using a constant input power of 100 mW in the expectation that saturation effects would be unimportant at this power level. Our subsequent measurements of saturation intensity (presented in a later section) indicate that this assumption is accurate at 150 torr with small errors being introduced at lower pressures. However, even at 50 torr, the errors introduced in the measured gain coefficient are less than 10 percent.

During the course of our measurements, care was taken to ensure that spontaneous emission noise and absorption by the cold gas were negligible factors. We also examined the discharge voltage at various times for signs of high-frequency oscillations and none were observed.

A. Small-Signal Gain versus Flow Rate

Before proceeding with gain measurements as a function of pressure, it is important to know the effects of gas flow on the gain. We have measured gain versus gas flow (measured in changes per second) at three different pressures; the gas mixture at each pressure has been adjusted for maximum gain. The results are shown in Fig. 8. The dashed line for each plot is an extension of the measured data to the sealed-off measured values of Abrams and Bridges [4]. At each pressure the gain rises rapidly, and then approaches a constant value for flow rates greater than ~200 changes/s. All subsequent gain measurements have been performed at flow rates of this magnitude.

B. Small-Signal Gain versus Pressure

In Fig. 9 we show values of gain measured as a function of pressure for gas mixtures optimized at 50, 100, and 150 torr. The flow rate for all measurements was kept constant at 200 changes/s. For reference purposes the gain is given in %/cm,

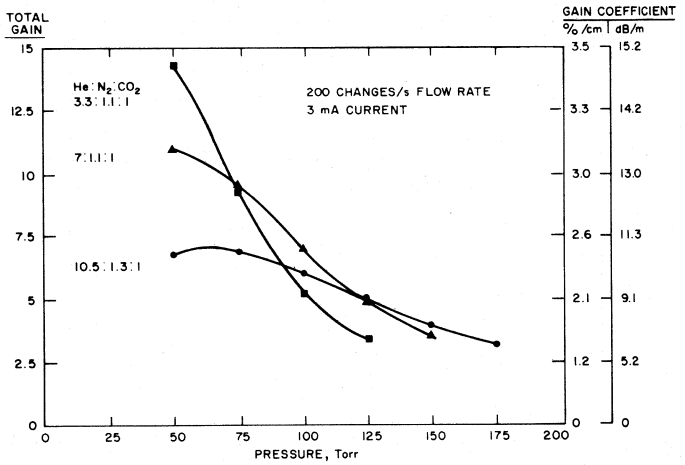

Fig. 9. Gain versus pressure at constant flow rate (200 changes/s) and current (3 mA), for mixtures shown.

dB/m, and overall gain for the device under investigation. The displayed data were taken at 3-mA current. In general, the gain at 2 mA and 4 mA is slightly lower. The data of Fig. 9 do not extend below 50 torr because we were not able to maintain the required flow rate in this range. However, measurements at approximately 120 changes/s yielded an overall gain of 17.5 at 38 torr (in a 3 : 1 : 1 mixture), corresponding to gain coefficients of 3.7%/cm, or 16.1 dB/m.

C. Measurement of Saturation Intensity

Many techniques for measuring the saturation intensity (using both oscillator and amplifier configurations) are available, and we have chosen one which we feel is particularly suitable to our experimental conditions. We make use of the same laser source (tuned to line center) used in the gain measurements, and adjust the attenuator to provide a variable power input in the range 0.1 to 1.0 W. The relation describing the interaction of such a source in the amplifier is given by (7), written explicitly in terms of laser power (with $\delta = 0$)

$$P_2(\nu_0) - P_1(\nu_0) = -P_s(\nu_0) \ln \frac{P_2(\nu_0)}{P_1} + P_s(\nu_0)\alpha_0 L. \qquad (27)$$

Thus, by measuring output power $P_2(\nu_0)$ for a range of input powers $P_1(\nu_0)$ and plotting $P_2(\nu_0) - P_1(\nu_0)$ as a function of $\ln [P_2(\nu_0)/P_1]$, we obtain a straight line with slope $-P_s(\nu_0)$. This technique is applicable for any range of input powers, but is most accurate when the range is large and appreciable saturation is produced.

Using the above technique, we have measured saturation power for five pressures in the range of 50 to 150 torr and for discharge currents of 2, 3, and 4 mA. The gas mixture at each pressure is that which produces maximum gain. For each setting of pressure and current, the data were plotted as described above. A straight line was then fitted (by the method of least squares) to each set of data points. The saturation power was obtained from the slope of each curve, and is plotted as a function of pressure (for each current) in Fig. 10. The saturation intensity may be obtained by dividing the power by πw^2, where w is the e^{-1} intensity radius of the Gaussian beam which best matches [6] the EH_{11} waveguide mode ($w/a = 0.455$).

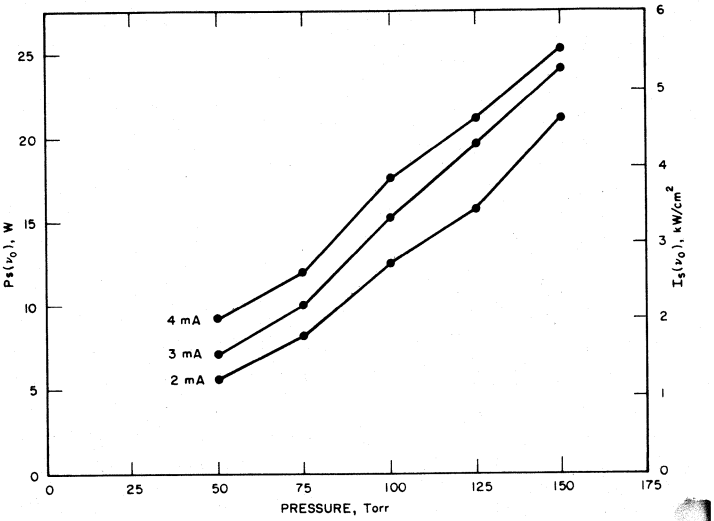

Fig. 10. Saturation power and intensity versus pressure (flow rate = 200 changes/s).

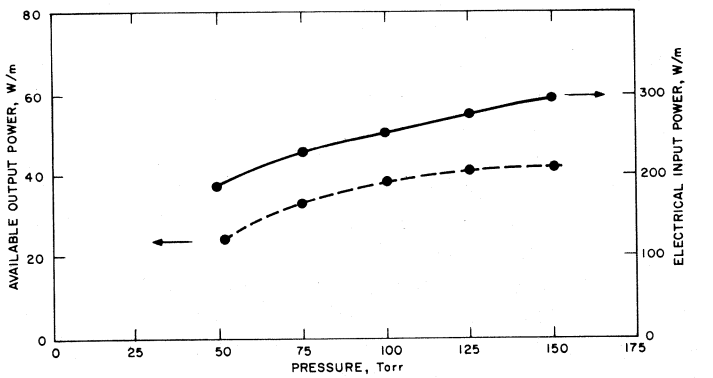

Fig. 11. Available output power and input electrical power versus pressure. Discharge current = 3 mA.

As expected, the saturation intensity increases with pressure (due to molecule-molecule collisions) and with current (due to electron-molecule collisions). The values of this parameter are approximately a factor of 2 lower than the measured values of Abrams and Bridges [4] for a sealed-off oscillator using He-CO_2 mixtures. The reasons for this discrepancy are not well understood; however, it is felt there may be some systematic errors in the previously published data.

In a highly saturated amplifier, one relevant measure of device performance is the power extraction capability (in watts per meter), given by the product of small-signal gain coefficient and the saturation power. In Fig. 11 we plot values of $a_0 P_s(\nu_0)$ as a function of pressure (at 3-mA current) using previously plotted values of gain and saturation power. We have also plotted measured values of electrical input power per unit length for the same condition. It is apparent that power extraction efficiencies as high as 20 percent are possible.

VII. Characterization of Full Scale Device

On the basis of the measurements described in the preceding sections, we are in a position to determine the amplifier length required to meet specific performance requirements. The length is related to other amplifier parameters by

$$\alpha_0 L = \gamma_2(\nu_0) + \ln \frac{\gamma_2(\nu_0)}{\gamma_1}. \tag{28}$$

Solving for L and writing in terms of power instead of intensity, we obtain

$$L = \frac{1}{\alpha_0}\left[\frac{P_2(\nu_0)}{P_s(\nu_0)} + \ln \frac{P_2(\nu_0)}{P_1}\right]. \tag{29}$$

As an example, in Fig. 12 we have made use of the above expression to plot the required length L as a function of line center output power $P_2(\nu_0)$ for three different pressures, using the gain and saturation power data of previous sections. We have assumed a constant 1-W input and a discharge current of 3 mA. The curves for 2 and 4 mA are very close to those plotted in Fig. 12. It should also be noted that the straight line nature of the plots in Fig. 12 follows directly from differentiation of (29), in the limit $P_2(\nu_0) >> P_s(\nu_0)$. The slope of each plot is just $[\alpha_0 P_s(\nu_0)]^{-1}$, or the inverse of the extractable power per unit length.

Using (11) we have also calculated the 3-dB amplifier linewidth for the range of parameters plotted in Fig. 12. We find that at 150 torr, $\Delta\nu_{3\,\mathrm{dB}} > 500$ MHz for the entire plotted range of output powers. At 100-torr pressure, $\Delta\nu_{3\,\mathrm{dB}} > 500$ MHz for output powers greater than 80 W. Finally, at 50 torr, we find $300 < \Delta\nu_{3\,\mathrm{dB}} < 500$ MHz over the entire plotted range of output powers. In each of these cases, the amplifier is strongly saturated at the output, resulting in significant power broadening of the amplifier bandwidth.

We see from Fig. 12 that the optimum amplifier pressure over the plotted range of output powers is near 100 torr. However, even at the optimum pressure, the required lengths range from 3 m (for 17-dB overall gain) to 7 m (for 23-dB overall gain). Thus the required amplifier length depends critically on the required system gain.

There are several refinements which can be made to further improve the amplifier performance. Most importantly, cooling of the amplifier is known to produce a significant improvement in small-signal gain coefficient, with a 50-percent increase at $-60°$C being typical [3]. Secondly, a double-pass configuration may be used to provide length reductions approaching a factor of 2.

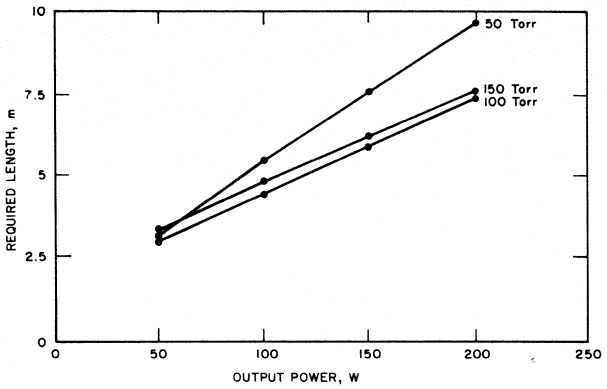

Fig. 12. Required length as a function of output power for a 1-W input.

VIII. Conclusions

We have shown that high-pressure waveguide laser devices provide a practical means for achieving high-gain wide-band amplification at 10.6 μm. Our study has included the analysis of high-gain saturated amplifiers, and experiments on a prototype 1-m device. As a result of this study, we are able to specify the design parameters required for construction of a device to meet specific performance goals.

Acknowledgment

The authors wish to acknowledge valuable technical discussions with G. Rupert.

References

[1] P. W. Smith, "A waveguide gas laser," *Appl. Phys. Lett.*, vol. 19, pp. 132–134, Sept. 1971.
[2] T. J. Bridges, E. G. Burkhardt, and P. W. Smith, "CO_2 waveguide lasers," *Appl. Phys. Lett.*, vol. 20, pp. 403–405, May 1972.
[3] E. G. Burkhardt, T. J. Bridges, and P. W. Smith, "BeO capillary CO_2 waveguide laser," *Opt. Commun.*, vol. 6, pp. 193–195, Oct. 1972.
[4] R. L. Abrams and W. B. Bridges, "Characteristics of sealed-off waveguide CO_2 lasers," *IEEE J. Quantum Electron.*, vol. QE-9, pp. 940–946, Sept. 1973.
[5] R. L. Abrams, "Gigahertz tunable waveguide CO_2 laser," *Appl. Phys. Lett.*, vol. 25, pp. 304–306, Sept. 1974.
[6] —, "Coupling losses in hollow waveguide laser resonators," *IEEE J. Quantum Electron.*, vol. QE-8, pp. 838–843, Nov. 1972.

Influence of Two-Photon Absorption on Second-Harmonic Generation in Semiconductors— Part I: Theoretical Analysis and Application to the Case of Tellurium

CHRISTIANE A. SCHWARTZ, MEMBER, IEEE, JEAN-LOUIS OUDAR, AND EDMOND M. BATIFOL

Abstract—**The competition between two-photon absorption and second-harmonic generation (SHG) in semiconductors is analyzed; particular attention is given to the linear absorption and change of phase-matching conditions caused by the two-photon induced free carriers. The system of equations is solved numerically in the case of tellurium, and this analysis enables prediction of an improvement of harmonic conversion efficiency when using shorter pulses.**

I. Introduction

ONE OF THE very few problems of second-order nonlinear optics which has not yet received a definite solution is the parametric oscillation in the medium infrared (5-30 μm). The frequency dependence of the parametric gain [1] makes the requirement on infrared materials for parametric oscillation quite drastic. Empirical and theoretical considerations show that noncentrosymmetric crystals with high refractive indices [2] are more likely to exhibit the required high nonlinear susceptibility. Since only low-gap semiconductors have these high refractive indices, this choice also selects the materials where multiphoton absorption easily occurs under the high power density necessary to reach a large conversion efficiency. Multiphoton absorption in solids promotes extra free carriers which in turn produce absorption (α) and refractive index variations and therefore together decrease the power density and break the phase-matching conditions. These effects, particularly strong for infrared wavelengths λ ($\alpha \propto \lambda^2$) can be more or less important depending on the carrier lifetime and the pulse duration. As a consequence the determination of maximum parametric gain must consider the competition of two nonlinear processes: harmonics generation and multiphoton absorption.

In this paper we wish to present a detailed analysis of the competition of second-order nonlinear processes and two-photon absorption in semiconductors.

In Part I, we consider the set of equations describing second-harmonic generation (SHG) in presence of two-photon absorption (TPA) as well as linear absorption and change of refractive indices induced by free carriers. This system is numerically solved in the case of tellurium. This crystal was chosen as an example for two reasons: a great number of experimental data is available on this material, and the multiphoton induced free carriers produce very strong effects. In the numerical analysis some unknown parameters are fitted to reproduce the experimental results of Gandrud and Abrams [3]. The same set of parameters enables one to explain other observations such as those made by Malz and Staupendhal [4], as well as our own. Then the model is used to predict the conversion efficiency for various experimental conditions. Two interesting results are obtained: the reduction of pulse duration leads to a significant decrease of the free carriers effects [5], and, at fixed pulsewidth, there is an optimum fundamental power density nearly independent of the total incident power.

In Part II[1] we test the analysis of Part I by measuring the absorption at 10.6 μm (CO_2 laser) induced in tellurium by 5-μm radiation (CO laser). The time dependence is analyzed by varying the delay between the two laser pulses. The power dependence is examined by varying independently the power of the two lasers. Then the frequency dependence is examined by varying the wavelength of the CO laser. These additional experimental data lead to a more precise analysis of the processes involved as well as the values of two-photon absorption coefficients in tellurium.

II. Equations Describing Simultaneous SHG and TPA in Semiconductors

Let us first give a brief summary of the experimental observation on SHG at high conversion efficiency in the medium infrared. First, a saturation of SHG is observed which cannot be explained only by power conversion from fundamental to harmonic frequencies. The observed depletion of the pump is much larger than the conversion efficiency (in $CdGeAs_2$ [6] 60-percent pump depletion for 15-percent efficiency; in tellurium [3] 70-percent pump depletion for 15-percent efficiency). In tellurium, a photoconductivity signal has been observed simultaneously with the laser pulse, indicating the creation of extra free carriers [3]. A shift and a deformation of phase-matching curve have also been mentioned [4]. Generally, the fundamental and harmonic pulse shapes are distorted: in the case of tellurium the distortion is assymmetric [3], leading to a narrowing of the pulses, conversely to $CdGeAs_2$ [6].

These observations strongly suggest that the mechanism is

Manuscript received February 15, 1975.

C. A. Schwartz was with Centre National d'Etudes des Télécommunications, 92220 Bagneux, France. She is now with Centre Commun d'Etudes de Télévision et Télécommunications, 35013 Rennes, France.

J.-L. Oudar and E. M. Batifol are with Centre National d'Etudes des Télécommunications, 92220 Bagneux, France.

[1] See pp. 623-629, this issue.

the following: at high conversion efficiency, the second-harmonic intensity becomes large enough to induce non-negligible TPA. Depending on the energy gap compared to the laser wavelength, two processes are possible: simultaneous absorption of 1) one photon from the fundamental beam and one from the harmonic, or 2) two photons at harmonic frequency. We symbolize henceforth the first process 1) by $(\hbar\omega_1 + \hbar\omega_2)$ and the second 2) by $(\hbar\omega_2 + \hbar\omega_2)$, where $\hbar\omega_1$ and $\hbar\omega_2$ are the fundamental and harmonic photon energies. We do not consider here another possibility, the process $(\hbar\omega_1 + \hbar\omega_1)$, for we assume the energy gap E_g is greater than $\hbar\omega_2 = 2\hbar\omega_1$. These absorptions create extra free carriers which in turn modify together the linear absorption and the refractive indices of the material.

To explain these observations, we build a model in the following way. We start from the usual system of equations describing SHG, slightly modified to include the aperture length effect. New terms taking TPA into account variation of refractive indices and of linear absorption due to induced free carriers are added. Then a rate equation for the evolution of induced free carriers population is coupled to the nonlinear system.

A. Set of Equations Describing SHG

The method of Boyd and Kleinman [7] is very powerful to describe focusing and aperture effects in SHG, but fails in taking into account the pump depletion. On the other hand, a plane-wave analysis in the line of Armstrong *et al.* [1] is more simple and well fitted to variations of the pump level.

These equations are

$$\frac{\partial \rho_1}{\partial z} = -C_0 \rho_1 \rho_2 \sin\theta - (\alpha_1/2)\rho_1$$

$$\frac{\partial \rho_2}{\partial z} = C_0 \rho_1^2 \sin\theta - (\alpha_2/2)\rho_2$$

$$\frac{\partial \theta}{\partial z} = 2C_0(\rho_2 - (\rho_1^2/2\rho_2))\cos\theta + \Delta k \qquad (1)$$

where $\rho_{1,2}$ are the electric field amplitudes, defined with the following notations: the indices 1 and 2 refer to the fundamental and harmonic beams and the plane-wave electric fields $\bar{E}_{1,2}(z, t)$ with $\bar{k}_1$ and $\bar{k}_2$ along z axis are

$$\bar{E}_{1,2}(z, t) = \tfrac{1}{2}\,\mathrm{Re}\,(\bar{E}_{1,2}\, e^{i(k_{1,2}z - \omega_{1,2}t)})$$

where

$$\bar{E}_{1,2} = \hat{u}_{1,2}\,\rho_{1,2}\, e^{i\phi_{1,2}}$$

$$\theta = 2\phi_1 - \phi_2 + \Delta k z$$

with

$$\Delta k = 2k_1 - k_2.$$

$\alpha_{1,2}$ are the absorption coefficients at $\omega_{1,2}$, the fundamental and harmonic frequencies. C_0 is equal to

$$C_0 = \frac{4\pi}{n_1 c}\,\omega_1\, d_{\mathrm{eff}}$$

where n_1 is the refractive index of the crystal at fundamental frequency, and d_{eff} is the effective SHG coefficient [7].

It is well known, from [7], that due to the focusing effect the variation of the harmonic power P_2, at phase-matching is

$$\begin{cases} P_2 \propto z^2, & \text{for } z \ll l_a, l_f \\ P_2 \propto z l_a, & \text{for } l_a \ll z \ll l_f \end{cases} \qquad (2)$$

where $l_a = \sqrt{\pi}\, w_0/\rho$ is the aperture length, w_0 is the minimum beam radius, ρ the walk-off angle; $l_f = \pi b/2$ where b is the confocal parameter.

Since in experimental configuration both strong focusing is required and large variations of pump level are observed, we choose to use the system (1) adequately modified to give the asymptotical behavior (2). This is performed in the following way. We replace the Gaussian beams by quasi-plane waves. When $z \ll l_a$, both treatments lead to the same result, i.e., the phase-matched second-harmonic power is proportional to z^2, when using the correspondence

$$\begin{cases} P_1 = \dfrac{\pi w_0^2}{2} I_1 = \dfrac{\pi w_0^2}{2}\dfrac{n_1 c}{8\pi}\rho_1^2 \\ P_2 = \dfrac{\pi w_0^2}{4} I_2 = \dfrac{\pi w_0^2}{4}\dfrac{n_2 c}{8\pi}\rho_2^2 \end{cases} \qquad (3)$$

and thus (1) lead to: $P_2 \propto z^2$ when $\Delta k = 0$ and P_1 remains constant.

For practical purposes, the same correspondence (3) is used even in the case $z \geqslant l_a$. This assumption leads to slight overestimation of the harmonic intensity of the fundamental beam axis, but a more sophisticated treatment would be too complicated. The relations $P_2 \propto \rho_2^2$ and $P_2 \propto z l_a$ when neglecting the pump depletion involve

$$\frac{\partial \rho_2}{\partial z} \propto z^{-1/2}.$$

Consequently, in order to obtain the asymptotic behaviors (2) when using (3), we replace C_0 in (1) by C, defined as follows:

$$\begin{cases} C = C_0, & \text{for } z \leqslant \gamma l_a \\ C = \dfrac{C_0}{2}\sqrt{\dfrac{l_a}{z}}, & \text{for } z > \gamma l_a. \end{cases} \qquad (4)$$

As (2) are only asymptotic, we adjust the numerical coefficient γ in such a way as to obtain the correct value of SHG efficiency when the pump can be taken as constant (γ is not far from one).

B. TPA and Induced Free Carriers

Whenever the fundamental photon energy exceeds the fourth part of the energy gap of the material ($\hbar\omega_1 > E_g/4$), new terms due to TPA must be introduced into (1). We consider the general case where both processes $(\hbar\omega_1 + \hbar\omega_2)$ and $(\hbar\omega_2 + \hbar\omega_2)$ can occur.

In the first process $(\hbar\omega_1 + \hbar\omega_2)$ the power absorption in a unit volume is proportional to the product of the fundamental

and harmonic intensities, whereas in $(\hbar\omega_2 + \hbar\omega_2)$ it is proportional to the square of the harmonic intensity. TPA can be described in terms of the imaginary part of the third-order nonlinear susceptibility χ_3''. The third-order polarizations $\bar{P}^{(3)}_{NL1}$ and $\bar{P}^{(3)}_{NL2}$ at fundamental and harmonic frequencies are

$$\begin{cases} \bar{P}^{(3)}_{NL1} = i\vec{\vec{\chi}}_3''(\omega_1, \omega_2, -\omega_2) \vdots \bar{E}_1 \bar{E}_2 \bar{E}_2^* \\ \bar{P}^{(3)}_{NL2} = i\vec{\vec{\chi}}_3''(\omega_2, \omega_1, -\omega_1) \vdots \bar{E}_2 \bar{E}_1 \bar{E}_1^* \\ \qquad + i\vec{\vec{\chi}}_3''(\omega_2, \omega_2, -\omega_2) \vdots \bar{E}_2 \bar{E}_2 \bar{E}_2^*. \end{cases} \tag{5}$$

We define two effective third-order coefficients by

$$\begin{cases} \Gamma_{12} = \hat{u}_1 \cdot \vec{\vec{\chi}}_3''(\omega_1, \omega_2, -\omega_2) \vdots \hat{u}_1 \hat{u}_2 \hat{u}_2 \\ \qquad = \hat{u}_2 \vec{\vec{\chi}}_3''(\omega_2, \omega_1, -\omega_1) \vdots \hat{u}_2 \hat{u}_1 \hat{u}_1 \\ \Gamma_{22} = \hat{u}_2 \cdot \vec{\vec{\chi}}_3''(\omega_2, \omega_2, -\omega_2) \vdots \hat{u}_2 \hat{u}_2 \hat{u}_2. \end{cases} \tag{6}$$

The energy densities W_1 and W_2 dissipated by the two beams in a unit volume of the crystal are given by

$$\begin{cases} \dfrac{dW_1}{dt} = \dfrac{\omega_1}{2} \Gamma_{12} \rho_1^2 \rho_2^2 \\ \dfrac{dW_2}{dt} = \left(\dfrac{dW_2}{dt}\right)_{12} + \left(\dfrac{dW_2}{dt}\right)_{22} = \dfrac{\omega_2}{2} \Gamma_{12} \rho_1^2 \rho_2^2 \\ \qquad + \dfrac{\omega_2}{2} \Gamma_{22} \rho_2^4. \end{cases} \tag{7}$$

Then the absorption coefficients due to TPA are

$$\begin{cases} \alpha_1' = \dfrac{4\pi}{n_1 c} \omega_1 \Gamma_{12} \rho_2^2 = \beta_{12} I_2 \\ \alpha_2' = \dfrac{4\pi}{n_2 c} \omega_2 (\Gamma_{12} \rho_1^2 + \Gamma_{22} \rho_2^2) = 2\beta_{12} I_1 + \beta_{22} I_2 \end{cases} \tag{8}$$

where

$$\beta_{12} = \frac{(8\pi/c)^2}{n_1 n_2} \frac{\omega_1}{2} \Gamma_{12}; \quad \beta_{22} = \left(\frac{8\pi}{n_2 c}\right)^2 \frac{\omega_2}{2} \Gamma_{22}$$

(these last expressions should be multiplied by 10^{13} if I_1 and I_2 are in megawatts per square centimeter—β in centimeters per megawatt). These instantaneous absorption terms must be added to the static absorption coefficients α_1 and α_2 in (1).

The last modification brought to (1) accounts for the TPA-induced free carriers. A rate equation for the induced carriers should include:

1) a source term, equal to the rate of the two-photon processes,
2) a diffusion term,
3) a recombination term, due to electron-hole pairs finite lifetime.

We assume that the two last terms lead to an exponential decay, with time constant τ. Since the transverse variations of the beam intensities are ignored in (1), there is, strictly speaking, no diffusion term. Actually, the initially Gaussian carrier distribution is spread by diffusion out of the focus region. This involves a diffusion time constant [3]

$$\tau_D = \frac{e w_0^2}{4 \mu k T}$$

where μ is the carrier mobility and T the temperature of the crystal. Therefore, the single time constant τ includes both contributions of τ_D and the carrier lifetime.

If N_e and N_h are the excess of electron and hole densities, the source term is

$$\frac{dN_e}{dt} = \frac{dN_h}{dt} = \frac{1}{\hbar\omega_2}\left(\frac{dW_2}{dt}\right)_{12} + \frac{1}{2\hbar\omega_2}\left(\frac{dW_2}{dt}\right)_{22} \tag{9}$$

as only one $\hbar\omega_2$ photon is absorbed in the process $(\hbar\omega_1 + \hbar\omega_2)$, while in the other process, two $\hbar\omega_2$ photons are absorbed.

Assuming the same decay time constant τ for electrons and holes, comparison of (7) and (9) leads to

$$\begin{cases} N_e = N_h = N \\ \dfrac{dN}{dt} = \dfrac{\Gamma_{12}}{2\hbar} \rho_1^2 \rho_2^2 + \dfrac{\Gamma_{22}}{4\hbar} \rho_2^4 - \dfrac{N}{\tau}. \end{cases} \tag{10}$$

The last step is now to describe the influence of the free carriers on the propagation of the two beams. As the absorption coefficients and refractive index variations due to free carriers are proportional to the carrier density, we define $\Sigma(\omega)$ and $\Lambda(\omega)$ as follows:

$$\begin{cases} \alpha_1'' = \Sigma(\omega_1) N \\ \alpha_2'' = \Sigma(\omega_2) N \\ \delta n_1 = \Lambda(\omega_1) N \\ \delta n_2 = \Lambda(\omega_2) N \end{cases} \tag{11}$$

where $\alpha_{1,2}''$ are the excess free carrier absorption coefficients at fundamental and harmonic frequencies and δn_1, δn_2 are the free carrier index variations at these frequencies. $\Sigma(\omega)$ corresponds to the carrier absorption cross section at ω frequency. Of course the contribution of the equilibrium carriers is already included in the static coefficients $\alpha_1, \alpha_2, n_1, n_2$ in (1).

The coefficients Σ and Λ can be estimated by means of the Drude model. In principle, this model may only lead to a rough estimate of Σ and Λ, but, as will be seen later, it gives fairly good results with tellurium, in regard of the dispersion of the available experimental data.

In the Drude model the dynamical conductivity is

$$\sigma(\omega) = e^2 \left(\frac{N_e}{m_e} \frac{\tau_e}{1 - i\omega\tau_e} + \frac{N_h}{m_h} \frac{\tau_h}{1 - i\omega\tau_h}\right) \tag{12}$$

where m_e and m_h are the electron and hole effective masses, τ_e and τ_h their relaxation times.

The absorption coefficient α_j'' is proportional to the real part σ_r of the conductivity

$$\alpha_j'' = \frac{4\pi}{n_j c}\,\sigma_r(\omega_j), \qquad j = 1, 2 \tag{13}$$

and the index variation δn_j is proportional to the imaginary part σ_i

$$\delta n_j = -\frac{2\pi}{n_j \omega_j}\,\sigma_i(\omega_j). \tag{14}$$

Thus, (11)-(14), together with $N_e = N_h = N$ and $\omega\tau_e, \omega\tau_h >> 1$ give $\Sigma(\omega_j)$ and $\Lambda(\omega_j)$

$$\Sigma(\omega_j) = \frac{4\pi}{n_j c}\,\frac{e^3}{\omega_j^2}\left(\frac{1}{m_h^2\mu_h} + \frac{1}{m_e^2\mu_e}\right)$$

$$\Lambda(\omega_j) = -\frac{2\pi}{n_j}\,\frac{e^2}{\omega_j^2}\left(\frac{1}{m_h} + \frac{1}{m_e}\right) \tag{15}$$

where

$$\mu_e = e\tau_e/m_e \quad \text{and} \quad \mu_h = e\tau_h/m_h.$$

Two effects can be expected from the index variation. First, as δn_j is frequency dependent ($\delta n_1 = 4\delta n_2$ in the Drude model), it induces a phase mismatch between the fundamental and harmonic waves [4]. In addition, if the incident beam is strongly focused ($w_0 \leqslant 100\ \mu$m), the refractive index gradient can cause self-defocusing. It will be seen in Part II that this effect may be quite important in some cases. Here we neglect self-defocusing, taking only the phase mismatch into account. Using $\delta n_1 = 4\delta n_2$ and (11), the induced phase mismatch Δk_i is

$$\Delta k_i = \frac{2\omega_1}{c}(\delta n_1 - \delta n_2) = \frac{3\omega_1}{2c}\,\delta n_1 = \frac{3\omega_1}{2c}\,\Lambda(\omega_1)N. \tag{16}$$

It is convenient to express Δk_i in terms of α_1'', thus keeping only one parameter proportional to the free carrier density, i.e., α_1''; using (13)-(15) we obtain

$$\Delta k_i = -\frac{3R}{4}\alpha_1'' \tag{17}$$

where $R = \sigma_i(\omega_1)/\sigma_r(\omega_1)$ is the ratio of imaginary to real part of the dynamical conductivity. When the relaxation times τ_e and τ_h are equal, the physical meaning of this dimensionless ratio is more apparent

$$R = \omega_1\tau_e = \omega_1\tau_h. \tag{18}$$

C. Equations Including SHG, TPA, and Free Carriers Effects

To describe the influence of TPA and of the induced free carriers, the SHG system (1) can be now modified in the following way:

a) α_j ($j = 1, 2$) becomes $\alpha_j + \alpha_j' + \alpha_j''$ using (8) and (11),
b) Δk becomes $\Delta k_e + \Delta k_i$ using (17) (Δk_e is any constant phase mismatch, depending on external conditions–crystal orientation, temperature, etc.),
c) the rate equation (10) is added to the original system (1) (we multiply each term of (10) by $\Sigma(\omega_1)$ to obtain $\partial\alpha_1''/\partial t$ using (11)).

With all these modifications, system (1) is replaced by

$$\begin{cases} \dfrac{\partial\rho_1}{\partial z} = -C\rho_1\rho_2\sin\theta - (\alpha_1 + D\rho_2^2 + \alpha_1'')\,\dfrac{\rho_1}{2} \\[2ex] \dfrac{\partial\rho_2}{\partial z} = C\rho_1^2\sin\theta - \left(\alpha_2 + 2D\rho_1^2 + D'\rho_2^2 + \dfrac{\alpha_1''}{4}\right)\dfrac{\rho_2}{2} \\[2ex] \dfrac{\partial\theta}{\partial z} = 2C\left(\rho_2 - \dfrac{\rho_1^2}{2\rho_2}\right)\cos\theta + \Delta k_e - \dfrac{3R}{4}\alpha_1'' \\[2ex] \dfrac{\partial\alpha_1''}{\partial t} = B\rho_1^2\rho_2^2 + B'\rho_2^4 - \dfrac{\alpha_1''}{\tau} \end{cases} \tag{19}$$

where C is defined in (4), R in (17), and

$$B = \frac{\Sigma(\omega_1)}{2\hbar}\,\Gamma_{12} \qquad B' = \frac{\Sigma(\omega_1)}{4\hbar}\,\Gamma_{22}$$

$$D = \frac{4\pi\omega_1}{n_1 c}\,\Gamma_{12} \qquad D' = \frac{4\pi\omega_2}{n_2 c}\,\Gamma_{22}.$$

An order of magnitude of these coefficients will be given in the next section where we apply this analysis to the case of tellurium.

Here we want to stress the importance of the free carrier terms compared to the pure TPA terms. Assume, for example, that the $(\hbar\omega_1 + \hbar\omega_2)$ process is predominant (which is the case when $B \sim B'$ and $\rho_1^2 >> \rho_2^2$). Under these conditions α_1'' is roughly proportional to $\rho_1^2\rho_2^2$, whereas α_1' (TPA term) is proportional to ρ_2^2. Therefore, at some fundamental intensity I_1^*, α_1'' and α_1' are nearly equal, and for $I_1 >> I_1^*$, the pure TPA term α_1' is negligible. Let us now estimate the value of I_1^* and for this purpose let us set an approximate expression for α_1''

$$\alpha_1'' \simeq B\rho_1^2\rho_2^2\tau_{\text{eff}}.$$

When evaluating α_1'' at the maximum of the pulse, τ_{eff} has two asymptotic expressions, depending on the relative value of τ (carrier lifetime) and Δt (pulsewidth)

$$\tau << \Delta t, \qquad \tau_{\text{eff}} \simeq \tau$$

$$\tau >> \Delta t, \qquad \tau_{\text{eff}} \simeq \frac{\Delta t}{2}.$$

The comparison of $\alpha_1' = (4\pi/n_1 c)\,\omega_1\,\Gamma_{12}\rho_2^2$ and $\alpha_1'' = (\Sigma(\omega_1)/2\hbar)\,\Gamma_{12}\,\tau_{\text{eff}}\rho_1^2\rho_2^2$ shows that the same magnitude is reached for

$$I_1^* = \frac{n_1 c}{8\pi}\,\rho_1^2 = \frac{\hbar\omega_1}{\Sigma(\omega_1)\,\tau_{\text{eff}}}. \tag{20}$$

The typical values for tellurium (see next section) of $\tau_{\text{eff}} = 100$ ns and $\Sigma(\omega_1) = 5 \times 10^{-17}$ cm^2 at 10.6 μm lead to $I_1^* \simeq 3.5$ kW/cm^2. So this situation is quite unusual: *the higher order effect (induced free carriers absorption) may easily be preponderant on the lower order effect (TPA).*

The very low value obtained for I_1^* is partly due to the frequency dependence of $\Sigma(\omega)$–according to the Drude model $\Sigma \propto \omega_1^{-2}$, leading to $I_1^* \propto \omega_1^3$.

III. Resolution and Comparison with Experimental Data on Tellurium

Solutions of system (19) have been computed in the case of SHG in tellurium at 10.6 μm. In a first step, the unknown parameters are fitted to reproduce the experimental results of Gandrud and Abrams [3]. Then the same set of parameters is used to explain other experimental observations. Before describing the procedure of numerical calculations and the results, let us discuss the case of SHG in tellurium using a CO_2 laser.

In this case both processes are possible: $(\hbar\omega_1 + \hbar\omega_2)$ and $(\hbar\omega_2 + \hbar\omega_2)$, since the bandgap is $E_g = 0.33$ eV and $\hbar\omega_1 = 0.177$ eV. B and B' are expected to be of the same order of magnitude (this is confirmed in Part II). Therefore, the first process is much more important when $\rho_1^2 >> \rho_2^2$. In order to reduce the number of parameters we neglect the contribution of the second process ($B' = D' = 0$). Since the free carriers terms are prevailing over the pure TPA terms, D cannot be adjusted separately. Hence the ratio B/D must be fixed, by a proper estimation of the free carrier absorption cross section $\Sigma(\omega_1)$, that we take equal to 5×10^{-17} cm^2 (for justification of this value, see Appendix).

With these assumptions, only three parameters are unknown—B, proportional to the two-photon absorption coefficient; R, related to the free carrier relaxation time; and τ the free carrier lifetime. C is easily calculated using [8] $d_{11} = 2.2 \times 10^{-6}$ ESU. Δk_e is another adjustable parameter which depends on the crystal orientation. In all the calculations where Δk_e is not specified, we used the value of Δk_e giving the maximum harmonic output, since one can assume that this optimization is made experimentally.

The numerical computation uses the following boundary conditions:

1) $\rho_2(t, z = 0) = 0$; $\alpha_1''(t = 0, z) = 0$; $\theta(t, z = 0) = \pi/2$;
2) the time variation of the incident electric field $\rho_1(t, z = 0)$ is approximated by a Gaussian pulse of given duration and maximum value.

At a given time t_i, the spatial integration is performed on the first three equations, using the previously calculated value $\alpha_1''(t_{i-1}, z)$. Then $\alpha_1''(t_i, z)$ is calculated by means of the last equation. It can be noticed that the calculation is rather simple, for the first three equations contain no time derivative: the pulse duration is very large compared to the transit time of the light through the crystal; in addition the last equation contains no spatial derivative: diffusion of the free carriers along z is negligible.

The three unknown parameters, B, R, and τ are adjusted to fit the results given in [3]. The main experimental data we have used are the time variation of P_2/P_1 during one pulse as a function of the instantaneous value of P_1, where P_2 is the harmonic output power and P_1 the fundamental input power. These experimental data are reproduced on Fig. 1, as well as the best fit we have obtained, with $B = 7$ ESU, $R = 25$, $\tau = 1$ μs.

The value of τ is not critical, and may be compared with the values of 0.5 μs measured in [3], and 0.4 μs obtained in Part II of this paper. The value of R is in good agreement with that estimated from the Drude model (with $\mu_h = 1000$ cm^2/V · s and $m_e = 0.2$ m, (18) leads to $R = 20$ at 10.6 μm). The value

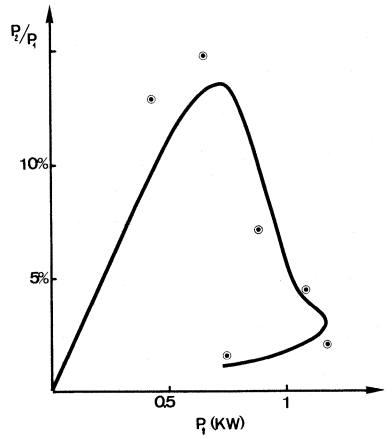

Fig. 1. Instantaneous variation of P_2/P_1 versus P_1 during one pulse. ⊙: Experimental data reproduced from [3]; ___: best fit calculated from system (19) with $B = 7$ ESU, $R = 25$, $\tau = 1$ μs (other input data according to the experimental conditions described in [3], i.e., crystal length is 9.8 mm, pulse duration of 200 ns, and beam radius $w_0 = 140$ μm).

of B corresponds to the third-order susceptibility: $\Gamma_{12} = 3 \times 10^{-10}$ ESU. It will be seen in Part II that this value is underestimated by our plane-wave treatment, since we have neglected the aperture length effects that are likely to appear not only on SHG but also in the TPA generation of carriers. Therefore, a better value of Γ_{12} (as well as Γ_{22}) will be given in Part II, where the new experimental data can be analyzed more precisely.

In Fig. 2 are reproduced some calculated curves of instantaneous conversion efficiency P_2/P_1, with the same fundamental peak power P_1 as in Fig. 1, but with different values of B, R, and τ. It is difficult to analyze the influence of each parameter separately, but some general trends are apparent in Fig. 2.

If all the processes were instantaneous ($\tau \to 0$), then the curve would show no loop. For a nonzero lifetime, the generated harmonic power is larger during the raising part than the decreasing part of the fundamental pulse, due to the accumulation of the carriers during the pulse. Consequently, the curve $P_2/P_1 = f(P_1)$ shows a loop, a smaller value of τ corresponding to a tighter loop, as is shown with $\tau = 20$ ns in Fig. 2.

The value of B fixes the magnitude of the total effect, whereas R describes the relative importance of the index variation and of the induced absorption. It can be seen in Fig. 2 that a larger value of R ($R = 50$) results in strong oscillations of the harmonic pulse, as can be expected from the variation of the phase-matching conditions during the pulse. B and R are independently adjustable parameters and we verified that the best fit also corresponds to the pump depletion of 70 percent experimentally observed [3].

With the same set of parameters as in Fig. 1, this analysis can now be used to explain some other experimental observations on SHG in tellurium. Nonsymmetrical harmonic pulse deformations with some oscillation at the end of the pulse can be observed with fundamental intensities near 10 MW/cm^2, as shown in Fig. 3(a). This kind of deformation is explained by our model, and Fig. 3(b) shows two calculated harmonic

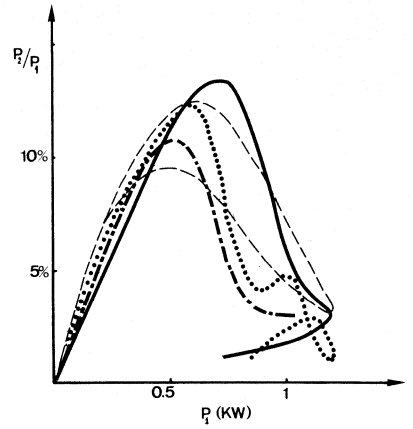

Fig. 2. Calculated curves of instantaneous P_2/P_1 versus P_1. ___: Best fit—same as Fig. 1; others: all parameters as above, except: – – –: τ = 20 ns; ●●●●●●●: R = 50; —·—: B = 17.5 ESU.

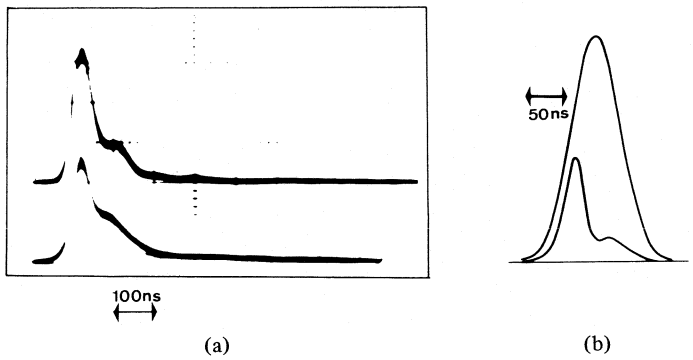

Fig. 3. Harmonic pulse shapes with $I_1 \simeq 10$ MW/cm^2. (a) Two experimental pulses (with slightly different propagation directions). (b) Calculated curves, with and without TPA.

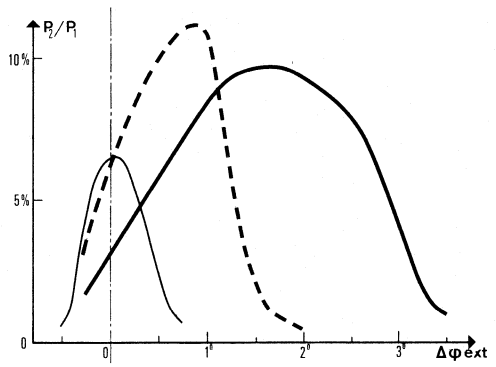

Fig. 4. Calculated phase-matching curves, using the best fitted parameters with 3 fundamental intensities: ——: 1 MW/cm^2; – – –: 4 MW/cm^2; ▬▬: 11 MW/cm^2. Other data are according to the experimental conditions of [4]: crystal length is 3.3 mm, pulse duration 280 ns, and beam radius w_0 = 170 μm. $\Delta\phi_{ext}$ = 0 corresponds to nominal phase matching.

pulse shapes, one without induced absorption, and the other with the free carrier effects. Intensity changes in the phase-matching angle are also observed [4]. Fig. 4 shows the calculated phase-matching curves for various pump intensities. Simultaneous shift of the maximum and broadening of the curve occur, in agreement with the results of Malz and Staupendhal [4].

In conclusion, the effect of the free carriers on SHG efficiency is summarized in Fig. 5, where the conversion efficiency is plotted at given fundamental power P_1 but increasing power density in three cases; without pump depletion [7] (curve 1), including pump depletion (curve 2), and finally with TPA induced free carriers (curve 3). Here it must be stressed that these curves are drawn *at constant power* P_1 (2.4 kW), which explains that in curve 2 the asymptotic value of P_2/P_1 is not 100 percent even in absence of any absorption.

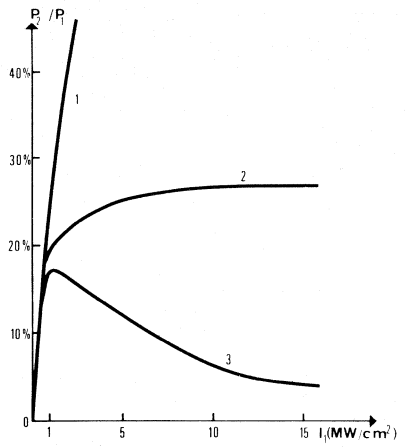

Fig. 5. Peak power conversion efficiency at P_1 = 2.4 kW as a function of power density I_1; 1 and 2 without TPA induced free carriers—1 neglecting pump depletion [6], 2 including pump depletion (see (1)); 3 calculated with system (19).

IV. Optimization of SHG Efficiency

This model provides a useful means to optimize the conversion efficiency of SHG in Te using a CO_2 laser. Two main results are obtained: at given pulse duration there is an optimum fundamental *power density*, and in addition the reduction of the pulse duration should appreciably increase the conversion efficiency.

A. Conversion Efficiency at Fixed Pulsewidth

The calculations have been performed with 120-ns fundamental pulsewidth (half-height), which is a typical value for the output pulses from low-pressure CO_2 lasers. The crystal length is 1 cm and the adjustable parameters have the same value as in Fig. 1.

In the usual case, the condition for optimum conversion efficiency is expressed in terms of geometrical quantities, e.g., focusing and double-refraction parameter [7]. In addition to these quantities, the TPA effects lead to consider an important parameter: the fundamental power density. The main result is that, as far as the conversion efficiency is concerned, there is an optimum fundamental power density, nearly independent of the total power incident on the crystal. This result is apparent on Fig. 6, where the peak power conversion efficiency is plotted as a function of intensity I_1, at different powers P_1 of the fundamental beam (each calculated value of P_2/P_1 has been optimized with respect to Δk_e). For instance, a curve at fixed power P_1, but increasing power density I_1, represents the variation of second-harmonic output with increasing focusing. It can be seen that the optimum I_1 is relatively low, between 1 and 2 MW/cm^2. In addition, with funda-

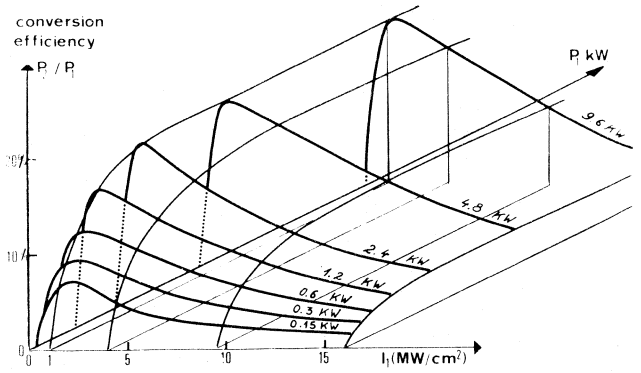

Fig. 6. Peak power conversion efficiency versus fundamental intensity I_1, at different powers P_1. Half maximum pulse duration is 120 ns.

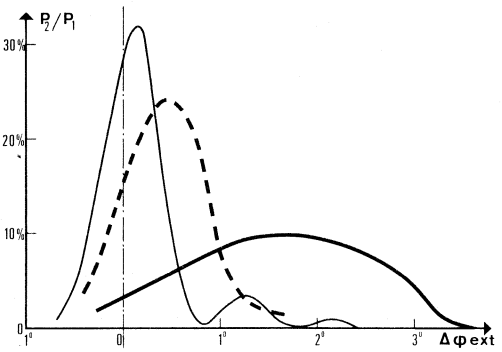

Fig. 7. Phase-matching curves at $I_1 = 11$ MW/cm^2 calculated with different half maximum pulse duration Δt: ——: $\Delta t = 1.2$ ns; – – –: $\Delta t = 12$ ns; ▬▬: $\Delta t = 280$ ns.

mental powers P_1 larger than 1.5 kW, the maximum conversion efficiency (15–17 percent) is practically independent of P_1. Thus experimentally, with increasing peak power it is necessary to increase the beam-waist size in order to keep I_1 around 1 MW/cm^2, and the only limit of the harmonic power generated is the size of the input face of the crystal, assuming the pump power is not limited (the same type of limitation occurs–at much higher intensity–when the harmonic generation is limited by the damage threshold instead of the TPA effects). With increasing fundamental power P_1 –in the range of 100 kW-1 MW–this model might slightly overestimate P_2/P_1, due to the fact that aperture length effects have been neglected in the TPA generation of free carriers.

B. Influence of Pulse Duration

It is clear from the above analysis that a long free carrier lifetime (which is the case in tellurium) results in an accumulation of the carriers during the pulse. In such a case, a reduction of the pulsewidth should increase the conversion efficiency. So we have made quantitative predictions about the efficiency that could be reached with shorter pulses. Fig. 7 shows the calculated phase-matching curves with 0.33-cm-long crystal and 5-kW fundamental power (11 MW/cm^2) at different pulsewidths. The 1-ns curve is practically the nominal phase-matching curve, indicating a large reduction of the free carriers density. This is confirmed in Fig. 8, which shows that the conversion efficiency with 1-ns pulses is not far from the efficiency that would be predicted without TPA.

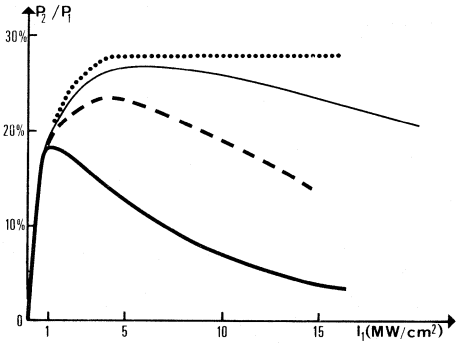

Fig. 8. Peak power conversion efficiency at $P_1 = 9.6$ kW as a function of power density I_1, calculated with different Δt: ——: $\Delta t = 1.2$ ns; – – –: $\Delta t = 12$ ns; ▬▬: $\Delta t = 120$ ns. Also shown (●●●●) is the curve calculated without TPA induced free carriers.

V. Conclusion

In Part I of this paper we have analyzed the second-harmonic generation in semiconductors in the presence of two-photon induced free carriers. For quantitative analysis the case of tellurium was considered. The model explains all the experimental data on SHG with a CO_2 laser. It can be also used to optimize the conversion efficiency. Two main results have been pointed out: first, the advantage of using shorter pulses to increase the harmonic conversion efficiency, and, second, the existence of an optimum fundamental intensity, near 1 MW/cm^2, practically independent of the total power incident on the crystal.

Appendix

We give here some details about the free carrier absorption cross section used in the text for tellurium at 10.6 μm. This free carrier absorption exhibits an important dichroism, due to intervalence band transition around 10 μm [9], [10]. This transition is forbidden for an electric field E perpendicular to the optic axis Z, so it need not be taken into account, because the only electric-field components involved in phase-matched SHG are E_Y at fundamental frequency and E_X at harmonic frequency (d_{XYY}). Therefore, the relevant value of $\Sigma(\omega)$ is the sum of the electron and hole absorption cross sections $\Sigma_e^{\perp}(\omega)$ and $\Sigma_h^{\perp}(\omega)$ for $E \perp Z$: $\Sigma(\omega) = \Sigma_h^{\perp}(\omega) + \Sigma_e^{\perp}(\omega)$.

The lack of experimental data makes it difficult to obtain a precise value of $\Sigma(\omega)$ for intrinsic tellurium at room temperature. With p-type extrinsic crystals the wavelength dependence is between $\lambda^{1.8}$ and $\lambda^{2.8}$ ([9] and [11]) at wavelengths greater than 15 μm. At 5 or 10 μm, the absorptions are slightly larger than the values extrapolated from longer wavelengths, but it is probably due to impurity transitions. At 20 μm and 300 K, the values of $\Sigma_h^{\perp}$ lie between 6.6×10^{-17} and 8.8×10^{-17} cm^2 in p-type crystals [9], [11], and $\Sigma_e^{\perp} + \Sigma_h^{\perp} \simeq 19 \times 10^{-17}$ cm^2 in intrinsic crystals [9].

So the cross section of electrons appears to be slightly larger than that of the holes. Thus it appears reasonable to take $\Sigma(\omega_1) = 5 \times 10^{-17}$ cm^2 at 10.6 μm, with an uncertainty of about 40 percent. It can be seen that the Drude model leads to the same estimation: with $\mu_e \simeq \mu_h \simeq 1000$ cm^2/V · s [12] and $m_h \simeq m_e \simeq 0.2$ m where m is the electron mass, (15) gives: $\Sigma = 6 \times 10^{-17}$ cm^2 at 10.6 μm.

REFERENCES

[1] J. A. Armstrong, N. Bloembergen, J. Ducuing, and P. S. Pershan, "Interactions between light waves in a nonlinear dielectric," *Phys. Rev.*, vol. 127, pp. 1918–1939, 1962.

[2] R. C. Miller, "Optical second harmonic generation in piezoelectric crystals," *Appl. Phys. Lett.*, vol. 5, pp. 17–19, 1964.

[3] W. B. Gandrud and R. L. Abrams, "Reduction in SHG efficiency in tellurium by photoinduced carriers," *Appl. Phys. Lett.*, vol. 17, pp. 302–305, 1970.

[4] D. Malz and G. Staupendhal, "Laser induced change of SHG phase-matching in tellurium," *Phys. Status Solidi* (b), vol. 51, pp. K51–K54, 1972.

[5] C. A. Schwartz and J. L. Oudar, "Optimization of second harmonic generation in tellurium in presence of photoinduced carriers," presented at CLEA, Washington, D.C., 1973.

[6] H. Kildal and J. C. Mikkelsen, "Efficient doubling and CW difference frequency mixing in the infrared using the chalcopyrite $CdGeAs_2$," *Opt. Commun.*, vol. 10, pp. 306–309, 1974; also R. L. Byer and H. Kildal (postdeadline paper), presented at CLEA, Washington, D.C., 1973.

[7] G. D. Boyd and D. A. Kleinman, "Parametric interaction of focused Gaussian light beams," *J. Appl. Phys.*, vol. 39, pp. 3597–3639, 1968.

[8] J. H. McFee, G. D. Boyd, and P. H. Schmidt, "Redetermination of the nonlinear optical coefficients of Te and GaAs by comparison with Ag_3SbS_3," *Appl. Phys. Lett.*, vol. 17, pp. 57–59, 1970.

[9] R. S. Caldwell, "Optical properties of tellurium and selenium," M.Sc. thesis, Purdue Univ., Lafayette, Ind., 1958.

[10] R. S. Caldwell and H. Y. Fan, "Optical properties of tellurium and selenium," *Phys. Rev.*, vol. 114, pp. 664–675, 1959.

[11] M. Selders, P. Gspan, and P. Grosse, "Polaron scattering of free carriers in tellurium," *Phys. Status Solidi* (b), vol. 47, pp. 519–528, 1971.

[12] W. Beyer, H. Mell, and J. Stuke, "Conductivity and thermoelectric power of trigonal Se_xTe_{1-x} single crystals," *Phys. Status Solidi* (b), vol. 45, pp. 153–170, 1971.

Influence of Two-Photon Absorption on Second-Harmonic Generation in Semiconductors— Part II: Measurement of Two-Photon Absorption in Tellurium

JEAN-LOUIS OUDAR, CHRISTIANE A. SCHWARTZ, MEMBER, IEEE, AND EDMOND M. BATIFOL

Abstract—**The effect of the free carriers generated by two-photon absorption in tellurium has been studied by using a CO_2 and a CO laser. Time and power dependence of the induced absorption has been measured, as well as the variation of the two-photon process with the wavelength of the CO laser. These observations confirm the assumptions of the analysis described in Part I.**

I. INTRODUCTION

THEORETICAL analysis of the influence of two-photon absorption (TPA) on second-harmonic generation (SHG) has been given in Part I[1] of this paper. It has been shown that the influence of photo-induced carriers is particularly important in small gap semiconductors, which is the case of tellurium. This analysis has explained previous experimental data on the limitation of conversion efficiency of SHG in tellurium at 10.6 μm. Nevertheless, many assumptions have been made and adjustable parameters have been introduced to give a quantitative account of the experimental data.

So, in order to confirm the validity of this model, the principal hypothesis has been checked directly by measuring the absorption at 10.6 μm (CO_2 laser) induced by a CO laser beam in a crystal of tellurium. The time dependence is analyzed by varying the delay between the two laser pulses. The power dependence is obtained by independently varying the power of the two lasers. Then the frequency dependence is examined by selecting different lines from the CO laser. Comparison of these data with the results of Part I confirms the principal assumptions of our analysis. It also enables a more detailed interpretation of some parameters that have been introduced; finally, a more reliable value of TPA coefficient in tellurium is obtained.

II. EXPERIMENTAL SETUP

The experiment has been performed by mixing the output beams of a CO_2 and a CO laser. These lasers are simultaneously Q switched by means of the same rotating mirror. The geometrical configuration is sketched on Fig. 1. The cavity of the CO_2 laser is ended by a Littrow-mounted diffraction grating, which allows a selection of each emitted rotational line. As the grooves of the grating are vertical and the axis of the rotating mirror is horizontal, a rotation of the grating around the vertical axis selects the emitted line, whereas a rotation around the horizontal axis is used to adjust the delay between the pulses of the two lasers within a small range of time (0–2 μs). Inside the cavity of the CO laser

Manuscript received February 15, 1975.

J.-L. Oudar and E. M. Batifol are with Centre National d'Etudes des Télécommunications, 92220 Bagneux, France.

C. A. Schwartz was with Centre National d'Etudes des Télécommunications, 92220 Bagneux, France. She is now with Centre Commun d'Etudes de Télévision et Télécommunications, 35013 Rennes, France.

[1] See pp. 616–623, this issue.

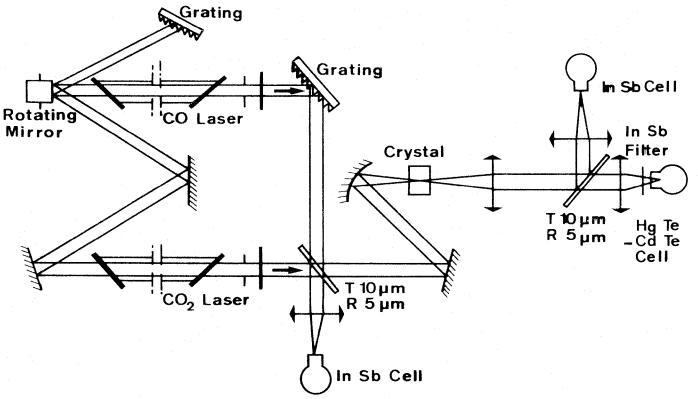

Fig. 1. Experimental arrangement for measuring TPA in tellurium.

there is no wavelength selection; the output beam is diffracted by a grating of 150 grooves per millimeter, which enables one to choose a small number of lines ($\Delta\lambda = 300$ Å) among the total spectrum of the laser output. The overlapping and colinearity of the two laser beams is achieved by a dielectric-coated germanium plate; then the beams are focused in the crystal by a concave mirror ($f = 10$ cm). Both lasers can be operated in the mode TEM_{00} and the spot size at focus was checked in these conditions. This measurement was performed for each laser by comparing the size of damages caused by the beam on a previously exposed Polaroid film, at different incident powers. The measured values agree within 30 percent with the calculated ones; we have obtained $w_1 = 100\ \mu m$ ($1/e^2$ radius) for the CO_2 laser and $w_2 = 65\ \mu m$ for the CO laser. The crystal of tellurium is 8 mm long and its optic axis is perpendicular to the beam axis. As the polarizations of the two beams are perpendicular to the optic axis, no three-wave interaction can be phase-matched; so in the following, we neglect all the effects due to second-order nonlinear processes. Behind the crystal, the beam is split by another germanium plate. The power at 5-6 μm is measured by an InSb photovoltaic detector; the power at 10.6 μm is detected by a Hg-CdTe detector in front of which an InSb filter stops any residual 5-6-μm radiation. Both signals from these detectors could be seen on an oscilloscope. The signal from the Hg-CdTe detector was detected by a gate integrator, and then recorded.

III. Experimental Results

When the pulses of the two lasers are simultaneous, the crystal transmission at 10.6 μm is greatly reduced in presence of the CO laser beam. We measured a reduction of transmission up to a factor 10, for some incident powers. At higher power levels, heating of the crystal became important and no reproducible data could be obtained.

In addition, the crystal transmission at 5-6 μm was also reduced by the presence of the CO_2 laser beam. The induced absorption at 5-6 μm was found smaller than the induced absorption at 10.6 μm, by a factor varying from 3 to 6. A factor of about 4 would be expected from the Drude model (free carrier absorption proportional to λ^2) but, as will be described hereafter, it depends also on the relative size and position of the two beams in the crystal. Therefore, we did not measure systematically the induced absorption at 5-6 μm and all the results given below concern the change of transmission at 10.6 μm. This induced absorption is the sum of two terms

$$\alpha_{ind} = \alpha_1' + \alpha_1'' = \beta_{12} I_2 + \Sigma(\omega_1) N \tag{1}$$

where β_{12} is the TPA coefficient and I_2 the power density at frequency ω_2; Σ is the free carrier absorption cross section at frequency ω_1 and N the induced free carrier density. As discussed in Part I, the first term is usually small compared to the free carrier term (when $I_1 \gg I_1^* = \hbar\omega_1/\Sigma(\omega_1)\tau_{eff}$); this is confirmed by the study of the power dependence of the induced absorption in the range of intensities where the effect can be observed.

The induced free carriers can be generated by two processes $-(\hbar\omega_1 + \hbar\omega_2)$ and $(\hbar\omega_2 + \hbar\omega_2)$, that is, absorption of one photon from each laser beam or two photons from CO laser beam. Each process can easily be observed separately from the other, for the first process is negligible when the intensity I_1 at frequency ω_1 is very small, while it is preponderant when I_1 is much greater than I_2.

A. Time Dependence

A convenient way to study the time dependence of the induced absorption is to gradually vary the delay between the pulses of the two lasers and to observe the variation of the absorption as a function of this delay.

Two different behaviors can be distinguished, depending on which process is preponderant. In the first case $(\hbar\omega_1 + \hbar\omega_2)$, the induced absorption occurs only when the two pulses are time-overlapping. This clearly proves that the free carriers are generated by simultaneous absorption of one photon from each laser. This behavior is sketched in Fig. 2(a). In this figure there has been schematically drawn a superposition of the oscilloscope traces of several transmitted pulses at 10.6 μm (lower trace), with gradually varying delay with respect to the CO laser pulse (upper trace). The incident peak powers are typically 1 kW at 10.6 μm and 6 W at 5.3 μm, outside the crystal.

Conversely, when the second process $(\hbar\omega_2 + \hbar\omega_2)$ is preponderant, some absorption remains after the end of the CO laser pulse. This is due to the fact that the induced free carriers are generated by the CO laser beam alone, the other beam acting merely as a probe. Fig. 2(b) shows what is obtained when superposing several pulses as in Fig. 2(a), but in this case the incident powers are 1 W at 10.6 μm and about 30 W at 5.3 μm.

The envelope of the transmitted pulse maxima at 10.6 μm provides a direct measurement of the lifetime of the free carriers. In order to get a more precise measurement we used the CO_2 laser operating in CW mode and observed the transient signal due to the induced absorption. The decay time constant is $\tau = 0.4\ \mu s$. This value is in good agreement with the measurement of Gandrud and Abrams [1] and not far from the estimate made in Part I from the analysis of instantaneous SHG conversion efficiency.

B. Power Dependence

We measured the relative value of the transmitted power at 10.6 μm when 1) both beams are sent together in the crystal and when 2) the CO laser beam is stopped by a shutter. The

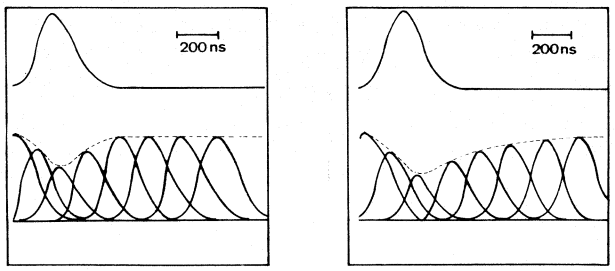

Fig. 2. Schematic diagram of the time dependence of the induced absorption. Superposition of several transmitted 10.6-μm pulses (lower trace), with variable delay with respect to the CO laser pulse (upper trace). (a) Free carriers generated by absorption of one photon from each laser ($\hbar\omega_1 + \hbar\omega_2$). (b) Free carriers generated by absorption of two-photons from CO laser ($\hbar\omega_2 + \hbar\omega_2$).

ratio T of these transmitted powers gives an average absorption coefficient $\langle\alpha\rangle$ defined by

$$T = e^{-\langle\alpha\rangle d} \tag{2}$$

where d is the thickness of the crystal. We point out that it is a mean value because the powers of the beams decrease along the crystal and therefore the free carrier density is also decreasing.

The wavelength selected from the CO laser was chosen near 5.3 μm to make easier the comparison with the SHG case. Figs. 3 and 4 give the variation of $\langle\alpha\rangle$ as a function of the incident peak powers P_1 (10.6 μm) and P_2 (5.3 μm) *inside* the crystal. The results were obtained under two different experimental conditions. Without selection of the fundamental TEM_{00} mode, the peak power of the CO laser is larger, and the process ($\hbar\omega_2 + \hbar\omega_2$) more easily observed. The results obtained in these conditions are given on Fig. 3. On the contrary, when operating the CO laser in the TEM_{00} mode, more precise absolute values can be expected; indeed the results, given in Fig. 4, are slightly different.

Two typical variations are apparent from these results: 1) with 5.3-μm power smaller than 5 W, the induced absorption coefficient $\langle\alpha\rangle$ is proportional to the product P_1P_2, 2) with 10.6-μm power smaller than 10 W, $\langle\alpha\rangle$ is proportional to the square of 5.3-μm power P_2.

In case 1) the major process is ($\hbar\omega_1 + \hbar\omega_2$), while the other process is preponderant in case 2). When $\langle\alpha\rangle$ is smaller than 0.5 cm^{-1}, the curves interpolated from the experimental points follow the simple relation

$$\langle\alpha\rangle = WP_1P_2 + W'P_2^2 \tag{3}$$

where W and W' are some coefficients, proportional to TPA coefficients β and free carrier cross section Σ. However, when $\langle\alpha\rangle$ is greater than 0.5 cm^{-1} this relation is not obeyed. This point will be discussed in the next section, when analyzing the results more precisely.

C. Wavelength Dependence of TPA

We measured the variation of the induced absorption as a function of the frequency ω_2 selected from the CO laser output; the other frequency ω_1 was kept constant. These measurements were made in the range of powers P_1 and P_2 where $\langle\alpha\rangle$ is smaller than 0.5 cm^{-1}, so that (3) is valid. In Fig. 5 is

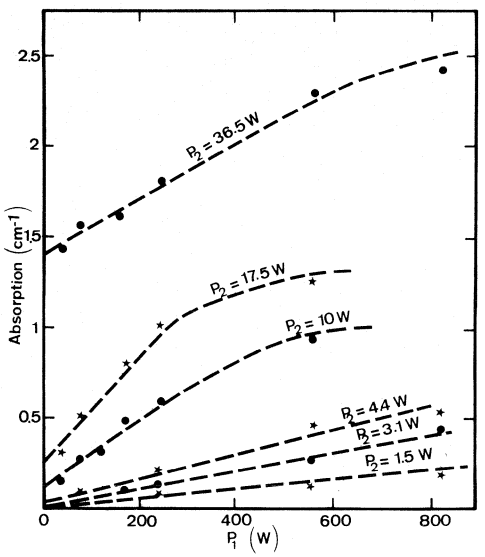

Fig. 3. Variation of the induced absorption $\langle\alpha\rangle$ as a function of the incident peak powers. Experimental points obtained with multimode CO laser operation. The dotted curves are interpolations of the experimental points.

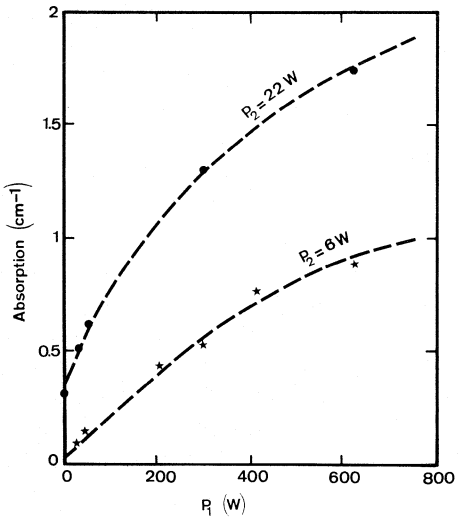

Fig. 4. Variation of $\langle\alpha\rangle$ as a function of incident peak powers. Experimental points and interpolating curves obtained with TEM_{00} CO laser.

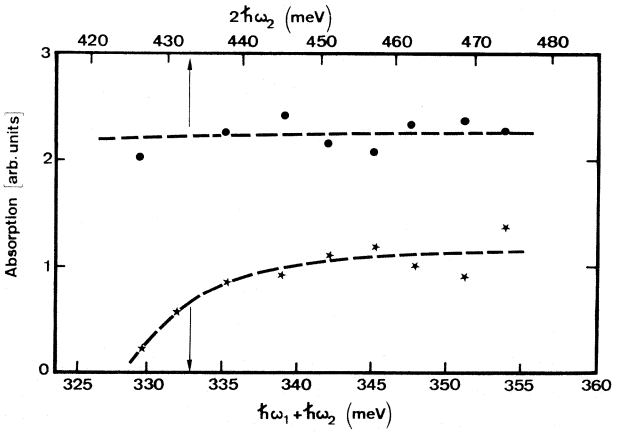

Fig. 5. Variation (at constant powers) of the induced absorption with the wavelength of the CO laser. Upper curve: ($\hbar\omega_2 + \hbar\omega_2$) process—Lower curve: ($\hbar\omega_1 + \hbar\omega_2$) process.

shown the variation of the coefficients W and W' as a function of $\hbar(\omega_1 + \omega_2)$ and of $2\hbar\omega_2$, respectively. It can be seen that W', related to the process $(\hbar\omega_2 + \hbar\omega_2)$, does not depend strongly on ω_2; besides, W becomes negligible when $\hbar(\omega_1 + \omega_2)$ approaches the value of 0.328 eV, which is the value of the energy gap E_g in tellurium [2], [3].

The symmetry properties of valence and conduction states near the minimum gap of tellurium indicate that "allowed-allowed" transitions can take place [4]. In this case, theoretical calculations [5] predict that the wavelength dependence of TPA should be $\propto(\hbar\omega_1 + \hbar\omega_2 - E_g)^{1/2}$ with parabolic energy bands, but the experimental uncertainties make the comparison with this theoretical dependence difficult. However, one can see in Fig. 5 that the agreement with this prediction is not too bad.

IV. Analysis of the Results

These experimental results are clearly understood within the frame of the previous analysis and they confirm the validity of the hypothesis made in Part I. Nevertheless, the power dependence of the induced absorption must be discussed more carefully, in order to compare the absolute values of induced absorption with the adjustable coefficient B, introduced in Part I, describing the probability of two-photon transition.

It has been seen in Figs. 3 and 4 that, above 0.5 cm^{-1}, the measured induced absorption is lower than the values that could be predicted using (3) with W and W' deduced from the smaller induced absorptions. One possible explanation is that what is measured is a mean absorption coefficient, which we have called $\langle\alpha\rangle$. This coefficient is expected to be smaller than the local absorption coefficient at the front plane of the crystal. So it seems that the departure from (3) is caused by the difference between $\langle\alpha\rangle$ and the front-plane induced absorption. In order to test this hypothesis we have calculated what should be the mean absorption, taking account for the decrease of the induced absorption coefficient along the crystal. To achieve this, one can use the system of equations (19) given in Part I (with $C = 0$ since here we neglect SHG). As the relative phase of the two waves is irrelevant here, these equations can simply be expressed in terms of the intensities I_1 and I_2 instead of the electric field amplitudes. One obtains

$$\frac{\partial I_1}{\partial z} = -(\alpha_1 + \alpha_1'' + \beta_{12} I_2) I_1 \tag{4a}$$

$$\frac{\partial I_2}{\partial z} = -\left(\alpha_2 + \left(\frac{\omega_1}{\omega_2}\right)^2 \alpha_1'' + \frac{\omega_2}{\omega_1}\beta_{12} I_1 + \beta_{22} I_2\right) I_2 \tag{4b}$$

$$\frac{\partial \alpha_1''}{\partial t} = \Sigma(\omega_1)\left(\frac{\beta_{12}}{\hbar\omega_1} I_1 I_2 + \frac{\beta_{22}}{2\hbar\omega_2} I_2^2\right) - \frac{\alpha_1''}{\tau} \tag{4c}$$

with the same notations as in Part I.

In this system the quantities I_1, I_2, and α_1'' are functions of x, y, z, and t. Thus an exact solution of this system would require a knowledge of the transverse variation (x, y) of the beam intensities I_1 and I_2 on the front plane of the crystal $(z = 0)$. As one set of experimental results was obtained with multimode CO laser operation, one can only expect an approximate description, due to incomplete knowledge of the transverse variations of the beams. This is why we use a simplified formulation of (4). First, we neglect the pure TPA terms, that is the terms $\beta_{12} I_1 I_2$ and $\beta_{22} I_2^2$ in (4a) and (4b), since we have shown they were very small compared to the terms containing α_1''. Second, we express the equations in terms of the powers P_1, P_2 of the beams, and an average absorption coefficient $\bar{\alpha}$, defined by

$$\iint \alpha_1'' I_1 \, dx \, dy = \bar{\alpha} \iint I_1 \, dx \, dy = \bar{\alpha} P_1. \tag{5}$$

Further we also assume that

$$\iint \alpha_1'' I_2 \, dx \, dy = \bar{\alpha} P_2$$

which is justified inasmuch as the spot sizes are not very different.

The integration of both terms of (4a) and (4b) with respect to x and y leads to

$$\begin{cases} \dfrac{\partial P_1}{\partial z} = -(\alpha_1 + \bar{\alpha}(z, t)) P_1 \\ \dfrac{\partial P_2}{\partial z} = -\left(\alpha_2 + \dfrac{\omega_1^2}{\omega_2^2}\bar{\alpha}(z, t)\right) P_2 \\ \dfrac{\partial \bar{\alpha}}{\partial t} = F P_1 P_2 + F' P_2^2 - \dfrac{\bar{\alpha}}{\tau} \end{cases} \tag{6}$$

where F and F' are proportional to β_{21} and β_{22}, respectively; the relations between these coefficients can be calculated in the case of Gaussian beams and the derivation will be given hereafter.

Numerical solutions of system (6) have been computed, with proper adjustment of F and F'. Then $\langle\alpha\rangle$ was derived by means of (2). The results are given in Figs. 6 and 7 together with the interpolated curves of Figs. 3 and 4. In Fig. 6 we used the values

$$F = 0.43 \times 10^4 \text{ cm}^{-1} \text{ s}^{-1} \text{ W}^{-2}$$

$$F' = 1.4 \times 10^4 \text{ cm}^{-1} \text{ s}^{-1} \text{ W}^{-2}$$

to fit the results of Fig. 3 (multimode CO laser), and in Fig. 7 the values

$$F = 1.2 \times 10^4 \text{ cm}^{-1} \text{ s}^{-1} \text{ W}^{-2}$$

$$F' = 2 \times 10^4 \text{ cm}^{-1} \text{ s}^{-1} \text{ W}^{-2}$$

were used to fit the results of Fig. 4 (TEM_{00} CO laser).

As was expected from qualitative arguments, the calculated curves are not straight lines, but their curvature is less pronounced than that of the experimental curves. So this model is not sufficient to explain the experimental results at high induced absorption.

We propose another explanation, taking into account the refractive index variation due to the free carriers. This variation gives rise to a considerable refractive index gradient which is thought to cause defocusing of the beams. This point was not investigated experimentally but a rapid estimate suggests that this effect may be important. Consider a Gaussian beam incident on the front face of the crystal $(z = 0)$. Assuming the shape of the amplitude profile to be unchanged (aberationless approximation [6]) the electric field amplitude E can be

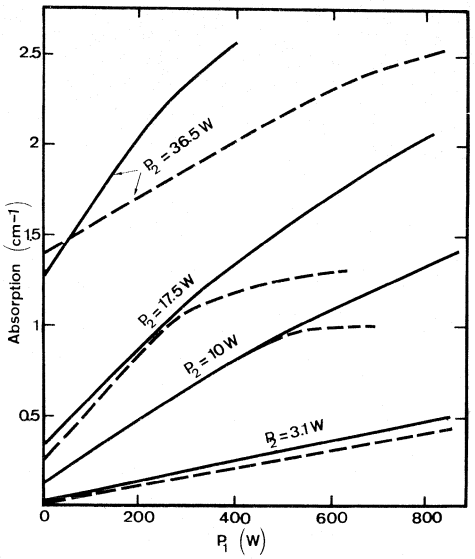

Fig. 6. Numerical solutions of system (6) with $F = 0.43 \times 10^4$ and $F' = 1.4 \times 10^4$ cm^{-1} s^{-1} W^{-2} (solid lines), together with the experimental curves of Fig. 3 (dotted lines).

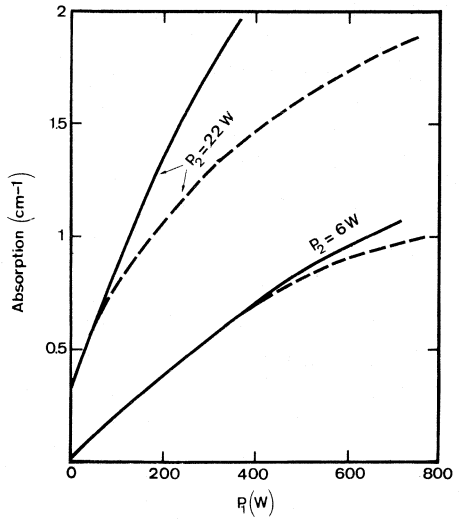

Fig. 7. Numerical solutions of system (6) with $F = 1.2 \times 10^4$ and $F' = 2 \times 10^4$ cm^{-1} s^{-1} W^{-2} (solid lines), together with the experimental curves of Fig. 4 (dotted lines).

written in the form

$$E(r,z) = \frac{E_0}{f(z)} \exp\left(-r^2/w_0^2 f^2(z)\right). \tag{7}$$

The refractive index is

$$n = n_0 + \delta n_0 \exp\left(-r^2/a_0^2\right) \tag{8}$$

where the second term is the variation induced by the free carriers in excess. When this term is approximated by $\delta n_0(1 - r^2/a_0^2)$, then $f(z)$ is given by

$$\frac{d^2 f}{dz^2} = \frac{-2}{a_0^2} f \frac{\delta n_0}{n_0}. \tag{9}$$

As δn_0 is negative (see (14) in Part I) the solution is

$$f = \cosh(\kappa z), \qquad \kappa = (-\delta n_0/n_0)^{1/2}/a_0.$$

Using the estimation of $\delta n_0/\alpha_1''$ made in Part I, one can calculate that when the induced absorption α_1'' at 10.6 μm is equal to 1 cm^{-1}, $\delta n_0 \simeq -2 \times 10^{-3}$; this leads to $\kappa = 4.5$ cm^{-1} with $a_0 = 45$ μm, which means that the *intensity of the CO_2 laser beam is reduced by a factor 2 after a length of only 2 mm in the crystal.*

So this quick estimate shows that very probably the effect of self-defocusing is responsible for the discrepancy between the experimental and calculated curves of Figs. 6 and 7, when $\langle\alpha\rangle \sim 1$ cm^{-1}. Nevertheless, in the limit of small induced absorptions any defocusing is expected to be negligible so that the results can be used to calculate the TPA coefficient in tellurium.

To achieve this it is necessary to derive the relation between the coefficients F and F' in (6) and the two-photon coefficients β_{12} and β_{22} of system (4). This derivation is only possible in a simple way when:

1) the intensity profile of the beams is known; that is why we will use only the data relative to TEM_{00} CO laser operation;
2) this profile is unchanged all along the crystal, which occurs when the induced free carrier density is so small that there is no defocusing, and only slight absorption takes place;
3) any diffusion of the free carriers is neglected.

Assume that these conditions are fulfilled, and that the intensities I_1 and I_2 can be written as

$$\begin{cases} I_1(x,y,z,t) = I_1^0(z,t)\, e^{-q_1(x^2+y^2)} \\ I_2(x,y,z,t) = I_2^0(z,t)\, e^{-q_2(x^2+y^2)} \end{cases} \tag{10}$$

where $q_1 = 2/w_1^2$ and $q_2 = 2/w_2^2$. Then, using (4c), α_1'' is the sum of two terms

$$\alpha_1'' = \alpha_{12}''(z,t)\, e^{-(q_1+q_2)(x^2+y^2)} + \alpha_{22}''(z,t)\, e^{-2q_2(x^2+y^2)} \tag{11}$$

where α_{12}'' and α_{22}'' are given by

$$\begin{cases} \dfrac{\partial \alpha_{12}''}{\partial t} = \Sigma(\omega_1) \dfrac{\beta_{12}}{\hbar\omega_1} I_1^0 I_2^0 - \dfrac{\alpha_{12}''}{\tau} \\ \dfrac{\partial \alpha_{22}''}{\partial t} = \Sigma(\omega_1) \dfrac{\beta_{22}}{2\hbar\omega_2} (I_2^0)^2 - \dfrac{\alpha_{22}''}{\tau}. \end{cases} \tag{12}$$

So, when using (5), (10), and (11) one readily obtains

$$\bar{\alpha} = \frac{q_1}{2q_1 + q_2} \alpha_{12}'' + \frac{q_1}{q_1 + 2q_2} \alpha_{22}''. \tag{13}$$

This equation shows that, due to the Gaussian beam shape, the absorption efficiency of the free carriers is divided by a factor depending on the relative sizes of the beams.

As $\bar{\alpha}$ is a linear combination of α_{12}'' and α_{22}'' the two equations (12) can be joined together to give

$$\frac{\partial \bar{\alpha}}{\partial t} = \frac{\Sigma(\omega_1)}{2 + w_1^2/w_2^2} \frac{\beta_{12}}{\hbar\omega_1} I_1^0 I_2^0 + \frac{\Sigma(\omega_1)}{1 + 2\, w_1^2/w_2^2} \frac{\beta_{22}}{2\hbar\omega_2} (I_2^0)^2 - \frac{\bar{\alpha}}{\tau}. \tag{14}$$

This equation is equivalent to the last equation of system (6), so F and F' are given by

$$\begin{cases} F = \dfrac{\Sigma(\omega_1)}{2 + w_1^2/w_2^2} \dfrac{\beta_{12}}{\hbar\omega_1} \dfrac{\pi^2}{4w_1^2 w_2^2} \\ F' = \dfrac{\Sigma(\omega_1)}{1 + 2\, w_1^2/w_2^2} \dfrac{\beta_{22}}{2\hbar\omega_2} \dfrac{\pi^2}{4w_2^4}. \end{cases} \tag{15}$$

To calculate β_{12} and β_{22} we use the values of F and F' relative to TEM_{00} CO laser operation (Figs. 4 and 7). With these values one obtains

$$\beta_{12} = 0.2 \text{ cm/MW}$$

$$\beta_{22} = 0.8 \text{ cm/MW}.$$

Let us now compare these values of TPA coefficients with other estimations or measurements on tellurium.

First an estimate of β_{12} is readily calculated from the results of Part I, where a good agreement with SHG data was obtained when using (19) of Part I with $B = 7$ ESU and $B' = 0$. With the simplifying assumption that the beams are collimated plane waves one can relate B to β_{12} and one obtains $\beta_{12} = (8\pi/c)^2 \cdot \hbar\omega_1 B/(n_1 n_2\, \Sigma(\omega_1))$. The numerical value is of the order of 10^{-2} cm/MW, which is much smaller than the value obtained here. This discrepancy is probably due to the crudeness of the collimated plane-wave approximation. We can see in (13) and (15) that, in the case of Gaussian beams, the effect of this transverse variation is *to reduce* the absorption by a geometrical factor (for instance $2 + w_1^2/w_2^2$). With the experimental conditions of phase-matched SHG, this situation is complicated by the influence of double refraction. Qualitatively, one can foresee that the reduction is more important than in the above case. Roughly speaking, the geometrical factor should depend on z, the correction being greater when z is larger than the "aperture length" ($z \gtrsim l_a$) due to a smaller overlap of the fundamental (extraordinary) and harmonic (ordinary) waves. So it is not surprising to encounter such a difference when making a plane-wave treatment as in Part I. But a more refined treatment would have involved much more complicated computations and we can consider the value of B given in Part I as an effective coefficient. In addition, the maximum SHG conversion efficiency does not depend critically on the exact value of B. For example, using $B = 100$ ESU instead of 7 ESU, 8-percent conversion efficiency is still predicted by our model in the case of tellurium.

Our value for β_{12} can also be compared to the estimate given by Malz *et al.* [7]. Their observations on photoconductivity led to $\beta_{12} \simeq 0.7 \times 10^{-2}$ cm/MW, which is also a very small value compared to ours. It should be noted that such discrepancies frequently occur between TPA measurements [8]-[10], due to the fact that the magnitude of the process is very sensitive to the mode structure (and hence the spatial intensity distribution) of the incident beam. In addition to a photoconductive signal proportional to the product of 5.3 μm and 10.6 μm intensities, these authors have also observed a signal when the crystal was irradiated with a CO_2 laser, even without second-harmonic phase matching. The generated free carriers were cubic in the laser intensity ($\propto I_1^3$) and this has been attributed to *three-photon absorption*. This contribution seems very unlikely, and we think that the second harmonic generated in the crystal—even in the case of phase mismatch—may have sufficient power density to induce TPA with the fundamental wave. The same cubic law is then expected since the harmonic intensity is $\propto I_1^2$. With a coherence length of $l_c = 106$ μm and the TPA coefficient $\beta_{12} = 0.2$ cm/MW, we find

$$dN_e = C I_1^3\, dt, \qquad \text{with } C = 430 \text{ cm}^3 \text{ W}^{-3} \text{ s}^{-1}.$$

This value is in quite good agreement with the experimental estimate [7] of $C \simeq 10^3$ cm^3 W^{-3} s^{-1}. So, the observation reported by Malz *et al.* is probably due to not-phase-matched SHG followed by TPA, rather than to a direct three-photon process.

V. Conclusion

In Part I, we have set up a system of equations to describe the competition between SHG and TPA in semiconductors, and particular attention has been given to the effects of the TPA-induced free carriers. It has been found that the numerical solution of these equations could give account of the experimental results of SHG in tellurium, with a suitable choice of three adjustable parameters. Then we have used these equations to make some predictions about the optimization of harmonic conversion efficiency. The results obviously show there exists an optimal value of the fundamental intensity, and make clear the advantage of using short pulses. For instance, conversion efficiency up to 25-30 percent could be obtained by using 1-ns pulses; so far, such a conversion has never been reached in the medium infrared.

Then, in Part II, owing to the number of unverified assumptions that had been made, we have reported a direct measurement of the absorption at 10 μm induced by an independent 5-μm beam. This experiment has confirmed the principal hypothesis made in Part I, and the three adjustable parameters have been related to some physical quantities of tellurium, namely, the TPA coefficient, and the lifetime and absorption cross section of the free carriers. In addition, this experiment has shown the importance of the free carriers induced by a CO laser beam alone—with 200-ns pulses, a 5.5-μm beam of only 100 kW/cm^2 is sufficient to induce a free carrier density of about 10^{15} cm^{-3}. So, as a consequence, it would be hopeless to attempt any parametric oscillation in tellurium using a 5-μm pump.

This conclusion can probably be extended to any semiconductor whose energy gap is smaller than twice the photon energy of the pump beam. A shorter carrier lifetime could reduce the free carrier density, but not enough; with a lifetime as short as 1 ns and approximately the same two-photon cross section as in tellurium, a pump intensity of 10 MW/cm^2 would induce 10^{17} carriers per cubic centimeter. The absorption caused by such a carrier density, nearly negligible in the visible range or the near infrared, would prevent parametric oscillation in the medium infrared. So this effect is a major obstacle to the use of small-gap semiconductors in parametric devices, in spite of their other advantages.

Acknowledgment

The authors wish to thank Dr. J. Jerphagnon for his stimulating interest during this work. They wish to acknowledge very fruitful discussions with Dr. D. S. Chemla, Dr. G. Rebmann,

and Dr. R. Eymard, and they would like to thank Dr. P. Kupecek and Dr. G. Duraffourg for their comments on the manuscript.

REFERENCES

[1] W. B. Gandrud and R. L. Abrams, "Reduction in SHG efficiency in tellurium by photoinduced carriers," *Appl. Phys. Lett.*, vol. 17, pp. 302–305, 1970.
[2] J. J. Loferski, "Infrared optical properties of single crystals of tellurium," *Phys. Rev.*, vol. 93, pp. 707–714, 1954.
[3] J. M. Debever, thesis, Paris, 1968.
[4] T. R. Bader and A. Gold, "Polarization dependence of two-photon absorption in solids," *Phys. Rev.*, vol. 171, pp. 997–1003, 1968.
[5] R. Braustein and N. Ockman, "Optical double-photon absorption in CdS," *Phys. Rev.*, vol. 134, pp. A499–A507, 1964.
[6] S. A. Akhmanov, R. V. Khokhlov, and A. P. Sukhorukov, "Self-focusing, self-defocusing and self-modulation of laser beams," in *Laser Handbook*. Amsterdam, The Netherlands: North Holland, 1972, pp. 1151–1228.
[7] D. Malz, M. Pöhler, and G. Staupendahl, "Multiphoton absorption in tellurium by irradiation of CO_2 laser pulses," *Phys. Status Solidi* (b), vol. 58, pp. K35–K38, 1973.
[8] C. C. Lee and H. Y. Fan, "Two-photon absorption and photoconductivity in GaAs and InP," *Appl. Phys. Lett.*, vol. 20, pp. 18–20, 1972.
[9] J. M. Doviak, A. F. Gibson, M. F. Kimmit, and A. C. Walker, "Two-photon absorption in indium antimonide at 10.6 μm," *J. Phys. C*, vol. 6, pp. 593–600, 1973.
[10] D. A. Kleinman, R. C. Miller, and W. A. Holland, "Two-photon absorption of Nd laser radiation in GaAs," *Appl. Phys. Lett.*, vol. 23, pp. 243–244, 1973.

Correspondence

Chirp Modulated CO_2 Waveguide Laser

ALEXANDER STEIN

Abstract—**Repetitive chirp modulation of a stable CO_2 waveguide laser yielded chirps of 75-MHz width and 2-μs duration. A demodulation technique is demonstrated which permits coherent detection of such a signal for periods extending over many chirps.**

With the development of CO_2 waveguide lasers of GHz tuning range [1], these devices are finding application as master oscillators in certain 10-μ radar systems, where one measures the fine structure in range and Doppler shift in analogy to high-resolution radar.

In considering the modulation formats of equivalent microwave radars, one finds that periodic chirp modulation is ideally suited for adaptation to optical systems [2].[1] Each returning chirp pulse yields the instantaneous range pattern, while the Doppler fine structure manifests itself in a slow variation of the optical phase which must be observed over an entire chirp train.

We report here the demonstration of a demodulation technique which permits the detection of slow phase variations in the presence of the much larger—but rapid and repetitive—phase excursions imparted by the chirps.

The device consisted of a 5-in-long BeO capillary tube with a 1.5-mm bore. Pyrex assemblies containing the electrodes, the evacuation port, and Brewster windows were epoxied to the capillary tube. This vessel was evacuated and back-filled with a mixture of He, CO_2, N_2, and Xe in the ratio 4:1:1:0.15 to a total pressure of 100 torr. A metallized, highly reflecting mirror of 15-cm radius of curvature and a dielectric multilayer mirror of 0.02 transmission with a 20-cm radius of curvature were placed at 14.5- and 19.5-cm distance, respectively, from either capillary aperture. An output power of 1.75 W was measured for this configuration. When an AR-coated 4-cm-long cadmium telluride modulator crystal was inserted between the metallized mirror and the plasma tube (and the mirror position adjusted for the effective change in reflector curvature) the output was reduced to 0.3 W. The sharp drop in power was caused by an increase in resonator loss from 0.04 to 0.12 per round trip upon insertion of the modulator; the round-trip gain was 0.19.

The CdTe crystal was cut for optimum phase modulation; i.e., the applied electrical field and the optical polarization were aligned with the ⟨111⟩, and the optical propagation direction with the ⟨110⟩ crystal axis [3]. The half-wave voltage for this modulator was V_0 = 6.9 kV, and the frequency shift for a voltage V

$$f_B = \frac{c}{2L}\frac{V}{V_0} \tag{1}$$

where c is the velocity of light and L the optical resonator length.

Maximum unambiguous frequency excursion, equal to the resonator free spectral range, is obtained at the half-wave voltage. For a cavity free spectral range of $c/2L$ = 300 MHz we attained a chirp width of 75 MHz at an output power of 0.3 W, while an equivalent extracavity modulation technique yielded 0.002 W of modulated optical power [4]. A proportionally larger chirp width can be attained by increasing the resonator free spectral range and/or the modulator voltage. The following describes the demodulation experiment which is a crucial part of the referenced lidar development.

In the experimental setup illustrated in Fig. 1, the master oscillator was chirped over 20 MHz by applying a ramp voltage, 0–500 V in 2 μs, to the crystal. (While a 75-MHz chirp width was obtained for a peak voltage of 1750 V, we reduced the voltage for the demodulation experiment to obtain a linear ramp.) The modulated laser output was optically mixed with the reference laser such that the IF signal swept from 10 to 30 MHz. The photoelectric sweep signal was first amplified and then mixed with a 20-MHz RF signal to yield a frequency sweep going through a zero beat. Fig. 2 shows an example of a demodulated chirp together with the modulation voltage. Note, one zero beat appears during the voltage ramp and a second one during flyback. We are interested in the signal value at the first zero beat and will show how it relates to the carrier phase.

The signal current at the RF-mixer output can be described by the expression

$$\begin{aligned} i &= i_0 \cos\left[-\Delta\omega t + \frac{\omega_B}{T}t^2 + \psi(t)\right] \\ &= i_0 \cos\left[\frac{\omega_B}{T}\left(t - \frac{\Delta\omega T}{2\omega_B}\right)^2 - \frac{\Delta\omega^2 T}{4\omega_B} + \psi(t)\right] \end{aligned} \tag{2}$$

where $\Delta\omega$ is the IF subcarrier; ω_B and T the chirp width and chirp period; and $\psi(t)$ is the phase modulation of interest. (In an actual lidar system master and local oscillators are locked

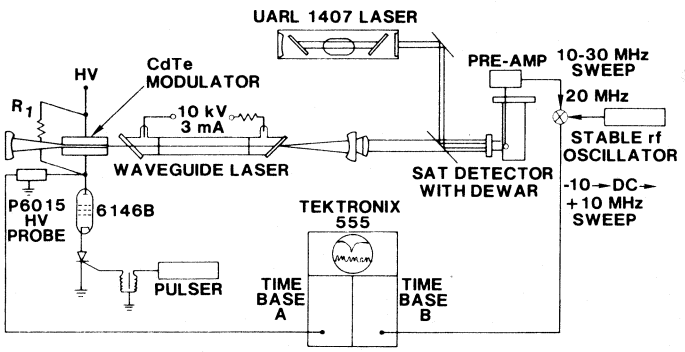

Fig. 1. Experimental setup for heterodyning of chirped waveguide laser and unmodulated references laser.

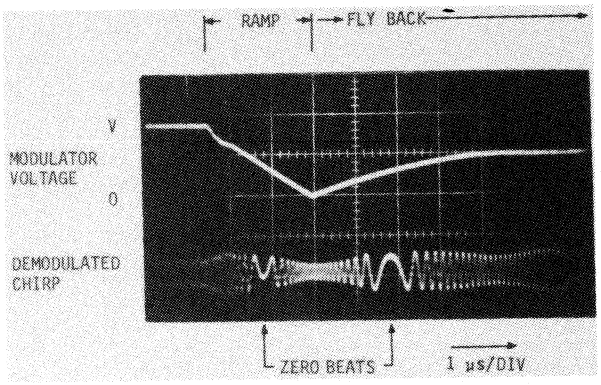

Fig. 2. Demodulated chirp.

Manuscript received January 20, 1975. This work was supported by ARPA/ONR under Contract N00014-73C-0086.

The author was with United Aircraft Research Laboratories, East Hartford, Conn. 06108. He is now with AIL, Cutler-Hammer, Melville, N.Y. 11746.

[1] Demonstrated in the ALCOR Radar System.

and $\psi(t)$ represents the modulation of the return signal's optical phase due to the Doppler signature of the target.) Note that a zero beat occurs at $t_1 = (\Delta\omega T/2\omega_B)$ and that the relative value of the signal current at that point determines $\psi(t_1)$ since the term $(\Delta\omega^2 T/4\omega_B)$ is known. The next chirp, which is a replica of the first one at a period τ later, yields

$$i = i_0 \cos\left[-\Delta\omega(t+\tau) + \frac{\omega_B}{T}t^2 + \psi(t+\tau)\right]$$
$$= i_0 \cos\left[\frac{\omega_B}{T}\left(t - \frac{\Delta\omega T}{2\omega_B}\right)^2 - \frac{\Delta\omega^2 T}{4\omega_B} - \Delta\omega\tau + \psi(t+\tau)\right] \quad (3)$$

where t is always counted from the beginning of each chirp. The zero beat occurs at $t_1 + \tau$ and the inverse cosine of the relative signal value at that point yields the phase value $\psi(t_1 + \tau)$ but for the known constant $-(\Delta\omega^2 T/4\omega_B) - \Delta\omega\tau$. For convenience, one may lock the chirp initiation to the IF carrier such that $\Delta\omega\tau = m2\pi$ ($m = 1, 2, \cdots$). In general we find for the nth chirp then

$$\psi(t_1 + n\tau) = \cos^{-1}\left[\frac{i(t_1 + n\tau)}{i_0}\right] + \frac{\Delta\omega^2 T}{4\omega_B}. \quad (4)$$

The phase modulation of interest is thus sampled through an entire train of chirp pulses. Precise chirp repetition is critical; as an example: for $(\Delta\omega/2\pi) = 10$ MHz, $\omega_B/2\pi = 75$ MHz, $T = 2$ μs, a 1-percent variation in chirp rate (ω_B/T) results in a phase error of 0.04 rad.

For an actual sampling circuit an electronic sampling window must be placed at zero beat; i.e., at time position t_1 after each ramp initiation.

From (2) we ascertain that the signal current at zero beat is essentially constant for a period $\delta t << \sqrt{(2\pi T/\omega_B)}$. For the chirp illustrated in Fig. 2, $T = 2 \times 10^{-6}$ s and $(\omega_B/2\pi) = 20$ MHz, yielding $\sqrt{(2\pi T/\omega_B)} = 300$ ns as a lower limit on the accuracy of the delay time t_1.

In summary, a demodulation technique previously used in microwave chirp radar [2] was demonstrated for a 10-μ system. This is an important step towards the construction of coherent lidars.

References

[1] R. L. Abrams, "Gigahertz tunable waveguide CO_2 laser," *Appl. Phys. Lett.*, vol. 25, pp. 304-306, Sept. 1, 1974.

[2] T. J. Gilmartin and W. E. Bicknell, private communication, Mass. Inst. Technol. Lincoln Labs., Lexington, Mass.

[3] I. D. Kaminow and E. H. Turner, "Electrooptic light modulators," *Proc. IEEE (A Joint Special Issue on Optical Electronics)*, vol. 54, pp. 1374-1390, Oct. 1966.

[4] W. E. Bicknell, private communication.

A Recirculating, Self-Contained DF/HF Pulsed Laser

D. W. FRADIN, P. P. CHENAUSKY, AND R. J. FREIBERG

Abstract—**The operation of the first self-contained, recirculating, electrically initiated, pulsed chemical laser is reported. A unique combination of scrubber beds selectively removes ground-state DF(HF) and other deleterious gases from the recirculating gas flow. By providing a small gas replenishment, it is possible to operate the laser for extended periods of time with little loss in power. The processes that degrade the power output in the absence of chemical scrubbing are discussed.**

The range of applications for pulsed HF/DF laser technology has been limited by the inherent safety hazards associated with both the laser fuels and the toxic laser exhaust. In addition, the weight and inconvenience of the vacuum pump needed for many conventional systems have precluded applications where portability is required. In recent years technological advances have provided specialized solutions to some of these problems. Such alternate fuel sources [1] as SF_6 have been successfully used in pulsed [2]-[4] and CW [5] HF/DF lasers operating at low and moderate power levels. In addition, chemical scrubber beds [6] have been found to be effective in reducing the concentrations of poisonous gases in the laser effluence. Despite these advances, conventional open-cycle HF/DF chemical lasers are generally bulky and poorly suited to applications outside the laboratory.

In this correspondence we report the successful operation of the first self-contained, recirculating DF/HF chemical laser. This laser, which utilizes a pulsed electrical discharge in a 95-torr mixture of SF_6 and either D_2 or H_2 [2]-[4], [7], provides solutions to several of the remaining problems that had previously prevented practical field applications of pulsed DF and HF lasers. In this system the laser effluence is chemically scrubbed within the low-pressure vacuum envelope, thereby removing the DF(HF) and other discharge by-products that tend to degrade laser action. The chemically scrubbed gas is then recirculated into the common laser cavity and discharge region. By providing a small replenishment of SF_6 and $D_2(H_2)$ to compensate for the gas removed in the scrubbing process, it is possible to operate the laser for long periods of time as a closed system. The recirculation and reclamation of the major portion of the premixed gas reduces the measured-gas consumption rate to less than 2 percent of that needed for comparable output power under open-cycle conditions. The bulky vacuum pump, required for conventional open-cycle chemical lasers, is replaced by a small gas circulator that is relatively lightweight [8]. In addition, details of operation in the recirculating mode provide insight into certain reaction mechanisms initiated with the laser discharge as well as aspects of the subsequent gas chemistry occurring within the vacuum envelope.

Fig. 1 summarizes the basic design of the DF/HF recirculating laser. The laser channel is a scaled-down version of the multipin electrical discharge of [3]. A gas mixture of 85-torr SF_6 and 10 torr of either D_2 or H_2 is normally used with this system. Voltage pulses of up to 32 kV with a 50 ns [full width at half maximum (FWHM)] duration provide a spatially averaged E/p of about 250 $Vcm^{-1}torr^{-1}$ at the peak of the discharge pulse. Output energies per pulse of up to 28 mJ with DF and 32 mJ with HF and electrical efficiencies of over 2 percent have been obtained in an active volume of 9 cm^3. After being

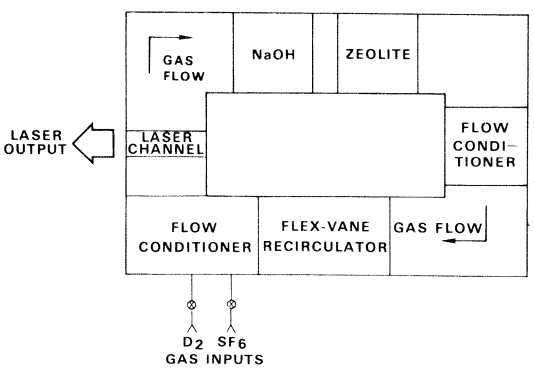

Fig. 1. Schematic of recirculating, self-contained DF chemical laser system.

Manuscript received January 21, 1975. This work was supported in part by the Defense Advanced Projects Agency and monitored by the Army Electronics Command.

The authors are with the United Technologies Research Center, East Hartford, Conn. 06108.

lased, the deexcited laser gas is convected out of the optical cavity and into the scrubber beds. In the experiments with DF reported here, solid pellets of NaOH and zeolite (Molecular Sieve type 5A) were used. Neither bed was cooled. The NaOH was used primarily to neutralize the DF in the circulating gas flow through the reaction DF + NaOH → NaF + DHO. The zeolite served to effectively remove the water vapor released in the neutralization process as well as any residual DF which was not converted by the NaOH. Small quantities of SF_6 and D_2 were replenished in the selectively scrubbed effluence prior to reentering the laser cavity. Gas-flow conditioning was employed to correct the nonuniform velocity profile of the gas flow.

Data demonstrating the efficacy of the scrubber beds are shown in Fig. 2. Although these data and the subsequent discussion apply specifically to the DF laser, virtually the same results were obtained with HF. With a total mass of NaOH and zeolite of approximately 450 g, the laser could be operated for 1 h, suffering a power loss of only about 19 percent. Under these conditions, the average power at the start of lasing was 0.13 W at a pulse-repetition frequency (PRF) of 10 Hz. When the beds were removed, about 30 percent of the power was lost during the first 2 min of operation, and the remaining power decayed exponentially with a time constant of about 5 min. In a similar experiment utilizing 290 g of zeolite and no NaOH, 1-h operation resulted in a 25-percent power loss. This result indicates that zeolite itself is very efficient in removing DF from the circulating flow.

For an average laser output of 0.13 W, the measured-gas replenishment rates for the DF laser were 1.6 torr/min of D_2 (or 2.7×10^{-4} moles/min) and 0.8 torr/min of SF_6 into a total gas ballast of 3.5 l. This replenishment rate exactly compensated for the pressure reduction in the system resulting from the gas removal by the scrubbing beds. The power output was generally much more sensitive to the D_2 replenishment rate than the SF_6 rate, and, in fact, no measurable power loss was observed over 15-min operating periods when only D_2 was replenished. Under the conditions of gas recirculation without electrical-discharge initiation, the gas pressure stayed constant without replenishment, thus indicating that the beds, as expected, removed neither SF_6 nor D_2 from the flowing gases.

The rapid loss in laser power exhibited by the data in Fig. 2 when the recirculating laser was operated without scrubber beds might be attributed to a combination of the following three processes: radiation trapping of the $v = 1$ to $v = 0$ transitions due to the accumulated ground-state DF molecules; vibrational relaxation of DF* by collisions with ground-state DF; and other processes in the active medium in which accumulated reaction by-products effectively reduce either the rate of fluorine-atom production or the rate of DF* formation.

A preliminary experiment was performed to assess the relative importance of radiative trapping processes in the temporal decay of the recirculating laser output when the beds were absent. These processes will occur predominantly in the $v = 1$ to $v = 0$ band whose lasing transitions initially comprise about 30 percent of the total laser output. The approximate magnitude of this effect is calculated from a simple argument. If no DF were lost from the recirculating gas flow, then after about 40 s of operation at a PRF of 10 Hz, the average concentration of accumulated ground-state DF in the gas ballast (3.5 l) would be equal to the instantaneous concentration of DF* created in the active medium (9×10^{-3} l) by a single electrical-discharge pulse. Under these conditions self-absorption from the ground-state DF should effectively quench lasing on the $1 \rightarrow 0$ band. In order to observe this selective quenching, the intensity of $P9(1 \rightarrow 0)$ laser transition, one of the most intense lines in the $1 \rightarrow 0$ band, was monitored with an Au:Ge detector and a 0.5-m Jarrel-Ash spectrometer. The temporal behavior of the laser transition was compared to a simultaneous measurement of the temporal decay of the total average laser power in the absence of gas scrubbing. As is shown in Fig. 3, the power in $P9(1 \rightarrow 0)$ did indeed fall rapidly to zero; in fact, more rapidly than the total laser power. The fact that several minutes of operation were required for the power loss as compared to the estimated time of 40 s is not surprising since this simple argument ignores both complications from rotational substructure and the fact that initially the DF molecules may be removed from the gas flow by reacting with the various surfaces in the recirculating flow channel.

Various vibrational transfer processes may also contribute to the power loss when the beds are removed. Because of the complexity of the physical and chemical mechanisms [7] occurring within the active medium and in the subsequent gas flow, the relative influence of such processes upon the temporal behavior of the laser output cannot be accurately determined without considerable analysis and additional experimental data. It is interesting to note, however, that the measured time constant of ~5 min for the DF-laser power loss would imply a vibrational energy-loss constant of about 8×10^5 s^{-1} $torr^{-1}$. This assumes that the rate of contamination buildup is equal to the estimated rate of DF formation (2.7×10^{-4} moles/min). By comparison, the measured vibrational energy-loss constant [9] for the self-deactivation of DF* ($v = 1$) by ground-state DF is only 0.24×10^5 s^{-1} $torr^{-1}$ at room temperature. This observation suggests that other vibrational deexcitation mechanisms may play an important role in the temporal decay of the DF-laser power when the gases are recirculated without scrubber beds. In order to more accurately assess the role of vibrational energy-loss processes, a mass-spectroscopic analysis is being conducted. The results of this study will be presented elsewhere.

In conclusion, a totally self-contained recirculating chemical laser has been successfully operated. This device operates by using room-temperature scrubber beds to selectively remove ground-state DF and other deleterious reaction by-products that would otherwise accumulate within the vacuum envelope. The viability of the recirculating chemical-laser device should

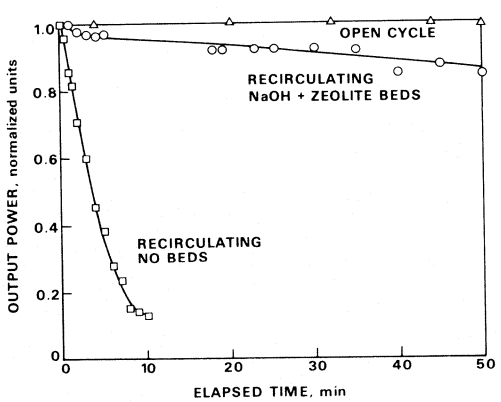

Fig. 2. Temporal dependence of normalized DF-laser output power.

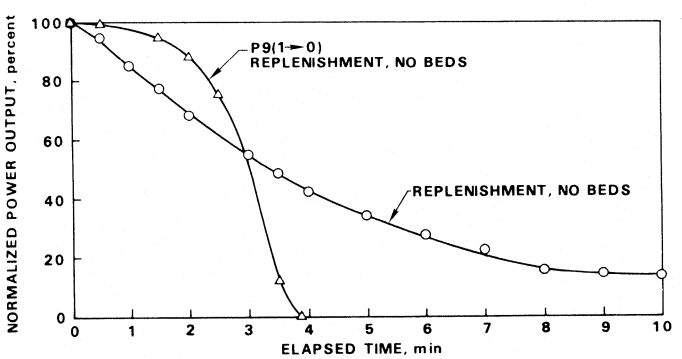

Fig. 3. Comparison of the temporal decay of the $P9(1 \rightarrow 0)$-line intensity with that of the total DF-laser output in the absence of gas scrubbing.

greatly expand the range of applications available for pulsed DF and HF laser systems.

ACKNOWLEDGMENT

The authors wish to thank F. R. Biancardi, Dr. R. Buser, Dr. H. Hieslmaier, Dr. J. J. Hinchen, Dr. L. Lynds, and Dr. R. M. Meinzer for helpful technical discussions. They also wish to thank M. Tamiso for his expert assistance during the experiments.

REFERENCES

[1] C. J. Ultee, "Pulsed hydrogen fluoride lasers," *IEEE J. Quantum Electron.* (Corresp.), vol. QE-6, pp. 647–648, Oct. 1970.

[2] H. Pummer and K. L. Kompa, "Investigation of a 1-J discharge-initiated HF laser," *Appl. Phys. Lett.*, vol. 20, p. 356, 1972.

[3] H. Pummer, W. Breitfeld, H. Wedler, G. Lement, and K. L. Kompa, "Parameter study of a 10-J hydrogen fluoride laser," *Appl. Phys. Lett.*, vol. 22, p. 319, 1973.

[4] a) R. G. Wenzel and G. P. Arnold, "A double-discharge-initiated HF laser," *IEEE J. Quantum Electron.* (Corresp.), vol. QE-8, pp. 26–27, Jan. 1972.
b) G. P. Arnold and R. G. Wenzel, "Improved performance of an electrically initiated HF laser," *IEEE J. Quantum Electron.* (Corresp.), vol. QE-9, pp. 491–493, Apr. 1973.

[5] J. J. Hinchen, "Operation of a small single-mode stable cw hydrogen fluoride laser," *J. Appl. Phys.*, vol. 45, p. 1818, 1974.

[6] A. C. Eckbreth, F. R. Biancardi, and R. J. Hall, U. S. Air Force Weapons Laboratories, UARL Final Rep. for Contract F29601-73-C-0027, June 1973.

[7] J. L. Lyman, "Computer model of the SF_6-H_2 electrical discharge chemical laser," *Appl. Opt.*, vol. 12, p. 2736, 1973.

[8] R. J. Wayne, C. J. Buczek, W. J. Green, and J. N. Elkins, "An airborne integrated CO_2 laser," in *Proc. 6th Department of Defense Conf.* (Colorado Springs, Colo., Mar. 1974).

[9] J. J. Hinchen, "Vibrational relaxation of hydrogen and deuterium fluorides," *J. Chem. Phys.*, vol. 59, p. 233, 1973.

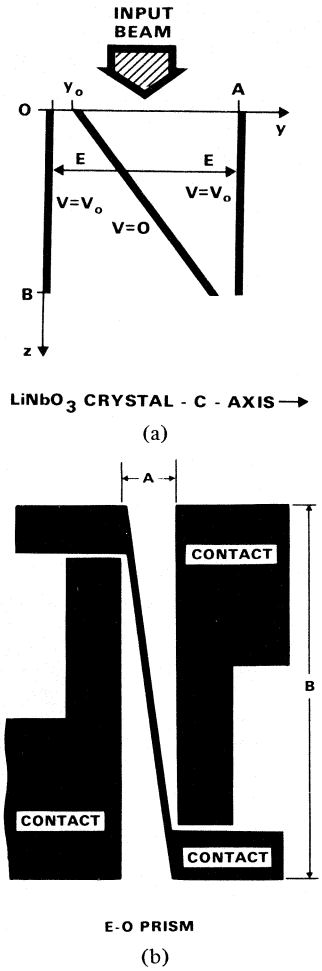

Fig. 1. Prism-electrode pattern. (a) Schematic. (b) Experimental.

A Planar Electrooptic-Prism Switch

I. P. KAMINOW AND L. W. STULZ

Abstract—**A novel electrode configuration for producing a prism-like deflector when applied to a planar optical waveguide is described. A prism deflector on a Ti-diffused $LiNbO_3$ waveguide was operated as a bipolar switch for electrode voltages of ±15 V.**

An electrooptically controlled prism deflector can serve as a multiport switch, the simplest example of which is a bipolar switch, which can also be operated as an optical shutter. We describe here an electrode pattern that can be applied to a planar optical waveguide in order to approximate an electrooptic prism in the planar geometry. The device is demonstrated using a titanium-diffused $LiNbO_3$ waveguide [1] operating at 0.633 μm as a bipolar switch requiring ±15 V for the two states. The electrode configuration is entirely different from those described earlier [2].

The prism-electrode pattern is illustrated schematically in Fig. 1(a). If we assume the width of the diagonal electrode to be much smaller than the separation A between the outer electrodes, then the distance from the left-hand electrode to the diagonal electrode is

$$d = y_0 + az \tag{1}$$

where a is the slope. The thickness of the planar waveguide is assumed to be much less than the spacing A. Hence the field $E_y(y, z)$ just below the surface of the crystal is [3]

$$E_y(y,z) = -\frac{V}{\pi}[y(d-y)]^{-1/2}, \qquad 0 < y < d$$

$$= +\frac{V}{\pi}[(A-y)(y-d)]^{-1/2}, \qquad d < y < A. \tag{2}$$

The electrooptically induced phase shift $\eta(y)$ for light polarized in the y direction and traveling along z at a given value of y is

$$\eta(y) = -\frac{\pi n_e^3 r_{33}}{\lambda}\int_0^B E_y(y,z)\,dz$$

$$= \eta_0 \begin{cases} \left(\dfrac{A-y_0-y}{y}\right)^{1/2} - \left(\dfrac{y_0-y}{y}\right)^{1/2}, & 0 < y < y_0 \\ \left(\dfrac{A-y_0-y}{y}\right)^{1/2} - \left(\dfrac{y-y_0}{A-y}\right)^{1/2}, & y_0 < y < A-y_0 \\ \left(\dfrac{y_0+y-A}{A-y}\right)^{1/2} - \left(\dfrac{y-y_0}{A-y}\right)^{1/2}, & A-y_0 < y < A \end{cases} \tag{3}$$

Manuscript received April 2, 1975; revised April 4, 1975.

The authors are with Bell Laboratories, Crawford Hill Laboratory, Holmdel, N.J. 07733.

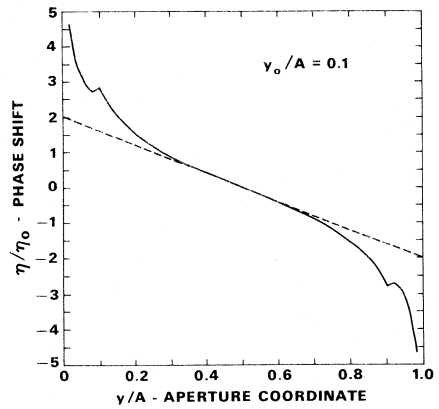

Fig. 2. Theoretical phase shift across electrode aperture and linear approximation for $y_0/A = 0.1$ (dashed).

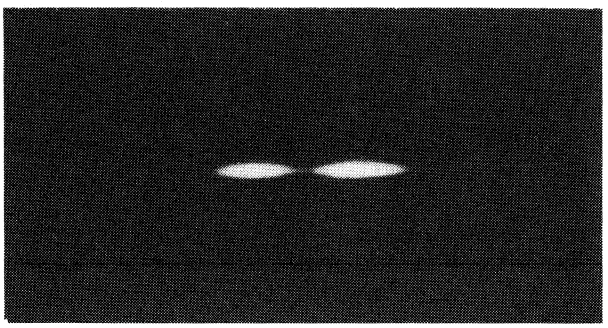

Fig. 3. Output spots for electrode voltages ± 15 V.

with

$$\eta_0 = \frac{2n_e^3 r_{33} V_0}{\lambda a} \tag{4}$$

where n_e is the extraordinary refractive index and r_{33} is the appropriate electrooptic coefficient.

In the approximation

$$y \approx A/2 \quad y_0 << A \quad a = A/B$$

the prismlike linear phase shift becomes

$$\eta(y) \approx 2\eta_0(1 - 2y/A). \tag{5}$$

This linear approximation is compared with the function (3) in Fig. 2 for $y_0/A = 0.1$. It can be seen that the approximation is satisfactory over about 70 percent of the aperture A.

The linear phase shift across the aperture causes the wavefronts to be rotated through a scan angle θ given by

$$\tan\theta = \frac{\lambda\eta(0)}{\pi n_e A} = \frac{4n_e^2 r_{33} B V_0}{\pi A^2}. \tag{6}$$

For a Gaussian beam having a diameter D at its waist, which is at the center of the prism, the beam angle between $1/e^2$ points is

$$\phi = \frac{4\lambda}{\pi n_e D} \tag{7}$$

and the number N of resolvable spots is, for small θ,

$$N = \frac{\theta}{\phi} = \frac{n_e^3 r_{33} B D V_0}{\lambda A^2}. \tag{8}$$

The experimental aluminum-electrode pattern shown in Fig. 1(b) was evaporated through a photolithographic mask onto a $LiNbO_3$ crystal having a Ti-diffused waveguide, approximately 1 μm thick, on its surface [1]. The effective prism-electrode dimensions are $A = 100$ μm, $B = 6$ mm, $y_0 = 10$ μm, and the width of the diagonal electrode is 5 μm. Light from a 0.633-μm laser was focused by a 14-cm lens and coupled into the guide by a rutile prism. The estimated waist diameter D is 66 μm.

Fig. 3 shows two well-resolved spots coupled through the output prism for applied voltages of ±15 V. According to (8) [with $n_e = 2.2$, $r_{33} = 3 \times 10^{-11}$ m/V, $B = 6$ mm, $D = 6.6$ μm, $V_0 = 30$ V (±15 V), $\lambda = 0.633$ μm, and $A = 100$ μm], we calculate $N = 0.6$ spots with $1/e^2$ resolution. It may be seen that this resolution criterion is more conservative than the usual Rayleigh criterion. For $N = 1$, the net required voltage is $V_0 = 50$ V (±25 V).

The switching voltage can be reduced at the expense of ease of alignment by using diffraction-limited electrode dimensions

$$A^2/B = \frac{4\lambda}{n_e \pi}, \qquad A = \sqrt{2}\, D. \tag{9}$$

Then

$$V_0 = \frac{4\sqrt{2}}{\pi} \frac{N\lambda^2}{n_e^4 r_{33} A} \tag{10}$$

which yields $V_0 = 20$ V (±10 V) for $N = 1$ and $A = 50$ μm.

Bipolar switches of the type described here might serve as elements of larger optical switching networks analogous to

electrical switching networks [4]. For this purpose, strip waveguides would have to be incorporated in the deflectors in order to interconnect the switches.

ACKNOWLEDGMENT

The authors wish to thank R. H. Bosworth for his help in producing the photomasks for the electrodes.

REFERENCES

[1] R. V. Schmidt and I. P. Kaminow, "Metal-diffused optical waveguides in $LiNbO_3$," *Appl. Phys. Lett.*, vol. 25, pp. 458–460, 1974.

[2] P. K. Tien, S. Riva-Sanseverino, and A. A. Ballman, "Light beam scanning and deflection in epitaxial $LiNbO_3$ electrooptic waveguides," *Appl. Phys. Lett.*, vol. 25, pp. 563–565, 1974.

[3] D. Marcuse, "Electrooptic coupling between TE and TM modes in anisotropic slabs," *IEEE J. Quantum Electron.*, to be published.

[4] N. T. Tsao-Wu, "Sorting and rearrangeable switching networks," *IEEE Trans. Commun. Technol. (Part I of Two Parts)*, vol. CT-19, pp. 596–600, Oct. 1971.

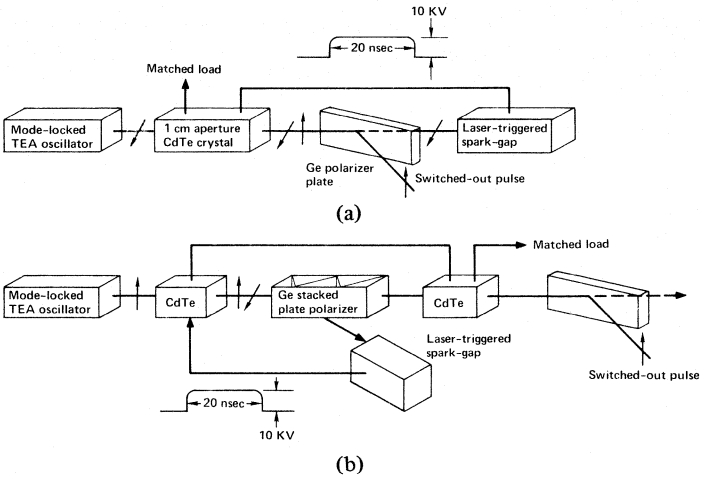

Fig. 1. (a) First pulse-selection system used for target experimentation. (b) Improved two-stage pulse-selection system.

Prepulse Extinction-Ratio Measurements on a CO_2-Laser System

K. R. MANES, D. L. SMITH, R. A. HAAS, AND S. S. GLAROS

Abstract—**Prepulse extinction-ratio measurements performed on two pulse-selection systems at the input and the output of a CO_2-amplifier chain are described.**

During laser-target interaction experiments with a 50-J 1.3-ns CO_2-laser system it rapidly became apparent that low-intensity prepulses were strongly affecting the target behavior. A TEA CO_2-oscillator mode locked by a Ge Brewster's-angle acoustooptic modulator produced a train of pulses which were directed into a switch-out system intended to select the largest pulse [1], [2]. The pulse-train envelope had the ~100-ns-duration gain-switched spike characteristic of TEA CO_2 lasers. The first series of target experiments used the pulse-selection technique indicated schematically in Fig. 1(a). Low-level pulses separated by 20 ns eventually produced enough ionization in the laser-triggered spark gap to cause it to close, launching a 10-kV square wave of 20-ns duration. When this voltage appeared across the CdTe electrooptic crystal, it caused the next mode-locked pulse's polarization to be rotated by $\pi/2$, and consequently that pulse was reflected off the output Brewster plate. Small alignment errors and residual strain-induced birefringence in the CdTe crystal prevented this pulse-selection system from having an adequate rejection ratio.

Fig. 2 shows the experimental arrangements used to determine the efficacy of this pulse-selection technique by measuring the ratio of the switched-out pulse amplitude to the immediately preceding mode-locked pulse amplitude; i.e., the prepulse extinction ratio. A photograph obtained with this apparatus is shown in Fig. 3. The Tektronix 519 oscilloscope was internally triggered by the prepulse entering the cooled Hg:Ge detector after traversing the 10-ns-long unattenuated leg. The next pulse, 10 ns later, is the switched-out pulse attenuated by calibrated CaF_2 plates. It was found that with

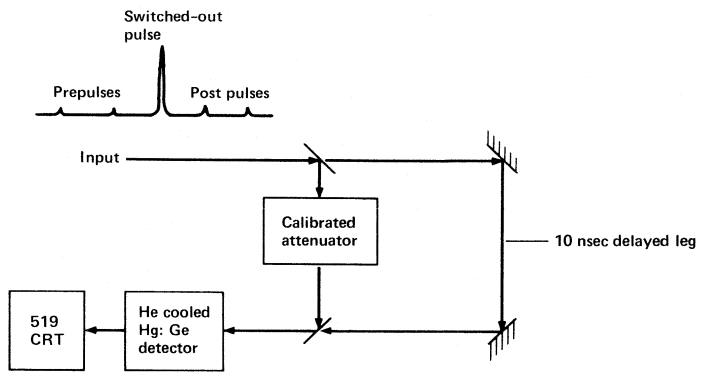

Fig. 2. Extinction-ratio measuring apparatus.

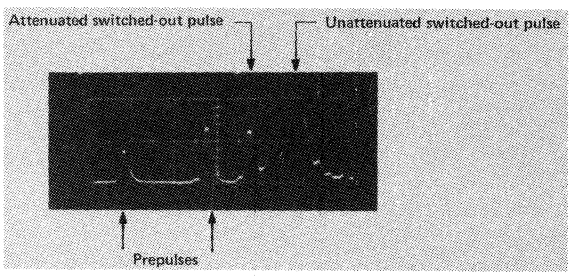

Fig. 3. Photograph obtained with apparatus indicated in Fig. 2.

the switch-out system shown in Fig. 1(a) an extinction ratio of $2 - 5 \times 10^4$ was typical. These pulses were directed into an amplifier chain consisting of 1 m of 4.5-cm clear-aperture TEA preamplifier, a Keplerian beam-expander followed by 1 m of 9-cm-aperture TEA amplifier, and finally two 11-cm clear aperture by 1-m-long cold-cathode electron-beam-sustained power amplifiers operated at two atmospheres. Upon emerging in the target area a portion of the laser signal was directed into another prepulse measuring apparatus identical to that described in Fig. 2. It was found that the saturation properties of the CO_2 amplifiers had deteriorated the extinction ratio to only 20–50. In fact, when this beam was focused to a nearly diffraction-limited spot $\lesssim 140\ \mu m$ in diameter on a 10-μm-thick CH_2 foil target, negligible

Manuscript received May 2, 1975. This work was performed under the auspices of the U.S. Energy Research and Development Administration.

The authors are with the University of California, Lawrence Livermore Laboratory, Livermore, Calif. 94550.

quantities of X-rays were observed even though the switched-out pulse contained 30–40 J. The target foil was disassembled prematurely by prepulses and was not there when the main pulse arrived.

In response to this problem, the switch-out system indicated in Fig. 1(b) was devised. Essentially, a second stage has been added. In principle, additional stages may be added until losses and mismatching degrade the 10-kV pulse. Synchronization between the 10-kV pulse and the optical pulse may be maintained by folding the optical path. Using the same evaluative technique, an extinction ratio of 2×10^6 was measured at the oscillator and 2×10^3 after amplification at the target. Separate measurements established that 10-μm CH_2 foils could survive irradiation by pulses with energies of $\sim$100 mJ. Consequently, it was not surprising to find that copious quantities of X-radiation, ions, and electrons were produced when the large switched-out pulse reached the thin CH_2 target.

The importance of establishing the integrity of fragile laser-fusion targets immediately prior to irradiation cannot be overemphasized [3]. The saturation property of CO_2 amplifiers which contributes to their relatively high efficiency also severely degrades the prepulse extinction ratio and can lead to premature target damage [4]. A two-stage switch-out system has been demonstrated which provides an extinction ratio at the target sufficiently large to permit laser–target interaction experiments with 10-μm-thick CH_2 foil targets.

References

[1] D. T. Davis, D. L. Smith, and J. S. Koval, "Generation of single 1-ns pulses at 10.6 μ," *IEEE J. Quantum Electron.* (Corresp.), vol. QE-8, pp. 846–848, Nov. 1972.

[2] F. Rheault, J. L. Lachambre, J. Gilbert, R. Fortin, and M. Blanchard, "Selection of a single pulse from a mode-locked TEA CO_2 laser," *Can. J. Phys.*, vol. 50, pp. 1867–1880, 1972.

[3] J. F. Holzrichter, D. R. Speck, and J. E. Swain, "Plasma development in low Z laser fusion targets," presented at the Plasma Physics Meet., Amer. Phys. Soc., Albuquerque, N. Mex., Oct. 28–31, 1974, Paper UCRL-75975.

[4] E. E. Stark, Jr., W. H. Reichelt, G. T. Schappert, and T. T. Stratton, "Nanosecond pulse amplification in very high gain C[illegible] amplifier systems," 1973 IEEE/OSA Conf. Laser Engineering and Applications, Washington, D.C., Postdeadline Paper.

Notes and Lines

New CO_2 Pumped CW Far-Infrared Laser Lines

D. A. JENNINGS, K. M. EVENSON, AND J. J. JIMENEZ

Abstract—**A single-frequency CW CO_2 laser has been used to pump ethyl alcohol, methyl chloride, ethyl chloride, and methylene chloride, generating 8 new CW far-infrared (FIR) laser lines from 254 to 1700 μm.**

Far-infrared (FIR) lasers are becoming useful radiation sources for use in spectroscopy, and many molecules exhibit lasing action when optically pumped with a CO_2 laser. We report here several new molecules and 8 new wavelengths to provide additional sources in this spectral region.

A single-frequency grating-tuned CW CO_2 laser, with a PZT for fine tuning, provided the pump source. Maximum power of 20 W in the 9.6-μm band with tuning from $P(8)$ to $P(42)$ and $R(8)$ to $R(36)$, and 40 W in the 10.6-μm band with tuning from $P(0)$ to $P(50)$ and $R(0)$ to $R(44)$ was obtained.

The FIR laser was of the waveguide design. The waveguide was a polished copper tube, of 14-mm diameter and 2.1 m long. The input and output mirrors were of copper and polished flat. FIR power was extracted through a 0.25-mm-thick fused-quartz window which covered a 2.5-mm coupling hole in the output mirror. The CO_2 pump radiation was focused through a salt window and through a 1-mm hole in the input mirror by a 6.4-cm focal-length germanium lens. The input mirror was moved via a micrometer from 1 to 5 mm from the end of the waveguide.

The FIR-laser radiation was detected by a quartz-window Golay cell with various attenuators between the FIR laser and the Golay cell, depending on the signal strength. The optimum pressure was in nearly all cases around 100-μm Hg. No attempt was made to determine the FIR-laser polarization relative to the CO_2-laser polarization.

The results of our measurements are summarized in Table I. The FIR power is listed as either M (medium) or W (weak) where $M \approx 0.1$ mW and $W \approx 0.01$ mW.

It is interesting to note that the ethyl alcohol line lased very well on vodka, gin, and rum, but it lased on only 1 line and rather weakly compared with methyl alcohol. It is quite obvious that there are better uses of ethyl alcohol.

TABLE I

Material	Wavelength μm	CO_2 Pumpline	Pressure μ Hg	Power
Ethyl Alcohol (C_2H_5OH)	396	9 P (32)	100	W
Methyl Chloride (CH_3Cl)	254	10 P (10)	100	M
	354	10 R (18)	100	W
	968	9 R (12)	100	W
Ethyl Chloride C_2H_5Cl	900	10 R (30)	100	M
	1350	10 R (30)	100	W
	1400	10 R (38)	100	
	1720	10 R (28)	100-200	M
Methylene Chloride CH_2Cl_2	258	10 P (26)	100	M

Manuscript received May 1, 1975.

D. A. Jennings and K. M. Evenson are with the Precision Laser Metrology Section, National Bureau of Standards, Boulder, Colo. 80302.

J. J. Jimenez is with the Centre National de la Recherche Scientifique and Bureau National de Metrologie, Paris, France. He is a guest worker at the Precision Laser Metrology Section, National Bureau of Standards, Boulder, Colo. 80302.

Contributors

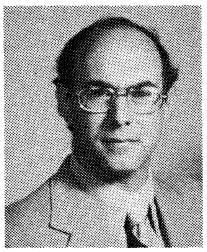

Richard L. Abrams (M'68) was born in Cleveland, Ohio, in 1941. He received the B.S. degree in engineering physics and the Ph.D. degree in applied physics from Cornell University, Ithaca, N.Y., in 1964 and 1968, respectively.

From February 1968 to September 1971 he was employed at Bell Laboratories, where he worked on optical communications, infrared modulators, infrared detectors, and CO_2 lasers. Since October 1971 he has been employed at the Hughes Research Laboratories, Malibu, Calif., as a Senior Staff Physicist and is Head of the Electro-Optics Section. He conducts research in the areas of optical modulation, communications, laser spectroscopy, and gas lasers.

Dr. Abrams is a member of the Americal Physical Society, Phi Kappa Phi, and Tau Beta Pi.

*

P. Avivi, photograph and biography not available at the time of publication.

*

Edward A. Ballik (A'56-M'60), for a photograph and biography please see page 313 of the June 1975 issue of this JOURNAL.

*

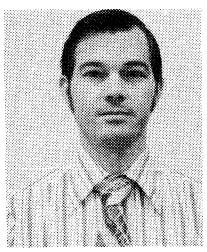

James D. Barry (S'66-M'72) was born in Washington, D.C., on February 8, 1942. He received the B.S. degree in applied physics, the M.S. degree in physics, and the Ph.D. degree in interplanetary space physics, all from the University of California, Los Angeles, in 1964, 1966, and 1969, respectively.

He has pursued research in the areas of interplanetary space physics, ionospheric plasma, and laser technology. He is currently at the Air Force Avionics Laboratory, Wright-Patterson Air Force Base, Ohio, where he is the Technical Director of the Air Force Program for Space Laser Communications. He has several patents in the laser area.

Dr. Barry is a member of the American Geophysical Union and Sigma Xi. He is Chairman of the DOD/NASA Optical Communications Working Group. He is also a member of several Department of Defense planning and coordinating committees in space laser communications, and serves on an advisory panel on medical applications of laser communications.



Edmond M. Batifol was born in Lozère, France, on November 20, 1930.

Since 1962 he has been involved in the development of laser sources and research in nonlinear optics in the Department of Physics and Electronics of the Centre National d'Etudes des Télécommunications, Bagneux, France.

*



Robert J. Coates (A'47-M'55-SM'56-F'71) was born in Lansing, Mich., on May 8, 1922. He received the B.S. degree in electrical engineering from Michigan State University, East Lansing, in 1943, the M.S. degree in electrical engineering from the University of Maryland, College Park, in 1948, and the Ph.D. degree in physics from The Johns Hopkins University, Baltimore, Md., in 1957.

From 1943 to 1959 he was at the U.S. Naval Research Laboratory engaged in millimeter-wave radio astronomy. Since 1959 he has been at the NASA Goddard Space Flight Center, Greenbelt, Md. He was Chief of the Space Data Acquisition Division, the Advanced Development Division, and the Advanced Data Systems Division at Goddard, developing antennas, RF systems, data handling and processing, and optical systems for spacecraft tracking and data acquisition. In 1974 he became the Senior Scientist of the Applications Directorate at Goddard, becoming responsible for the very long baseline interferometer and satellite laser tracking programs for determining tectonic-plate motions, geodesy, and earth dynamics.

Dr. Coates is a member of Tau Beta Pi, Phi Kappa Phi, Sigma Xi, t[illegible] American Physical Society, the American Geophysical Union, and t[illegible] American Association for the Advancement of Science.

*

Steven C. Cohen was born in New Kensington, Pa., on August 17, 1947. He received the B.S. degree in physics from Drexel University, Philadelphia, Pa., in 1970, and the M.S. and Ph.D. degrees in physics from the University of Maryland, College Park, in 1972 and 1973, respectively.

From 1966 to 1970 he was an undergraduate cooperative education student in the physical sciences at the NASA Goddard Space Flight Center, Greenbelt, Md. Since 1970 he has been a member of Goddard's Laser Technology Branch, where he has carried out research in heterodyne detection principles and applications, molecular energy-transfer theory, and gas-laser kinetics.

Dr. Cohen is a member of the American Physical Society, the Optical Society of America, Phi Kappa Phi, Sigma Xi, Sigma Pi Sigma, and Pi Mu Epsilon.



Anthony J. DiNardo was born in New York, N.Y., on June 14, 1941. He received the B.S. degree in electrical engineering from the City College of New York, in 1964, and the M.S. degree from the Polytechnic Institute of Brooklyn, Brooklyn, N.Y., in 1969.

He joined AIL, Melville, N.Y., in 1966 as an Electronics Engineer in the Applied Electronics Division. He is a Senior Engineer in the Infrared and Electro-Optics Department, and is engaged in the development of infrared receivers for radiometry, optical radar, and communications applications. He was Project Engineer on a NASA program which successfully developed and fabricated a unique infrared, 10.6-μm heterodyne radiometer (IHR). This program included the development of a new approach in analyzing the IHR's performance and the corroboration of the analysis with the experimental data in the field as well as in the laboratory. The IHR was employed for solar and atmospheric transmission measurements. He has performed in-depth computer studies of the Fraunhoffer diffraction patterns of an array of 10.6-μm coherent heterodyne mixers [illegible] determined the optimum optical photomixer geometry for maximum signal-to-noise performance. He has done complete systems modeling of heterodyne reception, heterodyne radiometry, and optical radar and analyzed these by computer-assisted variation of the key operational parameters. Previous to these assignments, he was engaged in the study of superconducting tunneling devices and superconducting filters. This work aimed at the development of a Josephson tunnel junction microwave mixer and a superconducting microwave microstrip reselector and filter for a cryogenic X-band receiver front end. Prior to joining AIL, he was associated with the Electronic Division of the General Dynamics Corporation from 1964 to 1966.

*

F. Dothan, photograph and biography not available at the time of publication.

*



Akira Fujisawa was born in Tokyo, Japan, on March 15, 1931. He received the B.S. degree in electrical engineering from Waseda University, Tokyo, in 1954.

He has since been employed at the 1st Research Center of the Technical Research and Development Institute, Japanese Defense Agency, Tokyo. Between 1954 and 1961 he was employed in R&D work on infrared equipment. During the academic year 1962 to 1963 he studied laser physics at Waseda University. He has since worked in fundamental and applied areas of solid and gaseous lasers as well as in the development of range finders, gated viewing systems, and underwater optical transmission systems. During a one year interval between 1965 and 1966 he was employed at the Night Vision Laboratory in Fort Belvoir, Va., and also spent the year 1974 at the U.S. Army Electronics Command Laboratories, Fort Monmouth, N.J., on an exchange program. He is the Chief of the Laser Project Team at TRDI.

*

Brian K. Garside, for a photograph and biography please see page 313 of the June 1975 issue of this JOURNAL.

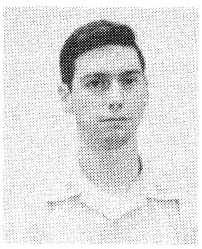

Chandler J. Kennedy was born in St. Louis, Mo., on June 12, 1943. He received the B.S. degree in physics from St. Louis University, St. Louis, the M.S. degree in engineering space physics from the Air Force Institute of Technology, Wright-Patterson Air Force Base, Ohio, and the Ph.D. degree in optical sciences from the University of Arizona, Tucson, in 1965, 1967, and 1972, respectively.

He has served in the Air Force since 1965 as a Physicist at the Air Force Weapons Laboratory, and as a Project Engineer and Deputy Program Manager at the Air Force Avionics Laboratory, Wright-Patterson Air Force Base. He is currently working in an advanced development program office for high data rate space laser communications and is engaged in applied research in solid-state lasers, nonlinear optics, and communication theory.

*

H. Keren, photograph and biography not available at the time of publication.

*

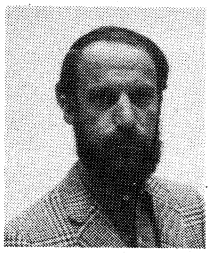

Marvin B. Klein was born in Perth Amboy, N.J., in 1942. He received the B.A. and B.S. degrees in electrical engineering from Brown University, Providence, R.I., in 1964, and the M.S. and Ph.D. degrees from the University of California, Berkeley, in 1965 and 1969, respectively.

While at the University of California, Berkeley, he conducted research on pulsed and CW ion lasers. From 1969 until 1973 he was at Bell Laboratories, Holmdel, N.J. His research activities included work on metal vapor ion lasers and CW dye lasers. Since 1973 he has been a member of the Technical Staff at the Hughes Research Laboratories, Malibu, Calif., where he has been engaged in research in waveguide gas lasers and amplifiers, and laser detection systems.

*

Chinlon Lin, for a biography, please see page 93 of the February 1975 issue of this JOURNAL.

*

John H. McElroy (S'63–M'66–SM'71) was born in Marion, Ohio. He received the B.S.E.E. degree from the University of Texas, Austin, and the M.E.E. degree from the Catholic University of America, Washington, D.C., where he is currently a part-time doctoral student.



From 1954 to 1957 he served with various U.S. Army airborne units, and from 1957 to 1963 he taught and prepared instructional materials on electronics, physics, and mathematics at the U.S. Army Air Defense School, Fort Bliss, Tex. Until 1966 he was a Research Assistant in the Quantum Electronics Research Laboratory of the University of Texas, where he assisted in research on laser-induced ionization of gases. Since joining the NASA Goddard Space Flight Center, Greenbelt, Md., in 1966, he has been responsible for developing laser systems and components for use in satellite data transmission and tracking.

Mr. McElroy is a member of the Optical Society of America, Tau Beta Pi, Eta Kappa Nu, and Omicron Delta Kappa, and an associate fellow of the American Institute of Aeronautics and Astronautics.

*

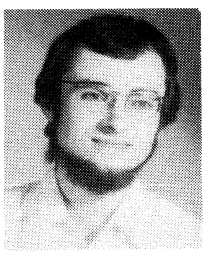

Jean-Louis Oudar was born in Lille, France, in 1949. He graduated from the Ecole Polytechnique of Paris, Paris, France, in 1970, and received the Diplôme d'Etudes Approfondies in solid state physics from the University of Orsay, Orsay, France, in 1972.

He is currently working in the Department of Physics and Electronics at the Centre National d'Etudes des Télécommunications (CNET), Bagneux, France, where he is interested in nonlinear optics and materials.

*

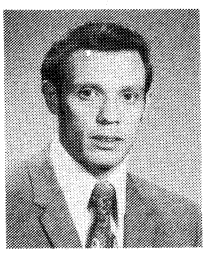

Aristotle Papayoanou was born in New York, N.Y., on July 7, 1936. He received the B.S. degree from the City College of New York and the M.S. and Ph.D. degrees in physics from the Stevens Institute of Technology, Hoboken, N.J., in 1958, 1965, and 1972, respectively.

Since 1961 he has been employed as a Research Physicist at the U.S. Army Electronics Command Laboratories at Fort Monmouth, N.J. Between 1961 and 1965 he performed research in ionospheric and radio wave physics. Since 1965 he has worked in various areas of laser physics including optical pumping, pulsed ion lasers, and CO_2 lasers. His thesis dealt with the Brillouin spectrum of laser light scattered by monomeric liquids.

*



Bernard J. Peyton (M'60–SM'69) was born in New York, N.Y., on April 11, 1937. He received the B.S. degree from the City College of New York, N.Y., in 1959, and the M.S. degree from the Polytechnic Institute of Brooklyn, N.Y., in 1964, both in electrical engineering.

He joined the Applied Electronics Division of AIL, a division of Cutler-Hammer, Inc., Melville, N.Y., in 1959. He is currently the Deputy Department Head of the Infrared and Electro-Optics Department, where he is responsible for and directs programs in the development of coherent and incoherent infrared receivers for communications, radar, atmospheric physics, and radiometric applications, the evaluation of a variety of detection techniques, and laser communications. He has investigated the noise properties and frequency-response characteristics of infrared photoconductors, photovoltaic diodes, and avalanche photodiodes. He previously worked on the development of advanced solid-state devices including maser, semiconductor, and ferrite components for the microwave and millimeter wavelength region, nonlinear up-conversion, radiometry, and microwave spectroscopy.

*

John Reid, for a photograph and biography please see page 315 of the June 1975 issue of this JOURNAL.

*



Christiane A. Schwartz (S'68–M'70) was born in Paris, France, in June 1947. She received a degree in electronic engineering from the Ecole Supérieure d'Electricité of Paris in 1969, and a Diplôme d'Etudes Approfondies in quantum optics from Orsay University, Orsay, France, in 1970, and the Diplôme de Docteur de 3° Cycle in 1973 for work on nonlinear devices based on tellurium.

She has worked in the Nonlinear Optics Department of the Centre National d'Etudes des Télécommunications, Bagneux, France. She is now with the Centre Commun d'Etudes de Télévision et Télécommunications, Rennes, France.

*

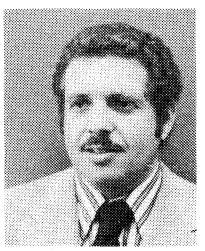

Malvin Carl Teich (S'62–M'66–SM'72) was born in New York, N.Y., on May 4, 1939. He received the S.B. degree in physics from the Massachusetts Institute of Technology, Cambridge, Mass., in 1961, the M.S. degree in electrical engineering from Stanford University, Stanford, Calif., in 1962, and the Ph.D. degree from Cornell University, Ithaca, N.Y., in 1966. While at M.I.T. he received the Frank W. and Carl S. Adams Memorial Scholarship, and at Cornell University he received the James Clerk Maxwell Fellowship and a Ford Foundation Grant.

He has held summer research positions at the Motorola Corporation, Rockwell International's Space and Information Systems Division, and the Mitre Corporation in 1959, 1961, and 1963, respectively. In the summer of 1960 he participated in a student technical exchange program at N.V. Philips Gloeilampenfabrieken in Eindhoven, The Netherlands. In 1966 he joined the M.I.T. Lincoln Laboratory, Lexington, Mass., where he was engaged in work on coherent infrared detection and modulation. In 1967 he became a Member of the Faculty of the Department of Electrical Engineering and Computer Science, Columbia University, New York, N.Y., where he is now teaching and pursuing his research interests in the areas of detection theory, quantum electronics, and optical communications.

Dr. Teich is a member of Sigma Xi, the American Physical Society, the American Society for Engineering Education, and the Optical Society of America. In 1969 he was the recipient of the IEEE Browder J. Thompson Award for his paper "Infrared Heterodyne Detection," and in 1974 was a Fellow of the John Simon Guggenheim Memorial Foundation.

Preface

THIS Special Issue of the IEEE JOURNAL OF QUANTUM ELECTRONICS is devoted to papers presented at the 4th Conference on Chemical and Molecular Lasers held in St. Louis, Mo., October 21-23, 1974. This conference was held in cooperation with the AIP/IEEE Joint Council on Quantum Electronics and the IEEE Quantum Electronics Council, and received financial support from the Chemistry Directorate of the Air Force Office of Scientific Research. The purposes of the Conference were principally to bring together people active in the area and to present new research results.

One hundred five papers were presented at the meeting; included in this JOURNAL are 7 full length papers and Digests of the remaining 98 papers. The work presented at the conference was grouped into sessions as follows.

MA: Electrically-Pumped Lasers
MB: New IR Laser Reactions
MC: Chemically-Pumped Electronic Transition Lasers
MD: Vibrational Energy Transfer
TA: Pulsed Chemical Lasers and Q-Switching
TB: CO Lasers
TC: Post-Deadline Papers
TD: Post-Deadline Papers
WA: Electronic Energy Transfer
WB: DF-CO_2 Lasers
WC: cw HF/DF Chemical Lasers I
WD: Laser-Controlled Chemistry
WE: Modeling and Theory
WF: cw HF/DF Chemical Lasers II

The work presented at the St. Louis Conference has undergone a continuous evolution since the 2nd Conference on Chemical and Molecular Lasers in 1969. Some subjects have continued as active areas through the 1974 Conference, notably CW HF/DF chemical lasers, CO chemical lasers, CO electric discharge lasers, vibrational energy transfer, and IR laser reactions. In the area of vibrational energy transfer, the recent work on collisions between vibrationally excited molecules and atoms is noteworthy. The area of collisional transfer lasers as represented by the DF-CO_2, H_2-HCl, and D_2-CO_2 systems continues to be an active area of research and, in the case of DF-CO_2, development. Supporting all of these is the continuing work in modeling of lasers.

The newer research areas represented at the 4th Conference on Chemical and Molecular Lasers include the search for visible chemical lasers and laser-induced or laser-controlled chemistry, with particular emphasis on isotope effects. The visible laser field was also represented in the papers on electrically pumped lasers; the work on electronic energy transfer is of importance to visible lasers.

Thanks are extended to the members of the Organizing Committee and the Program Committee listed below for their efforts on behalf of the conference.

Organizing Committee: D. P. Ames, *Chairman*; W. Q. Jeffers; J. D. Kelley, *Treasurer*; and T. J. Menne.
Program Committee: W. Q. Jeffers, *Chairman*; J. R. Airey; B. R. Bronfin; A. N. Chester; T. Cool; J. D. Kelley; G. Pimentel; and H. T. Powell.

The committee members and the reviewers of the full-length papers in this JOURNAL both gave generously of their time and efforts. Mrs. Judy Thomas handled the secretarial work associated with the Conference.

—W. Q. JEFFERS
Guest Editor

TA4—Characteristics of a High-Energy Hydrogen Fluoride (HF) Laser Initiated by an Intense Electron Beam

E. L. PATTERSON, MEMBER, IEEE, AND R. A. GERBER

Abstract—**The characteristics of a high-energy hydrogen fluoride (HF) laser and the effects of optical elements on beam quality and on energy extraction are described. The HF laser is initiated by injecting a 2-MeV electron beam into a mixture of SF_6 and C_2H_6. With 300-torr SF_6 and 30-torr C_2H_6, the radiated energy with a flat mirror on one end of the laser cell is ≈80 percent of the two-way energy when no mirrors are used. The effect of a confocal unstable resonator in providing collimation of the laser beam was studied. The maximum laser energy measured was 380 J in a 23-ns full width at half maximum (FWHM) pulse. The maximum electrical efficiency measured was 14 percent, which is about 60 percent of the maximum theoretical value.**

I. INTRODUCTION

THERE HAS recently been considerable interest in initiating hydrogen fluoride (HF) lasers by intense electron beams [1]-[8] because electron beams have been shown to be efficient in releasing fluorine atoms from fluorine compounds. Electron beams have been used to initiate HF lasers in mixtures of SF_6 and H_2 or C_2H_6 [1], [3], [5], [7], [8] and of H_2 and F_2 [2], [4], [6]. With electron beams it is possible to uniformly excite large laser volumes in nanosecond time scales. The availability of large electron beams has led to the production of high-energy HF lasers. Laser energies >200 J have been measured with SF_6 and C_2H_6 [1] and >2 kJ have been produced with H_2 and F_2 [2]. One of the major problems associated with the high-energy superradiant lasers reported in [1] and [2] is the poor optical beam quality of the amplified spontaneous emission. The purposes of this experiment are to determine the effect of optical feedback on a high-gain HF laser, to determine the characteristics of an electron-beam initiated laser, and to evaluate the electron-beam energy deposition and resulting excitation as a function of distance and pressure.

The laser described in [1] consisted of a straight tube with an absorber on one end. In that experiment, the maximum measured electrical efficiency η_e (η_e = laser energy out/deposited electron-beam energy) was about 8 percent from which a true electrical efficiency of 16 percent was inferred by assuming equal laser radiation in both directions. Access to both ends of the laser cell in the present experiment allows the verification of this inference. The electron beam was magnetically guided into the laser cell so that mirrors could be used at both ends. The electrons were transported along the laser-cell axis rather than transversely [6]-[8] because, for the reactant pressures of interest, the laser length is comparable to the stopping distance of the high-energy electrons. Detailed electron-beam deposition measurements were performed over the length of the laser cell. These measurements allow one to determine the optimum laser length for a given gas pressure. Other improvements over the experiments in [1] include detailed measurements of the laser spectrum as well as better laser-energy measurements as a function of gas mixtures and pressure. Total laser energy was measured in this experiment so that assumptions about beam uniformity are not required.

Manuscript received November 26, 1974; revised March 14, 1975. This work was supported by the Environmental Research and Development Agency.

The authors are with the Sandia Laboratories, Albuquerque, N. Mex. 87115.

II. EXPERIMENTAL APPARATUS

The experimental arrangement is shown in Fig. 1. The geometry is similar to that used with a smaller accelerator [3]. The table in Fig. 1 lists the conditions for two series of experiments described in this paper. In the first experiment, the laser medium was longer and the electron-beam energy was lower than in the second set of experiments. The active length is defined as the distance between the location where the electron beam enters the laser cell and where the residue of the beam is guided into the cell wall (near B_T in Fig. 1). The laser cell had a diameter of 14.9 cm giving laser volumes for the first and second series of experiments of 39 and 26.3 l, respectively. Measurements obtained on the first experiments were laser pulsewidths, delay times, spectra, energy as a function of SF_6 pressure for fixed C_2H_6/SF_6 ratio, and energy as a function of C_2H_6 concentration for fixed SF_6 pressure. The effect of a mirror on one end of the cell was also investigated. These same measurements, except for the spectra and variation of laser energy with ethane concentration, were repeated on the second experiments. In addition, an unstable optical resonator was used on the second series for a limited number of shots.

The REBA electron accelerator [2 MeV, 55 kA, 70-ns full width at half maximum (FWHM)] is the same as that used in [1] and [2]. The repetition rate of this machine is approximately ten shots per day. Magnetic-field coils around the laser cell and accelerator diode provide an axial magnetic field B_a to guide the electrons through the cell. The axial magnetic field was 2.0 and 2.5 kG, respectively, for the first and second series of experiments. Two coils in a Helmholtz configuration near the far end of the laser cell produced a transverse magnetic field B_T to guide the residue of the electron beam into the cell wall. GE-125 quartz [9] windows 0.51 cm thick and 16.5 cm in diameter sealed the ends of the laser cell.

Scientech [19] Model 36-0801 calorimeters having apertures of 20.3 cm were used to measure laser energy. All energy measurements discussed in this paper have been corrected for the 15-percent loss of the windows. This permits an accurate calculation of the electrical and chemical efficiencies. For the first experiments either a flat 15-cm-diam or a spherical 12.5-cm-diam (5-m-focal-length) mirror was used on the near end to

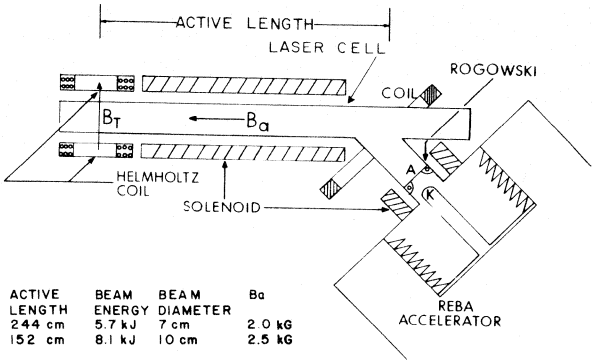

Fig. 1. Schematic view of the experimental apparatus.

compare with the case with no mirrors. In the second series a flat 15-cm-diam mirror on the near end and a confocal unstable resonator with a geometrical magnification of 2 were utilized. All mirrors were gold coated. Time-resolved measurements of the laser radiation were obtained with gold-doped germanium detectors [11] having a measured response time of about 1 ns. Time-integrated spectra were obtained for various conditions using a grating together with a focusing mirror and "footprint" paper [12]. Wavelength calibration was obtained by using the fourth and fifth orders of a He-Ne laser.

The electron-beam energy was measured at various gas pressures and positions in the laser cell using a total-stopping carbon calorimeter [13]. The accelerator diode current was measured with a fast Rogowski coil [14] and was time correlated with the laser detector signal.

III. Experimental Results and Discussion

The laser energy as a function of SF_6 pressure for a C_2H_6/SF_6 ratio of 0.10 and as a function of ethane concentration at an SF_6 pressure of 300 torr was measured to compare with the results reported in [1]. Since the optimum conditions were obtained in that experiment for a 0.10 ratio of C_2H_6/SF_6 at an SF_6 pressure of 300 torr, these conditions were used to obtain preliminary measurements. These measurements are shown in Fig. 2. The data associated with the lower curve in Fig. 2 are those taken with the long cell with either the flat or the 5-m-focal-length mirror. The same laser energy was obtained with either mirror because the *e*-beam excitation diameter was smaller than that of either mirror. The upper curve in Fig. 2 represents the data obtained with the short cell with the 15-cm-diam flat mirror on the near end. The laser energy is larger with the short cell because the electron-beam energy, and hence the deposition, was larger than in the long cell. In Fig. 2 the initial increase in laser energy with increasing SF_6 pressure is due to the increased fluorine atom concentration provided by the larger electron-beam energy deposition at higher pressures. This increase in energy deposition continues throughout the pressure range investigated. However, the deposition rate becomes increasingly nonuniform with axial position at SF_6 pressures above 200 torr causing a decrease in laser energy. At higher pressures the measured energy decreases because the nonuniform deposition effectively decreases the length and thus increases the divergence of this highly superradiant laser. Since the solid angle subtended by the laser

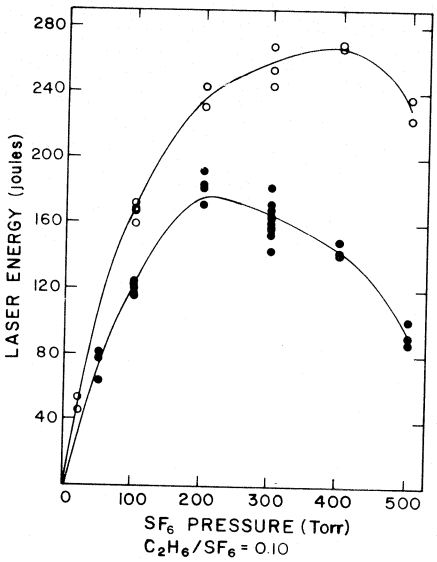

Fig. 2. Laser energy measured at the far end of the laser cell as a function of SF_6 pressure for a fixed C_2H_6/SF_6 ratio of 0.10. Mirror on near end. Closed circles are data taken with long (244-cm) cell; open circles are data taken with short (152-cm) cell.

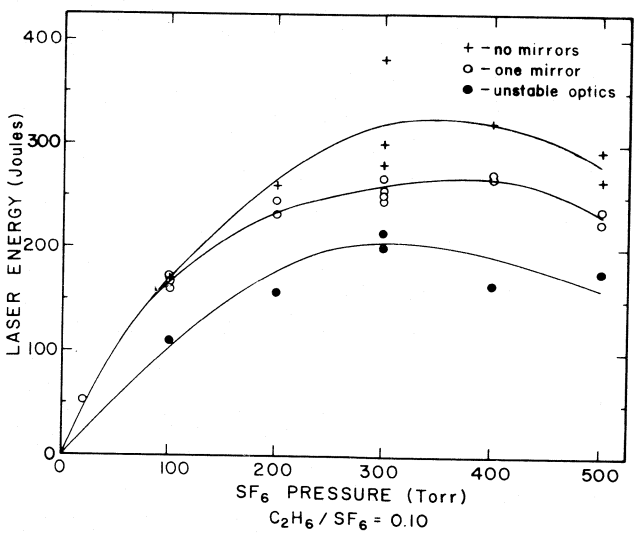

Fig. 3. Laser energy versus SF_6 pressure. Upper curve–sum of both ends with no mirrors. Middle curve–flat mirror on one end. Lower curve–unstable optics.

window is constant, a smaller portion of the total radiation can escape to be measured by the calorimeter. This same effect causes the maximum laser energy collected by the calorimeter to occur at an SF_6 pressure of 400 torr in the short tube as compared with 200 torr in the long tube.

Fig. 3 shows the effect of three optical configurations on the laser energy for the short cell. The upper curve represents the sum of the energies measured at each end of the laser cell at the various SF_6 pressures when no mirrors were used. A maximum energy of 380 J was obtained with 300-torr SF_6. The data associated with the middle curve are the same as those displayed in Fig. 2 for the energy measured at the far end with a flat mirror. The lower curve gives the energy measurements obtained with the confocal unstable resonator. These measurements were obtained after the convex mirror in the resona-

tor had been damaged by laser radiation. This damage, which began with the first shot, removed the gold coating from a 5-cm-diam area exposing the Kanigen coating on the copper mirror. Because of this damage, a direct comparison of energy obtained with the unstable optics and with the other optical arrangements cannot be expected. The total energy measured without mirrors is larger than that measured with the flat mirror by a factor of about 1.2. This ratio is consistent with values calculated for a uniformly excited superradiant laser [15]. The decrease in total laser energy with a flat mirror as compared to the two-way energy is primarily due to a decrease in the solid angle over which the radiation can escape from the cell. The mirror essentially doubles the length of the cell. For a medium excited uniformly in the axial direction, the backward-going and forward-going radiation should be equal. In the present experiment, the average ratio of the backward-to-forward radiation was 0.8.

Fig. 4 shows the measured laser energy as a function of C_2H_6 concentration for a fixed SF_6 pressure of 300 torr. These data were obtained with the long laser cell using the 5-m-focal-length mirror on the near end. The initial linear increase in laser energy with ratios of C_2H_6/SF_6 up to about 0.01 corresponds to approximately one 2.7-μ photon per initial ethane molecule. The abrupt saturation in laser energy with increasing ethane concentration is caused by the depletion of the free fluorine atoms. Following the argument of [1] and assuming that the entire measured electron-beam energy deposition was used to produce fluorine atoms, the time-integrated fluorine production was 8.2×10^{16} cm^{-3} at an SF_6 pressure of 300 torr. An ethane concentration equal to this F-atom density occurs for a relative concentration of 0.01. The fact that the optimum ethane concentration is about 0.02 rather than 0.01 is due to the decreased HF* formation rate as the fluorine and ethane are depleted. In [1] the maximum fluorine density at 300-torr SF_6 was about three times that calculated above, and the laser energy versus ethane concentration was maximum in the range from 0.06 to 0.10. This correlation was also observed in [3]. Therefore, the ethane concentration at maximum laser energy can serve as a rough indication of the free-fluorine production by the electron beam. The decrease in laser energy for ethane concentrations larger than optimum is due to HF* deactivation by C_2H_6. The decrease in laser pulsewidth with increasing C_2H_6 concentration can be explained by using the rate constant for deactivation of HF* by C_2H_6 [16]. The measured laser pulsewidth at half maximum (FWHM) for the data shown in Fig. 4 decreased from 120 ns at a C_2H_6/SF_6 ratio of 0.005 to 45 ns for a ratio of 0.3.

The relationship between the timing of the accelerator diode current and photodetector signals obtained with the short cell for various SF_6 pressures is shown in Fig. 5. The flat mirror was on the near end of the cell for these measurements. The amplitudes of the photodetector signals are not calibrated and are not all at the same sensitivity since various attenuators were required to prevent saturation of the detectors. The detector signals have been corrected in time to account for the optical transit time to the detector from the near end of the laser cell. The SF_6 pressures associated with the detector signals are shown above each trace. At low pressures there are two pulses. This behavior, which was also observed by Gross and Wesner [8], is probably due to relaxation oscillations. The average delay times between the electron-beam current and photodetector signal for an SF_6 pressure of 300 torr were 43 ns using no mirrors, 38 ns with one flat mirror, and 48 ns with the unstable resonator. As shown in Fig. 5, there was no systematic change in delay time with SF_6 pressure over the SF_6 pressure range from 100 to 500 torr. The delay time at an SF_6 pressure of 20 torr increased to 67 ns when no mirrors were used and to 45 ns when one flat mirror was used. The longer delay times at lower pressures are due to longer reaction times and to a reduced fluorine-atom production rate. The laser pulsewidth (FWHM) at 300-torr SF_6 as measured with the short cell varied between 10 and 50 ns with no correlation between pulsewidth and optical arrangement used. Part of the large variation in pulsewidth is due to the structure on the laser pulse.

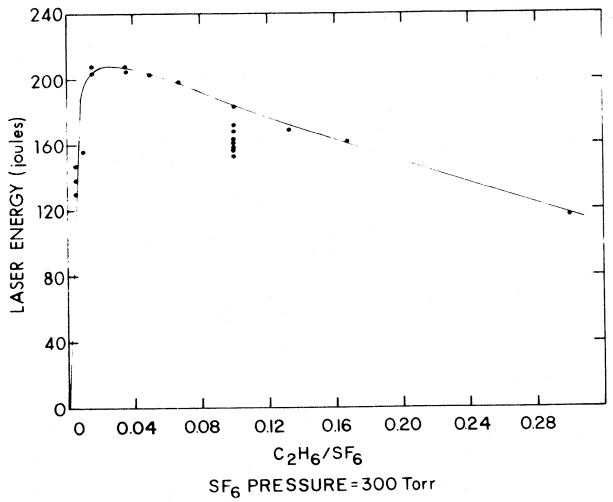

Fig. 4. Laser energy as a function of C_2H_6 concentration for a fixed SF_6 pressure of 300 torr for the long cell.

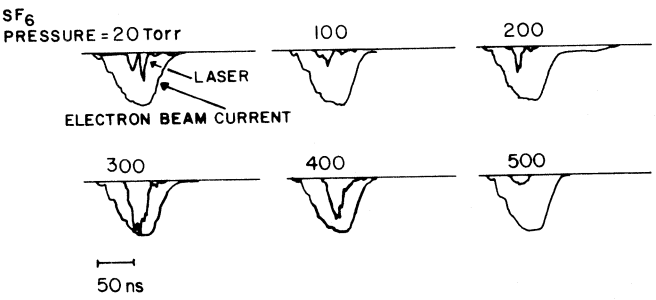

Fig. 5. Time-correlated electron-beam current and photodetector signals for the short cell with flat mirror on near end for $C_2H_6/SF_6 = 0.10$. SF_6 pressure in torr is shown above each trace.

The maximum divergence of the laser with and without a mirror, obtained by comparing the window diameter with the largest diameter of a damage pattern, was about equal to the geometrical divergence. In the case of the unstable resonator, damage patterns were taken on the first two shots with the film located first at a distance of 2.5 m from the convex mirror and then at a distance of 11.6 m. In both cases it was necessary, because of space limitations, to first turn the beam with a front surface aluminum mirror which was damaged during the shot. Fig. 6 shows the near-field radiation pattern obtained at various distances. The angular array of 6-mm-wide strips

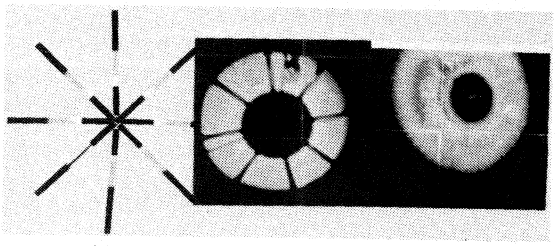

(a) (b) (c)

Fig. 6. Near-field radiation pattern with an unstable cavity. (a) Angular array located 37.5 cm from cavity. (b) Full pattern 2.5 m from cavity. (c) Full pattern 11.6 m from cavity.

shown in Fig. 6(a) was located in front of the turning mirror 37.5 cm from the convex mirror. The shadow cast by one of the three mirror-support struts is visible on one of the lower left spokes. The pattern shown in Fig. 6(b) was obtained at a distance of 2.5 m. The irregular shadow in the upper part was cast by a small pick-off mirror used to relay a portion of the laser beam to the photodetectors. The damage pattern shown in Fig. 6(c) was taken at a distance of 11.6 m from the cavity. Because of poor access to the location where the film was placed, it was not possible to locate the film perpendicular to the beam axis. This accounts for the noncircular shape of the pattern and the fact that the pattern is not centered on the film. The three light shadows were cast by the support web for the output mirror of the unstable optics. The central shadow has decreased in diameter to ≈5 cm from the original 7.5 cm at the mirror, and the spot of Arago [17] is visible in the center of this shadow. The maximum divergence obtained from Fig. 6(a) and (c) was 1.4 mrad. The significant result is that the unstable resonator was successful in controlling this highly superradiant medium to produce a collimated laser beam.

The laser spectrum was measured for several gas compositions in the long laser cell with a mirror on one end. Only *P*-branch transitions were observed. Identification and a qualitative comparative ranking of line strengths were assigned for the various transitions. The results of these measurements are shown in Table I. In this table *W*, *M*, and *S* refer to weak, medium, and strong lines. As would be expected from the exothermic energy release in the reaction $F + C_2H_6 \rightarrow HF^* + C_2H_5$, only the $v \leqslant 3$ levels are excited. A comparison of the line strengths for the given shots indicates that usually the intensity of lines forming a cascading series tends to increase with decreasing v. The largest number of transitions are observed for the lowest SF_6 pressure. The latter result is opposite to that observed previously using a transverse discharge with various electrode configurations [18].

In order to use the electrical efficiency of an electron-beam pumped laser to determine some important parameters of the laser, it is necessary to determine the amount of energy actually deposited in the gas. Measurements of the deposited energy will also allow an estimate of the efficiency of the electron beam in producing fluorine atoms from SF_6 molecules. Total-stopping calorimetric measurements were made as a function of distance in the long laser cell at various SF_6 pressures. Ethane was not mixed with the SF_6 because the small amounts of ethane do not greatly affect the beam propagation. In addition, if ethane is used, then the calorimeter also measures the laser energy which then must be taken into account to obtain the true electron-beam deposition. The results of the calorimetric measurements for the long cell and an axial magnetic field of 2 kG are shown in Fig. 7. The axial distance is the distance measured from the accelerator anode. The dashed line at 33 cm indicates the point at which the electron beam reaches the axis of the laser cell. Each point shown on the figure represents one shot. Some of the scatter of the data is due to shot-to-shot variations in beam energy. However, the large measurement errors at 50 cm are largely due to the calorimeter not measuring the entire beam energy at all pres-

TABLE I
OPTICAL TRANSITIONS OBSERVED FOR VARIOUS MIXTURES OF SF_6 AND C_2H_6

TRANSITION	λ	OBSERVED TRANSITIONS FOR C_2H_6/SF_6 PRESSURES (TORR)					
		5/300	30/300	90/300	10/100	50/500	4/20
$P_1(3)$	2.6083	W	-	-	W	-	W
$P_1(4)$	2.6396	M	M	M	M	-	M
$P_1(5)$	2.6726	M	M	M	M	-	M
$P_1(6)$	2.7074	M	S	M	M	M	M
$P_1(7)$	2.7440	S	S	S	M	S	M
$P_1(8)$	2.7825	S	S	S	S	S	S
$P_1(9)$	2.8230	-	-	-	M	-	S
$P_2(2)$	2.6962	-	-	-	-	-	W
$P_2(3)$	2.7274	W	-	W	M	-	M
$P_2(4)$	2.7604	S	-	W	M	W	M
$P_2(5)$	2.7952	S	M	M	M	S	S
$P_2(6)$	2.8318	M	S	S	M	S	S
$P_2(7)$	2.8705	S	S	M	M	M	S
$P_2(8)$	2.9111	S	M	M	M	M	S
$P_2(9)$	2.9539	-	M	-	M	-	S
$P_3(3)$	2.8542	W	W	-	M	-	M
$P_3(4)$	2.8889	M	M	M	M	-	M
$P_3(5)$	2.9256	M	M	M	M	M	M
$P_3(6)$	2.9644	M	M	M	M	M	M
$P_3(7)$	3.0052	M	M	W	M	W	M
$P_3(8)$	3.0482	M	M	-	M	-	M
$P_3(9)$	3.0936	-	-	-	W	-	W

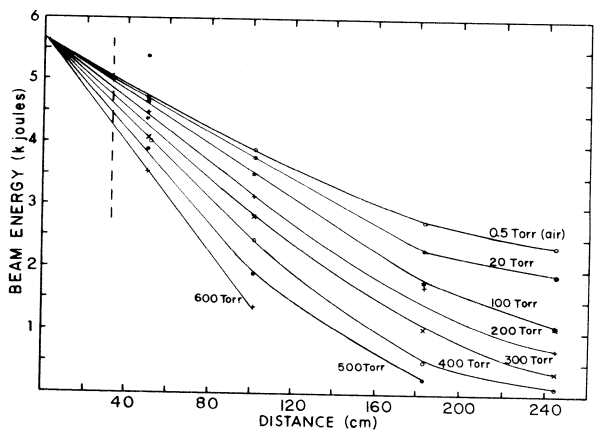

Fig. 7. Measured electron-beam energy as a function of distance, measured from the accelerator anode, for the long cell.

sures. This location is near the position where the electrons entered the laser cell. The segmented calorimeter did not always receive the entire beam energy because the electron trajectories in the magnetic field changed with pressure. The curves shown in Fig. 7 were for the most part drawn using the energy at the anode (0 cm) and the energy at the other three distances. As will be shown, the amount of energy actually deposited in the laser cell depends almost entirely on the deposition measurements at the distance of 244 cm. In addition to the propagation at various pressures of SF_6, the propagation in 0.5-torr air is also shown. These data taken with 0.5-torr air were obtained to determine the maximum beam propagation for this cell at a magnetic field of 2.0 kG. It has previously been shown that beam propagation efficiency is a maximum at about this pressure [19]. The measured beam energy shown in Fig. 7 follows an exponential decay with distance in 0.5-torr air and decreases monotonically with increasing SF_6 pressure at a given distance. A subsequent experiment using a straight tube showed that the propagation is very similar to that shown in Fig. 7. In fact, a comparison of the data shows that less than 5 percent of the beam was lost because of the bend.

Fig. 8 shows the percentage of beam energy lost as a function of density-length product. The percentage of the beam energy lost, given by the upper curves, is the difference between the measured beam energy at the anode and at each location shown on the curve. ρ is the density of gas in the cell. The data associated with curves labeled 50, 101, 183, and 244 cm were obtained from the curves in Fig. 7. The data labeled 152 cm were obtained with the short cell and an axial magnetic field of 2.5 kG. The lower solid curve is the beam-energy loss due to absorption calculated using a numerical one-dimensional computer code [20]. Results from this code are in good agreement with measurements under conditions where only deposition is important [21]. If there were no scattering of electrons out of the cell and no effect from the magnetic field, the deposited energy should only be a function of ρl. It is evident from the rapid decrease in beam energy with distance at 0.5 torr in Fig. 7, and from the large discrepancy between measured beam loss and calculated deposition in Fig. 8, that a large portion of the energy is lost by scattering to the wall. This scattering occurs because the magnetic field is not large enough to contain the electrons. The data shown by the crosses were obtained using a 140-cm-long straight cell similar to that of [1]. Starting from the upper cross, the magnetic-field values were 0, 2.0, and 4.5 kG. These points show that as the magnetic field is increased the measurements approach the calculated values. Fig. 8 shows that a determination of the deposited energy, using the difference between the energy at the anode and the measured energy at a given location, will be in error. This error will be greater for low magnetic fields and/or long laser cells. In order to take into account the amount of energy scattered to the cell walls, the energy deposited in the gas at a given SF_6 pressure is obtained by subtracting the energy measured at the given SF_6 pressure from that measured with 0.5-torr air. The energy loss at a pressure of 0.5-torr air is the amount of energy scattered to the wall since, at this pressure, less than 1 percent of the beam energy is actually deposited in the gas. This method of determining the deposited

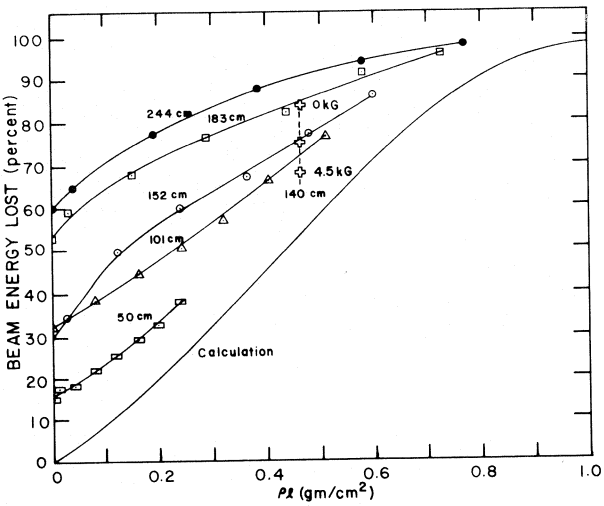

Fig. 8. Measured beam-energy loss and calculated beam absorption as a function of density-length product.

energy assumes that the scattering does not increase with cell length or with SF_6 pressure. Measurements show that scattering losses increase slightly with pressure and cell length; however, the difference between the value of the measured energy at 0.5 torr and at a given SF_6 pressure gives an upper bound to the amount of energy deposited.

Fig. 9 shows the beam-energy deposition, obtained in the manner just described, as a function of distance for the long laser cell. As was previously mentioned, the curves can be considered the upper bound on the true energy deposition in the gas. These data show that at low pressures the deposition is more or less linear with pressure over the full laser length. This means that the lasing medium is uniformly excited along the axis. At higher pressures the deposition rate decreases rapidly with increasing distance. At 600 torr, for example, most of the electron-beam energy is deposited in a length which is less than half the laser length. This nonlinear deposition with distance, along with the strong superradiance of the laser, accounts for the laser energy decrease with increasing SF_6 pressure in this experiment and that of [1]. The amount of energy actually deposited in the laser cavity is the difference between that deposited at 257 cm (extrapolated) and at 33 cm (shown by the dashed line in Fig. 9). From Fig. 9 the optimum laser length for a given reactant pressure can be determined if one uses uniform energy deposition as a criterion. Thus, for 2-MeV electrons, a laser length of 224 cm is about optimum for 200-torr SF_6 but this length decreases to 70 cm at 600 torr. Of course, the divergence angle of radiation will increase as the laser length is decreased.

Fig. 10 shows the electrical efficiencies obtained for several experiments as a function of SF_6 pressure and a C_2H_6/SF_6 ratio of 0.10. The electrical efficiency η_e was obtained by dividing the measured laser energy by the electron-beam energy deposited within the laser cavity. These are therefore minimum values of η_e since the upper bounds of deposited energy were used. Also shown are the efficiencies inferred in [1]. The maximum η_e observed is 14 percent compared to the maximum theoretical value of $\approx$24 percent [1]. The overall electrical efficiency of the laser is considerably less than that

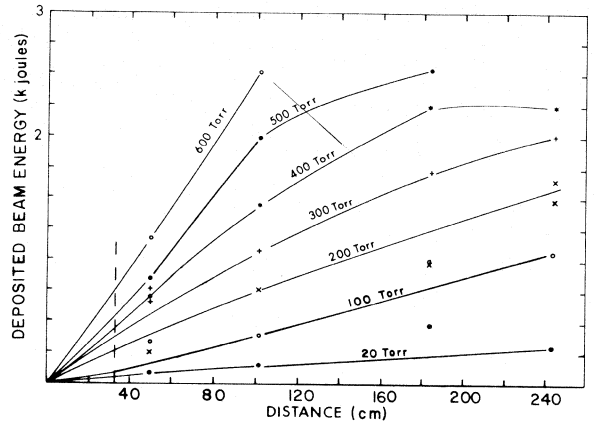

Fig. 9. Electron-beam energy deposition as a function of distance for the long cell.

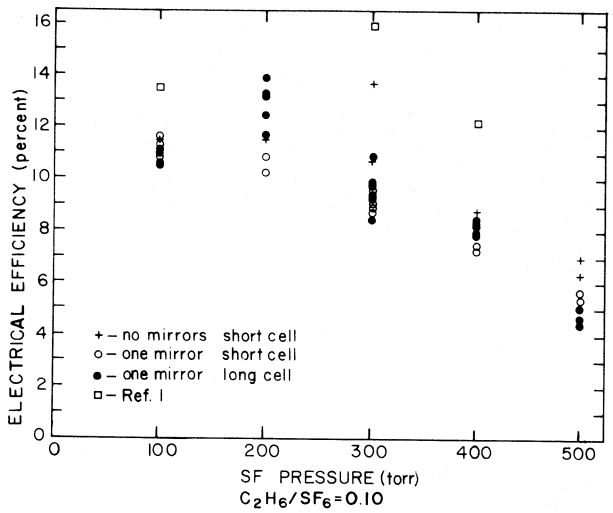

Fig. 10. Electrical efficiency η_e as a function of SF_6 pressure.

shown in Fig. 10 because the energy loss in the electron accelerator, the portion of the electron beam not used, and the energy required to produce the magnetic field have not been included. With the use of existing technology in building efficient electron-beam machines and by using transverse excitation, which uses no external magnetic field, it should be possible to obtain an overall electrical efficiency of >10 percent. The variation of efficiency with SF_6 pressure has the same general shape for all experimental conditions. Above 300 torr the decrease in efficiency is due to the decrease in laser energy caused by nonlinear electron-beam deposition.

The electrical efficiency can be used to determine several important parameters of the laser. The chemical efficiency (η_c) is defined as the fraction of the exothermic energy that appears as laser radiation. The dissociation efficiency (η_D) is the minimum energy required to produce a free fluorine atom divided by the actual energy expended in producing a free fluorine atom. The relationship between these three efficiencies is given by

$$\eta_c = \frac{\eta_e(75.9)\,[\mathrm{F}]}{\eta_D(38)\,[\mathrm{HF}^*]}. \tag{1}$$

The brackets denote the time-integrated production densities of F and HF* particles. The numerical quantities 75.9 and 38 are the endothermic and exothermic energies in kilocalories per mole associated with the reactions $SF_6 + e \rightarrow SF_5 + F + e$ and $F + C_2H_6 \rightarrow HF^* + C_2H_5$, respectively. For 300-torr SF_6 the maximum η_e observed was 14 percent. The maximum possible η_c, calculated in a manner similar to that used in [22], is 56 percent. This value is obtained by taking the percentage of the exothermic energy not remaining in the excited HF molecules after the inversion is terminated. The minimum η_c, obtained from (1) when [HF*] = [F] and $\eta_D = 1$, is 28 percent. That is, at least 28 percent of the exothermic energy appears as laser radiation. Using this range of values of η_c along with the measured laser energy, laser volume, and exothermic energy, one obtains 1.0×10^{17} cm$^{-3} \leqslant$ [HF*] $\leqslant 2.0 \times 10^{17}$ cm^{-3}. The maximum [F] is found by using the measured beam deposition, the laser volume, and the minimum energy required to produce a fluorine atom. The minimum density must be equal to the minimum [HF*] density. The limits on [F] turn out to be the same as those on HF*. The minimum value for [F] corresponds to at least 50 percent of the deposited energy being used to produce fluorine atoms. This means that the energy required to produce a free fluorine atom from SF_6 was less than 6.6 eV. This can be compared with the 4.5 eV reported in [8]. The values are in agreement since our value is an upper bound.

IV. Conclusions

The effects of optical elements on the operation of a high-energy HF laser have been investigated. The use of a single mirror on one end of the laser cell is found to reduce the laser energy to ≈80 percent of the value obtained when no mirrors are used. The effective control of the high-gain medium with a confocal unstable resonator has been demonstrated. A measured electrical efficiency of 14 percent was obtained. The minimum chemical efficiency for this laser was 28 percent. The overall efficiency ($\eta = (\eta_e \eta_c / \eta_e + \eta_c)$) for the laser is greater than 9.3 percent. Detailed measurements of electron-beam deposition in the laser gas provide a means for selecting an optimum laser length for a given operating pressure.

References

[1] R. A. Gerber and E. L. Patterson, "Intense electron-beam initiation of a high-energy hydrogen fluoride (HF) laser," *IEEE J. Quantum Electron.*, vol. QE-10, pp. 333–337, Mar. 1974.

[2] R. A. Gerber, E. L. Patterson, L. S. Blair, and N. R. Greiner, "Multi-kilojoule HF laser using intense-electron-beam initiation of H_2–F_2 mixtures," *Appl. Phys. Lett.*, vol. 25, p. 281, 1974.

[3] E. L. Patterson, R. A. Gerber, and L. S. Blair, "HF laser initiated by a 300-keV electron beam," *J. Appl. Phys.*, vol. 45, p. 1822, 1974.

[4] N. R. Greiner, L. S. Blair, and P. F. Bird, "A 0.2-GW pulsed H_2–F_2 chemical laser initiated by an electron beam," *IEEE J. Quantum Electron.* (Corresp.), vol. QE-10, pp. 646–647, Sept. 1974.

[5] C. P. Robinson, R. J. Jensen, and A. Kolb, "60-J pulses from an electron-beam-initiated SF_6–C_2H_6 chemical laser," *IEEE J. Quantum Electron.* (Notes and Lines), vol. QE-9, p. 963, Sept. 1973.

[6] R. Aprahamian, J. H. S. Wang, J. A. Betts, and R. W. Barth, "Pulsed electron-beam-initiated chemical laser operating on the H_2/F_2 chain reaction," *Appl. Phys. Lett.*, vol. 24, p. 239, 1974.

[7] R. Aprahamian, J. A. Betts, J. H. S. Wang, R. H. Herrett, and R. W. Barth, "Repetitively pulsed electron-beam-initiated chemical lasers from SF_6-H_2 and SF_6-D_2 mixtures," *Appl. Phys. Lett.*, vol. 24, p. 384, 1974.

[8] R. W. F. Gross and F. Wesner, "Electron-beam-initiated chemical laser in SF_6-H_2 mixtures," *Appl. Phys. Lett.*, vol. 23, p. 559, 1973.
[9] General Electric Company, Richmond Heights, Ohio.
[10] Scientech, Inc., Boulder, Colo.
[11] Barnes Engineering Company, Stanford, Conn.
[12] N. R. Greiner, G. P. Arnold, and R. G. Wenzel, "Rapid recording of infrared spectra from pulsed chemical lasers," *J. Appl. Phys.*, vol. 44, p. 3202, 1973.
[13] J. F. Schulze, Sandia Lab. Rep. SC-TM-69-298, 1969, unpublished.
[14] D. G. Pellinen and P. W. Spence, "A nanosecond risetime megampere current monitor," *Rev. Sci. Instrum.*, vol. 42, p. 1699, 1971.
[15] L. Allen and G. I. Peters, "Amplified spontaneous emission and external signal amplification in an inverted medium," *Phys. Rev. A*, vol. 8, p. 2031, 1973.
[16] K. G. Anlauf, P. H. Dawson, and J. A. Herman, "Relaxation of vibrationally excited HF in levels $v = 1$ and $v = 2$. II. By CH_4, C_2H_6, C_3H_8, C_2H_2, and C_2H_4," *J. Chem. Phys.*, vol. 58, p. 5354, 1973.
[17] R. J. Freiberg, P. P. Chenausky, and C. J. Buczek, "An experimental study of unstable confocal CO_2 resonators," *IEEE J. Quantum Electron.*, vol. QE-8, pp. 883–892, Dec. 1972.
[18] T. V. Jacobson and G. H. Kimbell, "Parametric studies of pulsed HF lasers using transverse excitation," *IEEE J. Quantum Electron. (Part II of Two Parts: 3rd Conference on Chemical and Molecular Lasers)*, vol. QE-9, pp. 173–181, Jan. 1973.
[19] P. A. Miller and J. B. Gerardo, "Relativistic electron beam propagation in high pressure gases," *J. Appl. Phys.*, vol. 43, p. 3008, 1972.
[20] J. A. Halbleib, Sandia Lab. Rep. SC-RR-720435, 1972, unpublished.
[21] G. J. Lockwood, G. H. Miller, and J. A. Halbleib, "Absolute measurement of low energy electron deposition profiles in semi-infinite geometries," *IEEE Trans. Nucl. Sci.*, vol. NS-20, pp. 326–330, 1973.
[22] W. H. Beattie, G. P. Arnold, and R. G. Wenzel, "Chemical efficiency in a pulsed HF laser," *Chem. Phys. Lett.*, vol. 16, p. 164, 1972.

TA5—H_2/F_2 Flame Propagation and Repetitively Pulsed Hydrogen Fluoride (HF) Chain-Reaction Chemical Laser

HAO-LIN CHEN, JACK D. DAUGHERTY, AND WALTER FYFE

Abstract—**The burning velocity and the nature of the H_2/F_2 flame at various gas compositions have been experimentally determined. It was found that reactions induced by a diffusion-type flame proceed rather slowly, but reactions triggered by a compression wave proceed with supersonic speed. Based on the measurements of gas stability, repetitive pulse operation of H_2/F_2 chemical lasers at atmospheric pressure has been achieved.**

The second and third explosion limits of $H_2 + F_2$ reactions in O_2/He mixtures were also studied experimentally to improve our understanding of the nature of a $H_2 + F_2$ explosion. The apparatus allowed the simultaneous time-resolved measurement of both gas pressure and temperature at the center of the spherical reaction vessel. It was found that, for fixed $H_2 + F_2$ total pressure and O_2 concentration, mixtures with higher F_2/H_2 ratios are less stable and explode at a lower temperature. It appears quite certain that molecular O_2 plays an important role in the chain termination reaction. However, the addition of CF_4, SF_6, or N_2 showed no effect on the boundaries of the H_2/F_2 explosion.

I. Introduction

ALTHOUGH the H_2/F_2 chain reaction is attractive for use in chemical lasers, and efficient single-pulse lasing systems have been demonstrated, no multipulse operation has ever been achieved. This is because of the difficulties encountered in 1) handling H_2/F_2 mixtures—their chemical stability against preignition, and 2) H_2/F_2 flame control—particularly in the suppression of self-sustained chemical reactions at the upstream end of the lasing cavity. These reactions are triggered by the detonation wave or flame originating from preceding lasing pulses. During the course of this study, two separate small-scale experiments have been conducted on each of these key problems. It was found that brief preignition stability over a wide range of parameters can be achieved with suitable additives. Using a small-scale flowing apparatus, we have also measured the H_2/F_2 flame speed for various gas mixtures and have demonstrated that repetitively pulsed operation in certain mixtures of H_2, F_2, O_2, and He is possible without producing detonation-wave propagation. The flame generated by preceding pulses could be completely quenched to permit repetitive pulse operation of H_2/F_2 chemical lasers at atmospheric pressure.

Ignition of the H_2/F_2 chemical reactions from the lasing medium to the unreacted regions could be triggered by the following three different mechanisms: 1) by diffusion of active centers like F, H, HF*, and H_2^* which initiate the chain or branched chain reaction; 2) by heat transport or diffusion of translationally hot molecules or atoms which heat up the gas and perturb the stationary reaction kinetics; and 3) by pressure waves propagating from the locally heated gases with supersonic speed, which changes the stationary reaction

Manuscript received November 28, 1974; revised February 3, 1975. This work was supported in part by the U.S. Air Force Weapons Laboratory, Air Force Systems Command, Kirtland Air Force Base, N. Mex. 87115, and in part by the Advanced Research Projects Agency under ARPA Order 0870 and Contract F296-1-73-0122.

H.-L. Chen was with the AVCO Everett Research Laboratory, Inc., Everett, Mass. 02149. He is now with the Lawrence Livermore Laboratory, Livermore, Calif. 94550.

J. D. Daugherty and W. Fyfe are with the AVCO Everett Research Laboratory, Inc., Everett, Mass. 02149.

kinetics. At constant volume condition, both mechanisms 2) and 3) could vary the pressure and temperature of reactants drastically and lead to explosive reactions. Since both mechanisms 1) and 2) are caused from gas diffusion, the propagation speed is normally very slow and less than that of the speed of sound in the mixture. Mechanism 3) could be very fast and is normally faster than the speed of sound. Grosse and Kirshenbaum [1] have systematically measured the diffusion-flame burning velocity of pure H_2/F_2 mixtures at 90 K, and a speed of 3.5×10^3 cm/s was reported. The estimated value at room temperature was about 10^4 cm/s. Similar measurements in He diluent show much slower burning velocities at lower $H_2 + F_2$ concentrations. In our present work, a maximum burning velocity of greater than three times the speed of sound in He was observed under some conditions.

To aid our understanding of the nature of H_2/F_2 explosions triggered by the compression wave, the second and third explosion limits of the $H_2 + F_2$ reaction in O_2/He mixtures were also studied experimentally. Simultaneously, time-resolve measurements were made of both the pressure and the gas temperature at the center of the spherical reaction vessel. In general, rapid exothermic gas reactions could lead to explosions in a closed vessel by two fundamentally different mechanisms. First, by thermal explosion; it arises from the self-heating of exothermic chemical reactions, and results directly from the imbalance between generation and transport of heat. This process depends strongly on the geometry of the reacting system, but not on the nature of the surface or detailed reaction mechanism. Second, by chain-branching explosion; it depends strongly on some particular chain-branching steps, the concentration of chain—or branching—inhibitors, or the nature of the reaction vessel surface. Kapralova and Chaikin [2a)] have demonstrated the nonthermal nature of the second explosion limit of a H_2/F_2 reaction at a total $H_2 + F_2$ pressure less than 0.05 atm. In this study, the total pressure of $H_2 + F_2$ is far above 0.05 atm, and a third limit was observed. In reducing the pressure from values below the third limit down to vacuum, the existence of a second limit, reported by Kapralova *et al.* [2b)], was also confirmed.

II. Experimental Apparatus and Procedures

A diagram of the experimental arrangements for the determination of H_2/F_2 explosion limits is shown in Fig. 1. The reaction vessel is a fully passivated stainless-steel 8-l sphere. Gases were admitted into the vessel through two separate tubes with small jet holes for the purpose of rapid mixing. The estimated mixing time was less than a few minutes. A thermal bath capable of temperature variations between -80 and 100°C was used for uniform variation of vessel temperature. Cu-Constantan thermocouples with response time less than 0.1 s were used to measure the temperature of the reactants. A Kistler pressure gauge with a rise time shorter than 10^{-3} s was used to monitor the pressure inside the vessel and to confirm the time of explosion. Both signals were displayed on synchronously swept X-Y recorders. All stainless-steel flanges were vacuum sealed by metal O rings.

Before each experiment, the reaction vessel was evacuated to 10^{-3}-mmHg pressure and then cooled down to -80°C. F_2/He/O_2 gases were also precooled to -80°C, then admitted separately into the vessel until a total pressure of 1 atm was reached. The gases were allowed to mix for at least $\frac{1}{2}$ h. For the determination of the conditions of the third limit, the temperature was slowly raised (about 0.5°C/min) by adjusting the temperature of the thermal bath until an explosion occurred. To locate the region of the second limit, mixtures of identical compositions and pressures were allowed to warm up to temperatures less than that of the third explosion limit. The pressure inside the vessel was then slowly reduced until explosion commenced.

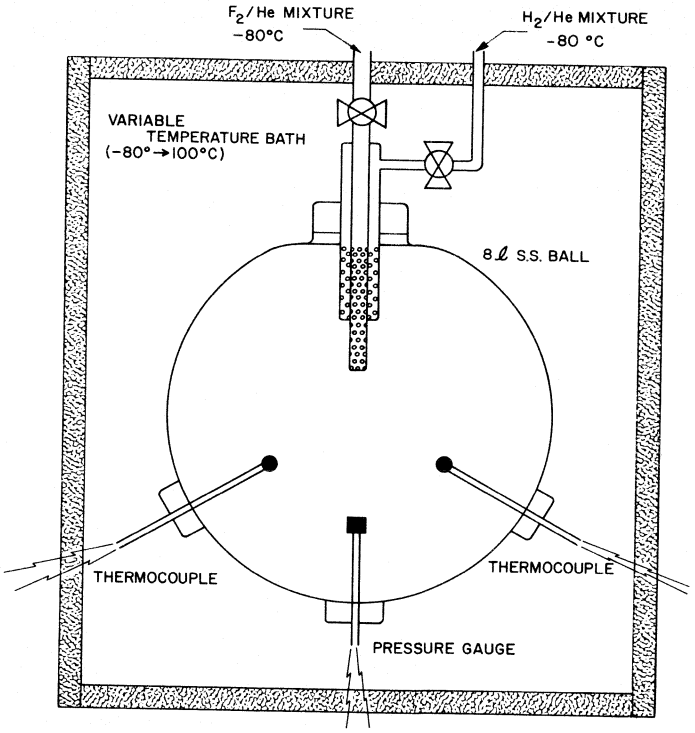

Fig. 1. Schematic diagram of apparatus used for determination of H_2 and F_2 explosion limits.

The small-scale flowing apparatus for flame-speed measurement is shown schematically in Fig. 2. Fluorine and hydrogen are each premixed with diluent helium in separate storage tanks at pressures of about 10 and 5 atm, respectively. During the experiment, fast-acting electrically operated valves, coupled with sonic metering orifices, open to admit these gases to a mixing manifold which distributes the gases in the mixing region in alternate sheets 2 mm thick as shown in Fig. 2. The cross section of this mixing region is 1.2×10 cm. The gases mix as they flow toward the test cell. From the test region, the gases flow into a dump tank. Three sets of viewing quartz windows were installed as shown in Fig. 2. In the cell, the reaction is initiated by a flash lamp located along the middle quartz window. The lamp is set to fire at a given time after the fast-acting valves open. The ultraviolet light from the lamp passes through quartz windows into the initiation section. Hg lamps emitting at 2537 Å and IP28 photomultiplier tubes coupled with 30-Å bandwidth filters located across the viewing windows are used to monitor the time history of the F_2 concentration. Kistler pressure gauges, mounted upstream and

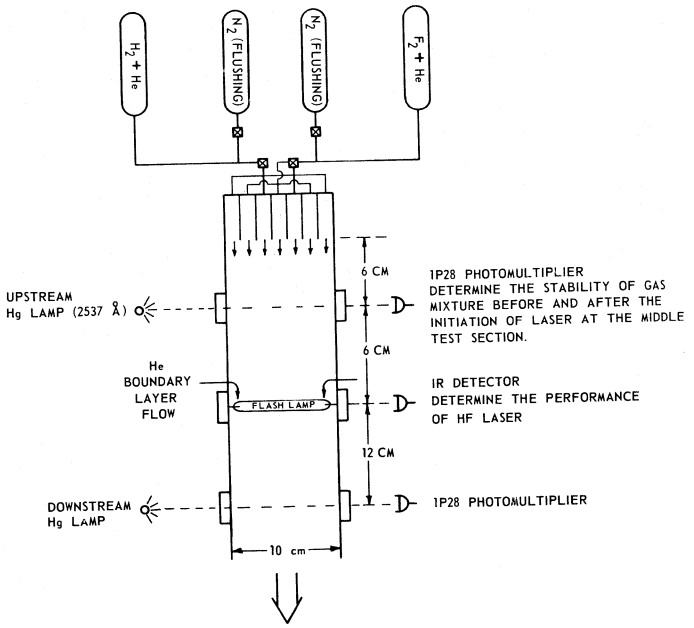

Fig. 2. Schematic diagram of apparatus used for the determination of the transient concentration of F_2 in the test cell as the reaction in the middle section was volumetrically triggered by a photolysis flashlamp. A change of F_2 concentration indicates chemical reaction in the mixture.

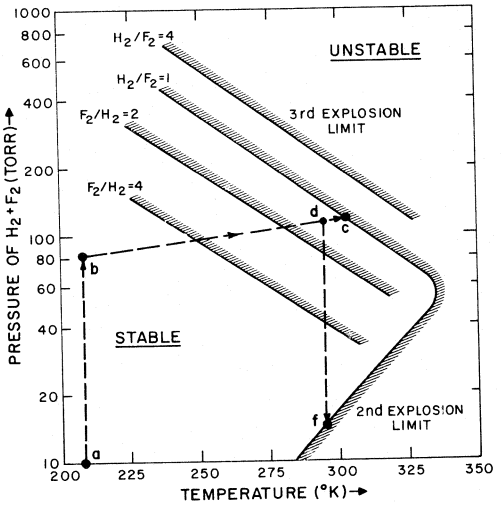

Fig. 3. The second and third explosion limits observed in H_2/F_2 mixture. The oxygen concentration was kept at 0.2 percent. The total pressure was 1 atm balanced by He. The reaction vessel was a fully passivated stainless-steel 8-l sphere. For determination of the third explosion limit for H_2/F_2 mixtures of stoichiometric H_2/F_2 ratio, the precooled H_2/He and F_2/O_2/He gases were first admitted into the vessel of same temperature (shown as line *ab*). The vessel was then allowed to warm up slowly until the explosion commenced (*bc*). For determination of the second explosion limit, an identical mixture was prepared and warmed up to point *d*. The reactant was then pumped down to lower pressure until explosion commenced (shown as line *df*).

downstream of the initiation section, are used to measure the pressure in the test cell and confirm the time of explosion if it occurs. Both the photomultiplier and pressure-gauge signals are displayed on oscilloscopes and photographed.

In the lasing experiments, the middle quartz windows were replaced by a Cu mirror with a 20-cm radius of curvature and a 20-percent output dielectric mirror. Measurements of the laser output energy were made with a calibrated calorimeter. The temporal variation of the laser duration was monitored with an InSb detector.

Matheson prepurified grade H_2 (99.95 percent), high purity grade He (99.99 percent), and high purity grade O_2 (99.95 percent), were used without further purification. In order to remove any HF contamination (~1 percent) in the Matheson F_2 gas (98 percent), it was passed through a NaF-HF adsorber prior to the preparation of the $F_2/He/O_2$ mixture. The final HF concentration in F_2 was found to be less than 0.1 percent.

III. Data

A. The H_2/F_2 Explosion Limits

Fig. 3 shows the data obtained with various $H_2/F_2/He/O_2$ mixtures. Lines *ab* and *bc* show the steps used to obtain the third-limit *P-T* data. Lines *ab*, *bd*, and *df* indicate the steps of locating regions for the second limit. It was found that for fixed O_2 concentration, the third explosion limit shifts toward higher *P-T* values as the H_2/F_2 ratio increases to values higher than stoichiometric (as shown in Fig. 3). For fixed H_2/F_2 compositions, the position of the third limit shifted to higher *P-T* values as more and more O_2 was added to the gases. The influence of other additives like SF_6, CF_4, and N_2 to the locations of the third limit was separately tested. Within the concentration range studied (<4 percent), no effect due to these additives was observed. The influence of the surface/volume ratio to the explosion boundary was also determined. By using a spherical vessel of 2-l volume, the third limit was found to be slightly shifted toward even higher pressures possibly due to heterogenous chemical reactions.

To determine the nature of the explosion—thermal or branching chain—simultaneous measurements of pressure and temperature were also made. Fig. 4 shows a typical pressure and temperature versus time record taken at pre-explosion conditions. The mixture was 5 percent H_2, 5 percent F_2, 0.2 percent O_2, and 89.8 percent He. It was found that within the response time of these measurements (for both second and third limit regions), the onset of the explosion was abrupt and no preexplosion temperature rise was observed.

B. The Results of H_2/F_2 Flame-Speed Measurements

By monitoring the time history of F_2 concentration across the viewing windows (see Fig. 2), the gas flow speeds were experimentally determined. For mixtures of 12 percent H_2, 4 percent F_2, and 84 percent He, a flow speed of (3.5 ± 1) 10^3 cm/s in our apparatus was observed. The speed varies as both gas density and tank pressure changes. The flame speed in $H_2/F_2/O_2$/He mixtures was found to depend strongly on its composition. In general, the flame speeds observed in mixtures containing a higher percentage of O_2 and larger H_2/F_2 ratios are slower than that of the gas flow speed. The data obtained in mixtures of lower O_2 concentration and larger F_2/H_2 ratios show flames propagated with supersonic speeds. For convenience, we shall call the former composition a weak-reaction mixture and the later one a strong-reaction mixture.

Fig. 5 shows the temporal intensity variation of 2537-Å

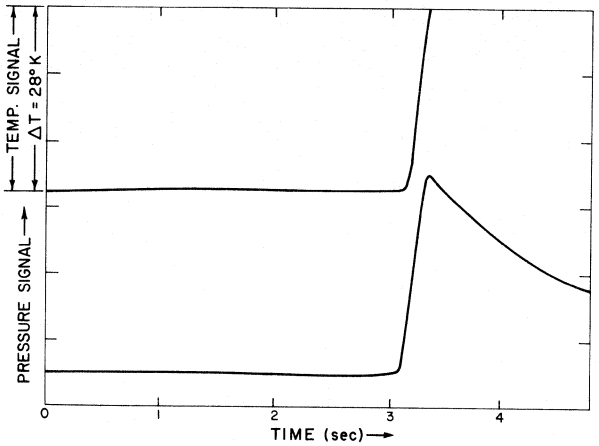

Fig. 4. The pressure and temperature time histories of H_2/F_2 reaction observed at the third explosion limit region. The upper trace shows the temperature signal and the lower trace shows the pressure pulse. No preexplosion heating was observed.

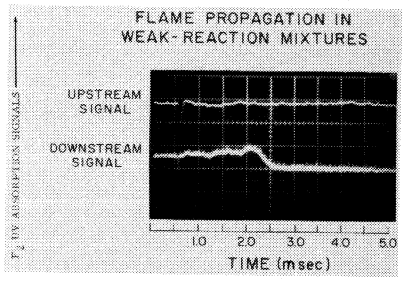

Fig. 5. Results of the transient chemical stability experiments in typical weak-reaction mixtures. The upper trace shows the transient F_2 concentration monitored at the upstream windows. The lower trace shows the signal monitored at the downstream windows. The first sharp spikes observed at each trace are the scattered light from the flashlamp. The gas composition was 12 percent H_2, 4 percent F_2, 0.4 percent O_2, and 83.6 percent He at a total pressure of 1 atm.

radiation transmitted through the two end windows monitored in a weak-reaction mixture. The gas composition was 12 percent H_2, 4 percent F_2, 83.6 percent He, and 0.4 percent O_2. The top trace, obtained at the windows upstream of the initiation section, shows no change in F_2 concentration. However, the observations at the downstream window show a decrease in F_2 absorption and hence concentration at about 1.7 ms after the initiation pulse. Since the distance between downstream windows and initiation section is about 12 cm and gas flow speed is about 3.5×10^3 cm/s, the flame velocity must also be about 3.5×10^3 cm/s. The fact that there was no apparent F_2 consumption at the upstream windows also indicates that the flame velocity for this mixture must be smaller than the flow speed.

Fig. 6 shows a set of temporal signals for a strong-reaction mixture observed at upstream, downstream, and initiation windows. The gas composition was 12 percent H_2, 8 percent F_2, 79.6 percent He, and 0.4 percent O_2. Consumption of F_2 was observed at all sections. The middle trace shows the disappearance of F_2 immediately after the flash. However, a delay of about 45 μs was observed at the downstream window, and 25 μs at the upstream window. Since the distance between windows is 12 and 6 cm, respectively (see Fig. 2), the flame speed induced in this strong-reaction mixture should be

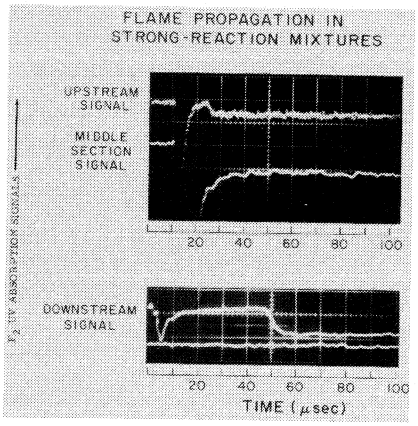

Fig. 6. Results of the transient chemical stability experiments in typical strong-reaction mixtures. The upper and middle traces show the F_2 concentration changes observed at the upstream and middle section windows, respectively. The lower trace shows the signal monitored at the downstream window. The first spikes resulting from flashlamp scattered light indicate the original triggering time of chemical reaction. The gas composition was 12 percent H_2, 8 percent F_2, 0.4 percent O_2, and 79.6 percent He at a total pressure of 1 atm.

about 2.4×10^5 cm/s or greater. Observations over extended time periods show that the upstream burning lasts for about 10 ms, but burning is sustained for more than 100 ms at downstream. By using He bleed gas to sweep out the residual gases, the duration of burning was found to be considerably shortened. Since the flame speed observed in the weak-reaction mixtures is far less than the speed of sound, flame propagation in these mixtures is probably the result of gas diffusion. The fact that the flame speed in strong-reaction mixtures was found to be far in excess of the speed of sound in gas indicates that flames in these mixtures must be propagated by a detonation wave.

C. Repetitively Pulsed H_2/F_2 Chain-Reaction Laser

For multipulse operation of H_2/F_2 chain-reaction lasers, the chemicals must stay unreacted before entering the laser cavity. Since the upstream chemicals of the strong-reaction mixtures are easily detonated by the preceding lasing pulses, they are not suitable for repetitive pulsing. Parametric determinations on the compositions that behave like strong-reaction mixtures were performed. Fig. 7 shows the short-term stability boundaries observed at various H_2, F_2, He, and O_2 compositions. These boundaries were found to shift toward higher $H_2 + F_2$ concentrations as more O_2 was added to the mixture. For a fixed O_2 concentration, the H_2-rich and F_2-lean mixtures are more stable and thus suitable for multipulse lasing.

Based on the flame data previously determined, lasing actions for weak-reaction mixtures at 10-pulses-per-second (pps) levels were successfully achieved. Fig. 8 shows the laser pulses, monitored by an InSb PEM detector, obtained in 4-percent F_2, 4-percent H_2, 91.6-percent He, and 0.4-percent O_2 mixtures. The total output energy is about 100 mJ/pulse. The laser active volume is $10 \times 1.2 \times 0.8$ cm or 10 cm^3 at atmospheric pressure. Thus a laser energy density of 10 J/l atm was demonstrated. Although the energy density obtained from this device is not optimum [3], the reproducibility between

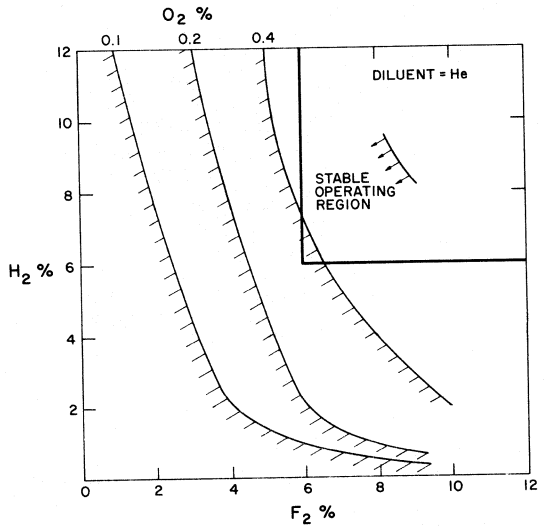

Fig. 7. Results of H_2 and F_2 short-term chemical stability mapping. Mixtures listed on the left of dashed curves are weak-reaction mixtures. The upstream reactant stays unreacted all the time. Mixtures listed on the right of dashed curves are strong-reaction mixtures. The upstream gas mixtures get detonated by the over pressure generated from the preceding laser pulse.

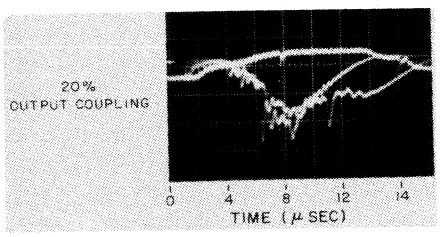

Fig. 8. The temporal behavior of HF laser outputs operated at 10-pps level. Only two pulses are shown. The flattened trace shows the transient F_2 concentration monitored at the He upstream windows. The time between pulses is about 80 ms. The decrease of F_2 concentration observed at the end of the flattened trace is due to the decrease of reactant supply pressure.

successive pulses is good. The repetition rate is design limited and could be improved to 100 pps or higher values.

IV. Discussion

A. On the Nature of H_2/F_2 Explosion

For exothermic chemical reactions in a closed spherical vessel and under conditions of conduction-dominated heat transport, the magnitude of preignition temperature rise at the center of the vessel can be approximated [4] as $\Delta T = 1.6RT_w^2/E$, where T_w is the temperature at the wall of the vessel, R is the gas constant, and E is the activation energy required for reaction. Adopting an upper limit of activation energy E of 10 kcal/mole [5] and T_w of 300 K, a preexplosion temperature rise of 28°C should be observed. Since no indication of preexplosion heating was observed, the explosion does not seem to be the result of thermal imbalance between chemical reaction and heat conduction. However, this does not rule out the possibility of a convection-controlled thermal explosion. The fact that the third limit was found to be shifted toward higher pressure, as a smaller reaction vessel was used, does indicate that the third explosion limit might still be a thermal one in nature.

It is generally believed that the first explosion limit is controlled by diffusion of the chain centers (F, H, and vibrationally excited H_2^*, HF* molecules) and hence, at low enough pressure (typically 0.01 atm or less, depending on the geometry of the reaction vessel), mixtures of H_2 and F_2 will be stable. The second explosion limit is postulated by Kapralova *et al.* [2b)], and is believed to be controlled by the branching reactions involving vibrationally excited HF* and H_2^* molecules

$$HF^* + F_2 \xrightarrow{k_1} HF + 2F \quad (1)$$

$$H_2^* + F_2 \xrightarrow{k_2} HF + H + F \quad (2)$$

and homogeneous chain-breaking reactions, like vibrational relaxation of HF*, H_2^*, or termolecular reaction of HO_2 formation

$$HF^* \text{ or } H_2^* + M \xrightarrow{k_3} HF \text{ or } H_2 + M + \Delta E \quad (3)$$

$$H + O_2 + M \xrightarrow{k_4} HO_2 + M. \quad (4)$$

Due to the similarity in P-T relations resulting from both thermal and branching-chain initiations at the high-pressure region, it is difficult to make a decisive interpretation for the third limit. Talroze *et al.* [6] proposed that the third limit might be triggered by the regeneration of chain centers through two-body reactions involving HO_2

$$HO_2 + F_2 \xrightarrow{k_5} HF + O_2 + F. \quad (5)$$

Adding excess F_2 into the $H_2/F_2/O_2/He$ mixture of stoichiometric H_2/F_2 ratio might result in three effects. First, it increases the overall heat-generation rate by enhancing reactions such as

$$F_2 \xrightarrow{\text{collisions}} 2F \quad (6)$$

$$H + F_2 \longrightarrow HF + F \quad (7)$$

where reaction (7) is the rate-limiting step involved in the H_2/F_2 chain reaction. Second, it decreases the overall thermal transport rate. Third, it increases the amount of F atoms that might be generated from reaction (5). Thus, for fixed $H_2/O_2/He$ concentrations at fixed temperature, increasing the F_2 concentration tends to lower the stability of the mixture. Since reaction (4) was thought to be the major chain termination reaction, its effect is quite straightforward. Therefore, the stable region (between the second and third limits) becomes wider as more O_2 molecules are added and narrower as the concentration of F_2 increases. With the limiting information on rate constants of the above-mentioned reactions [7]-[9] it is not possible to make precise quantitative modeling calculations or predictions about the explosion boundaries of $H_2 + F_2$ reactions. Since the boundary changes with the concentration of O_2 and not N_2, CF_4, or SF_6, molecular oxygen must have played an important role in chain-branching or breaking reactions and not merely served as an additional heat sink.

B. On the Nature of Flame Propagation

The characteristics of short-term gas stability in strong-reaction mixtures can be well explained by the long-term

explosion limits determined in Section III-A. The upstream reactant is originally stable and located at pressure-temperature conditions below the third limit. As the over pressure due to the preceding laser pulse arrives, the mixture changes into a different pressure-temperature relation and passes the boundary of the third explosion limit. Thus the reactant becomes unstable and reactive in nature. However, as more O_2 is added to the mixture, the boundary of the third explosion limit is pushed toward higher pressure and temperature. If the final pressure-temperature relation still falls within the boundary of the third explosion limit, the mixture will stay unreacted. Since the boundary of the third explosion limit lies at a region of higher pressure and temperature for H_2-rich and F_2-lean mixtures, a larger over pressure will be needed for triggering the reaction upstream.

Since the flame speeds measured in weak-reaction mixtures were found to be much slower than the gas flow speed (3.5×10^3 cm/s), the reactant at the upstream end will stay unreacted before entering the laser cavity. The flames must be propagated by diffusion mechanisms.

V. Conclusions

The two explosion limits (second and third) were studied experimentally in an apparatus which permits the simultaneous measurement of pressure and local gas temperature at the center of the spherical reaction vessel. No noticeable preexplosion heating was observed. For fixed $H_2 + F_2$ total pressure and O_2 concentration, mixtures with higher F_2/H_2 ratios are less stable and explode at lower temperature regions. Although there is not enough information available for the detailed explanation on the mechanism of H_2/F_2 explosions, molecular O_2 was observed to play an important role in the chain termination reaction. Additions of CF_4, SF_6, or N_2 showed no effect on the boundary of H_2/F_2 explosions.

In a separate small-scale flowing device, the flame propagation in H_2/F_2 was also studied. The short-term gas stability for various H_2/F_2/He and O_2 compositions was systematically determined. It was found that flames in weak-reaction mixtures are propagated by diffusion mechanism and in strong-reaction mixtures by detonation waves. Employing these weak-reaction mixtures, repetitive pulsing of H_2/F_2 lasers at atmospheric pressure was successfully demonstrated.

Acknowledgment

The authors wish to thank Dr. R. E. Center for his many helpful suggestions in the preparation of this manuscript.

References

[1] A. V. Grosse and A. D. Kirshenbaum, "The premixed hydrogen-fluorine flame and its burning velocity," *J. Amer. Chem. Soc.*, vol. 77, pp. 5012–5013, 1955.

[2] a) G. A. Kapralova and A. M. Chaikin, "Evidence for the nonthermal nature of the upper ignition limit in the reaction between fluorine and hydrogen," *Kinet. Katal.*, vol. 10, pp. 245–249, 1969.
b) G. A. Kapralova, E. M. Trofimova, and A. E. Shilov, "The upper ignition limit in the reaction of fluorine with hydrogen," *Kinet. Katal.*, vol. 6, pp. 977–981, 1965.

[3] H. L. Chen, R. L. Taylor, J. Wilson, P. Lewis, and W. Fyfe, "Atmospheric pressure pulsed HF chemical laser," *J. Chem Phys.*, vol. 61, pp. 306–318, 1974.

[4] N. J. Gerri and F. Kaufman, "The explosive decomposition of azomethane," in *Proc. 10th Int. Symp. Combustion*, 1965, pp. 227–235.

[5] N. Cohen, "A review of rate coefficients for reactions in the H_2/F_2 laser system," Aerospace Corp., El Segundo, Calif., Tech. Rep. TR-0172 (2779)-2, Sept. 1971.

[6] V. L. Talroze, G. K. Vasilev, and O. M. Batovskii, "Chemical lasers based on chain and branched-chain reactions," *Kinet. Katal.*, vol. 11, pp. 277–289, 1970.

[7] J. B. Levy and B. K. W. Copeland, "The kinetics of the hydrogen-fluorine reaction. II. The oxygen-inhibited reaction," *J. Phys. Chem.*, vol. 69, pp. 408–416, 1965.

[8] a) G. A. Kapralova, E. M. Margolina, and A. M. Chaikin, "Mechanism of the reaction of fluorine with hydrogen," *Dokl. Akad. Nauk. USSR*, vol. 198, pp. 634–637, 1971.
b) —, "Rate constants of several reactions of vibrationally excited hydrogen molecules in the reaction of fluorine with hydrogen," *Dokl. Akad. Nauk. USSR*, vol. 197, pp. 624–626, 1971.

[9] A. F. Dodonov, G. K. Laurovskaya, and V. L. Talroze, "Mass-spectroscopic measurement of the rate constant of elementary reactions. V. Reactions of hydrogen atoms with oxygen in the presence of H_2 and He," *Kinet. Katal.*, vol. 10, pp. 701–709, 1969.

TB3—Measurement of Vibrational-Vibrational Exchange of Highly Excited States of Diatomic Molecules where the Collisional Probability is Approaching Unity

YEHUDA NACHSHON, STUDENT MEMBER, IEEE, AND PAUL D. COLEMAN, FELLOW, IEEE

Abstract—An experimental method, employing a fast population perturbation technique, is described to measure the vibrational-vibrational (VV) collisional probability $P_{r,r-1}^{v,v+1}$ of a diatomic molecule for large vibrational quantum numbers r and v. The relaxation of the perturbed gain of a pair of vibrational levels is a function of the vibrational populations and VV rate constants $k_{r,r-1}^{v,v+1}$. The numerical inversion of the VV master rate equations determining this relaxation does not give unique value for $k_{r,r-1}^{v,v+1}$ (or $P_{r,r-1}^{v,v+1}$), but lower bounds can be evaluated and with empirical formulas, having several adjustable constants, it can be shown that probabilities of the order of unity are required to satisfy the experimental data. The method has been specifically applied to the CO molecule, but other molecules such as $HX(X = F, Cl, Br)$, NO, etc., could also be measured.

INTRODUCTION

IN MANY molecular laser systems, the excitation mechanism produces appreciable population of highly excited ground-electronic vibrational states. This is particularly true for chemical lasers using large exothermic reactions, i.e., the CO chemical laser employing the O + CS reaction where $\Delta H = 85$ kcal/mole. Energetically, CO vibrational excitation up to $v = 16$ is allowed. The peak in the vibrational population distribution has been experimentally measured [1]-[4] to be around $v = 12$ or 13 as seen in Fig. 1.

This means that the initial vibrational-vibrational (VV) energy exchange processes of importance

$$CO(r) + CO(v) \rightleftarrows CO(r-1) + CO(v+1) \tag{1}$$

will be for both r and v in the range 8-16. Hence a quantitative understanding and analysis of this laser system requires that the rate constants $k_{r,r-1}^{v,v+1}$ (or probabilities $P_{r,r-1}^{v,v+1}$) be known for large r and v. The probability is related to the rate constant by the expression $k_{r,r-1}^{v,v+1} = P_{r,r-1}^{v,v+1}\,\bar{\sigma}\bar{v}$, where $\bar{\sigma}$ is the hard sphere cross section and $\bar{v}$ is the average thermal velocity.

Previous experimental work [5]-[8] on VV collisions of CO has been for the case $P_{r,r-1}^{0,1}$, where the transition probability is small ($\leqslant 10^{-2}$). Theoretical calculations of $P_{r,r-1}^{0,1}$ have been made by Jeffers and Kelley [9], and calculations of $P_{r,r-1}^{v,v+1}$ have been reported by Rockwood *et al.* [10], Dawson and Tam [11], Dillon and Stephenson [12], and Kelley [13]. The last two papers also consider $P_{r,r-2}^{v,v+2}$ (i.e., a $\Delta v = \pm 2$ transition), which may become important, of large v and r.

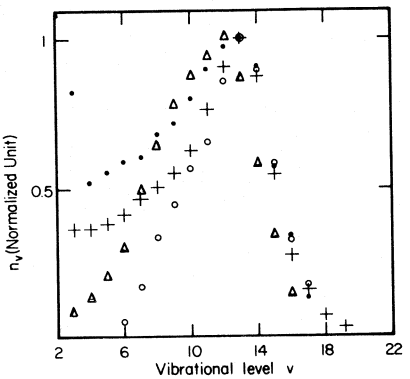

Fig. 1. Vibrational distribution from the chemical reaction $O + CS_2$. (○) Hancock *et al.* (○) Tsuchiya *et al.* (+) Powell and Kelley. (Δ) Djeu.

In this paper an experimental technique has been devised to measure $P_{r,r-1}^{v,v+1}$ for large r and v for a diatomic molecule. The method consists of first producing a peaked excited vibrational population of a diatomic molecule via a chemical reaction [14], specifically O + CS.

A short time (~ 16 μs) after electrical initiation and completion of the chemical reaction, the populations of a particular pair of CO vibrational levels are rapidly perturbed ($\leqslant 1$ μs) by means of a laser Q switch, i.e., $n_v \rightarrow n_v + \Delta n$ and $n_{v+1} \rightarrow n_{v+1} - \Delta n$. A CW CO probe laser, monitoring the gain of various pairs of vibrational levels, is used to measure the decay time of Δn. It is assumed that rotational equilibration exists and that the decay of Δn on the time scale of the experiment is determined solely by VV processes. The chemical mixture, prior to the chemical reaction, was 0.23-0.33 torr CS_2, 2.23 torr O_2, and 6.88 torr He, which should yield a large collision frequency for the CO product and a fast RT relaxation.

The calculation of the population perturbation Δn recovery time requires solving the master VV equations [15]

$$\frac{dn_v}{dt} = \sum_{r=1}^{\infty} \left(k_{r-1,r}^{v+1,v}\, n_{v+1}\, n_{r-1} - k_{r,r-1}^{v,v+1}\, n_v n_r\right) - \sum_{r=0}^{\infty} \left(k_{r,r+1}^{v,v-1}\, n_v n_r - k_{r+1,r}^{v-1,v}\, n_{v-1}\, n_{r+1}\right) \tag{2}$$

for the case where the populations of some particular levels,

Manuscript received November 21, 1974; revised March 11, 1975. This work was supported by the National Science Foundation under Grant GK4331, with equipment aid from the Industrial Affiliates Program on Physical Electronics, University of Illinois at Urbana-Champaign, Urbana, Ill.

Y. Nachshon was with the Electro-Physics Laboratory, Department of Electrical Engineering, University of Illinois at Urbana-Champaign, Urbana, Ill. 61801. He is now with the Israeli Defense Department, Haifa, Israel.

P. D. Coleman is with the Electro-Physics Laboratory, Department of Electrical Engineering, University of Illinois at Urbana-Champaign, Urbana, Ill. 61801.

for example, $n_{11} \rightarrow n_{11} - \Delta n$ and $n_9 \rightarrow n_9 + \Delta n$ have been been perturbed.

The solution of (2) will be of the form

$$-\frac{1}{\Delta n}\frac{d\Delta n}{dt} = f(k, n) = \frac{1}{\gamma_{v,v-1}}. \tag{3}$$

Over a 1-3-μs time interval, associated with the decay of Δn, the populations n_r will be essentially constant which in turn will make the function f (or decay constant γ which can be measured) essentially constant.

Since γ will depend on a large number of rate constants, a unique set of rate constants cannot be determined from a few measured γ's, i.e., the problem is underdetermined. However, a lower bound can readily be calculated for the maximum rate constants or an empirical formula, having several adjustable parameters, can be assumed and the parameters determined. These procedures lead to the results for CO that $P_{r,r-1}^{v,v+1} \geqslant 0.3$ for r and v of the order of 10.

Experiment

A schematic diagram of the experimental apparatus is shown in Fig. 2. The CW CO (LN_2) electrical laser, with a single-line single-mode output power of several milliwatts, is used as a gain probe for the pulsed Q-switched CO chemical laser. This CW CO probe signal is of sufficiently low intensity as to have negligible effect on the populations of the pairs of energy levels being examined. The signals from the two CO lasers are orthogonally polarized to make it convenient to separate the CW CO signal by means of the Brewster windows and 0.35-m spectrometer. An InSb (77 K · pV) detector (0.4-μs time constant), with a 2-mm-thick Te-crystal, AR coated for 5.4 μm, filter in front of it, is used to monitor the gain.

The electrically initiated pulsed Q-switched CO chemical laser consists of a 1-in OD glass tube with electrode spacing 122 cm. A 0.015-μF capacitor, charged to 30 kV is used to initiate a chemical reaction in a mixture of 0.23-0.33 torr CS_2, 2.23 torr O_2, and 6.88 torr He to form a vibrational population of excited CO, peaked around $v = 12$. A 500-l/min mechanical vacuum pump was used to exhaust the gases which were completely exchanged after each chemically initiating electrical discharge. It is assumed that no buildup of CO($v = 0$) was occurring, that the O + CS reaction proceeded to completion, and that no appreciable amounts of OCS or CS_2 were present at the time of Q switching.

The Q switching is accomplished by a rotating mirror (300 Hz) which is synchronized with the electrical pulse so as to produce a 16-μs delay between the two. Since the round-trip gain of the Q-switched laser system is about 200 percent, it is difficult to operate on a single laser line. Generally, two laser lines go simultaneously, but this does not cause any appreciable complication in the analysis of the data. Frequency selectivity and laser-line selection are achieved in both lasers by means of reflection gratings blazed at 5.18 μm.

Experimental Data

The gain α as a function of time was measured for a number of vibrational-rotational transitions, two different cases being displayed in Fig. 3.

With the $v = 11 \rightarrow 10$, $P(17)$ and $v = 10 - 9$, $P(23)$ transitions lasing in the Q-switched mode, the gains $\alpha_{12-11}\,P(13)$ and $\alpha_{9-8}\,P(12)$ were measured as shown in the oscilloscope traces of Fig. 3(a) and (b). The gain perturbation caused by the laser Q switching is seen to appear above the normal gain versus time curve. The short (<1 μs) Q-switch laser pulse perturbs the populations about 3 percent, but this is sufficient to observe a much larger perturbation of the gain.

The gain perturbations of α_{12-11} and α_{9-8} relax back to the normal gain curves with time constants γ_{12-11} and γ_{9-8} of 1.0 and 2.2 μs, respectively. The accuracy of these time-constant data is mainly limited by the length and decay time of the lasing Q-switched pulse, hence the error in determining γ_{12-11} is greater than that in γ_{9-8}. An estimate would be ± 0.2 μs for γ_{12-11} and ± 0.1 μs for γ_{9-8}. The gain curves of Fig. 3 are tracings from the oscilloscope pictures, which degrades the data somewhat. The quoted data were obtained from the oscilloscope pictures where the base line could be determined

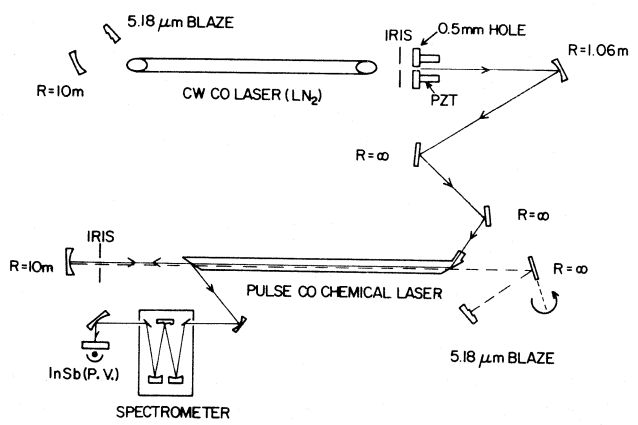

Fig. 2. Experimental configuration for measuring *VV* energy exchange on highly excited states of CO.

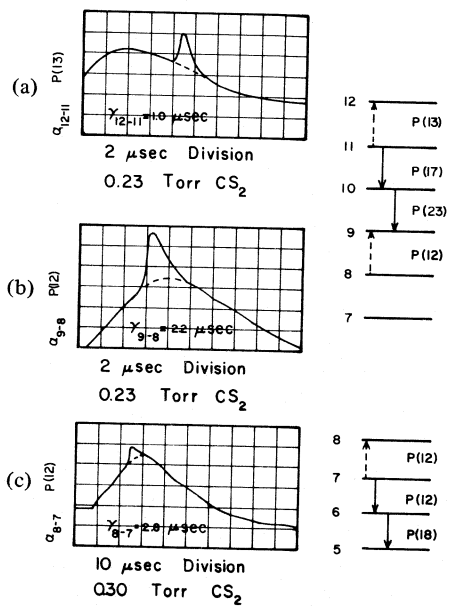

Fig. 3. The gain versus time for various P-branch transitions showing the effect of the vibrational population perturbation.

more accurately. However, the principal limitation on the accuracy of the data is the length of the Q-switched laser pulse.

With the $v = 7 \rightarrow 6$, $P(12)$ and $v = 6 \rightarrow 5$, $P(18)$ transitions lasing equally in the Q-switched mode, the decay constant of the $\alpha_{8-7}P(12)$ perturbed gain was determined from Fig. 3(c) to be 2.8 μs for the condition 0.30 torr CS_2. Over the pressure range 0.23-0.30 torr, the vibrational populations will scale as the pressure, i.e., $(n_r)_1/P_1 = (n_r)_2/P_2$. Hence, referring to (19), it is seen that $(\gamma_{8-7})_1 P_1 = (\gamma_{8-7})_2 P_2$, which will yield a value of 3.6 μs for γ_{8-7} at 0.23 torr, with an estimated error of ± 0.2 μs.

Population Distribution Measurement

It was seen from (3) that the decay constant $\gamma_{v,v-1}$ is a function of the rate constants k and the populations n_r during the time interval being considered. In order to obtain any information on the k's for a given $\gamma_{v,v-1}$, n_r must be measured.

The population distribution was determined by first measuring the gain $\alpha(J)$, $r = 9 \rightarrow 8$ for $8 \leqslant J \leqslant 16$, the P-branch transitions, and matching the experimental data to the theoretical gain curves computed from the expression [16]

$$\alpha(J)_{r,r-1} = \frac{\lambda^2 A_{r,r-1} S(\nu)}{8\pi kT} J \{n_r B_r \exp[-F(J-1)/kT] - n_{r-1} B_{r-1} \exp[-F(J)/kT]\} \quad (4)$$

where λ is the wavelength, A is the Einstein coefficient, $S(\nu)$ is the line-shape factor, B is the rotational constant, $F(J)$ is the rotational energy, k is the Boltzmann constant, and T is the translational-rotational temperature.

The problem in curve matching, using (4), is that three unknowns are present n_{r-1}, n_r (or $R = n_r/n_{r-1}$), and T. It would be desirable to obtain an independent estimate or measurement of the temperature or range of temperatures expected in the experiment to reduce the curve-fitting procedure to just two unknowns n_{r-1} and n_r.

One estimate of T can be made from a heat-balance calorimetric calculation. The pertinent chemical reactions are

$$O_2 + e \longrightarrow 2O + 117 \text{ kcal/mole} \quad (5)$$

$$O + CS_2 \xrightarrow[k_1]{} CS + SO - 32 \text{ kcal/mole} \quad (6)$$

$$O + CS \xrightarrow[k_2]{} CO + S - 85 \text{ kcal/mole} \quad (7)$$

along with the 1.4-cal electrical input from the charged capacitor.

The complete combustion of the 8.2×10^{-6} moles of CS_2 used in the experiment will require at least 8.2×10^{-6} moles of O_2 (12 percent dissociation) to be dissociated or a minimum of 1 cal of energy. Hence most of the electrical input will go into O_2 dissociation.

Assuming 25 percent of the 85 kcal/mole of reaction (7) goes into translation [1] and all of the 32 kcal/mole of reaction (6), the chemical energy input is 0.4 cal. Using 5 cal/mole for O_2 (7×10^{-5} moles) and SO (8.2×10^{-6} moles) and 3 cal/mole for He (2.4×10^{-4} moles) and S (8.2×10^{-6} moles), the temperature rise ΔT is estimated to be in the range 400-700 K.

A second estimate of the temperature can be obtained by measuring the overall $\Delta v = 1$ fluorescence of the excited $CO(v)$ produced by reaction (7) and determining the rise time which is dependent on the rate constants k_1 and k_2 and the chemical concentrations. This measurement with an InSb (Philco 301-77 K · pV) detector and an OCLI W-05050-9 wide-band interference filter yielded a time constant τ of 7 μs.

For a simple harmonic oscillator, the total fluorescent intensity for $\Delta v = 1$ transitions is independent of the VV energy-exchange process in the molecule [17]. It was found by Yardley [18] that a perturbation in the population of highly excited vibrational states of CO did not change the total fluorescence for $\Delta v = 1$ and that to see VV relaxation he had to examine $\Delta v = 2$ transitions. Hence the total fluorescent intensity for $\Delta v = 1$ transitions gives a good indication of the CO concentrations.

To relate the time constant τ to the rate constants, the rate equations for reactions (6) and (7) need to be solved.

$$\frac{dx}{dt} = k_1(a - x - y)(b - x) \quad \frac{dy}{dt} = k_2(x - y)(a - x - y) \quad (8)$$

where a and b are the initial concentrations of O and CS_2 and x and y are the concentrations of CS and CO.

Since $k_2 \gg k_1$ [19], then $dx/dt \simeq dy/dt$ and an approximate solution for y can be readily found to be

$$y \simeq \frac{a}{2}[1 - \exp(-2k_1 bt)] = \frac{a}{2}[1 - \exp(-t/\tau)]. \quad (9)$$

Hence, using the rate constant k_1 expression of Westenberg and DeHaas [19],

$$k_1 = 1.2 \times 10^{13} \exp(-525/T) = (2b\tau)^{-1} = 0.55 \times 10^{13} \text{ cm}^3 \text{ mole}^{-1} \text{ s}^{-1} \quad (10)$$

for $b = 1.3 \times 10^{-8}$ moles/cm^3, yielding a value of T of 680 K.

While these estimates of the temperature are not precise, they do suggest the theoretical gain curves be examined over the temperature range 700-1000 K. The end result of matching experimental and theoretical gain curves for $\alpha(J)$, $v = 9 \rightarrow 8$, gave a best fit for $T = 800$ K and $R = n_9/n_8$ of 1.10, from which the values of n_8 of 2.24×10^{14} and n_9 of 2.46×10^{14} cm^{-3} were obtained.

The curve-fitting details will now be summarized. Using the data $S(\nu_0) = 3.3 \times 10^{-9}$ s for a Voight profile [$S(\nu_0) = 4.3 \times 10^{-9}$ s for a pure Doppler line], $\lambda = 5.27 \times 10^{-4}$ cm, $A_{9,8} = 216.8$ s^{-1}, and $T = 800$ K, (4) can be rewritten for the case $r = 9$ as

$$\frac{\alpha(J)_{9,8}}{n_8} = 1.43 \times 10^{-17} J \{R_{9,8} B_9 \exp[-F(J-1)/556] - B_8 \exp[-F(J)/556]\} \text{ cm}^2. \quad (11)$$

The right-hand side of (11) is plotted in Fig. 4 as a function of J with the inversion ratio $R_{9,8} = n_9/n_8$ as a parameter. The experimental data for $\alpha(J)_{9-8}$ for various P-branch transitions are listed in Table I. These experimental gain data were superimposed on the theoretical gain curves of Fig. 4 by taking $\alpha(8)$

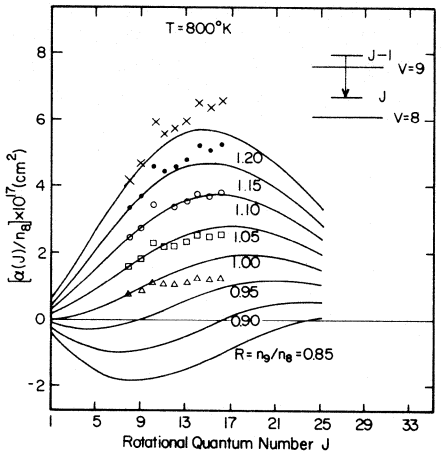

Fig. 4. The ratio of experimental gain α normalized to the vibrational population n_8 versus rotational quantum number J superimposed on theoretical curves.

TABLE I
EXPERIMENTAL DATA FOR $\alpha(J)_{9-8}$ FOR VARIOUS *P*-BRANCH TRANSITIONS

P(J)	$\alpha \times 10^3 cm^{-1}$	P(J)	$\alpha \times 10^3 cm^{-1}$	$n_8 \times 10^{-14} cm^{-3}$	$\alpha(8)/n_8 \times 10^{17}$
P(8)	5.41	P(13)	7.75	7.55	0.717
P(9)	6.03	P(14)	8.43	3.44	1.572
P(10)	7.68	P(15)	8.23	2.24	2.413
P(11)	7.20	P(16)	8.51	1.64	3.300
P(12)	7.42	-	-	1.31	4.130

and finding a value of n_8 (also listed in Table I) that matched the ratio $\alpha(8)/n_8$ to the various R parameter curves. Using these respective values of n_8, the remaining $\alpha(J)$ data were normalized to n_8 and plotted. It is seen that the experimental data most closely follow the $R_{9-8} = 1.10$ curve for the normalized density of n_8 of 2.24×10^{14} cm^3. Knowing n_8 and R_{9-8}, the value $n_8 = 2.24$, $n_9 = 2.46 \times 10^{14}$ was deduced. A similar matching of the data to theoretical curves for $T = 1000$ K, gave values $n_8 = 2.34$ and $n_9 = 2.64 \times 10^{14}$ mole/cm^3. Hence the curve-fitting procedure was not particularly sensitive to the temperature chosen. However, it is believed that the temperature can be estimated to be closer than 200 K and that 800 K gave the best fit which would suggest that error in determining the populations was less than 10 percent.

Next, by measuring the gain of the $P(12)$ transitions for $r \rightarrow r-1$ from $r = 6$ to 13, the values of n_r from $r = 6$ to 13 can be determined. This distribution of n_r, at 16 μs after initiation of the chemical reaction, is plotted in Fig. 5.

The vibrational distribution n_6-n_{13} at 16 μs after initiation of the chemical reaction is very similar to that of Fig. 1 since it has not had sufficient time to evolve. Hence to obtain values of n_r from $r = 5$ to 0 and $r = 13$ to 18, the measured curve has been extrapolated using Fig. 1 as a guide. The value of n_0 may be in question, but if all the n_r are summed, the total density of CO is 3×10^{15} cm^{-3} which would correspond to a pressure of 0.25 torr at 800 K. This pressure closely agrees with the experimental value so that assuming a value of $n_0 = 1.1 \times 10^{14}$ cm^{-3} does not seem to be incompatible.

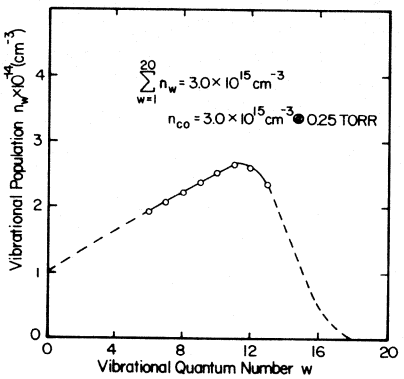

Fig. 5. The experimentally measured vibrational distribution of CO versus vibrational quantum number w, 16 μs after initiation of chemical reaction.

CALCULATION OF THE RATE CONSTANTS

At time $t = 16$ μs, when the chemical reaction was completed, the laser Q switch was applied which caused a perturbation in the CO vibrational populations. Referring to Fig. 3, in one case $P(17)_{11-10}$ and $P(23)_{10-9}$ were allowed to lase equally to produce gain perturbations of $\alpha_{12,11}$ and $\alpha_{9,8}$ as monitored by the probe CO laser.

This Q switching resulted in the population at $t = 16$ μs changing as follows:

$$n_{11} \longrightarrow n_{11} - \Delta n \quad n_{10} \longrightarrow n_{10} \quad n_9 \longrightarrow n_9 + \Delta n. \tag{12}$$

The gain $\alpha_{9,8}$ will be proportional to the population difference $[(n_9 + \Delta n) - n_8]$ so that

$$\frac{d}{dt}(\alpha_{9,8} + \Delta\alpha_{9,8}) \propto \frac{d}{dt}(n_9 + \Delta n - n_8). \tag{13}$$

If the population expressions of (12) are substituted into the master VV equation (2), the result is

$$\frac{d}{dt}(n_9 + \Delta n - n_8) = \left(\frac{d}{dt}(n_9 - n_8)\right)_{\Delta n=0} - \Delta n \left\{ 2(k^{9,10}_{9,8} + 2k^{9,8}_{9,10})n_9 + \sum_{\substack{r=1 \\ r\neq 9,11}}^{\infty} k^{9,10}_{r,r-1} n_r + 2 \sum_{\substack{r=0 \\ r\neq 9,11}}^{\infty} k^{9,8}_{r,r+1} n_r \right\} \tag{14}$$

from which the Δn term can be separated to yield

$$-\left(\frac{1}{\Delta n}\frac{d\Delta n}{dt}\right)_{9,8} = \frac{1}{\gamma_{9,8}} \tag{15}$$

where $\gamma_{9,8}$ is seen to be

$$\frac{1}{\gamma_{9,8}} = 2(k^{9,10}_{9,8} + 2k^{9,8}_{9,10})n_9 + \sum_{\substack{r=1 \\ r\neq 9,11}}^{\infty} k^{9,10}_{r,r-1} n_r + 2 \sum_{\substack{r=0 \\ r\neq 9,11}}^{\infty} k^{9,8}_{r,r+1} n_r. \tag{16}$$

A similar calculation yields for $\gamma_{12,11}$

$$\frac{1}{\gamma_{12,11}} = 2(k_{11,12}^{11,10} + 2k_{11,10}^{11,12})n_{11} + 2\sum_{\substack{r=1 \\ r\neq 9,11}}^{\infty} k_{r,r-1}^{11,12}\, n_r + \sum_{\substack{r=0 \\ r\neq 9,11}}^{\infty} k_{r,r+1}^{11,10}\, n_r. \quad (17)$$

Finally, if $P(12)_{7-6}$ and $P(18)_{6-5}$ were allowed to lase equally so that

$$n_7 \longrightarrow n_7 - \Delta n \quad n_6 \longrightarrow n_6 \quad n_5 \longrightarrow n_5 + \Delta n \quad (18)$$

the time constant $\gamma_{8,7}$ will be given by the expression

$$\frac{1}{\gamma_{8,7}} = 2(k_{7,8}^{7,6} + 2k_{7,6}^{7,8})n_7 + 2\sum_{\substack{r=1 \\ r\neq 5,7}}^{\infty} k_{r,r-1}^{7,8}\, n_r + \sum_{\substack{r=0 \\ r\neq 5,7}}^{\infty} k_{r,r+1}^{7,6}\, n_r. \quad (19)$$

As a set of algebraic equations in the rate constants, the three equations (16), (17), and (19) are greatly underdetermined since there are many more rate constants than equations. Hence a large number of sets of k's could, in principle, be found that would satisfy the three conditions. Nevertheless, without any recourse to a VV theory for the k's or a knowledge of the distribution of any set of k's, it is possible from a strictly mathematical argument to find a lower bound on the maximum k.

Consider any one of the three equations (17), (18), or (19) alone. For each equation, given the populations n_r and γ, there are a number of sets of k's, say $(k_{r,r-1}^{v,v+1})_j$ in which each $k_{r,r-1}^{v,v+1}$ is positive, that would satisfy the equations.

In each of these sets, there must be a maximum $(k_m)_j$. If one considers the maxima of all the sets, there must be a least maxima, say for the ith set, having the value $(k_m)_i$. This ith set is the distribution with all the k's equal, as can be seen from a simple example.

Let

$$a = bk_1 + ck_2 \quad (20)$$

where a, b, and c are positive constants. From a graph of (20), shown in Fig. 6, it is seen that the least maxima of k_1 and k_2 occurs when

$$k_1 = k_2 = \frac{a}{b+c} = \min\,(k_m)_i. \quad (21)$$

Any other pairs of k's will have one of the k's larger than the value of k given by (21). This argument can be extended to (17), (18), and (19).

If all the k's in (17) for the ith distribution are now placed by $(k_m)_i$, the following expression results:

$$(k_m)_j \geqslant (k_m)_i = \frac{1}{\gamma_{12,11}\left(3(n_{11} - n_9) - 2n_0 + 3\sum_{r=0}^{\infty} n_r\right)} = 1.0 \times 10^{-10}\ \mathrm{cm^3\,s^{-1}} \quad (22)$$

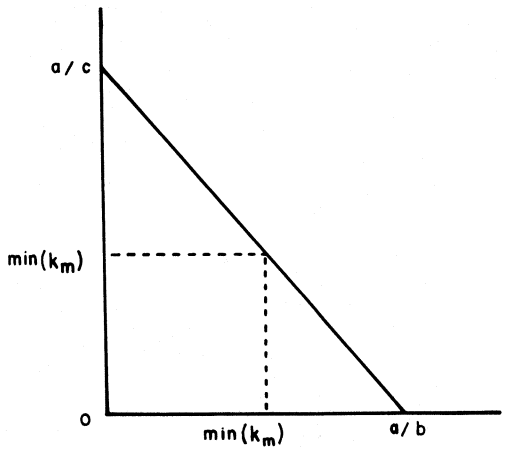

Fig. 6. Example of least maximum k's.

TABLE II
MEASURED VERSUS CALCULATED POPULATION PERTURBATION DECAY CONSTANT γ USING THE DATA $a = 3.60 \times 10^{-12}$ CM^{3}S AND $c = 0.35$

	γ_{CAL}	γ_{MEAS}
v → 12-11	1.08×10^{-6} sec	1.0×10^{-6} sec
v → 9-8	2.29	2.2
v → 8-7	3.65	3.6

corresponding to a probability $P_m \geqslant 0.3$ per hard sphere collision.

This probability, which is approaching unity, is the minimum of the least maximum probability distribution that will satisfy the equations, and it has been deduced without any appeal to any VV theory of any type.

If the VV theories, based on short-range [20] and long-range [21] (dipole-dipole interaction) potentials, are used as a guide to construct a simple empirical formula containing several adjustable parameters for the rate constants, another approximation can be made. For example, in most theories the probability per collision is proportional to the squares of the dipole matric elements of the transitions and has a maximum at resonance.

Hence the following empirical formula for the rate constant will be assumed:

$$k_{r,r-1}^{v,v+1} = a(v+1)r \exp\,[-c|v+1-r|] \quad (23)$$

where a and c are constants to be determined.

The results of using this formula in (16), (17), and (19) and the values obtained for a and c are given in Table II.

DISCUSSION

While there is a large body of literature on the theory of VV exchange in molecular collisions [22]-[24], few papers exist on the problem of exchange between highly excited states. Hence it is difficult to compare or relate the experimental work of this paper to a theory.

In most of the theoretical calculations, using both long- and short-range potentials, some perturbation technique is employed which usually requires that the interaction energy be small compared with the translational energy, and that the

transition probability be small compared with unity. Clearly, the experimental results of this paper can only be explained by taking the transition probabilities close to one, which makes comparing the results to a perturbation theory suspect.

Rockwood *et al.* [10] scaled the $k^{0,1}_{r,r-1}$ calculation of Jeffers and Kelley [9] on CO to obtain $k^{v,v+1}_{r,r-1}$ for $1 \leqslant r \leqslant 24$ and $0 \leqslant v \leqslant 10$, for a temperature of $T = 300$ K. Following the same procedure, a curve of $k^{9,10}_{r,r-1}$ versus r for $T = 800$ K was computed and plotted in Fig. 7. Superimposed on this figure is a plot of the empirical function $k^{9,10}_{r,r-1} = 10\,ar \exp[-c|10 - r|]$, whose constants were determined in this experiment. As will be noted, this empirical curve lies above the theory curve, with the peak values at $r = 10$ being 3.6×10^{-10} versus 2.45×10^{-10} $cm^3 s^{-1}$, for a rather good but perhaps coincidental fit.

Dillon and Stephenson [12] made a calculation of *VV* energy exchange which does not rely on the first Born approximation, and applied it to the dipole-dipole interaction of CO, taking the temperature to be 200 K. Their curves were not presented in the same form as those of Rockwood, but if the few data points that were available were plotted on a "Rockwood plot" of $k^{v,v+1}_{r,r-1}$ versus r, the results at 200 K would show values on resonance from one to two orders of magnitude lower while far-off resonance would show values substantially larger. There is no reason to believe that this disagreement would be substantially different at 800 K. Hence the experimental results of this paper correlate very poorly with Dillon and Stephenson's calculation.

Kelley [13], using a short-range potential, calculated a few values of $P^{v,v+1}_{r,r-1}$ for $r = 15$, $v = 13$ and $r = 21$, $v = 19$ for the collision of two diatomic molecules and obtained values as large as 0.35. If the long-range dipole-dipole interaction and the short-range interaction add in some positive manner, then Kelley would predict a total probability exceeding 0.35.

A point made by both Dillon and Stephenson and Kelley, which was not taken into account in this paper, is the probability for *VV* collisional exchanges for $\Delta v > \pm 1$, i.e., multiquantum vibrational-energy exchange. Dillon and Stephenson would predict $P^{v,v+2}_{r,r-2} \leqslant 0.1 P^{v,v+1}_{r,r-1}$ while Kelley would predict that $\Delta v = \pm 2$ transitions in CO would not be important for $v < 11$, and that a $k^{v,v+2}_{r,r-2}$ versus r curve would be sharply peaked compared to a $k^{v,v+1}_{r,r-1}$ versus r curve. If these predictions are valid, it would be difficult to see their effect on a measurement of perturbed gain decay constant γ within the experimental error.

Referring to the schematic vibrational-energy-level drawing of CO in the upper right part of Fig. 3, the gain α_{8-7} versus time was also measured. The perturbed part of the gain was also positive similar to that in Fig. 3(c). Since the population of level $v = 10$ was not perturbed, it could not transfer by a $\Delta v = 2$ *VV*-process additional perturbed population to level $v = 8$. However, level $v = 9$ could transfer additional perturbed population to level $v = 7$ by a $\Delta v = 2$ *VV* process. This would reduce the perturbed gain of α_{8-7} since it would compete with the $\Delta v = 1$ process from $v = 9$-8. These effects were not noted and hence it is concluded that the $\Delta v = 2$ processes were negligible in this experiment.

The question that always arises in this type of measurement is the effect of collision partners other than CO in the *VV* processes. Hancock and Smith [5] also addressed this problem in their paper, and it is believed that these effects are negligible in this work.

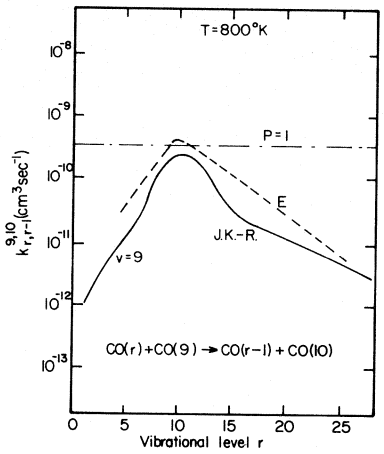

Fig. 7. Rate constants $k^{9,10}_{r,r-1}$ versus vibrational level r. The solid curve is an extrapolation of the work of Jeffers and Kelley and Rockwood *et al.* The dashed curve is a plot of the empirical formula $10\,ar \exp[-c|10 - r|]$.

The concentration of OCS that is present at 16 μs after initiation of the chemical reaction is negligible. Also the probability for the process

$$CO(v) + OCS(000) \longrightarrow CO(v - 1) + OCS(001) \qquad (24)$$

never exceeds 0.15 for all v [6].

The time scale of the gain perturbation measurements are in the range 1-2 μs. Hence the rate constants and/or the concentrations of the collision partners must be large to see an effect. Species such as He, O_2, or S do not satisfy these requirements [6].

Acknowledgment

The authors wish to thank J. T. Yardley, T. A. DeTemple, and L. H. Sentman for many discussions on the general problem of *VV* energy exchange. They also wish to thank their colleagues in the Electro-Physics Laboratory, in particular Y. Hirose, for their help.

References

[1] G. Hancock, C. Morley, and I. W. M. Smith, "Vibrational excitation of CO in the reaction: O + CS + CO + S," *Chem. Phys. Lett.*, vol. 12, pp. 193-196, 1971.

[2] S. Tsuchiya, N. Nielson, and S. H. Bauer, "Lasing action and relative populations of vibrationally excited carbon monoxide in pulsed-discharged carbon disulphide-oxygen-helium mixture," *J. Phys. Chem.*, vol. 77, pp. 2455-2464, 1973.

[3] H. T. Powell and J. D. Kelley, "Vibrational distribution of carbon monoxide from O + CS → S + CO(v)*," *J. Chem. Phys.*, vol. 60, pp. 2191-2192, 1974.

[4] N. Djeu, "Quantitative laser measurement of very small absorptions: Studies of the O + CS → CO(v) + S reaction," *J. Chem. Phys.*, vol. 60, pp. 4109-4115, 1974.

[5] G. Hancock and I. W. M. Smith, "Vibrational relaxation rates for CO($v \leqslant 13$) with CO($v = 0$), OCS, O_2 and He," *Chem. Phys. Lett.*, vol. 8, pp. 41-44, 1971.

[6] —, "Quenching of infrared chemiluminescence. 1: The rates of de-excitation of CO($4 \leqslant v \leqslant 13$) by He, CO, NO, N_2, O_2, OCS, N_2O, and CO_2," *Appl. Opt.*, vol. 10, pp. 1827-1842, 1971.

[7] H. T. Powell, "Vibrational relaxation of carbon monoxide using a

pulsed discharge," *J. Chem. Phys.*, vol. 59, pp. 4937–4941, 1973.
[8] Y. Fushiki and S. Tsuchiya, "Vibration to vibration energy transfer of CO in the states of $v = 2 \sim 9$," *Japan. J. Appl. Phys.*, vol. 13, p. 1043, 1974.
[9] W. Q. Jeffers and J. D. Kelley, "Calculations of *V-V* transfer probabilities in CO-CO collisions," *J. Chem. Phys.*, vol. 55, pp. 4433–4437, 1971.
[10] S. D. Rockwood, J. E. Brau, W. A. Proctor, and G. H. Canavan, "Time-dependent calculations of carbon monoxide laser kinetics," *IEEE J. Quantum Electron. (Part II of Two Parts: 3rd Conference on Chemical and Molecular Lasers)*, vol. QE-9, pp. 120–129, Jan. 1973.
[11] P. H. Dawson and W. S. Tam, "Vibrational energy transfer in carbon monoxide," *Can. J. Phys.*, vol. 50, p. 889, 1972.
[12] T. A. Dillon and J. C. Stephenson, "Multiquantum vibrational-energy exchange," *Phys. Rev. A*, vol. 6, pp. 1460–1468, 1972.
[13] J. D. Kelley, "Vibrational energy transfer processes in collisions between diatomic molecules," *J. Chem. Phys.*, vol. 56, pp. 6108–6117, 1972.
[14] C. Wittig, J. C. Hassler, and P. D. Coleman, "A CW carbon monoxide chemical laser," *J. Chem. Phys.*, vol. 55, pp. 5523–5532, 1971.
[15] C. E. Treanor *et al.*, "Vibrational relaxation of anharmonic oscillators with exchange-dominated collisions," *J. Chem. Phys.*, vol. 48, pp. 1798–1807, 1968.
[16] C. K. N. Patel, "Vibrational-rotational laser action in carbon monoxide," *Phys. Rev.*, vol. 141, pp. 71–82, 1966.
[17] K. E. Shuler, "Relaxation of an isolated ensemble of harmonic oscillators," *J. Chem. Phys.*, vol. 32, pp. 1692–1697, 1960.
[18] J. T. Yardley, "Vibrational energy transfer in CO-He lasers," *J. Chem. Phys.*, vol. 52, pp. 3983–3989, 1970.
[19] A. A. Westenberg and N. DeHaas, "Atom-molecule using ESR detection. V. Results for $O + OCS$, $O + CS_2$, $O + NO_2$, and $H + C_2H_4$," *J. Chem. Phys.*, vol. 50, pp. 707–719, 1969.
[20] R. N. Schwartz, Z. I. Slawsky, and K. F. Herzfeld, "Calculation of vibrational relaxation times in gases," *J. Chem. Phys.*, vol. 20, pp. 1591–1599, 1952.
[21] R. D. Sharma and C. A. Brau, "Energy transfer in near resonance molecular collisions due to long-range forces with applications to transfer of vibrational energy from ν_3 mode of CO_2 to N_2," *J. Chem. Phys.*, vol. 50, pp. 924–930, 1969.
[22] C. B. Moore, "Vibration-vibration energy transfer," *Ann. Rev. Phys. Chem.*, vol. 23, pp. 41–83, 1973.
[23] E. Weitz and G. Flynn, "Laser studies of vibrational and rotational relaxation in small molecules," *Ann. Rev. Phys. Chem.*, vol. 25, pp. 1–104, 1974.
[24] P. Borrël, "Relaxation processes in gases," *Advan. Mol. Relaxation Processes*, vol. I, pp. 69–108, 1967–1968.

TB4—Modeling of the CW CO Chemical Laser

H. V. LILENFELD, R. F. WEBBINK, W. Q. JEFFERS, MEMBER, IEEE, AND J. D. KELLEY

Abstract—**A computer code modeling the CS_2/O CW CO chemical laser (CL) is reported. The accuracy of the code has been tested by calculations of small-signal gain, output power, and chemical species densities in devices for which experimental data are available. Generally, good agreement is obtained. The code was also used to predict gain variations with diluent/fuel ratio, initial temperature, and cavity pressure.**

I. INTRODUCTION

MATHEMATICAL modeling of chemical and molecular lasers has been done for most of the important laser systems. Practically all of the work on chemical lasers (CL's) has concerned hydrogen halide lasers such as HCl and HF; early work was done on the pulsed HCl laser [1]-[3], followed by extensive and sophisticated efforts on the CW HF (or DF) laser [4]-[7]. The CW CO CL has received only limited analytical attention [8], [9]. This paper reports results on modeling of the CW CO CL; earlier publications documented the development of the model and computer code [10], [11]. The present version of this code is termed COMOD.

There are two important reasons to model CL systems. The first is to test the accuracy and completeness of the model's assumptions as to the phenomena occurring in laser devices. If good agreement with experimental laser performance is obtained, the model can be used to investigate the sensitivity of laser performance to variations in the values of parameters used; for example, variations in the rates of individual chemical reactions or collisional energy transfer processes. The second reason is the predictive function of laser modeling, that is, predictions of laser performance under conditions significantly different from those used in presently operating laser devices. An example of the predictive function which is particularly appropriate for CO CL's is the question of pressure scaling. The modeling code described in this paper predicts very favorable pressure scaling of the CO CL [10].

Briefly, the model described in Section II is chosen to approximate a transverse-flow CL. The fluid flow is one dimensional in that no gradients transverse to the flow direction are allowed. Mixing in the optical cavity region is described phenomenologically by an exponential mixing length. As the

Manuscript received March 14, 1975. This work was supported in part by the Defense Advanced Research Projects Agency under Contract DAAH01-72-C-0578, monitored by the Army Missile Command, and in part by the McDonnell Douglas Independent Research and Development Program.

H. V. Lilenfeld, W. Q. Jeffers, and J. D. Kelley are with the McDonnell Douglas Research Laboratories, McDonnell Douglas Corporation, St. Louis, Mo. 63166.

R. F. Webbink was with the McDonnell Douglas Research Laboratories, McDonnell Douglas Corporation, St. Louis, Mo. 63166. He is now with the Institute of Theoretical Astronomy, Cambridge University, Cambridge, England.

fuel and oxidizer streams mix, reactions are allowed to begin; concurrently, formation and relaxation of vibrationally excited CO (CO*) are calculated along with the resultant optical gain on CO transitions. Stimulated emission is treated by an amplifier model.

In Section III results from the modeling code are compared with experimental data. Detailed measurements of small-signal gain are available for a laser device [12], and it will be shown that such data provide a stringent test of the accuracy of the model. In fact, this comparison will be used to test various pumping reaction distributions which have been reported [13]-[15]. The code has also been used to model an existing laser [16]; again good agreement with experiment is obtained. Having tested the model by comparison to experiment, Section IV concludes with predictive results on the variations of small-signal gain with pressure, diluent-to-fuel mole ratio, and initial gas temperature.

II. Chemical Laser Model

The following is a condensed description of our model for a subsonic transverse-flow CL; more detailed discussions are available [10], [11], although the treatment of reaction chemistry and vibration-vibration (VV) relaxation rates described here differs somewhat from that presented in the earlier reports.

A. Fluid Flow and Mixing

The device geometry assumed in the model is shown in Fig. 1. The model starts with an initial set of chemical species $[A]$ in the major injector A at pressure and temperature p_A and T_A. This gas is injected through a slot of width w_A and length L transverse to the flow direction, which is taken to be the x axis, and expands into the cavity region at pressure p_{cav}; the expansion is assumed to be adiabatic. Given the initial stream area and cavity pressure, the initial species densities, temperature, and stream velocity v are obtained. At point $x = 0$, the stream encounters the transverse injector B containing species $[B]$ at p_B and T_B. At $x = 0$, the stream properties are recalculated assuming that $[A]$ and $[B]$ undergo instantaneous physical (but not chemical, *vide infra*) mixing and come to an internal pressure p_{cav}. The new stream quantities (e.g., width and flow velocity) are determined using conservation of mass, number of particles, degrees of freedom, x momentum, and energy. The model has the capability of describing two distinctly different fluid-flow situations. In the first, the cavity pressure p_{cav} is held constant. Temperature increases caused by heat liberated from chemical reactions expand the stream width while the stream velocity v remains constant. This describes a situation where the stream width is much smaller than the cavity width, and the stream is allowed to expand unbounded. In the second situation, the stream width is determined externally, and any heating effects cause a change in the stream velocity and internal pressure. This describes a situation where the stream width is determined by the cavity width. This mode has previously proved useful in describing the effect of supersonic nozzle cooling on a CW CO CL [11].

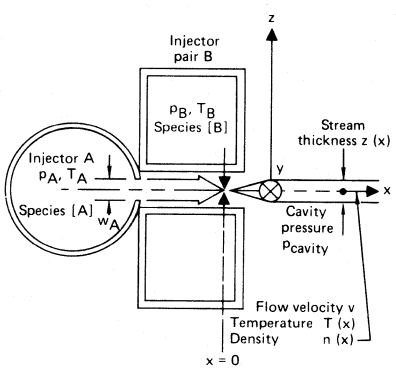

Fig. 1. Transverse-flow geometry and stream parameters used in the COMOD modeling code.

B. Chemical Reaction

Reactions between the species in $[A]$ and $[B]$ begin at $x = 0$, but to model the real situation of finite mixing rate, a phenomenological chemical mixing length l_{mix} is defined such that

$$\frac{d\xi_i}{dx} = \frac{n_i - \xi_i}{l_{mix}} - \frac{\xi_i}{z}\frac{dz}{dx} - \frac{\xi_i}{v}\frac{dv}{dx} \tag{1}$$

where n_i is the density of the ith reacting species in $[B]$ and ξ_i is that portion of n_i available for reaction with set $[A]$. The second term arises from stream expansion transverse to the flow, and the third term arises from changes in the stream velocity. The parameter l_{mix} can be estimated from experimental considerations and/or can be used as an adjustable parameter.

The model allows up to 20 chemical reactions involving up to 12 different species. In this study (see Table I), we used and compared a 3-reaction (reactions 1a, 2, 3) and 11-reaction (reactions 1-9) model. The rate constants used were experimental values, where available, or estimates. In computing stream

TABLE I
Reaction Kinetics for the $O/O_2/CS/CS_2$ Reaction System

	Reaction	ΔH [a,b]	Rate $k = AT^m \exp(-E_A/RT)$ A [c]	m	E_A [d]
1a.	$O + CS_2 \rightarrow CS + SO$	- 21	1.62×10^{-11} [19,20]	0	1.03 [19,20]
1b.	$O + CS_2 \rightarrow OCS + S$	- 54	1.8×10^{-12} [20]	0	1.03 [e]
1c.	$O + CS_2 \rightarrow CO + S_2$	- 83	2.0×10^{-12} [20]	0	1.03 [e]
2.	$O + CS \rightarrow CO^* + S$	- 84	7.9×10^{-11} [21]	0	1.03 [e]
3.	$S + O_2 \rightarrow SO + O$	- 5.5	2.2×10^{-12} [19]	0	0.00 [19]
4.	$SO + O + M \rightarrow SO_2 + M$	- 132	2.6×10^{-28} [f]	-1 [f]	0.00 [f]
5.	$SO + O_2 \rightarrow SO_2 + O$	- 13	3.0×10^{-13} [19]	0	5.60 [19]
6.	$CS + SO \rightarrow OCS + S$	- 33	6.7×10^{-11} [g]	0	4.0 [g]
7.	$O + OCS \rightarrow CO + SO$	- 51	6.8×10^{-11} [19]	0	5.08 [19]
8.	$S + CS_2 \rightarrow CS + S_2$	- 0	1.7×10^{-10} [f]	0	4.0 [f]
9.	$CS + O_2 \rightarrow OCS + O$	- 38	1.7×10^{-16} [23]	0	3.5 [23]

[a] Units of kcal/mole, values of heats of formation of all species except CS are taken from [17].
[b] Heat of formation for CS (65 kcal/mole) taken from [18].
[c] Units of cm^3 $molecule^{-1}$ s^{-1}, except 4 where units are cm^6 $molecule^{-2}$ s^{-1}.
[d] Units of kcal/mole.
[e] Estimate.
[f] Estimate in [22].
[g] Estimate by R. J. Richardson, private communication.

properties beyond injector B, account was taken of the influence of chemical reactions since the reactions change the stream composition and release heat. In calculating the reaction-generated heat release, allowance was made for the amount of energy stored in CO vibration. In most of the calculations reported here, the pumping reaction (number 2 in Table I) was assumed to form excited CO with the vibrational distribution labeled Powell and Kelley (PK) [14] in Fig. 2, although some comparison with results obtained with the Hancock, Morley, and Smith (HMS) [13] and Djeu (D) [15] distributions, also shown in Fig. 2, was also made.

C. Vibrational Relaxation

As the vibrationally excited CO is formed, collisional relaxation processes begin which modify the CO vibrational distribution as the gas mixture proceeds downstream. Thus the time-dependent or, equivalently, x-dependent CO vibrational state populations must be obtained by including the coupled rate equations for formation and relaxation into and out of each CO vibrational level. The model can treat up to 50 levels, but the calculations reported here include only the first 25 levels. In this treatment, only one quantum VV and vibration–translation (VT) process is allowed, and every species in the stream is considered separately as a relaxation partner with CO.

An important relaxation process is the redistribution of vibrational energy in the chemically pumped CO by VV transfer

$$\mathrm{CO}(m) + \mathrm{CO}(n) \rightarrow \mathrm{CO}(m-1) + \mathrm{CO}(n+1). \tag{2}$$

Probabilities for the general process in (2) were constructed from experimental measurements at 100 K (m = 2-7, n = 0) [25], 300 K (m = 2-11, n = 0) [24], [25], and 500 K (m = 2-12, n = 0) [25]. These experimental values were divided by m to obtain a reduced probability curve as a function of energy defect at each temperature. The three resulting curves were then extrapolated to m = 25, and the general temperature dependence for a given defect was obtained by fitting the three probability values to the functional form $P(T) = \exp(a + bT^{-1/3} + CT^{-1})$. The general probability, (2), was calculated by finding the appropriate defect and multiplying the reduced probability by m and n. For near resonance ($m \approx n$) with large m and n, perturbation-theory scaling with m and n leads to P values larger than unity. For large P, perturbation theory is inappropriate, and a more exact treatment [26] leads to a slower than linear increase in P with increasing m and n. To account for this, the probabilities were redefined as

$$P'(T) = \frac{P(T)}{1 + eP(T)} \tag{3}$$

with e = 2.72.

A similar procedure was used to obtain VV probabilities for $\mathrm{CO}(m) + M \rightarrow \mathrm{CO}(m-1) + M^*$. As an example, with M taken to be NO, the 300-K data [13] for m = 4-14 and for m = 1 [27] were converted to a reduced probability curve by dividing by m and using detailed balance to convert probabilities in the exothermic direction to endothermic probabilities. The curve was extrapolated to m = 25, and the temperature dependence was constructed, assuming that, for a given energy defect, the reduced endothermic probabilities vary with temperature in the same way as the CO–CO probabilities at that defect. The same procedure was used for M = O_2, NO, N_2, OCS, and N_2O with data taken from [13] and [27]. To treat CS_2 and SO_2 as transfer partners, the procedure must be modified since data are available only for CO(m = 1). For CS_2, the measured probability [28] at 300 K is 1.6×10^{-3}. If the transfer occurred to CS_2 (001), the defect would exceed 600 cm^{-1} and the probability would be expected to be much smaller than the measured value. We therefore assumed that transfer occurs to CS_2 (101) which is nearly resonant with CO(m = 1). The 300-K reduced probability curve was then generated by further assuming that the defect dependence is the same as that observed for CO–OCS VV transfer [13]; the general temperature dependence was obtained as described previously. For SO_2, the procedure was similar; the measured probability [28] for $\mathrm{CO}(1) + \mathrm{SO}_2 \rightarrow \mathrm{CO}(0) + \mathrm{SO}_2^*$ was used along the assumption that the SO_2 final state is the (011) state. For CS and SO, which are always in low concentration, no data are available, and the VV probabilities with CO were calculated from a simple short-range force theoretical model [29]. The VT probabilities for all species were calculated using standard SSH theory [30] with the range parameter l = 0.2 Å.

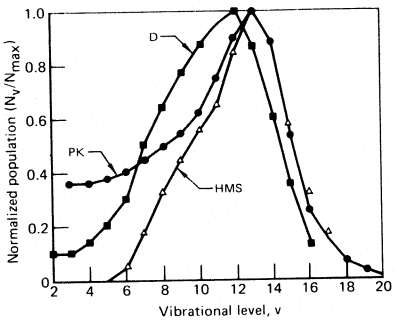

Fig. 2. Chemical distribution normalized to N_{max} = 1.0 versus vibrational level v for levels greater than v = 1. Curve labeled D is from [15], that labeled PK, from [14], and that labeled HMS, from [13].

D. Stimulated Emission

The calculation of laser output power was performed using an amplifier model; that is, an x-dependent input optical field is assumed to begin at some position x' and to vary with x. The optical path has a length L transverse to the flow direction x, and power is transferred from the medium to the field. The frequency spectrum of the field includes up to 50 P- or R-branch CO transition center frequencies, and the field intensities along the x direction may assume an arbitrary shape; Gaussian and step function intensity distributions have been the primary choices in our work. The program calculates the x-dependent optical gain coefficient, including Doppler and pressure broadening [31], for each transition of interest; the power transfer between the field and medium in an incremental distance dx along the flow is then calculated by a differential form of Beer's law

$$dP_{v,J} = I_{v,J}(x)\,[\exp(\alpha_{v,J}L) - 1]\,z(x)\,dx \tag{4}$$

TABLE II
INPUT CONDITIONS USED IN THE GAIN AND GAIN RELAXATION COMPARISON [12]

Injector A		mole/s
Flow rates	He	0.032
	O	0.001
	O_2	0.0156
P_A(Torr)	10	
T_A(K)	300	
Injector B		
Mole flow rates	CS_2	0.000526
P_B(Torr)	10	
T_B(K)	300	
Mixing length (cm)	0.5	
Cavity		
P_{cav}(Torr)	5.9	

where

$I_{v,J}(x)$ the input field intensity distribution for the transition with upper state v and lower state J;
$\alpha_{v,J}(x)$ the optical gain coefficient on the $v, J \pm 1 \rightarrow v-1$, J transition;
L the length of the stream in the y direction;
$z(x)$ the width of the stream in the z direction.

The total power delivered to the optical fields is then

$$P_{\text{rad}}(x) = \sum_{v,J} \int_{x'}^{x} \frac{dP_{v,J}}{d\xi}\, d\xi. \tag{5}$$

The saturating effects of the fields on the medium are accounted for following the technique described by Emanuel [32].

Additional quantities defined and computed are the vibrational power in the medium

$$\frac{dP_{\text{vib}}}{dx} = \overline{E}\,\frac{d\tilde{n}_{\text{CO}}}{dx}\, z(x)\, L v \tag{6}$$

and the chemical efficiency

$$\eta_{\text{chem}}(x) = \frac{P_{\text{rad}}(x)}{P_{\text{vib}}(x)} \tag{7}$$

where $\overline{E}$ is the average vibrational energy per CO molecule formed by the pumping reaction, assuming the PK distribution, $d\tilde{n}_{\text{CO}}/dx$ is the derivative of the CO density resulting only from chemical formation from reaction 2, Table I, and v is the stream flow velocity.

III. COMPARISON OF CALCULATIONS WITH EXPERIMENT

We have compared the predictions of the model for gain, gain relaxation, power output, species densities, and gas additive effects with the experimental results of various CO CL's with differing flow geometries [12], [16] in order to test the accuracy and completeness of the model and its usefulness in predicting experimental performance.

A. Comparison of Gain and Gain Relaxation Predictions with Experiment

The experimental results and flow geometry used for this set of calculations are those reported by Ultee and Bonczyk [12]. The flow rates and operating conditions used in this calculation are listed in Table II; the stream width was externally determined. For x less than 1.3 cm, dz/dx was set equal to 0.25. For x greater than 1.3 cm (the width of the flow channel), dz/dx was set equal to 0. The initial pressure in the stream was 5.9 torr and decreased less than 0.2 percent over the length of the calculation.

The gain calculated by this model will depend upon the choice of the vibrational distribution resulting from reaction 2 (Table I). A comparison was made between experimental results and the predicted gain coefficients resulting from three different experimentally determined distributions [13]-[15]. These distributions are in relatively good agreement for the higher vibrational levels ($v \geqslant 13$, see Fig. 2). The largest disagreement occurs in the lower vibrational levels. The results of this comparison are shown in Fig. 3. The HMS distribution overestimates the gain on all three lines and is clearly the least preferable. For the lowest two lines $P_7(13)$ and $P_9(11)$, the PK distribution gives the best agreement with experiment for maximum gain; gain relaxation, i.e., the rate of decrease of gain with distance downstream from the maximum, is approximately the same for all three distributions. For the highest measured line $P_{11}(10)$, the D distribution and the PK distribution yield nearly the same agreement with experiment for the maximum gain. The PK distribution was used in all subsequent calculations.

As a further check on the accuracy of the model, the J dependence of the gain on the $9 \rightarrow 8$ transition was compared with the experimental values at $x = 1.5$ cm. The results of this

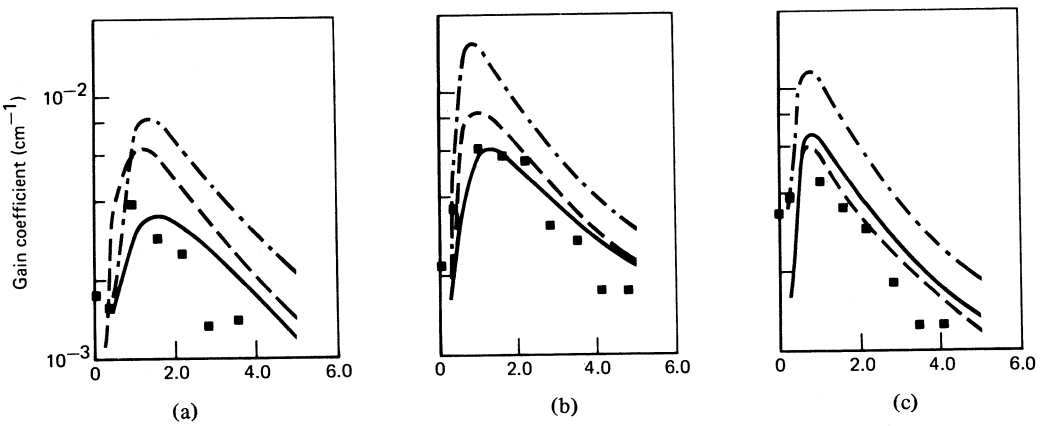

Fig. 3. Comparison of experimental and calculated gain coefficients as a function of distance downstream from the injector (cm). Three transitions are shown. (a) 7-6, $P(13)$. (b) 9-8, $P(11)$. (c) 11-10, $P(10)$. The calculations use three different initial vibrational distributions: ____PK, – – –D, and ____ ____HMS; ■ denotes data points from [12].

comparison are shown in Fig. 4. The prediction of maximum gain on $J = 12$ and the absolute value calculated agree with the experimental results within the reported experimental accuracy. The experimental and calculated values of the gain for J above and below the maximum differ appreciably. The temperature and inversion ratio predicted by the model for this position were 400 K and 1.1, respectively. An investigation of the J dependence of the gain with variable temperature and inversion ratios was made. For reasonable estimates of both of these quantities (i.e., inversion ratios from 0.95 to 1.3 and temperatures from 300 to 500 K), the calculations showed maximum gain variations of 9 percent from $J = 10$ to $J = 14$. Since no combination of inversion ratio and temperature in the gain equation could produce the large variations observed, we conclude that the actual error in the experimental data may be somewhat larger than suggested by the error bars of [12]. Alternatively, our model may overestimate the gain by ~20 percent; such a reduction in the calculated gain curve in Fig. 4 would improve the agreement.

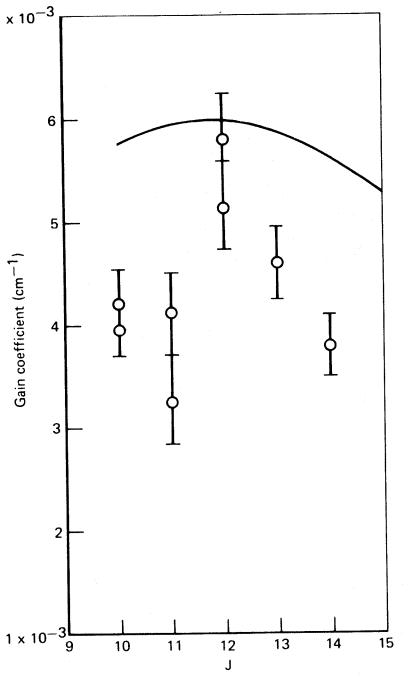

Fig. 4. J dependence of gain coefficient on the $9 \rightarrow 8$ transition at $x = 1.5$ cm. Experimental points are from [12].

B. Comparison of Predicted Output Power and Chemical Composition with Experiment

For this set of calculations, the geometry of a transverse-flow CO CL was used; experimental results are those of Jeffers and Wiswall [16]. The calculation was performed in the constant pressure mode at 5.2 torr, and the initial flow rates and injector conditions are listed in Table III. The amplifier fields used in this calculation are listed in Table IV; the field intensities were chosen to duplicate the intracavity flux of the experimental device. As a test of the degree of saturation of the medium by the input fields, the field intensities were increased by a factor of 3, resulting in an increase of only 25 percent in the calculated output power.

The effects of the chemical kinetics on predicted output power were investigated by comparison of calculations including all reactions listed in Table I with identical calculations using an abbreviated model including only three reactions (1a, 2, and 3 in Table I). These three reactions have been used previously to describe low-temperature CO CL's. The results of these calculations are listed in Table V. The predicted output power is reduced by inclusion of the eight additional reactions from 38.1 to 20.1 W. There are two important reasons for the reduced output power.

1) The inclusion of reactions 1b and 1c in the kinetics allows about about 20 percent of the CS_2 fuel to be consumed in forming the products OCS, S, S_2, and unexcited CO. This CS_2 would otherwise be available to form CS and subsequently excited CO via reaction 2. The net effect should be to reduce output power by about 20 percent.

2) The OCS formed efficiently relaxes the excited CO. The effect of OCS relaxation is shown in Fig. 5. Curve A shows the output power band spectrum predicted by the 11-reaction model ($x = 0 \rightarrow 1.5$ cm). Curve B shows the result of the

TABLE III
INPUT CONDITIONS USED IN THE OUTPUT POWER AND CHEMICAL COMPOSITION COMPARISON [16]

Injector A		mole/s
Flow rates	He	0.0208
	O_2	0.00511
	O	0.00093
p_A(Torr)	22	
T_A(K)	310	
Injector B		
Flow rates	CS_2	0.00076
	Ar	0.00355
p_B(Torr)	10	
T_B(K)	300	
Mixing length (cm)	0.5	
Cavity		
p_{cav}(Torr)	5.2	

TABLE IV
RADIATION FIELD USED IN OUTPUT POWER COMPARISON

Type of Field	Gaussian
Full width at half power	1.0 cm
Center position	1.5 cm
Peak intensity	70 W/cm^2
Transition (v, J)*	2, 20
	3, 15
	4, 15
	5, 15
	6, 15
	7, 14
	8, 15
	9, 9
	10, 9
	11, 8
	12, 10
	13, 13

*Denotes upper state v, lower state J.

TABLE V
COMPARISON OF THE 3- AND 11-REACTION MODELS

	3-Reaction Model	11-Reaction Model
Output Power (W)	38.1	20.1
Chemical Efficiency	0.233	0.179
Final Temperature (K)	536	557

11-reaction model where the CO relaxation rate by OCS has been set to zero. Finally, curve *C* shows the spectrum using the 3-reaction model, and thus effects from both OCS relaxation and additional chemical kinetics. The main effect of the OCS relaxation appears to be reduction of power on the lower bands.

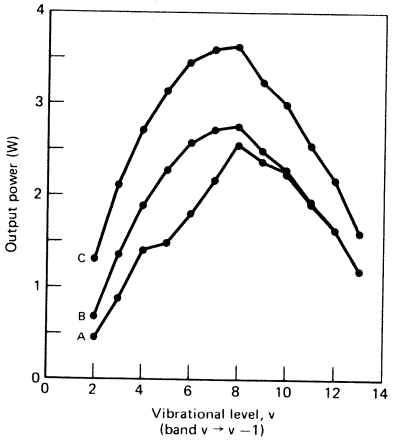

Fig. 5. Output power band spectrum from $0 \rightarrow 1.5$ cm for the 11- and 3-reaction models. Curve *A* represents results of the 11-reaction model; curve *B*, results of the 11-reaction model with the relaxation rate for OCS set to zero; and curve *C*, results of the 3-reaction model.

TABLE VI
COMPARISON OF 11-REACTION MODEL TO EXPERIMENT AT x = 1.5 CM

Species Densities (cm^{-3})	11-Reaction Model	Experiment[16]
He	6.0×10^{16}	6.4×10^{16}
CO	1.6×10^{15}	1.4×10^{15}
O_2	1.3×10^{16}	1.3×10^{16}
Ar	1.0×10^{16}	9.8×10^{15}
CS	3.3×10^{13}	2.7×10^{14}
SO	3.0×10^{15}	3.3×10^{14}
OCS	2.0×10^{14}	2.1×10^{14}
SO_2	1.0×10^{14}	2.3×10^{15}
CS_2	3.0×10^{14}	5.0×10^{14}
S_2O	---	1.1×10^{15}
Temperature (K)	557	520

To test the kinetics, we compared the chemical species densities and temperature predictions with the experimentally determined values. The comparison is shown in Table VI.

The good agreement between the model and experiment for the densities of the diluents (He and Ar) and O_2 indicates that the calculated stream width (z) at $x = 1.5$ is approximately correct. The CO densities in both model and experiment indicate that the formation of this species is virtually complete at this distance.

The OCS density predicted by the model is in good agreement with the experimental results. The predicted CS_2 density is in reasonably good agreement with experiment. Both model and experiment indicate that most of the CS_2 has been reacted. By adjusting the mixing length of the model (to about 0.8 cm), the model would be in better agreement with experiment. The model predicts a faster consumption rate for CS than the experiment shows. This comparison may suggest an error in the rate of reaction 2.

The predicted densities of the sulfur oxides (SO, SO_2, and S_2O) are in poorest agreement with the experiment. The mass spectroscopic results indicate more SO_2 and less SO than

predicted by the model. Lowering the activation energy of reaction 5 by an amount equal to one vibrational quanta of SO (i.e., assuming the SO produced by reaction 1a is vibrationally excited) fails to significantly influence the calculation. Thus this discrepancy remains, although we should point out that mass spectrometric sampling of radicals such as SO is very difficult and there is a possibility of forming SO_2 by wall reactions in the probe of the mass spectrometer. There is very little kinetic information on reactions forming S_2O in the chemical literature. Indeed, there are few possibilities of forming S_2O exothermically from any two-body reactions involving species found in the laser. Thus S_2O is not included in this laser kinetics code.

Finally, the temperature increase predicted by the model of 247 K (from 310 to 557 K) is in good agreement with the experimentally measured temperature rise of 210 K.

The addition of N_2O to the CO CL has been shown to increase total laser power and to shift the output power spectrum to lower bands [16]. This effect has been explained in terms of the N_2O-CO *VV* transfer probabilities [16]. The addition of N_2O to the laser modeling code does indeed increase the predicted output power from 20.0 W using Ar as the diluent to 35.1 W when N_2O is substituted for Ar. The output power band spectra for both the model and experiment are shown in Fig. 6. The calculation indicates that the power output increase occurs in the lower bands. The effect of power shift to the lower bands is clearly not as extensive as indicated by the experimental result. A possible cause of this discrepancy is the use of the amplifier field as an approximation to the laser oscillator. Table VII indicates, however, that the total power predicted by the model is in good agreement with experiment.

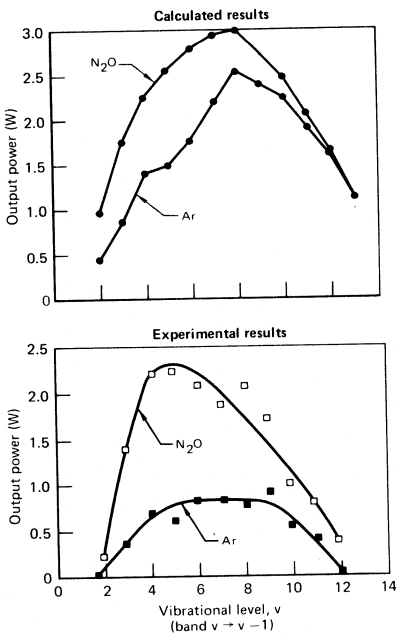

Fig. 6. Calculated output power band spectra with Ar and N_2O gas additives and the corresponding experimental results [16].

TABLE VII
PERFORMANCE COMPARISON BETWEEN MODEL AND EXPERIMENT

	11-Reaction Model	Experiment[16]
cw power (W)	35.1	28.8 (closed cavity)
Specific power (J/g)	77.1	65.5
Chemical efficiency (%)	.349	.211

IV. PREDICTIVE RESULTS

The small-signal gain [$\exp(\alpha_{v,J}L) - 1$] was investigated as a function of diluent/fuel ratio, injector temperature, and pressure.

The initial flow rates and flow geometry used in this set of calculations are listed in Table VIII. The flow rates of the reactants were held constant during all variations. The injector length was varied to ensure that the flow velocity was the same for all calculations (100 m/s).

A. Variation of Diluent/Fuel Flow Rates

It is useful to define a quantity β_F to represent the ratio of diluent flow rates to fuel flow rates by the following equation:

$$\beta_F = \frac{F(O_2) + F(N_2)}{F(CS_2)} \tag{8}$$

where $F(A)$ is the flow rate of chemical species A (in moles/s). The O_2 is included as a diluent in this definition since it is present in large excess compared with the other reactants in the $O/O_2/CS_2$ CL. The results of the variation of β_F on a typical vibrational band are listed in Table IX. The temperature increase as a result of chemical reactions in the flow stream is inversely proportional to the total heat capacity of the gases in the stream. Therefore, decreasing β_F increases the operating temperature of the laser. This in turn causes increases in the rates of the chemical reactions and the relaxation processes. The temperature increase also decreases the laser gain. Thus the maximum gain and the position of the maximum gain (determined by the chemical kinetics and relaxation processes) decrease monotonically with decreasing β_F. In some applications of high-power lasers, it is important to maximize the output power per unit mass flow. The maximum gain per unit mass flow for this system with nitrogen diluent occurs at $\beta_F = 25$.

The gain per unit mass flow can be further increased by using a lighter weight diluent like helium instead of nitrogen. Helium was therefore substituted for nitrogen in the model, and the results are shown in Fig. 7. The temperature rise in the laser is inversely proportional to the quantity η, which is defined by

$$\eta \equiv F(O_2)\, C_p(O_2) + F(\text{dil})\, C_p(\text{dil}) \tag{9}$$

where $C_p(A)$ is the constant pressure heat capacity of chemical species A in units of the gas constant R, and dil is either the chemical species N_2 or He. At identical values of η, a CL using either nitrogen or helium as diluent should produce nearly

TABLE VIII
INPUT CONDITIONS USED IN THE PREDICTIVE CALCULATIONS

Injector A		Mole/s
Flow rates	N_2	0.095 (β_F = 100)
	CS_2	0.001
	O_2	0.005
p_A(Torr)	35	
T_A(K)	300	
Injector B		
Flow rates	O	0.001
p_B(Torr)	10	
T_B(K)	300	
Cavity		
p_{cav}	5.0	

TABLE IX
RESULTS OF THE VARIATION OF β_F ON THE 7 → 6 BAND

β_F	Position of Maximum Gain (cm)	Temperature (K)	J_{max}	Gain	Gain/m (s/g)
100	4.8	362	11	.297	0.102
50	2.7	414	12	.206	0.136
25	1.5	495	13	.118	0.145
20	1.3	533	14	.094	0.140
15	1.0	568	14	.069	0.130

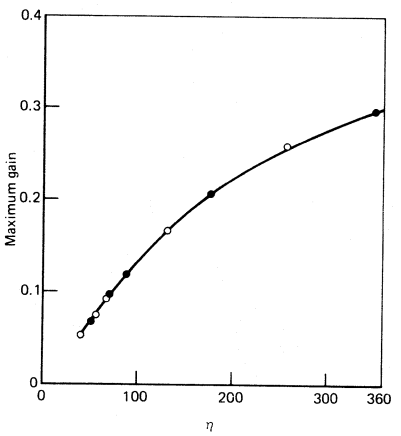

Fig. 7. Maximum gain with respect to both J line and downstream position for the 7 → 6 band versus η. • Calculations with N_2 diluent. ○ Calculations with He diluent. (The relative dependence of maximum gain for η for the other bands closely follows the illustrated band.)

equal output power; however, the specific output power will be greater using helium as the diluent.

B. Variation of Injector Temperature

The variation of gain with injector gas temperature is shown in Fig. 8. The gain decreases monotonically with increasing

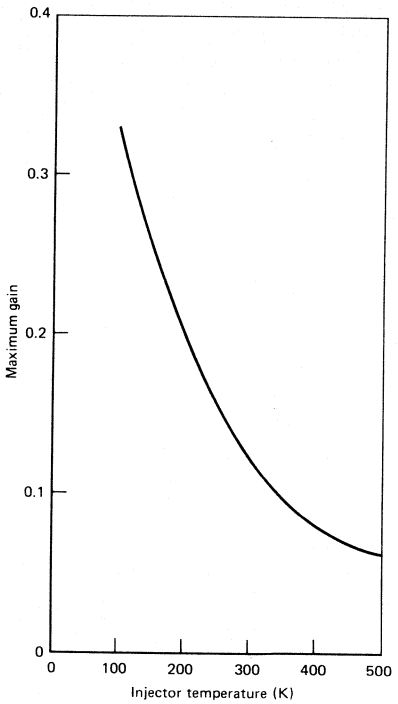

Fig. 8. Maximum gain (as in Fig. 7) versus injector temperature for the 7 → 6 band.

temperature. The calculation shows that cooling the CL medium should significantly enhance the small-signal gain.

C. Cavity Pressure Variations

The calculations of this section were designed to show the variation with cavity pressure of total gain produced by constant input flows of both reactants and diluents. As in the previous calculations of this section, the injector length was decreased with increasing pressure to maintain constant flow velocity. With constant relative amounts of input species, the rates of all two-body processes, including relaxation and chemical reactions, scale in the same way with total pressure. If only two-body processes were considered, the maximum gain in our calculation would be pressure independent; the downstream position of maximum gain on any transition would vary inversely with pressure. Processes which cause deviations from such simple pressure scaling are: 1) variations of mixing length with pressure; 2) pressure broadening of the optical line shape; and 3) three-body reactions.

The value chosen for the mixing length becomes an important consideration at pressures high enough so that mixing becomes slow compared with the chemical formation rates. To investigate the effect of mixing length on calculated laser performance, we performed two sets of calculations with pressure variations from 5 to 100 torr. In the first set, l_{mix} was taken to be 0.5 cm, a value which is appropriate to experimental devices [16]; in the second set, l_{mix} was 0.01 cm so that mixing would be rapid relative to the chemical formation rates even at 100 torr. The results of these calculations are shown in Fig. 9. Even at pressures as low as 10 torr, the in-

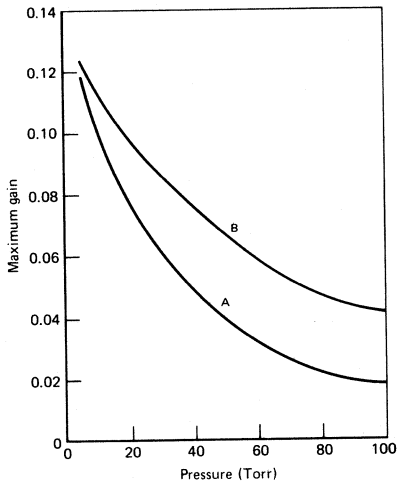

Fig. 9. Maximum gain (as in Fig. 7) versus cavity pressure for the $7 \rightarrow 6$ band. Curve A represents the calculations with $l_{mix} = 0.5$ cm. Curve B represents the calculations with $l_{mix} = 0.01$ cm.

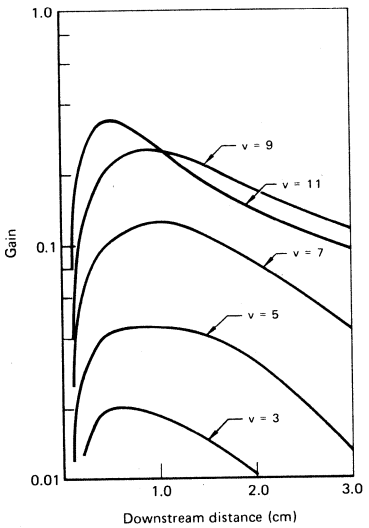

Fig. 10. Maximum gain with respect to J versus downstream position for the odd bands from $v = 3$ to $v = 11$ at 5 torr.

fluence of the 0.5-cm mixing length becomes noticeable and is increasingly important as the pressure increases. Thus mixing may be the dominant parameter determining the performance of CO CL's at high pressure.

The pressure scaling of gain relaxation is a second important effect on the operation of high-power laser systems. Gain as a function of downstream position is plotted in Fig. 10 for bands from $3 \rightarrow 2$ to $11 \rightarrow 10$. Gain relaxation after the maximum gain is reached occurs mainly by two-body collisional processes and hence will occur in a time inversely proportional to pressure. Table X shows the pressure-time products $(p \cdot \tau_{1/2})$ for gain to relax to one-half the maximum value for bands $2 \rightarrow 1$ up to $13 \rightarrow 12$. Comparison of the 5- and 100 torr $p \cdot \tau_{1/2}$ values for a given band shows deviations of less than 20 percent.

TABLE X
PRESSURE-TIME PRODUCTS FOR GAIN TO RELAX TO ONE-HALF ITS MAXIMUM VALUE

Band (v→v-1)	5 Torr $p \cdot \tau_{1/2}$ (ms Torr)	100 Torr $p \cdot \tau_{1/2}$ (ms Torr)
2	0.5	0.4
3	0.7	0.6
4	1.1	1.3
5	0.8	0.8
6	0.8	0.8
7	0.8	0.8
8	1.2	1.1
9	1.1	1.1
10	0.7	0.7
11	0.5	0.6
12	0.5	0.5
13	0.5	0.5

ACKNOWLEDGMENT

The authors wish to thank J. Putnam for his help in developing the computer code used in these calculations, and Dr. C. Ultee for furnishing additional information about his work cited in [12].

REFERENCES

[1] N. Cohen, T. A. Jacobs, G. Emanual, and R. L. Wilkins, "Chemical kinetics of hydrogen halide lasers 1. The H_2-Cl_2 system," *Int. J. Chem. Kinetics*, vol. 1, pp. 551–569, 1969.

[2] P. H. Corneil and J. V. V. Kasper, "Computer simulation of the HCl explosion laser," *IEEE J. Quantum Electron. (2nd Conference on Chemical and Molecular Lasers, Digest of Technical Papers)*, vol. QE-6, pp. 170–171, Mar. 1970.

[3] J. R. Airey, "Cl + HBr pulsed chemical laser: A theoretical and experimental study," *J. Chem. Phys.*, vol. 52, pp. 156–157, 1970.

[4] G. Emanuel, N. Cohen, and T. A. Jacobs, "Theoretical performance of an HF chemical cw laser," *J. Quant. Spectrosc. Radiat. Transfer*, vol. 13, pp. 1365–1393, 1973.

[5] W. S. King and H. Mirels, "Numerical study of a diffusion-type chemical laser," *AIAA J.*, vol. 10, pp. 1647–1654, Dec. 1972.

[6] B. R. Bronfin *et al.*, "Development of chemical laser computer models," United Aircraft Res. Lab., Tech. Rep. AFWL-TR-73-48, July 1973.

[7] J. Thoenes, A. J. McDanal, A. W. Ratliff, and S. D. Smith, "Chemical laser analysis development," Lockheed Missiles Space Co., Tech. Rep. RK-CR-73-2, Oct. 1973.

[8] R. J. Hall and B. R. Bronfin, "Influence of molecular energy transfer and reaction kinetic parameters on chemically pumped laser media," presented at the Conf. Molecular Energy Transfer, Cambridge, England, July 1971.

[9] C. Wittig, J. C. Hassler, and P. D. Coleman, "Continuous wave carbon monoxide chemical laser," *J. Chem. Phys.*, vol. 55, pp. 5523–5532, Dec. 15, 1971.

[10] W. Q. Jeffers, "Carbon monoxide chemical laser research," McDonnell Douglas Res. Lab. Rep. MDC Q0495, May 1973.

[11] T. J. Menne, "Laser kinetic data development," McDonnell Douglas Res. Lab. Rep. Q0510, Dec. 1973; MICOM Tech. Rep. RK-CR-73-7.

[12] C. J. Ultee and P. A. Bonczyk, "Performance and characteristics of a chemical CO laser," *IEEE J. Quantum Electron. (Part I of Two Parts)*, vol. QE-10, pp. 105–110, Feb. 1974.

[13] G. Hancock, C. Morley, and I. W. M. Smith, "Vibrational excitational CO in the reaction: O + CS → CO + S," *Chem. Phys. Lett.*, vol. 12, pp. 193–196, 1971.

[14] H. T. Powell and J. D. Kelley, "Vibrational distribution of carbon monoxide from O + CS → S + CO(v)*," *J. Chem. Phys.*, vol. 60, pp. 2191-2192, Mar. 1974.
[15] N. Djeu, "Quantitative laser measurement of very small absorptions: Studies of the O + CS → CO(v) + S reaction," *J. Chem. Phys.*, vol. 60, pp. 4109-4115, June 1, 1974.
[16] W. Q. Jeffers and C. E. Wiswall, "Experimental studies of the O/O_2/CS_2 CW CO chemical laser," *IEEE J. Quantum Electron.*, vol. QE-10, pp. 860-869, Dec. 1974.
[17] D. R. Stull and H. Prophet, *JANAF Thermochemical Tables*, 2nd ed. Washington, D.C.: U.S. GPO, 1971.
[18] H. Okabe, "Photodissociation of CS_2 in the vacuum ultraviolet; Determination of D: (SC-S)," *J. Chem. Phys.*, vol. 55, p. 4381, 1972.
[19] K. Schofield, "Evaluated chemical kinetic rate constants for various gas phase reactions," *J. Phys. Chem.* (Ref. Data), vol. 2, p. 25, 1973.
[20] I. R. Slagle, J. R. Gilbert, and D. Gutman, "Kinetics of the reaction between oxygen atoms and carbon disulfide," *J. Chem. Phys.*, vol. 61, p. 704, 1974.
[21] G. Hancock and I. W. M. Smith, "Infra-red chemiluminescence from vibrationally excited CO. Part 1—The reaction of atomic oxygen with carbon disulphide," *Trans. Faraday Soc.*, vol. 67, p. 2586, 1971.
[22] D. W. Howgate and T. A. Barr, Jr., "Dynamics of the CS_2-O_2 flame," *J. Chem. Phys.*, vol. 59, p. 2815, 1973.
[23] R. J. Richardson, "CS/O_2 flame reaction chemistry," *J. Phys. Chem.*, to be published.
[24] H. T. Powell, unpublished.
[25] —, "Vibrational relaxation of carbon monoxide using a pulsed discharge," *J. Chem. Phys.*, vol. 59, pp. 4937-4941, Nov. 1, 1973.
[26] J. D. Kelley, "Vibrational energy transfer processes in collisions between diatomic molecules," *J. Chem. Phys.*, vol. 56, pp. 6108-6117, June 15, 1972.
[27] W. H. Green and J. K. Hancock, "Measurement of CO(v = 1) vibrational energy transfer rates using a frequency-doubled CO_2 laser," *J. Chem. Phys.*, vol. 59, pp. 4326-4335, Oct. 15, 1973.
[28] J. K. Hancock, D. F. Starr, and W. H. Green, "Measurement of the rate of excitation and deactivation of OCS(001), N_2O(001), CS_2(001) and C_2N_2(00100) using laser excited CO as a pumping source," *J. Chem. Phys.*, vol. 61, pp. 3017-3025, Oct. 15, 1974.
[29] W. Q. Jeffers and J. D. Kelley, "Calculations of *V-V* transfer probabilities in CO-CO collisions," *J. Chem. Phys.*, vol. 55, pp. 4433-4437, Nov. 1, 1971.
[30] K. J. Herzfeld and T. A. Litovitz, *Absorption and Dispersion of Ultrasonic Waves.* New York: Academic, 1959.
[31] W. B. Lacina, "Kinetic model and theoretical calculations for steady state analysis of electrically excited CO laser amplifier system," Northrop Corporate Lab., Final Rep. NCL 71-32R, July 31, 1971.
[32] G. Emanuel, "Analytical model for a continuous chemical laser," *J. Quant. Spectosc. Radiat. Transfer*, vol. 11, pp. 1481-1520, 1971.

WA5—Laser-Excited Electronic-to-Electronic Energy Transfer in Sodium

HAO-LIN CHEN AND STEVE FRIED

Abstract—**Energy-transfer rates for the $E \rightarrow E$ process Na($^2P_{3/2}$) + Na ($^2S_{1/2}$) $\rightleftarrows$ Na ($^2P_{1/2}$) + Na ($^2S_{1/2}$) + ΔE = 17.2 cm^{-1} have been measured following direct excitation of specific ^2P levels with a pulsed tunable dye laser of 10^{-2}-Å linewidth and 5-ns duration. The cross sections for the forward and backward reactions at 272°C have been found by Pitre and Krause to be 250 ± 40 and 480 ± 80 Å, respectively.**

INTRODUCTION

THE DEVELOPMENT of an electronic-transition (visible or UV) gas-laser system for high-energy and high-efficiency applications has been one of the main interests in laser research for many years. In indirectly pumped laser systems, the energy-transfer rate must compete with the spontaneous-radiation rate. Since the radiative lifetimes of most known electronically excited states are rather short, between 10^{-7} and 10^{-9} s, a rapid energy-transfer rate for the upper lasing level is generally necessary. In order to measure these rates, the pulse length of the excitation source has to be sufficiently short compared with the radiative lifetime of the excited state. By using a Na resonance lamp and a Kerr-cell arrangement, Kibble *et al.* [1] have been able to generate 10-ns pulses of Na *D*-line radiation for measurement of Na (3^2P)-state lifetime. Using conventional resonance and sensitized fluorescence technique, Pitre and Krause [2] have also determinded the quenching, excitation, and doublet mixing cross sections of alkali metals. However, in order to avoid trapping of resonance radiation, all these measurements were carried out at extremely low alkali vapor pressures and at correspondingly low fluorescent intensity. In the case of near-resonant energy transfer, the small separation between the emitting lines presents additional experimental problems. In this work, by using a tunable laser of 10^{-2}-Å linewidth, we have developed a different method for measurement of these near-resonant energy-transfer processes at relatively high

Manuscript received November 11, 1974; revised March 7, 1975. This work was supported by the Advanced Research Projects Agency of the Department of Defense under Work Order 1180, and monitored by the U.S. Army Missile Command under Contract DAH01-72-C-0995.

H.-L. Chen was with the AVCO Everett Research Laboratory, Everett, Mass. 02149. He is now with the Lawrence Livermore Laboratory, Livermore, Calif. 94550.

S. Fried is with the AVCO Everett Research Laboratory, Everett, Mass. 02149.

metal vapor pressures. Instead of avoiding the imprisonment of radiation, we take advantage of the slow effective radiation loss and look at the wing radiations which directly reveal the translationally equilibrated populations of the excited states. In this paper, the experimental details on measurements of Na (^2P)-Na (^2S) collisional energy-transfer rates will be described.

Kinetic Scheme

The basic concept of the experiment was to selectively populate one particular excited state and to monitor the fluorescence from both the excited and collisionally transferred states. The vapor density was purposely kept at a level higher than 10^{13} atom/cm^3 to assure that the rate of radiation loss was kept small by the process of radiation trapping. Thus collision-dominated kinetics could be studied by monitoring the temporal intensity of untrapped radiation in the far wings from the excited states.

When a pure Na vapor is excited by a laser pulse of 5896 Å or 5890 Å, energy is transferred rapidly out of the excited ^2P to the other ^2P level of different J quantum number, by the processes of 1) electronic-to-electronic energy transfer between colliding atoms and/or 2) spin-orbital relaxation of the excited atom. For simplicity we shall consider only the three lowest states of Na $^2S_{1/2}$, $^2P_{3/2}$, and $^2P_{1/2}$. Sodium is excited by the laser photons of resonance frequency

$$\mathrm{Na}(^2S_{1/2}) + h\nu_{\mathrm{Laser}} \longrightarrow \mathrm{Na}(^2P_{3/2})$$

$$\mathrm{Na}(^2P_{3/2}) + \mathrm{Na}(^2S_{1/2}) \underset{k_{e'}}{\overset{k_e}{\rightleftharpoons}}$$

$$\cdot \begin{cases} \mathrm{Na}(^2P_{1/2}) + \mathrm{Na}(^2S_{1/2}) + \Delta E = 17.2\ \mathrm{cm}^{-1} \\ \mathrm{Na}(^2S_{1/2}) + \mathrm{Na}(^2P_{1/2}) + \Delta E = 17.2\ \mathrm{cm}^{-1}. \end{cases} \quad (1)$$

After the final equilibrated concentration ratio of

$$\frac{\mathrm{Na}(^2P_{3/2})}{\mathrm{Na}(^2P_{1/2})} = \frac{g_{3/2}}{g_{1/2}} \exp(-\Delta E/kT)$$

is reached, the electronic energy is subsequently depleted by energy transfer to translation in collisions with other Na atoms or by spontaneous radiations from the ^2P states

$$\mathrm{Na}(^2P_{3/2}) + \mathrm{Na}(^2S_{1/2}) \xrightarrow{k_{20}} 2\,\mathrm{Na}(^2S_{1/2}) + \Delta E$$
$$= 5890\ \text{Å} = 1.7 \times 10^4\ \mathrm{cm}^{-1} \quad (2)$$

$$\mathrm{Na}(^2P_{3/2}) \xrightarrow{k_{ir2}} \mathrm{Na}(^2S_{1/2}) + h\nu_{20} \quad (3)$$

$$\mathrm{Na}(^2P_{1/2}) + \mathrm{Na}(^2S_{1/2}) \xrightarrow{k_{10}} 2\,\mathrm{Na}(^2S_{1/2}) + \Delta E$$
$$= 5896\ \text{Å} = 1.7 \times 10^4\ \mathrm{cm}^{-1} \quad (4)$$

$$\mathrm{Na}(^2P_{1/2}) \xrightarrow{k_{ir1}} \mathrm{Na}(^2S_{1/2}) + h\nu_{10} \quad (5)$$

where k_{ir1}, k_{ir2} = [the imprisoned radiative lifetime of Na ($^2P_{1/2}$), Na($^2P_{3/2}$)]$^{-1}$, which is a constant for fixed vapor density and temperature.

The time dependence of the Na($^2P_{1/2}$) and Na($^2P_{3/2}$) concentrations is determined by the rate constants of (1)-(5). Each concentration can be described by a sum of two exponential decays [3]

$$\mathrm{Na}(^2P_{3/2})(t) = A \exp(-\lambda_1 t) + B \exp(-\lambda_2 t) \quad (6)$$

$$\mathrm{Na}(^2P_{1/2})(t) = D[-\exp(-\lambda_1 t) + \exp(-\lambda_2 t)]. \quad (7)$$

When the electronic-energy equilibration rates are faster than both the E-T and radiation losses, the λ_1 and λ_2 values can be approximated [3] as

$$\lambda_1 \approx [k_e\,\mathrm{Na}(^2S_{1/2}) + k_e'\,\mathrm{Na}(^2S_{1/2})] + \frac{k_e}{k_e + k_e'}$$
$$\cdot [k_{20}\,\mathrm{Na}(^2S_{1/2}) + k_{ir2}] + \frac{k_e'}{k_e + k_e'}$$
$$\cdot [k_{10}\,\mathrm{Na}(^2S_{1/2}) + k_{ir1}] \quad (8)$$

$$\lambda_2 \approx \frac{k_e}{k_e + k_e'} [k_{20}\,\mathrm{Na}(^2S_{1/2}) + k_{ir2}]$$
$$+ \frac{k_e'}{k_e + k_e'} [k_{10}\,\mathrm{Na}(^2S_{1/2}) + k_{ir1}] \quad (9)$$

$$(\lambda_1 - \lambda_2) \approx (k_e + k_e')\,\mathrm{Na}(^2S_{1/2})$$
$$= 1 + \frac{g_{3/2}}{g_{1/2}} \exp(-\Delta E/kT)]\, k_e\,\mathrm{Na}(^2S_{1/2}). \quad (10)$$

Thus, by measurement of λ_1 and λ_2 values at known Na ($^2S_{1/2}$) vapor pressure, it is possible to obtain the rate constants k_e and k_e'.

Experiment and Results

A simplified scheme of the experimental setup is shown in Fig. 1. The narrow-band tunable dye laser, side pumped by a nitrogen laser, emits about 5-μJ, 5-ns, and 10^{-2}-Å bandwidth pulses. Using an oscillator-amplifier arrangement, output energy of 50 μJ/pulse with similar beam quality was also obtained. The detailed laser setup is identical to that reported by Itzkan and Cunningham [4] and will not be described here.

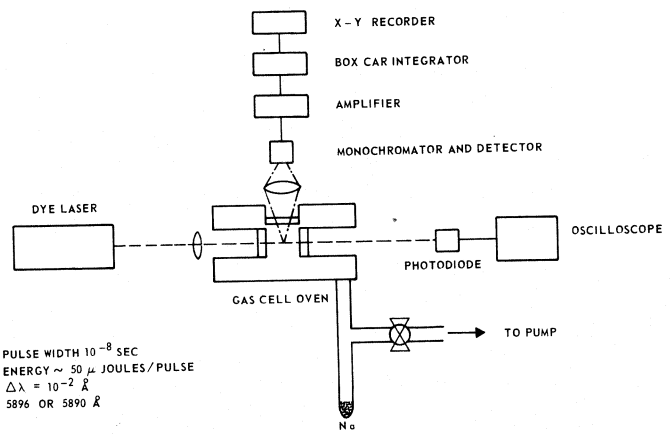

Fig. 1. Experimental apparatus for electronic energy-transfer experiments using a tunable dye laser.

The high-temperature fluorescence cell is constructed by three sapphire windows brazed in stainless-steel flanges which are sealed with the stainless-steel cell body by metal O rings. The cell is heated by an electric oven. The metallic Na reservoir is heated separately and kept at a temperature lower than that of the cell. The temperature of both the cell and reservoir are monitored by calibrated thermocouples. The vapor pressure of Na in the cell was determined from the temperature of the sidearm by means of Nesmeyanov's empirical equation and experimental data [5].

The pulse duration and energy were measured with a calibrated p-i-n photodiode. The signals were displayed on oscilloscopes and photographed. The final tuning of the excitation pulse was made by the fine adjustment of the etalon. For monitoring the resonance and sensitized fluorescence signals, a $f3.5$ light-collecting optics and $\frac{1}{4}$-m Jarrell-Ash monochromator fitted with a EMI 9529B photomultiplier were used. The signal was amplified and averaged with a PAR 160 boxcar integrator and displayed on the X-Y recorder. The overall electronic response time was less than 0.2 μs.

Typical fluorescence signals recorded by X-Y recorders are shown in Fig. 2. The cell temperature was 272°C and Na density of 8.2×10^{13} atom/cm^3. The lower trace shows the resonance-fluorescence signal from the Na($^2P_{1/2}$) state after the laser excitation. A rapid fall followed by a slower decay, as predicted by (6), was observed. The upper trace displays the sensitized fluorescence signal of Na($^2P_{3/2}$) after energy transfer from Na($^2P_{1/2}$). A fast rise and a slower decay was shown. This is again in agreement with the prediction of (7). Fig. 3(a) and (b) show the semilog plot of these data. Note that the τ_{fast} and τ_{slow} values deduced from both figures are almost identical. In exciting Na($^2P_{3/2}$) by laser pulses, a similar pattern of fluorescence signals was observed; namely, that the resonance-fluorescence signals were composed of two exponential decays and the sensitized fluorescence signal was found to rise exponentially and then decay with a slow rate. Data analysis adopting (10) yields k_e and k'_e values of $3.1 \pm 0.4 \times 10^7$ and $5.9 \pm 0.8 \times 10^7$ s^{-1}torr^{-1}, respectively. The error bars are caused mainly by uncertainties of vapor pressure of Na in the cell. The cross sections of these processes deduced from the relationship of $\sigma = k/v$ give 250 ± 40 Å [2],

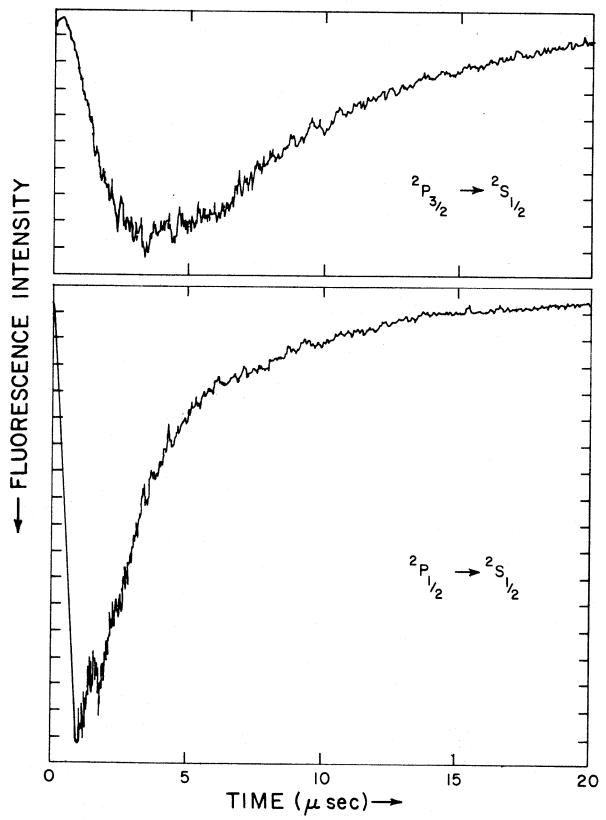

Fig. 2. Resonance and sensitized fluorescence signals of Na. The dye laser was tuned to 5896 Å. The upper trace shows the sensitized fluorescence signal of $^2P_{3/2}$-$^2S_{1/2}$ transition after laser excitation and collisional energy transfer. The bottom trace shows the resonance-fluorescence signal of $^2P_{1/2}$-$^2S_{1/2}$ transition.

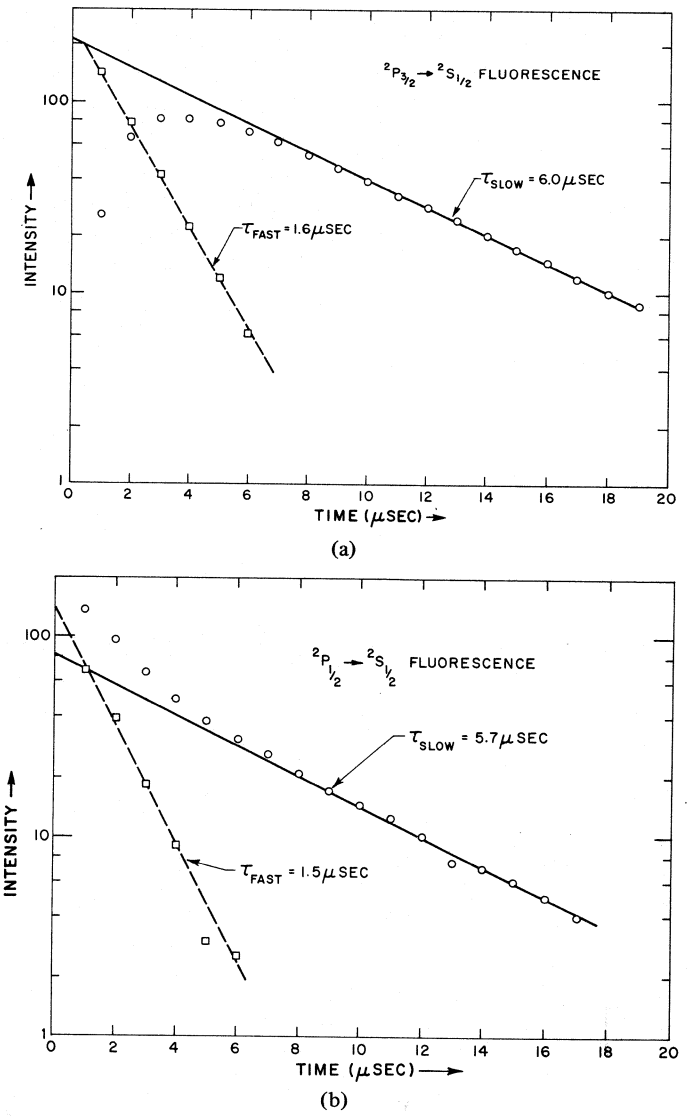

Fig. 3. Fluorescence signals analysis. (a) Semilog plot of sensitized fluorescence data. (b) Semilog plot of resonance fluorescence data. Note that the slopes of the semilog plot of both sensitized and resonance-fluorescence data are almost identical. The difference between the fluorescence trace during the first few microseconds and the solid line gives the squares (⊡) from which the τ_{fast} values are determined.

and 480 ± 80 Å [2] for transferring electronic energy from $^2P_{3/2}$ to $^2P_{1/2}$ and from $^2P_{1/2}$ to $^2P_{3/2}$, respectively. The large error bars are caused by additional uncertainty in the velocity profile or velocities of emitters.

The slow decay rate (λ_2) is believed to result mainly from the imprisoned radiative process and from *E-T* energy transfer or energy losses due to collisions with the wall. Calculations based on Milne's theory of radiation trapping [1], [6] for our experimental condition yields about 5-10 μs of imprisoned radiative lifetime, in good agreement with the observation of 6 μs.

Our measured total cross sections for $^2P_{1/2}$-$^2P_{3/2}$ mixing or the *E-E* energy-transfer process between excited and unexcited sodium atoms appears to be slightly smaller than that obtained from Pitre and Krause's data 283 Å [2] and 532 Å [2] at 151°C. The decrease in mixing cross sections in going from 283 Å [2] at 151°C to 250 Å [2] at 273°C appears to agree qualitatively with the theoretical prediction derived by Dashevskaya *et al.* [7] for the $^2P_{3/2}$-$^2P_{1/2}$ transition in the region of exchange interaction, where the total cross section decreases at $T^{-2/3}$. Of course, with the magnitude of the error bars, the limited number of data available and for the temperature ranges studied, it is difficult to draw any conclusion as to the dominating mechanism involved in the near-resonant electronic energy-transfer process in sodium. A wide temperature-variation study of these rates may provide a detailed mechanism on *E-E* energy transfer and the nature of the dominating interaction potential involved.

Owing to the very nature of radiation imprisonment in gas, caution should be exercised in obtaining *E-E* energy-transfer rate constants utilizing the "wing radiation" technique discussed previously. In order to assure translational equilibration and a slower rate of radiation loss, the vapor pressure of metal has to be kept at relatively high levels. However, it is also known that alkali metal dimerizes as the atomic density increases. For avoiding any possible complication introduced by atom-dimer collisions, it is important that the concentration of dimer in the vapor be kept at relatively low levels. Thus it is crucial that both the metallic vapor pressure and composition be accurately controlled.

References

[1] B. P. Kibble, G. Copley, and L. Krause, "Effect of imprisonment of radiation in sodium vapor on the measured lifetime of 3 ^2p states," *Phys. Rev.*, vol. 153-1, pp. 9-12, 1967.

[2] J. Pitre and L. Krause, "Sensitized fluorescence in vapors of alkali metals. X. Energy transfer in sodium-sodium collisions," *Can. J. Phys.*, vol. 46, pp. 125-128, 1968.

[3] H. L. Chen and C. B. Moore, "Vibration → rotation energy transfer in hydrogen chloride," *J. Chem. Phys.*, vol. 54, pp. 4072-4080, 1971.

[4] I. Itzkan and F. W. Cunningham, "Oscillator-amplifier dye-laser system using N_2 laser pumping," *IEEE J. Quantum Electron. (Part II of Two Parts: Special Issue on 1971 IEEE/OSA Conference on Laser Engineering and Applications)*, vol. QE-8, pp. 101-105, Feb. 1972.

[5] A. N. Nesmeyanov, *Vapor Pressure of the Elements*. New York: Academic, 1963.

[6] T. Holstein, "Imprisonment of resonance radiation in gas," *Phys. Rev.*, vol. 72, pp. 1212-1233, 1947.

[7] E. I. Dashevskaya, A. I. Voronin, and E. E. Nikitin, "Theory of excitation transfer in collisions between alkali atoms. I. Identical partners," *Can. J. Phys.*, vol. 47, pp. 1237-1248, 1969.

WB6—DF-CO_2 Transfer Laser Development

G. W. TREGAY, M. G. DREXHAGE, L. M. WOOD, AND S. J. ANDRYSIAK

Abstract—**Power extraction and chemiluminescence experiments have been conducted in the large-scale DF-CO_2 transfer chemical laser (TCL) (IRIS-I and IRIS-II) facility at Bell Aerospace Company (BAC). The modular design of the device allowed testing to be conducted with both a supersonic nozzle bank and also in subsonic flow with sonic injection for the deuterium. Power levels of 15 kW at 10.6 μ were obtained in IRIS-I (subsonic) employing an unstable resonator with a 50-percent output coupling ratio and cavity pressure of 35 torr. For IRIS-II (supersonic) somewhat lower power was obtained. In both systems the fluorine dissociation ($\alpha = F/F + 2F_2$) was less than 0.01. Chemiluminescent emission from HF and DF was monitored under zero-power conditions along an axis parallel to the laser-mirror axis. From the measured DF-concentration profiles it can be inferred that vibrationally excited DF is being produced throughout the cavity and, accordingly, the production of DF must be attributed largely to the chain reaction.**

Manuscript received November 28, 1974; revised March 19, 1975. The chemiluminescence measurements reported here were sponsored by the U.S. Air Force Weapons Laboratory, Air Force Systems Command, Kirtland Air Force Base, N. Mex., under Contract F29601-74-C-0100. This work contains data obtained at the IRIS Transfer Chemical Laser Facility at the Bell Aerospace Company.

The authors are with Textron Bell Aerospace, P.O. Box One, Buffalo, N.Y. 14240.

Introduction

At the Third Conference on Chemical and Molecular Lasers (May 1-3, 1972) the development of the transfer chemical laser (TCL) was briefly reviewed by Cool [1]. At that time, the maximum power that had been achieved from a DF-CO_2 TCL was 563 W [2]. In this instance, the device was operated in a subsonic mode with gaseous flow transverse to

the optical axis. Atomic fluorine was generated in a precombustor by means of the reaction

$$F_2 + NO = FNO + F.$$

Deuterium was injected into the flow containing He, CO_2, F_2, FNO, and F immediately upstream of the cavity. Chemical efficiences (ratio of output power to total energy available calculated from F_2 flow rate) in the neighborhood of 4 percent were obtained from the system. From this and other evidence, it was inferred that the D_2-F_2 reaction sequence was operating in a chain mode. From the results of this [2] and other studies [3], Cool [1] was able to make optimistic predictions that the DF-CO_2 TCL laser operated in supersonic modes. Thus chemical efficiencies of 5 percent and operating pressures high enough to allow recovery to atmospheric conditions were indicated. It was further pointed out that the achievement of these goals would require an extensive engineering effort.

A large subsonic device, IRIS, has recently been developed at the Bell Aerospace Company (BAC), with goals outlined by Cool [1] kept in mind. The device has an optical-gain path of 76 cm, and to date output powers in excess of 15 kW have been obtained. Efficient system operation has been demonstrated over a wide range of parameters, including pressures as high as 60 torr. The fabrication of the IRIS device has also been modified to allow for supersonic operation. To accomplish this, the D_2 spray bars of the subsonic device were incorporated into a nozzle bank designed for an exit velocity of Mach 1.75 at 15 torr. Although precombustor chemistry and the optics available for efficient power extraction severely restrict the operational parameters, 8 kW of outcoupled power has been obtained and lasing demonstrated at cavity pressures as high as 31 torr.

The successful operation of a large DF-CO_2 TCL in both the subsonic and supersonic modes makes it appropriate to address the question of the contribution of D_2-F_2 chain-reaction chemistry to the overall laser performance in much greater detail than has been done heretofore. Accordingly, experiments have been conducted at BAC which were designed to give quantitative information regarding concentration levels for the upper vibrational states of chemically produced DF within the cavity. From the rapid quenching of the DF chemiluminescence in the presence of CO_2 [4], [5], it was anticipated that the DF concentration would be greater than the detection limit of 10^{11} molecules/cm^3, only in the vicinity of DF production. Concentrations of DF ($v \geq 3$) in the range of 2×10^{11} to 10^{14} molecules/cm^3 were observed throughout the lasing zone, from which it can be inferred that the chain reaction is the dominant mechanism of DF production.

Experimental

IRIS Laser Facility

The power tests and chemiluminescence experiments described herein were conducted on the IRIS laser shown in Fig. 1. The IRIS-I precombustor injector contains 168 elements arranged in 28 linear rows. Each row contains 6 Fuel-Ox-Fuel triplet slots, shown to exhibit the most rapid mixing.

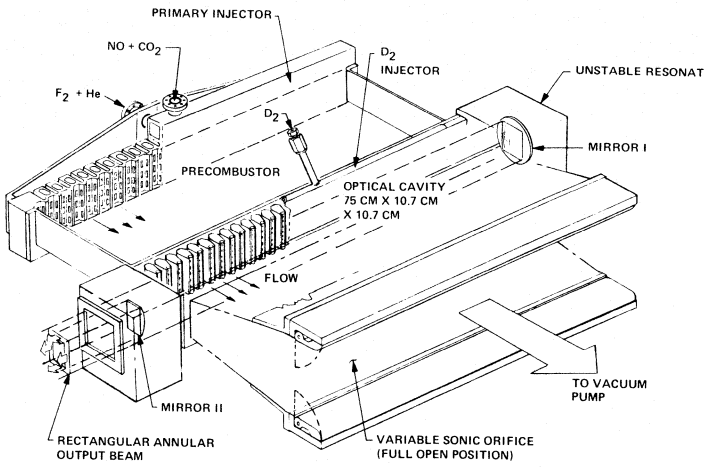

Fig. 1. IRIS laser.

Helium and fluorine comprise the oxidizer, and carbon dioxide and nitric oxide are the fuel materials. The F_2 and He as well as the CO_2 and NO are premixed prior to entering the injector in a mixer section immediately downstream of the individual gas-flow measurement sonic orifices. The precombustor consists of a rectangular TIG welded aluminum duct coated on the inside with Teflon to minimize the wall recombination. The combustor is uncooled and contains provisions for both pressure and static-temperature measurements along the combustor length. The nominal combustor length of 42 cm was derived from a complete combustor analysis to achieve a near steady-state reaction of the NO and F_2. Combustion test data substantiate the analyses performed, as indicated by the static temperature rise of the gas flow in the chamber.

The deuterium injection is accomplished through 4368 sonic orifices (0.028-cm diameter) contained in a 78-element array of 0.32-cm-diameter spray bars. Each spray bar contains two staggered rows of orifices which provides an effective orifice spacing of 0.18 cm. The spray-bar spacing is sufficiently fine (1 cm) to allow efficient penetration of the adjacent rows of D_2 sonic jets into the precombustor gas flow.

The optical cavity for IRIS is an area-defined flow channel of 5° half-angle divergence to compensate for heat release and thereby eliminate any risk of thermal choking in the flow channel. The optical-cavity portion of the flow channel measures 10.7×10.7 cm by 76 cm in width with provision for temperature and pressure measurements along the bottom wall. The optical-cavity pressure is regulated by a two-bladed variable-area sonic flow valve allowing optical-cavity pressure variation during a test from approximately 5 to 100 torr. The power-extraction optics consists of a confocal unstable resonator of 50-percent geometric output coupling. Several mirror arrangements are available for variation of beam cross-sectional area and geometry. The mirrors are uncooled copper with a nickel layer and silver coatings with thorium tetrafluoride overcoats. Power measurements are obtained by either close-coupling the beam onto a water-cooled copper calorimeter or outcoupling the beam to atmospheric pressure through NaCl or KCl windows and then onto a water-cooled aluminum calorimeter. These fast-response (1-s rise time) water-cooled

calorimeters were specially designed to operate in the range of 1-25 kW.

The IRIS-II device employs all of the IRIS-I components with the addition of a supersonic nozzle array. The deuterium-injector spray bars in IRIS-I form the base region of the IRIS-II supersonic nozzle array. The nozzle array fits over the D_2-injector spray bars. Although the IRIS-II nozzle array uses the IRIS-I optical cavity, the flow is not bounded by the flow channel and exists as a free jet. This is due in part to the large base region and the somewhat smaller supersonic nozzle height as compared to optical-cavity height. The IRIS-II flow reattaches to the flow-channel wall downstream of the optical-cavity section. Optical-cavity pressure is not finely controllable by the sonic throttling valve used for IRIS-I but is a function of precombustor operating pressure and heat release within the flow. The supersonic design Mach number is 1.75, which is quite low for an efficient system but is necessary due to chemical/gas dynamic limitations of the IRIS device. Specifically, precombustor chamber pressures less than 2 psia are desirable to minimize production of NOF, which markedly degrades laser performance, whereas cavity pressures greater than 15 torr are required to increase the chemical production rates sufficiently to confine most of the gain region within the optical cavity. The resulting 6:1 pressure ratio dictates a Mach number ~1.75.

Optical System

Spontaneous emission was monitored along an axis which was parallel to the laser mirror axis. The lens was stopped down to restrict the extent of the sample volume to less than 1 cm in the direction of the gas flow and the height varied from 2.5 to 6.5 cm over the test series. The table supporting the optical system was mounted on a translation stage, permitting the radiation to be monitored at any distance from 1 to 10.5-cm downstream. Measurements near the top of the cavity were made by displacing the optical axis 3.8 cm above the horizontal centerline of the cavity. The radiant energy emitted by the test gases was dispersed by a 0.3-m McPherson monochromator and detected by means of a RCA 7102 photomultiplier tube which was cooled to dry-ice temperatures. The signal was amplified with a high-impedance PAR amplifier, after which it was recorded on magnetic tape. A strip-chart recording was generated from the magnetic tape and used in the data reduction.

Spontaneous-Emission Measurements

Measurement of spontaneous emission originating from the upper vibrational levels is an established method [6]-[10] for obtaining concentrations of infrared active diatomic molecules. The relation between emission intensity and population is well known [11] and is reviewed briefly here. Two cases are considered: 1) determination of the population of a specific vibration-rotation state $N^{v',J'}$ from an isolated line; and 2) determination of $N^{v'}$ from unresolved lines. Rotational temperatures were obtained from the distribution of $N^{v',J'}$ in the conventional manner [6]-[9].

The intensity $I_{v,J}^{v',J'}$ due to a transition between an upper state designated by v', J' and a lower state v, J depends on the number of molecules in the initial state. The energy emitted in all directions by $N^{v',J'}$ molecules/cm^3 is given by the product of $N^{v',J'}$, the energy per photon $hc\nu$, and Einstein coefficient for spontaneous emission $A_{v,J}^{v',J'}$, i.e.,

$$I_{v,J}^{v',J'} = N^{v',J'}\, hc\nu\, A_{v,J}^{v',J'}. \tag{1}$$

An expression analogous to (1) can be derived for the relationship of vibrational populations $N^{v'}$ to the intensity of an entire vibrational-rotation band, i.e.,

$$I_v^{v'} = N^{v'}\, hc\nu_0\, A_v^{v'} \tag{2}$$

where ν_0 is the frequency of the band origin.

The Einstein coefficient for an entire vibration-rotation band $A_v^{v'}$ is related to that for an isolated rotational line of that band $A_{v,J}^{v',J'}$ by means of the following expression:

$$A_{v,J}^{v',J'} = A_v^{v'} \left(\frac{J+J'+1}{2}\right) (\nu/\nu_0)^3 F_{v,J}^{v',J'}. \tag{3}$$

Here $F_{v,J}^{v',J'}$ is the vibration-rotation interaction factor for the rotational line and $\frac{1}{2}(J+J'+1)$ is the associated line strength for a transition having on P and R branches.

It is desirable whenever possible to use single lines to determine $N^{v',J'}$; however, there are several instances where this may become difficult. For systems with HF or DF, partial pressures of several torr and long path lengths (10 cm or greater), an additional effect must be considered. Thus emission from one region may be absorbed by unexcited molecules in another (self-absorption) and (1) and (2) will not be valid [8]. This problem can be largely avoided by monitoring emission from the overtone bands which have smaller Einstein coefficients and by properly adjusting the depth of the media from which radiation is extracted. The Einstein coefficients [12] decrease rapidly with increasing v; for DF, $A_2^3 = 130\ s^{-1}$; $A_1^3 = 14\ s^{-1}$; and $A_0^3 = 0.18\ s^{-1}$. A compromise [6]-[8] which has been successfully used is to monitor the $\Delta v = 3$ bands of HF and the $\Delta v = 3$ and $\Delta v = 4$ bands of DF with one of the very sensitive near-infrared photomultiplier tubes. To resolve individual spectral lines, however, there must be sufficient intensity to reduce the spectrometer slit widths to obtain a resolution smaller than the line spacing. These conditions are more easily realized for HF with its large transition probability ($A_0^3 = 1.22\ s^{-1}$, rotational spacing ~50 cm^{-1}) than for DF ($A_0^3 = 0.18\ s^{-1}$, rotational spacing ~25 cm^{-1}).

If the individual lines are not resolved the vibrational population may still be determined from a group of lines [7], [10]. For the particular case of DF, the rotational constants are such that bandheads occur at $J' = 9$-10 in the R branch of the second and third overtone bands of DF. If the overlapping lines are properly accounted for, then the bandhead intensity is a specific fraction of the band intensity and therefore proportional to $N^{v'}$. Evaluation of the proportionality constant S involves a summation within the bandhead of the individual rotational line intensities weighted by the spectrometer slit function ϕ, which is evaluated at the bandhead frequency, i.e.,

$$S = \sum_{J'} [(\nu/\nu_0)^4 F_{v,J}^{v',J'} Q_{\text{rot}}^{-1} \tfrac{1}{2}(J+J'+1) \cdot \exp[-J'(J'+1) B_{v'} hc/(kT)]\ \phi(\nu_{\text{bandhead}} - \nu)]. \tag{4}$$

In practice the experimentally determined bandhead intensity must be corrected for the contribution of neighboring bands. For a single-band sequence this correction factor varies from 1.0 to 0.75 and must be determined numerically. The previous equations have been derived for radiation into a sphere; however, the spectrometric system collects only a small portion of the light emitted. By carefully defining the solid angle this fraction could be determined to within 10 percent.

Results and Discussion

Power Measurements

The output power of IRIS-I has been measured over a wide variation in pressure, gas composition, and mass flow (see Figs. 2 and 3). The interrelation of these parameters is complex; nevertheless, correlations can be pointed out to illustrate trends. As noted, the optical system is a 50-percent output-coupled unstable resonator with a large output beam (7.2 X 10 cm) or a small beam of 6.0 X 9.5 cm. Fig. 2 shows that the best performance at the low-pressure end of the operating range is obtained with the larger mirror set. The smaller beam more efficiently outcouples power from the narrower lasing zone present at pressures above 35 torr. At the highest pressures for this study (60 torr), the most power is obtained at high CO_2/F_2 ratios. The CO_2 in this instance acts as an added heat sink or diluent which keeps efficient chain operation from being affected by excessive heat release downstream. More power is obtained with high NO concentrations at pressures below 30 torr; whereas best high-pressure operation occurs at low NO levels (see Fig. 3). The product molecule NOF acts as a deactivator and also may take a minor part in the reaction; thus NOF acts to decrease the available power at high pressure.

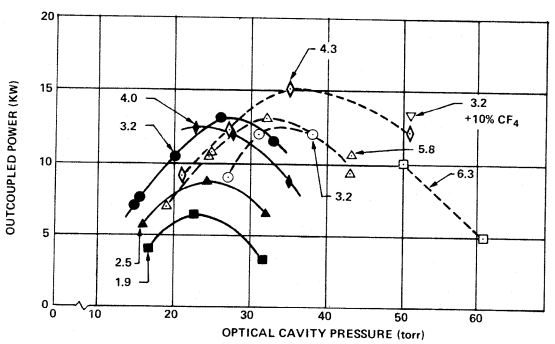

Fig. 2. IRIS-I: Effect of carbon dioxide flow rate on outcoupled power. The CO_2/F_2 ratios are noted in the figure. Closed symbols are for a beam size of 10 X 7.2 cm and open symbols are for a beam size of 9.5 X 6.0 cm. The mole ratio of NO to F_2 was held approximately constant at 0.22.

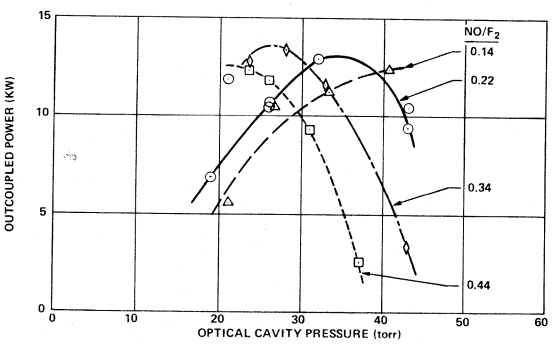

Fig. 3. IRIS-I: Effect of nitric oxide flow rate on outcoupled power. The beam size was 9.5 X 6.0 and the mole ratio of CO_2 to F_2 was held approximately constant at 5.8.

The intensity distribution within the outcoupled laser beam has been analyzed along the flow direction for a number of test conditions. Fig. 4 presents the intensity profile for the conditions which closely parallel those selected for IRIS-I chemiluminescence measurements. Interpretation of the power and intensity is largely a matter of proper evaluation of the chemical phenomena. Insertion of the chain TCL chemistry into any good one-dimensional laser model [13], [14] should provide a reasonable representation of the laser phenomena. Fig. 4 illustrates the comparison of two such analytical treatments with the experimental intensity data for an IRIS-I experiment at 41 torr. The experiment achieved 65 percent of the output power computed with the 1974 kinetic-rate review [14]. Similar results are obtained over the range of IRIS-I operational conditions.

As mentioned earlier, only a restricted range of flow conditions can be examined in IRIS-II and only a limited number of power tests have been conducted in supersonic flow (see Table I). The relative intensity distribution for one case is presented in Fig. 5 and exhibits a stretched power zone over that found

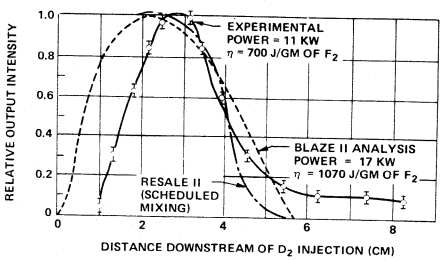

Fig. 4. IRIS-I: Typical beam-intensity profile. The test conditions were: precombustor pressure ~44 torr, optical-cavity pressure ~41 torr, and molar composition; 76.5 percent He, 3.1 percent F_2, 0.7 percent NO, 12.9 percent CO_2, and 6.8 percent D_2.

TABLE I
IRIS-II Power Tests

Power (kw)	Pressures		Molar Ratios		
	Precombustor (torr)	Optical Cavity (torr)	D_2/F_2	NO/F_2	CO_2/F_2
6.0	77.2	22.6	1.10	0.45	8.68
5.2	86.5	30.7	0.84	0.39	6.66
7.7	74.7	14.1	1.40	0.45	11.03

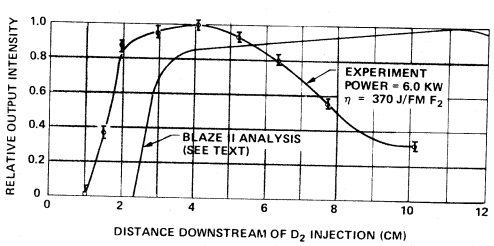

Fig. 5. IRIS-II: Typical beam-intensity profile. The test conditions were: precombustor pressure ~1.5 psia, optical-cavity pressure ~23 torr, and molar composition; 59.5 percent He, 3.6 percent F_2, 1.6 percent NO, 31.3 percent CO_2, and 3.9 percent D_2.

in the IRIS-I device. The 1-D analysis (1974 rates) for the flow predicts 6.5 kW can be extracted by 10 cm, but that a total of 12.5 kW should be obtained if the cavity were 25 cm long. Since 6.0 kW were extracted in this particular experiment over a 10-cm lasing length, it is likely that significantly better performance can be obtained from a supersonic transfer chemical laser.

Chemiluminescence Experiments

The primary objective of the chemiluminescence experiments was to measure the concentration of the upper vibrational levels of DF as a function of distance in both supersonic and subsonic flows. The mass flow, gas composition, and cavity pressure used in these tests are given in Table II. The supersonic case is similar to the test conditions given in Fig. 5, except that two-thirds of the CO_2 was replaced with nitrogen to keep the DF chemiluminescence from being completely quenched. The 10-percent CO_2 remaining in the mixture would have been sufficient for lasing if power extraction has been attempted with this gas composition. The subsonic case closely parallels the power test conditions given in Fig. 4. Emission from DF levels 3-11 were monitored along the centerline for both cases and also near the edge of the flow (3.8 cm above the cavity centerline) for the subsonic case.

Rotational temperature measurements were desired to further characterize the flow field. However, in neither subsonic nor supersonic flow was the intensity sufficient to resolve individual DF rotational lines with the present spectrometer configuration. A series of tests were conducted substituting H_2 for D_2, and thereby obtaining HF rotational temperatures in flows similar to the D_2 system. In an isentropic system at pressures of 20-40 torr, the rotational temperature of a diatomic molecule will approach the static translational temperature of the gas [8]. Where mixing limits the homogenity of the gas (as is the case here) the apparent rotational temperatures will be a weighted average over the temperature and concentration variations. Since the HF/DF is formed concurrently with heat release, the HF/DF concentration will be greater in the hotter regions and thus the apparent rotational temperature is likely to represent the upper extreme of the temperature fluctuations across the flow field [8].

The HF temperature profiles obtained for supersonic flow are presented in Fig. 6. The values shown represent an average of the HF-3-0, 4-1, and 5-2 bands weighted by the number of rotational lines utilized in each band. The rotational temperatures are about 20 percent above thermocouple measurement at the same distance downstream. It would be fortunate if a direct correlation between the temperatures of the hydrogen and deuterium systems could be made. However, the differences in kinetic-rate constants are significant enough to make this approach questionable. A more reasonable assumption is that deviation between actual temperature and those of the thermocouple would be in the same proportion for both HF and DF. On this basis, we estimate the equivalent rotational temperature of the DF system to be as depicted in Fig. 6.

TABLE II
TEST CONDITIONS FOR CHEMILUMINESCENCE MEASUREMENTS

Test	Cavity Pressure (torr)	Total Mass Flow (g/sec)	Composition (Mole Percent)						
			D_2	H_2	F_2	NO	CO_2	He	N_2
IRIS-II	21.5	382	3.9	–	3.4	1.6	10.5	58.8	21.8
	19	367	–	4.0	2.7	1.3	10.6	59.6	21.8
IRIS-I	39.6	171	6.5	–	3.1	0.7	9.7	80.1	–
	39.0	168	–	6.6	3.1	0.7	9.7	79.9	–

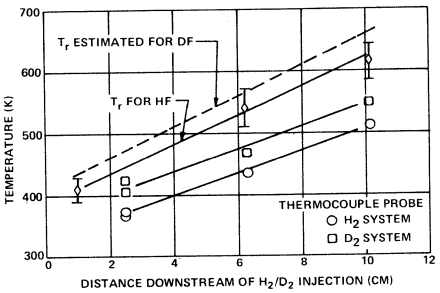

Fig. 6. IRIS-II: Comparison of temperature measurements for H_2 and D_2 systems.

In subsonic flow at 40 torr, an unusual situation arises. Thus, while thermocouple readings are similar for hydrogen and deuterium flows, there exist very large discrepancies between these temperatures and the corresponding HF rotational temperatures (see Fig. 7). The correlation of these values with mean gas temperature and also the analogous DF system presents a perplexing problem. The slower reaction rate of D_2 versus H_2 combined with the lower injection velocity of D_2 (for sonic injection) would moderate the rapid temperature rise observed with H_2. It is unlikely, however, that these effects would reduce the experimental HF temperature profile to values compatible with either the thermocouple values or the calculated DF temperature profile shown in Fig. 7. The temperature determined in BLAZE-II analyses (with revised kinetic rate review) are sensitive to the rate constant for the reaction[1]

$$D + FNO = DF + NO$$

which reduces the number of active chain carriers, and thereby slows the chain reaction. In view of such large discrepancies, the temperature profile in the DF system cannot be estimated with certainty. For purposes of data reduction the DF rotational temperature profile is assumed to be the same as the measured HF rotational temperature.[2]

The concentrations of the DF($3 \leqslant v \leqslant 11$) were determined from a band spectrum in which the major features were the

[1]The rate constant estimated in [14] is too large to account for the unpublished results of J. M. Herbelin of the Aerospace Corp., private communication, October 1974.

[2]The use of HF rotational temperatures in the DF system is, of course, a very crude approximation. Nevertheless, the error introduced in the calculated number density is still less than that associated with the transition probabilities.

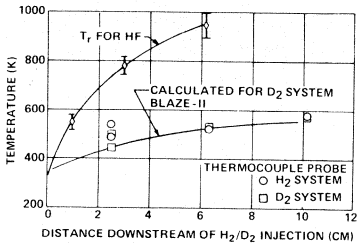

Fig. 7. IRIS-I: Comparison of temperature measurements for H_2 and D_2 systems.

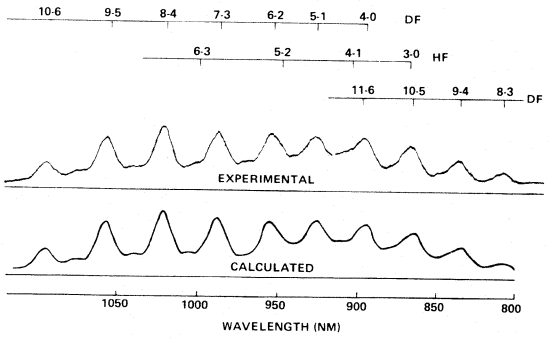

Fig. 8. DF vibrational-band system.

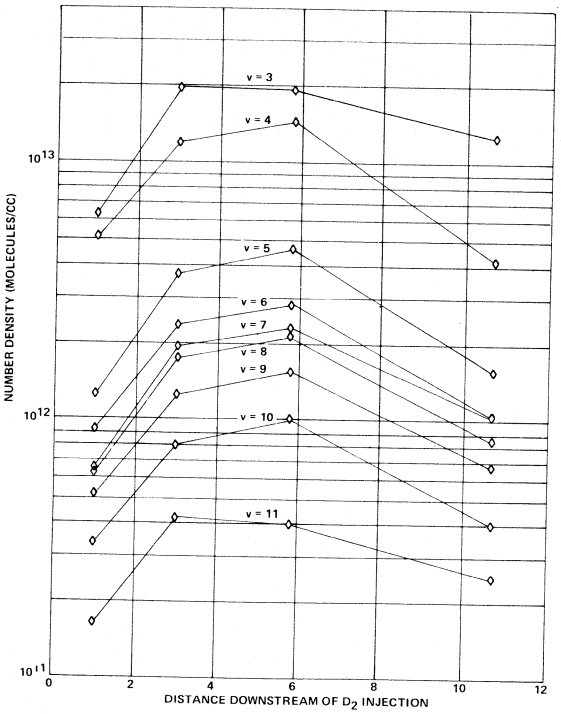

Fig. 9. IRIS-II: DF vibration populations. Test conditions are given in Table II.

R-branch bandheads (see Fig. 8). The accuracy with which the concentrations can be calculated depends on the rotational temperature and the complexity of the spectrum. For the bandpass of 10.6 nm employed in these experiments the maximum intensity of an isolated band is very insensitive to T_r. Rotational temperatures do, however, influence the extent of overlap between adjacent bands; thus a more accurate knowledge of the rotational temperature enters into data reduction as only a second-order correction. Use of an assumed rotational temperature greater than the actual value results in an overcorrection of band overlap, and consequently the actual DF concentrations will be slightly greater than the calculated value. The band spectrum is complex; however, if only a single-band sequence is present, such as DF $4 \rightarrow 0, 5 \rightarrow 1, 6 \rightarrow 2$, etc., the population of each level can be determined uniquely with a high degree of confidence. Interference by HF bands due to trace amounts of H_2 present in the D_2 will not contribute appreciably to the error due to small amounts of emission originating from HF. A serious problem does, however, arise in the overlap of the 4-0, 5-1, and 6-2 bands by the next overtone series. Concentrations of DF ($v = 10$, 11, and probably 12) are significant enough to cause appreciable interference in the bands selected for analysis. For this reason, it was necessary to use an iterative fit to the spectrum in the regions of 4-0, 5-1, and 6-2 bands. The population of DF ($v = 4$, 5, and 6), calculated from these bands are not unique due to uncertainties in the transition probabilities [12]. The populations of DF ($v = 7$-10) are calculated in a straightforward manner with the experimental error being less than that associated with the transition probability. The error associated with DF ($v = 3$) and DF ($v = 11$) increased slightly due to reduced sensitivity of the optical system in the region of the 3-0 and 11-7 bands.

The number densities of DF ($v = 3$-11), measured in supersonic flow, are presented in Fig. 9. The magnitude of the populations reach a maximum in the center of the cavity; however, the relative distribution of DF in the upper levels is virtually constant throughout the cavity. The large number of data points on Fig. 9 does not allow error brackets to be included in the figure; however, the uncertainties shown in Fig. 10 are applicable to the corresponding DF levels. DF-concentration measurements were obtained at three locations for one subsonic flow condition (Fig. 10). At each location the concentrations along the centerline were identical to those near the upper cavity wall. As with the supersonic case, the magnitude of the number density goes through a maximum, yet relative vibrational distribution, essentially unchanged from 1 to 6-cm downstream. The calculated DF vibrational distribution is in good agreement with the experimental values, especially in view of the complexity of the vibrational manifolds of the DF/CO_2 system. For comparison, the distribution of DF(v) was calculated assuming that only the fluorine atoms initially present in the flow reacted (cold reaction). In this case, upper DF levels are immediately quenched, and therefore it becomes obvious that the observed concentrations of DF(v) would be present only if DF is being produced throughout the cavity region via the chain reaction. The same argument would apply even at the higher flow velocities encountered in the supersonic case.

An independent verification of the contribution of the chain reaction to laser power can also be made from thermo-

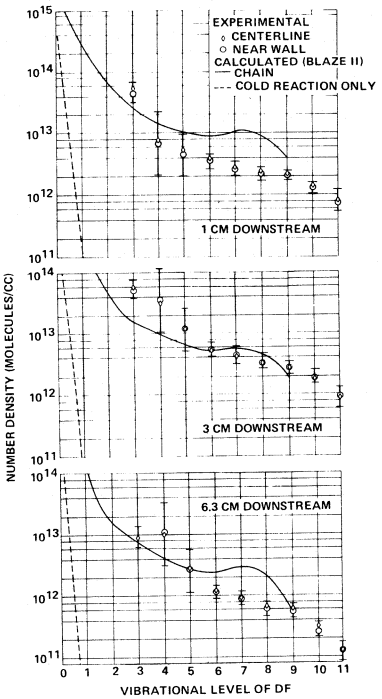

Fig. 10. IRIS-I: DF vibrational populations. Test conditions are given in Table II.

dynamic arguments. Taking the power measurement given in Fig. 4 as an example, the power that could be obtained from the initial fluorine-atom concentration is 0.5 kW. Similarly, incorporating chain-reaction chemistry and utilizing the reference flow rates allows one to compute a maximum theoretical value of 275 kW. A measured value of 11 kW is obtained in the experiment, again ruling out a dominant contribution from the "cold" reaction. Converting the experimental figures previously given to the conventional efficiency numbers provides an overall chemical efficiency of 4 percent for the chain laser in the reference experiment.

Conclusions

A large-scale DF-CO_2 TCL has been operated in both subsonic and supersonic flow. Output powers as high as 15 kW have been obtained and efficient operation has been demonstrated over a wide range of parameters, including pressures as high as 60 torr. The population profiles of the DF ($3 \leqslant v \leqslant 11$) have been determined by chemiluminescence measurements. In both subsonic and supersonic flows the concentrations are significantly greater than that derived from the initial concentration of fluorine atoms ($\alpha \equiv F/(F + 2F_2) < 0.01$), and accordingly the production of DF must be attributed largely to the chain reaction. This conclusion is substantiated by the fact that it is energetically impossible to attain the measured output power with the energy provided by the cold reaction alone.

Acknowledgment

The authors wish to thank Dr. G. Hager, Dr. D. Janiak, Dr. W. Solomon, and R. Agthe for their contributions to the successful completion of the project. They also wish to thank Dr. J. Blauer for reading the manuscript and for his suggestions.

References

[1] T. A. Cool, "The transfer chemical laser: A review of recent research," *IEEE J. Quantum Electron. (Part II of Two Parts: 3rd Conference on Chemical and Molecular Lasers)*, vol. QE-9, pp. 72–83, Jan. 1973.

[2] a) T. J. Falk, "Parametric studies of the DF-CO_2 chemical transfer laser," Cornell Aerospace Lab., Buffalo, N.Y., Rep. AFWL TR-71-96, June 1971.
b) —, "DF-CO_2 transfer laser development," Cornell Aerospace Lab., Buffalo, N.Y., Rep. AFWL-TR-72-169, June 1972.

[3] T. A. Cool, J. A. Shirley, and R. R. Stephens, "Operating characteristics of a transverse-flow DF-CO_2 purely chemical laser," *Appl. Phys. Lett.*, vol. 17, pp. 278–281, 1970.

[4] R. R. Stephens and T. A. Cool, "Vibrational energy transfer and de-excitation in the HF, DF, HF-CO_2 and DF-CO_2 systems," *J. Chem. Phys.*, vol. 57, pp. 5863–5878, 1972.

[5] J. R. Airey and I. W. M. Smith, "Quenching of infrared chemiluminescence: Rates of energy transfer from HF ($v \leqslant 5$) to CO_2 and HF, and from DF ($v \leqslant 3$) to CO_2 and HF*," *J. Chem. Phys.*, vol. 57, pp. 1669–1676, 1972.

[6] D. I. MacLean and G. W. Tregay, "Spectroscopic studies of low pressure hydrogen fluorine flames," in *Proc. 14th Int. Symp. Combustion* (The Combustion Institute, Pittsburgh, Pa., 1973), pp. 157–165.

[7] W. E. Dickinson, "A comparative spectroscopic study of low pressure $H_2 + F_2$ and $D_2 + F_2$ flames," Master's thesis, Boston College, Chestnut Hill, Mass., Aug. 1973.

[8] M. A. Kwok, R. R. Giedt, and R. H. Ueunten, "Development of the MESA spectroscopy experiment," Aerospace Corp., El Segundo, Calif., Rep. SAMSO-TR-74-2, Jan. 1971.

[9] J. T. Latimore *et al.*, "H_2-Cl_2 chemical laser program, Part One. CHEMLUM code for spectroscopic data analysis," TRW Systems Group, Redondo Beach, Calif., Rep. RK-CR-74-9, Jan. 1974.

[10] G. Hancock and I. W. M. Smith, "Quenching of infrared chemiluminescence. I: The rates of de-excitation of CO ($4 \leqslant v \leqslant 13$) by He, CO, NO, N_2, O_2, OCS, N_2 and CO_2," *Appl. Opt.*, vol. 8, pp. 1827–1842, 1971.

[11] G. Herzberg, *Molecular Spectra and Molecular Structure I. Spectra of Diatomic Molecules*. New York: Van Nostrand-Reinhold, 1950, ch. 3.

[12] R. E. Meredith and F. G. Smith, "Investigation of fundamental laser processes: Computation of vibration-rotation matrix elements for diatomic molecules," Univ. Michigan, Willow Run Lab., Ann Arbor, Rep. 84130-39-T, vol. II, Nov. 1971.

[13] G. Emanuel, "Resale-2, CO_2 and inhale," Aerospace Corp., El Segundo, Calif., Rep. SAMSO-TR-72-210, Aug. 1972.

[14] W. Baumann, J. A. Blauer, S. W. Zelazny, and W. C. Solomon, "Kinetic model and computer simulation of continuous wave DF-CO_2 chemical transfer lasers," *Appl. Opt.*, vol. 13, pp. 2823–2834, 1974. (The rates tabulated in this paper have been updated and will be published.)

WE5—Intermolecular Vibration-to-Vibration Energy Transfer in HF/DF(v = 1) + HF/DF(v = 1) ⟶ HF/DF(v = 0) + HF/DF(v = 2) Through the Formation of Dimers

HYUNG KYU SHIN

Abstract—A theory of vibration-to-vibration energy transfer is developed for HF/DF(v = 1) + HF/DF(v = 1) → HF/DF(v = 0) + HF/DF(v = 2) based on the model of dimer formation. This model is shown to be primarily responsible for the energy transfer below 500 K where a strong negative temperature dependence of energy-transfer rates is found; above this temperature the rapid rotational motion of the colliding molecules causes the energy exchange to take place with the result that the rate increases with temperature in a normal fashion. The model represents the low-temperature limit of the energy-transfer process, while the rapid rotational model gives the high-temperature limiting rate, so the overall collision process can be explained in terms of these two contributions. The sum takes a minimum value near 700 K in both HF + HF and DF + DF collisions.

Introduction

THE vibration-to-vibration (VV) energy-transfer process HF/DF(v = 1) + HF/DF(v = 1) → HF/DF(v = 0) + HF/DF(v = 2) + ΔE is of great importance in gas lasers and is responsible for the buildup of HF/DF(v = 2) in the laser pulse pumping of the first vibrational level. For this process the energy mismatches ΔE are only 180 and 91.6 cm^{-1} for HF + HF and DF + DF, respectively, so the energy-transfer rates may be very fast. Recent experimental studies [1]-[5] show the rate coefficient k to be about 10^{13} cm^3/mole · s near room temperature for both HF + HF and DF + DF and the inverse temperature dependence [4] of k for DF + DF in the temperature range of 295-739 K. In these collision systems, there are strong attractive forces acting between the colliding partners due to the presence of the hydrogen-bond interaction; the hydrogen-bond energy is known to be about 6 kcal/mole [6]. In the presence of such a strong attraction the colliding molecules can form a loosely bound complex, and unless the temperature is high, the loosely bound complex can exist with a long lifetime—much longer than the vibrational period of the molecule—thus causing an efficient energy exchange. However, such an energy-exchange process cannot be explained with the conventional vibration-to-translation (VT) [7] or vibration-to-rotation (VR) [8] energy-transfer theories.

It is the purpose of this paper to calculate the VV energy-transfer rates of HF/DF(v = 1) + HF/DF(v = 1) → HF/DF(v = 0) + HF/DF(v = 2) + ΔE on the basis of a mechanism that the energy exchange takes place through the formation of dimers [9]. In this model the molecules are considered to maintain the preferred orientation of the H · · · F interaction in the near-equilibrium configuration for an efficient VV energy transfer. While the molecules maintain the preferred orientation, they also undergo slow "back-and-forth" translational motion which is responsible for the removal of the energy mismatch ΔE, which is normally very small compared to vibrational quanta. We shall only consider zero-impact parameter collisions in treating the relative motion between two HF molecules. The result of this model will be compared with that of the complete rotational motion [8] of the colliding molecules.

Manuscript received November 18, 1974; revised March 7, 1975. This work was supported by the Directorate of Chemical Sciences, U.S. Air Force Office of Scientific Research, Grant AFOSR-72-2231, Theoretical Chemistry Group Contribution 1059.

The author is with the Department of Chemistry, University of Nevada, Reno, Nev. 89507.

Hydrogen-Bond Attraction

There are strong attractive forces, due to the hydrogen-bond interaction, between two HF molecules. The energetically preferred orientation for such strong attractions in the interaction of the H atom of one molecule, say $(HF)_1$, with F of the other, $(HF)_2$. Although this is not a favorable orientation for intermolecular VV energy transfer, because it represents the interaction of a light atom with a heavy atom of which the position is only slightly displaced from the equilibrium geometry, the presence of strong molecular attraction can allow the molecules to form dimers, thus causing them to remain in close proximity of each other for a long time for an efficient energy transfer. As temperature is raised, the thermal motion tends to destroy such an energetically favored orientation so the probability of energy transfer should decrease. Once we invoke the predominance of the hydrogen-bond attraction in the interaction of two HF molecules, the VR energy-transfer theory [8], which is based on the rapid, complete rotational motions of the colliding molecules, cannot therefore be applied to the present VV process, at least at low temperatures.

When the colliding molecules make complete rotational motions, two peripheral hydrogen atoms come into close range of each other. In this case, H of $(HF)_1$ is then in strong interaction with H of $(HF)_2$ in which both atoms are undergoing large displacements from the equilibrium bond distance, thus leading to an efficient intermolecular VV energy transfer [10]. The energy mismatch ΔE is now transferred to the rotational motion of the colliding partners (i.e., a VR mechanism). The overall process is then the combination of VV and VR mechanisms; *the VVR process*. Note that in this case two light atoms are squeezed close together by two heavy atoms, so the main interaction which causes the VVR energy transfer to take place is strongly repulsive, and that

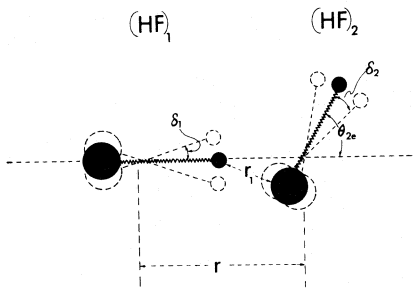

Fig. 1. Collision coordinates; the equilibrium orientation angles are taken as $\theta_{1e} = 0°$ and $\theta_{2e} = 60°$.

the hydrogen-bond energy for this configuration is negligible. The probability of energy transfer obtained for such a model should then increase with temperature in a "normal" fashion because of the increasing degree of the rotational motion of H atoms which leads to an efficient removal of the vibrational energy. In the VR model the molecular attractions do not make a large contribution to the energy transfer because, for the F-H $\cdots$ H-F encounter, which is the most favorable orientation for VV and VR energy transfer, the hydrogen-bond attraction is very weak, if not zero, and the dipole-dipole interaction becomes positive (i.e., repulsive). In [11] we have included, based on physical arguments, the hydrogen-bond and dipole-dipole attractions in the VR theory to investigate the self-relaxation of HF, but the study showed such a procedure to seriously overestimate the energy-transfer probability at low temperatures (~300 K) [12]. We should note that the hydrogen-bond energy of HCl is only about 2 kcal/mole [13], which is far less than that in HF, so the formation of the dimers may not be important in exchanging the vibrational energy intermolecularly even at low temperatures (~300 K). In fact, we have recently applied the VVR model, with the inclusion of the effects of hydrogen-bond and dipole-dipole attractions, to this system and found reasonable agreement between theory and experiment [10].

The collision coordinates of HF + HF in the near-equilibrium configuration are shown in Fig. 1. The equilibrium separation r_e is 2.79 Å, $\theta_{1e} = 0°$, and $\theta_{2e} = 60$-$70°$, [14]-[16]. The hydrogen bond is maintained through a strong interaction between H of $(HF)_1$ and F of $(HF)_2$. In the presence of such a bond, the molecules can neither make complete rapid rotational motion nor rapid translational motion; then the potential energy of the interaction of the molecules confined in the vicinity of the equilibrium coordinates θ_{1e}, θ_{2e}, and r_{1e} can be expressed in the exponential form

$$U(r_1) = D_0 \left[\exp\left(\frac{r_{1e} - r_1}{a}\right) - 2\exp\left(\frac{r_{1e} - r_1}{2a}\right)\right] \tag{1}$$

where r_1 is the H $\cdots$ F distance, D_0 is the hydrogen-bond energy (6 kcal/mole [6]), and a is a potential parameter. Since $r_e = 2.79$ Å [14] and the equilibrium bond distance is 0.917 Å, the H $\cdots$ F distance around the equilibrium separation can be approximated as $r_1 = r - q_F(d + x_1)\cos\theta_1 - q_H(d + x_2)\cos\theta_2$, where $q_{H,F} = m_{H,F}/(m_H + m_F)$, and x_1 and x_2 are the displacements of the bond distances of $(HF)_1$ and $(HF)_2$ from their equilibrium value d, respectively. In the dimer the molecules can make only small displacements from the equilibrium separation r_e; therefore, we can expand (1) as

$$U(r, \theta_1, \theta_2, x_1, x_2) = D_0(f_1 - 2f_2) + (f_1 - f_2)\left(\frac{r_e - r}{a}\right) + 2(f_1 - f_2/2)\left(\frac{r_e - r}{2a}\right)^2 + \cdots \tag{2}$$

where

$$f_1 = f_1(\theta_1, \theta_2, x_1, x_2) = \exp\left[\frac{r_{1e} - r_e}{a} + \frac{q_F(d + x_1)}{a}\cos\theta_1 + \frac{q_H(d + x_2)}{a}\cos\theta_2\right]$$

$$f_2 = f_2(\theta_1, \theta_2, x_1, x_2) = \exp\left[\frac{r_{1e} - r_e}{2a} + \frac{q_F(d + x_1)}{2a}\cos\theta_1 + \frac{q_H(d + x_2)}{2a}\cos\theta_2\right].$$

The orientational motion of the molecules in the dimer is confined to the immediate neighborhood of θ_{1e} and θ_{2e}, i.e., hindered rotational motion, and we shall neglect its coupling with the vibrational motion, as well as the back-and-forth motion, of individual molecules. However, such restricted rotational motion would modify the strength of the hydrogen-bond interaction; we shall discuss this aspect later. We can now replace the angles in (2) by their equilibrium values; i.e.,

$$f_1(\theta_{1e}, \theta_{2e}, x_1, x_2) = 1 + \frac{q_F x_1}{a}\cos\theta_{1e} + \frac{q_H x_2}{a}\cos\theta_{2e} + \frac{q_H q_F}{a} x_1 x_2 \cos\theta_{1e}\cos\theta_{2e} + \cdots \tag{3}$$

and a similar expression for $f_2(\theta_{1e}, \theta_{2e}, x_1, x_2)$. For $x_1 = x_2 = 0$, (2) reduces to $U(r, \theta_{1e}, \theta_{2e}, 0, 0) = D_0[((r_e - r)/2a)^2 - 1]$ as it should. In (3) the term which is responsible for the coupling between the vibrational motion of $(HF)_1$ and $(HF)_2$ is that containing the product x_1x_2, so the interaction potential energy which causes the VV energy transfer can be obtained from (2) and (3) as

$$U(r, \theta_{1e}, \theta_{2e}, x_1x_2) = D_0\left[\left(\frac{r_e - r}{2a}\right)^2 - 1\right] + \frac{1}{2}D_0\left[1 + \frac{3(r_e - r)}{2a}\right]\left(\frac{q_H q_F}{a^2}\right) x_1x_2 \cos\theta_{1e}\cos\theta_{2e} \equiv U_0(r) + U'(r, x_1x_2). \tag{4}$$

The potential energy $U_0(r)$ describes the relative motion of the centers of mass of the molecules in the dimer and determines the trajectory $r(t)$ of the collision in the neighborhood of the equilibrium separation. The orientation dependence should not then appear in the expression of $r(t)$. Since the molecules are loosely bound to each other in dimers, they make only slow translational motion back-and-forth in the neighborhood of r_e, this motion being responsible for the removal of the energy mismatch ΔE.

Energy-Transfer Probability

The probability of the vibrational transitions HF($v = 1$) + HF($v = 1$) → HF($v = 0$) + HF($v = 2$) + ΔE can be given by the expression [17], [18]

$$P_{11}^{02} = \left| \left\langle 02 \left| \exp\left[-\frac{i}{\hbar} \int_{-\infty}^{\infty} U'(r, x_1 x_2) \cdot \exp(i\Delta E t/\hbar)\, dt \right] \right| 11 \right\rangle \right|^2 . \tag{5}$$

To evaluate the vibrational matrix elements, we introduce the operators [19]-[21] $a_i^\dagger$ and a_i, which are Hermitian conjugates of each other satisfying the commutation relation $[a_i, a_i^\dagger] = 1$. The vibrational coordinates are then $x_i = (\hbar/2M\omega)^{1/2}(a_i^\dagger + a_i)$, $i = 1, 2$, where ω and M are the vibrational frequency ($2\pi\nu$) and the reduced mass of HF, respectively. By use of these operators we write the probability as

$$P_{11}^{02} = |\langle 02 |\exp\left[-iG(a_1^\dagger + a_1)(a_2^\dagger + a_2)\right]| 11\rangle|^2 \tag{6}$$

where

$$G = \left(\frac{3}{4M\omega}\right)\left(\frac{q_H q_F}{a^2}\right) \cos\theta_{1e} \cos\theta_{2e} \cdot \left[\int_{-\infty}^{\infty} D_0 \left(\frac{r_e - r}{2a}\right) \exp(i\Delta E t/\hbar)\, dt\right].$$

When we expand the exponential part and approximate as $\exp\left[-iG(a_1^\dagger + a_1)(a_2^\dagger + a_2)\right] \simeq 1 - iG(a_1^\dagger a_2^\dagger + a_1^\dagger a_2 + a_1 a_2^\dagger + a_1 a_2)$, (6) reduces to the first-order result $P_{11}^{02} = 2G^2$. This result will be used in the following derivation.

To evaluate the integral in the quantity G we write $U_0(r) = -D_0 + \frac{1}{2} f y^2$, where $f = D_0/2a^2$ and $y = r - r_e$. From the equation of motion $\mu\ddot{y} = -dU_0/dr = -fy$, where μ is the reduced mass of the collision system

$$t = (\mu/f)^{1/2} \int_{y_0}^{y} [(2E/f) - y^2]^{-1/2}\, dy$$

which gives [9]

$$\left(\frac{r_e - r}{2a}\right) = (E/D_0)^{1/2} \cos\left[(D_0/2\mu)^{1/2}(t/a)\right]. \tag{7}$$

Here we set $\frac{1}{2} f y_0^2 = E$, the initial relative energy. The dimer can therefore be treated as a "pseudo" oscillator with the force constant $f = D_0/2a^2$. When the colliding molecules are far apart (i.e., at large t) they undergo complete rotational motion which cannot be treated by the present model of dimer formation. When the molecules approach each other in the neighborhood of r_e, the rotational motion ceases and the dimer will be formed; thus the collision model restricts the limits of integration appearing in G to a narrow time interval, which is of the order of the vibrational period of the pseudooscillator τ. Equation (7) indicates that the displacement ($r_e - r$) of the pseudooscillator is maximum at $\tau = 0$. The displacement is zero at $-\tau/4$ and $\tau/4$. Therefore, the amplitude changes from zero at $-\tau/4$ to a maximum value at $\tau = 0$ and returns to zero at $\tau/4$. If we set $(D_0/2\mu)^{1/2}(t/a) = x$, then this one-half the period of vibration of the pseudooscillator corresponds to the range from $-\pi/2$ to $\pi/2$. During this period the amount of the energy mismatch ΔE, which is very small compared to the vibrational quantum of HF itself, can be effectively removed by the back-and-forth motion of the pseudooscillator. Therefore, we shall take the limits of the integration from $x = -\pi/2$ to $\pi/2$ to obtain the result [9], [22]

$$I = D_0 \int_{-\infty}^{\infty} \left(\frac{r_e - r}{2a}\right) \exp(i\Delta E t/\hbar)\, dt \simeq (2\mu E)^{1/2} \cdot a \int_{-\pi/2}^{\pi/2} \cos(x) \exp(isx)\, dx = \frac{(2\mu E)^{1/2} a\pi}{4} \cdot \frac{1}{B\left(\frac{3+s}{2}, \frac{3-s}{2}\right)} \tag{8}$$

where B is the beta-function and $s = (\Delta E a/\hbar)(2\mu/D_0)^{1/2}$. With this expression, the transition probability takes the form

$$P_{11}^{02}(E) = \left(\frac{3\pi q_H q_F}{8Ma\omega}\right)^2 \left[\frac{\cos\theta 1_e \cos\theta_{2e}}{B\left(\frac{3+s}{2}, \frac{3-s}{2}\right)}\right]^2 \mu E. \tag{9}$$

The structure of the dimer, or the pseudooscillator, under consideration is not rigid. The molecules in the dimer undergo hindered rotational motion about the equilibrium angles (θ_{1e}, θ_{2e}) and back-and-forth translational motion about the equilibrium separation (r_e). Because of these displacements from the equilibrium geometry, the attractive energy between two HF molecules in the dimer is less than the strength of the hydrogen bond D_0. We shall refer to this energy as the "effective" hydrogen-bond energy and denote it by D_0^*. The colliding molecules with the relative energy less than D_0^* will be attracted to each other to form a nonrigid dimer, so the initial collision energy is modified by D_0^*. This modification will have to be taken into consideration in averaging $P_{11}^{02}(E)$ over the distribution of initial collision energies. To determine the effective hydrogen-bond energy, we write

$$\bar{U}(r) = (2\pi)^{-2} \int_0^{2\pi} \int_0^{2\pi} U(r_1)\, d\theta_1\, d\theta_2 \tag{10}$$

where $U(r_1)$ is given by (1) and $r_1 = r - q_F d \cos\theta_1 - q_H d \cdot \cos\theta_2$ for $x_1 = x_2 = 0$. In the dimer, the molecules undergo small displacements (δ_1, δ_2) from θ_{1e} and θ_{2e}, so we can approximate $\cos\theta_1 = \cos(\theta_{1e} + \delta_1) \simeq (1 - \delta_1^2/2)\cos\theta_{1e}$ and $\cos\theta_2 = \cos(\theta_{2e} + \delta_2) \simeq (1 - \delta_2^2/2)\cos\theta_{2e} - \delta_2 \sin\theta_{2e}$. In

deriving these approximate relations, we took $\theta_{1e} \simeq 0$ and $\theta_{2e} = 60$–$70°$. With these expressions we now obtain

$$\bar{U}(r) = \frac{D_0}{(2\pi)^2}\left[\exp\left(\frac{r_e - r}{a}\right)\int_{-\infty}^{\infty}\exp\left(-\frac{q_F d}{2a}\delta_1^2\right)d\delta_1 \cdot\int_{-\infty}^{\infty}\exp\left(-\frac{q_H d\cos\theta_{2e}}{2a}\delta_2^2 - \frac{q_H d}{a}\sin\theta_{2e}\delta_2\right)d\delta_2 - 2\exp\left(\frac{r_e - r}{2a}\right)\int_{-\infty}^{\infty}\exp\left(-\frac{q_F d}{4a}\delta_1^2\right)d\delta_1 \cdot\int_{-\infty}^{\infty}\exp\left(-\frac{q_H d\cos\theta_{2e}}{4a}\delta_2^2 - \frac{q_H d}{2a}\sin\theta_{2e}\delta_2\right)d\delta_2\right] \tag{11}$$

in which we extended the integration limits from $-\infty$ to ∞ because of the steepness of the exponential functions. The result is

$$\bar{U}(r) = \frac{D_0}{2\pi}\left(\frac{a}{q_F d}\right)^{1/2}\left(\frac{a}{q_H d\cos\theta_{2e}}\right)^{1/2} \cdot\left[\exp\left(\frac{q_H d}{2a}\frac{\sin^2\theta_{2e}}{\cos\theta_{2e}}\right)\exp\left(\frac{r_e - r}{a}\right) - 4\exp\left(\frac{q_H d}{4a}\frac{\sin^2\theta_{2e}}{\cos\theta_{2e}}\right)\exp\left(\frac{r_e - r}{2a}\right)\right] \equiv D_0\left[\bar{A}\exp\left(\frac{r_e - r}{a}\right) - 2\bar{B}\exp\left(\frac{r_e - r}{2a}\right)\right]. \tag{12}$$

The equilibrium separation r_e^* of the dimer represented by the average energy $\bar{U}(r)$ is no longer r_e. This distance can be readily determined from (12) as $(r_e - r_e^*) = 2a \ln(\bar{B}/\bar{A})$. The effective hydrogen-bond energy is therefore

$$\bar{U}(r_e^*) = D_0\left[\bar{A}\exp\left(\frac{r_e - r_e^*}{a}\right) - 2\bar{B}\exp\left(\frac{r_e - r_e^*}{2a}\right)\right] \equiv -D_0^*. \tag{13}$$

The incident molecules with relative kinetic energies less than the effective hydrogen-bond energy D_0^* are primarily responsible for the production of dimers. The approaching molecules are attracted to each other through the potential energy well of depth D_0^*, and the dimers are confined to the well so the energy distribution should therefore be shifted to higher energy by the amount D_0^*. With the modification of the initial energy as $E + \bar{U}(r_e^*) = E - D_0^*$, we can therefore carry out the average of (9) over the Boltzmann distribution as

$$P_{11}^{02}(T) = (kT)^{-1}\int_0^{\infty} P_{11}^{02}(E)\exp\left[-(E - D_0^*)/kT\right]dE = \left(\frac{3\pi q_H q_F}{8Ma\omega}\right)^2\left[\frac{\cos\theta_{1e}\cos\theta_{2e}}{B\left(\frac{3+s}{2}, \frac{3-s}{2}\right)}\right]^2 \cdot \mu(kT + \Delta E/2)\exp(D_0^*/kT) \tag{14}$$

where $\Delta E/2$ is due to the symmetrization of the initial and final energies of the relative motion. Although it is less important, those collisions with $E > D_0^*$ can also produce the dimers; therefore, the integration limits are extended from 0 to ∞ in (14). The major contribution to the dimer formation comes from the energy range of 0-D_0^*. If the integral is evaluated over the latter limits, the result is smaller than that obtained from (14) by the factor $1 - [1 + D_0^*/(kT + \Delta E/2)] \cdot \exp(-D_0^*/kT)$. Since $D_0^* \gg kT$ near room temperature, this factor is very close to unity.

Numerical Results and Discussion

To calculate the vibrational energy-transfer probability $P_{11}^{02}(T)$, we shall use the following molecular and potential constants [23]: $\Delta E(\mathrm{HF}) = 180\ \mathrm{cm}^{-1}$; $\Delta E(\mathrm{DF}) = 91.6\ \mathrm{cm}^{-1}$; $\omega(\mathrm{HF}) = 7.45 \times 10^{14}\ \mathrm{s}^{-1}$; $\omega(\mathrm{DF}) = 5.47 \times 10^{14}\ \mathrm{s}^{-1}$; $d = 0.917$ Å; and $D_0 = 6$ kcal/mole. We choose the equilibrium orientation angles to be $\theta_{1e} = 0°$ and $\theta_{2e} = 60°$. The values of the potential parameter a are given in [11], and vary from 0.202 Å at 300 K to 0.183 Å at 2000 K, but (14) is only weakly dependent on the change of the value of a. We shall convert the calculated values of $P_{11}^{02}(T)$ to the rate coefficient k in units of cubic centimeters/mole · second through the expression $k = ZP_{11}^{02}(T) = 4.74 \times 10^{10} r^{*2}(T\mu^*)^{-1/2}P_{11}^{02}(T)/\mathrm{s} \cdot \mathrm{atm}$, where μ^* is the reduced mass in *amu*; we take [14] $r^* = 2.79$ Å. When this expression is multiplied by RT (i.e., $82T$), we obtain the rate coefficient in units of cubic centimeters/mole · second.

The model above developed is considered to represent the energy-transfer process at low temperatures. As the temperature increases, the molecules tend to undergo complete rotational motion so that the energy mismatch is transferred to the rotational motion of the colliding partner through the strong interaction of the peripheral hydrogen atoms; i.e., the VVR model. As the temperature is lowered, say below 1000 K, the molecules slow down their rotational motion, thus leading to less efficient rotational energy transfer. At such temperatures the effects of dipole-dipole and hydrogen-bond attractions can become important, thus leading to the situation that the molecules spend more time in those orientations for which the energy is small (i.e., more attractive). However, such orientations are due to the interaction of H of $(\mathrm{HF})_1$ with F of $(\mathrm{HF})_2$ for which orientation the intermolecular energy transfer is not efficient. In fact, in the VVR model the interaction energy between two peripheral H atoms dominates all other atom-atom interactions. Therefore, the application of the VVR model to low-temperature energy-transfer processes is unrealistic because the molecules can no longer undergo complete rotational motion. The introduction of the effects of dipole-dipole and hydrogen-bond energies in the model of complete rotational motion of colliding molecules has been discussed in [11], but the approach can produce a serious overestimate of the energy-transfer rate at lower temperatures. For example, for HF at 300 K we find $k = 1.5 \times 10^{14}\ \mathrm{cm}^3/\mathrm{mole} \cdot \mathrm{s}$, which is about five times the experimental data [1], [2] (see Fig. 2 shown below). When there are such strong attractive energies, however, it would not be possible to explain the process with the VVR model. On the other hand, the VVR model should describe the

energy-transfer process reasonably well at higher temperatures, but the effects of the dipole-dipole and hydrogen-bond attractions are now not important. Therefore, we shall compare the result of the dimer model with that of the VVR model which does not include the effects of dipole-dipole and hydrogen-bond energies. The probability for the latter model can be readily obtained from [10] in the form

$$P_{11}^{02}(T) = 8\left(\frac{\pi\phi\Delta E}{\hbar\omega}\right)^2 (1+\alpha)^4 \left(\frac{4\pi\chi}{3kT}\right)^{1/2} \cdot \exp\left[-\frac{3\chi}{kT} + \frac{4(D\chi)^{1/2}g}{\pi kT} + \frac{16Dg^2}{3\pi^2 kT} + \frac{\Delta E}{2kT}\right] \quad (15)$$

with

$$g = 2^{1/2}\,[Q_F^{-1}\sinh(Q_F/2) + Q_H^{-1}\sinh(Q_H/2)]\,/ \cdot (Q_F^{-1}\sinh Q_F + Q_H^{-1}\sinh Q_H)^{1/2}$$

$$\phi = (\cosh Q_F + \cosh Q_H)/ \cdot [\sinh Q_F + (Q_F/Q_H)\sinh Q_H] - Q_F^{-1}$$

$$\chi = [(M/2q_F)^{1/2}\pi(1+\alpha)(\Delta E/\hbar)akT]^{2/3}$$

$$\alpha = (9/2Q_F^2)\,[1 + (4/3Q_F^2)]$$

where $Q_{H,F} = q_{H,F}d/a$. In deriving the preexponential part of this expression, we have neglected some factors which are not significantly different from unity. We shall use (15) with D = 400 K [11] to calculate energy-transfer probabilities at higher temperatures.

In Fig. 2 we plot the calculated values of the rate coefficient k for *the dimer model* and that for *the VVR model* over the temperature range of 300-2000 K. The rate calculated from the dimer model is very large at room temperature and sharply decreases with rising temperature, while the VVR model gives large rates at higher temperatures but decreases rapidly as the temperature is lowered. At a given temperature the colliding molecules can transfer the vibrational energy through both the formation of dimers (i.e., the dimer model) and the rotational motion of the colliding partners (i.e., the VVR model). The sum of these two contributions should then represent the overall process taking place during collision at any temperature. In both mechanisms, the vibrational energy transfer takes place intermolecularly. In the dimer mechanism, the vibrational energy is transferred through the interaction of H of $(HF)_1$ with F of $(HF)_2$ in the neighborhood of the equilibrium separation under the influence of the strong hydrogen-bond *attraction*. On the other hand, in the VR mechanism, the vibrational energy transfer takes place through the interaction of H of $(HF)_1$ with H of $(HF)_2$; i.e., between two rapidly rotating peripheral atoms in the region of strong *repulsion*. In the dimer model, the energy mismatch is taken away by the relative translational motion of the colliding molecules which are loosely bound to each other, while in the VVR model it is transferred to the rotational motion of the colliding partner.

In Fig. 2 we show the sum of the probabilities calculated with the dimer and VVR models; the solid curve represents this sum. A probability minimum appears at 700 K; below this temperature the energy transfer through the formation of dimers dominates in the sum and the temperature dependence of the rate is negative. On the other hand, above 700 K the rotational motion of two colliding molecules becomes increasingly important and the VV process, as well as the removal of ΔE, takes place through the interaction of two peripheral hydrogen atoms. The calculation also shows that over the temperature range under consideration, the rate is fast (of order of 10^{13} cm^3/mole · s. Near room temperature, the calculated values are in reasonable agreement with the experimental data [1], [2]. Since experimental data at higher temperatures are not available at present, the negative temperature dependence between 300 and 700 K and the appearance of the probability minimum in the neighborhood of 700 K predicted by the present approach cannot be tested.

For DF, similar plots are made in Fig. 3; the overall rates calculated between 300 and 750 K are somewhat less than experimental data [3]-[5]. The negative temperature dependence of the experimental data is seen over this temperature range as in the HF system, the result being in agreement with the present calculation. A minimum value of the probability which is obtained by summing the results of the dimer and

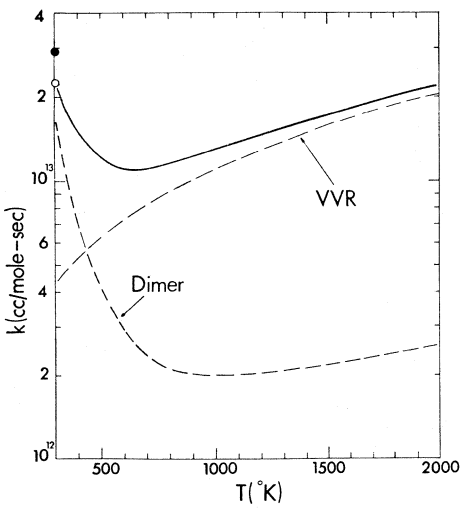

Fig. 2. Temperature dependence of the rate constant k for HF. Experimental data: ○, [1]; ●, [2].

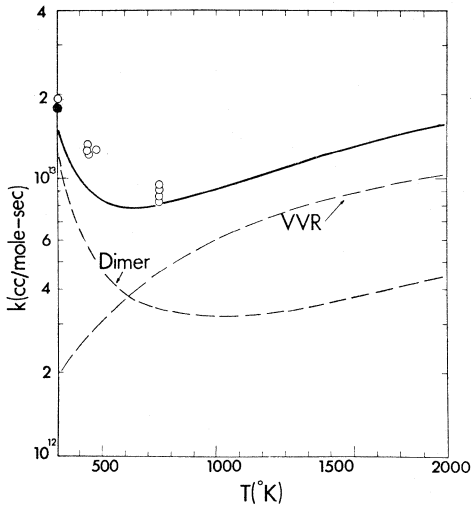

Fig. 3. Temperature dependence of the rate constant k for DF. Experimental data: ○, [3] and [4]; ●, [5].

VVR models occurs near 700 K. The probability starts to increase slowly at 750 K with rising temperature, but no experimental data are available to test such a temperature dependence.

By comparing Figs. 2 and 3 we find that the rates for HF are always larger than those for DF by a factor of about 1.5 over the entire temperature range under consideration in spite of the fact that the energy mismatch is smaller in DF + DF. As shown by broken curves, the VVR rate of HF, which is the major contribution to the sum at higher temperatures, is always greater than that of DF, the result being in accordance with the isotope effect predicted by the VR theory [8]. Note that the VVR approach is based on the rapid rotational motion of the colliding molecules, which is responsible for the isotope effect. As noted in the foregoing sections, the dimer rate dominates in the sum below 500 K. At such temperatures the dimer rate of HF is greater than that of DF.

Concluding Remarks

The VV energy transfer HF/DF($v = 1$) + HF/DF($v = 1$) → HF/DF($v = 0$) + HF/DF($v = 2$) at low temperatures has been examined with the hydrogen-bond dimer model. Because only a limited amount of experimental data is available, it is difficult to make a rigorous test of the present model. However, the model, which is admittedly a simplified one, has the advantage of conceptual and mathematical simplicity and gives the result which does seem to correspond to the observed rates. In particular, it gives a negative temperature dependence of the energy-transfer rate for DF + DF which essentially agrees with experiment. We may therefore state that at lower temperatures the VV energy transfer through the formation of dimers is primarily responsible for the overall process, whereas at higher temperatures, the major contribution to the energy transfer comes from the rapid rotational motion of HF molecules which leads to a strong interaction of two hydrogen atoms at close range. At a given temperature, the sum of these two contributions should represent the overall process. The sum takes a minimum value near 700 K.

References

[1] J. F. Bott, "HF vibrational relaxation measurements using the combined shock tube-laser-induced fluorescence technique," *J. Chem. Phys.*, vol. 57, pp. 96–102, 1972.

[2] R. M. Osgood, A. Javan, and P. B. Sackett, "Measurement of vibration-vibration energy transfer time in HF gas," *Appl. Phys. Lett.*, vol. 20, pp. 469–472, 1970.

[3] J. F. Bott and N. Cohen, "Temperature dependence of several vibrational relaxation processes in DF-CO_2 mixtures," *J. Chem. Phys.*, vol. 59, pp. 447–452, 1973.

[4] J. F. Bott, "Vibrational energy exchange of the DF($v = 2$) state with DF($v = 0$)," *Chem. Phys. Lett.*, vol. 23, pp. 335–338, 1973.

[5] K. Ernst, R. M. Osgood, A. Javan, and P. B. Sackett, "Measurement of the vibration-vibration exchange time ($v = 2$) for DF gas," *Chem. Phys. Lett.*, vol. 23, pp. 553–556, 1973.

[6] G. C. Pimentel and A. L. McClellan, *The Hydrogen Bond.* San Francisco: W. H. Freeman, 1960, p. 363.

[7] See, for example, D. Rapp and T. Kassal, "The theory of vibrational energy transfer between simple molecules in nonreactive collisions," *Chem. Rev.*, vol. 69, pp. 61–102, 1969.

[8] a) H. K. Shin, "Deexcitation of molecular vibration on collision: Vibration-to-rotation energy transfer in hydrogen halides," *J. Phys. Chem.*, vol. 75, pp. 1079–1090, 1971.
b) —, "Vibration-rotation-translation energy transfer in HF-HF and DF-DF," *Chem. Phys. Lett.*, vol. 10, pp. 81–85, 1971.

[9] —, "A collision model for the vibrational relaxation of hydrogen fluoride at low temperatures," *Chem. Phys. Lett.*, vol. 26, pp. 450–456, 1974.

[10] —, "Temperature dependence of the probability of vibration-vibration-rotation energy transfer in HCl($v = 2$) + HCl($v = 0$) → HCl($v = 1$) + HCl($v = 1$)," *J. Chem. Phys.*, vol. 60, pp. 2305–2309, 1974.

[11] —, "Vibration-to-rotation energy transfer in hydrogen fluoride: Effects of the dipole-dipole and hydrogen-bond interactions," *J. Chem. Phys.*, vol. 59, pp. 879–884, 1973.

[12] S. S. Fried, J. Wilson, and R. L. Taylor, "Measurement of the temperature dependence of the vibrational relaxation rate of HF and the effect of SF_6, N_2, and F_2 as diluents," *IEEE J. Quantum Electron. (Part II of Two Parts: 3rd Conference of Chemical and Molecular Lasers)*, vol. QE-9, pp. 59–64, Jan. 1973.

[13] D. H. Rank, P. Sitaram, W. A. Glickman, T. A. Wiggins, "Gas-phase complexes in hydrogen chloride," *J. Chem. Phys.*, vol. 39, pp. 2673–2677, 1963). (This paper reports the concentration of HCl dimers to be only one part in 50 000 at 195 K at a gas density of 0.36 amagat.)

[14] T. R. Dyke, B. J. Howard, and W. Klemperer, "Radiofrequency and microwave spectrum of the hydrogen fluoride dimer; A nonrid molecule," *J. Chem. Phys.*, vol. 56, pp. 2442–2454, 1972.

[15] Also see, a) P. A. Kollman and L. C. Allen, "Theory of the hydrogen bond: *Ab initio* calculations on hydrogen fluoride dimer and the mixed water-hydrogen fluoride dimer," *J. Chem. Phys.*, vol. 52, pp. 5085–5094, 1970.
b) G. H. F. Diercksen and W. P. Kraemer, "SCF MO LCGO studies on hydrogen bonding: The hydrogen flurode dimer," *Chem. Phys. Lett.*, vol. 6, pp. 419–422, 1970.
c) J. E. Del Bene and J. A. Pople, "Theory of molecular interaction. II. Molecular orbital studies of HF polymers using a minimal Slater-type basis," *J. Chem. Phys.*, vol. 55, pp. 2296–2299, 1971.

[16] D. R. Yarkony, S. V. O'Neil, H. F. Schaefer, C. P. Baskin, and C. F. Bender, "Interaction potential between two rigid HF molecules," *J. Chem. Phys.*, vol. 60, pp. 855–865, 1974.

[17] L. Landau and E. M. Lifschitz, *Quantum Mechanics.* Reading, Mass.: Addison-Wesley, 1965, pp. 140–143.

[18] H. K. Shin, "Vibration-to-vibration energy transfer in near-resonant collisions," *J. Chem. Phys.*, vol. 60, pp. 1064–1070, 1974.

[19] —, "Vibrational energy transfer in the hydrogen molecule-helium atom system," *J. Phys. Chem.*, vol. 75, pp. 4001–4011, 1971.

[20] J. D. Kelley, "Vibrational energy transfer processes in collisions between diatomic molecules," *J. Chem. Phys.*, vol. 56, pp. 6108–6117, 1972.

[21] T. A. Dillon and J. C. Stephenson, "Multiquantum vibrational-energy exchange," *Phys. Rev. A*, vol. 6, pp. 1460–1468, 1972.

[22] I. S. Gradshteyn and I. W. Ryzhik, *Table of Integrals, Series, and Products.* New York: Academic, 1965, p. 476.

[23] G. Herzberg, *Spectra of Diatomic Molecules.* Princeton, N.J.: Van Nostrand, 1967, pp. 536–537.

Digests of Technical Papers

SESSION MA

Electrically-Pumped Lasers
Monday, October 21, 8:30 A.M.

MA1. Electron Beam Excitation of Argon-Nitrogen Mixtures,[1] S. K. Searles and G. A. Hart,[2] *Naval Research Laboratory.*

Argon-nitrogen mixtures were excited with a pulsed 500 keV electron beam (e-beam). The N_2 $C(^3\pi_u)$ state was found to be populated efficiently. This state emits from $v = 0$ to $v = 0, 1, 2$ of the $N_2B(^3\pi_g)$ state at 3371, 3577, and 3805 Å, respectively. Laser emission at 3577 Å and side fluorescence at 3371, 3577, and 3805 Å were observed over a wide range of total pressures and mixture compositions. A kinetic model was developed to explain both the absolute magnitude and temporal dependence of the $N_2(C)$ population. In the model only the argon is directly pumped by the e-beam. This is justified by the high fraction of argon in the mixture. The key steps in the model include neutral excitation and ionization of the argon. Charge recombination produces an excited state of argon Ar* with unit yield. The Ar* transfers energy to N_2 to create $N_2(C)$. A comparison of absolute experimental fluorescence intensities from $N_2(C)$ with the model showed close agreement. The total pressure range was 200–5000 torr at $Ar:N_2$ ratios of 100, 20, and 10.

The energy transfer process also created a partial population inversion on the 3577 Å transition. Intense superfluorescence was detected from 400–5000 torr in a $Ar:N_2$ mixture of 20:1. A totally reflecting dielectrically coated mirror and a quartz window formed the laser cavity. Over a limited range of pressures laser action would occur with only two quartz windows serving as the laser cavity. Laser efficiency based on the calculated energy input measured by calorimetry was 0.4% while efficiency based on chemical dosimetry was somewhat lower.

[1] Work sponsored in part by DARPA.
[2] NRC-NRL Postdoctoral Research Associate 1973–present.

MA2. Laser Oscillation on the Green Bands of Xenon Oxide,[1] H. T. Powell, J. R. Murray, and C. K. Rhodes, *Lawrence Livermore Laboratory.*

Lasing has been achieved on the green bands of the XeO excimer using direct electron beam excitation of high pressure Xe with small additions of either O_2, CO_2, or N_2O. These bands are transitions between $^1\Sigma^+$ molecular levels correlating with the $^1S_0$ and $^1D_2$ metastable levels of atomic oxygen plus ground state Xe. The lasing wavelengths, near 5400 Å, are not far removed from the atomic oxygen, $^1S_0 - {}^1D_2$ line at 5577 Å since the bindings of the upper and lower levels are only about 0.06 and 0.33 eV respectively.[2] The XeO laser is representative of possible lasers based on the properties of the $O(^1S_1)$ metastable.[3,4]

A high pressure cell was irradiated by a 2×10 cm^2, 1 MeV electron beam lasting 50 ns. A Monte-Carlo electron trajectory calculation[5] predicts an energy deposition of approximately 1 J/cm^3 in the 50 cm^3 active volume. The optical cavity was formed by mirrors nominally 99.9% and 99% reflectivity which were separated by 15 cm. The operating pressures are from 10–15 atm of Xe and 5–15 Torr of added gas. Under these conditions the XeO fluorescence is characterized by a linear growth during the e-beam pulse, a sharp rise doubling its value at the end of the current, and then a decay with a half-life of 100 ns. The laser exhibits a smooth rise and fall with a maximum about 100 ns after the end of the e-beam and a FWHM of 75 ns. Using O_2, an output power of 75 kW and an output energy of 5 mJ have been measured with a calibrated photodiode.

Spectrograms with 0.2 Å resolution have been taken of both the XeO laser and fluorescence. For our pressures the $^1\Sigma^+ - {}^1\Sigma^+$ fluorescence extends over about 300 Å with a series of peaks associated with the various band heads, the 0–5 at 5377 Å and the 0–6 at 5433 Å being the most intense. The rotational lines are broadened and overlap producing only a small modulation in the spectral profile. The laser spectrum shows considerable narrowing. The strongest lasing occurs at the peaks of the fluorescence produced by the 0–5 and 0–6 band heads. The modulation of the gain caused by the rotational structure is greatly amplified in the laser spectrum.

The time dependence of the laser suggests that the output is limited by a low gain coupled with a short inversion lifetime rather than saturation effects. A sidelight monitor shows only a slight decrease in fluorescence caused by lasing which supports this conclusion. Further both the temporal and spectral data suggest that the gain is simply proportional to the fluorescence intensity indicating that the lower state population is negligible.

The authors are indebted for the contributions of numerous members of the Gas Laser Research and Gas Laser Technology groups and in particular to L. P. Bradley, T. Kan, and L. G. Schlitt.

MA3. Quasi-cw Laser Emission from the Second Positive Band of Nitrogen,[1] S. N. Suchard and D. G. Sutton, *The Aerospace Corp., El Segundo, Calif.*

Since the discovery of superradiant laser emission on the Second Positive band of nitrogen in 1964, there has been a considerable amount of research performed on this molecule in an attempt to increase the maximum output energy obtainable and the overall electrical efficiency. To this end several very difficult forms of initiation have been applied. The main difficulty that has arisen, however, has been caused by the ratio of the radiative lifetimes of the upper laser level ($C^3\pi_u$, $\tau_r = 40$ nsec) to the lower laser level ($B^3\pi_g$, $\tau_r = 5$–8 μs). Population inversion between $C^3\pi_u$ and $B^3\pi_g$ states can only take place during a time on the order of, but shorter than, the radiative lifetime of the $C^3\pi_u$ state.

This talk will report on the first observation of a Second Positive N_2 laser with a pulse length much longer than the radiative lifetime of the $C^3\pi_u$ state. Preliminary measurements of the temporal behavior of this laser indicate that it is operating in a "quasi-cw" manner and, in addition, the laser output is extremely sensitive to the alignment of the optical cavity placed around the discharge tube.

The primary difference between the N_2 laser which we are reporting upon and a "conventional" N_2 laser is the addition of SF_6 to the N_2 in the discharge region. Preliminary studies indicate that the SF_6 is extremely efficient at quenching the $B^3\pi_g$ state, thereby reducing the population of this state and "unblocking" the laser transition. Under our initiation conditions, the dis-

[1] This work was performed under the auspices of the Atomic Energy Commission.

[2] C. D. Cooper, G. C. Cobb, and E. L. Tolnes, *J. Mol. Spectrosc.*, vol. 7, p. 223, 1961.
[3] J. R. Murray and C. K. Rhodes, Lawrence Livermore Lab., Rep. UCRL-51455, 1973.
[4] J. R. Murray, H. T. Powell, and C. K. Rhodes, Paper P-8 VIII Int. Quantum Elect. Conf., 1974.
[5] L. G. Schlitt, private communication.

[1] This work reflects research supported by the Advanced Research Projects Agency of the Department of Defense under U.S. Air Force Space and Missile Systems Organization (SAMSO) Contract F04701-73-0074.

charge risetime is 130 ns; considerably longer than the radiative lifetime of the $C^3\pi_u$ state. Without addition of SF_6 to the N_2, no laser action is observed at a pressure of 50 torr. Upon adding SF_6 to a total pressure of 70 torr, non-superfluorescent N_2 laser emission is observed. Optimal laser output for 50 torr N_2 occurs at 50 torr of added SF_6.

We believe that the appearance of the N_2 laser action is a consequence of the "unblocking" of the lower laser level. Temporal measurements of the laser pulse indicate a risetime of 75 ns and a duration (FWHM) of 80 ns; these times are found to be independent of the SF_6/N_2 ratio, total pressure, and discharge voltage. The long duration of the pulse, in addition to the fact that the laser operates within optical cavity 3-m long (roundtrip transit time = 20 ns), strongly indicates a rapid deactivation of the $B^3\pi_g$ state.

Measurement of the laser pulse duration was also made using a discharge of twice the risetime (260 ns) and duration. These results showed that the laser pulse duration has also been extended by almost a factor of two. Since an increase in the discharge risetime would decrease the rate of pumping of the upper laser level, an experimental fact not observed, it appears as if the SF_6 is truly "unblocking" the N_2 laser bottleneck and allowing the laser to operate quasi-cw.

MA4. N_2 Infrared Laser Operation in an Electron Beam Controlled Discharge, L. Newman, T. A. DeTemple, and P. D. Coleman, *Electro-Physics Laboratory, University of Illinois, Urbana, Ill. 61801.*

Recently much interest has centered on the use of intense electron beams as the excitation source for gas lasers operating on electronic transitions. One possible alternate to this method would be to use an ionizer-sustainer discharge which has the advantage of depositing more energy into the gas than can be obtained conveniently from an electron beam. As a preliminary to applying this method to eximer, atomic, and transfer-type lasers, we have undertaken a study of the near-infrared first positive system N_2 laser (FPSL) operating in an ionizer-sustainer device.

Previous studies on the FPSL were concerned mainly with the temporal behavior of the pulse and the output power.[1,2] In this work we present a detailed parametric study of the FPSL operating in an ionizer-sustainer as well as results of a kinetic model for the laser system.

The significant findings to date are laser action up to 200 torr of pure N_2 (limited by the sustainer voltage available), pulse power in the tens of kW with pulsewidths ~ 150 ns and conversion efficiencies ~ .01%. In addition, the results of the kinetic model indicate that the metastable $A^3\Sigma_u^+$ population is comparable with that obtained with a direct electron beam excited system.[3] This in turn implies that the ionizer-sustainer mode of operation may be useful in studying transfer type lasers such as the N_2-NO system or the Ar-N_2 system for UV and IR transitions.[4,5]

[1] O. R. Wood *et al.*, *Appl. Phys. Lett.*, vol. 18, p. 261, 1971.
[2] T. J. Gleason *et al.*, *Appl. Phys. Lett.*, vol. 21, p. 267, 1972.
[3] D. J. Eckstrom, Stanford Research Inst., Rep. SRI MP73-1, 1973, unpublished.
[4] L. Y. Nelson *et al.*, *Appl. Phys. Lett.*, vol. 22, p. 79, 1973.
[5] S. K. Searles and G. A. Hart, *Appl. Phys. Lett.*, vol. 25, p. 79, 1974.

MA5. A New Pumping Technique and New V-V Transfer Molecule for the CS_2 Laser, L. Y. Nelson, C. H. Fisher, and S. R. Byron, *Mathematical Sciences Northwest, Inc., Seattle, Wash.*

The intractability of CS_2 in self-sustained discharges has discouraged additional experiments with this molecule beyond Patel's original report of a CS_2 laser in 1965.[1] His laser operated at low pressures (2 torr) in a flowing system in which the CS_2 was mixed with excited N_2 after it left the electrical discharge region. We have found that the laser emission Patel observed at 11.5 μm can also be produced by exciting directly mixtures of $He/N_2/CS_2$ or $He/CO/CS_2$ in a low $E/N(2 \times 10^{-16}$ V-cm^2), electron beam stabilized discharge. The discharge currents were limited to 1 A/cm^2 by the attachment rate of CS_2 (6×10^{-11} cm^3 sec^{-1}). It was found that gas mixtures containing CO provided far better laser output than those using N_2, which permitted laser operation at pressures up to one atmosphere for $He/CO/CS_2$ (75/24/1) mixtures. Helium, H_2, or D_2 was needed in the laser mixture for preferential de-excitation of the lower CS_2 laser level.

Laser assignments based on laser emission at 12.2 μm for 91 percent ^{13}C enriched samples, indicate that both the $001 \rightarrow 100$ and $01^11 \rightarrow 11^10$ transitions of $^{13}CS_2$ contribute to the lines observed. Line coincidences, which are very likely for these transitions in both $^{13}CS_2$ and $^{12}CS_2$ may be the cause of the anomalous laser intensity distribution among the rotational states observed at low pressures. For $^{12}CS_2$, the $02^01 \rightarrow 12^00$ and $101 \rightarrow 200$ transitions may also have line coincidences with $001 \rightarrow 100$. Our results with $He/CO/^{12}CS_2$ are not compatible with a laser assignment of $02^01 \rightarrow 12^00$ because the CO fundametnal (2143 cm^{-1}) is too far below the 02^01 level for effective V-V transfer.

The maximum laser output energy obtained with approximately 4 percent output coupling was 24 mj at 150 torr total pressure in a $He/CO/CS_2$ mixture. This corresponds to an energy of 0.4 j/l-atm and an electrical efficiency of 0.5 percent.

[1] C. K. N. Patel, *Appl. Phys. Lett.*, vol. 7, p. 273, 1965.

MA6. A Fifteen Atmosphere Electron-Beam-Controlled CO_2 Laser, N. W. Harris, F. O'Neill, and W. T. Whitney, *Naval Research Laboratory, Washington, D. C. 20375.*

High pressure molecular gas lasers are of interest because the broad bandwidth provided by the mutual overlapping of pressure broadened rotational lines will permit continuous frequency tuning of these devices. These high-power high-efficiency lasers will be useful as tunable infrared sources for isotope separation and laser induced chemistry applications. Highest gain has been achieved with atmospheric pressure CO_2 lasers using electron-beam-controlled discharges and we have recently reported[1] on the successful operation of a 15 atm. electron-beam-controlled CO_2 laser (active volume 22 cc).

In this paper we will describe the results of a more complete investigation of the gain characteristics of the high-pressure laser. Measurements were taken using a stabilized low pressure cw CO_2 laser. Gain results will be presented for a range of laser gas mixtures and for different settings of the probe laser wavelength. The dependence of the electric discharge properties and the gain pulse profile, on the gas composition will also be discussed. A multimode laser output of 1.2 J has been obtained from the above device for an overall efficiency of 2.5%. The peak laser power was ~50 MW.

The laser described[1] was powered by a high-current variable-parameter cold-cathode electron gun[2] designed primarily for use with large volume atmospheric pressure CO_2 amplifiers. We have recently constructed a more compact electron gun which has been successfully used to operate a bench top high-pressure laser. The operation of this device will be described and we will

[1] N. W. Harris, F. O'Neill, and W. T. Whitney, *Appl. Phys. Lett.*, vol. 25, p. 148, 1974.
[2] Manufactured by Maxwell Laboratories, Inc.

discuss recent experiments on the use of thin etalons to obtain frequency tuning of this laser.

MA7. Vibrational Excitation of HCl by Electron Impact, R. E. Center and H.-L. Chen, *AVCO Everett Research Lab., Inc.*

The direct electrical excitation of the vibrational mode of the hydrogen halides is of interest in the possible development of efficient electrically excited lasers in the 2.5 to 4.5 μ region. Stimulated emission from HF and DF has been recently observed[1] in experiments with direct electrical discharge excitation. However, there is a lack of information on the fundamental vibrational excitation cross sections for electron impact on the hydrogen halides. This paper presents a measurement of the vibrational excitation rate constant of HCl excited by electron impact. The experiments were performed in a uniform electron beam sustained discharge over the range of electron temperature from 0.3 eV to 1.7 eV. Mixtures of HCl, CO, and N_2 dilute in Ar were used in the discharge and the IR emission from the fundamental bands of HCl and CO were monitored. Typical mole fractions of HCl, CO, and N_2 were 0.003, 0.003, and 0.1, respectively, the N_2 being used to specify the electron distribution function. Under these conditions the vibrational excitation rate constant in the trace CO could be readily calculated based on previously measured cross-section data.[2] The vibrational excitation rate constant was then derived from the ratio of the simultaneous IR emission from both the CO and HCl taking into account the relevant V-V and V-T kinetics. A value of $(1.2 \pm .4) \times 10^{-8}$ cm^3/s was obtained for the vibrational rate constant in HCl at a mean electron temperature of 1 eV. It was also determined with the aid of a HCl absorption filter, that the dominant cross section was for the excitation of $v = 1$ with only 20% of the emission coming from levels $v \geqslant 2$.

[1] S. R. Byron, L. Y. Nelson, and G. J. Mullaney, *Appl. Phys. Lett.*, vol. 23, p. 565, 1973.
[2] M. J. W. Boness and G. S. Schulz, *Phys. Rev. A*, vol. 8, p. 2883, 1973.

MA8. Negative Ion Production and Influences in CO_2 Discharge Lasers, J. F. Prince, W. H. Long, Jr., and A. Garscadden, *Aerospace Research Laboratories, Wright-Patterson AFB, Ohio.*

Experiments on the effects of contaminants in CO_2 laser discharges and theoretical analyses of the properties of CO_2 molecular discharge lasers show that both the steady-state discharge properties and the stability of the plasma are very sensitive to the presence of negative ions. Scaling of these effects and the comparison of theoretical predictions with experiments depends upon the unambiguous identification of the ionic and neutral species that are generated under typical CO_2 laser discharge conditions. This identification has been accomplished using an on-line mass spectrometer to examine the negative ion, positive ion and neutral gas species in sealed-off and in slowly flowing CO_2-N_2-He cylindrical discharges (22mm i.d.). Measurements have been obtained of the equilibrium concentrations for given conditions and of the rate of change of the concentrations after turn-on of the discharge to a constant-current condition. For sealed-off operation at 10 mAcm^{-2}, the dominant negative ions are NO_2^-, O^-, NO_3^-, O_2^-, and CO_3^-. At very low current densities ($\sim$0.5 mAcm^{-2}) CO_3^- is the dominant negative ion, however, although the formation rate is very rapid it appears to saturate early with increasing current while the other negative ions increase in concentration. The dominant positive ions are typically NO^+, CO^+, O_2^+, and CO_2^+ with smaller amount of other species. The relative concentrations are strong functions of the discharge current, plasma homogeneity and the initial gas mixtures. The measurements have been obtained over the range 0.50 to 2 Torr for discharge currents 0.1 to 80 mA. The consequences of the negative ion formation on the impedance of the discharge, the power loading and gas heating are evaluated using a theoretical model of the positive column. The application of these results in predicting the onset of the attachment-detachment plasma instability will also be demonstrated.

SESSION MB

New IR Laser Reactions
Monday, October 21, 8:30 A.M.

MB1. Cyanide Radical Photodissociation and Predissociation Chemical Lasers: Molecular Electronic and Vibrational Laser Emissions, G. A. West and M. J. Berry, *Department of Chemistry, University of Wisconsin, Madison, Wis. 53706.*

Molecular electronic [$CN^*(A^2\Pi_3, v' = 0) \rightarrow CN(X^2\Sigma^+, v'' = 0, 1, 2)$] and vibrational [$CN\dagger(X^2\Sigma^+, v')^2 \rightarrow CN(X^2\Sigma^+, v' - 1)$, $v' = 5, 4, 3, 2$] cyanide radical laser emissions have been observed following photolysis of several cyanide parents [HCN, ClCN, BrCN, ICN, $(CN)_2$, CH_3NC, CF_3CN, C_2F_5CN] at $\lambda > 1550$ Å. In the electronic lasers, only Q_1 and P_1 branch transitions oscillate, indicating that rapid spin-orbit and rotational relaxations produce thermalized distributions within the $^2\Pi_1$, $v = 0$ and $^2\Pi_3$, $v = 0$ vibronic manifolds. From the highest gain transitions within the (0, 0), (0, 1), and (0, 2) CN* red bands, we find that electronic population inversions are total:

$$N_{A^2\Pi_i,v}/N_{X^2\Sigma^+,v''} \geqslant 1.6.$$

In the vibrational lasers, the highest gain transitions indicate that total vibronic population inversions are present:

$$(\text{e.g., } N_{v'=4}/N_{v''=3} \geqslant 1.2).$$

The electronic lasers can be quenched by high parent gas pressures or by addition of xenon and krypton.

We have used the observed laser transitions and their relative gain coefficients and quenching behaviors, together with spectroscopy and fluorescence experiments, to formulate a state-to-state photochemical reaction mechanism, *viz.*

$$RCN \xrightarrow{\hbar\omega} R + CN^*(A^2\Pi_i, v' = 0 \text{ primarily})$$
$$CN^*(A^2\Pi_i, v' = 0) + M \rightarrow CN(X^2\Sigma^+, v'' = 4 \text{ primarily}) + M.$$

In this mechanism, nascent photochemical products are formed with high electronic population inversion and *no* vibronic population inversion within the $A^2\Pi_i$ manifolds. Near-resonant collision-induced intersystem crossing preferentially populates $v = 4$ within the $X^2\Sigma^+$ electronic manifold.

We have treated electronic population inversions *via* state-to-state adiabatic correlation diagrams. In addition, we have calculated reaction product vibronic state distributions in photodissociative excitation of $CN^*(A^2\Pi_i, v')$, $CN^*(B^2\Sigma^+, v')$ and photosensitized excitation of $CN^*(B^2\Sigma^+, v')$ *via* a simple dynamical model. We find that photodissociation reactions are often very favorable candidates for molecular electronic chemical laser systems.

MB2. The Chloroethylene Photochemical Lasers: Vibrational Energy Content of the HCl Molecular Elimination Products, M. J. Berry, *Department of Chemistry, University of Wisconsin, Madison, Wis. 53706.*

Hydrogen chloride molecular vibrational laser emissions [$HCl\dagger$ $(X^1\Sigma^+, v') \rightarrow$

HCl ($X^1\Sigma^+$, $v'-1$), $v'=4, 3, 2, 1$] have been identified following flash photolysis of chloroethylenes ($CH_2=CHCl$, $CH_2=CDCl$, $CH_2=CCl_2$, *cis*-CHCl=CHCl, *trans*-CHCl=CHCl, $CHCl=CCl_2$) at $\lambda \geqslant 1550$ Å. Hydrogen chloride is produced as a vibrationally excited molecular photoelimination product:

$$\text{(e.g.,) } CH_2=CHCl \xrightarrow{\hbar\omega} HCl\dagger(v') + HC\equiv CH.$$

The grating selection technique [M. J. Berry, *J. Chem. Phys.*, vol. 59, p. 6229, 1973] has been used to measure relative gain coefficients of HCl vibration-rotation transitions, thereby permitting calculations of $HCl\dagger(v' \leqslant 4)$ product virbonic state distributions. The observed highly nonstatistical product vibronic state distributions are successfully matched by a bootstrap reaction dynamics model (M. J. Berry, *Chem. Phys. Lett.*, in press) which considers sudden structural distortion and intramolecular relaxation of HCl as it separates from acetylene or haloacetylene products in the primary photochemical act.

Chemical laser techniques have also been used to measure relative quantum yields of photochemical product types (e.g., the yield of chlorine atomic photodetachment relative to hydrogen chloride molecular photoelimination). In addition, spectroscopy experiments have been performed to determine the photochemical reactant states responsible for HCl elimination.

All available spectroscopic, photochemical, and product energy data are used to formulate a state-to-state photochemical reaction mechanism for HCl photoelimination from the chloroethylenes. Certain features of this mechanism operate in other elimination chemical lasers, such as those produced by the fragmentation of chemically activated fluoroethanes (e.g., $CH_3CH_2F\dagger \rightarrow HF\dagger + CH_2=CH_2$; *cf.* E. R. Sirkin and M. J. Berry, Paper G-2, VIII International Quantum Electronics Conference, San Francisco, Calif., June 11, 1974).

MB3. Temperature Dependence of the Vibrational Energy Distribution of HF Formed in the Reactions of NH with the Fluoromethanes, P. R. Poole and G. C. Pimentel, *Chemistry Department, University of California, Berkeley, Calif. 94720.*

Tandem chemical laser techniques[1] have been applied to study vibrational distributions of HF produced in the reactions of HN_3 photolysis products with the fluoromethanes, CH_3F, CH_2F_2, CHF_3, and CF_4. The reactions occurring are believed to be insertion of $NH(a^1\Delta)$ into the C-H and C-F bonds, with subsequent elimination of HF from the excited intermediate species. As well, there may be some fluorine atom abstraction by hot H atoms which may also be formed in the HN_3 photolysis.

$$NH + CHF_3 \longrightarrow CF_3NH_2^\dagger \longrightarrow CF_2=NH + HF$$

$$NH + CHF_3 \longrightarrow CF_2HNHF\dagger \longrightarrow CF_2=NH + HF.$$

Only the $v=1$ and $v=0$ HF vibrational levels are significantly populated in these systems. The N_1/N_0 vibrational population ratios for CF_4 and CF_3H are dissimilar but both decrease as temperature is raised. The opposite dependence is found for CF_2H_2 and CFH_3. The results have been interpreted in terms of characteristic temperature-dependent ratios for the isolated C-F and C-H insertion reactions, and in terms of the results obtained earlier for the $F+H_2$ and $F+D_2$ reactions.[2]

[1] M. J. Molina and G. C. Pimentel, *IEEE J. Quantum Electron.*, vol. QE-9, p. 65, 1973.

[2] R. D. Coombe and G. C. Pimentel, *J. Chem. Phys.*, vol. 59, p. 251 and p. 1535, 1973.

MB4. Rotational Chemical Lasers from HX Elimination Reactions, E. Cuellar and G. C. Pimentel, *Department of Chemistry, University of California, Berkeley, Calif. 94720.*

We have recently reported rotational laser emission from hydrogen fluoride elimination reactions, both from chemically activated $CH_3CF_3^\dagger$ and from photoexcited $CH_2CF_2^*$. The spectral range studied, 850 to 470 cm^{-1}, has been extended to 300 cm^{-1} and our search for laser emission at these longer wavelengths will be described. In addition, modifications to the system have been made to give a shorter flash pulse (1.2 μs rise time). We have also observed HF or HCl rotational laser emission in the photolysis of vinyl fluoride, vinyl chloride, and 1,1-dichloroethylene. In $CH_2=CHF$, HF laser transitions have been identified as $v=0$, $J=14\rightarrow13$, $v=0$, $J=13\rightarrow12$, and $v=1$, $J=14\rightarrow13$. In the case of the chloroethylenes, we have identified the following HCl transitions: $v=0$, $J=29\rightarrow28$ and $v=0$, $J=28\rightarrow27$ for CH_2CHCl, and $v=3$, $J=28\rightarrow27$ for $CH_2=CCl_2$. We believe that the most likely mechanism of excitation is that the HX molecules are probably born rotationally excited, with the implication that a substantial fraction of the available energy is being lodged in rotation. In addition, we feel that the rotational laser emission may be sustained after photolytic pumping has ended by near resonant $V\rightarrow R$ energy transfer processes. Preliminary results will also be presented on the rotational laser emission from HF produced in some F atom abstraction reactions.

MB5. HF Laser Emission and CO Population Distribution Studies of the $O(^3P)+CHF$ Reaction, R. G. Shortridge[1] and M. C. Lin.

HF stimulated emission was observed when mixtures of $CHFCl_2$ and SO_2 were subjected to flash photolysis above 165 nm. Vibrational analysis of the emission revealed that Δv ($2\rightarrow1$) and ($1\rightarrow0$) transitions were lasing. The effects of various additives (He, Ar, SF_6, D_2, N_2O, and CO_2), flash energy, temperature, and total pressure have been examined. Gas analysis of the flashed samples indicated the presence of CO, HCl, CO_2, and other minor sulfur-containing products. The observed HF laser emission is believed to result from the reaction

$$O(^3P) + CHF \longrightarrow HFCO\dagger \longrightarrow HF\dagger + CO$$

$$\Delta H^\circ \cong -181 \text{ kcal/mole.}$$

On account of the absence of CO emission and the small fraction of energy carried by HF (<10% on the basis of HF laser emission observed), the CO population distribution was measured by means of a cw CO laser. These experiments showed that CO was formed vibrationally excited up to $v=11$ without inversion.

HF laser emission was also observed in the flash-photolyzed mixtures of $CH_2FCl+SO_2$ and CHF_2Cl+SO_2. The pumping mechanisms of these two systems will also be discussed.

[1] NRC/NRL postdoctoral research associate (Aug. 1973–present).

MB6. Parametric Investigation of the Na-N_2O + CO Chemical Laser,[1] R. C. Benson, C. B. Bargeron, and R. E. Walker, *Johns Hopkins Applied Physics Lab.*

The effect of several parameters on the gain of the Na-N_2O + CO chemical laser system has been studied. The chemical reaction mechanism in its simplest form consists of the following reaction chain:

$$Na + N_2O \longrightarrow N_2 + NaO + 21.0 \text{ kcal/mole}$$

$$NaO + CO \longrightarrow CO_2 + Na + 66.2 \text{ kcal/mole.}$$

[1] Supported by the Department of the Navy.

The reaction proceeds rapidly at room temperature and is accompanied by intense sodium *D*-line chemiluminescence. At low combustion efficiencies (10–20%) and an excess of N_2O, the system lases at 10.8μ with N_2O as the optically active specie.[2] Helium is used as the diluent and as the carrier of the sodium vapor which is derived from thermally decomposing the easily handled NaN_3 powder. In a coaxial flow configuration, lasing has been achieved using potassium, rubidium, and cesium catalysts in addition to sodium; the laser performance with all catalysts is nominally the same. A transverse flow system has been constructed in order to probe the flame perpendicular to the flow axis. Gain measurements have been made along the reaction length as a function of the CO/N_2O ratio, combustion efficiency, pressure, and catalyst concentration. Experiments to date indicate that 15–30% of the chemical energy is available for laser pumping. In addition, several aspects of the chemical processes have been investigated. It has been determined that molecular oxygen is produced in a chain-breaking mechanism. Various species have been added to the flame in order to study their effect on the overall reaction. As expected, N_2 and Ar have no effect on the reaction process, but CO_2, O_2, and NO when added to the flame in concentrations of a few mole percent, are quite detrimental to the combustion efficiency. Preliminary studies on the kinetic processes occurring in the $Na-N_2O + CO$ chemical laser indicate that at least six chemical reactions need to be considered.

[2] D. J. Benard, R. C. Benson, and R. E. Walker, *Appl. Phys. Lett.*, vol. 23, p. 82, 1973.

MB7. Spectroscopic Studies of HCl‡ Producing Reactions,[1] –I. Cl + HI → HCl‡ + I, R. A. Carabetta and M. J. Linevsky, *Space Sciences Laboratory, General Electric Company, King of Prussia, Pa. 19406.*

An optional diagnostic technique has been developed for the study of vibrationally excited HCl produced by chemical reaction. Among the most efficient pumping reactions examined using this method was the exchange:

$$Cl + HI \longrightarrow HCl‡ + I \quad \Delta H = 32 \text{ kcal/mole.} \qquad (1)$$

Reaction (1) was studied using a subsonic flow reactor of rectangular cross section (1.5 cm × 15 cm) in which chlorine atoms, produced by microwave discharge in chlorine–helium mixtures, could be rapidly mixed ($t_{mix} \leqslant 15$ μs) with HI introduced into the laser section of the tube via an injector array. Associated optics were arranged to permit lasing and spectroscopic measurements to be made transverse to the gas flow. At a pressure of 3.6 torr, it was possible to couple 5 W of power from a Cl_2/HI/He mixture having the molar ratio 1/2.3/140. In these experiments, the Cl_2 flow rate was 0.51 millimoles/second and the average linear flow velocity was 166 m/s. Based on the spectroscopic measurements of the total HCl produced by reaction, the chemical efficiency of the system under conditions of maximum power was found to be 7.5%.

Measurements of the laser lines showed that the output consisted of a number of *P*-branch transitions from the $v = 3$, 2, and 1 levels of HCl^{35}; except for the appearance of several relatively weak lasing transitions from the HCl^{37} isotope, the spectra obtained were similar to those previously reported for (1) by Rosen, Sileo, and Cool[2] and others.

Spatially (time) resolved measurements of the spontaneous HCl‡ emission were carried out at ten positions along the flow reactor using a light gatherer/interferometer combination. The spectra obtained consisted of individual vibrational-rotational lines from HCl^{35} and HCl^{37}, and transitions were observed from $v = 5$ (a result of V-V pumping from lower v levels) through $v = 1$, from rotational levels $J = 0$ through 10. Typically, the spatial resolution of the optical system was 0.5 cm, which under the conditions of the experiment, represents a time resolution of about 30 μs.

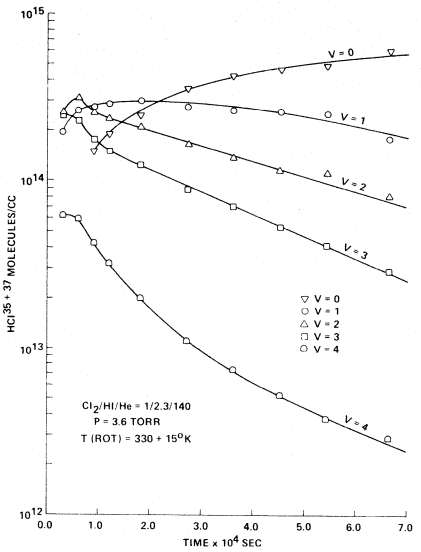

Fig. 1. Absolute HCl^{35+37} population profiles.

From the above data, the rotational temperature and relative HCl vibrational population distributions (for v's > 0) were obtained as a function of flow time. These relative concentrations were placed on an absolute bases from a knowledge of the threshold conditions for a given transition, the cavity loss, and the vibrational population ratios measured at threshold. Populations in $v = 0$ were obtained from an HCl mass balance and checked by a self-absorption technique involving the measurement of relative intensities of HCl^{35} and HCl^{37} for several *R*-branch transitions to the $v = 0$ level.

The resulting HCl profiles are shown in Fig. 1. The data shown were employed to compute the small-signal-gain for a number of transitions, the power output of the laser at several stations along the flow and to obtain estimates for V-T quenching of HCl‡. The calculated gain values were in good qualitative agreement with estimates of gain derived from the HCl^{35}/HCl^{37} isotopic intensity ratios observed in spontaneous emission for several *P*-branch transitions. The power calculations were in excellent agreement with measured power profiles.

MB8. Metal Atom Oxidation Lasers—A New Family of Chemical Lasers,[1] W. W. Rice, *Los Alamos Scientific Laboratory.*

At the time of the "3rd Conference on Chemical and Molecular Lasers" there were about six different chemical

[1] This work was supported by the Defense Advanced Research Projects Agency and monitored by the U.S. Army Missile Command.

[2] D. I. Rosen, R. N. Sileo, and T. A. Cool, "WB4—A spectroscopic study of CW chemical lasers," *IEEE J. Quantum Electron.*, vol. QE-9, pp. 163–172, Jan. 1973.

[1] Work performed under the auspices of the U. S. Atomic Energy Commission.

laser molecules (isotopic variations not considered). We wish to report a group of almost thirty additional chemical laser molecules from exothermic exchange reactions of the type suggested by J. C. Polanyi at the first "Conference on Chemical and Molecular Lasers": $M + XY \rightarrow MX^* + Y$ where M is a metal atom, XY is a gaseous oxidizer, and MX^* is an excited diatomic molecule.

These new laser molecules and their bond strength are as follows:

MX	D° (kJ/mol)	MX	D° (kJ/mol)	MX	D° (kJ/mol)
LiF	582	NiF	435	TaF	607
CO	1075	CuF	368	WO	674
CF	540	ZnF	364	WF	544
MgF	448	ZrN	561	PtF	–
AlF	669	ZrO	812	AuF	305
TiO	707	ZrF	615	PbF	314
TiF	619	MoO	519	UO	749
VO	615	MoF	502	UF	653
VF	536	AgF	347	UCl	615
FeF	448	TaO	824		

In the majority of these experiments exploding wire techniques were used to generate the metal atoms. However, one series of laser shots employed explosively shocked, grooved metal plates as metal vapor generators. In each experiment infrared emission lasting tens of microseconds was observed following the generation of metal atoms and the mixing of the metal vapor with oxidizers (O_2, Cl_2, F_2, and NF_3). With proper optical feedback strong infrared pulses, two to three orders of magnitude greater than the fluorescence level and $\leqslant 3$ μs duration, were observed.

These laser pulses appeared in the infrared spectral regions of the MX diatomic molecules. However, several systems lased at much shorter wavelengths than would be expected from the fundamental vibrational–rotational transitions within the MX electronic ground state. Thus population inversion among low lying electronic states is suggested.

MB9. Can We Beat F_2 & H_2 for HF Lasers?[1] G. L. Schott, S. W. Rabideau, A. V. Nowak, and R. W. Getzinger, *Los Alamos Scientific Laboratory.*

We explore potential new chain reaction mechanisms for pumping HF vibrational lasers by the basic process $F + HR \rightarrow HF^* + R$ (1). Our first starting point is the chain sequence, Reactions (1) and $R + F_2 \rightarrow RF + F$ (2). To avoid marginal-at-best stability of mixtures of hydrogenous fuels with elemental F_2, we tested possible reactions of difluorodiazine, N_2F_2, isomers with H atoms, $H + N_2F_2 \rightarrow HF^* + N_2 + F$(3), and other free radicals, e.g., $CF_3 + N_2F_2 \rightarrow CF_4 + N_2 + F$ (4), which regenerate an F atom exoergically. Reaction (3) was tested in a conventional fast flow mixing reactor with a TOF mass spectrometer, using H atoms from a microwave discharge. From the HF produced in 43 ms, we estimate k_3 as $10^{9.3}$ $cm^3 mol^{-1}$ s^{-1}, which is about 10^{-3} of the value of k_2 (R = H) at 300 K. Thus Reaction (3) appears too slow for a laser-pumping chain reaction. Occurrence of Reaction (4) or its CH_3 radical analog during near UV photolysis of CF_3I or CH_3I mixed with N_2F_2, was tested, using postreaction IR absorption for analysis. Since the N_2F_2 survived the photolytic decomposition of these iodides with little or no consumption, chains propagated by steps such as (4) appear far too slow to provide secondary F atoms for HF laser pumping.

In a second line of study, rapid branched chain reactions between fuels and undissociated F_2, producing F atoms, were sought. Here the starting point was the known, nonchain reaction pair $NO + F_2 \rightarrow FNO + F$ (5), $F + NO + M \rightarrow FNO + M$ (6). The guiding hypothesis is that strongly bound, polyatomic fluorides are formed by successive attack of incompletely fluorinated fragments upon F_2, as in Reaction (5), thus liberating several F atoms. These studies used a 24 mm i.d. conventional, low pressure, fast mixing flow apparatus of Al and sapphire, with reagents at 10–50 Pa partial pressure in an Ar carrier, and linear flows up to 10 m/s. The simplest reagents examined, besides NO, were PF_3, SF_4, and SO_2, which can each accommodate two F atoms in steps like (5) and (6). PF_3 reacted faster with F_2 than did NO, while SF_4 and SO_2 didn't react detectably in up to 0.1 s at 10 Pa partial pressures. Hydrogenous fuels were also tested. In approximate order of increasing speed, these were H_2, HBr, C_2H_6, H_2S, C_2H_4, HI, AsH_3, and PH_3. The reaction of H_2 with F_2 in the flow system behaved as a flame propagated by material and thermal transport, and not as a spontaneous reaction between original, room temperature reactants. The fastest of these reactions, with PH_3 and AsH_3, produced strong 2.5 μm and overtone HF emissions, plus near UV chemiluminescent bands from the respective $B^3\Pi - X^3\Sigma$ systems of PF and AsF, including many previously unreported PF bands with $v' - v'' \leqslant 7$. Our attempt at TOF mass monitoring of the $PH_3 + F_2$ system was stymied by accumulation of orange P-F polymer, but preliminary results showed PF_2 to be a major prompt gaseous product, and no higher fluorides.

[1] Work performed under the auspices of the U.S. Atomic Energy Commission.

SESSION MC

Chemically-Pumped Electronic Transition Lasers
Monday, October 21, 2:00 P.M.

MC1. Parametric Evaluation of Potential Electronic Transition Chemical Lasers,[1] D. G. Sutton and S. N. Suchard, *The Aerospace Corp., El Segundo, Calif.*

There has been intense interest over the past years in the demonstration of a chemically pumped electronic transition laser. A laser of this type would be similar to the well studied HF, HCl, HBr, and CO vibrational chemical lasers; however, the laser photons that would be extracted from the product molecules of the chemical reaction would be produced from electronic, not vibrational, transitions. Hence laser outputs would be expected in the visible and ultraviolet regions of the spectrum rather than the infrared.

The major difficulty faced by anyone contemplating the construction of such a laser is the lack of data crucial to the selection of an appropriate molecule and chemical reaction. Very few reactions have had their energy partitioning among available electronic states of the products characterized and little is known about the associated vibrational–rotational distributions. In addition, much more kinetic data, such as reaction rates, quenching and deactivation cross sections and radiative lifetimes is needed before accurate kinetic modeling can be used to help in the selection of suitable laser species.

There is available, however, a larger reservoir of spectroscopic data for dia-

[1] This work reflects research supported by the Advanced Research Projects Agency of the Department of Defense under U.S. Air Force Space and Missile Systems Organization (SAMSO) Contract F04701-73-0074.

tomic molecules.[2] It is our intention in this talk to exploit this information, with the aid of a static model, in order to isolate the parameters which influence the achievement of positive gain for electronic transitions in diatomic molecules.

Utilizing this generalized computer code which calculates the minimum reactive branching ratio required for a species to display optical gain, a parametric study was performed to ascertain which properties of the electronic potential curves of a diatomic molecule have the greatest effect on the suitability of this molecule as a potential electronic transition laser. The results of this study demonstrate that diatomic systems separate into different classes when the question of the minimum required reactive branching ratio is confronted. Using compiled molecular constants, this separation of molecular systems was translated into a determination of which vibrational level distribution class is most favorable for specific molecules to display optical gain. Potential laser candidates are pointed out.

[2] S. N. Suchard, "Spectroscopic constants for selected heteronuclear diatomic molecules," The Aerospace Corp., El Segundo, Calif., Tech. Rep. TR-0074(4641)-6, vol. I-III, May 1974.

MC2. Low Lying Excited Electronic States of BrCl and GeO, R. A. Harris, J. R. Lillis, *Air Force Weapons Laboratory*, J. A. Montgomery, Jr., *Columbia University*, and H. H. Michels, *United Aircraft Research Laboratories.*

Ab initio quantum mechanical calculations for the first 62 valence molecular states of GeO have been carried out using a valence configuration interaction method. A minimum basis set of Slater orbitals was used in conjunction with a complete set of valence configurations. Comparisons of theoretically determined spectroscopic constants and experimentally determined constants were made for those cases where experimental data exist. The results were also compared with theoretical calculations on CO and SiO.

Ab initio calculations have been completed for all molecular states of BrCl arising from the ground states of the separated atoms Br and Cl. A minimum basis set of Slater orbitals was used in conjunction with a complete set of valence configurations. Only two bound states were found to exist in the approximation used. These correspond to the $X^1\Sigma^+$ and the $a^3\pi$ electronic states. From the predicted ordering of the excited electronic states a correlation diagram is presented which aids in interpreting the observed predissociation in BrCl.

MC3. The Potential for Electronic Transition Lasers with Molecules from the Carbon Group Oxides, L. E. Wilson, S. G. Hadley, R. A. Harris, and G. Hager, *U.S. Air Force Weapons Laboratory, Kirtland AFB, N. Mex.*

Radiative electronic transitions between the lowest triplet and ground states of GeO and SiO have been studied as potential lasers. In order to observe the radiation we have employed the following chemical excitation scheme:

$$Si(^3P) + N_2O \longrightarrow N_2 + SiO$$

$$\Delta H = -150 \text{ kcal/mole}$$

$$Ge(^3P) + N_2O \longrightarrow N_2 + GeO$$

$$\Delta H = -130 \text{ kcal/mole.}$$

Due to spin conservation both reactions produce a triplet oxide product. The spectra of GeO and SiO, which appeared pale blue and violet to the eye, respectively, were recorded with a scanning spectrometer, photomultiplier and a lock in amplifier. We have assigned the emission spectrum of GeO to $a^3\Sigma^+ \rightarrow X^1\Sigma^+$ with $T_0 = 27\ 552\ \text{cm}^{-1}$ and $\omega_0' = 628\ \text{cm}^{-1}$. We have also assigned the emission spectrum of SiO to $a^3\Sigma^+ \rightarrow X^1\Sigma^+$ and $b^3\Pi \rightarrow X^1\Sigma^+$. Values of $T_0 = 33\ 409\ \text{cm}^{-1}$ for the $a \rightarrow X$ system, and $T_0 = 33\ 853\ \text{cm}^{-1}$ for the $b \rightarrow X$ system have been obtained.

The gain for vibrational transitions for the GeO $a^3\Sigma \rightarrow X^1\Sigma$ electronic transition have been calculated from the expression

$$\alpha = \left(\frac{\ln 2}{\pi}\right)^{1/2} \frac{\lambda_{21}^2}{\Delta\nu_0} \frac{A_{21}}{4\Pi} N_{JMAX}$$

where

$$A_{21} = \frac{\nu_{\nu'\nu''}^3 \left(\int \psi_{\nu'}\psi_{\nu''} d\tau\right)^2}{\tau \sum_{\nu''} \nu_{\nu'\nu''}^3 (\psi_{\nu'}\psi_{\nu''} d\tau)^2}.$$

The gain has been calculated by assuming the line is Doppler broadened and the vibrational levels have a Boltzmann population distribution. The A_{21} coefficient has been evaluated using Rydberg Klein potential energy curves in Schrodinger equation for nuclear motion. The Schrodinger equation was evaluated numerically and the integrals computed using a Simpson's rule method.

The requirements for producing a GeO laser on the $a \rightarrow X$ transition will be discussed. Estimates of radiative lifetimes will allow discussion of potential lasing from other carbon group oxides.

MC4. Studies of Visible Chemical Lasers Based on Reactions of Metal Atoms with Various Oxidizers,[1] D. J. Eckstrom, S. A. Edelstein, D. L. Huestis, M. Luria, B. E. Perry, and S. W. Benson, *Stanford Research Institute.*

As part of a program aimed at the development of visible chemical lasers, we have been studying the chemiluminescence of reactions of evaporated metal atoms with various oxidizers. Reactions that have been found to produce high photon yields now include: $Ba + N_2O$ (25%); $Ba + O_3$ (~35%); $Eu + N_2O$ (~20%); $Sm + N_2O$ (38%); and $Sm + F_2$ (61%). The peak yield usually occurs at a few torr pressure of inert gas, indicating that the initial reaction populates a reservoir state that does not radiate in the visible. We will discuss kinetic models of the $Ba + N_2O$ reaction that satisfactorily predict the variation of photon yield with pressure. Even in this well-studied reaction, however, we cannot specify the reservoir state with confidence.

Most of these flame spectra contain metal-atom emission. In the case of $Ba + N_2O$, however, when the reaction rates are increased to a level anticipated for laser threshold, the metal-atom emission becomes dominant at the expense of the diatomic emission. This energy-transfer rate is quite high, and may be an important quenching process for a diatomic upper laser level.

Experiments with $Ba + N_2O$ using a long-path burner (45 cm) in an optical cavity have not shown any evidence of gain in the 6000 to 8000 Å region.

[1] This work was sponsored by the Defense Advanced Research Projects Agency and monitored by the Army Missile Command.

MC5. Experimental Studies of Reaction Systems of Interest for Chemical Laser Operation at Short Wavelengths, M. S. Chou and T. A. Cool, *Department of Applied & Engineering Physics, Cornell University, Ithaca, N.Y. 14850.*

Experiments have been conducted to determine the feasibility of short duration pulsed discharges for the initiation of chemical reactions of potential interest for chemical laser operation at visible wavelengths. Double discharge preionization has been employed for rapid initiation of chemical reactions. The present technique accomplished uniform reaction on a time scale comparable to that (10^{-7} s) for spontaneous emission. Reaction initiation in pre-

mixed room temperature reagent combinations of several metal methyl compounds, $M(CH_3)_n$, with N_2O and O_2 have been extensively studied. High yields of metal atoms are provided by the reaction sequence

$$M(CH_3)_n + CH_3 \longrightarrow M(CH_3)_{n-1} + C_2H_6 \quad (1a)$$

$$\longrightarrow M(CH_3)_{n-1} + C_2H_4 + H_2. \quad (1b)$$

The observed visible chemiluminescence is believed to originate from the reactions

$$M + N_2O \longrightarrow N_2 + MO \quad (2)$$

or

$$M(CH_3) + O \longrightarrow MO + CH_3. \quad (3)$$

Spontaneous emission spectra have been recorded for several dozen reactant combinations which exhibit strong chemiluminescence. Photon yield measurements for the spectral region from 3000 Å to 9000 Å have been completed for several reagent combinations of interest.

The scope of application of discharge dissociation techniques for chemical laser reaction initiation with various reagent mixtures is discussed. Recent attempts at visible chemical laser operation with discharge reaction initiation are described.

MC6. Chemiluminescence and Photoluminescence Spectroscopy of the Barium Monohalides,[1] R. S. Bradford, Jr., and H. P. Broida, *University of California, Santa Barbara, Calif.*

In search of visible chemical laser candidates, Ba metal vapor, entrained in a flowing insert carrier gas, has been reacted with F_2, SF_6, Cl_2, Br_2, and I_2. Diatomic barium monohalides (BaX) have been produced in ground and electronic excited states. Bright green chemiluminescence flames occur at pressures from 0.1 to 10 Torr.

BaX chemiluminescent spectra, observed from 300–1100 nm have been corrected for absolute instrument response and are shown for the first time. The A through I electronic states have been found for BaF in emission where many high lying states were previously seen only in absorption. Vibrational structure is so closely spaced that there are more than 30 bands in a 6-mm spectral region. Rotational structure is only partially resolved with 0.01-nm resolution. Similar spectra are obtained from BaBr, BaCl, and BaI. New emission in the near infrared from BaBr and BaI is ascribed to transitions to the ground state from previously unobserved electronic states (analogous to A and B in BaF and BaCl). In BaBr, electronic state energies for B $^2\Sigma^+$, A $^2\Pi_{3/2}$ and A $^2\Pi_{1/2}$ have been found to be 11325, 10604, and 9980 cm^{-1}, respectively; while in BaI, corresponding values are 10417, 9921, and 9268 cm^{-1}, respectively.

Spectra of C $^2\Pi - X^2\Sigma^+$ transitions show thermal distributions in both vibration and rotation corresponding to population temperatures of approximately 3000 K for BaF and 2000 K for BaBr, BaCl, and BaI. BaX emission shows only slight dependence on pressure (0.1 to 10 Torr) and type of carrier gas (Ar, He, N_2).

Laser-induced photoluminescence has been observed with laser wavelengths of 496.5 and 514.5 in BaF; 488.0, 514.5, 520.8, and 530.8 in BaCl; as well as 514.5 and 520.8 nm in BaBr. Little pressure or carrier gas dependence has been found.

Production efficiencies into electronically excited states have been obtained from chemiluminescent spectra. BaX molecules are found to be produced with moderate efficiency into lower lying electronic states (80–98% in A and B) with an absolute efficiency of approximately 1 photon for each 100 reacted barium atoms. Electronic population temperatures obtained from efficiency measurements show trends similar to temperatures observed in vibration and rotation.

Electronically excited BaX species appear to be formed in two ways: 1) direct reaction, and 2) formation of long-lived BaX_2^* (asterisk indicates electronically excited) which then reacts with Ba to form BaX* + BaX. The second step allows equilibration of electronic, vibrational and rotational degrees of freedom as indicated by observed population temperatures.

[1] Work supported in part by Grant AFOSR-70-1851.

MC7. The Diatomic Oxides and Halides of Ca and Sr: Photon Yields and $A'^1\pi$ Molecular Constants,[1] G. A. Capelle, *The Aerospace Corporation*, and H. P. Broida, *University of California, Santa Barbara, Calif.*

The diatomic metal oxides and halides of Ca and Sr have been formed by reacting the respective metal vapors with N_2O, NO, O_2, C_3, Br_2, Cl_2, and F_2 in 1 to 10 torr of argon buffer gas. Photon yields for the chemiluminescent emission from these systems were measured in the region 250–1100 nm. Photon yields for CaO (A-X) emission were measured to be as high as 1% with N_2O at 1.2 torr total pressure. Sr + N_2O at the same pressure also gave a yield of slightly over 1% for A-X emission. Total photon yields for the calcium halides were strongest (up to 0.9%) with F_2 and weakest (0.03%) with Br_2. The greatest contribution to the total yield came from A-X photons (~74% at 1.2 torr); about 24% of the yield was due to B-X emission and the remainder (1–2%) from C-X. The corresponding numbers for strontium are similar.

With both Ca + N_2O and Sr + N_2O, the $A'^1\pi$-$X^1\Sigma$ system was observed where it had recently been predicted[2] to lie. Bandheads were measured in the 550-840 nm region and molecular constants were calculated. For CaO($A'^1\pi$) we found:

$$\nu_{00} = 8340(6)cm^{-1}$$
$$\omega_e = 545.7(8)$$
$$\omega_e\chi_e = 2.54(3)$$
$$B_e = 0.3372(67)cm^{-1}$$
$$\alpha_e = 0.0021(7)$$

and for SrO ($A'^1\pi$):

$$\nu_{00} = 9778(7)cm^{-1}$$
$$\omega_e = 468.7(1.4)$$
$$\omega_e\chi_e = 2.06(6)$$
$$B_e = 0.2548(18)cm^{-1}$$
$$\alpha_e = 0.0017(3)$$

These values are in good agreement with those found by Field[2] through the use of perturbation analysis.

[1] This work was supported in part by Air Force Office of Scientific Research Grants AFOSR-70-1851 and AFOSR-73-2565.

[2] R. W. Field, *J. Chem. Phys.*, vol. 60, p. 2400, 1974.

MC8. Production Efficiencies and Radiative Lifetime of FeO Produced in Low Pressure Flames,[1] J. B. West[2] and H. P. Broida, *Department of Physics, University of California, Santa Barbara, Calif.*

Chemiluminescent reactions between iron atoms and various oxidants are investigated[3,4] as possible mechanisms for electronic transition chemical lasers. Diatomic iron oxide (FeO) is produced[5] by reaction of either N_2O, O_3, NO_2, discharged O_2, or O_2 with iron vapor entrained in a flowing, inert carrier gas

[1] Work supported by NSF Grant GP-14011.

[2] Present address: National Bureau of Standards, Boulder, Colo. 80302.

[3] J. B. West, Ph.D. thesis, Univ. California, Santa Barbara, 1974.

[4] J. B. West and H. P. Broida, *J. Chem. Phys.*, in press.

[5] J. B. West, R. S. Bradford, Jr., J. D. Eversole, and C. R. Jones, *Rev. Sci. Instrum.*, in press.

(typically argon). Band emission from the infrared, orange, and blue systems of FeO is observed in chemiluminescent flames resulting from the reaction of Fe with O_3, N_2O, NO_2, or discharged O_2. Reaction of Fe with O_2 produces continuum-like emission of unidentified origin; however, laser photoluminescence studies confirm ground state FeO is present. Bands not previously reported are observed in flames of Fe reacting with O_3, N_2O, and discharged O_2. On the basis of vibrational spacings, some of these bands are ascribed to FeO.

Excited state production efficiencies (photon yield ≡ rate of photon emission from flame/rate of reaction of iron atoms) are measured for the band systems of FeO produced in the reactions of Fe with N_2O and O_3. For the reaction with N_2O at a pressure of 1.5 torr, photon yields for the infrared, orange, and blue systems of FeO are 0.7%, 0.15%, and 0.01%, respectively. Photon yields for these band systems produced in the reaction of iron with O_3 are about an order of magnitude greater.

Radiative lifetimes of FeO are measured by monitoring the decay of photoluminescence excited by a pulsed, tunable laser. Measurements on the 0, 0 band of the FeO orange system B at $\lambda = 579$ nm yield a lifetime of 450 ± 100 ns. A quenching rate constant for FeO by argon of $k = 3.4 \times 10^{-12}$ cm^3/s is found.

Reactions of Fe with Cl_2 and Br_2 produce only weak visible chemiluminescence. F_2 produces a bright blue flame with an unidentified, complex spectrum between 450 and 650 nm. Also, bands previously ascribed to FeF are observed near 330 nm. The photon yield for the unidentified emission between 450 and 650 nm is 1% at a pressure of 1.3 torr. No photoluminescence is observed from any of the lines of the argon ion laser or from a CW dye laser which is tunable between 570 and 620 nm. This observation indicates that the lower level of the visible emission could either be an electronically excited state or a high ground state vibrational level.

MC9. Population Inversions Measured in Alkali Metal-Halogen Reaction Systems, L. H. Hall, *Rocketdyne Division Rockwell International Corporation, Canoga Park, Calif.*

We have recently measured a number of population inversions in alkali metal atoms of the highly exothermic Cs + F_2 and Rb + F_2 reaction systems. The excitation process is probably a two-step process:

$$Cs + F_2 \longrightarrow CsF(v) + F$$

primary reaction

$$CsF(v) + Cs \longrightarrow CsF + Cs^*$$

transfer reaction.

The energy is initially created in vibrationally excited cesium fluoride and then is transferred to electric excitation of the cesium atom. Another reaction is possible based on the cesium dimer,

$$Cs_2 + F \longrightarrow CsF(v) + Cs^*$$

secondary reaction.

This reaction can create either vibrationally excited cesium fluoride or electronically excited cesium atoms. Under our experimental conditions (300°C initial reactant temperature, 1 torr total pressure, and 10:1 halogen to alkali metal ratio) only 1% of the cesium vapor is present in the form of dimers. We conclude that the secondary reaction is probably not a significant excitation mechanism in our experiments. The populations of the excited states of the alkali metal atoms were determined by chemiluminescence measurements combined with published values for the radiative oscillator strengths. For both the Cs + F_2 system and the Rb + F_2 system a substantial number of population inversions were measured indicating the potential for lasing at wavelengths as short as 1 micron. Parametric studies are currently underway on these and other alkali metal-halogen reaction systems.

MC10. F_2 Reactions as Possible Laser Candidates, S. J. Davis, G. Hager, S. G. Hadley, *Air Force Weapons Laboratory, Device Branch, Advanced Laser Technology Division, Kirtland AFB, N. Mex. 87117.*

Several chemiluminescent reactions involving molecular fluorine are being investigated in a flow tube apparatus. Reactions studied are those of I_2, Br_2, SiH_4, GeH_4, AsH_3, and PH_3 with F_2. The flames, produced in a concentric burner, are analyzed with a 1 m spectrometer and displayed on a strip-chart recorder via a phase sensitive detector. The $I_2 + F_2$ reaction yielded an orange appearing flame. The spectrum, which consisted of a series of red degraded bands extended from ~4500 to ~7000 Å. The chemiluminescence was due to the $A^3\Pi \rightarrow X^1\Sigma$ transition of IF. The mixing of Br_2 with F_2 produced no detectable emission. The reactions of F_2 with germane and silane yield extremely intense blue-violet flames. An analysis of the SiH_4, F_2 flame showed it to be due to the $A^2\Sigma^+ \rightarrow X^2\Pi$ SiF transition. It consists of a complex system of red degraded bands extending from ~4000 to ~4800 Å. The most intense bands are the vertical transitions (0, 0) and (1, 1) as expected from the near identical internuclear distances of the $A^2\Sigma^+$ and $X^2\Pi$ states. The possibility of an $a^4\Sigma^- \rightarrow X^2\Pi$ emission ($T = 29\,805$ cm^{-1}) was investigated but was not observed. The GeH_4, F_2 reaction was also spontaneous and the chemiluminescence was found to be due to $A^2\Sigma^+ \rightarrow X^2\Pi\,\frac{1}{2}$ and $A^2\Sigma^+ \rightarrow X^2\Pi\,\frac{3}{2}$ transitions. The large spin-orbit splitting (934 cm^{-1}) of the ground state leads to two subsystems each consisting of a series of red degraded bands. Strong $v'' = 0$ and $v'' = 1$ progressions were observed. Apparently, in both the GeH_4 and SiH_4 reactions, the fluorine strips the hydrogen, then we postulate that the following reactions occur:

$$Si + F_2 \longrightarrow SiF + F$$

$$\Delta H = -79 \pm 5 \text{ kcal/mole}$$

$$Ge + F_2 \longrightarrow GeF + F$$

$$\Delta H = -79 \pm 5 \text{ kcal/mole.}$$

The reactions of AsH_3 and PH_3 with F_2 yield what appears to be continuum spectra in the spectral region of ~3300 to 4700 Å. Further investigations of these two reactions are planned. RKR calculations have been performed for GeF and SiF using the known spectroscopic constants and are compared to the observed spectra. The calculated Franck–Condon factors are compared with those experimentally determined.

MC11. Metal-Oxident Flames: Visible Chemiluminescence Studies Using a Shock Tunnel Apparatus, P. B. Scott, S. Johnson, and G. Watson, *Xonics, Inc.*

A shock tube is used to vaporize metal (aluminum, boron, barium, carbon, copper, magnesium, silicon, strontium, titanium, uranium, tungsten, and zirconium have been used) powders in an argon gas carrier.[1] The argon-metal vapor mixture is then expanded through supersonic nozzles and an oxident (oxygen, nitrous oxide, chlorine or fluorine) mixes after injection downstream.

Flow duration is over 1 ms of steady flow and the resulting chemiluminescence is adequate to expose a spectral plate with 0.1 nm resolution. Emission spectra of numerous visible chemical laser candidates have been obtained. Systems of particular interest which produce strong spectra are as follows.

[1] S. Johnson *et al.*, *J. Chem. Phys.*, accepted for publication.

Metal	Oxident	Molecule	Electronic Transition	$\Delta\lambda$(nm)
B	N_2O	BO	$A^2\pi - X^2\Sigma$	320–550
	O_2	BO	$A^2\pi - X^2\Sigma$	320–550
Ba	N_2O	BaO	$A^1\Sigma - X^1\Sigma$	430–680
Cu	F_2	CuF	$A^1\pi, B^1\Sigma, C^1\pi - X^1\Sigma$	410–450
Si	N_2O	SiO	$D^1\pi - X^1\Sigma$, weak	230–300
	F_2	SiF	$A^2\Sigma - X^2\pi, C^2\pi$	410–460

The system can also be set up for laser gain observation or for lower state population measurements.

SESSION MD

Vibrational Energy Transfer
Monday, October 21, 2:00 P.M.

MD1. Vibrational Relaxation in HF and DF between 200-300°K,[1] J. K. Hancock and W. H. Green, *Naval Research Laboratory.*

Vibrational relaxation rates in HF-He and DF-He mixtures and pure DF samples have been measured between 200–300°K using the laser excited fluorescence technique. Rate constants are reported for the following collisional processes:

$$HF(v = 1) + HF \xrightarrow{k_{11}} 2HF + \Delta E = 3961\ cm^{-1}$$

$$HF(v = 1) + DF \xrightarrow{k_e + k_{12}} HF + DF(v = 1, 0) + \Delta E = 1055, 2906\ cm^{-1}$$

$$DF(v = 1) + DF \xrightarrow{k_{22}} 2DF + \Delta E = 2906\ cm^{-1}$$

$$DF(v = 1) + He \xrightarrow{k_{2m}} DF + He + \Delta E = 2906\ cm^{-1}.$$

The low temperature fluorescence cell consists of a stainless steel vacuum Dewar containing an internally mounted sample cell with appropriate window ports for the entrance and exit of the laser beam and collection of IR fluorescence. Gases to be studied were slowly flowed through coils surrounding the cold trap before entering the sample cell. Temperatures accurate to ±3 K were recorded using a Copper–Constantan thermocouple which had been calibrated with the known vapor pressure–temperature relationship of propane gas.

An HF TEA laser (<1 mj/pulse) was used as an excitation source for both the HF and DF measurements. A 2% HF impurity present in our DF sample cylinders was sufficient to allow direct DF($v = 1$) excitation through rapid V → V transfer from HF.

A summary of measured rates at 300 K and 200 K are listed in the table below (error limits shown are least squares values and indicate only the precision of the measured data).

System	Rate Constant	Temp. 300 K $k(sec^{-1}\ torr^{-1}) \times 10^4$	Temp. 200 K $k(sec^{-1}\ torr^{-1}) \times 10^4$
DF (pure gas)	k_{22}	1.77 ± 0.07	8
	$k_e + k_{12}$	7.2 ± 0.5	30
DF (dilute in He)	k_{22}	1.46 ± 0.09	6
	$k_e + k_{12}$	9.5 ± 0.4	30
	k_{2m}	$\leqslant 4 \times 10^{-3}$	$\leqslant 2 \times 10^{-3}$
HF (dilute in He)	k_{11}	4.7 ± 0.2	10–20

Preliminary temperature dependence results between 300 and 220 K suggest that room temperature rates increase only about a factor of two. Between 220 and 200 K, however, rates increase rapidly and vary nonlinearly with pressure. We report the asymptotic rates ($X_{HF,DF} \leqslant 0.005$) which represent the *slowest* rates measured in HF and DF at 200 K. At higher molefractions $0.005 \leqslant X_{HF,DF} \leqslant 0.015$, measured rates become up to five times faster.

Experiments are now in progress which will attempt to clarify some of the anomolous features of the low temperature relaxation measurements which have been observed.

MD2. DF* Laser Deactivation Kinetics, C. P. Wendelken, L. E. Wilson, C. Clendening, and J. Noetzel, *U.S. Air Force Weapons Laboratory, Kirtland AFB, N. Mex.*

Alternate reactant systems are being sought for combustion driven DF* lasers to replace the $H_2/F_2/D_2$ reactant system. Improved storage and handling are the primary reasons for this search, but the reduction of DF* deactivators in the laser cavity is also of major importance.

This paper presents results of a laboratory study of DF* deactivation rates by alternate laser reactants and their combustion products. The measurements were performed at 295 K using a flowing gas cell. Test species, diluent, and DF were mixed in a manifold with concentrations determined by differential pressure measurements. The DF was excited to the $V = 1$ state by a DF* pulse laser. The DF* deactivation rates were measured as a function of DF mole fraction; results were then extrapolated to zero mole fraction DF to obtain the deactivation rate of the test species.

Test species of interest include NF_3 for an oxidizer, C_2H_2, C_6H_6, and CS_2 for combustor fuels, DBr and deuterated hydrocarbons for cavity fuels, and N_2 and CF_4 products of the combustor reactants. The following DF rates were measured:

$$k_{DF^*-NF_3} = 4.86 \times 10^2\ s^{-1}\ torr^{-1};$$

$$k_{DF^*-N_2} = 7.3 \times 10^2\ s^{-1}\ torr^{-1};$$

$$k_{DF^*-CF_4} = 1.11 \times 10^3\ s^{-1}\ torr^{-1};$$

and

$$k_{DF^*-DBr} = 2 \times 10^4\ s^{-1}\ torr^{-1}.$$

A shortage of DF prevented measurement of DF* deactivation rates by the alternate combustor fuels at this time. To estimate the effect of alternate combustion fuels, HF* deactivation was measured. The following rates were obtained:

$$k_{HF^*-C_2H_2} = 3 \times 10^5\ s^{-1}\ torr^{-1};$$

$$k_{HF^*-C_6H_6} = 3.6 \times 10^5\ s^{-1}\ torr^{-1};$$

and

$$k_{HF-CS_2} = 1.6 \times 10^4\ s^{-1}\ torr^{-1}.$$

The DF rates are expected to be of the same order of magnitude.

Some preliminary conclusions may be drawn from these results. The HF*-hydrocarbon rates are extremely rapid; therefore, complete reaction of the fuel in the combustor is extremely important. On the other hand, the DF*-NF_3 rate is relatively low. Unreacted NF_3 would be relatively innocuous in the cavity. The DF*-DBr rate is essentially the same as DF*-DF so there is not advantage of either in the area of deactivation rates. The products formed have relatively low deactivation rates and should cause little problem in the cavity. Current operating

[1] This work was supported in part by AFWL under Contract 73-232.

characteristics of DF lasers with various fuels and oxidizers in both the combustor and the lasing cavity will be discussed.

MD3. Flow Tube Kinetics Studies: $DF(v) + HF$, $DF(v) + D_2$, and $HF(v) + H_2$ Systems,[1] M. A. Kwok and R. L. Wilkins, *The Aerospace Corporation.*

The medium pressure (1 torr), large diameter (10 cm) flow tube has been used to measure overall relaxation rates at room temperature for $DF(v) + HF$, $DF(v) + D_2$, and $HF(v) + H_2$ systems for $v = 1, 2, 3$, and 4. Computer model studies have been conducted on the kinetics of the $DF(v) + D_2$ and $HF(v) + H_2$ systems in order to predict the (VV) energy transfer rates for these systems which reproduce the observed overall rates.

The flow tube includes a side arm which provides the generation of F atoms by passing Ar diluent and SF_6 through a continuous RF discharge, and a movable fuel injector, which permits the reaction zone to be displaced with respect to a fixed optical station. Spectroscopic techniques monitor the emission (VR) bands of HF or DF. Average number densities of $HF(v)$ and $DF(v)$ exhibit exponential decays. From the sensitivity of the decays to HF, H_2, or D_2 concentrations, experimental rate coefficients can be determined.

As a trial experiment, the flow tube was used to measure HF vibrational deactivation of $HF(v)$ for $v = 1, 2$, and 3 and the measured rate coefficients are found to be in good agreement with reported experimental results.[2,3,4] Rate coefficients k_v for HF deactivation of $DF(v)$ are found to have a linear v dependence. The rate coefficients for vibrational de-excitation of $DF(v)$ by D_2 are found to have the values $(k_2/k_1) = 1.4$, $k_3/k_1 = 1.6$, and $k_4/k_1 = 1.8$, where $k_1 = 2.5 \times 10^{11}$ cm^3 mole^{-1} s^{-1}.

The rate coefficients for $HF(v) + H_2$ $(DF(v) + D_2)$ are determined by using a nonequilibrium chemistry flow model with three specialized components: 1) an H_2-HF (D_2-DF) VV rate package, 2) an HF-HF (DF-DF) VV rate package, and 3) a velocity profile adjustment. Of secondary importance, the HF-HF VV package must be included for the proper coupling behavior. An HF-HF VV rate package has been developed which fits known experimental data.[3] The model corrects for the paraboloid velocity profile which distorts the number density of $HF(v)$ or $DR(v)$ along the tube diameter. The successful H_2-HF VV rate package postulates strong multivibrational quantum processes, and uses a simple model to generate the required H_2-HF VV energy transfer rates.

[1] This work reflects research supported by the Air Force Weapons Laboratory (AFWL) under U.S. Air Force Space and Missile Systems Organization (SAMSO) Contract F04701-73-C-0074.

[2] J. R. Airey and I. W. M. Smith, *J. Chem Phys.*, vol. 57, p. 1669, 1972.

[3] R. M. Osgood, Jr., P. B. Sackett, and A. Javan, *J. Chem. Phys.*, vol. 60, p. 1464, 1974.

[4] Eight experiments for HF(1) + HF.

MD4. Rotational Relaxation of Hydrogen Fluoride,[1] J. J. Hinchen, *United Aircraft Res. Lab.*

Rotational relaxation effects in HF were observed with double resonance IR experiments that employed two single wavelength lasers. A pulsed laser is used to pump the population to a particular V, J level, and the absorption of stable CW laser radiation is used as a probe to determine the loss or arrival of population in specific V, J levels. Observations were made of collisional energy transfer by vibrational–translational, vibrational–vibrational, and rotational–rotational processes in HF. The results for V-T and V-V transfer are in agreement with data from laser-induced fluorescence experiments. Preliminary results will be described for the temporal behavior of the population distribution over rotational levels after the population was placed in a single level, and also for individual level rotational relaxation rates.

[1] This work was sponsored by the Air Force Office of Scientific Research and by the Naval Research Laboratory.

MD5. Relaxation of $HCl(v = 1)$ and $DCl(v = 1)$ by Cl and O Atoms, R. D. H. Brown, G. P. Glass, and I. W. M. Smith, *Department of Physical Chemistry, University Chemical Laboratories, Cambridge, England.*

$$Cl' + HCl''(v = 1) \rightarrow Cl'H(v = 0) + Cl'' \quad (1a)$$

$$Cl' + HCl''(v = 1) \rightarrow Cl' + HCl''(v = 0). \quad (1b)$$

Rate coefficients for the relaxation of $HCl(v = 1)$ and $DCl(v = 1)$ by Cl and O atoms have been determined experimentally by making time-resolved measurements of the vibrational fluorescence from these molecules following their excitation with a pulsed laser.

A discharge-flow system was used to produce a mixture of HCl, the atomic species, and Ar. O_2, diluted in Ar, was partially dissociated in a microwave discharge, and the flow of O atoms was measured by titration with NO_2. Where needed, Cl atoms were created by adding sufficient Cl_2 to convert the O atoms quantitatively to Cl through the reactions: $O + CL_2 \rightarrow ClO + Cl$ and $O + ClO \rightarrow O_2 + Cl$. HCl could be added through one of several inlets; the extent of the slow, thermal reaction between O and HCl[1] was minimized by adding the HCl just upstream of the window through which the fluorescence was observed.

The laser was a pulsed HCl chemical laser of the TE type. It produced ~2 mJ (the energy from the DCl laser was $\sim\frac{2}{3}$ mJ) of which $\gtrsim$60% was in the (1, 0) band. The radiation from the laser was directed along the axis of the flow tube. Infrared fluorescence was observed perpendicular to the direction of the laser beam using a cooled InSb detector (time response, 1 μs). The level of scattered light was low and it was unnecessary to use a narrow-band filter in front of the detector. This allowed us to use low HCl concentrations ($0.6 - 3 \times 10$ molecule cm^{-3}), which was particularly valuable in the O + HCl experiments since the extent of the thermal reaction could be reduced to negligible proportions at all but the highest temperature used (397 K). The main flow-tube was positioned in a lagged metal box which could be filled with coolant or heated oil.

In the absence of Cl or O, the HCl or DCl fluorescence decayed to half its initial intensity in ~3–4 ms. At the total pressures (~2 torr) in the flow tube, this was consistent with diffusion-controlled surface loss. Sufficient concentrations of either Cl or O could be added to reduce the lifetime of the vibrationally excited molecules to ~0.5 ms.

For $HCl(v = 1) + Cl$, rate coefficients have been determined for $263 \leqslant T \leqslant 397$ K. No distinction can, of course, be made between "reactive" and nonreactive processes, i.e.,

The data are matched quite well by the Arrhenius expression, $k_1 = (k_{1a} + k_{1b}) = 7.9 \times 10^{-11} \exp(-1.3 \text{ kcal mole}^{-1}/RT)$ cm^3 molecule^{-1} s^{-1}. Our value at 298 K, $k_1 = 8.8 \times 10^{-12}$ cm^3 molecule^{-1} s^{-1} is in good agreement with that of Craig and Moore[2] (11×10^{-12} cm^3 molecule^{-1} s^{-1}) and with more recent data from Moore's laboratory.[3] It appears that the value of k_1

[1] R. D. H. Brown and I. W. M. Smith, *Int. J. Chem. Kinetics*, in press.

[2] N. C. Craig and C. B. Moore, *J. Phys. Chem.*, vol. 75, p. 1622, 1971.

[3] G. Macdonald, C. B. Moore, I. W. M. Smith, and F. J. Wodarczyk, to be published.

obtained by Ridley and Smith[4] must be in error. The overall rate constants for deactivation of DCl($v = 1$) by Cl are approximately 0.6 k_1.

For HCl($v = 1$) + O, the reactive and nonreactive channels,

$$O + HCl(v = 1) \rightarrow OH + Cl \quad (2a)$$
$$O + HCl(v = 1) \rightarrow O + HCl(v = 0) \quad (2b)$$

are quite different, but they have not been distinguished in the present work. Measurements on HCl($v = 1$) between 196 and 397 K have given values of $k_1 = (k_{1a} + k_{1b})$ which can be fitted quite well to the expression, $k_1 = 8.2 \times 10^{-12} \exp(-1.3 \text{ kcal mole}^{-1}/RT)$ cm^3 molecule^{-1} s^{-1}. The rate coefficient at 298 K, 9.0×10^{-13} cm^3 molecule^{-1} s^{-1}, is four times smaller than that reported by Arnoldi and Wolfrum.[5] In the case of O atoms, DCl($v = 1$) is deactivated faster than HCl($v = 1$), the difference being greatest at 196 K where it amounts to a factor of two.

[4] B. A. Ridley and I. W. M. Smith, *Chem. Phys. Lett.*, vol. 9, p. 457, 1971.
[5] D. Arnoldi and J. Wolfrum, *Chem. Phys. Lett.*, vol. 24, p. 234, 1974.

MD6. Vibrational Relaxation in Potentially Reactive Collisions: Temperature and Isotope Effects, I. W. M. Smith, *Department of Physical Chemistry, University Chemical Laboratory, Cambridge, England.*

Vibrationally excited molecules appear to be deactivated much more rapidly by potentially reactive atoms (e.g., F, Cl, H, O) than by inert gases. This surely reflects differences in the intermolecular potentials. Two kinds of difference may be distinguished. First, the interaction between molecule and reactive atom may be characterized by more than one electronic potential: thus, Cl(^{2}P) + HCl ($^1\Sigma^+$) yields $^2\Pi$ and $^2\Sigma$ states in $C_{\infty v}$ symmetry and $2\,^2A' + {}^2A''$ in C_s symmetry. This may lead to an electronically nonadiabatic mechanism for energy transfer.[1] Secondly, the form of one or more of the potentials must reflect the possibility of chemical reaction, and this may lead to enhanced probabilities of energy transfer by an electronically adiabatic mechanism. In the present work, this possibility was investigated by means of classical trajectory calculations for systems modeled on HCl ($v = 1$) + Cl and DCl ($v = 1$) + Cl.

The simple LEPS expression was used to represent the potentials. The single adjustable parameter was chosen to give: a) a surface with a 6.2 kcal mole^{-1} barrier for H-atom transfer, and b) a surface with a 6.2 kcal mole^{-1} 'well', corresponding to a linear, symmetric, weakly bound collision complex. These choices were made to give a crude match with the two, apparently conflicting, pieces of empirical evidence[2,3] about the ClHCl potential. The general computational procedure was similar to that of Smith and Wood[4] except that all the initial collision parameters except E_{vib} were chosen by Monte Carlo methods, calculations being performed for $T = 1000$, 500, and 333.3 K.

For surface a), the calculated rate coefficients for deactivation were quite well-matched by Arrhenius expressions = $2.5 \times 10^{-11} \exp(-2.7 \text{ kcal mole}^{-1}/RT)$ cm^3 molecule^{-1} s^{-1} for HCl ($v = 1$) and $1.6 \times 10^{-11} \exp(-3.3 \text{ kcal mole}^{-1}/RT)$ cm^3 molecule^{-1} s^{-1} for DCl ($v = 1$). Compared with experimental values,[5] these are much too small and show too great a dependence on temperature and isotopic substitution. For both species on surface b), the rate coefficients were essentially independent of temperature and equal to 1.0×10^{-10} cm^3 molecule^{-1} s^{-1}. This time the absolute magnitude of the rate coefficients was too great and the temperature and isotope dependence too slight.

In view of the large discrepancy between the experimental results and both sets of calculated rate coefficients, a third series of calculations were carried out with the barrier for H-atom transfer adjusted to 1.9 kcal mole^{-1} The results of these calculations agreed quite well with those determined experimentally in regard to magnitude, temperature dependence, and isotope effect. It therefore seems that either the barrier on the ClHCl surface is lower than that deduced from the experiments of Klein *et al.*,[2] or possibly that an electronically nonadiabatic mechanism is operative. The latter seems somewhat unlikely as HCl is deactivated faster than DCl.

Some empirical evidence for a lower barrier for H-atom transfer in this system comes from comparing the activation energies for pairs of reactions involving OH and Cl. With H_2, CH_4, HBr, and HI these are similar, but the activation energy for OH + HCl → H_2O + Cl is only 1.0_6 kcal mole^{-1} [6] much less than the 6.6 kcal mole^{-1} given by Klein, Pensky, and Weston for ClCl* + HCl → Cl*H + Cl.

[1] E. E. Nikitin and S. Ya. Umanski, *Discuss. Faraday Soc.*, vol. 53, p.7, 1972.
[2] F. S. Klein, A. Pensky, and R. E. Weston, Jr., *J. Chem. Phys.*, vol. 41, p. 1799, 1964.
[3] P. N. Noble and G. C. Pimentel, *J. Chem. Phys.*, vol. 49, p. 3165, 1968.
[4] I. W. M. Smith and P. M. Wood, *Mol. Phys.*, vol. 25, p. 441, 1973.
[5] R. D. H. Brown, G. P. Glass, and I. W. M. Smith, previous paper.
[6] I. W. M. Smith and R. Zellner, *J. C. S. Faraday II*, vol. 70, p. 1045, 1974.

MD7. H Atom Deactivation of HF($v = 1$),[1] R. F. Heidner and J. F. Bott, *The Aerospace Corporation.*

Relaxation times of HF($v = 1$) by H atoms have been measured in a discharge flow tube. A microwave discharge dissociates the H_2 to give H atoms, and a small amount of HF is injected downstream to yield a gas mixture containing H atoms, H_2, HF, and He. The HF($v = 0$) is pumped to HF($v = 1$) by a pulsed HF laser. IR fluorescence from the HF($v = 1$) is monitored with and without the H atoms by switching on and off the microwave discharge. The H atom concentration is measured by a Pt-Rh catalytic probe with a calibrated recombination efficiency. We obtain a rate coefficient for HF($v = 1$) + H → HF($v = 0$) + H of $(1.4 \pm 1) \times 10^{11}$ cc/mole-s. This is lower by an order of magnitude than previous estimates of this rate and is much smaller than a similar measurement for HCl ($v = 1$) + H → HCl($v = 0$) + H. We have also measured rate coefficients for D + DF($v = 1$), D + HF($v = 1$) and H + DF($v = 1$).

[1] This work reflects research partly supported by Air Force Weapons Laboratory of the Department of Defense on U.S. Air Force Space and Missile Systems Organization (SAMSO) Contract F04701-73-C-0074.

MD8. Vibrational Deactivation of HF($v = 1$), DF($v = 1$), and HCl($v = 1$), by Collisions with Atoms, G. P. Quigley and G. J. Wolga, *Cornell University, Ithaca, N.Y. 14850.*

An experimental program has been set up to measure the rate of deactivation of hydrogen halide molecules by selected atomic collision partners. These rates are important for several reasons. First, within HX chemical laser media atoms are present as a result of the initiation means employed and due to chemical reactions that occur. Second, in general these deactivation rates have not previously been measured in the temperature range of laser operation. Finally, there is theoretical interest in the operative mechanisms that lead to these deactivations. Thus, the atoms selected for study include those that are found within chemical lasers as well as those whose deactivation efficiency should be compared in attempting to make correlations with theory.

The experimental approach employs a

fast, subsonic flow system. Laser induced fluorescence using a TEA pin-type chemical laser for excitation of the molecule to $v = 1$ is the chosen method for measurement of vibrational relaxation. Microwave paramagnetic resonance is employed to make absolute atomic density determinations using $O_2(^3\Sigma)$ and certain atoms as standards according to methods developed by Westenberg. Fast, digital signal averaging is employed to improve the precision of the results. The measurements to be reported were all done about 300 K.

The data to be reported concern the deactivation of: $HF(v = 1)$ by H, D, O, F, Cl, Br; $DF(v = 1)$ by H, D, O, F^-, Cl; $HCl(v = 1)$ by H, D, O, F, Cl. These rates will be correlated with other data in the literature and with such parameters as molecular dipole moments, atomic polarizability, and the reduced mass of the colliding complex. The theoretical position of I. I. Nikitin will be examined in light of our results and, in particular, his predictions of enhanced deactivation efficiency by atoms possessing orbital angular momentum degeneracy. Our work appears to broadly substantiate this position in that S state atoms such as H, D, and N are much less efficient deactivators of HF than is O, F, Cl, and Br. Among the halogen atoms deactivation efficiency increases in the order F, Cl, Br.

MD9. Vibrational Deactivation of $CO_2(^3\Sigma)$ by Collisions with Atoms, M. I. Buchwald and G. J. Wolga, *Cornell University, Ithaca, N.Y. 14850.*

The great interest in CO_2 lasers has prompted extensive investigation of the vibrational relaxation and energy transfer resulting from collisions between CO_2 and other molecules. In many types of CO_2 lasers atoms as well as molecules are present as a result of the excitation scheme employed. Few low temperature rates for the deactivation of the CO_2 upper level, $(00^\circ 1)$, by atoms have been available heretofore. The experimental work to be presented will describe our studies of the deactivation of $CO_2(00^\circ 1)$ by various atoms.

The experimental method employed is laser induced fluorescence on a flowing gas stream to measure vibrational relaxation, with microwave paramagnetic resonance to make absolute atom density determinations. In combination with known molecule-molecule deactivation rates this method has permitted us to determine or place upper bounds on a large number of atom-CO_2 rates. In the course of this work measurements have also been made on deactivation rates of certain atoms with $N_2(v = 1)$ and $CO(v = 1)$.

We shall report our studies of the deactivation of $CO_2(00^\circ 1)$ by H, D, O, N, F, and Cl. In addition we shall discuss our studies of $N_2(v = 1)$ deactivated by H and N and of $CO(v = 1)$ deactivated by H. This work was all done about 300 K.

In our discussion we shall contrast the relatively inefficient effects of S state atoms (H, D, N) with the relatively efficient effect of atoms possessing orbital angular momentum degeneracy (O, F, Cl). This distinction will be discussed in the light of I. I. Nikitin's theoretical prediction of deactivation enhancement by atoms possessing orbital degeneracy. We shall also contrast the relatively slow rates of deactivation of CO_2 with the more rapid deactivation of $HF(v = 1)$ by the same atomic collision partners. The advantages and limitations of our experimental method will be discussed as will the special problems attendant to slowly relaxing molecules like CO_2.

MD10. Vibrational Relaxation of N_2 and $CO_2(001)$ by Alkali Metal Atoms,[1] R. C. Benson, D. J. Benard, and R. E. Walker, *Johns Hopkins Applied Physics Lab.*

The efficient vibration-to-translation (V-T) relaxation of molecules by reactive atoms is of interest from both an experimental and a theoretical view. All results to date indicate that reactive atoms are at least an order of magnitude more efficient than typical molecules (e.g., CO, CO_2, N_2) in the vibrational relaxation of molecules. These high efficiencies cannot be explained by conventional theories and have been attributed to strong attractive intermolecular forces. We have devised a new technique to measure small signal gain and have applied this method to determine the V-T relaxation rates of N_2 and $CO_2(001)$ by alkali metal atoms. Basically the technique is to fluid-modulate trace amounts of CO_2 which are added to a fast-flowing, alkali metal-active N_2 mixture. The extremely fast resonant V-V transfer between $N_2(v = 1)$ and $CO_2(001)$ inverts the $CO_2(001)$ level which is then probed with a conventional CO_2 laser. By measuring the optical gain with and without the alkali metal, the V-T rates can be determined. The method is quite sensitive and gain changes as small as 0.1 percent can be measured. The effective rate,

$$k_{\text{eff}} = k_{N_2\text{-M}} + 0.914(X_{CO_2}/X_{N_2}) \cdot k_{CO_2\text{-M}},$$

for the coupled N_2 and CO_2 levels has been determined for $X_{CO_2}/X_{N_2} = 0.071$ and M = Li, Na, K and Cs: Li, $k_{\text{eff}} = 1500 \pm 500$; Na, $k_{\text{eff}} = 1400 \pm 200$; K, $k_{\text{eff}} = 4600 \pm 1000$; and Cs, $k_{\text{eff}} = 7900 \pm 2000$, all in units of $\text{torr}^{-1}\ \text{s}^{-1}$. In the case of Na, X_{CO_2} was also varied in order to determine the individual rates: $k_{N_2\text{-Na}} = 920 \pm 100\ \text{torr}^{-1}\ \text{s}^{-1}$ and $k_{CO_2\text{-Na}} = 8100 \pm 2000\ \text{torr}^{-1}\ \text{s}^{-1}$. These experimental rates differ by orders of magnitude from theoretically predicted values based on an ionic-intermediate curve-crossing model.[2]

[1] Supported by the Department of the Navy.

[2] E. R. Fisher and G. K. Smith, *Chem. Phys. Lett.*, vol. 6, p. 438, 1970.

MD11. Infrared Laser Enhanced Reactions: An Application of the Technique for the Measurement of V-T, and V-V Deactivation Rates in the 10_3 and O_3-SiF_4-O_2 Systems, A. Kaldor, *Corporate Research Labs, Exxon Research & Engineering Co.,* and W. Braun and M. J. Kurylo, *Physical Chemistry Div., National Bureau of Standards, Washington, D.C. 20234.*

A laser technique to study the chemical dynamics of vibrationally, excited species is described. The technique employs chemiluminescence and/or resonance fluorescence monitoring of the temporal or steady-state behavior of reactants or products in reactions of vibrationally excited (laser excited) species. In the chemiluminescence reaction of $O_3^\dagger$ with NO the method of measurement of deactivation (V-T) rates for vibrationally excited species is described, and rate constants for deactivation of $O_3^\dagger$ by He, Ar, H_2, N_2, O_2, H_2O, CO_2, SO_2, CH_4, and SF_6 are reported.

Rate Constants for the Deactivation $O_3^\dagger$ in the (100), (010), and (001) Manifold

Deactivant	$k(\text{cm}^3\ \text{molec}^{-1}\ \text{s}^{-1})$
Ar	$7.27 \pm 1.77 \times 10^{-15}$
O_2	$1.31 \pm 0.13 \times 10^{-14}$
N_2	$1.94 \pm 0.06 \times 10^{-14}$
He	$6.02 \pm 0.29 \times 10^{-14}$
CO_2	$1.06 \pm 0.08 \times 10^{-13}$
SO_2	$2.35 \pm 0.12 \times 10^{-13}$
CH_4	$4.83 \pm 0.44 \times 10^{-13}$
H_2	$1.18 \pm 0.07 \times 10^{-12}$
SF_6	$1.92 \pm 0.11 \times 10^{-12}$
H_2O	$3.53 \pm 0.24 \times 10^{-12}$

Rapid V-V energy transfer between SiF_4 and O_3 has been observed following laser excitation of either O_3 or SiF_4. In experiments where only the SiF_4 is vibrationally excited, the V-V transfer to O_3 and subsequent reaction of $O_3^\dagger$ with NO were used to obtain the rate constant for the V-T deactivation of $SiF_4^\dagger$ by O_2.

$$SiF_4^\dagger = O_2 \xrightarrow{h} SiF_4 + O_2$$

$k = 6.3 \pm 1.4$

$\times 10^{-13}$ cm^3 molec^{-1} s^{-1}.

Fractional modulation measurements of the chemiluminesence generated by the $O_3 + NO$ reaction were used in experiments where primarily the O_3 is excited to obtain the rate constant for the V-V energy transfer between $O_3^\dagger$ and SiF_4

$$O_3^\dagger + SiF_4 \xrightarrow{k} SiF_4^\dagger + O_3$$

$k = 3.8 \pm 0.5$

$\times 10^{-11}$ cm^3 molec^{-1} s^{-1}.

SESSION TA

Pulsed Chemical Lasers and Q-Switching
Tuesday, October 22, 8:30 A.M.

TA1. N_2F_4 as a Saturable Absorber of CO_2 Laser Radiation, R. D. Suart.

Tetrafluorohydrazine exhibits a moderately strong IR absorption spectrum around 10 microns. A cell containing low pressures of this gas, mixed with He, induced passive Q-switching of a continuous wave CO_2 laser when inserted into a frequency selective cavity. This effect was observed near the P and R branches of the CO_2 (0,0,1) to (1,0,0) laser system on all transitions accessible in the laser.

Experiments were performed in a 2.8 m long cavity with a 75 line/mm frequency tuning grating and a 98% reflectivity output mirror. The cavity contained a 30 cm long CO_2 gain tube and a 53 cm long, 2.5 cm bore absorption cell. The gain tube was capable of pumping the cavity to 150% of the threshold gain measured with the absorption cell empty.

Although ultra high resolution absorption spectra of N_2F_4 are not available, experiments with various pressures of N_2F_4 in the cavity suggest that there is not a great deal of fine structure in the absorption spectrum of this molecule near the R branch of the (0,0,1) → (1,0,0) transition. This follows from the fact that the absorption due to N_2F_4 required to reduce the cavity gain to threshold at each R branch transition lay on a smooth curve identical with the profile of small signal gains over the same transitions.

The introduction of larger pressures of N_2F_4 into the cell in a nonfrequency selective cavity forced the laser to oscillate on the (0,0,1) → (0,2,0) transitions near 9.4 microns. This occurs because the absorption due to N_2F_4 is less in this region. Oscillation can be forced on either the P or R branch of the 9.4 micron system depending on the N_2F_4 pressure, because of differing absorption intensities in each branch.

From the measured rise and fall times of the Q-switched pulse and the cavity photon lifetime, it was possible to compare the observed pulse shape to that predicted by the theory of Zsabo and Stein.[1] It was concluded that the absorption cross section for N_2F_4 is at least ten times greater than the cross section of stimulated emission by CO_2 (0,0,1) at the laser wavelengths.

The observed properties of N_2F_4 suggest that this molecule might be useful for the isolation of high power CO_2 laser amplifier sections, for passive mode locking of pulsed CO_2 lasers and for forcing CW lasers into the lower gain 9.4 micron laser system.

[1] A. Zsabo and R. A. Stein, *J. App. Phys.*, vol. 36, p. 1562, 1965.

TA3. Mixture Stability in High-Power Pulsed H_2-F_2 Chemical Lasers,[1] R. W. Getzinger, L. S. Blair, and N. R. Greiner, *Los Alamos Scientific Laboratory.*

Interest in using H_2-F_2 mixtures in high-power pulsed chemical lasers has focused attention on the problems of mixture stability. Because the output power increases with the chemical reaction rate, it is desirable to have high H_2-F_2 concentrations and a considerable temperature rise during the burn. Therefore, addition of other components to enhance stability should be minimized. Although mixture stability improves at low temperature, the design requirements and operation are simpler at room temperature. Furthermore, we need a variety of readily workable construction materials that are themselves stable in this harsh environment and do not cause instability in the mixture.

We wish to present the results of a systematic study of the behavior of atmospheric-pressure mixtures of H_2, O_2, and F_2 at ambient temperatures carried out to determine a range of conditions under which the reagents can be combined nonexplosively. The $P_1(7)$ line from an HF probe laser was used to monitor formation of hydrogen fluoride in the reaction cells during and, in the absence of explosion, for some 30 minutes after the mixing process. A detailed empirical calibration of beam transmission versus known partial pressure of HF in each of the gases of interest yielded pressure broadening parameters for the $P_1(7)$ line, and permitted determination of the absolute amount of HF formed during reaction.

In the absence of explosion conversion of reagents to HF during the period of observation was always less than 5%. Reaction to form HF was seen to take place "promptly" during mixing and at an essentially constant rate thereafter. The magnitudes of these two quantities increased together, and were clearly related to the difficulty of reproducibly bringing the reagents together without explosion. As little as 5% O_2 as the only additive was sufficient to prevent explosion in stoichiometric H_2/F_2 mixtures. The dependence of the reaction rate on partial pressure O_2, initial H_2/F_2 ratio, total gas density, and temperature was examined. Various considerations, including computations based on a plausible steady-state chemical mechanism with constant reagent concentrations and literature values for the pertinent rate coefficients, indicate that heterogeneous reaction steps significantly influence the long-term deterioration of the mixtures.

Stable mixtures could be made in contact with any of the following: Kel-F, Teflon, Viton, brass, aluminum, stainless steel, quartz, sapphire, or calcium fluoride. This list affords materials suitable for building H_2-F_2 lasers initiated by flash photolysis, electric discharge, or electron beams. Examples of each type have been built and successfully operated in this laboratory, including an e-beam initiated device 28 l in volume operated at 1.5 atm.

[1] Work performed under the auspices of the U.S. Atomic Energy Commission.

TA6. Chemically Pumped Hydrogen Fluoride Overtone Laser, J. F. Hon and J. R. Novak, *Rodketdyne Division/Rockwell International, Canoga Park, Calif. 91304.*

It has been shown by several workers that substantial fractions of the energy of reaction of F-atoms with H atom donors (HR) are distributed initially (primative distribution) into vibrationally excited states ranging from $v = 1$ to the highest v state possible for the energy available in a specific reaction. For a wide range of F plus HR reactions, this results in the population of $v = 3$ and higher. The gain on $\Delta v = 1$ transitions for HF can be quite high for these systems and a multitude of F + HR reactions have produced HF $\Delta v = 1$ lasing. Because the $\Delta v = 1$ transitions have very high gain, appreciable gain can be expected on $\Delta v = 2$ transitions although much lower than that of $\Delta v = 1$ transitions. Calculated[1] matrix elements for the low J, $v = 3 \rightarrow 1$ transitions are about 0.16 the values calculated for low J, $v = 2 \rightarrow 1$ transitions, so that for equivalent population inversion the overtone gain would be about 2.5×10^{-2} that of the fundamental. Provided that the optical resonator is sufficiently selective, there is no basic reason why $\Delta v = 2$ transitions should not be lasable, given a sufficiently long gain path. Indeed,

[1] R. E. Meredith and F. G. Smith, *Investigations of Fundamental Laser Process*, vol. II, Willow Run Laboratories, Nov. 1971 (ARPA Contract DAHC-15-67-C-0062).

$\Delta v = 2$ transitions have been reported for a DF chemical laser.[2] However, subsequent to this, no other overtone lasers have been reported in the literature.

Here we report the lasing of five overtone transitions in an electrical pulse-initiated chemically pumped HF laser. Chemical pumping of HF was achieved with a standard pin discharge laser employing SF_6 in the discharge to produce F atoms and HBr as the H atom donor. The discharge tube was 1 m long, terminated with CaF_2 Brewster angle windows and operated at low pressure ($\sim$1 torr). The optical resonator consisted of two 10-m radius dielectric-coated mirrors tuned for maximum reflectivity (>99.5%) at 1.3 μ. Published results on the primative vibrational distribution of HF(v) from the reaction of F with HBr indicate the relative rates[3]: $v = 0$, 0.2; $v = 1$, 0.62; $v = 2$, 1.00; $v = 3$, 0.9; $v = 4$, 0.67. Thus, $v = 3$ and $v = 4$ are well-populated initially. Lasing transitions corresponding to three $v = 3 \rightarrow 1$ transitions, P(3), P(4), and P(5), and two $v = 4 \rightarrow 2$ transitions, P(4) and P(5), were observed.

The overtone wavelengths observed and the transition assignments are shown in Table I. Also shown are the computed wavelengths. Transition assignments were made by comparing the two. The agreement, as assigned, with calculated wavelengths is quite good and this along with the J-value sequencing provides high confidence in the line assignments.

TABLE I
HF OVERTONE RESULTS

Observed (cm^{-1})	Assignment	Calculated[a]
7285 ± 1	3 ⟶ 1 P(3)	7284.3
7235	P(4)	7236.1
7187	P(5)	7185.2
6914	4 ⟶ 2 P(4)	6911.2
6864	P(5)	6862.0

[a]R. E. Meredith and F. G. Smith.[3]

[2]S. N. Suchard and G. C. Pimentel, *Appl. Phys. Lett.*, vol. 18, p. 530, 1971.
[3]N. Jonathan *et al.*, *Mol. Phys.*, vol. 22, p. 561, 1972.

TA7. Theoretical Investigation of the Effect of Rotational Nonequilibrium on Predicted Performance of Pulsed HF Chemical Lasers, J. J. T. Hough and R. L. Kerber, *Michigan State University, E. Lansing, Mich. 48824.*

A rate equation model is developed based on the interaction of the chemical kinetic and radiative phenomena within the active medium; the model simulates cavity transients such as the interaction of intensity and gain in the pulsed HF chemical laser. Calculations show that the growth in intensity is sufficiently slow that the gain may attain levels far above threshold before lasing begins. Intensity increases sharply after the gain is far above threshold causing the gain to drop rapidly and oscillate near the threshold value. This fluctuation in gain, which is a result of fluctuation in HF (v, J) populations, makes the calculations more sensitive to relaxation processes than has been shown by earlier constant gain models. The present model, which is capable of predicting time histories of intensities of laser transitions and chemical species concentrations is further expanded to study the effects of preferential pumping into rotational levels, rotational relaxation, and rotational nonequilibrium. Due to the length of the numerical calculations, this latter expansion was limited to the less complicated case of the SF_6/H_2 laser pumped by the $F + H_2$ reaction. Rotational relaxation is modeled by associating with each (v, J) state a relaxation time constant τ consistent with available experimental data and theoretical calculations. The results show that as the rotational relaxation rate decreases the laser output decreases and pulse energy is more uniformly distributed among the lasing transitions within a given band. The predicted time-resolved spectrum exhibits strong simultaneous lasing on many vibrational–rotational transitions; a situation that is found experimentally but cannot be predicted by earlier models. The normal J-shift pattern is also predicted. This unique model is capable of predicting the performance of lasers operating in the line-selected mode. A comparison is made of the output from a three transition cascade consisting of $P_1(8)$, $P_2(7)$, $P_3(6)$ with the same three transitions operated in the single-line mode. The sum of the output from the three single line calculations is just 65% of the output from the cascade.

TA8. Calculation of Rotational Nonequilibrium in a Pulsed HF Laser,[1] J. R. Creighton, *Lawrence Livermore Laboratory, Livermore, Calif. 94550.*

Several numerical models of the HF laser have been published.[2] These have generally assumed rotational equilibrium within each vibrational level and have used a steady-state (gain equals loss) model for lasing. We have developed a numerical model which extends these calculations by treating each vibrational–rotational state separately and allows rotational relaxation. This model can test the validity of assuming rotational equilibrium. The model also extends the calculations by using simplified semiclassical laser equations rather than the steady-state approximation.

The computer code produces waveforms for each P-branch transition. These waveforms are in good agreement with experimental waveforms from a pulsed $NF_3 + H_2$ laser initiated by a 70 ns discharge.[3,4] The calculated and experimental waveforms agree as to which transitions lase, the delay between initiation and laser turn on, and the shape and relative amplitudes of the individual waveforms, including spikes. The differences between calculated and experimental waveforms are comparable to the experimental variation from one shot to another.

The experiment used a mixture of 13 torr of NF_3 and 2.5 torr of H_2. The principal effect of the discharge was to dissociate a fraction of the NF_3 to produce atomic fluorine. Vibrationally excited hydrogen fluoride was produced by the reaction $F + H_2 \rightarrow HF + H$. The discharge volume was 0.50 m long and the output mirror was 8% reflective. The calculation used the same conditions, and the experimental and calculated output energies agreed when 1.25% dissociation of NF_3 was assumed.

The calculations show that rotational equilibrium at the translational temperature is not achieved, mainly because the chemical reaction pumps states with relatively large J. Near the end of the pulse, the rotational distribution approaches equilibrium; even then, the ratio of populations of adjacent states differs significantly from a Boltzmann factor.

The calculations also show a sizable delay between the time that a transition reaches threshold inversion and the time that lasing begins. This is followed by a spike in the laser intensity due to excess inversion. The P3 and P4 transitions are dominated by this spike. The calculation shows simultaneous lasing of several transitions, in agreement with experiment. Some J-shifting is also observed.

The interaction of all of the populations and laser intensities is portrayed in a computer generated 16-mm movie.

[3]R. K. Pearson, J. O. Cowles, G. L. Hermann, K. J. Pettipiece, and D. W. Gregg, III, *IEEE J. Quantum Electron.*, vol. QE-9, p. 723, 1973.
[4]R. K. Pearson, unpublished data.

[1]Work performed under the auspices of the U.S. Atomic Energy Commission.
[2]For example see: A. N. Chester, *J. Chem. Phys.*, vol. 53, p. 3595, 1970; G. Emanuel and J. S. Whittier, *Appl. Opt.*, vol. 11, p. 2047, 1972; J. R. Airey, *J. Chem. Phys.*, vol. 52, p. 156, 1970.

SESSION TB

CO Lasers
Tuesday, October 22, 8:30 A.M.

TB1. Chemically Pumped CO_2 and N_2O Lasers: $CO^{\dagger}/(CO_2 \cdot N_2O)$, A. B. Petersen and C. Wittig, *Electrical Engineering Department, University of Southern California.*

CO_2 and N_2O chemically pumped lasers are discussed. Excitation of the (001) state has been achieved by energy transfer from vibrationally excited CO ($CO^\dagger$). $CO^\dagger$ is produced in the chemical reaction: $O + CS \rightarrow CO^\dagger + S$. Both pulsed (flash photolysis initiated) and CW fluid mixing systems are discussed, and, in the pulsed systems, detailed small-signal gain measurements are presented. Because of energy transfer considerations, the $CO^\dagger/N_2O$ system appears more promising than $CO^\dagger/CO_2$. The stability of N_2O in the chemical system described in this work, compared to an electric discharge where irreversible dissociation occurs, makes the system quite attractive. It is shown that in addition to the enhancement of CO laser output by resonant energy transfer to triatomics such as N_2O, stimulated emission at the triatomic laser frequencies provides a further means of removing energy from the undesirable "bottleneck" in the CO system. This is the basis of a "bootstrap" operation of the $CO^\dagger/CO_2$ and $CO^\dagger/N_2O$ systems in which the total photon flux is enhanced through this coupling. This idea will be discussed in detail and experimental results will be presented. Kinetics of the systems will also be discussed in light of our data. Comparison between our results, theory, and other chemically pumped CO_2 and N_2O systems will be made with respect to important considerations such as efficiency, energy storage, etc.

TB2. Experimental Investigation of a Supersonic CO Electric Discharge Laser, M. J. Plummer, J. L. Wagner, and W. J. Glowacki, *Naval Ordnance Laboratory*.

A supersonic expansion offers a simple means of providing volume-type cooling of a gas to cryogenic temperatures. It has also been shown that a pulsed CO electric discharge laser operating at cryogenic temperatures is very efficient. It was therefore decided to investigate a CO laser where the gas is first cooled by a supersonic expansion and then flows through a discharge-cavity region where electrical power is added to the gas and optical power is extracted. To improve the stability and efficiency of the discharge, an e-beam-sustainer is used. While the laser is a CW device, it operates something like a pulsed device because at the typical flow velocities and cavity sizes used the gas residence time in the discharge is of the order of a few hundred microseconds.

In the NOL laser, the gas is cooled to 75 K by expansion through a supersonic nozzle and then flows through an e-beam (15 cm × 50 cm window) sustained discharge and optical cavity. The discharge volume (5 cm high × 50 cm wide × 15 cm in the flow direction) is 4.5 l and the optical volume (stable resonator) is 0.79 l and is centered 11.4 cm from the beginning of the discharge. A power output of 28 kW at 4.7 percent efficiency has been obtained. The pulse duration was 900 μs (three flow times) and is indicative of CW-type operation. Power outputs up to 67 kW have been obtained for 300 μs pulses (one flow time). Typical e-beam current densities used are 0.3 to 0.6 mA/cm^2 in the gas. The multiline spectral output ranges from 5.09 μ to 5.55 μ with the most intense lines being concentrated at the shorter wavelengths.

Input powers up to 600 kW have been achieved for CW-type operation (three to six flow times) and are presently arc limited. Preliminary results indicate substantial heating of the gas by the discharge.

Comparison of the experimental results with a theoretical CO kinetics model are made and future experiments include interferometry to look at the cavity density disturbances introduced by the supersonic flow and the discharge.

TB5. Near Single-Line Operation of a Free Burning $CS_2/O_2/N_2O$ Flame Laser with a Non-dispersive Optical Cavity, K. D. Foster, G. H. Kimbell, and D. R. Snelling, *Defence Research Establishment Valcartier*.

CO laser output spectra between 5 and 5.5 μm for the free-burning CS_2/O_2N_2O flame laser were examined. Under certain conditions of high O_2 and high N_2O flow, the spectra were found to be nearly single line in nature with most of the laser output occurring on the $P_{10-9}(17)$ line at 5.4265 μm. This is the same line that was reported to lase in a nearly single-line fashion in an electrically-assisted longitudinal CO chemical laser.[1]

Under certain conditions where the multiline power output was high (12 to 15 W), the $P_{10-9}(17)$, line was found to be absent from the laser output spectra. The multiline spectra showed that normally about 40 lines were lasing.

The explanation for the tendency to operate on a single line under certain conditions, which was proposed by Coleman and co-workers relied upon rapid V-V exchange between vibrationally-excited CO molecules. It was suggested that the coupling between vibrational levels of CO was so strong that lasing may occur on the line exhibiting the highest gain while other lines would be kept below threshold.

The fact that nearly single-line operation has been observed in the present purely chemical flame laser where conditions of temperature and pressure are very different from the above longitudinal laser, suggests that an additional explanation is required. It is proposed here, that the $P_{10-9}(17)$ line itself is somewhat unique since it is almost coincident with the $P_{9-8}(23)$ line. Linewidth calculations show that if the line-center separation of this line pair is within about 0.3 Å then the overlap in the line profiles is sufficient to cause an increase of more than 10% in the peak gain over that of the isolated lines. The anomalously high gain of the $P_{10-9}(17)$ line, such that near single-line operation can occur under very different experimental conditions, may thus be due to an overlap in the line profiles.

The unique behavior of the $P_{10-9}(17)$ has manifested itself previously in pulsed chemical CO lasers. In the first report of laser action in the CS_2/O_2 system in a flash photolysis system, Pollack[2] found the highest J value for any lasing band to be $J = 14$ except for the 10-9 band which was found to lase on the P(10), P(11), P(12), P(13), and P(17) lines. This anomalous presence of the $P_{10-9}(17)$ line was also observed in a TEA style pulsed CS_2/O_2 laser by Jacobson and Kimbell.[3]

[1] Y. Hiroše, Y. Nachshon, T. A. De Temple, and P. D. Coleman, *Appl. Phys. Lett.*, vol. 23, p. 195, 1973.

[2] M. A. Pollack, *Appl. Phys. Lett.*, vol. 8, p. 237, 1966.

[3] T. V. Jacobson and G. H. Kimbell, *J. Appl. Phys.*, vol. 41, p. 5210, 1970.

TB6. Role of Atomic Sulfur in the $O + CS_2$ Reaction, L. T. Cupitt and W. L. Gamble, *U.S. Army Missile Command*.

Preliminary and continuing experiments in our laboratory have demonstrated that one can observe both the atomic oxygen and atomic sulfur EPR resonances simultaneously in a reacting mixture of $O + CS_2$ if no O_2 is present. Atomic O is generated in a flowing system by the reaction $N + NO \rightarrow O + N_2$. The simultaneous measurement of concentrations of O, S, SO, etc. will, when fully analyzed, allow a severe test of some of the relative branching rates in the initial reactions of CS_2 with O. Some of the pertinent kinetic pathways are $CS_2 + O \rightarrow CS + SO$, $CS_2 + O \rightarrow COS + S$, and $CS + O \rightarrow CO + S$. This last reaction rate is reasonably well known. Measurement of SO_2 concentrations allow the O removal by means of $SO + O + M \rightarrow SO_2 + M$ to be monitored. The reaction of $O + COS$ is another method for O removal, but, because of its kinetic simplicity and

relative slowness, it should provide no complication to the analysis of the kinetic data.

We are unaware that anyone has ever observed resolved O and S resonances simultaneously in this system. The deposition of sulfur (or sulfur compounds) on the walls is the major uncertainty which we are having to deal with currently. The experiments are being conducted in a relatively fast flow system (velocities 10 to 100 m/s). The reaction tube is a 1.1 in diam quartz tube. Resolved O and S resonances are obtainable for overall pressures less than a torr.

Experimental results along with the theoretically predicted results using the accepted rate constants for the various reactions considered, will be presented.

TB7. Vibrational Deactivation and Atom Exchange in $O(^3P) + CO(^1\Sigma^+)$ Collisions,[1] J. D. Kelley, *McDonnell Douglas Research Laboratories*, and R. L. Thommarson, *McDonnell Douglas Astronautics Company*.

We report a quasiclassical Monte Carlo trajectory study of the electronic ground state $O(^3P) + CO(^1\Sigma^+)$ collision system. Oxygen atoms have been shown to effectively deactivate $CO(v = 1)$ above 1800 K with a collisional probability of about 10^{-2}, which is quite high relative to those values observed for chemically inert collision partners. The potential surface for this system is not purely repulsive, however, but can lead to O-atom exchange.

The observed activation energy for the exchange reaction was about 7 kcal/mole.[2] An energy barrier of about 5 kcal/mole for O, CO recombination to an excited triplet CO_2 was derived from spectroscopic studies;[3] the CO_2 is presumably in $^3B_2$ or $^3A_2$ at least initially.[3,4] These bent triplet CO_2 states represent spin-allowed intermediates for the $O(^3P) + CO(^1\Sigma^+)$ system when one considers that these states have A' and A'' symmetry, respectively, in the C_s point group. The three asymptotic states derived from $^3\Sigma_u^-$ and doubly degenerate $^3\Pi g$ for $O(^3P) \ldots . CO(^1\Sigma^+)$ also have A'' and A', A'' symmetry in the C_s group. Avoided crossings between the A' states and between the A'' states in the general C_s collision configuration then lead to two possible adiabatic surfaces which connect ground state reactants and the $^3B_2$ and $^3A_2$ states of CO_2. These states are bound by about 45 and 35 kcal/mole relative to the reactants.[4]

We have assumed that these adiabatic surfaces can be represented by one "effective" surface, and that an analytical representation can be constructed.[5] The resulting surface has an angle-dependent barrier for O-atom approach with a minimum height of 6.8 kcal/mole at an O-C-O angle of 120°; there is a basin corresponding to triplet CO_2 with $r_{eq.}$ (C-O) = 1.255 Å, an equilibrium angle of 120°, and a depth of 42 kcal/mole. Trajectories have been calculated for CO initially vibrating with energies corresponding to $v = 0$ and 1. Various initial collision energies and CO rotational energies were selected and averages taken over the other initial variables, e.g., impact parameter, orientation angles, etc., using Monte Carlo techniques.

Results thus far show that the calculated 1-0 deactivation rates from 2000–4000 K are in reasonably good agreement with Center's data,[6] i.e., about a factor of two faster over this temperature range. The calculated atom exchange rates for $CO(v = 0) + O$ are also within a factor of two of the data[2] taken from 300–400 K. The calculations predict a 1-0 deactivation rate of about 2.5×10^6 1 mole^{-1} s^{-1} at 300 K, which is about 2.5 times faster than the calculated atom exchange rate for $v = 0$.

[1] This research was conducted under the McDonnell Douglas Independent Research and Development Program.
[2] S. Jaffe and F. S. Klein, *Trans. Faraday Soc.*, vol. 62, p. 3135, 1966.
[3] M. A. A. Clyne and B. A. Thrush, *Proc. Roy. Soc.*, vol. A269, p. 404, 1962.
[4] N. W. Winter, C. F. Bender, and W. A. Goddard, III, *Chem. Phys. Lett.*, vol. 20, p. 489, 1973.
[5] A. E. Stearn and H. Eyring, *J. Chem. Phys.*, vol. 3, p. 778, 1935.
[6] R. E. Center, *J. Chem. Phys.*, vol. 58, p. 5230, 1973.

TB8. Vibrational Deactivation of CO Molecules by Atomic Oxygen, C. C. Davis and R. A. McFarlane, *Cornell University, Ithaca, N.Y. 14850.*

Measurements are being carried out on the rate at which atomic oxygen collisionally deactivates CO molecules in the $v = 1$ level of the electronic ground state. A grating tuned UV preionized $CO_2 : N_2 : He$ TEA laser which generates pulses of several hundred millijoules energy is operated at selectable rotational transitions in the $(001 \rightarrow 100)$ and $(001 \rightarrow 020)$ bonds of CO_2. Using a crystal of tellurium, phase-matched second-harmonic generation is obtained using the TEA laser as a driver and radiation at 4.6–5.4 μ is available for laser-induced fluorescence studies on molecules absorbing in this region.

The P(14) line of the CO fundamental at 2086 cm^{-1} is at twice the frequency of CO_2 P(24) of $(001 \rightarrow 020)$ at 1043 cm^{-1} and very substantial fractions of the second-harmonic energy can be absorbed in our fluorescence cell to populate the CO $v = 1$ level. Following illumination by the 300-ns second-harmonic pulse, the fluorescence on R-branch lines of CO $v = 1 \rightarrow v = 0$ is observed through a short wavelength pass filter by an InSb photovoltaic detector driving a Perry amplifier. The output is digitized using a Biomation Model 8100 Transient Digitizer and pulses are accumulated in a Northern Scientific Model 575 Signal Averager. Decay rates are determined by a least squares fit of the data to an appropriate exponential function.

The fluorescence cell is part of a flowing gas system and CO is injected upstream from the cell. At a point farther upstream from the CO injection molecular oxygen is introduced and passed through a microwave discharge to provide about 20% dissociation. Atomic oxygen concentration is measured using NO_2 titration at the plane of the cell. Absolute atomic concentrations will also be established with an X band E.P.R. system using molecular oxygen as a reference.

The contribution to the decay rate of CO ($v = 1$) due to atomic oxygen is determined from the increment in the observed decay rate as the microwave dissociation source is turned on. In addition to oxygen, measurements are planned using other atomic species and all data available at the time of the conference will be reported.

SESSION TC

Post-Deadline Papers
Tuesday, October 22, 2:00 P.M.

TC1. An Atomic Boron Laser—Pumping by Incomplete Autoionization or Ion-Electron Recombination, J. Stricker and S. H. Bauer, *Cornell University*.

Pulsed lasing was obtained from discharges in mixtures of He (≈10 torr) and a number of boron containing species (≈25 m torr). Discharge conditions for optimizing the output are briefly described. Lasing starts 20–50 μs after passage of the discharge pulse (≈1 μs halfwidth). By a suitable combination of filters that spanned the range 1 → 11 μm, we established that the radiation appeared only between 2 and 4 μm; a gold-doped germanium detector, cooled to liquid nitrogen, was used. We did not test for radiations outside the 1 to 11-μm range. With a calibrated 25 cm f.l. Spex grating monochromator fitted with 25-μm slits, a single line was found at 2777 ± 1.6 cm^{-1}; its width was less than or equal to the resolution of our instrument. *This frequency was unaffected by the reagents used* [B_2H_6, H_3BCO, B_5H_9, BBr_3]. The absence of any H/D

isotope shifts eliminated BH, BH_2, and BH_3 as emitters; this was later confirmed by the observed lasing from BBr_3/He mixtures. The possibility that the emitter is BHe^+ was eliminated by the absence of any $^{10}B/^{11}B$ isotope shift. We conclude that the emitter is atomic boron.

The appearance of a delay in the 20–50-μs range for an atomic laser is indicative of a multistep collisional mechanism. This was supported by our search for coincidence spacings among the term values for B I and B II. Reference to Moore's tables and the later work by Edlén *et al.* uncovered a single combination in the B I set which was close enough to be considered. The limiting ionization level for the doublet states is 66 928.10 ± 0.1 cm^{-1} [nf ^2F series], while $1s^2\ 2s^2\ 7s, {}^2S_{1/2}$ occurs at 64 156 ± ? cm^{-1}; i.e. 2772 ± ? cm^{-1} lower. The fact that two well-characterized states were observed above the ionization limit [$2s\ 2p^2, {}^2P_{3/2;1/2}$ at 72 547 and 72 535 cm^{-1}; $2p^3, {}^4S^0_{3/2}$ at 97 037 + x cm^{-1}] suggests that pumping may start by excitation to a metastable state above the ionization limit. Then, due to some perturbation, such as a distant collision, de-excitation to the ionization limit occurs but with the electron still captured (incomplete autoionization). Lasing occurs by induced transitions to the $1s^2\ 2s^2\ 7s, {}^2S_{1/2}$ state.

Dr. T. A. Cool called our attention to a second matching interval. Extrapolation *via* a linear Ritz formula indicates a term value of 61 381 cm^{-1} for the $1s^2\ 2s^2\ 5p, {}^2P_{3/2;1/2}$ state, which is 2775 cm^{-1} below 7s, $^2S_{1/2}$. Thus, the delay may be due to cascading from the incompletely autoionized states to $1s^2\ 2s^2\ 7s$, which is the upper lasing level, from which induced transitions are made to the 5p state. Finally, another possible route for populating states at the ionization limit is the capture of an electron by B^+ during a large impact-parameter encounter. The high sensitivity of lasing power to the pressure of B atom precursors suggests that populating the upper lasing level competes with other B atom or B^+ reactions.

TC2. Laser-Induced Photochemical Enrichment of Boron Isotopes, S. M. Freund, *Optical Physics Division, National Bureau of Standards, Washington, D.C.*, and J. J. Ritter, *Inorganic Materials Division, National Bureau of Standards, Washington, D.C.*

Mixtures of BCl_3 and H_2S are irradiated with 10.55-μm radiation (P(16) line of the 001-100 band of CO_2) from a TEA laser. This wavelength coincides with a strong B-Cl stretching transition in $^{11}BCl_3$. After several hours of irradiation it is found that the maximum ^{10}B to ^{11}B ratio of recovered gaseous boron containing material (primarily BCl_3) is 0.413 ± 0.004. The corresponding ratio of the BCl_3 starting material is 0.242 ± 0.002. The ^{10}B concentration has been increased from 19.5% to 29.2% by selectively exciting the $^{11}BCl_3$ with the laser radiation which causes it to react preferentially with the H_2S, forming a solid, and thereby increasing the ^{10}B concentration in the gas phase. Further, by irradiating a similar mixture with 10.18 μm (R(30) line of the 001-100 band of CO_2) it is found that the ratio changes to 0.1863 ± 0.002. This wavelength radiation coincides with a strong B-Cl stretching transition in $^{10}BCl_3$ which then reacts with the H_2S lowering its concentration to 15.7%. The thermal reaction between BCl_3 and H_2S, conducted under comparable conditions, proceeds very slowly yielding principally $HSBCl_2$. All laser experiments are performed in a small static system, and milligrams of enriched boron containing material are recovered. The principal products are a solid with negligible vapor pressure, the identification of which is not conclusive as yet, and HCl. Although the stoichiometry is somewhat uncertain at the moment, it is suspected that one mole of BCl_3 is consumed for every two moles of H_2S, liberating 2.5 moles of HCl.

TC3. Laser Induced Photochemical Enrichment of Chlorine Isotopes, M. Lamotte, H. J. Dewey, R. A. Keller, and J. J. Ritter, *National Bureau of Standards, Washington, D.C. 20234.*

Chlorine isotopic abundances were significantly altered by laser-induced selective excitation of particular isotopic species of thiophosgene followed by chemical reaction between electronically excited thiophosgene and diethoxyethylene. A CW argon ion laser was used to excite, primarily, the $CS^{37}Cl_2$ species while a tunable nitrogen pumped dye laser was used to excite the $CS^{35}Cl_2$ species. The extent of selective reaction was followed by analyzing the unreacted $CSCl_2$ mass spectrometrically. The intensities of the mass peaks of $CSCl^+$ at 79 and 81 were monitored as well as the parent peaks at masses 114, 116, and 118. The changes in the parent peaks are shown in Fig. 1. The percentage of ^{35}Cl in $CSCl_2$ was changed from the natural abundance value of 75% to either 64% or 80% in a single step. The extent of reaction required for various degrees of enrichment implies a loss in selectivity after the initial excitation.

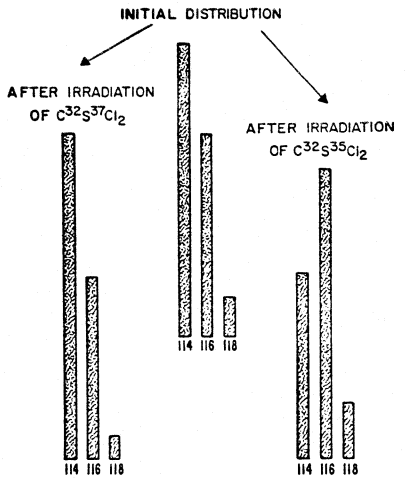

Fig. 1.

TC4. Laser Isotope Separation of Titanium-50 for Nuclear Reactor Applications, R. W. F. Gross, *The Aerospace Corporation, Los Angeles, Calif. 90009.*

The separation of titanium-50 by a two-step photodissociation with following chemical extraction process is proposed. It is suggested that titanium-50 could serve as a construction material for nuclear reactors, for instance, for cladding of reactor fuel elements. The laser separation process will be described in detail; it is based entirely on existing high-power laser sources. A preliminary cost estimate for the separation process indicates that titanium-50 could be economically competitive with zirconium, which is presently being used for such applications and at the same time be mechanically and structurally superior to zirconium.

TC5. Temperature Resolution of the Chemical Dynamics of the $O_3^\dagger$ + NO Reaction System, M. J. Kurylo, W. Braun, and C. Nguyen Xuan, *Physical Chemistry Division, National Bureau of Standards, Washington, D.C. 20234*, and A. Kaldor, *Corporate Research Laboratories, Exxon Research & Engineering Company, Linden, N.J. 07036.*

The rate constant for the decay of vibrationally excited ozone, $O_3^\dagger$, in the $O_3^\dagger$ + NO reaction system has been measured from 150 to 350 K. Vibrationally excited O_3 was produced in the asymmetric stretch normal mode by absorption of square-wave-modulated emission from a CO_2 laser tuned to the P(30) 9.6-μm transition. Under appropriate experimental conditions, a rapid V → V coupling process involving all three normal modes of O_3 is believed to set up a Boltzmann population distribution

between them. Reaction or relaxation of $O_3^\dagger$ out of this subset of normal modes is observed to proceed through a weighted average of rate constants. From the effects of temperature and buffer gas pressures it was determined that the predominant loss mechanism for the stretching mode(s) (ν_1 and/or ν_3) was via reaction with NO while the closely coupled ν_2 bending mode disappeared primarily via V → T deactivation by NO. The rate constant for the reaction channel (involving ν_1 and/or ν_3) is given by

$$k_{R2} = (2.0 \times 10^{-11}) \exp\left(\frac{-1107}{T}\right) \cdot \text{cm}^3 \text{ molec}^{-1} \text{ s}^{-1}$$

while that for V → T relaxation through ν_2 is

$$k_{R1} = (1.0 \times 10^{-13}) \exp\left(\frac{-39.2}{T}\right) \cdot \text{cm}^3 \text{ molec}^{-1} \text{ s}^{-1}.$$

The observations made in this study suggest the possibility of nonequilibrium among the vibrational modes under selected experimental conditions. This information is used in evaluating other measurements of this same reaction system and yield important conclusions suggestive of further research in chemical dynamics.

A comparison of the Arrhenius parameters for the above-mentioned reaction channel of $O_3^\dagger$ with parameters for the corresponding process involving thermal O_3 yields specific information about the effect of vibrational energy on the reaction dynamics.

TC6. High-Temperature Fast-Flow Reactor Studies of Metal Atom/N_2O Chemiluminescence,[1] W. Felder and A. Fontijn, *AeroChem Research Laboratories, Inc., Princeton, N.J. 08540.*

The AeroChem high-temperature (up to 2000 K) fast-flow reactor, previously used for reaction kinetic studies of metal atoms and metal monoxides with O_2, has been adapted for metal atom/N_2O chemiluminescence measurements. With this apparatus, spectroscopic and kinetic measurements are made under controlled and independently variable experimental conditions including reaction zone temperature, metal atom source temperature, total pressure, reagent partial pressure, and reaction time. Metal is evaporated from a suitable source in the upstream section of the flow tube, entrained in the bath gas and transported to the reaction zone, where N_2O is introduced in excess through a movable multiperforated ring. Measurements have been made on the reactions of N_2O with Sn, Ba, and Al.

Intense SnO chemiluminescence has been obtained from the Sn/N_2O reaction at 1000 K. A preliminary comparison of the total chemiluminescence intensity with the O/NO standard indicates a photon yield (branching ratio) for this reaction >20% from 300–750 nm. The spectrum exhibits transitions from the D, C, B, and A-X systems. The photon yields are $A > B > C \geqslant D$-X at all pressures studied, with the A-X (0, v'') bands accounting for ≈50% of the total light yield. The highest energy transition observed is the (5,0) $D^1\Pi$–$X^1\Sigma$ band at ≈310 nm, which agrees with $D_{\text{Sn-O}} \approx 5.7$ eV. Many band features especially for $\lambda > 550$ nm are not tabulated in the literature and have been shown to be A-X transitions. Initial kinetic and mechanistic studies indicate that the A and B-X photon yields and spectral distributions are pressure-independent from 3–50 torr. The yields of the C and D systems are enhanced by a factor of 2 as the pressure is increased over this range. The light producing reaction(s) have been shown to be first order in [Sn] and [N_2O]. The 1000 K value of the overall rate coefficient k for Sn + N_2O → all products, has been measured over a limited number of conditions (pressure, flow velocity, $[\text{Sn}]_{\text{initial}}$). The measurements indicate a $k \approx 10^{-12}$ ml molecule^{-1} s^{-1}, an usually low value suggesting the possibility of an electronic transition chemical laser system which is chemistry rather than mixing limited.

A test of the effect of temperature on the Ba/N_2O chemiluminescence was made by comparing the 350–750-nm spectra obtained under identical conditions at 500 and 1000 K at pressures from 0.7 to 20 torr. The comparisons show that the spectral distribution of the Ba/N_2O chemiluminescence at a given total density is temperature independent from 500–1000 K. Preliminary indications are that the total light yield also is independent of T over this range.

A search for 350–750 nm chemiluminescence from the Al/N_2O reaction was made. No chemiluminescence was observable at pressures of 0.7, 10, or 50 torr, T = 1000 K and reaction times from 0–10 ms. Simultaneous measurement of Al via atomic absorption verified that a rapid gas phase reaction with N_2O removes Al. From comparison with the Ba/N_2O chemiluminescence the photon yield is <0.05%. Thus this system does not appear to offer promise as a direct visible chemical laser pumping reaction.

[1] This work supported by the Office of Naval Research under Contract N00014-74-C-0327.

TC7. Direct Determination of the Yield of Electronically Excited Iodine Atoms, I($5^2P_{1/2}$), in the Flash Photolysis of Alkyl Iodides, T. Donohue and J. R. Wiesenfeld, *Cornell University, Ithaca, N.Y.*

The flash photolysis of alkyl iodides has been utilized to produce population inversions in the optically metastable, excited spin-orbit level, I($5^2P_{1/2}$) [≡I*], of the lowest electronic state of iodine. This inversion may be exploited in the construction of a high-gain pulsed laser operating on the transition, I* → I(λ = 1315 nm). A variety of iodides may be photolyzed in this system; their efficiencies appear to be a function of the alkyl group structure. In particular, photolysis of n-propyl iodide results in lasing action while that of iso-propyl iodide does not. This phenomenon has been ascribed to differences in the initial yields of I* for these isomers, although no quantitative results have been obtained. Here we describe experiments which permit the direct measurement of the initial photochemical yields of I and I* as a function of alkyl group structure. These yields are important parameters in modeling the performance of the I* laser.

Following the flash photolysis of the molecule under study using a 100 J Kr-filled discharge lamp, the I and I* atoms formed are monitored using time-resolved atomic absorption analysis. In this technique, the attenuation of the resonance transition, I($6^2P_{3/2} \leftarrow 5^2P_{1/2}$) at 2062 Å is used to obtain the temporal profile of the I* concentration while the transition at 1783 Å, I($6^2P_{3/2} \leftarrow 5^2P_{3/2}$), permits the corresponding measurement to be made on the concentration of ground state atoms. Typical photolysis mixtures contain *ca.* 0.2–20 μ of alkyl iodide and 20 torr of argon which acts as a buffer gas to prevent adiabatic heating of the photolysis mixture or pyrolysis of the source material. In addition, small quantities of H_2 (*ca.* 20–300 μ) are added to enhance the rate of the relaxation of I* to I. By varying this rate, it is possible to observe the concentration of I atoms following their formation both in the initial photolysis and subsequent relaxation of I* by H_2 and the relative initial yields of I* and I may be determined.

A number of alkyl iodides and their perfluorinated derivatives have been studied. These were extensively degassed and purified, and fractionally distilled under vacuum to remove such efficient quenchers of I* as O_2 and I_2. The yields of I* and the second-order rate coefficients for quenching of I* by the alkyl iodides are presented below.

Source	$\frac{[I^*]_0}{[I^*]_0 + [I]_0}$	k_Q (torr^{-1} s^{-1})
CH_3I	0.92 ± 0.02	2.2 ± 0.5 × 10^4
C_2H_5I	0.67 ± 0.10	2.2 ± 0.5 × 10^4
n-C_3H_7I	0.60 ± 0.10	3.0 ± 0.6 × 10^4
i-C_3H_7I	<0.10	–
CF_3I	0.90 ± 0.04	1.2 ± 0.2 × 10^1
n-C_3F_7I	>0.98	–
i-C_3F_7I	0.89 ± 0.02	–

At present, theory does not provide an explanation for the dramatic effect of structure on I* yield. Some possible approaches to this problem will be discussed.

TC8. Quantum Yields of O(^{1}S) from N_2O and S(^{1}S) from OCS in the Vacuum Ultraviolet, G. Black, R. S. Sharpless, and D. C. Lorents, *Stanford Research Institute.*

For laser fusion requirements, the ^{1}S states of the Group VI elements are of interest as possible high-energy lasers. One of the major problems with these excited states is associated with their production. It is desirable to find source molecules which yield these excited states with high efficiency at the wavelengths of the rare gas dimer emission. We have measured efficient production of O(^{1}S) from N_2O in the vicinity of the Ar_2 emission at 1260 Å and a high yield of S(^{1}S) from OCS in the vicinity of the Kr_2 emission at 1460 Å. The results are shown in Figs. 1 and 2.

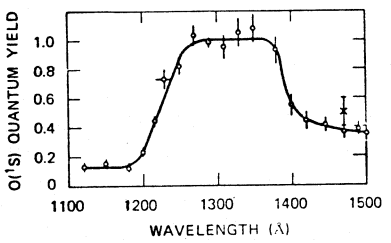

Fig. 1. Quantum yield of O(^{1}S) from N_2O.

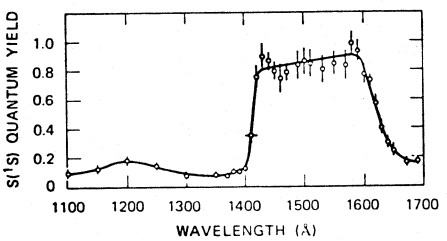

Fig. 2. Quantum yield of S(^{1}S) from OCS.

TC9. Xenon Oxide—The Kinetic Mechanism,[1] D. C. Lorents, D. L. Huestis, R. A. Gutcheck, R. M. Hill, and H. H. Nakano, *Stanford Research Institute.*

Laser action has recently been observed in the green band systems of XeO and KrO.[2] We report here our analysis of the reaction kinetics in e-beam pumped xenon–oxygen mixtures. The preliminary results of our experimental kinetic study were described previously.[3] Xe* and Xe_2^* have insufficient energy to produce O(^{1}S) from O_2 and must yield instead O(^{3}P) + O(^{1}D) or 2O(^{3}P). A second energy transfer from Xe_2^* to O(^{3}P) can then give O(^{1}S). The decay kinetics show mysterious features which are explained by the acceptance of this two-step excitation mechanism. Based on this mechanism various of the important rate coefficients have been determined from the kinetic data.

[1] This work was sponsored by the Defense Advanced Research Projects Agency through the Office of Naval Research.
[2] J. R. Murray, H. T. Powell, C. K. Rhodes, Paper P-8, VIII Int. Quant. Electronics Conf., 1974. H. T. Powell, J. R. Murray, C. K. Rhodes, preprint to *Appl. Phys. Lett.*, —, paper MA2, this conference.
[3] R. A. Gutcheck, R. M. Hill, D. L. Huestis, H. H. Nakano, and D. C. Lorents, *Bull. Amer. Phys. Soc.*, vol. 18, p. 1881, 1973.

TC10. Measurement of Pressure-Broadened Infrared Linewidths with an Optical Parametric Oscillator,[1] J. Wormhoudt, L. Marabella,[2] and J. I. Steinfeld, *Massachusetts Institute of Technology, Cambridge, Mass.*

A tunable, narrow-band infrared source is being used to probe the density dependence of infrared absorption lineshapes. The source consists of a commercial optical parametric oscillator pumped by a Q-switched ND: YAG laser. An internal etalon is used to narrow the infrared output to a linewidth of 0.005 cm^{-1} or better. Reference and sample beam intensities are detected by matched InSb detectors, put through a gated amplifier-integrator, and averaged on a computer.

Data obtained in these experiments will be used to test theoretical predictions of the density dependence of the absorption coefficient. The absorption coefficient at the line center is predicted to have the form $k(\nu_0) = A/\rho + B + C\rho + D\rho^2 + D'\rho^2 \ln \rho$, where ρ is the total gas density. The coefficients in this expansion, as well as non-Lorentzian behavior in the wings of the line, will be determined.

Experiments are being carried out on HCl gas in the presence of 1 to 100 atm of Ar, and will be extended to DF in the near future.

[1] Supported by the National Science Foundation.
[2] Present Address: Hughes Research, Culver City, Calif.

SESSION TD

Post-Deadline Papers
Tuesday, October 22, 2:00 P.M.

TD1. HCl/H_2 Gas Dynamic Laser Calculations, C. P. Holmes, *AFWL/DYT.*

An HCl/H_2 gas dynamic laser has been investigated with a computer program which couples the quasi-one-dimensional gas dynamic equations with an anharmonic oscillator vibrational kinetics model. Starting at the plenum, the gas flow parameters and vibrational level populations are calculated through a laval nozzle into the laser cavity where a Fabry–Perot power extraction model is used to produce HCl multiline radiation in the 4.0 to 4.7-μ range. Typical initial conditions have a 1/9 mole fraction ratio mixture of HCl/H_2 in a plenum at 100 atm and 3000 K. After an expansion to A/A* of 100, exothermic pumping creates a nonequilibrium distribution in the anharmonic vibrational levels of HCl resulting in partial inversions in the first ten to twelve levels with small signal gains of up to 0.6% cm^{-1}. With a laser cavity, specific energies of up to 30 kJ/lb were extracted representing about 10% of the total HCl/H_2 vibrational energy at the nozzle exit plane and only 0.35% of the total plenum energy. Calculations on a screened nozzle mixing GDL, similar to the CO_2/N_2 MGDL modeled by Holmes and Graham,[1] were performed. However, due to the large HCl/H_2 molecular weight ratio and the high expansion ratios needed to reduce the H_2 gas temperature, large temperature rises due to dissimilar gas mixing would not allow any partial inversions causing the small signal gain to remain negative. It is suggested that a much more efficient system with less severe plenum and

[1] C. P. Holmes and D. C. Graham, *Laser Digest*, AFWL-TR-74-241, 243, 1974.

expansion conditions could be realized by using an electron beam sustained discharge. The roles of atomic hydrogen and chlorine arising from thermal and electron induced dissociation should be studied. More information on the vibration relaxation rates are needed, particularly the H_2 to HCl VV transfer rate for which there is no experimental data.

TD2. A New Electric Discharge Gas Dynamic Laser, J. A. Stregack and B. L. Wexler, *Naval Research Laboratory, Washington, D.C. 20375.*

An electric discharge gas dynamic laser facility has been constructed to study the potential of several CW laser systems. The primary motivation is the development of lasers utilizing energy transfer from a molecule easily excited in a discharge to another molecule whose vibrational excitation rate by electron impact is not as favorable. Plenum excitation of one gas species is obtained in a dc glow discharge. The excited gas present in the plenum is then accelerated through an array of supersonic nozzles where the laser species is injected and mixes with the primary flow. Energy transfer and lasing occur in the supersonic region of the flow. Brewster-angle windows which extend 10 cm downstream from the nozzle exit plane enable a laser cavity or diagnostic apparatus to be positioned at a variable distance from the injection point. The optics are mounted on a motor-driven translation table so that continuous scans of the region downstream of the nozzle exit plane may be conveniently made. The present facility is versatile in that it may easily be operated with a subsonic cavity, with an RF discharge in the cavity region to augment the plenum discharge, with all gases premixed, or with any combination of these configurations.

As a result of studies of D_2 electrical excitation a D_2-CO_2 transfer laser has been produced with an output power in excess of 50 W and measured peak small signal gains of 0.015/cm. These results compare very favorably with those for a N_2-CO_2 laser run on the same apparatus. A He and D_2 mixture is excited in the plenum with CO_2 injected in the supersonic nozzle. The supersonic cavity pressure was 10 torr and the mixture used for peak laser performance was 0.06 CO_2/0.32 D_2/0.62 He. Due to the gasdynamic cooling, the peak gain occurs on the P(14) transition of the 10 μ band. This new laser clearly demonstrates the vibrational energy storage capability of D_2 excited by an electric discharge.

Other potential laser systems are being investigated and fluorescence data have been taken. These systems include D_2-HCl and CO-CS_2. The fluorescence indicate that the number densities of vibrationally excited CS_2 and HCl are comparable to CO_2 densities.

TD3. Pulsed, Electrically-Initiated, HF Chemical Lasers at Atmospheric Pressure, J. A. Mangano, R. Limpaecher, J. D. Daugherty, H.-L. Chen, and F. Russell, *Avco Everett Research Laboratory, Inc.*

Two methods of electrically initiating pulsed HF chemical lasing action with total lasing mixture pressures of 1 atm will be described. In the first method, a cold cathode electron gun produces an electron beam (130 keV, 10 A/cm^2, 200 ns, 10 cm $\times$ 25 cm) which is used to initiate various slowly flowing nonstoichiometric mixtures of H_2:F_2:He:O_2. The highest laser energy density obtained is 51 J/l-atm for a mixture of $[H_2]:[F_2]:[He]:[O_2] = 0.08:0.30:0.61:0.01$ mole fractions at 1 atm total pressure in a total active volume of 0.125. The corresponding electrical efficiency based on the actual electron beam energy deposited in the lasing mixture is 900%. Consideration of the uniformity of electron beam energy deposition and beam window losses indicates that overall electrical efficiencies of 100 to 200% should be achievable in a scaled device. The lasing pulse duration under these conditions was 2 μs. Experimental results with other nonstoichiometric mixtures of H_2:F_2:He:O_2 will also be presented.

In the second method, laser action is initiated with an electron beam-stabilized discharge. The electron gun used was identical to that described above except that the beam pulse duration was shortened to 140 ns. A spark gap-switched, capacitive discharge circuit has been used to supply the discharge energy. For the lasing mixture studies ($[H_2]:[F_2]:[Ar]:[He]:[O_2] = 0.03:0.06:0.35:0.555:0.005$ mole fractions), the duration of the stable discharge pulse (140 ns) was probably shorter than the time for which the positive and negative ion current density of the discharge became equal to the discharge electron current density, a necessary condition for high-initiation efficiency. Under these conditions, approximately 6 times more energy was introduced into the lasing mixture with the discharge than with just the electron beam. A laser output energy density of 25 J/l-atm has been obtained corresponding to an electrical efficiency of 72% if just the energy deposited into the lasing mixture is counted. This result represents an enhancement of 2.5 over the output energy density achieved with the 140 ns electron beam alone. In this experiment the direction of the discharge was aligned with the electron beam direction. The beam electrons entered the lasing mixture through an 80% open stainless steel wire screen. This scalable discharge geometry is compatible with high-speed transverse lasing mixture flow. Methods of improving the electron beam-stabilized discharge results are being pursued. These methods include increasing the discharge E/P and varying the relative concentrations of the present lasing mixture.

TD4. Continuous-Wave HF Chain Reaction Laser,[1] T. J. Sadowski, C. E. Kepler, B. R. Bronfin, M. D. Krosney, and R. Roback, *United Aircraft Research Laboratories, East Hartford, Conn. 0618.*

A theoretical and experimental investigation was conducted at the United Aircraft Research Laboratories to evaluate the performance potential of the HF/DF chain reaction laser, i.e., a laser operating under conditions which favor the production of vibrationally excited HF (or DF) via the "cold–hot" chain reaction sequence

$$\text{cold } F + H_2 \longrightarrow HF^* + H$$

$$\text{hot } H + F_2 \longrightarrow HF^* + F$$

$$\Delta H = 31.5 \text{ Kcal, } 75\% \text{ vib}$$

$$\Delta H = 97.9 \text{ Kcal, } 53\% \text{ vib.}$$

The program consisted of: theoretical calculations to aid in the selection of design conditions and laser operating conditions, laser power and gain tests of an 8-in nozzle array, and chemiluminescence-emission tests of a 1-in nozzle segment. The experiments were conducted with a mass heater to preheat the primary flow to temperatures sufficient to dissociate only a small fraction of the fluorine molecules to F-atoms, thereby initiating the chain reaction while inhibiting lasing under "cold" reaction conditions. Heating the flow by this means also eliminated combustion contaminants from the primary flow. The lasing tests were conducted in a constant-pressure free-jet cavity with closed-cavity optics. The laser power extracted from the media was

[1] Sponsored by the U.S. Army Missle Command Contract DAAH01-73-C-0321.

absorbed by the mirrors and measured calorimetrically.

On the basis of the experimental results achieved under this program and reported herein, it was concluded that continuous-wave chain-reaction lasing was achieved. This conclusion is supported by the achievement of a specific laser power of 3.8 kJ/g of F-atoms on vibrational transitions up to the 5th level, at laser cavity pressures up to 16 torr, and over extraction lengths up to 23 cm. It was further substantiated by emission spectroscopy measurements performed on a segment of the above nozzle which indicated that the chain reaction had proceeded to a significant extent for the above-operating conditions. This is the first known demonstration of such power extraction. A maximum average laser power of 3.9 kW was achieved during these tests. These results give encouragement to the possible achievement of the predicted potential of this laser system.

TD5. Subsonic cw Chemical Laser Emission from the Reaction of H-Atoms with Cl_2 in a Transverse Flow Laser, J. Wanner, *Department of Chemistry, University of Toronto, Toronto, Canada.*

The reaction of $H + Cl_2 \rightarrow HCl + Cl$ $-\Delta H^\circ_2 = 45$ kcal mole^{-1} has been employed in a longitudinal-flow laser to yield a total CW output of 1 mW.[1] The $H + Cl_2$ system is attractive as a source of CW HCl emission in view of the low-cost and moderately corrosive nature of the reagents, as compared with Cl + HI. The drawback lies in the low output power. In this work the same system has been examined in a transverse flow laser, and has produced 190-mW CW output.

The aluminum water-cooled laser flow chamber was a slightly scaled-up version of that described.[2] This laser body was kindly made available by T. A. Cool. The flow cross section measured 6.3 X 70 mm. The molecular reagent was injected transverse to the primary flow by means of two opposing arrays of thirty-two 0.3 mm diam orifices, spaced 2 mm apart. The transverse optical axis was 8 mm downstream from the injection orifices—the optimal position for HF lasing in the SF_6/H_2 system (the total HF power obtained with this setup was 3.5 W). One CaF_2 Brewster window and one internally mounted mirror were employed. The optical cavity comprised a 10-m radius spherical mirror and a 2-m spherical dielectric mirror, spaced 45 cm apart. Atomic hydrogen was formed in a 1.5-kW 2450-MHz microwave discharge.[3] The inside of the 19-mm ID quartz discharge tube was coated with Teflon. The pumping system was capable of 630 1/s, through 100 1/s was found to give the same total output power.

The flow rates at maximum output were He 27-m moles s^{-1}, H_2 1.5-m mole s^{-1}, Cl_2, 1.4-m moles s^{-1}. The pressure in the cavity was 6 torr. The total output ranged from 75 mW using a 0.2% coupler, to 190 mW using a 3.5% coupler. In contrast to the earlier study which yielded emission in $v(1\text{-}0)$ only,[1] the output with the present arrangement was in $v(1\text{-}0)$ (70%) and $v(2\text{-}1)$ (30%). Lasing was recorded in $P_{1-0}(3)$ to $P_{1-0}(8)$, and $P_{2-1}(4)$ to $P_{2-1}(7)$.

[1] T. A. Cool, R. R. Stephens, and J. A. Shirely, *J. Appl. Phys.*, vol. 41, p. 4033, 1970.
[2] R. R. Stephens and T. A. Cool, *Rev. Sci. Instr.*, vol. 42, p. 1489, 1971.
[3] D. I. Rosen, R. N. Sileo, and T. A. Cool, "A spectroscopic study of CW chemical lasers," *IEEE J. Quantum Electron.*, vol. QE-9, pp. 163-172, Jan. 1973.

TD6. Reaction Mechanism and Energy Distribution in a New Chemical Laser System: ClF_5-H_2, O. D. Krogh and G. C. Pimentel, *Chemistry Department, University of California, Berkeley, Calif. 94720.*

Stimulated vibration-rotation emission has been observed from both HF and HCl following flash photolysis of ClF_5-H_2-Ar mixtures. This new chemical laser is compared to the $ClF-H_2$ and ClF_3-H_2 chemical lasers to clarify the reaction mechanism. Applying tandem techniques we have put lower limits on the following population ratios for HCl, $N_1/N_0 > 1.8$, $N_2/N_1 > 1.5$, $N_3/N_2 > 0.76$, $N_4/N_3 > 0.61$ and for HF, $N_1/N_0 > 0.7$, $N_2/N_1 > 2.5$. The reaction:

$$H + ClF_4 \longrightarrow HCl^{\ddagger} + 2F_2,$$

$$\Delta H = -50 \text{ kcal/mole}$$

is probably contributing in the production of vibrationally excited HCl. This gives evidence for the existence of the radical ClF_4. Assuming that the above reaction is the only HCl producing reaction, the population ratios imply that more than 33% of the total energy available goes into vibrational excitation of HCl. Furthermore, the excitation of HCl to the $v = 4$ state would require that 62% of the total energy be channeled into vibration in a single reaction event. At least two and probably three different reactions produce vibrationally excited HF. One of these reactions (but not $F + H_2$) provides an unusual distribution of HF molecules over the rotational manifold as demonstrated by observation of $1 \rightarrow 0$ transitions up to $P_1(19)$, indicating rotational nonequilibrium.

TD7. Rotational Nonequilibrium in CW Chemical Lasers, L. H. Sentman, *University of Illinois and Bell Aerospace Company.*

By including the spontaneous emission term in the radiative transfer equation, an explicit expression for the radiation term in the species equation is obtained in terms of the fluid variables. With this description of the radiation field, the approach to saturation as well as the rapid decrease in α that occurs at cutoff is obtained. This formulation is used to study the role of rotational nonequilibrium in CW chemical lasers. A simplified chemical model in which the active species is a diatomic molecule with three vibrational levels that collide with an inert diluent is employed. The chemistry is described by an irreversible J-dependent pumping reaction, a set of J-dependent collisional deactivation reactions, and a set of J-dependent rotational relaxation reactions. The set of coupled nonlinear equations has been solved numerically for $J_{MAX} = 20$ (42 simultaneous equations). It is shown that the phenomena of J-shifting and the power being contained in the high J transitions are a consequence of the rotational equilibrium assumption. When rotational nonequilibrium is allowed to occur, several J transitions within a given vibrational band lase simultaneously, including R-branch transitions, which cut off when the initial total inversion is depleted. For the reference case (800 K), the transitions that contain most of the power are P6 to 12 with the strongest being 7, 8, and 9. The power is contained in those J transitions that are preferentially populated by the pumping reaction and the total power is decreased 20 to 30% from the rotational equilibrium value. As the ratio of the rate of rotational relaxation to the rate of collisional deactivation increases, the total power produced increases, the percent in the R branch decreases, the peak of the power distribution gradually shifts to higher J and eventually the phenomenon of J shifting occurs. As the temperature is decreased, the peak of the power distribution shifts to lower J. Comparison of these calculations for HF lasing on the $2 \rightarrow 1$ band with Hinchen's[1] and Kwok *et al.*[2] observations shows that the predicted

[1] J. J. Hinchen, *J. Appl. Phys.*, vol. 45, p. 1818, 1974.
[2] M. A. Kwok, R. R. Giedt, and R. W. F. Gross, *Appl. Phys. Lett.*, vol. 16, p. 386, 1970.

and observed peak power transitions are in agreement. The saturated R-branch transitions predicted by the present model agree with the observations of Green and Lin.[3] The agreement of these calculations with the observations of Chen *et al.*[4] who report lasing on P_3 through P_{16} for the $2 \rightarrow 1$ band in an atmospheric, pulsed HF laser supports their suggestion that rotational nonequilibrium is responsible for these observations.

[3] W. H. Green and M. C. Lin, *J. Chem. Phys.*, vol. 54, p. 3222, 1971.
[4] H. L. Chen, R. L. Taylor, J. Wilson, P. Lewis, and W. J. Fyfe, *Chem. Phys.*, vol. 61, p. 306, 1974.

TD8. Observation of Laser Action in CO Gas Excited Only with a Nuclear Reactor,[1] D. A. McArthur and P. B. Tollefsrud, *Sandia Labs.*

We report here what we believe is the first clear observation of lasing with only nuclear reaction product excitation. Lasing was observed on the vibrational bands of CO, when the CO was irradiated with an intense burst of fission fragments. No case of lasing under pure reactor excitation has been published, although reactor enhancement of electrically excited lasers has been observed. Since it appears possible to deposit at least ~1 mJ in a gas with a pulse ~100 μs wide using present fast burst reactors, it might now be possible to make very large lasers using only reactor excitation.

The laser apparatus for this experiment was mounted so that its axis was about 20 cm from the axis of the SPR-II reactor at Sandia Laboratories. This reactor produced a fast neutron flux $\sim 5 \times 10^{17}$ n/cm^2-s at the apparatus, in a pulse ~60 μs wide. The laser apparatus consisted of a vertically oriented cylinder divided into two chambers by a CaF_2 Brewster window. The lower chamber, immersed in liquid nitrogen, contained the laser gas (pure CO at ≈100 torr at 77 K), and a 20 cm long cylinder coated with enriched $^{235}U_3O_8$. The neutrons, partially moderated, caused fission fragments to emerge from the coating and excite the laser gas. A laser output mirror (reflectance = 96 or 98.5 percent) was mounted at the top of the upper chamber, while a totally reflecting mirror was mounted at the bottom of the lower chamber. The upper chamber was evacuated to provide insulation for the cold Brewster window. The laser output beam was focused by a mirror system onto a calorimeter and Ge:Au detector located about 15 m away, beyond the reactor shielding.

When the laser mirrors were aligned, a laser signal pulse about 1000 times larger than the background was observed in the Ge:Au detector. The signal peaked near the fast neutron pulse peak, and turned on and off rapidly as though a sharp threshold were being crossed. This signal disappeared if the CO was replaced by pure N_2, or if the output mirror was deliberately misaligned. The signal passed through a narrow-band interference filter centered at 5.24 μ, indicating lasing on the vibrational bands of CO. The measured laser pulse energy ($\sim 3 \times 10^{-4}$ J) was ten times larger than could possibly be explained by fluorescence from the gas.

Since the laser was operating near threshold, and since the calorimeter may not have intercepted the entire beam, the preliminary efficiency measurement (~0.2 percent) is believed to be a lower limit. Gain was also observed on ten CO laser transitions ranging in wavelength from 5.13 to 5.33 μ. Gain pulses ~80 μs wide were observed, with peak gains ~0.5%/cm. The relative gains on the 7-6, 9-8, and 10-9 bands are similar to those observed in low pressure, cooled CW CO lasers. To estimate the vibrational populations, we assumed a gas temperature and an approximate steady-state vibrational distribution to fit the gain data. For gas temperatures between 80 K and 150 K, gains of the observed magnitude were calculated, by assuming a vibrational excitation efficiency between 25 and 70 percent.

[1] This work supported by the U.S. Atomic Energy Commission.

TD9. Time Dependent Kinetics of CO-EDL with Multi-Level Pumping,[1] J. L. Boulnois and R. B. Miles, *Department of Aerospace and Mechanical Sciences, Princeton University, Princeton, N.J.*

In the conventional description of the CO-electric discharge laser, the pumping mechanism is assumed to be a combination of a direct electron excitation of the lower CO vibrational states followed by a redistribution of vibrational energy through inelastic self collisions; the deactivation mechanism is assumed to be the loss of vibrational energy to the translational degree of freedom through inefficient V-V and V-T collisions.[2,3] The translation energy mode of the CO-He mixture and the rotational degrees of freedom of CO are assumed to be in equilibrium at the same temperature.

The present kinetic model consists of a set of vibrational rate equations featuring the previous assumptions plus multilevel electron pumping. The equations are numerically solved in a time-dependent analysis including achievement of steady state. The production terms for the kinetic equations include single quantum V-V exchange collisions and V-T transfer collisions, spontaneous emission of radiation, and excitation by electron impact.[4] The electron coupling to the vibration energy mode is not restricted to the ground state, but rather a pumping scheme involving the entire vibrational ladder is assumed here. The electron impact rate coefficients are derived from the solutions given by Nighan,[5] then an extrapolation for the excitation and de-excitation rates for the range $v > 10$ is made along with the conservative assumption $k_{0 \rightarrow v} = k_{n \rightarrow n+v}$ to complete knowledge of all possible rates. At high pressures, where radiation deactivation is negligible, and low temperatures where the V-T processes only deactivate the highly excited states, the electron deactivation mechanism is believed to play an essential role among the middle levels above $v = 10$ where the population distribution is achieved through a competition of V-V fluxes with forward and reverse superelastic electron impact fluxes.

The initial effect of this multilevel pumping is to significantly populate all the vibrational levels in an extremely short time before the exchange collision redistribution proceeds. The next phase, which corresponds to the raising of the vibrational plateau, is slowed by reverse pumping losses whereby superelastic CO-electron collisions substantially inhibit V-V exchanges. Comparison between a steady-state distribution obtained with a limited pumping ($0 \rightarrow 10$) and one obtained with multilevel pumping indicates that the "knee" of the latter extends to higher vibrational quantum numbers because it is then controlled by a balance between V-V, electron pumping, and V-T deactivation. Following pulse termination, vibrational inversion builds up very rapidly under the drive of the anharmonic pumping through exchange colli-

[1] This work was supported by the Air Force Office of Scientific Research and NASA Ames Research Center.
[2] S. D. Rockwood, J. E. Brau, W. A. Proctor, and G. H. Canavan, "Time dependent calculations of carbon monoxide laser kinetics," *IEEE J. Quantum Electron.*, vol. QE-9, pp. 120-129, Jan. 1973.
[3] J. A. Lordi, S. J. Falk, and J. W. Rich, "Analytical studies of the kinetics of electrically excited continuously operating CO flow lasers," AIAA 7th Fluid and Plasma Dynamics Conf., Paper 74-563.
[4] W. B. Lacina, "Kinetic model and theoretical calculations for steady state analysis of electrically excited CO laser amplifier system," Northrop Corporate Lab. AD-729.235, Aug. 1971.
[5] W. L. Nighan, "Electron energy distributions and collision rates in electrically excited N_2, CO and CO_2," *Phys. Rev. A.*, vol. 2, 1970.

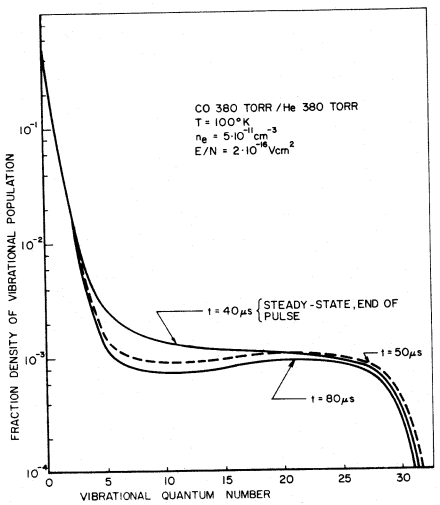

Fig. 1. Time evolution of a 40-μs pulse.

sions. Fig. 1 demonstrates that already 10 μs after pulse termination substantial total inversion has been achieved and persists with reasonable density for another few microseconds.

TD10. The Effects of Superelastic Collisions on Electron Energy Distributions in Vibrationally Excited CO Laser Mixtures, A. E. Greene, *Air Force Weapons Laboratory, Kirtland AFB, N. Mex. 87117.*

The dc Boltzmann equation, cast in a flux divergent form, has been solved to determine the electron energy distribution functions in vibrationally excited CO, CO-He, and CO-Ar mixtures. A brief explanation is given of the flux divergent Boltzmann equation formulation. Included in this formulation are ground state-to-excited state and excited-to-excited state inelastic and superelastic electron impact induced transitions among the first eight CO vibrational levels. The excited state populations used in this study were taken directly from predictions of e-beam sustained CO gas kinetic calculations. Once the electron energy distribution functions are determined, they are used to predict electron impact pumping rates and the partitioning of input energy between vibrational and electronic excitation, and ionization.

The results indicate that the effects of superelastic collisions are more pronounced in the CO-He and CO-Ar mixtures than in pure CO. Although the changes predicted for ground state-to-excited state electron impact pumping rates are, in some cases, quite significant, by far the most important effects are in the high-energy tail of the electron distributions. This can mean increases in the ionization rate of more than a factor of 20 implying that superelastic collisions may contribute significantly to ionization instabilities in CO lasers.

SESSION WA

Electronic Energy Transfer
Wednesday, October 23, 8:30 A.M.

WA1. Quenching Studies of Ar($^3P_0$, $^3P_2$) Metastable Atoms by Chlorine Atoms, D. L. King and D. W. Setser, *Kansas State University.*

A mixture of chlorine and argon excited by dc discharge has been shown to produce chlorine atom laser emission.[1] This presumably is a two-step process, the first being dissociation of Cl_2, followed by transfer of energy from electronically excited argon to chlorine atoms. Although the postulated excited state of argon is 4s $^1P_1$, the metastable states 4s $^3P_0$ and 4s $^3P_2$ could also be involved. We will report some results from a study of the interaction between molecular and atomic chlorine and these metastable states of argon, as measured by the flowing afterglow technique. In addition to the possible importance as a laser system, this work is an extension of quenching studies of argon metastables by atoms[2] and is important to development of theories of electronic energy transfer. For the atomic studies a 1–2% mixture of chlorine in helium was passed through a microwave discharge, producing ~15–20% dissociation. The argon (purified by molecular sieve traps) was passed through a dc discharge, producing the metastables $^3P_0$(11.723 eV) and $^3P_2$(11.548 eV) in a ratio of ~1:6. The two species were mixed concentrically and the emission was measured by a 0.75 m Jarrel Ash, Czerny-Turner monochromator equipped with a SSR photon counter and EMI 9558QA phototube. The observed chlorine atom emission was compared with emission from Kr, which has a known Ar* quenching cross section.[2] Calculations were performed to correct for branching from the excited Cl states. For Ar($^3P_0$) the quenching cross section thus derived is ≥ 6.2 Å^2; three different Cl manifolds are populated: 5p $^4p^0$, 5p $^4D^0$, and $^4p'$ $^2P^0$ in a ratio of roughly 0.3:0.25:0.45, respectively. This ratio showed little variation with pressure in the 1-3 torr range, indicating collisional quenching by argon is probably not important. For the Ar $^3P_2$, the quenching cross section based upon *observed* emissions is at least 4.6 Å^2. The product states from quenching of Ar($^3P_2$) could not be observed directly, since they are presumably the 5s and 3d manifolds of Cl, which emit to the 4p manifolds at wavelengths $\geq$ 10,000 Å or to the 3p at wavelengths $\leq$ 1150 Å. Neither wavelength region is measurable by our current apparatus. We observe only emission from the 4p chlorine manifolds, which probably are populated by cascading from the 5s and 3d levels. These emissions were mainly from quartet states, to be expected since branching from doublet states favors emission to the ground state at short (vac UV) wavelengths. The previously measured[2] total quenching cross section of Ar($^3P_2$) by Cl_2 is 95 Å^2. The known exit channels are formation of Cl(4s ^4P and ^2P) + Cl and molecular emission (either Cl_2* or ArCl*) continua in the vac UV (with maxima at 1737, 1687 and 1649 Å) and in the UV (with maximum at 2560 Å). The latter is a known Cl_2 band and is estimated to have 10% of the total cross section. Since the lower states of the continua are likely to be repulsive, the major fraction of the quenching by Cl_2 gives atoms.

[1] A. B. Dauger and O. M. Stafsudd, *IEEE J. Quantum Electron.*, vol. QE-6, p. 572, 1970.
[2] L. G. Piper, D. W. Setser, and J. E. Velazco, *J. Chem. Phys.*, vol. 59, p. 3323, 1973.

WA2. Quenching Studies of Xe($^3P_2$) Metastable Atoms, J. E. Velazco and D. W. Setser, *Kansas State University.*

Continuing the work previously reported from this laboratory,[1,2] we have extended the measurement of total quenching cross sections (thermal) of rare-gas metastable atoms to include Xe*($^3P_2$) with some light hydrocarbons and with the four fluoromethanes. Xenon metastable atoms were produced in a hollow cathode discharge by the reaction:

$$Ar^*(^3P_{0,2}; 11.5\text{–}11.7 \text{ eV}) + Xe \rightarrow Xe^*(^3P_2; 8.32 \text{ eV}) + Ar$$

with an efficiency of ~50%. Quenching measurements were made at room temperature in a flowing afterglow apparatus which had a flow velocity of 70–80 m s^{-1}; the decay of Xe*($^3P_2$) was monitored by absorption spectroscopy. The concentration of Xe*($^3P_0$; 9.54 eV) was below the detectable limit of absorption spectroscopy. The results are listed below and for comparison pur-

[1] L. G. Piper, J. E. Velazco, and D. W. Setser, *J. Chem. Phys.*, vol. 59, p. 3323, 1973.
[2] J. E. Velazco and D. W. Setser, *Chem. Phys. Lett.*, vol. 25, p. 197, 1974.

poses the ratios of the quenching cross sections for Xe* to the cross sections for quenching of $Ar^*(^3P_2)$ are listed; the units of k_Q are cm^3 $molec^{-1}$ s^{-1}.

Reagent	$k_Q \times 10^{11}$	$\sigma_Q(Å^2)$	$\sigma_Q(Xe^*)/\sigma_Q(Ar^*)$
C_5H_{12}	71.8	192	
C_4H_{10}	67.6	170	1.14
C_3H_8	54.2	123	0.92
C_2H_6	63.5	125	1.15
C_2H_4	58.2	110	1.11
C_2H_2	69.0	130	1.44
CH_4	32.5	49	1.09
CH_3F	44.4	91	
CH_2F_2	40.9	99	
CHF_3	0.2	0.6	~0.01
CF_4	≤0.03	<0.1	~0.01

The hydrocarbons were selected in order to cover a wide range of polarizabilities, as well as photoabsorption cross sections and ionization potentials.[1] An upper limit to the quenching cross section of Hg was established as ≤0.001 Å². The decay of $Xe(^3P_2)$ in Ar was characterized; the diffusion coefficient for Xe* in argon was found to be 70 cm^3 $torr$ s^{-1} and the first- and second-order decay constants in Ar are 3.8×10^{-16} cm^3 $molec^{-1}$ s^{-1} and 2.8×10^{-23} cm^6 $molec^{-2}$ s^{-1}, respectively. For some of the systems studied earlier,[2] e.g., N_2, CO, NO, and Cl_2, the distribution of exit channels, as measured by fluorescence, was observed. Previous results[3] were confirmed for N_2 and CO. The major quenching channel for Cl_2 is direct chemical reaction with formation of XeCl* which subsequently radiates to Xe + Cl; the resulting bound-free continuum emission peaks at 304 nm. Emission from XeF* and XeBr* also has been identified from direct reaction of $Xe(^3P_2)$ with fluorine and bromine containing compounds.

[3] D. H. Stedman and D. W. Setser, *J. Chem. Phys.*, vol. 52, p. 3957, 1970.

WA3. Studies of the Deactivation of Electronically Excited Iodine Atoms, D. H. Burde, R. A. McFarlane, and J. R. Wiesenfeld, *Cornell University, Ithaca, N.Y. 14850.*

The transition in atomic iodine at 1.315 μ takes place between the spin-orbit split levels of the electronic ground configuration: $I(5\ ^2P_{1/2}) \rightarrow I(5\ ^2P_{3/2}) + h\nu(1.315\ \mu)$. The system is being widely studied because of the very high energy pulses which can be obtained from flash-lamp pumped lasers. In addition, CW operation appears to be possible using collisional transfer of electronic energy to iodine atoms from excited molecular species produced chemically or in an electrical discharge. Modeling of the kinetics of these systems requires information on the rates at which energy is transferred from excited species to $I(5\ ^2P_{3/2})$ and the quenching rates for $I(5\ ^2P_{1/2})$ due to any other species present in the laser.

In this paper we report measurements on the deactivation of $I(5\ ^2P_{1/2})$ by I_2 using a new technique which is 2 to 3 orders of magnitude faster in time resolution than previous methods. It is possible in fact to observe the time development of the *appearance* of excited iodine atoms following the excitation of molecular iodine both above and below the dissociation limit of the $B^3\Pi_{0_u^+}$ electronic state.

The iodine is excited in a multiple reflection cell by a nitrogen laser pumped tunable dye laser which produces 10 ns pulses at a rate of 20 pps. The population of $I(5\ ^2P_{1/2})$ is monitored by observing the time dependence of the absorption of atomic line emission which is passed through the cell from an iodine lamp and which is observed using a McPherson Model 225 Vacuum Ultraviolet Monochromator tuned to 2062 Å. The photomultiplier signal is digitized using a Biomation Model 8100 Transient Digitizer and for each measurement approximately 10^4 pulses are accumulated in a Northern Scientific Model 575 Signal Averager. A variety of computer programs are used to carry out a least squares fit of the data to derive both a decay rate for $I(5\ ^2P_{1/2})$ and information on the time development of its appearance following the laser pulse.

By varying the I_2 pressure we have measured the second-order quenching rate coefficient for $I(5\ ^2P_{1/2})$ by I_2 as $kI_2 = (3.6 \pm 0.4) \times 10^{-11}$ cm^3 $molecule^{-1}$ s^{-1} which is nine times faster than that reported by Husain and co-workers.[1] Measurements of $I(5\ ^2P_{1/2})$ deactivation by other species are being carried out and similar measurements are planned for $Br(4\ ^2P_{1/2})$. Data available at the time of the conference will be presented.

[1] J. J. Deakin and D. Husain, *J. C. S. Faraday II*, vol. 68, p. 1603, 1972.

WA4. Kinetic Modeling of Photodissociation Iodine Laser Amplifiers,[1] C. E. Turner, Jr., and N. L. Rapagnani, *Lawrence Livermore Laboratory.*

A comprehensive kinetic model is described which predicts the time dependence of the inversion in iodine-laser energy-storage amplifiers over a wide range of helium diluent pressure. The high rare gas pressures (1–10 atm), which are required to control superfluorescence and produce bandwidths suitable for short pulse generation via collision broadening, significantly modify the chemical kinetics of the flash photolysis of fluorinated alkyl iodides (RI, e.g., CF_3I, C_3F_7I) because of lower temperature rise, fast thermalization of "hot" radicals and three-body effects. The model includes many of the typical two-body deactivation, recombination, and reaction mechanisms previously considered for low pressure analyses but it is appropriate to omit some uncertain reactions involving "hot" radicals. In addition, it is necessary to consider I_2 formation via three-body iodine atom recombination: (a) I + I + M, (b) I* + I + M, and (c) I* + I* + M, where the main catalysts (M) are He, I_2, and RI.

A major achievement of this modeling effort is the determination of a consistent set of rate equations and rate constants by critical examination of the experimental rate data coupled with an attempt to fit the detailed inversion history data of Hohla and Kompa[2] at P(He) = 0 and the inversion half-life data of Aldridge[3] at P(He) = 1 and 3 atm. An excellent fit to data is shown in Fig. 1. The agreement with Aldridge's data is also good. Since the various experimental conditions considered in the rate adjustment process emphasize different reactions, the overall confidence in the extrapolation capability is considerably enhanced.

Some important conclusions are: 1) it is unnecessary to invoke unknown chemical pumping processes[2] or diffu-

[1] Work performed under the auspices of the U.S. A. E. C.
[2] K. Hohla and K. L. Kompa, *Z. Naturforsch.*, vol. 27a, p. 938, 1972.
[3] F. T. Aldridge, to be published.

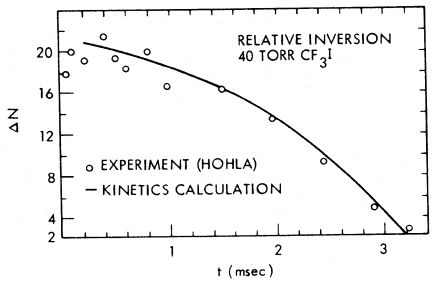

Fig. 1.

sion effects[4] to explain low pressure data; 2) the rate for reaction (b) with M = He may be only about a factor of five lower than that for (a); 3) reactions (c) can be neglected as expected theoretically; 4) for 10% dissociation of 10 torr C_3F_7I with a 10 μs FWHM pump pulse the model predicts a relatively weak dependence on the He diluent pressure, $T_{1/2}(\mu s) \sim 450/\sqrt{P(atm)}$, and 5) $T_{1/2}$ is principally determined by the formation rate of the main quencher, I_2.

[4] M. A. Gusinow *et al.*, *Chem. Phys. Lett.*, vol. 21, p. 197, 1973.

WA6. Electronic-to-Vibrational Energy Transfer Reactions: X* + CO (X = 0, I and Br), M. C. Lin and R. G. Shortridge.[1]

The vibrational distribution of CO produced from the following two electronic energy quenching reactions:

$$O(^1D) + CO(X\,^1\Sigma^+, v = 0) \xrightarrow{I} O(^3P) + CO(X\,^1\Sigma^+, v \leqslant 7)$$

$$I(5\,^2P_{1/2}) + CO(X\,^1\Sigma^+, v = 0) \xrightarrow{II} I(5\,^2P_{3/2}) + CO(X\,^1\Sigma^+, v \leqslant 3)$$

have been determined by means of infrared resonance absorption measurements employing a CW CO laser. The electronically excited $O(^1D)$ and $I(5\,^2P_{1/2})$ atoms were generated from the photodissociation of O_3 and CF_3I, respectively, above 200 nm:

$$O_3 + h\nu(\lambda \geqslant 200\text{ nm}) \longrightarrow O(^1D) + O_2(^1\Delta, {}^1\Sigma_g^+)$$

$$CF_3I + h\nu(\lambda \geqslant 200\text{ nm}) \longrightarrow I(5\,^2P_{1/2}) + CF_3.$$

The populations of CO produced in reactions (I) and (II) are given in Table I. The CO molecules formed in both reactions were found to be vibrationally excited up to the limits of available electronic energies carried by the excited atoms. A similar result was also observed in the $Br(4\,^2P_{1/2}) + CO$ ($v = 0$) reaction, in which absorption occurred only in the 1 → 2 band. The Br* atom was produced by the photodissociation of CF_3Br in the UV region.

For the O* + CO reaction, the efficiency of E → V energy transfer was determined to be 17%. Our present results were found to be inconsistent with the impulsive (half-collision) model.

[1] NRC/NRL Postdoctoral Research Associate (Aug. 1973–present).

TABLE I
RELATIVE RATE CONSTANTS FOR THE FORMATION OF CO(v) IN REACTIONS (I) AND (II)

v	0	1	2	3	4	5	6	7
k_v(I)	1.7[a]	1.0	0.51	0.33	0.20	0.12	0.068	0.0075
k_v(II)	–	1.0	0.094	0.043				

[a] Computed from the total quenching rate constant, determined by Heidner *et al.* (*J. C. S. Faraday Trans. II*, vol. 69, p. 927, 1973), and the extrapolated rate of formation of CO ($v = 0$) from the ln (N_v/N_1) versus [$G_0(v) - G_0(1)$] plot.

SESSION WB

$DF-CO_2$ Lasers
Wednesday, October 23, 8:30 A.M.

WB1. Electrically Initiated Pulse Chemical $DF-CO_2$ and DF Lasers,[1] T. O. Poehler and R. Turner, *Applied Physics Laboratory, Johns Hopkins U.*

While high energy outputs can be obtained from high-pressure pulsed $DF-CO_2$ chemical transfer lasers using optical initiation, the overall efficiency is low. Direct electrical initiation of the $D_2 + F_2$ reaction in a transverse discharge, with the potential advantage of much higher efficiency, has been studied for two excitation conditions: 1) a 150 ns wide current pulse; and 2) a 450 ns wide current pulse. The DF and $DF-CO_2$ lasers are nominally operated at 300–760 torr, static fill, with 2% D_2, 4.5% F_2, 6% O_2 (for stabilization), 6% CO_2 (when used) and 82–88% He.

In the $DF-CO_2$ laser, a 450-ns current pulse produces a 10.6-μm laser output beginning 7–12 μs after the start of current and usually consists of a series of spikes lasing 100–150 μs. The spikes are about 1 μs long, and occur at 3–4 μs intervals. The reaction pressure grows much less rapidly then in the flash initiated laser indicating a low initial F concentration or competing reactions with the chain reaction. There is no DF 3.8-μm laser output.

With 150-ns excitation, the laser output is completely different. With DF only, emission at 3.7–3.9 μm starts 0.3 μs after the current and the lines in order of occurrence are $P_3(4)$, $P_3(5)$, $P_3(6)$ (the strongest), and $P_3(7)$, followed by $P_4(5)$, $P_4(6)$, and $P_2(9)$. With CO_2 added, the initial output occurs 0.4 μs after the start of current and is at 10.6 μm—P(26), P(34), and P(42) of $00^\circ1\text{–}10^\circ0$. These are followed by 3.6-μm emission from $P_1(5)$ and $P_1(6)$. The main 10.6 μm follows at 4.8 μs from the P(20) and P(18) lines. If the laser is operated as a normal TEA laser, the 10.6-μm radiation occurs at 1.2 μs.

These results may be summarized as follows. With 450-ns excitation, the laser output is delayed as in flash initiation. With 150-ns excitation, DF alone lases first in the P branch from vibrational levels 3 to 2. The progressive transition to higher J's is probably the result of a temperature rise.[2] The 4 to 3 transitions occur after an inversion is produced by depletion of the lower level by the 3 to 2 transition. The $P_2(9)$ transition, which lases well after the peak of the 3-2 transitions, may be pumped by the 302 cascade. The pressure of inert gases has been observed to reduce the number of emission lines and reduce the equilibration time of the rotational temperature.[2]

The prompt 10.6-μm radiation in the case of the $DF-CO_2$ laser (in contrast to the delay with CO_2 only) is attributed to a collisional transfer of energy from DF to CO_2 with a rate constant of 6.0×10^5 s^{-1} $torr^{-1}$ with the result that the P_3 lines observed in DF only are missing. There is a significant difference in vibrational energy between the DF 3-2 transition and the CO_2 000-001 pump transition that may be taken up as rotational energy.[3] This energy transfer from DF in the V = 3 state will heavily populate the V = 2 states and produce the inversion responsible for the $P_2(1)$ and $P_2(2)$ lines. The P(18) and P(20) 10.6-μm lines observed later are presumably the result of excited DF formed as the chemical reaction proceeds.

[1] This work was supported by the Naval Ordinance Systems Command under Contract N00017-72-C-4401.

[2] K. L. Kompa, J. H. Parker, and G. C. Pimentel, *J. Chem. Phys.*, vol. 49, p. 4257, 1968.

[3] R. R. Stephens and T. A. Cool, *J. Chem. Phys.*, vol. 56, p. 5863, 1972.

WB2. Characteristics of a Supersonic DF-CO_2 Transfer Chemical Laser, J. A. Stregack and W. S. Watt, *Naval Research Laboratory.*

A CW supersonic DF-CO_2 transfer chemical laser has been developed which recovers to atmospheric pressure. The device is a modified combustion driven gas dynamic laser with added D_2-F_2 chemistry. A methane–oxygen pilot serves to catalyze the carbon monoxide–oxygen reaction which produces hot CO_2. Nitrogen and/or additional CO_2 are added to control the combustor conditions, and a mixture of fluorine and helium is injected downstream of the combustion zone. Plenum conditions range from 14–20 atm and 950–450 K which serve to partially dissociate the F_2 before the flow is accelerated to $M = 4.5$ through an array of supersonic nozzles. Two sets of nozzle arrays have been tested. The first injects the D_2 through a series of fine orifices immediately upstream of the nozzle throats. The mixing, chemical reaction, and energy transfer start near the throat and proceed through the nozzles and into the cavity region. The second nozzle configuration fully accelerates the flow prior to injection of D_2 at the nozzle exit plane. In this configuration, D_2-F_2 chemistry begins in the cavity. The cavity, a constant area flow channel, is connected at the downstream end to the converging section of a diffuser which enables the gas to recover to atmospheric pressure. Starting the diffuser is a prerequisite to laser operation.

The important chemistry is the D_2/F_2 chain reaction which produces vibrationally excited DF

$$F + D_2 \longrightarrow DF^* + D$$

$$D + F_2 \longrightarrow DF^* + F$$

the transfer of DF vibrational energy to CO_2

$$DF^* + CO_2(00^\circ 0) \longrightarrow DF + CO_2(00^\circ 1)$$

and the deactivation of the CO_2 upper laser level by species in the flow

$$CO_2(00^\circ 1) + M \longrightarrow CO_2(nm^l o) + M$$

$$M = HF, DF, \ldots .$$

Pumping of CO_2 by vibrational energy transfer from chemically produced DF has been observed but has been offset by deactivation due to by-products formed in the combustor.

For subsonic mixing of the D_2, the chemistry increases the laser power output over that during operation of the device as a gasdynamic laser. The enhancement is limited, however, by deactivation due to HF formed in the combustor as a by-product of methane combustion and prereaction in the injection and nozzle expansion region.

In the supersonic case the combustor conditions required to keep the diffuser started lead to incomplete CO oxidation prior to F_2 injection. The unburnt CO reacts with F_2 to form COF_2 and CF_4. This depletes the F_2 available for chemical pumping as well as introducing COF_2 which degrades CO_2 laser performance.

WB3. Supersonic Mixing DF-CO_2 Transfer Chemical Laser: Experiment, W. H. Evers, L. S. Forman, and J. J. Vieceli.

A multikilowatt, combustion driven, *supersonic mixing* transfer chemical laser has been operated efficiently (846 J/g available-fluorine, 40.1 kJ/1bm-total-flow) at high power levels (up to 2872 W) and moderate cavity pressures (up to 13 torr) in a small-scale laboratory device (1 in × 3 in nozzle-exit-area). The experimental apparatus is described in detail with emphasis on the unique method used for CO_2 injection. Performance variation with certain key-operating conditions (cavity pressure, CO_2 flow rate, available fluorine flow rate, and resonator configuration) is presented. In addition, performance variation over a narrow range of other variables (combustor temperature and laser cavity fuel (D_2) flow rate) is discussed. Comparisons are made between HF, DF, HF–CO_2, and DF–CO_2 lasing performance in the same device and conclusions are drawn about the operational characteristics of the four modes. Results obtained using alternate methods of CO_2 injection are also presented. The experimental data are discussed in terms of the physical bases for the observed trends; a more complete interpretation is presented in an accompanying paper on the theory of transfer chemical laser operation.

WB4. Supersonic Mixing DF-CO_2 Transfer Chemical Laser: Theory, J. J. Vieceli, W. H. Evers, and A. G. Negro.

A new analytical model, which represents both a significant conceptual improvement over previous models and a substantial reduction in computational requirements, has been developed for the DF-CO_2 transfer chemical laser and applied to evaluation of supersonic mixing device performance in light of recent data. Previous models for the DF-CO_2 transfer chemical laser have relied on a detailed state representation of the vibrational-level population densities of the species present (DF, CO_2, D_2). In the current model we assume that the population densities of each of the CO_2 vibrational modes can be described by a Boltzmann distribution vibrational temperature (an approach which has been demonstrated for the N_2-CO_2 gas dynamic laser). The existence of mode vibrational temperatures is both conceptually and quantitatively significant since, as would be expected physically, a mode vibrational temperature permits the population densities of each level within a particular vibrational mode to achieve a value representative of the total energy in that mode. This is clearly not the case with a detailed state model in which the $CO_2(001)$ is the highest vibrational level considered, while the effective vibrational temperature of the pumping species (DF) can easily be in excess of 5000 K. (The vibrational temperature of the pumping species (N_2) in the gas dynamic laser is typically only 1500 K.) Furthermore, inclusion of higher CO_2 vibrational levels into the detailed state model leads to an extremely unwieldy computation.

To apply the vibrational temperature concept, the kinetic rate equations are cast in an energy representation for which the dependent variables are the energies in $CO_2(\nu_1)$, $CO_2(\nu_2)$, $CO_2(\nu_3)$, $DF(v)$, and $D_2(v)$. Numerical solution of these equations in conjunction with mixing and power extraction represents a complete characterization of the lasing medium. The one-dimensional mixing model used is applicable to either laminar or turbulent mixing in either constant pressure or specified area flow fields. The interaction between the resonator and the lasing medium is considered using both geometric and physical optics.

Details of the model are presented and *results are compared* to experimental data for a supersonic mixing DF-CO_2 transfer chemical laser with a closed cavity stable resonator. In all cases, theoretical predictions compare favorably to the experimental data.

WB5. Kinetic Model and Computer Simulation of Continuous Wave DF-CO_2 Chemical Transfers Lasers, W. Baumann, J. A. Blauer, S. W. Zelazny, and W. C. Solomon, *Bell Aerospace Company Divison of Textron Inc., Buffalo, N.Y.*

Continuous wave DF-CO_2 chemical transfer has been investigated experimentally by Shirley, Falk *et al.*[1] and

[1] J. A. Shirley, R. N. Sileo, R. R. Stephens, and T. A. Cool, AIAA Paper 71-27, AIAA 9th Aerospace Sciences Meeting, N.Y., Jan. 1971; T. J. Falk, AF Tech. Rep. AFWL-TR-71-96, June 1973 and AFWL-72-169, June 1973.

more recently in our laboratory. Although all of these studies have employed the same chemical reagents, the experimental conditions used differ greatly. Thus, gaseous CO_2 and NO were added to a fluorine stream containing diluent (He or N_2) within a plenum chamber to provide, among other things, a source for atomic fluorine. The flow is directed past an array of deuterium injection ports into the optical cavity where lasing occurs. In order to better understand the available experimental results and use them to provide guidance to the designers of future devices, it is desirable to model such experiments analytically. Recent efforts of Kerber *et al.*[2] were confined to a consideration of pulsed devices. However, their success has encouraged us to attempt the mathematical description of the more complicated CW case with a consideration of the difficult subject of reagent mixing. We have successfully simulated much of the available experimental data for these devices. Our nonequilibrium model involves in excess of 150 individual chemical reactions and/or energy transfer processes and includes a simple description of mixing phenomena. The mixing model used is based upon the assumption that the fluid elements containing the oxidizer and fuel will mix through the eddy motion characteristic of a turbulent mixing layer. The process itself was characterized by two lengths the first being the distance required for a fluid lump to degrade in size to the point at which the transport properties and chemical reaction are significantly affecting the rate of the break-up; the second length scale represents the distance required for mixing to be complete. A direct comparison between the model and the available data demonstrates the chemical chain reaction mechanism chosen for input is quite adequate for most computational purposes. A moderate disagreement between experiment and theory can be shown to be primarily due to an inadequate description of the reagent mixing phenomena. The model developed reproduces in a quantitative way most of the salient features of the available data (e.g., the effect of cavity temperature, pressure, species mixture ratio, and flow Mach no.). Based upon the results of this study, it now appears that our present knowledge regarding the chemistry and physics of the DF-CO_2 transfer laser is adequate to allow for a reasonable mathematical description of a device which is based upon this system

[2] R. I. Kerber, N. Cohen, and G. Emanuel, "A kinetic model and computer simulation for a pulsed DF-CO_2 chemical transfer laser," *IEEE J. Quantum Electron.*, vol. QE-9, pp. 94–113, Jan. 1973.

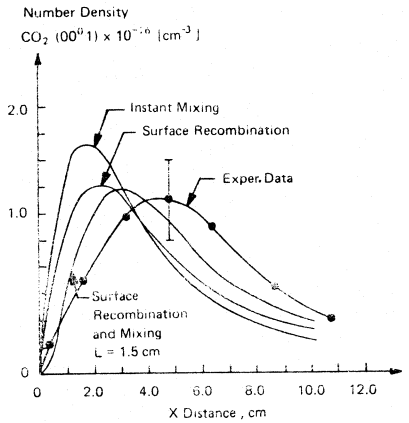

Fig. 1. Comparison of data by Shirley *et al.* with computed $CO_2(00^0 1)$ number densities.

and its operating in a continuous mode. In order to confirm the quantitative aspects discussed herein more data have been required. A more recent set of measurements for a chain reacting TCL have been conducted in our laboratory. These results have been obtained in a chain reacting device with a large mode volume and concomitant high output powers (15 kW). Power measurements and chemiluminescence data were compared to the newly developed model. The fit to the data from this large device confirms the validity of nonequilibrium models developed during the first part of the study. A typical comparison between observed and computed number densities in the upper laser level is shown in Fig. 1 for the data of Shirley *et al.*[1] Shown in this figure are the results computed not only for the case of instantaneous mixing but also the results to be expected when mixing phenomena as well as the effects of the recombination of atomic fluorine on the available surfaces are accounted for. We have estimated the losses due to surface recombination in line with the results of Ferrell *et al.*[3]

[3] J. E. Ferrell, R. M. Kendall, and H. Tong, AIAA Paper 73-643, AIAA 6th Fluid and Plasma Dynamics Conf., Palm Springs, Calif., July 1973.

SESSION WC

cw HF/DF Chemical Lasers I
Wednesday, October 23, 8:30 A.M.

WC1. Investigation of a Supersonic cw HF-Chain Laser, J. C. Cummings and C. M. Dube.

The successful demonstration of HF-chain-reaction lasing in a supersonic CW device will be discussed. Closed-cavity power in excess of 100 W has been obtained. Spectral identification of the laser radiation showed contributions from vibrational levels as high as $v = 5$ (this provides unequivocable evidence of chain reaction rather than the "cold reaction" alone). Chemiluminescent spectra have been recorded and used to determine profiles of small-signal gain, HF vibrational-band number densities, and rotational temperatures. Comparison of the experimental data with those from a detailed computer model[1] indicates discrepancies in power output and rotational temperature. Fluid-mechanical disturbances and/or thermal blockage within the cavity may be inhibiting the CW chain reaction from producing higher laser power.

Several tests have been conducted on the "hot reaction" alone. An arc heater was used to fully dissociate molecular hydrogen. Lasing power was observed and chemiluminescent spectra were recorded. Concentrations of the upper vibrational levels of HF were larger than those observed under chain-reaction conditions.

Since the first successful operation of a pulsed H_2-F_2 system was reported in 1969,[2] many such devices have been built. Standard pulse-initiation techniques dissociate ~1% of the fluorine in a mixture of H_2, F_2, and diluent. Until recently,[3] the only successful demonstrations of CW chain-reaction lasing were in subsonic flow devices.[4,5] However, no laser emission was observed for vibrational levels above $v = 2$.

The goal of our investigation was to study the CW chain laser in a supersonic mixing device. It has been necessary to run tests under a variety of conditions and with a variety of hardware since the number of parameters which can affect the lasing performance is even greater than for the HF "cold-reaction" laser. Several different initiation techniques (production of atomic fluorine), diluent gases, nozzle arrays, and optical-resonator configurations have been used during the investigation. Diagnostics include flow visualization, closed-cavity power, outcoupled lasing spectra, and chemiluminescent spectra.

[1] RESALE-3 Computer Code, developed by G. Emanuel, TRW Systems.
[2] O. M. Batovskii, G. K. Vasil'ev, E. F. Makarov, and V. L. Tal'rose, *Zh. Eksp. Teor. Fiz.*, vol. 9, p. 341, 1969.
[3] C. E. Kepler, T. J. Sadowski, R. Roback, and M. D. Krosney, MICOM Tech. Rep. RK-CR-75-4, July 1974.
[4] T. A. Cool, R. R. Stephens, and J. A. Shirley, *J. Appl. Phys.*, vol. 41, p. 4038, 1970.
[5] T. A. Cool, J. A. Shirley, R. N. Sileo, and R. R. Stephens, AIAA 9th Aerospace Sci. Meeting, N.Y., Jan. 25–27, 1971.

WC2. Spectroscopic Investigation of a Small-Scale cw HF Chain-Reaction Laser,[1] R. A. Meinzer and R. V. Steele, *United Aircraft Research Laboratories.*

[1] This work was supported by ARPA and was monitored by the U.S. Army Missile Command under Contract DAAH01-73-C-0321.

Investigation of the H_2-F_2 chain reaction demonstrated that it is effective as a method for efficiently generating vibrationally excited HF for a CW laser. These experiments were performed on a nozzle with an active area of 2 X 2 cm. Thermal dissociation of F_2 diluted in helium provided the small amount of F-atoms (1 mole %) needed to initiate the HF chain reaction downstream of a two-dimensional supersonic mixing nozzle. Chemiluminescent emission measurements were performed on the active medium and provided the HF vibrational population densities and rotational (static) temperatures. Interpretation of the emission data requires plotting the logarithm of the reduced emission intensity measured for each transition as a function of $J(J+1)$. A straight line plot is anticipated; after optical thickness effects were ruled out, the curvature that was experimentally observed was interpreted as indicating the presence of two temperatures within the flow field. One temperature corresponded to the rotational temperature that HF molecules would have if they had diffused into the unreacted primary gas stream and the second temperature corresponded to the anticipated temperature in the reaction zone. These conclusions are supported by the observation that the lower temperature (HF in unreacted, unmixed primary gas stream) remained constant with increasing distance downstream of the nozzle exit plane whereas the higher temperature (HF in reacting gas zone) increased. The associated vibrational population measurements provided a measurement of the degree of reaction that had occurred and the distribution of vibrational energy among the various vibrational levels. Vibrational levels up to $v = 6$ had significant populations ($\gtrsim 4 \times 10^{13}$ molecules/cc). The decrease in population with increasing vibrational level corresponded to the vibrational levels from $v = 2$ to $v = 6$ being in vibrational equilibrium at a temperature of approximately 5000 K. Use of optical thickness on the $v = 1 \rightarrow 0$ transitions allowed a measurement of ground state population to be made so that the total HF concentration could be determined. Comparison of the measured concentration with the amount of HF that would have been present if the chain reaction had gone to completion provided a quantitative estimate of the degree of reaction. At 10.6 cm downstream of the nozzle exit plane, the chain reaction had gone approximately 30% toward completion. Successful lasing tests were performed and the spectral content of the laser beam indicated that low J transitions were oscillating. This observation was consistent with gain calculations which had indicated that the gain arose from the HF that had diffused into the cool, unreacted primary gas stream.

WC3. Some Experimental Results with Stable Selected-Line Resonators in a Relatively High Gain cw HF Chemical Laser,[1] L. Boedeker, M. Foster, N. Nomiyama, L. Lynds, A. Angelbeck, and G. Wisner, *United Aircraft Research Laboratories.*

Fundamental transverse mode laser oscillations have been established in a CW HF chemical laser with stable single and multi selected-line resonators at power levels adequate for conducting subsequent saturation, cascade, selected-line power extraction and anomalous dispersion studies in separate CW chemical laser amplifiers. Good oscillator axial mode stability and control, amplitude stability, and near diffraction limited output were maintained, features of potential significance for the CW HF chemical laser. Requirements of power and gain for the selected line oscillator imply operation with a relatively high gain medium condition. Since the medium is predominantly Doppler broadened anomalous dispersion and frequency pulling effects are significant as discussed recently by Lynds.[2] The laser employs arc dissociation of SF_6, mixing of H_2 in a fine array nozzle, and supersonic expansion into the laser cavity. Stable single axial modes have been obtained for single vibration–rotation transitions in HF with a 37.5 cm PZT controlled Littrow grating cavity, and a 20 cm active optical path, at power levels near line center between 5 and 10 W per transition on P_2(2-8) and P_1(1-6). Mode widths, full width half power, were less than 80 MHz, however, the measurement may have been limited by the available finesse of the Fabry–Perot interferometer. Frequency stability was about ±15 MHz over 10 s. The full Doppler line width is about 300 MHz and the mode frequency was controllable over a range ±100 MHz about line center without significant introduction of a second axial mode. Amplitude stability was better than 3% rms over the frequency range investigated, 10 to 10^4 Hz. Long term drift (100 s) was less than 3%. Beam quality, as determined with focused integrated irradiance diagnostics was near diffraction limited for these single transitions. As the Littrow cavity was length tuned the laser power exhibited a Lamb dip near line center. Multi selected-line laser oscillator output was achieved using an intracavity grating, separate spherical total reflectors for each of up to three selected lines and a common flat dielectric output coupler. The three lines investigated were $P_2(3)$, $P_2(5)$, and $P_1(4)$. The extra length of this cavity relative to the Littrow for a 20 cm active path generally resulted in laser oscillation in HF on two simultaneous axial modes per transition. Selective simultaneous oscillation on combinations of two lines, including the cascade pair $P_2(3)$, $P_1(4)$, was observed with the Fabry–Perot scanning interferometer, which sets a lower limit to simultaneity here of ~100 MHz. Enhancement of laser output due to the cascade was not observed suggesting that significant saturation of the medium was not occurring.

WC4. High Field Saturation Phenomena in HF Chemical Amplifiers,[1] L. Lynds, M. C. Foster, and A. W. Angelbeck, *United Aircraft Research Laboratories.*

Amplification characteristics of five HF transitions: $P_2(3)$, $P_2(5)$, $P_2(6)$, $P_1(3)$, and $P_1(4)$ were investigated over three decades of intensity.[1] An arc-driven CW master oscillator with fine tuning capability provided the source of frequency-stable (±15 MHz) single line, single and double axial mode radiation with power outputs on the order of 5 W. Amplifier gain was generated by CW combustion driven supersonic flow devices utilizing the "cold" reaction, $F + H_2 \rightarrow HF(V, J) + H$. Two stages of amplification were used to obtain saturating power levels; measurements were performed relative to the second (final) stage. Small signal gains, $\langle g_0 \rangle$, and effective saturation parameters, I_s, measured at transition line centers with a single axial mode input were:

Transition	$\langle g_0 \rangle$ (cm^{-1})	I_s(W/cm^2)
$P_2(3)$	0.20	
$P_2(5)$	0.24	17-24
$P_2(6)$	0.16	8-12
$P_1(3)$	0.17	22-26
$P_1(4)$	0.17	

At sufficiently high intensity levels a single excitation line (double axial mode) induces superfluorescent radiation from the optically connected nonresonant

[1] This work was sponsored by the Advanced Research Projects Agency (ARPA) and monitored by the Air Force Weapons Lab., Air Force Systems Command, The United States Air Force, Kirtland Air Force Base, N. Mex.

[2] L. Lynds *et al.*, "Axial mode frequency–Pulling in an HF chemical oscillator," VIII IQEC, San Francisco, June 1974.

[1] Sponsored by ARPA Contract F29601-73-C-0072, "MOPA Systems for Chemical Lasers" and monitored by the Air Force Weapons Laboratory, Kirtland AFB, N. Mex.

vibrational–rotational level. The induced emission exhibits the following unique properties. It is: 1) continuous, 2) coaxial with the exciting beam, 3) coherent, 4) unidirectional in the direction of the propagation vector, and 5) the process has a specific threshold intensity. Experiments were performed on HF transitions $P_1(4)$ and $P_2(3)$ having a double-axial mode structure. Using $P_1(4)$ as the exciting line, $P_2(3)$ is induced at approximately 1300 W/cm^2. Rate of stimulated emission at this intensity level suggests that T_2 relaxation processes are on the order of 8×10^{-8} s which is equivalent to about 8 collisions. A 2 W $P_1(4)$ beam was boosted to 99 W in two stages of amplification. Near field measurements in the final stage indicate a e^{-1} diameter of 1.4 mm and a corresponding total intensity of 6000–7000 W/cm^2. Spectral distribution of output power (watts) is $P_1(4)$, 36.5; $P_2(3)$, 36.5; $P_2(4)$, 18 and $P_2(5)$, 8. Adjacent lines connected to the mutual vibrational level are also induced as a consequence of rapid rotational draining. Similar experiments were performed with $P_2(3)$ as the exciting transition. A kinetic model has been developed to describe the cascade dynamics of optically connected levels. The theoretical implications of these experiments will be discussed and compared to recent theoretical treatments on cooperative spontaneous emission superradiance.

WC5. Temporal Characteristics of Multiline-Multimode CF HF Chemical Lasers,[1] M. C. Foster, L. Lynds, and A. W. Angelbeck, *United Aircraft Research Laboratories.*

The temporal characteristics of a multiline-multimode CW HF chemical laser using a linear unstable resonator configuration have been investigated over a range of parametric flow conditions. Decoupled energy was separated into its spectral components with a dispersive element such that up to three lines could be simultaneously subjected to a detailed spectral and temporal analysis. Fabry–Perot interferometry high-frequency spectrum analysis and fast-amplitude detection provided a wide frequency range of mode analysis. Results indicate that the two dominant power transitions $P_2(5)$ and $P_1(6)$ fluctuate violently and randomly between zero and total power levels with an effective duty cycle far less than 100 percent. Maximum modulation excursions on these transitions were 55 and 100 percent, respectively. Total decoupled power collected from all transitions showed similar variations but tended to be more constant as a consequence of averaging. Amplitude variations display a distinct spiking tendency without periodic structure. When the optically connected transitions fire simultaneously, their high-frequency components (1 MHz to 100 MHz) tend to be correlated and periodic suggesting that optical-kinetic interactions are operative. The RF amplitude is 10 to 20 percent of the peak power. Frequency modulation of the RF envelope occurs at much lower frequencies and appears to be random and uncorrelated between the two investigated transitions. Several theoretical models for intermittent and periodic behavior within the dynamic range of experimental observables will be discussed. Mechanical driving forces and second-order optical phenomena such as population pulsations predicted from the Lamb equations[2] will be included in these considerations.

[1] Sponsored by ARPA Contract F29601-73-C-0072, "MOPA Systems for Chemical Lasers" and monitored by the Air Force Weapons Laboratory, Kirtland AFB, N. Mex.

[2] W. E. Lamb, Jr., *Phys. Rev.*, vol. 134, p. 1429, 1964.

SESSION WD

Laser-Controlled Chemistry
Wednesday, October 23, 8:30 A.M.

WD1. Laser Powered Homogeneous Pyrolysis,[1] W. H. Shaub and S. H. Bauer, *Cornell University.*

The large absorption cross sections for infrared radiation possessed by a few rather stable molecular species, their relatively fast vibration–translation relaxation times, and the availability of large laser fluxes at their characteristic frequencies can be effectively exploited to generate high bath temperatures for gas phase reactions under strictly homogeneous conditions. *Controlled* temperatures from 500–1500 K can be developed with a modest CO_2 laser. Rise times for heating are estimated to be in the millisecond range, with reaction times $\approx$10 s. Operating pressures [reagents, radiation absorber (generally, SF_6) and diluent] range from 10 to 100 torr. Thus, LPHP is complimentary to the single pulse-shock tube technique [rise time $\sim 10^{-8}$ s; reaction time $\sim 10^{-3}$ s] for obtaining product distributions in gas phase pyrolyses, and for measuring *relative* rates in the absence of hot walls, which may (and generally do) introduce catalytic effects. Further, LPHP is very simple and ideally suited for exploratory investigations of small amounts of reagent ($\approx 10^{-6}$ moles); also, sample cells may be heated externally to augment the vapor pressure of slightly volatile reagents. Conventional analytical procedures (gc, mass spec) are used to follow the course of pyrolysis.

The primary chemical kinetic parameters, the temperature and density of the reactants, have both spatial and temporal distributions. Computer programs were developed for $T(r, x; t)$, given the radial intensity distribution in the incident beam, the absorption coefficient of the SF_6 [as a function of density and the temperature for the anti-bleaching line, P(28)], as well as the mean heat capacity and thermal conductivity of the gas mixture. However, the computed profiles did not prove useful, since the effects of convection, which could not be included in the calculations, perturb the initial distribution significantly within a few milliseconds. Indeed, it proved practical to enhance convection so as to homogenize the sample composition. This was demonstrated experimentally by using a three-compartment cell with test mixtures irradiated in horizontal and vertical configurations. Chopping frequencies ranging from 100 Hz to 1 Hz gave the same product distributions. A practical procedure is to use a "chemical thermometer" to establish the mean *effective temperature* for a given experimental configuration. Examples showing how to measure relative rate constants for molecular conversions and the use of LPHP for qualitative determinations of product distributions as a function of temperature will be presented. For the former, the relative rates for $c \leftrightarrow t$ 2-butene; $c \leftrightarrow t$ 1,2-difluoro-ethene; $c \leftrightarrow t$ dichloro-ethene; cyclopropane; 1,4-cyclohexadiene were studied pairwise to demonstrate that the relative rates obtained by this technique are in agreement with literature values, as derived from single pulse-shock tube and conventional kinetic experiments. Finally, a number of high temperature conversions will be described to illustrate the utility of LPHP for flash thermolysis.

WD2. Infrared Laser Augmented Decomposition of H_3PBF_3, E. R. Lory and S. H. Bauer, *Cornell University*, and T. Manuccia, *Naval Research Laboratory.*

Consideration of v-v and v-T relaxation rates for polyatomic molecules subsequent to their vibrational excitation by currently available laser fluxes, led to a strategy for selecting reactants for which the possibility for successful

[1] Submitted by S. H. Bauer.

augmentation of reaction by infrared irradiation is optimized. Several criteria are listed. While these are shown to be useful guides, they do not constitute a sufficient set of conditions for predicting augmentation for reaction. The criteria were applied to the selection of a typical $2AB \rightarrow A_2 + 2B$ reaction; i.e., a self-scavenging system.

The thermochemistry, essential vibrational spectroscopy, and kinetic parameters for the H_3BPF_3 decomposition are briefly summarized. The experimental arrangement is described and the results of a series of runs with a CO_2 laser (10.6-μ band) are presented. That the augmented decomposition of H_3BPF_3 is due to specific vibrational excitation rather than to an overall temperature rise, or general vibrational excitation, such as developed through v-v transfer is demonstrated by the following: a) The extent of decomposition is dependent on the J value of the laser line used but not in proportion to its absorption coefficient; differences in energy between P(20), P(28), and P(30) are trivial, yet their relative chemical efficiencies differ by as much as a factor of 5. b) Collisional energy transfer to admixed H_3BCO does not appreciably raise the temperature of the latter, since there was no augmented decomposition of the carbonyl, which is as sensitive to rising temperatures as the phosphine adduct. Thus, the strategy of using low pressures to maintain the translational and rotational temperatures of the reactants at or near the wall temperature succeeded even though the radius of the cell was about four times the mean free path.

On the basis of the measured low-pressure absorption cross sections we concluded that under the high-flux conditions it is highly probable that most molecules which pass through the beam absorb at least one photon. However, the observation that the percent conversion depends on the laser power (as derived from log-log plots) indicates that for an H_3BPF_3 molecule to react at a translational temperature (25°C) it must carry at least two exciting quanta and that the absorption coefficient for the second photon must be at least an order of magnitude smaller than the first. Thus, the rate determining step is:

$$H_3B + H_3BPF_3^{(v \geqq 2)} = B_2H_6 + PF_3.$$

Similar studies with H_3BCO (9.6-μ band) showed no augmentation. No boron isotope effect (to within ±20%) was found for these self-scavenging systems.

WD3. Effects of Temperature and Buffer Gases on the Reactions of Nitric Oxide with Vibrationally Excited Ozone, R. J. Gordon[1] and M. C. Lin.

The reactions of nitric oxide and vibrationally excited ozone

$$NO + O_3(001) \xrightarrow{2a} NO_2^*(^2B_1) + O_2$$
$$\xrightarrow{2b} NO_2(^2A_1) + O_2$$

were studied in a rapidly flowing system. Ozone was excited with a pulsed CO_2 laser, and the enhanced NO_2^* emission was monitored with a photomultiplier.[2] The laser-induced signal had a double rise time followed by a slightly faster than exponential decay. The rapid rise rate is attributed to reactions (2a) and (2b), while the slower rise rate is attributed to the relaxation step,

$$O_3(001) + M \underset{-1}{\overset{1}{\rightleftharpoons}} O_3(010) + M$$

followed by the reactions

$$O_3(010) + M \xrightarrow{3a} NO_2^*(^2B_1) + O_2$$
$$\xrightarrow{3b} NO_2(^2A_1) + O_2.$$

The signal decay is due to consumption of excited ozone by chemical reaction and $V \rightarrow R/T$ relaxation. By changing the ozone concentration the gas temperature was varied from 300 to 450 K. The overall decay rate constant has a mean value of $1.1 \pm 0.2 \times 10^{11}$ cc/mole · s which appears to be independent of temperature (see Fig. 1). Most of the decay is due to the nonluminescence reaction, which has a rate constant of $9.6 \pm 1.2 \times 10^{10}$ cc/mole · s. From the analysis of the rise rates, we arrived at the conclusion that the rate constant $k_{2a} + k_{2b}$ is 60 ± 20% of $k_{3a} + k_{3b}$. The vibrational relaxation rates of ozone by various buffer gases (He, Ar, H_2, D_2, O_2, N_2, CO_2, N_2O, NO_2, and CH_4) were determined.

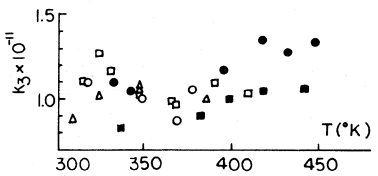

Fig. 1.

[1] NRC/NRL Postdoctoral Research Associate (1972-1973).

[2] R. J. Gordon and M. C. Lin, *Chem. Phys. Lett.*, vol. 22, p. 262, 1973.

SESSION WE

Modeling and Theory
Wednesday, October 23, 2:00 P.M.

WE1. Quasi-Equilibrium Vibrational Population Distributions for Anharmonic Molecular Lasers,[1] S. H. Lam and N. Papageorgis, *Princeton University.*

Theoretical predictions of vibrational population distributions, N_i ($i = 0, 1, \cdots$), are conventionally obtained by direct numerical integration of the master kinetic equations. For every operating condition of interest, a separate computation must be performed. In the present paper, we shall show that N_i of anharmonic diatomic molecules (such as CO and N_2) can be approximately represented by a two-parameter family of universal quasi-equilibrium distributions $N_i^{QE}(e_v, T; \ldots)$ provided the operating conditions satisfy the quasi-equilibrium assumptions. The parameters e_v and T are the vibrational energy per molecule and the translational–rotational temperature of the gas, respectively. The significant point is that $N_i^{QE}(e_v, T)$ depends only on molecular parameters and the V-V and V-T collision probabilities and is independent of the details of the operating conditions; thus for a given gas (or gas mixtures) the family of $N_i^{QE}(e_v, T)$'s can be computed once and for all. The parameter e_v is shown to be governed by a nonlinear relaxation equation of the form $de_v/dt = P - D$ $(e_v, T; \ldots)$ where P is the net rate of external input of vibrational energy per molecule and $D(e_v, T)$ is again a two-parameter family of universal functions which also can be computed once and for all. Sample calculations of N_i^{QE} (e_v, T) and $D(e_v, T)$ for CO and N_2 have been performed and are presented.

The present theory differs from the classical work of Treanor, Rich, and Rehm in that the dominance of V-T collisions over V-V collisions at sufficiently high vibrational levels is recognized. While the Treanor distribution is independent of any collision probabilities, the present N_i^{QE} depends on all the V-V and the V-T collision probabilities. The calculated results show that N_i^{QE} is approximately Treanor at low vibrational levels and is approximately Boltzmann (at temperature T) at high vibrational levels. In the intermediate levels, N_i^{QE} depends on the details of the V-V and V-T collision probabilities, particularly on the level scaling law of the nearly resonant V-V collision probabilities. In classical harmonic oscillator theories, $D(e_v, T)$ is given by $[e_v - e_v(T;$ Boltzmann$)]/\tau(T)$ where $\tau(T)$ depends

[1] This research is supported by the Air Force Office of Scientific Research Contract F44620-73-C-0059.

only on the V-T probabilities. The present results show that whenever N_i^{QE} departs substantially from a Boltzmann distribution, $D(e_v, T)$ is a strongly nonlinear function of e_v and its value depends mainly on the nearly resonant V-V probabilities.

WE2. Theoretical Performance of a V → V Transfer Laser,[1] R. Naismith and R. Cavalleri, *Atlantic Research Corp.*, and R. L. Taylor, P. Lewis, and J. D. Teare, *Physical Sciences Inc.*

This paper presents the results of a theoretical analysis applicable to a general class of gas dynamic vibration–vibration (V-V) transfer lasers. The concept is as follows: A hot pumping gas is expanded through a nozzle freezing the vibrational mode. The lasing gas is either mixed with the pump gas prior to the expansion or after the expansion. V-V pumping, both intermolecular and intramolecular, occurs in the flowing gas under the expansion conditions of high-vibrational temperature and low-translational temperature producing a non-Boltzmann vibrational distribution sufficient for high gain and lasing.

Two necessary requirements for this type of laser are that: 1) the pump gas must have a larger characteristic vibrational temperature than the lasing gas; and 2) the vibrational kinetics must be such that the V-V rates are much larger than the total deactivation processes in the gas.[2]

The hot pumping gas or pump/lase gas mixture can be produced by a variety of techniques such as combustion, electric discharge, or solid propellant-fueled gas generators.

As an example of such a V-V transfer laser, calculations have been performed for the H_2/HCl molecular system. Based on gas generator research performed at ARC, we believe that it is feasible to consider solid propellant gas generators for producing H_2 or H_2/HCl mixtures at temperatures up to 3000 K and pressures to 100 atm. A review of pertinent kinetic rate data for the H_2/HCl molecular system including the effects of H and Cl atoms has been performed, and a complete kinetic mechanism and rate package for these molecules considered as multilevel anharmonic oscillators developed.

The results of two types of analyses will be presented: 1) a harmonic oscillator kinetic model using premixed gas or instantaneous mixing in the throat region of the nozzle; and 2) an anharmonic kinetic model assuming premixed gas. These calculations indicate available energies in the cavity region of the flow of 100 kJ/lb of gas mixture. It is also clear that certain kinetic rates such as the H_2/HCl V-V transfer rate and HCl V-T rate for H-atoms are critical for this laser concept.

Some of the advantages of the H_2/HCl V-V transfer laser compared to chemical lasers are: the lower toxicity and corrosiveness of HCl compared to F_2 and HF, storable and compact fuels, transmission in the 4μ window, and use of the already highly developed GDL technology.

[1] This work was supported by the U.S. Army Missile Command, Huntsville, Ala.

[2] J. D. Teare, R. L. Taylor, and C. W. von-Rosenberg, Jr., *Nature*, vol. 225, pp. 240–243, 1970.

WE3. Theoretical Modeling of Saturation Effects in Laser Amplifiers,[1] R. Tripodi and B. Burdick, *United Aircraft Research Laboratories.*

A theoretical model has been developed to simulate the amplification of a laser beam passing through a chemical laser medium. The model treats the relevant kinetics, and couples these iteratively with a wave-optics calculation describing the propagation of the optical field. The complete cavity gas-dynamic problem is solved once for a description of such parameters as temperature, pressure and velocity. The calculation is done under an assumed flux loading in the range expected in the actual solution. These gas-dynamic parameters, not being strongly dependent on the flux loading, are then treated as known for subsequent calculations. Only the number densities of relevant emitter states need be calculated explicitly as a function of flux loading. This approximation results in a considerable savings of computer time with little sacrifice in accuracy. The optical calculations are, for the time being, restricted to two-dimensional geometries. The model has been applied to experiments carried on at United Aircraft Research Laboratories to study saturation effects in HF media. A specific case was selected, applicable to the $P_1(3)$ transition. Conditions were selected for the initial complete gas-dynamic calculation that resulted in reasonable agreement of predicted gas temperatures and HF number densities with experimental measurements. These conditions were then used in calculations of the amplification of laser beams of various sizes and initial powers. Since the calculations are restricted to two dimensions whereas the actual experiments were three dimensional, exact agreement was not expected. However, the results of the calculations should be comparable with experiment along a plane parallel to the flow direction through the center of the beam. This turns out to be the case, with predictions within 50% of the measurements for amplification over a 20-cm path. The model was used to evaluate the effects of varying beam size and focusing. Such factors can have a significant effect on the amplification of a given input power. For example, at low powers narrower parallel beams are amplified more than wider beams whereas at higher powers the opposite is true. Similarly focused beams with a varying diameter through the medium can also demonstrate differing degrees of amplification, depending upon the input power, degree of focusing, and location of the focal point. These effects and their impact upon the interpretation of experimental data will be discussed.

[1] This work was sponsored in part by the Advanced Research Projects Agency (ARPA) and monitored by the Air Force Weapons Laboratory, Air Force Systems Command, The United States Air Force, Kirtland Air Force Base, N. Mex.

WE4. Vibrational Relaxation of HCl (v = 1, 2, 3, and 6) by H- and Cl-Atoms,[1] R. L. Wilkins, *The Aerospace Corporation, El Segundo, Calif. 90045.*

Rate coefficients have been calculated for the collisional de-excitation of vibrationally excited HCl molecules by H- and Cl-atoms. Three-dimensional classical trajectories of the collisional dynamics of these reactions have been calculated by means of London–Eyring–Polanyi–Sato (LEPS) potential energy surfaces. The results of this study indicate: a) the rapid deactivation of vibrationally excited HCl by H- and Cl-atoms can be explained provided that bound complexes are postulated for both ClH_2 and HCl_2; b) H- and Cl-atom exchange provide efficient mechanisms for relaxing vibrationally excited HCl by Cl- and H-atoms, respectively; c) multiple quantum-transitions are important in these de-excitation processes; d) the major energy transfer processes are vibration to translation in the deactivation of HCl by H- atoms and vibration to rotation in the deactivation of HCl by Cl-atoms. The vibrational relaxation of HCl by H-atoms is faster than vibrational relaxation of HCl by Cl-atoms. Room temperature overall relaxation rates for HCl(v) by H-atoms are as follows: $k_2/k_1 = 1.7$, $k_3/k_1 = 2.5$, and $k_6/k_1 = 3.0$ where $k_1 = 3.0 \times 10^{13}$ cm^3 mole^{-1} s^{-1}.

For deactivation of HCl(v) by Cl-atoms, the room temperature overall relaxation rates are as follows: $k_2/k_1 = 1.5$, $k_3/k_1 = 2.2$, and $k_6/k_1 = 8.4$ where $k_1 = 4.5 \times 10^{12}$ cm^3 mole^{-1} s^{-1}. For v = 1, 2, and 3, these overall rates show

[1] This work reflects research supported by the Air Force Weapons Laboratory (AFWL) under U.S. Air Force Space and Missile Systems Organization (SAMSO) Contract F04701-73-C-0074.

a linear dependence with v. The potential energy wells predicted for the ClH_2 surface of −3.0 kcal/mole and for the HCl_2 surface of −0.77 kcal/mole have an effect on the collision dynamics across these surfaces as vibrational energy in the reagent is increased. The collision dynamics on the surface with the deeper potential-energy well is such that the deactivation rate for the reaction H + HCl(v = 6) shows a much smaller enhancement than does the deactivation rate for the reaction Cl + HCl(v = 6) where the potential energy well is not as deep. Increased vibrational energy in the reagents does not necessarily enhance the overall reaction rates in reactions that occur mostly by formation of collision complexes instead of by direct interaction. The results of the calculations are compared to the rates which have been determined experimentally for the de-excitation of HCl (v = 1, 2, and 3) by Cl-atoms and of HCl(v = 1) by H-atoms. Rate coefficients are provided for many reactions that have not been measured experimentally.

WE6. Investigation of the Computation of V-T and V-V Intermolecular Potentials, N. M. Witriol and J. D. Stettler, *Redstone Arsenal*, and J. R. Sabin and S. B. Trickey, *U. of Florida.*

We report model calculations based on semiempirical computer codes that give V-T and V-V short-range intermolecular potentials strikingly different from those normally chosen in traditional theories of energy exchange. Knowledge of such intermolecular energy transfer processes is essential to the computer modeling of gaseous lasers. Despite the recent outpouring of experimental determinations of such rates, a clear need exists for a quantitative theoretical procedure for their calculation. Sharma and co-workers have shown how to do this for vibrational (V-V) energy transfer mediated by long range multipole–multipole forces for cases in which the vibrational energy mismatch is small. Two of us have recently shown that short range forces can also contribute significantly to such processes. Also, short range forces are the primary origin of vibration–translation (V-T) energy exchange. Typically, the functional form and magnitude of these forces have been determined by the traditional theoretical approach of SSH. A purely repulsive exponential form is assumed and its parameters are obtained from a fit to the repulsive region of the Lennard–Jones potential determined from experimental transport properties. Ab initio calculations of V-T and V-V potentials have not previously been attempted for complicated systems such as N_2-CO_2 because of prohibitive computer costs which arise from the extensive configuration interaction calculations needed to achieve chemical accuracy. However, qualitative chemical behavior is often adequately modeled by semiempirical calculational procedures such as CNDO. We have obtained the V-T and V-V potentials for N_2 and the asymmetric stretch of CO_2 in the N_2-CO_2 system by use of CNDO/2. The intermolecular potential $V(R_{cm}, \rho_1, \rho_2)$ was obtained as

$$\begin{aligned} V(R_{cm}, \rho_1, \rho_2) &= E(R_{cm}, \rho_1, \rho_2) \\ &\quad - E(\infty, \rho_1 \rho_2) \\ &\simeq A_1 + A_2\rho_1 + A_3\rho_2 \\ &\quad + A_4\rho_1^2 + A_5\rho_2^2 \\ &\quad + A_6\rho_1\rho_2 \end{aligned}$$

where $E(R_{cm}, \rho_1, \rho_2)$ is the total CNDO energy of the N_2-CO_2 complex with intermolecular distance R_{cm} and vibrational mode expansions ρ_1 and ρ_2 for CO_2 and N_2, respectively. Although the changes in E were small (less than 0.1%), they were systematic, so that 25 values of V at a given R_{cm} (V at that R_{cm} frequently varying over a factor of two) were fit by the six A's to within 5% for R_{cm}'s of interest. The variation of the A's differed strikingly from that of a simple repulsive exponential. For A_2 through A_6, a variation of at least an order of magnitude occurs as a function of relative molecular orientation in a physically reasonable manner. For a collinear orientation, all A's exhibit an attractive region. The location of the minimum differs among the A's. In particular, A_2, A_4, and A_6 are still attractive at the room temperature classical turning point of A_1, the term governing elastic scattering. (It should be noted that the minimum of A_1 is substantially deeper than the experimental value.) Thus the predominant V-V potential for N_2-CO_2 and V-T potential for CO_2 in a collinear collision would have the form of an attractive force. Computations of other collision orientations show that all the A's are strongly orientation dependent and that none of the A's are well approximated by any of the others.

SESSION WF

CW HF/DF Chemical Lasers II
Wednesday, October 23, 2:00 P.M.

WF1. Relative Performance of Arc and Combustor Driven C.W. HF Lasers, G. L. Grohs and G. Emanuel.

A theoretical model for the HF cold-reaction continuous-wave laser is outlined, which combines the analyses of Mirels *et al.*[1] and Broadwell.[2] Lasing with finite-rate chemistry is considered in the laminar or turbulent mixing layer between parallel uniform oxidizer and fuel jets of finite width. The physical significance of the dimensionless scaling parameters is discussed. Scaling laws predicted by this model are then used to correlate experimental laser performance data obtained with both arc[3] and combustor[4] plenums. In the first case, the oxidizer stream contains atomic fluorine and inert diluent, while in combustor operation it also carries DF from the $D_2 + F_2$ combustion which provides the energy for fluorine dissociation.

Good correlations are obtained when the dominant deactivators of vibrationally excited HF are assumed to be H, HF, or F in arc operation, but DF in the combustor case. The laminar and turbulent models correlate the data equally well. It is shown that in typical arc driven cavities lasing is terminated by merging of adjacent mixing layers at the center line of the oxidizer jet, i.e., by the end of fluorine entrainment. Under otherwise equivalent conditions, operation with a combustor plenum results in a shorter lasing zone, ending before the mixing layers merge. Fluorine entrained downstream of the lasing zone is then wasted, and accounts for the factor 2 or 3 lower efficiencies observed.[5] In addition, the correlations indicate effective ratios of pumping rate to deactivation rate of 0(10) for the combustor, and larger for arc operation.

These observations can be explained if, in agreement with recent hydrogen atom kinetic experiments,[6] the fastest deactivation rate in an arc driven cavity is an order of magnitude slower than HF deactivation by DF. If the measured rate coefficients for the latter are accepted, theoretical estimates[7] for deactivation by H appear to be too fast by an order of magnitude. The large effective ratios of pumping rate to deactivation rate may be attributable to cascading. It is concluded that the efficiency of HF lasers driven by $D_2 + F_2$ combustion can be improved with smaller nozzles. To achieve powers comparable to arc-driven lasers, the combustion reaction should be replaced by one whose products are less effective in deactivating vibrationally excited HF.

[1] H. Mirels, R. Hofland, and W. S. King, *AIAA J.*, vol. 11, p. 156, 1973.
[2] J. E. Broadwell, *Appl. Opt.*, vol. 13, p. 962, 1974.
[3] H. Mirels and D. J. Spencer, *IEEE J. Quantum Electron.*, vol. QE-7, p. 501, 1971.
[4] Tests performed at TRW Systems Group under Contract F29601-73-C-0087, 1973.
[5] R. R. Giedt, paper submitted for 4th Conf. Chemical and Molecular Lasers, St. Louis, Mo., 1974.
[6] J. Bott, Aerospace Corp., private communication.
[7] R. L. Wilkins, *J. Chem. Phys.*, vol. 58, p. 2326, 1973.

WF2. Spectroscopic and Infrared Measurements on the Mesa CW HF (DF) Chemical Laser,[1] M. A. Kwok, R. R. Giedt, and E. F. Cross, *The Aerospace Corporation, Los Angeles, Calif. 90009.*

Results from the spatially, spectrally scanning, remotely controlled spectrograph are described; observations from the IR vidicon system are also given. The behavior of the free supersonic jet HF/DF laser medium is examined in He-F_2/D_2 laser systems with two types of nozzle banks, slit and axisymmetric. The spectrograph monitors number density for HF(3) along the line-of-sight N_2L, and the rotational temperature T_R at a large number of spatial points (X, Z). The data can be classified into three types: 1) transverse spatial scans along Z, 2) spatial scans along X, and 3) data at fixed X_0, Z_0. Different types of interpretations can be developed for three types.

The spectrograph system was designed to acquire spectroscopic data in a field environment with limited test duration. The HF 3-0 P-branch is observed at 8800 A. For these lines, the cavity is optically thin without atmospheric effects on the path. The sensitivity and fast time constants of photomultiplier tubes (S-1) can be used. Each P-branch is observed in 20 ms with a frequency of 10 spectra per second. A mirror system and laser chamber movements provide the (X, Z) displacements.

The Z-scans in N_3L and T_R permit an evaluation of jet uniformity in the direction transverse to the flow. This examines plenum uniformity since $N_3L(Z)$ will reflect the initial F/F_2 distribution and T_R will strongly manifest the exothermity from pumping reactions in the free jet. (The fuel distributions in the nozzle banks will also affect pumping reactions, but the $H_2(D_2)$ is found to be uniform.)

The X-scans provide information on downstream jet properties, which are especially sensitive to nozzle configurations. In particular, the jet static temperature (equated to T_R) has been found; this is important in understanding the reaction kinetics. With pressure measurements, mass density can be evaluated in a manner previously reported.[2] With Mach number information, the amount of reaction for a given nozzle bank can be estimated using jet calorimetry. The efficiency of mixing and reaction in the slit and axisymmetric nozzle can be compared. By running a flow condition with zero-power and with full-power loading in closed cavity conditions, a localized cooling effect can be observed; it is believed, on this upstream cavity edge, that most of the vibrational energy in HF(v) is extracted as photons.

Data at fixed (X_0, Z_0) can provide correlations of $\bar{N}_3L$ and T_R with laser performance parameters. An example is shown of the effect of DF from a F_2-D_2 combustor on an HF laser.[3]

Infrared TV pictures of the laser reaction zones, along the same line-of-sight as the spectrograph, have been obtained. The DF emission between 3.2 and 4.2 μ has been successfully observed.

[3] An estimate of the HF(3) + DF relaxation rate constant can be given.

WF3. Power and Pressure Recovery Measurements in High Mach Number Supersonic Chemical Lasers, J. C. Hyde and R. Knight.

The DF supersonic chemical laser (SCL) provides high power and high efficiency at a radiation wavelength with good atmospheric propagation properties. These devices require low pressure in the optical cavity to obtain high efficiency. The subsystem required to pump the exhaust gases from the cavity dwarfs the rest of the system unless a supersonic diffuser is used to recover a large fraction of the velocity head in the exhaust products. Diffuser recovery pressure is related to the combustor total pressure. Therefore, high-combustor pressure and low-cavity pressure (high Mach cavity entrance numbers) are required for an efficient compact system.

This paper discusses an experimental program investigating laser efficiency and pressure recovery in a high Mach number SCL. A set of Mach 7 nozzles was designed and fabricated using methods that have been shown to be successful at Mach numbers of 4 to 5. The nozzles were designed for helium, fluorine, and deuterium in the combustor, and hydrogen as the cavity fuel. The reactant flow rate was 12 g/s. Flat plat shrouds were positioned above and below the nozzles to contain the expansion in the cavity.

Closed cavity power was measured calorically on each of the water cooled mirrors in the stable oscillator. A probe was used to measure pitot pressure profiles at various distances from the cavity entrance. Most of the tests used D_2 as the combustor fuel to heat and dissociate the excess F_2, and H_2 as the cavity fuel and H_2, C_2H_6, or H_2S as the combustor fuel. The primary variables were diluent ratio, β, cavity fuel ratio, R_L, F_2 dissociation fraction, α, cavity pressure, P_L, and shroud angle θ. Unshrouded performance was most affected by P_L and β. Maximum power was obtained at $\beta = 6$ to 7 with a sharp drop in power outside the range.

Two tests were run using combustor fuels that produced significantly reduced concentrations of HF in the combustor products. Ethane produced slower mixing but less deactivation for a net longer lasing zone. Ethane combustion showed less decrease in power at high β and a 10% higher maximum power than H_2 combustion. H_2S combustion produced a 35% increase in power and produced high power at high β.

WF4. Experimental Comparison of CW Chemical Laser Gas Heaters and Nozzle Arrays,[1] R. R. Giedt, *The Aerospace Corporation, Los Angeles, Calif. 90009.*

Two important components of an HF/DF supersonic diffusion chemical laser configuration are the gas heater, traditionally an electric arc or a combustor, and the nozzle bank for accelerating the flow into the optical cavity, usually variations of a slit or axisymmetric array. Recent experiments at the MESA facility have been conducted with several combinations of an arc or combustor heater configured with one of four nozzles, two slit and two axisymmetric types. The discussion is limited to a comparison of specific experimental results for selected gas conditions and closed cavity lasing.

The performance of the two gas heaters, measured during tests with the same nozzle, an 18:1 expansion ratio axisymmetric array, was: maximum power 11.8 and 7.3 kW and at comparable high power levels, maximum chemical efficiency 7.0 and 4.6%, maximum specific power 120 and 45 kJ/lb., and maximum power peak at an optical axis position of 4.6 and 4.1 cm, for the arc and combustor, respectively. These data are part of a larger body of experimental and analytical evidence that DF combustion product is one of the few important deactivators of HF* in laser flows. In a previous arc versus combustor comparison, this deactivation factor was listed together with a nonuniformity of temperature detected in that combustor flow. The present advanced combustor has regenerative gas cooling so less energy is lost and thus there need be less DF in the flow (now uniform).

The four nozzles are compared in two steps. First, HF laser results from an axisymmetric versus a slit array, both coupled to the same arc, were 11.8 and 12.4 kW, respectively, closed cavity laser power for similar mass flows. Power profiles were sensitive to the faster mixing and therefore faster reac-

[1] This work reflects research supported by the Air Force Weapons Laboratory of the Department of Defense on U.S. Air Force Space and Missile Systems Organization (SAMSO) Contract F04701-73-C-0074.

[2] R. L. Varwig and M. A. Kwok, *AIAA J.*, vol. 2, p. 208, 1974.

[1] This work reflects research supported by the Air Force Weapons Laboratory of the Department of Defense on U.S. Air Force Space and Missile Systems Organization (SAMSO) Contract F04701-73-C-0074.

tion of the axisymmetric design. The slit nozzle-arc combination with longer mirrors produced 15 kW, HF, and DF. Second, higher expansion ratio slit and axisymmetric nozzle banks were matched in HF and DF lasing against the original axisymmetric nozzle, all tested with the combustor and the longer mirrors. These higher expansion ratio nozzles did not improve laser performance. One explanation for this, supported by some static temperature data, is that the $F + H_2$ reaction occurs mainly in the boundary layer and therefore the reaction zone does not see the core flow from the higher expansion. Another possible reason, supported by some pitot pressure data, is that the plenum (upstream of nozzle) pressure varies inversely as the throat area, and the increased expansion ratio was not able (because of boundary layer) to compensate for the higher plenum pressures used with the higher expansion ratio nozzles, thus causing higher static pressures in the lasing jet. However, the higher expansion ratio nozzles do show some evidence of a more extended lasing gain zone, and also a tolerance of high or "matched" optical cavity pressures with less degradation of DF power.

WF5. CW HF/DF Chemical Laser Spectral Diagnostics,[1] R. L. Varwig and M. A. Kwok, *The Aerospace Corporation, Los Angeles, Calif. 90009.*

Two spectrographic systems have been developed and applied to a number of diagnostic experiments on several CW HF/DF supersonic diffusion lasers. The experiments include spectroscopic determination of plenum temperature, and spatial mapping of HF(v)/DF(v) number densities and static temperatures in the lasing region. One system, using phase-lock techniques, has been designed for laboratory applications with high signal sensitivity at high spatial resolution commensurate with the spatial variations in the reaction zones of jets from the small supersonic nozzles employed in CW chemical lasers. It has been applied to the plenum temperature and jet mapping experiments. The second system is rapid spectrally, spatially scanning spectrograph intended for mapping flame zones in field applications where test duration is limited. Accordingly, signal sensitivity and spatial resolution are reduced. The spectrographic systems are described, experimental results are given and the two systems are compared.

The plenum temperature is important, because the degree of dissociation of fluorine containing compounds in the plenum and, hence, the free F atoms available for the HF reaction is dependent on temperature. The measurement is made by observing the rotational temperature of excited HF molecules formed in the hot plenum gas when it is seeded with trace amounts of H_2. The temperatures observed are generally higher than those predicted from the plenum pressure change when a fixed mass flow is heated. This may be expected since the latter value is actually a "throat estimate" back-computed to the plenum. Significant cooling can take place between plenum and throat; therefore, the measured values should be higher than the values predicted from the plenum pressure change associated with heating.

The laboratory spectrographic measurements made in the HF laser cavity have been aimed at getting the spreading rate of the reaction products, the temperature (from rotational temperature) and relative number density in each HF vibrational level. SF_6, heated by mixing with hot He diluent, provides the fluorine for the HF reaction. Data for both H_2 and D_2 fuel are reported and the spreading rates compared for similar flow conditions. From these data total inversion of HF is observed to occur at the nozzle exit plane close to the point where mixing between F and H_2 begins. Further downstream and further into the H_2 flow, the total inversion vanishes as a result of deactivation by HF and H_2. Rotational temperature measurements from the nozzle exit plane to two inches downstream (essentially the extent of the radiating cavity) are obtained as well as spreading rate over the same range. Spatial resolution obtained in these tests is about half mm which is adequate for observing the details of the flow including the differences in spreading rate for H_2 and D_2 fuel.

The spectrograph employed in field operation studies is also described. A special feature is the total remote control of the system. Complete spatial and spectral surveys of the flow field can be obtained in one short sequence. The overall uniformity of the medium is thus evaluated.

WF6. Analysis of Small-Scale DF Cold-Reaction CW Lasers,[1] R. V. Steele, R. A. Meinzer, and R. Roback, *United Aircraft Research Lab.*

Chemiluminescent emission spectroscopy and laser beam spectral content measurements performed with two different nozzle configurations have been used to characterize the resulting differences in the chemical laser media generated by the reaction of an F-atom with D_2 to form vibrationally excited DF. One nozzle design, which utilizes strips of conical nozzle elements, provided a relatively coarse grid of mixing elements while the other, which utilizes fine-scale nozzle elements with small base area, provided a fine grid; the former nozzle had a width of 4.0 cm and the latter a width of 1.7 cm. The long run times achievable with these nozzle segments facilitated making spectral diagnostic measurements. Vibrational populations and rotational temperatures were determined via emission spectroscopy as a function of the distance downstream of the nozzle for various gas compositions and static pressures. Comparison of the measured vibrational population distributions with the primitive vibrational distribution of the DF cold reaction provided an estimate of the degree of vibrational relaxation occurring in the laser medium. From this population and rotational temperature information, the small-signal gain profiles for the two nozzle configurations were also computed. In the case of the coarse grid mixing nozzle, the gains calculated on the basis of emission measurements showed good agreement with the results of gain probe measurements that were made on a larger version of the same nozzle design. Spectral content measurements were used in combination with the emission data to provide information on saturation and cascading in the presence of laser radiation. Spectral content measurements made with a high Q resonator gave evidence for cascading; the $4 \rightarrow 3$ transitions were observed to lase, whereas, the corresponding small-signal gain determined via emission spectroscopy was always below threshold. Estimates of the degree of saturation of optically connected levels can be obtained in part from the intensity distribution of lines observed in the laser output. For example, in one experiment the vibrational population ratio N_2/N_1 was observed to be 1.5 in the absence of lasing; whereas, with the laser operating, this ratio was estimated to be 0.6 from the observed lasing transitions. In addition, the small-signal gain calculations were combined with measurements of the extracted laser power to provide an estimate of the saturation intensity (200 W/cm^2). The measured spatial variation in vibrational population downstream of the nozzle exit plane has also been compared with calculations performed with the UARL one-dimensional chemical laser code and the exponential mixing length associated with the coarse-grid nozzle was estimated to be 10 cm. Furthermore, comparisons of the measured vibrational distributions with those predicted by the computer code provide a unique test of various V-V rate packages which have been proposed for the relaxation of the higher vibrational levels.

[1] This work reflects research supported by the Air Force Space and Missile System Organization (SAMSO) under Contract F04701-73-C-0074.

[1] This work was done under MICOM Contract DAAH01-73-C-0682.

Index to Authors

[NAME]	Paper	Page
Andrysiak, S. J.	WB6	672
Angelbeck, A.	WC3	713
Angelbeck, A. W.	WC4	713
Angelbeck, A. W.	WC5	714
Bargeron, C. B.	MB6	688
Bauer, S. H.	TC1	701
Bauer, S. H.	WD1	714
Bauer, S. H.	WD2	714
Baumann, W.	WB5	711
Benard, D. J.	MD10	697
Benson, R. C.	MB6	688
Benson, R. C.	MD10	697
Benson, S. W.	MC4	691
Berry, M. J.	MB1	687
Berry, M. J.	MB2	687
Black, G.	TC8	704
Blair, L. S.	TA3	698
Blauer, J. A.	WB5	711
Boedeker, L.	WC3	713
Bott, J. F.	MD7	696
Boulnois, J. L.	TD9	707
Bradford, Jr., R. S.	MC6	692
Braun, W.	MD11	697
Braun, W.	TC5	702
Broida, H. P.	MC6	692
Broida, H. P.	MC7	692
Broida, H. P.	MC8	692
Bronfin, B. R.	TD4	705
Brown, R. D. H.	MD5	695
Buchwald, M. I.	MD9	697
Burde, D. H.	WA3	709
Burdick, B.	WE3	716
Byron, S. R.	MA5	686
Capelle, G. A.	MC7	692
Carabetta, R. A.	MB7	689
Cavalleri, R.	WE2	716
Center, R. E.	MA7	687
Chen, H.-L.	MA7	687
Chen, H.-L.	TA5	648
Chen, H.-L.	TD3	705
Chen, H.-L.	WA5	669
Chou, M. S.	MC5	691
Clendening, C.	MD2	694
Coleman, P. D.	MA4	686
Coleman, P. D.	TB3	654
Cool, T. A.	MC5	691
Creighton, J. R.	TA8	699
Cross, E. F.	WF2	718
Cuellar, E.	MB4	688
Cummings, J. C.	WC1	712
Cupitt, L. T.	TB6	700
Daugherty, J. D.	TA5	648
Daugherty, J. D.	TD3	705
Davis, C. C.	TB8	701
Davis, S. J.	MC10	693
DeTemple, T. A.	MA4	686
Dewey, H. J.	TC3	702
Donohue, T.	TC7	703
Drexhage, M. G.	WB6	672
Dube, C. M.	WC1	712

[NAME]	Paper	Page
Eckstrom, D. J.	MC4	691
Edelstein, S. A.	MC4	691
Emanuel, G.	WF1	717
Evers, W. H.	WB3	711
Evers, W. H.	WB4	711
Felder, W.	TC6	703
Fisher, C. H.	MA5	686
Fontijn, A.	TC6	703
Forman, L. S.	WB3	711
Foster, K. D.	TB5	700
Foster, M.	WC3	713
Foster, M. C.	WC4	71
Foster, M. C.	WC5	71
Freund, S. M.	TC2	702
Fried, S.	WA5	699
Fyfe, W.	TA5	648
Gamble, W. L.	TB6	700
Garscadden, A.	MA8	687
Gerber, R. A.	TA4	642
Getzinger, R. W.	MB9	690
Getzinger, R. W.	TA3	698
Giedt, R. R.	WF2	718
Giedt, R. R.	WF4	718
Glass, G. P.	MD5	695
Glowacki, W. J.	TB2	700
Gordon, R. J.	WD3	715
Green, W. H.	MD1	694
Greene, A. E.	TD10	708
Greiner, N. R.	TA3	698
Grohs, G. L.	WF1	717
Gross, R. W. F.	TC4	702
Gutcheck, R. A.	TC9	704
Hadley, S. G.	MC3	69
Hadley, S. G.	MC10	693
Hager, G.	MC3	691
Hager, G.	MC10	693
Hall, L. H.	MC9	693
Hancock, J. K.	MD1	694
Harris, N. W.	MA6	686
Harris, R. A.	MC2	691
Harris, R. A.	MC3	691
Hart, G. A.	MA1	685
Heidner, R. F.	MD7	696
Hill, R. M.	TC9	704
Hinchen, J. J.	MD4	695
Holmes, C. P.	TD1	704
Hon, J. F.	TA6	698
Hough, J. J. T.	TA7	699
Huestis, D. L.	MC4	691
Huestis, D. L.	TC9	704
Hyde, J. C.	WF3	718
Jeffers, W. Q.	TB4	660
Johnson, S.	MC11	693
Kaldor, A.	MD11	697
Kaldor, A.	TC5	702
Keller, R. A.	TC3	702
Kelley, J. D.	TB4	660
Kelley, J. D.	TB7	701

[NAME]	Paper	Page
Kepler, C. E.	TD4	705
Kerber, R. L.	TA7	699
Kimbell, G. H.	TB5	700
King, D. L.	WA1	708
Knight, R.	WF3	718
Krogh, O. D.	TD6	706
Krosney, M. D.	TD4	705
Kurylo, M. J.	MD11	697
Kurylo, M. J.	TC5	702
Kwok, M. A.	MD3	695
Kwok, M. A.	WF2	718
Kwok, M. A.	WF5	719
Lam, S. H.	WE1	715
Lamotte, M.	TC3	702
Lewis, P.	WE2	716
Lilenfeld, H. V.	TB4	660
[illegible]illis, J. R.	MC2	691
[illegible]impaecher, R.	TD3	705
Lin, M. C.	MB5	688
Lin, M. C.	WA6	710
Lin, M. C.	WD3	715
Linevsky, M. J.	MB7	689
Long, Jr., W. H.	MA8	687
Lorents, D. C.	TC8	704
Lorents, D. C.	TC9	704
Lory, E. R.	WD2	714
Luria, M.	MC4	691
Lynds, L.	WC3	713
Lynds, L.	WC4	713
Lynds, L.	WC5	714
Mangano, J. A.	TD3	705
Manuccia, T.	WD2	714
Marabella, L.	TC10	704
McArthur, D. A.	TD8	707
McFarlane, R. A.	TB8	701
McFarlane, R. A.	WA3	709
Meinzer, R. A.	WC2	712
Meinzer, R. A.	WF6	719
[illegible]ichels, H. H.	MC2	691
Miles, R. B.	TD9	707
Montgomery, Jr., J. A.	MC2	691
Murray, J. R.	MA2	685
Nachshon, Y.	TB3	654
Naismith, R.	WE2	716
Nakano, H. H.	TC9	704
Negro, A. G.	WB4	711
Nelson, L. Y.	MA5	686
Newman, L.	MA4	686
Nguyen Xuan, C.	TC5	702
Noetzel, J.	MD2	694
Nomiyama, N.	WC3	713
Novak, J. R.	TA6	698
Nowak, A. V.	MB9	690
O'Neill, F.	MA6	686
Papageorgis, N.	WE1	715
Patterson, E. L.	TA4	642
Perry, B. E.	MC4	691
Petersen, A. B.	TB1	699
Pimentel, G. C.	MB3	688
Pimentel, G. C.	MB4	688
Pimentel, G. C.	TD6	706
Plummer, M. J.	TB2	700
Poehler, T. O.	WB1	710
Poole, P. R.	MB3	688
Powell, H. T.	MA2	685
Prince, J. F.	MA8	687
Quigley, G. P.	MD8	696
Rabideau, S. W.	MB9	690
Rapagnani, N. L.	WA4	709
Rhodes, C. K.	MA2	685
Rice, W. W.	MB8	689
Ritter, J. J.	TC2	702
Ritter, J. J.	TC3	702
Roback, R.	TD4	705
Roback, R.	WF6	719
Russell, F.	TD3	705
Sabin, J. R.	WE6	717
Sadowski, T. J.	TD4	705
Schott, G. L.	MB9	690
Scott, P. B.	MC11	693
Searles, S. K.	MA1	685
Sentman, L. H.	TD7	706
Setser, D. W.	WA1	708
Setser, D. W.	WA2	708
Sharpless, R. S.	TC8	704
Shaub, W. H.	WD1	714
Shin, H. K.	WE5	679
Shortridge, R. G.	MB5	688
Shortridge, R. G.	WA6	710
Smith, I. W. M.	MD5	695
Smith, I. W. M.	MD6	696
Snelling, D. R.	TB5	700
Solomon, W. C.	WB5	711
Steele, R. V.	WC2	712
Steele, R. V.	WF6	719
Steinfeld, J. I.	TC10	704
Stettler, J. D.	WE6	717
Stregack, J. A.	TD2	705
Stregack, J. A.	WB2	711
Stricker, J.	TC1	701
Suart, R. D.	TA1	698
Suchard, S. N.	MA3	685
Suchard, S. N.	MC1	690
Sutton, D. G.	MA3	685
Sutton, D. G.	MC1	690
Taylor, R. L.	WE2	716
Teare, J. D.	WE2	716
Thommarson, R. L.	TB7	701
Tollefsrud, P. B.	TD8	707
Tregay, G. W.	WB6	672
Trickey, S. B.	WE6	717
Tripodi, R.	WE3	716
Turner, Jr., C. E.	WA4	709
Turner, R.	WB1	710
Varwig, R. L.	WF5	719
Velazco, J. E.	WA2	708
Vieceli, J. J.	WB3	711
Vieceli, J. J.	WB4	711
Wagner, J. L.	TB2	700
Walker, R. E.	MB6	688
Walker, R. E.	MD10	697
Wanner, J.	TD5	706
Watson, G.	MC11	693
Watt, W. S.	WB2	711
Webbink, R. F.	TB4	660

[NAME]	Paper	Page
Wendelken, C. P.	MD2	694
West, G. A.	MB1	687
West, J. B.	MC8	692
Wexler, B. L.	TD2	705
Whitney, W. T.	MA6	686
Wiesenfeld, J. R.	TC7	703
Wiesenfeld, J. R.	WA3	709
Wilkins, R. L.	MD3	695
Wilkins, R. L.	WE4	716
Wilson, L. E.	MC3	691
Wilson, L. E.	MD2	694
Wisner, G.	WC3	713
Witriol, N. M.	WE6	717
Wittig, C.	TB1	699
Wolga, G. J.	MD8	696
Wolga, G. J.	MD9	697
Wood, L. M.	WB6	672
Wormhoudt, J.	TC10	704
Zelazny, S. W.	WB5	711

Contributors

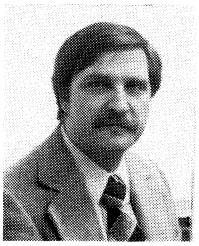

S. J. Andrysiak was born in Kaminoka, Poland, in 1942. He received the B.S.M.E. degree from Worcester Polytechnic Institute, Worcester, Mass., in 1964.

He has been with the Bell Aerospace Company, Division of Textron, Inc., Buffalo, N.Y., since 1966. He is presently in the High Energy Laser Technology Department, where he is working on advanced high-power transfer chemical lasers.

*

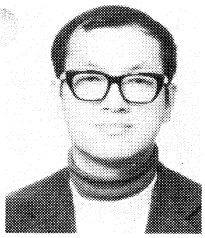

Hao-Lin Chen was born in Kiangsu, China, on February 24, 1941. He received the B.S. degree in chemical engineering from Tunghai University, Taichung, Taiwan, in 1962, and the Ph.D. degree in physical chemistry from Indiana University, Bloomington, in 1967.

He did his postdoctoral research at the University of California, Berkeley, from 1967 to 1969. He taught as an Assistant Professor at the Catholic University of America, Washington, D.C., from 1969 to 1972, where he conducted research on vibrational energy transfer in gas. He joined the AVCO Everett Research Laboratory in 1972, where he was principally concerned with research on high-power pulsed chemical lasers and electronic energy transfer of metal vapors. In February 1975 he joined the "Y" Division at Lawrence Livermore Laboratory, Livermore, Calif.

Dr. Chen is a member of the American Physical Society.

*

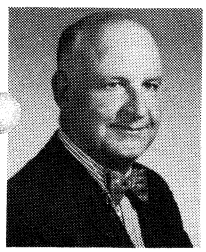

Paul D. Coleman (A'45-M'55-F'62) received the B.A. degree from Susquehanna University, Selinsgrove, Pa., the M.S. degree from Pennsylvania State University, University Park, and the Ph.D. degree from the Massachusetts Institute of Technology, Cambridge, in 1940, 1942, and 1951, respectively.

From 1942 to 1946 he was a Physicist with WADC, Dayton, Ohio, and AFCR, Cambridge, Mass., where he worked on radar countermeasures, antennas, and microwaves. In 1951 he came to the University of Illinois, Urbana, as an Associate Professor of electrical engineering where he established and has directed the Electro-Physics Laboratory. He is presently a Graduate Professor teaching and directing thesis research in the area of far-infrared physics, molecular and chemical lasers, quantum electronics, integrated optics, and optical properties of materials.

Dr. Coleman is a member of Sigma Xi, Pi Mu Epsilon, the American Physical Society, and the Optical Society of America. He is presently Treasurer of DRC, Chairman of the Quantum Electronics Council, a member of the International Scientific Radio Union Commission I, and Chairman of the MTT subcommittee on millimeter and submillimeter waves.

*

Jack D. Daugherty was born in Ottumwa, Iowa, on February 4, 1935. He received the B.S. degree in electrical engineering from Iowa State University, Ames, in 1957, and the M.S. and Ph.D. degrees from Purdue University, Lafayette, Ind., in 1963 and 1966, respectively. While at Purdue, he studied under a National Science Foundation Graduate Fellowship. He also attended the 1964 Princeton University Plasma Physics Summer Institute sponsored by a National Science Foundation Grant.



From 1957 to 1961 he was attached to Naval Reactors, U.S. Atomic Energy Commission, where he worked on the structural, electrical, and nuclear engineering of naval nuclear propulsion reactors. He joined AVCO Everett Research Laboratories, Everett, Mass., where he is currently Vice President for Laser Research, in 1966. As a Principal Research Scientist at AVCO Everett he conducted theoretical and experimental research in various areas of plasma physics, high-voltage electron devices, gas-discharge physics, and lasers. Since the invention of the E-beam sustained laser in 1969, he has concentrated his technical efforts on the development of high-power laser technology.

Dr. Daugherty is a member of the American Physical Society and several physics, engineering, and scholastic honor societies.

*



M. G. Drexhage was born in Luedenscheid, Germany. He received the B.S. degree in physics from the University of Jena, Jena, in 1935, and the M.S. degree in physics from the University of Goettingen, Goettingen, Germany.

He joined Bell Aerospace Company, Division of Textron Inc., Buffalo, N.Y., in 1953 and participated in the development of the Nike, Rascal, and Agena rocket systems; and the reaction control subsystems for the X-15, Mercury, and Centaur space vehicles. Currently, he is supervising the design, construction, and testing of two transfer chemical laser systems.

Dr. Drexhage received the AIAA award as "Aerospace Pioneer 1970."

*

Steve Fried, photograph and biography not available at the time of publication.

*



Walter Fyfe was born in Somerville, Mass., on November 6, 1929. He graduated from the Coyne Electrical and Technical School in 1951 and attended Northeastern University, Boston, Mass., and Boston University, Boston, Mass.

He was employed by the Bethlehem Steel Company Shipbuilding Division, Quincy, Mass., from 1952 to 1954, where he worked on radar and fire control systems. In 1955 he was employed by AVCO Everett Research Laboratory, Inc., Everett, Mass., where he has worked on numerous experiments in chemical kinetics, atomic physics, and laser research.

*

R. A. Gerber, photograph and biography not available at the time of publication.

*

W. Q. Jeffers (M'73) was born in Aurora, Nebr., on November 1, 1939. He received the S.B. degree in electrical engineering from the Massachusetts Institute of Technology, Cambridge, and the M.S. and Ph.D. degrees in electrical engineering from the University of Illinois, Urbana, in 1961, 1964, and 1967, respectively.



From 1961 to 1963 he was employed in the Research Division of McDonnell Aircraft Company, where he worked on microwave masers. He was in the Department of Electrical Engineering of the University of Illinois from 1963 through 1968 as a Research Assistant, Research Associate, and Assistant Professor. His thesis research at the University of Illinois was concerned with the water-vapor laser. He was associated with Hughes Research Laboratories, Malibu, Calif., in 1968, and rejoined McDonnell Douglas Research Laboratories, St. Louis, Mo., in 1969. His research interests have since been in the field of molecular and chemical lasers. He has been active in organizing the Conference on Chemical and Molecular Lasers in St. Louis in 1969, 1972, and 1974.

Dr. Jeffers is a member of Sigma Xi and the Optical Society of America.

*

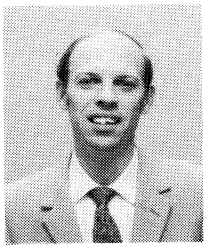

J. D. Kelley was born in Chicago, Ill., on July 30, 1937. He received the B.S. degree in chemistry from St. Louis University, St. Louis, Mo., and the Ph.D. degree in chemistry from Georgetown University, Washington, D.C., in 1959 and 1964, respectively.

From 1964 to 1967 he was with Brookhaven National Laboratory. In 1967 he joined the McDonnell Douglas Research Laboratories, where he is presently a Senior Scientist in the Radiation Sciences Laboratories, St. Louis, Mo. His research interests include molecular collision phenomena, chemical kinetics, and chemical lasers.

Dr. Kelley is a member of the American Chemical Society, Sigma Xi, and the American Association for the Advancement of Science.

*



H. V. Lilenfeld was born in Brooklyn, N.Y., on August 25, 1945. He received the B.S. degree in chemistry from the Polytechnic Institute of Brooklyn, N.Y., and the Ph.D. degree from the Massachusetts Institute of Technology, Cambridge, in 1966 and 1971, respectively.

From 1971 until 1972 he was a Research Associate at Brookhaven National Laboratory. Since 1972 he has been working at the McDonnell Douglas Research Laboratories in St. Louis, Mo. He is currently engaged in research in the kinetics and modeling of chemical lasers.

Dr. Lilenfeld is a member of the American Chemical Society, Sigma Xi, and Phi Lambda Upsilon.

*

Yehuda Nachshon (S'70) was born in Rehovoth, Israel, on November 18, 1943. He received the B.S. (Summa Cum Laude) and M.S. degrees in physics from the Technion–Israel Institute of Technology, Haifa, in 1968 and 1970, respectively, and the Ph.D. degree in electrical engineering from the University of Illinois, Urbana, in 1974. In 1970 he received a Technion scholarship and from 1970 to 1973 he had a Hebrew Technical Institute fellowship.

While at the University of Illinois, he was a Research Assistant in the Electro-Physics Laboratory. His professional interests have been in infrared physics and lasers, especially chemical and molecular lasers, optical pumping of infrared molecules, and energy exchange in molecular collision. He is presently in Haifa, Israel, working for the Israeli Defense Department.

Dr. Nachshon is a member of Sigma Xi and Phi Kappa Phi. He received the Best Student Award in his freshman and junior years as an undergraduate.

E. L. Patterson (S'60–M'64), photograph and biography not available at the time of publication.

*

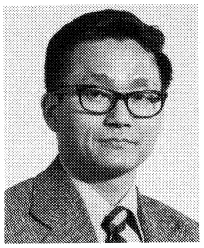

H. K. Shin was born in Korea. He came to the United States in 1957, where he received the B.A. and Ph.D. degrees in chemistry in 1959 and 1961, respectively, from the University of Utah, Salt Lake City.

From 1961 to 1962 he was a Research Chemist at the National Bureau of Standards, Washington, D.C. For the next two years he was a postdoctoral Research Fellow at Cornell University. Since 1965 he has been a member of the Faculty at the University of Nevada, Reno. His fields of research are the theory of molecular collisions, theory of collision-induced light scattering, and nonequilibrium rate processes.

Dr. Shin is a member of the American Chemical Society, the American Physical Society, the Korean Chemical Society, and Sigma Xi.

*

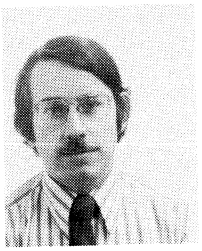

G. W. Tregay was born in Oak Ridge, Tenn., in 1945. He received the B.S. degree from the Massachusetts Institute of Technology, Cambridge and the Ph.D. degree in physical chemistry from Boston College, Boston, Mass., upon completing a spectroscopic investigation of low-pressure H_2/F_2 flames, in 1967 and 1972, respectively.

Since 1973 he has been employed at Bell Aerospace Company, Division of Textron Inc., Buffalo, N.Y., and is currently involved in both experimental and analytical studies of chemical laser systems.

Dr. Tregay is a member of the Combustion Institute and the American Chemical Society.

*

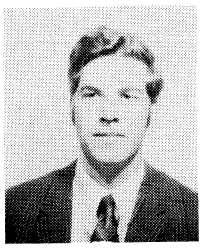

R. F. Webbink was born in Hutchison, Kans., on September 21, 1945. He received the B.S. degree in physics from the Massachusetts Institute of Technology, Cambridge, in 1967, and is presently completing work on the Ph.D. degree in theoretical astronomy at Cambridge University, Cambridge, England.

He worked at the McDonnell Douglas Research Laboratories immediately prior to, and following, service in the U.S. Navy from 1969 to 1972. He resumed a Marshall Scholarship at the Institute of Astronomy, Cambridge University, in October 1972. His current research includes calculations of the structure and evolution of close binary stars. He has been appointed Research Fellow in Astronomy and Astrophysics at the University of Illinois, Urbana, from August 1975.

Mr. Webbink is an associate member of Sigma Xi.

*

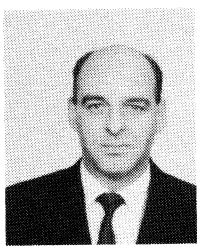

L. M. Wood was born in Evanston, Ill., in 1930. He received the B.S. degree from the University of Missouri at Rolla, Rolla, in 1956.

He has been with Bell Aerospace Company, Division of Textron Inc., Buffalo, N.Y., since 1959. He is currently working on optical cavity diagnostics for CW chemical lasers.

A Simplified Method for Predicting Unstable Resonator Mode Profiles

WILLIAM H. STEIER, SENIOR MEMBER, IEEE, AND GARY L. McALLISTER

Abstract—The qualitative features of the lowest order mode profile of an unstable resonator can be predicted by a simple technique based on Fresnel zone theory. The number of rings in the pattern and the occurrence of a local minimum or a local maximum on-axis can be predicted by computing the number of Fresnel zones subtended at the observation plane by the cavity aperture uniformly illuminated by a point source at the virtual focus. This technique has been verified by computer calculations of mode profiles both inside and external to the cavity for moderate Fresnel numbers. The results were also confirmed by experimentally measured mode profiles on an unstable cavity He-Xe laser. The predicted cyclic nature of the mode loss with cavity aperture diameter was also confirmed experimentally.

I. Introduction

NUMEROUS computer studies [1] of unstable resonators have shown complex mode patterns for even the lowest order modes. These patterns change rapidly as the cavity aperture size is changed, and prediction of the mode has, in general, required computer calculations. Any change in aperture size, or mirror spacing, or curvature has required another complete computer analysis to predict the mode shapes. In this paper we demonstrate a simple technique based on Fresnel zone theory [2] to predict the qualitative features of the mode profile and give experimental examples for moderately low equivalent Fresnel numbers.

The geometrical picture of unstable modes is that of spherical waves emanating from the virtual foci. This picture provides a first-order value for the cavity loss or mode eigenvalue and predicts a spherical phase front for the modes. Using this geometrical picture as a starting point, we have found that the number of rings in the pattern and the occurrence of a local minimum or local maximum in the on-axis intensity of the lowest order mode can be simply predicted by assuming the cavity aperture (generally the resonator mirror) to be uniformly illuminated by a spherical wave emanating from the virtual focus. By computing the number of Fresnel zones subtended by this aperture from any observation point inside or outside the cavity, these general features of the lowest order mode can be predicted at that point. In particular, if the observation point chosen is the opposite mirror, then the features of the resonator mode profile that would be calculated numerically can be predicted. This technique is demonstrated to work quite well when $2N_{eq}$ is odd, that is, away from a cavity loss degeneracy point [3]. Near a degeneracy point ($2N_{eq}$ even) the general mode features can be predicted in the same manner by assuming an additional corrective phase-front curvature to the aperture illumination.

Manuscript received August 15, 1974; revised April 22, 1975. This work was done at the Northrop Research and Technology Center, was supported in part by the Advanced Research Projects Agency, Department of Defense, and was monitored by the Office of Naval Research under Contract N00014-72-C-0043.

W. H. Steier is with the Department of Electrical Engineering, University of Southern California, Los Angeles, Calif. 90007.

G. L. McAllister was with the High Power Laser Program, Northrop Research and Technology Center, Hawthorne, Calif. 90250. He is now with the Exxon Nuclear Company, Richland, Wash. 99352.

II. Numerical Calculations

Diffraction calculations for near-field patterns of a uniformly illuminated circular aperture show series of concentric rings where the number of relative peaks in intensity in a scan taken along any diameter of the pattern is equal to the Fresnel number [4]. Furthermore, when the Fresnel number is even, there is a local minimum on-axis, and when it is odd, there is a local maximum on-axis. If the lowest order resonator mode has a phase profile which is approximately equal to that predicted by geometrical optics, and if the intensity profile varies slowly over the width of a Fresnel zone, then the general features of the mode profiles should show the same behavior as a uniformly illuminated aperture. That is, when the effective Fresnel number (which includes the spherical curvature of the illuminating wave) is even, there will be an on-axis dip in the intensity, and when it is odd, there will be peak. Also there will be a number of intensity peaks along a diameter equal to the effective Fresnel number. To demonstrate this, the mode patterns for the lowest loss mode of a symmetrical unstable resonator shown in Fig. 1 were computed using the Prony method described by Siegman and Miller [3]. The details of this computer code have been described in a previous paper [5]. Circular mirrors (with spherical surfaces) and cylindrical symmetry are assumed throughout. The modes were computed at an observation plane which can be inside or outside the cavity for the wave traveling from left to right. These computer results are compared to our simplified theory which is based on the effective Fresnel number N_{eff} at the observation plane for the mirror on the left when it is uniformly illuminated by a spherical wave from the virtual focus on the left. N_{eff} and N_{eq} are therefore defined by

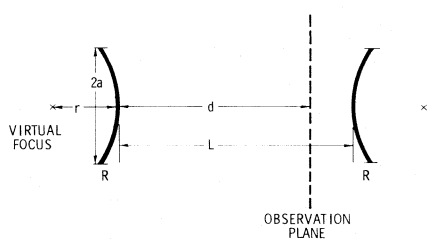

Fig. 1. Schematic diagram indicating the observation plane for calculating the intensity profile of a symmetric unstable resonator.

$$2N_{eq} = N(M - 1/M)$$

$$N_{eff} = N(L/r + L/d)$$

where

$N = a^2/L\lambda$	cavity Fresnel number;
a	radius of the cavity aperture;
L	mirror spacing;
R	mirror radius of curvature;
λ	wavelength;
g	$= 1 - L/R$;
$M = g + (g^2 - 1)^{1/2}$	cavity magnification;
$r = L/(M - 1)$	distance from the mirror to the virtual focus.

Fig. 2 illustrates the computed mode patterns at the plane of the mirrors with $N_{eq} = 1.5$ which is a minimum loss point for the lowest order mode and hence not near a mode degeneracy point as predicted by Siegman and Miller [3]. Modes for $N_{eff} = 4$ and 5 are shown. Since the modes are being calculated at the mirror, $d = L$ is used in calculating N_{eff}, and therefore $N_{eff} = NM$. It should be noted there that M is different for each example and they are therefore not normalized to the same radius. The tick mark on each curve denotes the respective mirror edge for each example, and the point where the normalized radius is 1.0 corresponds to a radius equal to the true cavity radius times the geometrical magnification. Fig. 3 shows similar mode profiles calculated for $N_{eq} = 0.5$. These results show that, at least for these low values of N_{eq}, the number of intensity peaks along a diameter of the pattern is equal to N_{eff} (the mode is symmetric about the center and hence the figures show $N_{eff}/2$ intensity peaks). Also the mode has a local minimum on-axis if N_{eff} is even and a local maximum on-axis if N_{eff} is odd. This is qualitatively the same as a simple diffraction calculation would have predicted for a point source at the virtual focus uniformly illuminating the mirror aperture.

Near a loss degeneracy point ($2N_{eq}$ is even) we have found that there are two distinct mode eigenfunctions with nearly the same mode loss (magnitude of the eigenvalue) but with different phase angles of the eigenvalue. This is in contrast to earlier published work with square apertures and slightly larger N_{eq} in which the mode eigenfunctions were also found to be degenerate. Numerous calculations have shown that the two modes have different intensity profiles and different phase-front radii; one is more concave than the geometrical wave and one is more convex in approximately equal amounts. We have found that near degeneracy our method is still applicable and that the mode features can be predicted by allowing the first-order-mode phase profile to be 90° advanced at the mirror edge relative to the geometric wave and by allowing the second-order-mode phase profile to be 90° retarded. This ±90° phase deviation would modify N_{eff} by ∓0.5 and would be expected to affect the number of rings observed in the intensity profile. Figs. 4 and 5 are the computed intensity and phase profiles

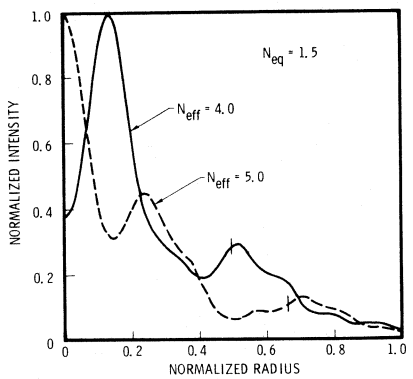

Fig. 2. Normalized mode intensity profile for a symmetric unstable resonator with $N_{eq} = 1.5$.

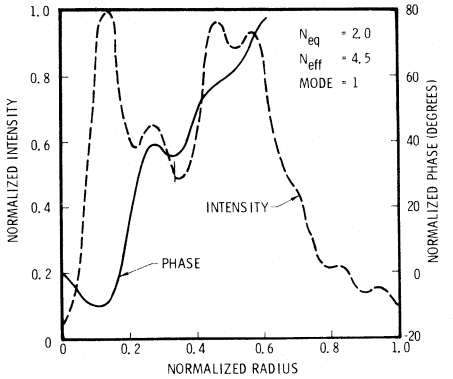

Fig. 4. Intensity and phase profiles for mode 1 of a symmetric unstable resonator at the loss degeneracy point $N_{eq} = 2.0$.

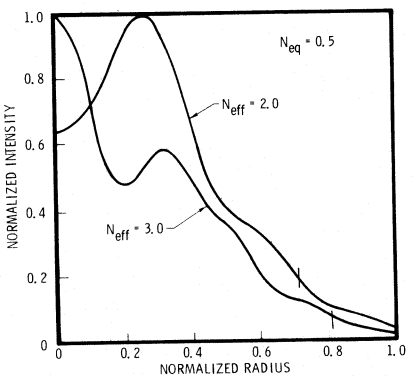

Fig. 3. Normalized mode intensity profiles for a symmetric unstable resonator with $N_{eq} = 0.5$.

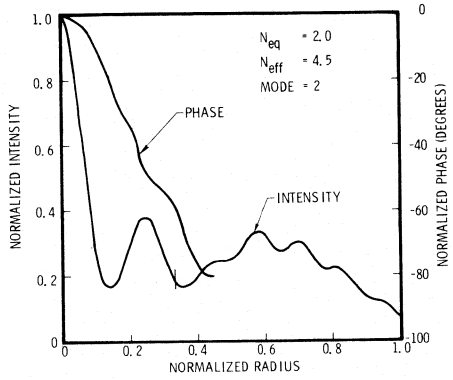

Fig. 5. Intensity and phase profiles for mode 2 of a symmetric unstable resonator at the loss degeneracy point $N_{eq} = 2.0$.

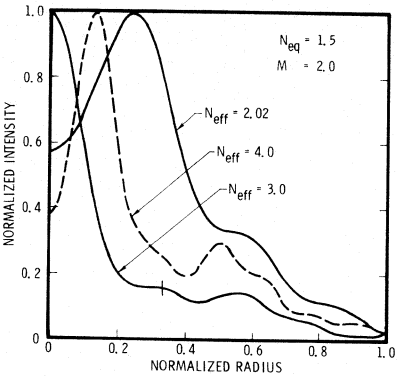

Fig. 6. Normalized intensity profiles for a symmetric unstable resonator at the mirror (N_{eff} = 4.0) and external to the cavity at the virtual focus (N_{eff} = 3.0) and at a distance far from the mirror (N_{eff} = 2.02).

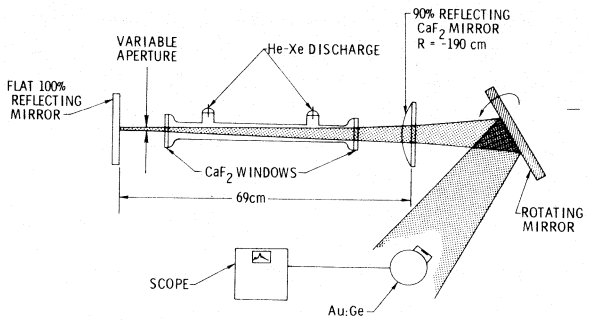

Fig. 7. Schematic diagram of the experimental configuration for measuring mode intensity profiles.

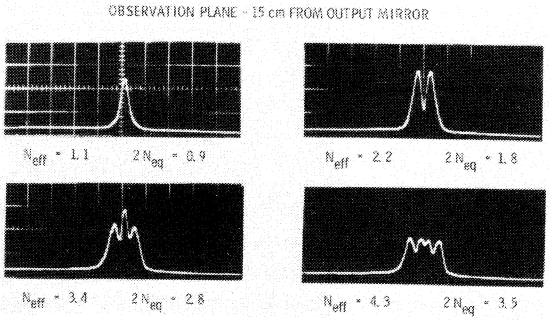

Fig. 8. Experimentally observed mode intensity profiles.

for, respectively, the first and second modes for N_{eq} = 2.0 and N_{eff} = 4.5, which is very near a mode crossing. As expected, the number of relative maxima along a diameter in the first mode is 4.5 - 0.5 = 4 and 4.5 + 0.5 = 5 in the second mode. The modes exhibited a smooth transition through the degeneracy point with the lowest mode phase front gradually assuming this additional curvature as $2N_{eq}$ increases from odd to even.

It is also possible to predict the mode profiles at other observation planes, and calculations have been made for the mode propagating outside the cavity. Fig. 6 shows examples for a symmetric resonator with N_{eq} = 1.5 and M = 2.0. The mode profile is shown at the plane of the opposite mirror (N_{eff} = 4), at the virtual focus (N_{eff} = 3), and far from the mirror (N_{eff} = 2.02). As expected, these profiles also follow the predicted shapes. These external calculations are particularly interesting at the virtual focus where $N_{eff} = 2N_{eq}$. A minimum in cavity loss occurs when $2N_{eq}$ is odd and hence corresponds to a relative peak in intensity at the virtual focus when the mode is extended outside the cavity. Likewise a maximum in cavity loss ($2N_{eq}$ even) corresponds to a minimum intensity at the virtual focus. Several papers [5], [6] have pointed out the importance of the virtual focus and this is another indication of the possible significance that a source at the virtual focus may play in acting as an equivalent source for the modes. Additional understanding of the importance of the virtual focus may yield further insight on unstable modes and increase our ability to make simplified predictions of their properties.

III. Experimental Results

An experimental study of the mode profiles was made using a longitudinal-discharge 3.5-μm He-Xe laser as shown in Fig. 7. This discharge tube was 25 cm long and 1 cm in diameter with sufficient gain to allow the use of an unstable resonator with a reasonably large magnification. One of the resonator mirrors was CaF_2 with -190-cm radius of curvature and coated for 90-percent reflectivity on its entire surface; the other mirror was flat and coated for 100-percent reflectivity. The mirrors were spaced at 69 cm to give a left to right cavity magnification of about 1.5 and a right to left cavity magnification of about 2.0. A variable-diameter leaf aperture was placed near the flat mirror and was the cavity-limiting aperture. Thus an equivalent symmetric unstable resonator (M = 3) can be defined as described by Siegman and Miller [3], and an N_{eq} can be calculated. The 10-percent transmission through the curved mirror was used to observe the mode pattern. The output was swept past a small Ge:Au detector by a rotating flat. The intensity profile was thus displayed in time on the oscilloscope trace.

The mode profiles were first observed in a plane 15 cm from the output mirror. The tube bore and the cavity axis were first carefully aligned with a He-Ne laser. With the xenon laser well above threshold, the cavity aperture was adjusted until a single bright spot with maximum intensity was obtained and the aperture diameter was measured. The aperture was then opened until the mode profile with the deepest minimum in the center was found, and again the aperture diameter was measured. This was continued up to a pattern having four intensity peaks in the scan. Typical observed mode profiles are shown in Fig. 8 with the calculated N_{eff} and cavity N_{eq}. The mode profiles were easily repeatable and in all cases exhibited a smooth transition between the patterns.

It is not possible with our experimental setup to obtain various combinations of integer values of $2N_{eq}$ and N_{eff} which would correspond to the computer results presented earlier. This would have required changing the cavity magnification by various combinations of mirror radii and spacings.

The detector was then moved to the virtual focus and the measurements repeated. The observed modes were very similar to Fig. 8, but to obtain the single peaked mode the aperture was adjusted for N_{eff} = 1.3; for two peaks, N_{eff} = 2.1, for three peaks, N_{eff} = 3.0, and for four peaks, N_{eff} = 4.1.

These results demonstrate that the general features of the

mode profiles can be predicted from N_{eff} both at the cavity mirror and at the virtual focus. In all cases the number of maxima in the pattern corresponds approximately to N_{eff}.

When the laser discharge current was reduced so that the laser was operating near threshold, the variation of the mode eigenvalue with N_{eq} as predicted by Siegman could be clearly demonstrated. As the cavity aperture was slowly opened, it was found that there were ranges of aperture diameters over which lasing occurred separated by ranges of diameters where no lasing was observed. As the discharge current was reduced still further, these ranges of diameters around which lasing occurred became narrower until the laser was below threshold for all aperture sizes. This is demonstrated in Fig. 9 in which the shaded areas correspond to ranges of N_{eq} where lasing did not occur. N_{eq} was calculated from the measured aperture diameters. Also shown in Fig. 9 are the mode losses calculated by the Prony method for the equivalent symmetric resonator ($M = 3.2$, $g = 1.76$). The lasing ranges clearly correspond to the ranges of N_{eq} where the losses are minimum, and the alternate lasing and nonlasing ranges demonstrate the cyclic nature of the loss of the lowest order mode.

Freiberg *et al.* [7] have reported mode profile measurements at a plane inside a CO_2 unstable resonator laser and in the far field. They also observed the cyclic nature of the eigenvalue.

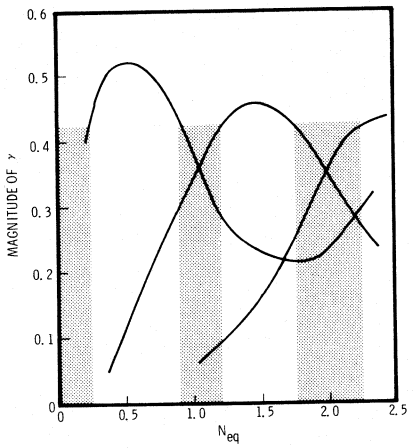

Fig. 9. Calculated magnitude of the mode eigenvalue γ for the experimental resonator used. The shaded zones indicate the regions below lasing threshold.

IV. Conclusions

It is concluded from these studies that the qualitative features of the fundamental mode for unstable resonators with reasonably low Fresnel numbers can be predicted on the basis of simple Fresnel zone theory. Both the mode shape within the cavity and the profile which would exist outside the cavity in the absence of the second mirror appear similar to the shape expected for a uniform spherical wave emanating from the virtual focus and illuminating the resonator aperture. The experimental loss also reaches a maximum when the equivalent Fresnel number is an integer in agreement with the calculations of Siegman and Miller [3]. This corresponds to the point where the effective Fresnel number computed at the virtual focus ($N_{eff} = 2N_{eq}$) is even and the on-axis intensity is minimum. Thus the resonator loss cycles with the same period as the relative intensity at the virtual focus giving further evidence to support the significance of the virtual foci. In a previous paper [5] it was pointed out that the fundamental mode could be optimized by minimizing the edge-wave diffraction at this point. It thus appears somewhat anomalous that the virtual foci, whose locations are given by geometrical optics, should be so significant in determining results based on diffraction theory. It is hoped that better understanding of these phenomena will make it possible to preempt with geometrical optics analyses many lengthy numerical calculations.

Acknowledgment

The authors wish to thank E. A. Maunders for vital laboratory assistance and measurements.

References

[1] A. E. Siegman, "Unstable optical resonators," *Appl. Opt.*, vol. 13, pp. 353-367, Feb. 1974.
[2] M. Born and E. Wolf, *Principles of Optics*. New York: Macmillan, 1964, p. 371.
[3] A. E. Siegman and H. Y. Miller, "Unstable optical resonator loss calculations using the Prony method," *Appl. Opt.*, vol. 9, pp. 2729-2736, Dec. 1970.
[4] F. Jenkins and H. White, *Fundamentals of Optics*. New York: McGraw-Hill, 1957, p. 359.
[5] G. L. McAllister, W. H. Steier, and W. B. Lacina, "Improved mode properties of unstable resonators with tapered reflectivity mirrors and shaped apertures," *IEEE J. Quantum Electron.*, vol. QE-10, pp. 346-355, Mar. 1974.
[6] Yu. A. Anan'ev, "Unstable resonators and their applications (Review)," *Sov. J. Quantum Electron.*, vol. 1, p. 565, May-June 1972.
[7] R. J. Freiberg, P. P. Chenausky, and C. J. Buczek, "An experimental study of unstable confocal CO_2 resonators," *IEEE J. Quantum Electron.*, vol. QE-8, pp. 882-892, Dec. 1972.

Characteristics of Optical Guided Modes in Multilayer Metal-Clad Planar Optical Guide with Low-Index Dielectric Buffer Layer

YOSHIHISA YAMAMOTO, STUDENT MEMBER, IEEE, TAKESHI KAMIYA, AND HISAYOSHI YANAI, SENIOR MEMBER, IEEE

Abstract—**The attenuation characteristics of a multilayer metal-clad optical guide, which is suitable for a mode filter or electrooptic devices, is investigated by the exact theory and the analytical approximation based on a perturbation technique. By using this approximation the dependences of the ohmic loss on the various waveguide parameters and the condition for the absorption peak of the TM mode are derived in closed form. Some remarks concerning the waveguide material and dimension for the design of the mode filter are also presented. The insertion loss at the abrupt junction between a normal (dielectric-clad) optical guide region and a metal-clad optical guide region is treated. Also the transformation of optical guided modes in the two kinds of tapered structures between the above two regions is examined.**

I. Introduction

A METAL-CLAD optical guide is suitable for electrooptic [1]-[3] or magnetooptic [4] devices because the metal cladding can be used for a part of electric circuits. This guide is also suitable for a mode filter because the ohmic loss of a TM guided mode is much larger than that of its TE counterpart [5]-[8].

In the former case of electrooptic or magnetooptic devices, it is important for the guided light to interact with the induced electric field effectively and not to be attenuated seriously due to the metal cladding. In the latter case of the mode filter, it is necessary to obtain a sufficient extinction ratio without introducing a significant loss in the transmitted light. Recently, Polky *et al.* pointed out that a TM guided mode exhibits an absorption peak as a function of the thickness of the low-index buffer layer in the multilayer structure shown in Fig. 1, and that this absorption peak is caused by the resonant coupling to the lossy surface mode [9], [20]. It is expected that a TE_0 mode filter having a high extinction ratio is obtained by utilizing this phenomenon. This multilayer structure was also proposed as one of the methods to decrease the ohmic loss for electrooptic devices [1], [10].

However, the dependences of the ohmic loss of each mode on the various waveguide parameters and the condition for the absorption peak of a TM guided mode, which are essential to the design of this guide, have not been sufficiently investigated yet. The first purpose of this paper is to investigate attenuation characteristics of the multilayer metal-clad optical guide by the analytical approximation based on a perturbation technique. The dependences of the attenuation constant on core-layer thickness, buffer-layer thickness, mode number, and refractive index difference between core and buffer layers are presented in closed form. By using these results, some remarks for the design of the mode filter are also presented. The exact solution of the eigenvalue equation by numerical analysis is used as a guide to assess the validity of this approximate solution.

Manuscript received December 27, 1974; revised April 22, 1975. This work was supported in part by the Oki Electric Company, and in part by the Toray Science Foundation.

The authors are with the Department of Electronic Engineering, Faculty of Engineering, University of Tokyo, 7-3-1, Hongo, Bunkyo-ku, Tokyo 113, Japan.

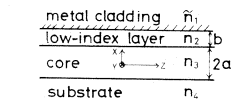

Fig. 1. A multilayer metal-clad planar optical guide with low-index dielectric buffer layer.

The insertion loss at the abrupt junction between a normal (dielectric-clad) optical guide region and a metal-clad optical guide region would also be an important problem for the two applications of this guide [11] previously mentioned. The tapered structure between two regions is needed for the reduction of this insertion loss. The second purpose of this paper is to examine this insertion loss at the abrupt junction and the transformation of optical guided modes in the tapered structures.

II. An Approximate Analysis of the Attenuation Characteristics

The guided mode in the multilayer metal-clad optical guide shown in Fig. 1 is assumed to propagate in the Z direction with a phase term $\exp[j(\omega t - k_z \cdot Z)]$, where k_z is the complex propagation constant. The mode characteristics are determined by applying the usual boundary-value technique, and k_z is expressed as solutions of the eigenvalue equation [10]

$$2au_3 = m\pi + \tan^{-1}\left(\gamma_{34}\frac{u_4}{-ju_3}\right) + \tan^{-1}\left[\gamma_{32}\frac{u_2}{u_3}\tan\left\{\tan^{-1}\left(\gamma_{21}\frac{u_1}{-ju_2}\right) - u_2 b\right\}\right] \quad (1)$$

where

$$\gamma_{pq} = \begin{cases} 1 & \text{TE mode} \\ \left(\dfrac{n_p}{n_q}\right)^2 & \text{TM mode} \end{cases} \quad (2)$$

$$u_l = k_0(n_l^2 - n^2)^{1/2}, \qquad l = 1 \sim 4 \quad (3)$$

$$n = \frac{k_z}{k_0} \equiv \frac{\beta - j\alpha}{k_0} \quad (4)$$

$$k_0 = \frac{2\pi}{\lambda} \quad (5)$$

where

$2a$ thickness of core layer;
b thickness of buffer layer;
u_l transverse wavenumber in each region;
n mode effective index;
m mode number.

The phase constant β and the attenuation constant α of each mode are obtained by the numerical analysis of the preceding transcendental equation concerning the complex propagation constant k_z, where the imaginary part of u_l is negative, and the real part of $\tan^{-1}$ ranges from 0 to π.

Figs. 2 and 3 show the attenuation constants of several modes versus the thickness of the core layer and the buffer layer, respectively. The solid line shows the exact solution by the numerical analysis of the eigenvalue, (1). Fig. 4 shows the change of the field distribution of TM guided modes at the various values of the buffer-layer thickness. The second lowest order TM guided mode (TM_1) in the multilayer structure exhibits the absorption peak and transforms continuously to the TM_0 mode in the single-layer structure [10]. The lowest order TM guided mode (TM_0) does not exhibit the absorption peak and transforms continuously to the surface mode [12] in the single-layer structure.

The second and the third terms of the right-hand side (RHS) of (1), which are the halves of the phase shifts of total internal reflection at both boundaries approach to $\pi/2$ for the well-guided TE modes, and the transverse wavenumber in the core layer, and the mode effective index are given in zeroth-order approximation by

$$u_3^{(0)} = \frac{(m+1)}{2a}\pi \tag{6}$$

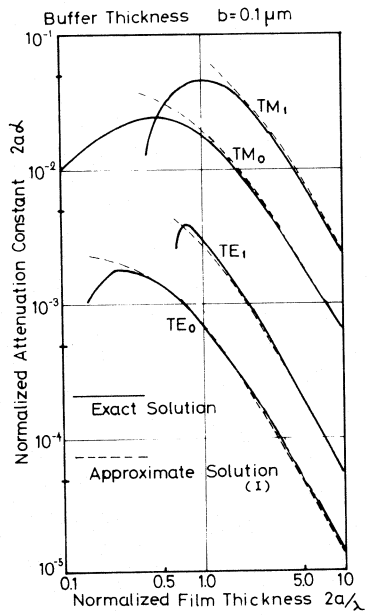

Fig. 2. The attenuation constants of several modes versus the core-layer thickness: —— indicates exact solution of the eigenvalue equation (1); ---- indicates approximate solution by (18). $n_1 = 1.2 - j7.0$ (for Al); $n_2 = 1.544$ (for Corning 7059 glass); $n_3 = 1.758$ (for Al_2O_3); $n_4 = 1.457$ (for SiO_2); and $\lambda = 0.633$ μm.

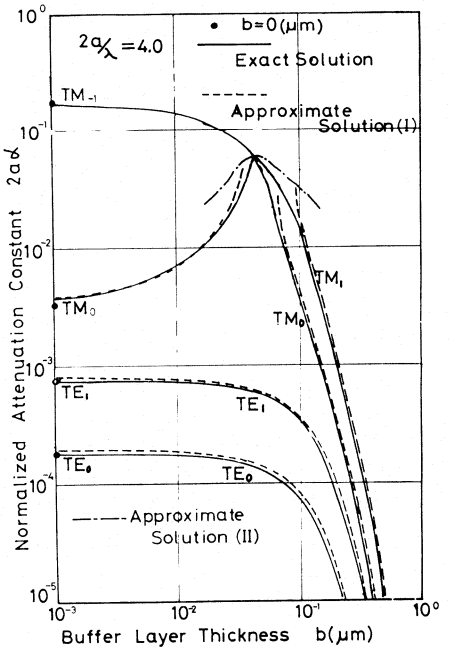

Fig. 3. The attenuation constants of several modes versus the buffer-layer thickness: —— indicates exact solution of the eigenvalue equation (1); ---- indicates approximate solution by (18); —·—· indicates approximate solution by (21). The numerical parameters are the same as those used in Fig. 2.

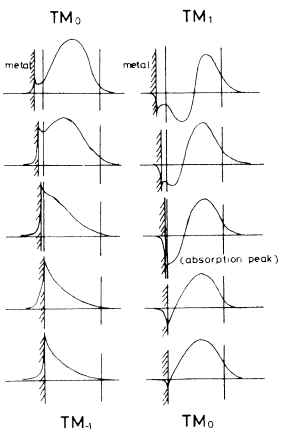

Fig. 4. The change of the transverse magnetic field distributions of the TM modes calculated by the exact solution of the eigenvalue equation (1). The numerical parameters are the same as those used in Fig. 3.

and

$$n^{(0)} = \left\{ n_3^2 - \frac{(m+1)^2}{4a^2k_0^2}\pi^2 \right\}^{1/2}. \tag{7}$$

Fig. 4 shows that this approximation is also valid for the well-guided TM modes except for the region just near the absorption peak. At the absorption peak, half of the phase shift of internal reflection at the buffer boundary is not $\pi/2$ but zero. The transverse wavenumber in other regions is given by

$$u_l^{(0)} = -jk_0\left\{ n_3^2 - \frac{(m+1)^2}{4a^2k_0^2}\pi^2 - n_l^2 \right\}^{1/2} = -ju_1^{(0)\prime}, \quad l = 2, 4 \tag{8}$$

and

$$u_1^{(0)} = k_0 \left\{ n_1^2 - n_3^2 + \frac{(m+1)^2}{4a^2 k_0^2} \pi^2 \right\}^{1/2} = u_1^{(0)\prime} - j u_1^{(0)\prime\prime} \quad (8a)$$

where $u_l^{(0)\prime}$, $u_1^{(0)\prime}$, and $u_1^{(0)\prime\prime}$ are real and positive. Substituting (8) and (8a) into (1), u_3 is given approximately by

$$u_3^{(1)} = (m+1)\pi \left[2a + \frac{1}{\gamma_{34} u_4^{(0)\prime}} + \frac{j}{\gamma_{32} u_2^{(0)\prime} \tan\left\{ \tan^{-1}\left(\gamma_{21} \frac{u_1^{(0)\prime} - j u_1^{(0)\prime\prime}}{-u_2^{(0)\prime}} \right) + j u_2^{(0)\prime} b \right\}} \right]^{-1}$$

$$\approx \frac{(m+1)\pi}{2a} \left[1 - \frac{\gamma_3}{2aU_4} - \frac{j\gamma_3}{2aU_2 \tan\left\{ \tan^{-1}\left(-\frac{U_1' + jU_1''}{U_2} \right) + jU_2^{(0)\prime} b \right\}} \right]$$

$$= \frac{(m+1)\pi}{2a} \left[1 - \frac{\gamma_3}{2aU_4} - \frac{\gamma_3 \{ \zeta_1 \exp(2u_2^{(0)\prime} b) - \zeta_2 \exp(-2u_2^{(0)\prime} b) - j4U_1' U_2 \}}{2aU_2 \{ \zeta_1 \exp(2u_2^{(0)\prime} b) + \zeta_2 \exp(-2u_2^{(0)\prime} b) + \zeta_3 \}} \right] \quad (9)$$

where

$$U_1 = U_1' + jU_1'' = \begin{cases} u_1^{(0)\prime} - j u_1^{(0)\prime\prime} & \text{TE mode} \\ \dfrac{u_1^{(0)\prime} - j u_1^{(0)\prime\prime}}{n_1^2} & \text{TM mode,} \end{cases}$$

U_1' and U_1'' are real (10)

$$U_l = \begin{cases} u_l^{(0)\prime} & \text{TE mode} \\ \dfrac{u_l^{(0)\prime}}{n_l^2} & \text{TM mode,} \quad l = 2, 4 \end{cases} \quad (11)$$

$$\gamma_3 = \begin{cases} 1 & \text{TE mode} \\ \dfrac{1}{n_3^2} & \text{TM mode} \end{cases} \quad (12)$$

$$\zeta_1 = U_1'^2 + U_1''^2 + U_2^2 - 2U_1'' U_2 \quad (13)$$

$$\zeta_2 = U_1'^2 + U_1''^2 + U_2^2 + 2U_1'' U_2 \quad (14)$$

$$\zeta_3 = 2(U_1'^2 + U_1''^2 - U_2^2). \quad (15)$$

The complex propagation constant k_z is given by

$$k_z \equiv \beta - j\alpha = k_0 \left\{ n_3^2 - \frac{u_3^{(1)2}}{k_0^2} \right\}^{1/2} \approx k_0 n_3 - \frac{u_3^{(1)2}}{2k_0 n_3}. \quad (16)$$

Using (9) and (10), the phase constant and the attenuation constant are given by

$$\beta = k_0 n_3 \left[1 - \frac{(m+1)^2 \pi^2}{8k_0^2 n_3^2 a^2} \left\{ 1 - \frac{(U_2 + U_4)\zeta_1 \exp(2u_2^{(0)\prime} b) + (U_2 - U_4)\zeta_2 \exp(-2u_2^{(0)\prime} b) + U_2 \zeta_3}{aU_2 U_4 (\zeta_1 \exp(2u_2^{(0)\prime} b) + \zeta_2 \exp(-2u_2^{(0)\prime} b) + \zeta_3)} \gamma_3 \right\} \right] \quad (17)$$

$$\alpha = \frac{(m+1)^2 \pi^2}{k_0 n_3 (2a)^3} \left\{ \frac{4U_1' \gamma_3}{\zeta_1 \exp(2u_2^{(0)\prime} b) + \zeta_2 \exp(-2u_2^{(0)\prime} b) + \zeta_3} \right\}. \quad (18)$$

On the other hand, Fig. 4 shows that the third term of the RHS of (1) is about zero for the TM guided mode near the absorption peak. So the transverse wavenumber in core layer and the mode effective index are given in zeroth-order approximation by

$$u_3^{(0)} = \frac{\left(m + \frac{1}{2}\right)\pi}{2a} \quad (19)$$

and

$$n^{(0)} = \left\{ n_3^2 - \frac{\left(m + \frac{1}{2}\right)^2}{4a^2 k_0^2} \pi^2 \right\}^{1/2}. \quad (20)$$

According to the procedure used in the former approximation, the attenuation constants of TM guided modes near the absorption peak are given by

$$\alpha = \frac{n_3}{k_0 \cdot 2a} \cdot \left\{ \frac{4U_1' U_2^2}{\zeta_1 \exp(2u_2^{(0)\prime} b) + \zeta_2 \exp(-2u_2^{(0)\prime} b) + \zeta_3} \right\} \quad (21)$$

where each parameter is given by replacing $(m+1)$ with $(m + \frac{1}{2})$ in (8), (8a), (10), (11), and (13)–(15).

The attenuation characteristics calculated by these two approximations are shown in Figs. 2 and 3. They show that the approximate solution by (18) is valid for the well-guided TE modes and the well-guided TM modes except for the region just near the absorption peak, and that the approximate solution by (21) is valid only for the well-guided TM modes just near the absorption peak. The attenuation characteristics of the second lowest order TM mode ($TM_0 \rightarrow TM_1$) is obtained by linking these two approximations to each other.

For the well-guided TE and TM modes in the multilayer

structure with the thick buffer layer, the dependence of the attenuation constant on the waveguide parameters is derived by (18)

$$\alpha \propto \frac{(m+1)^2}{(2a)^3}\lambda^2 \exp(-2u_2^{(0)\prime}b). \tag{22}$$

The $(m+1)^2$ and $(2a)^{-3}$ dependence of the attenuation constant is in agreement with the results which Reisinger showed theoretically and experimentally for the single-layer metal-clad optical guide [13]. The thickness of the buffer layer b_m at which the TM_m mode exhibits an absorption peak is given by equating the differential coefficient of (21) with respect to the buffer-layer thickness to zero and expressed as

$$b_m = \frac{1}{4u_2^{(0)\prime}} \ln\left(\frac{\xi_2}{\xi_1}\right). \tag{23}$$

This buffer layer thickness b_m is in agreement with that derived from the condition that the real part of the third term of the RHS of (1) is just zero (see Fig. 4).

III. Some Remarks for the Design of the Mode Filter

By using the results of Section II, the dependences of the extinction ratio of the mode filter on various waveguide materials and dimensions are investigated. Fig. 5(a)–(d) shows the attenuation constants of TE_0 mode and the second lowest order TM mode ($TM_0 \rightarrow TM_1$) versus the buffer-layer thickness for the various conducting materials. Optical constants of the conducting materials are presented in Table I. In Fig. 5(a), the approximate solutions are also presented. Fig. 6 shows the buffer-layer thickness b_m at which the second lowest order TM mode exhibits an absorption peak versus the refractive index difference between core and buffer layer for the various conducting materials. The approximate solution by (23) is in good agreement with the exact theory. Fig. 7 shows the extinction ratio of the TE_0 and TM_0 modes $\alpha_{TM_0}/\alpha_{TE_0}$ at the buffer-layer thickness b_m given in Fig. 6 versus the refractive index difference between core and buffer layer for the various conducting materials. In the case of the single-layer metal-clad mode filter, it was pointed out that a high extinction ratio can be obtained by using Ni or Al as the conducting material [14], but in the case of the multilayer metal-clad mode filter silver and gold are promising materials. In the single-layer structure of 1.0-μm core-layer thickness, the extinction ratio $\alpha_{TM_0}/\alpha_{TE_0}$ is about 2×10 for Ni, but in the multilayer structure of the same core-layer thickness, the extinction ratio is raised to 5×10^2 by using silver as the conducting material (see Fig. 7). Fig. 8 shows the attenuation constant of the second lowest order TM mode versus the refractive index difference. For the absorption modulator mentioned in [9], utilizing the attenuation characteristics of TM mode, the buffer layer consisting of the electrooptic material should be thick, and its refractive index should be nearly equal to that of the core layer in order to obtain a sufficient extinction ratio by the small change of the refractive index difference.

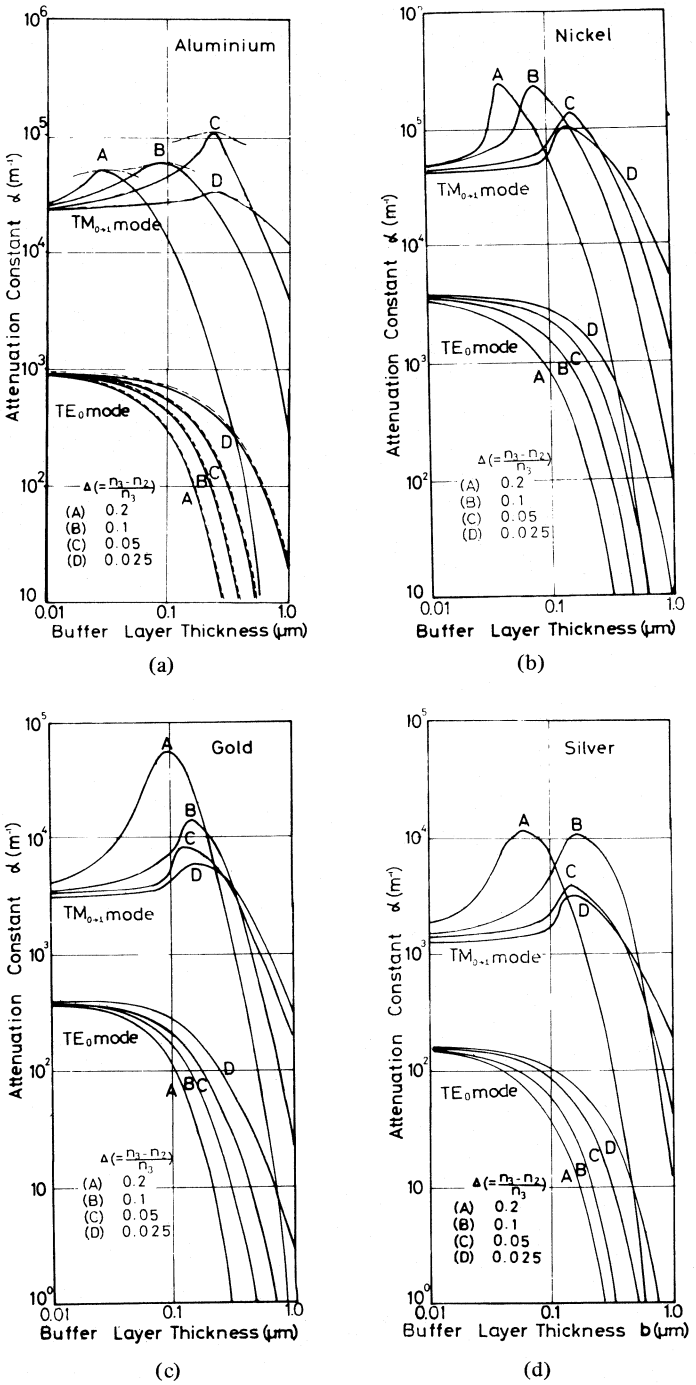

Fig. 5. The attenuation constants of TE_0 mode and the second lowest order TM mode ($TM_0 \rightarrow TM_1$) versus the buffer-layer thickness for the various conducting materials. $n_3 = 1.758$ (for Al_2O_3); $n_4 = 1.457$ (for fused quartz); and $2a = 1.0$ μm. (a) Aluminum. (b) Nickel. (c) Gold. (d) Silver.

TABLE I
Optical Constants of Conducting Materials [19]

Material	n	|k|
Aluminium	1.2	7.0
Gold	0.15	3.2
Nickel	2.0	3.8
Silver	0.065	4

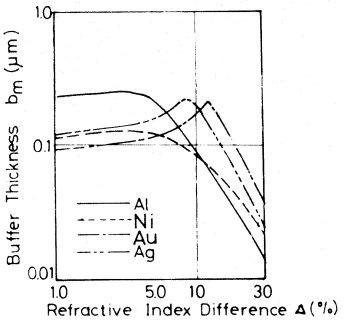

Fig. 6. The buffer-layer thickness b_m at which the second lowest order TM mode exhibits an absorption peak versus the refractive index difference between core and buffer layers for the various conducting materials by the exact solution. $n_3 = 1.758$ (for Al_2O_3); $n_4 = 1.457$ (for fused quartz); and $2a = 1.0$ μm.

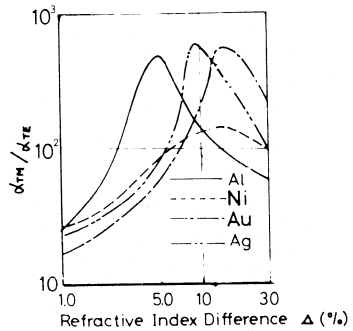

Fig. 7. The extinction ratio between the TE_0 mode and the second lowest order TM mode at the buffer-layer thickness b_m shown in Fig. 6 versus the refractive index difference between core and buffer layers for the various conducting materials. Silver and gold exhibit a very high extinction ratio. $n_3 = 1.758$ (for Al_2O_3); $n_4 = 1.457$ (for fused quartz); and $2a = 1.0$ μm.

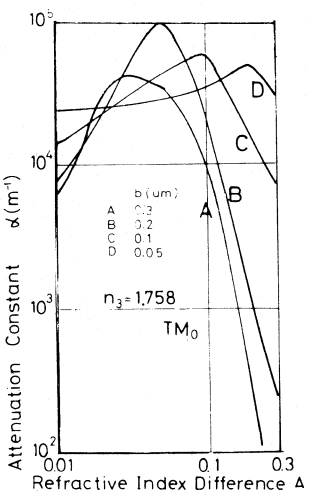

Fig. 8. The attenuation constants of TE_0 mode and the second lowest order TM mode versus the refractive index difference between core and buffer layers. $n_3 = 1.758$ (for Al_2O_3); $n_4 = 1.457$ (for fused quartz); $n_1 = 1.2 - j7.0$ (for Al); and $2a = 1.0$ μm.

IV. An Insertion Loss at the Abrupt Junction and a Transformation of Guided Modes in the Tapered Structure

The insertion loss at the abrupt junction between a normal (dielectric-clad) optical guide region and a metal-clad optical guide region shown in Fig. 9 is in general undesirable for the application to electrooptic devices or a mode filter. The coupling constants to the reflected guided mode, the transmitted guided mode, and the radiation modes are given by the boundary condition at the abrupt junction [15]. The boundary condition for the incident TE_0 mode is

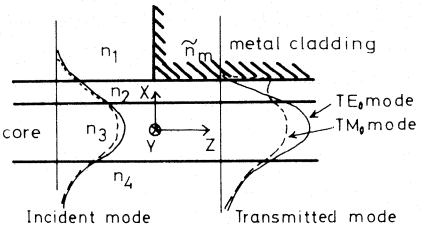

Fig. 9. The abrupt junction between a normal optical guide region and a metal-clad optical guide region.

$$E_y^{(i)} + a_r E_y^{(r)} + \int_{-k_0 n_4}^{0} q_r(\beta)\, E_y^{(r)}(\beta)\, d\beta = c_t E_y^{(t)} + \int_{0}^{k_0 n_4} q_t(\beta')\, E_y^{(t)}(\beta')\, d\beta' \tag{24}$$

$$H_x^{(i)} + a_r H_x^{(r)} + \int_{-k_0 n_4}^{0} q_r(\beta)\, H_x^{(r)}(\beta)\, d\beta = c_t H_x^{(t)} + \int_{0}^{k_0 n_4} q_t(\beta')\, H_x^{(t)}(\beta')\, d\beta' \tag{25}$$

where β and β' are the phase constants of the continuous radiation modes in the normal optical guide region and the metal-clad optical guide region, respectively. The superscripts i, r, and t indicate incident, reflected, and transmitted waves. The field components whose β and β' dependences are explicitly shown are radiation modes, and the other components belong to TE_0 guided mode. The TE higher mode is assumed to be cut off in both regions. The normalized condition for E_y is given by

$$-\frac{1}{2}\int_{-\infty}^{\infty} E_y H_x^*\, dx = \frac{\beta_0}{2\omega\mu_0}\int_{-\infty}^{\infty} |E_y|^2\, dx = 1 \tag{26}$$

$$-\frac{1}{2}\int_{-\infty}^{\infty} E_y(\beta_1) H_x(\beta_2)^*\, dx = \frac{\beta_2}{2\omega\mu_0}\int_{-\infty}^{\infty} \cdot E_y(\beta_1) E_y(\beta_2)^*\, dx = \delta(\beta_1 - \beta_2) \tag{27}$$

where β_0, β_1, and β_2 are the phase constants of each mode. If the coupling constant c_t which satisfies (24) and (25) is obtained, the insertion loss at the abrupt junction is given by

$$\frac{\Delta P}{P} = 1 - |c_t|^2 \tag{28}$$

where P is the power carried by the incident TE_0 mode. However, (24) and (25) are not solved exactly. We obtain the approximate solutions of c_t and a_r by neglecting the coupling coefficient q_r [15] and using the orthogonality of the modes

of the same waveguide. From (24) and (25)

$$c_t = \frac{\beta_i \beta_t}{\beta_i + \beta_t} \cdot \frac{1}{\omega \mu_0} \int_{-\infty}^{\infty} E_y^{(i)} E_y^{(t)*} \, dx \tag{29}$$

$$a_r = \frac{\beta_i - \beta_t}{\beta_i + \beta_t} \tag{30}$$

where β_i and β_t are the phase constants of the incident guided mode and the transmitted guided mode, respectively.

The coupling coefficients c_t and a_r for the TM_0 incident mode are in the same procedure given by

$$c_t = \frac{\beta_i \beta_t PQ}{\omega(\beta_i Q + \beta_2 P)} \tag{31}$$

$$a_r = \frac{(\beta_i - \beta_t)Q}{\beta_i Q + \beta_t P} \tag{32}$$

where

$$P = \int_{-\infty}^{\infty} \frac{1}{\epsilon^{(t)}(x)} H_y^{(i)} H_y^{(t)*} \, dx \tag{33}$$

$$Q = \int_{-\infty}^{\infty} \frac{1}{\epsilon^{(i)}(x)} H_y^{(i)} H_y^{(t)*} \, dx \tag{34}$$

where $\epsilon^{(i)}(x)$ and $\epsilon^{(t)}(x)$ are the dielectric constants of the normal optical guide region and the metal-clad optical guide region, respectively.

Fig. 10 shows the power-coupling coefficients of the TE_0 and TM_0 modes versus the buffer-layer thickness. The insertion loss of the TM_0 mode is larger than that of the TE_0 mode, which is attributed to the larger difference of the field distributions of the TM_0 mode between two regions compared with the TE_0 mode. The insertion losses of the TE_0 and TM_0 modes are decreased by increasing the thickness of the low-index buffer layer, which is well explained by the fact that the difference of the field distributions between two regions becomes small by increasing the thickness of the low-index buffer layer. However, the selection of buffer-layer thickness of the multilayer metal-clad optical guide regions should be determined by consideration for the performance of the devices. In the case of the electrooptic devices of multilayer structure, both the induced electric field strength and the ohmic loss of the guided modes are decreased by increasing the low-index buffer-layer thickness, and the optimum thickness exists. In the case of the mode filter, the buffer-layer thickness should be b_m given by (23), so that the other method to decrease the insertion loss is needed.

Two kinds of tapered structures to decrease the insertion loss at an abrupt junction are shown in Fig. 11. In the case of decreasing the thickness of the low-index buffer layer gradually as shown in Fig. 11(a), the TM_0 mode of the normal optical guide region transforms continuously to the TM_{-1} mode (surface mode) of the metal-clad optical guide region as discussed in Section II (see Fig. 4), and the maximum attenuation of this mode is caused in the single-layer structure ($b = 0$). In the case of increasing the metal-layer thickness

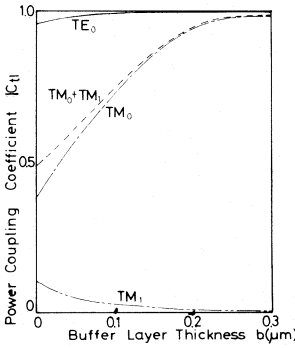

Fig. 10. The power coupling coefficient $|C_t|^2$ versus the buffer-layer thickness. The thickness of core layer is 0.4 μm. $n_1 = 1.0$; $n_2 = 1.480$; $n_3 = 1.680$; $n_4 = 1.480$; $n_m = 1.2 - j7.0$; and $\lambda = 0.633$ μm. The metal-clad optical guide of this dimension guides both the TM_0 and the TM_1 modes.

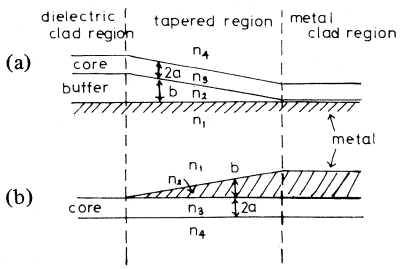

Fig. 11. Two kinds of tapered structure to decrease the insertion loss at the abrupt junction.

gradually shown in Fig. 11(b), the TM_0 mode of the normal optical guide region transforms continuously to the TM_0 mode of the metal-clad optical guide region as shown in Fig. 12, and the maximum attenuation of this mode is given in the multilayer structure ($b = b_m$). The changes of the mode effective index in these two kinds of tapered structures are shown in Fig. 13(a), (b). In the tapered structure shown in Fig. 11(a), the change of the mode effective index of the TM_0 mode is contrary to that of the TE_0 mode.

If the transverse boundary of the metal-clad optical stripline (MCOSL) [16], [17] is made by the tapered structure as shown in Fig. 14, the MCOSL of this structure guides only the TE mode, because the mode effective index of the metal-unclad region is lower than that of the metal-clad region for the TM mode; that is, this guide is a leaky waveguide for the TM mode. Fig. 15(a) shows the mode order converter only for TM modes. Fig. 14(b) shows the TE_0 mode selector of very high extinction ratio because the attenuation constant of the TM surface mode is very large.

V. Conclusion

The attenuation characteristics of the multilayer metal-clad optical guide are examined by the analytical approximation based on the perturbation technique, and the transformation of the guided mode in the tapered structures is also investigated. The main results presented in this paper follow.

1) The attenuation constants of the well-guided TM modes except for the region just near the absorption peak and the well-guided TE modes are expressed approximately by (18),

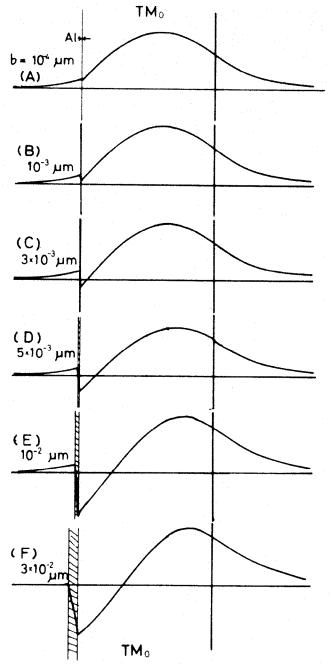

Fig. 12. The change of the transverse magnetic field distribution of the TM_0 mode for the gradual increase of the metal-layer thickness as shown in Fig. 11(b); (b = 0 μm).

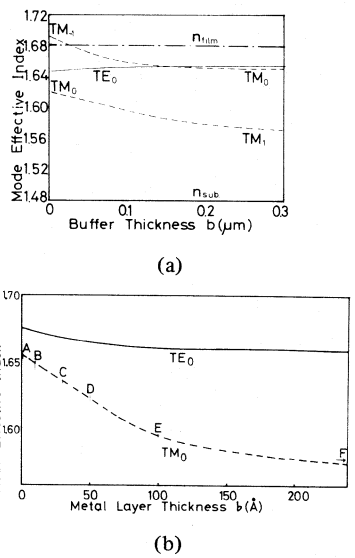

Fig. 13. (a) The mode effective index versus the buffer-layer thickness in the tapered structure shown in Fig. 11(a). $n_1 = 1.2 - j7.0$ (for Al); $n_2 = 1.48$; $n_3 = 1.68$; $n_4 = 1.48$; and $2a = 1.0$ μm. (b) The mode effective index versus the metal-layer thickness in the tapered structure shown in Fig. 11(b). $n_1 = 1.0$; $n_2 = 1.2 - j7.0$ (for Al); $n_3 = 1.68$; $n_4 = 1.48$; and $2a = 1.0$ μm.

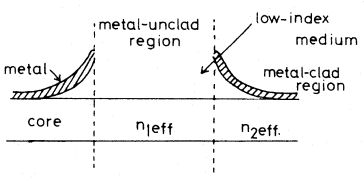

Fig. 14. MCOSL with the transverse boundary of the tapered structure. Only the E_{pq}^{y} (TE polarized) mode is confined in the metal-unclad region because of the effective index difference between the metal-unclad region and the metal-clad region.

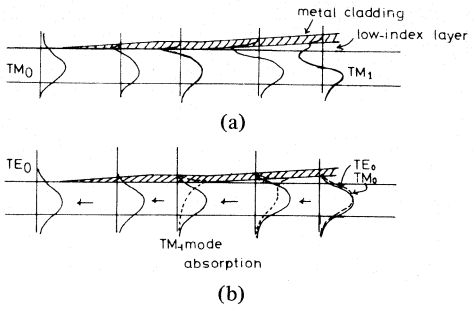

Fig. 15. (a) The mode order converter only for TM modes. (b) TE_0 mode filter having the high extinction ratio.

and the attenuation constants of the well-guided TM modes just near the absorption peak are expressed approximately by (21).

2) The attenuation constants of the well-guided TE and TM modes in the multilayer metal-clad optical guide with large buffer-layer thickness have the $(m+1)^2$, $(2a)^{-3}$, and $\exp(-2u_2^{(0)\prime}b)$ dependences for the mode number m, core-layer thickness $2a$, and buffer-layer thickness b, respectively.

3) The buffer-layer thickness b_m at which the TM_m mode exhibits an absorption peak is given by (23).

4) The extinction ratio between the TE and TM modes is increased by inserting the proper buffer layer between the metal cladding and the core layer. Silver and gold are promising materials for this multilayer mode filter.

5) The insertion loss at the abrupt junction between a normal optical guide region and a metal-clad optical guide region of the TM_0 mode is larger than that of the TE_0 mode because the difference of field distributions of the TM_0 mode between two regions is larger than that of the TE_0 mode.

6) In the tapered structure, decreasing the thickness of the low-index buffer layer gradually, the TM_0 mode of the normal optical guide region transforms continuously to the TM_{-1} mode (surface mode) in the metal-clad optical guide region, and the TM_1 mode of the normal optical guide region transforms continuously to the TM_0 mode in the metal-clad optical guide region. However, in the tapered structure, increasing the thickness of the metal layer gradually, the TM_0 mode in the normal optical guide region transforms continuously to the TM_0 mode in the metal-clad optical guide region.

Very recently, the waveguide polarizer using a birefringent material as a cladding was reported [18] in which the transmitted TE_0 mode is theoretically lossless. However, from the viewpoint of the integration with other waveguide components, the multilayer metal-clad optical guide polarizer investigated here seems to be superior. The mode filter of this structure cutting the higher modes by utilizing the $(m+1)^2$ dependence of the ohmic loss can be applied to the mode filter of the multimode optical fiber. The approximate analysis presented in this paper can be applied to the analysis of the multilayer lossy waveguide having a high-index semiconductor cladding such as Si or GaAs. Also in these structures, the attenuation constant of the TM mode is about ten times larger than that of its TE counterpart. This theoretical result shows that the mode-selecting photodetector which absorbs and

detects only the TM mode is constructed in the semiconductor substrate.

ACKNOWLEDGMENT

The authors wish to thank Prof. J. Hamasaki of the Institute of Industrial Science, University of Tokyo, for his critical discussion. The authors thank S. Ushio, S. Wako, and H. Mori of the Research and Development Center of the Oki Electric Company.

REFERENCES

[1] W. E. Martin, "Waveguide electro-optic modulation in II-VI compounds," *J. Appl. Phys.*, vol. 44, pp. 3703–3707, Aug. 1973.
[2] J. M. Hammer, D. J. Channin, and M. T. Duffy, "Fast electro-optic waveguide deflector modulator," *Appl. Phys. Lett.*, vol. 23, pp. 176–177, Aug. 15, 1973.
[3] H. F. Taylor, "Optical switching and modulation in parallel dielectric waveguides," *J. Appl. Phys.*, vol. 44, pp. 3257–3262, July 1973.
[4] P. K. Tien *et al.*, "Switching and modulation of light in magneto-optic waveguides of garnet films," *Appl. Phys. Lett.*, vol. 21, pp. 394–396, Oct. 15, 1972.
[5] Y. Takano and J. Hamasaki, "Propagating modes of a metal-clad-dielectric-slab waveguide for integrated optics," *IEEE J. Quantum Electron. (Part II of Two Parts–Special Issue on 1971 IEEE/OSA Conf. on Laser Engineering and Applications)*, vol. QE-8, pp. 206–212, Feb. 1972.
[6] Y. Suematsu *et al.*, "Fundamental transverse electric field (TE_0) mode selection in thin-film asymmetric light guide," *Appl. Phys. Lett.*, vol. 21, pp. 291–293, Sept. 1972.
[7] T. E. Batchman and S. C. Rashleigh, "Mode-selective properties of a metal-clad-dielectric-slab waveguide for integrated optics," *IEEE J. Quantum Electron.* (Corresp.), vol. QE-8, pp. 848–850, Nov. 1972.
[8] E. M. Garmire and H. Stoll, "Propagation losses in metal-film-substrate optical waveguides," *IEEE J. Quantum Electron.*, vol. QE-8, pp. 763–766, Oct. 1972.
[9] J. N. Polky and G. L. Mitchell, "Metal-clad planar dielectric waveguide for integrated optics," *J. Opt. Soc. Amer.*, vol. 64, pp. 274–279, Mar. 1974.
[10] A. Reisinger, "Characteristics of optical guided modes in lossy waveguides," *Appl. Opt.*, vol. 12, pp. 1015–1025, May 1973.
[11] I. P. Kaminow, W. L. Mammel, and H. P. Wever, "Metal-clad optical waveguides: Analytical and experimental study," *Appl. Opt.*, vol. 13, pp. 396–405, Feb. 1974.
[12] A. Otto and W. Sohler, "Modification of the total reflection modes in a dielectric film by one metal boundary," *Opt. Commun.*, vol. 3, pp. 254–258, June 1971.
[13] A. Reisinger, "Attenuation properties of optical waveguides with a metal boundary," *Appl. Phys. Lett.*, vol. 23, pp. 237–239, Sept. 1973.
[14] T. Takano and J. Hamasaki, "Approximate solutions of propagating modes of a metal-clad-dielectric-slab optical waveguide," *Trans. Inst. Electron. Commun. Eng. Japan*, vol. 56-A, pp. 385–392, July 1973.
[15] D. Marcuse, "Radiation losses of tapered dielectric slab waveguides," *Bell Syst. Tech. J.*, pp. 273–290, Feb. 1970.
[16] J. Hamasaki and K. Nosu, "Partially metal-clad-dielectric-slab waveguide for integrated optics," *IEEE J. Quantum Electron.*, vol. QE-10, pp. 822–825, Oct. 1974.
[17] Y. Yamamoto, T. Kamiya, and H. Yanai, "Propagation characteristics of partially metal clad optical guide–Metal clad optical strip line," *Appl. Opt.*, vol. 14, pp. 322–326, Feb. 1975.
[18] S. Uehara, T. Izawa, and H. Nakagome, "Optical waveguide polarizer," *Appl. Opt.*, vol. 13, pp. 1753–1754, Aug. 1974.
[19] D. Grey, Ed., *American Institute of Physics Handbook*. New York: McGraw-Hill, 1963, sec. 6g.
[20] A. Otto, "Excitation of nonradiative surface plasma waves in silver by the method of frustrated total reflection," *Z. Phys.*, vol. 216, pp. 398–410, 1968.

Theory of Mode Locking with a Slow Saturable Absorber

HERMANN A. HAUS, FELLOW, IEEE

***Abstract*—A closed-form solution is presented for the pulses of a homogeneously broadened laser mode locked by a saturable absorber of relaxation time much longer than the pulsewidth. With suitable approximations, the pulse shape is a secant hyperbolic. The system is described in terms of the linewidth ω_C of the system, the saturation energies of the saturable absorber and the laser medium, the ratio of saturable-absorber loss to resonator loss, and the ratio of cavity round-trip time and laser-medium relaxation time. The energy and width of the pulse are obtained as functions of these parameters. Graphs are presented for the operating regimes as bounded by the choice of the preceding parameters. The theoretical predictions are compared with second-harmonic-generation (SHG) autocorrelation traces of mode-locked dye-laser pulses.**

Manuscript received January 13, 1975.

The author is with Bell Laboratories, Holmdel, N.J. 07733, on leave from the Department of Electrical Engineering and the Research Laboratory of Electronics, Massachusetts Institute of Technology, Cambridge, Mass. 02139.

I. INTRODUCTION

EVEN THOUGH the literature on the theory of saturable absorber mode locking is extensive [1]-[14], no closed-form solution has been obtained for the mode-locked pulses ([11] gives a closed-form solution, but does not include the absorber modulation self-consistent with the temporal pulse shape). Of all publications only New's [14] addressed itself to the case when the saturable absorber has a long relaxation time compared with the pulse duration (slow absorber). This is the case of interest for subpicosecond pulse generation in dye lasers [15], [16]. New does not obtain a closed-form solution for the pulse shape. Here we present such a solution and explore the dependence of the pulse upon the system parameters. We also find conditions that have to be satisfied by the laser medium and the saturable absorber if stable mode locking is to be achieved.

In another paper [17] we have obtained a closed-form solution for a passively mode-locked system containing an absorber of fast relaxation time compared with the pulse duration. With solutions for the slow absorber as well as the fast absorber, one has covered two limiting cases which then in turn shed light on the general case for which no closed-form solution has been found as yet. It is true, though, that the most interesting case is the one when the mode-locked pulse is short compared with the relaxation time of the absorber, and this is the case covered in this paper.

The analysis makes the following assumptions and approximations.

1) The laser medium is homogeneously broadened.

2) A pulse passing through any one of the elements of the system, saturable absorber, gain medium, etc., is modified only slightly (say, 20-percent gain or loss) on one single pass. This assumption enables one to expand exponentials to first order in their argument.

3) The saturable-absorber and laser-medium gain coefficients, as functions of energy, may be expanded to second order in their (pulse-) energy dependence.

4) The dispersion of the system as a function of frequency may be expanded to second order in frequency (this assumption is legitimate if the laser pulse spectrum is narrow compared with the bandwidth of the system).

These assumptions enable one to get analytic solutions. Some conclusions reached by the present analysis will be shown to be independent of some of the assumptions.

Conditions necessary to achieve mode locking via a saturable absorber of long relaxation time have already been explored by New [14]. Our conditions are similar to his, but not precisely the same. The reasons for this are twofold.

1) New did not include the effect of bandwidth limitation upon the gain requirements. Bandwidth limitation "disperses" the pulse in the time domain, broadens it, and in so doing calls for adjustment of the gain conditions away from those that would have been obtained by disregarding the effect entirely.

2) In order to obtain the closed-form solution, we expand the exponential dependence of gain and absorption upon pulse energy up to second order. This introduces some approximation in our analysis which New did not need to make because he was not looking for closed-form solutions for the pulse shape.

In Section II we develop the basic equation, introducing explicit approximations. In Sections III and IV we establish the constitutive laws for the laser medium and saturable absorber starting with the rate equations. In Section V we solve the nonlinear integro-differential equation by expanding to second order the exponential dependence upon pulse energy of laser gain and absorber loss (parabolic approximation). We obtain two equations for the pulsewidth and pulse energy in terms of the system parameters. The best description of the operation of the system proves to be using the parameters of the net-gain parabola as carried out in Section VI. Section VII is devoted to a comparison between New's result and our analysis. Sections VIII and IX study the pulse shapes resulting from a nonparabolic dependence of net gain upon pulse energy. Finally, in Section X we discuss the relevance of the present theory to the dye-laser system.

II. The Fundamental Equation

The literature on mode locking analyzes the phenomenon either in the frequency domain, treating mode locking as injection locking of the axial cavity modes, or in the time domain. Passive mode locking is most conveniently analyzed in the time domain. The action on the mode-locked pulse within the laser cavity by any one of the components of the system is analyzed, and then the net modification of the pulse upon return to the starting reference plane is set equal to zero. This is the approach used here to arrive at the fundamental equation.

Consider an optical cavity with the laser medium near one end mirror and a saturable absorber near the other end mirror (Fig. 1). The absorber and laser medium are assumed to be "thin," i.e., the transit times through the laser medium and the saturable absorber are assumed to be short compared to the pulse duration. The pulse duration τ_p, in turn, is assumed to be short compared with the transit time through the cavity. We shall assume that the laser-medium and saturable-absorber bandwidths are broad compared to the pulse spectrum. Bandwidth limitation is provided by a linear passive element in the cavity (e.g., etalon). Also this assumption can be modified (within limits) as explained further on in this paper. At the start we assume a uniform intensity profile over the optical beam cross section. Later we show the generalization for treating nonuniform (Gaussian) beam profiles.

The positive-frequency part of the time-dependent electric field at the reference plane next to the laser medium is denoted by $v(t) \exp j\omega_0 t$, where $v(t)$ is the pulse envelope which is slowly time varying compared to $\exp j\omega_0 t$; ω_0 is a frequency near the center of the band, to be made more precise later. The Fourier transform is $v(\omega_k - \omega_0)$. The Fourier transform has a discrete spectrum with components spaced at $2\pi/T$, where T is the period of the mode-locked pulse train.

After passage through the laser medium, the pulse envelope is (see Fig. 1)

$$v_1(t) = e^{A(t)} v(t - T_1) \tag{1}$$

where $A(t)$, the gain coefficient for double passage through the laser medium, is a function of the integrated pulse power

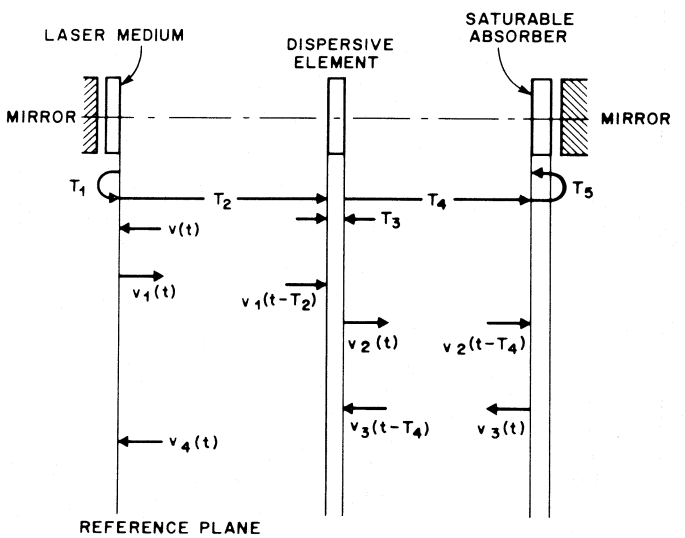

Fig. 1. Schematic of the laser cavity.

(time-dependent pulse energy) at the time t; T_1 is the time of travel through the absorber. The laser gain is assumed to be nondispersive but dependent upon the energy of the passing pulse. This is a necessary assumption if we want to obtain stable mode-locked solutions with a slow saturable absorber, an absorber whose relaxation time is slow compared to the pulse duration τ_p. After passage of a pulse the absorber has no chance of relaxing back to full absorption in a time corresponding to several pulsewidths. If the absorber remains "open," and the laser-medium gain itself is assumed to be time independent, there remains a net positive gain after passage of the pulse for a time corresponding to several pulsewidths. Now the response of the system to a perturbation is, in general, an operation in the time domain involving time derivatives, and hence growth or decay of a perturbation cannot be determined simply from the net-gain coefficient. However, if the perturbation is slow, i.e., has a narrow bandwidth compared to the system bandwidth, the response of the system is described by the net-gain coefficient of the system. With the saturable absorber open for a time corresponding to several pulsewidths, and the laser-medium gain unchanged, there is a net positive gain for a slow disturbance after the passage of the pulse. A steady-state solution found under such circumstances (and one does find such solutions) is unstable. Perturbations of the tail end of the pulse grow, and the pulse broadens, until its duration is limited by the relaxation of the absorber itself.

In order to obtain stable solutions, one must require that the net gain of the system be negative after passage of the pulse [14]. If the pulse is to be short compared with the absorber relaxation time, the gain can be shut off only through the action of the laser medium itself.

Next, the pulse passes through the bandwidth-limiting element (see Fig. 1). The spectrum of the pulse after passage is

$$v_2(\omega_k - \omega_0) = \exp\left[-j(\omega_k - \omega_0)(T_2 + T_3)\right] \cdot H(\omega_k)\, v_1(\omega_k - \omega_0) \tag{2}$$

where $H(\omega_k)$ is the Fourier transform of the transfer function of the element; T_2 is the time of travel between the laser medium and bandwidth-limiting element; T_3 is the delay in the element. The linear loss is included in $H(\omega_k)$ applied twice which, therefore, contains the factor $\exp - \omega_0 T_R/4Q$; T_R is the net round-trip time; Q is the optical cavity Q; and ω_0 is the center frequency of the cavity-mode spectrum. We shall assume that the loss goes up with deviation of frequency from the center frequency ω_0 of the cavity-mode spectrum which will be identified with ω_0 defined previously. The explicit frequency dependence of the loss factor is assumed to be

$$H(\omega_k) = \exp\left[-(\omega_0 T_R/4Q)\left(1 + \left(\frac{\omega_k - \omega_0}{\omega_C}\right)^2\right)\right] \tag{3}$$

where ω_C is the width of the loss "well" plotted versus frequency. Multiplication of $v(\omega_k - \omega_0)$ by $j(\omega_k - \omega_0)$ corresponds to operation by $d/dt - j\omega_0$ on $v(t) \exp j\omega_0 t$. The operation (2), using (4) gives in the time domain

$$v_2(t) = \exp\left(\left(-\frac{\omega_0 T_R}{4Q}\right)\left(1 - \frac{1}{\omega_C^2}\frac{d^2}{dt^2}\right)\right) v_1(t - T_2 - T_3). \tag{4}$$

When the pulse passes the saturable absorber, the envelope function becomes

$$v_3(t) = e^{-B(t)}\, v_2(t - T_4 - T_5) \tag{5}$$

where B is the loss coefficient, a function of the integrated power in the pulse, the time-dependent energy of the pulse; the delays T_4 and T_5 are shown in Fig. 1. Finally, after the pulse passes once more through the bandwidth-limiting element and returns to the reference plane it becomes

$$v_4(t) = \exp\left(\left(-\frac{\omega_0 T_R}{4Q}\right)\left(1 - \frac{1}{\omega_C^2}\frac{d^2}{dt^2}\right)\right) \cdot v_3(t - T_4 - T_3 - T_2). \tag{6}$$

We shall make some further approximations. We shall assume that the bandwidth of the pulse is sufficiently narrow, so that the exponential operators in (3) and (4) may be expanded to first order in $(\omega_k - \omega_0/\omega_C)^2$ or $-(1/\omega_C^2)\, d^2/dt^2$. Further, we shall assume that the modifications of the pulse in one pass through absorber or amplifier are sufficiently small so that all exponentials may be expanded to first order, and, also, in the functional dependence of B upon $v_3(t)$ this function may be replaced by $v(t - \Sigma_{i=1}^{5} T_i)$.

Introducing these approximations, we obtain for the change in the envelope $v(t)$ after one round trip

$$v_4(t) = \left[1 - \frac{\omega_0}{2Q} T_R \left(1 - \frac{1}{\omega_C^2}\frac{d^2}{dt^2}\right) + A(t) - B(t)\right] v(t - T_R) \tag{7}$$

where T_R is the cavity round-trip time, $T_R = T_1 + T_5 + 2(T_2 + T_3 + T_4)$. Now $v_4(t)$ need not be equal to $v(t)$ shifted by T_R, because some pulse shaping may lead to delays or advances of the pulse. Setting $v_4(t) = v(t - T_R + \delta T)$, and expanding to first order in δT, one finally obtains

$$\delta T \frac{dv}{dt} = -\frac{\omega_0}{2Q} T_R \left(1 - \frac{1}{\omega_C^2}\frac{d^2}{dt^2} - \left(\frac{2A(t)Q}{\omega_0 T_R}\right) + \left(\frac{2B(t)Q}{\omega_0 T_R}\right)\right) v. \tag{8}$$

This is the starting equation for our analysis. We shall introduce normalized parameters

$$\frac{2\omega_C \delta T}{\omega_0 T_R} Q \equiv \delta \tag{9}$$

$$g(t) \equiv \frac{2A(t)Q}{\omega_0 T_R} \tag{10}$$

$$\frac{Q}{Q_A(t)} \equiv \frac{2B(t)Q}{\omega_0 T_R} \tag{11}$$

where g may be interpreted as the gain coefficient of the laser medium normalized to the linear loss coefficient, δ is a time delay (or advance) parameter indicating whether the pulse repetition period deviates from the free-space round-trip time T_R, and Q_A is the Q of the saturable absorber.

Rewriting (8) one has

$$\left(1 + \frac{Q}{Q_A(t)} - g(t) - \frac{1}{\omega_C^2}\frac{d^2}{dt^2} + \frac{\delta}{\omega_C}\frac{d}{dt}\right)v = 0. \tag{12}$$

Note that

$$g_T(t) \equiv -\left(1 + \frac{Q}{Q_A(t)}\right) + g(t) \tag{13}$$

is the net-gain parameter, as determined from the combined loss and gain of the cavity (without dispersion), laser medium, and saturable absorber. This parameter plays a very important role in the mode-locking problem. We shall call it the net-gain function or the modulation function. In terms of g_T, (12) can be written

$$\left(g_T(t) + \frac{1}{\omega_C^2}\frac{d^2}{dt^2} - \frac{\delta}{\omega_C}\frac{d}{dt}\right)v = 0. \tag{14}$$

The same result can be obtained from a cavity-mode expansion, making the assumption of high Q (large growth and decay times of mode amplitudes due to the media in cavity). One advantage of the cavity-mode expansion approach [18] is that it permits the analysis of Gaussian modes (in the high-Q approximation). If only axial modes are present in the cavity, a situation assured by the use of mode-suppressing irises, and therefore the mode pattern is known to be Gaussian, then the nonlinear gain and loss parameters may be evaluated as integrals of the susceptibilities of the media in the cavity weighted by the mode patterns.

Note that the bandwidth-limiting element has introduced the operator $-(1/\omega_C^2)\,d^2/dt^2$ which is a diffusion operator (in time-"space"). This operator causes spreading of the pulse which, upon each transit, is compensated by the modulation function to restore the original pulsewidth. Because pulse diffusion or spreading can be caused by many different physical processes, we surmise that the final equation is relatively model independent.

III. The Saturable Absorber

Here we derive an expression for the time-dependent loss coefficient B (or inverse Q) of the absorber. This is proportional to the population difference n of the absorber

$$\frac{\partial n}{\partial t} = -\frac{n - n_e}{T_A} - \frac{\sigma_A}{\hbar\omega_0 A_A}|v(t)|^2\, n \tag{15}$$

where T_A is the relaxation time of the absorber; $|v(t)|^2$ is the square of the amplitude of the electric field within the absorber (normalized so that its square is equal to the sum of the powers in the counter-traveling waves); σ_A is the optical cross section; A_A is the beam cross section in the saturable absorber. In (15) a three-level system has been assumed with a fast relaxation of the upper level.

If the time dependence of the process to be considered is fast compared with T_A, then (15) can be replaced by

$$\frac{\partial n}{\partial t} = -\frac{\sigma_A|v(t)|^2}{\hbar\omega_0 A_A}\, n \tag{16}$$

with the integral

$$n = n^{(i)} e^{-\frac{E(t)}{E_A}} \tag{17}$$

where

$$E(t) \equiv \int^t |v(t)|^2\, dt \tag{18}$$

is the cumulative energy in the pulse

$$\frac{1}{E_A} \equiv \frac{\sigma_A}{\hbar\omega_0 A_A} \tag{19}$$

is the inverse saturation energy, and $n^{(i)}$ is the starting population difference. We shall assume that the saturable absorber relaxes completely *between pulses*, i.e., $T_A \ll T_R$, where T_R is the pulse repetition time. Then $n^{(i)} = n_e$.

The time-dependent inverse Q, as caused by the absorber, is proportional to the time-dependent population difference

$$\frac{Q}{Q_A(t)} = \frac{Q}{Q_A^0} e^{-\frac{E(t)}{E_A}} \tag{20}$$

where Q/Q_A^0 is the measure of the small-signal loading of the saturable absorber.

IV. The Laser Medium

The laser medium must possess a time-dependent gain in order to obtain stable pulses as explained previously. We shall assume that the bandwidth of the medium is much wider than the pulse bandwidth and that the relaxation time T_L of the laser medium is much longer than T_A, an assumption that is usually met in practice.

By a completely analogous argument as the one used for the saturable absorber, we find for the laser gain parameter g

$$g(t) = g^{(i)} e^{-\frac{E(t)}{E_L}} \tag{21}$$

where

$$\frac{1}{E_L} = \frac{\sigma_L}{\hbar\omega_0 A_L} \tag{22}$$

and $g^{(i)}$ is the gain before arrival of the pulse.

With (20) and (21) we have completed the description of the system. For any given $g^{(i)}$, Q/Q_A^0, E_A, and E_L one may plot g_T of (14) versus energy. This is an instructive plot which must be investigated before proceeding with the solution of (14). Fig. 2 shows $1 + (Q/Q_A)$ and $-g$ plotted versus energy. The net gain $g_T(E)$ is obtained by taking the difference between $1 + (Q/Q_A)(E)$ and $g(E)$. The figure shows an initial negative g_T. This is required because if gain preceded the pulse, the pulse would not be stable with respect to perturbations preceding it and would tend to "spread forward." The laser medium is assumed to be hard to saturate, $E_L \gg E_A$, so that over the energy range over which the saturable absorber is fully saturated, the laser-medium gain still decreases approximately linearly with energy.

One conclusion can be drawn immediately. Stability requires that

$$g^{(i)} < 1 + \frac{Q}{Q_A^0}. \tag{23}$$

If the medium relaxed fully between the pulses, $g^{(i)} = g_0$, the

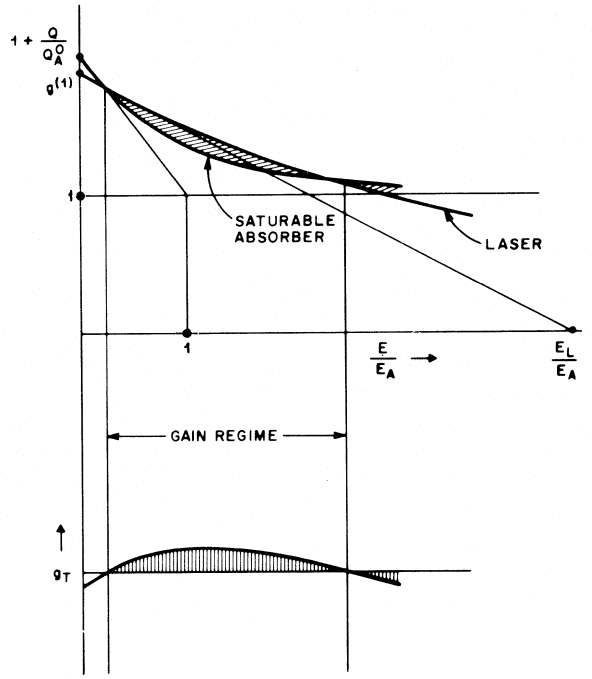

Fig. 2. (a) The saturable-absorber parameter Q/Q_A and laser gain as functions of energy. (b) The net gain g_T as a function of energy.

small-signal gain. But then $g_0 < 1 + (Q/Q_A^0)$, and the system could not get started. Therefore, one requires that $g_0 > 1 + (Q/Q_A^0) > g^{(i)}$, and hence the laser must not fully relax. This means that T_L must not be much shorter than T_R.

In order to relate $g^{(i)}$ to g_0, we note that $g^{(i)}$ decreases during the pulse to $g^{(i)} \exp -(E_0/E_L)$, where E_0 is the total pulse energy, and then relaxes back exponentially to $g^{(i)}$ within one cavity round-trip time T_R. The steady-state consistency requirements give

$$\left[g_0 - g^{(i)} \exp -\frac{E_0}{E_L}\right] e^{-\frac{T_R}{T_L}} = g_0 - g^{(i)}.$$

Solving for g_0 one has

$$g_0 = g^{(i)} \left(1 + \frac{E_0/E_L}{\exp (T_R/T_L) - 1}\right) \tag{24}$$

where we have expanded the exponential $\exp - E_0/E_L$ to first order in E_0/E_L, in anticipation of, and consistent with, the approximations made further on in this paper. If the laser medium is in the middle of the cavity, the round-trip time $T_R = 2L/c$ has to be replaced by L/c, as long as single pulsing occurs. Instead of the sum of the counter-traveling powers, one uses only one traveling component. Everything else is left unchanged.

V. The Solution

We are now ready to reenter (12) and write out all the terms. Using (20) and (21) we obtain

$$-\frac{Q}{Q_A^0} e^{-\frac{E}{E_A}} v = \left(1 - g^{(i)} e^{-\frac{E}{E_L}}\right) v + \frac{\delta}{\omega_C} \frac{d}{dt} v - \frac{1}{\omega_C^2} \frac{d^2}{dt^2} v \tag{25}$$

where E is defined by (18). This is a nonlinear integro-differential equation which looks quite complicated. A simple solution of the equation is obtained if we expand the exponentials into power series and break them off with second-order terms. This corresponds to representing the *net-gain curve* as shown in Fig. 2 by a parabola. Because $E_L \gg E_A$, one may break off the expansion of $\exp(-E/E_L)$ with the first-order term so that one obtains

$$0 = \left(\left(1 + \frac{Q}{Q_A^0} - g^{(i)}\right) - \left(\frac{Q}{Q_A^0} - g^{(i)} \frac{E_A}{E_L}\right) \frac{E}{E_A} + \frac{1}{2} \frac{Q}{Q_A^0} \left(\frac{E}{E_A}\right)^2\right) v + \frac{\delta}{\omega_C} \frac{dv}{dt} - \frac{1}{\omega_C^2} \frac{d^2}{dt^2} v. \tag{26}$$

A solution of this equation is

$$v = \frac{(V_0 E_A/2\tau_p)^{1/2}}{\cosh \frac{t}{\tau_p}} \tag{27}$$

where V_0 and τ_p are constants to be determined by substitution of (27) into (26), using the fact that

$$\frac{E}{E_A} = \frac{V_0}{2} \left(1 + \tanh \frac{t}{\tau_p}\right). \tag{28}$$

Note that V_0 is the normalized energy of the pulse, $V_0 = E_0/E_A$. Substituting (27) in (26), and setting the coefficients of the three hyperbolic functions equal to zero, we obtain three equations. To simplify notation we introduce two parameters, New's s parameter [14]

$$s \equiv \frac{E_L}{E_A} \tag{29}$$

and the saturable-absorber "loading" parameter

$$q \equiv \frac{Q}{Q_A^0}. \tag{30}$$

In terms of these parameters, the three characteristic equations become

$$(1 + q - g^{(i)}) - \frac{1}{2}\left(q - \frac{g^{(i)}}{s}\right) V_0 + \frac{1}{4} q V_0^2 - \frac{1}{\omega_C^2 \tau_p^2} = 0 \tag{31}$$

$$-\frac{1}{2}\left(q - \frac{g^{(i)}}{s}\right) V_0 + \frac{1}{4} q V_0^2 - \frac{\delta}{\omega_C \tau_p} = 0 \tag{32}$$

$$-\frac{1}{8} q V_0^2 + \frac{2}{\omega_C^2 \tau_p^2} = 0. \tag{33}$$

Equation (32) determines the detuning, once the pulse duration τ_p and pulse energy V_0 are determined from (31) and (33).

The net gain g_T as a function of normalized energy $U \equiv E/E_A$ has the dependence

$$g_T(U) = -(1 + q - g^{(i)}) + \left(q - \frac{g^{(i)}}{s}\right) U - \frac{1}{2} q U^2. \tag{34}$$

The pulse energy must satisfy the stability criterion that the net gain be negative after passage of the pulse

$$g_T(V_0) < 0. \tag{35}$$

Eliminating $1/\omega_C^2\tau_p^2$ from (31) and (33), one has

$$-(1+q-g^{(i)})+\left(q-\frac{g^{(i)}}{s}\right)\frac{V_0}{2}-\frac{3}{16}qV_0^2=0. \tag{36}$$

Equation (36) gives two solutions for V_0 for any choice of q, $g^{(i)}$, and s. The smaller of these two can be shown never to satisfy (35) and hence can be discarded.

Some constraints on the parameters may be gleaned directly from (34). In order to have loss before the pulse comes along, we must have

$$1+q-g^{(i)}>0. \tag{37}$$

The loss must be converted into gain with rising pulse energy, i.e., the coefficient $q-g^{(i)}/s$ must be positive

$$g^{(i)}<sq. \tag{38}$$

Fig. 3 shows pulsewidths versus small-signal gain computed for different saturable-absorber loadings $Q/Q_A^0=q$, at fixed s. For each value of q there are two limits on $g^{(i)}$ and V_0, as determined from (35) and (37). Hence there are two limiting values of g_0 obtained from (24). In between, the pulsewidth varies by not more than a factor of the order of 5/3, as explained further on in this paper.

VI. The Gain Parabola

It is convenient to analyze the problem in terms of parameters that are a direct measure of the net-gain parabola (34). We use the height H of the parabola at its maximum which is given by

$$H=\frac{1}{2}\left(1-\frac{g^{(i)}}{sq}\right)^2-\left(1+\frac{1}{q}-\frac{g^{(i)}}{q}\right). \tag{39}$$

Further, we use the curvature parameter (second derivative) of the parabola which is equal to q, and the displacement U_0 of the peak of the parabola from the origin of the energy scale

$$U_0=1-\frac{g^{(i)}}{sq}. \tag{40}$$

Note that U_0 is a weak function of $g^{(i)}$, whereas H is generally a strong function of $g^{(i)}$, because $g^{(i)}$ will generally lie close to $1+q$. This can be seen from the graph of Fig. 4. If $Q/Q_A^0=q\ll 1$, then the laser characteristic hinges around the "distant" point E_L/E_A on the abscissa, and its rotation as a function of $g^{(i)}$ is effectively a translation in the upper left-hand corner of the graph. This is the limit when U_0 is practically $g^{(i)}$ independent.

In terms of these parameters, we obtain for the pulse energy V_0, from (36)

$$-\tfrac{3}{8}V_0^2+U_0V_0-U_0^2+2H=0. \tag{41}$$

The equation for the net gain is

$$g_T(U)=-U^2+2U_0U-U_0^2+2H. \tag{42}$$

Note that the height of the parabola is limited on one hand by the fact that the net gain must be negative when $U=0$. This condition gives the maximum height H_0

$$H_0=\tfrac{1}{2}U_0^2.$$

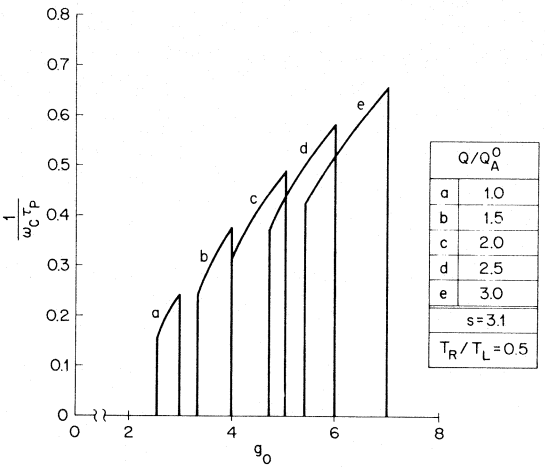

Fig. 3. Inverse pulsewidth versus g_0 with Q/Q_A^0 as parameter.

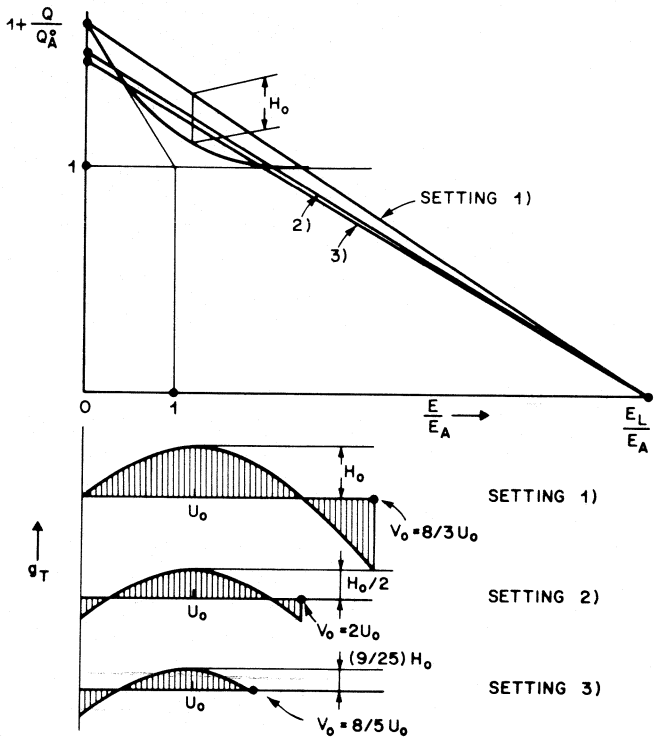

Fig. 4. Various settings of $g^{(i)}$.

TABLE I

Setting	Height H	Normalized Pulse Energy V_0	Normalized Inverse Pulse Width $\frac{1}{\omega_C\tau_p}$
1)	$H=\frac{1}{2}V_0^2=H_0$	$\frac{8}{3}U_0$	$\frac{2}{3}\sqrt{q}\,U_0$
2)	$H=\frac{1}{2}H_0$	$2U_0$	$\frac{1}{2}\sqrt{q}\,U_0$
3)	$H=\frac{9}{25}H_0$	$\frac{8}{5}U_0$	$\frac{2}{5}\sqrt{q}\,U_0$

The minimum height H is not zero, but rather has a positive value imposed by the fact that the pulse energy V_0, as obtained from (41), must satisfy the stability criterion (35). Table I summarizes the more important roots of (41). Case

1) has the largest energy and shortest pulsewidth. Case 2) is the case of symmetry, when the net gain g_T after passage of the pulse is equal to the net gain preceding the pulse. Case 3) is the case of minimum energy, smallest H, when the gain after the passage of the pulse just barely satisfies the stability requirement (35). The three settings for $g^{(i)}$ corresponding to these three cases are shown in Fig. 4.

Case 2) with $H = \frac{1}{2} H_0$ is one in which the loss before arrival of the pulse is equal to the loss after passage of the pulse and hence is a case of high symmetry. From (32), (40), and (41) we find that the detuning δ is zero for this case. We illustrate the conditions in Fig. 5. We show the secant hyperbolic pulse, its energy as a function of time, and the net gain g_T as a function of energy converted into a function of time. It is clear from the graph, and from a perusal of (14) with $\delta = 0$, that $g_T(t)$ plays a role of modulation function which enhances the pulse at its center and suppresses the wings of the pulse. The function $g_T(t)$ time modulates v just so as to compensate for the dispersive effect of the system. Note that the peak g_T at the time of maximum gain is equal and opposite to the g_T at the times before and after passage of the pulse.

Note from (33) and from Table I that the inverse pulsewidth is proportional to the pulse energy. The largest pulse energy equal to $2H_0$ is achieved in setting 1), with H_0 equal to the height of the gain parabola. Hence the largest achievable inverse pulsewidth, for given $g^{(i)}$, is proportional to the height H_0 of the gain parabola of setting 1). This gives a useful criterion for choice of laser medium and saturable-absorber parameters.

Further, we note from Table I that the largest pulse energy is $\frac{4}{3}$ times the distance (on the energy scale) between the zeros of the $g_T(U)$ curve. The smallest energy is $\frac{3}{5}$ times smaller than the largest energy.

To illustrate how the analysis may be applied to predict experimental variation of pulsewidth, we consider the case when q is varied at fixed s. This means that the absorber dye concentration is varied. Concurrently, the gain has to be readjusted by varying the pumping. Suppose that for each dye concentration the gain is adjusted for maximum pulse energy. Then $g^{(i)}$ is set equal to $1 + q$ [setting 1), Fig. 4]. From (40), with $g^{(i)} = 1 + q$, one may solve for q in terms of s and U_0. Using the value $V_0 = \frac{8}{3} U_0$ for setting 1) of Table I we may write for the pulsewidth

$$\omega_C \tau_p = \frac{4}{V_0} [s(1 - \tfrac{3}{8} V_0) - 1]^{1/2}. \tag{43}$$

The equation predicts zero pulsewidth when $\frac{3}{8} V_0 = s - 1$; however, this value corresponds to $q \to \infty$, and clearly the analysis breaks down in this unattainable limit. When $\frac{3}{8} V_0 \ll s - 1$, and thus $q \ll \infty$ we can approximate (43) by

$$\omega_C \tau_p = \frac{4(s-1)^{1/2}}{V_0}. \tag{44}$$

The pulsewidth varies inversely with the pulse energy. This finding should be compared with the prediction of Garmire and Yariv [12] who discussed the case of a relatively fast absorber, neglecting laser-medium dispersion.

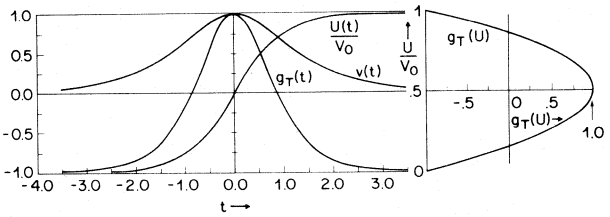

Fig. 5. Pulse amplitude, modulation function, and energy versus time, and g_T versus energy for the symmetric case; g_T is in units of $1/(\omega_C \tau_p)^2$; U and t are in units of τ_p.

Another experimental procedure may consist of varying the beam diameter in the absorber dye, followed by an adjustment of the laser pump to attain maximum energy and minimum pulsewidth. A beam cross-section change by a factor of x leads to a change of the s parameter by $1/x$, and the saturable-absorber loading parameter by x. Setting $s = s_0/x$ and $q = q_0 x$, one may again express x in terms of V_0 [setting 1)] and then write $\omega_C \tau_p$ in terms of V_0. The result is

$$\omega_C \tau_p = \frac{4}{V_0 [s_0 q_0 (1 - \frac{3}{8} V_0) - 1]^{1/2}}.$$

As long as $\frac{3}{8} V_0 \ll 1$, one finds again a variation of $\omega_C \tau_p$ proportional to the inverse pulse energy. When $\frac{3}{8} V_0 = 1 - 1/(s_0 q_0)$, one finds an infinite pulsewidth. This happens at $x = 0$, i.e., at zero beam diameter. This corresponds to the limit of no saturable-absorber action because of oversaturation.

VII. Correspondence with New's Results

To establish correspondence with New we have made the identifications displayed in Table II. Since we used New's notation in Section II, the entries are self-explanatory. Our Fig. 6 is a reevaluation of New's Fig. 2 in terms of the present theory. New put the laser medium at the center of the cavity, and for this reason we use (24) with T_R/T_L replaced by $T_R/2T_L$. Qualitatively, the two figures correspond to each other, whereas quantitatively there are discrepancies.

The discrepancies are accounted for by two facts.

1) We used an expansion for all exponentials.

2) In order to find the limiting regime of g_0, one must know the energy in the pulse. New computed the energy on the basis of the assumption that the net energy gain of the pulse be zero, disregarding medium dispersion. We took dispersion into account. Dispersion introduces an additional loss, and therefore the energy gained by the pulse, computed from $\int g_T(t) v^2 dt$ must be greater than zero. This criterion calls for a pulse energy different from that of New.

In order to show the difference in predicted energies in the pulse, using New's criterion on one hand, and our criterion (36) on the other hand, we plot Fig. 7. The figure shows the two limiting values of pulse energy obtained from New's criterion (as expressed in our notation, with expansion of the exponentials implied)

TABLE II

TABLE OF CORRESPONDENCE

New's Notation	Our Notation
$\beta_0 = \exp - 2B_0$	$\exp - \frac{\omega_0}{Q} q T_R$
$\gamma = \exp - 2\Gamma$	$\exp - \frac{\omega_0}{Q} T_R$
$g_0 = \alpha_0\beta_0\gamma$	$\exp \frac{\omega_0}{Q} T_R(g_0 - 1 - q)$
$\frac{\ln\beta_0}{\ln\gamma}$	q

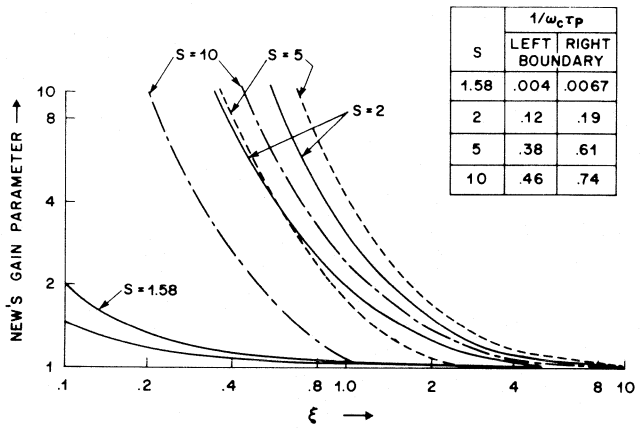

Fig. 6. Boundaries of allowed regimes of gain versus T_R/T_L. Plot corresponds to New's Fig. 2. In order to relate with New's case of a laser medium in cavity center, we multiply T_R/T_L in (24) by 0.5; Q/Q_A^0 = 1.76.

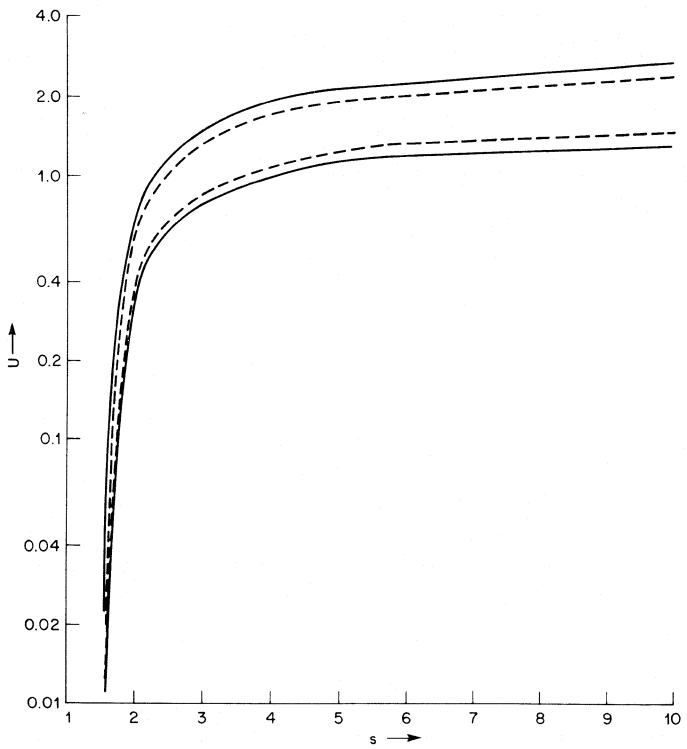

Fig. 7. The limiting energies computed on the basis of the two criteria (45) and (46), the latter is shown by a dashed line; Q/Q_A^0 = 1.76.

$$\int g_T(U)\, dU = 0 \tag{45}$$

and from our criterion (14)

$$\int g_T dU = \frac{1}{\omega_C^2 E_L} \int \left(\frac{dv}{dt}\right)^2 dt \tag{46}$$

which is automatically satisfied by (36).

The discrepancy is of the order of 10 percent, not a large effect. Hence, the major reason for discrepancies in the plots is our expansion of the exponentials. Note, however, that New's values for the losses and gain per pass are high compared with those occurring in the system of [16]. Hence the approximations made in this paper are better suited for the analysis of this experimental system than for a quantitative comparison with New's results.

It should be noted that Fig. 6 also gives a measure of pulsewidth versus the ξ parameter for a given g_0. A choice of g_0 chooses a horizontal line which intersects the s = const boundaries at two points. The rightmost boundary corresponds to a shorter pulsewidth than the leftmost. In between, the pulsewidth increases monotonically; the range of variation is of the order of 5/3.

VIII. Other Symmetric Pulse Shapes

We have concentrated on solutions for pulse shapes resulting from a parabolic g_T versus U-dependence. Experimentally, one finds shapes other than secant hyperbolics [16]. It behooves us, therefore, to look into the reasons for generating pulse shapes that are not secant hyperbolics. One could proceed by changing the $g_T(U)$ function to a dependence other than parabolic. Because the equation to be solved is a nonlinear integro-differential equation, with easy solution only if one guesses it, this route seems less desirable than the alternate one: one assumes a pulse shape and asks for the U-dependence of the modulation function g_T. We pursue here this second alternative. We use functional dependences that give us closed-form solutions while approximating the pulse shapes we are looking for.

In particular, we are interested in pulse shapes that have sharp peaks. We set

$$v = \frac{E_A^{1/2}}{(\cosh^2 u - a)^{1/2}} \tag{47}$$

where u is related to the time variable t by

$$\frac{t}{\tau} = u - a \tanh u \tag{48}$$

where τ is a time-scale parameter, and the a parameter lies in the range $0 < a < 1$. The pulse shape is a secant hyperbolic when $a = 0$, and becomes sharper at the time origin as $a \to 1$. Such a pulse shape has a dependence of energy upon time

$$U = \frac{1}{E_A} \int_{-\infty}^{t} v^2 dt = \tau[1 + \tanh u]. \tag{49}$$

One computes

$$-\frac{\tau^2}{v}\frac{d^2v}{dt^2} = \omega_C^2\tau^2 g_T(t)$$

$$= -\frac{\cosh^8 u - 2\cosh^6 u - a(3\cosh^4 u - 4\cosh^6 u)}{(\cosh^2 u - a)^4}. \quad (50)$$

Fig. 8 shows plots of v, U, and g_T versus time for different values of the a parameter and the corresponding plots of $g_T(U)$. We find that "sharp" pulses are generated by $g_T(U)$ dependences that have sharper peaks than parabolic. Now when a cavity is loaded heavily by the saturable absorber ($Q/Q_A^0 > 1$, compare Fig. 2), the $g_T(U)$ curve, aside from tending to become asymmetric, does acquire a peak that is sharper than the peak of a parabolic function. Hence heavy loading by the saturable absorber in an attempt to produce short pulses will also tend to produce pulses with sharp peaks. These pulses will have more energy content in their "tails" than secant hyperbolic pulses of comparable full width at half-intensity. This may be undesirable for some applications. One way of preventing the formation of pulses with sharp peaks, while maintaining strong saturable-absorber loading, is to use a combination of absorbing media. Through proper choice of saturation energies and small-signal loading factors (q) of the absorbers one may synthesize a more parabolic dependence of g_T upon U.

IX. Asymmetric Pulse Shapes

So far we have studied only symmetric mode-locked pulses resulting from (basically) symmetric $g_T(U)$ curves. To be sure, the parabolic $g_T(U)$ curve was not necessarily centered at the peak of the parabola. When this happened, detuning occurred, but the pulse was still symmetric. We shall now inquire into the reasons for the occurrence of asymmetric pulses.

We follow the procedure used in the preceding section. We postulate an asymmetric pulse shape and then explore what $g_T(U)$ curves are required to give these shapes.

We start by setting

$$v = \frac{E_A^{1/2}}{(\cosh^2 u + b\sinh u\cosh u + bu)^{1/2}} \quad (51)$$

and relate u to t by

$$\frac{t}{\tau} = u(1 + b\tanh u). \quad (52)$$

This "Ansatz" corresponds to asymmetric pulses with an energy

$$U = \frac{1}{E_A}\int_{-\infty}^{t} v^2 dt = \tau[1 + \tanh u]. \quad (53)$$

The modulation function $g_T(t)$ is obtained by straightforward algebra.

Fig. 9 shows a set of curves of $v(t)$, $g_T(t)$, and $U(t)$ for different b parameters, and the $g_T(U)$ curves. Note that all $g_T(U)$ curves are normalized to unity peak amplitude. Fig. 10 shows the half-power width of the pulses versus asymmetry parameter for constant peak amplitude of $g_T(U)$. We find that the width is not a very rapid function of asymmetry, indicating that the height of the asymmetric $g_T(U)$ curve is still a reasonable indication of pulsewidth.

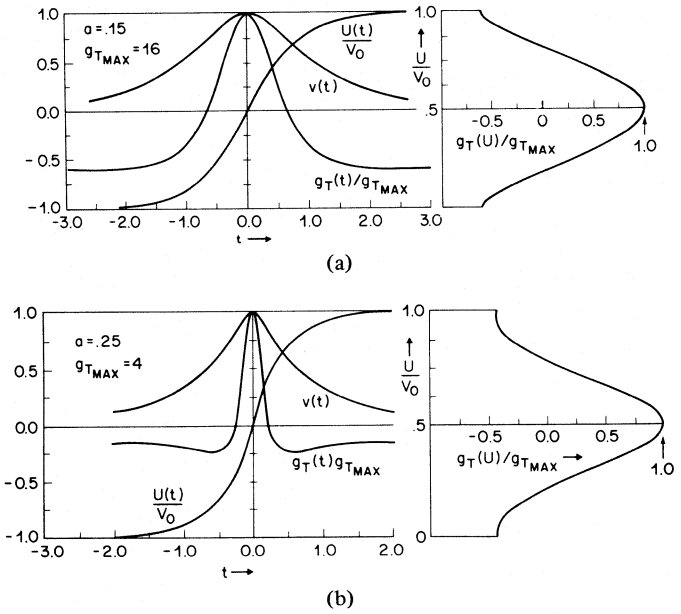

Fig. 8. Plots of pulse amplitude, modulation function $g_T(t)$, and energy versus time, and g_T versus energy for two values of parameter a. g_T is in units of $1/(\omega_C\tau)^2$; U and t are in units of τ.

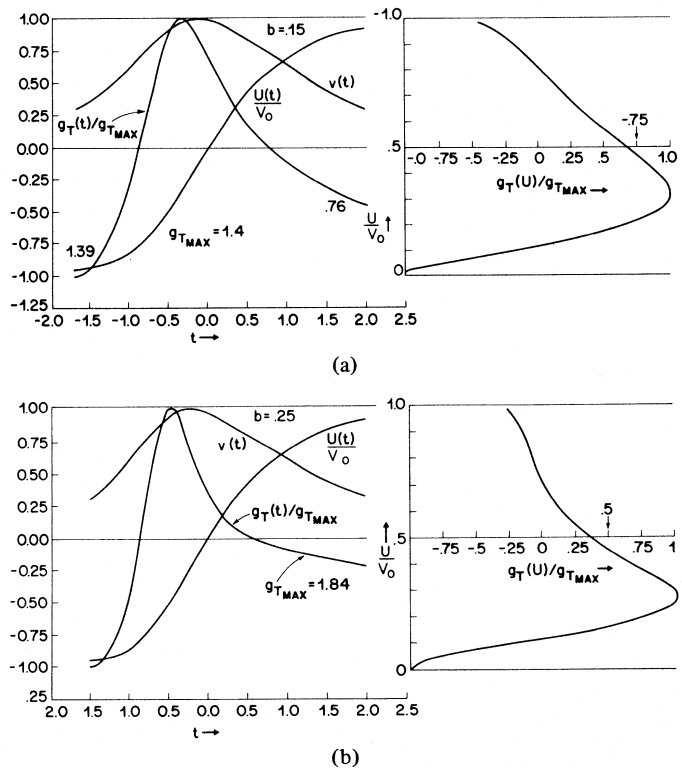

Fig. 9. Plots of pulse amplitude, modulation function $g_T(t)$, and energy versus time, and g_T versus energy for two values of parameter b. The maxima of $g_T(t)$ are in units of $1/(\omega_C\tau)^2$, U and t are in units of τ.

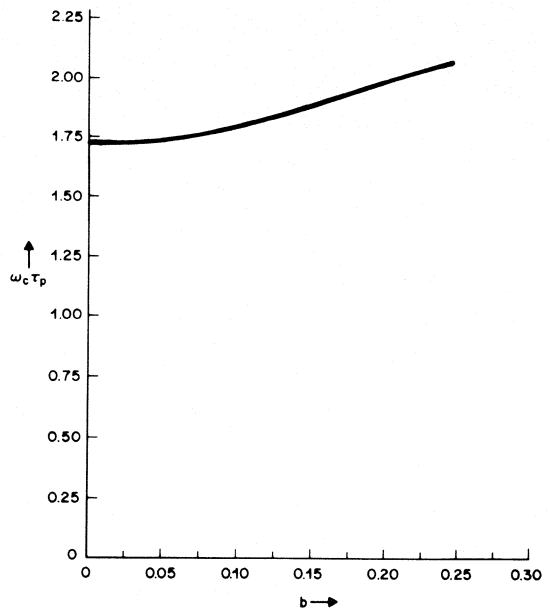

Fig. 10. Half-power widths versus b parameter for fixed peak modulation function, $g_{T\max} = 1$.

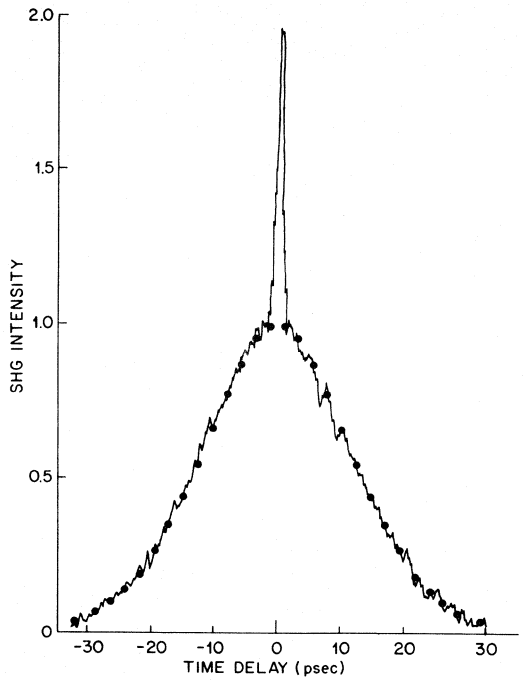

Fig. 11. Experimental correlation function for relatively long pulse.

X. Relevance to Dye-Laser System

We have dealt here with a rather idealized model which, hopefully, can give us insight into the mode locking of CW dye lasers. Some of the assumptions we made were necessary to obtain a closed-form solution, but, if dropped, do not change the qualitative conclusions.

Consider the assumption that Q/Q_A and g may be expanded in E/E_A. If this assumption is dropped, then the gain (or modulation) function $g_T(U)$ has a shape other than parabolic as a function of normalized energy U. We have seen that pulses result which may be peaked, or asymmetric depending upon the shape of $g_T(U)$. Yet, regardless of the detailed pulse shape, the leading and trailing edges of the pulse must be exponentials. This follows directly from (14), rewritten here for convenience

$$g_T[U(t)]\, v = \left(\frac{\delta}{\omega_C}\frac{d}{dt} - \frac{1}{\omega_C^2}\frac{d^2}{dt^2}\right) v. \tag{54}$$

Suppose we found the solution to this equation. Then a certain $g_T(U(t))$ would have been found. But for a known $g_T(U(t))$, (54) may be reduced by substitution of

$$v = V(t) \exp(\delta\omega_C t/2) \tag{55}$$

to a quantum problem of a particle of displacement $V(t)$ in a well

$$-g_T[U(t)] + \frac{\delta^2}{4}.$$

This well must be open on both sides, because $U(t)$ approaches constants for $t \to -\infty$ and $t \to +\infty$. Thus $V(t)$ must have exponential leading and lagging edges. This conclusion depends solely on the assumption that the operator $(1/\omega_C^2)d^2/dt^2$ represents satisfactorily the dispersion of the system.

In analyzing a mode-locked pulse train one makes the implicit assumption that mode locking is successful and all axial modes are in phase coherence with each other. This is not always the case as evidenced by the second-harmonic-generation (SHG) trace of Fig. 11 which was kindly supplied to the author by Dr. C. V. Shank and Dr. E. P. Ippen. The trace was taken under operating conditions such that only partial mode locking occurred. The SHG trace indicates that the pulse consists of a deterministic envelope $V(t)$ with a stochastic substructure $a(t)$

$$v(t) = V(t)a(t). \tag{56}$$

Can this pulse shape be explained by the theory presented here, or by a minor modification thereof?

When the pulse behaves as represented by (56), clusters of modes are locked, with random phases between clusters. The width of the envelope $V(t)$ is of the order of the average inverse bandwidth of the clusters. The saturable absorber and laser media relax slowly and hence are acted upon by the deterministic intensity envelope only. The time dependences of absorption and gain are, therefore, adequately described by the present analysis. The spreading mechanism, i.e., the diffusion term in (25), has to be reconsidered, however. Modes locked in clusters (in frequency space) spread in time if there are temporal shifts of the time envelopes of the clusters. Such temporal shifts are produced when the locking-range boundaries of the clusters fluctuate. When a diffusion term is introduced into the equation for $V^2(t)$, one finds again that the solution is a secant hyperbolic squared for $V^2(t)$.

The experimentally observed SHG trace for partial mode locking shows a pedestal and a coherence spike (Fig. 11). The pedestal is described very well by the correlation function of $1/\cosh^2(t/\tau_p)$ shown by the points in Fig. 11, with τ_p adjusted for a best match.

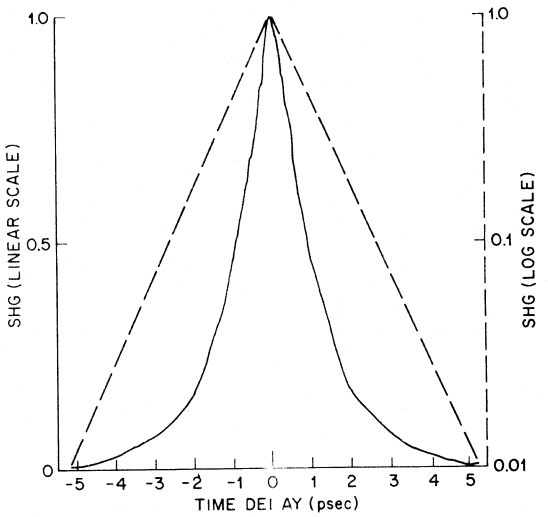

Fig. 12. Experimental correlation function for short pulse. Dashed curve is plotted on logarithmic scale.

When the mode locking is complete so that no coherence spike is visible, and much shorter pulse duration is achieved, the SHG traces assume the shape shown in Fig. 12 also supplied by Dr. Shank and Dr. Ippen. This correlation function cannot be fitted by the correlation function of a secant hyperbolic squared; it is too sharply peaked at the origin. The tails can be seen to be exponentials as predicted by theory. There are at least three different explanations for the deviation of the shape of the correlation function from that of a squared secant hyperbolic.

1) The pulse may not be Fourier-transform limited. The trace in Fig. 12 may be the merger of a coherence spike with the pedestal. The trace can be matched quite well under such an assumption, taking the spectrum of the substructure $a(t)$ of (56) to be that of a secant hyperbolic as well.

2) Deviation of the $g_T(U)$ function from a parabola may lead to asymmetric pulse shapes as explained in Section IX. The correlation function of a one-sided exponential can be fitted well to the trace of Fig. 12.

3) The short pulse may be affected by the nonnegligible time response of the upper and lower levels of the saturable absorber.

XI. Conclusions

By approximating the excess-gain curve versus energy by a parabola, we have obtained closed-form solutions for the problem of mode locking by a slow saturable absorber. The pulse shape is a hyperbolic secant. The analysis led to the following conclusions which hold for parabolic shapes of the $g_T(U)$ curve.

1) Inverse pulsewidths are porportional to the square root of the height above zero of the $g_T(U)$ curve. The widths are smallest when $g^{(i)} = 1 + Q/Q_A^0$, but are only $\frac{5}{3}$ times larger for the lowest allowed value of $g^{(i)}$.

2) The energy in the pulse is roughly $\frac{4}{3}$ times the distance (on the energy scale) between the zeros of the $g_T(U)$ curve.

For nonparabolic shapes of the $g_T(U)$ curve these conclusions follow.

3) Deviations from symmetry of the $g_T(U)$ curve do not affect the form of the solution of the pulsewidth drastically, but do lead to asymmetric pulse shapes.

4) "Peaking" of the $g_T(U)$ curve leads to sharply peaked pulses.

Acknowledgment

The author wishes to thank his students C. P. Ausschnitt and P. Hagelstein with whom many of the basic ideas presented in this paper have been worked out at M.I.T. However, theory did not make contact with physical reality until the author had the privilege of working closely with Dr. C. V. Shank and Dr. E. P. Ippen. Helpful suggestions by Dr. H. Kogelnik on changes in the manuscript are gratefully acknowledged. The careful reading of the manuscript by Dr. Shank and Dr. Ippen is greatly appreciated.

References

[1] V. S. Letokhov and V. N. Marzov, "Generation of ultrashort duration coherent light pulses," *Sov. Phys.–JETP*, vol. 25, pp. 862–866, 1967.
[2] V. S. Letokhov, "Formation of ultrashort pulses of coherent length," *JETP Lett.*, vol. 7, pp. 25–28, 1968.
[3] —, "Dynamics of generation of pulsed modelocking lasers," *Sov. Phys.–JETP*, vol. 27, pp. 746–751, 1968.
[4] —, "Generation of ultrashort light pulses in a laser with a nonlinear absorber," *Sov. Phys.–JETP*, vol. 28, pp. 562–568, 1969.
[5] —, "Ultrashort fluctuation pulses of light in a laser," *Sov. Phys.–JETP*, vol. 28, pp. 1026–1027, 1969.
[6] J. A. Fleck, "Modelocked pulse generation in passively switched lasers," *Appl. Phys. Lett.*, vol. 12, pp. 178–181, 1968.
[7] —, "Origin of short-pulse emission by passively switched lasers," *J. Appl. Phys.*, vol. 39, pp. 3318–3327, 1968.
[8] —, "Emission of pulse trains by Q-switched lasers," *Phys. Rev. Lett.*, vol. 21, pp. 131–133, 1968.
[9] —, "Ultrashort-pulse generation by Q-switched lasers," *Phys. Rev. B*, vol. 1, pp. 84–100, 1970.
[10] E. Mathieu and H. A. Weber, "A model for the evolution of short light pulses from noise," *Z. Angew. Math. Phys.*, vol. 22, pp. 458–465, 1971.
[11] J. R. Creighton and J. L. Jackson, "Simplified theory of picosecond pulses in lasers," *J. Appl. Phys.*, vol. 42, pp. 3409–3414, 1971.
[12] a) E. M. Garmire and A. Yariv, "Laser mode-locking with saturable absorbers," *IEEE J. Quantum Electron.*, vol. QE-3, pp. 222–226, June 1967.
b) —, "Correction to 'Laser mode-locking with saturable absorbers'," *IEEE J. Quantum Electron.*, vol. QE-3, p. 377, Sept. 1967.
[13] J. B. Gunn, "Spectrum and width of mode-locked laser pulses," *IEEE J. Quantum Electron.*, vol. QE-5, pp. 513–516, Oct. 1969.
[14] G. H. C. New, "Pulse evolution in mode-locked quasi-continuous lasers," *IEEE J. Quantum Electron. (Part I of Two Parts)*, vol. QE-10, pp. 115–124, Feb. 1974.
[15] A. Dienes, E. P. Ippen, and C. V. Shank, "A modelocked CW dye laser," *Appl. Phys. Lett.*, vol. 19, pp. 258–260, 1971.
[16] C. V. Shank and E. P. Ippen, "Subpicosecond kilowatt pulses from a mode-locked CW dye laser," *Appl. Phys. Lett.*, vol. 24, pp. 373–375, 1974.
[17] H. A. Haus, "Modelocking with a fast saturable absorber," *J. Appl. Phys.*, to be published.
[18] —, "A theory of forced mode locking," *IEEE J. Quantum Electron. (Part I of Two Parts)*, vol. QE-11, pp. 323–330, July 1975.

Low-Threshold, Transversely Excited NdP_5O_{14} Laser

STEPHEN R. CHINN, MEMBER, IEEE, JAMES W. PIERCE, AND HELMUT HECKSCHER

Abstract—We have measured the room-temperature lasing behavior of NdP_5O_{14} (NdPP) transversely pumped at 0.58-μm wavelength by a CW dye laser in an excitation geometry simulating that of an LED or laser diode. For a crystal 760 μm long, the lowest transverse threshold was 4 mW. From this threshold and a theoretical relationship between excitation efficiency and pump wavelength, we predict that a threshold of approximately 8.5 mW should be possible for excitation by an edge-emitting 0.8-μm wavelength LED. Using thin NdPP samples with reflecting back surfaces for better excitation efficiency should lower this threshold by ~60 percent, and give minimum optical-to-optical conversion efficiencies of ~3.5 percent.

I. Introduction

NEODYMIUM pentaphosphate (NdP_5O_{14}, abbreviated as NdPP), which has also been called Nd ultraphosphate, is a potentially useful laser material containing a high concentration of Nd^{3+} ions (4×10^{21} cm^{-3}) [1], [2]. Its Nd^{3+} emission cross sections, linewidths, and spontaneous lifetimes [3]-[6] are roughly comparable to those in 1-3 atomic percent Nd:YAG (Nd^{3+} concentration ~$1.4\text{-}4.2 \times 10^{20}$ cm^{-3}) [7]-[9]. Therefore the 10-30-fold increase in Nd^{3+} concentration in NdPP allows much shorter samples to yield useful gain-length products, and also results in much shorter absorption lengths, permitting efficient optical excitation of very small volumes.

Small efficient lasers emitting at 1.05 μm could have many applications as substitutes for low-power Nd:YAG lasers at this wavelength. In particular, miniature NdPP lasers would be well suited as sources for fiber-optic transmission systems, which have minimum absorption and scattering losses above 1 μm [10], [11]. Also NdPP lasers offer a possible solution to problems presently found with most semiconductor diode lasers, such as short operating lifetimes, poor mode aspect-ratios, and large beam divergence.

Excitation of Nd:YAG lasers by light-emitting diodes (LED's) or laser diodes results in lower thresholds and power consumption than excitation by the more conventional incandescent or discharge lamps. This paper reports on room-temperature lasing behavior of NdPP excited by a tunable CW dye laser in a transverse geometry that simulates a useful laser diode or LED excitation scheme. Using a simple model for the mode excitation appropriate to this configuration, we have computed a theoretical fit to our experimental data for threshold power versus excitation wavelength near 0.58 μm. From this model, we have calculated the threshold powers required for excitation in the 0.80-μm absorption region, which is of more practical interest because direct-gap, efficient 0.80-μm laser diodes and LED's are better developed than those emitting at 0.58 μm. Also the 0.80-μm band is the strongest Nd^{3+} absorption band in the visible and near infrared.

Manuscript received January 20, 1975; revised May 12, 1975. This work was sponsored by the Department of the Air Force.

The authors are with the Massachusetts Institute of Technology Lincoln Laboratory, Lexington, Mass. 02173.

II. Experimental Procedure and Results

The experimental apparatus, shown schematically in Fig. 1, was similar to those described by Weber *et al.* [1] and Danielmeyer *et al.* [2], except that we used a CW tunable dye laser as the excitation source. The dye was rhodamine 6G, whose output range includes the strong NdPP absorption band near 0.58 μm. The dye laser was excited by a CW argon-ion laser. The dye laser output was either interrupted by a tuning-fork chopper or used directly for CW pumping. The pump beam was expanded, passed through a 1-cm aperture, and focused on the NdPP sample at the center of a nearly spherical optical cavity having 5-cm radius input and output mirrors with reflectivities at 1.05 μm of nominally 100 percent and ~99.7 percent, respectively.

Two alternate excitation schemes were used. The first was collinear excitation [1], [2], with the pump beam focused on one end of the sample by a 10-cm focal length lens through the input mirror (transmitting at 0.58 μm). This configuration gave the lowest thresholds and was used for the initial alignment of the sample and cavity. For transverse excitation, a deflecting mirror diverted the pump beam to two other mirrors and then through two crossed cylindrical lenses to form a narrow-line image on one side of the sample. An enlarged sketch of the resulting excitation at the sample is shown in Fig. 2(a). The cylindrical lenses were first adjusted so that the horizontal length of the focused beam matched the sample length L in the lasing direction, and the beamwidth was as narrow as possible. This initial adjustment was performed

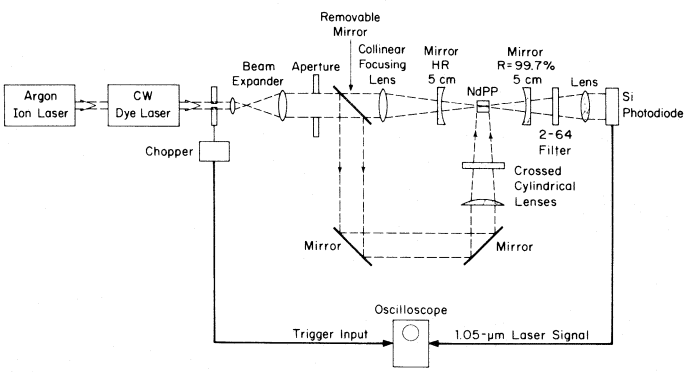

Fig. 1. Schematic diagram of experimental apparatus for optical excitation of a NdPP laser.

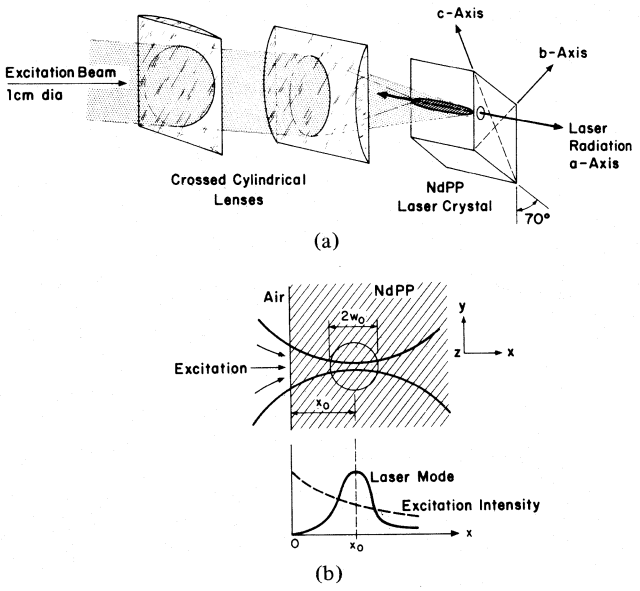

Fig. 2. (a) Enlarged view of transverse excitation at the NdPP laser crystal. (b) Diagram of the laser mode and transverse excitation intensity in the NdPP crystal.

visually by using a microscope with an infrared (IR) image converter to view the spontaneous emission at the beam focus. Fine angular adjustment of the output mirror was then performed by piezoelectric tuning of the mirror-mount micrometers. The mirror spacing and, consequently, the laser mode parameters were not changed from the collinear geometry. Both the excitation focus and transverse sample position were adjusted for minimum threshold. Then the threshold was measured as a function of pump wavelength, using a Si photodiode inserted in the beam outside the cavity to monitor the excitation power. In order to correct for losses due to the input optics, for both collinear and transverse cases the external photodiode was first calibrated against a calibrated detector placed at the sample position. In the data presented below the threshold powers refer to these measured incident powers. For the collinear geometry, the laser samples were long enough so that no significant amount of pump power was transmitted. Therefore, the absorbed power can be estimated by reducing the incident power by 5 percent, the Fresnel reflectivity of NdPP. Of course, for the transverse excitation case the most useful information is the amount of power absorbed in the region of the laser mode, which is discussed in the calculation below. Again, the data for transversely directed powers are the measured incident powers. Another Si photodiode, placed after the output mirror and preceded by an IR-transmitting visible-blocking Corning 2-64 glass filter, measured the 1.05-μm NdPP laser output.

The natural growth habit of the rhombohedral-prism-shaped NdPP crystals [Fig. 2(a)] made their use extremely convenient. Since both end *a* faces and the side excitation face were of very high optical quality, no sample preparation was necessary except for cleaning and cementing to a mounting pin. However, in an attempt to increase the transverse excitation efficiency by reflecting the transmitted pump light, we polished one sample to a thickness (t) of 78 μm, and placed the polished face against a small mirror. The mirror, fabricated from 100-μm-thick aluminized glass, had a length of 500 μm, slightly less than the sample length (565 μm) so as not to intercept the diverging laser mode. An as-grown platelet only 36 μm thick was also mounted in this fashion. This platelet had *a* faces parallel to the mirror surface, and the laser facets were cleaved normal to the *b* axis.

The general method used for growing NdPP crystals has been described by Danielmeyer *et al.* [12] and Hong [13], but we have found that there is some variation in crystal habit depending on specific growth conditions. To obtain the rhombohedral-prism-shaped samples, we used the following procedure. A 5-*g* charge of Nd_2O_3 was weighed into a 250-cm^3 Au crucible, and 200 cm^3 of 85-percent phosphoric acid was added slowly. The uncovered crucible was heated in a muffle furnace. The temperature was first raised to 250°C and held there for 50 h, then raised to 550°C in less than an hour and held there for 7 days. The excess liquid was poured off as quickly as possible (in about 1 min), and the crucible was returned to the hot furnace, which was shut off and cooled to room temperature in about 5 h. Any remaining polyphosphoric acid was removed by soaking the crucible in a beaker of cold, distilled water for about 24 h. Most of the cyrstals could then be washed from the crucible without applying any mechanical stress. The crystals obtained were rinsed several times with acetone and allowed to dry. After selection of the best crystals, followed by final cleaning with detergent, trichlorethylene, acetone, and methanol, the laser samples were cemented to pins for mounting on a goniometer in the optical cavity. These samples, typically about 0.5 × 0.5 × 0.5 mm^3, showed some internal growth striations under a microscope. Generally, however, these were faint enough and far enough apart so as not to degrade the laser operation significantly. The platelet 36 μm thick was selected from crystals grown by the same method as in the preceding, but using a 15-*g* charge of Nd_2O_3. It had no visible optical flaws.

The experimental data for transverse threshold $P_T(\lambda)$ versus pump wavelength λ for sample 1 (L = 760 μm) and sample 2 (L = 940 μm) are shown in Figs. 3 and 4, respectively. For sample 1 the collinear threshold P_C was 600 μW, and the minimum value of $P_T(\lambda)$ (found at λ = 0.58 μm), was 3.9 mW. Corresponding values for sample 2 were P_C = 720 μW and minimum $P_T(\lambda)$ = 4.8 mW.

The effects of reducing the thickness and reflecting the transmitted pump radiation are shown by the data for sample 3 (L = 565 μm, t = 78 μm) plotted in Fig. 5. Although P_C, 625 μW, was slightly higher than that of sample 1, the minimum $P_T(\lambda)$ = 2.7 mW was significantly lower. The output power, P_{out} (at 1.05 μm), as a function of optical input power, P_{in} (at 0.58 μm), was measured with 1.6-ms excitation pulses and 20-percent duty cycle. Sample 3 had a more efficient excitation geometry resulting in generally higher output power and power conversion efficiency than sample 1. With transverse excitation the best conversion efficiencies were 8.5 percent (sample 3) and 8 percent (sample 1) compared with 30-percent efficiency which we typically obtain with collinear pumping (and the same 99.7-percent reflector). Continuous lasing with up to 1-mW output power (3.5-percent efficiency) was also obtained, but thermal limitations made stable higher

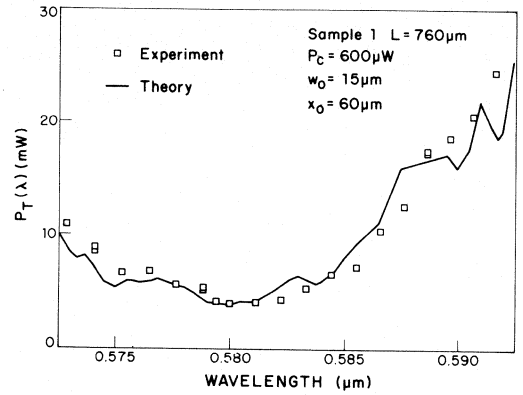

Fig. 3. Experimental and theoretical transverse pump threshold $P_T(\lambda)$ as a function of wavelength near 0.58 μm for NdPP sample 1, 760 μm long.

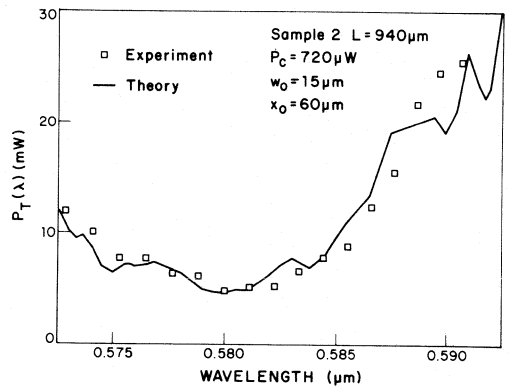

Fig. 4. Experimental and theoretical transverse pump threshold $P_T(\lambda)$ as a function of wavelength near 0.58 μm for NdPP sample 2, 940 μm long.

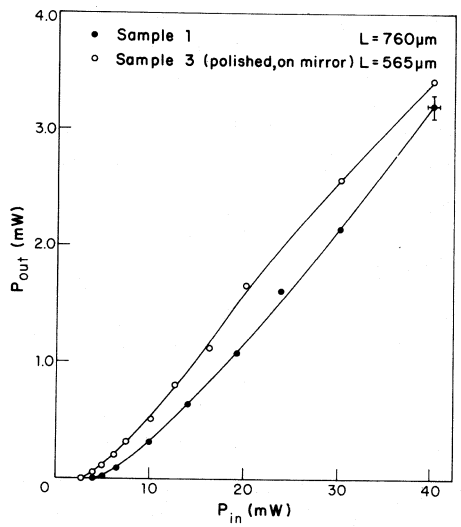

Fig. 5. Output power at 1.05 μm, P_{out}, as a function of transverse input power at 0.58 μm, P_{in}, for sample 1 (760 μm long) and for sample 3 (565 μm long) with reflecting back.

output powers difficult to achieve. The laser output for samples 1-3 was linearly polarized with the electric field parallel to the *b* axis, the orientation with highest stimulated emission cross section [5], [6].

To see whether an even thinner sample might be lased in the transverse configuration, we made measurements on sample 4,

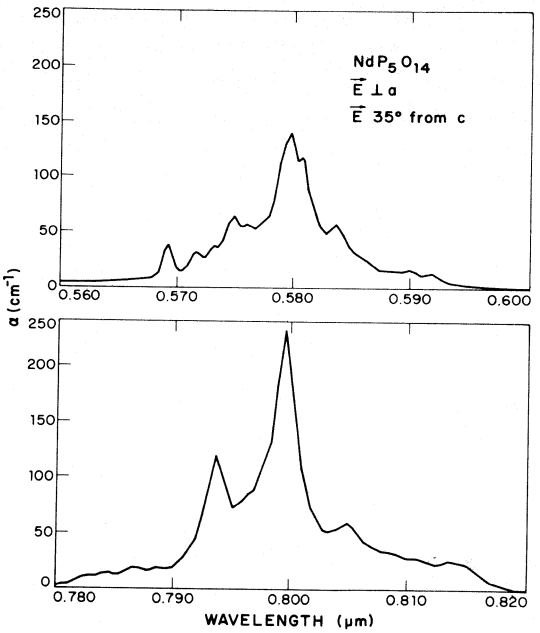

Fig. 6. Absorption coefficient α of NdPP as a function of wavelength near 0.58 and 0.80 μm. The electric field is polarized in the *y* direction of Fig. 2.

described in the preceding, with t = 36 μm and L = 290 μm. Like sample 3, this was mounted on a 500-μm-wide mirror, which may have partially vignetted the laser mode. Threshold values of P_C = 1.41 mW and minimum $P_T(\lambda)$ = 5.8 mW were found, with the laser output polarization parallel to the *c* axis, i.e., in the plane of the platelet. Singh *et al.* [5] and Huber *et al.* [6] have shown that the *c* polarization has approximately 50-percent smaller emission cross section and gain than the *b* polarization obtained with samples 1-3. This fact, along with vignetting of the laser mode, may explain the somewhat higher thresholds found for sample 4. However, the thickness of 36 μm seemed to be sufficient to give efficient absorption of the transverse pump radiation when the back-surface reflector was used.

Polarized optical transmission measurements were performed near 0.58 μm and 0.80 μm to obtain values of the absorption coefficient α for use in the theoretical calculations discussed below. These data were obtained with a double-beam spectrophotometer provided with a beam condenser to focus the transmitted light on the very small NdPP samples used. These samples were thin, as-grown platelets with the *a* axis normal to their broad faces. The transmission measurements were performed with the same electric field polarization as in the transverse excitation of the thicker laser samples, namely, E perpendicular to the *a* axis and rotated 35° from the *c* direction. The absorption coefficients computed from the measured transmission data are plotted in Fig. 6. (For convenience, α was evaluated at a limited number of wavelengths, and the resulting data points are connected by straight lines in the figure.)

III. Theoretical Calculations

A simplified model has been used to compute $P_T(\lambda)$. We assume that the width of the focused pump beam is sufficiently narrow compared to the NdPP laser mode diameter that no ex-

citation is lost in that dimension. Also we assume that both the mode and excitation are uniform along the axial direction. For these approximations, a simple one-dimensional integral gives the overlap, or effective gain, of the mode, as schematically indicated in Fig. 2(b). We define the additional parameters.

w_0 Gaussian laser mode radius;
x_0 depth of mode center from excitation face;
c_1 $= x_0/w_0$, $\rho = \alpha w_0/2$;
r radial coordinate for collinear geometry;
w_p collinear Gaussian pump beam radius at focus.

By computing the overlap of the excitation density and mode intensity for the transverse and collinear configurations (assuming complete absorption of the pump radiation in the collinear geometry) we find

$$P_T(\lambda) = P_C \left\{ \int_0^\infty \frac{4r \exp\left[-2r^2(1/w_p^2 + 1/w_0^2)\right]}{w_p^2}\, dr \right\} \cdot \left\{ \alpha \int_0^\infty \exp\left[-\alpha x - 2(x - x_0)^2/w_0^2\right] dx \right\}^{-1}$$

$$= P_C \left\{ (1 + w_p^2/w_0^2)\, \rho \exp\left[-\rho(2c_1 - \rho/2)\right] \sqrt{\pi/2} \cdot \left[\operatorname{erf}\left(\frac{2c_1 - \rho}{\sqrt{2}} \right) + 1 \right] \right\}^{-1}. \quad (1)$$

The pump radius, $w_p = 9 \pm 2$ μm, was determined experimentally by measuring the transmission through pinhole apertures of various diameters, assuming a Gaussian mode intensity. Equation (1) was used with the measured values of α, w_p, and P_C to calculate $P_T(\lambda)$ for samples 1 and 2. For sample 1, the mode parameters x_0 and w_0 were adjusted to give the curve best fitting the experimental data of Fig. 3 for λ near 0.58 μm. This curve, which was obtained with x_0 = 60 μm and w_0 = 15 μm, is shown in Fig. 3. We then used the same values of x_0 and w_0 to calculate $P_T(\lambda)$ for sample 2, again obtaining a good fit to the data, as shown in Fig. 4. This agreement is not surprising since the theoretical curves were found to be only moderately sensitive to the mode parameters over the physically reasonable range 50 μm $< x_0 <$ 75 μm and 10 μm $< w_0 <$ 20 μm. Note that P_C is an experimentally measured quantity (later, estimated for the 0.8-μm excitation), determined at a wavelength for total absorption of the pump radiation, and is not a function of λ.

The same values of x_0 and w_0 were also adopted in using (1) to predict $P_T(\lambda)$ for the Nd^{3+} absorption band peaking near 0.80 μm. The calculated curve for sample 1 is shown in Fig. 7. To obtain the value of P_C used in the calculations, 540 μW, the experimental value of 600 μW found at 0.58 μm was multiplied by 1.24 to allow for the increase in w_p [the first factor in (1)] and divided by 1.38 to allow for the decrease in energy per pump photon. For pumping at 0.80 μm, as at 0.58 μm, $P_T(\lambda)$ is relatively insensitive to the choice of laser mode parameters.

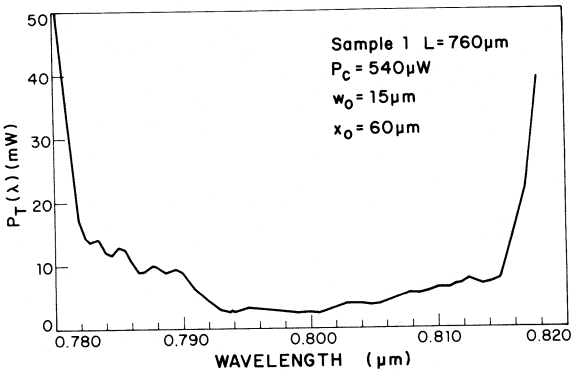

Fig. 7. Predicted transverse pump threshold $P_T(\lambda)$ versus excitation wavelength near 0.8 μm for a narrow-band source with a tightly focused beam (using sample 1).

The preceding calculations were made for a narrow-band pump. We now consider the case of wide-bandwidth pump radiation characterized by a spectral power density $\rho(\lambda)$. In a small wavelength interval $\delta\lambda$ the fraction of threshold attained will be $[\rho(\lambda)\, \delta\lambda/P_T(\lambda)]$. Therefore, the threshold condition is

$$\int \frac{\rho(\lambda)}{P_T(\lambda)}\, d\lambda = 1.$$

For simplicity we assume the pump radiation to have the normal distribution

$$\rho(\lambda) = \frac{P_\Sigma}{\Delta\lambda\sqrt{\pi}} \exp\left[-(\lambda - \lambda_0)^2/(\Delta\lambda)^2\right]$$

where

P_Σ total pump power;
λ_0 center wavelength of pump band.

The parameter $\Delta\lambda = \Delta\lambda_{1/2}/2\sqrt{\ln 2}$, where $\Delta\lambda_{1/2}$ is the full-width half-maximum (FWHM) interval. From this distribution, we find the wide-band pump power at threshold

$$P_\Sigma = \left\{ \int d\lambda \exp\left[-(\lambda - \lambda_0)^2/(\Delta\lambda)^2\right] / \left[\Delta\lambda\sqrt{\pi}\, P_T(\lambda)\right] \right\}^{-1}. \quad (2)$$

Numerical integration of (2) over the wavelength range 0.78–0.82 μm was used to compute P_Σ as a function of $\Delta\lambda_{1/2}$ as shown in Fig. 8 along with similar results for the 0.58-μm band. This plot shows that using wide-band LED's or laser diodes should not require an inordinate increase in pump power compared with a narrow-band source.

The threshold calculations in the preceding assume that the imaging geometry for the wide-band pump beam is the same as that of the dye laser. By suitable collection, collimation, and focusing optics it should be possible to achieve this type of beam geometry with narrow-junction edge-emitting laser diodes or LED's. However, it would be much simpler to place the narrow emitting junction region of the diode immediately next to or in contact with the NdPP crystal. The increase in power necessary in this configuration because of the pump beam diver-

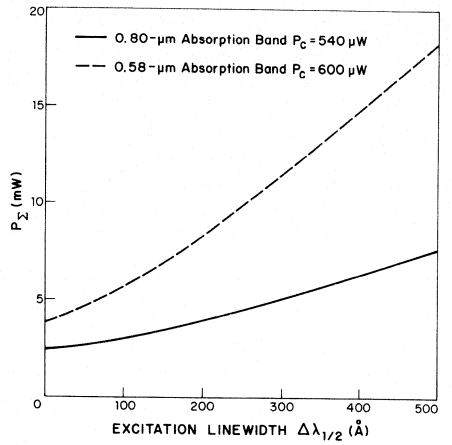

Fig. 8. Predicted transverse pump threshold P_Σ at 0.58 and 0.8 μm versus FWHM excitation bandwidth $\Delta\lambda_{1/2}$ for a tightly focused beam (using sample 1).

gence can be easily estimated by using an integration scheme [similar to the one used in deriving (1)] to evaluate the overlap along the y direction at $x = x_0$. The divergence is found to increase the threshold by the factor

$$\beta = \sqrt{1 + w_t^2(x = x_0)/w_0^2} \tag{3}$$

where $w_t(x = x_0)$ is the transverse pump beam radius along the y coordinate at the center of the NdPP laser mode. This expression confirms our earlier assumption that $\beta \simeq 1$ for diffraction-limited focusing of the dye laser beam along the y direction. For diode pumping, we take some typical parameters to estimate $w_t(x = x_0) \simeq [\lambda x_0/\pi w_t(x = 0)]$. For $\lambda = (0.8/n)$ μm = 0.5 μm (where the refractive index $n = 1.6$) and $w_t(x = 0) = 0.5$ μm, $w_t(x = x_0) \simeq x_0/3$. This calculation is approximate in that it uses simple diffraction theory to calculate the divergence from a source with height $2w_t \sim 1$ μm. This dimension is not an unreasonable estimate, either for high-radiance double-heterostructure (AlGa)As light-emitting diodes [14] (active region thickness ~2 μm, output power 3 mW for 50-μm-wide device) or for CW double-heterostructure (AlGa)As laser diodes [15] (active region thickness ~0.3 μm, output power 10 mW for 13-μm-wide device). In both cases, the output power densities should be sufficient for a small array of such narrow devices to exceed by several times our calculated thresholds. For the previous values $x_0 = 60$ μm and $w_0 = 15$ μm, (3) gives $\beta = 1.67$, a quite moderate price to pay for the convenience of this pumping configuration.

IV. Discussion

Certain refinements in the theory might give better agreement with experimental data.

1) We have implicitly assumed that the Gaussian laser mode is not truncated at the sample edge. Although this is probably a good approximation for $x_0 > 2w_0$, a condition satisfied in the present case, the truncation effect could be considered in a more exact model.

2) We have also neglected the variation of the laser mode in the z direction. Typical confocal parameter values, $(\pi w_0^2 n/\lambda) \simeq 1.2$ mm, are longer than the samples used, so that this is a good approximation, but the z variation could be taken into account.

3) Another factor which we have neglected is diffusion of the Nd^{3+} excitation. Theoretical analysis [16] shows that diffusion should be highest along the a axis; diffusion in this direction would not affect our results.

One reason for not attempting these refinements is that our experimental data are not sufficiently accurate to justify the additional mathematical complexity that would be required. Another reason is that our model may be only qualitatively correct to begin with, since it assumes excitation of the fundamental TEM_{00} mode. However, we did not observe a uniform symmetric mode unless apertures were introduced into the optical cavity. We believe that the output of this nearly unstable, almost spherical cavity is probably composed of several independent fundamental modes which are nearly collinear. Evidence for this is provided by the incoherent, rapidly fluctuating nature of the output relaxation oscillations observed with chopped excitation; in other NdPP collinearly pumped lasers, the relaxation oscillations are quite coherent and stable when care is taken to obtain a few well-defined modes. In any event, the simple model seems to provide a good, if phenomenological, fit to the data, and further sophistication in the theory is probably not warranted at present.

The results obtained for sample 3 mounted on a reflector are quite promising (Fig. 5). This sample shows a 60-percent reduction in the ratio of transverse to collinear thresholds over the thicker nonreflecting samples 1 and 2. The improved geometry also gives higher efficiency but seems to suffer more from thermal limitations on the output power at high levels. Presumably, this arises from the smaller sample volume and poorer heat dissipation, and should be reduced by establishing better thermal contact to a back reflector with increased thermal conductivity. The optical power conversion efficiency of sample 3 for excitation by a 300-Å bandwidth, 0.8-μm wavelength LED can be estimated from the efficiency of 8.5 percent measured with dye laser excitation. Dividing by a bandwidth factor of 2 (found from Fig. 8) and by the beam divergence factor $\beta = 1.67$, and multiplying by the photon energy factor 0.80 μm/0.58 μm = 1.38, we predict an efficiency ~3.5 percent.

In recent theoretical calculations, Singh *et al.* [5] claim that NdPP has no advantage over Nd:YAG for miniaturized lasers. This conclusion is reached on the basis of several factors, including the larger emission cross section [5]-[7], [9], longer fluorescent lifetime [5], [8], and smaller "resonant" loss (absorption from the thermally populated $^4I_{11/2}$ levels) in Nd:YAG. We do not disagree with their conclusion that an end- (collinearly) pumped Nd:YAG laser should have lower threshold than NdPP, although at the cost of a much longer crystal to insure efficient absorption of the pump radiation. However, we strongly disagree with their conclusions concerning side-pumped lasers. First, their own calculations [5, fig. 6] show that for "nonresonant" loss, L_0 (output coupling, scattering, etc.) exceeding 0.3 percent, NdPP has a lower threshold power density than 3-percent Nd:YAG. The differential output efficiency of the laser is inversely proportional to $[1 + L_i/$

$(\ln 1/R)]$, where L_i represents the internal part of the nonresonant loss, and R is the output mirror reflectivity (the other mirror is assumed to have $R \simeq 1$). Since in most lasers the internal loss exceeds a few tenths of a percent, one would generally desire an output transmission exceeding this loss to optimize the output power [17], and consequently would nearly always be in a regime where L_0 exceeded 0.3 percent, making NdPP the lower threshold material. Second, and perhaps more important, are the practical considerations of device size and total threshold powers (not power densities), which have been neglected by Singh *et al* [5]. The calculation in [5] for side-pumped lasers compares cases in which the excitation depth is an effective absorption length $1/\tilde{\alpha}_p$. Their value of $\tilde{\alpha}_p = 1.1$ cm^{-1} for Nd:YAG would give a laser 1 cm thick, hardly a miniaturized laser compared to 0.01-cm thickness, typical of NdPP. To be more specific, we have repeated our previous procedure, and measured the absorption coefficient of the 1-percent Nd:YAG for use in (1). After multiplying the measured α by three to apply to the case of 3-percent Nd:YAG we have calculated the ratio of transverse to collinear thresholds. Even after doubling the laser mode radius to 30 μm (compared to the NdPP results with $w_0 = 15$ μm) and placing the mode right at the edge of the crystal ($x_0 = 30$ μm) the *minimum* narrow-bandwidth threshold is 14 times higher than the collinear threshold. Increasing the bandwidth of the pump to 300 Å increases this value to 48 times the minimum narrow-band collinear threshold. The same factor for NdPP with a mode half the diameter, located 60 μm from the pump face, is only 9. Assuming that nonresonant losses dominate, one would expect nearly equal minimum collinear thresholds since the threshold power density is ~4 times lower for Nd:YAG (a factor of 2 from longer lifetime, and a factor of 2 from larger cross section), but the mode area is 4 times larger. With this choice of modes giving the same normalization factor, we find that the side-pumped NdPP threshold should be at least 5-6 times lower than for 3-percent Nd:YAG, and also enables use of a thinner device.

To verify that present NdPP crystal quality is good enough (scattering and extraneous loss much less than mirror-coupling losses) to allow a meaningful comparison with Nd:YAG for practical device applications, we have measured the differential quantum efficiency of a 1-mm-thick NdPP crystal using different output reflectors with transmission 0.3, 1.2, 2.2, and 5.7 percent. With collinear excitation, we have obtained *overall* power conversion efficiencies of 50 percent with the highest transmission mirror, and a value (corrected for sample reflectivity) of *differential* quantum efficiency $\eta \sim 95$ percent (within experimental error). Our data for η as a function of R show that $L_i \lesssim 0.3$ percent. This value is also consistent with estimates obtained from analysis of relaxation oscillations in the laser output, using chopped excitation.

A direct correspondence between our NdPP results and previous experimental work on diode-pumped Nd:YAG lasers is difficult because of the differences in laser geometries, modes, reflectivities, etc. Nevertheless, it should be useful to examine the device parameters of various diode-pumped Nd:YAG lasers to give some idea of the progress achieved in this area, and to serve as comparisons with the type of device we are considering in this paper. In Table I we summarize our experimental and predicted results along with some of the diode-pumped Nd:YAG results [18]-[24],[1] listed in approximately chronological order. These published results show the relative advantages of diode-pumped NdPP and Nd:YAG in different types of applications, which we have noted in the preceding. The most recent larger-scale (1.5-mm diameter × 30-50 mm long) Nd:YAG devices designed for maximum output power, such as those in items 9 and 10 (improved over similar, earlier versions in items 4-6) perform well in terms of power conversion efficiencies (even with a nonoptimum pump wavelength of 8680 Å for item 10). However, even after allowance for the different output couplers (i.e., 3 percent in item 10), the long absorption lengths and large volumes in these devices lead to high threshold powers. Reducing the device size would lower the threshold, but also the output power and efficiency. Such a trend is shown by the end-pumped devices of items 7 and 8. Here much smaller Nd:YAG rods (0.5-mm diameter × 6 mm long) are used, in an end-pumped geometry to allow greater pump absorption. The threshold powers are low, but the output is limited by the single end-pumping LED. Comparable thresholds should be obtainable with yet smaller, transversely pumped NdPP crystals, which would have the additional advantages of higher efficiency and larger output power obtained by using several diodes in a transverse pumping array. From our data, NdPP appears to offer the potential of performance superior to Nd:YAG for diode-pumped *miniature low-power* lasers, while for larger higher power ($\gtrsim$100-mW) devices, Nd:YAG probably will remain the better choice.

Low-threshold operation has also been demonstrated in an ion-laser excited Nd-doped silica fiber laser [25]. With a 1-cm-long 40-μm-core-diameter fiber end-pumped by an argon-ion laser emitting at 0.51 μm, a threshold of 1-2-mW absorbed power was obtained with 3-percent duty cycle. This system, like the end-pumped Nd:YAG lasers of [21] and [22], has the advantage of nearly complete absorption of the pump radiation, but requires moderately long lasers (several millimeters) and high-brightness excitation at the laser end face with area comparable to the cross section of the fiber core. Similar lasers using Nd-doped single-crystal YAG fibers have also been demonstrated [26]. The lasing parameters were close to those of the Nd:silica fiber lasers, and the same advantages and disadvantages mentioned in the preceding apply.

In order to make a more compact NdPP device the present input and output mirrors could be replaced by reflective coatings applied directly to the crystal lasing faces. A miniature cavity with smaller mode volume and better stability could be made using reflectors fabricated from coated, plane-polished

[1] We calculated the optical powers and efficiencies of [23] in Table I from the reported electrical input power by assuming 1-percent efficiency for the LED's, a conservative estimate. The actual thresholds were probably higher, and the efficiencies lower, than those listed.

TABLE I
COMPARISON OF NDPP LASERS AND DIODE-PUMPED ND:YAG LASERS

Laser Material	Ref.	Configuration	Pump	Temperature (K)	Duty Cycle and/or Pulse Duration	Optical Threshold Power (mW)	Optical Power Conversion Efficiency (%)
(1) NdPP	a	Side-pumped, nearly spherical external cavity; 0.3% output mirror	0.58 μm cw dye laser	300	20% (1 ms) cw	4 4	8.0 3.5
(2) NdPP	a	Same as (1), but with added pump reflector	Same as (1)	300	20%	2.7	8.5
(3) NdPP (calculated)	a	Same as (1)	Single 0.8 μm, 300Å bandwidth, edge-emitting LED	300	~20%	8.5 (calculated)	3.5 (calculated)
(4) Nd:YAG (1.5%)	18	Side-pumped cylindrical rod; external mirrors, 0.5% output; pump reflector	$GaAs_{1-x}P_x$ LED array	77	cw	~30	5
(5) Nd:YAG (1.5%)	19	Side-pumped cylindrical rod; polished mirrors, 0.4% output; elliptical pump reflector	$GaAs_{1-x}P_x$ LED array	270 150	cw cw	300 75	-- --
(6) Nd:YAG (1%)	20	Same as (5)	$GaAs_{0.85}P_{0.15}$ LED array	273 293	1 ms 1 ms	550 650	3.5 0.95
(7) Nd:YAG (1%)	21	End-pumped cylindrical rod; polished mirrors, HR output reflector	Single dome $GaAs_{1-x}P_x$ LED	300	2% (2 ms)	19	--
(8) Nd:YAG (1%)	22	Same as (7)	Same as (7)	88 300	2% (2ms) 98% (98ms)	6.2 6.2 19 (calculated)	0.2 0.09
(9) Nd:YAG (1%)	23	Side-pumped cylindrical rod; polished mirrors, 0.2% output; pump reflector with index-matching cylinder	$Ga_xAl_{1-x}As$ LED array	273	1% (500 μs) cw	~200 ~150	~7.5 ~5.5
(10) Nd:YAG	24	Side-pumped cylindrical rod; polished mirrors, 3% output; pump reflector	GaAs laser diode array	175	1.75% (500 ns)	1000	5.5

[a]Present work.

graded-index rods which simulate spherical mirrors [27]. Using a semiconfocal resonator should give optimum mode volume, stability, and ease of alignment. Since we have demonstrated the feasibility of efficient transverse pumping of NdPP platelets 36 μm thick, resembling thin-film or waveguide lasers, techniques such as distributed feedback might be considered for making an optical resonator compatible with planar, integrated optical circuits. The problems of NdPP crystal growth and device fabrication techniques still deserve much attention, but in view of the short time that this material has been studied for laser applications, present results are quite promising. Our present growth technique has yielded striation-free single domain perfect crystals up to 1 mm × 1 mm × 4 mm in size (this sample was used for the efficiency and loss measurements described in the preceding. The only polishing we have carried out has been for reducing the sample thickness in a side-pumped sample, with no degradation of the perpendicular lasing facets. Introduction of differently oriented domains [6], [28] can be a problem in polishing, but if no permanent defects are introduced, the domain walls should be removable by application of stress and/or heating above the monoclinic-orthorhombic phase transition temperature, 115°C [29]. Epitaxial growth of NdPP will probably be quite difficult, since few materials (except other pentaphosphates) can withstand the hot phosphoric acid growth melt. Nevertheless, NdPP lasers may still find applications in integrated optical circuits as thin hybrid elements added to a monolithic circuit containing other components, including diode excitation sources. Whether integrated or not, such small, efficient lasers should be useful as sources in fiber-optic communication systems and other areas requiring low-power lasers having mode quality and spectral output better than presently available semiconductor lasers. As past work has demonstrated [5], [30], (NdLa)PP may also offer many of the advantages of pure NdPP. With (NdLa)PP, a compromise between improved lifetime and lower resonant loss versus larger device size could be reached, depending on the particular desired properties and intended application.

In summary, we have obtained low-threshold operation of NdPP lasers transversely pumped at 0.58-μm wavelength with a CW dye laser. From a theoretical analysis of the data for threshold as a function of wavelength, we conclude that low-threshold operation at room temperature should also be possible with 0.8-μm excitation. For our example, a crystal 760 μm long (using 0.3-percent output mirror transmission), we predict quasi-CW transverse excitation thresholds at 0.8 μm of 4.4 mW and 8.5 mW, respectively, for 30-Å bandwidth (laser diode) and 300-Å bandwidth (LED) pumps in a very convenient, contact configuration. If quasi-CW sources are not available, short-pulsed sources having these average powers

should also be suitable. Using thin samples with back reflectors should lower these thresholds by ~60 percent. For designs with good heat-sinking, CW optical conversion efficiencies better than 3.5 percent should be possible with 0.8-μm 300-Å bandwidth excitation.

Acknowledgment

The authors wish to thank E. J. Delaney for assisting with the NdPP crystal growth, P. Moulton for help with the optical absorption measurements, and T. Lind for expert sample polishing. They also wish to thank A. J. Strauss for helpful comments and suggestions in preparing this paper.

References

[1] H. P. Weber, T. C. Damen, H. G. Danielmeyer, and B. C. Tofield, "Nd-ultraphosphate laser," *Appl. Phys. Lett.*, vol. 22, pp. 534–536, 1973.

[2] H. G. Danielmeyer, G. Huber, W. W. Krühler, and J. P. Jeser, "Continuous oscillation of a (Sc, Nd) pentaphosphate laser with 4 milliwatts pump threshold," *Appl. Phys.*, vol. 2, pp. 335–338, 1973.

[3] H. G. Danielmeyer and H. P. Weber, "Fluorescence in neodymium ultraphosphate," *IEEE J. Quantum Electron.*, vol. QE-8, pp. 805–808, 1972.

[4] H. P. Weber, P. F. Liao, and B. C. Tofield, "Emission cross section and fluorescence efficiency of Nd-pentaphosphate," *IEEE J. Quantum Electron.*, vol. QE-10, pp. 563–567, July 1974.

[5] S. Singh, D. C. Miller, J. R. Potopowicz, and L. K. Shick, "Emission cross section and fluorescence quenching of Nd^{3+} lanthanum pentaphosphate," *J. Appl. Phys.*, vol. 46, pp. 1191–1196, 1975.

[6] G. Huber, W. W. Krühler, W. Bludau, and H. G. Danielmeyer, "Anisotropy in the laser performance of NdP_5O_{14}," to be published.

[7] T. Kushida, H. M. Marcos, and J. E. Geusic, "Laser transition cross section and fluorescence branching ratio for Nd^{3+} in yttrium aluminum garnet," *Phys. Rev.*, vol. 167, pp. 289–291, 1968.

[8] H. G. Danielmeyer, M. Blätte, and P. Balmer, "Fluorescence quenching in Nd:YAG," *Appl. Phys.*, vol. 1, pp. 269–274, 1973.

[9] S. Singh, R. G. Smith, and L. G. Van Uitert, "Stimulated-emission cross section and fluorescent quantum efficiency of Nd^{3+} in yttrium aluminum garnet at room temperature," *Phys. Rev.*, vol. B10, pp. 2566–2572, 1974.

[10] D. B. Keck, P. C. Schultz, and F. Zimar, "Attenuation of multimode glass optical waveguides," *Appl. Phys. Lett.*, vol. 21, pp. 215–217, 1972.

[11] W. G. French, A. D. Pearson, G. W. Tasher, and J. B. MacChesney, "Low-loss fused silica optical waveguide with borosilicate cladding," *Appl. Phys. Lett.*, vol. 23, pp. 338–339, 1973.

[12] H. G. Danielmeyer, J. P. Jeser, E. Schönherr, and W. Stetter, "The growth of laser quality NdP_5O_{14} crystals," *J. Crystal Growth*, vol. 22, pp. 298–302, 1974.

[13] H. Y.-P. Hong, "Crystal structures of neodymium metaphosphate (NdP_3O_9) and ultraphosphate (NdP_5O_{14})," *Acta Crystallogr.*, vol. B30, pp. 468–474, 1974.

[14] M. Ettenberg, K. C. Hudson, and H. F. Lockwood, "High-radiance light-emitting diodes," *IEEE J. Quantum Electron.*, vol. QE-9, pp. 987–991, Oct. 1973.

[15] a) J. M. Hammer *et al.*, "Efficient modulation and coupling of CW junction laser light using electrooptic waveguides," *Proc. IEEE* (Lett.), pp. 325–326, Feb. 1975.
b) I. Ladany and H. Kressel, "The influence of device fabrication parameters on the gradual degradation of (AlGa)As CW laser diodes," *Appl. Phys. Lett.*, vol. 25, pp. 708–710, 1974.

[16] M. Blätte, H. G. Danielmeyer, and P. Ulrich, "Energy transfer and the complete level system of NdUP," *Appl. Phys.*, vol. 1, pp. 275–278, 1973.

[17] See, for example, the discussion in: A. E. Siegman, *An Introduction to Lasers and Masers*. New York: McGraw-Hill, 1971, pp. 431–437.

[18] R. B. Allen and S. J. Scalise, "Continuous operation of a YAlG:Nd laser by injection luminescent pumping," *Appl. Phys. Lett.*, vol. 14, pp. 188–190, 1969.

[19] F. W. Ostermayer, Jr., "$GaAs_{1-x}P_x$ diode pumped YAG:Nd lasers," *Appl. Phys. Lett.*, vol. 18, pp. 93–96, 1971.

[20] F. W. Ostermayer, Jr., R. B. Allen, and E. G. Dierschke, "Room-temperature CW operation of a $GaAs_{1-x}P_x$ diode-pumped YAG:Nd laser," *Appl. Phys. Lett.*, vol. 19, pp. 287–292, 1971.

[21] R. B. Chesler and D. A. Draegert, "Miniature diode-pumped Nd:YAIG lasers," *Appl. Phys. Lett.*, vol. 23, pp. 235–236, 1973.

[22] D. A. Draegert, "Single-diode end-pumped Nd:YAG laser," *IEEE J. Quantum Electron.*, vol. QE-9, pp. 1146–1149, Dec. 1973.

[23] G. I. Farmer and Y. C. Kiang, "Low-current-density LED-pumped Nd:YAG laser using a solid cylindrical reflector," *J. Appl. Phys.*, vol. 45, pp. 1356–1371, 1974.

[24] L. C. Conant and C. W. Reno, "GaAs laser diode pumped Nd:YAG laser," *Appl. Opt.*, vol. 13, pp. 2457–2458, 1974.

[25] J. Stone and C. A. Burrus, "Neodymium-doped silica lasers in end-pumped fiber geometry," *Appl. Phys. Lett.*, vol. 23, pp. 388–389, 1973.

[26] C. A. Burrus and J. Stone, "Single-crystal fiber optical devices: A Nd:YAG fiber laser," *Appl. Phys. Lett.*, vol. 26, pp. 318–320, 1975.

[27] J. C. Vanderleeden, "Resonant cavities with mirrors made from graded-index rods," *J. Appl. Phys.*, vol. 45, pp. 201–208, 1974.

[28] K. R. Albrand *et al.*, "Crystal structure of the laser material NdP_5O_{14}," *Mater. Res. Bull.*, vol. 9, pp. 129–140, 1974.

[29] H. Schulz, K.-H. Thiemann, and J. Fenner, "The high-temperature phase of NdP_5O_{14}," *Mater. Res. Bull.*, vol. 9, pp. 1525–1530, 1974.

[30] T. C. Damen, H. P. Weber, and B. C. Tofield, "NdLa pentaphosphate laser performance," *Appl. Phys. Lett.*, vol. 23, pp. 519–520, 1973.

Critically Index-Matched Second-Harmonic Generation in Multiple Crystals

F. M. LIBRECHT, STUDENT MEMBER, IEEE, AND G. E. FRANÇOIS

Abstract—A new method is presented for reducing the conversion-limiting effects of crystal anisotropy in critically index-matched second-harmonic generation (SHG). A number of crystals are put in series; adjacent crystals are oriented in such a way that their walkoff effects are opposite one another. The harmonic field and the harmonic power of a compensated two-crystal generator are calculated. Numerically computed curves show the dependence of the SH power on the mismatching of the crystals and on the focusing of a TEM_{00} laser beam. Theoretically predicted results are confirmed by experiment. As a typical result, the conversion efficiency of a compensated ADP generator (2 crystals, 1 cm each, in series) at optimum focusing is about twice the efficiency obtained with a single crystal of the same total length (2 cm, single crystal).

I. Introduction

THE second-harmonic generation (SHG) of coherent light in uniaxial nonlinear crystals has been studied extensively. Boyd and Kleinman [1] pointed out that the maximum conversion efficiency occurs when the angle of double refraction is zero. This condition is met by temperature tuning and occurs when the harmonic beam index matches the fundamental beam at 90° to the optic axis [2]. Commonly referred to as noncritical index matching, this type of matching is generally preferred to the critical index matching (angle tuning) for its higher harmonic conversion efficiency. Due to the thermal properties of the nonlinear material, there is for each type of harmonic generator a limited range of wavelengths that can be covered by temperature tuning. Outside of this range a critical matching technique with its lower conversion efficiency is required.

In this paper we show that the limitation of the conversion efficiency in critical index matching can be reduced by putting a number of crystals in series. Each crystal is critically index matched; any two adjacent crystals are oriented in such a way that their walkoff effects are opposite one another. Crystals in series were used in previous SHG studies [3]-[6], but never for the purpose of compensating for the walkoff effect at critical index matching.

In the following paragraphs we calculate the harmonic field and the harmonic power of a two-crystal harmonic generator put in the focus of a TEM_{00} laser beam. The crystals are assumed to belong to the XDP group; the calculations, however, can be adapted easily for other crystal classes. Theoretically predicted results on the effects of mismatching in the crystals and on the effects of focusing of the laser beam are confirmed by experiment.

Manuscript received January 24, 1975; revised May 15, 1975.

The authors are with the Catholic University of Leuven, Leuven, Belgium.

II. Harmonic Field and Harmonic Power of a Two-Crystal Harmonic Generator

Consider two ADP crystals of length $l/2$ in the focus of a Gaussian laser beam in the TEM_{00} mode (Fig. 1). The fundamental beam diameter at the beam waist is $2w_0$ ($1/e^2$ surface). The fundamental beam at frequency ω (wavelength = 632.8 nm) is introduced in each crystal as an ordinary wave index matched to the extraordinary second-harmonic wave (Type 1 index matching [7]). The input and output faces of each crystal are parallel. They are cut so that at approximately normal incidence the laser beam passes through the crystal in the critical index-matching direction z at an angle θ_m to the optic axis. The optic axis lies in the xz-plane. ρ is the angle of double refraction. The crystals are oriented in such a way that their walkoff effects are opposite one another. The origin $x = y = z = 0$ of the right-hand xyz-reference system is in the center of the nonlinear material. The medium surrounding the crystals is supposed to have the same refractive index as the crystal index at critical matching. Throughout the calculations we neglect the weak absorption at the fundamental and harmonic frequencies. We also neglect the depletion of the fundamental beam by the doubling process.

The description of the laser beam focused inside the harmonic generator is a straightforward problem since the beam is an ordinary wave and the crystal appears to it as an isotropic medium. We use Fourier analysis to decompose the fundamental beam into a sum of plane waves. The harmonic field generated in the first crystal is obtained from a well-known formal approach outlined by Boyd *et al.* [8] and applied by Bjorkholm [9]. This field propagates in the second crystal as an extraordinary wave. We assume that this extraordinary wave does not affect the harmonic generating process in the second crystal. So once more we use the formal theory of [9] to calculate the harmonic field generated in this second crystal.

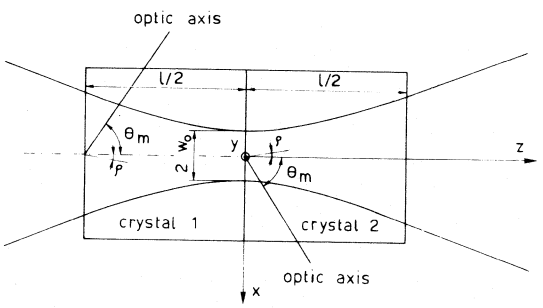

Fig. 1. Orientation of the ADP crystals of a compensated two-crystal harmonic generator in the focus of a TEM_{00} laser beam (wavelength = 632.8 nm). θ_m is the index-matching angle; ρ is the angle of double refraction.

The total harmonic field of the two-crystal generator is obtained by summing the harmonic contributions of the two crystals at the exit face of the second crystal. These harmonic contributions are individually described by an expression similar to [9, eq. (27)]. When the two crystals are tilted away from the index-matching direction by an angle Φ, Φ', respectively, we account for this by introducing additional mismatch terms (as defined in [9, eq. (54)]). Eventually, the total harmonic field at the exit face of the second crystal is written as follows:

$$E_{2\omega}(x, y, z = l/2) = E_{2\omega} \exp(ikl) \frac{\xi}{1 + i\xi} (I_p + I_q) \tag{1}$$

where

$$\xi = \frac{l}{b} \tag{2}$$

with b the confocal parameter ($b = kw_0^2$). The constant $E_{2\omega}$ has been defined by Bjorkholm [9]. It depends on the parameters of both the crystal and the laser beam. k is the propagation constant of the fundamental beam. I_p and I_q are integral expressions related to [9, eq. (27)]. They give the harmonic contributions at $z = l/2$ of the first and the second crystal, respectively.

$$I_p = \exp(-ik\rho\Phi' l) \cdot \int_0^1 \frac{\exp(-ipk\rho\Phi l) \exp\left[\dfrac{-2k[y^2 + (x - p\rho l/2 + \rho l/2)^2]}{b(1 + i\xi)}\right]}{-ipl/2 + b/2} dp \tag{3}$$

$$I_q = \int_0^1 \frac{\exp(-iqk\rho\Phi' l) \exp\left[\dfrac{-2k[y^2 + (x + q\rho l/2)^2]}{b(1 + i\xi)}\right]}{-iql/2 + b/2 + il/2} dq. \tag{4}$$

The difference between (3) and (4) arises from the fact that the harmonic contribution of the first crystal propagates in the second one as an extraordinary wave. The signs in front of the terms $pp l/2$ and $q\rho l/2$ in the second exponent of the integrands of (3) and (4), respectively, are determined by the orientation of the crystal optic axis with respect to the reference system. As the crystals are oriented in such a way that their walkoff effects are opposite (Fig. 1), the signs in front of the terms $pp l/2$ and $q\rho l/2$ are opposite too. The phase factor in front of the integral in (3) is a result of the mismatch Φ' in the second crystal.

Evaluating the harmonic field (1) in the far field outside the harmonic generator, greatly simplifies the calculation of the SH power $P_{2\omega}$, [1]. According to [1, eq. (2.13)], we transform the x- and y-coordinates into the variables s and s', and we define a parameter β. The SH power then reads

$$P_{2\omega} = KP_\omega^2 \frac{l^2\pi^2}{w_0^2\xi^2} F(\Phi, \Phi', \beta, \xi) \tag{5}$$

where

$$F(\Phi, \Phi', \beta, \xi) = \frac{2}{\pi^{1/2}} \int_{-\infty}^{+\infty} \exp(-4s^2) |H(s, \Phi, \Phi', \beta, \xi)|^2 \, ds \tag{6}$$

and

$$H(s, \Phi, \Phi', \beta, \xi) = \frac{\xi}{2\pi}\left[\int_0^1 \frac{\exp(-ik\rho\Phi lp) \exp(-4i\beta s\xi p)}{1 - i\xi p} dp + \int_0^1 \frac{\exp[-ik\rho\Phi' l(1 - q)] \exp[-4i\beta s\xi(1 - q)]}{1 + i\xi(1 - q)} dq\right]. \tag{7}$$

The definitions of H, K, and F are essentially the same as those given by [1, eqs. (2.16), (2.20), and (2.24)]. P_ω is the power at the fundamental frequency. From (5)-(7), and after integration with respect to s, the harmonic power can be written as a sum of four double integrations, each of them in a form like [9, eq. (32)] or [1, eq. (2.25)].

III. Theoretical and Experimental Study of the Harmonic Power as a Function of the Mismatching in the Crystals

In the weak focusing limit ($\xi << 1$), we have calculated $\pi^2 F(\Phi, \Phi', \beta, \xi)/\xi^2$ from (5) numerically as a function of the mismatch X_2 ($X_2 = k\rho l\Phi'$) in the second crystal at different values of the mismatch X_1 ($X_1 = k\rho l\Phi$) in the first crystal.

We have used Gaussian-Hermite quadrature formulas [10]. The results for $X_1 = 0$ and $X_1 = 1$ are given in Fig. 2. The maximum conversion efficiency occurs at nominal index matching ($X_1 = X_2 = 0$) in both crystals. The curve for $X_1 = 0$ is fully symmetric. A mismatch ($X_1 = 1$) in the first crystal

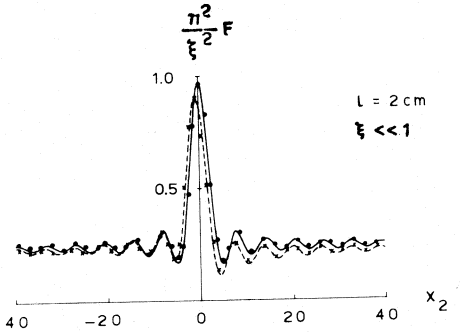

Fig. 2. Theoretical curves and experimental values of the SHG factor $\pi^2 F/\xi^2$, (5) in the weak focusing limit ($\xi << 1$, (2)) as a function of the mismatch X_2 in the second crystal at a given value of the mismatch X_1 in the first crystal: $X_1 = 0$, (solid line, dots); $X_1 = 1$, (dashed line, crosses). Total length l of nonlinear material: 2 cm.

results in an asymmetric curve and in a decrease of the maximum conversion efficiency.

In the experimental setup the first crystal is mounted in a gimbal; the second sits on a motor-driven rotating disk. An adjustable air gap remains between the crystals. Each crystal can be angle-tuned independently. Moreover, both crystals are provided with gold electrodes to fine tune the index-matching condition by means of the electrooptic effect.

The reflection and refraction effects at the crystal surfaces and the dispersion in the air gap between the crystals affect the expressions (5)-(7). Due to the air dispersion, a phase shift builds up between the harmonic wave and the square of the fundamental wave giving rise to a phase factor in front of the first integration of (7). In the weak focusing limit ($\xi \ll 1$), we have mounted the crystals at about 26 mm of each other to obtain a 2π phase shift, as can be derived from air refractive-index data [11]. On the other hand, tedious but straightforward calculations reveal that the reflection and refraction effects at the crystal surfaces do not affect the shape of the harmonic curve. Fig. 2 shows a close agreement between the experimental results and the theoretically predicted curves. The peak power in the experiment was arbitrarily taken to coincide with the theoretical peak.

At the point $\xi = 1$ (nearly optimal focusing) we have calculated the same curve: $\pi^2 F(\Phi, \Phi', \beta, \xi)/\xi^2$ as a function of the mismatch X_2 ($X_2 = k\rho l\Phi'$) in the second crystal. We have used an algorithm for automatic integration, based on the Gaussian and Kronrod quadrature formulas [12]. The results are given in Fig. 3. At nominal matching in the first crystal ($X_1 = 0$), the maximum efficiency occurs at a slight mismatch in the second crystal. A mismatch in the first crystal ($X_1 = 1$) shifts the maximum to other X_2 values. The amplitude of this maximum, however, does not change.

In the experimental setup the separation between the crystals is about 1 mm, resulting in a phase shift of $\pi/12$ between the harmonic wave and the square of the fundamental wave. As can be calculated from (5)-(7) this phase shift gives rise to a negligible additional asymmetry in the harmonic curve. The experimental results for $X_1 = 0$ are also shown in Fig. 3. Some quantitatively measurable features such as the peak width at half height and the ratio of the peak value to the value at X_2 values in excess of 30 are in good agreement. The overall agreement in the structure of the side maxima, however, is rather poor.

IV. Theoretical and Experimental Study of the Harmonic Power as a Function of the Focusing of the Laser Beam

We have calculated asymptotic and exact values of the harmonic power as a function of the focusing of the laser beam. The asymptotic values are listed in Table I. For comparison, the asymptotic values of a single crystal are listed in the same table.

In Fig. 4 the asymptotic solutions for a compensated two-crystal generator (2 ADP crystals, 1 cm each, in series) and for a single crystal (ADP, 2 cm) are shown on a log-log plot. This same figure also shows exact curves of the relative harmonic power $P_{2\omega}/KP_\omega^2$ calculated by Gaussian-Kronrod quadrature formulas [12]. At nearly optimal focusing, the conversion efficiency of a compensated two-crystal generator is about

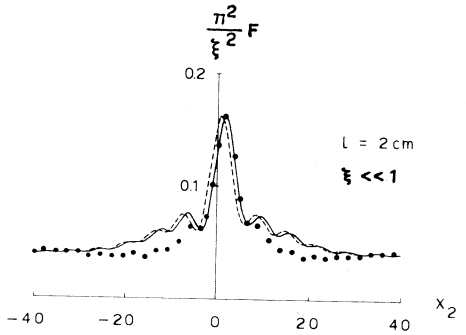

Fig. 3. Theoretical curves of the SHG factor $\pi^2 F/\xi^2$, (5) at nearly optimal focusing ($\xi = 1$, (2)) as a function of the mismatch X_2 in the second crystal at a given value of the mismatch X_1 in the first crystal: $X_1 = 0$, (solid line); $X_1 = 1$, (dashed line). Experimental results for $X_1 = 0$ are given by dots. Total length l of nonlinear material: 2 cm.

TABLE I
Harmonic Power of a Compensated Two-Crystal Harmonic Generator and of a Single Crystal of the Same Total Length

	Compensated Two-Crystal Generator	Single Crystal [1], [9]
$\xi \ll 1$ $\beta\xi \ll 1$	$P_{2\omega} = KP_\omega^2 (l^2/w_0^2)$	$P_{2\omega} = KP_\omega^2 (l^2/w_0^2)$
$\xi \ll 1$ $\beta\xi \gg 1$	$P_{2\omega} = KP_\omega^2 (l^2\pi^{1/2}/w_0^2\beta\xi)$	$P_{2\omega} = KP_\omega^2 (l^2\pi^{1/2}/2w_0^2\beta\xi)$
$\xi \gg 1$ $\beta \gg 1$	$P_{2\omega} = KP_\omega^2 [(1 + 2e^{-1}) l^2\pi^{3/2}/4w_0^2\beta\xi^2]$	$P_{2\omega} = KP_\omega^2 (l^2\pi^{3/2}/4w_0^2\beta\xi^2)$

Note: Asymptotic values.

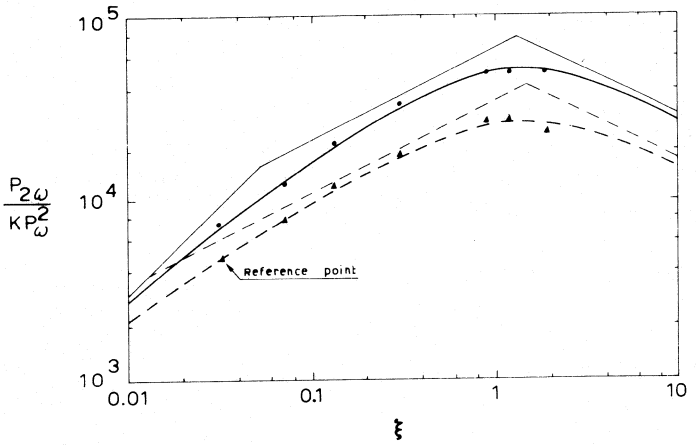

Fig. 4. Harmonic power as a function of focusing. Asymptotic and exact curves. Solid lines: 2 ADP crystals of 1 cm each in a compensated setup. Dashed lines: single ADP crystal of 2 cm. Dots: experimental values for a compensated, two-crystal generator (2 × 1 cm). Triangles: experimental values for a single crystal (1 × 2 cm). The reference point shown was chosen to coincide with the corresponding theoretical curve.

twice the efficiency obtained with a single crystal of the same total length.

The experimental results shown in Fig. 4 were obtained with an air gap in between the crystals of only 0.5 mm. The resulting phase shift of the harmonic wave with respect to the square of the fundamental wave was neglected. We have used a set of achromatic compound lenses ranging in focal length from 80 to 600 mm to vary the focusing parameter ξ. The power level at weak focusing ($\xi = 0.032$) in a single crystal was taken as a reference.

V. Multiple-Crystal Harmonic Generator

Increasing the number of crystals in a compensated arrangement, while keeping the total length of the harmonic generator constant, will further increase the peak doubling efficiency, as long as each crystal exceeds greatly the critical double-refraction length l_b, defined in [9, eq. (48)]. When the number of crystals increases to the point where each individual crystal is equal to or shorter than l_b, the doubling efficiency reaches a limit. This limit will take on the same value as for the noncritical index matching.

VI. Summary

In this paper, we have proposed a new method for reducing the conversion-limiting effects of crystal anisotropy in critically index-matched SHG by putting a number of crystals in series. Adjacent crystals have been oriented in such a way that their walkoff effects were opposite one another. The theoretically predicted doubling properties of a compensated two-crystal generator have been confirmed by experiment.

References

[1] G. D. Boyd and D. A. Kleinman, "Parametric interaction of focused Gaussian light beams," *J. Appl. Phys.*, vol. 39, pp. 3597–3639, July 1968.

[2] R. C. Miller, G. D. Boyd, and A. Savage, "Nonlinear optical interactions in $LiNbO_3$ without double refraction," *Appl. Phys. Lett.*, vol. 6, pp. 77–79, Feb. 1965.

[3] R. K. Chang, J. Ducuing, and N. Bloembergen, "Relative phase measurement between fundamental and second-harmonic light," *Phys. Rev. Lett.*, vol. 15, pp. 6–8, July 1965.

[4] N. J. Simon and N. Bloembergen, "Second-harmonic light generation in crystals with natural optical activity," *Phys. Rev.*, vol. 171, pp. 1104–1114, July 1968.

[5] J. J. Wynne and N. Bloembergen, "Measurement of the lowest-order nonlinear susceptibility in III–V semiconductors by second-harmonic generation with a CO_2 laser," *Phys. Rev.*, vol. 188, pp. 1211–1220, Dec. 1969.

[6] R. C. Miller and W. A. Nordland, "Absolute signs of nonlinear optical coefficients of polar crystals," *Opt. Commun.*, vol. 1, pp. 400–402, Mar. 1970.

[7] J. E. Midwinter and J. Warner, "The effects of phase matching method and of uniaxial crystal symmetry on the polar distribution of second-order nonlinear optical polarization," *Brit. J. Appl. Phys.*, vol. 16, pp. 1135–1142, Aug. 1965.

[8] G. D. Boyd, A. Ashkin, J. M. Dziedzic, and D. A. Kleinman, "Second harmonic generation of light with double refraction," *Phys. Rev.*, vol. 137, pp. A1305–A1320, Feb. 1965.

[9] J. E. Bjorkholm, "Optical second-harmonic generation using a focused Gaussian laser beam," *Phys. Rev.*, vol. 142, pp. 126–136, Feb. 1966.

[10] M. Abramowitz and I. A. Stegun, *Handbook of Mathematical Functions*. New York: Dover, 1965, p. 890.

[11] F. T. Arecchi and E. O. Schulz-Dubois, *Laser Handbook*. Amsterdam, The Netherlands: North-Holland, 1972, pp. 1479–1483.

[12] R. Piessens, "An algorithm for automatic integration," Appl. Math. Program. Div., Catholic Univ. Leuven, Leuven, Belgium, Rep. TW 13, Apr. 1973.

Electrooptic Coupling Between TE and TM Modes in Anisotropic Slabs

D. MARCUSE, FELLOW, IEEE

Abstract—**In an electrooptic crystal TE and TM modes can be coupled by application of a modulation voltage. Two types of modulators using anisotropic crystals are discussed. In the first type a voltage that is constant along the direction of wave propagation couples a guided mode to a radiation mode of the orthogonal polarization so that the radiation loss of the guided mode can be controlled by the applied voltage. The modulator of the second type uses voltage-controlled coupling between guided TE and TM modes. The computation of the coupling coefficients is outlined and numerical examples are plotted for $LiNbO_3$ and $LiTaO_3$ crystals.**

Introduction

CERTAIN electrooptic crystals are suitable for the fabrication of thin-film waveguides by diffusion methods [1]-[3]. Thin-film waveguides have been made by out-diffusion [1] as well as by in-diffusion [2], [3] of metal ions in $LiNbO_3$ and $LiTaO_3$. These crystals do not only have large electrooptic coefficients but they also are anisotropic. This anisotropy can be utilized to achieve phase matching between two modes coupled by the electrooptic effect without the need for imposing a periodicity on the coupling process. For example, it is possible to couple a guided TM mode to a TE radiation mode in $LiNbO_3$. The refractive indices of this material are for the ordinary index at $\lambda = 0.6328\ \mu m$ [4]

$$n_{o2} = 2.28 \tag{1}$$

and for the extraordinary index

$$n_{e2} = 2.17. \tag{2}$$

It has been demonstrated that doping may increase these indices to the following larger values in the guiding layer [1]:

$$n_{o1} = 2.29 \tag{3}$$

and

$$n_{e1} = 2.21. \tag{4}$$

Fig. 1 shows the possible values of the propagation constants β of the guided and radiation modes if the optical axis of the crystal is directed normal to its surface. The guided modes, one of which is indicated schematically in Fig. 1, have propagation constants whose values are bracketed by the plane-wave propagation constant $n_2 k$ of the substrate and the plane-wave propagation constant $n_1 k$ of the guiding layer. The radiation modes have propagation constants that are less than $n_2 k$ [5], [6]. If the guided TM mode is coupled to TE modes without the use of a periodic structure, phase matching requires that

Manuscript received February 4, 1975.
The author is with Bell Laboratories, Crawford Hill Laboratory, Holmdel, N.J. 07733.

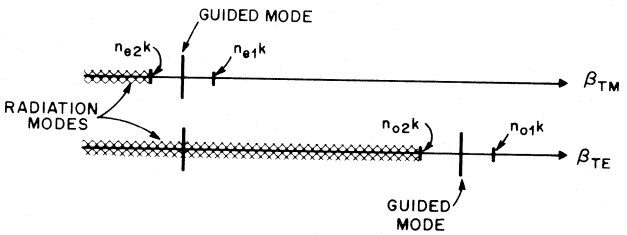

Fig. 1. This diagram shows the ranges of guided and radiation modes for TE and TM polarization for the case of $LiNbO_3$.

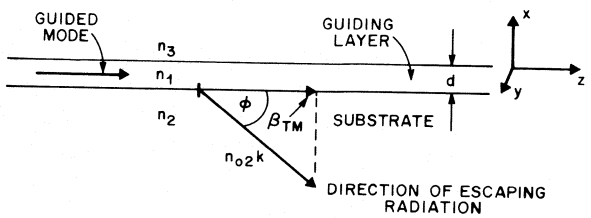

Fig. 2. Schematic of the asymmetric slab waveguide showing the angle at which radiation escapes into the substrate.

such coupling can occur only to a TE radiation mode whose propagation constant equals that of the guided TM mode. The angle at which the resulting radiation escapes into the substrate is given by [5], [6]

$$\cos\phi = \frac{\beta}{n_{o2}k} \tag{5}$$

with $\beta = \beta_{TM}$ as shown in Fig. 2. Coupling between the guided TM and TE radiation modes is caused by a change in the refractive index tensor induced by a dc electric field.

Coupling between a guided TM and guided TE mode is possible if the coupling coefficient is a periodic function whose periodicity, with spatial frequency θ, satisfies the relation [5], [6]

$$\theta = \beta_{TE} - \beta_{TM}. \tag{6}$$

In $LiTaO_3$ the situation is reversed because in this crystal the extraordinary refractive index n_e is larger than the ordinary index n_o

$$n_{o2} = 2.183$$

and

$$n_{e2} = 2.188. \tag{7a}$$

Doping may increase these indices to the following values in the guiding layer:

$$n_{o1} = 2.193$$

and

$$n_{e1} = 2.198. \tag{7b}$$

Fig. 3 shows a schematic diagram for this case. It is again assumed that the optical axis of the crystal is directed normal to its surface. Because the TE mode "senses" the ordinary refractive index the propagation constant of a guided TE mode can be matched to a TM radiation mode if

$$\beta_{TE} < n_{e2}k. \tag{8}$$

The radiation angle in the substrate is determined by the direction of power flow

$$\cos\phi = \frac{\beta}{(n_{e2}/n_{o2})\{n_{e2}^2k^2 + [(n_{o2}^2/n_{e2}^2) - 1]\,\beta^2\}^{1/2}} \tag{9}$$

with $\beta = \beta_{TE}$. The direction of power flow is not exactly perpendicular to the phase fronts for TM modes in this anisotropic crystal. The angle of escaping radiation is much smaller for the $LiTaO_3$ case. Coupling between guided TE and guided TM modes requires a periodic coupling process since an accidental overlap of a TE mode and a TM mode would involve modes of different symmetry whose coupling efficiency would be small. However, the period of the periodic coupling process can be much larger than in $LiNbO_3$ which is advantageous for the fabrication of electrodes.

The principal objective of this paper is the derivation of coupling coefficients for electrooptic coupling between TE and TM modes of anisotropic slab waveguides. These coupling coefficients are used to estimate the coupling efficiency for guided mode coupling to radiation into the substrate of the crystal and for the power exchange between guided modes. The field expressions for TE modes are the same as those of isotropic waveguides if the optical axis of the crystal is oriented perpendicular to the surface of the crystal. However, TM modes are different from those of isotropic guides. Expressions for the guided and radiation modes of TM polarization are presented.

Modes of the Anisotropic Slab

We consider a slab waveguide consisting of a thin film on a substrate. This waveguide is used as a model for integrated optics guides produced by diffusion of dopants into anisotropic crystals. The refractive index distributions of diffused guides do not have the step profile assumed here for simplicity. However, the asymmetric slab guide with piecewise constant discontinuous index distribution may be regarded as a reasonable first approximation to the more complicated graded index slabs.

Further, we assume throughout this paper that the optical axis of the uniaxial anisotropic crystal is oriented perpendicular to the guiding layer. The ordinary refractive index is "sensed" by electric-field components perpendicular to the optical axis. This means that electric-field components in the plane of the film are affected by the ordinary refractive index. The extraordinary refractive index, on the other hand, affects electric-field components parallel to the optical axis or, in our case, perpendicular to the plane of the film. TE modes in slab waveguides have only one electric-field component in the plane of the film perpendicular to their direction of propagation. TE modes are thus only affected by the ordinary refractive index and have the same field expressions as TE modes in isotropic slab waveguides. TM modes have electric-field components in the plane of the film and perpendicular to it. These fields are affected by the ordinary as well as the extraordinary refractive indices and are thus different from TM modes in isotropic slabs.

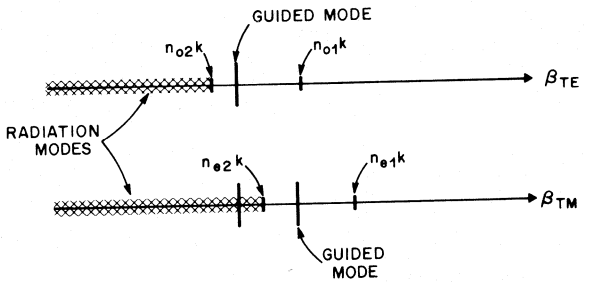

Fig. 3. This figure is similar to Fig. 1 but applies to the $LiTaO_3$ case.

The TE modes of the slab waveguide are well known [6]. Their H_x and H_z components are obtained from the E_y component by differentiation (the orientation of the coordinate system is shown in Fig. 2)

$$H_x = \frac{-i}{\omega\mu_0}\frac{\partial E_y}{\partial z} = \frac{-\beta}{\omega\mu_0}E_y \tag{10}$$

and

$$H_z = \frac{i}{\omega\mu_0}\frac{\partial E_y}{\partial x}. \tag{11}$$

The time dependence of the fields is assumed to be given by the function

$$\exp(i\omega t) \tag{12}$$

and μ_0 is the magnetic permeability of vacuum.

The E_y component of guided TE modes has the form

$$E_y = \begin{cases} A_g \exp(-\delta_e x), & \text{for } x \geqslant 0 \\ A_g\left(\cos\kappa_e x - \dfrac{\delta_e}{\kappa_e}\sin\kappa_e x\right), & \text{for } 0 \geqslant x \geqslant -d \\ A_g\left(\cos\kappa_e d + \dfrac{\delta_e}{\kappa_e}\sin\kappa_e d\right)\exp[\gamma_e(x+d)], & \text{for } x \leqslant -d. \end{cases} \tag{13}$$

The factor

$$\exp[i(\omega t - \beta z)] \tag{14}$$

($\beta = \beta_g$ for guided modes) is omitted from all the field equations for simplicity. The parameters appearing in (13) are defined as follows:

$$\kappa_e = (n_{o1}^2k^2 - \beta_{ge}^2)^{1/2} \tag{15}$$

$$\gamma_e = (\beta_{ge}^2 - n_{o2}^2k^2)^{1/2} \tag{16}$$

and

$$\delta_e = (\beta_{ge}^2 - n_{o3}^2k^2)^{1/2} \tag{17}$$

with

$$k = \omega\sqrt{\epsilon_0\mu_0} \tag{18}$$

(ϵ_0 is the dielectric permittivity of vacuum). The parameters (15)-(17) are not independent but must obey the eigenvalue equation

$$\tan \kappa_e d = \frac{\kappa_e(\gamma_e + \delta_e)}{\kappa_e^2 - \gamma_e\delta_e} \tag{19}$$

(d = film thickness). The mode fields are normalized with respect to a power parameter P that is chosen to be the same for all modes

$$A_g = \left\{\frac{4\omega\mu_0\kappa_e^2 P}{|\beta_{ge}|\left(d + \frac{1}{\gamma_e} + \frac{1}{\delta_e}\right)(\kappa_e^2 + \delta_e^2)}\right\}^{1/2}. \tag{20}$$

There are two types of radiation modes [6]. Modes of the first type show a standing-wave pattern in the substrate but have an exponential field decay in the region above the film provided we assume

$$n_{o1} > n_{o2} > n_{o3}. \tag{21}$$

These are the radiation modes of interest to us. There are modes of the second kind that have standing-wave patterns in the substrate as well as in the space above the film. The propagation constants of the modes of the second type obey the inequality

$$|\beta| < n_{o3}k. \tag{22}$$

These modes cannot be excited by constant electrooptic coupling since the phase-matching condition (6) requires a periodicity of the coupling process to couple guided modes to radiation modes in the range (22). Consequently, we limit our attention to radiation modes of the first kind whose propagation constants form a continuum in the range

$$n_3k < \beta < n_2k. \tag{23}$$

The E_y component of these radiation modes is given by

$$E_y = \begin{cases} A_r \exp(-\Delta_e x), & \text{for } x \geq 0 \\ A_r\left(\cos\sigma_e x - \frac{\Delta_e}{\sigma_e}\sin\sigma_e x\right), & \text{for } 0 \geq x \geq -d \\ A_r\left[\left(\cos\sigma_e d + \frac{\Delta_e}{\sigma_e}\sin\sigma_e d\right)\cos\rho_e(x+d)\right. & \\ \left. + \frac{\sigma_e}{\rho_e}\left(\sin\sigma_e d - \frac{\Delta_e}{\sigma_e}\cos\sigma_e d\right)\sin\rho_e(x+d)\right], & \\ \text{for } x \leq -d. & \end{cases} \tag{24}$$

The parameters are defined as follows:

$$\sigma_e = (n_{o1}^2k^2 - \beta^2)^{1/2} \tag{25}$$

$$\rho_e = (n_{o2}^2k^2 - \beta^2)^{1/2} \tag{26}$$

$$\Delta_e = (\beta^2 - n_{o3}^2k^2)^{1/2}. \tag{27}$$

There is no restriction on the allowed values of β except for the inequality (23). The amplitude coefficient is related to the power normalizing factor by the equation

$$A_r = \left\{\frac{4\omega\mu_0\rho_e^2\sigma_e^2 P}{\pi\beta[\rho_e^2(\sigma_e\cos\sigma_e d + \Delta_e\sin\sigma_e d)^2 + \sigma_e^2(\sigma_e\sin\sigma_e d - \Delta_e\cos\sigma_e d)^2]}\right\}^{1/2} \tag{28}$$

The power normalization factor P has a different physical interpretation for guided and for radiation modes. For guided modes P represents the power actually carried by the mode (24). The power carried by one individual radiation mode is infinite. For radiation modes P is a factor (with the dimension of power) that multiplies the δ-function in the orthogonality relation of these modes [6].

As already mentioned, the field expressions for TM modes of anisotropic slabs are different from those of isotropic waveguides [7], [8]. The derivation is straightforward and leads to the results quoted in the following. Assuming, as always in the case of slabs, that there is no variation in the y direction we obtain the field components E_x and E_z from

$$E_x = \frac{\beta}{n_e^2\omega\epsilon_0}H_y \tag{29}$$

and

$$E_z = \frac{i}{n_o^2\omega\epsilon_0}\frac{\partial H_y}{\partial x}. \tag{30}$$

The H_y component must be a solution of the reduced wave equation

$$\frac{\partial^2 H_y}{\partial x^2} + \frac{n_o^2}{n_e^2}(n_e^2k^2 - \beta^2)H_y = 0. \tag{31}$$

The guided TM modes are now obtained from the following solution for the H_y component:

$$H_y = \begin{cases} B_g\exp(-\delta_m x), & \text{for } x \geq 0 \\ B_g\left(\cos\kappa_m x - n_{o1}^2\frac{\delta_m}{\kappa_m}\sin\kappa_m x\right), & \\ & \text{for } 0 \geq x \geq -d \\ B_g\left(\cos\kappa_m d + n_{o1}^2\frac{\delta_m}{\kappa_m}\sin\kappa_m d\right)\exp[\gamma_m(x+d)], & \\ & \text{for } x \leq -d \end{cases} \tag{32}$$

with

$$\kappa_m = \frac{n_{o1}}{n_{e1}}(n_{e1}^2k^2 - \beta_{gm}^2)^{1/2} \tag{33}$$

$$\gamma_m = \frac{n_{o2}}{n_{e2}}(\beta_{gm}^2 - n_{e2}^2k^2)^{1/2} \tag{34}$$

and

$$\delta_m = (\beta_{gm}^2 - k^2)^{1/2}. \tag{35}$$

It was assumed that the region above the film is air with $n_{o3} = n_{e3} = 1$. In the case where the region above the film is not air we can easily obtain the generalization for an isotropic medium by replacing k with $n_3 k$ and by replacing all refractive indices by the ratios n/n_3.

The tangential field components H_y and E_z must remain continuous at the dielectric interfaces at $x = 0$ and $x = -d$. These boundary conditions lead to the eigenvalue equation

$$\tan \kappa_m d = \frac{n_{o1}^2 \kappa_m (\gamma_m + n_{o2}^2 \delta_m)}{n_{o2}^2 \kappa^2 - n_{o1}^4 \gamma_m \delta_m}. \tag{36}$$

The power carried by the mode (per unit length in y direction) is given by the general expression

$$P = \frac{1}{2} \operatorname{Re} \int_{-\infty}^{\infty} (\boldsymbol{E} \times \boldsymbol{H}^*)_z \, dx = \frac{1}{2} \frac{\beta_{gm}}{\omega \epsilon_0} \int_{-\infty}^{\infty} \frac{1}{n_e^2} |H_y|^2 \, dx. \tag{37}$$

This equation is used to express the mode amplitude B_g in terms of P

$$B_g = \left\{ \frac{4\omega\epsilon_0 P}{\beta_{gm}} \frac{n_{e1}^2 \kappa_m^2}{\kappa_m^2 + n_{o1}^4 \delta_m^2} \cdot \left[d + \frac{n_{o2}^2}{\gamma_m} \frac{n_{o2}^2 (n_{e1}^2/n_{e2}^2) \kappa_m^2 + n_{o1}^2 \gamma_m^2}{n_{o2}^4 \kappa_m^2 + n_{o1}^4 \gamma_m^2} + \frac{1}{\delta_m} \frac{n_{e1}^2 \kappa_m^2 + n_{o1}^2 \delta_m^2}{\kappa_m^2 + n_{o1}^4 \delta_m^2} \right]^{-1} \right\}^{1/2}. \tag{38}$$

For the reasons explained in the preceding we need only the TM radiation modes of the first kind. Their electric-field components are derived from (29), (30), and from the H_y component

$$H_y = \begin{cases} B_r \exp(-\Delta_m x), & \text{for } x \geq 0 \\ B_r \left(\cos \sigma_m x - n_{o1}^2 \frac{\Delta_m}{\sigma_m} \sin \sigma_m x \right), & \text{for } 0 \geq x \geq -d \\ B_r \left[\left(\cos \sigma d + n_{o1}^2 \frac{\Delta_m}{\sigma_m} \sin \sigma_m d \right) \cos \rho_m (x + d) \right. & \\ \left. + \frac{n_{o2}^2}{n_{o1}^2} \frac{\sigma_m}{\rho_m} \left(\sin \sigma_m d - n_{o1}^2 \frac{\Delta_m}{\sigma_m} \cos \sigma_m d \right) \right. & \\ \left. \cdot \sin \rho_m (x + d) \right], & \text{for } x \leq -d \end{cases} \tag{39}$$

with

$$\sigma_m = \frac{n_{o1}}{n_{e1}} (n_{e1}^2 k^2 - \beta^2)^{1/2} \tag{40}$$

$$\rho_m = \frac{n_{o2}}{n_{e2}} (n_{e2}^2 k^2 - \beta^2)^{1/2} \tag{41}$$

and

$$\Delta_m = (\beta^2 - k^2)^{1/2}. \tag{42}$$

The amplitude coefficient is expressed as

$$B_r = \left\{ \frac{4 n_{e2}^2 \omega \epsilon_0 \sigma_m^2 \rho_m^2 P}{\pi \beta} \cdot \left[\sigma_m^2 \left(\frac{n_{o2}^2}{n_{o1}^2} \sigma_m \sin \sigma_m d - n_{o2}^2 \Delta_m \cos \sigma_m d \right)^2 + \rho_m^2 (\sigma_m \cos \sigma_m d + n_{o1}^2 \Delta_m \sin \sigma_m d)^2 \right]^{-1} \right\}^{1/2}. \tag{43}$$

Mode Coupling

Coupling between the modes of an anisotropic dielectric optical waveguide is described by coupled-mode theory. The coupling coefficients can be approximated in the following way [9]-[11]:

$$K_{\mu\nu} = \frac{\omega}{4iP} \int_{-\infty}^{\infty} \boldsymbol{E}_\mu^* \cdot (\epsilon - \bar{\epsilon}) \cdot \boldsymbol{E}_\nu \, dx \tag{44}$$

provided that the dielectric tensors ϵ and $\bar{\epsilon}$ deviate only slightly from the unit tensor (times the isotropic dielectric constant) and that the dielectric tensor ϵ of the actual waveguide is very nearly the same as the z independent dielectric tensor $\bar{\epsilon}$ of an ideal guide whose modes are $\boldsymbol{E}_\nu$.

If we apply to the $LiNbO_3$ or $LiTaO_3$ crystal a dc electric-field E_{dc} in y direction simultaneously with a light field polarized in x direction, we obtain an electric polarization P_y of the anisotropic material in y direction. Similarly, we obtain an electric polarization P_x in x direction from the combination of the dc field in y direction and a light field in y direction. These polarizations can be expressed as [4, p. 56, eq. (2)]

$$P_y = -n_o^2 n_e^2 \epsilon_0 r_{51} E_{dc} E_x \tag{45}$$

$$P_x = -n_o^2 n_e^2 \epsilon_0 r_{51} E_{dc} E_y. \tag{46}$$

The relation

$$\epsilon \cdot \boldsymbol{E} = \bar{\epsilon} \cdot \boldsymbol{E} + \boldsymbol{P} \tag{47}$$

allows us to define the tensor

$$\epsilon - \bar{\epsilon} = \begin{pmatrix} 0 & \Delta\epsilon & 0 \\ \Delta\epsilon & 0 & 0 \\ 0 & 0 & 0 \end{pmatrix} \tag{48}$$

with

$$\Delta\epsilon = -n_o^2 n_e^2 \epsilon_0 r_{51} E_{dc}. \tag{49}$$

The coupling coefficient (44) can now be written in the form

$$K_{\mu\nu} = \frac{i\omega n_{o2}^2 n_{e2}^2 \epsilon_0 r_{51}}{4P} \int_{-\infty}^{0} E_{dc} (E_{\mu x}^* E_{\nu y} + E_{\mu y}^* E_{\nu x}) \, dx. \tag{50}$$

We have ignored the small differences between n_{o1} and n_{o2} and between n_{e1} and n_{e2}.

The dc electric field may be a function of x and z. In the simplest case shown in Fig. 4(a) it is generated by two parallel electrodes on the surface of the slab. In this case we approximate its x dependence by the expression

$$E_{dc} = E_0 \exp(x/D) \tag{51}$$

so that the dc field decays exponentially in the negative x direction. If the dc field is generated by opposing contact fingers shown in Fig. 4(b), we may write the fundamental spatial Fourier component of the field as

$$E_{dc} = E_0 \exp(x/D) \cos \theta z. \tag{52}$$

The y dependence of the fields is ignored. The amplitude factor E_0 must be regarded as a suitable average. The light wave is assumed to propagate in the space between the two metal electrodes in Fig. 4(a) and, correspondingly, also in the gap between the two rows of periodic electrodes in Fig. 4(b). Diffraction spreading tends to broaden the beam in the plane of the film so that additional guidance must be provided to form a rectangular strip guide that confines the light not only to the plane of the film but also to the narrow region between the metal electrodes. The dielectric waveguide is thus not truly a slab but a rectangular guide. However, the analysis is based on slab waveguide modes which are considered to be adequate approximations of the modes of the rectangular guide particularly if the beam confinement perpendicular to the slab is much narrower than in the plane of the slab. The device configurations shown in Fig. 4 were proposed by Schmidt and Kaminow [13].

The device sketched in Fig. 4(a) generates a dc electric field that is independent of the z coordinate. Coupling can thus only occur between two modes with equal propagation constants such as between a guided TM mode and a TE radiation mode according to Fig. 1 (in $LiNbO_3$). If the voltage is applied to the two electrodes power is converted from the guided TM mode to the TE radiation mode so that a light beam emerges in the substrate. The coupling efficiency of this device is best expressed in terms of the attenuation coefficient α of the guided mode. The attenuation is caused by power loss from the guided mode μ to the radiation modes ρ. High attenuation indicates good conversion efficiency. The power attenuation coefficient 2α is related to the coupling coefficient by the formula

$$2\alpha = 2\pi e(\theta) \frac{\beta}{\rho} |K_{\mu\rho}|^2 \tag{53}$$

with

$$e(\theta) = \begin{cases} 1 & \text{for } \theta = 0 \\ \frac{1}{4} & \text{for } \theta > 0. \end{cases}$$

Equation (53) is, of course, also applicable to the device of Fig. 4(b). The parameter ρ is defined by (26) for TE modes and by (41) for TM modes. The propagation constant β is

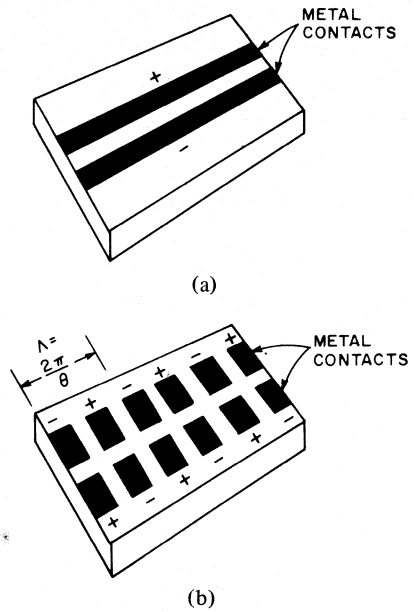

Fig. 4. Electrode configurations for electrooptic modulators. (a) Two continuous strips supply the voltage for a device that couples a guided mode to radiation. (b) Periodic electrodes are required for mode matching a guided TE and a guided TM mode.

given by

$$\beta = \beta_g \tag{54}$$

for the modulating field (51) and by

$$\beta = \beta_g - \theta \tag{55}$$

for the modulating field (52). These values for β must be used to compute the parameters of the radiation modes (25)-(27) and (40)-(42).

The electrode configuration in Fig. 4(b) can be used to convert a guided TE mode to a guided TM mode or vice versa or also for conversion from guided modes to radiation modes. The efficiency for conversion between guided modes is best expressed by the conversion length L that is required to couple all the power from one mode to the other. Defining

$$K_{\mu\nu} = 2\hat{K}_{\mu\nu} \cos \theta z \tag{56}$$

we obtain the total conversion length from the equation [6, p. 135, eq. (4.2-12)]

$$L = \frac{\pi}{2|\hat{K}_{\mu\nu}|}. \tag{57}$$

A useful approximation for L may be obtained by assuming that the field penetration depth D occurring in (52) is infinite and approximating the guided modes by plane waves. A straightforward analysis yields

$$L = \frac{2\pi}{(n_o n_e)^{3/2} k(r_{51} E_0)} \tag{58}$$

the approximation (58) is convenient for order of magnitude estimates of the total conversion length.

Substitution of the mode field expressions into (50) leads to

integrals that can be solved analytically. However, the resulting expressions are so long and unwieldy that they are omitted from this paper. All the relevant information is given in the preceding so that the evaluation of (50) is a simple matter of algebra.

The DC Electric Field

An idealized electrode configuration of Fig. 4(a) used to apply the dc electric field to the crystal is shown in Fig. 5. We have reversed the customary coordinate labels to obtain agreement with the coordinates used in Fig. 2. The metal electrodes are assumed to be infinitely thin and extend from $y = -\infty$ to $y = -a$ and from $y = a$ to $y = \infty$. The potential generated by these electrodes is given by the function $u(x, y)$ according to the formula [12] (the anisotropy of the material is ignored)

$$u + iv = \frac{V}{\pi} \arccos\left(\frac{y}{a} + i\frac{x}{a}\right). \tag{59}$$

The electric field follows from this potential equation

$$E_y = -\frac{\partial u}{\partial y} = \frac{V}{\pi\sqrt{2}} \frac{\{(a^2 + x^2 - y^2) + [a^4 + x^4 + y^4 + 2x^2y^2 + 2a^2(x^2 - y^2)]^{1/2}\}^{1/2}}{[a^4 + x^4 + y^4 + 2x^2y^2 + 2a^2(x^2 - y^2)]^{1/2}} \tag{60}$$

and

$$E_x = -\frac{\partial u}{\partial x} = \frac{V}{\pi\sqrt{2}} \frac{\{-(a^2 + x^2 - y^2) + [a^4 + x^4 + y^4 + 2x^2y^2 + a^2(x^2 - y^2)]^{1/2}\}^{1/2}}{[a^4 + x^4 + y^4 + 2x^2y^2 + a^2(x^2 - y^2)]^{1/2}}. \tag{61}$$

V is the potential difference between the electrodes. These field expressions apply to the region $-a < x < a$. For $|x| > a$ the sign of the inner square root in the numerator of (60) and (61) must be reversed.

The complicated field expressions (60) and (61) simplify substantially in the planes $x = 0$ and $y = 0$. We obtain for the plane of the electrodes $x = 0$

$$E_x = 0 \tag{62}$$

and

$$E_y = \frac{V}{\pi(a^2 - y^2)^{1/2}}. \tag{63}$$

In the vertical plane halfway between the two electrodes at $y = 0$ we have

$$E_x = 0 \tag{64}$$

and

$$E_y = \frac{V}{\pi(a^2 + x^2)^{1/2}}. \tag{65}$$

Fig. 6 shows a comparison between the function $(1 + x^2)^{-1/2}$ and the exponential function $\exp(-0.4x)$. It is apparent that the exponential function is a reasonable approximation to the electric-field distribution (65) over the entire range shown in Fig. 6. Therefore, we may approximate (65) in the form

$$E_y = \frac{V}{\pi a} \exp\left(-0.4\frac{|x|}{a}\right). \tag{66}$$

The field penetration depth D defined by (51) and (52) is thus expressed in terms of the electrode separation $2a$ as follows:

$$D = 2.5a \tag{67}$$

and the amplitude coefficient of the field can be expressed in terms of the applied voltage

$$E_0 = \frac{V}{\pi a}. \tag{68}$$

We use the field expression (66) as an approximation for the electrode field of Fig. 4(a) and

$$E_y = \frac{V}{\pi a} \exp\left(-0.4\frac{|x|}{a}\right)\cos\theta z \tag{69}$$

as an approximation for the field of the electrode configuration shown in Fig. 4(b).

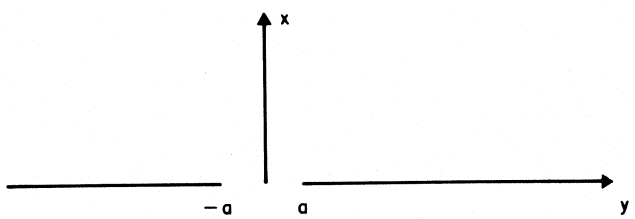

Fig. 5. Idealized geometry for establishing the field distribution generated by the electrodes shown in Fig. 4.

Numerical Examples

The electrooptic coefficient is [4, p. 113]

$$r_{51} = \begin{cases} 28 \times 10^{-12}\ \text{m/V}, & \text{for } LiNbO_3 \\ 20 \times 10^{-12}\ \text{m/V}, & \text{for } LiTaO_3 \end{cases} \tag{70}$$

at the helium-neon laser wavelength of 0.633 μm.

The power loss coefficient 2α is shown in normalized form in Fig. 7 as a function of $kd = 2\pi d/\lambda$. The solid curves of Fig. 7 represent the loss for different values of the field penetration depth D/λ. The dotted line in the figure shows the angle at which the radiation escapes into the substrate. The figure is drawn for the case of the lowest order guided TM mode losing power to a TE radiation mode due to electrooptic coupling in $LiNbO_3$.

In order to keep the modulating voltage low it is desirable to maintain close electrode spacing. For this reason we consider the case $D/\lambda = 1$. The peak of the curve with $D/\lambda = 1$ occurs at $kd = 5.52$, with $\lambda = 0.633$ μm. Thus we need a slab guide with a thickness $d = 0.56$ μm. Using (67) and $D/\lambda = 1$ we obtain the electrode spacing $2a = 0.51$ μm. This small spacing cannot be realized with present-day fabrication methods.

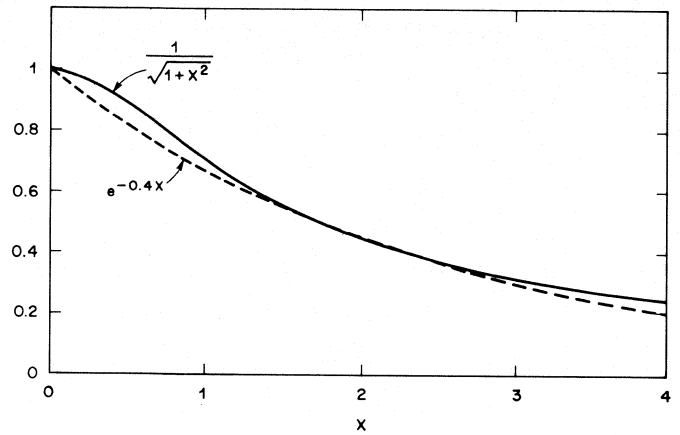

Fig. 6. Comparison between the electric field in the midway plane of the electrode of Fig. 4(a) and an exponential function.

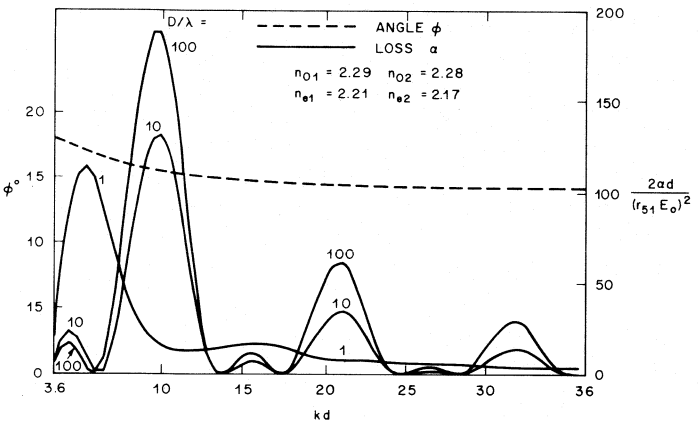

Fig. 7. Normalized loss coefficient as a function of $kd = 2\pi d/\lambda$. The solid curves apply to the loss coefficient and are labeled by different values of the normalized field penetration depth D/λ. The dotted curve represents the angle at which radiation escapes into the substrate. The figure applies to the $LiNbO_3$ case with $n_{o1} = 2.29$, $n_{o2} = 2.28$, $n_{e1} = 2.21$, and $n_{e2} = 2.17$.

Next we consider the amount of attenuation that we may achieve for the guided TM mode. A voltage of $E_a = 30\,000$ V/cm causes breakdown in dry air. Equation (68) yields for this value and the preceding electrode spacing the electrode voltage $V = 2.4$ V. For $LiNbO_3$ we obtain from (70) $r_{51}E_0 = 8.4 \times 10^{-5}$. Using a path length of $L = 1$ cm we have $L/d = 1.8 \times 10^4$. At the peak of the $D/\lambda = 1$ curve of Fig. 7 we have $2\alpha d/(r_{51}E_0)^2 = 114$ so that we obtain for the attenuation caused by electrooptic coupling to radiation, $2\alpha L = 0.014$ Np = 0.063 dB. This example shows that a modulator based on electrooptic radiation loss in $LiNbO_3$ is not efficient even for an idealized design. If it were possible to increase the modulation voltage the modulator could be improved because the attenuation is proportional to the square of the applied modulating voltage.

The situation is more hopeful for a device based on $LiTaO_3$. Fig. 8 applies to this case. The peak of the $D/\lambda = 1$ curve appears at $kd = 9.2$ requiring a slab thickness $d = 0.93$ μm ($\lambda = 0.633$ μm). The electrode spacing is unchanged, $2a = 0.51$ μm. However, the normalized value of the attenuation constant is much higher for this case because the attenuation escapes into the substrate at a much smaller angle, $2\alpha d/(r_{51}E_0)^2 = 3800$. From (70) we have for $LiTaO_3$ with

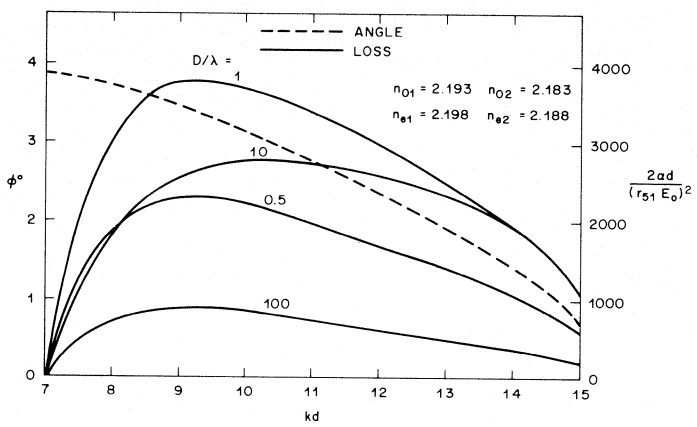

Fig. 8. Similar to Fig. 7, this figure applies to the $LiTaO_3$ case, $n_{o1} = 2.193$, $n_{o2} = 2.183$, $n_{e1} = 2.198$, and $n_{e2} = 2.188$.

$E_0 = 30\,000$ V/cm the value $r_{51}E_0 = 6 \times 10^{-5}$ so that the peak value of the attenuation for $L = 1$ cm is in this case $2\alpha L = 0.15$ Np = 0.65 dB. This value is far more favorable than the corresponding figure for the $LiNbO_3$ case. If it were possible to double the applied voltage, a value of $2\alpha L = 0.6$ Np would be obtained so that approximately 50 percent of the guided mode power could be radiated into the substrate.

Figs. 9 and 10 apply to electrooptic mode conversion from a guided TE mode to a guided TM mode or vice versa. The figures show the normalized total exchange length L (required for complete exchange of power from one mode to the other) as a function of kd. The parameter D/λ (normalized field penetration depth) is again used to label the curves. The dotted line shown in the figures gives the period length Λ of the periodic electrodes shown in Fig. 4(b). Fig. 9 applies to $LiNbO_3$ and Fig. 10 to $LiTaO_3$. It is immediately apparent that the coupling efficiency is comparable in both cases. A small value of L is desired for an efficient modulator. More important than the coupling efficiency is the required electrode spacing $\Lambda = 2\pi/\theta$ that follows from (6). (It must be remembered that the values of Λ—as all other values—were calculated from a slab waveguide model. A diffused guide has different dispersion characteristics and, therefore, different values of Λ.) The $LiTaO_3$ case, Fig. 10, leads to much larger, more easily manageable electrode spacings so that we concentrate on this case. The curves in Figs. 9 and 10 labeled $D/\lambda = \infty$ were calculated from the plane-wave model that leads to (58). It is apparent that the curves for large values of D/λ, that were calculated from the coupled-mode theory, asymptotically assume the same values predicted by the plane-wave model. Only for small values of kd does the plane-wave model yield inaccurate results since the rapid increase caused by the cutoff behavior of the guided modes is not included in the plane-wave analysis.

A modulator based on mode coupling between guided waves is more efficient for large values of D/λ. This is not surprising since the modulating field penetrates deeper into the waveguide if D/λ is large. The fluctuations in the radiation loss curves of Figs. 7 and 8 are caused by interference effects that are absent for guided mode interaction. Large values of D/λ are obtained by large electrode spacings. However, it is advantageous to keep the electrode spacing small in order to reduce the required modulating voltage.

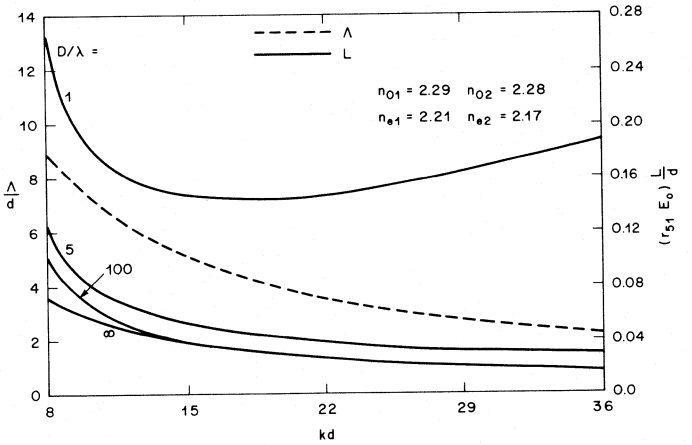

Fig. 9. Normalized power exchange length L as a function of kd for different values of the normalized field penetration depth D/λ, solid curves. The dotted curve gives the normalized length Λ/d of the electrode period. This figure applies to $LiNbO_3$ with $n_{o1} = 2.29$, $n_{o2} = 2.28$, $n_{e1} = 2.21$, and $n_{e2} = 2.17$.

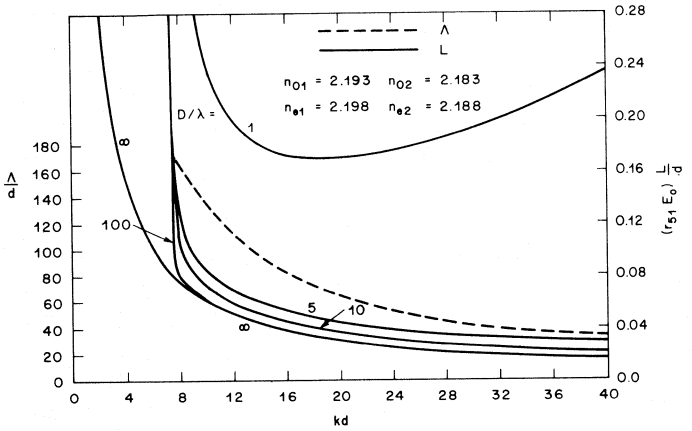

Fig. 10. Same as Fig. 9 for $LiTaO_3$ with $n_{o1} = 2.193$, $n_{o2} = 2.183$, $n_{e1} = 2.198$, and $n_{e2} = 2.188$.

Table I shows numerical values for the required gap spacing $2a$ between the modulating electrodes, the modulating voltage V (provided that $E_0 = 30\,000$ V/cm), and the length L required for total power exchange between the lowest order guided TE and TM modes for several values of D/λ. The values in Table I are taken from Fig. 10 and are based on a slab width of $d = 2$ μm and $\lambda = 0.633$ μm. The length for one period of the periodic electrode spacing is $\Lambda = 130$ μm.

Table I shows that complete conversion of power is easily obtainable over short distances. A modulator based on power conversion between guided modes is thus far more attractive than the modulator based on radiative power loss discussed in the preceding.

Conclusions

We have discussed the performance of two different types of electrooptic modulators. The modulator of the first type couples a guided TE or TM mode to radiation modes that are polarized orthogonally to the polarization of the guided wave. This type of modulator requires a modulating voltage that need not be periodic in the direction of wave propagation.

TABLE I

$\frac{D}{\lambda}$	2a(μm)	V(volts)	L(cm)
1	0.51	2.4	0.57
5	2.53	11.9	0.15
10	5.06	23.84	0.12
100	50.6	238.5	0.10

Note: This table shows the spacing $2a$ between contact pairs and the required modulating voltage to achieve complete conversion from a guided TE to a guided TM mode (or vice versa) over a distance L for a $LiTaO_3$ crystal for preselected values of D/λ. It is assumed that the electric-field strength is $E_0 = 30\,000$ V/cm, that the slab thickness is $d = 2$ μm corresponding to $kd = 19.85$. The length of the fundamental period of the periodic electrodes is $\Lambda = 130$ μm.

Numerical examples for $LiNbO_3$ and $LiTaO_3$ show that the efficiency of this type of modulator is marginal. In $LiTaO_3$ approximately 14 percent of the guided wave power may be coupled out of the guide by a dc field of $E_0 = 30\,000$ V/cm applied via two contact strips that are 1 cm long. If the voltage could be increased by a factor of 2 about 50 percent of the power could be coupled out. For $LiNbO_3$ the situation is even less favorable.

The modulator of the second type uses a (spatially) periodically varying applied voltage whose period (of approximately 100 μm for $LiTaO_3$) is adjusted to match the phases of the two guided waves. Complete conversion of power from a TE to a TM mode (or vice versa) is possible over distances ranging from 0.1 cm to about 0.6 cm. This type of modulator is capable of 100-percent modulation with an applied voltage of a few volts. To achieve amplitude modulation one of the two guided modes must be suppressed before reaching the detector. This can be done in several ways. For example, it is possible to taper the width of the guiding film to such a thickness that one of the modes exceeds its cutoff condition while the other mode remains guided. The cutoff mode would radiate out of the film in a very short distance. A metal layer on top of the guiding film introduces more loss to the TM mode than to the TE mode so that suppression of the TM mode is possible in this way [14]. An efficient method of mode suppression consists of a periodic grating deposited on top of the guiding film. This grating can be adjusted to couple one of the two guided modes to radiation resulting in very high radiation losses without appreciably affecting the other mode.

Acknowledgment

The author wishes to thank I. P. Kaminow who contributed to this paper not only by posing the problem but also during the course of many interesting conversations.

References

[1] I. P. Kaminow and J. R. Carruthers, "Optical waveguiding layers in $LiNbO_3$ and $LiTaO_3$," *Appl. Phys. Lett.*, vol. 22, pp. 326-328, Apr. 1973.

[2] J. M. Hammer and W. Phillips, "Low loss single-mode optical waveguides and efficient high-speed modulators of $LiNb_xTa_{1-x}O_3$ and $LiTaO_3$," *Appl. Phys. Lett.*, vol. 24, pp. 545-547, June 15, 1974.

[3] R. V. Schmidt and I. P. Kaminow, "Metal-diffused optical waveguides in $LiNbO_3$," *Appl. Phys. Lett.*, vol. 25, pp. 458–460, Oct. 15, 1974.
[4] I. P. Kaminow, *An Introduction to Electrooptic Devices*. New York: Academic, 1974.
[5] D. Marcuse, *Light Transmission Optics*. New York: Van Nostrand-Reinhold, 1972.
[6] D. Marcuse, *Theory of Dielectric Optical Waveguides*. New York: Academic, 1974.
[7] V. Ramaswamy, "Propagation in asymmetrical anisotropic film waveguides," *Appl. Opt.*, vol. 13, pp. 1363–1371, June 1974.
[8] ——, "Ray model of energy and power flow in anisotropic film waveguides," *J. Opt. Soc. Amer.*, vol. 64, pp. 1313–1320, Oct. 1974.
[9] A. Yariv, "Coupled-mode theory for guided-wave optics," *IEEE J. Quantum Electron.*, vol. QE-9, pp. 919–933, Sept. 1973.
[10] T. P. Sosnowski and G. D. Boyd, "The efficiency of thin-film optical-waveguide modulators using electrooptic films or substrates," *IEEE J. Quantum Electron.*, vol. QE-10, pp. 306–311, Mar. 1974.
[11] D. Marcuse, "Coupled mode theory for anisotropic optical waveguides," *Bell Syst. Tech. J.*, vol. 54, pp. 985–995, July/Aug. 1975.
[12] S. Ramo and J. R. Whinnery, *Fields and Waves in Modern Radio*, 2nd ed. New York: Wiley, 1964, p. 137.
[13] R. V. Schmidt and I. P. Kaminow, private communication.
[14] Y. Suematsu *et al.*, "Fundamental transverse electric field (TE_0) mode selection for thin-film asymmetric light guides," *Appl. Phys. Lett.*, vol. 21, pp. 291–293, Sept. 15, 1972.

Gain Characteristics of a Multiatmosphere UV-Preionized CO_2 Laser

A. J. ALCOCK, MEMBER, IEEE, ROBERT FEDOSEJEVS, AND ANDREW C. WALKER

Abstract—**The small-signal gain of a transverse-discharge UV-preionized CO_2 laser has been investigated at pressures in the 1–15-atm range. Measurements were carried out on the $P(18)$ and $R(16)$ lines of both the 10.4- and 9.4-μm bands, and data on the pressure dependence of the peak gain and gain rise time are presented. The results demonstrate that small-signal gains in excess of 5-percent cm^{-1} are readily obtained at pressures of $\sim$ 12 atm and confirm that the relaxation times of the energy levels relevant to laser action scale inversely with pressure. In addition, it is found that the gain of both R branches increases more rapidly with pressure than that of the P branches, while there are indications that the 9.4- and 10.4-μm gain values become comparable at pressures of $\sim$ 15 atm. The experimental results have been compared with the dependence of gain on pressure predicted by a relatively simple theoretical model. On the basis of this model it is found that the experimentally determined gain rises more rapidly with pressure than one would expect and a number of possible reasons for this discrepancy are discussed.**

I. Introduction

SINCE the inherent advantages of operating molecular lasers at extremely high pressures were first pointed out [1]–[3], a number of experimental approaches have successfully demonstrated CO_2-laser action at pressures well in excess of 1 atm. The excitation techniques employed include fast, ultrahigh-voltage discharges [4], electron-beam-sustained discharges [5], optical pumping [6], and UV preionized [7] and "double-discharge" configurations [8]. However, only three of these methods [5]–[7] have so far permitted operation at pressures higher than 10 atm, with the highest reported operating pressure (50 atm) being attained by means of an electron-beam-sustained discharge [5]. An interesting feature of molecular lasers at such high pressures is the overlapping of the individual rotational lines caused by pressure broadening. In the case of CO_2, significant overlap occurs at pressures of the order of 10 atm and the individual vibrational-rotational lines merge into a single continuous gain spectrum. As a result the gain at any particular wavelength is the sum of contributions from several nearby rotational lines and thus it is pressure dependent even though the pump energy per unit-volume pressure is maintained constant. This is in contrast to the low-pressure (20 torr–2 atm) situation where pressure broadening of the individual rotational lines maintains a constant ratio of bandwidth to molecular density, and hence results in the gain being almost independent of pressure.

Although a number of authors have discussed the effects of line broadening [9] and calculations of the high-pressure gain spectrum have been published [10], there has been little effort to compare the predicted behavior with experimental data. Recently, gain measurements for a 15-atm electron-beam-controlled device were reported by Harris *et al.* [11]; however, the only study which has dealt specifically with the effect of pressure on gain has been that of Basov *et al.* [12]. In the case of an electron-beam-sustained device, these authors were able to show that the gain is proportional to the pump energy density per atmosphere and that the gain lifetime is inversely proportional to pressure for pressures up to 20 atm. In the present paper we wish to describe an experimental study of a transverse-discharge UV-preionized CO_2 laser capable of operation at pressures as high as 15 atm. Small-signal gain measure-

Manuscript received February 18, 1975; revised April 28, 1975.

A. J. Alcock is with the Division of Physics, National Research Council of Canada, Ottawa, Ont., Canada.
R. Fedosejevs was with the Division of Physics, National Research Council of Canada, Ottawa, Ont., Canada. He is now with the University of Toronto, Toronto, Ont., Canada.
A. C. Walker was with the Division of Physics, National Research Council of Canada, Ottawa, Ont., Canada. He is now with the Department of Physics, University of Essex, Colchester, Essex, England.

ments have been carried out on the $P(18)$ and $R(16)$ lines of both the 10.4- and 9.4-μm bands at pressures ranging from 1 to 15 atm, and the results compared with the dependence of pressure on gain predicted by a simple theoretical model.

II. Experimental Details

Aside from a minor modification to the preionization system, the main features of the multiatmosphere CO_2 laser have been described in an earlier publication [7]. UV radiation is provided by a series of small (~2 mm long) arcs formed between tungsten electrodes running parallel to the 26-cm-long main discharge electrodes; however, unlike the device described in [7], a second preionizer array has been added to permit illumination from both sides of the main discharge volume. Although no additional energy is required for the larger number of arcs, this symmetrical illumination scheme has resulted in a significant improvement in the laser's performance. The main discharge is energized by a five-stage Marx Bank operating at charging voltages ranging from 30 to 80 kV. Thus, for the 0.7-cm interelectrode gap, the nominal E/p values cover the range 14.3 kV/cm · atm to ~70 kV/cm · atm and correspond to pump energy densities between 30 and 500 J/l · atm. Over this range stable operation, with a gas-mixture composition of 1:1:8, $CO_2:N_2:He$, is achieved at pressures anywhere between 1 and 15 atm.

Gain measurements were made by operating the laser with Brewster-angled NaCl windows and probing the active region with radiation from a grating-tuned CW CO_2 laser having an output power of ~2 W. The experimental setup is shown in Fig. 1. After checking the wavelength of the CW laser output the probe beam was chopped and directed through the gain medium. It was then focused onto a liquid-N_2-cooled, photoconductive, Ge:Au detector. The latter had a measured rise time of ~50 ns, when suitably matched into both channels of a Tektronix 556, dual-beam oscilloscope, and allowed full temporal resolution of the gain pulses. The chopped signal was displayed on a slow sweep while the other oscilloscope beam was triggered from this sweep after an appropriate delay. The start of the second sweep triggered the CO_2-laser discharge and the delay was set so that this coincided with an "on" period of the chopped probe beam. In this manner a value for the power of the probe beam could be recorded while at the same time displaying the gain pulse on a fast sweep. Fig. 2 shows an example of a typical gain measurement. It should be noted that the diameter of the probe beam corresponded approximately to the 0.7-cm laser aperture and hence the results obtained are average gain values for the whole active area.

III. Experimental Results

The gain of the laser was measured on the $P(18)$ and $R(16)$ lines of both the 9.4- and 10.4-μm transitions over the pressure range of 1-15 atm and at various pump energies. The gas mixture was kept constant with a composition of 1:1:8, $CO_2:N_2:He$. Each gain measurement was made by averaging six shots of the laser, the greatest shot-to-shot variations being observed at the extremes of the ranges covered; e.g., near 15 atm and at maximum energy input.

Fig. 3 shows one set of peak gain measurements for the

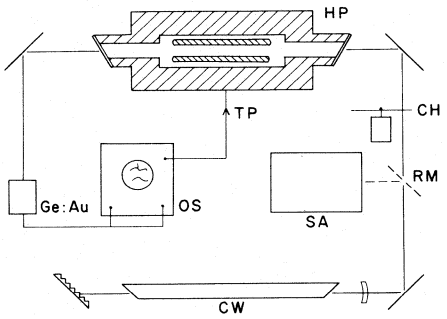

Fig. 1. Experimental arrangement used for multiatmosphere gain measurements. Legend: CW—grating-tuned probe laser; RM—removable beam-sampling mirror; SA—spectrum analyzer; CH—chopper; HP—high-pressure laser; Ge:Au—gold-doped germanium detector; OS—oscilloscope; TP—trigger pulse to laser.

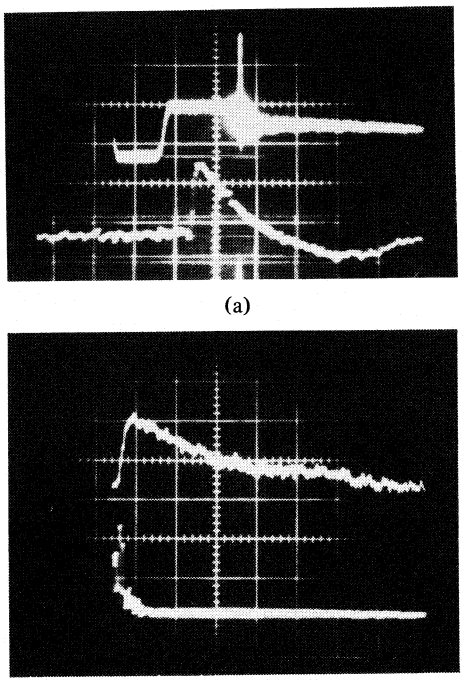

(a)

(b)

Fig. 2. (a) Upper trace—Typical gain pulse superimposed on chopped CW laser signal (sweep speed 1 ms/div). Lower trace—Gain pulse displayed on faster (1 μs/div) sweep. Vertical scale 20 mV/div for both traces; laser pressure 12 atm; input energy density 110 J/l · atm. (b) Upper trace—12-atm gain pulse displayed on 500 ns/div sweep. Lower trace—Pickup from main-discharge current indicating duration of excitation pulse (sweep speed 500 ns/div).

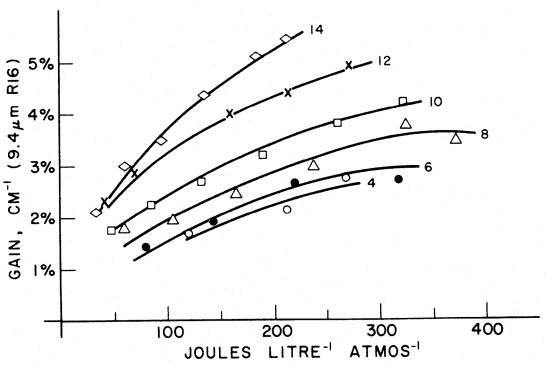

Fig. 3. Peak gain measurements for the 9.4-μm $R(16)$ line showing dependence on laser gas pressure and pump energy density.

9.4-μm $R(16)$ line. This shows that the peak gain increases with pressure, above 1 atm, and that gain values of more than 5-percent cm^{-1} can be readily obtained at pressures over 12 atm. Maximum gain occurs at pump energy densities of approximately 300 J/l · atm. A similar set of data was obtained for the other laser lines investigated.

Fig. 4 is a summary of the experimentally measured gain for the four laser lines studied, given a constant energy input of 200 J/l · atm.

As expected from the closer spacing of the rotational lines, the R-branch gain increases relatively more with increasing pressure than that of the P-branch lines. Fig. 4 also shows that the 10.4- and 9.4-μm gain values approach one another at the higher pressures. The measurement accuracy of these relative effects is estimated to be within a 5-percent error margin; however, it should be noted that the absolute measurement accuracy of the peak gain values is of the order of ± 0.005 cm^{-1}.

A study was also made of the pressure dependence of the rise time of the gain pulse [Fig. 2(b)]. The result is shown in Fig. 5 and indicates a linear relationship between pressure and the reciprocal rise time. The limit of this proportionality is reached when the rise time of the gain becomes comparable to the pumping time. In our laser this occurs at a pressure of ~15 atm where the gain was observed to rise to its peak value in only 80 ns. The duration of the gain pulse [full width at half maximum (FWHM)] also varies inversely with pressure and is usually about ten times larger than the pulse rise time. These observations show that, as expected, the relaxation times of the energy levels relevant to laser action scale inversely with pressure. This agrees with the results of Basov *et al.* [12] who showed, using an electron-beam-controlled CO_2 laser, that the product of inversion lifetime and pressure remains constant over the pressure range from 3 to 20 atm.

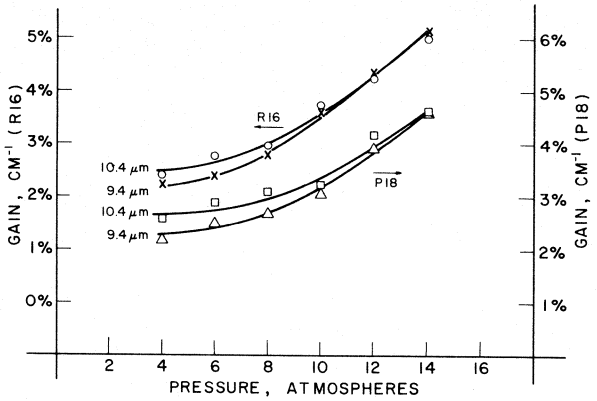

Fig. 4. Summary of gain measurements for the $P(18)$ and $R(16)$ lines of both the 9.4- and 10.4-μm bands showing the measured pressure dependence at a constant pump energy density of 200 J/l · atm.

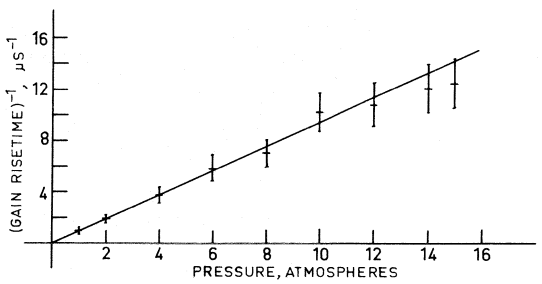

Fig. 5. Plot of inverse-gain rise time as a function of pressure.

IV. Theoretical Model

As mentioned previously (Section I) the high-pressure gain at any particular wavelength consists of contributions from a number of adjacent vibrational-rotational transitions. In the case of the 10.4- and 9.4-μm CO_2-laser bands, these transitions occur between rotational sublevels of the $(00^\circ 1)$ upper vibrational level and the $(10^\circ 0)$ and $(02^\circ 0)$ lower vibrational levels, respectively. Within each laser band the P branch and R branch correspond to transitions from upper states with rotational quantum numbers of $J-1$ and $J+1$, respectively, to a lower state with a rotational quantum number of J; however, due to the symmetry of CO_2, there are no antisymmetric rotational levels [13], and thus all of the laser transitions occur between an upper level with odd J and a lower level with even J. For the individual vibrational-rotational transitions the gain coefficient at a frequency ν is given by

$$\alpha_J(\nu) = \frac{c^2}{8\pi\nu_J^2} A_{21} \left(n_2 - \frac{g_2}{g_1} n_1\right) g(\nu - \nu_J) \tag{1}$$

where ν_J is the frequency at the line center; A_{21} is the spontaneous transition probability; n_2 and n_1 are the populations of the upper and lower states, respectively; g_2 and g_1 are the degeneracies of the upper and lower levels; and $g(\nu - \nu_J)$ is the line-shape function. The number densities of the upper and lower levels are related to the total population densities N_2 and N_1 of the upper and lower vibrational levels by

$$n_i = N_i \left(\frac{2hcB_i}{kT}\right) g_i \exp\left[-B_i J_i (J_i + 1)\frac{hc}{kT}\right]_{i=1,2} \tag{2}$$

where J_2 and J_1 are the rotational quantum numbers for the upper and lower levels, respectively; B_2 and B_1 are the rotational constants for the upper and lower levels, respectively; and T is the rotational temperature. The line shape at high pressures is assumed to be a collision-broadened Lorentzian with a FWHM of $\Delta\nu_L$, and thus

$$g(\nu - \nu_J) = \frac{2\Delta\nu_L}{\pi} \frac{1}{4(\nu - \nu_J)^2 + \Delta\nu_L^2}. \tag{3}$$

The spontaneous-transition probability is given by

$$A_{21} = \frac{64\pi^4 \nu_J^3}{3hc^3 g_2} |R_{12}|^2 S_J \tag{4}$$

where $|R_{12}|^2$ is the vibrational contribution to the matrix element, and S_J is the rotational contribution to the matrix element equal to J for the P branch and $J+1$ for the R branch.

Thus the gain coefficient of transition J is given, for the P branch, by

$$\alpha_J(\nu) = A\nu_J J \left\{R \exp\left[-B_2 J(J-1)\frac{hc}{kT}\right] - \exp\left[-B_1 J(J+1)\frac{hc}{kT}\right]\right\} g(\nu - \nu_J) \tag{5}$$

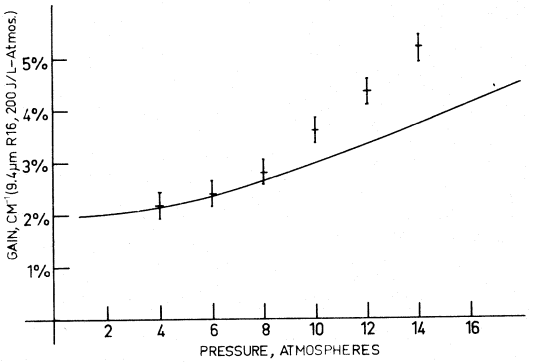

Fig. 6. Experimentally determined pressure dependence of gain for the 9.4-μm $R(16)$ transition at a constant energy input of 200 J/l · atm. The continuous line shows the calculated pressure dependence based on a collision-broadening coefficient of 3.5 GHz/atm.

and for the R branch, by

$$\alpha_J(\nu) = A\nu_J [J+1] \left\{ R \exp\left[- B_2 (J+1)(J+2) \frac{hc}{kT} \right] - \exp\left[- B_1 J(J+1) \frac{hc}{kT} \right] \right\} g(\nu - \nu_J) \quad (6)$$

where $R = (N_2 B_2 / N_1 B_1)$ is almost equal to the inversion ratio and

$$A = \frac{16\pi^3}{3kT} |R_{12}|^2 N_1 B_1 .$$

Taking line overlap effects into account, the total gain at any frequency is given by

$$\alpha(\nu) = \sum_J \alpha_J(\nu). \quad (7)$$

Substituting measured values for the rotational constants [14] and line frequencies [15], (5)-(7) were used to compute the CO_2 gain spectra and, in the case of no line overlap, the results were normalized to give $\alpha = 1$ on the peak of the 10.4-μm $P(20)$ transition and $\alpha = 0.74$ on the peak of the 9.4-μm $P(20)$ transition. The factor of 0.74 was calculated from (5) assuming equal linewidths for both bands and using values for the vibrational matrix elements given by Cousin *et al.* [16].

The small-signal gain of atmospheric-pressure transverse-discharge lasers has been investigated experimentally by Robinson [17], Girard *et al.* [18], and Singer [19] and their measurements yield inversion-ratio values between 16 and 30 and rotational temperatures ranging from 325 to 435 K. However, measurements carried out with electron-beam-sustained amplifiers [20], [21] indicate considerably lower values (2.5-10) for the inversion ratio, and for the computed spectra presented in this paper a rotational temperature of 325 K was used together with an inversion ratio of 4.0 for the 10.4-μm band. Assuming thermodynamic equilibrium for the (10°0) and (02°0) levels at 325 K, the inversion ratio for the 9.4-μm band becomes 2.54. Although the assumed values are quite low, the shape of the gain spectrum is not highly dependent on this ratio and the chosen value gives a gain maximum between $P(18)$ and $P(20)$ on the 10.4-μm band.

The linewidths can be determined from the collision-broadening coefficients (GHz [FWHM]/atm) and partial pressures P(atm), of the gases present in the laser discharge, by using

$$\Delta\nu_L = \beta_{CO_2} P_{CO_2} + \beta_{N_2} P_{N_2} + \beta_{He} P_{He} = \beta_{eff} P_{tot}. \quad (8)$$

However, the collision-broadening coefficients are temperature dependent ($\Delta\nu \propto PT^{-1/2}$) and their values must be corrected for the gas temperature in the discharge.

V. Comparison of Experimental Data and Theoretical Predictions

A critical parameter in the calculation of the pressure dependence of the laser gain is clearly the value taken for the line-broadening coefficient (β_{eff}). Many values have been published and by taking a weighted average of 12 of these results a value of 5.4 GHz/atm is obtained for pure CO_2. A similar review of the published data by Judd [22] yielded a value in agreement with this figure. In the case of mixtures of CO_2 and other gases, fewer data are available; however, relative broadening coefficients for N_2 and He have been measured by Patty *et al.* [23] and reduce β_{eff} by a factor of ~0.65 for our laser gas mixture (10-percent CO_2, 10-percent N_2, 80-percent He), giving a value of 3.5 GHz/atm (FWHM). This figure used with the theory described in Section IV allows calculation of the variation with pressure of the laser gain at a particular wavelength. Fig. 6 shows the experimentally determined gain values for the 9.4-μm $R(16)$ transition at a number of pressures. The calculated pressure dependence is shown as a continuous line and has been normalized to agree with the low-pressure experimental values where the effect of line overlap is not significant. This implies an assumption that the population-inversion ratio remains constant provided the energy input per unit-volume-pressure does not change. Such an assumption is compatible with the observed proportionality between pressure and molecular relaxation rates, and seems particularly appropriate for the 8-14-atm pressure range where the nominal value of E/p does not vary significantly (37-49 kV/cm · atm). As can be seen from Fig. 6, a serious discrepancy exists between theory and experiment. A similar disagreement is found to occur at the other three wavelengths investigated, and in all cases the

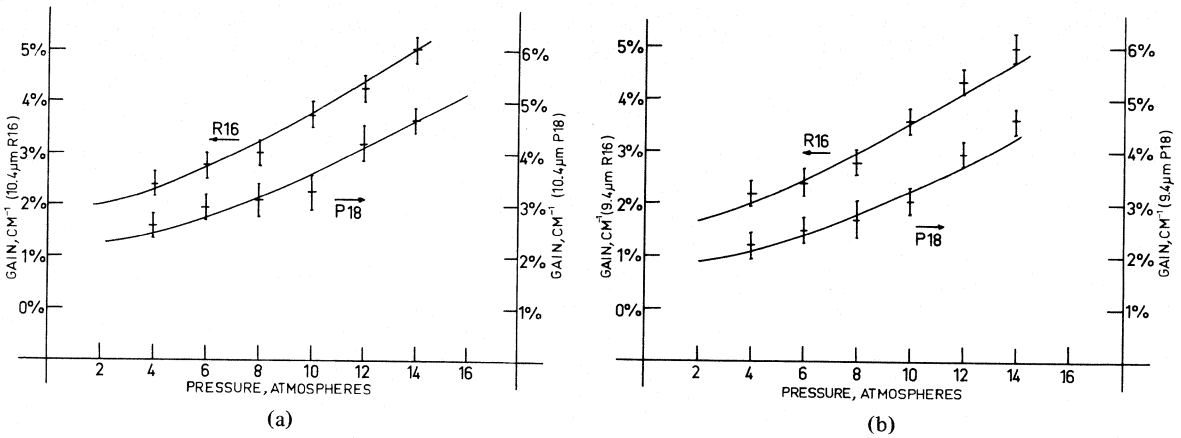

Fig. 7. (a) Measured pressure dependence of gain for the 10.4-μm, $P(18)$, and $R(16)$ lines. (Pump energy density is 200 J/l · atm.) The continuous line shows the calculated pressure dependence for a collision-broadening coefficient of 5.3 GHz/atm. (b) Measured pressure dependence of gain for the 9.4-μm, $P(18)$, and $R(16)$ lines. (Pump energy density is 200 J/l · atm.) The continuous line shows the calculated pressure dependence for a collision-broadening coefficient of 6.1 GHz/atm.

gain increases more rapidly with pressure than the theory predicts.

The failure of our theoretical model to agree with experiment may be attributable to the use of an incorrect value for the line-broadening coefficient as there is a large spread in the data on which the average is based (~40 percent). However, those values published more recently and obtained by more accurate techniques [24] are all close to the value we have used and imply that our choice of broadening coefficient is not unreasonable. In spite of this, an attempt was made to obtain a fit between theory and experiment by taking β_{eff} to be an adjustable parameter. The closest fit is shown in Fig. 7(a) for the $R(16)$ and $P(18)$ lines of the 10.4-μm transition and corresponds to an assumed value of β_{eff} of 5.3 GHz/atm. Similarly, Fig. 7(b) shows the best fit to experimental data taken for the 9.4-μm transitions using $\beta_{eff} = 6.1$ GHz/atm. Coincidentally, both of these latter values correspond to some preliminary results of CO_2 linewidth measurements made available to us by Meyer and Rhodes [25]; however, these values are exceptionally high and in a published account of this work have been revised downwards [26]. Although they no longer explain our results, Meyer's data do indicate that the collision-broadening coefficient is larger for the 9.4-μm transitions than for the 10.4-μm transitions, and therefore agree qualitatively with our experimental observations. Nevertheless, noting that the experimental fit of Fig. 7(a) and (b) is far from perfect and considering the large number of publications giving β_{eff} values of approximately 3.5 GHz/atm, we feel it is unlikely that this value is significantly in error.

Although they are not in agreement with the majority of measured values, the high values for β_{eff} previously mentioned do permit our theoretical model to approximate the experimentally measured pressure dependence of the laser gain. Thus, in calculating the gain spectrum at high pressures, it would seem appropriate to use these values for β_{eff}. The resulting computer calculation yielded the spectrum shown in Fig. 8(a) and (b). As can be seen, considerable smoothing of the rotational bands occurs as one changes from a pressure of 1-10 atm. It should further be noted that, unlike the results of a similar calculation by Chang and Tavis [10], a more realistic estimation of the population inversion ($N_2/N_1 = 4$) results in a higher gain on the R branches than on the P branches at pressures of the order of 10 atm. This result is confirmed experimentally by the observation that the laser always oscillates on an R-branch transition when operated at pressures over 8 atm. Furthermore, when operated as a simple oscillator [7] the laser has a strong tendency to generate 9.3-μm radiation, an effect which is compatible with the effective β value being higher for the 9.4-μm transitions than the 10.4-μm transitions.

VI. Discussion

A similar discrepancy between calculated and observed optical properties of high-pressure CO_2 has been reported by Christiansen *et al.* [27]. Studying the transmission of 10.6-μm radiation through CO_2 at pressures up to 18 atm, these authors found that the absorption increased faster with pressure than predicted by theory. As possible explanations for this result they proposed: 1) an incorrect choice for the broadening coefficient; 2) that the rotational line shape may not be Lorentzian; and 3) the existence of collisionally induced absorption effects. All of these explanations could be applied to our gain measurements, but there is little evidence to determine the validity of any particular one.

The atmospheric-pressure gain measurements reported recently by Singer [19] have particular relevance since they have revealed that the gain on certain lines (e.g., $P(20)$ of the 10.4-μm band) is ~10 percent higher than that predicted by the theoretical population distribution. The explanation for this effect is based on the coincidence in wavelength between

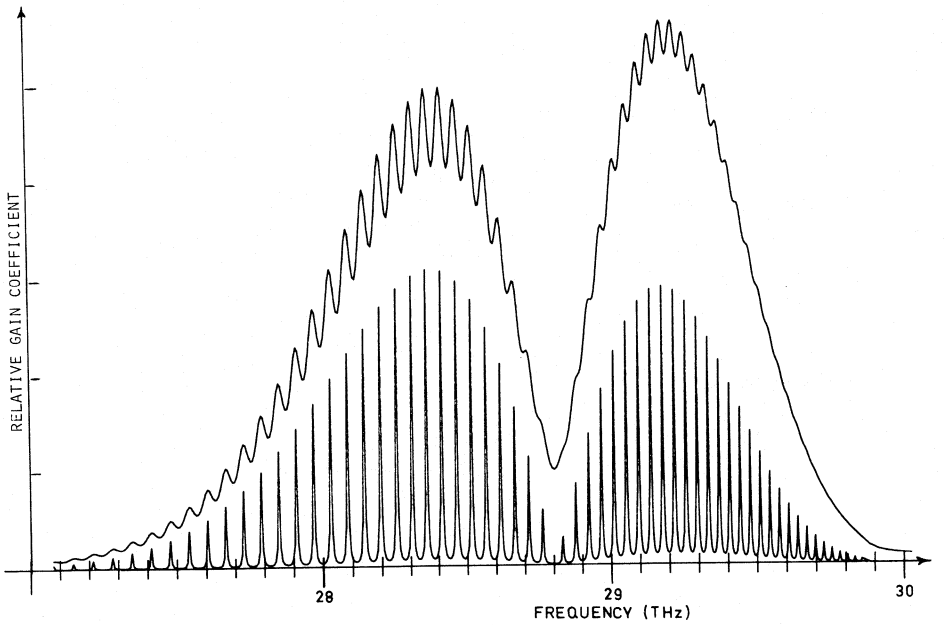

(a)

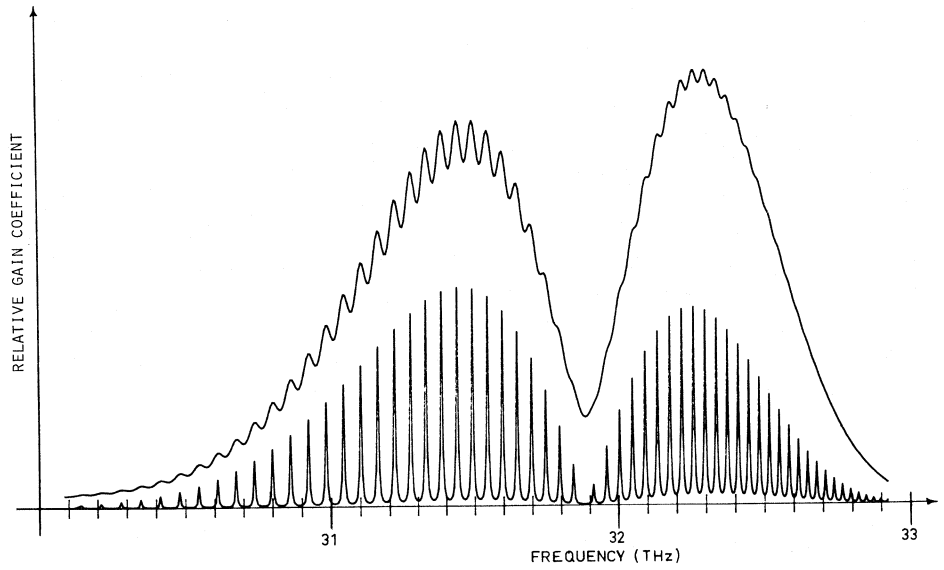

(b)

Fig. 8. (a) Upper curve–Computed 10.4-μm gain spectrum for $p \sim 10$ atm. Values of 4.0 and 53 GHz were used for the inversion ratio and collision-broadened linewidth, respectively. Lower curve–Low-pressure gain spectrum ($p \sim 1$ atm). (b) Upper curve–Computed 9.4-μm gain spectrum for $p \sim 10$ atm. Values of 2.54 and 61 GHz were used for the inversion ratio and collision-broadened linewidth, respectively. Lower curve–Low-pressure gain spectrum ($p \sim 1$ atm).

this particular line and a corresponding transition among the higher CO_2 energy levels. Thus some of the energy stored in these "hot bands" becomes available and leads to an enhancement of the gain for this individual line. Clearly, at higher pressures the probability of such a coincidence increases when all the lines are broadened and will lead to an increasing contribution to the gain from overlapping hot-band transitions.

This effect could account for the observation that the gain at 14 atm is ~40 percent higher than the value predicted by theory and might also explain the discrepancy between our observations and the 15-atm data of Harris *et al.* [11] who found that maximum gain occurred for the $R(16)$ line of the 10.4-μm band. Indeed, assuming an appreciable population inversion among the upper CO_2 levels, such an effect must occur. A numerical calculation, including the contribution from hot-band transitions, would follow closely that described in Section IV with the final summation including the terms due to all relevant transitions. However, a detailed determination of the relative population inversion between the various upper levels requires a fairly sophisticated model for the excitation process. For this reason we have not attempted to confirm this explanation theoretically. Futhermore, it should be noted that this cannot be the explanation for the anomalous pressure dependence obtained from the CO_2 absorption studies [27] as these were performed at room temperature, and hence with a negligible population of the upper energy levels. A

similar argument would also apply to an explanation based on a pressure-dependent population-inversion ratio, and thus there is little reason to doubt the assumption mentioned in Section V.

In conclusion, therefore, it is clear that more detailed investigations, capable of determining the true linewidth and line shape at high pressures, coupled with a knowledge of the direct effect of collisions on the stimulated-emission cross section will be required before a complete explanation for our experimental observations can be given.

Note Added in Proof: An investigation of the gain spectrum of a 14-atm CO_2 laser has been reported recently (J. L. Miller, A. H. M. Ross, and E. V. George, "Gain spectrum of a high pressure CO_2 laser," *Appl. Phys. Lett.*, vol. 26, pp. 523-526, 1975). The data presented indicate that the high-pressure gain spectrum is modified significantly by overlapping higher lying vibrational bands.

Acknowledgment

The authors wish to thank Dr. M. C. Richarson for valuable discussions. They also wish to thank K. Leopold and W. J. Orr for their continuing technical support.

References

[1] V. N. Bagratashvili, I. N. Knyazev, and V. S. Letokhov, "On the tunable infrared gas lasers," *Opt. Commun.*, vol. 4, pp. 154-156, 1971.

[2] N. G. Basov *et al.*, "Gas lasers at high pressures," *JETP Lett.*, vol. 14, pp. 285-288, 1971.

[3] N. G. Basov, E. M. Belenov, V. A. Danilychev, and A. F. Suchkov, "Possibility of producing tunable, infrared gas lasers," *JETP Lett.*, vol. 14, pp. 375-376, 1971.

[4] D. J. Hidson, V. Makios, and R. W. Morrison, "Transverse CO_2 laser action at several atmospheres," *Phys. Lett.*, vol. 40A, pp. 413-414, 1972.

[5] N. G. Basov *et al.*, "Electro-ionization lasers," presented at the Symp. High Power Molecular Lasers, Laval Univ., Quebec, P.Q., Canada, May 15-17, 1972, unpublished; also *Sov. Phys.-JETP*, vol. 37, pp. 58-64, July 1973.

[6] T. Y. Chang and O. R. Wood, II, "Optically pumped 35-atm. CO_2 laser," *Appl. Phys. Lett.*, vol. 23, pp. 370-372, 1973.

[7] A. J. Alcock, K. Leopold, and M. C. Richardson, "Continuously tunable high-pressure CO_2 laser with UV photopreionization," *Appl. Phys. Lett.*, vol. 23, pp. 562-564, 1973.

[8] M. Blanchard *et al.*, "Superatmospheric double-discharge CO_2 laser," *J. Appl. Phys.*, vol. 45, pp. 1311-1314, 1974.

[9] B. S. Patel and P. Swarup, "Rotational line overlap in CO_2 laser transitions," *J. Phys. D: Appl. Phys.*, vol. 6, pp. 1670-1673, 1973.

[10] N.-C. Chang and M. T. Tavis, "Gain of high-pressure CO_2 lasers," *IEEE J. Quantum Electron.*, vol. QE-10, pp. 372-375, Mar. 1974.

[11] N. W. Harris, F. O'Neill, and W. T. Whitney, "Operation of a 15-atm. electron-beam-controlled CO_2 laser," *Appl. Phys. Lett.*, vol. 25, pp. 148-151, 1974.

[12] N. G. Basov, V. A. Danilychev, O. M. Kerimov, and A. S. Podsosonnyi, "Population inversion in the active medium of an electroionization CO_2 laser at a working mixture pressure up to 20 atmospheres," *JETP Lett.*, vol. 17, pp. 102-104, 1973.

[13] G. Herzberg, *Molecular Spectra and Molecular Structure–II. Infra-red and Raman Spectra of Polyatomic Molecules.* New York: Van Nostrand, 1945, pp. 379-384.

[14] T. J. Bridges and T. Y. Chang, "Accurate rotational constants of $C^{12}O_2^{16}$ from measurement of CW beats in bulk GaAs between CO_2 vibrational-rotational laser lines," *Phys. Rev. Lett.*, vol. 22, pp. 811-814, 1969.

[15] K. M. Baird, H. D. Riccius, and K. J. Siemsen, "CO_2 wavelengths and the velocity of light," *Opt. Commun.*, vol. 6, pp. 91-95, 1972.

[16] C. Cousin, C. Rossetti, and C. Meyer, "Spectroscopie avec source laser. Etude des transitions de vibration-rotation, $\nu_3 - \nu_1, \nu_3 - 2\nu_2$ et $(\nu_3 + \nu_2) - (\nu_1 + \nu_2)$ de l'anhydride carbonique," *C. R. Acad. Sci.*, vol. 268, ser. B, pp. 1640-1643, 1969.

[17] A. M. Robinson, "Gain distribution in a CO_2 TEA laser," *Can. J. Phys.*, vol. 50, pp. 2471-2474, 1972.

[18] G. Girard, M. Huguet, and M. Michon, "High-power double-discharge TEA laser medium diagnostic," *IEEE J. Quantum Electron.* (Corresp.), vol. QE-9, pp. 426-428, Mar. 1973.

[19] S. Singer, "Observation of anomalous gain coefficients in TEA double discharge CO_2 lasers," presented at the 8th Int. Quantum Electronics Conf., San Francisco, Calif., June 10-13, 1974; also in *IEEE J. Quantum Electron.*, vol. QE-10, pp. 829-831, Nov. 1974.

[20] C. A. Fenstermacher, M. J. Nutter, W. T. Leland, and K. Boyer, "Electron-beam-controlled electrical discharges as a method of pumping large volumes of CO_2 laser media at high pressure," *Appl. Phys. Lett.*, vol. 20, pp. 56-60, 1972.

[21] B. J. Feldman, "Short-pulse multiline and multiband energy extraction in high-pressure CO_2-laser amplifiers," *IEEE J. Quantum Electron.*, vol. QE-9, pp. 1070-1078, Nov. 1973.

[22] O. P. Judd, "Line broadening and level shift of vibration-rotation transitions in a CO_2 gas mixture," Hughes Res. Rep. 452, Aug. 1971.

[23] R. R. Patty, E. R. Manring, and J. A. Gardner, "Determination of self-broadening coefficients of CO_2 using CO_2 laser radiation at 10.6 μ," *Appl. Opt.*, vol. 7, pp. 2241-2245, 1968.

[24] R. L. Abrams, "Broadening coefficients for the $P(20)$ CO_2 laser transition," *Appl. Phys. Lett.*, vol. 25, pp. 609-611, 1974.

[25] T. W. Meyer and C. K. Rhodes, "High resolution pressure broadening studies in CO_2," *IEEE J. Quantum Electron. (1973 IEEE/OSA Conference on Laser Engineering and Applications: Digest of Technical Papers)*, vol. QE-9, pp. 636-637, June 1973; also T. W. Meyer, private communication.

[26] T. W. Meyer, "Line broadening and collisional studies in CO_2 using the techniques of saturation spectroscopy," Univ. California, Lawrence Livermore Lab. Rep. UCRL-51561.

[27] W. H. Christiansen, G. J. Mullaney, and A. Hertzberg, "Absorption in CO_2 at 10.6 μ with rotational line overlap," *Appl. Phys. Lett.*, vol. 18, pp. 385-387, 1971.

A Compact Sealed Pulsed CO_2 TEA Laser

DONALD S. STARK, PETER H. CROSS, AND HARRY FOSTER

Abstract—A compact sealed pulsed CO_2 TEA laser with an operational life exceeding 10^6 pulses has been developed. It provides single-mode output pulses of 1.0-MW peak power in 50-ns full width at half maximum (FWHM) and total energy 110 mJ in 2 μs. The output beam emerges from an 8.5-mm-diam aperture with a full-angle divergence of 3.5 mrad, which is less than 1.5 times the diffraction limited value. With a different optical resonator system, the corresponding multimode output exceeds 1.4 MW in 80 ns with a total energy of 300-500 mJ delivered in 4 μs and with a beam divergence of about 10 mrad. These output levels, corresponding to 15-25 J/l, are obtained for a pulse repetition frequency of 2 Hz and are maintained after initial conditioning, even in lasers tested to 2×10^6 pulses. Hitherto, prolonged sealed operation was not possible because the glow discharge degraded into arcs. This has been overcome in the present device by the addition of small quantities of carbon monoxide and hydrogen to the basic CO_2-N_2-He-laser gas mixture before seal-off.

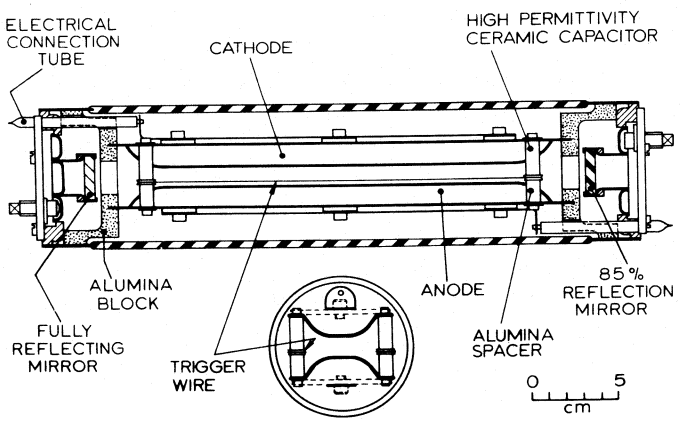

Fig. 1. Sealed pulsed CO_2 TEA laser.

Introduction

THE generation of high-power pulses by TEA CO_2 lasers using flowing-gas mixtures (CO_2-N_2-He) has been extensively described in the literature [1]-[5], but thus far there have been no published reports of the successful operation of sealed devices of this type. The major obstacle has been the early onset of arcing between the electrodes, due to the accumulation of gaseous reaction products of the electrical discharge. In a flowing-gas system these are swept out of the discharge region. This paper describes the development of a compact sealed TEA CO_2 laser in which the peak power output exceeds 1 MW and operational lives greater than 10^6 pulses are reliably obtained. The design is outlined in the following, together with a description of the techniques which have made the development possible. The compactness and portability of this device greatly widen the range of possible applications compared with those of previous TEA lasers requiring bulky and immobile gas handling equipment.

Description of the Laser

The sealed laser is derived from the double-discharge laser described by Pearson and Lamberton [4], [5], in which a uniform pulsed electrical discharge is produced in a flowing gas at atmospheric pressure between two parallel Rogowski-profiled electrodes. The natural tendency to arc is countered by the use of subsidiary discharges between "trigger" wires and the anode. These cause ultraviolet irradiation of the cathode surface, so producing the diffuse photoemission of electrons necessary for the creation of a uniform discharge at high pressures.

Manuscript received February 25, 1975; revised May 22, 1975. This paper was reprinted with permission of the Controller, HMSO, London, England, 1975.

The authors are with the Ministry of Defence, Procurement Executive, Services Electronics Research Laboratory, Baldock, Herts. SG7 6NG, England.

The design of the sealed laser is shown in Fig. 1. Two pressed nickel electrodes are spaced so as to form a discharge volume of cross section 10×10 mm and of length 200 mm. Two trigger wires are placed close to the anode and are supported on ceramic posts separating the electrodes. The insulators between the wires and the cathode are made of a high-permittivity ceramic while those spacing the wires from the anode are of alumina. In this way, capacitative coupling of the trigger wires to the cathode is achieved inside the laser envelope. This eliminates the additional electrical lead-through seals which are normally needed for the connection of external capacitors, thus reducing the size of the device. Energy for the discharge is provided by a 12-nF condenser, charged to about 25 kV and connected across the main electrodes via a triggered sparkgap. The energy in the auxiliary discharges between the trigger wires and the anode is maintained at an optimized low level by limiting the capacity between each wire and the cathode to 45 pF.

The envelope of the laser is made of glass and expansion-matched NiFeCo alloy, and is designed so that the principal joints are argon-arc welds. Low-inductance electrical connections to the main electrodes are made at opposite ends of the envelope via copper tubes which also serve to flow gas through the laser during initial testing. The laser is ultimately sealed by squeezing off these tubes. The principal dimensions of the laser and typical operating parameters are summarized in Table I.

Development

Each laser went through a processing schedule which commenced with a period of outgassing on a high-vacuum pumping system. This was followed by operation as a laser using a flowing-gas mixture at atmospheric pressure for at least 10^4 pulses in order to stabilize the uniformity of the discharge before seal-off.

TABLE I
DIMENSIONS AND TYPICAL OPERATING CONDITIONS OF SEALED TEA LASERS

Length of laser (mm)	380
Diameter of laser (mm)	81
Discharge dimensions (mm)	200 × 10 × 10
Optical-cavity length (mm)	281
Reflectivity of output window (percent)	85
Main storage capacitance (nF)	12
Charging voltage (kV)	20–27
Input energy (J)	2.4–4.4
Proportions of principal gases (CO_2–N_2–He)	1:1:5

During operation, either sealed or with a flowing gas, the output energy was continuously monitored using a calibrated thermopile and the output waveform was measured using a photon-drag detector. At intervals, samples of gas were transferred to a mass spectrometer for analysis.

Initial Experiments

In the development of the sealed laser, several different electrode materials were assessed experimentally. Lasers containing stainless-steel electrodes operated well with flowing gases (a 1:1:5, CO_2–N_2–He mixture being used, typically) but arcing between the main electrodes commenced soon after seal-off and became persistent after 10^3–10^4 pulses. It was not possible to significantly prolong the life of the device by varying the proportions of gas mixture. In the hope of increasing the photoemission of electrons from the cathode and hence preventing arcing, several lasers containing electrodes with varying degrees of controlled surface oxidation were assessed. These produced no significant improvement in life, however.

After the onset of arcing, analyses of the residual free gas in several sealed lasers showed that significant amounts of carbon monoxide and oxygen had accumulated. These were presumably produced by the dissociation of carbon dioxide according to the reversible equation

$$CO_2 \rightleftharpoons CO + O.$$

In general, between 0.1 and 0.4 percent of oxygen and 1–2 percent of carbon monoxide were found. Neither ozone nor oxides of nitrogen were observed to the detection sensitivity limits of 100 parts per million (ppm) for NO and NO_2 and 0.2 percent for N_2O. This does not rule out the possibility that concentrations of these gases below the detection limit are important. Moreover, little is known about the lifetime of ozone in the laser environment and it is possible that some was present originally.

To determine whether oxygen or carbon monoxide was associated with arcing, lasers were operated with flowing gases and various proportions of oxygen and carbon monoxide were added separately and in combination. It was found that more than 5 percent of carbon monoxide could be flowed before arcing commenced, whereas the levels of oxygen which led to arcing were 0.1–0.5 percent, i.e., similar to those found in degraded sealed lasers. Moreover, if these concentrations of oxygen were present, the addition of carbon monoxide did not prevent arcing. It therefore appeared desirable to minimize the presence of oxygen.

The stainless-steel electrodes used in the initial experiments were replaced by nickel pressings in the hope of catalyzing the recombination of carbon monoxide and oxygen back to carbon dioxide at the electrode surfaces. This change led to a significant improvement, and operational lives of 4×10^3–1×10^5 pulses were obtained (though mostly at the lower end of this range). This was not necessarily the result of catalytic action since there are other differences between the nickel and stainless-steel electrodes; for example, in the nature of inclusions in the metal surface. The best discharges and the longest lives were achieved when the distance between the electrodes varied by less than 0.02 mm. All subsequent lasers were therefore made with this degree of precision.

Gaseous Additives

In order to limit the generation of oxygen, three basic approaches were considered. The first was to introduce some mechanism for the selective removal of oxygen; for example, by diffusion through a heated silver tube. The second was to seal the laser with added carbon monoxide in order to bias the reaction equation in the backward direction and thus to discourage the dissociation of carbon dioxide. The third approach was to use a form of gaseous catalysis. The aim of this would be to cause each oxygen atom to recombine with a carbon monoxide molecule preferably before it could combine with another oxygen atom to form a stable oxygen molecule. It was thought that in a sealed device operating at atmospheric pressure a gaseous catalyst would be more effective than a solid surface, since the mean free path for collisions between gas molecules is very small ($\simeq 5 \times 10^{-5}$ mm) compared with the interelectrode distance.

The first of these three approaches (the selective removal of oxygen) was rejected since this would probably encourage the dissociation of carbon dioxide by inhibiting the reverse reaction. The second was assessed in a series of experiments in which lasers were sealed after the addition of carbon monoxide in various proportions between 1.25 and 6.6 percent. The best concentration was found to be 4.6 percent, and even this produced only a tenfold increase in life. Failure of the device again came through arcing rather than a reduction of output.

For the third approach (the addition of a gaseous catalyst) it was felt that hydrogen might be suitable since it had been shown by Carbone [6] and Wittemann [7] to be effective in producing long lives in sealed CW lasers operating at pressures up to 2.7 kPa. Although the mechanisms limiting the life of

low-pressure lasers are very different (for example, there is no arcing problem due to the generation of oxygen), they share the requirement that the dissociation of carbon dioxide should be limited.

The reactions proposed by Wittemann for the possible effect of hydrogen are as follows. There would always be present some oxygen atoms derived from the basic dissociation equation

$$CO_2 \rightleftharpoons CO + O.$$

Hence OH radicals would be formed thus

$$O + H \rightleftharpoons OH.$$

This would be followed by reactions which could be summarized as follows:

$$CO + OH \rightleftharpoons CO_2 + H.$$

Hence, in effect, the oxygen and carbon monoxide would be recombined to form carbon dioxide and the hydrogen would be available to repeat the cycle.

It was not known whether such a catalytic effect would be appreciable at atmospheric pressure. To assess this approach, a series of experiments were performed in which a laser was sealed off with varied proportions of hydrogen between 0.19 and 2.5 percent. The results showed that the addition of hydrogen in suitable proportions prolonged life by a factor exceeding 10 but that, though arcing was prevented, the output dropped rapidly. It was interesting to note that even when the proportion of oxygen had risen as high as 1.2 percent, there was no arcing in the presence of a suitable concentration of hydrogen. On the other hand, if the proportion of hydrogen exceeded about 0.6 percent, not only was the steady decline in output even more rapid but there was a tendency to arc towards the end. Higher concentrations of hydrogen resulted in arcing even though the proportion of oxygen was much lower than normal.

It appeared, then, that though carbon monoxide and hydrogen each prolonged life, hydrogen in appropriate concentrations inhibited arcing but allowed the output to fall to very low levels, whereas carbon monoxide maintained the output but ultimately permitted arcing. The possibility that the simultaneous addition of both gases would combine the benefits of each was assessed experimentally by sealing the laser successively with mixtures of both gases in varied proportions. This was successful in that a suitable mixture gave a very great increase in life. The output remained constant at a high level and there was virtually no arcing.

Operational Life

To establish the effectiveness of the mixture of hydrogen and carbon monoxide, life tests were performed at a pulse-repetition frequency (PRF) of 2 Hz on a first batch of seven substantially identical lasers, initially without the additives. All of these became very difficult to operate within about 10^4 pulses, since the operational voltage range became extremely narrow and variable. It was possible by careful control of the voltage, PRF, etc., to process only two lasers through this very difficult initial period and these ultimately provided more than 2×10^6 consecutive satisfactory pulses. The remaining five failed, however, due to persistent arcing within about 10^4 pulses. These were opened and resealed with the H_2-CO additives. All then operated satisfactorily from the outset and showed no deterioration after 1×10^6-2×10^6 pulses each. Thus the effectiveness of the H_2-CO mixture in promoting long lives was established and all subsequent lasers were therefore sealed off with its prior addition. Fourteen sealed lasers have now each operated for 4×10^5-2.5×10^6 pulses. Some of these were pulsed continuously while others were deliberately interrupted for periods of up to a month. Optical stability was good; retuning of the mirrors was seldom needed, even after transportation. In all cases, the performance was unchanged at the termination of the test.

Fig. 2 is a graph of output peak power as a function of the number of pulses of sealed operation for one multimode laser. The scale on the pulse-number axis is divided into two parts, that nearest the origin being on an expanded scale to show the details of the initial fall in output following seal-off, while later the scale is compressed to demonstrate the long-term stability of the output. The first point on the graph is for flowing gas (with H_2-CO additive) and subsequent points are after seal-off. The immediate initial fall is partly due to the fact that the laser was sealed off at atmospheric pressure, while in flowing conditions the pressure in the laser was slightly above atmospheric because of the impedance of pipes and taps. The output peak power measurements were made at 2 Hz throughout. At this PRF the output power and energy were the same as for single-shot pulses. All the points on the graph relate to measurements made at the same instantaneous voltage ($\simeq$21 kV) in order to give a valid comparison of the output at different times. However, in between these spot measurements the laser was operated at voltages up to 27 kV and output levels around 1.5 MW as indicated. After a rapid drop during the initial 5×10^3 pulses following seal-off, the peak power output efficiency was substantially constant over the next 2×10^6 pulses.

Tests were also performed on the pulse-to-pulse repeatability of the output by photographing a large number of successive output-power traces displayed on an oscilloscope, using a single exposure. Fig. 3 is a typical photograph of one hundred consecutive traces from a sealed laser after 5×10^5 pulses, and shows that the output peak power was constant within ± 10 percent.

During prolonged sealed operation, a dark grayish film developed upon the surface of the anode but not on the cathode. An analysis of the film from a laser which was still operating satisfactorily after 2.4×10^6 pulses showed that it consisted almost entirely of oxygen and nickel in roughly equal atomic proportions. The thickness was approximately 1 $\mu g/mm^2$ ($\simeq$200 nm). These results suggest the presence of a high concentration of negative oxygen-bearing ions within the discharge. The possible significance of this is discussed later.

The shelf life of sealed lasers exceeds one year. Thus far

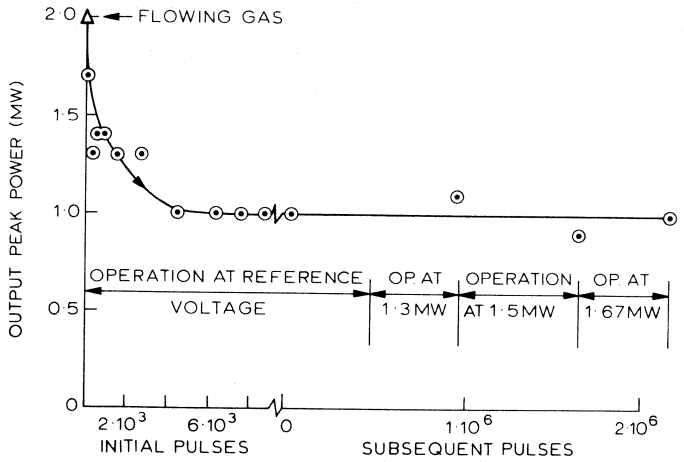

Fig. 2. Peak power output (multimode) as a function of the number of pulses of sealed operation.

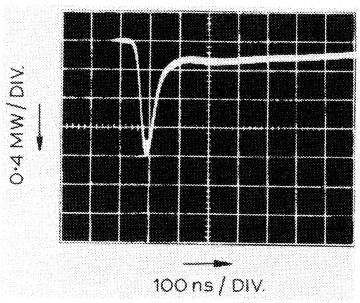

Fig. 3. Power output waveform of 100 superimposed pulses for a multimode laser after 5×10^5 pulses.

no laser has failed on the shelf, so that the upper limit is not known.

Output Mode Properties

Nine out of the fourteen life-tested sealed lasers contained a concave fully reflecting mirror and a plane output window, so that the output was multimode. Typically, at the end of 2×10^6 pulses the output peak power exceeded 1.5 MW. This was contained within a "spike" of duration 80-ns full width at half maximum (FWHM), followed by a "tail" of 3–4 μs. The total output energy was 300–500 mJ/pulse depending upon the operating voltage, corresponding to an energy per unit volume of 15–25 J/l and an optical conversion efficiency of about 10 percent. The beam divergence, defined as the full angular width at $1/e^2$ of the peak intensity, was measured as about 10 mrad.

Five of the sealed lasers contained two plane mirrors and an 8.5-mm-diam aperture, thus giving a single-mode (TEM_{00}) output. After 10^6 pulses at 2 Hz, the output peak power was still 1.0 MW contained in a 50-ns spike (FWHM), followed by a tail of about 2 μs. The beam divergence was 3.0 mrad, which is less than 1.3 times the diffraction-limited value. Fig. 4 shows a typical plot of beam energy density against radial distance in the optical far field, and shows that the distribution is approximately Gaussian, as expected for single-mode operation. The corresponding total energy was 100 mJ/pulse, which

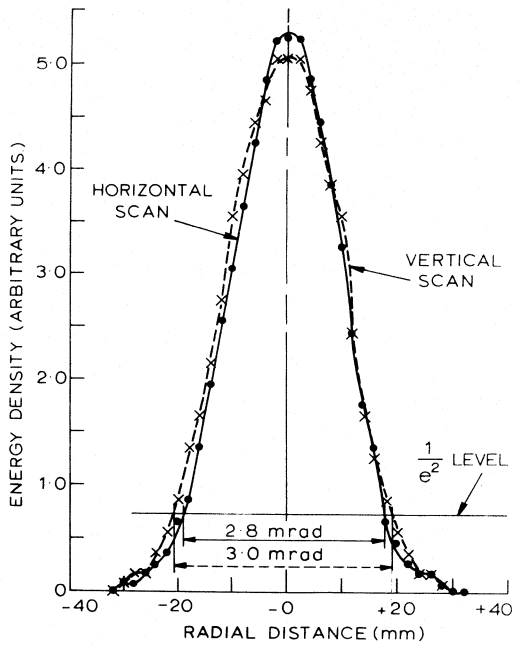

Fig. 4. Beam energy density of a single-mode laser as a function of radial distance in the optical far field. (Output peak power = 1 MW. Measurement distance = 13.35 m.)

was about one third of that from similar multimode lasers. Thus the output energy reduction in a single-mode laser is considerably greater than the peak power reduction. This is because of the sharper output spike and shorter tail as expected in single-mode operation.

Discussion

The development of arcing in sealed lasers may be explained in terms of the work of Nighan *et al.* [8] who have made a theoretical study of the discharge stability conditions for CO_2-N_2-He gas mixtures at low pressures ($\simeq$2.7 kPa). Their work shows that a high proportion of negative ions (predominantly O^- and CO_3^-) is present, and that the discharge becomes unstable if the ratio Nn/Ne between the negative ion and the electron concentrations (Nn and Ne, respectively) lies within a certain range of values. The presence of carbon monoxide influences this ratio; for example, by the associative detachment reaction

$$O^- + CO \longrightarrow CO_2 + e.$$

It is probable that hydrogen has a similar effect. Deutsch [9] has reported that the addition of hydrogen to a double-Rogowski TE laser operating with flowing gas led to a more uniform discharge and suppressed the formation of arcs.

Assuming that these principles are applicable at atmospheric pressure (and the analysis of the oxide surface film on the sealed laser anode is consistent with the presence of oxygen-bearing negative ions), it is probable that one role of the hydrogen and carbon monoxide is to control the Nn/Ne ratio right from the outset, thereby maintaining conditions for arc-free operation. The last statement is validated by analyses of the residual gases at the end of the life tests in the two

lasers which had operated for 10^6 pulses without the additives. These analyses showed that the residual hydrogen and carbon monoxide levels were similar to those found in life-tested lasers which had been sealed off with the H_2-CO mixture. In other words, the proper levels of carbon monoxide and hydrogen in the two lasers had been accidentally obtained early in the tests. Presumably, the carbon monoxide was produced by dissociation of carbon dioxide while the hydrogen was derived from water vapor and outgassing of the electrodes, etc.

In general, the concentrations of the carbon monoxide, oxygen, and hydrogen in lasers which had survived 10^4 pulses without arcing were very similar to those in lasers surviving 10^6 pulses and more. This was true whether or not hydrogen and carbon monoxide were added initially. It appears, therefore, that in satisfactory lasers an equilibrium composition is established within about 10^4 pulses. This is consistent with the fact that the laser output remains substantially constant between 10^4 and 10^6 pulses.

Acknowledgment

The authors wish to thank their colleagues at the Services Electronics Research Laboratory who made contributions to this development; in particular, M. R. Harris, P. R. Pearson, V. G. Roper, and M. J. Wright. They also wish to thank Dr. E. W. Blackmore of the Admiralty Materials Laboratory for performing the electrode film analyses.

References

[1] R. Dumanchin and J. Rocca-Serra, "Electronique quantique," *C. R. Acad. Sci.*, vol. 269B, pp. 916–917, 1969.
[2] A. J. Beaulieu, "Transversely excited atmospheric pressure CO_2 lasers," *Appl. Phys. Lett.*, vol. 16, pp. 504–505, 1970.
[3] A. K. LaFlamme, "Double discharge excitation for atmospheric pressure CO_2 lasers," *Rev. Sci. Instrum.*, vol. 41, pp. 1578–1581, 1970.
[4] H. M. Lamberton and P. R. Pearson, "Improved excitation technique for atmospheric pressure CO_2 lasers," *Electron. Lett.*, vol. 7, pp. 141–142, 1971.
[5] P. R. Pearson and H. M. Lamberton, "Atmospheric pressure CO_2 lasers giving high output energy per unit volume," *IEEE J. Quantum Electron. (Special Issue on 1971 IEEE/OSA Conference on Laser Engineering and Applications)*, vol. QE-8, pp. 145–149, Feb. 1972.
[6] R. J. Carbone, "Long-term operation of a sealed CO_2 laser," *IEEE J. Quantum Electron.*, vol. QE-3, pp. 373–375, Sept. 1967.
[7] W. J. Wittemann, "Sealed-off high-power CO_2 lasers," *Phillips Tech. Rev.*, vol. 28, pp. 287–296, 1967.
[8] W. L. Nighan, W. J. Wiegand, and R. A. Haas, "Ionisation instability in CO_2 laser discharges," *Appl. Phys. Lett.*, vol. 22, pp. 579–582, 1973.
[9] T. F. Deutsch, "Effect of hydrogen on CO_2 TEA lasers," *Appl. Phys. Lett.*, vol. 20, pp. 315–316, 1972.

Optimization of a Laser Communications System Using Electrooptic Modulation

ARMAND L. WAKSBERG, SENIOR MEMBER, IEEE

Abstract—**An analysis is made of the optimum carrier-to-noise ratio (CNR) that can be obtained from a laser communications system using external polarization electrooptic modulation and avalanche diode detection. The analysis is not restricted to low-modulation index but covers the range up to the maximum possible modulation. Alternate definitions of modulation index are given in terms of communication concepts. Finally, some practical uses of the results are discussed.**

I. Introduction

In a previous publication [1] a study was made of the maximum signal power that can be obtained from electrooptic modulation of lasers using internal and external polarization modulation. In this paper, we shall consider the optimum carrier-to-noise ratio (CNR) that could be obtained from a laser communications system using external polarization, electrooptic modulation, and avalanche diode detection. The analysis is not restricted to low-modulation index but covers the range up to the maximum possible modulation. Alternate definitions of modulation index are given in terms of communication concepts. Finally, some practical uses of the results are discussed.

Manuscript received March 7, 1975; revised April 28, 1975. This work was supported in part by the Canadian Government under Defense Industrial Research Grant 9751-11.

The author is with RCA Research Laboratories, Ste-Anne de Bellevue, P. Q., Canada.

II. System Analysis

The type of system that is being considered is shown in Fig. 1. It consists, on the transmitter side, of a laser producing a polarized beam of power P_l, an electrooptic modulator properly oriented, a phase shifter, an analyzer, and a telescope. The receiver includes a telescope, an avalanche-type diode, and a preamplifier. It is assumed that maximum modulation of the laser beam is permissible even though strong nonlinearity will be produced. This is because the resulting intensity modulation can be used to generate a subcarrier which can itself be modulated by any convenient modulation scheme such as FM,

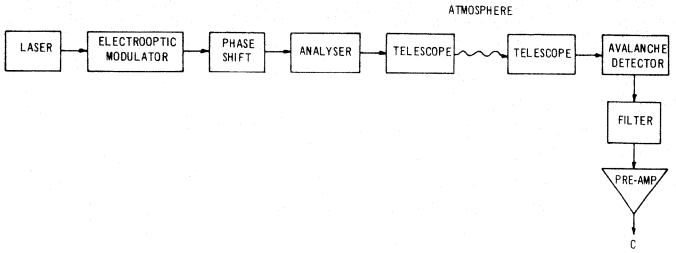

Fig. 1. Schematic diagram of a laser communication system.

PM, or PCM. Nonlinear effects would then become inconsequential. In our subsequent derivations, CNR will refer to that subcarrier which modulates the laser beam.

A. Modulation System

The type of modulation envisaged is a standard external polarization modulation using an electrooptic crystal as modulator. The output power P_0 in this case is given by [2]

$$P_0 = P_l \sin^2 \Gamma/2 \tag{1}$$

where P_l is the laser output power and Γ is the phase difference between the two electrooptic axes of the crystal.

A modulation voltage $V_m(\omega) = V_m \cos \omega_m t$ applied to such a crystal would produce a modulation in the power of the laser beam given by

$$P_0 = CP_l \{\tfrac{1}{2}[1 - \cos(\Gamma_b)J_0(\Gamma_m)] + \sin(\Gamma_b)J_1(\Gamma_m)\cos \omega_m t + \cdots\} \tag{2}$$

where the series is expanded only to the fundamental frequency. Other terms are eliminated by proper filtering. J_n is the Bessel function of order n. $\Gamma = \Gamma_b + \Gamma_m \cos \omega_m t$ is the total phase difference along the two electrooptic axes of the crystal made up of a constant bias term Γ_b and a modulated term of amplitude Γ_m and circular frequency ω_m. The constant term can be the result of natural birefringence or a dc voltage applied to the crystal, while the modulated term is produced by the modulating voltage $V_m \cos \omega_m t$ through the relation $\Gamma_m = KV_m$ with K a constant. Finally, C is the coupling coefficient of the polarization coupler which extracts the cross polarized part of the beam ($\leqslant 1$).

B. Modulation Indices

In order to relate our results to the magnitude of the modulation impressed on the carrier, possible definitions of modulation indices have to be given explicitly. Also the functional relation between these indices and the phase modulation (Γ_m) should be obtained. The power output versus phase shift relation is shown in Fig. 2.

If an optical bias Γ_b is chosen and a drive modulation Γ_m is applied, the output light modulation would fluctuate between $P_{\max}$ and $P_{\min}$ in a manner similar to that depicted in the figure. This is what would be observed on a scope if the light is detected by a typical square law detector. The modulation is obviously not sinusoidal but is given by (2). Three modulation indices suggest themselves and will now be defined.

Peak-to-Peak Modulation Index m_p: This is probably the simplest modulation index as it can be obtained directly from

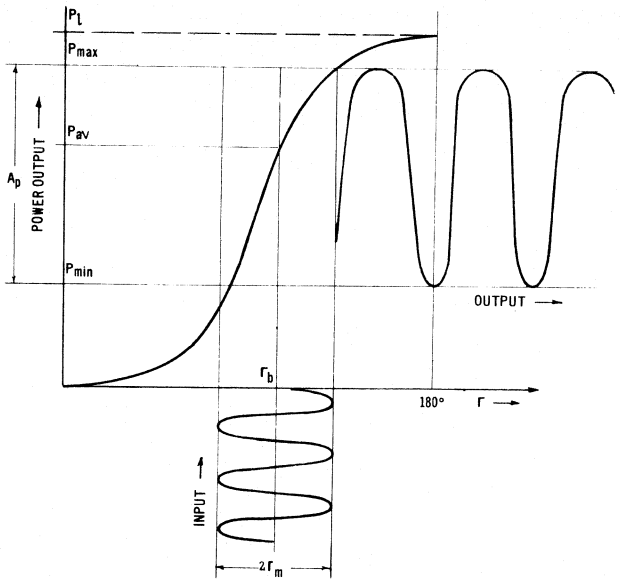

Fig. 2. Electrooptic modulation.

the scope output. We thus define the peak-to-peak modulation index as

$$m_p = \frac{P_{\max} - P_{\min}}{P_{\max}} = \frac{A_p}{P_{\max}} = \frac{2 \sin \Gamma_p \sin \Gamma_m}{1 - \cos(\Gamma_b + \Gamma_m)}. \tag{3}$$

Amplitude Modulation Index m_a: It is possible to define an amplitude modulation index m_a such that

$$m_a = \frac{P_{\max} - P_{\min}}{2/P_a} = \frac{\sin \Gamma_b \sin \Gamma_m}{1 - \cos \Gamma_b}, \quad \text{for } \Gamma_m \leqslant \frac{\pi}{2} \tag{4}$$

where P_a is that output power that would be obtained when Γ_m is reduced to zero.

Efficiency Factor ξ: A third modulation index, here called the efficiency factor ξ, is defined as the ratio of the total laser power which is being modulated at the signal frequency ω to the average nonmodulated part of the laser power, i.e.,

$$\xi = \frac{2 \sin(\Gamma_b)J_1(\Gamma_m)}{1 - \cos(\Gamma_b)J_0(\Gamma_m)}. \tag{5}$$

It can be shown that this term is directly related to the efficiency of the modulation being used.

Comparison Between the Indices: Probably the best way to compare the three indices is by means of a graph as shown in Fig. 3. Measurement of one modulation index thus permits the determination of the other two and the corresponding phase drive.

C. Detection

For detection, it is assumed that a standard avalanche detector is used. It is shown in [3] that the carrier power, noise power, and power CNR for these devices is given by

$$C = (P_R(\omega_m)R_0M)^2 \frac{R_L}{2} \tag{6}$$

$$N = \{2q(I_{ds} + (\bar{P}_R R_0 F_s + I_{db}F_d)M^2 + i_{na}^2(\omega_m)\}BR_L \tag{7}$$

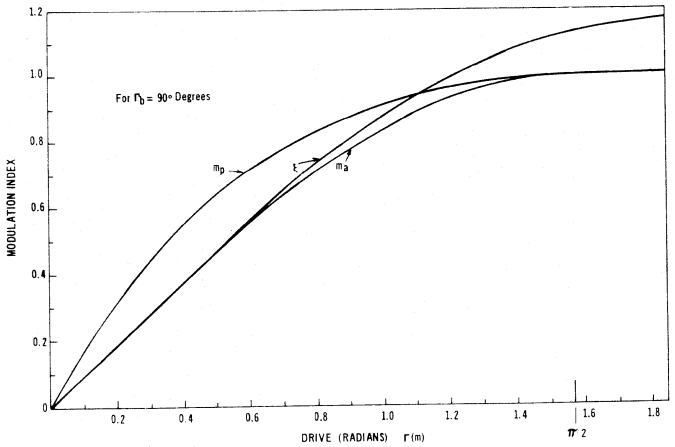

Fig. 3. Modulation indices versus phase angle drive.

$$\frac{C}{N} = \frac{(P_R(\omega_m)R_0M)^2/2}{\{2q[I_{ds} + (\bar{P}_R R_0 F_s + I_{db}F_d)M^2] + i_{na}^2(\omega_m)\}B} \tag{8}$$

where $P_R(\omega_m)$ is the received amplitude of the modulated power of the laser beam at the carrier frequency (at the detector), $\bar{P}_R$ is the received average dc component of laser power at the detector where

- R_0 unity-gain responsivity;
- M gain ($M = 1$ in the case of nonmultiplying photodiode);
- q electronic charge;
- I_{ds} that component of the dark current (usually the surface component) which is not multiplied, typically, $I_{ds} \approx 10^{-7}$ A for an RCA #C30817 diode;
- I_{db} that component of the dark current (usually the bulk-generated dark current) which undergoes multiplication, $I_{db} = 10^{-10}$ A for this diode;
- B noise bandwidth;
- i_{na}^2 equivalent mean-square noise current of the amplifier and biasing circuit;
- F_d detector effective excess noise factor appropriate to the multiplication of the dark current I_{db};
- F_s detector effective excess noise factor appropriate to the multiplication of the photocurrent (we assume that the radiation due to background and signals are at the same wavelength);
- R_L load resistance.

In the case of typical reach-through avalanche diodes [4]

$$F_s \approx F_d = k_e M + \left(2 - \frac{1}{M}\right)(1 - K_e) \tag{9}$$

where K_e is an effective weighted ionization rate ratio and depends on the particular diode. It is equal to 0.02 for the RCA #C30817

$$R_0 = \frac{q\eta}{h\nu}$$

where η is the efficiency of the diode and is about 70 percent for this diode.

- h Planck's constant.
- ν Laser frequency.

It shall be assumed here that the system under consideration has a gain bandwidth wide enough that it does not need to be taken into account in the calculation.

A bandpass filter introduced at the output of the detector, centered at the frequency of interest (ω_m), will produce a power signal [from (2)] of

$$P_R(\omega_m) = P_R \sin(\Gamma_b) J_1(\Gamma_m) \tag{10}$$

while the dc component is

$$\bar{P}_R = \frac{P_R}{2}(1 - \cos(\Gamma_b) J_0(\Gamma_m)) \tag{11}$$

where $P_R = TCP_l$ is the received power at the detector when $\Gamma_b = 180°$, $\Gamma_m = 0$. T is the transmission loss coefficient going from the modulator output to the detector. It includes all optical and atmospheric losses. By making the proper substitutions, the CNR becomes

$$\frac{C}{N} = \frac{(P_R \sin(\Gamma_b) J_1(\Gamma_m) R_0 M)^2/2}{\left\{2q\left\{I_{ds} + \left(\frac{P_R}{2}[1 - \cos(\Gamma_b)J_0(\Gamma_m)]R_0 + I_{db}\right)\left[k_e M + \left(2 - \frac{1}{M}\right)(1 - k_e)\right]M^2\right\} + \frac{4KT}{R_L}\right\}B}. \tag{12}$$

D. Optimization Carrier-to-Noise Ratio

It is evident that for best systems performance, one should strive to maximize the CNR at the receiving end. An examination of (12) will reveal that for high CNR, the laser power and coupling coefficient should be a maximum. Usually, the driving voltage limitation sets a limit on the driving phase Γ_m. In a real situation, the laser beam power will be attenuated by the intervening optics and atmosphere between laser and detector. In the calculation of CNR, we shall therefore set the received power P_R and the driving phase Γ_m as the independent variables. Optimization will then result by choosing the dc bias Γ_b and gain M so as to make the CNR a maximum.

Because of the complexity of (12) optimization has to be carried out using a computer. The avalanche diode considered here is a well-proven "reach-through" diode of a type such as an RCA #C30817. The standard load of $R_L = 50\ \Omega$ is used for the computation and a bandwidth of 30 MHz is assumed. The results of the optimization calculations are plotted in Figs. 4-7.

In Fig. 4 the optimum CNR is plotted as a function of the received power P_R for various modulation drive Γ_m. It can be seen that the amount of drive can have a marked effect on the CNR. In fact, a factor of about 9 in Γ_m (which is equivalent to the same factor in drive voltage) will produce a ratio of about 30 in CNR.

To obtain the optimum CNR for any other bandwidth than 30 MHz, simply multiply the CNR by 30 MHz and divide by the required bandwidth B. Fig. 5 is a plot of carrier signal and output noise as a function of received power. This is done for various Γ_m. The values are those obtained under maximum

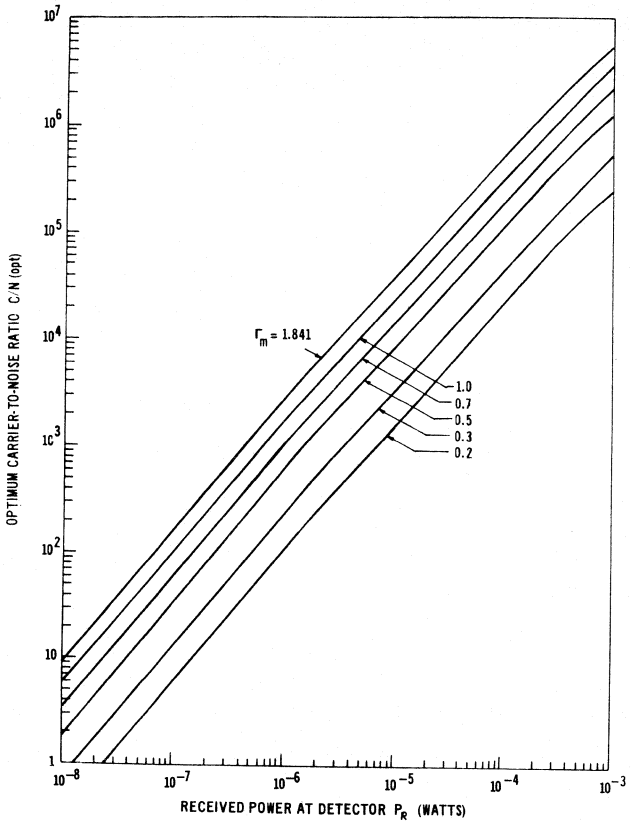

Fig. 4. Optimum CNR as a function of received power P_R for various signal drive Γ_m.

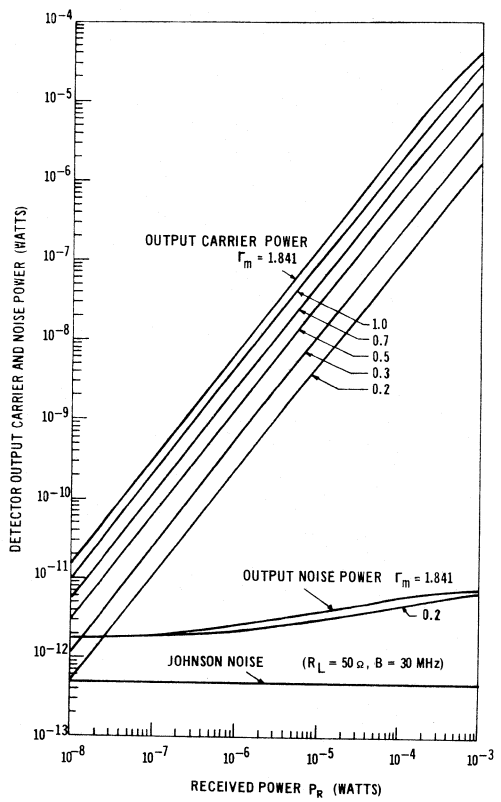

Fig. 5. Carrier and noise levels at detector output as a function of received power P_R and various signal drives Γ_m.

CNR. For reference purposes, the Johnson noise reference level is also put on the same graph.

In Fig. 6 the optimum avalanche diode gain M is plotted against the received power. As before, this is done for various Γ_m.

Fig. 7 is a plot of the optimum optical bias Γ_b as a function of P_R for various Γ_m.

Finally, Fig. 8 gives the maximum CNR as a function of Γ_m for various P_R.

III. Discussion of Results

Calculations using the curves in Fig. 4 result in a CNR which is approximately proportional to $P_R^{1.3}$ for $0.4 < \Gamma_m < 1.3$. The effect of drive (Γ_m) is important and Fig. 8 shows that the optimum CNR varies linearly with Γ_m in the interval $0.4 < \Gamma_m < 1.3$. Within some narrow limits it is possible to trade P_R for larger Γ_m although the former has a larger effect and is not limited in magnitude as is Γ_m. It is also observed that once Γ_m reaches about 1.4, 90 percent of the maximum attainable CNR has been achieved. Trying to obtain greater CNR by driving the modulator harder becomes a venture of diminishing return. For example, to go from $\Gamma_m = 1.4$ to its maximum value of 1.841 means an increase in voltage requirement of about 30 percent, i.e., an increase

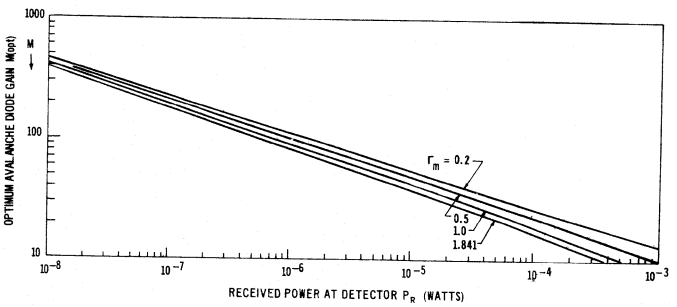

Fig. 6. Optimum avalanche detector gain (M) as a function of received power (P_R) for various signal drives (Γ_m).

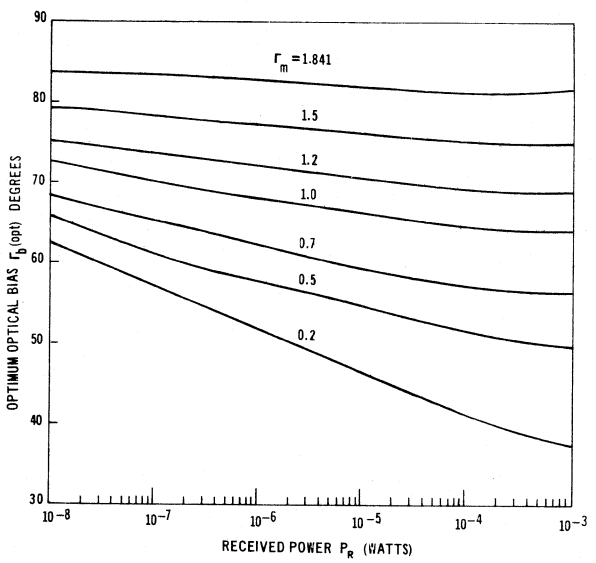

Fig. 7. Optimum optical bias (Γ_b) as a function of received power (P_R) for various signal drives (Γ_m).

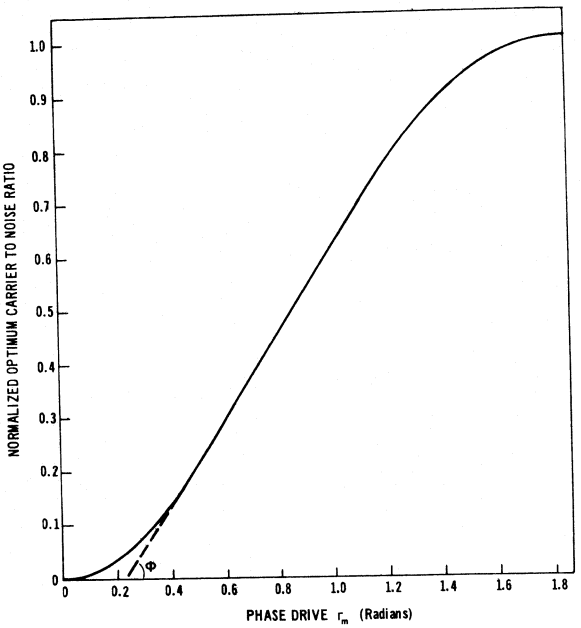

Fig. 8. Normalized CNR as a function of drive Γ_m.

drive power requirement of 70 percent. The benefit in CNR is only about 10 percent.

The optical bias required for optimum CNR is seen from Fig. 7 to be always below 90°. In fact, for small drive, the optical bias should be well below that point. The reason for this can be understood qualitatively if it is realized that although the maximum modulated power would occur for $\Gamma_b = 90°$, the average (dc) radiation component is very high at this point—specifically, it is equal to $P_R/2$ (see Fig. 2). The values of Γ_b given in Fig. 7 are thus a compromise between the size of the signal and the noise level produced by the dc component of the signal which results in the maximum possible CNR.

Consequently, in a practical situation, it is important to know the drive Γ_m and the expected received power in order to control the optical bias for optimum operation.

A. Practical Use of Results

In the design of a practical system it is most important to be able to predict its performance. For example, knowing the power output of a laser, the modulation index, and the loss through the atmosphere, it is possible to predict the absolute signal strength at the detector (P_R). The optimum CNR to be expected can then be obtained from Fig. 4.

In another example, let us suppose a communication system has been built and prediction of its performance under various conditions is required. This can be obtained by first measuring the laser power received by the avalanche detector using a power meter or a calibrated diode at the place of the detector. The power reading when the modulator phase is adjusted for maximum output (no RF modulation) gives the value of P_R. Knowing the drive Γ_m, it is now possible to determine the optimum CNR for this situation (using Fig. 4).

If a certain CNR is required, it is possible to obtain through Figs. 4 or 8 the required modulation drive Γ_m (or modulation index from Fig. 2). If the effect of the link distance or the weather can be evaluated, new values for P_R can be calculated and optimum CNR obtained using Fig. 4.

Acknowledgment

The author wishes to thank Dr. McIntyre and Dr. J. Conradi for their helpful discussions concerning the avalanche diodes as well as Dr. Bachynski for his kind support.

References

[1] A. L. Waksberg, "A comparative evaluation between internal and external polarization modulation of lasers," *IEEE J. Quantum Electron.*, vol. QE-9, pp. 1086–1097, Nov. 1973.
[2] M. Ross, *Laser Receivers*. New York: Wiley, 1966.
[3] P. P. Webb, R. J. McIntyre, and J. Conradi, "Properties of avalanche photodiodes," RCA Tech. Rep. MNLDO74-TR-002, 1974; also RCA Application Notes C30817.
[4] J. Conradi, private communication.

Interferometric Studies of Mode-Locked Nd^{3+}:Glass Lasers

RAJIV R. SHAH, STUDENT MEMBER, IEEE, THOMAS A. RABSON, MEMBER, IEEE, AND DAE M. KIM

Abstract—**A general technique for measuring the electric-field vector of the ultrashort pulses from mode-locked laser systems is described. The technique is applied to perhaps the most difficult laser to analyze, the dye mode-locked Nd^{3+}:glass laser whose pulses change rapidly in bandwidth and amplitude, are chirped, and can occur in quite short pulse trains. The results of these measurements indicate a rather rapid change in the phases between modes, and a plot of the phase change as a function of mode frequency has been obtained.**

I. Introduction

NUMEROUS TECHNIQUES have been developed for analysis of the output of mode-locked lasers [1]. The technique to be reported here is unusual in its inherent simplicity and the fact that its basic concepts are rooted in classical optics modified to take into account the transient nature of the output of mode-locked Nd^{3+}:glass lasers. The methods used so far are two- and three-photon fluorescence [2]-[4], second- and third-harmonic generation [5]-[7], time-resolved spectroscopy [8], [9], and photographing with ultrafast streak cameras with picosecond time resolution [10], [11]. The information obtained from all but the time-resolved spectroscopy method is limited mainly to the spectral- or temporal-intensity profiles of the picosecond pulses. However, the phase of the mode-locked field is equally important since the typical mode-locked output from pulsed lasers does not usually reach a steady state and such phenomena as chirping, partial mode locking, and substantial change of pulse characteristics from pulse to pulse even within a single firing of the laser are known to exist in mode-locked Nd:glass lasers. Cross-correlation measurements between two different lasers have been used to measure the time duration of one of the mode-locked HeNe lasers, and it was suggested that the technique be applied to mode-locked Nd^{3+}:glass lasers [12]. The necessity of having one unchirped laser was also mentioned in [12], whereas our technique only requires the cross correlation of two pulses in the pulse train of a single laser in order to obtain relative phase information.

One can measure the amplitude and frequency of the cavity modes which are present in the output pulse of a mode-locked laser by various well-known spectroscopic methods including the use of a Michelson interferometer (MI), which essentially gives the autocorrelation of the pulse. However, to determine completely the nature of the pulse, one must also determine the relative phase of the different modes in the pulse. These phases do not change appreciably throughout the duration of the pulse (usually less than 10 ps). It is shown in this paper how one can obtain by numerical techniques the relative phase change from one pulse to another from the experimentally determined cross correlation of the two pulses. If the form of one of the pulses in the train is known, then by forming the cross correlation of it with other pulses, the form of the other pulses can be determined. In addition to the cross correlation, the bandwidth and mode amplitude of the unknown pulses must be measured. The theory and experimental results of techniques involving time-resolved linear interferometry are presented herein. Specifically, it is pointed out that the measurements of fringe visibilities of auto- and cross correlations of Nd^{3+}:glass lasers can lead to information regarding: 1) the pulse bandwidth as well as the fraction and nature of the noise present; 2) the change of bandwidth between two successive pulses; and, finally, 3) the evolution of the relative phase of modes in any region of the pulse train. An interferometric technique of this kind, performed in different regions of the pulse train, combined with the fact that the pulses in the rising edge of the train are usually bandwidth limited [2], [9], can ultimately lead to the calculation of the time-dependent phase dispersion which occurs throughout the pulse train.

In Section II we present an outline of the theory of auto- and cross correlation of short pulses. The experimental procedures for measuring these functions are described in Section III. The numerical analysis of the experimental data and the final results are presented in Section IV.

II. Theory

The fringe visibility (FV) as measured by the MI (sketched in Fig. 1) is given by

$$\mathrm{FV} = \frac{I_{\max} - I_{\min}}{I_{\max} + I_{\min}} \tag{1}$$

where the total registered intensity

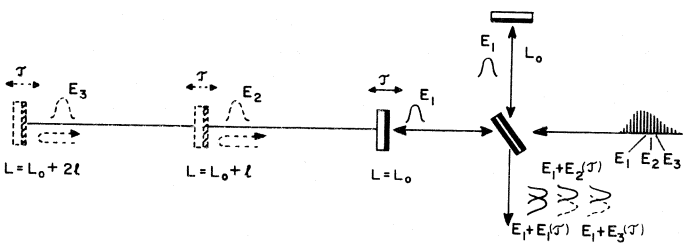

Fig. 1. Schematic representation of the MI as used for measuring auto- and cross correlations. L_0 is the distance of the fixed mirror from the beamsplitter and l is the optical length of the laser cavity. E_1, E_2, E_3 are any three consecutive pulses in the pulse train. τ is the differential displacement of the movable mirror.

Manuscript received March 11, 1975. This work was supported in part by the National Science Foundation.

The authors are with the Department of Electrical Engineering, Rice University, Houston, Tex. 77001.

$$I = \int_{-\infty}^{\infty} dt \langle |E_i(t) + E_j(t+\tau)|^2 \rangle \quad (2)$$

consists of the linear superposition of the time-delayed electric field of the same ($i = j$) or different pulses ($i \neq j$).

A. Autocorrelation

For the case of autocorrelation, for which $i = j$, the net registered intensity can be expressed in terms of the power spectrum of the electric field as

$$I(\tau) = 2\,\mathrm{Re} \int d\omega [\,|\langle \mathcal{E}(\omega) \rangle|^2 + \langle |\epsilon(\omega)|^2 \rangle]\ [1 + e^{-i\omega\tau}]. \quad (3)$$

Here we have partitioned the field power spectrum into the mode-locked signal $|\langle \mathcal{E}(\omega) \rangle|^2$ and random noise $|\epsilon(\omega)|^2$ to include the effect of noise on fringe visibility since the output pulse is generally accompanied by noise due to imperfect mode-locking. Upon inserting (3) into (1), we obtain

$$\mathrm{FV} = \frac{\left| \int dw [\,|\langle \mathcal{E}(\omega) \rangle|^2 + \langle |\epsilon(\omega)|^2 \rangle]\ e^{-i(\omega - \omega_0)\tau} \right|}{\int dw [\,|\langle \mathcal{E}(\omega) \rangle|^2 + \langle |\epsilon(\omega)|^2 \rangle]} \quad (4)$$

where ω_0 is the central frequency of the emission.

From (4) note that by measuring the FV of the field autocorrelation one can distinguish the nature of noise present in the mode-locked pulses. For instance, for the case of white noise, the FV will go to zero for large delay time τ. The same is true if the bandwidth of the noise is of the same order of magnitude as that of the mode-locked signal within the broad gain profile. If, on the other hand, the bandwidth of the noise is much less than that of the signal, the FV will not go to zero even for large T. Additionally, one can also obtain the fraction of power present in the noise and the ratio of bandwidths of two successive pulses. These points will be pursued further in the following sections.

B. Cross Correlation

For the case of cross correlation between two pulses in the same pulse train, the FV can be analyzed in the same way as in the autocorrelation. In this case, however, there exist two important differences: a) the two pulses can have different power spectra, i.e., bandwidths, which can be measured separately by autocorrelation techniques (see Section IV); and b), more importantly, the relative phase difference existing between the modes of the two pulses under consideration can significantly modify the FV profile. Because the FV curves for cross correlation are quite sensitive to relative mode phase, they can be used to measure these phases.

Thus we may write in this case

$$\mathrm{FV} = \frac{\left| \mathcal{S}(\tau) + \int \{\langle |\epsilon(\omega)|^2 \rangle\}_{\mathrm{av}}\, e^{-i(\omega - \omega_0)\tau}\, d\omega \right|}{\int d\omega [\{|\langle \mathcal{E}(\omega) \rangle|^2\}_{\mathrm{av}} + \{\langle |\epsilon(\omega)|^2 \rangle\}_{\mathrm{av}}]}. \quad (5)$$

Here $\{|\langle \mathcal{E}(\omega) \rangle|^2\}_{\mathrm{av}}$, $\{\langle |\epsilon(\omega)|^2 \rangle\}_{\mathrm{av}}$ represent, respectively, the powers in the mode-locked signal and noise averaged over the two interfering pulses, and the signal portion of FV

$$\mathcal{S}(\tau) \equiv \int |\langle \mathcal{E}_1(\omega) \rangle|\, |\langle \mathcal{E}_2(\omega) \rangle|\, e^{i\Delta\chi(\omega)}\, e^{-i(\omega - \omega_0)\tau}\, d\omega \quad (6)$$

contains explicitly the relative phase between the two pulses

$$\Delta\chi(\omega) = \chi_1(\omega) - \chi_2(\omega). \quad (7)$$

III. Auto- and Cross-Correlation Measurements

A. Experimental Setup

The experimental systems for generation and measurement of picosecond pulses are depicted schematically in Fig. 2. The setup consists of 1) a mode-locked Nd^{3+}:glass laser; 2) a triangular two-photon-fluorescence (TPF) monitoring arrangement; 3) a diffraction spectrometer; and 4) a photodiode-oscilloscope detection system. In addition, the arrangement necessary for time-resolved interferometry includes: 1) a Michelson interferometer (MI); 2) an image-converter camera (ICC); 3) a laser-triggered spark gap (LTSG); and 4) a 17-m optical delay path.

The laser cavity consists of two plane-wedge mirrors with 99- and 65-percent reflectivities. The active medium is an Owens Illinois Type ED2 Nd:glass rod 20.5 cm long, 1 cm in diameter, and cut at Brewster angles at both ends. The rod was pumped by an ILC helical xenon flashlamp. The cavity was made to oscillate in the TEM_{00} mode by inserting a 3-5-mm spatial filter into the cavity. Mode locking was achieved using Eastman Kodak dyes A-9860 in 1,2-dichloroethane or A-9740 in chlorobenzene.

Small fractions of the laser output were sampled to monitor: a) the TPF in a 10^{-2}-M solution of rhodamine-6 G in ethanol using a triangular arrangement; b) the spectra of the pulse trains on Kodak 1Z plates at the output of a Jarrel Ash Series 70-000 3.4-m Ebert grating spectrograph with a first-order reciprocal linear dispersion of 5.0 Å/mm; and c) the intensity profiles of pulse trains using an ITT F-4000 biplanar vacuum photo-diode detector displayed on a Tektronix 7904 oscilloscope.

The rest of the beam was allowed to reach the MI after traveling a distance of 17 m in air (effective delay ≈ 55 ns). The movable arm of the interferometer could be moved through a distance $L = L_0 + 2l$, where l is the optical length of the cavity and L_0 is the distance of the fixed mirror from the beamsplitter. The movable mirror was mounted on a translation stage provided with a micrometer gauge to allow small, accurately measured dispalcements. The output of the MI was viewed through a TRW Instruments STL Model 1D ICC with an S-1 spectral response tube and fitted with a Model 7B high-speed streak unit. Fast and efficient triggering of the ICC was achieved by using an LTSG. A small fraction of the beam focused with a short focal-length lens was used to trigger the spark gap. The LTSG delays were typically less than 40 ns.

The experimental setup described previously allowed simultaneous recording of the TPF, the spectrum, the intensity profile, and streaked interference fringes of the mode-locked laser output.

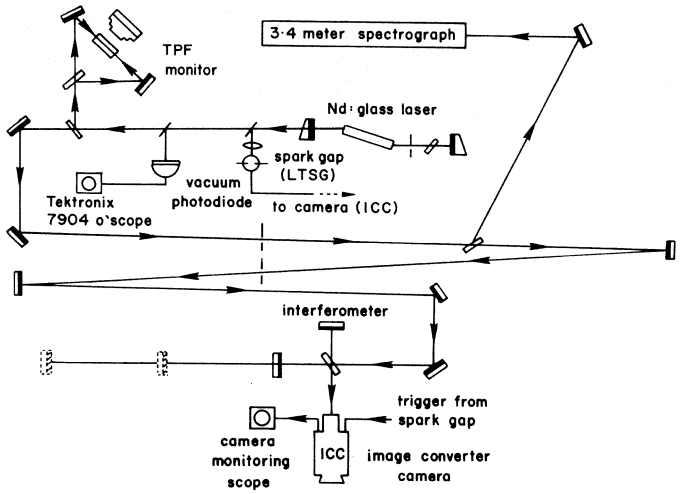

Fig. 2. Experimental arrangement for generation and measurement of picosecond pulses. In addition to the MI and ICC necessary for measuring time-resolved correlations, the experimental setup includes a TPF monitor and a 3.4-m spectrograph.

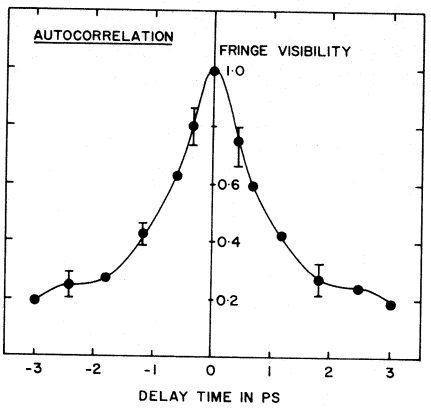

Fig. 3. Measured FV as a function of delay time τ for autocorrelation.

B. Techniques

Reproducible regular pulse trains were obtained under carefully controlled conditions. High peak power, short pulse trains were generated using a concentrated mode-locking dye solution and pumping voltages approximately 20 percent above threshold. The optical length of the cavity as determined by adjacent-pulse cross correlation TPF was 74.8 cm. Pulse trains generated under these conditions were typically of 100–150-ns duration. Spectral widths were determined from the microdensitometer records of the processed photographic plates. Photographs of the TPF taken with an $f = 5.6$ cm, 1:1.3 camera were similarly analyzed with a microdensitometer.

Since the interference patterns were obtained for pulses with durations $\sim 10^{-12}$ s, the arms of the interferometer had to be equal to within a fraction of a millimeter. The ICC was triggered by a high-voltage pulse (~ 600 V) obtained from the LTSG. For pulse trains of 100–150-ns duration and a triggering accuracy $\leqslant 40$ ns of the spark gap, exposures could be obtained only on some shots of the laser for a 2-m delay path. This indicated that the region of observation was close to the tail of the pulse train. Introducing a 17-m delay path shifted the region of observation further up in the pulse train. The ICC was operated without the objective lens and with a slit in front of the photocathode. The streaking rate of the ICC was 50 mm/20 ns and the direction of sweeping was parallel to that of the fringes.

Time-resolved interference patterns were recorded on Kodak Royal X-Pan film. The film was developed using Acufine developer. Under conditions of operation and processing identical to that in the actual experiment, the characteristic curve for the film was plotted using density steps from the Kodak photographic step tablet. From the microdensitometer traces of the interference fringes and the characteristic curve of the film, the values of intensity maxima, minima, and hence of FV were obtained. For each setting of the interferometer arm (zero, one, or two cavity transit-time delays) values of FV were obtained for various values of the differential delay τ between the interferometer arms. Simultaneously, the TPF, the spectrum, and the intensity profile were recorded for each value of τ.

C. Results

The pulse trains were of 100–150-ns duration, consisting of 20–30 pulses. Typical widths for the time-integrated spectra ranged between 9 and 15 cm^{-1} and the time-integrated TPF widths were between 2 and 5 ps. In each interference pattern from the ICC, four sets of interference fringes were obtained corresponding to four consecutive pulses in the same pulse train as in [13]. From these pictures one can obtain the difference in sharpness of the sets of fringes for different delay times.

In Fig. 3 the measured autocorrelation fringe visibility as a function of differential delay time τ in the arms of the interferometer is plotted. The pulses in a streaked picture are any four consecutive pulses in the region of the pulse train being probed limited by the accuracy of the triggering system. Note in particular that the FV does not fall off to zero for large delay time. From this curve one can determine the bandwidth of the mode-locked signal and can also infer the nature as well as the power fraction of noise, as will be explicitly presented in the next section. In addition, by comparing the FV for any two successive sets of fringes in a streaked interference pattern one can obtain the change of bandwidth between two successive pulses.

In Fig. 4 we present the FV curves for cross correlation between two consecutive pulses. The substantial difference in the general shape of this curve as compared to that of autocorrelation clearly demonstrates the relative phase dispersion existing between two consecutive pulses. This will be elaborated upon in Section IV. Experimentally measured values of FV for the correlation of pulses separated by two cavity transit times are given in Fig. 5. For this case, due to the rapid variation of the FV values within the delay-time intervals used (which are the same as in Figs. 3 and 4) one should take the curve with data points connected qualitatively. However, the significance of this curve will be explained later.

IV. Analysis and Conclusions

In interpreting the autocorrelation fringe visibility, we approximate the actual power spectrum of the mode-locked signal and nosie with, in general, different bandwidths. Inas-

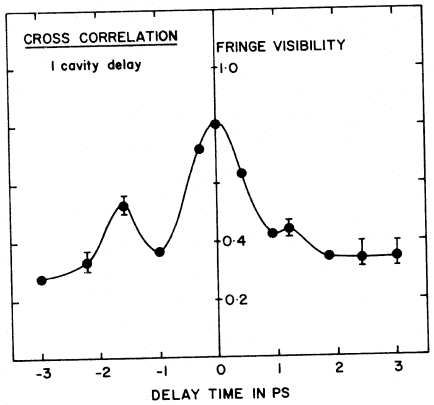

Fig. 4. Measured FV as a function of differential delay time τ for 1 cavity-delay cross correlation.

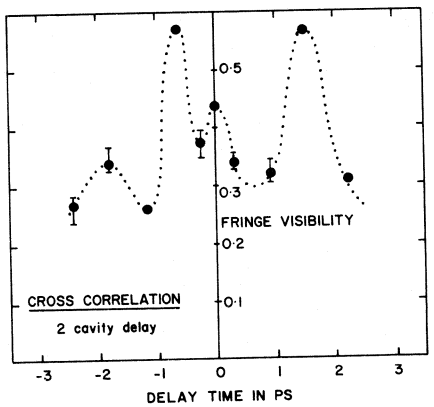

Fig. 5. Measured values of FV as a function of differential delay time τ for 2 cavity-delay cross correlation. The dotted curve represents the experimental values connected only qualitatively, due to rapid variation of FV within the delay-time intervals used.

much as the main information contained in this FV is the bandwidth, our Gaussian approximation with the corresponding bandwidth determined to fit the data optimally is a reasonable assumption. Needless to say, this approximation is not essential. However, any improvement in actual data fitting does not lead to substantial change in the information to be obtained. Hence (4) can now be written as

$$\mathrm{FV} = [e^{-\beta\tau_p^2} + f]\ [1+f]^{-1} \tag{8}$$

where the dimensionless time parameter τ_p is scaled with respect to picosecond unit ($\tau_p = \Delta\Omega t$, $\Delta\Omega = 10^{12}$) and β is the correspondingly scaled bandwidth of the signal. In view of the fact that the autocorrelation curve (Fig. 3) does not fall off to zero but reaches a constant value for a large delay time, it is clear that the bandwidth of the noise is much less than that of the signal. Thus we may, to a good approximation, take the time dependence of noise to be essentially constant f in the τ_p scale, in which case f represents the power fraction of noise with respect to signal power.

By optimally fitting (8) to our autocorrelation data we find that $f = 0.25$ and $\beta = 1.125$. This means that about 75 percent of the laser output power goes into the mode-locked optical pulses whose spectral bandwidth is approximately 10 cm^{-1}. These values for f and β fit the data to within 3-percent error (Fig. 6).

We next consider the cross correlation, first between two pulses separated by one cavity transit time. In so doing, we

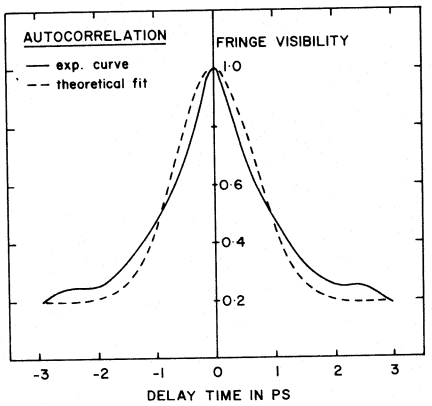

Fig. 6. Comparison of experimental and theoretical plots of autocorrelation FV as a function of differential delay time τ. Fit to data within 3.2 percent.

take the total power and fraction of noise in these two pulses to be the same. This is a good approximation considering the fact that the pulses are two consecutive pulses in a single pulse train. We point out, however, that the bandwidths of these two pulses are substantially different from each other. Their ratio is to be estimated by measuring the autocorrelation FV for two consecutive sets of fringes for a given delay time in a single streaked autocorrelation interference pattern. Bandwidth modulation of this kind has also been previously observed by Duguay *et al.* with a different technique [2].

As mentioned earlier, the relative phase dispersion existing between these two pulses can affect significantly the FV curve for cross correlation. In order to obtain this phase dispersion, we first represent the relative phase as

$$\Delta\chi(\omega) = a \sin K\left(\frac{\omega-\omega_0}{\Delta\Omega}\right) + b \cos K\left(\frac{\omega-\omega_0}{\Delta\Omega}\right). \tag{9}$$

Here, the parameters a, b, and K (scaled with respect to picosecond units) will be determined in such a way that the ensuing theoretical expression fits optimally the experimental data. The fit to data will undoubtedly improve if we increase the number of available parameters by adding more terms in (9) such as the harmonic terms. But as will become clear later, (9) is adequate for the analysis of our data.

Upon inserting (9) into (5) and (6), with the identity

$$e^{iz\sin\theta} = \sum_{n=-\infty}^{\infty} J_n(z)\, e^{in\theta}$$

with J_n representing nth-order Bessel function, we find, as in the case of autocorrelation,

$$\mathrm{FV} = \left(\frac{2r}{1+r^2}\right)^{1/2} [1+f]^{-1}\ [f + |\delta(\tau_p)|] \tag{10}$$

with

$$\delta(\tau_p) = \sum_{\pm} \{[A_0 e^{-\gamma\tau_p^2} + A_{\pm 1} e^{-\gamma(\tau_p \pm K)^2} + A_{\pm 2} e^{-\gamma(\tau_p \pm 2K)^2}] + i[B_{\pm 1} e^{-\gamma(\tau_p \pm K)^2} + B_{\pm 2} e^{-\gamma(\tau_p \pm 2K)^2}]\} \tag{11}$$

$$\gamma = 2r^2\beta/[1+r^2] \tag{12}$$

and

$$A_0 = J_0(a)\,J_0(b)$$
$$A_{\pm 1} = \pm J_0(b)J_1(a)$$
$$A_{\pm 2} = J_0(b)\,J_2(a) - J_0(a)\,J_2(b)$$
$$B_{\pm 1} = J_0(a)\,J_1(b)$$
$$B_{\pm 2} = \pm J_1(a)\,J_1(b). \tag{13}$$

Here r denotes the ratio of bandwidth of these pulses.

We take the values $f = 0.25$ and $r = 1.74$ appearing in (10) as obtained from the autocorrelation data to fit the theoretical expression to the cross-correlation curve. Numerical analysis of one cavity delay cross correlation was performed by varying the parameters a, b, and K. The best fit is obtained for $a = -0.23$, $b = 0.77$, and $K = 1.555$, in which case the error is 2.5 percent (see Fig. 7). In Fig. 8 we show the relative phase dispersion corresponding to this best fit. The shape of this phase curve shows explicitly that there exist both positive- and negative-frequency chirping as well as a substantial degree of nonlinear phase dispersion occurring within the bandwidth of the mode-locked signal. This rapid change in phase and bandwidth is understandable considering the fact that the pulses investigated here lie near the peak amplitude region of short high-power pulse trains.

We also applied our analysis to previously reported data obtained under different conditions [13]. The auto- and one cavity-delay cross correlation FV's reported therein were measured for the case of 1) long pulse trains of durations 400–500 ns, and 2) the region of investigation long after the start of the pulse train. The results of the analysis are shown in Figs. 9–11. The bandwidth of the pulse is 23 cm^{-1}, the fraction of noise power $f = 28$ percent, and the ratio of bandwidths of two successive pulses, $r = 1.2$. The main difference lies in the cross correlation, and hence the phase-dispersion curve. Note that in this case there is essentially no relative

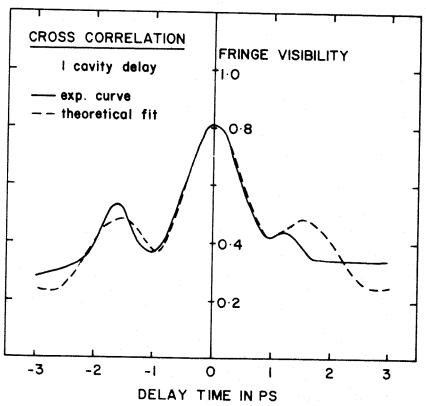

Fig. 7. Comparison of experimental and theoretical plots of 1 cavity-delay cross correlation FV as a function of differential delay time τ. Fit to data within 2.5 percent.

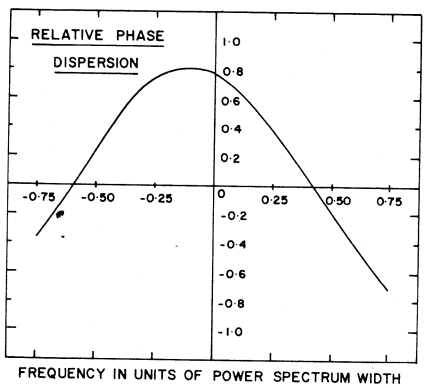

Fig. 8. Relative phase dispersion plotted in frequency units of power-spectrum bandwidth. The shape of the curve demonstrates the existence of positive- and negative-frequency chirping as well as substantial degree of nonlinear phase dispersion in the peak amplitude region of short high-power pulse trains. The region of the curve near $\Delta\omega = 0$ is most important because the amplitude of the modes is largest there.

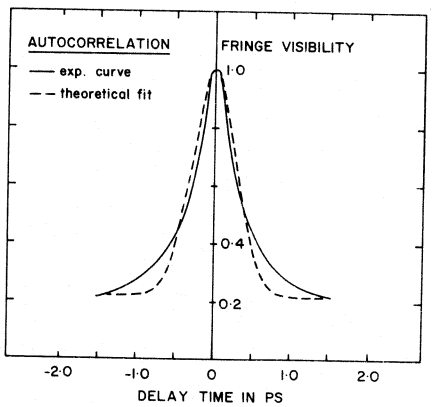

Fig. 9. Comparison of experimental and theoretical plots of autocorrelation FV as a function of differential delay time τ for the data reported in [13]. Fit to data within 2.5 percent.

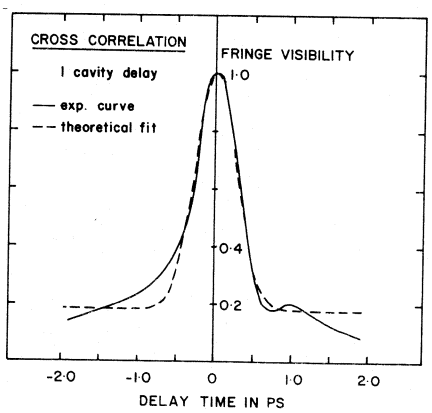

Fig. 10. Comparison of experimental and theoretical plots of 1 cavity-delay cross correlation FV as a function of differential delay time τ for the data reported in [13]. Fit to data within 6.2 percent.

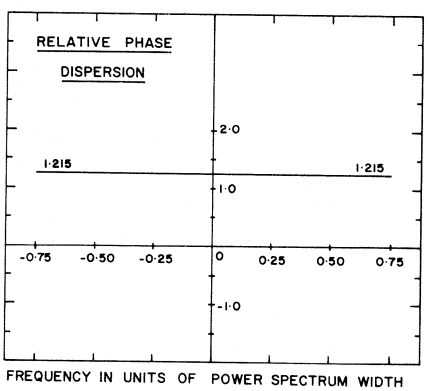

Fig. 11. Relative phase dispersion in frequency units of power-spectrum bandwidth for the data reported in [13]. Essentially, there is no phase dispersion. Phase change is constant for pulses in the tail region of long quasi-continuous pulse trains.

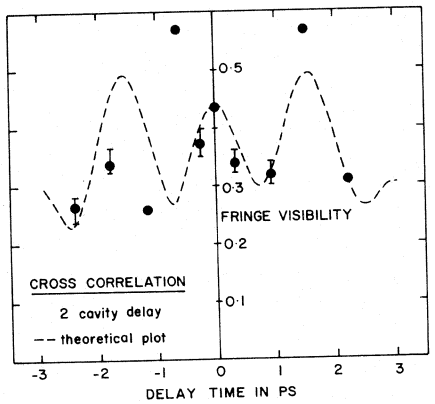

Fig. 12. Theoretical and experimental fringe visibilities for 2 cavity-delay cross correlation. The experimental points of Fig. 8 have been included for comparison. The theoretical curve was obtained by extrapolation of the analysis for 1 cavity-delay cross correlation with the parameter values calculated for Fig. 10.

phase dispersion, which tends to indicate that the pulses in the latter part of the train of such quasi-continuous pulse trains are almost identical in phase.

Since, as was pointed out earlier, the experimental curve for cross correlation between pulses that are two cavity transit times apart should be taken only qualitatively (see Section III), we did not carry out explicit numerical analysis. Instead, we have assumed that in the region of the pulse train investigated, the phase dispersion and bandwidth modulation between any two successive pulses remain the same. Hence we extrapolated our analysis for one cavity delay correlation by taking the relative phase dispersion to be $2\Delta\chi$ and the net ratio between bandwidths to be r^2. The resulting FV is plotted in Fig. 12 together with the data points. The agreement between these two curves lends some degree of confidence to the techniques of analysis.

The train of pulses produced by a mode-locked Nd:glass laser have been difficult to measure and analyze because of the short duration of the pulse train, the rapid variation from pulse to pulse, and the fact that they possessed subpicosecond substructure and internal frequency chirping. It is shown in this paper that the auto- and cross-correlation data obtained by time-resolved linear interferometry can make it possible to determine accurately the changes in mode phase and amplitude taking place from pulse to pulse. If the initial pulses are measured to be minimum bandwidth pulses, as they are in most systems, then the succeeding pulses are consequently known. As a result, the method of measurement and analysis presented here is especially valuable for determining the form of the output pulses from a Nd^{3+}:glass mode-locked laser system.

References

[1] D. J. Bradley and G. H. C. New, "Ultrashort pulse measurements," *Proc. IEEE*, vol. 62, pp. 313–345, Mar. 1974.

[2] M. A. Duguay, J. W. Hansen, and S. L. Shapiro, "Study of the Nd:glass laser radiation," *IEEE J. Quantum Electron.*, vol. QE-6, pp. 725–743, Nov. 1970.

[3] R. J. Harrach, "Determination of ultrashort pulse widths by two-photon fluorescence patterns," *Appl. Phys. Lett.*, vol. 14, pp. 148–151, Mar. 1969.

[4] P. M. Rentzepis, C. J. Mitschele, and A. C. Sanman, "Measurement of ultrashort pulses by three photon fluorescence," *Appl. Phys. Lett.*, vol. 17, pp. 122–125, Aug. 1970.

[5] H. P. Weber, "Method for pulsewidth measurement of ultrashort light pulses generated by phase-locked lasers using nonlinear optics," *J. Appl. Phys.*, vol. 38, pp. 2231–2235, Apr. 1967.

[6] P. P. Bey, J. F. Giuliani, and H. Rabin, "Phase-matched optical harmonic generation in liquid media employing anomalous dispersion," *IEEE J. Quantum Electron. (Special Issue on the 1968 International Quantum Electronics Conference: Part II)*, vol. QE-4, pp. 932–939, Nov. 1968.

[7] R. C. Eckardt and C. H. Lee, "Optical third harmonic measurements of subpicosecond light pulses," *Appl. Phys. Lett.*, vol. 15, pp. 425–427, Dec. 1969.

[8] A. J. DeMaria, D. A. Stetser, and W. H. Glenn, Jr., "Ultrashort light pulses," *Science*, vol. 156, pp. 1557–1568, June 1967.

[9] A. J. DeMaria, W. H. Glenn, Jr., M. J. Brienza, and M. E. Mack, "Picosecond laser pulses," *Proc. IEEE*, vol. 57, pp. 2–25, Jan. 1969.

[10] D. J. Bradley, B. Liddy, W. Sibbett, and W. E. Sleat, "Picosecond electron-optical chronography," *Appl. Phys. Lett.*, vol. 20, pp. 219–221, Mar. 1972.

[11] M. Ya. Schelev, M. C. Richardson, and A. J. Alcock, "Image-converter streak camera with picosecond resolution," *Appl. Phys. Lett.*, vol. 18, pp. 354–357, Apr. 1971.

[12] R. W. Uhlhorn and D. F. Holshouser, "Cross-correlation detection of subnanosecond optical pulses," *IEEE J. Quantum Electron.*, QE-6, pp. 775–782, Dec. 1970.

[13] H. J. Ruiz, J. J. Turner, and T. A. Rabson, "Interpulse coherence of picosecond pulses," *Opt. Commun.*, vol. 6, pp. 435–437, Dec. 1972.

Correspondence

Generation of a Short Optical Pulse of Arbitrary Shape and Phase Variation

ELI YABLONOVITCH

Abstract—**It is shown that the problem of generating an optical pulse of arbitrary shape and phase may be reduced to the problem of producing an arbitrary spectral filter. This generalizes the short-pulse generation techniques, which are based on the laser breakdown switch, as the active element. We examine the extent to which any desired filter may be realized in practice, and some examples are given.**

INTRODUCTION

In recent years there has been great progress in the generation of short optical pulses by techniques that do not depend upon mode locking. Instead, they depend on the laser breakdown switch [1] which cuts off transmission with a fall time in the picosecond range. This step function is then converted into a short optical pulse by transmission through an appropriate spectral filter as shown in Fig. 1.

Among the types of optical filters which have been suggested are the Michelson interferometer [2], the Fabry–Perot etalon [3], the grating monochromator [4], and resonant-material absorbers [5]. Each of these filters produces a pulse with a characteristic shape and phase variation. In this correspondence we will turn the problem around: For a given pulse shape we will derive the specific spectral transmittance function which is required to generate it.

Thus the problem of generating an optical pulse of arbitrary shape and phase may be reduced to the problem of producing an arbitrary spectral filter. Furthermore, we will examine the extent to which any desired filter may be realized in practice.

Fig. 1 is a block diagram showing the basic concept of short-pulse generation from a laser spark. A long-pulse laser produces a breakdown plasma between a lens pair. This blocks off transmission of the beam, thereby amplitude modulating it. In the frequency domain, sidebands are associated with the amplitude modulation. The spectral filter rejects the incident laser wavelength but transmits the sidebands produced at the instant of breakdown. After the plasma has fully formed, again nothing is transmitted. Thus a step function is converted into a short pulse.

THEORY

Let $E(t)$ represent the incident laser pulse whose duration is assumed to be much longer than any of the other times of interest in this problem. We will choose $t = 0$ as the instant at which the plasma forms, blocking off the beam. Then the electric field of the light wave transmitted through the lens pair may be represented as

$$E(t) = 1, \quad \text{for } -\infty < t < 0$$

$$E(t) = 0, \quad \text{for } 0 < t < \infty \tag{1}$$

i.e., a step-function amplitude modulation. This electric field

Manuscript received February 3, 1975. This research was supported by the Advanced Research Projects Agency under Contract DAHC 15-73-G-16.

The author is with the Gordon McKay Laboratory, Harvard University, Cambridge, Mass. 02138.

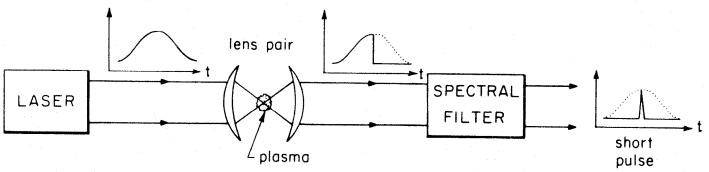

Fig. 1. A block diagram of the basic laser breakdown pulse-shaping scheme. The spectral filter rejects all but the plasma-induced sidebands on the laser pulse.

may also be written in terms of its Fourier amplitude

$$E(\omega) = \frac{1}{\sqrt{2\pi}} \int_{-\infty}^{\infty} E(t) \exp(i\omega t)\, dt$$

$$E(\omega) = \frac{1}{\sqrt{2\pi} i\omega}. \tag{2}$$

(In this correspondence, the factor $\exp\{i\omega_0 t\}$ in the time dependence of the electric field will be suppressed. Frequencies ω are generally measured relative to ω_0, the center frequency of the laser, unless otherwise noted.)

From (2) we see that the sidebands of the step-function amplitude modulation fall off inversely with the frequency shift from line center.

Let $G(\omega)$ represent the electric-field spectral transmittance function of the optical filter. $G(\omega)$ has both an amplitude and a phase and should be distinguished from the intensity transmission function $|G(\omega)|^2$ which has no phase information. The output electric field in the frequency domain $E_0(\omega)$ is then simply $G(\omega)\, E(\omega)$ or, using (2),

$$E_0(\omega) = \frac{G(\omega)}{\sqrt{2\pi} i\omega}. \tag{3}$$

The output pulse in the time domain is simply the inverse Fourier transform of (3).

Equation (3) determines the output field amplitude for a given spectral transmittance function. The relationship may readily be inverted

$$G(\omega) = \sqrt{2\pi} i\omega E_0(\omega). \tag{4}$$

This tells us the function G, which is required to produce a desired output pulse of Fourier amplitude $E_0(\omega)$. Equation (4) is the central result of this correspondence. It may also be written

$$G(\omega) = \int_{-\infty}^{\infty} \exp(i\omega t) \frac{dE_0(t)}{dt}\, dt \tag{5}$$

which expresses $G(\omega)$ directly in terms of the output field in the time domain $E_0(t)$.

To satisfy causality, $G(\omega)$ must be analytic in the upper half-plane. This requires $([dE_0(t)]/dt) = 0$ for $t < 0$; i.e., no change in output until the spark forms. We will make the stronger restriction $E_0(t) = 0$ for $t < 0$, thereby both satisfying causality and demanding that $G(0) = 0$. This last condition ensures that the incident laser beam does not leak through the filter in the absence of a spark.

EXAMPLES

a) What spectral filter is required to produce a δ-function pulse? A δ-function pulse has Fourier amplitude $E_0(\Delta\omega)$ = constant, independent of frequency over its bandwidth. (In this section we will use the sumbol $\Delta\omega$ to distinguish relative frequency from absolute frequency ω; i.e., $\Delta\omega = \omega - \omega_0$.) Using (4) the transmittance function should be

$$G(\Delta\omega) = \sqrt{2\pi}\, i\Delta\omega \times \text{constant}. \tag{6}$$

Thus we require a filter whose transmittance is linearly proportional to the frequency difference from the laser frequency. It turns out that a quarter-wave antireflection coating, when used in reflection, has precisely this behavior over a wide bandwidth (see Fig. 2)

$$\text{reflection coefficient} = \frac{E_R}{E_{in}} = \frac{1-n}{1+n}\left[1 + \exp\left\{\frac{i2nt\omega}{c}\right\}\right]. \tag{7}$$

Using the condition for zero reflection at the laser frequency, (7) becomes

$$\frac{E_R}{E_{in}} = \frac{1-n}{1+n}\left[1 - \exp\left\{\frac{i\pi\Delta\omega}{\omega_0}\right\}\right].$$

If $\Delta\omega \ll \omega_0$, then we may expand the exponential in a power series keeping only the first two terms

$$\frac{E_R}{E_{in}} = i\pi\frac{(1-n)}{(1+n)}\frac{\Delta\omega}{\omega_0} \tag{8}$$

which is the required functional form.

It is interesting to note in passing that a filter described by (8), or equivalently (6), is an optical differentiator. Its output is the time derivative of its input. This is proven in the Appendix.

b) What spectral filter is required to produce a rectangular pulse of duration T? Such a pulse has a Fourier amplitude

$$E_0(\Delta\omega) = \frac{1}{\sqrt{2\pi}i\Delta\omega}\left[\exp(i\Delta\omega T) - 1\right].$$

Therefore, the required spectral transmittance function is

$$G(\Delta\omega) = \sqrt{2\pi}\, i\Delta\omega E_0(\Delta\omega) = \left[\exp(i\Delta\omega T) - 1\right]. \tag{9}$$

A Michelson interferometer [2], used as shown in Fig. 3, and adjusted for destructive interference of the output beam, satisfies (9). In particular

$$\frac{E_0}{E_{in}} = \left[1 - \exp(i\omega T)\right] = \left[1 - \exp(i\omega_0 T)\exp(i\Delta\omega T)\right].$$

Destructive interference at the laser frequency requires $\exp\{i\omega_0 T\} = 1$, where T is the difference in optical path between the two arms of the interferometer. Therefore, the Michelson interferometer satisfies (9).

c) What spectral filter is required to produce an exponentially decaying pulse of time constant τ? Such a pulse has a Fourier amplitude

$$E_0(\Delta\omega) = \frac{\tau}{\sqrt{2\pi}\,(1 - i\Delta\omega\tau)}.$$

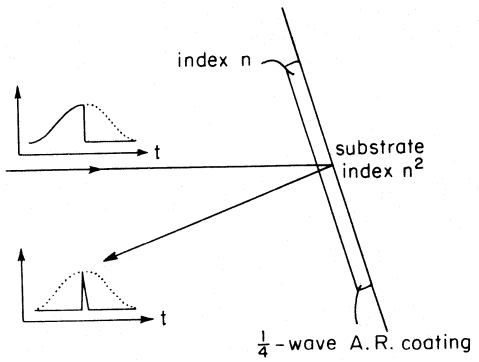

Fig. 2. A quarter-wave antireflection coating, when used in reflection, acts as an optical differentiator (see Appendix). It converts the step function into a δ-function pulse.

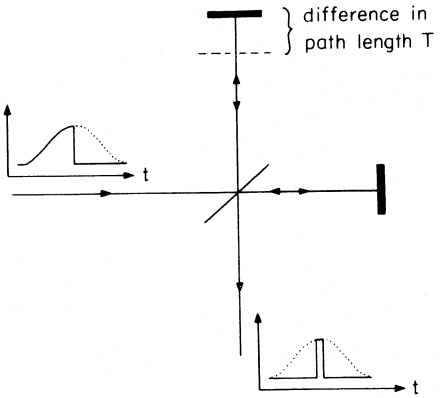

Fig. 3. A Michelson interferometer is used to generate a rectangular pulse of duration T which is the difference in path length between the two arms of the interferometer.

Therefore, the required spectral transmittance function is

$$G(\Delta\omega) = \sqrt{2\pi}\, i\Delta\omega E_0(\Delta\omega) = \frac{i\Delta\omega\tau}{1 - i\Delta\omega\tau}. \tag{10}$$

Such an optical filter may be realized as shown in Fig. 4. It requires two filter elements in series, the $G(\Delta\omega)$ of the combination being the product of the individual G's. One element is simply an optical differentiator (see the Appendix), such as the quarter-wave antireflection coating which supplies the factor $i\Delta\omega$ to the numerator. The other element is a Michelson interferometer, this time adjusted for equal-length arms. In one of the arms is an optically thin, homogeneously broadened, resonant absorber. It is readily shown that such an element contributes the factor $(1 - i\Delta\omega\tau)$ in the denominator of (10). The homogeneous linewidth of the absorber is $1/\tau$. If it is off-resonance, then an oscillatory decaying pulse is produced. A somewhat different pulse shape was recently generated by using an optically thick resonant medium as the filter [5].

DISCUSSION

The previously given examples are meant to indicate the generality of the pulse-shaping approach being proposed here. Since spectral filters are linear elements, many of them may be combined in series to produce the required transmittance function. There is great versatility in using media, both resonant and nonresonant, as filtering elements.

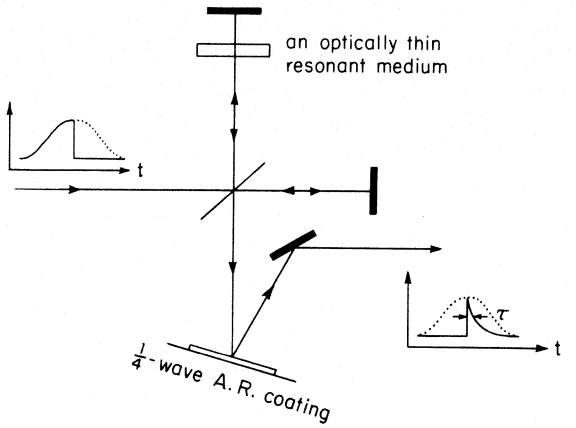

Fig. 4. A composite filter element, consisting of a Michelson interferometer and a quarter-wave antireflection coating used in series. An optically thin resonant medium of homogeneous linewidth $1/\tau$ unbalances one of the arms of the interferometer. The output is an exponentially decaying pulse of time constant τ.

A type of filter which was not mentioned in the previously given examples, but which has great potential, is the multilayer dielectric-coated interference filter. These are now mainly used in bandpass applications, for which only $|G(\omega)|^2$ is important. If designed to take account of both the phase and amplitude of $G(\omega)$, they could be used in pulse-shaping applications. It should be possible to closely approximate any given function by using enough layers. Complicated pulse shapes, such as those which have been proposed for laser fusion [6], may require computer design to optimize the layer spacing and other parameters.

Practical Limitations

There are, of course, practical limitations to these pulse-generation techniques. For example, many of the filters which we have been discussing have the property of zero transmission at the center laser wavelength; i.e., $G(0) = 0$. This is important for rejecting the laser light at $t < 0$ before the breakdown spark has formed. In practice, a perfect null is not always possible and the rejection may not be 100-percent complete.

Another limitation is related to the finite fall time T of the light as it passes through the breakdown plasma. Equation (1) assumes an instantaneous fall time, which is only approximate. In particular, (2) is correct only for frequency shifts $\Delta\omega \lesssim 1/T$. Therefore, the techniques described in this correspondence are useful for generating pulses whose overall frequency spectrum is no wider than $2/T$. Understandably, it is not possible to generate pulses which are shorter than the fall time T. Recent measurements indicate that T is in the picosecond range for CO_2-laser-produced plasmas. There is speculation that even faster fall times are possible.

Conclusion

We have shown that the problem of generating an arbitrary optical pulse $E(t)$ may be reduced to the problem of producing a matched filter as given by (5). Some examples of specific pulse shapes and their matching filters were also presented.

Appendix

We wish to show that a filter whose spectral transmittance function is described by (6) acts as an optical differentiator. By definition

$$E_{\text{out}}(\omega) = \sqrt{2\pi}\, i\omega E_{\text{in}}(\omega).$$

Taking the inverse Fourier transform

$$E_{\text{out}}(t) = \int_{-\infty}^{\infty} i\omega \exp(-i\omega t)\, E_{\text{in}}(\omega)\, d\omega$$

$$= -\frac{d}{dt}\int_{-\infty}^{\infty} \exp(-i\omega t)\, E_{\text{in}}(\omega)\, d\omega$$

$$= -\frac{d}{dt} E_{\text{in}}(t).$$

Therefore, the output of such a filter is the time derivative of its input. Several such filters may be used in series to obtain higher order derivatives.

References

[1] E. Yablonovitch, "Self-phase modulation and short-pulse generation from laser-breakdown plasmas," *Phys. Rev.*, vol. A10, pp. 1888–1895, Nov. 1974.

[2] a) A. Szoke, J. Goldhar, H. P. Grieneisen, and N. A. Kurnit, "Generation of variable length laser pulses in the subnanosecond region," *Opt. Commun.*, vol. 6, pp. 131–134, Oct. 1972.
b) D. Milam *et al.*, "Production of intense subnanosecond pulses by cavity dumping," *IEEE J. Quantum Electron.*, vol. QE-10, pp. 20–25, Jan. 1974.

[3] M. Duguay, private communication.

[4] a) E. Yablonovitch, "Spectral broadening in the light transmitted through a rapidly growing plasma," *Phys. Rev. Lett.*, vol. 31, pp. 877–879, Oct. 1973.
b) ——, "Self-phase modulation of light in a laser-breakdown plasma," *Phys. Rev. Lett.*, vol. 32, pp. 1101–1104, May 1974.

[5] E. Yablonovitch and J. Goldhar, "Short CO_2 laser pulse generation by optical free induction decay," *Appl. Phys. Lett.*, vol. 25, pp. 580–582, Nov. 1974.

[6] J. Nuckolls, L. Wood, A. Thiessen, and G. Zimmerman, "Laser compression of matter to super-high densities: Thermonuclear (CTR) applications," *Nature*, vol. 239, pp. 129–142, Sept. 1972.

Excitation of Cold Cavity Modes in a Coupling-Modulated CO_2 Laser

A. L. SCHOLTZ

Abstract—**The amplitudes of cold longitudinal cavity modes excited as an unwanted side effect of coupling modulation were studied in a CO_2 laser. Experimental observations agree well with the results of an analytical approach treating the effect of coupling modulation on the cavity field as loss modulation.**

Introduction

Intracavity coupling modulation [1] is an efficient method to modulate CO_2 lasers [2]–[4]. With this modulation scheme, the unwanted excitation of cold cavity modes is of particular interest [5], [6]. Cold modes are longitudinal modes of the optical resonator which do not coincide with the laser transition. They can be excited by any kind of intracavity modulation if the modulating frequency f_m is approximately an integer multiple of the cavity mode spacing $c/2l$ (l

Manuscript received February 25, 1975; revised May 20, 1975. This work was supported by the Fonds zur Förderung der wissenschaftlichen Forschung as part of project Elektronik in Nachrichtentechnik und Automatisierung.

The author is with the Institut für Hochfrequenztechnik, Technische Hochschule, Vienna, Austria.

is the optical length of the cavity). In the case of coupling modulation, the cold modes distort the modulated output signal by reducing the sideband amplitude, as has been observed in He–Ne lasers [7]. However, no experimental data concerning inherently single-mode lasers, such as the CO_2 laser, have been reported up to now. This correspondence reports on the first experimental study of the excitation of cold modes by coupling modulation of the CO_2 laser. In particular we investigate the relative amplitudes of the cold modes adjacent to the active mode. A theory is presented which predicts these amplitudes in good agreement with the experimental observations.

Theory

The well-known scheme of coupling modulation [1] is shown in Fig. 1. The relation between the optical field $E_i \cos \omega t$ incident on the modulator and the perpendicular field component E_c produced after two passes through the modulator is [6]

$$E_c(t) = E_i \sin \Gamma(t) \sin \omega t. \tag{1}$$

Here $\Gamma(t)$ is the single-pass phase retardation induced by the modulating signal via the electrooptic effect. The power extracted from the incident optical field follows as:

$$P_c(t) = \tfrac{1}{2}\,[1 - \cos 2\Gamma(t)] \quad P_i = c_m(t)\,P_i \tag{2}$$

where P_c and P_i correspond to E_c and E_i, respectively, and c_m is the coupling coefficient. Evidently, coupling modulation introduces time-varying cavity losses. This suggests extension of the theory of loss modulation, as derived by McDuff and Harris [8], to calculate the amplitudes of the cold modes which are excited by coupling modulation as an unwanted side effect. Without loss of generality, calculations can be restricted to the lowest resonant modulation frequency $f_m \doteq c/2l$.

For sinusoidal modulation with a voltage $V(t) = V_0 + V_m \sin \omega_m t$ applied to the modulator, the phase retardation is

$$\Gamma(t) = \Gamma_0 + \Gamma_m \sin \omega_m t \tag{3}$$

and, with (2) and (3), the coupling coefficient becomes

$$c_m(t) = \tfrac{1}{2}\,[1 - J_0(2\Gamma_m) \cos (2\Gamma_0)] + J_1(2\Gamma_m) \sin (2\Gamma_0) \sin \omega_m t - \cdots. \tag{4}$$

The single-pass power loss introduced by the modulator $\alpha_m(t)$ may be defined in the form

$$\alpha_m(t) = \alpha_a(1 + m \sin \omega_m t) \tag{5}$$

where α_a is the time-average single-pass power loss introduced by the modulator and m is the depth of the time-dependent loss variations. For $\Gamma_0, \Gamma_m \ll 1$, (2), (4), and (5) yield

$$\alpha_a = [1 - J_0(2\Gamma_m) \cos (2\Gamma_0)]/4 \tag{6}$$

and

$$m = 2J_1(2\Gamma_m) \sin (2\Gamma_0)/[1 - J_0(2\Gamma_m) \cos (2\Gamma_0)]. \tag{7}$$

Note that m is equal to the depth of modulation of the coupled-out signal when no coupling to cold modes takes place, as can be seen from (7) and (4). Now assuming that the single-pass power loss α of the cavity does not depend on the frequency, further, that the modulator is located near one of the cavity mirrors (see Fig. 1), a calculation similar to [8] can be performed. The two cold modes next to the active one, both having the same amplitude E_1, are of main interest; all others are negligible if one considers only first-order effects. One obtains

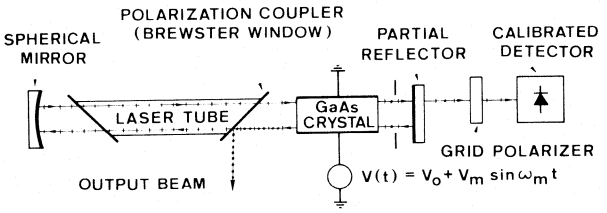

Fig. 1. Experimental setup used for cold-mode coupling measurements. States of polarization parallel and perpendicular to the laser oscillation are indicated by dashes and dots, respectively. A conventional coupling modulation arrangement is modified by replacing the flat mirror by a 6.1-percent transmission partial reflector. A small fraction of the cavity field is passed through a grid polarizer to a SAT HgCdTe detector, whereas the modulated signal beam is directed to an absorber. In order to prevent oscillation of higher order transverse modes, an aperture of 3-mm diameter is inserted near the partial reflector.

$$\frac{E_1}{E_0} = \frac{\alpha + \alpha_a}{m\alpha_a} - \left(\left(\frac{\alpha + \alpha_a}{m\alpha_a}\right)^2 - 1\right)^{1/2} \tag{8}$$

where E_0 is the amplitude of the active mode. For $\alpha_a \ll \alpha \ll 1$, (8) takes the simple form

$$E_1/E_0 = m\alpha_a/(2\alpha). \tag{9}$$

In this limit, E_1/E_0 increases linearly 1) with the modulation depth m of the introduced loss and 2) with the ratio of the average introduced loss α_a to the cavity loss α.

For modulation frequencies other than the resonant one, E_1/E_0 decreases according to the frequency response of the cold cavity [5].

Experiment

The relative amplitudes of the cold modes were measured in an experimental setup shown in Fig. 1. A CO_2–N_2–He laser containing a water-cooled flowing-gas discharge tube (500-mm active length, 10-mm inside diameter (ID), 10-torr total pressure, 10-mA discharge current) was used. The optical resonator (length 1080 mm) consisted of a spherical mirror and a plane 6.1-percent transmission partial reflector. A Lansing lock-in stabilizer was used to maintain stable operation at the center of one molecular transition. The modulator consisted of a $5 \times 5 \times 50\text{-mm}^3$ GaAs crystal. The fact that one mirror is a partial reflector has no effect on the modulation mechanism other than increasing the cavity loss to a total of $\alpha = 0.29$.

A fraction of the cavity field emerges through the partial reflector and contains components polarized parallel and perpendicular to the active mode, as indicated in Fig. 1 by dashes and dots, respectively. The presence of cold modes in the cavity results in amplitude modulation of the parallel component. In order to isolate this effect, the perpendicular component is suppressed by an IGP 225 grid polarizer. Keeping in mind that $E_1/E_0 \ll 1$, a square-law detector can be used to measure E_1/E_0. A SAT HgCdTe detector, type C1, served for this purpose and had been calibrated [9] previously in an external modulation setup.

Fig. 2 shows the results of typical measurement runs. Choosing $V_0 = 300$ V and $V_m = 177$ V ($V_m = 78$ V) one obtains $m = 1$ ($m = 0.5$) and $\alpha_a = 6.1 \times 10^{-3}$ ($\alpha_a = 5.4 \times 10^{-3}$) with the electrooptic data of GaAs as given in [10]. Here and in the following, values in parentheses correspond to $m = 0.5$. The measured relative cold-mode amplitudes versus frequency indicated by circles closely follow the normalized frequency response of the cavity, calculated for $\alpha = 0.29$. The resonant values of $E_1/E_0 = 0.0170$ ($E_1/E_0 = 0.0079$) are higher than the calculated maxima $E_1/E_0 = 0.0103$ ($E_1/E_0 = 0.0046$). The

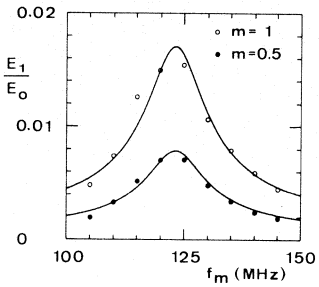

Fig. 2. Relative cold-mode amplitude E_1/E_0 versus frequency. The cases $m = 1$ ($m = 0.5$) correspond to $V_m = 177$ V ($V_m = 78$ V) and to $\alpha_a = 6.1 \times 10^{-3}$ ($\alpha_a = 5.4 \times 10^{-3}$), with $V_0 = 300$ V kept constant. The single-pass cavity power loss was $\alpha = 0.29$. Measured values indicated by circles closely follow the frequency response of the cold laser cavity calculated for this power loss and normalized for best fit.

difference is probably due to the finite extinction ratio [11] of the external modulator used to calibrate the detector; it is readily explained assuming an extinction ratio of some 600, which agrees well with the data for GaAs given in [11]. This explanation is further supported by the following observation: The ratio of the values of E_1/E_0 associated with $m = 1$ and $m = 0.5$, respectively, was measured to be 2.15 in good agreement with 2.24, which results from (8).

From the preceding one can conclude that the presented approach predicts the amplitudes of cold modes excited by coupling modulation with good accuracy. The results of the analysis should prove useful in the design of low-distortion wide-band communication systems.

ACKNOWLEDGMENT

The author wishes to thank Dr. E. Bonek and Dr. G. Schiffner for stimulating discussions.

REFERENCES

[1] K. Gürs and R. Müller, "Breitband-Modulation durch Steuerung der Emission eines optischen Masers (Auskoppelmodulation)," *Phys. Lett.*, vol. 5, pp. 179–181, July 1963.

[2] A. L. Waksberg, "A comparative evaluation between internal and external polarization modulation of lasers," *IEEE J. Quantum Electron.*, vol. QE-9, pp. 1086–1097, Nov. 1973.

[3] N. McAvoy, J. Osmundson, and G. Schiffner, "Broadband CO_2 laser coupling modulation," *Appl. Opt.*, vol. 11, pp. 473–474, Feb. 1972.

[4] E. Bonek and H. Korecky, "Intracavity millimeter-wave coupling modulation of a CO_2 laser," *Appl. Phys. Lett.*, vol. 25, pp. 740–741, Dec. 1974.

[5] M. DiDomenico, Jr., "Small-signal analysis of internal (coupling-type) modulation of lasers," *J. Appl. Phys.*, vol. 35, pp. 2870–2876, Oct. 1964.

[6] I. P. Kaminow, "Internal modulation of optical masers (bandwidth limitations)," *Appl. Opt.*, vol. 4, pp. 123–127, Jan. 1965.

[7] F. R. Nash and P. W. Smith, "Broadband optical coupling modulation," *IEEE J. Quantum Electron.*, vol. QE-4, pp. 26–34, Jan. 1968.

[8] O. P. McDuff and S. E. Harris, "Nonlinear theory of the internally loss-modulated laser," *IEEE J. Quantum Electron.*, vol. QE-3, pp. 101–111, Mar. 1967.

[9] K. K. Chow and W. B. Leonard, "Efficient octave-bandwidth microwave light modulators," *IEEE J. Quantum Electron.*, vol. QE-6, pp. 789–793, Dec. 1970.

[10] I. P. Kaminow, "Measurements of the electrooptic effect in CdS, ZnTe, and GaAs at 10.6 microns," *IEEE J. Quantum Electron.*, vol. QE-4, pp. 23–26, Jan. 1968.

[11] J. F. Figueira, "Extinction ratios of GaAs and CdTe electro-optical modulators," *IEEE J. Quantum Electron.* (Corresp.), vol. QE-10, pp. 572–573, July 1974.

A Comment on the Theory of Mode Locking and Frequency Doubling

C. J. KENNEDY

Abstract—**The time-domain theory of the mode-locked and frequency-doubled laser by J. Falk depends greatly on the particular Gaussian approximation to the pulse transmitted from the frequency doubler. This correspondence examines an alternative approximation which appears to be a better fit to the actual pulse shape and which gives substantially different results for pulsewidth.**

Probably the most important aspect of any theory which proposes to explain the characteristics of the mode-locked and intracavity frequency-doubled laser is that which predicts the pulsewidth given the depth of modulation of the mode locker and other laser parameters. For communication system purposes, the pulsewidth is defined at a low relative intensity such as $1/e^2$, or 10-percent power width, because pulse-gating modulation techniques lose efficiency rapidly when the gate width is less than $1/e^2$, or 10-percent width of the laser pulse.

The time-domain approach to this laser system involves the balancing mechanisms for a hypothetical pulse making a round trip in the laser cavity. Let us refer our time coordinate to the center of the pulse ($t = 0$) and assume for simplicity that the round-trip time of the pulse is synchronized with the peak transmission of the loss modulator. Also let us assume that the gain medium has a negligible tendency to broaden the pulse. *It is a general rule that the total losses as a function of time referred to the center of the pulse must be constant for a steady-state pulse of whatever shape* [3]. Otherwise the shape of the pulse will vary with time until a steady state is reached. Mathematically, this relation may be stated as

$$\alpha + \alpha_{ML}(t) + \alpha_{FD}(t) = g \tag{1}$$

where α represents continuous losses, α_{ML} is the time-dependent mode-locker loss, α_{FD} is the time-dependent frequency-doubler loss, and g is the saturated gain. (All are single-pass power quantities.) The time dependance of α_{ML} and α_{FD} may be expanded in a power series, but we shall retain only the second order in t. It has been shown by Kuizenga and Siegman [1] that

$$\alpha_{ML}(t) \simeq \delta_l \omega_m^2 t^2/2 \tag{2}$$

where δ_l is the modulation depth and ω_m is $2\pi C/2L$.

However, α_{FD} depends on the exact functional form of the incident and transmitted pulses to the frequency doubler. Since the peak losses in intracavity frequency doubling are very small (~0.5 percent), it is reasonable to approximate with a Gaussian pulse both the input and output of the doubler. There are several ways to choose the Gaussian fit to the output. The loss is proportional to the intensity of the input pulse and, for small conversion efficiency, one obtains Falk's [2] analysis

$$I'(t) = I(t)\,[1 - (k/2)^2 I(t)]^2 \tag{3}$$

where $I(t)$ is the intensity envelope of the mode-locked pulse. If $I(t)$ is Gaussian, then the output $I'(t)$ must be approximated by a Gaussian. Letting

$$I(t) = I_0 e^{-2\gamma t^2} \tag{4}$$

Manuscript received March 4, 1975; revised May 16, 1975.

The author is with the Advanced Development Program 405B, Space Laser Communications, U.S. Air Force Avionics Laboratory, Wright-Patterson Air Force Base, Ohio 45433.

we show in Fig. 1 the incident and transmitted pulses for an exaggerated conversion efficiency of 38 percent to show the effects of various fits to the non-Gaussian $I'(t)$. The curve labeled "output" is the approximation of (3) to the actual shape, which is a sech^2 function.

Falk fits this function with a Gaussian that matches the height and curvature of $I'(t)$ at $t = 0$. This fit is shown against $I'(t)$ in Fig. 1 and is labeled "Fit 1." Fit 1 is a better match than it appears in Fig. 1, because, for small conversion efficiency, the mismatch in height is much less. However, Fit 1 is considerably broader at the $1/e^2$ points than $I'(t)$. The excess broadening of Fit 1 remains significant even for the more realistic conversion efficiency of 1 percent, although the percentage of broadening per pass is reduced. Since the action of the frequency doubler to broaden pulses is balanced exactly by the loss modulator in the steady state, a slight excess broadening may be significant when it is to be balanced against a small loss modulation depth. Consequently, we would expect the broadening tendencies of the frequency-doubler model to be greater than the real world. The fitted function is

$$I_f(t) = I_0 e^{-k^2 I_0/2}\, e^{-2\gamma(1-k^2 I_0/2)\, t^2}. \tag{5}$$

The time-dependent loss is then

$$\alpha_{SH}(t) = k^2 I_0/2 - k^2 I_0 \gamma t^2. \tag{6}$$

Substituting into (1), we find that this expression becomes independent of t when

$$\frac{\delta_e \omega_m^2}{2} = k^2 I_0 \gamma. \tag{7}$$

If we note that

$$\alpha_{SHG} = \frac{k^2 I_0}{2\sqrt{2}} \tag{8}$$

we have

$$\gamma = \frac{\delta_l \omega_m^2}{4\sqrt{2}\,\alpha_{SHG}} \tag{9}$$

and since the 10-percent full-frequency-doubled pulsewidth is

$$\tau_g = \sqrt{\frac{\ln 10}{\gamma}} = \frac{2\sqrt{\sqrt{2}\ln 10}}{\omega_m}\left(\frac{\alpha_{SHG}}{\delta_l}\right)^{1/2} \tag{10}$$

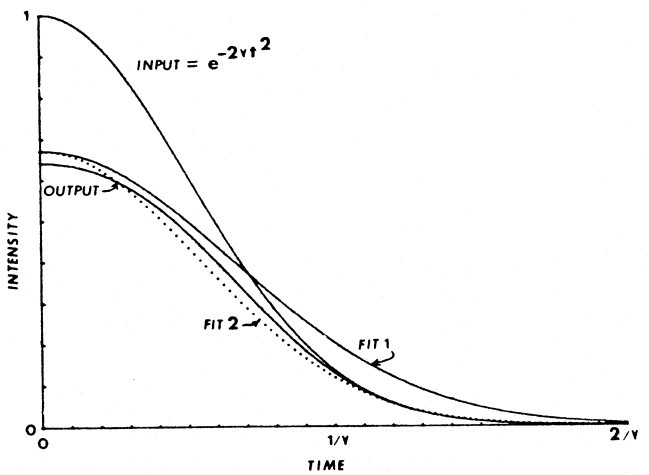

Fig. 1. Gaussian approximations to the transmitted pulse of the frequency doubler. The functions of the output pulse, Fit 1, and Fit 2 are given in the text.

which is precisely Falk's result, in the limit that gain–bandwidth broadening is negligible in comparison with frequency-doubling broadening.

However, if we were to choose a fitted Gaussian which matched $I'(t)$ closely at both $t = 0$ and the $1/e^2$ point, one might obtain what we refer to as "Fit 2" in Fig. 1, or

$$I_f(t) = I_0 e^{-k^2 I_0/2}\, e^{-2\gamma(1-k^2 I_0/6) t^2}. \tag{11}$$

Now α_{SH} is

$$\alpha_{SH}(t) = k^2 I_0/2 - k^2 I_0 \gamma t^2/3 \tag{12}$$

from which we obtain

$$\tau_g = \frac{2}{\omega_m}\sqrt{\frac{\sqrt{2}\ln 10}{3}}\left(\frac{\alpha_{SHG}}{\delta_l}\right)^{1/2} \tag{13}$$

which is $1/\sqrt{3}$ times the pulsewidth obtained for Fit 1.

In conclusion, the theoretical pulsewidth seems to be very sensitive to the curve fit employed. The final word must come from a general analysis or a careful experiment to determine the coefficient of $(\alpha_{SHG}/\delta_l)^{1/2}/\omega_m$. A more exact analysis has been performed by Bernecker [3] which deserves consideration since a Gaussian pulse is not assumed. However, Bernecker's theory ignores the effect of gain broadening and possible etalon effects, which occur in practical laser systems, which will alter the functional form of the pulse.

References

[1] D. J. Kuizenga and A. E. Siegman, "FM and AM mode locking of the homogeneous laser–Part I: Theory," *IEEE J. Quantum Electron.*, vol. QE-6, pp. 694–708, Nov. 1970.

[2] J. Falk, "A theory of the mode-locked, internally frequency-doubled laser," *IEEE J. Quantum Electron.*, vol. QE-11, pp. 21–31, Jan. 1975.

[3] O. Bernecker, "Limitations for mode-locking enhancement of internal SHG in a laser," *IEEE J. Quantum Electron.*, vol. QE-9, pp. 897–900, Sept. 1973.

Holocoupler: A Novel Coupler for Optical Circuits

H. NISHIHARA, S. INOHARA, T. SUHARA, AND J. KOYAMA

Abstract–**A novel type of optical coupler, which is based on the principle of holography, is designated as "holocoupler," and the potentiality of application is stressed. The holocouplers for optical fibers are fabricated for demonstration, and the experimental results are presented.**

Recent developments of optical communication systems require various types of couplers for optical devices, such as light-emitting sources, transmission circuits and lines, modulators, and detectors. Optical couplers currently in use may be classified into three groups: 1) direct couplers; 2) wave-vector converting couplers; and 3) wavefront converting couplers. The prism coupler [1] and the grating coupler [2] may belong to group 2), and the holocoupler is a typical example of group 3). "Holocoupler" has been given by the authors as a general name for couplers whose working principle is based on holography. The idea of holographic coupling and resolution capabilities have been demonstrated for a thin-film waveguide by Ash *et al.* [3], whereas the holographic mode discriminator [4] has been proposed for optical fibers. The purpose of this

Manuscript received March 24, 1975; revised June 5, 1975.

The authors are with the Faculty of Engineering, Osaka University, Suita, Osaka, Japan.

correspondence is to point out some interesting properties of the holocoupler, and to report some experimental results when holocouplers were used as direct coupling elements for optical fibers.

The holocoupler corresponds to the hologram in holography, and therefore the feature of the wavefront conversion is attributed to the holographic principle. Just as the reference wave is diffracted into the signal wave by a hologram, the wavefront of the input signal is converted into that of the output signal by a holocoupler, as shown in Fig. 1, where the wavefronts of the input and output signals are not necessarily planar or spherical, but can be arbitrary. Because of this wavefront-conversion property, the feasibility of various performances can be expected of the holocoupler. Some of the properties are as follows.

1) Easy fabrication of lens holocoupler of the arbitrary F number and the arbitrary focal length.

2) The mode-conversion holocoupler, which can convert, for example, the modes of an optical fiber of the round cross section into those of a thin-film integrated circuit.

3) The mode-filter holocoupler: the wave-conversion efficiency is low when the illuminating wavefront is other than what has been used for making the hologram.

4) The sharp-corner holocoupler, as shown in Fig. 2(a).

5) The multibranching holocoupler, which can couple one line into several lines of a different cross section, as shown in Fig. 2(b).

6) Compound holocouplers, which reduce the requirement of accurate alignment for line connection, as shown in Fig. 2(c).

In addition, replicas of a holocoupler can be easily produced only by the optical method [5], and the copying method provides some degree of freedom for choosing the material and the light source.

Since the highest diffraction efficiency may be expected in a hologram of the volume and phase type [6], the conversion efficiency of the holocoupler of this type has been approximately analyzed for the arrangement, as shown in Fig. 1, by means of the coupled-mode technique. It has been found that one can theoretically predict a maximum value of 100 percent by choosing the appropriate values of the relevant parameters. These values will be reported elsewhere.

Here two typical holocouplers are briefly described, with some preliminary experimental results for demonstration. We have used the materials and techniques of holography for fabrication.

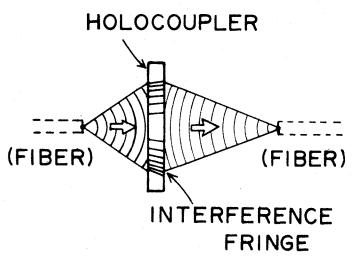

Fig. 1. Illustration of the principle of the holocoupler.

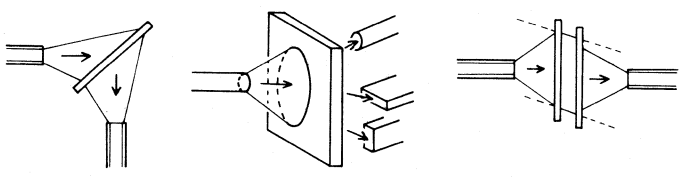

Fig. 2. Several types of holocouplers. (a) Sharp-corner holocoupler. (b) Branching holocoupler. (c) Compound holocoupler with accurate alignment not required.

The first example is a branching holocoupler for coupling a multimode fiber with two fibers, as shown in Fig. 3(a). The input and output fibers are arranged so that this holocoupler may also have the property of a sharp-corner holocoupler. In fabrication, a He–Ne laser beam was divided into three beams: one beam was made diverging and the other two were made converging by lenses in such a way that each beam may have the same cone angle as that of a beam emerging from each fiber end which is to be coupled. Unfortunately, the holocoupler cannot be made practical by using the radiation field from a multimode fiber because of the random mutual interference of a few hundred modes during the exposure time. The authors, however, have found theoretically that the conversion efficiency is reduced by only less than 1 percent, even if a hologram fabricated by a spherical reference wave is illuminated by a diverging wave from a multimode fiber. The material used was a high-resolution photographic plate (Kodak 649F) with a gelatin thickness of 15 μm. The plate was bleached after processing. A photograph of the resulting output pattern is shown in Fig. 3(b). The conversion efficiency for each output beam is approximately 15 percent.

The second example is a mode-conversion holocoupler—that is, a holocoupler between a fiber and an optical integrated circuit, as shown in Fig. 4. The material used was the amorphous semiconductor films of As_2S_3. The 5145-Å line of an Ar-ion laser was used for fabrication, and the 6328-Å line of a He–Ne laser was used for coupling. The beam from a fiber of 100-μm diameter was successfully converted into a beam of 150 × 800-μm^2 rectangular cross section, as shown in Fig. 4(b), with a conversion efficiency of approximately 20 percent.

In spite of the theoretical prediction, unfortunately, the maximum available conversion efficiency would be 60 percent at most, in practice, which is less than the value reported in direct coupling. Therefore, the holocoupler would be better

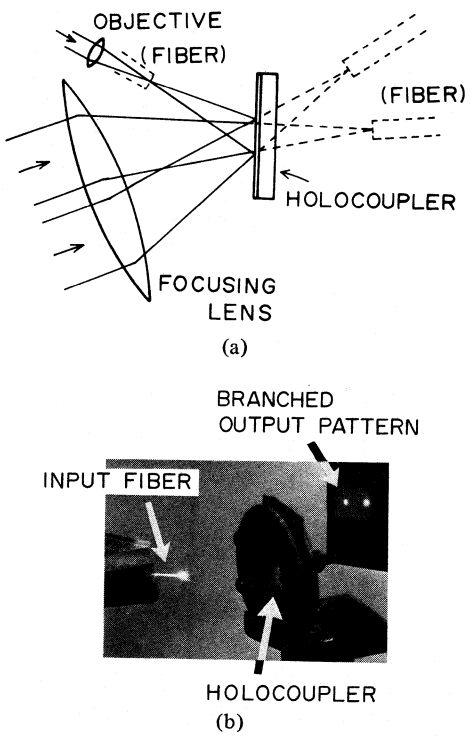

Fig. 3. The branching holocoupler. Fiber diameter: 100 μm; light-emitting cone angle: 6°; size of holocoupler: 4 mmϕ; the output-beam diameters were measured to be less than 100 μm. (a) Fabrication arrangement. (b) Coupling arrangement.

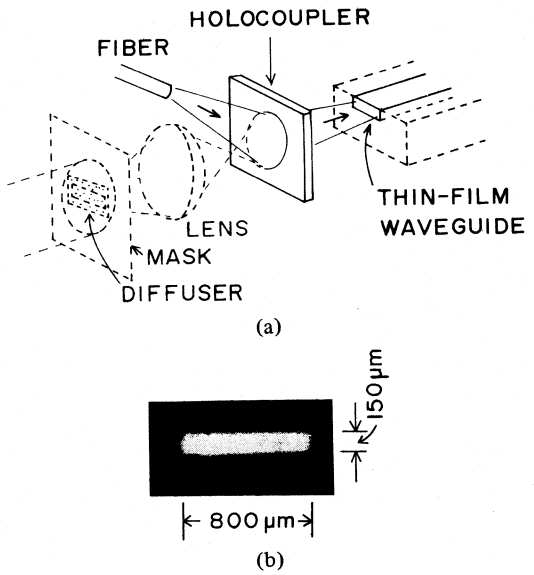

Fig. 4. The holocoupler for a fiber and an optical integrated circuit. Some of the optical components used for fabrication are drawn by dotted lines in (a). (a) Coupling arrangement. (b) Output pattern.

applied to complex wavefront-converting processes, as, for example, the conversion from a light-emitting diode (LED) or a semiconductor injection laser to a fiber, since the conversion efficiency would be much improved compared with the amount (the order of 1 percent) that is attained by the direct-coupling method. In the process of fabrication, the recently developed technique of computer-generated holograms and kinoforms should be taken into consideration, thus providing more possibilities of various types of holocouplers. Since the holocoupler has the capability of making feasible the complicated and functional couplings of optical fibers, integrated circuits, and elements, it shows promise for future optical communication systems.

References

[1] P. K. Tien, R. Ulrich, and J. R. Martin, "Modes of propagating light waves in thin deposited semiconductor films," *Appl. Phys. Lett.*, vol. 14, pp. 291–294, May 1969.
[2] H. Kogelnik and T. P. Sosnowski, "Holographic thin film couplers," *Bell Syst. Tech. J.*, vol. 49, pp. 1602–1608, Sept. 1970.
[3] E. A. Ash, E. Seaford, O. Soares, and K. S. Pennington, "Holographic coupler for integrated optics," *Appl. Phys. Lett.*, vol. 24, pp. 207–208, Feb. 15, 1974.
[4] S. Kapany and B. Burke, *Optical Waveguides.* New York: Academic, 1972, ch. 6.
[5] T. Suhara, H. Nishihara, and J. Koyama, "The modulation transfer function in hologram copying process," *Opt. Commun.*, vol. 14, pp. 35–38, May 1975.
[6] H. Kogelnik, "Coupled wave theory for thick hologram gratings," *Bell Syst. Tech. J.*, vol. 48, pp. 2909–2947, Nov. 1969.

Coupling Considerations for Ring Resonators

ALAN C. ECKBRETH

Abstract—**Analyses of the extraction efficiency from traveling-wave (ring) resonators indicate that for media with low gain-length product ($g_0 l$), the coupling fraction from a properly designed ring resonator must be substantially lower than that employed in equivalent standing-wave (linear) configurations.**

Manuscript received April 7, 1975: revised May 7, 1975.
The author is with the United Technologies Research Center, East Hartford, Conn. 06108.

Introduction

Recently, much attention has been directed toward the use of stable [1] and unstable [2] ring resonators for both dye- and molecular-laser applications. Unstable-ring geometries are particularly attractive for large-volume molecular-laser applications because of their characteristically large mode volumes and their design flexibility in regard to the expansion optics. It is also anticipated that unstable rings will be increasingly applied to dye lasers. This follows from the order-of-magnitude increase in beam quality obtained by Ewanizky [3] employing a linear unstable resonator on a flashlamp-pumped dye laser. However, for dye-laser applications which employ intracavity tuning or spectrum-condensing elements, purely collimated beam regions are desired, such as are provided in unidirectional confocal unstable ring resonators. Freiberg *et al.* [2] have experimentally shown that the fractional output coupling exhibited by standing-wave and traveling-wave unstable-resonator configurations is the same when the equivalent Fresnel numbers, appropriately defined, are equal. However, the optical extraction efficiency from traveling-wave resonator configurations can be substantially below that obtainable in the equivalently coupled standing-wave resonator. Physically, from a wave viewpoint, this is due to the fact that, in the traveling-wave case, the optical flux makes only one pass through the active medium prior to coupling; whereas, in the standing-wave case, two passes are made through the medium prior to extraction. It is the purpose of this correspondence to compare quantitatively the extraction efficiency obtainable in traveling-wave geometries with that characteristic of standing-wave configurations and to calculate the optimum coupling to employ in traveling-wave geometries, i.e., that coupling which maximizes power extraction from the medium.

Traveling-Wave Extraction Efficiency

A generalized traveling-wave configuration is displayed in Fig. 1. Solid lines indicate reflecting elements, e.g., mirrors, denoted by M, gratings; and dashed lines indicate partially transmitting elements, e.g., windows, lenses, prisms, etalons, denoted by O. In the analysis which follows, it will be assumed that the ring is operating in a unidirectional fashion, achieved, for example, by inclusion of a feedback mirror M_S to suppress the reverse traveling wave. The output coupler C would normally be provided by either a partially transmitting reflector (stable geometries) or an annular coupler (unstable configurations). In the latter case, the degree of coupling is determined by the magnification and equivalent Fresnel number in accordance with [2] and [4]. In the active medium, the traveling waves will be assumed to be collimated (e.g., confocal unstable rings) and having a uniform intensity profile. The analysis will be similar to that of Rigrod [5] for standing-wave geometries.

In Fig. 2 the traveling-wave configuration of Fig. 1 is replaced by the equivalent periodic system. The active medium will be assumed to be homogeneously broadened and characterized by a spatially uniform small-signal gain g_0 and saturation parameter I_s. β is the traveling-wave flux normalized to the saturation flux. The optical elements between the output

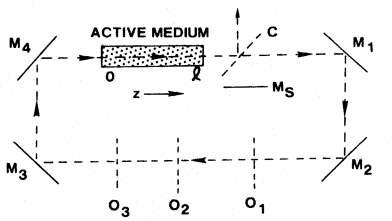

Fig. 1. Typical traveling-wave resonator configuration. Solid lines indicate reflecting elements; dashed lines partially transmitting elements. The active region is shown shaded. Unidirectional operation is achieved by means of the mirror M_S placed behind the coupler.

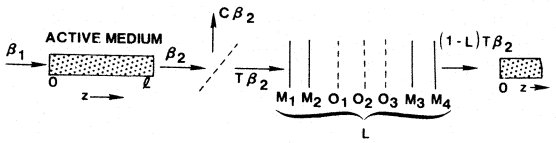

Fig. 2. Equivalent periodic system for Fig. 1 traveling-wave resonator.

coupler and active medium are lumped into a general element of loss L, or equivalently a "transmissivity" of $(1 - L)$. Integrating the gain equation (1)

$$\frac{1}{\beta}\frac{d\beta}{dz} = g = \frac{g_0}{1+\beta} \tag{1}$$

from 0 to l and applying the boundary conditions (2)

$$\beta_1 = (1 - L)T\beta_2$$
$$\beta_{\text{out}} = C\beta_2 \tag{2}$$

leads to the following expression for the normalized output flux:

$$\beta_{\text{out}} = \frac{C}{1 - T(1 - L)}\{g_0 l + \ln T(1 - L)\} \tag{3}$$

where T and C are the fractions of flux incident on the coupler which are transmitted and extracted, respectively. The extraction efficiency, i.e., the output power normalized to the total available optical power, namely $g_0 I_s A l$, where A is the cross-sectional area of the medium, is thus given by

$$\eta_e^{\text{TW}} = \frac{C}{1 - T(1 - L)}\left\{1 + \frac{\ln T(1 - L)}{g_0 l}\right\}. \tag{4}$$

It is important to note that the traveling-wave extraction efficiency would be decreased from the values calculated using (4) if loss elements are situated in the region between the output end of the active medium and the coupler. Thus it is best to configure the ring with all of the loss elements between the coupler and the input end of the active medium, i.e., in the area of least flux as shown in Fig. 1. In those instances, e.g., due to geometric constraints, where loss elements occur on either side of the coupler, the extraction efficiency becomes

$$\eta_e^{\text{TW}} = \frac{C(1 - L_1)}{1 - (1 - L_1)(1 - L_2)T}\left\{1 + \frac{\ln T(1 - L_1)(1 - L_2)}{g_0 l}\right\} \tag{5}$$

where L_1 is the lumped loss situated between the output end of the active medium and the coupler, and L_2 is the lumped loss between the coupler and input to the medium.

Extraction-Efficiency Comparisons

Following an analysis similar to that in [5] it can be shown that the extraction efficiency from the asymmetric (extraction only from one end) standing-wave resonator depicted in Fig. 3 is

$$\eta_e^{\text{SW}} = \frac{C(1 - L)\sqrt{1 - A}}{[1 - (1 - L)\sqrt{(1 - A)(1 - A - C)}]\,[(1 - L)\sqrt{1 - A} + \sqrt{1 - A - C}]}\left\{1 + \frac{\ln (1 - L)\sqrt{(1 - A)(1 - A - C)}}{g_0 l}\right\} \tag{6}$$

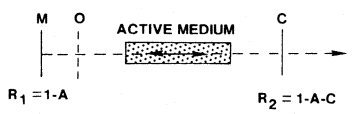

Fig. 3. Standing-wave configuration containing a discrete lumped-loss element O.

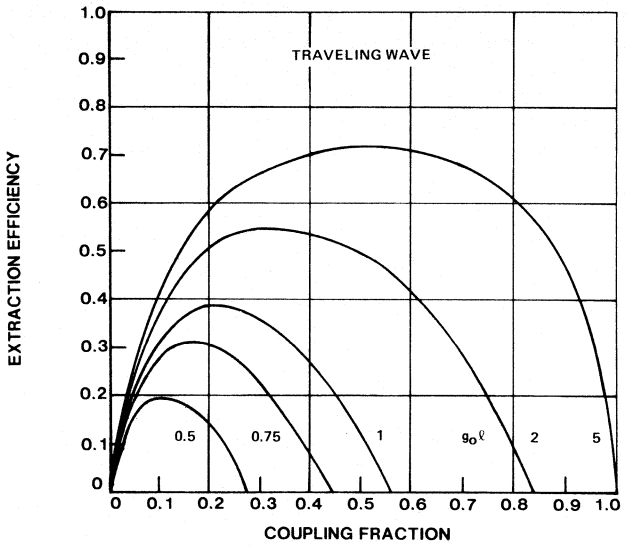

Fig. 4. Traveling-wave extraction efficiency variation with output coupling fraction for various $g_0 l$ products for Fig. 1 configuration containing only one optical element O with single-pass loss of 10 percent. All other optical elements are assumed to have an absorption loss of 1 percent.

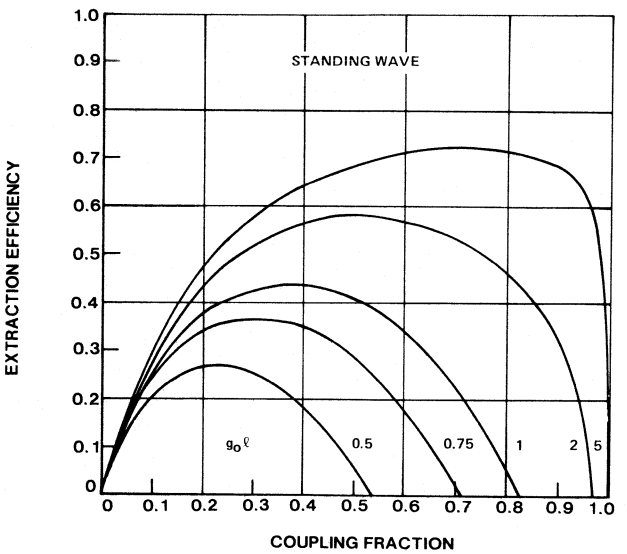

Fig. 5. Standing-wave extraction efficiency variation with output coupling for various $g_0 l$ products for Fig. 3 configuration. Optical element O is assumed to posses a single-pass loss of 10 percent. All other optical elements are assumed to have an absorption loss of 1 percent.

where C is the fractional coupling from the cavity, and L is the single-pass loss of optical element O. Both mirrors are assumed to possess equal absorption coefficients A.

As an example, Figs. 4 and 5 compare the extraction efficiencies obtainable from equivalent traveling-wave and standing-wave configurations, respectively, as a function of coupling for various (small-signal gain) (active-medium length) products. For both cases, all mirrors, including the couplers, were assumed to have an absorption coefficient A equal to 0.01. The results displayed in Fig. 4 correspond to the Fig. 1

ring configuration containing only one such optical element O, e.g., a tuning etalon, which is assumed to possess a single-pass loss of 10 percent. Hence, in (4), $(1 - L) = (0.99)^4 \cdot (0.90) = 0.86$. The Fig. 5 results for the equivalent standing-wave cavity correspond to the Fig. 3 configuration in which optical element O is assumed, as in the traveling-wave example, to have a single-pass loss L, (6), of 10 percent.

Comparing Figs. 4 and 5, it is seen that for high $g_0 l$ products (i.e., > 2), the traveling- and standing-wave cases exhibit comparable performance in regard to maximum extraction efficiency and optimal coupling. However, for low $g_0 l$ values, generally less than 2, these differences become pronounced, particularly with respect to the selection of the output-coupling fraction. The optimal-coupling fraction for the traveling-wave case is generally about half of the value found optimal in the standing-wave case. The maximum extraction efficiency obtainable in the traveling-wave configuration is decreased by about 5 percent ($g_0 l = 2$) to 25 percent ($g_0 l = 0.5$) from that obtainable in the equivalent standing-wave case. However, if the optimal coupling fraction for standing-wave geometries is employed on an equivalent $g_0 l$ traveling-wave configuration, significant decreases in extraction efficiency will occur for low $g_0 l$ media, i.e., $g_0 l < 2$. Accordingly, care must be exercised in the design of traveling-wave resonators to avoid overcoupling the active medium.

References

[1] G. Marowsky and F. Zaraga, "A comparative study of dye prism ring lasers," *IEEE J. Quantum Electron.*, vol. QE-10, pp. 832–837, Nov. 1974.

[2] R. J. Freiberg, P. P. Chenausky, and C. J. Buczek, "Asymmetric unstable traveling-wave resonators," *IEEE J. Quantum Electron. (Part II of Two Parts: Special Issue on 1973 IEEE/OSA Conference on Laser Engineering and Applications)*, vol. QE-10, pp. 279–289, Feb. 1974.

[3] T. F. Ewanizky, "An unstable-resonator flashlamp-pumped dye laser," *Appl. Phys. Lett.*, vol. 25, pp. 295–297, Sept. 1974.

[4] A. E. Siegman and H. V. Miller, "Unstable optical resonator loss calculations using the Prony method," *Appl. Opt.*, vol. 9, pp. 2729–2736, Dec. 1970.

[5] W. W. Rigrod, "Saturation effects in high-gain lasers," *J. Appl. Phys.*, vol. 36, pp. 2487–2490, Aug. 1965.

Nonradiative Relaxation of Rare-Earth Ions in Silicate Laser Glass

C. B. LAYNE, W. H. LOWDERMILK, AND M. J. WEBER

Abstract—**Rates for nonradiative decay by multiphonon emission are measured for rare-earth ions in silicate laser glass and used to estimate quantum efficiencies.**

Three important properties of lasers doped with rare-earth ions are determined by the nonradiative decay rates of the excited states of these ions. First, the pump conversion efficiency[1] is large when the nonradiative decay rate from the pump band to the upper laser level is much greater than the rate for radiative decay from the pump band. Second, for a high radiative quantum efficiency, the nonradiative decay rate from the upper laser level should be small compared to the radiative rate. And third, for a four-level laser system, the relaxation rate of the terminal laser level is important in determining the saturation flux for a laser pulse of given duration. We have determined the nonradiative decay rates for rare-earth ions doped into Owens-Illinois ED-4 glass in order to estimate these properties. ED-4, a widely used commercial laser glass, is a silicate glass modified by the addition of LiO_2, CaO, and Al_2O_3. When doped with Nd^{3+}, this glass is designated as ED-2.

The lifetime of an excited state is determined by all the competing radiative and nonradiative decay processes; the latter include decay by both ion–ion interactions and the emission of phonons. To reduce the probability of nonradiative decay by ion-pair interactions in this work, the rare-earth concentrations of our samples were less than 1 mol%. When the energy gap between the excited ionic energy level and the next-lower level is greater than the energy of the most energetic lattice vibration, the nonradiative decay must involve the emission of several phonons. The multiphonon relaxation rates among the $4f^n$ levels of rare-earth ions have been investigated in many crystals including several laser materials [2]. These studies have shown that, in these high-order processes, the detailed features of the electronic states and phonon modes involved in the transition average out. Thus the multiphonon decay is adequately described in many cases by the stimulated emission of phonons, all of a single frequency ω, leading to a decay rate of the form

$$W_{NR} = Ce^{-\alpha \Delta E}[n(\omega, T) + 1]^p \tag{1}$$

where C and α are constants characteristic of the host material, ΔE is the energy gap to the next-lower ionic level, and $p = \Delta E/\hbar\omega$ is the number of phonons which must be emitted in order to conserve energy in the transition. The explicit temperature dependence of W_{NR}, through the Bose-Einstein occupation number $n = (e^{\hbar\omega/kT} - 1)^{-1}$, provides a way to determine experimentally the number and energy of the phonons involved in the decay process.

It has been established that the nonradiative decay of rare-earth ions in crystals involves emission of the highest energy phonons in the lowest order, and therefore most probable, process consistent with energy conservation and the lattice vibrational spectrum [2]. The highest energy vibrations of a lattice are, in general, the most localized modes characterized by the short-range order of the material. This statement is borne out by the similarity of the infrared and Raman spectra of vitreous materials and their crystalline polymorphs. One would expect that the nonradiative decay of rare-earth ions in glasses would also be dominated by these highest energy lattice vibrations. The glass-lattice vibrational frequencies of ED-4 may be obtained from the Raman spectrum [3]. The highest frequency band at 900–1100 cm^{-1} is attributed to the Si–O–Si

Manuscript received April 28, 1975. This work was performed under the auspices of the U.S. Energy Research and Development Administration.

The authors are with the University of California, Lawrence Livermore Laboratory, Livermore, Calif. 94550.

[1] Our definitions of pump conversion efficiency and radiative quantum efficiency differ from conventions used by other authors [1]. We separate the total efficiency into two parts: 1) pump conversion efficiency is defined as the number of ions in the upper laser level divided by the number of absorbed pump photons, and 2) radiative quantum efficiency is defined as the fraction of ions in the upper laser level which decay radiatively. Both concentration quenching and multiphonon relaxation may decrease radiative quantum efficiency. The present measurements pertain only to the multiphonon contribution, while previous measurements determined the product of pump conversion efficiency and radiative quantum efficiency including concentration quenching.

stretching mode of the silicate-lattice network. Based on a fit to our measurements of the temperature dependence of W_{NR} using (1), we conclude that this highest frequency vibrational mode plays the dominant role in the nonradiative decay. We have found in addition that the strength of ion-lattice coupling in glasses is about the same as it is in crystals. Consequently, since the highest vibrational frequencies of the glass lattice are much greater than the highest phonon frequencies of most crystals, the multiphonon decay rates in glasses are much greater than in crystals.

In order to establish the dependence of the nonradiative decay rate on the energy gap, the rates for eight excited states of four different trivalent rare-earth ions in ED-4 glass were measured. The decay rates were determined from measurements of the transient fluorescence following pulsed selective excitation. Two different laser sources were used to excite the various ionic energy levels. One source was a Nd:YAG laser which produced a 100-mJ pulse at 1.06 μm with a duration of 1 ns. This pulse was used to produce pulses at the second- and third-harmonic frequencies by frequency doubling and mixing in KD*P. The second source was a tunable $LiNbO_3$ optical parametric oscillator which was pumped by the frequency-doubled output of a Chromatix Nd:YAG laser with a pulse duration of 200 ns. (Details of the experimental apparatus and techniques used will be published elsewhere.) The total fluorescence decay rate measured in this experiment consists of both a radiative and a nonradiative contribution. Fortunately, the measured rates in ED-4 were much larger than the estimated radiative rates, and thus the latter were neglected.

The measured nonradiative decay rates for the various ionic energy levels are plotted in Fig. 1 as a function of the energy gap to the next lower level. An approximate exponential dependence on the energy gap, independent of the rare-earth ion or electronic level, is obtained. This systematic dependence can be used to estimate the nonradiative decay rates from other rare-earth energy levels of interest in ED-4. The exponential dependence of the decay rate should not, however, be extrapolated to values of the energy gap corresponding to the excitation of less than approximately two quanta of the highest frequency lattice vibrational mode. For relaxation processes involving only one or two vibrational quanta, the averaging effect of high-order processes is not present, and in this case the decay rate is expected to depend on the details of the electronic state and vibrational mode excited in the decay. This effect is apparent in the deviation from the exponential fit of the decay rate for the $^4G_{7/2}$ level of Nd^{3+} with an energy gap of 1400 cm^{-1}. The results shown in Fig. 1, of course, apply only to the silicate glass. The characteristic vibrational frequencies of other glasses are significantly different, leading to large variations of the nonradiative decay rates [4].

We conclude by applying the results of this experiment to the Nd^{3+}-doped ED-2 glass to estimate the pump conversion efficiency, the radiative quantum efficiency of the $^4F_{3/2}$ upper laser level, and the lifetime of the $^4I_{11/2}$ terminal laser level. Since the nonradiative rate depends exponentially on the energy gap, the decay time from the optical pump bands to the $^4F_{3/2}$ level is determined by the largest energy gap encountered in the cascade. The largest gap, of approximately 2300 cm^{-1}, occurs below the $^2P_{3/2}$ level. The fluorescence lifetime of this level was measured to be 50 ns. The radiative lifetimes of all the excited states in the pump bands have been calculated using the Judd–Ofelt intensity parameters for ED-2 [5]. These lifetimes are all longer than 10^{-5} s. Thus, since ion-pair interactions are believed to be negligible, the pump conversion efficiency is found to be greater than 99 percent. The nonradiative decay rate for the $^4F_{3/2}$ level, based on the extrapolation shown in Fig. 1 to an energy gap of 4800 cm^{-1},

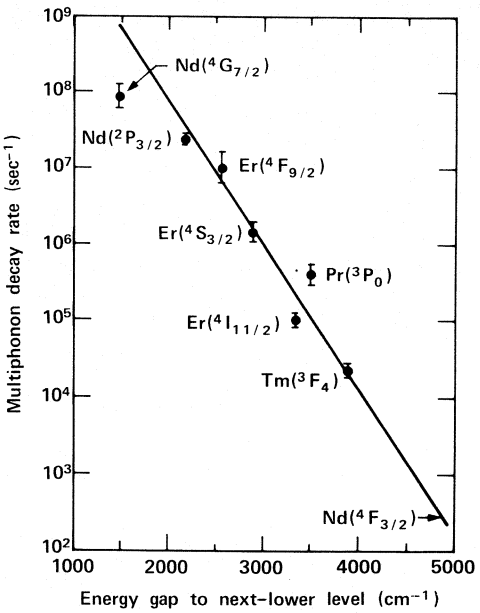

Fig. 1. Multiphonon decay rates as a function of energy gap to the next-lower level for rare-earth ions in ED-4 silicate glass at 300 K. The extrapolation to the Nd ($^4F_{3/2}$) nonradiative rate is indicated.

is estimated to be 200 s^{-1}. The radiative decay rate for this level is about 3×10^3 s^{-1}, leading to a radiative quantum efficiency of approximately 95 percent in the absence of concentration quenching. An estimate of the radiative quantum efficiency which is in agreement with this value was obtained from measurements of the temperature dependence of the fluorescence lifetime of the $^4F_{3/2}$ level. This temperature dependence arises from thermal population and decay of levels above the $^4F_{3/2}$ in addition to the temperature dependence of W_{NR} shown in (1). This result is, however, less accurate since the change in the measured rate over the available temperature range is small compared to the uncertainty in the measurement. Finally, the lifetime of the $^4I_{11/2}$ terminal level with a gap of 1500 cm^{-1} is predicted to be approximately 10 ns. This value is in good agreement with estimates based on attempts to measure this lifetime directly [6].

REFERENCES

[1] a) L. G. DeShazer and L. G. Komai, "Fluorescence conversion efficiency of neodymium glass," *J. Opt. Soc. Amer.*, vol. 55, pp. 940–944, Aug. 1965.
b) R. A. Brandewie and C. L. Telk, "Quantum efficiency of Nd^{3+} in glass, calcium tungstate, and yttrium aluminum garnet," *J. Opt. Soc. Amer.*, vol. 57, pp. 1221–1225, Oct. 1967.

[2] L. A. Riseberg and M. J. Weber, "Relaxation phenomena in rare-earth luminescence," in *Progress in Optics*, vol. XIV. Amsterdam, The Netherlands: North-Holland, 1975, in press.

[3] R. W. Hellwarth, J. Cherlow, and T. Yang, "Origin and frequency dependence of nonlinear optical susceptibilities of glasses," *Phys. Rev.*, vol. 11, pp. B964–B967, Jan. 1975.

[4] W. H. Lowdermilk, C. B. Layne, and M. J. Weber, "Nonradiative relaxation of rare earth ions in glasses: (II) Dependence on vibrational spectrum," *Bull. Amer. Phys. Soc.*, vol. 20, ser. II, p. 448, Mar. 1975.

[5] W. F. Krupke, "Optical properties of ED-2 laser glass," Univ. Calif., Lawrence Livermore Lab., Livermore, Calif., Int. Rep. UCIR-714, Dec. 1973.

[6] a) D. K. Duston, "Factors influencing the gain in neodymium doped laser glass," Ph.D. dissertation, Rensselaer Polytech. Inst., Troy, N.Y., May 1969.
b) V. V. Grigoryants *et al.*, "Determination of τ_{21} relaxation time of $^4I_{11/2}$ level of neodymium ions in glass," *Zh. Prikl. Specktrosk.*, vol. 14, pp. 73–77, Jan. 1971.

Comments on "Picosecond Optical Sampling"

JAMES D. MACOMBER

Abstract—**An optical sampler recently reported by Vogel *et al.* is revealed to have been invented six and one-half years previously by Macomber.**

In the above paper,[1] a device designed to measure "single-shot" optical events by multiple sampling was reported. Each sampling channel is fed by a mirror in the path of the beam: the signals from the several channels are then fed into optical fibers of different lengths which serve as delay lines. The amount of delay of the signal increases from one channel to the next so as to reduce the effective rise time of the event. The signals may then be processed at a rate which does not exceed the rise time of commercially available photodetectors and oscilloscopes.

Manuscript received May 12, 1975.

The author is with the Department of Chemistry, Louisiana State University, Baton Rouge, La. 70803.

[1] G. C. Vogel, A. Savage, and M. A. Duguay, *IEEE J. Quantum Electron.*, vol. QE-10, pp. 642–646, Sept. 1974.

The purpose of this correspondence is to publicize the fact that the device in question had actually been invented six and one-half years before the submission date of the subject manuscript. On June 16, 1967 I wrote an invention disclosure, subsequently submitted to the Department of Health, Education, and Welfare (DHEW) in accordance with the terms of Grant 1 RO1 NB 07891-01 RAD (although the grant did not officially begin until September 1, 1967). A patent application was filed by DHEW on February 10, 1969, and the patent [1] was awarded on July 27, 1971.

The device described in the subject paper is identical not only in its general purpose, but also in the details of the construction of most of its various parts. Therefore, there is no doubt that the two devices are identical. There is no evidence, however, that the authors knew of my work prior to the publication of theirs—indeed, they are to be congratulated for building and testing the device which I conceived so long ago. But perhaps your readers might be interested in knowing that "Great minds think alike!"

References

[1] J. D. Macomber, "Method and apparatus for analyzing traveling light waves," U.S. Patent 3 596 104, July 27, 1971.

Notes and Lines

Long-Pulse Generation in Rhodamine-6G Pumped by a CO_2-Laser-Heated Plasma

ROBERT T. BROWN

Abstract—**Results obtained using a laser-heated plasma as the pumping source for a dye laser are described. A small dye laser using a cylindrical close-coupled pumping arrangement was operated at various xenon pressures. Dye-laser pulses with 20-ns rise times and 800-ns pulsewidths were obtained.**

It has recently been shown [1], [2] that a laser-heated xenon plasma is potentially a very effective pumping source for a dye laser. In [1] lasing was obtained using a close-coupled arrangement with no pumping cavity, but it was found that the dye-laser pulse terminated prematurely, apparently due to thermal distortions in the dye solution. If this effect were to persist in large-scale breakdown-pumped dye lasers, it would severely limit the potential efficiency of this approach. This note describes results obtained with a somewhat different pumping arrangement in which the dye-laser pulse shape tended to follow the TEA pumping pulse shape, indicating that efficient coupling with breakdown pumping should be possible.

Breakdown-pumped dye-laser studies were carried out using a dye cell 3 mm in diameter by 7 cm long, as shown in Fig. 1.

Manuscript received May 7, 1975.

The author is with the United Technologies Research Center, East Hartford, Conn. 06108.

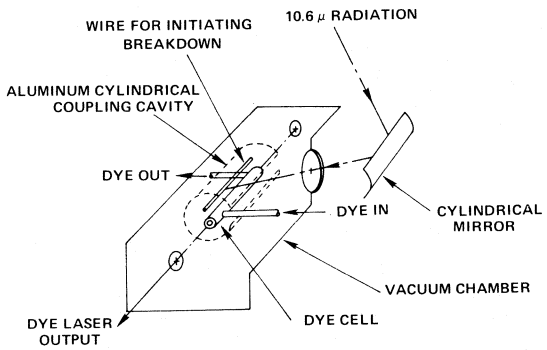

Fig. 1. Experimental arrangement used in breakdown-pumped dye-laser studies.

A thin tungsten wire for initiating the breakdown was located adjacent to the cell, near the centerline of a cylindrical close-coupled pumping cavity. The dye cell, coupling cavity, and wire were contained in a chamber filled with xenon at various pressures, and the 10.6-μ radiation was focused onto the wire with a 6-cm focal-length mirror. The dye-laser cavity consisted of plane-parallel mirrors separated by 17 cm, with one total reflector and an 80-percent reflecting output coupler.

Fig. 2 shows typical pulses from the TEA pumping laser and corresponding pulses from the dye laser, operating with a 3×10^{-3}-M solution of rhodamine-6G in ethanol and a xenon pressure of 20 torr. The pulse in Fig. 2(c) had an energy of $\sim$0.3 mJ, a circular near-field pattern with a diameter of 4 mm, and a full-angle beam divergence of 5 mrad. It can be seen

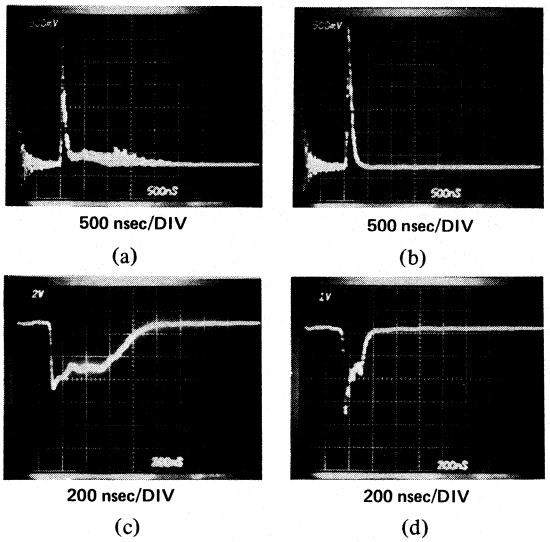

Fig. 2. Pulse shapes. (a) 10.6-μ TEA laser pulse with nitrogen. (b) TEA laser pulse without nitrogen. (c) Dye-laser pulse shape corresponding to (a). (d) Dye-laser pulse shape corresponding to (b).

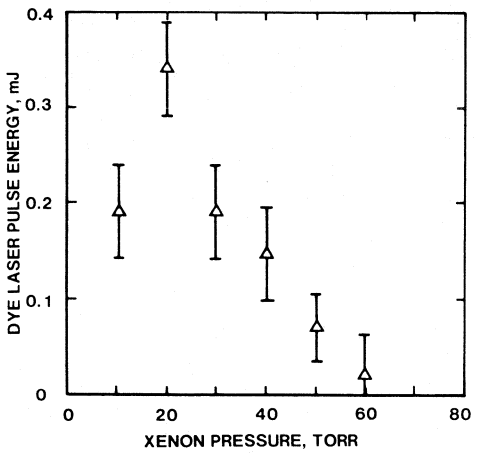

Fig. 3. Laser pulse energy at various xenon pressures.

from these traces that the pumping which occurred during the tail of the 10.6-μ pulse was still well above threshold, and that the dye-laser pulse length was comparable to the intense portion of the 10.6-μ pulse.

Photographs showed that the laser-heated plasma was not cylindrical, as originally intended, but instead had a rather complicated wedge shape of roughly the same dimensions as the 10.6-μ laser focal volume. Because of this, the coupling between the plasma and the dye cell was not efficient. However, even with this preliminary arrangement, a dye-laser output energy of 0.5 mJ was obtained for 1.0 J of 10.6-μ energy. Improved coupling geometries are currently being studied.

Fig. 3 shows the laser energy for various xenon pressures, and, as expected, based on [2], shows a maximum at pressures well below those used in conventional xenon flashlamps.

References

[1] W. T. Silfvast and O. R. Wood, II, "A 3400 Å p-terphenyl dye laser pumped by a CO_2 laser produced plasma," *Appl. Phys. Lett.*, vol. 26, pp. 447-449, 1975.

[2] —, "Comparison of radiation from laser-produced and dc-heated plasmas in xenon," *Appl. Phys. Lett.*, vol. 25, pp. 274-277, 1974.

Observation of Stimulated Emission at 0.3159 μm in the Nitrogen Second-Positive System at Room Temperature

JOHN S. KRUGER

Abstract—**Pulsed electrical discharges in pure nitrogen have produced laser oscillation on an ultraviolet band of the nitrogen triplet system not previously reported above liquid-nitrogen temperature.**

This note reports observation of laser oscillation on the $C^3\pi_u$–$B^3\pi_g$ (1–0) band in nitrogen at room temperature. This band is one of three laser bands that have been seen in the second-positive system (C–B electronic–vibrational transitions) of nitrogen.

Oscillation in the ultraviolet was first reported on the 0–0 band (0.3371 μm) of the second-positive system by Heard [1]. Lasing in the 0–0 and 0–1 (0.3577-μm) bands was observed by Kaslin and Petrash [2] and Massone *et al.* [3]. By cooling the walls of the discharge tube with liquid nitrogen, Kaslin and Petrash [4] were also able to detect a new oscillation on the 1–0 band (0.3159 μm). With electron-beam-pumped Ar–N_2 mixtures Searles and Hart [5] and Ault *et al.* [6] reported lasing on the 0–1 and 0–2 (0.3805) and 0–1 bands, respectively. The present work noted this band at room temperature, in nitrogen alone, with a conventional longitudinally excited discharge.

In this work pulsed electrical discharges were produced in commercial-grade (water-pumped) nitrogen at about 3 torr, flowing at < 1 Standard l/h. The laser discharge tube had an 8-mm ID, with 40 cm of plasma length along the laser axis. The tube was fitted with fused-silica Brewster's-angle windows and tungsten electrodes. A 2.4-nF ceramic capacitor was charged to 20 kV and then discharged via a triggered spark gap through the laser tube at an 11-Hz repetition rate. The resonant cavity was formed by two highly reflecting Ag-coated mirrors placed 50 cm apart. One mirror was flat and the other was a 2.17-m-radius hole-coupled spherical mirror, which served as the output mirror.

The oscillation from the laser was detected through a 1-m Czerny–Turner spectrometer with a thermoelectrically cooled S-1 photomultiplier. Table I summarizes the results obtained for both spontaneous and stimulated emission on all three second-positive-system bands. The spontaneous emission was distinguished from the stimulated emission by blocking the rear cavity reflector and noting a drop in detected intensity of several orders of magnitude.

TABLE I
ULTRAVIOLET BANDS OBSERVED IN NITROGEN AT ROOM TEMPERATURE IN A LONGITUDINALLY EXCITED DISCHARGE

Emission Band	Band Edge λ_{vac} (μm)	Relative Spontaneous Intensity	Relative Stimulated Intensity	Optimum N_2 Pressure (Torr)
1-0	0.3159	0.01*	3	3.2
0-0	0.3371	0.10	300	3.0
0-1	0.3577	0.07	30	2.5

*Comparable to fluctuations in photomultiplier dark current.

Manuscript received May 15, 1975.

The author is with the Harry Diamond Laboratories, 2800 Powder Mill Rd., Adelphi, Md. 20783.

REFERENCES

[1] H. G. Heard, "Ultraviolet gas laser at room temperature," *Nature*, vol. 200, p. 667, 1963.

[2] V. M. Kaslin and G. G. Petrash, "Rotational structure of ultraviolet generation of molecular nitrogen," *Sov. Phys.–JETP Lett.*, vol. 3, pp. 55–57, 1966 (Transl.: *Pis'ma Zh. Eksp. Teor. Fiz.*, vol. 3 pp. 88–92, Jan. 15, 1966).

[3] C. A. Massone, M. Garavaglia, M. Gallardo, J. A. E. Calatroni, and A. A. Tagliaferri, "Investigation of a pulsed molecular nitrogen laser at low temperature," *Appl. Opt.*, vol. 11, pp. 1317–1328, June 1972.

[4] V. M. Kaslin and G. G. Petrash, "Effect of temperature on the properties of pulsed laser action on electron transitions in diatomic molecules," *Sov. Phys.–JETP*, vol. 27, pp. 561–567, Oct. 1968 (Transl.: *Zh. Eksp. Teor. Fiz.*, vol. 54, pp. 1051–1063, Apr. 1968).

[5] S. K. Searles and G. A. Hart, "Laser emission at 3577 and 3805 Å in electron-beam-pumped Ar-N_2 mixtures," *Appl. Phys. Lett.*, vol. 25, pp. 79–82, July 1, 1974.

[6] E. R. Ault, M. L. Bhaumik, and N. T. Olson, "High-power Ar-N_2 transfer laser at 3577 Å," *IEEE J. Quantum Electron.* (Corresp.), vol. QE-10, pp. 624–626, Aug. 1974.

Contributors

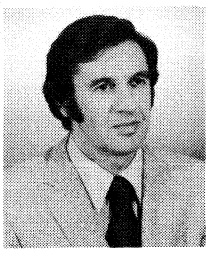

A. J. Alcock (S'58–M'59) was born in Glasgow, Scotland, on February 3, 1938. He received the B.Sc. degree in electrical engineering from the University of Toronto, Toronto, Ont., Canada, and the Dr. Phil. degree in engineering science from Oxford University, Oxford, Oxon., England, in 1959 and 1965, respectively.

Since 1965 he has been with the Physics Division of the National Research Council of Canada, Ottawa, Ont., and is currently Head of the Laser and Plasma Physics Section. His principal research interests include laser plasma interactions, high-pressure gas lasers, plasma diagnostics, and the measurement of ultrashort laser pulses.

Dr. Alcock is a member of the American Physical Society and the Canadian Association of Physicists.

*

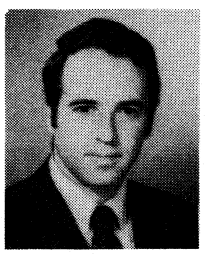

Stephen R. Chinn (M'75) was born in Baltimore, Md., on November 20, 1942. He received the B.S. and M.S. degrees in electrical engineering and the Ph.D. degree in electrical science and engineering from the Massachusetts Institute of Technology, Cambridge, Mass., in 1965 and 1970, respectively.

He has worked in the areas of electron paramagnetic resonance, magnetism, and Raman scattering. In 1970 he became a postdoctoral fellow at the Massachusetts Institute of Technology Lincoln Laboratory, Lexington, Mass., and since 1971 has been a member of the staff there, studying semiconductor lasers.

Dr. Chinn is a member of the American Physical Society, Tau Beta Pi, Eta Kappa Nu, and Sigma Xi.

*

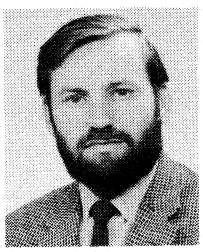

Peter H. Cross was born in London, England, in 1928. He received the H.N.C. in mechanical engineering and the H.N.C. in applied physics in 1950 and 1964, respectively.

Since 1949 he has been engaged in microwave-tube and CO_2-laser research at the Services Electronics Research Laboratory, United Kingdom Ministry of Defence, Baldock, Herts., England. Engineering design has been a hobby since childhood.



Robert Fedosejevs was born in Ottawa, Ont., Canada, on November 5, 1952. He received the B.Sc. degree in physics from the University of Toronto, Ont., Canada, in 1973. He is currently pursuing the Ph.D. degree in the area of laser-produced plasmas at the same university.

For the year following his graduation he worked on high-pressure CO_2 lasers and CO_2-laser-produced plasmas with the Division of Physics, the National Research Council of Canada, Ottawa, Ont., Canada.

Mr. Fedosejevs is a member of the American Physical Society and the Canadian Association of Physicists.

*



Harry Foster was born in Yorkshire, England, in 1918. He received a Final City and Guilds of London Institute certificate at the City of Leeds Institute, Leeds, England, in 1939.

From 1940 to 1945 he was engaged on the development of microwave valves at the Admiralty Signal and Radar Establishment. In the postwar years he joined the Royal Naval Scientific Service and worked on the development of magnetrons and klystrons at the Services Electronics Research Laboratory, Mininstry of Defence, Baldock, Herts., England. Since 1960 he has been engaged on gas-laser projects at the same laboratory, and is at present a Section Leader of a team working on the development of carbon-dioxide lasers.

Mr. Foster is a fellow of the Institute of Physics.

*

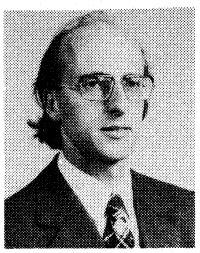

G. E. François was born in Ghent, Belgium, on June 30, 1936. He received the degree of engineer from the State University of Ghent, Ghent, Belgium, in 1960, and the M.S. and Ph.D. degrees from Stanford University, Stanford, Calif., in 1962 and 1965, respectively, while on a CRB Graduate Fellowship from the Belgian American Educational Foundation.

He worked for one year for the Belgian National Scientific Foundation (NFWO) following his graduation from the State University of Ghent. During the summer of 1965 he worked as a Research Associate at Stanford University, where he was involved in work on nonlinear

optics. Since 1967 he has been a Professor at the Catholic University of Leuven, Leuven, Belgium. His areas of research include nonlinear optics and, more generally, laser applications.

Dr. François is a member of the Optical Society of America, Sigma Xi, KVIV, and AIG.

*

Hermann A. Haus (S'50–A'55–SM'58–F'62), for a photograph and biography please see page 377 of the July 1975 issue of this JOURNAL.

*



Helmut Heckscher was born in Hamburg, Germany, where he received his primary education. He received the B.S. degree in physics from the University of Wisconsin, Madison, in 1950.

He came to the United States in 1940, where he served as an officer in Military Intelligence. Since graduating, he has worked on research and development projects at Battelle Memorial Institute, Itek Corporation, Technical Operations, and, currently, at the Massachusetts Institute of Technology Lincoln Laboratory, Lexington, Mass. He has been granted five U.S. patents in the field of imaging systems.

*

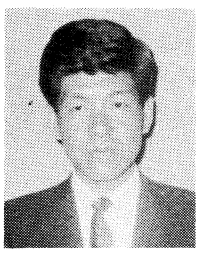

Takeshi Kamiya was born in Tokyo, Japan, on July 19, 1939. He received the B.E., M.E., and Ph.D. degrees in applied physics from the University of Tokyo, Tokyo, Japan, in 1963, 1965, and 1970, respectively.

In 1968 he joined the staff of the Department of Electronic Engineering at the University of Tokyo, and since 1969 he has been an Associate Professor at the University of Tokyo, where he has been engaged in quantum electronics and optoelectronics fields. Currently, he is working on semiconductor lasers and integrated optics.

Dr. Kamiya is a member of the Physical Society of Japan, the Japan Society of Applied Physics, the Institute of Electronics and Communication Engineers of Japan, and the Institute of Electrical Engineers of Japan.

*



Dae M. Kim was born in Korea on April 22, 1938. He received the B.S. degree in physics from Seoul National University, Seoul, Korea, in 1960, and the M.S. and Ph.D. degrees in physics from Yale University, New Haven, Conn., in 1965 and 1967, respectively.

He was at the Massachusetts Institute of Technology from 1967 to 1970, the first two years as a postdoctoral research associate, and the last year as an Instructor in Physics. He joined the Department of Electrical Engineering at Rice University, Houston, Tex., in 1970, as an Assistant Professor. He is currently an Associate Professor of Electrical Engineering. His research interests are mode-locked lasers, light-heating spectroscopy, and parametric excitation of plasma lines.

Dr. Kim is a member of the American Physical Society and Sigma Xi.



F. M. Librecht (S'68–M'70–S'70) was born in Oudenaarde, Belgium, on September 7, 1945. He received the degree of engineer and the doctor's degree, both from the Catholic University of Leuven, Leuven, Belgium, in 1969 and 1974, respectively.

He holds a fellowship of the Belgian National Scientific Foundation (NFWO) at the Laboratory of Telecommunications, Microwaves and Lasers of the Catholic University of Leuven. His research interests include nonlinear optics and optical communications.

*

D. Marcuse (M'58–F'73), for a photograph and biography please see page 179 of the April 1975 issue of this JOURNAL.

*

Gary L. McAllister, for a photograph and biography please see page 314 of the June 1975 issue of this JOURNAL.

*

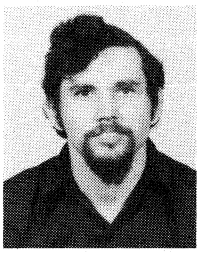

James W. Pierce was born in Sandwich, Mass., on September 25, 1943. He received the B.S. degree in chemistry from Worcester Polytechnic Institute, Worcester, Mass., in 1965, and the Ph.D. degree in chemistry from Brown University, Providence, R.I., in 1970.

He has worked in preparative and structural chemistry of transition metal and rare-earth oxides and fluorides, correlating structure and composition with optical, magnetic, and transport properties. At the Massachusetts Institute of Technology Lincoln Laboratory, Lexington, Mass., his primary emphasis has been on rare-earth fluorides and oxides for infrared-to-optical up-conversion and on improved laser hosts.

*



Thomas A. Rabson (S'54–M'60) was born in Houston, Tex., on July 31, 1932. He received the B.A. and B.S. degrees in electrical engineering, and the M.A. and Ph.D. degrees in physics, all from Rice University, Houston, Tex., in 1954, 1955, 1957, and 1959, respectively.

Since 1959 he has been with the Department of Electrical Engineering, Rice University, and is currently a Professor of Electrical Engineering. His research interests are in mode-locked lasers, photorefractive effects, submillimeter waves, and semiconductor physics.

Dr. Rabson is a member of the American Physical Society, the Optical Society of America, Tau Beta Pi, and Sigma Xi.

*

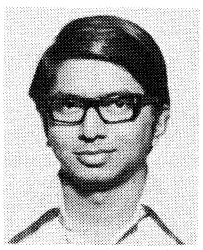

Rajiv R. Shah (S'74) was born in Pulgaon, Maharashtra, India, on July 11, 1953. He received the B.Sc. degree in physics from the University of Poona, Poona, India, in 1972, and the M.S. degree in electrical engineering from Rice University, Houston, Tex., in 1974.

In 1969 he was selected as a National Science Talent Search Scholar by the Government of India and was awarded a scholarship for pursuing studies in physics while at the University of Poona. Also, under the same program, he par-

ticipated in advanced summer training institutes at Jodhpur, Vishakapatnam, and Bangalore, India, in 1970, 1971, and 1972, respectively. He is currently working towards the Ph.D. degree in electrical engineering in the area of holographic storage of data on crystals at Rice University, Houston.

Mr. Shah is a student member of the American Physical Society and the Optical Society of America.

*

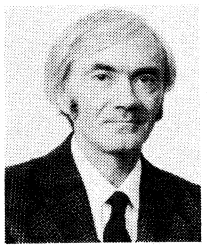

Donald S. Stark was born in Calcutta, India, in 1925. He received the B.Sc. degree in physics from the University of London, London, England, in 1944.

After holding posts at the Research Department of EMI Ltd., Hayes, England, and at the City College of Technology, Liverpool, England, he has been working since 1951 at the Services Electronics Research Laboratory of the United Kingdom Ministry of Defence, Baldock, Herts., England. He has been principally engaged in research and development in the fields of vacuum physics, neutron generators, and (currently) CO_2 lasers.

*



William H. Steier (S'58-M'60-SM'72) was born in Kendallville, Ind., on May 25, 1933. He received the B.S. degree in electronic engineering from Evansville College, Evansville, Ind., in 1955, and the M.S. and Ph.D. degrees, both in electrical engineering, from the University of Illinois, Urbana, in 1957 and 1970, respectively.

From 1960 to 1962 he was an Assistant Professor in the Department of Electrical Engineering, University of Illinois. From 1962 to 1968 he was a member of the Technical Staff, Bell Telephone Laboratories, Holmdel, N.J. He is currently a Professor of Electrical Engineering, University of Southern California, Los Angeles. He is also a Consultant to the Northrop Corporate Laboratories, Hawthorne, Calif. In September 1970, he became Chairman of the Department of Electrical Engineering–Electro-Physics at USC. He has been active in research in millimeter waves, optical transmission lines, coherent optical devices, and air-pollution monitoring.

Dr. Steier is a member of Eta Kappa Nu and Sigma Xi.

*



Armand L. Waksberg (M'63-SM'70) received the B.Sc. degree in honors mathematics and physics and the M.Sc. degree in physics from McGill University, Montreal, P.Q., Canada, in 1956 and 1960, respectively.

He joined Canadair in 1956, where he worked on aerodynamic and dynamic problems of aircraft, as well as performing system studies on various vehicles. In 1960 he joined the Canadian Aviation Electronics Research and Development Department, where he worked on various electronic systems. He joined the Research Laboratories of RCA Limited, Ste-Anne de Bellevue, P. Q., in 1963. He has made theoretical studies of the He-Ne laser system, noise in lasers, detection of weak laser signals, and the feasibility of laser pumping with monoenergetic electrons. Experimental studies have included work on off-axis laser modes, measurement of high-speed detectors, and side-light properties of lasers. More than 25 papers have been published on these subjects. More recently, he has developed techniques to stabilize CO_2 lasers, and he is currently working on laser communication experiments.

*

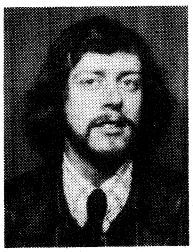

Andrew C. Walker was born in Harrow, England, on June 24, 1948. He received the B.A. degree in physics, the M.Sc. degree in quantum electronics, and the Ph.D. degree in physics, all from Essex University, Colchester, Essex, England, in 1969, 1971, and 1973, respectively. His Ph.D. research was based on an investigation of the photon drag effect.

In 1972 he joined the Laser and Plasma Physics group at the National Research Council of Canada, Ottawa, as a postdoctoral fellow, and worked on high-pressure CO_2 lasers and the generation and detection of short, 10-μm radiation pulses. He is currently an SRC fellow at Essex University, and his research interests include high-pressure and waveguide CO_2 lasers.

*



Yoshihisa Yamamoto (S'75) was born in Tokyo, Japan, on November 21, 1950. He received the B.E. degree in electrical engineering from the Tokyo Institute of Technology, Tokyo, Japan, and the M.E. degree in electronic engineering from the University of Tokyo, Tokyo, Japan, in 1973 and 1975, respectively. He has been working toward the Ph.D. degree in electronic engineering at the University of Tokyo; his current interest is in integrated optics.

Mr. Yamamoto is a member of the Institute of Electronics and Communication Engineers of Japan and the Japan Society of Applied Physics.

*



Hisayoshi Yanai (M'57-SM'63) was born in Okayama, Japan, on May 19, 1920. He received the B.E. degree in electrical engineering from the University of Tokyo, Tokyo, Japan, in 1942, and the Ph.D. degree in electrical engineering from the University of Tokyo in 1953 for research on measurements of dielectric properties in the delta-modulation wave region. From 1954 to 1955 he studied at the Institute of Technology, Munich, Germany.

In 1945, after three years of military service, he joined the staff of the Electrical Engineering Department at the University of Tokyo. In 1947 he became an Associate Professor, and since 1960 he has been a Professor at the University of Tokyo, where he is currently concerned with semiconductor devices, integrated circuits, and optoelectronics. He has published a number of research papers and articles in the area of semiconductor devices and circuits, especially in the microwave region.

Dr. Yanai received the Paper Award for two of these papers and the Distinguished Services Award from the Institute of Electronics and Communication Engineers of Japan for his excellent research works in 1970. He is a member of the Institute of Electrical Engineers of Japan, the Institute of Electronics and Communication Engineers of Japan, and the German Society of Electrical Engineers.



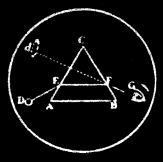

1975 IEEE/OSA Conference on Laser Engineering and Applications

May 28–30, 1975

Washington Hilton Hotel
Washington, D.C.

Joint Sponsors:
IEEE Quantum Electronics Council
and
Optical Society of America

Digest of Technical Papers

1975 IEEE/OSA Conference on Laser Engineering and Applications

Washington, D.C., May 28–30, 1975

Session 1

Wednesday, May 28, 1975 9:00-11:45 A.M.

Dye Lasers

Chairman: John P. Goldsborough, *Spectra-Physics Inc., Mt. View, Calif. 94040*

1.1 A 3400 Å Dye Laser and a 1.315 μm Photodissociation Laser Efficiently Pumped by a CO_2 Laser-Produced Plasma,

W. T. Silfvast and O. R. Wood II, *Bell Telephone Laboratories, Holmdel, N. J. 07733*

(15 min)

A cylindrically shaped CO_2 laser-produced plasma has been used to optically pump lasers in gases[1] and organic dyes. Using a transverse pumping arrangement, a 3400 Å p-terphenyl dye laser[2] was optically pumped by UV radiation from a xenon plasma produced with a high pressure pulsed CO_2 laser. Dye laser output powers greater than 10 kW at 3400 Å, in an active length of 4.2 cm, were produced by a 10.6 μm input pulse energy of 5.6 joules. In addition, more than 30 kW of laser power has been obtained at 5875 Å from Rh6G using the same pumping geometry. Laser action has also been obtained at 1.315 μm by photodissociation of C_3F_7I.[1] In this case, the laser output intensity was measured to be at least a factor of 5 greater than that obtained using a linear flashlamp. The potential scaling of CO_2 laser-produced plasmas to larger dimensions, higher repetition rates and shorter risetimes makes them an attractive alternative to a conventional flashlamp as sources for optical pumping.

A spectral radiance of 2 W/mm²-ster-nm at 230 nm from an elongated xenon plasma can be produced by focused 10.6 μm laser radiation for input energies/length of 0.8 Joules/cm. In the ultraviolet region (2000-3000 Å) the spectral radiance for a laser-produced plasma in xenon gas is 2-3 times greater than that produced by a xenon flashlamp of comparable size and input energy.[3] Thus, for a CO_2 laser that is 30 percent efficient in converting electrical energy to 10.6 μm radiation,[4] the two pumping sources would be approximately equal in overall efficiency. Furthermore, since the rate of increase of ultraviolet emission with increasing input energy is much greater for the laser-produced plasma than for a flashlamp (for input energies up to 0.8 Joules/cm,[3] this comparison is expected to improve with increasing input energy, eventually favoring the laser-produced plasma source. While the risetime of a CO_2 laser-produced plasma source is a function of the 10.6 μm input power, even for the modest CO_2 laser energies used in the present experiment, risetimes less than 5 nsec can readily be achieved.

Dye laser pumping was accomplished by focusing the output from a high pressure pulsed CO_2 laser having a 2.5 × 5 cm rectangular cross-section with a 7.5 cm focal length cylindrical lens onto an aluminum target inside a cell filled with xenon gas. An approximately cylindrically shaped plasma, 4.5 cm in length, was formed in xenon gas adjacent to a 0.9 cm × 0.9 cm × 4.5 cm quartz cuvette which had been filled with a solution of p-terphenyl in cyclohexane. Stimulated emission was observed from a layer of dye solution immediately inside the 0.9 cm × 4.5 cm side window of the cuvette.

For initiation of an iodine photodissociation laser, a laser-produced plasma was formed in xenon gas adjacent to a 4 mm diameter quartz tube (30 cm in length) filled with i-C_3F_7I. For comparison with the lawer-produced plasma, an E G & G FX38C linear flashlamp was mounted adjacent to the laser tube. This lamp, having approximately the same dimensions as those of the laser-produced plasma, was excited with an electrical pulse of comparable duration to the CO_2 laser pulse and with the same energy input per unit length.

The application of this technique to other gases (particularly other chemical lasers), liquids (particularly other organic dyes), and solids is strongly indicated. In systems having high gains and very short lifetimes, the possibility of traveling-wave optical pumping using laser-produced plasma sources also seems possible.

1.2 Subnanosecond Tunable Dye Laser Pulse Generation by Controlled Resonator Transients,

Chinlon Lin and C. V. Shank, *Bell Telephone Laboratories, Holmdel, N. J. 07733*

(15 min)

We describe a general technique for generating a single subnanosecond pulse from a laser pumped dye laser. Our technique makes use of the resonator transients which are in the form of damped relaxation oscillations or "spiking," a well known phenomenon observed and studied extensively in solid state masers and lasers.[1] These resonator transients are a consequence of the interaction between the excess population inversion and the photons in the cavity.

Fig. 1 shows the observed transient behavior of a N_2 laser-pumped 7-diethylamino-4-methylcoumarin dye laser at various levels of the pumping power. The damped relaxation oscillations are clearly seen. For this experiment a dye

[1] G. Birbaum, *Optical Masers*. New York: Academic Press, 1964, p. 51.

Fig. 1. (i) N_2 laser pumping pulse, time scale 2 ns/cm; (ii)-(iv): observed dye laser pulse as the pump power is decreased from (ii) to (vi). Time scale: 1 ns/cm, except for (ii) which is 2 ns/cm. Photon cavity decay time of the dye laser is ~50 psec.

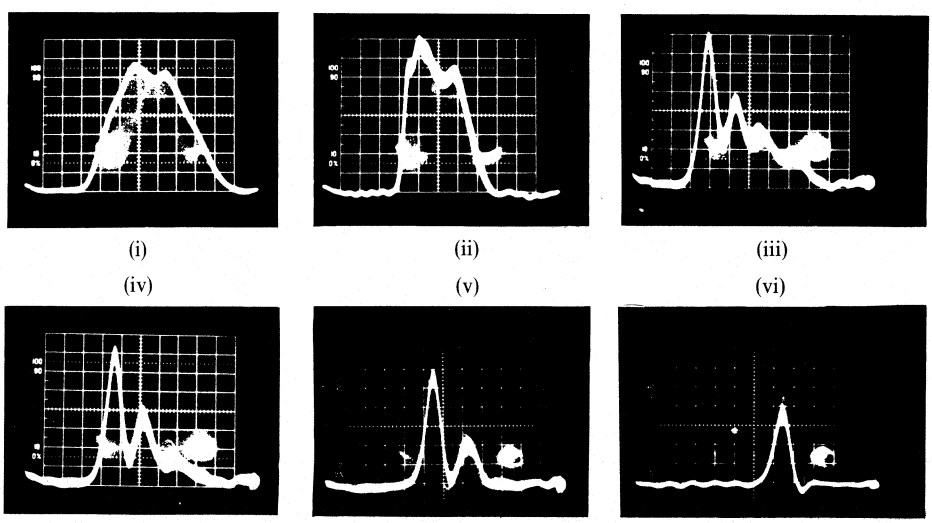

[1] W. T. Silfvast, L. H. Szeto and O. R. Wood II, *Appl. Phys. Lett.*, vol. 25, p. 593, 1974.

[2] G. A. Abakumov, A. P. Simonov, V. V. Fadeev, L. A. Kharitonov and R. V. Kokhlov, *JETP Lett.*, vol. 9, p. 9, 1969; H. W. Furumoto and H. L. Ceccon, *IEEE J. Quantum Electron.*, vol. QE-6, p. 262, 1970.

[3] W. T. Silfvast and O. R. Wood II, *Appl. Phys. Lett.*, vol. 25, p. 274, 1974.

[4] T. F. Stratton, G. F. Erickson, C. A. Fenstermacher, and E. O. Swickard, *IEEE J. Quantum Electron.*, vol. QE-9, p. 157, 1973.

cell of 1 cm length is used with its uncoated windows to form a cavity, with a photon cavity decay time of ~50 psec. Similar behavior is observed in all laser dyes we tested under appropriate conditions. The characteristics of these damped relaxation oscillations and their functional dependence are found to have good qualitative agreement with computer solutions of the coupled rate equations.[2] This study leads to the applications using the idea of controlled transient response of laser-pumped dye lasers. By proper control of photon cavity decay time and the level of pumping one can vary not only the number of oscillation periods but also the pulse duration, as is evident from computer solutions as well as experimental observations. Based on this general technique of controlled resonator transients we have demonstrated generation of high repetition rate subnanosecond pulses tunable in the near UV and the visible region from N_2 laser-pumped dye lasers.

[2] H. Statz and G. A. deMars, *Quantum Electronics*, ed. C. H. Townes. New York: Columbia University Press, 1960, p. 531.

1.3 Picosecond Pulse Generation, Amplification and Nonlinear Mixing with a Synchronous Mode-Locked Dye Laser Pumped by Nd:YAG, L. S. Goldberg and C. A. Moore,[1] *Naval Research Laboratory, Washington, D.C. 20375*

(15 min)

Dye lasers pumped by mode-locked lasers can emit very short pulses in exact time synchronization with the pump pulses when their respective cavity lengths are matched. We report studies with a streak camera of picosecond pulse formation in a synchronously mode-locked dye laser pumped by a frequency doubled, passively mode-locked Nd:YAG laser. We have used the synchronous nature of this source to operate a high gain short-pulse dye amplifier, and to generate tunable short pulses of near transform limited bandwidth in the UV and IR spectral regions by nonlinear mixing.

The performance of the synchronous dye laser replicates the main features of the Nd:YAG pump source, namely high repetition rate, fundamental-mode beam quality, high peak power, and uniform pulse trains. The dye laser comprises a two-mirror linear cavity with Brewster-angle dye flow cell and narrow gap Fabry-Perot etalon tuning element. It is longitudinally pumped by pulse trains of 1 mJ energy at 532 nm. Significant performance characteristics obtained for the dye laser are: (1) pulse duration of 12 psec, nearly 1/3 as short as the pump pulses; (2) transform limited bandwidth of 2 cm^{-1}, readily achieved with two Fabry-Perot etalons; (3) wavelength tunability of 549-662 nm, using rhodamine 6G, rhodamine B, and crestyl violet perchlorate laser dyes; (4) energy conversion efficiency of 15% untuned (R6G), 5% transform limited bandwidth; (5) pulse temporal characteristics independent of lasing wavelength; requiring no saturable absorbing dyes.

The temporal character of the dye laser pulses was found to depend critically on adjustment of the relative lengths of dye and pump cavities. At cavity match, a recycling of population through the lasing states was discovered to occur in the dye medium during simultaneous passage of intense pump and dye pulses. This effect enhances the efficiency of energy extraction from the pump pulses, but causes the dye pulse length to approximate the 30 psec duration of the pump. For deviations of cavity length from match, a pronounced asymmetry in conversion efficiency and temporal character of the pulses was observed, depending on whether the circulating dye pulses arrived at the dye cell earlier or later than the gain. The shortest pulses of 12 psec duration were generated when the dye cavity length was slightly longer than match, where the process of gain depletion could operate free of recycling effects. Dye pulses sampled from different portions of a single mode-locked train, and displayed simultaneously on the streak camera, showed progressive shortening as the pulse train developed.

The suitability of synchronous pumping to short-pulse dye amplification was studied. A dye amplifier cell was pumped with amplified and doubled 1.06 μm pulses separately available from the Nd:YAG laser. An optical delay line permitted the adjustment of the relative arrival times of the pump and dye pulses at the amplifier cell. In the initial measurements a peak small-signal gain of 100 and a saturated gain of 4 were obtained using R6G. No significant changes in dye pulse length were observed for a single pass through the amplifier cell under gain saturation conditions.

The intense 1.06 μm and 532 nm pulses were individually sum- and difference-frequency mixed with the synchronous dye laser output in non-linear crystals of ADP and $LiIO_3$. The spectral ranges obtained by mixing and by frequency doubling were 270-331 nm and 362-408 nm in the UV and 1.1-1.7 μm and 2.7-5.6 μm in the IR. Efficiencies of 20% and 2% were measured for the conversion of the dye pulse train energy to the UV and IR when mixing with the 1.06 μm pulse train. Thus, the synchronous mode-locked dye laser with the use of nonlinear methods is capable of generating intense picosecond duration pulses of minimum bandwidth that are tunable over substantial spectral regions.

[1] NRC-NRL Postdoctoral Research Associate.

1.4 Energy Transfer Processes in Organic Dye Laser Mixtures, S. A. Ahmed, J. S. Gergely, and D. Infante, *Electrical Engineering Department, City College of New York, New York, N. Y. 10031*

(15 min)

Energy transfer processes in organic dye mixtures in solutions have received some consideration in the past.[1,2] This paper presents the results of an experimental study on energy transfer processes in organic dye mixtures. The work includes the study of simultaneous laser action at three primary colors from a mixture of three dyes.

Quantitative measurements demonstrated that in a mixture of two or more laser dyes in a solution, excitation energy may be very efficiently transferred from an excited molecule of one dye species to an unexcited molecule of another species, and that process may be repeated successively to a third and fourth dye with the excitation energy being efficiently cascaded to longer wavelengths.[3]

In the first series of experiments carried out, we were concerned with dye mixtures from which simultaneous laser outputs at useful spectral combinations could be obtained. Coumarine, Acriflavine and Rhodamine B constituted a mixture from which dye laser outputs could be obtained at three primary colors. The absorption bands of Acriflavine and Rhodamine B overlap the flourescence bands of the Coumarine and the Acriflavine respectively. This overlap in the energy gaps of these dyes would permit, in principle, excitation energy transfer from Coumarine to the Acriflavine and from the Acriflavine to Rhodamine B either by collisions or optically.

It was therefore possible to use the 337.1 nanometer output of an N_2 laser to excite the Coumarine dye and obtain excitation transfer to, and simultaneous emission (including laser emission) from all three dyes.

The optimum concentrations for three color laser operation with a 1 mm optical path length were found to be: Coumarine -5×10^{-3} molar, Acriflavine -1×10^{-4} molar, Rhodamine B -1.5×10^{-4} molar. Excitation for the front surface fluorescence measurements was by means of the 365.0 nanometer output obtained from a mercury discharge lamp. This is absorbed by the Coumarine, which transfers excitation to the Acriflavine, which in turn transfers excitation to the Rhodamine B.

The different concentration used for each of the three dyes arises from the fact that the excitation source for laser action in the dye mixture was the N_2 laser output at 337.1 nanometers. The absorption of this pump light was therefore predominantly by the Coumarine dye, hence its large concentration requirements relative to its other two dyes. With the three dye mixture, laser action was obtained simultaneously at three wavelengths, centered at 440, 490 and 620 nanometers. These outputs could be individually tuned over a range of approximately 6 nanometers.

That excitation transfer is the predominant mechanism for exciting laser action in the Acriflavine and Rhodamine B is confirmed by the fact that it was not possible to obtain laser action from Acriflavine alone, at any concentration, using the 337.1 nanometer N_2 laser output for excitation; while laser action by direct excitation (at 337.1 nanometers) of Rhodamine B alone was

[1] P. Bied-Charreton *et al.*, *G. R. Acad. Sc.*, Paris, vol. 268, pp. 1377-80, May 1969.

[2] C. E. Moeller, C. M. Verber and A. H. Adelman, *Appl. Phys. Lett.*, vol. 18, p. 278, 1971.

[3] S. A. Ahmed, J. S. Gergely and D. Infante, *J. Chem. Phys.*, vol. 61, no. 4, p. 1584, 1974.

found to require an order of magnitude higher concentration of Rhodamine B (with the optical arrangement used).

Experiments were also carried out on several pairs of dye mixtures, including Dichlorofluorescein as donor and Rhodamine B and DODC as acceptors, and using the 488.0 nanometer output of an argon ion laser to excite the donor alone. The results showed that excitation transfer rates were related (i) to the overlap of absorption and emission spectra of the acceptor and donor dyes respectively and (ii) to the dye concentration.

The efficiency of excitation transfer, as measured by the total fluorescent quantum yield for the mixture, over the quantum yield for the donor dye alone was found to be ~90% for single step transfer. This was the case for several of the dyes tested, including those used for three color laser operation.

The high efficiency of the energy transfer processes makes the use of dye mixtures attractive for a variety of applications including three color lasers for display purposes, and for increasing the efficiency of flashlamp pumped dye laser systems by utilizing more effectively the wide spectral output of the pump bands.

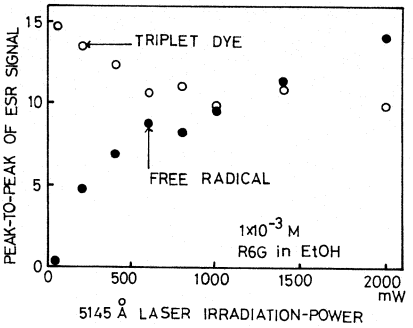

Fig. 2. 5145 Å laser-irradiation-power dependences of the peak-to-peak esr signals due to the triplet-dyes and of those due to the photoinduced free radicals after degradation.

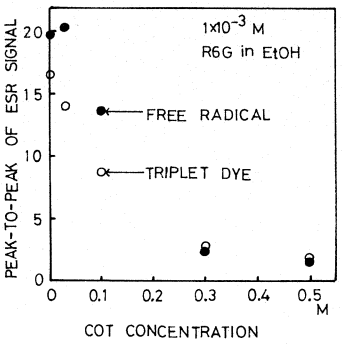

Fig. 3. COT concentration dependences of the peak-to-peak esr signals due to the triplet-dyes before degradation and of those due to the free radicals after UV irradiation.

1.5 Investigation of Photodegradation Mechanism in Laser Dyes by Detection of Triplet-Molecules and Free Radicals Induced by Laser Light,

Mikio Yamashita and Hiroshi Kashiwagi, *Electrotechnical Laboratory, Tokyo, Japan,* and Hidenori Ikeda, *Keio University, Yokohama, Japan*

(15 min)

Photodegradation of organic dyes has severely limited the life of the laser, but the degradation mechanism is not yet well understood. The study on the degradation has been made so far by measuring changes in the absorption and fluorescent spectra of the dye solution before and after photodegradation. We are investigating the photodegradation mechanism by a quite different method where laser-induced free radicals and triplet-dyes are directly monitored at 77 K using an esr technique during and after laser irradiation. In comparison with measuring optical spectra our method has the following merits; (1) the dye molecules in the first triplet excited state and the photochemically produced free radicals can be directly detected, and (2) this method is much more sensitive for the photochemical paramagnetic-products in the dye solution.

Each dye – R6G, RB, RS, AR, and FDS – from the Eastman Kodak and Tokyo Kasei Kogyo Cos., was dissolved in ethanol, methanol or DMSO at 1×10^{-3} M concentration. The oxygen-free solution was outgassed by a freeze-thaw process and sealed in a 4 mm-o.d. quartz tube. Both the esr spectra of the H_{min} line corresponding to $\Delta m = \pm 2$ transitions in the triplet-dyes and of the free radicals induced by laser light were recorded with a Varian E-4 spectrometer with an optical transmission cavity. The glassy solution, cooled by inserting into liquid nitrogen in a quartz Dewar, was irradiated by an unfocused beam with the UV (3511 + 3638 Å) or 5145 Å wavelength of an Ar ion laser.

At first it was found that continuous excitation for several minutes by UV or 5145 Å beams produced the esr signals of the free radicals and decreased the intensity of the H_{min} line which is proportional to the triplet-dye concentration. These phenomena appeared in the case of UV excitation under less excitation-power and -time than in the case of visible excitation, and the shapes of the spectra due to the free radicals produced were different, as shown in Fig. 1. The peak-to-peak esr signals due to the free radicals produced after laser irradiation with 5145 Å for five minutes and those due to the triplet-dyes (which were recorded during irradiation of 5145 Å beam with very low power after the degradation) are given as a function of the continuous irradiation power in Fig. 2.

Furthermore, the investigation of the effects of different dyes (R6G, RB, RS, AR, and FDS) and solvents (ethanol, methanol, and DMSO) on the UV laser-produced radical-spectra has shown the spectrum shape depends on the solvent molecule but hardly depends on the molecular structure of the dye. The dependence of the peak-to-peak radical signals on the triplet molecular concentrations was examined for 1×10^{-3} M ethanolic R6G solutions with different COT concentrations after UV irradiation, as shown in Fig. 3. From these results, we consider that the chemical reaction between the triplet-dye molecules and the solvents dissolving the dye causes the photodegradation of the dye solution and produces the free radicals.

Fig. 1. Observed laser-induced derivative esr spectra of free radicals in 1×10^{-3} M ethanolic R6G solution at 77 K.

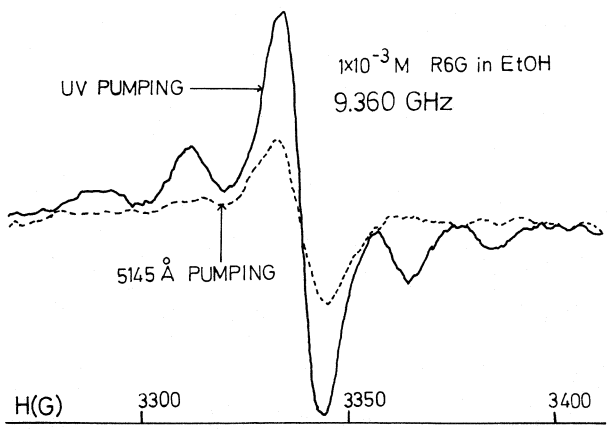

1.6 Lasing Efficiency and Photochemical Stability of Laser Dyes Spanning the Infrared Spectral Region 710-950 nm,

P. E. Oettinger, *Thermo Electron Corp., Waltham, Mass. 02154,* C. F. Dewey, Jr., *MIT, Cambridge, Mass. 02139*

(15 min)

Although substantial effort has been devoted analyzing lasing dyes in the 300-700 nm near UV and visible spectral regions, near IR (700-1000 nm) dyes are less well researched.[1-5] Such

[1] Y. Miyazoe and M. Maeda, *Appl. Phys. Lett.*, vol. 12, p. 206, 1968.
[2] L. D. Derkacheva, A. I. Krymova, A. F. Vompe, and I. I. Levkoev, *Opt. and Spectr.*, vol. 25, p. 404, 1968.
[3] Y. Miyazoe and M. Maeda, *Opto-Electr.*, vol. 2, p. 227, 1970.
[4] A. Hirth, J. Faure, and D. Lougnot, *Opt. Comm.*, vol. 8, p. 318, 1973.
[5] J. P. Webb and F. G. Webster, presented at 8th Int. Quantum Electronics Conf., June 1974.

long wavelength dyes consist, in general, of long polymethine chains, which because of their fragility decompose readily when exposed to radiation. Since all lasing dyes are at present excited by radiative sources, it is important to know their photochemical stability to the exciting photons. Optimum dyes would be those with the highest combination of lasing efficiency and resistance to photochemical bleaching.

Using a 5 pps, 50 nsec Q-switched, multimode ruby laser with output averaging 1.4 MW per pulse, we angle-pumped (14°) a 1 or 2 mm long quartz spectroscopic cell sequentially filled with a number of dye-solvent mixtures. A UV blocking filter shielded the dye from the bleaching effects of nondesirable high frequency radiation of the ruby laser's flash lamp. The cell formed the active region of either a broad band lasing cavity composed of a fully reflecting mirror and a 45 % reflecting output coupler, or a narrower band (5 Å) oscillator wherein the fully reflecting mirror was replaced by a 600 1/mm grating. Output measurements from this cavity determined the dye lasing efficiency. The observed degree of absorption of the incident ruby by the dye before and after exposure to 1500 ruby pulses was used to calculate the number of dissociated dye molecules per ruby photon absorbed, i.e. the probability of bleaching of the dye. The experiments included four new Kodak modified tricarbocyanine salt IR dyes[5] containing ring structures to strengthen the normally chain-like molecules against bleaching. Our results show that three (IR-125, 132, 144) of the four are substantially more photochemically resistant than other molecules we analyzed. However, one of the new dyes (Kodak 123), although lasing well, shows only average photochemical stability. Sixteen of the best dyes were studied in detail. Of these the following seven dyes cover the entire spectral region 710-950 nm: 3, 3′-dimethyl-2, 2′-(5, 5′-dimethyl)-thiathiazolinotricarbocyanine iodide (710-735 nm); 3, 3′-diethyl-2, 2′-oxatricarbocyanine iodide (725-770 nm); Eastman Kodak IR-123 (765-815 nm); 3, 3′-diethyl-2, 2′-thiatricarbocyanine bromide (DTTC Bromide) (810-830 nm) 3, 3′-diethyl-2, 2′-(5, 5′-dimethoxy)-thiatricarbocyanine iodide (820-875 nm); Eastman Kodak IR-125 (840-920 nm); 3, 3′-diethyl-12-acetoxy-2, 2′-thiatetracarbocyanine perchlorate (920-950 nm); The optimum solvent for these dyes was found to be DMSO. Lasing efficiencies for 2 (10^{-4}) M concentrations varied from 18 to 43%. Bleaching probabilities ranged from 1.2 (10^{-5}) to 3.0 (10^{-4}). Quality factors, Q, defined as the ratio of the lasing efficiency to bleaching probability, varied from 1.3 to 11.7.

1.7 Transverse Flow Flashlamp Pumped Dye Laser, H. W. Friedman and R. G. Morton, *Avco Everett Research Laboratory, Inc., Everett, Mass.*

(15 min)

Pulsed operation of flashlamp pumped dye lasers at high repetition rates is usually limited to a frequency roughly equal to the reciprocal of dye interchange time. By flowing the dye at a given rate transverse to the laser axis, the maximum pulse repetition rate is increased over that of the axial configuration by essentially the aspect ratio of the laser channel, i.e., by length/diameter.

A transverse flow dye laser pumped by two linear flashlamps in a close coupled configuration has been built. The lamps are water cooled and easily replaceable without disturbing dye seals or optical alignment.

The laser system is comprised of three sections: the laser head with pulse modulator, liquid flow system, and power supply. The cross section of the laser channel resembles that of a convergent-divergent nozzle and discourages the onset of parasitic modes. The linear, xenon filled flashlamps are housed in trough shaped reflectors which also serve as the cooling water channel and low inductance current return path. No adhesive or epoxy seals are used and hence the laser is compatible with a wide variety of solvents. The side windows may be pyrex or one of the varieties of quartz and are interchangeable to control the UV content of the flashlamp light. Optical distortions arising from temperature gradients in the lasing medium are minimized by thermal insulation and boundary layer control. A high voltage pulse preionizes each flashlamp prior to the main discharge to increase the lamp performance and lifetime and to facilitate triggering as the lamps age. Thyratron switchgear is used for both the preionization and main discharge to insure good pulse to pulse reproducibility and low jitter. Spectral narrowing and tuning are achieved with a telescope and multiprism ring.

The transverse flow dye laser operates at a repetition rate of up to 100 Hz and with smaller bore lamps, up to 500 Hz. An average power level of 6 watts (Rhodamine 6G at 30 Hz) under broadband conditions and 3 watts at a bandwidth of 2 Å has been achieved. The pulse duration varies from one-half to one microsecond depending upon the choice of discharge capacitance and the beam divergence is typically a few milliradians.

The performance of water/alcohol mixtures of several dyes has been tested. A general reduction in beam divergence and bandwidth has been observed with water/methanol solvent mixtures as compared to 100% methanol. The spectral brightness of Rhodamine 6G, for example, is increased by 40% using a 30% water/70% methanol solvent over that of 100% methanol. A similar enhancement in spectral brightness occurs with solvent mixtures of 50% water/50% alcohol but at this point the average power is falling off.

Results with water/alcohol solvent mixtures indicate that potential safety problems associated with storage and handling of large volumes of alcohol may be substantially reduced without loss of laser efficiency or beam quality.

1.8 Thermo-Optical Limitations on High Average Power Dye Lasers,[1] O. G. Peterson, A. A. Pease, and W. M. Pearson, *Lawrence Livermore Laboratory, Livermore, Calif. 94550*

(15 min)

The application of organic dye lasers to isotope separation requires the simultaneous achievement of high average power and single mode, spectrally narrow output, $\Delta\lambda/\lambda = 10^{-6}$. Previously reported narrow line lasers[2] have been limited to low average powers to minimize thermal effects which severely restrict single mode operation. This represents the ultimate limitation on the scalability of dye lasers to high average powers.

This limit is critically dependent upon the properties of the solvent used for the lasing molecules. The most sensitive of these properties is the variation of refraction index with temperature. The solvent of choice is usually water because of its large heat capacity and small variation of index with temperature.

The determination of the high average power limit must be based on an evaluation of the efficiency of the laser at some suitable operating

[1] This work was performed under the auspices of the U.S. Atomic Energy Commission.

[2] H. Walther, *Physica Scripta*, vol. 9, p. 297, 1974.

Fig. 1.

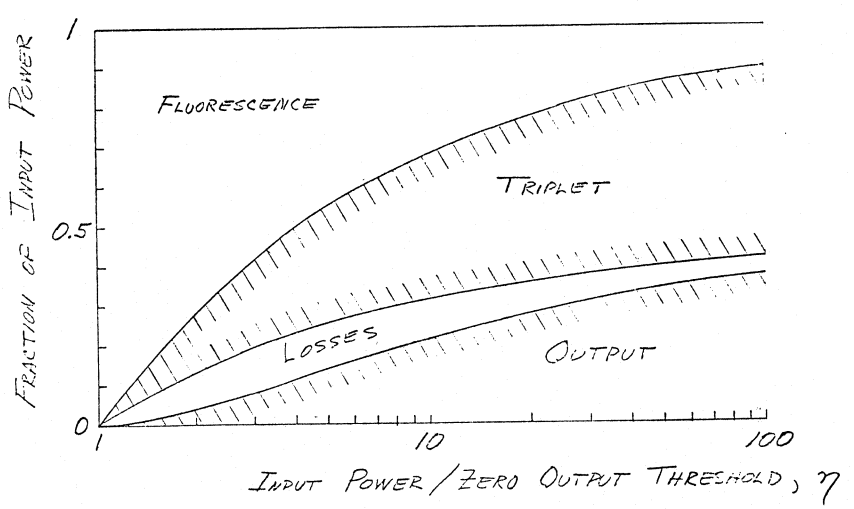

point. The fraction of absorbed quanta that are contributing to fluorescence, triplet state absorption, non-dye resonator losses and useful output have been calculated and are displayed as a function of input power in Fig. 1. These calculations were based on the dye parameters characteristic of rhodamine 6G and assumed that the laser inversion, n^*/n, is proportional to the sum of the resonator losses, L, and the output transmission, T; $n^*/n \propto (L + T)$. The distribution of power depends on evaluating the optimum output coupling at each value of the input power. It was found that this optimum output coupling was independent of effects due to dye triplet state. The mirror transmission then reduces to the familiar[3] $T = (P\tau L/K)^{1/2} - L$ where P is the input power per cross-sectional area of laser bore and τ is the dye fluorescence lifetime.

From the figure it is clear that a dye laser should be operating with a minimum input intensity of ten times the zero output threshold. For incoherently pumped lasers where pumping intensity is limited, this becomes the operating point of choice. At this point the output coupling is twice the internal resonator losses and the laser intensity in the resonator is approximately twice the saturation value. The fraction of the input quanta that are converted into useful output is then 20% while 40% goes into solution heating via triplet state absorption.

Using this operating point together with published efficiency data on flashlamps,[4] dyes,[5] and pumping cavities[6] the ultimate output efficiency of narrow line dye lasers has been estimated to be 0.1%. Similarly, the solution heat load has been estimated to be 3% of the input power.

Only a limited amount of energy can be absorbed by a given volume of solvent before the lasing wavelength is shifted more than the specified limit. For a pulsed laser this limit implies a maximum pulse length which is of the order of 1 to 20 μs for the excitation intensities required for dye lasers.

The time required for the thermally induced optical inhomogenities to become significant has been measured interferometrically. A Michelson interferometer has been set up to probe the active volume of the laser under lasing conditions. Data will be presented from this time resolved interferometry and compared with the predictions made using the steady state values of the thermo-optic parameters of the dye solvent. Comparisons will be made between different solvent systems under different levels of excitation. These experiments provide the basic parameters which allow calculations to be made setting limits on the maximum average power available from single mode dye lasers.

[3] A. E. Siegman, *Introduction of Lasers and Masers.* New York: McGraw-Hill.

[4] M. E. Mack, *Appl. Opt.*, vol. 13, p. 46, 1974.

[5] K. H. Drexhage, *Dye Lasers*, ed. F. P. Schäfer. New York: Springer-Verlag, 1973.

[6] C. Bowness, *Appl. Opt.*, vol. 4, p. 103, 1965.

1.9 A Free Stream Jet for High Power Dye Lasers,[1] R. J. Foley, T. C. Kuklo, and O. G. Peterson, *Lawrence Livermore Laboratory, Livermore, Calif. 94550*

(15 min)

High-power, narrow linewidth tunable dye lasers are required for laser isotope separation processes. Although high-power lasers exist, the combination of high power and narrow linewidth, of the order $(\Delta\lambda/\lambda) \approx 10^{-6}$ have been difficult to achieve since the linewidth stability is easily destroyed by temperature and velocity fluctuations[2] within the dye solutions. In enclosed dye cells, the excitation intensities required for high laser output have introduced thermal gradients into the dye fluid as a result of the low heat transfer in the boundary layer at the cell wall.

To eliminate the thermal problems at the boundary, a free jet stream of liquid dye solution has been investigated as a substitute for the dye cell in the laser cavity. A geometry was investigated which would be applicable to high average power, incoherently pumped dye lasers. For this application it is necessary to have the excitation illumination direction, solution flow, and laser mode axes mutually perpendicular. The excitation is focused through the air-liquid interface. The edges of the jet stream are bounded by quartz plates which serve as windows for the laser emission. Jet streams 76 mm in width have been investigated with thickness varying from 1 to 3 mm. To be effective in the laser the surface of the liquid-air interface must not distort the focus of the excitation illumination. Also, the jet must be stable at liquid flow velocities large enough to replace the dye solution in the active volume between every flash of a pulsed laser. Most importantly, the clear aperture in the direction of the laser mode axis must be essentially identical to the stream thickness.

The development of a nozzle and flow system that is capable of establishing a stable free stream jet is quite complex. Exact analytical solutions to describe the jet velocity profile and surface wave phenomena are difficult to obtain. However, hydrodynamic theories have been helpful in establishing guidelines for an experimental approach.

An experimental evaluation of three nozzle configurations was performed to establish the merits of each. The configurations tested were: (1) flow between two long parallel planes with 90° edges at the exit and width to thickness ratios of 20:1; (2) orifice flow with knife edges at the exit; and (3) flow from a converging slit. This testing established the magnitude of the effects of several parameters on the production of surface waves on the jet stream, namely: (a) fabrication imperfections of the nozzle; (b) end window contacts; (c) hydraulic pulsations and supply plenum turbulence; and (d) air friction.

The configuration with slot flow between long parallel planes has given the highest quality planar surfaces at fluid velocities up to 6 m/sec. The surface quality was improved by fabricating a nozzle with parallel planar walls and optical quality finishes on the walls and exit edges. The hydraulic pulsations and fluid turbulence were damped by use of a fluid accumulator and grids at the nozzle entrance. The fluid/air friction instabilities for a water jet have a critical relative velocity of $\Delta V \approx 6.5$ m/sec.[3] For velocity above this, a reduction of the air pressure in the region of the jet stream has reduced this surface effect.

The jet stream clear apertures were evaluated for each design over a range of Reynold's numbers in the laminar and turbulent regions by the use of laser interferometry. The laminar flow jets produce the highest quality surfaces, however, the clear aperture is not adversely effected by the transition into the turbulent regime.

Results will be presented on the operation of the jet in a flashlamp pumped dye laser. The laser output was measured as a function of solution flow rate to evaluate the reduction in coupling efficiency caused by scattering of the excitation illumination from turbulence induced surface waves.

[1] This work was performed under the auspices of the U. S. Atomic Energy Commission.

[2] H. W. Schröder, H. Welling, B. Wellegehausen, *Appl. Phys. Lett.*, vol. 1, p. 343, 1973.

[3] H. Lamb, *Hydrodynamics.* New York: Dover, 1945, p. 462.

1.10 High Power Dye Lasers (*Invited*), W. H. Glenn, W. Morey, and C. Ferrar, *United Aircraft Research Labs., East Hartford, Conn. 06108*

(30 min)

A review of the mechanisms limiting high power operation of dye lasers will be given. The operation of a flash lamp pumped dye laser with greater than 40 watts average output power will be described.

Session 2

Wednesday, May 28, 1975 9:00-11:45 A.M.

General Applications—I

Chairman: R. A. Hella, *Avco Everett Research Lab., Everett, Mass. 02149*

2.1 Streak Camera Studies Using Picosecond Pulses of Photosynthesis and Plastic Scintillators. S. L. Shapiro, V. H. Kollman, R. C. Hyer, and A. J. Campillo,[1] *Los Alamos Scientific Laboratory, Los Alamos, N. M. 87544*

(15 min)

Picosecond laser techniques provide a unique opportunity to monitor the initial steps in photosynthetic processes. We have used a streak camera to study the fluorescent decay times of

[1] Work performed under the auspices of the U. S. Atomic Energy Commission.

several photosynthetic systems including the blue green algae *anacystis nidulans* and also *chlorella pyrenoidosa*. We have found that the high efficiencies for the conversion of solar energy is related to the high concentration of pigment dye molecules in cells. Specifically, the low quantum efficiency of these species can be simulated by mixing component dye species in a cell in about the same concentration and proportions present in the live cells.

An experimental result showing the fluorescence decay curves for chlorophyll *a* at two different concentrations is shown in Fig. 1. Chlorophyll *a* is present in living cells in about a concentration of 0.1 M. The decay time for this molecule in chloroform was measured to be as short as 10 ± 5 psec at 0.1 M concentration. Living cells show similar decay characteristics, and *anacystis nidulans* decays smoothly in intensity with a lifetime of 75 ± 10 psec. Careful calibration shows that the decay curves for photosynthetic species and for pigments at high concentrations are not exponential, but are very nearly of the same form as predicted by Förster.[2] The concentration quenching mechanism responsible for the observed fluorescent decay curves will be discussed.

Previous measurements on fluorescent decay times for *anacystis nidulans* and *chlorella pyrenoidosa* have indicated longer lifetimes than we report. Our results are more in accord with the known quantum efficiencies, and are made possible by the improvement in technique because of the application of the streak camera.

There has been much interest lately in resolving events on the picosecond time scale; however, it has been generally believed in the literature[3] that the typical fluorescent risetimes of commercial plastic scintillators were at best 300 ps. The measured risetime of NE 102, for example, under excitation of picosecond bursts of beta radiation was 0.9 ns in Ref. 3. Recently, however, Duguay and Olsen[4] have measured much faster fluorescent risetimes (~ 60 ps) when exciting NE 102, a commonly used plastic scintillator, with ultrashort bursts of X-ray radiation. This result has great potential importance as these scintillators can be used with optical gates or streak cameras to resolve ultrafast high-energy events. We have excited NE 102 with picosecond light pulses in an attempt to resolve any risetime discrepancy. We find that the risetime of the resulting 4200 Å fluorescence is less than 50 and 20 ps, for 0.265 and 0.353 μm, respectively. The rapid risetime of the observed fluorescence cannot be explained by pure radiative transfer of the energy between the dye molecules but is consistent with the Förster mechanism.[2] Our results are consistent with Duguay and Olsen.[4]

The experiment consists of a mode-locked Nd:glass laser which emits pulses of about 8-ps duration at 1.06 μm. These pulses are frequency doubled and/or summed in two consecutive

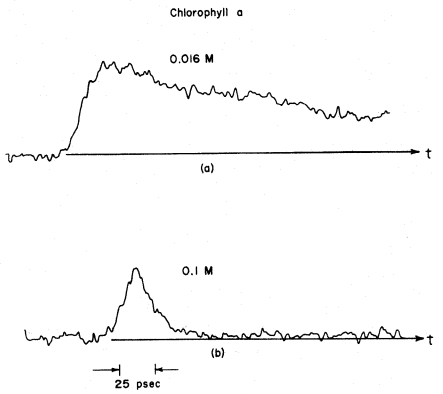

Fig. 1. Densitometer traces of streak photographs of chlorophyll *a* in chloroform showing strong dependence of fluorescent lifetime with concentration. 1(a) and 1(b) show, respectively, concentrations of 0.016 and 0.1 Molar.

KDP crystals to produce 0.353- and 0.265-μm radiation. Due to the dispersive properties of KDP, it is necessary to use a short fourth harmonic crystal (~ 3 mm) to insure that the resultant 0.265-μm pulses are not temporally stretched. We estimate that our exciting pulses were 10 ps in duration (FWHM). These harmonic pulses then excite the sample (thickness 0.3 mm) which emits fluorescence which is collected by a glass lens onto the slit of a LASL streak camera. Because of limitations inherent in the collection of light, the resolution of the 0.265- and 0.353-μm excited fluorescence was limited to about 50 ps and 20 ps, respectively. Data were recorded on both Polaroid and Kodak 2484 film.

The function of a ternary scintillator, composed of a solvent (x) and two solute dye molecules, is to convert the energy supplied by a particle or electromagnetic wave into the emission of light waves in a wavelength range best adapted for photomultiplier sensitivity. The energy first goes to the main constituent X, is then transferred nonradiatively to the primary solute molecule Y, and is finally transferred to the molecule Z which emits light near 4200 Å. In our experiment, the 0.353-μm radiation was used to directly excite molecule Z while the 0.265-μm radiation excites both X and Y molecules. The risetime of the resulting fluorescence at 4200 Å thus gives a measure of the nonradiative transfer time. A typical result is shown in Fig. 1.

The rapid risetimes of the fluorescence observed, i.e. <50 and <20 ps for 0.265- and 0.353-μm excitation respectively, cannot be explained by pure radiative transfer of the energy between the dye molecules. Rather, as first pointed out by Förster,[2] a nonradiative dipole-dipole interaction can account for the very rapid observed transfer times.

[2] T. Förster, *Z. Naturf.*, vol. 4A, p. 321, 1949.

[3] P. B. Lyons and J. Stevens, *Nucl. Instr. Methods*, vol. 114, p. 313, 1974.

[4] M. A. Duguay and J. N. Olsen, *IEEE J. Quantum Electron.*, (in press).

2.2 High-Speed Radiation Camera Using a PTM Ruby Laser and Hydrated Electron Absorption Phenomena,[1] Gerald W. Coutts and LaMar B. Olk, *Lawrence Livermore Laboratory, Livermore, Calif. 94550*

(15 min)

High-speed radiation cameras typically employ fast scintillators and framing cameras constructed of electronically shuttered image-intensifier arrays. With these systems, high-speed photographs of pulsed radiation sources are possible. For such systems, the meaningful time resolution is limited by the 1.7-ns fluorescence lifetime of the scintillator material and by the gating potential of commercial image intensifiers. To avoid these limitations, we have developed an ultra-high-speed radiation camera which makes use of the photo-absorption phenomena associated with the hydrated electron and of the picosecond pulses obtainable from a mode-locked dye laser.

Previous work has shown that the photo-absorption phenomena of the hydrated electron can be used as a sub-nanosecond pulse dosimetry mechanism. Acidic aqueous solutions can function as absorption mechanisms which convert rapidly changing radiation patterns into corresponding optical absorption patterns. Separate, time-resolved, high-resolution images of these transient absorption patterns can be transferred to photographic film with short laser pulses. The effective exposure time for the transferred image is limited by the absorption center lifetime and the width of the sampling laser pulse. Since mode-locked laser pulses of less than 5 ps can be obtained, the potential time resolution for such a system should be about 20 ps. The potential time resolution for such a system is far superior to existing scintillator-type framing camera systems.

In order to investigate the technical difficulties and develop the technique associated with the radiation camera outlined above, we have built and operated a 12-frame camera. A frame exposure time of 2.5 ns is achieved with a Pulse Transmission Mode (PTM) ruby laser. An optical beam-splitter delay arrangement provides 12 frames with an interframe time of 3 ns (3×10^8 frames per second). With this radiation camera, we have obtained photographs of a 60 ns (FWHM) burst of high-energy electrons absorbed in an aqueous cell.

Employment of a mode-locked dye laser and electronically gated image intensifiers has yielded a second-generation camera which obtains picosecond images and minimizes the synchronization problems inherent in the first-generation system. With the synchronization problems minimized, a six-frame camera with picosecond exposures and a 1-ns interframe time has been made a useful diagnostic tool. With this picosecond framing camera, we have obtained six frames containing 66- and 400-ps images of a 3-ns burst of high-energy electrons absorbed in an aqueous cell. These photographs contain previously unavailable information concerning the time-resolved electron-energy spectrum of a 706 Febetron.

[1] Work performed under the auspices of the U. S. Atomic Energy Commission.

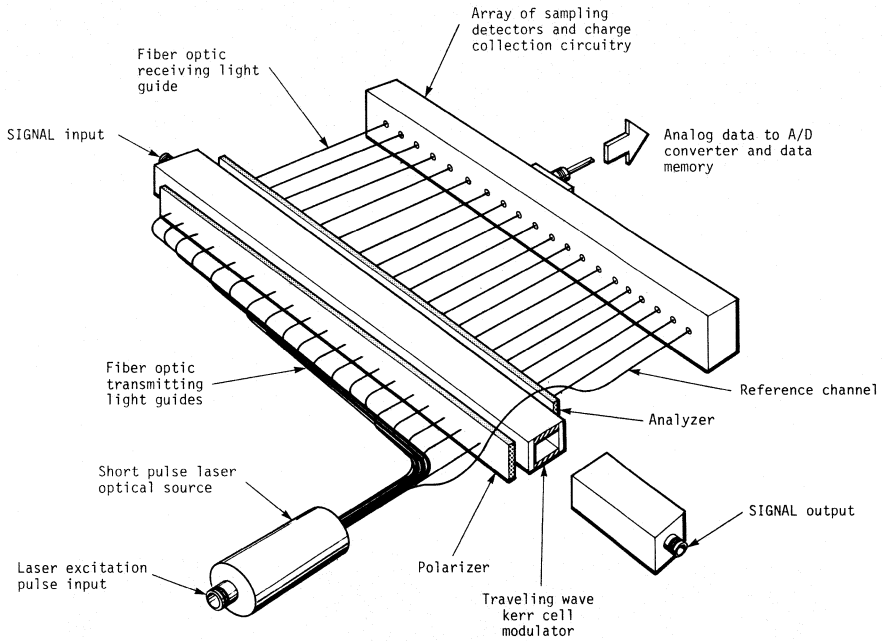

Fig. 1. Functional components of OSTA system.

2.3 Laser Applications in Surgery (*Invited*), T. G. Polanyi, *American Optical Co., Framingham Center, Mass.*

(30 min)

No summary.

2.4 The Tunable Laser—An In-Vivo Biological Probe (*Invited*), A. Lewis, *Cornell University, Ithaca, N. Y.*

(30 min)

No summary.

2.5 Medical Diagnostic Measurements Using Lasers (*Invited*), G. Benedek, T. Tanaka, and R. Cohen, *Department of Physics, Massachusetts Institute of Technology, Cambridge, Mass.*

(30 min)

No summary.

2.6 Optical Sampling Transient Analyzer (OSTA) System,[1] Terence J. Davies and Melvin A. Nelson, *EG&G, Goleta, Calif. 93017*

(15 min)

The OSTA data acquisition system, shown in Fig. 1, has been developed to measure and digitally record the time-amplitude characteristics of a fast, high-voltage, large-dynamic-range, single transient electrical signal. It has a bandwidth response of about 1 GHz. A typical signal of interest might range in amplitude from about 10 V to many kilovolts, and in time from a few nanoseconds to tens of nanoseconds duration.

The system takes successive 350 ps-wide samples of a signal every 350 ps, or longer as desired, and converts the samples to a digital number. The number of amplitude samples that can be taken by the present system is 21, but the technique will accommodate many times that number of samples.

Duration of the sampling window is determined by the selected sampling interval in combination with the number of samples taken. Sampling intervals from 350 ps to 2 ns, or a total signal window as narrow as 7 ns to as wide as 40 ns for all samples are provided for in the present system. Time resolution between signal samples is better than 50 ps, and amplitude resolution is 0.1 percent.

Sensitivity of the present system (equivalent "trace width" sensitivity) is approximately 10 V. This is not a fundamental limit. The system will measure signal amplitudes to the breakdown limit of the electro-optical modulator (greater than 20 kV).

Using the OSTA technique, the sensitive sampling circuitry is completely isolated electrically from the input signal since sampling is carried out on the optical analog of the input signal. The input signal is unaffected by the sampling process and later signal values do not affect the sampled data. Also, the dynamic measurement range of the sampling circuitry is independent of the signal voltage and is always within prescribed limits.

The four major subsystems that constitute the OSTA system are an electro-optical modulator assembly, a short-pulse laser subsystem, optoelectronic charge-collection circuitry, and digitizing and recording apparatus. The diagnostic signal being measured is connected to the traveling wave Kerr cell-type electro-optical modulator, which appears electrically as a section of liquid-dielectric transmission line. The electrical signal passes down the cell at a velocity of approximately 5 cm per nanosecond, where nitro-benzene is the dielectric fluid. The electrical signal then passes out of the cell and into a get-lost line for further measurement or termination. This line is also used to connect a dc bias voltage source to the Kerr cell. Bias enhances the signal sensitivity of the cell.

When the signal to be measured is present in the cell, a short-pulse laser is triggered to emit a single high-intensity 350-ps wide optical sampling pulse. This pulse is divided into multiple sampling pulses by directing it onto one end of a fiber optic light guide bundle which is separated at its other end into a multiplicity of individual light guides, each a different length and each directed through the Kerr cell at a different point along its body. The graduated length variations cause the sampling pulses to arrive at each Kerr cell location at a different time. This preselected time difference determines the signal sampling rate.

Optical transmission at each sampling point (in conjunction with polarizer and analyzer) is a function of the instantaneous voltage across the cell electrodes at that sampling point. Hence, the sampling pulse intensities transmitted through the cell are optical analogs of that voltage. Each sample is collected into a separate light guide and channeled to its own semiconductor detector. There, the optical flux is converted to electrical charge and temporarily stored using charge-hold circuitry for the time required to multiplex all analog samples into a digitizer. The digitized data are stored in a memory and printed out on command, or transmitted to permanent storage in a computer memory where the electrical input signal amplitude at each sampled point can be reconstructed and other processing and analysis effected.

[1] This work was performed under the auspices of the U. S. Atomic Energy Commission.

2.7 Raindrop Measurements by Holography, V. N. Zakharov, L. N. Rasoumov, E. M. Birger, and S. P. Karlov, *USSR*

(15 min)

(Received late; see page 82.)

Session 3

Wednesday, May 28, 1975 9:00-11:45 A.M.

Information Processing and Display

Chairman: Robert Adler, *Zenith Radio Corp., Chicago, Ill.*

Organizer: Emmett Leith, *University of Michigan, Ann Arbor, Mich.*

3.1 Progress in Optical Information Processing (*Invited*), Junichi Shimada, *Electrotechnical Laboratory, Ministry of International Trade and Industry, Tanashi, Tokyo, Japan*

(30 min)

No summary.

3.2 A Near Real-Time Coherent Optical Processing System Using Two Itek PROM Devices,[1] S. Iwasa, *Itek Corporation, Lexington, Mass. 02173*

(15 min)

A near real-time coherent optical processing system has been demonstrated using two Itek PROM devices[2] and a TV monitor. The PROM (Pockels Readout Optical Modulator) is a recyclable electro-optic device for image storage developed by Itek. A reflection-type device was placed in the input plane as an incoherent-to-coherent image converter, and a transmission-type device in the Fourier transform plane as a laser addressed programmable Fourier filter. A video camera with a TV monitor was placed in the output plane for the observation of the filtered images.

A scene is incoherently imaged on, and stored in, the first PROM from a transparency using the 436 nm line of a mercury arc lamp. A He-Ne laser 633 nm line coherently reads out the stored scene and the optics is so arranged that the Fourier transform of the scene falls on the location of the second PROM. Preprogrammed filter patterns are generated on the second PROM by means of a krypton laser 476 nm line, an electronic programmable pattern generator, an electro-optic modulator and an *xy* deflection system composed of an acousto-optic deflector and a galvanometer. The intensity-only filter patterns include wedges, circles, rings and spirals. The PROM device is capable of electrically reversing the image contrast; therefore, a wedge pattern provides either a slit or a line-stop in the Fourier plane. Similarly, a circle provides either a high pass or a low pass; a ring, a band pass or a band rejection. The spiral pattern generates a transmission function proportional to the square of the spatial frequency and is used to demonstrate spatial differentiation (edge enhancement). The TV camera monitors the reconstructed scene before and after the programmable filtering operation.

In the present experiment, the first PROM is exposed at an energy density of about 200 ergs/cm^2 typically, in less than 1/10 sec with a 100 W mercury lamp. Concurrently, one programmed pattern is generated on the second PROM in about one second. The erasure and prepoling of the devices take approximately 3 msec. The total cycle therefore takes one second plus the inspection duration on the TV monitor. The slow speed of the present electronic pattern generator is the limiting factor. With improved instrumentation, the processor should operate at a much faster rate. Needless to say, a scene can be entered into the first PROM via another laser addressed scanning system allowing full automation of the processor.

[1] This work supported under Army Contract No. DAAK02-74-C-0029.

[2] Sato Iwasa and Julius Feinleib, "The PROM Devices in Optical Processing Systems," *Opt. Eng.*, vol. 13, p. 235, 1974.

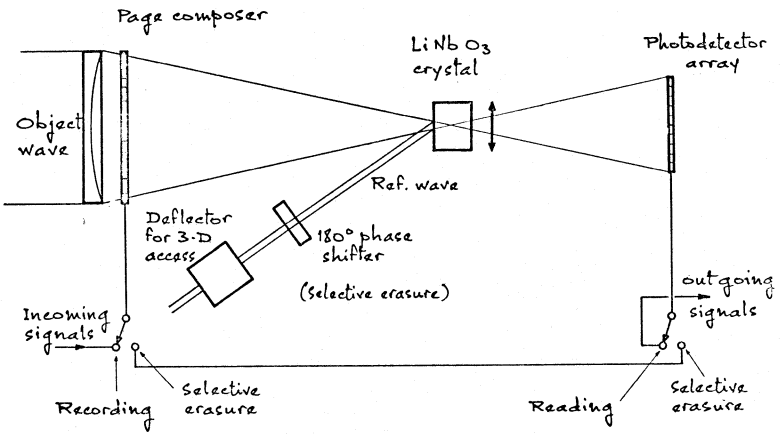

Fig. 1.

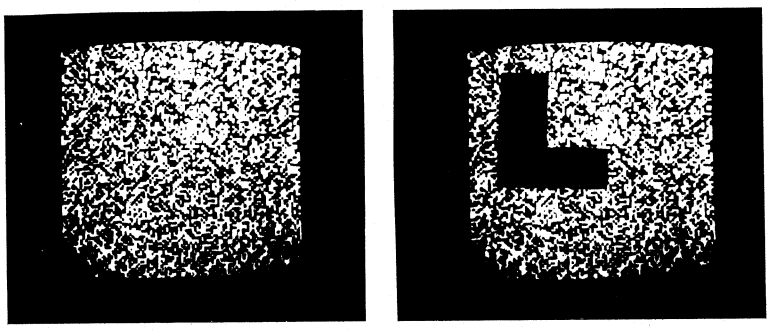

(a) (b).

Fig. 2.

3.3 Selective Erasure and Parallel Processing in Holograms Superimposed in $LiNbO_3$ Crystal, J. P. Huignard, J. P. Herriau, F. Micheron, and J. M. Rouchon, *Thomson-CSF, Laboratoire Central de Recherches, Orsay, France*

(15 min)

It has been demonstrated that high storage densities can be achieved by recording three-dimensional holograms stacked in photosensitive electrooptic crystals. Nevertheless, read-write operations in such optical memories are limited by existing erasure techniques; optical and thermal erasures are both bulk processes, which do not discriminate between different volume holograms.

We report a new technique which provides selective erasure of any hologram superimposed in the crystal volume, and selective erasure of any block in a recorded data set. This technique is called a coherent erasure since it is based on recording a hologram complementary to the one to be erased; this we obtain by recording the same object as previously recorded, but with a 180° phase shift in the reference wave. This operation is shown to cancel refractive index changes induced during recording.

Experiments were performed in reduced $LiNbO_3$:Fe single crystals, which show strongly asymmetrical write-erase cycles. Erasure during continuous readout, at the recording wavelength, requires a light energy density much larger than for recording. When using the coherent erasure technique, the write-erase cycle becomes quite symmetrical. The number of such write-erase cycles achievable in the same volume of the crystal is limited to an order of ten by scattering effects which occur after long exposure to a coherent light beam.

This technique can be used in a read-write optical memory, as described in Fig. 1. Different holograms $H_1 \dots H_i \dots H_n$ of objects $O_1 \dots O_i \dots O_n$ are superimposed in the $LiNbO_3$ crystal, using, for example, a liquid crystal page composer. Erasure of the hologram H_i is achieved as follows. The corresponding object O_i is reconstructed on the photodetector array, and the out-going electrical signals are used for composition of O_i on the page composer. A 180° phase shift is introduced in the reference wave, and O_i is recorded with the same geometrical conditions as used for the first recording. This operation results in complete erasure of H_i only.

Coherent erasure can be applied to a block b_i of data contained in O_i. After having reconstructed O_i on the photodetector array, the part corresponding to b_i in the electrical signals is used to recompose b_i. Recording b_i with the 180° phase shift erases b_i in the object O_i. Demonstration of this partial erasure is given in Fig. 2; (a) shows the reconstruction on a TV camera of the recorded object, and (b) the reconstruction with partial erasure. We have shown that such partial erasure can be achieved in any hologram superimposed in the crystal volume.

When an object O_1 has been recorded, recording an object O_2 under the same geometrical conditions, but with a 180° shift, produces

erasure of common parts of O_1 and O_2. This operation provides the difference between O_1 and O_2, and the Boolean Exclusive OR between two digital objects. Since the Boolean OR is easily obtained by recording successively two digital objects, any Boolean operation can be performed by combinations of these two operations. This is the first demonstration of parallel processing between data blocks optically recorded in a three dimensional storage material.

3.4 Laser Color Video Printer Breadboard, R. E. Baldwin, B. G. Fike, and J. H. Ladd, *Eastman Kodak Company Research Laboratories, Rochester, N. Y. 14650*

(15 min)

The laser color video printer breadboard was built to investigate the effect of laser raster exposure upon conventional color photographic materials; to demonstrate feasibility to read a color negative and to expose a color print in synchronism by a single raster; to determine what factors limit print quality; and to determine what factors limit throughput rate. The photometer section of the breadboard scans a $2\frac{1}{4} \times 2\frac{1}{4}$ inch color negative with a single 2560-line raster by means of two galvanometers. Simultaneously, the printer section of the breadboard exposes an 8×10 inch color print. The red, green, and blue wavelengths for negative photometry and for print exposure are 647, 521, and 476 nanometers, all from one 0.4-watt krypton ion laser. A color video signal processor is inserted between photometer and acousto-optic modulator.

If throughput rate for such a printer were limited only by the red, green, and blue radiant power available from the laser, printing rate could be about one 8×10 inch print per second. However, total time per print in the breadboard is determined by the speed of and the mass carried by the fast galvanometer. Exposure time is about 2.5 microseconds per picture element and the raster is completed in about 20 seconds.

Galvanometer instability and pincushioning are compensated for in the breadboard by scanning the negative and exposing the print simultaneously with two-faced mirrors mounted on the two galvanometers. To a first approximation, timing jitter between adjacent scan lines and nonlinearity of individual scan lines do not degrade picture quality because "identical" jitter and nonlinearity occur both at the negative plane and at the paper plane. Nevertheless, print sharpness and resolution are limited primarily by the size and flatness of the two mirror faces carried by the fast galvanometer. These two mirror faces do not fill the entrance pupils of the two special achromatized lenses in the scanner and printer optics.

A set of 8×10 inch color prints were exposed in a conventional optical enlarger. Replicate color negatives were printed on the laser color video printer breadboard. Direct visual comparison of the 8×10 inch prints permits the following inferences: (1) D_{max} in the optical prints is noticeably higher than in the laser prints. This is a consequence of video signal processing parameters, not inherent in laser prints. (2) The optical prints are definitely sharper. (3) Small, whitish "noise" spots appear on the laser prints, but not on the optical prints. The spots would be eliminated if the laser photometer were to have diffuse, rather than specular, collection of the light transmitted by the color negative. (4) Laser prints have the same color saturation and can provide about the same color balance as optical prints. However, some exposure of the green-sensitive layer from the 476-nanometer blue wavelength produces orangish yellows.

The breadboard includes electronic circuits by which to generate a variety of line and dot patterns for raster studies, and to generate a set of 64 colored patches with set proportions of red, green, and blue exposure. The patch generator has been used for sensitometric exposure experiments with many kinds of color photographic films and papers. The sensitometry has disclosed some speed and contrast shifts for 2.5-microsecond exposures of products which are customarily exposed at 1/50 second. However, macro densitometry of patches from laser exposures of the products tested showed no sensitometric phenomena which would discourage laser raster exposure of color photographic films and papers. Indeed, the point-to-point signal processing possible in such a printer offers potential advantages not attainable in any conventional optical printer.

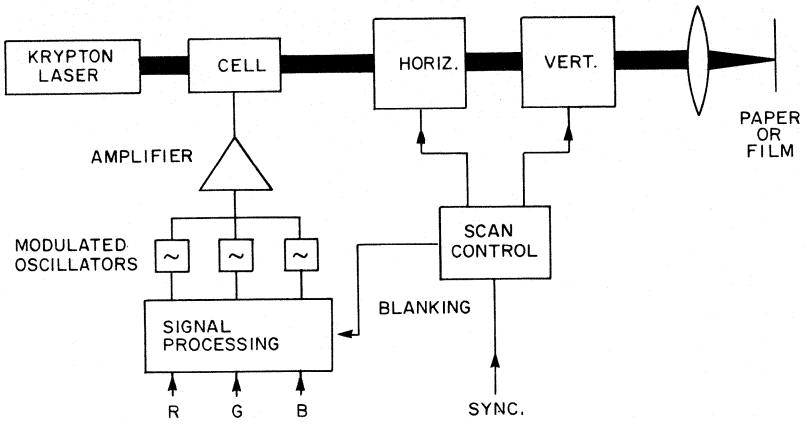

Fig. 1. Laser printer concept.

3.5 Interferometric Measurement and Display of Ultrasonic Waves, R. Mezrich, K. F. Etzold, and D. Vilkomerson, *RCA Laboratories, Princeton, N. J. 08540*

(15 min)

The optical arrangement for a new system[1] to measure and display ultrasonic waves is described. Using interferometric techniques, combined with a deflection method, displacement amplitudes as small as .05 Å, over apertures as large as 150 mm and with submillimeter lateral resolution can be observed. The system also includes a simple but effective open loop method to stabilize the interferometer and at the same time minimize the flatness requirements of the optical elements used.

The arrangement is schematically shown in Fig. 1. The basic structure is that of the Michelson interferometer. One mirror is a thin flexible metallized membrane, or pellicle, suspended in the water bath, and through which the acoustic waves pass. The pellicle is transparent to the acoustic waves, so its motion at every point is almost exactly equal to the displacement amplitude of the acoustic wave at that point. The second mirror is external to the water tank.

A deflection system, using mirror galvanometers, is included in the pellicle leg of the interferometer and is arranged so the virtual pivot point of the orthogonal deflections is at the front focal point of lens L_4. As the beam is scanned the light is normally incident on the pellicle and is thus reflected back through the optical system to interfere with the light from the reference mirror.

A component of the interference is proportional to the motion of the pellicle, and hence displacement amplitude of the acoustic wave. This component is measured and then processed for display. Maximum response occurs when the light from the pellicle and reference are in phase quadrature. To obtain this maximum response, even in the presence of thermal or mechanical disturbances, the reference mirror is vibrated or "wiggled" with a maximum excursion of at least $\lambda/4$ (which causes a $\lambda/2$ phase shift). At least once per cycle of the "wiggler" the relative phase between the pellicle and reference must pass through 90°; by peak detecting the output (which is maximum at this point) the response is as if the system were stable and always in quadrature. The frequency of the "wiggler" must be large compared to the frequency components of material velocities, but low enough so that high harmonics of the wiggler do not fall into the signal band. To measure acoustic frequencies in the range from .5 to 10 MHz, wiggler frequencies of 20-100 KHz are used. A further benefit of the use of the wiggler is that the requirement on optical flatness is reduced; with its use, a pellicle flatness of 3

[1] *IEEE Ultrasonic Symposium*, Milwaukee, Wisconsin, November 1974.

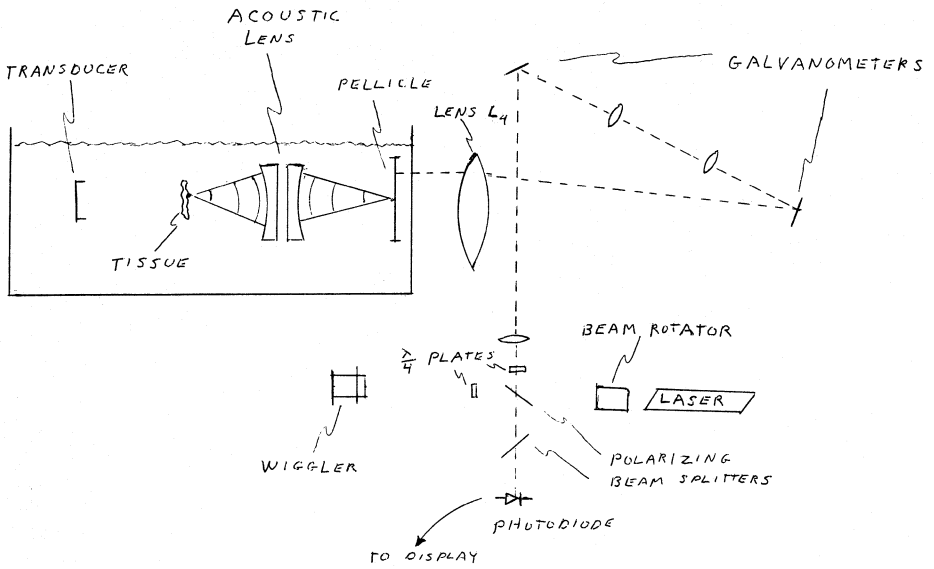

Fig. 1.

waves/inch gives 90% of the response of an ideally flat mirror.

To isolate the laser from the interferometer, and to provide means for varying the beam balance in the two legs, a polarizing beam splitter (PBS) with a quarter wave plate in each leg of the interferometer is used. The polarization angle of the incident beam is varied to change the beam balance. A second PBS is used to analyze the interference. By using both outputs from this second PBS, which has a 180° relative phase shift, the response is doubled and common mode noise is minimized.

This system, with associated electronics and display circuitry, has been used to measure and display ultrasonic waves, and some examples are given. It is being used to measure ultrasonic transducer response, to measure and display the interaction between biologic tissue and ultrasound, and as an aid in the design of ultrasonic lenses. In this paper we want to stress the optical design of the system and discuss other applications in the measurement of small motions of mechanical objects.

3.6 Wideband Guided - Wave Acoustooptic Bragg Devices Using Multiple Tilting Surface Acoustic Waves,[1] C. S. Tsai, M. A. Alhaider, LeT. Nguyen, and B. Kim, *Department of Electrical Engineering, Carnegie-Mellon University, Pittsburgh, Pa. 15213*

(15 min)

Experimental results with guided-wave acoustooptic devices, utilizing coplanar Bragg diffractions, have suggested that these devices are capable of performing a number of important functions such as deflection/switching, modulation and spectrum analysis of rf signals.[2] However, all of the various forms of the devices which have been reported employ only a single surface acoustic wave (SAW) interdigital transducer and, therefore, a single SAW. The inherent limitation of devices which employ a single interdigital transducer is a relatively small acoustic bandwidth and thus a small device bandwidth. A further limitation is that in order to achieve a large device bandwidth (assuming a sufficiently large acoustic bandwidth) the aperture of the acoustic wave must be chosen very small. This in turn results in a drastic decrease in diffraction efficiency. Recently, we have explored a wideband device configuration which employs multiple tilting SAWs which are staggered in their center frequency and tilted in their propagation direction, and have achieved some preliminary experimental results.[3] For example, by employing just two tilting SAWs on a *Y*-cut $LiNbO_3$ out-diffused waveguide, a bandwidth of 200 MHz at 50% diffraction efficiency was obtained, requiring a total electric driving power of only 200 mW.[3] This performance figure greatly exceeds those obtained in previous devices which employ only a single SAW.[2]

We report in this paper theoretical results relating to the wideband device configuration, namely, guided-wave Bragg diffraction from multiple tilting SAWs, and a number of new experimental results which serve to verify the theoretical predictions, including the performance characteristics of a device which is capable of a 300 MHz bandwidth. In addition, the results of a number of experiments which are designed to demonstrate the potential applications of this type of wideband device are presented.

The theoretical results have established the relevant device parameters as well as the important design considerations. Experiments using two to four tilting SAWs on single-mode *Y*-cut $LiNbO_3$ out-diffused waveguides were carried out to verify the theoretical predictions. In particular, the theory and experiments have established the relationships among the three most important design parameters required for large bandwidth: acoustic angular spread of individual SAW, tilting angle between adjacent SAWs and the phase difference between adjacent SAWs. In one of the wideband units being studied, a device bandwidth of 300 MHz has been achieved, requiring a total electric driving power of 350 mw at 50% diffraction efficiency. Also, a diffraction efficiency as high as 85%, requiring a total electric driving power of 197 mw, has been obtained with one of the lower bandwidth units. A further reduction in the electric driving power should be possible by connecting matching networks to the transducers. A device bandwidth of 300 MHz enables the device to deflect a guided-light beam of 1 cm aperture into 862 resolvable spot diameters with a switching time of 2.8 μs. Equivalently, the same device is capable of switching a guided-light beam into 10 beam positions with a switching time of 33 ns. The devices being studied consistently provide a through-put coupling efficiency of greater than 20% and good optical beam quality.

The experiments that have been designed to demonstrate the potential applications of the wideband guided-wave acoustooptic Bragg devices include: 1) RF spectrum analysis, 2) multiport beam deflection and switching, 3) optical pulse modulation, and 4) signal processing of RF signals. Some of the performance figures obtained are reported.

3.7 Multichannel Interferometry, C. R. Pond and P. D. Texeira, *The Boeing Aerospace Company, Seattle, Wash. 98124*

(15 min)

The multichannel interferometer[1] is well suited for applications requiring simultaneous measurements over several optical paths. A substantially improved version of the referenced interferometer has been used as a dilatometer to measure the coefficient of thermal expansion of low expansion composite structural forms ($\alpha \simeq 10^{-8}$ cm/cm−°K) during the engineering phase of the Large Space Telescope (LST) metering truss development program.

[1] This work was supported jointly by the ONR and the NSF.

[2] *See* for example, L. Kuhn *et al., Appl. Phys. Lett.*, vol. 17, p. 265, 1970; Y. Ohmachi, *J. Appl. Phys.*, vol. 44, p. 3928, 1973; R. V. Schmidt *et al., Appl. Phys. Lett.*, vol. 28, p. 417, 1973; J. F. Weller *et al., Topical Meeting on Integrated Optics*, Paper WA9-1, Jan. 21-24, 1974; C. S. Tsai *et al.*, Paper D.12, *Integrated Optics and Fiber Optics Communication Conference*, NELC, San Diego, Calif., May 15-17, 1974 (unpublished); K. W. Loh and W. S. C. Chang, presented at the *NSF Meeting on Optical Communication Systems*, University of Illinois, Nov. 14-15, 1974; E. Lean *et al.*, presented at the 1974 *Ultrasonics Symposium*, Milwaukee, Wisc., Nov. 11-14.

[3] C. S. Tsai *et al.*, "A high performance acoustooptic guided-light beam device using two tilting surface acoustic waves," to be published in *Appl. Phys. Lett.*

[1] C. R. Pond, M. H. Horman, and P. D. Texeira, *Appl. Opt.*, vol. 7, p. 2144, 1971.

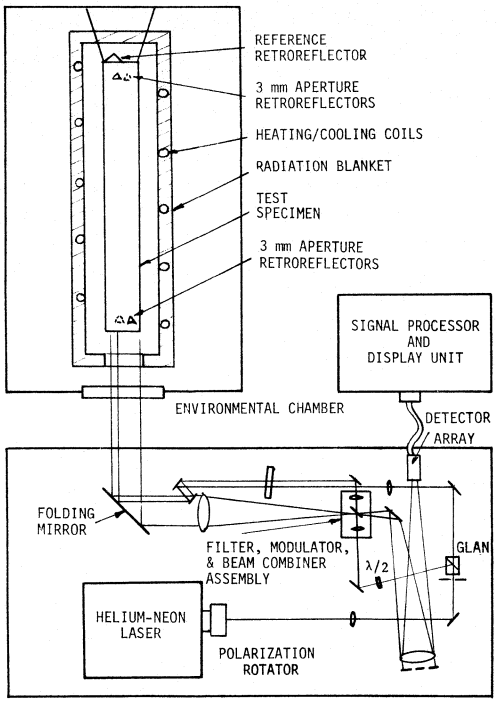

Fig. 1. Multichannel Interferometer setup for dilatometry.

The multichannel interferometer consists of several parallel fringe counting interferometers with a single laser as the source. Common optical elements – modulator, beamsplitters, collimator, folding mirrors, etc. – are used to reduce environmental effects. A common reference beam eliminates errors due to variation in reference beam path length.

Fig. 1 shows the basic configuration of the interferometer as used for dilatometry. (The folding mirror will be replaced by an array of seven adjustable mirrors when the interferometer is used for testing the full scale LST truss.) The laser is a single frequency, stabilized helium-neon laser. The polarization rotator, Glan prism, and $\lambda/2$ plate form a variable, low loss beamsplitter for optimizing the relative power in the signal and reference beams. The reference beam is retroreflected at the test specimen to compensate for gross relative motion between the interferometer and the specimen.

The interferometer employs a novel electro-optical element (designated FMC for filter-modulator-combiner) which performs the functions of spatially filtering the beams, modulating the relative phase of the signal and reference beams, and combining the reference with the signal beams that return from the test specimen. The FMC consists of a 1.5 mm square glass plate, 0.2 mm thick, mounted on the end of a piezoelectric bender and held between two 10x microscope objectives. A 7×10 micron elliptical mirror is deposited on either side of the glass plate, using microcircuit fabrication techniques. These mirrors are the reflection analog of a pinhole spatial filter, where the input signal and reference beams (parallel polarization) are focused onto the elliptical mirrors. The filtered beams are reflected near Brewster's angle, while the unfiltered light passes through the glass. The mirrors are offset so the filtered reference beam coincides with the return signal beams, insuring misalignment between the input beams. This effectively prevents feedback into the laser. The relative phase modulation needed for bidirectional fringe counting is provided by a low voltage drive on the bender.

The outgoing signal beam is spatially filtered and recollimated to 5 cm diameter. Small cube corner reflectors at each test point reflect signal beams back to the spatial filter, forming diffraction patterns that are large compared to the filter mirror. The obstruction loss is less than 1%. Specimen orientation variation necessitates two retroreflectors at each end. The spherical mismatch in the signal and reference wavefronts is removed by fine adjustment of the collimating lens. The detector array is seven phototransistors. The signal processor produces an up or down pulse for each 90% phase change between signal and reference beam. These $\lambda/8$ increments are accumulated in the display unit which provides binary coded decimal output in addition to a decimal display.

3.8 Optical Video Disks (*Invited*), Eric Spitz, *Central Research Laboratory, Thomson-CSF, Domaine de Corbeville, France*

(30 min)

The optical video disk is expected to become a new, inexpensive medium capable of carrying information, educational or entertainment material. Players and disks now under development in a number of laboratories handle information densities of about 10^8 bits/cm^2. This paper reviews the fundamental considerations and optical design principles of these developmental systems, discusses the problems encountered and describes the solutions presently envisaged.

3.9 A Holographic Video Disk: An Alternative Approach to Optical Video Disks, Y. Tsunoda, K. Tatsuno, and Y. Takeda, *Central Research Laboratory, Hitachi, Ltd., Tokyo, Japan*

(15 min)

One of the problems with optical video disks employing FM coding is the precise focusing and tracking adjustment needed in a player intended for use in the home. To resolve this problem, a holographic video disk is proposed and examined at a fundamental stage.

Construction of the player is explained in Fig. 1. A disk of 300 mm diameter contains 54,000 holograms, each of which stores luminance, chrominance and sound codes in a small area of 1 mm diameter. The extremely high packing density is realized by combining the random phase sampling technology[1] with the

[1] Y. Tsunoda and Y. Takeda, *Appl. Opt.*, vol. 13, p. 2046, 1974.

Fig. 1. Basic concept of the holographic video disk player.

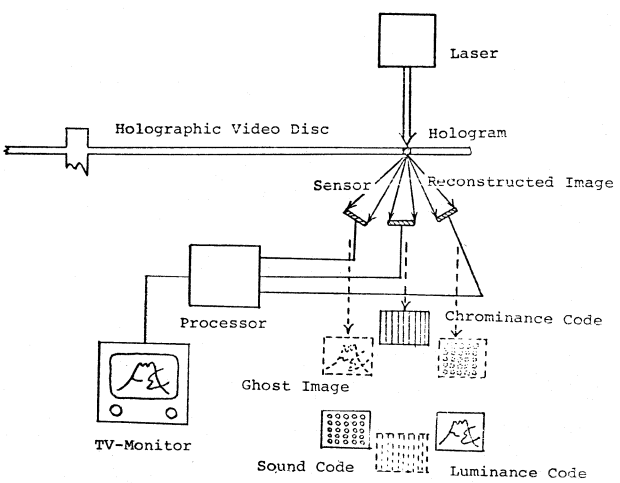

method of coherent superposition of holograms. Interference between the ghost images and the reconstructed images is eliminated by setting the incident angles of the three information light waves in three axially symmetric directions. Reconstructed images are focused on the image sensors (such as solid state sensor arrays) whose output signals are processed and displayed on a TV monitor. As a light source, a compact laser is used. There is no need for precise focusing or tracking of the laser beam. To obtain rotational immobility of successively reconstructed images, the laser waves are chopped or directly modulated.

To clarify the above design considerations, several fundamental experiments were carried out.

Photoresist was selected as the storage medium in order to make a master disk for duplication by stamping. The restricted dynamic range of the photoresist was controlled by pre-exposure. For the luminance and the chrominance signals, conventional EVR coding was used. The sound signal was converted into sampled pulse code modulation. The optical axes of these three information signals onto the hologram plane formed an angle of 120° with each other. For each information signal a sampling mesh and a random phase shifter were closely attached and set in the optical path of a He-Cd laser (4416 Å). Almost all of the light energy of the information signals was uniformly distributed in the restricted hologram area. The diameter of the hologram was related to the diameter of the sampling hole by the Rayleigh Criterion. As a result, the three information signals could be stored in a hologram of 1 mm in diameter without speckle noise. More than two thousand holograms were arranged on a photoresist disk to give several minutes of play of motion pictures in color. The signal-to-noise ratio of the reconstructed images was found to be 38 ± 2 db in both single and superimposed holograms. Continuous rotation of the disk at 6 RPM gave color motion pictures and sound on a TV monitor. Each hologram had information corresponding to 1/30 seconds. Chopped illumination of each hologram facilitated smooth motion of the pictures and assured immobility.

Session 4

Wednesday, May 28, 1975 1:30-5:00 P.M.

Solid State Lasers

Chairman: L. G. DeShazer, *University of Southern California, Los Angeles, Calif.*

Organizer: A. J. Glass, *Lawrence Livermore Laboratory, Livermore, Calif.*

4.1 Active Mirror: An Alternative Design for a High Power Nd:Glass Amplifier, J. Hoose and J. Soures, *University of Rochester, Laboratory for Laser Energetics, Rochester, N. Y. 14627*
(15 min)

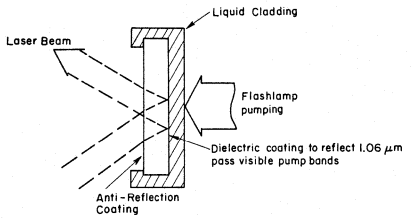

Fig. 1. Schematic of active mirror amplifier.

At present only two general types of amplifiers are being used in high energy short pulse glass laser systems. These are the face pumped disk[1,2] and large diameter rod[3] amplifiers. The inherent disadvantages of the open face disk geometry are:

(i) Relatively low pumping efficiencies,

(ii) Maintenance problems due to high light flux loading on the interior surfaces of the amplifier, and

(iii) Low repetition rates due to the relatively slow air cooling.

The basic drawbacks of rod amplifiers are:

(i) Stored energy is not as high as with disk amplifiers,

(ii) Repetition rates are also low due to thermal lensing and thermally induced stress birefringence.

In an attempt to overcome some of these problems, we have re-examined a relatively old design, the active mirror.[4] The principle of operation of such an amplifier is shown in Fig. 1. This design combines the advantages of the larger diameter possible with disk amplifiers, with the characteristic higher efficiencies attained by rod amplifiers. In addition, because it lends itself to liquid cooling, considerably higher repetition rates could probably be achieved with this type of amplifier than with either rods or open disks. The possible problem areas of such a design are:

(i) Possible coating damage due to large pump fluxes,

(ii) Warping of the disks due to heating, and

(iii) Possible beam deflection due to flashlamp induced acoustic shock incident on active mirror.

[1] J. M. McMahon, J. L. Emmett, J. F. Holzrichter, and J. B. Trenholme, *J. Quantum Electron.*, vol. QE-9, p. 992, 1973.

[2] M. Lubin, J. Soures, and L. Goldman, *J. Appl. Phys.*, vol. 44, p. 347, 1973.

[3] J. Soures, S. Kumpan, and J. Hoose, *Appl. Opt.*, vol. 13, p. 2081, 1974.

[4] J. P. Chernoch, U. S. Patent 3,525,053, August 28, 1970.

Several prototype amplifiers of this design have been built and tested. The largest unit tested so far utilizes a 15 × 10 × 1.4 cm thick slab of ED-2 laser glass. It was found that average stored energy densities in excess of 0.6 J/cm^3 could be achieved with pumping efficiencies well over 1%. At these flux levels no coating damage has been observed for hundreds of shots.

The results of experiments to measure beam distortion and deflection will be reported and the staging of a large glass laser system utilizing active mirror amplifiers will be discussed.

4.2 Face-Pumped Mirror-Like Structure as an Alternative to Disk Amplifiers, G. Bret, M. C. Hurand, and J. C. Boltz, *Energetic S. A., Vigneux, France*
(15 min)

In the design of high energy, high power, light amplifiers, efficiency and reliability are of prime importance. Reliability depends strongly on the self trapping of small scale spatial fluctuations related to the nonlinear index of refraction. This effect can be limited by using high gain systems and low power density beams.

In conventional design, where pumping efficiency is poor, increasing the overall efficiency requires an increased extraction efficiency, accomplished by raising the power density in the beam.

It is easy to understand that a design with a much larger pumping efficiency would permit a now impossible trade-off, by lowering the power density, giving a much better reliability, but still keeping the total efficiency at an acceptably high level.

We have studied a structure made of a plate of glass coated on one side with a dielectric mirror which is transparent to the pump light, but reflects the 1.06 μm light to be amplified. A sketch of the design is given on Fig. 1, where *F* is an array of linear flash lamps, *M*1 is a mirror reflecting the 1.06 μm light to be amplified, but transparent for the pumping light, and *G* is a disk of Owens-Illinois glass 2.5 cm in thickness with a 3% neodymium concentration. The figure also indicates the system that was used to measure the gain of the design using the known variations of gain of a rod amplifier *A*, together with a second mirror *M*. Data are presented showing the linear increase of measured small-signal gain with pump energy, and of energy

Fig. 1. Design of face-pumped mirror-like structure.

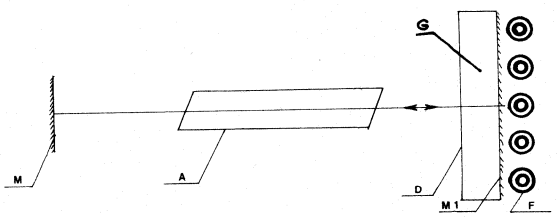

stored per unit surface area with pump energy per unit surface area. These data show that a maximum pumping efficiency of 2% is possible. This represents a nearly ten-fold increase compared with standard disk designs.

Such a system is very promising for large beam amplification since it is scalable. Several problems related to mirror deformation, induced birefringence, cooling and pump light filtering have been solved, and will be discussed during the presentation of this paper.

4.3 Tailoring Nd-Doped Glasses for Laser Applications: Dependence of Induced-Emission Cross Sections on Composition,[1] R. R. Jacobs and M. J. Weber, *Lawrence Livermore Laboratory, Livermore, Calif. 94550*

(15 min)

The spectroscopic and optical properties of Nd laser glasses are dependent upon the chemical composition of the host. Thus it is possible, by compositional changes, to tailor Nd glasses for specific laser applications. We have conducted an extensive program directed toward the development of an optimal Nd^{3+} glass medium for laser fusion experiments. Many glasses have been investigated, ranging from simple fused silica to complex multi-component oxide glasses. In these studies, the induced-emission cross section for the $^4F_{3/2} \rightarrow {}^4I_{11/2}$ lasing transition was varied by a factor of four as a result of changes in glass composition.

Radiative intensities in Nd-doped glasses are analyzed using the Judd-Ofelt theory of electric-dipole transition probabilities for rare-earth ions. In this treatment the line strength for a transition between two J states is expressed as a sum of three terms involving products of matrix elements and phenomenological intensity parameters $\Omega_2, \Omega_4, \Omega_6$. The latter are determined experimentally from a least-squares-fit of absorption spectra. These parameters, in turn, are used to calculate the probabilities for optical transitions between any electronic states of interest and hence properties such as absorption intensities, fluorescence intensities, branching ratios, and radiative lifetimes can be evaluated. By combining the results of these intensity calculations with linewidth data from emission spectra, induced-emission cross sections are obtained.

Recently Krupke[2] applied the Judd-Ofelt model to predict induced-emission cross sections at ≈ 1.06 μm for four Nd-doped silicate laser glasses with results which were in good agreement with experiment. We have extended Krupke's technique to investigate a large variety of possible laser glasses. The Judd-Ofelt parameters are found to depend upon the specific ions used both as glass network formers and network modifiers. As an example, measurements of alkali alkaline-earth silicate glasses have shown a systematic trend in the absorption and emission properties as the network modifying ions are varied. By changing the alkali ion in the series K_2O-Na_2O-Li_2O, both the Ω's and the predicted transition probabilities increase with decreasing ion size. The result is in agreement with the experimental determinations of cross section by Sarkies *et al.*[3] and fluorescence lifetime data of Rapp.[4] Another example of the use of the Judd-Ofelt model is to evaluate the branching ratios of the fluorescence from the $^4F_{3/2}$ state to the ^4I states of Nd^{3+}. These ratios can be expressed in terms of the ratio of intensity parameters Ω_4/Ω_6. Thus to optimize the emission intensity for a particular transition, appropriate compositional changes can be made to obtain, as nearly as possible, the desired Ω values. Variations in the emission wavelengths and peak induced-emission cross sections for the $^4F_{3/2} \rightarrow {}^4I_{11/2}$ and $^4F_{3/2} \rightarrow {}^4I_{13/2}$ transitions of several different glass compositions will be presented and compared with commercial laser glasses.

In addition to silicate glasses, the intensity parameters have been determined for several borate, silicate, phosphate, germanate, tellurite, aluminate, and titanate glasses. Changes in the Judd-Ofelt parameters for these glass compositions will be discussed with respect to their usefulness in designing glasses for specific laser applications.

Finally, the intensity parameters for any Nd glass medium can be used to determine the optical pumping efficiency, radiative lifetime, saturation parameter, and probability for parasitic oscillation in large amplifier disks. These considerations, which are important for arriving at an overall figure of merit for a laser glass, will be discussed in connection with a final selection of glass composition.

[1] This work was performed under the auspices of the U. S. Atomic Energy Commission.

[2] W. F. Krupke, *IEEE J. Quantum Electron.*, vol. QE-10, p. 450, 1974.

[3] P. H. Sarkies, J. N. Sandoe, and S. Parke, *J. Phys. D: Appl. Phys.*, vol. 4, p. 1642, 1971.

[4] C. F. Rapp, "Physics of electronic ceramics," Part B, edited by L. L. Hench and D. B. Dove (M. Dekker, New York, 1972), p. 1011.

4.4 2.06 μm Laser Performance and Design Options for Rangefinder and Illuminator Applications,[1] D. P. Devor, *Hughes Research Laboratories, Malibu, Calif. 90265*

(15 min)

The highest unit rod volume laser efficiency occurs for Ho^{3+} ($^5I_7 \rightarrow {}^5I_8$) output from Er-Tm sensitized Ho:YLF. Spectrally broad, high optical density pump bands and high laser efficiency result from Er-Tm sensitization. These effects allow large reductions in design scale in addition to other new design options for sources using $Y_{1-x-y-z}Er_xTm_yHo_zLiF_4$. Operating at 2.06 μm, laser applications include efficient, alternative wavelength sources for target designator/illuminators and eye-safe rangefinders for both civilian and military devices.

[1] Supported in part under U. S. Army Electronics Command contract.

Ho:YLF is easily and rapidly grown using a reactive atmosphere crystal growth process. A 6-hr growth cycle Czochralski ingot yields several laser rods of glass-like optical quality. Because of easy growth, systematic variation of ion concentrations x-y-z has been possible and allowed study of effects on laser performance. Horizontal Bridgman crystal growth method can be used for large scale, inexpensive rod production when x-y-z values are fixed. Thermal and elastic properties of birefringent Ho:YLF are satisfactory. Maximum power dissipation of fracture stress limit is 60% of the Nd:YAG value.

New laser design options result from significant changes in laser performance occurring with variation of Er-Tm sensitizer concentrations x-y and Ho activator concentration z. Trade-offs can be made for pump-band optical densities, laser threshold, slope efficiency, and output pulse power. Design options therefore occur for choice of pump lamp and lamp parameters, resonator configuration, rod dimensions, and cooling system. The options are generally interdependent. Optimum Er-Tm-Ho concentrations exist for particular laser applications of Ho:YLF.

Rod colling requirements have more flexibility for 2.06 μm laser design than for similar performance Nd:YAG systems. The Ho:YLF laser transition terminal level is 300 cm^{-1} above ground and is thermally populated at 300°K. For ambient temperature operation the minimum possible metastable level excitation necessary for laser gain requires 2.4 J per unit rod volume (cm^3) per atomic percent Ho concentration. For light weight, portable sources where minimum laser threshold is an important system requirement, a small diameter laser rod will also minimize rod thermal gradients. With simple lamp-rod imaging optics, rod and lamp dimensions are 1-to-1 and reliable lamp performance requires about a 1 mm bore lamp, implying a minimum 1 mm rod diameter. Selective variation of rod diameter depends on efficiency of rod pump light absorption. Consequently, pump level optical densities and efficient pump-to-metastable level energy transfer requirements provide additional design constraints.

The Ho:YLF pump band spectral distribution covers 90% of a pulsed xenon lamp spectral output. Respective Er^{3+}, Tm^{3+} and Ho^{3+} levels account for 45, 13, and 42% of the spectral distribution of pump levels. Threshold consideration requires modest Ho concentration, indicating variation of Er concentration for control of pump band optical density. Although Tm^{3+} levels weakly contribute to pump light absorption, Tm concentration is necessary for fast pump-to-metastable energy transfer rate. Extensive recorded data on Ho:YLF concentration effects indicate an Er-Tm-Ho energy transfer interaction contrasting with results reported for other ion interaction systems. However, the data do provide empirical criteria satisfactory for laser design for specific application requirements.

For a heavy system with low duty-cycle requirements, such as high output energy rangefinders, a design option different from threshold minimization occurs. The Ho:YLF x-y-z con-

centration performance data show a cross-over where laser slope efficiency improves although threshold also increases.

4.5 Barium Sodium Niobate Acoustooptic Mode-Locker/Frequency-Doubler (AOML/FD) for Nd:YAG,[1]

R. R. Rice and G. H. Burkhart, *McDonald-Douglas Astronautics Company East, St. Louis, Mo. 63166*

(15 min)

One highly promising space laser communication system utilizes a frequency doubled Nd:YAG laser transmitter mode-locked at 500 MHz. In such a laser, intracavity acoustooptic loss modulation is superior to electrooptic phase modulation for achieving narrow mode-locked pulses and stable operation, and resonator loss must be minimized for maximum efficiency. We have developed an acoustooptic mode-locker and frequency doubler (AOML/FD) that uses a single barium sodium niobate (BSN) crystal to both frequency double and acoustooptically mode-lock a Nd:YAG laser. Thus, one intracavity component is eliminated.

A typical AOML/FD unit measures only 4.5 cm × 4.2 cm × 1.9 cm. A BSN crystal was cut in the form of a rectangular parallelopiped 5 mm × 5 mm × 2 mm with the crystal axes parallel to the edges. The 2 mm × 5 mm faces normal to the *c*-axis were polished flat and parallel to form the acoustic resonator. A longitudinal transducer was bonded to one of the *c*-faces using a vacuum cold welding technique, and the transducer was mechanically polished for half wave resonant operation at 250 MHz. The thin upper electrode was sputtered on and connected to the RF matching section. The RF matching was accomplished by a novel transmission line technique involving line sections having different characteristic impedance. The crystal was mounted in a solid copper heat sink fitted with heater windings, a thermistor, and a thermocouple. The faces normal to the *b*-axis were AR coated for both 1.06 μm and 0.53 μm.

The acoustooptic figure of merit (FOM) for BSN was measured by the method of Dixon and Cohen.[2] For longitudinal acoustic waves propagating down the *c*-axis (001) direction, the FOM relative to fused silica was 2.07 and 7.25 for light polarized perpendicular ("O") and parallel ("E") to the *c*-axis, respectively. The longitudinal acoustic velocity down the *c*-axis was 6250 M/S, and the temperature coefficient of longitudinal phase velocity was -3.1×10^{-4}/°C. For light propagating normal to the *c*-axis polarized "O" for efficient SHG and with the sound column propagating at an angle θ to the *c*-axis in the *a*-*c* plane, the angular dependence of the FOM is $A \cos^2\theta + B \sin^2\theta$ for longitudinal waves and $C \sin 2\theta$ for shear waves, where $A:B:C \simeq 1:.2:2.5$.

[1] The experimental results reported have been accomplished as part of the USAF 405B Space Communications Program.

[2] R. W. Dixon and M. G. Cohen, *Appl. Phys. Lett.*, vol. 9, p. 205, 1966.

TABLE 1
PERFORMANCE CHARACTERISTICS OF TYPICAL AOML/FD UNIT

Polarization	1.06 "O" wave 0.53 "E" wave
RF frequency	250 MHz
Transducer conversion loss	0.5-0.1 dB
Diffraction efficiency (Time averaged @ 1.06 μm)	3.0-3.5%/W, polarized 1 *c*-axis
Effective SHG coherence length	$>0.9l$ @ 1W RF, $>0.8l$ @ 2W RF
Ratio diff. loss Resonant:antiresonant	<2:1
Optical insertion loss*	0.1-0.3% (No RF)
External Bragg angle	2.43°
Angular width of diffraction peak (1.06 μm)	0.75°
Angular width of SHG vs angle	−4° @ 1.0W RF
Oven temperature peak SHG	−75°C @ 1.0W RF
Temperature width of SHG vs temperature	−2°C @ 1.0W RF

*BSN crystals grown under Air Force contract by Union Carbide Corporation.

Operation was well within the Bragg regime, and the diffracted intensity showed a $\text{sinc}^2 x$ dependence on the angle of incidence. The external Bragg angle was 2.43°, and the measured external half width was 0.75° for 1.06μm light, consistent with the 3.8 mm sound column length. The SHG showed a nearly ideal $\text{sinc}^2 x$ dependence on temperature and on angle of incidence. Longitudinal thermal gradients produced by RF heating distort the SHG versus temperature curves and reduce the effective SHG coherence length, but careful thermal design minimized this effect. In Table I, we summarize the performance characteristics of a typical AOML/FD.

Excellent results were routinely obtained in laser operation using an AOML/FD to mode-lock and frequency double a Nd:YAG laser. SH power outputs greater than 200 mW have been achieved, and SH conversion efficiency greater than 70% were achieved in properly designed resonators. The 1.06 μm pulse width depends on the modulation depth and the SH conversion efficiency.[3] In general, the pulse-width decreases as modulation depth increases or the SH conversion decreases. Under typical operating conditions, at 150 mW SH output (~70% SH conversion efficiency) with 2W RF drive, a 1.06 μm pulse width of about 300 ps (FWHM) is obtained.

[3] J. Falk, submitted for publication.

4.6 Solar-Pumped, Mode-Locked, Frequency-Doubled Nd:YAG Laser,[1]

Joel Falk, L. Huff[2] and Joseph D. Taynai, *GTE Sylvania Inc., Electronic Systems Group—Western Division, Electro-Optics Organization, Mountain View, Calif. 94042*

(15 min)

Direct solar pumping of a Nd:YAG laser permits the construction of a long life, low prime-power laser that is useful for a satellite-borne optical communications transmitter. We report recent progress in the development of a frequency-doubled, solar-pumped laser to be used for space communications. Improvements reported here for the first time include: (1) the simultaneous mode-locking and internal frequency-doubling of the solar pumped laser; (2) achievement of average power outputs of 5.6 watts multimode and 2.05 watts TEM_{00} mode at 1.06 μm; (3) construction of a laser structure and collecting optics that are designed to meet weight, vibration and temperature specifications appropriate to a satellite environment, i.e., construction of a preliminary space qualified laser.

The solar pumped laser (shown schematically in Fig. 1) consists of a telescope and sunlight

[1] This work was supported by Air Force Contract F33615-74-C-1062, as a part of the Advanced Development Program 405B, Air Force Avionics Laboratory, Wright-Patterson Air Force Base, Ohio.

[2] Now at University of Dayton, Dayton, Ohio.

Fig. 1. The solar pumped laser.

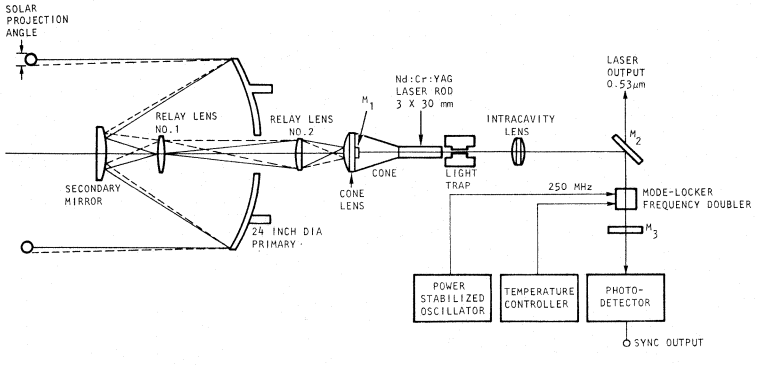

TABLE I
SUN-PUMPED LASER: OUTPUT POWERS

λ	Multimode	TEM_{00} CW	TEM_{00}: Mode Locked
1.06 μm	5.6 W	2.05 W	0.4 W
0.53 μm*	–	0.5 W	0.16 W

*Solar-simulator results.

collection assembly, and an L shaped optical cavity which contains a conductively cooled Nd:YAG laser rod, an internal focusing lens, and a barium sodium niobate crystal that is used both for mode locking and frequency doubling of the laser. The laser, aside from the collecting telescope, is designed to occupy 200 in^3 and weigh approximately 10 lbs.

The solar light collection assembly uses a series of optical elements to efficiently end pump the laser rod. The pump light is collected by a telescope whose dielectric secondary mirror is highly reflecting for wavelengths within the Nd:YAG 0.40 μm to 0.90 μm pump bands and has low reflectivity for $\lambda > 0.90$ μm. This filtering reduces the thermal load on the laser rod. The output of the telescope is relayed by three lenses to a hollow condensing cone which concentrates the light on the 3 mm diameter × 30 mm long Nd:YAG or Nd:Cr:YAG laser rod. The residual sunlight not absorbed by the laser rod (approximately 50 watts) is collected in a light trap. Heat from the light trap as well as the condensing cone and laser rod is conductively transferred to heat pipes.

The heat sink that cools the laser rod contacts it over its entire circumference. In spite of this circular symmetry, the non-uniform cooling of the heat sink produces preferred laser polarizations parallel and perpendicular to the direction of heat flow from the heat sink. This unusual laser polarization behavior has important consequences for the operation of a conductively cooled laser and will be discussed in detail.

Various concentration Nd:YAG and Nd:Cr:YAG laser rods have been evaluated in the solar pumped laser. The use of Cr as a co-dopant to Nd increases the fraction of sunlight absorbed in the laser rod and, because of excitation transfer to the upper laser level of the Nd^{+3} ion, increases the laser efficiency. Laser rods with 1% Nd, 0.1% Cr doping have yielded the highest laser output.

The laser is simultaneously frequency-doubled and acoustooptically modelocked using a single 5 × 2.5 × 5 mm barium sodium niobate crystal. This acoustooptic mode-locker frequency doubler, developed at McDonnell-Douglas Astronautics East, will be described in detail elsewhere.

The L shaped resonator structure allows efficient combination of the 0.53 μm beams generated in two directions within the $Ba_2NaNb_5O_{15}$ frequency doubler crystal. The focal length and location of the intracavity lens are selected to provide a maximum TEM_{00} mode size in the laser rod and a beam size in the $Ba_2NaNb_5O_{15}$ crystal that will provide maximum output power at 0.53 μm.

The performance of the solar-pumped laser has been evaluated both directly pumped by sunlight and pumped by a high pressure Xe arc lamp whose output approximates that of the solar spectrum. The power outputs achieved at 0.53 μm and 1.06 μm for both CW and mode-locked operation are given in Table I. These represent the highest output powers observed to date from a solar-pumped laser at either wavelength. The solar pumped results were achieved with a 24 inch diameter collecting aperture.

The 0.53 μm results given in Table I represent the results of preliminary experiments. Extensive work at 0.53 μm is in progress and will be reported in detail.

4.7 Lamp-Pumped Engineering Feasibility Model Laser Subsystem,[1] Dan J. Radecki, *GTE Sylvania, Inc., Mountain View, Calif. 94042*

(15 min)

We report on the state of development of the lamp-pumped Nd:YAG Laser Subsystem for use in a 1 GBPS Space Communication System. The Engineering Feasibility Model (EFM) Laser Subsystem incorporates components and techniques which have been developed over the past five years at various laboratories including GTE Sylvania, McDonnell-Douglas Astronautics-East, and ILC Technology Incorporated, for the Air Force Advanced Development Program 405B. Previous theoretical and experimental work has been reported elsewhere.

The EFM Laser Subsystem includes a mode-locked and frequency-doubled Nd:YAG laser operating at 500 Mpps. A heat-pipe cooling system effectively transfers heat generated in the conduction-cooled rod and infrared heat generated by the K-Rb pump lamps to a simulated space radiator. The associated electronics include an automatic power controlled alkali-metal lamp power supply, a power controlled RF drive for the mode-locker, a frequency doubling crystal oven controller, and a photo detector, bias supply, and amplifiers which provide a clock output for the remainder of the communication system. The laser system specifications are listed in Table I.

The heart of the system is the preliminary space qualified model (PSQM) laser head. Modelocking and simultaneous frequency doubling is accomplished with a $Ba_2NaNb_5O_{15}$ (BSN) acoustooptic loss modulator developed at MDAC-E, whose performance characteristics are reported elsewhere. A monolithic invar structure supports all of the internal components and maintains cavity length stability within required tolerances over an operating temperature range of 20°C ± 5°C. Unique lockable mirror mounts utilizing beryllium-copper flexures have been developed which maintain alignment over wide temperature variations and survive sinusoidal vibration to 5 g's. The pump cavity has dielectric cold-mirror inserts bonded to copper cavity inner walls. The coatings are highly reflecting at Nd:YAG absorption band wavelengths and transmit unwanted IR wavelength light to the conduction cooled cavity walls where it is absorbed and conducted away. A 4 × 63 mm Nd:YAG rod is indium bonded over one-third of its surface area to a copper heat sink. A folded-cavity resonator design with an intracavity lens, is used to obtain the maximum TEM_{00} mode volume in the rod simultaneously with the optimum mode diameter in the BSN crystal giving maximum second-harmonic generation. In addition to mode-size control, the folded cavity configuration is used to obtain the second-harmonic generated in

[1] This work was supported by the Advanced Development Program 405B, Air Force Avionics Laboratory, Wright-Patterson Air Force Base, Ohio, through a subcontract from McDonnell Douglas Astronautics Company-East, Contract No. Y3E-247R.

TABLE I
LASER SYSTEM SPECIFICATIONS

Intensity profile	TEM_{00} mode, Gaussian
Wavelength	0.53 μm
Power output	150 mW
Pulse repetition rate	500 MHz ±50 kHz
Pulse duration	300 pico-seconds
Amplitude stability	±2%
Polarization	100:1 horizontal (±1°)
Prime power	300 watts reservoir heater/lamp 15 watts – control/drive electronics
Weight (laser head)	14 lbs.
Operating temperature	20°C ±5°C
Vibration (non-operating)	5g, sinusoidal sweep, 2 oct/min 10 to 2000 Hz

both directions as useful laser output.

The primary pump-lamp being developed for use in the laser is a 5 mm ID × $2\frac{1}{2}$ inch arc length potassium-rubidium alkali-metal vapor lamp. Development problems prevent reporting of final results as of this writing. However, they are expected to be available at the time this paper is formally presented. Preliminary testing in an EFM prototype laser with 280 watts input has resulted in 70 mW of second harmonic output with a 280 picosecond pulse duration.

In addition to preliminary K-Rb lamp data, a large amount of data has been obtained with a more optimal laser configuration, utilizing a water-cooled krypton lamp which is mechanically interchangeable with the K-Rb lamp. With the input power adjusted to give an unsaturated laser gain which is equivalent to that observed when pumping with a K-Rb lamp (~2.9%), a power output of 120 mW with a pulse duration of 350 picoseconds has been obtained. Reduction of the rod temperature to 0°C should provide power output in excess of 150 mW. These results compare favorably with theoretical predictions based on Kennedy's[2] and Falk's[3] analysis of the mode-locked frequency doubled laser.

[2] C. J. Kennedy, "Mode domain analysis of the mode-locked and frequency-doubled laser: Homogeneous medium without spatial hole burning," to be published in *IEEE J. Quantum Electron.*

[3] J. Falk, "A theory of the mode-locked, internally frequency-doubled laser," to be published in *IEEE J. Quantum Electron.*

4.8 CW Pumping of Nd:YAG with Electrodeless Arc Lamps,[1] D. A. Huchital and G. N. Steinberg, *The Perkin-Elmer Corp., Norwalk, Conn. 06852*

(15 min)

In many applications, the utility of CW-Nd:YAG lasers is limited by the short life of the krypton-arc pumping source. It is shown that most failures of arc lamps arise at the electrodes and the associated, fused-silica-to-metal seals, and that the electrodes are essentially irrelevant to the pumping mechanism.

The pumping of Nd:YAG lasers with electrodeless krypton arc lamps is described. It is established that power output levels and overall efficiencies comparable to that achieved with conventional lasers are obtained while lifetime and reliability of the device is markedly improved.

The arc lamps are toroidal and are located either adjacent to the laser rod or surrounding it. Electrical energy at 27 MHz is coupled to the lamp by an induction coil acting as the primary of a transformer of which the arc lamp is a single-turn secondary winding.

Factors influencing the coupling efficiency are analyzed. The electric field necessary to maintain the arc is usually of the order of some tens of volts per centimeter, which translates to some tens of thousands of volts across the coupling coil. Generation of such voltages requires radio-frequency currents of the order of thirty or forty amperes and since the skin depth of copper conductors is approximately 10^{-3} cm at these frequencies, the problem of joule heating losses in the coupling coil is not trivial. However, it is shown that by proper design, electrical coupling efficiency of 80% or more is achievable.

Both lamp and laser rod are surrounded by a diffusely reflecting surface which contains the pump energy until it can be absorbed by the rod. The optical coupling is analyzed both theoretically and experimentally. It is shown that a high value of diffuse reflectivity is essential, since a change in reflectivity of 2% can reduce laser output by 50%. A further constraint is imposed by the requirement that the reflectivity remain high for thousands of hours in a UV-rich environment.

It is shown that coupling efficiencies of 35% and 65% are achieved for 4 mm and 6 mm diameter laser rods respectively. These values are comparable to those achievable in the usual elliptical imaging geometry.

A medium power laser which developed 25 watts multimode and 10 watts TEM_{00} for 1.5 kW of RF power is described. A controlled life test was performed in which the arc was extinguished and reignited regularly in the course of 1000 hours of continuous operation. At the administrative termination of the test the power output has decreased by only a few percent. Lasers capable of developing 80 watts multimode and 20 watts TEM_{00} are also described.

The issue of RF power supply and efficiency has also been addressed. Both high-level-oscillator and master-oscillator-power-amplifier configurations have been considered. A single tube unit will be described which generates 1.5 kW of radio-frequency energy with 67% efficiency.

[1] Sponsored in part by the Air Force Avionics Laboratory.

4.9 Laser Diode Pumped Nd^{3+}:YAG Laser,[1] C. W. Reno, *RCA, Advanced Technology Laboratories, Camden, N. J. 08102*

(15 min)

GaAs and complex structure AlGaAs laser diodes offer attractive pump sources for low power Nd^{3+}:YAG lasers. Their output spectra are narrow and can be matched to various lines of the Nd absorption spectra. The "high" radiance of the source when combined with a novel coupling scheme leads to efficient pumping. Absorption efficiencies of 50% have been achieved into the YAG rod using the 8680 Å absorption line for a 1.5 mm diameter rod and side pumping.

Fig. 1 shows output power versus rod temperature for the laser operating TEM_{00} with various output couplings. The pump source consisted of two GaAs homojunction arrays at 175°K heat sink temperature. Total input power to the laser drivers was 50 watts. Output in this case consisted of pulses at a rate of 35 kHz.

A second experiment shows the output waveform using 14 AlGaAs LOC laser subarrays at a heat sink temperature of 250°K and driven in sequence at an average rate of 70 kHz for each subarray with each subsequent subarray driven when the preceding one is turned off (14 arrays at 70 kHz each are approximately 1 MHz total). Of significance is the CW output with ripple components almost wholly restricted to frequencies less than the master clock rate of 1 MHz. This is in accordance with published theoretical results.[2] The output wavelength of the AlGaAs was 8850 Å which matches a major absorption line of the Nd^{3+}:YAG. The average output power was about 40 mW. The technical approach and capability for the construction of an AlGaAs LOC laser pumped Nd^{3+}:YAG laser of greater than 100 mW CW TEM_{00} output for a 250°K heat sink and 50 watt input power now exists.

[1] This project was partially supported by NASA Goddard under contract NAS5-23281.

[2] H. G. Danielmeyer, "Low frequency dynamics of homogeneous four level CW laser," *JAP*, vol. 41, pp. 4014-4018.

4.10 Picosecond-Pulse, Fieldable Frequency-Doubled Nd:YAG Laser System for Ultra-Precision Ranging,[1] E. G. Erickson and L. L. Harper, *GTE Sylvania Inc., Mountain View, Calif. 94042*

(15 min)

A unique picosecond-pulse Nd:YAG laser system has been developed for NASA for use in precision satellite ranging applications. It is the

Fig. 1. Power output vs. temperature.

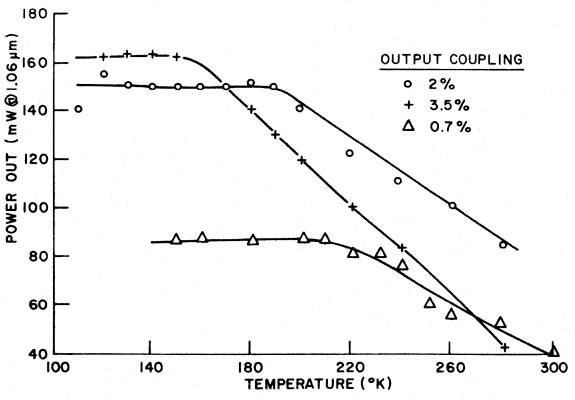

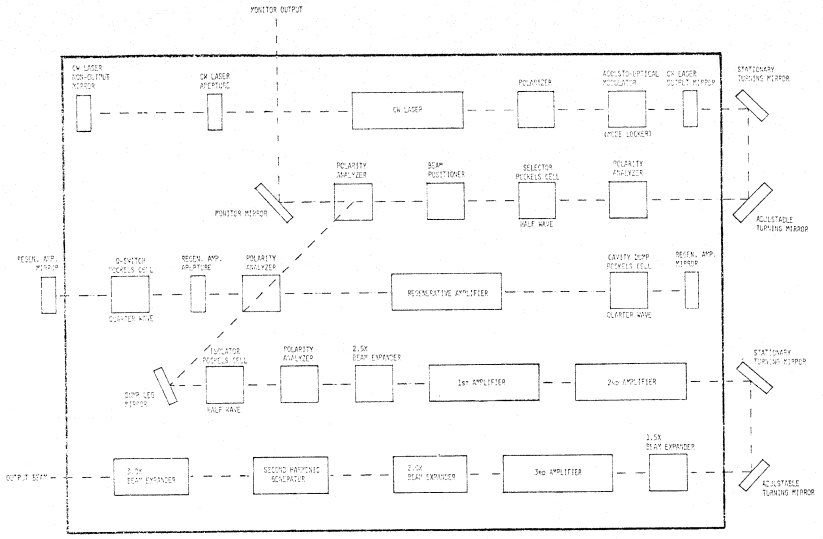

Fig. 1. Optical system diagram.

first frequency-doubled, picosecond-pulse Nd:YAG laser designed and packaged for stable operation in a field environment. This system emits an adjustable 100 to 1000 picosecond pulse containing 0.25 joule at 532 nanometers or 0.60 joule at 1064 nanometers. The pulse repetition rate is variable from 1.0 to 5.0 pps and the pulse-to-pulse amplitude stability is $\pm 5\%$. The output beam diameter is 3.6 centimeters and the divergence is less than 200 microradians. These performance characteristics are maintained for altitudes between sea level and 15,000 feet, temperatures between 40°F and 125°F, and a relative humidity up to 50%. The laser system also maintains performance in the vibration environment of a mobile electronic van. The basic design concept of this system is the regenerative amplification of a single mode-locked pulse from a CW, mode-locked, Nd:YAG laser.

The laser transmitter is a sealed unit measuring 13 in × 26 in × 56 in and consists of an electronic deck and an optical deck and support structure. The optical deck and support structure is fabricated entirely from invar for thermal stability. The heat exchanger and operator console are contained in identical cabinets measuring 60 in × 24 in × 27 in. The operator console contains a pulsed laser power supply, a CW laser power supply, and a control unit.

The optical train of the picosecond-pulse fieldable laser system is diagrammed in Fig. 1. This train consists of 33 optical subassemblies all mounted to the invar optical deck. The CW Nd:YAG laser generates 2.5 watts of TEM_{00} mode radiation modelocked at 150 megahertz. The single pulse energy is 16.7 nanojoules, the pulse duration is nominally 200 picoseconds, and the pulse spacing is 6.67 nanoseconds. The extraction and amplification of a single 16.7 nanojoule pulse is accomplished in three steps. First, a pulse train consisting of approximately 15 pulses is electrooptically switched into the regenerative amplifier by the selector Pockels cell. Second, all pulses in the train, except the first pulse, are electrooptically switched back out of the regenerative amplifier by the Q-switch Pockels cell. Third, the single pulse remaining in the regenerative amplifier is electrooptically switched out by the cavity dump Pockels cell after a suitable delay to allow multi-pass amplification to 5 millijoules. The fourth Pockels cell, in conjunction with the polarizers immediately preceeding and following it in the optical train, functions as an optical isolator between the regenerative and single-pass amplifiers. Following this isolator are three beam expanders and three single-pass amplifiers as shown in Fig. 1. The 5 millijoule output of the regenerative amplifier is amplified to 100 millijoules by two 0.25-inch diameter Nd:YAG amplifiers which is in turn amplified to 600 millijoules by a 0.375-inch Nd:YAG diameter amplifier. A 18 mm × 18 mm × 10 mm CD*A crystal frequency-doubles this output to 0.25 joules of 532 nanometer radiation. The final 3.0x power beam expander collimates both the green and IR beams to less than 0.2 milliradians.

The advantages for field systems of the above-outlined approach for achieving the stated output performance will be discussed. This discussion will include the presentation of the techniques for pulse-width adjustment and the circumvention of laser damage.

[1] This work has been supported by NASA Goddard Space Flight Center under Contract NAS5-20030.

4.11 A Negative-Branch Unstable Resonator Nd:YAG Laser,

T. F. Ewanizky and J. M. Craig, *Combat Surveillance & Target Acquisition Laboratory, US Army Electronics Command, Fort Monmouth, N. J. 07703*

(15 min)

Numerous publications describing the application of various forms of the positive-branch unstable resonator have been presented in recent years.[1] These applications have been virtually restricted to large bore, high energy gas or chemical laser systems, exploiting the primary feature of unstable resonators—good beam quality over an arbitrarily large mode volume.

Based on previously successful experience[2] with rhodamine 6G as a laser medium, we investigated the properties and beam quality of a Q-switched Nd:YAG laser employing a negative-branch form of confocal, unstable resonator. The Nd-YAG laser was flashlamp excited and of moderate dimension and input energy and normally fitted with the conventional plane mirror-porro prism cavity. In a comparison we found that the negative-branch unstable resonator equalled the plane mirror cavity in energy extraction from the excited medium, however produced near diffraction-limited beam divergence.

The far-field intensity profile of the Nd:YAG unstable resonator system was detected by a linear array of pyroelectric elements. The measured angular divergence to the first, second, and third intensity minima corresponded, within a few percent to the far-field angles predicted by theory for a Fraunhofer diffraction pattern produced by an appropriately dimensioned annular source.[3]

Burn patterns made by the beam in the near-field were of high contrast and evolution through the Fresnel regime of diffraction could be clearly traced, implying a high degree of coherence of the emitted radiation. Experiments performed with both normal and Q-switched modes of oscillation gave substantially identical results in beam quality.

[1] A. E. Siegman, *Appl. Opt.*, vol. 13, p. 353, 1974, and references contained therein.

[2] T. F. Ewanizky, *Appl. Phys. Lett.*, vol. 25, p. 295, 1974.

[3] M. Born and E. Wolf, *Principles of Optics*. Oxford: Pergamon Press, 4th edit., 1970, p. 417.

TABLE I
COMPARISON OF UNSTABLE RESONATOR WITH PARALLEL PLANE MIRROR RESONATOR

	Unstable*	Plane
Full-angle beam divergence	0.4×10^{-3} rad	2.2×10^{-3} rad
Pulse duration FWHM	1×10^{-8} sec	1.3×10^{-8} sec
Beam radiance	6×10^{13} W/cm^{2}sr	1.7×10^{12} W/cm^{2}sr

*Beam divergence and radiance of central maximum in far-field pattern.

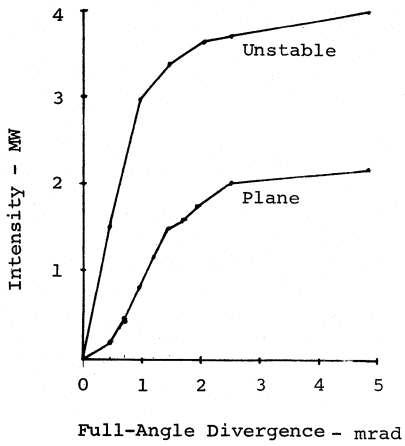

Fig. 1. Integrated angular intensity distribution.

Fig. 1 illustrates the measured angular intensity distribution of the Q-switched laser using either the unstable or parallel-plane mirror resonators and pertinent parameters are compared in Table I.

A significant practical advantage of the negative-branch unstable resonator was found in its relative insensitivity to angular misalignment. Initial alignment could be easily achieved and maintained over long periods without resort to special components.

In conclusion, we have found that efficient energy extraction and near diffraction-limited beam quality together with stable, non-critical alignment could be achieved with a negative-branch unstable resonator applied to a Q-switched Nd:YAG laser. Comparison of experimental results clearly shows the superiority of the unstable resonator form over the conventional parallel-plane mirror system.

4.12 Laser Transition Measurements for Nd-Glass, E. M. Dianow, A. Ya Karasik, L. S. Kornienko, A. M. Prokhorov, I. A. Shcherbakov, *USSR*

(15 min)

(Received late; see page 83)

Session 5

Wednesday, May 28, 1975 1:30-5:00 P.M.

Tunable Lasers and Isotope Separation

Chairman: O. Judd, *Los Alamos Scientific Laboratory, Los Alamos, N. M. 87544*

5.1 Applications of Tunable Infrared Lasers (*Invited*), P. L. Kelley, *MIT Lincoln Lab., Lexington, Mass.*

(30 min)

No summary.

5.2 Tunable $Hg_{1-x}Cd_xTe$ Infrared Lasers, J. P. Sattler, B. A. Weber, and J. Nemarich, *Harry Diamond Laboratories, Adelphi, Md. 20783*

(15 min)

We report on the development of new magnetically-tunable infared lasers using the semiconductor alloy $Hg_{1-x}Cd_xTe$. Tunable spin-flip Raman lasing and tunable recombination lasing have been obtained from this material using chopped-CW and TEA CO_2 lasers for optical pumping.

Semiconductor band theory and experimental results have indicated that crystals of $Hg_{1-x}Cd_xTe$ with small band gaps should have highly tunable Raman and recombination radiation, owing to the small conduction band effective mass. In addition, by selecting the appropriate composition of this material with respect to a pump-laser line, one should be able to reduce the spin-flip lasing threshold because of resonant enhancement effects. Our experiments indicate that these expectations are indeed warranted for this material, which offers great promise as a tunable infrared laser. Initial measurements using a TEA CO_2 pump laser have yielded a large first-Stokes tuning rate of $3.4\ cm^{-1}/kG$[1].

The experiments with the chopped-CW source utilized a conventional grating-tunable CO_2 laser that produced 2 W in the TEM_{00} mode. The output beam was externally chopped to a 2% duty cycle at 73 Hz to reduce crystal heating. This radiation with $E_p \| H$ was focused using a 26-cm focal length Ge lens onto the $Hg_{1-x}Cd_xTe$ crystal held at 12 K on a cold finger in a superconductive magnet. The crystal was a 0.5 × 3 × 6-mm parallelopiped, and was pumped in collinear geometry parallel to the 3-mm length and perpendicular to H. The crystal had an n-type carrier concentration of $5.4 \times 10^{14}\ cm^{-3}$, a mobility of $1.1 \times 10^5\ cm^2/V\text{-sec}$ and a cadmium fraction, x, of 0.234. The output radiation was analyzed using a 0.5 m spectrometer, a Ge:Cu detector, and a lock-in amplifier. The spin-flip radiation could be produced using all pump lines of the CW laser from the $P(16)$ to the $P(30)$ of the (00°1-02°0) band. Using the 9,52-μm line, the emission tuned from 9.67 to 9.96 μm by varying the magnetic field from 4 to 13 kG. A greater tuning range was obtained with the TEA laser pump.[1] The threshold for stimulated emission was measured to be 150 mW, corresponding to an intensity of $200\ W/cm^2$. The output polarization was perpendicular to the pump polarization in accordance with spin-flip selection rules.

The recombination radiation was observed for all CW-CO_2 laser pump lines between 9.22 and 9.55 μm. When using the 9.22-μm pump line, the emission tuned from 9.59 to 9.36 μm by varying the magnetic field from 0 to 20 kG. Various cavity modes could be selectively excited by adjusting the focusing and alignment of the pump laser beam with respect to the crystal faces. The wavelength, polarization, and output power of the recombination radiation depended on the magnetic field and pump wavelength.

The tuning data of these lasers for $Hg_{0.766}Cd_{0.234}Te$ have been analyzed using band theory, and the effective-mass ratio has been determined to be 9.77×10^{-3}. This value compares favorably with those obtained by other experimenters using other techniques for similar alloy ratios. The results obtained are used to project the tuning behavior of $Hg_{1-x}Cd_xTe$ crystals with different x-factors and electrical parameters.

[1] J. P. Sattler, B. A. Weber, and J. Nemarich, *Appl. Phys. Lett.*, vol. 25, p. 491, 1974.

5.3 A Highly Stabilized, Tunable CW Dye Laser and an Accurate Determination of the Rydberg Constant, J. B. West, R. L. Barger, and T. C. English, *National Bureau of Standards, Boulder, Col. 80302*

(15 min)

Recently it has been demonstrated[1] that remarkable frequency stability may be obtained from a CW dye laser. By using a wide-band (0-100 kHz) servo system to lock the dye laser frequency to a transmission fringe of a high finesse optical cavity, residual frequency fluctuations of less than 50 kHz for short times (20 μ sec) and 100 Hz for long times (10 sec) were obtained. However, due to thermal fluctuations in the reference optical cavity, long term drifts on the order of 1.5 MHz/min were observed.

Modifications to the laser system have resulted in a significant improvement in performance.[2] A high optical quality dye jet has replaced the dye cell and wavelength tuning is now accomplished using a tilted birefringent filter. Lasing in a single longitudinal cavity mode is achieved with two intracavity etalons. Error signals for the frequency control servo are derived from the signal difference between the transmission fringe of an external high finesse cavity and a reference beam bypassing the cavity. Low frequency corrections (0-1 kHz) are applied directly to the laser output mirror using a piezioelectric driver. High frequency corrections (1 kHz-5 MHz) are applied by varying the voltage across a deuterated KDP crystal in the laser cavity. Present frequency fluctuations are 1 kHz for short times and 300 Hz for 300 seconds. Long term frequency drifts are virtually eliminated by locking the length of the servo cavity to a fringe of a 3.39 μm He-Ne local oscillator laser which is frequency-offset-locked to a methane stabilized laser.[3] By using this technique, the long term frequency drifts of the dye laser should approach that of the methane-stabilized laser (about a part in 10^{13}), and the variable frequency-offset-locking technique allows the dye laser frequency to be tuned over 2.5 GHz while stabilized to this degree.

The amplitude of the dye laser output is stabilized to one part in 10^4 with a high speed

[1] R. L. Barger, M. S. Sorem, and J. L. Hall, *Appl. Phys. Lett.*, vol. 22, p. 573, 1973.

[2] R. L. Barger, J. B. West, and T. C. English, in preparation.

[3] R. L. Barger and J. L. Hall, *Phys. Rev. Lett.*, vol. 22, p 4, 1969.

servo system which uses an ADP crystal and linear polarizer combination. Present plans call for the entire dye laser and servo cavity to be enclosed in a pressure box. This will allow continuous pressure tuning of the laser over a 0.2 nm wavelength range without disturbing the frequency servo lock.

Presently, experiments are in progress which use this stabilized laser to saturate the Balmer α transition of the hydrogen atom. The result of these experiments should be a significant improvement in the accuracy of the Rydberg constant. Saturation of the transition in a beam offers specific advantages over experiments done with a discharge. In particular, shifts and broadening due to collisions and the Stark effect should be nearly eliminated. For these reasons, our experiments use a beam of metastable hydrogen atoms.

An RF discharge is used to produce ground state hydrogen atoms which are then collimated using a multichannel array of 5 μm diameter capillary tubes. Metastable hydrogen atoms (2^2S) are produced by bombarding ground state atoms with electrons near threshold energy ($\approx$11 eV). Metastable atoms in the beam are detected downstream by applying a dc electric quenching field. A photomultiplier tube monitors the resulting Lyman-α emission which is proportional to the number of metastable atoms in the beam. Laser saturation of the hydrogen 2^2S-3^2P transition occurs just upstream from the detector. Thus, the saturation is observed as a decrease in the Lyman-α emission.

The laser wavelength is measured with a frequency-controlled Fabry-Perot interferometer[4] which is accurate to about 10^{-5} order.

Saturation of the 2^2S-3^2P transition should provide a linewidth on the order of 30 MHz. If, however, the 3^2P state is used as an intermediate state and an RF field is simultaneously applied to induce transitions from the 3^2P to 3^2S state, a linewidth of 1 MHz should be realized.[5] After careful corrections for systematic errors, this method should provide an accuracy of at least one part in 10^9 for the Rydberg constant.

[4] R. L. Barger and J. L. Hall, *Appl. Phys. Lett.*, vol. 22, p. 196, 1973.

[5] D. E. Roberts and E. N. Fortson, *Phys. Rev. Lett.*, vol. 31, p. 1539, 1973.

5.4 Laser Stimulation of Chemical Reactions (*Invited*), R. Deslattes, *National Bureau of Standards, Gaithersburg, Md.*

(30 min)

No summary.

5.5 Laser Isotope Separation (*Invited*), B. B. Snavely, *Lawrence Livermore Laboratory, Livermore, Calif. 94550*

(30 min)

No summary.

5.6 Application of Photodeflection to Spectroscopy,[1] A. F. Bernhardt,[2] D. E. Duerre, J. R. Simpson, and L. L. Wood, *Lawrence Livermore Laboratory, Livermore, Calif. 94550*

(15 min)

The laser deflection of a single isotopic component of an atomic beam has recently been demonstrated. The technique relies on the selective absorption of laser beam photons by one isotopic component of an atomic beam to transfer momentum from the laser beam to that component. In a well-collimated atomic beam, the momentum acquired by many absorption and spontaneous re-emission events per atom will be sufficient to deflect the isotopic component out of the original beam.

This physical separation permits mass analysis of the deflected beam and highly reliable mass assignment of various isotopic hyperfine components. In addition, peaks from different isotopic components which cannot be relatively resolved optically, can be unequivocally resolved from the associated mass spectrometer data. A plot of mass peak height as a function of laser frequency gives a separate absorption curve for each mass number. The isotopic hyperfine structure of the barium 5536 Å resonance was investigated in this manner. Frequency shifts for all peaks of isotopes 134 through 137 were measured relative to 138 with $\leqslant$8 MHz error. The natural linewidth of the transition is 20 MHz. The absorption peaks of ^{134}Ba, ^{136}Ba and ^{135}BaF = 5/2, which could not be resolved optically, were resolved from the mass spectromer data. This is the first experimental resolution of these peaks.

The accuracy of the photodeflection method of spectroscopy is limited by reading error of the reference peak and the peaks plotted from mass spectrometer data. In the limit of a spectrum analyzer of great finesse and negligible laser linewidth, this method has an accuracy of about one tenth the natural linewidth of the transition. Since the natural linewidth of 5535 Å Ba resonance is $\sim$20 MHz, it would be possible to achieve an accuracy of about $\pm$2 MHz in the determination of the hyperfine structure of this resonance line.

The separation efficiency in the barium experiment has been measured. A simple expression for this efficiency has also been derived. The most important parameter in this expression is the branching ratio into the metastable 6s5d $^1D_2$ state from the upper 6s6p $^1P_1$ level of the 5536 Å resonance. The deflection process terminates for a given atom when it decays into the $^1D_2$ level rather than returning to the ground state. The previously accepted value for this ratio is 1/24. This would imply a separation efficiency in our experiment of less than 10^{-4}. Instead, we measured an efficiency of more than 70%. Our result implies that the accepted branching ratio of 1/24 is high by just over a factor of 30.

[1] Work performed under the auspices of the U. S. Atomic Energy Commission.

[2] Also Fannie & John Hertz Foundation Fellow at the Dept. of Applied Science, University of California, Davis-California.

5.7 Experimentally Measured Photoionization Cross Sections and Excited State Lifetimes in Uranium Vapor,[1] R. W. Solarz, *Lawrence Livermore Laboratory, Livermore, Calif. 94550*

(15 min)

The chemistry and spectroscopy of uranium are especially complicated and a complete knowledge of the behavior of this important element is required in order to assess the promise of various schemes for an isotope separation process. Some of the parameters needed for assessing the varied approaches are, for example, hyperfine splittings, lifetimes, bound state absorption cross sections, and relative photoionization cross sections from laser populated excited states. Until now most of the available spectroscopic information has been obtained using classical techniques such as high resolution absorption spectroscopy. Attempts to analyze the resulting spectra have been partially successful; nonetheless much of the data has defied analysis making it clear that alternate experimental approaches are required. While there is currently an excellent line list available for the U I and U II systems, many levels have not been assigned. In addition little information exists concerning hyperfine structure and no data exists on lifetimes, ionization cross sections, and high lying levels of the neutral and ionized species. Furthermore there are several experimental problems unique to the uranium system which require attention in any experimental set-up. This paper will present recent laser spectroscopic experiments aimed at measuring lifetimes and photoionization cross sections in uranium vapor. Experiments to map out high lying odd parity levels in uranium will also be presented.

It is well known that most isotope separation schemes, whether employing physical or chemical extraction processes, require a relatively long-lived laser populated level in order to function at peak efficiency. In a search for such long-lived states we have begun a systematic effort to map the lifetimes of uranium levels in the visible region of the excitation spectrum. A uranium oven operated at about 2000°C provides a cloud of primarily $^5L_6^\circ$ ground state and $^5K_5^\circ$, 620 cm^{-1} populated vapor. A Molectron commercial N_2 pumped dye laser is used to bring either population to a predetermined excited state. The resulting fluorescence decay is monitored through a half meter monochromator-phototube-boxcar arrangement. Advantages of this method over alternate techniques will be discussed and the experimental results presented.

Also well known is that a primary difficulty in a two step photoionization process is that the cross sections for ionization are typically quite small resulting in the requirement of a large laser for the second state of the separation process. In order to minimize this requirement an experiment to determine relative photoionization cross sections in uranium vapor has been carried out. In this experiment a high temperature uranium oven is again utilized. The resulting

[1] This work was performed under the auspices of the U. S. Atomic Energy Commission.

uranium beam is brought to a preselected excited state by a CW dye laser and simultaneously struck by a 3 Å bandwidth UV source which is swept in wavelength. Ions are counted as a function of UV intensity and wavelength with the result that relative photoionization cross sections from laser populated levels are obtained.

Finally, brief mention will be made of a two photon experiment which is designed to uncover and assign high lying odd parity levels in uranium vapor. The experiment is one which takes advantage of the black body radiation which is normally a hindrance in optical spectroscopy. In this experiment a chopped CW laser beam excites the vapor to a preselected even parity level. The black body radiation is monitored through a slow monochromator phase-sensitive detection scheme. Detected modulations of the black body radiation are interpreted as absorption of laser populated levels into high lying odd parity states. Reasons for the difficulty in assigning such levels via classical techniques will be outlined and the importance of such assignments will be discussed.

The impact of the above measurements on various isotope separation proposals will be outlined.

5.8 Selective Isotope Excitation of CuI,[1] C-Y. R. Wu and D. A. Dows, *Department of Chemistry, University of Southern California, Los Angeles, Calif. 90007*

(15 min)

Resonance fluorescence (RF) occurs when a molecule absorbs a photon and subsequently emits a photon from the same excited state reached in absorption, i.e. before energy transfer to other excited states can take place. The phenomenon is normally observed only for gases at pressures low enough so that collisions do not occur during the fluorescence lifetime. Analysis of the RF can yield information about the excited and ground states of the molecule.

We have carried out studies of the resonance fluorescence of copper iodide (CuI) vapor, exciting the RF with Argon ion laser radiation at 5145, 5017, 4880 and 4579 Å. The laser was operated single mode in order to obtain narrow lines which would excite only single upper state levels. RF was observed using a Spex double monochromator. Ground state parameters obtained from the analysis of the observed spectra are in agreement with existing literature data. The rotational constant in the excited state of the A-bands, which has not been previously obtained, was found from combination of data from several different excitations.

By adjusting the intracavity etalon to select different modes within the gain curve of the 5145 Å line, three distinct patterns of fluorescence, one much stronger than the other two, can be seen. Fig. 1(a) shows the excitation spectrum for fluorescence at 19176 cm^{-1} versus modes of the 5145 Å line. Fig. 1(b) is the fluorescence spectrum of the first Stokes bands taken with multi-mode excitation. The doublets *A-A* and *B-B*, and the remaining singlet, are obtained when single mode excitation at the corresponding points *A*, *B* and *C* in Fig. 1(a) is used. In Fig. 1(b) one may notice that the sharp RF lines are superimposed on a broader background spectrum, which we call the normal fluorescence (NF).

The sample consists of solid CuI with a small amount of excess Cu metal (to suppress I_2, a strongly fluorescent molecule under Argon laser excitation), in a quartz cell. When the sample temperature is below about 300°C all the fluorescence is NF, i.e. a banded spectrum similar to the absorption spectrum in general appearance is seen. As the temperature is increased the sharp RF lines begin to show up superimposed on the NF. The intensity of the sharp lines increases more rapidly with temperature than does the NF. This may be understood if the degree of trimer-monomer dissociation increases as the temperature rises. In the temperature range studied (about 300 550°C) the dominant species is the trimer, and the total pressure is below 0.1 Torr. We assume that absorption of light by the trimer results in monomer emission from a large number of excited levels.

From the ground state rotational and vibrational constants and the RF spectra excited by the 5145 Å Argon line, the sequences of doublets corresponding to *A-A* and *B-B* in Fig. 1(a) are assigned to the R(70) and P(44) rotational line absorptions in the 0 ← 1 A-band of $Cu^{65}I$. The singlets corresponding to absorption of the mode at *C* arise from excitation in the 0 ← 1 A-band of $Cu^{63}I$. The rotational constant of the A-band excited state is found to be 0.0676 cm^{-1} (compare the ground-state value of 010735 cm^{-1}).

The assignments and isotopic species being excited by other Argon laser lines are summarized in Table I. As shown in this table, one may preferentially excite a particular isotopic species of CuI to an excited state from which chemical reaction, sequential two-photon dissociation or resonance-pressure deflection could possibly be used to conduct a practical isotope separation of Cu^{63} and Cu^{65}.

TABLE I

Line	Assignment	System	Isotope
5145	0 ← 1 P(44)	*A*	65
	0 ← 1 R(70)	*A*	65
	0 ← 1	*A*	63
5017	3 ← 2 J = 127	*A*	65
4880	2 ← 7 J = 75	*C*	63
	4 ← 0	*A*	63

[1] Supported by the National Science Foundation.

Fig. 1. (a) Excitation spectrum of 19176 cm^{-1} fluorescence of CuI as a function of longitudinal mode of laser operation in the 5145 Å line. Mode separation in 143 MHz. (b) Fluorescence in the first Stokes band of CuI excited by multimode 5145 Å radiation.

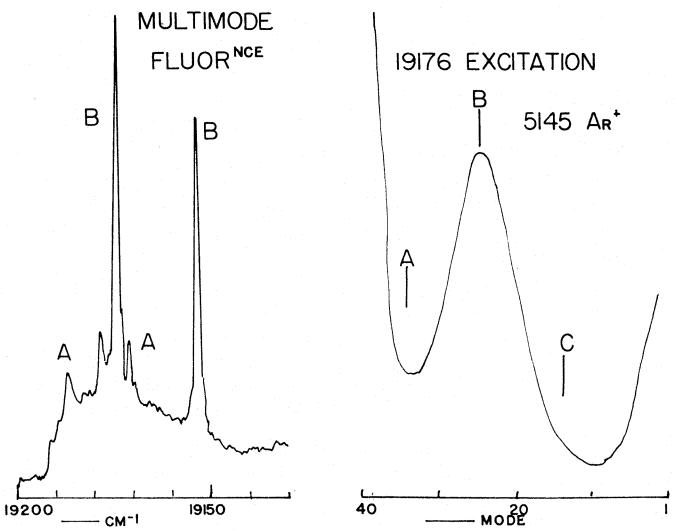

5.9 Isotope Selective Chemical Reactions of BC_{13} Molecule in a Strong Infrared Laser Field, R. V. Ambartzumyan, V. S. Letokhov, E. A. Rialov, and V. V. Chekalin, *USSR*

(15 min)

No summary.

Special Session 1:00 PM

5.10 The Relevance of Lasers in the Energy Shortage *(Invited)*, E. Teller, *Lawrence Livermore Laboratory, Livermore, Calif. 94550*

(30 min)

(Received late; see page 83)

Session 6

Wednesday, May 28, 1975 1:30-5:00 P.M.

General Applications I

Chairman: M. I. Cohen, *Western Electric, Princeton, N. J. 08540*

6.1 Automatic Laser Inspection/Laser Repair System for Masks, D. L. Fehrs, D. F. Munro and J. D. Cuthbert, *Bell Telephone Laboratories, Inc., Allentown, Pa. 18103*, and G. S. Yanochko, *Western Electric Co., Allentown, Pa. 18103*

(15 min)

The high degree of perfection required of chrome masks used in the manufacture of hybrid integrated circuits (HIC's) can be achieved only when thorough inspection and suitable repair procedures are made an integral part of the mask fabrication process.

Chrome masks for HIC's have patterned areas of up to $\sim 3\frac{1}{2}$ in $\times$ $4\frac{1}{4}$ in and pattern options include a large number of *regular* geometric shapes (lines, circles, squares, etc.) occurring at an unlimited number of orientations. Common defects consist of extraneous chrome spots, pinholes, and other defects which are in general irregular in shape. Comparative techniques would in principle seem to provide the simplest way to inspect such patterns. Our studies have shown that such techniques are indeed feasible; however, they are unattractive because of the complex procedures required to align one pattern with respect to the other with sufficient accuracy. Furthermore, comparative methods are excluded when one-of-a-kind masks are made.

For inspection and repair of chrome masks for HIC's we have taken the *noncomparative* approach shown in Fig. 1. No critical mask alignment is required since the mask is scanned using a *single* focussed laser spot. At any given instant the light transmitted and diffracted from a given point on the mask is collected, immobilized by a descan mirror, and then directed into the optical processing head. The processing head divides the beam into segments to allow a determination of the radial and angular characteristics of the diffraction patterns. If the laser spot size is arranged to be smaller than the minimum feature size on the pattern then the "regular" nature of valid features results in diffraction patterns with a limited set of radial and angular characteristics. With few exceptions pattern defects result in anomalous diffraction patterns having radial and angular characteristics which fall outside the set unique to valid features.

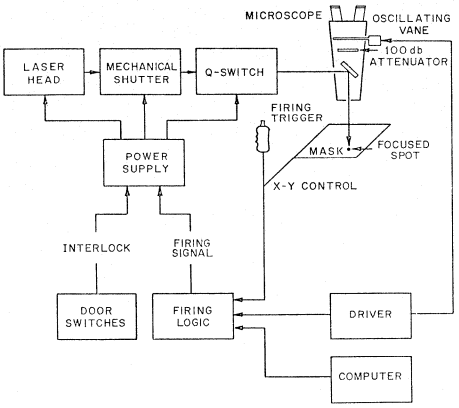

Fig. 2.

The position of both the scanned laser spot and the translation table are at all times encoded so that, once a defect is detected, its position can be stored in a minicomputer. After the entire mask has been scanned the plate is transferred to a motorized *x-y* stage which, under the control of the minicomputer, moves defect locations into the field of view of a microscope/laser machining system shown in Fig. 2. For removal of extraneous chrome spots, the operator centers the defect on the crosshairs of the microscope and then fires the machining laser. Pinholes are touched up with epoxy.

Compared with the old procedure of visual inspection and manual repair of chrome masks for HIC'S, the newly automated procedure is superior in terms of both speed and reliability.

6.2 Correction of Mask Defects by Laser Beam, F. Lee and J. Mitchell, *RCA, Somerville, N. J. 08876*

(15 min)

Microprocessors and other high density large scale integrated circuits now are made on silicon substrates measuring over 200 mils square. The standard $2\frac{1}{4}$ in wafer used in the industry can contain less than 50 of these devices. Masks are used for photolithographic processing of the wafers. Masks with 50 to 100 defects were acceptable for use with small area devices where each wafer could contain 1000 to 2000 pieces. Such masks would cause very low yield on large scale integrated circuits.

In order to improve masks, one must first define the defects. These are of three types, glass plate flaws, excess material in the information part of the mask such as black spots or overrun, and voids or breaks in this material. Perfect glass plates are obtainable. Voids cannot easily be filled in. Excess material, however, can be removed by laser beam. This excess material is the cause of perhaps forty percent of the defects. With perfect glass plates and use of laser beams to eliminate excess material, the masks may be made at least twice as good as present masks. While this improvement might not double the yield, it would certainly improve it.

With the end in mind of producing nearly perfect masks, a xenon laser was used to vaporize thin films of chrome, iron oxide, and emulsion. The laser is a pulsed xenon laser with a 0.5 microsecond pulse at 150 microjoules. The repetition rate is one to thirty pulses per second. Spot size is adjustable from one to twenty microns, and the optical system allows convenient identification of the defects and alignment of the beam.

Use of the laser for soft emulsions necessitates adjusting simultaneously the spot size and the attenuation of the power supply, to reduce spalling of the glass underneath.

The use of the laser for improving masks used for the RCA microprocessor is shown in a series of photomicrographs. These pictures show a mask defect and the mask after correction by laser beam. The improvement in yield from one set of wafers using the corrected masks over a second set of wafers using the uncorrected masks is given.

6.3 A Precision, High Speed Galvanometer Deflection System, D. P. Jablonowski and J. Raamot, *Western Electric Co., Engineering Research Center, Princeton, N. J. 08540*

(15 min)

An *X-Y* galvanometer deflection system capable of high precision in a random access mode of operation is described in this report. Beam positional information in digitized form is obtained by employing a Ronchi grating with a sophisticated optical detection scheme. This information is used in a control interface to locate the beam to the required precision. The system is characterized by high accuracy at maximum speed and is designed for operation in a variable environment, with particular attention placed on thermal insensitivity.

The present system configuration provides a 100 mm $\times$ 100 mm field size with a scan lens which produces a 25 μ spot size in its back focal plane, resulting in a 4000 $\times$ 4000 spot array. Address structure is located on 1.25 μ centers, implying an 80,000 $\times$ 80,000 address. The sys-

Fig. 1.

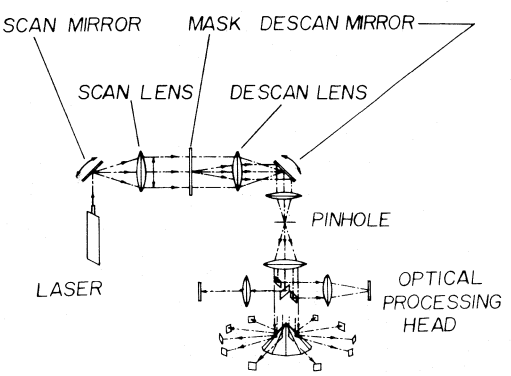

tem is capable of positioning the center of the 25 μ spot to any field address with a precision of ± 5 μ (1 part in 20,000). It is also configured to operate in a scan mode between any two field points while maintaining the same ± 5 μ precision. Scan rate is 50 cm/sec, a speed limited by the present laser and, to a lesser degree, the control interface.

The optical system consists of the basic beam deflection components – laser, X and Y galvanometers, and scan lens – plus the required grating for position monitoring. Beam position detection is accomplished by combining a low power CW (detection) beam of a different wavelength with the primary (recording) beam. By superimposing the two beams before detection, both will be focused to the same field position. A dichroic beam splitter placed beyond the scan lens will send the primary beam to a recording or machining plane, and the low power CW beam to the grating plane. Detectors record the modulated waveforms that result as the beam moves across the grating surface. To obtain directional information, two signals (a sine and cosine) are obtained for each axis. Fine resolution is obtained by dividing the waveform into 16 segments. Our waveform, corresponding to 40 μ, provides a final detection resolution capability of 2.5 μ.

A unique interference optical scheme is employed for detection. The low power beam is shaped by a special aperture prior to its combination with the primary beam. By so doing, the grating is used as a modulator of light amplitude, rather than light intensity. Diffraction orders produced by the grating interfere at the detectors, resulting in an intensity modulation that is an exact cosine. By controlling the spatial phase distribution of the beam, a sine waveform is also obtained. The use of circularly polarized light with linear polarizers at the detectors provides a constant 90° phase relationship over the full field. Because light amplitude modulation is employed, the period of the output signal is halved. thereby providing twice the resolution. In addition, detection with the interference method provides excellent phase stability, and is insensitive to dust or defects on the grating surface.

Control of the beam position is accomplished by sending the positional information to a control interface. A PDP-15 computer provides input data. The control interface is used primarily to *predict* the beam position when shaped driving waveforms are applied to the galvanometers. If the prediction is correct, the beam is accurately placed at the desired location. If the prediction is incorrect, the positional information is used to make a second prediction; this process will continue until the beam position is correct within the specified tolerances. By employing this philosophy instead of the standard servo control, high accuracy has been achieved without materially sacrificing system speed.

Since all positional information is obtained from the grating, absolute positional accuracy is directly related to grating accuracy. Precision rulings, therefore, are used in the system. Their stability results in excellent accuracies for a wide variety of environmental variations, including temperature.

This precision galvanometer deflection system has been used for generating thin film photomasks in a manner that has been previously described.[1] A high power Q-switched YAG laser is deflected by the galvanometers to selectively machine a metallic thin film from a glass substrate. The result is a one-step process for generating the mask, thereby eliminating photolithography and its inherent disadvantages. The use of the system in this particular application has verified its operation as a precision, high speed galvanometer deflection system.

[1] J. Raamot and V. J. Zaleckas, "Laser pattern generation using X-Y beam deflection," *App. Opt.*, vol. 13, p. 1179, 1974.

6.4 Distance and Thickness Measurement by Laser Beams (*Invited*), E. Klement and V. Bodlaj, *Siemens Co., Munchen, Germany.*
(30 min)

No summary.

6.5 Laser Interferometric Check-out of Granite Surface Plates, H. J. Rabal,[1] J. J. Lunazzi, and M. Garavaglia, *Departamento de Física, Universidad Nacional de La Plata, La Plata, Argentina*
(15 min)

This communication reports on the successful results obtained with the application of a grazing incidence triangular interferometer to check the quality of a granite surface plate for metrological inspections. The interferometer can be used when the surface is completely free and in such a case the observed fringes reveal details located between the successive points adjusted by the autocollimation method. The most important feature is that the interferometer can be used when the granite surface is occupied with metrological inspection pieces. In this case, it is possible to measure the deformation of the granite plate due to the weight of those pieces and subsequently to apply the appropriate correction to the observed figures. Experiments performed on a Johansson laboratory grade AA black diabase plate show that its surface reflectivity depends upon the incidence angle and polarization plane of the impinging light. A maximum reflectivity of about 20% was observed when the incidence angle ranged from 0° to 26.5°. Such a maximum was achieved with the polarization plane parallel to the granite surface. Optical flats or the Twyman-Green interferometer cannot be used in the surface inspection because these instruments work at normal incidence. Optical flats present another difficulty: the tremendously large difference in their reflectivity compared with that of the

[1] Member of the Laboratorio de Ensayos de Materiales e Investigaciones Tecnológicas de la Provincia de Buenos Aires, Argentina.

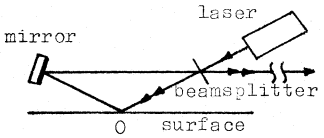

Fig. 1.

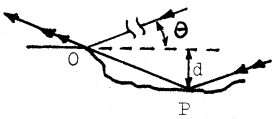

Fig. 2.

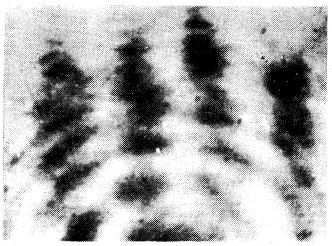

(a)

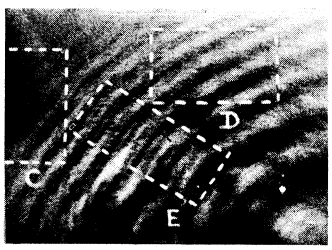

(b)

Fig. 3.

diabase. The grazing incidence triangular interferometer works in the following way: The laser beam is divided into two rays by using a beamsplitter, the beam passing through it is directed to the granite surface making an angle of less than 20° with it, the reflection of the granite surface is collected by a high-quality first-surface plane mirror and directed to the beamsplitter to combine with the reference beam. If the optical path difference is less than the coherent length of the laser light, interference fringes are observed directly with the naked eye, projected onto a screen, or photographed. Fig. 1 shows a line drawing of the experimental installation. Fig. 2 shows the behavior of a parallel laser beam in the vicinity of a depression on the granite surface.

The geometrical analysis of this situation results in the following expressions for the optical path difference or the phase difference: $\Delta x = d \sin \theta$, or $\Delta \Psi = 2\pi d \sin \theta$, respectively. The factor $\sin \theta$ acts like a damping term reducing the sensitivity of the interferometer and consequently permitting the observation of simple interferograms of the granite surface whose microstructure is several times larger than the wavelength used. Fig. 3 reproduces interferograms obtained with a 2 mW He-Ne laser and

photographed with a 35-mm camera using panchromatic film. Fig. 3(a) shows fringes produced by the reflection on a stainless steel plane block gauge located on the granite surface, while Fig. 3(b) shows fringes produced by the granite surface itself. It is very easy to separate regions *C*, *D* and *E* which correspond to a plane, to a convex or concave surface and to a valley surrounded by borders or its specular image, respectively. To decide about the sign of the surface the beamsplitter must be moved to observe the corresponding behavior of the fringes. When the granite surface plate was loaded with 500 N at an extremity a fringe shift of two fringes was clearly observed at 80 cm from that point. Such a fringe shift corresponds to a deformation of about 4 μm.

6.6 Paper withdrawn

6.7 Laser Generated R. C. Networks, M. A. Saifi, *Western Electric Co., Engineering Research Center, Princeton, N. J.,* and O. T. Masopust, *Western Electric Co., Chicago, Ill.*
(15 min)

An important application of series resistive-capacitive (R.C.) networks is that of providing protection for electrical contacts during closure. These networks are normally made with discrete resistors and capacitors. The high voltage rating (typically 250 V) of these capacitors requires use of either polyester film-metal foil sandwich construction or metallized polyester films. This paper describes a new technique for generating integrated series R.C. networks by laser machining nonconductive paths in metallized polyester films.

The laser generated networks have only $\frac{1}{9}$ the volume of the comparable discrete component networks. To determine their suitability for long life applications, several networks were subjected to one billion pulses of 250 V under actual operating conditions but at an accelerated rate. None of the networks showed any degradation in either physical or electrical characteristics.

A typical laser machined pattern for a series R.C. network is shown in Fig. 1. Machining is done with a *Q*-switched YAG laser (1.06 μm wavelength) during the capacitor winding operation. The two capacitor plates consist of 6 μm thick polyester films metallized with .04 μm thick zinc coating. The low frequency resistance value of this network largely depends upon the length and width of the segment between the two laser machined lines. Since the resistance is generated in a capacitively coupled region of the plates, its electrical characteristics are essentially that of a distributed R.C. network.

The network reliability under operating conditions is largely dependent upon the electrical isolation provided by the laser machined line. Good adherence of the metal film at the edges of the machined line is required, with no loose

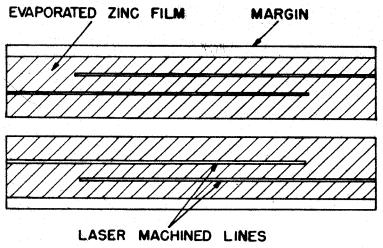

Fig. 1. A resistance pattern produced by machining metallized mylar.

metal particles. This entails careful control of the laser pulse intensity and spot overlap. A further restriction on the laser machining parameters is imposed by the fact that the 6 μm thick polyester film (the dielectric body of the network) should not be thermally damaged due to evaporating metal film.

An important laser parameter is the machining threshold intensity. This was determined by studying the machined spot structure as a function of radiation intensity. Additional information on the threshold intensity was obtained by monitoring the beam transmitted through the opaque metal film while machining with a single *Q*-switched pulse. The intensity at which the transmission occurs near the end of the pulse is defined as the threshold intensity. For an .04 μm thick zinc on the polyester film and for 70 ns long laser pulse the experimentally determined threshold intensity is 0.45×10^6 W/cm^2. This compares well with the 0.35×10^6 W/cm^2 threshold intensity determined from the machining model discussed by Maydan.[1] Considering the simplifying assumptions of the model and the experimental errors, the agreement is good.

It is shown that machining with intensities much above the threshold value is desirable. This reduces the width of the molten zone and also maintains a practically constant line width ($\pm 2\%$) for the nominal $\pm 5\%$ pulse to pulse stability of the commercially available lasers.

Other aspects of this process, such as the system schematic, and in particular the characteristics of various integrated R.C. networks generated by this technique will be discussed.

[1] D. Maydan, *Bell Sys. Tech. J.*, vol. 50, p. 1761, 1971.

6.8 Applications of Lasers to Integrated Circuit Fabrication (*Invited*), B. A. Unger, *Bell Laboratories, Holmdel, N. J.*
(30 min)

No summary.

6.9 Lasers in Supermarket Point of Sale Systems (*Invited*), L. Dickson and R. L. Soderstrom, *IBM Corp., Rochester, Minn.*
(30 min)

In April of 1973, the Supermarket Industry adopted the Universal Product Code (UPC) and associated bar code symbol. This symbol will ultimately appear on more than 90% of all items sold in supermarkets, and is a major factor in the development of more efficient supermarkets. The UPC symbol, designed to be read by an optical scanner at the checkout counter, contains manufacturer, item, and size information. When the label is scanned, the decoded information is transmitted to an in-store computer which retrieves, from its memory, the price of the item. This information is rapidly transmitted back to the checkout counter where item description and price are produced simultaneously on the display and the customer receipt. All of this, of course, occurs at millisecond rates.

The heart of such a system is an accurate, reliable optical scanner. However, selection of a linear bar code and the establishment of stringent scanner performance specifications by the Supermarket Industry placed heavy burdens on scanner development programs. One of the early labels proposed for the UPC symbol was the circularly symmetric bull's-eye label. Designing a scanner for this label is a much easier task since it simply requires a single linear scan. But the industry committee rejected this symbol in favor of the linear bar code, mainly because the latter can be free of objectionable ink smear, when printed in the proper orientation, in an on-the-fly printing process. The bull's-eye label will always have smear problems regardless of pattern orientation during printing.

After adopting the symbol, the Supermarket Industry established performance specifications for label-reading scanners. Among the specifications were the following requirements. The scanner must be able to read labels: (1) which may vary in size from 0.8 × nominal to 2.0 × nominal; (2) crossing the scan window at a maximum velocity of 100 inches per second; (3) in any orientation in the scan window plane; (4) under normal store lighting conditions, (5) up to one inch above the scan window. These requirements can only be met by a laser scanner. Even then, developing a reliable, accurate scanner is no mean task.

The UPC symbol is actually two separate half-symbols which are independently read and combined in the terminal. Each half-symbol is oversquare, that is, the half-symbol dimension parallel to the bars is greater than the dimension perpendicular to the bars. This allows the half-symbol to be read by a minimum of two orthogonal scan lines regardless of symbol orientation in the plane of the scan window. The amount of oversquare combined with the 100 inches per second maximum item velocity determines the pattern repetition rate which in turn establishes the video rate at the detector.

Minimum optical requirements of the scanner call for a focused spot size of 0.2 mm to 0.25 mm and a depth of field of at least 25 mm. Use of a laser allows rejection of ambient light via the use of a narrow band filter on the detector. Specular reflection can be minimized by proper geometrical considerations or totally eliminated by using a polarized laser. Finally, typical scan repetition rates result in detector video rates of several MHz for the smallest label.

A variety of scanner systems have been developed by a number of manufacturers to read the UPC symbol. Scan patterns include

(1) single, large X, (2) multiple X's, (3) stitch-bar, (4) sinusoidal and (5) Lissajous. Each has its merits.

We will discuss the general problems in the development of a supermarket scanner and our specific solutions to these problems.

Session 7

Thursday, May 29, 1975 8:45 – 11:45 AM

Spectroscopy and UV Lasers

Chairman: R. A. Andrews, *Naval Research Laboratory, Washington, D.C.*

7.1 A Dye Laser Spectrometer for the Analysis of Pulsed Vacuum Arcs,[1] P. J. Hargis, Jr. and M. M. Robertson, *Sandia Laboratories, Albuquerque, N. M. 87115*

(15 min)

The high degree of spectral purity and high peak power available from pulsed tunable dye lasers allows detailed spectroscopic measurements to be made on the plasma formed by a pulsed vacuum arc discharge. The dye laser spectrometer we have developed for analyzing these plasmas is used to obtain three spectroscopic measurements: (1) transmittance of the dye laser radiation through the plasma, (2) the absorption line profile, and (3) the lifetime of laser induced fluorescence radiation. Neutral and ionized atomic number densities and electron number densities are unfolded from these measurements which are all obtained with one pulse from the dye laser.

A schematic diagram of the dye laser spectrometer is shown in Fig. 1. The N_2 pumped dye laser used in the spectrometer is based on the Hansch design. Using the dye α-NPO, the tuning range of the dye laser extends from 387 nm to 415 nm. When tuned to the 399.8 nm TiI resonance line, the dye laser output is a 10 kW peak power, 5 ns duration, 0.025 nm FWHM spectral width pulse of 3 mrad full angle divergence. The transmittance of the dye laser radiation through the plasma is measured from the ratio of the outputs from diodes D1 and D2. Radiation transmitted through the plasma is passed through a Fabry-Perot interferometer with a free spectral range of 0.05 nm. A 500 element image intensified diode array placed in back of the interferometer intercepts the Fabry-Perot ring pattern which is used to measure the spectral distribution of the transmitted radiation. Because of the good resolution of the diode array (5×10^{-4} nm) and broad bandwidth of the dye laser radiation (2.5×10^{-2} nm) in comparison with that of a typical absorption line (2×10^{-3} nm), this technique is used to measure the absorption line profile with one pulse from the dye laser. The time distribution of the laser induced fluorescence radiation is monitored by PMT2. A narrow-band filter (F2) is used to restrict the spectral bandwidth of the radiation detected by this tube. The visible radiation (200 nm to 900 nm) emitted by the plasma is monitored by PMT1. A spectrograph with a 1000 element diode array mounted at the exit slit is used to tune the dye laser radiation to absorption lines of the plasma constituents using a hollow cathode lamp. The arc is mounted on an x, y, z translator so that the spatial distribution of constituents in the plasma can be measured. The measurements reported below were obtained with a spatial resolution of 0.5 mm. When desired, much better spatial resolution can be obtained.

[1] Work supported by the U. S. Atomic Energy Commission.

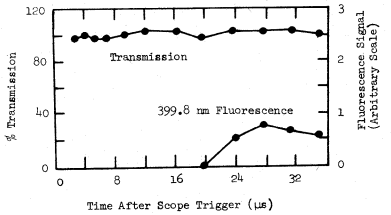

Fig. 2. Experimentally observed transmission and fluorescence signals at 399.8 nm.

An example of the results obtained with this spectrometer is shown in Fig. 2. These measurements were made on the plasma formed by the discharge between a Ti anode and kovar cathode. The dye laser was tuned on and off the 399.8 nm TiI resonance line ($a^3F_4 \rightarrow y^3F_4^0$). The fluorescence signal shows the expected 20 ns decay of the $y^3F_4^0$ level. Fig. 2 is a plot of the time distribution of the peak value of the 399.8 nm fluorescence signal. No signal is seen in the transmitted radiation (ratio of D2 to D1) since its detectivity limit corresponds to a number density of $\sim 10^{11}/cm^3$. These results show that buildup of neutral Ti atoms does not occur until very late in the lifetime of the arc. The early history of the arc is dominated by the presence of ionized Ti atoms.

Fig. 1. Schematic diagram of the dye laser spectrometer.

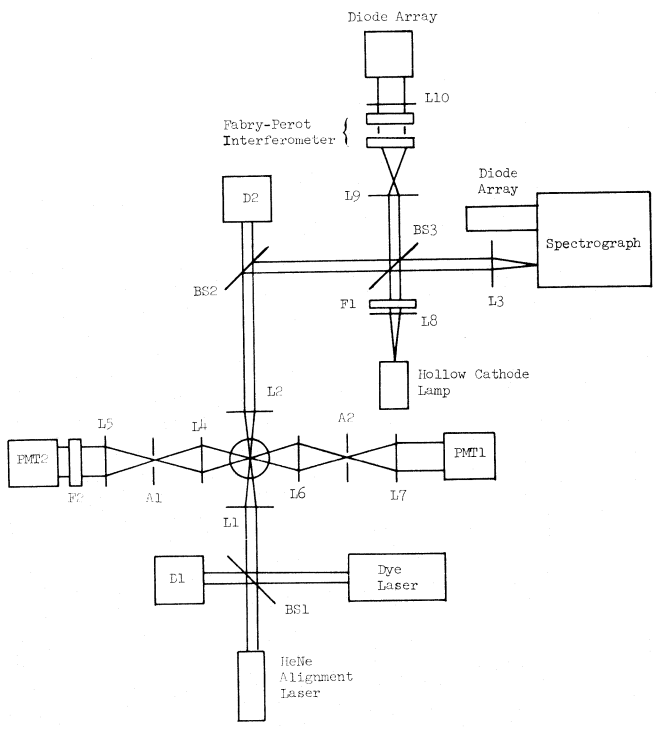

7.2 Collisional Studies of $^{12}CH_3F$ Using Doppler Free Two Photon Absorption Techniques, W. K. Bischel, P. J. Kelly, and C. K. Rhodes, *Lawrence Livermore Laboratory, Livermore, Calif. 94550*

(15 min)

The technique of Doppler broadening reduction in two photon absorption via oppositely directed photons which has been previously demonstrated in atomic vapors[1] is especially interesting in molecular applications. Not only will this method provide new and detailed spectroscopic information about molecules, but it will also reveal additional information about molecular collision processes.

We have therefore extended this technique to a molecule ($^{12}CH_3F$) using two fixed frequency CW CO_2 lasers operating in combination with molecular Stark tuning. In particular we have utilized the near coincidences of the P14 and P30 lines of the 9.4 μm branch with the $R(1, 1)$

[1] F. Biraben, B. Cagnac, and G. Grynberg, *Phys. Rev. Lett.*, vol. 32, p. 643, 1974; M. D. Levenson and N. Bloembergen, *Phys. Rev. Lett.*, vol. 32, p. 645, 1974; J. E. Bjorkholm and P. F. Liao, *Phys. Lett.*, vol. 33, p. 128, 1974.

TABLE I
TRANSITIONS OBSERVED FOR THE CASE $J, K = 1,1 \rightarrow 2,1 \rightarrow 3,1$

Transition Magnetic Quantum Number M_I	M_N	M_F	Polarization Between Laser and Stark Field ν_1	ν_2	Relative Coupling	Resonant Stark Field (V/cm)
−1	−1	−1	∥	∥	100	358
0	1	1	⊥	∥	50	1758
−1	0	0	⊥	∥	20	295
−1	−2	−2	⊥	∥	63	454
0	1	2	⊥	⊥	33	849
−1	0 −2	−1	⊥	⊥	28	358
−1	−2	−3	⊥	⊥	97	622

TABLE II
PRESSURE BROADENING AND PRESSURE SHIFT DATA

Transition Magnetic Quantum Number M_I	M_N	M_F	Perturbing Molecule	Pressure Broadening (MHz/Torr)	Pressure Shift (MHz/Torr)
−1	−1	−1	CH_3F	41.3	2.1
			CF_3I	41.0	0.0
			He	5.0	0.0
−1	−2	−3	CH_3F	40.1	2.1
			He	4.9	0.0

transition of the $0 \rightarrow \nu_3$ band and the $R(2, 1)$ transition of the $\nu_3 \rightarrow 2\nu_3$ band.[2] Shown in Table I are the transitions observed to date for the above described case. The column describing the relative coupling is determined from the magnitude of the direction cosine matrix elements associated with the two photon absorption cross section.

Through the use of phase sensitive detection methods, we were able to accurately determine the broadening and center frequency measurements at various pressures for different perturbers and for different polarizations between the laser and Stark fields. This information is listed in Table II. The pressure broadening mechanisms constitute those processes which transfer angular momentum. These mechanisms are of the energy changing (T_1) type and include molecular reorientation and rotational transitions. The shift of the resonant frequency is determined by the difference in the collisional perturbations on the initial and final states of the transition under investigation. Elaboration on the aforementioned processes are presented and compared with the results of Table II.

[2] S. M. Freund, G. Duxbury, M. Römheld, J. T. Tiedje, and T. Oka, *J. Mol. Spectrosc.*, vol. 52, p. 38, 1974.

7.3 Sub-Picosecond Optical Chronoscopy, D. J. Bradley and W. Sibbett, *Imperial College, London, England*

(20 min)

Streak cameras based on the photocathode extraction electrode principle[1] have permitted the direct linear measurement of ultra-short laser pulse durations with a time resolution as short as ~2 psec.[2] For several ultra-short pulse

[1] D. J. Bradley. U. K. patent 1329977 (1973), U. S. patent 3761614 (1973).

[2] D. J. Bradley and G. H. C. New, *Proc. IEEE*, vol. 62, p. 313, 1974 and references therein.

TABLE I

	Photochron I	Photochron II
Phosphor spatial resolution		
static	8 lp/mm	18 lp/mm
streaked	5 lp/mm	10 lp/mm
Electron-optical magnification	×3.6	×2
Photocathode extraction field	6 kV cm^{-1}	20 kV cm^{-1}

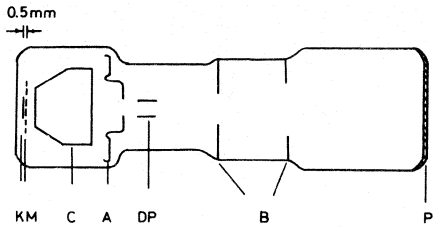

Fig. 1. Electrode configuration of Photochron II streak tube. Photocathode K, Extraction Mesh M, Deflection Plates DP, Phosphor P.

interaction studies, including self-phase modulation and transient Raman scattering, resolution has proved inadequate. In the last year at Imperial College we have further developed the technique of chronoscopy, to what is probably the practical limit of electron-optical technology, to achieve sub-picosecond time-resolution. For some applications of picosecond light pulses, particularly in photo-chemistry and X-ray laser studies, sub-picosecond time-resolution has to be maintained throughout the spectrum of sensitivity of the photocathode. The extraction mesh electric-field strength must be sufficiently greater than that necessary to produce the desired time-resolution with radiation of wavelength close to the photo-cathode cut-off. To permit such a substantial increase in the photocathode extraction electric-field strength we redesigned the electron-optics of the original Photochron tube,[1,2] at the same time improving the spatial resolution to increase the information content and to reduce triggering jitter. The resultant reduction in magnification also increased the recording speed. With this new Photochron II tube, direct sub-picosecond time-resolution was first achieved.[3]

Fig. 1 shows the tube electrode arrangement which is similar to that employed in the Photochron I tube. The mesh-photocathode separation is reduced to 0.5 mm and with an applied mesh-voltage of 1 kV the photocathode field strength is 20 $kVcm^{-1}$. Comparison of the performance characteristics is given in Table I. The reduced magnification produces a speed gain of ×3 while the improved streak spatial resolution increases the information content by ×2, for the same streaking speed, and reduces the jitter by the same factor. The Krytron deflection voltage ramp circuit has also been improved to increase the writing speed to $> 2 \times 10$ cm sec^{-1} and to reduce the jitter to < 50 psec. Photochron II tubes with S1 and S20 cathodes have been constructed[4] to the new design and tested.

In an effort to demonstrate directly the sub-picosecond time-resolution capability of the camera we made many streak records of a mode-locked Rhodamine 6G dye laser. Occasionally in the initial laser intensity fluctuation two equal intensity spikes occur close together. This fluctuation pattern then develops[5] to produce a suitable time-resolution test pulse (Fig. 2). The

[3] P. R. Bird, D. J. Bradley and W. Sibbett, Proc. of XI High Speed Photography Congress, London, 1974.

[4] By Instrument Technology Ltd.

[5] D. J. Bradley, *Opto-Electronics*, vol. 6, p. 25, 1974, and references therein.

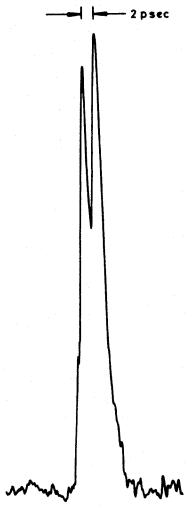

Fig. 2. Microdensitometer trace (linear density scale) of dye laser pulse showing subpicosecond time-resolution.

recorded width of each peak is 1 picosecond and a camera instrumental width of 0.5 psec is unambiguously determined. At selected wavelengths sub-picosecond resolution down to 0.1 picosecond is obtained, depending upon the type of photocathode employed. With the higher light gain the range of usefulness of a camera employing the Photochron II tube is extended to weaker light sources. As a result the art of time measurement of light pulses is again ahead of the techniques of ultra-short pulse generation. Test measurements employing transient Raman generated sub-picosecond pulses will be discussed and a new camera system employing fibre-optic coupling to a channel plate intensifier array will be described. Results with VUV sensitive tubes will also be reported.

7.4 Application of Picosecond Optical Pulses (*Invited*), C. V. Shank and E. P. Ippen, *Bell Laboratories, Holmdel, N. J.*

(30 min)

No summary.

7.5 Optically Pumped Infrared Transfer Lasers[1] (*Invited*), T. F. Deutsch and H. Kildal, *Lincoln Laboratory, Massachusetts Institute of Technology, Lexington, Mass. 02173*

(30 min)

No summary.

[1] This work was supported by the Department of the Air Force and the U. S. Atomic Energy Commission under a subcontract from the Los Alamos Scientific Laboratory.

7.6 Optically Pumped Superfluorescent Na_2 Molecular Laser, M. Henesian, R. L. Herbst, and R. L. Byer, *Stanford University, Stanford, Calif. 94305*

(15 min)

Using a *Q*-switched internally doubled Nd:YAG laser operating at 0.473 μm, we have optically pumped molecular Na_2 and observed superfluorescent laser emission on a series of green and yellow molecular transitions. The observed superfluorescent gain agrees with our calculated gains for the B band based on an upper state lifetime of 64 nsec.[1] Sodium vapor was contained in a 10 cm long heat pipe with helium and argon used as a buffer gas. Na_2 vapor pressures up to 1 torr at buffer gas pressures of up to 50 torr have been used. The threshold pump energy was approximately 500 μJ in a 1.5 cm^{-1} bandwidth which overlapped a large number of absorbing molecular transitions. The high gain and low threshold energy indicate that flashlamp pumping should be possible.

Unlike recently demonstrated molecular vapor phase dye lasers, the Na_2 molecular laser is stable against dissociation. We have also observed laser action on the Na_2 A band at 0.75 μm to 0.85 μm when pumped at 0.659 μm. Laser action on the A band has recently been reported in Japan.[2] Extension of laser operation to the other alkali diatomic molecules gives the possibility of obtaining quasi tunable laser operation over the entire visible to near infrared spectral range.

[1] M. McClintock, W. Demtroder and R. N. Zare, *J. Chem. Phys.*, vol. 51, p. 5509, 1969.

[2] M. Jyumonji, T. Kobayasi and H. Inaba, Spring Meeting of Japanese Society of Applied Physics, April 1974, paper nos. 2a-A-11.

7.7 Behavior of the First and Second Positive Emission in the N_2/SF_6 Laser, S. N. Suchard, R. F. Heidner, III, and D. G. Sutton, *The Aerospace Corp., El Segundo, Calif. 90245*

(15 min)

Recently, several of us reported the observation of a long pulse nitrogen second positive laser.[1] The primary differences between this nitrogen laser and those that have been reported previously is the addition of SF_6 to the laser gas and the duration of the observed laser pulse. In a conventional nitrogen second positive laser, pulse durations on the order of 5-15 nsec have been observed[2]; however, in the N_2/SF_6 laser, pulse durations longer than 75 nsec have been measured.[1] Experimental measurements of the effect of SF_6 on the behavior of both the first and second positive band systems in N_2 will be discussed.

The discharge apparatus utilized for the fluorescence, superfluorescence, and laser measurements of the N_2/SF_6 mixtures has been described previously.[1] It consists of two 1.5 m Lucite pipes fitted with a double helix of 470 ohm resistors. One of the helices forms the anode of a pulsed power supply and the other helix is connected to ground. This configuration results in 502 pin-pair opposed electrodes across a 2-cm gap. For the laser experiments, an optical cavity was formed around the discharge tube by a concave Al coated mirror with a 12 m focal length and a variety of partially transmitting flat output couplers. For the flowtube measurements of the deactivation of specific electronic-vibrational levels of N_2 by SF_6, the apparatus employed was similar to that described by Setser,[3] using a conventional nitrogen first positive laser as a pump source to produce $B^3\Pi_g$ state N_2.

Experimental measurements of the relative output intensity of the N_2/SF_6 laser on the first positive and second positive bands of N_2 as a function of the added SF_6 have provided some insight into the role of the SF_6 in the laser. Fig. 1 displays the relative first and second positive laser outputs as a function of the added SF_6. The first and second positive laser outputs were normalized within themselves and not relative to each other; the second positive emission is approximately 10^2 more intense than the first positive emission. With 50 Torr N_2 in the laser cavity and no SF_6, no laser emission is observed at any discharge voltage below 120 KV, the

[1] S. N. Suchard, L. Galvan and D. G. Sutton, "Quasi-CW laser emission from the second positive band of nitrogen," to be published.

[2] B. Godard, *IEEE J. Quantum. Electron.*, vol. QE-10, pp. 147-153, 1974, and references therein.

[3] J. A. Meyer, D. H. Klosterboer and D. W. Setser, *J. Chem. Phys.*, vol. 55, pp. 2084-91, 1971.

Fig. 1. Relative first and second positive N_2 laser emission as a function of added SF_6. N_2 pressure = 50 Torr, discharge voltage = 60 kv, output coupling = 92%.

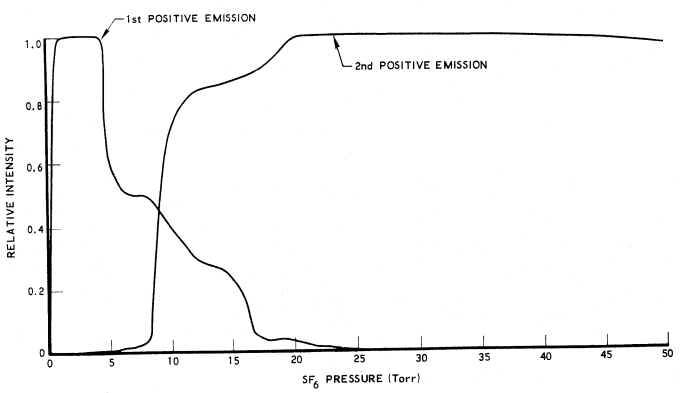

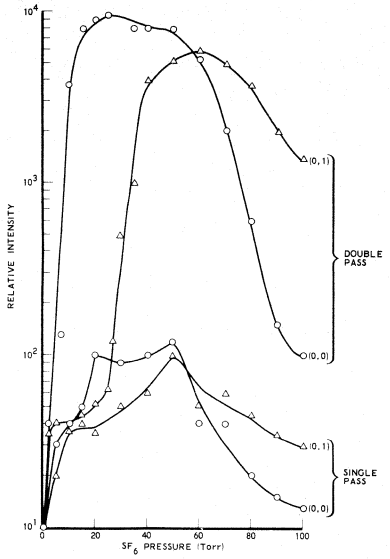

Fig. 2. (0, 0) and (0, 1) bands of the N_2 second positive system under both single and double pass conditions as a function of the added SF_6. N_2 pressure = 50 Torr, discharge voltage = 100 kv.

highest voltage accessable with the apparatus. As SF_6 is added, the mixture very quickly reaches threshold on the first positive ($B^3\Pi_g$-$A^3\Sigma_u^+$) bands. Continued addition of SF_6 quenches the first positive laser emission and the second positive ($C^3\Pi_u$-$B^3\Pi_g$) laser reaches threshold. Addition of more SF_6 has only a small effect upon the second positive laser output until the SF_6 pressure approaches 70 Torr, where a slow falloff of relative intensity is observed.

These changes in the relative laser intensities upon addition of SF_6 can possibly be explained in terms of increased pumping of the upper laser levels and electronic deactivation of the lower laser levels by the SF_6. Addition of SF_6 to a nonelectronegative gas causes the average electron energy in the discharge, to increase, hence increasing the rate of pumping of the upper laser levels. Addition of more SF_6 quenches the first positive laser, even though the rate of pumping of the $B^3\Pi_g$ state should have been increased. This fact, in addition to the temporal history of the N_2/SF_6 laser, indicates the $B^3\Pi_g$ state is being deactivated by the SF_6.

Fig. 2 presents spectrally resolved results of the relative emission of the (0, 0) and (0, 1) bands of the second positive system as a function of SF_6 pressure under both single pass and double pass conditions. Gain is not observed on other second positive bands. It is interesting to note the change-over in intensities of the two bands as the SF_6 is increased. Since both transitions originate from the same upper laser level these results indicate that the rates of electronic and vibrational deactivation of the $B^3\Pi_g$ states are different.

Flowtube experiments are now underway to measure the deactivation of the different vibrational levels of both the $B^3\Pi_g$ and $C^3\Pi_u$ states by SF_6 under non-discharge conditions. The results of these experiments will be used in conjunction with the laser results in order to elucidate the operating mechanisms of the N_2/SF_6 laser.

7.8 Collision-Induced Auroral Line Lasers,

H. T. Powell, J. R. Murray and C. K. Rhodes, *Lawrence Livermore Laboratory, Livermore, Calif. 94550*

(15 min)

Laser oscillation has been recently reported[1] on the green bands of the XeO and KrO excimers correlating with the 5577 Å, $^1S - {}^1D$, auroral line of atomic oxygen. As previously described an electron beam was used to excite a mixture of Xe and Kr at several atmospheres pressure containing a few Torr of oxygen bearing species. Stimulated emission has now been achieved from ArO at 5577 ± 1 Å; time dependent gain measurements have been made of all three excimer systems using a CW dye laser; and the parameters of these lasers have been investigated with respect to their suitability as lasers for fusion.

The radiative lifetime of the $^1S - {}^1D$, electric quadrupole transition of an isolated oxygen atom is 0.8 s. However, the overall transition probability for unresolved green emission is known to exhibit a linear dependence on buffer gas pressure. This collision-induced emission phenomenon is believed caused[2] by the formation of weakly bound excimers of $O(^1S)$ (binding $\leqslant 500$ cm^{-1}) where the proximity of another specie causes the forbidden atomic transition to become a dipole allowed molecular emission, $^1\Sigma^+ - {}^1\Sigma^+$ or $^1\Sigma^+ - {}^1\pi$. The overall radiative lifetime is dictated by the fraction of $O(^1S)$ bound in such excimers and is typically 10-100 μs at the rare gas pressures used.

The molecular emission spectrum depends, of course, on the binding between the additive gas and $O(^1S)$ and $O(^1D)$. In xenon a vibrationally banded emission centered at 5450 Å having a halfwidth of 200 Å is observed while for Kr and Ar the emissions are diffuse, violet degraded bands centered at 5577 ± 1 Å having a 30 Å halfwidth. At the typical operating pressures the rotational lines are merged giving a continuum spectrum.

The intensity and time dependence of collision-induced emission has been studied for O_2-rare gas mixtures excited by a 2 × 10 cm, 1 MeV electron beam with variable currents of 1-50 kA. The fluorescence decays exponentially with a rate depending on both rare gas and O_2 pressure as well as excitation level. This evidence suggests that the quenching in such mixtures is usually dominated by three body processes involving an $O(^1S)$, an $O(^3P)$, and a rare gas atom. In pure Ar, Kr, or Xe, collision-induced emission is believed the primary deactivation channel of $O(^1S)$. Inversion is produced by the rapid deactivation of $O(^1D)$ in the high pressure rare gas.

Single-pass gain measurements have been made using a tunable CW dye laser. During the *E*-beam pulse the medium is highly absorbing throughout the visible ($\alpha_{abs} \geqslant 0.5$ cm^{-1}); only in the afterglow does gain appear within the emission bandwidth ($\alpha_{gain} \leqslant 0.01$ cm^{-1}). The absorption has been tentatively ascribed to ground state molecular ions. Their decay after the current pulse is highly dependent on gas purity and apparently involves subtle ionic processes.

The energy storage in the green has been computed from both fluorescence intensity and gain measurements. A value of ~10 J liter^{-1} with an overall efficiency of ~1% of the *E*-beam deposition is consistent with both measurements for all three rare gases. The excitation mechanism has not been determined, however, the process $0(^3P) + e \rightarrow 0(^1S)$ is not inconsistent with these results.

7.9 Ion Laser Performance and Spectroscopy—New Pulsed and CW Transitions below 3000 Å

J. B. Marling, *Lawrence Livermore Laboratory, Livermore, Calif. 94550*

(15 min)

The performance and spectroscopy of ion lasers has been investigated below 3000 Å. Many new pulsed ion laser transitions were found below 2500 Å, several of which exhibited anomalously high peak power for ion lasers, as indicated in Table I. Additionally, CW operation has been observed below 3000 Å for the first time, principally in third spectrum noble gas transitions.

Investigations of pulsed ion laser performance and spectroscopy was performed with a 7 mm bore, 150 cm arc length tube, with electrical driver specially designed for short duration, high peak current excitation pulses. Third, fourth, and fifth spectrum laser transitions were observed with excitation pulses of 250 ns FWHM and up to 10,000 amp/cm^2. Current saturation of third spectrum transitions was observed near 5000 amp/cm^2. Fourth spectrum transitions in krypton and xenon did not exhibit current saturation. Wavelengths of new and previously known transition were measured to about 0.006 Å, and relative peak powers were measured in order to identify the strong transitions. Results of this investigation are presented in Table I.

CW operation of several ion laser transitions has been observed below 3000 Å for the first time. Data on observed CW transitions, threshold current values and output performance in watts are presented. Principally, the strong

[1] H. T. Powell, J. R. Murray, and C. K. Rhodes, *Appl. Phys. Lett.*, vol. 25, p. 730, 1974.

[2] D. L. Cunningham and K. C. Clark, *J. Chem. Phys.*, vol. 61, p. 1118, 1974 and references therein.

TABLE I
PULSED ION LASER PERFORMANCE AND SPECTROSCOPY IN ULTRAVIOLET

Ion Type	Measured Wavelength in Air, Ångstroms	Peak Power Output Watts
Ne III	2180.922 ± .004	17
Ne V	2265.7 ± 1.	2
Ne IV[a]	2358.033 ± .005	75
Ne IV	2373.231 ± .008	1
Ne III[a]	2473.441 ± .005	140
Ne III[a]	2677.963 ± .008	150
Ne III[a]	2678.735 ± .008	100
Ne III[a]	2866.762 ± .005	5
Ar IV[a]	2624.935 ± .009	8
Ar III[a]	2753.914 ± .008	11
Ar III[a]	2855.413 ± .005	9
Ar IV[a]	2912.928 ± .008	16
Ar IV[a]	2926.272 ± .003	4
Ar III[a]	3002.664 ± .008	42
Kr IV	2191.979 ± .006	600
Kr IV	2254.694 ± .008	80
Kr IV	2338.526 ± .006	8
Kr IV[a]	2664.424 ± .010	21
Kr IV[a]	2741.405 ± .008	27
Kr III[a]	3049.667 ± .012	18
Kr III[a]	3124.395 ± .008	6
Kr III[a]	3239.512 ± .005	14
Xe III	2315.363 ± .006	1400
Xe IV[a]	2691.969 ± .006	5
Xe III[a]	3079.738 ± .012	32
Xe IV[a]	3246.922 ± .005	260
Xe IV[a]	3330.869 ± .015	330
Xe III[a]	3454.248 ± .004	22
XE IV[a]	3645.478 ± .008	3600

[a] *See* P. K. Cheo and H. G. Cooper, *J. Appl. Phys.*, vol. 36, pp. 1862-1865, 1965.

third spectrum noble gas transitions in Table I were observed in CW operation. Data were taken from a 3.5 mm segmented tungsten bore laser at anode currents up to 55 amperes.

7.10 Co-Axial Electron-Beam Pumped VUV Laser Oscillators and Amplifiers, E. G. Arthurs, D. J. Bradley, C. B. Edwards, A. I. Ferguson, D. R. Hull, M. H. R. Hutchinson, C. C. Ling, and M. W. McGeoch, *Imperial College, London, England*

(15 min)

High pressure, quasi-molecular noble gas VUV lasers have many potential applications in photochemistry, plasma diagnostics, and for the generation of XUV lasers either by nonlinear interactions or by direct pumping of appropriate plasma media. In these and other applications, efficient oscillator and amplifier systems are required to produce tunable frequency, low divergence beams in variable duration pulses, covering the nanosecond to picosecond temporal range. For photochemical studies a moderate power (~1 MW) high repetition rate oscillator would be particularly valuable.

Earlier oscillator systems employed transverse pumping with indefinite and variable active media cross-sections and pumping energies of several hundreds of joules were required. To produce an efficient and convenient laser system with low energy pumping (<10 J), yet with megawatt power, we designed and constructed a coaxial diode electron-beam system.[1] Mirror damage limited this laser, employing 10 kTorr Xenon gas, to peak powers of ~1 MW. The 3 nsec 60 π (10 KA, 600 KV) generator has been altered to produce a 5 nsec, 20 J output pumping pulse of 0.5 MeV electrons. The coaxial diode has also been reconstructed so that both ends of the tubular anode are open (Fig. 1) and there is adequate space to insert various mirror-disperser combinations. With the increased gain an output power of 3 MW (10 mJ) is readily obtained with an $AlMgF_2$ mirror and a single plate BaF_2 resonant reflector. The upper power limit is still set by damage to the mirrors and the output window. By inserting a dispersive prism (quartz, BaF_2 or sapphire) the laser spectral bandwidth (<1 nm) is tunable from 170 nm to 175 nm. At present thermal effects[1] limit the repetition rate and a gas flow system has been designed to permit up to 10 pps operation. While the overall efficiency of the oscillator is

[1] D. J. Bradley, D. R. Hull, M. H. R. Hutchinson and M. W. McGeoch, *Opt. Commun.*, vol. 11, p. 335, 1974.

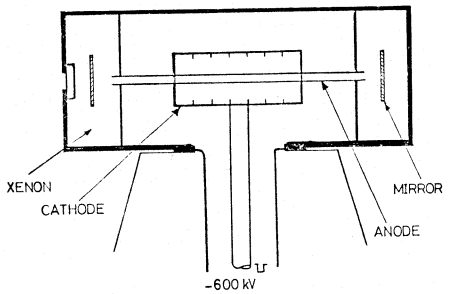

Fig. 1. Details of open-ended coaxial diode construction.

~0.1% the energy storage efficiency is ~10% with gains of ~0.25 cm^{-1}. The high storage capacity and well defined geometry of the coaxial diode system has been scaled to construct an efficient amplifier with a pumping duration of 20 nsec and a single pass gain of ~150, for an incident 1 MW pulse. Amplification of picosecond pulses is also being investigated, the initial pulse being produced by generation of the 4th harmonic of a mode-locked ruby laser using consecutive stages of second harmonic generation and four wave mixing in magnesium vapour.

Investigations with frequency shifted picosecond tunable pulses from dye lasers will be described, together with spectroscopic studies of the atomic and molecular excited states. The latest results obtained with other noble gases and gas mixtures in these systems are also reported.

Session 8

Thursday, May 29, 1975 8:45-11:45 A.M.

Laser Fusion I

Chairman: W. F. Krupke, *Lawrence Livermore Laboratory, Livermore, Calif. 94550*

Organizer: E. Beckner

8.1 Characterization of Optical Nonlinearity in Transparent Dielectrics and Implications for Fusion Laser Design (*Invited*), A. J. Glass, E. J. Goodwin, and J. B. Trenholme, *Lawrence Livermore Laboratory, Livermore, Calif. 94550*

(30 min)

In the design of a large glass laser for fusion experiments, the principal limitation of high power, short pulse operation is imposed by the index nonlinearity of the laser material. This includes not only the laser glass, but also any other transparent solid dielectric material present in the optical path, including Faraday rotators, lenses, beam splitters, and polarizers. Insofar as it is possible to choose materials for use in a fusion laser, those materials with the lowest index nonlinearity are clearly preferred.

The index nonlinearity arises from several

sources. The main contribution is from the direct electronic nonlinearity. In most glasses, this comprises from 75 to 90 percent of the total nonlinear index. Other contributions arise from Raman-active modes of the medium, two-photon resonances, and changing anomalous dispersion. Estimates of the importance of these contributions for laser materials will be given. The compositional dependence of the index nonlinearity for optical materials will be discussed.

In a high power laser, the presence of index nonlinearity gives rise to both self-focusing of the beam as a whole, and beam breakup (small-scale self focusing). Recent experimental results on both beam breakup and whole beam distortion will be reviewed and compared with theoretical analyses. In order to maintain the optical quality of the beam, the integrated nonlinear index along the optical path, given by the parameter

$$B = (2\pi/\lambda n_0)\int n_2 < E^2 > dz \qquad (1)$$

must be kept below a critical value. We will discuss the maximum tolerable value of B, and its dependence on gain staging, spatial filtering, and apodization.

In subsequent papers in this session, various aspects of the problem of beam quality control will be examined in detail.

8.2 Loss of Focusable Energy Due to Small-Scale Nonlinear Effects, E. S. Bliss, G. E. Sommargren, and H. J. Weaver, *Lawrence Livermore Laboratory, Livermore, Calif. 94550*

(15 min)

The nonlinear growth of small-scale intensity and phase irregularities on an intense laser pulse is predicted by linearized instability theory[1] and is well documented experimentally.[2,3] In a large laser system the resulting intensity and phase profiles are complicated and not easily characterized in detail. Qualitatively, linear propagation theory predicts that the far field diffraction pattern of a beam which has experienced this sort of spatial breakup will contain significant energy outside of the diffraction limited spot size of the corresponding unperturbed beam.[4] We report two sets of experiments to determine the effect of small-scale beam breakup on the focusing properties of an initially high quality beam propagating through the simplest possible system, a single unpumped rod of ED-2 laser glass.

In the first experiment a collimated input pulse containing up to 0.75 J in approximately 100 psec (FWHM) with a $1/e$ beam diameter of 1 cm propagates through a 50 cm long sample rod. The near and far field profiles of the pulse are then compared with those of an identical beam which propagated around the rod. Severe beam breakup is evident in the near-field of the transmitted beam, and at the focus of a 1 meter lens some distortion of the transmitted beam can be seen. However, the most dramatic far field effect is that the fraction of input energy which is contained within a 500 μr angular aperture at the focus decreases dramatically with increasing pulse intensity, which is consistent with the angular distribution of light predicted by linearized instability theory for a beam experiencing small-scale beam breakup.

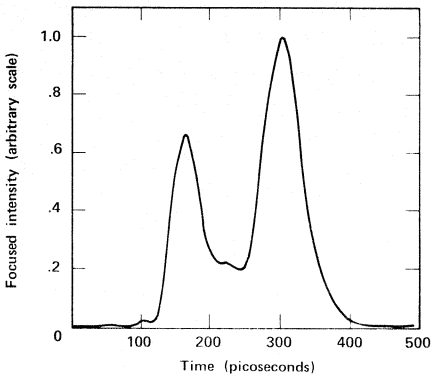

Fig. 1. Temporal distortion in the far field.

The preceding observations are based on temporally and spatially integrated measurements. Since the modulation of the beam profile grows exponentially with intensity and the loss from the focal spot increases nonlinearly with modulation depth, the fraction lost at the temporal and spatial peak of a pulse is expected to be considerably larger than the average over the whole pulse. Severe temporal and spatial distortion could occur as a result of preferentially depleting the high intensity parts of the pulse. Recognition of this fact led us to conduct a second set of experiments with a streak camera added. The streak photographs show obvious distortion of an intense pulse's temporal profile in the focal plane. In fact, above a certain value of intensity, growing losses are seen to overcome further increases in input intensity leading to a minimum in the focused on-axis intensity at the peak of the input pulse as seen in Fig. 1. Detailed measurements of the far field distribution of power as a function of instantaneous input intensity over an angular aperture of up to 3 mr will be presented, and the relative contributions of small-scale breakup and whole-beam self-focusing[5] to the results will be discussed.

The far field effects described here strongly suggest the use of one or more strategically placed spatial filters to remove accumulating beam breakup in a large system. These results also demonstrate the necessity of using target diagnostics capable of determining how much energy actually reached the target and to what extent the spatial and temporal profiles of the focused beam were altered by nonlinear propagation effects in the laser.

[1] V. I. Bespalov and V. I. Talanov, *JETP Lett.*, vol. 3, p. 307, 1966.

[2] A. J. Campillo, S. L. Shapiro, and B. R. Suydam, *Appl. Phys. Lett.*, vol. 23, p. 628, 1973.

[3] E. S. Bliss, D. R. Speck, J. F. Holzrichter, J. H. Erkkila, and A. J. Glass, *Appl. Phys. Lett.*, vol. 25, p. 448, 1974.

[4] J. W. Goodman, *Introduction to Fourier Optics.* New York: McGraw-Hill, 1968, pp. 65-70.

[5] A. J. Campillo, R. A. Fisher, R. C. Hyer, and S. L. Shapiro, *Appl. Phys. Lett.*, vol. 25, p. 408, 1974.

8.3 Focusing Properties of an Aberrated Laser Beam, J. T. Hunt and R. G. Nelson, *Lawrence Livermore Laboratory, Livermore, Calif. 94550*

(15 min)

The focal volume properties of an intense, aberrated light beam are of great importance in laser fusion experiments. Computer simulation studies of the beam for the prototype laser developed at Lawrence Livermore Laboratory indicate the beam as a whole accumulates two distinct types of phase distortion in traversing the laser. One of the phase distortions is classical astigmatism[1] and it is independent of both time and beam intensity, and therefore it can be corrected. This aberration results from the expanding beam passing through a refracting medium whose surface normal is not parallel to the optical axis of the laser. The source of the second type of phase distortion is the intensity dependent portion of the index of refraction of both the pumped medium and the transparent optical components of the laser system through which the beam passes. This aberration depends upon both the temporal and spatial properties of the intensity distribution of the laser beam. However, for the system configurations and intensity profiles considered, the bending of the light rays is small due to the nonlinear index of refraction. The condition of no bending of the light rays over the path of propagation leads to an unchanging intensity profile and a phase distortion whose spatial profile is identical to the intensity profile. The magnitude of the phase distortion, B, is given by

$$B = \frac{2\pi}{\lambda_0}\int \frac{\Delta n}{n} dl \qquad (1)$$

where Δn is the nonlinear index change and λ_0 is the wavelength of the light in a vacuum. The integration path is along the trajectory of the ray at the center of the beam.

A computer code has been developed to investigate the effect that this second type of distortion has on the focused beam properties. The computational algorithm utilizes the self-similar propagation modes which were discovered in laser cavity work.[2] These modes or functions are orthonormal with respect to the scalar product

$$<f, g> = \int_{-\infty}^{\infty}\int_{-\infty} f^* g \, dxdy, \qquad (2)$$

where f^* denotes the complex conjugate of f. These modes are a complete set of functions in the infinite spatial domain (x,y).

The Laguerre-Gaussian modes are the appropriate propagation modes if the laser beam has circular symmetry. These modes are characterized by three parameters; the transverse beam size or waist, $w(z)$, the radius of curvature of the phase front $R(z)$, and the model phase $\phi_m(z)$.[3]

[1] M. Born and E. Wolf, *Principles of Optics.* Oxford: Permagon Press, 1970, p. 214.

[2] A. G. Fox and T. Li, "Resonant modes in a laser interferometer," *Bell System Tech. J.*, vol. 40, p. 453, March 1961.

[3] Maitland and Dunn, *Laser Physics*, North-Holland, 1969, p. 157.

The dependence of these propagation parameters on the propagation coordinate z is given by the expressions

$$w^2(z) = w_0^2[1 + (z/kw_0^2)^2] \quad (3)$$

$$R(z) = z\left[1 + \left(\frac{kw_0^2}{z}\right)\right] \quad (4)$$

$$\phi_m = (2m + 1)\tan^{-1}\left[\frac{kw_0^2}{z}\right] \quad (5)$$

where w_0^2 is the beam size parameter in the focal plane.

Since these modes are a complete set, the transverse wave function or field ψ can be decomposed into these functions; i.e.

$$\psi = \sum_m \gamma_m \Gamma^m \quad (6)$$

where Γ^m is the mth Laguerre-Gaussian mode.

The computational algorithm truncates the infinite series expressed by (6) after the first N terms. The set of N complex coefficients, $\{\gamma_m\}$, and the waist size w are obtained by minimizing the residual F, where

$$F = \int_0^{2\pi}\int_0^{\infty}\left|\psi - \sum \gamma_m \Gamma^m\right|^2 r dr d\phi \quad (7)$$

The radius of curvature of the phase front associated with the Laguerre-Gaussian modes is chosen equal to the radius of curvature of the beam that is to be propagated. After the beam parameters and the set of complex coefficients $\{\gamma_m\}$ are calculated in one transverse plane they are obtained in any other plane using (3)-(5).

This algorithm has been used to calculate the diffracted light rays and the intensity distribution throughout the focal volume of the focused laser beam for various proposed beam intensity distributions. The effect of nonlinear phase distortions of $0 \geqslant B \leqslant 4\pi$ on the focused beam characteristics will be shown.

8.4 A High Energy Spatial Filter for Removal of Small Scale Beam Instabilities in High Power Solid State Lasers,

W. W. Simmons, S. Guch, Jr., F. Rainer, and J. E. Murray, *Lawrence Livermore Laboratory, Livermore, Calif. 94550*

(15 min)

We have fabricated and measured the performance of an evacuated 10 cm aperture spatial filter using the LLL prototype solid state laser CYCLOPS. In this paper we shall discuss the rationale for this filter, its design and construction, and its transmission characteristics for high power laser pulses incident upon it. In conclusion, we shall present data gathered from the entire CYCLOPS chain, illustrating the impact and importance of spatial filtering upon the design and performance of large solid state laser amplifiers.

It is now well known that for pulses with high enough intensity, I, the nonlinear index of refraction of the propagating medium (amplifier laser glass in situations of interest here) will cause small scale beam amplitude and phase irregularities to grow with propagation distance. In one formulation of the instability problem,[1] a small, one dimensional intensity modulation of spatial wave number K, superimposed upon a uniform intensity background, will undergo approximately exponential growth with gain coefficient g given by $g = K(\gamma I - K^2\lambda^2/16\pi^2)^{1/2}$, where I is the background beam intensity in watts/cm^2, γI is the nonlinear part of the index of refraction, and λ is the wavelength.

In the simplest application of this formula to an amplifier, the instability, assumed to initiate at $z = 0$, will grow by an amount $\exp[B(K)]$, where $B(K) = \int g(K)\,dz$. For an amplifier chain such as CYCLOPS, K scales toward smaller wave numbers as z increases, due to beam divergence. Including the effect of divergence in the integration for the CYCLOPS amplifier (the geometry is shown in Fig. 1), we find that a reasonable approximate first representation of the result is a flat spatial spectrum;

$$B(K) = bP, \qquad K < K_{co} = aP^{1/2},$$

where P is the instantaneous power at the spatial filter input, and a and b are constants that depend upon the details of the amplifier staging.

The spatial filter is an element which transmits only those spatial frequency components with $K < K_{sf}$ (including, of course, the main beam). Thus if $K_{sf} < K_{co}$, some of the instabilities are removed from the ongoing beam before they can propagate further. If we assume that $\rho(K)$ is the initial distribution of instabilities, that each ripple grows independently, and that the net fractional power parametrically[2] removed from the main beam is small, then the instantaneous transmission of the spatial filter can be expressed in the approximate form

$$T_p = 1 - \int_{K_{sf}}^{K_{co}} \rho(K)\exp B(K)\,dK.$$

[1] V. I. Bespalov and V. I. Talanov, *JETP Lett.*, vol. 3, p. 307, 1966.

[2] R. Y. Chiao, P. L. Kelley, and E. Garmire, *Phys. Rev. Lett.*, vol. 17, p. 1158, 1966.

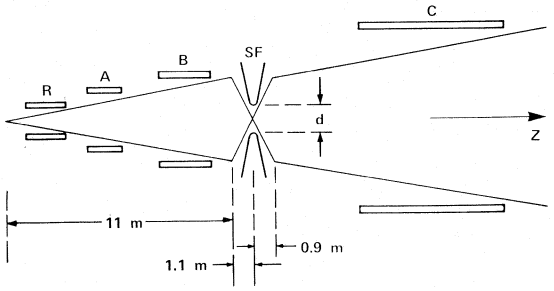

Fig. 1. Foreshortened schematic of CYCLOPS amplifier chain, showing extreme beam rays and pertinent dimensions. Amplifier stages are as follows: R = rods, 24 mm C.A.; A = disk amp, 3.6 cm C.A.; B = disk amp, 8.8 cm C.A.; C = disk amp, 20 cm C.A.; SF = spatial filter. Beam diameter at spatial filter input is 9.5 cm; pinhole diameter $d = K_{SF}/270$.

We have compared measured transmissions, as a function of peak power P_p, for several K_{sf}, with phenomenological transmission functions based upon time integrated versions of T_p. As an example of our results, for $P_p = 170$ GW and $K_{sf} = 10$ cm^{-1}, $T = 0.71$, while for $K_{sf} = 17$ cm^{-1}, $T = 0.93$. The ripple distribution thus appears to maximize (at this power level) for $K \simeq 10$-20 cm^{-1}.[3] This conclusion is confirmed by inspection of time integrated beam profile photographs.

These and other time-resolved results to be presented imply an upper limit for *focusable* peak power from any large amplifier chain, which is dependent primarily upon final amplifier aperture size. This limit can be approached through careful amplifier staging and judicious use of spatial filters throughout the chain.

[3] J. McMahon, 20th Annual IEDM, Washington, D.C., December 1974.

8.5 Enhanced Parasitic Suppression in Large Aperture Disk Lasers Using Liquid Edge Claddings,

S. Guch, Jr., *Lawrence Livermore Laboratory, Livermore, Calif. 94550*

(15 min)

Development of large aperture Nd:glass disk laser systems requires extreme care in suppression of parasitic oscillations. Current designs employ solder glass claddings applied to disk edges to absorb fluorescence, reducing reflection back into the disk and minimizing regenerative amplification. Present claddings have significant limitations, including poor refractive index matching to the base glass, insufficient absorption at 1.06 μm, large bubble and crystalline inclusion content, and lack of reproducibility in application. Calculations of parasitic thresholds indicate that these claddings may limit αD, the product of small signal gain coefficient (α) and disk major axis dimension (D) to a maximum value near 2.5. In the present work, a liquid edge cladding system with excellent index matching to laser glasses and satisfactory fluorescence absorption was successfully developed and employed in a high performance large aperture disk laser amplifier.

A detailed survey of candidate liquids revealed that solutions of zinc iodide with

refractive index of up to 1.63 at 1.06 μm could be prepared, handled, and employed with common laser amplifier materials. While an excellent index match to laser glasses, zinc iodide solutions possess negligible absorption at 1.06 μm. Two procedures were developed to correct this deficiency. Addition of nickel chloride provided a capability for fluorescence absorption of 4.6 cm^{-1} in a solution of 1.58 refractive index at 1.06 μm. Alternatively, coating of the inner surface of the liquid containment channel with chrome black was found to produce equally satisfactory suppression of parasitic oscillations.

Preliminary evaluation of the liquid concept was accomplished using two small disk amplifier test modules. Successful testing in over 600 laser firings led to integration of the design in a high performance, 20 cm clear aperture disk laser amplifier. A zinc iodide solution of 1.58 refractive index at 1.06 μm was employed. Limitations on disk holder size restricted the cladding flow channel sufficiently to require use of an extrinsic chrome black absorber alone for fluorescence absorption. The fluid flow channel was sealed on the disk faces using standard "o" ring seals. Disk holders used were slightly bulkier than for solid edge clad designs, reducing amplifier clear aperture by approximately 5%. The fluid system, configured to allow continuous circulation, suffered no leaks within the laser head in over 120 laser firings.

Amplifier performance was evaluated through small signal gain measurements. These measurements determined the maximum value of αD attainable for comparison with similar results obtained with two different solid edge claddings. The solid clad disks reached an αD value of 2.55, while the liquid system achieved a peak αD of 3.05, an increase of approximately 20%. This represents a significant improvement in energy storage capability and efficiency over that attainable with curent solder glass edge claddings. These results indicate both the superior parasitic suppression and the practicality of liquid edge claddings in large aperture Nd:glass disk laser amplifiers.

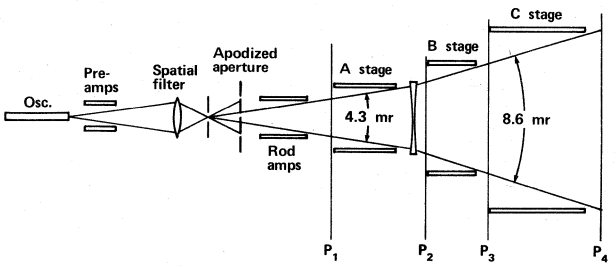

Fig. 1. Schematic of CYCLOPS amplifier, illustrating limiting rays along the beam path and delineating important subsystem blocks. Energy measurements and near-field photography are employed at positions P_1, P_2, P_3 and P_4.

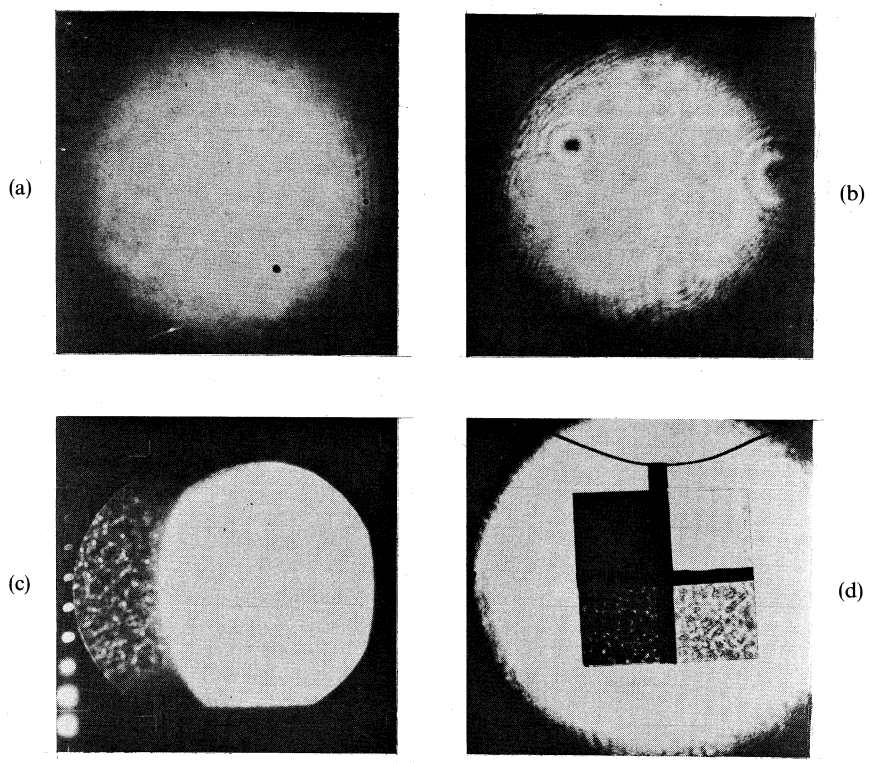

Fig. 2. Typical integrated beam profiles at $P_1(a)$, $P_2(b)$, $P_3(c)$ and $P_4(d)$.

TABLE I
INTERSTAGE ENERGY, PEAK PULSE POWER, AND (APPROXIMATE) PEAK AXIAL INTENSITY FOR SHOT #20, OCTOBER 14, 1974

Station	E	P_p^*	$I^\dagger$
P_1 (A stage input)	1.09 J	5.2 GW	3 GW/cm^2
P_2 (B stage input)	5.48 J	26.0 GW	4 GW/cm^2
P_3 (C stage input)	50.0 J	240.0 GW	6 GW/cm^2
P_4 (output)	274.0 J	1.3 TW	10 GW/cm^2

* Streak camera measured FWHM temporal pulse duration = 210 ps.
† Computed from measured P_p, beam diameter, and energy profile discounting hot spot energy content.

8.6 Terawatt Laser Performance, W. W. Simmons, F. Rainer, R. D. Boyd, C. C. Fetterman, and J. A. Glaze, *Lawrence Livermore Laboratory, Livermore, Calif. 94550*
(15 min)

The LLL solid state laser CYCLOPS was constructed as a single chain prototype unit for advanced multi-arm laser systems intended for laser fusion experiments. It has been operated through its 20 cm clear aperture amplifier stages (C stages), and is presently undergoing performance characterization with a 10 cm aperture spatial filter inserted just prior to the C stages. In this paper we shall present details of CYCLOPS performance to date, including near and far field beam profiles, stage gains, and time-resolved power measurements. Details of CYCLOPS staging and examples of system performance are presented in the following summary.

Staging has been described previously[1] and is summarized in Fig. 1. The oscillator, Nd:glass preamps, spatial filter, apodized aperture, and 2.5 cm clear aperture rod amplifiers deliver a pulse of nominal energy 0.5-1.0 joules contained within a Gaussian temporal envelope of FWHM duration 150-200 ps to the disk amplifiers. The apodized aperture imposes the desired intensity profile (both exp. $-r^5$ and quadratic aperture functions have been employed) and divergence

[1] Lawrence Livermore Laboratory Laser Fusion Semiannual Report, July-December 1973, p. 19.

(4.3 mrad full angle) upon the beam. The three rod amplifiers are protected from self oscillation by Faraday rotators and rooftop multilayer dielectric polarizers following each rod. This combination provides more than 25 dB of isolation per rod against back reflections.[2]

Each amplifier stage (*A*, *B*, and *C*) consists of 12 disks, 2 multilayer polarizers, and one Faraday rotator. Clear apertures are as follows: *A* stage, 3.6 cm; *B* stage, 8.8 cm; *C* stage, 20 cm. The energy storage required is approximately 1.6 MJ (for all disk stages).

At each of the diagnostic stations (P_1, P_2, P_3, and P_4), approximately 5% of the beam is back reflected from both front and back surfaces of the Faraday rotator glass, which is tilted at 5° from the beam line for this purpose. One of these beams is directed into a calorimeter; the other is used for obtaining near or far field beam information photographically. Data from a number of shots has been analyzed and will be discussed during the talk. As a representative example, we present the results of a single shot in Table I. Corresponding near field beam profiles are shown in Fig. 2.

The major problems encountered in CYCLOPS operation to date have been associated with maintenance of disk surface quality in the presence of hard optical pumping from the flashlamps. Small, flashlamp-induced damage sites act as sources for small scale beam breakup, ultimately leading to self focused filaments and component damage. Discussion of spatial filtering for control of small scale instability growth, will be presented in another paper at this meeting.

[2] G. W. Leppelmeier and W. W. Simmons, 7th European Conference on Plasma Production by High Power Lasers, Garching, Germany, April 1974.

8.7 10 Kilojoule SHIVA Laser System for Fusion Experiments at LLL (*Invited*), T. J. Gilmartin, R. O. Godwin, J. W. Davis, W. F. Hagen, C. H. Hurley, G. W. Leppelmeier, G. J. Linford, J. O. Myall, W. C. O'Neal, and J. B. Trenholme, *Lawrence Livermore Laboratory, Livermore, Calif. 94550*
(30 min)

Large, multi-beam, neodymium glass laser systems are playing an important role in near term laser fusion experiments. Although the primary purpose of these laser fusion experiments is to demonstrate inertial confinement of a thermonuclear reaction in a manner which is ultimately scalable to commerical power generation, there are many intermediate scientific goals. These goals include: understanding plasma physics associated with high power laser and matter interactions; developing fuel target design models; designing and fabricating efficient targets; advancing the state of laser/optics engineering; and developing reactor chambers. Several significant laser fusion programs in pursuit of these goals are currently underway.

In describing the capability of the fusion glass laser systems, several parameters are important. The energy yield from a thermonuclear reaction with reactor fuel targets of solid D-T (deuterium-tritium) is critically dependent on the illumination geometry and the focusable power available from the laser system. However, the yield from the currently used experimental targets, glass bubbles containing gaseous D-T, is also dependent on the energy output of the laser system. Since nonlinear optical effects limit the flux in the laser output aperture, a fourth important system parameter is the area of the total system aperture. The Lawrence Livermore Laboratory 10 kilojoule SHIVA laser system, the highest performance glass laser system currently on the drawing boards in the U. S., will be described in detail.

The detailed laser system performance requirements are determined by the characteristics of the fuel target. The size and shape of the target and its sensitivity to nonuniformity in the illumination determine the accuracy with which the laser beams must be apodized, aligned and focused. The temporal response of the target determines the laser pulse shape and the accuracy of synchronism required among the illuminating beams. For example, the 20 beam SHIVA laser system will give an initial illumination uniformity of $\pm 10\%$ over 4π. This will require that the beams be aligned to within 2% and focused within 5% of the target diameter, typically 100 to 500 μm. Simple pulses 100 psec long must be synchronized to within 10 psec (3 mm) and the relative power output in the several laser beams must be within 5%. As the laser system power increases, larger targets can be burned and the absolute beam alignment tolerance is relaxed. With fewer faster (lower f/ # beams) the alignment tolerance may be relaxed because the achievable illumination uniformity is already poorer.

In addition to the linear optical alignment requirements, nonlinear optical effects which deflect the beams, move the focal plane, modify the beam apodization near focus, and temporally modulate the pulse shape, must be minimized. A brief discussion of these effects vis-à-vis the illumination and alignment requirements of fusion laser systems with emphasis on the SHIVA system will be given.

Finally, since these large laser systems contain literally hundreds of laser amplifiers, thousands of flashlamps and energy storage capacitors, and large part counts of all components, reliability and maintainability are essential. A brief discussion will highlight the engineering aspects of the major subsystems, including the laser space frame, control and data management, energy storage and power conditioning, and the target chamber.

8.8 Production of Specially Tailored Laser Pulses, S. K. Vartapetov, V. I. Vovchenko, I. K. Krasujk, S. G. Lukishova, P. P. Pashinin, and A. M. Prokhorov, *USSR*
(15 min)

(Received late; see page 83)

Session 9

Thursday, May 29, 1975 8:45-11:45 A.M.

Pollution Monitoring and Remote Sensing

Chairman: S. F. Jacobs, *Optical Sciences Center, University of Arizona, Tucson, Ariz.*

9.1 Measurement of Atmospheric Absorption Using Solar Infrared Heterodyne Radiometer and Its Application to the Knowledge of Pollutant Densities, B. Christophe and D. Camus, *S.A.T., Paris, France,* and J. Gay and A. Journet, *C.E.R.G.A., Grasse, France*
(15 min)

The object of this experiment is to use the Solar Infrared Heterodyne Radiometer to measure the atmospheric absorption at high resolution. It is a technique which has been described by J. McElroy[1] and has been applied before[2] to measure vertical absorption. We wish to describe here an experiment to measure the variation of the absorption coefficient with altitude and therefore obtain pollutant concentration.

The beat signal produced in the mixer between the sun and the local oscillator radiations are detected and analysed in connection with the rising of the sun. The signal depends only on the integrated absorption path in the atmosphere given by:

$$k(v,Z) = \int_0^\infty \frac{k(v,h)\,dh}{\sqrt{1 - \left(\frac{R}{R+h}\right)^2 \sin^l Z}}$$

in which formula, h is the altitude, R the earth radius and Z the zenithal angle of the observed object. The technique gives k as a function of the zenithal angle and by inversion of the above integral equation one can recover $k(v,h)$, the absorption function of the altitude.

[1] J. H. McElroy, "Infrared heterodyne solar radiometry," *Appl. Opt.*, vol. 11, p. 1619, 1972.

[2] S. R. King, D. T. Hodges, T. S. Hartwick and D. H. Barker, "High-resolution atmospheric transmission measurements using a laser heterodyne radiometer," *Appl. Opt.*, vol. 12, p. 1106, 1973.

Fig. 1.

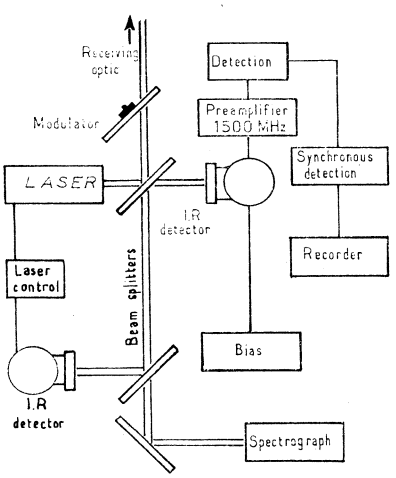

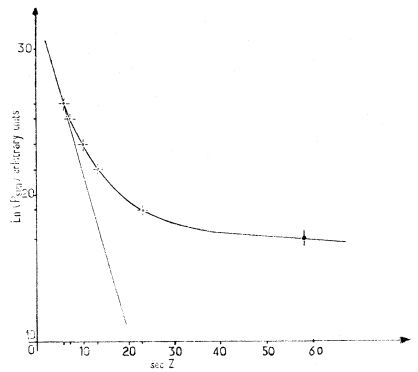

Fig. 2. Graph of the recieved solar power versus the secant of the zenith angle. Taken 29 Oct. with P22.

The detection chain (Fig. 1) consists of a Telescope following an heliostat, a beam splitter, a CO_2 laser, as local oscillator (which is tunable over 40 transitions between 9.2 and 11.2 μ), a Hg Cd Te photovoltaic mixer with a bandwidth larger than 1 GHz followed by an amplifier Avantek and a synchronous detection. When the local oscillator photon current shot noise is preponderant, the signal to noise ratio is given by:[4,5]

$$\frac{S}{N} = Q\chi(B\tau)^{1/2}Tf[\exp h\nu/kT - 1]^{-1}$$

Q is the quantum efficiency, χ the wave mixing factor,[3] B the equivalent bandwidth, τ the integration time, Tf the optical transmission, ν the local oscillator frequency, T the source temperature. In our experiment the theoretical S/N is 34 dB taking $\chi = Tf = 1$ and we have measured $(S/N) = 20$ dB.

One of the results obtained is shown on Fig. 2 and using measurements at low sec z can lead to the vertical transmission which was for this day of 80% on P_{22}. The use of high number sec z, enables us to observe the repartition of CO_2 or any absorbant in the atmosphere (Ozone for example). To improve experimental results and obtain the excitation of CO_2, we can also measure absorption on all rotational lines and also obtain measurements at low altitude by looking away from the center line (1.5 GHz).

This technique used to obtain information on pollutants is different from any other technique using IHR[6,7] since it needs an outside atmosphere source.

It has the advantage, however, to have a better sensitivity and it enables us to measure the altitude of the polluted layer.

[3] H. T. Yura, "Optical heterodyne signal power obtained from finite sized source of radiation," *Appl. Opt.*, vol. 13, p. 150, 1974.

[4] A. E. Siegman, "The antenna properties of optical heterodyne receivers," *Proc. IEEE*, vol. 54, p. 1350, 1966.

[5] J. Gay, A. Journet, B. Christophe and A. Robert, "Heterodyne detection of blackbody radiation," *Appl. Phys. Lett.*, vol. 22, p. 448, 1973.

[6] R. T. Menzies, "Remote detection of SO_2 and CO_2 with a heterodyne radiometer," *Appl. Phys. Lett.*, vol. 22, p. 592, 1973.

[7] R. T. Menzies and M. S. Shumate, "Air pollution: remote detection of several pollutant gases with a laser heterodyne radiometer," *Science*, p. 570, May 1974.

9.2 Ambient Air Pollutant Measurements with a Bistatic, Heterodyne System, R. T. Menzies and M. S. Shumate, *Jet Propulsion Laboratory, California Institute of Technology, Pasadena, Calif. 91103*

(15 min)

We have performed several ambient-air monitoring experiments in the Pasadena, California area with a bistatic, long path differential absorption technique. Both cube corner reflection and diffuse reflection from ordinary surfaces were used to provide the return signal. Two pollutants were monitored over a round trip path of nearly one kilometer: nitric oxide and ozone. The transmitter used in the nitric oxide monitoring experiments was a CW $C^{12}O^{16}$ laser. The laser lines chosen to interact with NO were the 7-6 band, $P(15)$ line at 1052.194 cm^{-1} and the 9-8 band, $P(9)$ line at 1900.049 cm^{-1}. The transmitter used to monitor ozone was a CW $C^{12}O_2^{16}$ laser. The $C^{12}O_2^{16}$ laser 00°1-II band, $P(14)$ line at 1052.194 cm^{-1} interacts strongly with the ozone ν_3 band. This line and several other P-branch lines up to $P(24)$ were used in the experiments. Both lasers were stabilized with Invar cavity spacers and fitted with gratings for line-to-line tuning capability.

Heterodyne detection is an effective means of obtaining high sensitivity to a weak return laser signal in a bistatic system. In this system, the Dicke-type heterodyne radiometer could easily detect a return laser signal from a Lambertian reflector surface at a distance of 0.5 km, whose reflectivity was 1%, when only a few milliwatts of power were transmitted. The heterodyne radiometer was operated with a beat frequency of a few MHz and an IF bandwidth of 1 MHz. The detection system was also operated in a homodyne mode, i.e., there was no frequency shift between the local oscillator and return signal frequencies. The comparative sensitivity of the homodyne mode was degraded somewhat by gain variations in the amplifiers and by excess local oscillator noise in the frequency region near the chopping frequency. However it is a simpler technique to employ in certain cases and still provides high sensitivity.

Ozone and nitric oxide were monitored during several days, some of which showed the obvious signs of photochemical smog. Typical plots of the daily concentration trends agreed with the classic pattern of NO buildup during early morning hours and subsequent decay via photochemical reactions, with O_3 concentrations peaking in the early afternoon hours. A 2% differential absorption could normally be detected, the limitation being mainly due to atmospheric turbulence. This corresponded to a sensitivity of less than 0.02 ppm average concentration for both ozone and nitric oxide. Smaller differential absorption signals can be detected with modifications in the optics and processing electronics. However, the initial limitation in accuracy, expecially for NO measurements, was found to be due to water vapor differential absorption at the laser wavelengths. Inadequate knowledge of water vapor absorption led to inaccuracies of the order of 0.1 ppm for NO measurements. Independent water vapor absorption measurements were made which reduced this source of error considerably. The accuracy of the laser measurements was substantiated with supporting data from chemiluminescent monitors of NO and O_3.

Plans are in progress to convert this pollutant monitoring technique to an airborne system, with a downward pointing transmitter. With such an instrument, one can obtain altitude profiles of pollutants, with high sensitivity at all altitude levels. Because the instrument can operate effectively with short integration times, high spatial resolution can be achieved also.

9.3 Absorption of CO_2 Laser Radiation by Water Vapor, M. S. Shumate and L-G. Rosengren, *Jet Propulsion Laboratory, Pasadena, Calif. 91103*

(15 min)

In recent years, the proliferation of optical systems that utilize carbon dioxide lasers has produced considerable interest in the effects of atmospheric absorption upon CO_2 laser radiation. One of the most common constituents of the atmosphere, water vapor, can have a sizable effect upon operation of these laser systems. In this present work, we report measurements of the absorption coefficients of water vapor at the emission lines of the normal isotope of carbon dioxide, $C^{12}O_2^{16}$. The measurements were made using an acoustically resonant optoacoustic detector, at room temperature, with an atmospheric pressure background of air.

Measurements of water vapor absorption at CO_2 laser wavelengths has been previously reported by McCoy, *et al.*,[1] and by Trusty.[2] The most interesting feature of their results was a nonlinear variation in the absorption coefficient with a change in the partial pressure of water vapor. Benedict and Kaplan[3] have presented a detailed theoretical prediction of the dependence of water vapor absorption with pressure that differs significantly from McCoy, *et al.*, and Trusty's results. Furthermore, the values they report are not in agreement with each other. These discrepancies together with the need for accurate absorption coefficients on several CO_2 laser lines motivated the present investigation.

The experimental technique used for our measurements utilized an acoustically resonant optoacoustic detector, or spectrophone, in conjunction with a passive stabilized, grating tunable carbon dioxide laser. The optoacoustic detector was constructed in a cylindrical shape out of pyrex glass, with barium fluoride infrared windows. The detector has a first order radial

This paper represents the results of one phase of research carried out by the Jet Propulsion Laboratory, California Institute of Technology, under Contract Number NAS 7-100, sponsored by the National Aeronautics and Space Administration.

[1] J. H. McCoy, D. E. Rensch, and R. K. Long, *Appl. Opt.*, vol. 8, p. 1471, 1969.

[2] G. L. Trusty, "Absorption measurements of the 10.4 micron region using a CO_2 laser," Dissertation, Ohio State University, 1972.

[3] W. S. Benedict and L. D. Kaplan, *J. Quantum Spectrosc. Radiat. Transfer*, vol. 4, p. 453, 1964.

resonant frequency at 2.8 KHz, and used a conventional condenser microphone mounted in the detector side wall as a pressure transducer. With the laser radiation modulated by a mechanical chopper, and using a commercial lock-in amplifier, the minimum detectable absorption strength was 2×10^{-5} m^{-1}

The optoacoustic detector was attached to a vacuum station that permitted evacuation of the detector prior to filling. Since water vapor adsorbs to almost all materials, care was taken to assure that the walls of the system were saturated with water vapor before admitting dry air to the detector. Four different water vapor partial pressures were used: 5, 10, 15, and 20 torr. The detector was then filled with dry air to a final pressure of 730 torr. Measurements were made with a laser operating on the $P(10)$-$P(32)$ and $R(10)$-$R(32)$ lines of the 00°1-02°0 band and the 00°1-10°0 band of the normal isotope of carbon dioxide, $C^{12}O_2^{16}$.

In order to measure the contribution to the detector signal that was due just to the water vapor, background signals were measured using a detector fill of only dry air at the same laser wavelengths. Thus, the contributions to the signal caused by CO_2 and trace contaminants in the dry air could be subtracted. Background signals due to window absorption effects are likewise cancelled out of the final result.

The results obtained with the apparatus described consistently showed larger absorption coefficients for water vapor than have been previously reported. Furthermore, the variation in absorption with water vapor pressure was linear, to within the accuracy of our method. This result supports the theory of Benedict and Kaplan. The paper will present a detailed description of the experimental apparatus, including the procedures followed to minimize the effects of water vapor adsorption on the optoacoustic detector walls. A detailed analysis of the error sources will be presented.

9.4 Progress in Laser Radar *(Invited)*, H. Inaba, *Research Inst. of Electrical Communication, Tohoku University, Sendai, Japan*
(30 min)

No summary.

9.5 A Laser Doppler Velocimeter for Remote Power Plant Effluent Measurements, C. R. Miller and C. M. Sonnenschein, *Raytheon Co., Sudbury, Mass. 01776* and W. F. Herget, *Environmental Protection Agency, Research Triangle Park, N. C. 27711*
(15 min)

A CO_2 Laser Doppler Velocimeter (LDV) System was assembled into a mobile test van and field tested during the weeks of 23-30 August 1974 and 12-19 January 1975 to prove the feasibility of remotely detecting and measuring the velocity of effluents from the smoke stacks of power plants. The LDV was a coaxial homodyne system which detected the Doppler shift, $\Delta\nu_D$, on the 10.6 μ radiation backscattered from the smoke stack effluents. Since the angle, α, between the smoke stack and the transmitted laser beam was known, the velocity, v, of the effluent could be determined from the equation:

$$v = (\lambda/2 \cos \alpha) \cdot \Delta\nu_D$$

A block diagram of the effluent detection system is shown in Fig. 1. The optical portion of the system consisted of a 20 W CW CO_2 laser; a Mach-Zehnder interferometer; a 12-inch diameter, f/8 telescope; and a copper doped Germanium detector. This equipment was mounted on a common base plate which was in turn shock mounted to a support table to isolate against vibration. The transmitted beam was directed to the target by an 18-inch elliptical scanning mirror. The system could be scanned over $\pm 10°$ angles in both elevation and azimuth before coarse mirror adjustments became necessary. The system was bore-sighted to an alignment telescope and it was found that pointing accuracies of 0.2 mrad were easily maintained.

Fig. 1. Block diagram of effluent detection system.

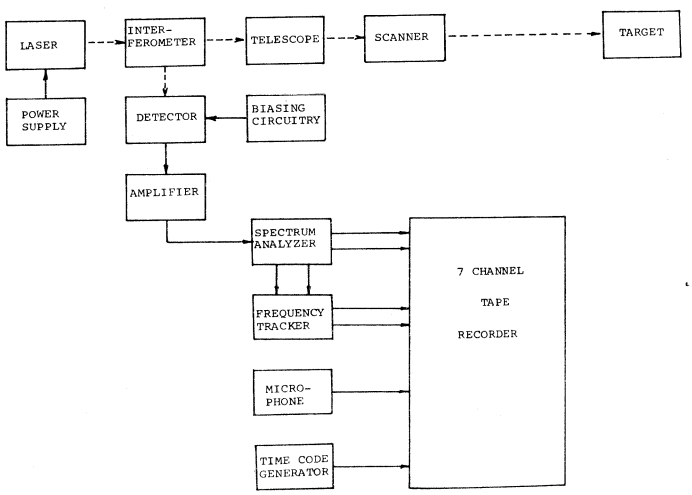

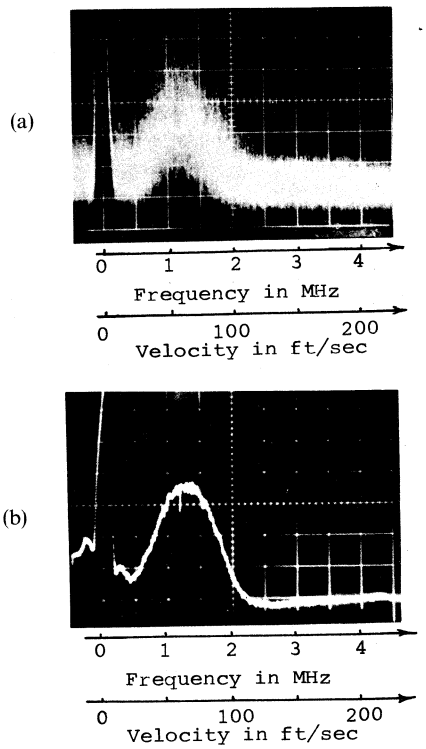

Fig. 2. (a) 2 second duration photograph of the spectral distribution of effluent backscatter signals. (b) Spectral distribution of effluent backscatter signals after 7 seconds of signal averaging.

The *IF* Doppler signals were detected in a shot noise limited detector and after amplification were displayed on a spectrum analyzer. The spectrum analyzer's vertical output was recorded on magnetic tape for further processing.

Overall system efficiency was measured by calibrating the LDV against a standard target of known reflectivity. This calibration allowed estimates of the effluent backscatter coefficient, $\beta(\pi)$, to be made.

A variety of measurements were made against a smoke stack at the River Bend Steam Plant of Duke Power in Mt. Holley, North Carolina.[1] Duke uses electrostatic precipitators to remove the larger particles from their stacks. Under typical operating conditions the plume is invisible with an opacity of about 3-10%. Effluent backscatter signals were detected across a 1310 ft range at an elevation angle of 10° (α = 80°). Typical spectrum analyzer waveforms are shown in Fig. 2(a) and 2(b). These photographs indicate the spectral distribution of smoke stack effluent backscatter signals before and after signal averaging. Effluent velocities were measured as a function of power load conditions to be in the 100 to 140 ft/sec range. Estimates of the effluent backscatter coefficient have been made. Velocity profile measurements above the

[1] W. F. Herget, C. R. Miller, and C. M. Sonnenschein, "Remote measurement of power plant stack effluent velocity," to be published.

stack lip had a variety of distributions with the velocities varying from 80 to 160 ft/sec.

Two areas currently under investigation are the effect of plume turbulence on the LDV signal and the relationship between backscatter signal strength and plume opacity.

The authors would like to acknowledge the cooperation of Duke Power Co. in these measurements. The technical assistance of R. E. Schaaf of Raytheon Co., R. M. Huffaker of NASA MSFC, and J. A. Thompson of Physical Dynamics was greatly appreciated. This work was supported by the EPA and NASA.

9.6 Performance of a CO_2 Laser Vortex Detection System, C. M. Sonnenschein and C. A. DiMarzio, *Raytheon Co., Sudbury, Mass. 01776*, and H. Jeffreys, *NASA, Marshall Space Flight Center, Huntsville, Ala. 35812*

(15 min)

Two CO_2 laser Doppler velocimeters have been built to detect and measure the characteristics of aircraft trailing vortices. The systems, currently operating at Kennedy International Airport, use a CO_2 laser in a heterodyne configuration to determine the transport and velocity distribution of the vortex flow field. The optical portion consists of a CW laser, a Mach-Zehnder interferometer, a 12-inch telescope that focuses and scans in range, an output mirror that scans in elevation, and a shot noise limited Hg:Cd:Te detector. Following the detector is a sophisticated signal processor, a PDP-11 computer, several tape recorders, and displays.

The system operates by propagating a laser beam into the atmosphere and collecting the Doppler shifted signal scattered by aerosols naturally suspended. A signal at the Doppler frequency is obtained by detecting the superposition of the scattered signal and a stable local oscillator. The presence of a vortex is determined by high frequency components in the detector output.

The signal processor frequency analyzes the signal. The signal at each frequency is integrated and recorded on a high speed tape. Since there are 104 distinct frequency channels and a typical integration time is 2 msec, this produces approximately 50,000 pieces of data per second.

In order to reduce the data stream, the signal processor performs other functions. An amplitude threshold can be set to remove the noise floor and a velocity threshold discriminates against the ground wind. Data from the thresholded spectrum indicating the maximum velocity, the highest signal amplitude and its frequency, and the number of filters excited are recorded and processed by a computer in real time.

Results from both thresholded and raw data have been analyzed in detail. Calibration measurements against a spinning wheel have shown excellent repeatibility. Signal - to - noise ratio measurements against the atmosphere have been carried out to yield an atmospheric backscatter coefficient.

The vortex is an extended target, whose area is much greater than the system resolution. The vortex position is obtained by an algorithm that locates the centroid of the maximum intensities above appropriately selected amplitude and velocity thresholds. Vortex tracks from hundreds of aircraft landing at Kennedy have been collected and several will be presented. A comparison of vortex locations obtained from the two systems show an average error of less than 10 ft.

The authors would like to acknowledge the assistance of the many agencies, companies, and people who made this work possible. The program was funded by NASA, Huntsville, and the FAA, both of whom provided valuable technical assistance. The equipment was built and operated by personnel from Raytheon Company and Lockheed Missiles and Space Company. M&S Computing provided the computer hardware and much of the software, and Physical Dynamics, Inc., helped in the data evaluation.

9.7 Resonant Doppler Velocimeter, R. B. Miles, *Aerospace and Mechanical Sciences Department, Princeton University, Princeton, N. J. 08540*

(15 min)

Tunable narrow linewidth laser sources permit the inclusion of resonant absorption and fluorescence among the tools for analysis of gas flow and turbulence. The concept may be demonstrated by the introduction of trace amounts of sodium vapor into a helium or nitrogen flow. A narrow bandwidth tunable dye laser incident in the direction opposed to the flow is absorbed at the Doppler shifted resonant frequency, and the light is reradiated by the sodium atom after some characteristic time equal to or shorter than the natural lifetime of 16.3 n sec. The detected fluorescence intensity for optically thin sodium may be correlated with the absorption constant, the maximum occurring when the tunable laser is matched to the Doppler corrected resonant absorption linecenter of the observed region. Measurement of the laser frequency, then, yields the velocity of the observed region. Pressure and temperature discontinuities such as shock waves and boundary layers are observable as intensity variations, rendering this tool a convenient device for qualitative flow visualization as well as quantitative measurements.

The Doppler shift for sodium is 1.7 MHz for each meter/sec of flow velocity. Since the natural linewidth is 9.8 MHz, the limiting resolution of the resonant Doppler technique is several meters/sec. Pressure and thermal broadening will substantially increase the minimum velocity sensitivity, depending on the particular configuration chosen. Several experimental configurations with their minimum velocity resolution and other pertinent information are given in Table I for helium and nitrogen.

Further extensions of this tool beyond the flow visualization and average velocity measurements are obvious. The atoms or molecules will microscopically follow the flow field; thus the thermally broadened linewidth, while to some

TABLE I
CALCULATED PARAMETERS FOR VARIOUS WIND TUNNEL CONFIGURATIONS

	Helium				Nitrogen		
Mach number	8	10	16	20.7	2.9	10	20
Stagnation pressure (atmospheres)	20	108	20	102	6.8	50	100
Stagnation temperature (°Kelvin)	300	256	300	297	291	10000	2000
Free stream velocity (meters/sec)	1725	1606	1753	1748	616	1407	2027
Velocity sensitivity	±3%	±7%	±0.6%	±0.6%	±49%	±2.3%	±1.1%
Velocity correction (meters/sec)	+27	+67	+1.8	+3.3	−1128	−9.3	−0.2
Fluorescence per atom (photons/sec)	6.33×10^4	2.58×10^4	3.68×10^5	3.30×10^5	2.45×10^2	1.08×10^5	1.99×10^5
Maximum sodium density (atoms/cc)	4.69×10^{10}	1.15×10^{11}	8.06×10^9	9.01×10^9	2.91×10^{11}	2.05×10^{10}	1.47×10^{10}
Maximum detected signal from 1 cc (watts)	2.5×10^{-6}	2.5×10^{-6}	2.5×10^{-6}	2.5×10^{-6}	6.0×10^{-8}	1.9×10^{-6}	2.5×10^{-6}
Mass flow ratio	1.7×10^7	2.3×10^7	1.3×10^7	2.8×10^7	6.1×10^7	1.1×10^7	5.1×10^5

extent obscuring the average velocity, yields a microscopic static temperature profile. The frequency difference between the fluorescent light and the incident laser suggests methods for measuring Reynolds shear stress, and variations of the absorption line with velocity, temperature, and pressure fluctuations suggest methods for turbulence measurement.

9.8 Remote Measurement of Ozone by Resonance Raman Scattering and Differential Absorption, C. M. Penney, *General Electric Corporate Research & Development, Schenectady, N. Y. 12301*

(15 min)

We have measured the absolute magnitude, spectral distribution and depolarization of resonance Raman scattering[1] from ozone excited in its dissociative Hartley absorption band between 286 and 294 nm. These measurements were accomplished using a line-narrowed doubled dye laser, 3/4 meter Spex monochromator and timing/photon-counting detection, providing 5 nsec incident pulses with spectral bandwidth less than 0.1 nm and scattered light resolutions of 0.1 nm and 5 nsec. Measurements of absolute magnitude were obtained by comparison of Raman scattering signals from O_3 and O_2 and an auxiliary absolute measurement of the O_2 scattering cross section using techniques described previously.[2] Typical results shown in Fig. 1 reveal a progression of harmonics characteristic of the type of resonance Raman scattering described by Holzer, Murphy and Bernstein[1] in their observations on halogen molecules excited above the dissociation limit. We find that the cross section for scattering into the $\nu_1(+\nu_3?)$ is 1.1×10^{-26} cm^2/sr $\pm$ 20% for excitation at 286.6 nm. This is 600 times stronger than the ordinary Raman scattering from O_2 excited at the same wavelength. Also, the cross section appears to increase in proportion to the absorption coefficient over the observed spectral range. In the case of ozone, the harmonics appear to arise from both the ν_1 and ν_3 vibrations, revealing in the latter case an expected breaking of selection rules for ordinary Raman scattering. The overall characteristics of the ozone scattering are consistent with the distinctions between scattering and fluorescence which are set forth in Ref. 1.

These results are used to compare the resonance Raman scattering and differential absorption techniques for remote, spatially-resolved LIDAR measurements of ambient ozone near the ground, and in its stratospheric layer roughly between altitudes of 10 and 30 km. Raman LIDAR directly observes the ozone, which is a minor species (10 ppb to 10 ppm), ideally providing a signal directly proportional to ozone concentration. Differential absorption LIDAR determines ozone concentration from

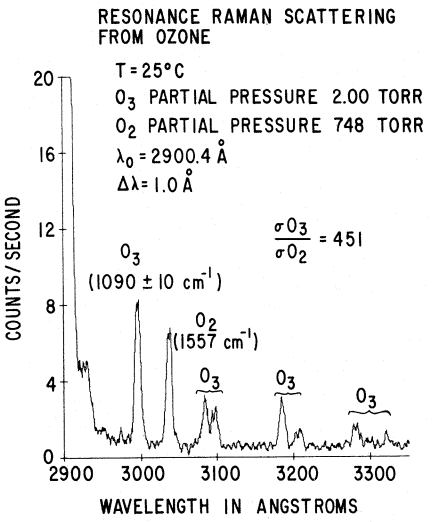

Fig. 1. Resonance Raman scattering from ozone.

the difference between two signals, a situation that, in general, is less favorable from signal-to-noise (S/N) considerations. However, since differential absorption LIDAR is based on scattering from a major species and can use a stronger scattering process (Rayleigh vs Raman scattering) it often provides a substantial S/N advantage. We shall show how the general expressions for S/N differ for the two techniques and use the general and specific results to establish that ozone is a particularly favorable target for ground-based and satellite-based differential absorption LIDAR measurements.

9.9 Paper withdrawn.

[1] W. Holzer, W. F. Murphy and H. J. Bernstein, *J. Chem. Phys.*, vol. 52, p. 399, 1970.

[2] C. M. Penney, R. L. St. Peters and M. Lapp, *J. Opt. Soc. Amer.*, vol. 64, p. 712, 1974.

9.10 Laser Optoacoustic Detection of Explosive Vapors,[1] P. C. Claspy, Y-H. Pao, S. Kwong, and E. Nodov, *Department of Electrical Engineering and Applied Physics, Case Western Reserve University, Cleveland, Ohio 44106*

(15 min)

The illegal use of explosives in public crimes has reached a level such that a critical need exists for a method of detection of the presence of such materials in locations such as airports and postal facilities. While effective methods for indirect detection using tagging schemes have been proposed, a reliable method for direct detection of the explosive vapors in the presence of normal atmospheric pollutants is still required. This paper presents the results of the application of a laser optoacoustic detector to the direct detection problem. The results indicate that such a device can provide a sensitive, reliable direct detection system.

The laser optoacoustic detector makes use of a cell containing an air sample which is suspected to contain the vapor to be detected. The cell is illuminated with chopped infrared radiation of a wavelength known to be absorbed by the vapor being sought. If that vapor is present in the sample, a periodic heating of the gas in the cell occurs. The resulting pressure fluctuations are then detected with a sensitive capacitive microphone which has been placed in the cell. Kreuzer, *et al.*,[2] have reported the application of usch a device to the detection of low molecular weight pollutants in the atmosphere. In performing direct detection of explosive vapors, consideration must be given to several factors in addition to the determination of the optoacoustic spectrum of the materials. These factors include:

1) a strong tendency of all explosive molecules to adhere to the surface of most materials;

2) the low vapor pressure of most explosives (vapor pressure of TNT at 20°C $\approx 10^{-6}$ Torr;

3) the problem of interference by pollutant gases normally found in the atmosphere.

The detector used in this experiment was an acoustically resonant device of the same general type as those used by Dewey[3] and by Goldan and Goto.[4] Our detector, however, is designed such that the dominant acoustic mode is a mixture of the fundamental radial mode of the large diameter cylindrical end sections and the fundamental longitudinal mode of a small diameter coaxial cylindrical microphone. The microphone is thus a part of the resonant system rather than a perturbation to it. The cell design provides acoustic amplification of the small signals which result from very low vapor concentrations (typically 0.01 ppm or less). In addition, to reduce the tendency for surface absorption of the explosive molecules the cell is operated at a nominal temperature of 50°C. The light source was a dry ice cooled CW CO laser which could be grating tuned over the wavelength region from 5.8 microns to 6.7 microns. This tuning range coincides with the symmetrical stretching vibration of the NO_2 group which is present in all of the explosives studied. A fixed set of 16 laser lines, spanning the above spectral range, was used to study all explosives. This set of lines was also used to determine the spectra of five common atmospheric pollutants, which included water vapor, methane, butane, nitrogen dioxide, and nitric oxide. Of these only nitrogen dioxide appears to offer potential interference with the explosive spectra.

TABLE I
EXPLOSIVE OPTOACOUSTIC SPECTRA (NORMALIZED)

Wavelength (microns)	EGDN + 10% NG	PETN
6.626	2.4	1.2
6.539	4.8	1.7
6.466	0.6	0.8
6.408	2	0.9
6.367	1.6	0.5
6.313	0	0.1
6.258	0.7	0
6.214	1.6	0.3
6.175	5.6	4.0
6.133	3.6	0.8
6.063	10.9	1.9
6.003	100.	2.5
5.942	61.8	2.0
5.881	6.7	5.5

Eight explosives were investigated in the course of this program. These include nitroglycerine, ethylene glycol dinitrate (EGDN), dinitrotolnene (DNT), trinitrotoluene (TNT), TOVEZ, dynamite, cyclotrimethylene trinitramine (RDX), and pentaerythritol tetranitrate (PETN). Normalized optoacoustic spectra for three of these explosives are given in Table I. Our high resolution optoacoustic spectra show good agreement with the low resolution data reported by Pristera, *et al.*[5]

Our results demonstrate the feasibility of direct laser optoacoustic detection of explosive vapors in the atmosphere at partial pressures of 10^{-6} Torr or less in the presence of normal atmospheric pollutants.

[1] This work was supported by the Law Enforcement Assistance Administration through subcontract with the Aerospace Corporation.

[2] L. B. Kreuzer, N. D. Kenyon, and C. K. N. Patel, *Science*, vol. 177, pp. 347-349, 1972.

[3] C. F. Dewey, Jr., R. D. Kamm, and C. E. Hackett, *Appl. Phys. Lett.*, vol. 23, pp. 633-635, 1973.

[4] P. D. Goldan and K. Goto, *J. Appl. Phys.*, vol. 45, pp. 4350-4355, 1974.

[5] F. Pristera, M. Halik, A. Castelli, and W. Fredericks, *Anal. Chem.*, vol. 32, pp. 495-508, 1960.

9.11 Some Applications of Zeeman Tunable Gas Lasers for High Resolution Spectroscopy, M. V. Dubovic, A. P. Shkadarevich, and A. P. Voytovich, *USSR*

(15 min)

No summary.

Session 10

Thursday, May 29, 1975 1:30-5:00 P.M.

Guided Waves

Chairman: H. Kressel, *RCA Laboratories, Princeton, N. J.*

Organizer: J. E. Goell, *ITT Electro-Optical Products Division, Roanoke, Va.*

10.1 Guided-Wave Modulators (*Invited*), I. P. Kaminow, *Bell Telephone Laboratories, Holmdel, N. J.*

(30 min)

No summary.

10.2 Monolithic Integrated Optical Devices (*Invited*), F. Reinhardt and R. A. Logan, *Bell Telephone Laboratories, Murray Hill, N. J.*

(30 min)

No summary.

10.3 Epitaxially Grown Single Crystal KTN for Thin Film Optical Modulators,[1] R. E. Fontana, Jr., D. J. Epstein and A. Linz, *Center for Materials Science and Engineering and Department of Electrical Engineering, Massachusetts Institute of Technology, Cambridge, Mass. 02139*

(15 min)

We report here on the growth, by liquid phase epitaxy, of single crystal thin films of potassium tantalate niobate (KTN), and the preliminary evaluation of these films as light guides and modulators. The material KTN exists over the complete solid solution range $0 \leqslant x \leqslant 1$ in the formula $KTa_{1-x}Nb_xO_3$, and exhibits a ferroelectric state for all compositions except those close to $x = 0$. By suitable choice of x the cubic-to-tetragonal ferroelectric transition can be made to occur near room temperature. Advantage of the enhanced electrooptic coefficients[2] accompanying the transition has been taken in designing room temperature bulk electrooptic devices[3] characterized by a particularly low half-wave voltage. Typically, this voltage is a factor ten smaller than for comparable devices using $LiNbO_3$ or $LiTaO_3$.[3,4]

[1] This work was supported by the Advanced Research Projects Agency under Contract DAHC-15-73-C-0316.

[2] The electrooptic coefficients referred to here and elsewhere in the discussion are those relating the index change to the applied electric field.

[3] F. S. Chen, J. E. Geusic, J. G. Skinner, S. K. Kurtz, and S. H. Wemple, *J. Appl. Phys.*, vol. 37, p. 388, 1966.

[4] R. T. Denton, F. S. Chen, and A. A. Ballman, *J. Appl. Phys.*, vol. 38, p. 1611, 1967.

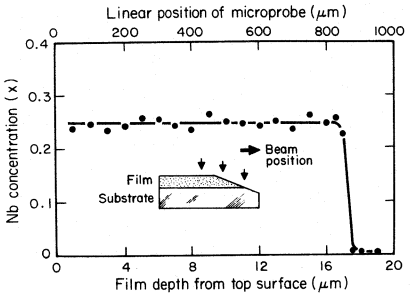

Fig. 1. Nb concentration in $KTa_{1-x}Nb_xO_3$ vs. film depth as determined from microprobe results of a lapped film-substrate.

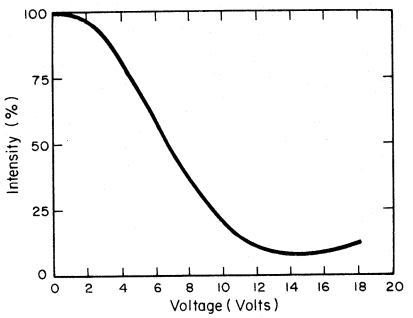

Fig. 2. Central beam light intensity for KTN modulator vs. applied d.c. voltage. Results are for a TE_0 mode in a 26 mole percent Nb film at 633 nm.

Because the index of refraction of KTN increases with increasing Nb concentration it is possible to obtain light guiding in thin films of KTN^+ (higher Nb concentration) grown on KTN^- (lower Nb concentration) substrate. By combining the high electrooptic effect available in this system with the more favorable geometry associated with thin film devices it becomes possible to fabricate electrooptic modulators requiring only a few volts for full modulation. Our materials effort has focussed on films with Nb content less than 40 mole percent. For this compositional range, KTN is paraelectric at room temperature, with cubic symmetry and a quadratic electrooptic effect. The index of refraction, the cubic lattice constant and the cubic-tetragonal Curie temperature all increase with increasing Nb content.

To obtain KTN waveguiding structures we have grown KTN single crystal films on (100) potassium tantalate ($KTaO_3$) substrates by liquid phase epitaxy. We employ a dipping method similar to that used for growing magnetic garnet films.[5] Because $KTaO_3$ has the lowest index of refraction in the KTN system, any composition $x > 0$ grown on this substrate will support guided modes. We grow from a melt containing a non-stoichiometric ratio of K_2CO_3, Ta_2O_5, and Nb_2O_5; a 7 mole percent excess of K_2CO_3 serves as the flux. Using a 60:40 mole ratio of Nb:Ta in the melt, we have obtained, by varying the growth temperature, films with Nb content ranging from $x = 0.11$ to 0.28.

The compositional uniformity of our films has been verified by electron-beam microprobe techniques. Fig. 1 shows the results for a 17 μm thick film lapped at 1°. Within experimental accuracy the film-substrate interface appears to be abrupt. After growth, the films are carefully polished to reduce the film thickness to 3-5 μm in order to limit the number of guided modes. Rutile prisms were used to couple the light into and out of the films.

For a 26 mole percent Nb film, electrooptic modulation of guided modes with an interdigital beam deflector has been achieved at 633 nm. The interdigital electrodes were 3 mm long with 25 μm wide fingers spaced 50 μm center-to-center. Fig. 2 shows the central beam output intensity as a function of d.c. voltage for an input TE_0 mode. An applied d.c. voltage of 15 volts, corresponding to a maximum surface electric field of 6000 volts/cm, gives 90% amplitude modulation. An improved electrode pattern now being fabricated (with 8 μm finger width and gap spacing) should reduce this voltage to about 5 volts. A further reduction in drive voltage should be possible by using KTN films in the range $x = 0.33$ to $x = 0.38$ thereby placing the Curie point closer to room temperature and, accordingly, increasing the value of the electrooptic coefficients.

The wide range of dielectric, optical and electrooptical properties available in the KTN system provides a design flexibility not possessed by other electrooptic materials thus far considered for thin film optics. In particular, it should be possible in this system to fabricate, by multiple dip liquid phase epitaxy, multilayered thin film structures which can be used for a host of applications including filters, switches, couplers and deflectors.

[5] E. A. Giess, J. D. Kuptsis, and E. A. White, *J. Crystal Growth*, vol. 16, p. 36, 1972.

10.4 Diffused Two-Dimensional Optical Waveguides in GaAs, E. Garmire,[1] D. Lovelace, G. H. B. Thompson, *Standard Telecommunication Laboratories, Ltd., Harlow, Essex England*

(15 min)

In this talk we describe the first studies of passive optical waveguide properties of diffused stripe geometry pn junctions in GaAs. The two-dimensional waveguides were ~2 μm deep and had widths varying from 2 to 6 μm. Single mode propagation at 1.15 μm was observed in both fundamental and first order modes, depending on stripe width. Photographs of guided light profiles and cleaved and stained end faces will be shown. These results indicate that diffusion is a convenient method of fabricating two-dimensional optical waveguides in GaAs.

The stripe pn junctions were fabricated by zinc diffusion into *n*-type GaAs through SiO_2 stripe masks, resulting in surface hole concentrations of 10^{19} cm^{-3}. We studied first the properties of planar diffused guides, comparing measured light profiles to theoretical ones. We assume that contributions to the refractive index

[1] Present address: University of Southern California, University Park, Los Angeles, Calif. 90007.

profile come from the free-carrier population, due only to plasma effects. The diffusion profile causes the hole concentration to decrease linearly from its surface value down to zero at the 2 μm depletion depth. At depths below the depletion layer, the electron population grows linearly until it reaches its substrate value. To calculate the resulting refractive index profile, we used the fact that the plasma contribution of the holes is ten times smaller than that of the same density of electrons. To calculate approximate mode profiles, averaged square refractive index profiles were assumed (typical values were $\Delta n \sim 0.01$). Excellent agreement was obtained between the theoretical guided light intensities and the measured profiles, both in position and width of the intensity peaks. Several diffusion depths and substrate carrier concentrations were studied, including a sample which was just below waveguide cutoff. From these experiments we were able to determine that after free-carrier contributions are subtracted, zinc-diffused GaAs has the same refractive index as n-type substrates (to <0.0006) at 1.15 μm.

With an understanding of planar guides, we can compare two-dimensional guided light profiles with theory. Because of the nature of diffusion, the width of the stripe junction depends strongly on the depth at which it was measured. We define an effective guide width measured at a depth corresponding to the peak of the guided light distribution. It should be pointed out that the pn junction width at the surface is larger than the SiO_2 mask stripe width because of diffusion under the edges of the mask. It is an interesting fact that for our range of stripe widths and diffusion depths, the effective guide width was the same as the mask stripe width in all cases. Using this effective width and refractive index profiles determined by plasma effects, we calculated theoretical transverse guided light profiles. We found excellent agreement between the theory and experiment for all our stripe widths, varying from 2 to 6 μm, and for first order modes as well as fundamental modes.

The results of both planar and stripe guides tell us that diffused pn junction optical waveguides in GaAs at 1.15 μm can be understood by considering free-carrier effects only. There is no evidence for additional effects, such as are observed near the lasing wavelength.

Crucial to the possible use of these guides for integrated optics is the question of optical losses. In the guides studied so far, the losses have been quite high, with an exponential loss coefficient the order of 15 cm^{-1}. This is because the surface hole concentration was still fairly large. We found agreement between this guided wave loss and an estimation based on measured bulk losses in p and n GaAs at 1.15 μm. These losses are much larger than estimates based on purely free carrier loss. The bulk loss measurements allow us to estimate how low the loss can be made by lowering the surface hole concentration. As an example, diffusion with a surface zinc concentration of 5×10^{18} cm^{-3} into n-type 4×10^{18} cm^{-3} GaAs to a depletion depth of 1 μm will have roughly the same average refractive index profile as the guides we report here and an estimated loss of less than 2 cm^{-1}.

Because zinc-diffused guides will usually have a substantial number of holes, their losses will always be relatively high. However, they have the advantage of being easy to fabricate, without requiring ion implantation or epitaxy. Furthermore, because of the pn junction, they are electrically active and may be used to make channel waveguide modulators. We feel that this technique for fabricating optical waveguides in GaAs will have many important applications.

10.5 Planar Optical Waveguides in Ion-Implanted ZnTe, S. Valette, G. Labrunie, J-C. Deutsch and J. Lizet, *Laboratoire d'Electronique et de Technologie de l'Informatique, Centre d'Etudes Nucléaires de Grenoble, Grenoble Cedex, France*

(15 min)

Zinc telluride (ZnTe) is a II-VI semi-conductor compound exhibiting physical properties particularly interesting for the achievement of monolithic integrated optical circuits of signal transmission and processing: 1) a direct gap allowing laser emission in the visible[1] ($\lambda_g \simeq 0.55$ μm at 300°K or in the near infrared with the ternary compound $Cd_xZn_{1-x}Te$, 2) the best electrooptical figure of merit of all semiconductor compounds,[2,3] 3) and very favorable photodetection properties.[4]

We present a preliminary study concerning the achievement, by ion-implantation of various ion species, of planar optical waveguides integrated in ZnTe.

Wafers have been implanted with boron, helium, and protons, under energies of 240 keV.

Doses ranging from 10^{13} to 2.10^{14} cm^{-2} (boron), from 5.10^{13} to 5.10^{14} cm^{-2} (helium) and from 10^{14} to 10^{15} cm^{-2} (protons) have been tried up to now. He-Ne laser ($\lambda = 6328$ Å) and dye laser ($\lambda = 5800$-6100 Å) beams are then coupled into the waveguides by means of a GaP prism,[5] and the propagation constants β of the guided modes are measured with the m-lines.[6] The experimental results will be presented in details.

Waveguides obtained under these conditions are characterized by thicknesses in the range 3-7 μm and a mean relative index variation $\Delta n/n$ of about 10^{-3}. Two contributions have been separated in this index variation: Δn_c due to the carriers compensation and Δn_d due to the defects induced in the crystal by implantation.

It can be noticed that:

1) Δn obtained in the guides is equal to Δn_d for low substrate carrier densities N_S ($N_S < 10^{17}$ cm^{-3}) because $\Delta n \gg \Delta n_c$ as deduced from usual expression.[7]

2) Observations achieved on samples with N_S ranging between 2.10^{15} cm^{-3} and 2.10^{18} cm^{-3} lead to the following conclusions: for high values of N_S (and particularly $N_S > 3.10^{17}$ cm^{-3}), propagation constants (and therefore substrate indices) are lower, and many more modes can be observed.

Elsewhere, losses in the range 1-5 db/cm have been measured at 0.633 μm for low order modes without any thermal annealing. This can be partly due to the fact that waveguides are somewhat buried, but also to a very low intrinsic absorption in the implanted guide.

[1] A. N. Vlasov, G. S. Kosina and O. B. Ferodova, *Soviet Phys. JETP*, vol. 25, p. 283, 1967.

[2] T. R. Sliker and J. M. Jost, *J. Opt. Soc. Amer.*, vol. 56, p. 130, 1966.

[3] D. B. Hall, Report NELC/TR 1861, Naval Electronics Laboratory Center, San Diego, Calif. 92152.

[4] T. D. Larsen, C. F. Varotto and D. A. Stevenson, *J. Appl. Phys.*, vol. 43, p. 172, 1972.

[5] S. Valette, G. Labrunie and J. Lizet, submitted for publication.

[6] P. K. Tien, R. Ulrich and R. J. Martin, *Appl. Phys. Lett.*, vol. 14, p. 291, 1969.

[7] E. Garmire, H. Stoll, A. Yariv, and R. G. Hunsperger, *Appl. Phys. Lett.*, vol. 21, p. 87, 1972.

Fig. 1. Coupling an He-Ne laser beam into an ion-implanted ZnTe planar waveguide by means of a Gap prism (under the match).

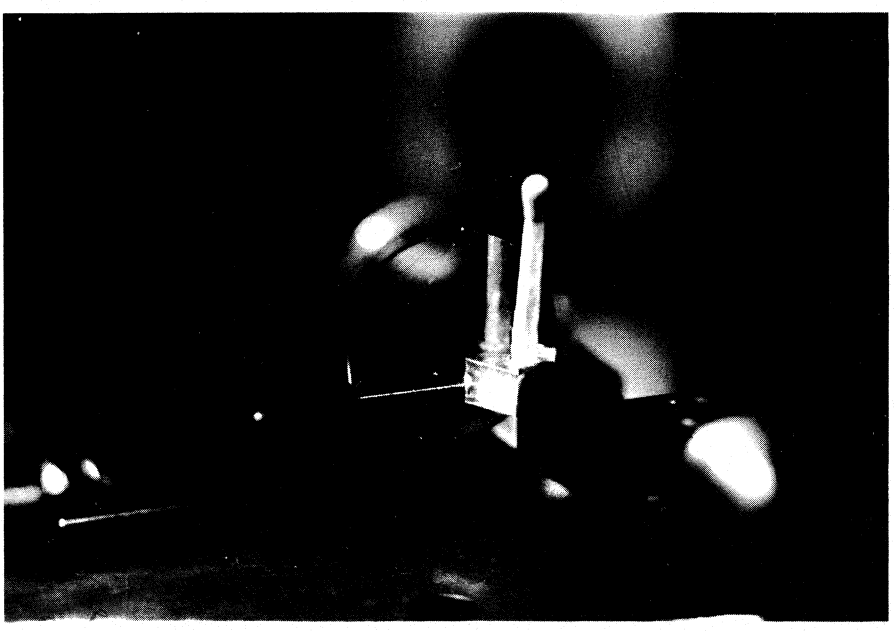

Finally, index profiles have been determined by a well-known microscopic interferometry method.[8] Results will be presented as a function implantation conditions.

The authors wish to thank J. C. Pfister, B. Schaub, J. Marine and C. Roussel for helpful suggestions and comments during this work, which has been partly supported by the Direction des Recherches et Moyens d'essais under contract no. 74/392.

[8] W. E. Martin, *Appl. Opt.*, vol. 13, p. 2112, 1974.

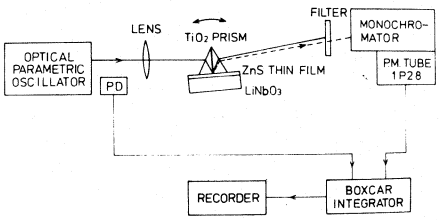

Fig. 1. Experimental setup of phase-matched SHG in a ZnS polycrystalline thin film waveguide evaporated on an x-cut $LiNbO_3$ substrate. The output of an optical parametric oscillator was used for the fundamental beam.

10.6 Phase-Matched SHG in Thin-Film Nonlinear Optical Waveguide Incorporated with Substrate Nonlinearity,

H. Ito and H. Inaba, *Research Institute of Electrical Communication, Tohoku University, Sendai, Japan*

(15 min)

For nonlinear optical effects in guided wave structures, such as SHG and optical parametric coupling, interaction can take place through either the optical nonlinearity of the substrate or of the film. Most of the previous work was performed using only the substrate nonlinearity, because of the difficulty of fabricating single-crystal thin films of sufficient optical quality. Recently we reported phase-matched SHG in an oriented polycrystalline ZnS film deposited on a glass substrate.[1] However, it should be pointed out that deposited nonlinear thin films have a great advantage in that the combination of film and substrate can be selected to make the interaction most efficient. As an evidence of the feasibility of this novel idea, we present in this paper the experimental verification of phase-matched SHG in a guided wave structure utilizing the nonlinearities inherent in both the thin film and the substrate made by the deposition of polycrystalline ZnS thin film on a $LiNbO_3$ single crystal substrate. Tunable optical parametric oscillator in the near infrared region was employed for a fundamental input.

For a ZnS thin film waveguide fabricated by vacuum deposition on an x-cut $LiNbO_3$ substrate, the (111) plane was found to be oriented parallel to the surface of the substrate by X-ray analysis. The calculation of the effective second-order nonlinearity $<d^2>$ of the oriented ZnS thin film waveguide was performed by fixing the [111] direction normal to the substrate surface. For the case of TE modes for both the fundamental and harmonic waves (TE + TE → TE), $(i/3)d_{14}^2$ is evaluated for $<d^2>$ of the oriented ZnS thin film.

In the optical waveguide, nonlinear interactions of optical waves can be phase-matched by utilizing proper mode dispersion. Taking into account the transverse spatial coupling coefficient and other experimental parameters of the ZnS-$LiNbO_3$ optical waveguide, the phase-matchable mode combination of TE_0 for fundamental and TE_2 for harmonic waves was selected for 1.1 μm-SHG. The estimated phase-matched film thickness was around 0.8 μm. The thickness of the ZnS film was controlled by a calibrated thin-film deposition monitor to within an accuracy of 200 Å. The precise control of the phase-matching condition was realized by means of a coherent tunable optical source for the fundamental.

[1] H. Ito, N. Uesugi and H. Inaba, *Appl. Pays. Lett.*, vol. 25, p. 385, 1974.

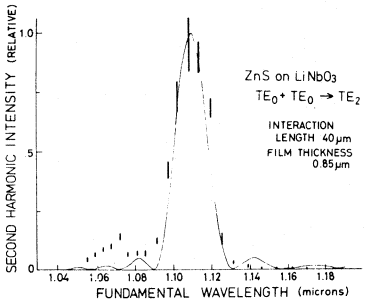

Fig. 2. The dependence of the phase-matched second harmonic intensity in the ZnS-$LiNbO_3$ waveguide on the fundamental wavelengths from the optical parametric oscillator. The interaction occurred between the TE_0 mode for the fundamental and TE_2 for the harmonic.

Phase-matched SHG was performed using the experimental setup shown in Fig. 1. In this experiment, the coupling and decoupling prisms were placed closely to each other, and a Chromatix optical parametric oscillator operated at the wavelength region of 1.1 μm was employed as the fundamental. The complete phase-matching profile as a function of fundamental wavelength is shown in Fig. 2. It is known from the result that the phase-matched wavelength is 1.11 μm for this ZnS film. From this wavelength, the thickness of the waveguide for SHG of 1.11 μm fundamental is calculated to be 0.85 μm, while the deposition monitor gives 0.82 μm. The input fundamental power in front of the prism coupler was nearly 70 W, and measured decoupled SH power was 5 μW. The theoretical value for SHG is estimated to be 23 μW, which is within the experimental error. Based upon the measured tuning curve in Fig. 2, the effective interaction length was calculated to be about 40 μm from mismatching behavior of nonlinear interaction between propagating modes. The solid curve in Fig. 2 corresponds to this length. From the fact that the spot size of the fundamental beam on the film was approximately 45 μm (the interaction length was restricted by the prism couplers) and the coherence length of the interaction was only about 5 μm for 1.1 μm-SHG, the calculated effective interaction length seems quite realistic.

Although most of the fundamental energy was confined in the ZnS film for the selected combination of the propagating modes in this experiment, the collaboration of both the nonlinearities of the film and substrate were demonstrated for the first time. Hence, the capability of phase-matched SHG in oriented polycrystalline thin film waveguides formed on nonlinear substrates suggests attractive applications of various nonlinear thin film materials for use in optical integrated circuits.

10.7 Integrated Optical Silicon Photodiode Array,[1]

J. T. Boyd and C. L. Chen, *Department of Electrical Engineering, University of Cincinnati, Cincinnati, Ohio 45221*

(15 min)

We describe the fabrication and operation of integrated optical silicon photodiode arrays. These structures consist of a relatively low-loss KPR optical waveguide[2] ($n = 1.61$) deposited on a layer of SiO_2 ($n = 1.46$) which in turn is grown on a silicon substrate. Utilizing an n-type substrate with an epitaxially-grown intrinsic layer, a row of p-type diffusions form a diode array. A profile of this structure is shown in Fig. 1. Note that over most of the Si surface the SiO_2 layer is sufficiently thick so that there is no significant coupling of optical energy from the waveguide into the Si substrate. However, as light propagates into the detector region the SiO_2 layer is tapered to a much smaller thickness, allowing significant optical coupling into the Si substrate to occur in this region. In the detector region the waveguide structure thus has the same configuration and behaves in the same manner as the prism-coupler, the detector region being formed in the coupling prism. Because of the similarity with the prism coupler, the detector region can be designed so that essentially complete transfer of optical energy from the waveguide to the detector region occurs.[3] Allowing light to optically tunnel into the detector region in this manner avoids reflection loss associated with previous designs of integrated optical detectors.[4,5,6] The present waveguide-detector design also allows use of a thicker SiO_2 layer in the detector region so that only a small fraction of the light would couple to the detector; the remainder would continue to propagate. Such a structure would be useful for continuous beam monitoring.

[1] Supported in part by the National Science Foundation and the Harry Diamond Laboratories, Department of the Army.

[2] H. W. Weber, *et al.*, *Appl. Phys. Lett.*, vol. 20, p. 143, 1972.

[3] J. H. Harris *et al.*, *IEEE Trans. MTT*, vol. 19, p. 269, 1971.

[4] D. B. Ostrowski *et al.*, *Appl. Phys. Lett.*, vol. 22, p. 463, 1973.

[5] W. Duncan *et al.*, *Opt. Commun.*, vol. 10, p. 371, 1974.

[6] G. E. Stillman *et al.*, *Appl. Phys. Lett.*, vol. 25, p. 36, 1974.

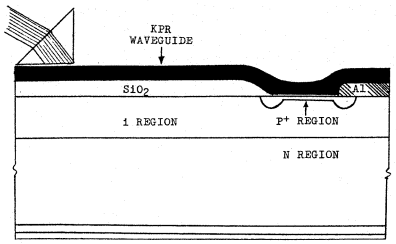

Fig. 1. Profile of waveguide-photodiode structure.

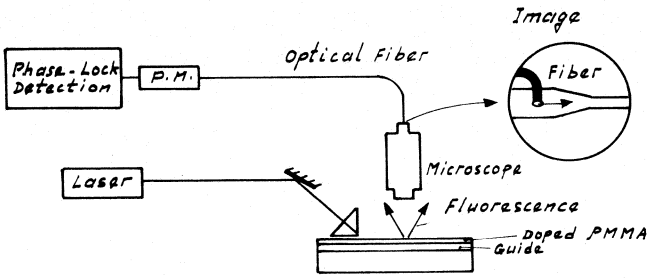

Fig. 1. Schematic of fluorescent light measurement.

The detector array structures described above have been fabricated using the established processes of silicon device technology. A special etching procedure is necessary to properly form the tapered region. A diffused guard ring structure is incorporated in order to improve device performance. Formation of the waveguide utilized a previously described procedure.[2]

Operation of one of the integrated optical photodiode array structures is illustrated in Fig. 2. On the right portion of the Si wafer a row of photodiode bonding pads is visible. The detector region is directly adjacent to each bonding pad. On the left portion of the Si wafer a prism coupler (n_p = 1.8) couples He-Ne laser light into the optical waveguide. By viewing scattered light we see that the light beam propagates until it reaches the detector region. As the transverse extent of the light beam is greater than the detector width, only the central portion is absorbed, as illustrated in Fig. 2. Light outside this central portion continues to propagate between adjacent devices, finally terminating at a scratch intentionally introduced. The bright spots at the scratch provide a qualitative indication that the waveguide is characterized by low propagation losses. Experimental results regarding light coupling and propagation as well as photodiode responsivity and device quantum efficiency will be discussed. We will also discuss array geometry with regard to performance in integrated Fourier optical processing systems.

We acknowledge the technical assistance provided by J. T. Garrett.

10.8 Visualization of Optical Fields in Integrated Optical Tapers and Bifurcations, D. B. Ostrowsky, A. M. Roy and B. Séjourné, *Thomson-CSF, Orsay, France*

(15 min)

In this paper we report the first detailed quantitative measurements of optical fields propagating in passive integrated optical components.

The components were fabricated by direct electron beam writing in PPS, an electron resist which serves as an optical waveguide[1] (n = 1.57). The optical fields of guided 6328 Å light were visualized by depositing a thin (~2000 Å) Rhodamine B doped PMMA film on the guiding structure and observing the anti-stokes fluorescence (5900 Å) induced by the guided light.[2]

The fluorescence (which is directly proportional to the local guided intensity) was measured using the device schematized in Fig. 1.

A scanning fiber optic probe is used which accepts light emitted from a 1 to 5 μm diameter (depending upon the magnifying power of the objective) region of the structure being observed and transports this light to a photomultiplier.

Among the components examined to date we wish to report on: triangular transitions between wide and narrow guides (Fig. 2(a); bifurcations dividing light from one guide into two separate guides (Fig. 2(b).

In the first case we have measured the power density augmentations one can obtain in passing from 20, 10 and 5 μm wide guides to 5, 2 and 1 μm waveguides.

Power density augmentations of 30% have been attained for a 20-5 μm transition.

In the second case we have measured the

Fig. 2. Waveguide-photodiode operation. Note that only the central portion of the light beam encounters the diode region.

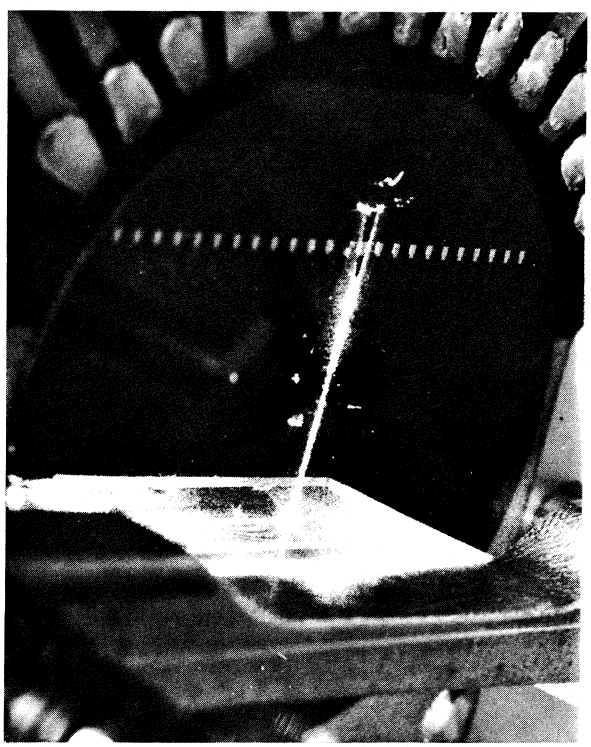

[1] D. B. Ostrowsky *et al.*, *Appl. Opt.*, vol. 13, p. 636, 1974.

[2] D. B. Ostrowsky, A. M. Roy and J. Sevin, *Appl. Phys. Lett.*, vol. 24, p. 553, 1974.

Fig. 2. Integrated optical components. (a) transition; (b) bifurcation.

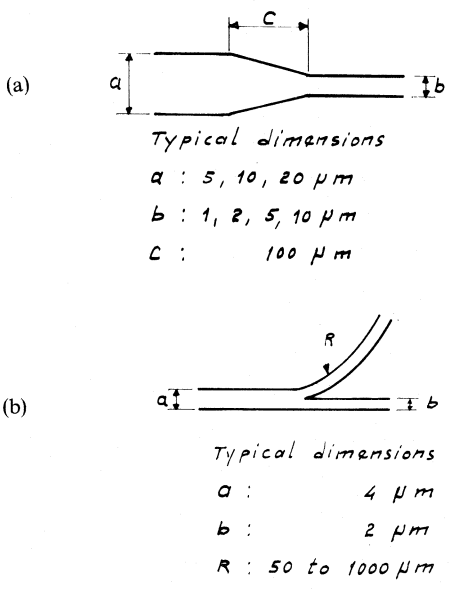

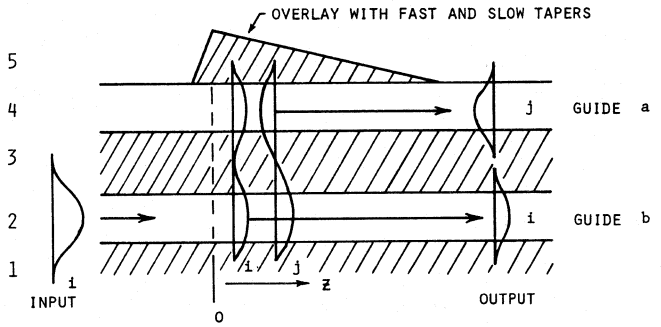

Fig. 1. Evolution of local normal modes in 3-dB coupler.

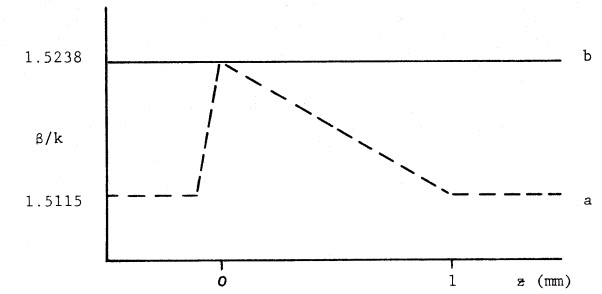

Fig. 2. Effective indices for the modes of the guides taken separately.

polarization dependence of the fraction of light which passes into each of the arms of the bifurcation. Typically TM modes have a tendency to continue in the straight section and TE modes have a tendency to leave via the curved section. Discrimination ratios of up to 80% have been measured.

10.9 A New Optical 3-dB Coupler, W. K. Burns, A. F. Milton, E. J. West and A. B. Lee, *Naval Research Laboratory, Washington, D.C. 20375*

(15 min)

Three-dB couplers or power dividers are expected to be important components in optical waveguide amplitude modulators or switches which operate by interferring two phase-shifted guided waves.[1] The conventional 3-dB coupler operates by maintaining a degree of velocity synchronism between two coupled waveguides over a coupling length L. Fabrication tolerances pose a difficult problem in construction of such a coupler, since the necessary length L for 50-50 power division between the coupled guides depends on the coupling constant. Also the degree of synchronism must be maintained over the coupling length L.

We propose a novel device which allows 50-50 power division between two coupled waveguides with reduced fabrication tolerances. It requires a degree of mode synchronism only at a single point, and the exact length of the coupler is not critical. The coupler (Fig. 1) consists of two coupled, planar waveguides with a small section of overlaid superstrate which makes that section of the device symmetrical. The overlay is introduced abruptly and removed slowly by constructing it with fast and slow tapers. Precise mode synchronism between the two guiding regions is required only at $z = 0$ where the overlay is introduced. Sections of the device without the overlay are nonsynchronous.

In the local normal mode picture, operation of the coupler is as follows. An input local normal mode from the left, confined to guide b, propagates to the point $z = 0$ where synchronism between the two guides is abruptly introduced. At this point the symmetrical (i) and anti-symmetrical (j) local normal modes of the coupled structure are excited, each with one-half of the input power. Synchronism is then slowly removed so that modal evolution causes mode i to select guide b, while mode j selects guide a. Since this operation is slow, the 50-50 power division between i and j is retained, and 3-dB coupling is achieved.

To analyze this coupler we revert to a coupled mode theory formulism and recognize the coupler's similarity to a tapered velocity coupler, divided at the point of mode synchronism. The slow and fast tapers must be designed to provide negligible and cumulative mode conversion between the two local normal modes respectively.[2] The slope of the slow and fast tapers must satisfy respectively,

$$\left|\frac{d\Delta\beta}{dz}\right|_{-} \leqslant .8KK^* \quad \text{and} \quad \left|\frac{d\Delta\beta}{dz}\right| \geqslant 150KK^*. \quad (1)$$

Here $\Delta\beta = \beta_a - \beta_b$ and K are the coupled mode theory synchronism and coupling coefficients. Effective indices for the modes associated with the individual guiding regions, a and b, are shown in Fig. 2. A second design requirement is for the local normal modes to contain essentially all their power in a single guiding region at each end of the coupler where $\Delta\beta$ is large. In particular if we allow 1% of the local normal mode power to be in the second guide then at both ends we must maintain:

$$\left|\frac{K}{\Delta\beta}\right| \leqslant .1 \quad (2)$$

We have chosen an experimental system of 7059 glass guiding layers and SiO_2 cladding layers. Indices in Fig. 1 are $n_1 = 1.457$, $n_2 = n_4 = 1.561$, $n_3 = 1.476$, $n_5 = 1.476$ or 1. Layer thicknesses that satisfy (2) are $d_2 = .525$ μm, $d_3 = .76$ μm, $d_4 = .5$ μm, $d_5 = 1$ μm. Then $|\Delta\beta/k| = .012$, (where $k = 2\pi/,6328$ μm), in the non-synchronous regions. Application of (1) then requires that the fast and slow tapers have lengths of $\leqslant 5.4$ μm and $\geqslant 1.0$ mm respectively. These taper lengths have been experimentally achieved by photolithographic and sputter etching techniques for the fast taper and by masking techniques for the slow taper. Prism coupling measurements of mode effective indices are in progress and experimental results of power transfer will be reported.

[1] F. Zernike, "Integrated optic switch," Topical Meeting on Integrated Optics, New Orleans, 1974.

[2] A. F. Milton and W. K. Burns, "The design of tapered velocity couplers for integrated optics," to be published.

Session 11

Thursday, May 29, 1975 1:30-5:00 P.M.

Laser Fusion II

Chairman: A. J. Alcock, *National Research Council, Ottawa, Canada*

Organizer: E. Beckner, *Sandia Laboratories, Albuquerque, N. M.*

11.1 The Pulsed High Power Iodine Laser Asterix III, G. Brederlow, K. J. Witte, E. Fill, K. Hohla, and R. Volk, *Max-Planck-Institut für Plasmaphysik, EURATOM-Association, Garching, W. Germany*

(15 min)

A system description and first results of the high power iodine laser Asterix III, designed to yield an output energy of 1 kJ in 1 ns is given. This laser ($\lambda = 1.315$ μ) is an optically pumped single-beam version intended for use in laser fusion investigations.

The system consists of a mode-locked oscillator and three amplifiers. The oscillator delivers a mode-locked pulse train from which a single pulse is extracted by means of a pulse cutting system. The beam divergence is 0.8 mrad in keeping with the TEM_{00} mode of the oscillator. The pulse length is dependent on the gas pressure and varies between 3 and 0.7 ns. The first amplifier has an internal diameter of 2.5 cm and

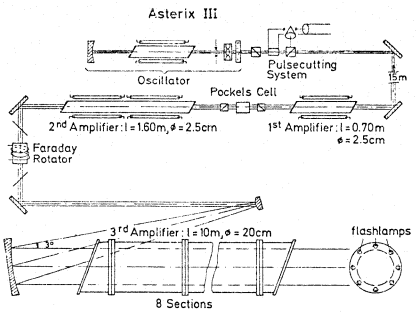

Fig. 1. Schematic set-up of Asterix III.

is located 15 m behind the oscillator. This distance is chosen such that the beam emanating from the oscillator and widening owing to its natural divergence fits the diameter of the amplifier tube. The second amplifier has the same internal diameter as the first one. It is optically isolated from the latter by a Pockels cell. Behind the second amplifier the beam is expanded from 2.5 cm to 20 cm by means of an off-axis Cassegrain system. The distance between the second and third amplifier is about 50 m. Optical isolation is further improved by means of a Faraday rotator.

The third amplifier provides the actual energy amplification. The input energy of 6 J is supposed to be amplified here to about 1 kJ. This amplifier consists of a stainless steel tube assembled from eight sections with an active length of 1 m each.

While the oscillator and the first and second amplifiers consist of quartz tubes pumped by external flashlamps, the third amplifier has the flashlamps inside the metal tube, there being eight lamps in each section with an energy intake of 5 kJ each.

The laser medium in the amplifiers consists of a mixture of C_3F_7I and CO_2. The partial pressure of the C_3F_7I is chosen such that the most uniform possible illumination of the amplification cross-section is ensured. The partial pressure of the CO_2 for the individual amplifier, on the other hand, is chosen such that the stimulated emission cross-section is reduced so much that the maximum small signal amplification of which the amplifier is capable is not exceeded.

The oscillator, the pulse cutting system and the first and second amplifiers could be taken over with appropriate modifications from Asterix II, the 100 J/l ns pulse laser. The choice of the final concept for the third amplifier, however, required a number of basic investigations.

We measured the inversion profile as a function of the C_3F_7I pressure and of the pumping energy. It turned out that at a C_3F_7I pressure of 4 Torr the inversion at the edge is 15% higher than in the center. Reducing the C_3F_7I pressure makes the inversion profile more homogeneous but also decreases the energy stored. At the pressure value mentioned the energy stored per section is 210 J at a capacitor energy of 37 kJ. The storable energy increases at the same rate as the pump energy.

In order to keep the storable energy at the required value, CO_2 has to be added in such an amount that the small signal amplification V_{th} of which the amplifier is capable is not exceeded. Extrapolation of measurements made with two sections yielded a value of $V_{th} \approx 10^5$ for all eight sections.

The optical homogeneity of the active medium will be disturbed by shock waves caused by the evaporation of deposits on the walls by the pump light. These waves propagate with low supersonic speed ($V = 0.3$ mm/μs) towards the center of the tube. Therefore the pumping time of this amplifier should not exceed 20 μs.

With the results reported the conditions under which the entire system has to be operated are known. As the laser is scheduled for completion in the next two months, first experimental results on the performance of the complete system can be expected soon.

11.2 Pressure Broadening and Saturation Behaviour of the Iodine Laser, W. Fuss and K. Hohla, *Max-Planck-Institut für Plasmaphysik, EURATOM-Association, Garching, W. Germany*

(15 min)

Storable energy of a high power laser is inversely proportional to the maximum of the stimulated emission cross section σ. Addition of a foreign gas broadens the emission line by collision and thereby lowers σ. In the iodine laser line complications arise from its hyperfine structure (hfs). Whereas for a single hfs line, $1/\sigma$ linearly depends on the partial pressures P_i,

$$1/\sigma = \beta_0 + \sum_i \beta_i P_i$$

no simple relationship can be expected if overlap of lines varies. In this case also the saturation behavior changes: The saturation energy per cm^2

$$e_s = \frac{h\nu}{\sigma(1 + g_u/g_l)}$$

can no longer be calculated with the level degeneracies g_u and g_l of a single transition. We were able to determine the saturation energy as well as the degeneracy factors – and thereby σ – as functions of the pressures of some gases [Ar, N_2, CO, CO_2, SF_6, CF_3Br, C_3F_7I, CF_2Cl_2, $(CF_3)_2$ CO]. The saturation energy e_s has been determined by measuring high and low signal gain (V and V_{lo}) and the input energy e_{in}, using the equation

$$V = \frac{e_s}{e_{in}} \ln\left(1 + \left[\exp\frac{e_{in}}{e_s} - 1\right] V_{lo}\right)$$

Because the spectrum is inhomogeneous, only a fraction a can respond to a single input frequency. The saturation energy must then be written

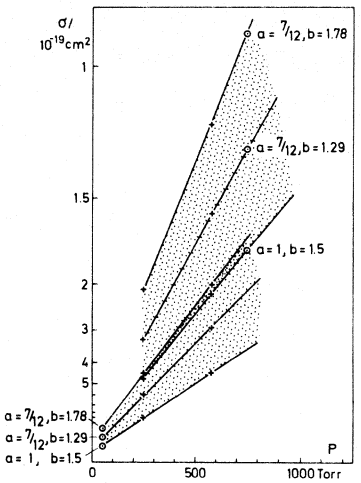

Fig. 1. $1/\sigma$ as a function of pressure (50 torrs C_3F_7I; balance CO_2); Θ "absolute" measurements based on e_s assuming different a and b parameters; + relative measurements based on the high and low pressure values, respectively.

$$e_s = a\frac{h\nu}{b\sigma},$$

where $b = 1 + g_u/g_l$. If a/b is known, σ can be calculated from e_s. Furthermore we determined relative σ values at different pressures from the ratios $\log V(p)/\log V(p_0)$ (V = low signal gain). These ratios of $\sigma(p)/\sigma(po)$ are independent of the respective a/b value at the pressure p. These ratios can be multiplied by $\sigma(p_0)$ calculated from e_s inserting all possible values of a and b. In the figure this has been done with two different values of p_0. It turns out that the measurements are only consistent if $a = 7/12$, $b = 1.78$ at low pressure and $a = 1$, b = 1.5 at high p_0. These a and b parameters are valid for ns pulses, by which they have been measured. a/b rises for longer pulses by the influence of relaxations between hfs sublevels as well as by the recombination of the radicals (from photolysis) with ground state iodine atoms.

For all gases investigated, $1/\sigma$ plotted versus pressure results in straight lines. This yet unexplained fact is not expected because the overlap of the hfs lines can be calculated to vary considerably over the respective pressure range.

For the purpose of energy storage CO_2 seems to be the best compromise between pressure broadening and deactivation of I*. At one atmosphere of CO_2 about 7 J cm^{-3} can be stored, hfs is extensively blurred, the energy can be extracted by a short single frequency input pulse, and amplification of pulses shorter than 100 ps should be possible. The "broadening coefficient" β_{CO_2} is by a factor of two higher than the Ar value. Our $\beta_{Ar} = 3.55 \cdot 10^{-15}$ cm^{-2} $Torr^{-1}$ compares favorably with former measurements.[1]

[1] F. T. Alridge, *Appl. Phys. Lett.*, vol. 22, p. 180, 1973; V. S. Zujev, V. A. Katulin, V. Ju. Nosac, and O. Ju. Nosac, *ZETF*, vol. 62, p. 1673, 1972.

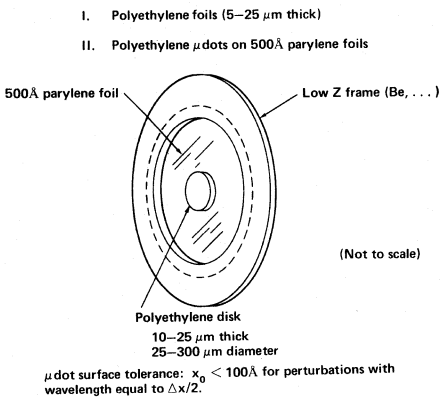

Fig. 1. Slab acceleration targets.

11.3 "Valkyrie," A CO_2 Laser System for Laser Fusion Experiments,[1] K. R. Manes, *Lawrence Livermore Laboratory, Livermore, Calif. 94550*

(15 min)

The Livermore CO_2 laser system, Valkyrie, was constructed to provide an experimental facility capable of delivering 50 J in a diffraction limited beam at 10.6 μm in ~1 nsec. This device has met all of its design goals and is in operation as a target irradiation facility. On a typical day, Valkyrie provides 40 J ± 10% in ~1 nsec at a repetition rate limited by the time required to replace targets.

In order to design Valkyrie a CO_2 amplifier modeling computer program predicted the output of individual amplifier modules. This information was fed into a laser system simulation routine in order to determine amplifier staging. Once specified and manufactured, Valkyrie's amplifiers were subjected to an exhaustive series of tests. Small signal gain as a function of gas mixture, E/n, pump pulse duration, and spatial position was measured.

Valkyrie's oscillator employs a specially designed UV preionized TFA gain medium (Lumonics 142A), a Ge Brewster's angle acoustooptic mode-locker, and an NaCl etalon as an output mirror. This oscillator generates a burst of 1 nsec duration pulses with peak pulse energies in excess of 50 mJ distributed reproducibly among ~six rotational lines centered on the $P20$ transition of the 10.4 μm band. A single pulse is selected by a switch-out assembly consisting of a laser triggered spark gap and CdTe Pockel's cells. The pulse is then directed through a second Lumonics 142A which serves as a preamplifier and into a 3× Keplerian beam expander with a spatial filter at its focus. Expended and collimated, the pulse propagates through a nine centimeter aperture UV-preionized TEA amplifier (Lumonics 602A) followed by two eleven centimeter aperture cold-cathode E-beam sustained amplifiers operated at two atmospheres. Emerging in the target area, the pulse contains ~50 J in 1 nsec with an approximately Gaussian spatial intensity distribution. Two NaCl beamsplitters which are wedged and anti-reflection coated with NaF on one face provide diagnostic beams for intensity profile, energy, temporal character and spectral measurements. The main beam is finally focussed to an ~80 μm diameter spot by an f/2 aspheric NaCl lens mounted inside a spherical vacuum vessel. When this laser-target chamber system became available in September, attention was concentrated on assembling and calibrating diagnostics, suppressing parasitic oscillations, and other laser system related problems.

By December X-ray spectral measurements, ion studies and electron spectral measurements were underway on CD_2 and CH_2 targets. Slab acceleration studies are planned for the first months of 1975. In these experiments, targets such as that illustrated in Fig. 1 will be illuminated from one side by the laser and the development of plasma density and temperature gradients as a function of time will be recorded.

[1] Work performed under the auspices of the Atomic Energy Commission.

11.4 Measurement of Beam Quality from Short Pulse CO_2 Lasers,[1] I. Liberman, *Westinghouse Research Laboratories, Pittsburgh, Pa.*, and M. J. Bennett, J. J. Hayden, and S. Singer, *Los Alamos Scientific Laboratory, Los Alamos, N. M. 87544*

(15 min)

Lasers built for fusion application must not only be capable of delivering high power, but this power must be focused onto extremely small pellets. The minimum laser spot size obtainable is known from well established diffraction theory. However, in high power laser systems, phase distortion due to apertures, imperfections in large optics, inhomogeneities in heated active laser media, etc., results in laser beam quality which can deviate significantly from the diffraction limit. This paper describes two methods of measuring the beam quality of a nominal 1 J, 1 ns, CO_2 TEA laser oscillator preamplifier chain which drives a 2.5 kJ amplifier for fusion application.

The mode-locked oscillator and switch-out crystal provide about a 5 mJ 1.6 ns single pulse and about 0.1 mJ total of unwanted mode-locked pulses. The output beam is expanded and amplified by two nearly identical TEA laser discharge volumes having a 3.5 cm square discharge region and each discharge length being about 1.3 m. At the output of the second preamplifier the gain medium is saturated and we assume (somewhat inaccurately) for purposes of comparing measured results with theory that the desired output beam has a uniform intensity across a 3.5 cm diameter circle. The measured total energy is about 2 J of which 1.5 J is in a single 1.6 ns pulse.

Using our primary method for measuring the laser optical quality, the beam is focused with a 1.5 m focal length mirror. A grating is placed about 30 cm after this mirror. The grating diffracts the beam into multiple orders with each order of essentially identical shape, but different intensity.[2] The grating spacing is .180 cm with an open width of .033 cm resulting in a transmission, T, of 18.3%. From elementary grating diffraction theory the intensity of the first five orders relative to the zero order are .89, .63, .33, .10, .008 respectively. At the focal plane of the diffracted spots a film of UV sensitized Kalvar 100 is placed. The properties of this film have been extensively studied[3] and it has been found that it has a resolution greater than 100 l/mm and a calibrated energy density range of ~0.75-3.1 J/cm^2. Under the existing experimental conditions, exposed spots are observed for the zero and first four orders. Since the diffracted intensity variations overlap the dynamic range of the Kalvar film, a composite spot pattern is obtained. A smooth transition from spot pattern to spot pattern requires multiplying the recorded 1st to 4th order intensities by .91, .62, .37, and .15 respectively, which agrees reasonably well with the grating formula calculation. After multiplying the energy by T^{-2} the results show that the focal spot without the grating present has a peak energy density of 433 J/cm^2 and that at 30 J/cm^2, the lowest energy density measured, the spot radius is 0.55 mm. The diffraction limited spot is calculated to have a peak energy density of 761 J/cm^2 and an Airy disk radius of 0.55 mm. Therefore, based on the ratio of peak energy densities, the beam is 1.76 times diffraction limited.

The second measurement depends on knowing the breakdown strength of argon vs. pressure. Rockwood[4] has calculated this function which agrees favorably with the measured results of Alcock[5] and Franzen.[6] Our measurement of breakdown threshold of 225 Torr from a 1.5 J, 1.6 ns pulse focused in an argon cell with a 2.5 m focal length mirror results in a peak power density of 7.1×10^{10} W/cm^2. The diffraction limited power is calculated to be 12.8×10^{10} W/cm^2. Therefore from this measurement the beam is 1.80 times the diffraction limit.

The two methods agree with each other to better than the accuracy of each measurement. These techniques are a rapid, relatively simple, accurate way of measuring the optical quality of a broad range of high powered lasers.

[1] This work was performed under the auspices of the U. S. Atomic Energy Commission and the Westinghouse Electric Corporation.

[2] R. W. O'Neil, *et al.*, *Appl. Opt.*, vol. 13, p. 314, 1974.

[3] J. Manning and Q. Klingler, "Kalvar Film Report," EG&G report LAO-196 under AEC contract AT (29-1)1183, Los Alamos, N. M., Oct. 1974.

[4] S. Rockwood, unpublished.

[5] A. J. Alcock and M. C. Richardson, *Phys. Rev. Lett.*, vol. 21, p. 667, 1968.

[6] D. L. Franzen, *Appl. Phys. Lett.*, vol. 21, p. 62, 1972.

11.5 The LASL 2-5 kJ CO_2 Short-Pulse Laser System (*Invited*), S. Singer, *Los Alamos Scientific Laboratory, Los Alamos, N. M. 87544*

(30 min)

The design and performance of the LASL CO_2 2.5 kJ laser will be described. It is intended to deliver to a target system two 35 cm diameter beams, with 1250 J per beam in a 1 nsec pulse,

focused to an intensity of 10^{15} W/cm^2. The system will be used to study techniques of gain suppression and target isolation as well as laser-plasma interaction at 10.6 μm at energy inputs an order of magnitude larger than previously available. This laser system will form the basis for the LASL 10 kJ laser now under construction.

11.6 The Physics of Laser Fusion (*Invited*), G. H. McCall, *Los Alamos Scientific Laboratory, Los Alamos, N. M. 87544*

(30 min)

The results and interpretation of laser fusion experiments at 1.06 μ and 10.6 μ will be presented.

11.7 Investigations of Laser Fusion by CO_2 Laser, C. Yamanaka, M. Yokoyama, S. Nakai, M. Matoba, and C. Yamabe, *Institute of Laser Engineering, Osaka University, Osaka, Japan*

(15 min)

Experiments on laser plasma interaction using a CO_2 laser (wavelength 10.6 μm) give us detailed information on the interaction mechanisms. The feasibility of laser fusion is going to require high power CO_2 lasers. For this purpose we have been developing a high power E-beam controlled CO_2 laser system with 200 J output in one nsec and a double discharge CO_2 laser of 100 J in 100 nsec. For the former, to improve the energy extraction we have made a two band, multiline TEA laser oscillator and also investigated the high pressure ($\sim$15 atm) *E*-beam CO_2 laser oscillator.

The *E*-beam controlled CO_2 laser system consists of the following parts: oscillator, with Ge acoustooptical mode locker in the cavity; GaAs optical shutter combined with Ge polarizer to select one pulse from the mode-locked pulse train, or to chop out a pulse of nsec duration from *Q*-switched pulse; pre-amplifier; *E*-beam controlled main amplifier stages of No. 1 (5 cm × 5 cm × 80 cm), No. 2 (10 cm × 10 cm × 100 cm) and No. 3 (20 cm × 20 cm × 200 cm).

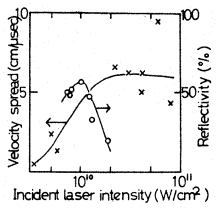

Fig. 1. Variation of reflectivity and velocity spread of blow-off plasma against incident laser intensity.

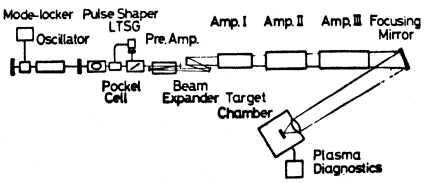

Fig. 2. *E*-beam controlled CO_2 laser system, 200 J, 1 ns.

For the experiments on laser interaction with plasma, we have used various diagnostic methods. They are an X-ray pinhole camera to make an X-ray image of the target, thermofluorescence X-ray dosimeter, and scintillator photomultiplier combinations with different absorbers to analyze X-ray energy, incident and reflected beam monitors to measure the reflectivity at the plasma surface, time of flight measurements by charge collectors, interferometric measurements to measure the plasma density and measurements of higher harmonic components in reflected light.

We measured the reflectivity for the frequency ω_0 and back scattering of frequency $2\omega_0$. The reflectivity at frequency ω_0 showed a maximum ($\sim$56%) at a laser power intensity of about 1.1×10^{10} W/cm^2, and above this value, the reflectivity decreased (Fig. 1). It was also observed that the velocity spread of ions, that may indicate the ion temperature of blow-off plasma, increased at the incident laser power intensity which showed the decrease of the reflectivity.

The electron temperature was also estimated from the X-ray measurements. The plasma seemed to be heated by the anomalous absorption due to parametric instability. Energetic X-rays were also observed due to high energy electrons.

For the alternative study of the absorption mechanism, we use a double discharge TEA CO_2 laser and the dense plasma of a plasma focus device as a target plasma. A Mather type coaxial cylindrical gun with maximum available input energy 14 KJ (12 μF, 50 kV) was used. Preliminary experiments show enhancement of X-ray emission from the plasma focus with CO_2 laser irradiation. Neutron measurements are also made.

The arrangement of our *E*-beam controlled CO_2 laser system is shown in Table I and Fig. 2.

11.8 A Nd Laser System Developed for Target Irradiation Studies at the Lawrence Livermore Laboratory,[1] D. R. Speck and J. F. Holzrichter, *Lawrence Livermore Laboratory, Livermore, Calif. 94550*

(15 min)

The LLL JANUS laser uses a Nd:YAG oscillator and Nd:glass amplifiers to provide one and two beam irradiation of laser fusion targets with 100 pico-second duration pulses. The system is constructed from components which are under development at LLL for the planned 10 KJ laser system (SHIVA). It is devoted to irradiation experiments to study the physics of laser plasma interaction and to evaluate laser fusion target designs.

The JANUS system consists of a dye mode-locked Nd:YAG oscillator, a Nd:YAG preamplifier, beam shaping optics, three 25 mm × 250 mm Nd:glass rod preamplifiers with optical isolators and a series of Nd:glass disk amplifiers with Faraday rotator optical isolators. Two sizes of disk amplifiers are used; the "A" size with a 35 mm clear aperture containing 6 15 mm thick brewster angle disks, and the "B" size with an 85 mm clear aperture containing 6 23.5 mm thick brewster angle disks. Prepulses and amplified spontaneous emission which cause premature target damage are controlled with bleachable dye cells. Their use will be discussed.

The principal design criterion used in assembling the system has been to minimize self-focusing effects which limit the output of short pulse glass lasers. This has been done by maintaining a temporally and spatially smooth pulse and by minimizing the integrated gain for the growth of self-focusing instabilities, *B*, through the amplifier train;[2]

$$B = \frac{8\pi^2}{\lambda_{vac} C} \int_0^z \frac{n_2}{n_0} I \, dZ.$$

The pulse is spatially smoothed and shaped

TABLE I
E-BEAM CONTROLLED CO_2 LASER SYSTEM "GEKKO II"

	Oscillator TEA	Pre-Amp. TEA	Amp.-I Hot Cathode	Amp.-II Cold Cathode	Amp.-III Cold Cathode
Active size (cm)	2.5 × 2.5 × 60	2.5 × 2.5 × 60	5 × 5 × 80	10 × 10 × 100	20 × 20 × 200
Volume (l)	0.4	0.4	2	10	80
Pressure (atm)	1	1	2	2	2
Pumping energy	62 J	62 J	10 kJ	67.5 kJ	180 kJ
Output power (ns pulse)	1 mJ	0.5 J	5 J	50 J	200 J

[1] Work performed under the auspices of the U. S. Atomic Energy Commission.

[2] Bliss, Speck, Holzrichter, Erkkila, and Glass, *Appl. Phys. Lett.*, vol. 25, p. 448, 1974.

before it enters the amplifier system with a spatial filter and apodized aperture. The shape generated is $I(r) = I_0 e^{-(r/r_0)^5}$ which propagates the length of the amplifier free of diffraction irregularities. B is minimized by employing high gain amplifiers, minimizing the length of glass in components, minimizing losses and by proper staging.

Experimentally it is observed that the energy which can be focused onto fusion targets is limited by beam break-up. This arises from self focusing instabilities. Beam break-up is manifested by: 1) high intensity spots in the beam which may be many times the average intensity and cause damage to components, 2) an apparent decrease in amplification of the chain resulting from losses caused by filament formation, and, 3) a catastrophic increase in focal spot size caused by self-induced phase distortions as the beam breaks-up. These three effects have been observed; (3) is particularly important in limiting the energy coupled to small targets employed in laser fusion. Time integrated and time resolved far field photographs of the JANUS output have been taken and the fraction of the beam energy intercepted by fusion targets has been measured as the output energy increases. This data will be presented and correlated with the gain for instability growth, B.

11.9 Laser Plasma Interaction Studies at LLL,[1] J. F. Holzrichter, H. G. Ahlstrom, and R. A. Haas, *Lawrence Livermore Laboratory, Livermore, Calif. 94550*

(15 min)

This paper describes the results of studies which are being pursued on the interaction of high intensity laser radiation with laser fusion targets. The purpose of these studies is to provide an experimental basis for achieving efficient laser fusion. Two lasers, a 20 Joule, 100 psec Nd:glass laser system (JANUS) and a 30 Joule, 1 nsec CO_2 laser (VALKYRIE), have been used for the irradiation experiments. Both of these systems are described elsewhere.

The main thrust of the experiments has been to account for optical propagation and energy transport in fusion targets which are smaller than 200 μ Dia. Accurate measurements of the absorption, reflection and transmission of the optical energy are most important because they determine the overall energy balance. The absorbed energy is subsequently partitioned into fluid motion (electrons and ions), X-rays, and eventually neutrons. The results of absorption and energy distribution measurements will be described.

Detailed studies on the focusing properties of the 1.06 μ laser beam from the Janus system have been carried out by time resolving the focal spot of an f/1 lens. It has been found that the focal spot is well behaved at a power output of 0.1 terrawatt. As the laser power is raised above this level, the beam begins to break up. Little additional beam energy is stopped by the target and the scattered radiation completely confuses the target interaction experiments.

Another problem arises when optical energy reaches the target before the main laser pulse. This radiation can alter the target and make the experimental results meaningless. Amplified spontaneous emission (ASE) levels above 10 mJ and laser pre-pulses above 0.1 mJ can damage fusion targets. The Janus system when not isolated will produced 20 mJ of ASE and 1.0-2.0 mJ prepulses. Examples of these problems and corrective techniques will be given.

In order to determine the energy budget in targets, the incident and scattered energy fluxes have been measured. The energy scattered backward and forward, into the focusing lenses, and energy scattered into a 2π steradian parabola is measured with calorimeters. Energy scattered into the remaining 2π steradian is detected with photodiodes. Accounting for all scattered energy indicates that for some of these targets greater than 60% of the incident laser radiation is absorbed. The details of optical propagation experiments in these targets, with particular emphasis on refraction and time resolved transmission will be described. Also details concerning the X-ray emission and plasma motion will be presented.

Laser produced plasmas vary in temperature from $\sim$100 ev to $\sim$2.3 keV. As a consequence X-ray radiation is the most useful diagnostic for determining the state of the target. A variety of techniques have been developed at LLL and elsewhere to diagnose this radiation. They include absolute X-ray spectrometry, from <1 keV to 80 keV, X-ray imaging with <7 micron resolution at 1 keV, and time resolution of <100 psec at 1 keV. These diagnostics are being employed to determine the state of glass ball fusion targets and metal foil X-ray targets. The X-ray performances of these targets will be described.

The most important objective of our experiments is to cause target compressions which will lead to efficient laser fusion. Such compressions (>1000 $\times$ solid density) require a detailed knowledge of the conversion of optical radiation to plasma motion. To this end, the motion of thin slab targets is observed while they are being irradiated by intense laser radiation. In these experiments streak camera photography and interferometric techniques are employed in concert with ion and X-ray diagnostics to measure the evolution of the accelerated foil. Because the motion of a thin slab simulates the motion of a thin shell section, the effect of fluid instabilities, electron preheat effects, etc., which would occur in an imploding shell can be observed. Experiments to date show that the slab motion is governed by high energy electron preheat of the back surface. Effects due to the initial breakdown of the target have also been observed.

Special Session 4:30 P.M.

11.10 Optical Communications in Perspective (*Invited*), R. Kompfner, *Stanford University, Stanford, Calif. and Oxford Univeristy, England*

(30 min)

No summary.

[1] Work performed under the auspices of the U. S. Atomic Energy Commission.

Session 12

Thursday, May 29, 1975 1:30-5:00 P.M.

Laser Machining and Material Processing

Chairman: Larry Osterink, *GTE Sylvania, Mountain View, Calif.*

12.1 High Power CO_2 Lasers for Industrial Applications (*Invited*), R. Hella, *Avco Corp., Everett, Mass.*

(30 min)

No summary.

12.2 Laser Processing in the Automotive Industry (*Invited*), M. Yessik and D. J. Schmatz, *Scientific Research Staff, Ford Motor Co., Dearborn, Mich. 48121*

(30 min.)

The types of laser processing of interest to the automotive industry fall into three categories: cutting and drilling, surface hardening, and welding. The desirability of using a laser for these applications is mainly the result of the high power densities, the ability to control precisely both the total power and the power density, and the small size and ease of manipulation of the beam. Because of the need for high average power outputs, in addition to the high power densities, the continuous CO_2 lasers have received the most attention for these applications.

Laser cutting and drilling is of interest for a wide variety of materials including metals, ceramics, plastics, rubber, and composites. The major advantages are simplified fixturing, fast cutting rates, and no limitation on the configuration of the cut. The particular characteristics of the oxygen-assisted laser cutting of steel are narrow kerf widths, small heat-affected zones and little or no slag. One potential application is the automatic cutting of option holes in the dash panel. Advantages of this system are greater precision in the location and size of the holes and the ability to cut other-than-circular holes. A laser-drilling application presently under development involves the drilling of the oil-metering holes in a rifle-bore camshaft. The high hardenability of the iron makes conventional drilling or punching very difficult, but does not affect the laser-drilling process.

Laser hardening has two major advantages over conventional techniques. The first is the ability to localize the hardening at the exact spot where it is needed. This minimizes the total heat input to the material and thus eliminates the distortions which often accompany other hardening techniques. Second is the ability to apply the heat to otherwise inaccessible areas, for example, small bores or complicated shapes not amenable to induction hardening. Both of these advantages stem from the small size and ease of manipulation of the beam. A particular applica-

tion presently under investigation is the hardening of the inner bore of the gray iron valve guides. The hardening is achieved through a solid-state transformation with no melting of the surface. No measurable distortion is produced and thus no additional machining is required.

Laser welding has similar advantages to the other laser processes: no contact with the work, small heat-affected zones, easy manipulation of the beam and high processing speeds. In addition, because of the deep penetrations obtainble, laser welds do not require the use of filler metals. The effect of the laser weld on the metallurgical structure is highly dependent on the particular material being welded, and as a result, some metals are much more amenable to laser welding than others. A potential laser welding application is the joining of a stack of laminations to form a motor stator. Another welding application which has reached the pilot-operation stage is the welding together of several stamped panels to form a car underbody. In both of these applications, the automated motion of the beam is of major importance.

A more extensive review of our current laser processing interests are to be published shortly.[1]

[1] M. Yessik and D. J. Schmatz, *Metal Progress*, May 1975.

12.3 Influence of Spatial Intensity Distribution of Laser Beam on Deep Welding Geometry, V. Boedecker and K.-H. Drake, *Institut für Angewandte Materialforschung, Bremen, Institut für Angewandte Physik, T.-U. Hannover*

(15 min)

With laser beams of high power and high power density the deep penetration welding effect can be obtained. Early models describing the influence of beam parameters on the welding geometry have been made for electron beam welding. In these theoretical models, the incident beam is considered to be parallel and the intensity distribution of the focussed beam is neglected. Therefore, in calculating the welding zone geometry, one can get information about the welded volume but not the depth and width of the fusion zone.

In this paper we present a new theoretical model describing the influence of welding parameters on the total welding geometry. This theory includes the welding velocity and the thermophysical properties of the material as well as the spatial intensity distribution of the focused laser beam. These considerations are valid for deep welding capillaries which are surrounded by a zone of molten metal.

To calculate the geometry of the fusion zone, the whole laser beam is divided into many small parts. Then the shape of the deep welding capillary results from the equilibrium condition that the energy of such a small beam incident on a small area of the capillary wall must be transported by heat conduction from this area. The temperature of the capillary wall is the vaporizing temperature of the material.

From these conditions a formula can be derived describing the total geometry of the vapor filled channel and the melting zone as a function of the welding velocity, the thermophysical properties of the material, and the spatial intensity distribution of the beam. This formula includes also the distance between the focal plane of the welding lens and the workpiece. Furthermore, the broadening of the beam due to scattering effects at the plasma cloud surrounding the welding zone can be considered. Also, estimations about the effects of non-constant temperatures within the capillary are possible.

The influence of all the above mentioned parameters on deep welding geometry has been calculated and proved by experimental investigations. Measurements have been carried out with high power lasers and with electron beams. The experimental results are in good agreement with the theory.

From this theory the optimum degree of focussing to get the desired welding geometry as a function of laser power, beam divergence and all the other welding parameters can be calculated.

12.4 Investigations on Laser-Welding, M. Montanarini and J. Steffen, *LASAG SA, Thun, Switzerland*

(15 min)

Laser welding has become an important process in many industrial production lines, since the laser promises several advantages compared with conventional welding means. The thermal influence of material outside the welding deposit is extremely low because of the short heating duration ($\simeq 1$ msec). The physical properties of the material are not influenced and therefore thermal sensitive materials, as e.g. springy, hard and brittle materials or magnets, can be welded.

The laser also overcomes certain problems of welding dissimilar materials with different thermal or electrical properties; however, the metallurgical problems of intermixing (formation of intermetallic compounds) and the resulting effects as reduced strength, generation of hot cracks, etc. have not yet been studied satisfactorily.

This paper presents some investigations on the influence of different laser parameters on the intermixing of dissimilar materials. The different intermixing states and some intermetallic compounds were detected in the weld with an electron beam microprobe analysis. By this analysis the most endangered zone (that is, the intermetallic interlayer between the deposit and the basic material) could be studied.

As a result of these investigations, a procedure to improve the weldability and the welding strength of materials showing bad weldability is demonstrated. This procedure is characterized by adding a welding agent to the weld and by intermixing it homogeneously in the deposit. Different metallurgical problems, such as formation of hot cracks and material softening, could be avoided by choosing appropriate agent materials.

As an example, a weld between a spring (Co, Cr, Ni, Fe-alloy) and a Fe piece was realized by adding Nb as welding agent. Laser parameters were suitably adapted in order to get a homogeneous Nb distribution in the deposit. In that way the difference of hardness between the deposit and the basic material is diminished and the weldability is improved.

This laser procedure differs from conventional techniques by the possibility to control the intermixing and recrystallization by an appropriate time performance of the laser emission. In addition the laser technique offers a larger selection of different welding partners. Control of the laser emission also allows one to influence the shape and the size of the weld and gives the possibility to optimize the constructive conditions.

12.5 Formation of SiC Heating Elements Using a CO_2 Laser, F. J. Hierholzer, *Emerson Electric Corp., St. Louis, Mo. 63136*

(15 min)

High-temperature resistors or heating elements are formed using a 250 watt CO_2 laser. The resistor elements are fabricated by placing particulate SiC grains into a "boat." An X-Y table moves the boat beneath the focused 10.6 μ beam. After the programmed motion is complete, the boat is removed from the X-Y table. A pair of tweezers is used to lift the resistor element from the remaining SiC grains. A metallization of the two ends of the resistor element completes the fabrication process.

The electrical properties of the resulting heating elements or resistors are measured by soldering or "clipping" leads to each of the two metallized regions. With heavily nitrogen doped (N type semiconductive) SiC, voltage, current and temperature of the resistors with increasing AC 60 Hz voltage show a slight negative temperature coefficient of resistance until a temperature of about 1400°F is reached. From 1400°F to 2600°F the resistor has a positive temperature coefficient of resistance. When the SiC is heavily aluminum doped (P type semiconductive), the resistor has a positive temperature coefficient of resistance throughout the entire temperature span. With either the P or N doped SiC the resistors had a resistance tracking from unit to unit (using the same material) during laser fabrication very close to $\pm 1\%$.

The CO_2 laser beam has a 10.6 μ wavelength which is almost completely absorbed by the SiC particles in the "boat." The beam strikes the surface of the particles in the boat and almost instantaneously raises the temperature of the SiC particles within the beam pattern to their sublimation temperature of about 2300°C. The SiC "burns" with a small flame within the energy beam and this temperature was measured using an optical pyrometer. The beam essentially "burns" a hole into the SiC powder and creates a cloud of SiC vapor as well as a deep "valley" in the powder. When the laser beam transverses the

surface of the SiC grains, this SiC vapor settles upon the clean SiC grains and "grows" the grains together. A self-bonded SiC heating element results. In addition to the "valley" and the "core" of the heating element, a "rind" is formed which when compared to the "core" is non-conductive. The "rind" is bonded together primarily by SiO_2 which is rapidly formed when SiC is heated above 1800°C in air.

Not all particle sizes of SiC will form a heating element using a laser beam of 250 watts CW. Particle sizes of 5 microns or less will not form a cohesive element. Particle sizes of 300 microns or greater will not bond together well.

12.6 Use of Pulsed Laser Treatment to Change Physical Properties of Metals and Semiconductors, I. Ya. Dekhtar, L. I. Ivanov, N. V. Karlov, A. M. Prokhorov, and N. N. Rykalin, *USSR*

(15 min)

(Received late; see page 83)

12.7 Laser Spot Welding and Real Time Evaluation, M. A. Saifi and S. J. Vahaviolos, *Western Electric Co., Inc., Engineering Research Center, Princeton, N. J. 08540*

(15 min)

This paper will discuss a technique for laser welding of insulated copper wires to terminal posts, and real time analysis of weld quality by stress wave emission (SWE) tests. The copper wire is 0.3 mm diameter polyurethane insulated and the terminal material used in this study is a Cu-Ni alloy commercially known as Monel. Typical welding (100 watt pulsed YAG welding system) parameters are: pulse length – 3.5 ms, energy/pulse – 10 joules, spot size – 1 mm.

The utility of this material combination is best illustrated by discussing the welding process as a function of time during the laser pulse. The beam is focused on the terminal shoulder. Its absorption causes an increase in the Monel's surface temperature and a transfer of heat towards the Monel-Cu interface. Surface temperature and depth of the melt zone can be estimated.[1,2] The calculations show that for a 0.3 mm thick shoulder, the surface reaches its vaporization temperature (3000°C), and the molten zone penetrates to the Monel-Cu interface within 1 to 1.5 ms. Since the melting point of Monel is about 150°C higher than that of copper, (with comparable specific heats) this results in rapid melting of the copper wire (insulation is burned out instantaneously) and wetting of the Monel surface with copper. In general, the melting point of copper rich Monel is always lower than that of Monel and higher than that of copper. Furthermore, the high thermal conductivity of copper soaks in the heat from the terminal and inhibits a rapid-rise in its temperature, which would tend to cause evaporation and welding instability.

We have found this Monel/Copper system to consistently produce good quality welds. The structure of the weldment was studied by the usual metalographic techniques which will be discussed. The welds were also pull tested, and the wire strength in close proximity to the weld was found to be over 50% of the original wire strength.

In many applications it is important to determine the weld quality during the welding cycle. This is particularly important in order to realize the full potential of high speed spot welding now possible with high repetition rate pulsed lasers. We have investigated SWE[3] during the laser welding cycle. As a criterion of weld quality, we have successfully used the number of zero crossings over a biased line, generally known as SWE counts. We have found good correlation within a well defined narrow band.

We will discuss in detail a model which describes the welding process, and the results of the SWE tests.

[1] R. H. Fairbanks, Sr., and C. M. Adams, Jr., "Laser beam fusion welding," *Welding J.* (Welding Research Supplement) 43:97-102S, March 1964.

[2] M. I. Cohen and J. P. Epperson, "Applications of lasers to microelectronic fabrication," *Electron Beam and Laser Beam Technology*, pp. 139-86, 1968.

[3] R. S. Sharpe, ed., *Research Techniques in Nondestructive Testing*. New York: Academic Press, 1970, Chapter 2.

12.8 Pulsed Laser Welding of Clad Metals, S. R. Bolin, *Raytheon Co., Waltham, Mass. 02154*

(15 min)

Pulsed laser welding is a widely accepted technique of metal joining. It is estimated that over 100 machines are in operation in this country. The advantages over conventional welding techniques (low heat input, welding of inaccessible locations, noncontact, etc.) are extensively detailed elsewhere.

High reflectivity materials have proven intractable to pulsed laser welding due to the large energy required to overcome reflective losses.

The approach taken here is to investigate the use of a high reflectivity base material clad with a layer of material of lower reflectivity which can be alloyed into the base material.

Literature suggests that welding may be promoted in highly reflective materials by application of a nonreflective coating to the metal surface. From a practical standpoint, this is effective only if the coating material will not contaminate the weld joint and if the coating is not removed by the laser pulse.

As the cladding material is not removed by the laser pulse, but rather is alloyed into the welded joint, the cladding and base materials must be metallurgically compatible. Pure copper sheet clad with a thin layer of nickel provides a most desirable combination to demonstrate this. Because the reflectivity of copper is much higher than that of nickel, approximately one fourth the energy required to weld bare copper is required for clad copper. Due to the wide range of solid solutions formed between copper and nickel, and the high cooling rates of laser welds, welds are of very high quality.

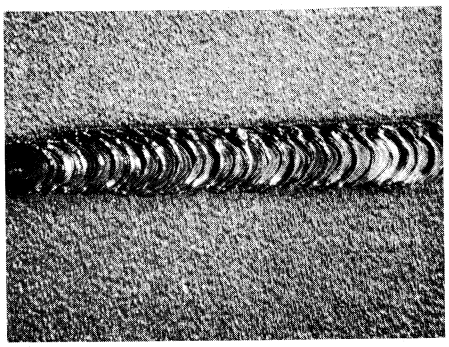

Fig. 1. Weld seam in nickel clad copper.

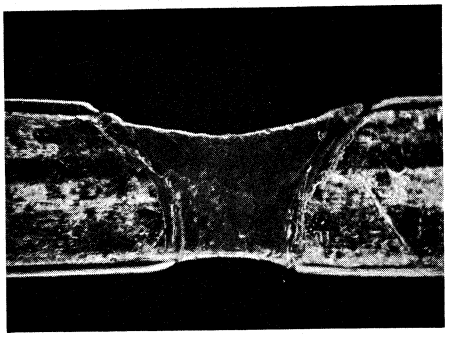

Fig. 2. Cross section of weld in nickel clad copper showing full penetration.

Fig. 1 shows a butt weld produced by overlapping spot welds. The material is pure copper 0.48 mm thick clad with .04 mm of pure nickel. A cross section of the same weld is shown in Fig. 2. Laser parameters were two pulses per second, each pulse being 9 milliseconds long, 18 joules energy. When the same conditions were used on unclad copper, only superficial melting occurred with no weld joint.

A unique feature observed in pulsed laser welding of clad materials is that penetration may be substantially increased by either slowing the advance of the laser or making multiple passes. This occurs as a result of increased alloying as the material is remelted by subsequent laser pulses. The penetration shown in Fig. 2 was achieved by applying 2 pulses in each position; penetration from a single pulse was typically about 0.23 mm.

The same material has also given good results for terminals and where lap welds are required. In production applications, the cladding material need only be placed in the actual weld area, thus reducing cost. This technique should be easily applicable to gold and silver. Application to aluminum may prove more difficult in terms of finding an appropriate cladding material which will alloy well with aluminum.

12.9 Change of Reflectivity of Metallic Surfaces during Irradiation by CO_2-TEA Laser Pulses, J. F. Ready, *Honeywell Corporate Research Center, Bloomington, Minn. 55420*
(15 min)

The reflectivity of metallic surfaces can undergo large changes during irradiation by high power laser pulses. This factor is important for applications involving welding and drilling, because it affects the amount of laser energy that actually is absorbed by the surface. It is especially significant for CO_2 lasers, because the initial reflectivity of metallic surfaces tends to be very high at the CO_2 laser wavelength. Despite the fact that this phenomenon has been recognized for some time, there is little quantitative data on how the reflectivity changes during irradiation.

We measured the change in reflectivity of metallic surfaces as a function of time during irradiation by pulses from a CO_2-TEA laser operating at 10.6 μ. The pulse duration could be varied from 100 nanoseconds (FWHM) to several microseconds by varying the gas mixture in the laser. The laser power density at the target could be varied up to 3×10^8 W/cm^2.

The reflectivity was monitored by a second probing beam from a low power continuous CO_2 laser, which used a grating reflector to control the wavelength at 9.6 μ. This beam was focused onto the same area struck by the TEA laser pulse. The amount of 9.6 μ light reflected from the surface was monitored by a fast pyroelectric detector or by a photovoltaic mercury cadmium telluride detector. The 9.6 μ probing beam was separated from scattered 10.6 μ radiation by interference filters. We measured both the specular reflectivity and the diffuse reflectivity within a specified solid angle surrounding the specularly reflected beam. Additional measurements of the transmission of the blowoff material were made and the reflectivity results were corrected for absorption therein. The results yielded the reflectivity of the target surface as a function of time during irradiation. The target assembly was contained in a vacuum chamber so that the ambient air pressure could be varied. In addition, measurements were made of the absorptivity and of the hemispherical diffuse reflectivity on areas which had been irradiated by the TEA laser. These latter measurements were not time-resolved.

Fig. 1 shows the specular reflectivity of a stainless steel target as a function of the number of laser shots incident on a given area. The laser power density was 3×10^8 W/cm^2 and the laser pulse duration was around 3 microseconds. At one atmosphere ambient air pressure, it requires several hundred shots to produce an appreciable change in reflectivity. This is because a laser-supported detonation wave is kindled in front of the target, which absorbs much of the incoming laser energy. At reduced ambient pressures, the shielding is diminished and the effect on the surface is increased. For pressures below 10 torr, the specular reflectivity can drop to low values in a single shot. For a shorter laser pulse ($\sim$100 nanoseconds) the results are qualitatively similar to those shown in Fig. 1, but it requires a larger number of laser pulses to produce a given decrease in specular reflectivity. For an aluminum target, the results are also qualitatively similar, but the effect is somewhat less, presumably because of the greater initial value of the reflectivity.

The time resolved data show that, in cases where a substantial decrease in reflectivity occurs in a single shot, there is a rapid drop over a period of several hundred nanoseconds. For the longer laser pulses, the specular reflectivity continues to decrease slowly for several microseconds.

The data on diffuse reflectivity indicate that the diffuse reflectivity within a given solid angle surrounding the specular angle first increases and later decreases. Simultaneously, the total diffuse reflectivity increases. This indicates that the diffuse scattering moves into a progressively larger cone of solid angles. For a well damaged steel surface (specular reflectivity $\lesssim 0.001$), the total hemispherical reflectivity is ~ 0.85. The absorptivity has increased to 0.15, as compared to an initial value of 0.025.

"This work was supported by the Air Force Office of Scientific Research under contract F44620-73-C-0022."

Fig. 1. Specular reflectivity at 10 μ of a stainless steel target after it has been struck by the indicated number of TEA laser shots at 3×10^8 w/cm^2. Ambient air pressure is indicated.

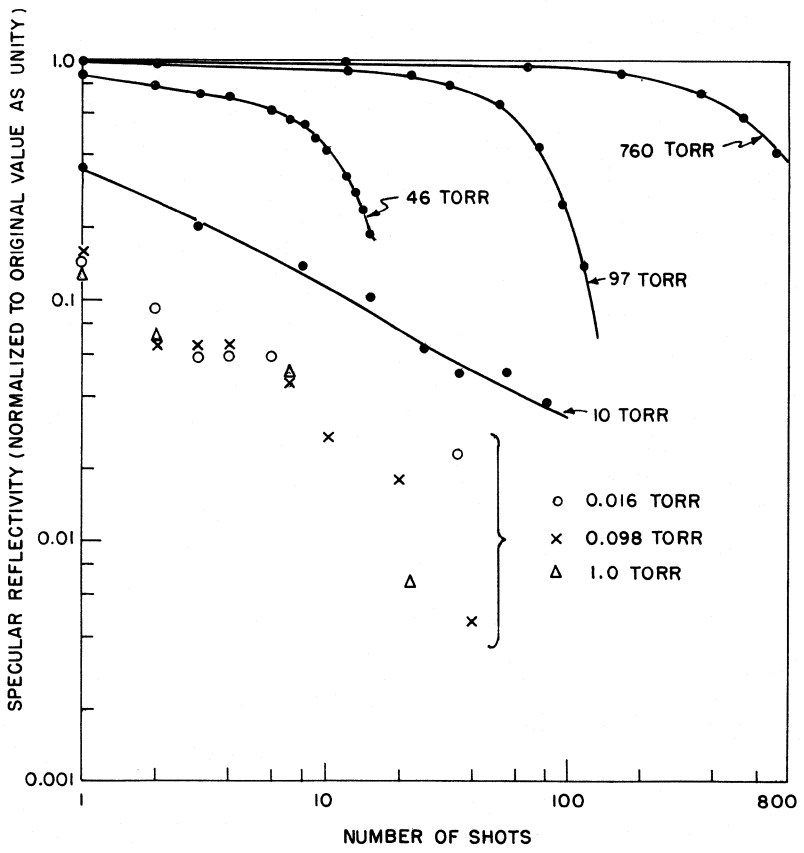

12.10 Laser Heating of Metallic Surfaces,[1] S. Marcus, J. E. Lowder, S. Manlief, and D. L. Mooney, *MIT, Lincoln Laboratory, Lexington, Mass. 02173*
(15 min)

In those laser applications which involve heating of metals, the heating efficiency is characterized by the thermal coupling coefficient, i.e., the ratio of absorbed to incident energy. We report here the use of fast-response, thin-film thermocouples to measure temperature histories with microsecond time response. These thermocouples, whose junctions can be positioned at various points in the target less than 1 μm from the surface, can thus be used to obtain coupling coefficients for pulsed-laser irradiation with both temporal and spatial resolution. We have used this technique to investigate coupling to both copper and aluminum targets as a function of laser intensity, and have found in each case a marked increase in coupling when the intensity was sufficient to cause breakdown on the target surface.

In order to measure surface temperature changes outside the focal spot ($\approx$2 mm), a target incorporating a linear array of five thermocouples was used, each thermocouple separated by 3.2 mm. The source of laser radiation was a pulsed electron-beam laser capable of producing approximately 5 joules at 10.6 μm in 10-100 μsec pulses. After passing through a KCl beam-splitting wedge, used to monitor the pulse shape and energy, the beam was focused on the middle thermocouple of the target. A photomultiplier viewing parallel to the target surface was used to detect plasma luminosity.

The thermal coupling with no detectable plasma formation at the target surface was first measured by attenuating the incident laser

[1] This work is supported by the Advanced Research Projects Agency of the Department of Defense.

intensity to less than 10^5 W/cm^2. Under these conditions, a temperature increase was registered on the middle thermocouple only. Upon increasing the laser intensity to the point where surface-induced breakdown occurred ($\sim 10^6$ W/cm^2), temperature increases were sensed by all five thermocouples. A plot of distance from the middle thermocouple vs. arrival time of the thermal disturbance shows that the disturbance spreads outward at supersonic velocities typical of blast wave expansion, much too fast to be due to surface conduction. The observed time delay also indicates that the plasma heating of the target is predominantly due to electron conduction or very short range radiative transfer.

The instantaneous front surface heating rate of metallic surfaces may be determined by measuring the front surface temperature history and then calculating the heating rate with the relation[2]

$$F(0,t) = \frac{K}{\sqrt{\pi k}} \int_0^t \frac{\frac{d}{dt'} T(0,t')}{\sqrt{t - t'}} dt'$$

for the case of a thermocouple located at the absorbing surface.

After the absorbed flux is extracted from the data for each thermocouple, it is integrated in time to give a radial profile of the absorbed energy fluence. This profile, which can be fit to an exponential, is in turn integrated spatially to give the total absorbed laser energy. In the case where no plasma is generated, the absorbed energy is simply the product of absorbed fluence and the measured focal spot area. In each case, the thermal coupling coefficient is defined as the ratio of absorbed to incident laser energy.

The coupling coefficients thus determined for copper and aluminum are shown below:

Surface	Low Intensity	With Breakdown
Aluminum	.039	.27
Copper	.036	.33

It is seen that for both these metals, there is a large coupling enhancement when laser-induced breakdown occurs.

We are currently extending our technique to investigate spot size scaling, using a 500-joule laser. In addition, other metallic surfaces of interest are being investigated.

[2] H. S. Carslaw and J. G. Jaeger, *Conduction of Heating Solids*. Oxford: Clarendon, 1959.

Session 13-A

Thursday, May 29, 1975 8:00-10:00 P.M.

Post-Deadline Papers

Chairman: A. S. Halsted, *Hughes Aircraft Co., Culver City, Calif.*

Session 13-B

Thursday, May 29, 1975 8:00-10:00 P.M.

Post-Deadline Papers

Chairman: H. Kogelnik, *Bell Laboratories, Holmdel, N. J.*

Session 14

Friday, May 30, 1975 8:45-11:45 A.M.

Radar and Propagation

Chairman: W. B. Bridges, *California Institute of Technology, Pasadena, Calif.*

14.1 A Pulsed UV Rangefinder, T. P. Davis and M. A. Nelson, *EG&G, Inc., Santa Barbara Operations, Goleta, Calif. 93017*

(15 min)

There are many applications for a rangefinder capable of operation against moving targets over distances of a few kilometers with a range precision of less than a meter. A system based on a pulsed UV source has been developed in this laboratory. Key to the performance of the instrument is a unique source, which generates short, intense pulses of UV at 337 nm by amplified spontaneous emission from electrically excited nitrogen.[1] In rangefinder applications, this source offers a number of advantages: 1) an inherently eye-safe wavelength; 2) high peak power; 3) very short pulse duration; 4) high PRF's; 5) reasonable atmospheric transmission; 6) multiplier phototube detectors available with high efficiency at the operating wavelength.

The prototype instrument reported here has demonstrated these advantages. A description of the instrument and preliminary evaluation results follow.

The rangefinder consists of a transmitter and receiver mounted on a common optical rail, plus associated power supplies and readout. The transmitter includes the pulsed nitrogen laser, a 200 mm focal-length quartz collimating lens, and a 45° turning mirror. The lens provides beam divergence of slightly less than 5 milliradians, and the turning mirror mount gives convenient alignment of the transmitted beam with the receiver.

The latter consist of a Newtonian reflector with a 10 cm diameter f/2 primary mirror. A 1 mm stop at the primary focus provides a field of view matching that of the transmitter. A field lens images this stop onto the photocathode of the detector. A line filter with 100 Å bandwidth and peak transmission of about 40% at 337 nm is positioned ahead of the field lens. A 4 × finder telescope is rigidly attached to and aligned with the receiver.

[1] E. T. Gerry, *Appl. Phys. Lett.*, vol. 7, 1965.

The laser power supply is a special unit which furnishes a 30 kV pulse to the laser head at rates up to about 50 pps. The receiver power supply furnishes 1000 V to the detector PMT. For preliminary evaluation, readout was by fast oscilloscope.

The prototype instrument was tested against various targets. A highway sign at 890 meters presented an adventitious "cooperative" target in the form of two 8 cm diameter glass reflector buttons normal to the line of sight. The receiver noise was immeasurably small compared to the return signal. At this same range, a concrete bridge yielded a return signal-to-noise ratio of about 80. A simplified analysis[2] of this situation leads to a predicted signal-to-noise ratio of about 100, which is in good agreement with the measured value.

The eye hazards associated with a pulsed UV nitrogen laser have been analyzed in detail in an earlier document.[3] The wavelength of the nitrogen laser is such as to minimize both these hazards. The rangefinder here studied is safe at all ranges.

Preliminary results from measurements made with the prototype system described support the conclusion that range precision of tens of centimeters can be achieved at ranges of at least one kilometer. The instrument is compact, rugged, and readout is relatively simple. Most importantly, the system does not present a significant eye hazard.

[2] T. P. Davis and M. A. Nelson, EG&G SBO Report No. S-85-TP, December 1973.

[3] T. W. Nybakken and T. P. Davis, EG&G SBO Report No. S-531-R, March 1970.

14.2 A Phase-Comparison Monopulse Laser Rangefinder/Altimeter, G. Ammon, D. Herzog, C. Reno, and H. Zadell, *Advanced Technology Laboratories, RCA Corp., Camden, N. J. 08102*

(15 min)

A unique laser rangefinder was developed as part of a Precision Hover Sensor for the flight control system of a Heavy Lift Helicopter. This sensor provides the pilot with the capability, without visual reference to the ground, to position the helicopter and load to a prescribed heading at any height above the terrain from 25 to 125 feet and within 4 inches of a reference point near the ground. In addition the sensor provides hands off capability to maintain a given hover position of the aircraft's center of gravity to within 4 inches in the vertical and horizontal directions.

This laser rangefinder measures absolute altitude to within 4 inches and changes in altitude from a desired hover point with a resolution of 0.5 inch. In addition the rangefinder provides a velocity output which can detect rates as small as one inch per second.

The rangefinder uses an eye-safe GaAs pulsed injection laser for an optical source and a silicon avalanche photodiode for a detector. Both of these units are temperature controlled with

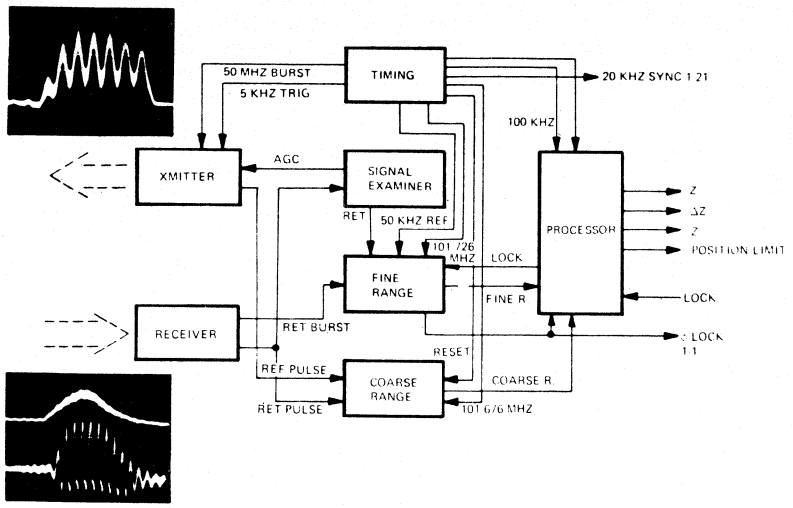

Fig. 1. Laser rangefinder.

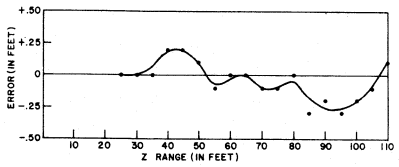

Fig. 2. Absolute range error vs. range.

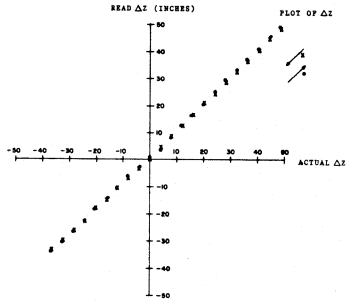

Fig. 3. Measured Z vs. actual.

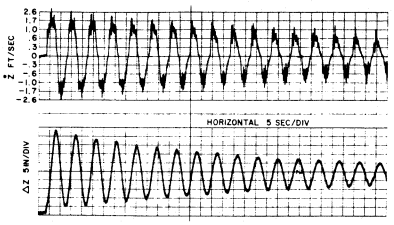

Fig. 4. Velocity and position change outputs with pendulum target.

thermoelectric modules to maintain a constant laser output wavelength and a constant photodiode gain level. Fig. 1 shows a functional diagram of the rangefinder along with some important waveforms.

The pulsed output from the laser is modulated with approximately five cycles of a 100 MHz sinewave. This is accomplished by driving an acoustooptic modulator with 30 watts of 50 MHz RF during the time the laser is being pulsed. The modulated laser output is focused into a narrow beam and transmitted towards the ground and reflected back to the receiver. The laser receiver detects this modulated signal and separates it into pulse and burst waveforms.

The absolute range to the target is determined by measuring the time of flight of the laser pulse. The laser output is sampled as it is transmitted with a silicon photodiode and amplifier. This signal, the reference pulse, and the detected return pulse are processed in two identical circuit channels in the coarse range circuitry and the time difference is measured with a digital time interval counter. The results of many measurements are averaged to yield an overall accuracy of 4 inches. Fig. 2 shows a plot of measured absolute range error versus range.

Range changes or fine range information is obtained by comparing the phase of the 100 MHz burst signal as it is transmitted with the phase of the return burst. A gated phase-locked loop is used to obtain a continuous 100 MHz signal which has the same phase relationship as the return burst. This signal is then phase-compared to the signal which modulates the laser to yield fine range information with a resolution of 0.5 inch. Fig. 3 shows a plot of measured range change versus actual as a target was moved away from a reference position.

Velocity information is obtained by differentiating the high resolution fine range measurement. Fig. 4 shows the rangefinder Z and $\dot{Z}$ outputs while operating off of a large pendulum which was pulled 24 inches from its rest position and released.

This rangefinder combines the advantages of both pulsed and CW systems to provide a system with unique capabilities. Operating in a pulsed mode allows the range to be measured unambiguously. It also allows the use of gating techniques to discriminate multiple targets or to blank out backscatter. Modulating the pulse with a sinewave enables the use of phase detection to obtain a very high resolution range change measurement. The 0.5 inch capability is equivalent to a time interval of about 85 picoseconds.

14.3 A Laser Precision Hover Sensor for HLH Helicopter,

D. G. Herzog and G. Ammon, *Advanced Technology Laboratories, RCA Corp., Camden, N. J. 08102* and C. Stephenson, *Boeing Vertol Co., Philadelphia, Pa. 19142*

(15 min)

A Heavy Lift Helicopter is being designed to have a load handling capability up to 73,000 lbs. (80% of a Boeing 707-320c capability). Specific use is for cargo handling from truck, rails and even ships under running conditions in high sea state. Damage easily reuslts from mishandling of large loads thereby requiring the helicopter to have the capability of "freezing" in mid-air or dynamically matching the motion of a heaving deck. An experimental sensor and performance is described.

Concept drawing Fig. 1 shows the sensor beams illuminating two areas beneath the helicopter: (1) an outer 20 ft. diameter region used to measure translation characteristics in a plane parallel to the ground (Δx, Δy, $\dot{x}\dot{y}$) via image

Fig. 1. Precision hover sensor beam patterns from the helicopter.

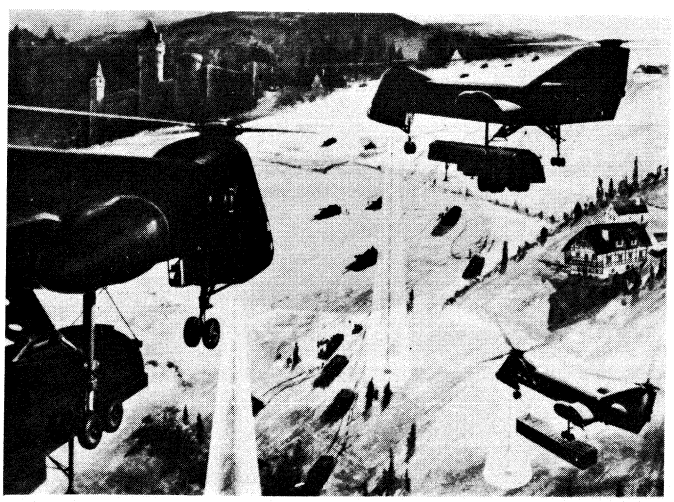

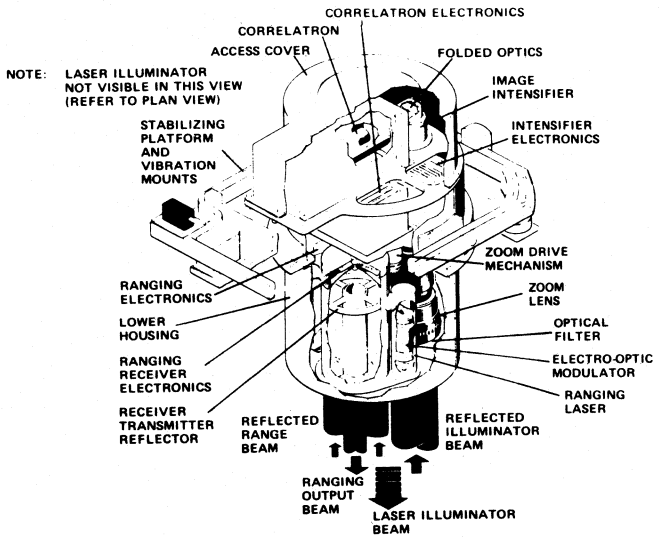

Fig. 2. Concept of precision hover sensor.

TABLE I
PERFORMANCE CHARACTERISTICS

Hover precision (ΔX, ΔY, ΔZ)	1.0 in
Detectable velocities ($\dot{X}$, $\dot{Y}$, $\dot{Z}$)	2.0 in/s
Data bandwidth	10 Hz
Beep interval (X, Y, Z)	1.0 in
Creep interval ($\dot{X}$, $\dot{Y}$,$\dot{Z}$)	1-18 in/s
Maximum displacement (X, Y, Z)	$\pm$4.0 ft
Altitude	25-125 ft
Lock-on and relock-on time	1.0 s
Hover time (nominal)	10 min

correlation tracking and (2) an inner (dotted) 3 inch area used to measure altitude characteristics (Z, ΔZ, $\dot{Z}$) via a very precise pulse sinewave modulated laser rangefinder.

Table 1 summarizes the sensor's performance. Fig. 2 is a concept description of the sensor including the pendulum referenced gyro stabilized against helicopter pitch and roll induced errors.

Upon "hover position initiation" the scene below is electronically stored as a reference and all future scene information is dynamically compared in a special correlation tracker using all the scene information rather than depending on particular highlights, edges, patterns or beacons. Cooperation from the ground is highly undesirable because of extra logistic and communication problems.

Micro-positional control is provided by allowing the pilot to offset the sensor by 1 inch offset intervals (beeps) and continuous velocity offsets (creeps) without having the sensor relock up to 2 feet. Beyond 2 feet, automatic relock occurs allowing the helicopter to "walk" over extended distances.

Figure 3 is a block diagram and points out how the problems of all-weather, day/might and heavy dust environment (particularly because of the downwash of large rotor blades) were addressed by using a very narrow pulsed GaAlAs illuminator and an ultra-fast gated intensifier to provide the required images to the correlation tracker. Thus backscatter was rejected from the image and a "punchthrough" of very dusty environment that would eliminate normal seeing of the ground down to pathlength as small as 15 feet was simulated on the ground.

Fig. 3. Functional block diagram of PHS system.

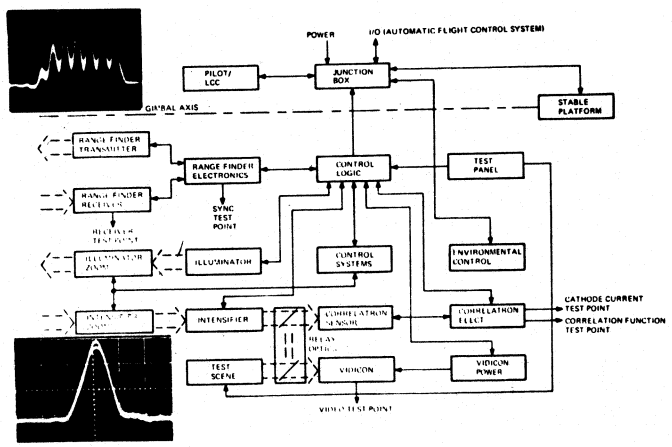

The correlation tracker (closest substitute for the combination human eye-nerves-brain) uses a GAC system, conceptually shown in Fig. 4, operates using an electron storage meash for the initial scene which is then used to multiply the dynamic scene electron image producing the auto-correlation value. By use of a hill climbing servo the dynamic image is deflected to maintain a maximum output. The deflection is the linearized position offset Δx and Δy. Pick off before deflection feedback intergration provides velocities ($\dot{x}$ and $\dot{y}$). Typical error functions are shown in Fig. 5.

The zoom optical system on the illuminator and intensifier maintain the illuminated and tracked scene to 20 feet diameter independent of the altitude (information obtained from rangefinder) of the helicopter thereby maintaining a constant calibration for the tracker. The experimental performance will be presented.

The rangefinder optical pulse (Fig. 3) shows the 5000 pps, 50 ns pulse width, 100 MHz modulated transmitted waveform. Coarse ranging is provided with a time-of-flight measurement using the silicon avalanche detector and counter to process the pulse to 3 inch accuracy. The 100 MHz modulated signal is stripped from the pulse and its phase is compared to the transmitted phase to obtain the 0.5 inch position and 1 inch/sec velocity precision at an error output bandwidth of 10 Hz.

Even though substantial problems were encountered with scene lock on these problems are not insurmountable and excellent stablization and meaneuvering potential of the HLH helocpter was demonstrated using available high constrast ground scenes. Movies taken from the aircraft will be shown.

14.4 Polarization Reference Imaging Systems: Basic Principles,[1] W. P. Brown, Jr., and T. R. O'Meara, *Hughes Research Laboratories, Malibu, Calif. 90265*

(15 min)

Polarization reference imaging (PRIM) systems are a new approach to achieving diffraction-limited imaging through a turbulent atmosphere, with laser target illuminators. They may be implemented either as add-ons to existing telescopes or as large-baseline optical arrays.

The approach is fundamentally different from that employed in competitive adaptive optical systems in that neither rubber mirrors nor electrooptic compensation is employed. Conceptually, the approach is closest to on-axis holography in that one or more bright target glints provide the reference which beats against the image wavefront and, by virtue of an (essentially) common path, cancels the propagation and/or optical figure errors. However, the fold-over problems of on-axis holography are completely avoided, even though the reference typically falls near the middle of the image. Further, photographic film is not employed to record the resultant fringe patterns.

[1] Work partially supported by DARPA contract no. DAAH01-73-C-0629 and monitored through U. S. Army Missile Command, Redstone Arsenal, Ala.

In a PRIM system, a cooperative laser transmits two polarization states which are at two closely spaced wavelengths, or are otherwise distinctly modulated. The image information is obtained from the depolarized portion of the diffusely reflected component of one of these polarization states. The reference information is obtained from the nondepolarized return of the other polarization state. Since the initial polarization states are at different frequencies, the image and reference signals produce a heterodyne beat in the detector output at a difference frequency. From another viewpoint, the image and reference components generate a fringe pattern at the receiver aperture plane which is modulated at the beat or difference frequency. This fringe pattern is sampled by an array of receivers, either in the aperture plane or (with conventional telescopes) at an image of the aperture plane. We will show that the beat frequency output of each receiver is a sample of the Fourier transform of the irradiance distribution of the target. Further, we will show that these samples are unaffected by atmospheric turbulence, given target isoplanatic assumptions.

The samples obtained from each receiver must be further processed in order to generate an image. In the present system, the receiver output at the beat frequency is synchronously detected and A/D converted. These digital samples are then inverse transformed to generate a true image of the target. The inverse transform may be computed in (substantially) real time if desired. Operation at both visible wavelengths and at 10.6 μm will be considered; each has advantages for certain applications.

Key problem areas to be discussed are (1) signal-to-noise ratio and S/N optimization, (2) target reflectivity characteristics, (3) techniques for reducing the required number of sampling receivers, and (4) operation with multiple glint references.

Computer simulations of a visible PRIM system will be discussed in a companion paper: 14.5 "Polarization reference imaging system: computer simulation studies" by D. Y. Tseng.

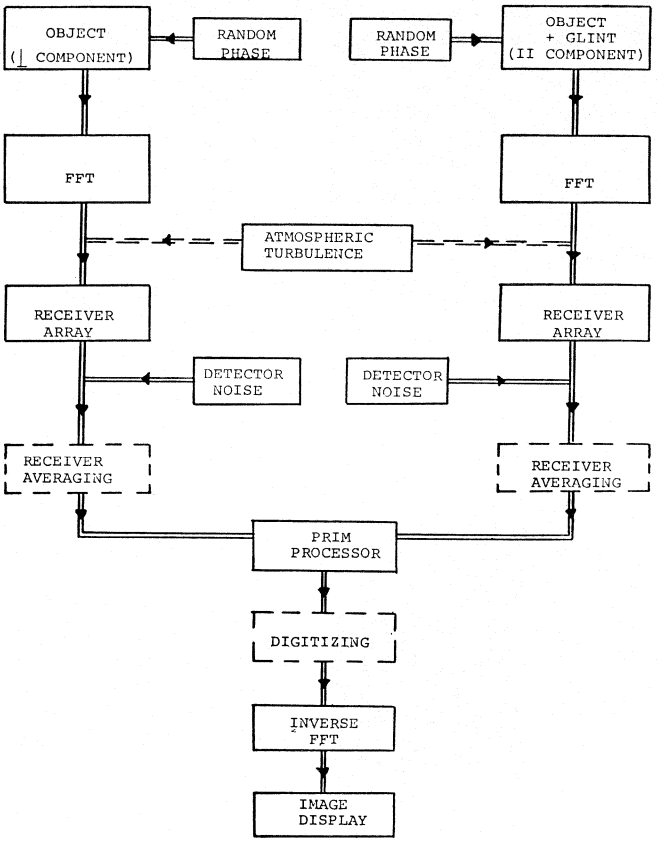

Fig. 1. Block diagram of PRIM simulation computation.

14.5 Polarization Reference Imaging System: Computer Simulation Studies,[1] D. Y. Tseng, *Hughes Research Laboratories, Malibu, Calif. 90265*

(15 min)

The polarized and coherent output characteristic of lasers can be utilized to eliminate image distortion caused by atmospheric turbulence. One approach which takes advantage of this characteristic is the Polarization Reference Imaging (PRIM) system. It has the capability of achieving diffraction limited image resolution through turbulent atmosphere. The basic principles and analytic details of the PRIM concept are presented in a companion paper: 14.4 "Polarization reference imaging system: basic principles," by W. B. Brown, Jr. and T. R. O'Meara.

This paper presents a comprehensive computer simulation study of the PRIM system. The simulation scheme incorporates all of the system parameters of interest, such as signal-to-noise ratio, glint amplitude, glint distribution, system aperture size, and receiver size. Speckle effects are also included. The simulation study was carried out using a DEC/PDP-10 digital computer. A block diagram of the computational scheme is shown in Fig. 1. The PRIM-processed reconstructed images, exhibited as grey-scale displays on a CRT, were evaluated extensively as a function of system parameters. An example of a turbulent image and the corresponding PRIM-processed diffraction-limited image is shown in Fig. 2.

The PRIM-processed images will be shown as a function of the system parameters, some of which have been listed above. The image quality dependence on particular parameters will be displayed and discussed in detail. Conclusions drawn on the values and ranges of system parameters which produce good quality images based on the computer simulation studies will be presented.

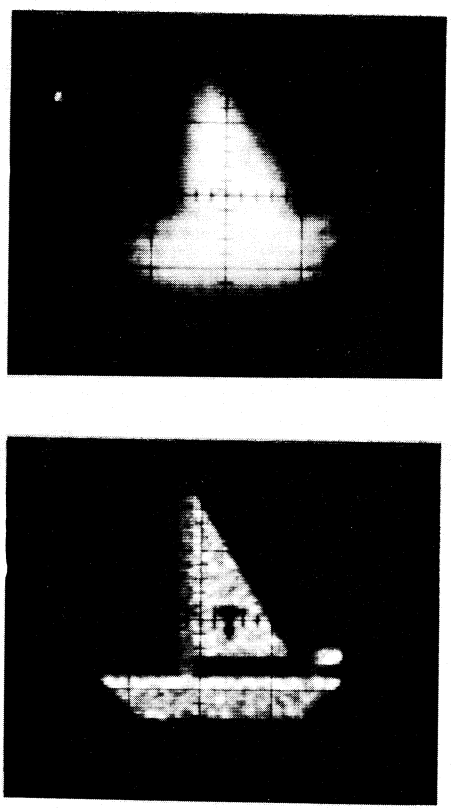

Fig. 2. Top: turbulent image. Bottom: PRIM processed image.

[1] Work supported by DARPA contract no. F30602-74-C-0227 and monitored through Rome Air Development Center, N. Y.

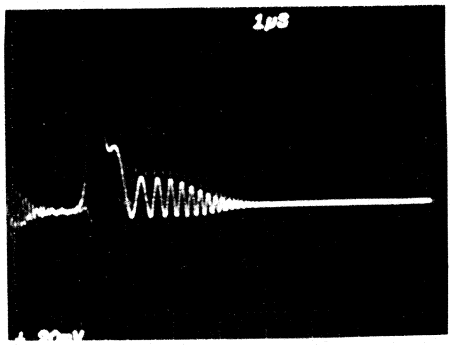

Fig. 1. Time resolved beat frequency between TEA laser and stable CW laser.

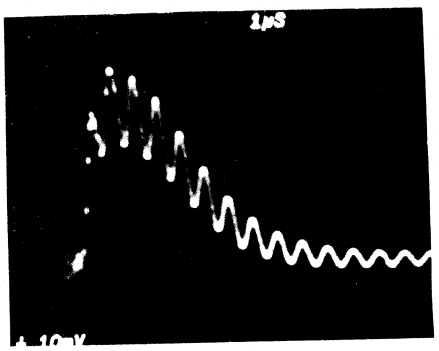

Fig. 2. Time resolved beat frequency between hybrid laser and stable CW laser.

14.6 Temporal Coherence Measurements of a Double Discharge CO_2 TEA Laser, R. I. Rudko, *Raytheon Research Division, Waltham, Mass. 02154*

(15 min)

The CO_2-TEA laser, because of its high peak powers, high efficiency, and relatively small size, is an attractive device to use as a laser radar transmitter. However, if it is to be used in a Doppler rader or any other type of radar which uses coherent detection, the temporal coherence of the laser must be good enough to meet the system requirements. The object of this investigation was to measure the temporal coherence of a CO_2-TEA laser, including frequency chirp during a single pulse and pulse-to-pulse repeatibility; determine the causes of any lack of coherence; and see whether any improvements can be made.

Initial measurements were carried out on a simple double-discharge TEA laser in a stable optical frame. An SF_6 cell, grating, and aperture were used to force the laser into single radial and longitudinal mode operation. The output of this laser was heterodyned with the output of a stable single-frequency CW laser whose frequency was offset by several MHz from the TEA laser oscillation frequency. A typical result for the time-resolved beat frequency between these two lasers is shown in Fig. 1. The frequency chirp rate in this case is more than several MHz/μsec.

Next, measurements were made on a hybrid CO_2 laser consisting of the same TEA laser used in the initial measurements along with a low pressure CW laser inside the same optical cavity. In this case, the grating and the SF_6 cell were not needed to force the laser to run single longitudinal mode. In addition, the low pressure CW laser provided the aperturing for single radial mode operation. The output of this laser was then heterodyned with the stable single-frequency CW laser with a typical result for the time-resolved beat frequency between these two lasers shown in Fig. 2. In this case, the frequency chirp rate is less than 100 kHz/μsec, considerably better than that observed with the TEA laser by itself. In addition, the initial gain-switched spike, which usually occurs at the beginning of the TEA laser pulse, does not occur with the hybrid laser because of the CW power which exists in the cavity before the pulse. Furthermore, the output pulse occurs with less delay after the current pulse.

The frequency chirp on the output of these lasers is caused by an index of refraction change as a function of time in the laser gas. This index change could be caused by various effects such as resonance or anomalous dispersion, plasma electron density variation, gas dissociation, or gas density variation. It is believed that the major effect comes from gas density variations. The reduced chirp observed with the hybrid laser apparently results from the fact that its pulse occurs earlier in time, before density variations start.

14.7 Chirp Measurement of CO_2 TEA Laser Using Interferometric Pulse Delay Techniques, H. Hieslmair, C. J. Bickart, and J. N. Fulton, *Combat Surveillance & Target Acquisition Laboratory, US Army Electronics Command, Fort Monmouth, N. J. 07703*

(15 min)

Several authors[1-3] have measured the frequency chirp of a TEA-CO_2 laser pulse by observing the chirp of the beat signal between the TEA laser pulse and a stable CW CO_2 laser. In this paper the frequency chirp of a TEA laser pulse is observed by beating one part of the laser pulse with a delayed part of the same laser pulse. This is experimentally accomplished by using a Michelson type interferometer with a large path difference in the two arms. Fig. 1 illustrates the experimental arrangement. The TEA laser cavity is defined by a gold coated mirror of 1.6 m radius and a flat 60% reflecting germanium mirror with an intracavity aperture to control the transverse mode pattern. A low inductance 0.01 μF capacitor charged to 20 kV is discharged through the 25 cm long flat electrodes with a Rogowski profile via a triggerable spark gap.

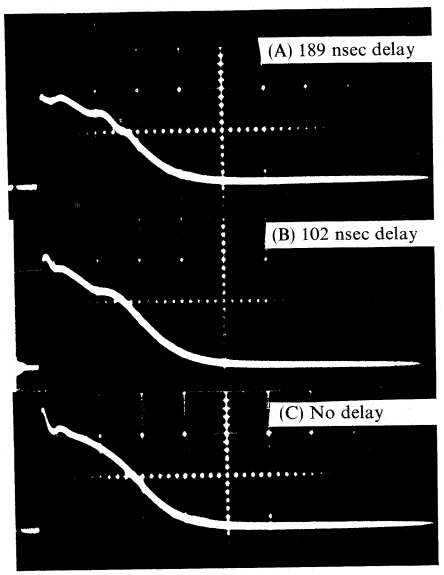

Fig. 2. Beatnote between delayed pulses (timescale: 1 microsecond/Div.).

Curve A and B of Fig. 2 show typical time resolved beat signals superimposed on the TEA laser pulse. In curve A the long arm was 28.3 m long which corresponds to a time delay of 189 ns long which corresponds to a time delay of 189 ns. The beat signal is 1.4 MHz, which corresponds to a frequency chirp of 7.5 MHz/μs. On curve B the time delay is 102 ns and a lower frequency beat signal than in A is obtained, which corresponds to a comparable frequency chirp of 7.8 MHz/μs. In curve C of Fig. 2 the two arms of the interferometer were of equal length. No beat note can be observed. The above figures of frequency chirp correspond to results obtained with a helical pin type TEA laser of comparable length as reported by Stiehl, *et al.*[1] The potential of using the tail of a TEA laser pulse as a local oscillator for the return signal of the same pulse in radar applications will be discussed.

[1] W. A. Stiehl and P. W. Hoff, *Appl. Phys. Lett.*, vol. 22, p. 680, 1973.
[2] J. A. Weiss and J. M. Schnur, *Appl. Phys. Lett.*, vol. 22, p. 453, 1973.
[3] R. Rudko, private communication.

Fig. 1. Experimental arrangement.

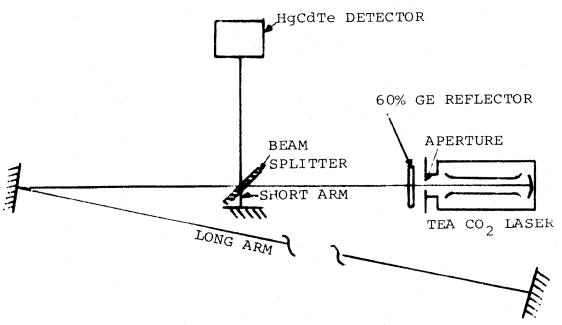

14.8 Review of High Power Laser Propagation (*Invited*), F. G. Gebhardt, *United Aircraft Research Laboratories, East Hartford, Conn.* (30 min)

No summary.

14.9 Recent Advances in Multidither Coherent Optical Adaptive Techniques (COAT),[1] J. E. Pearson, *Hughes Research Laboratories, Malibu, Calif. 90265*

(15 min)

High power optical beams propagating in the atmosphere can experience severe distortions caused by two effects: atmospheric turbulence (a linear process) and thermal blooming (a power-dependent or nonlinear process). Coherent Optical Adaptive Techniques (COAT) have been proposed to compensate for both types of distortion and at present appear to be essential for efficient utilization of high power 10.6 μm and 3.8 μm lasers now being developed. Early prototype 3- and 7-element multidither COAT systems reported at the 1973 CLEA meeting[2] have been superseded by a more advanced 18-element visible wavelength system.[3] Recent outdoor range tests with this system[4] have proven conclusively that multidither COAT can nearly eliminate the linear beam distortions caused by atmospheric turbulence and by static optical system errors. This paper reports the results of preliminary experimental investigations aimed at answering two of the remaining fundamental questions about COAT: (1) What are the limitations on a COAT system's ability to compensate for nonlinear thermal blooming distortions? (2) How do diffuse or multi-glint moving targets affect the performance of a multidither COAT system in compensating for turbulence and blooming?

All measurements were made with the 18-element COAT system[3] in a laboratory environment. The optical path and blooming distortions are properly scaled, however, so that the results are directly applicable to longer ranges at 3.8 μm and 10.6 μm by use of well-developed scaling laws. The turbulence distortions are not accurately scaled, but are reasonably characteristic of the magnitude and spectrum of atmospheric turbulence.

In studying target effects, the important parameters are γ_{RT}, the ratio of the receiver resolution to that of the transmitter and β_{RT}, the ratio of the receiver to transmitter area. Our studies have used single pinhole receivers ($\gamma_{RT} < 1$, $\beta_{RT} < 1$) and multiple pinhole and annular receivers ($\gamma_{RT} > 1$, $0.5 < \beta_{RT} < 5$). The targets studied to date have included single and multiple glints (both resolved and unresolved) and diffuse surfaces (curved scotchlite).

Initial experiments, supported by computer simulation,[5] have indicated little, if any, COAT correction for thermal blooming. Initial speculation on reasons for the lack of correction have emphasized the finite number of transmitter elements, the fact that the strongest blooming distortions do not correspond to phase changes at the transmitter, and the possibility that a high speed (1000 Hz) multidither servo is not the optimum correction algorithm for thermal blooming. The results of more refined experimental studies in both gas and liquid blooming media will be presented. In addition, we will discuss the limitations of using transmitter phase control to compensate for thermal blooming distortions.

Recent computer simulations[6] have indicated that returns from moving multiglint or diffuse targets can contain significant amplitude modulations which could swamp the COAT error signals and thus disable or "confuse" the COAT system. Our initial observations without turbulence and with single pinhole receivers ($\gamma_{RT} < 1$, $\beta_{RT} < 1$) have supported this conclusion for diffuse targets, but have been contrary to it for multiple, unresolved glint targets. When using larger receivers ($\gamma_{RT} > 1$, $\beta_{RT} > 1$) or multiple pinhole or annular receivers, we see no target effects; the COAT system performs exactly the same as with a single retroreflecting glint. The detailed results and conclusions from these experiments and from experiments which include the effects of turbulence and blooming will be presented along with the results of studies using "calibrated surface" targets of different shapes.

[1] Work supported by DARPA contract no. F30602-75-C-0001 and monitored through Rome Air Development Center, N. Y.

[2] W. B. Bridges, *et al.*, paper presented at May 1973 CLEA meeting. Also *Appl. Opt.*, vol. 13, p. 291, 1974.

[3] J. E. Pearson, "Coherent optical adaptive techniques (COAT)," Quarterly report no. 5, DARPA contract F30602-73-C-0248, Dec. 1974.

[4] J. E. Pearson, *et. al.*, "Atmospheric turbulence compensation using coherent optical adaptive techniques," OSA Topical Meeting on Optical Propagation through Turbulence, Boulder, Colo., July 1974.

[5] W. P. Brown, unpublished.

[6] G. Gurski and R. F. Ogrodnik, "Target return – adaptive aperture system interaction effects (U)," first DoD Conference on High Energy Laser Technology, San Diego, Calif., October 1974.

Session 15

Friday, May 30, 1975 **8:45-11:45 A.M.**

Gas Lasers

Chairman: R. L. Abrams, *Hughes Research Laboratories, Malibu, Calif.*

15.1 DC Pump Sources for the Optically Pumped 546.1 nm Hg Laser,[1] N. Holmes, *Microwave Laboratory, Stanford University, Stanford, Calif. 94305*

(15 min)

Djeu and Burnham[2] have reported operation of an optically pumped CW Hg laser at 546.1 nm, using the two-step optical pumping scheme shown in Fig. 1, and employing a low-pressure RF-excited mercury lamp coaxial with the laser tube. The laser tube contains, in addition to the Hg vapor, nitrogen at a pressure of 10-100 torr to produce quenching of the 6^3P_2 lower laser level. Djeu and Burnham's analysis showed that for sufficient pumping at 253.7 nm the laser power output should be proportional, with high quantum efficiency, to the available pump power at 404.7 nm.

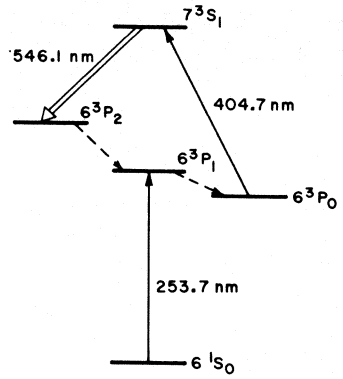

Fig. 1. Important energy levels of HgI for Hg-N_2 laser.

We are presently developing efficient Hg pump lamps intended to obtain CW operation in this same system with separate, replaceable, dc-excited lamps. Highly luminous and efficient Hg 253.7 nm emission is readily obtained in low-pressure (~10 mtorr) Hg resonance lamps. Efficient Hg 404.7 nm emission, however, is obtained from higher-pressure Hg arc lamps, in which the 253.7 nm radiation is strongly self-absorbed. The required line-center Hg 253.7 nm emission from these higher-pressure lamps is, in fact, almost totally absorbed and self-reversed at line center by cooler Hg vapor near the lamp walls. Hence, separate 253.7 resonance lamps and 404.7 nm arc lamps in a double-elliptical pump cavity appear to be desirable for optimum pumping.

A series of measurements on dc arc discharge lamps are being conducted to optimise tube geometry, discharge conditions and Hg pressure for maximum line-center 404.7 nm radiation. Computer modelling is being employed to guide the experimental studies. To date, best results have been obtained with a quartz arc tube of 4 mm i.d. with an arc length of 70 cm. Dispenser cathodes are employed, and argon is added to facilitate starting. The mercury vapor pressure is controlled by a small air-cooled heat sink on the tube wall. At a mercury pressure of ~25 torr and a power input of 400 W this lamp delivers ~1% of this power in the central lobe of the 404.7 nm line, or an ~10× improvement over typical low-pressure lamps. Use of isotopically pure even isotope mercury should increase this power by ~40%. Further increases in Hg pressure lead to self-absorption and broadening effects that limit the useful line-center output at 404.7 nm.

To test these lamps a mercury laser using a polished aluminum double-elliptical cavity 80 cm long is being built. Results of these experiments and their applications will be discussed.

[1] Work supported by AFOSR: F44620-71-C-0053.

[2] N. Djeu and R. Burnham, *Appl. Phys. Lett.*, vol. 25, p. 350, 1974.

15.2 Electron-Beam-Driven Chemical Lasers (*Invited*), J. B. Gerardo, *Sandia Laboratories, Albuquerque, N. M.*

(30 min)

Results will be presented of electron-beam-driven chemical lasers, with emphasis on HF laser output from high-pressure mixtures of $H_2 + F_2$. The physics of electron-beam deposition in gases and the subsequent chemical reactions leading to laser action will be stressed. Experimental results include: parametric studies of gas mixtures, cavity effects, and pilot beam studies.

15.3 Lasing at 5578.5 Å in *E*-Beam Excited Kr/O_2 Mixtures, A. W. Johnson, F. W. Bingham, and J. K. Rice, *Sandia Laboratories, Albuquerque, N. M. 87115*

(15 min)

The ^1S-^1D transition of oxygen (as well as other isoelectronic elements) has in principle many favorable attributes for use as the very high power laser necessary for compression of pellets in the laser fusion program. Some of these attributes are 1) statistical weight of upper level less than lower level; 2) relatively long-lived upper energy level; 3) energy extractable in one line; 4) visible wavelength; 5) cross-section of $\sim 10^{-19}$ cm^2 at low gas pressure; and 6) potentially efficient excitation by electron beam. One of the most critical unknown parameters is the behavior of the gain cross-section at the high pressures necessary for efficient utilization of electron-beam machine.

A relativistic-electron-beam machine has produced lasing action at 5578.5 ± 0.3 Å in mixtures of high-pressure krypton ($\leq 1.25 \times 10^4$ torr) and molecular oxygen (~ 5 torr). The upper state of the lasing transition is associated with the lowest ^1S state of atomic oxygen; the transition occurs in either the isolated atomic oxygen or the KrO molecule. The electron beam energy is deposited primarily in the Kr atoms and Kr_2 molecules. This energy transfers to O_2, forming $O(^1S)$.

The 0.7-MeV, 50-nsec electron beam, from a long carbon cathode, was approximately 100 cm long and 5 cm wide. The laser axis was parallel to the cathode in the 100 cm dimension. The electronic energy deposited in the gas at the optical axis of the laser was determined by evaluating the density of Kr_2^* formed by the electron beam with no O_2 present. The total density of Kr_2^* was $\sim 2 \times 10^{16}$ cm^{-3} at 250 psi of krypton.

Mirrors with reflectivities of 99.8% and ~96% were mounted on the two ends of the laser cavity 125 cm apart. The radiation spontaneously emitted perpendicular both to the laser axis and to the direction of the E-beam was monitored by a photodiode after being filtered by a broadband filter. Studies using a spectrometer indicated that the only significant radiation transmitted by the filter was in a band near the 5577 Å atomic line of oxygen; this band arises from perturbation of the atomic line by Kr atoms. The total radiation emitted through the higher-transmission mirror was also monitored with a photodiode and an interference filter (5577 ± 5 Å). Fig. 1 shows both the laser light and the spontaneously emitted light.

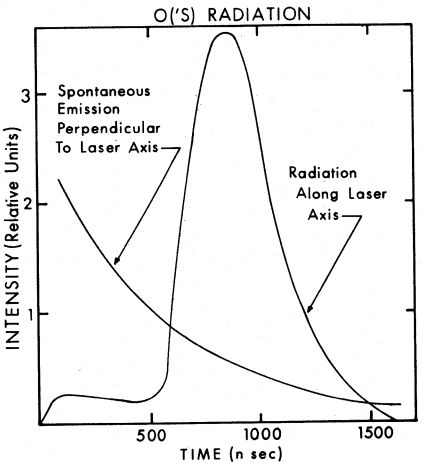

Fig. 1. Laser light and spontaneous emitted light from a mixture of 5 torr of O_2 and 1.25×10^4 torr of krypton.

The net gain of the lasing medium was evaluated in two ways. The total radiation intensity I emitted spontaneously in the 5578 Å band was 6×10^{18} photons/sec cm^3 at 600 nsec after the start of the E-beam pulse. The spectral width ν_w of the spontaneously emitted radiation was measured to be 2.5×10^{11} hertz. The gain coefficient g is evaluated from

$$g = \frac{\lambda^2}{8\pi} \frac{I}{\nu_w} = 1.5 \times 10^{-3} \text{ cm}^{-1}$$

for a wavelength λ of 5578 Å. Since the excited length of laser medium along the axis of the laser was 100 cm, the total gain per pass G is 15%.

The laser growth observed in Fig. 1 furnishes the second estimate of G. An approximation to the net gain is $\exp(g_N ct)$ where g_N is the net gain coefficient and t is the time the lasing pulse spends in the active volume for a given growth of laser intensity. To obtain the gain per pass of the lasing medium, a correction must be made to account for the mirror losses and for the fact that the excited laser medium does not completely fill the volume between the mirrors. The second estimate for G is 10% per pass. Within the accuracy of the present measurements, the two estimated values of G are in agreement.

15.4 A Discharge Heated Copper Vapor Master Oscillator Power Amplifier, R. S. Anderson, B. G. Bricks, L. W. Springer, and T. W. Karras, *GE Space Sciences Laboratory, King of Prussia, Pa.*

(15 min)

The copper vapor laser emitting at 5105 Å and 5782 Å is potentially a high power, high efficiency visible laser. In practice, however, its efficiency has been limited by the energy required to vaporize copper and its output power has been limited by superradiant losses associated with the high gain of the laser. Recent experiments at our laboratories have attacked these two problems directly and have produced some interesting results.

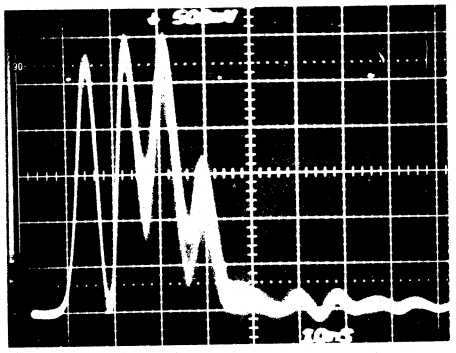

Fig. 1. 5105 Å laser pulse at copper densities $> 10^{16}$ cm^{-3}.

Copper lasers[1,2,3] generally require two sources of input energy. One source vaporizes the copper and the second source produces an electrical discharge and inversion in this vapor. The efficiency of the laser can be increased by using the electrical discharge energy to vaporize the copper, completely eliminating the first energy source. This type of laser, first demonstrated by Isaev,[4] has been built at our laboratories.[5,6]

This laser uses a high density alumina tube whose walls have been lined with thin copper foil. Refractory metal tubes inserted into both ends of the alumina serve as electrodes. This combination of electrodes and alumina tubes is surrounded by radiation shields and placed in a vacuum chamber such that buffer gases can be added inside the tubing while maintaining the outside regions at very low pressures.

An inductively charged capacitor bank is discharged between the electrodes through the buffer gas using a hydrogen thyratron as the switch. The discharge heats the alumina tube to temperatures up to 1800°C, producing copper vapor densities of 3×10^{16}/cm^3, the highest thus far reported in a copper vapor laser. This same discharge also produces a transient inversion in the copper producing very strong superradiance and lasing.

Using this design, a 2 watt average power copper laser operating at 6 kHz has been pro-

[1] T. W. Karras, R. S. Anderson, B. G. Bricks, T. E. Buczacki, and L. W. Springer, "Copper vapor generator," AFWL TR-73-133, 1973.

[2] W. T. Walter, "40 KW pulsed copper laser," *Bull. Am. Phys. Soc.*, vol. 12, p. 90, 1967.

[3] G. R. Russell, N. M. Nerheim, and T. J. Pwirotto, "Supersonic electrical-discharge copper vapor laser," *Appl. Phys. Lett.*, vol. 21, p. 565, 1972.

[4] A. A. Isaev, M. A. Kazaryan, and G. G. Petrash, "Effective pulsed copper-vapor laser with high average generation power," *JETP Lett.*, vol. 16, p. 27, 1972.

[5] R. S. Anderson, L. W. Springer, B. G. Bricks, and T. W. Karras, "A high current density pulsed metal vapor laser," presented at 1974 Gaseous Electronics Conference, Houston, Tex.

[6] R. S. Anderson, L. W. Springer, B. G. Bricks, and T. W. Karras, "Discharge heated copper vapor laser," to be published.

duced. This corresponded to a specific energy density of 40 $\mu J/cm^3$/pulse. The efficiency of the entire system was 0.2 percent considering all the input energy to the system. In addition, this laser has operated for periods of 12 hours unattended at power levels greater than 1 watt.

The discharge current pulses used in these experiments were long, varying between 125 nsec and 175 nsec. The laser pulse moreover, occurred within the first 25 nsec of the current pulse at a time when the current densities were 100 Amp/cm^2.

The laser pulse at low copper densities ($< 3 \times 10^{15}$ cm^{-3}) is approximately 20 nsec. FWHM with little structure, but as the copper density increases, the pulse assumes a modulated structure, and at densities greater than 10^{16} cm^{-3}, it is composed of four distinct 5-6 nsec spikes (Fig. 1). Interferometric studies of the laser indicate that each pulse is a slightly different frequency.

This laser is highly superradiant and indications are that a large fraction of the inversion energy is lost due to radial superradiance. To compound this problem, optical feedback is provided by the walls of the alumina tubing, further increasing radial losses. A Master Oscillator Power Amplifier (MOPA) configuration has been constructed to reduce the losses. In this configuration, a laser pulse from the oscillator is present in the amplifier when inversion is attained. The presence of the oscillator field results in stimulated emissions preferentially in the direction of this field. This produces amplification of the oscillator pulse, preventing radial superradiance losses, and permits higher extraction of the available energy in the amplifier compared to a simple oscillator.

This MOPA configuration has been initially tested using a low power oscillator (100 mW) with a pulse width of 20 nsec FWHM. The amplifier was very similar to the oscillator and produced 225 mW with a 20 nsec modulated pulse when operated as a laser. When operated in a MOPA configuration, the output power rose to 450 mW and the output pulse narrowed to a single 5 nsec peak.

This increase in output presumably was produced by stimulated emission of the inverted atoms along the optic axis which would otherwise have radially superradiated.

Further tests using a higher power oscillator and a higher gain amplifier are being conducted. Better synchronization of oscillator pulse and amplifier discharge will also be used. A substantial increase in specific energy density, laser power, and efficiency are expected.

Special thanks to B. Fox and T. E. Buczacki for their excellent help.

15.5 High Repetition Rate Flowing Copper Vapor Laser, B. G. Bricks, T. W. Karras, T. E. Buczacki, L. S. Springer, and R. S. Anderson, *GE Space Sciences Laboratory, King of Prussia, Pa.*

(15 min)

A flowing metal vapor laser suitable for high repetition rate, fast-discharge operation has been constructed and is now undergoing study.

The fundamental technology, originally reported elsewhere,[1] is based upon a copper vapor generator that provides the flowing metal. The generator consists of a thin graphite channel ($0.005'' \times 0.260'' \times 5.0''$) fed at both ends by reservoirs filled with copper. One side of the channel has an array of a large number of 0.015″ holes. Surface tension forces prevent the flow of liquid copper through the holes. When the generator is heated by currents above ~200 amperes, liquid copper flows from the reservoirs into the channel. Copper is vaporized at the hole array and flows into the optical cavity.

Neon is present as a buffer gas, and this reduces the flow so that vapor densities in the range of 10^{15}-10^{16} cm^{-3} can be maintained for periods of an hour. This gas also serves to carry the discharge.

Transverse discharge electrodes are oriented perpendicular to both the optical axis and the direction of flow of metal vapor. A low-inductance transmission line-vacuum feedthrough integrates the internal electrode configuration with the external discharge circuitry. In the design of the feedthrough, particular effort was taken to minimize the circuit inductance, to withstand the thermal loading, and to confine the electrical discharges to the laser cavity.

Oscillation is obtained by discharging a capacitor (0.5-20 nF) through a quenching spark gap switch.[2,3] This capacitor is run in bursts of 50-1000 pulses since it is pulse-charged by a 1.0 μF capacitor. With charging resistance < 3 KΩ, discharge rates above 100 kHz can be achieved. Also, with the 0.5 nF capacitor, discharge pulses of ~10 ns FWHM (as measured by Pearson Model 4100 current probe and Tektronix 7904 oscilloscope) have been obtained. It is observed that as long as the discharge time is less than that required for streamer formation, the discharge will fill a volume 10 cm × 0.6 cm in cross section and 1.4 cm long.

Lasing and supperadiant emission have been obtained at both 5105 Å and 5782 Å. Using a clear glass output mirror, pulse energies up to 10 $\mu J/cm^3$ have been measured. Increasing specific energy was found to correlate with increasing copper vapor density, current density, and initial capacitor voltage.

High repetition rate capability was also found to follow from increasing capacitor voltage. Thus, lasing could not be obtained at rates above a few kHz when the discharge voltage (5.0 nF) was ~2 kV. However, at 5 kV, the range was extended to 15 kHz with no reduction in the specific output energy per pulse. At this voltage, oscillation was also observed up to 70 kHz with a corresponding decrease in pulse amplitude.

The presence of Ne as a buffer limits the copper vapor flow velocity to about 200 cm/sec. Thus, the same copper atoms must be reused from pulse to pulse within a burst. Consequently, some mechanism is active in quenching the metastable lower laser state. We suggest that collisions of the second kind between electrons and the metastables are responsible for the quenching. Thus, for the conditions of Fig. 1, enough metastables were deexcited to allow attainment of laser threshold after ~14 μs and full deexcitation was reached after ~ 67 μs.

The authors would like to acknowledge the support of DARPA and AFWL under contract F29601-74-C-0048 and the suggestions and support of C. E. Anderson.

15.6 Frequency-Stable, Single-Mode CW Chemical Lasers for Mid-IR Heterodyne Applications, R. J. Freiberg and J. J. Hinchen, *United Aircraft Research Laboratories, East Hartford, Conn. 06108*

(15 min)

The multiline capability coupled with the mid-IR atmospheric transmission associated with CW chemical lasers, results in their being potentially very attractive sources for applications such as laser communications and frequency-diversity ladars. Moreover, in contrast to CO_2 lasers, chemical lasers require electrical energy only to initiate the chemical reaction rather than to sustain lasing. Consequently, with the inherently higher efficiencies available, potential reductions in the overall size and weight of the chemical laser and its peripheral electronics exist. However, mid-IR systems have not at the present time become serious contenders with 10.6 μ systems due to the unavailability of a suitable CW frequency-stable, single-mode mid-IR local oscillator required by the heterodyne receiver.

The present paper explores the feasibility of employing a low power CW, electrically initiated, chemical mixing laser[1] as a local oscillator for middle-infrared laser heterodyne applications. In the chemical mixing laser, atomic fluorine is produced by a dc electrical discharge in a flowing gas mixture of SF_6 and He. Molecular hydrogen or deuterium, which is subsequently mixed downstream in the subsonic gas flow, reacts with the atomic fluorine to produce the vibrationally excited lasing species. Laser power is extracted slightly downstream of the mixing region using a resonator whose optical axis is oriented transverse to the gas flow. Single fundamental mode operation is achieved by employing intracavity irises to discriminate against higher order transverse modes and by employing a cavity length which is sufficiently short such that only a single longitudinal mode can exist within the Doppler broadened linewidth.

The frequency stability of the chemical mixing laser output is limited primarily by the mechanical properties of the resonator in conjunction with the variations of the active medium initiated by the turbulent gas mixing. The long term frequency stability of these devices was investi-

[1] T. W. Karras, R. S. Anderson and B. G. Bricks, "A spectroscopic study of a high flow copper vapor laser," *Bull. Am. Phys. Soc.*, vol. 19, p. 153, 1974.

[2] F. Frungle, *High Speed Pulse Technology*. New York: Academic Press, 1965.

[3] T. W. Karras and W. E. Austin, "High repetition rate metal vapor lasers," final report to contract N0014-73-C-0042, 1973.

[1] J. J. Hinchen, *J. Appl. Phys.*, vol. 45, p. 1818, 1974.

gated using a scanning Fabry-Perot interferometer. The data consisted of multiple scans of a single Fabry-Perot fringe which were photographically recorded over various exposure times. The frequency variations exhibited by these multiple traces indicate that over a period of 1 sec, long term frequency stabilities of better than 3 parts in 10^8 are achievable with a relatively straight forward resonator design. Similar data obtained over shorter time durations indicated an approximate inverse square root dependence upon the observation time. For times shorter than 100 msec, the frequency stability was less than 1 part in 10^8 and could not be resolved by the present scanning Fabry-Perot technique.

The frequency spectrum produced by heterodyning two identical HF mixing lasers, both operating on P_2-1 (6), was displayed on a low frequency spectrum analyzer. The data indicated that the frequency stability of the present device is predominantly limited by the low frequency disturbances coupled to the mechanical resonator structure from the environment and not by the mixing within resonator medium. Consequently, significantly better frequency stability should be attainable by further sophistication of the resonator's mechanical properties before the influence of the active medium imposes limitations upon the device's performance.

To evaluate the suitability of these chemical lasers for applications such as laser communications, where frequency and amplitude stability is required over very long time periods, active stabilization techniques were investigated. A particularly attractive technique which was developed is that of locking the HF laser output to the minimum of the Lamb dip by using active dither stabilization. The laser cavity was tuned in frequency such that the dither was symmetrically applied about the minimum of the Lamb dip which was located at the center of the 300 MHz Doppler broadened gain curve. A comparison of the open and close loop performance of the chemical laser was made. In the open loop mode when the cavity length was changed due to thermal or mechanical influences, substantial variations in both the intensity and frequency of the laser were observed. However, when the laser was actively locked to the Lamb dip by means of an electronic servo system, the laser intensity and frequency remained constant within the limits associated with the dither stabilization over periods in excess of an hour and for a wide range of conditions.

Data will also be presented comparing the performance of a premixed, CW electrically-initiated, chemical laser[2] with that of the chemical mixing laser and the suitability of these CW chemical lasers as frequency-stable local oscillators for mid-IR heterodyne applications will be discussed.

[2] C. J. Buczek, R. J. Freiberg, J. J. Hinchen, P. P. Chenausky, and R. J. Wayne, *Appl. Phys. Lett.*, vol. 17, p. 514, 1970.

15.7 Recirculating DF/HF Chemical Lasers Suitable for Portable System Applications,[1] P. P. Chenausky, R. J. Freiberg, and D. W. Fradin, *United Aircraft Research Laboratories, East Hartford, Conn. 06108*

(15 min)

The recent demonstration of a self-contained, pulsed recirculating DF laser (Ref. 2 and 3) has extended the range of potential applications for DF and HF chemical lasers. This device, which uses a unique combination of pellet beds to scrub the laser effluence directly in the gas flow channel, circumvents the safety and convenience problems associated with open-cycle operation. Furthermore, because a light weight gas blower can be used instead of the heavy vacuum pump required by conventional systems, the recirculating laser is well suited for portable operation. In this paper, work that extends the basic feasibility demonstration of Refs. 2 and 3 is described. The operating characteristics of the recirculating DF laser are investigated in detail, and various component design trade-offs are considered. A portable laboratory recirculating pulse DF laser system that uses unstable resonator optics and a specially designed flex-vane blower is described. Finally, it is shown that with proper modification the recirculating mode of operation is also feasible for certain types of CW DF/HF chemical lasers.

The design parameters for the scrubber beds are discussed as a function of average laser power, pulse repetition frequency and period of recirculating operation. In particular, experimental relationships relating required bed volume to total optical energy output are presented for various scrubber bed designs. Scrubber bed designs which are capable of rejuvenation are also considered. A comparison between recirculating pulsed laser operation with DF and HF is made. This data indicates that only slightly higher average powers are attainable from the HF system.

Using the basic pulsed laser design described in Refs. 2 and 3, a portable recirculating SF_6/D_2 laser system has been built. This laser, which operates at average power levels of about 1 W, contains a specially designed, light weight flex-vane blower. Unstable resonator optics are used with this device in order to extract substantially all the optical power available from a multimode stable resonator but in a single unstable resonator mode. High-resolution beam quality measurements indicate that near diffraction-limited operation has been achieved.

The feasibility of operating a CW DF/HF chemical laser in a recirculating mode is discussed. It is shown that a CW premixed SF_6/D_2 can be operated as a recirculating laser using a gas channel design that is fundamentally the same as that used with the pulsed DF chemical laser. Chemical scrubber beds and gas flow requirements are discussed. Possible designs for operating a CW SF_6/D_2 mixing laser in the recirculating self-contained mode are also considered.

The results of this work demonstrate that safe, fully portable DF/HF chemical lasers using the recirculating mode of operation can be developed. Such systems may considerably expand the range of applications for chemical laser technology.

[1] Portions of this work were supported by the Defense Advanced Projects Agency and monitored by the Army Electronics Command.

[2] D. W. Fradin, P. P. Chenausky, and R. J. Freiberg, *Appl. Phys. Lett.*, to be published.

[3] R. J. Freiberg, P. P. Chenausky, and D. W. Fradin, *Digest IEEE Electron Devices Meeting*, paper 9.7, Washington, D.C., December 1974.

15.8 A New Look at Unstable Resonators, C. Santana and L. B. Felsen, *Polytechnic Institute of New York, Brooklyn, N. Y. 11201*

(15 min)

Unstable resonators have traditionally been analyzed by numerical solution of the resonator integral equation. These numerical solutions have exhibited some very peculiar behavior of the eigenmode losses and eigenmode fields which have not been adequately explained. It has been realized that these peculiarities are intimately connected with diffraction caused by the edges of the mirror configuration, but it has not been possible to isolate and quantify edge diffraction effects in a simple way.

In an earlier paper,[1] it has been shown that the unstable resonator problem can be attacked by a new method whereby the resonator configuration is regarded as a waveguide in the direction transverse to the resonator axis. Guided modes capable of propagating in this waveguide are reflected, transmitted (by radiation) and coupled at the resonator edges, which thus appear explicitly as constituent building blocks in the eigenmode resonance equation. By postulating a mechanism of selective coupling between two adjacent waveguide modes, it was found possible to produce and explain the intricate interweaving of the resonator eigenmode loss curves obtained previously by what have been referred to as "brute-force numerical methods."[2] The same approach, but without the quantitative formulation of the mode coupling concept, was followed recently (and independently) in the Soviet literature.[3]

In the earlier work,[1] which dealt with sharp-edged cylindrical mirrors of hyperbolic shape, emphasis was placed on small equivalent Fresnel numbers N_{eq}; the analysis accordingly contained approximations (for example, the local modeling of the edge configuration) suitable for this range of parameters. An attempt was made to extend the range of applicability to moderately large N_{eq}. But to achieve agreement with the numerically produced data,[4] it was necessary to make some heuristic modifications of the formulas. While the results[1] predicted correctly

[1] L. W. Chen and L. B. Felsen, *IEEE J. Quantum Electron.*, vol. QE-9, p. 1102, 1973.

[2] A. E. Siegman, *Appl. Opt.*, vol. 13, p. 353, 1974.

[3] G. N. Vinokurov, V. V. Lyubimov, and I. B. Orlova, *Opt. Spektrosk*, vol. 34, p. 741, 1973.

[4] R. L. Sanderson and W. Streifer, *Appl. Opt.*, vol. 8, p. 2129, 1969.

the intricate interweaving of the eigenmode loss curves, there was a question concerning the validity, or not, of the low-loss detached mode for sufficiently large N_{eq}.

To understand the cause of the difficulty in the earlier work[1] with respect to large values of N_{eq}, the analysis has been re-examined, with emphasis on two of the essential constituents that appear in the eignemode resonance equation: the waveguide mode reflection coefficient due to the modal caustic near the resonator axis, and the waveguide mode reflection coefficient due to the edges of the mirrors. Improved and more accurate formulas for both reflection coefficients have been developed. When these are inserted into the eigenmode resonance equation and the procedure described previously[1] is followed, it is found that the resonance curves for the uncoupled waveguide modes now are changed in such a way as to predict clearly the existence of a detached resonator eigenmode for sufficiently large N_{eq}. In the earlier study (see Sec. VI of ref. 1, the solution of the uncoupled-mode resonance equation did not exhibit unambiguously the possibility of eigenmode detachment whence the verification of that phenomenon was left unresolved. The present more accurate analysis confirms completely and quantitatively all aspects of the numerical solution of the resonator integral equation,[4] for small and large Fresnel numbers, without the need for heuristic assumptions. Thus, the original theory of Chen and Felsen[1] has been proved adequate for furnishing unstable resonator eigenmode behavior for small and large N_{eq} in terms of the simple model of either a single resonant waveguide mode (near eigenmode loss minima) or two coupled resonant waveguide modes (in high-loss regions). Numerical comparisons to that effect will be presented.

The theory has also been extended to circular mirrors of hyperbolic shape. The waveguide modes are now found to be solutions of Whittaker's differential equation. When a resonance equation for azimuthally symmetric fields is constructed by the method used for the cylindrical mirror case, and when caustic and edge reflection coefficients are calculated by the improved methods alluded to above, one finds that the solutions of the eigenmode resonance equation reproduce completely the curves of Siegman and Miller[5]; our analysis confirms the absence of a low-loss detached mode in this instance. It is to be noted that our improved method predicts naturally, and within the same basic framework, the existence of a detached eigenmode for cylindrical mirrors and the absence of such a mode for circular mirrors. This does not appear to be the case for other analytical procedures.[6]

The waveguide method can be extended to accommodate resonators filled with inhomogeneous media and with media exhibiting a gain profile. Necessary modifications of the analysis are discussed.

[5] A. E. Siegman and H. Y. Miller, *Appl. Opt.*, vol. 9, p. 2729, 1970.

[6] P. Horwitz, *J. Opt. Soc. Am.*, vol. 63, p. 1528, 1973.

15.9 A 700 Meter Long Mode-Locked Argon Ion Laser,[1] P. P. Tripathi and R. H. Lovberg, *Institute of Geophysics and Planetary Physics, University of California, San Diego, La Jolla, Calif. 92037*

(15 min)

A visible argon ion laser, on the high gain 4880 Å transition, has been made to operate in a long vacuum optical cavity. Single frequency CW operation was achieved. The laser was also actively amplitude-modulated to produce mode-locked pulses, at a repetition rate of 204 kHz. Also, by utilizing electrooptical feed back[2] self-sustained mode-locked pulse opeartion was achieved.

The only other very long cavity lasers reported in literature[3,4] were operated at infrared wavelengths; Xenon at 3.508 μ, and Nd:YAG at 1.064 μ. These utilized long atmospheric cavities, and reflecting optics for beam expansion. It appears that in those experiments actively mode-locked pulses were not achieved; however in [4], evidence of self-locking of the modes in the pulsed Nd:YAG laser is indicated.

Our long laser project was undertaken as a feasibility study for making a device for measuring geophysical strain accumulated in the earth's crust. The basic principle of this device is the following: It is essentially a long laser of cavity length L in which the longitudinal modes separated in frequency by $c/2L$ are actively phase-locked with each other by utilizing electrooptical feed back. Then it becomes possible to measure L very precisely, by frequency measurement of a higher harmonic of $c/2L$, say at 100 MHz. A 10-second integration time can then produce data accurate to 1 part in 10^9. As opposed to optical interferometric method,[5] this device would preserve absolute strain value in case of a seismic event strong enough to cause power failure.

The present system consists of an approximately 700 meter long evacuated pipe with windows on the ends. Refractive optics are used for beam expansion and retro-reflection. (See Fig. 1.) Optical gain is provided by a conventional size (20 cm long × 2 mm bore diameter) laser discharge tube (Hughes 3066H Ar^+ laser head) located at one end. Because of many inherent sources of loss per round trip in the long laser configuration, a high gain laser medium is essential.

The frequency spacing ($c/2L$) of the longitudinal modes for this cavity is near 200 kHz, which is much less than the expected Lorentzian line width of 500 MHz for the Ar^+ laser transition; it can therefore be expected that the spectral cross-relaxation (CR) should be strong, inhibiting oscillation of all modes except one at the line center. However, initially, intermode beats at $n(c/2L)$ were observed for n up to 5. The appearance of these beats was rather random in time. This can be explained with the hypothesis of energy being pumped into these cavity modes because of the nonlinear coupling through the laser plasma, as the discharge current fluctuated with its inherent 60 Hz ripple. An additional experiment indicated that the amount of energy in these side modes was at least 5 orders of magnitude lower than the central mode. The intermode beats vanished and true single frequency operation was obtained on switching to dc supply for heating the laser cathode filament, eliminating the source of the 60 Hz ripple in the discharge current.

Intra-cavity Pockels cell was utilized to provide loss modulation at intermode beat frequency $c/2L$ (= 204 kHz). Mode-locked pulses of width 1 μsec at a repetition period of about 5 μsec were obtained. Modulation at c/L produced two pulse operation, and thus an effective repetition period of 2.5 μsec and a pulse width of 0.5 μsec.

These optical pulses were detected by a photodetector, amplified, properly delayed and fed back to the modulator, closing the feed back loop. Self-regeneratively driven mode-locked-pulse operation was achieved. This experimental evidence indicates that it is possible to further engineer this long laser into operating in its original concept of measuring the strain in the earth's crust.

[1] This work was supported by NSF Grant GA36234.

[2] G. R. Huggett, *Appl. Phys. Lett.*, vol. 13, p. 186, 1968.

[3] G. J. Linford, E. R. Peressini, W. R. Sooy, and M. L. Spaeth, *Appl. Opt.*, vol. 13, p. 379, 1974.

[4] G. J. Linford and L. W. Hill, *Appl. Opt.*, vol. 13, p. 1387, 1974.

[5] J. Berger and R. H. Lovberg, *Science*, vol. 170, p. 296, 1970.

15.10 High Pressure Gas Lasers, V. A. Danilychev, *USSR*

(15 min)

No summary.

Session 16

Friday, May 30, 1975 8:45-11:45 A.M.

Semiconductor and Miniature Solid State Lasers

Chairman: P. L. Kelley, *Lincoln Laboratories, MIT, Lexington, Mass. 01741*

Organizer: H. Kressel, *RCA Laboratories, Princeton, N. J. 08540*

16.1 A Review of Molecular Beam Epitaxy for Optoelectronic Applications (*Invited*), A. Y. Cho, *Bell Telephone Laboratories, Murray Hill, N. J.*

(30 min)

No summary.

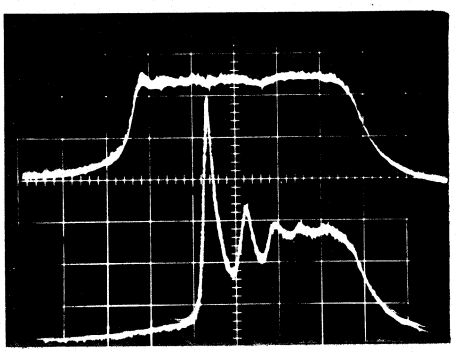

Fig. 1. Output response of diode *A* with (upper trace) and without light injection (lower trace) 1.0 nsec/div.

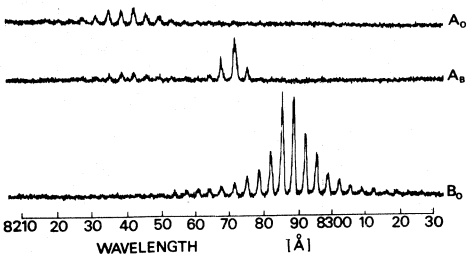

Fig. 2. Spectra of the output from the two diodes. The ordinates of diodes *A* and *B* are different from each other.

16.2 Suppression of Relaxation Oscillation in Semiconductor Lasers, R. Lang and K. Kobayashi, *Central Research Laboratories, Nippon Electric Co., Ltd., Kawasaki-shi, Japan*

(15 min)

Semiconductor lasers are considered to be especially desirable sources for optical communication systems because of their unique characteristics including the ability to be modulated directly by varying the injection current. Direct modulation of the output intensity of a GaAs laser at a rate of 46 GHz has been reported.[1] However, the practical rate has been limited to several hundred MHz, owing to the serious distortion of the output signal caused by relaxation oscillations, or spiking, in the modulated output. We have analyzed various schemes for suppression of these oscillations and found that optical injection,[2] where a small amount of external radiation is continuously injected into resonant modes of the laser cavity, is quite effective.

Computer simulation indicates that the light injection can improve the response characteristics in pulse modulation in the following fashion: i) the height of the initial spike and the delay of the onset of lasing is reduced, ii) the residual relaxation oscillation damps faster. In addition, stabilization of the output wavelength is expected due partly to selective excitation of laser modes by the injected light.

The effectiveness of the light injection method has been confirmed in a series of experiments which employed two GaAs DH lasers. The two lasers (diode *A* and *B*) were excited by current pulses of 10 nsec duration, and a small portion of the output of diode *B* was fed into diode *A*. Care was taken to insure that diode *B* was lasing stably when diode *A* was excited. In Fig. 1 the output responses of diode *A* are compared. With light injection (upper trace), suppression of the relaxation oscillation is seen to take place. Typical output spectra are shown in Fig. 2. The spectra of diode *A* with and without light injection from diode *B*, having spectrum B_O, are denoted respectively as A_B and A_O. In A_B, spectral peaks appear in the wavelength region where the closest matching of the characteristics of the two diodes are attained.

In conclusion, the light injection method has been shown to be effective in suppressing relaxation oscillation. Although the small amount of optical injection sufficient for the effective suppression can be achieved without difficulty employing a separate laser diode as the external source, the alignment problem may be eliminated by using, for example, a double section diode with two independent optical cavities. With the use of this technique, the practical upper limit for the rate of direct modulation of semiconductor lasers is expected to increase greatly.

[1] S. Takamiya, *et al.*, *Proc. IEEE*, vol. 56, p. 135, 1968.
[2] A. B. Fowler, *J. Appl. Phys.*, vol. 35, p. 2275, 1964.

16.3 Spatially Coherent Radiation from an Array of Three GaAs Lasers—Phase Controlled or Free Running Mode,[1] E. M. Philipp-Rutz, *IBM Corp., Federal Systems Division, Gaithersburg, Md. 20760*

(15 min)

A spatially coherent GaAs laser with an external optical cavity and transverse mode control, using a single laser diode, has been described previously.[2] Also, a technique was reported[3] of phase coherent coupling three GaAs lasers in a monolythic array, with the objective of obtaining higher optical power in the spatially coherent mode. In this paper, the phase controlled mode of spatially coherent beam formation, reported previously,[3] is compared with the free running mode which recently has been verified experimentally. While in the phase controlled mode the far-field of the spatially coherent radiation is an interference pattern with the zero-order and also the first-

[1] This work was partly supported by NASA contract NES830543.
[2] E. M. Philipp-Rutz, *IEEE Quantum Electr.*, vol. QE-8, p. 632, 1972.
[3] E. M. Philipp-Rutz, 1974 IEEE Int. Semiconductor Laser Conf., Atlanta, Ga.

Fig. 1. GaAs laser device with three-laser array.

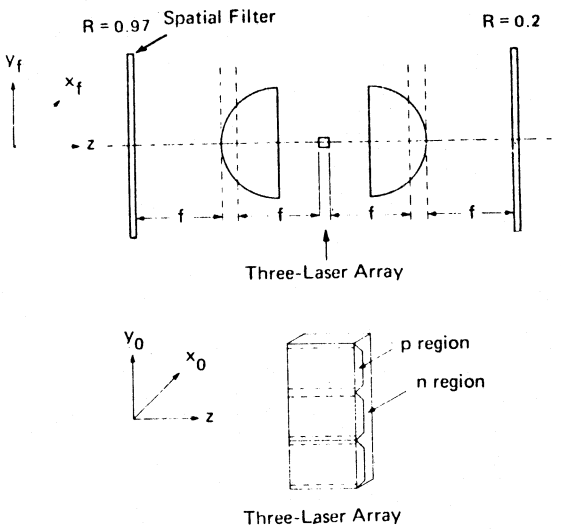

Fig. 2. Field distribution of three-laser array at second focal plane of internal lenses.

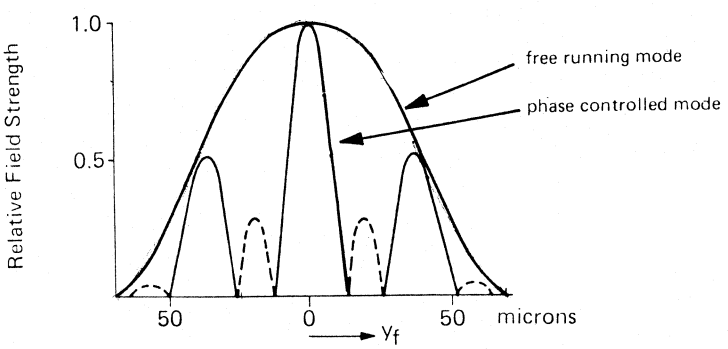

order grating lobes, in the free running mode the far-field has a single maximum and no grating lobes.

For spatially coherent radiation, the GaAs lasers in the monolythic array, with their mirror faces antireflection coated, are operated with an external optical cavity. The cavity is built of spherical lenses and plane mirrors, as shown in Fig. 1. The laser array and the plane mirrors are placed at the focal planes of the internal lenses. A spatial filter which selects the spatially coherent mode is formed by one or several highly reflecting strips on one of the plane mirrors of the cavity.

The transverse mode control makes use of the Fourier transform property of the lenses in the optical cavity. The transformation of the field of each laser in the array by the internal lenses, yields the identical amplitude distribution at the second focal plane. Since the waves from the lasers in the array, at the second focal plane of each lens, occupy the same space, the resultant field distribution is determined by the phase relations among the waves. When the waves are all in phase, their superposition at the second focal plane will result in an interference pattern, as shown in Fig. 2. (Fig. 2 was computed for an array of 3 lasers where the junction of each laser is 180 microns wide and the spacing between centers is 230 microns.)

To select the phase controlled mode of the three laser array, a spatial filter is used in the external optical cavity, formed by three gold stripes of 25.5 microns width which are spaced 12.5 microns apart. The spatial filter reflects only the dominant in-phase components of the interference function in Fig. 2. The Fraunhofer diffraction pattern of the laser array, when restored by an external lens, is similar to the interference function in Fig. 2.

For most system applications, the energy contained in the first-order grating lobes cannot be utilized. In the phase controlled mode the off-axis lobes cannot be eliminated, though, by making the spacings between lasers smaller, the energy in these lobes can be reduced. The free running mode of a laser array yields a single spatially coherent beam without grating lobes. To select the free running mode a spatial filter is used in the optical cavity which only controls the field of each laser to be in the lowest order transverse mode; it does not influence the phase angles of the fields. The spatial filter at the second focal plane of one of the internal lenses, is formed by a single gold strip of 120 microns width. The spatial filter reflects nearly the entire field of each of the lasers in the array. This type of spatial filter which does not reproduce an interference function, does not exert any control other than the transverse mode selection. Without control the longitudinal modes of the laser array with the external optical cavity, have slowly varying amplitudes and phase angles. These variations are random. The fluctuations of an optical field, resulting from the summation of randomly phased, monochromatic waves with randomly varying amplitudes, are completely random. The random fluctuations of the optical fields of the lasers in the array prevent the formation of a stationary interference pattern. The field distribution at the output mirror of the optical cavity is that shown in Fig. 2.

The Fraunhofer diffraction pattern of an array of lasers in the free running mode, when restored by an external lens, has a single beam along the optical axis of the internal lenses and no grating lobes.

We have synthesized the far-field distributions of the laser array in our laboratory by the use of two external lenses. The synthesized far-fields of the three laser array in the phase controlled mode and in the free running mode were measured. They are similar to the distributions in Fig. 2. In both modes the optical peak pulse power, measured at room temperature, was close to 5 watts; 3 times the power of a single laser in the array.

16.4 Reliable Laser Diodes: A Status Report (*Invited*), H. Kressel, *RCA Laboratories, Princeton, N. J.*

(30 min)

No summary.

16.5 Packaged Semiconductor Lasers for Optical-Fiber Transmission, M. Takusagawa, K. Hori, H. Ishikawa, H. Takanashi, T. Toge, and T. Kudo, *Fujitsu Laboratories Ltd., Kawasaki, Japan*

(15 min)

In the application of semiconductor lasers to optical-fiber transmission, it is important to obtain stable laser output power for long times over a wide temperature range. Since the light emitted from the semiconductor laser goes in two directions it is possible to use the output from one end as the transmitted signal and from the other for feedback control through the operating current or temperature. A new method of packaging semiconductor lasers which is appropriate to obtaining constant laser output power has been developed. The method of packaging has been presented elsewhere.[1] This paper describes the characteristics of the packaged laser, the methods of automatic optical-power control, and the results obtained.

GaAlAs DH laser was packaged with a fiber F_s for signal transmission and a fiber F_c for signal monitoring. The two fibers are directly coupled with the DH lasers. We used F_s and F_c with numerical apertures of 0.14 and 0.5, core diameters of 90 μm and 570 μm, and lengths of 10 cm and 6 mm, respectively. The curves of output from F_s and F_c vs diode current were similar. The DH lasers used were modified stripe-geometry planar structures whose stripe width was 15-30 μm.[2] The wavelength was 0.80-0.85 μm. The lasers operate stably over 5000 hrs with very slight increase of threshold current when the output from F_s is larger than 1 mW. Several packaged lasers exhibited stable operation for over 3000 hrs. Significant relative changes were not observed between the output from F_s and that from F_c. The characteristics of the long lived packaged lasers will be shown.

We examined two methods of automatic optical-power control, namely, control of operating current and control of operating temperature by changing the current of thermo-electric elements on which the packaged laser was mounted. The output from F_c was detected by a photodiode and the signal compared with a given standard voltage. The current of the laser diode or the thermo-electric elements was controlled to give a zero voltage difference with the reference.

In the control of operating current of the laser diode, constant output at room temperature ($\sim$1 mW) has been obtained from F_s for over 1000 hrs. When the temperature of the packaged laser was changed from 10 to 70°C, low thermal-resistance diodes showed constant output ($\sim$1 mW) from F_s by the automatic optical-power control technique.

In the control of operating temperature, the fluctuation of the output from F_s was kept below 5% with the environmental temperature range of 10 to 40°C. In this temperature range no change was observed in a light pulse waveform modulated at 100 Mb/s. The thermal response time of the experimental system was about 200 sec which was good enough to follow the slow change of optical power.

The comparison between the two methods will be discussed.

16.6 Progress in Nd-Pentaphosphate Lasers, H. P. Weber, B. C. Tofield,[1] and P. F. Liao, *Bell Telephone Laboratories, Holmdel, N. J. 07733*

(15 min)

Nd-pentaphosphate (NdP_5O_{14}) is a high Nd-concentration material, well suited for fabrication of miniaturized optically pumped lasers.[2] We report here new results concerning material characteristics and laser properties.

A direct measurement of energy-diffusion distance is reported, based on a novel measurement technique.[3] An upper limit of 32 nm along the supposedly fast migration direction[4] is determined. This value is too small to significantly influence laser emission.

The quasi-orthorhombic symmetry of the crystals is shown to undergo a second order phase transition into orthorhombic symmetry

[1] T. Yamaoka, *et al.*, Topical Meeting on Optical Fiber Transmission, Williamsburg, Va. 1975.

[2] H. Yonezu, *et al.*, *Japanese J. Appl. Phys.*, vol. 12, p. 1585, 1973.

[1] Present address: Materials Physics Div., AERE, Harwell Didcot, Oxfordshire, OX11 ORA, England.

[2] For a review and references see e.g. B. C. Tofield, H. P. Weber, T. C. Damen, and P. F. Liao, *J. Solid State Chem.*, Jan. 1975.

[3] H. P. Weber and P. F. Liao, *JOSA*, vol. 64, p. 1337, 1974.

[4] G. Huber, J. P. Jeser, W. W. Krühler, and H. G. Danielmeyer, *IEEE J. Quantum Electron.*, vol. QE-10, p. 766, 1974.

at 174°C. The transition is directly observed by the disappearance of the twin boundaries at that temperature. At room temperature, ferroelastic movement[5] of the twin boundaries is observed. A shear stress of σ = kN/m^2, produces this ferroelastic reorganization. This stress is two orders of magnitude lower than has been reported for any other material and allows undesired twin boundaries to be easily removed mechanically.

A CW NdP_5O_{14} laser was pumped with a Kr laser and had a threshold of 1.6 mW. By monitoring the fluorescence light a precise value for the internal quantum efficiency, η can be obtained, yielding for this laser $\eta = 63\%$.

Bistable operation between oscillating and nonoscillating regimes was observed as a result of a thermal lens created in the pumped zone. If feedback is temporarily blocked during pumping, this lens becomes strong and makes the nearly concentric Nd laser resonator unstable, so that stimulated emission cannot build up after removing the blockage. If the pump beam is temporarily blocked, the crystal cools and when the blockage is removed, laser action is reinstated. The resonator then remains in the stable regime, because the stimulated emission competes with nonradiative quenching processes (cooling effect via stimulated emission). The temperature increase above room temperature for the two situations is measured using Raman spectroscopy. From the intensity variation of an anti-Stokes line of a probe beam, temperature increases of 18° and 11°C for the nonlasing and lasing situations are established. From these values we determine a fluorescence quenching rate of 68% for the upper laser state. This number is in close agreement with the value of 62.5% found by interpretation of lifetimes for different x in $Nd_xLa_{1-x}P_5O_{14}$ and supports observed concentration independence of the emission cross section.[6] It is in disagreement with suggested[4] lifetime shortening due to increased emission cross section when $x = 1$.

Heat development per unit volume in $Nd_{0.5}La_{0.5}P_5O_{14}$ would be reduced by 2/3; whereas because of reduced quenching, the small signal gain for equal pump power should be twice as high. These facts together with the absence of any advantage due to strong energy diffusion in undiluted NdP_5O_{14} renders the less concentrated material more attractive for device applications.

[5] S. C. Abrahams, *Mat. Res. Bull.*, vol. 6, p. 881, 1971.

[6] S. Singh, D. C. Miller, J. R. Potoponics, and L. K. Shick, *J. Appl. Phys.*, March 1975.

16.7 Low - Threshold, Transversely - Excited NdP_5O_{14} Laser,[1] S. R. Chinn, J. W. Pierce, and H. Heckscher, *Lincoln Laboratory, MIT, Lexington, Mass. 02173*

(15 min)

We have measured room-temperature CW lasing thresholds of NdP_5O_{14} (NdPP) excited by a dye laser. The pump beam was incident on the sample in a direction perpendicular to the lasing axis, simulating the geometry for excitation by a narrow-junction, edge-emitting LED or laser diode.

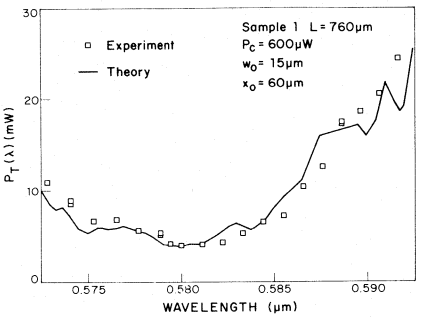

Fig. 1. Experimental and theoretical transverse pump threshold, $P_T(\lambda)$, as a function of wavelength near 0.58 μm for NdPP sample #1, 760 μm long.

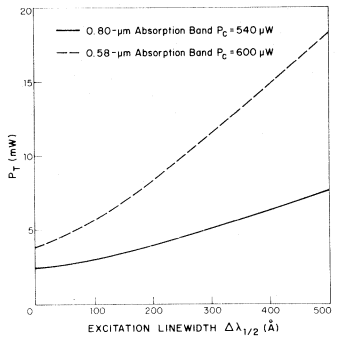

Fig. 2. Theoretical transverse pump threshold vs. FWHM excitation bandwidth, $\Delta\lambda_{1/2}$, for NdPP sample #1 using a tightly focused pump beam.

The NdPP laser crystal was located at the center of a nearly-spherical optical cavity having mirrors with nominally 100% and 99.7% reflectivity at the lasing wavelength, 1.052 μm. The pump radiation was focused on the side of the sample by two crossed cylindrical lenses to form a narrow line image parallel with the NdPP laser mode. By tuning the Rhodamine 6G dye laser about the wavelength of peak absorption at 0.580 μm, we have measured the threshold as a function of pump wavelength from 0.575 to 0.590 μm. Typical minimum thresholds were 4 mW at the absorption line center, increasing to 25 mW at wavelengths 0.01 μm away (Fig. 1). With 20% duty-cycle, quasi-CW excitation, we have measured power conversion efficiencies ~8% at output powers ~3 mW.

Using a simple theoretical model, we have obtained a good fit to the experimental data for threshold vs pump wavelength. In this treatment, the calculated transverse threshold, $P_T(\lambda)$, was normalized to the experimentally measured collinear-pumping threshold at 0.58 μm, P_C (typically six times smaller than the transverse value). Using measured values for the pump absorption coefficient, and adjustable parameters for the laser mode waist, w_0, and depth, x_0, inside the crystal, we calculated the values of $P_T(\lambda)$ shown in Fig. 1 (the results were relatively insensitive to the choice of w_0 and x_0 over a wide range of these parameters). This analysis was then used to calculate thresholds for wider-bandwidth pump sources, such as LED's or laser diodes, emitting near 0.80 μm, a favorable wavelength for electro-luminescent device operation and the location of the strongest absorption band in NdPP. The threshold vs pump bandwidth calculations for the dye-laser configuration are shown in Fig. 2. Taking account of the larger pump beam divergence from a semiconductor light source placed next to the laser crystal, it is estimated that thresholds ranging from 4 mW for an extremely narrow-band laser pump, to 8.5 mW for a 300 Å (FWHM) bandwidth LED, should be attainable with our present 760 μm long NdPP sample.

We have also succeeded in lowering the threshold and increasing the laser efficiency by using a thin NdPP sample mounted on an aluminized surface which reflected any transmitted pump radiation back into the sample. With this arrangement a transverse threshold (at 0.58 μm) of 2.7 mW was obtained, with a reduction of 60% in the ratio of transverse/collinear threshold. A sample only 36 μm thick also lased in this configuration, indicating a possible compatibility with integrated optical technology.

In preliminary experiments, we have obtained laser action in NdPP using a single $Al_xGa_{1-x}As$ laser diode provided by RCA. The diode was cooled to obtain the desired 8000 Å wavelength, and driven by 300 μs current pulses to avoid heating. This pulse length was sufficient to produce quasi-CW NdPP lasing. The pump radiation was collected by a single f/.9 lens and focused transversely on the room-temperature NdPP sample, mounted as described above. Because of the non-optimum diode dimensions and collection optics, the overall performance was degraded. Nevertheless, we have obtained thresholds of 12.4 mW for the thick 760 μm long sample and 7.2 mW for the thin sample described above. The respective optical power conversion efficiencies were 7.5% and 6.8%. Detuning the pump wavelength to 7930 Å increased the threshold for the thin sample only to 7.9 mW, in good qualitative agreement with the wavelength dependence described by our theory.

16.8 CW Laser Operation of $LiNdP_4O_{12}$ by Transverse Pumping, T. Yamada and K. Otsuka, *Musashino Electrical Communication Laboratory, Nippon Telegraph and Telephone Public Corp., Musashino-shi, Tokyo, Japan*

(15 min)

One of the laser materials in which the Nd ion is a constituent of the compound[1] is lithium neodymium tetraphosphate ($LiNdP_4O_{12}$, abbreviated as LNP). The crystal belongs to the monoclinic system (pseudo-orthorhombic system). The Nd content is 4.37 × 10^{21} cm^{-3} and

[1] This work was sponsored by the Department of the Air Force.

[1] T. Yamada, K. Otsuka, and J. Nakano, *J. Appl. Phys.*, vol. 45, Nov. 1974.

TABLE I
CRYSTAL DIMENSIONS AND OBSERVED CHARACTERISTICS OF LNP LASER

dimensions (mm)								
l	t	w	P_{th}	ω_0	L_c	η	σ_s	σ_1
2.57	0.44(2)	2.0	168 mW	61 μm	0.10(3)	0.37(5)	0.04	3.0×10^{-19} cm^2
3.67	0.44(5)	2.0	196	66	0.12(1)	0.40	0.04(5)	3.3×10^{-19}

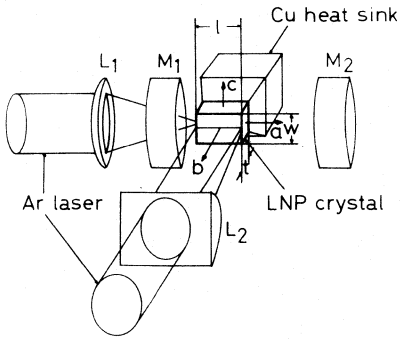

Fig. 1. Experimental arrangement of CW LNP laser.

the fluorescent lifetime is 120 μs at room temperture. The single crystals of about $5 \times 5 \times 5$ mm^3 have been obtained by the top-seeded Kyropoulos method from a melt.

The largest effective emission cross section at the line peak [1.047(7) μm] was spectroscopically determined with a 25 μm thick plate, employing the method described by Singh *et al.*,[2] as 3.2×10^{-19} cm^2 for the electric vector parallel to the pseudo-orthorhombic c-axis.

The present paper reports the characteristics of LNP CW laser transversely pumped with Ar laser to know the power requirement of LED to lase LNP.

Two polished crystals with different lengths were used for the experiment (Table I). The experimental setup as well as the crystal mounting are shown in Fig. 1. The laser cavity consisted of mirror M_1 [radius curvature r_1 = 20 cm, transmittance at 1.047(7) μm T_1 = 0.1, 1%] and mirror M_2(r_2 = 9 cm, T_2 = 0.1, 1, 2%) separated by about 9 cm. The crystal was placed just in front of M_1 and pumped by Ar laser (5145 Å) longitudinally or transversely through a circular lens L_1 or a cylindrical lens L_2. The transverse pumping efficiency η was measured by the ratio of threshold P_{th} between these two pumping geometries. The spot size ω_0 was approximately determined by using the equation $\eta = 2 \sinh (2.1\alpha\omega_0) \exp(-\alpha D)$, where α is the absorption coefficient of pump light and D is the distance between the crystal surface and the center axis of the oscillating beam. Here, α is 23 cm^{-1} for the light polarized along c-axis and D was 200 μm. The round-trip loss L_c was directly measured by the change of threshold with T_1 and T_2.

The results obtained are shown in Table I, where T_1 and T_2 were fixed as 0.1 and 1%, respectively. In Table I, σ_s is the slope efficiency and σ_1 is the effective emission cross section calculated using the listed data. The values of σ_1 agreed with that obtained spectroscopically.

The LNP laser emission was linearly polarized along c-axis.

The propagation loss of the lasing crystal α_c was calculated from the two measured L_c as 0.0084 mm^{-1}, which is mainly attributed to the self-absorption of inverse $^4I_{11/2} \rightarrow {}^4F_{3/2}$ transition.

Comparing the threshold of the two crystals, the threshold power per unit crystal length p_{th} was found to decrease from 65 mW/mm to 53 mW/mm, because $p_{th} \propto \alpha_c + \beta_c/2l$, where β_c is the transmission loss of the cavity mirrors plus the diffraction loss and l is the crystal length.

Since the absorption coefficient of LNP, as in the case of NdP_5O_{14},[3] is about 30 times higher than that of Nd:YAG, the Nd-compound laser transversely pumped by LEDs is considered to be a candidate as a light source in an optical communication system. From the data in Table I the optical power of LEDs to lase a 5 mm LNP crystal is calculated as 30 mW/mm ($\omega_0 \approx 70$ μm).

[2] S. Singh, R. G. Smith, and L. G. Van Uitert, *Phys. Rev. B*, vol. 10, p. 2566, 1974.

[3] H. G. Danielmyer and H. P. Weber, *IEEE J. Quantum Electron.*, vol. QE-8, p. 805, 1972.

16.9 Application of CW AlGaAs Injection Lasers in Electrooptical Technology (*Invited*), I. Gorog, P. V. Goedertier, J. D. Knox, I. Ladany, J. P. Wittke, and A. H. Firester, *RCA Laboratories, Princeton, N. J. 08540*
(30 min)

AlGaAs heterojunction laser diodes have been successfully used in scanning systems. System design concepts and performance characteristics will be described.

Session 17

Friday, May 30, 1975 1:30-5:00 P.M.

Modulators, Parametric and Nonlinear Optical Devices

Chairman: J. A. Giordmaine, *Bell Laboratories, Murray Hill, N. J.*

17.1 GaAs Electrooptic Channel-Waveguide Modulator, J. C. Campbell and F. A. Blum, *Texas Instruments Incorporated, Dallas, Tex. 75222*
(15 min)

We report a new type of high-speed GaAs channel-waveguide modulator for integrated optical circuits (IOC's). These devices utilize the electrooptic effect to (1) confine light in the vicinity of a narrow Schottky-barrier strip and/or (2) modulate the trapped beam.

A schematic diagram of the electrooptic channel-waveguide modulator is shown in Fig. 1. A planar asymmetric waveguide is formed by growing a 2-3 μm thick, lightly-doped ($N_d \sim 10^{15}$/cm^3) GaAs epitaxial layer on a heavily-doped ($N_d \sim 10^{18}$/cm^3) {100} GaAs substrate. Schottky barriers are then made by opening narrow strips parallel to the y axis (see Fig. 1) in an oxide mask using standard photoresist techniques and selectively electroplating Pt-Au contacts. For the crystal orientation indicated in Fig. 1, GaAs is biaxial i.e., if an electric field is applied in the z direction, the electrooptic contribution to the refractive index, for a wave polarized along x is

$$\Delta n_{eo} = (n_0^3 r_{41} E_z)/2$$

where r_{41} is the linear electrooptic coefficient and E_x is the electric field strength. At zero bias, light propagating in the epitaxial layer spreads out laterally along the x direction. When the Schottky-barrier strip is reverse biased much of the light coupled into the waveguide is trapped under the metal contact, (Fig. 1) because of the electrooptic contribution to the refractive index in that region. This scheme permits confinement in the x direction as well as the z direction thus forming a channel-waveguide. If the applied voltage is modulated, the signal seen by a small aperture receiver such as an optical fiber is amplitude modulated.

Light is coupled into the waveguide by focus-

Fig. 1.

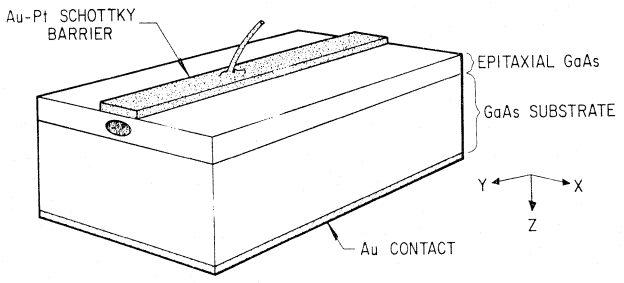

ing a 1.06 μm Nd:YAG laser beam onto the cleaved edge of the waveguide. To observe the electrooptic channeling effect, a magnified image of the near field intensity pattern at the waveguide output is focused on an infrared vidicon and displayed on a T.V. monitor. When the input laser beam is focused directly underneath the Schottky barrier at zero bias, little light emerges from the waveguide because of the high attenuation associated with the Pt-Au contact. When 40 V reverse bias is applied to the Schottky barrier, the output intensity increases by a factor of 18. A loss coefficient of 3-8 cm^{-1} has been determined for these waveguides by measuring the transmission of several lengths of the same sample.

The time response of an electrooptic channel waveguide operating as a modulator is determined by focusing the output on an RCA 7102 photomultiplier and driving the device with a delay line pulser having a 2 nsec rise time. A phototube limited rise time of 5 nsec has been measured for a 21 μm wide device implying a minimum bandwidth of 150 MHz. The combined capacitance of this modulator and the transistor header to which it is attached is 7 pF. This gives an RC time constant across 50 Ω of 0.35 nsec and a projected bandwidth of 900 MHz. The actual device capacitance is estimated to be 5 pF, yielding an ultimate bandwidth limitation of 1.2 GHz. With a reverse bias of 40 V, the modulator current is less than 1 mA. For the measured bandwidth of >150 MHz, the required modulator power per unit bandwidth is <300 μW/MHz.

17.2 Electrooptic Modulation in Grain-Oriented ZnO Films,[1] Chenming Hu, *Massachusetts Institute of Technology, Cambridge, Mass. 02139*

(15 min)

Most of the waveguide electrooptic modulators that have been reported to date involved the use of single crystal films.[2] It appears that sputtered or evaporated polycrystalline films would be easier to fabricate and more versatile in forming composite systems with other optical films or metal electrodes. Gia Russo *et al.*[3] have investigated sputtered $LiTaO_3$ modulators and found that the effective electrooptic coefficients of the films were only a few percent of the single crystal value, presumably due to the randomness of the polycrystalline structure.

However, many materials, notably ZnO and CdS, are known to form grain oriented polycrystalline films, usually with the *c*-axis of the crystallites perpendicular to the substrate (Fig. 1). This is the case whether the substrate is glass, single crystal, or metal.[4] Utilizing this fact, it

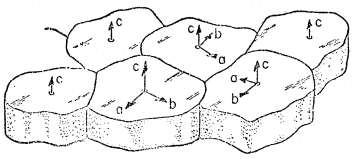

Fig. 1. Grain oriented polycrystalline film.

should be possible to construct polycrystalline modulators that have nearly the same electrooptic coefficient, and voltage and power requirement as single crystal modulators.

We have sputtered a series of ZnO films on glass slides under varying conditions in a dc diode sputtering system. Besides the usual parameters such as pressure and sputtering rate, the temperature of the substrate during the sputtering process was found to be an important parameter. Heating the substrate to 300°C resulted in highly aligned films, which also had lower waveguide losses. X-ray diffraction studies indicated that the *c*-axes of the crystallites were 97% aligned within two degrees. The optical waveguide loss was around 25 dB cm^{-1} at 6328 Å and could be reduced to 10 dB cm^{-1} by slightly polishing the film surface.

On the surface of a rather thick ZnO film (1.8 μm) we defined a silver interdigital electrode having 8 μ line width and 1.2 mm long by a photoresist-lifting technique. Both the thick film and the silver metal were chosen to minimize the effect of the electrodes on the waveguide modes. A 6328 Å laser beam was coupled into the TEO mode (Fig. 2), directed to pass under the electrode at the proper Bragg angle, and then coupled out by a second prism. The transmitted and diffracted beam intensities were measured as functions of the applied voltage. The results were fit to the formula

$$\frac{I_{diffracted}}{I_{incident}} = \left(\frac{\pi L}{2\lambda} n_0^3 \gamma_{13} E_3\right)$$

to determine the electrooptic coefficient γ_{13}. Because of the uncertainty in E_3, γ_{13} could only be estimated to be 1×10^{-12} m/v, which is close to the bulk value of 1.4×10^{12} m/v.

In order to measure the electrooptic coefficient more accurately the ZnO film should be sandwiched between two electrodes and, probably, buffer films. Such geometry will also result in more savings of the modulator power requirement.

Fig. 2. Modulator configuration.

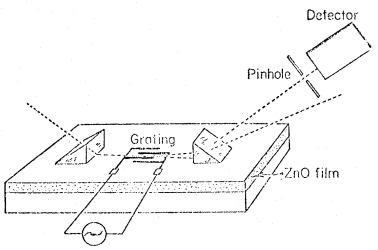

17.3 Resonant Piezo-Electrooptic Modulation, D. Halido[1] and Raoul Weil, *Technion-Israel Institute of Technology, Haifa, Israel*

(15 min)

Resonant Piezo-electrooptic (RPEO) modulation is achieved when an electrooptic modulator is operated at its piezo-electric resonance. The resonant frequency is a function of the material properties and the geometry of the modulator. When a device is operated in this mode, full modulation can be achieved with several orders of magnitude less voltage than needed in the usual electrooptic mode. Because the device is resonant, it has a narrow bandwidth.

In a previous paper[2] an experimental study of RPEO modulation was presented along with a one dimensional theory. The theory gave only order of magnitude agreement with the measurements on samples of the geometry used. In the present paper, experiments are reported of measurements on samples which have plate geometry (sides greater than 10 times the thickness) and for which the one dimensional theory actually applies. This allows us not only to verify the soundness of the theoretical model, but also to determine one of the elastooptic coefficients. Furthermore, the effect of mechanically loading the samples is studied with a view of looking at the increase in bandwidth obtainable by this method. Finally it is shown that the RPEO modulator does not require an external oscillator to drive it.

Experiments were performed on the modulation of a CO_2 laser beam. The modulating single crystals were suitably oriented plates of semi-insulating GaAs.

The effect of applying "heavy" electrodes (silver paint) on a crystal was calculated by use of an electrical equivalent circuit obtained through the application of the schemes described by Mason[3] for piezo-electric crystals. Measurements were made of the Q of the crystal and of the voltage, V_π, at which the samples become optical half wave plates, as a function of electrode thickness. A good fit was obtained between the experimental and calculated curves. Specifically, the V_π curves show a flat region in which the crystal's own attenuation is the dominant factor, and a linear region where the attenuation increases linearly with electrode thickness. An increase of electrode thickness from 7 microns to 40 microns of silver paint resulted in a bandwidth increase from 300 Hz to 3200 Hz in a crystal whose resonant frequency was 1.4 MHz. The half wave voltage increased from 5.0 volts to 61 volts. The accuracy of the measurements was $\pm 10\%$. The same crystal, operated as a wide band electrooptic modulator, would have a V_π of 5000 V.

Our measurements also yielded a value of

[1] Work supported by NSF Grant GK-42072.

[2] J. M. Hammer, D. J. Channin, and M. T. Duffy, *Appl. Phys. Lett.*, vol. 23, p. 176, 1973.

[3] D. P. Gia Russo and S. C. Kumar, *Appl. Phys. Lett.*, vol. 23, p. 229, 1973.

[4] N. F. Foster, *J. Vacuum Sciences and Tech.*, vol. 6, 1969.

[1] Present address: P. O. Box 1, Kiriat Motzkin, Israel.

[2] R. Weil and D. Halido, "Resonant-piezo-electro-optic light modulation," *J. Appl. Phys.*, vol. 45, p. 2258, 1974.

[3] W. Mason, *Electro-Mechanical Transducers and Wave Filters*, New York: Van Nostrand, 1948, pp. 230-241.

$(8.6 \pm 1.3) \times 10^{-2}$ for the elastooptic coefficient p_{44} of GaAs at 10.3 μ and room temperature. This is consistent with, but more precise than, the value of $(9.9 \pm 5) \times 10^{-2}$ obtained from measurements by Carleton and Soref.[4]

In principle, because the modulator crystal is operated at resonance, it can be used as both the load and the controlling element of an oscillator circuit. To verify this, a simple one transistor oscillator was built. It is shown that, optically, the performance of the RPEO modulator is the same when self or externally driven. As expected, self drive also prevents drift from the resonant frequency.

[4] H. R. Carleton and R. A. Soref, "Modulation of 10.6 laser radiation by ultrasonic diffraction," *Appl. Phys. Lett.*, vol. 9, p. 110, 1966.

17.4 High Repetition-Rate (kHz) Lithium Iodate Optical Parametric Oscillator,[1] E. O. Ammann, *GTE Sylvania, Mountain View, Calif. 94042*

(15 min)

Lithium iodate has previously been used successfully in optical parametric oscillators by several different workers.[2-5] Past oscillator experiments have utilized flash-pumped lasers to pump the oscillator, and hence operation has been limited to relatively low pulse repetition rates. In this paper, we report on a lithium iodate optical parametric oscillator operating at kHz pulse repetition rates. This oscillator has yielded the first substantial average output powers ob-obtained from a lithium iodate parametric oscillator.

The configuration used for the oscillator is shown in Fig. 1. An internal oscillator configuration[6] is employed, with the lithium iodate crystal placed inside a Nd:$YA1O_3$ laser operating at 1.08 μm. The laser is continuously pumped by two krypton-arc lamps and is repetitively Q-switched by a fused quartz acoustooptic Q-switch. Three different lithium iodate crystals have been employed; each is 15 mm long and has AR coati: gs on its faces. Rotation of the lithium iodate crystal produces angle tuning of the oscillator. The oscillator resonator consists of two flat mirrors which are separate from the crystal and which are independently adjustable. The oscillator mirror separation is approximately 19 mm.

[1] This work was supported by the Air Force Avionics Lab., Air Force Systems Command, Wright-Patterson AFB, Ohio.

[2] L. S. Goldberg, *Appl. Phys. Lett.*, vol. 17, p. 489, 1970.

[3] A. J. Campillo and C. L. Tang, *Appl. Phys. Lett.*, vol. 19, p. 36, 1971.

[4] L. S. Goldberg, presented at VII Int. Quant. Electr. Conf., paper L.2, May 1972.

[5] A. J. Campillo, *IEEE J. Quantum Electron.*, vol. QE-8, p. 809, 1972.

[6] E. O. Ammann, J. M. Yarborough, M. K. Oshman, and P. C. Montgomery, *Appl. Phys. Lett.*, vol. 16, p. 309, 1970.

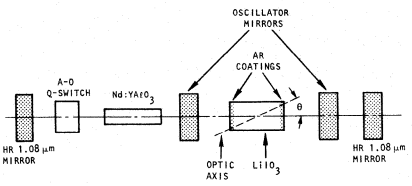

Fig. 1. Configuration of lithium iodate internal optical parametric oscillator.

Parametric oscillation has been obtained both near degeneracy and well away from degeneracy. In the near-degeneracy case, a doubly-resonant configuration was used, with the left and right-hand oscillator mirrors of Fig. 1 being HR and 5% transmitting, respectively, in the 2.16 μm region. The lithium iodate AR coatings were centered at 1.3 μm. Strong parametric oscillation was observed, with average power outputs of up to 530 mW obtained (signal and idler combined) at a repetition rate of 5 kHz. For comparison purposes, the Q-switched laser output power was measured with all oscillator components in the laser cavity, but with oscillation extinguished. For this test, one of the laser HR mirrors was replaced by a 4% transmitting mirror. The 1.08 μm average output power obtained was 1.1 watts, which indicates that approximately 50% of the available 1.08 μm power is being converted to tunable oscillator output. The oscillator output was tuned via crystal rotation over the entire mirror reflectivity range from 1.98 to 2.37 μm. The output spectrum was quite broad, however, due to the nearly vertical slope of the tuning curve near degeneracy (Fig. 2).

Doubly-resonant lithium iodate oscillator experiments were also carried out in the 3 to 4 μm region of the spectrum using a second lithium iodate crystal (designated 2B). This crystal was fabricated at a slightly larger phase-matching angle than the first crystal. The mirrors employed were HR over the signal range (1.45 to 1.65 μm) and approximately 10% transmitting over the idler range. Rotation of the crystal provided continuous tuning of the output from 3.25 μm through 4.05 μm. The best average output power obtained thus far in this range is 50 mW at a 5 kHz repetition rate.

Measured and calculated tuning curves for the lithium iodate parametric oscillator are shown in Fig. 2. The measured points were obtained from oscillator experiments and from sum-frequency generation experiments utilizing the output from a lithium niobate parametric oscillator.[6] The slight offset of about 0.1° between the curves for the two lithium iodate crystals used is within the 0.15° accuracy with which their orientations are known. The calculated tuning curve makes use of unpublished Sellmeier equations of Byer and Herbst.[7]

Experiments have also been carried out using 15 mm long crystals in which we attempted (unsuccessfully) to obtain parametric oscillation in the 4.5-4.9 μm region. These experiments are being continued using longer crystals, and using multiple crystals. The results of the continuing experiments will be reported.

[7] R. L. Byer and R. L. Herbst, private communication.

Fig. 2. Calculated and measured tuning curves for the lithium iodate parametric oscillator.

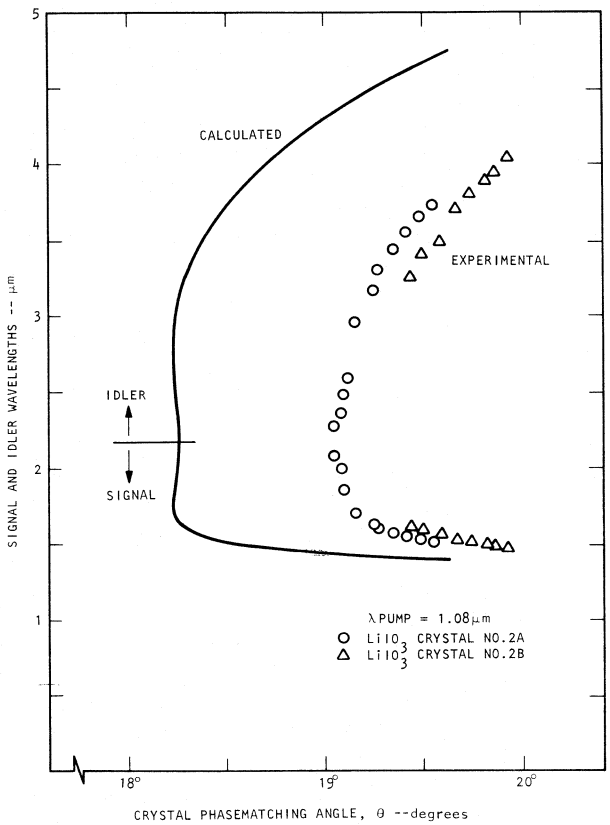

TABLE I
EXPERIMENTAL DATA: ADP PARAMETRIC AMPLIFIER PUMPED AT 266 NM

Input Wavelength (nm)	Laser Medium	Complement Line (nm)	Input Power (mW)	Output Power (kW)
476.5	Ar	602.3	35	4-6
488.0	Ar	584.7	70	2-9
501.7	Ar	566.2	5	1.5-4
514.5	Ar	550.8	60	3-7
530.9	Kr	533.2	35	~5(estimated)
568.2	Kr	500.2	15	~2
632.8	He-Ne	458.9	19	2-4
647.1	Kr	451.7	70	4-6
676.4	Kr	438.5	10	~2

17.5 Generation of Frequency-Stable, Narrow-band Optical Pulses by High Gain Parametric Amplification, G. A. Massey and J. C. Johnson, *Oregon Graduate Center, Beaverton, Oreg. 97005*

(15 min)

This paper describes a method of obtaining brief, intense pulses with narrow spectral linewidths, diffraction-limited divergences, and accurately controlled frequencies, by amplifying the output of a low power reference light source in a traveling-wave parametric amplifier. Using intense pump pulses at 266 nm (the 4th harmonic of the Nd:YAG laser) in crystals of ammonium dihydrogen phosphate, it has been demonstrated that traveling-wave gains as high as 10^{11} per pass at visible frequencies can be achieved.[1,2] Previously these high gains have been used to produce beams of nearly collimated parametric fluorescence, but light generated in this manner typically has had a spectral spread in the range 0.5 to 5 nm. However, the effective fluorescence noise input in these amplifiers is of the order of 10^{-6} W or less, and it is therefore easy to obtain an external optical signal input which exceeds the zero-point noise by several orders of magnitude, even on a continuous basis, from gas or dye lasers. We have used this approach to produce frequency-stable pulses from 438.5 nm to 676.4 nm by injecting CW gas laser signals into an ADP parametric amplifier pumped by 10 nsec pulses at 266 nm.

Table I shows the results of preliminary experiments. Input light was obtained from transitions of a mixed-gas Ar-Kr ion laser and from a He-Ne laser. The spectral spread of the pump was about 3 GHz, and that of the gas laser varied from 1.5 GHz for Ne to about 8 GHz for one of the Ar lines. The pump light was focused to produce a gain of 10^5 to 10^6 in a 6-cm ADP crystal. The visible output pulse lengths were between 1 and 2 ns, with bandwidths less than 0.01 nm, and the beam was diffraction limited. Since both signal and idler frequencies are generated, a new "complement" wavelength at the difference frequency between the pump and the input frequencies appears in the output. In each case output measurements were performed on the complement line to avoid interference with the CW input.

This technique has obvious applications in radar and in pulse-probe experiments in which coherence must be preserved between an exciting pulse and a probe signal applied later to the system under study.

We have performed similar experiments in which the input light was parametric fluorescence filtered by a Fabry-Perot etalon, and we are now beginning experiments with a mode-locked pump beam which will permit higher gains without optical damage to the amplifier.

This work is supported by the National Science Foundation under Grant GK-40812.

[1] J. M. Yarborough and G. A. Massey, *Appl. Phys. Lett.*, vol. 18, p. 438, 1971.

[2] A. H. Kung, *Appl. Phys. Lett.*, vol. 25, p. 653, 1974.

17.6 A Tunable Collinear Acoustooptic Filter for the Intermediate Infrared Using Single Crystal Tl_3AsSe_3,[1] J. D. Feichtner, M. Gottlieb and J. J. Conroy, *Westinghouse Research Laboratories, Pittsburgh, Pa. 15235*

(15 min)

The tunable collinear acoustooptic filter was first proposed by Harris and Wallace[2] and later realized by Harris and his co-workers using $LiNbO_3$ and $CaMoO_4$.[3,4,5] Noncollinear and walkoff-type tunable acoustooptic filters have been investigated by Chang[6,7] and by Yano and Watanabe.[8]

The materials used for these first filters have limited applicability in the infrared for two reasons. The acoustic power density required for 100% transmission at band center increases as λ_0^2, and their acoustooptic efficiency is such that at the longer wavelengths this power density causes excessive heating. In addition, such oxide materials generally exhibit strong lattice absorption beginning at about 4.5 μm, becoming opaque at longer wavelengths.

Tl_3AsSe_3, a single crystal material of the sulfosalt group, was first investigated as a nonlinear optical material,[9] but we also found that like many materials of this group, its low acoustic velocity and high refractive index yielded favorable infrared acoustooptic properties. It also is one of a small number of single crystal materials with the proper symmetry (Tl_3AsSe_3 belongs to crystal class 3 m) for collinear tunable acoustooptic filter operation.

The filter was designed to operate in the reflection mode, as shown in Fig. 1. Collimated polarized light from the source at the right traverses an MgF_2 Rochon Prism, from which it enters the Tl_3AsSe_3 crystal, traveling parallel to the Tl_3AsSe_3 crystal *a*-axis. The light is reflected back from an evaporated aluminum layer at the far end of the crystal and reverses its path. Interaction with the phase-matched col-

[1] Work supported in part by Advanced Research Projects Agency, monitored by Air Force Materials Laboratory, LP, under Contract no. F33615-72-C-1976.

[2] S. E. Harris and R. W. Wallace, *JOSA*, vol. 59, p. 744, 1969.

[3] S. E. Harris, S. T. K. Nieh and D. K. Winslow, *Appl. Phys. Lett.*, vol. 15, p. 325, 1969.

[4] S. E. Harris, S. T. K. Nieh and R. J. Feigelson, *Appl. Phys. Lett.*, vol. 17, p. 223, 1970.

[5] S. T. K. Nieh and S. E. Harris, *JOSA*, vol. 62, p. 672, 1972.

[6] I. C. Chang, *Appl. Phys. Lett.*, vol. 25, p. 323, 1974.

[7] I. C. Chang, *Appl. Phys. Lett.*, vol. 25.

[8] T. Yano and A. Watanbe, Paper X.9, VIII Intl. Quantum Electronics Conf., San Francisco, 1974.

[9] J. D. Feichtner and G. W. Roland, *Appl. Opt.*, vol. 11, p. 993, 1972.

Fig. 1. Experimental set up for an infrared tunable acoustoptic filter using Tl_3AsSe_3.

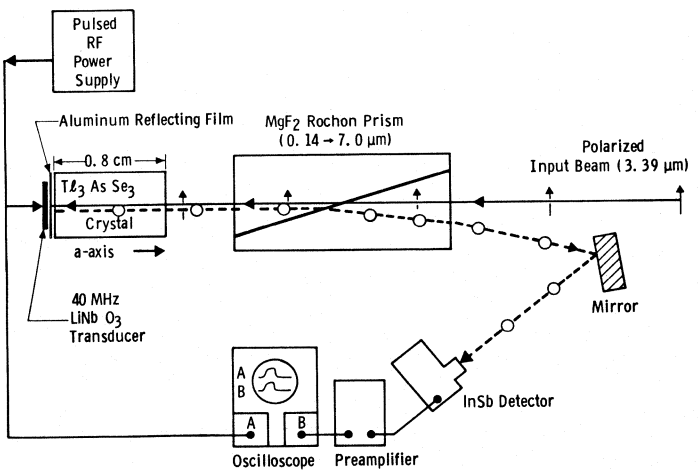

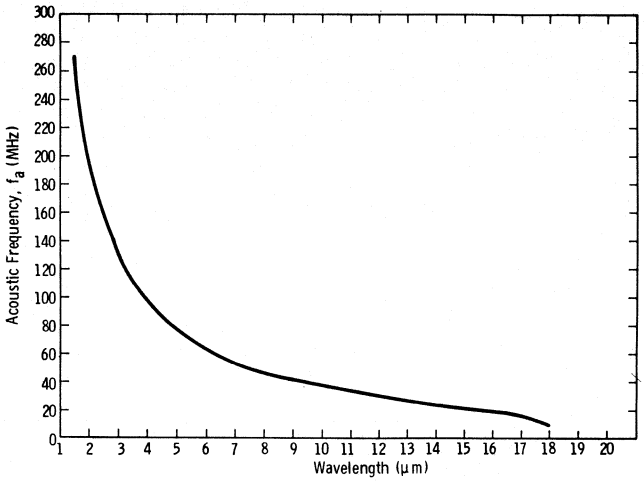

Fig. 2. Theoretical tuning curve for a collinear tunable acoustooptic filter based on Tl_3AsSe_3.

linear longitudinal acoustic wave, generated by a $LiNbO_3$ transducer bonded to the Al reflecting layer, diffracts part of the light beam into the orthogonal polarization. In retracing its path back through the MgF_2 Rochon Prism, this 90° rotated polarization component is spatially separated from the incident component, picked off by a mirror, and reflected to an InSb detector. The diffracted signal is displayed on an oscilloscope along with the pulsed acoustic signal applied to the transducer.

A tuning curve for the filter, calculated from the relation

$$f = \frac{v_{acoustic}(n_o - n_e)}{\lambda}$$

is shown in Fig. 2. It can be seen that tuning can be achieved over the range of transparency of crystal Tl_3AsSe_3 (1.3 μm to 18 μm) with acoustic frequencies ranging from about 300 MHz (at 1.3 μm) to 22 MHz (at 18 μm).

Experimental verification of the tuning curve has been achieved at two wavelengths, 3.39 μm and 5.3 μm. In the first experiment, a 40 MHz $LiNbO_3$ transducer operating on the 3rd harmonic at 120 MHz was used to tune the filter pass band to the 3.39 μm wavelength of a He-Ne laser. The measured required acoustic frequency of 115.65 MHz is in agreement with the value calculated. The acoustic power density required to give 20% transmission for 1.6 cm crystal path length at the peak of the filter pass band was 60 mW/mm², in order of magnitude agreement with the calculated value. This can be compared with the higher calculated required power density in $CaMoO_4$ for the same crystal path length of 133 mW/mm². In the second experiment, the frequency doubled output of a CO_2 laser, at 5.3 μm, was used as the infrared source. The measured acoustic frequency was 72 MHz, in agreement with the calculated value.

In the configuration of Fig. 1, the filter is potentially operable out to 7 μm, which is the limit of transparency of the MgF_2 prism. Efficient birefringent polarizing elements operating beyond 7 μm will be required if the filter is to be operated in the reflection mode at longer wavelengths. However, we have also designed mission-type filters using Tl_3AsSe_3.

Potential applications of a tunable infrared filter, which include infrared spectroscopy, pollution monitoring, and infrared laser frequency selection, will also be discussed.

17.7 Electrooptical Compensation for Self-Heating in CD*A During SHG, D. Hon, *Hughes Aircraft Co., Culver City, Calif. 90230* (15 min)

Self-heating in a second harmonic generating (SHG) crystal tends to disrupt the phase-matching (PM) condition and could cause serious output instabilities. This limitation of the power each crystal can handle is well known. The optical absorptivities of many crystals increase significantly *during* SHG. For CD*A, α exceeds 7% cm^{-1}! Even a preprogrammed oven could not manage this problem for input powers ≥5 or 6 watts, particularly in the presence of ambient temperature fluctuations. Our solution is electrooptical compensation. The E-O effect on SHG has been known.[1,2] In this paper. this principle is analyzed and its application in solving the self-heating problem in CD*A is reported.

The optimal orientation of CD*A (a KDP isomorph) for SHG is a 45° z-cut.[3] The 1.06 μ is polarized ⊥ to, while the 0.53 μ ∥ to the z-axis. An E-field ΔE applied in the z direction rotates the x and y axes by 45° in their own plane, and the new principal indices are

$$\begin{pmatrix} nx \\ ny \end{pmatrix} = n_0 \pm (n_0^3 \Delta E/2)(r_{63} + p_{66}d_{36}),$$

$$n_z = n_e \text{ (unchanged)} \quad (1)$$

where the symbols are standard.[4,5] If the ΔE pulse duration is short compared to the typical mechanical response time of the crystal bulk of 1-2 × 10^{-5} sec, contribution from the $p_{66}d_{36}$ term vanishes and one has a "clamped" E-O effect. (1) describes an electrooptical mechanism to fine-tune the SHG phase-match condition.

Pulsed E-fields were applied to the crystal synchronously with the laser pulses. The resultant SHG efficiency versus temperature curves are illustrated in Fig. 1. The E-fields translated the zero-field curve horizontally. Two families of curves were obtained for the two representative pulsewidths of ~200 ns (clamped) and ~200 μs (unclamped). From such SHG versus T curves, and with (1) and the familiar equation[4]

$$P_\omega^2/(P_\omega^2)_{max} = \sin^2(\Delta Kl/2)/(\Delta Kl/2)^2$$

for the relative SHG efficiency as a function of crystal length l and phase-mismatch $\Delta K = K_{2\omega}$, we obtained

[1] J. P. Van der Ziel, *Appl. Phys. Lett.*, vol. 5, p. 27, 1964.

[2] B. H. Soffer and I. M. Winer, *Appl. Phys. Lett.*, vol. 24A, p. 5, 1967.

[3] R. C. Miller, G. D. Boyd, and A. Savage, *Appl. Phys. Lett.*, vol. 6, 1965.

[4] *See* e.g., A. Yariv, *Quantum Electronics*. New York: John Wiley & Sons, 1967.

[5] J. F. Nye, *Physical Properties of Crystals*. New York and London: Oxford University Press, 1957.

Fig. 1. 200 μsec pulses. ΔE = 0, ±.85, ±1.8, ±2.75, ±3.25 kV/cm.

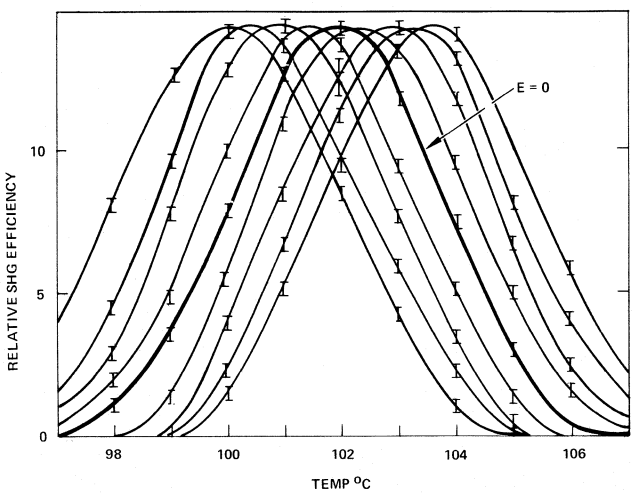

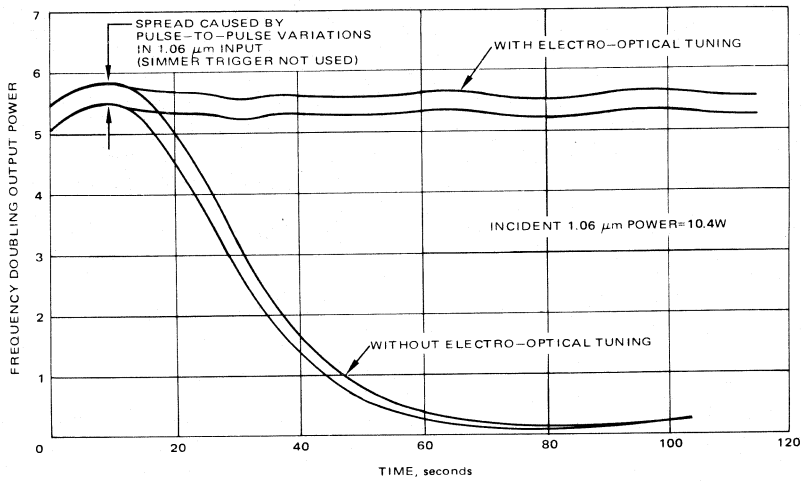

Fig. 2.

$$r_{63} = 14.1 \pm .4 \times 10^{-10} \text{ cm/V}$$

and

$$p_{66}d_{36} = 10.2 \pm .4 \times 10^{-10} \text{ cm/V}$$

for $T_{PM} \sim 102°C$, in good agreement with conventional measurements.

The 200 μs E-field pulses were modulated and the SHG output was monitored. A feedback loop was built which compensates electrooptically for self-heating in the crystal. A 0.52 J/15 ns/20 Hz laser was used with an uncoated 1 × 1 × 2 cm CD*A housed in a Hughes-built dry oven with maximum thermal conductivity and minimum thermal mass. The output normally vanished after one minute – long compared with other oven types (Fig. 2). But E-O compensation kept it steady indefinitely at an efficiency of 57% (Fresnel reflection considered). The response time of the loop was four times faster than the maximum self-heating rate of ~0.5°C/sec. The E-field range of ±5 kV corresponded to ±~3°C. But additional circuitry from the loop control the oven temperature to provide a total compensation range of 20°C. Ambient fluctuations of ±60°C has not affected the performance.

This technique will work for considerably higher powers than the equipment-limited 10.4 W reported here until severe crystal temperature gradients ultimately drop the efficiency. E-O compensation should be useful also for other SHG materials and, perhaps, parametric oscillators too.

The author thanks E. Woodbury, W. Ng, G. Atchison, R. Wyeth, R. Farnsworth and C. Smith for their contributions.

17.8 Use of a Resonant Atomic Dispersion to Convert Frequency Modulated CW Light into a Train of Subnanosecond Pulses, J. E. Bjorkholm, E. H. Turner, and D. B. Pearson, *Bell Telephone Laboratories, Holmdel, N. J. 07733*

(15 min)

A frequency modulated pulse of electromagnetic radiation can be compressed (pulsewidth reduced and peak power correspondingly increased) by passing it through a medium or structure which has group velocity dispersion. This is the basis of chirp radar and similar schemes have been suggested for compressing pulses of light. Atomic vapors exhibit very strong group velocity dispersion for frequencies close to a resonance transition. Grischkowsky has recently made use of this fact to reshape and compress (to nsec pulsewidths) frequency modulated pulses of near-resonance light from a pulsed dye laser by passing them through rubidium vapor.[1] In our work we demonstrate the conversion of near-resonance CW light, from a CW dye laser, into a train of repetitive subnanosecond pulses by sinusoidally frequency modulating the light and then passing it through sodium vapor. The light was modulated using a $LiNbO_3$ electrooptic modulator driven at 200 MHz and the resulting pulses occurred once every 5 nsec. The sharpest pulses we obtained had a 240 psec pulsewidth and a peak power of 6.3 times the input power; average power was 77% of the input power. By varying the light frequency (on a scale of GHz) and the strength of the modulation, pulsewidths from 250 psec to 2 nsec could easily be obtained. The experimental pulses are in excellent quantitative agreement with computer calculations carried out using linear dispersion theory. Detailed comparison of calculation with experiment will be given.

The pulse trains are very reproducible and quite controllable. With precisely tunable CW dye lasers now commerically available, the technique we have demonstrated is a useful and simple way of obtaining continuous trains of repetitive short pulses in the vicinity of atomic resonance lines.

[1] D. Grischkowsky, *Appl. Phys. Lett.*, vol. 25, p. 566, 1974.

17.9 Conversion Efficiency and Pulse Shortening of a Frequency Tripled, Subnanosecond, 1.06 μm Pulse,[1] D. T. Attwood, E. L. Pierce, and L. W. Coleman, *Lawrence Livermore Laboratory, Livermore, Calif. 94550*

(15 min)

The interferometric study of plasmas produced by high intensity, subnanosecond pulses from a Nd laser, requires short wavelength, short duration probing pulses. Because of very steep density gradients within these plasmas, it is very important that the probe pulse be at least frequency tripled if critical electron densities for 1.06 μm are to be studied; shorter wavelengths are desirable. In addition, the temporal duration of the probe pulse should be short so as to minimize fringe smearing within the interferometer due to plasma density contour motion. In this paper we report high conversion efficiency of 1.06 μm pulses to 3547 Å,[2] as well as the concomittant shortening of the pulse.

The schematic diagram in Fig. 1 illustrates the procedure for obtaining synchronous frequency tripled probe pulses. A mode locked Nd laser produces a nominal 1 joule, 150 ps pulse at 1.06 μm which is used for target irradiation. A small portion of this radiation is split off and frequency doubled in an angle tuned KDP crystal. Fifty percent energy conversion to 5320 Å is regularly obtained with an incident 1.06 μm intensity of 10^9 W/cm^2. Type II phase matching is then employed to frequency mix the unconverted fundamental and its harmonic in a second KDP crystal. An overall energy conversion efficiency of 30% is regularly obtained for the frequency tripling process. Pulse shortening has

[1] This work was performed under the auspices of the U. S. Atomic Energy Commission.

[2] A. H. Kung, J. F. Young, G. C. Bjorklund, and S. E. Harris, *Phys. Rev. Lett.*, vol. 29, p. 985, 1972.

Fig. 1. Schematic diagram showing target irradiation as well as the generation of a frequency tripled probe pulse.

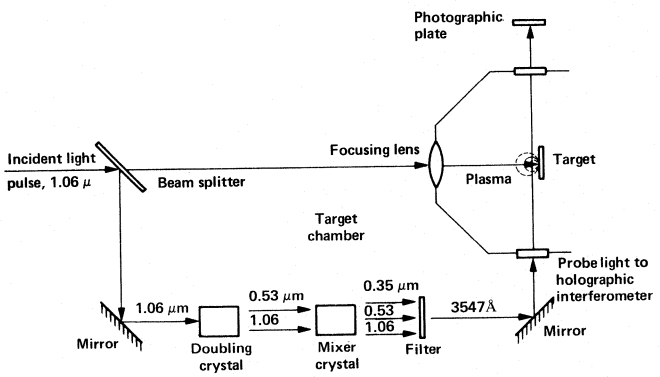

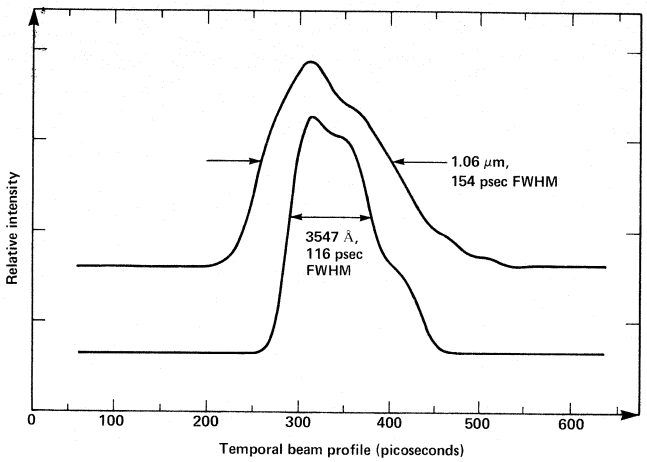

Fig. 2. Pulse compression via frequency tripling in KDP crystals. Incident 1.06 μm intensity of 10^9 W/cm^2; overall energy conversion of 32%.

been observed in this configuration by using two 10 ps resolution streak cameras[3] to simultaneously measure temporal profiles of the 1.06 μm and 3547 Å radiation. A sample of the incident 1.06 μm pulse was made to multiply reflect from a calibrated mirror pair giving a series of 1.06 μm pulses of known amplitude rations which were then recorded with the S-1 photocathode streak camera.[4] A similar mirror pair was used in conjunction with an S-20 streak camera to record the 3547 Å pulse. A sample result of these experiments, obtained simultaneously with the multiple exposure technique, is shown in Fig. 2 for an incident 1.06 μm intensity of 10^9 W/cm^2 and an overall energy conversion of 32%. The frequency tripled pulse displays a 25% temporal compression for this single laser firing.

The authors acknowledge the assistance of Dr. H. J. Weaver and Dr. E. Bliss of our Laboratory, and acknowledge helpful conversations with Dr. A. Kung and Dr. S. Harris of Stanford University.

[3] S. W. Thomas, G. R. Tripp, and L. W. Coleman, in *Proc. 10th International Conf. on High Speed Photography*, (National Association of Technical Research, Paris, 1972), 127.

[4] H. J. Weaver, E. S. Bliss, and G. E. Sommargren, Laser Fusion Program Annual Report, 1974, Lawrence Livermore Laboratory, Livermore, Calif. 94550.

17.10 A Transient Induced Grating System for Measuring Ultrafast Photo-Induced Phenomena,[1] A. E. Siegman, D. J. Kuizenga, and D. W. Phillion, *Stanford University, Stanford, Calif. 94305*

(15 min)

We have previously developed a continuously pumped, repetitively Q-switched, mode-locked Nd:YAG laser which produces bursts of 20 to 30 several hundred kilowatt pulses of ~60 psec duration, at repetition rates up to 500 Hz. A z-cut $LiNbO_3$ switch driven by a photodiode, fast logic circuitry and an avalanche transistor chain selects a single pulse from each burst. The resulting train of 500 single pulses per second is doubled to 532 nm with >35% efficiency in an elliptically focused $LiIO_3$ crystal, and can be doubled again to 266 nm in an ADP crystal. The output from this system has the stability, reliability and spectral purity of a CW mode-locked laser, at a usefully high repetition rate and power level, though with pulsewidths still rather wider than in flash-pumped saturable-absorber lasers or CW dye lasers.

Pulses at any of the wavelengths from this laser can be sent into the stroboscopic transient-induced-grating optical system shown in Fig. 1. Time-coincident excitation pulses in the two excitation beams arrive at an angle of a few degrees in an experimental sample (here a rotating dye cell) to create a transient interference pattern or transient hologram. The resulting photo-induced grating of excited states, free carriers, excitons, or other photo-excited phenomenon is then probed by a delayed probe pulse from a variable delay line. By measuring the diffracted probe beam intensity averaged over many pulses, while slowly varying the time delay, one can measure the decay of the photo-excited phenomenon in stroboscopic fashion.

The chart recording in Fig. 1 shows the decay of a transient grating induced by $S_0 \rightarrow S_1$ absorption at 532 nm in Rhodamine 6G. The decay curve is accurately fit by two exponential terms, first the orientational relaxation of preferentially aligned molecules with $\tau_{rot} \approx 150$ psec, then the fluorescent decay of S_1 molecules with $\tau_{fl} \approx 4$ nsec.

A variety of further studies of transient phenomena involving excitons, nonlinear phenomena, excited states, and energy transfer processes are now being undertaken with this system. Special advantages of the transient grating method for studying fast photophysical phenomena include improved sensitivity and background rejection; the ability to sense excited-state dispersive or phase-grating effects as well as excited state absorption; the ability to separate diffusion effects from lifetime effects by varying the grating periodicity; and the ability to study anisotropic diffusion effects.

[1] Work supported by National Science Foundation.

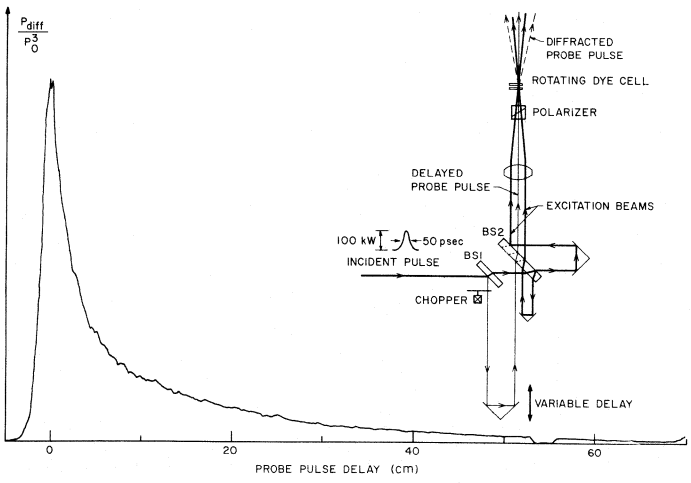

Fig. 1. Chart recording showing the decay of a transient induced grating produced by mode-locked pulses in a Rhodamine 6G solution in alcohol, and the optical system used to excite and probe the transient grating.

17.11 Self Defocusing of Mode Locked Nd: YAG Pulses in Cesium Vapor, R. H. Lehmberg, J. Reintjes, and R. C. Eckardt, *Naval Research Laboratory, Washington, D. C. 20375*

(15 min)

In a recent publication, we reported the observation of self defocusing of mode-locked 1.06 μ pulses in Cs vapor.[1] Here, we report a measurement of the negative nonlinear refractive index responsible for this effect ($n_2 = 1.5 \times 10^{-30}$ N), and the first observation of its use in compensating the self focusing that occurs in other transparent materials. Since the useful output power from large Nd laser systems is limited by self focusing due to the laser glass ($n_2 \approx 1.6 \times 10^{-13}$ esu), these experiments suggest the possibility of increasing this power by using Cs vapor for compensation; e.g., one could

[1] R. H. Lehmberg, J. Reintjes and R. C. Eckardt, *Appl. Phys. Lett.*, vol. 25, p. 374, 1974; NRL Memorandum Report 2932.

TABLE 1
COMPARISON OF MEASURED AND THEORETICAL NONLINEAR REFRACTIVE INDICES
$n_2/N \times 10^{30}$ (esu)

	Experimental	Three Level Model Resonant	Three Level Model Exact	Miles & Harris JQE 9, 470 (1973)
↑	-1.5 ± 0.2	-1.84	-1.95	-0.66
↻	-0.35 ± 0.04	-0.29	-0.38	

insert Cs cells at various stages of the glass amplifier chain.

At 1.06 μ, the nonlinear susceptibility of Cs vapor is determined almost entirely by interaction between the $|6s> \equiv |0>$ ground state and the $|6p> \equiv |1>$ and $|7s> \equiv |2>$ levels. We have shown that in the case of linearly polarized light, the nonlinear susceptibility can be analyzed into two distinct contributions.[1] The predominant one arises from the polarization $\rho_{02}(t)$ due to the two photon resonance between $|6s>$ and $|7s>$. The other term, which is also negative at 1.06 μ, arises from induced population changes between the $|6s>$ and $|6p>$ levels, and is analogous to the nonlinear refractive effects observed by Grischkowsky and Armstrong.[2]

In this experiment, where the pulses are much shorter than the inverse linewidth of $|6p>$, the nonlinear contribution to the refractive index becomes

$$\sigma n^{NL} = n_2 <E^2(t)>, \qquad (1)$$

where

$$n_2 = -\frac{2\pi}{h^3}\left[\frac{1}{(\nu_{10} - \nu)^2(2\nu - \nu_{20})} + \frac{1}{(\nu_{10} - \nu)^3}\right] N, \qquad (2)$$

$E(t)$ is the optical field of frequency $\nu = c/\lambda$, N is the atomic number density, μ_{ij} the dipole matrix element between levels $|i>$ and $|j>$, and ν_{ij} the corresponding frequency splitting. Nonresonant contributions have been ignored in (2), since at 1.064 μ, $\nu/c = 9398$ cm^{-1}, while $(\nu_{10} - \nu)/c = 2149$ cm^{-1} and $(2\nu - \nu_{20})/c = 260$ cm^{-1}. For circularly polarized radiation, the $|0> \rightarrow |1> \rightarrow |2>$ transition is not allowed, and only the second term of (2) remains nonvanishing. With longer pulses, one would obtain additional contributions to δn^{NL} proportional to the integrated intensity.[1]

In order to measure n_2 vs. N we studied the self-defocusing of mode-locked Nd:YAG pulses in a 100 cm long Cs vapor cell at several densities between $N = .080 \times 10^{17}$ and $.32 \times 10^{17}$ cm^{-3}. The input beam was a single 35 psec pulse of 1.1 mm $1/e$ diameter and 50-60 MW peak power. The output beam profile was recorded by imaging the exit window of the cell onto a silicon photodiode array. In analyzing the data, we used the constant shape approximation,[3] and numerically integrated the instantaneous profile over the pulse duration. We then chose the value of n_2 that gave the best theoretical fit to the measured profile. The results for linear and circular polarization are compared with theory in Table 1. The second column is obtained from (2), the third includes the nonresonant contributions to n_2, and the fourth is the value calculated by Miles and Harris.[4] The theory is in good agreement with these measurements, with the remaining discrepancy possibly due to the theoretical value of μ_{12} used in the calculation.

In the compensation experiment, a 2 cm long cell of CS_2 was inserted 45 cm from the entrance window of the Cs cell, and the beam profile was measured at the exit window. With 1 mJ pulses and no Cs in the cell, the (FWHM) width was 0.96 mm. With a Cs density of $.13 \times 10^{17}$ cm^{-3} and similar pulses, this width increased to 1.07 mm, which is close to the 1.12 mm width measured in the absence of both Cs and the CS_2. The Cs vapor thus appears to effectively compensate for the CS_2; however, no attempt was made to optimize this. Further experiments are currently in progress, and conditions required for practical application of Cs vapor compensation will be discussed at length.

[2] D. Grischkowsky and J. A. Armstrong, *Phys. Rev. A*, vol. 6, p. 1566, 1972.

[3] S. A. Akhmanov, R. V. Khokhlov and A. P. Sukhorukov, *Laser Handbook*, vol. 2, edited by F. T. Arecchi and E. O. Schulz-Dubois. Amsterdam: North Holland, 1972.

[4] R. B. Miles and S. E. Harris, *IEEE J. Quant. Electron.*, vol. QE-9, p. 470, 1973.

17.12 A High Power Isolator for the 10 Micron Region Employing Interband Faraday Rotation in Germanium,[1] C. M. Phipps, Jr.[2] and S. J. Thomas,[2] *Lawrence Livermore Laboratory, Livermore, Calif. 94550*

(15 min)

A crucial element in the design of high power CO_2 laser systems is the provision of adequate interstage isolation. Previously, the free carrier Faraday effect in InSb has been employed to build low power isolators for the 9-10 micron region.[3-5] We report the construction and testing of a room temperature, high power isolation device based on the interband Faraday effect in intrinsic Ge.

The interband isolator has four principal advantages with respect to the earlier free carrier devices:

1. *Freedom from 2 photon absorption.* The 10.6 micron 2 photon absorption coefficient in InSb $\kappa_2 = 16 \pm 5$ cm^{-1} per MW/cm^2, with a threshold at 10^5 W/cm^2, preventing the use of this material at higher power levels.[6]

2. *Scalability.* Germanium of suitable purity is available in apertures as large as 30 cm, whereas InSb is not.

3. *Excellent Isolation Figure.* Tests with CW and pulsed probe lasers showed an isolation figure of 40 dB with our device. This improvement is due to the higher uniformity of rotation which is achieved with bound carriers vs. doped donor impurities in a crystal lattice.

4. *Decoupling of Rotation and Absorption.* Free carrier rotation and absorption are directly coupled, their ratio depending only on mobility and magnetic field strength. This is not true for the interband Faraday effect.

For frequencies well below the gap frequency of the semiconductor, the interband Faraday

[1] Work performed under the auspices of the U. S. Atomic Energy Commission.

[2] Presently with Los Alamos Scientific Laboratory, Los Alamos, N. M. 87544.

[3] J. H. Dennis, *IEEE J. Quantum Electron.*, vol. QE-3, p. 416, 1967.

[4] W. T. Boord, Y. H. Pao, F. W. Phelps and P. C. Claspy, *IEEE J. Quantum Electron.*, vol. QE-10, p. 273, 1974.

[5] W. E. Bickell, L. R. Tomaseta and D. H. Bates, paper X.11, 8th Internat. Quantum Electron. Conf., San Francisco, June 1974.

TABLE I
SUMMARY OF ISOLATOR PERFORMANCE

	9.55 μ	10.59 μ	deg/kG cm
Verdet coefficient V:	0.094	0.079	deg/kG cm
dV/VdT:	0.12	0.05	%/deg C
B for 45° rotation:	39.9	47.4	kG
Figure of merit Q: (high power)	–	66	deg/dB
Isolation level A_r: (high power)	–	41.2	dB
Isolation level A_r: (CW)	–	35.5	dB

rotation is isotropic in a cubic crystal, and is given by[7]

$$\frac{\Theta}{B} = \frac{5A\gamma\,\omega^2}{64C\,\varepsilon_g}^{7/2} \quad \text{rad/cm gauss} \qquad (1)$$

A and γ are constants determined by the band parameters and the spin-orbit coupling in the presence of a magnetic field, and ε_g is the energy gap for direct transitions. For frequencies well below the energy gap, the intrinsic absorption in materials such as Ge and CdTe is dominated by residual free carrier effects and lattice absorption in the 10 micron region. In Ge, the ratio of the hole to electron absorption cross-sections is about 43,[8] but the hole transition absorption will bleach at intensities in excess of 10 MW/cm^2, leaving only the lattice absorption $\alpha_0 = 0.013$ cm^{-1},[9] which is not dependent on B to first order. Decoupling of rotation and absorption should permit figures of merit as large as 2×10^3 deg/dB for some interband materials.[10]

The isolator rotation medium for this study was a cylinder 12 cm long and 2.7 cm in diameter, cut from Ge single crystal with a maximum 10^{12} cm^{-3} impurity concentration. End faces were polished and AR coated for minimum reflectivity. The magnetic field was generated by a 5 cm bore uncompensated pulsed solenoid. 45 degree rotation was achieved 450 sec after firing the associated 8 kJ capacitor bank, corresponding to a peak on-axis field of 49 kgauss. The polarizer and analyzer each employed four wedged germanium plates. Their measured crossed extinction was -51 dB.

Detailed measurements of isolator performance were made at 9.55 μ and 10.59 μ wavelengths, in the temperature range 260 to 300 degrees C. These are summarized in Table I. In the Table, V is the Verdet coefficient Θ/B, and Q is the figure of merit, with units of degrees rotation per dB loss.

[6] J. M. Doviak, A. F. Gibson, M. F. Kimmitt and A. C. Walker, *J. Phys. C*, vol. 6, p. 593, 1973.

[7] B. Lax and J. G. Mavroides, *Semiconductors and Semimetals*, vol. 3, p. 321, 1967.

[8] P. J. Bishop and A. F. Gibson, *Appl. Opt.*, vol. 12, p. 2549, 1973.

[9] A. F. Gibson, C. A. Rosito, C. A. Raffo and M. F. Kimmitt, *Appl. Phys. Lett.*, vol. 21, p. 356, 1972.

[10] C. R. Phipps, Jr., and S. J. Thomas, *Appl. Phys. Lett.*, vol. 25, p. 313, 1974.

Session 18

Friday, May 30, 1975 **1:30-5:00 P.M.**

CO_2 Lasers

Chairman: R. I. Rudko, *Raytheon Research Division, Waltham, Mass.*

Organizer: L. A. Weaver, *Westinghouse Research Laboratories, Pittsburgh, Pa.*

18.1 High Energy CO_2 Laser Pumped by a UV Sustained Discharge,[1] R. C. Lind, *Hughes Research Laboratories, Malibu, Calif. 90265* (15 min)

The ultraviolet sustained electric discharge has been proposed as an alternative to the E-beam sustained discharge for conditioning CO_2 laser plasmas.[2] A key question concerning this approach is scalability. This paper presents results of a program currently in progress whose objective is demonstration of UV sustained discharge pumping in a 40 liter active volume.

At the present time, the only method successfully developed to achieve high-energy, long-pulse optical output from atmospheric pressure electric-discharge molecular-gas laser systems requires a discharge in which the electron production is controlled separately from the vibrational excitation process. In particular, operation with an electric field below that required for avalanche ionization (E/p < 6 kV/cm-atm) coupled with a large background electron density (> 10^{12}/cm^3) created by an auxiliary ionization source is used. The current technique for the production of the background electron density uses an E-beam as the auxiliary ionization source.[3]

The importance of the UV sustained approach results from elimination of the E-beam and its associated high voltage gun, fragile foil, and X-ray production characteristics and its replacement by a source of UV radiation. The UV radiation from this source produces the required electron density in the laser volume by photoionizing a small amount of low ionization potential seed gas which is added to the 1 atm laser mixture.

Using this technique on a small scale device, with tri-n-propylamine as the seed gas, we earlier demonstrated output energy densities of 50 J/l-atm with pulse lengths greater than 20 μsec.[4] Additionally, we have determined that the wavelength range of 1200-1700 Å is responsible for the observed photoionization, and we have conjectured that the mean free path for this radiation, which is determined by absorption in both the CO_2 and the seed gas, is about 8 cm for an optimum laser mixture of 2.5/47.5/50 (CO_2/N_2/He). This suggests that laser devices with electrode separations up to 16 cm should be feasible. The practical limits on scaling must however be established experimentally.

A large scale, UV-sustained CO_2 laser device has been constructed using the measured mean free path as a guideline to device size with the objective of determining the scaling limits. The device consists of a large metal vacuum enclosure in which Bruce contoured electrodes are housed. A high energy (up to 50 kJ, 80 kV) dc storage bank is used to provide the sustainer voltage to the electrodes. Two UV sources, located behind metal screens which form the discharge electrode surfaces irradiate the discharge volume. Each UV source consists of 40 rows of cascaded arc discharges, each row energized by its own low inductance capacitor. The active discharge area is 20 × 100 cm^2 and the electrode gap dimension is adjustable up to a maximum spacing of 20 cm providing a maximum active volume of 40 l.

There were three objectives of the experimental program. These are: (1) energy extraction measurements using a stable cavity, (2) energy and beam quality measurements using an unstable resonator, and (3) a characterization of the medium quality using holographic interferometry and spatially resolved gain measurements.

A significant portion of objectives (1) and (3) has been achieved at this time. Extensive stable cavity energy extraction measurements have been carried out over a wide range of conditions with an electrode gap of 6 cm. Using a 25% hole coupled output mirror and a 60 m radius of curvature total reflector, an output energy of 200 J in a 30 μsec pulse has been achieved. This corresponds to approximately 30 J/l-atm energy density. Additional measurements with an electrode spacing of 10 cm are currently underway and will be reported.

The medium quality of the device is affected by the UV flux distribution, acoustic waves produced by the UV sources, and by thermally induced medium inhomogeneities. To establish the uniformity of the discharge gain profile measurements with a spatial resolution of less than 2 mm have been performed in both the width (20 cm) and height dimension. Measurements taken to date indicate a uniform gain (at a magnitude of about 0.7%/cm) distribution in both dimensions. In addition, holographic interferometry measurements were taken with a Q-switched, single mode ruby laser. Time sequenced holograms, taken at appropriate intervals after discharge initiation will be discussed.

On the basis of the performance data the feasibility of replacing E-beam sustainers with UV sustained plasma conditioning will be discussed.

[1] This investigation was supported in part by ARPA/ONR contract no. N00014-73-C-0287.

[2] R. C. Lind and J. Y. Wada, 26th Gaseous Electronics Conf., Wisconsin, 1973, papers BB1 and BB2; R. C. Lind, W. M. Clark, J. Y. Wada, VIII QEC Conf., San Francisco, 1974, paper W.3.

[3] J. D. Daugherty, E. R. Pugh, and O. H. Douglas-Hamilton, "A stable, scalable, high pressure gas discharge as applied to the CO_2 laser," *Bull. Amer. Phys. Soc.*, vol. 17, p. 399, 1972.

[4] R. C. Lind, J. Y. Wada, G. J. Dunning, W. M. Clark, "A long-pulse, high-energy CO_2 laser pumped by an ultraviolet-sustained electric discharge," *IEEE J. QE*, vol. QE-10, pp. 818-820, 1974.

18.2 Photo Ionization Parameters for TEA Lasers, H. J. J. Seguin, D. McKen, and J. Tulip, *University of Alberta, Edmonton, Alberta, Canada* (15 min)

There has recently been a revival of interest in photoionization processes as a result of the application of this technique to CO_2 lasers. Of special interest has been the emission spectra of various ultraviolet sources, propagation of ionizing radiation, and photoelectron density production in a CO_2 laser environment. These

parameters are of particular relevance both for a fuller understanding of the basic mechanisms involved, and an optimum exploitation of the technique in large scale high powered devices.

The paper describes the measurement techniques adopted and the results obtained in an extended investigation of some of the more salient parameters associated with the application of ultraviolet photoionization processes in TEA-CO_2 lasers. In particular, the points to be examined will include:

(a) A brief presentation of previous photoelectron density data obtained with microwave diagnostics. Electron density and ionization decay times are given as a function of pressure for several laser host gases and mixtures. Plasma density and penetration depths are measured in relation to UV source parameters. The effects of selected "seed" additives on photoionization is demonstrated.

(b) Details of a recent study on a variety of UV spark sources, specific data with respect to emission spectrum, time evolution of radiation and the influence of circuit parameters are given. Complementary emission-absorption measurements obtained in laser host gases clearly identify the useful source emission bands.

(c) Measurements of UV source wavelength emission with corresponding photoelectron production are also presented. This investigation, which utilizes specialized charge collection apparatus fitted to a monochromator, identifies the source emission bands which dominate the photoionization process in a CO_2 laser gas environment. The photoionization vs. wavelength data so obtained specifies a one-step process as the dominant mechanism in this type of laser. A dramatic increase in the useful portion of the spark source emission spectrum is clearly shown when low ionization threshold additives are used. These results are in good agreement with microwave diagnostic photoionization enhancement measurements reported earlier.

In general the data obtained from these investigations provided further insight into the primary mechanisms involved in photoinitiated TEA lasers, and in addition has yielded design criteria for the development of more efficient UV sources. Details of such a UV device employing a simple plasma jet geometry are also given.

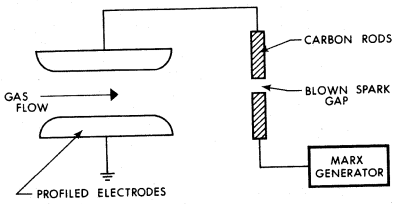

Fig. 1. Discharge region is preconditioned with UV radiation from the Marx generator gaps.

gases is low, the gaps are arranged as a Marx generator. Such an arrangement has routinely provided in excess of 100 kV at the profiled electrodes. The gaps are well coupled by UV radiation so that triggering at the first gap produces a clean jitter free pulse. Charging of the storage capacitors up to a voltage of 20 kV, is performed using a diode-inductor set. The Marx generator will free run as a relaxation oscillator or can be triggered at frequencies up to 4000 pps. This maximum frequency corresponds to a flow velocity of 40 m/s. The storage capacitors may be varied up to 0.1 μF and the hold-off inductors up to 30 mH. For discharge energies of more than a few joules a capacitor across the profiled electrodes is needed to delay the growth of voltage at the electrodes. Without this arcing will occur.

A 50 cm long and 3 cm square cross-section flow discharge is formed between the two profiled graphite electrodes. The pulse repetition frequency and the energy per pulse are power supply limited to 12 kW. A typical operating situation for the gas flow velocity of 40 m/s is shown below.

Typical Discharge Conditions
CO_2, N_2, H_e; 1, 1, 8

Supply voltage	4 kV
Supply current	3A
Storage capacitors	0.06 μF
Hold-off inductors	2 mH
Energy pulse	14 J
Repetition rate	900 pps
Pulse duration	0.9 μs
Peak current	1200 A

The discharge will operate without arcing with up to 15% CO_2 and 30% N_2 under these conditions.

The discharge duration can be increased by simply introducing an inductor between the Marx generator and the discharge.[1] The long discharge period allows glow to arc transitions time to form[2] so that reduced energy density is necessary. Two techniques have been found useful in stretching the discharge period. A small capacitor in parallel with the stretching inductor will provide a starting "kick." The low impedance path through the capacitor provides a large initial current which "forms" the discharge. This technique has permitted the discharge of 15 joules over 20 μs without arcing. The judicious choice of an inductor across the electrodes will eliminate post arcing, (small arcs which form in the discharge tail). We conclude however, that pulse stretching is best achieved by operating the discharge at sub-atmospheric pressure.

An extended structure has been constructed which provides a flow velocity of 100 m/s and has a power capacity of 50 kW. This will be used to investigate the effect of preionisation from the previous pulse which occurs at high repetition rates.

[1] O. P. Judd and J. Y. Wada, *IEEE J. Quantum Electron.*, vol. QE-10, p. 12, 1974.
[2] W. L. Nighan and W. J. Wiegand, *Appl. Phys. Lett.*, vol. 25, pp. 633-636, 1974.

18.4 Efficient Preionization Scheme for High Gain CW CO_2 Waveguide TE Laser, O. R. Wood II, P. W. Smith, C. R. Adams, and P. J. Maloney, *Bell Telephone Laboratories, Holmdel, N. J. 07733*

(15 min)

Using a preionization scheme based on the Malter effect, quasi-continuous gains of peak value 6.6%/cm at 10.6 μm have been produced in a 1 mm^2 cross-section waveguide TE laser[1] by loading up to 500 J/L-atm into a 145 torr CO_2 laser mixture at an E/P = 6 V/cm-torr. Electron number density and field strength can be controlled independently, as is the case with

[1] P. W. Smith, P. J. Maloney, and O. R. Wood, II, *Appl. Phys. Lett.*, vol. 23, p. 524, 1973.

18.3 High Repetition Rate TEA Laser Discharge Using an Integrated Preionisation and Switching Technique, J. Tulip, H. J. J. Seguin, and W. Faszer, *University of Alberta, Edmonton, Alberta, Canada*

(15 min)

This paper describes a high pressure, high repetition rate pulsed discharge technique which integrates UV preionization with voltage switching. The essence of the technique is shown in Figs. 1 and 2. The switching is performed using spark gaps within the flowing laser gases. Seven gaps are arranged transverse to the profiled electrodes several cm from the downstream edge. Because the hold-off voltage of the laser

Fig. 2. Marx generator is placed in the flowing laser gases.

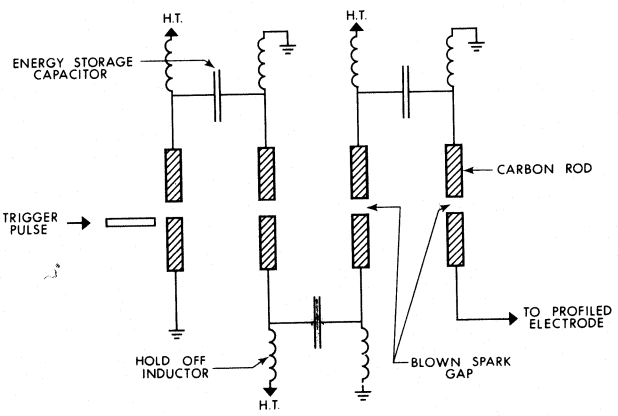

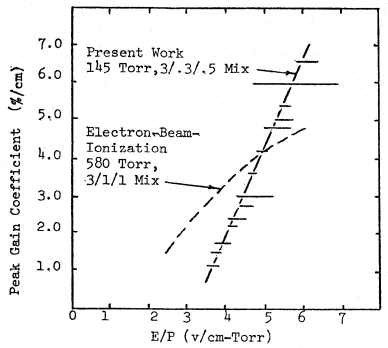

Fig. 1.

electron-beam-ionization.[2] This scheme, similar to one used previously by J. P. Reilly[3] and A. E. Hill,[4] differs from previous work, in that, in the present device the proximity of metal and insulating waveguide walls play an important role in discharge preionization, stabilization, and cooling. A 10 cm long waveguide TE CO_2 laser, based on this excitation scheme, should be capable of generating CW output powers in the range 10-100 watts.

A hollow waveguide of 1 mm^2 cross-section was constructed with slabs of fused quartz and metal in such a way that multiple transverse discharges could be formed inside the waveguide. A solid block of polished copper comprised one wall of the waveguide. A sandwich made up of alternate slabs of aluminum and quartz (each 1 mm thick) comprised the opposite waveguide wall. The remaining waveguide walls were formed by fused quartz slabs whose edges had been polished.

A train of 20 nsec duration high-voltage pulses (4-8 kV) applied (transverse to the waveguide axis) between the aluminum slabs (acting as cathodes) and the copper block (acting as an anode) increases the electron density from a low initial value (left over from the previous pulse) to a high peak value ($1\text{-}3 \times 10^{12}$ cm^{-3}). This high level of ionization is thought to result from a combination of efficient secondary emission from the aluminum cathode (the Malter effect) and electron multiplication due to the high electric fields present. After the ionizing pulse, a continuous electric field applied between the aluminum slabs (now acting as anodes) and the copper block (now acting as a cathode), with E/P = 3.5 – 6.5 V/cm-torr, provides the electron energy needed to vibrationally excite N_2 and CO_2 molecules during the recombination period. This electric field results in energy loadings from 50 to 500 J/L-atm without arc breakdown and values for peak gain from 1.2 to 6.6%/cm. The gain rises to this peak value some 70 μsec after the start of the ionizing pulse and has an overall duration of 150 μsec. Hence, at pulse repetition frequencies of 5-10 kHz nearly continuous gain can be obtained.

A comparison of the peak gain coefficient versus E/P for the present device and for an electron-beam-controlled discharge[2] is shown in Fig. 1. Possible extension of this technique to higher operating pressures and, hence, to higher projected CW output powers will be discussed.

[2] C. A. Fenstermacher, VII Int. Quantum Electron. Conf., Montreal, Quebec, Canada, 1972.

[3] J. P. Reilly, *J. Appl. Phys.*, vol. 43, p. 3411, 1972.

[4] A. E. Hill, *Appl. Phys. Lett.*, vol. 22, p. 670, 1973.

18.5 Discharge Scaling Studies for a Continuously Operating Fast Flow Electrically Excited (Coffee) Laser, S. A. Wutzke, L. H. Taylor, J. L. Pack, T. V. George, and L. A. Weaver, *Westinghouse Research Laboratories, Pittsburgh, Pa. 15235*

(20 min)

Discharge scaling studies of a unique dc CO_2 (COFFEE) laser excitation scheme are described. The COFFEE laser is excited with a high-pressure, self-sustained glow discharge. The glow is produced between a multipin cathode and a planar anode. Current flow is mutually perpendicular to both the gas flow and the optical axis. The discharge is stabilized by the gas flow and by a ballast resistor connected in series with each cathode pin. The high-pressure continuous glow has been successfully scaled to a 10 cm square aperture along the optical axis. The experiments were performed in a closed-loop flow tunnel using a 10 × 10 × 10 cm discharge module. The cathode pin density was 1 pin/cm^2 and the electrode gap was varied between 2 and 10 cm. Flow velocities up to 150 m/sec were used.

Discharge parameterization experiments and computer simulations have been performed over a broad range of the primary variables. Specific input powers up to 115 J/1-atm (110 kJ/1b) were obtained with input power densities up to 50 W/cm^3 of discharge volume. No fundamental scaling limit has been encountered for electrode spacings up to 10 cm.

If one keeps the input power per unit volume (jE) constant in order to maintain uniform excitation, the gas temperature rises almost linearly along the flow direction, causing the gas density to decrease nonlinearly. Since the glow discharge operates at nearly constant E/N, the E field decreases in the same manner as N. In order to hold jE constant, the current density (j) must increase linearly along the gas flow direction. This is easily accomplished in the COFFEE laser by adjusting the cathode row currents.

The operating E/N for the discharge was measured as a function of j/N, ratio of current density to total gas density. The upstream values agreed with the predictions of Lowke *et al.*[1] obtained from a steady state balance between electron generation and loss mechanisms. An upstream E/N of 2.6×10^{-16} V-cm^2 was measured for a 1 CO_2:7 N_2:30 He gas mixture, and decreased by as much as 50% through the downstream portion of the discharge.

Small-signal gain measurements were performed to determine the spatial uniformity of the electrical excitation and its dependence on the operational parameters. The gain was nearly constant as a function of the distance (8 cm) between anode and cathode, and increased in value as the gas was convected through the excitation region. Peak gains of 0.25%/cm were measured for 10 CO_2 : 70 N_2 :200 He:2 H_2 gas mixtures with a current density of approximately 15 mA/cm^2. In general the peak gain varied linearly with current and approximately inversely with total pressure. Small amounts of hydrogen introduced into the laser gas mixture improved the long term discharge stability when operating near the glow-to-arc threshold, and caused a tolerable decrease in small-signal gain.

A six-temperature, CO_2 laser kinetics computer program was developed to simulate excitation and relaxation processes in the COFFEE laser mixture as a function of downstream distance. Computed gain agreed well in magnitude and spatial dependence with measured values. The gas temperature rise was calculated to be 47°K in 25 cm without mirrors, but was reduced to 36°K with mirrors due to extraction of the laser energy. Laser outputs of 21 kW at 11% efficiency are predicted for an 8 cm × 10 cm × 140 cm excitation region with a total current of 14 A.

The measured input power for an 8 cm × 10 cm × 10 cm volume was 24 kW, which is over 200 kW/m of cavity length. Since the discharge operates near the optimum E/N values for efficient excitation and provides sufficient gain for efficient energy extraction, the COFFEE laser concept appears to be scalable to the multikilowatt levels predicted by the computer simulations.

[1] J. J. Lowke, A. V. Phelps and B. W. Irwin, *J. Appl. Phys.*, vol. 44, p. 4664, 1973.

18.6 Multigigawatt Peak-Power Generation from a Tandem of TEA-CO_2 Lasers, P. A. Bélanger and J. Boivin, *Laval University, Quebec, Canada*

(15 min)

A new simple method has been successfully demonstrated for obtaining multigigawatt, ns pulses from a tandem of two TEA-CO_2 lasers. In operation, the first laser[1] is conventionally mode-locked using an acoustooptic modulator and serves as a master oscillator for the system. A propylene attenuator drastically reduces the signal from this first laser before it is optically coupled to the second by means of a small hole (500 microns) pierced in the spherical mirror. The second or slave oscillator is the same type of high-energy laser as the first and is of approximately the same length (±2 cm). Its excitation is electronically controlled through a time delay circuit so that the laser medium presents the low gain value when the pulse train from the master oscillator arrives.

The output of the tandem unit under optimum conditions (which can consistently be achieved) is depicted in Fig. 1. The pulse train resembles in every respect that which would be obtained from ordinary mode-locking but with the peak power now attaining 4 gigawatts.

[1] J. L. Lachambre, J. Gilbert, F. Rheault, R. Fortin and M. Blanchard, *IEEE J. Quantum Electron.*, vol. QE-9, p. 459, 1973.

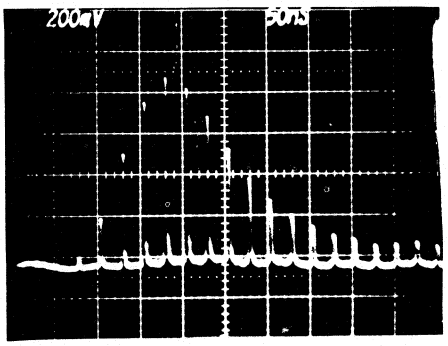

Fig. 1. Output of tandem unit under optimum conditions.

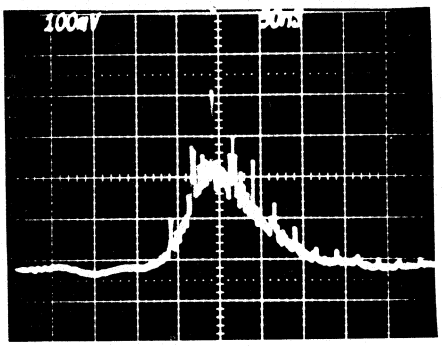

Fig. 2. Output of tandem unit with excess attenuation.

Fig. 2 illustrates the importance of determining the proper attenuation of the propylene cell. In this figure, the attenuation was too strong and the input signal to the slave was below the noise for spontaneous emission. If the input signal is too strong, the gain switching effect of the second laser is then attenuated. Optimum conditions were determined by varying the pressure of the propylene in the 30 cm cell.

It has been experimentally verified that this system works just as well as long as the ratio of the length of the first laser to that of the second forms a simple ratio: $2, \frac{1}{2}, \frac{2}{3}, \ldots$. This permits the use of higher energy slave oscillators without complication. The operation with unstable resonators has also been demonstrated.

Another variation which has been successfully demonstrated is the injection of a unique pulse into the second laser. This has been accomplished using a GaAs active polarizer followed by a saturable absorber (SF_6) to further attenuate the unwanted peaks.

This new method for producing multigigawatt pulses imposes itself not only by its reliability but by its simplicity. Its potential is far from being fully developed as no critical experimental limitations are as yet evident. In fact, we are confident of some achieving much better results with a very 400 joule slave oscillator in an unstable configuration for the resonator.

18.7 Multiline Operation of a CO_2 Oscillator/Amplifier System,[1] J. F. Figueira, W. H. Reichelt, G. T. Schappert, and B. Feldman, *Los Alamos Scientific Laboratory, Los Alamos, N. M. 87544*

(15 min)

In the design of large volume, high energy CO_2 laser systems, the overall system efficiency has a substantial inpact on the design and cost of the laser. It has been shown by previous theoretical and experimental work at LASL and elsewhere that the efficiency for amplifying nanosecond CO_2 laser pulses is limited by the rotational relaxation rates within the upper and lower lasing levels for oscillator/amplifier systems operating on a single rotational line. Theoretical studies have shown that increased efficiency is obtained if the oscillator/amplifier system is designed to operate on multiple rotational lines of the CO_2 laser transistion.

In this paper we report the results of an experimental and theoretical study comparing the efficiency of energy extraction from a CO_2 amplifier system operating on a single rotational line and one operating on multiple rotational lines. The input oscillator was of a hybrid design utilizing both high pressure (600 torr) and low pressure (20 torr) gain sections. By use of an intercavity absorption cell containing SF_6 this oscillator could be operated on either a single line ($P(20)$ 10.4 μm branch) or multiple line ($R(14)$, $R(16)$ and $R(18)$ of the 10.4 μm branch) with equal energies. Operation could be obtained on both the 9.4 μm branch or the 10.4 μm branch. From the gain swtich output pulse from this oscillator, a single nanosecond pulse was generated with an electrooptical gating technique. The amplifier system consisted of two stages of electron beam pumped gain volumes, 1 m long each, operated at a total pressure of 600 torr with a small signal gain coefficient of 4.4%/cm at $P(20)$ of the 10.4 μm branch. Input and output energies, pulse time histories and frequency distribution of the output radiation were monitored.

A theoretical analysis of multiline energy extraction, based on a model of random rotational relaxation (no ΔJ selection rule) has been performed. Applied to the above experimental conditions, such calculations predict a 50% increase in energy output and a pulse narrowing resulting in a factor of two higher peak intensity. A comparison of theory and experiment will be given.

[1] Work performed under the auspices of the U. S. Atomic Energy Commission.

18.8 Parametric Studies of a Multiband CO_2 Laser,[1] J. F. Figueira, G. T. Schappert, S. Singer, and S. J. Thomas, *Los Alamos Scientific Laboratory, Los Alamos, N. M. 87544*

(15 min)

In a previous paper[2] the authors have described the performance characteristics of a CO_2 oscillator capable of operating on multiple rotational lines and multiple vibrational bands. In this paper we report on a more detailed extension of this work. The experimental arrangement consisted of a conventional UV preionized TEA-CO_2 laser equipped with an intercavity gaseous absorption cell. The output energy was monitored with band pass filters and a disk calorimeter. Pulse time histories were measured using a scanning 0.75 m grating monochrometer equipped with a fast pyroelectric detector readout to a dual beam 500 MHz oscilloscope. Time integrated pulse energies were also obtained using the grating monochrometer. A 2 cm long Brewster angle intercavity absorber cell was filled with various pressures of SF_6 and the output spectra from the oscillator was measured. For a typical operating condition the output consisted of eight rotational lines, three on the 9.4 μm branch and five on the 10.4 μm branch. It was found that when the cell pressure was maintained at 15 torr, the $R(14)$, $R(16)$, $R(18)$ lines of the 10.4 μm branch and the $P(22)$ line of the 9.4 μm branch were found to contain equal energy. At 15 torr pressure the output energy from the multiline operation was essentially the same as the output energy with the SF_6 cell evacuated. As the cell pressure was increased the total output energy stayed approximately constant, but the ratio of 9 μm energy to 10 μm energy increased linearly with SF_6 pressure.

When the laser output intensity was examined several interesting features were noticed. For low SF_6 pressure ($P < 10$ torr) the 10 μm radiation consisted of a gain switched spike followed by a low level N_2 repumping tail with 30-50% of the total energy contained within the gain switched envelope, The 9 μm radiation under the same conditions consisted of a low level gain switched peak, followed 300-400 ns later by a 2 μs burst of radiation. Less than 5% of the total energy on the 9 μm band was contained within the gain switched peak. By increasing the SF_6 pressure it was possible to equalize the peak gain switched intensities in both bands, however over 50% of the total energy occurred in the 9.4 μm tail.

The variation of the output intensity with laser frequency was also observed using different gaseous absorbers, suggesting that the effect is not due to the absorption process but rather is a result of the pumping dynamics of the CO_2 laser. These experimental results are compared with the computational results derived from a simple kinetic model of the CO_2 laser gain.

In conclusion we have made a parametric study of a multiband CO_2 laser. It was found that the gain and lasing dynamics of this system cause the multiband output intensities to vary greatly with lasing wavelength.

[1] Work supported by the U. S. Atomic Energy Commission.

[2] G. T. Schappert and J. F. Figueira, "A multiband CO_2 oscillator," in press, *Opt. Commun.*

18.9 A Frequency Tunable 15 Atmosphere CO_2 Laser, F. O'Neill and W. T. Whitney, *Naval Research Laboratory, Washington, D. C. 20375*

(15 min)

High pressure ($\sim$15 atm) CO_2 lasers are presently of interest because of their possible use as tunable sources of coherent radiation in

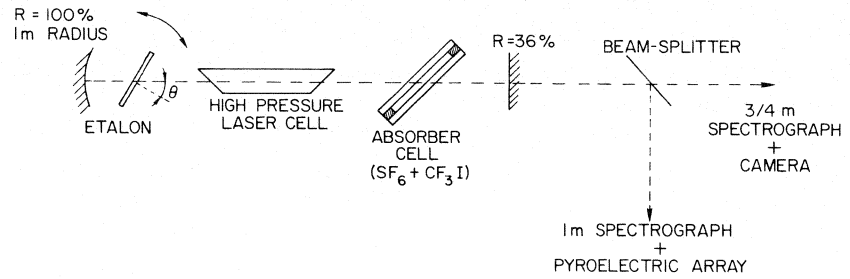

Fig. 1. Experimental arrangement used for interferometric tuning of 15 atm CO_2 laser.

the 9-11 μm spectral region. In view of their higher operating power and efficiency, these lasers will have a significant advantage over presently available tunable infrared sources for applications such as laser induced chemistry, isotope separation and infrared up-conversion studies. We have previously described[1] the characteristics of a cold-cathode electron-beam-controlled CO_2 laser which is suitable for operation at pressures up to 15 atm and in this paper we discuss experiments on frequency tuning of the laser using a Fabry-Perot etalon as a dispersive element in the laser resonator. The experimental arrangement used for this work is shown in Fig. 1.

Frequency tuning of the laser is obtained by using a 1.5 cm diameter, 0.9 mm thick, ZnSe solid etalon. The refractive index of ZnSe is 2.4 giving an etalon free spectral range ~ 2.3 cm^{-1}. The etalon was coated on both sides with 47% reflectivity dielectric coatings giving a finesse ~ 4. A gas absorber cell (thickness ~ 1 cm) is placed in the cavity and by filling it to a pressure of 50 torr with equal parts of SF_6 and CF_3I the laser is restricted to oscillation on the *R* branch of the 10.4 μm band of CO_2. The spectral behavior of the laser is monitored simultaneously using an Optical Engineering Spectrum Analyzer and a 1 m Czerny-Turner spectrograph. The laser is frequency tuned by rotating the etalon in a vertical plane and by changing the etalon angle θ (Fig. 1) over the range 0°-9° the laser wavelength is varied over one free spectral range (~ 2.3 cm^{-1}). The tuned laser spectral width is <0.2 cm^{-1} and an output energy ~ 100 mJ has been obtained for a laser peak power ~ 5 MW. This is higher than has been achieved with a diffraction grating tuned laser[2] and should be limited only by the same damage criteria as for dielectric coated mirrors. Even though the finesse of the etalon is only 4 the device was still selective enough to narrow the lasing linewidth by more than an order of magnitude and give smooth tuning over two of the CO_2 rotational lines.

Present experiments are aimed at obtaining tunable single longitudinal mode operation of the laser throughout the complete gain spectrum of CO_2. This will be achieved by using a number of interferometers simultaneously in the laser cavity. In addition the usefulness of this laser as a spectroscopic tool will be demonstrated and we will describe experiments on the measurement of absorption lines in various gases.

[1] N. W. Harris, F. O'Neill and W. T. Whitney, *Appl. Phys. Lett.*, vol. 25, p. 148, 1974.

[2] A. J. Alcock, K. Leopold, and M. C. Richardson, *Appl. Phys. Lett.*, vol. 23, p. 562, 1973.

18.10 Suppression of Self-Oscillations in High-Gain CO_2 Amplifiers, P. Lavigne, J. L. Lachambre, and J. Gilbert, *Defence Research Establishment Valcartier, Courcelette, P. Q. Canada*

(15 min)

A major problem encountered in the design of high-gain CO_2 laser chains for generating short powerful pulses at 10.6 μm is the suppression of self-excitation arising from the amplification of spontaneous noise in the gain medium. Besides depriving the amplifier of its gain by destroying the inversion prior to the passage of the pulse to be amplified, self-excitation may in some conditions cause permanent damage to the optical components of the system. One promising way of ensuring stability against self-stimulation of the spontaneous noise is the inclusion of optical isolators between successive amplifier stages.

This paper will report the results of an experimental investigation of the use of the gas combination N_2F_4/C_2H_5OH as an interstage saturable filter. In this system the saturable gas N_2F_4 plays the role of an amplitude discriminator in the CO_2 laser band centered at 10.6 μm transmitting pulses of high intensity and preventing self-stimulation of the spontaneous noise while C_2H_5OH acts as selective absorber compensating for the limited absorption bandwidth of N_2F_4.

Direct transmission measurements performed with a low resolution spectrophotometer indicate that N_2F_4 has five strong absorption bands between 900 and 1050 cm^{-1} spanning the *P* and *R* branches of the 00°1-10°0 emission transition of CO_2 and also a portion of the *P* branch of the 00°1-02°0 transition. C_2H_5OH is essentially transparent in this region but absorbs strongly in the 00°1-02°0 band. The transmission characteristics of N_2F_4 and C_2H_5OH were also examined with a CW CO_2 laser beam over a large number of rotational transitions near 10.6 μm and 9.6 μm. The variations in the absorption of the laser radiation was found to be in good agreement with the measured low resolution spectrum. It was verified, in particular, that for pressures above 1 torr N_2F_4 does not have any narrow absorption dips that coincide with the CO_2 laser lines examined. Given the complexity of the N_2F_4 band system, this suggests that the absorption spectrum is formed by a continuum of overlapping lines in the pressure range of interest. The measured value of the small-signal absorption coefficient of N_2F_4 on the *P*(20) line of CO_2 is 0.021 cm^{-1} torr^{-1}.

The transmission of nanosecond pulses as a function of pulse intensity and gas pressure has been studied experimentally. The experiment was carried out by irradiating a 20-cm absorption cell filled with N_2F_4 at pressures between 1 and 20 torr using as a source a mode-locked laser with a single pulse selector followed by a multistage amplifier. At high intensity levels the pulse transmission exhibits a residual absorption which varies linearly with pressure over the pressure range 1-14 torr. When fully bleached the residual absorption absorption of N_2F_4 at *P*(20) line is approximately 0.003 cm^{-1} torr^{-1}.

Preliminary experiments were performed with the object of determining the isolation effectiveness of the N_2F_4/C_2H_5OH system in a practical amplifier chain. The test amplifier consisted of 4 sections of grid-type double-discharge excitation having each a 100-cm active length and an effective apertured cross-section of 15 cm^2. The measured linear amplification coefficient was 0.045 cm^{-1} and the overall gain of the complete chain reached 10^8. The two absorbing gases were contained in separate cells fitted with NaCl windows which were placed between the second and third stage of the amplifier. The N_2F_4 and C_2H_5OH cells were 30-cm and 50-cm long respectively. With 35 torr of N_2F_4 and 21 torr of C_2H_5OH, the amplifier was found to be completely free of oscillation when placed between two partially transparent mirrors of 50% reflection. This experiment served to confirm that the absorption spectrum of the isolator has a smooth contour covering the full emission bandwidth of the CO_2 molecule. Using as driving source a mode-locked laser with single-pulse switchout, pulses of 2 ns duration have been delivered to a 4% reflecting target at an energy of 7 joules without damaging the optical components. It is estimated that somewhat less than 50% of the energy carried by the pulse incident on the isolator was consumed in the bleaching of the N_2F_4 absorber. In these experiments, the isolation from target backscatter was achieved by a gaseous breakdown scheme.

The simplicity of construction together with the high resistance to optical damage and the easy adaptability to large cross-section amplifiers make this isolator attractive for high-gain CO_2 laser chains. Further tests on energy extraction, saturation and recovery time are in progress and available results will be reported.

18.11 Gain Recovery After Saturation in Short-Pulse CO_2 Amplifiers,[1] G. T. Schappert, J. S. Ladish, W. T. Leland, and M. J. Kircher, *Los Alamos Scientific Laboratory, Los Alamos, N. M. 87544*

(15 min)

Since the small signal gain of a laser power amplifier is also a measure of the stored energy, one can observe the pulse energy extraction and subsequent repumping by monitoring the small

[1] Work performed under the auspices of the U. S. Atomic Energy Commission.

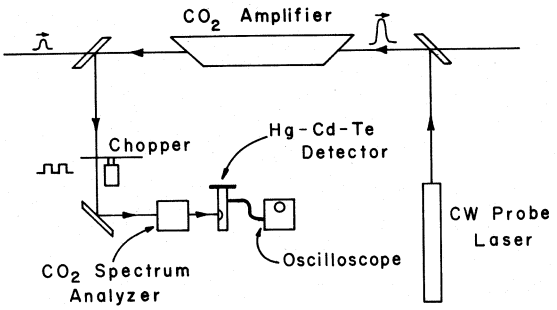

Fig. 1. Experimental layout.

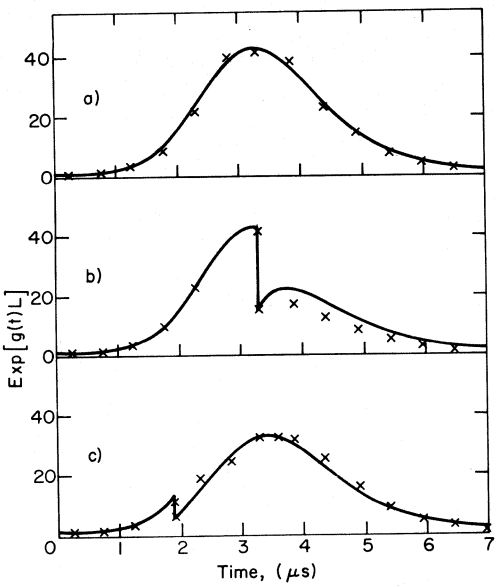

Fig. 2. Small signal gain.

signal gain as the energy is extracted. We have performed such measurements on a high pressure CO_2 power amplifier and have analyzed the results on the basis of a 4 temperature kinetics model.

Fig. 1 shows the experimental layout. A 1.5-1.8 ns (FW 1/e) pulse ($P(20)$, 10.6 μm) of 200-400 mJ energy traverses a 1 meter 1800 torr ($3/\frac{1}{4}/1$: $He/N_2/CO_2$ mixture), E-beam pumped CO_2 amplifier, extracting about 2 joules of energy. A tunable CW CO_2 laser monitors the small signal gain. This signal is chopped, passed through a CO_2 spectrum analyzer, detected by a Hg-Cd-Te photo-voltaic detector and displayed on an oscilloscope. Isolation between the CW signal and the pulse is a serious concern in this experiment because the CW signal, corresponding to 100 mW power, must be isolated from the pulse power ($\sim 10^9$ watt). To facilitate this isolation, the CW signal and the pulse traverse the amplifier in opposite directions. Furthermore, the CW laser is tuned to a line ($R(18)$, 10.26 μm) which differs from the pulse so that further isolation is achieved with the spectrum analyzer.

Fig. 2 shows the results of the experiment. The solid curve represents the calculated small signal gain, $\exp(g(t)L)$, as a function of time. In Fig. 2(a) we show the time history of the small signal gain in the amplifier. In Fig. 2(b), a saturating pulse goes through the amplifier at a gain maximum. The drop in stored energy and subsequent repumping are clearly shown. Similarly, Fig. 2(c) shows a pulse extracting energy from the amplifier about 1.4 μs before gain maximum. The experimental data transposed from scope traces are shown as points on each picture and are in good agreement with the results predicted by the kinetics model.

In comparing theory and experiment, the adjustable parameter is the fraction of the available energy extracted. For 1 ns pulses, rotational relaxation prevents some of the 100-001 vibrational population difference from contributing in the energy extraction. We find a good fit with about 0.8 of the available vibrational energy extracted. This cannot be compared directly with the drop in gain shown in Figs. 2(b) and 2(c). Within the time resolution of the experiment (20 ns) and the time scale of the kinetics model (50 ns), the population transferred from 001 into 100 by the saturating pulse is redistributed within the symmetric and bending modes, so that both experimentally, and in the kinetics model, one does not record the absolute minimum in inversion due to pulse amplification.

Session 19

Friday, May 30, 1975 1:30-5:00 P.M.

Optical Communications—Fibers and 10.6 μm

Chairman: T. Li, *Bell Laboratories, Holmdel, N. J. 07733*

19.1 Optical Fiber Communications—Potential Applications (*Invited*), J. E. Goell, *ITT Electro-Optical Products Division, Roanoke, Va.*

(30 min)

Recent technological advances will allow the use of fiber optics to transmit signals in a variety of commercial and military systems. This paper gives projections of performance and describes several potential applications.

19.2 Progress of Optical Communications in Japan (*Invited*), G. Marubayashi, *Electrical Communications Laboratory, NTT, Japan*

(30 min)

The status of optical communications research and development in Japan will be reported.

19.3 Measured Dispersion in Long Multimode Fiber Waveguides With and Without Joints, C. Kao, G. Bickel, and M. Maklad, *ITT Electro-Optical Products Division, Roanoke, Va. 24019*

(15 min)

Dispersion in Multimode Fibers arises from the intrinsic group velocity characteristics of each propagating mode, the material dispersion and the differences in modal velocities. For a particular waveguide under a specific launching condition the signal pulse will initially be carried by a particular mixture of propagating modes which is by and large constant along the pulse duration. As this pulse propagates the pulse shape will be modified by the dispersion effects. For an ideal guide there is no mode coupling, so that as the higher order modes are delayed relative to the lower order modes, the pulse will broaden. The start of the pulse will eventually be made up by the energy carried in the lower order modes and the tail in the higher order modes. The pulse broadening will be proportional to length and pulse shape will be governed by the relative energy carried by each mode. For a practical guide, bending, stress and structural imperfections cause mode coupling; in other words, the energy carried by each mode is given to other modes, including radiative modes, and in turn receives energy from other modes. This gives rise to the effect that the velocity of the energy propagation will have an average value and its deviation will be de-

creasing at a rate proportional to $\sqrt{L}$. Hence, the pulse spread will increase at a rate proportional to $\sqrt{L}$. There will also be radiative losses. An equilibrium situation will arise when each part of the pulse energy will be carried in a mixture of modes undergoing continuous conversion as it propagates. Before this equilibrium is reached, the pulse shape undergoes complex changes from its initial state when the pulse will have a particular mixture of propagating modes along its duration, through successive stages when the modal delay causes pulse shape changes and pulse broadening.

The distance required for equilibrium may vary from fiber to fiber. It is the spectral distribution and the spectral content of the coupling discontinuities which govern the rate and type of equilibrium. For fiber waveguides with imperfections which can cause gross modal conversion distributed along its length, equilibrium may not be established.

This paper presents the results of an experimental study of dispersion in long multimode fiber waveguides.

The fiber waveguides under study are made by a chemical vapor deposition process. The resulting fibers have a numerical aperture of approximately 0.2. Fibers of various lengths are studied including one of 4 km length.

Measurements have been carried out on a dispersion measuring apparatus consisting of a GaAs laser source switched at low repetition rate by a subnanosecond pulse and a fast detector. The optical output has a subnanosecond rise edge and the principal pulse has a duration of 1 ns. The optical output is launched into the fiber with adjustable numerical aperture from 0.1 to 0.2.

Various fiber lengths from 2 meters to 1 km are measured for dispersion. A particular fiber is destructively tested by successive reduction of length. This serves to check the consistency between different fibers. A 4 km fiber is also destructively tested to study equilibrium effect. It is then rejoined by couplers of different tolerances. The gross discontinuities are introduced by the couplers. The equilibrium effects are again studied.

The transient behaviors are discussed.

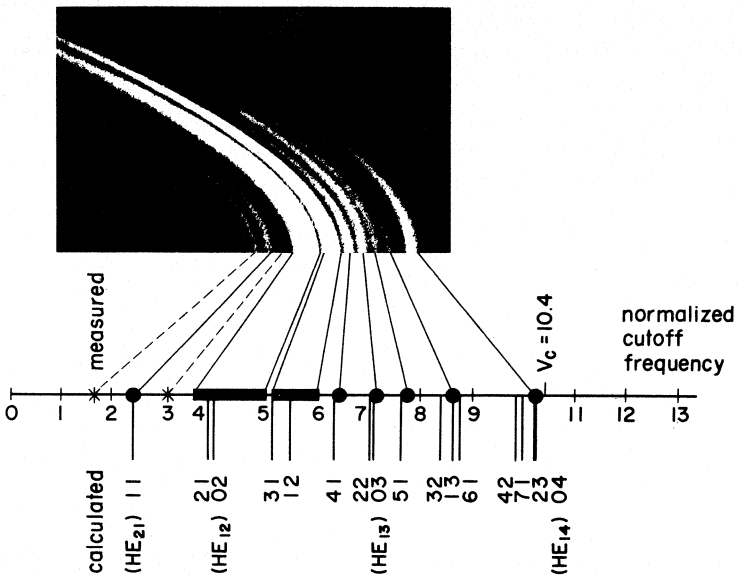

Fig. 1. Mode identification of multimode cladded fiber using mode analyzer. $(lm) = HE_{l+1,m}, EH_{l-1,m}$ $(l \neq 1)$; $(1m) = HE_{2m}, TE_{0m}, TM_{0m}$.

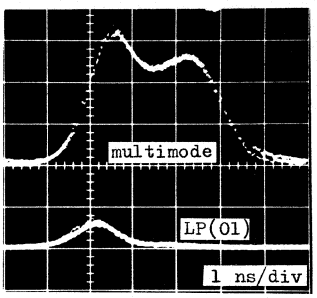

Fig. 2.

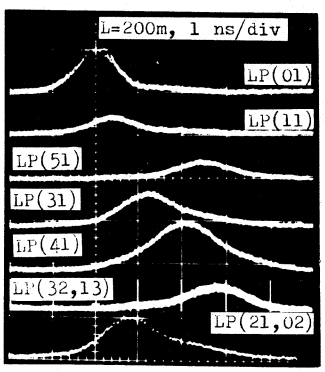

Fig. 3.

19.4 Mode Analysis of Multimode Fibers, T. Ozeki, T. Ito, and T. Tamura, *Toshiba Research and Development Center, Kawasaki, Japan*

(15 min)

For analysis of propagating mode characteristics of multimode fibers, it is desired to realize the identification of modes and the measurement of mode amplitude distribution. Also, the direct measurement of group delay of each propagating mode is important to improve the fabrication techniques of graded index fibers.

It is found that a linearly-tapered section can be used as a mode analyzer for multimode fibers. The tapered section immersed in oil radiates the cutoff modes in coaxially stacked conical sheaths. When a screen is placed in parallel with the axis of the conical sheaths, the sections of these conical sheaths appear as a group of hyperbolas. The apexes of the hyperbolas correspond to the normalized cutoff frequencies of multimode fiber as shown in Fig. 1.

The mode analyzer using the linearly-tapered section with a ring spatial filter makes it possible to measure the group delay of each propagating mode of multimode fibers. The output from a mode-locked He-Ne laser operating at 0.633 μm was injected into the fiber through a $\times 40$ microscope objective and the output pulses from the fiber became widened due to mode dispersion of a clad fiber as shown in the upper trace of Fig. 2. The lower trace in Fig. 2 shows the output pulse component carried in the He_{11} mode, which is detected separately by the mode analyzer. Fig. 3 shows relative group delays of several modes of a clad fiber with the normalized frequency of 10.4. The measured group delays show good agreement with the calculated values based on the dispersion equation.[1]

The mode conversion in the clad fiber is measured quantitatively by using mode filters. A biconical taper as a mode filter has the insertion loss of 0.2 dB for the HE_{11} mode and the rejection ratios of more than 20 dB for the higher order modes. The amount of mode conversion from the HE_{11} mode to the higher order modes is measured to be 0.3 dB for the clad fiber with a core diameter of 12.5 μm, an outside diameter of 72 μm and for the length of 300 m at a bend radius of 15 cm. The pulse broadening due to mode reconversion or mode mixing cannot be detected within the time resolution of ~ 100 ps.

[1] D. Gloge, "Weakly guiding fibers," *Appl. Opt.*, vol. 10, p. 2252, 1971.

19.5 An Optical-Fiber Cable Fault Location Method, Y. Ueno and M. Shimizu, *Nippon Electric Company, Ltd., Yokohama, 226 Japan*

(15 min)

For the construction of an optical-fiber cable transmission system, it is necessary to develop efficient optical cable inspection methods. As practical inspection methods, there are "reflection methods" and "transmission methods" including pulse distortion method and conventional optical loss measuring method. During experimental inspection of a 600 m long SELFOC fiber in which faults exist, distinct pulse distortion is observed. "Reflection methods" including those methods which stand on the same principles of optical radars and sonars,

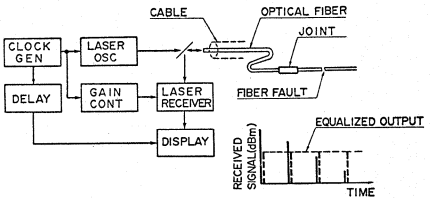

Fig. 1. Block diagram.

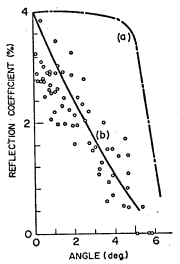

Fig. 2. Reflection coefficient.

have a merit of indicating the location of the fault.

An optical fiber fault location method using the optical pulse radar scheme is studied in detail, comparing with other methods. Optical fiber cables are tested by an experimental inspection set and effective data are obtained for the improvement of the cabling process and of the cable structure. The set is also applied to the study of the cable laying work (see Fig. 1).

In optical fibers the decay of optical pulse signals occurs exponentially to the transmission length, while available optical input power is limited by the stimulated Brillouin scattering effect.[1] Those effects and the reflection coefficient at the fault surface define the maximum detectable range. The reflection coefficient at a fault surface of an optical fiber is calculated and measured, as a function of the inclination angle between the surface and the optical axis, as shown in Fig. 2. In this figure, (a) indicates estimated value based on launching angle characteristics, (b) indicates estimated value based on geometrical optics, and the dots illustrate experimentally-measured data. The measurement is made using a mode-locked He-Ne laser and 1.5 m long SELFOC fibers.

In the block diagram shown in Fig. 1, optical pulses which are transmitted through the optical fiber and reflected at the joints and the fiber fault, are received by the optical receiver and displayed in a CRT display. The reflected signal from a joint which is nearer than the fiber fault becomes intense noise. A gain control method which increases the receiver gain synchronizing to the pulse transmission, is employed to equalize the input signals and to reduce the effect of the noise signals from the joints. Range gating is also an important technique to improve the signal-to-noise ratio. Ranging resolution can be improved by pulse shifting method or random pulsation method in which range is expressed as a statistical value of many samples.

A maximum detection range of 3 km is estimated in a ranging resolution of 2.5 m, assuming that an optical power of 0.5 W is launched into an optical fiber which has a loss of 10 dB/km. In practice, the output power of available lasers and the coupling efficiency to the optical fiber define the detection range. Reflected signal from an optical fiber fault at a distance of 1.4 km is observed by the experimental set with a GaAlAs laser diode. The input optical pulse peak power and wavelength of the laser are 0.2 W and 0.83 μm respectively, and the optical fiber loss is 17 dB/km.

[1] R. G. Smith, *Appl. Opt.*, vol. 11, p. 2489, 1972.

19.6 A 40 Mb/s and a 400 Mb/s Repeater for Fiber Optic Communications,

Y. Ueno and Y. Ohgushi, *Nippon Electric Company, Ltd., Yokohama, 226 Japan*

(15 min)

The high-performance feedback-type amplifier which makes front-end equalization unnecessary has been studied. Using amplifiers of this type, a 40 Mb/s repeater and a 400 Mb/s repeater have been built and tested for an optic PCM communication system.

The minimal optical power of the feedback-type amplifier (c.f. Fig. 1) is acquired using Personick's method[1] as follows.

$$P \text{ required} = \frac{1}{2T}(Q)^{(2+x)/(1+x)} \cdot [(Z)^{x/2+2x}(r_1)^{x/2+2x}(r_2)^{2+x/1+x}]\frac{\hbar\Omega}{\eta} \quad (1)$$

$$Z = \frac{T}{e^2}\left[S_I + 2k\theta\left(\frac{1}{R_b}+\frac{1}{R_f}\right) + S_E\left(\frac{1}{R_b}+\frac{1}{R_a}-\frac{1}{R_f}\right)\right]I_2 + \frac{(2\pi C_T)^2 S_E I_3}{Te^2} \quad (2)$$

where R_f = a feedback resistance and other symbols are used as in Ref. 1. And it is shown that we can obtain without a front-end equalizer the same performance as that of the equalizer-type integrating amplifier, if we make the feed back resistance sufficiently large.

A 40 Mb/s regenerative repeater (Fig. 1) using the feedback-type amplifier has been constructed with a 55 dB loss margin. The preamplifier is built using a 40 dB bipolar transistor amplifier, including the first stage bipolar transistor whose bias current is 0.5 mA, and a 68 kΩ feedback resistance. The gain of the main amplifier is 40 dB with 30 dB AGC. The total capacitance is 10 pF with the APD. The quantum efficiency of this APD is 70% and the excess noise coefficient is 0.5. The laser diode used here is a GaAs DH type which is driven by 200 mA current pulses. The optical output power is 0 dBm (average) at the panel connecter. The error performance of this repeater is plotted in Fig. 2. Good agreement with theoretical calculations represented by the solid line is obtained.

A 400 Mb/s repeater has also been built (Fig. 1). The 36 dBm loss margin has been obtained in this case. In higher bit-rate range, we can reduce the value of R_f without increasing noise. So, a 680 ohm feedback resistance is selected. The gain of the preamplifier is 20 dB. The first stage of this preamplifier is a bipoler transister whose collector current is 2 mA. And the total input capacitance is 13 pF with the APD. The quantum efficiency of this APD is 40% and its excess noise coefficient is 0.38. The driving condition of the laser diode is different from the case of 40 Mb/s. The 100 mA dc bias current is applied in order to reduce the delay between optical pulses and driving pulses. The

[1] S. D. Personick, "Receiver design for digital fiber optic communication systems, Part I and II," *Bell System Tech. J.*, vol. 52, pp. 843-886, July-August, 1973.

Fig. 1. A block diagram of repeaters.

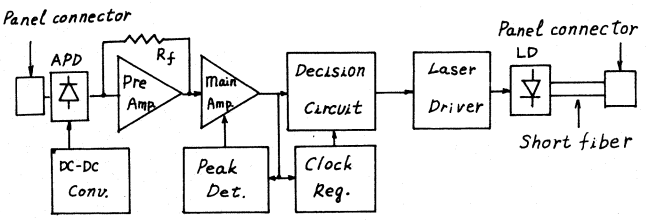

Fig. 2. Error rate performance.

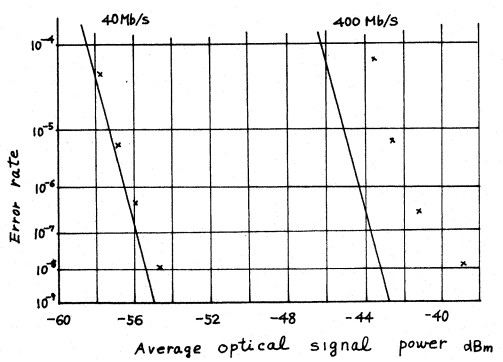

100 mA pulse current is added to this bias current. The output optical power from the panel optical connecter is −3 dBm (average). Experimental results of the error-rate performance is plotted in Fig. 2. The solid line is from theoretical calculations according to (2). In this case good agreement with theory is not obtained without taking into account the 3 dB power penalty due to the intersymbol interferences caused by the APD.

19.7 Planar HgCdTe Photodiodes for Wideband Heterodyne Detection at 10.6 μm, [1] D. L. Spears, I. Melngailis, and T. C. Harman, *Lincoln Laboratory, Massachusetts Institute of Technology, Lexington, Mass. 02173*

(15 min)

ZnS films have been found to provide a sufficiently good mask for mercury diffusion to enable selective diffusions to be carried out in HgCdTe for the fabrication of planar photodiodes. Such *n*-on-*p*-type diodes, with 100 μm and 150 μm diameter clear active areas, have shown quantum efficiencies as high as 60% (uncoated) at 10.6 μm with a frequency cut-off well in excess of 1 GHz. Evaluated as detectors in a blackbody heterodyne radiometer, they have displayed a sensitivity within a factor of 3 of that of an ideal detector over a 0.5 GHz bandwidth.

Diodes were fabricated from 0.1 Ω-cm, *p*-type HgCdTe (19% CdTe) material which was mechanically lapped and polish-etched in 25% Br-methanol to a wafer thickness of about 0.2 mm. A 0.5 μm layer of ZnS was then RF-sputtered onto the wafer and openings etched in the layer with 5% HCl. A 5 μm deep, low carrier concentration *n*-type layer was produced in the open regions by a 30-minute, 240°C Hg-vapor diffusion in a sealed ampoule. The ZnS diffusion mask automatically passivated the edge of the *n-p* junction. Indium bonding pads were formed off the active region of the device. After gold plating the back contact, the wafer was diced and the devices mounted in microwave packages as shown in Fig. 1.

Electrical characteristics of these planar diodes are similar to etched mesa diodes,[2] having forward resistances of 5 to 10 ohms and reverse dynamic resistances of 200 to 1000 ohms. Most of the devices have shown a soft reverse breakdown starting at about 0.5 volts, apparently due to the high electric field at the perimeter of the planar structure. However, these planar devices, which have no surface passivation other than the ZnS diffusion mask, have shown no sign of electrical degradation over a period of more than 15 months.

Diodes made from three different HgCdTe crystals exhibited cut-off wavelengths ranging from 12.5 to 14.5 μm. Generally, the quantum efficiency was found to be almost constant from 3 μm to within 1 μm of the cut-off wavelength.

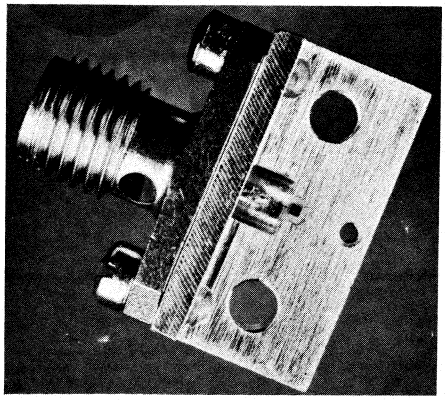

Fig. 1. HgCdTe photodiode in high frequency package. Cover plate is removed to show details.

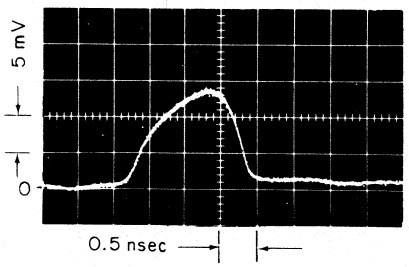

Fig. 2. HgCdTe photodiode response to a 1-nsec CO_2 laser pulse produced by an electrooptic modulator.

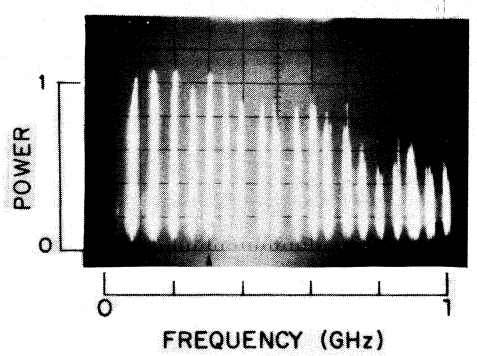

Fig. 3. Beat signals between a PbSnTe diode laser and CO_2 laser detected by a HgCdTe photodiode. Each line of the multiple exposure photograph corresponds to a different diode laser wavelength.

With a small reverse bias the peak quantum efficiencies of these uncoated diodes were typically 40 to 60%.

Detector response to a 1-nsec CO_2 laser pulse revealed RC limited response times of less than 1-nsec with only 100 to 200 mV reverse bias. With 500 mV bias, many devices had a fall time of less than 0.5 nsec, as shown in Fig. 2, which was the response time of the test equipment. Frequency response was also measured by detecting the heterodyne beat signal between a tunable PbSnTe diode laser and a CO_2 laser as the diode laser line was tuned through the CO_2 laser wavelength. Fig. 3 shows some typical results.

Blackbody heterodyne measurements[3] outlined schematically in Fig. 4 were used to obtain high frequency sensitivity information. By inserting a microwave mixer and low-pass filter between the preamplifier and RF detector, photodiode frequency response was measured by scanning the microwave local oscillator. With a 300°C blackbody temperature a signal to noise ratio of over 100 was observed with 1 sec integration time and 1.4 GHz bandwidth. This is within a factor of 7 of that expected for an ideal radiometer. With a 0.5 GHz bandwidth the detector-preamplifier combination performed within a factor of 3 of ideal, which is well over twice the sensitivity previously reported for HgCdTe diodes.[4] Only about p.5 mW of laser power was needed for quantum noise limited operation.

[1] This work was sponsored by the Department of the Air Force.

[2] D. L. Spears, T. C. Harman, and I. Melngailis, Solid State Research Report, Lincoln Laboratory, M.I.T. (1973:2), p. 2.

[3] E. D. Hinkley and P. L. Kelley, *Science*, vol. 171, p. 635, 1971.

[4] J. Gay, A. Journet, B. Christophe, and M. Robert, *Appl. Phys. Lett.*, vol. 22, p. 448, 1973.

Fig. 4. Schematic diagram of the blackbody heterodyne detection setup used to evaluate high frequency HgCdTe photodiodes.

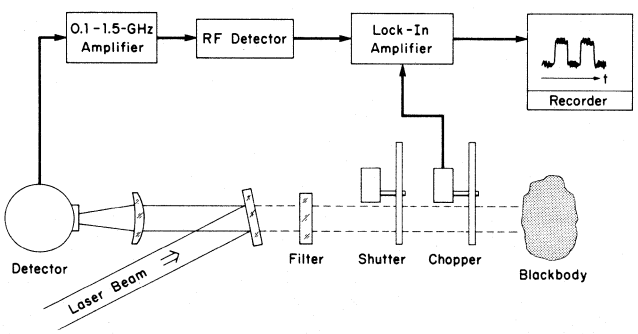

19.8 A Ten-Micrometer Receiver Subsystem for Wideband Space Communications, F. E. Goodwin and T. A. Nussmeier, *Hughes Aircraft Company, El Segundo, Calif.*

(15 min)

The need for wideband data relay system between satellites in space has fostered the development of 10 micrometer laser communication components over the past five years. This

paper reports the test results of an engineering model heterodyne receiver terminal for a synchronous satellite. The terminal would ostensibly serve as the receiver portion of a wideband relay link from a low altitude user satellite such as ERTS.

The receiver subsystem is comprised of components developed by a number of contractors and integrated at Hughes Space and Communications Group.[1]

An opto-mechanical design has been achieved which can operate with negligible distortion while directly exposed to the sun. This will permit the receiver to operate while tracking the transmitter signal across a solar background, a great operational advantage over other optical system concepts. The opto-mechanical portion of the receiver made almost entirely of beryllium weighs less than 30 pounds including waveguide laser local oscillator and radiation cooler. The electronics are rack-mounted at present.

The folded-Gregorian optical system utilizes a coarse pointing flat mirror having a field range of $\pm 20°$, and a set of orthogonal fine pointing mirrors having a field range of $\pm 0.1°$. Acquisition is achieved by commanding the coarse pointing mirror to within 0.1° of the transmitter beacon and searching by a raster scan pattern over the fine pointing field range. After initial pointing, the raster search routine takes less than six seconds. When the signal is sensed by the optical heterodyne detector, an RF carrier is developed in the IF amplifier which triggers a threshold and stops the search. Tracking of the incoming signal is then achieved by conical scanning of the fine pointing mirrors.

Doppler shifts of up to ± 700 MHz are encountered due to the relative velocity of a low altitude and synchronous spacecrafts. These Doppler shifts are accommodated through a wideband optical mixer and tracking RF electronics. For initial acquisition of a low altitude spacecraft, the receiver is commanded to be centered near the expected incoming signal frequency. Frequency acquisition takes place if the signal is within 85 MHz of the receiver band center.

The laser transmitter modulation format is double-sideband suppressed carrier modulation, and detection is achieved in the receiver by phase-lock or product detection of the IF signal. Data rates of 300 MBps can be accommodated by the receiver. Bit-error-rate measurements agree with theoretical within a factor of 1 dB for a bit error rate of 10^{-6}.

The optical mixer (detector) is cooled in space through the use of a radiation cooler to a temperature of approximately 100 to 120°K. In the laboratory, a temperature controlled Joule-Thompson cooler is used to simulate the space temperature.

Optical transmitter signals are simulated in the laboratory through the use of a breadboard laser transmitter using intracavity coupling modulation. The transmitter signal is attenuated to a level of approximately 10^{-15} W which compares with a receiver pre-detection NEP of 2×10^{-17} W.[2]

[1] Contributors to the effort are Hughes Research Laboratories (structural frame and waveguide laser local oscillator), Airborne Instrument Laboratory (Doppler tracking receiver electronics), Airborne Instrument Laboratory (Heterodyne receiver front end), Hughes Electro-Optical Division (optical design), and Hughes Space and Communications Group (opto-mechanical and servo system.)

[2] The work described in this paper was supported under NASA Goddard Space Flight Center Contracts Numbers NAS 5-21859, NAS 5-23183, NAS 5-23119, NAS 5-20623, and NAS 5-20018.

19.9 Wideband Heterodyne Receiver for CO_2 Laser Communication Link,[1] B. J. Peyton, T. Flattau, J. Wolczok, J. Mellars, and R. A. Lange, *AIL, a Division of Cutler-Hammer, Melville, N. Y. 11746*

(15 min)

This paper reports on an extremely wide bandwidth of a 10.6 μm infrared heterodyne receiver which has been developed for use in an engineering model of a simulated CO_2 space-borne communications link. For the link considered, the transmitter and the local oscillator (LO) are operated on the same laser transition. For low-altitude-satellite to synchronous-satellite and low-altitude-satellite to ground links, the transmitted signal is Doppler-shifted due to the difference in the relative velocity of the two stations.[2] The resultant Doppler frequency shift (Δf_d) varies with time and, hence, must be frequency tracked by either (a) a spectrally wide laser LO which can be rapidly tuned at infrared wavelengths, or (b) a heterodyne receiver which employs a fixed frequency laser LO and a wideband IF network which can be rapidly scanned using RF techniques. This latter type of communications receiver which utilizes RF tuning to handle the Doppler frequency offset has been adopted. Some design considerations for wideband infrared heterodyne receivers have previously been reported.[3] An electronic receiver back-end accepts the output of the heterodyne receiver front end and tracks the Doppler shifted signal so as to maintain a constant second IF at 1500 MHz. The receiver has a 300 megabit data capacity, which is compatible with the 400 MHz instantaneous IF bandwidth.

In order to prevent communication data distortion due to data foldover when $\Delta f_d < 200$ MHz, the laser LO in the heterodyne receiver front end is frequency offset by a minimum of 200 MHz with respect to the frequency of the laser transmitter. As the satellite passes through the zenith position, the polarity of the laser LO offset frequency is reversed.

A heterodyne receiver with an IF response up to 1200 MHz is required for the communications link, having a maximum Doppler frequency of 750 MHz, an IF bandwidth of ± 200 MHz, as well as a minimum IF offset of 250 MHz between the received carrier frequency and the LO frequency.

Heterodyne receiver measurements have been carried out over the 77° to 130°K temperature range to simulate operation with a passive radiative cooler which might be employed in an

[1] This work was sponsored by NASA Goddard Space Flight Center, Greenbelt, Md.

[2] J. McElroy, N. McAvoy, H. Richards, T. McGunigal and G. Schiffner, "Carbon dioxide laser communications systems for near-earth applications," *Proc. IEEE Int. Conf. on Communications*, pp. 22-27 to 22-37, San Francisco, June 1970.

[3] B. J. Peyton, A. J. DiNardo, G. K. Kanischak, F. R. Arams, R. A. Lange and E. W. Sard, "High-sensitivity receiver for infrared laser communications," *IEEE J. Quantum Electron.*, vol. QE-8, p. 252, 1972.

Fig. 1. Measured heterodyne receiver sensitivity.

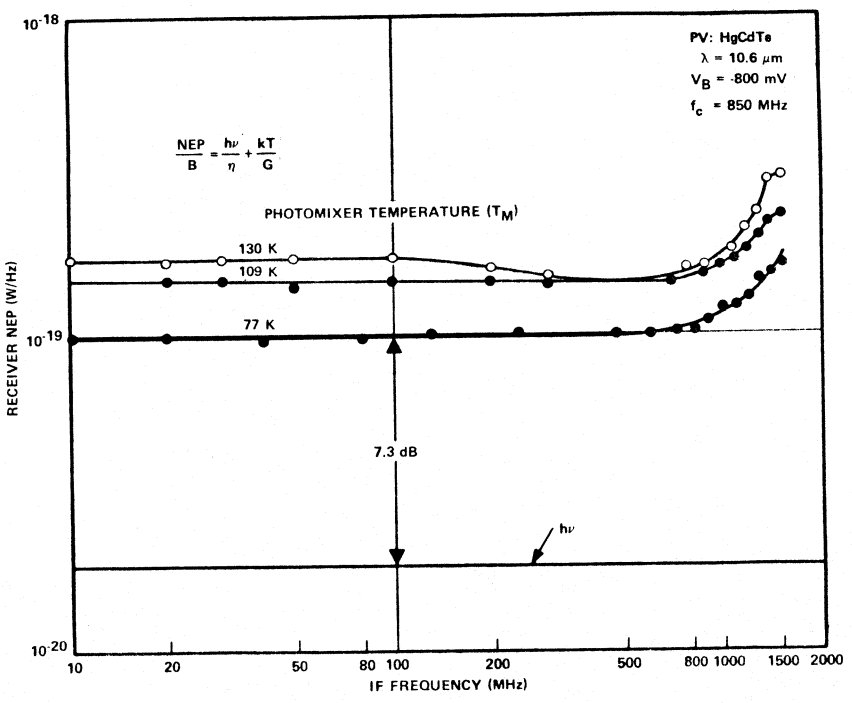

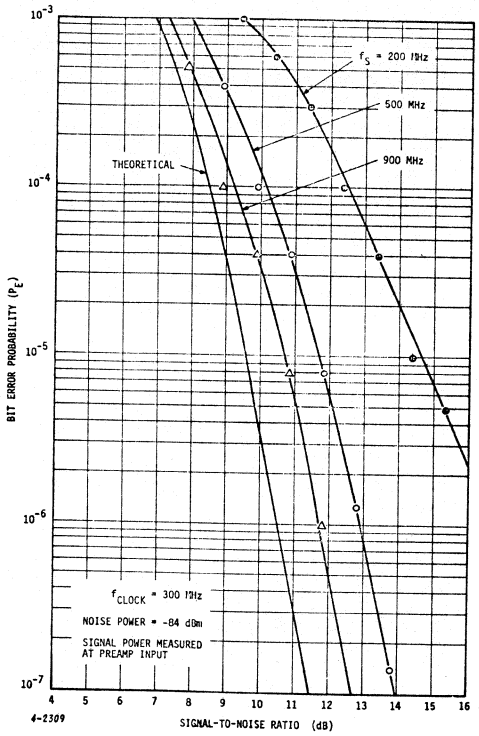

Fig. 2. Measured bit error probabilities of receiver back-end.

operational satellite receiver system. Measurement results indicate that efficient heterodyne operation can be obtained at photomixer temperatures up to 130°K and IF frequencies up to 1500 MHz for selected photo-mixer-IF preamplifier combinations. The heterodyne receiver NEP was measured as a function of IF offset at photomixer temperatures of 77°K, 109°K and 130°K with maximum incident laser LO power. The measured results (Fig. 1) indicate that the NEP near 20 MHz for an applied bias voltage of $V_B = -800$ mV is 1.0×10^{-19} W/Hz at $T_M =$ 77 K, 1.5×10^{-19} W/Hz at 109°K and increases to 1.75×10^{-19} W/Hz at 130°K. The receiver NEP improves slightly near IF = 700 MHz due to optimum impedance matching between the photomixer and the IF preamplifier, and then degrades slightly with increasing IF due to a decrease in the photomixer gain and an increase in the IF preamplifier noise. For an IF of 1500 MHz the receiver NEP is 1.65×10^{-19} W/Hz at 77 K, 2.35×10^{-19} W/Hz at 109°K and increases to 3×10^{-19} W/Hz at 130°K.

The signal entering the receiver back-end from the PV HgCdTe photomixer has a carrier frequency which can range between 250 and 1000 MHz (a greater than 20 MHz/sec rate of change can be tracked) depending upon the Doppler frequency shift encountered. It is binary double-sideband amplitude modulated with the carrier being suppressed on the order of 20 dB below the total signal power (which is nearly equivalent to binary phase shift keying). The receiver configuration employs a signal squaring tracking loop to provide the coherent reference required for optimum signal demodulation.

The bit error probabilities measured at a data rate of 300 megabits/second are given in Fig. 2 for carrier frequencies (off-set plus Doppler shift frequencies) of 200 MHz, 500 MHz, and 900 MHz. The increasing error probabilities at the lower carrier frequencies are attributable to the higher levels of signal image and VCO leakage powers appearing at the output of the second IF filter.

TABLE I

Run	Diversity Array σ_T^2	Diversity Array σ_χ^2	Diversity Array P_E	Photon Bucket σ_χ^2	Photon Bucket P_E
Low turbulence	0.696	0.087	1.97×10^{-3}	0.027	1.06×10^{-3}
High turbulence	6.32	0.044	9.19×10^{-5}	0.053	1.00×10^{-4}

σ_T^2 = theoretical point detector variance; σ_χ^2 = measured variance; P_E = bit error probability.

19.10 Direct-Detection Diversity Receiver for Optical Communication through the Atmosphere, C. M. McIntyre, J. R. Dunphy, and J. R. Kerr, *Oregon Graduate Center, Beaverton, Oreg. 97005*

(15 min)

Optical communications systems operating in the atmosphere are subject to the degrading effects of, among other things, clear air turbulence.[1] This phenomenon causes fading due to beam wander and scintillation.[2] In the case of a large beam diameter at the receiver (or when a tracking transmitter[3] is used to cancel wander) scintillation constitutes the dominant fading mechanism with a dynamic range that can approach 80 dB (defined on the photo current signal) in a small receiver. Recent experimental[4] and theoretical[5] results have revealed that under conditions of high turbulence, a transverse spatial correlation exists in the received field such that the aperture averaging expected in a large aperture receiver[6] is not completely effective. Under these conditions, an array of small aperture receivers, separated to ensure independent sampling of the received field, is expected to outperform a large aperture receiver of equivalent area.

In order to demonstrate the capability of this diversity array for overcoming the deleterious effects of atmospheric turbulence, a receiver designed to operate with a binary on-off transmitter (operating at 4880 Å) has been installed on our 1.6 kilometer field test facility. The receiver consists of: i) a four-element horizontal array, with each element composed of a 4 cm diameter lens, semiconductor detector, and preamplifier, and ii) a 25 cm diameter "photon bucket" with its associated detector and preamplifier for direct comparison. The array receiver contains electronics for processing and adding the elemental signals. Both the diversity array and the photon bucket feed common decision making electronics and then logic circuits that compare the receiver decision with a reference that is hard wired from the transmitter. The receiver decision is made by comparing the received signal (integrated over the duration of a bit interval) with an adaptive threshold that is derived by averaging the received signal over a time that is long compared to a bit interval, but short compared to the atmospheric fluctuations. The site is instrumented to record meteorological conditions; C_N^2 (a point measurement of the strength of turbulence); σ_l^2 (log amplitude variance of the received field) for i) a point detector ii) a single element of the diversity array iii) the sum of the four array elements and iv) the photon bucket; the correlation between adjacent elements of the array; and the system error probability.

Typical results are indicated in the table. During periods of low turbulence, when the transverse spatial correlation described above is not evidenced, the photon bucket outperforms the diversity array as expected due to the larger area. Note the lower variance and error probability for the photon bucket. However, under conditions of high turbulence, the diversity array constitutes a more efficient system. Note that with only one tenth of the area, the array receiver has a comparable variance and error probability. In low turbulence, the diversity array performs as well as a photon bucket with the same area, while in high turbulence the diversity array performs as well as a photon bucket with 10 times the area.

19.11 Application of Lasers with Folded Optical Delay Line in Optical Communication Systems, L. S. Kornienko, N. V. Krovtsov, E. G. Lariontsev, N. I. Naumkin, and V. N. Serkin, *USSR*

(15 min)

No summary.

[1] D. L. Fried and R. A. Schmeltzer, *Appl. Opt.*, vol. 6, p. 1729, 1967.

[2] V. I. Tatarskii, *Wave Propagation in a Turbulent Medium.* New York: McGraw-Hill, 1961.

[3] J. R. Dunphy and J. R. Kerr, *J. Opt. Soc. Am.*, vol. 64, p. 1015, 1974.

[4] J. R. Dunphy and J. R. Kerr, *J. Opt. Soc. Am.*, vol. 63, p. 981, 1973.

[5] H. T. Yura, *J. Opt. Soc. Am.*, vol. 64, p. 59, 1974.

[6] D. L. Fried, *J. Opt. Soc. Am.*, vol. 57, p. 169, 1967.

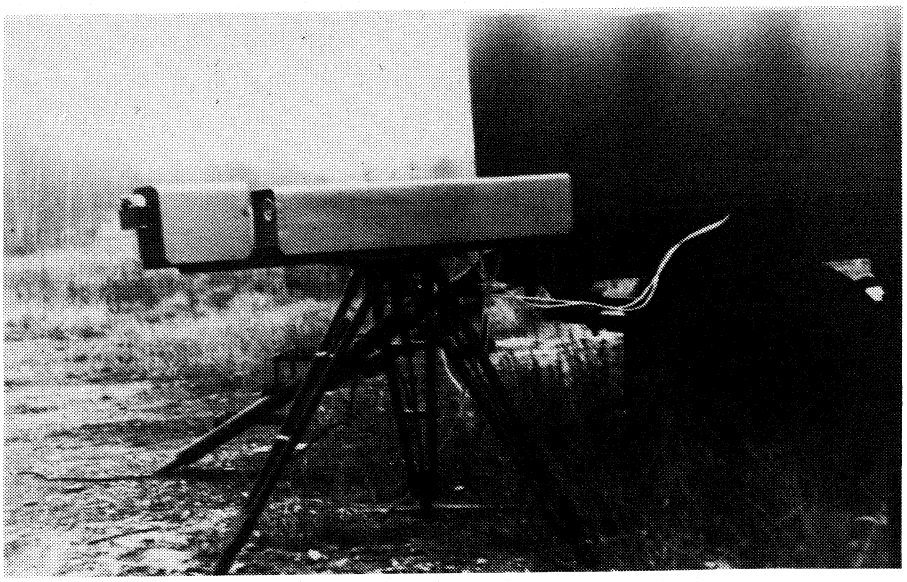

Fig. 1. Field unit in a working position.

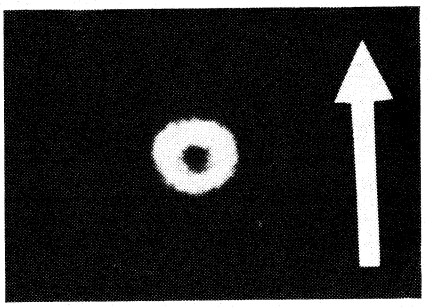

(a)

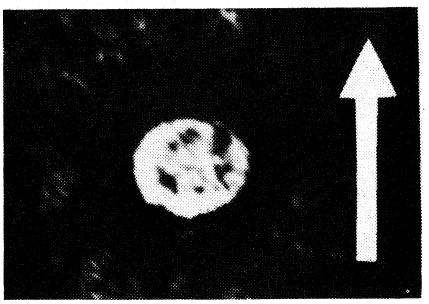

(b)

Fig. 2. Real image with mean diameters. a) 225 μ; b) 345 μ; picture magnification of 42×.

2.7 Rain Drop Measurements by Holography, V. M. Zakharov, L. N. Rasoumov, E. M. Birger, and S. P. Karlov, *Department of Hydrometeorology, Moscow, USSR*

(15 min)

At present rain drops are studied by a number of methods. Among the most frequently used methods are: filter paper; intercepting rain drops with cells filled with vaseline or castor oil; photographic recording; and a photoelectrical method, which is the most effective one at present.

In this work a method of pulsed holography which has been applied successfully to aerosol observations by a number of authors[1,2] was utilized for rain drop studies. These measurements were made with a holographical unit, laboratory operation of which has already been reported.[3] To test a working capacity of the unit in field measurements, atmospheric precipitation studies were begun in October, 1974. When processing the results of preliminary field experiments we did not undertake the task of determining integral characteristics of precipitation, but studied the form of rain drops and determined their typical size in rain of various intensities.

Fig. 1 shows a field unit in a working position. Its lens variant was capable of sounding in a 20-200 cm^3 volume while a lenseless one was within 1 litre. The time of exposure was determined by a ruby oscillator pulse length which could operate in a free generation mode ($\tau = 10^{-4}$ sec) as well as with Q-switching ($\tau = 2.0.10^{-8}$ sec). Holographical recording was made on holographical films with a resolution of not less than 1200 lines/mm and high contrast phototechnical films with a 270-450 lines/mm resolution.

When a droplet passed close enough to a photographic plate we managed to reconstruct both holographical images, bright and contrasting. When it appeared far from a plate (> 15 cm), it was impossible to observe a virtual image. The image reconstructed by the usual scheme was photographed through a microscope with variable magnification. Fig. 2 shows real images of rain drops with mean diameters of 225 and 345 μ. The total magnification is 42×. An observed eccentricity (meaning a vertical to horizontal drop size ratio) showed significant differences. In Fig. 2(a) and (b), its values are 0.95 and 0.87, respectively. From the known mean diameters stabilized fall velocities were calculated. The empirical relations from papers[4] were applied.

The most typical sizes and velocities of droplets for low intensity rain are shown in Table I. Fig. 2(a) and (b) corresponds to cases 3 and 4.

Small exposure values limit essentially the number of droplets which can be detected simultaneously. Indeed, at droplet concentration of an order of 10^3 m^{-3} which is the case in mean intensity rains, only one droplet is detected in the volume of interest simultaneously.

This causes the necessity of increasing the volume several times at such concentrations or lower concentrations. The technical difficulties of realizing such systems grow significantly and from our point of view can hardly be justified. Evidently, a sampling method is more effective in this case. However, at concentration exceeding 10^3 m^{-3} a method of pulsed holography is rather useful for obtaining information about size and form of rain drops. It should be noted that no other method except photography can provide data on droplet form.

The unit with which the results presented here were obtained detects particles with 10 μ diameters with certainty. This is by an order of magnitude lower than is provided by a photographic recording, not to mention the fact that pulsed holography in addition to sounding large volumes fits high aerosol velocities much better.

TABLE I

	Cases				
	1	2	3	4	5
Eccentricity	1.00	1.00	0.95	0.87	0.83
Mean droplet diameter μ	45	98	225	345	638
Stabilized fall velocity M/sec	–	0.25	0.9	1.4	2.6

[1] B. A. Silverman, B. J. Thompson, and J. H. Ward, "A laser fog disarometer," *J. Appl. Meteor.*, vol. 3, no. 6, 1964.

[2] A. K. Brice, "Fog drop-size distribution measured with a hologram camera," *J. Appl. Meteir.*, vol. 10, no. 3, 1971.

[3] E. M. Birger and L. N. Razoumov, "Holographical Recording of Moving Water Aerosol," *Sixth Conf. on Laser Atmospheric Studies*, September 1974, p. 193.

[4] H. B. Wobus, F. W. Murray, and L. R. Koenig, "Calculation of the terminal velocity of water drops," *J. Appl. Meteor.*, vol. 10, no. 4, 1971.

4.12 Measurement of the Cross Section for Stimulated Emission in Neodymium-Doped Glasses, E. M. Dianov, A. Ya. Karasik, L. S. Kornienko, A. M. Prokhorov, and I. A. Shcherbakov, *P. N. Lebedev Physical Institute, Academy of Sciences, Moscow, USSR.*

A knowledge of the cross section for stimulated emission (σp) of an active medium is needed in designing laser systems. But this value is difficult to measure, to within a sufficient accuracy, in the case of a four-level system and great nonuniform broadening of spectral lines, which is the case nonuniform broadening of spectral lines, which is the case with neodymium-doped glasses, so that measurement results strongly differ with authors. In the present paper a method for measuring the cross section for stimulated emission of neodymium in the glass, based on spectral absorbance and fluorescence measurements at helium temperature, is suggested. An absorption associated with a transition between the lowest components of the ground and excited states, which are the Kramers doublets, is measured and the Einstein coefficient for spontaneous transition is determined. The same transition is taken in the resonance fluorescence spectrum and it is used to normalize the whole fluorescence spectrum. This procedure requires a precision measurement of spectral distribution of the fluorescence energy over a wide wavelength range (0.85–1.8 μm), a technique which has been also developed by the authors. The values of σp have been determined for a number of silicate- and phosphate-based glasses. In the latter σp is much higher (maximum $4.6.10^{-20}$ cm^2) than in the former (maximum $2.4.10^{-20}$ cm^2). Most of the glasses studied exhibit a low thermooptic constant, thereby providing a highly directional laser beam. It follows from the above considerations that a measurement of σp by the method suggested will necessarily require the Einstein coefficient for radiative transitions. This makes it possible to determine the radiative lifetime of the metastable state. On the other hand, knowing σp, the effective fluorescence linewidth of laser transition and the ratio of fluorescence energies of all radiative transitions, one can calculate the radiative lifetime of the excited state. We have performed such calculations for the glasses for which all these data are available in the literature. All the values of σp practically proved to yield a radiative quantum efficiency from the metastable state of neodymium of over unity. Sometimes it is far more than unity. In other words, the radiative lifetime determined in the above way turns out to be shorter than the directly measured values. This circumstance uniquely suggests that the values of σp presented elsewhere are overrated. So, we have analyzed the spectroscopic methods available for determining σp. The analysis has revealed that in all the cases calculations of σp based on the experimental spectroscopic data inexplicitly assume equal probabilities of transitions connecting the Stark components of the ground and excited states. We have shown that under this assumption, the total probability of transition, and hence its cross section, can be either overrated or underrated. The experimental investigation of the ground state structure of neodymium in the glass has shown that the spectroscopic methods available tend, as a rule, to provide too high values of σp, which is the case.

5.10 The Relevance of Lasers in the Energy Shortage, E. Teller, *Lawrence Livermore Laboratory, Livermore, Calif. 94550.*

Laser fusion has captured the popular imagination as an energy source of the future. The idea is simple, but the difficulties are enormous. A thousandfold compression of the thermonuclear fuel permits an explosion approximately one millionth the size that is predicted by theory in the uncompressed liquid fuel. But appropriate lasers will be hard to develop. The symmetry needed to establish the high compression is a great challenge and even after feasibility is established, an engineering development of exceptional difficulty will have to follow.

It is more probable that lasers will make a contribution in the energy crisis by means of separating isotopes. Remarkable progress has been made on the separation of uranium isotopes, but it must be remembered that today the cost of separating uranium isotopes accounts for only 5% of the cost of generating electricity by a nuclear reactor.

The really great influence of lasers may be due to the separation of the hydrogen isotope. Today the heavy water reactor appears to be an interesting alternative, but it is handicapped by the high cost and scarcity of heavy water. Laser separation of hydrogen isotopes could decrease this cost to a fraction of its present value and could therefore revolutionize the deployment of reactors.

Laser fusion will come too late. Uranium separation will make a marginal contribution. Heavy water production may however have a thorough influence on the energy economy.

8.8 Production of Specially Tailored Laser Pulse, S. K. Vartapetov, V. I. Vovchenko, I. K. Krasjuk, S. G. Lukishova, P. P. Pashinin, and A. M. Prokhorov, *P. N. Lebedev Physical Institute of the Academy of Sciences of the USSR, Moscow, USSR.*

The production of laser light with the intensity grown according a specified law by a regenerative amplifier is considered. Formulas estimating the required amplifier characteristics due to desired light pulse parameters are presented. The combined method of control of the amplification coefficient by means of electrooptical cell and saturated filter is analysed.

The preliminary experimental results for the case of generation of a number of light pulses with growing amplitudes are represented.

12.6 Use of Pulsed Laser Treatment to Change Physical Properties of Metals and Semiconductors, I. Ya. Dekhtar, L. I. Ivanov, N. V. Karlov, A. M. Prokhorov, and N. N. Rykalin, *P. N. Lebedev Physical Institute, Academy of Sciences of the USSR, Moscow, USSR.*

The possibility of using the shock waves generated by absopriton of laser pulse irradiation in the surface layers of metals, semiconductor and skin layers which form under laser influence to change physical properties of the substances is considered.

The data are listed on the nature of radiative defects appearing in metals and semiconductors generated by the travelling shock waves caused by laser irradiation. Use of laser pulse irradiation to strength metals and alloys is shown to be promising.

The effect of laser pulse irradiation on electrical properties of semiconductor silicium and germanium single crystal whiskers is considered. An anomalous drop of electroresistence in such crystals is found when treated with shock waves.

The data are listed on the influence of laser pulse irradiation upon superconductivity. The effect of considerable change of transition temperature was found. It is discussed due to crystallo-chemical reactions stimulated by point defects caused by laser irradiation or (and) by methastable phase formation caused by fast laser heating and subsequent fast cooling.

Post-Deadline Sessions

Papers Included in Regular Daytime Sessions

4.10 CW and Self-Q-Switched Laser Operation of Nd:YVO_4, L. G. DeShazer, *University of Southern California, Los Angeles, Calif. 90007,* and A. W. Tucker, M. Birnbaum, and C. L. Fincher, *Aerospace Corp., El Segundo, Calif. 90245.*

High-efficiency low-threshold solid-state laser oscillators are needed for many communication and ranging applications. Until recently, Nd:YAG material has been the only choice for such oscillators, even though Nd:YAG lasers did not meet many system requirements. Last year, an experimental material, Nd:YVO_4 (yttrium orthovanadate), was shown to outperform Nd:YAG in a pulsed-lamp pumping configuration.[1] However, advances in Nd:YVO_4 laser development have been hindered by the lack of large-sized (3 × 30 mm) laser-grade crystals. This current scarcity resulted from control difficulties in the vanadate crystal growth; these difficulties have been identified and procedures are now being taken to grow large crystals.[2]

Meanwhile, we initiated a laser testing program to carefully evaluate the performance of Nd:YVO_4 lasers relative to Nd:YAG. Since only relatively small crystals (5 × 5 mm) of Nd:YVO_4 were available (in fact, we used only spectroscopic samples), we based our test program on solid-state lasers pumped by a CW argon-ion laser. All results were obtained with the pump at 5145 Å only, and soft-focused (25 cm fL) into the crystal through the back mirror. The pump beam waist was 180 μm, increasing only slightly over distances of 1 cm on either side of the focus. Incident pump powers up to 10 W were available.

Many advantages, both experimental and theoretical and sometimes surprising, were realized by this laser pumping procedure. The experimental advantages are centered on the longitudinal excitation ("end pumping") of the crystals which confined the laser-active region to a well-defined volume. Thus the best optical quality crystalline region could be chosen for the laser experiments, escaping obstruction by large inclusions and cracks. Further, this restricted active region leads to an effective resonator aperture producing single transverse mode (TEM_{00}) performance of the crystal laser. The effective aperture is, in fact, *tapered* ("soft aperture") due to the smooth intensity profile of the pump beam. In addition, confinement of the gain to a small volume avoids the parasitic laser oscillations which usually depump solid-state lasers in the high pumping regime. It was noted that dye lasers do not have all of these advantages.

Many advantages in the theoretical analysis of the input–output power curves are accrued by this well-controlled performance. Since the mode volume is fixed and the pump power absorbed is simply measured, the input–output (P versus W) followed the theoretical linear plot $P = P_s\,[(W/W_{th}) - 1]$, instead of the S-shaped curve common for flash-lamp pumping. The dependence of threshold power (W_{th}) upon mirror reflectivity was accurately determined to be $KW_{th} = -\ln(R_1R_2) + 2L\alpha$. Thus the loss coefficient α was determined from the intercept at $W_{th} = 0$. Only two difficulties occurred: a slight variation in the data was produced by optical feedback into the gas laser (a Faraday isolator is currently being constructed), and the back mirror can be damaged by the pump beam if its transmission is below 80 percent at 5145 A.

Therefore, in this manner, the input–output power characteristics were measured for pulsed quasi-CW (1 pulse per second), N and CW lasers of Nd:YVO_4 and YAG at both 1.0640 and 1.3395 μm. The threshold, slope efficiency (versus output reflectivity), gain, and loss were determined for both crystals. A comparison of the laser performance of a spectroscopic sample of Nd:YVO_4 (4.8 mm, 1 percent Nd) and a laser rod of Nd:YAG (13 mm, 1 percent Nd) will be presented. Resonator length was 1–2 cm and plane mirrors were used with reflectivities from 65 to 99 percent 1 W of Nd:YVO_4 laser output was obtained in CW operation at 1.0640 μm, 100 percent plane polarized (parallel to the optic axis) with 4.5 W absorbed at 5145 A. The 1.06-μm laser cross section of Nd:YVO_4 is 30×10^{-19} cm^2, which is 4.6 times greater than that of Nd:YAG. The intrinsic loss coefficient at 1.06 μm was measured to be 0.16 cm^{-1} for YVO_4 and 0.012 cm^{-1} for YAG. This high loss for YVO_4 is mainly due to the scattering from small inclusions of iridium metal and gaseous voids; the theoretical loss limit was calculated from spectroscopy to be 0.009 cm^{-1}. Undoubtedly, this loss will not be present in future YVO_4 material. Calculations based upon measured values showed that if the Nd:YVO_4 loss coefficient at 1.06 μm were equal to that measured in the Nd:YAG rod, the CW laser threshold of the vanadate would be less than half that observed for the garnet. Maximum slope efficiency was measured to be 25 percent at 20 percent output coupling.

1.34-μm CW operation of Nd:YVO_4 and YAG lasers was obtained where the laser emission was plane polarized for vanadate and unpolarized for YAG. Nd:YVO_4 clearly outperformed YAG at this wavelength and had an output of 0.35 W for 4.8 W of 5145-A pump power absorbed. The 1.34-μm laser cross section of Nd:YVO_4 was 3.6×10^{-19} cm^2, which is *18 times* greater than that of Nd:YAG at 1.32 μm. The 1.06 μm oscillation was suppressed by having mirror reflectivities below 10 percent for that wavelength.

Self-Q-switched operation of Nd:YVO_4 was observed at 1.06 and 1.34 μm, but not for Nd:YAG. These are the *first* observations of self-Q-switched operation of a Nd laser at room temperature.[3] Most of the data were obtained with the Nd:YVO_4 sample misaligned by 25 arcmin from the resonator axis. Pulsewidths of 40 ns were observed, with peak powers over 1000 times greater than the CW output of the laser. Our observations imply that the vanadate laser could operate in a repetitively Q-switched mode simply by misalignment of the resonator mirrors or rod.

[1] L. G. DeShazer *et al.*, *IEEE J. Quantum Electron.* vol. QE-10, p. 683, 1974.

[2] L. R. Rothrock, Union Carbide Corp., private communication.

[3] M. Birnbaum and C. L. Fincher, *Proc. IEEE*, vol. 57, p. 804, 1969.

6.6 Soil Compaction Checks by Means of a Laser Device, Panagiotis A. Drakatos, *Polytechnic Institute, University of Patras, Patras, Greece.**

The absorption of longitudinal sound waves by the soil surface is a function of soil compaction and depends on its elastic and plastic properties. The longitudinal waves are created by a vibrating machine during soil compaction.

The present method uses a vibrating compactor (see 4 of Fig. 1) which operates at various frequencies f from a fixed

*Present address: 1807 Ford Parkway, St. Paul, Minn. 55116.

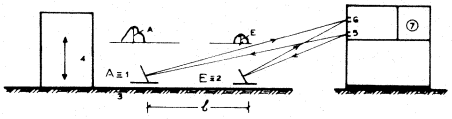

Fig. 1. A view of experimental arrangement for measuring the amplitude ($A \equiv 1$), ($E \equiv 2$), and the frequency (f) of the longitudinal waves during soil compaction. Mirrors: 1, 2. Soil for compaction: 3. Vibrating machine: 4. Laser device: 5. Detectors 6. Oscilloscope: 7.

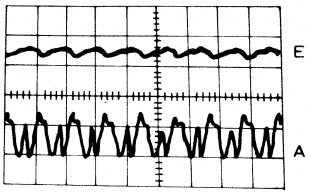

Fig. 2. Soil vibrations measured by means of laser device. A: Mirror nearest to the vibrating machine. E: Mirror farthest from the vibrating machine.

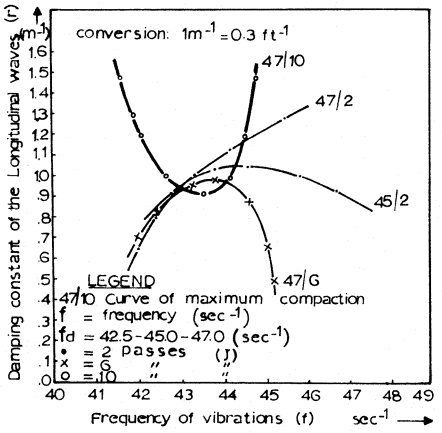

(a)

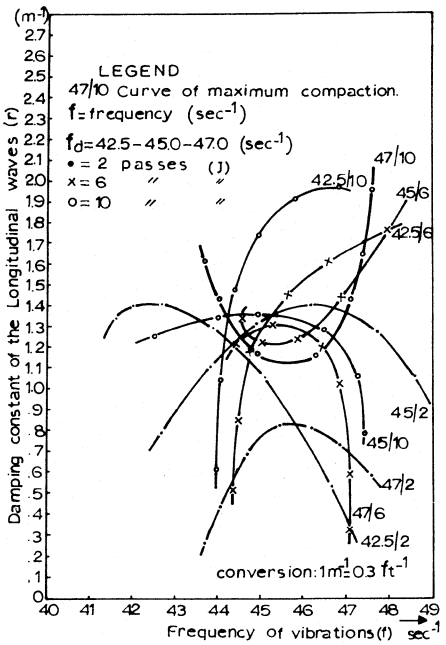

(b)

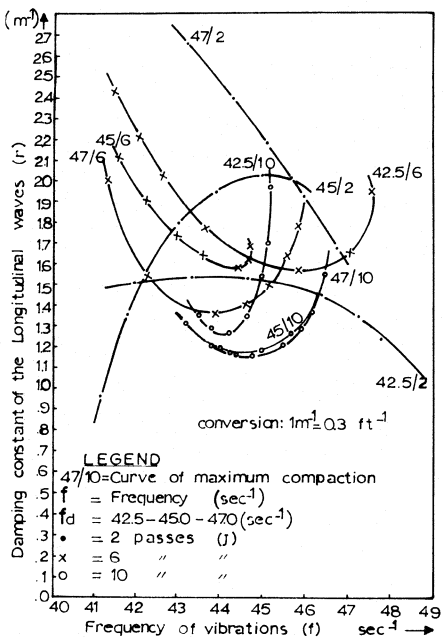

(c)

Fig. 3. Changes in the damping constant r of the longitudinal wave on the surface of compacted soil as a function of the vibrating machine's frequency of vibration f. (a) Sand. (b) Clay. (c) Clay and sand.

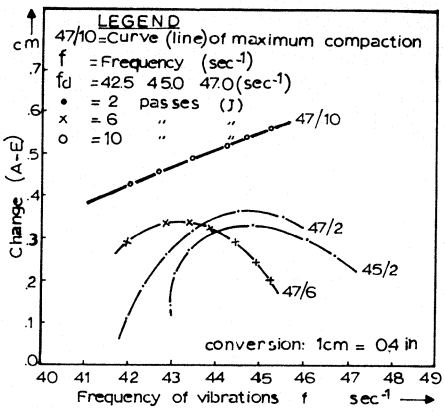

(a)

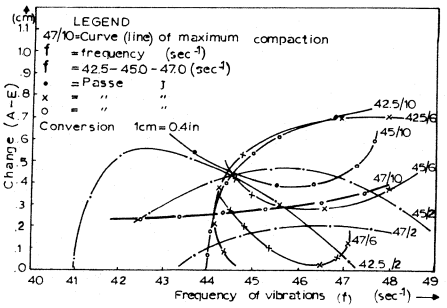

(b)

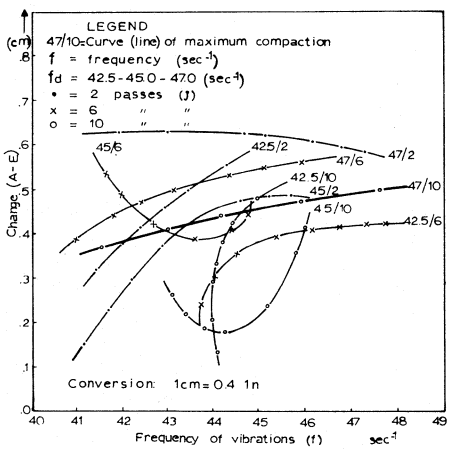

(c)

Fig. 4. The change (A-E) of the longitudinal wave on the surface of compacted soil as a function of the vibrating machine's frequency of vibration f. (a) Sand. (b) Clay. (c) Clay and sand.

position on compacted soil and a specially operated laser device (5 of Fig. 1) to measure the amplitudes of the sound wave, A and E, (Fig. 5. 1 and 2), and the frequency of vibration f as well as the vibration frequency f_d of the vibrating machine during soil (3 of Fig. 1) compaction (frequency of compaction).

It is achieved by directing the laser beam on the mirrors (1 and 2 of Fig. 1). The beam is reflected and enters the detectors (6 of Fig. 1) as measured by the oscilloscope (7 of Fig. 1). Forms of these signals are shown on Fig. 2. If the distance between the mirrors ($A \equiv 1$), ($E \equiv 2$) is l, then the damping constant of these waves is $r = (1/l) \ln (A/E)$.

In Fig. 3(a)-(c), is shown the change r as a function of frequency f as well as in Fig. 4(a)-(c), the change (A-E) as a function of f, after each pass J of the vibrating machine. Thus, for a given compactor, the following question arises: What should constitute the basis for predetermining the number of passes J of the

TABLE I
SOIL COMPACTION PARAMETERS

Soil	$r_{min}(m^{-1})$	J	$f(sec^{-1})$	$f_d(sec^{-1})$
Sand	0.9	10	43.5	47.0
Clay	1.105	10	45.7	47.0
Clay and Sand	1.15	10	44.75	47.0

machine in order to achieve the desired soil density at a given depth?

The minimum values obtained [Fig. 3 (a)-(c)] for the damping constant r on three kinds of soil was found as listed in Table I. The values r_{min}, J, f, and f_d in Table I correspond to the maximum desired density values.

Referring to the graphs [Fig. 4(a)-(c)] of (*A-E*), it is noticed that the curve $f_d = 47\ s^{-1}$, $J = 10(47/10)$ has a linear change in the frequencies and passes of the compactor, with which the maximum compaction is achieved. However, in the other frequencies and passes the change is not linear and a high instability of these changes is noticed due to the nonuniformity of the soil.

The preceding method for checking the quality of compaction can be applied in the study of construction of roads, electrical cable-carrying ditches, or water pipes, and numerous other projects. It constitutes an original and precise method and its implementation is simple and inexpensive.

10.10 Convolution Using Guided Acoustooptical Interaction in As_2S_3 Waveguides, K. W. Loh, W. S. C. Chang, and R. A. Becker, *Washington University, St. Louis, Mo. 63130.*

Acoustic surface waves (ASW's) have been used to achieve convolution by a number of researchers.[1-10] Use of acoustooptical (AO) interaction for convolution in the bulk medium was reported by Squire *et al.*[11] and Damon *et al.*[12] The signal-to-noise ratio and the dynamic range of the bulk convolver are low because the AO diffraction is not very efficient. Bragg diffraction of optical guided waves (OGW's) by ASW's can be very efficient in thin-film waveguides, e.g., As_2S_3 film deposited on top of a $LiNbO_3$ substrate.[13-14] Convolution by guided AO interaction may yield large dynamic range or time bandwidth product. More importantly, it will allow us to carry out signal processing in thin-film waveguides which may have many applications in single-mode optical-fiber communication systems in the future. We report here the first experimental observation of the convolution by the OGW-ASW interactions in the As_2S_3-$LiNbO_3$ waveguide.

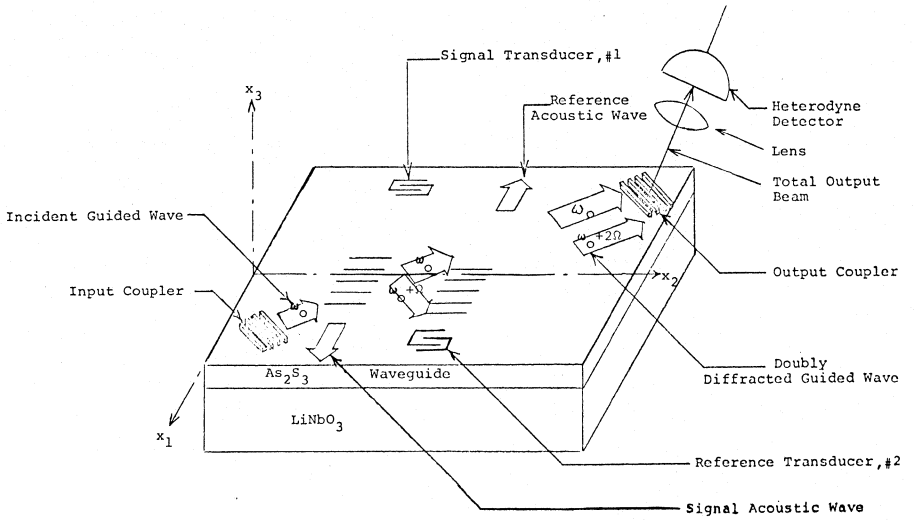

Fig. 1. Illustration of OGW-ASW convolver.

Fig. 1 illustrates the OGW-ASW convolver. For Bragg diffraction with less than 10-percent efficiency, the spatial amplitude distribution (i.e., the x_2 variation) of the OGW diffracted by the ASW of the first transducer will be proportional to the power distribution of the acoustic surface wave in the x_2 direction, i.e., $P_1(x_2)$. The ASW from the second transducer is again phase matched to the diffracted beam. Thus the spatial amplitude distribution of the twice-diffracted beam will be proportional to the product of the power distribution of the two acoustic surface waves in the x_2 direction [i.e., $P_1(x_2) \cdot P_2(\tau - x_2)$]. The twice-diffracted beam is parallel to the incident beam. It is also shifted in angular frequency by 2 ($\Omega_0 \pm \Delta\Omega$) where Ω_0 is the center frequency of the ASW and $\Delta\Omega$ is the frequency bandwidth of the ASW signal. Therefore the electrical output signal in the frequency range $2(\Omega_0 \pm \Delta\Omega)$ from an optical heterodyne receiver will be proportional to the integrated product of $P_1(x_2)P_2(\tau - x_2)$, i.e., it is proportional to the convolution of P_1 and P_2.

Experimentally, a set of ASW transducers is fabricated first on the $LiNbO_3$ substrate. A layer of As_2S_3 film is then sputter deposited on top of the entire structure. OGW at the 1.06-μm wavelength is coupled in and out by means of a pair of GaP prisms. When CW RF power is applied to one pair of the transducers, we obtain a maximum Bragg diffraction efficiency of 93 percent at 3 mW of ASW power (30 mW of electric power). When a 200-ns rectangular pulse is applied to both sets of transducers, a convolved triangular pulse is detected by the oscilloscope through the heterodyne detector. The theoretically predicted dynamic range and time bandwidth of such a convolver are quite high. However, OGW wavefront distortion observed by us in the As_2S_3 waveguide is very bad; this has prevented us from realizing the theoretical predicted performances. Theoretical and preliminary experimental data will be presented in this paper.

[1] L. O. Svaasand, *Appl. Phys. Lett.*, vol. 15, p. 300, 1969.
[2] C. F. Quate and R. B. Thompson, *Appl. Phys. Lett.*, vol. 16, p. 494, 1970.
[3] M. Luukkala and G. S. Kino, *Appl. Phys. Lett.*, vol. 18, p. 393, 1971.
[4] P. Pas, M. N. Araghi, and W. C. Wang, *Appl. Phys. Lett.*, vol. 21, p. 152, 1972.
[5] C. W. Lee and R. L. Gunshor, *Appl. Phys. Lett.*, vol. 20, p. 288, 1972.
[6] G. Sagnes, C. Roustand, and M. Rouzeyre, *Appl. Phys. Lett.*, vol. 21, p. 527, 1972.
[7] J. Smith, E. Stern, A. Bers, and J. Cafarella, *Proc. IEEE Ultrasonics Symp.*, p. 142, 1973.
[8] M. Yamanishi and T. Kawamura, *Proc. IEEE Ultrasonics Symp.*, p. 228, 1972.
[9] L. P. Solie, *Proc. IEEE Ultrasonics Symp.*, p. 175, 1973.
[10] G. S. Kino *et al., IEEE Trans. Microwave Theory Tech.*, vol. MTT-21, p. 244; 1973.
[11] W. D. Squire, H. J. Whitehouse, and J. M. Alsup, *Proc. Electro-Optics Int. Conf.*, England, p. 153, 1971.
[12] R. W. Damon, W. T. Maloney, and D. H. McMahon, "Interaction of light with ultra sound," in *Physical Acoustics*, W. P. Mason and R. N. Thurston, Ed. New York: Academic, p. 273 (170).
[13] Y. Ohmachi, *J. Appl. Phys.*, vol. 44, p. 3928, 1973.
[14] E. G. H. Lean, Acoustooptical interactions in guided wave structures," in *Introduction to Integrated Optics*, M. K. Burnoski, Ed. New York: Plenum, 1973, ch. 14.

14.10 Atmospheric Transmission Measurements at HF/DF Laser Wavelengths,* S. R. King, F. I. Shimabukuro, E. E. Reber, and D. J. Spencer, *Electronics Research Laboratory, The Aerospace Corporation, Los Angeles, Calif. 90009.*

The measurement of atmospheric attenuation of laser radiation for an earth-to-space path presents difficult experimental problems. We have developed an earth-based system capable of making these measurements at HF and DF laser wavelengths. Experimental results for several laser lines will be presented. The heart of the absorption measurement system is a near quantum noise limited (QNL) optical heterodyne radiometer. This radiometer is similar to one previously used to make atmospheric transmission measurements at CO_2 laser frequencies.[1] The present radiometer utilizes a photovoltaic HgCdTe infrared detector as the optical mixer and a stable CW HF/DF laser as the local oscillator. The construction of this type of laser has been described elsewhere[2] with the exception that mode control apertures are permanently positioned within the optical cavity to ensure TEM_{00q} mode operation. Single-line output power is typically 100 mW.

The use of an optical heterodyne radiometer to measure atmospheric transmission has been discussed by McElroy.[3] Briefly, the sun is used as a source and the variation in received solar power with zenith angle yields the attenuation coefficient for a vertical transmission path through the entire atmosphere. The advantages of an optical heterodyne radiometer over a conventional spectrometer for this measurement are extremely high spectral resolution ($\lambda/\Delta\lambda > 10^6$) and precise knowledge of measurement wavelength relative to laser wavelength. The importance of these two properties is evident when the rapid variation of atmospheric transmission with wavelength is examined.[4]

One of the inherent difficulties in achieving QNL optical heterodyne detection is the requirement for a stable local oscillator. At CO_2 laser frequencies this problem has been solved by a number of workers. However, to our knowledge, this is the first reported work showing near QNL performance at HF laser frequencies. Fig. 1 shows predicted and measured radiometer performance as a function of laser local-oscillator induced current in the HgCdTe mixer. Much of the discrepancy between experiment and theory is caused by electromagnetic interference from the laser discharge. Although this source of noise has been reduced by over three orders of magnitude, it is still a problem because of the proximity of the laser and detector electronics in our laboratory setup. Increasing the local oscillator power would appear to be the solution to improving radiometer performance. Unfortunately, the mixer current responsivity decreases for currents above ~0.5 mA, destroying the linear relationship between radiometer output voltage and local oscillator power. Using 0.5 mA as the optimum local oscillator current, the radiometer performance (therefore the mixer performance) is seen to be within a factor of ~9 of predicted performance.

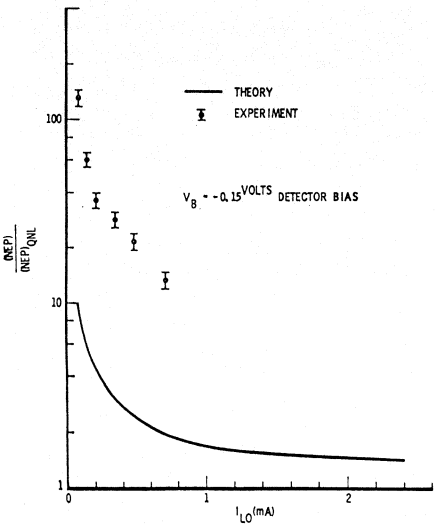

Fig. 1. Radiometer performance at HF P_2 (8).

Atmospheric transmission measurements using the previously described radiometer are presently being conducted at El Segundo, Calif. Fig. 2 shows the results of two typical radiometer measurements performed at HF laser wavelengths. High and low transmission lines have been displayed to demonstrate both the wide dynamic range and high sensitivity of this system. Theory predicts a straight line on this plot; the attenuation coefficient for zenith transmission through the entire atmosphere is given by the slope. Scatter in the data is seen to be small. A statistical analysis shows the standard error for these measurements to be ~3 percent of the measured values. A comparison of these measured values will be made with predicted values using the line atlas compiled by McClatchey *et al.*[5] Results of measurements at laser wavelengths where high transmission is found will be presented.

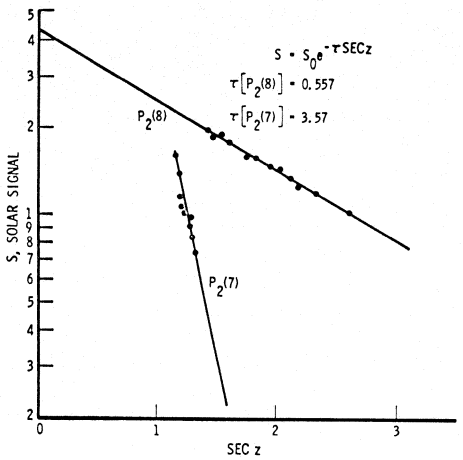

Fig. 2. HF IR transmission. T = 17.6°C, P = 763 torr, RH = 0.42.

*This work was supported by the Defense Advanced Research Projects Agency.

[1] S. R. King, D. T. Hodges, T. S. Hartwick, and D. H. Barker, *Appl. Opt.*, vol. 6, p. 1106, 1973.

[2] J. J. Hinchen, *J. Appl. Phys.*, vol. 45, p. 1818, 1974.

[3] J. H. McElroy, *Appl. Opt.*, vol. 11, p. 1619, 1972.

[4] D. J. Spencer, G. C. Denault, and H. H. Takimoto, *Appl. Opt.*, vol. 13, p. 2855, 1974.

[5] R. A. McClatchey *et al.*, Air Force Cambridge Res. Labs., Mass., Environmental Res. Paper 434, AFCRL-TR-73-0096, 1973.

14.11 Frequency Stabilization and Absolute Frequency Measurements of a CW HF/DF Laser,* R. S. Eng† and D. L. Spears, *Lincoln Laboratory, Massachusetts Institute of Technology, Lexington, Mass. 02173.*

By mixing the CW output of an HF/DF laser and a frequency-doubled CO laser, we have measured the frequency of one HF laser line relative to the second harmonic of a CO laser line with an uncertainty of about ±5 MHz. The absolute frequency of the HF line is then obtained from the absolute frequency of the CO laser line which has recently been measured to about ±2.5 MHz. Extension of this measurement to other HF and DF laser lines can easily be made. The HF and DF lasers are useful high-power lasers important in atmospheric propagation, optical communications, and optical pumping applications. In particular, the heterodyne technique enabled

*This work was sponsored by the Department of the Air Force.

†Present address: Block Engineering, Inc., 19 Blackstone Street, Cambridge, Mass. 02139.

us to successfully stabilize the frequency and to some extent the amplitude of the HF laser to a much higher degree, and at the same time it provided a convenient way to study the effects of electric discharge, kinetic reactions, and gas dynamics on the laser stability.

The experimental setup consisted of CW grating controlled highly stable CO and less stable HF lasers, each operating in a single longitudinal TEM_{00} mode with piezoelectric tuning of the output mirror. The 0.5-W CO laser was focused into a $AgGaSe_2$ nonlinear crystal generating a second harmonic frequency. The second harmonic beam was collimated and then combined with the HF laser beam. The combined beam was focused on a high-speed HgCdTe detector to generate a beat signal. The beat signal was externally mixed with a microwave oscillator and the resulting IF signal was amplified and fed into a spectrum analyzer. The lasers were tuned to line centers by cavity tuning. For the second harmonic of the $P_9(16)$ line of $^{12}C^{16}O$ and the $P_0(6)$ line of HF, a 30-dB signal-to-noise beat signal of 10 783.43 ± 5.1 MHz was obtained from 10 independent measurements. This yields an absolute frequency of 110 725 697.37 ± 7 MHz for the $P(6)$ line of the 1–0 band of HF laser, which is about two orders of magnitude more accurate than the existing grating value.

Since the accuracy of the absolute frequency measurement depended greatly on the success of stabilizing the HF laser frequency, great care was taken to minimize transmission of pump vibration and acoustic noises to the laser cavity. The HF laser was a small electric discharge transverse-flow mixing laser with $H_2:SF_6:O_2:He$ pressures of 2:4:3:1 torr. It was pumped by a 40-ft^3/min mechanical pump. An amplitude fluctuation of about 1 percent was observed for a single-line output power of about 150 mW. With both lasers free running, a short-term jitter of ±5 MHz was observed in the beat signal. The rate of jitter had a strong low-frequency component due to periodic pump-speed variation, and weaker components as high as 2 kHz were present. A feedback loop consisting of a 70-MHz frequency discriminator and an operational amplifier was used to reduce the short-term jitter to about ±500 kHz, as seen in Fig. 1, and greatly increase the long-term stability. The short-term frequency instability is believed due to the nature of the SF_6 discharge, rapid gas mixing, and kinetic reactions, although some acoustic noise and structural resonances cannot be excluded.

The servo loop had a very high dc gain and a bandwidth of about 300 Hz limited by resonances in the piezoelectric element. A higher frequency piezoelectric element and a parallel phase-lock loop could be used to reduce the jitter to below 100 kHz. Since frequency modulation is not used, this technique of stabilization is especially useful in optical communications and radar applications.

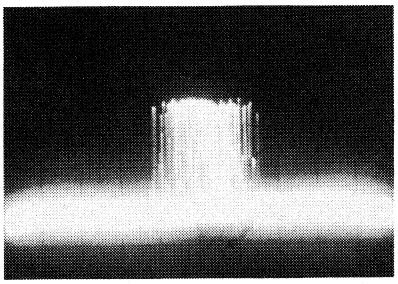

Fig. 1. Beat signal between HF and frequency-doubled CO laser. Horizontal scale: 500 kHz/div. Vertical scale: 10 dB/div. Linewidth is about 1 kHz; 1-s exposure time.

15.10 Determination of Argon Oxide 558-nm Laser Parameters, William M. Hughes, *Los Alamos Scientific Laboratory, Los Alamos, N. Mex. 87544,* T. Olsen and R. Hunter, *Maxwell Laboratories, Incorporated, San Diego, Calif. 92123.*

Experiments have been conducted using high-power vacuum-ultraviolet (VUV) flash photolysis of N_2O to produce $O(^1S_0)$. Measurements of the gain profile and the pressure and time dependence of the gain and excited state lifetime have been made. A two-chamber apparatus was employed where one chamber was used as a flashlamp.

A 50 × 1 cm^2 MgF_2 window array transmitted the VUV into a second independent chamber containing a mixture of N_2O and high-pressure argon. The complication of *in situ* processes such as electron collisions and ion recombination are removed, the volumetric deposition of energy and temperature rise can be readily characterized, the gas pressures and types in the flashlamp and experimental chambers can be independently optimized, and flashlamp background can be minimized by the spatial positioning of detectors.

The flashlamp is driven by a 40-ns pulse from a 50-cm cathode electron beam. Approximately 1.5 J of transmitted VUV has been calorimetrically measured in the second chamber. The gain of the medium is probed by a pulsed tunable dye laser (150 kW, 5 ns, 0.01 nm). The dye laser pulse is injected into a stable cavity which is constructed in the high-pressure region. The exponential decay of the trapped radiation is monitored on the far side of the cavity by a photodiode. Cavities with roundtrip losses of ~1.3 percent have been constructed. Oscillograms of the photodiode signal are taken and changes in the roundtrip loss of 0.1 percent or 10^{-5} cm^{-1} are apparent.

Roundtrip gains of 3 percent have been observed and yield greater than net break even gain. An early loss period of ~200-ns duration has been observed and appears to be broad banded and depend on the N_2O pressure. The gain profile is wide (~1.5 nm full width at half maximum), exhibits a blue wing, and is peaked slightly to the blue of the atomic line. This profile is consistent with discharge spectra of $Ar + O_2$ mixtures which exhibit vibrational–rotational structure, and strongly suggests that the gain is due to stabilized molecules rather than collisional (pseudomolecular) stimulation.

The upper state lifetime is inversely proportional to N_2O pressure and is independent of argon pressure within the limits used. The gain appears to be linearly proportional to argon pressure. If one estimates $n(^1S_0)$ production, then the effective stimulated-emission cross section can be calculated from the experimentally determined gain to be $\sigma_{EFF} = K\sigma = 3 \times 10^{-20}$ cm^2, where K is the fraction of $O(^1S_0)$ found in the molecular state and σ is the real stimulated-emission cross section. Assuming that $K = 10^{-2}$ at room temperature and 2.8 MPa (400 psia) Ar, then $\sigma \approx 3 \times 10^{-18}$ cm^2.

15.11 Optically Pumped 15.90-μm SF_6 Laser,* H. R. Fetterman and W. E. Barch, *Lincoln Laboratory, Massachusetts Institute of Technology, Lexington, Mass. 02173,* H. R. Schlossberg, *Air Force Cambridge Research Laboratory, Bedford, Mass. 01730.*

Optically pumped molecular lasers, oscillating on vibrational transitions, offer a promising means of achieving wavelength diversity in the infrared. Although numerous molecules have absorption bands coinciding with existing pulsed lasers (e.g., CO_2, HBr), to date only simple linear molecules,[1] optically pumped, have lased on vibrational tran-

*This work was sponsored by the Department of the Air Force.

[1](a) T. Y. Chang and T. J. Bridges, *Appl. Phys. Lett.*, vol. 23, p. 370, 1972. (b) H. R. Schlossberg and H. R. Fetterman, *Appl. Phys. Lett.*, vol. 26, p. 316, 1975.

sitions. We report here the first example of this type of lasing in a nonlinear molecule. Laser radiation has been generated at 15.90 μm from SF_6 by optical pumping with a pulsed CO_2 laser. Analysis of this laser indicates that it is the first optically pumped laser involving a two-photon pumping process.

In recent experiments,[2] significant sulfur isotope separation has been achieved using only a high-intensity CO_2 laser pulse whose 10.6-μm wavelength overlaps the ν_3 band of SF_6. Other important photochemical and isotope separation applications will require high-intensity infrared lasers at different wavelengths. Our 15.90-μm output falls within the ν_3 band of UF_6.[3]

Several sealed experimental laser cells were used in this study ranging from 1 to 3 in in diameter and having either internal mirrors or Brewster windows. A typical system, shown in Fig. 1, used a configuration of mirrors and lenses to focus the pump CO_2 laser beam into a hole coupled laser cavity. Simultaneous pumping with both $P(12)$ and $P(14)$ of the 10-μm CO_2 laser was required to obtain oscillation. Each of the CO_2 laser input pulses was typically about 200 ns long and each had a peak power of about 300 kW. The optically pumped laser pulse had a halfwidth of about 1 μs, was delayed from the CO_2 pulses from 3 to 8 μs, and had a measured wavelength of 15.9005 ± 0.0005 μm (628.74 ± 0.02 cm^{-1}). Operating pressures, measured using a capacitance manometer, were critical and depended on the particular cavity. As indicated in Fig. 2, the peak signal occurs (in a 3-in-diam cell) at 55 m·torr of SF_6. Addition of He or H_2 gas to the SF_6 quenched the 15.90-μm radiation at pressures of approximately 100 m·torr.

The low pressures and pulse delays in our experiments preclude vibrational relaxation as a mechanism for population inversion. At 40 m·torr of pure SF_6, for example, VV relaxation[4] takes about 27 μs. Without invoking a VV relaxation mechanism, it is not possible to assign the lasing transition on the basis of a single photon absorption. This and the necessity for two pump wavelengths imply that the upper laser level is populated via absorption of two photons. The induced transition rate at our intensity levels can be shown to be much

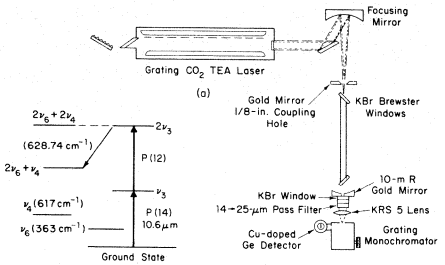

Fig. 1. Lasing from optically pumped vibration levels.

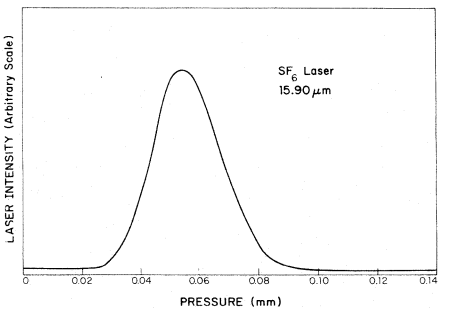

Fig. 2.

greater than $1/T_2$ (T_2, the phase coherence time, is 600 ns at 40 m·torr), indicating that direct two-photon absorption with a near-resonant intermediate state can be an important process. The possible energy levels in a two-photon absorption (simultaneous or stepwise) pumping followed by 15.90-μm laser emission can be limited greatly from considerations of odd/even symmetry of the SF_6 vibrations. A plausible model which meets all constraints is that the $2\nu_3$ level of SF_6 is pumped via near resonance of ν_3, and lasing takes place from $2\nu_3$ to $\nu_2 + \nu_4$. The latter transition could be reasonably strong because of a Fermi resonance between $2\nu_3$ and $\nu_2 + 2\nu_4$, the ν_4 band being strongly allowed. Alternatively, the Fermi resonant state could be $2\nu_6 + 2\nu_4$ and the final laser state $2\nu_6 + \nu_4$ as shown in the insert of Fig. 1.

While the quantum efficiency from 10 to 16 μm in our initial experiments is relatively small, the interpretive model suggested previously would allow high efficiencies in an optimized system. Higher pumping levels could be achieved by better temporal and spatial coincidence and increased power of the two pump laser lines. With stronger optical pumping, a greater degree of rotational relaxation (induced, for example, by a rare gas) could be tolerated and would produce some tunability of the output by lasing from adjacent rotational states. Alternatively, by using two independent CO_2 lasers with a greater choice of pump wavelengths, it may be possible to excite other states of SF_6, leading to additional wavelength selection.

[2](a) R. V. Ambartzumian, Y. A. Gorokhov, V. S. Letokhov, and G. N. Makarov, *Pis'ma Zh. Eksp. Teor. Fiz.*, vol. 21, p. 375, 1973 (in Russian). (b) J. L. Lyman, R. J. Jensen, J. Rink, C. P. Robinson, and S. D. Rockwood, to be published.

[3]R. S. McDowell, L. B. Asprey, and R. T. Paine, *J. Chem. Phys.*, vol. 61, p. 3571, 1974.

[4]J. T. Knudtson and G. W. Flynn, *J. Chem. Phys.*, vol. 58, p. 1467, 1973.

17.13 Low-Power CW Generation of Coherent Anti-Stokes Raman Radiation in CH_4 Gas

J. J. Barrett and R. F. Begley, *Materials Research Center, Allied Chemical Corporation, Morristown, N.J. 07960.*

We report the first observation of coherent antistokes Raman scattering (CARS) generated by CW lasers in methane gas. Up to the present time, all four frequency mixing experiments have been performed using high-power (typically $>$ 1 kW) pulsed lasers. In comparison with pulsed lasers, CW lasers have the advantage of better frequency and amplitude stability facilitating accurate experimental measurements over long time spans.

A CW jet-stream dye laser, which was pumped collinearly by the 514.53-nm line of an argon-ion laser, consisted of a folded six-mirror astigmatically compensated resonator. The 514.53-nm beam entered the dye laser cavity through a multilayer dielectric mirror which had high transmissivity over the range of 470-530 nm and high reflectivity over the range of 560-650 nm. A pair of 30-cm radius mirrors in the dye laser cavity was used to produce a focus in a gas cell with Brewster angle windows containing 1 atm of methane. All of the mirrors of the dye laser cavity had high reflectivity over the range 560-650 nm. Wavelength selection in the dye laser cavity was accomplished by use of a prism for coarse tuning and a thin solid etalon for fine tuning. The laser linewidth was about 0.1 cm^{-1}. The coherent antistokes radiation was transmitted by the second 30-cm-radius mirror which had high transmissivity at ω_A and high reflectivity at ω_P and ω_S. It was filtered and then detected by a cooled RCA 8850 photomultiplier tube operated in the pulse counting mode.

The vacuum wavenumber ω_P of the 514.53-nm line is 19429.79 cm^{-1} and the observed Raman frequency shift for the ν_1 band of CH_4 is 2916.7 cm^{-1}. The Stokes and antistokes vacuum wavenumbers are 16513.09 cm^{-1} and 22346.49 cm^{-1}, respectively. By using data in the literature, the value of the differential Raman scattering cross section for the ν_1 band was calculated to be 2.52×10^{-30} cm^2/sr molecule and the value of Γ is 0.9 cm^{-1}. The bulk resonance susceptibility $N\chi_R$ for the ν_1 band of CH_4 is 1.75×10^{-14} cm^3/erg. In our experiment, the interaction length at the beam focus was 1.04 cm and the interaction area 4.01×10^{-6} cm^2. The measured powers in the pump and Stokes beams were 0.46 and 0.21 W, respectively. The amount of Stokes power within the interaction volume was 0.036 W. The antistokes power was

calculated to be 2.18×10^{13} W or 4.90×10^{5} photons/s which is in good agreement with the observed value of 5.72×10^{5} photons/s.

A theoretical comparison of the coherent antistokes signal from CH_4 with the Stokes signal generated by spontaneous (ordinary) Raman scattering from CH_4 was made. For input powers of less than 1 W (typical of the power levels used in this experiment), the coherent antistokes Raman signal is less than the spontaneous Raman Stokes signal scattered into a collection solid angle defined by $f/1$ optics. However, since the coherent antistokes signal has the spatial characteristics of a laser beam rather than being scattered into 4 π sr, it is possible to collect efficiently nearly all of the coherent antistokes signal. At an input power of 28.4 W, the coherent antistokes power and the ordinary Stokes power are equal for this calculation in methane.

18.12 Energy Extraction Improvement in Nanosecond Pulse TEA-CO_2 Lasers,* J. C. Farcy, A. Fertal, M. Huguet, G. Girard, and M. Michon, Laboratoires de Marcoussis, Centre de Recherches de la C.G.E., 91460 Marcoussis, France.

Energy extraction efficiency is of fundamental importance in CO_2 short pulse amplifiers. It is well known that the extracted energy is lower for shorter pulses: there is roughly a ratio of 10 between energies extracted at 1 μs and at 1 ns at atmospheric pressure.[1] Transfer times become too long with respect to pulse duration, and increasing pressure is a convenient but partial solution.

Improved energy extraction for nanosecond pulses can be obtained in two ways. First, by using a multiline–multiband (9.6 + 10.6 μ) oscillator, we observe a 35-percent increase. Second, an original setup uses several passes through the same active medium; the time delay between each pass of the same nanosecond pulse is long enough to allow good rotational and vibrational relaxation to take place so as to obtain energy extraction similar to that for longer pulse duration; an upper limit of 400-percent increase could be theoretically achieved.

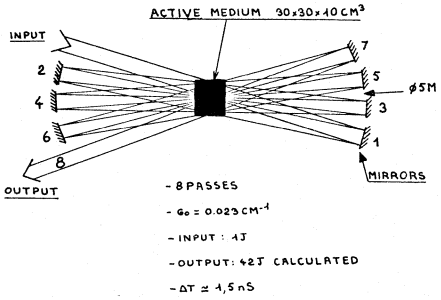

Fig. 1. Multipass amplifier.

I. Multiline and Multiband Operation

We used a 3.7-m-long oscillator mode locked by a 20-MHz acoustooptical germanium modulator. The optical cavity is made up of a gold coated mirror and a ClNa flat. The multiline (10.6 μ) and multiband (10.6 + 9.6 μ) operation is obtained through an angle tunable Fabry–Perot placed inside the optical cavity. The lines are controlled by an Opt. Eng model 16A spectrophotometer. A double gallium arsenide shutter provides a single pulse with an extinction ratio of about 10^5. Energy up to 1.5 J is provided by three double-discharge amplifiers, and is used as input into the atmospheric-pressure test amplifier, whose gain is chosen to be exactly 10 dB (0.023 cm^{-1}) for 1 m.

Energy extracted from the test amplifier versus input energy density up to 0.35 J/cm^2 shows 16- and 35-percent increase for multilines (10.6 μ) and multiband (10.6 and 9.6 μ) operation, respectively. Results are compared to a theorical model by Feldman.

II. Multipass Extraction

By allowing the time delay between passes of the same pulse through the active medium to be longer than relaxation times, stored energy in the laser level of interest can be regenerated and more energy can be theoretically extracted.

An atmospheric double-discharge 30 × 30 × 10-cm^3 amplifier is set up (Fig. 1) at the center of a circle 5 m in diameter. Seven mirrors insure multiple reflection so that time delay between passes is about 15 ns. In this way, energy is extracted 8 times successively, corresponding to 120-ns operation. Mirrors and amplifier medium are installed in the same Plexiglass housing to avoid window losses; the entire volume is occupied by the gas mixture. The 0.023 cm^{-1} small-signal gain provides a total gain of 24 dB so that a theorical 42-J output could be obtained for 1-J input.

Such a multipass system should be of great interest for pulses even shorter ($\leqslant$ 1 ns). Moreover, its principle might be applied to all gas lasers which cannot deliver their energy rapidly.

18.13 Multikilowatt CO_2 Laser Utilizing Plasma Injection, R. McLeary, R. E. Whitcher, and P. J. Beckwith, *Materials Research Laboratories, Department of Defence, Maribyrnong, Vic. 3032, Australia.*

The "plasma-injection" technique has been shown[1] to be suitable for obtaining uniform continuous discharges in CO_2-laser gas mixtures at pressures up to 1 atm. In this technique, preionization of the laser discharge volume is achieved by the injection of ionized gas from a secondary discharge. A typical plasma injector has a suitable gas, e.g., N_2, ionized in a small arc discharge originating on the pin electrode, and forced at sonic velocity into the main discharge region. The remaining constituents of the laser gas mix flow radially inwards and are mixed with the preionized gas in the main discharge region. The power dissipated in the preionizing discharge is about 20 percent of the main discharge power and the mass flow rate of gas through the preionizer is about 25 percent of the total. The main discharge characteristics are sensitive to polarity with higher conductances and power inputs obtained with the polarity shown. This asymmetry was most pronounced at low values of preionizing current, and could be due to the ease with which electrons can be extracted from what is essentially a plasma cathode. The main discharge has a positive slope resistance the value of which decreases as the amount of preionization is increased. Discharge power densities of up to 150 kW/l at pressures up to 1 atm have been achieved by the use of this technique.

A laser has been constructed in which 200 of these plasma injectors are arranged along the 3.2-m length, with the discharge axes perpendicular to the optical axis. Consecutive discharge axes were rotated by approximately 45° in a plane normal to the optical axis. Each discharge length was 28 mm, making the total discharge volume approximately

*This work was performed under contract from the Commissariat à l'Energie Atomique.

[1] G. Girard, J. C. Farcy, M. Michon, and P. Vincent, *IEEE J. Quantum Electron.*, vol. QE-11, June 1975.

[2] M. S. Piltch, *Opt. Commun.*, vol. 7, Apr. 1973.

[3] B. J. Feldman, *IEEE J. Quantum Electron.*, vol. QE-9, Nov. 1973.

[1] R. McLeary, P. J. Beckwith, and W. E. K. Gibbs, "Uniform continuous discharges and CO_2-laser action at atmospheric pressure by plasma injection," *IEEE J. Quantum Electron*, vol. QE-10, pp. 649–651, Sept. 1974.

TABLE I
PERFORMANCE OF CW PLASMA-INJECTION CO_2 LASER

Pressure	33 kPa (250 Torr)
Gas Mixture	5 CO_2:76 N_2: 19 He
Mass Flow (Total)	500 g/s
Discharge Power (incl. preionizing)	70 kW
Power Output	7.5 kW
Efficiency	10.7%

2 l. As the input and hence output power density is very high in this type of device, diffraction coupling of the output from a stable resonator system was used to minimize damage to the resonator components. Although oscillation was achieved at atmospheric pressure, the efficiency was low ($<$ 1 percent) due to the combination of low small-signal gain and perturbation of the resonator by turbulence in the gas flow. Operation at pressures less than atmospheric was achieved by the use of a 10-m^3 vacuum dump tank.

Table I gives typical performance data at a pressure of 33 kPa (250 torr) where an output power of 7.5 kW at an electrical efficiency of over 10 percent was obtained. Comparison of the operating parameters of this laser with those of conventional convection-cooled types shows that the plasma-injection technique allows efficient high-power operation to be obtained at considerably higher pressures and without the use of a large proportion of He in the gas mixture.

19.11 Application of Laser with Folded Optical Delay Line in Optical Communication Systems, L. S. Kornienko, N. V. Kravtsov, E. G. Lariontsev, N. I. Naumkin, and V. N. Serkin, Moscow, USSR.

The mode-locked lasers have been used in optical communication systems.[1,2] By using a folded optical delay line in a laser cavity, one can easily change the cavity length L and the pulse repetition time $T = 2L/c$. Energy, time, and spectral characteristics of such lasers depend on the cavity length.

The peak intensity of CW laser mode-locked pulses increases significantly with increasing cavity length. In lasers with saturable absorber, the cavity length variation results in a change of mode-locked pulse duration, pulse peak intensity, contrast ratio, number of pulses in a chain, and the pulse chain duration[3-5]. With increased cavity length, the nonlinear distortions of the mode-locked pulses induced by self-focusing and self-phase modulating are significantly reduced.

Properties of such lasers have been investigated in ruby with saturable absorbers and CW YAG:Nd^{3+} lasers. It is shown that a mode-locked laser with a folded optical delay line has some advantages for application in communication systems, namely the possibility of pulse repetition frequency variation, increased contrast ratio, pulse intensity, and spectral width variation.

[1](a)R. T. Denton and T. S. Kinsel, *Proc. IEEE*; vol. 56, p. 140, Feb. 1968. (b) T. S. Kinsel and R. T. Denton, *Proc. IEEE*, vol. 56, p. 146, Feb. 1968.

[2]K. Otsuka and T. Kimura, *IEEE J. Quantum Electron.*, vol. QE-8, p. 23, Jan. 1972.

[3]E. L. Klochan, L. S. Kornienko, N. V. Kravtsov, E. G. Lariontsev, and N. I. Naumkin, *Kvantovaya Elektronika*, no. 5, p. 47, 1973.

[4]V. M. Dytynko, L. S. Kornienko, and N. V. Kravtsov, *RIE*, vol. 16, p. 450, 1971.

[5]E. G. Lariontsev and V. N. Serkin, *Kvantovaya Electronika*, vol. 1, p. 2166, 1974.

Session 13-A

Thursday, May 29, 1975
8:00-10:00 P.M.

Post-Deadline Papers

Chairman: A. S. Halsted, *Hughes Aircraft Co., Culver City, Calif.*

13.A1 Observation of Fluorescence Narrower than the Natural Linewidth, H. M. Gibbs, *Bell Laboratories, Murray Hill, N.J. 07974*, and T. N. C. Venkatesan, *Brooklyn College, City University of New York, New York, N.Y.*, and *Bell Laboratories, Murray Hill, N.J. 07974.*

We report the first direct observation of fluorescence narrower than the natural linewidth.[1] It was shown by Weisskopf[2] and popularized by Heitler that the fluorescence from a two-level system subjected to monochromatic radiation has the same spectral profile as the excitation.[3] From the points of view of conservation of energy and of a driven classical oscillator, this result is trivial.[4] However, persons accustomed to associating (via the Heisenberg Uncertainty Principle) a width $\Delta\nu = (2\pi\tau)^{-1}$ with a state of lifetime τ, often find this prediction surprising. This is because absorption and reemission are often treated as distinct processes. If the excitation is much shorter than the lifetime, such a treatment is justified and the reemitted radiation has the natural linewidth. On the other hand, if monochromatic excitation is used, the excitation and reemission processes must be treated as a single coherent process, yielding narrower-than-natural fluorescence for all intensities low enough to avoid power broadening.

In the present experiment, a fluorescence width less than half of the natural width was seen. An atomic beam of Mg, the 200-nW second-harmonic beam of a stabilized CW dye laser, and the detection axis of a spherical Fabry–Perot interferometer formed mutally perpendicular axes. Apertures limited the solid angles and reduced the $\approx$4000-MHz Doppler width to about 20 MHz. The 80-MHz linewidth[5] of the Mg 2852-Å $^1S_0$-to-$^1P_1$ transition then easily exceeded the composite detection width including the Doppler width, the 10-MHz instrumental width of the scanning spherical Fabry–Perot with small aperture, and the laser jitter of less than 5 MHz.

This direct demonstration of narrower-than-natural linewidth fluorescence points the way to careful studies of the details of the spontaneous-emission spectral profile. Sensitivity to distortion in lineshape of order α^2 would permit a test of quantum electrodynamic radiation corrections.[6]

[1]Hanle effect signals half the natural linewidth have been seen using monochromatic excitation: W. Rasmussen, R. Schieder, and H. Walther, *Opt. Commun.*, vol. 12, p. 315, 1974. Without natural-linewidth resolution it has been shown that emission occurs at the frequency of off-resonance excitation: L. S. Ditman, Jr., R. W. Gammon, and T. D. Wilkerson, *Opt. Commun.*, vol. 13, p. 154, 1975.

[2]V. Weisskopf, *Ann. Phys.*, vol. 9, p. 23, 1931.

[3]W. Heitler, *The Quantum Theory of Radiation.* New York: Oxford, 1954, pp. 196–203. Heitler does not include broadening of the ground state by repeated absorption: see F. K. Lamb and D. Ter Haar, *Phys. Rep.*, vol. 2, p. 253, 1971, and A. Omont, E. W. Smith, and J. Cooper, *Astrophys. J.*, vol. 175, p. 185, 1972. We saw power broadening in Na, but the intensities were too low in the Mg experiment.

[4]See, for example, M. O. Scully and M. Sargent, III, *Phys. Today*, vol. 25, p. 38, 1972.

[5]The $^1P_1$ lifetime is known to be 2 ns to a few percent: See references in W. H. Smith and H. S. Liszt, *J. Opt. Soc. Amer.*, vol. 61, p. 938, 1971.

[6]See pp. 348-353 of Heitler[3] in the preceding.

13.A2 High-Repetition-Rate H_2 Vacuum-Ultraviolet Laser Applications: Photoionization and Excitation of Luminescence, V. S. Antonov, I. N. Knyazev, V. S. Letokhov, and V. G. Movshev, *Institute of Spectroscopy, Academy of Sciences, Moscow, Akademgorodok, 142092 USSR.*

Development of the repetitively pulsed H_2 laser suitable for physical experiments[1,2] made it possible to carry out experiments on photoionization of molecules and excitation of luminescence of crystals by using vacuum-ultraviolet (VUV) laser radiation.

Experiments were carried out by using a repetitively pulsed H_2 VUV laser at 13 transitions $\lambda \sim 1610$ A with a 10-Hz repetition rate, ~1-ns laser pulse duration and 0.1-mW average power. The H_2-laser photon energy is sufficient for ionization of 50 percent of the elements, a substantial portion of organic compounds, and also for excitation of luminescence of crystals.

In the photoionization experiments methylaniline and dimethylaniline were choosen because of their comparatively low ionization energy (7.36 and 7.1 eV) and relatively high vapor pressure at room temperature (0.4 and 0.5 torr, respectively). Laser radiation was directed on the photoionization cells through a set of buffer volumes with LiF, BaF_2, or MgF_2 windows. The buffer volumes were filled with pure hydrogen at atmospheric pressure to prevent breakdown from the laser as well as to decrease leakage currents. The transmission of laser radiation through the system and the alignment of the cells were controlled by use of a luminescent screen.

The mean photocurrent in dimethylaniline approached 0.5 μA. Check experiments were carried out by using nitrogen UV laser radiation with the photon energy 3.7 eV, as well as by using H_2 laser radiation and helium- or oxygen-filled photoionization cells. In these experiments there was no current in the photoionization cell circuit. The maximum registered photocurrent is 0.2–0.3 μA. A rough estimate of the photoionization current in dimethylaniline gives a value of 0.25 μA, assuming a photoionization output of 0.1 and neglecting by photoelectron recombination.

H_2-laser radiation can be used in attempts to increase sensitivity of photoionization mass spectrometers and to develop basically new methods of molecular detection. The mean probability of molecular photoionization in the case of using a H_2 VUV laser with the aforementioned parameters approaches 10^{-4} s^{-1}. That is three orders of magnitude more than in the available photoionization mass spectrometers. By using the two-step laser photoionization method, it is possible to develop photoionization methods of molecular detection with sensitivity 10^4–10^5 molecules. Some details of the photoionization experiments can be found in Andreyev *et al.*[3]

The luminescence of crystals was excited by using focused H_2 VUV laser radiation and recording by a monochromator and phototube with known spectral response. The system allows sensitive monitoring of the luminescence with a quantum efficiency ~1 percent. The main limitations in this respect are connected with the false signal induced by the excitation system of the laser and scattering of the spontaneous radiation of the pulsed discharge in the region $\lambda \lesssim 2000$ Å in the crystal. The luminescence of sapphire, ZnS, NaCl, and other crystals was investigated. A strong 2300-Å peak of luminescence was observed in NaCl at 88 K.

High-repetition-rate Verner band 1200-Å H_2 VUV laser action was observed. Detailed spectral investigations of stimulated and spontaneous H_2 VUV radiation were carried out by using a 6.6-m VUV spectrograph of the Institute of Spectroscopy. The overall number of registered VUV laser lines in H_2 is ~100. The 1200-Å H_2 VUV laser is also a prospective laser for photoionization experiments and excitation of luminescence.

[1] V. S. Antonov, I. N. Knyazev, V. S. Letokhov, and V. G. Movshev, *JETP Lett.*, vol. 17, p. 545, 1973.

[2] I. N. Knyazev, V. S. Letokhov, and V. G. Movshev, 8th Int. Quantum Electronics Conf. Digest, San Francisco, Calif., June 10–13, 1974.

[3] S. V. Andreyev, V. S. Antonov, I. N. Knyazev, V. S. Letokhov, and V. G. Movshev, *Phys. Lett.*, to be published.

13.A3 Laser Action on the XeF $^2\Sigma \rightarrow {}^2\Sigma$ Band at 3540 Å,* J. J. Ewing and C. A. Brau, *Avco Everett Research Laboratory, Inc., Everett, Mass. 02149.*

We report here lasing at 3540 Å on a molecular band of XeF. Electronically excited XeF is formed when F_2/Xe/Ar mixtures are irradiated with a pulsed electron beam. This is a new laser operating on a member of a new class of molecules, the noble gas monohalides. These diatomic molecules are characterized by weakly bound or nonbound covalent lower levels having molecular symmetries $^2\Sigma_{1/2}$ and $^2\Pi_{1/2,3/2}$. The upper laser level of these species is ionic in nature, having the polarity Xe^+F^-. The lowest ionic state of noble gas monohalides has the molecular symmetry $^2\Sigma_{1/2}$, and is usually strongly bound relative to the lowest excited states of the free atoms.[1] Fig. 1 shows estimated potential energy curves for XeF. The lasing transition in XeF reported here terminates on high lying vibrational levels of the weakly bound lower state.

The excited XeF can be formed in two ways. First, xenon excited states, formed in our experiments by energy transfer from Ar* and Ar_2^*, can react with F_2 to directly produce the excited monofluoride[2]:

$$Xe^* + F_2 \rightarrow XeF^* + F.$$

Reactions of this type have large cross sections and a high probability of reaction leading to excited states. A second important pumping channel is the rapid termolecular recombination of Xe^+ ions with F^- ions,[3] both of which can be formed in these *e*-beam excited mixtures.

The laser experiments were performed in an aluminum cell with aligned quartz flats as optical windows and an aluminized Mylar foil as the window for the electron beam. The electron beam is formed by pulse charging a cold cathode gun to about 300 kV. With an anode–cathode spacing of 0.511 in, the current density through the foil is about 150 A/cm^2, over a 1.5 × 15 cm^2 area. The electron-beam pulse duration is 100 ns with approximately 15-ns rise and fall times.

The optical cavity was formed by two 1-m radius-of-curvature maximum reflectors separated by 30 cm. The output coupling at 3540 Å was $\frac{1}{2}$ percent per window. The beam output at one end was attenuated by a factor of 500 and was directed onto an ITT FW128 photodiode. The output passing through the other reflector was taken onto a spectrograph for wavelength analysis.

Fig. 2 shows the time history of the XeF stimulated emission as monitored by the photodiode for a mixture of F_2/Xe/Ar having mole fractions 0.001/0.003/0.996 at a total pressure of 70

*This work was supported by ARPA/ONR through Contract N00014-75-C-0063.

[1] J. J. Ewing and C. A. Brau, "Emission spectrum of XeI* in electron beam excited Xe/I_2 mixtures," *Phys. Rev. A*, to be published, June 1975.

[2] J. E. Velazco and D. W. Setser, *J. Chem. Phys.*, vol. 62, p. 1990, 1975.

[3] J. J. Thompson, *Phil Mag.*, vol. 47, p. 337, 1924.

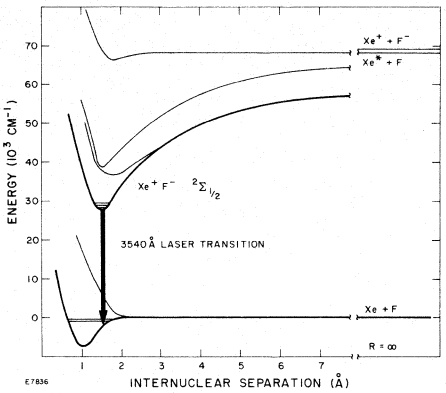

Fig. 1. Potential energy curves for xenon fluoride.

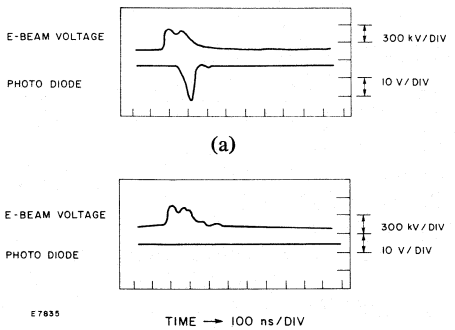

Fig. 2. XeF laser time history. (a) Lasing. (b) Mirror blocked.

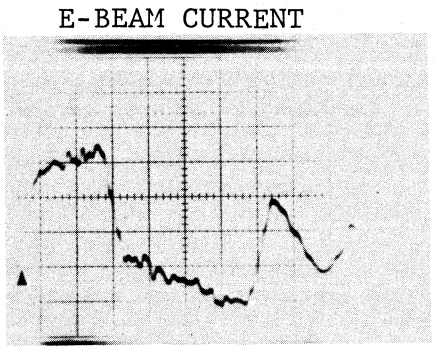

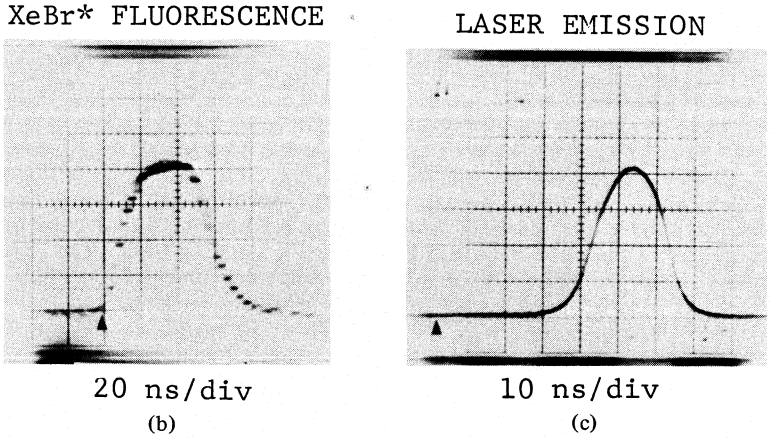

Fig. 1. Temporal comparison of the *e*-beam excitation pulse (a), side fluorescence viewed through a 250–390-nm filter (b), and laser emission (c).

psia. The stimulated emission signal in this case is 100 times larger than the spontaneous emission signal. A comparison of microdensitometer tracings of spontaneous and stimulated emission from XeF shows that the spectrum of laser light emitted from the cavity is narrowed compared to that of the spontaneous emission.

13.A4 A New Excimer Laser,† S. K. Searles and G. A. Hart,* *Naval Research Laboratory, Washington, D.C. 20375.*

Previous excimer lasers have been confined to stimulated emission from Xe_2^*, Kr_2^*, Ar_2^*, XeO*, and KrO*. Recent studies[1] confirmed the existence of a new class of excimers RX* where R is a rare gas atom, X is a halogen atom, and * denotes the first excited electronic state of the molecule. We wish to report the first rare-gas halide excimer laser. The kinetics of this laser are described by a three-step mechanism

$$e + Xe \longrightarrow Xe^* + e \quad (1)$$

$$Xe^* + Br_2 \longrightarrow XeBr^* + Br \quad (2)$$

$$XeBr^* \longrightarrow Xe + Br + h\nu\,(281.8\text{ nm}). \quad (3)$$

Xe* generated by a high-energy electron-beam device[2] reacts with Br_2 at a gas kinetic rate to produce XeBr* which undergoes a bound-free transition.

The experimental results consist of fluorescence (side emission) measurements for Xe with 0.01–4-percent Br_2 over the range 10–3000 torr and stimulated emission data from a 760-torr-Xe–3.8-torr-Br_2 mixture. Very close agreement with the observed fluorescence was obtained with an energy deposition and chemical kinetics model. This model indicates that the two key rate constants are given by $k_2 = (2.0 \pm .4) \times 10^{-9}$ cm^3/molecule · s and $k_3 = (5.7 \pm .8) \times 10^7$ s^{-1}. In addition, a preliminary value of 8×10^{-10} cm^3/molecule · s was found for the quenching of XeBr* by Br_2. This quenching puts a severe limit on the partial pressure of Br_2 in a potential laser mixture.

A low-loss optical cavity consisting of >99.5-percent reflectivity mirrors and aligned normal incidence windows was used to search for laser emission in gas mixtures displaying the most intense fluorescence. Laser emission was observed from a 760-torr-Xe–3.8-torr-Br_2 mixture. Proof of laser emission is as follows.

1) Laser emission disappeared when the far mirror was blocked.

2) The laser spectrum was less than 0.75 nm wide at 281.8 nm while the fluorescence is a banded continuum over the range 230–360 nm.

3) As indicated in Fig. 1, the laser full width at half maximum (FWHM) is much less than the fluorescence FWHM.

At present, laser emission is near threshold with a peak power of about 100 W. It is expected that the power of this new laser can be significantly increased and that it can also be made to operate as a tunable high-power laser in this wavelength region of photochemical interest.

†This work was supported in part by DARPA.

*NRC-NRL Postdoctoral Research Associate, 1973-present.

[1](a) J. E. Velazco and D. W. Setser, *J. Chem. Phys.*, vol. 62, p. 1990, 1975. (b) M. F. Golde and B. A. Thrush, *Chem. Phys. Lett.*, vol. 29, p. 486, 1974. (c) J. J. Ewing and C. A. Brau, to be published.

[2]S. K. Searles and G. A. Hart, *Appl. Phys. Lett.*, vol. 25, p. 79, 1974.

13.A5 Broad-Band Continuously Tunable High-Pressure CO_2 Laser: Use for Excitation of Molecules and in Molecular Spectroscopy, V. N. Bagratashvili, I. N. Knyazev, V. S. Letokhov, and V. V. Lobko, *Institute of Spectroscopy, Academy of Sciences, Moscow, Akademgorodok, 142092 USSR.*

The main characteristics of the modified version of a high-pressure CO_2 laser[1] with continuous frequency tuning on P and R branches of laser transitions are presented. A 3-pass resonator was used to obtain continuous frequency tuning at 5-atm $CO_2:N_2 = 1:2$ mixture of gas with $0.5 \times 4 \times 50$ cm^3 active volume excited by a nonself-sustained gas discharge with preionization of the laser volume by high-energy electrons. At 1-atm gas pressure, a superluminescent mode of operation was observed proving the high overall amplification of the system.

Spectral measurements carried out with an accuracy of 0.01 cm^{-1}, by using a mechanically scanned Fabry–Perot interferometer, gave a spectral width of 0.05 cm^{-1} for the laser radiation. Completely continuous frequency tuning was observed in the region $J'' = 10$–24, while partial continuous tuning occurred for $J'' = 6$–32. For the partial frequency tuning, a spectral range of 90 cm^{-1} was covered. The laser pulse energy was of the order of 0.1 J.

Focused frequency-tuned laser radiation with a power density of 10^9 W/cm^2 was used to excite visible luminescence of molecules, ethylene in particular. Molecular ethylene was chosen for experiments due to the existence of a strong absorption band with developed rotational structure which covers the whole laser tuning range. This enables one to investigate the variation of luminescence intensity over a spectral range of 150 cm^{-1}. To observe the instantaneous state of the luminescence, a phototube is illuminated by the radiation from the region of the lens caustic.

The narrow-band tuning of the laser frequency in the wings of the ethylene absorption band gives no noticeable resonances for the excitation of luminescence, while the simultaneously measured linear absorption of the molecule reveals strong variations in accordance with the rotational structure of the band. In the case of broad-band laser frequency tuning, an excitation resonance of the luminescence was observed in the Q-branch region. The spectral width of the excitation peak is 10 cm^{-1} and is proportional to the square root of the laser pulse energy.

The existence of an excitation peak for the Q-branch luminescence indicates a definite correlation between the luminescence intensity and average absorption in a particular region of the band with an interval of averaging of some cm^{-1}. There is no correlation between the intensity of luminescence and absorption in the case of laser frequency scanning in a narrow interval about 1 cm^{-1} at any region of the band, including Q branch. These facts indicate the effective averaging of the rotational structure of the spectrum in the process of excitation of luminescence. The observed Q-branch excitation resonance of luminescence can be qualitatively interpreted in the framework of a radiative excitation mechanism of molecules in a strong field. The observed averaging of the spectral characteristics of a molecular gas occurs perhaps due to modulation splitting and corresponding broadening of the spectral lines during pulsed coherent saturation of molecular quantum states in a strong field. The broadening of molecular lines caused by coherent pulsed saturation at 10^9 W/cm^2 is 3 cm^{-1}, which is in rough agreement with the experimentally measured spectral width of the Q-branch excitation resonance for luminescence. In practice, the spectral width of the Q-branch luminescence resonances gives the value of the vibrational band isotopic shift required for isotopically selective dissociation. Some details of this experiment can be found in Bagratashvili *et al.*[2]

The first experiments were carried out by using a continuously tuned CO_2 laser and an optoacoustical detector to register weak absorption spectra of small amounts of molecular gases. By using this system, the absorption spectra of HDS in natural H_2S (10^{-2} percent of content) as well as some other molecules were detected.

[1] V. N. Bagratashvili, I. N. Knyazev, Yu. A. Kudryavtsev, and V. S. Letokhov, *Opt. Commun.* vol. 9, p. 135, 1973.

[2] V. N. Bagratashvili, I. N. Knyazev, V. S. Letokhov, and V. V. Lobko, *Opt. Commun.*, to be published.

13.A6 Laser Emission at 1.32 μm from Atomic Iodine Produced by Electrical Dissociation of CF_3I,* L. D. Pleasance and L. A. Weaver, *Westinghouse Research Laboratories, Pittsburgh, Pa. 15235.*

We have been investigating the dissociation of molecules by electron impact into excited electronic states. The objective of this research is the development of dissociation lasers with the potentially high excitation efficiencies and volume scaling characteristics of electrical discharges. In this paper we report the observations of laser emission at 1.32 μm from atomic iodine produced by the electrical dissociation of CF_3I. These observations are the first reported evidence that population inversions can be produced on this transition by volume electrical processes. These results raise the possibility of generation of atomic iodine lasers by electrical excitation with improved volume scaling and efficiency.

The excited atomic iodine is produced by dissociation of the CF_3I following an inelastic collision with an electron:

$$CF_3I + e^- \rightarrow CF_3I^* + e^-$$

$$CF_3I^* \rightarrow CF_3 + I^*.$$

This process is analogous to that found for excitation by photodissociation. Electrons with energies $\gtrsim$4.3 eV are required to excite the same predissociative state of CF_3I.

Fast pulse discharges between planar electrodes (TEA laser discharge) were used in this investigation. The active discharge volume is $2 \times 2 \times 50$ cm or 200 cm^3. Stable volume discharges have been obtained in mixtures of a few percent of CF_3I with N_2, Ar, or He buffer gases at total pressures of 50–300 torr. The discharge was driven by a single 20-nF capacitor charged to between 10 and 35 kV and connected to the electrodes by a triggered spark gap. This power supply produced a current pulse in the form of a damped sinusoid with a width of ~150 ns full width at half maximum (FWHM) for the first half-cycle.

Fig. 1 shows the laser output measured with an InSb detector for a discharge in 0.18 torr of CF_3I mixed with 70-torr N_2. The laser emission consists of one or more pulses delayed by 50–100 μs with respect to the discharge pulse. The small initial pulse at the beginning of the trace is laser emission from a nitrogen line emitted during the discharge pulse. No structure has been observed within each laser pulse to the time resolution of the detector (~0.5 μs). The laser intensity increases with both CF_3I pressure and discharge current density. The delay to the onset of lasing decreases with increasing laser intensity.

We have tentatively identified the mechanism responsible for the delay in the appearance of laser emission as the decay of the population in the lower laser level by the recombination reaction

$$CF_3 + I^\circ \rightarrow CF_3I^\dagger$$

where $CF_3I^\dagger$ is a vibrationally excited ground electronic state of CF_3I.

The energy output of the laser under the conditions of Fig. 1 was measured

*This work was supported in part by the Air Force Office of Scientific Research under Contract F44620-73-C-0046.

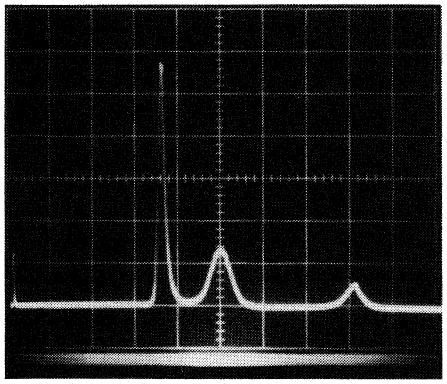

Fig. 1. Laser emission on the $I(^2P_{1/2}) \rightarrow I(^2P_{3/2})$ transition at 1.32 μm from a CF_3I-N_2 discharge; $P_{CF_3I} = 0.18$ torr, $p_{N_2} = 70$ torr, and $J = 32$ A$\cdot$ cm^{-2}. Time increases from left to right at 20 μs per major division. The initial pulse on the left is a N_2 laser line emitted during the excitation pulse. The duration of the discharge is ~0.5 μs.

with a calibrated thermopile. This measurement gave a value of 0.3 mJ which corresponds to an efficiency of 0.1 percent. Further improvements in efficiency are anticipated. Measurements of the dissociation rate gave a value of 2×10^{-8} cm^3/s at $E/N \simeq 9 \times 10^{-16}$ V-cm^2.

These results indicate that electrical dissociation of the perfluoro-iodides may represent an attractive alternative to flashlamp excitation of iodine lasers.

13.A7 A TE Copper Iodide Laser, J. A. Piper and C. E. Webb, *Clarendon Laboratory, Oxford, England.*

Substitution of copper halide vapor for the vapor of elemental copper allows operation of the potentially high-efficiency pulsed laser transitions of neutral copper at substantially reduced temperatures.[1-4] To date, the only reported experiments on copper halide lasers have been carried out with *longitudinally* excited discharge tubes. The performance of these devices in some cases suffers severely because of the erratic and irreproducible nature of the discharge path.[3,4] Consequently, it would appear difficult to scale longitudinal discharge tubes to large active volumes while retaining the essential qualities (high current and fast rise time) of the excitation pulse.

Laser tubes in which the discharge is *transverse* to the optical axis should not have these disadvantages since discharge paths can be kept short and well defined. The discharge circuit can take the form of parallel low-inductance loops, and it should therefore be possible to scale these devices to large active volumes to obtain high laser pulse energies. Unfortunately, design of transverse-discharge tubes for operation even at the relatively low temperatures (typically 500°C) appropriate to copper halide lasers is complicated by the problem of differential expansion between metal electrodes and the nonconducting material of the discharge vessel. This problem has been overcome in the present tube by segmenting the electrodes into short sections, free to expand independently. Discharge uniformity along the length of the electrode structure is promoted by providing each section with a separate current lead-through and using as a localized energy source a distributed capacitor array.

The main body of the laser is constructed from a heavy-wall fused silica tube. The electrode structure is formed by two rows of semicircular cross-sectional stainless-steel bars giving an active discharge volume approximately 700 mm long $\times$ 25 mm high $\times$ 5 mm wide. The device is capable of operation at temperatures in excess of 700°C. Experiments to date have been conducted with copper iodide vapor and neon as a buffer gas. The laser is operated in the double-pulse mode[2,4] in which the first discharge pulse dissociates the copper iodide molecules and thus provides a supply of copper atoms in the volume which are then excited by the second pulse. The circuit incorporates two independently triggered spark gaps which successively transfer energy from separate storage capacitors into the common dump capacitor array.

Although the gain is sufficient for observation of strong superradiant emission at both 5106 and 5782 Å, maximum laser output energy is obtained with an optical cavity comprising a high-reflecting mirror and an uncoated silica blank. Best laser performance occurs for pulse separation times 50–60 μs, copper iodide evaporation temperatures 480–500°C, and buffer-gas (neon) pressures about 100 torr, but satisfactory performance is obtained over a wide range of discharge parameters, including buffer-gas pressures up to 1 atm. The laser pulse duration is about 25 ns full width at half maximum (FWHM) and highest output energies achieved to date are 10 μJ/cm^3/pulse (active volume $\approx$ 100 cm^3) at conversion efficiencies, which compare favorably with those of the longitudinally excited copper halide lasers. A high degree of laser stability is indicated by excellent shot-to-shot reproducibility. Although no attempt has been made as yet to optimize the electrode profiles, the operating characteristics suggest the device can be scaled to large active volumes and input energies.

13.A8 High-Repetition-Rate TEA Laser System for Closed-Cycle Operation with Ultrapure Gases, Robert A. Olson, Dennis Grosjean, and Benjamin Sarka, Jr., *Systems Research Laboratories, Inc., Dayton, Ohio 45440,* Alan Garscadden and Peter Bletzinger, *Aerospace Research Laboratories, Wright-Patterson Air Force Base, Ohio 45433.*

A fast-flow high-pressure laser system capable of closed-cycle operation with ultrapure gases has been developed. The ultrahigh-vacuum properties of the system permit long gas-fill lifetime, as demonstrated by an undiminished laser output three weeks after filling. In experiments with He–Xe at a pressure of 700 torr, lasing was achieved at 2.03, 2.65, and 3.65 μm simultaneously. The laser pulses occurred predominantly during the afterglow of the 100-ns discharge pulse and lasted up to 5 μs after the discharge. Average output power was found to be a linear function of pulse-repetition frequency (PRF) up to 10 kHz. Multiline, multimode, average output power was $\approx$0.5 W at 10 kHz for a charging voltage of 10 kV and a discharge length of $\approx$12 cm. The rectangular output beam had approximately the same cross section as the discharge, viz., 1×3 cm^2.

The flowing gas system consists of a closed loop, constructed from 6-in-OD ultrahigh-vacuum components, through which gas is circulated by an axial fan. The fan is driven externally by a 400-Hz motor coupled to a Ferrofluidic rotary vacuum seal which maintains vacuum integrity at a fan rotation speed of 11 000 rpm. The gas-flow loop is initially evacuated through a 6-in valve by a 500-l/s vertical turbomolecular pump. Research-grade gases are admitted to the system from a gas manifold equipped with ultrapure gas regulators and ultrahigh-vacuum valves.

Converging and diverging transitions channel the flow into and out of a region of rectangular cross section where Rogowski-profile electrodes are located. The Lamberton-Pearson[1] configuration

[1] C. S. Liu, E. W. Sucov, and L. A. Weaver, *Appl. Phys. Lett.*, vol. 23, p. 92, 1973.
[2] C. J. Chen, N. M. Nerheim, and G. R. Russell, *Appl. Phys. Lett.*, vol. 23, p. 514, 1973.
[3] L. A. Weaver, C. S. Liu, and E. W. Sucov, *IEEE J. Quantum Electron.*, vol. QE-10, p. 140, 1974.
[4] I. Liberman, R. V. Babcock, C. S. Liu, T. V. George, and L. A. Weaver, *Appl. Phys. Lett.*, vol. 25, p. 334, 1974.

[1] H. M. Lamberton and P. R. Pearson, *Electron. Lett.*, vol. 7, p. 141, 1971.

is employed with upstream and downstream preionization wires being located at the electrode midplane. The transverse interelectrode flow speed is calculated from the velocity pressure as measured with a pitot-static probe located upstream of the converging transition. The flow speed through a 1-cm electrode gap is 250 ft/s for the 250-ft^3/min flow achieved with atmospheric-pressure helium.

The high-repetition-rate pulser which drives the laser discharge utilizes a thyratron-switched low-inductance energy-storage capacitor charged through a tetrode pulse modulator. The tetrode isolates the charging supply from the thyratron during each pulse and permits control of the charging time and duty cycle, thereby ensuring uniform energy storage per pulse and sufficient thyratron interpulse recovery time. CaF_2 windows oriented at the Brewster angle were used for optical coupling to the discharge, and a 1-m confocal cavity was formed by a total reflector and an output mirror having 10-percent transmission from 4.4 to 5.4 μm.

For laser media such as the rare gases which are adversely affected by small amounts of impurities such as N_2, O_2, and H_2O, this system is particularly suitable because of its low background-impurity level. Since high-pressure laser action has been reported for all of the rare gases,[2,3] an evaluation of the performance of the ultrapure closed-cycle system for the rare-gas mixtures He–Ne, He–Ar, He–Kr, Kr–Xe, Ar–Xe, and Ar–Kr will be made.

[2]S. E. Schwartz, T. A. DeTemple, and R. Targ, *Appl. Phys. Lett.*, vol. 17, p. 305, October 1, 1970.

[3]O. R. Wood, E. G. Burkhardt, M. A. Pollack, and T. J. Bridges, *Appl. Phys. Lett.*, vol. 18, p. 112, February 15, 1971.

13.A9 A Scalable High-Speed Switch for High-Power CO_2 Laser Radiation, A. J. Alcock, P. B. Corkum, D. J. James,* and K. Leopold, *Division of Physics, National Research Council of Canada, Ottawa, Canada.*

Fast switching of high-power 10-μm radiation by optically induced carriers in a semiconductor sample has been demonstrated. Initial studies carried out with a single-mode CO_2 TEA laser and a 2-ns ruby laser pulse have resulted in the generation of synchronized ~2-ns pulses at 0.7- and 10-μm wavelength. One application of this technique is the selection of a single pulse from the mode-locked output of a high-power CO_2 laser.

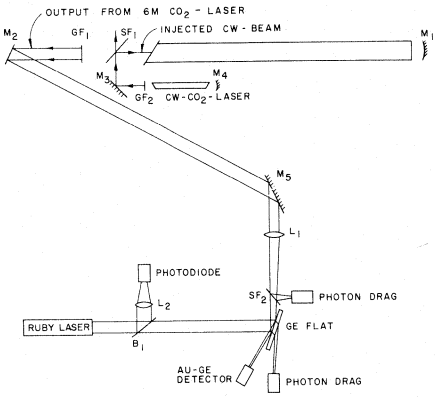

Fig. 1.

Techniques now exist for generating extremely high-power mode-locked pulses of CO_2 laser radiation.[1,2] For many applications it is desirable to select a single pulse from the train, and although several switching techniques are limited to relatively low power.

We have developed a switching technique which is readily scalable to large apertures and should thus allow the selection of extremely high-power pulses. Alternatively, the technique can be used to generate a gated 10-μm pulse in synchronism with the output of a visible laser. The switching element consists of a slab of germanium which is irradiated by a ruby laser pulse. Absorption of this radiation creates free carriers in the germanium[3-5] with sufficient density that a pulse of CO_2 laser radiation may be completely reflected. If the CO_2 laser pulse is plane polarized and incident on the germanium at Brewster's angle, high contrast switching may be achieved.

Fig. 1 shows the experimental arrangement used to investigate reflection switching. A single axial mode CO_2 laser pulse, of 200-ns duration, was generated by injecting the radiation from a low-power CW CO_2 laser into the resonator of a helical p-i-n TEA laser. The plane-polarized 10-μm radiation of ~2-MW peak power was incident at Brewster's angle on the polished surface of a slab of polycrystalline n-type germanium. A 2-ns pulse of ruby laser radiation [Fig. 2(b)] was also incident on the semiconductor and gave rise to a short pulse of reflected 10-μm radiation [Fig. 2(d)]. At a peak ruby laser intensity of ~20 MW/cm^2, the reflected 10-μm power was essentially equal to the incident power and the contrast ratio of the switch was ~300. At this ruby laser intensity damage to the germanium was not observed at CO_2 laser intensities of ~20 MW/cm^2. A decrease in transmission was also observed [Fig. 2(c)] with a fall time of approximately 2 ns and a significantly longer recovery time.

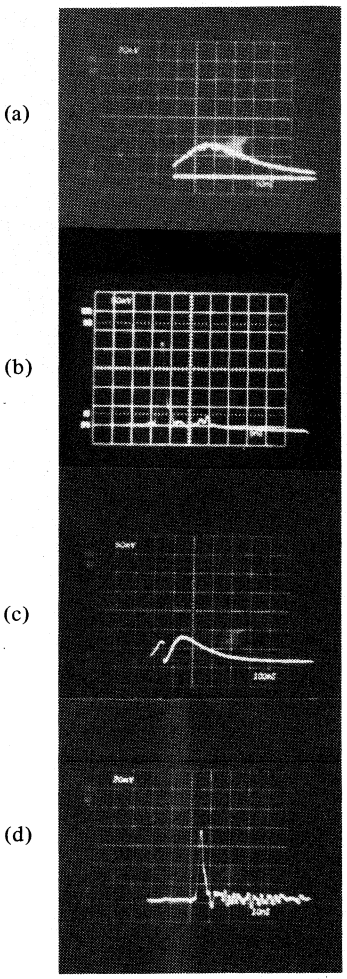

Fig. 2. (a) Incident CO_2 laser pulse; 50 ns/div. (b) Incident ruby laser pulse; 5 ns/div. (c) Transmitted CO_2 laser pulse; 100 ns/div. (d) Reflected CO_2 laser pulse; 10 ns/div.

More detailed investigations are now in progress. However, the aforementioned results clearly indicate the potential of this new approach to the control of high-power CO_2 laser radiation.

[1]P. A. Belanger and J. Boivin, *Phys. Can.*, vol. 30, p. 47, 1974.

[2]P. E. Dyer and D. J. James, *Appl. Phys. Lett.*, vol. 26, p. 331, 1975.

[3]W. R. Sooy *et al.*, *Appl. Phys. Lett.*, vol. 5, p. 54, 1964.

[4]G. N. Galkin *et al.*, *JETP Lett.*, vol. 7, p. 69, 1968.

[5]D. H. Auston and C. V. Shank, *Phys. Rev. Lett.*, vol. 32, p. 1120, 1974.

*Permanent address: Department of Applied Physics, University of Hull, Hull, England.

13.A10 A Direct Nuclear-Pumped Ne–N_2 Laser,* R. J. DeYoung, W. E. Wells, J. T. Verdeyen, and G. H. Miley, *Nuclear Engineering Program and Department of Electrical Engineering, University of Illinois at Urbana/Champaign, Urbana, Ill. 61801.*

Within the past year, rapid progress has been made in research on direct nuclear pumping of gas lasers. Workers at both Sandai[1] and Los Alamos[2] previously obtained lasing in CO and He–Xe, respectively, using a uranium-235 coating on the inner surface of the laser cell, demonstrating the feasibility of reactor-driven nuclear-pumped lasers. The present paper describes a new nuclear-driven laser that utilizes a boron-10 coating, Ne–N_2 gas, and provides simultaneous output at 8629 and 9393 Å in nitrogen. This laser has several distinctive features, namely the neutron flux, i.e., power input at threshold requirement is the lowest reported to date for nuclear pumping and the wavelengths fall into an attractive region in the near infrared (versus far-infrared output from the earlier lasers).

The experiment employed a 2.5-cm ID quartz laser tube containing a 60-cm section of aluminum tubing, coated on the inner surface with boron-10. The cell was placed next to the core of the Illinois TRIGA reactor such that thermal neutrons bombarding the boron coating caused emission of MeV α and Li^7-ions. These ions, in turn, ionized and excited the lasing gas. Pressure and concentration studies were carried out by utilization of a vacuum system attached to the laser external to the reactor. Lasing occurred at pressures above 75-torr Ne with very low partial pressures of N_2.

Fig. 1 shows a scope photograph of the laser output superimposed on the neutron pulse time history. The laser cavity was chopped by means of a small electric motor with fan blades which alternatively blocked and unblocked the back mirror. The large change in signal, among other things, clearly verifies that lasing occurred.[3] Note that the lasing

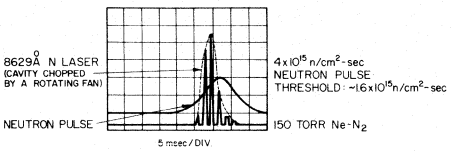

Fig. 1. Direct Ne–N_2 nuclear-pumped laser.

threshold took place at $\sim 1.6 \times 10^{15}$ neutrons/cm^2 · s, the lowest threshold of any nuclear-pumped laser to date. Since the neutron pulsewidth is much longer than the atomic and molecular processes taking place in the gas, this can be viewed as a near steady-state laser.

In summary, the significant results of this research are as follows.

1. For the first time nuclear pumping of a Ne–N_2 gas has been achieved at 8629 and 9393 Å. These transitions are at shorter wavelengths than previously reported lasers of this type. This is attractive since the photon energy is compatible with existing technology in optical components.
2. Lasing took place over 6 ms within the 10-ms neutron pulse, implying near steady-state laser operation.
3. A boron-10 coating was used, and this is the first nuclear laser using such a coating.
4. The lasing threshold was $\sim 10^{15}$ neutron/cm^2 · s, giving ~ 5 kW/l, the lowest threshold yet reported for nuclear pumping. A lower flux threshold could be expected with the more energetic ions from a uranium coating.

Because nuclear-pumped lasers can potentially be scaled up to quite high pressures and volumes, thus power levels,[4,5] such lasers must receive serious consideration for application requiring high powers.

*This work was sponsored by ERDA under Contract AT (11-1) 2007.

[1]D. A. McArthur and P. B. Tollefsrud, "Observation of laser action in CO gas excited only by fission fragments," *Appl. Phys. Lett.*, vol. 26, p. 187, Feb. 1975.

[2]H. H. Helmick, J. Fuller, and R. T. Schneider, "Direct nuclear pumping of a helium–xenon laser," *Appl. Phys. Lett.*, vol. 26, p. 327, Mar. 1975.

[3]R. J. DeYoung, M. A. Akerman, W. E. Wells, and G. H. Miley, "Studies of radiation-induced plasmas," presented at the 2nd IEEE Conf. Plasma Science, May 1975, Paper 3D2.

[4]G. H. Miley, "Direct pumping of lasers by fusion reactors," *Trans. Amer. Nuc. Soc.*, vol. 15, 1972.

[5]W. E. Wells, "Laser-pellet fusion by energy feedback to a direct nuclear pumped auxiliary laser," presented at the 2nd IEEE Conf. Plasma Science, May 1975, Paper 3D4.

Session 13-B

Thursday, May 29, 1975
8:00–10:00 P.M.

Post-Deadline Papers

Chairman: H. Kogelnik, *Bell Laboratories, Holmdel, N.J.*

13.B1 Fourier-Transform Holograms with X-Rays,* H. Mahr, *Cornell University, Ithaca, N.Y. 14853*, Benno Reuter, *Gesellschaft für Strahlen und Umweltforschung, Munich, Germany.*

We have recorded lensless Fourier transform[1] holograms of simple plane objects using X-rays at 44.8 Å (carbon K_α radiation). The generation of the hologram with an incoherent pointlike X-ray source was made possible through the use of a Fresnel zone plate. The zone plate acted very much like a beam splitter in that the zeroth-order radiation passing the zone plate provided the object illumination while the focused first-order radiation served as the reference point source, similar to an optical analog experiment. Original holograms were reconstructed with the visible light from a He–Ne laser to provide a 150-times enlarged image of the object taken at 44.8 Å.

Characteristic K_α radiation of carbon was generated inside a scanning electron microscope by focusing the electron beam onto a thick polished graphite target. The microscope was run at 21 kV in order to get currents of $2\text{–}4 \times 10^{-7}$ A and a small target spot size. Minimum spot size was monitored via the resolution of the scanning-electron-microscope picture of the graphite target. From experiments testing its coherence, the X-ray source size was estimated to be 2–4 μm.

X-rays emitted from the pointlike source were focused into the object plane with a Fresnel zone plate of focal length $f = 7.73$ cm for $C\text{–}K_\alpha$ radiation at 44.85 Å. A pointlike reference image of the source was obtained in the object plane at about twice the focal distance from the zone plate. About 10 percent of the intensity incident on the zone plate was transmitted into the point reference. Undeflected X-ray light proceeded through the zone plate and illuminated the object surrounding the point reference source with about 25 percent of the intensity incident on the zone plate. The superposition of this radiation, transmitted and diffracted by the object, with the reference beam produces the hologram in the film plane a distance c from the object plane.

An object that we found most suitable for a first test of the method is part of

*This work was supported by the U.S. Office of Naval Research and by the National Science Foundation through the Materials Science Center at Cornell University.

[1](a) G. W. Stroke, *An Introduction to Coherent Optics and Holography.* New York: Academic, 1966. (b) J. T. Winthrop and C. R. Worthington, *Phys. Lett.*, vol. 15, p. 124, 1965.

another zone plate, having 19 open zones in a gold foil of 440-μm diameter. if we center the reference beam through a slitlike "torn area," a "single-sided" object hologram of part of the zone rings in the right-half circle area is produced, and no superposition of the real and virtual images occurs in the reconstruction process.

Holograms were recorded with Eastman Kodak SWR film. A typical exposure laster between 20 and 40 min. We estimate that about 10^{-14} W of characteristic X-radiation was passing through the reference point and that the film received about 0.1 erg/cm^2 exposure in 30 min. This value agrees well with a measured exposure value of 0.3 erg/cm^2 (for $D = 0.6$) at 1200 Å.

Throughout the experiment, we were guided by results obtained with an optical analog setup. The image of a carbon arc source, filtered near 5800 Å with appropriate interference filters, served as a visible analog of the X-ray source of variable source size and spectral width.

The great advantage of the optical simulation was that holograms could easily be recorded under differing conditions of source size, spectral width of the source, intensity ratio of reference and object beam, steepness, graininess, and resolution of recording films, etc. By comparison with the X-ray holograms and through efforts to reconstruct these holograms, we found that the properties of the recording medium posed the most stringent conditions on the successful recording and reconstruction of X-ray holograms.

Reconstruction of the holograms was performed with a point reference source derived from a He–Ne laser at 6328 Å at approximately the distance c of the recording. A virtual image (magnified by the ratio of the wavelengths used in reconstruction and recording, or, $\lambda_{vis}/\lambda_x \approx 150$) could be seen by eye in the point reference plane or could be photographed.

The main problem with the reconstruction of the X-ray holograms was the low contrast of SWR film and the noise produced by the graininess of the film. Separate tests showed that a resolution of 120 lines/mm of SWR film is sufficient to record an object area within a radius of about 80 μm. Because of the low contrast and the graininess, the noise level in the reconstruction is much higher than the light level of the reconstructed image but for the brightest features.

Numerous tests, both with X-rays and optical simulation, were performed to determine the minimum conditions of coherence, ratio of reference to object intensity, resolution, and H–D curve of the recording material. With these minimum conditions established, we can now predict the minimum requirements for X-ray holography with laserlike sources in the vacuum–ultraviolet and X-ray region, as well as with synchrotron sources below 100 Å.

13.B2 Application of Electronically Scanned Semiconductor Lasers in Optical Data Processing, Yu M. Popov, *Lebedev Physical Institute, Moscow, USSR.*

No summary.

13.B3 Low-Divergence Beams from Grating-Coupled Composite-Guide Heterostructure GaAlAs Diode Lasers, R. D. Burnham, D. R. Scifres, and W. Streifer, *Xerox Palo Alto Research Center, Palo Alto, Calif. 94304.*

We report room-temperature operation of a new heterostructure diode laser which emits low-divergence grating-coupled output beams. The large output-beam divergence of conventional diode lasers is caused by their small emission aperture. Our device contains two closely spaced GaAs layers; one is electrically pumped, the other is corrugated. The corrugation scatters light out of the device at large angles to the waveguide plane, and since the light is emitted along the entire length of the laser, low-divergence output beams (in one dimension) are obtained.

A schematic diagram is shown in Fig. 1. The two waveguide layers (n-GaAs and active p-GaAs) are separated by a thin layer of n-$Ga_{0.7}Al_{0.3}As$. Light is generated by carrier injection into the p-GaAs active layer, but depending on the transverse mode excited, it spreads into the region occupied by the grating which is fabricated between the n-GaAs and n-$Ga_{0.7}Al_{0.3}As$ layers. This structure was chosen both for its usefulness in integrated optics and because the grating is not directly adjacent to the active region. In our experience, fabrication of the grating in the active layer causes undesirable nonradiative recombination.

Fig. 2 illustrates TE modes in the structure of Fig. 1. Since the TE_0 mode is primarily confined to the unpumped n-GaAs layer, it will experience little gain and is unlikely to lase. The TE_1 and TE_2 modes, however, do have sufficient overlap with the active region. The light in these modes also extends into the grating region and is therefore coupled out.

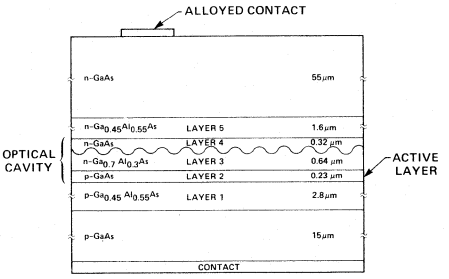

Fig. 1. Schematic diagram grating-coupled composite-guide diode laser.

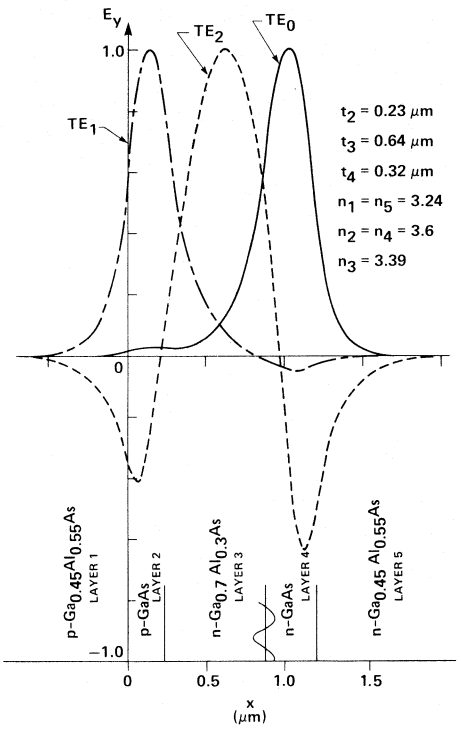

Fig. 2. TE mode patterns of composite-guide laser structure.

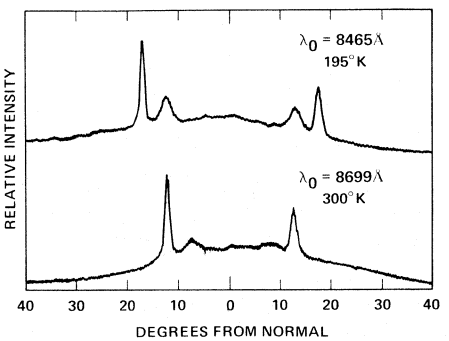

Fig. 3. Angular scan of the far-field radiation pattern of a grating-coupled composite-guide laser.

Scans of the grating-coupled far-field radiation pattern emitted through the n-side of a typical diode laser are shown in Fig. 3. At 30 K the center laser wavelength is 8699 Å at 15 A, which is twice the threshold current. Two strong beams are observed at angles of ± 12.4°

from the junction normal. Symmetric beams produced by the right and left traveling waves of the laser were always observed. However, the observed intensity of these beams is not equal. We believe this results from nonuniform pumping, as indicated by near-field observations with an IR microscope. Also observed were two weak beam modes at angles of ± 8.2°. At 195 K we also observe a total of four 8465-Å beams at ± 17.2° and ± 12.5°. All radiation was highly polarized with the E field parallel to the corrugations, which indicates that TE modes excite the radiation field. Calculations of beam angles and angular divergence agree well with the observations.

13.B4 Electrically Switched Optical Directional Coupler: COBRA, M. Papuchon, Y. Combemale, X. Mathieu, D. B. Ostrowsky, L. Reiber, A. M. Roy, B. Séjourné, and M. Werner, *Thomson–Compagnie Générale de Télégraphie sans Fil–L. C. R., 91401 Orsay, France.*

We report the realization, in titanium diffused lithium niobate,[1,2] of an integrated optical switch/modulator consisting of an active directional coupler with a novel electrode configuration (COBRA configuration: from Commutateur Optique Binaire Rapide).[3]

Switched directional coupler configurations previously suggested (but not, to our knowledge, fabricated) were based on the use of initially resonant coupled guides and three electrodes which permit changing the guide indices in opposite directions via applied, opposed electric fields, to destroy the resonance[4] in an optimum fashion. If one of the guides is initially excited, one can control the fraction of light leaving the coupler in each guide by switching between the resonant and nonresonant condition. We have used, however, the configuration shown in Fig. 1 in which there are only two electrodes, situated directly upon the guides. With the C axis of the crystal normal to the guide surface, the opposed direction of the vertical components of the fringing field in the two guiding regions gives the desired opposed index changes. The effect is maximal for TM polarized waves due to the large r_{zzz} electrooptic coefficient of $LiNbO_3$. Other

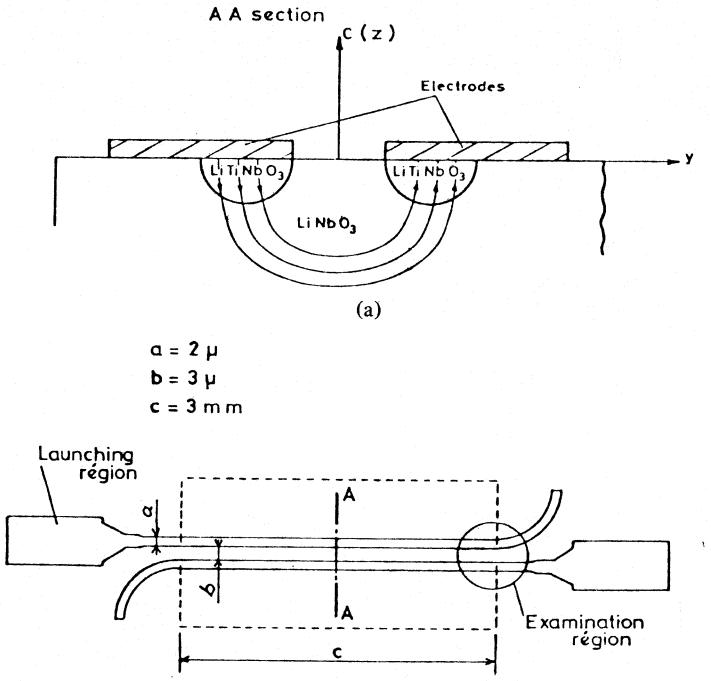

Fig. 1. COBRA.

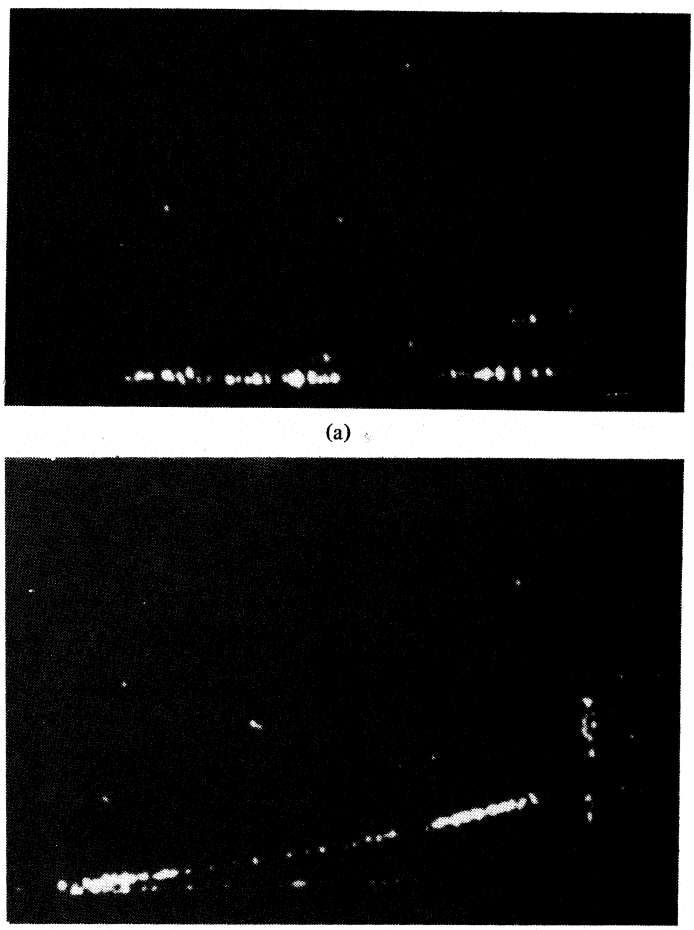

Fig. 2. (a) $V = 0$ V. (b) $V = 6$ V.

[1] J. M. Hammer and W. Phillips, *Appl. Phys. Lett.*, vol. 24, p. 545, 1974.
[2] R. V. Schmidt and I. P. Kaminow, *Appl. Phys. Lett.*, vol. 25, p. 458, 1974.
[3] M. Papuchon *et al.*, *Compt. Rend. ACSC*, to be published.
[4] S. Kurazono, K. Inasaki, and N. Kanagai, *Elec. Commun. Jap.*, vol. 55, p. 103, 1972.

effects, which we shall discuss, also occur due to the form of the fringing field and the other coefficients.

Approximately 500 Å of titanium was RF sputtered onto the $LiNbO_3$ surface. This Ti was then masked and etched[5] to obtain the guide configuration in the Ti [Fig. 1(b)]. The Ti was then diffused into the $LiNbO_3$ in an O_2 atmosphere[6] at 1100°C for approximately 11 h to form the guide structure.

Directional couplers fabricated in this way were examined by exciting one of the guides (using a rutile prism coupler) and observing (via fluorescence[7] or scattered light) the energy exchange between the guides. Typical coupling lengths observed for couplers formed from 2-μm-wide Ti strips were approximately 500 μm for a 2-μm guide separation, and 1 mm for a 3-μm guide separation. Since the final configuration chosen had a 3-mm coupling length and a 3-μm separation, we expect that in the resonant condition (0 V applied) nearly all the guided energy, at the exit end, will be in the guide which was not initially excited, and this is, indeed, observed.

The electrodes were prepared by RF sputtering a 2000-Å-thick gold film onto the structure and masking and ion etching this film to form two 1 × 3-mm electrodes separated by 3 μm at the coupler center.

Light from an argon laser was coupled into the upper guide (Fig. 1) from the left, and the light diffused out of the guides at the output end was observed as various voltages were applied. In Fig. 2(a) we see that with 0 V applied most of the light is, as expected, in the guide which was not initially excited. With 6 V applied [Fig. 2(b)] most of the light has switched back to the upper initially excited guide.

The switching was, as expected, more efficient for TM than for TE polarized waves and, despite the incomplete switching observed, we believe these results validate the COBRA principle.

[5]D. B. Ostrowsky, M. Papuchon, A. M. Roy, and J. Trotel, *Appl. Opt.*, vol. 13, p. 636, 1974.

[6]W. Phillips, private communication.

[7]D. B. Ostrowsky, A. M. Roy, and J. Sevin, *Appl. Phys. Lett.*, vol. 24, p. 553, 1974.

13.B5 NdLa Pentaphosphate Fiber Laser, H. P. Weber, P. F. Liao, B. C. Tofield,* and P. M. Bridenbaugh, *Bell Laboratories, Holmdel, N.J. 07733.*

*Present address: Materials Physics Division, Atomic Energy Research Establishment, Harwell, Didcot, Oxon., England.

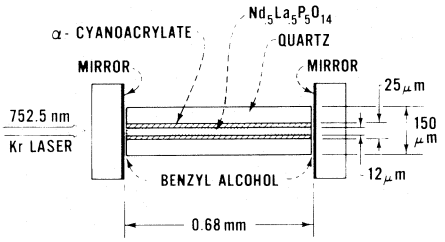

Fig. 1

We report the first successful operation of a laser using the high Nd concentration material $Nd_{0.5}La_{0.5}P_5O_{14}$ in the form of a single crystal fiber. The fiber serves both as the amplifying medium and as a waveguide.

The high concentration of Nd^{3+} ions in $Nd_{0.5}La_{0.5}P_5O_{14}$ (2×10^{21} cm^{-3}) means the length of the laser can be kept to a minimum with a resulting decrease in the number of longitudinal modes and in the total loss due to scattering from imperfections at the interface between the crystalline core and cladding. High concentration materials are also well suited for transverse pumping schemes.

Our laser was constructed with a single crystal fiber of cross-sectional area a = 12 × 12 μm and length l = 0.68 mm. The crystal was used as grown from phosphoric acid, as grown crystalline fibers are of excellent optical quality and their side faces are smooth. The axis of the fibers corresponds to the crystallographic a axis. The laser was constructed by cementing the pentaphosphate fiber into a hollow quartz fiber with alpha cyanoacrylate (see Fig. 1). The end faces were then polished and external mirrors were placed against the polished faces. To reduce loss at the mirror interface, it was immersed in benzyl alcohol.

The pentaphosphate laser was longitudinally pumped at room temperature with the 752.5-nm beam of a Kr^+ ion laser. True CW operation was obtained with a threshold of 10 mW of absorbed power. Calculated gain for this amount of absorbed power is 1.9/pass, which implies a loss of about 50 percent/pass. The diffraction loss in the absence of waveguiding would have been 90 percent and would have far exceeded the calculated gain at threshold. Hence waveguiding was an essential feature of the laser. The 50-percent loss probably resulted from scatter due to an imperfect interface between the fiber and the alpha cyanocrylate cement. We calculate that a reduction of this loss to 1 percent/pass would result in a threshold of 160 μW of absorbed power for the present geometry.

13.B6 An Organic-Dye Light Gate, David W. Vahey, *Battelle Columbus Laboratories, Columbus, Ohio 43201.*

The phenomenon of optically induced dichroism in organic-dye solutions[1] is the basis for a light gate that we have found to be competitive with the optical Kerr gate of Duguay and Hansen.[2] In our experiments, a helium–neon laser beam is partially transmitted through two crossed polarizers when there is a solution of cryptocyanine–glycerin between the polarizers, and when this solution is partially bleached by a giant ruby-laser pulse. A comparison to the optical Kerr gate is afforded by simply employing CS_2 in place of the dye.

We found that probe transmission through the dichroic device was relatively insensitive to variations in exciting intensity throughout the range ~2–20 MW/cm^2 (see Fig. 1). Over the same range the CS_2 gate transmission varied by a factor ~100. Moreover, the CS_2 gate transmission was less than that of the dye gate at intensities up to 10 MW/cm^2. These features make organic dyes attractive candidates for gates triggered by repetitively pulsed lasers that may have low peak power and some pulse-to-pulse instability. Dye light gates may also be useful at intensities beyond 10 MW/cm^2, since they employ solvents that do not exhibit the self-focusing nonlinearities of CS_2 and other molecules that display the optical Kerr effect.

Dyes are candidates as gating materials because they preferentially absorb light that is polarized along a certain molecular axis. A solution that is partially bleached by an intense pulse will tend to contain excited molecules aligned parallel to the optical polarization and unexcited molecules aligned normal to this direction. The result is a dichroism that can rotate the plane of polarization of a probe beam, enabling some component to pass through a pair of crossed polarizers. At increasingly high radiation intensities, this dichroism is quenched as all dye molecules are maintained in the excited state. Consequently, gating action may be terminated by raising the light intensity as well as by removing it. This feature should make the dye gate competitive with the CS_2 device even in the picosecond regime, despite the fact that the reorientational and excited-state relaxation times of dyes may be as large as nanoseconds. Computer simu-

[1](a) K. B. Eisenthal and K. H. Drexhage, *J. Chem. Phys.*, vol. 51, p. 5702, 1969. (b) C. V. Shank and E. P. Ippen, *Appl. Phys. Lett.*, vol. 26, p. 63, 1975.

[2]M. A. Duguay and J. W. Hansen, *Appl. Phys. Lett.*, vol. 15, p. 192, 1969.

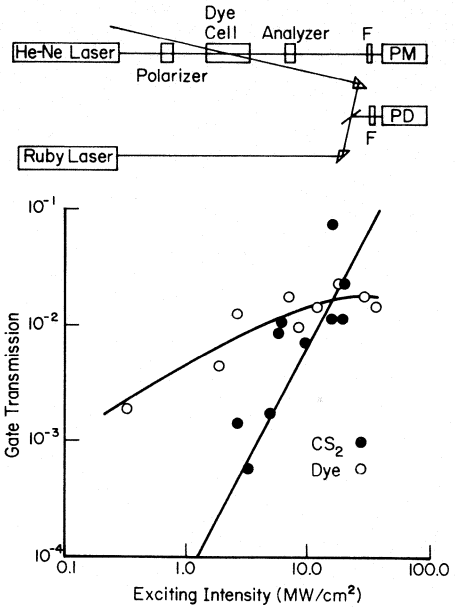

Fig. 1

lations suggest that a dye light gate based on induced anisotropy of gain can have a 0.5-ps rise time and a 3-ps open time when triggered by 10^9 W/cm^2, 10-ps pulses.

Although our experiments were not sensitive to the limiting resolution of the dye gate, we were able to observe intensity quenching of gating action on a nanosecond time scale. Triggering pulses of ~20-ns full width at half maximum duration and ~20 MW/cm^2 peak intensity occasionally passed 10–15-ns helium–neon laser signals during both the rise and fall of the exciting pulse, with little or no output during the time of peak intensity. The rise time of the gated output was as short as 5 ns, or only one-third the rise time of the ruby-laser excitation.

13.B7 On the Possibility of Isotope Selection through Selective Excitation of Molecular Vibrations, E. P. Markin, *Lebedev Physical Institute, Moscow, USSR.*

No summary.

13.B8 Macroscopic Isotope Separation of Uranium by Selective Photoionization, Sam A. Tuccio, Richard J. Foley, James W. Dubrin, and Oscar Krikorian, *Lawrence Livermore Laboratory, Livermore, Calif. 94550.*

The enrichment of uranium in milligram quantities has been obtained by using selective photoionization. In this experiment, a vapor stream of natural uranium was irradiated by two colinear laser beams to selectively photoionize ^{235}U atoms. The ions were then electrostatically separated from the neutral atoms and collected on a beryllium plate.

For the selective photoionization process, ^{235}U atoms were excited by the 3781-Å output from a xenon ion laser and then ionized by UV radiation from a krypton ion laser. The 3781-Å emission line from XeIII overlaps a uranium transition, initiating from a low-lying metastable level at 620 cm^{-1}. At an operating temperature of 2600 K, this level has a thermal population of approximately 27 percent. The 3781-Å transition in uranium has a ^{235}U–^{238}U isotope shift of 3 GHz. The emission bandwidth of the xenon laser used, approximately 4 GHz full width at half maximum, overlaps both the ^{235}U and ^{238}U absorption lines. A temperature-stabilized intracavity etalon with 10-percent reflective surfaces was used to narrow the xenon bandwidth to ~0.3 GHz and tune the output wavelength to excite ^{235}U only. The tuned output power of the laser was 70 mW. The krypton laser used had a nominal output power of 1 W, total, from the two UV lines at 3075 and 3564 Å.

The optical arrangement of the experiment was such that a vacuum chamber with Brewster-angle windows, housing the uranium source, was placed between the xenon and krypton lasers and was intracavity to the krypton laser. The output mirror of the xenon laser acted simultaneously as an output coupler for the xenon laser and a high reflector for the krypton laser. With this arrangement, the krypton laser radiation circulating through the vacuum chamber was 30 W. Both lasers used for this experiment were modified Spectra-Physics Model 170 Argon-Ion Lasers.

The uranium source consisted of a cylindrical oven, approximately 10 cm long, operating at a temperature of ~2600 K. Effusion of uranium vapor from a 1-mm by 8-cm exit slit provided an atom density of about 3×10^{13} cm^{-3} at the slit. The xenon and krypton ion laser beams, colinear and focused to about 0.2 mm, passed over the oven, parallel and adjacent to the exit slit.

A technique was developed to prevent contamination of the Brewster windows on the vacuum chamber by uranium vapor deposition and other vacuum system contaminants. Normally, significant contamination would occur within a few minutes of operation time. A quasi-static pressure of 0.5 torr of xenon gas was maintained at the inner-window surface by flowing xenon through an aluminum tube with a 3-mm bore, situated between the window and the uranium oven. Also a dc discharge was maintained in the xenon gas in a short region near the window. Adequate vacuum-pumping speed provided an overall chamber pressure of about 2×10^{-5} torr. With this technique, no observable contamination of the windows was incurred with several hours of running time.

Photoionized ^{235}U atoms generated at the oven exit slit were separated from the uranium vapor stream by the electric field produced by a beryllium collector plate, biased at −1500 V, located near the exit slit. The ions were deflected into roughly parabolic trajectories and made a deposition on the collector plate in an area of approximately 5 mm by 8 cm. Thermally ionized ^{238}U atoms emanating from the oven were also attracted to the plate, thereby diluting the collected ^{235}U sample. The neutral uranium atoms were allowed to condense onto a water-cooled U-shaped copper block located above the oven exit slit.

A 4-mg sample of uranium was collected in about 2 h. Mass spectrographic analysis showed the sample to be enriched to reactor grade quality, which is about 3-percent ^{235}U.

The macroscopic separation of uranium isotopes has been obtained by selective photoionization. This experiment was performed as part of a program to investigate the viability of laser separation processes based upon atomic vapors. Further experimental studies will be necessary to ascertain the economics of such systems.

13.B9 Two-Photon Laser Isotope Separation of Atomic Uranium—Spectroscopic Studies,† Excited State Lifetimes, and Photoionization Cross Sections, G. S. Janes, I. Itzkan, C. T. Pike, R. H. Levy,* and L. Levin,** *Avco Everett Research Laboratory, Inc., Everett, Mass. 02149.*

†This work was supported by Jersey Nuclear-Avco Isotopes, Inc., Bellevue, Wash.

*Present address: Exxon Nuclear Company, Inc., Bellevue, Wash.

**Present address: P.O. Box 9001, Beer-Cheva, Israel.

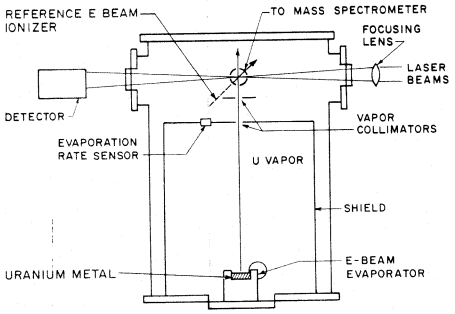

Fig. 1. Schematic diagram of vapor source and vacuum chamber.

One of the more attractive laser-isotope-separation schemes[1] involves the use of atomic uranium vapor. This paper describes experimental studies at low particle density which demonstrate selective two-step excitation and ionization of atomic uranium vapor and, additionally, measure a number of relevant parameters such as photoionization cross sections and state lifetimes. The apparatus should also prove to be a useful tool for the spectroscopic study of other atomic vapors as well.

In this experiment, uranium atoms are excited and ionized by light from short pulse-tuned lasers. The ions are detected and analyzed by a mass spectrometer. The vacuum tank is shown schematically in Fig. 1. Uranium vapor is produced at the bottom of the tank by electron beam evaporation. Only a small fraction of the vapor passes through a hole in the top of the shield and reaches the sensitive region of the mass spectrometer. The tuned laser light is provided by either a pair of pulsed dye laser systems or else by a single pulsed dye laser system for excitation followed by a pulsed nitrogen laser (3371 Å) for ionization. The exciter consists of two synchronized nitrogen lasers which transversely pump a dye oscillator and a dye amplifier. The dye oscillator is basically an Avco "Dial-A-Line"® laser with some tuning modifications.[2] The wavelength and linewidth of this dye laser are determined by the grating used as the rear reflector of the oscillator and two Fabry–Perot etalons. This combination of elements gave an oscillator linewidth of about 0.02 Å. A lens focuses the oscillator output into the amplifier. The wavelength of the exciter laser is monitored with both a standard 1.25-m spectrometer and a Fabry–Perot spectrometer. The ionizer and exciter beams are combined with a dichroic mirror prior to entering the vacuum tank through a window. A lens is used to focus this light into the sensitive region of the quadrupole mass spectrometer where it intercepts the uranium atoms. The total number of ions per pulse produced by two-step laser photoionization was small; however, the time of production was known precisely. By counting single ions, using digital logic, and multiplexing the mass spectrometer between U^{238} and U^{235}, it was possible to not only measure isotope ratios as a function of exciter wavelength, but also to estimate and correct for background effects and for ions produced by single photons. These results are shown in Fig. 2 where we demonstrate 50-percent enrichment of atomic uranium. The

[1] R. H. Levy and G. S. Janes, "Method of and apparatus for the separation of isotopes," U.S. Patent 3 772 519, Nov. 13, 1973.

[2] I. Itzkan and F. W. Cunningham, *IEEE J. Quantum Electron.*, vol. 8, p. 101, 1972.

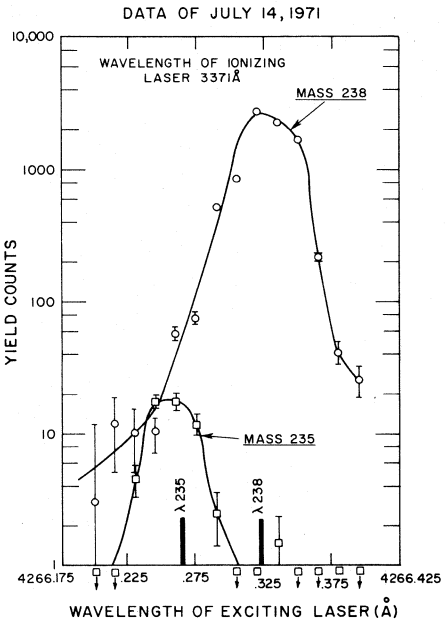

Fig. 2. Measurements of the two-step laser-induced "yield" for mass 235 and mass 238 as a function of the wavelength of the exciting laser. These data include corrections for background and for single photon yields. The error bars are due to counting statistics. Note that 50-percent enrichment has been obtained.

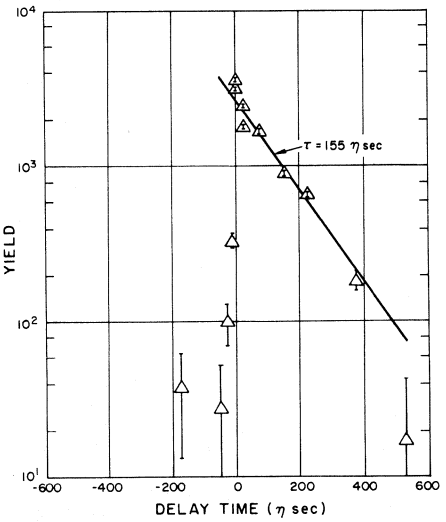

Fig. 3. Measurement of the counting rate yield due to two-step photoionization of uranium as a function of the delay between the exciting and the ionizing laser pulses. The error bars shown are due to counting statistics. The mean life of the excited state is seen to be close to 150 ns.

TABLE I
LIFETIMES OF SOME EXCITED STATES WITH LARGE ISOTOPE SHIFTS

Energy (cm^{-1})	Exciting Wavelength in Air (Å)	J	Isotope Shift	Lifetime (nsec)
23 572	4241.1	6	-.076	60
23 433	4266.3	5	-.057	155
23 212	4306.8	5	-.080	170
22 862	4372.8	6	-.061	135
22 583	4426.9	6	-.055	130
22 056	4532.6	6	-.081	300

raw data without background correction yielded a 30-percent enrichment.

Excited state lifetimes have been measured by observing yields as a function of the delay between the two laser pulses. These results are given in Fig. 3 and in Table I. In addition, for an excitation wavelength of 4266.325 Å the variation of two-step photoionization efficiency was measured as a function of the wavelength of the ionizing laser. The maximum yield at an ionizing wavelength of 3609 Å corresponded to a cross section of $2 \times 10^{-17}\ G_L/G\ \text{cm}^2$ where G is the linewidth of the optical transition and G_L is the laser linewidth. The ionization potential of uranium was determined to be 6.187 ± 0.002 eV.

13.B10 Isotopic Enrichment by Multiple Absorption of CO_2 Laser Radiation, J. L. Lyman, R. J. Jensen, J. P. Rink, C. P. Robinson, and S. D. Rockwood, *Los Alamos Scientific Laboratory, University of California, Los Alamos, N. Mex. 87544.*

The polyatomic molecules of SF_6, BCl_3, CF_2Cl_2, and SiF_4 have been irradiated in the presence of H_2 and N_2 with intense CO_2 laser pulses. All four of the polyatomic molecules underwent isotopically selective reactions with regard to the elements S, B, C, and Si, respectively.

The CO_2 laser was a conventional double-discharge design that delivered 0.5–2 J in a 200-ns gain switched pulse, the output depending upon the laser transition selected. Laser emission could be tuned to selected lines of both the 9 and 10-μ bands by means of a diffraction grating in the optical cavity. The radiation was focused with $f/1.5$ lenses into brass sample cells containing the gas mixtures. The products and residual reagents were analyzed with IR spectrophotometry and a quadrupole mass spectometer.

Mixtures containing 10-percent SF_6 and 90-percent H_2 were irradiated with the $P(16)$, $P(20)$, and $P(32)$ lines of the 10.6-μ band. All lines lie within the ν_3 absorption band of $^{32}S\ F_6$ and yielded comparable enrichment of the residual gas in $^{34}S\ F_6$.[1] The enrichment factor β is defined as $\beta = R/R_0$ where R_0 is the normal isotope ratio and R is the isotope ratio of the unreacted material following irradiation. Fig. 1(a) displays β as a function of the number of laser pulses parametric in the total gas pressure. In all cases, β was observed to increase linearly with the number of laser shots. However, for a fixed number of shots β increases as exp $(1/p)$, as shown in Fig. 1(b).

Similar experiments were performed with BCl_3, SiF_4, and CF_2Cl_2. All three species were irradiated with a CO_2 laser frequency that coincides with a strong absorption band of one isotopic form of the central atom. In all cases, depletion of the isotopic form irradiated was observed. The pressure dependence of β was similar to SF_6; however, enrichment factors of only about 2–5 were achieved. Both BCl_3 and SiF_4 showed evidence of an isotopic rescrambling reaction within the product gases. In all cases, the quantity of material enriched was on the order of 50–100 μg.

The mechanism of the isotopically selective absorption process and subsequent chemistry is still under investigation.

Two models under current consideration are 1) sequential selective absorption of n laser quanta followed by collisional dissociation of the excited molecules. The dominant collisional process would probably be anharmonic pumping by VV collisions or 2) sequential selective absorption of n quanta followed by multiphoton to absorption. Present data tend to support the latter model. Any theoretical model should consider the high peak power and related electric field at the focus along with the very large density of states ($>> 10^5\ \text{cm}^{-1}$) present in polyatomic molecules with more than a few quanta of excitation.

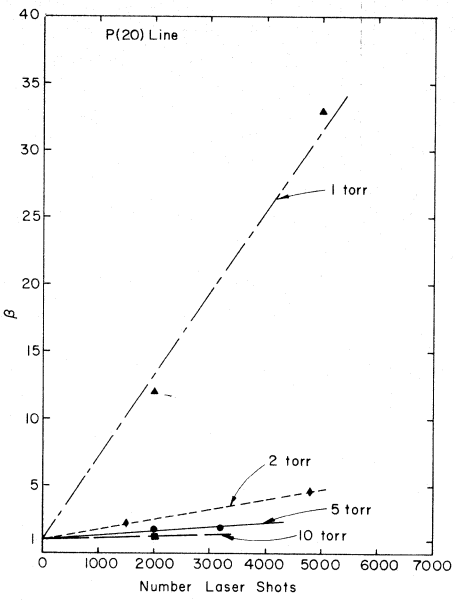

(a)

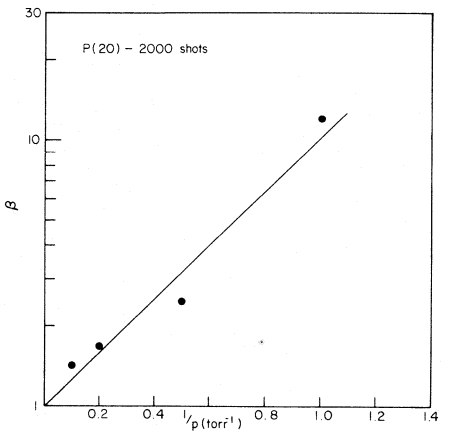

(b)

Fig. 1.

[1] Prior to completion of the SF_6 experiments, we were informed that Ambartzumian *et al.* had obtained, in a similar experiment, very high enrichment of ^{34}S. (R. N. Zare, private communication).

CLEA '75 Conference Committee

A. J. DeMaria, *Co-Chairman*
United Aircraft Research Labs
East Hartford, Connecticut

D. R. Whitehouse, *Co-Chairman*
Raytheon Company
Waltham, Massachusetts

A. S. Halsted, *Program Co-Chairman*
Hughes Aircraft Company
Culver City, California

H. Kogelnik, *Program Co-Chairman*
Bell Laboratories
Holmdel, New Jersey

A. Morandiere, *Conference Manager*
Courtesy Associates
Washington, D. C.

R. Andrews, *Treasurer*
Naval Research Laboratory
Washington, D. C.

M. J. Brienza, *Publicity*
United Aircraft Corp.
Norwalk, Connecticut

Lewis Winner, *Exhibits Manager*
New York, New York

A. Likely, *Press Relations*
American Institute of Physics
New York, New York

W. J. Schreibeis, *Safety*
Bell Laboratories
Murray Hill, New Jersey

CLEA '75 Steering Committee

IEEE

L. K. Anderson
Bell Telephone Laboratories
Murray Hill, New Jersey

F. R. Arams
LNR Communications
Farmingdale, New York

D. E. Caddes
Oximetrix
Mountain View, California

P. D. Coleman
University of Illinois
Urbana, Illinois

P. O. Clark
ARPA
Arlington, Virginia

A. G. Fox
Bell Telephone Laboratories
Murray Hill, New Jersey

E. I. Gordon
Bell Telephone Laboratories
Murray Hill, New Jersey

W. K. Kahn
George Washington University
Washington, D. C.

OSA

W. B. Bridges
California Institute of Technology
Pasadena, California

A. J. DeMaria
United Aircraft Research Labs
East Hartford, Connecticut

P. Franken
University of Arizona
Tucson, Arizona

J. W. Goodman
Stanford University
Stanford, California

D. R. Herriott
Bell Telephone Laboratories
Murray Hill, New Jersey

H. Kogelnik
Bell Laboratories
Holmdel, New Jersey

R. V. Pole
IBM Corporation
San Jose, California

D. C. Sinclair
University of Rochester
Rochester, New York

CLEA '75 Program Committee

A. S. Halsted, *Co-Chairman*
Hughes Aircraft Company
Culver City, California

H. Kogelnik, *Co-Chairman*
Bell Laboratories
Holmdel, New Jersey

R. L. Abrams
Hughes Research Laboratories
Malibu, California

R. Adler
Zenith Radio Corporation
Chicago, Illinois

A. J. Alcock
National Research Council
Ottawa, Canada

R. A. Andrews
Naval Research Laboratory
Washington, D. C.

P. Avizonis
AFWL/AR
Albuquerque, New Mexico

E. Beckner
Sandia Laboratories
Albuquerque, New Mexico

W. B. Bridges
California Institute of Technology
Pasadena, California

C. J. Buczek
United Aircraft Research Laboratories
East Hartford, Connecticut

R. L. Byer
Stanford University
Stanford, California

M. Cohen
Western Electric
Princeton, New Jersey

A. J. DeMaria
United Aircraft Research Laboratories
East Hartford, Connecticut

L. G. Deshazer
University of Southern California
Los Angelos, California

J. Giordmaine
Bell Laboratories
Murray Hill, New Jersey

J. Goell
IT&T
Roanoke, Virginia

J. P. Goldsborough
Spectra Physics, Inc.
Mountain View, California

R. Hella
Avco-Everett Research Labs
Everett, Massachusetts

S. F. Jacobs
University of Arizona
Tucson, Arizona

O. P. Judd
Los Alamos Scientific Lab
Los Alamos, New Mexico

N. V. Karlov
Lebedev Physical Institute
Moscow, U.S.S.R.

P. L. Kelley
Massachusetts Institute of Technology
Lexington, Massachusetts

H. Kressel
RCA Corporation
Princeton, New Jersey

W. F. Krupke
Lawrence Livermore Labs
Livermore, California

E. Leith
University of Michigan
Ann Arbor, Michigan

Tingye Li
Bell Laboratories
Holmdel, New Jersey

L. Osterink
GTE Sylvania, Inc.
Mountain View, California

R. I. Rudko
Raytheon Research Div.
Waltham, Massachusetts

B. B. Snavely
Lawrence Livermore Labs
Livermore, California

C. M. Strickley
Advanced Research Project Agency
Arlington, Virginia

W. Streifer
Xerox Corporation
Palo Alto, California

Teiji Uchida
Nippon Electric Co., Ltd.
Kawasaki, Japan

L. A. Weaver
Westinghouse Research Labs
Pittsburgh, Pennsylvania

D. R. Whitehouse
Raytheon Company
Waltham, Massachusetts

CLEA '75 Program Subcommittee for Japan

T. Uchida, *Chairman*
Nippon Electric Co., Ltd.
Kawasaki, Japan

H. Inaba
Tohoku University
Sendai, Japan

J. Hamasaki
Tokyo University
Tokyo, Japan

K. Sakurai
National Electrotechnical Laboratory
Tokyo, Japan

Y. Suematsu
Tokyo Institute of Technology
Tokyo, Japan

Y. Furukawa
Nippon Telegraph and Telephone Public Corporation
Tokyo, Japan

CLEA '75 Program Subcommittee for USSR

N. V. Karlov, *Chairman*
Lebedev Physical Institute
Moscow, U.S.S.R.

CLEA '75 European Advisory Committee

O. Hintringer
Siemens A. G.
Munich, W. Germany

E. Spitz
Thomson-CSF
Corbeville, France

C. E. Webb
Oxford University
Oxford, England

IXth INTERNATIONAL CONFERENCE 1976

QUANTUM ELECTRONICS

AMSTERDAM the NETHERLANDS JUNE 14–18, 1976

SPONSORS: EUROPEAN PHYS. SOC., DUTCH PHYS. SOC., PHYSICA (Neth.), A.I.P. and I.E.E.E. through the JOINT COUNCIL on QUANT. ELECTR. (USA)

TOPICS:
- Physics and chemistry with lasers
- Laser-induced isotope separation and chemical reactions
- Interaction of extremely intense radiation with matter
- Laser spectroscopy and environmental measurements
- Advances in coherent light sources
- Photon statistics and coherence effects
- Nonlinear optics, modulators and detectors
- New optical materials
- Integrated optics and guided waves

EXHIBITION: – During the conference at the congress site

CALL FOR PAPERS:

Both invited and contributed papers will be presented; working language in English. Original papers, not previously published or presented, are sollicited in the above mentioned areas.

Instructions are given in the call for papers available from the secretary of the Organizing Committee. Also local organisations will distribute the call for papers.

The authors are requested to submit both a 35-word abstract and a 500-word summary of their paper to the Technical Program Committee.

Deadline for contributions: December 15, 1975

Chairman Technical Program Committee
Prof. Dr. O. Svelto
c/o Prof. Dr. H. J. Frankena
Dept. Applied Physics
University of Technology
Lorentzweg 1
Delft/the Netherlands

Local Program Committee USA/Canada
Dr. J. A. Armstrong
IBM Thomas J. Watson
Research Center
P.O. Box 218
Yorktown Heights
NY 10598

Secretary Organizing Committee
Dr. J. Langelaar
Lab. for Physical Chemistry
University of Amsterdam
Nieuwe Prinsengracht 126
Amsterdam-C/
the Netherlands

REGISTRATION For a smooth organization, advance registration is highly desirable. Advance registration fee: Dfl 175,-; deadline April 14, 1976. Registration fee after April 14, 1976: Dfl. 275,-

GENERAL INQUIRIES
to be directed to Dr. Langelaar only.

Efficient and Practical Hydrogen Vacuum Ultraviolet Laser

I. N. KNYAZEV, V. S. LETOKHOV, AND V. G. MOVSHEV

Abstract—**Investigations of the hydrogen vacuum ultraviolet (VUV) laser carried out in the Institute of Spectroscopy of the USSR Academy of Sciences are reviewed. Data for VUV TEA H_2 and D_2 lasers at gas pressure up to 2 atm and for low-pressure high-repetition rate hydrogen lasers are presented. The upper limit quantum system efficiency for both gas discharge and *e*-beam excitation of H_2 lasers is discussed. The possibility of obtaining CW operation of the H_2-VUV laser is also discussed.**

I. Introduction

THE vacuum ultraviolet (VUV) region is very attractive for many laser applications. The electronic absorption and photoionization bands of most molecules occur in this region. In this wavelength region, the laser frequency becomes comparable with the electron plasma oscillation frequency for plasmas having charged particle concentrations of about 10^{22} cm^{-3}. The nonlinear resonance effects on the short wavelength electron transitions of atoms and molecules are increased sharply in this region. Intensive coherent VUV radiation can be utilized to optically excite tunable lasers which can in turn be utilized to investigate the ultraviolet (UV) region near the VUV cutoff limit. This region is presently unexplored by coherent radiation techniques. The most important laser parameter for the VUV photochemistry applications is the laser's average power output. Molecular excitation rates of the order of 10^{-3} molecules/h can be achieved with a laser having an average power output of 0.1 W. A power density over 1 MW/cm^2 is required for most optical pumping experiments. High power levels and comparatively high coherency are also required for performing nonlinear optical experiments. Lasers having efficiencies greater than 0.1 percent are suitable for most practical applications.

VUV laser action is presently obtained by *e*-beam excitation of condensed inert gases [1] and by frequency multiplying visible high peak power laser pulses [2], [3]. VUV laser action has been obtained by utilizing high current *e*-beam excitation of the bound-free transitions of gaseous xenon, krypton, and argon [4]. Unfortunately, lasers utilizing relativistic *e*-beam excitation present high radiation danger to the operators and the overall efficiency of the frequency multiplying laser systems is too small to be practical.

One of the most attractive VUV laser systems is the hydrogen laser [5]. The low-inductance single-shot self-sustained discharges obtained with solid-state dielectric switches [6] or with the nanosecond pulsed *e* beams [7] are widely used for exciting lasers. The average output power for the solid-state dielectric switch excited laser systems is limited to approximately 1 μW. The low average power is determined by the ratio of the laser pulse energy to the time interval required for the replacement of the dielectric in the switch.

The basic characteristics of the H_2-VUV quantum system are favorable for the conversion of electron excitation energy to the VUV laser emission energy (Table I). Effective electronic excitation cross sections of the upper laser states are comparable with the effective cross section of ionization and the total nonelastic losses of the hydrogen molecule. The ratio of laser radiation quantum energy to the excitation energy is higher than that for a CO_2 laser. The Doppler linewidth of the H_2 spontaneous radiation is four orders of magnitude less than the luminescence bandwidth of rare gas excimers. The parameter $g_{0v'}g_{v'v''}\beta_{v'J'}S_{J'J''}$ in the expression for gain, connected with the splitting of molecular electronic states into a system of vibrational-rotational sublevels, is about 10^{-2} for the H_2 laser transitions.[1]

The molecular hydrogen laser system is, therefore, capable of excellent performance. This performance at the present is far from being realized. The excessively high probability of radiative decay causes the inverted population to have an extremely short lifetime of ~1 ns. Effectively depositing the excitation energy into the active medium during such a short period of time is a rather difficult task. Low-inductance systems utilizing solid-state dielectric switches provide the formation of excitation pulses with appropriate parameters, but these systems are rather inconvenient in practice. The quantitative data on the limiting value of the excitation efficiency of laser states by *e*-beam excitation are still unknown. The operation of VUV lasers at high-repetition rates is important in order for these lasers to be widely utilized.

The main purpose of this paper is to report more precise measurements of the limiting parameters of the H_2 laser. The experimental results obtained with a single-shot TEA H_2-VUV laser and with a high-repetition rate low-pressure hydrogen laser are given. The upper limit of the laser states excitation efficiency for self-sustained discharges and for *e*-beam excitation is presented. The problem of the CW hydrogen VUV laser is also discussed.

II. Single-Shot TEA H_2-VUV Laser

A. Experimental Arrangement

The experimental arrangement of the TEA H_2-VUV laser used in our investigations is shown in Fig. 1. The 0.006 × 1 × 30-cm^3 laser volume was excited by a transverse discharge in the bipolar plane Blumlein line with a varied profile and a dielectric film switch. The probability of the corona discharge

Manuscript received September 30, 1974.

The authors are with the Institute of Spectroscopy, Academy of Sciences, Moscow, USSR.

[1] The characteristic values of Franck–Condon factors for the Lyman band system are $g_{0v'} = 0.07$, $g_{v'v''} = 0.3$, the Honle–London factor $S_{J'J''} = 0.5$, the parameter of rotational population $\beta_{v'J'} = 0.5$.

TABLE I
CHARACTERISTICS OF THE H_2 LASER QUANTUM SYSTEM

	Wavelength λ (Å)	Linewidth $\Delta\nu$ (cm^{-1})	$h\nu$ / E_{OK}	Effective Excitation Cross Section σ_{OK}^{max} (cm^2)	Effective Ionization Cross Section σ_{oi}^{max} (cm^2)
Lyman Bands	1600	0.6	0.65	$5.5.10^{-17}$	10^{-16}
Werner Bands	1200	0.8	0.85	4.10^{-17}	10^{-16}

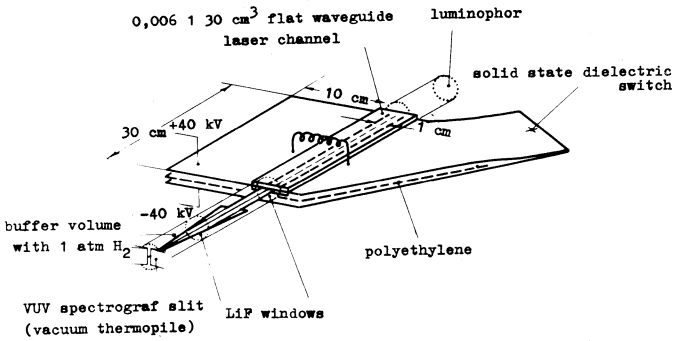

Fig. 1. H_2-VUV laser experimental arrangement.

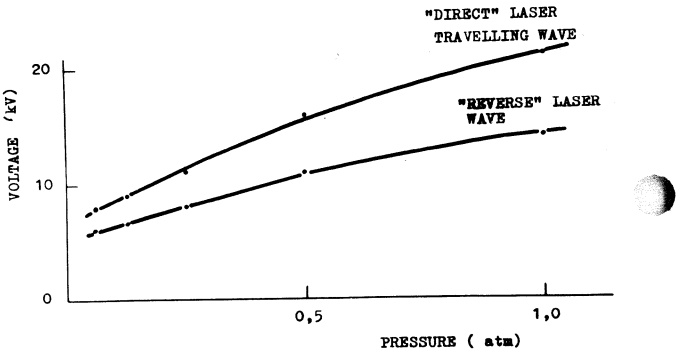

Fig. 2. Threshold voltage versus pressure behavior.

initiation (or surface breakdown) is sharply decreased by using the bipolar charging of the plates to $\pm V/2$. At voltages of $\lesssim 100$ kV, the bipolar charging of the plates is a more convenient solution of the surface breakdown problem compared with the distilled water or oil filled systems approach.

The mechanical initiation of the electrical breakdown of a polyethylene film by an electromagnetic (EM) striker was used. The traveling-wave excitation was provided by designing the pulse forming wing of the Blumlein line at a certain angle to the optical axis of the laser cell. A capacitive voltage divider with a time constant less than ~0.2 ns and the N2-7 oscillograph were used to measure the voltage pulse at the cell. The distinguishing feature of the system was the very narrow laser channel ($h = 60\ \mu$) which provided the high current density and a satisfactory spatial homogeneity of the discharge. The narrow channel also provided a comparatively large effective voltage pulse duration in the discharge gap. As a result, the conditions for laser excitation improved greatly. Copper foil electrodes having a thickness of 50 μ and polished edges were held fixed with epoxy adhesive at a distance $l = 1 \pm 0.05$ cm between polished glass plates. These plates had a rather high reflectivity for beams traveling at a small angle to the laser optical axis and thus formed a peculiar plane waveguide for the short-wave laser radiation. The Fresnel number for the laser volume was 7×10^{-2}.

The laser pulse energy was measured by a calibrated vacuum thermopile connected to the laser cell through a buffer volume (see Fig. 1). The volume was filled with hydrogen at 1 atm in order to prevent electric breakdown to the thermopile. The absence of the false signals was controlled by filling the volume with oxygen. For visual observation of the laser radiation, the rear window of the thermopile was covered by a thin layer of sodium salycilate.

The laser spectrum was measured by means of a VMS-1 spectrograph with an accuracy of 0.1 A. The laser radiation was directed from the cell through the LiF window and the intermediate vacuum tube with a LiF lens to the entrance slit of the spectrograph.

B. Experimental Results

For pressures up to 2 atm and with the operating voltage slightly over threshold, the radiation from the laser cell was unidirectional. The intensity ratio of the forwards and backwards beams was more than 10. The radiation divergence in the plane of the laser cell was 2° and about 1° in the direction perpendicular to the cell. For a pressure change of one order of magnitude (i.e., 0.1-1 atm), the threshold voltage only increases by a factor of 2-2.5 (Fig. 2). Near threshold, laser action was observed as a "reverse" traveling wave towards the commutator. At higher voltages, the unidirectional superluminescence traveling wave in the "forward" direction was observed. For the optimum excitation conditions, $p = 0.1$ atm and $V = 5$ kV, the laser pulse energy was 0.5 mJ. The laser energy remained constant with a diminishing of the wing length to several centimeters. The energy stored by the line for this case was about 0.1 J and the corresponding measured maximum efficiency was 0.5 percent. The formation of the superluminescence traveling wave for a 30-cm active length corresponds to the laser pulse duration of approximately 0.5 ns yielding a peak power of more than 1 MW and a power density of approximately 200 MW/cm^2 at the exit laser opening (Table II).

The densitograms of the H_2 and D_2 superluminescence spectra on the $B'\Sigma_u^+ \rightarrow X'\Sigma_g^+$ transition are given in Figs. 3 and 4. Five new laser lines have been observed in hydrogen, including two lines $P(3)$ (11, 14) and $R(1)$ (8, 14) ending in the last vibrational state $v'' = 14$ of H_2 close to the dissociation limit, as well as five new laser lines in D_2. The measured wavelengths of the new laser lines and their identification are given in Table III.

The laser spectrum differed greatly from the spontaneous

TABLE II
PARAMETERS OF THE TEA SINGLE-SHOT H_2-VUV LASER

λ	1610 Å
Maximum Laser Energy	0.5 mJ
Pulse Duration	0.5 nsec
Peak Power	1 MW
Peak Output Power Density	200 MW/cm^2
Efficiency	0.5%
Maximum H_2 Pressure	2 atm
Timer Interval Between Laser Pulses	10 to 60 sec
Mean Laser Power	$\lesssim$ 10 μW

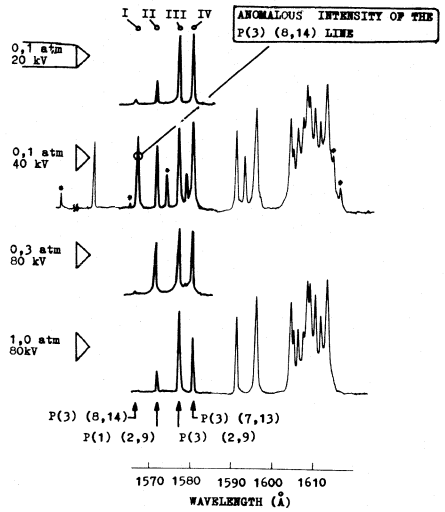

Fig. 3. Densitometer trace of the H_2-VUV laser spectra. The new laser lines are denoted by an asterisk.

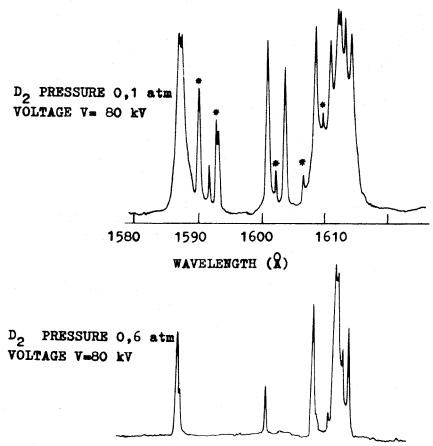

Fig. 4. Densitometer trace of D_2-VUV laser spectra. The new laser lines are denoted by an asterisk.

radiation from the same cell by the line intensity ratio and the number of observed transitions. The 1:0.7 characteristic intensity ratio for P and R branch lines of spontaneous radiation was not observed for the laser radiation. Luminescence occurs mainly at the P branch and there are no lines of the R branch in the spectrum, as a rule. The line intensity ratio for ortho- and paramodification of hydrogen was observed to be severely distorted. Radiation was observed on only a relatively few lines. Only 23 lines were observed in the laser cell spectra compared with the hundreds of electronic vibrational-rotational lines normally observed in the transitions of the Lyman hydrogen band system in the spontaneous radiation.

The specific intensity ratio of the laser lines remained almost constant at various hydrogen pressures and charging voltages of the Blumlein line (see Fig. 3). The lines $P(3)$ (8,14) and $P(3)$ (7,13) (I and IV in Fig. 3) which end at levels close to the dissociation limit were observed to be exceptions to this rule. It is convenient to take the lines $P(1)$ (2,9) and $P(3)$ (2,9) (II and III in Fig. 3) with the rather deep-lying lower vibrational levels as the comparison lines. The line $P(3)$ (8,14) is weaker than the line $P(1)$ (2,9) at p = 0.1 atm and at low voltages. At higher voltages, the $P(3)$ (8,14) line becomes comparable in intensity with the strongest lines of the spectrum and becomes more intensive than line II. Increasing the gas pressure resulted in decreasing the laser lines' intensities, especially for the $P(3)$, (8,14) and the $P(3)$ (7,13) lines. The latter becomes weaker than line III. At a low gas pressure, the ratio between intensities of the two last lines become inversed.

The rise time of the voltage pulse applied to the laser cell τ_f is dependent on the width of the forming line (Fig. 5). For a narrow line, τ_f is determined by the commutation time of the solid-state dielectric switch. In our experiment, it was in the range of 0.3–0.6 ns. In a line with variable profile, the voltage transformation illustrated by Fig. 6 was observed.

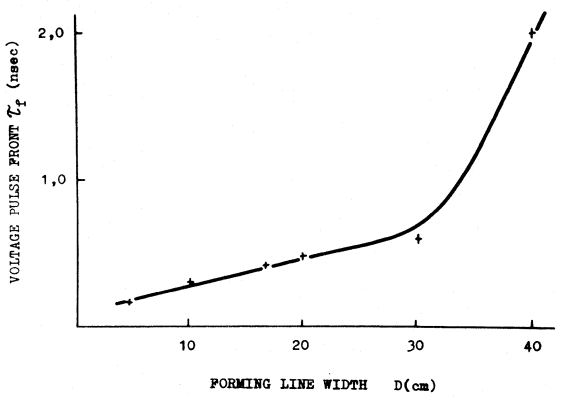

Fig. 5. Voltage pulse rise time applied to the laser cell as a function of Blumlein linewidth.

TABLE III
NEW LASER LINES OF THE H_2 AND D_2 LYMAN LASER

	H_2					D_2				
λ (Å)	1494.2	1565.5	1574.3	1614.8	1616.5	1589.9	1592.3	1602.1	1606.3	1609.5
Transition	P(3)(11,14)	R(1)(8.14)	P(2)(2,9)	P(4)(5,12)	P(5)(5,12)					

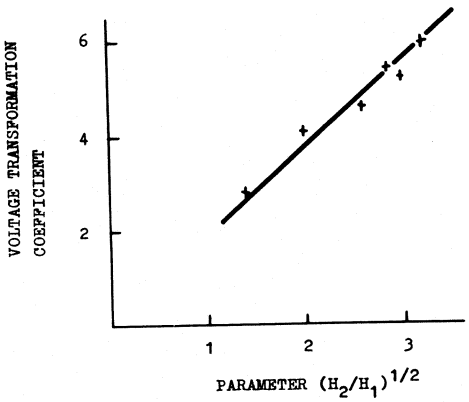

Fig. 6. Peak voltage transformation coefficient versus line thickness ratio near the laser cell and the commutator.

C. Discussion of the Results

Comparatively high operating performance of the single-shot H_2 laser was obtained by using supernarrow laser channels, choosing an optimum width of the line, and operation at a sufficiently high voltage. In the narrow channel, a high current density $j_{max} = V^{max}/\rho S = 10^5$ A/cm^2 was obtained. For this condition, a rather long effective pulse duration of high electrical field in the discharge, $\tau \sim \gamma_0^{-1} \ln (l/h)$, was achieved; $S = b \cdot h$ is the cross section of the discharge gap perpendicular to current direction; γ_0 is the electron avalanche growth constant; ρ is the wave impedance; and $\epsilon = 2.2$.

The single-channel switch forms in the two-dimensional line a circular wave of voltage having a width b, with variable amplitude, and having a maximum $-V$ at the commutation point. This wave is attenuated as $1/r$ as it propagates down the line. It is reflected from the rear and side edges of the line. The experimental results show that the wave becomes approximately a plane at a distance $2B$. The rise time of this wave depends on the commutation time of the switch and on the formation time of the plane wave. The quantitative analysis of the discharge wave propagation is difficult because of the necessity of solving a two-dimensional wave equation in a limited space. The main conclusion reached from the experimental data is that despite the more complicated process of wave formation in a plane line, the amplitude of the resultant wave at distance $\gtrsim 2b$ is equal to V as in a one-dimensional line. In other words, the line is recharged completely.

The voltage transformation was experimentally observed for the line with a variable profile (Fig. 6). The ratio of transformation for a linear line is $V_2/V_1 = 2(\rho_2/\rho_1)^{1/2}$ where V_1, ρ_1, V_2, ρ_2 are the voltage and wave impedance at the points 1 and 2. The factor of 2 arises due to a reflection at the open end. In accordance with the previously mentioned wave formation, the voltage transformation in a plane line may be described by the same expression with wave impedance ρ_1 averaged over the length of the wave formation. For constant wave impedance $\rho_1 = 377 H_1/b(\epsilon)^{1/2}$, where H_1 (centimeters) is the distance between the plates at the beginning of the line. For a constant linewidth, the transformation ratio is

$$K = 2\sqrt{\frac{\rho_2}{\rho_1}} = 2\sqrt{\frac{H_2}{H_1}}$$

where H_2 is the distance between the plates at the end of line. The expression is consistent with the diagram in Fig. 6.

Let us now consider the intensity anomalies of the laser lines terminating near the dissociation limit. Potential curves of some electronic states of molecular hydrogen are illustrated in Fig. 7(a). The radiation lifetimes of the upper laser states are $\tau^B = 0.8$ ns, $\tau^C = 0.6$ ns [9]. The lifetimes of the lower laser states at gas pressures $p \lesssim 0.3$ atm are determined by the wall diffusion with the characteristic time $\tau_d = (h/\pi)^2/D = 10^{-3}$ s ($p = 1$ cm). For pressures $p \gtrsim 0.3$ atm, the lifetimes of the lower laser states are determined by the vibrational-translational relaxation with the corresponding time of the order of the VT relaxation time for the lower molecular levels $\tau_{VT} = 5 \times 10^{-4}$ s · atm [10]. Thus the H_2 laser operates on the typical self-terminated scheme.

The peculiar feature of the hydrogen laser is the decay of the upper laser state $B'\Sigma_u^+$ on the vibrational-rotational levels of the ground state near the dissociation limit [Fig. 7(a) and (b)]. Laser action is observed on the last stable level of the hydrogen molecule $v'' = 14$, $J'' = 3$, located only 48 cm^{-1} below the H_2 dissociation limit. This suggests that the dissociative depletion of the lower laser states is possible with the corresponding interpretation of observed anomalies. The dissociative depletion of laser states has been considered in our paper [12] in connection with the problem of the four-level hydrogen laser.

The intensity of superluminescence is proportional to the excitation rate of the upper laser state. The relative electron excitation rate of vibrational-rotational levels within the laser electronic state does not change sufficiently with the gas pressure and voltage on the discharge gap. Corresponding specific intensity ratio of superluminescence lines should remain constant. An increase in gas pressure results in a relative intensification of intermolecular processes including the molecular dissociation from vibrationally excited states near the dissociation limit.

The depletion of the vibrationally excited molecules is possible due to collisional transitions to the unstable rotational states lying above the dissociation limit and subjected to the rotational predissociation. For laser states lying within kT from the dissociation limit, a direct collisional transition to a continuous state is also possible. The existence of unstable states is connected with the rotational deformation of the potential energy curve of the ground state. The curve of effective potential energy $V_J(r) = V(r) + J(J+1)h^2/2\mu\rho^2$ passes through the maximum [Fig. 7(b)] in the region of large internuclear distances and then approaches gradually the dissociation energy $V(\infty)$; ($V(r)$ is the molecular potential energy without regard to the rotation, and μ is the reduced mass). The rotational levels $J'' = 4,5$, $v'' = 14$ are located above the dissociation limit but below the maximum of the corresponding curve $V_J(r)$. The nonradiative lifetime for these levels due to the tunneling to a repulsive state is of the order $\tau \sim T_{vib}/D^* = 10^{-11}$ s [13] with the corresponding natural linewidth of 0.6 cm^{-1} compared with the Doppler width; T_{vib} is the period of molecular vibration and D^* is the tunneling coefficient. The corresponding comparatively narrow lines have been observed in the spontaneous radiation spectrum [11]. The states $J'' = 6$, $v'' = 14$ overlie the maximum effective potential. The lines terminating on these states have not

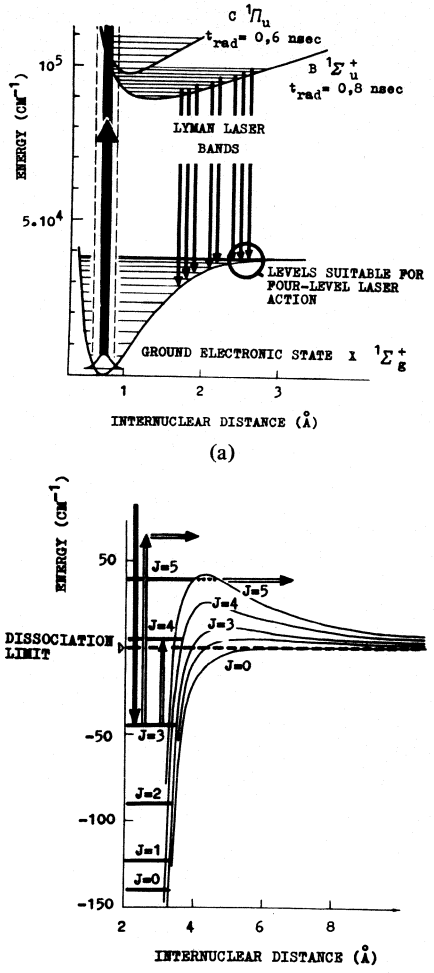

Fig. 7. (a) Potential energy curves of H_2. Lower laser level structure near the dissociation limit (circled) see Fig. 7(b) for details. (b) Energy levels of last excited vibrational state of H_2 $v'' = 14$. Dotted horizontal line denotes dissociation limit of ground state. Downward vertical line corresponds to the observed laser action on the last stable molecular level $v'' = 14, J'' = 3$.

been observed in spontaneous spectra due to the excessive natural width caused by fast molecular dissociation.

The collisional lifetime of the $v'' = 14$, $J'' = 3$ level is approximately equal to $\tau_{14,3}^{coll} \approx 4.5 \times 10^{-11}$ s · atm. At $p \gtrsim 0.05$ atm $\tau_{14,3}^{coll}$ becomes less than the radiative lifetime of the upper laser states $\tau^B = 0.8$ ns, and the four-level laser action can take place on the line $P(3)$ (8,14). The lifetime of inversion population on this transition is no longer limited by the value τ^B. Depending on the experimental conditions, at a rather long excitation pulse duration, this lifetime may be much longer than that for the rest of the self-terminated transitions. The corresponding anomalous behavior of the line intensity should show up in the superluminescence spectra. This behavior is determined mainly by the temporal dependence of the excitation rate of the laser electronic states $f_{0K}(t) = N_0 n_e(t) \langle \sigma_{0K} v \rangle t$.

The absence of a rather strong superluminescence line $P(3)$ (8,14) at $\rho \gtrsim 0.3$ atm and a considerable attenuation of the line $P(3)$ (8,13) at $p = 1$ atm indicate that gain is rapidly decreased for transitions terminating on the vibrational-rotational levels $v'' = 13,14$ of the ground state near the dissociation limit. The collisional broadening for these levels is the biggest

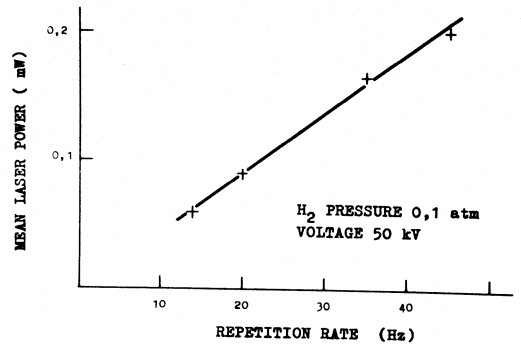

Fig. 8. Characteristics of high-repetition rate H_2-VUV laser. Average power versus repetition rate.

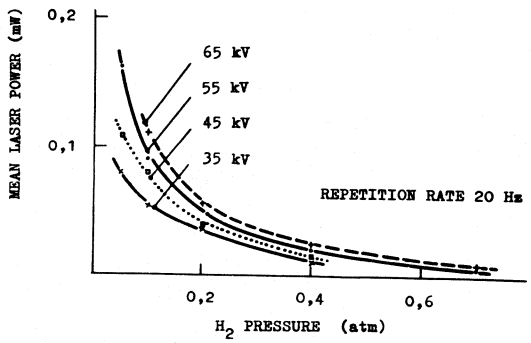

Fig. 9. Average power output versus H_2 pressure.

and accounts for the observed intensity drop for the broadening parameter ~0.3 cm^{-1} atm^{-1}.

The single-shot hydrogen laser with a solid-state dielectric switch is very inconvenient in practice because of the necessity of changing the dielectric film. The mean laser output for a 1-min average time of changing the dielectric switch is about 10 μW. A comparatively high voltage $\gtrsim$40 kV is needed for laser operation. In this case, the film width should be about 20 cm. For higher voltages, two changeable films are needed. Changing of the films in this case is a rather complicated operation with certain difficulties in mechanization. In this connection, the high-repetition rate H_2-VUV laser with the gas discharge spark-gap commutator is of particular interest.

III. High-Repetition Rate H_2-VUV Laser

A. Experiment

A high-repetition rate pulsed output was obtained by triggering a SF_6 spark gap pressurized at 9 atm. The measured commutation time of the spark gap was slightly longer than 1 ns. The repetition pulse rate was usually operated up to 50 Hz. The mean laser power output was directly proportional to the repetition rate (Fig. 8). The laser power increased with increasing voltage and decreased with increasing gas pressure (Fig. 9). At pressures below 40 mmHg, the system could not be operated because of breakdown. The maximum attained laser power was about 0.4 mW at $f = 45$ Hz and the laser pulse energy was about 10 μJ. The laser output power decreased with increasing dielectric film thickness of the transmission line [Fig. 10(a)]. Decreasing the length of the wings of the transmission line below $l \lesssim 8$ cm [Fig. 10(b)] begins to decrease the laser output power. The efficiency of the system was 0.03 percent (Table IV).

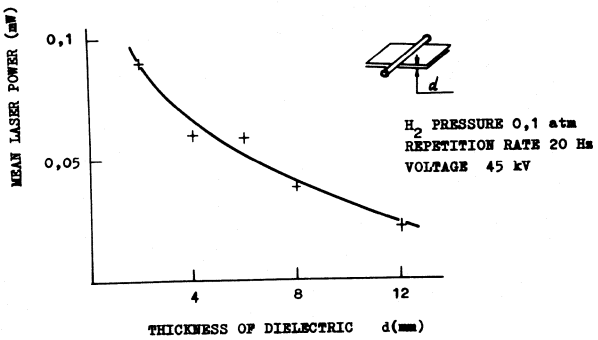

(a)

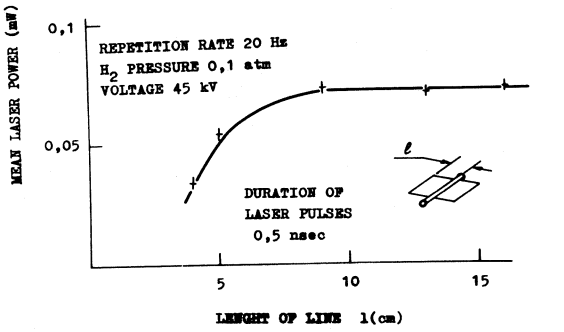

(b)

Fig. 10. (a) Average power output dependence on the Blumlein line thickness. (b) Average power versus Blumlein line length.

TABLE IV
PARAMETERS OF HIGH-REPETITION RATE H_2-VUV LASER

λ	1610 Å
Mean Power	0.4 mW
Repetition Rate	50 Hz
Laser Pulse Duration	0.5 nsec
Peak Power	20 kW
Optimal Pressure	30 torr
Efficiency	0.03%

B. Discussion of the Results

The observed decrease in the laser output power with pressure results from the reduction in the electric field to pressure ratio (E/P) and with the corresponding reduction of the $\langle \sigma v \rangle$ parameter which determines the excitation rate of the laser levels. For fixed (E/P), the laser power increases with increasing laser gas pressure up to a range of approximately 0.1 atm. Beyond this gas pressure, the laser power remains constant. At higher pressures, the molecular quenching of excited electronic states appears to be significant. The probability of quenching is related to the radiative decay probability A at gas pressure p (atmospheres) and to the effective quenching cross section q (square centimeters) by the relationship

$$\sigma_q p = A/2.7 \times 10^{19} vp$$

where $v = 2 \times 10^5$ cm/s is the gas-kinetic velocity of the molecules at room temperature. There is no accurate data available on the value σ_q for B state of molecular hydrogen. This cross section is apparently of the same order of magnitude as for the gas-kinetic cross section [14]. The quenching is substantial in this case at a gas pressure about 0.1 atm.

The region of relatively high pressures $p \gtrsim 0.05$–0.1 atm is unsuitable because of the short time interval τ with respect to the high electrical field existing in the discharge channel where τ is inversely proportional to the rate of electron avalanche growth $\gamma_0 = N_0 \langle \sigma_{01} v \rangle$. Effective excitation of laser states is attained provided the $\langle \sigma v \rangle$ coefficient is a maximum at least during the laser pulse length Δt. This at once sets a limit on the molecular concentration $N_0 \lesssim N_0^*$. For higher molecular concentration, the time interval τ becomes shorter than Δt and the excitation efficiency of the laser states decreases. It should be noted that the same situation may also hold for the nitrogen laser as well as for any other laser excited by a self-sustained discharge.

The laser pulse duration is about 0.5 ns as stated in Fig. 10(b). Laser action in a system having short plates for the transmission line is of particular interest in connection with the ones desired to develop advanced small-size excitation systems for such lasers. As it follows from Fig. 10(a), the wave impedance of the line should be decreased. The limit is set by the electrical strength of available materials.

The laser pulse energy for a discharge system having a spark-gap commutator is approximately one order of magnitude less than for lasers having solid-state switches. This occurs because of two factors. The rise time of the voltage pulse exciting the laser cell is longer for the gas-discharge switch. This is equivalent to considerably decreasing the line charging voltage which, of course, leads to a corresponding decrease in the laser output pulse energy. The wave impedance of the gas discharge switch is comparatively high. As a result, the current density in the active volume is much smaller than when a solid-state switch is utilized. This results in decreasing gain and output laser power.

The average laser power may be substantially increased by pulse charging the line up to a voltage of 150–200 kV. Capacitors of 50–100 pF can be charged to such voltage without much difficulty. The cross section and the active volume of the laser cell can also be increased at the same time in order to obtain higher laser pulse energies. If high-repetition rate high-pressure spark-gap commutators are developed, the average laser output power can be increased by the operation of the laser at higher repetition rates. The repetition rate can be increased up to at least a few kilohertz without physical limitations. Forced cooling of the electrodes and the cell walls can be performed to remove the effects of gas heating on the redistribution of gain on the rotation–vibrational lines of the band, as well as on the tendency to increase the Doppler linewidth. A principal limitation is encountered with the H-atom recombination rate and with the depletion of the long-lived lower laser states. The corresponding characteristic times are of the order of the molecular wall diffusion time $\tau_d = (\Delta/\pi)^2 D^{-1} = 3 \times 10^{-7}$ s, where $\Delta = 10^{-2}$ cm and $D = 10$ cm/s at $p = 0.1$ atm. Thus even with present laser cells, an average power of about 30 mW can be attained at a repetition rate of 5 kHz. This is

quite sufficient for many applications for this laser. The major limitation at present is mainly with the commutator. For satisfactory laser operation, the stored electrical energy of a few tenths up to a few joules should be commutated at high-repetition rates. The development of commutators with the required parameters is essentially alleviated due to the smallness of the commutated electrical energy.

The hydrogen laser considered in the preceding operates on a three-level scheme. The main disadvantage of this scheme is an extremely short lifetime for the inversion population of ~1 ns. This short lifetime causes many difficulties. It is difficult to use the resonator effectively. This involves the necessity of having a high gain in the active medium in order to utilize the superluminescence mode of operation. The laser coherence for this mode of operation in this case is comparatively poor. Requirements on pumping power are respectively increased. The consequences are heavy demands on the excitation system. As a result, the alternative four-level laser excitation scheme is of specific interest. The excitation systems for such schemes may have ordinary parameters. Before discussing this scheme, we should consider the limiting efficiency of the H_2 laser quantum-mechanical system.

IV. The Limiting Excitation Efficiency of the Hydrogen Laser Levels

The H_2-VUV laser is excited at present by using nanosecond self-sustained discharge and relativistic electron beams. To choose optimum excitation conditions, it is necessary to have information on the excitation efficiency of the hydrogen laser levels excited by e beam or in a gas discharge. The high energy electronic excitation is of interest also in connection with the existence of accelerated electrons in discharges having rather low pressures under high voltages. These electrons may also substantially affect the laser states population.

The excitation efficiency of the B and C states [Fig. 7(a)] in the electronic energy region $0 \lesssim \epsilon \lesssim 10^2$ eV is considered by using the data on effective cross sections of electron excitation of rotational σ_r [15], [16] and vibrational σ_v [16], [17] levels of the ground state, triplet [18], [19] electronic states $a\,^3\Sigma_g^+$, $b\,^3\Sigma_u^+$, and $c\,^3\Pi_u$ with the total effective cross section σ_d. Excitation of triplet states and a subsequent radiation decay leads to molecular dissociation. We used also the data on the effective excitation cross sections of the laser states σ_{0B}, σ_{0C} [20], the singlet electronic state $E'\Sigma\sigma_{0E}$ [21], ionization with H_2^+ ion formation [22], and the data on the effective elastic collision cross section of electrons with hydrogen molecules σ_e [16].

The energy losses of electrons in nanosecond pulsed discharges occur through collisions of electrons with hydrogen molecules in the ground state. Relative energy losses in the kth collisional process are

$$\chi_K^{\text{disch}} = \frac{\langle \sigma_{0K} v \rangle \epsilon_{0K}}{\Sigma_J \langle \sigma_{0j} v \rangle \epsilon_{0j} + \left\langle \int_0^{(\epsilon-\epsilon_{0i})/2} \epsilon_s \sigma_{0i}(\epsilon, \epsilon_s)\, d\epsilon_s \cdot v \right\rangle}. \quad (1)$$

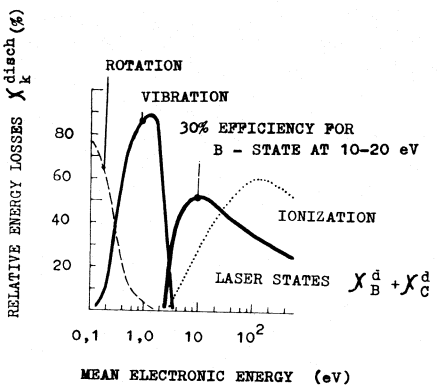

Fig. 11. Excitation efficiency of the H_2 molecular states in the gas discharge versus the mean electron energy.

Fig. 11 shows losses χ_K^{disch} versus the electron energy. At low electron energy of $\epsilon \lesssim 6$ eV, results of numerical calculations [16] are used. For 6 eV $\lesssim \epsilon \lesssim$ 100-eV energy range, effective cross sections are averaged over the Maxwellian velocity distribution of the electrons. The losses on the kinetic energy of the secondary electrons, given by the right-hand term of the denominator in (1), become substantial at $\epsilon \gtrsim 70$ eV. The maximum excitation efficiency of laser states $\chi_B^d + \chi_C^d = 50$ percent is achieved at the mean electron energy of about 10-20 eV (Fig. 11). Efficiency decreases rapidly with diminishing electric field ϵ, especially in the region $\epsilon < 5$ eV. Electronic energy over 10 eV is attained at $E/p \gtrsim 500$ V · cm^{-1} torr^{-1}. This value of electronic energy is maintained during 0.6 ns at a gas pressure $p = 0.05$ atm for a system having a wave impedance of 1 Ω for the storage line. In the following quasi-CW phase of the discharge, the mean energy $\epsilon \sim$ 2-3 eV is established in accordance with the charged particle balance in the volume. Losses of electrons and positive ions are caused by volume recombination and ambipolar diffusion. The excitation efficiency of the laser states for this phase is insufficient due to comparatively low electron energy.

The excitation efficiency of the H_2 laser states by high energy electron beam is convenient to consider on the basis of a simplified model. The optimal use of the e-beam energy is achieved in the case of complete stoppage of the electrons in the laser volume V. The corresponding conversion efficiency of the total energy of e beam to the kth electronic state excitation energy may be considered over all the volume V during the current pulse. There is no need in this case for detailed study of the space-time pattern of the electronic energy losses and the approximate analytical analysis becomes possible. The addition of energy losses of the various electrons during the generations process were implicitly used to simplify the analysis. The rather precise set of data on the effective electron cross sections available at present for many atoms and molecules makes it possible to consider the problem using characteristics of particular collisional processes.

Laser states are excited in the process of energy loss of primary and secondary electrons. To determine the total efficiency κ^K, it is convenient to introduce the following value:

$$\kappa^K = \frac{\sigma_{0K}\epsilon_{0K}}{(1/N_0 v)(d\epsilon/dt)} = \frac{\sigma_{0K}\epsilon_{0K}}{(1/N_0)(d\epsilon/dx)}$$

$$\sqrt{\frac{1}{N_0}}\frac{d\epsilon}{dx} = \Sigma_m \sigma_{0m}\epsilon_{0m} + \delta_e + \int_0^{(\epsilon-\epsilon_{0i})/2} \epsilon_s \sigma_{0i}(\epsilon, \epsilon_s)\, d\epsilon_s + \int_0^{\epsilon} \epsilon_b \sigma_b(\epsilon, \epsilon_b)\, d\epsilon_b. \quad (2)$$

The parameter κ^K is the average part of the energy expended by the monoenergetic electrons with the initial energy in the range ϵ, $\epsilon + d\epsilon$ at distance dx on the kth collisional process. The balance equation for the mean electron energy is used in (2). The parameter κ^K does not depend strictly on time and position coordinates and is only a function of energy. Terms in the denominator are, respectively, excitation of quantum states and ionization, elastic losses, losses on the secondary electron kinetic energy, and bremsstrahlung radiation. In (2), v is the velocity of electrons and $d\epsilon/dx$ is the "ionization" losses of the electrons. At comparatively low electronic energies, elastic losses are $\delta_l = 2m\sigma_l\epsilon/M$, where m and M are the mass of the electron and atom/molecule, respectively, and σ_l is the effective cross section of the elastic collisions. The mean energy loss of electrons in elastic collisions with nuclei at energies in the range 10^3-10^5 eV are negligible due to the rapid drop of the corresponding differential scattering cross section with angle.

The parameter κ^K is plotted in Fig. 12 against the electron energy.[2] In the nonrelativistic energy region, approximately up to 0.2-0.4 MeV, the first two terms in the power expansion of the effective cross sections of the optically allowed transitions and ionization, calculated in the Born approximation, may be used (expansion on powers of ϵ^{-1})

$$\sigma_{0K} = \sigma^0_{0K}\frac{\epsilon_K}{\epsilon}\ln\frac{\epsilon}{\epsilon_K}. \quad (3)$$

In (3) $\sigma^0_{0B} = 1.5 \times 10^{-16}$ cm^2, $\sigma^0_{0C} = 1.1 \times 10^{-16}$ cm^2, and $\sigma^0_{0i} = 3.5 \times 10^{-16}$ cm^2. The experimental data on ionization [22] are described by (3) with an accuracy of 20 percent over the entire energy region of $10^2 \lesssim \epsilon \lesssim 10^4$ eV where measurements have been carried out. For the relativistic energy region $\epsilon \gtrsim 0.2$-0.4 MeV, the following approximation can be used [24]:

$$\sigma^r_{0K} \simeq \sigma^0_{0K}\frac{\epsilon_{0K}}{mv^2}\ln\left[\frac{mv^2}{2\epsilon^2_{0K}}\frac{\epsilon'}{(1-\beta^2)}\right] \quad (4)$$

where m is the rest mass of electron, $\epsilon' = mc^2[(1-\beta^2)^{-1/2} - 1]$, and $\beta = v/c$.

General control of used approximations for the effective cross sections of the electronic collisional processes in hydrogen can be carried out by using the known data on energetic losses of electrons $d\epsilon/dx$ [24] according to the relation ($\epsilon \lesssim 60$ MeV)

[2] Index K takes the following values: $r, v, d, B, C, E, i, i^d, b$, and e.

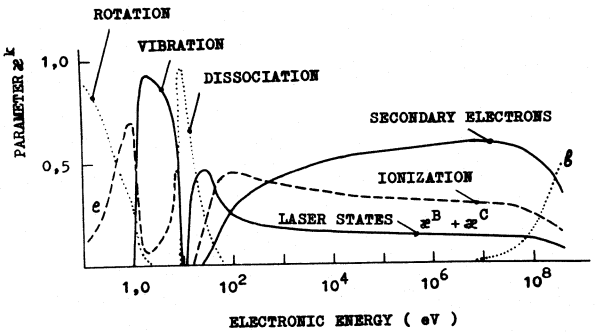

Fig. 12. Parameter κ^K dependence on energy: e—elastic collisions; b—bremsstrahlung radiation.

$$10^6\frac{\rho}{N_0}\frac{d\epsilon}{dx} = \Sigma_m \sigma_{0m}\epsilon_{0m} + \int_0^{(\epsilon-\epsilon_{0i})/2} \epsilon_s \sigma_{0i} \cdot (\epsilon, \epsilon_s)\, d\epsilon_s = \delta(\epsilon) \quad (5)$$

where $d\epsilon/dx$ (in MeV/cm^{2}g^{-1}), and $\rho = 9.10^{-5}$g $\cdot$ cm^{-3} is the density of hydrogen. The chosen effective cross sections provide descriptions of the energetic losses of electrons over a wide energy region with an accuracy of <10 percent (Fig. 13). Maximum deviations occur in a relativistic region of $\epsilon \gtrsim 1$ MeV. The energetic dependence of the effective ionization cross section $\sigma_{0i}(\epsilon, \epsilon_s)$ have substantial effect on the curves at high electronic energies. The inverse square dependence increases electronic energy losses at 1 MeV approximately 1.5 times (the curve 1 in Fig. 13). More precise results are obtained with index 2.1 [24].

The maximum excitation efficiency of B and C laser states $\kappa^B + \kappa^C \simeq 50$ percent is achieved at the electronic energy about 30 eV (Fig. 12). The efficiency drops quickly with energy and for 10 keV $\lesssim \epsilon \lesssim$ 10 MeV the efficiency is stabilized at a level $\kappa^B + \kappa^C = 14$ percent. Main energetic losses, up to 55 percent, are accounted for by the kinetic energy of the secondary electrons. In the ultrarelativistic energy region $\epsilon \gtrsim 60$ MeV, the bremsstrahlung radiation becomes a dominating channel of losses, and the excitation efficiency of the laser states drops drastically (Fig. 12). The excitation efficiency of vibration levels and triplet electronic states by the primary electrons is extremely low, of order of the ratio of molecular state energy to the initial electronic energy.

The excitation efficiency of the kth collisional process by completely stopping groups of electrons with initial energy in the interval ϵ, $\epsilon + d\epsilon$ is approximately

$$\kappa^K_0 = \frac{1}{\epsilon}\int_0^t N_0 \sigma_{0K} V \epsilon_{0K} dt = \frac{1}{\epsilon}\int_0^{\epsilon} \kappa^K d\epsilon \quad (6)$$

(t_0—time of complete stoppage of electrons). The change of variables $t = t(\epsilon)$ is used here according to the electronic energy balance equation. The electronic energy distribution function is changed for the stopping electrons and the effective width of the function $\Delta\epsilon$ is increased. The effective cross sections of ionization and laser states excitation (allowed optical transitions) at $\epsilon \gtrsim 200$ eV vary rather slowly in

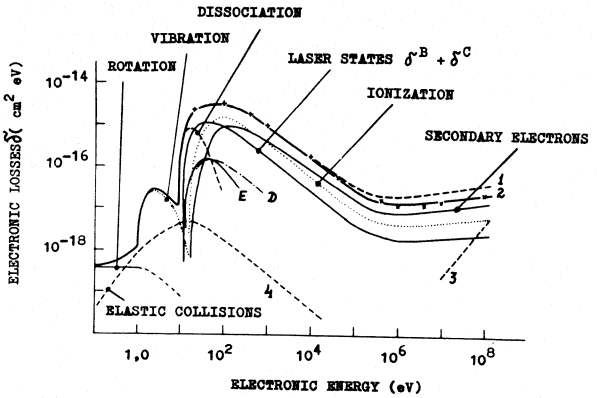

Fig. 13. Energy losses of electrons in H_2. 1—total losses for inverse square dependence of $\sigma_{0i}(\epsilon_1 \epsilon_s)$ from energy. 2—total losses for index 2, 1. 3—bremsstrahlung losses. 4—elastic collisions with nucleus. E, D—singlet electronic states.

the energy range $\Delta\epsilon$. Electrons lose energy by small portions $\sim\epsilon_{0i}$, considerable changes of energy in processes with secondary electrons are unlikely. This fact justifies to some extent the use in (6) of the product $\sigma_{0K}(\epsilon)v(\epsilon)$ at the mean electron energy ϵ instead of the coefficient $\langle\sigma_{0K}V\rangle_t$ averaged over the time-dependent electron velocity distribution.

The interaction of the primary electrons with the gas yields secondary electrons with considerable kinetic energy. These electrons also cause ionization and excitation. Part of the kinetic energy is transmitted to the secondary electrons of the following generations. Overall excitation of the electronic states is determined by the primary electrons and the secondary electrons of all generations.

The basic characteristics of secondary electrons of successive generations are the following: the total number of electrons in jth generation n_j, the energy distribution function of electrons φ_j, the total initial kinetic energy of electrons W_j, the maximum energy of electrons ϵ_j^{max}, and the excitation efficiency of kth process. Table V gives recurrent relations for these parameters, including an approximate expression for the energy distribution function of the electrons. All parameters are integral in time and space for given electron generation.

The total conversion efficiency of energy of the monochromatic electron beam with the energy ϵ_0 to the kth inelastic process, including secondary electrons, is

$$\kappa^K(\epsilon_0) = \frac{1}{W_0}\sum_{j=0} W_j\kappa_j^K = \sum_{j=0}\kappa_j^K\prod_{l=0}^{j-1}\kappa_l^s. \qquad (7)$$

The kinetic energy of the second generation electrons is ~15 percent of that of primary electron beam. The total kinetic energy of the third generation is ~2.0 percent of the initial energy of the electron beam. Fig. 14 shows the energetic dependence of total efficiency κ^K. At energies $\epsilon > 10^3$ eV, the parameters κ^K vary rather slightly. For this energy range, a certain relation between effective cross sections as well as between energetic losses for basic inelastic processes is established. The total efficiency of excitation for laser states of the Lyman and Werner band systems is somewhat less than 30 percent; κ^B = 16 percent, κ^C = 13 percent. Half of the total

TABLE V
TRANSITIONS SUITABLE FOR CW VUV LASER ACTION (LYMAN BANDS)

Band	Parameter $f_{v'v''} \times 10^2$	Line	Wave Length (Å)
	Molecular Hydrogen		
(8,14)	2.02	P(2)	1567.525
		P(3)	1567.249
		P(4)	1566.431
(10,14)	0.83	P(2)	1518.184
		P(3)	1518.005
		P(4)	1517.343
(11,14)	0.89	P(2)	1495.686
		P(3)	1495.565
		P(4)	1495.012
		P(5)	1494.190
	Molecular Deuterium		
(11-20)	P(2)	P(2)	1596.249
		P(3)	1596.115
		P(4)	1595.772
(12,21)		P(1)	1580.193

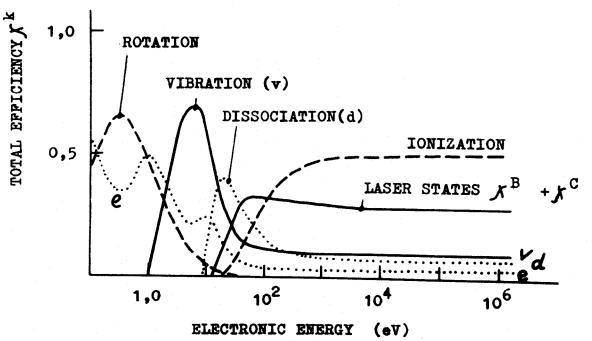

Fig. 14. The total excitation efficiency of molecular states of H_2 by electrons in dependence on the initial electronic energy. e—elastic collisions. For $\epsilon \lesssim 30 \div 50$ eV approximate data are given.

energy is expended on ionization; about 7 percent on excitation of triplet electronic states. Obtained results can be controlled by comparison with the mean energy $\bar{\epsilon}$, needed for ion pair formation. This value is almost constant over wide energy region of primary electrons [23], and for hydrogen it is $\bar{\epsilon}$ = 36.5 eV. For considered scheme $\bar{\epsilon} = \epsilon_0/n = \epsilon_{0i}/\chi^i = 3$/eV ($n = \chi^i\epsilon_0/\epsilon_{0i}$ is the total number of secondary electrons produced by the primary electron). The agreement with the approximate calculations is quite satisfactory.

Performed analysis shows that the H_2-VUV laser quantum system converts the energy of e beams into the excitation energy of laser electronic states with the efficiency approximating a limiting value. Complete absorption of electrons in the laser volume is a basic condition for the effective use of electron beam energy in hydrogen. Decreasing the electron path by increasing gas pressure is possible only to a certain limit.

This limit is connected with the quenching of electronic stages and collisional broadening of the amplification lines. The electronic path decreases rapidly with diminishing of electronic energy in proportion to $l \propto \epsilon^{1.8}$. At low electronic energy, the main difficulties are connected with the injection of e beam into the laser volume and with the ability to attain a sufficient value of electronic current. It becomes necessary to use thin separating foils with thickness of 1-10 μ.

For optimal usage of the e-beam energy, the special confining systems of high-speed electrons in the active volume can be used along with methods mentioned in the preceding. Such systems are of particular importance at low gas pressure. In a simple transverse excitation system with magnetic field H = 1 kG directed along the active medium the Larmor radius of electrons with energy ϵ = 100 keV, $r = mvc/eH$ is 1 cm. Although the general picture of high energy electron scattering in a rather rarefied gas at $p \sim 0.1$-1.0 atm in a magnetic field is not clearly understood, one should expect from qualitative considerations a sharp reduction of the volume, where electronic energy is absorbed.

It is difficult at present to draw a certain conclusion in favor of self-sustained gas discharge or e-beam excitation methods for H_2-VUV laser. At present, self-sustained discharges are preferred due to the absence of effective e-beam confining systems. In small volumes with narrow laser channels, a higher specific pumping power up to 10 GW/cm^3 is obtained in gas discharges at low-pressure $p \sim 0.1$ atm.

V. On the CW H_2-VUV Laser

A. Depletion of the Lower Laser Levels

Four-level laser system of molecular hydrogen and deuterium [12] is one of the most promising for CW laser action in the VUV region due to the rather small spectral width of amplification lines ~0.6 cm^{-1} and to the corresponding comparatively low-threshold pumping energy. The practical realization of this most favorable CW VUV laser scheme is obviously a rather difficult problem. In connection with this difficulty, it is useful to consider the main kinetic processes in the scheme in some detail.

The potential energy curve of the upper state of the Lyman band hydrogen laser is highly displaced about the ground state towards long internuclear distances [Fig. 7(a)]. The result is intensive transitions to the highly excited molecular levels of the ground (lower laser) state located within kT from the dissociation limit. There are three basic mechanisms of effective depletion of these levels. Depletion of H_2 levels v'' = 14, J'' = 4,5 overlying the dissociation limit has been already considered in the preceding. It occurs due to the rotational predissociation. Dissociation in molecular collisions and depletion due to VT relaxation are also effective. The nonradiative lifetime of the levels at optimum conditions may be much less than the radiative lifetime of the upper laser levels. At moderate pumping power of molecular hydrogen in gas discharge or by CW e beam, the population of the upper laser state is determined mainly by the electronic excitation rate, radiative decay, and molecular quenching. Population of lower laser levels depends on the radiative decay rate of the upper electronic states, dissociation rate, atomic hydrogen recombination, as well as VV and VT relaxation of the vibrational level system of the ground electronic state. The most critical for CW laser action is concentration of atomic hydrogen in the discharge. This concentration is determined by electronic dissociation rate of the molecules and by the atomic recombination rate on chamber walls and during triple molecular collisions in the gas volume.

The probability of predissociation of the levels v'' = 14, J'' = 4,5, and $W^{pr}_{v''J''} = D_{v''J''}/T_{\text{vib}}$ is about two orders of magnitude more than that of radiative decay of the higher laser states. Calculations of bound-bound and bound-free transitions probabilities for molecular states are the dissociation limit is a rather difficult task of molecular-collision physics [25]. A close bound between vibration and rotation involves certain difficulties in studying the problem. The molecular vibration amplitude is not small compared with the range of intermolecular forces. The Massey parameter $\xi = 4\pi^2\,\Delta\epsilon/\alpha v h \sim 1$ ($\Delta\epsilon$—transition energy, α—constant of exponential interaction potential, v—molecular velocity). The last two circumstances present essential difficulties in using perturbation theory. The exact form of the interaction potential for vibrationally excited molecules and molecules in the ground state is unknown. The corresponding population equations are strongly bound due to rather high transition probability, and it is very difficult to solve them even by numerical methods.

Particular problems, related to dissociation, are usually considered by assuming the coefficients $\langle \sigma_{v''J'',d}\, v\rangle$ for levels $v''J''$ in the immediate vicinity of the dissociation limit to be

$$\langle \sigma_{v''J'',d}\, v\rangle = \kappa \langle \sigma_l v\rangle \exp\left(-\epsilon_{v''J'',d}/kT\right) \tag{8}$$

where σ_l is the effective cross section of elastic collisions, $\epsilon_{v''J'',d}$ is the dissociation energy for the state $v''J''$, and κ is the arbitrary parameter of the order of 1. This corresponds to the dissociation cross section

$$\sigma_{v''J'',d} = \begin{cases} \kappa\sigma_l, & \epsilon \geqslant \epsilon_{v''J'',d} \\ 0, & \epsilon < \epsilon_{v''J'',d} \end{cases} \tag{9}$$

for collisions along the center line.

Levels v'' = 14, J'' = 0, 1, 2, 3 of H_2, and v'' = 20, 21 of D_2 lying within kT($T \simeq 300$ K) below the dissociation limit are subjected to direct transitions to continuous spectrum during molecular collisions with the probability

$$W^d_{v''J''} = \kappa v/\tau^*_{0vi} = \kappa\sqrt{2}\, N_0 \pi (r_0 + r_{v''})^2\, vp,$$

$$N_0 = 2.7 \times 10^9 \text{ cm}^{-3}$$

where r_0, $r_{v''}$ are effective radii of molecules in ground and excited states, v is the molecular velocity, and parameter $\kappa \simeq 1$ is the dissociation probability of excited molecules during collisions. For v'' = 14 of hydrogen, the probability $W^d_{v''J''}$ exceeds the value A_{BX} at gas pressure $p \gtrsim 40$ mmHg.

VT relaxation is an effective depletion mechanism of molecular levels nearby the dissociation limit. The corresponding probability calculated in [26] by using the anharmonic oscillator model is

$$W^{\text{VT}}_{v''J''} \simeq \kappa P/\tau^*_{0v'}, \qquad \kappa \simeq 1.$$

An effective action of the two last mechanisms of collisional depletion is provided at gas pressure $\gtrsim$ 40 mmHg.

B. Population of Laser States

The stationary population of the upper laser state $v'J'$ under amplification mode of operation with excitation by electrons at moderate pumping power depends mainly on the excitation rate of the electronic state $N_0 f_{0B}$, radiative decay, and molecular quenching of level $v'J'$ with probabilities A_{BX} and $W_{B\cdot P}$, respectively (Fig. 15)

$$N^B_{v'} = N_0 f_{0B} g^{BX}_{0v'} \beta^{BX}_{0J'} / (A_{BX} + W_{B\cdot P}). \tag{10}$$

Population of lower laser levels is determined mainly by radiative decay of B state, volume recombination of hydrogen atoms with the concentration N_H, and by the total depletion probability

$$W_{v''J''} = W^{pr}_{v''J''} + W^{d}_{v''J''} + W^{VT}_{v''J''}$$

$$N_{v''J''} = \left[\sum_{v'J'} N^B_{v'J'} A_{BX} g^{BX}_{v'v''} S^{BX}_{J'J''} / (2J^1 + 1) + \delta N_H^2 N_0 K^{vol}_{rec} \right] W^{-1}_{v''J''} \tag{11}$$

where δ is the relative recombination yield of molecules on level $v''J''$, $K^{vol}_{rec} = 5.10^{-33}$ cm^6 s^{-1} [27]—the volume recombination constant of hydrogen atoms at room temperature. The influence of radiative decay of C state is negligible due to the smallness of the corresponding Franck-Condon factors. The contribution of the highly excited electronic states B', C', d is of no importance due to small value of the oscillator strength of these transitions. For levels near the dissociation limit, the population rate from the underlying vibrational states due to VV exchange is negligible since at gas temperature T = 300-700 K, the probability of VV exchange is small compared with that of VT relaxation.

The H-atom concentration is determined by the molecular dissociation rate connected with excitation of singlet and triplet states $\simeq N_0 f_{0D}$, volume and surface recombination as well as by nonrecombination processes which decrease H-atom concentration with the total probability R^*

$$N_H^2 N_0 K^{vol}_{rec} + N_H R = N_0 f_{0D} \tag{12}$$

where $R = R^{wall}_{rec} + R^*$. The molecular dissociation rate is determined by excitation of the repulsion $b\,^3\Sigma^+_u$ state, radiative decay of the $c\,^3\Pi_u$ state, and by the total bound-free radiative decay rate of $B\,^1\Sigma^+_u$ state with emission of the Herzberg continum [28]

$$N_0 f_{0d} \simeq N_0 f_{0b} + \frac{N_c A_c b}{A_c b + W_c \cdot p} + \frac{N_0 f_{0b} \kappa_{cont}}{A_B + W_B P}. \tag{13}$$

Chemical bonding and gas pumping are examples of effective nonrecombination processes resulting in decreasing the H-atom concentration. Use of volume recombination with this purpose is inexpedient since this channel leads to increasing the lower laser level population. In the case of surface recombination, the excess energy of the recombined molecules is transferred to the walls and the lower laser levels remain empty. The atomic recombination probability on the walls of the cylindrical cell of radius r_0 is $R^{wall}_{rec} = D(2.4/r_0)^2\,\gamma$. The parameter γ is the recombination probability of atoms during collision with the walls. For various wall materials, it ranges from 10^{-2} to 0.5 [29].

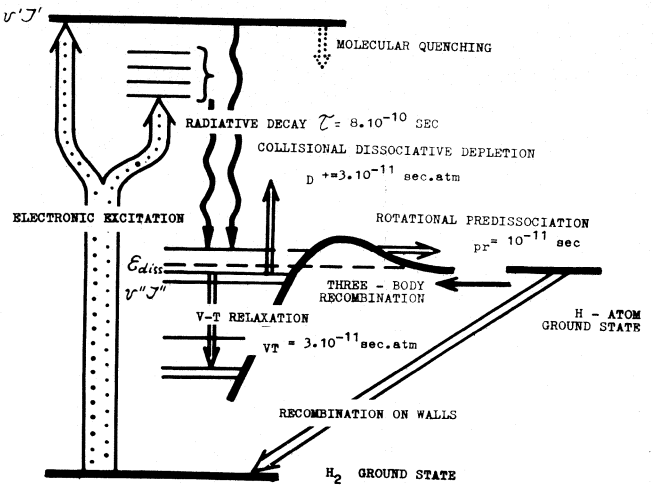

Fig. 15. Population scheme of CW H_2-VUV laser.

There are two criteria which should be fulfilled to obtain CW laser action. The requirements are applied on the excitation rate of the B state (and hence on the absolute intensity of spontaneous radiation of the laser transitions) and on the rate of decreasing the H-atom concentration. The basic condition is excess of gain over losses $K^{v'J'}_{v''J''} \gtrsim \kappa$, where

$$K^{v'J'}_{v''J''} = \mu^{v'J'}_{v''J''} P \cdot f_{0B} \left[1 - (\chi^{v'J'}_{v''J''})^{rad}\, w^{-1} - \chi_{rec} \frac{f_{0B} P^2}{R^2 w} \right] \tag{14}$$

$$\mu^{v'J'}_{v''J''} = \frac{\lambda^2 g_{0v'} g_{v'v''} \beta_{0J'} S_{J'J''} (\pi \ln 2)^{1/2} N_0}{4\pi^2 \Delta\nu_d (1 + \gamma^0 P (\pi \ln 2)^{1/2} / \Delta\nu_d)\,(2J^1 + 1)\,[1 + (W_q \cdot P / A_{BX})]} \tag{15}$$

where p (atmospheres), χ denotes numerical parameters, $w = W_{v''J''}/A_{BX}$, γ_0 is the collisional broadening parameter, $\kappa = l^{-1} \ln(1 - R)$, l is the active medium length, and R is the reflection coefficient.

In the plane of the parameters, (f, R) in logarithmic scale, the region of CW laser action corresponds approximately to a sector limited from below by the straight line $f_{min} = \kappa/\mu^{v'J'}_{v''J''}$ and from above by $f_{max} = wR^2/p^2\,\chi_{rec}$ (Fig. 16). The lower line corresponds to the threshold amplification for $N_{v''} = 0$, to the minimum excitation rate f_{0B} and the minimum spontaneous radiation power P_{min} of laser line. For the $P(4)$ (8,14) band line of pure paramodification $P_{min} = K \cdot 1.7 \times 10^3$ W/cm^3. For active medium length l = 1 m and losses of 20 percent, P_{min} = 3.4 W/cm^3. The upper line on the graph corresponds to a decrease of the gain to threshold at high pumping rate due to intense recombination population of the

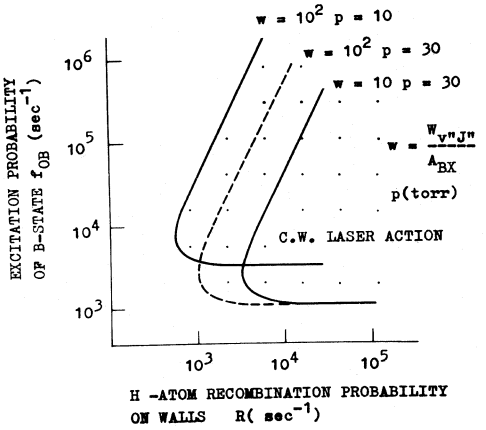

Fig. 16. Criterion of the CW H_2-VUV laser action on the $P(4)$ (8,14) line of pure parahydrogen.

lower laser levels. The minimum value of effective recombination rate

$$R_{\min} = \left(\frac{\kappa w \chi_{\text{rec}} P}{\mu_{v''J''}^{v'J'}}\right)^{1/2} \frac{2}{w - \chi_{\text{rad}}} \tag{16}$$

is of the order of 5×10^2-5×10^3 s^{-1}.

The most appropriate conditions for attaining the previously mentioned minimum rates of CW excitation and recombination could be created apparently in narrow gas discharge channels. Table V gives the wavelength of transitions suitable for CW VUV laser action in hydrogen and deuterium.

VI. Conclusion[3]

The quantum-mechanical system of the H_2-VUV laser as it is shown in this paper is characterized by rather high limiting operating laser parameters. The problem is to approach these laser parameters in practice.

In gas discharges, the effective excitation of the H_2-VUV laser can be carried out apparently only at comparatively low pressure $p \lesssim 0.05$-0.1 atm. At higher pressures, the electric field and the mean electronic energy in the discharge drop rapidly in a time interval less than the laser pulse duration. The result is low efficiency of excitation.

The main problems in practice are connected with the extremely short lifetime of the inversion population ~1 ns. These problems can be completely removed by using the four-level collisional scheme of excitation. The optimal pressure range for this scheme is rather high $p \gtrsim 0.1$ atm. The most favorable excitation conditions can be attained by using e-beam systems with electron trapping. The excitation efficiency in this case, unlike the gas-discharge systems, remains constant during the current pulse irrespective of the pressure. The region of optimum pressure depends on the value of the molecular quenching cross section of excited molecular states of hydrogen. Observed laser action in pure H_2 at 2-atm pressure is certain evidence in favor of rather high optimal pressures. Molecular quenching of laser states may be substantially decreased by the addition of inert gases such as He. In this case, the effective collisional depletion of the lower laser states is provided. The four-level laser action in H_2 could be obtained apparently also on bound-free Lyman transition on Herzberg continuum [28].

The four-level bound-bound transitions of H_2 and D_2 are favorable for achieving the CW VUV laser action on several lines in the region of 1500-1600 Å. The use of supernarrow laser channels yield high probability for wall recombinations and should be used to obtain the needed H-atom recombination rate. Simultaneously, high electronic energy should be provided in the active medium. CW pumping can be carried out by using some sort of gas discharge CW electronic beam. Pure parahydrogen is expedient to use in first experiments.

The wavelength of H_2-VUV laser is near the absolute wavelength limit about 700-1000 Å for neutral atomic and molecular laser systems without photoionization absorption from the ground state. The H_2 electronic transition $D \rightarrow X$ in the region about 900 Å near the photoionization limit remains unstudied. The effective electronic excitation cross section of D state is probably an order of magnitude less than that of the B state. A strong radiative population of the lower levels from B and C states apparently presents some difficulties for obtaining population inversion.

Small-size high-repetition rate gas discharge excited H_2-VUV laser with mean power of even several milliwatts will have wide applications in laboratory experiments. Unlike the e-beam excited inert gas excimer systems, this laser is absolutely free of penetrating radiation danger. The laser can be used in investigations of laser VUV photochemistry, including isotopic-selective processes. Dynamic and spectral features of luminescence of the complex molecular systems including biologically active materials can be carried out. Luminescence and photoionization detection of small admixtures in gases, optical pumping of lasers with continuous frequency tuning in the range 1800–3000 Å can also be performed. Applications will be expanded for these lasers in the future in accordance with the growth of the average and the peak laser power and with the simplifcation of the excitation techniques.

[3] After this paper was submitted, similar spectroscopic results were reported by R. W. Dreyfus and R. T. Hodgson, "Molecular-hydrogen laser: 1098-1613 Å," *Phys. Rev.*, vol. 9, pp. 2635-2648, 1974.

References

[1] N. G. Basov, V. A. Danilychev, I. N. Popov, and D. D. Khodkevich, "Laser operating in the vacuum region of the spectrum by excitation of liquid xenon with an electron beam," *JETP Lett.*, vol. 12, pp. 329-331, 1970.

[2] A. G. Akamanov *et al.*, "Generation of coherent radiation at λ = 2120 Å by cascade frequency conversion," *JETP Lett.*, vol. 10, pp. 154-157, 1969.

[3] S. E. Harris and R. B. Miles, "Proposed third-harmonic generation in phase-matched metal vapors," *Appl. Phys. Lett.*, vol. 19, pp. 385–387, Nov. 1971.

[4] a) H. A. Koehler, L. I. Ferderber, D. L. Redhead, and P. I. Ebert, "Stimulated VUV emission in high pressure xenon excited by high-current relativistic electron beams," *Appl. Phys. Lett.*, vol. 21, pp. 198–200, Sept. 1972.
b) P. W. Hoff, I. C. Swingle, and C. K. Rhodes, "Demonstration of temporal coherence, spatial coherence, and threshold effects in the molecular xenon laser," *Opt. Commun.*, vol. 8, pp. 128–131, June 1973.

[5] P. A. Bazhulin, I. N. Knyazev, and G. G. Petrash, "On the possibility of stimulated emission in the far ultraviolet," *Sov. Phys.–JETP*, vol. 23, pp. 649–650, Sept. 1965.

[6] a) R. W. Waynant, J. D. Shipman, R. C. Elton, and A. W. Ali, "Vacuum ultraviolet laser emission from molecular hydrogen," *Appl. Phys. Lett.*, vol. 17, pp. 383–384, Nov. 1970.

b) R. T. Hodgson, "Vacuum-ultraviolet laser action observed in the Lyman bands of molecular hydrogen," *Appl. Phys. Lett.*, vol. 25, pp. 494–497, Aug. 1970.
[7] R. T. Hodgson and R. W. Dreyfus, "Vacuum-UV laser action observed in H_2 Werner bands; 1161–1240 Å," *Phys. Rev. Lett.*, vol. 28, pp. 536–539, Feb. 1972.
[8] V. S. Antonov, I. N. Knyazev, V. S. Letokhov, and V. G. Movshev, "Hydrogen laser in vacuum ultraviolet at atmospheric pressure," *JETP Lett.*, vol. 17, pp. 393–395, 1973.
[9] J. E. Hesser, "Absolute transition probabilities in ultraviolet molecular spectra," *J. Chem. Phys.*, vol. 48, pp. 2518–2535, Mar. 1968.
[10] J. H. Kiefer and R. W. Lutz, "Vibrational and relaxation of hydrogen," *J. Chem. Phys.*, vol. 44, pp. 668–672, Jan. 1966.
[11] G. Herzberg and L. L. Howe, "The Lyman bands of molecular hydrogen," *Can. J. Phys.*, vol. 51, pp. 867–887, May 1973.
[12] I. H. Knyazev, V. S. Letskhov, and V. G. Moushev, "TEA N_2 UV laser with reduced spectra," *Opt. Commun.*, vol. 6, pp. 250–252, Nov. 1972.
[13] I. Tobias and J. Vanderslice, "Potential energy curves for the $X^1\Sigma_g^+$ and $B^1\Sigma_u^+$ states of hydrogen," *J. Chem. Phys.*, vol. 35, pp. 1852–1855, Nov. 1961.
[14] E. H. Fink, D. L. Akins, and C. B. Moore, "Energy transfer in monochromatically-excited hydrogen ($B^1\Sigma_u^+$). I. Excitation processes, electronic quenching, and vibrational energy transfer," *J. Chem Phys.*, vol. 56, pp. 900–915, Jan. 1972.
[15] A. Dalgarno and R. J. Henry, "The rotational excitation of molecular hydrogen by slow electrons," *Proc. Phys. Soc.* (London), vol. 85, pp. 679–684, 1965.
[16] A. G. Englehardt and A. V. Phelps, "Elastic and inelastic collision cross sections in hydrogen and deuterium from transport coefficients," *Phys. Rev.*, vol. 131, pp. 2115–2128, Sept. 1963.
[17] A. V. Phelps, "Rotational and vibrational excitation of molecules by low-energy electrons," *Rev. Mod. Phys.*, vol. 40, pp. 399–410, Apr. 1968.
[18] S. J. B. Corrigan, "Dissociation of molecular hydrogen by electron impact," *J. Chem. Phys.*, vol. 43, pp. 4381–4386, Dec. 1965.
[19] S. P. Khare, "Excitation of hydrogen molecule by electron impact III. Singlet-triplet excitations," *Phys. Rev.*, vol. 157, pp. 107–112, May 1967.
[20] —, "Excitation of hydrogen molecules by electron impact," *Phys. Rev.*, vol. 149, pp. 33–37, Sept. 1966.
[21] R. Roscoe, "The excitation of the hydrogen molecule by electron impact," *Phil. Mag.*, vol. 31, pp. 349–362, 1941.
[22] L. J. Kieffer and G. H. Dunn, "Electron impact ionization cross-section data for atoms, atomic ions, and diatomic molecules: I. Experimental Data," *Rev. Mod. Phys.*, vol. 38, pp. 1–35, Jan. 1966.
[23] A. Dalgarno, *Atomic and Molecular Processes*, (Pure and Applied Science Ser.), vol. 13, D. Bates, Ed. New York: Academic, 1962.
[24] a) L. Pages, E. Bertel, H. Joffre, and L. Sklavenitis, "Energy loss, range, and bremsstrahlung yield for 10-KEV to 100-MEV electrons in various elements and chemical compounds," *At. Data*, vol. 4, pp. 1–127, Mar. 1972.
b) C. B. Opal, W. K. Peterson, and E. C. Beaty, "Measurements of secondary-electron spectra produced by electron impact ionization of a number of simple gases," *J. Chem. Phys.*, vol. 55, pp. 4100–4106, Oct. 1971.
[25] E. E. Nikitin, "Theory of elementary atomic-molecular processes in gases," in *Chemistry*, Moscow, 1970.
[26] J. H. Kiefer, "Effect of VV transfer on the rate of diatomic dissociation," *J. Chem. Phys.*, vol. 57, pp. 1938–1956, Sept. 1972.
[27] V. H. Shui and J. P. Appleton, "Gas-phase recombination of hydrogen. A comparison between theory and experiment," *J. Chem. Phys.*, vol. 55, pp. 3126–3132, Oct. 1971.
[28] A. Dalgarno, G. Herzberg, and T. L. Stephens, "A new continuous emission spectrum of the hydrogen molecule," *Astrophys. J.*, vol. 162, pp. L49–L53, Oct. 1970.
[29] A. Gelb and S. K. Kim, "Theory of atomic recombination on surfaces," *J. Chem. Phys.*, vol. 55, pp. 4935–4939, Nov. 1971.

Mass Spectroscopy of the HCN-Laser Plasma

HANS J. SCHÖTZAU AND FRITZ KNEUBÜHL

Abstract—**We have measured for the first time the chemical composition of the HCN-laser discharge plasma. The results show the important role of hydrogen in the HCN laser. Additional experiments with different gas mixtures prove that hydrogen molecules are necessary for population inversion in the HCN laser.**

I. Introduction

LOW-PRESSURE discharges in molecular gases containing constituents of compounds made-up of hydrogen, carbon, and nitrogen show stimulated emission in the far-infrared and submillimeter-wave regions [1]. The strongest emission occurs at a wavelength of $\lambda = 337$ μm. Lide and Maki [2], [3] and Hocker and Javan [4], [5] identified this emission with the vibrational–rotational transition of the HCN molecule

$$(11^10),\ J = 10 \longrightarrow (04^00),\ J = 9.$$

However, the mechanism of the excitation of this stimulated emission is still unknown.

Usually, the HCN-laser discharge is sustained in molecular gas mixtures, e.g., CH_4 and N_2. In these mixtures the laser-active HCN molecules are formed in the low-pressure plasma. Hitherto, the formation of the laser-active molecules could not be demonstrated. However, it could be shown that chemical reactions strongly influence the laser action. This is shown by the possibility of excitation and suppression of the higher resonator modes of the 337-μm emission [6] by variation of the gas mixture. In addition, some emissions in the submillimeter-wave region are not yet explained, e.g., the emission of C/H/N compounds at wavelengths of $\lambda = 201$, 211, and 223 μm [7], the radiation of CH_3SH [8] and

Manuscript received October 1, 1974; revised May 30, 1975. This work was supported by the "Schweizerischer Nationalfonds."

H. J. Schötzau was with the Solid State Physics Laboratory, Swiss Federal Institute of Technology, Zurich, Switzerland. He is now with the European Space Research and Technology Centre, Domeinweg, Noordwijk, The Netherlands.

F. Kneubühl is with the Solid State Physics Laboratory, Swiss Federal Institute of Technology, Zurich, Switzerland.

CH_3SCN [9] at the wavelength of 337 and 336.1 μm, respectively, as well as those of the [ICN-H_2] gas mixtures at wavelengths between 169 and 774 μm [9].

For these reasons we studied the chemical reactions in the plasma of the HCN laser with the aid of a quadrupole mass spectrometer.

II. The Experimental Arrangement

A CW HCN laser was used for the mass-spectroscopic measurements. The discharge tube of the HCN laser was water-cooled and the two plane-parallel mirrors of the resonator were separated by a distance of about 150 cm and had diameters of 6 cm. Using a special hollow cathode [10], the longitudinal electric discharge with a length of 110 cm can be sustained for a range of discharge currents between 0.1 and 2 A and at gas pressures up to 3 torr. The gas passes through the resonator with a slow flow rate. The laser radiation is coupled out by a 18-μm-thick Mylar foil tilted at an angle of 45° relative to the tube axis. A Unicam–Golay detector is used for the measurements of the laser output power. The resonator can be tuned to the different resonator modes by a variation of the resonator length [9]. A part of the gas is bled out near the cathode by a small aperture of diameters of 50–250 μm. The working pressure in the chamber of the mass spectrometer, Balzers QMG 101, is of the order of magnitude of 10^{-5}-10^{-4} torr, depending on the actual pressure in the laser tube. The different out-streaming gas species are ionized in the ion source of the quadrupole mass spectrometer at a distance of 20 cm from the hole. The electrons from the ion source have a mean energy of about 90 eV. Since we are interested in the neutral particles only (the degree of ionization is of the order of 10^{-6}), and we have used these results as a starting point for additional experiments, the system was not calibrated.

A. The Gas Mixtures and the Mass Spectrum

The laser emission at a wavelength of 337 μm can be observed with different gas mixtures, e.g., CH_3CN [11], [$(C_2H_5)_2O + N_2$] [12], C_2H_5CN [13], [$CH_3CN + NH_3$] [14], [$CH_4 + N_2$] [15], and [$CH_4 + NH_3$] [16]. On the other hand, the [$C_2H_2 + N_2$] mixture was found to be laser inactive [17]. For our experiments we selected the following three types of laser gases.

1) [CH_4-N_2]: This gas mixture used in the HCN laser gives a high laser output power.

2) [C_2H_6-, C_2H_4-, C_2H_2-N_2]: The sequence of hydrocarbons allows a variation of the hydrogen content in the plasma.

3) HCN: No chemical reaction is necessary for the formation of the laser-active molecules as in 1) and 2).

For the interpretation of the mass spectra of the laser plasma of the previously given gas mixtures, the following facts have to be taken into account.

1) Molecules with the same ratio of mass/charge = m/q are indistinguishable.

2) The ion source of the QMG generates ions as well as dissociation products, e.g.,

$$CH_n + e^- \longrightarrow CH_{n-1} + e^- + H.$$

3) Ion–molecule reactions take place in the chamber of the quadrupole analyzer. As an example, mass-spectroscopic studies of pure CH_4 frequently show new compounds CH_5 and H_2 besides the products of dissociation: CH_3, CH_2, CH, and C [18], [19].

a) *Ion source:*

$$CH_n + e^- \longrightarrow CH_n^+ + 2e^-$$

$$CH_n + e^- \longrightarrow CH_{n-1} + e^- + H.$$

b) *Secondary reactions:*

$$CH_3^+ + CH_4 \longrightarrow C_2H_5^+ + H_2$$

$$CH_4^+ + CH_4 \longrightarrow CH_5^+ + CH_3.$$

Therefore, the mass-spectroscopic data of the HCN-laser plasmas had to be checked by other experiments.

III. Experiments

A. The [CH_4-N_2] System

The mass-spectrometric measurements of the [CH_4-N_2] discharge, which yields a high laser intensity, show the formation of new molecules (Figs. 1 and 2)

$$CH_4 + N_2 \xrightarrow{\text{discharge}} H,\ \boxed{H_2},\ H_3,\ NH_x, N_2H_y, \cdots, N, N_2,\ CH_x, C_2H_y, \cdots,\ CN,\ \boxed{HCN}.$$

(0.5 torr; 0.8 A)

The concentration of HCN molecules is small compared to the concentration of hydrogen which is the main product of these reactions. The observation of the formation of higher hydrocarbons agrees well with other experiments [20]. The new compounds are generated by different processes [18] [20]-[22], for example.

1) *The Formation of Hydrogen:*

$$CH_4 + e^- \longrightarrow CH_3 + H + e^-$$

$$H + H + M \longrightarrow M^* + H_2.$$

2) *The Formation of Higher Hydrocarbons:*

$$CH_3^+ + CH_4 \longrightarrow C_2H_5^+ + H_2.$$

3) *The Formation of Hydrocyanic Acid:*

$$CH_3 + N \longrightarrow HCN + 2H.$$

The observation of H_3 ions can probably be attributed to the ion-molecule reaction in the ion source

$$H_2^+ + H_2 \longrightarrow H_3^+ + H.$$

Fig. 3 shows the concentration of different molecules as a function of the discharge current. The CH_4 concentration decreases with increasing current, whereas the hydrogen concentration increases. The HCN concentration achieves a maximum at the threshold current of the laser emission. The highest value of the laser intensity coincides with the maxi-

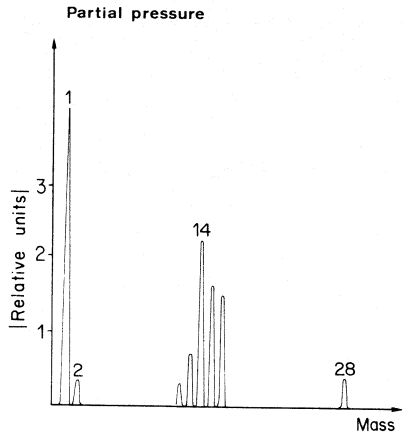

Fig. 1. Mass spectrum of the gas mixture $[CH_4:N_2] \simeq [7{:}7$ torr $\cdot$ l $\cdot$ min$^{-1}]$ at a pressure of 0.5 torr without an electrical discharge. The following masses can be identified by the ratio mass/charge: H(1); H_2(2); C(12); CH(13); N(14): CH_2(14); N_2(28/2); CH_3(15); CH_4(16); N_2(28).

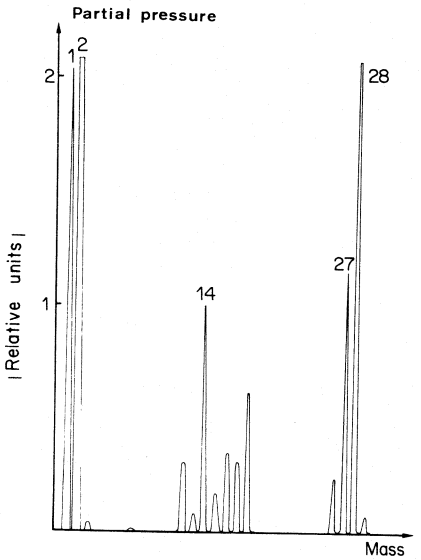

Fig. 2. Mass spectrum of the gas mixture $[CH_4:N_2] \simeq [7{:}7$ torr $\cdot$ l $\cdot$ min$^{-1}]$ at a pressure of 0.5 torr and discharge current of 0.8 A.

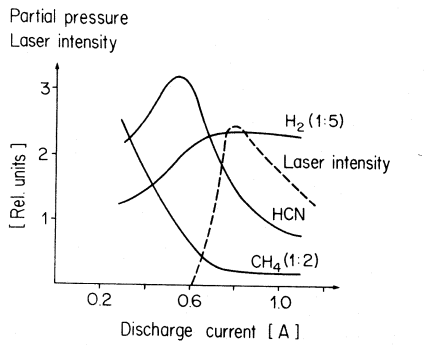

Fig. 3. The partial pressures of CH_4, H_2, and HCN and the laser intensity of the 337-μm emission of the gas mixture $[CH_4:N_2] \simeq [7{:}7$ torr $\cdot$ l $\cdot$ min$^{-1}]$ as a function of the discharge current at a total pressure of 0.5 torr.

mum concentration of hydrogen molecules. It does not correspond to the HCN maximum.

B. The $[C_2H_6$-, C_2H_4-, C_2H_2-$N_2]$ System

The observed influence of hydrogen on the laser intensity was investigated with the $[C_2H_4$-$N_2]$ system.

The addition of H_2 molecules to the optimum $[C_2H_4$-$N_2]$ gas mixture, i.e., the mixture which has the highest laser intensity, lowers the output power of the HCN laser (Fig. 4(a)). Therefore, the optimum content of the concentration of hydrogen characterizes the laser maximum.

The laser emission of another laser-active gas mixture is enhanced (Fig. 4(b)) and a laser-inactive gas composition (Fig. 4(c)) is enabled to emit the 337-μm radiation by the external addition of hydrogen.

A discharge containing a similar concentration of carbon and nitrogen gives rise to the 337-μm HCN-laser emission after addition of a sufficient amount of hydrogen. The maximum of the laser intensity occurs in a plasma with a ratio of the constituents near

$$C{:}H{:}N \cong 1{:}2{:}1.$$

The study of the $[C_2H_2$-$N_2]$ gas mixture enabled us to determine the influence of the addition of hydrogen on the chemistry in the plasma and on the collision processes involved in the laser emission. In agreement with Stafsudd *et al.* [17] we find the $[C_2H_2$-$N_2]$ mixture laser inactive. Fig. 5(a) shows that the addition of hydrogen makes possible the 337-μm emission. To demonstrate the importance of H_2 in the HCN laser, a part of the hydrogen is replaced by deuterium [23]. The D_2 molecules have no influence on the formation of the HCN. The possible generation of DCN molecules gives no contribution to the 337-μm HCN emission [3], [5]. Among the significant observations are the onset as well as the enhancement of the 337-μm emission of the

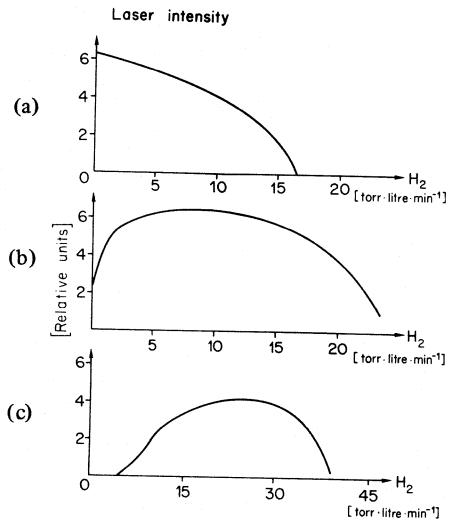

Fig. 4. Laser intensity of the 337-μm emission of the $[C_2H_4:N_2]$ gas mixtures as a function of the addition of H_2. (a) $[C_2H_4:N_2] \simeq [10{:}5$ torr $\cdot$ l $\cdot$ min$^{-1}]$, $p_{tot} \sim 0.5$ torr. (b) $[C_2H_4:N_2] \simeq [7{:}5$ torr $\cdot$ l $\cdot$ min$^{-1}]$, $p_{tot} \sim 0.4$ torr. (c) $[C_2H_4:N_2] \simeq [4{:}5$ torr $\cdot$ l $\cdot$ min$^{-1}]$, $p_{tot} \sim 0.3$ torr.

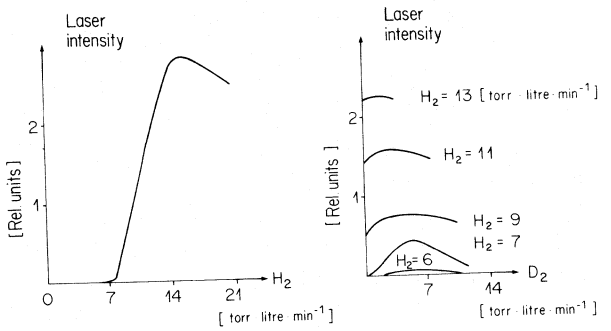

Fig. 5. The dependence of the 337-μm emission of the [C_2H_2:N_2] gas mixture of the hydrogen and deuterium addition. (a) Addition of hydrogen. (b) Addition of hydrogen and deuterium.

[C_2H_2-N_2-H_2] mixture by the addition of deuterium (Fig. 5(b)).

An enhancement of the laser radiation by the addition of helium, which has the same mass as deuterium, was not observed. In addition, the various publications on the influence of He on the HCN laser do not all reach similar conclusions [7], [14], [24]-[27].

The [C_2H_6-, C_2H_4-, C_2H_2-N_2] gas mixtures have a different content of hydrogen as well as different chemical bonds (single, double, triple, respectively). The smaller abundance of hydrogen can be compensated for by external addition of H_2, as shown above. Then the laser intensity is identical for all systems. However, these optimum mixtures have different threshold discharge currents at which laser oscillation occurs. Therefore, the electrical input power for the laser threshold differs for the gas mixtures previously mentioned.

Fig. 6 shows that the formation energies of the CH radical are correlated with the minimum input power required for the laser threshold.

C. The HCN System

To our knowledge, pure HCN gas as an active medium has only been used in a pulsed laser system [1], [28]. Pure HCN gas is desirable for the study of the laser mechanism in the CW HCN laser since no chemical reaction is necessary for the formation of the HCN molecules. The mass-spectroscopic studies demonstrate that the HCN molecules are not stable in a dc glow discharge since they are dissociated by electron impact [28], [30].

Our experiments showed that the emission in the CW laser occurs only if hydrogen is added to the HCN gas. The H_2 molecules tend to suppress the dissociation of HCN.

Furthermore, the same experiments were carried out with the pulsed HCN laser as described in [9]. The laser tube was filled with pure HCN of about 0.3 torr and sealed afterwards. Then a series of pulsed discharges were initiated. In agreement with Turner and Poehler [28], the 337-μm emission is observed after the first electrical excitation. Subsequently, the laser intensity increases to a value twice as large as the initial intensity (Fig. 7).

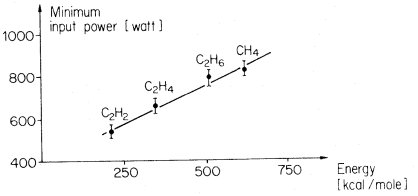

Fig. 6. The correlation between the threshold of the input power of the 337-μm emission and the energy of formation of CH radical for the different gas mixtures.

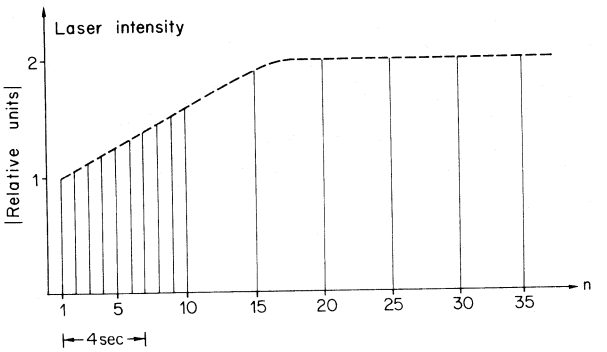

Fig. 7. The laser intensity of the 337-μm emission of pure HCN gas in a sealed-off system as a function of the electrical excitations n. Initial HCN pressure: $p = 0.32$ torr. Voltage: $V = 30$ kV. Pulse repetition rate: $f = 1.75$ Hz. Length of the resonator: $L = 432$ cm.

IV. Interpretation of the Experiment

The measurements of the chemical composition of the HCN-laser plasma with the aid of a quadrupole mass spectrometer, as well as the related experiments with the different gas compositions, show the important role of hydrogen in the HCN laser (Figs. 2-4).

The experiment with the [C_2H_2-N_2] gas demonstrates that hydrogen (or deuterium) is required as a collision partner of the HCN molecules to yield the laser emission (Fig. 5).

Flournoy and Nelson [31] showed that the metastable vibrational state of hydrogen $H_2(v = 1)$ and deuterium $D_2(v = 1)$ transfer their energy to the HCN molecule. On the other hand, long-lived electronic states of H_2, H, and N_2 near 11 eV [32] can also excite the levels of HCN in this energy range by resonance processes [33]. These levels increase the inversion population of the HCN molecules by relaxation effects. The metastable states of helium are near an energy of 19 eV, which is higher than the energy of ionization of the HCN at 13.9 eV [34]. Therefore, a resonance energy transfer is excluded. But the helium can change the gas temperature, and thus the chemical reactions in the discharge through its high heat conductivity.

The gas composition with the lowest threshold for laser oscillation also possesses the highest efficiency. Fig. 6 shows the correlation of the formation of CH radical and threshold input power. The existence of these radicals or CH^+ radical ions in a low-pressure discharge is established in [35]. The CH radical is essential in the plasma chemistry as a carrier of carbon in the gas phase. This observation agrees well with

the theory of chemical equilibrium in these plasmas developed by Vepřek [36]. Its adaptation to the HCN-laser plasma predicts the presence of these radicals for the chemical formation of HCN molecules [37].

Continuous discharges in pure HCN gas are laser-inactive, whereas the [HCN-H_2] gas mixture shows stimulated emission. On the other hand, the 337-μm radiation can be observed in pulsed discharges in pure HCN gas. However, the efficiency of this system is enhanced by the plasma-generated hydrogen. This observation proves that electron impact is not the main mechanism of the excitation of the HCN molecules, since the HCN concentration is lowered after each electrical pulse, whereas the laser intensity increases (Fig. 7).

The excitation of the HCN molecules is enhanced by molecule-molecule (H_2-HCN) collisions. The measurements of the time behavior of the gain of the pulsed HCN laser by Yamanaka *et al.* [38] support this fact, as well as the time delay between the electrical excitation and the beginning of the laser emission [9], [39], [40].

V. Conclusion

Mass-spectroscopic measurements are useful for the study of molecular far-infrared gas-laser discharges. Our experiments on the HCN-laser plasma with a quadrupole mass spectrometer, as well as experiments with different gas mixtures, have proved that molecular hydrogen is required as a collision partner for the 337-μm emission of the HCN laser. Furthermore, pulsed discharges in pure HCN gas confirmed that electron impact can be excluded as the main mechanism for the generation of the population inversion of the HCN laser.

Acknowledgment

The authors wish to thank Prof. H. Schneider (Fribourg), Prof. B. Lengyel (Northridge, Calif.), Prof. W. Känzig (Zurich), Prof. W. Rieder (Vienna), Dr. S. Vepřek (Zurich), and Dr. E. Hugentobler (Fribourg) for active support and discussions. They also wish to thank E. Griesshaber, Ch. Grathwohl, H. J. Mahler, B. Adam, W. Herrmann, and B. Nussberger for their help.

References

[1] H. A. Gebbie, F. D. Findlay, N. W. B. Stone, and J. A. Ross, "Interferometric observations on far infra-red stimulated emission sources," *Nature*, vol. 202, pp. 169–170, Apr. 1964.

[2] D. R. Lide and A. G. Maki, "On the explanation of the socalled CN laser," *Appl. Phys. Lett.*, vol. 11, pp. 62–64, July 1967.

[3] A. G. Maki, "Assignment of some DCN and HCN laser lines," *Appl. Phys. Lett.*, vol. 12, pp. 122–124, Feb. 1968.

[4] L. O. Hocker and A. Javan, "Absolute frequency measurements on the new CW HCN submillimeter laser lines," *Phys. Lett.*, vol. 25A, pp. 489–490, Oct. 1967.

[5] —, "Absolute frequency measurements of new CW DCN submillimeter laser lines," *Appl. Phys. Lett.*, vol. 12, pp. 124–125, Feb. 1968.

[6] H. J. Schötzau and F. K. Kneubühl, "Chemical excitation and suppression of HCN-laser modes," *Phys. Lett.*, vol. 46A, pp. 415–416, Jan. 1974.

[7] L. E. S. Mathias, A. Crocker, and M. S. Wills, "Laser oscillations at submillimeter wavelengths from pulsed gas discharges in compounds of hydrogen, carbon and nitrogen," *Electron. Lett.*, vol. 1, pp. 45–46, Apr. 1965.

[8] H. J. Schötzau, R. Crettol, E. Griesshaber, and F. K. Kneubühl, "Experiments on the generation of 10^{12} Hz sound with the aid of a pulsed CH_3CN-CH_3SH submillimeterwave laser," in *Proc. Symp. Submillimeter Waves* (Brooklyn, N.Y., 1970), vol. XX, pp. 431–436.

[9] H. Steffen and F. K. Kneubühl, "Resonator interferometry of pulsed submillimeter-wave lasers," *IEEE J. Quantum Electron.*, vol. QE-4, pp. 992–1008, Dec. 1968.

[10] H. J. Schötzau, Ch. Grathwohl, F. K. Kneubühl, and E. Griesshaber, "A water-cooled hollow cathode for continuous HCN-laser," *Z. Angew. Math. Phys.*, vol. 22, pp. 778–779, 1971.

[11] G. T. Flesher and W. M. Müller, "Submillimeter gas laser," *Proc. IEEE (Special Issue on Millimeter Waves and Beyond)*, vol. 54, pp. 543–546, Apr. 1966.

[12] S. F. Dyubko, V. A. Svich, and R. A. Valitov, "Submillimeter CW gas laser," *JETP Lett.*, vol. 6, pp. 80–81, Aug. 1967.

[13] S. Kon, M. Yamanaka, J. Yamamoto, and H. Yoshinaga, "Experiments on a far infrared CN laser," *Japan. J. Appl. Phys.*, vol. 6, pp. 612–619, May 1967.

[14] W. M. Müller and G. T. Flesher, "Continuous-wave submillimeter oscillation in discharges containing C, N, and H or D," *Appl. Phys. Lett.*, vol. 10, pp. 93–94, Feb. 1967.

[15] O. M. Stafsudd and Y. C. Yeh, "The CW gain characteristics of several gas mixtures at 337 μm," *IEEE J. Quantum Electron.*, vol. QE-5, pp. 377–380, July 1969.

[16] B. McCaul, private communication.

[17] O. M. Stafsudd, F. A. Haak, and K. Radisavljevic, "Laser action in selected compounts containing C, N, and H or D," *IEEE J. Quantum Electron.*, vol. QE-3, pp. 618–620, Nov. 1967.

[18] B. D. Blaustein, "Chemical reactions in electrical discharges," in *Advances in Chemistry*, ser. 80, 1969.

[19] F. H. Field and D. P. Beggs, "Reversible reactions of gaseous ions. III. Studies with methane at 0.1–1.0 torr and 77–300°K," *J. Amer. Chem. Soc.*, vol. 93, pp. 1585–1591, Apr. 1971.

[20] H. W. Eckert and G. Eckert-Reese, "Ueber die Reaktionen von Aethan in einer Glimmentladung," *Forschungsber. Landes Nordrhein-Westfalen*, no. 1554, Apr. 1968.

[21] F. K. McTaggart, *Plasma Chemistry in Electrical Discharges*. New York: Elsevier, 1967.

[22] N. S. Perucho, *Organic Reactions in Electrical Discharges*, Consultants Bureau, New York, 1968.

[23] H. J. Schötzau, H. J. Mahler, and F. K. Kneubühl, "Mass spectroscopy of HCN-laser plasmas with H_2 and D_2," *Phys. Lett.*, vol. 38A, p. 286, Feb. 1972.

[24] R. Volk, "Operating conditions of a CW cyanide laser with mixtures of methane, nitrogen and helium as working medium," *Phys. Lett.*, vol. 42A, pp. 321–322, Dec. 1972.

[25] R. T. Ulrich, T. J. Bridges, and M. A. Pollack, "Variable metal mesh coupler for far infrared lasers," *Appl. Opt.*, vol. 9, pp. 2511–2516, Nov. 1970.

[26] O. Gehre, "Aufbau und Betrieb eines HCN-Lasers für Streuung an Wellen in stationären Plasmen," *Inst. Plasmaphysik Garching*, Munich, vol. IV, p. 39, July 1972.

[27] G. E. Morris, C. S. Brand, H. Jacobs, and T. R. Mooney, "Chemical mixtures in submillimeter lasers," U. S. Army Electron. Command, Electron. Components Lab., Fort Monmouth, N.J., ECOM 3039, 1968.

[28] R. Turner and T. O. Poehler, "Characteristics of the HCN laser radiation at high excitation currents," *J. Appl. Phys.*, vol. 42, pp. 3819–3826, Sept. 1971.

[29] D. P. Stevenson, "Ionization and dissoziation by electron impact: Cyanogen, hydrogen cyanide, and cyanogen chloride and the dissoziation energy of cyanogen," *J. Chem. Phys.*, vol. 18, pp. 1347–1351, Oct. 1950.

[30] T. F. Moran and W. H. Hamill, "Cross sections of ion-permanent-dipole reactions by mass spectrometry," *J. Chem. Phys.*, vol. 39, pp. 1413–1422, Sept. 1963.

[31] J. M. Flournoy and L. Y. Nelson, "Vibrational excitation of HCN," *Chem. Phys. Lett.*, vol. 6, pp. 512–524, Sept. 1970.

[32] J. B. Hasted, *Physics of Atomic Collisions*, 2nd ed. London: Butterworth, 1971.

[33] W. C. Price, "The absorption spectra of formaldehyde and hydrogen cyanide in the far ultraviolet," *Phys. Rev.*, vol. 46, p. 529, Sept. 1934.

[34] F. H. Field and J. L. Franklin, *Electron Impact Phenomena*. New York: Academic, 1970.
[35] S. Vepřek, "Chemical evaporation and deposition of solids in a nonisothermal plasma; Chemical transport of carbon," *J. Cryst. Growth*, vol. 17, pp. 101–116, 1972.
[36] —, "Statistical model of chemical reactions in nonisothermal low pressure discharges," *J. Chem. Phys.*, vol. 57, pp. 952–959, July 1972.
[37] H. J. Schötzau and F. Kneubühl, "Parameters and chemistry of the HCN-laser plasma," *Appl. Phys.*, vol. 6, pp. 25–30, Feb. 1975.
[38] M. Yamanaka, T. Yamauchi, and H. Yoshinaga, "Time behaviour of pulsed gain at 337 μm of HCN laser," *Japan. J. Appl. Phys.*, vol. 10, pp. 1601–1603, Nov. 1971.
[39] P. D. Coleman, "Far-infrared molecular lasers," *IEEE J. Quantum Electron. (Part II of Two Parts: 3rd Conference on Chemical and Molecular Lasers)*, vol. QE-9, pp. 130–138, Jan. 1973.
[40] S. Kunstreich and J. P. Lesieur, "Switch-on delay time of a cw-HCN-laser," *Opt. Commun.*, vol. 13, pp. 17–20, Jan. 1975.

Ultraviolet Ion Laser Performance and Spectroscopy—Part I: New Strong Noble-Gas Transitions Below 2500 Å

JOHN B. MARLING, MEMBER, IEEE

Abstract—**The performance and spectroscopy of UV ion lasers have been investigated to 1850 Å, the limit of available mirrors. New anomalously strong transitions of about 1-kW peak power were found in Xe IV? at 2315.357 Å and Kr IV at 2191.916 Å. The shortest wavelength new laser transition was Kr IV at 1949.623 Å. Wavelengths were measured for 25 new and many previously known UV laser transitions to about 0.006 Å. Optimum output in watts was also measured as a function of bore current density and gas pressure. All measurements were taken from a 7-mm-bore 150-cm-arc-length tube designed for low electrical inductance providing current excitation pulses with 250-ns full width at half maximum (FWHM).**

I. Introduction

MANY APPLICATIONS requiring the practical use of UV ion lasers, such as in photochemistry, have been hampered because of a lack of experimental performance parameters. Wavelengths of the laser transitions, measured to within the Doppler width (about 1 pm) are required, as well as relative laser performance based on optimized current density and gas pressure. An excellent tabulation of known ion laser transition is given in the *Handbook of Lasers* [1], relative performance of CW UV ion lasers is given by Fendley [2], as well as literature by the commercial vendors of ion lasers. The first systematic investigation of pulsed ion lasers in the UV was the original survey by Cheo and Cooper [3], but the only real comparative performance data on pulsed ion lasers below 400 nm are the recent results of Tucker and Birnbaum [4] on Xe, Ar, Kr, O, N, and the earlier work by Cheo and Cooper on fluorine, phosphorus, and chlorine [5]. The measured wavelength accuracy of pulsed ion lasers was about 0.06 Å, which was generally sufficient to permit classification of the lines according to known spectroscopic data for energy levels.

The available literature suggested that observations of laser transitions below 300 nm were limited by a lack of suitable mirrors in this region. Therefore, dielectric mirrors to permit laser-cavity reflectivity $R_1 \cdot R_2 > 0.8$ were obtained to investigate UV lasing down to 185 nm in noble gases. Investigation of possible ion laser transitions down to 200 nm in other elements will be reported in a future article [6]. The lower wavelength limit of ion laser transitions is currently 155 nm in carbon IV, recently observed as impurity laser emission in a mirrorless traveling-wave transverse-discharge system [7].

Since ion lasers provide convenient, stable high-intensity wavelength sources referenced to atomic transitions, they are ideal for investigations involving coincidences to within the Doppler bandwidth, e.g., with other atomic or molecular systems. Such applications require, however, that the transition wavelengths be experimentally known to 1 pm or better. Therefore, an order-of-magnitude better accuracy in measuring the wavelengths of known UV ion laser transitions was attempted. In addition, it is generally useful to know which transitions are the strongest, so the relative performance of all the UV ion lines was optimized with bore current and pressure as parameters. Such work also provided information on ionic assignment of the unclassified laser transitions. For the strong transitions of Kr IV 219 nm and Xe IV? 231.5 nm, first observed in this study, various output mirror reflectivities were also evaluated.

In order to investigate UV ion lasers, high bore currents are necessary, since most UV transitions occur in the doubly and triply ionized species. Therefore, the ion-laser discharge circuit was designed for minimum inductance, permitting peak bore current densities of 10 000 A/cm^2 to be obtained with a 0.03-μF capacitor charged to 23 kV, the highest charging voltage utilized. Circuit inductance was about 350 nH, permitting

Manuscript received March 10, 1975; revised May 13, 1975. This work was performed under the auspices of the U.S. Atomic Energy Commission.

The author is with the Lawrence Livermore Laboratory, University of California, Livermore, Calif. 94550.

a nearly critically damped current pulse with rise time of 80 ns and full width at half maximum (FWHM) which varied between 200–300 ns (depending on the gas used). This short excitation pulse definitely affected the types of ion laser transitions observed to be strongest, which will be discussed further in the section on experimental results.

It is suggested that the simple design of the laser system used in this work (relative to electron-beam or traveling-wave excitation systems) may make the entire chemical UV laser spectrum accessible to the general investigator, who may be limited by budget and interest in construction of the very sophisticated lasers previously needed for short-wavelength generation.

II. Experimental Procedure

A. Laser Design

In order to achieve high current densities with minimum pulse energy, a very low inductance, ultrahigh-speed electrical discharge is necessary. Therefore, the laser and electrical-driver circuit were designed with an all-coaxial geometry with minimum spacing between discharge-current conductors. The 0.03-μF capacitor was charged to positive high voltage, then switched to ground, using an EG&G Model HY3202 hydrogen thyratron in a grounded-grid configuration and laser tube geometry. The cathode received the negative high-voltage pulse from the capacitor. The anode was connected to ground by means of a several mill aluminum-foil sheet wrapped closely around the laser bore from the anode to within a few inches of the cathode, where it was connected to the capacitor housing, as shown in Fig. 1. Both cathode and anode were solid indium and coaxial with a hole in the center of each for the passage of the laser light. The tube was of quartz, graded to borosilicate glass to permit a Kovär ring for electrical contact to the indium cold cathode and anode.

To achieve a high pulse repetition rate without large resistive charging losses, an inductive resonant charging circuit was chosen, as shown in Fig. 2. The resonant charging time was $\pi\sqrt{LC} \approx 1.6$ ms for the 10-H charging inductor used, permitting repetition rates up to 600 pulses per second (pps) without loss of pulse voltage. Use of resonant charging naturally also offers the advantage of permitting twice the power-supply voltage to be applied to the discharge capacitor C_2, provided the source capacitor C_1 in the power supply is about an order of magnitude larger than C_2. The diodes in series with the charging inductor hold the voltage on C_2 after it resonantly swings to twice the supply voltage. (It is, of course, necessary that the inductor core of L_1 be chosen such that the charging inductor stores enough energy to swing C_2 to twice the power-supply voltage.)

The cathode end of the capacitor C_2 is held to dc ground by means of the small inductor L_2 (about 1 mH), which completes the charging circuit for C_2. This small inductor, in series with a 100-W 100-Ω resistor, permits an alternate discharge path for the applied high voltage in the event the discharge in the laser tube fails to occur. The values were chosen so that slight ringing of the discharge current occurs, in order to turn off the thyratron.

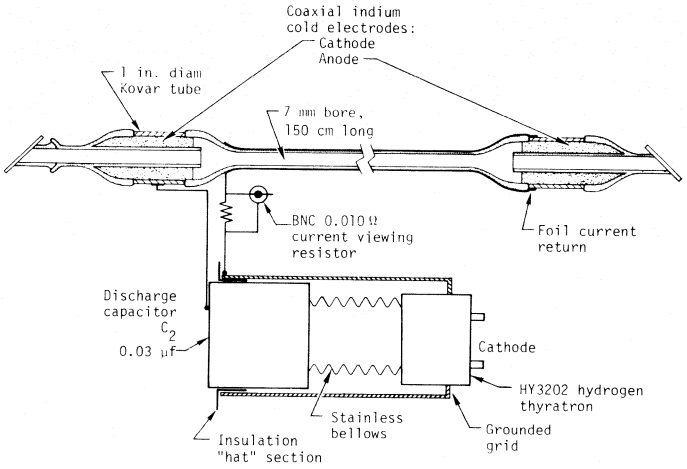

Fig. 1. Ion laser tube and electrical-driver configuration.

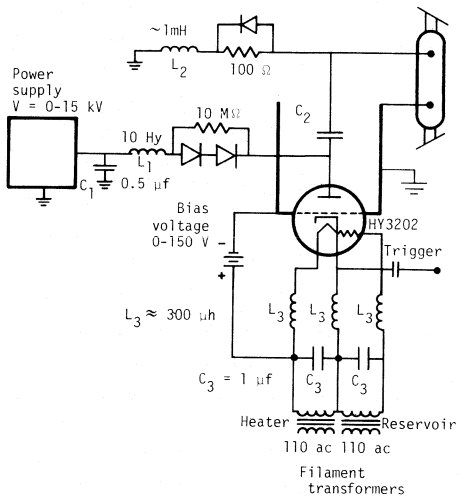

Fig. 2. Schematic diagram of electrical-driver circuit for high repetition-rate operation of pulsed ion laser.

Prepulsing of flashlamps is generally beneficial in establishing a low inductance discharge path [8]. Therefore, an ionization prepulse was applied to the cathode several microseconds before the thyratron was switched on. This was especially helpful in gases such as xenon that lase best at relatively low operating pressures. It was also indispensible if operation at low pulse voltages were desired, such as necessary for study of the singly ionized laser transitions. Generally, operation below 10-kV peak pulse voltage required a prepulse for steady discharges. Fig. 3 illustrates in block diagrams the various circuit modules as well as the gas-handling layout for the laser.

The dielectric mirrors used in this study had a 10-m concave radius for all wavelengths investigated in the range 200–600 nm. For examination of laser transitions down to about 220 nm, a standard laser configuration with suprasil quartz Brewster windows was satisfactory. However, below this wavelength the Brewster windows were eliminated by mounting the laser mirrors directly exposed to the plasma, which also eliminated possible losses by oxygen absorption in air. Vacuum seals were achieved by O rings, and mirror adjustment was achieved by connecting the mirror holder to the laser tube by a small sec-

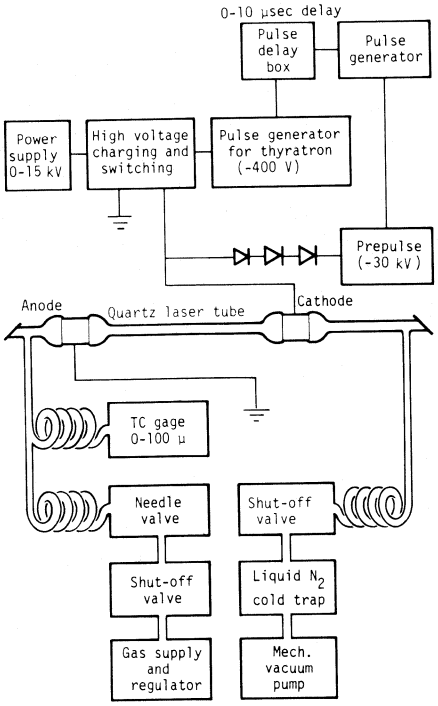

Fig. 3. Block diagram of mechanical and electrical layout for the pulsed ion laser.

tion of flexible stainless-steel bellows. However, the mirror holder must be insulated from ground, since the stainless bellows can be at a high voltage during discharge.

Gas pressure was monitored by a 100-μ full-scale thermocouple guage, and by a Schultz-Phelps ionization guage for the range 10^{-3}-500 μ; the measured pressures have been converted to absolute pressure according to conversion charts supplied by the manufacturers. Gas was continuously pumped out of the tube at the cathode end from a valved orifice through a helical gas coil (to prevent alternate discharge paths) into a liquid-nitrogen cold trap. Gas was supplied continuously at the anode end to maintain the desired operating pressure, which was monitored at the anode end. Pressure was regulated by means of a high-vacuum all-welded bellows-type needle valve. Gas was research grade (or reagent grade, if liquids were used) and held at slightly above atmospheric pressure by means of a high-purity stainless-steel regulator. As would be expected, contamination by foreign gases was noted to be completely absent, and any residual contaminants initially present were quickly swept away by the flowing gases. However, a liquid-nitrogen cold trap is essential to isolate the laser system from the vacuum pumping station, since contamination by pump oil (in an untrapped system) was found to suppress laser lines below 250 nm.

B. Spectroscopic Procedure

Spectroscopic wavelength measurement of wavelengths was performed on a 1-m scanning spectrometer using a 1200-lines/mm grating blazed for 1.2 μ, first order. Thus measurements were performed in the fourth-seventh order, permitting a resolution of 0.015 Å (1.5 pm) near 3000 Å, and a readability of spontaneous- or laser-emission line centers to 0.2 pm (0.002 Å), by comparison to wavelength calibration sources, such as hollow-cathode atomic-emission lamps.

Reference light was supplied by a series of atomic hollow-cathode lamps, such as iron, titanium, etc., and passed through a mechanical light chopper, then combined with the laser light on a beam-splitter and admitted into the spectrometer. The combined laser and reference light, modulated at the frequencies of the mechanical light chopper and laser repetition rate, was detected by a photomultiplier at the spectrometer exit. Two lock-in amplifiers then provided signals which were combined for presentation on a strip-chart recorder. Knowledge of the spectrometer scan rate, grating order used, and strip charge speed permitted display at a known linear dispersion. Values typically of 1-2 pm/cm of chart paper were used for ease in comparing the center of the laser peak to the center of the atomic reference emission peaks. Fig. 4 shows a typical data presentation used to determine laser wavelength, in this case Xe IV? 231.5 nm.

Since higher orders of dispersion were used, it was always possible to find a good atomic reference line within $\frac{1}{2}$ Å of the laser line, on the strip-chart display. This is because the laser line in one order was often near some atomic line (generally in a lower grating order), as seen by the photomultiplier. The values for the refractive index of air as needed in conversion to vacuum wavenumbers were taken from the *Tables of Wavenumbers* [9]. Iron, titanium, neon, or argon provided most of the reference wavelengths for laser-wavelength determination, and reference wavelengths to 7 or 8 significant digits were taken from *Tables of Spectral Lines of Neutral and Ionized Atoms* [10]. If one of these four elements did not provide a good reference line sufficiently near the laser line being measured, then a satisfactory reference line could always be found

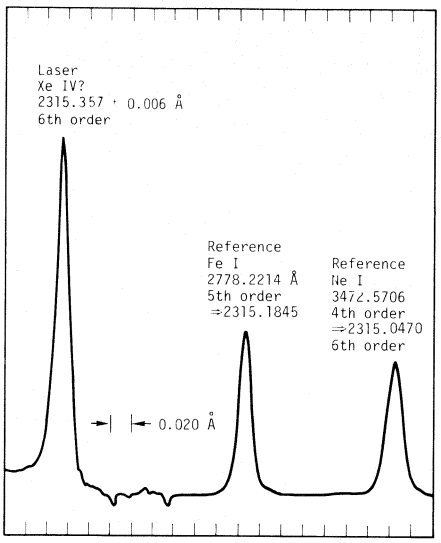

Fig. 4. Laser-wavelength calibration by simultaneous strip-chart display of laser wavelength and hollow-cathode-lamp reference wavelengths measured in air.

from the transition elements such as cobalt, manganese, etc., with reference wavelength to six significant digits taken from *Tables of Spectral-Line Intensities* [11]. Thus most laser wavelengths appearing in Tables I-VI could be specified to an accuracy of 0.01 Å or better.

Performance of the various laser lines was measured on a silicon photodiode calibrated in absolute units (milliamps per watt) throughout the spectral range of interest. Response and calibration below 3000 Å was achieved by removing the glass cover of the photodiode, thereby exposing the silicon surface directly to the incident laser light. Attenuation was achieved by use of quartz neutral-density (ND) filters, with absorption measured to 200 nm. (Typical absorption of these commercial ND filters varies by up to a factor of 3 in the range 200-400 nm.)

The laser pulses were displayed on a dual-beam oscilloscope simultaneously with the current pulse from the laser discharge. The current-pulse display on the scope was obtained by a 0.010-Ω current-viewing resistor placed in the current return of the laser tube, indicated in Fig. 1. The laser operated at 10 pps for all spectroscopic and performance measurements. For performance analysis of each line, if several oscillated simultaneously for a given set of mirrors, the laser output was reflected off a small, 1200-lines/mm grating. The first- or second-order reflection of the laser beam detected at a distance of several feet was generally sufficient to resolve adjacent laser lines at the 1-cm-aperture photodiode detector. Multiple laser lines closely separated in wavelength, such as oxygen at 375 nm or neon at 268 nm, were resolved for relative performance with the scanning spectrometer. Then absolute performance of the group was measured with the photodiode, as before. Performance was determined by generating a family of curves of output as a function of pulse voltage (i.e., current density) for different pressure settings. Generally, performance was fairly sensitive to pressure settings, and many lines could tolerate only a factor of 2 pressure variation for oscillation.

III. Experimental Results and Discussion

Experimental results are presented first for the noble gases, since they are generally the richest in laser transitions. Helium was tried, but no transitions were observed in the range 215-400 nm. The other noble gases generally exhibited laser action approximately every 10 nm throughout the portion of the UV between 200 and 400 nm. The gases are presented in order of increasing atomic weight for each column investigated of the periodic table.

A. Neon

Neon is characterized by many higher ionization states exhibiting laser action below 3000 Å. The results of neon-laser performance and spectroscopy are presented in Table I. Eleven new laser transitions were found in the range 202-261 nm. All the new transitions for neon satisfied the commonly observed characteristic of laser transitions $\Delta J = \Delta L$ [12], and all the observed neon transitions were $3p$-$3s$. The new transitions were classified directly by reference to *Tables of Spectral Lines of Neutral and Ionized Atoms* [10]. The shortest wavelength neon transitions occurred at 202 nm for Ne IV $3p\ ^2D^0 \rightarrow 3s\ ^2D$, as indicated in Table I. Both transitions of this doublet were observed to lase, but the member with the highest value of J was strongest, as was the case for all other laser transitions observed in this study to occur from the same multiplet. The Ne IV 202-nm transition was strong and would lase even using Brewster windows and intracavity air between the mirrors and laser. The transition at 206.5 nm exhibited high gain and was stronger than indicated in Table I, since nonoptimum output mirror reflectivity was used. This transition also exhibited a low threshold for laser action similar to the Ne III transitions at 247 and 268 nm. However, efforts at classification of the 206.5-nm transition were inconclusive and the ionic classification is either Ne III or Ne IV. The Ne V 2265.7-Å laser line was the only transition observed in this investigation that was definitely classified as a laser transition from a quadruply

TABLE I
NEON ULTRAVIOLET LASER TRANSITIONS

Measured Wavelength in Air Angstroms	Classification	Prior Reference	Optimized Pressure & Current Density J amp/cm^2	P_μ	Output Reflector	Peak Power Output-Watts
2018.424 ±.01	NeIV(^{1}D)3p $^2D^0_{3/2}$→3s $^2D_{3/2}$	New			92%	0.5* Est.
2022.186 ±.005	NeIV(^{1}D)3p $^2D^0_{5/2}$→3s $^2D_{5/2}$	New	>8000 A/cm^2	21	92%	50* Est.
2065.304 ±.01	NeIII or NeIV	New	~6500 A/cm^2	18	50%	40*
2177.705 ±.005	NeIII(^{2}D^0)3p $^3P_1$→3s $^3D^0_2$	New			84%	0.5* Est.
2180.858 ±.005	NeIII(^{2}D^0)3p $^3P_2$→(^{2}D^0)3s $^3D^0_3$	New	5700 A/cm^2	23μ	85%	17
2265.7[a]	NeV(^{2}P^0)3p $^3D_3$→3s $^3P^0_2$	New	>7500 A/cm^2	20μ	88%	2
2285.793 ±.005	NeIV(^{1}D)3p $^2F^0_{7/2}$→3s $^2D_{5/2}$	New	5200 A/cm^2	20μ	90%	0.4
2352.554 ±.005	NeIV(^{3}P)3p $^4D^0_{5/2}$→3s $^4P_{3/2}$	New			85%	0.5 Est.
2357.980 ±.005	NeIV(^{3}P)3p $^4D^0_{7/2}$→3s $^4P_{5/2}$	3	5700 A/cm^2	20μ	85%	75
2373.200 ±.01	NeIV	New	5200 A/cm^2	20μ	85%	0.8
2473.398 ±.005	NeIII(^{2}D^0)3p $^1D_2$→3s $^1D^0_2$	3	5700 A/cm^2	30μ	80%	140
2609.982 ±.01	NeIII(^{2}D^0)3p $^3F_4$→3s $^3D^0_3$	New		10	86%	1 Est.
2613.4 ±0.1	NeIII(^{2}D^0)3p $^3F_3$→3s $^3D^0_2$	New			86%	<0.1
2677.918 ±.01	NeIII(^{4}S^0)3p $^3P_{2,0}$→3s $^3S^0_1$	3, 12	5700 A/cm^2	30μ	~40%	250 150 Est.
2678.690 ±.01	NeIII(^{4}S^0)3p $^3P_1$→3s $^3S^0_1$	3, 12				100 Est.
2777.634 ±.005	NeIII(^{2}D^0)3p $^3D_3$→3s $^3D^0_3$	12		10	89%	0.2 Est.
2866.726 ±.005	NeIII(^{2}D^0)3p $^1F_3$→3s $^1D^0_2$	3	4000 A/cm^2	25μ	91%	5
3319.745 ±.01	NeII(^{1}D)3p $^2P^0_{1/2}$→3s $^2D_{3/2}$	22, 3	3000 A/cm^2	13μ	77%	6
3323.745 ±.005	NeII(^{3}P)3p $^2P^0_{3/2}$→3s $^2P_{3/2}$	12, 23			77%	23
3345.446 ±.02	NeII(^{1}D)3p $^2P^0_{3/2}$→3s $^2D_{5/2}$	12, 23	3400 A/cm^2	13μ	78%	8
3378.256 ±.01	NeII(^{3}P)3p $^2P^0_{1/2}$→3s $^2P^0_{1/2}$	12, 23	3400 A/cm^2	13μ	78%	21
3392.799 ±.01	NeII(^{3}P)3p $^2P^0_{3/2}$→3s $^2P_{1/2}$	12, 23	3200 A/cm^2	25μ	78%	0.9

[a]Wavelength taken from [10].
*Mirrors directly exposed to the plasma; Brewster window absent.

ionized atom, and it was observed only at the upper limits of applied voltage. Unfortunately, laser operation at these settings was not sufficiently reliable for precise wavelength measurement, so the value from [10] is reported here. The most interesting aspect of neon is the strength indicated in Table I of the four lasing transitions at 236, 247, 267.8, and 267.9 nm. These were previously observed [3], [12], but it was not generally appreciated how strong they could be with suitable low-loss dielectric mirrors. High intrinsic gain was indicated by the peak power of Ne III at 247 nm, which dropped only 40 percent as the output mirror reflectivity was lowered from 80 to 35 percent. Similar high intrinsic gain was also exhibited by the other three neon lasing transitions at 236, 267.8, and 267.9 nm. The Ne III transitions appeared to saturate at about 5700 A/cm^2 in the short-pulse regime, and were generally 5 times stronger than the strong Ne II transitions near 330 nm. Saturation of Ne II under the same short excitation regime appeared at about 3000 A/cm^2, considerably higher than other singly ionized noble-gas laser transitions.

The two previously unclassified neon transitions at 247 and 289 nm have been tentatively classified as members of the Ne III singlet system. Motivation for this tentative classification appears justified by examination of characteristic isoelectronic laser transitions as indicated in Table II. Examination of Table II illustrates several other interesting features. First, it shows that isoelectronic atomic transitions are remarkably consistent in exhibiting similar laser properties. Entry *A* indicates five isoelectronic laser transitions for $3p\ ^3D_3 \rightarrow 3s\ ^3P^0_2$, and predicts furthermore that the transitions in F IV and Ne V should be quite strong at sufficiently high current densities. Entries *B* and *C* suggest possible new laser transitions at short wavelengths (see also Subsection E). Laser action was subsequently observed in Ne IV at 202 nm (see Table I), verifying entry *C* of Table II. However, laser action expected at 187.5 nm (entry *B* of Table II) was not observed, even at 10 000-A/cm^2 current density and with mirror reflectivity $R_1 \cdot R_2 > 0.95$ at 187.5 nm. However, a new transition in argon with the same electronic configuration was observed at 251.3 nm, as indicated in Table III. Entries *F*–*J* in Table II indicate that the given classifications of Ne III (247 and 287 nm in the Ne III singlet system) are plausible. Furthermore, it suggests that the Ne III transition at 268 nm is likely to be a strong CW transition as well.

B. Argon

Results of spectroscopic and performance investigation of argon are presented in Table III. Five new laser transitions were measured. However, efforts to achieve laser emission expected at 191.4 nm were not successful. This transition corresponds to Ar III $4p\ ^3P_2 \rightarrow 3d\ ^3D^0_3$ and should lase based

TABLE II
Isoelectronic Sequences for Laser Transitions Ending with Neon

Transition	Ion Type and Emission Wavelength in Angstroms				
A. $(^2P^0)3p\ ^3D_3 \cdot 3s\ ^3P^0_2$	NeV 2265.7 Pulsed laser[a]	FIV 2826.13 Pulsed laser[5]	OIII 3759.88 Strong pulsed laser[b]	NII 5679.56 Strong pulsed laser[12]	CI 10691.2 CW laser[1]
B. $(^3P)3p\ ^4S^0_{3/2} \cdot 3s\ ^4P_{5/2}$	NeIV 1875.26 Laser not observed	FIII 2484.36[10] Laser not yet observed	OII 3749.47 Strong pulsed laser[b]	NI 7468.31[10] Laser not yet observed	
C. $(^1D)3p\ ^2D^0_{5/2} \cdot 3s\ ^2D_{5/2}$	NeIV 2022.19[10] Strong pulsed laser[a]	FIII 2759.58 Pulsed laser[5]	OII 4351.28 Strong pulsed laser[4,20]	NI 9187.45[10] Laser not yet observed	
D. $(^3P)3p\ ^4D^0_{7/2} \cdot 3s\ ^4P_{5/2}$	NeIV 2357.98 Strong pusled laser[a]	FIII 3121.51 Strong pulsed laser[5]	OII 4649.14 Pulsed laser[12]	NI 8680.27[10] Laser not yet observed	
E. $(^3P)3p\ ^2D^0_{5/2} \cdot 3s\ ^2P_{3/2}$	NeIV 2363.28[10] Laser not yet observed	FIII 3174.13 Strong pulsed laser[5]	OII 4414.88 Strong pulsed laser[4,20]	NI 9392.8 CW laser[1]	
F. $(^2D^0)3p\ ^1D_2 \cdot 3s\ ^1D^0_2$	NeIII[c] 2473.40 Strong pulsed laser[a]	FII 3202.75 Pulsed laser[5]	OI 7156.80[10] Laser not yet observed		
G. $(^4S^0)3p\ ^3P_2 \cdot 3s\ ^3S_1$	NeIII 2677.92 Strong pulsed laser[a]	FII 4024.72 Strong pulsed laser[5]	OI 8446.36 CW laser[1]		
H. $(^4S^0)np\ ^3P_2 \cdot ns\ ^3S_1$ n = 3, 4, 5, 6	NeIII 2677.92 Strong pulsed laser[a]	ArIII 3511.12[d] Strong pulsed and CW laser[2]	KrIII 3507.39 Strong pulsed[e] and CW laser[2]	XeIII 3781.01 Pulsed[f] and CW laser[2]	
I. $(^2D^0)3p\ ^1F_3 \cdot 3s\ ^1D_2$	NeIII[c] 2866.73 Pulsed laser	FII 4299.18[10] Laser not yet observed	OI 8820.4 Pulsed laser[1]		
J. $(^2D^0)\ np\ ^1F_3 \cdot ns\ ^1D_2$ n=3, 4, 5, 6	NeIII[c] 2866.73 Pulsed laser	ArIII 3637.89 Strong pulsed[d] and CW[2] laser	KrIII 4067.37 CW laser[2]	XeIII 4673.68 Pulsed[f] and CW[1] laser	

[a]See Table I.
[b]See Table VI.
[c]Proposed classification.
[d]See Table III.
[e]See Table IV.
[f]See Table V.

TABLE III
Argon Ultraviolet Laser Transitions

Measured Wavelength in Air Angstroms	Classification	Prior Reference	Optimized Pressure & Current Density: J Amp/cm^2	Optimized Pressure & Current Density: P	Output Reflector	Peak Power Output-Watts
2113.982 ±.005	ArIV	New	>8000 A/cm^2	12μ	91%	20*
2248.840 ±.005	ArIV	New	>8000 A/cm^2	7μ	90%	10*
2513.298 ±.02	ArIV(^{3}P)4p $^4S^0_{3/2}$→4s $^2P_{5/2}$	New	>8000	6μ	90%	6*
2621.377 ±.005	ArIV(^{1}D)4p $^2D^0_{3/2}$→4s $^2D_{3/2}$	New	~8000 A/cm^2	9μ	85%	10* Est.
2624.882 ±.01	ArIV(^{1}D)4p $^2D^0_{5/2}$→4s $^2D_{5/2}$	3	>7800 A/cm^2	9μ	85%	8, 30*
2753.884 ±.005	ArIII($^2D^0$)4p $^1D_2$→4s $^1D^0_2$	12,3,CW-27	~7300 A/cm^2	6μ	88%	11
2855.374 ±.005	ArIII($^2D^0$)4p $^3P_1$→4s $^3D^0_2$	New	5400 A/cm^2	5μ	92%	0.2
2884.216 ±.005	ArIII($^2D^0$)4p $^3P_2$→4s $^3D^0_3$	22,3,CW-27	6200 A/cm^2	5μ	92%	9
2912.924 ±.005	ArIV(^{3}P)4p $^2D^0_{5/2}$→4s $^2P_{3/2}$	12,3	~7000 A/cm^2	10μ	92%	16
2926.227 ±.003	ArIV(^{3}P)4p $^2D^0_{3/2}$→4s $^2P_{1/2}$	12,3	~7000 A/cm^2	12μ	92%	4
3002.642 ±.01	ArIII($^2P^0$)4p $^1P_1$→3d $^1D^0_2$	12,3,CW-27	6200 A/cm^2	10μ	91%	42
3511.13 ±.06	ArIII($^4S^0$)4p $^3P_2$→4s $^3S^0_1$	20,12-λ	~7200 A/cm^2	10μ	60%	1000-s
3514.15 ±.06	ArIII($^4S^0$)4p $^3P_1$→4s $^3S^0_1$	20,12-λ	~6200 A/cm^2	7μ	60%	5 Est.
3637.86 ±.04	ArIII($^2D^0$)4p $^1F_3$→4s $^1D^0_2$	20,12-λ	5700 A/cm^2	8μ	60%	240
4579. 4765. 4880. 4965. 5017. 5145.	Strong Visible Argon Lines	ArII	24	~500 A/cm^2	6	90%	64 all lines

*Mirrors directly exposed to the plasma; Brewster windows absent.
[S]Superradiant laser action noted.
[CW]Transitions newly observed in CW operation, [27].

TABLE IV
KRYPTON ULTRAVIOLET LASER TRANSITIONS

Measured Wavelength in Air Angstroms	Classification	Prior Reference	Optimized Current Density & Gas Pressure		Output Reflector	Peak Output Power-Watts
1949.623 ±.01[a]	KrIV	New	>9000 A/cm^2	7μ	97%	15*
2051.082 ±.003	KrIV	New		8μ	98%	1* Est.
2191.916 ±.005	KrIV	New	>9800 A/cm^2	8μ	76%	600
2254.638 ±.005	KrIV	New	>7800 A/cm^2	6μ	90%	80
2338.478 ±.01	KrIV	New	>7800 A/cm^2	13μ	86%	8
2417.843 ±.005	KrIII or KrIV	New	6200 A/cm^2	8μ	84%	0.2
2649.357 ±.005	KrIV	3		10μ	82%	0.1* Est.
2664.398 ±.010	KrIV	3	>7800 A/cm^2	10μ	85%	21
2741.380 ±.01	KrIV	3	>7500 A/cm^2	11μ	90%	27
3049.704 ±.02	KrIII	12, 3	~6200 A/cm^2	11μ	90%	18
3124.363 ±.01	KrIII($^2D^0$)5p $^1D_2$→5s $^1D^0_2$	3, CW-27	5400 A/cm^2	8μ	87%	6
3239.512 ±.005	KrIII($^2P^0$)5p $^1D_2$→5s $^1P^0_1$	12,3,CW-27	5400 A/cm^2	11μ	75%	14
3507.420 ±.01	KrIII($^4S^0$)5p $^3P_2$→5s $^3S^0_1$	12	6200 A/cm^2	8μ	60%	130
3564.20 ±.06	KrIII($^4S^0$)5p $^3P_1$→5s $^3S^0_1$	12-λ	4000 A/cm^2	7μ	80%	0.3
7435.764 ±.01	KrII(^1D)4d $^2D_{5/2}$→(^3P)5p $^4D^0_{5/2}$	25-s	>7800 A/cm^2		45%	400-s

*Mirrors directly exposed to the plasma; Brewster windows absent.
[a]Vacuum wavelength = 1950.26 Å (51 275.0 cm^{-1}).
[s]Superradiant laser action observed.
[CW]Transitions newly observed in CW operation, [27].

on sharing the same highly populated $4p\ ^3P_2$ level with the very strong Ar 351.1-nm laser transition, as well as having a lower level strongly coupled to the $3p^5\ ^3P_2$ ground state, necessary requirements for a strong ion laser. Laser action at 191.4 nm would require suppression of the 351.1-nm emission; therefore, mirrors were tried with $R_1 \cdot R_2 \geqslant 0.96$ at 191 nm and $R_1 \cdot R_2 < 0.005$ at 351 nm. Laser action was still strong at 351.1 nm and absent at 191 nm, implying excessive population of the $3d\ ^3D^0_3$ level by a different mechanism. All the argon transitions below 300 nm were similar in performance, except for the 285.5-nm laser transition, which was 100 times weaker, as indicated in Table III. The new transition at 285.5 nm does illustrate the common characteristic of pulsed lasers, namely that for transitions between the same multiplets, the transition with highest value of J in the upper level will be strongest. This is also indicated in the relative laser strengths of the Ar IV lines at 291 and 293 nm, Ar III at 351.1 and 351.4 nm, and Ar IV 262.1 and 262.5 nm.

Examination of Table III also indicates the unusually high peak power obtainable from the strong Ar III 351-nm transition. The optimized measured peak power of 1 kW is nearly two orders of magnitude stronger than the other argon transitions, except Ar III 364 nm. It was interesting to note that the saturation current density for the Ar III transitions occurred at about 6000 A/cm^2, which was roughly ten times greater than the saturation current density of 500 A/cm^2 noted for the strong visible Ar II transitions. The peak power of these Ar II visible transitions is also indicated in Table III for comparison.

The new short-wavelength argon transitions at 211 and 225 nm remain incompletely classified, although ionic classification as Ar IV appears correct, based on their laser performance at high current densities as indicated in Table III.

The previously unclassified [1] argon transitions at 275 and 300 nm have been tentatively classified as members of the Ar III singlet system, based on comparison with known isoelectric laser transitions in chlorine [5]. These tentative classifications await further spectroscopic verification.

C. Krypton

Results of spectroscopic and performance evaluation of the krypton UV laser transitions are presented in Table IV. Six new transitions were measured below 250 nm. The shortest wavelength of all laser transitions observed in this study was Kr IV 195.0 nm and is technically in the vacuum UV. It is also the shortest wavelength of any laser transition produced by a simple z-pinch excitation scheme. The laser transition, Kr IV 219 nm, is unusual because of its high peak power and high gain of at least several decibels/meter. In this respect, its performance resembles the strong Xe IV transitions discussed in the next section.

The performance of Kr IV 219 nm plotted against peak bore current density is shown in Fig. 5. Also shown is a similar plot for the other strong UV krypton transition, Kr III at 351 nm. It can be seen that saturation occurs for the Kr III transition around 6000 A/cm^2, while the transition at 219 nm was still increasing in power at 10 000 A/cm^2. Lack of apparent saturation in output power with increasing current density is the basis for classification of the krypton transitions at 195, 205, 219, 225, 234, 266, and 274 nm as occurring in Kr IV. The remaining transitions decreased in output power with increasing current density, with saturation occurring near 6000 A/cm^2, as indicated in Table IV. The new transition at 225 nm is also strong, and low gas pressures result in the best operation.

Fig. 6 shows oscilloscope traces of the output signal of

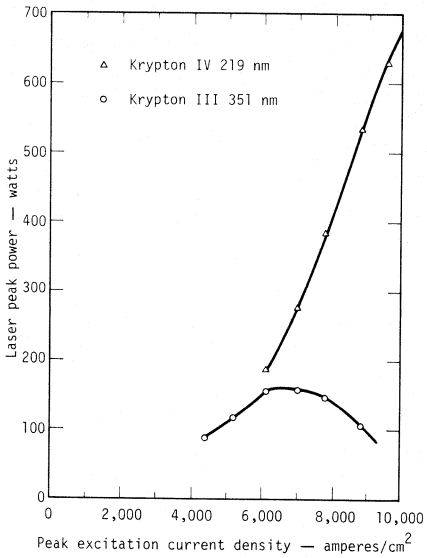

Fig. 5. Peak laser power in krypton at 219 and 351 nm plotted as a function of peak excitation current density.

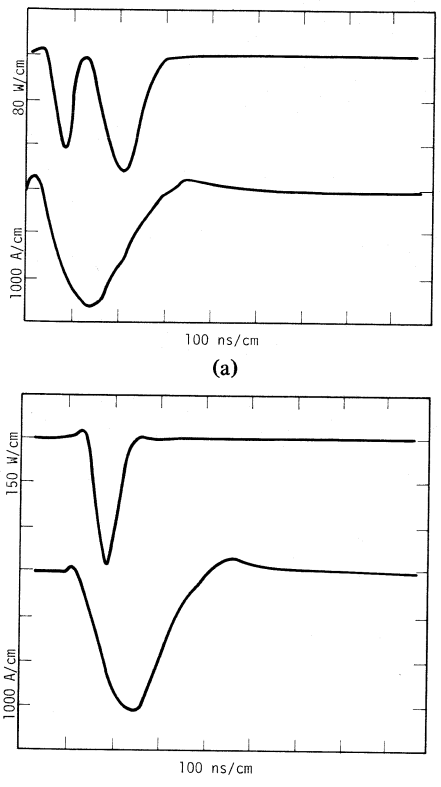

Fig. 6. Temporal display of krypton-ion laser output and excitation current pulse at 219 and 744 nm. (a) Upper trace: Laser emission in krypton IV at 219 nm (second pulse only). Lower trace: Excitation current pulse. (b) Upper trace: Laser emission in krypton II at 744 nm. Lower trace: Excitation current pulse.

Kr IV 219 nm compared to the bore current of the excitation discharge. The first pulse is due to a superradiant transition at Kr II 7435.764 Å. The performance and wavelength of this near-infrared transition is also included in Table IV because of its high gain and high available peak power of several hundred watts. Fig. 6 additionally shows that the premature termination of the Kr II 744-nm transition occurs before the excitation pulse has reached maximum. Examination of Table IV also indicates that many of the Kr UV laser transitions still remain unclassified and that further spectroscopic investigation is required. The previously observed Kr III transition at 337 nm [12], [2] was not observed in this study, presumably due to the nature of the short excitation pulse used, which was generally an order of magnitude shorter than the excitation-pulse duration used by previous investigators. It is interesting to note that krypton exhibits laser action about once every 10 nm throughout the UV from 355 to 195 nm.

D. Xenon

Xenon is perhaps the most interesting of the pulsed noble-gas ion lasers because of its large number of strong transitions, due principally to Xe IV throughout the UV and visible spectral regions. Results of spectroscopic and lasing-performance investigations of xenon UV and selected visible transitions are presented in Table V. Three new transitions were observed below 260 nm and are tentatively attributed to Xe IV, as discussed below. The xenon-laser transition at 223 nm was found to be very erratic in performance, with shot-to-shot output varying by a factor of 5. It was found to lase only in the afterglow, with onset of lasing occurring 400 ns after termination of the excitation current discharge. Lasing duration was 400 ns, twice as long as all other xenon-ion transitions. Thus it could be a transition in Xe III, since third-spectrum xenon transitions did exhibit some lasing in the afterglow, as discussed below. The 231.5-nm transition is unusual in being both short in wavelength and also high in peak output power, and is exceeded in power only by the anomalously strong Xe IV 365-nm line at high current densities. In addition, it exhibited high gain, since lasing power output was higher using a 50-percent reflector than employing either 75- or 90-percent reflectors to couple out from the cavity. On the bases of high gain and output power, it resembles the Xe IV transitions, but its output power appeared to saturate at current densities corresponding to Xe III transitions (see Fig. 7). However, the strong Xe 231.5-nm transition seemed to show some anti-correlation with the strong Xe IV 365-nm transition. This might explain why this potentially high-gain laser line was not seen earlier [6], where the use of aluminized mirrors [6] permitted oscillation at 365 nm, hence suppressing oscillation at 231.5 nm. This problem is avoided with dielectric mirrors. On this basis the 231.5-nm transition would have ionic classification as Xe IV. All the Xe IV laser transitions continued to increase in power at the highest current densities tested. The Xe 231.5-nm output power as a function of current density is compared with Xe IV 365 nm in Fig. 7. Fig. 8 compares the output versus current density for Xe IV 269 nm and Xe III 308 nm. Here there is clear saturation occurring for the Xe III 308-nm transition at about 5000 A/cm^2, while the 269-nm output power continues to increase with increasing current density, suggesting the 269-nm transition should be attributed to Xe IV and the 308-nm transition to Xe III. This conclusion is in agreement with a recent study of xenon-laser ionic assignments [13] regarding the Xe III assignment at 308 nm. However, this earlier study [13] assigns the 269-nm

TABLE V
XENON ULTRAVIOLET LASER TRANSITIONS

Measured Wavelength in Air Angstroms	Classification	Prior Reference	Optimized Current Density & Gas Pressure		Output Reflector	Peak Output Power - Watts
2232.442 ±.003	XeIII or XeIV	New	~8000 A/cm^2	5μ	90%	10-50* Erratic
2315.357 ±.005	XeIII or XeIV	New	~5700 A/cm^2	5μ	50%	1400
2526.664 ±.003	XeIV	New	>10,000 A/cm^2	9μ	90%	24*
2691.939 ±.005	XeIV	3	>8500 A/cm^2	10μ	70%	5
3079.738 ±.02	XeIII	3, CW-27	5200 A/cm^2	5μ	90%	32
3246.922 ±.005	XeIV	3	>8500 A/cm^2	5μ	73%	260
3305.957 ±.005	XeIII?	3,12	~4300 A/cm^2	6μ	76%	5
3330.869 ±.02	XeIV	3	>8000 A/cm	5μ	77%	330
3454.248 ±.005	XeIII ($^2D^o$)6p $^1D_2$-6s $^1D^o_2$	3	5200 A/cm^2	5μ	78%	22
3645.478 ±.01	XeIV	22,3	>8500 A/cm^2	7μ	60%	3600
3780.990 ±.02	XeIII($^4S^o$)6p $^3P_2$-6s $^3S^o_1$	12,3	~4200 A/cm^2	5μ	92%	2
4060.48 ±.06	XeIII($^2P^o$)6p $^3[2]_1$-5d $^2[5]_1$	12-CW	4400 A/cm^2	7μ	74%	20
4305.75 ±.03	XeIV	12,14-CW	>8000 A/cm^2	11μ	84%	1000
4673.73 ±.06	XeIII($^2D^o$)6p $^1F_3$-6s $^1D^o_2$	12-CW	>6800 A/cm^2	11μ	92%	3
4954.18 5007.80 5159.08 5260.17 5352.90 5394.60	±.03 XeIV	12,14-CW	>9400 A/cm^2	11μ	60%	6500 all lines

*Mirrors directly exposed to the plasma; Brewster windows absent.
CWTransitions newly observed in CW operation, [27].

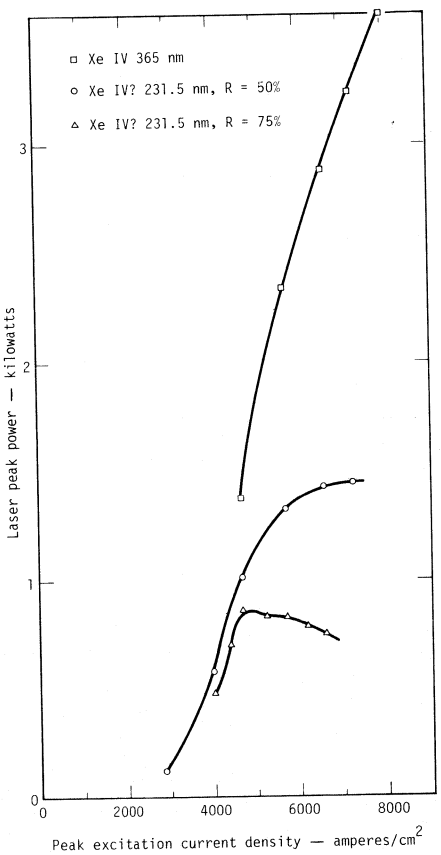

Fig. 7. Peak laser output power in xenon at 231.5 and 365 nm as a function of peak excitation current density.

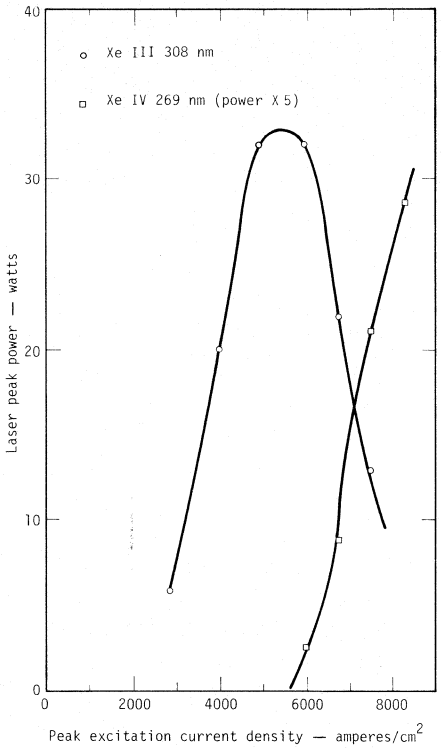

Fig. 8. Peak laser output power in xenon at 269 and 308 nm as a function of peak excitation current density.

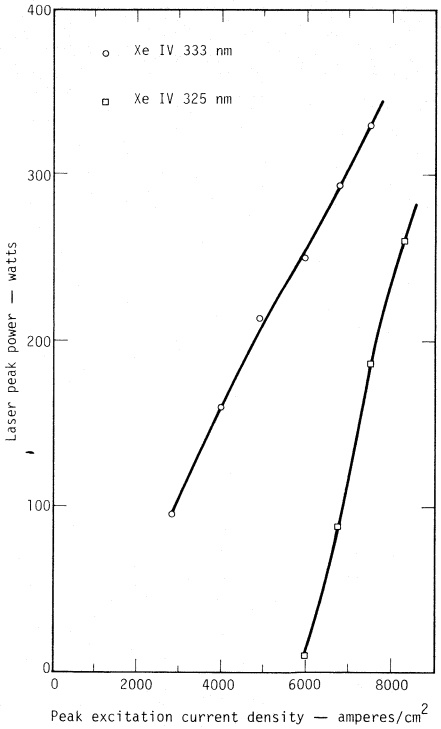

Fig. 9. Peak laser output power in xenon at 325 and 333 nm as a function of peak excitation current density.

transition to Xe III, which cannot be justified, based on the apparent lack of saturation of this transition at high current densities, as indicated in Fig. 8. However, ionic assignments of the other xenon-laser transitions given earlier [13] are in agreement with the ionic assignments given in this study. The possible existence of a xenon transition at 298.4 nm in [1], [12], and [13] appears to be ruled out; a careful search at this wavelength was negative. However, the very strong oxygen transition at 2983.86 Å (see Table VI) is the likely source of this line as an impurity from the oxide cathode used in [12]. The use of indium cold electrodes precluded such oxygen contamination in this investigation.

Fig. 9 shows the output-power performance of the xenon transitions at 325 and 333 nm, plotted against current density. Neither transition exhibited clear saturation at the highest current densities tested, again suggesting that both belong to the Xe IV spectrum. Therefore, the assignment of the xenon 325-nm transition to Xe III $(^2P^0)\ 6p\ ^3D_3 \rightarrow 5d\ ^3D^0_3$, [3], must be in error. In confirmation of this, the measured wavelength of 3246.922 ± 0.005 Å is rather clearly outside the calculated Xe III wavelength of 3246.84, but in agreement with the originally measured wavelength of 3246.94 Å [3]. Similarly, apparent power saturation at a current density of about 4000 A/cm² would classify the xenon 330.6-nm transition in the Xe III spectrum. It may be noted that the transitions at 345, 378, and 406 nm with known Xe III classifications exhibited similar peak powers and similar apparent saturation current densities of about 4500 A/cm².

The strong Xe IV visible transitions are also included in Table V for comparison. The violet line at 430.6 nm again exhibited the high peak power of about 1 kW characteristic of these fourth-spectrum xenon transitions. Saturation current density was not reached in this investigation, and exceeds 8000 A/cm², substantiating the Xe IV assignment proposed earlier [13]-[15]. The strong Xe IV green lines were measured simultaneously and each averaged about 1-kW peak power; current saturation was not reached at 9400 A/cm². Relative strengths for the individual lines are given in [16] and [17], and a thorough parametric study is given [18].

The temporal behavior of typical xenon-ion-laser transitions is presented in Fig. 10 for the transitions at 231.5 and 308 nm, and in Fig. 11 for the transitions at 345 and 365 nm. For the short current excitation pulse used in this investigation, lasing began about 150 ns after onset of the current excitation pulse, and terminated with the current pulse for the Xe IV transitions; all Xe IV transitions exhibited similar temporal behavior, with 100-ns FWHM. The Xe III transitions often continued to lase during the afterglow for about 100–300 ns. This is well illustrated by the 308-nm transition; laser pulse FWHM was typically 200 ns for all Xe III transitions in this investigation.

Again examination of Table V reveals the large number of xenon-laser transitions that remain incompletely classified, and further investigation is certainly warranted.

E. Oxygen and Nitrogen

The atmospheric gases oxygen and nitrogen were investigated for relative performance of their UV and several visible laser transitions. Results of this investigation are presented in

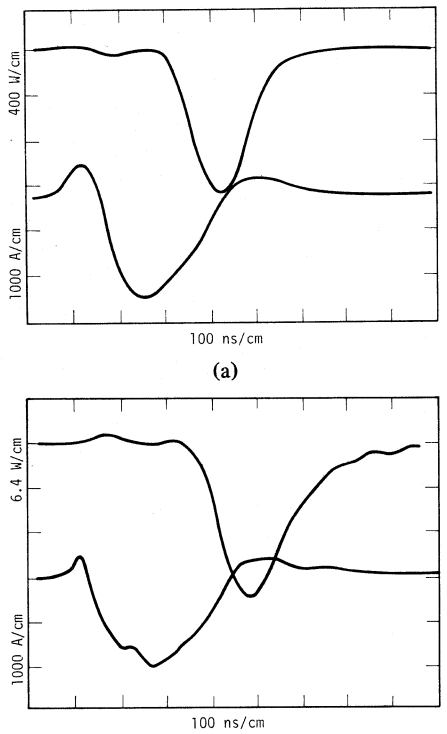

Fig. 10. Temporal display of xenon-ion-laser output pulse shape and corresponding excitation current pulse at 231.5 and 308 nm. (a) Upper trace: Laser emission in xenon IV? at 231.5 nm. Lower trace: Excitation current pulse. (b) Upper trace: Laser emission in xenon III at 308 nm. Lower trace: Excitation current pulse.

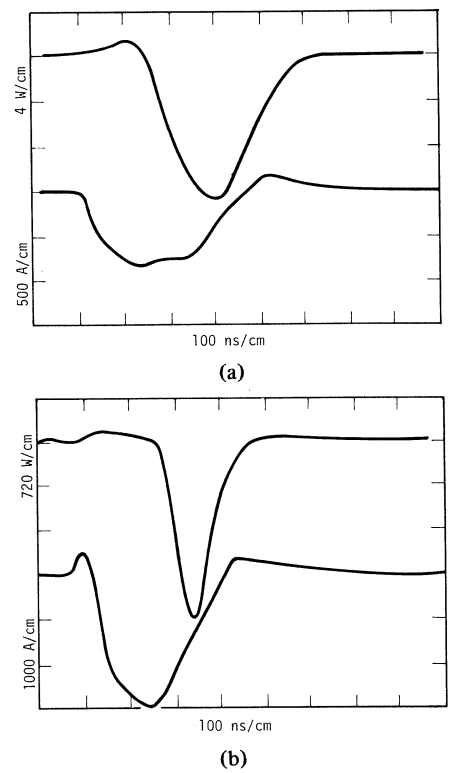

Fig. 11. Temporal display of xenon-ion-laser output pulse shape and corresponding excitation current pulse at 345 and 365 nm. (a) Upper trace: Laser emission in xenon III at 345 nm. Lower trace: Excitation current pulse. (b) Upper trace: Laser emission in xenon IV at 365 nm. Lower trace: Excitation current pulse.

Table VI. In oxygen no new transitions were observed between 215 and 298 nm, the first entry in Table VI; the recently observed O V 2781.04-Å laser transition [19] was not visually detected in this study using fluorescent paper, i.e., peak power was less than 0.1 W. The accuracy of the measured wavelengths, except as indicated in Table VI, is that reported by previous investigators [3], [20], [21]. One new transition was measured at 375.7 nm, and is the remaining member of the laser triplet O III $3p\ ^3D_{3,2,1} \rightarrow 3s\ ^3P_{2,1,0}$, for which $\Delta J = \Delta L = -1$. The O III transition at 559 nm was also included since it exhibited high peak power in this investigation.

The temporal behavior of the oxygen transitions was similar to the XE III transitions discussed in Subsection D. All exhibited FWHM of about 200 ns, with onset of lasing occurring 200 ns after onset of current excitation. However, significantly different temporal behavior occurred for the O III 375-nm triplet and O III 559 nm. For these four transitions, onset of lasing occurred in the afterglow 200 ns after termination of current excitation. The duration of lasing was typically 700-ns FWHM. Thus the energy content of these O III transitions was comparable to the strong Xe IV transitions.

The oxygen transition O II 374.9 nm exhibited "normal" behavior with 180-ns FWHM. It is to be noted that O II 374.9 nm is the strongest of all singly ionized laser transitions. Examination of the isoelectronic sequence for this transition, namely $(^3P)3p\ ^4S_{3/2} \rightarrow 3s\ ^4P_{5/2}$, would predict strong laser transitions in F III at 2484.36 Å and Ne IV at 1875 Å, which are under investigation [6] (see also Subsection A).

The oxygen-blue transitions were observed to be very weak with the short-pulse excitation used here and parametric data on performance are not reported, but are given in [4] for 4-μs-duration current excitation pulses.

Nitrogen was investigated for UV ion laser transitions, but the spectrum between 215 and 348 nm was unproductive of laser transitions. However, the only observed UV transition, N IV at 347.9 nm, exhibited high peak power of 400 W. The other nitrogen UV transitions [1] were not observed. The transition N III at 409.7 nm was also very strong and exhibited nearly superradiant behavior. Some of the known nitrogen-blue-laser transitions [1] were observed in this investigation and are included in Table VI. The wavelength of N III 451.1 nm was remeasured more accurately than previously reported [1], [20] and confirms the given classification [20]. Similar to oxygen, the nitrogen-blue transitions apparently favor longer pulse current excitation, and more complete relative performance data were reported earlier [4].

IV. Conclusion

Investigation of pulsed UV ion lasers has permitted measurement of the emission wavelengths to generally better than 0.01 Å. In addition, 25 new laser transitions were observed below 2700 Å, including transitions in Xe IV? 231.536 nm and Kr IV 219.192 nm, both of which exhibited peak pulsed powers of about 1 kW. The shortest wavelength transition was Kr IV at 194.962 nm at the edge of the vacuum UV. Measurement of peak laser power as a function of bore current density has yielded current saturation of 4000-6000 A/cm^2 for third-spectrum ion lasers, thus permitting ionic classification of the

TABLE VI
OXYGEN AND NITROGEN ULTRAVIOLET LASER TRANSITIONS

Measured Wavelength in Air Angstroms	Classification	Prior Reference	Optimized Current Density & Gas Pressure		Output Reflector	Peak Output Power - Watts
2983.86 ±.06	$OIII(^2P^o)3p\ ^1D_2 \rightarrow 3s\ ^1P^o_1$	12,3-λ	4200 A/cm^2	18μ	91%	17
3047.15 ±.06	$OIII(^2P^o)3p\ ^3P_2 \rightarrow 3s\ ^3P^o_2$	12,3-λ	4800 A/cm^2	19μ	90%	32
3063.46 ±.06	$OIV(^1S)3p\ ^2P^o_{3/2} \rightarrow 3s\ ^2S_{1/2}$	3-λ	4800 A/cm^2	17μ	90%	18
3749.47 ±.04	$OII(^3P)3p\ ^4S^o_{3/2} \rightarrow 3s\ ^4P_{5/2}$	20-λ	∿3100 A/cm^2	15μ	80%	135
3754.68 ±.04	$OIII(^2P^o)3p\ ^3D_2 \rightarrow 3s\ ^3P^o_1$	20-λ	4800 A/cm^2	25μ	80%	105
3754.257 ±.005	$OIII(^2P^o)3p\ ^3D_1 \rightarrow 3s\ ^3P^o_0$	New	∿4800 A/cm^2	25μ	80%	5 est.
3759.89 ±.05	$OIII(^2P^o)3p\ ^3D_3 \rightarrow 3s\ ^3P^o_2$	20-λ	4800 A/cm^2	25μ	80%	170
5592.37 ±.06	$OIII(^2P^o)3p\ ^1P_1 \rightarrow 3s\ ^1P^o_1$	20,12-λ	4800 A/cm^2	30μ	58%	180
3478.76 ±.06	$NIV\ (^2S)3p\ ^3P^o_2 \rightarrow 3s\ ^3S_1$	20-λ	4800 A/cm^2	16μ	80%	400
4097.27 ±.06	$NIII(^1S)3p\ ^2P^o_{3/2} \rightarrow 3s\ ^2S_{1/2}$	20-λ	3900 A/cm^2	11μ	50%	230
4103.36 ±.02	$NIII(^1S)3p\ ^2P^o_{1/2} \rightarrow 3s\ ^2S_{1/2}$	20,21-λ			50%	10 est.
4510.888 ±.015	$NIII(^3P^o)3p\ ^4D_{5/2} \rightarrow 3s\ ^4P^o_{3/2}$	20			92%	0.1 est.
4514.86 ±.03	$NIII(^3P^o)3p\ ^4D_{7/2} \rightarrow 3s\ ^4P^o_{5/2}$	20,21-λ	2800 A/cm^2	16μ	92%	7
4630.51 ±.02	$NII(^2P^o)3p\ ^3P_2 \rightarrow 3s\ ^3P^o_2$	20,21-λ	2300 A/cm^2	8μ	92%	15

new and previously unclassified laser transitions. Seven of these third-spectrum transitions between 275 and 324 nm have been recently observed in CW operation [27] with thresholds of about 500 A/cm^2. Optimum output performance characteristics were determined as functions of excitation current density and gas pressure for all the ion-laser transitions below 400 nm observed to lase with short-duration (250 ns) current excitation pulses. Comparison of isoelectronic sequences has permitted tentative classification of some unclassified UV transitions in neon and argon, but many krypton and xenon laser lines still remain unclassified. Investigation of pulsed UV ion laser transitions in other gases will be reported in a subsequent article [6].

Thus a simple z-pinch capacitive-discharge laser system has been described which produces laser emission completely spanning the chemical UV from 195–300 nm in 25 new and 15 previously known laser transitions in the four noble gases. Performance is equally good on many previously known laser transitions above 300 nm. In addition, system reliability permits operation for days continuously, with a system lifetime between 10^8 and 10^9 shots. This should make this kind of ion laser a powerful and reliable research tool for generation of laser light throughout the chemical UV.

ACKNOWLEDGMENT

The author wishes to thank W. R. Call and W. E. Elsholz for expert technical assistance in laser construction and glass blowing, respectively. He also wishes to thank L. L. Wood, M. L. Spaeth, and W. W. Simmons for helpful suggestions.

REFERENCES

[1] "Ionized gas lasers," in *Handbook of Lasers*, R. J. Pressley, Ed., Chemical Rubber Co., Cleveland, Ohio, 1971, ch. 7, pp. 242-277.
[2] J. R. Fendley, Jr., "Continuous UV lasers," *IEEE J. Quantum Electron. (Special Issue on 1968 International Quantum Electronics Conference: Part I)*, vol. QE-4, pp. 627-631, Oct. 1968.
[3] P. K. Cheo and H. G. Cooper, "Ultraviolet ion laser transitions between 2300 and 4000 Å," *J. Appl. Phys.*, vol. 36, pp. 1862–1865, 1965.
[4] A. W. Tucker and M. Birnbaum, "Pulsed-ion laser performance in nitrogen, oxygen, krypton, xenon, and argon," *IEEE J. Quantum Electron.* (Notes and Lines), vol. QE-10, pp. 99–100, Jan. 1974.
[5] P. K. Cheo and H. G. Cooper, "UV and visible laser oscillations in fluorine, phosphorous, and chlorine," *Appl. Phys. Lett.*, vol. 7, pp. 202–204, 1965; also, H. P. Palenius, "The identification of some Si and Cl laser lines observed by Cheo and Cooper," *Appl. Phys. Lett.* (Corrections), vol. 16, pp. 5–8, 1966.
[6] J. B. Marling, to be published.
[7] R. W. Waynant, "Vacuum ultraviolet laser emission from CIV," *Appl. Phys. Lett.*, vol. 22, pp. 419–420, 1973.
[8] M. H. Hornstein and V. E. Derr, "Prepulse enhancement of a flashlamp pumped dye laser," *Appl. Opt.*, vol. 13, pp. 2100–2104, 1974.
[9] *Tables of Wavenumbers*, vol. I, *2000 Å to 7000 Å* (NBS Monograph 3). Washington, D.C.: U.S. Government Printing Office, 1960.
[10] *Tables of Spectral Lines of Neutral and Ionized Atoms*, A. R. Striganov and N. S. Sventitskii, Ed. New York: Plenum, 1968.
[11] *Tables of Spectral-Line Intensities*, pt. I (NBS Monograph 32). Washington, D.C.: U.S. Government Printing Office, 1961.
[12] W. B. Bridges and A. N. Chester, "Visible and UV laser oscillation at 118 wavelengths in ionized neon, argon, krypton, oxygen, and other gases," *Appl. Opt.*, vol. 4, pp. 573–580, 1965.
[13] E. Gallego Lluesma, A. A. Tagliaferri, C. A. Massone, M. Garavaglia, and M. Gallardo, "Ionic assignment of unidentified xenon laser lines," *J. Opt. Soc. Amer.*, vol. 63, pp. 362–364, 1973.
[14] M. Gallardo, M. Garavaglia, A. A. Tagliaferri, and E. Gallego Lluesma, "About unidentified ionized Xe laser lines," *IEEE J. Quantum Electron.* (Corresp.), vol. QE-6, pp. 745–747, Nov. 1970.
[15] W. B. Bridges and A. W. Chester, "Comments on the identification of some xenon ion laser lines," *IEEE J. Quantum Electron.* (Notes and Lines), vol. QE-7, pp. 471–472, Sept. 1971.
[16] A. Papayoanou and I. Gumeiner, "High power laser action in high current pinched discharges," *Appl. Phys. Lett.*, vol. 16, pp. 5–8, 1970.
[17] J. P. Wheeler, "New xenon laser line observed," *IEEE J. Quantum Electron.* (Notes and Lines), vol. QE-7, p. 429, Aug. 1971.
[18] W. W. Simmons and R. S. Witte, "High-power pulsed xenon ion lasers," *IEEE J. Quantum Electron.*, vol. QE-6, pp. 466–469, July 1970.
[19] Y. Hashino, Y. Katsuyama, and K. Fukuda, "Laser oscillation of O V in Z-pinch discharge," *Japan. J. Appl. Phys.*, vol. 12, p. 470, 1973.
[20] R. A. McFarlane, "Laser oscillation on visible and ultraviolet transitions of singly and multiply ionized oxygen, carbon and nitrogen," *Appl. Phys. Lett.*, vol. 5, pp. 91–93, 1964.
[21] R. B. Allen, R. B. Starnes, and A. A. Dougal, "A new pulsed ion laser transition in nitrogen at 3995 Å," *IEEE J. Quantum Elec-*

tron. (Notes and Lines), vol. QE-2, p. 334, Aug. 1966.
[22] L. Dana, P. Laures, and R. Rocherolles, "Raies laser ultraviolettes dans le neon, l'argon, et le xenon," *C. R. Acad. Sci.*, vol. 260, pp. 481–484, 1965.
[23] K. G. Ericsson and L. R. Lidholt, "Superradiant transitions in argon, krypton, and xenon," *IEEE J. Quantum Electron.* (Corresp.), vol. QE-3, p. 94, Feb. 1967.
[24] W. B. Bridges, "Laser oscillation in singly ionized argon in the visible spectrum," *Appl. Phys. Lett.*, vol. 4, pp. 128–130, 1964; also Erratum, *Appl. Phys. Lett.*, vol. 5, p. 39, 1964.
[25] V. A. Tolkachev, "Super-radiant transitions in Ar and Kr," *Zh. Prikl. Spektrosk*, vol. 8, pp. 746–749, May 1968.
[26] C. E. Moore, *Atomic Energy Levels*, vol. I (NBS Monograph 35). Washington, D.C.: U.S. Government Printing Office, 1971.
[27] J. B. Marling and J. R. Simpson, "Continuous ultraviolet lasers below 3000 angstroms," to be published.

Production of Electronically Excited Iodine Atoms, $I(^2P_{1/2})$, Following Injection of HI into a Flow of Discharged Oxygen

ROBERT J. PIRKLE, J. R. WIESENFELD, CHRISTOPHER C. DAVIS, GEORGE J. WOLGA, MEMBER, IEEE, AND ROSS A. McFARLANE, MEMBER, IEEE

Abstract—**The emission from the transition $I^*(5\ ^2P_{1/2}) \rightarrow I(5\ ^2P_{3/2})$ at 1.315 μm following injection of HI into a microwave-discharged He/O_2 flow has been studied. Relative $I^*(5\ ^2P_{1/2})$ emission intensities have been recorded as a function of HI and O_2 flow rates and as a function of time after injection. Pulsed gain measurements using an iodine photodissociation laser as a source show that the ratio, $N_{I^*}/(N_I + N_{I^*}) \approx 0.15$–$0.25$, is less than that required for population inversion. This observation will be discussed in terms of known chemical processes involving $O(^3P)$, HI, $O_2(^1\Delta_g)$, and iodine atoms.**

I. Introduction

STUDIES of the atomic-iodine emission generated when HI is injected into a microwave-discharged flow of molecular oxygen have indicated [1] that the atomic iodine may exhibit population inversion on the transition $I^*(5\ ^2P_{1/2}) \rightarrow I(5\ ^2P_{3/2}) + h\nu$ (7603 cm^{-1}). In such a system, atomic iodine is generated by the reactions

$$O + HI \xrightarrow{k_{1a}} OH + I, \qquad \Delta H = -31 \frac{\text{kcal}}{\text{mole}} \tag{1a}$$

$$O + HI \xrightarrow{k_{1b}} OH + I^*, \qquad \Delta H = -10 \frac{\text{kcal}}{\text{mole}} \tag{1b}$$

Manuscript received April 14, 1975. This work was supported by the U.S. Army Research Office and by the Cornell Materials Science Center through the use of Central Facilities.

R. J. Pirkle is with the Laboratory of Plasma Studies, Cornell University, Ithaca, N.Y. 14853.
J. R. Wiesenfeld is with the Department of Chemistry, Cornell University, Ithaca, N.Y. 14853.
C. C. Davis is with the School of Applied and Engineering Physics and Materials Science Center, Cornell University, Ithaca, N.Y. 14853.
G. J. Wolga and R. A. McFarlane are with the School of Electrical Engineering and Laboratory of Plasma Studies, Cornell University, Ithaca, N.Y. 14853.

with rapid establishment of the equilibrium

$$O_2(^1\Delta_g) + I \underset{k_{-2}}{\overset{k_2}{\rightleftharpoons}} + O_2(^3\Sigma_g^-) + I^*, \qquad \Delta H = -0.8 \frac{\text{kcal}}{\text{mole}} \tag{2}$$

and the initial branching ratio, k_{1a}/k_{1b}, determining the relative populations of the two atomic-iodine states. The equilibrium constant, $K_2 = k_2/k_{-2}$, has been calculated [2] to be 2.94 at 273 deg. Given sufficient initial concentrations of $O_2(^1\Delta_g)$, the atomic-iodine transition may be inverted via electronic-energy transfer from $O_2(^1\Delta_g)$.

Using the computed value of the equilibrium constant, the fraction of oxygen molecules initially in the $O_2(^1\Delta_g)$ state

$$\frac{[O_2(^1\Delta_g)]_0}{[O_2(^1\Delta_g)]_0 + [O_2(^3\Sigma_g^-)]_0} \tag{3}$$

required to achieve the desired inversion

$$\frac{[I(^2P_{1/2})]}{[I(^2P_{3/2})]} > 0.5 \tag{4}$$

may be shown to lie in the range 0.15–0.20, depending on k_{1a}/k_{1b} and the absolute concentrations of atomic iodine and molecular oxygen present. Both atomic oxygen, $O(^3P)$ and excited molecular oxygen, $O_2(^1\Delta_g)$ are conveniently produced by passing a flow of molecular oxygen in a suitable diluent such as He or Ar through a microwave-excited discharge tube. The amount of $O_2(^1\Delta_g)$ produced in such a flow has been investigated by several authors [3]–[9] and the range of reported values overlaps the requirement mentioned previously. Here this system is studied as a possible candidate for a continuous laser on the 1.315-μm atomic-iodine transition.

II. Experimental Procedure and Results

A. Spontaneous Emission

We have observed the emission at 1.315 μm from I* generated under conditions similar to those previously described. A schematic diagram of the apparatus used in our study is presented in Fig. 1. Microwave excitation of a flowing mixture of He and O_2 in a 2.5-cm-ID quartz tube was provided by a Litton Industries 2450-MHz 1-kW magnetron coupled into a 1-m section of a *C*-band waveguide. The cross-sectional dimensions of the flow were expanded to match those of the reaction chamber (1.2 X 21.6 cm) in a transition region designed to insure uniform flow. The transition region was lined with Teflon-coated foil to minimize recombination of oxygen atoms. Hydrogen iodide was injected into the discharged oxygen flow using an injector[1] which consisted of 76 sections of ~0.08-cm stainless-steel syringe tubing separated by 0.24 cm and mounted vertically in the reaction chamber. In each injector, seven ~0.013-cm holes admitted the HI in a direction normal to the discharged flow. Fused-quartz windows were mounted at Brewster's angle and emission was observed transverse to the flow. The flow of gases through the reaction chamber was maintained by a 450-ft^3/min blower backed by an 80-ft^3/min mechanical pump. Flow velocities of 90–95 m/s were measured in the reaction chamber at total pressures of 7–10 torr.

The emission was chopped at ~200 Hz and dispersed using a 1/2-m Jarrell-Ash monochromator before being detected with a room-temperature PbS detector. At wavelengths greater than 1.0 μm, the only emission observed was a single line at 1.315 μm, the wavelength corresponding to the transition $I(5\,^2P_{1/2}) \rightarrow I(5\,^2P_{3/2})$. In order to maximize the observed signal, the monochromator was replaced with a narrow bandpass filter [104 Å full width at half maximum (FWHM)] centered at 1.313 μm. The output of the PbS detector was monitored with a PAR-HR8 lock-in amplifier.

In Fig. 2, the observed relative I* emission intensity is presented as a function of HI flow at optimum O_2 and He flows. The ratio He:O_2:HI at maximum I* emission was found to be 40:3:1. The I* emission as a function of total molecular-oxygen flow is shown in Fig. 3. The more rapid initial increase may be attributed to maximization of the $O(^3P)$ and $O_2(^1\Delta_g)$ concentrations followed by a slower decrease as the excess $O_2(^3\Sigma_g^-)$ deactivates I*. The emission intensity decreases slowly with a decrease in He flow. We determined that the emission was slightly less intense when Ar was substituted for He. The emission intensity was proportional to discharge power at low power but quickly became constant and further increases in discharge power had no effect.

Shown in Fig. 4 is the relative I* emission intensity as a function of time after injection. The emission peaks sharply at ~75 μs after injection and decreases rapidly thereafter. The rapid decrease in I* emission at later times implies that significant deactivation processes are of considerable importance and overwhelm the equilibrium pumping mechanism (2). Such processes include diffusion of $I(5\,^2P_{1/2})$ to the

[1]The design of the injector was suggested by Prof. T. A. Cool.

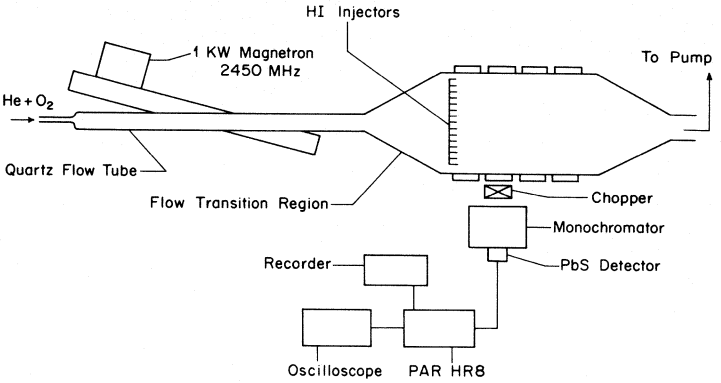

Fig. 1. A schematic diagram of the flow system used for atomic-iodine spontaneous-emission studies at 1.315 μm under various flow conditions.

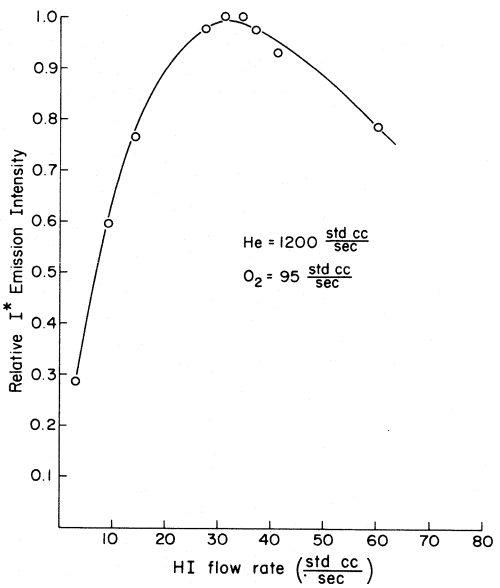

Fig. 2. A plot of $I^*(^2P_{1/2})$ spontaneous emission at 1.315 μm as a function of HI flow rate at optimized He and O_2 flow rates.

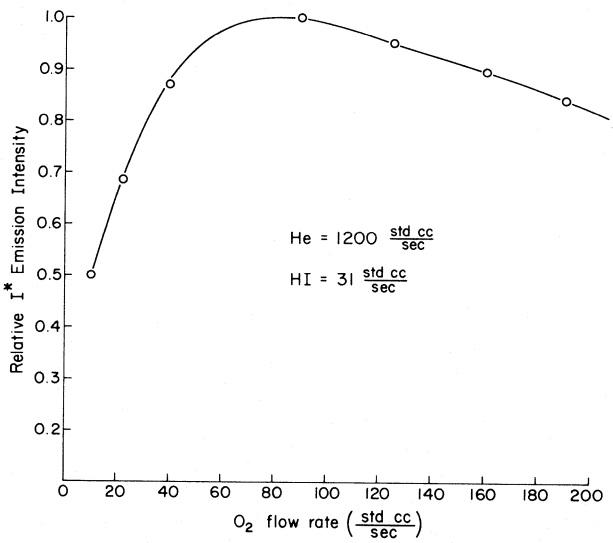

Fig. 3. A plot of $I^*(^2P_{1/2})$ spontaneous emission at 1.315 μm as a function of O_2 flow rate at optimized He and HI flow rates.

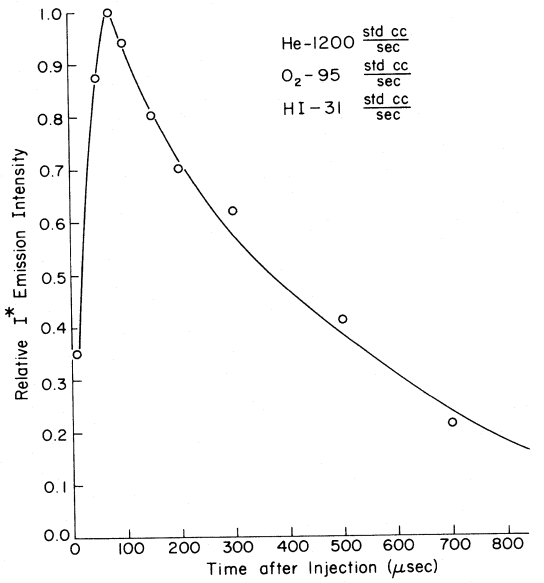

Fig. 4. A plot of $I^*(^2P_{1/2})$ spontaneous emission at 1.315 μm as a function of time after injection of HI into the discharged-oxygen flow.

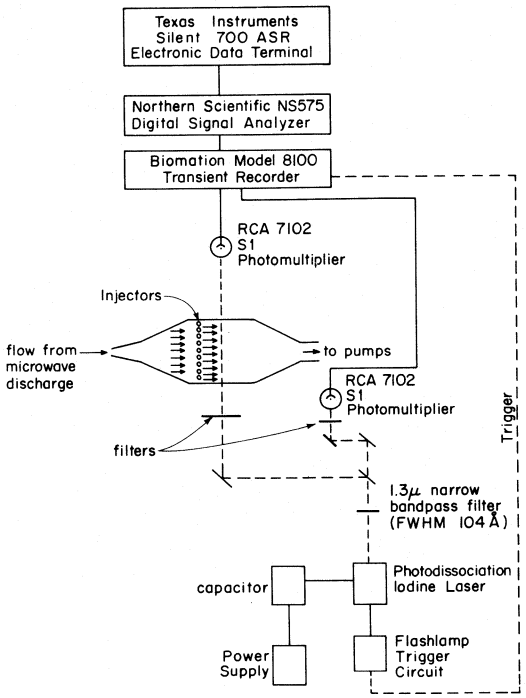

Fig. 5. A schematic diagram of the apparatus used to measure pulsed single-pass gain (absorption).

walls of the reaction chamber accompanied by efficient deactivation. In addition, the presence of the intense yellow-green fluorescence of $I_2(B^3\pi_{0^+u})$ suggests a significant concentration of I_2 which is a very rapid quencher of $I(5\ ^2P_{1/2})$ [10]. Furthermore, the presence of unreacted HI due to imperfect mixing would also result in deactivation [11] of the excited atomic iodine. These observations point to the importance of transverse-flow operation when systems of this type are considered as potential chemical lasers.

B. Absorption Measurements

In view of the intense emission observed from this system and previous reports of large I^* populations generated in similar experiments [1], we have carried out pulsed gain experiments to determine the fraction, $f(I^*)$, of atomic iodine present in the I^* state

$$f(I^*) = \frac{N_{I^*}}{N_{I^*} + N_I} \tag{5}$$

where N_{I^*} and N_I are number densities of I^* and I, respectively. A schematic diagram of the apparatus used in these experiments is shown in Fig. 5. The optical source was an iodine photodissociation laser which used n-C_3F_7I at a pressure of 10 torr as a source of atomic iodine. The laser consisted of a quartz tube of 10-mm ID and 30 cm in length. The central 15-cm portion of this tube was enclosed in a polished-aluminum elliptical cavity where it was irradiated with the output of an ILC 10L6 linear xenon flashlamp. A 200-μF capacitor bank charged at voltages up to 2 kV (an input energy of 400 J) was discharged through the flashlamp and a 20-μH series inductor to yield a pumping flash of ~140-μs FWHM. At charging voltages of 2 kV, we have calculated the peak flashlamp current to be ~1100 A and the peak magnetic field at the laser tube to be ±40 G. At these low magnetic fields, shifts of the hyperfine lines are considerably smaller than the Doppler width of the zero-field lines (251 MHz at 300 K) [13]. The output of the photodissociation laser under these conditions of low input energy and small magnetic field is almost certainly on the $F' = 3 \rightarrow F'' = 4$ hyperfine component only [12]-[15].

The laser output was passed through the 1.3-μm narrow bandpass filter to minimize scattered flashlamp radiation reaching the detectors. The laser pulse was then split using quartz flats and attenuated using neutral-density filters. One portion of the split signal was sent through the reaction chamber of the flow system and both portions of the signal were monitored using RCA-7102 (S-1) photomultiplier tubes. The integrated outputs ($\tau_{RC} = 0.05$ s) of the photomultipliers were recorded simultaneously using a Biomation 8100 transient recorder which transferred a digital representation of each transient signal to a Northern Scientific NS575 digital signal analyzer.

In a typical experiment the outputs of the photomultipliers were recorded with only discharged oxygen and helium in the reaction chamber. Changes in the relative output of each photomultiplier were then recorded when HI was injected into the discharged flow. Results from one such experiment are shown in Fig. 6. A small decrease in the output of the photomultiplier monitoring the transmission through the reaction chamber (lower trace in each photograph) is clearly evident when HI is injected and corresponds to absorption of the laser pulse. Similar data for a variety of HI and O_2 inputs, and at a number of distances downstream of the HI injectors, were also recorded. Under all sets of conditions small (3-8 percent) absorptions were observed; errors in a single measurement were 0.3-0.4 percent. No changes in these observations occurred when the laser-pulse intensity through the reaction chamber was changed by a factor of 10^2.

The accuracy of the absorption measurements was checked

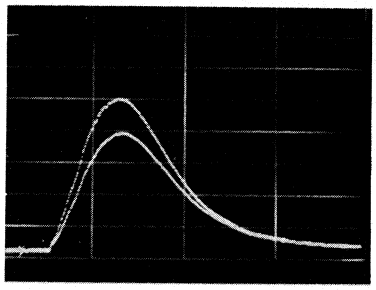

135 μs

He = 1200 std. cc/s
O_2 = 95 std. cc/s

(a)

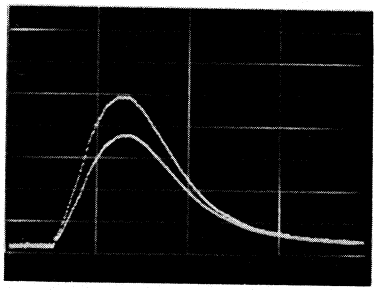

135 μs

He = 1200 std. cc/s
O_2 = 95 std. cc/s
HI = 31 std. cc/s

(b)

Fig. 6. Scope traces showing reference-laser pulse (upper curve) compared to pulse through flow cavity (lower curve). (a) The curves are characteristic of the flowing medium under optimized conditions, but without HI. (b) The pulse through the flow cavity (lower curve) has been attenuated following the addition of HI.

by measuring the attenuation of the laser pulse when a clean quartz flat was placed in front of one of the photomultipliers. The calculated reflection coefficient of quartz at 1.315 μm is 6.6 percent; while the measured attenuation was 6.5 ± 0.3 percent.

Finally, we have premixed O_2 with the HI before injection and noted a decrease in spontaneous-emission intensity with a simultaneous increase in absorption. From a single absorption measurement, the population difference, ΔN, may be calculated from

$$\Delta N = 12/7 \frac{\ln I_0/I}{\alpha_0 L} \tag{6}$$

where $\Delta N = 1/2N_I - N_{I^*}$, L is the absorption path length, and α_0 is given by

$$\alpha_0 = 1/4\pi\left(\frac{\ln 2}{\pi}\right)^{1/2} \lambda^2 \frac{A_{34}}{\Delta\nu_D} \tag{7}$$

where λ is the transition wavelength and $\Delta\nu_D$ is its Doppler width. A_{34} is the Einstein coefficient for spontaneous emission on the $I^*(F = 3) \rightarrow I(F = 4)$ transition. The use of this coefficient and the factor of 12/7 in (6) arise because the probe laser operates on the $F' = 3 \rightarrow F'' = 4$ transition and thus only directly measures $\Delta N_{34} = \frac{7}{9}(I(F'' = 4)) - (I^*(F' = 3))$.

The increase in ΔN found when O_2 is premixed with the injected HI resulted from the quenching of I^* to I by the excess O_2. Assuming that the fractional decrease in observed spontaneous emission corresponds to the fractional decrease in the I^* population, the observed increase in ΔN, $\Delta(\Delta N)$ is directly related to the I^* population before addition of undischarged O_2, $N^0_{I^*}$, as

$$\Delta(\Delta N) = 3/2XN^0_{I^*} \tag{8}$$

where X is the fractional decrease in spontaneous-emission intensity. Using $N^0_{I^*}$ from (8) and $\Delta N^0 (= \frac{1}{2} N^0_I - N^0_{I^*})$ calculated from absorption data when no undischarged O_2 was added, N^0_I may easily be calculated. Thus the fraction of atomic iodine initially in the $^2P_{1/2}$ state may be calculated from (5). It is noteworthy that (5) is independent of A_{34} and $\Delta\nu_D$ since these terms occur in both the numerator and denominator and cancel.

Data from several experiments yielded values of $f(I^*)$ in the range 0.15–0.25. The uncertainty in these figures is at least a factor of 2 since the uncertainty in a single absorption measurement was a significant fraction of the total increase in observed absorption (typically, 1.5–3.0 percent). It may be noted, however, that the observation of absorption rather than gain clearly demonstrates that $f(I^*) < 0.33$, the minimum figure corresponding to population inversion.

III. Conclusions

We have determined that the atomic iodine generated when HI is injected into a discharged He/O_2 flow does not exhibit population inversion on the transition $I(5\,^2P_{1/2}) \rightarrow I(5\,^2P_{3/2})$ at 1.315 μm. However, the large population of excited species produced in this system, $f(I^*) = 0.15$–0.25, suggest that the equilibrium pumping mechanism (2) is indeed efficient and that given larger initial concentrations of $O_2(^1\Delta_g)$, the atomic-iodine transition previously discussed might well be inverted via electronic-energy transfer. To this end, a search for new sources of singlet molecular oxygen seems justified.

References

[1] P. Cadman and J. C. Polanyi, "Production of electronically excited atoms, $H + HI \rightarrow H_2 + I^*$ $(^2P_{1/2})$," *J. Phys. Chem.*, vol. 72, pp. 3715–3721, 1968.

[2] R. G. Derwent and B. A. Thrust, "The radiative lifetime of the metastable iodine atom $I(5^2P_{1/2})$," *Chem. Phys. Lett.*, vol. 9, pp. 591–592, 1971.

[3] A. M. Winer and K. D. Bayes, "The decay of $O_2(a^1\Delta)$ in flow experiments," *J. Phys. Chem.*, vol. 70, pp. 302–304, 1966.

[4] R. L. Brown, "Effects of impurities on the production of oxygen atoms by a microwave discharge," *J. Phys. Chem.*, vol. 71, pp. 2492–2495, 1967.

[5] A. M. Falick, B. H. Mahan, and R. J. Myers, "Paramagnetic resonance spectrum of the $^1\Delta_g$ oxygen molecule," *J. Chem. Phys.*, vol. 42, pp. 1837–1838, 1965.

[6] A. K. MacKnight, Air Force Weapons Lab., Albuquerque, N. Mex., private communication.

[7] L. Elias, E. A. Ogryzlo, and H. I. Schiff, "The study of electrically discharged O_2 by means of isothermal calorimetric detector," *Can. J. Chem.*, vol. 37, pp. 1680–1689, 1959.

[8] J. T. Herron and H. I. Schiff, "A mass spectrometric study of

normal oxygen and oxygen subjected to electrical discharge," *Can. J. Chem.*, vol. 36, pp. 1159–1170, 1958.
[9] S. N. Foner and R. L. Hudson, "Metastable oxygen molecules produced by electrical discharges," *J. Chem. Phys.*, vol. 25, pp. 601–602, 1956.
[10] D. H. Burde, R. A. McFarlane, and J. R. Wiesenfeld, "Quantum efficiencies for the production of electronically excited iodine atoms I($5p^5\ ^2P_{1/2}$) following laser photolysis of I_2 near 5000 Å," *Phys Rev. A.*, vol. 10, pp. 1917–1920, 1974.
[11] R. J. Donovan and D. Husain, "Electronically excited iodine atoms: Pt. 2–I($5\ ^2P_{1/2}$) in the photolysis of hydrogen iodide," *Trans. Faraday Soc.*, vol. 62, pp. 1050–1055, 1962.
[12] I. M. Belousova, V. M. Kiselev, and V. N. Kurzenkov, "Induced emission spectrum of atomic iodine due to the hyperfine structure of the transition $^2P_{1/2} - {}^2P_{3/2}$ (7603 cm^{-1})," *Opt. Spectrosc.* (USSR), vol. 33, pp. 112–114, 1972.
[13] V. S. Zuev, V. A. Katulin, V. Yu. Nosach, and O. Yu. Nosach, "Investigation of the luminescence spectrum of atomic iodine ($^2P_{1/2} - {}^2P_{3/2}$) laser transition," *Sov. Phys.–JETP*, vol. 35, pp. 870–873, 1972.
[14] W. C. Hwang and J. V. V. Kasper, "Zeeman effects in the hyperfine structure of atomic iodine photodissociation laser emission," *Chem. Phys. Lett.*, vol. 13, p. 511, 1972.
[15] I. M. Belousova, B. D. Bobrov, V. M. Kiselev, V. N. Kurzenkov, and P. I. Krepostnov, "Photodissociative I^{127} laser in a magnetic field," *Sov. Phys.–JETP*, vol. 38, pp. 258–263, 1974.

Far Infrared Frequency Synthesis with Stabilized CO_2 Lasers: Accurate Measurements of the Water Vapor and Methyl Alcohol Laser Frequencies

F. RUSSELL PETERSEN, KENNETH M. EVENSON, DONALD A. JENNINGS, JOSEPH S. WELLS, KENYA GOTO, AND JUAN J. JIMÉNEZ

Abstract–**A far infrared (FIR) frequency synthesis technique using saturated-absorption stabilized CO_2 lasers and a point-contact diode has been used to measure frequencies of a number of strong CW H_2O, D_2O, and CH_3OH laser lines. The first frequency measurements of the 79-μm H_2O, the 73- and 108-μm D_2O, and 11 CO_2-pumped CW $^{12}CH_3{}^{16}OH$ laser lines are reported. This measurement is the first demonstration of the general usefulness of CO_2 lasers for accurate synthesis of FIR frequencies.**

Manuscript received April 28, 1975.

F. R. Petersen, K. M. Evenson, D. A. Jennings, and J. S. Wells are with the Precision Laser Metrology Section, National Bureau of Standards, Boulder, Colo. 80302.
K. Goto is with the Toshiba Research & Development Center, Tokyo Shibaura Electric Company Ltd., Kawasaki, Japan.
J. J. Jiménez is with the Precision Laser Metrology Section, National Bureau of Standards, Boulder, Colo. 80302, on leave from the Laboratoire Primaire de Métrologie des Fréquences, Bureau National de Métrologie, Paris, France, and Centre National de la Recherche Scientifique, Paris, France.

DIRECT laser frequency measurements are made by frequency harmonic generation and mixing in nonlinear diodes and crystals [1], [2]. At longer far infrared (FIR) wavelengths, frequency beats between a high harmonic of a klystron and the laser line have been observed. For instance, the 337-μm HCN line has been beat with the 12th harmonic of a *V* band klystron in a commercially available diode [3], the 118.8-μm CH_3OH line has been beat with the 33rd harmonic of a *V* band klystron in a Schottky diode [4], and the 84-μm H_2O line has been beat with the 401st harmonic of a high quality *X* band klystron in a Josephson junction [5].

While this procedure is desirable insofar as it directly connects the unknown laser frequency with an easily measurable microwave frequency (and consequently to excellent frequency standards), there are a number of serious and as yet unresolved limitations. For instance, as the laser frequency increases, the harmonic number of necessity must

increase. Consequently, severe requirements are imposed on the spectral purity of the microwave source [6] as well as on the S/N capability of the harmonic generator and mixing device. While very low noise, spectrally pure oscillators together with detectors such as the Josephson junction may extend the present microwave multiplication limit, there is a current need for accurate frequency measurement in the intermediate and near infrared (IR) spectral region.

Frequencies greater than the FIR have in fact been measured; the current highest measurement is 148 THz [7]. In these experiments a chain of lasers was used to extend frequency measurements from a microwave oscillator to that of the highest laser frequency. In this chain, the nth harmonic of one laser was mixed with the next higher frequency. By using such a chain of lasers it was possible to reduce the mixing order[1] to less than 14 [3]. This procedure was necessary because the S/N decreased rapidly with increasing harmonic number [1].

This technique has been eminently successful, but for wide application, has suffered from a number of drawbacks. First, the limited number of known laser sources makes it difficult to reduce the unknown-laser synthesized-frequency difference to within the range of commonly available microwave oscillators. Second, stability and reproducibility of many laser oscillators are poor; in these cases, highly accurate measurements require continuous frequency monitoring of the lower frequency lasers during the measurement process. And finally, some of the known CW laser oscillators cannot produce, in a compact device, the power required for effective harmonic generation in a point-contact diode.

Many of these problems can be eliminated if two stabilized CO_2 lasers are chosen to synthesize the IR frequencies,[2] as shown schematically in Fig. 1. The unknown laser frequency is then given by the expression

$$\nu_L = l\nu_1 + m\nu_2 + n\nu_{\mu w} \pm \nu_B.$$

Here ν_L is the unknown laser frequency, ν_1 and ν_2 are frequencies of CO_2 lasers operating in either the 9.4- or 10.4-μm bands, $\nu_{\mu w}$ is a microwave frequency (X band or less), and ν_B is the beat frequency measured with a spectrum analyzer. l, m, and n are small positive or negative integers such that the mixing order is less than about 10. The CO_2 laser is chosen because every line in each of the two laser bands can be stabilized to a narrow saturated-absorption feature very close to the true molecular frequency [9]. These frequencies are reproducible to within 2 parts in 10^{-10}, and the laser stability is good, e.g., [3]

$$\delta\nu/\nu = 3 \times 10^{-11}, \quad \text{for} \quad \tau = 1 \text{ s}.$$

Absolute frequency measurements of two CO_2 lines, one in each band [3], coupled with a remeasurement of the rotational constants [10] resulted in absolute frequencies for

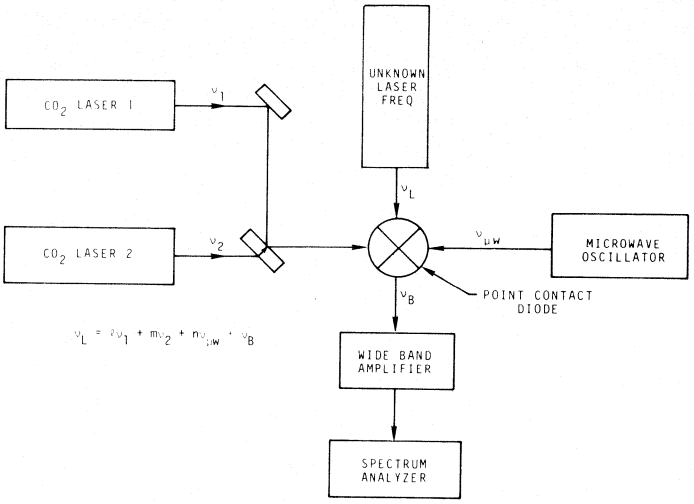

Fig. 1. Schematic diagram of the two-CO_2 laser frequency synthesis experiment.

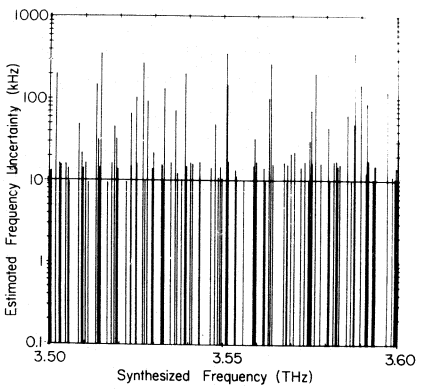

Fig. 2. Difference spectrum from the fundamentals of the first 60 lines in both the 9.4- and 10.4-μm bands of CO_2. The frequency interval taken here, 3.5–3.6 THz, is typical of much of the total frequency range covered. Estimated uncertainty for each synthesized frequency is plotted on the vertical scale.

most of the $^{12}C^{16}O_2$ laser lines with a fractional uncertainty of about 1×10^{-9} [11]. Thus, with this technique, the CO_2 lasers can be regarded as secondary frequency standards, and the measured frequency is related to the primary Cs frequency standard through experiments establishing the CO_2 molecular constants. As a result, a comb of over 100 accurately known, reproducible, and highly stable laser frequencies, all with adequate power for harmonic generation, exists in the band from 27 to 33 THz.

If the use of two stabilized $^{12}C^{16}O_2$ lasers is considered for frequency synthesis, then many thousands of additional discrete frequencies can be generated. For instance, over 7000 frequencies in the band from 0.025 to 5.8 THz, most with an uncertainty less than 30 kHz, can be produced from differences of the fundamentals of the first 60 lines in both the 9.4- and 10.4-μm bands. As an example, Fig. 2 shows this difference spectrum in the interval from 3.5 to 3.6 THz. If, in addition, sums as well as differences of harmonics from each CO_2 laser are used, then the covered frequency band is greatly extended. In fact, semiuniform frequency coverage from 0.025 to 100 THz can be attained with a mixing order less

[1]The mixing order is defined as the sum of the absolute values of the harmonic numbers of all the coherent oscillators being mixed in the diode.

[2]A multiple CO_2 laser frequency synthesis technique has been proposed for relating CO_2 frequencies to the microwave standard without the use of other lasers in the synthesis chain. See [8].

than ten. In most cases, the CO_2 combination will produce a frequency that comes within 10 GHz of the one desired. With low mixing orders, S/N ratios which are adequate for precision frequency measurements can be expected.

In order to demonstrate the experimental worthiness of this idea, we have used this CO_2 frequency synthesis technique to measure the frequencies of a number of strong CW H_2O, D_2O [12], and CH_3OH [13]-[16] laser lines. Some of these have been measured before by other synthesis techniques [4], [5], [17]-[21] and consequently provide useful comparison with the present measurements. Other motivation stems from the use of laser lines from these molecules for laser magnetic resonance spectroscopy [22], [23], radio astronomy, detector evaluation, and possible standards applications.

Four CO_2 lasers, similar to those described previously [3], were used in the experiment. Two of the lasers were frequency locked to standing-wave saturation dips observed in the 4.3-μm fluorescent radiation emanating from intracavity absorption cells [9]. Pressure in each absorption cell was 0.035-0.040 torr. No corrections to the CO_2 frequencies were made for pressure, power, or other shifts since these were considered negligible compared to other uncertainties in the experiment. The two $^{12}C^{16}O_2$ lasers used to synthesize $\nu_1 - \nu_2$ were offset locked by about 2.5 MHz from the absorption stabilized lasers. This procedure reduced the width of the beat signal caused by the frequency modulation required for line center locking. In each case, the estimated 1-standard-deviation uncertainty in $\nu_1 - \nu_2$ was less than 30 kHz and did not contribute significantly to the uncertainty in the measured frequency.[3] Power from each synthesis laser was adjusted to be about 100 mW.

The 8-m-long water vapor laser has also been described previously [3] and in this experiment was filled with H_2 and water vapor to a total pressure of 0.6 torr in a 3:2 ratio. In each measurement, the frequency of the water vapor laser was manually adjusted to the maximum power point of the laser gain curve. Power from the water vapor laser depended on the isotope as well as the transition and ranged from 0.5 to 50 mW.

The other CW FIR laser lines were produced by optically pumping a low-pressure methyl alcohol cell in a waveguide configuration [24] with a 2-m $^{12}C^{16}O_2$ laser. The polished-copper cylindrical waveguide cavity, which was also the gas cell, was 14 mm in diameter and 2 m long. Both end mirrors were flat, with one being movable for tuning purposes. CO_2 pump radiation was focused through a 1-mm-diameter hole in the movable input mirror by a 6.4-cm focal length germanium lens. FIR power was coupled out of the other end mirror through a 2.5-mm-diameter hole. Methyl alcohol vapor pressure ranged from 0.1 to 0.25 torr. The FIR laser had a tuning range of 3-16 MHz, which was both mode and wavelength dependent. Output power ranged from about 0.1 to 10 mW.

All lasers were focused onto the tungsten-nickel point-contact diode with short focal length lenses; microwave power was received from a simple antenna placed close to the diode. The beat frequency between the FIR laser and appropriate harmonic combination of CO_2 lasers and klystron was amplified and subsequently measured with a 1.2-GHz spectrum analyzer.

The CO_2 synthesis combination[4] together with the measured frequencies of four H_2O and three D_2O laser lines are presented in Table I. Although many CO_2 synthesis combinations often exist for any given FIR frequency, the lowest mixing order was usually chosen. However, in the case of the 28-μm line, a high mixing order was deliberately chosen for the purpose of measuring the S/N ratio. In spite of this high mixing order (9), the S/N observed on a spectrum analyzer with a predetection bandwidth of 30 kHz and a video bandwidth of 10 kHz was still greater than 25 dB. The uncertainty in each measured frequency was estimated to be ± 1 MHz, mainly because of difficulty in determining the center of the Doppler and pressure-broadened laser gain curve (10-20 MHz wide). In the third column, measured frequencies have been converted to vacuum wavenumbers with $c = 299\,792\,458$ m/s ($\delta c/c = \pm 4 \times 10^{-9}$), [25].[5]

Two other experiments were performed which did not use the CO_2 laser, but which gave results in good agreement with the results obtained here. In one, the difference frequency between two water vapor lasers oscillating on 78 and 79 μm, respectively, was beat with a 30-GHz klystron. The measured frequency was 31.298(3) GHz, in good agreement with 31.2968(2) GHz obtained with the CO_2 synthesis technique. In the other a 2-m-long water vapor laser oscillating on 28 μm which exhibited a Lamb dip was mixed with the 12th harmonic of a 337-μm HCN laser, of known frequency [3], and a 29-GHz klystron. The frequency of the Lamb dip was found to be within 1 MHz of the top of the gain curve and in good agreement with the results in Table I.

These two results together with previous measurements by other synthesis techniques are listed for comparison at the bottom of Table I. There is general agreement within the estimated experimental errors. The measurements most reproducible and closest to the true molecular frequency are those in which the water vapor laser frequency was set to the center of the Lamb dip. Although the Lamb dip is not necessarily in the center of the gain curve when the laser is operated at maxi-

[3]Tables of frequencies are given in [11]. Since uncertainties in the rotational constants are correlated, the estimated standard deviation of a frequency difference involves use of the variance-covariance matrix obtained from a least squares fit of the rotational constants to experimental data. The calculation here used experimental data from [10]. A NBS publication giving CO_2 synthesis combinations and estimated errors for the FIR spectral region is in preparation.

[4]Here and again in Table II, the subscripts I and II refer to the CO_2 10.4- and 9.4-μm bands, respectively, and are derived from the spectroscopic notation for the lower vibrational level of the laser transition.

[5]This value of c has been recommended by the Consultative Committee for the Definition of the Meter at their meeting in the Bureau Internationale des Poids et Mesures, Sevres, France, and by the International Astronomical Union, Fifteenth General Assembly, Sydney, Australia.

TABLE I
MEASURED FREQUENCIES FOR H_2O AND D_2O LASER LINES

WATER VAPOR LASER LINE λ (μm)	MEASURED FREQUENCY (MHz) (UNCERTAINTY: ± MHz)	VACUUM WAVENUMBER (cm^{-1})	$^{12}C^{16}O_2$ SYNTHESIS COMBINATION
H_2O			
28[a]	10 718 068.3	357.516 276	$^3P_{II}$ (10) - ^3P_I (28)
78[b]	3 821 771.3	127.480 567	R_{II} (14) - P_I (16)
79[c]	3 790 474.5	126.436 620	R_{II} (10) - P_I (18)
119[d]	2 527 952.0	84.323 402	P_{II} (8) - R_I (16)
D_2O			
73[e]	4 120 984.3	137.461 240	R_{II} (22) - P_I (22)
84[f]	3 557 147.1	118.653 665	P_{II} (12) - P_I (30)
108	2 783 066.6	92.833 109	R_{II} (10) - R_I (26)

Note: Vacuum wavenumbers were calculated from the measured frequencies with $c = 299\,792\,458$ m/s ($\delta c/c = \pm 4 \times 10^{-9}$). The CO_2 synthesis combination with appropriate harmonic numbers is also listed for each measurement. In each case, the estimated 1-standard-deviation uncertainty in the CO_2 synthesized frequency was less than 30 kHz. Microwave frequencies up to 16 GHz were used. A total uncertainty of ±1.0 MHz has been assigned to each water vapor frequency, mainly because of the difficulty in determining the center of the Doppler and pressure-broadened laser gain curve.

[a]Evenson *et al.*, 10 718 073(2) MHz [17]. From HCN laser, 10 718 068.6(5) MHz (Lamb dip). Blaney *et al.*, 10 718 068.71(3) MHz [18] (Lamb dip).

[b]Evenson *et al.*, 3 821 775(3) MHz [17]. McDonald *et al.*, 3 821 774.4(3.0) MHz [5].

[c]From 78–79-μm difference, 3 790 477(3) MHz.

[d]Frenkel *et al.*, 2 527 952.8(1) MHz [19] (Lamb dip). Hocker and Javan, 2 527 954.0 MHz [20].

[e]The 72.7-μm line was the only CW line oscillating in our laser near this wavelength. Reference [12] reports CW oscillation at 71.9, but not at 72.7 μm.

[f]Hocker *et al.*, 3 557 143(2) MHz [21].

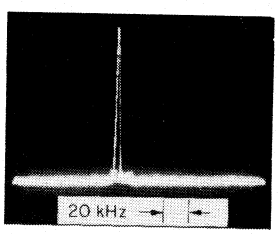

Fig. 3. Beat note at 54 MHz between the 118.8-μm CH_3OH laser line and the synthesized frequency. The spectrum analyzer was set for linear response with RF and video bandwidths of 3 and 10 kHz, respectively. The dc impedance of the diode was 550 Ω.

mum power, the shift between these two points appears to be less than 1 MHz.

A beat signal observed in the measurement of the 118.8-μm methyl alcohol line is shown in Fig. 3. *S/N* ratios varied from 10 to 20 dB. The frequency measurements along with corresponding CO_2 synthesis combinations are presented in Table II. Each CH_3OH line is identified by wavelength and CO_2 pump line. Here wavelengths were calculated from these measured frequencies and in some cases differ slightly from previously published values. In the third column, measured frequencies have been converted to vacuum wavenumbers. Methyl alcohol vapor pressure for each measurement is also given. In each case, the alcohol laser frequency was set to the center of the gain curve. Uncertainty in this procedure resulted in the assignment of a ±0.5-MHz error to each frequency measurement. In comparison, other measurement errors were considered negligible. The CH_3OH frequencies have not been corrected for any type of frequency shift.

The 170.6- and 118.8-μm lines have been measured previously by direct frequency multiplication from the microwave region [4]. The two results 1757.526(6) and 2522.78(1) GHz, are in excellent agreement with the values obtained here.

These measurements demonstrate the feasibility of synthesizing any frequency in the FIR with two $^{12}C^{16}O_2$ lasers and a microwave oscillator (*X* band or less). If, in addition, each $^{12}C^{16}O_2$ laser is stabilized to a narrow standing-wave saturated-absorption resonance in $^{12}C^{16}O_2$ itself, then the estimated fractional uncertainty in the synthesized frequency is less

TABLE II
MEASURED FREQUENCIES OF 13 METHYL ALCOHOL LASER LINES

METHYL ALCOHOL LASER LINE λ (μm)	MEASURED FREQUENCY (MHz) (UNCERTAINTY: ±0.5 MHz)	VACUUM WAVENUMBER (cm^{-1})	ALCOHOL LASER VAPOR PRESSURE (Torr)	CO_2 PUMP LINE	CO_2 FREQUENCY SYNTHESIS COMBINATION
70.5	4 251 668.7	141.820 403	0.10	P_{II} (34)	R_{II} (30) - P_I (22)
96.5	3 105 936.8	103.602 901	0.20	R_{II} (10)	R_{II} (20) - R_I (18)
118.8[a]	2 522 781.6	84.150 935	0.10	P_{II} (36)	P_{II} (14) - R_I (8)
163.0	1 838 839.3	61.337 076	0.10	R_I (38)	P_{II} (20) - R_I (36)
170.6[b]	1 757 526.3	58.624 765	0.10	P_{II} (36)	P_{II} (30) - R_I (24)
232.9	1 286 999.5	42.929 683	0.20	R_{II} (10)	R_{II} (32) - P_{II} (24)
250.8	1 195 433.9	39.875 383	0.16	R_I (34)	R_I (34) - P_I (20)
251.1	1 193 727.3	39.818 455	0.20	R_I (38)	R_I (34) - P_I (20)
369.1	812 195.4	27.091 924	0.10	P_{II} (16)	R_I (10) - P_I (22)
392.1	764 642.6	25.505 733	0.15	P_{II} (36)	R_{II} (6) - P_{II} (24)
469.0	639 184.6	21.320 902	0.25	R_I (38)	P_I (8) - P_I (32)
570.6	525 427.5	17.526 375	0.15	P_{II} (16)	P_{II} (18) - P_{II} (36)
699.4	428 628.5	14.297 508	0.10	P_{II} (34)	R_I (38) - R_I (14)

Note: Vacuum wavenumbers were calculated from the measured frequencies with $c = 299\,792\,458$ m/s ($\delta c/c = \pm 4 \times 10^{-9}$). The 1-standard-deviation-type uncertainty for each frequency measurement is estimated to be ±0.5 MHz. The alcohol laser vapor pressure along with the CO_2 pump line are also given. The final column lists the two-laser CO_2 frequency synthesis combination. In each case, the estimated 1-standard-deviation uncertainty in the CO_2 synthesized frequency was less than 30 kHz.

[a] Fetterman *et al.*, 2522.78(1) GHz [4].

[b] Fetterman *et al.*, 1757.526(6) GHz [4].

than a few parts in 10^9. As a result, the accuracy of a measurement is often limited by the reproducibility of the unknown laser frequency. While other combinations and types of lasers can and have been used for frequency synthesis in the past, two stabilized CO_2 lasers by virtue of their large number of lines, high efficiency, simplicity, and excellent frequency reproducibility appear to be the most promising at present.[6] Since the 2nd and 3rd harmonics of CO_2 have been used to measure CO laser [27] and methane stabilized He-Ne laser frequencies [3], respectively, it is expected that the two-laser CO_2 frequency synthesis technique can be extended to even higher frequencies. Experiments to determine the highest mixing order which will produce usable signals are in progress in anticipation of demonstrating usefulness of this frequency synthesis technique to 100 THz.

ACKNOWLEDGMENT

The authors wish to thank M. Lojko for his contribution in producing the CO_2 frequency synthesis tables.

REFERENCES

[1] E. Sakuma and K. M. Evenson, "Characteristics of tungsten-nickel point contact diodes used as laser harmonic-generator mixers," *IEEE J. Quantum Electron.*, vol. QE-10, pp. 599–603, Aug. 1974.

[2] F. Zernike and J. E. Midwinter, *Applied Nonlinear Optics* (Pure and Applied Optics Ser.). New York: Wiley, 1973.

[3] K. M. Evenson *et al.*, "Accurate frequencies of molecular transitions used in laser stabilization: The 3.39 μm transition in CH_4 and the 9.33- and 10.18-μm transitions in CO_2," *Appl. Phys. Lett.*, vol. 22, pp. 192–195, 1973.

[4] H. R. Fetterman, B. J. Clifton, P. E. Tannenwald, and C. D. Parker, "Submillimeter detection and mixing using Schottky diodes," *Appl. Phys. Lett.*, vol. 24, pp. 70–72, 1974.

[5] D. G. McDonald *et al.*, "Four-hundredth-order harmonic mixing of microwave and infrared laser radiation using a Josephson junction and a maser," *Appl. Phys. Lett.*, vol. 20, pp. 296–299, 1972.

[6] F. L. Walls and A. DeMarchi, "RF spectrum of a signal after frequency multiplication; Measurement and comparison with a simple calculation," *IEEE Trans. Instrum. Meas.*, to be published.

[7] D. A. Jennings, F. R. Petersen, and K. M. Evenson, "Extension of absolute frequency measurements to 148 THz: Frequencies of the 2.0 and 3.5 μm Xe laser," *Appl. Phys. Lett.*, vol. 26, pp. 510–511, 1975.

[8] B. G. Whitford, J. K. Siemsen, H. D. Riccius, and K. M. Baird, "New frequency measurements and techniques in the 30 THz region," *IEEE Trans. Instrum. Meas.*, vol. IM-23, pp. 535–539, Dec. 1974.

[9] C. Freed and A. Javan, "Standing-wave saturation resonances in the CO_2 10.6μ transitions observed in a low-pressure room-temperature absorber gas," *Appl. Phys. Lett.*, vol. 17, pp. 53–56, 1970.

[10] F. R. Petersen, D. G. McDonald, J. D. Cupp, and B. L. Danielson, "Rotational constants for $^{12}C^{16}O_2$ from beats between Lamb-dip-stabilized lasers," *Phys. Rev. Lett.*, vol. 31, pp. 573–576, 1973.

[11] ——, in *Laser Spectroscopy*, R. G. Brewer and A. Mooradian, Ed. New York: Plenum, 1974.

[12] W. S. Benedict, M. A. Pollack, and W. J. Tomlinson, III, "The water-vapor laser," *IEEE J. Quantum Electron.*, vol. QE-5, pp. 108–124, Feb. 1969.

[13] T. Y. Chang, T. J. Bridges, and E. G. Burkhardt, "cw submillimeter laser action in optically pumped methyl fluoride, methyl alcohol, and vinyl chloride gases," *Appl. Phys. Lett.*, vol. 17, pp. 249–251, 1970.

[14] D. T. Hodges, R. D. Reel, and D. H. Barker, "Low-threshold CW submillimeter- and millimeter-wave laser action in CO_2-laser-pumped $C_2H_4F_2$, $C_2H_2F_2$, and CH_3OH," *IEEE J. Quantum Electron.* (Notes and Lines), vol. QE-9, pp. 1159–1160, Dec. 1973.

[15] R. J. Wagner, A. J. Zelano, and L. H. Ngai, "New submillimeter laser lines in optically pumped gas molecules," *Opt. Commun.*, vol. 8, pp. 46–47, 1973.

[6] It has been assumed that $^{12}C^{16}O_2$ by itself has an adequate number of laser lines for the frequency synthesis process. However, there may be occasions when use of other CO_2 isotopes is advantageous. The frequencies of these isotopes can be measured with the same accuracy as $^{12}C^{16}O_2$. See, for example, [26].

[16] H. E. Radford, "New CW lines from a submillimeter waveguide laser," *IEEE J. Quantum Electron.*, vol. QE-11, pp. 213–214, May 1975.
[17] K. M. Evenson, J. S. Wells, L. M. Matarrese, and L. B. Elwell, "Absolute frequency measurements of the 28- and 78-μm cw water vapor laser lines," *Appl. Phys. Lett.*, vol. 16, pp. 159–161, 1970.
[18] T. G. Blaney, C. C. Bradley, G. J. Edwards, and D. J. E. Knight, "Absolute frequency measurements of a Lamb-dip stabilised water vapor laser oscillating at 10.7 THz (28 μm)," *Phys. Lett.*, vol. 43A, pp. 471–472, 1973.
[19] L. Frenkel, T. Sullivan, M. A. Pollack, and T. J. Bridges, "Absolute frequency measurement of the 118.6-μm water-vapor laser transition," *Appl. Phys. Lett.*, vol. 11, pp. 344–345, 1967.
[20] L. O. Hocker and A. Javan, "Laser harmonic frequency mixing of two different far infrared laser lines up to 118 μ," *Phys. Lett.*, vol. 26A, pp. 255–256, 1968.
[21] L. O. Hocker, J. G. Small, and A. Javan, "Extension of absolute frequency measurements to the 84 μ range," *Phys. Lett.*, vol. 29A, pp. 321–322, 1969.
[22] M. Mizushima, K. M. Evenson, and J. S. Wells, "Laser magnetic resonance of the NO molecule using 78-, 79-, and 119-μm H_2O laser lines," *Phys. Rev.*, vol. 5A, pp. 2276–2287, 1972.
[23] C. J. Howard and K. M. Evenson, "Laser magnetic resonance study of the gas phase reactions of OH with CO, NO, and NO_2," *J. Chem. Phys.*, vol. 61, pp. 1943–1952, 1974.
[24] D. T. Hodges and T. S. Hartwick, "Waveguide laser for the far infrared (FIR) pumped by a CO_2 laser," *Appl. Phys. Lett.*, vol. 23, pp. 252–253, 1973.
[25] *Proc. Conf. Consultative Committee for the Definition of the Meter*, Bureau Internationale des Poids et Mesures, Sevres, France, 1973; also J. Terrien, "International agreement on the value of the velocity of light," *Metrologia*, vol. 10, p. 9, 1974; also presented at the International Astronomical Union, Fifteenth General Assembly, Sydney, Australia, Aug. 1973; also *Information Bulletin 31*, International Astronomical Union, Jan. 1974.
[26] C. Freed, A. H. M. Ross, and R. G. O'Donnell, "Determination of laser line frequencies and vibrational-rotational constants of the $^{12}C^{18}O_2$, $^{13}C^{16}O_2$, and $^{13}C^{18}O_2$ isotopes from measurements of CW beat frequencies with fast HgCdTe photodiodes and microwave frequency counters," *J. Mol. Spectrosc.*, vol. 49, pp. 439–453, 1974.
[27] R. S. Eng, H. Kildal, J. C. Mikkelsen, and D. L. Spears, "Determination of absolute frequencies of $^{12}C^{16}O$ and $^{13}C^{16}O$ laser lines," *Appl. Phys. Lett.*, vol. 24, pp. 231–233, 1974.

Correspondence

Time-Resolved Output Spectrum from a Hydrogen Fluoride Laser Using Mixtures of SF_6 and HI

N. R. GREINER

Abstract—**The time-resolved spectrum from a transverse-discharge hydrogen fluoride (HF) laser using a mixture of SF_6 and HI is reported. Because this spectrum matches that from a high-pressure H_2-F_2 laser, and because the SF_6-HI mixture is chemically stable, this laser should be a suitable and convenient source for probing H_2-F_2 amplifiers.**

In studying laser amplifiers, it is desirable to have an oscillator with output at all of the wavelengths where the amplifier has gain. H_2-F_2 chemical lasers lase on six vibrational levels, each containing several rotational levels [1], [2]. In further investigating transverse pulsed discharges in SF_6-HI mixtures [3], [4], we have found that this hydrogen fluoride (HF) laser medium provides an oscillator output spectrum that matches the spectrum from the high-pressure H_2-F_2 laser [2]. Furthermore, a large number of the transitions lase simultaneously. The greater stability of SF_6-HI mixtures makes them more convenient to use than H_2-F_2 mixtures.

The laser tube and the Marx bank have been described [5]. We used triggered spark gaps and a confocal unstable resonator with a magnification of 2, but dispensed with the double discharge. 2.5-cm-diam irises placed outside the tube allowed lasing only from the volume defined by the resonator. Individual spectral lines were isolated with a 0.5-m JaCo monochromator, and the pulse shapes were monitored with Ge:Au detectors (10–90-percent rise times, 3 ns) and displayed on oscilloscopes (10–90-percent rise times, 7 ns).

The HI was taken from a cylinder and condensed in a U tube cooled with dry ice to separate it from the H_2 impurity. It was then evaporated at dry-ice temperature into a stainless-steel tank, leaving behind the I_2 impurity. SF_6 was added to the tank to make the desired mixture. These mixtures gave good laser output after storage for a couple of weeks at room temperature. The laser tube was filled, fired, and evacuated as quickly as possible to avoid the reaction of HI with the materials in the tube.

The greatest output energies (0.5–0.8 J) and the best stability were obtained with mixtures containing 4–5 mol-percent HI. At 3.5 mol-percent HI the output ranged from 0 to 0.5 J, and at 9 mol percent the output was about 0.3 J. All of the work reported in the following was done with 4 mol-percent HI. The output energy was greatest when the tube was filled to 1.33×10^4 Pa (100 torr) with the mixture. At 8×10^3 and 2.4×10^4 Pa the average energies were 0.2 and 0.3 J, respectively. The richest output spectra were also observed at 1.33×10^4 Pa.

Fig. 1 shows the time-resolved spectrum at 1.33×10^4 Pa. Each transition is referenced to the spectrally unresolved (total) pulse to show how the transitions overlap in time. The decrease in peak power with increasing v is partly due to the decrease in grating efficiency at longer wavelengths. Absolute comparisons would also require knowledge of the detector efficiency at the different wavelengths, which we do not have. Comparisons within a vibrational band are somewhat more valid, so we can say that the transitions shown in Fig. 1 are the most important for a given band because a search with both a spectrograph [6] and the monochromator showed no other detectable transitions.

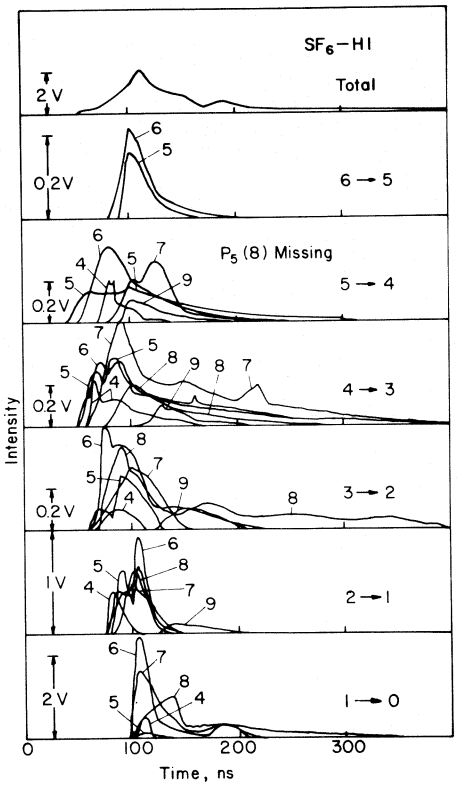

Fig. 1. Time-resolved HF laser line intensities from an SF_6 (12.8 kPa)-HI (0.53 kPa) mixture. The arrows on the right show the change in the vibrational quantum number, and the numbers on the curves show the rotational quantum number in the final vibrational state. These are all *P*-branch transitions. The peak power in the undispersed beam is 10 MW.

The sequence in which the levels begin to emit suggests cascading from $v = 5$ down to $v = 1$. This idea is supported by the observed vibrational distribution among the products of the reaction F + HI, which is strongly peaked at $v = 5$, [7]. It is interesting that nearly all of the transitions within a vibrational band turn on simultaneously. This suggests that lasing occurs before the molecule has a chance for much rotational relaxation [8]. Finally, we note the period of ~20 ns (from 100 to 120 ns in Fig. 1), during which all but two of the transitions are lasing. This feature makes this laser attractive for the stimulation of short-pulse high-pressure H_2-F_2 amplifiers, where many transitions have gain, but only for a few nanoseconds.

Manuscript received April 17, 1975; revised June 12, 1975. This work was performed under the auspices of the U.S. Atomic Energy Commission.

The author is with the Los Alamos Scientific Laboratory, University of California, Los Alamos, N. Mex. 87544.

ACKNOWLEDGMENT

The author wishes to thank P. Bird, L. Blair, J. McGurn, J. Young, and F. Archuleta for their help, comments, and encouragement during this work.

REFERENCES

[1] S. N. Suchard, "Lasing from the upper vibrational levels of a flash-initiated H_2-F_2 laser," *Appl. Phys. Lett.*, vol. 23, pp. 68-70, 1973.
[2] N. R. Greiner, "Laser action from atmospheric-pressure H_2-F_2 mixtures made at 300 K," *IEEE J. Quantum Electron.* (Corresp.), vol. QE-9, pp. 1123-1124, Nov. 1973.
[3] T. V. Jacobson and G. H. Kimbell, "Transversely pulse-initiated chemical lasers: Preliminary performance of the HF system," *Chem. Phys. Lett.*, vol. 8, pp. 309-311, 1971.
[4] S. W. Mayer, D. Taylor, and M. A. Kwok, "HF chemical lasing at higher vibrational levels," *Appl. Phys. Lett.*, vol. 23, pp. 434-436, 1973.
[5] R. G. Wenzel and G. P. Arnold, "A double-discharge-initiated HF laser," *IEEE J. Quantum Electron.* (Corresp.), vol. QE-8, pp. 26-27, Jan. 1972.
[6] N. R. Greiner, G. P. Arnold, and R. G. Wenzel, "Rapid recording of infrared spectra from pulsed chemical lasers," *J. Appl. Phys.*, vol. 44, pp. 3202-3204, 1973.
[7] N. Johnathan, C. M. Melliar-Smith, S. Okuda, D. H. Slater, and D. Timlin, "Initial vibrational energy level distributions determined by infrared chemiluminescence II. The reaction of fluorine atoms with hydrogen halides," *Mol. Phys.*, vol. 22, pp. 561-574, 1971.
[8] J. J. T. Hough and R. L. Kerber, "Theoretical investigation of the effect of rotational nonequilibrium on predicted performance of pulsed HF chemical lasers," presented at the 4th Conf. Chemical and Molecular Lasers, St. Louis, Mo., Oct. 1974, Paper TA7, to be published.

Continuous Oscillation of a Lithium Neodymium Tetraphosphate Laser with 200-μW Pump Threshold

KENJU OTSUKA AND TOMOAKI YAMADA

Abstract—**Room temperature CW oscillation of a lithium neodymium tetraphosphate ($LiNdP_4O_{12}$) (LNP) laser with thresholds in the fractional milliwatt range is reported. With a 5145-Å pump, observed threshold was 200 μW and the slope efficiency was 43 percent.**

Recently, Danielmeyer *et al.* reported continuous oscillation of a $(Nd,Y)P_5O_{14}$ laser with a pump threshold of 1 mW [1]. We reported quasi-continuous oscillation of a lithium neodymium tetraphosphate $LiNdP_4O_{12}$ (LNP) laser pumped longitudinally as well as transversely with an argon laser [2], [3]. We present here the CW operation of a LNP laser with thesholds in the submilliwatt range. The measured minimum threshold of 200 μW is, to our knowledge, the lowest obtained with any laser material.

An argon laser ($\lambda = 5145$ Å) served as a pump. A platelet-like LNP crystal of 0.3-mm thickness, which absorbed 50 percent of the pump light, was pumped longitudinally. The resonator consisted of mirrors M_1 (radius of curvature $R_1 = \infty$; transmission at 1.047_7 μm, $T_1 = 0.1$ percent; transmission at 5145 Å, $T' = 83$ percent) and M_2 ($R_2 = 9$ cm, $T_2 = 0.1$, 1.2, 2, 3 percent) separated by about 9 cm. The cavity was nearly semiconcentric. The mirror M_2 was movable back and forth precisely by the motor-driven micrometer screw. The crystal was cemented by a heat-sink compound on the mirror M_1. The focal length of the lens focusing the pump beam was 5 cm and the pump light was focused on an area smaller than the beam-waist spot size of the LNP laser.

Manuscript received April 22, 1975.

The authors are with the Musashino Electrical Communication Laboratory, Nippon Telegraph and Telephone Public Corporation, Musashino-shi, Japan.

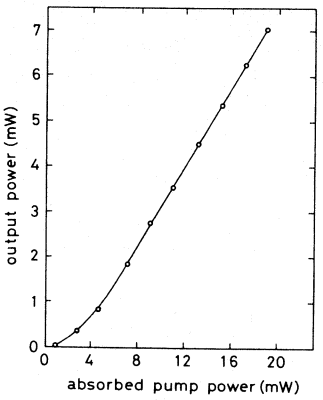

Fig. 1. The output power through the mirror M_2 ($T_2 = 1.2$ percent) as a function of the absorbed pump power at 5145 Å.

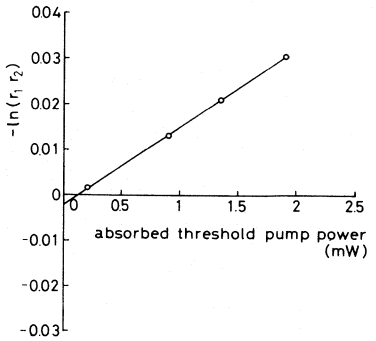

Fig. 2. The laser threshold as a function of $-\ln(r_1 r_2)$, where r_1 and r_2 are the mirror reflectivities.

The output power through the mirror M_2 is shown in Fig. 1 as a function of the absorbed pump power at 5145 Å, where T_1 and T_2 were fixed at 0.1 and 1.2 percent, respectively. The threshold was $P_{th} = 920$ μW and the slope efficiency was 43 percent.

The round-trip loss of the cavity L_c was directly measured by the change of threshold with $-\ln(r_1 r_2)$, where r_1 and r_2 are mirror reflectivities. The round-trip loss L_c consists of propagation loss of the crystal, transmission losses of two cavity mirrors, and diffraction loss. From Fig. 2, the round-trip loss, except the transmission losses of the mirrors, is found to be 0.002. The minimum threshold of 200 μW was obtained when T_1 and T_2 were fixed at 0.1 percent. From the slope of the measured line, the round-trip gain per absorbed pump power g is determined as 1.67×10^{-2} mW^{-1}.

The output-beam spot size of the LNP-laser radiation was measured as a function of the distance from the mirror M_2, as is shown in Fig. 3(a), and we estimated the spot size at the mirror M_2 as $w_m = 1.5$ mm. With $w_m = 1.5$ mm and $R_2 = 9$ cm, the oscillating-beam spot size in the 0.3-mm-thick LNP crystal was calculated in Fig. 3(b). From Fig. 3(b), the beam spot size averaged over the crystal is found to be $w_a = 20$ μm.

The round-trip gain G is given by [4]

$$G = 2\,\Delta N \sigma_l L_{\text{crystal}}$$

$$\Delta N = P_{\text{th}} \tau_f / h\nu \pi w_a^2 L_{\text{crystal}} \qquad (1)$$

where ΔN is the absorbed Nd ion density, σ_l is the effective emission cross section, L_{crystal} is the crystal length, τ_f is the fluorescence lifetime, h is Planck's constant, and ν is the pump frequency.

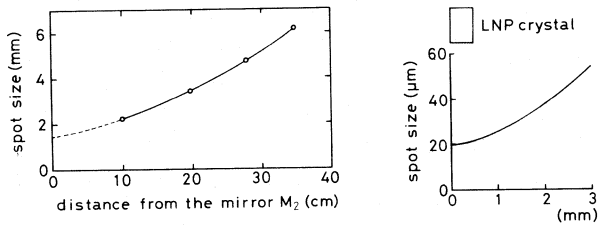

(a) (b)

Fig. 3. The oscillating-beam spot size of the LNP laser. (a) The output-beam spot size as a function of the distance from the mirror M_2 ($R_2 = 9$ cm). (b) The oscillating-beam spot size in the LNP crystal. The mirror spacing is about 9 cm and the crystal is attached on the mirror M_1.

TABLE I
OBSERVED CHARACTERISTICS OF LNP LASER

thickness	w_a	η	$P_{th,m}$	g (obs.)	g (calc.)
0.3 mm	20 μm	0.5	200 μW	1.67×10^{-2} mW^{-1}	1.59×10^{-2} mW^{-1}
0.7	22	0.8	370	1.43×10^{-2}	1.32×10^{-2}

Note: $P_{th,m}$ is the observed minimum threshold and η is the pumping efficiency.

The oscillation threshold is obtained when

$$G = L_c. \tag{2}$$

From (1) and (2), the oscillation threshold is given by

$$P_{th} = L_c h\nu\pi w_a^2 / 2\sigma_l \tau_f. \tag{3}$$

Therefore one obtains the round-trip gain per absorbed pump power g as follows:

$$g = G/P_{th} = L_c/P_{th} = 2\sigma_l \tau_f / h\nu\pi w_a^2. \tag{4}$$

With $\sigma_l = 3.2 \times 10^{-19}$ cm^2 [5], $\tau_f = 120$ μs [6], $\nu = 5.8 \times 10^{14}$ Hz, and $w_a = 20$ μm, g is calculated as 1.59×10^{-2} mW^{-1}. This is in good agreement with the value of 1.67×10^{-2} mW^{-1} obtained from Fig. 2.

Then we pumped a LNP of 0.7-mm thickness, which absorbed 80 percent of the pump light, in the same cavity configuration. The observed minimum threshold was 370 μW when T_1 and T_2 were fixed at 0.1 percent. The obtained results are shown in Table I together with those for the 0.3-mm-thick LNP.

In conclusion, we have obtained continuous operation of a $LiNdP_4O_{12}$ laser with a pump threshold of 200 μW at 5145 Å. There is good agreement between theory and experiment. If we convert our result to the light-emitting-diode (LED) pumping ($\lambda = 0.8$ μm), the threshold power for a LED to lase a LNP crystal is calculated as 130 μW, assuming $w_a = 20$ μm.

ACKNOWLEDGMENT

The authors wish to thank Dr. N. Niizeki and Dr. H. Iwasaki for their encouragement and valuable criticism.

REFERENCES

[1] H. G. Danielmeyer, G. Huber, W. W. Krühler, and J. P. Jeser, "Continuous oscillation of a (Sc, Nd) pentaphosphate laser with 4 milliwatts pump threshold," *Appl. Phys.*, vol. 2, pp. 335-338, Dec. 1973.
[2] K. Otsuka, T. Yamada, J. Nakano, T. Kimura, and M. Saruwatari, "Lithium neodymium tetraphosphate laser," *J. Appl. Phys.*, June 1975, to be published.
[3] K. Otsuka and T. Yamada, "Transversely pumped LNP laser performance," *Appl. Phys. Lett.*, vol. 26, pp. 311-313, Mar. 15, 1975.
[4] M. Birnbaum and J. A. Gelbwachs, "Stimulated-emission cross section of Nd^{3+} at 1.06 μ in $POCl_3$, YAG, $CaWO_4$, ED-2 glass and LG55 glass," *J. Appl. Phys.*, vol. 43, pp. 2335-2338, May 1972.
[5] K. Otsuka, T. Yamada, M. Saruwatari, and T. Kimura, "Spectroscopy and laser oscillation properties of lithium neodymium tetraphosphate," *IEEE J. Quantum Electron. (Part I of Two Parts)*, vol. QE-11, pp. 330-335, July 1975.
[6] T. Yamada, K. Otsuka, and J. Nakano, "Fluorescence in lithium neodymium ultraphosphate single crystals," *J. Appl. Phys.*, vol. 45, pp. 5096-5097, Nov. 1974.

Induced-Emission Cross Sections for the $^4F_{3/2} \rightarrow {}^4I_{13/2}$ Transition in Neodymium Laser Glasses

RALPH R. JACOBS AND MARVIN J. WEBER

Abstract—**Induced-emission cross sections for the $^4F_{3/2} \rightarrow {}^4I_{13/2}$ transition of Nd^{3+} in several commercial and experimental laser glasses have been determined using spectroscopic data and the Judd-Ofelt treatment of electric-dipole transition probabilities.**

Recently, Krupke [1] determined the induced-emission cross section for the $^4F_{3/2} \rightarrow {}^4I_{11/2}$ transition of Nd^{3+} in four silicate laser glasses using spectroscopic data and the Judd-Ofelt treatment of crystal-field-induced electric-dipole transition probabilities. We have utilized this approach to determine the cross sections for the $^4F_{3/2} \rightarrow {}^4I_{13/2}$ transition of Nd^{3+} in several silicate and phosphate glasses. These results can be used to evaluate Nd^{3+} laser action at longer wavelengths,[1] ≈1.3-1.4 μm, and to estimate losses due to amplified spontaneous emission in large Nd:glass amplifiers arising from $^4F_{3/2} \rightarrow {}^4I_{13/2}$ transitions.

In Fig. 1, the $^4F_{3/2} \rightarrow {}^4I_{13/2}$ fluorescence spectrum of Nd^{3+} is shown for two silicate glasses (ED-2 and LG 650) and one phosphate glass (P-107) at 300 K.[2] These spectra typify the variations of line shape and position observed for the different glasses investigated. In all cases, the emission bands were inhomogeneously broadened and asymmetric. Fluorescence was excited using a frequency-doubled Nd:YAG laser (≈150-ns pulsewidth at 532 nm) and observed with a 0.3-m grating monochromator equipped with a PbS detector and boxcar integrator. The detection system was calibrated for relative spectral response using a quartz-tungsten-iodine standard lamp. The spectral resolution was ≈3 nm.

The peak induced-emission cross sections σ_p for Nd^{3+} were determined from the expression

$$\sigma_p(\lambda_p) = \frac{\lambda_p^4}{8\pi c n^2 \Delta\lambda_{\text{eff}}} A(^4F_{3/2} \rightarrow {}^4I_J) \tag{1}$$

Manuscript received April 28, 1975. This work was performed under the auspices of the U.S. Energy Research and Development Administration.

The authors are with the Lawrence Livermore Laboratory, University of California, Livermore, Calif. 94550.

[1] Nd^{3+} laser oscillation arising from $^4F_{3/2} \rightarrow {}^4I_{13/2}$ transitions has been reported for glasses and crystals. See, for example, M. J. Bina and C. R. Jones, "Some characteristics of neodymium lasers operating in the $\lambda = 1.35$ μm range," *Opt. Commun.*, vol. 7, pp. 400-401, Apr. 1973, and references therein.

[2] Reference to a company or product name does not imply approval or recommendation of the product by the University of California or the U.S. Energy Research and Development Administration to the exclusion of others that may be suitable.

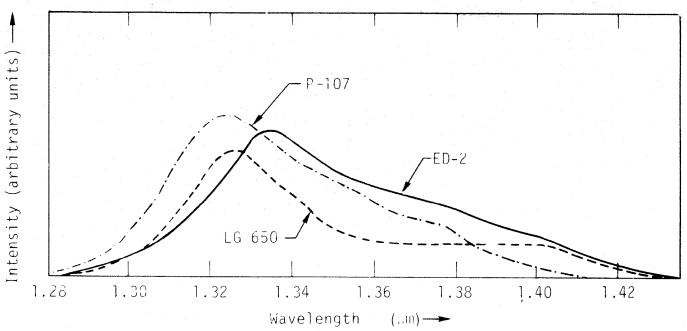

Fig. 1. Room-temperature fluorescence spectra of Nd^{3+} for the $^4F_{3/2} \rightarrow {}^4I_{13/2}$ transition in silicate (ED-2, LG 650) and phosphate (P-107) glasses. The individual curves are each corrected for the spectral response of the detection apparatus but, for clarity of presentation, the individual intensity scales are different.

where λ_p is the wavelength of the fluorescence peak, n is the refractive index at λ_p, and $\Delta\lambda_{eff}$ is the effective bandwidth. The last quantity was obtained by integration of the fluorescence band [1] and was so determined since, as previously noted, the fluorescence spectra were asymmetric. The spontaneous-emission probability A for transitions to the Jth multiplet was calculated using the Judd–Ofelt intensity parameters Ω_2, Ω_4, and Ω_6 for crystal-field-induced electric-dipole transitions. These intensity parameters were obtained from a least squares fit of measured absorption intensities, as described in [1]. The agreement between measured and calculated absorption linestrengths was generally good with rms deviations of $\lesssim 5$ percent. Details of the spectral intensities, resulting Ω parameters, and variations of induced-emission cross sections with glass composition will be presented in a future publication [2].

Measured bandwidths, peak wavelengths, and cross sections of the $^4F_{3/2} \rightarrow {}^4I_{13/2}$ transition for several commercial and experimental silicate and phosphate glasses are summarized in Table I. The sources of the glasses were as follows: 3669A—American Optical; LSG-91H, LSG-95, LHG-5—Hoya; P-25, P-107—Kigre; L-41—National Bureau of Standards; ED-2, ED-8—Owens-Illinois; and LG 650—Schott. Most of the phosphate glasses are experimental. P-25 and L-41, which are K_2O–BaO–P_2O_5 and MgO–Al_2O_3–P_2O_5 glasses, respectively, are included since they represent the extremes of the cross sections observed thus far in phosphate glasses. The uncertainties in the listed λ_p and σ_p values are estimated to be ±2 nm and ±10 percent, respectively. Included in the final column of Table I, for comparison, are the peak cross sections for the $^4F_{3/2} \rightarrow {}^4I_{11/2}$ transition. The stated values of this latter cross section for ED-2 and LSG-91H are in good agreement with the corresponding results in [1] which, in turn, agree with available experimental determinations.

A check was made on the internal consistency of the σ_p values in Table I via a separate determination of the ratio of the cross sections at ≈ 1.06 μm to that at ≈ 1.33 μm for representative silicate and phosphate glasses. An expression for calculating such a cross section ratio has been given by Singh *et al.* [3]. In addition to index and wavelength factors, it contains the ratio of corrected peak fluorescence intensities for the two bands. To within the stated accuracy of the σ_p values listed in Table I (±10 percent), the results of this method agreed with the corresponding ratio of cross sections evaluated using (1).

Whereas the $^4F_{3/2} \rightarrow {}^4I_{13/2}$ fluorescence spectra and cross sections for the lithium-alkaline earth-silicates ED-2, ED-8, LSG-91H, and LSG-95 are similar, they differ significantly from the potassium-heavier alkaline-earth-silicates 3669A and LG 650. In the phosphate glasses, the cross sections

TABLE I
EFFECTIVE BANDWIDTH $\Delta\lambda_{eff}$, PEAK FLUORESCENCE WAVELENGTH λ_p, AND INDUCED-EMISSION CROSS SECTION σ_p FOR THE $^4F_{3/2} \rightarrow {}^4I_{13/2}$ TRANSITION IN NEODYMIUM LASER GLASSES

	$^4F_{3/2} \rightarrow {}^4I_{13/2}$			$^4F_{3/2} \rightarrow {}^4I_{11/2}$
Glass	$\Delta\lambda_{eff}$(nm)	λ_p(μm)	$\sigma_p(10^{-20}$ cm$^2)$	$\sigma_p(10^{-20}$cm$^2)$
Silicates				
3669A	53	1.326	0.30	1.2*
LSG-91H	64	1.335	0.65	2.7
LSG-95	58	1.335	0.78	2.8
ED-2	67	1.335	0.72	2.9
ED-8	63	1.334	0.82	3.1
LG 650	52	1.325	0.31	1.1
Phosphates				
LHG-5	49	1.323	0.94	3.9
P-25	45	1.324	1.1	4.7
P-107	55	1.324	0.89	3.9
L-41	54	1.320	0.50	1.9

*Result from [1].

for both the $^4F_{3/2} \rightarrow {}^4I_{13/2}$ and $^4F_{3/2} \rightarrow {}^4I_{11/2}$ transitions can be larger than in the silicates. This is due to a combination of narrower emission bandwidths and larger Ω values. For all glasses studied, the peak cross sections for transitions to the $^4I_{13/2}$ state are about one-fourth as large as those to $^4I_{11/2}$, the saturation flux being correspondingly higher. The cross section to $^4I_{15/2}$, however, is very much smaller due to the small transition matrix element (the fluorescence branching ratio to $^4I_{15/2}$ is <0.01) and the larger splitting of the $J = 15/2$ manifold and resulting increased bandwidth.

Finally, it should be noted that the *net* cross sections for stimulated emission may be smaller than those given in Table I because of excited state absorption from $^4F_{3/2}$. While this is predicted [1] to be a small effect at ≈ 1.06 μm, it may not be at ≈ 1.33 μm since calculated linestrengths from $^4F_{3/2}$ to $^4G_{7/2}$, $^2K_{13/2}$ are approximately one-half as large as those to $^4I_{13/2}$. Detailed estimates of this excited state absorption require information about the spectral overlap of the absorption and emission profiles which are presently not available.

ACKNOWLEDGMENT

The authors wish to thank Dr. J. Paisner for performing the spectral calibration of the fluorescence detection apparatus. They also wish to thank C. Dobler, J. Lynch, and R. Morgret for their excellent assistance in the data acquisition and reduction.

REFERENCES

[1] W. F. Krupke, "Induced-emission cross sections in neodymium laser glasses," *IEEE J. Quantum Electron.*, vol. QE-10, pp. 450–457, Apr. 1974.

[2] R. R. Jacobs and M. J. Weber, "Tailoring Nd-doped glasses for laser applications: Dependence of induced-emission cross sections on composition," presented at the 1975 IEEE/OSA Conf. Laser Engineering and Applications, Washington, D.C., May 1975, to be published.

[3] S. Singh, R. G. Smith, and L. G. Van Uitert, "Stimulated emission cross section and fluorescent quantum efficiency of Nd^{3+} in yttrium aluminum garnet at room temperature," *Phys. Rev. B*, vol. 10, pp. 2566–2572, Sept. 1974.

Performance of a Compact Sealed 200-W CO_2 Laser

THEODORE S. FAHLEN

Abstract—**The performance characteristics of a compact (3-ft^3) TEM_{00}-mode single-wavelength CO_2 laser are described. The optic axis, gas flow velocity, and glow discharge are mutually orthogonal in the sealed-off laser head. The laser produces up to 300 W of TEM_{00}-mode 10.6-μm power.**

In this correspondence, the design and performance characteristics of a compact 200-W CW CO_2 laser head are described. To our knowledge, this CO_2 laser head is the smallest yet built that operates in this power regime. In order to obtain high CW power output from this compact sealed CO_2 laser, the laser head utilized a rapid recirculating gas flow, a stable folded optical cavity, and a unique CW glow discharge configuration. The advantages of using a rapid recirculating gas flow to increase the obtainable power per unit length of discharge by convectively cooling the active gas of high-power CW CO_2 lasers have been discussed previously [1]–[3]. The use of a folded optical cavity allows a long optical cavity length to be contained in a short structure. The long cavity length not only provides sufficient gain length for high output power, but also allows single-wavelength operation to be obtained [4] without the use of intracavity wavelength selectors (such as a diffraction grating) with their inherent losses. The stable optical resonator provides a TEM_{00} mode beam. The unique electrode configuration provides a stable dc glow discharge of high power density without additional radio-frequency, ultraviolet, or electron-beam sources of ionization.

The laser head dimensions are 24 in long, 16 in high, and 13.5 in wide. The 3-ft^3 head weighs 97 lb. A vaneaxial blower contained within the vacuum enclosure circulates the laser gas through the discharge region at a velocity of 50 m/s and then through a gas-to-liquid heat exchanger, also contained within the vacuum enclosure.

The optical cavity and electrode configuration are shown schematically in Fig. 1. The cathode consists of a copper tube, 1.59 cm in diameter and 33 cm long located above and upstream of the first optical beam. The anode, located directly below the optical cavity, consists of 18 copper strips, each 8.06 cm long by 1.19 cm wide and separated by 0.51 cm. Each individual anode pad is resistively ballasted with 1.4 kΩ. Both the cathode and anode are water cooled.

The optical cavity consists of two flat highly reflective folding mirrors, separated by 42 cm, a highly reflective non-output mirror of 20-m radius of curvature, and a flat output mirror of 48-percent transmission at 10.6 μm. The intracavity beam is folded to pass nine times through the discharge region. The resulting total optical-cavity length of this stable resonator is 3.9 m.

The optimum gas mixture, in terms of laser efficiency, was found to be 25-torr He, 10-torr N_2, and 2.5-torr CO_2.

The laser output power and efficiency are plotted as a function of input current in Fig. 2. The laser efficiency is defined as the laser output power divided by the total power delivered to the laser head. The maximum power attained was 300 W. The total power input includes the 215 W of power required to run the vaneaxial blower but not the power lost in the ballast resistors as no attempt was made to minimize the ballast resistance. The maximum current input, limited by arc formation in the positive column of the discharge, was about 5 A, corresponding to an input power density to the positive column of 5.8 W/cm^3.

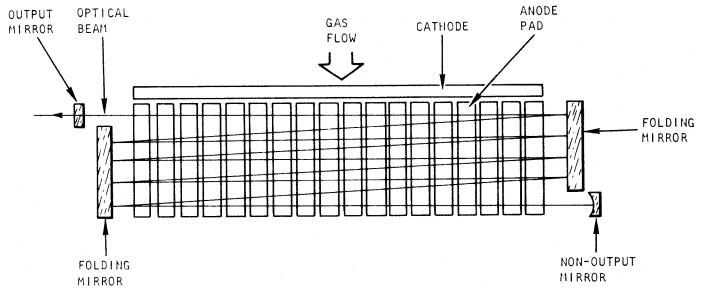

Fig. 1. Diagram of discharge and optical path region.

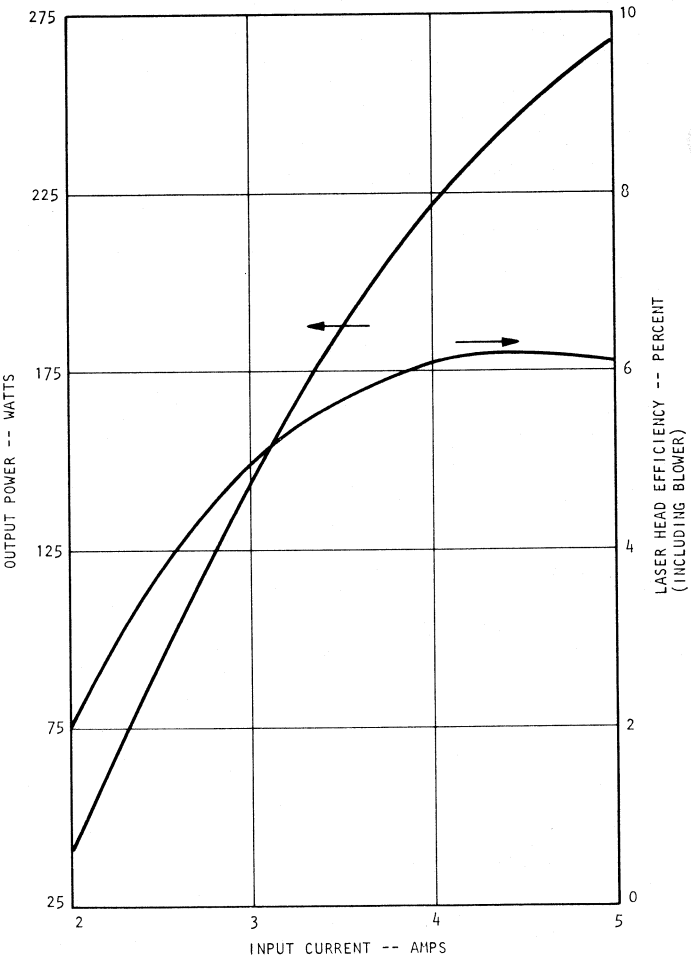

Fig. 2. Laser power and efficiency versus input current.

The laser output wavelength was measured to be 10.59 μm, corresponding to the $P(20)$ laser transition. Single-wavelength operation is obtained by virtue of the long length of the resonant cavity [4] so that no intracavity wavelength discriminating elements are required. Single-wavelength operation remained invariant as mirror alignment and applied current were varied.

The transverse mode quality of the laser was measured by scanning a small aperture through the beam in the far field as imaged by a lens. The output of a Au:Ge detector collecting the energy passing through the aperture was then displayed on an oscilloscope. The beam profile was found to be Gaussian (TEM_{00}). The full angular beam divergence θ to the $1/e^2$ in-

Manuscript received May 12, 1975. This work was supported by the Air Force Systems Command under Wright-Patterson Air Force Base Contract F33615-74-C-1056.

The author is with the Electro-Optics Organization, GTE Sylvania, Inc., Mountain View, Calif. 94042.

tensity radius was also measured with the scanning aperture and oscilloscope, and was found to be 1.6 ± 0.3 mrad.

The laser was designed to operate in a sealed-off condition, i.e., no gas was added to the system once it was filled with the proper gas mix. It was found experimentally that the power monotonically decreased from 230 to 200 W after 1 h of continuous operation at 4 A of input current, corresponding to a power decrease of 13 percent/h.

The primary factor causing the output power to diminish with time is the degradation of the laser gas mixture. One known effect is that the action of the discharge decomposes CO_2 molecules into CO and O_2. It has been shown [5] that the presence of O_2 molecules in the mix is detrimental to laser action. Furthermore, the formation of oxides of the various components within the vacuum shell tends to reduce the partial pressure of O_2 in the laser. To maintain chemical equilibrium, more CO_2 dissociates and the laser output power decreases. It was found that the power output did not decrease unless the laser was operated. Therefore, outgassing or air leakage without the presence of a discharge (or heat from the discharge) does not affect the rate of power decrease. It is then concluded that the rate of power decrease depends on some chemically contaminating reaction among the various gases and components within the vacuum shell brought about by the action of the discharge. Adding a slow-flow continuous-gas-replenishment system to the laser would drastically reduce the rate of power degradation but would add complexity to the system.

ACKNOWLEDGMENT

The author wishes to thank M. L. Conroy for his expert technical assistance.

REFERENCES

[1] W. B. Tiffany, R. Targ, and J. D. Foster, "Kilowatt CO_2 gas transport laser," *Appl. Phys. Lett.*, vol. 15, pp. 11-73, Aug. 1969.
[2] T. F. Deutsch, F. A. Horrigan, and R. I. Rudoko, "CW operation of high-pressure flow CO_2 lasers," *Appl. Phys. Lett.*, vol. 15, pp. 88-97, Aug. 1969.
[3] A. J. DeMaria, "Review of CW high-power CO_2 lasers," *Proc. IEEE*, vol. 61, pp. 731-748, June 1973.
[4] M. W. Sasnett and R. S. Reynolds, "Single-wavelength CO_2 laser without dispersive elements," *IEEE J. Quantum Electron.* (Corresp.), vol. QE-7, pp. 372-373, July 1971.
[5] J. A. Howe, "Effect of foreign gases on the CO_2 laser: *R*-branch transitions," *Appl. Phys. Lett.*, vol. 7, pp. 21-22, July 1965.

Guided-Wave Acoustooptic FM Modulator

C. P. CHRISTENSEN, W. H. STEIER, AND R. BASU

Abstract—**Phase modulation of guided optical waves by longitudinal sound is observed in a thin-film modulator of simple construction. The dependence of modulation sideband amplitudes upon acoustic strain is investigated, and device performance is found to be close to that predicted by theory.**

Manuscript received May 13, 1975. This work was supported by the Joint Services Electronics Program through the Air Force Office of Scientific Research (AFSC).

The authors are with the Department of Electrical Engineering, University of Southern California, Los Angeles, Calif. 90007.

Acoustooptic modulation schemes suitable for use in integrated optics have been the subject of several recent investigations. Bragg deflection of guided light by acoustic surface waves [1], mode conversion by bulk shear waves [2], as well as phase modulation by bulk longitudinal and shear waves have been reported [3]. Acoustic devices can often use amorphous or multicrystal films which are in general use as guiding layers for integrated optics and hence have the advantage of possibly using the same material for the wave-guiding layer and the modulator. In this correspondence we discuss a simple FM modulator design based upon the interaction of light and longitudinal sound in a thin-film waveguide.

The physical construction of the experimental device is shown in Fig. 1. A 35° Y-cut $LiNbO_3$ transducer is bonded with phenylbenzoate to the bottom of a glass substrate (n_2 = 1.51) and operated at its seventh overtone frequency of 62 MHz. Bulk longitudinal waves generated by the transducer travel through the substrate and successive overlayers of Corning 7059 sputtered glass (n_1 = 1.57, thickness = 0.6 μ), solution deposited silica film [4], (n_0 = 1.44, thickness = 1 μ), and sputtered aluminum (thickness = 25 μ). The layer thicknesses are chosen so that acoustic reflection at the aluminum–air interface produces a standing acoustic wave which has a peak at the sputtered glass layer. The sputtered glass film acts as an optical waveguide which is isolated from the aluminum overlayer by the low-index silica film. Light is introduced into the waveguide by means of prism couplers, and the guided optical waves are then phase modulated at the acoustic frequency primarily through the photoelastic effect. Qualitative results for a somewhat similar modulator utilizing an acoustic traveling wave to produce phase modulation have been given by Brandt *et al.* [3]. However, use of a standing wave geometry produces almost pure phase modulation with little AM and increases the efficiency of the device by a factor of 4, since the bandwidth of a modulator of this type is approximately that of the acoustic transducer.

This bulk acoustic wave and guided optical wave interaction is not expected to have an increased modulation efficiency over the more conventional acoustooptic interaction in which the light is not guided. Increased efficiency requires also guiding the sound as in acoustic surface waves. However, this device gives almost pure FM or PM modulation, which is difficult to achieve in interactions where both the sound and light are guided waves, or in interactions where both the sound and light are not guided waves.

The modulator output spectrum was observed with an optical hetrodyne arrangement which is similar to that used by Kaminow [5]. Examples of spectra are shown in Fig. 2. Acoustic strain in the substrate was monitored by propagating an He-Ne laser beam through the glass substrate bulk and observing the intensity of the zeroth diffraction order during the sound pulse. The standing wave diffraction results of Sanders [6] were then used to obtain the acoustic strain from the diffraction measurements.

The efficiency of a modulator of this type can be accurately

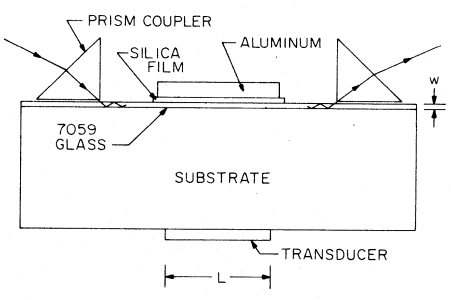

Fig. 1. Thin-film FM modulator construction (not to scale).

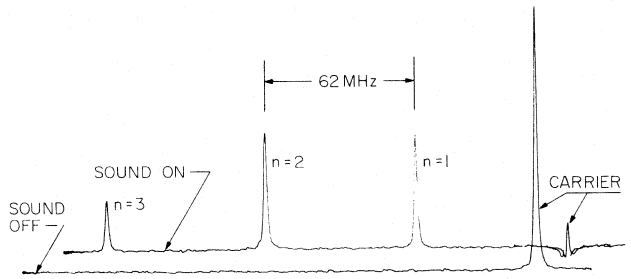

Fig. 2. Modulator output spectra obtained in the absence of an acoustic field and with an acoustic intensity corresponding to $\delta\phi = 2.55$.

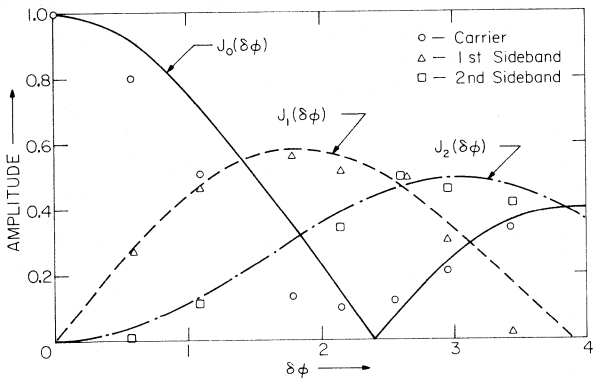

Fig. 3. Amplitude of the carrier and first two sidebands as a function of phase shift $\delta\phi$. Equation (1) was used to obtain $\delta\phi$ from the acoustic strain measured by light scattering in the substrate bulk.

estimated by using the characteristic equation of a planar waveguide [7]. For TE waves we find the phase shift corresponding to an acoustic strain S to be

$$\delta\phi = \frac{-kLS}{2\bar{\beta}\,[kw + (1/b_0) + (1/b_2)]} \left\{ n_1^4\, p_{12}^{(1)} \left[kw + \frac{b_0}{b_0^2 - b_1^2} + \frac{b_2}{b_2^2 - b_1^2} \right] + \frac{n_0^4\, p_{12}^{(0)}\, b_1^2}{b_0\,(b_1^2 - b_0^2)} + \frac{n_2^4\, p_{12}^{(2)}\, b_1^2}{b_2\,(b_1^2 - b_2^2)} + 2b_1^2\, kw \right\} \tag{1}$$

where n_i and $p_{12}^{(i)}$ are, respectively, the refractive index and photoelastic coefficient of the ith medium. The acoustic overlayer is taken to be medium zero, the optical guide to be medium 1, and the substrate as medium 2. $\bar{\beta}$ is given by the ratio of the optical waveguide propagation constant to the free-space propagation constant k. The width of the optical guide is taken to be w, the length of the interaction region to be L, and $b_i^2 = \bar{\beta}^2 - n_i^2$. The first three terms in brackets on the right side of (1) arise from modulation of the refractive indices of the three media, while the fourth term is due to modulation of the waveguide thickness. A result similar to (1) can be derived for TM waves.

Using the measured strain values in (1) with $p_{12}^{(0)} \cong p_{12}^{(1)} \cong p_{12}^{(2)} = 0.24$ and $L = 7.4$ mm, we find $\delta\phi = 3.0 \times 10^4 S$ where $\delta\phi$ is in radians. Since hetrodyne detection was used, the measured amplitude of the nth sideband should be proportional to $J_n(\delta\phi)$. The sideband amplitudes and the acoustic strain were measured at several levels of input sound power and compared to these theoretical predictions in Fig. 3. The results show the modulator is working as predicted and is producing a largely FM output spectrum.

The effect of the reflected acoustic wave on the bandwidth of the transducer can be eliminated by a small angle between the transducer and the guiding layer in the plane perpendicular to the light propagation. If the substrate is sufficiently thick, the reflected acoustic wave will be offset from the transducer and can be conveniently absorbed. The modulation power per unit bandwidth of our modulator was largely determined by the transducer efficiency; the achievable modulation efficiency, as discussed earlier, is expected to be the same as bulk acousto-optic modulators [8].

At high acoustic intensities we have also observed beam deflection phenomena similar to those described by Brandt *et al.* [3], in which the distribution of light in the plane of the waveguide is altered by the presence of the acoustic beam. Although the total optical power in the mode remains constant, scattering from the central portion of the m line into the wings and the converse effect have both been observed. The central spot intensity, however, fluctuated by about 15 percent at most, and modulator operation was not significantly affected. Variations in strain phase or amplitude in the waveguide plane could perturb the light distribution in the waveguide, but experimental verification of this is difficult and was not attempted.

In summary, we have demonstrated the feasibility of a guided-wave FM modulation technique employing an acoustic standing wave. The modulator output spectrum has been shown to be very close to that predicted by theory.

References

[1] R. V. Schmidt, I. P. Kaminow, and J. R. Carruthers, "Acousto-optic diffraction of guided optical waves in $LiNbO_3$," *Appl. Phys. Lett.*, vol. 23, pp. 417–419, 1973.
[2] M. L. Shah, "Fast acousto-optical waveguide modulators," *Appl. Phys. Lett.*, vol. 23, pp. 75–77, 1973.
[3] G. B. Brandt, M. Gottlieb, and J. J. Controy, "Bulk acoustic wave interaction with guided optical waves," *Appl. Phys. Lett.*, vol. 23, pp. 53–54, 1973.
[4] Emulsitone Co., 411 E. Willow St., Milburn, N. J. 07041.
[5] I. P. Kaminow, "Barium titanate light phase modulator," *Appl. Phys. Lett.*, vol. 7, pp. 123–125, 1965.
[6] F. H. Sanders, *Can. J. Res., Sect. A*, vol. 14, pp. 158–171, 1936.
[7] P. K. Tien and R. Ulrich, "Theory of prism-film coupler and thin-film light guides," *J. Opt. Soc. Amer.*, vol. 60, pp. 1325–1337, 1970.
[8] D. Maydan, "Acoustooptic pulse modulators," *IEEE J. Quantum Electron.*, vol. QE-66, pp. 15–24, Jan. 1970.

Second-Harmonic Generation in Birefringent Crystals by a Gaussian Beam with an Elliptical Cross Section

F. M. LIBRECHT AND J. A. SIMONS

Abstract—**The theory of second-harmonic generation (SHG) in birefringent crystals by a Gaussian beam with an elliptical cross section is developed in the assumption of no depletion of the fundamental beam. This study reveals that the doubling efficiency at optimum elliptical focusing is higher than at optimum circular focusing.**

The second-harmonic generation (SHG) of coherent light in birefringent crystals by a focused Gaussian beam with a circular cross section has been studied extensively [1]–[3]. At increasing focusing, the critical index-matching condition is affected considerably. This critical index matching occurs only in the plane of the direction of propagation z and the

Manuscript received May 27, 1975. F. M. Librecht holds a fellowship of the Belgisch Nationaal Fonds voor Wetenschappelijk Onderzoek.

The authors are with the Microwaves and Laser Division, Department of Electrical Engineering, Katholieke Universiteit Leuven, Heverlee, Belgium.

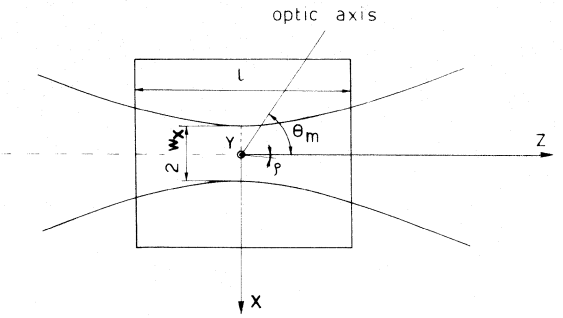

Fig. 1. Orientation of an ADP crystal in the focus of a Gaussian laser beam with an elliptical cross section.

crystal optic axis, commonly called the walkoff plane (Fig. 1). By changing the shape of the laser beam into an elliptical cross section, it is possible to focus more tightly in the nonwalkoff plane (yz plane) without affecting the critical index matching in the walkoff plane. This has been applied to parametric oscillation [4] and to SHG [5]. However, a rigorous analysis of SHG by a Gaussian beam with an elliptical cross section is not available. We therefore develop, in this correspondence, the theory of SHG by an elliptical Gaussian beam, assuming no depletion of the fundamental beam by the doubling process. As a result, using ADP crystals with a length of a few centimeters for the doubling of the 632.8-nm He–Ne light, we point out that the doubling efficiency at optimum elliptical focusing is about 25 percent higher than at optimum circular focusing.

Consider an ADP crystal of length l in the focus of a Gaussian laser beam with an elliptical cross section (Fig. 1). The beam diameters at $z = 0$ are $2w_x$ and $2w_y$ in the x and y directions, respectively. The fundamental beam is introduced in the crystal as an ordinary wave phase matched to the extraordinary second-harmonic wave. The input and output faces of the crystal are parallel and are cut so that at approximately normal incidence the laser beam passes through the crystal in the critical index-matching direction z, at an angle θ_m to the optic axis. The optic axis lies in the xz plane. ρ is the angle of double refraction. The medium surrounding the crystals is supposed to have the same refractive index as the crystal at the fundamental frequency.

The electromagnetic field of a Gaussian beam with an elliptical cross section is described by Carter [6]. In the paraxial approximation, the electric field at the fundamental frequency ω can be derived from [6, eq. (11)]

$$E_\omega(x,y,z) = E_\omega (z_{Rx} z_{Ry})^{1/2} \exp(ikz) \cdot \frac{\exp\left\{-\frac{k}{2}\left[x^2/(z_{Rx}+iz) + y^2/(z_{Ry}+iz)\right]\right\}}{(z_{Rx}+iz)^{1/2}\,(z_{Ry}+iz)^{1/2}} \tag{1}$$

where

$$z_{Rx} = \frac{kw_x^2}{2} \tag{2a}$$

$$z_{Ry} = \frac{kw_y^2}{2}. \tag{2b}$$

The constant E_ω is the fundamental electric-field amplitude in the origin, and k is the propagation constant in the crystal.

We calculate the generated harmonic field following the well-known formal approach [1], [7]. We assume no depletion of the fundamental beam by the doubling process and we neglect any absorption at the fundamental and harmonic frequencies. We take into account the additional mismatch term when the crystal is tilted away from the index-matching direction by a small angle Φ (as mentioned in [1, eq. (54)]). Eventually, the harmonic power is calculated by integrating the z component of the time-averaged Poynting's vector over the beam cross section. Describing the ellipticity of the laser beam by the parameter

$$\alpha = \frac{w_y}{w_x} \tag{3}$$

and defining a focusing parameter

$$\zeta = \frac{l}{\alpha k w_x^2} \tag{4}$$

the harmonic power $P_{2\omega}$ at the exit face ($z = l/2$) of the crystal is written as

$$P_{2\omega} = KP_\omega^2 \frac{k^2 w_x w_y}{4} \int_{-\zeta}^{+\zeta} dv \int_{-\zeta}^{+\zeta} dv' \frac{\exp\left[2ik\rho\Phi\alpha z_{Rx}(v-v')\right] \exp\left\{-\left[\rho^2\alpha^2 z_{Rx}^2 (v-v')^2/w_x^2\right]\right\}}{\left\{1+i\left[(1+\alpha^2)/\alpha\right] v - v^2\right\}^{1/2} \left\{1-i\left[(1+\alpha^2)/\alpha\right] v' - v'^2\right\}^{1/2}}. \tag{5}$$

P_ω is the power of the fundamental beam. K is a constant depending on the type of the crystal and on the fundamental frequency ω (as defined by [3, eq. (2.20)]). When $\alpha = 1$, our result (5) agrees with [1, eq. (31)] and with [3, eqs. (2.22), (2.23), (2.25)].

We calculated asymptotic and exact values of $P_{2\omega}/KP_\omega^2$, (5) as a function of w_x. The asymptotic values are listed as follows:

$$\zeta \ll 1 \qquad \frac{\rho l}{w_x} \ll 1 \qquad \frac{P_{2\omega}}{KP_\omega^2} = \frac{l^2}{\alpha w_x^2} \tag{6a}$$

$$\zeta \ll 1 \qquad \frac{\rho l}{w_x} \gg 1 \qquad \frac{P_{2\omega}}{KP_\omega^2} = \frac{\pi^{1/2} l}{\rho\alpha w_x} \tag{6b}$$

$$\zeta \gg 1 \qquad \frac{\rho k w_x \alpha}{2} \gg 1 \qquad \alpha < 1 \qquad \frac{P_{2\omega}}{KP_\omega^2} = \frac{\alpha\pi^{1/2} k w_x}{\rho} \cdot K(1-\alpha^4) \tag{6c1}$$

$$\alpha > 1 \qquad \frac{P_{2\omega}}{KP_\omega^2} = \frac{\pi^{1/2} k w_x}{\alpha\rho} \cdot K(1-\alpha^{-4}) \tag{6c2}$$

$$\zeta \gg 1 \qquad \frac{\rho k w_x \alpha}{2} \ll 1 \qquad \frac{P_{2\omega}}{KP_\omega^2} = \pi^2 \alpha k^2 w_x^2. \tag{6d}$$

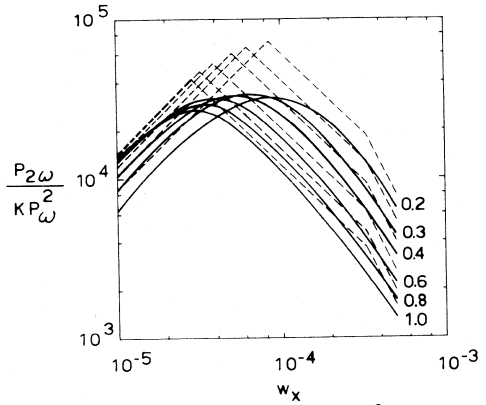

Fig. 2. Asymptotic and exact curves of $P_{2\omega}/KP_\omega^2$ (5) as a function of the beam radius w_x in the x direction for an ADP crystal with a length of 2 cm and for different values of the parameter α, (3).

$K(1-\alpha^4)$ and $K(1-\alpha^{-4})$ are complete elliptic integrals of the first kind [8]. When $\alpha = 1$ (circular cross section) our asymptotic solutions agree with the asymptotic solutions of [1] and [3]. We calculated the exact values by using an algorithm based on the Gaussian and Kronrod quadrature formulas [9].

In Fig. 2 we plotted asymptotic and exact curves on a log-log plot for an ADP crystal with a length of 2 cm and for different values of the parameter α, (3). The maximum doubling efficiency at optimum focusing occurs when α equals $\frac{1}{3}$. This maximum is not a critical function of the parameter α. The optimum shaping and focusing of the laser beam results in a 25-percent increase of the doubling efficiency with regard to the optimum focusing condition of a Gaussian beam with a circular cross section. When the length of the crystal takes on values from 1 to 4 cm, the doubling efficiency varies from 22 to 26 percent. The optimum shaping of the laser beam with these crystals is obtained when α is about $\frac{1}{3}$.

In the experimental setup, we combined commercial spherical and cylindrical lenses to shape and focus the TEM_{00} beam of a 15-mW He–Ne laser. In Table I some experimental results for an ADP crystal with a length of 2 cm are compared with theoretically predicted values.

In summary, depending on the type and the length of the nonlinear crystal, this study reveals a small increase of doubling efficiency (e.g., ADP, 2 cm, 25-percent increase) by using an optimum focused laser beam with an optimum elliptical cross section instead of using an optimum focused circular beam.

TABLE I
THEORETICAL AND EXPERIMENTAL VALUES OF THE RATIO OF $(P_{2\omega}/KP_\omega^2)_{\alpha=\alpha}$ TO $(P_{2\omega}/KP_\omega^2)_{\alpha=1}$ FOR DIFFERENT VALUES OF α WHEN $(w_x w_y)^{1/2} = 7.5 \times 10^{-5}$ M

α	$\frac{(P_{2\omega}/KP_\omega^2)_{\alpha=\alpha}}{(P_{2\omega}/KP_\omega^2)_{\alpha=1}}$ Theoretical	$\frac{(P_{2\omega}/KP_\omega^2)_{\alpha=\alpha}}{(P_{2\omega}/KP_\omega^2)_{\alpha=1}}$ Experimental
0.4	1.49	1.47 ± 0.05
0.25	1.66	1.64 ± 0.05
0.2	1.74	1.69 ± 0.05

REFERENCES

[1] J. E. Bjorkholm, "Optical second-harmonic generation using a focused Gaussian laser beam," *Phys. Rev.*, vol. 142, pp. 126–136, Feb. 1966.

[2] D. A. Kleinman, A. Ashkin, and G. D. Boyd, "Second-harmonic generation of light by focused laser beams," *Phys. Rev.*, vol. 145, pp. 338–379, May 1966.

[3] G. D. Boyd and D. A. Kleinman, "Parametric interaction of focused Gaussian light beams," *J. Appl. Phys.*, vol. 39, pp. 3597–3639, July 1968.

[4] D. Kuizenga, "Optimum focusing conditions for parametric gain in crystals with double refraction," *Appl. Phys. Lett.*, vol. 21, pp. 570–572, Dec. 1972.

[5] V. D. Volosov, "Effect of laser and medium parameters on second-harmonic generation," *Sov. Phys.–Tech. Phys.*, vol. 14, pp. 1652–1658, June 1970.

[6] W. H. Carter, "Electromagnetic field of a Gaussian beam with an elliptical cross section," *J. Opt. Soc. Amer.*, vol. 62, pp. 1195–1201, Oct. 1972.

[7] G. D. Boyd, A. Ashkin, J. M. Dziedzic, and D. A. Kleinman, "Second-harmonic generation of light with double refraction," *Phys. Rev.*, vol. 137, pp. A1305–A1320, Feb. 1965.

[8] M. Abramowitz and I. A. Stegun, *Handbook of Mathematical Functions*. New York: Dover, 1965, p. 590.

[9] R. Piessens, "An algorithm for automatic integration," Appl. Math. Programming Div., Katholieke Univ. Leuven, Leuven, Belgium, Rep. TW 13, Apr. 1973.

Notes and Lines

New Visible Laser Transitions in Ba I and Ba II

K. U. BARON AND B. STADLER

Abstract—**Three new visible laser transitions at λ = 7120 Å in Ba I and at λ = 6496.9 and 6141.7 Å in Ba II have been observed in a pulsed discharge with Xe, Ne, and He as carrier gas. A new all-metal hollow-cathode design was used.**

Manuscript received April 2, 1975.

The authors are with the Institut für Angewandte Physik, Universität Heidelberg, 6900 Heidelberg, Germany.

New laser transitions of barium vapor at 7120, 6496.9, and 6141.7 Å have been observed in a pulsed discharge. The laser lines were identified as the following transitions [1]:

7120 Å:

$6p'\,^1D_2$ [23074.4 cm^{-1}] – $5d\,^3D_1$ [9033.98 cm^{-1}]

in Ba I

6496.9 Å:

$6p\,^2P^0_{1/2}$ [20261.5 cm^{-1}] – $5d\,^2D_{3/2}$ [4873.85 cm^{-1}]

in Ba II

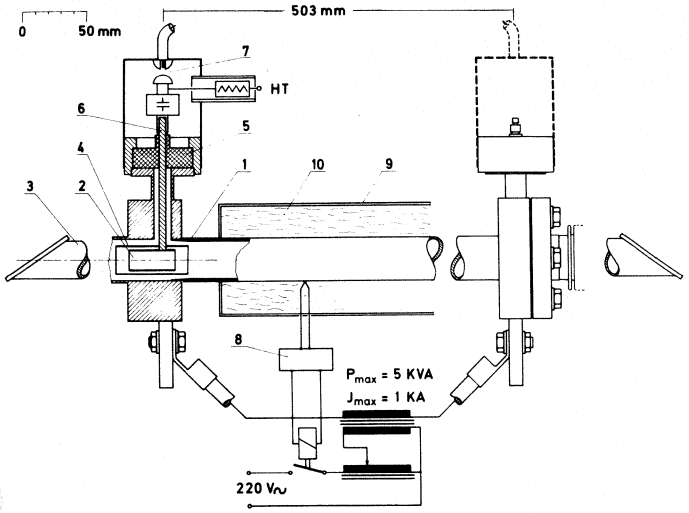

Fig. 1. Experimental laser tube. 1: Hollow cathode. 2: Hollow anode. 3: Brewster window. 4: Protective quartz tube. 5: Glass vacuum seal. 6: Electrical feedthrough (quartz tube isolated). 7: Triggered pressurized spark gap. 8: Temperature controller. 9: Metallic heat reflector. 10: Thermal isolation.

6141.7 Å:

$$6p\ ^2P^0_{3/2}\ [21952.4\ \text{cm}^{-1}] - 5d\ ^2D_{5/2}\ [5674.82\ \text{cm}^{-1}]$$

in Ba II.

We believe these are the first visible laser transitions in barium to be excited. So far only infrared lines of barium in the wavelength range longer than 1.13 μ have been observed [2]. The two laser transitions in Ba II, which seem promising for spectroscopic light sources, were suggested by Walter *et al.* [3] in 1966.

The discharge was excited inside a heated hollow-cathode structure (about 50 cm long with a 2.8-cm bore), suitable for materials of low vapor pressure. The cathode was manufactured of a nickel-chromium alloy (Sanicro 31[1]), which proved rather resistant against liquid alkaline earths and many other materials. This alloy has sufficient mechanical strength even at 1000°C and did not exhibit any deterioration after more than 200 h of operation. The hollow cathode served as vacuum envelope and was directly heated. Two hollow anodes placed inside of overlapping quartz tubes were located at the water-cooled headflanges of the envelope (see Fig. 1).

Laser action was observed with the following parameters in our experiments:

1) temperature of the hollow cathode: 710–900°C;
2) carrier gas: He at 0.4 torr, Ne at 0.1 torr, Xe at 0.04–0.1 torr;
3) pulse excitation: capacitive discharge through triggered spark gap (C = 500–9000 pF, charged up to 25 kV), either applied to both anodes, or only to one of them while dc current (I = 50–2000 mA) was supplied to the other one;
4) optical resonator: concave mirror ($f = 2m$) and plane mirror; all lines mentioned and, in addition, a laser line at 1.13 μ [2] have been also observed in superradiance;
5) operating time with 5 g of Ba: $\geqslant$ 5 h;
6) peak pulse power: $\approx$ 10 W;
7) pulse length: $\approx 10^{-8}$ s.

ACKNOWLEDGMENT

The authors wish to thank Prof. G. zu Putlitz for his suggestion of this work. They also wish to thank Prof. P. E. Toschek and his co-workers for helpful discussions and technical assistance.

[1] Sandvikstahl GmbH, Düsseldorf, Germany.

REFERENCES

[1] C. E. Moore, *Atomic Energy Levels* (NBS Circular 467), vol. III, pp. 131–135, 1958.

[2] P. Cahuzac, "Nouvelles raies laser infrarouges dans la vapeur de baryum," *Phys. Lett.*, vol. 32 A, pp. 150–151, June 1970.

[3] W. T. Walter, N. Solimene, M. Piltch, and G. Gould, "Efficient pulsed gas discharge lasers," *IEEE J. Quantum Electron. (1966 International Quantum Electronics Conference)*, vol. QE-2, pp. 474–479, Sept. 1966.

New Far-Infrared Laser Lines from CO_2-Laser-Pumped CH_3OH Gas by Using a Copper Waveguide Cavity

ATSUO TANAKA, MASANOBU YAMANAKA, AND HIROSHI YOSHINAGA

Abstract—**Eleven new far-infrared (FIR) laser lines have been observed from CH_3OH pumped by a CO_2 laser. These lines are ranged from 78 to 694 μm and are obtained by using a copper waveguide cavity.**

A large number of far-infrared (FIR) laser lines have been observed in CH_3OH [1]–[5] and CD_3OD [6] by means of optical pumping. Recently, Radford [7] reported some new CW lines in CH_3OH from a FIR waveguide laser [5], [8]. We have observed independently new laser lines from CH_3OH [9], of which some lines are the same as those found by Radford [7]. In this note, we report eleven new FIR laser lines from CH_3OH pumped by a CO_2 laser. These lines are successfully obtained by using a waveguide cavity with internal end plates.

The FIR cavity consisted of a 1-m-long copper tube of 12-mm ID and two flat copper end plates. Each plate had a coupling hole of 1.5-mm diameter at the center. One plate was translated like a piston to tune the cavity [5]. The pump CO_2 laser had the cavity length of 5.5 m and Littrow configuration of the grating. The CO_2 laser was internally chopped with a 25-percent duty factor at 480 Hz, and then the CO_2 laser beam, coupled out through the zeroth-order reflection of the grating, was chopped once more with a 50-percent duty factor at 20 Hz. The signal from a Golay detector was fed into a lock-in amplifier tuned to the chopping frequency of the pump laser beam at 20 Hz. The response of the Golay detector was assumed to be flat in the 10-μm–1-mm spectral region and calibrated near 10 μm.

Table I shows the experimental results obtained in this study. The previously reported 1217-μm line [5], which was also obtained using the 1-m-long waveguide cavity of 12-mm ID, is listed for completeness. The wavelength of these lines was measured in air by means of a scanning mesh Fabry–Perot interferometer [10] within an accuracy of ± 3 μm, where the wavelength once measured was compared with that of a known laser line. The three laser lines with a dagger coincide, within experimental errors, with those found by Radford [7]. Since the piston-type end plate as an end mirror and the smaller diameter of coupling hole can lower the threshold pump power [5], [9], it seems that these FIR laser lines, not found otherwise, were obtained by using this type of waveguide cavity even for relatively lower pump power.

Manuscript received June 27, 1975.

The authors are with the Department of Applied Physics, Osaka University, Yamada-Kami, Suita, Osaka 565, Japan.

TABLE I
EXPERIMENTAL RESULTS IN OPTICALLY PUMPED FIR CH_3OH WAVEGUIDE LASER

FIR WAVELENGTH (μm)	CO_2 PUMP LINE (μm)	PUMP POWER (W)	FIR POWER (mW)	PRESSURE* (mTorr)	THRESHOLD PUMP POWER (W)
211 495	R(4) 10.365	10 10	0.3 0.01	330 450	3 3
78 694	R(16) 10.274	10 10	0.2 0.01	280 280	4 2
242†	R(34) 10.159	10	0.3	240	2
163† 469†	R(38) 10.136	10 10	0.3 0.06	160 200	0.3 0.3
98	R(40) 10.125	10	0.03	400	8
121 251	R(44) 10.105	9 9	0.01 0.01	220 220	9 5
274	R(46) 10.095	8	0.03	210	8
286	R(48) 10.085	7	1	320	0.4
165 417	P(14) 9.504	5 5	0.03 0.01	100 100	3 1
1217**	P(16) 9.520	5	0.01	130	2

*The pressure at which the FIR output power shows the maximum for that pump power.
**See [5].
†See [7].

In conclusion, if we adopt this low-loss waveguide cavity with internal end plates, numerous new laser lines in the FIR will be expected from some available polar molecules optically pumped by the existing CO_2 or N_2O laser.

REFERENCES

[1] T. Y. Chang, T. J. Bridges, and E. G. Burkhardt, "cw submillimeter laser action in optically pumped methyl fluoride, methyl alcohol, and vinyl chloride gases," *Appl. Phys. Lett.*, vol. 17, pp. 249–251, 1970.

[2] H. R. Fetterman, H. R. Schlossberg, and J. Waldman, "Submillimeter lasers optically pumped off resonance," *Opt. Commun.*, vol. 6, pp. 156–159, 1972.

[3] R. J. Wagner, A. J. Zelano, and L. H. Ngai, "New submillimeter laser lines in optically pumped gas molecules," *Opt. Commun.*, vol. 8, pp. 46–47, 1973.

[4] D. T. Hodges, R. D. Reel, and D. H. Barker, "Low-threshold CW submillimeter- and millimeter-wave laser action in CO_2-laser-pumped $C_2H_4F_2$, $C_2H_2F_2$, and CH_3OH," *IEEE J. Quantum Electron.* (Notes and Lines), vol. QE-9, pp. 1159–1160, Dec. 1973.

[5] A. Tanaka, A. Tanimoto, N. Murata, M. Yamanaka, and H. Yoshinaga, "Optically pumped far-infrared and millimeter wave waveguide lasers," *Japan. J. Appl. Phys.*, vol. 13, pp. 1491–1492, 1974.

[6] S. Kon, E. Hagiwara, T. Yano, and H. Hirose, "Far-infrared laser action in optically pumped CD_3OD," *Japan. J. Appl. Phys.*, vol. 14, pp. 731–732, 1975.

[7] H. E. Radford, "New CW lines from a submillimeter waveguide laser," *IEEE J. Quantum Electron.*, vol. QE-11, pp. 213–214, May 1975.

[8] D. T. Hodges and T. S. Hartwick, "CO_2 laser-pumped far infrared (FIR) waveguide laser," *Appl. Phys. Lett.*, vol. 23, pp. 252–253, 1973.

[9] A. Tanaka, Ph.D. dissertation, Osaka Univ., Osaka, Japan, Mar. 1975.

[10] K. Sakai, T. Fukui, Y. Tsunawaki, and H. Yoshinaga, "Metallic mesh bandpass filters and Fabry-Perot interferometer for the far-infrared," *Japan. J. Appl. Phys.*, vol. 8, pp. 1046–1055, 1969.

Contributors

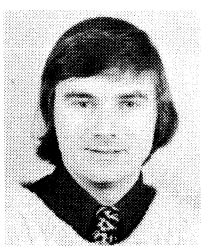

Christopher C. Davis was born in Manchester, England, on July 7, 1944. He received the B.A. and M.A. degrees from Trinity College, Cambridge, England, in 1965 and 1970, respectively, and the Ph.D. degree in physics from the University of Manchester, Manchester, in 1970. His doctoral research involved studies of excitation and relaxation processes in noble-gas lasers.

From 1969 to 1973 he was a Research Associate in the Department of Physics at the University of Manchester, where he carried out research on atomic-iodine gas-discharge lasers, electronegative plasmas, and atomic-iodine photodissociation lasers. Since 1973 he has been at Cornell University, Ithaca, N.Y., where he is currently a Research Associate in the Materials Science Center. His current research interests include photodissociation and chemical lasers, photochemical kinetics, and molecular-energy transfer.

Dr. Davis is a member of the Institute of Physics (London).

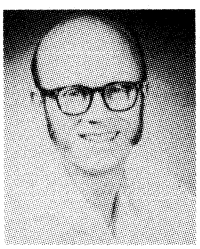

Kenneth M. Evenson was born in Wisconsin. He received the B.S. degree from Montana State University, Bozeman, and the M.S. and Ph.D. degrees from Oregon State University, Corvallis, in 1955 and 1963, respectively.

He was a Fulbright Scholar at Tübingen University, from 1955 to 1956. Since 1963 he has been with the National Bureau of Standards, Boulder, Colo.

Dr. Evenson is a member of the American Physical Society. He has received the Department of Commerce Silver Medal and the National Bureau of Standards Stratton Award.

*

Kenya Goto was born in Fukushima, Japan, on November 3, 1938. He received the B.E. degree in electronics engineering from Tohoku University, Sendai, Japan, in March 1963.

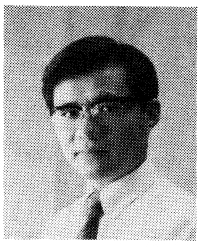

Since April 1963 he has been a member of the Research Staff in the Laser Group at Toshiba Research & Development Center, Tokyo Shibaura Electric Company Ltd., Kawasaki, Japan, where he developed high repetition rate giant pulse Nd:YAG lasers and laser radars for air pollution monitoring. From 1973 to 1975 he was a Guest Worker at the Quantum Electronics Division of the National Bureau of Standards, Boulder, Colo., and a Research Associate at the Department of Physics and Astrophysics, University of Colorado, Boulder. His primary concerns in research at Toshiba are in laser spectroscopy and its application to isotope separation.

Mr. Goto is a member of the Optical Society of America.

*

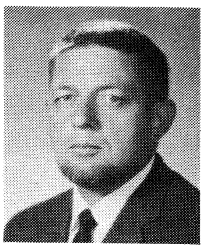

Donald A. Jennings was born in Stanton, Mich., on October 30, 1930. He received the B.S. degree from Central Michigan College of Education, Mount Pleasant, in 1954, the M.S. degree from Michigan State University, East Lansing, in 1958, and the Ph.D. degree in physics from the University of Colorado, Boulder, in 1962.

He began work at the Boulder Laboratories, National Bureau of Standards, Boulder, Colo., in 1961 as a Physicist, and has worked in the fields of gamma-ray spectroscopy, laser spectroscopy, nonlinear optics, Raman and Brillouin scattering, dye-laser technology (both pulsed and CW), and laser frequency area. The work in calorimetric laser measurements has led to the development of probably the most precise method available for determining the energy of a laser pulse.

Dr. Jennings is a member of the American Physical Society. He received a Department of Commerce Gold Medal Award in 1970 for his work in calorimetric laser measurements.

*

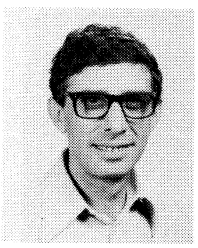

Juan J. Jiménez was born in Madrid, Spain, on April 17, 1935. He received a degree in telecommunication engineering from the Escuela Tecnica Superior de Ingenieros de Telecomunicacion (ETSIT), Madrid, the equivalent of the M.S. degree in physics from the University of Toulouse, Toulouse, France, and the equivalent of the Ph.D. degree from the University of Paris Sud, Orsay, France, in 1964, 1967, and 1974, respectively.

From 1966 to 1968 he was a Visiting Engineer at Centre National d'Etudes des Télécommunications (CNET), Issy-les-Moulineaux, France, where he worked on the tunnel diode microwave equivalent circuit and noise in frequency multipliers. In 1968 he joined the Institut d'Electronique Fondamentale, Orsay University, where he worked on superconducting cavities and developed a new microwave frequency standard: The superconducting cavity stabilized oscillator (SCSO). He has contributed to the research of low-noise microwave mixers and amplifiers, Schottky diodes, and MESFET, by cooling. His research areas also include the study of noise in oscillators and the related instrumentation. Currently, he is Associate Director of the Laboratoire Primaire de Métrologie des Fréquences (LPMF) which is part of the Bureau National de Métrologie (BNM), Paris, France, where he is engaged in basic research and development of stabilized lasers and infrared detectors. He is also Chargé de Recherche au Centre National de la Recherche Scientifique (CNRS), Paris. During 1975 he is a Visiting Scientific Guest with the Precision Laser Metrology Section, National Bureau of Standards (NBS), Boulder, Colo.

Dr. Jiménez is a member of the French Physical Society and the French "Société des Electriciens, des Electroniciens et des Radioélectriciens" (SEE), Paris.



Fritz Kneubühl was born in Zurich, Switzerland, on March 7, 1931. He received the Diploma and the Ph.D. (physics) degrees, both from the Swiss Federal Institute of Technology (ETH), Zurich, in 1955 and 1959, respectively. In 1959 he spent the summer as a Ramsay Memorial Fellow at University College, London, England. The following year he spent as Graeflin Fellow in the Chemistry Department at The Johns Hopkins University, Baltimore, Md.

At the end of 1960 he entered the Solid State Physics Laboratory at the ETH, Zurich, where he was appointed Privatdozent in 1963, Assistant Professor in 1967, Associate Professor in 1970, and Full Professor of Physics in 1972. Before 1963 he was engaged in gaseous microwave spectroscopy and in paramagnetic resonance. From 1964 to the present he has been engaged in submillimeter-wave and infrared physics: i.e., spectroscopy of solids and liquids, longitudinally and transversely excited HCN, ICN, and CO_2 lasers, laser interaction with solids, spectral thermal emission and blackbody radiation, thermal imaging, and balloon-borne solar spectroscopy.

Dr. Kneubühl is a member of the Swiss and the European Physical Society. From 1967 to 1971 he acted as the Secretary of the Swiss Physical Society.

*

I. N. Knyazev, photograph and biography not available at the time of publication.

*

V. S. Letokhov, photograph and biography not available at the time of publication.

*

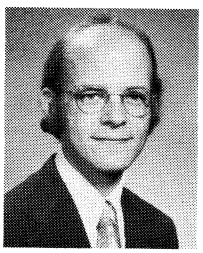

John B. Marling (M'72) was born in Cumberland, Md., on September 19, 1946. He received the B.S. degree in physics from the Georgia Institute of Technology, Atlanta, in 1967, and the M.S. and Ph.D. degrees, both in applied science, from the University of California at Davis/Livermore, in 1968 and 1971, respectively. He was a Hertz Fellow from 1967 to 1971.

In 1971 he joined the professional staff at the AVCO Everett Research Laboratory, Everett, Mass., and worked on high-power tunable dye-laser development as part of the program for laser isotope separation of uranium. During 1973 he joined the staff at Stanford Research Institute, Menlo Park, Calif., to help develop high-power dye lasers for atmospheric probing. Later in 1973 he joined the Physics Department staff at the Lawrence Livermore Laboratory, Livermore, Calif., where he has been responsible for the research and development of laser methods leading to improved isotope separation of deuterium and other light atoms. Photopredissociation of formaldehyde is being currently investigated, and highly selective laser separation of deuterium from natural abundance HDCO is described in a recent article. Short wavelength pulsed and CW ion-laser development was a by-product of the need for wavelength-stable ultraviolet laser sources for photochemistry and isotope separation.

*

Ross A. McFarlane (S'52-M'71) was born in Toronto, Ont., Canada, on June 10, 1931. He received the B.Sc. degree in physics from McMaster University, Hamilton, Ont., Canada, in 1953, and the M.S.

and Ph.D. degrees in physics from McGill University, Montreal, P. Q., Canada, in 1955 and 1959, respectively.

From 1959 to 1961 he was a member of the Division of Space and Research, Research Laboratory of Electronics at the Massachusetts Institute of Technology, engaged in research on broad-band microwave masers. In 1961 he joined the Bell Laboratories in Murray Hill, N.J., where he worked on atomic and molecular-gas lasers and precision spectroscopy. He joined the Faculty of Cornell University, Ithaca, N.Y., in 1969, and is currently Professor of Electrical Engineering. His current research interests include molecular-energy transfer, chemical lasers, and photochemical kinetics.

*

V. G. Movshev, photograph and biography not available at the time of publication.

*

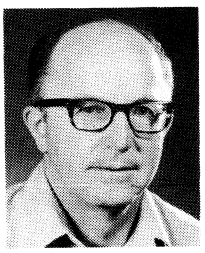

F. Russell Petersen was born in DeSmet, S. Dak., on August 21, 1930. He received the B.S. degree from the South Dakota School of Mines and Technology, Rapid City, and the Ph.D. degree from the University of California, Berkeley, both in physics, in 1952 and 1961, respectively.

In 1961 he joined the National Bureau of Standards, Boulder, Colo., where he initially conducted molecular beam research. For the last five years he has been engaged in various CO_2 laser stabilization and IR frequency synthesis programs.

Dr. Petersen is a member of the American Physical Society.

*

Robert J. Pirkle received the B.S. and M.S. degrees in chemistry from Auburn University, Auburn, Ala., in 1963 and 1965, respectively, and the Ph.D. degree in physical chemistry, from the University of Western Ontario, London, Ont., Canada, in 1972. He studied the visible electronic spectrum of NO_2 while at this last university.

From 1965 to 1969 he worked in the Molecular Spectroscopy Branch of the Physical Sciences Laboratory DR&D at the U.S. Army Missile Command, Redstone Arsenal, Ala. From 1972 through 1974 he worked as a Postdoctoral Associate in the Laboratory for Plasma Studies at Cornell University, Ithaca, N.Y., where he studied several chemical-laser systems and also the photodissociation iodine laser. He is currently studying the kinetics of electronically excited atomic species in the Department of Chemistry at Cornell University.

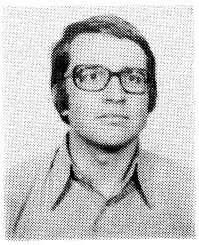

Hans J. Schötzau was born in Augst, Switzerland, on January 21, 1944. He received the Diploma in physics and the Ph.D. degree, both from the Swiss Federal Institute of Technology (ETH), Zurich, Switzerland, in 1968 and 1973, respectively.

From 1968 to 1975 he was with the Solid State Physics Laboratory of the ETH, where he was engaged in the study of infrared lasers. He is currently an ESRO-Postdoctoral Fellow at the European Space Research and Technology Centre (ESTEC), Noordwijk, The Netherlands, where he is working on submillimeter heterodyne receivers.

*

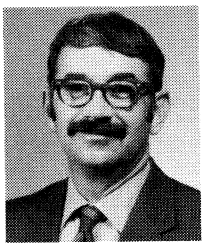

Joseph S. Wells was born in Meade, Kans., on March 19, 1930. He received the B.S. and M.S. degrees from the Kansas State University of Agriculture and Applied Science, Manhattan, in 1956 and 1958, respectively, and the Ph.D. degree in physics from the University of Colorado, Boulder, in 1964.

He joined the staff of the Boulder Laboratories, National Bureau of Standards, Boulder, Colo., in 1958, where he is now employed in the Time and Frequency Division and is concurrently a Professor Adjoint in the Department of Physics at the University of Colorado.

Dr. Wells is a member of the American Physical Society and Sigma Xi.

*

J. R. Wiesenfeld, photograph and biography not available at the time of publication.

*

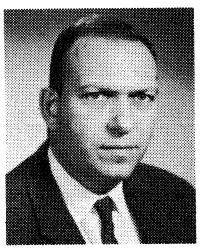

George J. Wolga (M'71) received the B. Eng. Phys. degree from Cornell University, Ithaca, N.Y., in 1953, and the Ph.D. degree in physics from the Massachusetts Institute of Technology, Cambridge, in 1957.

He was an Instructor and Assistant Professor of Physics at the Massachusetts Institute of Technology through 1961 when he returned to Cornell University where he is now Professor of Electrical Engineering and Applied Physics. He spent 1968–1969 at the Naval Research Laboratory, where he was Branch Head of the Laser Physics Branch. His current research interests are tunable infrared lasers, molecular-energy transfer and relaxation as studied with lasers, laser-induced chemistry, and the development and study of new laser systems.

Frequency-Domain Analysis of the Mode-Locked and Frequency-Doubled Homogeneous Laser

C. J. KENNEDY

Abstract—A frequency-domain analysis of the mode-locked intracavity frequency-doubled laser is pursued. An expression for pulsewidth is derived based upon basic laser parameters and the nonlinear coupling of the frequency doubler. It is found that mode locking induces an additional loss to the cavity even in the ideal case, so that the frequency-doubled output power at optimum coupling is less than an optimally coupled fundamental frequency laser with identical losses.

Introduction

MODE-LOCKED visible lasers have considerable potential as ultrahigh data rate communication lasers. One such device is the intracavity frequency-doubled and mode-locked Nd:YAG laser. Communication efficiency with such a laser-based system depends greatly on obtaining the greatest average power at 0.53 μm while at the same time maintaining short pulsewidth. Experience has shown, however, that high power and short pulses are antithetical; that is, an effort to produce higher power also leads to longer pulses. In an effort to enhance our predictive capability for these lasers, the author has embarked on an attempt to treat the laser system theoretically.

In this attempt, we are encouraged by the previously successful analyses of mode-locked lasers by Kuizenga and Siegman [1a)], McDuff and Harris [1b)], Haken and Pauthier [1c)], and Nelson [1d)]. The analyses of Nelson and Kuizenga represent two different approaches to the mode-locking problem. Nelson describes the field in terms of discrete mode amplitudes and phases, while Kuizenga considers the propagation of a quasi-general pulse through a complete round trip through the laser. The pulse is assumed to be Gaussian, a fact which was demonstrated by Nelson to be the lowest order solution to the mode-locking equations. The introduction of intracavity second-harmonic generation (SHG) was treated in a somewhat qualitative way by Hitz and Osterink [2], but their reasoning is essential to a physical understanding of the interaction between the mode locker and frequency doubler.

Fundamentals of the Analysis

McDuff and Harris have arrived at a self-consistency equation for mode locking using the original laser theory of Lamb [3]. We will take the liberty of adding a term which represents the loss and phase shift involved in SHG, or using their notation,

$$\alpha_c(E_{n+1} + E_{n-1}) + E_n(G_n - \alpha - \alpha_a - \alpha_n^{(2)} - i\dot{\phi}\tau + in\Delta\nu\tau - i\psi_n) = 0 \tag{1}$$

where E_n is the complex electric field of the nth mode, α_c is the intermode coupling coefficient due to loss modulation, G_n is the saturated round-trip amplitude gain, α is the double-pass field amplitude loss, α_a is the continuous mode-locker loss, $\dot{\phi}$ is an overall constant rate phase shift, $\Delta\nu$ is the detuning of the laser cavity from the mode-locker frequency, τ is the cavity round-trip time, ψ_n is the round-trip residual phase shift for the nth mode, and $\alpha_n^{(2)}$ is the (complex) term describing the fraction of amplitude loss (phase shift) encountered by the nth mode on a round trip. Since SHG is a nonlinear process, $\alpha_n^{(2)}$ is dependent on all other mode amplitudes in a complicated fashion, hence the coupling of the N different mode equations is hopelessly elaborate. To this dilemma we propose the following solution. Let

$$E_n = E \exp\left[-(\delta + i\xi)n^2\right] \tag{2}$$

where δ and ξ are parameters which describe the width and frequency chirp of the mode-locked spectrum, be an adequate trial solution for the coupled-mode equations. A Gaussian distribution of the mode amplitude and phases allows for the possible presence of pulse chirping, and represents a close approximation of actual distributions in experimental mode-locked frequency-doubled lasers [4]. The Fourier transform of (2) represents the time-domain pulses, or

$$E(t) = E\sqrt{\frac{\pi}{\delta + i\xi}} \exp\left[-\frac{\Omega^2 t^2}{4(\delta + i\xi)}\right]. \tag{3}$$

We define the pulsewidth $\hat{t}$ to be the full $1/e^2$ width, or

$$\hat{t} = \frac{4}{\Omega}\sqrt{\frac{(\delta^2 + \xi^2)}{\delta}} \tag{4}$$

where $\Omega = 2\pi C/2L$. Also the time-averaged circulating intensity of the laser is the sum over the time-averaged intensity of each mode (the cross terms of $\langle(\Sigma_n E_n(t))^2\rangle$ vanish)

$$I = \frac{1}{2}\sqrt{\frac{\epsilon}{\mu_0}}\sum_n |E_n|^2 = \frac{1}{2}|E|^2\sqrt{\frac{\pi\epsilon}{2\delta\mu_0}}. \tag{5}$$

Equation (2) may then be substituted into (1) once the form of $\alpha_n^{(2)}$ has been determined, the equation expanded in powers of n, and coefficients of like powers of n equated. Expansion to second order in n gives us three complex equations in three unknowns. Taken together with the assumption of ideal mode locking, this is sufficient to produce a solution for E, δ, and ξ as a function of basic laser parameters, which completely specifies the spectrum and chirping of a steady-state mode-locked pulse in this laser.

Manuscript received July 29, 1974; revised July 15, 1975.

The author was with the Air Force Avionics Laboratory, Wright Patterson Air Force Base, Ohio 45433. He is now with SAMSO/DY (Program 405B), Los Angeles Air Force Station, El Segundo, Calif. 90009.

Second-Harmonic Term

The SHG loss may be derived in the time domain from the double-pass expression for fundamental (1.06 μm) loss (see Appendix B for the relation between κ and fundamental properties of the doubling medium),

$$\Delta E(t) = -\kappa E(t)\,|E(t)|^2 \tag{6}$$

or, using (3),

$$\Delta E(t) = \frac{-\kappa E\,|E|^2\,\pi^{3/2}}{[(\delta^2+\xi^2)(\delta+i\xi)]^{1/2}} \exp\left[-\Omega^2 t^2 \frac{(3\delta - i\xi)}{4(\delta^2+\xi^2)}\right]. \tag{7}$$

Transforming to the mode domain,

$$\Delta E_n = \frac{-\kappa E\,|E|^2\,\pi}{[(\delta+i\xi)(3\delta - i\xi)]} \exp\left[-\frac{\delta^2+\xi^2}{3\delta - i\xi} n^2\right]. \tag{8}$$

Since the field loss per round trip is defined by

$$\alpha_n^{(2)} = -\frac{\Delta E_n}{E_n} \tag{9}$$

we have, after choosing the phase of E to make the coefficient of the exponential real,

$$\alpha_n^{(2)} = \frac{\pi\kappa\,|E|^2}{[(9\delta^2+\xi^2)(\delta^2+\xi^2)]^{1/4}} \cdot \exp\left[\frac{2\delta(3\delta^2 - \xi^2 + 4i\delta\xi)}{9\delta^2+\xi^2} n^2\right]. \tag{10}$$

We note the positive (for $\xi = 0$) real coefficient of n^2, which causes the loss for outlying modes to be greater than for the central modes. This must ultimately result in a narrower spectrum and broader pulses, depending on the nonlinear coupling coefficient κ.

The second-harmonic laser output (bidirectional) is

$$\begin{aligned} I_{sh} &= \sum_n 2\alpha_n^{(2)} I_n \\ &= \frac{\pi\kappa\sqrt{\epsilon/\mu_0}\,|E|^4}{[(9\delta^2+\xi^2)(\delta^2+\xi^2)]^{1/4}} \cdot \sum_n \exp\left[-\frac{4\delta(3\delta^2+\xi^2 - 2i\delta\xi)}{9\delta^2+\xi^2} n^2\right] \\ &= \frac{\pi^{3/2}\,\kappa\sqrt{\epsilon/\mu_0}\,|E|^4}{[(9\delta^2+\xi^2)(\delta^2+\xi^2)]^{1/4}} \left[\frac{9\delta^2+\xi^2}{4\delta(3\delta^2+\xi^2)}\right]^{1/2} \end{aligned} \tag{11}$$

for small ξ.

Finally, we note that since $\alpha_n^{(2)}$ is dependent on $|E|^2$ and the latter quantity has a Gaussian (TEM_{00}) spatial dependence, the average loss over the Gaussian mode, rather than the peak loss at mode center, should be included in the coupled-mode equations. The average differs from the peak loss by a factor of $\frac{1}{2}$; therefore this factor is included in subsequent expressions for $\alpha_n^{(2)}$.

Gain and Saturation

The present paper is concerned with the class of homogeneously broadened lasers which are not subject to spatial hole burning [5], or those in which the effects of spatial hole burning are negligible. Consequently, the expression for saturated gain in our laser is

$$G_n = g_0[1 - n^2(\Omega/\gamma)^2]/(1 + I/I_s) \tag{12}$$

where I_s is the saturation intensity, g_0 the unsaturated gain, and γ is the half-gain angular frequency halfwidth of the homogeneously broadened (Lorentzian) line. In this case,

$$\psi_n = gn\frac{\Omega}{\gamma} \tag{13}$$

where g is the saturated gain at line center. The necessary elements for a prediction of laser performance are now present. Implicit in the analysis is the assumption of ideal mode locking, which is to say, the pulse arrives at the modulator precisely at peak transmission and the mode spectrum is concentric with the gain spectrum. Otherwise more variables would be needed to specify the intracavity field.

Solution to the Equations

Upon substitution of E_n, G_n, and ψ_n and $\alpha_n^{(2)}$, the self-consistency equation becomes

$$\begin{aligned} 2\alpha_c e^{-(\delta+i\xi)} \cosh[2(\delta+i\xi)n] &= -g + \alpha + \alpha_a + i\dot{\phi}\tau - in\Delta\nu\tau + gn^2\left(\frac{\Omega}{\gamma}\right)^2 - ign\frac{\Omega}{\gamma} \\ &\quad + \frac{\pi}{2}\frac{\kappa\,|E|^2 \exp\left[\frac{2\delta(3\delta^2 - \xi^2 + 4i\delta\xi)\,n^2}{9\delta^2+\xi^2}\right]}{[(9\delta^2+\xi^2)(\delta^2+\xi^2)]^{1/4}}. \end{aligned} \tag{14}$$

Expanding the functions to second order in n, equating like orders, and using (5) to obtain $|E|^2$ in terms of I results in the following three equations:

$$2\alpha_c e^{-(\delta+i\xi)} = -g + \alpha + \alpha_a + i\dot{\phi}\tau + \sqrt{\frac{2\pi\mu_0\delta}{\epsilon}}\frac{\kappa I}{[(9\delta^2+\xi^2)(\delta^2+\xi^2)]^{1/4}} \tag{15a}$$

$$-\Delta\nu\tau = g\left(\frac{\Omega}{\gamma}\right) \tag{15b}$$

$$4\alpha_c e^{-(\delta+i\xi)}(\delta+i\xi)^2 = g\left(\frac{\Omega}{\gamma}\right)^2 + \sqrt{\frac{2\pi\mu_0\delta}{\epsilon}} \cdot \frac{\kappa I}{[(9\delta^2+\xi^2)(\delta^2+\xi^2)^{1/4}} \cdot \frac{2\delta(3\delta^2 - \xi^2 + 4i\delta\xi)}{9\delta^2+\xi^2}. \tag{15c}$$

Physically, the significance of these three equations is that of conservation equations. Equation (15a) (real) represents the conservation of mode amplitude through a round trip; (15b) represents the conservation of pulse position with respect to the modulator phase; (15c) (real) represents the conservation of spectral width; and (15c) (imaginary) conserves pulse chirp.

The imaginary part of (15c) is

$$4\alpha_c e^{-\delta}\left[2\delta\xi\cos\xi-(\delta^2-\xi^2)\sin\xi\right]$$
$$=\sqrt{\frac{2\pi\mu_0\delta}{\epsilon}}\,\frac{\kappa I}{[(9\delta^2+\xi^2)(\delta^2+\xi^2)]^{1/4}}\cdot\frac{8\delta^2\xi}{9\delta^2+\xi^2} \quad (16)$$

which has the solution $\xi = 0$. Other solutions are possible, however, and one must consider the physical significance of this equation. A term is notably absent, which takes the chirping which results from pulse propagation through a dispersive medium into account. This omission results from the approximations made in the derivation of the self-consistency equation (i.e., the second-time derivative of the polarization is neglected). The existence of physical solutions with $\xi \neq 0$ may be possible due to the small progressive chirp induced by the passive (and active) medium. This is an interesting line of investigation which we will not pursue further in this paper.

Proceeding with the $\xi = 0$ case, we see that (15) becomes, for small δ (many modes oscillating)

$$2\alpha_c(1-\delta)-\alpha_a-\alpha=-g+\sqrt{\frac{2\pi\mu_0}{3\epsilon\delta}}\,\kappa I \quad (17a)$$

$$4\alpha_c\delta^2=g(\Omega/\gamma)^2+\frac{2}{3}\sqrt{\frac{2\pi\mu_0}{3\epsilon\delta}}\,\kappa I\delta. \quad (17b)$$

Ideally, $2\alpha_c = \alpha_a$; thus

$$g=\alpha+\sqrt{\frac{2\pi\mu_0}{3\epsilon\delta}}\,\kappa I+2\alpha_c\delta. \quad (18)$$

We may pause here to check the form of our equations by reducing the problem to the nonfrequency doubled case. The pulsewidth should then reduce to a form which is equivalent to those of other authors.

If we let $\kappa = 0$ in (17b) and (18), we have

$$\delta=\frac{\Omega}{\gamma}\cdot\left(\frac{g}{4\alpha_c}\right)^{1/2} \quad (19)$$

or

$$\hat{t}=\frac{4}{\Omega}\left(\frac{\Omega}{\gamma}\right)^{1/2}\left(\frac{g}{4\alpha_c}\right)^{1/4} \quad (20)$$

which is equivalent to the expression derived by Kuizenga and Siegman.

When the SHG loss is the dominant spectrum-narrowing mechanism and (Ω/γ) is negligible, (17b) yields the expression

$$\hat{t}=\frac{4}{\Omega}\left(\sqrt{\frac{2\pi\mu_0}{3\epsilon}}\,\frac{\kappa I}{6\alpha_c}\right)^{1/3}. \quad (21)$$

Proceeding to solve for E, or equivalently I, we multiply (18) by $2\delta/3$ and subtract from (17b), obtaining

$$4\alpha_c\delta^2=g\left(\frac{\Omega}{\gamma}\right)^2+(g-\alpha-2\alpha_c\delta)\frac{2\delta}{3}. \quad (22)$$

Since $(\Omega/\gamma)^2$ is small in Nd:YAG, the foregoing equation reduces to

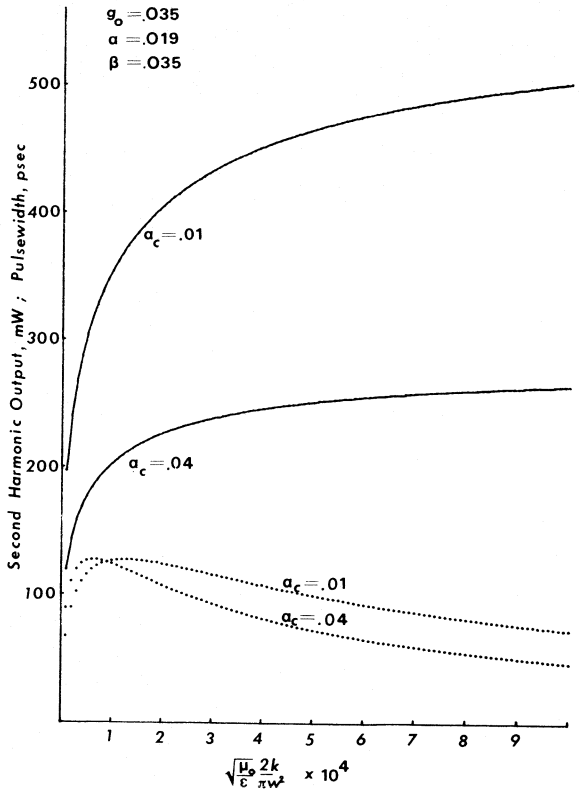

Fig. 1. 1.06-μm pulsewidth (solid) and output power (dotted) versus nonlinear coupling for two values of mode-locker coupling, plotted for the case where gain bandwidth broadening is negligible.

$$g=\alpha+8\alpha_c\delta \quad (23)$$

or, using the gain saturation relation for homogeneous lasers

$$I=I_s\left[\frac{g_0}{8\alpha_c\delta+\alpha}-1\right] \quad (24)$$

which may be substituted into (21) and the result solved for $\hat{t}$ or δ. Such a solution is illustrated in Fig. 1, which displays 0.53-μm power and 1.06-μm pulsewidth versus κ for several values of α_c.

Optimum Coupling

Equation (21) may be manipulated to show that

$$3\sqrt{6}\,\alpha_c\delta=\alpha_{SHG}$$

where α_{SHG} is the single-pass power fraction converted to the second harmonic defined (see Appendix B) by

$$P_{SH}=2\alpha_{SHG}P$$

and P_{SH} and P are the total second-harmonic power and circulating fundamental power, respectively. Equation (24) indicates that some constant factor ($q = 8/3\sqrt{6}$) which is greater than unity enters the gain saturation equation such that

$$P=\frac{1}{\beta}\left[\frac{g_0}{\alpha+q\alpha_{SHG}}-1\right] \quad (25)$$

where β is the power saturation parameter.

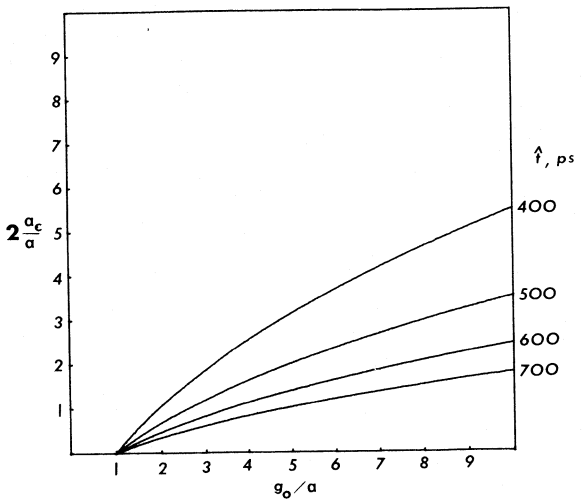

Fig. 2. Curves of modulation strength versus pumping ratio for constant pulsewidth. Optimum second-harmonic coupling is assumed.

It may be shown by differentiating P_{SH} with respect to α_{SHG} that optimum α_{SHG} is (the asterisk denotes an optimized value)

$$\alpha^*_{SHG} = \frac{1}{q}\left[\sqrt{g_0\alpha} - \alpha\right]. \tag{26}$$

This is the familiar expression for output coupling except for the $1/q$. Furthermore, it may be shown that the optimum second-harmonic power is

$$P^*_{SH} = \frac{1}{q\beta}\left[\sqrt{g_0} - \sqrt{\alpha}\right]^2. \tag{27}$$

The conclusion is that mode-locked second-harmonic operation is never as efficient as mode-locked fundamental operation, even for an ideal lossless SHG crystal. Only $1/q$, or 91 percent of the fundamental, can be converted. Physically, this is due to the extra pulse broadening induced by the frequency doubler which causes greater losses to the loss modulator. These extra losses reduce the efficiency of the laser.

The optimum nonlinear coupling is obtained by using the fact, disclosed in Appendix B, that

$$\alpha_{SHG} = \frac{2\kappa P}{\pi w^2}\sqrt{\frac{\mu_0}{\epsilon}}\frac{2\tau}{\sqrt{\pi}\,\hat{t}}. \tag{28}$$

Substituting the optimal values of α_{SHG} and P into the above relation, we obtain

$$\left[\frac{2\kappa}{\pi w^2}\sqrt{\frac{\mu_0}{\epsilon}}\right]^* \frac{2\tau}{\sqrt{\pi}\,\hat{t}} = \frac{\alpha\beta}{q} \tag{29}$$

where once again we denote the optimized quantity (in brackets) by an asterisk. This relationship is amply demonstrated in Fig. 1 where the peak second-harmonic power occurs at a coupling of $\alpha\beta/q$ divided by the mode-locking enhancement factor $2\tau/\sqrt{\pi}\,\hat{t}$.

Pulsewidth at Optimum Coupling

Having derived the optimum value for α_{SHG}, we may proceed to find the pulsewidth for an optimally coupled laser. From (26) and (28) we deduce the optimum value of

$$\kappa I\sqrt{\frac{\mu_0}{\epsilon}} = \frac{\sqrt{\pi}\,\hat{t}}{2\tau}\frac{3\sqrt{6}}{8}\left[\sqrt{g_0\alpha} - \alpha\right]. \tag{30}$$

Inserting this relation in (21) produces the result

$$\hat{t} = \frac{4}{\Omega}\left[\frac{\alpha}{8\alpha_c}\left(\sqrt{\frac{g_0}{\alpha}} - 1\right)\right]^{1/2}. \tag{31}$$

We may invert this expression to yield the depth of modulation necessary to produce a given pulsewidth, or

$$\frac{\alpha_c}{\alpha} = \frac{2}{\Omega^2\hat{t}^2}\left(\sqrt{\frac{g_0}{\alpha}} - 1\right). \tag{32}$$

This relation is plotted in Fig. 2 for various pulsewidths in a laser where $\Omega = 2\pi \cdot 5 \times 10^8\ s^{-1}$.

Fig. 2 is most essential in engineering a given laser system for communications use. Modulation requirements usually set an upper limit on pulsewidth. For instance, pulse gated binary modulation at 5×10^8 bit/s using a modulator of 1.5-ns rise time leaves room for a 0.53-μm pulsewidth of only 500 ps (or 700 ps at 1.06 μm). If the gain-to-loss ratio is 5 (achievable in a sun-pumped laser), then a modulation depth of 1 percent at a loss of 1 percent is necessary to obtain this pulsewidth. This is well within the performance range of acoustooptic devices. But if a pulsewidth of 300 ps is necessary to accommodate a slower modulator (or in higher m-ary formats), then at least 3-percent depth of modulation ($= 2\alpha_c$) becomes necessary. This modulation depth may not be practical due to acoustic heating effects in the loss modulator.

The problem of achieving optimum coupling consists of obtaining the proper value of $(\sqrt{\mu_0/\epsilon})\,2\kappa/\pi w^2$. Since κ depends only on physical parameters, only the phase-matching length is variable to a degree. Thus the beam waist is our only adjustable parameter to obtain proper coupling. Typically, it is necessary to provide a laser resonator with an intracavity lens in order to accommodate small beams in the doubling crystal to large beam diameters in the gain medium. Movement of this lens can provide some adjustability of the parameter over a small range, but usually many resonator configurations must be tried before one is assured of optimum coupling. Equation

(29) emphasizes the necessity of measuring α and β accurately to ascertain the optimum value of nonlinear coupling. The actual value of nonlinear coupling in any given configuration may then be measured either by measuring output power and pulsewidth and using formula (B2) in Appendix B or by measuring the relaxation time of the perturbed laser after the analysis of [7]. Optimum w may then be predicted and an optimal design generated to achieve this using resonator theory.

Comparison with Time-Domain Theories

Falk [8] and Kennedy [9] have devised theories which approach this laser system from the time domain. The results of these analyses are pulsewidth formulas similar to (21) which differ only in the coefficient of $(\kappa I/\alpha_c)^{1/3}$. The pulsewidth may also be expressed in terms of α_{SHG} as

$$\hat{t} = \frac{4}{\Omega}\left(\frac{1}{3}\sqrt{\frac{2}{3}}\right)^{1/2}\left(\frac{\alpha_{SHG}}{\delta_l}\right)^{1/2} \quad \text{[frequency domain]}$$

$$\hat{t} = \frac{4}{\Omega}2^{1/4}\left(\frac{\alpha_{SHG}}{\delta_l}\right)^{1/2} \quad \text{[time domain of Falk]}$$

$$\hat{t} = \frac{4}{\Omega}\left(\frac{\sqrt{2}}{3}\right)^{1/2}\left(\frac{\alpha_{SHG}}{\delta_l}\right)^{1/2} \quad \text{[time domain of Kennedy]}$$

where $\delta_l = 2\alpha_c$ is the depth of modulation of the loss modulator. The numerical results of the three theories are thus quite different, and this difference becomes important in determining maximum theoretical efficiency of mode locking and frequency doubling. In Falk's theory the factor q turns out to be $\sqrt{2}$, limiting the conversion efficiency to 0.7. This is understandable because, all other things being equal, this time-domain theory predicts much broader pulses which have a higher loss on transmission through the mode locker. The higher losses are reflected in a lowered efficiency. The second time-domain theory predicts a pulse which is shorter than Falk's theory but longer than the frequency-domain theory. One would expect that its conversion limit would lie between 0.7 and 0.9.

Physically, q is the ratio of the peak second-harmonic loss to the average, and in the real world depends on the actual pulse shape which is non-Gaussian. Bernecker's theory [10] predicts a sine^2 dependence when broadening due to gain bandwidth and etalon effects is absent. However, real lasers frequently contain these effects in significant amounts and the factor q is altered. This value may be measured experimentally, provided very fast photodiodes are available at both the fundamental and second harmonic by comparison of the pulse shapes at these frequencies.

Conclusions

The theoretical model we have chosen for the mode-locked frequency-doubled laser predicts some rather basic behavioral patterns. First, the pulsewidth becomes significantly broader as one approaches the optimum second-harmonic output, which leads to increased mode-locker losses. It is these additional losses which cause the optimum power of these lasers to be less than their nonmode-locked counterparts. Secondly, any alteration of laser parameters which increases output power also broadens the pulses if α_c is kept constant. Increasing α_c always decreases pulsewidth, but slowly compared to decreasing cavity length.

Experimental verification of this theory is possible using a technique which measures the relaxation oscillations associated with a nonlinear loss [7]. This technique offers the possibility of measuring g_0, α, β, and κ in a pair of measurements of relaxation phenomena. The author will soon publish the results of these experiments on a frequency-doubled mode-locked Nd:YAG laser.

Appendix A
Transformed Modes

The time-domain representation of the mode distribution

$$E_n = Ee^{-(\delta + i\xi)n^2}$$

must have the following properties.

1) The peak field in the time domain must equal the sum of the complex mode amplitudes.

2) The time-integrated average intensity in the time domain must equal the sum of the average intensities of the individual modes.

3) The mode-locking enhancement to SHG must be $2\tau/\sqrt{\pi}\,\hat{t}$. Since

$$\sum_n E_n = \sum_n Ee^{-(\delta + i\xi)n^2} \simeq E\sqrt{\frac{\pi}{\delta + i\xi}}$$

then from property 1 we observe

$$E(t) = E\sqrt{\frac{\pi}{\delta + i\xi}}\exp\left[-\frac{\Omega^2 t^2}{4\delta}\right]. \tag{A1}$$

The second property demands that energy be conserved under transformation. The total time-averaged intensity of all modes is

$$\sum_n |E_n|^2 = |E|^2\sqrt{\frac{\pi}{2\delta}}$$

which must equal

$$\frac{1}{\tau}\int_{-\infty}^{\infty} dt\,|E(t)|^2 = |E|^2\,\frac{2\pi}{\tau\Omega}\sqrt{\frac{\pi}{2\delta}}.$$

And the condition is satisfied by the form chosen for $E(t)$.

The final condition is a check on the validity of the method of obtaining the mode-dependent SHG loss $\alpha_n^{(2)}$. It is easily demonstrated that the SHG power converted from a Gaussian pulse of width $\hat{t}$ is $2\tau/\sqrt{\pi}\,\hat{t}$ times the SHG power converted from a square pulse of width τ and the same total energy.

Appendix B
Second-Harmonic Output Power

Assuming perfect phase matching, the equations describing SHG for a single mode are [6]

$$\frac{dE_1}{dz} = -i\,\frac{\omega}{2}\sqrt{\frac{\mu_0}{\epsilon}}\,dE_3E_1^*$$

$$\frac{dE_3}{dz} = -i\frac{\omega}{2}\sqrt{\frac{\mu_0}{\epsilon}}\,dE_1^2.$$

If E_1 is undepleted (small SHG), then

$$E_3(z) = -i\frac{\omega}{2}\sqrt{\frac{\mu_0}{\epsilon}}\,dE_1^2 z$$

and

$$\Delta E_1 = -\frac{\omega^2}{4}\frac{\mu_0}{\epsilon}d^2E_1\,|E_1|^2\,\frac{L^2}{2}$$

where L is the phase-matched crystal length. Equation (6) then implies that

$$\kappa = \frac{\omega^2}{8}\frac{\mu_0}{\epsilon}d^2L^2.$$

Since

$$I_{SH} = \frac{1}{2}\sqrt{\frac{\epsilon}{\mu_0}}\,|E_3|^2$$

and

$$E_3(L) = -\frac{i\omega}{2}\sqrt{\frac{\mu_0}{\epsilon}}\,dE_1^2\,L$$

then

$$I_{SH} = 4\kappa I^2\sqrt{\frac{\mu_0}{\epsilon}}.$$

This applies only to the center of the Gaussian mode. Total output power is obtained by integrating over the intensity in the mode of waist w at the doubling crystal, or

$$P_{SH} = \frac{\pi w^2}{4}\cdot 4\kappa I^2\sqrt{\frac{\mu_0}{\epsilon}}.$$

Hence

$$P_{SH} = \frac{4\kappa}{\pi w^2}P^2\sqrt{\frac{\mu_0}{\epsilon}}. \tag{B1}$$

Simplifying (11) for $\xi = 0$, we obtain the full expression for a mode-locked laser

$$I_{SH}(r) = \frac{1}{2}\left(\frac{\pi}{\delta}\right)^{3/2}\kappa\,|E|^4\,e^{-4(r/w)^2}\sqrt{\frac{\epsilon}{\mu_0}}.$$

Hence it can be shown that

$$P_{SH} = \frac{4\kappa}{\pi w^2}\sqrt{\frac{\mu_0}{\epsilon}}\,\frac{2\tau}{\sqrt{\pi}\,\hat{t}}\,P^2. \tag{B2}$$

Comparing this with (B1) shows a mode-locking enhancement factor of the proper amount.

Acknowledgment

The author wishes to thank J. Falk, whose review of this paper greatly enhanced its clarity.

References

[1] a) D. J. Kuizenga and A. E. Siegman, "FM and AM mode locking of the homogeneous laser—Part I: Theory," *IEEE J. Quantum Electron.*, vol. QE-6, pp. 694–708, Nov. 1970.
b) O. P. McDuff and S. E. Harris, "Nonlinear theory of the internally loss-modulated laser," *IEEE J. Quantum Electron.*, vol. QE-3, pp. 101–111, Mar. 1967.
c) H. Haken and M. Pauthier, "Nonlinear theory of multimode action in loss modulated lasers," *IEEE J. Quantum Electron.*, vol. QE-4, pp. 454–459, July 1968.
d) T. J. Nelson, "A coupled-mode analysis of mode locking in homogeneously broadened lasers," *IEEE J. Quantum Electron. (Part I of Two Parts)*, vol. QE-8, pp. 29–33, Feb. 1972.

[2] C. B. Hitz and L. M. Osterink, "Simultaneous intracavity frequency doubling and mode-locking in a Nd:YAG laser," *Appl. Phys. Lett.*, vol. 18, p. 378, 1971.

[3] W. E. Lamb, Jr., "Theory of an optical maser," *Phys. Rev.*, vol. 134, p. A1429, 1964.

[4] C. J. Kennedy, "Pulse chirping in a Nd:YAG laser," *IEEE J. Quantum Electron.* (Corresp.), vol. QE-10, pp. 528–530, June 1974.

[5] T. Kimura, K. Otsuka, and M. Saruwatari, "Spatial hole-burning effects in a Nd^{3+}:YAG laser," *IEEE J. Quantum Electron.*, vol. QE-7, pp. 225–230, June 1971.

[6] A. Yariv, *Quantum Electronics*. New York: Wiley, 1968, pp. 348–351.

[7] C. J. Kennedy and J. D. Barry, "Stability of an intracavity frequency-doubled Nd:YAG laser," *IEEE J. Quantum Electron.*, vol. QE-10, pp. 596–599, Aug. 1974.

[8] J. Falk, "A theory of the mode-locked, internally frequency-doubled laser," *IEEE J. Quantum Electron.*, vol. QE-11, pp. 21–31, Jan. 1975.

[9] C. J. Kennedy, "A comment on the theory of mode locking and frequency doubling," *IEEE J. Quantum Electron.* (Corresp.), vol. QE-11, pp. 793–794, Sept. 1975.

[10] O. Bernecker, "Limitations for mode-locking enhancement of internal SHG in a laser," *IEEE J. Quantum Electron.*, vol. QE-9, pp. 897–900, Sept. 1973.

Self-Focusing Phenomena in Air–Glass Laser Structures

C. JAMES ELLIOTT AND BERGEN R. SUYDAM, MEMBER, IEEE

Abstract—**The effect of the air space on self-focusing instability growth rates has been considered for glass laser systems. The situation may be viewed as a min-max problem in which the air space may be adjusted to minimize the fastest growing instability. A solution exists to the min-max problem which reduces the problem to the solution of a single transcendental equation. Solutions to this equation indicate that, at most, a 10-percent reduction in the effective value of the nonlinear index of refraction can occur.**

IN THE PAST the growth rate for optical instabilities such as small-scale self-focusing has been computed [1]-[4] for various models of a glass laser all of which involve a solid piece of material as the nonlinear medium. We extend the calculations to include the effect of an air gap separating a periodic structure of glass disks each of thickness z_g and separation z_a. In this calculation we do not take into account divergence of the beam, finite extent of the beam, gain of the media, nor do we correctly account for disk surfaces which are at a tilt relative to the optical axis. Rather we model the glass disks as being perpendicular to the optical axis and as having antireflecting optical coatings which introduce no phase change to the propagating beam. This model simulates Brewster angle interfaces with a simple geometry.

We find that in no case do the instabilities grow faster than in the solid glass ($z_a = 0$). We may describe the maximum growth rate in the presence of an air space by an effective nonlinear index of refraction $n_{2\,\mathrm{eff}}$, which is lower than the actual nonlinear index n_2. We find that up to a point the thicker the glass disk, the lower $n_{2\,\mathrm{eff}}$. At most an effective 10-percent reduction in the nonlinear index can be achieved by the optimal spacing. For an instability growth of one e-folding length as is representative of a conventional disk system, this reduction is 5 percent.

For the purposes of this analysis, we use the results of the general formalism by Suydam [2], [3] for self-focusing. Given the quasi-optical approximation to the wave equation

$$(2i\omega/v)\partial E/\partial z = \nabla_\perp^2 E + \gamma |E|^2 E \tag{1}$$

where v is the velocity of light in the medium, and ω is the angular frequency of the light, and where the change in index of refraction at frequency ω experienced by a small amplitude test wave is

$$\delta n = \tfrac{1}{2}\omega^{-2} v c \gamma |E|^2$$

the perturbed field of the plane wave solution may be written

$$E = A_0(1 + u\cos k_x x \cos k_y y) \cdot \exp i(\phi_0 + q \cos k_x x \cos k_y y) \tag{2}$$

where u perturbs the amplitude and q perturbs the phase. Using the relationship between ϕ_0 and A_0, Suydam has found for the case of no gain

$$\begin{aligned} (2\omega/v)(du/dz) &= -k^2 q \\ (2\omega/v)(dq/dz) &= (k^2 - 2\gamma A_0^2)u \\ k &= (k_x^2 + k_y^2)^{1/2}. \end{aligned} \tag{3}$$

These equations indicate that the growth of the fractional perturbation u with a transverse wavenumber k is

$$u = c_0 \exp(\alpha z) + c_1 \exp(-\alpha z) \tag{4}$$

where the growth rate α is given by

$$\alpha = (vk/2\omega)(2\gamma A_0^2 - k^2)^{1/2}. \tag{5}$$

The parameter z is the distance into the medium and c_0 and c_1 are free constants. We use this result in conjunction with boundary conditions to derive a propagation or scattering matrix which relates the growth coefficients $\bar{c}_0$ and $\bar{c}_1$ in a second piece of glass shown in Fig. 1 to those in the first by

$$\begin{bmatrix} \bar{c}_0 \\ \bar{c}_1 \end{bmatrix} = \begin{bmatrix} T_{11} & T_{12} \\ T_{21} & T_{22} \end{bmatrix} \begin{bmatrix} c_0 \\ c_1 \end{bmatrix} \tag{6}$$

where T_{ij} is determined by the matching procedure.

The boundary conditions on the electric field envelope at a plane perpendicular antireflecting interface are that the intensity and phase are continuous. More precisely, the electric field envelope is written as in (2), and these conditions require that in a medium with dielectric constant ϵ, $(\epsilon)^{1/2}A_0^2$ and ϕ_0 are continuous as well as u and q. The quantities u and q are determined by (3), where $v = c(\epsilon)^{-1/2}$ so that continuity of q demands a jump discontinuity in du/dz given by

$$(du/dz)_0 = (\epsilon_1/\epsilon_0)^{1/2}(du/dz)_1. \tag{7}$$

We must now do the matching. Three of the matching regions are shown in Fig. 1. We need only consider these three regions in a periodic problem since the transformation matrix will simply be raised to powers to represent the additional

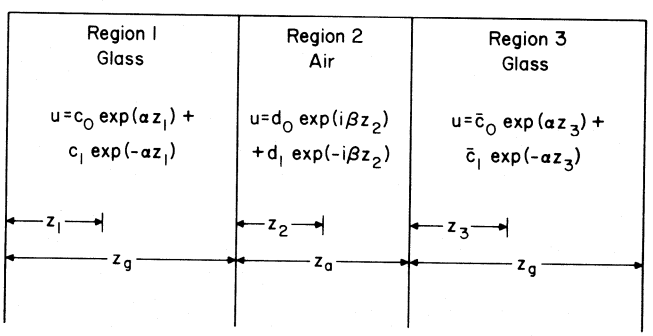

Fig. 1. The three regions in the matching which are joined by the required continuity of u and the discontinuity in its derivative given by (7).

Manuscript received January 3, 1975. This work was performed under the auspices of the U. S. Atomic Energy Commission.

The authors are with the Los Alamos Scientific Laboratory, University of California, Los Alamos, N. Mex. 87544.

structures. In region 2, the air space, the value of q is imaginary since no self-focusing occurs there. The procedure in solving the problem is identical to the quantum mechanical barrier penetration problem and will not be given here. The results are that

$$T_{ij} = \frac{1}{\cos\theta} \cdot \begin{bmatrix} \cos(\beta z_a + \theta)\exp(\alpha z_g), & -\sin\beta z_a \\ \sin\beta z_a, & \cos(\beta z_a - \theta)\exp(-\alpha z_g) \end{bmatrix} \tag{8}$$

where

$$\theta = \cos^{-1}[2/(\alpha c/\beta v) + (\beta v/\alpha c)]$$

and

$$\beta = vk^2/2\omega$$

also $|T| = 1$. It is the largest eigenvalue of this matrix which gives the growth of the instability.

We find that the two eigenvalues of our transformation matrix are given by

$$\lambda_{\pm}^2 - 2F\lambda_{\pm} + 1 = 0 \tag{9}$$

where F is half the trace of the matrix

$$F = (\tfrac{1}{2})(T_{11} + T_{22}). \tag{10}$$

The product of the two eigenvalues is unity and their average is F. If F^2 is less than unity the eigenvalue is complex but has unity modulus. For F^2 larger than unity, the largest eigenvalue in absolute value λ is

$$\lambda = |F|\,[1 + (1 - F^{-2})^{1/2}] \tag{11}$$

which increases as $|F|$ increases. It is convenient to rewrite F in the form

$$F = \cos(\bar{z}\rho x^2)\cosh(\bar{z}y) + (1 - x^2)y^{-1}\sin(\bar{z}\rho x^2)\sinh(\bar{z}y) \tag{12}$$

$$y = x(2 - x^2)^{1/2}$$
$$\bar{z} = (vk_0^2/2\omega)z_g$$
$$\rho = n_g z_a/n_a z_g$$
$$x = k/k_0. \tag{13}$$

The expression in parentheses for $\bar{z}$ is the peak growth rate α_0 in solid glass; the quantity ρ is a normalized aspect ratio; and x is the transverse wavenumber normalized to the wavenumber k_0 which has the peak growth in the solid. We may look at $\bar{z}$ as being a measure of the glass thickness; $\rho\bar{z}$, a measure of the air space; and x, a measure of the transverse wavenumber of the perturbation.

In order to minimize self-focusing in this system, we may cast the analysis in the form of a min-max problem [5] in which self-focusing chooses the value of k to maximize damage (growth of instabilities) in the glass, and in which we choose the normalized aspect ratio which minimizes our loss. We wish to find

$$\lambda_{mm}(\bar{z}) = \min_{\rho}\max_{x} |\lambda(x, \rho, \bar{z})|. \tag{14}$$

It turns out that our optimal strategy does not occur at a saddle point of λ so that the usual analytical methods do not apply. However, we can ask: if we were to choose the worst value of ρ, what would our damage be? This is the max-max problem which does have a simple solution given in the Appendix. The worst we can do is the same as we did with no air space, i.e.

$$\max\max |\lambda(x, \rho, \bar{z})| = \max_{x} |\lambda(x, 0, \bar{z})| = \exp(\bar{z}). \tag{15}$$

This says that the worst case is solid glass.

A simple analogy may help us understand the min-max problem. Consider the model problem of finding the lowest constant altitude constant latitude flight path across the United States. For each latitude we find the highest altitude and then we examine this value for each east-to-west route to find the lowest of these. A typical terrain of our self-focusing problem is shown in Fig. 2; the ridges are the analogs of the mountain ranges of the United States. Latitude corresponds to the value of $\rho\bar{z}$ and longitude to x.

When we look at a side view of the terrain of our problem we see it as in Fig. 3. The important thing to notice is that the optimal point (lowest point on the envelope), occurs where two ridges have the same height at a latitude of $\rho\bar{z} = 1.5708$; *the optimal point is not a saddle point of* F. Here at increasing latitude one ridge is decreasing in height and the other is increasing in height; the inevitable crossing is the optimal point.

We may set down these observations in terms of three conditions on F. First and second, we demand we are on two ridges, one at $x_1, \rho, \bar{z}$ and the other at $x_2, \rho, \bar{z}$. This requires extrema in x and may be written

$$F_1(x_1, \rho, \bar{z}) = F_1(x_2, \rho, \bar{z}) = 0 \tag{16}$$

where the subscript 1 indicates partial differentiation with respect to the first argument. Third, we demand the two ridges be of equal height

$$|F(x_1, \rho, \bar{z})| = |F(x_2, \rho, \bar{z})|. \tag{17}$$

These equations possess solutions for all values of $\bar{z}$. These are

$$\rho\bar{z} = \pi/2, \quad x_1^2 + x_2^2 = 2. \tag{18}$$

The preceding two conditions guarantee the equality of F at x_1 and x_2, and F_1 at x_1 and x_2.

The remaining degree of freedom is fixed by a single transcendental equation which dictates we are on a ridge. The condition is

$$F_1(x_1, \pi/2\bar{z}, \bar{z}) = 0 \tag{19}$$

and this serves to determine x_1 where by convention x_1 is chosen less than unity and x_2 greater than unity. One method of solving for x_1 is to isolate the root of (19) to the nearest 0.01 and then apply Newton's method successively.

The preceding results indicate: First, that at the optimal point there are two spot sizes (values of k^{-1}), one smaller and one larger than the optimal spot in solid glass, which now have

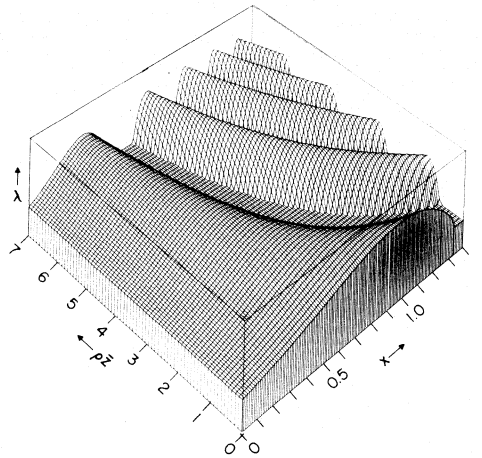

Fig. 2. A projection plot of the surface $|\lambda(x, \rho, 1)|$ which is analogous to the terrain of the United States high above the west coast. The flat regions correspond to $|F|$ less than unity, where $|\lambda|$ is taken to be unity. The ridges are analogous to mountain ranges.

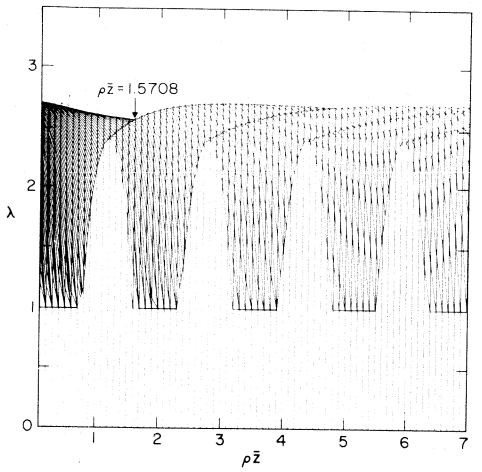

Fig. 3. A picture plot view of the terrain from the east coast ($x = +\infty$). The closest part of the plot corresponds to $x = \sqrt{2}$. Here we wish to find the lowest point at which we can see daylight; this point is indicated by the arrow.

optimal growth rates. The spot which is smaller is never smaller in radius by more than $(2)^{-1/2}(x_2 \leqslant 2^{1/2})$. The larger of the two spots increases in size if the air gap remains fixed and the width of the glass diminishes ($\bar{z} \to 0$). These results are shown in Fig. 4 where we plot x_1 and x_2 versus $\bar{z}$. As we expect, as $\bar{z}$ becomes large (ρ becomes small) we recover the solid glass results. Second, examination of the results shows us that many very thin glass structures are just as bad as one very thick glass structure—the growth rates are the same as in solid glass, the worst possible case. In between these extremes we must get the best improvement in performance of the glass. We may describe the performance by an effective value $n_{2\,\mathrm{eff}}$ of the nonlinear index which is lower than the actual value n_2 and given in terms of the growth of the instability λ_{mm} by

$$\lambda_{mm} = \exp\,(n_{2\,\mathrm{eff}}\bar{z}/n_2). \tag{20}$$

The fractional decrease $(n_2 - n_{2\,\mathrm{eff}})/n_2$ is shown in Fig. 5. As we expected a maximum decrease occurs and this corresponds to at most a 10-percent decrease in the value of n_2.

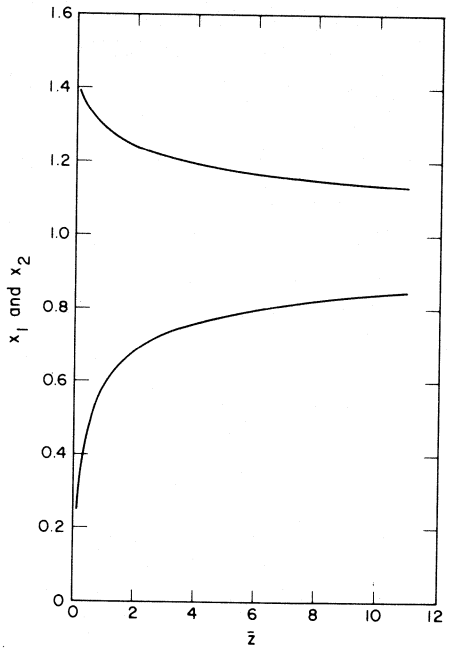

Fig. 4. A plot of $x_1(\bar{z})$ and $x_2(\bar{z})$ for the optimal solutions. Here $x_1^2 + x_2^2 = 2$ and x_1 are determined by (19). Knowing x_1 and x_2 we can then find the magnitude of both the transverse k vectors which give the optimal growth.

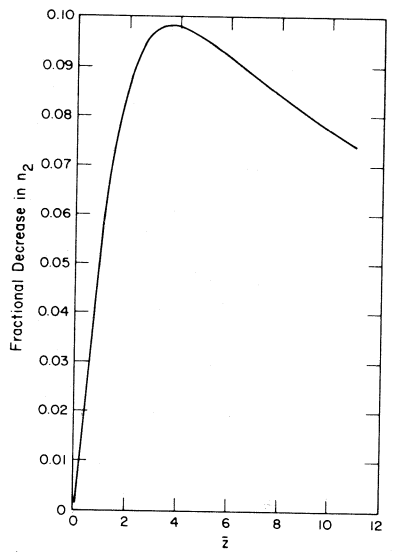

Fig. 5. The fractional decrease $(n_2 - n_{2\,\mathrm{eff}})/n_2$ in terms of $\bar{z}$ at the optimal solution. For large and small values of $\bar{z}$ there is no improvement over the worst possible case (solid glass); in between there is a maximum improvement of less than 10 percent.

In conclusion we find that periodic air-glass laser structures can at best account for a 10-percent improvement in the effective value of n_2 for small-scale self-focusing. This result should be contrasted with the result for the beam as a whole [6], [7] (large-scale self-focusing) in which the air spaces aggravate the self-focusing problem. In regards to small-scale self-focusing, these results indicate that consideration of the air space is a minimal design factor in glass-disk lasers, and that previous models which ignored these effects were adequate for many design purposes.

APPENDIX

The Max-Max Problem

We wish to find F_{mm} defined by

$$F_{mm} = \max_{\rho} \max_{x} |F(x, \rho, \bar{z})|. \tag{A1}$$

First we note that unlike the min-max problem, the two max operations commute so that

$$F_{mm} = \max_{x} \max_{\rho} |F(x, \rho, \bar{z})|. \tag{A2}$$

We may easily determine $\max_\rho |F|$ since ρ appears only as sines and cosines; that is, F of (12) may be written

$$F = C(x, \bar{z}) \cos [\rho \bar{z} x^2 + \theta (x, \bar{z})] \tag{A3}$$

where

$$\theta(x, \bar{z}) = -\tan^{-1} \{(1 - x^2) x^{-1} (2 - x^2)^{-1/2} \cdot \tanh [\bar{z} x (2 - x^2)^{1/2}]\} \tag{A4}$$

and

$$C(x, \bar{z}) = [\cosh^2 \bar{z} y + y^{-2} (1 - x^2)^2 \sinh^2 \bar{z} y]^{1/2} \tag{A5}$$

and y is given in (13). Only the amplitude $C(x, \bar{z})$ determines the maximum since the cosine factor can never exceed unity

$$\max_{\rho} |F| = C(x, \bar{z}). \tag{A6}$$

Examination of the structure of C indicates that it is monotonically increasing in y and that the maximum of C occurs at the peak value of y of unity where x is also unity and

$$F_{mm} = \max_{x} C(x, \bar{z}) = \cosh (\bar{z}). \tag{A7}$$

The growth rate which corresponds to F_{mm} is governed by (11) and it indicates that the worst possible ρ gives a growth rate of

$$\cosh (\bar{z}) [1 + (1 - \cosh^{-2} \bar{z})^{1/2}] = \exp \bar{z} \tag{A8}$$

which is the growth rate in solid glass. The worst possible growth rates occur at

$$\rho \bar{z} = n\pi - \theta (1, \bar{z}) = n\pi, \qquad n = 0, 1, 2, \cdots. \tag{A9}$$

We may see these peaks in the projection plot of Fig. 3.

ACKNOWLEDGMENT

The authors wish to thank O. D. Judd for helpful suggestions with the organization of this paper.

REFERENCES

[1] V. I. Bespalov and V. I. Talanov, "Filamentary structure of light beams in nonlinear liquids," *Pis'ma Zh. Eksp. Teor. Fiz.*, vol. 3, pp. 471–476, June 15, 1966; also (English transl., pp. 307–310).

[2] B. R. Suydam, "Self-focusing of very powerful laser beams," in *Laser Induced Damage in Optical Materials* (Special Publication 387), A. J. Glass and A. H. Guenther, Ed. Washington, D. C.: National Bureau of Standards, 1973.

[3] —, "Self-focusing of very powerful laser beams II," *IEEE J. Quantum Electron.*, vol. QE-10, pp. 837–843, Nov. 1974.

[4] C. J. Elliott, "Gain saturation and self-focusing considerations in the design of optical amplifiers," *Appl. Phys. Lett.*, vol. 24, pp. 91–93, Jan. 1974.

[5] J. M. Danskin, *The Theory of Max-Min and Its Application to Weapons Allocation Problems* (*Econometrics and Operations Research*) *V*, M. Beckmann *et al.*, Ed. New York: Springer, 1967, pp. 1–9 and 34–41.

[6] K. A. Brueckner and J. E. Howard, "Self-focusing and saturation in disk amplifiers," in *Laser Induced Damage in Optical Materials* (Special Publication 387), A. J. Glass and A. H. Guenther, Ed. Washington, D. C.: National Bureau of Standards, 1973.

[7] C. J. Elliott and D. B. Henderson, "A new computer technique for non-linear optical problems," *J. Appl. Phys.*, Jan. 1975.

Coupling Coefficients for Distributed Feedback Single- and Double-Heterostructure Diode Lasers

WILLIAM STREIFER, SENIOR MEMBER, IEEE, DONALD R. SCIFRES, MEMBER, IEEE, AND ROBERT D. BURNHAM

Abstract—**We compute coupling coefficients for TE modes as a function of tooth height, active layer thickness, and Bragg scattering order in single-heterostructure (SH) and double-heterostructure (DH) distributed feedback (DFB) diode lasers for a variety of corrugation shapes. In particular, equations for rectangular, sinusoidal, and triangular shapes are evaluated; the last both in the symmetric and sawtooth cases. It is shown that the coupling coefficient for rectangular and sawtooth gratings decreases much less rapidly with increasing Bragg order than do the sinusoidal and symmetric triangular.**

I. Introduction

DISTRIBUTED FEEDBACK (DFB) lasers differ from conventional lasers in that feedback is provided by a distributed periodic spatial variation in gain, refractive index, and/or geometry, rather than by discrete reflectors. The analysis of these devices [1] has been carried out as a function of the coupling coefficient κ, which describes the degree to which oppositely going waves transfer energy. Generally, κ has been expressed in terms of refractive index and/or gain variations, but in many cases there exist instead periodic corrugations which perturb the light. To employ the results of Kogelnik and Shank [1] for thresholds and frequencies of pure DFB lasers or similar results for DFB lasers with external reflectors [2]-[4] to geometries which employ corrugations [5]-[7], one must relate the coupling coefficients to the corrugations. This task has been formally carried out by several authors [8]-[10] using a perturbation procedure in which modes of the unperturbed structure are examined in their interaction with the corrugation. To date no extensive evaluation of the resulting integrals has been carried out except for square shaped corrugations, and therefore, no detailed comparisons of different corrugation shapes exist in the literature. Furthermore, the unperturbed mode fields used in many previous calculations were not chosen optimally and the published results are somewhat inaccurate. It is our purpose, therefore, in writing this paper to present analytic and numerical results for TE-mode coupling coefficients for various tooth shapes and Bragg scattering orders m using a more accurate formulation. We consider rectangular, sinusoidal, triangular, and sawtooth shapes in detail, but the methods employed are shown to be valid for other shapes as well. The derived formulas apply to both GaAs and dye DFB lasers, but are evaluated herein only for GaAs/GaAlAs SH's and DH's.

Manuscript received January 13, 1975; revised July 9, 1975.
The authors are with the Xerox Palo Alto Research Center, Palo Alto, Calif. 94304.

II. Analytic Results

In three-layer laser structures, as illustrated in Fig. 1, there exist right and left going TE and TM modes coupled by the corrugations. A perturbation analysis is used to obtain an expression for the coupling coefficients produced by the corrugations and thereby permit one to predict thresholds and lasing wavelengths as described in [1]-[4]. The result of the perturbation analysis, as given in [10], for TE modes is

$$\kappa = \frac{k_0^2}{2\beta N^2} \int_{\text{corrugation}} \Delta\,[n^2(x,z)]\; \mathcal{E}^2(x)\, dx \tag{1}$$

where κ is the coupling coefficient, $k_0 = 2\pi/\lambda_0$ (the free-space wavenumber), β is the TE-mode propagation constant, $\mathcal{E}$ is the y component of the unperturbed E-field, and N^2 is a normalization constant given by

$$N^2 = \int_{-\infty}^{\infty} \mathcal{E}^2(x)\, dx. \tag{2}$$

As shown in the following only the negative spatial harmonic of $\Delta\,[n^2(x,z)]$ (which is the perturbation in refractive index of the corrugation) appropriate to the Bragg scattering is to be retained.

In [10] the full guide width t (see Fig. 1) was employed to compute the unperturbed mode field $\mathcal{E}$, but as shown in [11], this can lead to inaccurate excessively high coupling coefficients. The optimal unperturbed mode $\mathcal{E}$ is that of a related four-layer structure (see [11]); however, we have found that one can obtain adequate accuracy without excessive complexity by judiciously choosing the unperturbed guide boundary at $t' < t$. We choose t' such that the volume of n_1 material extending into region 2 just equals the volume of n_2 material extending into region 1. The symbol t' thus refers to the distance from the n_2-n_3 interface to the line

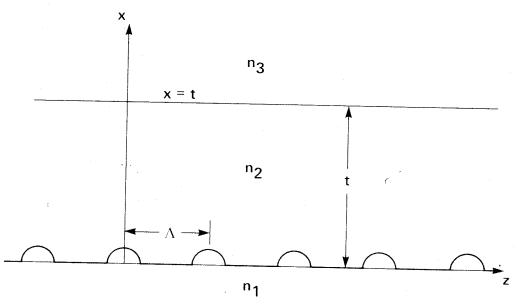

Fig. 1. Three-layer DFB laser structure.

shown in Fig. 2. That line is positioned such that the areas labeled A and B are equal. It is not coincident with the base of the teeth as in [10], [12], [13]. The unperturbed mode $\mathcal{E}(x)$ is then

$$\mathcal{E}(x) = \begin{cases} \exp(qx), & x \le 0 \\ \cos(hx) + (q/h)\sin(hx), & 0 \le x \le t' \\ [\cos(ht') + (q/h)\sin(ht')]\exp[-p(x-t')], & t' \le x \end{cases} \quad (3)$$

where

$$q = \sqrt{\beta^2 - n_1^2 k^2} \quad (4a)$$

$$h = \sqrt{n_2^2 k^2 - \beta^2} \quad (4b)$$

$$p = \sqrt{\beta^2 - n_3^2 k^2} \quad (4c)$$

and where β is found by solving

$$\tan(ht') = \frac{h(q+p)}{h^2 - pq} \quad (5)$$

and

$$N^2 = \int_{-\infty}^{\infty} \mathcal{E}^2(x)\,dx = \frac{(h^2+q^2)(t'+q^{-1}+p^{-1})}{2h^2}. \quad (6)$$

Consider now a single corrugation as shown in Fig. 2. Here

$$\Delta[n^2(x,z)] = \begin{cases} n_1^2 - n_2^2, & \text{in area } A \\ n_2^2 - n_1^2, & \text{in area } B \end{cases} \quad (7)$$

and $w_i(x)$, $i = 1, 2, 3, 4$ describe the tooth boundary. If any of these functions are not single valued the tooth shape can be decomposed into two or more curves with single valued boundaries and the results superimposed.

Since $\Delta[n^2(x,z)]$ is periodic in z it is expanded in a Fourier series whose coefficients depend on x. After some manipulation we obtain

$$\Delta[n^2(x,z)] = \begin{cases} (n_1^2 - n_2^2)\left[\dfrac{w_2(x) - w_1(x)}{\Lambda} - \dfrac{i}{2\pi}\sum_{m=-\infty}^{\infty}\dfrac{1}{m}\right. \\ \quad \{\exp[i2\pi m w_2(x)/\Lambda] \\ \quad\quad - \exp[i2\pi m w_1(x)/\Lambda]\} \\ \quad\quad \left.\cdot \exp(-i2\pi m z/\Lambda)\right], \quad x > 0 \\ (n_2^2 - n_1^2)\left[\dfrac{w_4(x) - w_3(x)}{\Lambda} - \dfrac{i}{2\pi}\sum_{m=-\infty}^{\infty}\dfrac{1}{m}\right. \\ \quad \{\exp[i2\pi m w_4(x)/\Lambda] \\ \quad\quad - \exp[i2\pi m w_3(x)/\Lambda]\} \\ \quad\quad \left.\cdot \exp(-i2\pi m z/\Lambda)\right], \quad x < 0 \end{cases} \quad (8)$$

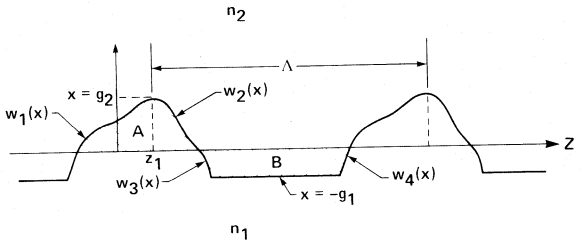

Fig. 2. Illustrating the functions defining tooth shape.

and so

$$\kappa = \frac{-ik_0^2(n_1^2 - n_2^2)}{4\pi\beta m N^2}\left\{\int_0^{g_2} \{\exp[i2\pi m w_2(x)/\Lambda] - \exp[i2\pi m w_1(x)/\Lambda]\}\,\mathcal{E}^2(x)\,dx - \int_{-g_1}^{0} \{\exp[i2\pi m w_4(x)/\Lambda] - \exp[i2\pi m w_3(x)/\Lambda]\}\,\mathcal{E}^2(x)\,dx\right\} \quad (9)$$

where, as shown in Fig. 2, g_1 and g_2 are the maximum tooth heights in media 1 and 2, respectively, and m is the Bragg scattering order.

Rectangular Grating

For rectangular teeth $w_2(x) = -w_1(x) = w/2$, $w_3(x) = w/2$, $w_4 = \Lambda - w/2$, and the area averaging conditions yields

$$g_1 = wg/\Lambda \quad (10)$$

and

$$g_2 = (1 - w/\Lambda)g \quad (11)$$

where g is the total tooth height. After integration (9) becomes

$$\kappa = \frac{k_0^2(n_1^2 - n_2^2)}{4\pi\beta m N^2}\sin\left(\frac{\pi m w}{\Lambda}\right)\left\{g_2 + \frac{\sin(2g_2h)}{2h} + \frac{q}{h^2}\cdot[1 - \cos(2g_2h)] + \frac{q^2}{h^2}\left[g_2 - \frac{\sin(2g_2h)}{2h}\right] + \frac{1}{q}[1 - \exp(-2qg_1)]\right\} \quad (12)$$

where q, h, and p are defined by (4a)-(4c).

In (12) the quantities β, N^2, q, and h all depend on the unperturbed geometry, i.e., n_1, n_2, n_3, and $t' = t - g_1$ as well as the transverse mode number. The dependence on Bragg order m is completely represented by the multiplicative factor

$$\frac{\sin(\pi m w/\Lambda)}{m}. \quad (13)$$

Clearly, κ can be zero for integral values of mw/Λ, but gen-

erally it decreases as $1/m$. Finally, the dependence on tooth height is given by the bracketed expressions, which for $2g_1h$, $2g_2h \ll 1$ reduces to $2g_1 + 2g_2 = 2g$. The dependence of κ on the various parameters is discussed more completely in [14].

Sinusoidal Grating

The tooth profile for sinusoidal teeth is

$$x = (g/2)\cos(2\pi z/\Lambda) \tag{14}$$

and so

$$w_2(x) = -w_1(x) = \frac{\Lambda}{2\pi}\cos^{-1}\left(\frac{2x}{g}\right) \tag{15a}$$

and

$$[w_4(x) - \Lambda/2] = -[w_3(x) - \Lambda/2] = \frac{\Lambda}{2\pi}\cos^{-1}\left(-\frac{2x}{g}\right) \tag{15b}$$

where it is understood that

$$0 < \cos^{-1}(U) < \pi/2.$$

The boundary line for the unperturbed modes bisects the corrugation and (9) is then

$$\kappa = \frac{k_0^2(n_1^2 - n_2^2)}{2\pi\beta m N^2}\left\{\int_0^{g/2} \sin\left[m\cos^{-1}(2x/g)\right]\mathcal{E}^2\,dx - (-1)^m\int_{-g/2}^{0}\sin\left[m\cos^{-1}(2x/g)\right]\mathcal{E}^2\,dx\right\}. \tag{16}$$

The integrals in (16) can be evaluated numerically or analytically by using trigonometric identities for $\sin[m\cos^{-1}(2x/g)]$ and expanding $\mathcal{E}^2(x)$ in power series. Details of the latter procedure and evaluation of the integrals are too lengthy to be included herein. The results for $m = 1, 2, 3$, and 4 are in the form

$$\kappa = \frac{k_0^2(n_1^2 - n_2^2)}{\beta N^2}\begin{cases}\frac{g}{8}S_1\\ \frac{g^2}{64}S_2\\ \frac{g^2}{60\pi}S_3\\ \frac{g^3}{420\pi}S_4\end{cases} \tag{17}$$

where S_i, $i = 1, 2, 3, 4$ are summations whose first terms are $S_1 = 1, S_2 = S_3 = q$, and $S_4 = (q^2 - h^2)/2$.

Symmetric Triangular Grating

Consider next a symmetric triangular grating defined by

$$w_1(x) = w_4(x) - \Lambda = \frac{x\Lambda}{2g} - \frac{\Lambda}{4} \tag{18a}$$

and

$$w_2(x) = w_3(x) = \frac{x\Lambda}{2g} + \frac{\Lambda}{4}. \tag{18b}$$

The integrals which result upon substitution in (9) are in standard form and are easily evaluated to yield

$$\kappa = \frac{k_0^2(n_1^2 - n_2^2)}{4\pi\beta m N^2}g\left\{\left(1 + \frac{q^2}{h^2}\right)\frac{[1 - \cos(\pi m/2)]}{\pi m} + \frac{q}{h}\frac{2}{[(2gh)^2 - (\pi m)^2]}[2gh\sin(\pi m/2) - \pi m\sin(gh)] - \left(1 - \frac{q^2}{h^2}\right)\frac{\pi m}{[(2gh)^2 - (\pi m)^2]}[\cos(gh) - \cos(\pi m/2)] - \frac{2(-1)^m}{[(2gq)^2 + (\pi m)^2]}[2gq\sin(\pi m/2) - \pi m\cos(\pi m/2) + \pi m e^{-gq}]\right\}. \tag{19}$$

Since $\sin(\pi m/2) = 0$ for m even and $\cos(\pi m/2) = 0$ for m odd many terms in (19) vanish for particular Bragg diffraction orders. In general, however, $\kappa \to 1/m^2$ with increasing order.

Sawtooth Grating

The sawtooth grating is defined by

$$w_1(x) = w_4(x) = x\Lambda/g \tag{20a}$$

and

$$w_2(x) = -w_3(x) = \Lambda/2. \tag{20b}$$

The integral (9) again is in standard form, and we find

$$\kappa = \frac{k_0^2(n_1^2 - n_2^2)}{8\pi\beta m N^2}\left\{g\left[\frac{(u-1)v_1}{2\pi m} + \frac{\pi m}{2d_1}\cdot\left\{v_2(1 - uC_1) - \frac{2uq}{h}S_1\right\} + \frac{\pi m}{d_2}(1 - uE_1)\right] - i\left[\frac{u}{2}\left\{v_1 g + \frac{2q}{h^2}(1 - C_1) + \frac{v_2}{h}S_1\right\} - \frac{g^2 h}{2d_1}\left\{\frac{2q}{h}(1 - uC_1) + uv_2S_1\right\} - \frac{qg^2}{d_2}(1 - uE_1) + \frac{u}{q}(1 - E_1)\right]\right\} \tag{21}$$

where

$$C_1 = \cos(gh), \quad S_1 = \sin(gh), \quad E_1 = \exp(-qg) \tag{22a}$$

$$v_1 = (1 + q^2/h^2), \quad v_2 = (1 - q^2/h^2) \tag{22b}$$

$$d_1 = (gh)^2 - (\pi m)^2, \quad d_2 = (gq)^2 + (\pi m)^2 \tag{22c}$$

and

$$u = (-1)^m. \tag{22d}$$

An examination of (21) reveals that $|\kappa| \to 1/m$ with increasing

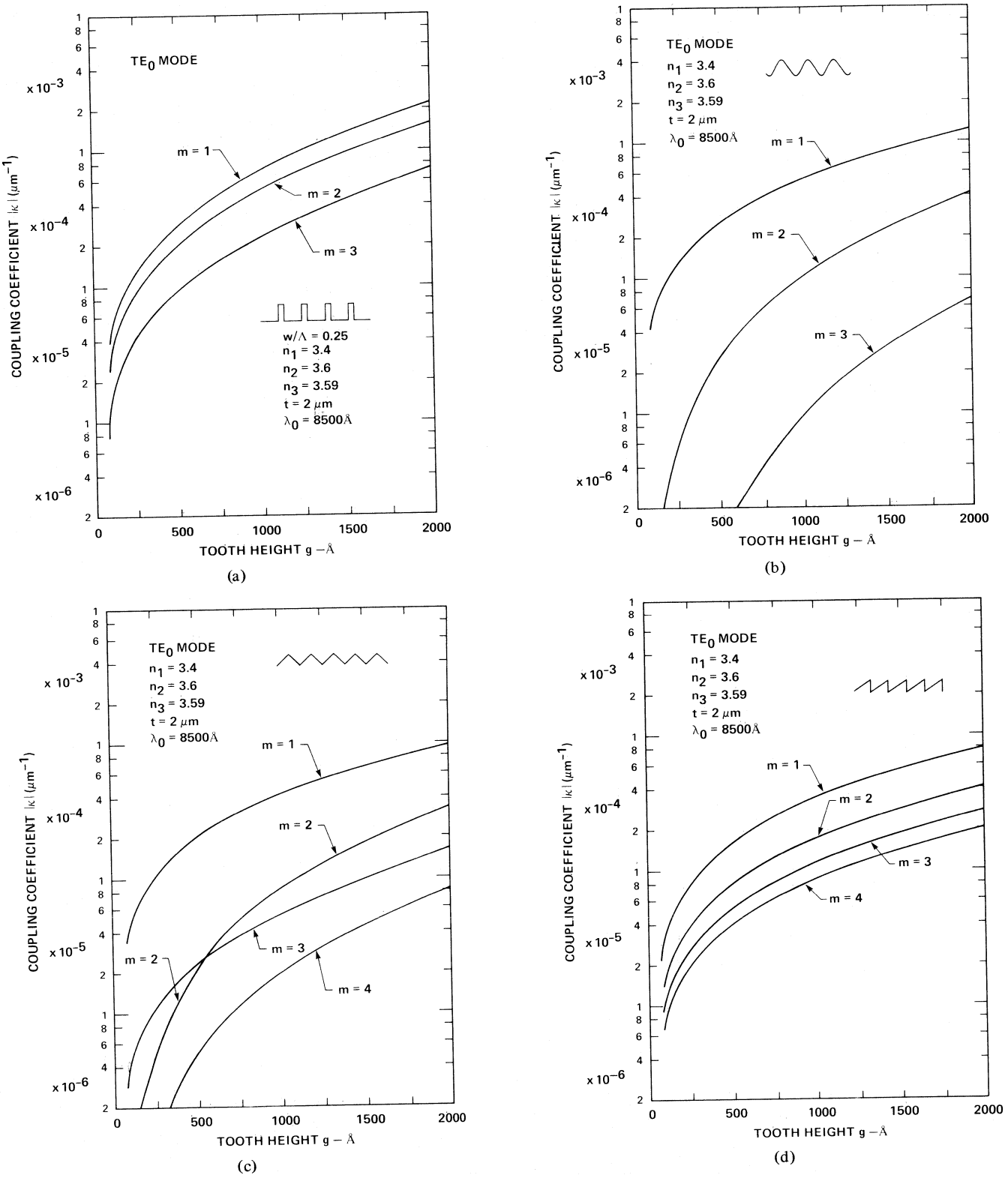

Fig. 3. Coupling coefficient versus tooth height with Bragg order as a parameter for TE_0 mode in a SH geometry. (a) Rectangular grating. (b) Sinusoidal grating. (c) Symmetric triangular grating. (d) Sawtooth grating.

m and for $gh, gq \ll 1$

$$|\kappa| \approx \frac{k_0^2(n_1^2 - n_2^2)}{8\pi\beta m N^2} g \tag{23}$$

where only the dominant inverse power of m has been retained.

III. Numerical Results

Fig. 3(a)-(d) are plots of coupling coefficient versus tooth height g in a SH GaAs DFB laser geometry for the four corrugation shapes discussed in the preceding. Interestingly enough, κ for $m = 1$ is not strongly dependent on tooth shape.

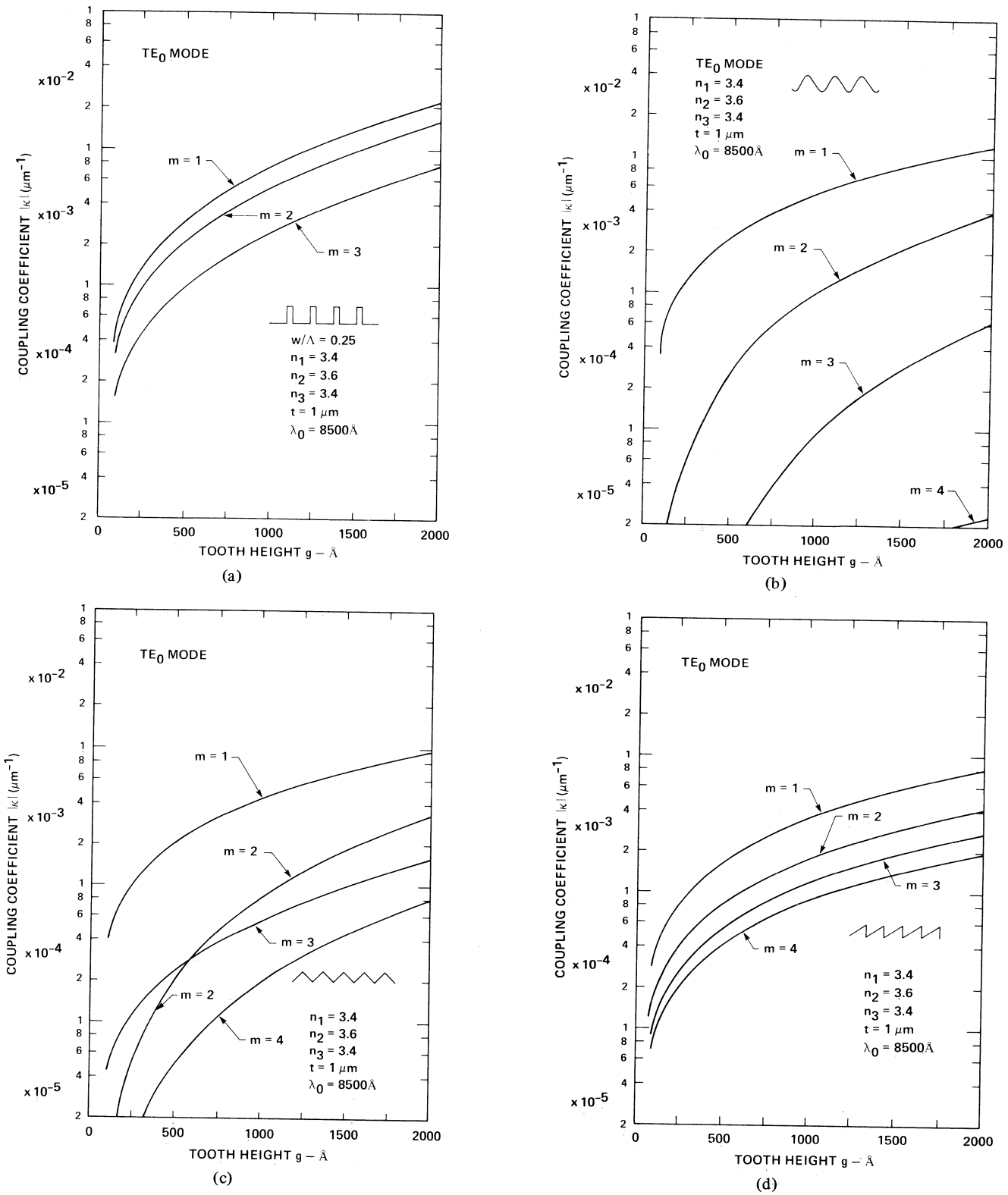

Fig. 4. Coupling coefficient versus tooth height with Bragg order as a parameter for TE_0 mode in a DH geometry. (a) Rectangular grating. (b) Sinusoidal grating. (c) Symmetric triangular grating. (d) Sawtooth grating.

With increasing m the coupling constants for rectangular ($w/\Lambda = 0.25$) and sawtooth gratings decrease at approximately the same rate and that decrease is much less rapid than those for the triangular and sinusoidal gratings. The coupling coefficient for rectangular teeth with $m = 4$ is zero because the factor (13) is zero. Physically, when mw/Λ is an integer, reflections from the parallel vertical tooth boundaries are exactly a half-wavelength out-of-phase and therefore cancel. It is likely that $|\kappa|$ for any tooth shape with discontinuities will decrease with Bragg order at approximately the same

rate as the rectangular and sawtooth gratings. The coupling coefficient for sinusoidal teeth decreases most rapidly and for $m = 4$ values of $|\kappa|$ are all less than the lowest point on the graph. For symmetrical triangular teeth $|\kappa|$ also decreases quickly and exhibits other interesting behavior. In this case with m odd, $\kappa \propto g$ for small g, whereas with $m = 2$, $\kappa \propto g^2$ for small g; as g increases, however, the latter exceeds the former above approximately $g = 550$ Å.

Consider next the aspect ratios. Since it is often the period Λ which largely determines the maximum tooth height, one may well ask, given a fixed aspect ratio of tooth height to period, what Bragg order will maximize κ? Clearly, for rectangular and sawteeth dividing tooth height and period by m reduces κ by a greater factor. Thus, other considerations aside, one need not (in these cases) strive for lowest order Bragg scattering. Of course, this result is predicated on the assumption of constant aspect ratio, particular tooth shapes (since it is invalid in the other cases), and finally the neglect of other phenomena such as radiation losses to the lower order Bragg scattering modes.

In Fig. 4(a)-(d) we plot similar curves for the lowest order transverse mode TE_0 in a DH geometry ($n_1 = n_3 = 3.4$, $n_2 = 3.6$, and $t = 1.0$ μm). As a result of the stronger confinement and smaller thickness the coupling coefficients exceed those for the SH geometry by more than an order of magnitude. For the particular refractive indices and thickness given in the preceding the DH geometry will actually allow additional transverse electric modes to propagate, the TE_1 and TE_2. In Fig. 5(a) and (b) we plot $|\kappa|$ versus tooth height for the TE_1 mode with rectangular ($w/\Lambda = 0.25$) and symmetric triangular corrugations, respectively. Values of $|\kappa|$ are roughly a factor of 3 greater than for the TE_0 mode in the same geometry. It should be noted that the grating period Λ must be adjusted somewhat to resonate these higher order transverse modes [13]-[15]. Also as shown in [13] and [15], depending on t, $|\kappa|$ may continue to increase with transverse mode number.

DFB lasers have also been shown to produce highly collimated beams by radiation from the grating [16]-[19]. For single beam output [19] it is best to employ the grating in the 2nd Bragg order, i.e., $m = 2$ and optimum output coupling may well occur for symmetric triangular or sawtooth gratings [20]. With $m = 2$, $\Lambda \simeq 2300$ Å, and so $g = 1150$ Å and $g = 2300$ Å will give teeth with a 45° slope for symmetric triangular or sawtooth gratings, respectively. We plot $|\kappa|$ versus t for four transverse (TE) modes in a DH geometry with a symmetric triangular grating in Fig. 6. The TE_1, TE_2, and TE_3 modes all exhibit a more complex $|\kappa|$ versus t dependence then shown in Fig. 6. In Fig. 7 we plot $|\kappa|$ versus t for a small range of t just above cutoff for the TE_2 mode. The behavior illustrated can be explained mathematically by studying (19). As t increases the bracketed expression changes from positive to negative at which point $|\kappa|$ passes through zero. Physically, there is destructive interference from different parts of the tooth which exactly cancel for a particular value of t. This phenomenon is not of great significance since it is probably desirable to resonate the transverse modes well above cutoff.

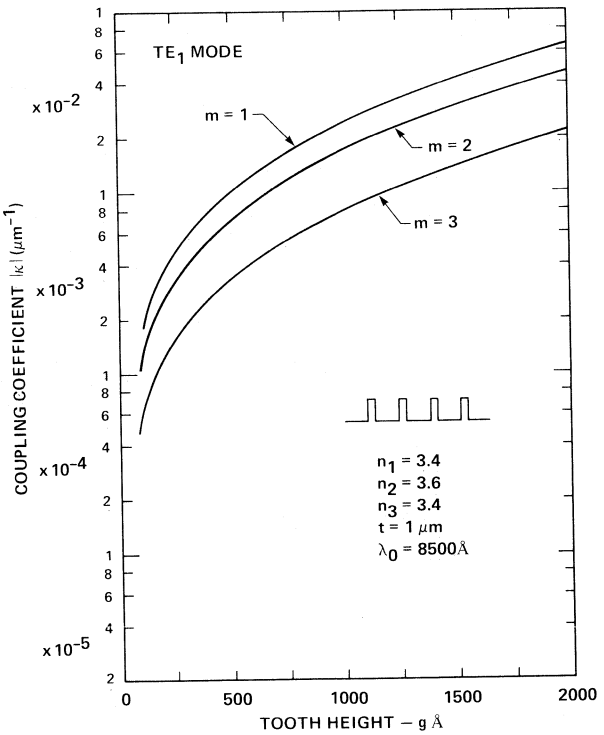

(a)

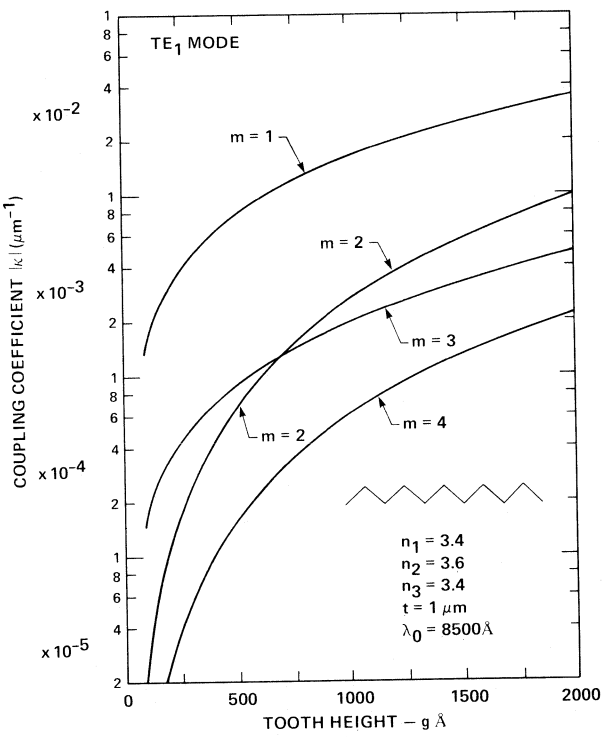

(b)

Fig. 5. Coupling coefficient versus tooth height with Bragg order as a parameter for the TE_1 mode in a DH geometry. (a) Rectangular grating. (b) Symmetric triangular grating.

IV. Remarks

The computed values of coupling coefficients for TE modes presented in the preceding for rectangular, sinusoidal, triangular, and sawtooth corrugation shapes in both SH and DH

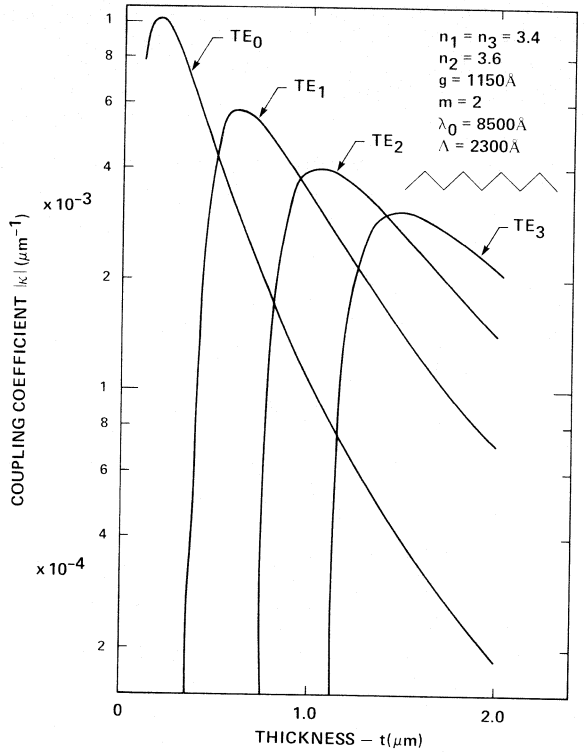

Fig. 6. Coupling coefficient versus thickness for transverse modes in a DH geometry with a symmetric triangular grating.

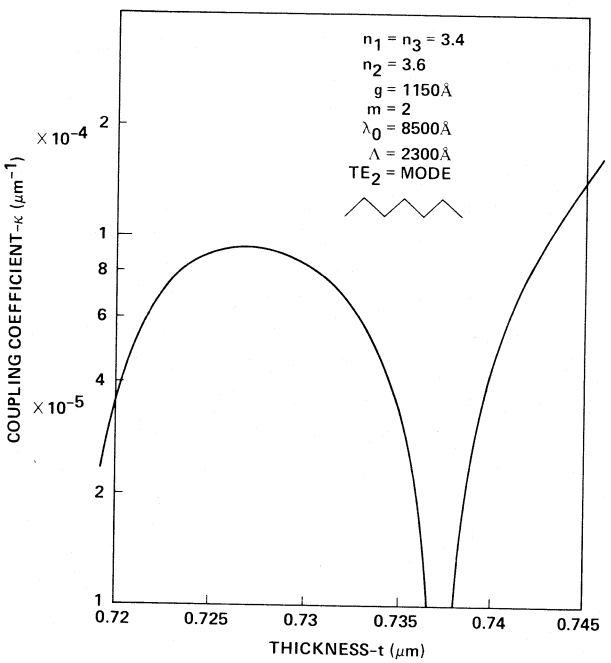

Fig. 7. Detail of the TE_2 mode shown in Fig. 6.

laser diodes are based on a perturbation analysis, which uses a more accurate unperturbed mode field than heretofore published.

References

[1] H. Kogelnik and C. V. Shank, "Coupled mode theory of distributed feedback lasers," *J. Appl. Phys.*, vol. 43, pp. 2327–2335, 1972.

[2] S. R. Chinn, "Effects of mirror reflectivity in a distributed-feedback laser," *IEEE J. Quantum Electron.*, vol. QE-9, pp. 574–580, June 1973.

[3] W. Streifer, D. R. Scifres, and R. D. Burnham, "Longitudinal modes in distributed feedback lasers with external mirrors," *J. Appl. Phys.*, vol. 46, pp. 247–249, 1975.

[4] W. Streifer, R. D. Burnham, and D. R. Scifres, "Effect of external reflectors on longitudinal modes of distributed feedback lasers," *IEEE J. Quantum Electron.*, vol. QE-11, pp. 154–161, Apr. 1975.

[5] D. R. Scifres, R. D. Burnham, and W. Streifer, "Distributed-feedback single heterojunction GaAs diode laser," *Appl. Phys. Lett.*, vol. 25, pp. 203–206, 1974.

[6] M. Nakamura *et al.*, "GaAs-GaAlAs double-heterostructure distributed feedback diode lasers," *Appl. Phys. Lett.*, vol. 25, pp. 487 and 488, 1974.

[7] P. Zory, "Leaky wave thin film laser," in *Dig. Tech. Papers, Integrated Optics Topical Meeting of the Optical Society of America*, Feb. 1972, pp. ThA2-1–ThA2-2.

[8] D. Marcuse, "Mode conversion caused by surface imperfections of a dielectric slab waveguide," *Bell Syst. Tech. J.*, vol. 48, pp. 3187–3215, 1969.

[9] S. Wang, "Proposal of periodic layer waveguide structures for distributed lasers," *J. Appl. Phys.*, vol. 44, pp. 767–780, 1972.

[10] A. Yariv, "Coupled-mode theory for guided-wave optics," *IEEE J. Quantum Electron.*, vol. QE-9, pp. 919–933, Sept. 1973.

[11] K. Handa, S. T. Peng, and T. Tamir, "Improved perturbation analysis of dielectric gratings," *Appl. Phys.*, vol. 5, p. 325, 1975.

[12] H. Stoll and A. Yariv, "Coupled-mode analysis of periodic dielectric waveguides," *Opt. Commun.*, vol. 8, pp. 5–8, 1973.

[13] W. Streifer, R. D. Burnham, and D. R. Scifres, "Coupling coefficients and propagation constants in guided wave distributed feedback lasers," *J. Appl. Phys.*, vol. 46, pp. 946–948, 1975.

[14] R. D. Burnham, D. R. Scifres, and W. Streifer, "Single heterostructure distributed-feedback GaAs-diode lasers," *IEEE J. Quantum Electron. (Part II of Two Parts)*, vol. QE-11, pp. 439–449, July 1975.

[15] J. E. Bjorkholm and C. V. Shank, "Distributed-feedback lasers in thin-film optical waveguides," *IEEE J. Quantum Electron.*, vol. QE-8, pp. 833–838, Nov. 1972.

[16] Zh. I. Alferov *et al.*, "Semiconductor laser with extremely low divergence of radiation" (in Russian), *Sov. Phys.–Semicond.*, vol. 8, pp. 832–833, 1974; also (in English), *Sov. Phys.–JETP*, pp. 541 and 542.

[17] P. Zory, "Laser oscillation in leaky corrugated optical waveguides," *Appl. Phys. Lett.*, vol. 22, pp. 125–128, 1973.

[18] K. O. Hill and A. Watanabe, "Passive-core corrugated-waveguide laser," *Appl. Opt.*, vol. 12, pp. 430–433, 1973.

[19] D. R. Scifres, R. D. Burnham, and W. Streifer, "Observation of highly collimated laser beams from electrically pumped SH GaAs/GaAlAs distributed feedback lasers," *Appl. Phys. Lett.*, vol. 26, pp. 48–50, 1975.

[20] S. T. Peng and T. Tamir, "Directional blazing of waves guided by asymmetric dielectric gratings," *Opt. Commun.*, vol. 11, pp. 405–409, 1974.

Characteristics of Room-Temperature 2.3-μm Laser Emission from Tm^{3+} in YAG and $YAlO_3$

JOHN A. CAIRD, MEMBER, IEEE, LARRY G. DESHAZER, AND JOHN NELLA

Abstract—The relaxation of low-lying excited states of Tm^{3+} ions doped in YAG, $YAlO_3$, and Y_2O_3 due to photon and phonon emission is studied theoretically. Stimulated emission cross sections (integrated over frequency), fluorescence lifetimes, and radiative quantum efficiencies are calculated and their implications for laser operation on the 2.3-μm $^3F_4 \rightarrow {}^3H_5$ line of Tm^{3+} are discussed. The calculations, based on a few phenomenological parameters which have been determined by others, are easily generalizable to other host materials and other rare-earth (RE) ions.

Room-temperature pulsed laser emission from Tm^{3+} ions near 2.3 μm was observed on one line in Tm:Cr:YAG, and on four lines in Tm:Cr:$YAlO_3$. Lower oscillation thresholds were generally obtained in the $YAlO_3$ rods, consistent with the theory presented. A threshold of 31 J was obtained with a Tm:Cr:$YAlO_3$ rod at 2.274 μm. In the free-running pulsed mode, peak power levels up to several hundred watts and total output energies up to 12 mJ/pulse were observed. Other general, observed operating characteristics are discussed.

I. INTRODUCTION

THE STRONG, sharp line fluorescence from transparent crystals doped with rare-earth (RE) ions has long been recognized. As a result, these materials have been used extensively as active media in optically pumped laser devices. The choice of RE crystal combinations for use as laser materials has generally been made empirically, but quantitative theories have been used increasingly in recent years to evaluate RE laser materials. In 1968, Riseberg, Moos, and Partlow [1] discussed the application of multiphonon relaxation data to the design of quantum electronic devices. Subsequently, Moos [2] has described a three parameter model for calculating these nonradiative transition rates. Since the early 1970's the techniques developed by Judd [3] and Ofelt [4] (the J-O model) have been used in several studies to calculate radiative transition rates in RE laser materials [5]-[8]. The combination of these theories into a general evaluation procedure was proposed by Krupke [9] and has been used to study a large number of actual and potential laser devices [10]-[12]. The pertinent calculations will be described here for three thulium-doped crystals.

The need for additional laser sources operating in the 2-2.5-μm atmospheric window led to a search for a suitable RE/host system [13], [14]. As will be shown, the $^3F_4 \rightarrow {}^3H_5$ fluorescence of trivalent thulium (Tm^{3+}) was found to have characteristics favorable to laser action around 2.3 μm. A Tm:Cr:$YAlO_3$ laser rod was subsequently fabricated, and pulsed oscillation was demonstrated on two lines near 2.3μm [14], [15]. Additional study of this system has led to the observation of new laser lines, reported here, at 2.27 and 2.32 μm in Tm:Cr:$YAlO_3$ and at 2.32 μm in Tm:Cr:YAG. The pertinent energy manifolds are depicted in Fig. 1, where the sensitizing function of the Cr^{3+} ions is indicated. Laser oscillation on $^3H_4 \rightarrow {}^3H_6$ transitions has been previously reported in Tm:Cr:YAG at 2.01 μm and in Tm:YAG at 1.88 and 2.01 μm [16]. The latter part of this paper discusses the characteristics of the observed $^3F_4 \rightarrow {}^3H_5$ laser emission (e.g., wavelength, threshold, polarization, and efficiency), along with the prospects for improved performance and CW operation.

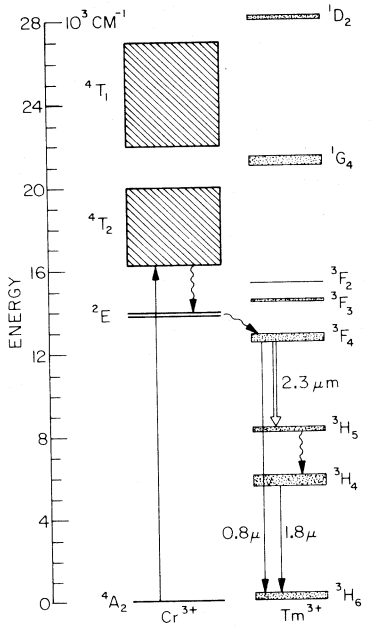

Fig. 1. Energy level diagram of the 2.3-μm Tm^{3+} laser sensitized with Cr^{3+} (after Hobrock [14]).

II. THEORETICAL CONSIDERATIONS

Since the 2.3-μm thulium laser was developed as a result of the previously mentioned theoretical work, the relevant calculations will be described here. This will show, by example, how the theories are applied, and will be compared qualitatively with the experimental results. Some of the parameters used, which will be described, were only estimated when the original analysis was performed [13], but have

Manuscript received March 27, 1975. This work was supported in part by independent research and development funds, Hughes Aircraft Company, Culver City, Calif. 90230.

J. A. Caird is with the Department of Physics, University of Southern California, Los Angeles, Calif. 90007, and with Hughes Aircraft Company, Culver City, Calif. 90230.

L. G. DeShazer is with the Center for Laser Studies, University of Southern California, Los Angeles, Calif. 90007.

J. Nella is with Hughes Aircraft Company, Culver City, Calif. 90230.

subsequently appeared in the literature. The discussion will be limited to thulium-doped $YAlO_3$, YAG, and Y_2O_3, since these are the only materials for which a full set of parameters is currently available.

A. Radiative Transitions

The spontaneous emission rate between two nondegenerate energy levels due to dipolar processes is given by

$$A(\alpha,\beta)=\frac{64\pi^4}{3h\bar{\lambda}^3}\chi|\langle\alpha|\boldsymbol{D}|\beta\rangle|^2 \tag{1}$$

where $\bar{\lambda}$ is the mean wavelength of the transition and $\boldsymbol{D}$ is the electric or magnetic dipole operator. In (1), χ is a factor which corrects for the local effective field and increased density of electromagnetic states seen by an atomic system embedded in a dielectric medium. If a dielectric with refractive index n has zero magnetic susceptibility, there is no effective field correction for magnetic dipole emission and χ is given by n^3 due to the increased density of final states of the electromagnetic field. In such cases it can be shown, in the tight binding limit, that the first-order correction factor for electric dipole emission is $\chi=n(n^2+2)^2/9$ [17].

In laser devices another very important parameter is the cross section for stimulated emission which for nondegenerate levels is equal to the absorption cross section. The integrated cross section Σ can be related to the spontaneous emission rate [18]

$$\Sigma(\alpha,\beta)\equiv\int\sigma(\nu)d\nu=\frac{\bar{\lambda}^2}{8\pi n^2 c}A(\alpha,\beta) \tag{2}$$

where ν has been taken in wavenumbers ($\nu=1/\lambda$). In (2) the factor n^2 takes into account the reduced velocity of light in the medium along with the increased density of states. From (1) and (2) the integrated cross section is given by

$$\Sigma(\alpha,\beta)=\frac{8\pi^3}{3hc\bar{\lambda}}\frac{\chi}{n^2}|\langle\alpha|\boldsymbol{D}|\beta\rangle|^2. \tag{3}$$

For RE ions doped in crystals the $2J+1$ levels associated with a state of total angular momentum J are only split by a few hundred wavenumbers, so that experimental observations often involve averages over them. The total transition rate from level α to all components β of level $|bJ'\rangle$ is given by

$$A(\alpha,bJ')=\sum_{\beta}A(\alpha,\beta). \tag{4}$$

Then if the individual components α of level $|aJ\rangle$ are equally populated, the observed decay rate will be the average over the upper manifold. Thus the observed rate is

$$A(aJ,bJ')=\frac{1}{(2J+1)}\sum_{\alpha,\beta}A(\alpha,\beta) \tag{5}$$

which, using (1), becomes

$$A(aJ,bJ')=\frac{64\pi^4\chi}{3h\bar{\lambda}^3(2J+1)}\sum_{\alpha,\beta}|\langle aJ\alpha|\boldsymbol{D}|bJ'\beta\rangle|^2. \tag{6}$$

Similarly, the observed integrated emission cross section is

$$\Sigma(aJ,bJ')=\frac{8\pi^3}{3hc\bar{\lambda}(2J+1)}\frac{\chi}{n^2}\sum_{\alpha,\beta}|\langle aJ\alpha|\boldsymbol{D}|bJ'\beta\rangle|^2. \tag{7}$$

The results predicted by these equations can be in error to some extent when the equal population assumption is strongly violated.

Fundamental to the calculation of these quantities are the dipole matrix elements. Formulas for the magnetic dipole matrix elements can be found in standard texts [19]. The electric dipole matrix elements in the J-O model [3], [4] can be written as

$$\sum_{\alpha,\beta}|\langle aJ\alpha|\boldsymbol{D}|bJ'\beta\rangle|^2=e^2\sum_{t=2,4,6}\Omega_t|\langle aJ\|U^t\|bJ'\rangle|^2 \tag{8}$$

where the Ω_t are intensity parameters, usually derived empirically, and the $\langle\|U^t\|\rangle$ are reduced matrix elements of the angular unit tensor operators in the atomic $4f^n$ configuration. Intensity parameters have been published for Tm^{3+} in YAG [12], $YAlO_3$ [20], and Y_2O_3 [21] and are listed in Table I. A computer program was written to calculate the required matrix elements [10] using techniques described by Judd [22]. The wave functions for Tm^{3+} derived by Krupke and Gruber [23] were used to compute the unit tensor operator matrix elements, listed in Table II, between low-lying energy levels. Table III lists the resulting integrated emission cross sections and spontaneous emission rates calculated for each material, including both electric and magnetic dipole contributions. In a previous study [10], [11] it was found that many RE transitions with Σ values greater than 10^{-18} cm have produced laser emission provided that the relaxation of the upper level by other mechanisms is sufficiently slow, that is, provided that its radiative quantum efficiency is sufficiently high.

B. Nonradiative Transitions

For low-RE dopant concentrations the dominant nonradiative relaxation mechanism is multiphonon emission. According to Moos [2] the multiphonon relaxation rate can be approximated by

$$R(a)=Be^{-\alpha\Delta E_a}\left\{1+\left[\exp\left(\frac{E_p}{kT}\right)-1\right]^{-1}\right\}^{\frac{\Delta E_a}{E_p}} \tag{9}$$

where B, α, and E_p are characteristic of the host crystal, with negligible dependence on the dopant ion. In (9), ΔE_a is the energy gap between level a and the next lower level. The bracketed factor in (9) accounts for increased transition rates

TABLE I
INTENSITY PARAMETERS FOR Tm^{3+} IN YAG, $YAlO_3$, AND Y_2O_3

	Ω_2 (10^{-20} cm^2)	Ω_4 (10^{-20} cm^2)	Ω_6 (10^{-20} cm^2)
Tm:YAG	0.7	1.2	0.5
Tm:$YAlO_3$	0.67	2.30	0.74
Tm:Y_2O_3	4.07	1.46	0.61

TABLE II
MATRIX ELEMENTS FOR Tm^{3+}

Upper State	Lower State	$\langle U^2\rangle^2$	$\langle U^4\rangle^2$	$\langle U^6\rangle^2$
$^3H_4$	$^3H_6$	0.527	0.718	0.228
$^3H_5$	$^3H_4$	0.089	0.125	0.905
	$^3H_6$	0.107	0.231	0.638
$^3F_4$	$^3H_5$	0.011	0.480	0.004
	$^3H_4$	0.129	0.133	0.213
	$^3H_6$	0.249	0.118	0.608
$^3F_3$	$^3F_4$	0.081	0.344	0.264
	$^3H_5$	0.629	0.347	0.
	$^3H_4$	0.002	$< 10^{-3}$	0.167
	$^3H_6$	0.	0.316	0.841
$^3F_2$	$^3F_3$	0.004	0.075	0.
	$^3F_4$	0.287	0.163	0.074
	$^3H_5$	0.	0.290	0.583
	$^3H_4$	0.311	0.056	0.044
	$^3H_6$	0.	$< 10^{-3}$	0.258

TABLE III
COMPUTED INTEGRATED CROSS SECTIONS AND RADIATIVE TRANSITION RATES FOR Tm^{3+} IN $YAlO_3$, Y_2O_3, AND YAG

Upper State	Lower State	Tm:$YAlO_3$ $\Sigma(10^{-18}$ cm)	Tm:$YAlO_3$ A(sec^{-1})	Tm:Y_2O_3 $\Sigma(10^{-18}$ cm)	Tm:Y_2O_3 A(sec^{-1})	Tm:YAG $\Sigma(10^{-18}$ cm)	Tm:YAG A(sec^{-1})
$^3H_4$	$^3H_6$	2.43	210	3.74	311	1.44	110
$^3H_5$	$^3H_4$	0.45	9	0.49	9	0.29	5
	$^3H_6$	1.99	374	2.11	380	1.38	299
$^3F_4$	$^3H_5$	1.17	61	0.85	42	0.68	31
	$^3H_4$	0.97	131	1.39	180	0.67	80
	$^3H_6$	2.22	972	3.91	1643	1.49	578
$^3F_3$	$^3F_4$	0.51	4	0.49	4	0.30	2
	$^3H_5$	1.91	198	4.82	478	1.29	118
	$^3H_4$	0.63	134	0.59	121	0.51	96
	$^3H_6$	4.96	2827	3.60	1971	2.83	1425
$^3F_2$	$^3F_3$	0.08	~0	0.07	~0	0.06	~0
	$^3F_4$	0.53	8	1.25	19	0.36	5
	$^3H_5$	2.65	331	1.89	226	1.49	164
	$^3H_4$	1.24	301	4.64	1080	0.99	212
	$^3H_6$	1.05	653	0.85	503	0.67	364

at elevated temperatures due to emission stimulated by thermal phonons of energy E_p. This factor may be neglected at temperatures for which E_p is much greater than kT.

Transition rates due to multiphonon emission have been measured in YAG [24], $YAlO_3$ [25], and Y_2O_3 [26], [27]. Estimates of the parameters B, α, and E_p based on these data are listed in Table IV. Using these parameters the measured rates are typically within a factor of 2 of the rates predicted by (9). The predicted multiphonon decay rates for the low-lying thulium energy levels are given in Table V for each crystal. The energy gaps ΔE_a were found from the absorption spectra of Tm:Y_2O_3 [28] and Tm:$YAlO_3$ [14]. For the purposes of this calculation, the energy gaps for Tm:YAG were assumed to be equal to those of Tm:$YAlO_3$. The transition rates for the $^3F_2$ level are not expected to be accurate since the energy gap ΔE_a is less than E_p.

C. Quantum Efficiencies and Conclusions

When the RE-ion doping level is on the order of one atomic percent or less, concentration-dependent nonradiative relaxation mechanisms such as ion-pair relaxation can generally be neglected. In such cases the nonradiative lifetime τ_n is given by

$$\frac{1}{\tau_n(a)} = R(a). \tag{10}$$

The radiative lifetime τ_r of the level is defined as

$$\frac{1}{\tau_r(a)} = \sum_b A(a, b) \tag{11}$$

where the J's of (6) have been dropped for simplicity. The total lifetime τ is found from

$$\frac{1}{\tau(a)} = \frac{1}{\tau_n(a)} + \frac{1}{\tau_r(a)} \tag{12}$$

and the radiative quantum efficiency is given by

$$\eta_a = \frac{\tau(a)}{\tau_r(a)}. \tag{13}$$

These quantities were calculated for each crystal using the results from Tables III and V and are listed in Table VI.

It is evident that only the $^3H_4$ and $^3F_4$ energy levels have high radiative quantum efficiencies, and can be expected to fluoresce strongly. The previously observed $^3H_4 \rightarrow {}^3H_6$ laser emission has been noted in Section I. Here we are interested in the $^3F_4 \rightarrow {}^3H_5$ transitions around 2.3 μm. Table VI shows that the $^3F_4$ level should fluoresce in all three crystals, though somewhat more weakly in YAG. The integrated cross section of the $^3F_4 \rightarrow {}^3H_5$ transition is highest in $YAlO_3$ (Table III) which is not surprising since for this transition the $(U^{(4)})^2$ matrix element is by far the largest (Table II), while the largest Ω_4 parameter occurs in $YAlO_3$ (Table I). Additional advantages predicted for $YAlO_3$ include the fastest decay rate of the lower laser level and the fastest rate of energy transfer between the ^3F states.

However, there are additional factors to consider in choosing a laser crystal, which cannot be discussed quantitatively at present. An examination of the Tm^{3+} energy level diagram (see Fig. 1) shows the shortage of energy levels above the $^3F_4$ state which can be used for optical pumping. Efficient flashlamp to laser energy conversion therefore requires sensi-

TABLE IV
ESTIMATED MULTIPHONON PARAMETERS FOR $YAlO_3$, Y_2O_3, AND YAG

crystal	B (sec^{-1})	α (10^{-3} cm)	E_p (cm^{-1})
$YAlO_3$	6.5×10^9	4.7	600
Y_2O_3	4.0×10^8	4.2	550
YAG	1.0×10^8	3.2	700

TABLE V
CALCULATED MULTIPHONON EMISSION RATES

Excited State	Tm:$YAlO_3$		Tm:Y_2O_3		Tm:YAG
	$\Delta E(cm^{-1})$	$R(sec^{-1})$	$\Delta E(cm^{-1})$	$R(sec^{-1})$	$R(sec^{-1})$
$^3H_4$	5272	2×10^{-1}	4818	1.2	5.9
$^3H_5$	2273	1.8×10^5	2069	8.7×10^4	7.7×10^4
$^3F_4$	3829	1.4×10^2	3639	1.4×10^2	5.8×10^2
$^3F_3$	1499	6.5×10^6	1519	8.2×10^5	8.9×10^5
$^3F_2$	399	10^9	337	10^8	3×10^7

TABLE VI
CALCULATED LIFETIMES AND QUANTUM EFFICIENCIES

Excited State	Tm:$YAlO_3$		Tm:Y_2O_3		Tm:YAG	
	τ(sec)	η	τ(sec)	η	τ(sec)	η
$^3H_4$	4.8×10^{-3}	1.00	3.2×10^{-3}	1.00	8.6×10^{-3}	0.95
$^3H_5$	5.6×10^{-6}	.002	11.5×10^{-6}	.005	13×10^{-6}	.003
$^3F_4$	$.77 \times 10^{-3}$	.89	$.55 \times 10^{-3}$	.93	$.79 \times 10^{-3}$	.54
$^3F_3$	$.15 \times 10^{-6}$	.0005	1.2×10^{-6}	.003	1.1×10^{-6}	.002
$^3F_2$	1×10^{-9}	$\sim 10^{-6}$	10×10^{-9}	$\sim 2 \times 10^{-5}$	30×10^{-9}	$\sim 2 \times 10^{-5}$

tization by one or more additional dopants. In this case, trivalent chromium ions provide broad absorption bands in the visible and efficient energy transfer to the ^3F multiplet of thulium [16], [29]. In YAG the pulsed threshold for $^3H_4 \rightarrow {}^3H_6$ laser emission in thulium was reduced by a factor of 7 when the crystal was co-doped with chromium [16]. The effect is expected to be even greater for $^3F_4 \rightarrow {}^3H_5$ transitions because none of the transferred energy is lost to $^3F_4 \rightarrow {}^3H_6$ fluorescence at 0.8 μm (see Fig. 1).

Chromium can be doped in YAG and $YAlO_3$ where it enters the lattice substitutionally at Al^{3+} sites, but it cannot be doped in Y_2O_3. For this reason YAG and $YAlO_3$ were considered the prime candidate hosts for the 2.3-μm thulium laser. In these crystals it is possible that the overriding factor affecting laser performance is the $Cr^{3+} \rightarrow Tm^{3+}$ energy transfer efficiency. Factors affecting this energy transfer, such as energy-level proximity and orbit-lattice coupling strengths, vary from crystal to crystal, and there is no applicable predictive theory. Also, it was felt that none of the existing experimental data on energy transfer were conclusive enough to make a decision on that basis alone.

On the basis of considerations presented so far, the prime candidate laser material was Tm:Cr:$YAlO_3$. Laser rods of this type were fabricated first, and laser action near 2.35 μm was demonstrated [14], [15]. However, because of the advanced growth technology of high-optical-quality YAG crystals, and the uncertainties regarding Cr^{3+} sensitization, a rod of Tm:Cr:YAG was also fabricated for testing.

TABLE VII
LASER ROD STATISTICS

Rod	Material	Dimensions (mm)	at.% Tm^{3+}	at.% Cr^{3+}	Rod Axis
A	Tm:Cr:$YAlO_3$	5 x 50	1.0	0.25	<112>
B	Tm:Cr:$YAlO_3$	3 x 50	1.0	0.25	<112>
C	Tm:Cr:$YAlO_3$	3 x 75	1.0	0.75	<111>
D	Tm:Cr:YAG	3 x 50	1.0	0.10	- -

III. EXPERIMENTAL RESULTS

Long-pulse laser tests were performed at room temperature with three rods of Tm:Cr:$YAlO_3$ and one rod of Tm:Cr:YAG, all antireflection coated at 2.3 μm. Pertinent rod statistics are listed in Table VII. The orientation of the $YAlO_3$ rods used in these experiments was determined through the Laue backscatter method of X-ray diffraction. The absorption spectrum of each Tm:Cr:$YAlO_3$ rod was compared to that determined by Weber [29] to derive the doping levels of the rods. The doping levels listed in Table VII assume distribution coefficients of 1.0 for Tm^{3+} and 2.5 for Cr^{3+} in Weber's Czochralski-grown $YAlO_3$ samples. The Cr^{3+} doping level in the YAG rod was determined by comparison of the rod's absorption spectrum to that of a Cr^{3+}:YAG sample with known concentration [30]. The Tm^{3+} concentration in the YAG rod is listed according to the manufacturer's specifications (Union Carbide, Crystal Products Department), but was not determined here for lack of an adequate standard of comparison. The accuracy of the concentrations listed in Table VII is estimated to be ±10 percent.

Most experiments were performed with linear xenon flashlamps (ILC7L3 or ILC7L4) in elliptical pump cavities, and highly reflective (99+ percent) mirrors spaced 25 cm apart. Flashlamp pulses were limited to 1 ms or less in duration to minimize losses due to spontaneous relaxation of the upper laser level. A summary of the thresholds and polarizations of the observed laser lines appears in Table VIII. Thresholds for rods *A* and *B* were very similar, so the 2.27- and 2.32-μm entries have been omitted for rod *A*. The 2.35-μm doublet was resolved for rod *A* at about twice threshold, but the thresholds of the individual lines were not obtained since the signal level near threshold was too small to allow their resolution. The ILC flashlamps used had an inside diameter of 7 mm and were about 1 in longer than the laser rods so that the actual thresholds should be somewhat less than the reported electrical input energies. When rod *B* was pumped by a 450-torr xenon flashlamp with a 3-mm × 1-in luminous volume (ILC L-3F1G) in a 1-in pump cavity, laser action was observed at 44-J input. A threshold of 31 J was measured in the same cavity using a 1200-torr krypton flashlamp of the same dimensions.

Since the Stark splittings of Tm^{3+} in YAG were not determined, the specific laser transition was not identified for this

TABLE VIII
2.3-μM THULIUM LASER CHARACTERISTICS

Laser Rod	Transition (and Symmetries)	Wavelength (microns)	Polarization	Threshold (Joules)	Flashlamp
A:<112> $YAlO_3$	$^3F_4a(\Gamma_1) \rightarrow {}^3H_5a(\Gamma_2)$	2.354	π	144	ILC7L3
	$^3F_4a(\Gamma_1) \rightarrow {}^3H_5b(\Gamma_1)$	2.355	σ	144	ILC7L3
B:<112> $YAlO_3$	$^3F_4c(\Gamma_1) \rightarrow {}^3H_5a(\Gamma_2)$	2.274	π	64	ILC7L3
	$^3F_4c(\Gamma_1) \rightarrow {}^3H_5a(\Gamma_2)$	2.274	π	44	ILC L-3F1G
	$^3F_4c(\Gamma_1) \rightarrow {}^3H_5a(\Gamma_2)$	2.274	π	31	1200 Torr Kr
	$^3F_4b(\Gamma_2) \rightarrow {}^3H_5a(\Gamma_2)$	2.318	σ	132	ILC7L3
	$^3F_4a(\Gamma_1) \rightarrow {}^3H_5a,b(\Gamma_2,\Gamma_1)$	2.353	π,σ	110	ILC7L3
C:<111> $YAlO_3$	$^3F_4c(\Gamma_1) \rightarrow {}^3H_5a(\Gamma_2)$	2.274	π	94	ILC7L4
	$^3F_4b(\Gamma_2) \rightarrow {}^3H_5a(\Gamma_2)$	2.318	σ	188	ILC7L4
	$^3F_4a(\Gamma_1) \rightarrow {}^3H_5a,b(\Gamma_2,\Gamma_1)$	2.353	π,σ	325	ILC7L4
D:YAG	$^3F_4 \rightarrow {}^3F_5$	2.324	Un.	200	ILC7L3

Note: Stark split levels are labeled $a, b, c, \cdots$, in order of increasing energy.

host. In $YAlO_3$, thulium enters the lattice on Y^{3+} sites with reflection symmetry (C_s) in the plane normal to the c axis [14]. As a result, the atomic wave functions are either even (Γ_1) or odd (Γ_2) under reflection in this plane, and $\Gamma_i \rightarrow \Gamma_j$ transitions are either σ polarized (in the reflection plane) if $i=j$, or π polarized (parallel to the c axis) if $i \neq j$. The Tm^{3+} energy levels in $YAlO_3$ and their reflection symmetries were determined previously at 4 K [14]. However, the identification of the room-temperature laser transitions is not straightforward since the energy levels shift slightly with temperature. The laser line polarizations are useful in making these identifications.

Since $YAlO_3$ is a biaxial crystal, the laser resonator modes tend to be polarized along the major and minor axes of the cross section of the Fresnel ellipsoid cut normal to the rod axis. In rods cut along one major crystal axis, these modes are polarized along the other two major axes. A calculation of the expected polarization directions in ⟨111⟩ $YAlO_3$ was performed using previously determined refractive indices [31]. When referred to the projection of the c axis in the plane normal to the ⟨111⟩ direction the mode angles were predicted to be $-16.4°$ and $+73.6°$. Measurements of the observed laser line polarizations were consistent with this calculation ($\pm 10°$), the prime source of error being caused by the transfer of the laser rod from the X-ray goniometer to the laser cavity. In each rod, laser emission at 2.318 μm was polarized in the polarization mode farthest from the c axis projection, indicating σ polarization. The other lines were all polarized in the mode closest to the c axis, but since the rod axes were far from normal to the c axis, it cannot be concluded that they are all π polarized.

It should be noted here that the 2.27-μm line showed the lowest threshold in all rods because a high-reflectivity curved reflector was available at that wavelength to construct a folded confocal resonator. The resulting reduction of losses led to reduced thresholds. No curved mirror with high reflectivity (99+ percent) at 2.35 μm was available, so plane parallel mirrors were used.

When plane mirrors with achromatic reflectivity (99+ percent) in the 2–2.4-μm region were used, the 2.27-μm line had the lowest threshold in the ⟨111⟩ rod, while the two lines near 2.35 μm (unresolved) had the lowest threshold in the ⟨112⟩ rods. This indicates that the 2.27-μm line is π polarized since its relative threshold is increased when the c axis is closer to the direction of propagation. Comparison of the observed wavelengths with the Tm^{3+} energy levels [14] shows that the two closely spaced lines near 2.35 μm probably emanate from the same upper laser level and terminate on neighboring levels of opposite symmetry indicating one π- and one σ-polarized line. These arguments along with the 4-K energy levels [14] were used to determine the transitions listed in Table VIII and depicted in Fig. 2.

In the ⟨112⟩ axis rods it was possible to suppress 2.35-μm oscillation by using a 49-cm-radius mirror with 5-percent transmission at this wavelength, but only 0.35-percent transmission at 2.27 μm. In the anisotropic $YAlO_3$ medium, the wave vectors of the two orthogonal polarization modes are not parallel (unless propagation is along a major crystallographic axis) so that the optimum resonator alignment is not the same for both polarizations. It was found that tuning between the 2.27- and 2.32-μm lines which are of opposite polarization could be achieved by changing the alignment of the 49-cm-radius mirror. This effect was not observed when using flat mirrors. All of the available mirrors had higher reflectivity at

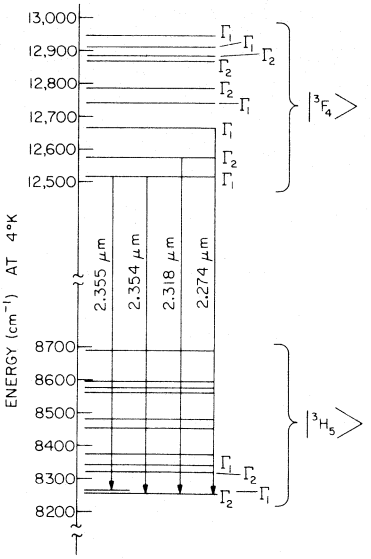

Fig. 2. $^3F_4$ and $^3H_5$ energy levels in Tm:$YAlO_3$ (4 K) and associated room-temperature laser transitions.

2.27 μm than at 2.35 μm, so it was not possible to suppress 2.27-μm oscillation in the ⟨111⟩ rod. As a result of the competing 2.27-μm laser emission, the observed 2.35-μm oscillation threshold was much higher in that rod.

The two lines near 2.35 μm were first reported to lie at 2.348 and 2.349 μm [14], [15]. The wavelengths of these lines appear to be very sensitive to operating conditions, especially with respect to the rod temperature. In the present work the average wavelength of these lines was found to be 2.353 μm under normal conditions, as indicated in Table VIII, for rods *B* and *C*. When the spectrometer slits were narrowed in an attempt to resolve the two lines, the flashlamp energy was increased to maintain the signal level. This had the effect of increasing the temperature of the convectively air-cooled rod with a resulting further increase in the wavelengths of this line pair to 2.354 and 2.355 μm. Fig. 3 is an oscilloscope display showing the resolved laser-line pair. The total scan time was approximately 1 h with the laser fired once per minute. The upper trace is a set of wavelength markers from the spectrometer at 2.3526, 2.3546, and 2.3566 μm (left to right). The lower trace gives the laser energy at the spectrometer's output slit as a function of wavelength. The signal level was held between shots by a boxcar integrator.

The laser output energy was measured as a function of flashlamp energy for rod *A* at 2.274 μm. The results appear in Fig. 4. In this experiment the flashlamp's luminous volume dimensions (7 × 75 mm) were considerably larger than the laser rod (5 × 50 mm). Therefore, the actual efficiency is estimated to be about twice as high as measured. A folded confocal resonator was used with 0.35-percent output coupling. This is undoubtedly a severely undercoupled condition, so that considerably higher efficiency should be obtainable through proper resonator design alone. The measurements were made with a PbS detector whose integrated output was calibrated in volts/joule using a repetitively pulsed Ho:YAG laser at 2.1 μm illuminating a MgO block. The average power, about 1 W, of

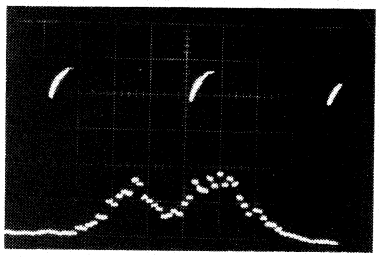

Fig. 3. Tm:Cr:$YAlO_3$ laser emission spectrum near 2.35 μm. The calibration markers are at 2.3526, 2.3546, and 2.3566 μm (left to right).

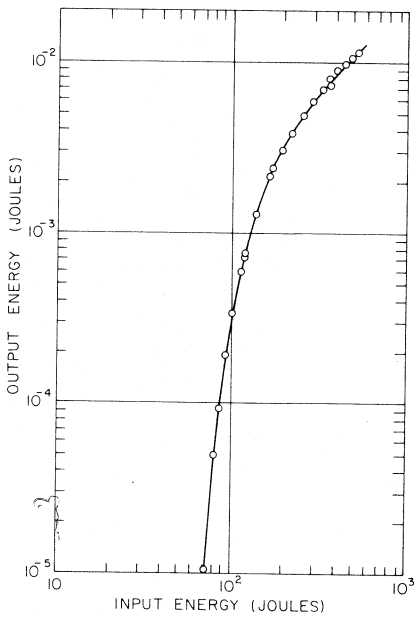

Fig. 4. Tm:Cr:$YAlO_3$ laser output energy at 2.274 μm versus electrical energy to flashlamp (0.35-percent output coupling).

the Ho:YAG laser was measured with a calibrated thermopile. The energy per pulse is given by $P_{avg} \cdot T$ where T is the pulse period. The slight increase in PbS response from 2.1 to 2.3 μm was also taken into account.

A fast InAs detector was calibrated for peak power (volts/watt) in the same manner as described above. Here the Ho:YAG peak power is given by $P_{avg} \cdot T/\tau$, where τ is the effective pulsewidth. The output of the Tm:Cr:$YAlO_3$ laser consisted of a train of relaxation oscillation spikes, typical of non-*Q*-switched insulating crystal lasers. The peak power of the pulses in the train was found to be several hundred watts.

IV. Summary and Conclusions

The long-pulse 2.3-μm laser characteristics of four thulium laser rods have been investigated at room temperature. The $YAlO_3$ rods showed lower oscillation thresholds in all cases. This is consistent with the theoretical results of Section II, if the $Cr^{3+} \rightarrow Tm^{3+}$ energy transfer efficiency is assumed to be approximately equal for YAG and $YAlO_3$. For π-polarized lines in $YAlO_3$, the gain should vary as the squared cosine of the angle between the *c* axis and the polarization direction. The *c* axis makes angles of approximately 45° and 30° with the ⟨111⟩ and ⟨112⟩ directions, respectively. Rods grown

normal to the c axis (⟨mn0⟩) should, therefore, have thresholds for π lines which are factors of 2 and 4 lower than the ⟨111⟩ and ⟨112⟩ rods, respectively. This would indicate a pulsed threshold on the order of 8 J for the 2.274-μm line with the 1200-torr krypton lamp, other things being equal.

A relatively low CW threshold is expected at room temperature for several reasons. First, the pulsed threshold is relatively low compared to other insulating crystal lasers. Second, the lower laser level lifetime is significantly shorter than that of the upper level. In addition, the thermal population of the lower laser level is negligible.

One factor which may adversely affect the CW operation is the long lifetime of the $^3H_4$ energy level. There are several possible schemes for dealing with this problem. The addition of ions such as Pr^{3+}, Eu^{3+}, Tb^{3+}, etc., would reduce the $^3H_4$ lifetime by nonradiative ion-pair interaction as, for example, was done with the $^5I_7$ level of Ho^{3+} by Johnson and Guggenheim [32]. Care would have to be taken so that the $^3F_4$ lifetime is not also reduced. A second possibility would be to take advantage of potential excited-state absorption by the $^3H_4$ state. Examination of the energy levels in Fig. 1 shows that a neodymium laser might be able to pump $^3H_4 \rightarrow {}^3F_2$ transitions in the 1.06-μm wavelength region. Finally, if the crystal temperature is lowered, laser action on the $^3H_4 \rightarrow {}^3H_6$ transitions might be obtained simultaneously around 1.9 μm to deplete $^3H_4$ population. This would result in a very interesting double laser line device.

Laser action on $^3H_4 \rightarrow {}^3H_6$ transitions has not yet been reported for Tm:$YAlO_3$, but reference to Table III shows that this transition's cross section should be higher in $YAlO_3$ than in YAG where CW emission was observed with a 160-W threshold at 85 K [16]. If only $^3H_4 \rightarrow {}^3H_6$ laser emission is considered, the threshold in $YAlO_3$ might be higher than in YAG because the fractional energy lost to $^3F_4 \rightarrow {}^3H_6$ fluorescence is $\sim A(^3F_4 \rightarrow {}^3H_6) \cdot \tau(^3F_4)$ which from Tables III and VI is predicted to be 75 percent in $YAlO_3$ as opposed to only 46 percent in YAG. However, if the $^3F_4 \rightarrow {}^3H_5$ laser action is obtained simultaneously, a portion of the loss to fluorescence would be avoided. Thus simultaneous oscillation would be beneficial to both laser lines.

The other significantly developed solid-state lasers in the 2–2.5-μm atmospheric window are Ho^{3+}:YAG at 2.1 μm and Dy^{2+}:CaF_2 at 2.36 μm. In both of these lasers the terminal laser levels are in the ground-state manifold so that efficient operation requires cryogenic cooling. The minimal cooling which the Tm:Cr:$YAlO_3$ laser might require makes it a reasonable alternative for many applications. It is likely that other transitions in the $^3F_4 \rightarrow {}^3H_5$ group (see Fig. 2) can be made to lase by using an intracavity dispersive element, with potential wavelengths from 2.2 to 2.6 μm. In an ⟨mn0⟩ rod, tuning between π and σ lines such as 2.274 and 2.355 μm could be achieved by simply rotating a polarizer or Brewster plate inside the laser cavity. Although the efficiency achieved in these experiments was fairly low, improvements are expected when attempts are made at optimization. In the final analysis the added energy savings due to reduced cooling requirements must also be considered.

Acknowledgment

The authors wish to thank Dr. W. F. Krupke for his efforts and analysis which were essential to the initiation of this research. They also wish to thank the Crystal Products Department, Union Carbide Corporation, for donation of the original ⟨112⟩ $YAlO_3$ laser rods.

References

[1] L. A. Riseberg, H. W. Moos, and W. D. Partlow, "Multiphonon relaxation in laser materials and applications to the design of quantum electronic devices," *IEEE J. Quantum Electron. (Special Issue–1968 Int. Quantum Electronics Conf.: Part I)*, vol. QE-4, pp. 609–612, Oct. 1968.

[2] H. W. Moos, "Spectroscopic relaxation processes of rare earth ions in crystals," *J. Luminescence*, vols. 1 and 2, pp. 106–121, 1970.

[3] B. R. Judd, "Optical absorption intensities of rare-earth ions," *Phys. Rev.*, vol. 127, pp. 750–761, Aug. 1962.

[4] G. S. Ofelt, "Intensities of crystal spectra of rare-earth ions," *J. Chem. Phys.*, vol. 37, pp. 511–520, Aug. 1962.

[5] W. F. Krupke, "Radiative transition probabilities within the $4f^3$ ground configuration of Nd:YAG," *IEEE J. Quantum Electron.*, vol. QE-7, pp. 153–159, Apr. 1971.

[6] —, "Assessment of a promethium YAG laser," *IEEE J. Quantum Electron.* (Corresp.), vol. QE-8, pp. 725–726, Aug. 1972.

[7] —, "Induced-emission cross sections in neodymium laser glasses," *IEEE J. Quantum Electron.*, vol. QE-10, pp. 450–457, Apr. 1974.

[8] J. A. Caird and L. G. DeShazer, "Analysis of laser emission in Ho^{3+}-doped materials," *IEEE J. Quantum Electron.*, vol. QE-11, pp. 97–99, Mar. 1975.

[9] W. F. Krupke, private communication.

[10] J. A. Caird, "Rare-earth laser engineering program," AF Avionics Lab., Wright Patterson AFB, Ohio, AFAL-TR-73-323 (Contract F 33615-72-C-2038), Final Rep., 1973.

[11] —, "Theoretical analysis of rare-earth laser materials," presented at the 1974 Spring Meeting of the Optical Society of America, Washington, D. C., Apr. 21–25, 1974; summary in *J. Opt. Soc. Amer.*, vol. 64, p. 535, Apr. 1974.

[12] W. F. Krupke, "New rare-earth quantum electronic devices: A calculational approach," presented at the 1974 IEEE Region 6 Conf., Albuquerque, N. Mex., Apr. 24–26, 1974.

[13] —, "2.4 micron laser in Tm:YAG or $YAlO_3$," Hughes Aircraft Co., Culver City, Calif., independent research and development program (unpublished), 1970.

[14] L. M. Hobrock, "Spectra of thulium in yttrium orthoaluminate crystals and its four level laser operation in the middle infrared," Ph.D. dissertation, Univ. Southern Calif., Los Angeles, 1972.

[15] L. M. Hobrock *et al.*, "Four-level operation of Tm:Cr:$YAlO_3$ laser at 2.35 microns," in *Digest Tech. Papers, 7th Int. Quantum Electronics Conf.* (Montreal, P. Q., Canada), May 8–11, 1972.

[16] L. F. Johnson, J. E. Geusic, and L. G. Van Uitert, "Coherent oscillations from Tm^{3+}, Ho^{3+}, Yb^{3+} and Er^{3+} ions in yttrium aluminum garnate," *Appl. Phys. Lett.*, vol. 7, pp. 127–129, Sept. 1965.

[17] D. L. Dexter, "Theory of the optical properties of imperfections in nonmetals," in *Solid State Physics*, vol. 6, F. Seitz and D. Turnbull, Ed. New York: Academic, 1958.

[18] W. B. Fowler, and D. L. Dexter, "Relation between absorption and emission probabilities in luminescent centers in ionic solids," *Phys. Rev.*, vol. 128, pp. 2154–2165, Dec. 1962.

[19] B. G. Wybourne, *Spectroscopic Properties of Rare Earths*. New York: Interscience, 1965, ch. 4, p. 98.

[20] M. J. Weber, T. E. Varitimos, and B. H. Matsinger, "Optical intensities of rare-earth ions in yttrium orthoaluminate," *Phys. Rev. B*, vol. 8, pp. 47–53, July 1973.

[21] W. F. Krupke, "Optical absorption and fluorescence intensities in several rare-earth-doped Y_2O_3 and LaF_3 single crystals," *Phys. Rev.*, vol. 145, pp. 325–337, May 1966.

[22] B. R. Judd, *Operator Techniques in Atomic Spectroscopy*. New York: McGraw-Hill, 1963.

[23] W. F. Krupke and J. B. Gruber, "Optical-absorption intensities of rare-earth ions in crystals: The absorption spectrum of thulium

ethyl sulfate," *Phys. Rev.*, vol. 139, pp. A2008–A2016, Sept. 1965.
[24] G. M. Zverev, G. Ya. Kolodnyi, and A. M. Onishchenko, "Nonradiative transitions between levels of trivalent rare-earth ions in yttrium-aluminum garnate crystals," *Sov. Phys.–JETP*, vol. 33, pp. 497–501, Sept. 1971.
[25] M. J. Weber, "Multiphonon relaxation of rare-earth ions in yttrium orthoaluminate," *Phys. Rev. B*, vol. 8, pp. 54–64, July 1973.
[26] —, "Radiative and multiphonon relaxation of rare-earth ions in Y_2O_3," *Phys. Rev.*, vol. 171, pp. 283–291, July 1968.
[27] L. A. Riseberg, and H. W. Moos, "Multiphonon orbit-lattice relaxation of excited states of rare-earth ions in crystals," *Phys. Rev.*, vol. 174, pp. 429–438, Oct. 1968.
[28] J. B. Gruber, W. F. Krupke, and J. M. Poindexter, "Crystal-field splitting of trivalent thulium and erbium *J* levels in yttrium oxide," *J. Chem. Phys.*, vol. 41, pp. 3363–3377, Dec. 1964.
[29] M. J. Weber, "Chromium-rare earth energy transfer in $YAlO_3$," *J. Appl. Phys.*, vol. 44, pp. 4058–4064, Sept. 1973.
[30] —, private communication.
[31] K. W. Martin and L. G. DeShazer, "Indices of refraction of the biaxial crystal $YAlO_3$," *Appl. Opt.*, vol. 12, pp. 941–943, May 1973.
[32] L. F. Johnson and H. J. Guggenheim, "Electronic- and phonon-terminated laser emission from Ho^{3+} in BaY_2F_8," *IEEE J. Quantum Electron.*, vol. QE-10, pp. 442–449, Apr. 1974.

Amplified Spontaneous Emission and Signal Amplification in Dye-Laser Systems

U. GANIEL, MEMBER, IEEE, A. HARDY, G. NEUMANN, MEMBER, IEEE, AND D. TREVES, MEMBER, IEEE

Abstract—**Transversely pumped dye-laser systems are investigated theoretically and experimentally. A set of coupled rate equations for the excited-state population densities and for the photon fluxes in both directions, at all wavelengths, is presented. Both the temporal and spatial dependence of these quantities are accounted for. The equations are solved numerically for a variety of practical situations, and analytical approximations for some limiting cases are discussed. The results describe the dependence of the amplified-spontaneous-emission (ASE) output flux on pumping rate, the spectral narrowing process, and the effects of gain saturation. It is found that under practical laboratory conditions the gain of such dye systems saturates rapidly. Consequently, at high pumping rates the output varies linearly with pump intensity, and the conversion efficiency from pump to ASE photons approaches unity. The performance of dye-laser amplifiers is described by the same set of equations, and the gain characteristics of such systems are analyzed as a function of input signal intensity and pumping rate. The theoretical calculations are compared with the results of a set of experiments, and good agreement is found. The operation characteristics of a dye-laser amplifier are evaluated and utilized in the design of a narrow-band oscillator-amplifier system.**

I. Introduction

EVER SINCE the first successful operation of organic dye lasers [1], these systems have become the subject of intensive research.[1] Many dye systems exhibit high gains even when pumped by flashlamps where the pumping rates are relatively low [2]. Much higher pumping rates can be achieved in laser-pumped systems, and this approach has been used extensively both in pulsed systems and in CW operation, which to date has been achieved only with a laser as the pumping source [3]. In high-gain systems, particularly under strong pumping conditions, consideration of the phenomenon of amplified spontaneous emission (ASE) [4][2] becomes all important for understanding the behavior of such systems. This is true in particular for dye solutions when excited in a transverse pumping configuration [5]. In such systems the spontaneous emission is amplified as it propagates along the excited medium, and even without feedback the emitted radiation exhibits "laserlike" properties, i.e., low divergence and spectral narrowing. Operation of dye solutions in this ASE mode has been reported in recent years [6]. The effect of ASE must also be considered in analyzing the gain characteristics of dye oscillator-amplifier systems, where the ASE can interfere with the process of amplification of the input signal, causing excessive background noise in the output.

Spectral narrowing in ASE was treated in the past by various authors. Yariv and Leite [7] considered a simple model in which they calculated an approximate expression for the narrowing of the spectrum of the spontaneous emission, due to the gain profile of the medium at which it originates. Saturation was not accounted for in this model. Casperson and Yariv [8] dealt with spectral narrowing in lasers at steady state, extending their treatment to include saturation in amplifiers

Manuscript received April 16, 1975.

U. Ganiel, A. Hardy, and D. Treves are with the Department of Electronics, the Weizmann Institute of Science, Rehovot, Israel.
G. Neumann is with Tadiran, Israel Electronic Industries, on leave from the Department of Electronics, the Weizmann Institute of Science, Rehovot, Israel.

[1] A number of excellent review articles appear in F. P. Schäfer, Ed. *Dye Laser*.. New York: Springer, 1973.

[2] ASE is often referred to as "superradiance," although this term should probably be reserved for a completely different phenomenon, discussed first by Dicke [4a)].

by the amplified radiation. These authors obtained analytic results for certain limiting cases, and their results apply mainly to high-gain gas lasers with a Doppler-broadened gain profile. Casperson [9], [10] extended these results by including in the rate equations the effect of power flow in both directions, which was absent in previous treatments. Allen and Peters [11] considered ASE and amplification of external signals. Their discussion concentrated on high-gain gas-laser systems (mainly the 3.39-μ transition in He-Ne), and solutions of the relevant rate equations were obtained and fitted to experimentally determined parameters. The relevant level scheme in dye systems is generally more complex (ground-state absorption, triplet-state effects, etc.), and some of the assumptions which apply to the experimental situation in gas lasers cannot be made for dye-laser systems. Thus the extensive work of Allen and Peters [11] cannot be applied directly in the investigation of these systems. ASE in dye lasers has not been analyzed in detail in the past. Most authors dealing with dye-laser oscillators follow the approach introduced by Sorokin *et al.* [12] in which rate equations are written down for the (single-mode) photon density, the population inversion, and the triplet-state population. With various modifications, this approach was followed also by Keller [13] and by Pappalardo *et al.* [14]. In this approach the quantities are all assumed to be uniform along the cavity. Since in many laser-pumped dye-laser systems the gain is very high, and consequently the optimum output coupling rather large (in some cases a ~4-percent-reflectivity quartz wedge gives the highest output [15]), this assumption is probably invalid for such systems. Weber and Bass [16] and Snavely [17], on the other hand, considered rate equations for the populations at threshold in order to calculate the gain. They did not include stimulated emission in these equations, and hence saturation effects are excluded from this description. Recently, Atkinson and Pace [18] introduced a more complete approach, including also frequency selective elements in their analysis. Again, they assume all quantities uniform along the cavity, an approximation which, as already mentioned, can introduce serious errors in cases of high output coupling (see [19]).[3]

Dye-laser amplifiers have been considered by a number of investigators. Huth [20] measured the gain of a flashlamp-pumped rhodamine 6G (R6G) laser. His data fit into the weak pumping regime, below saturation by ASE or by the injected signal. Hence his results could be fit to calculated gain coefficients which are uniform along the medium. Shank *et al.* [21] described an elegant gain-measurement scheme in which the gain is extracted from direct measurement of the ASE. Their method, however, applies only in the regime of weak enough pumping where no saturation occurs. More recently, Flamant and Meyer [22] studied the steady-state gain of a flashpumped dye amplifier. They recognize the importance of the spatial dependence of the gain along the active medium. Spontaneous emission is excluded from their photon flux equation. Their results are thus valid only for strong enough input signals, so that the competing effect of ASE can be ignored.

In this work we shall treat the problem of a transversely pumped dye medium. Rate equations will be written in a general form so that numerical solutions can be obtained from them for both pure ASE and laser-amplifier situations. Both the temporal and spatial dependence will be accounted for so that no *a priori* assumptions will be needed concerning the magnitude of either the pumping intensity or the laser radiation. In Section II we present the rate equations and explain the details of the physical model used. Section III is devoted to a discussion of the solutions for ASE with no external input. The behavior of the solutions at the various regimes of pumping rates is explained with an emphasis on its physical significance. Some analytical approximations, which are helpful for anticipating the results in certain limiting cases, are also derived. In Section IV the characteristics of dye-laser amplifiers are discussed, and again the discussion is based both on numerical solutions of the rate equations and on some analytical approximations which are shown to be valid on physical grounds. Section V deals with a set of experiments which were aimed at checking the theory and obtaining the characteristics of the operation of dye-laser amplifiers. Finally, a narrow-band output oscillator-amplifier system is described.

II. Rate Equations

The energy level scheme we shall consider is shown schematically in Fig. 1. S_0 is the lowest singlet vibration-rotation manifold, S_1 is the first excited (electronic) singlet manifold, and T_1 is the first triplet manifold. Higher excited manifolds (S_i, T_i, $i > 1$) are not shown since radiationless transitions back to S_1 (or T_1) are known to be fast ($\sim 10^{-12}$-10^{-11} s) on the time scales of interest to us [23]. Nonradiative decay within each manifold is also a fast process, so that only the lowest level populations within each manifold will be considered. We assume a transversely excited region of length L and width $2r$ ($r \ll L$), so that the pump power $P(t)$ is uniformly incident on an area $A = 2rL$. Reduction of $P(t)$ in the transverse direction (into the medium) due to absorption is neglected. This assumption is not expected to affect the results appreciably, and it reduces the complication of the numerical treatment considerably.

Let $I^+(x,t,\lambda)$ be the photon flux per unit wavelength (photon $\cdot$ s^{-1} cm^{-3}) at coordinate x ($0 \leqslant x \leqslant L$), time t, and wavelength λ, propagating in the $+x$ direction, and let $I^-(x,t,\lambda)$ be the corresponding quantity for the radiation propagating in the $-x$ direction. Then the following coupled set of rate equations holds for the photon flux and populations:

$$\frac{\partial N_1(x,t)}{\partial t} = W(t)N_0(x,t) - \tau^{-1}N_1(x,t) - N_1(x,t)\int \sigma_e(\lambda)\,[I^+(x,t,\lambda) + I^-(x,t,\lambda)]\,d\lambda + N_0(x,t)\int \sigma_{01}(\lambda)\,[I^+(x,t,\lambda) + I^-(x,t,\lambda)]\,d\lambda \quad (1)$$

[3] For reflectivities of $R \gtrsim 50$ percent, the approximation of uniform gain coefficient along the medium is reasonable, but for low reflectivities it is no longer valid.

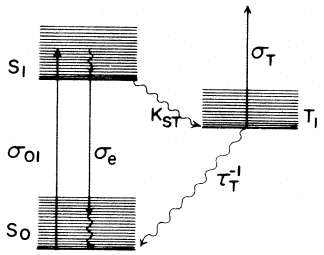

Fig. 1. Energy level scheme assumed in the calculation. Straight arrows denote radiative transitions, wiggled arrows denote radiationless transitions.

$$\frac{\partial N_T(x,t)}{\partial t} = K_{ST}N_1(x,t) - \tau_T^{-1}N_T(x,t) \tag{2}$$

$$N_0(x,t) + N_1(x,t) + N_T(x,t) = N \tag{3}$$

$$\pm\frac{d}{dx}[I^{\pm}(x,t,\lambda)] = N_1(x,t)\sigma_e(\lambda)I^{\pm}(x,t,\lambda) + \tau^{-1}N_1(x,t)E(\lambda)g^{\pm}(x) - \sigma_{01}(\lambda)N_0(x,t)I^{\pm}(x,t,\lambda) - \sigma_T(\lambda)N_T(x,t)I^{\pm}(x,t,\lambda). \tag{4}$$

The quantities in (1)-(4) are defined as follows. $N_i(x,t)$, $i = 0, 1, T$, is the population density (molecules $\cdot$ cm^{-3}) in S_0, S_1, and T_1. $W(t)$ is the pumping rate, given generally by

$$W(t) = [P(t)/A]\int\sigma_{01}(\lambda)f(\lambda)(\lambda/hc)\,d\lambda \tag{5}$$

where $\sigma_{01}(\lambda)$ is the absorption cross section (cm^2) from S_0 to S_1 at wavelength λ, and $f(\lambda)$ is the normalized spectral distribution of the pump radiation ($\int f(\lambda)d\lambda = 1$). τ is the lifetime of the S_1 state in the absence of stimulated emission. $\sigma_e(\lambda)$ is the stimulated-emission cross section, given by[4]

$$\sigma_e(\lambda) = [\lambda^4 E(\lambda)]/8\pi c\eta^2\tau \tag{6}$$

where $E(\lambda)$ is the $S_1 \rightarrow S_0$ fluorescence spectrum normalized so that $\int E(\lambda)d\lambda = \Phi$, Φ being the quantum efficiency, η is the refractive index of the dye solution, K_{ST} is the $S_1 \rightarrow T_1$ intersystem crossing rate (s^{-1}), and τ_T is the T_1 lifetime. $g^{\pm}(x)$ are geometrical factors which determine the fraction of the spontaneous emission which is emitted into the solid angle at which the output aperture is seen from position x in the medium. $\sigma_T(\lambda)$ is the absorption cross section from T_1 to higher triplet states. In (1), the first term describes excitation by the pump source from S_0 to S_1, the second term accounts for spontaneous decay from S_1 via all available channels, the third term describes the effect of stimulated emission by radiation of all wavelengths on N_1, and the last term gives the rate of increase of N_1 due to self-absorption by ground-state molecules. Equation (2) describes the temporal evolution of N_T by intersystem crossing $S_1 \rightarrow T_1$ and by relaxation to the ground state. In (4), $(d/dx)I^{\pm} = (\partial/\partial x)I^{\pm} \pm (\eta/c)(\partial/\partial t)I^{\pm}$. The terms in (4) describe, in that order, stimulated emission, spontaneous emission into the appropriate solid angle, absorption from the ground state, and triplet-state absorption. Variations in the transverse dimension of $I^{\pm}$ and N_i are not accounted for in this model. It is assumed that the active region is a cylinder of radius r, within which the rate of excitation is constant. Hence we have

$$g^{+}(x) = \tfrac{1}{2}\{1 - (L-x)/[(L-x)^2 + r^2]^{1/2}\}$$
$$g^{-}(x) = \tfrac{1}{2}\{1 - x/(x^2 + r^2)^{1/2}\}. \tag{7}$$

As long as the depth of the excited region is of the same order of magnitude as its width $2r$ ($\ll L$), its exact geometric shape is not too important, and $g^{\pm}$ will have the same x dependence. Equations (1)-(4) are written for a homogeneously broadened medium so that the same $N_1(x,t)$ is assumed for the interaction with radiation at all wavelengths λ within the fluorescence band.

Equations (1)-(4) were solved numerically on an IBM 370/165 computer for a large variety of practical solutions. We chose a solution of the dye rhodamine 6G (R6G) in ethanol for our computations since the material parameters for this system are well known. The parameters needed for the computation are given in Table I. The geometry was chosen to correspond to our experimental arrangement (see Section V), $L = 1$ cm, $r = 0.02$ cm. Although various pumps and dye concentrations were studied, we shall report here only on our studies for a nitrogen-laser-pumped dye solution. The pump is monochromatic ($\lambda_p = 337.1$ nm, $\sigma_{01}(\lambda_p) = 2.4 \times 10^{-17}$ cm^2), and a dye concentration of $N = 3 \times 10^{18}$ cm^{-3} (5×10^{-3} mol $\cdot$ l^{-1}) is used.

For a monochromatic pump source, $W(t) = \sigma_{01}(\lambda_p)I_p(t)$, $I_p(t)$ being the pump photon flux (photons $\cdot$ cm^{-2}s^{-1}). The

TABLE I
PARAMETERS USED IN THE COMPUTATIONS

Quantity	Numerical value	Reference
1) Material parameters (R6G)		
τ	5.5×10^{-9} [sec.]	24
η (ethanol)	1.36	
$E(\lambda)$	Figure 9 in reference	17
$\sigma_{01}(\lambda)$	Figure 9 in reference	17
K_{ST}	3.4×10^{6} [sec.$^{-1}$]	25
τ_T	2.5×10^{-7} [sec.]	25
$\sigma_T(\lambda)$	Figure 7 in reference	26
2) Parameters used in our numerical example		
L	1 [cm.]	
r	2×10^{-2} [cm.]	
λ_p (pump wavelength)	337.1 [nm]	
$\sigma_a(\lambda_p)$	2.4×10^{-17}[cm^2]	
N	5×10^{-3}(mole/liter) = 3×10^{18} [cm^{-3}]	
3) Conversion of pump power to pumping rate (W) for conditions given above		
1 KW $\rightarrow$ 25 KW.cm^{-2} $\rightarrow$ W = 10^6 [sec.$^{-1}$]		

[4]See [17]. $\sigma_e(\lambda)$ given in (6) differs from Snavely's expression by a factor of η^{-3}. This difference was already noted previously (see [21]).

analysis is somewhat simplified by assuming $I_p(t)$ to be of a square wave form in t. For fast rise-time pumps this is a reasonable approximation, so that in the following discussion we write $W(t) = W$ for $0 \leqslant t \leqslant T$, T being the pump pulsewidth. If T is large enough so that steady state is reached $((\partial/\partial t) = 0)$, we have from (1)-(4)

$$N_1(x) = N\{W + \int \sigma_{01}(\lambda)\,[I^+(x,\lambda) + I^-(x,\lambda)]\,d\lambda\}/ \cdot \{W(1 + K_{ST}\tau_T) + \tau^{-1} + \int [\sigma_{01}(\lambda) \cdot (1 + K_{ST}\tau_T) + \sigma_e(\lambda)]\,[I^+(x,\lambda) + I^-(x,\lambda)]\,d\lambda\} \tag{8}$$

$$N_T(x) = N_1(x) K_{ST}\tau_T. \tag{9}$$

By direct integration we have

$$I^+(x,\lambda) = I^+(0,\lambda)\exp\left[\int_0^x \alpha(\xi,\lambda)d\xi\right] + E(\lambda)\tau^{-1}\int_0^x dy N_1(y) g^+(y) \cdot \exp\left[\int_y^x \alpha(\xi,\lambda)d\xi\right] \tag{10}$$

$$I^-(x,\lambda) = I^-(L,\lambda)\exp\left[\int_x^L \alpha(\xi,\lambda)d\lambda\right] + E(\lambda)\tau^{-1}\int_x^L dy N_1(y) g^-(y) \cdot \exp\left[\int_x^y \alpha(\xi,\lambda)d\xi\right] \tag{11}$$

where

$$\alpha(\xi,\lambda) = [\sigma_e(\lambda) + \sigma_{01}(\lambda)]\,N_1(\xi) + [\sigma_{01}(\lambda) - \sigma_T(\lambda)]\,N_T(\xi) - \sigma_{01}(\lambda)N. \tag{12}$$

The first term on the right-hand side in (10) and (11) describes the amplified input signal while the second results from ASE. The gain of the medium at steady state is conveniently defined as

$$G(\lambda) = \exp\left[\int_0^L \alpha(\xi,\lambda)d\xi\right]. \tag{13}$$

In a general situation (8)-(13) are obviously not very useful, and (1)-(4) have to be solved numerically on a computer. In the following we shall use (8)-(13) as a starting point for discussing a number of limiting cases of practical interest.

III. Amplified Spontaneous Emission

A. Dependence of the ASE on Pumping Rate

In most pulsed laser-pump sources (nitrogen laser, Q-switched Nd^{3+}:YAG or ruby, and their harmonics, etc.), the pumping pulse is short (~5-30 ns) compared to K_{ST}^{-1}, so that the effect of triplet states is negligible since no appreciable population $N_T(x)$ can build up.[5] We shall therefore assume henceforth $N_T = 0$ in our analysis. The steady-state assumption, introduced previously, is still reasonable, as will be discussed in the following, and it is certainly a very good one for strong pumping sources which are of main interest here.

In Fig. 2 we plot the results of the numerical calculation of the ASE, assuming no triplet-state population. In the graph giving the results with no ground-state absorption ($\sigma_{01}(\lambda) = 0$)[6] one clearly discerns the fluorescence region, which is the regime of weak pumping rates. In this region $N_1(x)$ remains so low that there is practically no stimulated emission, and the output consists of that part of the total fluorescence which is collected at the output aperture. Therefore, in the transverse pumping configuration, the conversion efficiency from absorbed pump photons to output is very low.

As the pump rate increases, there is a smooth transition to a regime in which the output increases exponentially with W. This is obviously due to the effect of stimulated emission. It should be noted, however, that there is no discontinuity in the graph so that the concept of threshold for the onset of ASE [11] is mainly qualitative.

As indicated in Fig. 2, this exponential regime spans only about one order of magnitude of pumping intensities since the exponential dependence of $G(\lambda)$ on W causes $I^{\pm}$ to grow very quickly with W and saturation becomes important. (In the numerical example (Fig. 2), the output increases by a factor of $\sim 10^4$ as W changes from 3×10^5 to 3×10^6.)

With $\sigma_{01}(\lambda) = 0$, $I^{\pm}(\lambda)$ peaks at the peak of $E(\lambda)$ (~555 nm for R6G), but spectral narrowing sets in [7], [8]. The approximate analytical treatment by Yariv and Leite [7] is adequate in this regime, but its validity breaks down as soon as saturation effects become important. In the present treatment, $E(\lambda)$ is not available to us in analytical form, so no attempt was made to analyze this effect beyond numerical evaluation of $I^{\pm}(\lambda)$ as a function of λ. In the numerical computation, the fluorescence band of R6G (520-630 nm) was divided into segments of 5 nm each.[7] In Fig. 2 the effect of spectral narrowing is indicated by the difference between the curve describing the total photon flux and the curve giving the photon flux within a 5-nm bandwidth around the peak of the ASE. The stronger the pumping, the closer these two curves become, indicating that a larger portion of the radiation is concentrated in the central bandwidth.

The conversion efficiency from pump photons to $I^{\pm}$ is still low at the lower end ($W \gtrsim 2 \times 10^5$) of the exponential regime,

[5] This assumption is definitely invalid for flashlamp-pumped dye lasers, where the pulses are in the microsecond regime (see [13], [14]), or for CW dye lasers, where the triplet-state populations are of primary importance.

[6] In some dyes, such as 4 methyl-umbelliferone [21], the emission and absorption bands do not overlap so that $\sigma_{01} = 0$ is a realistic assumption. This is definitely not the situation for R6G, but we deal with it nonetheless since it helps in understanding the physical behavior of the system.

[7] Finer divisions were used in trial runs, and this increased the computer time needed significantly. We found that the division into segments of 5 nm was adequate, and no substantial information was gained by using a finer grid in λ.

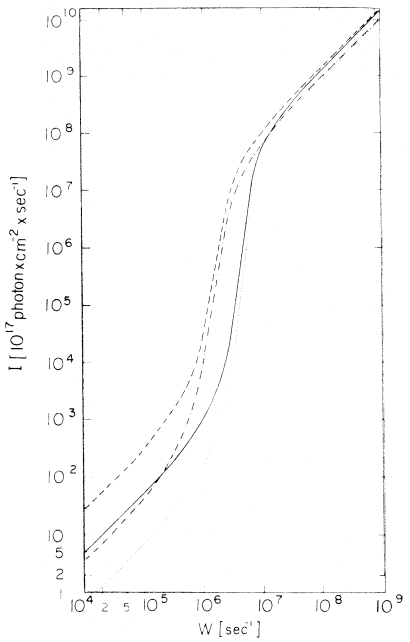

Fig. 2. Calculated ASE output (I) as a function of pumping rate (W), for R6G with parameters listed in Table I. ····· photon flux within a bandwidth of 5 nm around the peak of the ASE spectrum with $\sigma_{01} \neq 0$. -·-·- photon flux within a bandwidth of 5 nm around the peak of the ASE assuming $\sigma_{01} = 0$. ——— total photon flux with $\sigma_{01} \neq 0$. ----- total photon flux with $\sigma_{01} = 0$.

but it grows rather quickly with W as the strong pumping regime is approached.

For still larger values of W, saturation causes the dependence of $I^{\pm}$ on W to become weaker than exponential. In our numerical example, with $\sigma_{01} = 0$, about one more decade in W (2×10^6-2×10^7) spans this transition region in which this dependence changes from exponential to linear.

The effect of ground-state absorption ($\sigma_{01} \neq 0$) is twofold. First, it shifts the peak of the ASE towards longer wavelengths where σ_{01} is smaller. In our numerical example the spectrum peaks at 590 nm for $W \leqslant 10^5$ (s^{-1}), but as W becomes larger the peak gradually shifts towards shorter wavelengths. For $W > 5 \times 10^6$ (s^{-1}), the peak appears at $\lambda = 575$ nm, and it remains at this wavelength for all higher values of W for which calculations were performed. Note that at the peak of the fluorescence ($\lambda = 555$ nm) the absorption cross section is $\sigma_{01} = 0.11\sigma_e$, with $\sigma_e = 3.2 \times 10^{-16}\,\mathrm{cm}^2$, while at the peak of the ASE ($\lambda = 575$ nm), $\sigma_{01} \sim 0.008\ \sigma_e$, with $\sigma_e = 1.8 \times 10^{-16}\,\mathrm{cm}^2$.

The second effect of ground-state absorption is to lower the conversion efficiency at *low* pumping rates. At higher pumping rates this effect becomes less pronounced until at high enough values of W the efficiency is the same whether $\sigma_{01} \neq 0$ or $\sigma_{01} = 0$. This can be shown analytically as follows. Starting from (4), we have, with $N_T = 0$,

$$\frac{d}{dx}[I^+(x,\lambda) - I^-(x,\lambda)] = N_1(x)\,[\sigma_e(\lambda) + \sigma_{01}(\lambda)]\,[I^+(x,\lambda) + I^-(x,\lambda)] + \tau^{-1}N_1(x)E(\lambda)[g^+(x) + g^-(x)] - \sigma_{01}(\lambda)N[I^+(x,\lambda) + I^-(x,\lambda)]. \quad (14)$$

Integration over λ yields

$$\frac{d}{dx}[I^+(x) - I^-(x)] = N_1(x)\int[\sigma_e(\lambda) + \sigma_{01}(\lambda)]\,[I^+(x,\lambda) + I^-(x,\lambda)]\,d\lambda + \tau^{-1}N_1(x)\,[g^+(x) + g^-(x)]\,\Phi - N\int\sigma_{01}(\lambda)\,[I^+(x,\lambda) + I^-(x,\lambda)]\,d\lambda \quad (15)$$

where $I^{\pm}(x) = \int I^{\pm}(x,\lambda)d\lambda$. Since the triplet-state population is neglected, we have from (8)

$$N_1(x) = N\left\{W + \int\sigma_{01}(\lambda)\,[I^+(x,\lambda) + I^-(x,\lambda)]\,d\lambda\right\}\Big/ \cdot\left\{W + \tau^{-1} + \int[\sigma_{01}(\lambda) + \sigma_e(\lambda)]\,[I^+(x,\lambda) + I^-(x,\lambda)]\,d\lambda\right\}. \quad (16)$$

Substituting (16) into (15) we obtain

$$\frac{d}{dx}[I^+(x) - I^-(x)] = N_0(x)W - \tau^{-1}N_1(x) \cdot \{1 - [g^+(x) + g^-(x)]\,\Phi\}. \quad (17)$$

For large values of W ($W \gtrsim \tau^{-1}$) stimulated emission becomes the dominant process. Over most of the medium (except a narrow region around $x = L/2$ which we shall discuss later) we can assume $\int[\sigma_{01}(\lambda) + \sigma_e(\lambda)]\,[I^+(x,\lambda) + I^-(x,\lambda)]\,d\lambda \gg \tau^{-1} + W$ so that $N_1(x) \ll N$. This leads to the approximation

$$\frac{d}{dx}[I^+(x) - I^-(x)] \simeq WN \quad (18)$$

and since with no external signal $I^+(L) = I^-(0)$, we have

$$I^+(L) = I^-(0) \simeq \tfrac{1}{2}WNL. \quad (19)$$

This means that the total ASE output becomes linear with pumping intensity, and the conversion efficiency from absorbed pump photons to ASE approaches unity. This conclusion holds even in the presence of ground-state absorption, in spite of the shift of the peak of the ASE to longer wavelengths, where σ_e is smaller. This decrease in σ_e is compensated for by the fact that the excited-state (S_1) population $N_1(x)$ is higher than what it would have been if σ_{01} were zero. The net gain thus obtained overall (stimulated emission minus ground-state absorption) becomes equal to what it would have been for $\sigma_{01} = 0$.

Note that when excited-triplet-state absorption is neglected, as is done here based on the preceding arguments, and the quantum efficiency Φ is close to unity, there is practically no mechanism for loss of photons. In other words, the overall conversion efficiency from absorbed pump photons to photons emitted by the dye solution, including both ASE and fluorescence, is always close to unity. At low pumping rates, however, most of the emitted photons go into (unamplified) fluorescence. As the pumping rate increases, more and more of the photons are emitted into the ASE mode. For the values used in our numerical example, we find that (19) is a very good

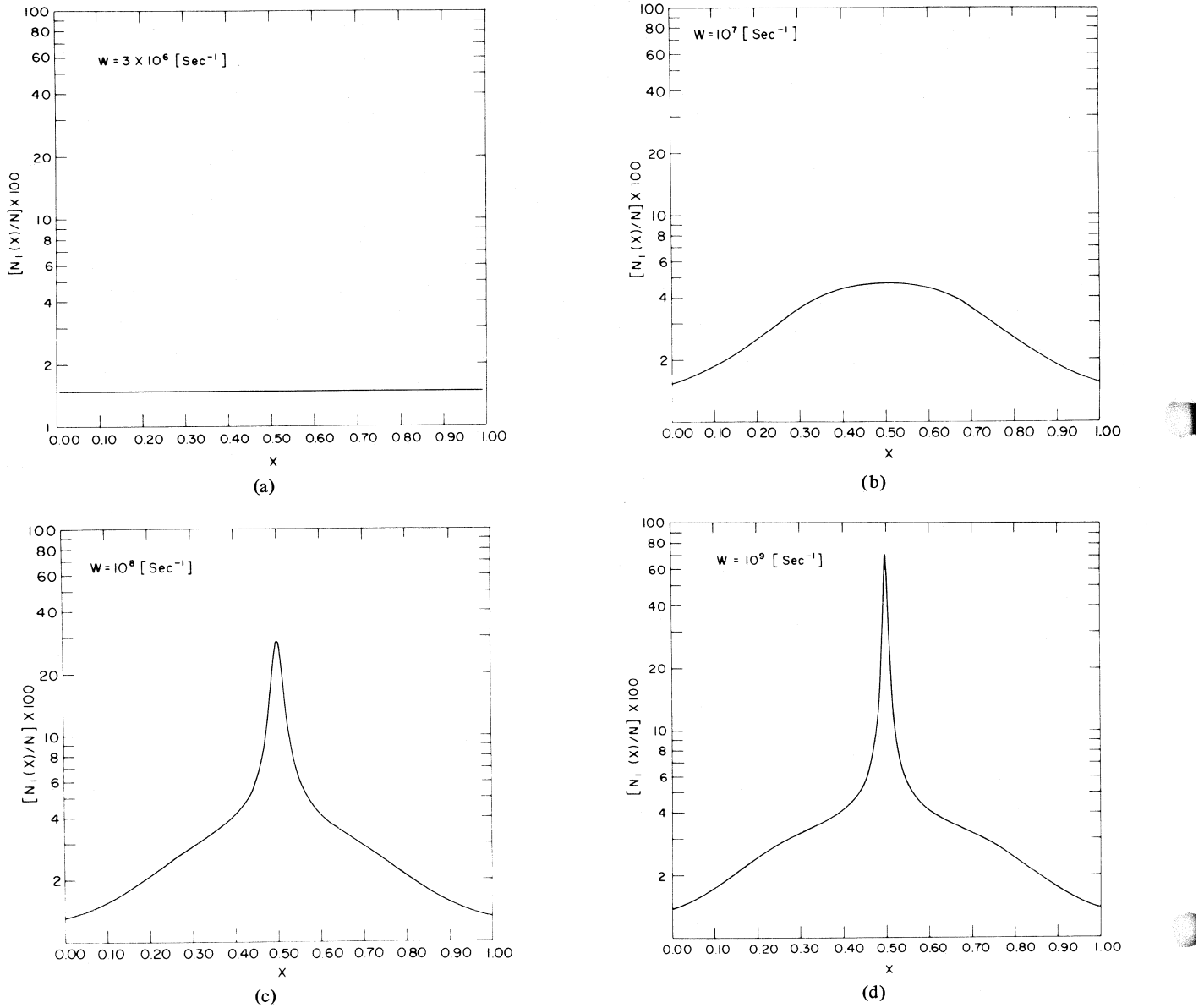

Fig. 3. Excited-state population ($N_1(x)$) in percent of total concentration (N), as a function of position in the medium (x), for various pumping rates. Material parameters are listed in Table I. (a) $W = 3 \times 10^6$ (s^{-1}). (b) $W = 10^7$ (s^{-1}). (c) $W = 10^8$ (s^{-1}). (d) $W = 10^9$ (s^{-1}).

approximation at pumps for which $W > 2 \times 10^7$ (Fig. 2) (corresponding to intensities above ~ 500 kW $\cdot$ cm^{-2} at 337.1 nm, or ~ 20 kW for the geometry we deal with).

The process of spectral narrowing, which starts already in the exponential regime, continues to take place in the saturated regime, as can be clearly seen from Fig. 2. For $W = 10^9$, about 70 percent of the total radiation is contained within the bandwidth of 5 nm around the peak of the spectrum. The rate of spectral narrowing with increasing W is much slower here than in the exponential (intermediate pumping) regime, as is obvious from Fig. 2. This fact agrees with the analysis of Casperson and Yariv [8] for a homogeneously broadened medium.

B. Spatial Distribution of the Gain: $N_1(x)$

Let us consider the saturated (strong pumping) regime first, and values of x in the vicinity of $x = L$. By symmetry, the same considerations will apply for $x \sim 0$. From (18) and (19) we have

$$I^+(x) = I^-(x) + WN(x - L/2), \quad (x \sim L). \tag{20}$$

For $x \sim L$, $I^+(x) \gg I^-(x)$, so that we obtain from (16)

$$N_1(x) \sim [1 + \bar{\sigma}_{01} N(x - L/2)] / [(\bar{\sigma}_e + \bar{\sigma}_{01}) \cdot (x - L/2)], \quad (x \sim L) \tag{21}$$

where $\bar{\sigma}_{01}$ and $\bar{\sigma}_e$ are some appropriate weighted average values of $\sigma_{01}(\lambda)$ and $\sigma_e(\lambda)$ over the bandwidth for which $I^+(\lambda)$ is significantly large. Equation (21) and a similar one for $x \sim 0$ (obtained by replacing x by $L - x$ on the right-hand side) are useful approximations at the edges of the medium at strong pumping intensities, and show $N_1(x)$ to be independent of W. On the other hand, we know from the previous discussion that the total output (whether $\sigma_{01} = 0$ or $\sigma_{01} \neq 0$) is proportional to W in this regime, so that for λ in the region of the spectral peak, $\int_0^L \alpha(\lambda, \xi) d\xi$ must increase with W approximately with a

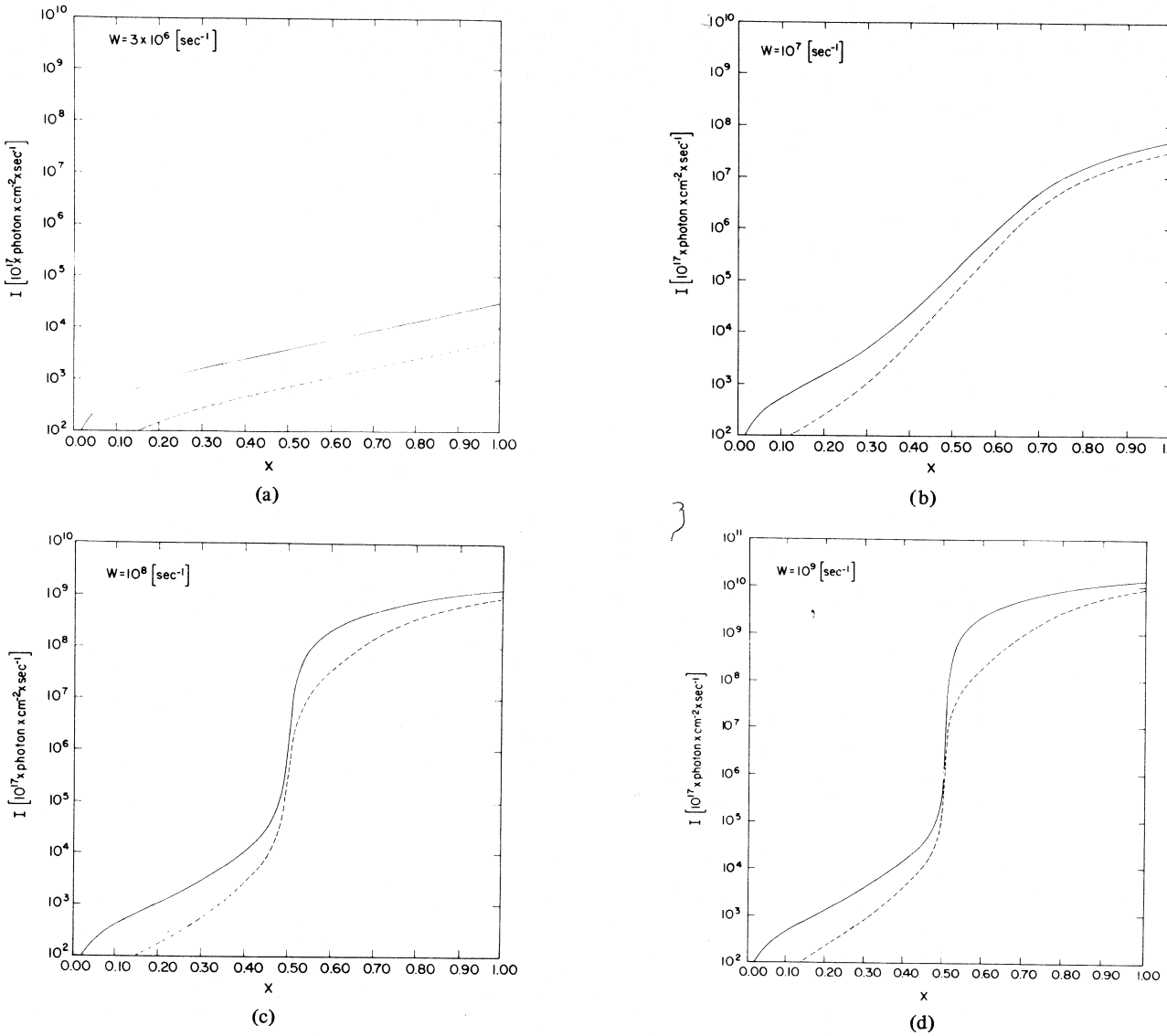

Fig. 4. Photon flux (I) as a function of position in the medium for various pumping rates. Only $I^+(x)$ is plotted. Solid line–total flux. Broken line–photon flux within 5 nm around the peak of the ASE spectrum. Material parameters are listed in Table I. (a) $W = 3 \times 10^6$ (s^{-1}). (b) $W = 10^7$ (s^{-1}). (c) $W = 10^8$ (s^{-1}). (d) $W = 10^9$ (s^{-1}).

logarithmic dependence, as can be seen by a detailed analysis of (10). This increase comes about mainly by an increase of $N_1(x)$ in the central region of the medium, where $I^+(x) + I^-(x)$ is smaller than at the edges. The behavior of $N_1(x)$ for various values of W is plotted in Fig. 3. At the low and intermediate pumping regimes, where saturation is not important yet, $N_1(x)$ is constant along the medium. However, as W increases and saturation effects become important, the function $N_1(x)$ develops a peak around $x = L/2$. It is seen clearly that at $x \sim 0$ and $x \sim L$, for large W, $N_1(x)$ does not change much, but the central peak increases sharply so as to render the correct total gain [(12), (13)]. This particular behavior of $N_1(x)$ (or a similar behavior of the fractional gain $\alpha(x, \lambda)$) comes about by the simultaneous effect of I^+ and I^-.

A similar effect to the one described here has been described by Allen and Peters [11] who calculated the saturated gain coefficient for a He-Ne (3.39-μm) system as a function of position in the medium. However, as pointed out by these authors, observation of this central peak is not feasible in laboratory He-Ne. In the dye system we consider, our calculations show that the peak in $N_1(x)$ should be easily observable in the laboratory.

In the discussion leading to the approximation (18), we have assumed $N_1(x) \ll N$ over most of the region $0 \leqslant x \leqslant L$. Around $x = L/2$ this assumption fails, but although (18) is not valid in the vicinity of $x = L/2$, our numerical analysis shows that the integrated result (19) is still a very good approximation. This is explained by the fact that the central region, where $N_1(x)$ becomes large, is very narrow so that it does not appreciably affect the integration leading from (18) to (19). The narrow region around $x = L/2$ is, however, of primary importance in the evolution of the intensity. Consider $I^+(x)$ in the strong pumping region. It starts from fluorescence at $x = 0$ and increases rather slowly with x, since for $0 < x < L/2 - \epsilon$ (with ϵ some typical half-width of the central peak) $N_1(x)$ is quenched to small values by the intense $I^-(x)$. As we enter the central peak region, $N_1(x)$ becomes large and $I^+(x)$ increases very rapidly. Once we move out of the central peak

$(x > L/2 + \epsilon)$, $I^+(x)$ is already very large, $N_1(x)$ accordingly small, and the growth becomes approximately linear with x. The same behavior is exhibited by $I^-(x)$, which is the mirror image of $I^+(x)$ around $x = L/2$. This qualitative description is verified by the numerical results shown in Fig. 4, where we plot $I^+(x)$ for various pumping rates W. Clearly, the larger W, the more the behavior fits the previously given description.

It should be emphasized that this spatial behavior of $N_1(x)$ and of $I^{\pm}(x)$ is typical of ASE, and a different behavior is expected in the case of a laser oscillator. There $I^+(0)$ and $I^-(L)$ are not zero, and due to the feedback from the mirrors both $I^+(x)$ and $I^-(x)$ reach high values all over the medium. Since at steady state $1 - R_1R_2G^2 \simeq 0$ in a laser (R_1, R_2 are the mirror reflectivities), G is much smaller than in the case of ASE, and hence $N_1(x)$ is also much smaller. The problem of a laser oscillator will be treated in more detail elsewhere.

C. Temporal Behavior

All the discussion in Sections III-A and III-B, as well as Figs. 2–4, refer to steady-state solutions. In cases where the pumping pulse has a temporal width of ~10 ns, the validity of the steady-state assumption may be questioned. In the weak and intermediate pumping regimes (unsaturated regime, $W \lesssim 5 \times 10^6$ s^{-1}), and assuming very fast rise times of the pump pulse, the typical time constant for the evolution of $N_1(x, t)$ to steady state is $\sim\tau$. The evolution of $I^+(L, t, \lambda)$ (or $I^-(0, t, \lambda)$) is not exponential, in general. For very weak pumps, $I^+(L, t)$ is simply proportional to $N_1(t)$, and hence approaches steady state exponentially at the same rate as $N_1(t)$. For W in the intermediate regime, $N_1(x, t)$ still evolves exponentially in time, but since $I^+(L, t, \lambda)$ depends approximately exponentially on the integral of $N_1(x)$ along the medium, it will approach steady state more slowly than N_1. The exact details depend on the particular set of parameters which are used in the calculation. In general, it can be stated that in the exponential regime ($5 \times 10^5 < W < 5 \times 10^6$), the intensities $I^{\pm}$ will reach steady state more slowly than an exponential with a time constant τ (typical times of 2τ–4τ were found to elapse before $I^+(L, t, \lambda)$ reached ~70 percent of its steady-state value). The situation is different at strong pumps (saturated regime) since there the stimulated-emission terms begin to dominate the temporal evolution of both $N_1(x, t)$ and of $I^{\pm}(x, t, \lambda)$ very quickly. As a result, steady state is reached at times much shorter than τ. For the numerical parameters chosen as previously, we find that for $W = 10^8$ equilibrium is reached in less than 2 ns, whereas at $W = 10^9$ the system is at steady state already after 0.5 ns. Hence for intense laser-pump sources, with pulses of ~10 ns, the steady-state description is certainly a good approximation to the actual physical situation.

IV. Dye-Laser Amplifiers

The general expressions (10) and (11) are valid as before, but here we shall consider an input signal given by $I^+(0, \lambda)$ such that $I^+(0, \lambda) \neq 0$ over some bandwidth $\Delta\lambda$.

A useful concept in dealing with amplifiers in general is the equivalent noise input signal. In the systems we consider, background noise is inherently present in the form of spontaneous emission, so we have a distributed noise source. Let us define $I_0(\lambda)$ such that

$$\sigma_e(\lambda) I_0(\lambda) N_1 = E(\lambda)\tau^{-1} g N_1 \tag{22}$$

where $g = g^+(0)$. This can be interpreted to mean that $I_0(\lambda)$ is that input photon flux per unit wavelength for which the rate of stimulated emission equals the rate of spontaneous emission into the same spatial mode [in (4)]. Using (6), we have

$$I_0(\lambda) = 8\pi\eta^2 g c/\lambda^4 \tag{23}$$

so that $I_0(\lambda)$ depends only on wavelength and on the geometrical configuration, and not on the particular gain medium. Typically, for $g = 10^{-4}$, $I_0(\lambda) \sim 10^{17}$ [photon · cm^{-2} s^{-1}/Å] in the visible, or ~35 [mW · cm^{-2}/Å].

Assuming first $\sigma_{01} = 0$ and an input signal of $I^+(0, \lambda) = pI_0(\lambda)$, we obtain from (10) and (11), neglecting triplet states as before,

$$\begin{aligned} I^+(L, \lambda) &= pI_0(\lambda)G(\lambda) + I_0(\lambda)[G(\lambda) - 1] \\ I^-(0, \lambda) &= I_0(\lambda)[G(\lambda) - 1] \end{aligned} \tag{24}$$

where $G(\lambda) = \exp[\sigma_e(\lambda) \int_0^L N_1(\xi) d\xi]$. In deriving (24), we assumed $g^{\pm}(x) = g^+(0) = g$. This approximation can be seen to be valid if the contribution of fluorescence to $I^{\pm}(x, \lambda)$ is important mainly at the edges of the medium. This is indeed the situation for large enough values of W. The weak pumping regime, for which this assumption is not correct, is of no practical interest in amplifier applications since there $G \simeq 1$.

In cases of interest for amplifier applications, $G(\lambda) \gg 1$ so that $I_0(\lambda)$ represents an input signal ($p = 1$) for which the output at wavelength λ is double its value with no input, which justifies its identification as a noise equivalent input signal. In (24) the second term on the right-hand side represents the background due to ASE, while the first term is the amplified input signal. One can therefore define the amplified signal to background noise $S/N \simeq p$.

The amplification is properly given by $G(\lambda)$ since

$$G(\lambda) I^+(0, \lambda) = I^+(L, \lambda, \text{total}) - I^+(L, \lambda, \text{background}). \tag{25}$$

In the *exponential regime* and in the *strong pumping* regime, $G(\lambda) \gg 1$ for not-too-large input signals. When the input signal is small, i.e., when

$$\sigma_e(\lambda) I^+(0, \lambda) \Delta\lambda < \int \sigma_e(\lambda') I_0(\lambda') d\lambda' \tag{26}$$

(the integration performed over the fluorescence bandwidth) $G(\lambda)$ will be approximately equal to its value in the absence of an input signal since the population of the excited state is then unaffected by the addition of the input signal. Hence the *small-signal gain* at each wavelength is simply proportional to the ASE output at that wavelength in the absence of an input signal (24), except for a weak λ^{-4} dependence (23). As p becomes larger, saturation by the amplified signal will cause a decrease in $G(\lambda)$. However, even in this case one sees from (24) that $S/N \simeq p$ (provided G is still large enough).

When $\sigma_{01}(\lambda) \neq 0$, we obtain from (10), assuming again

$$I^+(0,\lambda) = pI_0(\lambda),$$

$$I^+(L,\lambda) = pI_0G(\lambda) + I_0(\lambda)\{\sigma_e(\lambda)/[\sigma_e(\lambda) + \sigma_{01}(\lambda)]\}[G(\lambda) - 1] + I_0(\lambda)\sigma_{01}(\lambda) \cdot N\{\sigma_e(\lambda)/[\sigma_e(\lambda) + \sigma_{01}(\lambda)]\} \int_0^L \cdot \exp\left[\int_y^L \alpha(\xi,\lambda)\,d\xi\right] dy \quad (27)$$

where $G(\lambda) = \exp[\int_0^L \alpha(\xi,\lambda)\,d\xi]$, $\alpha(\xi,\lambda)$ is defined in (12), and we assume as before $N_T(\xi) = 0$. This expression is similar to (24), the two last terms on the right-hand side representing the background due to ASE. In Fig. 5 we plot the calculated values of $G(\lambda)$, as a function of $I^+(0,\lambda)$, for a wide range of pump intensities W. In the calculation we concentrated on amplification of narrow-band signals, assuming an input signal with a bandwidth of 0.05 nm at a wavelength of $\lambda = 575$ nm, which is the peak of the ASE spectrum and hence the peak of $G(\lambda)$ at all pump intensities for which $W > 3 \times 10^6$. It turns out that also in this case the small-signal gain is approximately proportional to the ASE output at the same wavelength. Since spectral narrowing of this output is significant at high pump intensities, the small-signal gain of a dye-laser amplifier will drop sharply away from the peak of the ASE (see also Section V). In Fig. 5 the initial range of values for which $G(\lambda)$ is independent of the input is clearly seen. For higher input signals there is a gradual decrease of $G(\lambda)$ with increasing inputs.

Finally, for very high input signals, such that

$$\sigma_e(\lambda)I^+(0,\lambda)\,\Delta\lambda >> \int I_0(\lambda')\sigma_e(\lambda')\,d\lambda' \quad (28)$$

and high pumping rates, $G(\lambda)$ becomes inversely proportional to $I^+(0,\lambda)$, as is expected in the regime where the conversion efficiency is close to unity. This can also be shown analytically as follows. Integrating (17) with $I^+(0) = I^+(0,\lambda)\,\Delta\lambda$, $I^-(L) = 0$, yields

$$I^+(L) - I^+(0) + I^-(0) = W \int_0^L N_0(x)\,dx - \tau^{-1} \int_0^L N_1(x)\{1 - [g^+(x) + g^-(x)]\Phi\}\,dx. \quad (29)$$

The assumption (28) means that $I^-(x)$ is quenched to negligible values everywhere in the medium so that $I^-(0)$ can be neglected in (29). Furthermore, the high pumping-rate assumption means that $WN_0(x) >> \tau^{-1}N_1(x)$ so that (29) simplifies to

$$I^+(L) \simeq I^+(0) + WNL \quad (30)$$

from which

$$G(\lambda) \simeq 1 + NWL/I^+(0) \quad (31)$$

so that as long as $G(\lambda) >> 1$, it is inversely proportional to $I^+(0)$, as stated in the preceding. The strong signal regime was also treated by Flamant and Meyer [22] in their study of the dependence of the total gain of a flashlamp-pumped dye-laser amplifier on its length.

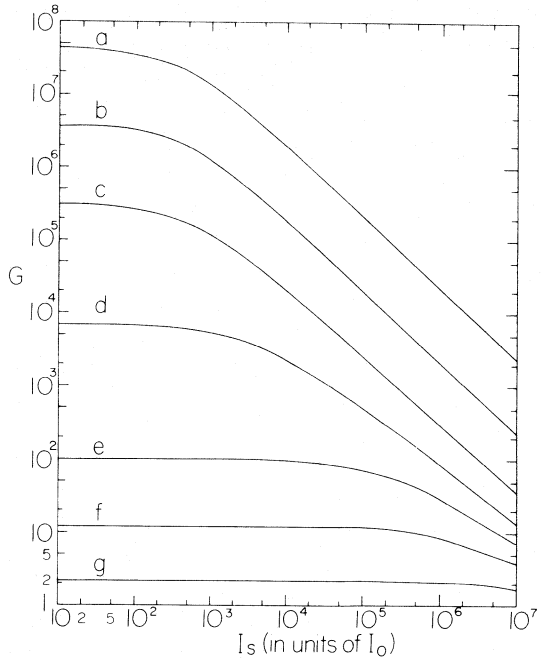

Fig. 5. Calculated gain (G) of a dye-laser amplifier as a function of input signal (I_S). I_S is given in units of I_0 [in (23)]. A bandwidth of 0.05 nm is assumed at $\lambda = 575$ nm. Material parameters are listed in Table I. (a) $W = 5 \times 10^8$ (s^{-1}). (b) $W = 5 \times 10^7$ (s^{-1}). (c) $W = 10^7$ (s^{-1}). (d) $W = 5 \times 10^6$ (s^{-1}). (e) $W = 3 \times 10^6$ (s^{-1}). (f) $W = 2 \times 10^6$ (s^{-1}). (g) $W = 10^6$ (s^{-1}).

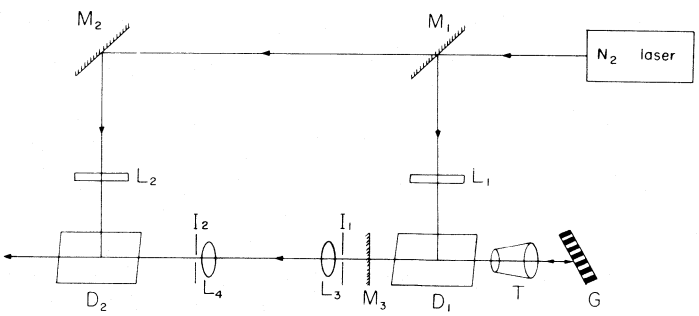

Fig. 6. Experimental setup. M_1—beam-splitting mirror for $\lambda = 337.1$ nm. M_2—totally reflecting mirror at $\lambda = 337.1$ nm. L_1, L_2—cylindrical lenses ($f = 50$ nm). G—reflection grating. T—telescope (magnification; 20×). D_1—oscillator dye cell. M_3—output coupler. I_1, I_2—iris diaphragms. L_3—collimating lens. L_4—focusing lens. D_2—amplifier dye cell.

V. Experiment

A. Experimental Setup

Our experiments were performed using the setup shown schematically in Fig. 6. The pump beam of a longitudinally excited pulsed nitrogen laser ($\lambda = 337.1$ nm, full width at half maximum (FWHM) of 8 ns) is divided by the beam-splitting mirror M_1 into two beams with equal intensities. The two beams pump transversely a laser oscillator and an amplifier. One beam is focused by the cylindrical lens L_1

(focal length 50 mm) into the dye cell D_1. The dye cell is wedged at 8° to prevent feedback by reflection from the cell's windows. D_1 in conjunction with the output coupler M_3 (a quartz wedge), the telescope T (magnification: 20X) and the grating G form the dye-laser oscillator. The part of the pump beam which is transmitted by M_1 is reflected by the mirror M_2 through the cylindrical lens L_2 into the dye cell D_2. L_2 and D_2 are identical to their counterparts in the oscillator branch of the system. The cylindrical lenses focus the nitrogen laser beam to a strip of 1 cm by 4×10^{-2} cm on the dye cell, centered in a 3-cm-long dye region. The optically pumped dye cell D_2 forms the amplifier in the system. Optical coupling between the oscillator and the amplifier is accomplished through a lens system L_3 and L_4. Lens L_3 is used to collimate the oscillator output and lens L_4 focuses it into the amplifier. The diaphragms are used for spatial filtering. The parallelogram $M_1M_2D_2D_1$ provides equal path length for the paths $M_1D_1D_2$ and $M_1M_2D_2$. This assures temporal overlap in the amplifier between the pump beam and the input beam from the oscillator to the amplifier. With this simple configuration, the problem of synchronization, which is very critical when the oscillator and the amplifier are pumped by two different nitrogen lasers [27], is easily overcome. Throughout the experiment, we used a concentration of 5×10^{-3} mole · l^{-1} rhodamine 6G in ethanol.

B. Measurements of the ASE

The first experiment we performed consisted of measuring the total ASE output of the dye cell D_2 as a function of pump power. To this end the mirror M_1 was removed from the system. In Fig. 7 we show the results of this experiment. The circles represent the measured total photon flux, averaged over the pulse length (total pulse energy divided by the FWHM of the pulse), as a function of pumping rate W. The absorption cross section of rhodamine 6G at 337.1 nm is $\sigma_a = 2.4 \times 10^{-17}$ cm^2, and with a pumped area of 0.04 cm^2 the pumping rate W is related to the nitrogen laser power P by $W(s^{-1}) = 10^6 P(\text{kW})$ (see Table I). Again, P is the average of the measured nitrogen laser power. The experimental results are compared to the steady-state solutions of (1)-(4) (solid curve), assuming, however, $N_T = 0$. As previously discussed, this is an appropriate approximation at high pumping rates. At low pumping rates, steady state may not be reached during the short pump pulses, so that one would expect the measured values to be somewhat below the calculated ones. The absorption depth $(\sigma_a N)^{-1}$ at the dye concentration used is 1.4×10^{-2} cm. This dimension was used for calculating the ASE photon flux I (photons · cm^{-2} s^{-1}) from the measured ASE power. As the dye region in D_2 is 3 cm long, self-absorption of the ASE in the pumped dye region must be taken into account. The computer calculations used to generate the continuous curve took into consideration the fact that the ASE generated in the 1-cm-long excited region is attenuated by traveling through 1 cm of unpumped region. No adjustable parameters were used in the calculation. The measurements could be performed accurately over two decades of W. As seen in Fig. 7, there is good agreement between theory and experiment. We conclude that the model analyzed in Section III gives a satisfactory description of the physical situation.

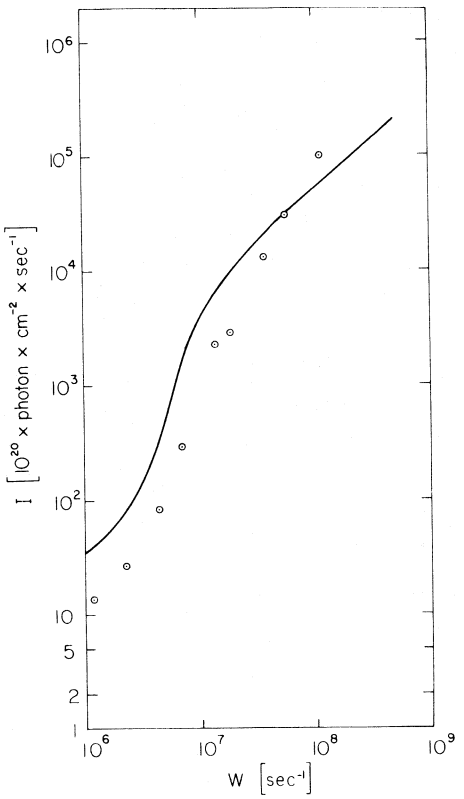

Fig. 7. ASE output (I) as a function of pumping rate (W). Circles denote experimentally measured values; the solid curve is calculated as explained in the text.

C. Gain Measurements

In order to measure the gain of the dye amplifier as a function of the signal input for various amplifier pumping rates, we replaced the mirror M_1 in the dye system. In this arrangement the oscillator output serves as the amplifier input. By placing calibrated filters between M_1 and M_2, and L_3 and L_4, both the amplifier pump rate and the amplifier input could be easily controlled. In this experiment G was a ruled grating with 1200 lines/mm and the oscillator linewidth was 5×10^{-2} nm. The oscillator temporal FWHM was 5 ns. The experiment was performed with the oscillator tuned at 595 nm since at this wavelength the amplifier output was largest. This wavelength is considerably larger than $\lambda = 555$ nm, the fluorescence peak, and it reflects the tradeoff between gain and self-absorption in our oscillator-amplifier system. The experimental data and a calculated curve are shown in Fig. 8.

In order to compare the experimental data with the theoretical calculation, the data were corrected to account for self-absorption in the unpumped regions of the amplifier cell. The dashed curve is calculated for the highest pumping rate used ($W = 6.9 \times 10^7$ s^{-1}, corresponding to ~70-kW nitrogen laser power), and again no adjustable parameters are used in the calculation. The difference between the calculated and the corresponding experimental curve represents a difference of at most 15 percent in the value of $\int_0^L \alpha(\xi, \lambda) d\lambda$ [(12), (13)]. This

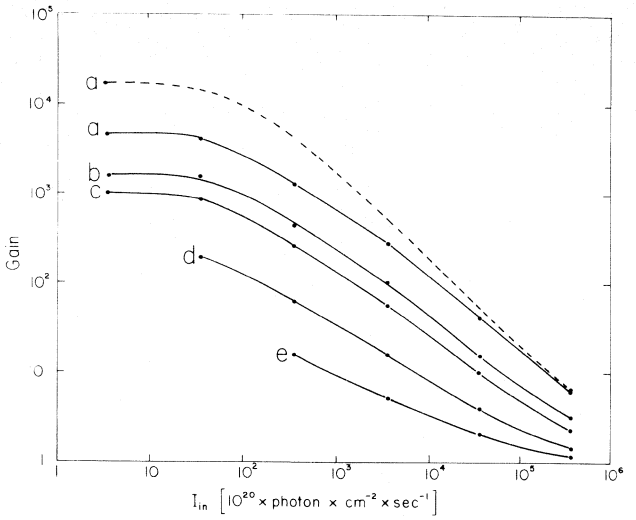

Fig. 8. Measured gain of a R6G amplifier, at $\lambda = 595$ nm, as a function of input photon flux (I_{in}), for various pumping rates. Points represent the measured values, and the solid curves are hand drawn through them. The dashed curve is calculated for the value of W that corresponds to the highest pumping rate. (a) $W = 6.9 \times 10^7$ (s^{-1}). (b) $W = 3.4 \times 10^7$ (s^{-1}). (c) $W = 2.2 \times 10^7$ (s^{-1}). (d) $W = 1.2 \times 10^7$ (s^{-1}). (e) $W = 6.9 \times 10^6$ (s^{-1}).

represents a much better fit than one would expect in view of the uncertainty of the constants used in the calculation and the approximation of the model. The behavior of the experimental curves in Fig. 8 agrees with the description given in Section IV and these curves are qualitatively similar to the theoretical curves shown in Fig. 5. For very small input signals the gain is constant, but as the input signal becomes more intense saturation effects reduce the gain. As explained previously in (31), at high pump rates and high enough input signals, the gain becomes approximately proportional to the pump rate and inversely proportional to the signal input.

D. Narrow-Band Amplification

From Fig. 8 it can be seen that with the amplifier pumped by 70 kW, its peak power output at 5950 Å (with $\Delta\lambda = 5 \times 10^{-2}$ nm) was 40 kW for an input of 6.7 kW. However, for a 20-dB attenuation of the input signal the amplifier output is reduced by 3 dB only. Consequently, if a Fabry-Perot etalon is placed in the space between the lenses L_3 and L_4, we can expect to greatly reduce the linewidth of the dye system without suffering a serious reduction in the power output. As already noted by Hänsch [5b)], in nitrogen-laser-pumped systems, the oscillator linewidth will not be much smaller than that of the intracavity Fabry-Perot filter because of the short duration of the pulse. However, a high-finesse intracavity etalon causes an appreciable reduction of the oscillator narrow-band output power due to insertion losses. We therefore found it advantageous for further line narrowing to place the etalon between the oscillator and amplifier stages of the system. We replaced the ruled grating in Fig. 6 by a holographic grating with 2900 lines/mm, and placed a Fabry-Perot etalon with a free spectral range of 2×10^{-2} nm and a reflective finesse of 20 between the lenses L_3 and L_4. With the amplifier pumped by 70 kW, this system gave an output peak power of 20 kW at 595 nm with a linewidth of $\Delta\lambda = 2 \times 10^{-3}$ nm. These results demonstrate that a dye-laser oscillator-amplifier system is a convenient tool for generating high-power narrow-band emission.

REFERENCES

[1] P. P. Sorokin and J. R. Lankard, "Stimulated emission observed from an organic dye chloroaluminum phtalocyanine," *IBM J. Res. Develop.*, vol. 10, pp. 162–163, Mar. 1966.

[2] M. H. Gassman and H. Weber, "Flashlamp-pumped high gain laser dye amplifiers," *Opt. Electron.*, vol. 3, pp. 177–184, 1971.

[3] B. B. Snavely, "Continuous wave dye lasers," in *Dye Lasers*, F. P. Schäfer, Ed. New York: Springer, 1973, ch. 2.

[4] a) R. H. Dicke, "Coherence in spontaneous radiation processes," *Phys. Rev.*, vol. 93, pp. 99–110, Jan. 1954.
b) L. Allen and G. I. Peters, "Superradiance, coherence brightening and amplified spontaneous emission," *Phys. Lett. A*, vol. 31, pp. 95–96, Feb. 1970.

[5] a) G. Capelle and D. Phillips, "Tuned nitrogen laser pumped dye laser," *Appl. Opt.*, vol. 9, pp. 2742–2745, Dec. 1970.
b) T. W. Hänsch, "Repetitively pulsed tunable dye laser for high resolution spectroscopy," *Appl. Opt.*, vol. 11, pp. 895–989, Apr. 1972.

[6] a) M. E. Mack, "Superradiant traveling-wave dye laser," *Appl. Phys. Lett.*, vol. 15, pp. 166–168, Sept. 1969.
b) S. L. Chin and G. Bedard, "High efficiency superradiant traveling-wave dye laser," *Opt. Commun.*, vol. 3, pp. 299–300, July 1971.
c) C. Lin, T. K. Gustafson, and A. Dienes, "Superradiant picosecond laser emission from transversely pumped dye solution," *Opt. Commun.*, vol. 8, pp. 210–215, July 1973.

[7] A. Yariv and R. C. C. Leite, "Super radiant narrowing in fluorescence radiation of inverted populations," *J. Appl. Phys.*, vol. 34, pp. 3410–3411, Nov. 1963.

[8] L. W. Casperson and A. Yariv, "Spectral narrowing in high-gain lasers," *IEEE J. Quantum Electron. (Part I of Two Parts)*, vol. QE-8, pp. 80–85, Feb. 1972.

[9] L. W. Casperson, "Saturation and power in a high-gain gas laser," *IEEE J. Quantum Electron.* (Corresp.), vol. QE-9, pp. 250–252, Feb. 1973.

[10] —, "Spectral narrowing in double-pass superradiant lasers," *Opt. Commun.*, vol. 8, pp. 85–87, May 1973.

[11] L. Allen and G. I. Peters, "Amplified spontaneous emission and external signal amplifications in an inverted medium," *Phys. Rev. A*, vol. 8, pp. 2031–2047, Oct. 1971. (See also a series of articles by the same authors, cited in [11, ref. 1]).

[12] a) P. P. Sorokin, J. R. Lankard, E. C. Hammond, and V. L. Moruzzi, "Laser pumped stimulated emission from organic dyes: Experimental studies and analytical comparisons," *IBM J. Res. Develop.*, vol. II, pp. 130–147, Mar. 1967.
b) P. P. Sorokin, J. R. Lankard, V. L. Moruzzi, and E. C. Hammond, "Flashlamp pumped organic-dye lasers," *J. Chem. Phys.*, vol. 48, pp. 4726–4741, May 1967.

[13] R. A. Keller, "Effect of quenching of molecular triplet states in organic dye lasers," *IEEE J. Quantum Electron.*, vol. QE-6, pp. 411–416, July 1970.

[14] R. Pappalardo, H. Samelson, and A. Lempicki, "Calculated efficiency of dye lasers as a function of pump parameters and triplet lifetimes," *J. Appl. Phys.*, vol. 43, pp. 3776–3787, Sept. 1972.

[15] U. Ganiel and G. Neumann, "Power output coupling in a dye laser pumped by a nitrogen laser," *Opt. Commun.*, vol. 12, pp. 5–7, Sept. 1974.

[16] M. J. Weber and M. Bass, "Frequency- and time-dependent gain characteristics of dye lasers," *IEEE J. Quantum Electron.*, vol. QE-5, pp. 175–188, Apr. 1969.

[17] B. B. Snavely, "Flashlamp-excited organic dye lasers," *Proc. IEEE*, vol. 57, pp. 1374–1390, Aug. 1969.

[18] J. B. Atkinson and F. P. Pace, "The spectral linewidth of a flashlamp-pumped dye laser," *IEEE J. Quantum Electron.*, vol. QE-9, pp. 569–574, June 1973.

[19] W. W. Rigrod, "Saturation effects in high gain lasers," *J. Appl. Phys.*, vol. 36, pp. 2487–2490, Aug. 1965.

[20] B. G. Huth, "Direct gain measurements of an organic dye ampli-

fier," *Appl. Phys. Lett.*, vol. 16, pp. 185–188, Feb. 1970.
[21] C. V. Shank, A. Dienes, and W. T. Silvfast, "Single pass gain of Exciplex 4-MU and Rhodamine 6G dye laser amplifiers," *Appl. Phys. Lett.*, vol. 17, pp. 307–309, Oct. 1970.
[22] P. Flamant and Y. J. Meyer, "Steady-state gain equation in a flashpumped dye amplifier," *Opt. Commun.*, vol. 7, pp. 146–149, Feb. 1973.
[23] F. P. Schäfer, "Principles of dye laser operation," in *Dye Lasers*, F. P. Schäfer, Ed. New York: Springer, 1973, sec. 1.3, pp. 28–32.
[24] M. E. Mack, "Measurements of nanosecond fluorescence decay times," *J. Appl. Phys.*, vol. 39, pp. 2483–2485, Apr. 1968.
[25] J. P. Webb, W. C. McColgin, O. G. Peterson, D. L. Stockman, and J. G. Eberly, "Intersystem crossing rate and triplet state lifetime for a lasing dye," *J. Chem. Phys.*, vol. 53, pp. 4227–4229, Dec. 1970.
[26] D. N. Dempster, T. Morrow, and M. F. Quinn, "The photochemical characteristics of Rhodamine 6G-ethanol solutions," *J. Photochem.*, vol. 2, pp. 343–359, 1973/1974.
[27] I. Itzkan and F. W. Cunningham, "Oscillator–amplifier dye-laser system using N_2 laser pumping," *IEEE J. Quantum Electron. (Part II of Two Parts. Special Issue on 1971 IEEE/OSA Conference on Laser Engineering and Applications)*, vol. QE-8, pp. 101–105, Feb. 1972.

Theory of the Nitrogen Laser Excited by a Relativistic Electron Beam

DAVID A. McARTHUR AND J. W. POUKEY

Abstract—**The 3371-Å nitrogen laser power produced by a relativistic electron beam propagating into nitrogen gas is calculated. The excitation contribution of cascade electrons is found to be negligible, compared to the excitation caused by plasma electrons drifting in the inductive electric field produced by the beam. The extensive experimental data on nitrogen are used wherever possible in the calculation, and the sensitivity of the calculation to the various input data is given. The mechanism of excitation by plasma electrons alone yields agreement within experimental uncertainty for such parameters as the peak laser power, the laser pulsewidth and delay, and the dependence of the laser power on gas pressure. For a larger drift tube radius, the plasma electron mechanism predicts higher power and a different pressure dependence, in agreement with experimental trends. In calculating the laser power, the beam propagation details, excitation to the upper and lower laser levels, collisional quenching, a threshold for amplified spontaneous emission, and excitation and deexcitation by plasma electrons are included, but coherent dipole moment effects are neglected.**

I. Introduction

PULSED relativistic electron beams [1]–[4] have recently been used to excite laser action in gases such as N_2 and H_2, providing intense sources of short wavelength radiation useful in applications such as plasma heating and spectroscopy. The theory of such laser action has not been treated in detail, probably because the interaction of a relativistic electron beam with an initially neutral gas is complex, involving strong spatial and time variations of the plasma parameters [5]. It has been proposed that in the case of the N_2 laser, excitation proceeds via a cascade of secondary electrons produced in ionization events caused by the primary beam electrons, the presence of an electric field in the beam-produced plasma being of little importance [2].

Manuscript received May 15, 1975.
The authors are with the Sandia Laboratories, Albuquerque, N. Mex. 87115.

In order to understand the propagation of relativistic electron beams, a detailed model of the plasma produced by the beam was recently developed for the well-understood case of N_2 gas [5], [6]. In this model, the electrons produced initially by the primary beam drift through the weakly ionized N_2 gas, because the plasma contains an axial electric field. The electric field in the relativistic electron beam case is the inductive electric field caused by the rapidly rising beam current waveform. As a result of this drift process, the initial secondary electrons acquire a new energy distribution determined by the electric field and the gas pressure. The measured transport coefficients of this distribution can then be used to calculate the resulting avalanche ionization and further plasma current production in the gas. The additional plasma current caused by avalanche ionization subtracts from the primary beam current, tending to reduce the inductive electric field, and eventually "shutting off" the avalanche ionization process. Fig. 1 shows representative waveforms of the beam current (I_b), plasma current (I_p), and net current ($I_n = I_b - I_p$). The resulting plasma properties thus vary rapidly in space and time. Without adjustable parameters, the model has been shown to describe the measured net current waveform well for beams of different peak currents and energies, over a wide pressure range [6].

The detailed time- and space-dependent plasma properties provided by the model can equally well be applied to the N_2 laser situation, provided accurate measurements of the excitation cross sections to the upper and lower laser levels are available. In this paper detailed calculations are made for the case studied experimentally by Patterson [7], with certain simplifying assumptions concerning the calculation of the laser power since we are primarily concerned with identifying the excitation mechanism. Preliminary calculations have already been reported briefly [8], and also a summary of more com-

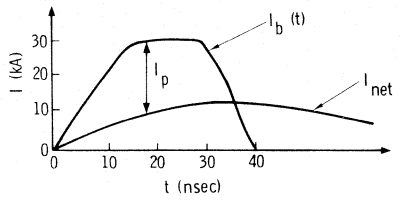

Fig. 1. Representative current waveforms produced by a high-current electron beam propagating into neutral gas. I_p changes sign near the end of the I_b pulse (the plasma electrons reverse direction at late times).

plete calculations [9]. In Section II we describe the additional measurements made by Patterson to define the primary beam characteristics, in Section III we describe the laser model, in Section IV the comparison between theory and experiment, and in Section V we present our conclusions.

II. Measurement of Primary Beam Characteristics

Reference [7] describes the measurement of the laser output power and pulsewidth as a function of the nitrogen pressure, the primary beam current, and the length of the laser tube. Since lasing occurs primarily on the rapidly rising initial part of the net current waveform, the measured velocity v_b of the primary beam front is used [7]. For an accurate calculation of the laser power additional details about the primary beam are needed, because of the long drift tube length L and the relatively small tube radius r_0 (see Fig. 2). The plasma current and the electric field depend on the radial shape $S(r)$ of the primary beam if the beam radius is comparable to r_0 [6]. Representative time-averaged functions $S(r)$ measured with 4-chlorostyrene films [7] are shown in Fig. 3. Finally, the primary electron beam current I_b is attenuated exponentially (within the experimental error of ±10 percent), with a characteristic decay length Λ

$$I_b(z) = I_b(0) \exp(-z/\Lambda).$$

Λ was measured as a function of the N_2 pressure P by comparing the peak $I_b(z > 0)$ with the simultaneously measured peak anode current $I_b(0)$, for two values of z (see Fig. 4).

III. The Laser Model

The net current model of [6] permits the calculation of the plasma current density j_{pz} and the electric field E_z as a function of radius r and length z along the laser tube, assuming cylindrical symmetry. At high gas pressure and low electron density, E_z controls the characteristic electron energy ϵ_k, and thus the relative excitation to the upper and lower laser levels. To a good approximation ϵ_k is a function of (E_z/N_g), where N_g is the initial density of N_2 molecules [6]. E_z and j_{pz} are calculated from a varying primary beam current density j_{bz} which includes the effects of the measured beam front velocity v_b, shape $S(r)$, and beam loss length Λ (see Section II)

$$j_{bz}(r, z, t) = S(r)\, I_b \left(t - \frac{z}{v_b}\right) \exp(-z/\Lambda) \qquad (1)$$

where I_b is the primary beam current measured at the anode, corresponding to $z = 0$. The calculated j_{pz} and E_z yield calculated plasma electron excitation rates X_u and X_l to the upper and lower laser levels, respectively, which are discussed in Section III-A. In Section III-B we discuss the calculation of the laser power which results from these excitation rates.

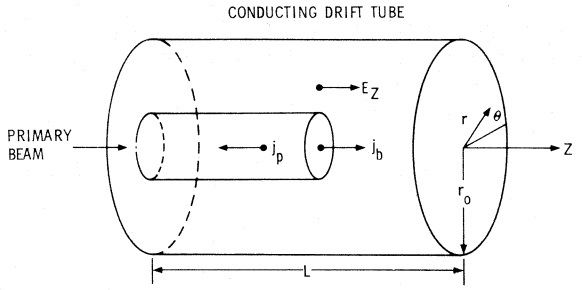

Fig. 2. Geometry of beam and drift tube.

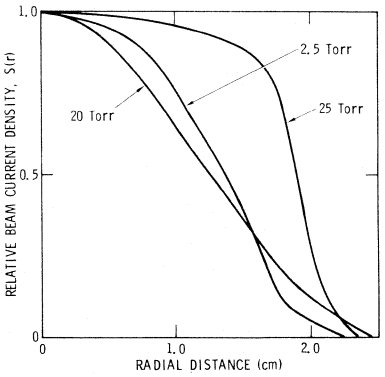

Fig. 3. Measured radial variation of average beam current density, for several pressures.

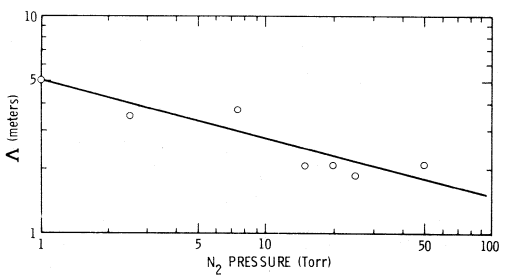

Fig. 4. Measured beam loss parameter Λ, as a function of nitrogen pressure at constant axial magnetic field.

A. Calculation of the Excitation Rates X_u, X_l

The 3371-Å N_2 laser transitions occur between rotational levels of the $v' = 0$ vibrational state of the $C^3\Pi_u$ electronic level (denoted here by the subscript u), and the $v'' = 0$ vibrational state of the $B^3\Pi_g$ electronic level (denoted by the subscript l). The rates X_u and X_l are given in general by

$$X_{u,l} = n_s N_g \langle \sigma_{u,l} v \rangle = j_{pz} N_g \langle \sigma_{u,l} v \rangle / ew \qquad (2)$$

where σ_u, σ_l, respectively, are the energy-dependent electron excitation cross sections, v is the velocity of a plasma electron of energy ϵ, w is the drift velocity of the electron distribution, n_s is the plasma electron density, and e is the electron charge. $\langle \sigma v \rangle$ represents the average of the product σv over the distribu-

tion of plasma electron energies, given by

$$\langle \sigma v \rangle \propto \int_0^\infty \sigma \epsilon^{1/2} f(\epsilon)\, d\epsilon \tag{3}$$

where $f(\epsilon)$ is the electron distribution function. In the general case, it would be necessary to solve the Boltzmann transport equation to obtain $f(\epsilon)$ as a function of E_z/N_g. However, in the case of excitation to the $C^3\Pi_u$ and $B^3\Pi_g$ levels of N_2, we are able to use experimental data for $\langle \sigma_u v \rangle$, and to obtain $\langle \sigma_l v \rangle$ approximately from calculated $f(\epsilon)$ [10].

Legler [11] has measured a transport coefficient δ_0 for N_2, which is analogous to the Townsend first ionization coefficient, and is closely related to $\langle \sigma_u v \rangle$. The light emitted from several vibrational states of the $C^3\Pi_u$ level was observed as a function of the E_z/N_g present in the weakly ionized gas. δ_0 is related to $\langle \sigma_u v \rangle$ by [11]

$$\langle \sigma_u v \rangle = K \delta_0 w / N_g \tag{4}$$

where K is a correction factor to remove contributions from $C^3\Pi_u$ vibrational levels with $v' > 0$. Since the $v' = 1, 2$, and 3 levels comprise most of the unwanted contribution [11], K is given by

$$K = \left(\sum_{v'=0}^{3} \left[\left(\frac{\sigma_{Cv'}}{\sigma_{C0}} \right) \sum_{v''=0}^{9} P_{v'v''}\, \eta_{v'v''} \right] \right)^{-1} = 0.53. \tag{5}$$

Here $\sigma_{Cv'}$ is the measured peak cross section for electron excitation to the v' level of the C state [12], the $P_{v'v''}$ are the measured relative probabilities of emission from the v' level to the various v'' levels of the B state ($\Sigma_{v''} P_{v'v''} \equiv 1$) [13], and $\eta_{v'v''}$ is the photomultiplier quantum efficiency at the wavelength of the $v' \rightarrow v''$ band, relative to the average value used by Legler in determining δ_0. At $E_z/N_g \sim 6 \times 10^{-15}$ V · cm^2 it is possible that a small contribution ($\sim$ 5 percent) may be present from the $B^2\Sigma_u^+$ level of the N_2^+ ion, but this effect is smaller than the errors in most of the input data to the model, and can be ignored. The resulting function $\langle \sigma_u v \rangle / w$ is shown in Fig. 5, as a function of E_z/N_g.

No measurement of the corresponding transport coefficient for the lower laser level has been made, presumably because of the long radiative lifetime of the $B^3\Pi_g$ level, the long wavelengths of the bands originating from the $B^3\Pi_g$ level, and the presence of important cascade contributions from the $C^3\Pi_u$ levels which would result from a broad electron energy distribution [13]. Measurements have, however, been made of the excitation cross sections $\sigma_{Bv''}$ to several vibrational levels of the $B^3\Pi_g$ state, as a function of the precisely defined energy of an electron beam [12], [14], [15]. From the calculations of [10] it can also be seen that for $\epsilon \gtrsim 3.5$ eV in N_2, $f(\epsilon)$ is given approximately over a wide range of E_z/N_g by

$$f(\epsilon) \cong A' \epsilon^{1/2} \exp(-\epsilon/\epsilon_k') \quad (\epsilon \gtrsim 3.5 \text{ eV}) \tag{6}$$

where A' and ϵ_k' are independent of ϵ but do depend on E_z/N_g. Note that the single exponential form of $f(\epsilon)$ is retained even when several sharp thresholds of inelastic processes are crossed, ϵ_k' is equal to the measured electron characteristic energy ϵ_k

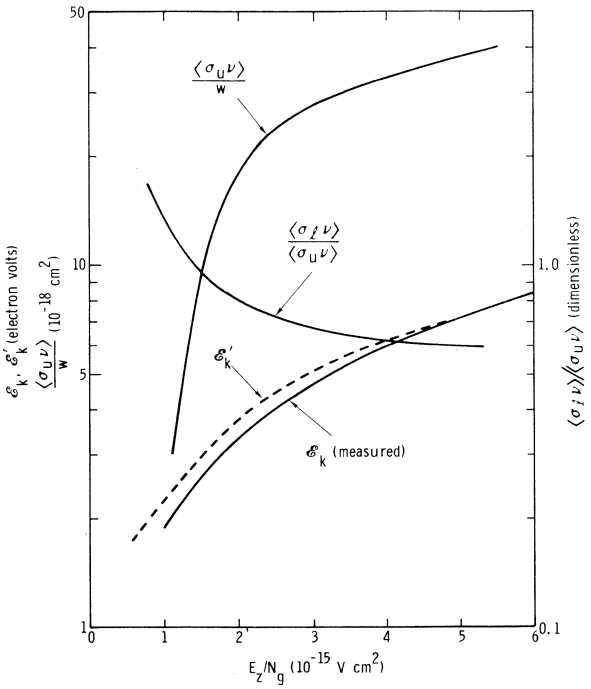

Fig. 5. Variation with E_z/N_g of transport coefficients used to calculate excitation to upper and lower laser levels. The curve labeled ϵ_k shows the experimentally measured characteristic energy of the electron distribution [10].

within <20 percent over the range of large $\langle \sigma_u v \rangle / w$ (see Fig. 5), but A' depends strongly on E_z/N_g and the set of cross sections used to calculate $f(\epsilon)$. On the other hand, A' does not appear in the ratio $\langle \sigma_l v \rangle / \langle \sigma_u v \rangle$ for a particular value of E_z/N_g, since it can be taken outside the integral in (3) and cancels in the ratio

$$\frac{\langle \sigma_l v \rangle}{\langle \sigma_u v \rangle} \cong \frac{\int_0^\infty d\epsilon \sigma_{B0} \epsilon \exp(-\epsilon/\epsilon_k')}{\int_0^\infty d\epsilon \sigma_{C0} \epsilon \exp(-\epsilon/\epsilon_k')}. \tag{7}$$

Thus a calculation of the ratio depends on knowledge of excitation cross sections and the parameter ϵ_k', which at high E_z/N_g is nearly equal to the measured characteristic energy ϵ_k, and is available at lower E_z/N_g from the calculations of [10] (see Fig. 5).

To calculate the ratio $\langle \sigma_l v \rangle / \langle \sigma_u v \rangle$, we use the measurements of [16] for the shape of σ_{C0}. σ_{B0} as measured directly contains cascade contributions from the $C^3\Pi_u$ level [14], [15]. The σ_{B3} cross section has been corrected for cascade contributions in [14], so the shape of this "corrected" σ_{B3} was used for the shape of σ_{B0}. In calculating the ratio it is important to have correct *relative* magnitudes for σ_{B0} and σ_{C0}; since [12] appears to take more accurate account of the long lifetime of the $B^3\Pi_g$ level in measuring $\sigma_{Bv''}$, we use [12] for the peak cross sections for both σ_{B0} and σ_{C0}. (An alternative shape for σ_{B0} can be obtained from the measured $v' = 9$ to $v'' = 6$ transition cross section [15], which has negligible cascade. This shape is only 25 percent wider than that assumed in the preceding and results in little change in the calculated ratio.) The resulting ratio $\langle \sigma_l v \rangle / \langle \sigma_u v \rangle$ is shown in Fig. 5 as a function of

E_z/N_g.[1] Since the uncertainties in ϵ_k', σ_{C0}, and σ_{B0} are $\lesssim$20 percent [10]-[12], we estimate that $\langle\sigma_l v\rangle/\langle\sigma_u v\rangle$ is accurate to ±20 percent for $E_z/N_g \geq 10^{-15}$ V · cm^2. Therefore

$$X_l = n_s N_g \left(\frac{\langle\sigma_l v\rangle}{\langle\sigma_u v\rangle}\right)\langle\sigma_u v\rangle. \tag{8}$$

1) Excitation by Cascade Electrons: Thus far we have considered only excitation by the swarm of plasma electrons produced by avalanche or primary electron ionization, which have an energy distribution determined by E_z/N_g. However, there exist two groups of electrons which would have energies $\gtrsim$10 eV even if I_b were so small that $E_z \cong 0$ as follows: a) the energetic primary electrons; and b) the distribution of energetic "first secondary" electrons produced when primary electrons ionize N_2 molecules. The primary electrons have negligible probability of undergoing the electron-exchange type of collision required to excite an N_2 molecule from the singlet ground state to the triplet laser levels, because of their high energy [17]. The "first secondary" electrons, on the other hand, have an energy distribution $\rho_f(\epsilon)$ extending to low energies [18] and thus have an appreciable probability of exciting the triplet laser levels. The "first secondary" electrons are assumed to be responsible for essentially all the laser excitation in the model of Dreyfus and Hodgson [2]. The amount of excitation to the upper laser level by these first secondary electrons can be estimated because ρ_f changes slowly with primary electron energy and is roughly constant in shape above a primary electron energy of a few kiloelectronvolts. The relative ionization contribution η_f of these first secondary electrons in N_2 has been measured [19]

$$\dot{N}_{ip} \propto (1 + \eta_f)\,\sigma_{ip0}$$

where $\dot{N}_{ip}$ is the total primary electron ionization rate, σ_{ip0} is the ionization cross section for the primary electrons alone, and $\eta_f = 1.8 \pm 0.7$. The relative contribution ξ_f for excitation to the upper laser level can be estimated from the distribution ρ_f, the cross section σ_{C0} [12], [16], and the N_2 ionization cross section σ_i [20]

$$\frac{\xi_f}{\eta_f} = \frac{\int_0^\infty \sigma_{C0}(\epsilon)\rho_f(\epsilon)\epsilon^{1/2}\,d\epsilon}{\int_0^\infty \sigma_i(\epsilon)\rho_f(\epsilon)\epsilon^{1/2}\,d\epsilon} \cong 0.05.$$

(This ratio is also in rough agreement with the ratio of $C^3\Pi_u$ excitation to ionization which has been measured to be 0.092 for 4.3-MeV α particles incident on N_2 [21].) The function $\rho_f(\epsilon)$ yields a calculated value of η_f which is ≈ 0.8 rather than the 1.8 measured. This discrepancy may be real, corresponding to an added contribution from cascading high-ϵ electrons in ρ_f. Therefore, in our estimate of this small contribution, we use $2\xi_f/\eta_f$. Thus the estimated excitation rate by first secondary electrons at a given point in the gas is

$$X_{uf} \cong \frac{2\xi_f}{\eta_f}\frac{\eta_f \dot{N}_{ip}}{(1+\eta_f)} \tag{9}$$

where $\dot{N}_{ip}$ is the total ionization rate by primary and first secondary electrons. Using calculated values of X_u and $\dot{N}_{ip}$, we find $X_u/X_{uf} \cong 100$ at the peak of the laser pulse at 1.5- and 7.5-torr N_2, and $X_u/X_{uf} = 30$ at $P = 50$ torr where the primary and plasma avalanche ionization rates are comparable. Therefore, excitation by first secondary electrons appears to be a small effect compared to plasma excitation, and we therefore neglect excitation by primary electrons throughout the pulse, even when $X_u = 0$. The neglect of primary electron cascade excitation and the dominance of plasma electron excitation is in strong contrast to the model presented by Dreyfus and Hodgson [2]. The difference between the two models will be discussed further in Section IV.

We also neglect excitation by collisions between excited molecules, which may influence the plasma parameters significantly late in the primary beam pulse [22], because the calculated laser pulse occurs close to the beginning of the primary beam pulse.

2) Distribution of Molecules Among Sublevels: Each vibrational state of the C and B levels is split into multiplet components, into rotational levels denoted by the rotational quantum number J, and into two Λ-doublet components [23]. In calculating the small-signal gain for each possible laser transition we assume equal populations of the three multiplets, we ignore the small Λ-doublet splitting and the associated alternation of intensities caused by varying nuclear spin state degeneracies [24] (at most a ±35-percent effect in the small-signal gain, and a much smaller effect in the total power, as discussed as follows in Section IV), and we assume for the rotational levels a Boltzmann distribution with a temperature equal to the gas temperature T. Over most of the pressure range of interest here (1.5 torr $\leq P \leq$ 50 torr [7]), the measured N_2 rotational relaxation time τ_r ($\cong$ 370 ns/P(torr) [25]) is greater than the laser pulsewidth, so that rotational relaxation effects during lasing are small. For 0.5 torr $\lesssim P \lesssim$ 3 torr experiments [26], [27] have shown that the assumption of a rotational temperature close to the initial gas temperature describes the intensities of the lasing transitions well, although this approximation may begin to fail at $P \cong$ 30 torr [24]. Because the plasma model is already sufficiently complex and the peak of the measured laser power occurs at $\approx$10 torr, we ignore high-pressure rotational relaxation effects.

B. Calculation of the Laser Power

We are concerned primarily with the laser excitation mechanism, and therefore with the order of magnitude of the laser power, and the dependence of the laser power on such parameters as the gas pressure, drift tube diameter, and the primary beam current. We therefore neglect several details of the lasing process which are expected to make relatively small changes in the laser pulse shape and peak power. We neglect the possibility of laser beams directed both parallel to the primary electron beam (forward wave), and antiparallel to the primary

[1] As a check on the numerical integration and $f(\epsilon)$ used to obtain $\langle\sigma_l v\rangle/\langle\sigma_u v\rangle$, δ_0 was calculated as a function of E_z/N_g, using the calculated ϵ_k' and A' from [10]. The shape of the resulting δ_0 was equal to that of the data of [11] or the calculations of [10] within ±15 percent.

beam (backward wave). In the traveling-wave-excited H_2 laser, more than 90 percent of the laser energy is emitted in the forward direction [28]. In the electron-beam-excited N_2 laser [2], more than 65 percent of the energy is emitted in the forward direction, even if the weak second laser pulse observed is assumed to be a backward wave and the Ti anode reflectivity is included. Based on these experiments we assume that all laser energy is emitted in the forward direction.

Finally, we neglect coherent dipole moment effects analogous to self-induced transparency [29]. These are expected to be important to an exact treatment because for $P < 50$-torr N_2 the phase memory time T_2 is greater than the laser pulsewidth τ_L (we estimate that $T_2^{-1} \cong \tau_r^{-1} + \tau_{su}^{-1}$, where $\tau_{su} = 38$ ns is the spontaneous lifetime of the upper laser level). For T_2 much greater than the preparation time of an inversion, it has been observed [30] that the laser pulse is considerably delayed and has a pulsewidth which depends strongly on the inversion density, even if the initial inversion density is constant in space and time. However, our case differs considerably from that of [30] because the excitation is incoherent and because the delay time τ_D and the radiation damping time τ_R are much shorter even if coherent excitation is assumed. From the gain calculations described in the following and in [30], we can estimate that $\tau_D \cong 1$ ns and $\tau_R \cong 0.1$ ns, at a time of 2 ns after the gain becomes nonzero. Since τ_D and τ_R are much shorter than the risetime of the gain pulse, the laser pulse shape is likely to be determined to a large extent by the excitation pulse shape. To treat this in detail would require a considerable generalization of the theory of [30], which is beyond the scope of this paper. We therefore use rate equations to calculate the population of the upper and lower laser levels, calculate the small-signal gain, and assume that lasing begins on a particular transition when a threshold value of the gain is reached, as explained in detail in the following.

We neglect the slowing of the laser pulse in the high-gain region of the laser tube where the laser transition is not yet saturated [31], because the high-gain region is much shorter than the laser length for the most intense laser lines (estimates show that this is about a 10-percent effect). Estimates show that some of the larger Zeeman splittings in the applied magnetic guide field are of the same size as the Doppler linewidth; these splittings are ignored in the model, however, because the calculated power is relatively insensitive to the precise magnitude of the gain, and because many of the Zeeman splittings are small.

The laser field extracts energy efficiently from the excited laser medium only if the laser intensity I_J on a particular rotational transition is of the order of a threshold intensity I_1. This intensity, which corresponds to the onset of a constant and maximum dI_J/dz rather than exponential growth, is much greater than the saturation intensity I_S because the N_2 laser lines are inhomogeneously broadened in this pressure region. The experimental N_2 laser saturation studies of Leonard [32] show that efficient energy extraction begins at a threshold gain $\exp(G_0)$, where

$$G_0 \equiv \int \alpha dz \cong 13 \tag{10}$$

and α is the small-signal gain coefficient. The saturation threshold condition is most important at high and low pressures where the gain is lower and many lines are prevented from efficient laser action. If no backward laser wave exists, the region near the anode will never become saturated; then the laser power from an element of laser volume is assumed to be zero unless the element is located a distance

$$z > z_{sJ}(r, t) \tag{11}$$

from the anode, where z_{sJ} is a saturation threshold length given by

$$\int_0^{z_{sJ}(r,t_0)} \alpha_{gJ}\left(r, z', t_0 + \frac{z'}{c}\right) dz' = G_0. \tag{12}$$

Here α_{gJ} is the small-signal gain of the P-branch transition originating from the Jth rotational level of the $C^3\Pi_u v' = 0$ state in one of the multiplet components, and t_0 is the laboratory frame time at which the light beam of interest left the anode region ($z = 0$). z_{sJ} is a strong function of t and r because of variations in the plasma properties which determine α_{gJ}.

Laser action is assumed to occur only on the P-branch transitions because of the rotational distribution discussed in Section III-A, which results in slightly less gain for the R-branch transitions. The P-branch transitions will reach the saturation threshold first and because of competition will further decrease the gain on the R-branch transitions, resulting in only P-branch lasing. Experiments also show that only a few R-branch lines [24] and one Q-branch line [26] lase weakly.

The gain α_{gJ} is calculated from

$$\alpha_{gJ} = \frac{1}{3}\left(\frac{\ln 2}{\pi}\right)^{1/2} \frac{B_{00} S_J \lambda^2}{4\pi \tau_{su} \Delta\nu_D}\left[\frac{N_{CJ}}{(2J+1)} - \frac{N_{BJ+1}}{(2J+3)}\right] \tag{13}$$

where the $\frac{1}{3}$ factor accounts for the multiplet splitting, $S_J \cong J$ [33], $\tau_{su} = 3.8 \times 10^{-8}$ s is the spontaneous lifetime of the upper laser level [13], $B_{00} = 0.49$ is the relative probability of the $v' = 0$ to $v'' = 0$ transition, $\lambda = 3371$ Å is the average laser wavelength, N_{CJ} and N_{BJ+1} are the populations of the upper and lower laser levels of the Jth P transition (if we neglect the multiplet splitting), and $\Delta\nu_D$ is the Doppler linewidth

$$\Delta\nu_D = \frac{2}{\lambda}\left(\frac{2kT\ln 2}{M}\right)^{1/2}.$$

Here T is the translational temperature in degrees kelvin and M is the molecular mass of the N_2 molecule.

The populations are obtained from the equations

$$\frac{dN_{CJ}}{dt} \cong f_J X_u - \frac{N_{CJ}}{\tau_u} - \frac{N_{CJ}D}{\tau_{su}} + K' D N_{BJ} \frac{B_{00}}{\tau_{su}} \exp\left(-\frac{h\nu}{\epsilon_k}\right), \quad (0 \leqslant J \leqslant 20) \tag{14a}$$

and

$$\frac{dN_{BJ}}{dt} \cong f_J X_l - \frac{N_{BJ}}{\tau_l} + \frac{K'' B_{00} N_{CJ}}{\tau_{su}}[1 + D], \quad (1 \leqslant J \leqslant 21). \tag{14b}$$

X_l and X_u are the excitation rates discussed in Section III-A and τ_u and τ_l are the total lifetimes of the upper and lower laser levels, respectively, including collisional deactivation [34], [11][2]

$$\tau_u^{-1} = \tau_{su}^{-1} + 0.036 \times 10^7 P\,\mathrm{s}^{-1} \quad (15a)$$

$$\tau_l^{-1} = \tau_{sl}^{-1} + 0.245 \times 10^7 P\,\mathrm{s}^{-1} \quad (15b)$$

$\tau_{sl}^{-1} = 1.12 \times 10^5$ s^{-1} [12], and P is the N_2 pressure in torr. f_J gives the relative rotational populations

$$f_J = x(2J+1)\exp\left[-xJ(J+1)\right] \quad (16)$$

where $x = Bhc/kT$, $B = 2.01$ cm^{-1} is the rotational level constant for the N_2 ground state [23], h is Planck's constant, k is Boltzmann's constant, and T is the rotational temperature, which is assumed equal to the translational temperature.

On the right-hand side of (14a), the third term ($\propto D$) represents the effect of collisional deexcitation of the upper laser level to all the $B^3\Pi_g(v'')$ levels by plasma electrons, and the fourth term ($\propto K'D$) represents the excitation of molecules from the $B^3\Pi_g(v'')$ levels to the upper laser level by plasma electrons. On the right-hand side of (14b) the third term ($\propto K''$) represents spontaneous emission from the $C^3\Pi_u(v')$ levels into the lower laser level, and the fourth term ($\propto K''D$) represents collisional deexcitation from the $C^3\Pi_u(v')$ levels into the lower laser level. To uncouple the equations for different J values, the further approximation required to obtain (14) is that terms such as

$$\left[\frac{J}{2J+1} + \left(\frac{N_{CJ+2}}{N_{CJ}}\right)\left(\frac{J+1}{2J+5}\right)\right] \cong 1$$

for those J values having the peak small-signal gain and contributing most of the laser energy ($J \approx 8$). Using (16) and assuming $T = 300$ K, this approximation is satisfied for the strongest laser lines to $\approx \pm 10$ percent, which is within the experimental error of other input data to the problem. In calculating contributions from other vibrational levels the measured $P_{v'v''}$ are used [see (5)] and it is assumed that excitation to various vibrational levels is proportional to the measured $\sigma_{Cv'}$ and $\sigma_{Bv''}$ [12]. For example

$$K' = \sum_{v''=0}^{4}\left(\frac{\lambda_{0v''}}{\lambda_{00}}\right)^3\left(\frac{P_{0v''}}{P_{00}}\right)\left(\frac{\sigma_{Bv''}}{\sigma_{B0}}\right) \cong 4.8$$

where $\lambda_{0v''}$ is the wavelength of the transition form the $C^3\Pi_u \cdot (v' = 0)$ level to the $B^3\Pi_g(v'')$ level. By a similar calculation, $K'' = 1.57$. The function D is given by

$$D = \frac{7.33}{\epsilon_k^{1/2}}\left(\frac{n_s}{10^{15}\ \mathrm{cm}^{-3}}\right)P\left(\frac{h\nu}{\epsilon_k}\right)$$

where $h\nu$ is the energy of a 3371-Å photon and $P(y)$ is a tabulated function associated with the effective Gaunt factor [35]. Deexcitation of the lower laser level by plasma electrons is neglected because it is smaller than the molecular collisional deexcitation rate at all pressures.[2] The net excitation from the $A^3\Sigma$ state to the $B^3\Pi_g$ state by plasma electrons is expected to be small, since the B–A energy difference is much smaller than ϵ_k during the laser pulse, and since the A state population is expected to be comparable to the B state population.

Typical calculated z_{sJ} are shown in Fig. 6, as a function of the laboratory frame time t_{sat} when the condition of (12) is satisfied (note that the saturation condition is not defined at a given point until the beam reaches it). The straight line shows the progress of the electron beam front down the laser tube. Regions of the laser tube far from the anode saturate as soon as the beam arrives, because of the gain acquired at smaller z. The region near $z = 0$ never saturates, and the unsaturated region is larger for lines with lower gain. As the pressure is varied from $\approx$10 torr the gain becomes lower and less energy is extracted efficiently from the anode region, which has the largest stored energy density because of the exponential primary beam loss. z_{sJ} increases later in the pulse as the small-signal gain again decreases, either because of spontaneous emission losses from the upper laser level or because of decreasing excitation. Because of the radial variation of α_{gJ}, the central portion of the tube may be lasing, yet the region near the walls may be far from threshold and can even be absorbing because of a low ϵ_k which preferentially excites the lower laser level. In an actual laser [7] light waves can propagate at appreciable angles to the drift tube axis and could possibly extract some energy from the lower gain regions even though they do not satisfy (12). Our model does not attempt to treat the angular details because of the complexity of the problem. Calculations with $G_0 = 0$ (which include on-axis contributions from low-gain J transitions as well as the contributions from off-axis regions) show that the peak laser power increases by about a factor of 2 over the $G_0 = 13$ case. Therefore, including the off-axis regions can increase the peak power at most by a factor of 2.

For particular volume element at distance z, when $z_{sJ} < z$ equations (14) are no longer valid because they neglect satura-

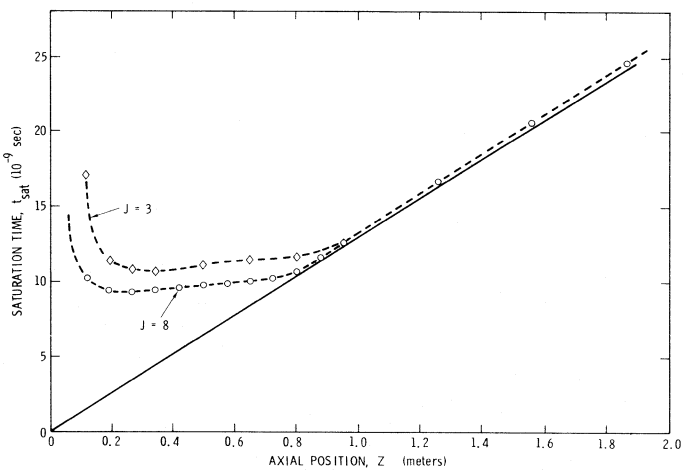

Fig. 6. Dependence of the saturation time t_{sat} on the axial position z, for the $P(4)$ and $P(9)$ laser transitions at $r = 0$ and 15-torr N_2. The higher gain line saturates earlier and leaves a smaller portion of the laser tube unsaturated. The straight line is the beam front trajectory.

[2] The collisional deactivation rate has been measured to ±30 percent only for the $v'' = 3$ vibrational level of the B state [11]; this value is used for the $v'' = 0$ level.

tion. The laser power per unit volume is then calculated from equations similar to those of Gerry [36] and Ali *et al.* [37], in which it is assumed that laser action almost equalizes the populations of the upper and lower laser levels. The equations used here include the degeneracies $g_u = 2J + 1$ and $g_l = 2J + 3$, quenching through collisions with other N_2 molecules, and by the coefficient X_l the recent careful measurements of excitation to the lower laser level.

If two new variables N_J and ΔN_J are defined

$$N_J = \frac{1}{2}\left(\frac{N_{CJ}}{g_u} + \frac{N_{BJ+1}}{g_l}\right) \tag{17a}$$

and

$$\Delta N_J = \frac{1}{2}\left(\frac{N_{CJ}}{g_u} - \frac{N_{BJ+1}}{g_l}\right) \tag{17b}$$

then saturation of the laser transition corresponds to a small value of the saturated population difference ΔN_J, and N_J is the average population per degenerate rotational level. If P_J is the rate of stimulated transitions per unit volume required to maintain ΔN_J at its low value in the presence of excess excitation to the upper level, the equations for N_J and P_J become

$$(g_u + g_l)\dot{N}_J = (f_J X_u + f_{J+1} X_l) - \left(g_u\left[\tau_u^{-1} + \frac{D}{\tau_{su}} - \frac{K'' B_{00}}{\tau_{su}}(1 + D)\right] + g_l\left[\tau_l^{-1} - \frac{K' B_{00} D \exp\left(-\frac{h\nu}{\epsilon_k}\right)}{\tau_{su}}\right]\right) N_J \tag{18a}$$

and

$$P_J = \frac{1}{2}\left[(f_J X_u - f_{J+1} X_l) - \bar{g}\,(f_J X_u + f_{J+1} X_l)\right] - \frac{N_J}{2}\left[g_u\left(\tau_u^{-1} + \frac{D}{\tau_{su}}\right)(1 - \bar{g}) + \frac{g_u K'' B_{00}}{\tau_{su}} \cdot (1 + D)(1 + \bar{g}) - g_l \frac{K' B_{00} D \exp\left(-\frac{h\nu}{\epsilon_k}\right)}{\tau_{su}}(1 - \bar{g}) - \frac{g_l}{\tau_l}(1 + \bar{g})\right] \tag{18b}$$

where $\bar{g} = (g_u - g_l)/(g_u + g_l) = -1/2(J + 1)$. The Jth level here includes all three multiplet transitions, since they all have the same threshold according to (13). The initial conditions for (18) are obtained from the solutions of (14) at the instant $t_{sat}(z, r)$ when z_{sJ} becomes less than the particular z of interest. The initial value of ΔN_J represents stored energy which we assume is released from each volume in an initial laser pulse of constant width = 1.0 ns, which is estimated from the calculated small-signal gain and the calculations of [30]. The detailed calculations show that the maximum contribution to the peak power because of the energy stored in a particular transition is $\lesssim 5$ percent of the peak laser power. Energy extraction from a volume element ceases when $P_J \lesssim 0$, which corresponds to the onset of absorption; for $P \lesssim 15$ torr, absorption begins typically as $\dot{I}_b$ begins to decrease after the initial rise of I_b.

The laser power per unit length at the position z along the drift tube, dP_L/dz, is given by

$$\frac{dP_L}{dz} = h\nu \int_0^{r_0} 2\pi r dr \sum_J{}' P_J(r, t) \tag{19}$$

where the prime on the summation indicates that at a given r, only those J are summed over for which $P_J > 0$ and which satisfy (11). Fig. 7 shows dP_L/dz at two pressures, in relation to the primary beam current I_b and the net current I_n at the same axial position.

The detailed shape of dP_L/dz depends strongly on both the time variation of j_{pz} and E_z/N_g, and on the upper and lower laser level lifetimes τ_u and τ_l. The peak values of dP_L/dz are similar at the two pressures, but the widths of the pulses differ with the details of E_z and j_{pz}. The structure on the initial dP_L/dz pulse at 20 torr is sensitive to the structure on the measured I_b. At $P \gtrsim 20$ torr the laser is no longer self-terminating, the collisional quenching of the lower laser level[2] resulting in a second dP_L/dz pulse at $t = 45$ ns, and a small nonvanishing dP_L/dz throughout the primary current pulse. The second dP_L/dz pulse, which is not observed experimentally and will be discussed further in the following, results from the increase of E_z/N_g as the net current decreases late in the I_b pulse.

To obtain the laser power P_L emitted from the end of the laser tube, we sum contributions from each axial element dz, phased in time according to the speed of light in vacuum since the gain is saturated above the threshold [31]

$$P_L(z = L, t) = \int_0^L dz' \frac{dP_L}{dz'}\left(z', t - \frac{(L - z')}{c}\right). \tag{20}$$

The peak value, full width at half maximum (FWHM), and the delay of P_L relative to the I_b pulse are compared in Section IV with the measurements of Patterson [7].

IV. Comparison with Experiment

In contrast with the experimental tests of the net current model [5], [6], in the laser experiment it is not possible to measure for the same electron beam pulse both the laser power and the detailed input data required to calculate the laser pulse. Therefore, we have neglected shot-to-shot variations, and compare calculated and measured laser powers under the same nominal conditions of pressure, magnetic field, beam current, etc. The experimental variations in the electron beam input data to the calculation result in some scatter in the theoretically calculated laser powers.

Fig. 8 shows typical laser pulse shapes calculated from the model of Section III for the experimental conditions of [7], assuming a gas temperature $T = 300$ K. At the zero of time the primary electron beam enters the drift chamber through the anode. To obtain the delay before lasing [7], the time required for a light pulse to travel the length of the drift chamber (6.3 ns) must be subtracted from the times of Fig. 8. This yields the calculated delay curve shown in Fig. 9, which has a weak pressure dependence which is opposite to the measured dependence [7]. This difference is not understood at present

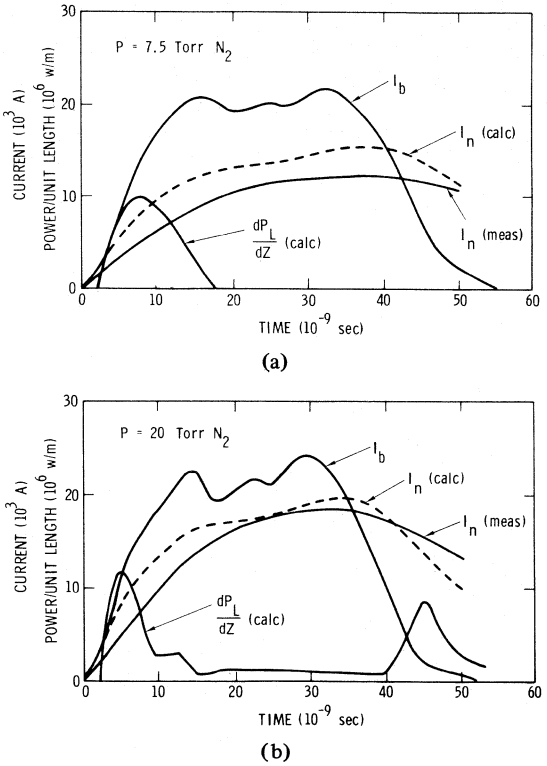

Fig. 7. Time relationship between the measured beam and net currents, and the calculated net current and laser power per unit length, at one axial position. The second pulse of laser power at $t = 45$ ns for 20 torr results from collisional quenching of the lower laser level and an increase of E_z as the net current decays late in the beam pulse.

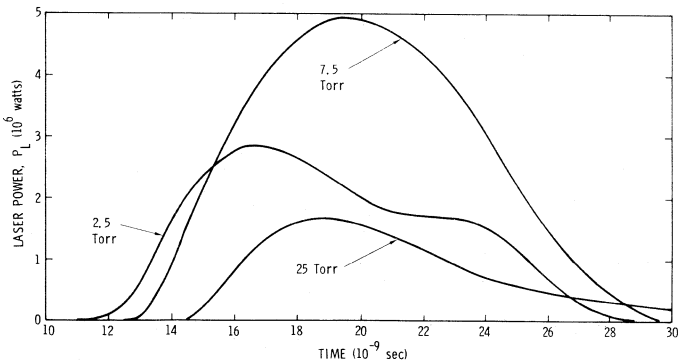

Fig. 8. Calculated laser pulses at end of laser tube, for three representative pressures. The electron beam enters the laser tube (length 2 m) at $t = 0$. $T = 300$ K.

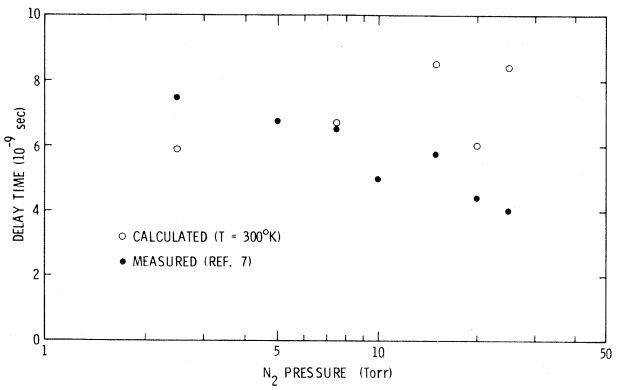

Fig. 9. Pressure dependence of time delay between beginning of laser pulse as seen at end of drift tube, and entrance of beam into laser tube.

but may be associated with the simplified threshold model or the difference between the calculated and measured net current curves in Fig. 7. (It is possible that some plasma is trapped ahead of the primary beam by the longitudinal magnetic field, providing some preionization.) However, the average calculated delay equals the average measured delay within 25 percent. The pulse shapes are similar to the measured shape shown in [7, fig. 2(e)], except that at very high pressures the calculated laser pulse has a longer tail, which probably results from the assumed collisional deactivation of the lower laser level.[2] The weak structure (shown, for example, in the 2.5-torr laser pulse of Fig. 8) is sensitive to the details of the measured I_b time dependence.

Fig. 10 shows the comparison between the calculated peak laser power P_p for $T = 300$ K and 550 K, and the measured peak power [7]. By exciting N_2 gas with a Nereus electron beam and measuring the spectrum of the N_2^+ ion 3914-Å band, a crude measurement of the rotational temperature T was made [38]. Within the experimental error T ranges from 340 to 550 K at $P = 2$ torr, thus providing the choice of temperatures used in the calculation. Most of the experimental points fall between the calculated points for the two temperatures. The pressure at which maximum power occurs agrees with experiment within 30 percent, the magnitude of peak power agrees within 40 percent, and the pressure width agrees within 15 percent. These errors are quite reasonable in view of the experimental errors in several of the input parameters to the calculation. The calculated power does not approach zero as fast as the experiment at high and low pressures, perhaps because of the simple threshold approximation.

Fig. 11 shows the calculated laser pulsewidth τ_L as a function of pressure, compared to the experimentally measured pulsewidth. There is considerable scatter in the calculated pulsewidth, perhaps because the pulse shape is sensitive to the measured primary beam velocity and current waveform. Averaging the calculated and measured pulsewidths between 2.5 and 25 torr shows that the average calculated pulsewidth is ~20 percent higher than the measured average pulsewidth for $T = 300$ K, and ~10 percent higher if $T = 550$ K.

Although these calculations involve no adjustable parameters, they require a large number of experimentally measured

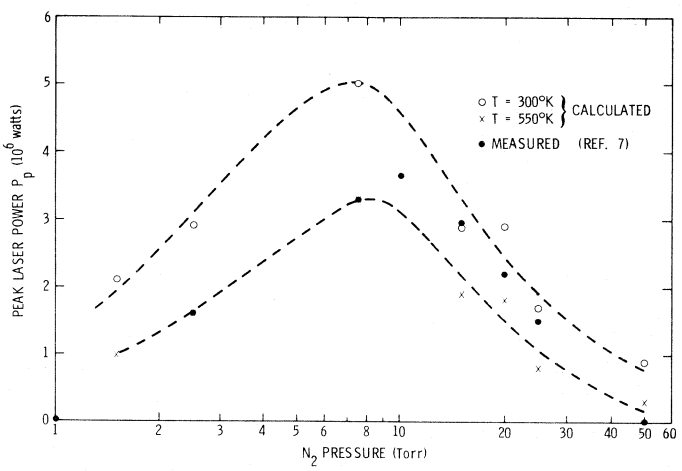

Fig. 10. Pressure dependence of peak laser power. The dashed lines are smooth curves through the calculated points.

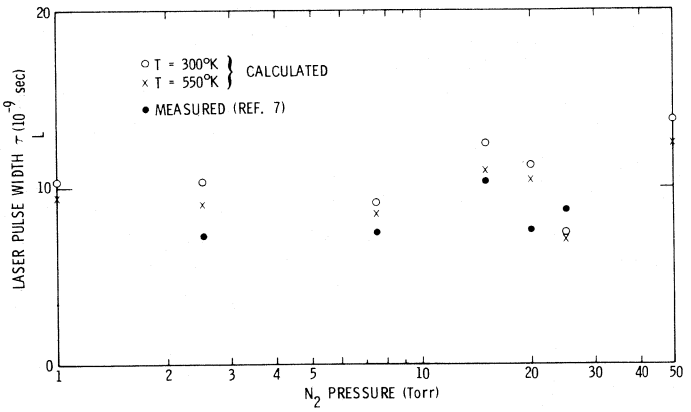

Fig. 11. Pressure dependence of laser pulsewidth (FWHM).

parameters of the laser gas and the electron beam propagation process. It is therefore of interest to know how sensitive the calculation is to each parameter. The sensitivity of the plasma calculation to the gas-discharge parameters of the gas has been discussed in [6]. Table I shows the sensitivity of the calculation to those parameters associated mainly with the laser; Figs. 12 and 13 give the variation of those parameters not characterized by a simple formula. The magnitude of variation in the parameter (Variation Factor in Table I) corresponds to the expected magnitude of experimental uncertainty, except for the parameters r_0, $S(r)$, and I_b, where reasonable but arbitrary variations were used. The "Change Factors" for τ_L and P_p in Table I represent the ratio of the new τ_L or P_p with the varied parameter, to the value of τ_L or P_p in the reference calculation at $P = 15$ torr. From Table I, it can be seen that the laser power is most sensitive to $\langle\sigma_l v\rangle/\langle\sigma_u v\rangle$, r_0, $S(r)$, v_b, and T; it is relatively insensitive to G_0, τ_u^{-1}, and τ_l^{-1}. The experimental uncertainties in $\langle\sigma_l v\rangle/\langle\sigma_u v\rangle$, $S(r)$, v_b, and I_b are clearly large enough to account for the discrepancies remaining between the calculated and measured τ_L and P_p in Figs. 10 and 11.

If we assume $G_0 = 0$ [8], the calculated power at 7.5-torr N_2 is a factor of 2 higher than for the present assumption of $G_0 = 13$. Since Table I also shows that the calculated power varies slowly for $G_0 > 13$, we believe that the error resulting from our simple threshold gain assumption does not greatly affect the magnitude of the calculated power.

The experiments in [4] used a 10-cm-diameter drift tube rather than the 5-cm-diameter tube used in [7]. The maximum laser power obtained from the larger tube was about a factor of 5 higher than for the smaller drift tube, and the peak power occurred at a pressure twice as high as for the smaller tube. No detailed measurements of Λ, v_b, or $S(r)$ were made in [4], so it is difficult to make an accurate calculation of the laser power for this case. The trend of the laser power with increasing r_0 can, however, be obtained roughly by doubling r_0, using the same primary beam parameters as in Figs. 10 and 11. The resulting P_p and τ_L are shown in Figs. 14 and 15. (No point is shown at 1.5 torr for the larger tube since the longitudinal electric field is so large that plasma electron runaway can occur and the model no longer holds [6].) The largest P_p is more than a factor of 2 higher and P_p has not begun to decrease even at 50 torr, while the calculated pulsewidth is only about 8 percent larger. This clearly indicates the trends of a

TABLE I
NUMERICAL SENSITIVITY STUDIES

Parameter	Variation Factor	Change Factor τ_L	Change Factor P_p
Reference Calculation	1.0	1.0	1.0
$\langle\sigma_l v\rangle/\langle\sigma_u v\rangle$	0.5	1.06	2.34
r_o	2.0	1.04	1.95
S(r)	see Fig. 12	.82	.54
T	1.67	.88	.68
α_{gJ}	0.50	.88	.76
v_b	1.25	.77	1.26
I_b	see Fig. 13	.85	.82
τ_l^{-1}	[a]	1.02	1.16
τ_u^{-1}	[b]	.93	.90
G_o	1.29	.96	.92
Λ	1.10	----	1.17

[a] τ_l^{-1} was replaced by $(0.0112 + 0.32P) \times 10^7$ s^{-1}.
[b] τ_u^{-1} was replaced by $(2.63 + 0.072P) \times 10^7$ s^{-1}.

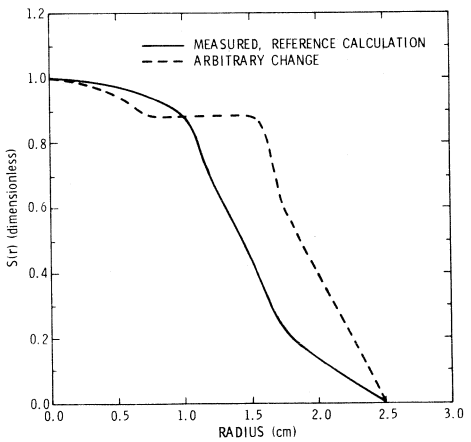

Fig. 12. $S(r)$ functions used to check sensitivity of calculation.

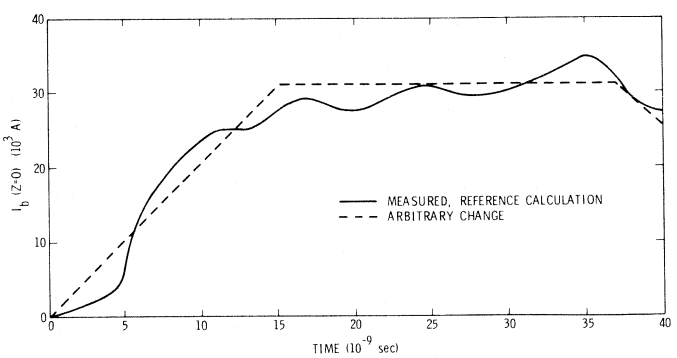

Fig. 13. $I_b(t)$ functions used to check sensitivity of calculation.

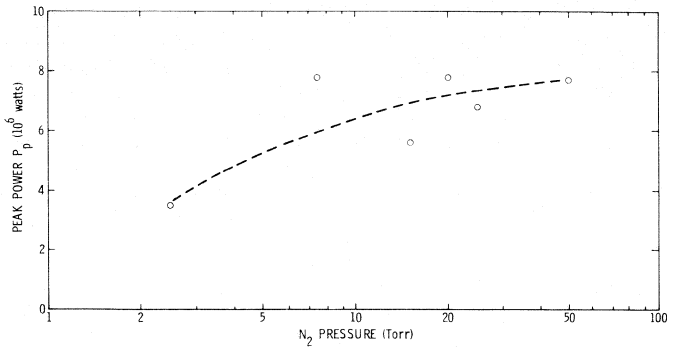

Fig. 14. Pressure dependence of calculated peak laser power, for r_0 doubled with no other changes.

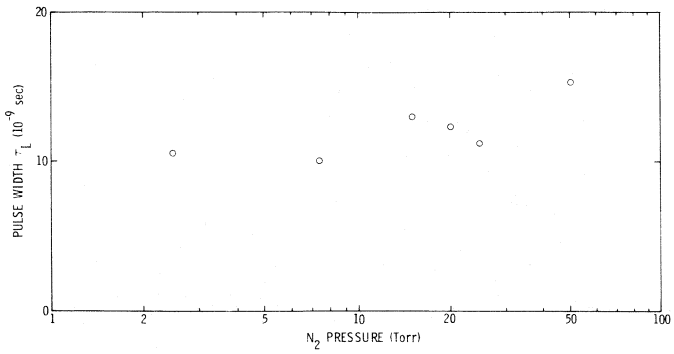

Fig. 15. Pressure dependence of calculated laser pulsewidth (FWHM), for r_0 doubled with no other changes.

larger power and a higher pressure at which the peak power occurs, as seen in [4].

In their earlier work on N_2, Dreyfus and Hodgson [2] find good agreement between their measured energy and a calculated laser energy assuming only cascade electron excitation. However, [2] overestimates by a factor of 2.5 the relative contribution of secondary electrons to ionization, compared to the careful measurements of Hirsch *et al.* [39]. They also neglect excitation to the lower laser level, and the fact that at low pressures the laser transition is self-terminating so that only one-half the excess atoms in the upper state can undergo stimulated emission before the gain vanishes. These effects would reduce their calculated energy output by a factor of 0.24. In addition, estimates of their output intensity based on their data range from 15 to 50 kW/cm^2, which is not much greater than the measured 3371-Å saturation intensity of [32] (~30 kW/cm^2); this implies that energy is probably not extracted efficiently from the first ~1 m of the drift tube, decreasing the estimate of output energy by a factor of ~0.5. Including collisional quenching of the upper laser level and the fact that all rotational lines probably do not lase, yields a further factor of ~0.4. Thus a more realistic treatment of the details of the lasing process itself yields for the cascade mechanism alone an output energy $\sim 0.05 \times 10^3$ ergs/cm^2, far below the observed energy.

On the other hand, the estimated E_z/N_g at 20 torr, if this beam fills the drift tube, is $\sim 8 \times 10^{-15}$ V · cm^2, which means that at 20 torr the plasma electrons can multiply by a factor of 10 in ≈ 0.5 ns [6]. This can make a significant plasma contribution to the excitation of $C^3\Pi_u$ light, since the plasma current is so much more efficient at exciting these levels.

V. Conclusions

This represents the first calculation of laser excitation by a relativistic electron beam which includes the effects of the beam-produced electric field on the beam-induced plasma. The plasma properties calculated with the net current model of [6] yield calculated laser powers which agree well with experiment, if the simplifying assumption is made that all laser power is emitted in the forward direction. The calculation is most sensitive to the following laser model parameters: 1) the excitation coefficients to the lower and upper laser levels, as a function of the E_z/N_g at a point in the gas; and 2) those parameters ($S(r)$, I_b, v_b, and r_0) which are most important in determining the plasma electron density and the E_z/N_g in the gas. Incidental results of these calculations are the following.

1) The net current model of [6] can be used to calculate the net current with reasonable accuracy even in the presence of a longitudinal magnetic guide field.

2) The plasma properties produced by the model appear to be accurate near the front of the primary beam pulse, in view of the correct magnitude of the calculated laser power.

In contrast to [2], the calculation neglects excitation by primary electrons and energetic cascade electrons, which are estimated to produce at most a 3-percent effect; in addition, the cascade electron mechanism is unable to explain the variation of laser power with drift tube radius and the rapid decrease of power at high pressures.

The 3371-Å N_2 laser transition is perhaps unusual because the primary electrons themselves cannot directly excite the laser transition. The H_2 laser studied in the later work of Dreyfus and Hodgson [2] represents a case in which the primary electrons *can contribute directly* to excitation of the laser levels. However, the cascade electron model yields less power than is observed (even assuming that all molecules excited to the upper laser level yield laser energy), and is unable to explain in detail the multiple laser pulses and the laser power emitted near the end of the primary beam pulse [2]. Our calculations for N_2 show that excitation by plasma electrons is dominant, and that under some conditions a second laser pulse can appear as the plasma current decays following the primary beam pulse. It is therefore possible that the plasma electrons are making important contributions to the H_2 laser as well. Other lasers may, however, be dominated by primary electron cascade, especially at pressures $\gtrsim 1$ atm where little plasma current flows.

Note Added in Proof: J. W. Dreyer and D. Perner (*Chem. Phys. Lett.*, vol. 16, pp. 169-173, Sept. 15, 1972) have measured the collisional quenching of the lower laser level. Using this lower quenching rate in the calculation decreases τ_L by ~15 percent and P_p by ~30 percent at higher pressures. These trends yield slightly better agreement with experiment for the 300 K temperature assumption (see Figs. 10 and 11).

Acknowledgment

The authors wish to thank E. L. Patterson, who cooperated by making additional measurements to test the model.

REFERENCES

[1] M. Clerc and M. Schmidt, "Emissions stimulees des systemes premier et deuxieme positifs de N_2, produites par radiolyse impulsionelle," *C. R. Acad. Sci.*, ser. B, vol. 272, pp. 668–671, Mar. 1971.

[2] a) R. W. Dreyfus and R. T. Hodgson, "Electron-beam excitation of the nitrogen laser," *Appl. Phys. Lett.*, vol. 20, pp. 195–197, Mar. 15, 1972.
b) —, "Relativistic electron-beam pumped UV gas lasers," *J. Vac. Sci. Technol.*, vol. 10, pp. 1033–1036, Nov./Dec. 1973.

[3] a) R. T. Hodgson and R. W. Dreyfus, "Electron-beam excitation of vacuum ultraviolet hydrogen laser," *Phys. Lett.*, ser. A, vol. 38, pp. 213–214, Jan. 31, 1972.
b) —, "Vacuum-UV laser action observed in H_2 Werner bands: 1161–1240 Å," *Phys. Rev. Lett.*, vol. 28, pp. 536–539, Feb. 28, 1972.

[4] E. L. Patterson, J. B. Gerardo, and A. W. Johnson, "Intense-electron-beam excitation of the 3371-Å N_2 laser system," *Appl. Phys. Lett.*, vol. 21, pp. 293–295, Sept. 15, 1972.

[5] D. A. McArthur and J. W. Poukey, "Return current induced by a relativistic electron beam propagating into neutral gas," *Phys. Rev. Lett.*, vol. 27, pp. 1765–1768, Dec. 27, 1971.

[6] —, "Plasma created in a neutral gas by a relativistic electron beam," *Phys. Fluids*, vol. 16, pp. 1996–2004, Nov. 1973.

[7] E. L. Patterson, "Parametric study of superradiant laser action in molecular nitrogen excited by a high-energy electron beam," *J. Appl. Phys.*, vol. 44, pp. 3193–3197, July 1973.

[8] D. A. McArthur and J. W. Poukey, "Theory of the nitrogen laser excited by an intense relativistic electron beam," *Bull. Amer. Phys. Soc.*, ser. II, vol. 17, p. 1032, Nov. 1972.

[9] —, "Theory of plasma electron contribution to the electron-beam-excited nitrogen laser," *Phys. Rev. Lett.*, vol. 32, pp. 89–92, Jan. 21, 1974.

[10] A. G. Engelhardt, A. V. Phelps, and C. G. Risk, "Determination of momentum transfer and inelastic collision cross sections for electrons in nitrogen using transport coefficients," *Phys. Rev.*, vol. 135, pp. A1566–A1574, Sept. 14, 1964.

[11] W. Legler, "Anregung von UV-strahlung in Stickstoff und Wasserstaff durch einen Elektronenschwarm," *Z. Phys.*, vol. 173, pp. 169–183, Apr. 1963.

[12] D. E. Shemansky and A. L. Broadfoot, "Excitation of N_2 and N_2^+ systems by electrons–II; Excitation cross sections and N_2 1PG low pressure afterglow," *J. Quant. Spectrosc. Radiat. Transfer*, vol. 11, pp. 1401–1439, 1971.

[13] —, "Excitation of N_2 and N_2^+ systems by electrons–I; Absolute transition probabilities," *J. Quant. Spectrosc. Radiat. Transfer*, vol. 11, pp. 1385–1400, 1971.

[14] J. W. McConkey and F. R. Simpson, "Electron impact excitation of the $B^3\Pi_g$ state of N_2," *J. Phys.*, ser. B, vol. 2, pp. 923–929, Sept. 1969.

[15] P. N. Stanton and R. M. St. John, "Electron excitation of the first positive bands of N_2 and of the first negative and Meinel bands of N_2^+," *J. Opt. Soc. Amer.*, vol. 59, pp. 252–260, Mar. 1969.

[16] D. J. Burns, F. R. Simpson, and J. W. McConkey, "Absolute cross sections for electron excitation of the second positive bands of nitrogen," *J. Phys.*, ser. B, vol. 2, pp. 52–64, Jan. 1969.

[17] H. S. W. Massey and E. H. S. Burhop, *Electronic and Ionic Impact Phenomena (Collision of Electrons with Atoms)*, vol. I, 2nd ed. New York: Oxford, 1969, p. 455.

[18] C. B. Opal, W. K. Peterson and E. C. Beaty, "Measurements of secondary-electron spectra produced by electron impact ionization of a number of simple gases," *J. Chem. Phys.*, vol. 55, pp. 4100–4106, Oct. 15, 1971.

[19] M. N. Hirsch, E. Poss, and P. N. Eisner, "Absolute fluorescence yields of 3914-Å photons from N_2 and air excited by relativistic electrons," *Phys. Rev.*, ser. A, vol. 1, pp. 1615–1626, June 1970.

[20] D. Rapp and P. Englander-Golden, "Total cross sections for ionization and attachment in gases by electron impact," *J. Chem. Phys.*, vol. 43, pp. 1464–1479, Sept. 1, 1965.

[21] I. Tatisheff, "Specific excitation of N_2 ($C^3\Pi_u$) and specific ionization by 4.3 MeV α particles," *J. Chem. Phys.*, vol. 52, pp. 503–508, Jan. 1970.

[22] D. A. McArthur and J. W. Poukey, "Interaction of relativistic electron beam with neutral gas," Sandia Laboratories, Albuquerque, N. Mex., Rep. SC-RR-72 0841, Jan. 1973.

[23] G. Herzberg, *Molecular Spectra and Molecular Structure*, vol. I, 2nd ed. Princeton, N.J.: Van Nostrand, 1950.

[24] J. H. Parks, D. R. Rao, and A. Javan, "A high-resolution study of the $C^3\Pi_u \rightarrow B^3\Pi_g$ (O,O) stimulated transitions in N_2," *Appl. Phys. Lett.*, vol. 13, pp. 142–144, Aug. 15, 1968.

[25] a) A. M. Cazabat-Longequeue, "Etude de la relaxation rotation-translation dans les gaz au moyen de l'effect Brillouin," *C. R. Acad. Sci.*, ser. B, vol. 272, pp. 607–610, Mar. 8, 1971.
b) K. F. Herzfeld and T. A. Litovitz, *Absorption and Dispersion of Ultrasonic Waves* (Pure and Applied Physics Ser.), vol. 7. New York: Academic, pp. 205–239, 1959.

[26] C. A. Massone *et al.*, "Investigation of a pulsed molecular nitrogen laser at low temperature," *Appl. Opt.*, vol. 11, pp. 1317–1328, June 1972.

[27] T. Kasuya and D. R. Lide, "Measurements on the molecular nitrogen pulsed laser," *Appl. Opt.*, vol. 6, pp. 69–80, Jan. 1967.

[28] R. W. Waynant, J. D. Shipman, Jr., R. C. Elton, and A. W. Ali, "Vacuum ultraviolet laser emission from molecular hydrogen," *Appl. Phys. Lett.*, vol. 17, pp. 383–384, Nov. 1, 1970.

[29] S. L. McCall and E. L. Hahn, "Self-induced transparency," *Phys. Rev.*, vol. 183, pp. 457–485, July 10, 1969.

[30] N. Skribanowitz, I. P. Herman, J. C. MacGillivray, and M. S. Feld, "Observation of Dicke superradiance in optically pumped HF gas," *Phys. Rev. Lett.*, vol. 30, pp. 309–312, Feb. 19, 1973.

[31] L. Casperson and A. Yariv, "Pulse propagation in a high-gain medium," *Phys. Rev. Lett.*, vol. 26, pp. 293–295, Feb. 8, 1971.

[32] D. A. Leonard, "Saturation of the molecular nitrogen second positive laser transition," *Appl. Phys. Lett.*, vol. 7, pp. 4–6, July 1, 1965.

[33] A. Budo, "Intensitatsformeln fur die Triplettbanden," *Z. Phys.*, vol. 105, pp. 579–587, 1937.

[34] K. Mitchell, Los Alamos Rep. LA-4248, 1969.

[35] H. Van Regemorter, "Rate of collisional excitation in stellar atmospheres," *Astrophys. J.*, vol. 136, pp. 906–915, July–Nov. 1962.

[36] E. T. Gerry, "Pulsed-molecular-nitrogen laser theory," *Appl. Phys. Lett.*, vol. 7, pp. 6–8, July 1, 1965.

[37] A. W. Ali, A. C. Kolb, and A. D. Anderson, "Theory of the pulsed molecular nitrogen laser," *Appl. Opt.*, vol. 6, pp. 2115–2119, Dec. 1967.

[38] D. A. McArthur, Sandia Laboratories, unpublished data.

[39] M. N. Hirsch, P. N. Eisner, and J. A. Slevin, "Ionization and attachment in O_2 and airlike N_2:O_2 mixtures irradiated by 1.5 MeV electrons," *Phys. Rev.*, vol. 178, pp. 175–181, Feb. 5, 1969.

Surface-Wave Radiation Loss from Curved Dielectric Slabs and Fibers

EDWARD F. KUESTER, STUDENT MEMBER, IEEE, AND DAVID C. CHANG, MEMBER, IEEE

Abstract—**A newly developed systematic procedure to calculate the real and imaginary parts of the change in propagation constant of a surface-wave mode on a curved open waveguide of general cross section is used here to determine these quantities for the TE modes of an asymmetric slab waveguide and for all the modes of an optical fiber. Comparison of these results with the existing literature points up the care which must be taken in making approximations in this problem, since errors of significant factors in the radiation loss have been made in previous work.**

I. Introduction

With increased interest in optical fibers and integrated optical devices as practical means of communication, one problem which has received considerable interest recently is that of the continuous radiation loss from a section of curved optical waveguiding structure [1]-[7]. Unfortunately, the results obtained by different analyses do not always agree, and the difference is in some cases a very large factor (see [6] and Section III below). In [6] and [7], the authors have developed a general, systematic technique for the calculation of this radiation loss on an arbitrary curved surface-wave structure. In the present paper, this technique is applied to the TE modes of an asymmetric slab waveguide and to all the modes of a curved optical fiber. In the process, it will be seen how the approximations made in some of the existing analyses can lead to serious errors in the expression for the radiation loss.

II. Expression for Radiation Loss on an Arbitrary Waveguide

In [6] and [7], a general method is presented for the determination of the change in the real and imaginary parts of the propagation constant for a surface-wave mode due to uniform curvature, if the fields and propagation constant of the straight waveguide mode are known. We present here only the results of that analysis; the interested reader should consult [6] or [7] for details of the derivation.

We consider the surface waveguide shown in Fig. 1, bent uniformly with radius R in a plane perpendicular to the $\hat{z}$-direction as shown. If we define the normalized propagation constant ν through an implied field dependence of $\exp \cdot (i\omega t - ik_0 \nu R\theta)$, where $k_0 = \omega(\mu_0 \epsilon_0)^{1/2}$ is the free-space wavenumber, then the correction to the real part of the propagation constant ν_0 for a given surface-wave mode of a corresponding straight waveguide is [6], [7]

$$\text{Re}\,[k_0(\nu - \nu_0)] = \Delta/P + O(1/R^2) \tag{1}$$

Manuscript received May 21, 1975; revised July 1, 1975. This research was supported by the Air Force Office of Scientific Research (AFSC) under Grant AFOSR-72-2417.

The authors are with the Electromagnetics Laboratory, Department of Electrical Engineering, University of Colorado, Boulder, Colo. 80302.

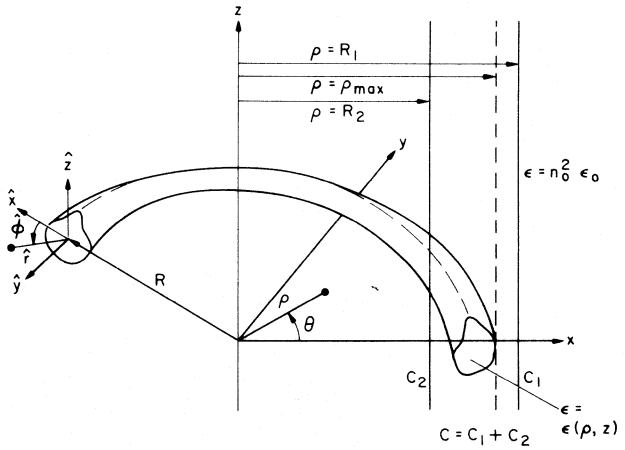

Fig. 1. Section of curved optical waveguide with Cartesian coordinate system (x, y, z), cylindrical system (ρ, θ, z), local Cartesian system $(\hat{x}, \hat{y}, \hat{z})$, and local cylindrical system $(\hat{r}, \hat{\phi}, \hat{y})$.

where

$$\Delta = \frac{1}{R}\int_S \hat{x}\left[2k_0\nu_0(E_{0\hat{z}}H_{0\hat{x}} - E_{0\hat{x}}H_{0\hat{z}}) + i\left(H_{0\hat{y}}\frac{\partial E_{0\hat{z}}}{\partial \hat{x}} - E_{0\hat{z}}\frac{\partial H_{0\hat{y}}}{\partial \hat{x}} + H_{0\hat{z}}\frac{\partial E_{0\hat{y}}}{\partial \hat{x}} - E_{0\hat{y}}\frac{\partial H_{0\hat{z}}}{\partial \hat{x}}\right)\right] dS \tag{2}$$

$$P = 2\int_S \bar{a}_{\hat{y}} \cdot [\bar{E}_0 \times \bar{H}_0]\, dS. \tag{3}$$

Here S is the (infinite) cross section of the straight waveguide, the fields $\bar{E}_0$ and $\bar{H}_0$ are unperturbed fields of the surface-wave mode being considered on the straight waveguide and $(\hat{x}, \hat{y}, \hat{z})$ describe a "local" set of Cartesian coordinates as shown in Fig. 1.

The correction to the imaginary part of ν_0 (which gives the attenuation of the mode due to continuous radiation loss) is given by

$$\text{Im}\,[k_0(\nu - \nu_0)] = -(c/P)\,\{1 + O(1/R)\} \tag{4}$$

where P is given by (3) and

$$c = \frac{2\pi\omega}{k_0^2 n_0^3}\left(\frac{\pi\lambda_0}{k_0 R}\right)^{1/2}[\epsilon_0 n_0^2 \tilde{E}^2(0) + \mu_0 \tilde{H}^2(0)] \cdot \exp(-2\tau). \tag{5}$$

In (5), n_0 is the index of refraction of the medium exterior to the waveguide, $\lambda_0 = (\nu_0^2 - n_0^2)^{1/2}$ is a measure of the field

decay outside the guide

$$\tau = \tau_0 - \frac{R\Delta}{2P} \ln\left(\frac{\nu_0 - \lambda_0}{\nu_0 + \lambda_0}\right) \tag{6a}$$

$$\simeq \tau_0 + \frac{R\Delta}{P}\left[\frac{\lambda_0}{\nu_0} + \frac{1}{3}\frac{\lambda_0^3}{\nu_0^3} + \cdots\right] \tag{6b}$$

$$\tau_0 = -k_0 R\left[\lambda_0 + \frac{\nu_0}{2} \ln\left(\frac{\nu_0 - \lambda_0}{\nu_0 + \lambda_0}\right)\right] \tag{7a}$$

$$\simeq \frac{1}{3} k_0 R \frac{\lambda_0^3}{\nu_0^2} \tag{7b}$$

and finally,

$$\left.\begin{matrix}\tilde{E}(0)\\ \tilde{H}(0)\end{matrix}\right\} = \frac{k_0 n_0}{2\pi} \exp(k_0 \lambda_0 \hat{x}) \int_{-\infty}^{\infty} \left.\begin{matrix}E_{0\hat{z}}(\hat{x}, \hat{z})\\ H_{0\hat{z}}(\hat{x}, \hat{z})\end{matrix}\right\} d\hat{z} \tag{8}$$

represent a kind of averaged amplitude for the $\hat{z}$-components of the field, with $\hat{x}$ chosen at just outside the waveguide at the location corresponding to $\rho = \rho_{\max}$ in Fig. 1. It can be shown that the expression (8) is independent of the choice of $\hat{x}$ following from the fact that $\bar{E}_0$ and $\bar{H}_0$ must satisfy the scalar wave equation outside the guide [6]. It is to be noted from (6) and (7) that the Δ/P correction to τ (which, since it is multiplied by R, is $O(1)$ by (1)-(3)) must be calculated before the c/P correction in (4) may be evaluated. We further note that the expressions in (6b) and (7b) hold for $\lambda_0/\nu_0 \ll 1$, which is typical for optical waveguides, while (6a) and (7a) are applicable to a more general case subject only to the condition on (5) that $(\lambda_0^3 k_0 R) \gg 1$, [6], [7].

III. TE Modes of an Asymmetric Slab Waveguide

The treatment of slab waveguides by this method is simplified somewhat, since the surface integrals in (2) and (3) reduce to line integrals and the expression for c, instead of (5), can be reduced to a field evaluation at a single point, because the slab fields are independent of $\hat{z}$ [6]

$$c = \frac{\lambda_0}{k_0 n_0^2} [\epsilon_0 n_0^2 \tilde{E}_{0\hat{z}}^2 + \mu_0 \tilde{H}_{0\hat{z}}^2] \exp(-2\tau) \tag{9}$$

where τ is given by (6) and (7). The condition for the validity of (9) can also be relaxed to $(\lambda_0 kR) \gg 1$, rather than $(\lambda_0^3 kR) \gg 1$. The expressions for $\tilde{E}_{0\hat{z}}$ and $\tilde{H}_{0\hat{z}}$ are simply given as

$$\left.\begin{matrix}\tilde{E}_{0\hat{z}}\\ \tilde{H}_{0\hat{z}}\end{matrix}\right\} = \left.\begin{matrix}E_{0\hat{z}}\\ H_{0\hat{z}}\end{matrix}\right\} \exp[k_0 \lambda_0 \hat{x}]. \tag{10}$$

We now examine the TE modes of an asymmetric slab waveguide. If we locate $\hat{x} = 0$ at the center of the slab, the fields are given by [8, p. 9]

$$E_{0\hat{z}} = \begin{cases} -A \exp[-k_0\lambda_0(\hat{x} - d/2)], & \hat{x} \geq d/2 \quad \text{(I)} \\ -A\left[\cos K_0(\hat{x} - d/2) - \dfrac{k_0\lambda_0}{K_0} \sin K_0(\hat{x} - d/2)\right], & -d/2 \leq x \leq d/2 \quad \text{(II)} \\ -A\left[\cos K_0 d + \dfrac{k_0\lambda_0}{K_0} \sin K_0 d\right] \exp[\gamma_0(\hat{x} + d/2)], & \hat{x} \leq -d/2 \quad \text{(III)} \end{cases}$$

with

$$H_{0\hat{y}} = \frac{1}{i\omega\mu_0} \frac{\partial E_{0\hat{z}}}{\partial \hat{x}} \qquad H_{0\hat{x}} = \frac{k_0 \nu_0}{\omega\mu_0} E_{0\hat{z}}$$

and all other field components vanishing. Here

$$K_0 = k_0(n_1^2 - \nu_0^2)^{1/2}$$

$$\gamma_0 = k_0(\nu_0^2 - n_2^2)^{1/2}$$

$$\lambda_0 = (\nu_0^2 - n_0^2)^{1/2}$$

where n_0, n_1, and n_2 are the indices of refraction in regions I, II, and III, respectively. The parameters γ^{-1} and $(k_0\lambda_0)^{-1}$ therefore have the physical meaning of penetration depths of a specific mode into the two exterior regions of the waveguide. Continuity of $H_{0\hat{y}}$ results in the eigenvalue equation

$$k_0\lambda_0(K_0 \cos K_0 d + \gamma_0 \sin K_0 d) = K_0(K_0 \sin K_0 d - \gamma_0 \cos K_0 d).$$

The P-integral is calculated in [8, p. 14]

$$P = \frac{A^2 k_0 \nu_0 L_e (n_1^2 - n_0^2)}{\omega\mu_0(n_1^2 - \nu_0^2)}, \qquad L_e = d + \frac{1}{\gamma_0} + \frac{1}{k_0\lambda_0}.$$

From (2), Δ can be expressed as

$$\Delta = \frac{1}{R}\left\{\frac{1}{\omega\mu_0} \int_{-\infty}^{\infty} \hat{x}\left[k_0^2(\nu_0^2 + n^2) E_{0\hat{z}}^2 + \left(\frac{\partial E_{0\hat{z}}}{\partial \hat{x}}\right)^2\right] d\hat{x}\right\}.$$

After considerable algebra, this can be shown to be

$$\Delta = \frac{k_0^2 \nu_0^2 A^2 (n_1^2 - n_0^2) L_e}{2\omega\mu_0 R(n_1^2 - \nu_0^2)}\left[\frac{1}{k_0\lambda_0} - \frac{1}{\gamma_0}\right].$$

Thus the real part Δ/P of the correction to $k_0\nu_0$ from (1) is simply

$$\frac{\Delta}{P} = \frac{k_0\nu_0}{2R}\left(\frac{1}{k_0\lambda_0} - \frac{1}{\gamma_0}\right). \tag{11}$$

As expected, this correction is zero in the symmetric case ($k_0\lambda_0 = \gamma_0$). Equation (11) is identical to the phase correction found by Chang and Barnes [3] for the asymmetric slab.

The quantity c can be found from (9) as

$$c = \frac{A^2}{\omega\mu_0} k_0\lambda_0 \exp(k_0\lambda_0 d) \exp(-2\tau)$$

where τ is given by (6) and (7). From (11), then, the attenuative correction becomes, for $\lambda_0/\nu_0 \ll 1$,

$$-i\frac{c}{P} = -i\frac{\lambda_0(n_1^2 - \nu_0^2)}{\nu_0 L_e(n_1^2 - n_0^2)} \exp\left[-\frac{2}{3} k_0 R \frac{\lambda_0^3}{\nu_0^2} - k_0\lambda_0\left(\frac{1}{k_0\lambda_0} - \frac{1}{\gamma_0}\right) + k_0\lambda_0 d\right]. \tag{12}$$

Once again, this is in agreement with [3], if the reference point $\hat{x} = 0$ is changed and the errors in [3, eq. (26)] are noted.[1] However, (12) differs from the result obtained by Marcuse in [2] by a factor of $\exp(-[1 - k_0\lambda_0/\gamma_0])$. As noted in [3], the extra term in the exponent resulting from the asymmetry, which does not appear in [2], can be quite significant in the case when the penetration depths γ_0^{-1} and $(k_0\lambda_0)^{-1}$ on the two sides of the slab are very different.

IV. Modes of the Step-Index Optical Fiber

We consider here the "simplified" modes of the step-index optical fiber with $n = n_0$ for $\hat{r} > a$ and $n = n_1$ for $\hat{r} < a$, as discussed by Marcuse [8]. These simplified modes assume that $(n_1 - n_0)/n_0 \ll 1$, and what is more, assume convenient forms quite naturally in the Cartesian coordinate system [8, pp. 62-77]. There exist two orthogonally polarized mode types in this approximation. One is polarized with the electric field in the $\hat{z}$ direction

$$E_{0\hat{z}} = -AJ_m(\kappa\hat{r})\cos(m\hat{\phi} - \phi_0), \qquad \hat{r} < a$$
$$= -AQ_m(\nu_0)K_m(k_0\lambda_0\hat{r})\cos(m\hat{\phi} - \phi_0), \qquad \hat{r} > a$$

$$H_{0\hat{x}} = -\frac{\nu_0 A}{\zeta_0} J_m(\kappa\hat{r})\cos(m\hat{\phi} - \phi_0), \qquad \hat{r} < a$$
$$= -\frac{\nu_0 A}{\zeta_0} Q_m(\nu_0)K_m(k_0\lambda_0\hat{r})\cos(m\hat{\phi} - \phi_0), \qquad \hat{r} > a$$

$$E_{0\hat{y}} = \frac{iA\kappa}{2k_0\nu_0}[J_{m+1}(\kappa\hat{r})\sin((m+1)\hat{\phi} - \phi_0) + J_{m-1}(\kappa\hat{r})\sin((m-1)\hat{\phi} - \phi_0)], \qquad \hat{r} < a$$
$$= \frac{iA\lambda_0}{2\nu_0} Q_m(\nu_0)[K_{m+1}(k_0\lambda_0\hat{r})\cdot\sin((m+1)\hat{\phi} - \phi_0) - K_{m-1}(k_0\lambda_0\hat{r})\cdot\sin((m-1)\hat{\phi} - \phi_0)], \qquad \hat{r} > a$$

$$H_{0\hat{y}} = \frac{iA\kappa}{2\omega\mu_0}[J_{m+1}(\kappa\hat{r})\cos((m+1)\hat{\phi} - \phi_0) - J_{m-1}(\kappa\hat{r})\cos((m-1)\hat{\phi} - \phi_0)], \qquad \hat{r} < a$$
$$= -\frac{iA\lambda_0}{2\zeta_0} Q_m(\nu_0)[K_{m+1}(k_0\lambda_0\hat{r})\cdot\cos((m+1)\hat{\phi} - \phi_0) + K_{m-1}(k_0\lambda_0\hat{r})\cdot\cos((m-1)\hat{\phi} - \phi_0)], \qquad \hat{r} > a.$$

Here

$$Q_m(\nu_0) = J_m(\kappa a)/K_m(k_0\lambda_0 a)$$
$$\zeta_0 = [\mu_0/\epsilon_0]^{1/2}$$
$$\kappa = k_0(n_1^2 - \nu_0^2)^{1/2}$$

and ϕ_0 is an angle defining the orientation of the field maxima. The other mode type is polarized with the electric field in the $\hat{x}$ direction

$$E_{0\hat{x}} = AJ_m(\kappa\hat{r})\cos(m\hat{\phi} - \phi_1), \qquad \hat{r} < a$$
$$= AQ_m(\nu_0)K_m(k_0\lambda_0\hat{r})\cos(m\hat{\phi} - \phi_1), \qquad \hat{r} > a$$

$$H_{0\hat{z}} = \frac{\nu_0 A}{\zeta_0} J_m(\kappa\hat{r})\cos(m\hat{\phi} - \phi_1), \qquad \hat{r} < a$$
$$= -\frac{\nu_0 A}{\zeta_0} Q_m(\nu_0)K_m(k_0\lambda_0\hat{r})\cos(m\hat{\phi} - \phi_1), \qquad \hat{r} > a$$

$$E_{0\hat{y}} = \frac{iA\kappa}{2k_0\nu_0}[J_{m+1}(\kappa\hat{r})\cos((m+1)\hat{\phi} - \phi_1) - J_{m-1}(\kappa\hat{r})\cos((m-1)\hat{\phi} - \phi_1)], \qquad \hat{r} < a$$
$$= \frac{iA\lambda_0}{2\nu_0} Q_m(\nu_0)[K_{m+1}(k_0\lambda_0\hat{r})\cdot\cos((m+1)\hat{\phi} - \phi_1) + K_{m-1}(k_0\lambda_0\hat{r})\cdot\cos((m-1)\hat{\phi} - \phi_1)], \qquad \hat{r} > a$$

$$H_{0\hat{y}} = \frac{iA\kappa}{2\omega\mu_0}[J_{m+1}(\kappa\hat{r})\sin((m+1)\hat{\phi} - \phi_1) + J_{m-1}(\kappa\hat{r})\sin((m-1)\hat{\phi} - \phi_1)], \qquad \hat{r} < a$$
$$= \frac{iA\lambda_0}{\zeta_0} Q_m(\nu_0)[K_{m+1}(k_0\lambda_0\hat{r})\cdot\cos((m+1)\hat{\phi} - \phi_1) - K_{m-1}(k_0\lambda_0\hat{r})\cdot\cos((m-1)\hat{\phi} - \phi_1)], \qquad \hat{r} > a$$

where ϕ_1 is another orientation angle. For either mode type the eigenvalue equation can be given in two equivalent forms [8, p. 68]

$$\kappa J_{m+1}(\kappa a)/J_m(\kappa a) = k_0\lambda_0 K_{m+1}(k_0\lambda_0 a)/K_m(k_0\lambda_0 a)$$
$$\kappa J_{m-1}(\kappa a)/J_m(\kappa a) = -k_0\lambda_0 K_{m-1}(k_0\lambda_0 a)/K_m(k_0\lambda_0 a)$$

and the P-integral (3) is also known [8, p. 70]

$$P = e_m \frac{A^2}{\zeta_0\lambda_0^2}\pi a^2\nu_0(n_1^2 - n_0^2)\,|J_{m-1}(\kappa a)\,J_{m+1}(\kappa a)| \qquad (13)$$

where $e_m = 1$ for $m \neq 0$, and $e_0 = 2\cos^2\phi_{0,1}$. Note that a lowest order mode of the $m = 0$ class corresponds to the dominant HE_{11} mode. Arbitrarily polarized modes may be constructed by multiplying an $\hat{x}$-mode by $\cos\phi_2$ and adding it to the corresponding $\hat{z}$-mode multiplied by $-\sin\phi_2$, where ϕ_2 is the angle of polarization. Such a mode will have the same P value as the $\hat{x}$ or $\hat{z}$ modes separately, except for the case $m = 0$, where we must take $e_0 = 2[\cos^2\phi_0\sin^2\phi_2 + \cos^2\phi_1\cos^2\phi_2]$.

Since m is an integer, it may be readily seen by examining (2) that Δ must vanish by reason of the angular dependences of the various field components. Thus we may immediately go about calculating the attenuation. We shall need the spectrum function for $K_m(k_0\lambda_0\hat{r})\exp(\pm im\phi)$ in order to calculate $\tilde{E}(0)$ and $\tilde{H}(0)$. We may start from an integral representation for K_m [9]

$$K_m(k_0\lambda_0\hat{r}) = \tfrac{1}{2}\int_{-\infty}^{\infty}\exp(-k_0\lambda_0\hat{r}\cosh t - mt)\,dt.$$

[1] Some typographical mistakes are seen in their expression; specifically the exponential term in (26) should be $\exp(-k\lambda_0\delta)$ instead of $\exp(-2k\nu_0\lambda_0\delta/3)$.

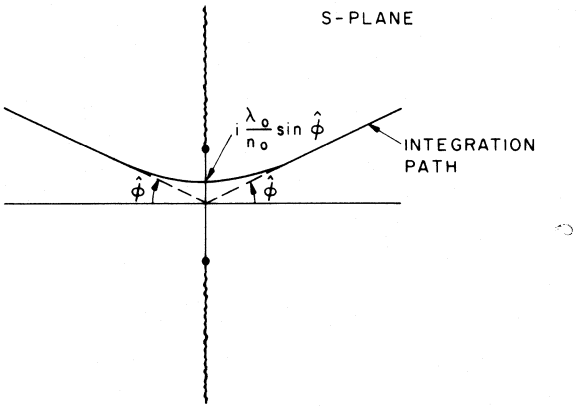

Fig. 2. Integration path in s plane for $K_m(k_0\lambda_0\hat{r})$. Branch points occur at $s = \pm i\lambda_0/n_0$.

Letting $t = \Psi - i\hat{\phi}$, $\hat{x} = \hat{r}\cos\hat{\phi}$, and $\hat{z} = -\hat{r}\sin\hat{\phi}$

$$K_m(k_0\lambda_0\hat{r}) = \tfrac{1}{2}\int_{-\infty+i\hat{\phi}}^{\infty+i\hat{\phi}} \exp\left[-k_0\lambda_0(\hat{x}\cosh\Psi + i\hat{z}\sinh\Psi) - m\Psi + im\hat{\phi}\right] d\Psi .$$

Further changing variables to $n_0 s = \lambda_0 \sinh\Psi$, so that $\lambda_s = \lambda_0\cosh\Psi$ and $n_0 ds = \lambda_s d\Psi$, where $\lambda_s = (\nu_0^2 - n_0^2)^{1/2}$ and $k = k_0 n_0$ gives

$$K_m(k_0\lambda_0\hat{r}) = \tfrac{1}{2}\int_{-\infty\exp(-i\hat{\phi})}^{\infty\exp(i\hat{\phi})} \left[\exp\left(-k_0\lambda_s\hat{x} - iks\hat{z} - m\,\mathrm{arcsinh}\,(n_0 s/\lambda_0) + im\phi\right)\right]\left(\frac{n_0 ds}{\lambda_s}\right).$$

We choose the branch cuts in the s plane from the branch points at $\lambda_s = 0$ to go along the positive and negative imaginary axes as shown in Fig. 2. The present integration path may be deformed back to the real axis because we are interested only in angles $|\hat{\phi}| < \pi/2$. Thus

$$K_m(k_0\lambda_0\hat{r}) = \int_{-\infty}^{\infty} \exp\left(-k_0\lambda_s\hat{x} - iks\hat{z} + im\hat{\phi}\right)\cdot\left(\frac{n_0}{2\lambda_s}\right)\left(\frac{\lambda_0}{n_0 s + \lambda_s}\right)^m ds.$$

Removing $\exp(im\hat{\phi})$ to the left side of this equation, we recognize that the right side is now an inverse Fourier transform, which we may invert again to give (using similar reasoning if m is replaced by $-m$)

$$\frac{k_0 n_0}{2\pi}\int_{-\infty}^{\infty} K_m(k_0\lambda_0\hat{r})\exp(\pm im\hat{\phi})\exp(iks\hat{z})\,d\hat{z} = \frac{n_0}{2\lambda_s}\left(\frac{n_0 s + \lambda_s}{\lambda_0}\right)^{\pm m}\exp(-k_0\lambda_s\hat{x}) \tag{14}$$

so that $\tilde{E}(0)$ and $\tilde{H}(0)$ may be obtained for the arbitrarily polarized mode of the previous paragraph by setting $s = 0$ in (14) and using the appropriate combinations of $\exp(\pm im\hat{\phi})$

$$\tilde{E}(0) = AQ_m(\nu_0)\frac{n_0}{2\lambda_0}\sin\phi_2\cos\phi_0$$

$$\tilde{H}(0) = -\frac{\nu_0}{\zeta_0}AQ_m(\nu_0)\frac{n_0}{2\lambda_0}\cos\phi_2\cos\phi_1 .$$

As a result, from (5), and since no correction from (6) need be made, we have

$$c = \frac{A^2}{\omega\mu_0}\left(\frac{\pi\lambda_0}{k_0 R}\right)^{1/2} Q_m^2(\nu_0)\frac{\pi}{2n_0\lambda_0^2}\left[n_0^2\sin^2\phi_2\cos^2\phi_0 + \nu_0^2\cos^2\phi_2\cos^2\phi_1\right]\exp(-2\tau_0) \tag{15}$$

where, as always,

$$\tau_0 \simeq \tfrac{1}{3}k_0 R\lambda_0^3/\nu_0^2$$

and the expression for $Q_m(\nu_0)$, as mentioned earlier, equals

$$Q_m(\nu_0) = J_m(\kappa a)/K_m(k_0\lambda_0 a), \qquad \kappa = k_0(n_1^2 - \nu_0^2)^{1/2}.$$

For the case $m = 0$, since $n_0 \simeq \nu_0$, we have that the attenuation is essentially independent of polarization and mode orientation, and is given by (making use of the eigenvalue equation)

$$-\frac{ic}{P} = -ik_0\left(\frac{\pi}{k_0 R}\right)^{1/2}\exp(-2\tau_0)\cdot\frac{(n_1^2 - \nu_0^2)\,n_0}{4\nu_0 k_0^2 a^2(n_1^2 - n_0^2)\lambda_0^{3/2}K_1^2(k_0\lambda_0 a)}f(\phi_0,\phi_1,\phi_2) \tag{16}$$

where

$$f(\phi_0,\phi_1,\phi_2) = 1 + \frac{\lambda_0^2}{n_0^2}\cdot\frac{\cos^2\phi_2\cos^2\phi_1}{\sin^2\phi_2\cos^2\phi_0 + \cos^2\phi_2\cos^2\phi_1} \simeq 1$$

since $\lambda_0/n_0 \ll 1$. This is exactly Lewin's result for the HE_{11} mode [4].[2] For the mode very far from cutoff, $k_0\lambda_0 a \gg 1$ and $\kappa a \simeq p_{0,1}$, i.e., the first zero of J_0. In this case we have

$$-i\frac{c}{P} \simeq -\frac{i}{2}k_0\left(\frac{1}{\pi k_0 R}\right)^{1/2}\exp(-2\tau_0 + 2k_0\lambda_0 a)\cdot\frac{p_{0,1}^2\,n_0}{n_1 k_0^3 a^3\lambda_0^{5/2}}.$$

[2] An error of a factor of 2 appeared in Lewin's original paper [4], which has subsequently been corrected.

This result differs from that of Arnaud [5] in two significant ways: 1) the additional $2k_0\lambda_0 a$ term in the exponent; and 2) the presence of R instead of $R + a/\lambda_0^2$ under the square-root sign. These differences are accounted for in the conclusion.

For $m \neq 0$, a similar procedure gives

$$-i\frac{c}{P} = -ik_0\left(\frac{\pi}{k_0 R}\right)^{1/2} \exp(-2\tau_0)\, \frac{(n_1^2 - \nu_0^2)\, n_0\, g(\phi_0, \phi_1, \phi_2)}{2\nu_0 k_0^2 a^2 (n_1^2 - n_0^2)\, \lambda_0^{3/2}\, |K_{m+1}(k_0\lambda_0 a)\, K_{m-1}(k_0\lambda_0 a)|} \tag{17}$$

where

$$g(\phi_0, \phi_1, \phi_2) = \sin^2\phi_2 \cos^2\phi_0 + \frac{\nu_0^2}{n_0^2}\cos^2\phi_2 \cos^2\phi_1. \tag{18}$$

This result seems to indicate that, unlike the $m = 0$ modes, these modes have both polarization and orientation-dependent losses. However, [10], we may recover the approximate $EH_{m-1,n}$ (respectively, $HE_{m+1,n}$) modes by setting $\phi_1 = \phi_0 + \pi/2$ or $\phi_1 = \phi_0 + 3\pi/2$ and $\phi_2 = \pi/4$ or $5\pi/4$ (respectively, $\phi_2 = 3\pi/4, 7\pi/4$); so that for these cases

$$g(\phi_0, \phi_1, \phi_2) = \frac{1}{2}\left[1 + \frac{\lambda_0^2}{n_0^2}\sin^2\phi_0\right] \simeq \frac{1}{2}$$

and again this result agrees with that obtained by Lewin [4]. The TE_n and TM_n modes are included as a special case of the $EH_{m-1,n}$ modes for $m = 1$. Note that all exact modes of the fiber have loss which is essentially independent of the polarization and orientation,[3] but that approximate composite $m \geq 1$ modes can be constructed using (18) to minimize the radiation (e.g., $\phi_0 = \phi_1 = \pi/2$).

V. Conclusion

The results (11) and (12) for the TE modes of the asymmetric slab are both dependent on the term $[(k_0\lambda_0)^{-1} - \gamma_0^{-1}]$, which is a measure of the asymmetry of the guide, and may in fact be an extremely sensitive function of the guide parameters [3]. These results agree with those of [3] obtained by directly perturbing the eigenvalue equation. The result of Marcuse [2] omits the asymmetry term in the attenuation constant, and the possibility of a factor of 2 or 3 difference between the two results indicates the importance of retaining the first-order correction in (6). In addition, we note that the choice of the location of $\hat{x} = 0$ (i.e., the definition of R) relative to the slab will have an effect on the phase constant which amounts to a referral of the phase velocity to the location $\hat{x} = 0$. However, the only change in the attenuation constant is a change in R (occurring in τ_0) by the appropriate amount, so that it is clear that the $k_0\lambda_0 d$ term appearing in the exponent is not removable by a redefinition of R.

The results of Section IV agree with Lewin's analysis [4] as previously noted. The apparent discrepancies with Arnaud's [5] result, in which a limiting case is treated, can be seen [12] to be a result of a referral of the propagation constant to the outer boundary, ratner than to the center of the fiber, as has been done here. This accounts for the factor $\exp(2k_0\lambda_0 a)$ discussed in Section IV, while the remaining discrepancy can be explained by Arnaud's use of an approximate spectrum function instead of the exact one obtained in Section IV. From the restrictions given in Section II on (5), this difference must be negligible so that the present result agrees with the case treated in [5].

Finally, it will be noted that (5) predicts a dependence of $R^{-1/2}$ for the attenuation of any finite cross-section guide. As pointed out in [6], field approximations which are not somehow averaged [as, e.g., in (8)] do not generally give satisfactory results, and in particular Marcatili's analysis of the rectangular cross-section guide [1] is in error by at least this term (in fact, to his approximations, the bending loss behaves as if the guide were a slab).

[3] This is a consequence of the fact (shown by Arnaud [11]) that the formulas obtained for the "simplified" modes of the fiber follow from the scalar Helmholtz equation.

Acknowledgment

The authors wish to thank Prof. L. Lewin for the idea of the spectral-function treatment of the waveguide fields which forms the basis of this approach and for many fruitful discussions. They also wish to thank Prof. S. Maley for his helpful comments and discussions, and Dr. J. A. Arnaud for his kind criticisms and comments.

References

[1] E. A. J. Marcatili, "Bends in optical dielectric guides," *Bell Syst. Tech. J.*, vol. 48, pp. 2103–2132, 1969.
[2] D. Marcuse, "Bending losses of the asymmetric slab waveguide," *Bell Syst. Tech. J.*, vol. 50, pp. 2551–2563, 1971.
[3] D. C. Chang and F. S. Barnes, "Reduction of radiation loss in a curved dielectric slab waveguide," Dep. Elec. Eng., Univ. Colorado, Boulder, *Sci. Rep. No. 2* (AFOSR-72-2417), 1973.
[4] L. Lewin, "Radiation from curved dielectric slabs and fibers," *IEEE Trans. Microwave Theory Tech.*, vol. MTT-22, pp. 718–727, July 1974.
—, "Correction to 'Radiation from curved dielectric slabs and fibers,'" *ibid.*, vol. MTT-23, p. 779, Sept. 1975.
[5] J. A. Arnaud, "Transverse coupling in fiber optics–Part III: Bending losses," *Bell. Syst. Tech. J.*, vol. 53, pp. 1379–1397, 1974.
[6] D. C. Chang and E. F. Kuester, "General theory of surface wave propagation on a curved optical waveguide or arbitrary cross-section," Dep. Elec. Eng., Univ. Colorado, Boulder, *Sci. Rep. No. 11* (AFOSR-72-2417), 1975.
[7] —, "Radiation and propagation of a surface-wave mode on a curved open waveguide of arbitrary cross-section," *Radio Sci.*, submitted for publication.
[8] D. Marcuse, *Theory of Dielectric Optical Waveguides.* New York: Academic, 1974.
[9] I. S. Gradshteyn and I. M. Ryzhik, *Table of Integrals, Series and Products.* New York: Academic, 1965, p. 309.
[10] D. Marcuse, *Light Transmission Optics.* New York: Van Nostrand-Reinhold, 1972, pp. 337–339.
[11] J. A. Arnaud, "Transverse coupling in fiber optics–Part II: Coupling to mode sinks," *Bell Syst. Tech. J.*, vol. 53, pp. 675–696, 1974.
[12] —, "Comments on 'Radiation from curved dielectric slabs and fibers,'" *IEEE Trans. Microwave Theory Tech.*, to be published.

Behavior of First- and Second-Positive Emission in the N_2/SF_6 Laser

STEVEN N. SUCHARD, DAVID G. SUTTON, AND R. F. HEIDNER, III

Abstract—**Experimental results for the behavior of the emission of the discharge-excited first- and second-positive bands of N_2 and flow-tube measurements for the deactivation of the $A^3\Sigma_u^+$ and $B^3\Pi_g$ levels of N_2 by SF_6 are presented. The results of both these experiments are used to explain the operating mechanisms of the N_2/SF_6 laser.**

I. Introduction

SUPERFLUORESCENT laser emission on the second-positive band of the nitrogen molecule $C^3\Pi_u$-$B^3\Pi_g$ was first reported in 1964 [1]. Since that time, many novel attempts have been made to increase both the maximum energy that can be extracted as laser emission and the overall electrical efficiency with which the laser can be operated [2]-[9]. To date, the maximum energy that has been extracted from an N_2 laser is on the order of 20 mJ from a discharge-initiated system [7] and 250 mJ from an electron-beam-initiated Ar/N_2 laser [10]. More energy has been extracted from the electron-beam-initiated N_2 laser; however, because of the inefficient coupling of the initiation source to the active volume by electron-beam initiation, the "wall-plug" electrical efficiency of the electron-beam-initiated device is several orders of magnitude smaller than the discharge device, which has an efficiency ≈ 0.1 percent.

The principal difficulty encountered in the investigation of N_2 lasers is the exceedingly small ratio of the radiative lifetime of the upper laser level $C^3\Pi_u$ to that of the lower laser level $B^3\Pi_g$, i.e., $\tau_C/\tau_B \approx 4 \times 10^{-3}$. Because of this small ratio, it is imperative that the time in which the laser inversion is produced be short with respect to the radiative lifetime of the upper state. If this pumping criterion is not met, the inversion will be destroyed by spontaneous decay of the upper state and laser threshold cannot be attained.

Recently, several of the authors reported quasi-continuous-wave (CW) laser action on the second-positive band of the nitrogen molecule by TEA discharges in a mixture of N_2/SF_6 [6], [9]. They also reported that laser emission was extremely sensitive to the alignment of the optical cavity formed about the discharge tube in contradistinction to "normal" superfluorescent N_2 laser emission. At that time, it was hypothesized that the operating mechanism for this laser could be explained solely by deactivation of the lower laser level $B^3\Pi_g$ by the SF_6 molecule. Laser and fluorescence measurements performed in this laboratory and interpretations of the results of others [7], [8] are reported in order to explain the kinetic mechanisms inherent to the N_2/SF_6 system.

Manuscript received May 29, 1975. This work reflects research supported by the Energy Research and Development Administration under Contract AT(04-3)-1056.

The authors are with the Aerospace Corporation, El Segundo, Calif. 90245.

II. Experimental

The experiments performed for this study fall into three distinct but interrelated categories. In the first type of experiment, the fluorescent and superfluorescent emission from both the first-positive $B^3\Pi_g$-$A^3\Sigma_u^+$ and second-positive bands of N_2 were measured as a function of the total system pressure and the N_2/SF_6 ratio. In the second type, the temporally and spectrally resolved laser emission from N_2/SF_6 mixtures were measured. In the third, measurements were performed to investigate the electronic and vibrational deactivation of the $A^3\Sigma_u^+$ and $B^3\Pi_g$ states of N_2 by SF_6 in a flowing afterglow apparatus similar to the one described by Meyer *et al.* [11].

A. Fluorescence, Superfluorescence, and Laser Measurements

The discharge apparatus employed for the fluorescence, superfluorescence, and laser experiments has been described briefly elsewhere [12]. The discharge tube consists of a 3-m Lucite pipe fitted with a double helix of 470-Ω resistors. Each helix consists of 502 resistors with one wire lead penetrating the 1-in-ID tube at equally spaced intervals. The other lead is tied to a common bus line. One helix is connected through the bus bar to ground, and the other helix forms the anode of a pulsed power supply consisting of a 0.014-μF capacitor bank triggered at 1 Hz by a spark gap (EG & G GP-14B). The capacitor is connected to a dc power supply (Universal Voltronics BAL 130-5.5) capable of delivering 130 kV. This configuration results in 502 pin-pair electrodes being opposed across a $\frac{3}{4}$-in gap. Actually, the tube is formed from two equal sections connected in the middle, where provision is made for evacuation by a mechanical pump. The ends of the tube are sealed by CaF_2 windows at Brewster's angle. The gas mixture from a metered manifold flows into the tube from both ends (Fig. 1).

For the fluorescence and superfluorescence measurements, the detection apparatus consisted of an optical multichannel analyzer with a calibrated wavelength dispersive element placed between the emission source and the detection section [Tektronix 7J20 rapid scan spectrometer (RSS)]. The spectral range of this instrument is from 2500 to 11 000 Å, which permits observation of both the first- and second-positive bands of N_2. Analog output from the RSS was stored and displayed on a storage oscilloscope (Tektronix 7704A), and photographs of the display were taken as a permanent record. In order to determine the linearity of the wavelength dispersive element, the RSS was calibrated by means of known

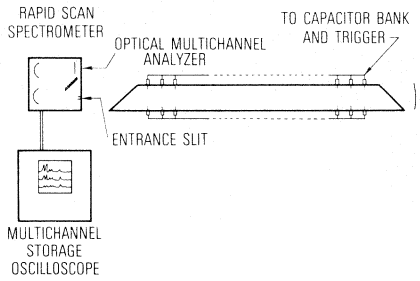

Fig. 1. Discharge apparatus used for fluorescence and laser experiments.

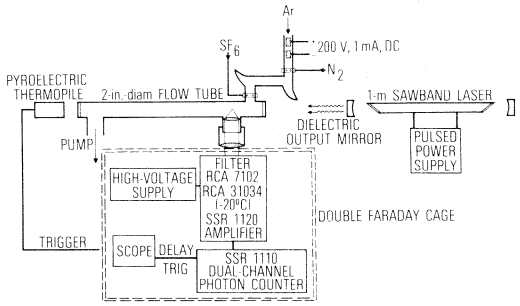

Fig. 2. Fast-flow apparatus including hollow cathode lamp for generating Ar metastables and apparatus for pumping and detection of first-positive laser-induced fluorescence.

spectral lines from a Hg pen-ray lamp and a F(I) laser [13]. For measurements of the second-positive bands, the wavelength region $3000 \leqslant \lambda \leqslant 5000$ Å was monitored, and for the first-positive bands, the region $7000 \leqslant \lambda \leqslant 11\,000$ Å. Measurements were made of both band systems under both single- and double-pass conditions. For the double-pass measurements, an Al-coated mirror aligned along the optical axis of the discharge tube was placed on the end of the discharge tube opposite the detection system.

In order to perform the laser measurements, an optical cavity was formed about the discharge tube by an internal-cavity totally reflecting concave mirror of focal length 450 in and an external-cavity totally reflecting flat mirror with a 1-mm-diam coupling hole. Both mirrors were Au coated for laser measurements in the infrared (IR) and were replaced by identical Al-coated mirrors for the study of the second-positive laser. These mirrors were spaced 6 in from the end windows, which yielded a 3.2-m-long laser cavity. Output from the laser entered a screen room and was split into two beams by a NaCl flat at 45° to the beam. The reflected beam from the flat was monitored with an InSb photovoltaic detector operated at 77 K (Barnes Engineering). The transmitted portion of the laser beam was directed to a $\frac{1}{2}$-m monochromator (McKee-Pederson) equipped with an IR grating blazed at 10 μm. Output from the monochromator was focused onto an identical InSb detector or a Ge:Au detector (Raytheon) by an Au-coated 8-in-radius of curvature mirror. Measured detector response was monitored by an oscilloscope (Tektronix 7704) to be less than 100 ns. Ultraviolet (UV) emission was monitored with a photodiode (RCA 1P28) at the exit slit of the monochromator. Energy measurements were made with a pyroelectric joulemeter (Molectron J3-05).

B. Fast-Flow System for Laser-Induced Fluorescence Measurement of $N_2(B^3\Pi_g, v)$ Kinetics

The fast-flow system geometry (Fig.2) closely resembles the apparatus used by Meyer *et al.* [11] in the $N_2(A^3\Sigma_u^+)$ kinetics study. $N_2(A)$, primarily in $v = 0, 1$, is prepared by collisions of N_2 with Ar metastable atoms. The $N_2(A)$ molecules are rapidly pumped from the upstream mixing region into a 2-in-diam flow tube. Pressure and mass-flow measurements, as well as gas-purification techniques have been previously described [14]. $N_2(A)$ concentrations of $\sim 5 \times 10^9$ molecules/cm^3 can be prepared in this manner.

A small fraction (~1 percent) of the molecules are pumped to the $B^3\Pi_g$ state by selected first-positive band laser excitation; the (0, 0) band at 1.05 μm and the (1, 0) band at 8912 Å were used in this study. The width of the pumping pulse was small (~80 ns) with respect to the time during which $B \rightarrow A$ fluorescence was monitored (3-80 μs). No cascading processes occurred since only a single vibrational state of $B^3\Pi_g$ was pumped.

The laser-introduced $B \rightarrow A$ fluorescence was detected with a cooled S1 photomultiplier (RCA 7102; -20C) in conjunction with an SSR 1100 dual-channel photon counter. This instrument was used as a photon-counting box-car integrator and has a 1-μs minimum gate width. One channel measured the fluorescence signal as a function of time following the laser pulse. The reference channel was opened 100 μs after the signal channel in order to count dark pulses, scattered light, and any small $B \rightarrow A$ signal that might occur as a result of the very fast energy pooling between two $N_2(A)$ molecules [15]. Although this latter rate is $\sim 1 \times 10^{-9}$ cm^3/molecule^2 · s, this term can amount to only 5 photons/cm^3 · s emitted in all $B \rightarrow A$ bands. By comparison, the detected fluorescence signal is 2×10^6 photons/s.

III. Results

A. Discharge Fluorescence Measurements

Nitrogen first- and second-positive band fluorescent and superfluorescent emission was monitored as a function of both the N_2/SF_6 ratio and the total system pressure. Specifically, with a fixed N_2 pressure, the emission intensity and shape of all the bands of a given system were monitored as a function of the added SF_6. The N_2 pressure was then changed, and the measurements repeated as a function of added SF_6. The dynamic range of the RSS was such that the peak intensities of all the bands monitored could be measured directly.

1) First-Positive Bands: Measurements on the first-positive band system were performed on the (0, 0), (1, 0), (2, 1), (2, 0), (3, 1), and (4, 2) bands. Other bands could have been used for these measurements; however, the ones chosen allowed the extraction of relative changes in population information from $v = 0$-4 of the $B^3\Pi_g$ state. Typical data for these bands are given in Fig. 3. These experiments were performed with a N_2 pressure of 50 torr and a discharge voltage of 100 kV under double-pass conditions. Because the sensitivity of the Si vidicon in the RSS drops off rapidly beyond 1.0 μm, the (0, 0) band was only observable under double-pass

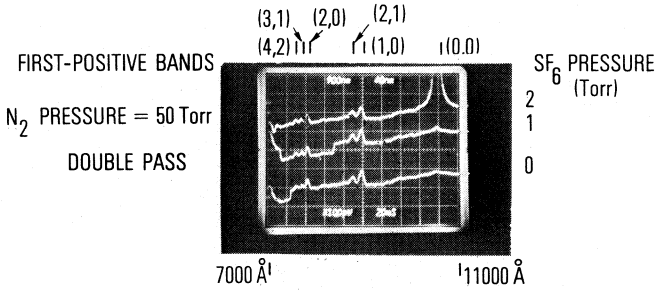

Fig. 3. Fluorescence data from the first-positive bands as a function of added SF_6. (N_2 pressure = 50 torr, discharge voltage = 100 kV, double-pass conditions.)

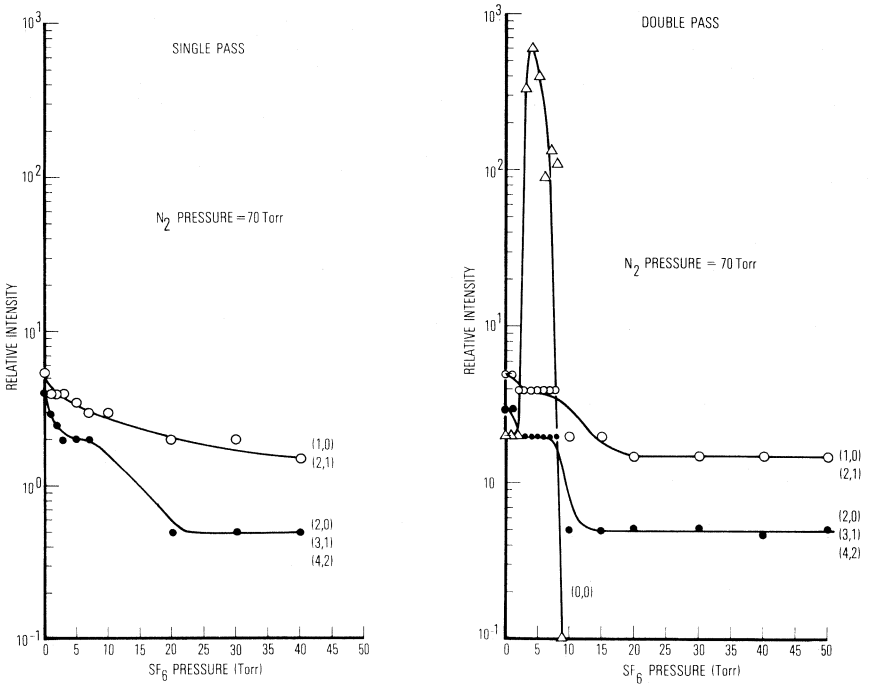

Fig. 4. Relative first-positive fluorescence intensity as a function of added SF_6. (a) Single-pass conditions. (b) Double-pass conditions. (N_2 pressure = 70 torr, discharge voltage = 100 kV.)

conditions where it would superfluoresce. Reduced data for the intensity change in the first-positive emission under both single- and double-pass conditions as a function of added SF_6 are given in Fig. 4(a) and (b). Again, the N_2 pressure was fixed at a constant 70 torr, and the discharge voltage at 100 kV. The addition of SF_6 to the N_2 decreases the intensity of all of the first-positive bands, except the (0, 0) band, by a factor of 5-10. This decrease in intensity was found to be essentially the same for all the N_2 pressures investigated.

As the N_2 pressure was increased from 30 to 70 torr, the pressure of SF_6 that had to be added to the N_2 in order to achieve the maximum superfluorescnece on the (0, 0) band also increased. The N_2/SF_6 ratio required for maximum (0, 0) superfluorescence, however, remained nearly constant at ~17.

In Fig. 4(a) and (b), single curves only are used to represent the $\Delta v = 1$ and $\Delta v = 2$ transitions, respectively. It was determined that the shape of the fluorescence intensity versus added SF_6 curves is the same for each member of a Δv progression. The relative intensities of the members of a Δv progression were found to decrease with increasing v'. The curves represent the lowest member of each progression. Previously measured excitation cross sections for the production of the vibrational levels of the $B^3\Pi_g$ state by e-N_2 collisions indicate that the vibrational levels of maximum population correspond to $v = 2$-4 [16]. The fluorescence measurements made in this study do not correlate with these results; however, since the RSS integrates the signal that it sees over the entire discharge time, it is not surprising that the measured vibrational distributions appear to be equilibrated.

2) Second-Positive Bands: For the fluorescence intensity versus added SF_6 measurements of the second-positive emission, the (0, 0), (0, 1), (0, 2), (0, 3), (1, 3), and (1, 4) bands were monitored. Typical experimental data for these bands are given in Fig. 5. These measurements were performed with a fixed N_2 pressure of 70 torr and a discharge voltage of 100 kV under single-pass conditions. The jumps observed in the

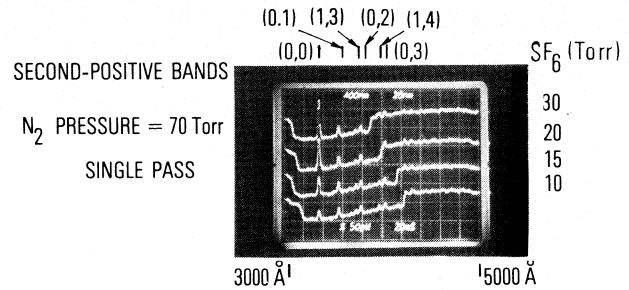

Fig. 5. Fluorescence data from second-positive bands as function of added SF_6. (N_2 pressure = 70 torr, discharge voltage = 100 kV, single-pass conditions.)

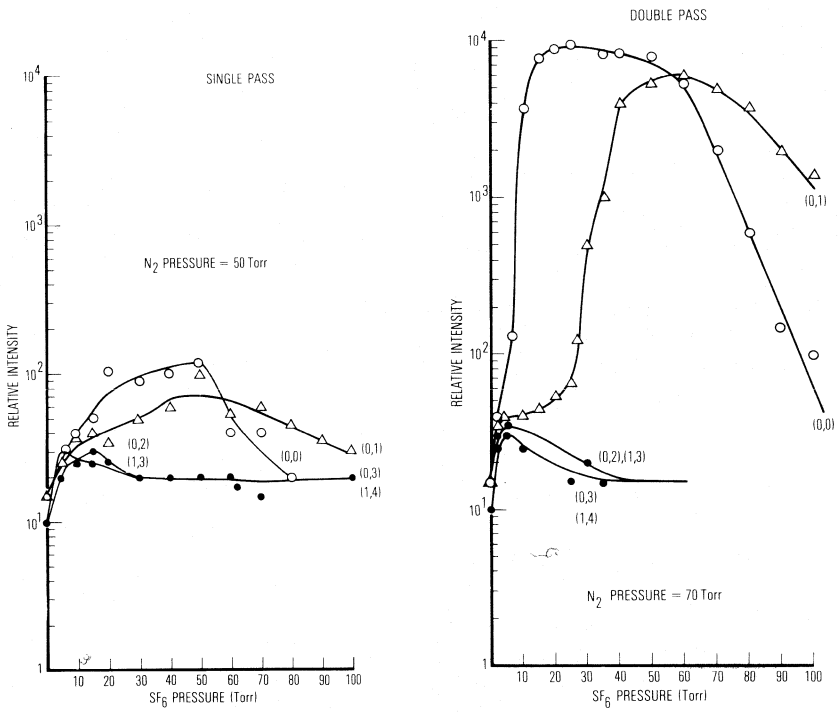

Fig. 6. Relative second-positive fluorescence intensity as function of added SF_6. (a) Single-pass conditions. (b) Double-pass conditions. (N_2 pressure = 70 torr, discharge voltage = 100 kV.)

signal baseline are not the result of radiation but electrical pickup by the RSS of the initiation discharge. A more complete display of the reduced experimental data is given in Fig. 6(a) and (b) for both single- and double-pass conditions. As in the case of the first-positive emission, only the lowest member of a given Δv progression is plotted in Fig. 5(a) and (b). The fluorescence intensities from the higher members of a progression decrease with increasing v'. Measured excitation cross sections for the vibrational levels of the $C^3\Pi_u$ state by e-N_2 collisions indicate that the vibrational level of maximum population will be $v' = 0$, decreasing with increasing v' [17]. The results of this study support this conclusion.

There are several interesting phenomena that are apparent in Fig. 6(a) and (b). The intensities of all Δv progressions increase by at least a factor of 2 as the SF_6 pressure is increased from 0 to 10 torr. Above 10-torr added SF_6, the intensities of the $\Delta v = -2$ and -3 progressions decrease; however, they do not decrease to the intensity level of the N_2 without SF_6. The (0, 0) and (0, 1) bands behave quite differently; the intensities of both of these bands continue to increase with added SF_6. This increase in intensity on only these two bands is a strange phenomenon. If it were caused only by an increase in the population of the $v = 0$ level of the $C^3\Pi_u$ state, an increase in intensity on all (0, v') bands of the second-positive system would be observed [18]. The reason for this anomalous intensity increase was found when the discharge voltage was lowered to below 75 kV. Below this voltage, the intensities of the (0, 0) and (0, 1) bands follow those of the $\Delta v = -2$ and -3 progressions. Above 75 kV, there must be sufficient gain in both the (0, 0) and (0, 1) bands such that they display single-pass superfluorescence. The realization that both the (0, 0) and (0, 1) bands display single-pass superfluorescence also helps to explain the crossover in intensities of the (0, 0) and (0, 1) band intensities at high SF_6 pressures.

A more detailed explanation of this effect is given in Section IV.

Three additional features of the second-positive emission are the following.

1) The (0, 0) band reaches its maximum intensity with 20-torr added SF_6, independent of N_2 pressure.

2) The condition under which the intensities of the (0, 0) and (0, 1) bands become equal always corresponds to $N_2/SF_6 \approx 1.0$.

3) The condition under which the (0, 1) band intensity maximizes corresponds to $N_2/SF_6 \approx 0.8$.

B. Laser Emission from N_2/SF_6 Discharges

The triplet states below 11.5 eV are *ungerade* except for the $B^3\Pi_g$ state (Fig. 7). All electric-dipole allowed transitions must, therefore, involve the B state, which includes the three laser systems $C \rightarrow B$, $B \rightarrow A$, and $W \rightarrow B$. In addition to these bands, a band laser emission near 1.82 μm and a single line at 3.355 μm also have been observed; however, these have not been positively identified. These lasers are affected by the addition of SF_6 in different ways (Fig. 8). The assignment of the 1.82-μm band to the $B(4) \rightarrow A(8)$ band is tentative. The lasers are molecular bands, which when inspected under high resolution consist of many lines except for the single line at 3.355 μm.

The electronic transitions identified in laser emission are given in Fig. 9. The 1.82-μm laser behaves temporally as a function of N_2 and SF_6 in a manner similar to the first-positive group lasers; consequently, these four bands are considered to be one laser system. Because it has not been identified, the 3.355-μm line will not be discussed.

In pure nitrogen, the lasers in Fig. 9 can be made to oscillate, except the second-positive bands. The relative laser intensities of each as a function of N_2 pressure are shown in Fig. 10. These measurements have been normalized so that the peak intensity of each band is 1.0. No comparison between individual bands is implied. The first-positive laser bands behave as the 1.822-μm line shown in Fig. 10.

The $W \rightarrow B \rightarrow A$ laser system is similar to the $C \rightarrow B \rightarrow A$ system observed with the addition of SF_6 in that the B state plays an intermediate role. In addition to the wavelength, however, there are other important distinctions. Neither of the McFarlane $W \rightarrow B$ bands III and IV [19], [20] (Fig. 10) are observed to lase unless they are preceded by first-positive laser action (Fig. 11). In addition, calculated electron impact cross sections for the excitation of the W state are lower at all energies than the corresponding cross sections for the B state [21]. This implies that the W and B states are strongly coupled through collisions with ground state N_2. Inversion requires $B \rightarrow A$ lasing to empty the low laser levels $B(v = 0, 1)$.

The $W(2) \rightarrow B(1)$ laser oscillates over a wider N_2 pressure range than the $W(1) \rightarrow B(0)$, which indicates that the inversion between the latter two levels is more susceptible to annihilation by collisions. Observation of the second-positive laser, which has oscillations terminating on the same two levels, i.e., $B(v = 0, 1)$, supports this conclusion.

The effect of SF_6 on discharges containing 10- and 50-torr N_2 was examined. At the lower N_2 pressure, the $W \rightarrow B$ and first-positive lasers are operative; at the higher pressure, only the first-positive laser is operative. With the addition of a

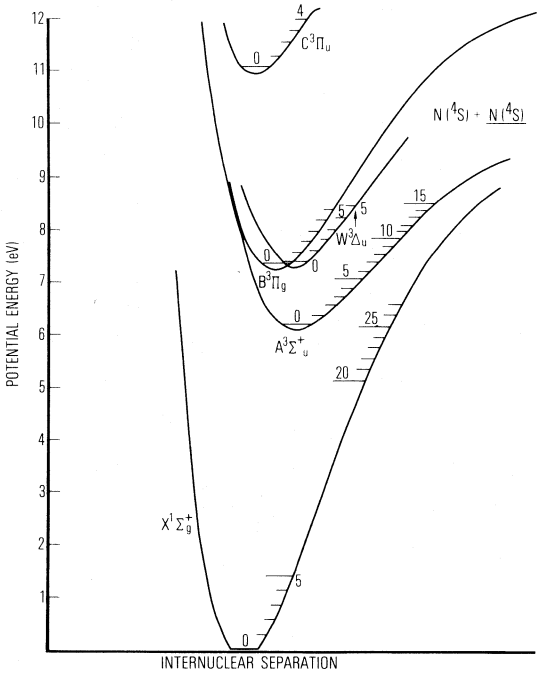

Fig. 7. Potential energy curves of the triplet states relevant to the N_2/SF_6 laser system.

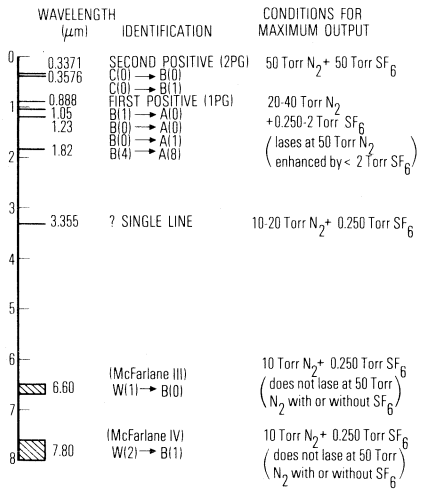

Fig. 8. Observed laser oscillations in N_2/SF_6 discharges.

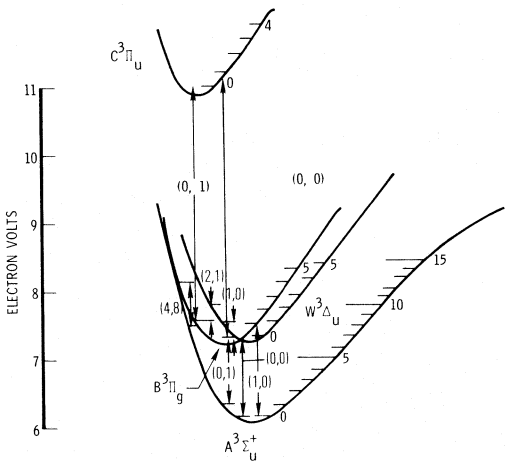

Fig. 9. Nitrogen transitions observed in laser emission.

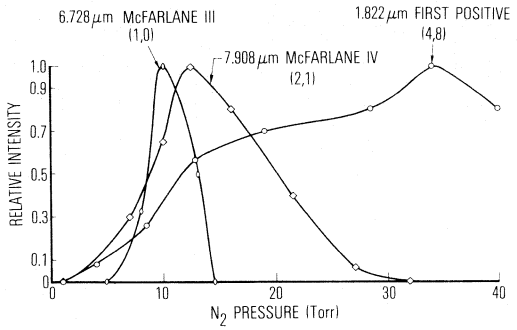

Fig. 10. Relative laser intensities as function of N_2 pressure.

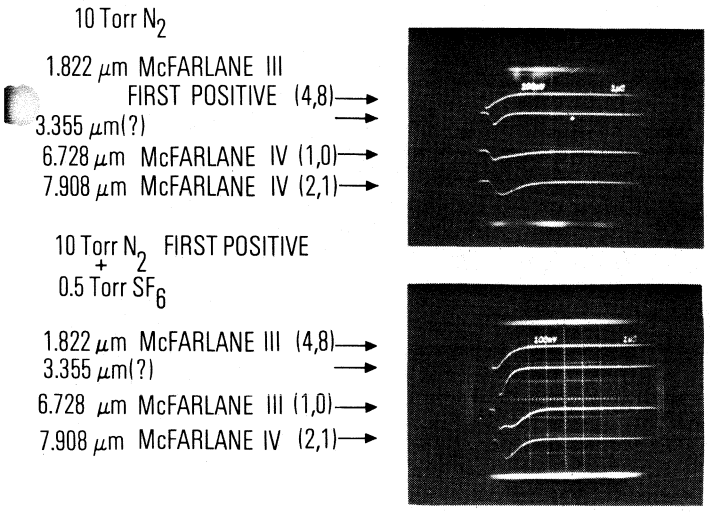

Fig. 11. Time-resolved nitrogen-laser emission at 10-torr N_2 and 10-torr N_2 + 0.5-torr SF_6.

minimum of 8-torr SF_6, the second-positive laser is observed. The results of the addition of SF_6 to discharges containing 10-torr N_2 are shown in Fig. 12. The effects on laser intensity are qualitatively similar to those produced, when the nitrogen pressure is varied; however, they are much more pronounced.

The laser transitions are enhanced, go through a maximum, and are quenched as successively more SF_6 is introduced. The $W(1) \rightarrow B(0)$ laser intensity peaks and is quenched at lower SF_6 pressures than the $W(2) \rightarrow B(1)$. Only 0.5-torr SF_6 is required to quench the $W(1) \rightarrow B(0)$ laser, while 5 torr of additional N_2 is required for the same result. A similar effect is also found for the $W(2) \rightarrow B(1)$ laser. Clearly, SF_6 is more efficient in quenching the inversion between these states than N_2.

At 50-torr N_2, with between 8- and 25-torr SF_6, both the first- and second-positive lasers oscillate. As shown in Fig. 13, however, the time to threshold for the first-positive laser follows that of the second-positive laser. Consequently, first-positive laser action can play no role in creating or maintaining inversion on the $C \rightarrow B$ transitions.

As shown in Fig. 14, up to 5 torr of SF_6 added to the 50-torr N_2 augments the peak intensity of the first-positive oscillations. Above 5 torr, however, further SF_6 addition results in a monotonic decline in first-positive laser power. At 8-torr SF_6, the second-positive laser reaches a threshold and increases in peak power until a broad maximum is reached at 25-torr SF_6.

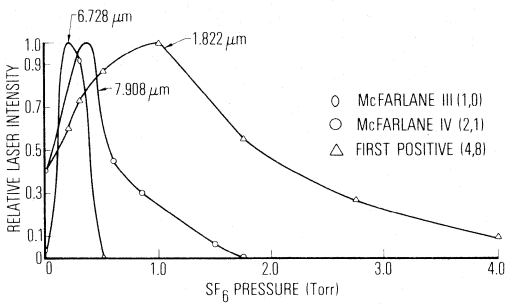

Fig. 12. Relative laser intensities as function of SF_6 pressure at 10-torr N_2.

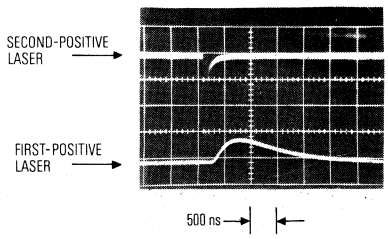

Fig. 13. Time sequencing of the first- and second-positive N_2 lasers at 50-torr N_2 + 14-torr SF_6.

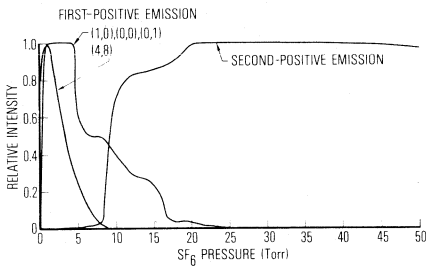

Fig. 14. Relative laser intensities as function of SF_6 pressure at 50-torr N_2.

The relative energy of the most intense second-positive laser oscillations as a function of SF_6 is shown in Fig. 15. The broad maximum in second-positive laser power is an artifact of the simultaneous decrease in the (0, 0) transition with an increase in the (0, 1) transition. These transitions both originate from the same upper state, and the Franck-Condon factor for the (0, 0) transition is approximately 30 percent larger than for the (0, 1) transition; thus the SF_6 is more effective at deactivating the $v = 1$ level of the B state than the $v = 0$ level. This conclusion is supported by the laser-induced fluorescence measurements given in Section IV.

C. *Laser-Induced Fluorescence Measurements*

Laser-induced fluorescence data for $B, v = 0$ and $B, v = 1$ are given in Figs. 16 and 17, respectively. Obviously, $B, v = 0$ has more than one decay time, while $B, v = 1$ appears to have one decay time, at least over the first decade of signal. Secondary and tertiary decay times have been observed previously when $B^3\Pi_g$ kinetics have been examined by pulsed-electric discharge techniques [22]-[24]. Since cascading (electronic and vibrational) processes occur in such experiments, only the first decay time has been considered as significant. Although our $B, v = 0$ kinetic data are similar to the data of several of these experiments, neither the cascading nor any "active nitrogen"

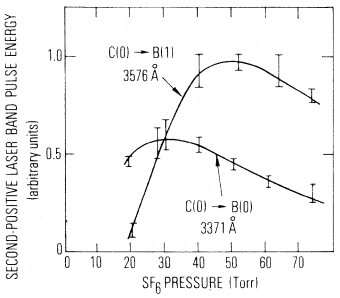

Fig. 15. Pulse energies of second-positive (0, 0) and (0, 1) bands as function of SF_6 pressure at 50-torr N_2.

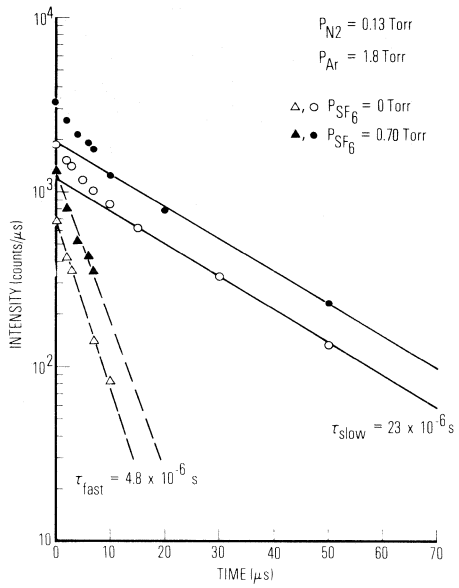

Fig. 16. Laser-induced fluorescence for (0, 0) band decay of $N_2(B^3\Pi_g, v=0)$. (Open circles are data for 1.8-torr Ar and 0.13-torr N_2. Closed circles are for the same Ar and N_2 partial pressures with 0.7 torr of SF_6. A double exponential curve fit gives identical decay times, $\tau_1 = 4.8$ μs and $\tau_2 = 23$ μs.)

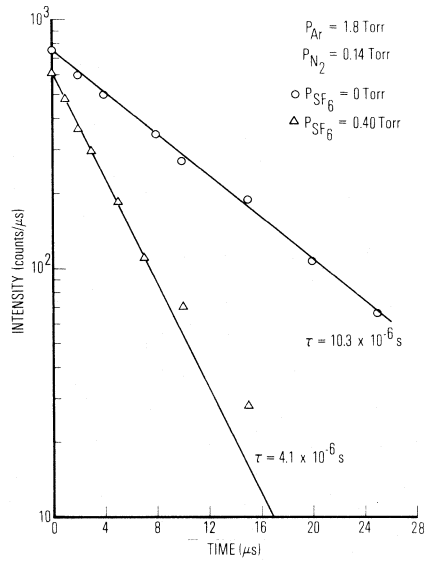

Fig. 17. Laser-induced fluorescence for (1, 0) band decay of $N_2(B^3\Pi_g, v=1)$. (Circles are data for 1.8-torr Ar and 0.14-torr N_2. Triangles are for the same Ar and N_2 partial pressures with 0.4 torr of SF_6. Decay times are 10.3 μs and 4.1 μs, respectively.)

afterflow effects [24] were observed in this study. The data of this study are consistent with a model in which strong collisional equilibrium of $N_2(B^3\Pi_g)$ and $N_2(W^3\Delta_u)$ is followed by relatively weak electronic quenching of the coupled B, W system. Analyzing the data in this manner reveals a longer radiative lifetime for $B^3\Pi_g$, $v=0$ than that reported by Jeunehomme [22].

The latest work by Benesch and Saum [25] on the spectroscopy of the $W^3\Delta_u$ state indicates that $v=0$ lies 73 cm^{-1} above $v=0$ for the $B^3\Pi_g$ state. Therefore, it is proposed [14] that the two decay times in Fig. 16 represent an equilibration between B, $v=0$ and W, $v=0$ (first decay) followed by loss of energy as a result of quenching and radiation by the coupled B, W system (second decay). The mathematical formalism applicable to these kinetics was developed by Chen and Moore [26] to deal with $V \rightarrow V$ transfer in HCl/DCl mixtures. It has been expanded subsequently [27], [28] to deal with vibrational energy exchange between diatomics with a close energy resonance.

The following kinetic processes are relevant to the quenching of $N_2(B, v=0)$ by Ar and N_2:

$$N_2(B, v=0) + Ar \underset{k_{-1}}{\overset{k_1}{\rightleftharpoons}} N_2(W, v=0) + Ar \tag{1}$$

$$N_2(B, v=0) + N_2 \underset{k_{-2}}{\overset{k_2}{\rightleftharpoons}} N_2(W, v=0) + N_2 \tag{2}$$

$$N_2(B, v=0) \xrightarrow{k_3} N_2(A^3\textstyle\sum_u^+) + h\nu \tag{3}$$

$$N_2(B, v=0) + Ar \xrightarrow{k_4} N_2(A, X) + Ar \tag{4}$$

$$N_2(B, v=0) + N_2 \xrightarrow{k_5} N_2(A, X) + N_2 \tag{5}$$

$$N_2(W, v=0) + Ar \xrightarrow{k_6} N_2(A, X) + Ar \tag{6}$$

$$N_2(W, v=0) + N_2 \xrightarrow{k_7} N_2(A, X) + N_2. \tag{7}$$

The solution of these equations has been given previously [26] and may be written

$$N_2(B, v=0) = A \exp(-\lambda_1 t) + B \exp(-\lambda_2 t) \tag{8}$$

where λ_1 and λ_2 are the reciprocals of the measured fast and slow relaxation times. Various approximations can be made that give tractable expressions for λ_1 and λ_2 in terms of the rate coefficients for processes (1)-(7). The two most useful expressions are [26], [28]

$$\lambda_1 + \lambda_2 = k_3 + (k_2 + k_{-2} + k_5 + k_7)(N_2) + (k_1 + k_{-1} + k_4 + k_6)(Ar) \tag{9}$$

$$\lambda_2 \approx \frac{k_3}{(K_e + 1)} + \frac{(k_6 K_e + k_4)}{(K_e + 1)}(Ar) + \frac{(k_1 K_e + k_5)}{(K_e + 1)}(N_2) \tag{10}$$

where

$$K_e = k_1/k_{-1} = k_2/k_{-2} = (Q^W_{ROT}/Q^B_{ROT}) \exp(-\Delta E/kT).$$

Q_{ROT} is the rotational partition function, $\Delta E(\sim 73\ cm^{-1})$ is the energy difference between W, $v=0$ and B, $v=0$, and K_e is ~ 0.78.

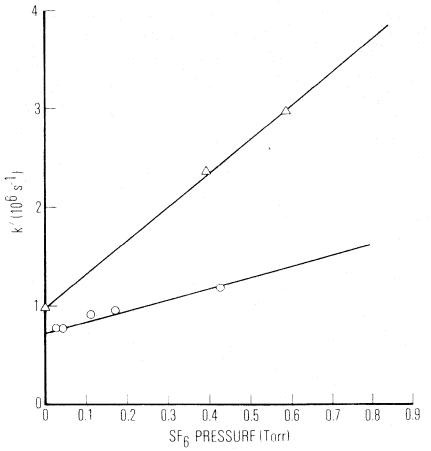

Fig. 18. Comparison of $N_2(B^3\Pi_g, v=1)$ quenching by SF_6 (triangles) and N_2 (open circles). (The derived rate coefficients are 1×10^{-11} and 3×10^{-12} cm^3/molecule · s, respectively.)

The following resulting rate coefficients for processes (1)-(7) have been previously discussed [14] and are presented here for reference only:

$$k_1 = 4 \times 10^{-13}\ \text{cm}^3/\text{molecule} \cdot \text{s}$$

$$k_2 = 7 \times 10^{-12}\ \text{cm}^3/\text{molecule} \cdot \text{s}$$

$$k_3 = 1 \times 10^{5}\ \text{s}^{-1}$$

$$0.56k_4 + 0.44k_6 \leqslant 1 \times 10^{-14}\ \text{cm}^3/\text{molecule} \cdot \text{s}$$

$$0.56k_5 + 0.44k_7 = 2 \times 10^{-12}\ \text{cm}^3/\text{molecule} \cdot \text{s}.$$

The conclusion to be drawn is that N_2 equilibrates $N_2(B)$ and $N_2(W)$ approximately 20 times more rapidly than Ar. Furthermore, N_2 electronically quenches the coupled B, W system more than 200 times faster than does Ar. Qualitatively, we have found no measurable effect of SF_6 on the N_2 $B, v=0$) relaxation rate.

With $N_2(B, v=1)$ assumed to have only one decay time (Fig. 17), the quenching rate of this state has been plotted versus N_2 and SF_6 in Fig. 18. These data must be regarded as preliminary. The rate coefficients derived from these data are

$$k_{SF_6}^{N_2(B,v=1)} = 1 \times 10^{-11}\ \text{cm}^3/\text{molecules} \cdot \text{s}$$

$$k_{N_2}^{N_2(B,v=1)} = 3 \times 10^{-12}\ \text{cm}^3/\text{molecules} \cdot \text{s}.$$

Although the product states are not known at this time from the kinetics, it is hoped that studies where one state is pumped and a second vibrational state is monitored as a function of time will be pursued.

When SF_6 is added, the population of $N_2(B, v=0)$ increases by a factor of 2 at all times following the laser pulse (Fig. 16). This results from vibrational relaxation in the $A^3\Sigma_u^+$ state since the $(A, v=1)/(A, v=0)$ measured by Setser *et al.* [29] downstream of the Ar* + N_2 flame persists at a ratio of 1. Qualitatively, SF_6 vibrationally but not electronically quenches the $A^3\Sigma_u^+$ state.

IV. Conclusions

The fluorescence, superfluorescence, and laser data were obtained in the range 0-60 torr of added SF_6. The experimental results, however, are more meaningful when considered in terms of two distinct ranges, i.e., 0-10 torr of added SF_6 and 10-60 torr of added SF_6. In the 0-10-torr SF_6 range, a complicated superposition of energy transfer processes, discharge impedance matching, and possibly new pumping processes is evident. These effects may reflect the altered electron energy distribution in the discharge or even direct excitation of SF_6 and subsequent energy transfer to N_2. In the 10-60-torr SF_6 range, results can be explained on the basis of the detailed energy transfer processes measured by the first-positive laser-induced fluorescence technique.

In 10-60-torr SF_6 range, it was observed that the (0, 1) second-positive, double-pass superfluorescence became more intense than the (0, 0) double-pass superfluorescence at a SF_6/N_2 ratio of ~1. This could not occur unless the $v=1$ level of $N_2(B)$ was being quenched to the $v=0$ level. The laser-induced fluorescence results indicate that this quenching rate $R = k_{SF_6}(SF_6) = 2 \times 10^7\ \text{s}^{-1}$ for an SF_6 pressure of 60 torr. The inverse of this rate (~50 ns) is comparable to the time to threshold (~100 ns) and the width (~100 ns) of the second-positive laser pulse in this system.

The behavior of double-pass superfluorescence on the (0, 0) first-positive band is not as clearly defined since it occurs entirely in the 0-10-torr SF_6 range. Nevertheless, the time to threshold (~300 ns) and the laser pulsewidth (~1 μs) for conditions of maximum (0, 0) output ($P_{SF_6} \approx 3$ torr) are very closely defined by the $N_2(B, v=1)$ relaxation time by SF_6 ($1/R \approx 1$ μs). Not until quantitative kinetic information concerning the $N_2(A)$ vibrational relaxation by SF_6 is available, can the first-positive laser performance be accurately predicted. Nevertheless, a comparison of the first-positive single-pass fluorescence to first-positive double-pass superfluorescence indicates that the addition of SF_6 results in vibrational cascading from $v>0$ to $v=0$ of the B state. The effect is probably more pronounced than indicated in Fig. 4(a) since increased C-state pumping in the 0-10-torr SF_6 range provides an additional B-state pumping term, i.e., $C \rightarrow B$ spontaneous and stimulated emission.

Analysis of the detailed fluorescence and laser behavior in the 0-10-torr SF_6 range is difficult, at best. In Fig. 6(a), the second-positive single-pass fluorescence increases by a factor of 2-3 with the addition of <5 torr of SF_6. Since this increase occurs on bands originating on $C^3\Pi_u$, $v=1$ as well as $v=0$, a new C-state pumping term is clearly indicated. Quite the opposite is indicated for single-pass fluorescence on the first-positive bands in the 0-10-torr SF_6 range. These observations indicate the possibility that some of the C-state production is two-step excitation involving either $B^3\Pi_u$ or $A^3\Sigma_u^+$ as an intermediate. Selective excitation of $C^3\Pi_u$ by SF_6* could also explain these results. Simpson *et al.* [30] found a strong peak in the energy loss spectrum for SF_6 at 11.5 eV, which is at threshold for $N_2(C^3\Pi_u)$ production. A final pumping possibility is ion recombination involving N_2^+ and SF_6^-, which is exoergic by 14 eV. The second-positive (0, 0) band always reaches a maximum intensity at 20 torr of added SF_6. This implies that SF_6-induced pumping processes in the 0-10-torr SF_6 range are being overtaken by the vibrational cascading into $B, v=0$ at the higher SF_6 pressures of the 10-60-torr SF_6 range.

The performance of the $W^3\Delta \rightarrow B^3\Pi_g$ laser is extremely

interesting in light of the proposed model for $B^3\Pi_g$, $v=0$ relaxation. Laser action is only observed at low N_2 pressures (<10 torr), and even at low pressures, the $B \rightarrow A$ transition always reaches threshold first, followed immediately by $W \rightarrow B$ laser action. These observations indicate that W and B are strongly coupled by N_2 collisions, i.e., $R = 2 \times 10^6$ s^{-1} at 10 torr of N_2 for B, $v=0 \rightarrow W$, $v=0$, and that stimulated emission is the only mechanism by which the lower state $B^3\Pi_g$ can be removed rapidly enough to invert the $W \rightarrow B$ transition. SF_6 helps both $W \rightarrow B$ (1, 0) and (2, 1) when added in extremely small amounts. This is clearly a 0-10-torr SF_6 range discharge effect rather than a kinetic relaxation effect by SF_6. Interestingly, $W \rightarrow B$ (1, 0) turns on first and then shuts off rather quickly with added SF_6. $W \rightarrow B$(2, 1) turns on later and shuts off more slowly with SF_6. In that sense, the behavior is qualitatively like that of the (0, 0) and (0, 1) $C \rightarrow B$ laser transitions.

Acknowledgment

The authors wish to thank P. Valenzuela, L. Galvan, and C. Gardner for their assistance in the fabrication and operation of the experimental apparatus.

References

[1] H. G. Heard, "High power ultraviolet gas laser," *Bull. Amer. Phys. Soc.*, vol. 9, p. 65, 1964.

[2] L. Y. Nelson, G. J. Mullaney, and S. R. Byron, "Superfluorescence in N_2 and H_2 electron-beam-stabilized discharges," *Appl. Phys. Lett.*, vol. 22, pp. 79-80, 1973.

[3] B. W. Woodward, V. J. Ehlers, and W. C. Lineberger, "A reliable, repetitively pulsed, high power nitrogen laser," *Rev. Sci. Instr.*, vol. 44, pp. 882-887, 1973.

[4] B. Godard, "A simple high-power large efficiency N_2 ultraviolet laser," *IEEE J. Quantum Electron. (Part II of Two Parts)*, vol. QE-10, pp. 147-153, Feb. 1974.

[5] S. K. Searles and G. A. Hart, "Laser emission at 3577 and 3805 Å in electron-beam-pumped Ar-N_2 mixtures," *Appl. Phys. Lett.*, vol. 25, pp. 79-82, 1974.

[6] S. N. Suchard, L. Galvan, and D. G. Sutton, "Nitrogen second positive laser emission utilizing pin initiation," presented at the 1st Summer Colloq. Electronic Transition Lasers, Santa Barbara, Calif., June 17-19, 1974.

[7] J. I. Levatter and S. C. Lin, "High-power generation from a parallel-plate-driven pulsed nitrogen laser," *Appl. Phys. Lett.*, vol. 25, pp. 703-705, 1974.

[8] C. S. Willett and D. M. Litynski, "Power increase of N_2 UV and IR lasers by addition of SF_6," *Appl. Phys. Lett.*, vol. 26, pp. 118-121, 1975.

[9] S. N. Suchard, L. Galvan, and D. G. Sutton, "Quasi-cw laser emission on the second positive band of nitrogen," *Appl. Phys. Lett.*, vol. 26, pp. 521-523, 1975.

[10] E. R. Ault, M. L. Bhaumik, and N. T. Olson, "High-power Ar-N_2 transfer laser at 3577 Å," *IEEE J. Quantum Electron.* (Corresp.), vol. QE-10, pp. 624-626, Aug. 1974.

[11] J. A. Meyer, D. H. Klosterboer, and D. W. Setser, "Energy transfer reactions of $N_2(A^3\Sigma_u^+)$. IV. Measurement of the radiative lifetime and study of the interaction with olefins and other molecules," *J. Chem. Phys.*, vol. 55, pp. 2084-2091, 1971.

[12] D. G. Sutton, L. Galvan, P. R. Valenzuela, and S. N. Suchard, "Atomic laser action in rare gas-SF_6 mixtures," *IEEE J. Quantum Electron.* (Corresp.), vol. QE-10, pp. 54-57, Jan. 1975.

[13] M. A. Kovacs and C. J. Ultee, "Visible laser action in fluorine I," *Appl. Phys. Lett.*, vol. 17, pp. 39-40, 1970.

[14] R. F. Heidner, III, D. G. Sutton, and S. N. Suchard, "Kinetic study of $N_2(B^3\Pi_g, v)$ utilizing laser-induced fluorescence," to be published.

[15] G. N. Hays and H. J. Oskam, "Population of $N_2(B^3\Pi_g)$ by $N_2(A^3\Sigma_u^+)$ during the nitrogen afterglow," *J. Chem. Phys.*, vol. 59, pp. 1507-1516, 1973.

[16] J. W. McConkey and F. R. Simpson, "Electron impact excitation of the $B^3\Pi_g$ state of N_2," *J. Phys. B (At. Mol. Phys.)*, vol. 2, pp. 923-929, 1969.

[17] D. J. Burns, F. R. Simpson, and J. W. McConkey, "Absolute cross section for electron excitation of the second positive bands of nitrogen," *J. Phys. B (At. Mol. Phys.)*, vol. 2, pp. 52-64, 1969.

[18] R. N. Zare, E. O. Larsson, and R. A. Berg, "Franck-Condon factors for electronic band systems of molecular nitrogen," *J. Mol. Spectrosc.*, vol. 15, pp. 117-139, 1965.

[19] R. A. McFarlane, "Precision spectroscopy of new infrared emission system of molecular nitrogen," *IEEE J. Quantum Electron.*, vol. QE-2, pp. 229-232, Aug. 1966.

[20] H. L. Wu and W. Benesch, "Evidence for the $^3\Delta_u \rightarrow B^3\Pi_g$ transition in N_2," *Phys. Rev.*, vol. 172, pp. 31-35, 1968.

[21] D. C. Cartwright, "Total cross sections for the excitation of the triplet states in molecular nitrogen," *Phys. Rev.*, vol. A2, pp. 1331-1348, 1970.

[22] M. Jeunehomme, "Transition moment of the first positive band system of nitrogen," *J. Chem. Phys.*, vol. 45, pp. 1805-1811, 1966.

[23] H. J. Hartfuss and A. Schmillen, "Über das Abklingen der ersten positiven Gruppe des N_2 und der Asundi-Banden des CO," *Z. Naturforsch. A*, vol. 23a, pp. 722-726, 1968.

[24] D. E. Shemansky and A. L. Broadfoot, "Excitation of N_2 and N_2^+ systems by electrons. II. Excitation cross sections and N_2 1PG low pressure afterglow," *J. Quant. Spectrosc. Radiat. Transfer*, vol. 11, pp. 1401-1439, 1971.

[25] W. M. Benesch and K. A. Saum, "The $W^3\Delta_u$ state of molecular nitrogen," *J. Phys. B (At. Mol. Phys.)*, vol. 4, pp. 732-738, 1971.

[26] H.-L. Chen and C. B. Moore, "Vibration rotation energy transfer in hydrogen chloride," *J. Chem. Phys.*, vol. 54, pp. 4072-4079, 1971.

[27] J. K. Hancock and W. H. Green, "Vibrational deactivation of HF($v=1$) in pure HF and in HF-additive mixtures," *J. Chem. Phys.*, vol. 57, pp. 4515-4529, 1972.

[28] J. F. Bott, "Relaxation of HF ($v=1$) and DF ($v=1$) by H_2 and D_2," *J. Chem. Phys.*, vol. 61, pp. 2530-2535, 1974.

[29] D. W. Setser, D. H. Stedman, and J. A. Coxon, "Chemical applications of metastable argon atoms, IV. Excitation and relaxation of triplet states of N_2," *J. Chem. Phys.*, vol. 53, pp. 1004-1020, 1970.

[30] J. A. Simpson, C. E. Kuyatt, and S. R. Mielczarek, "Absorption spectrum of SF_6 in the far ultraviolet by electron impact," *J. Chem. Phys.*, vol. 44, pp. 4403-4404, 1966.

Correspondence

Rotational-Vibrational Line Competition in a Dual-Polarization CO_2 Laser

N. E. BUHOLZ

Abstract—**A dual-polarization CO_2 laser can be caused to operate such that the two polarization modes correspond, respectively, to different rotational-vibrational lines. Interline competition effects, similar to those described previously, here also result in a mode power change with optical frequency which can be utilized as a convenient and sensitive optical frequency discriminant.**

The central component of an active laser stabilization system is the optical frequency discriminant, i.e., some quantity which changes with the laser frequency and which can be converted into a corresponding voltage increment. To be usable, the discriminant must have a noise level which is below the desired degree of stabilization, and it should have a flat frequency response in the band of laser modulation frequencies which are to be actively corrected by the system. Such a discriminant is potentially available in the case of CO_2 lasers through utilization of some of the special properties of a dual-polarization CO_2 laser. This type of laser, as first discussed by White and Gerber [1], [2], has in its output beam two polarization modes, linearly and orthogonally polarized, corresponding to an ordinary $c/2L$ cavity mode. The two modes are typically separated in frequency by a few megahertz. This behavior is produced by introducing a birefringent element into a laser cavity which is otherwise polarization isotropic. White and Gerber also demonstrated that it is possible through use of an intracavity modulator to force simultaneous oscillation of these modes within some narrow (~MHz) frequency band near the line center. It is found, under these conditions, that as the laser frequency is swept across line center, the modes exchange power content in a roughly linear manner. The slope of the power change with frequency may be adjusted by altering the modulator drive level. An optical frequency discriminant may thus be obtained through utilization of this mode power change with frequency. This behavior occurs because of gain competition effects which exist between the modes as they oscillate in a single rotational-vibrational line.

In contrast, Mocker [3] has shown that competition leading to the same sort of see-saw mode power exchange occurs when two modes oscillate on different vibrational-rotational lines. His experiments were performed using a CO_2 ring laser, in which the two modes were linearly and orthogonally polarized, and corresponded to opposite directions in the ring cavity. He also demonstrated similar competition effects in a single polarization linear laser using a heterodyne arrangement. In the latter case, to produce a usable discriminant one must separate the radiation corresponding to the two lines using some sort of dispersive arrangement since there is only a single polarization in the output.

We have also observed such line competition effects, but we utilized a dual-polarization CO_2 laser. The behavior is essentially the same as that described by Mocker, except that here we have a linear laser in which the "*s*" polarization, for example, may oscillate on the $P(18)$ line, and the "*p*" polarization may oscillate on the $p(20)$ line. The discriminant may be obtained simply by passing the output beam through a polarizer. In stabilized operation, then, the laser operates in two lines simultaneously, with the radiation corresponding to the two lines appearing primarily in orthogonal polarizations.

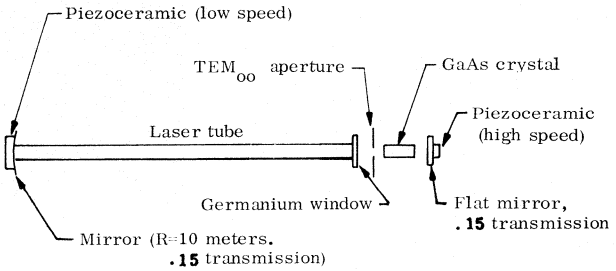

Fig. 1. Dual polarization CO_2 laser.

In the dual-polarization laser case, there appear to be certain advantages to using this discriminant over that provided by modulation near a single line center. First, the laser can presumably be constructed with fewer intracavity elements since no modulator is required. Second, it is desirable in sensitive heterodyne receiver applications to have a spectrally "clean" local oscillator (LO) beam.[1] This is difficult to obtain in the single line case, but is readily observed in the dual line case, the only probable contaminant being the radiation at the competing rotational-vibrational line frequency, which is one or more units of ~55 GHz away. The final advantage is connected with the slope and frequency response of this discriminant. Preliminary tests have shown that the slope $\Delta p/\Delta f$ can be as much as $\times 3$ greater than that obtainable with line center operation, and there are no anomalous amplitude and phase characteristics in its frequency response, as are also found in the line center case [4].

The dual-polarization laser from which these results were obtained is shown schematically in Fig. 1. This is a configuration which was used for line center operation and is not the optimum one for exploitation of the dual line discriminant. The GaAs crystal, which is the intracavity modulator in the line center scheme, is stressed mechanically as well, in order to produce the birefringence offset. The offset frequency is ~7 MHz. Piezoceramics located as shown provide optical frequency control, and an output of ~1.2-W total is obtained from each end of the laser. The laser tube is a Coherent Radiation model 42L and utilizes the standard laser mix (82:13.5:4.5, $He:N_2:CO_2$) with flow rate of 0.3 l/min and pressure of 20 torr. Excitation is provided by dc currents of ~10 mA flowing between cathodes located at the ends of the tube and the centrally located anode.

The photograph in Fig. 2 represents the power variation in each polarization mode as the laser frequency is swept through the crossover region. It was obtained by placing Ge:Au detectors on the output beams from each end after passing the beams through polarizers which were oriented along the two

Manuscript received December 12, 1974; revised July 10, 1975.

The author is with Lockheed Missiles & Space Company, Sunnyvale, Calif. 94088.

[1] Spectrally "clean" as used here means that there is no detectable RF beat note in the heterodyne detector due to the presence of more than one optical frequency in the laser (LO) output.

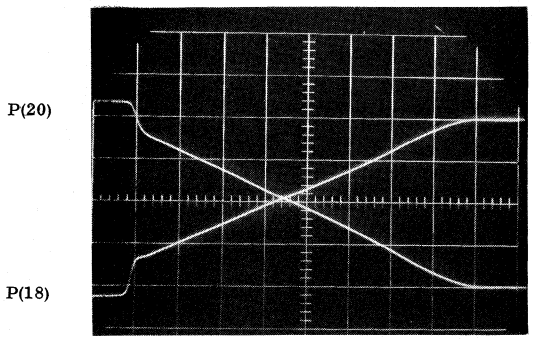

Fig. 2. Polarization mode power variation with laser frequency.

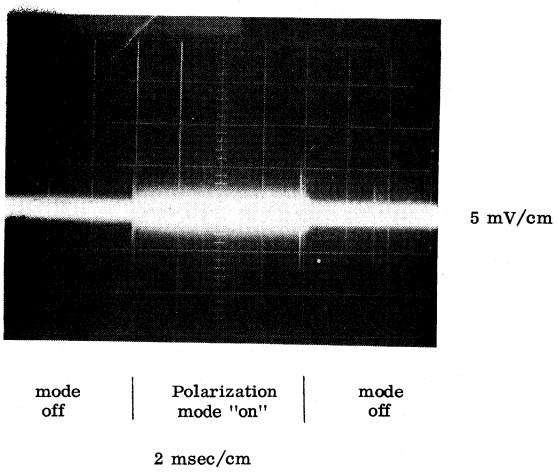

Fig. 3. Detector output $\times 100$ for one polarization mode output (approximately square wave) showing detector shot noise, amplifier noise, and polarization spectral purity.

orthogonal polarization directions. As is indicated in the figure, the two polarization modes correspond to the $P(18)$ and $P(20)$ rotational-vibrational lines (λ = 10.57, 10.59 μ, respectively). This was determined with a spectrum analyzer in place of the detectors. Also, as indicated, the slope of these traces in terms of volts per increment in laser frequency is ~6 mV/kHz. The magnitude of this slope depends upon the detector responsivity and the total power available at the detector, and so is a result of this particular experimental configuration. Thus in principle the slope may be increased if more sensitivity is required. For these detectors and the 6-mV/kHz slope, the detector self-noise level corresponds to a sensitivity limit of ~30 Hz of optical frequency deviation.

The frequency response characteristics of this discriminant in the range 0–10 kHz were obtained using a small sinusoidal drive on the high speed piezoceramic and observing the discriminant response with an hp 5480B averaging oscilloscope. The response was found to be completely flat in this range, unlike that of the discriminant established at line center using internal modulation.

As a final check, the laser output was tested for spectral "purity" using a HgCdTe photo diode placed after a polarizer oriented along one of the polarization mode directions.[1] The detector output was amplified and displayed on an oscilloscope, and the bandwidth of this arrangement was 250 kHz–20 MHz. During this experiment, the laser was swept sinusoidally in frequency such that each polarization mode was switched alternately "on" and "off" at the 60-Hz sweep rate. Thus in Fig. 3, which is a photograph of the oscilloscope display, we have an "on time" interval in which detector shot noise plus amplifier noise occurs, and an "off time" in which there is only amplifier noise. Since there is no beat note present during the mode on time, single frequency operation is indicated. The spikes in the photograph have been identified as transients with frequency near 250 kHz which originate in the amplifier.

In conclusion, we have observed the same rotational-vibrational competition effects which were reported earlier by Mocker, but we utilized a dual-polarization CO_2 laser, a device which is not a ring laser, but which can oscillate in two mutually orthogonal polarization modes, the two corresponding, respectively, to different rotational-vibrational lines. This provides a convenient optical frequency discriminant, some of the properties of which are that it has adequate sensitivity, good frequency response, is simple to obtain and utilize, and it allows active stabilization to be applied such that a single frequency output suitable for heterodyne receiver applications may be generated.

REFERENCES

[1] M. B. White and W. D. Gerber, "Mode-locked dual-polarization operation of a CO_2 laser," *IEEE J. Quantum Electron.*, vol. QE-7, pp. 445–450, Sept. 1971.

[2] —, "Frequency modulation of a self-mode-locked dual-polarization CO_2 laser," *IEEE J. Quantum Electron.*, vol. QE-7, pp. 577–578, Dec. 1971.

[3] H. W. Mocker, "Rotational level competition in CO_2 lasers," *IEEE J. Quantum Electron. (Special Issue on 1968 International Quantum Electronics Conference: Part II)*, vol. QE-4, pp. 769–776, Nov. 1968.

[4] N. E. Buholz, "Dual mode CO_2 laser stabilization," Lockheed Missiles & Space Company, Inc., Sunnyvale, Calif., LMSC Rep. D/425832, July 1974, unpublished.

A Copper Laser Using CuI Vapor

I. SMILANSKI, L. A. LEVIN, AND G. EREZ

Abstract—**A simple CuI double-pulsed laser was built. The dependence of power output on the delay between the two excitation pulses, temperature, and the type of buffer gas has been investigated. The laser pulse duration was measured.**

Some recent papers [1], [2] have reported on metal vapor lasers operating at relatively low temperatures, utilizing the fact that the vapor pressures of some metal salts are higher than those of the metal itself.

Laser excitation is produced in two stages; in the first stage a discharge pulse dissociates the metal salt vapor to produce metal atoms, and in the second stage a second discharge pulse pumps these atoms to the upper laser levels. The minimum delay between the two pulses is determined by the time the metal atoms, produced in the excited state, require to decay to the ground state. The maximum delay time is determined by the recombination time of the dissociated molecules. An inert buffer gas is used to maintain the discharge and to keep the windows clean. The type and the pressure of the gas have an important influence on the laser's characteristics.

In this work the dependence of power output on delay time, temperature, and type of buffer gas have been investigated, and the laser pulse duration was measured. The power output was compared for two pumping capacitors.

The active part of the laser was constructed of a quartz tube, 2.5 cm in diameter and 30 cm long, enclosed in a tubular furnace. The rest of the laser tube, outside the furnace, was constructed of Pyrex with tubular aluminium electrodes. The Brewster windows were supported on short tubes with ground glass joints. The vacuum connection was in the cold zone, enabling fast gas exchange and easy pressure control. The diameter of the Brewster windows (1.2 cm) determined the beam diameter. The tube was operated under static vacuum conditions, as it was found unnecessary to change the buffer gas continuously. The discharge was always homogeneous and reproducible, as long as the buffer gas was reasonably clean.

The optical resonator consisted of a flat maximum reflectivity broad-band dielectric mirror, and a flat dielectric output coupling mirror, 1 m apart. Lasing was achieved at both 5106- and 5782-Å wavelengths simultaneously. The divergence of the beam was about 1.5 mrad. Under optimum conditions the laser operated without mirrors due to its high gain, but with a much larger divergence.

Manuscript received March 14, 1975.

The authors are with Atomic Energy Commission, Nuclear Research Centre-Negev, Beer-Sheva, Israel.

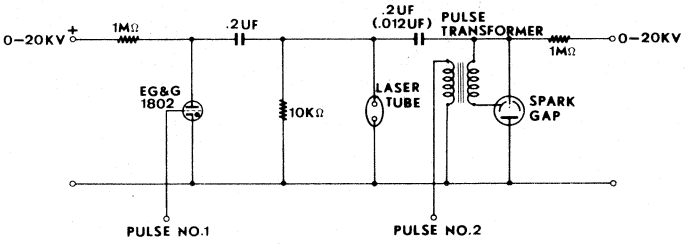

Fig. 1. Double-pulse power supply circuit.

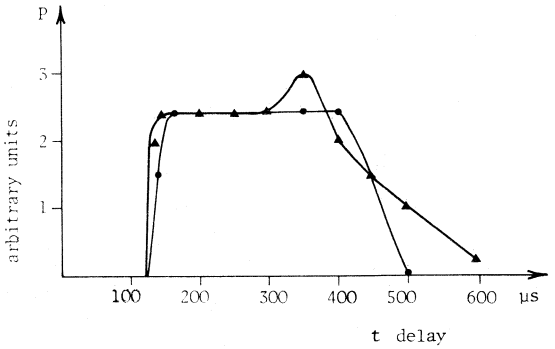

Fig. 2. Power output as function of delay time. •–20 torr He; ▲–7-torr He.

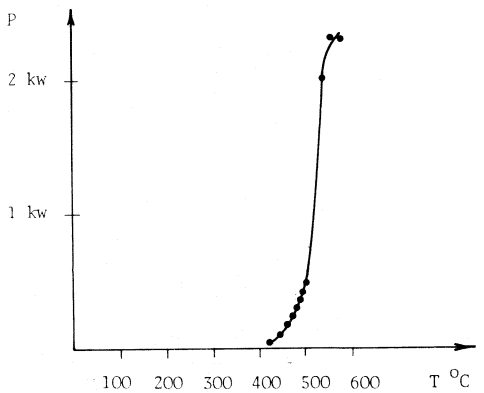

Fig. 3. Power output as function of furnace temperature. T_d = 200 μs; 7-torr He; C_{dis} = 0.2 μF; V_{dis} = 6 kV. C_{pump} = 0.012 μF; V_{pump} = 12 kV.

The electrical circuit used for the excitation is shown in Fig. 1. Separate high-voltage supplies enabled independent control of the dissociation and the pumping voltages. The maximum operating rate was 30 pps (power supply limited). The electrical leads to the tube were as short and as thick as possible.

Dependence of power output on delay time is shown in Fig. 2, and on temperature in Fig. 3 for helium buffer gas. At temperatures higher than 588°C [3] CuI melts and diffuses quickly to the colder parts of the tube. However, the laser was operated for 40 h at 550°C, with a high output, using only 5-g CuI. Power measurements were made with an EGG radi-

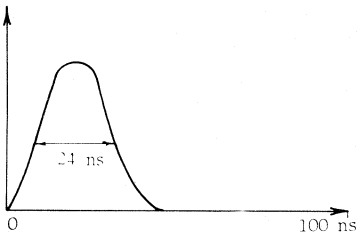

Fig. 4. Time dependence of the laser pulse.

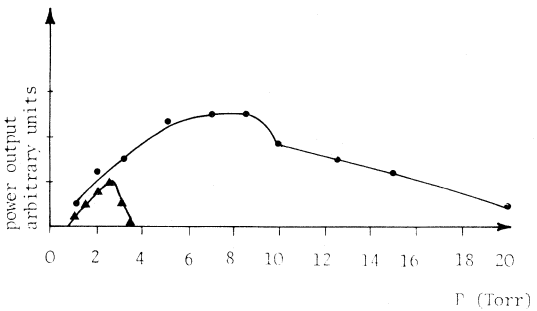

Fig. 5. Power output as function of buffer gas pressure at optimum delay. ▲—Ar; ●—He; $T = 500°C$; $T_d(\text{He}) = 200\ \mu s$; $T_d(\text{Ar}) = 450\ \mu s$.

ometer, model 585. Measurements of pulse shape and duration (Fig. 4) were made with a p-i-n diode terminated by 50 Ω and a Model 475 Tektronix oscilloscope.

The pulsewidth reported here, 24 ns, is an order of magnitude wider than that reported by Liberman *et al.* [4]. This width is consistent with the observation that laser operation was dependent on the existence of a cavity, whose roundtrip time was 7 ns. This time is also nearer to that reported for other copper lasers [5], including a CuCl vapor laser [2].

We have also investigated power dependence on pressure and type of buffer gas (Fig. 5). Lasing was achieved more easily and over a wider pressure range with helium than with argon. The minimum dissociation pulse voltage required to operate the laser with helium was about 7 kV, while with argon 16 kV was necessary. There was no difference in minimum pumping voltage [6]. The reason for the dissociation voltage difference seems to be the higher electron temperature achieved in the helium discharge. Both higher voltage and lower pressure were needed to achieve lasing in argon. Thus it would seem that a hollow cathode configuration would improve the performance of the CuI vapor laser [7].

Reducing the pumping capacitor from 0.2 to 0.012 μF increased the power output by 20 percent, which suggests that the reduced rise time compensated the reduced overall charge, such that in both cases the current during the first 25 ns was about the same.

ACKNOWLEDGMENT

The authors wish to thank A. Dagan for his expert glassblowing.

REFERENCES

[1] A. A. Isaev, M. A. Kazaryan, and G. G. Petrash, "Mechanism of pulsed lasing of the green thallium line in a thallium iodide vapor discharge," *Opt. Spectra*, vol. 31, pp. 180–183, 1971.
[2] C. J. Chen, N. M. Nerheim, and G. R. Russell, "Double discharge copper vapor laser with copper chloride as a lasant," *Appl. Phys. Lett.*, vol. 23, pp. 514–515, Nov. 1, 1973.
[3] N. N. Sidgwick, *The Chemical Elements and Their Compounds*. New York: Oxford, 1950.
[4] I. Liberman *et al.*, "High repetition-rate copper iodide laser," *Appl. Phys. Lett.*, vol. 25, pp. 334–335, 1974.
[5] C. M. Ferrar, "Copper-vapor laser with closed-cycle transverse vapor flow," *IEEE J. Quantum Electron.* (Corresp.), vol. QE-9, pp. 856–857, Aug. 1973.
[6] —, "Buffer gas effects in a rapidly pulsed copper vapor laser," *IEEE J. Quantum Electron.* (Corresp.), vol. QE-10, pp. 655–657, Sept. 1974.
[7] W. K. Schuebel, "New CW laser transitions in singly ionized cadmium and zinc," *IEEE J. Quantum Electron.* (Notes and Lines), vol. QE-6, pp. 654–655, Oct. 1970.

On the Stability of Modes in a Laser Resonator with an Active Medium

G. J. ERNST AND W. J. WITTEMAN

Abstract—**A discussion is given on the stability of laser modes; particularly for those in active resonators having negative gain profiles.**

One of the most fundamental properties of any laser resonator is the fact that radiation generated in a laser is only present in a number of stable well-defined (sometimes of very complex structure) amplitude and phase distributions of the electromagnetic field at certain frequencies. In a normal continuous or quasi-continuous wave oscillator these stable distributions are independent or quasi-independent of time and they are called the modes of the resonator. The characteristics of a mode are fully determined by the geometry and

Manuscript received March 17, 1975; revised July 28, 1975.
The authors are with the Department of Applied Physics, Twente University of Technology, Enschede, The Netherlands.

optical properties of the cavity and by the plasma parameters of the active medium. Immediately after the discovery of the laser, the mode patterns of the system were the subject of intensive and detailed study. In this respect, the papers of Fox and Li [1] and Kogelnik and Li [2] can be regarded as classics. Also, for unstable resonators, comprehensive studies have been made (see, for example, the survey paper of Siegman [3]). These papers, dealing only with passive resonators, have value mainly because of the excellent fit shown between the experimentally observed intensity patterns of small cavities and the theoretical calculations. The stability of such modes and how such a mode builds up in time, however, are only fragmentarily studied.

In a recent publication [4] we calculated the mode structure of active resonators for the case where diffraction losses are small, starting from the basic work of Kogelnik [5]. We found that for a stationary state an eigenmode with a Gaussian distribution satisfies the boundary conditions for any quadratic radial gain profile; positive as well as negative ones. As a stability criterion we used the existence of an eigenmode. The justification for the stability of the calculated modes comes, of course, from experiments. For instance, it is not difficult to achieve a high-gain CW CO_2 laser oscillating in the fundamental mode [6]. For such a CO_2 system the small-signal gain has, at high-power excitation conditions due to thermal heating, a minimum in the center of the tube [7]. Moreover, because of saturation, the high intensity of the beam in the center of the tube lowers the actual gain considerably, so that in such a system a large negative gain profile (with the smaller gain at the axis of the tube) exists. Still, from the theoretical point of view, there seems to be doubt about the stability of modes in laser systems with a negative profile, because Casperson [8] and, somewhat similarly, Ganiel and Silberberg [9] try to prove mode instability for such laser systems.

In [8] and [9] the authors describe essentially the behavior of an arbitrary Gaussian pattern through a sequence of identical amplifiers and then they apply the conclusions to an oscillator. Amplifiers only transform the beam parameters by the medium and optical components, but there is no resonance effect. The absence of a resonance condition is the essential difference between an oscillator and an amplifier. For a high-quality oscillator there is the extra condition that only those fields can bounce back and forth for which the phases are not changed after a round trip through the resonator. This means that radiation that does not fit in eigenmodes of the oscillator, because of frequency, amplitude, or phase distributions, will not be amplified to a substantial level. Following the time behavior of a radiation field in an oscillator these nonfitting parts of the field can be neglected as compared with the fitting parts of the field.

A procedure to determine the time behavior can be as follows (this procedure can describe stability as well as the starting process). Suppose in a laser oscillator a certain field distribution is present at a given time t_0. When looking for stability of a mode this time point will be chosen just after a disturbance has taken place. Also spontaneously emitted radiation will be present. This radiation is in general distributed over both space and frequency.

A part of this field can be expanded in terms of the cavity eigenmodes having specific frequencies. The remaining part will disappear anyhow due to interference because of the lower quality factor of the resonator for this remaining field. Thus only the part of the radiation field that is expanded into the cavity eigenmodes can be amplified to a reasonable level.

The time behavior of the strengths of these expanded modes is rather complex. The time-dependent intensity of a mode is subject to diffraction losses, available gain, out-coupling losses, competition effects, etc. In the steady state, however, the strength of each mode comes from the equilibrium between the gain and all relevant losses. Some modes may even disappear. This, for instance, may be the case because they are below threshold, or because a finite aperture discriminates higher order modes due to higher diffraction losses. In this way, it is possible that one observes only a zero-order mode with low diffraction losses. Then the radial intensity pattern can to a good approximation be described by the infinte aperture theory; i.e., a pure Gaussian distribution as given in [4]. Anyhow, whatever the gain profile and the cavity parameters are, as long as eigenmodes can be found for such a system stable oscillations will be obtained.

References

[1] A. G. Fox and T. Li, "Resonant modes in a maser interferometer," *Bell Syst. Tech. J.*, vol. 40, pp. 453–488, Mar. 1961.

[2] H. Kogelnik and T. Li, "Laser beams and resonators," *Proc. IEEE (Special Joint Issue on Optical Electronics with Applied Optics)*, vol. 54, pp. 1312–1329, Oct. 1966.

[3] A. E. Siegman, "Unstable optical resonators," *Appl. Opt.*, vol. 13, pp. 353–367, Feb. 1974.

[4] G. J. Ernst and W. J. Witteman, "Mode structure of active resonators," *IEEE J. Quantum Electron.*, vol. QE-9, pp. 911–918, Sept. 1973.

[5] H. Kogelnik, "On the propagation of Gaussian beams of light through lenslike media including those with a loss or gain variation," *Appl. Opt.*, vol. 4, pp. 1562–1599, Dec. 1965.

[6] W. J. Witteman, "High-power single-mode CO_2 laser," *IEEE J. Quantum Electron. (Special Issue on 1968 Int. Quantum Electronics Conf.: Part II)*, vol. QE-4, pp. 785–788, Nov. 1968.

[7] P. K. Cheo and H. G. Cooper, "Gain characteristics of CO_2 laser amplifiers at 10.6 microns," *IEEE J. Quantum Electron.*, vol. QE-3, pp. 79–84, Feb. 1967.

[8] L. W. Casperson, "Mode stability of lasers and periodic optical systems," *IEEE J. Quantum Electron.*, vol. QE-10, pp. 629–634, Sept. 1974.

[9] U. Ganiel and Y. Silberberg, "Stability of optical resonators with an active medium," *Appl. Opt.*, vol. 14, pp. 306–309, Feb. 1975.

Fuels for a Premixed Pulsed HCl Laser

T. J. MANUCCIA, J. A. STREGACK, AND W. S. WATT

Abstract—**HCl pulsed chemical lasing was obtained from several premixed R-Cl/HI mixtures when initiated by a transverse pulsed discharge. The relative merits of these mixtures were compared to a premixed H_2/Cl_2 mixture. For a constant stored electrical energy several mixtures have been found which give higher specific power than the H_2/Cl_2 system. In addition, it has been possible to run some of these improved mixtures without diluent with no laser performance degradation.**

The first pulsed chemical HCl laser was reported by Kasper and Pimentel [1] in 1965. Since then, several workers [2]–[7] have studied various fuel systems which produced HCl lasers using both flashlamp and pulsed discharge initiation

Manuscript received June 9, 1975; revised July 21, 1975. This work was partially supported under ARPA Order 2062.

The authors are with the Laser Physics Branch, Optical Sciences Division, Naval Research Laboratory, Washington, D.C. 20375.

TABLE I

	PARTIAL PRESSURES OF OPTIMUM CONDITION (TORR)	LASER OUTPUT (NORMALIZED TO H_2/Cl_2)	SPECIFIC OUTPUT (OUTPUT/MOLE-NORMALIZED TO H_2/Cl_2)
$H_2/Cl_2/He$	(40/20/3)	1.0	1.0
$HI/CCl_2F_2/He$	(1/10/3)	4.0	18.0
$HI/CCl_4/He$	(1/7/3)	4.5	25.8
$HI/CF_3CCl_3/He$	(0.6/7.0/3)	3.1	18.4
$HI/TiCl_4/He$	(3.4/10/3)	1.0	3.8
$HI/TiCl_4$	(3.5/10)	3.0	14.0
$HI/PCl_3/He$	(2.0/4.2/3)	.4	2.7

of the chemical reactions. However, no attempt to quantify the relative merits of these fuel systems has been undertaken. Consequently, an investigation of many of the fuel systems previously studied as well as several new fuels was undertaken to compare their relative merits in producing HCl laser radiation.

Typically, pulsed HCl lasers operate using either the H_2/Cl_2 mixture which has the assumed reaction sequence

$$Cl + H_2 \longrightarrow HCl + H \quad -1 \text{ kcal/mole} \tag{1}$$

$$H + Cl_2 \longrightarrow HCl^* + Cl \quad +45 \text{ kcal/mole} \tag{2}$$

or the HI/Cl_2 system which operates on the two exothermic reactions

$$H + Cl_2 \longrightarrow HCl^* + Cl \quad +45 \text{ kcal/mole} \tag{3}$$

$$Cl + HI \longrightarrow HCl^* + I \quad +32 \text{ kcal/mole.} \tag{4}$$

In the H_2/Cl_2 system, endothermic reaction (1) is slow on the time scale of the laser pulse and therefore contributes neither to the production of excited HCl nor to the supply of H atoms for reaction (2). The requisite H atoms must come directly from the dissociation of H_2 in the discharge. HI is a better source of atomic hydrogen than H_2 and one would expect the HI/Cl_2 system to be more efficient. However, premixing of HI and Cl_2 is difficult to perform without spontaneous reaction. Alternate chlorine sources, R–Cl, were sought which would be sufficiently reactive so that the resulting HI/R–Cl mixture would outperform the H_2/Cl_2 system and, in addition, could be premixed with HI.

The laser used in the present study is a transverse electrical pin discharge laser which is constructed from aluminum tubing. The discharge region was 100 cm long with 100 evenly spaced ballasted (1 kΩ, 1 W) cathodes (Stupkopf connectors electrically isolated from the outer tube) located approximately 2.5 cm from a hemicylindrical brass anode. The electrical initiation of the chemical reactions was provided by repetitive discharge (typically 1 pps) of a 0.0027-μF capacitor charged to a voltage of 30 kV. The optical cavity was formed by two gold mirrors, one of which had an on-axis 0.5-mm hole through which the output power was coupled. The pairs of gases were premixed before entering the laser region and a small amount of He was injected as window purge. Laser radiation was detected with a Ge:Au detector. As the pulse shapes were very similar when each of the fuel–oxidizer mixtures was optimized, performance was determined from peak pulse heights.

Initial experiments performed on the apparatus gave the result that the H_2/Cl_2 mixture produced laser power which was about one order of magnitude greater than the HI/Cl_2 mixture. There was clear evidence of prereaction in the HI/Cl_2 system which could explain its lower power. An additional factor is that vibrational excitation of the H_2 or production of Cl* in the discharge for the H_2/Cl_2 experiment could make reaction (1) exothermic and promote chain behavior, with a subsequent increase in H_2/Cl_2 laser output. Efficient electron impact excitation of H_2 has been observed [8].

In order to compare the merits of the various fuels, an initial screening was performed by adding the proposed chlorine atom source to an HCl laser operating on the H_2/Cl_2 system. These runs were made with the laser operating chlorine lean such that the effect of the new chlorine source would be as large as possible. Those fuels which either enhanced or did not degrade lasing were CCl_4, CCl_3H, PCl_3, $COCl_2$, $TiCl_4$, $SOCl_2$, $SnCl_4$, CCl_3CH_3, CCl_2CHCl, CCl_2F_2, CF_3CCl_3, and C_6H_5Cl. As a result of this screening, several of these systems and one other have led to HCl lasing in premixed R–Cl/HI systems. New Cl atom sources not previously reported in the literature which produced HCl laser emission are $SiCl_4$, $SnCl_4$, CF_3CCl_3, CCl_3CH_3, CCl_2CHCl, C_6H_5Cl, PCl_3, and $TiCl_4$. In addition, lasing was observed using CCl_4 [7], CCl_3H [7], $SOCl_2$ [6], and CCl_2F_2 [7] as had been previously reported.

By optimizing conditions for each pair of fuels (at constant stored electrical energy), it has been possible to identify those fuel sources that operate at higher specific powers (power out per mole of reactants) than the H_2/Cl_2 system. These improved laser fuels and their optimized operating characteristics are summarized in Table I. The H_2/Cl_2 mixture preferred to operate in the range $0.5 < H_2:Cl_2 < 15$ with optimum operation occurring at a fuel to oxidizer ratio of 2. The HI/R–Cl mixtures all optimized at fuel-to-oxidizer ratios below 0.5 and lasing could never be maintained beyond a ratio of 2.0. The previously reported experiments [7] on the HI/CCl_4 and HI/CCl_2F_2 systems were performed under conditions of high helium dilution (>90 percent). In the present experiments these fuel mixtures were run with less than 3 torr of He, which plays little or no part in the kinetics. For example, laser power was not affected when all helium was removed from the CCl_2F_2/HI system. One anomalous effect was observed when the output more than doubled when the 3 torr of He were removed from the $TiCl_4$/HI system.

As reported by Taylor [7], HF and HCl lasing occurred simultaneously for the CCl_2F_2/HI mixture. In the present experiments, for the optimum HCl lasing conditions the HCl laser output was approximately 2.5 times that of HF.

REFERENCES

[1] J. V. V. Kasper and G. C. Pimentel, "HCl chemical laser," *Phys. Rev. Lett.*, vol. 14, pp. 352–354, 1965.

[2] J. R. Airey, "A new pulsed I-R chemical laser," *IEEE J. Quantum Electron.* (Notes and Lines), vol. QE-3, p. 208, May 1967.

[3] T. F. Deutsch, "New infrared laser transitions in HCl, HBr, DCl, and DBr," *IEEE J. Quantum Electron.* (Notes and Lines), vol. QE-3, pp. 419–421, Oct. 1967.

[4] C. B. Moore, "An electrically pulsed HCl laser," *IEEE J. Quantum Electron.*, vol. QE-4, p. 52, Feb. 1968.

[5] M. C. Lin, "HCl chemical laser from $H + Cl_2O$," *Chem. Phys. Lett.*, vol. 7, pp. 209–210, Oct. 15, 1970.

[6] J. R. English, III, H. C. Gardner, R. W. Mitchell, and J. A. Merritt,

"HCl chemical lasers with $SOCl_2$, SO_2Cl_2, Cl_2CNCl, and ClCN," *Chem. Phys. Lett.*, vol. 16, pp. 180–182, Sept. 15, 1972.
[7] D. Taylor, S. W. Mayer, and S. N. Suchard, "HCl chemical lasing with HI and chloro compounds," *IEEE J. Quantum Electron.* (Corresp.), vol. QE-10, pp. 389–390, Mar. 1974.
[8] J. A. Stregack and B. L. Wexler, "A new electric discharge gas-dynamic laser," presented at the 4th Conf. Chemical and Molecular Lasers, St. Louis, Mo., Oct. 21–23, 1974.

Contributors

Robert D. Burnham, for a photograph and biography please see page 178 of the April 1975 issue of this JOURNAL.

*



John A. Caird (S'75–M'75) was born in Brooklyn, N.Y., on December 24, 1947. He received the B.S. degree in electrical engineering from Rutgers University, New Brunswick, N.J., in 1969, the M.S. degree in physics from the University of California, Los Angeles, in 1971, and the Ph.D. degree in physics from the University of Southern California, Los Angeles, in 1975.

Since 1969 he has been with the Laser Division of Hughes Aircraft Company, Culver City, Calif., and completed his graduate studies under the company's work-study fellowship program. His research activities have centered on the development of laser sources and the analysis of rare-earth laser materials.

Dr. Caird is a member of Eta Kappa Nu, Tau Beta Pi, and the Optical Society of America.

*



David C. Chang (S'65–M'67) was born in Hupeh, China, on September 9, 1941. He received the B.S. degree in electrical engineering from Cheng Kung University, Tainan, Taiwan, China, and the M.S. and Ph.D. degrees in applied physics from Harvard University, Cambridge, Mass., in 1961, 1963, and 1967, respectively.

From 1963 to 1967 he was a Research Assistant at the Gordon McKay Laboratory, Harvard University. He joined the University of Colorado, Boulder, in 1967 and is now a Professor of Electrical Engineering. In 1972 he was a Visiting Professor at Queen Mary College, University of London, London, England. Currently, he is also a guest worker with the theoretical studies group at the Environmental Research Laboratory, NOAA/DOC.

Dr. Chang is a member of Sigma Xi and the International Scientific Radio Union Commission VI. He is currently Chairman of the IEEE-MTT-S15 Subcommittee on Microwave Theory.

*

Larry G. DeShazer, for a photograph and biography please see page 119 of the March 1975 issue of this JOURNAL.

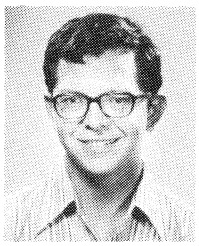

C. James Elliott was born on January 2, 1943. He attended Lafayette College, Easton, Pa., from 1960 to 1962, and received the A.B. degree in mathematics-physics from Yale College, New Haven, Conn., and the Ph.D. degree in engineering and applied science from Yale University, in 1964 and 1972, respectively. He also attended the Summer Institute in Space Science at Columbia University, N.Y., in 1962.

He joined the Los Alamos Scientific Laboratory, University of California, Los Alamos, N. Mex., in 1972 to work in laser-driven-fusion energy research. His professional interests include discharge physics and kinetics, nonlinear optical propagation, coherence phenomena, and numerical and computational analysis.

Dr. Elliott received the Barge Prize in Mathematics in 1962.

*

U. Ganiel (A'71–M'72) was born in Rehovot, Israel, on September 6, 1936. He received the M.Sc. degree from the Hebrew University of Jerusalem, Jerusalem, Israel, and the Ph.D. degree from the Weizmann Institute of Science, Rehovot, both in physics, in 1963 and 1968, respectively.

He did research in the fields of atomic spectroscopy, nuclear quadrupole resonance, Mössbauer spectroscopy, and magnetism. He spent a year as a Visiting Research Physicist at Carnegie-Mellon University, Pittsburgh, Pa., where he worked in Mössbauer spectroscopy. He was a Research Fellow at the California Institute of Technology for two years (1970–1971), where he worked in the field of nonlinear optics. Since 1971 he has been on the faculty of the Department of Electronics of the Weizmann Institute, where he has been working on various laser systems, problems in optical resonator theory, and specifically, on tunable dye laser systems.

Dr. Ganiel is a member of the American Physical Society and the Israel Physical Society.

*



A. Hardy was born in Hungary on February 9, 1942. He received the B.Sc. and M.Sc. degrees from the Hebrew University of Jerusalem, Jerusalem, Israel, and the Ph.D. degree in applied physics from the Weizmann Institute of Science, Rehovot, Israel, in 1966, 1969, and 1975, respectively. His Ph.D. dissertation was in the area of optical diffraction theory.

Since April 1975 he has been with the Department of Electronics, the Weizmann Institute of Science, where he has been working on dye laser systems and some problems in optical resonator theory.

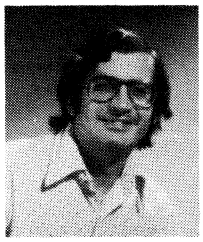

R. F. Heidner, III, was born in Corpus Christi, Tex., on July 22, 1944. He received the B.A. degree in chemistry from Rice University, Houston, Tex., and the Ph.D. degree in physical chemistry from the University of California at Los Angeles, in 1966 and 1972, respectively.

From 1972 to 1973 he was a National Science Foundation Postdoctoral Fellow with the Department of Physical Chemistry, Cambridge University, England. In 1973 he joined the Aerospace Corporation, El Segundo, Calif., where he worked on gas phase chemical kinetics relevant to chemical and energy transfer lasers.

Dr. Heidner is a member of the American Physical Society, Sigma Xi, and Phi Lambda Upsilon.

*

C. J. Kennedy, for a photograph and biography please see page 639 of the August 1975 issue of this JOURNAL.

*

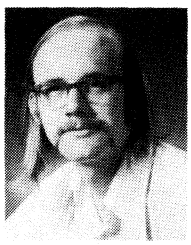

Edward F. Kuester (S'73) was born in St. Louis, Mo., on June 21, 1950. He received the B.S.E.E. degree from Michigan State University, East Lansing, Mich., in 1971, and is currently working towards the Ph.D. degree at the University of Colorado, Boulder.

He has been a Research Assistant at the University of Colorado since 1972.

Mr. Kuester is a student member of the Optical Society of America.

*

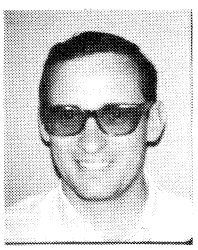

David A. McArthur was born in Meridian, Miss., on August 14, 1938. He received the B.S. degree in physics from the University of Arizona, Tucson, and the Ph.D. degree in physics (nuclear magnetic resonance) from the University of California, Berkeley, in 1960 and 1967, respectively. He attended the University of Munich, Germany, from 1960 to 1961 on a Fulbright Scholarship.

He was a member of the Technical Staff at Bell Laboratories, Holmdel, N.J., from 1967 to 1969 where he worked in far-infrared nonlinear optics using the water vapor laser. Since 1969 he has been a member of the technical staff at Sandia Laboratories, Albuquerque, N. Mex., where he has worked experimentally on optical techniques to measure the current, voltage, charge deposition, and plasma properties of relativistic electron beams. He has also worked on theoretical models of the plasma created and laser action induced by intense electron beams. More recently, he has experimentally studied the excitation of laser media by nuclear reactions, using laboratory nuclear reactors.

John Nella was born in Brooklyn, N.Y., on July 10, 1947. He received the B.S. degree in electrical engineering from the Polytechnic Institute of Brooklyn, Brooklyn, N.Y., in 1968, the M.S. degree in electrical engineering from the California Institute of Technology, Pasadena, in 1969, and the Ph.D. degree in electrophysics from the Polytechnic Institute of Brooklyn, Brooklyn, N.Y., in 1972.

Since 1972 he has been with the Laser Division of Hughes Aircraft Company, Culver City, Calif., where he has been engaged in the development of new coherent optical sources.

*



G. Neumann (M'74) was born in Petach-Tivka, Israel, on September 14, 1943. He received the B.A. degree in physics from Queens College, CUNY, N.Y., and the Ph.D. degree in optics from the Institute of Optics, University of Rochester, Rochester, N.Y., in 1965 and 1970, respectively.

From 1970 to 1971 he was a postdoctoral fellow with the Department of Physics, Hebrew University of Jerusalem, Jerusalem, Israel, working on thermally excited CO_2 lasers. Since 1970 he has been with the Department of Electronics, the Weizmann Institute of Science, Rehovot, Israel, where he has been working on tunable dye lasers, multiple wavelength dye lasers, nitrogen lasers, and dye doped polymers. For the present he is on leave of absence at Tadiran, Israel Electronic Industries.

*

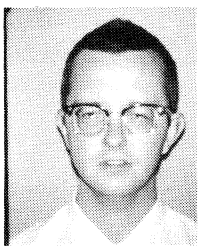

J. W. Poukey was born in Indianapolis, Ind., on February 17, 1940. He received the B.S., M.S., and Ph.D. degrees in physics, all from the University of Wisconsin, Madison, in 1961, 1963, and 1966, respectively.

He has been associated with Sandia Laboratories, Albuquerque, N. Mex., since 1967. He has done theoretical research in various areas of plasma physics, including gas discharges, neutron tube design, and computer simulation of space-charge flow and plasma instabilities. His current work is concerned with the theory and simulation of relativistic electron beams and their interaction with gases and plasmas.

Dr. Poukey is a member of the American Physical Society.

*

Donald R. Scifres (M'74), for a photograph and biography please see page 180 of the April 1975 issue of this JOURNAL.

*

William Streifer (S'56–M'58–SM'73), for a photograph and biography please see page 180 of the April 1975 issue of this JOURNAL.

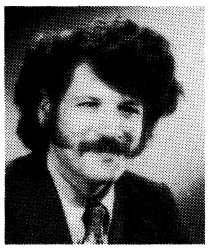

Steven N. Suchard was born in Chicago, Ill., on February 8, 1944. He received the B.S. degree in chemistry from the University of California at Berkeley, and the Ph.D. degree in chemical physics from the Massachusetts Institute of Technology, Cambridge, in 1965 and 1969, respectively. During his graduate career he was awarded a NASA Traineeship from 1965 to 1968 and an NIH Predoctoral Fellowship from 1968 to 1969.

From September 1969 to September 1970 he was a Postdoctorate Research Fellow in the College of Chemistry at the University of California at Berkeley, where his work involved the demonstration of the first hydrogen halide chemical laser to operate on an overtone transition. He joined the Aerophysics Laboratory of the Aerospace Corporation, El Segundo, Calif., in October 1970, and has studied pulse-chain and transfer chemical lasers and chemically pumped electronic transition lasers.

Dr. Suchard is a member of the American Physical Society.

*

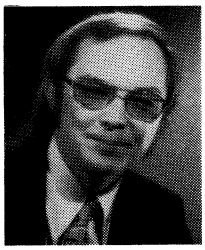

David G. Sutton was born in San Francisco, Calif., on April 17, 1944. He received the B.S. degree in chemistry from the University of California, Berkeley, in 1966. In 1967 he entered the graduate school in chemistry at the Massachusetts Institute of Technology, Cambridge. He was a National Institutes of Health Predoctoral Fellow from 1967 to 1970, when he received the Ph.D. degree in physical chemistry.

He was a Research Associate with the Department of Chemistry, Massachusetts Institute of Technology, Cambridge. He is now with the Aerospace Corporation, El Segundo, Calif. His research interests include molecular spectroscopy, gas phase energy transfer, and gas lasers.

Dr. Sutton is a member of the American Physical Society and Sigma Xi.

*

Bergen R. Suydam (M'72), for a photograph and biography please see page 315 of the June 1975 issue of this JOURNAL.

*

D. Treves (M'69) was born in Italy on June 29, 1930. He received the B.Sc., M.S., and Ph.D. degrees, all in electrical engineering, from the Haifa Technion, Israel, in 1953, 1956, and 1958, respectively.

Since 1953 he has been associated with the Weizmann Institute and has been involved in the study of magnetization processes; magnetic materials, magnetooptic memories, and laser systems. He spent several years in the United States as a Research Associate at Pomona College, Claremont, Calif., as a member of the Technical Staff at Bell Laboratories, Murray Hill, N.J., at the Ampex Research Laboratory at Redwood City, Calif., and as World Trade Exchange Fellow at IBM, San Jose, Calif. At present he is a Professor with the Department of Electronics, the Weizmann Institute, Rehovot, Israel.

IXth INTERNATIONAL CONFERENCE 1976

QUANTUM ELECTRONICS

AMSTERDAM the NETHERLANDS JUNE 14–18, 1976

SPONSORS: EUROPEAN PHYS. SOC., DUTCH PHYS. SOC., PHYSICA (Neth.), A.I.P. and I.E.E.E. through the JOINT COUNCIL on QUANT. ELECTR. (USA)

TOPICS:
- Physics and chemistry with lasers
- Laser-induced isotope separation and chemical reactions
- Interaction of extremely intense radiation with matter
- Laser spectroscopy and environmental measurements
- Advances in coherent light sources
- Photon statistics and coherence effects
- Nonlinear optics, modulators and detectors
- New optical materials
- Integrated optics and guided waves

EXHIBITION: – During the conference at the congress site

CALL FOR PAPERS:

Both invited and contributed papers will be presented; working language in English. Original papers, not previously published or presented, are sollicited in the above mentioned areas.

Instructions are given in the call for papers available from the secretary of the Organizing Committee. Also local organisations will distribute the call for papers.

The authors are requested to submit both a 35-word abstract and a 500-word summary of their paper to the Technical Program Committee.

Deadline for contributions: December 15, 1975

Chairman Technical Program Committee
Prof. Dr. O. Svelto
c/o Prof. Dr. H. J. Frankena
Dept. Applied Physics
University of Technology
Lorentzweg 1
Delft/the Netherlands

Local Program Committee USA/Canada
Dr. J. A. Armstrong
IBM Thomas J. Watson
Research Center
P.O. Box 218
Yorktown Heights
NY 10598

Secretary Organizing Committee
Dr. J. Langelaar
Lab. for Physical Chemistry
University of Amsterdam
Nieuwe Prinsengracht 126
Amsterdam-C/
the Netherlands

REGISTRATION For a smooth organization, advance registration is highly desirable. Advance registration fee: Dfl 175,-; deadline April 14, 1976. Registration fee after April 14, 1976: Dfl. 275,-

GENERAL INQUIRIES

to be directed to Dr. Langelaar only.

IMPORTANT NEW BOOKS FROM THE IEEE PRESS

Books of Selected Reprints are available in clothbound and low-cost, durable, IEEE members' paperbound editions.

Just Published

FREQUENCY SYNTHESIS: Techniques and Applications.

Edited by Jerzy Gorski-Popiel, *M.I.T. Lincoln Laboratory*. 1975. 184 pages. Illustrated. ISBN—087942-039-1

This book is written for the practicing engineer faced with a need to learn about, design, or apply modern frequency synthesizers. Many advances in frequency synthesis have been made in recent years, and a variety of systems have been developed, which may be broadly divided into those using direct, indirect, and all-digital techniques. This volume describes the basic properties of synthesizers, compares the three approaches on the basis of performance and complexity, presents case studies in sufficient detail to permit the reader to confidently apply and design synthesizers, and discusses alternate configurations and the characterization and measurement of noise. Each of the six chapters was written by an expert in the subject discussed.

CONTENTS: Preface, Applications of Frequency Synthesizers, Contemporary Frequency Synthesis Techniques, Direct Frequency Synthesis, Phase-Locked Loop Frequency Synthesizers, Digital Frequency Synthesizers, Hybrid Configurations and Frequency Stability, Subject Index.

	Order No.	Nonmember	Member
Clothbound	PC00463	$11.95	$8.95

Just Published

DATA COMMUNICATIONS VIA FADING CHANNELS

Edited by Kenneth Brayer, *The MITRE Corporation*. 1975. 520 pages. Illustrated. A Book of Selected Reprints. ISBN—Clothbound 0-87942-047-2; Paperbound 0-97942-048-0

The functioning of numerous aspects of modern society is dependent on the communication of data over fading channels. Now, after years of rapid development, there is a stabilization in the underlying technology, so this collection of papers appears at a fortuitous time. The papers included were carefully selected to summarize the relevant principles of propagation, modulation, signaling, and coded diversity techniques. In Part I, the fundamentals of propagation are presented, along with details of the effects of fading and multipath. The basics of signaling for the non-fading channel are covered in Part II, followed by papers extending the coverage to fading multipath channels and to diversity techniques. Part III treats error control coding. A bibliography of over 500 citations in included.

CONTENTS: Introduction, The Fading Channel, Digital Signaling on the Fading Channel, Error Control (Coded Diversity) for the Fading Channel, Bibliography, Author Index. A total of 35 reprinted papers.

	Order No.	Nonmember	Member
Clothbound	PC00422	$17.95	$13.45
Paperbound	PP00430		$ 9.00

Just Published

LITERATURE IN DIGITAL SIGNAL PROCESSING: Author and Permuted Title Index (Revised and Expanded Edition)

Edited by Howard D. Helms, James F. Kaiser, Lawrence R. Rabiner, *Bell Laboratories*. 1975. 216 pages. Illustrated. ISBN—Clothbound 0-87942-051-0; Paperbound 0-87942-052-9.

This is a much-needed volume, since a great deal of publication activity has taken place in the field of digital processing since the previous edition was issued. It provides comprehensive coverage of digital filtering and spectral analysis, and selected titles from related areas are included. All told, 1,872 books, conference records, reports, theses, and papers are listed, an increase of 160% over the earlier edition. The book is divided into three sections: permuted title index, in which titles are listed consecutively under key words; author-title index, with all the papers of a given author listed under his name; and a complete listing of all titles indexed by year, edition number, and serial number.

CONTENTS: Introduction, Permuted Title Index, Author Index, List of References.

	Order No.	Nonmember	Member
Clothbound	PC00448	$12.95	$9.70
Paperbound	PP00455		$6.50

To order, use this handy coupon. **PR-T**

IEEE Service Center
445 Hoes Lane, Piscataway, N.J. 08854.

Please send me the IEEE PRESS books whose ORDER NUMBERS I have entered below. My check, made payable to IEEE, is enclosed. (Residents of New Jersey please add 5% state sales tax.)

Order No.	Units	Total Price
	Amount	

IEEE No.

Print Name

Address

City State/Country Zip

OTHER RECENT TITLES

COMPUTER COMMUNICATIONS

Edited by Paul E. Green, Jr., *IBM*, and Robert W. Lucky, *Bell Laboratories*. 1975. 624 pages. Illustrated. A Book of Selected Reprints. ISBN—Clothbound 0-87942-041-3; Paperbound 0-87942-042-1. This book treats systems through which the resources of the modern computer are made available to many remote users.

CONTENTS: Introduction, The Computer Communications Environment, System Elements, Digital Transmission Media, Total Systems, Author and Subject Indexes. A total of 60 reprinted papers.

	Order No.	Nonmember	Member
Clothbound	PC00380	$17.95	$13.45
Paperbound	PP00398		$ 9.00

NONLINEAR NETWORKS: Theory and Analysis

Edited by Alan N. Willson, Jr., *UCLA*. 1975. 408 pages. Illustrated. A Book of Selected Reprints. ISBN — Clothbound 0-87942-045-6; Paperbound 0-87942-046-4. The papers reprinted in this volume provide a comprehensive review of research on the theory of nonlinear networks.

CONTENTS: Introduction, 23 Reprinted Papers, Author Index.

	Order No.	Nonmember	Member
Clothbound	PC00406	$16.95	$12.70
Paperbound	PP00414		$ 8.50

Near-UV Spectral Efficiency of High-Current Xenon Flashlamps

M. A. GUSINOW

Abstract—**A discussion is given of the limiting spectral efficiency of flashlamps that are used to pump lasers. Absolute measurements indicate that 4.5 percent of the capacitor-bank energy appears as radiant energy in the region 2500–2900 Å (the nominal pump band of the iodine photodissociation laser) for the flashlamps studied in this work. A large portion of the radiation in this band is due to bound–bound processes and not solely recombination radiation and bremsstrahlung as is usually assumed.**

Introduction

Intense light sources have been the subject of considerable study for many years. Since the invention of the laser there has been a greater emphasis on increasing the efficiency of high-power light sources. Higher efficiency light sources for neodymium glass (and YAG) and iodine photodissociation lasers are of interest because both of these lasers are prime candidates for laser-fusion studies. The net efficiency of these lasers is dependent upon the efficiency of converting electrical energy to radiation in the appropriate laser pump bands. A variety of schemes have been proposed to increase the pump efficiency; for example, dyes that are effectively broad-band absorbers which fluoresce at the pump-band wavelength [1] and the use of an alkali metal vapor in the flashlamp proper [2] where the alkali metal fluoresces in the appropriate pump band.

The goal of the present work is the study and determination of the physical mechanisms pertinent to the spectral efficiency of pulsed high-current gas-filled flashlamps. The spectral efficiency is defined as the ratio of the photon flux in the appropriate pump bands to the total (over all frequencies emitted) photon flux. The primary interest of the present work is the near-UV spectrum, 2500–2900 Å. While many papers and reviews [3], [4] have been published on the subject of flashlamps, some flashlamp phenomena are still not well understood. The complexity and many-faceted aspects of a spark discharge are overwhelming from an analytical viewpoint. Modeling of such a system cannot be seriously considered at present because there are so many processes and as yet undetermined quantities. This last statement is not meant to imply that calculations cannot be done to elucidate certain macroscopic features of such a discharge [5]-[9], but means only that understanding, for example, certain aspects such as the detailed spectral behavior is not, at present, quantitatively possible.

A flashlamp of the sort considered here consists of a highly ionized plasma medium contained in a quartz tube. The maximum intensity available from such a medium is determined by the radiation emitted from a backbody at the plasma temperature.[1] This latter statement is a consequence of Kirchhoff's law and it is applicable when radiative equilibrium applies and there is no net transfer of heat. Its applicability is subject to certain restrictions concerning plasma uniformity and equilibration times ([10] contains an excellent discussion of this question). It will be assumed that Kirchhoff's law is valid for the conditions studied in this work. Consequently, for a given temperature, the maximum radiation within any spectral region is given by the intensity from a blackbody at that temperature, regardless of the makeup of the plasma, i.e., independent of any dopants such as alkali metals. It is important to note that for a given spectral band there is an optimum blackbody temperature that maximizes the percentage of the total radiation appearing in that band. The temperature for maximizing the photon flux from a blackbody in the wavelength band λ_1-λ_2 is given by [11]

$$kT_{\text{opt}} = \frac{(hc/\lambda_2)\,[(\lambda_2/\lambda_1) - 1]}{3 \ln (\lambda_2/\lambda_1)}. \tag{1}$$

For example, if one considers the pump bands of the iodine laser to be from 2500 to 2900 Å, then T_{opt} = 18 000 K, and 8.6 percent of the total photon flux appears in the specified pump band. The neodymium glass laser has pump bands at several locations that result in 1.06-μ laser radiation [12]. It is not possible to maximize all of these bands simultaneously but an approximate maximization results in $T_{\text{opt}} \approx$ 7000 K and 15 percent of the radiation appears in the pump bands. Of course, account must also be taken of the actual quantum efficiency in the absorption bands. Dopants to the flashlamp can increase the brightness of the flashlamp in that they may enhance the coupling between the electrical energy deposited in the gas and the energy radiated. Specifically, they can increase the plasma temperature. They can also radiate preferentially in certain regions of the spectrum.

That high-current gas-filled flashlamps can closely radiate as effective blackbodies within restricted spectral limits has been illustrated by the opacity measurements in [13] and [14]. Additional evidence for the preceding was presented in [15]. In that work it was assumed that the plasma was fully ionized, radiated as a blackbody, and that the source of energy was Joule heating of the plasma. The result was an

Manuscript received May 8, 1975; revised May 15, 1975, and July 28, 1975. This work was supported by the Energy Resource and Development Administration.

The author is with the Sandia Laboratories, Albuquerque, N. Mex. 87115.

[1] One can define a variety of temperatures; however, for the work discussed here only two need be considered: 1) the excitation temperature which is defined in terms of the bound-state population densities; 2) the electron temperature. It is the electron temperature that determines the recombination and bremsstrahlung radiation. As a rule, the excitation temperature is not unique, but in the limit of collisional equilibrium, the excitation temperature equals the plasma electron temperature.

expression for the temperature of such a system [15], [16]

$$T = 603\ (jR^{1/2})^{4/11} \tag{2}$$

where j is the current density in the plasma in amperes · centimeter^{-2}, R is the tube radius in centimeters, and T is the temperature in degrees Kelvin. It was found that this idealization agreed with a number of experiments from different laboratories under a variety of conditions.[2] The temperature in (2) as related to actual experiments refers to the radiation color temperature and in this work will be assumed to approximate the electron temperature.

Experiment

The experiments to be discussed were performed by discharging a 13.8-μF capacitor through a flashlamp. The arrangement is shown in Fig. 1. The inner diameters of the flashlamps ranged from 8 to 16 mm with an interelectrode spacing of 30–35 cm. The gases were one of the following: helium, neon, argon, or xenon. The measurements consisted of recording the current through the discharge and the emitted radiation in the spectral range of 2500–2900 Å. The spectral measurements were done in two ways: 1) by recording the time-integrated emission on type 55 P/N film with a spectrograph; 2) by using a 0.3-m monochromator and on a shot-to-shot basis making measurements over the aforementioned spectral range at specified times after discharge initiation. The monochromator was completely calibrated including measuring the slits with a microscope and checking the instrumental line shape and width as a function of slit width and height. The photomultiplier was an EMI type 9635QB which has a bialkali cathode and a Spectrosil window. All measurements were taken with a 20-μ slit width which corresponded to an instrumental width of 0.24 Å. This slit width was used for the calibrations and experiment so that the illuminated photocathode area was constant. All attenuation of the radiation was done with neutral density filters in order to avoid saturation and detector nonlinearities. The neutral density filters were calibrated on a Cary 14 spectrophotometer. The Corning 7-54 filter eliminated scattered visible radiation in the monochromator. The wavelength calibration of the optical system (including the monochromator–photomultiplier combination) was done by utilizing an irradiance standard (a General Electric quartz iodide 200-W lamp) and a photodiode (EMP Model 543-09-00) calibrated absolutely at 2537 Å. The irradiance standard was used for relative spectral calibration while the calibrated photodiode was used for the absolute calibration. Thus the relative spectral calibration in the spectral band of interest and an absolute calibration at 2537 Å result in an absolutely calibrated system at each wavelength. The precision of the spectral measurements is estimated to be ±12 percent. (This precision accounts for the uncertainties in the irradiance standard, the calibrated photodiode, the errors introduced in the system calibration, and experimental reproducibility.) The discharge current was monitored with a calibrated current-viewing resistor. The current temporal shape was approximately triangular, reaching its peak in 1[illegible] μs with a base of about 30 μs.

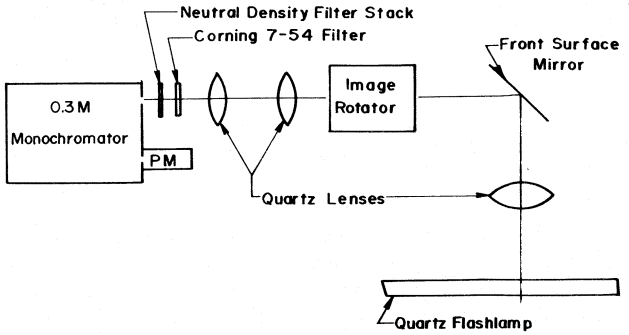

Fig. 1. The experimental arrangement utilized for spectral observations.

Results

A typical result is shown in Fig. 2. (Notice that the brightness is per unit surface area of the flashlamp.) From these types of data it was concluded that nominally (4.50 ± 0.54 percent) of the capacitor-bank energy appeared as radiation in the range 2500–2900 Å. In order to obtain the total emitted radiation it was assumed that the flashlamp radiated uniformly in both the azimuthal as well as the axial direction. To test the accuracy of this assumption would require reasonably extensive high-speed photographic measurements (as a function of flashlamp parameters) which were not available for this experiment. A measurement of the plasma resistivity was consistent with a temperature of 21 000 K (assuming the plasma to be fully ionized [16]) while (2) predicted 24 000 K. A blackbody at this temperature would radiate about 6.7 percent of its total energy in this wavelength range. If one asks for the optimum percentage of energy radiated in th[illegible] interval, then the number is about 10.5 percent at a blackbody temperature of about 14 000 K. It is important to point out that (1) is obtained by maximizing photon flux and not energy. If one seeks to optimize the blackbody photon flux in the specified bandpass, (1) predicts $T = 18\,000$ K as being the appropriate temperature. The experiment indicates that the intensity for a typical xenon-filled flashlamp is within a factor of 3 (except in the vicinity of 2500 and 2800 Å) of a blackbody (at a temperature of 24 000 K) in this spectral range.

Fig. 3 shows a comparison of the radiation from xenon and argon discharges (on a relative scale) for nominally the same current. The main difference is in the spectral intensity distributions at the shorter wavelengths. On an absolute scale, xenon is brighter than argon. Fig. 4 shows the effect of increasing the argon pressure at about the same discharge current level. Again, the prime effect is to enhance the intensity of the shorter wavelengths. This short wavelength enhancement compared to longer wavelengths is likely due to the fact that the longer wavelengths approach the blackbody limit before the shorter wavelengths as pressure and current are increased. This last statement could be recast into a discussion concerning the absorption as a function of wavelength [18], [19].

[2] In [17] experimental measurements coupled with the radiant emittance of a blackbody yielded an expression $T = 1435\ (jR^{1/2})^{2/7}$. This expression and (2) differ by about 12 percent for the conditions of the present work.

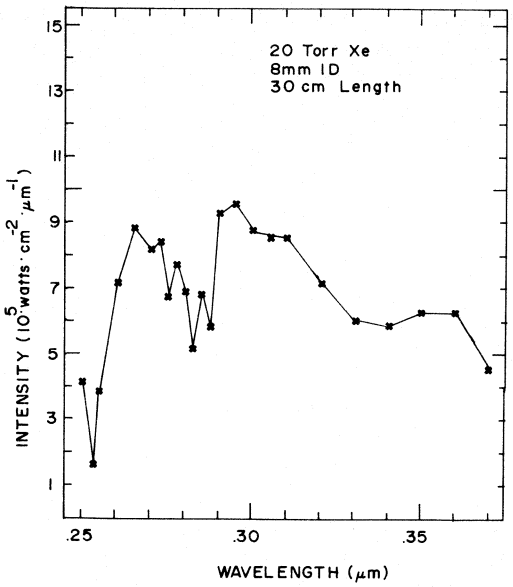

Fig. 2. The flashlamp surface brightness as a function of wavelength at 10 μs after initiation of the main discharge for an 8-mm-ID xenon-filled tube. The peak current was 20 kA.

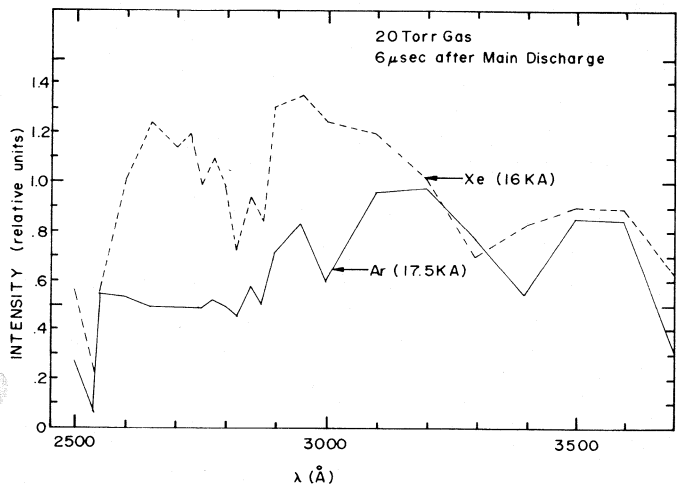

Fig. 3. The relative spectral intensities from xenon and argon discharges at nominally the same currents.

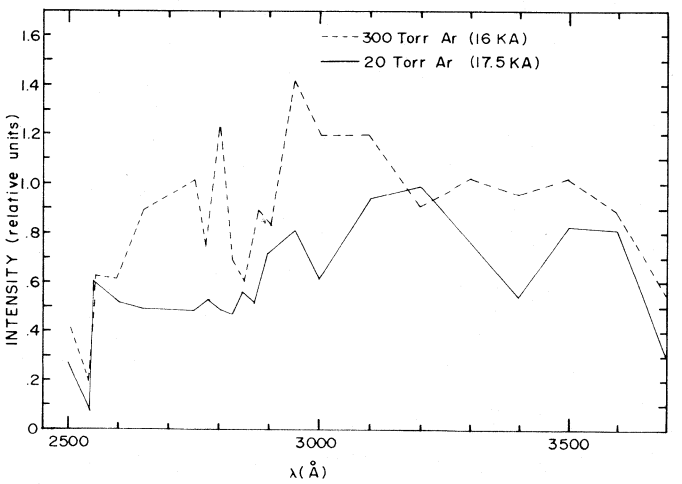

Fig. 4. The relative spectral intensities from argon discharges at nominally the same current but different pressures.

The UV spectral efficiency measured in this work is consistent with the results of [20] and [21].

It has been noticed that a double discharge technique [22] seems to produce enhanced efficiencies for UV emission. The double discharge technique utilizes a long (duration) relatively low-current discharge which is followed, after some time, by a short high-current discharge. Although there is no quantitative information concerning the physical mechanisms involved, the enhancement may be due to several effects, among which are: 1) metastable atoms produced by the weak (simmer) discharge; 2) UV photons produced by the simmer discharge [23]; or 3) a diffuse plasma produced by the simmer. The results of an experiment are shown in Fig. 5 in which the light output around 2800 Å was measured both with and without the simmer discharge. An interference filter with a center wavelength of 2800 Å and a bandpass of 200 Å was used for this latter experiment. It can be seen that the enhancement produced by the simmer is less at higher main-discharge peak currents. (The simmer current at the time of the main-discharge peak current was 10 A.) Shown in Fig. 6(a) and (b) are the spectra (uncorrected for film response) for a helium discharge with the main discharge only and the simmer discharge only. The strong emission lines in the simmer spectra and the absorption lines in the main-discharge spectra are due to silicon from the walls [4].

The data discussed previously establish that the emitted radiation is within a factor of 3 (in the near UV) of an equivalent blackbody at a temperature determined by the discharge current density [(2)]. For laser excitation purposes, it would be beneficial to increase the radiation up to the blackbody limit without utilizing higher capacitor-bank energies. In order to evaluate how this can be accomplished, it is necessary to evaluate the physical mechanisms producing the radiation. Fig. 7 is a photograph of a xenon spectrum. This picture represents the time-integrated flux (over a 30-μs interval). The presence of some strong absorption lines upon what

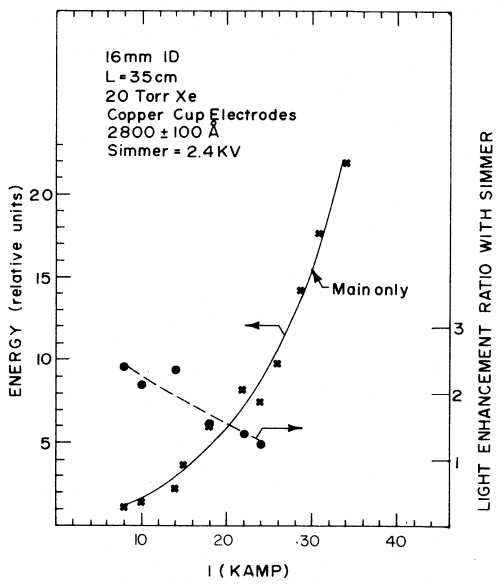

Fig. 5. The energy from a xenon-filled flashlamp (without a simmer discharge) and the light enhancement in a band centered at 2800 A due to applying a simmer discharge.

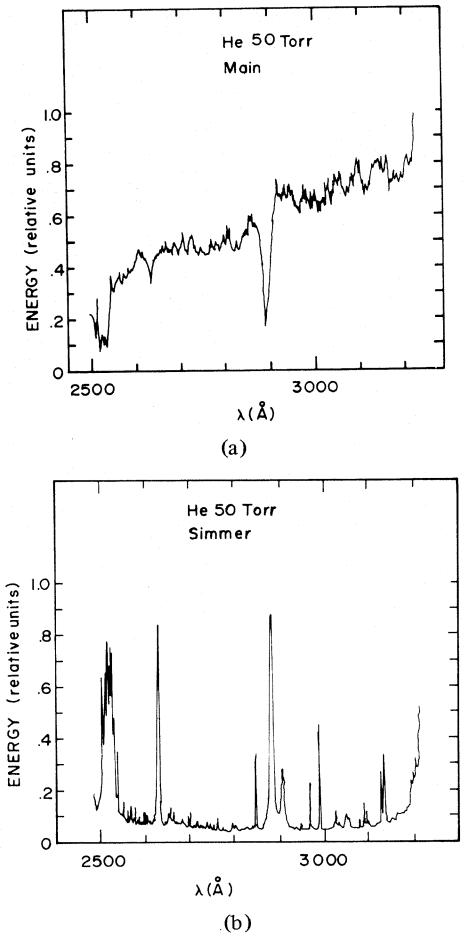

Fig. 6. (a) The spectra (uncorrected for film response) from the main discharge. (b) The spectra (uncorrected for film response) from the simmer discharge.

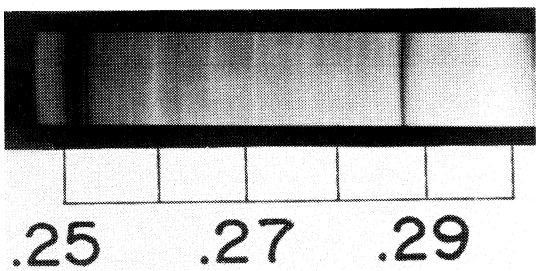

Fig. 7. A photograph of a xenon spectrum emanating from an 8-mm-ID flashlamp filled to 20 torr and 8-mm ID. The current pulse is about 30 μs long and has a peak of 20 kA. The wavelength is indicated in microns.

appears to be a continuum dominates the spectrum. The absorption lines are all due to silicon from the quartz inner surface (depending upon the discharge conditions, these absorption lines can also appear in emission). The data of Fig. 2 were taken at discrete wavelength intervals and then connected with straight lines. Except at points where line radiation is located, this procedure seems reasonably justified (in view of the time-integrated spectrogram). With a few exceptions this "continuum" has been designated in many works as being due completely to recombination and bremsstrahlung radiation. For the temperatures with which one is typically concerned in xenon-filled flashlamps (≈2-3 eV), the contribution of bremsstrahlung is small and the primary mechanism for producing continuum radiation is due to two-body radiative recombination. The continua due to bremsstrahlung and recombination are given by the following equation [24]:

$$\epsilon(\nu, T) = 6.3 \times 10^{-47}(kT)^{-1/2} N_e \sum_{i=1}^{\infty} N_i Z_i^2 \xi_i(\nu) \text{ erg} \cdot \text{s}^{-1} \cdot \text{cm}^{-3} \cdot \text{sr}^{-1} \cdot (\text{s}^{-1})^{-1} \quad (3)$$

where T is the electron temperature in degrees Kelvin, N_e is the electron density in units of cm^{-3}, N_i is the ion density of the ith ionization stage, and ν is the frequency. The radiation brightness $\epsilon(\nu, T)$, is a function of ν through the function $\xi_i(\nu)$ which accounts for deviations from a hydrogenic atom. The function $\xi_i(\nu)$ has been calculated [24] with a number of simplifying assumptions. The continuum calculated in [24] has a smooth character which is not in complete agreement with the jagged appearance predicted by more exact calculations and experiments concerning recombination radiation. It was also shown in [24] that the function $\xi(\nu)$ for ions of the same element but of different ionization stages approaches unity with increasing Z, i.e., the system becomes more hydrogenic. With increasing Z it is found that $\xi(\nu) \to 1$, but not monotonically. Equation (3) assumes that the lowering of the ionization potential and the shift of the photoionization threshold due to the presence of the plasma may be neglected. The derivation of (3) also assumes the validity of Kirchhoff's law as well as Saha equilibrium.

It is possible to predict T from (2) and it remains to find N_e and N_i. A reasonable approach to estimating N_e is via the Stark broadening of selected plasma spectral lines. In the case of xenon, there is not adequate information available to do this. The next option is to add the appropriate impurities and measure their spectral widths. Helium was added; however, due to the considerably lower ionization potential of xenon the helium was not excited (to within the sensitivity of the measurement). Hydrogen was added (about 2 percent) and an attempt was made to look at H_α and H_β emission. However, H_β was too weak relative to the continuum, and H_α, while stronger, was in the close proximity of silicon lines. It was not possible to use the silicon lines because they were not emitted from the volume but rather from the vicinity of the plasma-quartz interface and under appropriate conditions appear as absorption lines rather than emission lines.

As an approach to estimating the degree of ionization for the xenon discharge, a helium discharge was looked at under conditions of the same tube size, gas pressure, and capacitor energy. The peak current in the helium discharge was 30 kA and was underdamped. The peak current in the xenon discharge was 20 kA and was only slightly underdamped compared to the helium discharge. The current in the helium discharge peaked at 10 μs after initiation of the discharge and it was not possible to make a measurement until 20 μs due to a delay in the emission of HeI radiation. At this time, the spectral half-width of the HeI 5876-Å line was measured to be ≈20 Å which corresponded to 5.5×10^{17} electrons $\cdot$ cm^{-3}

[25]. (The instrumental width was 0.24 Å while the maximum Doppler width is estimated to have been 0.3 Å. Both were neglected and the measured width was taken to be due to Stark broadening.) At 40 μs the half-width was 16.5 Å with a shift of about 1.5 Å to the blue. The width measurement corresponded to 4.6×10^{17} cm^{-3} while the displacement corresponded to 4.2×10^{17} cm^{-3}. At an initial pressure of 20-torr helium and completely stripped helium atoms, the maximum electron density would be 1.3×10^{18} cm^{-3}. However, for electron temperatures of several electron volts, one does not expect significant quantities of HeIII (doubly ionized helium). If thermal equilibrium prevailed, Saha equilibrium would predict an electron density (and HeII) of 5.0×10^{17} cm^{-3} at an electron temperature of 28 000 K. (For the peak current in the helium discharge, (2) predicts 28 000 K.) For the xenon medium and a temperature of 24 000 K, Saha thermal equilibrium would predict the dominant heavy species to be XeII and XeIII. Again, one can place an approximate upper limit to the electron density which would be about 1.3×10^{18} cm^{-3}. It is to be expected on the basis of the ionization potentials that a xenon plasma would result in a higher electron density than a helium plasma under the same conditions. Consequently, it seems reasonable to place the electron density for the xenon plasma near the time of peak current between $5.0\text{-}13 \times 10^{17}$ cm^{-3}. If one considers the plasma to be in approximate thermal equilibrium, then the Saha relationship would predict $N_e = 9.0 \times 10^{17}$ cm^{-3} for $T = 24\,000$ K (i.e., the plasma is essentially fully ionized). So, assuming the plasma to consist of only XeII and XeIII ions ($N_e = \Sigma N_i$), it is found that the energy predicted to be radiated in the wavelength range 2500-2900 Å is 4.3 J. In calculating this quantity $\xi_i(\nu)$ was taken to be three [24]. This value is for neutral xenon and, as stated in [24], the higher stages of xenon ionization will have values of $\xi(\nu)$ closer to unity. The flashlamp was assumed to radiate from the whole tube volume, i.e., a cylinder 8-mm ID and 30 cm long. It has been assumed that over the time considered the electron density follows the discharge current. On this basis, 4.3 J is an approximate upper limit. It is to be noted that experimentally the continuum contributed 56 J for the wavelength range 2500-2900 Å. There is a discrepancy between the calculations and experiment of a factor of 13. Of course, there are a number of assumptions concerned with the calculations and the interpretation of the experiment, and consequently, it is not clear exactly how large the discrepancy actually is. In [26] there was a considerable discrepancy between electron densities interpreted from continuum and line-broadening measurements (the former predicted higher densities than the latter); [27] noted similar discrepancies. The results of [26] and [27] are consistent with those of the present work.

Consider Fig. 8, which is a schematic of the xenon line spectra in the near-UV regions of interest. All the lines indicated are due to XeII and XeIII which is consistent with the foregoing estimate of the ion makeup of the plasma at 24 000 K. Also consider that it is usual at the plasma densities and temperature nominally of interest that lines may be broadened from 10 to 100 Å and shifted by several

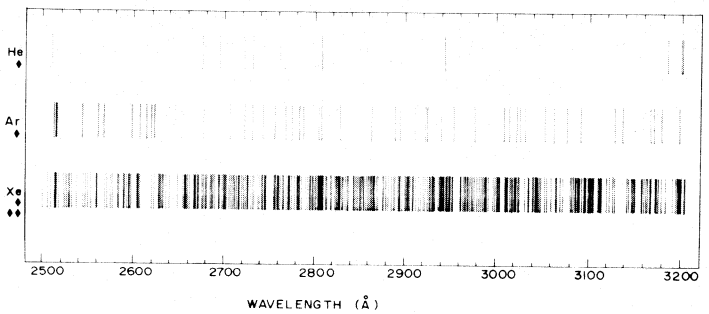

Fig. 8. A schematic representation of the location of the spectral line radiation for several important atoms. ♦ indicates [32], ♦♦ indicates [33] and [34].

angstroms. All of this, taken with the present discrepancy between calculation and experiment and the discrepancies noted in [26] and [27], strongly suggests that the so-called continuum is not due solely to free-free and free-bound processes, but a considerable portion may be due to bound-bound processes [3], [27]-[30], with the usual discrete appearance smeared out. The schematic representation of Fig. 8 cannot be taken by itself. These atoms are all capable of forming diatoms [23], [31] and, as such, one can expect molecular emission which, due to the strong plasma fields, will be very diffuse. Upon consideration of spectral broadening and displacement only, it is evident why one might expect He and Ar not to produce as bright a continuum as Xe. (It must be noted that the calculations presented in [24] would predict the same relative behavior for these gases on the basis of continuum emission alone.) Consequently, we have a situation where line radiation evidently contributes a large portion of the radiation. (The calculations presented in [29] and [30] substantiate these results.) This gives a hint as to how one might enhance the near-UV spectral efficiency. In particular, dopants that have strong and/or plentiful line spectra in this region can be used to increase the line radiation in the wavelength band of interest. The spectral enhancement produced by dopants has been demonstrated [35] which lends support to the thesis concerning the contribution of line radiation to the near-UV spectrum.

Conclusion

The limiting spectral efficiency of flashlamps used to pump lasers is determined by the emission from a blackbody at the same temperature as the flashlamp plasma. The results of such considerations are: the maximum spectral efficiency for pumping an iodine photodissociation laser occurs for an electron plasma temperature of 18 000 K with 8.6 percent of the total photon flux appearing in the pump band (2500-2900 Å). Similar considerations for the limiting efficiency of a neodymium glass laser result in a required plasma temperature of approximately 7000 K with 15 percent of the radiation appearing in the pump bands.

The double-discharge technique of Emmett and Schawlow [22] was investigated. The results of this study indicate that there is indeed an enhancement of the near-UV emission when utilizing a double discharge; however, the enhancement is dependent upon the relative magnitude of the simmer- and

main-discharge currents. Specifically, the enhancement ratio decreases (at fixed simmer current) with increasing main-discharge current.

Absolute measurements of the emission spectra and consideration of the origins of the radiation suggest that a large percentage of the near-UV emission in typical xenon-filled flashlamps is line radiation rather than continuum radiation due to bremsstrahlung and two-body radiative recombination as is usually assumed. The flashlamps studied in this work were typified by discharge current densities of 40 kA · cm^{-2} and electron temperatures of 24 000 K.

Acknowledgment

The author wishes to thank G. R. Schuster for efforts in the experimental aspects above and beyond the call of duty.

References

[1] J. M. Drake, E. M. Tam, and R. I. Morse, "The use of light converters to increase the power of flashlamp-pumped dye lasers," *IEEE J. Quantum Electron. (Part I of Two Parts)*, vol. QE-8, pp. 92–94, Feb. 1972.

[2] W. T. Bayha, J. E. Creedon, and S. Schneider, "Alkali-vapor light sources as optical pumps for Nd:YAG lasers," *IEEE Trans. Electron Devices*, vol. ED-17, pp. 612–616, Aug. 1970.

[3] I. S. Marshak, "Strong current pulse (spark) discharges in gas, used in pulsed light sources," *Sov. Phys.–Usp.*, vol. 5, pp. 478–514, 1962.

[4] M. P. Vanyukov and A. A. Mak, "High intensity pulsed light sources," *Sov. Phys.–Usp.*, vol. 66, pp. 137–155, 1958.

[5] S. I. Braginskii, "Theory of the development of a spark channel," *Sov. Phys.–JETP*, vol. 34, pp. 1068–1074, 1958.

[6] A. F. Aleksandrov, I. S. Marshak, and A. A. Rukhadze, "Radiating discharges confined by walls," *Sov. Phys.–Tech. Phys.*, vol. 19, pp. 308–313, 1974.

[7] C. H. Church, R. G. Schlecht, I. Liberman, and B. W. Swanson, "Studies of highly radiative plasmas using the wall-stabilized pulsed arc discharge," *AIAA J.*, vol. 4, pp. 1947–1953, 1966.

[8] N. G. Basov *et al.*, "Strong gas discharges. II–A description of the dynamics of a strong discharge in a gas by means of a self-similar solution of the gas dynamics equations with nonlinear thermal conductivity," *Sov. Phys.–Tech. Phys.*, vol. 15, pp. 624–630, 1970.

[9] J. W. Poukey, J. B. Gerardo, and M. A. Gusinow, "Properties of an afterflow helium plasma," *Phys. Rev.*, vol. 179, pp. 211–226, 1969.

[10] R. W. P. McWhirter, "Spectral intensities," in *Plasma Diagnostic Techniques*, R. H. Huddlestone and S. L. Leonard, Ed. New York: Academic, 1965, ch. 5, pp. 227–233.

[11] M. A. Gusinow, "Efficiency of flashlamp excited lasers," Sandia Labs., Albuquerque, N. Mex., Rep. SLA-73-0905, Sept. 1973.

[12] R. F. Woodstock, "Commercial laser glasses," in *Handbook of Lasers*, R. J. Pressley, Ed. Chemical Rubber Co., Cleveland, Ohio, 1971, ch. 11, p. 361.

[13] J. F. Holzrichter and J. L. Emmett, "Design and analysis of a high brightness axial flashlamp," *Appl. Opt.*, vol. 8, pp. 1459–1465, 1969.

[14] M. P. Vanyukov, A. A. Mak, and A. I. Sedykova, "Limiting brightness of a spark discharge channel," *Sov. Phys.–Dokl.*, vol. 135, pp. 1237–1239, 1969.

[15] M. A. Gusinow, "Effective blackbody temperature of high-current gas filled flashlamps," *J. Appl. Phys.*, vol. 44, pp. 4567–4568, 1973.

[16] —, "The electrical characteristics of high current gas filled flashlamps," Sandia Labs., Albuquerque, N. Mex., Rep. SLA-73-0352, Mar. 1973.

[17] S. L. Andreev and V. E. Gavrilov, "Radiative energy losses from a dense xenon plasma" (Transl.), *Teplofiz. Vys. Temp.*, vol. 8, pp. 190–192, 1970.

[18] A. P. Dronov, A. G. Svirodov, and N. N. Sobolev, "The continuous emission spectra of krypton and xenon behind a shock wave," *Opt. Spectrosc.* (USSR), vol. 12, pp. 383–389, 1962.

[19] J. L. Emmett, A. L. Schawlow, and E. H. Weinberg, "Direct measurement of xenon flashlamp opacity," *J. Appl. Phys.*, vol. 35, pp. 2601–2604, 1964.

[20] A. D. Klementov and G. V. Mikhailov, "Investigation of emission of xenon flashlamps in short pulse operation," *J. Appl. Spectrosc.* (USSR), vol. 9, pp. 1177–1180, 1968.

[21] A. F. Aleksandrov *et al.*, "Dynamics and radiation of direct high-current discharges in the atmosphere," *Sov. Phys.–JETP*, vol. 34, pp. 979–987, 1972.

[22] J. L. Emmett and A. L. Schawlow, "Enhanced ultraviolet output from double-pulsed flashlamps," *Appl. Phys. Lett.*, vol. 2, pp. 204–206, 1963.

[23] P. Gloersen, "Some unexpected results of shock-heating xenon," *Phys. Fluids*, vol. 3, pp. 857–870, 1960.

[24] L. M. Biberman and G. E. Norman, "Continuous spectra of atomic gases and plasma," *Sov. Phys.–Usp.*, vol. 10, pp. 52–90, 1967.

[25] I. I. Sobel'man, *Introduction to the Theory of Atomic Spectra*. New York: Pergamon, 1970, p. 455.

[26] A. A. Mak, "Measurement of electron concentrations by the intensity of the continuum radiation in a spark discharge," *Sov. Phys.–Tech. Phys.*, vol. 6, pp. 67–71, 1961.

[27] H. N. Olsen, "Partition function cutoff and lowering of the ionization potential in an argon plasma," *Phys. Rev.*, vol. 124, pp. 1703–1708, 1961.

[28] M. P. Vanyukov, A. A. Mak, and V. R. Muratov, "Time resolved spectra of the radiation from a spark discharge in inert gases," *Opt. Spectrosc.* (USSR), vol. 6, pp. 8–10, 1959.

[29] L. M. Biberman, V. S. Vorob'ev, and G. E. Norman, "Energy emitted in spectral lines by a plasma at equilibrium," *Opt. Spectrosc.* (USSR), vol. 14, pp. 176–179, 1963.

[30] V. S. Vorobyov and G. E. Norman, "Energy radiated in spectral lines by an equilibrium plasma, II," *Opt. Spectrosc.* (USSR), vol. 17, pp. 96–100, 1964.

[31] W. Roth and P. Gloersen, "Shock-tube study of luminosity in xenon," *J. Chem. Phys.*, vol. 29, pp. 820–824, 1958.

[32] A. N. Zaidel' *et al.*, *Tables of Spectral Lines*. New York: Plenum, 1970.

[33] J. Humphreys, "Second spectrum of xenon," *J. Res. Nat. Bur. Stand.*, vol. 22, pp. 19–53, 1936.

[34] —, "Third spectrum of xenon," *J. Res. Nat. Bur. Stand.*, vol. 16, pp. 639–648, 1936.

[35] M. A. Gusinow, "The enhancement of the near UV flashlamp spectra with special emphasis on the iodine photodissociation laser," *Opt. Commun.*, to be published.

A High-Power Pulsed Xenon Ion Laser as a Pump Source for a Tunable Dye Laser

LAIRD D. SCHEARER

Abstract—**An inexpensive pulsed xenon ion laser with peak power outputs up to 4 kW has been constructed and used as a pump source for a tunable rhodamine 6G dye laser with a 0.25-Å bandpass in the yellow-red range of the spectrum. The dye laser is tunable from 5465 to 6300 Å. Over 50 W are obtained at the peak of the tuning range.**

I. Introduction

THERE has been considerable recent interest in the pulsed xenon ion laser [1]-[4]. The interest stems primarily from the simplicity of a high-gain laser system which is capable of relatively high peak power emission in the blue-green region of the spectrum accompanied by relatively long pulsewidths. We have investigated the properties of a high-power pulsed xenon ion laser and its use as a pump source for a tunable dye laser. Peak pulse powers of 4 kW and pulse durations up to 1 μs have been obtained in a 120-cm X 4-mm xenon discharge at pressures between 5 and 30 m · torr. The high peak power available in the xenon laser has enabled us to use it as a pump source for a rhodamine 6G dye laser which is tunable from 5465 to 6300 Å with a 0.25-Å bandwidth. At the peak of the dye laser output, ~ 5750 Å, we obtain over 50 W of peak power with 500-ns pulsewidths.

In the sections following we describe the operating characteristics of our pulsed xenon laser and its use as a pump source in the design and construction of the tunable dye laser system.

II. Xenon Ion Laser

Data obtained in earlier work on this type laser system are summarized in Table I along with the results of our work. It is important to note that, based on the volume of the excited gas, the work reported here represents a substantial improvement in both the peak pulse power and pulse duration obtained. In particular, we compare the results of our work with that of Hänsch *et al.* [3]. It was the report of their work on the xenon laser and dye laser that provided the initial motivation for the work we report here. The particular aspect of the Hänsch *et al.* work which attracted our attention was the low construction cost and simplicity of design of the xenon laser and the dye laser system.

The only work which reports a higher peak power than that reported here is that of Gundersen and Harper [4] who obtained approximately 80-kW peak pulse power. Their laser tube, however, was over 10 ft in length with a bore area approximately 20 times greater than the one we used.

TABLE I
SUMMARY OF RECENT WORK ON PULSED XENON ION LASERS

Workers	Active length (cm)	Bore diameter (mm)	Total Peak Power (W)	Pulse width μs
Hoffmann and Toschek[1]	175	5.0	380	0.6 - 1.5
Simmons and Witte[2]	150	2.3	900	
	300	3.0	1,300	0.5 - 5
	30	1.5	100	
Hansch, Schawlow and Toschek[3]	120	4.0	300	0.3
Gundersen and Harper[4]	300	17.0	80,000	0.11 - 0.2
This work	120	4.0	4,000	0.1 - 1.5

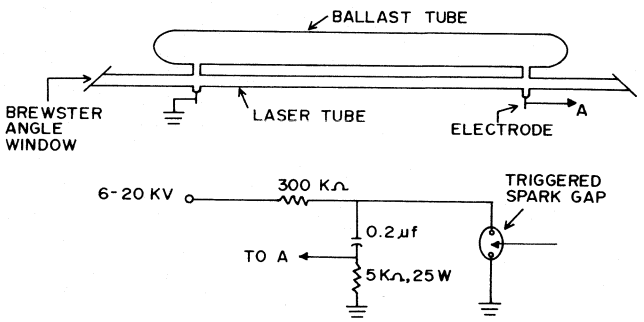

Fig. 1. Pulsed xenon ion laser and electrical discharge circuit.

The active length of the discharge tube was 120 cm with a bore diameter of 4 mm. The laser tube length was supplemented by an additional 25 cm at each end between the internal electrodes and the windows which terminated the laser tube. The electrodes are high-current indium cathodes constructed by melting pure indium metal around the tungsten electrodes [5]. The additional spacing between the electrodes and Brewster windows was provided to reduce the possibility of window contamination by sputtering of the metal at the electrodes. The laser tube also included a ballast tube as shown in Fig. 1.

We utilized a number of electrical circuits for the pulsed excitation of the laser discharge tube. The first method and probably the simplest we utilized was that described by Hänsch *et al.* in their report on the xenon laser [3]. The power supply consisted of a 15-kV 60-mA high-voltage transformer of the type used to excite neon signs and a bank of twenty-two 500-pF capacitors connected across the transformer terminals and laser electrodes. In this condition the laser tube discharged at a 120-Hz rate, i.e., on each half-cycle.

With an 80-percent output reflector in place we obtained

Manuscript received June 16, 1975. This work was supported in part by the Air Force Office of Scientific Research under Contract 2672, and in part by the Office of Naval Research under Contract N00014-75C-0477.

The author is with the Department of Physics, University of Missouri at Rolla, Rolla, Mo. 65401.

results identical with those reported by Hänsch *et al.* [3]. There were eight visible lines observed in laser emission ranging from the violet at 4306 Å to the orange at 5956 Å. The maximum peak power output obtained was 300 W with laser pulsewidths up to 350 ns.

With the circuit described previously the pulse repetition rate was erratic with many skipped pulses. We had additional difficulty with periodic failure of the doorknob capacitors. As a result of these difficulties we abandoned this excitation method and constructed a spark-gap-triggered discharge. The important features of the spark gap are its exceptionally low inductance, its capacity for holding off high voltages, and when it does break down, its capacity of transferring large quantities of electrical charge. Our triggered spark gap has properties similar to those of commercial manufacture.

The capacitive discharge circuit is shown as part of Fig. 1. When the properties of the laser system were evaluated with this circuit we obtained a substantial increase in both peak power and laser pulse duration.

The peak pulse power obtained and the pulsewidth as a function of the charging voltage on a 0.2-μF capacitor are shown in Fig. 2. These data were obtained when the laser pressure was optimized for maximum power. Table II summarizes typical peak powers obtained for seven of the eight observed transitions.

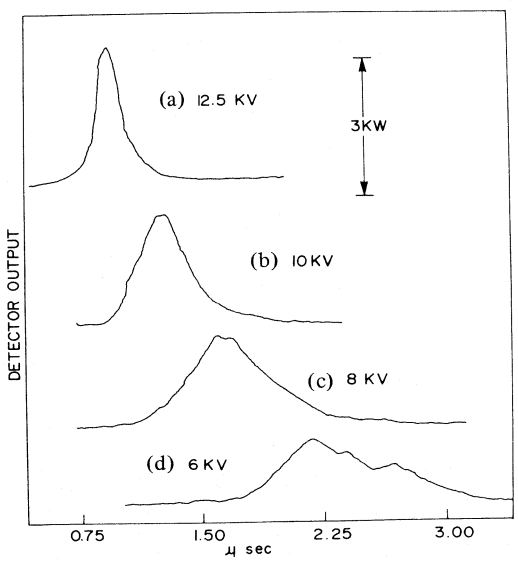

Fig. 2. Laser pulse shapes obtained at various charging voltages for a 0.2-μF capacitor. The curves were obtained with a high-speed silicon photodiode and a PAR boxcar integrator. The scale shown on the horizontal axes represents time delays after a trigger pulse is applied to the spark gap.

TABLE II
PEAK POWER ON OBSERVED LASER LINES

Wavelength (Å)	Peak power (watts)
5956	110
5395	480
5353	800
5260	680
5190	250
4954	800
4306	50

This laser system was capable of repetition rates from single shot up to 30 Hz. The upper limit is determined by the present capacity of our power supply. From the energy-per-pulse measurement and the repetition rate one can obtain the *average* laser power output. The highest average power we obtained was approximately 20 mW.

The data shown were obtained with an 80-percent broadband reflecting output mirror. In an effort to determine the optimum output coupling we repeated the power measurements for output mirror reflectivities of 98, 50, and 20 percent. At 98 percent, the power output was reduced by a factor of 2. At 20 percent the output power was down an order of magnitude, while with the 50-percent mirror similar results were obtained. We thus conclude that the mirror reflectivity required for optimum power output lies between 50 and 80 percent.

The availability of substantial laser output power even with mirrors which transmit 80 percent of the incident optical energy is an indication of the relatively large gain of several of the laser transitions. This in turn suggests that relatively lossy elements can be inserted in the optical cavity while still maintaining laser action. As a next step in this work the addition of a nonlinear crystal in the optical cavity is planned to attempt intracavity frequency doubling of the Xe ion laser emission.

III. The Tunable Dye Laser Cavity

Several dye laser cavitites have been developed in the past for use in CW dye laser applications. In these systems one needs a cavity design which provides an intracavity focus to meet the pumping requirements. In CW systems pump power is at a premium and the pump beam is generally focused to a small spot to provide a high energy density within the dye. One also desires a long cavity length as well, for tuning purposes.

Cavity configurations which satisfy these requirements are resonators with an internal lens or the equivalent three-mirror cavity [6].

Hänsch *et al.* constructed a three-mirror resonator and pumped the dye with the output of their pulsed xenon ion laser. With rhodamine 6G dye they obtained 12 W of peak power at 5700 Å. The resolution of the dye laser emission they reported as <100 Å. However, they did not include a frequency-selective element inside the dye laser cavity. Consequently, the dye laser output was not tunable and their laser output had poor resolution.

The three-mirror resonator of [6] was modified slightly by replacing the flat mirror (1) by a 1200-l/mm grating in Littrow mount as shown in Fig. 3. Mirrors 1 and 2 are highly reflective over a broad band and have radii of curvature of 5 and 10 cm, respectively. When the mirrors are separated by 10 cm there is a tightly focused spot at the center of the 2 mirrors. At this point a cell of thickness 1 mm containing a 10^{-3} M solution of rhodamine 6G dye in ethanol is inserted at Brewster's angle. The dye is contained in a sealed cell. It

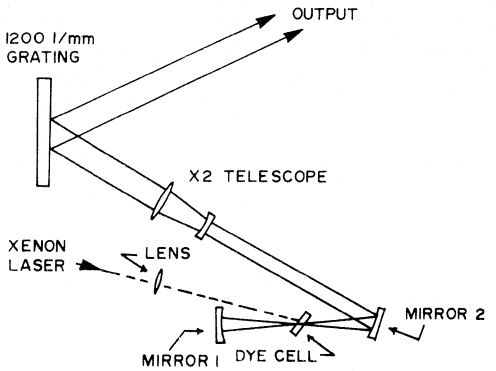

Fig. 3. The astigmatic dye cavity. A 1200-l/mm grating is used as the output reflector.

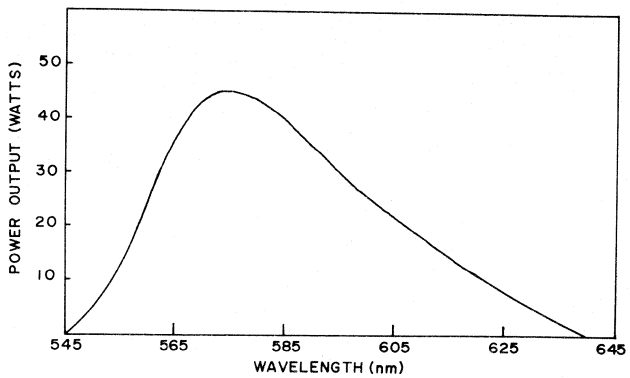

Fig. 4. Power tuning curve for rhodamine 6G. Bandwidth is less than 0.25 Å over entire range. Pulsewidth is 350 ns. Pump power is approximately 1.6 kW.

was found unnecessary to flow the dye. The grating is located 25 cm from mirror 2. A two-power telescope is used inside the cavity as shown to expand the beam on the grating.

The xenon ion laser light is focused on the dye cell by a 20-cm fL spherical lens as shown. When properly adjusted the dye system lases with no difficulty. The dye output is taken from the zero-order diffraction from the grating which was blazed for 5000 Å. No system degradation over many days was observed by using a sealed dye cell containing 0.1 ml at repetition rates to 30 Hz.

With the dye laser system described in the preceding section pumped by our xenon ion laser we were able to obtain substantially higher peak power outputs from the dye laser than that reported by Hänsch *et al.* In addition, the presence of the grating permits tuning of the dye laser output and results in a much higher resolution of the laser emission.

Our tuning width with rhodamine 6G ranged from approximately 5465 to 6300 Å, with a bandwidth of less than 0.25 Å. The peak output power at the center of the tuning range was 50 W. The dye laser pulsewidth was slightly shorter (~20 percent) than the xenon pump pulse. The power tuning range we obtained for rhodamine 6G is shown in Fig. 4. The dye laser gain pumped by the xenon laser is sufficiently great that the system lases even when a clear quartz plate is used as the output reflector.

This is the first reported instance of a tunable dye pumped by a repetitively pulsed xenon ion laser. Without the telescope, the dye laser bandwidth was about 2 Å with a peak power output of 100 W at the center of the tuning range.

Rhodamine B dye was used also; contrary to expectations it did not provide operation further into the red than rhodamine 6G. This may be more a property of the dye mirrors and grating used which were standard commercial reflectors for rhodamine 6G than any inherent difficulties with the pumping source.

The attractive features of this xenon pumped dye laser are the relatively high repetition rates and the relatively long pulsewidths available in a simple, inexpensive system. The 0.25-Å bandpass obtainable with the grating telescope combination should make this a valuable tool in atomic spectroscopy. We also note that a considerable improvement in the efficiency of the system and the bandwidth should be possible by using coated optics in the telescope and, in general, by upgrading the quality of the components.

Acknowledgment

The author wishes to thank W. Hoffman and S. Price for assistance in the design and construction of the lasers.

References

[1] V. Hoffman and P. Toschek, "New laser emission from ionized xenon," *IEEE J. Quantum Electron.* (Notes and Lines), vol. QE-6, p. 757, Nov. 1970.

[2] W. W. Simmons and R. S. Witte, "High-power pulsed xenon ion lasers," *IEEE J. Quantum Electron.*, vol. QE-6, pp. 466–469, July 1970.

[3] T. W. Hänsch, A. L. Schawlow, and P. Toschek, "Simple dye laser repetitively pumped by a xenon ion laser," *IEEE J. Quantum Electron.* (Corresp.), vol. QE-9, pp. 553–554, May 1973.

[4] M. Gundersen and C. D. Harper, "A high-power pulsed xenon ion laser," *IEEE J. Quantum Electron.* (Notes and Lines), vol. QE-10, p. 1160, Dec. 1973.

[5] W. W. Simmons and R. S. Witte, "New cold cathode for pulsed ion laser," *IEEE J. Quantum Electron.* (Corresp.), vol. QE-6, pp. 648–649, Oct. 1970.

[6] H. W. Kogelnick, E. P. Ippen, A. Dienes, and C. V. Shank, "Astigmatically compensated cavities for CW dye laser," *IEEE J. Quantum Electron.*, vol. QE-8, pp. 373–379, Mar. 1972.

Correspondence

Electrooptic Q Switching of the Nd:YVO_4 Laser Without an Intracavity Polarizer

MICHAEL BASS

Abstract—**An explanation of the excellent Q-switched lasing of Nd:YVO_4 at pump levels many times threshold with no intracavity polarizer is presented. A small wedge between the laser rod's end faces, coupled with the material's high birefringence, enables the rod to act as its own intracavity polarizer. This results in a simplification of the Q-switched optical resonator and can be applied to other birefringent laser materials.**

Pulse-pumped Nd:YAG lasers are often Q switched using the Pockels-cell–Glan-polarizer combination shown in Fig. 1(a). Since the host material is optically isotropic, both the Pockels cell and the Glan polarizer must be placed in the optical cavity to prevent premature lasing or prepulsing. As indicated in Fig. 1(a), when the voltage applied to the Pockels cell produces a one-quarter-wave, $\lambda/4$, phase retardation at the laser wavelength, the light reflected from the 100-percent R-cavity mirror enters the Glan polarizer polarized so that it is not transmitted. The combination of intracavity Pockels cell and Glan polarizer thus spoils the cavity Q by isolating the 100-percent R mirror from the optical resonator. When the voltage applied to the Pockels cell is reduced to zero, there is no phase retardation, the cavity Q is restored, and an intense Q-switched pulse of laser light is produced.

A significant simplification of the Q-switched laser could be achieved if the optical resonator did not require an intracavity polarizer for prepulse-free operation. This was attempted by McClung and Hellwarth [1] for a ruby laser and by Weber *et al.* [2] for a Nd:$YAlO_3$ laser. In both of these referenced cases, the authors attempted to use the anisotropic properties of the laser gain in a crystalline host to prevent premature oscillation in the laser cavity.

Consider a laser cavity where the active medium has gain for light polarized in one direction only. After two complete round trips through this cavity with no intracavity polarizer and $\lambda/4$ voltage applied to the Pockels cell [see Fig. 1(b)], a condition for oscillation can be reached. If this condition

$$(R_1)^2 \exp(2\beta_H l) = 1$$

is met, there will be prepulsing. Here R_1 is the output mirror reflectivity, β_H is the net laser gain [β_H is assumed to be zero for light polarized normal to the figure in Fig. 1(b)], and l is the length of pumped medium. At threshold for lasing with no voltage applied to the Pockels cell, the oscillation condition is

$$R_1 \exp(2\beta_{Th} l) = 1.$$

Thus $\beta_H = 2\beta_{Th}$ and so no holdoff is possible at pump levels which produce a gain equal to twice that at threshold. This is in agreement with the results in [1] and [2]. Recently, however, prepulse-free electrooptic Q switching of Nd:YVO_4 with no intracavity polarizer was reported at pump levels as high as eight times threshold [3] (see Fig. 2). Since the anisotropic gain of the laser crystal cannot account for such excellent performance, the explanation must lie elsewhere.

Manuscript received June 25, 1975. This work was supported by the U.S. Army Electronics Command under Contract DAAB07-74-C-0104.

The author is with the Center for Laser Studies, University of Southern California, Los Angeles, Calif. 90007.

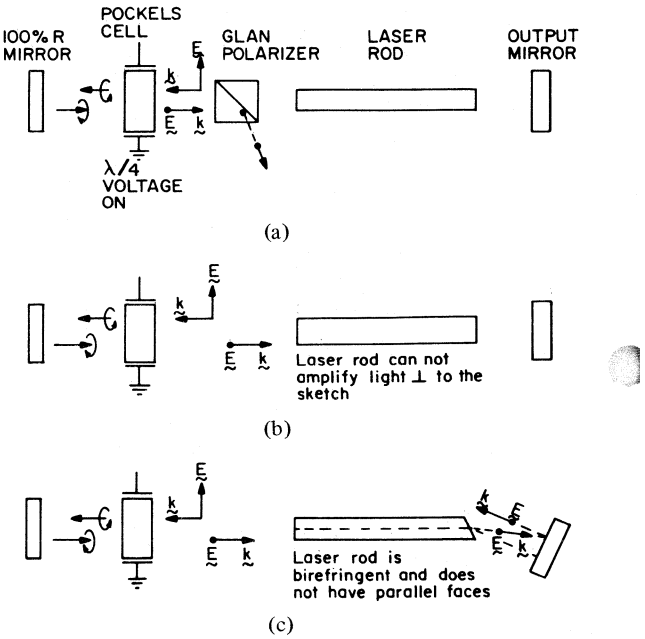

Fig. 1. Electrooptically Q-switch configurations. (a) A Pockels-cell–Glan-polarizer combination in a Nd:YAG laser cavity. (b) A Pockels cell only in a cavity which has a strong polarization-dependent gain. (c) A Pockels cell in a cavity where the laser rod is slightly wedged and strongly birefringent.

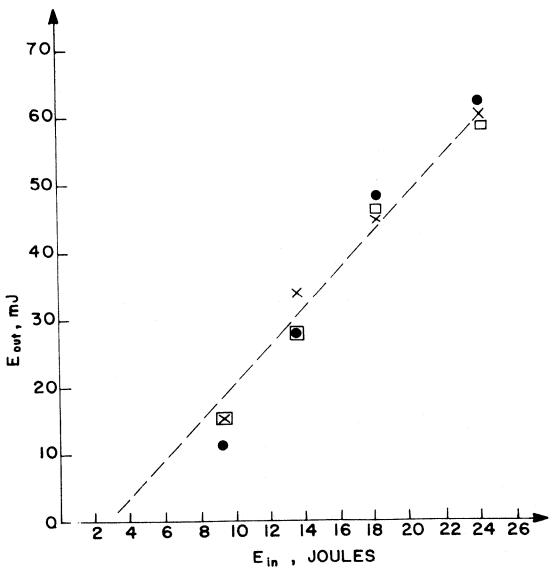

Fig. 2. Q-switched laser output versus input energy from Nd:YVO_4 using a Pockels-cell Q switch and no intracavity polarizer. The output reflector was 3 percent R at 10.6 μm. × indicates Pockels-cell Q-switched data. • indicates long-pulse lasing with Pockels cell in cavity. □ indicates long-pulse lasing, empty cavity. Rod dimensions were 3 × 30 mm, and a small gold-plated single-ellipse pump cavity was used. This figure is reproduced from [3].

The Nd:YVO_4 laser rod studied in [3] was inadvertently polished so that its flat end faces were wedged with respect to each other by $\sim 6 \times 10^{-3}$ rad. This, coupled with the very strong birefringence of the YVO_4 host ($n_O = 1.958$ and $n_e = 2.168$ at 1.06 μm^3), permitted the laser rod to act as its

own intracavity polarizer. To understand the importance of the wedge between the rod faces consider that if the flat, 0.25-percent R faces had been parallel, laser action would have occurred between the rod faces at pump levels ~3.5 times that required for lasing in the main optical resonator. Since no oscillations at all were reported with the optical-cavity mirrors misaligned, the wedge between the rod faces is sufficient to prevent unwanted lasing, and therefore is a critical factor in determining the properties of the Nd:YVO_4 laser.

Suppose, for simplicity, that the face of the rod nearest the 100-percent R mirror was normal to the rod axis and that the other face was misaligned by the wedge angle (6×10^{-3} rad) [see Fig. 1(c)]. Since the cavity mirrors were aligned for best long-pulse lasing, they were oriented so that light polarized parallel to the direction having maximum gain propagated parallel to the rod axis. In [3] the rod was nominally cut with its axis parallel to the crystalline a axis and, since maximum gain in Nd:YVO_4 occurs for light polarized parallel to the optic axis, light which propagated as an extraordinary ray in the laser rod was that which could oscillate.

When the Pockels cell voltage was on, light reflected from the 100-percent mirror entered the rod as an ordinary ray. As it left the Nd:YVO_4 rod it was not refracted far enough to be normal to the output mirror, and so no premature oscillations were possible. For the wedge angle of 6×10^{-3} rad of the Nd:YVO_4 laser rod in [3], the extraordinary ray would have been refracted by 14×10^{-3} rad and the ordinary ray by 11.8×10^{-3} rad. The resulting 2.2×10^{-3} rad (0.126°) misalignment would have been sufficient to prevent prepulsing, and thus explains the excellent results reported.

The observation that a suitably birefringent laser crystal can be prepared so that it can act as its own intracavity polarizer for electrooptic Q switching can lead to great simplification in Q-switched laser systems. This was demonstrated in the present correspondence for Nd:YVO_4, and can be adapted to the design of other birefringent laser crystals.

ACKNOWLEDGMENT

The author wishes to thank Dr. K. M. Leung and Dr. L. G. DeShazer for fruitful conversations.

REFERENCES

[1] F. J. McClung and R. W. Hellwarth, "Giant optical pulsations from ruby," *J. Appl. Phys.*, vol. 33, pp. 828–829, Mar. 1962.

[2] M. J. Weber, M. Bass, K. Andringa, R. R. Monchamp, and E. Comperchio, "Czochralski growth and properties of $YAlO_3$ laser crystals," *Appl. Phys. Lett.*, vol. 15, pp. 342–345, Nov. 1969.

[3] M. Bass, L. G. DeShazer, and U. Ranon, "Evaluation of Nd:YVO_4 and Ho:Er:Tm:YVO_4 as pulse pumped Q-switched lasers," U.S. Army Electronics Command, Fort Monmouth, N.J., Semi-Annu. Rep. ECOM-74-0104-1.

3547-Å Pumped Parametric Oscillation in RD*A

K. KATO

Abstract—**Efficient parametric oscillation in a deuterated rubidium dihydrogen arsenate (RD*A) crystal has been achieved by pumping with the third harmonic of a Nd:YAG laser. A peak power as high as 1.2 MW at 7095 Å and peak powers in excess of 0.5 MW from 6470 to 7850 Å have been obtained.**

Manuscript received July 7, 1975.

The author is with the 1st Research Centre, Japan Defence Agency, Nakameguro 2-2-1, Meguro, Tokyo, Japan.

It has been reported by Adhav and Wallace [1] that a deuterated rubidium dihydrogen arsenate (RD*A) crystal is 90° phase matchable for frequency doubling of dye-laser radiation at 7000–7100 Å. A frequency-tripled Nd:YAG-laser radiation at 3547 Å can be, in principle, used to pump parametric oscillators using the same nonlinear crystal with a 90° phase-matching condition. In this correspondence we wish to report the first observation of parametric oscillation in RD*A pumped by the third harmonic of a Nd:YAG laser.

The 25.5-mm-long 45°z 90°y-cut RD*A crystal used in this experiment was supplied from Quantum Technology Ltd., and they estimate that the degree of deuteration in RD*A is approximately 90 percent. Measurements of the transmission curves of this crystal were made by a Hitachi FPS-3T spectrophotometer. The 50-percent transmission range was approximately from 2700 to 14 800 Å. The transmission loss at 10 642, 5321, and 3547 Å was measured by means of the fundamental, second, and third harmonics of a Nd:YAG laser. The absorption loss per centimeter was approximately 5 percent at 10 642 Å, 2 percent at 5321 Å, and 5 percent at 3547 Å which are similar to the values reported for a normal RDA crystal [2].

Fig. 1 is a schematic diagram of the experimental setup. The basic pump source was a repetitively Q-switched Nd:YAG oscillator–amplifier system working in the TEM_{00} transverse mode and in 2–4 axial modes with a peak power of 50 MW and 12-ns pulse duration. The 10-ns 22-MW second-harmonic radiation at 5321 Å generated from a temperature-tuned deuterated cesium dihydrogen arsenate (CD*A) crystal [3] was frequency mixed with the transmitted fundamental radiation in a rubidium dihydrogen phosphate (RDP) crystal [4] orientated for type-1 phase matching at room temperature. The third-harmonic radiation at 3547 Å was characterized by a peak power of 11 MW and 8-ns pulse duration. The spatial profile of the 5-mm-diam third-harmonic beam was close to Gaussian having an angular divergence of 0.95 mrad. As shown in Fig. 1, the third-harmonic beam was physically separated from the fundamental and second harmonic by a fused-silica prism and was used to pump the temperature-controlled RD*A parametric generator crystal through a high-quality Glan polarizer incorporated in the 8-cm-long optical cavity and the output beam was coupled through an uncoated sapphire etalon. A flat, dielectric-coated rear mirror had 99.9-percent reflectivity from 5600 to 8200 Å. The effective pump power incident on the generator crystal was 7 MW. Since a single-pass parametric gain greater than 11 is necessary for the oscillator to reach threshold, due to the 86-percent output coupling of sapphire etalon and the 20-percent transmission loss through the Glan polarizer and RD*A crystal, the pump-power density at the generator crystal was increased up to 200 MW/cm^2 by means of an inverted telescope having an angular magnification of 2.5.

The output wavelengths of the oscillator were analyzed by a 1-m-grating spectrograph when the crystal temperature was varied from 97 to 110°C. Fig. 2 shows the resulting

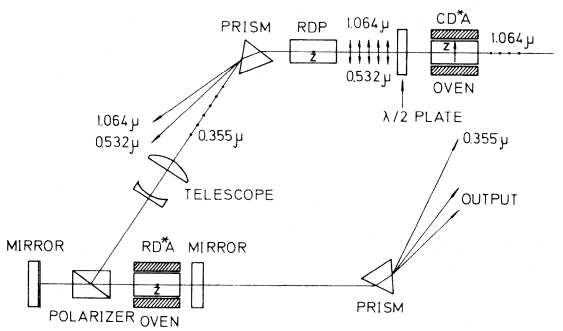

Fig. 1. Schematic diagram of experimental setup.

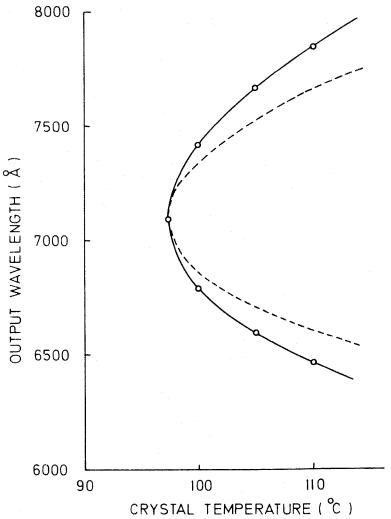

Fig. 2. Temperature tuning characteristics for the RD*A parametric oscillator pumped by 3547-Å radiation. The dashed line is the theoretical curve.

temperature-tuning curve of the RD*A parametric oscillator measured with constant pump power of 7 MW and a pulse repetition rate of 10 pulses per second (pps). The dashed line is the theoretical curve calculated from

$$\Delta\omega = k(\Delta T)^{1/2} \tag{1}$$

where

$$k^2 = (\omega_p/2)(d(n_p^e - n_s^o)/dT)/(dn_s^o/d\omega) \tag{2}$$

ω_p is the pump frequency, and n_p and n_s are the refractive indices at pump and signal, respectively. The parameters used for calculation are $\omega_p = 2.82 \times 10^4$ cm^{-1}, $d(n_p^e - n_s^o)/dT = 1.2 \times 10^{-5}$ °C^{-1}, which was deduced from the temperature bandwidth of the second-harmonic tuning curve of dye-laser radiations, and $dn_s^o/d\omega = 2 \times 10^{-6}$ cm^{-1}, which was extrapolated from the data on the refractive indices reported by Adhav [5]. The lack of agreement between theoretical and experimental curves is probably due to the difference in thermal gradients between the optical region in the crystal and the oven. The spectral bandwidth of the oscillator output was approximately 50 Å when the generator crystal was tuned to degeneracy at 7095 Å, decreasing to less than 10 Å when tuned a few hundred angstroms away from degeneracy. Although no attempt was made to reduce the bandwidth of the oscillator output, substantial reduction in the bandwidth can be expected through insertion of Fabry–Perot etalons between the high-reflectivity mirror and the Glan polarizer.

The temporal behavior of the oscillator output pulses was measured through a fused-silica prism and a high-speed photodiode-oscilloscope system having an overall rise time of less than 1 ns. With this system we have observed that the pulse shape of the oscillator output was nearly symmetric, with a pulse duration of approximately 2 ns at full width at half maximum (FWHM). Average output powers as high as 25 mW were measured near degeneracy at 7095 Å at a pump power of 7 MW and a pulse repetition rate of 10 pps. The corresponding peak output power was approximately 1.2 MW. With the oscillator tuned away from degeneracy, peak powers in excess of 0.5 MW were observed at signal and idler frequencies, respectively.

Following analyses previously used by Yarborough and Massey [6] and Massey and Elliott [7] we have estimated the parametric gain from the ratio of the observed output power to the optical noise [8] given by

$$P_f/P_i = (R_m(1 - \epsilon)^2 G)^m \tag{3}$$

where

$$P_i = h\nu B \tag{4}$$

R_m is the output mirror reflectivity, ϵ is the total transmission loss through the Glan polarizer and RD*A crystal, G is the single-pass parametric gain, m is the number of round trips during the growth of the output pulse, $h\nu$ is the signal or idler photon energy per single spatial mode, and B is the output bandwidth. For a wavelength of 7095 Å and a spectral bandwidth of 50 Å, P_i is approximately 5.9×10^{-6} W. Taking the values of $P_f = 1.2 \times 10^6$ W, $R_m = 0.14$, and $\epsilon = 0.2$, we obtain $G = 57$ for $m = 16$. Comparison of this parameter can be made by the value deduced from the following expression [9]:

$$G = \tfrac{1}{4} \exp(2gl) \tag{5}$$

where l is the crystal length and

$$g = d_{36}(4\pi/c)^{3/2}(2(\omega_s\omega_i/n_s^o n_i^o n_p^e)S)^{1/2}. \tag{6}$$

In (6), d_{36} is the nonlinear optical constant of RD*A and S is the pump-power density at the crystal. Using the following values, $S = 200$ MW/cm^2, $\omega_s = \omega_i = \omega_p/2 = 1.41 \times 10^4$ cm^{-1}, $n_s^o = n_i^o = n_p^e = 1.548$, and taking d_{36}(RD*A) $= 1.02 \times 10^{-9}$ ESU which was deduced from frequency doubling of dye-laser radiations, we find from (6) that $g = 0.76$ cm^{-1}. The corresponding single-pass parametric gain is 12 which is considerably lower than the previous estimate. The discrepancy between these two results may arise from the inaccuracy in the pump-power density and from the simplifying assumption used to calculate the optical noise power. However, we note that an increase in g by a factor of 1.4 would bring the two results in equality.

The spatial profile of the 2-mm-diam oscillator output beam exhibited some inhomogeneous structure due probably to the structural flaws in the RD*A crystal.

The system described in the preceding has been operated for several hours without noticeable deterioration in the output power, although the RD*A crystal exhibited some surface damage which seemed to be associated with the light scratches remaining from polishing.

In summary, we have reported the efficient operation of a RD*A parametric oscillator in the visible to near infrared using the third harmonic of a Nd:YAG laser as a pump source.

ACKNOWLEDGMENT

The author wishes to thank M. Yanada of Nippon Electric Company for his technical assistance in the transmission loss measurements of RD*A.

REFERENCES

[1] R. S. Adhav and R. W. Wallace, "Second harmonic generation in 90° phase-matched KDP isomorphs," *IEEE J. Quantum Electron.* (Corresp.), vol. QE-9, pp. 855–856, Aug. 1973.

[2] K. Kato, "Frequency conversion of Nd:YAG laser radiation in RDA," *Opt. Commun.*, vol. 13, pp. 93–95, 1975.

[3] —, "Second-harmonic generation in CDA and CD*A," *IEEE J. Quantum Electron.* (Corresp.), vol. QE-10, pp. 616–618, Aug. 1974.

[4] —, "Efficient uv generation at 3547 Å in RDP," *Appl. Phys. Lett.*, vol. 25, pp. 342–343, 1974.

[5] R. S. Adhav, "Some physical properties of single crystals of normal and deuterated rubidium dihydrogen arsenate," *Brit. J. Appl. Phys.*, ser. 2, vol. 2, pp. 177–182, 1969.

[6] J. M. Yarborough and G. A. Massey, "Efficient high-gain parametric generation in ADP continuously tunable across the visible spectrum," *Appl. Phys. Lett.*, vol. 18, pp. 438–440, 1971.

[7] G. A. Massey and R. A. Elliott, "Tunable infrared parametric generation in cesium dihydrogen arsenate," *IEEE J. Quantum Electron.* (Corresp.), vol. QE-10, pp. 899–900, Dec. 1974.

[8] D. A. Kleinman, "Theory of optical parametric noise," *Phys. Rev.*, vol. 174, pp. 1027–1041, 1968.

[9] S. E. Harris, "Tunable optical parametric oscillators," *Proc. IEEE*, vol. 57, pp. 2096–2113, Dec. 1969.

Contributors

M. A. Gusinow was born in Chicago, Ill., on September 17, 1939. He received the B. S. degree from the University of Arizona, Tucson, and the Ph.D. degree from the University of Illinois, Urbana, both in electrical engineering, in 1961 and 1966, respectively.

From 1966 to 1967 he held a postdoctoral appointment at the Joint Institute for Laboratory Astrophysics, Boulder, Colo. Since 1967 he has been a member of the staff at Sandia Laboratories, Albuquerque, N. Mex. His research interests are gaseous electronics and lasers.

Dr. Gusinow is a member of Phi Eta Sigma, Pi Mu Epsilon, Tau Beta Pi, Sigma Pi Sigma, and the American Physical Society.

Laird D. Schearer was born in Allentown, Pa., in 1931. He received the Ph.D. degree in physics from Rice University, Houston, Tex., in 1966.

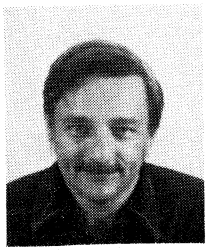

From 1959 to 1971 he was a member of the technical staff and later, Senior Scientist with the Central Research Laboratories, Texas Instruments, Dallas, Tex. In 1971 he joined the faculty of the University of Missouri at Rolla, Rolla, as Professor of Physics and Chairman of the Department of Physics. His principal interests are in atomic physics: optical pumping, energy transfer collisions, and spectroscopy.

Dr. Schaerer is a fellow of the American Physical Society, and a member of the Division of Electron and Atomic Physics, AAAS, Phi Kappa Phi, Sigma Xi, and is currently secretary of the Gaseous Electronics Conference.

1975 Index
IEEE Journal of Quantum Electronics
Vol. QE-11

This index covers all items – papers, correspondence, reviews, etc. – that appeared in this periodical during 1975, and items from prior years that were commented upon or corrected in 1975. The index is divided into an Author Index and a Subject Index, both arranged alphabetically.

The *Author Index* contains the primary entry for each item; this entry is listed under the name of the first author and includes coauthor names, title, location of the item, and notice of corrections and comments if any. Cross-references are given from each coauthor name to the name of the corresponding first author. The location of the item is specified by the journal name (abbreviated), year, month, inclusive pages, and microfiche code. [The microfiche code, given in parentheses following the inclusive pages, consists of four characters to be interpreted as follows: the first character identifies the microfiche number within the set of fiches for the issue; the second character identifies the row in which the first frame of the particular item is located; and the last two characters designate the position of that frame within the row.]

The *Subject Index* contains several entries for each item, each consisting of a subject heading, modifying phrase(s), first author's name, and location of the item. For information on coauthors, title, comments and corrections if any, etc., it is necessary to refer to the Author Index. Some generic subject headings are used in this index in addition to the usual technical headings, e.g., *Books* (books reviewed in this periodical), *Bibliographies* (both papers that are bibliographies and any other papers which contain more than 50 references), *Conferences* (technical meetings a substanial number of whose abstracts or papers have appeared in this periodical), and *Special Issues* (issues of this periodical devoted primarily to a specific subject). The Subject Index includes subject cross-references as required by the subject matter.

AUTHOR INDEX

A

Abrams, Richard L., *see* Klein, Marvin B.; *J-QE 75 Aug* 609-615 (1D01)
Adams, C. R., *see* Wood, O. R., II; *J-QE 75 Sep* 72D-73D (2G04)
Adams, M. J., *see* Thomas, Ben; *J-QE 75 Jul* 528-532 (3D10)
Adams, M. J., *see* Gründorfer, Stephan; *J-QE 75 Jul* 532-537 (3D14)
Ahlstrom, H. G., *see* Holzrichter, J. F.; *J-QE 75 Sep* 46D (2E06)
Ahmed, S. A., J. S. Gergely, and D. Infante; Energy transfer processes in organic dye laser mixtures (CLEA 75 Abstr.); *J-QE 75 Sep* 2D-3D (1B04)
Aiki, K., *see* Nakamura, Michiharu; *J-QE 75 Jul* 436-439 (2E02)
Alcock, A. J., Robert Fedosejevs, and Andrew C. Walker; Gain characteristics of a multiatmosphere UV-preionized CO_2 laser; *J-QE 75 Sep* 767-773 (1D03)
Alcock, A. J., P. B. Corkum, D. J. James, and K. Leopold; A scalable high-speed switch for high-power CO_2 laser radiation (CLEA 75 Abstr.); *J-QE 75 Sep* 96D (3A13)
Aldridge, F. T.; Stimulated-emission cross section and inversion lifetime in a three-atmosphere iodine photodissociation laser (Corresp.); *J-QE 75 May* 215-216 (1C09)
Aleksanian, A. G., I. A. Poluektov, and Y. M. Popov; Theory of optical gain and threshold properties of semiconductor lasers; *J-QE 74 Mar* 297-305 (1A03) *Correction, J-QE 75 Jul* 375 (1E05)
Alferov, Z. I., V. M. Andreyev, S. A. Gurevich, R. F. Kazarinov, V. R. Larionov, M. N. Mizerov, and E. L. Portnoy; Semiconductor lasers with the light output through the diffraction grating on the surface of the waveguide layer; *J-QE 75 Jul* 449-451 (2F01)
Alhaider, M. A., *see* Tsai, C. S.; *J-QE 75 Sep* 10D (2B12)
Alimonda, A. S., *see* Burnham, R. D.; *J-QE 75 Jul* 418-420 (2C12)
Allario, Frank, Clayton H. Bair, and Jack F. Butler; Resolution spectral measurements of SO_2 from 1176.0 to 1265.8 cm^{-1} using a single PbSe laser with magnetic and current tuning; *J-QE 75 May* 205-209 (1B13)
Ammann, E. O.; High repetition-rate (kHz) lithium iodate optical parametric oscillator (CLEA 75 Abstr.); *J-QE 75 Sep* 65D (2F11)
Ammon, G., D. Herzog, C. Reno, and H. Zadell; A phase-comparison monopulse laser rangefinder/altimeter (CLEA 75 Abstr.); *J-QE 75 Sep* 50D-51D (2E10)
Ammon, G., *see* Herzog, D. G.; *J-QE 75 Sep* 51D-52D (2E11)
Anderson, R. S., L. Springer, B. G. Bricks, and T. W. Karras; A discharge heated copper vapor laser (Corresp.); *J-QE 75 Apr* 172-174 (1D12)
Anderson, R. S., B. G. Bricks, L. W. Springer, and T. W. Karras; A discharge heated copper vapor master oscillator power amplifier (CLEA 75 Abstr.); *J-QE 75 Sep* 56D-57D (2F02)
Anderson, R. S., *see* Bricks, B. G.; *J-QE 75 Sep* 57D (2F03)
Andreyev, V. M., *see* Alferov, Z. I.; *J-QE 75 Jul* 449-451 (2F01)
Andrysiak, S. J., *see* Tregay, G. W.; *J-QE 75 Aug* 672-678 (2C06)
Angelbeck, A., *see* Boedeker, L.; *J-QE 75 Aug* 713 (2F05)
Angelbeck, A. W., *see* Lynds, L.; *J-QE 75 Aug* 713-714 (2F05)
Angelbeck, A. W., *see* Foster, M. C.; *J-QE 75 Aug* 714 (2F06)
Antonov, V. S., I. N. Knyazev, V. S. Letokhov, and V. G. Movshev; High-repetition-rate H_2 vacuum-ultraviolet laser applications: Photoionization and excitation of luminescence (CLEA 75 Abstr.); *J-QE 75 Sep* 92D (3A09)
Arthurs, E. G., D. J. Bradley, C. B. Edwards, A. I. Ferguson, D. R. Hull, M. H. R. Hutchinson, C. C. Ling, and M. W. McGeoch; Co-axial electron-beam pumped VUV laser oscillators and amplifiers (CLEA 75 Abstr.); *J-QE 75 Sep* 28D (2D02)
Asakawa, K., M. Kondo, Y. Ohta, F. Saito, and T. Yamazaki; Multimode Bragg diffractions in an ion-exchanged optical waveguide with a sputter-etched periodic surface corrugation (Corresp.); *J-QE 75 Jun* 304-306 (1F12)
Asami, Yoshihiro, *see* Fujii, Kan-Ichi; *J-QE 75 Mar* 111-114 (1B03)
Attwood, D. T., E. L. Pierce, and L. W. Coleman; Conversion efficiency and pulse shortening of a frequency tripled, subnanosecond, 1.06 μm pulse (CLEA 75 Abstr.); *J-QE 75 Sep* 68D-69D (2F14)
Auston, D. H., *see* Johnson, A. M.; *J-QE 75 Jun* 283-287 (1E05)
Avivi, P., *see* Keren, H.; *J-QE 75 Aug* 590-594 (1B10)

B

Bachert, H., P. G. Eliseev, M. A. Manko, V. P. Strahov, S. Raab, and Chan Min Thay; Multimode operation and mode-locking effect in injection lasers; *J-QE 75 Jul* 507-510 (3C03)
Bagratashvili, V. N., I. N. Knyazev, V. S. Letokhov, and V. V. Lobko; Broad-band continuously tunable high-pressure CO_2 laser: Use for excitation of molecules and in molecular spectroscopy (CLEA 75 Abstr.); *J-QE 75 Sep* 94D (3A11)
Bailey, William F., *see* Bletzinger, Peter; *J-QE 75 Jul* 317-323 (1A03)
Bair, Clayton H., *see* Allario, Frank; *J-QE 75 May* 205-209 (1B13)
Baldwin, R. E., B. G. Fike, and J. H. Ladd; Laser color video printer breadboard (CLEA 75 Abstr.); *J-QE 75 Sep* 9D (2B11)
Ballik, Edward A., *see* Garside, Brian K.; *J-QE 75 Jun* 264-270 (1C14)
Ballik, Edward A., *see* Garside, Brian K.; *J-QE 75 Aug* 583-589 (1B03)
Barch, W. E., *see* Fetterman, H. R.; *J-QE 75 Sep* 88D-89D (3A05)
Barger, R. L., *see* West, J. B.; *J-QE 75 Sep* 18D-19D (2C06)
Bargeron, C. B., *see* Benson, R. C.; *J-QE 75 Aug* 688-689 (2D08)
Barnes, P. A., *see* Casey, H. C., Jr.; *J-QE 75 Jul* 467-470 (2G05)
Baron, K. U., and B. Stadler; New visible laser transitions in Ba I and Ba II (Note); *J-QE 75 Oct* 852-853 (1D08)
Barrett, J. J., and R. F. Begley; Low-power CW generation of coherent anti-Stokes Raman radiation in CH_4 gas (CLEA 75 Abstr.); *J-QE 75 Sep* 89D-90D (3A06)
Barry, James D., and Chandler J. Kennedy; Thermooptical effects of intracavity $Ba_2Na(NbO_3)_5$ on a frequency-doubled Nd:YAG laser; *J-QE 75 Aug* 575-579 (1A13)
Bass, Michael; Electrooptic Q switching of the Nd:YVO_4 laser without an intracavity polarizer (Corresp.); *J-QE 75 Dec* 938-939 (1A12)
Basu, R., *see* Christensen, C. P.; *J-QE 75 Oct* 849-850 (1D05)
Batifol, Edmond M., *see* Schwartz, Christiane A.; *J-QE 75 Aug* 616-623 (1D08)
Batifol, Edmond M., *see* Oudar, Jean-Louis; *J-QE 75 Aug* 623-629 (1E01)
Bauer, S. H., *see* Stricker, J.; *J-QE 75 Aug* 701-702 (2E07)
Bauer, S. H., *see* Shaub, W. H.; *J-QE 75 Aug* 714 (2F06)
Bauer, S. H., *see* Lory, E. R.; *J-QE 75 Aug* 714-715 (2F06)
Baumann, W., J. A. Blauer, S. W. Zelazny, and W. C. Solomon; Kinetic model and computer simulation of continuous wave DF–CO_2 chemical transfers lasers (CHEMLAS 74 Digest); *J-QE 75 Aug* 711-712 (2F03)
Becker, R. A., *see* Loh, K. W.; *J-QE 75 Sep* 86D (3A03)
Beckwith, P. J., *see* McLeary, R.; *J-QE 75 Sep* 90D-91D (3A07)
Begley, R. F., *see* Barrett, J. J.; *J-QE 75 Sep* 89D-90D (3A06)
Beisser, F. A., and D. J. Eilenberger; Pumping of red continuous-wave laser dyes (Corresp.); *J-QE 75 Jul* 372 (1E02)

Bélanger, P. A., and J. Boivin; Multigigawatt peak-power generation from a tandem of TEA-CO_2 lasers (CLEA 75 Abstr.); *J-QE 75 Sep* 73D-74D
Benard, D. J., *see* Benson, R. C.; *J-QE 75 Aug* 697 (2E03)
Bennett, M. J., *see* Liberman, I.; *J-QE 75 Sep* 44D (2E04)
Benson, R. C., C. B. Bargeron, and R. E. Walker; Parametric investigation of the Na–N_2O + CO chemical laser (CHEMLAS 74 Digest); *J-QE 75 Aug* 688-689 (2D08)
Benson, R. C., D. J. Benard, and R. E. Walker; Vibrational relaxation of N_2 and CO_2(001) by alkali metal atoms (CHEMLAS 74 Digest); *J-QE 75 Aug* 697 (2E03)
Benson, S. W., *see* Eckstrom, D. J.; *J-QE 75 Aug* 691 (2D11)
Bernhardt, A. F., D. E. Duerre, J. R. Simpson, and L. L. Wood; Application of photodeflection to spectroscopy (CLEA 75 Abstr.); *J-QE 75 Sep* 19D (2C07)
Berry, M. J., *see* West, G. A.; *J-QE 75 Aug* 687 (2D07)
Bett, T. H., *see* Smith, A. L. S.; *J-QE 75 Jul* 335-340 (1B07)
Bickart, C. J., *see* Hieslmair, H.; *J-QE 75 Sep* 54D (2E14)
Bickel, G., *see* Kao, C.; *J-QE 75 Sep* 76D-77D (2G08)
Bicknell, W. E., L. R. Tomasetta, and R. H. Kingston; 10.6-μm FM-chirp radar using narrow-band correlation detection (Corresp.); *J-QE 75 Jun* 308-311 (1G02)
Bidichand, K., *see* Kurnit, N. A.; *J-QE 75 Apr* 174-176 (1D14)
Bingham, F. W., *see* Johnson, A. W.; *J-QE 75 Sep* 56D (2F02)
Birger, E. M., *see* Zakharov, V. M.; *J-QE 75 Sep* 82D (2G14)
Birnbaum, M., *see* DeShazer, L. G.; *J-QE 75 Sep* 84D (3A01)
Bischel, William K., *see* Fisher, Robert A.; *J-QE 75 Jan* 46-52 (1D06)
Bischel, W. K., P. J. Kelly, and C. K. Rhodes; Collisional studies of $^{12}CH_3F$ using Doppler free two photon absorption techniques (CLEA 75 Abstr.); *J-QE 75 Sep* 24D-25D (2C12)
Bjorkholm, J. E., E. H. Turner, and D. B. Pearson; Use of a resonant atomic dispersion to convert frequency modulated CW light into a train of subnanosecond pulses (CLEA 75 Abstr.); *J-QE 75 Sep* 68D (2G01)
Bjorklund, Gary C.; Effects of focusing on third-order nonlinear processes in isotropic media; *J-QE 75 Jun* 287-296 (1E09)
Black, G., R. S. Sharpless, and D. C. Lorents; Quantum yields of O(^{1}S) from N_2O and S(^{1}S) from OCS in the vacuum ultraviolet (CHEMLAS 74 Digest); *J-QE 75 Aug* 704 (2E10)
Blair, L. S., *see* Getzinger, R. W.; *J-QE 75 Aug* 698 (2E04)
Blauer, J. A., *see* Baumann, W.; *J-QE 75 Aug* 711-712 (2F03)
Bletzinger, Peter, David A. LaBorde, William F. Bailey, William H. Long, Jr., Peter D. Tannen, and Alan Garscadden; Influence of contaminants on the CO_2 electric-discharge laser; *J-QE 75 Jul* 317-323 (1A03)
Bletzinger, Peter, *see* Olson, Robert A.; *J-QE 75 Sep* 95D-96D (3A12)
Bliss, E. S., G. E. Sommargren, and H. J. Weaver; Loss of focusable energy due to small-scale nonlinear effects (CLEA 75 Abstr.); *J-QE 75 Sep* 29D (2D03)
Blum, F. A., *see* Doerbeck, F. H.; *J-QE 75 Jul* 464-467 (2G02)
Blum, F. A., *see* Campbell, J. C.; *J-QE 75 Sep* 63D-64D (2F09)
Blum, Joseph M., J. C. McGroddy, Paul G. McMullin, K. K. Shih, Archibald W. Smith, and J. F. Ziegler; Oxygen-implanted double-heterojunction GaAs/GaAlAs injection lasers; *J-QE 75 Jul* 413-418 (2C07)
Bluyssen, H. J. A., Robert E. McIntosh, A. F. van Etteger, and Peter Wyder; Pulsed operation of an optically pumped far-infrared molecular laser; *J-QE 75 Jul* 341-348 (1B13)
Boedecker, V., and K.-H. Drake; Influence of spatial intensity distribution of laser beam on deep welding geometry (CLEA 75 Abstr.); *J-QE 75 Sep* 47D (2E07)
Boedeker, L., M. Foster, N. Nomiyama, L. Lynds, A. Angelbeck, and G. Wisner; Some experimental results with stable selected-line resonators in a relatively high gain CW HF chemical laser (CHEMLAS 74 Digest); *J-QE 75 Aug* 713 (2F05)
Bogatov, A. P., P. G. Eliseev, and B. N. Sverdlov; Anomalous interaction of spectral modes in a semiconductor laser; *J-QE 75 Jul* 510-515 (3C06)
Boivin, J., *see* Bélanger, P. A.; *J-QE 75 Sep* 73D-74D
Bolin, S. R.; Pulsed laser welding of clad metals (CLEA 75 Abstr.); *J-QE 75 Sep* 48D (2E08)
Boltz, J. C., *see* Bret, G.; *J-QE 75 Sep* 12D-13D (2B14)
Bortfeld, David P.; Mode-dependent retardation in (Ga,Al)P waveguide modulators (Corresp.); *J-QE 75 Mar* 108-110 (1A14)
Bott, J. F., *see* Heidner, R. F.; *J-QE 75 Aug* 696 (2E02)
Boulnois, J. L., and R. B. Miles; Time dependent kinetics of CO-EDL with multi-level pumping (CHEMLAS 74 Digest); *J-QE 75 Aug* 707-708 (2E13)
Boyd, J. T., and C. L. Chen; Integrated optical silicon photodiode array (CLEA 75 Abstr.); *J-QE 75 Sep* 40D-41D (2D14)
Boyd, R. D., *see* Simmons, W. W.; *J-QE 75 Sep* 31D-32D (2D05)
Bradford, R. S., Jr., and H. P. Broida; Chemiluminescence and photo-luminescence spectroscopy of the barium monohalides (CHEMLAS 74 Digest); *J-QE 75 Aug* 692 (2D12)
Bradley, D. J., and W. Sibbett; Sub-picosecond optical chronoscopy (CLEA 75 Abstr.); *J-QE 75 Sep* 25D-26D (2C13)
Bradley, D. J., *see* Arthurs, E. G.; *J-QE 75 Sep* 28D (2D02)
Bradley, Lorne L. T., *see* Panarella, Emilio; *J-QE 75 May* 181-185 (1A03)
Brau, C. A., *see* Ewing, J. J.; *J-QE 75 Sep* 92D-93D (3A09)
Braun, W., *see* Kaldor, A.; *J-QE 75 Aug* 697-698 (2E03)
Braun, W., *see* Kurylo, M. J.; *J-QE 75 Aug* 702-703 (2E08)
Brederlow, G., K. J. Witte, E. Fill, K. Hohla, and R. Volk; The pulsed high power iodine laser Asterix III (CLEA 75 Abstr.); *J-QE 75 Sep* 42D-43D (2E02)
Bret, G., M. C. Hurand, and J. C. Boltz; Face-pumped mirror-like structure as an alternative to disk amplifiers (CLEA 75 Abstr.); *J-QE 75 Sep* 12D-13D (2B14)
Bricks, B. G., *see* Anderson, R. S.; *J-QE 75 Apr* 172-174 (1D12)
Bricks, B. G., *see* Anderson, R. S.; *J-QE 75 Sep* 56D-57D (2F02)
Bricks, B. G., T. W. Karras, T. E. Buczacki, L. S. Springer, and R. S. Anderson; High repetition rate flowing copper vapor laser (CLEA 75 Abstr.); *J-QE 75 Sep* 57D (2F03)
Bridenbaugh, P. M., *see* Weber, H. P.; *J-QE 75 Sep* 100D (3B03)
Broida, H. P., *see* Bradford, R. S., Jr.; *J-QE 75 Aug* 692 (2D12)
Broida, H. P., *see* Capelle, G. A.; *J-QE 75 Aug* 692 (2D12)
Broida, H. P., *see* West, J. B.; *J-QE 75 Aug* 692-693 (2D12)
Bronfin, B. R., *see* Sadowski, T. J.; *J-QE 75 Aug* 705-706 (2E11)
Brown, R. D. H., G. P. Glass, and I. W. M. Smith; Relaxation of HCl($v=1$) and DCl($v=1$) by Cl and O atoms (CHEMLAS 74 Digest); *J-QE 75 Aug* 695-696 (2E01)
Brown, Robert T.; Long-pulse generation in Rhodamine-6G pumped by a CO_2-laser-heated plasma (Note); *J-QE 75 Sep* 800-801 (1F08)
Brown, W. P., Jr., and T. R. O'Meara; Polarization reference imaging systems: Basic principles (CLEA 75 Abstr.); *J-QE 75 Sep* 52D-53D (2E12)
Browne, P. G., *see* Smith, A. L. S.; *J-QE 75 Jul* 335-340 (1B07)
Buchwald, M. I., and G. J. Wolga; Vibrational deactivation of $CO_2(^3\Sigma)$ by collisions with atoms (CHEMLAS 74 Digest); *J-QE 75 Aug* 697 (2E03)
Buczacki, T. E., *see* Bricks, B. G.; *J-QE 75 Sep* 57D (2F03)
Buholz, N. E.; Rotational–vibrational line competition in a dual-polarization CO_2 laser (Corresp.); *J-QE 75 Nov* 917-919 (1E07)
Burde, D. H., R. A. McFarlane, and J. R. Wiesenfeld; Studies of the deactivation of electronically excited iodine atoms (CHEMLAS 74 Digest); *J-QE 75 Aug* 709 (2F01)
Burdick, B., *see* Tripodi, R.; *J-QE 75 Aug* 716 (2F08)
Burkhart, G. H., *see* Rice, R. R.; *J-QE 75 Sep* 14D (2C02)
Burnham, R. D., D. R. Scifres, J. C. Tramontana, and A. S. Alimonda; Striped-substrate double-heterostructure lasers; *J-QE 75 Jul* 418-420 (2C12)
Burnham, R. D., D. R. Scifres, and W. Streifer; Low-divergence beams from grating-coupled composite-guide heterostructure GaAlAs diode lasers (CLEA 75 Abstr.); *J-QE 75 Sep* 98D-99D (3B01)
Burnham, Robert D., *see* Streifer, William; *J-QE 75 Apr* 154-161 (1C08)
Burnham, Robert D., Donald R. Scifres, and William Streifer; Single-heterostructure distributed-feedback GaAs-diode lasers; *J-QE 75 Jul* 439-449 (2E05)
Burnham, Robert D., *see* Streifer, William; *J-QE 75 Nov* 867-873 (1A13)
Burns, William K., and A. Fenner Milton; Mode conversion in planar-dielectric separating waveguides; *J-QE 75 Jan* 32-39 (1C06)
Burns, William K., *see* Hocker, G. Benjamin; *J-QE 75 Jun* 270-276 (1D06)
Burns, W. K., A. F. Milton, E. J. West, and A. B. Lee; A new optical 3-dB coupler (CLEA 75 Abstr.); *J-QE 75 Sep* 42D (2E02)
Burrus, C. A., *see* Lee, T. P.; *J-QE 75 Jul* 432-435 (2D12)
Butler, Jack F., *see* Allario, Frank; *J-QE 75 May* 205-209 (1B13)
Butler, J. K., H. Kressel, and I. Ladany; Internal optical loss in very thin CW heterostructure laser diodes; *J-QE 75 Jul* 402-408 (2B10)
Byer, R. L., *see* Henesian, M.; *J-QE 75 Sep* 26D (2C14)
Byer, Robert L., *see* Choy, Michael M.; *J-QE 75 Jan* 40-45 (1C14)
Byron, S. R., *see* Nelson, L. Y.; *J-QE 75 Aug* 686 (2D06)

C

Caird, John A., and Larry G. DeShazer; Analysis of laser emission in Ho^{3+}-doped materials; *J-QE 75 Mar* 97-99 (1A03)
Caird, John A., Larry G. DeShazer, and John Nella; Characteristics of room-temperature 2.3-μm laser emission from Tm^{3+} in YAG and $YAlO_3$; *J-QE 75 Nov* 874-881 (1B06)
Campbell, J. C., *see* Doerbeck, F. H.; *J-QE 75 Jul* 464-467 (2G02)
Campbell, J. C., and F. A. Blum; GaAs electrooptic channel-waveguide modulator (CLEA 75 Abstr.); *J-QE 75 Sep* 63D-64D (2F09)
Campillo, A. J., *see* Shapiro, S. L.; *J-QE 75 Sep* 5D-6D (2B07)
Camus, D., *see* Christophe, B.; *J-QE 75 Sep* 32D-33D (2D06)
Capelle, G. A., and H. P. Broida; The diatomic oxides and halides of Ca and Sr:photon yields and $A'^1\pi$ molecular constants (CHEMLAS 74 Digest); *J-QE 75 Aug* 692 (2D12)
Carabetta, R. A., and M. J. Linevsky; Spectroscopic studies of HCl* producing reactions (CHEMLAS 74 Digest); *J-QE 75 Aug* 689 (2D09)
Carman, Robert L., *see* Moran, Michael J.; *J-QE 75 Jun* 259-263 (1C09)
Casey, H. C., Jr., A. Y. Cho, and P. A. Barnes; Application of molecular-beam epitaxial layers to heterostructure lasers; *J-QE 75 Jul* 467-470 (2G05)
Cavalleri, R., *see* Naismith, R.; *J-QE 75 Aug* 716 (2F08)
Center, R. E., and H.-L. Chen; Vibrational excitation of HCl by electron impact (CHEMLAS 74 Digest); *J-QE 75 Aug* 687 (2D07)
Chang, David C., *see* Kuester, Edward F.; *J-QE 75 Nov* 903-907 (1D07)
Chang, W. S. C., *see* Loh, K. W.; *J-QE 75 Sep* 86D (3A03)
Channin, D. J., *see* Hammer, Jacob M.; *J-QE 75 Apr* 138-148 (1B06)
Chen, Bor-Uei, and C. L. Tang; Generation of second harmonic UV radiation using a nonlinear substrate coated with a UV absorbing thin film waveguide (Note); *J-QE 75 Apr* 177-178 (1E03)
Chen, C. L., *see* Boyd, J. T.; *J-QE 75 Sep* 40D-41D (2D14)
Chen, Hao-Lin, and Steve Fried; Laser-excited electronic-to-electronic energy transfer in sodium; *J-QE 75 Aug* 669-672 (2C03)
Chen, H.-L., *see* Center, R. E.; *J-QE 75 Aug* 687 (2D07)
Chen, H.-L., *see* Mangano, J. A.; *J-QE 75 Aug* 705 (2E11)
Chenausky, P. P., R. J. Freiberg, and D. W. Fradin; Recirculating DF/HF chemical lasers suitable for portable system applications (CLEA 75 Abstr.); *J-QE 75 Sep* 58D (2F04)
Chinn, S. R., J. W. Pierce, and H. Heckscher; Low-threshold, transversely-excited NdP_5O_{14} laser (CLEA 75 Abstr.); *J-QE 75 Sep* 62D (2F08)
Chinn, Stephen R., James W. Pierce, and Helmut Heckscher; Low-threshold, transversely excited NdP_5O_{14} laser; *J-QE 75 Sep* 747-754 (1B11)
Cho, A. Y., *see* Casey, H. C., Jr.; *J-QE 75 Jul* 467-470 (2G05)
Chou, M. S., and T. A. Cool; Experimental studies of reaction systems of interest for chemical laser operation at short wavelengths (CHEMLAS 74 Digest); *J-QE 75 Aug* 691-692 (2D11)
Choy, Michael M., Salim Ciraci, and Robert L. Byer; Bond-orbital model for second-order susceptibilities; *J-QE 75 Jan* 40-45 (1C14)
Christensen, C. P., W. H. Steier, and R. Basu; Guided-wave acoustooptic FM modulator (Corresp.); *J-QE 75 Oct* 849-850 (1D05)
Christophe, B., D. Camus, J. Gay, and A. Journet; Measurement of atmospheric absorption using solar infrared heterodyne radiometer and its application to the knowledge of pollutant densities (CLEA 75 Abstr.); *J-QE 75 Sep* 32D-33D (2D06)
Ciraci, Salim, *see* Choy, Michael M.; *J-QE 75 Jan* 40-45 (1C14)
Claspy, P. C., Y-H. Pao, S. Kwong, and E. Nodov; Laser optoacoustic detection of explosive vapors (CLEA 75 Abstr.); *J-QE 75 Sep* 37D (2D11)
Clendening, C., *see* Wendelken, C. P.; *J-QE 75 Aug* 694-695 (2D14)
Coates, Robert J., *see* Peyton, Bernard J.; *J-QE 75 Aug* 569-574 (1A03)
Cohen, Steven C., *see* Peyton, Bernard J.; *J-QE 75 Aug* 569-574 (1A03)
Coleman, J. J., N. Holonyak, Jr., M. J. Lubowise, P. D. Wright, W. O. Groves, and D. L. Keune; Liquid phase epitaxial $In_{1-x}Ga_xP_{1-z}/GaAs_{1-y}nP_y$ heterojunction lasers; *J-QE 75 Jul* 471-476 (2G09)

Coleman, L. W., *see* Attwood, D. T.; *J-QE 75 Sep* 68D-69D (2F14)
Coleman, Paul D., *see* Nachshon, Yehuda; *J-QE 75 Aug* 654-660 (2B02)
Coleman, P. D., *see* Newman, L.; *J-QE 75 Aug* 686 (2D06)
Combemale, Y., *see* Papuchon, M.; *J-QE 75 Sep* 99D-100D (3B02)
Comerford, L. D., *see* Zory, P.; *J-QE 75 Jul* 451-457 (2F03)
Conroy, J. J., *see* Feichtner, J. D.; *J-QE 75 Sep* 66D-67D (2F12)
Conwell, Esther M.; 'Buried modes' in planar media with nonmonotonically varying index of refraction (Corresp.); *J-QE 75 May* 217-218 (1C11)
Cool, T. A., *see* Chou, M. S.; *J-QE 75 Aug* 691-692 (2D11)
Corkum, P. B., *see* Alcock, A. J.; *J-QE 75 Sep* 96D (3A13)
Coutts, Gerald W., and LaMar B. Olk; High-speed radiation camera using a PTM ruby laser and hydrated electron absorption phenomena (CLEA 75 Abstr.); *J-QE 75 Sep* 6D (2B08)
Craig, J. M., *see* Ewanizky, T. F.; *J-QE 75 Sep* 17D-18D (2C05)
Creighton, J. R.; Calculation of rotational nonequilibrium in a pulsed HF laser (CHEMLAS 74 Digest); *J-QE 75 Aug* 699 (2E05)
Cross, E. F., *see* Kwok, M. A.; *J-QE 75 Aug* 718 (2F10)
Cross, Peter H., *see* Stark, Donald S.; *J-QE 75 Sep* 774-778 (1D10)
Cross, Peter S., and William G. Oldham; Theory of optical-gain measurements; *J-QE 75 May* 190-197 (1A12)
Cuellar, E., and G. C. Pimentel; Rotational chemical lasers from H*X* elimination reactions (CHEMLAS 74 Digest); *J-QE 75 Aug* 688 (2D08)
Cummings, J. C., and C. M. Dube; Investigation of a supersonic CW HF-chain laser (CHEMLAS 74 Digest); *J-QE 75 Aug* 712 (2F04)
Cupitt, L. T., and W. L. Gamble; Role of atomic sulfur in the $O+CS_2$ reaction (CHEMLAS 74 Digest); *J-QE 75 Aug* 700-701 (2E06)
Cuthbert, J. D., *see* Fehrs, D. L.; *J-QE 75 Sep* 21D (2C09)

D

Daugherty, J. D., *see* Mangano, J. A.; *J-QE 75 Aug* 705 (2E11)
Davies, Terence J., and Melvin A. Nelson; Optical sampling transient analyzer (OSTA) system (CLEA 75 Abstr.); *J-QE 75 Sep* 7D (2B09)
Davis, C. C., and R. A. McFarlane; Vibrational deactivation of CO molecules by atomic oxygen (CHEMLAS 74 Digest); *J-QE 75 Aug* 701 (2E07)
Davis, Christopher C., *see* Pirkle, Robert J.; *J-QE 75 Oct* 834-838 (1C04)
Davis, J. W., *see* Gilmartin, T. J.; *J-QE 75 Sep* 32D (2D06)
Davis, S. J., G. Hager, and S. G. Hadley; F_2 reactions as possible laser candidates (CHEMLAS 74 Digest); *J-QE 75 Aug* 693 (2D13)
Davis, T. P., and M. A. Nelson; A pulsed UV rangefinder (CLEA 75 Abstr.); *J-QE 75 Sep* 50D (2E10)
Dekhtar, I. Ya., L. I. Ivanov, N. V. Karlov, A. M. Prokhorov, and N. N. Rykalin; Use of pulsed laser treatment to change physical properties of metals and semiconductors (CLEA 75 Abstr.); *J-QE 75 Sep* 83D (2G14)
DeShazer, Larry G., *see* Caird, John A.; *J-QE 75 Mar* 97-99 (1A03)
DeShazer, Larry G., *see* Caird, John A.; *J-QE 75 Nov* 874-881 (1B06)
DeShazer, L. G., A. W. Tucker, M. Birnbaum, and C. L. Fincher; CW and self-*Q*-switched laser operation of Nd:YVO_4 (CLEA 75 Abstr.); *J-QE 75 Sep* 84D (3A01)
DeTemple, T. A., *see* Newman, L.; *J-QE 75 Aug* 686 (2D06)
Deutsch, J-C., *see* Valette, S.; *J-QE 75 Sep* 39D-40D (2D13)
Devor, D. P.; 2.06 μm laser performance and design options for rangefinder and illuminator applications (CLEA 75 Abstr.); *J-QE 75 Sep* 13D-14D (2C01)
Dewey, C. F., Jr., *see* Oettinger, P. E.; *J-QE 75 Sep* 3D-4D (2B05)
Dewey, H. J., *see* Lamotte, M.; *J-QE 75 Aug* 702 (2E08)
DeYoung, R. J., W. E. Wells, J. T. Verdeyen, and G. H. Miley; A direct nuclear-pumped Ne–N_2 laser (CLEA 75 Abstr.); *J-QE 75 Sep* 97D (3A14)
Dianov, E. M., A. Ya. Karasik, L. S. Kornienko, A. M. Prokhorov, and I. A. Shcherbakov; Measurement of the cross section for stimulated emission in neodymium-doped glasses (CLEA 75 Abstr.); *J-QE 75 Sep* 83D (2G14)
Dickson, L., and R. L. Soderstrom; Lasers in supermarket point of sale systems (CLEA 75 Abstr.); *J-QE 75 Sep* 23D-24D (2C11)
DiMarzio, C. A., *see* Sonnenschein, C. M.; *J-QE 75 Sep* 35D (2D09)
DiNardo, Anthony J., *see* Peyton, Bernard J.; *J-QE 75 Aug* 569-574 (1A03)
Doerbeck, F. H., K. L. Lawley, F. A. Blum, and J. C. Campbell; Monolithic $Ga_{1-x}In_xAs$ diode lasers; *J-QE 75 Jul* 464-467 (2G02)
Dothan, F., *see* Keren, H.; *J-QE 75 Aug* 590-594 (1B10)
Dows, D. A., *see* Wu, C.Y. R.; *J-QE 75 Sep* 20D (2C08)
Drakatos, Panagiotis A.; Soil compaction checks by means of a laser device (CLEA 75 Abstr.); *J-QE 75 Sep* 84D-86D (3A01)
Drake, K.-H., *see* Boedecker, V.; *J-QE 75 Sep* 47D (2E07)
Drexhage, M. G., *see* Tregay, G. W.; *J-QE 75 Aug* 672-678 (2C06)
Dube, C. M., *see* Cummings, J. C.; *J-QE 75 Aug* 712 (2F04)
Dubrin, James W., *see* Tuccio, Sam A.; *J-QE 75 Sep* 101D (3B04)
Duerre, D. E., *see* Bernhardt, A. F.; *J-QE 75 Sep* 19D (2C07)
Duffy, Michael T., *see* Hammer, Jacob M.; *J-QE 75 Apr* 138-148 (1B06)
Duguay, M. A., and J. N. Olsen; Observations of picosecond X-ray pulses (Corresp.); *J-QE 75 Apr* 170-172 (1D10)
Duguay, Michel A., *see* Vogel, Gerald C.; *J-QE 74 Sep* 642-646 (1B02)
Dumke, W. P.; The angular beam divergence in double-heterojunction lasers with very thin active regions; *J-QE 75 Jul* 400-402 (2B08)
Dunphy, J. R., *see* McIntyre, C. M.; *J-QE 75 Sep* 81D (2G13)
Dyment, John C., *see* Garel-Jones, P.; *J-QE 75 Jul* 408-413 (2C02)

E

Eckardt, R. C., *see* Lehmberg, R. H.; *J-QE 75 Sep* 69D-70D (2G01)
Eckbreth, Alan C.; Coupling considerations for ring resonators (Corresp.); *J-QE 75 Sep* 796-798 (1F04)
Eckstrom, D. J., S. A. Edelstein, D. L. Huestis, M. Luria, B. E. Perry, and S. W. Benson; Studies of visible chemical lasers based on reactions of metal atoms with various oxidizers (CHEMLAS 74 Digest); *J-QE 75 Aug* 691 (2D11)
Edelstein, S. A., *see* Eckstrom, D. J.; *J-QE 75 Aug* 691 (2D11)
Edwards, C. B., *see* Arthurs, E. G.; *J-QE 75 Sep* 28D (2D02)
Eicher, Hermann; Third-order susceptibility of alkali metal vapors; *J-QE 75 Apr* 121-130 (1A03)
Eichler, H., G. Schick, and W. Wiesemann; Realization of a mode-selective three-mirror reflector (Corresp.); *J-QE 75 Apr* 168-170 (1D08)
Eilenberger, D. J., *see* Beisser, F. A.; *J-QE 75 Jul* 372 (1E02)
Eliseev, P. G., *see* Bachert, H.; *J-QE 75 Jul* 507-510 (3C03)
Eliseev, P. G., *see* Bogatov, A. P.; *J-QE 75 Jul* 510-515 (3C06)
Elliott, C. James, and Bergen R. Suydam; Focusing phenomena in air–glass laser structures; *J-QE 75 Nov* 863-866 (1A09)
Elliott, R. A., *see* Massey, G. A.; *J-QE 75 Jul* 358-364 (1D02)
Emanuel, G., *see* Grohs, G. L.; *J-QE 75 Aug* 717 (2F09)
Eng, R. S., and D. L. Spears; Frequency stabilization and absolute frequency measurements of a CW HF/DF laser (CLEA 75 Abstr.); *J-QE 75 Sep* 87D-88D (3A04)
English, T. C., *see* West, J. B.; *J-QE 75 Sep* 18D-19D (2C06)
Epstein, D. J., *see* Fontana, R. E., Jr.; *J-QE 75 Sep* 38D (2D12)
Erez, G., *see* Smilanski, I.; *J-QE 75 Nov* 919-920 (1E09)
Erickson, E. G., and L. L. Harper; Picosecond-pulse, fieldable frequency-doubled Nd:YAG laser system for ultra-precision ranging (CLEA 75 Abstr.); *J-QE 75 Sep* 16D-17D (2C04)
Ernst, G. J., *see* Witteman, W. J.; *J-QE 75 May* 198-204 (1B06)
Ernst, G. J., and W. J. Witteman; On the stability of modes in a laser resonator with an active medium (Corresp.); *J-QE 75 Nov* 920-921 (1E10)
Etzold, K. F., *see* Mezrich, R.; *J-QE 75 Sep* 9D-10D (2B11)
Evenson, Kenneth M., *see* Petersen, F. Russell; *J-QE 75 Oct* 838-843 (1C08)
Evenson, K. M., *see* Jennings, D. A.; *J-QE 75 Aug* 637 (1F01)
Evers, W. H., L. S. Forman, and J. J. Vieceli; Supersonic mixing DF–CO_2 transfer chemical laser: Experiment (CHEMLAS 74 Digest); *J-QE 75 Aug* 711 (2F03)
Evers, W. H., *see* Vieceli, J. J.; *J-QE 75 Aug* 711 (2F03)
Ewanizky, T. F., and J. M. Craig; A negative-branch unstable resonator Nd:YAG laser (CLEA 75 Abstr.); *J-QE 75 Sep* 17D-18D (2C05)
Ewing, J. J., and C. A. Brau; Laser action on the XeF $^2\Sigma \rightarrow ^2\Sigma$ band at 3540 Å (CLEA 75 Abstr.); *J-QE 75 Sep* 92D-93D (3A09)

F

Fahlen, Theodore S.; Performance of a compact sealed 200-W CO_2 laser (Corresp.); *J-QE 75 Oct* 848-849 (1D04)
Falk, Joel; A theory of the mode-locked, internally frequency-doubled laser; *J-QE 75 Jan* 21-31 (1B09)
Comments by Kennedy, C. J.; *J-QE 75 Sep* 793-794 (1F01)
Falk, Joel, and C. Breck Hitz; Pulsewidth of the mode-locked, internally frequency-doubled laser; *J-QE 75 Jul* 365-367 (1D09)
Falk, Joel, L. Huff, and Joseph D. Taynai; Solar-pumped, mode-locked, frequency-doubled Nd:YAG laser (CLEA 75 Abstr.); *J-QE 75 Sep* 14D-15D (2C02)
Farcy, J. C., *see* Girard, G.; *J-QE 75 Jun* 241-247 (1B05)
Farcy, J. C., A. Fertal, M. Huguet, G. Girard, and M. Michon; Energy extraction improvement in nanosecond pulse TEA-CO_2 lasers (CLEA 75 Abstr.); *J-QE 75 Sep* 90D (3A07)
Faszer, W., *see* Tulip, J.; *J-QE 75 Sep* 72D (2G04)
Fedosejevs, Robert, *see* Alcock, A. J.; *J-QE 75 Sep* 767-773 (1D03)
Fehrs, D. L., D. F. Munro, J. D. Cuthbert, and G. S. Yanochko; Automatic laser inspection/laser repair system for masks (CLEA 75 Abstr.); *J-QE 75 Sep* 21D (2C09)
Feichtner, J. D., M. Gottlieb, and J. J. Conroy; A tunable collinear acoustooptic filter for the intermediate infrared using single crystal Tl_3AsSe_3 (CLEA 75 Abstr.); *J-QE 75 Sep* 66D-67D (2F12)
Felder, W., and A. Fontijn; High-temperature fast-flow reactor studies of metal atom/N_2O chemiluminescence (CHEMLAS 74 Digest); *J-QE 75 Aug* 703 (2E09)
Feldman, B., *see* Figueira, J. F.; *J-QE 75 Sep* 74D (2G06)
Felsen, L. B., *see* Santana, C.; *J-QE 75 Sep* 58D-59D (2F04)
Ferguson, A. I., *see* Arthurs, E. G.; *J-QE 75 Sep* 28D (2D02)
Ferrar, C., *see* Glenn, W. H.; *J-QE 75 Sep* 5D (2B07)
Fertal, A., *see* Farcy, J. C.; *J-QE 75 Sep* 90D (3A07)
Fetterman, C. C., *see* Simmons, W. W.; *J-QE 75 Sep* 31D-32D (2D05)
Fetterman, H. R., W. E. Barch, and H. R. Schlossberg; Optically pumped 15.90-μm SF_6 laser (CLEA 75 Abstr.); *J-QE 75 Sep* 88D-89D (3A05)
Figueira, J. F., W. H. Reichelt, G. T. Schappert, and B. Feldman; Multiline operation of a CO_2 oscillator/amplifier system (CLEA 75 Abstr.); *J-QE 75 Sep* 74D (2G06)
Figueira, J. F., G. T. Schappert, S. Singer, and S. J. Thomas; Parametric studies of a multiband CO_2 laser (CLEA 75 Abstr.); *J-QE 75 Sep* 74D (2G06)
Fike, B. G., *see* Baldwin, R. E.; *J-QE 75 Sep* 9D (2B11)
Fill, E., *see* Brederlow, G.; *J-QE 75 Sep* 42D-43D (2E02)
Fincher, C. L., *see* DeShazer, L. G.; *J-QE 75 Sep* 84D (3A01)
Firester, A. H., *see* Gorog, I.; *J-QE 75 Sep* 63D (2F09)
Fisher, C. H., *see* Nelson, L. Y.; *J-QE 75 Aug* 686 (2D06)
Fisher, Robert A., and William K. Bischel; Pulse compression for more efficient operation of solid-state laser amplifier chains—Part II; *J-QE 75 Jan* 46-52 (1D06)
Flattau, T., *see* Peyton, B. J.; *J-QE 75 Sep* 80D-81D (2G12)
Foley, Richard J., *see* Tuccio, Sam A.; *J-QE 75 Sep* 101D (3B04)
Foley, R. J., T. C. Kuklo, and O. G. Peterson; A free stream jet for high power dye lasers (CLEA 75 Abstr.); *J-QE 75 Sep* 5D (2B07)
Fonstad, C. G., *see* Tomasetta, L. R.; *J-QE 75 Jul* 384-390 (2A06)
Fontana, R. E., Jr., D. J. Epstein, and A. Linz; Epitaxially grown single crystal KTN for thin film optical modulators (CLEA 75 Abstr.); *J-QE 75 Sep* 38D (2D12)
Fontijn, A., *see* Felder, W.; *J-QE 75 Aug* 703 (2E09)
Forman, L. S., *see* Evers, W. H.; *J-QE 75 Aug* 711 (2F03)
Foster, Harry, *see* Stark, Donald S.; *J-QE 75 Sep* 774-778 (1D10)
Foster, K. D., G. H. Kimbell, and D. R. Snelling; Near single-line operation of a free burning CS_2/O_2N_2O flame laser with a non-dispersive optical cavity (CHEMLAS 74 Digest); *J-QE 75 Aug* 700 (2E06)
Foster, Kenneth D., George H. Kimbell, and David R. Snelling; Near single-line operation of a free-burning $CS_2/O_2/N_2O$ flame laser with a nondispersive optical cavity; *J-QE 75 Jun* 253-258 (1C03)
Foster, M., *see* Boedeker, L.; *J-QE 75 Aug* 713 (2F05)
Foster, M. C., *see* Lynds, L.; *J-QE 75 Aug* 713-714 (2F05)
Foster, M. C., L. Lynds, and A. W. Angelbeck; Temporal characteristics of multiline–multimode CF HF chemical lasers (CHEMLAS 74 Digest); *J-QE 75 Aug* 714 (2F06)
Fradin, D. W., *see* Chenausky, P. P.; *J-QE 75 Sep* 58D (2F04)
François, G. E., *see* Librecht, F. M.; *J-QE 75 Sep* 755-758 (1C05)

Freiberg, R. J., and J. J. Hinchen; Frequency-stable, single-mode CW chemical lasers for mid-IR heterodyne applications (CLEA 75 Abstr.); *J-QE 75 Sep* 57D-58D (2F03)
Freiberg, R. J., *see* Chenausky, P. P.; *J-QE 75 Sep* 58D (2F04)
Freund, S. M., and J. J. Ritter; Laser-induced photochemical enrichment of boron isotopes (CHEMLAS 74 Digest); *J-QE 75 Aug* 702 (2E08)
Fried, Steve, *see* Chen, Hao-Lin; *J-QE 75 Aug* 669-672 (2C03)
Friedman, H. W., and R. G. Morton; Transverse flow flashlamp pumped dye laser (CLEA 75 Abstr.); *J-QE 75 Sep* 4D (2B06)
Fujii, Kan-Ichi, Tsutomu Takahashi, and Yoshihiro Asami; Hollow-cathode-type CW white light laser (Corresp.); *J-QE 75 Mar* 111-114 (1B03)
Fujisawa, Akira, *see* Papayoanou, Aristotle; *J-QE 75 Aug* 579-583 (1A13)
Fulton, J. N., *see* Hieslmair, H.; *J-QE 75 Sep* 54D (2E14)
Fuss, W., and K. Hohla; Pressure broadening and saturation behavior of the iodine laser (CLEA 75 Abstr.); *J-QE 75 Sep* 43D (2E03)

G

Galvan, L., *see* Sutton, D. G.; *J-QE 75 Jan* 54-57 (1D14)
Galvan, L., *see* Sutton, D. G.; *J-QE 75 Feb* 92 (1C02)
Galvan, L., *see* Sutton, D. G.; *J-QE 75 Jun* 312 (1G06)
Gamble, W. L., *see* Cupitt, L. T.; *J-QE 75 Aug* 700-701 (2E06)
Ganiel, U., A. Hardy, G. Neumann, and D. Treves; Amplified spontaneous emission and signal amplification in dye-laser systems; *J-QE 75 Nov* 881-892 (1B13)
Garavaglia, M., *see* Rabal, H. J.; *J-QE 75 Sep* 22D-23D (2C10)
Garel-Jones, P., and John C. Dyment; Calculations of the continuous-wave lasing range and light-output power for double-heterostructure lasers; *J-QE 75 Jul* 408-413 (2C02)
Garmire, E., D. Lovelace, and G. H. B. Thompson; Diffused two-dimensional optical waveguides in GaAs (CLEA 75 Abstr.); *J-QE 75 Sep* 38D-39D (2D12)
Garscadden, A., *see* Prince, J. F.; *J-QE 75 Aug* 687 (2D07)
Garscadden, Alan, *see* Bletzinger, Peter; *J-QE 75 Jul* 317-323 (1A03)
Garscadden, Alan, *see* Olson, Robert A.; *J-QE 75 Sep* 95D-96D (3A12)
Garside, Brian K., John Reid, and Edward A. Ballik; Studies of the inversion and lower leval relaxation in pulsed TE CO_2 discharges; *J-QE 75 Jun* 264-270 (1C14)
Garside, Brian K., John Reid, and Edward A. Ballik; TE CO_2 laser pulse decay and molecular relaxation rates; *J-QE 75 Aug* 583-589 (1B03)
Gay, J., *see* Christophe, B.; *J-QE 75 Sep* 32D-33D (2D06)
Gelbwachs, Jerry, and Thomas S. Hartwick; Radiation-pressure separation of molecules and atoms (Corresp.); *J-QE 75 Jan* 52-54 (1D12)
George, T. V., *see* Wutzke, S. A.; *J-QE 75 Sep* 73D (2G05)
Gerardo, J. B.; Electron-beam-driven chemical lasers (CLEA 75 Abstr.); *J-QE 75 Sep* 56D (2F02)
Gerber, R. A., *see* Patterson, E. L.; *J-QE 75 Aug* 642-648 (2A04)
Gergely, J. S., *see* Ahmed, S. A.; *J-QE 75 Sep* 2D-3D (1B04)
Gerritsen, H. J., and G. Nienhuis; Standing-wave effect in laser-saturation experiments or when 2 is less than 1 (Corresp.); *J-QE 75 Apr* 174 (1D14)
Getzinger, R. W., *see* Schott, G. L.; *J-QE 75 Aug* 690 (2D10)
Getzinger, R. W., L. S. Blair, and N. R. Greiner; Mixture stability in high-power pulsed H_2–F_2 chemical lasers (CHEMLAS 74 Digest); *J-QE 75 Aug* 698 (2E04)
Gibbs, H. M., and T. N. C. Venkatesan; Observation of fluorescence narrower than the natural linewidth (CLEA 75 Abstr.); *J-QE 75 Sep* 91D (3A08)
Giedt, R. R., *see* Kwok, M. A.; *J-QE 75 Aug* 718 (2F10)
Gilbert, J., *see* Lavigne, P.; *J-QE 75 Sep* 75D (2G07)
Gilmartin, T. J., R. O. Godwin, J. W. Davis, W. F. Hagen, C. H. Hurley, G. W. Leppelmeier, G. J. Linford, J. O. Myall, W. C. O'Neal, and J. B. Trenholme; 10 kilojoule SHIVA laser system for fusion experiments at LLL (CLEA 75 Abstr.); *J-QE 75 Sep* 32D (2D06)
Girard, G., J. C. Farcy, M. Michon, and P. Vincent; Experiments and theory on energy extraction in an atmospheric-pressure CO_2 amplifier with 60 ns–1 μs pulses; *J-QE 75 Jun* 241-247 (1B05)
Girard, G., *see* Farcy, J. C.; *J-QE 75 Sep* 90D (3A07)
Glaros, S. S., *see* Manes, K. R.; *J-QE 75 Aug* 635-636 (1E13)
Glass, A. J., E. J. Goodwin, and J. B. Trenholme; Characterization of optical nonlinearity in transparent dielectrics and implications for fusion laser design (CLEA 75 Abstr.); *J-QE 75 Sep* 28D-29D (2D02)
Glass, G. P., *see* Brown, R. D. H.; *J-QE 75 Aug* 695-696 (2E01)
Glaze, J. A., *see* Simmons, W. W.; *J-QE 75 Sep* 31D-32D (2D05)
Glenn, W. H., W. Morey, and C. Ferrar; High power dye lasers (CLEA 75 Abstr.); *J-QE 75 Sep* 5D (2B07)
Glenn, William H.; The fluctuation model of a passively mode-locked laser; *J-QE 75 Jan* 8-17 (1A10)
Glowacki, W. J., *see* Plummer, M. J.; *J-QE 75 Aug* 700 (2E06)
Godwin, R. O., *see* Gilmartin, T. J.; *J-QE 75 Sep* 32D (2D06)
Goedertier, P. V., *see* Gorog, I.; *J-QE 75 Sep* 63D (2F09)
Goell, J. E.; Optical fiber communications—Potential applications (CLEA 75 Abstr.); *J-QE 75 Sep* 76D (2G08)
Goldberg, L. S., and C. A. Moore; Picosecond pulse generation, amplification and nonlinear mixing with a synchronous mode-locked dye laser pumped by Nd:YAG (CLEA 75 Abstr.); *J-QE 75 Sep* 2D (1B04)
Gonda, Shun-Ichi, and Seiji Mukai; Degradation and intensity fluctuations in CW AlGaAs double-heterostructure junction lasers; *J-QE 75 Jul* 545-550 (3E13)
Gondhalekar, A., N. R. Heckenberg, and E. Holzhauer; The mechanism of single-frequency operation of the hybrid-CO_2 laser; *J-QE 75 Mar* 103-108 (1A09)
Goodwin, E. J., *see* Glass, A. J.; *J-QE 75 Sep* 28D-29D (2D02)
Goodwin, F. E., and T. A. Nussmeier; A ten-micrometer receiver subsystem for wideband space communications (CLEA 75 Abstr.); *J-QE 75 Sep* 79D-80D (2G11)
Gordon, R. J., and M. C. Lin; Effects of temperature and buffer gases on the reactions of nitric oxide and vibrationally excited ozone (CHEMLAS 74 Digest); *J-QE 75 Aug* 715 (2F07)
Gorog, I., P. V. Goedertier, J. D. Knox, I. Ladany, J. P. Wittke, and A. H. Firester; Application of CW AlGaAs injection lasers in electrooptical technology (CLEA 75 Abstr.); *J-QE 75 Sep* 63D (2F09)
Goto, Kenya, *see* Petersen, F. Russell; *J-QE 75 Oct* 838-843 (1C08)
Gottlieb, M., *see* Feichtner, J. D.; *J-QE 75 Sep* 66D-67D (2F12)
Green, W. H., *see* Hancock, J. K.; *J-QE 75 Aug* 694 (2D14)
Greene, A. E.; The effects of superelastic collisions on electron energy distributions in vibrationally excited CO laser mixtures (CHEMLAS 74 Digest); *J-QE 75 Aug* 708 (2E14)
Greenhow, R. C., and A. J. Street; Mode locking the Nd:glass laser with BDN: Measurements of dye recovery times and laser pulse lengths (Corresp.); *J-QE 75 Jan* 59-60 (1E05)
Greiner, N. R., *see* Getzinger, R. W.; *J-QE 75 Aug* 698 (2E04)
Greiner, N. R.; Time-resolved output spectrum from a hydrogen fluoride laser using mixtures of SF_6 and HI (Corresp.); *J-QE 75 Oct* 844-845 (1C14)
Grohs, G. L., and G. Emanuel; Relative performance of arc and combustor driven CW HF lasers (CHEMLAS 74 Digest); *J-QE 75 Aug* 717 (2F09)
Grosjean, Dennis, *see* Olson, Robert A.; *J-QE 75 Sep* 95D-96D (3A12)
Gross, R. W. F.; Laser isotope separation of titanium-50 for nuclear reactor applications (CHEMLAS 75 Digest); *J-QE 75 Aug* 702 (2E08)
Groves, W. O., *see* Coleman, J. J.; *J-QE 75 Jul* 471-476 (2G09)
Gründorfer, Stephan, *see* Thomas, Ben; *J-QE 75 Jul* 528-532 (3D10)
Gründorfer, Stephan, M. J. Adams, and Ben Thomas; *H*-pulsing: A transient effect in $GaAs/Ga_xAl_{1-x}As$ injection lasers; *J-QE 75 Jul* 532-537 (3D14)
Guch, S., Jr., *see* Simmons, W. W.; *J-QE 75 Sep* 30D (2D04)
Guch, S., Jr.; Enhanced parasitic suppression in large aperture disk lasers using liquid edge claddings (CLEA 75 Abstr.); *J-QE 75 Sep* 30D-31D (2D04)
Gurevich, S. A., *see* Alferov, Z. I.; *J-QE 75 Jul* 449-451 (2F01)
Gusinow, M. A.; Near-UV spectral efficiency of high-current xenon flashlamps; *J-QE 75 Dec* 929-934 (1A03)
Gutcheck, R. A., *see* Lorents, D. C.; *J-QE 75 Aug* 704 (2E10)

H

H_2/F_2 flame propagation and repetitively pulsed hydrogen fluoride (HF) chain-reaction chemical laser; *J-QE 75 Aug* 648-653 (2A10)
Haas, R. A., *see* Manes, K. R.; *J-QE 75 Aug* 635-636 (1E13)
Haas, R. A., *see* Holzrichter, J. F.; *J-QE 75 Sep* 46D (2E06)
Hadley, S. G., *see* Wilson, L. E.; *J-QE 75 Aug* 691 (2D11)
Hadley, S. G., *see* Davis, S. J.; *J-QE 75 Aug* 693 (2D13)
Hagen, W. F., *see* Gilmartin, T. J.; *J-QE 75 Sep* 32D (2D06)
Hager, G., *see* Wilson, L. E.; *J-QE 75 Aug* 691 (2D11)
Hager, G., *see* Davis, S. J.; *J-QE 75 Aug* 693 (2D13)
Hakki, B. W.; Near-field emission from GaAs double-heterostructure laser mirrors; *J-QE 75 Apr* 149-154 (1C03)
Halido, D., and Raoul Weil; Resonant piezo-electrooptic modulation (CLEA 75 Abstr.); *J-QE 75 Sep* 64D-65D (2F10)
Hall, L. H.; Population inversions measured in alkali metal–halogen reaction systems (CHEMLAS 74 Digest); *J-QE 75 Aug* 693 (2D13)
Hambenne, J. B., and M. Sargent, III; Physical interpretation of bistable unidirectional ring-laser operation (Corresp.); *J-QE 75 Feb* 90-92 (1B14)
Hammer, Jacob M., D. J. Channin, Michael T. Duffy, and Clyde C. Neil; High-speed electrooptic waveguide grating modulator using epitaxial ZnO; *J-QE 75 Apr* 138-148 (1B06)
Hancock, J. K., and W. H. Green; Vibrational relaxation in HF and DF between 200–300°K (CHEMLAS 74 Digest); *J-QE 75 Aug* 694 (2D14)
Hardy, A., *see* Ganiel, U.; *J-QE 75 Nov* 881-892 (1B13)
Hargis, P. J., Jr., and M. M. Robertson; A dye laser spectrometer for the analysis of pulsed vacuum arcs (CLEA 75 Abstr.); *J-QE 75 Sep* 24D (2C12)
Harman, T. C., *see* Spears, D. L.; *J-QE 75 Sep* 79D (2G11)
Harper, L. L., *see* Erickson, E. G.; *J-QE 75 Sep* 16D-17D (2C04)
Harrach, Robert J.; Effect of rotational and intramode vibrational coupling on short-pulse amplification in CO_2; *J-QE 75 Jul* 349-357 (1C07)
Harris, Jay H., *see* Heiblum, Mordehai; *J-QE 75 Feb* 75-83 (1A13)
Harris, N. W., F. O'Neill, and W. T. Whitney; A fifteen atmosphere electron-beam-controlled CO_2 laser (CHEMLAS 74 Digest); *J-QE 75 Aug* 686-687 (2D06)
Harris, R. A., J. R. Lillis, J. A. Montgomery, Jr., and H. H. Michels; Low lying excited electronic states of BrCl and GeO (CHEMLAS 74 Digest); *J-QE 75 Aug* 691 (2D11)
Harris, R. A., *see* Wilson, L. E.; *J-QE 75 Aug* 691 (2D11)
Hart, G. A., *see* Searles, S. K.; *J-QE 75 Aug* 685 (2D05)
Hart, G. A., *see* Searles, S. K.; *J-QE 75 Sep* 93D (3A10)
Hartwick, Thomas S., *see* Gelbwachs, Jerry; *J-QE 75 Jan* 52-54 (1D12)
Haus, Hermann A.; A theory of forced mode locking; *J-QE 75 Jul* 323-330 (1A09)
Haus, Hermann A.; Theory of mode locking with a slow saturable absorber; *J-QE 75 Sep* 736-746 (1A14)
Hayashi, K., *see* Suematsu, Y.; *J-QE 75 Jul* 457-460 (2F09)
Hayden, J. J., *see* Liberman, I.; *J-QE 75 Sep* 44D (2E04)
Heckenberg, N. R., *see* Gondhalekar, A.; *J-QE 75 Mar* 103-108 (1A09)
Heckscher, H., *see* Rossi, J. A.; *J-QE 75 Jul* 538-545 (3E06)
Heckscher, H., *see* Chinn, S. R.; *J-QE 75 Sep* 62D (2F08)
Heckscher, Helmut, *see* Chinn, Stephen R.; *J-QE 75 Sep* 747-754 (1B11)
Heiblum, Mordehai, and Jay H. Harris; Analysis of curved optical waveguides by conformal transformation; *J-QE 75 Feb* 75-83 (1A13)
Heidner, R. F., and J. F. Bott; H atom deactivation of HF($v=1$) (CHEMLAS 74 Digest); *J-QE 75 Aug* 696 (2E02)
Heidner, R. F., III, *see* Suchard, S. N.; *J-QE 75 Sep* 26D-27D (2C14)
Heidner, R. F., III, *see* Suchard, Steven N.; *J-QE 75 Nov* 908-916 (1D12)
Henesian, M., R. L. Herbst, and R. L. Byer; Optically pumped superfluorescent Na_2 molecular laser (CLEA 75 Abstr.); *J-QE 75 Sep* 26D (2C14)
Henningsen, J. O., and H. G. Jensen; The optically pumped far-infrared laser: Rate equations and diagnostic experiments; *J-QE 75 Jun* 248-252 (1B12)
Herbst, R. L., *see* Henesian, M.; *J-QE 75 Sep* 26D (2C14)
Herget, W. F., *see* Miller, C. R.; *J-QE 75 Sep* 34D-35D (2D08)
Herriau, J. P., *see* Huignard, J. P.; *J-QE 75 Sep* 8D-9D (2B10)
Hertel, Ingolf V., and Aleksandar S. Stamatović; Spatial hole burning and oligo-mode distance control in CW dye lasers; *J-QE 75 May* 210-212 (1C04)
Herzog, D., *see* Ammon, G.; *J-QE 75 Sep* 50D-51D (2E10)
Herzog, D. G., G. Ammon, and C. Stephenson; A laser precision hover sensor for HLH helicopter (CLEA 75 Abstr.); *J-QE 75 Sep* 51D-52D (2E11)
Hierholzer, F. J.; Formation of SiC heating elements using a CO_2 laser (CLEA 75 Abstr.); *J-QE 75 Sep* 47D-48D (2E07)

Hieslmair, H., C. J. Bickart, and J. N. Fulton; Chirp measurement of CO_2 TEA laser using interferometric pulse delay techniques (CLEA 75 Abstr.); *J-QE 75 Sep* 54D (2E14)
Hill, R. M., *see* Lorents, D. C.; *J-QE 75 Aug* 704 (2E10)
Hinchen, J. J.; Rotational relaxation of hydrogen fluoride (CHEMLAS 74 Digest); *J-QE 75 Aug* 695 (2E01)
Hinchen, J. J., *see* Freiberg, R. J.; *J-QE 75 Sep* 57D-58D (2F03)
Hitz, C. Breck, *see* Falk, Joel; *J-QE 75 Jul* 365-367 (1D09)
Hocker, G. Benjamin, and William K. Burns; Modes in diffused optical waveguides of arbitrary index profile; *J-QE 75 Jun* 270-276 (1D06)
Hohla, K., *see* Brederlow, G.; *J-QE 75 Sep* 42D-43D (2E02)
Hohla, K., *see* Fuss, W.; *J-QE 75 Sep* 43D (2E03)
Holmes, C. P.; HCl/H_2 gas dynamic laser calculations (CHEMLAS 74 Digest); *J-QE 75 Aug* 704-705 (2E10)
Holmes, N.; Dc pump sources for the optically pumped 546.1 nm Hg laser (CLEA 75 Abstr.); *J-QE 75 Sep* 55D (2F01)
Holonyak, N., Jr., *see* Coleman, J. J.; *J-QE 75 Jul* 471-476 (2G09)
Holzhauer, E., *see* Gondhalekar, A.; *J-QE 75 Mar* 103-108 (1A09)
Holzrichter, J. F., *see* Speck, D. R.; *J-QE 75 Sep* 45D-46D (2E05)
Holzrichter, J. F., H. G. Ahlstrom, and R. A. Haas; Laser plasma interaction studies at LLL (CLEA 75 Abstr.); *J-QE 75 Sep* 46D (2E06)
Hon, D.; Electrooptical compensation for self-heating in CD*A during SHG (CLEA 75 Abstr.); *J-QE 75 Sep* 67D-68D (2F13)
Hon, J. F., and J. R. Novak; Chemically pumped hydrogen fluoride overtone laser (CHEMLAS 74 Digest); *J-QE 75 Aug* 698-699 (2E04)
Hoose, J., and J. Soures; Active mirror: An alternative design for a high power Nd:glass amplifier (CLEA 75 Abstr.); *J-QE 75 Sep* 12D (2B14)
Hori, K., *see* Takusagawa, M.; *J-QE 75 Sep* 61D (2F07)
Hough, J. J. T., and R. L. Kerber; Theoretical investigation of the effect of rotational nonequilibrium on predicted performance of pulsed HF chemical lasers (CHEMLAS 74 Digest); *J-QE 75 Aug* 699 (2E05)
Hsieh, J. J., *see* Rossi, J. A.; *J-QE 75 Jul* 538-545 (3E06)
Hu, Chenming; Electrooptic modulation in grain-oriented ZnO films (CLEA 75 Abstr.); *J-QE 75 Sep* 64D (2F10)
Huchital, D. A., and G. N. Steinberg; CW pumping of Nd:YAG with electrodeless arc lamps (CLEA 75 Abstr.); *J-QE 75 Sep* 16D (2C04)
Huestis, D. L., *see* Eckstrom, D. J.; *J-QE 75 Aug* 691 (2D11)
Huestis, D. L., *see* Lorents, D. C.; *J-QE 75 Aug* 704 (2E10)
Huff, L., *see* Falk, Joel; *J-QE 75 Sep* 14D-15D (2C02)
Hughes, William M., T. Olsen, and R. Hunter; Determination of argon oxide 558-nm laser parameters (CLEA 75 Abstr.); *J-QE 75 Sep* 88D (3A05)
Huguet, M., *see* Farcy, J. C.; *J-QE 75 Sep* 90D (3A07)
Huignard, J. P., J. P. Herriau, F. Micheron, and J. M. Rouchon; Selective erasure and parallel processing holograms superimposed in $LiNbO_3$ crystal (CLEA 75 Abstr.); *J-QE 75 Sep* 8D-9D (2B10)
Hull, D. R., *see* Arthurs, E. G.; *J-QE 75 Sep* 28D (2D02)
Hunt, J. T., and R. G. Nelson; Focusing properties of an aberrated laser beam (CLEA 75 Abstr.); *J-QE 75 Sep* 29D-30D (2D03)
Hunter, R., *see* Hughes, William M.; *J-QE 75 Sep* 88D (3A05)
Hurand, M. C., *see* Bret, G.; *J-QE 75 Sep* 12D-13D (2B14)
Hurley, C. H., *see* Gilmartin, T. J.; *J-QE 75 Sep* 32D (2D06)
Hutchinson, M. H. R., *see* Arthurs, E. G.; *J-QE 75 Sep* 28D (2D02)
Hyde, J. C., and R. Knight; Power and pressure recovery measurements in high Mach number supersonic chemical lasers (CHEMLAS 74 Digest); *J-QE 75 Aug* 718 (2F10)
Hyer, R. C., *see* Shapiro, S. L.; *J-QE 75 Sep* 5D-6D (2B07)

I

IEEE Quantum Electronics Council; Special issue on Semiconductor Laser Conference; *J-QE 75 Jul, Pt. II* 381-568 (2A03)
IEEE Quantum Electronics Council; Special issue on Chemical and Molecular Laser Conference; *J-QE 75 Aug, Pt. II* 641-722 (2A03)
Ikeda, Hidenori, *see* Yamashita, Mikio; *J-QE 75 Sep* 3D (2B05)
Inaba, H., *see* Ito, H.; *J-QE 75 Sep* 40D (2D14)
Infante, D., *see* Ahmed, S. A.; *J-QE 75 Sep* 2D-3D (1B04)
Inohara, S., *see* Nishihara, H.; *J-QE 75 Sep* 794-796 (1F02)
Inoue, Morio, *see* Itoh, Kunio; *J-QE 75 Jul* 421-426 (2D01)
Ishida, Katsuhiko, *see* Nishizawa, Jun-Ichi; *J-QE 75 Jul* 515-519 (3C11)
Ishikawa, H., *see* Takusagawa, M.; *J-QE 75 Sep* 61D (2F07)
Ito, H., and H. Inaba; Phase-matched SHG in thin-film nonlinear optical waveguie incorporated with substrate nonlinearity (CLEA 75 Abstr.); *J-QE 75 Sep* 40D (2D14)
Ito, Ryoichi, Hisao Nakashima, Seigo Kishino, and Osamu Nakada; Degradation sources in GaAs–AlGaAs double-heterostructure lasers; *J-QE 75 Jul* 551-556 (3F05)
Ito, T., *see* Ozeki, T.; *J-QE 75 Sep* 77D (2G09)
Itoh, Kunio, Morio Inoue, and Iwao Teramoto; New heteroisolation stripe-geometry visible-light-emitting lasers; *J-QE 75 Jul* 421-426 (2D01)
Itzkan, I., *see* Janes, G. S.; *J-QE 75 Sep* 101D-102D (3B04)
Ivanov, L. I., *see* Dekhtar, I. Ya.; *J-QE 75 Sep* 83D (2G14)
Iwasa, S.; A near real-time coherent optical processing system using two Itek PROM devices (CLEA 75 Abstr.); *J-QE 75 Sep* 8D (2B10)

J

Jablonowski, D. P., and J. Raamot; A precision, high speed galvanometer deflection system (CLEA 75 Abstr.); *J-QE 75 Sep* 21D-22D (2C09)
Jacobs, Ralph R., and Marvin J. Weber; Induced-emission cross sections for the $^4F_{3/2} \rightarrow {}^4I_{13/2}$ transition in neodymium laser glasses (Corresp.); *J-QE 75 Oct* 846-847 (1D02)
Jacobs, R. R., and M. J. Weber; Tailoring Nd-doped glasses for laser applications: Dependence of induced-emission cross sections on composition (CLEA 75 Abstr.); *J-QE 75 Sep* 13D (2C01)
James, D. J., *see* Alcock, A. J.; *J-QE 75 Sep* 96D (3A13)
Janes, G. S., I. Itzkan, C. T. Pike, R. H. Levy, and L. Levin; Two-photon laser isotope separation of atomic uranium—Spectroscopic studies, excited state life-times, and photoionization cross sections (CLEA 75 Abstr.); *J-QE 75 Sep* 101D-102D (3B04)
Javan, A., *see* Kurnit, N. A.; *J-QE 75 Apr* 174-176 (1D14)
Jeffers, W. Q., *see* Lilenfeld, H. V.; *J-QE 75 Aug* 660-669 (2B08)
Jeffers, W. Q., *Guest ed.*; Preface to special issue; *J-QE 75 Aug* 641 (2A03)
Jeffreys, H., *see* Sonnenschein, C. M.; *J-QE 75 Sep* 35D (2D09)
Jennings, D. A., K. M. Evenson, and J. J. Jimenez; New CO_2 pumped CW far-infrared laser lines (Note); *J-QE 75 Aug* 637 (1F01)
Jennings, Donald A., *see* Petersen, F. Russell; *J-QE 75 Oct* 838-843 (1C08)
Jensen, H. G., *see* Henningsen, J. O.; *J-QE 75 Jun* 248-252 (1B12)
Jensen, R. J., *see* Lyman, J. L.; *J-QE 75 Sep* 103D (3B06)
Jimenez, J. J., *see* Jennings, D. A.; *J-QE 75 Aug* 637 (1F01)
Jiménez, Juan J., *see* Petersen, F. Russell; *J-QE 75 Oct* 838-843 (1C08)
Johnson, A. M., and D. H. Auston; Microwave switching by picosecond photoconductivity; *J-QE 75 Jun* 283-287 (1E05)
Johnson, A. W., F. W. Bingham, and J. K. Rice; Lasing at 5578.5 Å in *e*-beam excited Kr/O_2 mixtures (CLEA 75 Abstr.); *J-QE 75 Sep* 56D (2F02)
Johnson, J. C., *see* Massey, G. A.; *J-QE 75 Sep* 66D (2F12)
Johnson, S., *see* Scott, P. B.; *J-QE 75 Aug* 693-694 (2D13)
Journet, A., *see* Christophe, B.; *J-QE 75 Sep* 32D-33D (2D06)

K

Kaldor, A., W. Braun, and M. J. Kurylo; Infrared laser enhanced reactions: An application of the technique for the measurement of V–T, and V–V deactivation rates in the O_3 and O_3-SiF_4-O_2 systems (CHEMLAS 74 Digest); *J-QE 75 Aug* 697-698 (2E03)
Kaldor, A., *see* Kurylo, M. J.; *J-QE 75 Aug* 702-703 (2E08)
Kaminow, I. P., *see* Schmidt, R. V.; *J-QE 75 Jan* 57-59 (1E03)
Kaminow, I. P., and L. W. Stulz; Nd:$LiNbO_3$ laser (Corresp.); *J-QE 75 Jun* 306-308 (1F14)
Kaminow, I. P., and L. W. Stulz; A planar electrooptic-prism switch (Corresp.); *J-QE 75 Aug* 633-635 (1E11)
Kamiya, Takeshi, *see* Yanai, Hisayoshi; *J-QE 75 Jul* 519-524 (3D01)
Kao, C., G. Bickel, and M. Maklad; Measured dispersion in long multimode fiber waveguides with and without joints (CLEA 75 Abstr.); *J-QE 75 Sep* 76D-77D (2G08)
Karasik, A. Ya., *see* Dianov, E. M.; *J-QE 75 Sep* 83D (2G14)
Karlov, N. V., *see* Dekhtar, I. Ya.; *J-QE 75 Sep* 83D (2G14)
Karlov, S. P., *see* Zakharov, V. M.; *J-QE 75 Sep* 82D (2G14)
Karras, T. W., *see* Anderson, R. S.; *J-QE 75 Apr* 172-174 (1D12)
Karras, T. W., *see* Anderson, R. S.; *J-QE 75 Sep* 56D-57D (2F02)
Karras, T. W., *see* Bricks, B. G.; *J-QE 75 Sep* 57D (2F03)
Kashiwagi, Hiroshi, *see* Yamashita, Mikio; *J-QE 75 Sep* 3D (2B05)
Kato, K.; 3547-Å pumped high-power dye laser in the blue and violet (Corresp.); *J-QE 75 Jul* 373-374 (1E03)
Kato, K.; 3547-Å pumped parametric oscillation in RD*A (Corresp.); *J-QE 75 Dec* 939-941 (1A13)
Katzir, A., *see* Nakamura, Michiharu; *J-QE 75 Jul* 436-439 (2E02)
Kawakami, Shojiro, and Shigeo Nishida; Perturbation theory of a doubly clad optical fiber with a low-index inner cladding; *J-QE 75 Apr* 130-138 (1A12)
Kazarinov, R. F., *see* Alferov, Z. I.; *J-QE 75 Jul* 449-451 (2F01)
Keller, R. A., *see* Lamotte, M.; *J-QE 75 Aug* 702 (2E08)
Kelley, J. D., *see* Lilenfeld, H. V.; *J-QE 75 Aug* 660-669 (2B08)
Kelley, J. D., and R. L. Thommarson; Vibrational deactivation and atom exchange in $O(^3P) + CO(^1\Sigma^+)$ collisions (CHEMLAS 74 Digest); *J-QE 75 Aug* 701 (2E07)
Kelly, P. J., *see* Bischel, W. K.; *J-QE 75 Sep* 24D-25D (2C12)
Kennedy, Chandler J., *see* Barry, James D.; *J-QE 75 Aug* 575-579 (1A13)
Kennedy, C. J.; *J-QE 75 Sep* 793-794 (1F01)
Comments on Falk, Joel; A theory of the mode-locked, internally frequency-doubled laser; *J-QE 75 Jan* 21-31 (1B09)
Kennedy, C. J.; Frequency-domain analysis of the mode-locked and frequency-doubled homogeneous laser; *J-QE 75 Nov* 857-862 (1A03)
Kepler, C. E., *see* Sadowski, T. J.; *J-QE 75 Aug* 705-706 (2E11)
Kerber, R. L., *see* Hough, J. J. T.; *J-QE 75 Aug* 699 (2E05)
Keren, H., P. Avivi, and F. Dothan; The influence of oxygen on CO-laser performance; *J-QE 75 Aug* 590-594 (1B10)
Kerr, J. R., *see* McIntyre, C. M.; *J-QE 75 Sep* 81D (2G13)
Keune, D. L., *see* Coleman, J. J.; *J-QE 75 Jul* 471-476 (2G09)
Kim, B., *see* Tsai, C. S.; *J-QE 75 Sep* 10D (2B12)
Kim, Dae M., *see* Shah, Rajiv R.; *J-QE 75 Sep* 783-788 (1E05)
Kimbell, George H., *see* Foster, Kenneth D.; *J-QE 75 Jun* 253-258 (1C03)
Kimbell, G. H., *see* Foster, K. D.; *J-QE 75 Aug* 700 (2E06)
Kimura, Tatsuya, *see* Otsuka, Kenju; *J-QE 75 Jul* 330-334 (1B02)
King, D. L., and D. W. Setser; Quenching studies of $Ar(^3P_0, {}^3P_2)$ metastable atoms by chlorine atoms (CHEMLAS 74 Digest); *J-QE 75 Aug* 708 (2E14)
King, S. R., F. I. Shimabukuro, E. E. Reber, and D. J. Spencer; Atmospheric transmission measurements at HF/DF laser wavelengths (CLEA 75 Abstr.); *J-QE 75 Sep* 87D (3A04)
Kingston, R. H., *see* Bicknell, W. E.; *J-QE 75 Jun* 308-311 (1G02)
Kircher, M. J., *see* Schappert, G. T.; *J-QE 75 Sep* 75D-76D (2G07)
Kirkby, P. A., *see* Thompson, G. H. B.; *J-QE 75 Jul* 481-488 (3A05)
Kirkby, P. A.; Dislocation pinning in GaAs by the deliberate introduction of impurities; *J-QE 75 Jul* 562-568 (3G02)
Kishino, Seigo, *see* Ito, Ryoichi; *J-QE 75 Jul* 551-556 (3F05)
Klein, Marvin B., and Richard L. Abrams; 10.6-μm waveguide laser power amplifier; *J-QE 75 Aug* 609-615 (1D01)
Kneubühl, Fritz, *see* Schötzau, Hans J.; *J-QE 75 Oct* 817-822 (1B01)
Knight, R., *see* Hyde, J. C.; *J-QE 75 Aug* 718 (2F10)
Knox, J. D., *see* Gorog, I.; *J-QE 75 Sep* 63D (2F09)
Knyazev, I. N., *see* Antonov, V. S.; *J-QE 75 Sep* 92D (3A09)
Knyazev, I. N., *see* Bagratashvili, V. N.; *J-QE 75 Sep* 94D (3A11)
Knyazev, I. N., V. S. Letokhov, and V. G. Movshev; Efficient and practical hydrogen vacuum ultraviolet laser; *J-QE 75 Oct* 805-817 (1A03)
Kobayashi, K., *see* Lang, R.; *J-QE 75 Sep* 60D (2F06)
Kolb, W. P.; Five-year operation of a He–Ne laser (Corresp.); *J-QE 75 Jul* 374-375 (1E04)
Kollman, V. H., *see* Shapiro, S. L.; *J-QE 75 Sep* 5D-6D (2B07)
Kondo, M., *see* Asakawa, K.; *J-QE 75 Jun* 304-306 (1F12)
Kornienko, L. S., *see* Dianov, E. M.; *J-QE 75 Sep* 83D (2G14)
Kornienko, L. S., N. V. Kravtsov, E. G. Lariontsev, N. I. Naumkin, and V. N. Serkin; Application of laser with folded optical delay line in optical communication systems (CLEA 75 Abstr.); *J-QE 75 Sep* 91D (3A08)

Koyama, J., *see* Nishihara, H.; *J-QE 75 Sep* 794-796 (1F02)
Krasjuk, I. J., *see* Vovchenko, V. I.; *J-QE 75 Sep* 83D (2G14)
Kravtsov, N. V., *see* Kornienko, L. S.; *J-QE 75 Sep* 91D (3A08)
Kressel, H., *see* Butler, J. K.; *J-QE 75 Jul* 402-408 (2B10)
Krikorian, Oscar, *see* Tuccio, Sam A.; *J-QE 75 Sep* 101D (3B04)
Krogh, O. D., and G. C. Pimentel; Reaction mechanism and energy distribution in a new chemical laser system: ClF_3–H_2 (CHEMLAS 74 Digest); *J-QE 75 Aug* 706 (2E12)
Krosney, M. D., *see* Sadowski, T. J.; *J-QE 75 Aug* 705-706 (2E11)
Kruger, John S.; Observation of stimulated emission at 0.3159 μm in the nitrogen second-positive system at room temperature (Note); *J-QE 75 Sep* 801-802 (1F09)
Krupka, D. C.; Selection of modes perpendicular to the junction plane in GaAs large-cavity double-heterostructure lasers; *J-QE 75 Jul* 390-399 (2A12)
Krupka, D. C., and Thomas L. Paoli; Transverse mode control of junction lasers optically coupled to single-mode fibers; *J-QE 75 Jul* 503-507 (3B13)
Ksmiya, Takeshi, *see* Yamamoto, Yoshihisa; *J-QE 75 Sep* 729-736 (1A07)
Kudo, T., *see* Takusagawa, M.; *J-QE 75 Sep* 61D (2F07)
Kuester, Edward F., and David C. Chang; Surface-wave radiation loss from curved dielectric slabs and fibers; *J-QE 75 Nov* 903-907 (1D07)
Kuizenga, D. J., *see* Siegman, A. E.; *J-QE 75 Sep* 69D (2G01)
Kuklo, T. C., *see* Foley, R. J.; *J-QE 75 Sep* 5D (2B07)
Kurnit, N. A., S. J. Tubbs, K. Bidichand, L. W. Ryan, Jr., and A. Javan; Photopreionization of the 3371-Å pulsed N_2 laser (Corresp.); *J-QE 75 Apr* 174-176 (1D14)
Kurylo, M. J., *see* Kaldor, A.; *J-QE 75 Aug* 697-698 (2E03)
Kurylo, M. J., W. Braun, C. Nguyen, and A. Kaldor; Temperature resolution of the chemical dynamics of the $O_3^+ + NO$ reaction system (CHEMLAS 74 Digest); *J-QE 75 Aug* 702-703 (2E08)
Kwok, M. A., and R. L. Wilkins; Flow tube kinetics studies: $DF(v) + HF$, $DF(v) + D_2$, and $HF(v) + H_2$ systems (CHEMLAS 74 Digest); *J-QE 75 Aug* 695 (2E01)
Kwok, M. A., R. R. Giedt, and E. F. Cross; Spectroscopic and infrared measurements on the mesa CW HF (DF) chemical laser (CHEMLAS 74 Digest); *J-QE 75 Aug* 718 (2F10)
Kwok, M. A., *see* Varwig, R. L.; *J-QE 75 Aug* 719 (2F11)
Kwong, S., *see* Claspy, P. C.; *J-QE 75 Sep* 37D (2D11)

L

LaBorde, David A., *see* Bletzinger, Peter; *J-QE 75 Jul* 317-323 (1A03)
Labrunie, G., *see* Valette, S.; *J-QE 75 Sep* 39D-40D (2D13)
Lachambre, J. L., *see* Lavigne, P.; *J-QE 75 Sep* 75D (2G07)
Lacina, William B., and Gary L. McAllister; Scaling generalizations for a CO electric laser; *J-QE 75 Jun* 235-241 (1A13)
Lacina, William B.; Effects of near-resonance self-absorption on CO laser kinetic modeling; *J-QE 75 Jun* 297-302 (1F05)
Ladany, I., *see* Butler, J. K.; *J-QE 75 Jul* 402-408 (2B10)
Ladany, I., *see* Gorog, I.; *J-QE 75 Sep* 63D (2F09)
Ladd, J. H., *see* Baldwin, R. E.; *J-QE 75 Sep* 9D (2B11)
Ladish, J. S., *see* Schappert, G. T.; *J-QE 75 Sep* 75D-76D (2G07)
Lam, S. H., and N. Papageorgis; Quasi-equilibrium vibrational population distributions for anharmonic molecular lasers (CHEMLAS 74 Digest); *J-QE 75 Aug* 715-716 (2F07)
Lamotte, M., H. J. Dewey, R. A. Keller, and J. J. Ritter; Laser induced photochemical enrichment of chlorine isotopes (CHEMLAS 74 Digest); *J-QE 75 Aug* 702 (2E08)
Lang, R., and K. Kobayashi; Suppression of relaxation oscillation in semiconductor lasers (CLEA 75 Abstr.); *J-QE 75 Sep* 60D (2F06)
Lange, R. A., *see* Peyton, B. J.; *J-QE 75 Sep* 80D-81D (2G12)
Larionov, V. R., *see* Alferov, Z. I.; *J-QE 75 Jul* 449-451 (2F01)
Lariontsev, E. G., *see* Kornienko, L. S.; *J-QE 75 Sep* 91D (3A08)
Lavigne, P., J. L. Lachambre, and J. Gilbert; Suppression of self-oscillations in high-gain CO_2 amplifiers (CLEA 75 Abstr.); *J-QE 75 Sep* 75D (2G07)
Lawley, K. L., *see* Doerbeck, F. H.; *J-QE 75 Jul* 464-467 (2G02)
Layne, C. B., W. H. Lowdermilk, and M. J. Weber; Nonradiative relaxation of rare-earth ions in silicate laser glass (Corresp.); *J-QE 75 Sep* 798-799 (1F06)
Lee, A. B., *see* Burns, W. K.; *J-QE 75 Sep* 42D (2E02)
Lee, F., and J. Mitchell; Correction of mask defects by laser beam (CLEA 75 Abstr.); *J-QE 75 Sep* 21D (2C09)
Lee, T. P., C. A. Burrus, B. I. Miller, and R. A. Logan; $Al_xGa_{1-x}As$ double-heterostructure rib-waveguide injection laser; *J-QE 75 Jul* 432-435 (2D12)
Leheny, Robert F., and Jagdeep Shah; Amplification and excited state absorption in longitudinally pumped laser dyes; *J-QE 75 Feb* 70-74 (1A08)
Lehmberg, R. H., J. Reintjes, and R. C. Eckardt; Self defocusing of mode locked Nd:YAG pulses in cesium vapor (CHEA 75 Abstr.); *J-QE 75 Sep* 69D-70D (2G01)
Leland, W. T., *see* Schappert, G. T.; *J-QE 75 Sep* 75D-76D (2G07)
Leopold, K., *see* Alcock, A. J.; *J-QE 75 Sep* 96D (3A13)
Leppelmeier, G. W., *see* Gilmartin, T. J.; *J-QE 75 Sep* 32D (2D06)
Letokhov, V. S., *see* Antonov, V. S.; *J-QE 75 Sep* 92D (3A09)
Letokhov, V. S., *see* Bagratashvili, V. N.; *J-QE 75 Sep* 94D (3A11)
Letokhov, V. S., *see* Knyazev, I. N.; *J-QE 75 Oct* 805-817 (1A03)
Levin, L., *see* Janes, G. S.; *J-QE 75 Sep* 101D-102D (3B04)
Levin, L. A., *see* Smilanski, I.; *J-QE 75 Nov* 919-920 (1E09)
Levy, R. H., *see* Janes, G. S.; *J-QE 75 Sep* 101D-102D (3B04)
Lewis, P., *see* Naismith, R.; *J-QE 75 Aug* 716 (2F08)
Liao, Paul F., *see* Smith, Peter W.; *J-QE 75 Feb* 84-89 (1B08)
Liao, P. F., *see* Weber, H. P.; *J-QE 75 Sep* 61D-62D (2F07)
Liao, P. F., *see* Weber, H. P.; *J-QE 75 Sep* 100D (3B03)
Liberman, I., M. J. Bennett, J. J. Hayden, and S. Singer; Measurement of beam quality from short pulse CO_2 lasers (CLEA 75 Abstr.); *J-QE 75 Sep* 44D (2E04)
Librecht, F. M., and G. E. François; Critically index-matched second-harmonic generation in multiple crystals; *J-QE 75 Sep* 755-758 (1C05)
Librecht, F. M., and J. A. Simons; Second-harmonic generation in birefringent crystals by a Gaussian beam with an elliptical cross section (CLEA 75 Abstr.); *J-QE 75 Oct* 850-852 (1D06)
Lilenfeld, H. V., R. F. Webbink, W. Q. Jeffers, and J. D. Kelley; Modeling of the CW CO chemical laser; *J-QE 75 Aug* 660-669 (2B08)
Lillis, J. R., *see* Harris, R. A.; *J-QE 75 Aug* 691 (2D11)
Limpaecher, R., *see* Mangano, J. A.; *J-QE 75 Aug* 705 (2E11)
Lin, C., *see* Smith, Peter W.; *J-QE 75 Feb* 84-89 (1B08)
Lin, Chinlon; Near-infrared dye laser emission from ultraviolet nitrogen-laser-pumped dye solutions (Note); *J-QE 75 Jan* 61 (1E07)
Lin, Chinlon; Studies of relaxation oscillations in organic dye lasers; *J-QE 75 Aug* 602-609 (1C08)
Lin, Chinlon, and C. V. Shank; Subnanosecond tunable dye laser pulse generation by controlled resonator transients (CLEA 75 Abstr.); *J-QE 75 Sep* 1D-2D (2B03)
Lin, M. C., *see* Shortridge, R. G.; *J-QE 75 Aug* 688 (2D08)
Lin, M. C., and R. G. Shortridge; Electronic-to-vibrational energy transfer reactions: X* + CO(X = O, I and Br) (CHEMLAS 74 Digest); *J-QE 75 Aug* 710 (2F02)
Lin, M. C., *see* Gordon, R. J.; *J-QE 75 Aug* 715 (2F07)
Lind, R. C.; High energy CO_2 laser pumped by a UV sustained discharge (CLEA 75 Abstr.); *J-QE 75 Sep* 71D (2G03)
Linevsky, M. J., *see* Carabetta, R. A.; *J-QE 75 Aug* 689 (2D09)
Linford, G. J., *see* Gilmartin, T. J.; *J-QE 75 Sep* 32D (2D06)
Ling, C. C., *see* Arthurs, E. G.; *J-QE 75 Sep* 28D (2D02)
Linz, A., *see* Fontana, R. E., Jr.; *J-QE 75 Sep* 38D (2D12)
Lizet, J., *see* Valette, S.; *J-QE 75 Sep* 39D-40D (2D13)
Lobko, V. V., *see* Bagratashvili, V. N.; *J-QE 75 Sep* 94D (3A11)
Logan, R. A., *see* Lee, T. P.; *J-QE 75 Jul* 432-435 (2D12)
Logan, R. A., and F. K. Reinhart; Integrated GaAs–$Al_xGa_{1-x}As$ double-heterostructure laser with independently controlled optical output divergence; *J-QE 75 Jul* 461-464 (2F13)
Loh, K. W., W. S. C. Chang, and R. A. Becker; Convolution using guided acoustooptical interaction in As_2S_3 waveguides (CLEA 75 Abstr.); *J-QE 75 Sep* 86D (3A03)
Long, W. H., Jr., *see* Prince, J. F.; *J-QE 75 Aug* 687 (2D07)
Long, William H., Jr., *see* Bletzinger, Peter; *J-QE 75 Jul* 317-323 (1A03)
Loree, T. R., L. M. Sherman, and J. M. Thorne; Amplification of the 1.32 μm line in Nd:YAG (Corresp.); *J-QE 75 Jul* 371-372 (1E01)
Lorents, D. C., *see* Black, G.; *J-QE 75 Aug* 704 (2E10)
Lorents, D. C., D. L. Huestis, R. A. Gutcheck, R. M. Hill, and H. H. Nakano; Xenon oxide—The kinetic mechanism (CHEMLAS 74 Digest); *J-QE 75 Aug* 704 (2E10)
Lory, E. R., S. H. Bauer, and T. Manuccia; Infrared laser augmented decomposition of H_3PBF_3 (CHEMLAS 74 Digest); *J-QE 75 Aug* 714-715 (2F06)
Lovberg, R. H., *see* Tripathi, P. P.; *J-QE 75 Sep* 59D (2F05)
Loveberg, R. V., Eric R. Wooding, and Michael L. Yeoman; Pulse stretching and shape control by compound feedback in a *Q*-switched ruby laser; *J-QE 75 Jan* 17-21 (1B05)
Lovelace, D., *see* Garmire, E.; *J-QE 75 Sep* 38D-39D (2D12)
Lowder, J. E., *see* Marcus, S.; *J-QE 75 Sep* 49D-50D (2E09)
Lowdermilk, W. H., *see* Layne, C. B.; *J-QE 75 Sep* 798-799 (1F06)
Lubowise, M. J., *see* Coleman, J. J.; *J-QE 75 Jul* 471-476 (2G09)
Lukishova, S. G., *see* Vovchenko, V. I.; *J-QE 75 Sep* 83D (2G14)
Lunazzi, J. J., *see* Rabal, H. J.; *J-QE 75 Sep* 22D-23D (2C10)
Luria, M., *see* Eckstrom, D. J.; *J-QE 75 Aug* 691 (2D11)
Lyman, J. L., R. J. Jensen, J. P. Rink, C. P. Robinson, and S. D. Rockwood; Isotopic enrichment by multiple absorption of CO_2 laser radiation (CLEA 75 Abstr.); *J-QE 75 Sep* 103D (3B06)
Lynds, L., *see* Boedeker, L.; *J-QE 75 Aug* 713 (2F05)
Lynds, L., M. C. Foster, and A. W. Angelbeck; High field saturation phenomena in HF chemical amplifiers (CHEMLAS 74 Digest); *J-QE 75 Aug* 713-714 (2F05)
Lynds, L., *see* Foster, M. C.; *J-QE 75 Aug* 714 (2F06)

M

Macomber, James D.; *J-QE 75 Sep* 800 (1F08)
Comments on Vogel, Gerald C., Albert Savage, and Michel A. Duguay; Picosecond optical sampling; *J-QE 74 Sep* 642-646 (1B02)
Mahr, H., and Benno Reuter; Fourier-transform holograms with X-rays (CLEA 75 Abstr.); *J-QE 75 Sep* 97D-98D (3A14)
Maklad, M., *see* Kao, C.; *J-QE 75 Sep* 76D-77D (2G08)
Maloney, Patrick J., *see* Smith, Peter W.; *J-QE 75 Feb* 84-89 (1B08)
Maloney, P. J., *see* Wood, O. R., II; *J-QE 75 Sep* 72D-73D (2G04)
Manes, K. R., D. L. Smith, R. A. Haas, and S. S. Glaros; Prepulse extinction-ratio measurements on a CO_2-laser system (Corresp.); *J-QE 75 Aug* 635-636 (1E13)
Manes, K. R.; 'Valkyrie'—A CO_2 laser system for laser fusion experiments (CLEA 75 Abstr.); *J-QE 75 Sep* 44D (2E04)
Mangano, J. A., R. Limpaecher, J. D. Daugherty, H.-L. Chen, and F. Russell; Pulsed, electrically-initiated, HF chemical lasers at atmospheric pressure (CHEMLAS 74 Digest); *J-QE 75 Aug* 705 (2E11)
Manko, M. A., *see* Bachert, H.; *J-QE 75 Jul* 507-510 (3C03)
Manlief, S., *see* Marcus, S.; *J-QE 75 Sep* 49D-50D (2E09)
Manuccia, T., *see* Lory, E. R.; *J-QE 75 Aug* 714-715 (2F06)
Manuccia, T. J., J. A. Stregack, and W. S. Watt; Fuels for a premixed pulsed HCl laser (Corresp.); *J-QE 75 Nov* 921-923 (1E11)
Marabella, L., *see* Wormhoudt, J.; *J-QE 75 Aug* 704 (2E10)
Marcus, S., J. E. Lowder, S. Manlief, and D. L. Mooney; Laser heating of metallic surfaces (CLEA 75 Abstr.); *J-QE 75 Sep* 49D-50D (2E09)
Marcuse, D.; Light scattering from periodic refractive-index fluctuations in asymmetric slab waveguides; *J-QE 75 Apr* 162-168 (1D02)
Marcuse, D.; Electrooptic coupling between TE and TM modes in anisotropic slabs; *J-QE 75 Sep* 759-767 (1C09)
Marling, J. B.; Ion laser performance and spectroscopy—New pulsed and CW transitions below 3000 Å (CLEA 75 Abstr.); *J-QE 75 Sep* 27D-28D (2D01)
Marling, John B.; Ultraviolet ion laser performance and spectroscopy—Part I: New strong noble-gas transitions below 2500 Å; *J-QE 75 Oct* 822-834 (1B06)
Marubayashi, G.; Progress of optical communications in Japan (CLEA 75 Abstr.); *J-QE 75 Sep* 76D (2G08)
Masopust, O. T., *see* Saifi, M. A.; *J-QE 75 Sep* 23D (2C11)

Massey, G. A., and R. A. Elliott; The optically gated dye cell—A high-speed shutter and pulse shaper; *J-QE 75 Jul* 358-364 (1D02)
Massey, G. A., and J. C. Johnson; Generation of frequency-stable, narrowband optical pulses by high gain parametric amplification (CLEA 75 Abstr.); *J-QE 75 Sep* 66D (2F12)
Mathieu, X., *see* Papuchon, M.; *J-QE 75 Sep* 99D-100D (3B02)
Matoba, M., *see* Yamanaka, C.; *J-QE 75 Sep* 45D (2E05)
McAllister, Gary L., *see* Lacina, William B.; *J-QE 75 Jun* 235-241 (1A13)
McAllister, Gary L., *see* Steier, William H.; *J-QE 75 Sep* 725-728 (1A03)
McArthur, D. A., and P. B. Tollefsrud; Observation of laser action in CO gas excited only with a nuclear reactor (CHEMLAS 74 Digest); *J-QE 75 Aug* 707 (2E13)
McArthur, David A., and J. W. Poukey; Theory of the nitrogen laser excited by a relativistic electron beam; *J-QE 75 Nov* 892-902 (1C10)
McCall, G. H.; The physics of laser fusion (CLEA 75 Abstr.); *J-QE 75 Sep* 45D (2E05)
McElroy, John H., *see* Peyton, Bernard J.; *J-QE 75 Aug* 569-574 (1A03)
McFarlane, R. A., *see* Davis, C. C.; *J-QE 75 Aug* 701 (2E07)
McFarlane, R. A., *see* Burde, D. H.; *J-QE 75 Aug* 709 (2F01)
McFarlane, Ross A., *see* Pirkle, Robert J.; *J-QE 75 Oct* 834-838 (1C04)
McGee, T. J., and F. X. Powell; On the mechanism of the $N(^4S)+CS_2$ reaction: N_2–CO_2 laser pumping from the products of the $N(^4S)+CS_2$ reaction (Corresp.); *J-QE 75 Jun* 302-304 (1F10)
McGeoch, M. W., *see* Arthurs, E. G.; *J-QE 75 Sep* 28D (2D02)
McGroddy, J. C., *see* Blum, Joseph M.; *J-QE 75 Jul* 413-418 (2C07)
McIntosh, Robert E., *see* Bluyssen, H. J. A.; *J-QE 75 Jul* 341-348 (1B13)
McIntyre, C. M., J. R. Dunphy, and J. R. Kerr; Direct-detection diversity receiver for optical communication through the atmosphere (CLEA 75 Abstr.); *J-QE 75 Sep* 81D (2G13)
McKen, D., *see* Seguin, H. J. J.; *J-QE 75 Sep* 71D-72D (2G03)
McLeary, R., R. E. Whitcher, and P. J. Beckwith; Multikilowatt CO_2 utilizing plasma injection (CLEA 75 Abstr.); *J-QE 75 Sep* 90D-91D (3A07)
McMullin, Paul G., *see* Blum, Joseph M.; *J-QE 75 Jul* 413-418 (2C07)
Meinzer, R. A., and R. V. Steele; Spectroscopic investigation of small-scale CW HF chain-reaction laser (CHEMLAS 74 Digest); *J-QE 75 Aug* 712-713 (2F04)
Meinzer, R. A., *see* Steele, R. V.; *J-QE 75 Aug* 719 (2F11)
Mellars, J., *see* Peyton, B. J.; *J-QE 75 Sep* 80D-81D (2G12)
Melngailis, I., *see* Spears, D. L.; *J-QE 75 Sep* 79D (2G11)
Menyuk, N., A. S. Pine, and A. Mooradian; Efficient InSb laser with resonant longitudinal optical pumping; *J-QE 75 Jul* 477-481 (3A01)
Menzies, R. T., and M. S. Shumate; Ambient air pollutant measurements with a bistatic, heterodyne system (CLEA 75 Abstr.); *J-QE 75 Sep* 33D (2D07)
Mezrich, R., K. F. Etzold, and D. Vilkomerson; Interferometric measurement and display of ultrasonic waves (CLEA 75 Abstr.); *J-QE 75 Sep* 9D-10D (2B11)
Michels, H. H., *see* Harris, R. A.; *J-QE 75 Aug* 691 (2D11)
Micheron, F., *see* Huignard, J. P.; *J-QE 75 Sep* 8D-9D (2B10)
Michon, M., *see* Girard, G.; *J-QE 75 Jun* 241-247 (1B05)
Michon, M., *see* Farcy, J. C.; *J-QE 75 Sep* 90D (3A07)
Miles, R. B., *see* Boulnois, J. L.; *J-QE 75 Aug* 707-708 (2E13)
Miles, R. B.; Resonant Doppler velocimeter (CLEA 75 Abstr.); *J-QE 75 Sep* 35D-36D (2D09)
Miley, G. H., *see* DeYoung, R. J.; *J-QE 75 Sep* 97D (3A14)
Miller, B. I., *see* Lee, T. P.; *J-QE 75 Jul* 432-435 (2D12)
Miller, C. R., C. M. Sonnenschein, and W. F. Herget; A laser Doppler velocimeter for remote power plant effluent measurements (CLEA 75 Abstr.); *J-QE 75 Sep* 34D-35D (2D08)
Milton, A. F., *see* Burns, W. K.; *J-QE 75 Sep* 42D (2E02)
Milton, A. Fenner, *see* Burns, William K.; *J-QE 75 Jan* 32-39 (1C06)
Mitchell, J., *see* Lee, F.; *J-QE 75 Sep* 21D (2C09)
Mizeraczyk, Jerzy K.; On saturation mechanisms in PC He–Cd^+ lasers (Corresp.); *J-QE 75 May* 218-220 (1C12)
Mizerov, M. N., *see* Alferov, Z. I.; *J-QE 75 Jul* 449-451 (2F01)
Montanarini, M., and J. Steffen; Investigations on laser-welding (CLEA 75 Abstr.); *J-QE 75 Sep* 47D (2E07)
Montgomery, J. A., Jr., *see* Harris, R. A.; *J-QE 75 Aug* 691 (2D11)
Mooney, D. L., *see* Marcus, S.; *J-QE 75 Sep* 49D-50D (2E09)
Mooradian, A., *see* Menyuk, N.; *J-QE 75 Jul* 477-481 (3A01)
Moore, C. A., *see* Goldberg, L. S.; *J-QE 75 Sep* 2D (1B04)
Moran, Michael J., Chiao-Yao She, and Robert L. Carman; Interferometric measurements of the nonlinear refractive-index coefficient relative to CS_2 in laser-system-related materials; *J-QE 75 Jun* 259-263 (1C09)
Morey, W., *see* Glenn, W. H.; *J-QE 75 Sep* 5D (2B07)
Morosini, A. C., *see* Paoli, Thomas L.; *J-QE 75 Jul* 525-527 (3D07)
Morton, R. G., *see* Friedman, H. W.; *J-QE 75 Sep* 4D (2B06)
Mourou, Gerard; Spectral hole burning in dye solutions; *J-QE 75 Jan* 1-8 (1A03)
Movshev, V. G., *see* Antonov, V. S.; *J-QE 75 Sep* 92D (3A09)
Movshev, V. G., *see* Knyazev, I. N.; *J-QE 75 Oct* 805-817 (1A03)
Mukai, Seiji, *see* Gonda, Shun-Ichi; *J-QE 75 Jul* 545-550 (3E13)
Munro, D. F., *see* Fehrs, D. L.; *J-QE 75 Sep* 21D (2C09)
Murray, J. E., *see* Simmons, W. W.; *J-QE 75 Sep* 30D (2D04)
Murray, J. R., *see* Powell, H. T.; *J-QE 75 Aug* 685 (2D05)
Murray, J. R., *see* Powell, H. T.; *J-QE 75 Sep* 27D (2D01)
Myall, J. O., *see* Gilmartin, T. J.; *J-QE 75 Sep* 32D (2D06)

N

Nachshon, Yehuda, and Paul D. Coleman; Measurement of vibrational–vibrational exchange of highly excited states of diatomic molecules where the collisional probability is approaching unity; *J-QE 75 Aug* 654-660 (2B02)
Naismith, R., R. Cavalleri, R. L. Taylor, P. Lewis, and J. D. Teare; Theoretical performance of V→V transfer laser (CHEMLAS 74 Digest); *J-QE 75 Aug* 716 (2F08)
Nakada, Osamu, *see* Ito, Ryoichi; *J-QE 75 Jul* 551-556 (3F05)
Nakai, S., *see* Yamanaka, C.; *J-QE 75 Sep* 45D (2E05)
Nakamura, Michiharu, K. Aiki, J. Umeda, A. Katzir, A. Yariv, and H. W. Yen; GaAs–GaAlAs double-heterostructure injection lasers with distributed feedback; *J-QE 75 Jul* 436-439 (2E02)
Nakano, H. H., *see* Lorents, D. C.; *J-QE 75 Aug* 704 (2E10)
Nakashima, Hisao, *see* Ito, Ryoichi; *J-QE 75 Jul* 551-556 (3F05)
Namizaki, H.; Transverse-junction-stripe lasers with a GaAs p-n homojunction; *J-QE 75 Jul* 427-431 (2D07)
Naumkin, N. I., *see* Kornienko, L. S.; *J-QE 75 Sep* 91D (3A08)
Negro, A. G., *see* Vieceli, J. J.; *J-QE 75 Aug* 711 (2F03)
Neil, Clyde C., *see* Hammer, Jacob M.; *J-QE 75 Apr* 138-148 (1B06)
Nella, John, *see* Caird, John A.; *J-QE 75 Nov* 874-881 (1B06)
Nelson, L. Y., C. H. Fisher, and S. R. Byron; A new pumping technique and new V–V transfer molecule for the CS_2 laser (CHEMLAS 74 Digest); *J-QE 75 Aug* 686 (2D06)
Nelson, M. A., *see* Davis, T. P.; *J-QE 75 Sep* 50D (2E10)
Nelson, Melvin A., *see* Davies, Terence J.; *J-QE 75 Sep* 7D (2B09)
Nelson, R. G., *see* Hunt, J. T.; *J-QE 75 Sep* 29D-30D (2D03)
Nemarich, J., *see* Sattler, J. P.; *J-QE 75 Sep* 18D (2C06)
Neumann, G., *see* Ganiel, U.; *J-QE 75 Nov* 881-892 (1B13)
Newman, L., T. A. DeTemple, and P. D. Coleman; N_2 infrared laser operation in an electron beam controlled discharge (CHEMLAS 74 Digest); *J-QE 75 Aug* 686 (2D06)
Nguyen, C., *see* Kurylo, M. J.; *J-QE 75 Aug* 702-703 (2E08)
Nguyen, LeT., *see* Tsai, C. S.; *J-QE 75 Sep* 10D (2B12)
Nienhuis, G., *see* Gerritsen, H. J.; *J-QE 75 Apr* 174 (1D14)
Nishida, Shigeo, *see* Kawakami, Shojiro; *J-QE 75 Apr* 130-138 (1A12)
Nishihara, H., S. Inohara, T. Suhara, and J. Koyama; Holocoupler: A novel coupler for optical circuits (Corresp.); *J-QE 75 Sep* 794-796 (1F02)
Nishizawa, Jun-Ichi, and Katsuhiko Ishida; Injection-induced modulation of laser light by the interaction of laser diodes; *J-QE 75 Jul* 515-519 (3C11)
Nodov, E., *see* Claspy, P. C.; *J-QE 75 Sep* 37D (2D11)
Noetzel, J., *see* Wendelken, C. P.; *J-QE 75 Aug* 694-695 (2D14)
Nomiyama, N., *see* Boedeker, L.; *J-QE 75 Aug* 713 (2F05)
Novak, J. R., *see* Hon, J. F.; *J-QE 75 Aug* 698-699 (2E04)
Nowak, A. V., *see* Schott, G. L.; *J-QE 75 Aug* 690 (2D10)
Nussmeier, T. A., *see* Goodwin, F. E.; *J-QE 75 Sep* 79D-80D (2G11)

O

Oettinger, P. E., and C. F. Dewey, Jr.; Lasing efficiency and photochemical stability of laser dyes spanning the infrared spectral region 710–950 nm (CLEA 75 Abstr.); *J-QE 75 Sep* 3D-4D (2B05)
Ohgushi, Y., *see* Ueno, Y.; *J-QE 75 Sep* 78D-79D (2G10)
Ohta, Y., *see* Asakawa, K.; *J-QE 75 Jun* 304-306 (1F12)
Oldham, William G., *see* Cross, Peter S.; *J-QE 75 May* 190-197 (1A12)
Olk, LaMar B., *see* Coutts, Gerald W.; *J-QE 75 Sep* 6D (2B08)
Olsen, J. N., *see* Duguay, M. A.; *J-QE 75 Apr* 170-172 (1D10)
Olsen, T., *see* Hughes, William M.; *J-QE 75 Sep* 88D (3A05)
Olson, Robert A., Dennis Grosjean, Benjamin Sarka, Jr., Alan Garscadden, and Peter Bletzinger; High-repetition-rate TEA laser system for closed-cycle operation with ultrapure gases (CLEA 75 Abstr.); *J-QE 75 Sep* 95D-96D (3A12)
O'Meara, T. R., *see* Brown, W. P., Jr.; *J-QE 75 Sep* 52D-53D (2E12)
O'Neal, W. C., *see* Gilmartin, T. J.; *J-QE 75 Sep* 32D (2D06)
O'Neill, F., *see* Harris, N. W.; *J-QE 75 Aug* 686-687 (2D06)
O'Neill, F., and W. T. Whitney; A frequency tunable 15 atmosphere CO_2 laser (CLEA 75 Abstr.); *J-QE 75 Sep* 74D-75D (2G06)
Ostrowsky, D. B., *see* Papuchon, M.; *J-QE 75 Sep* 99D-100D (3B02)
Otsuka, K., *see* Yamada, T.; *J-QE 75 Sep* 62D-63D (2F08)
Otsuka, Kenju, Tomoaki Yamada, Masatoshi Saruwatari, and Tatsuya Kimura; Spectroscopy and laser oscillation properties of lithium neodymium tetraphosphate; *J-QE 75 Jul* 330-334 (1B02)
Otsuka, Kenju, and Tomoaki Yamada; Continuous oscillation of a lithium neodymium tetraphosphate laser with 200-μW pump threshold (Corresp.); *J-QE 75 Oct* 845-846 (1D01)
Oudar, Jean-Louis, *see* Schwartz, Christiane A.; *J-QE 75 Aug* 616-623 (1D08)
Oudar, Jean-Louis, Christiane A. Schwartz, and Edmond M. Batifol; Influence of two-photon absorption on second-harmonic generation in semiconductors —Part II: Measurement of two-photon absorption in tellurium; *J-QE 75 Aug* 623-629 (1E01)
Ozeki, T., T. Ito, and T. Tamura; Mode analysis of multimode fibers (CLEA 75 Abstr.); *J-QE 75 Sep* 77D (2G09)

P

Pack, J. L., *see* Wutzke, S. A.; *J-QE 75 Sep* 73D (2G05)
Panarella, Emilio, and Lorne L. T. Bradley; Controlled timewise redistribution of laser energy; *J-QE 75 May* 181-185 (1A03)
Pao, Y-H., *see* Claspy, P. C.; *J-QE 75 Sep* 37D (2D11)
Paoli, Thomas L.; Noise characteristics of stripe-geometry double-heterostructure junction lasers operating continuously—Part I: Intensity noise at room temperature; *J-QE 75 Jun* 276-283 (1D12)
Paoli, Thomas L.; Depolarization of the lasing emission from CW double-heterostructure junction lasers; *J-QE 75 Jul* 489-494 (3A13)
Paoli, Thomas L.; A new technique for measuring the thermal impedance of junction lasers; *J-QE 75 Jul* 498-503 (3B08)
Paoli, Thomas L., *see* Krupka, D. C.; *J-QE 75 Jul* 503-507 (3B13)
Paoli, Thomas L., José E. Ripper, A. C. Morosini, and N. B. Patel; Suppression of intensity self-pulsations in CW junction lasers by frequency-selective optical feedback; *J-QE 75 Jul* 525-527 (3D07)
Paoli, Thomas L., *Guest ed.*; Introduction: Semiconductor lasers—1975; *J-QE 75 Jul* 381 (2A03)
Papageorgis, N., *see* Lam, S. H.; *J-QE 75 Aug* 715-716 (2F07)
Papayoanou, Aristotle, and Akira Fujisawa; Theory of porous wall capillary tubes for flowing gas lasers; *J-QE 75 Aug* 579-583 (1A13)
Papuchon, M., Y. Combemale, X. Mathieu, D. B. Ostrowsky, L. Reiber, A. M. Roy, B. Séjourné, and M. Werner; Electrically switched optical directional coupler: COBRA (CLEA 75 Abstr.); *J-QE 75 Sep* 99D-100D (3B02)
Pashinin, P. P., *see* Vovchenko, V. I.; *J-QE 75 Sep* 83D (2G14)
Patel, N. B., *see* Paoli, Thomas L.; *J-QE 75 Jul* 525-527 (3D07)
Patterson, E. L., and R. A. Gerber; Characteristics of a high-energy hydrogen fluoride (HF) laser initiated by an intense electron beam; *J-QE 75 Aug* 642-648 (2A04)

Pearson, D. B., *see* Bjorkholm, J. E.; *J-QE 75 Sep* 68D (2G01)
Pearson, J. E.; Recent advances in multidither coherent optical adaptive techniques (COAT) (CLEA 75 Abstr.); *J-QE 75 Sep* 55D (2F01)
Pearson, W. M., *see* Peterson, O. G.; *J-QE 75 Sep* 4D-5D (2B06)
Pease, A. A., *see* Peterson, O. G.; *J-QE 75 Sep* 4D-5D (2B06)
Penney, C. M.; Remote measurement of ozone by resonance Raman scattering and differential absorption (CLEA 75 Abstr.); *J-QE 75 Sep* 36D (2D10)
Perry, B. E., *see* Eckstrom, D. J.; *J-QE 75 Aug* 691 (2D11)
Petersen, A. B., and C. Wittig; Chemically pumped CO_2 and N_2O lasers: $CO^+/(CO_2{\cdot}N_2O)$ (CHEMLAS 74 Digest); *J-QE 75 Aug* 699-700 (2E05)
Petersen, Alan B., and Curt Wittig; NaCl surface reaction in chemical-laser devices (Corresp.); *J-QE 75 Mar* 110-111 (1B02)
Petersen, F. Russell, Kenneth M. Evenson, Donald A. Jennings, Joseph S. Wells, Kenya Goto, and Juan J. Jiménez; Far infrared frequency synthesis with stabilized CO_2 lasers: Accurate measurements of the water vapor and methyl alcohol laser frequencies; *J-QE 75 Oct* 838-843 (1C08)
Peterson, O. G., A. A. Pease, and W. M. Pearson; Thermo-optical limitations on high average power dye lasers (CLEA 75 Abstr.); *J-QE 75 Sep* 4D-5D (2B06)
Peterson, O. G., *see* Foley, R. J.; *J-QE 75 Sep* 5D (2B07)
Peyton, Bernard J., Anthony J. DiNardo, Steven C. Cohen, John H. McElroy, and Robert J. Coates; An infrared heterodyne radiometer for high-resolution measurements of solar radiation and atmospheric transmission; *J-QE 75 Aug* 569-574 (1A03)
Peyton, B. J., T. Flattau, J. Wolczok, J. Mellars, and R. A. Lange; Wideband heterodyne receiver for CO_2 laser communication link (CLEA 75 Abstr.); *J-QE 75 Sep* 80D-81D (2G12)
Philipp-Rutz, E. M.; Spatially coherent radiation from an array of three GaAs lasers—Phase controlled or free running mode (CLEA 75 Abstr.); *J-QE 75 Sep* 60D-61D (2F06)
Phillion, D. W., *see* Siegman, A. E.; *J-QE 75 Sep* 69D (2G01)
Phipps, C. M., Jr., and S. J. Thomas; A high power isolator for the 10 micron region employing interband Faraday rotation in germanium (CLEA 75 Abstr.); *J-QE 75 Sep* 70D-71D (2G03)
Pierce, E. L., *see* Attwood, D. T.; *J-QE 75 Sep* 68D-69D (2F14)
Pierce, James W., *see* Chinn, Stephen R.; *J-QE 75 Sep* 747-754 (1B11)
Pierce, J. W., *see* Chinn, S. R.; *J-QE 75 Sep* 62D (2F08)
Pike, C. T., *see* Janes, G. S.; *J-QE 75 Sep* 101D-102D (3B04)
Pimentel, G. C., *see* Poole, P. R.; *J-QE 75 Aug* 688 (2D08)
Pimentel, G. C., *see* Cuellar, E.; *J-QE 75 Aug* 688 (2D08)
Pimentel, G. C., *see* Krogh, O. D.; *J-QE 75 Aug* 706 (2E12)
Pine, A. S., *see* Menyuk, N.; *J-QE 75 Jul* 477-481 (3A01)
Piper, J. A., and C. E. Webb; A TE copper iodide laser (CLEA 75 Abstr.); *J-QE 75 Sep* 95D (3A12)
Pirkle, Robert J., J. R. Wiesenfeld, Christopher C. Davis, George J. Wolga, and Ross A. McFarlane; Production of electronically excited iodine atoms, $I(^2P_{1/2})$, following injection of HI into a flow of discharge oxygen; *J-QE 75 Oct* 834-838 (1C04)
Pleasance, L. D., and L. A. Weaver; Laser emission at 1.32 μm from atomic iodine produced by electrical dissociation of CF_3I (CLEA 75 Abstr.); *J-QE 75 Sep* 94D-95D (3A11)
Plourde, Bertrand E., *see* Webb, J. Pierce; *J-QE 75 Mar* 114-119 (1B06)
Plummer, M. J., J. L. Wagner, and W. J. Glowacki; Experimental investigation of a supersonic CO electric discharge laser (CHEMLAS 74 Digest); *J-QE 75 Aug* 700 (2E06)
Poehler, T. O., and T. O. Turner; Electrically initiated pulse chemical DF–CO_2 and DF lasers (CHEMLAS 74 Digest); *J-QE 75 Aug* 710 (2F02)
Pond, C. R., and P. D. Texeira; Multichannel interferometry (CLEA 75 Abstr.); *J-QE 75 Sep* 10D-11D (2B12)
Poole, P. R., and G. C. Pimentel; Temperature dependence of the vibrational energy distribution of HF formed in the reactions of NH with the fluoromethanes (CHEMLAS 74 Digest); *J-QE 75 Aug* 688 (2D08)
Portnoy, E. L., *see* Alferov, Z. I.; *J-QE 75 Jul* 449-451 (2F01)
Poukey, J. W., *see* McArthur, David A.; *J-QE 75 Nov* 892-902 (1C10)
Powell, F. X., *see* McGee, T. J.; *J-QE 75 Jun* 302-304 (1F10)
Powell, H. T., J. R. Murray, and C. K. Rhodes; Laser oscillation on the green bands of xenon oxide (CHEMLAS 74 Digest); *J-QE 75 Aug* 685 (2D05)
Powell, H. T., J. R. Murray, and C. K. Rhodes; Collision-induced auroral line lasers (CLEA 75 Abstr.); *J-QE 75 Sep* 27D (2D01)
Prince, J. F., W. H. Long, Jr., and A. Garscadden; Negative ion production and influences in CO_2 discharge lasers (CHEMLAS 74 Digest); *J-QE 75 Aug* 687 (2D07)
Prokhorov, A. M., *see* Dianov, E. M.; *J-QE 75 Sep* 83D (2G14)
Prokhorov, A. M., *see* Vovchenko, V. I.; *J-QE 75 Sep* 83D (2G14)
Prokhorov, A. M., *see* Dekhtar, I. Ya.; *J-QE 75 Sep* 83D (2G14)

Q

Quigley, G. P., and G. J. Wolga; Vibrational deactivation of HF($v=1$), DF($v=1$), and HCl($v=1$), by collisions with atoms (CHEMLAS 74 Digest); *J-QE 75 Aug* 696-697 (2E02)

R

Raab, S., *see* Bachert, H.; *J-QE 75 Jul* 507-510 (3C03)
Raamot, J., *see* Jablonowski, D. P.; *J-QE 75 Sep* 21D-22D (2C09)
Rabal, H. J., J. J. Lunazzi, and M. Garavaglia; Laser interferometric check-out of granite surface plates (CLEA 75 Abstr.); *J-QE 75 Sep* 22D-23D (2C10)
Rabideau, S. W., *see* Schott, G. L.; *J-QE 75 Aug* 690 (2D10)
Rabson, Thomas A., *see* Shah, Rajiv R.; *J-QE 75 Sep* 783-788 (1E05)
Radecki, Dan J.; Lamp-pumped engineering feasibility model laser subsystems (CLEA 75 Abstr.); *J-QE 75 Sep* 15D-16D (2C03)
Radford, Harrison E.; New CW lines from a submillimeter waveguide laser; *J-QE 75 May* 213-214 (1C07)
Rainer, F., *see* Simmons, W. W.; *J-QE 75 Sep* 30D (2D04)
Rainer, F., *see* Simmons, W. W.; *J-QE 75 Sep* 31D-32D (2D05)
Rapagnani, N. L., *see* Turner, C. E., Jr.; *J-QE 75 Aug* 709-710 (2F01)
Rasoumov, L. N., *see* Zakharov, V. M.; *J-QE 75 Sep* 82D (2G14)
Ready, J. F.; Change of reflectivity of metallic surfaces during irradiation by CO_2-TEA laser pulses (CLEA 75 Abstr.); *J-QE 75 Sep* 49D (2E09)
Reber, E. E., *see* King, S. R.; *J-QE 75 Sep* 87D (3A04)
Reiber, L., *see* Papuchon, M.; *J-QE 75 Sep* 99D-100D (3B02)
Reichelt, W. H., *see* Figueira, J. F.; *J-QE 75 Sep* 74D (2G06)
Reid, John, *see* Garside, Brian K.; *J-QE 75 Jun* 264-270 (1C14)
Reid, John, *see* Garside, Brian K.; *J-QE 75 Aug* 583-589 (1B03)
Reinhart, F. K., *see* Logan, R. A.; *J-QE 75 Jul* 461-464 (2F13)
Reintjes, J., *see* Lehmberg, R. H.; *J-QE 75 Sep* 69D-70D (2G01)
Reno, C., *see* Ammon, G.; *J-QE 75 Sep* 50D-51D (2E10)
Reno, C. W.; Laser diode pumped Nd^{3+}:YAG laser (CLEA 75 Abstr.); *J-QE 75 Sep* 16D (2C04)
Reuter, Benno, *see* Mahr, H.; *J-QE 75 Sep* 97D-98D (3A14)
Rhodes, C. K., *see* Powell, H. T.; *J-QE 75 Aug* 685 (2D05)
Rhodes, C. K., *see* Bischel, W. K.; *J-QE 75 Sep* 24D-25D (2C12)
Rhodes, C. K., *see* Powell, H. T.; *J-QE 75 Sep* 27D (2D01)
Rice, J. K., *see* Johnson, A. W.; *J-QE 75 Sep* 56D (2F02)
Rice, R. R., and G. H. Burkhart; Barium sodium niobate acoustooptic mode-locker/frequency-doubler (AOML/FD) for Nd:YAG (CLEA 75 Abstr.); *J-QE 75 Sep* 14D (2C02)
Rice, W. W.; Metal atom oxidation lasers—A new family of chemical lasers (CHEMLAS 74 Digest); *J-QE 75 Aug* 689-690 (2D09)
Rink, J. P., *see* Lyman, J. L.; *J-QE 75 Sep* 103D (3B06)
Ripper, José E., *see* Paoli, Thomas L.; *J-QE 75 Jul* 525-527 (3D07)
Ritter, J. J., *see* Freund, S. M.; *J-QE 75 Aug* 702 (2E08)
Ritter, J. J., *see* Lamotte, M.; *J-QE 75 Aug* 702 (2E08)
Roback, R., *see* Sadowski, T. J.; *J-QE 75 Aug* 705-706 (2E11)
Roback, R., *see* Steele, R. V.; *J-QE 75 Aug* 719 (2F11)
Robertson, M. M., *see* Hargis, P. J., Jr.; *J-QE 75 Sep* 24D (2C12)
Robinson, C. P., *see* Lyman, J. L.; *J-QE 75 Sep* 103D (3B06)
Rockwood, S. D., *see* Lyman, J. L.; *J-QE 75 Sep* 103D (3B06)
Rosengren, L-G., *see* Shumate, M. S.; *J-QE 75 Sep* 33D-34D (2D07)
Rossi, J. A., J. J. Hsieh, and H. Heckscher; The gain profile and time-delay effects in external-cavity-controlled GaAs lasers; *J-QE 75 Jul* 538-545 (3E06)
Rouchon, J. M., *see* Huignard, J. P.; *J-QE 75 Sep* 8D-9D (2B10)
Roy, A. M., and B. Séjourné; Visualization of optical fields in integrated optical tapers and bifurcations (CLEA 75 Abstr.); *J-QE 75 Sep* 41D-42D (2E01)
Roy, A. M., *see* Papuchon, M.; *J-QE 75 Sep* 99D-100D (3B02)
Rudko, R. I.; Temporal coherence measurements of a double discharge CO_2 TEA laser (CLEA 75 Abstr.); *J-QE 75 Sep* 54D (2E14)
Russell, F., *see* Mangano, J. A.; *J-QE 75 Aug* 705 (2E11)
Ryan, L. W., Jr., *see* Kurnit, N. A.; *J-QE 75 Apr* 174-176 (1D14)
Rykalin, N. N., *see* Dekhtar, I. Ya.; *J-QE 75 Sep* 83D (2G14)

S

Sabin, J. R., *see* Witriol, N. M.; *J-QE 75 Aug* 717 (2F09)
Sadowski, T. J., C. E. Kepler, B. R. Bronfin, M. D. Krosney, and R. Roback; Continuous-wave HF chain reaction laser (CHEMLAS 74 Digest); *J-QE 75 Aug* 705-706 (2E11)
Saifi, M. A., and O. T. Masopust; Laser generated *RC* networks (CLEA 75 Abstr.); *J-QE 75 Sep* 23D (2C11)
Saifi, M. A., and S. J. Vahaviolos; Laser spot welding and real time evaluation (CLEA 75 Abstr.); *J-QE 75 Sep* 48D (2E08)
Saito, F., *see* Asakawa, K.; *J-QE 75 Jun* 304-306 (1F12)
Santana, C., and L. B. Felsen; A new look at unstable resonators (CLEA 75 Abstr.); *J-QE 75 Sep* 58D-59D (2F04)
Sargent, M., III, *see* Hambenne, J. B.; *J-QE 75 Feb* 90-92 (1B14)
Sarka, Benjamin, Jr., *see* Olson, Robert A.; *J-QE 75 Sep* 95D-96D (3A12)
Saruwatari, Masatoshi, *see* Otsuka, Kenju; *J-QE 75 Jul* 330-334 (1B02)
Sattler, J. P., B. A. Weber, and J. Nemarich; Tunable $Hg_{1-x}Cd_xTe$ infrared lasers (CLEA 75 Abstr.); *J-QE 75 Sep* 18D (2C06)
Savage, Albert, *see* Vogel, Gerald C.; *J-QE 74 Sep* 642-646 (1B02)
Schappert, G. T., *see* Figueira, J. F.; *J-QE 75 Sep* 74D (2G06)
Schappert, G. T., *see* Figueira, J. F.; *J-QE 75 Sep* 74D (2G06)
Schappert, G. T., J. S. Ladish, W. T. Leland, and M. J. Kircher; Gain recovery after saturation in short-pulse CO_2 amplifiers (CLEA 75 Abstr.); *J-QE 75 Sep* 75D-76D (2G07)
Schearer, Laird D.; A high-power pulsed xenon ion laser as a pump source for a tunable dye laser; *J-QE 75 Dec* 935-937 (1A09)
Schick, G., *see* Eichler, H.; *J-QE 75 Apr* 168-170 (1D08)
Schicketanz, D., and G. Zeidler; GaAs-double-heterostructure lasers as optical amplifiers; *J-QE 75 Feb* 65-69 (1A03)
Schlossberg, H. R., *see* Fetterman, H. R.; *J-QE 75 Sep* 88D-89D (3A05)
Schmatz, D. J., *see* Yessik, M.; *J-QE 75 Sep* 46D-47D (2E06)
Schmidt, R. V., and I. P. Kaminow; Acoustooptic Bragg deflection in $LiNbO_3$ Ti-diffused waveguides (Corresp.); *J-QE 75 Jan* 57-59 (1E03)
Scholtz, A. L.; Excitation of cold cavity modes in a coupling-modulated CO_2 laser (Corresp.); *J-QE 75 Sep* 791-793 (1E13)
Schott, G. L., S. W. Rabideau, A. V. Nowak, and R. W. Getzinger; Can we beat F_2 and H_2 for HF lasers? (CHEMLAS 74 Digest); *J-QE 75 Aug* 690 (2D10)
Schötzau, Hans J., and Fritz Kneubühl; Mass spectroscopy of the HCN-laser plasma; *J-QE 75 Oct* 817-822 (1B01)
Schwartz, Christiane A., Jean-Louis Oudar, and Edmond M. Batifol; Influence of two-photon absorption on second-harmonic generation in semiconductors —Part I: Theoretical analysis and application to the case of tellurium; *J-QE 75 Aug* 616-623 (1D08)
Schwartz, Christiane A., *see* Oudar, Jean-Louis; *J-QE 75 Aug* 623-629 (1E01)
Scifres, Donald R., *see* Streifer, William; *J-QE 75 Apr* 154-161 (1C08)
Scifres, Donald R., *see* Burnham, Robert D.; *J-QE 75 Jul* 439-449 (2E05)
Scifres, Donald R., *see* Streifer, William; *J-QE 75 Nov* 867-873 (1A13)
Scifres, D. R., *see* Burnham, R. D.; *J-QE 75 Jul* 418-420 (2C12)
Scifres, D. R., *see* Burnham, R. D.; *J-QE 75 Sep* 98D-99D (3B01)
Scott, P. B., S. Johnson, and G. Watson; Metal-oxidant flames: Visible chemiluminescence studies using a shock tunnel apparatus (CHEMLAS 74 Digest); *J-QE 75 Aug* 693-694 (2D13)
Searles, S. K., and G. A. Hart; Electron beam excitation of argon–nitrogen mixtures (CHEMLAS 74 Digest); *J-QE 75 Aug* 685 (2D05)
Searles, S. K., and G. A. Hart; A new excimer laser (CLEA 75 Abstr.); *J-QE 75 Sep* 93D (3A10)
Seguin, H. J. J., D. McKen, and J. Tulip; Photoionization parameters for TEA lasers (CLEA 75 Abstr.); *J-QE 75 Sep* 71D-72D (2G03)

Seguin, H. J. J., *see* Tulip, J.; *J-QE 75 Sep* 72D (2G04)
Séjourné, B., *see* Roy, A. M.; *J-QE 75 Sep* 41D-42D (2E01)
Séjourné, B., *see* Papuchon, M.; *J-QE 75 Sep* 99D-100D (3B02)
Sentman, L. H.; Rotational nonequilibrium in CW chemical lasers (CHEMLAS 74 Digest); *J-QE 75 Aug* 706-707 (2E12)
Serkin, V. N., *see* Kornienko, L. S.; *J-QE 75 Sep* 91D (3A08)
Setser, D. W., *see* King, D. L.; *J-QE 75 Aug* 708 (2E14)
Setser, D. W., *see* Velazco, J. E.; *J-QE 75 Aug* 708-709 (2E14)
Shah, Jagdeep, *see* Leheny, Robert F.; *J-QE 75 Feb* 70-74 (1A08)
Shah, Rajiv R., Thomas A. Rabson, and Dae M. Kim; Interferometric studies of mode-locked Nd^{3+}:glass lasers; *J-QE 75 Sep* 783-788 (1E05)
Shank, Charles V., *see* Smith, Peter W.; *J-QE 75 Feb* 84-89 (1B08)
Shank, C. V., *see* Lin, Chinlon; *J-QE 75 Sep* 1D-2D (2B03)
Shapiro, S. L., V. H. Kollman, R. C. Hyer, and A. J. Campillo; Streak camera studies using picosecond pulses of photosynthesis and plastic scintillators (CLEA 75 Abstr.); *J-QE 75 Sep* 5D-6D (2B07)
Sharpless, R. S., *see* Black, G.; *J-QE 75 Aug* 704 (2E10)
Shaub, W. H., and S. H. Bauer; Laser powered homogeneous pyrolysis (CHEMLAS 74 Digest); *J-QE 75 Aug* 714 (2F06)
Shcherbakov, I. A., *see* Dianov, E. M.; *J-QE 75 Sep* 83D (2G14)
She, Chiao-Yao, *see* Moran, Michael J.; *J-QE 75 Jun* 259-263 (1C09)
Sherman, L. M., *see* Loree, T. R.; *J-QE 75 Jul* 371-372 (1E01)
Shih, K. K., *see* Blum, Joseph M.; *J-QE 75 Jul* 413-418 (2C07)
Shima, Yasuji, *see* Tsukada, Toshihisa; *J-QE 75 Jul* 494-498 (3B04)
Shimabukuro, F. I., *see* King, S. R.; *J-QE 75 Sep* 87D (3A04)
Shimizu, M., *see* Ueno, Y.; *J-QE 75 Sep* 77D-78D (2G09)
Shin, Hyunk Kyu; Intermolecular vibration-to-vibration energy transfer in $HF/DF(v=1)+HF/DF(v=1) \rightarrow HF/DF(v=0)^{+}$ $HF/DF(v=2)$ through the formation of dimers; *J-QE 75 Aug* 679-684 (2C13)
Shortridge, R. G., and M. C. Lin; HF laser emission and CO population distribution studies of the $O(^3P)+CHF$ reaction (SHEMLAS 75 Digest); *J-QE 75 Aug* 688 (2D08)
Shortridge, R. G., *see* Lin, M. C.; *J-QE 75 Aug* 710 (2F02)
Shumate, M. S., *see* Menzies, R. T.; *J-QE 75 Sep* 33D (2D07)
Shumate, M. S., and L-G. Rosengren; Absorption of CO_2 laser radiation by water vapor (CLEA 75 Abstr.); *J-QE 75 Sep* 33D-34D (2D07)
Sibbett, W., *see* Bradley, D. J.; *J-QE 75 Sep* 25D-26D (2C13)
Siegman, A. E., D. J. Kuizenga, and D. W. Phillion; A transient induced grating system for measuring ultrafast photo-induced phenomena (CLEA 75 Abstr.); *J-QE 75 Sep* 69D (2G01)
Silfvast, W. T., and O. R. Wood, II; A 3400 Å dye laser and a 1.315 μm photodissociation laser efficiently pumped by a CO_2 laser-produced plasma (CLEA 75 Abstr.); *J-QE 75 Sep* 1D (2B03)
Simmons, W. W., S. Guch, Jr., F. Rainer, and J. E. Murray; A high energy spatial filter for removal of small scale beam instabilities in high power solid state lasers (CLEA 75 Abstr.); *J-QE 75 Sep* 30D (2D04)
Simmons, W. W., F. Rainer, R. D. Boyd, C. C. Fetterman, and J. A. Glaze; Terawatt laser performance (CLEA 75 Abstr.); *J-QE 75 Sep* 31D-32D (2D05)
Simons, J. A., *see* Librecht, F. M.; *J-QE 75 Oct* 850-852 (1D06)
Simpson, J. R., *see* Bernhardt, A. F.; *J-QE 75 Sep* 19D (2C07)
Singer, S., *see* Liberman, I.; *J-QE 75 Sep* 44D (2E04)
Singer, S.; The LASL 2.5 kJ CO_2 short-pulse laser system (CLEA 75 Abstr.); *J-QE 75 Sep* 44D-45D (2E04)
Singer, S., *see* Figueira, J. F.; *J-QE 75 Sep* 74D (2G06)
Smilanski, I., L. A. Levin, and G. Erez; A copper laser using CuI vapor (Corresp.); *J-QE 75 Nov* 919-920 (1E09)
Smith, A. L. S., T. H. Bett, and P. G. Browne; The effects of gas additives on TEA CO_2 lasers; *J-QE 75 Jul* 335-340 (1B07)
Smith, Archibald W., *see* Blum, Joseph M.; *J-QE 75 Jul* 413-418 (2C07)
Smith, D. L., *see* Manes, K. R.; *J-QE 75 Aug* 635-636 (1E13)
Smith, I. W. M., *see* Brown, R. D. H.; *J-QE 75 Aug* 695-696 (2E01)
Smith, I. W. M.; Vibrational relaxation in potentially reactive collisions: Temperature and isotope effects (CHEMLAS 74 Digest); *J-QE 75 Aug* 696 (2E02)
Smith, Peter W., Paul F. Liao, Charles V. Shank, C. Lin, and Patrick J. Maloney; The POPOP dye vapor laser; *J-QE 75 Feb* 84-89 (1B08)
Smith, P. W., *see* Wood, O. R., II; *J-QE 75 Sep* 72D-73D (2G04)
Snelling, David R., *see* Foster, Kenneth D.; *J-QE 75 Jun* 253-258 (1C03)
Snelling, D. R., *see* Foster, K. D.; *J-QE 75 Aug* 700 (2E06)
Soderstrom, R. L., *see* Dickson, L.; *J-QE 75 Sep* 23D-24D (2C11)
Soiarz, R. W.; Experimentally measured photoionization cross sections and excited state lifetimes in uranium vapor (CLEA 75 Abstr.); *J-QE 75 Sep* 19D-20D (2C07)
Solomon, W. C., *see* Baumann, W.; *J-QE 75 Aug* 711-712 (2F03)
Sommargren, G. E., *see* Bliss, E. S.; *J-QE 75 Sep* 29D (2D03)
Sonnenschein, C. M., *see* Miller, C. R.; *J-QE 75 Sep* 34D-35D (2D08)
Sonnenschein, C. M., C. A. DiMarzio, and H. Jeffreys; Performance of a CO_2 laser vortex detection system (CLEA 75 Abstr.); *J-QE 75 Sep* 35D (2D09)
Soures, J., *see* Hoose, J.; *J-QE 75 Sep* 12D (2B14)
Spears, D. L., I. Melngailis, and T. C. Harman; Planar HgCdTe photodiodes for wideband heterodyne detection at 10.6 μm (CLEA 75 Abstr.); *J-QE 75 Sep* 79D (2G11)
Spears, D. L., *see* Eng, R. S.; *J-QE 75 Sep* 87D-88D (3A04)
Speck, D. R., and J. F. Holzrichter; A Nd laser system developed for target irradiation studies at the Lawrence Livermore Laboratory (CLEA 75 Abstr.); *J-QE 75 Sep* 45D-46D (2E05)
Spencer, D. J., *see* King, S. R.; *J-QE 75 Sep* 87D (3A04)
Spitz, Eric; Optical video disks (CLEA 75 Abstr.); *J-QE 75 Sep* 11D (2B13)
Springer, L., *see* Anderson, R. S.; *J-QE 75 Apr* 172-174 (1D12)
Springer, L. S., *see* Bricks, B. G.; *J-QE 75 Sep* 57D (2F03)
Springer, L. W., *see* Anderson, R. S.; *J-QE 75 Sep* 56D-57D (2F02)
Stadler, B., *see* Baron, K. U.; *J-QE 75 Oct* 852-853 (1D08)
Stamatović, Aleksandar S., *see* Hertel, Ingolf V.; *J-QE 75 May* 210-212 (1C04)
Stark, Donald S., Peter H. Cross, and Harry Foster; A compact sealed pulsed CO_2 TEA laser; *J-QE 75 Sep* 774-778 (1D10)
Steele, R. V., *see* Meinzer, R. A.; *J-QE 75 Aug* 712-713 (2F04)
Steele, R. V., R. A. Meinzer, and R. Roback; Analysis of small-scale DF cold-reaction CW lasers (CHEMLAS 74 Digest); *J-QE 75 Aug* 719 (2F11)
Steffen, J., *see* Montanarini, M.; *J-QE 75 Sep* 47D (2E07)
Steier, W. H., *see* Christensen, C. P.; *J-QE 75 Oct* 849-850 (1D05)
Steier, William H., and Gary L. McAllister; A simplified method for predicting unstable resonator mode profiles; *J-QE 75 Sep* 725-728 (1A03)
Stein, Alexander; Chirp modulated CO_2 waveguide laser (Corresp.); *J-QE 75 Aug* 630-631 (1E08)
Steinberg, G. N., *see* Huchital, D. A.; *J-QE 75 Sep* 16D (2C04)
Steinfeld, J. I., *see* Wormhoudt, J.; *J-QE 75 Aug* 704 (2E10)
Stephenson, C., *see* Herzog, D. G.; *J-QE 75 Sep* 51D-52D (2E11)
Stettler, J. D., *see* Witriol, N. M.; *J-QE 75 Aug* 717 (2F09)
Stolen, Rogers H.; Phase-matched-stimulated four-photon mixing in silica-fiber waveguides; *J-QE 75 Mar* 100-103 (1A06)
Strahov, V. P., *see* Bachert, H.; *J-QE 75 Jul* 507-510 (3C03)
Street, A. J., *see* Greenhow, R. C.; *J-QE 75 Jan* 59-60 (1E05)
Stregack, J. A., and B. L. Wexler; A new electric discharge gas dynamic laser (CHEMLAS 74 Digest); *J-QE 75 Aug* 705 (2E11)
Stregack, J. A., and W. S. Watt; Characteristics of a supersonic DF–CO_2 transfer chemical laser (CHEMLAS 74 Digest); *J-QE 75 Aug* 711 (2F03)
Stregack, J. A., *see* Manuccia, T. J.; *J-QE 75 Nov* 921-923 (1E11)
Streifer, W., *see* Burnham, R. D.; *J-QE 75 Sep* 98D-99D (3B01)
Streifer, William, Robert D. Burnham, and Donald R. Scifres; Effect of external reflectors on longitudinal modes of distributed feedback lasers; *J-QE 75 Apr* 154-161 (1C08)
Streifer, William, *see* Burnham, Robert D.; *J-QE 75 Jul* 439-449 (2E05)
Streifer, William, Donald R. Scifres, and Robert D. Burnham; Coupling coefficients for distributed feedback single- and double-heterostructure diode lasers; *J-QE 75 Nov* 867-873 (1A13)
Stricker, J., and S. H. Bauer; An atomic boron laser—Pumping by incomplete autoionization or ion-electron recombination (CHEMLAS 74 Digest); *J-QE 75 Aug* 701-702 (2E07)
Stulz, L. W., *see* Kaminow, I. P.; *J-QE 75 Jun* 306-308 (1F14)
Stulz, L. W., *see* Kaminow, I. P.; *J-QE 75 Aug* 633-635 (1E11)
Suart, R. D.; N_2F_4 as a saturable absorber of CO_2 laser radiation (CHEMLAS 74 Digest); *J-QE 75 Aug* 698 (2E04)
Suchard, S. N., *see* Sutton, D. G.; *J-QE 75 Jan* 54-57 (1D14)
Suchard, S. N., *see* Sutton, D. G.; *J-QE 75 Feb* 92 (1C02)
Suchard, S. N., *see* Sutton, D. G.; *J-QE 75 Jun* 312 (1G06)
Suchard, S. N., and D. G. Sutton; Quasi-CW laser emission from the second positive band of nitrogen (CHEMLAS 74 Digest); *J-QE 75 Aug* 685-686 (2D05)
Suchard, S. N., *see* Sutton, D. G.; *J-QE 75 Aug* 690-691 (2D10)
Suchard, S. N., R. F. Heidner, III, and D. G. Sutton; Behavior of the first and second positive emission in the N_2/SF_6 laser (CLEA 75 Abstr.); *J-QE 75 Sep* 26D-27D (2C14)
Suchard, Steven N., David G. Sutton, and R. F. Heidner, III; Behavior of first- and second-positive emission in the N_2/SF_6 laser; *J-QE 75 Nov* 908-916 (1D12)
Suematsu, Y., M. Yamada, and K. Hayashi; Integrated twin-guide AlGaAs laser with multiheterostructure; *J-QE 75 Jul* 457-460 (2F09)
Suhara, T., *see* Nishihara, H.; *J-QE 75 Sep* 794-796 (1F02)
Sutton, David G., *see* Suchard, Steven N.; *J-QE 75 Nov* 908-916 (1D12)
Sutton, D. G., L. Galvan, P. R. Valenzuela, and S. N. Suchard; Atomic laser action in rare gas-SF_6 mixtures (Corresp.); *J-QE 75 Jan* 54-57 (1D14)
Sutton, D. G., L. Galvan, and S. N. Suchard; New laser oscillation in the oxygen atom (Corresp.); *J-QE 75 Feb* 92 (1C02)
Sutton, D. G., L. Galvan, and S. N. Suchard; Two-electron laser transition in Sn(I)? (Note); *J-QE 75 Jun* 312 (1G06)
Sutton, D. G., *see* Suchard, S. N.; *J-QE 75 Aug* 685-686 (2D05)
Sutton, D. G., and S. N. Suchard; Parametric evaluation of potential electronic transition chemical lasers (CHEMLAS 74 Digest); *J-QE 75 Aug* 690-691 (2D10)
Sutton, D. G., *see* Suchard, S. N.; *J-QE 75 Sep* 26D-27D (2C14)
Suydam, Bergen R., *see* Elliott, C. James; *J-QE 75 Nov* 863-866 (1A09)
Suydam, B. R.; Effect of refractive-index nonlinearity on the optical quality of high-power laser beams; *J-QE 75 Jun* 225-230 (1A03)
Sverdlov, B. N., *see* Bogatov, A. P.; *J-QE 75 Jul* 510-515 (3C06)

T

Takahashi, Tsutomu, *see* Fujii, Kan-Ichi; *J-QE 75 Mar* 111-114 (1B03)
Takanashi, H., *see* Takusagawa, M.; *J-QE 75 Sep* 61D (2F07)
Takeda, Y., *see* Tsunoda, Y.; *J-QE 75 Sep* 11D-12D (2B13)
Takeuchi, Nobuo; Photon-echo behavior in the presence of extreme inhomogeneous broadening; *J-QE 75 Jun* 230-235 (1A08)
Takusagawa, M., K. Hori, H. Ishikawa, H. Takanashi, T. Toge, and T. Kudo; Packaged semiconductor lasers for optical-fiber transmission (CLEA 75 Abstr.); *J-QE 75 Sep* 61D (2F07)
Tamura, T., *see* Ozeki, T.; *J-QE 75 Sep* 77D (2G09)
Tanaka, Atsuo, Masanobu Yamanaka, and Hiroshi Yoshinaga; New far-infrared laser lines from CO_2-laser pumped CH_3OH gas by using a copper waveguide cavity (Note); *J-QE 75 Oct* 853-854 (1D09)
Tang, C. L., *see* Chen, Bor-Uei; *J-QE 75 Apr* 177-178 (1E03)
Tannen, Peter D., *see* Bletzinger, Peter; *J-QE 75 Jul* 317-323 (1A03)
Tatsuno, K., *see* Tsunoda, Y.; *J-QE 75 Sep* 11D-12D (2B13)
Taylor, L. H., *see* Wutzke, S. A.; *J-QE 75 Sep* 73D (2G05)
Taylor, R. L., *see* Naismith, R.; *J-QE 75 Aug* 716 (2F08)
Taynai, Joseph D., *see* Falk, Joel; *J-QE 75 Sep* 14D-15D (2C02)
Teare, J. D., *see* Naismith, R.; *J-QE 75 Aug* 716 (2F08)
Teich, Malvin Carl; Multiphoton optical heterodyne detection; *J-QE 75 Aug* 595-602 (1C01)
Teller, E.; The relevance of lasers in the energy shortage (CLEA 75 Abstr.); *J-QE 75 Sep* 83D (2G14)
Teramoto, Iwao, *see* Itoh, Kunio; *J-QE 75 Jul* 421-426 (2D01)
Texeira, P. D., *see* Pond, C. R.; *J-QE 75 Sep* 10D-11D (2B12)
Thay, Chan Min, *see* Bachert, H.; *J-QE 75 Jul* 507-510 (3C03)
Thomas, Ben, M. J. Adams, and Stephan Gründorfer; A comprehensive model for *Q* switching in semiconductor lasers; *J-QE 75 Jul* 528-532 (3D10)
Thomas, Ben, *see* Gründorfer, Stephan; *J-QE 75 Jul* 532-537 (3D14)
Thomas, S. J., *see* Phipps, C. M., Jr.; *J-QE 75 Sep* 70D-71D (2G03)
Thomas, S. J., *see* Figueira, J. F.; *J-QE 75 Sep* 74D (2G06)

Thommarson, R. L., *see* Kelley, J. D.; *J-QE 75 Aug* 701 (2E07)
Thompson, G. H. B., P. A. Kirkby, and J. E. A. Whiteaway; The analysis of optical scattering in double-heterostructure and five-layer heterostructure (GaAl)As/GaAs injection lasers; *J-QE 75 Jul* 481-488 (3A05)
Thompson, G. H. B., *see* Garmire, E.; *J-QE 75 Sep* 38D-39D (2D12)
Thorne, J. M., *see* Loree, T. R.; *J-QE 75 Jul* 371-372 (1E01)
Tofield, B. C., *see* Weber, Heinz P.; *J-QE 75 Jul* 368-370 (1D12)
Tofield, B. C., *see* Weber, H. P.; *J-QE 75 Sep* 61D-62D (2F07)
Tofield, B. C., *see* Weber, H. P.; *J-QE 75 Sep* 100D (3B03)
Toge, T., *see* Takusagawa, M.; *J-QE 75 Sep* 61D (2F07)
Tollefsrud, P. B., *see* McArthur, D. A.; *J-QE 75 Aug* 707 (2E13)
Tomasetta, L. R., *see* Bicknell, W. E.; *J-QE 75 Jun* 308-311 (1G02)
Tomasetta, L. R., and C. G. Fonstad; Lead–tin telluride double-heterojunction laser diodes: Theory and experiment; *J-QE 75 Jul* 384-390 (2A06)
Tramontana, J. C., *see* Burnham, R. D.; *J-QE 75 Jul* 418-420 (2C12)
Tregay, G. W., M. G. Drexhage, L. M. Wood, and S. J. Andrysiak; DF–CO_2 transfer laser development; *J-QE 75 Aug* 672-678 (2C06)
Trenholme, J. B., *see* Glass, A. J.; *J-QE 75 Sep* 28D-29D (2D02)
Trenholme, J. B., *see* Gilmartin, T. J.; *J-QE 75 Sep* 32D (2D06)
Trickey, S. B., *see* Witriol, N. M.; *J-QE 75 Aug* 717 (2F09)
Tripathi, P. P., and R. H. Lovberg; A 700 meter long mode-locked argon ion laser (CLEA 75 Abstr.); *J-QE 75 Sep* 59D (2F05)
Tripodi, R., and B. Burdick; Theoretical modeling of saturation effects in laser amplifiers (CHEMLAS 74 Digest); *J-QE 75 Aug* 716 (2F08)
Tsai, C. S., M. A. Alhaider, LeT. Nguyen, and B. Kim; Wideband guided-wave acoustooptic Bragg devices using multiple tilting surface acoustic waves (CLEA 75 Abstr.); *J-QE 75 Sep* 10D (2B12)
Tseng, D. Y.; Polarization reference imaging system: Computer simulation studies (CLEA 75 Abstr.); *J-QE 75 Sep* 53D (2E13)
Tsukada, Toshihisa, and Yasuji Shima; Thermal characteristics of buried-heterostructure injection lasers; *J-QE 75 Jul* 494-498 (3B04)
Tsunoda, Y., K. Tatsuno, and Y. Takeda; A holographic video disk: An alternative approach to optical video disks (CLEA 75 Abstr.); *J-QE 75 Sep* 11D-12D (2B13)
Tubbs, S. J., *see* Kurnit, N. A.; *J-QE 75 Apr* 174-176 (1D14)
Tuccio, Sam A., Richard J. Foley, James W. Dubrin, and Oscar Krikorian; Macroscopic isotope separation of uranium by selective photoionization (CLEA 75 Abstr.); *J-QE 75 Sep* 101D (3B04)
Tucker, A. W., *see* DeShazer, L. G.; *J-QE 75 Sep* 84D (3A01)
Tulip, J., *see* Seguin, H. J. J.; *J-QE 75 Sep* 71D-72D (2G03)
Tulip, J., H. J. J. Seguin, and W. Faszer; High repetition rate TEA laser discharge using an integrated preionization and switching technique (CLEA 75 Abstr.); *J-QE 75 Sep* 72D (2G04)
Turner, C. E., Jr., and N. L. Rapagnani; Kinetic modeling of photodissociation iodine laser amplifiers (CHEMLAS 74 Digest); *J-QE 75 Aug* 709-710 (2F01)
Turner, E. H., *see* Bjorkholm, J. E.; *J-QE 75 Sep* 68D (2G01)
Turner, T. O., *see* Poehler, T. O.; *J-QE 75 Aug* 710 (2F02)

U

Ueno, Y., and M. Shimizu; An optical-fiber cable fault location method (CLEA 75 Abstr.); *J-QE 75 Sep* 77D-78D (2G09)
Ueno, Y., and Y. Ohgushi; A 40 Mb/s and a 400 Mb/s repeater for fiber optic communications (CLEA 75 Abstr.); *J-QE 75 Sep* 78D-79D (2G10)
Umeda, J., *see* Nakamura, Michiharu; *J-QE 75 Jul* 436-439 (2E02)

V

Vahaviolos, S. J., *see* Saifi, M. A.; *J-QE 75 Sep* 48D (2E08)
Vahey, David W.; An organic-dye light gate (CLEA 75 Abstr.); *J-QE 75 Sep* 100D-101D (3B03)
Valenzuela, P. R., *see* Sutton, D. G.; *J-QE 75 Jan* 54-57 (1D14)
Valette, S., G. Labrunie, J-C. Deutsch, and J. Lizet; Planar optical waveguides in ion-implanted ZnTe (CLEA 75 Abstr.); *J-QE 75 Sep* 39D-40D (2D13)
van Etteger, A. F., *see* Bluyssen, H. J. A.; *J-QE 75 Jul* 341-348 (1B13)
Varwig, R. L., and M. A. Kwok; CW HF/DF chemical laser spectral diagnostics (CHEMLAS 74 Digest); *J-QE 75 Aug* 719 (2F11)
Velazco, J. E., and D. W. Setser; Quenching studies of $Xe(^3P_3)$ metastable atoms (CHEMLAS 74 Digest); *J-QE 75 Aug* 708-709 (2E14)
Venkatesan, T. N. C., *see* Gibbs, H. M.; *J-QE 75 Sep* 91D (3A08)
Verdeyen, J. T., *see* DeYoung, R. J.; *J-QE 75 Sep* 97D (3A14)
Vieceli, J. J., *see* Evers, W. H.; *J-QE 75 Aug* 711 (2F03)
Vieceli, J. J., W. H. Evers, and A. G. Negro; Supersonic mixing DF–CO_2 transfer chemical laser: Theory (CHEMLAS 74 Digest); *J-QE 75 Aug* 711 (2F03)
Vilkomerson, D., *see* Mezrich, R.; *J-QE 75 Sep* 9D-10D (2B11)
Vincent, P., *see* Girard, G.; *J-QE 75 Jun* 241-247 (1B05)
Vogel, Gerald C., Albert Savage, and Michel A. Duguay; Picosecond optical sampling; *J-QE 74 Sep* 642-646 (1B02)
Comments by Macomber, James D.; *J-QE 75 Sep* 800 (1F08)
Volk, R., *see* Brederlow, G.; *J-QE 75 Sep* 42D-43D (2E02)
Vovchenko, V. I., I. J. Krasjuk, S. G. Lukishova, P. P. Pashinin, and A. M. Prokhorov; Production of specially tailored laser pulse (CLEA 75 Abstr.); *J-QE 75 Sep* 83D (2G14)

W

Wagner, J. L., *see* Plummer, M. J.; *J-QE 75 Aug* 700 (2E06)
Waksberg, Armand L.; Optimization of a laser communications system using electrooptic modulation; *J-QE 75 Sep* 778-782 (1D14)
Walker, Andrew C., *see* Alcock, A. J.; *J-QE 75 Sep* 767-773 (1D03)
Walker, R. E., *see* Benson, R. C.; *J-QE 75 Aug* 688-689 (2D08)
Walker, R. E., *see* Benson, R. C.; *J-QE 75 Aug* 697 (2E03)
Wanner, J.; Subsonic CW chemical laser emission from the reaction of H-atoms with Cl_2 in a transverse flow laser (CHEMLAS 74 Digest); *J-QE 75 Aug* 706 (2E12)
Watson, G., *see* Scott, P. B.; *J-QE 75 Aug* 693-694 (2D13)
Watt, W. S., *see* Stregack, J. A.; *J-QE 75 Aug* 711 (2F03)
Watt, W. S., *see* Manuccia, T. J.; *J-QE 75 Nov* 921-923 (1E11)
Weaver, H. J., *see* Bliss, E. S.; *J-QE 75 Sep* 29D (2D03)
Weaver, L. A., *see* Wutzke, S. A.; *J-QE 75 Sep* 73D (2G05)
Weaver, L. A., *see* Pleasance, L. D.; *J-QE 75 Sep* 94D-95D (3A11)
Webb, C. E., *see* Piper, J. A.; *J-QE 75 Sep* 95D (3A12)
Webb, J. Pierce, F. Glenn Webster, and Bertrand E. Plourde; Sixteen new IR laser dyes (Corresp.); *J-QE 75 Mar* 114-119 (1B06)
Webbink, R. F., *see* Lilenfeld, H. V.; *J-QE 75 Aug* 660-669 (2B08)
Weber, B. A., *see* Sattler, J. P.; *J-QE 75 Sep* 18D (2C06)
Weber, Heinz P., and B. C. Tofield; Heating in a CW Nd–pentaphosphate laser; *J-QE 75 Jul* 368-370 (1D12)
Weber, Horst, *see* Wilbrandt, Robert; *J-QE 75 May* 186-190 (1A08)
Weber, H. P., B. C. Tofield, and P. F. Liao; Progress in Nd-pentaphosphate lasers (CLEA 75 Abstr.); *J-QE 75 Sep* 61D-62D (2F07)
Weber, H. P., P. F. Liao, B. C. Tofield, and P. M. Bridenbaugh; NdLa pentaphosphate fiber laser (CLEA 75 Abstr.); *J-QE 75 Sep* 100D (3B03)
Weber, Marvin J., *see* Jacobs, Ralph R.; *J-QE 75 Oct* 846-847 (1D02)
Weber, M. J., *see* Jacobs, R. R.; *J-QE 75 Sep* 13D (2C01)
Weber, M. J., *see* Layne, C. B.; *J-QE 75 Sep* 798-799 (1F06)
Webster, F. Glenn, *see* Webb, J. Pierce; *J-QE 75 Mar* 114-119 (1B06)
Weil, Raoul, *see* Halido, D.; *J-QE 75 Sep* 64D-65D (2F10)
Wells, Joseph S., *see* Petersen, F. Russell; *J-QE 75 Oct* 838-843 (1C08)
Wells, W. E., *see* DeYoung, R. J.; *J-QE 75 Sep* 97D (3A14)
Wendelken, C. P., L. E. Wilson, C. Clendening, and J. Noetzel; DF* laser deactivation kinetics (CHEMLAS 74 Digest); *J-QE 75 Aug* 694-695 (2D14)
Werner, M., *see* Papuchon, M.; *J-QE 75 Sep* 99D-100D (3B02)
West, E. J., *see* Burns, W. K.; *J-QE 75 Sep* 42D (2E02)
West, G. A., and M. J. Berry; Cyanide radical photodissociation and predissociation chemical lasers: Molecular electronic and vibrational laser emissions (CHEMLAS 74 Digest); *J-QE 75 Aug* 687 (2D07)
West, J. B., and H. P. Broida; Production efficiencies and radiative lifetime of FeO produced in low pressure flames (CHEMLAS 74 Digest); *J-QE 75 Aug* 692-693 (2D12)
West, J. B., R. L. Barger, and T. C. English; A highly stabilized, tunable CW dye laser and an accurate determination of the Rydberg constant (CLEA 75 Abstr.); *J-QE 75 Sep* 18D-19D (2C06)
Wexler, B. L., *see* Stregack, J. A.; *J-QE 75 Aug* 705 (2E11)
Whitcher, R. E., *see* McLeary, R.; *J-QE 75 Sep* 90D-91D (3A07)
Whiteaway, J. E. A., *see* Thompson, G. H. B.; *J-QE 75 Jul* 481-488 (3A05)
Whitney, W. T., *see* Harris, N. W.; *J-QE 75 Aug* 686-687 (2D06)
Whitney, W. T., *see* O'Neill, F.; *J-QE 75 Sep* 74D-75D (2G06)
Wiesemann, W., *see* Eichler, H.; *J-QE 75 Apr* 168-170 (1D08)
Wiesenfeld, J. R.; Direct determination of the yield of electronically excited iodine atoms, $I(5^2P_{1/2})$, in the flash photolysis of alkyl iodides (CHEMLAS 74 Digest); *J-QE 75 Aug* 703-704 (2E09)
Wiesenfeld, J. R., *see* Burde, D. H.; *J-QE 75 Aug* 709 (2F01)
Wiesenfeld, J. R., *see* Pirkle, Robert J.; *J-QE 75 Oct* 834-838 (1C04)
Wilbrandt, Robert, and Horst Weber; Fluctuations in mode-locking threshold due to statistics of spontaneous emission; *J-QE 75 May* 186-190 (1A08)
Wilkins, R. L., *see* Kwok, M. A.; *J-QE 75 Aug* 695 (2E01)
Wilkins, R. L.; Vibrational relaxation of HCl ($v=1$, 2, 3, and 6) by H- and Cl-atoms (CHEMLAS 74 Digest); *J-QE 75 Aug* 716-717 (2F08)
Wilson, L. E., S. G. Hadley, R. A. Harris, and G. Hager; The potential for electronic transition lasers with molecules from the carbon group oxides (CHEMLAS 74 Digest); *J-QE 75 Aug* 691 (2D11)
Wilson, L. E., *see* Wendelken, C. P.; *J-QE 75 Aug* 694-695 (2D14)
Wisner, G., *see* Boedeker, L.; *J-QE 75 Aug* 713 (2F05)
Witriol, N. M., J. D. Stettler, J. R. Sabin, and S. B. Trickey; Investigation of the computation of V–T and V–V intermolecular potentials (CHEMLAS 74 Digest); *J-QE 75 Aug* 717 (2F09)
Witte, K. J., *see* Brederlow, G.; *J-QE 75 Sep* 42D-43D (2E02)
Witteman, W. J., and G. J. Ernst; On the saturation effects and start jump of Gaussian modes in oscillators; *J-QE 75 May* 198-204 (1B06)
Witteman, W. J., *see* Ernst, G. J.; *J-QE 75 Nov* 920-921 (1E10)
Wittig, C., *see* Petersen, A. B.; *J-QE 75 Aug* 699-700 (2E05)
Wittig, Curt, *see* Petersen, Alan B.; *J-QE 75 Mar* 110-111 (1B02)
Wittke, J. P., *see* Gorog, I.; *J-QE 75 Sep* 63D (2F09)
Wolczok, J., *see* Peyton, B. J.; *J-QE 75 Sep* 80D-81D (2G12)
Wolga, George J., *see* Pirkle, Robert J.; *J-QE 75 Oct* 834-838 (1C04)
Wolga, G. J., *see* Quigley, G. P.; *J-QE 75 Aug* 696-697 (2E02)
Wolga, G. J., *see* Buchwald, M. I.; *J-QE 75 Aug* 697 (2E03)
Wood, L. L., *see* Bernhardt, A. F.; *J-QE 75 Sep* 19D (2C07)
Wood, L. M., *see* Tregay, G. W.; *J-QE 75 Aug* 672-678 (2C06)
Wood, O. R., II, *see* Silfvast, W. T.; *J-QE 75 Sep* 1D (2B03)
Wood, O. R., II, P. W. Smith, C. R. Adams, and P. J. Maloney; Efficient preionization scheme for high gain CW CO_2 waveguide TE laser (CLEA 75 Abstr.); *J-QE 75 Sep* 72D-73D (2G04)
Wooding, Eric R., *see* Loveberg, R. V.; *J-QE 75 Jan* 17-21 (1B05)
Woolhouse, G. R.; Degradation in injection lasers; *J-QE 75 Jul* 556-561 (3F10)
Wormhoudt, J., L. Marabella, and J. I. Steinfeld; Measurement of pressure-broadened infrared linewidths with an optical parametric oscillator (CHEMLAS 74 Digest); *J-QE 75 Aug* 704 (2E10)
Wright, P. D., *see* Coleman, J. J.; *J-QE 75 Jul* 471-476 (2G09)
Wu, C.Y. R., and D. A. Dows; Selective isotope excitation of CuI (CLEA 75 Abstr.); *J-QE 75 Sep* 20D (2C08)
Wutzke, S. A., L. H. Taylor, J. L. Pack, T. V. George, and L. A. Weaver; Discharge scaling studies for a continuously operating fast flow electrically excited (COFFEE) laser (CLEA 75 Abstr.); *J-QE 75 Sep* 73D (2G05)
Wyder, Peter, *see* Bluyssen, H. J. A.; *J-QE 75 Jul* 341-348 (1B13)

Y

Yablonovitch, Eli; Generation of a short optical pulse of arbitrary shape and phase variation (Corresp.); *J-QE 75 Sep* 789-791 (1E11)
Yamabe, C., *see* Yamanaka, C.; *J-QE 75 Sep* 45D (2E05)
Yamada, M., *see* Suematsu, Y.; *J-QE 75 Jul* 457-460 (2F09)
Yamada, T., and K. Otsuka; CW laser operation of $LiNdP_4O_{12}$ by transverse pumping (CLEA 75 Abstr.); *J-QE 75 Sep* 62D-63D (2F08)
Yamada, Tomoaki, *see* Otsuka, Kenju; *J-QE 75 Jul* 330-334 (1B02)
Yamada, Tomoaki, *see* Otsuka, Kenju; *J-QE 75 Oct* 845-846 (1D01)
Yamamoto, Yoshihisa, Takeshi Ksmiya, and Hisayoshi Yanai; Characteristics of optical guided modes in multilayer metal-clad planar optical guide with low-index dielectric buffer layer; *J-QE 75 Sep* 729-736 (1A07)

Yamanaka, C., M. Yokoyama, S. Nakai, M. Matoba, and C. Yamabe; Investigations of laser fusion by CO_2 laser (CLEA 75 Abstr.); *J-QE 75 Sep* 45D (2E05)
Yamanaka, Masanobu, *see* Tanaka, Atsuo; *J-QE 75 Oct* 853-854 (1D09)
Yamashita, Mikio, Hiroshi Kashiwagi, and Hidenori Ikeda; Investigation of photodegradation mechanism in laser dyes by detection of triplet-molecules and free radicals induced by laser light (CLEA 75 Abstr.); *J-QE 75 Sep* 3D (2B05)
Yamazaki, T., *see* Asakawa, K.; *J-QE 75 Jun* 304-306 (1F12)
Yanai, Hisayoshi, Mitsuhiro Yano, and Takeshi Kamiya; Direct modulation of a double-heterostructure laser using a Schottky-barrier-gate Gunn-effect digital device; *J-QE 75 Jul* 519-524 (3D01)
Yanai, Hisayoshi, *see* Yamamoto, Yoshihisa; *J-QE 75 Sep* 729-736 (1A07)
Yano, Mitsuhiro, *see* Yanai, Hisayoshi; *J-QE 75 Jul* 519-524 (3D01)
Yanochko, G. S., *see* Fehrs, D. L.; *J-QE 75 Sep* 21D (2C09)
Yariv, A., *see* Nakamura, Michiharu; *J-QE 75 Jul* 436-439 (2E02)
Yen, H. W., *see* Nakamura, Michiharu; *J-QE 75 Jul* 436-439 (2E02)
Yeoman, Michael L., *see* Loveberg, R. V.; *J-QE 75 Jan* 17-21 (1B05)
Yessik, M., and D. J. Schmatz; Laser processing in the automotive industry (CLEA 75 Abstr.); *J-QE 75 Sep* 46D-47D (2E06)
Yokoyama, M., *see* Yamanaka, C.; *J-QE 75 Sep* 45D (2E05)
Yoshinaga, Hiroshi, *see* Tanaka, Atsuo; *J-QE 75 Oct* 853-854 (1D09)

Z

Zadell, H., *see* Ammon, G.; *J-QE 75 Sep* 50D-51D (2E10)
Zakharov, V. M., L. N. Rasoumov, E. M. Birger, and S. P. Karlov; Rain drop measurements by holography (CLEA 75 Abstr.); *J-QE 75 Sep* 82D (2G14)
Zeidler, G., *see* Schicketanz, D.; *J-QE 75 Feb* 65-69 (1A03)
Zelazny, S. W., *see* Baumann, W.; *J-QE 75 Aug* 711-712 (2F03)
Ziegler, J. F., *see* Blum, Joseph M.; *J-QE 75 Jul* 413-418 (2C07)
Zory, P., and L. D. Comerford; Grating-coupled double-heterostructure AlGaAs diode lasers; *J-QE 75 Jul* 451-457 (2F03)

SUBJECT INDEX

A

Absorption; **cf.** Infrared propagation, absorbing media; Laser absorbers; Optical propagation, absorbing media
Acoustic bulk waves
interferometric measurement and display. *Mezrich, R., J-QE 75 Sep* 9D-10D (2B11)
Acoustic bulk-wave devices
FM acoutooptic modulators; optical-guided-wave modulator using standing wave. *Christensen, C. P., J-QE 75 Oct* 849-850 (1D05)
Acoustic diffraction; **cf.** Acoustic surface-wave diffraction
Acoustic filters; **cf.** Acoustooptic filters
Acoustic signal processing; **cf.** Acoustic surface-wave signal processing
Acoustic surface-wave convolution
optical guided wave–acoustic surface-wave interactions in thin-film As_2S_3 guide on $LiNbO_3$ substrate. *Loh, K. W., J-QE 75 Sep* 86D (3A03)
Acoustic surface-wave diffraction
guided-wave Bragg diffraction from multiple tilting surface acoustic waves. *Tsai, C. S., J-QE 75 Sep* 10D (2B12)
light deflectors; $LiNbO_3$ acoustooptic Bragg deflectors with low electrical drive power requirements. *Schmidt, R. V., J-QE 75 Jan* 57-59 (1E03)
Acoustic surface-wave effects
optical planar waveguides; light scattering from periodic refractive-index fluctuations. *Marcuse, D., J-QE 75 Apr* 162-168 (1D02)
shock wave effects in laser-irradiated semiconductors and metals. *Dekhtar, I. Ya., J-QE 75 Sep* 83D (2G14)
Acoustic surface-wave signal processing; **cf.** Acoustic surface-wave convolution
Acoustooptic devices
explosive vapor detectors. *Claspy, P. C., J-QE 75 Sep* 37D (2D11)
mode locker/frequency doubler for Nd:YAG lasers. *Rice, R. R., J-QE 75 Sep* 14D (2C02)
Acoustooptic filters
Tl_3AsSe_3 tunable colllinear filters for intermediate infrared. *Feichtner, J. D., J-QE 75 Sep* 66D-67D (2F12)
Acoustooptic light deflectors
$LiNbO_3$ Bragg deflectors with low electrical drive power requirements. *Schmidt, R. V., J-QE 75 Jan* 57-59 (1E03)
Acoustooptic modulation
guided-optical-wave FM modulator using acoustic standing wave. *Christensen, C. P., J-QE 75 Oct* 849-850 (1D05)
Aerodynamic testing; **cf.** Gas flow visualization
Aerospace simulation; **cf.** Gas flow visualization
Aircraft; **cf.** Helicopters
Aircraft control
helicopters; precision hover sensor for heavy lift helicopter. *Herzog, D. G., J-QE 75 Sep* 51D-52D (2E11)
Aircraft wakes
vortex detection system using CO_2 laser Doppler velocimeter. *Sonnenschein, C. M., J-QE 75 Sep* 35D (2D09)
Air pollution monitoring
ambient-air pollutant measurements using bistatic heterodyne system. *Menzies, R. T., J-QE 75 Sep* 33D (2D07)
pollution concentration variations with altitude; measurement using solar infrared heterodyne radiometer. *Christophe, B., J-QE 75 Sep* 32D-33D (2D06)
power plant effluent measurements; remote measurements using laser Doppler velocimeter. *Miller, C. R., J-QE 75 Sep* 34D-35D (2D08)
Altimetry; **cf.** Optical distance measurement
Aluminum
laser-heated surfaces; thermal coupling coefficient. *Marcus, S., J-QE 75 Sep* 49D-50D (2E09)
Aluminum alloys/compounds; **cf.** Gallium alloys/compounds
Amplifiers; **cf.** Laser amplifiers; Optical amplifiers; Feedback amplifiers
Arc heating
Cu vapor laser produced by discharge heating. *Anderson, R. S., J-QE 75 Apr* 172-174 (1D12)
Arc lamps
Kr arc lamps; electrodeless lamp for CW pumping of Nd:YAG lasers. *Huchital, D. A., J-QE 75 Sep* 16D (2C04)
Argon; **cf.** Noble gases
Arsenic alloys/compounds, devices
As_2S_3 optical planar waveguides; convolution using optical guided wave–acoustic surface-wave interactions. *Loh, K. W., J-QE 75 Sep* 86D (3A03)
Atmospheric pollution; **cf.** Air pollution
Atmospheric radio propagation; **cf.** Optical radio propagation meteorological factors
Automobiles
laser materials processing in automotive industry. *Yessik, M., J-QE 75 Sep* 46D-47D (2E06)
Automotive industry; **cf.** Automobiles
Avalanche diodes
laser communications system using external polarization electrooptic modulation and avalanche diode detection; optimum carrier-to-noise ratio. *Waksberg, Armand L., J-QE 75 Sep* 778-782 (1D14)

B

Barium alloys/compounds, devices
$Ba_2NaNb_5O_{15}$ acoustooptic mode locker/frequency doubler for Nd:YAG lasers. *Rice, R. R., J-QE 75 Sep* 14D (2C02)
$Ba_2Na(NbO_3)_5$ intracavity frequency-doubling elements in Nd:YAG lasers; thermooptical effects. *Barry, James D., J-QE 75 Aug* 575-579 (1A13)
lasers; BaF, BaCl, BaBr and BaI electronic-transition chemical lasers. *Bradford, R. S., Jr., J-QE 75 Aug* 692 (2D12)
lasers; BaO electronic-transition chemical laser. *Scott, P. B., J-QE 75 Aug* 693-694 (2D13)
Beams; **cf.** Laser beams
Beam deflection; **cf.** Beam steering
Beam steering
laser beam deflection by precision galvanometer deflection system. *Jablonowski, D. P., J-QE 75 Sep* 21D-22D (2C09)
Biological cells
photosynthetic processes; streak camera studies of fluorescent decay times. *Shapiro, S. L., J-QE 75 Sep* 5D-6D (2B07)
Boron devices
lasers; pulsed lasers pumped by incomplete autoionization or ion–electron recombination. *Stricker, J., J-QE 75 Aug* 701-702 (2E07)
Boron alloys/compounds
BCl_3 isotopic enrichment by multiple absorption of CO_2 laser radiation. *Lyman, J. L., J-QE 75 Sep* 103D (3B06)
Boron alloys/compounds, devices
lasers; BO electronic-transition chemical laser. *Scott, P. B., J-QE 75 Aug* 693-694 (2D13)
Bragg scattering; **cf.** Distributed feedback lasers
Bromine compounds/mixtures, devices
lasers; excited electronic states of BrCl electronic-transition lasers. *Harris, R. A., J-QE 75 Aug* 691 (2D11)
Bulk waves; **cf.** Acoustic bulk waves

C

Cadmium devices; **cf.** Gas lasers
Cadmium alloys/compounds, devices
HgCdTe planar photodiodes for wideband heterodyne detection at 10.6 μm. *Spears, D. L., J-QE 75 Sep* 79D (2G11)
Cadmium alloys/compounds, devices; **cf.** Semiconductor defects
Calcium devices; **cf.** Gas lasers, molecular
Cameras
radiation cameras; ultra-high-speed camera using hydrated electron photoabsorption phenomena and mode-locked-dye-laser picosecond pulses. *Coutts, Gerald W., J-QE 75 Sep* 6D (2B08)
Camera tubes; **cf.** Image sensors
Carbon alloys/compounds
CH_4 gas; generation of coherent anti-Stokes Raman scattering by CW lasers. *Barrett, J. J., J-QE 75 Sep* 89D-90D (3A06)
Carbon dioxide lasers
2.5 kJ short-pulse system. *Singer, S., J-QE 75 Sep* 44D-45D (2E04)
aircraft vortex detection system using CO_2 laser Doppler velocimeter. *Sonnenschein, C. M., J-QE 75 Sep* 35D (2D09)
beam quality of short-pulse lasers; measurement. *Liberman, I., J-QE 75 Sep* 44D (2E04)
chemical lasers using $N + CS_2$ reaction. *McGee, T. J., J-QE 75 Jun* 302-304 (1F10)
chemical lasers using energy transfer from vibrationally excited CO. *Petersen, A. B., J-QE 75 Aug* 699-700 (2E05)
chirp-modulated waveguide lasers; demodulation technique. *Stein, Alexander, J-QE 75 Aug* 630-631 (1E08)
$CO_2(00°1)$ level; vibrational deactivation by H, D, O, N, F and Cl atoms. *Buchwald, M. I., J-QE 75 Aug* 697 (2E03)
cold cavity modes; amplitudes of modes excited by coupling modulation. *Scholtz, A. L., J-QE 75 Sep* 791-793 (1E13)
compact sealed 200-W laser. *Fahlen, Theodore S., J-QE 75 Oct* 848-849 (1D04)
contaminant gases; effects on CO_2–N_2–He electric-discharge lasers. *Bletzinger, Peter, J-QE 75 Jul* 317-323 (1A03)
contaminant gases; effects on flowing-gas TEA lasers. *Smith, A. L. S., J-QE 75 Jul* 335-340 (1B07)
continuously operating fast flow electrically excited (COFFEE) lasers; discharge scaling studies. *Wutzke, S. A., J-QE 75 Sep* 73D (2G05)
continuously tunable high-pressure lasers; use in molecular spectroscopy and excitation of luminescence. *Bagratashvili, V. N., J-QE 75 Sep* 94D (3A11)
CS_2/O_2 chemical lasers; flash photolysis-produced surface reactions on NaCl Brewster windows. *Petersen, Alan B., J-QE 75 Mar* 110-111 (1B02)
CW chemical transfer lasers; model. *Baumann, W., J-QE 75 Aug* 711-712 (2F03)

D_2–CO_2 transfer lasers; electric discharge gas dynamic laser. *Stregack, J. A., J-QE 75 Aug* 705 (2E11)
DF–CO_2 chemical transfer lasers; supersonic CW laser which recovers to atmospheric pressure. *Stregack, J. A., J-QE 75 Aug* 711 (2F03)
DF–CO_2 chemical transfer lasers; supersonic mixing laser experiments. *Evers, W. H., J-QE 75 Aug* 711 (2F03)
DF–CO_2 chemical transfer lasers; supersonic mixing laser theory. *Vieceli, J. J., J-QE 75 Aug* 711 (2F03)
DF–CO_2 electrically initiated pulsed chemical lasers. *Poehler, T. O., J-QE 75 Aug* 710 (2F02)
DF–CO_2 transfer chemical lasers; power extraction and chemiluminescence experiments in large-scale IRIS laser. *Tregay, G. W., J-QE 75 Aug* 672-678 (2C06)
Doppler velocimeters for remote power plant effluent measurements. *Miller, C. R., J-QE 75 Sep* 34D-35D (2D08)
far-infrared frequency synthesis using stabilized CO_2 lasers; application in laser line frequency measurements. *Petersen, F. Russell, J-QE 75 Oct* 838-843 (1C08)
frequency tuning of 15-atm electron-beam-controlled lasers. *O'Neill, F., J-QE 75 Sep* 74D-75D (2G06)
high-energy lasers pumped by nultraviolet sustained electric discharges; scalability. *Lind, R. C., J-QE 75 Sep* 71D (2G03)
high-pressure lasers; 15-atm electron-beam-controlled laser. *Harris, N. W., J-QE 75 Aug* 686-687 (2D06)
hybrid laser with active medium consisting of TEA and low-pressure gain sections; mechanism of single-frequency operation. *Gondhalekar, A., J-QE 75 Mar* 103-108 (1A09)
isotopic enrichment of polyatomic molecules by multiple absorption of laser radiation. *Lyman, J. L., J-QE 75 Sep* 103D (3B06)
materials processing applications in automotive industry. *Yessik, M., J-QE 75 Sep* 46D-47D (2E06)
metallic surface irradiation by CO_2–TEA lasers; changes in surface reflectivity. *Ready, J. F., J-QE 75 Sep* 49D (2E09)
molecular decomposition; infrared-laser-augmented decomposition of H_3BPF_3. *Lory, E. R., J-QE 75 Aug* 714-715 (2F06)
multiatmosphere transverse-discharge ultraviolet-preionized lasers; small-signal gain at pressures in 1–15-atm range. *Alcock, A. J., J-QE 75 Sep* 767-773 (1D03)
multiband lasers; parametric study. *Figueira, J. F., J-QE 75 Sep* 74D (2G06)
N_2 and CO_2(001) vibration-to-translation relaxation by alkali metal atoms. *Benson, R. C., J-QE 75 Aug* 697 (2E03)
negative ions in discharge lasers; formation and effects. *Prince, J. F., J-QE 75 Aug* 687 (2D07)
plasma-injection CW lasers with multikilowatt power output. *McLeary, R., J-QE 75 Sep* 90D-91D (3A07)
pulsed laser gain dynamics; model. *Garside, Brian K., J-QE 75 Jun* 264-270 (1C14)
pulsed lasers; multigigawatt, ns pulses from tandem of two TEA lasers. *Bélanger, P. A., J-QE 75 Sep* 73D-74D
pulsed TEA lasers; compact sealed laser. *Stark, Donald S., J-QE 75 Sep* 774-778 (1D10)
Q-switched lasers; passive *Q*-switching by N_2F_4 absorption cells. *Suart, R. D., J-QE 75 Aug* 698 (2E04)
radiation absorption by water vapor. *Shumate, M. S., J-QE 75 Sep* 33D-34D (2D07)
rotational–vibrational line competition in dual-polarization laser. *Buholz, N. E., J-QE 75 Nov* 917-919 (1E07)
semiconductor device fabrication; SiC high-temperature resistor fabrication using CO_2 lasers. *Hierholzer, F. J., J-QE 75 Sep* 47D-48D (2E07)
switching of high-power output radiation using light-activated Ge switches. *Alcock, A. J., J-QE 75 Sep* 96D (3A13)
TEA laser pulse frequency chirp; measurement using interferometric pulse delay techniques. *Hieslmair, H., J-QE 75 Sep* 54D (2E14)
TEA lasers; discharge technique that integrates ultraviolet preionization with voltage switching. *Tulip, J., J-QE 75 Sep* 72D (2G04)
TEA lasers; ultraviolet photoionization parameters. *Seguin, H. J. J., J-QE 75 Sep* 71D-72D (2G03)
temporal coherence of double-discharge TEA lasers. *Rudko, R. I., J-QE 75 Sep* 54D (2E14)
transversely excited lasers; laser dynamics model including rotational coupling effects. *Garside, Brian K., J-QE 75 Aug* 583-589 (1B03)
transversely excited CW lasers; high-gain waveguide laser using preionization scheme based on Malter effect. *Wood, O. R., II, J-QE 75 Sep* 72D-73D (2G04)

Carbon dioxide laser amplifiers
energy extraction by short-duration input pulses; effect of rotational and intramode vibrational coupling. *Harrach, Robert J., J-QE 75 Jul* 349-357 (1C07)
energy extraction from atmospheric-pressure lasers using 60 ns–1 μs pulses. *Girard, G., J-QE 75 Jun* 241-247 (1B05)
energy extraction from atmospheric-pressure lasers for nanosecond input pulses. *Girard, G., J-QE 74 Dec* 901-902 (1D09) ♦
energy extraction improvement in ns-pulse TEA lasers. *Farcy, J. C., J-QE 75 Sep* 90D (3A07)
gain recovery in short-pulse high-pressure amplifiers after saturation. *Schappert, G. T., J-QE 75 Sep* 75D-76D (2G07)
high-power electron-beam-controlled system for laser fusion. *Yamanaka, C., J-QE 75 Sep* 45D (2E05)
multiple rotational line operation for increased efficiency. *Figueira, J. F., J-QE 75 Sep* 74D (2G06)
prepulse extinction-ratio measurements on pulse-selection systems. *Manes, K. R., J-QE 75 Aug* 635-636 (1E13)
self-oscillation suppression in high-gain amplifiers using interstage optical isolators. *Lavigne, P., J-QE 75 Sep* 75D (2G07)
Valkyrie system for laser fusion experiments. *Manes, K. R., J-QE 75 Sep* 44D (2E04)
waveguide CW power amplifiers. *Klein, Marvin B., J-QE 75 Aug* 609-615 (1D01)

Carbon monoxide lasers
chemical lasers; computer modeling code for CS_2O CW laser. *Lilenfeld, H. V., J-QE 75 Aug* 660-669 (2B08)
chemical lasers; $CS_2/O_2/N_2O$ flame laser featuring nearly single-line operation. *Foster, Kenneth D., J-QE 75 Jun* 253-258 (1C03)
CO($v=1$) vibrational deactivation by atomic oxygen. *Davis, C. C., J-QE 75 Aug* 701 (2E07)
CS_2/O_2 chemical laser; role of atomic S. *Cupitt, L. T., J-QE 75 Aug* 700-701 (2E06)
$CS_2/O_2/N_2O$ chemical flame laser; near single-line operation in 5–5.5 μm region. *Foster, K. D., J-QE 75 Aug* 700 (2E06)
electric discharge lasers; time-dependent kinetics of multilevel pumping. *Boulnois, J. L., J-QE 75 Aug* 707-708 (2E13)
electron energy distributions in vibrationally excited CO, CO–He and CO–Ar mixtures; effects of superelastic collisions. *Greene, A. E., J-QE 75 Aug* 708 (2E14)
excitation by nuclear reactor products. *McArthur, D. A., J-QE 75 Aug* 707 (2E13)
kinetic modeling of high-pressure lasers; effects of resonance self-absorption. *Lacina, William B., J-QE 75 Jun* 297-302 (1F05)
O_2 additions to CO–He mixtures; effects on laser performance. *Keren, H., J-QE 75 Aug* 590-594 (1B10)
$O(^3P)+CO(^1\Sigma^+)$ collisions; vibrational deactivation and atom exchange. *Kelley, J. D., J-QE 75 Aug* 701 (2E07)
O* + CO and I* + CO electronic-to-vibrational energy transfer reactions. *Lin, M. C., J-QE 75 Aug* 710 (2F02)
scaling generalizations for high-pressure electric-discharge lasers. *Lacina, William B., J-QE 75 Jun* 235-241 (1A13)
supersonic electric discharge laser. *Plummer, M. J., J-QE 75 Aug* 700 (2E06)
vibrational–vibrational collision probability measurements on CO molecule. *Nachshon, Yehuda, J-QE 75 Aug* 654-660 (2B02)

Cathode-ray oscilloscopes
optical sampling oscilloscope for picosecond laser pulse displays. *Vogel, Gerald C., J-QE 74 Sep* 642-646 (1B02) ♦

Cavity resonators; **cf.** Laser resonators
Cell biology; **cf.** Biological cells
Cerenkov radiation; **cf.** Ultraviolet generation

Cesium
negative nonlinear refractive index of Cs vapor at 1.06 1gmm; use in compensation of self-focusing in other transparent materials. *Lehmberg, R. H., J-QE 75 Sep* 69D-70D (2G01)
vapor; third-order susceptibility. *Eicher, Hermann, J-QE 75 Apr* 121-130 (1A03)

Cesium alloys/compounds, devices
CD*A second-harmonic generating crystals; electrooptic compensation for self-heating. *Hon, D., J-QE 75 Sep* 67D-68D (2F13)

Cesium devices
lasers; electronic-transition chemical laser using Cs + F_2 reaction system. *Hall, L. H., J-QE 75 Aug* 693 (2D13)

Chemical and Molecular Lasers Conference
papers and abstracts from Oct. 1974 conference, *J-QE 75 Aug, Pt. II* 641-722 (2A03)
special issue on Oct. 1974 conference; foreword. *Jeffers, W. Q., Guest ed., J-QE 75 Aug* 641 (2A03)

Chemical lasers
electronic-transition chemical lasers using reactions of I_2, Br_2, SiH_4, GeH_4, AsH_3 or Ph_3 with F_2. *Davis, S. J., J-QE 75 Aug* 693 (2D13)

Chemical lasers; **cf.** Gas lasers

Chemistry
B isotope enrichment by laser-induced photochemical process. *Freund, S. M., J-QE 75 Aug* 702 (2E08)
Cl isotope enrichment by laser-induced photochemical process. *Lamotte, M., J-QE 75 Aug* 702 (2E08)
molecular decomposition; infrared-laser-augmented decomposition of H_3BPF_3. *Lory, E. R., J-QE 75 Aug* 714-715 (2F06)
nitric oxide reactions with laser-excited ozone. *Gordon, R. J., J-QE 75 Aug* 715 (2F07)
photochemistry; isotopic enrichment by multiple absorption of CO_2 laser radiation. *Lyman, J. L., J-QE 75 Sep* 103D (3B06)
pyrolysis; laser-powered homogeneous pyrolysis. *Shaub, W. H., J-QE 75 Aug* 714 (2F06)

Chirp modulation
CO_2 waveguide lasers; demodulation technique for chirp-modulated laser. *Stein, Alexander, J-QE 75 Aug* 630-631 (1E08)

Chirp radar; **cf.** Pulse compression-radar
Chlorine devices; **cf.** Gas lasers
Communication systems; **cf.** Optical communication; Satellite communication

Communication system fault diagnosis
optical fiber communication; fiber fault location method. *Ueno, Y., J-QE 75 Sep* 77D-78D (2G09)

Conferences; **cf.** Chemcial and Molecular Lasers Conference; Laser Engineering and Applications Conference; Semiconductor Laser Confererence

Consumer products
universal product code symbol; optical scanners using lasers for reading. *Dickson, L., J-QE 75 Sep* 23D-24D (2C11)

Control systems; **cf.** Feedback systems; Vehicle control
Convolution; **cf.** Acoustic surface-wave convolution

Copper
laser-heated surfaces; thermal coupling coefficient. *Marcus, S., J-QE 75 Sep* 49D-50D (2E09)
welding of Cu wires to Monel terminal posts; laser welding. *Saifi, M. A., J-QE 75 Sep* 48D (2E08)

Copper alloys/compounds
CuI vapor; selective isotope excitation by Ar ion laser excitation. *Wu, C.Y. R., J-QE 75 Sep* 20D (2C08)

Copper alloys/compounds, devices
lasers; CuF electronic-transition chemical laser. *Scott, P. B., J-QE 75 Aug* 693-694 (2D13)
Monel terminal posts; laser welding of insulated Cu wires to posts. *Saifi, M. A., J-QE 75 Sep* 48D (2E08)

Copper alloys/compounds, devices; **cf.** Gas lasers
Couplers; **cf.** Laser couplers; Optical couplers
Crime; **cf.** Law enforcement
Crystal defects; **cf.** Semiconductor defects

♦ **Check author entry for later corrections/comments**

Crystal growth
KTN; single-crystal thin-film growth by liquid-phase epitaxy. *Fontana, R. E., Jr., J-QE 75 Sep* 38D (2D12)
Crystal growth; **cf.** Semiconductor growth
CW lasers
AlGaAs double-heterostructure junction lasers; depolarization of lasing emission. *Paoli, Thomas L., J-QE 75 Jul* 489-494 (3A13)
Ar ion lasers using 700-m-long cavity. *Tripathi, P. P., J-QE 75 Sep* 59D (2F05)
buried-heterostructure lasers with GaAs active regions completely buried in GaAlAs; thermal properties. *Tsukada, Toshihisa, J-QE 75 Jul* 494-498 (3B04)
CO_2 laser amplifiers; high-power 10.6-μm waveguide amplifier. *Klein, Marvin B., J-QE 75 Aug* 609-615 (1D01)
CO_2 lasers; compact sealed 200-W laser. *Fahlen, Theodore S., J-QE 75 Oct* 848-849 (1D04)
CO_2 lasers; multikilowatt laser using plasma injection. *McLeary, R., J-QE 75 Sep* 90D-91D (3A07)
CO_2 transversely excited lasers; high-gain waveguide laser using preionization scheme based on Malter effect. *Wood, O. R., II, J-QE 75 Sep* 72D-73D (2G04)
CO chemical laser; computer modeling code for CS_2/O laser. *Lilenfeld, H. V., J-QE 75 Aug* 660-669 (2B08)
coherent anti-Stokes Raman scattering; generation by CW lasers. *Barrett, J. J., J-QE 75 Sep* 89D-90D (3A06)
cresyl violet perchlorate laser; pumping using dye mixture and tandem systems. *Beisser, F. A., J-QE 75 Jul* 372 (1E02)
DF–CO_2 chemical transfer lasers; model. *Baumann, W., J-QE 75 Aug* 711-712 (2F03)
DF–CO_2 supersonic chemical transfer lasers. *Stregack, J. A., J-QE 75 Aug* 711 (2F03)
DF cold-reaction lasers; analysis of small-scale laser. *Steele, R. V., J-QE 75 Aug* 719 (2F11)
DF/HF chemical lasers; portable lasers using recirculating mode of operation. *Chenausky, P. P., J-QE 75 Sep* 58D (2F04)
double-heterostructure stripe-geometry junction lasers; room-temperature intensity noise characteristics. *Paoli, Thomas L., J-QE 75 Jun* 276-283 (1D12)
double-heterostructure GaAs/GaAlAs lasers with oxide-insulated stripe geometry; CW lasing range and light-output power. *Garel-Jones, P., J-QE 75 Jul* 408-413 (2C02)
dye lasers stabilized by frequency locking to high-finesse optical cavity; frequency fluctuations of 1 kHz for short times and 300 Hz for 300 s. *West, J. B., J-QE 75 Sep* 18D-19D (2C06)
far-infrared lasers; CO_2-pumped laser lines from 254 to 1700 μm. *Jennings, D. A., J-QE 75 Aug* 637 (1F01)
GaAs/GaAlAs double-heterojunction lasers; internal optical loss in very thin lasers. *Butler, J. K., J-QE 75 Jul* 402-408 (2B10)
GaAs/GaAlAs double-heterojunction visible-light-emitting lasers using heteroisolation stripe geometry. *Itoh, Kunio, J-QE 75 Jul* 421-426 (2D01)
H_2 vacuum ultraviolet lasers. *Knyazev, I. N., J-QE 75 Oct* 805-817 (1A03)
HCl chemical lasers; transverse-flow laser using $H+Cl_2$ reaction. *Wanner, J., J-QE 75 Aug* 706 (2E12)
HF chain-reaction lasers in supersonic mixing device. *Cummings, J. C., J-QE 75 Aug* 712 (2F04)
HF chain-reaction lasers; generation of vibrationally excited HF. *Meinzer, R. A., J-QE 75 Aug* 712-713 (2F04)
HF chemical lasers; temporal characteristics of multiline–multimode lasers. *Foster, M. C., J-QE 75 Aug* 714 (2F06)
HF chemical lasers; transverse mode oscillations in lasers with stable selected-line resonators. *Boedeker, L., J-QE 75 Aug* 713 (2F05)
HF chemical mixing lasers; CW lasers as local oscillators for middle-IR heterodyne applications. *Freiberg, R. J., J-QE 75 Sep* 57D-58D (2F03)
HF/DF chain-reaction lasers. *Sadowski, T. J., J-QE 75 Aug* 705-706 (2E11)
HF/DF lasers; frequency stabilization and absolute frequency measurements. *Eng, R. S., J-QE 75 Sep* 87D-88D (3A04)
HF/DF supersonic chemical lasers; spectroscopic and infrared measurements. *Kwok, M. A., J-QE 75 Aug* 718 (2F10)
HF/DF supersonic chemical lasers; gas heater and nozzle array performance. *Giedt, R. R., J-QE 75 Aug* 718-719 (2F10)
HF/DF supersonic diffusion chemical lasers; spectrographic systems for diagnostic experiments. *Varwig, R. L., J-QE 75 Aug* 719 (2F11)
HF lasers; arc- and combustion-driven laser performance. *Grohs, G. L., J-QE 75 Aug* 717 (2F09)
Hg lasers; dc-excited Hg pump lamps for operation at 546.1 nm. *Holmes, N., J-QE 75 Sep* 55D (2F01)
hydrogen halide chemical lasers; rotational nonequilibrium. *Sentman, L. H., J-QE 75 Aug* 706-707 (2E12)
InSb lasers; tunable lasers optically pumped in longitudinal geometry. *Menyuk, N., J-QE 75 Jul* 477-481 (3A01)
$LiNdP_4O_{12}$ lasers; transversely pumped laser. *Yamada, T., J-QE 75 Sep* 62D-63D (2F08)
$LiNdP_4O_{12}$ lasers with 200-μW pump threshold. *Otsuka, Kenju, J-QE 75 Oct* 845-846 (1D01)
N_2 lasers; quasi-CW second-positive laser using SF_6 additions to N_2 in discharge region. *Suchard, S. N., J-QE 75 Aug* 685-686 (2D05)
NdLa pentaphosphate fiber lasers. *Weber, H. P., J-QE 75 Sep* 100D (3B03)
Nd:YAG lasers; pumping with electrodeless Kr arc lamps. *Huchital, D. A., J-QE 75 Sep* 16D (2C04)
Nd:YVO_4 lasers. *DeShazer, L. G., J-QE 75 Sep* 84D (3A01)
noble-gas ion lasers; CW operation below 3000 Å. *Marling, J. B., J-QE 75 Sep* 27D-28D (2D01)
self-induced intensity pulsations from junction lasers; suppression by frequency-selective optical feedback. *Paoli, Thomas L., J-QE 75 Jul* 525-527 (3D07)
submillimeter emission from optically pumped waveguide gas lasers. *Radford, Harrison E., J-QE 75 May* 213-214 (1C07)
supersonic CO electric discharge laser. *Plummer, M. J., J-QE 75 Aug* 700 (2E06)
transverse-junction-stripe lasers with GaAs homojunction sandwiched between GaAlAs layers. *Namizaki, H., J-QE 75 Jul* 427-431 (2D07)
CYCLOPS amplifier; **cf.** Laser amplifiers

D

Defocusing; **cf.** Laser-beam focusing
Deformation; **cf.** Strain
Delay lines
optical communication systems; mode-locked lasers using folded optical delay lines. *Kornienko, L. S., J-QE 75 Sep* 91D (3A08)
Demodulation; **cf.** Optical demodulation
Detection; **cf.** Demodulation
Deuterium halide lasers; **cf.** Hydrogen halide lasers
Dielectric waveguides; **cf.** Optical waveguides
Diffraction; **cf.** Acoustic diffraction; Optical diffraction
Digital communication; **cf.** PCM
Digital integrated circuits
masks for integrated-circuit fabrication; correction of defects using laser beam. *Lee, F., J-QE 75 Sep* 21D (2C09)
Dilatometry; **cf.** Length measurement
Diodes; **cf.** Semiconductor diodes
Diode lasers; **cf.** Semiconductor lasers
Dislocations; **cf.** Semiconductor defects
Displacement measurement
motions as small as .05 Å; interferometric measurement and display of ultrasonic waves. *Mezrich, R., J-QE 75 Sep* 9D-10D (2B11)
Distance measurement; **cf.** Optical distance measurement
Distributed-feedback lasers
coupling coefficients for TE modes in single- and double-heterostructure diode lasers. *Streifer, William, J-QE 75 Nov* 867-873 (1A13)
GaAs/GaAlAs double-heterostructure injection lasers; pulsed operation between 80 and 150 K. *Nakamura, Michiharu, J-QE 75 Jul* 436-439 (2E02)
GaAs/GaAlAs double-heterostructure lasers; corrugated grating-coupled laser with low-divergence output normal to waveguide plane. *Zory, P., J-QE 75 Jul* 451-457 (2F03)
GaAs lasers; single-heterostructure electrically pumped lasers. *Burnham, Robert D., J-QE 75 Jul* 439-449 (2E05)
longitudinal modes; effect of external reflectors. *Streifer, William, J-QE 75 Apr* 154-161 (1C08)
Diversity communication
optical radio communication under turbulent conditions. *McIntyre, C. M., J-QE 75 Sep* 81D (2G13)
Doppler measurements
$^{12}CH_3F$; pressure broadening and pressure shift coefficient measurements using Doppler-free two-photon absorption techniques. *Bischel, W. K., J-QE 75 Sep* 24D-25D (2C12)
aircraft vortex detection system using CO_2 laser Doppler velocimeter. *Sonnenschein, C. M., J-QE 75 Sep* 35D (2D09)
gas flow measurement and visualization using resonant Doppler velocimeter. *Miles, R. B., J-QE 75 Sep* 35D-36D (2D09)
power plant effluent measurements; remote measurements using laser Doppler velocimeter. *Miller, C. R., J-QE 75 Sep* 34D-35D (2D08)
Dyes
BDN; recovery times for transient bleaching; mode locking of Nd:glass lasers. *Greenhow, R. C., J-QE 75 Jan* 59-60 (1E05)
cryptocyanine in methanol; spectral hole burning in absorption band. *Mourou, Gerard, J-QE 75 Jan* 1-8 (1A03)
light gates using optically induced dichroism in organic-dye solutions. *Vahey, David W., J-QE 75 Sep* 100D-101D (3B03)
optically gated dye cells for optical pulse shaping; saturable absorber dye dynamics. *Massey, G. A., J-QE 75 Jul* 358-364 (1D02)
Dye lasers
amplified spontaneous emission and signal amplification in transversely pumped lasers. *Ganiel, U., J-QE 75 Nov* 881-892 (1B13)
cresyl violet perchlorate in methanol; small-signal gain in longitudinally pumped solutions. *Leheny, Robert F., J-QE 75 Feb* 70-74 (1A08)
cresyl violet perchlorate laser; pumping using dye mixture and tandem systems. *Beisser, F. A., J-QE 75 Jul* 372 (1E02)
CW lasers stabilized by frequency locking to high-finesse optical cavity; frequency fluctuations of 1 kHz for short times and 300 Hz for 300 s. *West, J. B., J-QE 75 Sep* 18D-19D (2C06)
energy transfer processes in organic dye mixtures; simultaneous laser actions at the primary colors from three-dye mixture. *Ahmed, S. A., J-QE 75 Sep* 2D-3D (1B04)
high-power lasers; mechanisms limiting operation. *Glenn, W. H., J-QE 75 Sep* 5D (2B07)
high-power lasers; thermally induced optical inhomogeneities in active volume. *Peterson, O. G., J-QE 75 Sep* 4D-5D (2B06)
high-power lasers using free jet stream of liquid dye solution. *Foley, R. J., J-QE 75 Sep* 5D (2B07)
infrared dyes; lasing efficiency and photochemical stability in spectral region 710–950 nm. *Oettinger, P. E., J-QE 75 Sep* 3D-4D (2B05)
infrared lasers; near-IR emission from 16 new flashlamp-pumped dyes. *Webb, J. Pierce, J-QE 75 Mar* 114-119 (1B06)
infrared lasers; superradiant near-IR emission from ultraviolet-pumped dye solutions. *Lin, Chinlon, J-QE 75 Jan* 61 (1E07)
oligo-mode distance control using spatial hole burning. *Hertel, Ingolf V., J-QE 75 May* 210-212 (1C04)
photodegradation of organic laser dyes; study using esr detection of laser-induced triplet molecules and free radicals. *Yamashita, Mikio, J-QE 75 Sep* 3D (2B05)
pulsed high-repetition-rate lasers; transverse-flow laser pumped by linear close-coupled flashlamps. *Friedman, H. W., J-QE 75 Sep* 4D (2B06)
pulse generation; subnanosecond tunable pulse generation in N_2-laser-pumped lasers using controlled resonator transients. *Lin, Chinlon, J-QE 75 Sep* 1D-2D (2B03)
relaxation oscillations and initial spikes in N_2 laser-pumped dye lasers; tunable nanosecond pulse generation in UV and visible region. *Lin, Chinlon, J-QE 75 Aug* 602-609 (1C08)
resonant Doppler velocimeters for gas flow measurement and visualization. *Miles, R. B., J-QE 75 Sep* 35D-36D (2D09)

Rhodamine-6G lasers; long-pulse generation in laser pumped by Co_2-laser-heated plasma. *Brown, Robert T., J-QE 75 Sep* 800-801 (1F08)
spectrometer for analysis of pulsed vacuum arcs. *Hargis, P. J., Jr., J-QE 75 Sep* 24D (2C12)
synchronous mode-locked laser pumped by frequency-doubled, passively mode-locked Nd:YAG laser; picosecond pulse generation. *Goldberg, L. S., J-QE 75 Sep* 2D (1B04)
terphenyl dye laser; optical pumping by UV radiation from CO_2-laser-produced Xe plasma. *Silfvast, W. T., J-QE 75 Sep* 1D (2B03)
tunable Rhodamine-6G dye laser; high-power pulsed Xe ion laser as pump source. *Schearer, Laird D., J-QE 75 Dec* 935-937 (1A09)
vapor laser using organic scintillator dye POPOP. *Smith, Peter W., J-QE 75 Feb* 84-89 (1B08)
visible lasers; high-power blue and violet lasers pumped by third harmonic of Nd:YAG laser. *Kato, K., J-QE 75 Jul* 373-374 (1E03)

E

Earth
soil compaction quality checking using lasers. *Drakatos, Panagiotis A., J-QE 75 Sep* 84D-86D (3A01)
Electrical dissociation pumping; **cf.** Gas lasers
Electric discharge pumping; **cf.** Gas lasers
Electric heating; **cf.** Arc heating
Electric variables measurement; **cf.** Pulse measurements
Electroluminescent devices; **cf.** Light-emitting diodes
Electromagnetic diffraction; **cf.** Optical diffraction
Electromagnetic propagation; **cf.** Optical propagation
Electromagnetic pulse generators
microwave and millimeter-wave pulse generation using Si optoelectronic switches. *Johnson, A. M., J-QE 75 Jun* 283-287 (1E05)
Electromagnetic radiation effects
microwave radiation effects; isotope separation using radiation pressure. *Gelbwachs, Jerry, J-QE 75 Jan* 52-54 (1D12)
Electromagnetic reflection; **cf.** Optical reflection
Electromagnetic refraction; **cf.** Optical refraction
Electron-beam pumping; **cf.** Gas lasers
Electrooptics
self-heating compensation in CD*A crystals during second-harmonic generation. *Hon, D., J-QE 75 Sep* 67D-68D (2F13)
Electrooptics; **cf.** Pockels effect
Electrooptic modulation
(Ga,Al)P optical planar waveguide modulators; mode-dependent modulation. *Bortfeld, David P., J-QE 75 Mar* 108-110 (1A14)
GaAs channel-waveguide modulators. *Campbell, J. C., J-QE 75 Sep* 63D-64D (2F09)
KTN single-crystal thin-film modulators. *Fontana, R. E., Jr., J-QE 75 Sep* 38D (2D12)
laser communications system using external polarization electrooptic modulation and avalanche diode detection; optimum carrier-to-noise ratio. *Waksberg, Armand L., J-QE 75 Sep* 778-782 (1D14)
mode coupling; electrooptic coupling between TE and TM modes in anisotropic slab waveguides. *Marcuse, D., J-QE 75 Sep* 759-767 (1C09)
optical planar waveguide modulators using grain-oriented polycrystalline ZnO film. *Hu, Chenming, J-QE 75 Sep* 64D (2F10)
resonant piezo-electrooptic modulation. *Halido, D., J-QE 75 Sep* 64D-65D (2F10)
ZnO optical planar waveguide modulators. *Hammer, Jacob M., J-QE 75 Apr* 138-148 (1B06)
Electrooptic switches
optical planar waveguide switches; electrode configuration for producing prism-like deflector on guide. *Kaminow, I. P., J-QE 75 Aug* 633-635 (1E11)
Energy transfer; **cf.** Relaxation processes
Environmental pollution; **cf.** Air pollution
Epitaxial growth; **cf.** Semiconductor growth
Excimer lasers; **cf.** Noble gas lasers, molecular
Excitation of lasers; **cf.** Laser excitation
Explosions
explosive vapor detection using laser optoacoustic detector. *Claspy, P. C., J-QE 75 Sep* 37D (2D11)

F

Fabrication; **cf.** Integrated-circuit fabrication; Laser materials-processing applications; Semiconductor device fabrication
Fabry–Perot interferometers
laser tuning;-frequency tunable 15-atm electron-beam-controlled CO_2 laser. *O'Neill, F., J-QE 75 Sep* 74D-75D (2G06)
Fading channels; **cf.** Diversity communication
Faraday effect
infrared isolators; Ge high-power isolator for 10 μm region using interband Faraday effect. *Phipps, C. M., Jr., J-QE 75 Sep* 70D-71D (2G03)
Far infrared; **cf.** Submillimeter-wave (300–3000 GHz)
Fault diagnosis; **cf.** Communication system fault diagnosis
Feedback amplifiers
optical fiber communication repeaters; 40-Mb/s and 400-Mb/s repeaters using feedback-type amplifiers. *Ueno, Y., J-QE 75 Sep* 78D-79D (2G10)
Feedback lasers; **cf.** Distributed-feedback lasers
Feedback systems
frequency-selective optical feedback; suppression of self-induced intensity pulsations from CW junction lasers. *Paoli, Thomas L., J-QE 75 Jul* 525-527 (3D07)
Nd:glass lasers; light emission control. *Panarella, Emilio, J-QE 75 May* 181-185 (1A03)
Q-switched ruby lasers; pulse shaping by compound feedback. *Loveberg, R. V., J-QE 75 Jan* 17-21 (1B05)
Fiber optics; **cf.** Optical fibers
Fiber waveguides; **cf.** Optical fiber waveguides
Filters; **cf.** Acoustic filters; Acoustooptic filters; Optical filters
Flashlamps
pulsed high-current gas-filled flashlamps; near-ultraviolet spectral efficiency. *Gusinow, M. A., J-QE 75 Dec* 929-934 (1A03)
Flight control; **cf.** Aircraft control
Fluid flow; **cf.** Gas flow
Fluorescence
$LiNdP_4O_{12}$. *Otsuka, Kenju, J-QE 75 Jul* 330-334 (1B02)
narrower-than-natural linewidth fluorescence in Mg atomic beams subjected to CW dye laser radiation. *Gibbs, H. M., J-QE 75 Sep* 91D (3A08)
streak camera studies in photosynthetic systems and plastic scintillators. *Shapiro, S. L., J-QE 75 Sep* 5D-6D (2B07)
FM
guided-optical-wave modulator using acoustic standing wave. *Christensen, C. P., J-QE 75 Oct* 849-850 (1D05)
FM pulse-compression methods; **cf.** Chirp modulation
Focusing; **cf.** Laser-beam focusing
Food industry
universal product code symbol; laser scanners for reading. *Dickson, L., J-QE 75 Sep* 23D-24D (2C11)
Fourier transforms
holograms of simple plane objects; recording using X-rays. *Mahr, H., J-QE 75 Sep* 97D-98D (3A14)
Frequency conversion
laser frequency doubling; mode-locked lasers with internal frequency doubling. *Falk, Joel, J-QE 75 Jan* 21-31 (1B09) ♦
Frequency conversion; **cf.** Optical frequency conversion
Frequency-domain analysis
lasers; mode-locked intracavity frequency-doubled laser. *Kennedy, C. J., J-QE 75 Nov* 857-862 (1A03)
Frequency modulation; **cf.** FM
Frequency multiplication; **cf.** Frequency conversion
Frequency stability; **cf.** Laser frequency stability
Frequency synthesizers
far-infrared frequency synthesis using saturated-absorption stabilized CO_2 lasers and point-contact diode. *Petersen, F. Russell, J-QE 75 Oct* 838-843 (1C08)
Fusion; **cf.** Nuclear fusion

G

Gallium alloys/compounds
GaAs; dislocation pinning by Group III or V impurities. *Kirkby, P. A., J-QE 75 Jul* 562-568 (3G02)
GaAs; elastooptic coefficient p_4. *Halido, D., J-QE 75 Sep* 64D-65D (2F10)
Gallium alloys/compounds, devices
(Ga,Al)P optical planar waveguide modulators; mode-dependent modulation. *Bortfeld, David P., J-QE 75 Mar* 108-110 (1A14)
GaAs channel-waveguide modulators. *Campbell, J. C., J-QE 75 Sep* 63D-64D (2F09)
GaAs diffused optical strip waveguides. *Garmire, E., J-QE 75 Sep* 38D-39D (2D12)
GaAs modulators; resonant piezo-electrooptic modulator. *Halido, D., J-QE 75 Sep* 64D-65D (2F10)
GaAs or AlGaAs laser diode array pumping of Nd:YAG lasers. *Reno, C. W., J-QE 75 Sep* 16D (2C04)
optical waveguides; rib structure for transverse-mode control in injection lasers. *Lee, T. P., J-QE 75 Jul* 432-435 (2D12)
Gallium alloys/compounds, lasers
AlGaAs CW double-heterostructure lasers; intensity fluctuation changes after degradation. *Gonda, Shun-Ichi, J-QE 75 Jul* 545-550 (3E13)
AlGaAs double-heterostructure diode lasers; rib-guide optical-waveguide structure for transverse-mode control. *Lee, T. P., J-QE 75 Jul* 432-435 (2D12)
AlGaAs double-heterostructure junction lasers; depolarization of lasing emission. *Paoli, Thomas L., J-QE 75 Jul* 489-494 (3A13)
AlGaAs multiheterostructure laser with integrated twin guide. *Suematsu, Y., J-QE 75 Jul* 457-460 (2F09)
buried-heterostructure lasers with GaAs active regions completely buried in GaAlAs; thermal characteristics and CW operation. *Tsukada, Toshihisa, J-QE 75 Jul* 494-498 (3B04)
double-heterostructure GaAs/GaAlAs lasers with oxide-insulated stripe geometry; CW lasing range and light-output power. *Garel-Jones, P., J-QE 75 Jul* 408-413 (2C02)
GaAlAs composite-guide heterostructure diode lasers; grating-coupled laser with low-divergence beams. *Burnham, R. D., J-QE 75 Sep* 98D-99D (3B01)
GaAlAs double heterostructure lasers; packaged lasers for optical-fiber transmission. *Takusagawa, M., J-QE 75 Sep* 61D (2F07)
GaAlAs–GaAs heterostructure lasers; optical-absorption loss in double-heterostructure and five-layer devices. *Thompson, G. H. B., J-QE 75 Jul* 481-488 (3A05)
GaAlAs heterojunction lasers; scanning system applications. *Gorog, I., J-QE 75 Sep* 63D (2F09)
GaAs–AlGaAs double-heterostructure lasers; integrated taper-coupled laser for optical coupling of active and passive waveguide sections. *Logan, R. A., J-QE 75 Jul* 461-464 (2F13)
GaAs–AlGaAs double-heterostructure lasers using molecular-beam epitaxy layers. *Casey, H. C., Jr., J-QE 75 Jul* 467-470 (2G05)
GaAs–AlGaAs double-heterostructure lasers; dark-line defect sources and propagation. *Ito, Ryoichi, J-QE 75 Jul* 551-556 (3F05)
GaAs–AlGaAs double-heterostructure lasers; direct modulation using Schottky-barrier-gate Gunn-effect digital device. *Yanai, Hisayoshi, J-QE 75 Jul* 519-524 (3D01)
GaAs–AlGaAs injection lasers; dark-line defects causing degradation. *Woolhouse, G. R., J-QE 75 Jul* 556-561 (3F10)
GaAs distributed-feedback lasers; effect of external reflectors on longitudinal modes. *Streifer, William, J-QE 75 Apr* 154-161 (1C08)
GaAs double-heterostructure laser amplifiers. *Schicketanz, D., J-QE 75 Feb* 65-69 (1A03)
GaAs double-heterostructure laser mirrors; near-field emission. *Hakki, B. W., J-QE 75 Apr* 149-154 (1C03)

GaAs double heterostructure lasers; suppression of relaxation oscillations by light injection method. *Lang, R., J-QE 75 Sep* 60D (2F06)
GaAs/GaAlAs double-heterojunction lasers; internal optical loss in very thin CW lasers. *Butler, J. K., J-QE 75 Jul* 402-408 (2B10)
GaAs/GaAlAs double-heterojunction lasers; stripe formation using oxygen-ion implantation. *Blum, Joseph M., J-QE 75 Jul* 413-418 (2C07)
GaAs/GaAlAs double-heterostructure lasers; stripe-geometry laser with current-confining channel formed prior to heterostructure layer growth. *Burnham, R. D., J-QE 75 Jul* 418-420 (2C12)
GaAs/GaAlAs double-heterojunction visible-light-emitting lasers using heteroisolation stripe geometry. *Itoh, Kunio, J-QE 75 Jul* 421-426 (2D01)
GaAs/GaAlAs double-heterostructure injection lasers with distributed feedback; pulsed operation between 80 and 150 K. *Nakamura, Michiharu, J-QE 75 Jul* 436-439 (2E02)
GaAs/GaAlAs double-heterostructure lasers; corrugated grating-coupled laser with low-divergence output normal to waveguide plane. *Zory, P., J-QE 75 Jul* 451-457 (2F03)
GaAs/GaAlAs heterojunction lasers; grating-coupled lasers with low-divergence output through plane parallel to waveguide layer. *Alferov, Z. I., J-QE 75 Jul* 449-451 (2F01)
GaAs/GaAlAs single-heterostructure injection lasers; *H*-pulsing. *Gründorfer, Stephan, J-QE 75 Jul* 532-537 (3D14)
GaAs injection lasers; multimode operation and mode-locking. *Bachert, H., J-QE 75 Jul* 507-510 (3C03)
GaAs large-cavity double-heterostructure lasers; mode selection perpendicular to junction plane. *Krupka, D. C., J-QE 75 Jul* 390-399 (2A12)
GaAs lasers; distributed-feedback single-heterostructure electrically pumped lasers. *Burnham, Robert D., J-QE 75 Jul* 439-449 (2E05)
GaAs lasers; spatially coherent radiation from three-laser arrays in phase-controlled or free-running mode. *Philipp-Rutz, E. M., J-QE 75 Sep* 60D-61D (2F06)
GaAs single-, double- and large-optical cavity heterostructure lasers; gain profile and time-delay effects in external-cavity-controlled lasers. *Rossi, J. A., J-QE 75 Jul* 538-545 (3E06)
InGaPAs–GaAsP single-heterojunction laser diodes; LPE growth and properties. *Coleman, J. J., J-QE 75 Jul* 471-476 (2G09)
monolithic GaInAs homojunction diode lasers. *Doerbeck, F. H., J-QE 75 Jul* 464-467 (2G02)
transverse-junction-stripe lasers with GaAs homojunction sandwiched between GaAlAs layers. *Namizaki, H., J-QE 75 Jul* 427-431 (2D07)

Gas discharges; **cf.** Plasmas

Gas flow

flowing-gas capillary lasers; gas flow in porous wall tube system. *Papayoanou, Aristotle, J-QE 75 Aug* 579-583 (1A13)

Gas flow measurement

resonant Doppler velocimeters using tunable narrow-bandwidth dye lasers. *Miles, R. B., J-QE 75 Sep* 35D-36D (2D09)

Gas flow visualization

resonant Doppler velocimeters using tunable narrow-bandwidth dye lasers. *Miles, R. B., J-QE 75 Sep* 35D-36D (2D09)

Gas lasers

$Ar–N_2$ mixtures; excitation using pulsed electron beams. *Searles, S. K., J-QE 75 Aug* 685 (2D05)
BO, BaO, CuF, SiO and SiF electronic-transition chemical lasers. *Scott, P. B., J-QE 75 Aug* 693-694 (2D13)
Chemical and Molecular Lasers Conference; papers and abstracts from Oct. 1974 conference, *J-QE 75 Aug, Pt. II* 641-722 (2A03)
chemical laser amplifiers; theoretical model. *Tripodi, R., J-QE 75 Aug* 716 (2F08)
chemical lasers for operation at visible wavelengths; reaction initiation by short-duration pulsed discharges. *Chou, M. S., J-QE 75 Aug* 691-692 (2D11)
chemical lasers; laser technique for studying dynamics of vibrationally excited species. *Kaldor, A., J-QE 75 Aug* 697-698 (2E03)
CuI vapor lasers; transversely excited pulsed laser. *Piper, J. A., J-QE 75 Sep* 95D (3A12)
Cu vapor lasers; CuI double-pulsed laser. *Smilanski, I., J-QE 75 Nov* 919-920 (1E09)
Cu vapor lasers; discharge-heated master oscillator power amplifier. *Anderson, R. S., J-QE 75 Sep* 56D-57D (2F02)
Cu vapor lasers; flowing laser for high repetition rate, fast-discharge operation. *Bricks, B. G., J-QE 75 Sep* 57D (2F03)
CW submillimeter emission from optically pumped waveguide lasers. *Radford, Harrison E., J-QE 75 May* 213-214 (1C07)
electronic-transition chemical lasers; parametric evaluation of potential diatomic molecules. *Sutton, D. G., J-QE 75 Aug* 690-691 (2D10)
flowing-gas capillary lasers; porous wall tube system. *Papayoanou, Aristotle, J-QE 75 Aug* 579-583 (1A13)
HF chemical lasers; electron-beam-driven H_2+F_2 high-pressure mixtures. *Gerardo, J. B., J-QE 75 Sep* 56D (2F02)
I lasers; pressure broadening and saturation behavior of Asterix III pulsed high-power laser. *Fuss, W., J-QE 75 Sep* 43D (2E03)
I lasers; pulsed high-power Asterix III laser for laser fusion experiments. *Brederlow, G., J-QE 75 Sep* 42D-43D (2E02)
I photodissociation lasers; photodissociation of C_3F_7I by UV radiation from CO_2-laser-produced Xe plasma. *Silfvast, W. T., J-QE 75 Sep* 1D (2B03)
metal vapor lasers; electronic-to-electronic energy transfer rates in Na vapor. *Chen, Hao-Lin, J-QE 75 Aug* 669-672 (2C03)
N_2 lasers; photopreionization of pulsed lasers. *Kurnit, N. A., J-QE 75 Apr* 174-176 (1D14)
$Na–N_2O+CO$ chemical laser; parametric study of gain. *Benson, R. C., J-QE 75 Aug* 688-689 (2D08)
output intensity; three-dimensional analysis of Gaussian mode interactions with laser transitions. *Witteman, W. J., J-QE 75 May* 198-204 (1B06)
photodissociation I laser amplifiers; kinetic model. *Turner, C. E., Jr., J-QE 75 Aug* 709-710 (2F01)
resonators; eigenmode loss behavior of unstable resonators with cylindrical and circular mirrors at small and large Fresnel numbers. *Santana, C., J-QE 75 Sep* 58D-59D (2F04)
Sn(I) lasers. *Sutton, D. G., J-QE 75 Jun* 312 (1G06)
visible chemical lasers using reactions of evaporated metal atoms with various oxidizers. *Eckstrom, D. J., J-QE 75 Aug* 691 (2D11)
V–T and V–V intermolecular potential computation; application to $N_2–CO_2$ system. *Witriol, N. M., J-QE 75 Aug* 717 (2F09)

Gas lasers; **cf.** Dye lasers; Noble-gas lasers

Gas lasers, atomic

ArO lasers; parameters of flash-photolyzed $N_2O–Ar_2$ mixtures. *Hughes, William M., J-QE 75 Sep* 88D (3A05)
B lasers; pulsed lasers pumped by incomplete uatoionization or ion–electron recombination. *Stricker, J., J-QE 75 Aug* 701-702 (2E07)
Cl atom lasers; quenching of Ar metastable atoms by Cl atoms and molecules in dc-discharge-excited Cl–Ar mixtures. *King, D. L., J-QE 75 Aug* 708 (2E14)
Cs and Rb electronic-transition chemical lasers; population inversions. *Hall, L. H., J-QE 75 Aug* 693 (2D13)
Cu vapor laser produced by discharge heating. *Anderson, R. S., J-QE 75 Apr* 172-174 (1D12)
Group VI element (^1S) lasers; production of $O(^1S)$ from N_2O and $S(^1S)$ from OCS. *Black, G., J-QE 75 Aug* 704 (2E10)
Hg lasers; dc-excited Hg pump lamps for CW operation at 546.1 nm. *Holmes, N., J-QE 75 Sep* 55D (2F01)
I lasers; 1.32 μm emission from atomic I produced by electrical dissociation of CF_3I. *Pleasance, L. D., J-QE 75 Sep* 94D-95D (3A11)
I lasers; deactivation of electronically excited I atoms. *Burde, D. H., J-QE 75 Aug* 709 (2F01)
I* lasers; direct measurement of initial yields of I and I* atoms in flash-photolyzed alkaly iodides. *Wiesenfeld, J. R., J-QE 75 Aug* 703-704 (2E09)
I lasers; emission at 1.315 μm following injection of HI into microwave-discharge He/O_2 flow. *Pirkle, Robert J., J-QE 75 Oct* 834-838 (1C04)
I photodissociation lasers; stimulated-emission cross section and inversion lifetime. *Aldridge, F. T., J-QE 75 May* 215-216 (1C09)
O(I) atomic lasers with emission at 2.652 μm. *Sutton, D. G., J-QE 75 Feb* 92 (1C02)
O lasers using $^1S–^1D$ transition; lasing at 5578.5 Å in relativistic-electron-beam excited Kr_2/O_2 mixtures. *Johnson, A. W., J-QE 75 Sep* 56D (2F02)

Gas lasers, atomic; **cf.** Noble-gas lasers

Gas lasers, ionic

Ba vapor lasers; visible laser transitions at 7120 Å in Ba I and at 549.9 and 6141.7 Å in Ba (II). *Baron, K. U., J-QE 75 Oct* 852-853 (1D08)
$He–Cd^+$ lasers emitting CW white light; single-gun hollow cathode tube with three-color outputs. *Fujii, Kan-Ichi, J-QE 75 Mar* 111-114 (1B03)
$He–Cd^+$ lasers; saturation mechanisms of power output. *Mizeraczyk, Jerzy K., J-QE 75 May* 218-220 (1C12)

Gas lasers, ionic; **cf.** Noble-gas lasers

Gas lasers, molecular

anharmonic diatomic molecular lasers; quasi-equilibrium vibrational population distributions. *Lam, S. H., J-QE 75 Aug* 715-716 (2F07)
BaF, BaCl, BaBr and BaI electronic-transition chemical lasers. *Bradford, R. S., Jr., J-QE 75 Aug* 692 (2D12)
calcium and strontium oxide and halide chemical lasers; photon yields in 250–1100 nm region and $A'^1\pi$ molecular constants. *Capelle, G. A., J-QE 75 Aug* 692 (2D12)
CH_3F far-infrared laser; pulse characteristics of optically pumped laser. *Bluyssen, H. J. A., J-QE 75 Jul* 341-348 (1B13)
CH_3OH far-infrared lasers; four-level rate equation model and output power expression for optically pumped laser. *Henningsen, J. O., J-QE 75 Jun* 248-252 (1B12)
CH_3OH lasers; far-infrared lines from CO_2-laser-pumped laser. *Tanaka, Atsuo, J-QE 75 Oct* 853-854 (1D09)
CS_2 lasers; $He/N_2/CS_2$ or $He/Co/CS_2$ mixtures directly excited in electron-beam-stabilized discharge. *Nelson, L. Y., J-QE 75 Aug* 686 (2D06)
cyanide radical photodissociation and predissociation chemical lasers; molecular electronic and vibrational lasers. *West, G. A., J-QE 75 Aug* 687 (2D07)
diatomic molecules; vibrational–vibrational collision probability measurements for large vibrational quantum numbers. *Nachshon, Yehuda, J-QE 75 Aug* 654-660 (2B02)
FeO electronic-transition chemical lasers. *West, J. B., J-QE 75 Aug* 692-693 (2D12)
GeO and SiO electronic-transition chemical lasers. *Wilson, L. E., J-QE 75 Aug* 691 (2D11)
H_2O, D_2O and CH_3OH lasers; measurement of line frequencies using far-infrared frequency synthesis technique. *Petersen, F. Russell, J-QE 75 Oct* 838-843 (1C08)
H_2 vacuum ultraviolet lasers; use in photoionization and excitation of luminescence experiments. *Antonov, V. S., J-QE 75 Sep* 92D (3A09)
H_2 vacuuum ultraviolet lasers; single-short TEA laser, high-repetition rate laser and CW laser. *Knyazev, I. N., J-QE 75 Oct* 805-817 (1A03)
HCN lasers; role of hydrogen. *Schötzau, Hans J., J-QE 75 Oct* 817-822 (1B01)
metal atom/N_2O visible chemical lasers; luminescence. *Felder, W., J-QE 75 Aug* 703 (2E09)
metal atom oxidation chemical lasers using exothermic exchange reactions; 30 new laser molecules. *Rice, W. W., J-QE 75 Aug* 689-690 (2D09)
N_2 lasers; 3371-Å laser power produced by relativistic electron-beam propagation. *McArthur, David A., J-QE 75 Nov* 892-902 (1C10)
N_2 lasers; first- and second-positive emission from N_2/SF_6 laser. *Suchard, Steven N., J-QE 75 Nov* 908-916 (1D12)
N_2 lasers; near-infrared first positive system laser using ionizer-sustainer discharge excitation. *Newman, L., J-QE 75 Aug* 686 (2D06)
N_2 lasers; quasi-CW second-positive laser using SF_6 additions to N_2 in discharge region. *Suchard, S. N., J-QE 75 Aug* 685-686 (2D05)
N_2 lasers; stimulated emission at 0.3159 μm in second-positive system at room temperature. *Kruger, John S., J-QE 75 Sep* 801-802 (1F09)
N_2O chemical lasers using energy transfer from vibrationally excited CO. *Petersen, A. B., J-QE 75 Aug* 699-700 (2E05)
N_2/SF_6 lasers; first and second positive band emission. *Suchard, S. N., J-QE 75 Sep* 26D-27D (2C14)
Na_2 molecular lasers; optically pumped superfluorescent laser. *Henesian, M., J-QE 75 Sep* 26D (2C14)
SF_6 lasers; optically pumped laser emitting at 15.90 μm. *Fetterman, H. R., J-QE 75 Sep* 88D-89D (3A05)

vibrationally excited molecules; deactivation by potentially reactive atoms. *Smith, I. W. M., J-QE 75 Aug* 696 (2E02)
vibration–vibration transfer lasers; theoretical performance. *Naismith, R., J-QE 75 Aug* 716 (2F08)
Gas lasers, molecular; **cf.** Carbon dioxide lasers; Carbon monoxide lasers; Hydrogen halide lasers; Noble-gas lasers
Gates; **cf.** Logic gates
Geophysical measurements
strain in earth's crust; measurement using 700-m long mode-locked Ar ion laser. *Tripathi, P. P., J-QE 75 Sep* 59D (2F05)
Germanium devices
optical isolators; high-power isolators for 10 μm region using interband Faraday effect. *Phipps, C. M., Jr., J-QE 75 Sep* 70D-71D (2G03)
switches; fast switching of high-power CO_2 laser radiation by optically induced carriers. *Alcock, A. J., J-QE 75 Sep* 96D (3A13)
Germanium alloys/compounds, devices
lasers; excited electronic states of GeO electronic-transition lasers. *Harris, R. A., J-QE 75 Aug* 691 (2D11)
lasers; GeO electronic-transition chemical lasers. *Wilson, L. E., J-QE 75 Aug* 691 (2D11)
Glass
Nd-doped laser glasses; tailoring for specific applications by compositional changes. *Jacobs, R. R., J-QE 75 Sep* 13D (2C01)
silicate laser glass; nonradiative relaxation of rare-earth ions. *Layne, C. B., J-QE 75 Sep* 798-799 (1F06)
Glass devices
lasers for nuclear fusion; refractive index nonlinearity of transparent dielectric material. *Glass, A. J., J-QE 75 Sep* 28D-29D (2D02)
Glass devices; **cf.** Neodymium:glass lasers; Solid lasers
Gunn devices
Schottky-barrier-gate digital device for direct modulation of GaAs–AlGaAs double-heterostructure lasers. *Yanai, Hisayoshi, J-QE 75 Jul* 519-524 (3D01)

H

Harmonic generation; **cf.** Optical harmonic generation
Heating; **cf.** Electric heating
Helicopters
flight control; hover sensor for heavy lift helicopter. *Herzog, D. G., J-QE 75 Sep* 51D-52D (2E11)
Heterodyne detection; **cf.** Optical heterodyne detection
Heterodyning; **cf.** Optical heterodyning
Heterojunctions; **cf.** Semiconductor heterojunctions
Holmium; **cf.** Rare earths
Holographic memories
erasure techniques; selective erasure of holograms superimposed in $LiNbO_3$ crystals. *Huignard, J. P., J-QE 75 Sep* 8D-9D (2B10)
Holographic recording
Fourier-transform holograms of simple plane objects; recording using X-rays. *Mahr, H., J-QE 75 Sep* 97D-98D (3A14)
optical video disks. *Tsunoda, Y., J-QE 75 Sep* 11D-12D (2B13)
Holography
optical waveguide couplers; holographic couplers for optical fiber and planar waveguides. *Nishihara, H., J-QE 75 Sep* 794-796 (1F02)
rain drop measurements using pulsed holography technique. *Zakharov, V. M., J-QE 75 Sep* 82D (2G14)
Hybrid integrated circuits
masks for fabrication; automatic laser inspection/repair system. *Fehrs, D. L., J-QE 75 Sep* 21D (2C09)
Hydrogen
isotope separation using lasers. *Teller, E., J-QE 75 Sep* 83D (2G14)
Hydrogen halide lasers
CW chemical lasers; rotational nonequilibrium. *Sentman, L. H., J-QE 75 Aug* 706-707 (2E12)
DF cold-reaction lasers; analysis of small-scale laser. *Steele, R. V., J-QE 75 Aug* 719 (2F11)
DF/HF chemical lasers; portable lasers using recirculating mode of operation. *Chenausky, P. P., J-QE 75 Sep* 58D (2F04)
DF* lasers; deactivation kinetics in combustion driven lasers using alternates for H_2/Fd′D_2 reactant system. *Wendelken, C. P., J-QE 75 Aug* 694-695 (2D14)
DF lasers; electrically initiated pulsed chemical laser. *Poehler, T. O., J-QE 75 Aug* 710 (2F02)
$DF(\nu)+HF$, $DF(\nu)+D_2$ and $HF(\nu)+H_2$ systems; room temperature relaxation rates. *Kwok, M. A., J-QE 75 Aug* 695 (2E01)
DF supersonic chemical lasers; power and pressure recovery measurements in high-Mach-number lasers. *Hyde, J. C., J-QE 75 Aug* 718 (2F10)
H_2–F_2 high-power pulsed chemical lasers; mixture stability and construction materials. *Getzinger, R. W., J-QE 75 Aug* 698 (2E04)
H_2/HCl V–V transfer lasers; theoretical performance. *Naismith, R., J-QE 75 Aug* 716 (2F08)
HCl chemical lasers; spectroscopic measurements of Cl+HI→•∜/▼⟨+| 1/8 1/4∼ ∜/5/8∞⊗⊥. *Carabetta, R. A., J-QE 75 Aug* 689 (2D09)
HCl chemical lasers; transverse-flow laser using $H+Cl_2$ reaction. *Wanner, J., J-QE 75 Aug* 706 (2E12)
HCl/H_2 gas dynamic laser calculations. *Holmes, C. P., J-QE 75 Aug* 704-705 (2E10)
HCl lasers; measurement of pressure-broadened infrared linewidths in HCl–Ar mixtures. *Wormhoudt, J., J-QE 75 Aug* 704 (2E10)
HCl lasers; vibrational excitation by electron impact. *Center, R. E., J-QE 75 Aug* 687 (2D07)
HCl molecular vibrational lasers; chloroethylene photochemical laser. *Berry, M. J., J-QE 75 Aug* 687-688 (2D07)
HCl molecules; deactivation of vibrationally excited molecules by H and Cl atoms. *Wilkins, R. L., J-QE 75 Aug* 716-717 (2F08)
$HCl(\nu=1)$ and $DCl(\nu=1)$; rate coefficients for relaxation by Cl and O atoms. *Brown, R. D. H., J-QE 75 Aug* 695-696 (2E01)
$HCl(\nu=1)+Cl$ and $DCl(\nu=1)+Cl$ systems; vibrational relaxation in potentially reactive collisions. *Smith, I. W. M., J-QE 75 Aug* 696 (2E02)
HCl pulsed chemical lasers; premixed R–Cl/HI fuel mixtures initiated by transverse pulsed discharge. *Manuccia, T. J., J-QE 75 Nov* 921-923 (1E11)
HF and HCl chemical lasers; reaction mechanism and energy distribution in flash-photolyzed Cl_5–H_2 system. *Krogh, O. D., J-QE 75 Aug* 706 (2E12)
HF and HCl rotational laser emission from elimination reactions. *Cuellar, E., J-QE 75 Aug* 688 (2D08)
HF chain-reaction lasers; supersonic CW laser. *Cummings, J. C., J-QE 75 Aug* 712 (2F04)
HF chain-reaction lasers; generation of vibrationally excited HF for CW laser. *Meinzer, R. A., J-QE 75 Aug* 712-713 (2F04)
HF chemical laser amplifiers; amplification characteristics of 5 transitions. *Lynds, L., J-QE 75 Aug* 713-714 (2F05)
HF chemical lasers; electron-beam-initiated laser using mixture of SF_6 and C_2H_6. *Patterson, E. L., J-QE 75 Aug* 642-648 (2A04)
HF chemical lasers; electrically initiated pulsed atmospheric lasers. *Mangano, J. A., J-QE 75 Aug* 705 (2E11)
HF chemical lasers; repetitively pulsed operation of chain-reaction lasers. *H_2/F_2 flame propagation and repetitively pulsed hydrogen fluoride (HF) chain-reaction chemical laser, J-QE 75 Aug* 648-653 (2A10)
HF chemical lasers; temporal characteristics of multiline–multimode CW lasers. *Foster, M. C., J-QE 75 Aug* 714 (2F06)
HF chemical mixing lasers; CW lasers as local oscillators for middle-IR heterodyne applications. *Freiberg, R. J., J-QE 75 Sep* 57D-58D (2F03)
HF CW chemical lasers; transverse mode oscillations in lasers with stable selected-line resonators. *Boedeker, L., J-QE 75 Aug* 713 (2F05)
HF, DF and HCl chemical lasers; hydrogen halide molecule deactivation by atomic collisions. *Quigley, G. P., J-QE 75 Aug* 696-697 (2E02)
HF/DF chain-reaction CW lasers. *Sadowski, T. J., J-QE 75 Aug* 705-706 (2E1
HF/DF lasers; atmospheric transmission measurements. *King, S. R., J-QE 75 Sep* 87D (3A04)
HF/DF lasers; frequency stabilization and absolute frequency measurements. *Eng, R. S., J-QE 75 Sep* 87D-88D (3A04)
HF/DF lasers; intermolecular vibration-to-vibration energy transfer by dimer formation. *Shin, Hyunk Kyu, J-QE 75 Aug* 679-684 (2C13)
HF/DF supersonic chemical lasers; spectroscopic and infrared measurements. *Kwok, M. A., J-QE 75 Aug* 718 (2F10)
HF/DF supersonic chemical lasers; gas heater and nozzle array performance. *Giedt, R. R., J-QE 75 Aug* 718-719 (2F10)
HF/DF supersonic diffusion chemical lasers; spectrographic systems for diagnostic experiments. *Varwig, R. L., J-QE 75 Aug* 719 (2F11)
HF–He and DF–He mixtures and pure DF samples; vibrational relaxation between 200 and 300°K. *Hancock, J. K., J-QE 75 Aug* 694 (2D14)
HF lasers; arc- and combustion-driven CW laser performance. *Grohs, G. L., J-QE 75 Aug* 717 (2F09)
HF lasers; emission and CO population distribution studies of $O(^3P)+CHF$ reaction. *Shortridge, R. G., J-QE 75 Aug* 688 (2D08)
HF lasers; lasing of overtone transitions in electrical pulse-initiated chemical laser. *Hon, J. F., J-QE 75 Aug* 698-699 (2E04)
HF lasers using mixtures of SF_6 and HI; time-resolved spectrum from transverse-discharge laser. *Greiner, N. R., J-QE 75 Oct* 844-845 (1C14)
HF lasers; vibrational distributions of HF formed in reactions of HN_3 photolysis products with fluoromethanes. *Poole, P. R., J-QE 75 Aug* 688 (2D08)
$HF(\nu=1)$ deactivation by H atoms. *Heidner, R. F., J-QE 75 Aug* 696 (2E02)
HF pulsed chemical lasers; effect of rotational nonequilibrium on predicted performance. *Hough, J. J. T., J-QE 75 Aug* 699 (2E05)
HF pulsed chemical lasers; rotational nonequilibrium. *Creighton, J. R., J-QE 75 Aug* 699 (2E05)
HF; rotational relaxation effects. *Hinchen, J. J., J-QE 75 Aug* 695 (2E01)
HF vibrational lasers; potential new chain reaction mechanisms for pumpin
Schott, G. L., J-QE 75 Aug 690 (2D10)

I

Image processing
near-real-time coherent processing system. *Iwasa, S., J-QE 75 Sep* 8D (2B10)
Image sensors
streak camera tubes; Photochron II tube. *Bradley, D. J., J-QE 75 Sep* 25D-26D (2C13)
universal product code symbol; optical scanners using lasers for reading. *Dickson, L., J-QE 75 Sep* 23D-24D (2C11)
Imaging; **cf.** Holography; Photography; Radar imaging; Radiography
Impurities; **cf.** Semiconductor impurities
Indium alloys/compounds; **cf.** Gallium alloys/compounds
Indium alloys/compounds, devices; **cf.** Semiconductor lasers
Infrared (0.70–100 μm); **cf.** Submillimeter-wave (300–3000 GHz)
Infrared absorption; **cf.** Infrared propagation, absorbing media
Infrared demodulation
CO_2 waveguide lasers; demodulation technique for chirp-modulated laser. *Stein, Alexander, J-QE 75 Aug* 630-631 (1E08)
wideband heterodyne detection at 10.6 μm using planar HgCdTe photodiodes. *Spears, D. L., J-QE 75 Sep* 79D (2G11)
Infrared filters
Tl_3AsSe_3 acoustooptic filters; tunable collinear filter for intermediate infrared. *Feichtner, J. D., J-QE 75 Sep* 66D-67D (2F12)
Infrared generation
picosecond pulse generation using synchronous mode-locked dye laser and nonlinear mixing; tunable pulses over 1.1–1.7 μm and 2.7–5.6 μm. *Goldberg, L. S., J-QE 75 Sep* 2D (1B04)
Infrared isolators; **cf.** Optical isolators
Infrared lasers
2.3-μm Tm^{3+} lasers; room-temperature pulsed emission from Tm:Cr:YAG and Tm:Cr:$YAlO_3$ lasers. *Caird, John A., J-QE 75 Nov* 874-881 (1B06)
BaF, BaCl, BaBr and BaI electronic-transition chemical lasers. *Bradford, R. S., Jr., J-QE 75 Aug* 692 (2D12)
B atomic lasers; pulsed lasers pumped by incomplete autoionization or ion–electron recombination. *Stricker, J., J-QE 75 Aug* 701-702 (2E07)
calcium and strontium oxide and halide chemical lasers; photon yields in 250–1100 nm region and $A'^1\pi$ molecular constants. *Capelle, G. A., J-QE 75 Aug* 692 (2D12)

CH_3F far-infrared laser; pulse characteristics of optically pumped laser. *Bluyssen, H. J. A., J-QE 75 Jul* 341-348 (1B13)
CH_3OH lasers; far-infrared lines from CO_2-laser-pumped CH_3OH gas. *Tanaka, Atsuo, J-QE 75 Oct* 853-854 (1D09)
CS_2 lasers; $He/N_2/CS_2$ or $He/Co/CS_2$ mixtures directly excited in electron-beam-stabilized discharge. *Nelson, L. Y., J-QE 75 Aug* 686 (2D06)
cyanide radical photodissociation and predissociation chemical lasers; molecular electronic and vibrational lasers. *West, G. A., J-QE 75 Aug* 687 (2D07)
DF and DF–CO_2 electrically initiated pulsed chemical lasers. *Poehler, T. O., J-QE 75 Aug* 710 (2F02)
dye lasers; lasing efficiency and photochemical stability of infrared dyes in spectral region 710–950 nm. *Oettinger, P. E., J-QE 75 Sep* 3D-4D (2B05)
He–Xe mixtures; simultaneous lasing at 2.03, 2.65 and 3.65 μm in fast-flow high-pressure system for closed-cycle operation. *Olson, Robert A., J-QE 75 Sep* 95D-96D (3A12)
HgCdTe magnetically tunable lasers; tunable spin-flip and recombination lasers using optical pumping. *Sattler, J. P., J-QE 75 Sep* 18D (2C06)
Ho:YLF lasers; 2.06 μm laser performance and design options for rangefinder and illuminator applications. *Devor, D. P., J-QE 75 Sep* 13D-14D (2C01)
I lasers; 1.32 μm emission from atomic I produced by electrical dissociation of CF_3I. *Pleasance, L. D., J-QE 75 Sep* 94D-95D (3A11)
I lasers; emission at 1.315 μm following injection of HI into microwave-discharge He/O_2 flow. *Pirkle, Robert J., J-QE 75 Oct* 834-838 (1C04)
I photodissociation lasers; 1.315 μm emission from C_3F_7I optically pumped by UV radiation from CO_2-laser-produced Xe plasma. *Silfvast, W. T., J-QE 75 Sep* 1D (2B03)
metal atom oxidation chemical lasers using exothermic exchange reactions; 30 new laser molecules. *Rice, W. W., J-QE 75 Aug* 689-690 (2D09)
N_2 lasers; near-infrared first positive system laser using ionizer-sustainer discharge excitation. *Newman, L., J-QE 75 Aug* 686 (2D06)
Na_2 molecular lasers; optically pumped superfluorescent laser. *Henesian, M., J-QE 75 Sep* 26D (2C14)
Nd:$LiNbO_3$ lasers; emission at 1.0845 μm. *Kaminow, I. P., J-QE 75 Jun* 306-308 (1F14)
Nd:YVO_4 lasers. *DeShazer, L. G., J-QE 75 Sep* 84D (3A01)
Ne–N_2 lasers; direct nuclear pumped laser with simultaneous output at 8629 and 9393 Å. *DeYoung, R. J., J-QE 75 Sep* 97D (3A14)
O(I) atomic lasers with emission at 2.652 μm. *Sutton, D. G., J-QE 75 Feb* 92 (1C02)
rate equation model and output power expression for optically pumped far-infrared laser. *Henningsen, J. O., J-QE 75 Jun* 248-252 (1B12)
SF_6 lasers; optically pumped laser emitting at 15.90 μm. *Fetterman, H. R., J-QE 75 Sep* 88D-89D (3A05)
Sn(I) lasers; two-electron transition at 1.061 μm. *Sutton, D. G., J-QE 75 Jun* 312 (1G06)

Infrared lasers; **cf.** Carbon dioxide lasers; Dye lasers; Hydrogen halide lasers; Neodymium:solid lasers

Infrared propagation, absorbing media
atmospheric absorption measurements using solar infrared heterodyne radiometer. *Christophe, B., J-QE 75 Sep* 32D-33D (2D06)
CO_2 laser radiation; absorption by water vapor. *Shumate, M. S., J-QE 75 Sep* 33D-34D (2D07)
infrared absorption lineshapes; measurement of pressure-broadened lines using optical parametric oscillator. *Wormhoudt, J., J-QE 75 Aug* 704 (2E10)
N_2F_4 absorption cells for passive Q-switching of CO_2 lasers. *Suart, R. D., J-QE 75 Aug* 698 (2E04)

Infrared propagation, absorbing media; **cf.** Infrared radio propagation

Infrared radio communication
receivers; 10-μm optical heterodyne receiver for satellite communication. *Goodwin, F. E., J-QE 75 Sep* 79D-80D (2G11)
receivers; wideband 10.6-μm heterodyne receiver for CO_2 laser satellite communications link. *Peyton, B. J., J-QE 75 Sep* 80D-81D (2G12)

Infrared radiometry
heterodyne radiometer for solar radiation and atmospheric transmissivity measurements. *Peyton, Bernard J., J-QE 75 Aug* 569-574 (1A03)

Infrared radio propagation
atmospheric absorption measurements using solar infrared heterodyne radiometer. *Christophe, B., J-QE 75 Sep* 32D-33D (2D06)
atmospheric transmissivity measurements in 9–11-μm band using heterodyne radiometer. *Peyton, Bernard J., J-QE 75 Aug* 569-574 (1A03)

Infrared spectroscopy
SO_2 spectral measurements using single magnetic- and current-tuned PbSe laser. *Allario, Frank, J-QE 75 May* 205-209 (1B13)

Infrared waveguides
GaAs diffused optical strip waveguides; single-mode propagation at 1.15 μm in fundamental and first-order modes. *Garmire, E., J-QE 75 Sep* 38D-39D (2D12)

Injection lasers; **cf.** Semiconductor lasers

Inspection
masks for hybrid integrated circuit fabrication; automatic laser inspection/repair system. *Fehrs, D. L., J-QE 75 Sep* 21D (2C09)

Integrated circuits; **cf.** Digital integrated circuits; Hybrid integrated circuits

Integrated-circuit fabrication
mask defects; correction using laser beam. *Lee, F., J-QE 75 Sep* 21D (2C09)
mask generation; precision galvanometer laser-beam deflection system. *Jablonowski, D. P., J-QE 75 Sep* 21D-22D (2C09)
masks for hybrid integrated circuit fabrication; automatic laser inspection/repair system. *Fehrs, D. L., J-QE 75 Sep* 21D (2C09); Integrated optics

Integrated optics
monolithic GaInAs homojunction diode lasers. *Doerbeck, F. H., J-QE 75 Jul* 464-467 (2G02)
Si photodiode arrays. *Boyd, J. T., J-QE 75 Sep* 40D-41D (2D14)
waveguide transitions and bifurcations; optical field propagation. *Roy, A. M., J-QE 75 Sep* 41D-42D (2E01)

Integrated optics; **cf.** Optical planar waveguides; Optical strip waveguides

Interferometry; **cf.** Optical interferometry

Iodine devices; **cf.** Gas lasers

Ion implantation
stripe formation in GaAs/GaAlAs double-heterojunction lasers. *Blum, Joseph M., J-QE 75 Jul* 413-418 (2C07)
ZnTe optical planar waveguides. *Valette, S., J-QE 75 Sep* 39D-40D (2D13)

Ionization; **cf.** Photoionization

Ion lasers; **cf.** Gas lasers; Solid lasers

Iron alloys/compounds, devices
lasers; FeO electronic-transition chemical lasers. *West, J. B., J-QE 75 Aug* 692-693 (2D12)

Isolators; **cf.** Optical isolators

Isotope separation
^{235}U isotope separation using selective photoionization. *Tuccio, Sam A., J-QE 75 Sep* 101D (3B04)
Cu^{63} and Cu^{65}; selective isotope excitation of CuI by Ar ion laser excitation. *Wu, C.Y. R., J-QE 75 Sep* 20D (2C08)
laser deflection of single isotopic component of atomic beam; application to particle spectroscopy. *Bernhardt, A. F., J-QE 75 Sep* 19D (2C07)
laser separation of U and H isotopes. *Teller, E., J-QE 75 Sep* 83D (2G14)
laser separation process for Ti-50. *Gross, R. W. F., J-QE 75 Aug* 702 (2E08)
radiation-pressure separation. *Gelbwachs, Jerry, J-QE 75 Jan* 52-54 (1D12)
U; photoionization cross section and excited state lifetime measurements in U vapor. *Solarz, R. W., J-QE 75 Sep* 19D-20D (2C07)
U; selective two-step laser excitation and photoionization of atomic U vapor. *Janes, G. S., J-QE 75 Sep* 101D-102D (3B04)

J

Japan
optical communication research and development. *Marubayashi, G., J-QE 75 Sep* 76D (2G08)

Junction lasers; **cf.** Semiconductor lasers

Junctions; **cf.** Waveguide junctions

K

Krypton; **cf.** Noble gases

L

Lamps
Hg pump lamps for optically pumped Hg laser. *Holmes, N., J-QE 75 Sep* 55D (2F01)
K–Rb pump lamps for Nd:YAG lasers. *Radecki, Dan J., J-QE 75 Sep* 15D-16D (2C03)

Lamps; **cf.** Arc lamps; Flashlamps

Lanthanum; **cf.** Rare earths

Lasers; **cf.** CW lasers; Distributed-feedback lasers; Dye lasers; Gas lasers; Infrared lasers; Liquid lasers; Pulsed lasers; Raman lasers; Ring lasers; Semiconductor lasers; Solid lasers; Submillimeter-wave lasers; Ultraviolet lasers; Visible lasers; Waveguide lasers

Laser absorbers
N_2F_4 absorption cells for passive Q-switching of CO_2 lasers. *Suart, R. D., J-QE 75 Aug* 698 (2E04)
slow saturable absorber mode locking; closed-form solution for pulses. *Haus, Hermann A., J-QE 75 Sep* 736-746 (1A14)

Laser amplifiers
chemical laser amplifiers; theoretical model. *Tripodi, R., J-QE 75 Aug* 716 (2F08)
Cu vapor lasers; discharge-heated master oscillator power amplifier. *Anderson, R. S., J-QE 75 Sep* 56D-57D (2F02)
CYCLOPS amplifier performance. *Simmons, W. W., J-QE 75 Sep* 31D-32D (2D05)
CYCLOPS amplifier; removal of small-scale beam instabilities using spatial filter. *Simmons, W. W., J-QE 75 Sep* 30D (2D04)
dye-laser amplifiers; gain of transversely pumped lasers. *Ganiel, U., J-QE 75 Nov* 881-892 (1B13)
dye-laser amplifiers; high gain short-pulse-laser amplifiers using synchronous pumping. *Goldberg, L. S., J-QE 75 Sep* 2D (1B04)
GaAs double-heterostructure lasers. *Schicketanz, D., J-QE 75 Feb* 65-69 (1A03)
HF chemical laser amplifiers; amplification characteristics of 5 transitions. *Lynds, L., J-QE 75 Aug* 713-714 (2F05)
JANUS Nd:glass laser system for laser fusion experiments. *Speck, D. R., J-QE 75 Sep* 45D-46D (2E05)
Nd:glass amplifiers; active mirror high-power amplifier. *Hoose, J., J-QE 75 Sep* 12D (2B14)
Nd:glass amplifiers; face-pumped mirror-like structure. *Bret, G., J-QE 75 Sep* 12D-13D (2B14)
Nd:glass laser amplifier chains; optical pulse compression. *Fisher, Robert A., J-QE 75 Jan* 46-52 (1D06)
Nd:glass lasers; parasitic oscillation suppression in large aperture disk lasers using liquid edge cladding. *Guch, S., Jr., J-QE 75 Sep* 30D-31D (2D04)
noble-gas lasers; vacuum ultraviolet lasers pumped by coaxial diode electron-beam system. *Arthurs, E. G., J-QE 75 Sep* 28D (2D02)
photodissociation I laser amplifiers; kinetic model. *Turner, C. E., Jr., J-QE 75 Aug* 709-710 (2F01)
SHIVA 10-kilojoule system at Lawrence Livermore Laboratory. *Gilmartin, T. J., J-QE 75 Sep* 32D (2D06)

Laser amplifiers; **cf.** Carbon dioxide laser amplifiers

Laser applications
chemistry; infrared-laser-augmented decomposition of H_3BPF_3. *Lory, E. R., J-QE 75 Aug* 714-715 (2F06)
chemistry; laser-induced photochemical enrichment of B isotopes. *Freund, S. M., J-QE 75 Aug* 702 (2E08)
chemistry; laser-induced photochemical enrichment of Cl isotopes. *Lamotte, M., J-QE 75 Aug* 702 (2E08)
chemistry; laser-powered homogeneous pyrolysis. *Shaub, W. H., J-QE 75 Aug* 714 (2F06)
chemistry; reactions of nitric oxide with vibrationally excited ozone. *Gordon, R. J., J-QE 75 Aug* 715 (2F07)

energy-crisis applications in nuclear fusion and isotope separation. *Teller, E., J-QE 75 Sep* 83D (2G14)
explosive vapor detection using laser optoacoustic detector. *Claspy, P. C., J-QE 75 Sep* 37D (2D11)
helicopters; precision hover sensor for heavy lift helicopter. *Herzog, D. G., J-QE 75 Sep* 51D-52D (2E11)
isotope separation by selective photoionization. *Tuccio, Sam A., J-QE 75 Sep* 101D (3B04)
isotope separation; laser deflection of single isotopic component of atomic beam for particle spectroscopy. *Bernhardt, A. F., J-QE 75 Sep* 19D (2C07)
isotope separation; photoionization cross section and excited state lifetime measurements in U vapor for separation process evaluation. *Solarz, R. W., J-QE 75 Sep* 19D-20D (2C07)
isotope separation; selective isotope excitation of CuI by Ar ion laser excitation. *Wu, C.Y. R., J-QE 75 Sep* 20D (2C08)
isotope separation; selective two-step excitation and photoionization of atomic U vapor. *Janes, G. S., J-QE 75 Sep* 101D-102D (3B04)
isotope separation; two-step photodissociation process for Ti-50. *Gross, R. W. F., J-QE 75 Aug* 702 (2E08)
molecular spectroscopy and excitation of luminescence using continuously tunable high-pressure CO_2 lasers. *Bagratashvili, V. N., J-QE 75 Sep* 94D (3A11)
nuclear fusion; development of optimum glass for Nd:glass lasers. *Jacobs, R. R., J-QE 75 Sep* 13D (2C01)
nuclear fusion; laser fusion at 1.06 μm and 10.6 μm. *McCall, G. H., J-QE 75 Sep* 45D (2E05)
nuclear fusion; optical pulse-shaping for laser-driven fusion. *Massey, G. A., J-QE 75 Jul* 358-364 (1D02)
nuclear fusion; pellet compression using electron-beam excited Kr/O_2 mixtures. *Johnson, A. W., J-QE 75 Sep* 56D (2F02)
nuclear fusion; refractive index nonlinearity of transparent dielectric material in glass lasers. *Glass, A. J., J-QE 75 Sep* 28D-29D (2D02)
photochemistry; isotopic enrichment by multiple absorption of CO_2 laser radiation. *Lyman, J. L., J-QE 75 Sep* 103D (3B06)
photoionization and luminescence excitation using H_2 vacuum ultraviolet lasers. *Antonov, V. S., J-QE 75 Sep* 92D (3A09)
printers for color photography. *Baldwin, R. E., J-QE 75 Sep* 9D (2B11)
radiation cameras; ultra-high-speed camera using hydrated electron photoabsorption phenomena and mode-locked-dye-laser picosecond pulses. *Coutts, Gerald W., J-QE 75 Sep* 6D (2B08)
rangefinder and illuminator applications; Ho:YLF 2.06 μm laser performance and design applications. *Devor, D. P., J-QE 75 Sep* 13D-14D (2C01)
soil compaction quality checking. *Drakatos, Panagiotis A., J-QE 75 Sep* 84D-86D (3A01)
streak camera studies of fluorescence in photosynthetic systems and plastic scintillators. *Shapiro, S. L., J-QE 75 Sep* 5D-6D (2B07)
supermarket industry; laser scanner for reading universal product code symbol. *Dickson, L., J-QE 75 Sep* 23D-24D (2C11)

Laser applications; **cf.** Laser materials-processing applications; Laser plasma generation; Optical communication; Optical measurements; Optical radar

Laser beams
aberrated-beam focusing properties. *Hunt, J. T., J-QE 75 Sep* 29D-30D (2D03)
amplification of beams passing through chemical laser medium; theoretical model. *Tripodi, R., J-QE 75 Aug* 716 (2F08)
CO_2 lasers; measurement of beam quality of short-pulse lasers. *Liberman, I., J-QE 75 Sep* 44D (2E04)
deflection by precision galvanometer deflection system. *Jablonowski, D. P., J-QE 75 Sep* 21D-22D (2C09)
instabilities in CYCLOPS laser amplifier; removal using spatial filter. *Simmons, W. W., J-QE 75 Sep* 30D (2D04)
low-divergence beams from grating-coupled composite-guide heterostructure GaAlAs diode lasers. *Burnham, R. D., J-QE 75 Sep* 98D-99D (3B01)

Laser-beam effects; **cf.** Laser radiation effects

Laser-beam focusing
focusable energy; loss due to small-scale nonlinear effects. *Bliss, E. S., J-QE 75 Sep* 29D (2D03)
self dofocusing of mode-locked 1.06 μm pulses in Cs vapor; negative nonlinear refractive index and self-focusing compensation in other materials. *Lehmberg, R. H., J-QE 75 Sep* 69D-70D (2G01)
self-focusing; effects on optical quality of high-power beams. *Suydam, B. R., J-QE 75 Jun* 225-230 (1A03)
self-focusing instability growth rates in glass laser systems; effect of air space. *Elliott, C. James, J-QE 75 Nov* 863-866 (1A09)
third-order nonlinear processes in isotropic media; effects of focusing. *Bjorklund, Gary C., J-QE 75 Jun* 287-296 (1E09)

Laser communication; **cf.** Optical communication

Laser couplers
GaAs–AlGaAs double-heterostructure lasers; integrated taper-coupled laser for optical coupling of active and passive waveguide sections. *Logan, R. A., J-QE 75 Jul* 461-464 (2F13)
ring lasers; comparison of traveling-wave and standing-wave resonator extraction efficiencies. *Eckbreth, Alan C., J-QE 75 Sep* 796-798 (1F04)

Laser diodes; **cf.** Semiconductor lasers

Laser Engineering and Applications Conference
digests of papers from 1975 conference, *J-QE 75 Sep* 1D-103D (2B03)

Laser excitation
standing-wave effect in laser pumping. *Gerritsen, H. J., J-QE 75 Apr* 174 (1D14)

Laser excitation; **cf.** *Specific types of laser*

Laser frequency stability
CW dye lasers; frequency stabilization by frequency locking to high-finesse optical cavity. *West, J. B., J-QE 75 Sep* 18D-19D (2C06)
HF/DF lasers. *Eng, R. S., J-QE 75 Sep* 87D-88D (3A04)

Laser heating effects; **cf.** Laser applications; Laser thermal factors

Laser machining; **cf.** Laser materials-processing applications

Laser materials-processing applications
automotive industry. *Yessik, M., J-QE 75 Sep* 46D-47D (2E06)
masks for hybrid integrated circuit fabrication; automatic laser inspection/repair system. *Fehrs, D. L., J-QE 75 Sep* 21D (2C09)
masks for integrated-circuit fabrication; correction of defects using laser beam. *Lee, F., J-QE 75 Sep* 21D (2C09)
masks for integrated-circuit fabrication; generation using precision galvanometer deflection system. *Jablonowski, D. P., J-QE 75 Sep* 21D-22D (2C09)
metallic surfaces; reflectivity changes during irradiation by CO_2-TEA lasers. *Ready, J. F., J-QE 75 Sep* 49D (2E09)
RC network generation. *Saifi, M. A., J-QE 75 Sep* 23D (2C11)
semiconductor device fabrication; SiC high-temperature resistor fabrication using CO_2 lasers. *Hierholzer, F. J., J-QE 75 Sep* 47D-48D (2E07)
welding; effect of welding parameters on deep welding geometry. *Boedecker, V., J-QE 75 Sep* 47D (2E07)
welding of dissimilar materials; effect of laser parameters on material intermixing. *Montanarini, M., J-QE 75 Sep* 47D (2E07)
welding of insulated Cu wires to Monel terminal posts; real-time analysis of weld quality. *Saifi, M. A., J-QE 75 Sep* 48D (2E08)
welding; pulsed laser welding of high-reflectivity materials. *Bolin, S. R., J-QE 75 Sep* 48D (2E08)

Laser measurement applications; **cf.** Optical measurements

Laser measurements
beam quality of short-pulse CO_2 lasers. *Liberman, I., J-QE 75 Sep* 44D (2E04)
chemical lasers; laser technique for studying dynamics of vibrationally excited species. *Kaldor, A., J-QE 75 Aug* 697-698 (2E03)
$CO_2(00°1)$ level deactivation in CO_2 lasers by H, D, O, N, F and Cl atoms. *Buchwald, M. I., J-QE 75 Aug* 697 (2E03)
CO_2 TEA lasers; temporal coherence measurements of double-discharge laser. *Rudko, R. I., J-QE 75 Sep* 54D (2E14)
energy extraction from atmospheric-pressure CO_2 amplifiers using 60 ns–1 μs pulses. *Girard, G., J-QE 75 Jun* 241-247 (1B05)
energy transfer rates; laser-excited electronic-to-electronic transfer in Na vapor. *Chen, Hao-Lin, J-QE 75 Aug* 669-672 (2C03)
gain in pulsed CO_2 lasers; ratio of upper to lower level populations. *Garside, Brian K., J-QE 75 Jun* 264-270 (1C14)
HF/DF supersonic diffusion chemical lasers; spectrographic systems for diagnostic experiments. *Varwig, R. L., J-QE 75 Aug* 719 (2F11)
I* lasers; direct measurement of initial yields of I and I* atoms in flash-photolyzed alkaly iodides. *Wiesenfeld, J. R., J-QE 75 Aug* 703-704 (2E09)
junction laser thermal impedance measurement. *Paoli, Thomas L., J-QE 75 Jul* 498-503 (3B08)
laser line frequency measurements; far-infrared frequency synthesis technique using stabilized CO_2 lasers. *Petersen, F. Russell, J-QE 75 Oct* 838-843 (1C08)
N_2 and $CO_2(001)$ vibration-to-translation relaxation by alkali metal atoms. *Benson, R. C., J-QE 75 Aug* 697 (2E03)
near-field emission measurements on GaAs double-heterostructure laser mirrors. *Hakki, B. W., J-QE 75 Apr* 149-154 (1C03)
nonlinear refractive-index coefficient of laser-system materials; interferometric measurement. *Moran, Michael J., J-QE 75 Jun* 259-263 (1C09)
optical gain–absorption in active media; amplified spontaneous emission measurement technique. *Cross, Peter S., J-QE 75 May* 190-197 (1A12)
picosecond pulses; optical sampling technique. *Vogel, Gerald C., J-QE 74 Sep* 642-646 (1B02) ♦
prepulse extinction-ratio measurements on CO_2 laser amplifier chains. *Manes, K. R., J-QE 75 Aug* 635-636 (1E13)
stimulated emission in Nd-doped glass; measurement of cross section. *Dianov, E. M., J-QE 75 Sep* 83D (2G14)
temperature measurement in optically pumped NdP_5O_{14} laser using Raman spectroscopy. *Weber, Heinz P., J-QE 75 Jul* 368-370 (1D12)

Laser measurements; **cf.** Optical measurements

Laser modes
asymmetric spectral-mode interaction in semiconductor lasers. *Bogatov, A. P., J-QE 75 Jul* 510-515 (3C06)
cold cavity modes in coupling-modulated CO_2 laser. *Scholtz, A. L., J-QE 75 Sep* 791-793 (1E13)
GaAs injection lasers; multimode operation and mode-locking. *Bachert, H., J-QE 75 Jul* 507-510 (3C03)
HF CW chemical lasers; transverse mode oscillations in lasers with stable selected-line resonators. *Boedeker, L., J-QE 75 Aug* 713 (2F05)
longitudinal mode selection in He–Ne lasers using mode-selective three-mirror reflector. *Eichler, H., J-QE 75 Apr* 168-170 (1D08)
oligo-mode distance control in CW dye lasers using spatial hole burning. *Hertel, Ingolf V., J-QE 75 May* 210-212 (1C04)
selection perpendicular to junction plane in GaAs large-cavity double-heterostructure lasers. *Krupka, D. C., J-QE 75 Jul* 390-399 (2A12)
stability in active laser resonators. *Ernst, G. J., J-QE 75 Nov* 920-921 (1E10)
transverse-mode control in injection lasers by rib-guide optical-waveguide structure. *Lee, T. P., J-QE 75 Jul* 432-435 (2D12)
transverse mode control in multimode double-heterostructure junction lasers optically coupled to single-mode fibers. *Krupka, D. C., J-QE 75 Jul* 503-507 (3B13)

Laser noise
semiconductor lasers; intensity noise characteristics of CW double-heterostructure stripe-geometry lasers. *Paoli, Thomas L., J-QE 75 Jun* 276-283 (1D12)

Laser plasma generation
CO_2 laser amplifier chains; prepulse extinction-ratio measurements on pulse-selection systems. *Manes, K. R., J-QE 75 Aug* 635-636 (1E13)
CO_2 laser amplifiers; high-power electron-beam-controlled system for laser fusion. *Yamanaka, C., J-QE 75 Sep* 45D (2E05)
CO_2 lasers; 2.5 kJ short-pulse system. *Singer, S., J-QE 75 Sep* 44D-45D (2E04)
CO_2 lasers; Valkyrie system for laser fusion experiments. *Manes, K. R., J-QE 75 Sep* 44D (2E04)
dye laser pumped by CO_2-laser-heated plasma. *Brown, Robert T., J-QE 75 Sep* 800-801 (1F08)
JANUS Nd:glass laser system for laser fusion experiments. *Speck, D. R., J-QE 75 Sep* 45D-46D (2E05)
optical propagation and energy transport in fusion targets. *Holzrichter, J. F., J-QE 75 Sep* 46D (2E06)
optical pumping of lasers using UV radiation from CO_2-laser-produced Xe plasma. *Silfvast, W. T., J-QE 75 Sep* 1D (2B03)
X-ray pulses emitted by laser-produced plasma; pulse-duration measurement. *Duguay, M. A., J-QE 75 Apr* 170-172 (1D10)

Laser processing applications; **cf.** Laser materials-processing applications

Laser pulse amplifiers; **cf.** Laser amplifiers

♦ **Check author entry for later corrections/comments**

Laser pulses; **cf.** Optical pulses; Pulsed lasers; *Q*-switching
Laser radiation effects
metallic surfaces; reflectivity changes during irradiation by CO_2-TEA lasers. *Ready, J. F., J-QE 75 Sep* 49D (2E09)
metals and semiconductors; physical property changes in laser-pulse-irradiated material. *Dekhtar, I. Ya., J-QE 75 Sep* 83D (2G14)
Laser radiation effects; **cf.** Laser applications
Laser resonators
negative-branch unstable resonator Nd:YAG laser. *Ewanizky, T. F., J-QE 75 Sep* 17D-18D (2C05)
three-mirror reflector; single-mode operation of six-mode He–Ne laser. *Eichler, H., J-QE 75 Apr* 168-170 (1D08)
unstable resonator mode profiles; prediction of fundamental mode features using Fresnel zone theory. *Steier, William H., J-QE 75 Sep* 725-728 (1A03)
unstable resonators; eigenmode loss behavior of resonators with cylindrical and circular mirrors at small and large Fresnel numbers. *Santana, C., J-QE 75 Sep* 58D-59D (2F04)
Laser thermal factors
buried-heterostructure lasers with GaAs active regions completely buried in GaAlAs; CW operation. *Tsukada, Toshihisa, J-QE 75 Jul* 494-498 (3B04)
dye lasers; high-power lasers using free jet stream of liquid dye solution. *Foley, R. J., J-QE 75 Sep* 5D (2B07)
dye lasers; thermally induced optical inhomogeneities in active volume of high-power lasers. *Peterson, O. G., J-QE 75 Sep* 4D-5D (2B06)
explosive vapor detection by laser illumination of air sample suspected of containing vapor. *Claspy, P. C., J-QE 75 Sep* 37D (2D11)
GaAs/GaAlAs double-heterostructure injection lasers with distributed feedback; pulsed operation between 80 and 150 K. *Nakamura, Michiharu, J-QE 75 Jul* 436-439 (2E02)
metallic surfaces; thermal coupling coefficient for laser-heated surfaces. *Marcus, S., J-QE 75 Sep* 49D-50D (2E09)
NdYAG lasers; mode-locked lasers using liquid absorbers. *Wilbrandt, Robert, J-QE 75 May* 186-190 (1A08)
Nd:YAG lasers; thermooptical effects of intracavity $Ba_2Na(NbO_3)_5$ crystal on frequency-doubled lasers. *Barry, James D., J-QE 75 Aug* 575-579 (1A13)
optical-pumping-induced heating in CW NdP_5O_{14} lasers; bistable laser operation. *Weber, Heinz P., J-QE 75 Jul* 368-370 (1D12)
thermal impedance of junction lasers; measurement. *Paoli, Thomas L., J-QE 75 Jul* 498-503 (3B08)
Laser tuning
CO_2 15-atm electron-beam controlled lasers; frequency tuning using Fabry–Perot interferometers. *O'Neill, F., J-QE 75 Sep* 74D-75D (2G06)
CO_2 lasers; continuously tunable high-pressure lasers. *Bagratashvili, V. N., J-QE 75 Sep* 94D (3A11)
dye lasers; tunable subnanosecond pulse generation from N_2-laser-pumped dye laser in near UV and visible region. *Lin, Chinlon, J-QE 75 Aug* 602-609 (1C08)
HgCdTe magnetically tunable lasers; tunable spin-flip and recombination lasers using optical pumping. *Sattler, J. P., J-QE 75 Sep* 18D (2C06)
InSb lasers; CW lasers optically pumped in longitudinal geometry. *Menyuk, N., J-QE 75 Jul* 477-481 (3A01)
monolithic GaInAs homojunction diode lasers. *Doerbeck, F. H., J-QE 75 Jul* 464-467 (2G02)
pulsed dye lasers; subnanosecond tunable pulse generation in N_2-laser-pumped lasers using controlled resonator transients. *Lin, Chinlon, J-QE 75 Sep* 1D-2D (2B03)
Laser welding; **cf.** Laser materials-processing applications
Law enforcement
explosive vapor detection using laser optoacoustic detector. *Claspy, P. C., J-QE 75 Sep* 37D (2D11)
Lead alloys/compounds, devices; **cf.** Semiconductor lasers
Length measurement
dilatometry using multichannel interferometer. *Pond, C. R., J-QE 75 Sep* 10D-11D (2B12)
Lidar; **cf.** Optical radar
Light...; **cf.** Optical...
Light-activated switches; **cf.** Light-triggered switches
Light-beam focusing; **cf.** Laser-beam focusing
Light deflectors; **cf.** Acoustooptic light deflectors
Light-emitting diodes
$LiNdP_4O_{12}$ laser pumping using LEDs; optical power requirements. *Yamada, T., J-QE 75 Sep* 62D-63D (2F08)
Light modulation; **cf.** Optical modulation
Light-triggered switches
Ge switches for fast switching of high-power CO_2 laser radiation. *Alcock, A. J., J-QE 75 Sep* 96D (3A13)
microwave switches using bulk photoconductivity produced in Si transmission lines by picosecond optical pulses. *Johnson, A. M., J-QE 75 Jun* 283-287 (1E05)
Linear FM; **cf.** Chirp modulation
Liquid lasers
CW far-infrared lasers using ethyl alcohol, methyl chloride, ethyl chloride and methylene chloride. *Jennings, D. A., J-QE 75 Aug* 637 (1F01)
Liquid lasers; **cf.** Dye lasers
Lithium
vapor; third-order susceptibility. *Eicher, Hermann, J-QE 75 Apr* 121-130 (1A03)
Lithium alloys/compounds
$LiNdP_4O_{12}$; optical absorption, fluorescence, and laser characteristics. *Otsuka, Kenju, J-QE 75 Jul* 330-334 (1B02)
Lithium alloys/compounds, devices
$LiIO_3$ optical parametric oscillators operating at kHz pulse repetition rates. *Ammann, E. O., J-QE 75 Sep* 65D (2F11)
$LiNbO_3$ acoustooptic light deflectors with low electrical drive power requirements. *Schmidt, R. V., J-QE 75 Jan* 57-59 (1E03)
$LiNbO_3$ planar optical waveguides; electrooptic-prism switch. *Kaminow, I. P., J-QE 75 Aug* 633-635 (1E11)
optical directional couplers; $LiNbO_3$ integrated optical switch/modulator using electrical switching. *Papuchon, M., J-QE 75 Sep* 99D-100D (3B02)
Lithium alloys/compounds, devices; **cf.** Neodymium:solid lasers
Logic devices; **cf.** Optical logic devices
Logic gates
light gates using optically induced dichroism in organic-dye solutions. *Vahey, David W., J-QE 75 Sep* 100D-101D (3B03)
Losses; **cf.** Waveguide losses
LSI; **cf.** Digital integrated circuits
Luminescence; **cf.** Photoluminescence

M

Machining; **cf.** Laser materials-processing applications
Magnetic field effect
InSb lasers; CW tunable lasers optically pumped in longitudinal geometry. *Menyuk, N., J-QE 75 Jul* 477-481 (3A01)
Mass spectroscopy
HCN-laser discharge plasma. *Schötzau, Hans J., J-QE 75 Oct* 817-822 (1B01)
Materials processing; **cf.** Laser materials-processing applications; Laser plasma generation
Measurements; **cf.** Electric variables measurement; Geophysical measurements; Laser measurements; Mechanical variables measurement; Optical measurements; Thermal variables measurement; Time measurement
Mechanical variables measurement; **cf.** Displacement measurement; Fluid flow measurement; Length measurement; Strain measurement
Memories; **cf.** Holographic memories
Mercury devices
laser pump lamps. *Holmes, N., J-QE 75 Sep* 55D (2F01)
Mercury devices; **cf.** Gas lasers
Mercury alloys/compounds, devices
HgCdTe planar photodiodes for wideband heterodyne detection at 10.6 μm. *Spears, D. L., J-QE 75 Sep* 79D (2G11)
Mercury alloys/compounds, devices; **cf.** Semiconductor lasers
Mesa devices
lasers; monolithic GaInAs homojunction diode lasers. *Doerbeck, F. H., J-QE 75 Jul* 464-467 (2G02)
Metal radiation effects
laser pulse irradiation effects on metals and semiconductors. *Dekhtar, I. Ya., J-QE 75 Sep* 83D (2G14)
laser radiation effects on metallic surface reflectivity. *Ready, J. F., J-QE 75 Sep* 49D (2E09)
Metal vapor lasers; **cf.** Gas lasers
Meteorological factors
rain drop measurements using pulsed holography technique. *Zakharov, V. M., J-QE 75 Sep* 82D (2G14)
Meteorological factors; **cf.** Optical radio propagation meteorological factors
Microstrip switches
Si switches using bulk photoconductivity produced by picosecond optical pulses. *Johnson, A. M., J-QE 75 Jun* 283-287 (1E05)
Microwave radiation effects/safety; **cf.** Electromagnetic radiation...
Microwave switches; **cf.** Microstrip switches
Middle infrared; **cf.** Infrared (0.70–100 μm)
Mode-locked lasers
Ar ion lasers using 700-m-long cavity. *Tripathi, P. P., J-QE 75 Sep* 59D (2F05)
fluctuation model of passive mode locking; ultrashort pulse generation. *Glenn, William H., J-QE 75 Jan* 8-17 (1A10)
forced mode locking of homogeneously broadened lasers in frequency and time domains. *Haus, Hermann A., J-QE 75 Jul* 323-330 (1A09)
frequency-domain analysis of intracavity frequency-doubled lasers. *Kennedy, C. J., J-QE 75 Nov* 857-862 (1A03)
frequency doubling; internal doubling in amplitude-modulated lasers. *Falk, Joel, J-QE 75 Jan* 21-31 (1B09) ♦
GaAs injection lasers; multimode operation and mode-locking. *Bachert, H., J-QE 75 Jul* 507-510 (3C03)
internally frequency-doubled Nd:YAG lasers; output pulse duration variations. *Falk, Joel, J-QE 75 Jul* 365-367 (1D09)
Nd:glass lasers; pulse lengths. *Greenhow, R. C., J-QE 75 Jan* 59-60 (1E05)
Nd:YAG lasers; mode-locking threshold above normal lasing threshold. *Wilbrandt, Robert, J-QE 75 May* 186-190 (1A08)
Nd:YAG lasers; solar-pumped lasers with simultaneous frequency doubling and mode locking. *Falk, Joel, J-QE 75 Sep* 14D-15D (2C02)
Nd:YAG lasers using $Ba_2NaNb_5O_{15}$ acoustooptic mode locker/frequency doubler. *Rice, R. R., J-QE 75 Sep* 14D (2C02)
optical communication systems using mode-locked lasers with folded optical delay lines. *Kornienko, L. S., J-QE 75 Sep* 91D (3A08)
output pulses; analysis of ultrashort pulses using time-resolved linear interferometry. *Shah, Rajiv R., J-QE 75 Sep* 783-788 (1E05)
pulses of lasers mode-locked with slow saturable absorbers; closed-form solution. *Haus, Hermann A., J-QE 75 Sep* 736-746 (1A14)
Modes; **cf.** Laser modes
Modulation; **cf.** Optical modulation
Molecular lasers; **cf.** Liquid lasers
Monel; **cf.** Copper alloys/compounds
Monitoring; **cf.** Air pollution monitoring
Multiprocessing; **cf.** Parallel processing

N

Near infrared; **cf.** Infrared (0.70–100 μm)
Neodymium alloys/compounds
$LiNdP_4O_{12}$; optical absorption, fluorescence, and laser characteristics. *Otsuka, Kenju, J-QE 75 Jul* 330-334 (1B02)
Neodymium alloys/compounds, devices; **cf.** Solid lasers
Neodymium:glass lasers
amplifiers; active mirror high-power amplifier. *Hoose, J., J-QE 75 Sep* 12D (2B14)
amplifiers; face-pumped mirror-like structure. *Bret, G., J-QE 75 Sep* 12D-13D (2B14)
amplifiers; parasitic oscillation suppression in large aperture disk amplifiers using liquid edge cladding. *Guch, S., Jr., J-QE 75 Sep* 30D-31D (2D04)
ED-2 silicate laser glass; pump conversion efficiency. *Layne, C. B., J-QE 75 Sep* 798-799 (1F06)
glass; tailoring for specific applications by compositional changes. *Jacobs, R. R., J-QE 75 Sep* 13D (2C01)

♦ **Check author entry for later corrections/comments**

JANUS system for laser fusion experiments. *Speck, D. R., J-QE 75 Sep* 45D-46D (2E05)
laser amplifier systems; SHIVA 10-kilojoule system at Lawrence Livermore Laboratory. *Gilmartin, T. J., J-QE 75 Sep* 32D (2D06)
light emission; laser energy redistribution using electronic feedback circuit. *Panarella, Emilio, J-QE 75 May* 181-185 (1A03)
mode-locked lasers; ultrashort output pulse analysis using time-resolved linear interferometry. *Shah, Rajiv R., J-QE 75 Sep* 783-788 (1E05)
Nd^{3+}; $^4F_{3/2} \rightarrow {}^4I_{13/2}$ laser glasses; induced-emission cross sections. *Jacobs, Ralph R., J-QE 75 Oct* 846-847 (1D02)
pulse compression methods for amplifier chains. *Fisher, Robert A., J-QE 75 Jan* 46-52 (1D06)
pulse lengths from mode-locked lasers. *Greenhow, R. C., J-QE 75 Jan* 59-60 (1E05)
stimulated emission in Nd-doped glass; measurement of cross section. *Dianov, E. M., J-QE 75 Sep* 83D (2G14)

Neodymium:solid lasers
$LiNbO_3$ lasers. *Kaminow, I. P., J-QE 75 Jun* 306-308 (1F14)
Nd:YVO_4 lasers; CW and self-*Q*-switched operation. *DeShazer, L. G., J-QE 75 Sep* 84D (3A01)
Nd:YVO_4 lasers; electrooptic *Q*-switching without intracavity polarizer. *Bass, Michael, J-QE 75 Dec* 938-939 (1A12)

Neodymium:YAG lasers
frequency-doubled lasers; thermooptical effects of intracavity $Ba_2Na(NbO_3)_5$ crystal. *Barry, James D., J-QE 75 Aug* 575-579 (1A13)
frequency-doubled mode-locked lasers using $Ba_2NaNb_5O_{15}$ acoustooptic mode locker/frequency doubler. *Rice, R. R., J-QE 75 Sep* 14D (2C02)
lamp-pumped subsystem for 1 gbps satellite communication system. *Radecki, Dan J., J-QE 75 Sep* 15D-16D (2C03)
mode-locked internally frequency-doubled lasers; output pulse duration variations. *Falk, Joel, J-QE 75 Jul* 365-367 (1D09)
mode-locked lasers with internal frequency doubling. *Falk, Joel, J-QE 75 Jan* 21-31 (1B09) ♦
mode-locking threshold above normal lasing threshold. *Wilbrandt, Robert, J-QE 75 May* 186-190 (1A08)
pumping by GaAs or AlGaAs laser diode arrays. *Reno, C. W., J-QE 75 Sep* 16D (2C04)
pumping with electrodeless Kr arc lamps. *Huchital, D. A., J-QE 75 Sep* 16D (2C04)
Q-switched lasers using negative-branch unstable resonator. *Ewanizky, T. F., J-QE 75 Sep* 17D-18D (2C05)
satellite ranging systems; picosecond-pulse, fieldable Nd:YAG laser system. *Erickson, E. G., J-QE 75 Sep* 16D-17D (2C04)
single-pass gains at 1.32 μm. *Loree, T. R., J-QE 75 Jul* 371-372 (1E01)
solar-pumped lasers with simultaneous internal frequency doubling and mode locking. *Falk, Joel, J-QE 75 Sep* 14D-15D (2C02)
third-harmonic radiation pumping of high-power visible dye lasers. *Kato, K., J-QE 75 Jul* 373-374 (1E03)

Neon; **cf.** Noble gases
Networks; **cf.** *RC* networks

Neutron radiation effects
Ne–N_2 lasers; direct nuclear pumped laser with simultaneous output at 8629 and 9393 Å. *DeYoung, R. J., J-QE 75 Sep* 97D (3A14)

Nickel alloys/compounds, devices
Monel terminal posts; laser welding of insulated Cu wires to posts. *Saifi, M. A., J-QE 75 Sep* 48D (2E08)

Niobium alloys/compounds, devices; **cf.** Neodymium:solid lasers
Nitrogen devices; **cf.** Gas lasers
Nitrogen compounds/mixtures, devices; **cf.** Gas lasers

Noble-gas devices
lamps; CW pumping of Nd:YAG lasers with electrodeless Kr arc lamps. *Huchital, D. A., J-QE 75 Sep* 16D (2C04)

Noble-gas lasers
Ar–SF_6 and He-SF_6 mixtures; pulsed-laser action on atomic transitions. *Sutton, D. G., J-QE 75 Jan* 54-57 (1D14)
fast-flow high-pressure system for closed-cycle operation with ultrapure gases; high-repetition-rate TEA system. *Olson, Robert A., J-QE 75 Sep* 95D-96D (3A12)
He–Ne lasers; five-year operation of laser using metal–ceramic discharge tube. *Kolb, W. P., J-QE 75 Jul* 374-375 (1E04)
He–Ne lasers; mode-selective three-mirror reflector for single mode operation. *Eichler, H., J-QE 75 Apr* 168-170 (1D08)
Ne–N_2 lasers; direct nuclear pumped laser with simultaneous output at 8629 and 9393 Å. *DeYoung, R. J., J-QE 75 Sep* 97D (3A14)
$Xe^*(^3P_2)$ metastable atoms; quenching with light hydrocarbons and fluoromethanes. *Velazco, J. E., J-QE 75 Aug* 708-709 (2E14)
XeO lasers; lasing on green bands using direct electron beam excitation of high pressure Xe with small additions of O_2, CO_2 or N_2O. *Powell, H. T., J-QE 75 Aug* 685 (2D05)
XeO lasers; reaction kinetics in electron-beam pumped Xe–O_2 mixtures. *Lorents, D. C., J-QE 75 Aug* 704 (2E10)

Noble-gas lasers, ionic
Ar ion lasers; CW laser using 700-m-long cavity. *Tripathi, P. P., J-QE 75 Sep* 59D (2F05)
pulsed Xe laser; operating characteristics and use as pump source for tunable Rhodamine-6G dye laser. *Schearer, Laird D., J-QE 75 Dec* 935-937 (1A09)
ultraviolet lasers; noble-gas transitions below 2500 Å. *Marling, John B., J-QE 75 Oct* 822-834 (1B06)
ultraviolet lasers; pulsed and CW transitions below 3000 Å. *Marling, J. B., J-QE 75 Sep* 27D-28D (2D01)

Noble-gas lasers, molecular
vacuum ultraviolet laser oscillators and amplifiers; pumping by coaxial diode electron-beam system. *Arthurs, E. G., J-QE 75 Sep* 28D (2D02)
XeBr* excimer lasers; 281.8-nm emission from electron-beam-excited Xe/Br_2 mixture. *Searles, S. K., J-QE 75 Sep* 93D (3A10)
XeF lasers; 3540-Å emission from electron-beam-excited F_2/Xe/Ar mixtures. *Ewing, J. J., J-QE 75 Sep* 92D-93D (3A09)
XeO, KrO, and ArO excimer lasers; collision-induced emission in electron-beam-excited O_2–rare gas mixtures. *Powell, H. T., J-QE 75 Sep* 27D (2D01)

Noise; **cf.** Laser noise
Nonlinear optics; **cf.** Laser absorbers; Optical propagation, nonlinear media

Nuclear fusion
JANUS Nd:glass laser system for laser fusion experiments. *Speck, D. R., J-QE 75 Sep* 45D-46D (2E05)
laser amplifier systems; SHIVA 10-kilojoule system at Lawrence Livermore Laboratory. *Gilmartin, T. J., J-QE 75 Sep* 32D (2D06)
laser-beam focusing; aberrated beams. *Hunt, J. T., J-QE 75 Sep* 29D-30D (2D03)
laser-driven fusion; pulse shaping using optically gated dye cell. *Massey, G. A., J-QE 75 Jul* 358-364 (1D02)
laser fusion. *Teller, E., J-QE 75 Sep* 83D (2G14)
laser fusion at 1.06 μm and 10.6 μm. *McCall, G. H., J-QE 75 Sep* 45D (2E05)
laser fusion; optical propagation and energy transport in fusion targets. *Holzrichter, J. F., J-QE 75 Sep* 46D (2E06)
laser fusion; pellet compression using electron-beam-excited Kr/O_2 mixtures. *Johnson, A. W., J-QE 75 Sep* 56D (2F02)
lasers; Asterix III pulsed high-power I laser. *Brederlow, G., J-QE 75 Sep* 42D-43D (2E02)
lasers; pressure broadening and saturation behavior of Asterix III pulsed high-power I laser. *Fuss, W., J-QE 75 Sep* 43D (2E03)
lasers; refractive index nonlinearity of transparent dielectric material in glass lasers. *Glass, A. J., J-QE 75 Sep* 28D-29D (2D02)
Nd:glass lasers; development of optimum glass. *Jacobs, R. R., J-QE 75 Sep* 13D (2C01)

O

Optical amplifiers; **cf.** Laser amplifiers; Optical parametric amplifiers

Optical communication
in Japan; status of research and development. *Marubayashi, G., J-QE 75 Sep* 76D (2G08)
mode-locked lasers using folded optical delay lines; optical communication system applications. *Kornienko, L. S., J-QE 75 Sep* 91D (3A08)

Optical communication; **cf.** Infrared communication; Optical radio communication

Optical couplers
optical waveguides; holographic couplers for optical fiber and planar waveguides. *Nishihara, H., J-QE 75 Sep* 794-796 (1F02)

Optical couplers; **cf.** Laser couplers; Optical directional couplers; Optical planar waveguide couplers
Optical deflectors; **cf.** Light deflectors

Optical demodulation
laser communications system using external polarization electrooptic modulation and avalanche diode detection; optimum carrier-to-noise ratio. *Waksberg, Armand L., J-QE 75 Sep* 778-782 (1D14)

Optical demodulation; **cf.** Infrared demodulation; Optical heterodyne detection

Optical diffraction
Bragg diffraction; noncollinear multimode diffraction in ion-exchanged optical planar waveguides with periodic surface corrugation. *Asakawa, K., J-QE 75 Jun* 304-306 (1F12)

Optical directional couplers
$LiNbO_3$ integrated optical switch/modulator; COBRA electrically switched coupler. *Papuchon, M., J-QE 75 Sep* 99D-100D (3B02)

Optical distance measurement
altimetry; laser rangefinder for heavy-lift-helicopter precision hover sensor. *Ammon, G., J-QE 75 Sep* 50D-51D (2E10)
laser rangefinders; Ho:YLF laser performance and design options. *Devor, D. P., J-QE 75 Sep* 13D-14D (2C01)
rangefinders using pulsed ultraviolet N_2 laser. *Davis, T. P., J-QE 75 Sep* 50D (2E10)
satellite ranging systems; picosecond-pulse, fieldable Nd:YAG laser system. *Erickson, E. G., J-QE 75 Sep* 16D-17D (2C04)

Optical fiber communication
fault location method for fibers. *Ueno, Y., J-QE 75 Sep* 77D-78D (2G09)
potential applications. *Goell, J. E., J-QE 75 Sep* 76D (2G08)
repeaters; 40-Mb/s and 400-Mb/s repeaters using feedback-type amplifiers. *Ueno, Y., J-QE 75 Sep* 78D-79D (2G10)

Optical fiber waveguides
couplers; holographic optical couplers for fiber–fiber or fiber–thin-film waveguide coupling. *Nishihara, H., J-QE 75 Sep* 794-796 (1F02)
dispersion in long multimode guides. *Kao, C., J-QE 75 Sep* 76D-77D (2G08)
doubly clad W-type fibers; leaky mode characteristics below cutoff; group velocity and power flow distribution slightly above cutoff. *Kawakami, Shojiro, J-QE 75 Apr* 130-138 (1A12)
four-photon mixing; phase-matched-stimulated mixing in silica-fiber waveguides. *Stolen, Rogers H., J-QE 75 Mar* 100-103 (1A06)
lasers; packaged GaAlAs double heterostructure lasers. *Takusagawa, M., J-QE 75 Sep* 61D (2F07)
mode analysis of multimode fibers using linearly tapered section. *Ozeki, T., J-QE 75 Sep* 77D (2G09)
surface-wave radiation loss for all modes. *Kuester, Edward F., J-QE 75 Nov* 903-907 (1D07)

Optical filters
optical pulse generation by laser breakdown switch technique; production of filters. *Yablonovitch, Eli, J-QE 75 Sep* 789-791 (1E11)
spatial filter for removal of small-scale beam instabilities in CYCLOPS laser. *Simmons, W. W., J-QE 75 Sep* 30D (2D04)

Optical frequency conversion
frequency tripling of 1.06 μm subnanosecond pulses to 3547 Å. *Attwood, D. T., J-QE 75 Sep* 68D-69D (2F14)
Nd:YAG lasers; solar-pumped lasers with simultaneous frequency doubling and mode locking. *Falk, Joel, J-QE 75 Sep* 14D-15D (2C02)
Nd:YAG lasers using $Ba_2NaNb_5O_{15}$ acoustooptic mode locker/frequency doubler. *Rice, R. R., J-QE 75 Sep* 14D (2C02)

Optical frequency conversion; **cf.** Optical harmonic generation; Optical heterodyning; Optical mixers

Optical harmonic generation
frequency-doubled Nd:YAG lasers; thermooptical effects of intracavity $BaNa(NbO_3)_5$ crystal. *Barry, James D., J-QE 75 Aug* 575-579 (1A13)
phase-matched second-harmonic generation in ZnS optical planar waveguides using film and substrate nonlinearities. *Ito, H., J-QE 75 Sep* 40D (2D14)

♦ **Check author entry for later corrections/comments**

second-harmonic generation; effect of two-photon absorption in semiconductors. *Schwartz, Christiane A., J-QE 75 Aug* 616-623 (1D08)
second-harmonic generation in Te; effect of two-photon absorption. *Oudar, Jean-Louis, J-QE 75 Aug* 623-629 (1E01)
second-harmonic generation; reduction of conversion-limiting effects of crystal anisotropy in critically index-matched generation. *Librecht, F. M., J-QE 75 Sep* 755-758 (1C05)
second-harmonic generation in CD*A crystals; electrooptical compensation for self-heating. *Hon, D., J-QE 75 Sep* 67D-68D (2F13)
second-harmonic generation in birefringent crystals by Gaussian beam with elliptical cross section. *Librecht, F. M., J-QE 75 Oct* 850-852 (1D06)
second-harmonic ultraviolet Cerenkov radiation generation. *Chen, Bor-Uei, J-QE 75 Apr* 177-178 (1E03)

Optical heterodyne detection
10.6-μm wideband receiver for CO_2 laser satellite communications link. *Peyton, B. J., J-QE 75 Sep* 80D-81D (2G12)
10-μm receiver for satellite communication. *Goodwin, F. E., J-QE 75 Sep* 79D-80D (2G11)
chirp-modulated CO_2 waveguide lasers. *Stein, Alexander, J-QE 75 Aug* 630-631 (1E08)
multiphoton absorption heterodyne receivers; detector response, signal-to-noise ratio, minimum detectable power. *Teich, Malvin Carl, J-QE 75 Aug* 595-602 (1C01)
wideband heterodyne detection at 10.6 μm using planar HgCdTe photodiodes. *Spears, D. L., J-QE 75 Sep* 79D (2G11)

Optical heterodyning
IR heterodyning; CW HF chemical mixing lasers as local oscillators for mid-IR applications. *Freiberg, R. J., J-QE 75 Sep* 57D-58D (2F03)
radiometers; optical heterodyne radiometers for atmospheric transmission measurements at HF/DF laser wavelengths. *King, S. R., J-QE 75 Sep* 87D (3A04)

Optical interferometry
dilatometry using multichannel interferometer. *Pond, C. R., J-QE 75 Sep* 10D-11D (2B12)
grazing incidence triangular laser interferometer; application to checkout of granite surface plate quality. *Rabal, H. J., J-QE 75 Sep* 22D-23D (2C10)
laser pulse measurements; analysis of ultrashort pulses from mode-locked lasers using time-resolved linear interferometry. *Shah, Rajiv R., J-QE 75 Sep* 783-788 (1E05)
nonlinear refractive-index coefficient of laser-system materials; interferometric measurement. *Moran, Michael J., J-QE 75 Jun* 259-263 (1C09)

Optical interferometry; **cf.** Fabry–Perot interferometers

Optical isolators
CO_2 high-gain amplifiers; suppression of self-oscillations using interstage optical isolators. *Lavigne, P., J-QE 75 Sep* 75D (2G07)
infrared isolators; Ge high-power isolator for 10 μm region using interband Faraday effect. *Phipps, C. M., Jr., J-QE 75 Sep* 70D-71D (2G03)

Optical logic devices
gates; light gates using optically induced dichroism in organic-dye solutions. *Vahey, David W., J-QE 75 Sep* 100D-101D (3B03)

Optical measurements
ambient-air pollutant measurements using bistatic heterodyne system. *Menzies, R. T., J-QE 75 Sep* 33D (2D07)
electrical signals; optical sampling transient analyzer for fast, high-voltage, single transient signals. *Davies, Terence J., J-QE 75 Sep* 7D (2B09)
pollution concentration variations with altitude; measurement using solar infrared heterodyne radiometer. *Christophe, B., J-QE 75 Sep* 32D-33D (2D06)
rain drop measurements using pulsed holography technique. *Zakharov, V. M., J-QE 75 Sep* 82D (2G14)
strain in earth's crust; measurement using 700-m long mode-locked Ar ion laser. *Tripathi, P. P., J-QE 75 Sep* 59D (2F05)
ultrafast photoinduced phenomena; measurement using transient induced grating system. *Siegman, A. E., J-QE 75 Sep* 69D (2G01)

Optical measurements; **cf.** Laser measurements; Optical distance measurement; Optical interferometry; Optical pulse measurements; Optical spectroscopy; Optical velocimeters

Optical memories; **cf.** Holographic memories

Optical mixers
tunable short pulse generation in infrared and ultraviolet using synchronous mode-locked dye laser. *Goldberg, L. S., J-QE 75 Sep* 2D (1B04)

Optical mixers; **cf.** Optical heterodyning

Optical modulation; **cf.** Acoustooptic modulation; Electrooptic modulation

Optical parametric amplifiers
optical pulse generation by pulsed parametric amplification of noble gas laser emission. *Massey, G. A., J-QE 75 Sep* 66D (2F12)

Optical parametric oscillators
infrared source for infrared absorption line-shape measurements. *Wormhoudt, J., J-QE 75 Aug* 704 (2E10)
$LiIO_3$ oscillators operating at kHz pulse repetition rates. *Ammann, E. O., J-QE 75 Sep* 65D (2F11)
RD*A parametric oscillators; efficient operation in visible to near infrared using third harmonic of Nd:YAG laser as pump source. *Kato, K., J-QE 75 Dec* 939-941 (1A13)

Optical planar waveguides
bend losses in curved guides; conformal transformation analysis. *Heiblum, Mordehai, J-QE 75 Feb* 75-83 (1A13)
Bragg diffraction; noncollinear multimode diffraction in ion-exchanged guide with periodic surface corrugation. *Asakawa, K., J-QE 75 Jun* 304-306 (1F12)
buried modes in guides with nonmonotonically varying index of refraction. *Conwell, Esther M., J-QE 75 May* 217-218 (1C11)
KTN single-crystal thin-film guides. *Fontana, R. E., Jr., J-QE 75 Sep* 38D (2D12)
mode conversion in planar-dielectric separating waveguides. *Burns, William K., J-QE 75 Jan* 32-39 (1C06)
modes in diffused guides of arbitrary index profile; phase constants. *Hocker, G. Benjamin, J-QE 75 Jun* 270-276 (1D06)
multilayer metal-clad guides with low-index dielectric buffer layer; attenuation characteristics. *Yamamoto, Yoshihisa, J-QE 75 Sep* 729-736 (1A07)
rib-waveguide structure for transverse-mode control in injection lasers. *Lee, T. P., J-QE 75 Jul* 432-435 (2D12)
second-harmonic generation in ZnS thin-film guides using nonlinearities in film and substrate. *Ito, H., J-QE 75 Sep* 40D (2D14)
slab waveguides; light scattering from periodic refractive-index fluctuations in asymmetric guides. *Marcuse, D., J-QE 75 Apr* 162-168 (1D02)
surface-wave radiation loss for TE modes in asymmetric slab waveguides. *Kuester, Edward F., J-QE 75 Nov* 903-907 (1D07)
ZnTe ion-implanted guides. *Valette, S., J-QE 75 Sep* 39D-40D (2D13)

Optical planar waveguide components
convolvers; optical guided wave–acoustic surface-wave interactions in thin-film As_2S_3 guide on $LiNbO_3$ substrate. *Loh, K. W., J-QE 75 Sep* 86D (3A03)
electrooptic switches; electrode configuration for producing prism-like deflector on planar optical waveguide. *Kaminow, I. P., J-QE 75 Aug* 633-635 (1E11)
modulators; electrooptic modulator using grain-oriented polycrystalline ZnO film. *Hu, Chenming, J-QE 75 Sep* 64D (2F10)
modulators; GaAs electrooptic channel-waveguide modulator. *Campbell, J. C., J-QE 75 Sep* 63D-64D (2F09)
modulators; mode-dependent modulation in (Ga,Al)P modulators. *Bortfeld, David P., J-QE 75 Mar* 108-110 (1A14)
modulators; ZnO electrooptic grating modulator. *Hammer, Jacob M., J-QE 75 Apr* 138-148 (1B06)

Optical planar waveguide couplers
3-dB couplers with noncritical length and mode synchronization only at single point. *Burns, W. K., J-QE 75 Sep* 42D (2E02)
holographic optical couplers for fiber waveguide–thin-film waveguide coupling. *Nishihara, H., J-QE 75 Sep* 794-796 (1F02)

Optical planar waveguides
mode coupling in anisotropic slab waveguides; electrooptic coupling between TE and TM modes in $LiNbO_3$ and $LiTaO_3$. *Marcuse, D., J-QE 75 Sep* 759-767 (1C09)

Optical propagation; **cf.** Infrared propagation; Optical radio propagation; Optical waveguides

Optical propagation, absorbing media
laser fusion targets; optical propagation and energy transport. *Holzrichter, J. F., J-QE 75 Sep* 46D (2E06)
$LiNdP_4O_{12}$; optical absorption characteristics. *Otsuka, Kenju, J-QE 75 Jul* 330-334 (1B02)

Optical propagation, absorbing media; **cf.** Infrared propagation, absorbing media

Optical propagation, guided; **cf.** Optical waveguides

Optical propagation, nonlinear media
four-photon mixing; phase-matched-stimulated mixing in silica-fiber waveguides. *Stolen, Rogers H., J-QE 75 Mar* 100-103 (1A06)
laser beam focusing; effect of small-scale beam breakup. *Bliss, E. S., J-QE 75 Sep* 29D (2D03)
second-order susceptibilities; bond-orbital model for tetrahedral compounds. *Choy, Michael M., J-QE 75 Jan* 40-45 (1C14)
third-order nonlinear processes in isotropic media; effects of focusing. *Bjorklund, Gary C., J-QE 75 Jun* 287-296 (1E09)
third-order susceptibility of alkali metal vapors. *Eicher, Hermann, J-QE 75 Apr* 121-130 (1A03)

Optical propagation, nonlinear media; **cf.** Optical resonance

Optical propagation, refraction; **cf.** Optical refraction

Optical propagation, turbulent media; **cf.** Optical radio propagation meteorological factors

Optical pulses
CO_2 laser amplifier pulse-selection systems; prepulse extinction-ratio measurements. *Manes, K. R., J-QE 75 Aug* 635-636 (1E13)
laser pulses; energy extraction from CO_2 laser amplifiers using 60 ns–1 μs pulses. *Girard, G., J-QE 75 Jun* 241-247 (1B05)
laser pulses; energy redistribution using electronic feedback circuit. *Panarella, Emilio, J-QE 75 May* 181-185 (1A03)
laser pulses; optical sampling technique for picosecond pulses. *Vogel, Gerald C., J-QE 74 Sep* 642-646 (1B02) ♦
Nd:glass lasers mode-locked with BDN; pulse lengths. *Greenhow, R. C., J-QE 75 Jan* 59-60 (1E05)

Optical pulse amplifiers; **cf.** Laser amplifiers

Optical pulse compression
1.06 μm subnanosecond pulse shortening and frequency tripling to 3547 Å. *Attwood, D. T., J-QE 75 Sep* 68D-69D (2F14)
Nd:glass laser amplifier chains. *Fisher, Robert A., J-QE 75 Jan* 46-52 (1D06)

Optical pulse generators
laser pulses with increasing intensity; generation using regenerative amplifier. *Vovchenko, V. I., J-QE 75 Sep* 83D (2G14)
Na vapor; conversion of CW dye laser light into train of repetitive subnanosecond pulses using resonant atomic dispersion. *Bjorkholm, J. E., J-QE 75 Sep* 68D (2G01)
pulsed parametric amplification of noble gas laser emission; frequency-stable, narrow-band pulses from 438.5 nm to 676.4 nm. *Massey, G. A., J-QE 75 Sep* 66D (2F12)
short pulses of arbitrary shape and phase; generation by laser breakdown switch technique. *Yablonovitch, Eli, J-QE 75 Sep* 789-791 (1E11)

Optical pulse generators; **cf.** Pulsed lasers

Optical pulse measurements
laser pulses; analysis of ultrashort pulses from mode-locked lasers using time-resolved linear interferometry. *Shah, Rajiv R., J-QE 75 Sep* 783-788 (1E05)
laser pulses; measurement of CO_2 TEA laser pulse frequency chirp using interferometric pulse delay techniques. *Hieslmair, H., J-QE 75 Sep* 54D (2E14)
subpicosecond measurements using Photochron II streak camera tube. *Bradley, D. J., J-QE 75 Sep* 25D-26D (2C13)

Optical pulse shaping
dye cells; optically gated cells using bleachable liquid dyes. *Massey, G. A., J-QE 75 Jul* 358-364 (1D02)
laser pulse shaping; *Q*-switched ruby laser with compound feedback. *Loveberg, R. V., J-QE 75 Jan* 17-21 (1B05)

Optical pumping; **cf.** Laser excitation

Optical radar
FM-chirp radar; high-resolution radar ranging at 10.6 μm. *Bicknell, W. E., J-QE 75 Jun* 308-311 (1G02)

♦ **Check author entry for later corrections/comments**

imaging; diffraction-limited imaging through turbulent atmosphere using polarization reference imaging system. *Brown, W. P., Jr., J-QE 75 Sep* 52D-53D (2E12)
imaging through turbulent atmosphere; computer simulation of polarization reference imaging system. *Tseng, D. Y., J-QE 75 Sep* 53D (2E13)
laser infrared radar (LIDAR); demodulation technique for chirp-modulated CO_2 waveguide laser. *Stein, Alexander, J-QE 75 Aug* 630-631 (1E08)
LIDAR measurements of ozone using resonance Raman scattering and differential absorption techniques. *Penney, C. M., J-QE 75 Sep* 36D (2D10)
multidither coherent optical adaptive techniques for compensation of turbulence and blooming distortions. *Pearson, J. E., J-QE 75 Sep* 55D (2F01)
transmitters; temporal coherence of double-discharge CO_2 TEA laser. *Rudko, R. I., J-QE 75 Sep* 54D (2E14)

Optical radiation effects
isotope separation using radiation pressure. *Gelbwachs, Jerry, J-QE 75 Jan* 52-54 (1D12)

Optical radiation effects; cf. Laser radiation effects; Ultraviolet radiation effects

Optical radio communication
diversity receiver for turbulent conditions. *McIntyre, C. M., J-QE 75 Sep* 81D (2G13)
laser communications system using external polarization electrooptic modulation and avalanche diode detection; optimum carrier-to-noise ratio. *Waksberg, Armand L., J-QE 75 Sep* 778-782 (1D14)
satellite communication; lamp-pumped Nd:YAG laser subsystem for 1 gbps system. *Radecki, Dan J., J-QE 75 Sep* 15D-16D (2C03)
transmitters; solar-pumped Nd:YAG laser transmitter for satellite communication. *Falk, Joel, J-QE 75 Sep* 14D-15D (2C02)

Optical radio propagation meteorological factors
CO_2 laser radiation; absorption by water vapor. *Shumate, M. S., J-QE 75 Sep* 33D-34D (2D07)
diversity receiver for optical communication under turbulent conditions. *McIntyre, C. M., J-QE 75 Sep* 81D (2G13)
HF/DF laser radiation; atmospheric transmission measurements. *King, S. R., J-QE 75 Sep* 87D (3A04)
infrared; atmospheric transmissivity measurements in 9–11-μm band using heterodyne radiometer. *Peyton, Bernard J., J-QE 75 Aug* 569-574 (1A03)
optical radar imaging through turbulent atmosphere using polarization reference imaging system. *Brown, W. P., Jr., J-QE 75 Sep* 52D-53D (2E12)
optical radar imaging through turbulent atmosphere using polarization reference imaging system; computer simulation. *Tseng, D. Y., J-QE 75 Sep* 53D (2E13)
optical radar; multidither coherent optical adaptive techniques for compensation of turbulence and blooming distortions. *Pearson, J. E., J-QE 75 Sep* 55D (2F01)

Optical recording; cf. Holographic recording

Optical reflection
metallic surfaces; reflectivity changes during irradiation by CO_2-TEA lasers. *Ready, J. F., J-QE 75 Sep* 49D (2E09)

Optical refraction
Cs vapor; negative nonlinear refractive index at 1.06 μm. *Lehmberg, R. H., J-QE 75 Sep* 69D-70D (2G01)
glass lasers for nuclear fusion; refractive index nonlinearity of transparent dielectric material. *Glass, A. J., J-QE 75 Sep* 28D-29D (2D02)
nonlinear refractive-index coefficient of laser-system materials; interferometric measurement. *Moran, Michael J., J-QE 75 Jun* 259-263 (1C09)

Optical resonance
photon-echo behavior in presence of extreme inhomogeneous broadening. *Takeuchi, Nobuo, J-QE 75 Jun* 230-235 (1A08)

Optical scattering
GaAlAs–GaAs heterostructure lasers; optical-absorption loss in double-heterostructure and five-layer devices. *Thompson, G. H. B., J-QE 75 Jul* 481-488 (3A05)
optical planar waveguides; light scattering from periodic refractive-index fluctuations. *Marcuse, D., J-QE 75 Apr* 162-168 (1D02)

Optical scattering; cf. Raman scattering

Optical signal processing
near-real-time coherent processing system. *Iwasa, S., J-QE 75 Sep* 8D (2B10)

Optical spectroscopy
$^{12}CH_3F$; pressure broadening and pressure shift coefficient measurements using Doppler-free two-photon absorption techniques. *Bischel, W. K., J-QE 75 Sep* 24D-25D (2C12)
cryptocyanine in methanol; spectral hole burning in absorption band. *Mourou, Gerard, J-QE 75 Jan* 1-8 (1A03)
dye laser spectrometer for analysis of pulsed vacuum arcs. *Hargis, P. J., Jr., J-QE 75 Sep* 24D (2C12)
laser diagnostic spectrographic systems. *Varwig, R. L., J-QE 75 Aug* 719 (2F11)
molecular spectroscopy using continuously tunable high-pressure CO_2 lasers. *Bagratashvili, V. N., J-QE 75 Sep* 94D (3A11)
Rydberg constant determination using highly stabilized CW dye laser. *West, J. B., J-QE 75 Sep* 18D-19D (2C06)

Optical spectroscopy; cf. Infrared spectroscopy

Optical strip waveguides
diffused guides in GaAs. *Garmire, E., J-QE 75 Sep* 38D-39D (2D12)

Optical strip waveguide components
lasers; AlGaAs multiheterostructure laser with integrated twin guide. *Suematsu, Y., J-QE 75 Jul* 457-460 (2F09)

Optical surface waves
radiation loss from asymmetric slab waveguides and optical fibers. *Kuester, Edward F., J-QE 75 Nov* 903-907 (1D07)

Optical tracking
satellites; ranging systems using picosecond-pulse, fieldable Nd:YAG laser system. *Erickson, E. G., J-QE 75 Sep* 16D-17D (2C04)

Optical velocimeters
aircraft vortex detection system using CO_2 laser Doppler velocimeter. *Sonnenschein, C. M., J-QE 75 Sep* 35D (2D09)
laser Doppler velocimeters for remote power plant effluent measurements. *Miller, C. R., J-QE 75 Sep* 34D-35D (2D08)
resonant Doppler velocimeters using tunable narrow-bandwidth dye lasers; gas flow measurement and visualization. *Miles, R. B., J-QE 75 Sep* 35D-36D (2D09)

Optical waveguides
optical field propagation in integrated optical transitions and bifurcations. *Roy, A. M., J-QE 75 Sep* 41D-42D (2E01)

Optical waveguides; cf. Optical fiber waveguides; Optical planar waveguides; Optical strip waveguides

Optical waveguide communication; cf. Optical fiber communication

Organic dye lasers; cf. Dye lasers

Oscillators; cf. Optical parametric oscillators

Oscillator frequency stability; cf. Laser frequency stability

Oscilloscopes; cf. Cathode-ray oscilloscopes

Oxygen devices; cf. Gas lasers

Oxygen
ozone; remote measurement by resonance Raman scattering and differential absorption. *Penney, C. M., J-QE 75 Sep* 36D (2D10)

Ozone; cf. Oxygen

P

Parallel processing
holograms superimposed in $LiNbO_3$ crystals. *Huignard, J. P., J-QE 75 Sep* 8D-9D (2B10)

Parametric amplifiers; cf. Optical parametric amplifiers

Paremetric oscillators; cf. Optical parametric oscillators

Particle spectroscopy
photodeflection method; laser deflection of single isotopic component of atomic beam followed by mass analysis of deflected beam. *Bernhardt, A. F., J-QE 75 Sep* 19D (2C07)

PCM
abbr. of Pulse-code modulation

PCM communication
optical fiber communication repeaters; 40-Mb/s and 400-Mb/s repeaters using feedback-type amplifiers. *Ueno, Y., J-QE 75 Sep* 78D-79D (2G10)

Perturbation methods
optical fiber waveguide analysis using perturbation theory. *Kawakami, Shojiro, J-QE 75 Apr* 130-138 (1A12)

Photochemistry; cf. Chemistry

Photoconducting devices
microwave switches using bulk photoconductivity produced in Si transmission lines by picosecond optical pulses. *Johnson, A. M., J-QE 75 Jun* 283-287 (1E05)

Photodetector arrays
Si photodiode arrays; integrated optical array. *Boyd, J. T., J-QE 75 Sep* 40D-41D (2D14)

Photodetectors; cf. Photodiodes

Photodiodes
HgCdTe planar photodiodes for wideband heterodyne detection at 10.6 μm. *Spears, D. L., J-QE 75 Sep* 79D (2G11)
Si integrated optical arrays. *Boyd, J. T., J-QE 75 Sep* 40D-41D (2D14)

Photodissociation; cf. Gas lasers

Photography
printers for color photography; laser color video printer. *Baldwin, R. E., J-QE 75 Sep* 9D (2B11)

Photoionization
isotope separation; selective photoionization of ^{235}U atoms by laser beam irradiation. *Tuccio, Sam A., J-QE 75 Sep* 101D (3B04)
isotope separation; selective laser two-step excitation and photoionization of atomic U vapor. *Janes, G. S., J-QE 75 Sep* 101D-102D (3B04)
laser-generated photoionization; experiments using H_2 vacuum ultraviolet lasers. *Antonov, V. S., J-QE 75 Sep* 92D (3A09)
U; photoionization cross section measurements. *Solarz, R. W., J-QE 75 Sep* 19D-20D (2C07)

Photoionization; cf. Gas lasers

Photoluminescence
laser-excited lumiinescence; continuously tunable high-pressure CO_2 lasers. *Bagratashvili, V. N., J-QE 75 Sep* 94D (3A11)
laser-excited luminescence; experiments using H_2 vacuum ultraviolet lasers. *Antonov, V. S., J-QE 75 Sep* 92D (3A09)

Photon echoes; cf. Optical resonance

Photosynthesis; cf. Biological cells

Piezoelectric semiconductor devices
ZnO optical planar waveguide modulators. *Hammer, Jacob M., J-QE 75 Apr* 138-148 (1B06)

Plasma diagnostics
laser probe pulses; 1.06 μm subnanosecond pulse shortening and frequency tripling to 3547 Å. *Attwood, D. T., J-QE 75 Sep* 68D-69D (2F14)
pulsed vacuum arcs; analysis using dye laser spectrometer. *Hargis, P. J., Jr., J-QE 75 Sep* 24D (2C12)

Plasma generation; cf. Laser plasma generation

Pockels effect
light emission control in Nd:glass lasers. *Panarella, Emilio, J-QE 75 May* 181-185 (1A03)
Q-switching of Nd:YVO_4 lasers without intracavity polarizer. *Bass, Michael, J-QE 75 Dec* 938-939 (1A12)
ZnO optical planar waveguide modulators. *Hammer, Jacob M., J-QE 75 Apr* 138-148 (1B06)

Pollution; cf. Environmental pollution

Potassium
vapor; third-order susceptibility. *Eicher, Hermann, J-QE 75 Apr* 121-130 (1A03)

Potassium alloys/compounds, devices
KTN optical planar waveguides and modulators. *Fontana, R. E., Jr., J-QE 75 Sep* 38D (2D12)

Potassium devices
lamps; K–Rb pump lamps for Nd:YAG lasers. *Radecki, Dan J., J-QE 75 Sep* 15D-16D (2C03)

Power dividers
optical planar waveguides; mode conversion in planar-dielectric separating guides. *Burns, William K., J-QE 75 Jan* 32-39 (1C06)

Power generation
power plant effluent measurements. *Miller, C. R., J-QE 75 Sep* 34D-35D (2D08)

Power stations; cf. Power generation

Pulse amplifiers; **cf.** Optical pulse amplifiers
Pulse-code modulation; **cf.** PCM
Pulse-compression methods; **cf.** Optical pulse compression
Pulse-compression radar
FM-chirp radar; high-resolution radar ranging at 10.6 μm. *Bicknell, W. E., J-QE 75 Jun* 308-311 (1G02)
Pulsed lasers
2.3-μm Tm^{3+} lasers; room-temperature pulsed emission from Tm:Cr:YAG and Tm:Cr:$YAlO_3$ lasers. *Caird, John A., J-QE 75 Nov* 874-881 (1B06)
Ar–SF_6 and He-SF_6 mixtures; pulsed-laser action on atomic transitions. *Sutton, D. G., J-QE 75 Jan* 54-57 (1D14)
B atom lasers; pumping by incomplete autoionization or ion–electron recombination. *Stricker, J., J-QE 75 Aug* 701-702 (2E07)
CH_3F far-infrared laser; pulse characteristics of optically pumped laser. *Bluyssen, H. J. A., J-QE 75 Jul* 341-348 (1B13)
CO_2 laser amplifiers; energy extraction improvement in ns-pulse TEA lasers. *Farcy, J. C., J-QE 75 Sep* 90D (3A07)
CO_2 laser gain dynamics; model. *Garside, Brian K., J-QE 75 Jun* 264-270 (1C14)
CO_2 TEA lasers; compact sealed laser. *Stark, Donald S., J-QE 75 Sep* 774-778 (1D10)
CO_2 TEA lasers; multigigawatt, ns pulses from tandem of two lasers. *Bélanger, P. A., J-QE 75 Sep* 73D-74D
CO_2 TE lasers; laser dynamics model including rotational coupling effects. *Garside, Brian K., J-QE 75 Aug* 583-589 (1B03)
CuI vapor lasers; transversely excited laser. *Piper, J. A., J-QE 75 Sep* 95D (3A12)
DF and DF–CO_2 electrically initiated chemical lasers. *Poehler, T. O., J-QE 75 Aug* 710 (2F02)
DF lasers; portable recirculating system. *Chenausky, P. P., J-QE 75 Sep* 58D (2F04)
dye lasers; high-repetition-rate transverse-flow laser pumped by linear close-coupled flashlamps. *Friedman, H. W., J-QE 75 Sep* 4D (2B06)
dye lasers; long-pulse generation in Rhodamine-6G laser pumped by CO_2-laser-heated plasma. *Brown, Robert T., J-QE 75 Sep* 800-801 (1F08)
dye lasers; picosecond pulse generation in synchronous mode-locked laser pumped frequency-doubled, passively mode-locked Nd:YAG laser. *Goldberg, L. S., J-QE 75 Sep* 2D (1B04)
dye lasers; subnanosecond tunable pulse generation in N_2-laser-pumped lasers using controlled resonator transients. *Lin, Chinlon, J-QE 75 Sep* 1D-2D (2B03)
dye lasers; tunable subnanosecond pulse generation from N_2-laser-pumped dye laser in near UV and visible region. *Lin, Chinlon, J-QE 75 Aug* 602-609 (1C08)
GaAs/GaAlAs double-heterojunction visible-light-emitting lasers using hetero-isolation stripe geometry. *Itoh, Kunio, J-QE 75 Jul* 421-426 (2D01)
GaAs/GaAlAs double-heterostructure injection lasers with distributed feedback; operation between 80 and 150 K. *Nakamura, Michiharu, J-QE 75 Jul* 436-439 (2E02)
H_2–F_2 high-power chemical lasers; mixture stability and construction materials. *Getzinger, R. W., J-QE 75 Aug* 698 (2E04)
H_2 vacuum ultraviolet lasers. *Knyazev, I. N., J-QE 75 Oct* 805-817 (1A03)
HF chemical lasers; effects of rotational nonequilibrium on predicted performance. *Hough, J. J. T., J-QE 75 Aug* 699 (2E05)
HF chemical lasers; electrically initiated atmospheric lasers. *Mangano, J. A., J-QE 75 Aug* 705 (2E11)
HF chemical lasers; repetitively pulsed operation of chain-reaction lasers. *H_2/F_2 flame propagation and repetitively pulsed hydrogen fluoride (HF) chain-reaction chemical laser, J-QE 75 Aug* 648-653 (2A10)
HF chemical lasers; rotational nonequilibrium. *Creighton, J. R., J-QE 75 Aug* 699 (2E05)
H-pulsing in GaAs/GaAlAs single-heterostructure injection lasers. *Gründorfer, Stephan, J-QE 75 Jul* 532-537 (3D14)
I lasers; pressure broadening and saturation behavior of Asterix III pulsed high-power laser. *Fuss, W., J-QE 75 Sep* 43D (2E03)
I lasers; pulsed high-power Asterix III laser for laser fusion experiments. *Brederlow, G., J-QE 75 Sep* 42D-43D (2E02)
mode-locked internally frequency-doubled lasers; output pulse duration variations. *Falk, Joel, J-QE 75 Jul* 365-367 (1D09)
N_2 lasers; photopreionization. *Kurnit, N. A., J-QE 75 Apr* 174-176 (1D14)
noble-gas ion lasers; pulsed transitions below 3000 Å. *Marling, J. B., J-QE 75 Sep* 27D-28D (2D01)
self-induced intensity pulsations from CW junction lasers; suppression by frequency-selective optical feedback. *Paoli, Thomas L., J-QE 75 Jul* 525-527 (3D07)
transverse-junction-stripe lasers with GaAs homojunction sandwiched between GaAlAs layers. *Namizaki, H., J-QE 75 Jul* 427-431 (2D07)
Pulsed lasers; **cf.** Mode-locked lasers; *Q*-switched lasers
Pulse generators; **cf.** Optical pulse generators
Pulse measurements
optical sampling transient analyzer for fast, high-voltage, single transient electrical pulses. *Davies, Terence J., J-QE 75 Sep* 7D (2B09)
X-ray pulses emitted by laser-produced plasma; pulse-duration measurement. *Duguay, M. A., J-QE 75 Apr* 170-172 (1D10)
Pulse measurements; **cf.** Optical pulse measurements
Pulse shaping; **cf.** Optical pulse shaping
Pumping of lasers; **cf.** Laser excitation
Pyrolysis; **cf.** Chemistry

Q

***Q*-switched lasers**
CO_2 lasers; passive *Q*-switching by Na_2F_4 absorption cells. *Suart, R. D., J-QE 75 Aug* 698 (2E04)
Nd:YAG lasers using negative-branch unstable resonator. *Ewanizky, T. F., J-QE 75 Sep* 17D-18D (2C05)
Nd:YVO_4 lasers; electrooptic *Q*-switching without intracavity polarizer. *Bass, Michael, J-QE 75 Dec* 938-939 (1A12)
Nd:YVO_4 lasers; self-*Q*-switched operation. *DeShazer, L. G., J-QE 75 Sep* 84D (3A01)
pulse shaping in ruby lasers. *Loveberg, R. V., J-QE 75 Jan* 17-21 (1B05)
semiconductor laser theory. *Thomas, Ben, J-QE 75 Jul* 528-532 (3D10)

R

Radar; **cf.** Optical radar
Radar imaging
optical radar; diffraction-limited imaging through turbulent atmosphere using polarization reference imaging system. *Brown, W. P., Jr., J-QE 75 Sep* 52D-53D (2E12)
optical radar imaging through turbulent atmosphere; computer simulation of polarization reference imaging system. *Tseng, D. Y., J-QE 75 Sep* 53D (2E13)
Radar transmitters
optical radar transmitters; temporal coherence of double-discharge CO_2 TEA laser. *Rudko, R. I., J-QE 75 Sep* 54D (2E14)
Radiation effects
CO laser excitation by nuclear reaction products. *McArthur, D. A., J-QE 75 Aug* 707 (2E13)
Radiation effects; **cf.** Electromagnetic radiation effects; Metal radiation effects; Neutron radiation effects; Optical radiation effects; Semiconductor device radiation effects
Radio communication; **cf.** Optical radio communication
Radio communication transmitters
optical communication transmitters; Nd:YAG transmitter for satellite communication laser. *Falk, Joel, J-QE 75 Sep* 14D-15D (2C02)
Radiography; **cf.** X-ray imaging
Radiometry
optical heterodyne radiometer for atmospheric transmission measurements at HF/DF laser wavelengths. *King, S. R., J-QE 75 Sep* 87D (3A04)
solar infrared heterodyne radiometer; atmospheric absorption measurements yielding pollutant concentrations. *Christophe, B., J-QE 75 Sep* 32D-33D (2D06)
Radiometry; **cf.** Infrared radiometry
Radio propagation meteorological factors; **cf.** Optical radio propagation meteorological factors
Rain; **cf.** Meteorological factors
Raman lasers
HgCdTe magnetically tunable lasers; tunable spin-flip and recombination lasers using optical pumping. *Sattler, J. P., J-QE 75 Sep* 18D (2C06)
Raman scattering
coherent anti-Stokes scattering in CH_4 gas; generation by CW lasers. *Barrett, J. J., J-QE 75 Sep* 89D-90D (3A06)
ozone; resonance Raman scattering. *Penney, C. M., J-QE 75 Sep* 36D (2D10)
Raman spectroscopy
temperature measurement in optically pumped NdP_5O_{14} laser. *Weber, Heinz P., J-QE 75 Jul* 368-370 (1D12)
Ranging; **cf.** Distance measurement
Rare-earth ion lasers; **cf.** Solid lasers
Rare gases; **cf.** Noble gases
***RC* networks**
integrated series networks generated by laser machining. *Saifi, M. A., J-QE 75 Sep* 23D (2C11)
Recording; **cf.** Optical recording; Video recording
Reflection; **cf.** Optical reflection
Refraction; **cf.** Optical refraction
Relaxation processes
CO_2 lasers; vibrational deactivation of $CO_2(00°1)$ level by H, D, O, N, F and Cl atoms. *Buchwald, M. I., J-QE 75 Aug* 697 (2E03)
CO_2 TE lasers; laser dynamics model including rotational coupling effects. *Garside, Brian K., J-QE 75 Aug* 583-589 (1B03)
$CO(v=1)$ vibrational deactivation by atomic oxygen. *Davis, C. C., J-QE 75 Aug* 701 (2E07)
DF* lasers; deactivation kinetics in combustion driven lasers using alternates for H_2/Fd'D_2 reactant system. *Wendelken, C. P., J-QE 75 Aug* 694-695 (2D14)
$DF(v)+HF$, $DF(v)+D_2$ and $HF(v)+H_2$ systems; room temperature relaxation rates. *Kwok, M. A., J-QE 75 Aug* 695 (2E01)
dye lasers; relaxation oscillations and initial spikes. *Lin, Chinlon, J-QE 75 Aug* 602-609 (1C08)
gas lasers; deactivation of vibrationally excited molecules by potentially reactive atoms. *Smith, I. W. M., J-QE 75 Aug* 696 (2E02)
HCl molecules; deactivation of vibrationally excited molecules by H and Cl atoms. *Wilkins, R. L., J-QE 75 Aug* 716-717 (2F08)
$HCl(v=1)$ and $DCl(v=1)$; rate coefficients for relaxation by Cl and O atoms. *Brown, R. D. H., J-QE 75 Aug* 695-696 (2E01)
HF–He and DF–He mixtures and pure DF samples; vibrational relaxation between 200 and 300°K. *Hancock, J. K., J-QE 75 Aug* 694 (2D14)
$HF(v=1)$ deactivation by H atoms. *Heidner, R. F., J-QE 75 Aug* 696 (2E02)
$HF(v=1)$, $DF(v=1)$ and $HCl(v=1)$ vibrational deactivation by atomic collisions. *Quigley, G. P., J-QE 75 Aug* 696-697 (2E02)
HF pulsed chemical lasers; effect of rotational nonequilibrium on predicted performance. *Hough, J. J. T., J-QE 75 Aug* 699 (2E05)
HF pulsed chemical lasers; rotational nonequilibrium. *Creighton, J. R., J-QE 75 Aug* 699 (2E05)
HF; rotational relaxation effects. *Hinchen, J. J., J-QE 75 Aug* 695 (2E01)
I lasers; deactivation of electronically excited I atoms. *Burde, D. H., J-QE 75 Aug* 709 (2F01)
N_2 and $CO_2(001)$ vibration-to-translation relaxation by alkali metal atoms. *Benson, R. C., J-QE 75 Aug* 697 (2E03)
$O_3^+ + NO$ reaction system; rate constant for O_3^{++} decay from 150 to 350 K. *Kurylo, M. J., J-QE 75 Aug* 702-703 (2E08)
$O(^3P)+CO(^1\Sigma^+)$ collisions; vibrational deactivation and atom exchange. *Kelley, J. D., J-QE 75 Aug* 701 (2E07)
silicate laser glass; nonradiative relaxation of rare-earth ions. *Layne, C. B., J-QE 75 Sep* 798-799 (1F06)
$Xe^*(^3P_2)$ metastable atoms; quenching with light hydrocarbons and fluoromethanes. *Velazco, J. E., J-QE 75 Aug* 708-709 (2E14)
Relay systems; **cf.** Wire communication repeaters
Remote sensing
ozone measurements using resonance Raman scattering and differential absorption. *Penney, C. M., J-QE 75 Sep* 36D (2D10)
power plant effluent measurements; remote measurements using laser Doppler velocimeter. *Miller, C. R., J-QE 75 Sep* 34D-35D (2D08)

Repeaters; **cf.** Wire communication repeaters
Resistors
SiC high-temperature resistors; fabrication using CO_2 lasers. *Hierholzer, F. J., J-QE 75 Sep* 47D-48D (2E07)
Resonance; **cf.** Optical resonance
Resonators; **cf.** Laser resonators
Ring lasers
bistable unidirectional operation. *Hambenne, J. B., J-QE 75 Feb* 90-92 (1B14)
coupling; comparison of traveling-wave and standing-wave resonator extraction efficiencies. *Eckbreth, Alan C., J-QE 75 Sep* 796-798 (1F04)
Rubidium
vapor; third-order susceptibility. *Eicher, Hermann, J-QE 75 Apr* 121-130 (1A03)
Rubidium alloys/compounds, devices
RD*A optical parametric oscillators. *Kato, K., J-QE 75 Dec* 939-941 (1A13)
Rubidium devices
lamps; K–Rb pump lamps for Nd:YAG lasers. *Radecki, Dan J., J-QE 75 Sep* 15D-16D (2C03)
lasers; electronic-transition chemical laser using $Rb + F_2$ reaction system. *Hall, L. H., J-QE 75 Aug* 693 (2D13)
Ruby lasers
pulse shaping in *Q*-switched lasers. *Loveberg, R. V., J-QE 75 Jan* 17-21 (1B05)

S

Sampled signals
optical sampling transient analyzer for fast, high-voltage, single transient electrical pulses. *Davies, Terence J., J-QE 75 Sep* 7D (2B09)
Satellite communication
optical communication transmitters; Nd:YAG laser transmitter. *Falk, Joel, J-QE 75 Sep* 14D-15D (2C02)
optical communication; lamp-pumped Nd:YAG laser subsystem for 1 gbps system. *Radecki, Dan J., J-QE 75 Sep* 15D-16D (2C03)
receivers; 10-μm optical heterodyne receiver for synchronous satellite. *Goodwin, F. E., J-QE 75 Sep* 79D-80D (2G11)
receivers; wideband 10.6-μm heterodyne receiver for CO_2 laser satellite communications link. *Peyton, B. J., J-QE 75 Sep* 80D-81D (2G12)
Satellite tracking
ranging systems; picosecond-pulse, fieldable Nd:YAG laser system. *Erickson, E. G., J-QE 75 Sep* 16D-17D (2C04)
Scanning; **cf.** Imaging
Scattering; **cf.** Optical scattering
Schottky-barrier devices
Gunn effect digital device for direct modulation of GaAs–AlGaAs double-heterostructure lasers. *Yanai, Hisayoshi, J-QE 75 Jul* 519-524 (3D01)
Scintillation detectors
fluorescent rise times in plastic scintillators; streak camera studies. *Shapiro, S. L., J-QE 75 Sep* 5D-6D (2B07)
Second-harmonic generation; **cf.** Optical harmonic generation
Self-focusing; **cf.** Laser-beam focusing
Self-pulsing lasers; **cf.** Pulsed lasers
Self-*Q*-switching; **cf.** *Q*-switched lasers
Semiconductor defects
dark-line and dark-spot defects in GaAs–AlGaAs double-heterostructure lasers. *Ito, Ryoichi, J-QE 75 Jul* 551-556 (3F05)
dislocation networks (dark-line defects) producing degradation in injection lasers; network development model. *Woolhouse, G. R., J-QE 75 Jul* 556-561 (3F10)
dislocation pinning in GaAs by group III or V impurities. *Kirkby, P. A., J-QE 75 Jul* 562-568 (3G02)
Semiconductor devices; **cf.** Piezoelectric semiconductor devices; Semiconductor plasma devices
Semiconductor device fabrication
GaAs lasers; single-heterostructure distributed-feedback lasers. *Burnham, Robert D., J-QE 75 Jul* 439-449 (2E05)
lasers; monolithic GaInAs homojunction diode lasers. *Doerbeck, F. H., J-QE 75 Jul* 464-467 (2G02)
resistors; fabrication of high-temperature SiC resistors using CO_2 lasers. *Hierholzer, F. J., J-QE 75 Sep* 47D-48D (2E07)
Semiconductor device fabrication; **cf.** Ion implantation; Semiconductor growth
Semiconductor device noise
lasers; intensity noise characteristics of continuously operating stripe-geometry double-heterostructure junction lasers. *Paoli, Thomas L., J-QE 75 Jun* 276-283 (1D12)
Semiconductor device radiation effects
laser pulse irradiation effects on metals and semiconductors. *Dekhtar, I. Ya., J-QE 75 Sep* 83D (2G14)
Semiconductor device thermal factors; **cf.** Laser thermal factors
Semiconductor diodes; **cf.** Avalanche diodes
Semiconductor doping; **cf.** Semiconductor impurities
Semiconductor growth
liquid-phase epitaxial growth of GaAs–AlGaAs double-heterostructure tsper-coupled lasers. *Logan, R. A., J-QE 75 Jul* 461-464 (2F13)
LPE InGaPAs–GaAsP single-heterojunction laser diodes. *Coleman, J. J., J-QE 75 Jul* 471-476 (2G09)
Semiconductor heterojunction devices; **cf.** Gallium alloys/compounds, devices; Gallium alloys/compounds, lasers; Semiconductor lasers
Semiconductor impurities
dislocation pinning in GaAs by group III or V impurities. *Kirkby, P. A., J-QE 75 Jul* 562-568 (3G02)
Semiconductor Laser Conference
papers from Nov. 1974 conference, *J-QE 75 Jul, Pt. II* 381-568 (2A03)
special issue on Nov. 1974 conference; foreword. *Paoli, Thomas L., Guest ed., J-QE 75 Jul* 381 (2A03)
Semiconductor lasers
asymmetric spectral-mode interaction due to stimulated scattering of laser radiation. *Bogatov, A. P., J-QE 75 Jul* 510-515 (3C06)
distributed-feedback single- and double-heterostructure diode lasers; coupling coefficients for TE modes. *Streifer, William, J-QE 75 Nov* 867-873 (1A13)
double-heterojunction lasers with very thin active regions; angular beam divergence. *Dumke, W. P., J-QE 75 Jul* 400-402 (2B08)
double-heterostructure stripe-geometry lasers operating continuously at room temperature; intensity noise characteristics. *Paoli, Thomas L., J-QE 75 Jun* 276-283 (1D12)
double-heterostructure lasers; dislocation pinning by deliberately added impurities. *Kirkby, P. A., J-QE 75 Jul* 562-568 (3G02)
HgCdTe magnetically tunable lasers; tunable spin-flip and recombination lasers using optical pumping. *Sattler, J. P., J-QE 75 Sep* 18D (2C06)
InSb lasers; CW tunable lasers optically pumped in longitudinal geometry. *Menyuk, N., J-QE 75 Jul* 477-481 (3A01)
light output intensity modulation using injected laser beams. *Nishizawa, Jun-Ichi, J-QE 75 Jul* 515-519 (3C11)
optical theory for highly doped semiconductors; spontaneous emission and threshold property calculations. *Aleksanian, A. G., J-QE 74 Mar* 297-305 (1A03) ♦
PbSe lasers; current- and magnetic-tuned laser for SO_2 infrared spectral measurements. *Allario, Frank, J-QE 75 May* 205-209 (1B13)
PbSnTe double-heterojunction laser diodes; threshold current densities. *Tomasetta, L. R., J-QE 75 Jul* 384-390 (2A06)
Q-switching theory. *Thomas, Ben, J-QE 75 Jul* 528-532 (3D10)
relaxation oscillations in modulated output; suppression by light injection method. *Lang, R., J-QE 75 Sep* 60D (2F06)
self-induced intensity pulsations from CW junction lasers; suppression by frequency-selective optical feedback. *Paoli, Thomas L., J-QE 75 Jul* 525-527 (3D07)
thermal impedance measurement. *Paoli, Thomas L., J-QE 75 Jul* 498-503 (3B08)
transverse mode control in multimode double-heterostructure junction lasers optically coupled to single-mode fibers. *Krupka, D. C., J-QE 75 Jul* 503-507 (3B13)
Semiconductor lasers; **cf.** Gallium alloys/compounds, lasers
Semiconductor plasma devices
microwave switches using bulk photoconductivity produced in Si transmission lines by picosecond optical pulses. *Johnson, A. M., J-QE 75 Jun* 283-287 (1E05)
Semiconductor switches
Ge light-triggered switches for fast switching of high-power CO_2 laser radiation. *Alcock, A. J., J-QE 75 Sep* 96D (3A13)
microwave switches using bulk photoconductivity produced in Si transmission lines by picosecond optical pulses. *Johnson, A. M., J-QE 75 Jun* 283-287 (1E05)
Sensors
hover sensor for heavy lift helicopter. *Herzog, D. G., J-QE 75 Sep* 51D-52D (2E11)
SF_6
isotopic enrichment by multiple absorption of CO_2 laser radiation. *Lyman, J. L., J-QE 75 Sep* 103D (3B06)
N_2 lasers; quasi-CW second-positive laser using SF_6 additions to N_2 in discharge region. *Suchard, S. N., J-QE 75 Aug* 685-686 (2D05)
SF_6; **cf.** Gas lasers, molecular
Shock waves; **cf.** Acoustic surface-wave effects
Signal analysis
optical sampling transient analyzer for fast, high-voltage, single transient electrical pulses. *Davies, Terence J., J-QE 75 Sep* 7D (2B09)
Signal processing; **cf.** Acoustic signal processing; Optical signal processing
Signal sampling; **cf.** Sampled signals
Silicon devices
microwave switches using bulk photoconductivity produced in Si transmission lines by picosecond optical pulses. *Johnson, A. M., J-QE 75 Jun* 283-287 (1E05)
photodiode arrays; integrated optical array. *Boyd, J. T., J-QE 75 Sep* 40D-41D (2D14)
Silicon alloys/compounds
SiF_4 isotopic enrichment by multiple absorption of CO_2 laser radiation. *Lyman, J. L., J-QE 75 Sep* 103D (3B06)
Silicon alloys/compounds, devices
lasers; SiO and SiF electronic-transition chemical lasers. *Scott, P. B., J-QE 75 Aug* 693-694 (2D13)
lasers; SiO electronic-transition chemical lasers. *Wilson, L. E., J-QE 75 Aug* 691 (2D11)
SiC high-temperature resistors; fabrication using CO_2 lasers. *Hierholzer, F. J., J-QE 75 Sep* 47D-48D (2E07)
Slab waveguides; **cf.** Optical planar waveguides
Sodium
vapor; third-order susceptibility. *Eicher, Hermann, J-QE 75 Apr* 121-130 (1A03)
Sodium devices
lasers; electronic-to-electronic energy transfer rates in Na vapor. *Chen, Hao-Lin, J-QE 75 Aug* 669-672 (2C03)
optical pulse generators; conversion of CW dye laser light into train of repetitive subnanosecond pulses using resonant atomic dispersion in Na vapor. *Bjorkholm, J. E., J-QE 75 Sep* 68D (2G01)
Sodium devices; **cf.** Gas lasers
Sodium alloys/compounds, devices
$Ba_2NaNb_5O_{15}$ acoustooptic mode locker/frequency doubler for Nd:YAG lasers. *Rice, R. R., J-QE 75 Sep* 14D (2C02)
$Ba_2Na(NbO_3)_5$ intracavity frequency-doubling elements in Nd:YAG lasers; thermooptical effects. *Barry, James D., J-QE 75 Aug* 575-579 (1A13)
NaCl Brewster windows in CS_2/O_2 chemical lasers; surface reactions produced by flash photolysis. *Petersen, Alan B., J-QE 75 Mar* 110-111 (1B02)
Soils; **cf.** Earth
Solar energy applications
laser pumping; solar-pumped Nd:YAG laser. *Falk, Joel, J-QE 75 Sep* 14D-15D (2C02)
Solar radiation
measurements using infrared heterodyne radiometer. *Peyton, Bernard J., J-QE 75 Aug* 569-574 (1A03)
Solid lasers
2.3-μm Tm^{3+} lasers; room-temperature pulsed emission from Tm:Cr:YAG and Tm:Cr:$YAlO_3$ lasers. *Caird, John A., J-QE 75 Nov* 874-881 (1B06)
glass laser systems; effect of air space on self-focusing instability growth rates. *Elliott, C. James, J-QE 75 Nov* 863-866 (1A09)
Ho:solid lasers; laser transitions. *Caird, John A., J-QE 75 Mar* 97-99 (1A03)

♦ Check author entry for later corrections/comments

Ho:YLF lasers; 2.06 μm laser performance and design options for rangefinder and illuminator applications. *Devor, D. P., J-QE 75 Sep* 13D-14D (2C01)
$LiNdP_4O_{12}$ lasers; CW laser with 200-μW pump threshold for 5145-Å pump. *Otsuka, Kenju, J-QE 75 Oct* 845-846 (1D01)
$LiNdP_4O_{12}$ lasers; CW operation of transversely pumped laser. *Yamada, T., J-QE 75 Sep* 62D-63D (2F08)
$LiNdP_4O_{12}$ lasers; quasi-continuous action. *Otsuka, Kenju, J-QE 75 Jul* 330-334 (1B02)
NdLa pentaphosphate fiber lasers. *Weber, H. P., J-QE 75 Sep* 100D (3B03)
NdP_5O_{14} lasers; material characteristics and laser properties. *Weber, H. P., J-QE 75 Sep* 61D-62D (2F07)
NdP_5O_{14} lasers; optical-pumping-induced heating resulting in bistable laser operation. *Weber, Heinz P., J-QE 75 Jul* 368-370 (1D12)
NdP_5O_{14} lasers; threshold and efficiency of transversely excited laser. *Chinn, S. R., J-QE 75 Sep* 62D (2F08)
NdP_5O_{14} transversely excited lasers; room-temperature lasing behavior. *Chinn, Stephen R., J-QE 75 Sep* 747-754 (1B11)
nonlinear refractive-index coefficient of laser-system materials; interferometric measurement. *Moran, Michael J., J-QE 75 Jun* 259-263 (1C09)
quantum efficiencies of lasers using rare-earth-doped silicate glass. *Layne, C. B., J-QE 75 Sep* 798-799 (1F06)

Solid lasers; **cf.** Neodymium:solid lasers; Ruby lasers; Semiconductor lasers
Special issues
Chemical and Molecular Lasers Conference; papers and abstracts from Oct. 1974 conference, *J-QE 75 Aug, Pt. II* 641-722 (2A03)
Semiconductor Laser Conference; papers from Nov. 1974 conference, *J-QE 75 Jul, Pt. II* 381-568 (2A03)
Spectroscopy; **cf.** Mass spectroscopy; Optical spectroscopy; Particle spectroscopy; Raman spectroscopy
Spin-flip lasers; **cf.** Raman lasers
Spontaneous emission
amplified spontaneous emission in transversely pumped dye lasers. *Ganiel, U., J-QE 75 Nov* 881-892 (1B13)
mode-locking threshold in Nd:YAG lasers above normal lasing threshold. *Wilbrandt, Robert, J-QE 75 May* 186-190 (1A08)
optical gain–absorption in active media; amplified spontaneous emission measurement technique. *Cross, Peter S., J-QE 75 May* 190-197 (1A12)
Strain measurement
granite plate deformation; measurement using grazing incidence triangular laser interferometer. *Rabal, H. J., J-QE 75 Sep* 22D-23D (2C10)
Strontium devices; **cf.** Gas lasers, molecular
Submillimeter-wave (300–3000 GHz); **cf.** Infrared (0.70–100 μm)
Submillimeter-wave lasers
CO_2-pumped CW laser lines from 254 to 1700 μm. *Jennings, D. A., J-QE 75 Aug* 637 (1F01)
CW emission from optically pumped waveguide gas lasers. *Radford, Harrison E., J-QE 75 May* 213-214 (1C07)
Sulfur devices; **cf.** Gas lasers
Sulfur alloys/compounds
SO_2 infrared spectral measurements using single magnetic- and current-tuned PbSe laser. *Allario, Frank, J-QE 75 May* 205-209 (1B13)
Sulfur hexafluoride; **cf.** SF_6
Superconductivity
laser pulse radiation effects. *Dekhtar, I. Ya., J-QE 75 Sep* 83D (2G14)
Surfaces
granite surface plate quality checkout using grazing incidence triangular laser interferometer. *Rabal, H. J., J-QE 75 Sep* 22D-23D (2C10)
metallic surface reflectivity changes during irradiation by CO_2–TEA laser. *Ready, J. F., J-QE 75 Sep* 49D (2E09)
metallic surfaces; thermal coupling coefficient for laser-heated surfaces. *Marcus, S., J-QE 75 Sep* 49D-50D (2E09)
NaCl Brewster windows in CS_2/O_2 chemical lasers; surface reactions produced by flash photolysis. *Petersen, Alan B., J-QE 75 Mar* 110-111 (1B02)
Surface waves; **cf.** Optical surface waves
Switches; **cf.** Electrooptic switches; Light-triggered switches; Semiconductor switches; Waveguide switches

T

TEA lasers; **cf.** Gas lasers
Tellurium
second-harmonic generation; effect of two-photon absorption. *Schwartz, Christiane A., J-QE 75 Aug* 616-623 (1D08)
second-harmonic generation; effect of two-photon absorption. *Oudar, Jean-Louis, J-QE 75 Aug* 623-629 (1E01)
Temperature measurement
junction laser temperature rise as function of average electrical power supplied to device. *Paoli, Thomas L., J-QE 75 Jul* 498-503 (3B08)
metallic surface temperatures in laser-irradiated material; measurement using thin-film thermocouples. *Marcus, S., J-QE 75 Sep* 49D-50D (2E09)
Raman spectroscopy measurement in optically pumped NdP_5O_{14} laser. *Weber, Heinz P., J-QE 75 Jul* 368-370 (1D12)
Thallium alloys/compounds, devices
Tl_3AsSe_3 acoustooptic filters; tunable collinear filter for intermediate infrared. *Feichtner, J. D., J-QE 75 Sep* 66D-67D (2F12)
Thermal factors; **cf.** Laser thermal factors
Thermal variables measurement
dilatometry using multichannel interferometer. *Pond, C. R., J-QE 75 Sep* 10D-11D (2B12)
Thermal variables measurement; **cf.** Temperature measurement
Thin-film waveguides; **cf.** Optical planar waveguides
Time measurement
subpicosecond optical chronoscopy; Photochron II streak camera tube. *Bradley, D. J., J-QE 75 Sep* 25D-26D (2C13)
Tin alloys/compounds, devices; **cf.** Semiconductor lasers
Titanium
isotope separation; laser separation process for Ti-50. *Gross, R. W. F., J-QE 75 Aug* 702 (2E08)
Tracking; **cf.** Satellite tracking
Transfer lasers; **cf.** Gas lasers, molecular
Transforms; **cf.** Fourier transforms
Transient analysis
optical sampling transient analyzer for fast, high-voltage, single transient electrical pulses. *Davies, Terence J., J-QE 75 Sep* 7D (2B09)
Transitions; **cf.** Waveguide transitions
Transmitters; **cf.** Radar transmitters; Radio communication transmitters
Transversely excited lasers; **cf.** Gas lasers; Solid lasers
Traveling-wave lasers; **cf.** Ring lasers
Tunable filters
Tl_3AsSe_3 acoustooptic filters; tunable collinear filter for intermediate infrared. *Feichtner, J. D., J-QE 75 Sep* 66D-67D (2F12)
Turbulent media; **cf.** Optical radio propagation meteorological factors

U

Ultrasonic...; **cf.** Acoustic...
Ultraviolet generation
Cerenkov radiation generation; second-harmonic generation. *Chen, Bor-Uei, J-QE 75 Apr* 177-178 (1E03)
picosecond pulse generation using synchronous mode-locked dye laser and nonlinear mixing; tunable pulses over 270–331 nm and 362–408 cm. *Goldberg, L. S., J-QE 75 Sep* 2D (1B04)
Ultraviolet lasers
dye lasers; 3400 Å terphenyl dye laser pumped by UV radiation from CO_2-laser-produced Xe plasma. *Silfvast, W. T., J-QE 75 Sep* 1D (2B03)
dye lasers; tunable subnanosecond pulse generation from N_2-laser-pumped dye laser in near UV and visible region. *Lin, Chinlon, J-QE 75 Aug* 602-609 (1C08)
electronic-transition chemical lasers; parametric evaluation of potential diatomic molecules. *Sutton, D. G., J-QE 75 Aug* 690-691 (2D10)
H_2 lasers; use in photoionization and luminescence excitation experiments. *Antonov, V. S., J-QE 75 Sep* 92D (3A09)
H_2 vacuuum ultraviolet lasers; single-short TEA laser, high-repetition rate laser and CW laser. *Knyazev, I. N., J-QE 75 Oct* 805-817 (1A03)
N_2 lasers; 3371-Å laser power produced by relativistic electron-beam propagation. *McArthur, David A., J-QE 75 Nov* 892-902 (1C10)
N_2 lasers; stimulated emission at 0.3159 μm in second-positive system at room temperature. *Kruger, John S., J-QE 75 Sep* 801-802 (1F09)
N_2 pulsed lasers; photopreionization. *Kurnit, N. A., J-QE 75 Apr* 174-176 (1D14)
noble gas ionic lasers; transitions below 2500 Å. *Marling, John B., J-QE 75 Oct* 822-834 (1B06)
noble-gas ion lasers; pulsed and CW transitions below 3000 Å. *Marling, J. B., J-QE 75 Sep* 27D-28D (2D01)
noble-gas lasers pumped by coaxial diode electron-beam system. *Arthurs, E. G., J-QE 75 Sep* 28D (2D02)
pulsed dye lasers; subnanosecond tunable pulse generation in N_2-laser-pumped lasers using controlled resonator transients. *Lin, Chinlon, J-QE 75 Sep* 1D-2D (2B03)
rangefinders using pulsed ultraviolet N_2 laser. *Davis, T. P., J-QE 75 Sep* 50D (2E10)
XeBr* excimer lasers; 281.8-nm emission from electron-beam-excited Xe/Br_2 mixture. *Searles, S. K., J-QE 75 Sep* 93D (3A10)
XeF lasers; 3540-Å emission from electron-beam-excited $F_2/Xe/Ar$ mixtures. *Ewing, J. J., J-QE 75 Sep* 92D-93D (3A09)
Ultraviolet radiation effects
photoionization in TEA CO_2 lasers. *Seguin, H. J. J., J-QE 75 Sep* 71D-72D (2G03)
Uranium
^{235}U isotope separation using selective photoionization. *Tuccio, Sam A., J-QE 75 Sep* 101D (3B04)
isotope separation; photoionization cross section and excited state lifetime measurements in U vapor for separation process evaluation. *Solarz, R. W., J-QE 75 Sep* 19D-20D (2C07)
isotope separation; selective two-step excitation and photoionization of atomic U vapor. *Janes, G. S., J-QE 75 Sep* 101D-102D (3B04)
isotope separation using lasers. *Teller, E., J-QE 75 Sep* 83D (2G14)

V

Vehicle control; **cf.** Aircraft control
Velocity measurement; **cf.** Optical velocimeters
Video recording
optical video disks. *Spitz, Eric, J-QE 75 Sep* 11D (2B13)
optical video disks; holographic disk. *Tsunoda, Y., J-QE 75 Sep* 11D-12D (2B13)
Visible lasers
Ar ion lasers; CW laser using 700-m-long cavity. *Tripathi, P. P., J-QE 75 Sep* 59D (2F05)
ArO lasers; parameters of flash-photolyzed N_2O–Ar_2 mixtures. *Hughes, William M., J-QE 75 Sep* 88D (3A05)
BaF, BaCl, BaBr and BaI electronic-transition chemical lasers. *Bradford, R. S., Jr., J-QE 75 Aug* 692 (2D12)
Ba vapor lasers; visible laser transitions at 7120 Å in Ba I and at 549.9 and 6141.7 Å in Ba (II). *Baron, K. U., J-QE 75 Oct* 852-853 (1D08)
BO, BaO, CuF, SiO and SiF electronic-transition chemical lasers. *Scott, P. B., J-QE 75 Aug* 693-694 (2D13)
BrCl and GeO electronic-transition lasers; excited electronic states. *Harris, R. A., J-QE 75 Aug* 691 (2D11)
calcium and strontium oxide and halide chemical lasers; photon yields in 250–1100 nm region and $A'^1\pi$ molecular constants. *Capelle, G. A., J-QE 75 Aug* 692 (2D12)
chemical lasers; reaction initiation by short-duration pulsed discharges. *Chou, M. S., J-QE 75 Aug* 691-692 (2D11)
chemical lasers using reactions of evaporated metal atoms with various oxidizers. *Eckstrom, D. J., J-QE 75 Aug* 691 (2D11)
cresyl violet perchlorate laser; pumping using dye mixture and tandem systems. *Beisser, F. A., J-QE 75 Jul* 372 (1E02)
Cu vapor lasers; discharge-heated master oscillator power amplifier. *Anderson, R. S., J-QE 75 Sep* 56D-57D (2F02)
dye lasers; high-power blue and violet lasers pumped by third harmonic of Nd:YAG laser. *Kato, K., J-QE 75 Jul* 373-374 (1E03)

dye lasers; pulsed Xe ion laser pump for tunable Rhodamine-6G laser. *Schearer, Laird D., J-QE 75 Dec* 935-937 (1A09)
dye lasers; tunable subnanosecond pulse generation from N_2-laser-pumped dye laser in near UV and visible region. *Lin, Chinlon, J-QE 75 Aug* 602-609 (1C08)
electronic-transition chemical lasers; parametric evaluation of potential diatomic molecules. *Sutton, D. G., J-QE 75 Aug* 690-691 (2D10)
electronic-transition chemical lasers using reactions of I_2, Br_2, SiH_4, GeH_4, AsH_3 or Ph_3 with F_2. *Davis, S. J., J-QE 75 Aug* 693 (2D13)
FeO electronic-transition chemical lasers. *West, J. B., J-QE 75 Aug* 692-693 (2D12)
GaAs/GaAlAs double-heterojunction lasers using heteroisolation stripe geometry. *Itoh, Kunio, J-QE 75 Jul* 421-426 (2D01)
GeO and SiO electronic-transition chemical lasers. *Wilson, L. E., J-QE 75 Aug* 691 (2D11)
He–Cd^+ lasers emitting CW white light; single-gun hollow cathode tube with three-color outputs. *Fujii, Kan-Ichi, J-QE 75 Mar* 111-114 (1B03)
Hg lasers; dc-excited Hg pump lamps for CW operation at 546.1 nm. *Holmes, N., J-QE 75 Sep* 55D (2F01)
metal atom/N_2O chemical lasers; luminescence. *Felder, W., J-QE 75 Aug* 703 (2E09)
Na_2 molecular lasers; optically pumped superfluorescent laser. *Henesian, M., J-QE 75 Sep* 26D (2C14)
O lasers using ^1S–^1D transition; lasing at 5578.5 Å in relativistic-electron-beam excited Kr_2/O_2 mixtures. *Johnson, A. W., J-QE 75 Sep* 56D (2F02)
pulsed dye lasers; subnanosecond tunable pulse generation in N_2-laser-pumped lasers using controlled resonator transients. *Lin, Chinlon, J-QE 75 Sep* 1D-2D (2B03)
XeO lasers; lasing on green bands using direct electron beam excitation of high pressure Xe with small additions of O_2, CO_2 or N_2O. *Powell, H. T., J-QE 75 Aug* 685 (2D05)
XeO lasers; reaction kinetics in electron-beam pumped Xe–O_2 mixtures. *Lorents, D. C., J-QE 75 Aug* 704 (2E10)

W

Wave diffraction; **cf.** Optical diffraction
Waveguides; **cf.** Optical waveguides
Waveguide communication; **cf.** Optical waveguide communication
Waveguide junctions
optical waveguide junctions; optical field propagation in integrated optical bifurcations. *Roy, A. M., J-QE 75 Sep* 41D-42D (2E01)
Waveguide junctions; **cf.** Waveguide transitions
Waveguide lasers
AlGaAs multiheterostructure laser with integrated twin guide. *Suematsu, Y., J-QE 75 Jul* 457-460 (2F09)
chirp-modulated CO_2 lasers; demodulation technique. *Stein, Alexander, J-QE 75 Aug* 630-631 (1E08)
CO_2 laser amplifiers; high-power CW 10.6-μm amplifier. *Klein, Marvin B., J-QE 75 Aug* 609-615 (1D01)
CO_2 transversely excited lasers; high-gain CW laser using preionization scheme based on Malter effect. *Wood, O. R., II, J-QE 75 Sep* 72D-73D (2G04)
CW submillimeter emission from optically pumped gas lasers. *Radj Harrison E., J-QE 75 May* 213-214 (1C07)
flowing-gas capillary lasers; porous wall tube system. *Papayoanou, Aris... J-QE 75 Aug* 579-583 (1A13)
GaAlAs double heterostructure packaged lasers for optical-fiber transmission *Takusagawa, M., J-QE 75 Sep* 61D (2F07)
optical waveguide lasers; grating-coupled composite-guide heterostructure GaAlAs diode lasers with low-divergence beams. *Burnham, R. D., J-QE 75 Sep* 98D-99D (3B01)
Waveguide losses
optical waveguide bend losses; conformal transformation analysis of curved guides. *Heiblum, Mordehai, J-QE 75 Feb* 75-83 (1A13)
Waveguide switches
electrooptic switches for optical planar waveguides; electrode configuration fo producing prism-like deflector on guide. *Kaminow, I. P., J-QE 75 Aug* 633-635 (1E11)
Waveguide transitions
optical waveguide transitions; optical field propagation in integrated optical transitions. *Roy, A. M., J-QE 75 Sep* 41D-42D (2E01)
Wave propagation; **cf.** Optical propagation
Welding; **cf.** Laser materials-processing applications
Wire communication repeaters
optical fiber communication repeaters; 40-Mb/s and 400-Mb/s repeaters using feedback-type amplifiers. *Ueno, Y., J-QE 75 Sep* 78D-79D (2G10)

X

Xenon; **cf.** Noble gases
X-ray generators
laser-produced plasma; duration of emitted X-ray pulses. *Duguay, M. A., J-QE 75 Apr* 170-172 (1D10)
X-ray imaging
Fourier-transform holograms of simple plane objects; recording using X-ra... *Mahr, H., J-QE 75 Sep* 97D-98D (3A14)

Y

YAG lasers; **cf.** Neodymium:YAG lasers; Solid lasers
$YAlO_3$ lasers; **cf.** Solid lasers
YLF lasers; **cf.** Solid lasers
YVO_4 lasers; **cf.** Neodymium:solid lasers

Z

Zinc alloys/compounds, devices
ZnO modulators; waveguide electrooptic modulator using grain-oriented polycrystalline film. *Hu, Chenming, J-QE 75 Sep* 64D (2F10)
ZnO optical planar waveguide modulators. *Hammer, Jacob M., J-QE 75 Ap* 138-148 (1B06)
ZnS optical planar waveguides; phase-matched second-harmonic generat using nonlinearities in film and substrate. *Ito, H., J-QE 75 Sep* 40D (2D
ZnTe optical planar waveguides fabricated by ion implantation. *Valette, S J-QE 75 Sep* 39D-40D (2D13).